Conference on Modelling Fluid Flow (CMFF'15)
The 16th International Conference on Fluid Flow Technologies
Budapest, Hungary, September 1-4, 2015

HEAT TRANSFER ENHANCEMENT OF A BIODIESEL HEATER

Chamil Abeykoon

Division of Applied Science, Computing and Engineering, Glyndwr University, Mold Road, Wrexham, LL11 2AW, United Kingdom.
Tel.: +44 1978293067, E-mail: c.abeykoon@glyndwr.ac.uk

ABSTRACT

Issues of fuel preparation are quite crucial in many industrial/transport applications. Some fuels may not be ready to use in their raw state and hence are required to pre-processed, particularly to increase the temperature to the required level, prior to the combustion stage. For this purpose, two major types of fuel heaters are used: in-line type that attached to the fuel pipes and off-line type that attached outside the fuel tank. This work is aimed to consider an in-line counter flow heater used in marine applications and to propose modifications to improve its performance. After considering several heat transfer enhancement techniques, a twisted-tube insert was chosen to be used. Then, theoretical calculations were performed with and without heat transfer enhancement for a set task. The results showed that the required length of the heater can be reduced by 83.9% only introducing a twisted-tube instead of a plain tube. Usually, pressure drop increases with a twisted-tube but a reduction of pressure drop also can be observed in this work due to the reduction of the required length of the heater. Also, a reduction of the heater's manufacturing cost should be achieved with a twisted-tube to perform the same task compared to a plain tube. Therefore, the use of twisted-tubes within these type of heaters will provide substantial benefits particularly to design compact heat exchangers but with improved performance.

Keywords: Heat exchanger, Heat transfer enhancement, Biodiesel, Modelling, Twisted-tube

NOMENCLATURE

A	[m^2]	Surface area
C_p	[J.kg^{-1}.K^{-1}]	Specific heat capacity at constant pressure
d	[m]	Diameter
h	[W.m^{-2}.K^{-1}]	Convective heat transfer coefficient
k	[W.m^{-1}.K^{-1}]	Thermal conductivity
L	[m]	Length
$\dot{m}$	[kg. s^{-1}]	Mass flow rate
Nu	[-]	Nusselt number
Pr	[-]	Prandtl number
$\dot{q}$	[W]	Heat transfer rate
Re	[-]	Reynolds number
t	[m]	Thickness
T	[^{o}C]	Temperature
ΔT_{lm}	[^{o}C]	Log mean temperature difference
U	[W.m^{-2}.K^{-1}]	Overall heat transfer coefficient
V	[m.s^{-1}]	Velocity
ρ	[m^3/kg]	Density
μ	[Pa.s]	Viscosity

Subscripts and Superscripts

c	Cold fluid flow
h	Hot fluid flow
i	Inlet conditions
o	Outlet conditions

1. INTRODUCTION

Heat transfer can occur through several mechanisms such as conduction, convection, radiation, etc. Usually, the heat is naturally released to the surroundings from systems/machines by means of one or many of these ways. However, the forced cooling is a requirement of removing the additional heat generated in some applications to ensure the effective/efficient operation. In such applications, heat exchanges are commonly used for removing the additional or unnecessary heat. Usually, heat exchangers remove the heat of a particular medium by allowing it to absorb into another heat transfer medium such as water, oil, air, etc. Currently, numerous heat exchanging techniques are available and are widely used in the applications such as refrigeration, air conditioning, automobiles, process industry, solar water heating, thermal power plants, and so forth. In some particular applications, heat exchangers which are bulky in size have to be used based on the amount of the heat required to be removed or added for a given time to maintain the desirable temperature limits. However, the size of the components or machines has become a major consideration in the modern industrial world due to the constraints such as space limitations, maintenance requirements, manufacturing cost, portability, appearance, etc. Therefore, the size of the heat exchangers has also become a critical factor which would decide the size of some particular machines/plants. Under such circumstances, extensive researches have been focused over the last few decades to reduce the size and fabrication cost of the heat exchangers [1-7].

This work is aimed to explore the possible strategies of enhancing the performance of a biodiesel heater (used with internal combustion engines) to reduce its typical size while maintaining its efficiency in the same or a higher level. The typical low- or medium-speed marine engines use fuel heaters which are quite large in size and hence the possible reductions of their sizes and weight, while having the same/higher performance, would be invaluable. A biodiesel heater was considered due to its timely importance of using more green fuels particularly in marine applications. Currently, a number of heat transfer enhancement techniques are used in practical applications. However, some of these heat transfer techniques may not be used with biodiesel heaters due to the constraints such as high viscosity and density of the biodiesel. After choosing a suitable heat transfer enhancement technique, theoretical calculations can be performed to determine the required length of the heater with and without the enhancement technique to evaluate the efficacy of the selected technique. Regardless the possible improvements of heat transfer performance (i.e., the reduction of the length), pressure drop may be increased and this may cause to increase the required pumping power. Hence, the increase of both the heat transfer performance and the pumping power should be estimated and compared before making any judgement on the overall worthiness of the newly proposed technique.

1.1. Biodiesel

Biodiesels are type of environmentally friendly biofuels which are made from vegetable oils (e.g., rapeseed, soy, palm, coconut, etc. oils) or animal fat and are used to replace petroleum diesel fully or partially. They are good alternatives to conventional fuels due to their environmental friendliness [8] and the best fit with new regulations imposed by International Maritime Organisation (IMO) [9]. From chemical standpoint, biodiesel is a mixture of methyl and/or ethyl monoalkyl esters of long-chain fatty acids (saturated and unsaturated). Also, it can be used in pure or blended form with petrol/diesel [10]. Depending on the amount of the biodiesel in the blend it has different commercial names:

- B100: 100% biodiesel
- B20, B5, B2: 20%, 5%, 2% of biodiesel with 80%, 95%, 98% of petro-diesel, respectively.

Blends with low biodiesel content (2-20%) could be used in normal diesel engines without any modifications. Others require certain engine modifications to avoid troubles during performance and maintenance [11]. Biodiesels are light solvents and hence they keep fuel tank and feed/injection systems clean. Moreover, because of their acidic nature, they require storage tanks and supplying systems made from corrosion-resistant materials or with a specific coating. Moreover, biodiesels' lubricity help to reduce engine wear and hence to increase its lifetime. It was indicated that B5 blend provides 50% of less wear scars than petro-diesel. Higher Cetane number and oxygen content (11%) provide better combustion as well as a shorter ignition delay and hence a lower emission rates [10]. The overall impact of biodiesels on engine performance is well-described by BioMer [10]. Apart from the toxicity and the pre-preparatory requirements, another limitation of the biodiesels is the cost. The average price of B100 is 3.08 $/Gal when diesel costs 2.54 $/Gal. Blends B5 and B20 are quite cheaper (2.55 and 2.69 $/Gal, respectively) but still expensive than diesel. Moreover, it requires special engine modifications, which incur extra cost, that provides high resistant to corrosion, additional fuel preparation processes, etc [11]. However, wide spreading of biodiesels as a marine fuel is ensured by its low emission rate. The National Renewable Energy Lab [11] has reported that the use of biodiesel in conventional diesel engines provide significant reduction of unburned hydrocarbons (HC), exhaust (i.e., particulate matter) and carbon monoxide (CO) in comparison with the emissions from high sulphur diesels which occurs due to 11% of oxygen (by weight) in biodiesel fuels that allows the complete burning of fuel. Also, the use of biodiesel has been become much popular due to the strict regulations imposed recently by the IMO [9]. These regulations have significantly reduced the allowed SO_x and NO_x pollution levels and consequently, they force to consider of minimizing the use of conventional marine fuels. New regulations state that NO_x emissions in new ships that would be built in 2016 should be reduced almost in 5 times comparing with those that exist from year 2000. A 3 times of reduction of SO_x emissions is also expected during the same time period. In fact, some marine engine manufactures have already been preparing for using biodiesel fuels [11]. However, most of them have been using blends that contain only 5-20% of the biodiesel.

1.2. Biodiesel heating

As was mentioned earlier, biodiesels' cloud point is usually higher than petro-diesels and hence the use of various additives as well as heating during exploitation should be required, particularly in cold weather conditions. Previous studies [12] recommended that heating of biodiesel in tanks, pipes and separators or using of chemical additives prior to use in ship power plants. Also they have proposed a number of possible heating techniques. One possibility is that a heater attached on the outer surface of the fuel tank as shown in Figure 1.

Figure 1: Heater for biodiesel storage tanks [12]

This heater is made as a flexible wide ribbon worn on the fuel tank externally. It comprises a heating element sandwiched between two layers of fiberglass with silicone rubber. These types of heaters do not need to be installed in the fuel system and they are compact, corrosion/moisture/chemical resistant. However, they can be used only on small vessels powered by biodiesel. Also, typical electrical heaters that can be attached to any metal surface would also be used in fuel heating. Their aluminium heat exchange surface can heat the fuel by converting it from gel to a liquid and to maintain the fuel at the desired temperature.

ArcticFox Company has introduced pipes with integrated heating elements which prevent solidification of the fuel inside pipelines. These in-line fluid warmers are double-pipe shell-and-tube heat exchangers and the warm water is taken from the engine cooling system which flows in the inner tube while heating biodiesel fuel that flows in the shell-side. All surfaces in contact with the biodiesel are made from stainless steel to avoid corrosion and to eliminate contamination of the fuel. This construction is fairly simple in manufacturing, installation and maintenance. Moreover it uses the heat removed by the engine cooling system (hence to save the power required for heating) that would be otherwise lost [13]. Stainless steel (at least 11% of Chromium by weight) is the most commonly used material for biodiesel fuel system/equipment while Nickel or Molybdenum also could be added for improving the corrosion resistance [14].

2. ADDITION OF SWIRL TO THE SHELL-AND-TUBE HEAT EXCHANGERS

In general, heat transfer enhancement methods can be classified into three major types [15, 16]:

Active methods: These involve in improving the heat transfer rate via techniques that require extra external power sources, for example, mechanical aids, injection and suction of the fluid, surface-fluid vibration, jet impingement, use of electrostatic fields, etc. However, these methods may have limitations in practical applications due to their requirement of external power sources.

Passive methods: These perform their function passively (i.e., without any involvement of external power sources) by enhancing the heat transfer with various possible techniques such as the use of surface coatings, rough/extended/twisted surfaces, swirl-flow generators across the flow, additives with heat transferring mediums, etc. These methods seem to be attractive in practical applications particularly due to their simplicity and low cost.

Compound methods: If a system uses any two or more active or passive methods to improve the rate of heat transfer, it is known as a compound method.

In fact, the performance of heat exchangers can be improved passively by addition of swirl [17]. The use of twisted tapes/tubes is a good way of adding swirl to the fluid flow and two types of swirl flow devices are widely popular in the industry: continuous and decaying swirl flow devices. In a continuous swirl flow, the swirling motion exists over the whole length of the tube (e.g., twisted-tapes, twisted-tubes and wire coil inserts) while the heat transfer coefficient and pressure drop keep constant with the axial distance [18-21]. In a decaying swirl flow, the swirl motion is generated at the entrance of the tube and decays along the flow path (e.g., radial guide vane swirl generators, snail swirl generators and the tangential flow injection devices) while the heat transfer coefficient and pressure drop decrease with the axial distance [22-23]. To enhance the rate of heat transfer, it is required to increase the convective heat transfer coefficient and this can be achieved by increasing the convection coefficient or/and by increasing the convective surface area. Schematic diagrams showing some of the possible methods of improving the rate of heat transfer are presented in Figures 2-8.

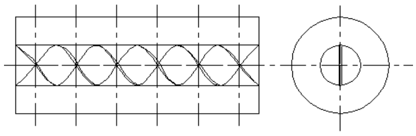

Figure 2: A twisted-tape placed inside the tube

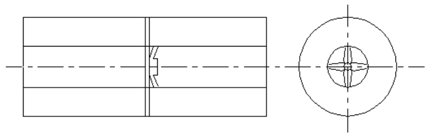

Figure 3: A propeller placed inside the tube

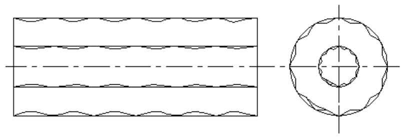

Figure 4: A shell and a tube with wavy surfaces

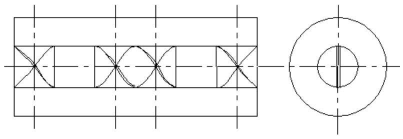

Figure 5: Spiral windings placed inside the tube

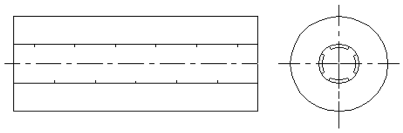

Figure 6: A tube surface with obstacles

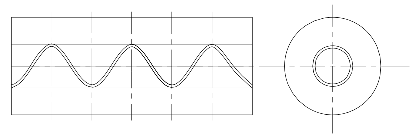

Figure 7: A helical coil placed inside the tube

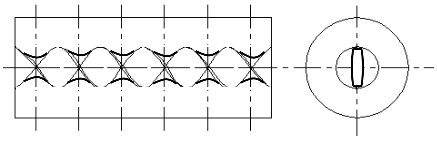

Figure 8: A twisted-tube inside the shell

In this study, a passive heat transfer enhancement method was used particularly due to its simplicity and low implementation cost. After evaluating several possibilities, a twisted-tube insert was identified as an efficient method as it can increase the convection coefficient by introducing swirl into both fluid flows inside the tube and shell. A twisted-tube is a periodically twisted pipe through 360º which can be fabricated relatively easily and economically and provides good heat transfer performance as well [10]. Here, the introduction of a tangential velocity component increases the speed of the flow. Therefore, twisted-tubes would be an economical, simple and efficient way of adding swirl to the fluid flows. In this work, the heat transfer enhancement of a double-tube biodiesel heater is considered with a twisted inner tube. In fact, such a technique could also be applied in multi-tube heaters as well (Figure 9). Evidently, due to the space limitations, it would be difficult to use the baffles in this type of heat exchanger. Therefore, the tubes should be subjected to a unique forming process that provides an oval cross-section with a superimposed helix as shown in Figures 9 and 10. Then, each tube is firmly supported by the adjacent tubes without baffles (i.e., baffle free tube support) while allowing the fluids to swirl freely along the outer surface as shown in Figure 9. Tube forming process ensures that the tube wall thickness stays constant as well as the material yield point is not exceeded thereby retaining mechanical integrity. By allowing required connections with other systems, tube ends are formed in round shape.

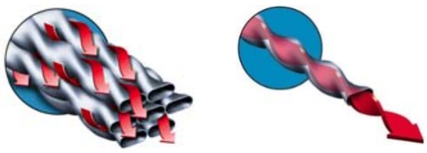

Figure 9: Schematics showing the flow arrangements inside and outside of a twisted-tube [10]

There are a few possible ways of assembling twisted-tubes in a bundle and seven possible constructions are shown in Figure 10. As was mentioned by Morgan [10], some bundles can include up to 5000 tubes leading of up to 1.8 m in diameter and length of up to 2.5 m.

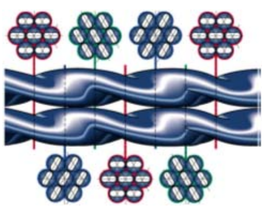

Figure 10: Arrangements of twisted-tube bundles [10]

Some of the major advantageous of heat exchangers with twisted-tubes are that they do not have baffles and hence a less pressure drop and also can have significant reduction of tube vibrations which is a common problem of other types. Also, they are good in thermal effectiveness and less susceptible to fouling. Furthermore, comprehensive review studies on the methods of enhancing of heat transfer with swirl generators [16] and also other possible techniques in heat transfer augmentation [24-29] can be found in the literature.

3. MODELLING

3.1. Case study details

A schematic of the double-pipe biodiesel heater considered in this work is shown in Figure 11.

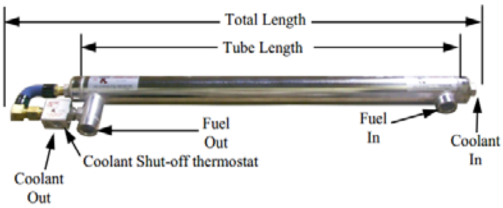

Figure 11: ArcticFox LCC in-line fluid warmer [13]

Heat exchanger type: a double tube heat exchanger with a concentric flow and concentric pipes
Fluid inside the inner tube (hot fluid): water from the engine cooling system
Fluid inside the shell (cold fluid): biodiesel B100
Material (tube and shell): stainless steel
Enhancement technique: twisted inner tube

Table 1. Major parameters of the heat exchanger

Parameter	Unit	Water (Hot fluid)	Biodiesel (cold fluid)
Diameter of the tubes (d_i ,d_o)	m	0.028	0.05
Mass flow rate (m)	kg/s	0.1	0.04
Inlet temperature (T_i)	°C	85	30
Outlet temperature (T_o)	°C	-	80
Specific heat capacity (C_p)	kJ/kg·K	4197	2067
Prandtl number (Pr)	-	2.22	5.66
Viscosity (μ)	10^{-6} Pa·s	355	1,383
Thermal conductivity (k)	W/m·K	0.670	0.154
Density (ρ)	kg/m^3	972	875

Assumptions:

- Negligible heat losses to the surroundings.
- Negligible kinetic and potential energy changes.
- Constant properties of fluids and fully-developed conditions for the cold and hot fluid flows.
- Negligible fouling factors.

Shell and tube diameters were chosen according to the dimensions provided by the ArcticFox [13]. Mass flow rate of biodiesel was decided by fuel consumption requirements of the most widely-used marine internal combustion engines. The mass flow rate of the water (hot fluid) was chosen based on the heat transfer requirements to heat-up the biodiesel till the desired temperature [30]. Usually, B100 biodiesel blend is kept in storage tanks at 25-30 ^oC and must be delivered to engines at 70-85 ^oC to ensure the efficient performance of the engine [12]. Since the hot fluid is taken from the engine cooling system its temperature is also known and taken as 85 ^oC for this study. The outlet temperature of the hot fluid would be figured out later from the energy balance equation. Specific heat capacity, Prandtl number, viscosity and thermal conductivity values were taken from the literature [11, 31]. For calculations, it would also be necessary to know tubes' material parameters. The heat exchanger is made from stainless steel (thickness = 1 mm and thermal conductivity 16.5 W/m·K) due to its good resistance to corrosion. A schematic of the heat exchanger and the corresponding temperature-distance (T-x) graph are shown in Figure 12.

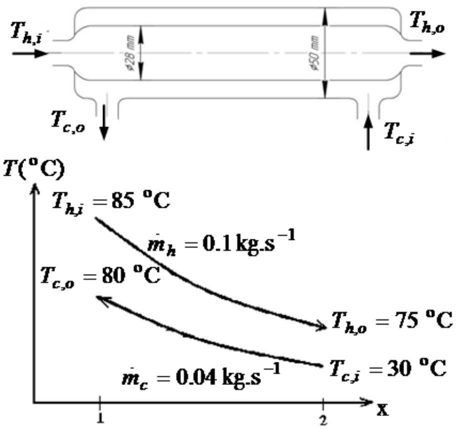

Figure 12: Model of the heat exchanger with the corresponding temperature-distance diagram

Flow conditions based on the Reynolds number (*Re*) [31-33]: Laminar flow: $Re < 2000$

Transitional flow: $2000 < Re < 4000$

Turbulent flow: $Re > 4000$

Dittus-Boelter (DB) correlations which represent the relationship between the Nusselt number (*Nu*), Reynolds number (*Re*) and Prandtl number (*Pr*) are given by Eqs. (1) and (2) [31]:

$$Nu = 0.023 \times Re^{0.8} \times Pr^{0.4} \text{ (Turbulent flows} \quad (1)$$

$$Nu = 0.023 \times Re^{0.8} \times Pr^{1/3} \text{ (Transitional flows)} \quad (2)$$

3.2. Estimation of the heat exchanger length without an enhancement technique

The required rate of heat transfer, $\dot{q}$, (i.e., the heat that should be added to the cold fluid to reach the specified outlet temperature) can be obtained from the overall energy balance of the cold fluid, Eq. (3):

$$\dot{q}_c = \dot{m}_c \times C_{p,c} \times (T_{c,o} - T_{c,i}) \quad (3)$$

$$\dot{q}_c = 0.04 \times 2132 \times (80 - 30) = 4264 \text{ W}$$

By assuming that there is no any heat loss to the surroundings, $\dot{q}_h = \dot{q}_c$, and hence for the hot fluid:

$$\dot{q}_h = \dot{m}_h \times C_{p,h} \times (T_{h,i} - T_{h,o}) \quad (4)$$

$$4264 = 0.1 \times 4197 \times (85 - T_{h,o})$$

$$T_{h,o} = 74.9 \ ^oC \approx 75 \ ^oC$$

Then, the log-mean temperature difference is:

$$\Delta T_{lm} = \frac{(T_{h,i} - T_{c,o}) - (T_{h,o} - T_{c,i})}{ln\left(\frac{(T_{h,i} - T_{c,o})}{T_{h,o} - T_{c,i})}\right)} \quad (5)$$

$$\Delta T_{lm} = \frac{(85-75)-(80-30)}{ln\left(\frac{85-75}{80-30}\right)} = 24.9 \ ^oC$$

Reynolds number of the hot fluid inside the tube:

$$Re = \frac{4 \times \dot{m}_h}{\pi \times d_i \times \mu_h} = \frac{4 \times 0.1}{\pi \times 0.028 \times 313 \times 10^{-6}} = 14{,}528 \quad (6)$$

Therefore, the hot fluid flow is turbulent and hence the Nusselt number is given by Eq. (1):

$$Nu = 0.023 \times Re^{0.8} \times Pr^{0.4}$$

$$Nu = 0.023 \times 14{,}528^{0.8} \times 2.22^{0.4} = 67.6$$

Then, the heat transfer coefficient for water (hot fluid) in the inner tube can be obtained by Eq. (7):

$$h_h = \frac{Nu \times k_h}{d_i} = \frac{67.6 \times 0.670}{0.028} = 1{,}617.6 \text{ W.m}^{-2}.\text{K}^{-1} \quad (7)$$

For the cold fluid flow (biodiesel) inside the shell:

$$Re = \frac{4 \times \dot{m}_c}{\pi \times (d_i + d_o) \times \mu_c} \quad (8)$$

$$Re = \frac{4 \times 0.04}{\pi \times (0.028 + 0.05) \times 1383 \times 10^{-6}} = 472.1$$

Therefore, shell flow is laminar and Nusselt number was chosen from the tables provided in the literature [1] which was noted as 5.63. Then, heat transfer coefficient is given by Eq. (9):

$$h_c = \frac{Nu \times k_h}{(d_o - d_i)} = \frac{5.63 \times 0.154}{(0.05 - 0.028)} = 39.4 \text{ W.m}^{-2}.\text{K}^{-1} \quad (9)$$

Eventually, the overall convection coefficient (*U*) could be obtained from Eq. (10):

$$U = \frac{1}{\left(\frac{1}{h_h}\right) + \left(\frac{1}{h_c}\right) + \left(\frac{t_{tube\,wall}}{k_{tube\,wall}}\right)} \quad (10)$$

$$U = \frac{1}{\left(\frac{1}{1618}\right) + \left(\frac{1}{39.4}\right) + \left(\frac{0.001}{16.5}\right)} = 38.4 \text{ W.m}^{-2}.\text{K}^{-1}$$

where $t_{tube\,wall}$ is the thickness of the tube wall and $k_{tube\,wall}$ is the thermal conductivity of the tube material. Therefore, the required length (*L*) of the heat exchanger tube for this particular set task is:

$$L = \frac{q}{U \times \pi \times d_i \times \Delta T_{lm}} \quad (11)$$

$$L = \frac{4264}{38.4 \times \pi \times 0.028 \times 24.9} = 50.7 \ m$$

3.3. Estimation of the heat exchanger length with an enhancement technique

In this work, inserting of twisted-tubes was used as the heat transfer enhancement technique. By using twisted-tubes instead plain tubes, Nusselt number can be increased in both fluid flows and hence the heat transfer rate would increase. The relationship between Nusselt number and Reynolds number for twisted-tubes with different twisting ratios (S/d) is illustrated in Figure 13.

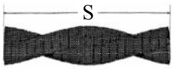

S – Pitch, S/d – Twisting Ratio

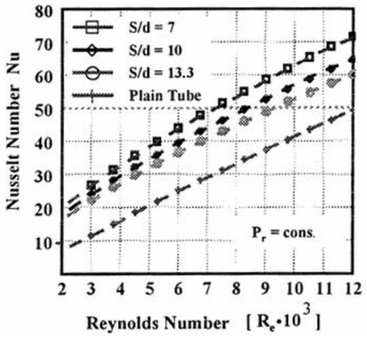

Figure 13: The dependence of Nusselt number *(Nu)* on Reynolds number and twisting ratio [2]

The percentage increase of Nusselt number with different twisting ratios (S/d) can be determined as below based on the information given in Figure 13.

For the hot fluid inside the tube (Re = 14,528):

$S/d = 13.3$

$$\%\,increase\,of\;Nu = \left(\frac{71-60}{60}\right)\times 100\% = 18.3\%$$

$S/d = 10$

$$\%\,increase\,of\;Nu = \left(\frac{75-60}{60}\right)\times 100\% = 25.0\%$$

$S/d = 7$

$$\%\,increase\,of\;Nu = \left(\frac{83-60}{60}\right)\times 100\% = 38.3\%$$

For the cold fluid inside the shell (Re = 472.1):

$S/d = 13.3$

$$\%\,increase\,of\;Nu = \left(\frac{6-1}{1}\right)\times 100\% = 500\%$$

$S/d = 10$

$$\%\,increase\,of\;Nu = \left(\frac{8-1}{1}\right)\times 100\% = 700\%$$

$S/d = 7$

$$\%\,increase\,of\;Nu = \left(\frac{10-1}{1}\right)\times 100\% = 900\%$$

Then, by following the same method presented in section 3.2, the required length of the heat exchanger with twisted-tubes can be calculated, with new Nusselt numbers achieved with different twisting ratios, for the same task.

The use of twisted-tubes to increase the heat transfer rate will affect the axial pressure drop along the heat exchanger. The change of friction factor (f) with Reynolds number and twisting ratio is given in Figure 14 [2]. The pressure drops (ΔP) along the heat exchanger with a plain tube and twisted-tubes were also calculated (for Re = 14,528 and Re = 472) with Darcy-Weisbach equation given in Eq. (12):

$$\Delta P = f \times \frac{L}{d} \times \frac{\rho}{2} \times V^2 = f \times \frac{L}{d} \times \frac{\rho}{2} \times \left(\frac{\dot{m}}{\rho A}\right)^2$$

$$\Delta P = \frac{f \times L \times \dot{m}^2}{2 \times d \times \rho \times A^2} \qquad (12)$$

Then, new values calculated for twisted-tubes with different twisting ratios are presented in Table 2.

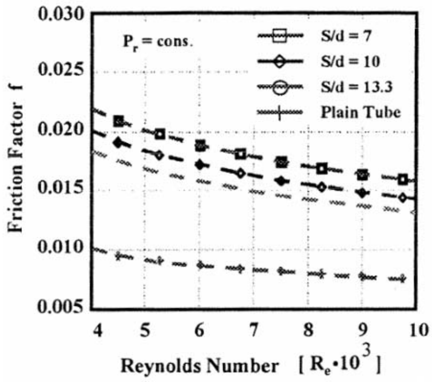

Figure 14: The dependence of friction factor on Reynolds number and twisting ratio [2]

Table 2. Parameters of the heat exchanger after adding a twisted-tube

S/d	**13.3**	**10**	**7**
	Tube flow (hot fluid)		
Nu	79.97	84.05	93.49
h_h (W.m^{-2}.k^{-1})	1914	2022	2237
ΔP (Pa)	66.67	53.25	48.67
	Shell flow (cold fluid)		
Nu	28.15	39.41	50.67
h_c (W.m^{-2}.k^{-1})	197.1	275.9	354.7
ΔP (Pa)	6.42	5.21	4.52
U (W.m^{-2}.k^{-1})	176.7	239.2	300.6
L *(m)*	11.01	8.14	6.48

4. DISCUSION

A comparison of the required heat exchanger length with and without heat transfer enhancement to perform the same task is shown in Figure 15. Clearly, the heat exchanger length has reduced considerably with twisted-tubes where the higher the twisting ratio the lower the required length. Also, with twisted-tubes, the axial pressure drops along both the shell and tube show reductions as shown in Table 2 and Figure 16 which should lead to decrease the required pumping power as well.

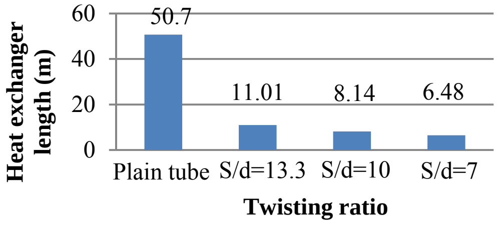

Figure 15: The required length of the heat exchanger with different tubes to perform the same task

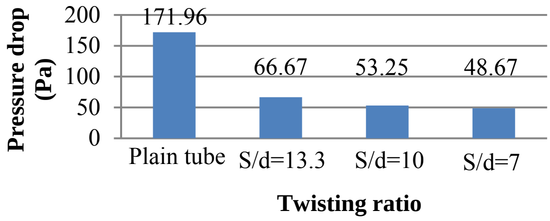

Figure 16: The axial pressure drop along the different tubes to perform the same task

A comparison of the major parameters of the heat exchanger with a plain tube and a twisted-tube with a twisting ratio (S/d) of 10 is given in Table 3.

Table 3. Parameters of the heat exchanger with a plain tube and a twisted-tube (S/d=10)

Parameter	Plain tube	Twisted-tube (S/d=10)	Reduction or Increment (%)
U (W.m^{-2}.K^{-1})	38.4	239.2	↑ 522.9
Nu - tube flow	67.6	84.05	↑ 24.3
Nu - shell flow	5.63	39.41	↑ 600
ΔP- tube flow	171.96	53.25	↓ 69.0
ΔP- shell flow	18.56	5.21	↓ 71.9
Required Length, L (m)	50.7	8.14	↓ 83.9

The results show that the rate of heat transfer has increased by a percentage of 522.9% with a twisted tube (S/d=10) leading to a 83.9 % reduction of the required length of the heat exchanger to perform the same task. Therefore, it is clear that the inserting of twisted-tubes is an effective way to enhance the rate of heat transfer in heat exchangers and hence to reduce their size (i.e., heat exchangers which are compact in size) to perform a particular task. Moreover, the fabrication cost of the heat exchanger may be reduced considerably with the addition of swirl to the fluid flows inside the tube and shell. In fact, the case study presented in this work considered a heat exchanger with a single tube. However, the shell-and-tube heat exchangers which are commonly used in industrial applications include a number of tubes inside the shell. Thus, the addition of swirl to flows of such heat exchangers with multiple tubes may provide further improvements of the rate of heat transfer and hence further reductions to the fabrication cost as well.

The design and fabrication of twisted-tubes are relatively simple and also there is no need of any additional modification to the shell for inserting these tubes. Therefore, the inserting of twisted-tubes is a highly compatible technique for industrial applications. However, one of the disadvantages of this technique is that the possible increase of the pressure drop which should lead to demand more power to pump the fluid inside the tubes and shell. However, for this work, the pressure drops along both the shell and tube show reductions of 71.9% and 69.0% respectively with a twisted-tube (S/d=10) due to the reduction of the required length. In general, some of the major factors which should be taken into account as the addition of swirl for designing of compact heat exchangers are:

- The space requirements/limitations to position the heat exchanger
- Simplicity, effectiveness and the access requirements of the swirl generator/s
- Design and fabrication cost of the heat exchanger with and without swirl
- The level of increase/decrease of the pressure drop with the addition of swirl
- The level of increase/decrease of the required pumping power with the addition of swirl

Overall, it seems that the inserting of twisted-tubes is a cost effective and an efficient technique for enhancing the rate heat transfer and hence to design compact heat exchangers.

5. CONCLUSIONS

This study was mainly focused on investigating strategies to improve the performance of a biodiesel heater (i.e., a shell-and-tube heat exchanger) by the addition of swirl. A number of possible methods of adding swirl were evaluated and then a twisted-tube insert was selected to use. A case study was presented for calculating the increase of rate of heat transfer, the reduction of the required length of the tube and increase/decrease of the pressure drop with twisted-tubes with different twisting ratios. The results confirmed that the twisted-tubes are one of the simple and effective techniques to improve the rate of heat transfer without involving complex modifications to the typical design of shell-and-tube heat exchangers. In general, it showed that the size of the heat exchanger can be reduced considerably by introducing swirl to the tube and shell flows by inserting twisted-tubes and also the fabrication cost may be reduced significantly due to the reduction of the required length. Usually, the axial pressure drop along the tube and shell should be increased with a twisted-tube due to the increase of swirl motion and hence the required pumping power would also increase. However, the results of this work showed that the pressure drop has decreased with the twisted-tubes, due to the reduction of the heat exchanger length, to perform same task and hence the required power for pumping of fluids should also be decreased which is another advantage. Further studies are underway to explore more on the effective and economical strategies to enhance the rate of heat transfer to design compact heat exchangers. Also, computational fluid dynamics approaches will be used in the modelling work.

REFERENCES

[1] Lunsford K. M., “Increasing heat exchanger perfomance”, Bryan Research and Engineering, Inc., Bryan, Texas, USA.

[2] Ljubicic B., “Testing of Twisted-tube exchangers in transition flow regime”, Brown Fintube Company, Koch Industries, Houston, USA.

[3] Thantharate V., and Zodpe D. B., “Experimental and numerical comparison of heat transfer Performance of Twisted Tube and Plain Tube heat exchangers”, *Int. Journal of Scientific & Engineering Research*, 4 (7), 1107-1113, 2010.

[4] Siddique M., Khaled A. R. A., Abdulhafiz N. I., and Boukhary A. Y., “Recent advances in heat transfer enhancements: A review report”, *Int. Journal of Chemical Engineering,* 2010.

[5] Nagayach N. K., and Agrawal A. B., “Review of heat transfer augmentation in circular and non-circular tube”, *Int. Journal of Engineering Research & Applications,* 2 (5), pp. 796-802, 2012.

[6] Yang S., Zhang L., and Xu H., “Experimental study on convective heat transfer and flow resistance characteristics of water flow in twisted elliptical tubes”, *Applied Thermal Engineering,* 31 (14-15), pp 2981-2991, 2011.

[7] Tan X-H, Zhu D-S., Zhou G-Y., and Zeng L-D., “Experimental and numerical study of convective heat transfer and fluid flow in twisted ovel tubes”, *Int. Journal of Heat & Mass Transfer,* 55 (17-18), pp. 4701-4710, 2012.

[8] Opdal O. A., and Hojem F.M., “Biofuels in Ships”, ZERO emission organisation, Oslo, 2007.

[9] “Prevention of air pollution from ships”, International Maritime Organisation, 2010, [Online] Available at: http://www.imo.org/OurWork/Environment/Pollution Prevention/AirPollution/Pages/Air-Pollution.aspx. [Last viewed: 20/08/2014].

[10] BioMer, “Biodiesel demonstration and assessment for tour boats in the old port of Montreal and Lanchine Canal National Historic Site”, 2005.

[11] Nayyar M. P., “The use of biodiesel fuels in the U.S. marine industry”, PRIME, Inc., 2010.

[12] Горбов В. М., and Митенкова В. С., “Альтернативные топлива в судовой энергетике”, *Николаев: НУК*, 2012.

[13] Arctic Fox, “In-line fluid warmers,” Delano, USA.

[14] Calister W. D., and Rethwisch D. G., “*Material Science and Engineering: An Introduction*”., John Willey & Sons, 1940.

[15] Kumar C. N. and Murugesan P., “Review on twisted-tapes heat transfer enhancement”, *Int. Journal of Scientific & Engineering Research*, 3 (4), pp. 1-9, 2012.

[16] Kumbhar D. G. and Sane N. K., “Heat transfer enhancement in a circular tube twisted with swirl generator: A review”, *Proc. of the 3rd Int. Conf. on Advances in Mechanical Engineering*, pp 188-192, Gujarat, India, January 4-6, 2010.

[17] Eiamsa-ard S., and Promvonge P., “Enhancement of heat transfer in a tube with regularly-spaced helical tape swirl generators, *Solar energy*, 78 (4), pp. 483-494, 2005.

[18] Manglik R. M. and Bergles A. E., “Heat transfer and pressure drop correlations for twisted-tape inserts in isothermal tubes, Part I: Laminar flows”, *ASME Journal of Heat Transfer*, 115 (4), pp. 881–889, 1993.

[19] Manglik R. M., and Bergles A. E., “Heat transfer and pressure drop correlations for twisted-tape inserts in isothermal tubes: Part II-Transition and turbulent flows”, *ASME Journal of Heat Transfer*, 115 (4), pp. 890–896, 1993.

[20] Hong S. W., and Bergles A. E., “Augmentation of laminar flow heat transfer in tubes by means of twisted-tape inserts”, *ASME Journal of Heat Transfer*, 98, pp. 251–256, 1976.

[21] Eiamsa-ard S., Thianpong C. and Promvonge P., “Experimental investigations of heat transfer and pressure drop characteristics of flow through circular tube fitted with regularly-spaced twisted-tape”, *The Joint Int. Conf. on Sustainable Energy and Environment*, Thailand, pp 18-22, 2004.

[22] Chang F. and Dhir V. K., “Mechanisms of heat transfer enhancement and slow decay of swirl in tubes using tangential injection”, *Int. Journal Heat Fluid Flow*, 16 (2), pp. 78–87, 1995.

[23] Yildiz C., Bicer Y. and Pehlivan D., “Influence of fluid rotation on the heat transfer and pressure drop in double pipe heat exchangers”, *Applied Energy*, 54 (1), pp. 49–56, 1996.

[24] Siddique M., Khaled A.-R. A., Abdulhafiz N. I., and Boukhary A. Y., “Recent advances in heat transfer enhancements: A review report”, *Int. Journal of Chemical Engineering*, vol. 2010, Article ID 106461, 28 pages, 2010.

[25] Dewan A., Mahanta P., Raju K. S., and Kumar P. S., “Review of passive heat transfer augmentation techniques”, *Proc. of the IMechE -Part A: Journal Power and Energy*, 218 (7), pp 509-527, 2004.

[26] Gupta A., and Uniyal M., “Review of heat transfer augmentation through different passive intensifier methods”, *OSR Journal of Mechanical and Civil Engineering*, 1 (4), pp. 14-21, 2012.

[27] Nagayach N. K., and Agrawal A. B., “Review of heat transfer augmentation in circular and non-circular tube”, *Int. Journal of Engineering Research and Applications*, 2 (5), pp. 796-802, 2012.

[28] Ganorkar A. B., and Kriplani V. M., “Review of heat transfer enhancement in different types of extended surfaces”, *Int. Journal of Engineering Science & Technology*, 3 (4), pp. 3304-3313, 2011.

[29] Stone K., and Vanka S. P., “Review of literature on heat transfer enhancement in compact heat exchangers”, [Online] Available at: https://ideals.illinois.edu/bitstream/handle/2142/11540/TR105.pdf?sequence=2, [Last viewed:20/08/14].

[30] Горбов В. М., “Енциклопедія суднової енергетики”, *Миколаїв: НУК*, 2010.

[31] Incropera F. P. and Dewitt D. P., “*Fundamentals of heat and mass transfer*, John Wiley and Sons, 2001.

[32] “Laminar and Turbulent flows in pipes”, [Online] Available at: http://www.cs.cdu.edu.au/homepages/jmitroy/eng243/sect09.pdf, [Last viewed: 03/03/2013].

[33] Subramanian R. S., “Heat transfer to or from a fluid flowing through a tube”, [Online], Available at: http://web2.clarkson.edu/projects/subramanian/ch302/notes/Convective%20Heat%20Transfer%201.pdf, [Last viewed: 03/03/2013].n

Conference on Modelling Fluid Flow (CMFF'15)
The 16th International Conference on Fluid Flow Technologies
Budapest, Hungary, September 1-4, 2015

PIV MEASUREMENTS OF THE VORTEX RING STATE OF THE MAIN ROTOR OF A HELICOPTER

Wit STRYCZNIEWICZ[1], Katarzyna SURMACZ[2]

[1]Institute of Aviation, Krakowska 110/114, 02-256 Warsaw, Poland, Tel. (+48) 22 846 00 11, E-mail. wit.stryczniewicz@ilot.edu.pl
[2]Institute of Aviation, Warsaw, Poland, E-mail. katarzyna.surmacz@ilot.edu.pl

ABSTRACT

Measurements of the flow field around a main rotor of a helicopter in a low-speed wind tunnel have been performed using Particle Image Velocimetry (PIV). The aim of the research was to investigate conditions known as settling with power (vortex ring state, VRS). VRS occurs when the velocity of upward flow of air through a rotor is close to the value of the induced velocity at the rotor disc (i.e. in descent flight of a helicopter). In order to provide the necessary conditions for development of VRS we set the rotation axis of the main rotor of a helicopter in the axis of symmetry of the wind tunnel's test section. We present 2D vector velocity field of the investigated flow measured by PIV technique Results provide a visualization of the vortex ring state and show the development of the VRS. The center of the vortex ring shifts its position from back to front of the rotor. Presented results are in agreement with theory and can be used for visualization and deeper understanding of the VRS development mechanism.

Keywords: helicopter aerodynamics, vortex ring state, low-speed wind tunnel tests, PIV

NOMENCLATURE

D	[m]	diameter of the main rotor
TF	[]	turbulence factor
$\underline{\underline{U}}$	[m/s]	vector velocity filed
v	[*m/s*]	horizontal velocity component
v_i	[*m/s*]	induced velocity
u	[*m/s*]	vertical velocity component
w	[*m/s*]	upward flow velocity
τ	[%]	turbulence intensity

1. INTRODUCTION

Helicopter aerodynamics depends on the interaction between the flow induced by the main rotor and the flow of air resulting from the movement of the helicopter. In the most conditions of vertical flight, like hovering or ascending flight the flow through the rotor is definite. There is a well-defined slipstream [1]. However, in descent flight when the flow induced by the rotor and the upward flow are oppositely directed the recirculation of air may occur. This conditions lead to development of vortex ring system that engulfs the rotor. (Fig. 2.) This state is known as settling with power (VRS, vortex ring state).

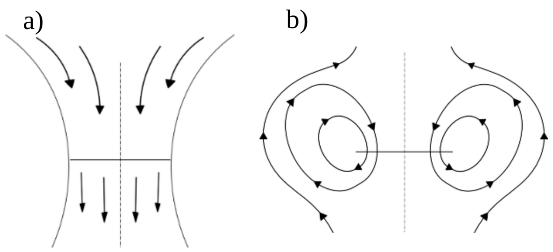

Figure 1. Flow through rotor: a) hover b) vortex ring state in vertical descent

The vortex ring state in a descent flight is prone to form in case when the upward flow velocity w and the velocity of the induced flow v_i have similar values. The theoretical range of the VRS occurrence is w=(0,5-1,5)v_i. The development of recirculation zone in a vortex ring state causes serve loss of lift of the main rotor. The settling with power condition is especially dangerous during landing of the helicopter. The development of VRS was responsible for accidents involving many different types of helicopters (Hughes 269C (2000), Robinson R-22 (2002), MH-60 (2011)) and tiltrotors (V-22 Osprey (2000)). Therefore the need for detailed investigation of this phenomenon is still valid by means of experimental tests

[2],[12],[13],[14] and numerical simulations [3],[4],[5],[6].

In the present paper the results of the PIV measurements of the flow field around a helicopter's main rotor has been presented. The results include velocity fields, scalar fields of velocity magnitude and streamlines patterns of the observed vortex ring state. The path of the vortex ring center close to the rotor is presented in all stages of the VRS occurrence. Results demonstrate the development of VRS and give the information about the time scale of the phenomenon.

2. METHOD

In order to provide the necessary conditions for development of VRS the rotation axis of the main rotor of a helicopter (model) was set in the axis of the wind tunnel's test section (Figure 2.). It means that the flow induced by the rotor and the flow generated by the wind tunnel was oppositely directed. Measurements were performed using a Particle Image Velocimetry (PIV) method [2]. The flow was investigated in proximity of the tip of the blade where the center of the vortex ring was expected to occur.

2.1. Experimental setup

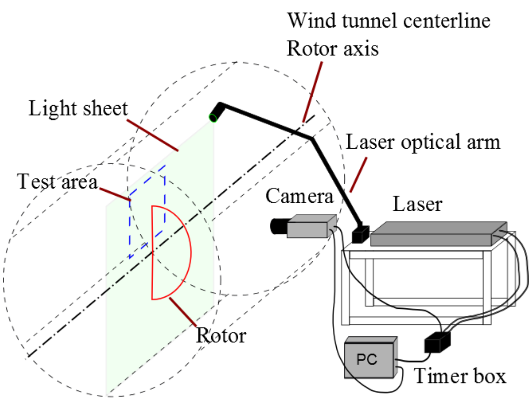

Figure 2. Experimental setup

The experimental setup consisted of closed-circuit low speed wind tunnel and the model of a helicopter. The test section of the wind tunnel has a diameter of 1,5 m and length of 2 m. The wind speed range is from 10 m/s to 40 m/s. The turbulence intensity measured for empty test section is τ=0,5%, while the turbulence level TF=1,425. The helicopter was fixed to the test section of the wind tunnel using a pillar.

The model of a helicopter (T-REX 450 PRO Super Combo) has a two blade rotor powered by an electric drive. The diameter of main rotor is D=0.710 m. The pitch angle of the blades can be changed during the test in range 0 to 10°. The maximum rotational speed of the main rotor is 2400 rpm and the maximum induced velocity of the rotor in hover is approximately 6 m/s.

2.2. PIV setup

The PIV system consisted of dual-cavity solid-state (Nd:YAG) pulse laser and digital camera. The lightsheet was formed by set of cylindrical lenses. The Canon EF 35 mm f 1:1.4 lenses for the camera were used. The seeding was produced by seeding generator form DEHC oil. Since the VRS is an unsteady phenomenon we set the temporal resolution of the measurements to the maximum value of 7 Hz. In order to measure velocities in a range 1 m/s to 10 m/s the time delay between illumination pulses was set to 80 µs. The measurement area of the PIV system included the area above the tip of the blades (Fig. 6.). Measurements were performed with three sizes of the PIV test region (380x380, 400x400, 450x450 mm). The 2D vector velocity fields of the flow from the acquired images were obtained with use of DynamicStudio software. The Adaptive Correlation scheme with initial size of the interrogation windows 128x128 pixels was applied for the analysis. The final integration windows size was 64x64 pixels with 50% window overlap. The outlier vectors and missing data was removed in post-processing with use of average and median filtering. The system was calibrated use of calibration target approach.

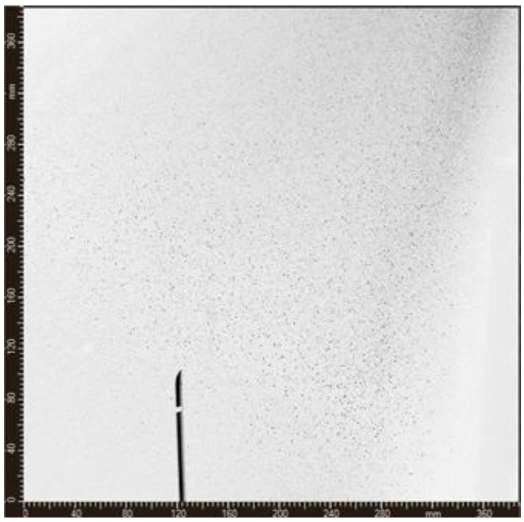

Figure 3. Observation area of the PIV system. View with seeding and the tip of the blade

2.3. Validation of the PIV system settings

The PIV system setup was validated in two tests. First test was designed to validate the settings of the PIV system for measurements of the speed of air in the wind tunnel. The free-stream velocity was measured by PIV system and compared the results of the velocity measured by the pitot tube in the wind tunnel test section. The second test of the PIV system setup involved the measurement of the induced flow velocity. In this test the induced flow velocity was measured by the PIV system and the vane anemometer. Both tests proved that the PIV system settings were proper (see Table 1.).

Table 1. Comparison of the inducted velocity measured with PIV and vane anemometer

the pitch angle of the blades [°]	Velocity v_i [m/s] Measured by vane anemometer	PIV Velocity v_i [m/s]
0	0.75	0.8
2	0.59	-
4	0.05	2.1
6	3.4	3.5
8	5.9	5.9
10	7	7.1
8	5.4	5.6
6	3.3	3.2
4	2	2
2	0.5	-
0	0.75	0.75

3. RESULTS

Toroidal rings around the main rotor of a helicopter formed in each test. Since the conditions for development of the VRS was appropriate only at the lowest speed of the wind tunnel (before reaching the minimum velocity of the free-stream or slowing down the air in the tunnel to minimum value of free-stream velocity after turning of the wind tunnel's engine), only one set of speeds was tested: w ≅ 8 m/s and vi ≅ 6 m/s.

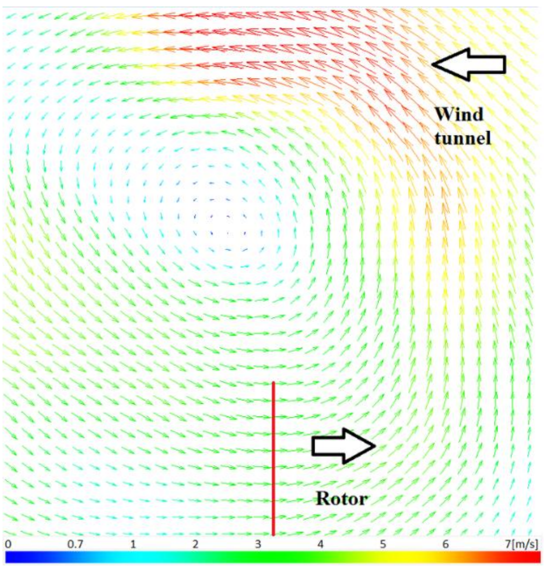

Figure 4. 2D vector velocity field presenting observed vortex ring state

The results show the velocity distribution in the PIV test region in form of 2D vector velocity field in meters per second (see Figure 4.). It is an example of the flow pattern in vortex ring state. Directions of the free-stream flow and induced flow are marked by black arrows. The figure shows the blade tip and the vortex which the core is located above the blade.

3.1. Rotational flow condition

In order to distinguish between rotational and irrotational characteristic of the flow following condition need to calculate for all velocity field:

$$\nabla \times \underline{\underline{U}} = 0 \tag{1}$$

For irrotational flow the curl of the velocity field, given by equation 1, is equal to zero. The flow is considered to be potential. This is the case for most of investigated flow in the wind tunnel test section (for example the flow over an airfoil).

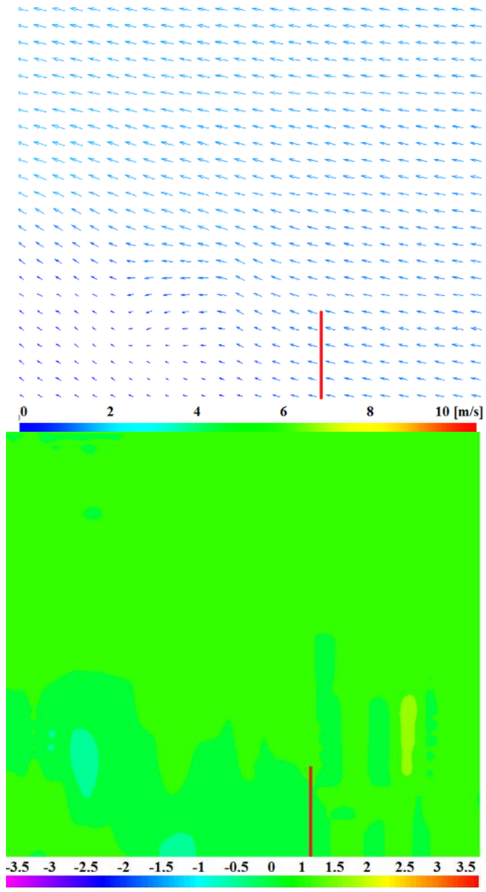

Figure 5. Visualization of the rotational condition (bottom) and the corresponding vector velocity field (upper) case of translational flow of air over a rotor. Values of rotational flow condition are equal to zero

In case of rotational flow the like vortex flow the expression (1) is not equal to zero. Therefore in order to verify if investigated flow is rotational the following condition needs to be fulfilled for 2D velocity field

$$\frac{\partial v}{\partial x} - \frac{\partial u}{\partial y} \neq 0 \qquad (2)$$

The equation (2) was calculated from measured velocity fields. In cases when the velocity vectors were forming a vortex pattern the condition (2) was fulfilled.

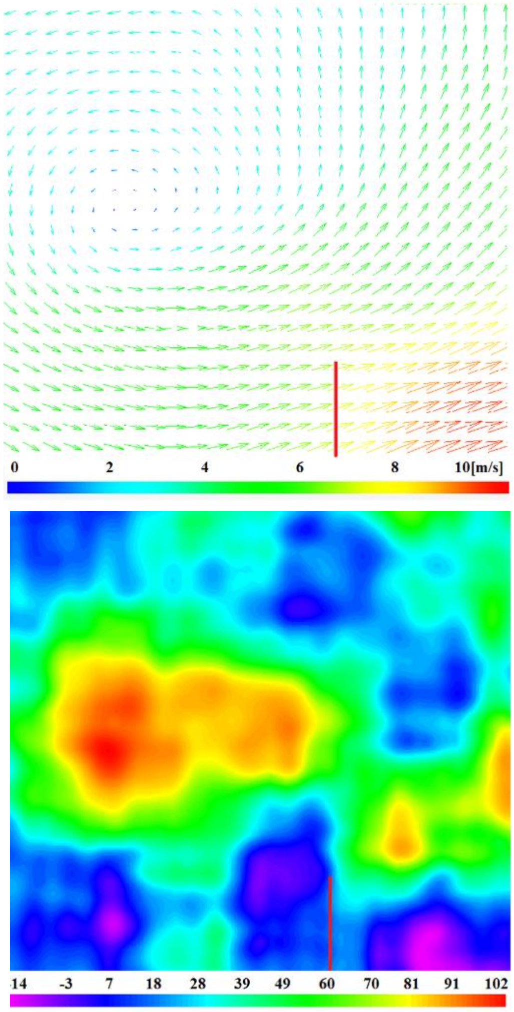

Figure 5. Visualization of the rotational condition (bottom) and the corresponding vector velocity field (upper) case of rotational flow of air over a rotor. The highest values at the bottom image corresponds to highest vorticity in the vortex core.

3.3. Streamlines

In order to ensure clear recognition of the vortex structure the streamlines pattern was calculated from the 2D vector velocity fields. Streamlines form a vortex pattern on consecutive frames (see Figure 6). The results show the development of the vortex ring state on two consecutive frames. The position and size of the vortex core had changed. The streamlines visualization shows the changing nature of the flow in VRS region.

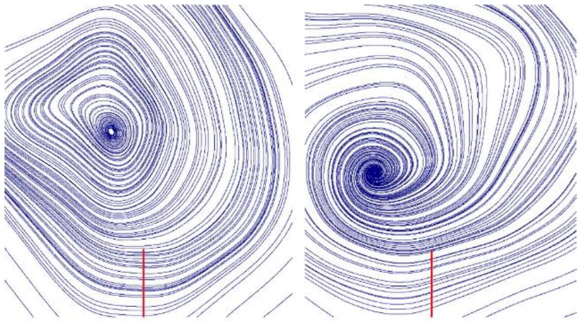

Figure 6. Streamlines patterns of the vortex ring state on two consecutive frames. The vortex ring shifts its position in correspondence to the rotor's plane.

3.3. Development of VRS

In order to track the center of the vortex the maps of the velocity magnitude was analysed. The assumed was that the center of the vortex is placed at the position of the minimum of the local velocity. The vortex center changes the position on the consecutive frames.

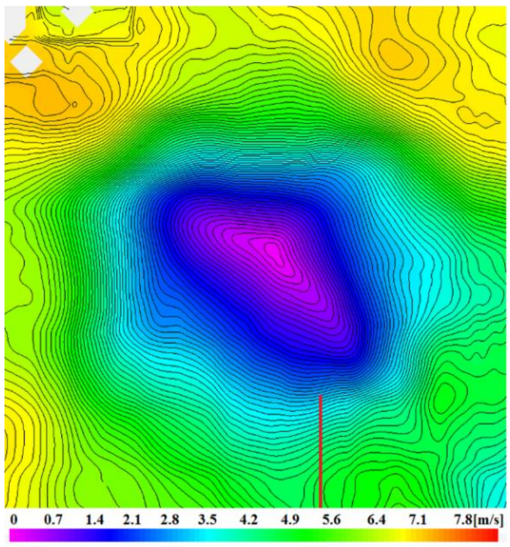

Figure 7. Scalar map presenting the velocity magnitudes of the flow during the development of vortex ring state. The lowest values of the velocity magnitude can be observed at vortex core.

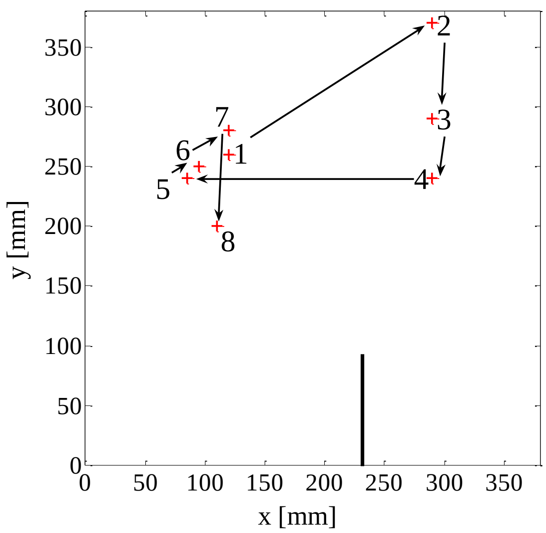

Figure 8. Consecutive positions of the vortex ring center. The black line indicates the position of the blade's tip. Firstly the position of the vortex core travels form region above the rotor's plane to region underneath. Secondly reverse transition is observed. The measurement frequency is 7 Hz.

4. SUMMARY

In the recent years, the use of helicopters increased. Determination of limits on the use provides acceptable levels of safety. One of the restrictions for use of the helicopter is the vortex ring state boundary. Research on the issue of the VRS is intended to increase the safety and reliability of helicopters. The results of experimental and numerical analyses show that the real area of the occurrence of VRS can be a little different than the theoretical area (the VRS develops in some cases earlier and can take longer than in the theoretical). The experimental results presented in this paper are part of the work carried out on the vortex ring state phenomenon. The conditions of axial flight of a helicopter were considered. Helicopter flights were performed in the vicinity and inside the area of the VRS.

Tests proved that PIV method is a reliable tool for an investigation of flow around the rotor of a helicopter in a controlled wind tunnel conditions. The aim of presented research was to investigate the development of the vortex ring state of the main rotor of a helicopter. The development of VRS was observed using with non-intrusive velocity measurement method in a low speed wind tunnel. The visualization of a flow field provided information about the changing nature of the flow in vortex ring state conditions. The 2D vector velocity field of the investigated flow was obtained. The settings of the PIV system was validated and results of PIV velocity measurements was compared with the vane anemometer indications. Good agreement of the results in most cases was obtained (see Table 1).

The presented experiment permitted the quantitative and qualitative an analysis of VRS phenomena. In order to get insight on development of VRS, the vortex ring center was traced on consecutive frames. The velocity of the vortex ring center was in range 0,5 to 1,5 m/s. The time of the VRS occurrence for the experimental conditions was in range 0,5 to 2 seconds. The position of the vortex ring center changed between frames. It is worth to notice that the region identified as a vortex core of the VRS structure was observed in a region above and underneath the rotor's plane and it was traversing freely during development and demise vortex (See Figure 8). Although the sampling frequency of the PIV system was relatively low (7Hz) it was possible to observe the development and demise of VRS in controlled laboratory conditions and to characterise the movement of the vertex ring canter. The speed of freestream in the wind tunnel was not constant during the experiment. It was decreasing form value above the condition of VRS occurrence to zero. This allowed to observed the process of development and demise of investigated phenomenon. Nevertheless in such conditions continuous observation of the VRS was not possible.

Due to the technical limitations of the laser the sampling frequency was 7 Hz. Higher sampling frequency would provide more accurate information of the vortex core trajectory. The field of view of the PIV system cameras do not allowed to visualise the whole investigated structure.

The research will be continued with use a stereo-PIV system and a strain gauge balance in order to acquire more detailed understanding of VRS phenomenon development. Also the field of view will be enlarged due to application of special optics. In the future, experimental results will be compared with results of CFD calculations which are currently performed in Institute of Aviation [4].

REFERENCES

[1] Adrian R. J. Twenty Years Of Particle Image Velocimetry, 2005, *Experiments in Fluids* 39, pp. 159-169.

[2] Dress J., and Hendal W. P., 1951, Airflow Patterns In The Neighbourhood Of Helicopter Rotors, *Aircraft engineering*, vol. 23(266), pp. 107-111.

[3] Florczuk W., 2009, CFD Hover Analysis Of W-3 Falcon Rotorcraft For Different Upstream Air Conditions, *Transactions of the Institute of Aviation*, Vol. 201, pp. 67-80.

[4] Grzegorczyk K., 2009, An Analysis of Vortex Ring State on the Rotorcraft, *Transactions of the Institute of Aviation*, Vol. 201, pp. 52-66.

[5] Grzegorczyk K., Helicopter flight simulation close to safety limits conditions, Mechanics in Aviation nr ML-XV, 2012
[6] Grzegorczyk K., 2013, Analysis of influence of helicopter descent velocity changes on the phenomena of vortex ring state, Postępy Nauki i Techniki, Vol. 7., pp. 35-41.
[7] Leishman J. G., 2000, *Principles of helicopter aerodynamics*, Cambridge University Press.
[8] Raffel M., Willert C.E., Wereley S.T., Kompenhans J., 2007, *Particle Image Velocimetry – A practical Guide*, 2nd ed., Springer.
[9] Ruchała P., 2013, The Measurement and Control System in the T-1 Wind Tunnel, *Transactions of the Institute of Aviation*, Vol. 232,. pp. 63-78.
[10] Stryczniewicz W., 2012, Development of Particle Image Velocimetry Algorithm, *Problems of Mechatronics*, Vol. 9, pp. 41-54.
[11] Stryczniewicz W., Surmacz K., 2014, Investigations of the Vortex Ring State of the Main Rotor of a Helicopter, *Transactions of the Institute of Aviation*, Vol. 235, pp. 17-27.
[12] Wielgus S., 1963, „Sprawozdanie z prób w locie śmigłowca SM-1 w stanie pierścienia wirowego", *Technical Report*, Institute of Aviation
[13] Wiśniowski W., 2014, Twenty Years of Light Aircraft and Safety Program, *Transactions of the Institute of Aviation*, Vol. 236, pp. 7-25.
[14] Vad, J., and Bencze, F., 1998, "Three-Dimensional Flow in Axial Flow Fans of Non-Free Vortex Design", *Int J Heat Fluid Flow*, Vol. 19, pp. 601-607.

Conference on Modelling Fluid Flow (CMFF'15)
The 16th International Conference on Fluid Flow Technologies
Budapest, Hungary, September 1-4, 2015

A NUMERICAL STUDY OF THE THREE-DIMENSIONAL INCOMPRESSIBLE ROTOR AIRFLOW WITHIN A TESLA TURBINE

Constantin Schosser[1], Michael Pfitzner[2]

[1] Corresponding Author. Technische Thermodynamik, MB 5.1, Universität der Bundeswehr München, Werner-Heisenberg-Weg 31, 85577 Neubiberg, E-mail: constantin.schosser@unibw.de
[2] Institut für Thermodynamik, LRT 10, Universität der Bundeswehr München, Werner-Heisenberg-Weg 31, 85577 Neubiberg, E-mail: michael.pfitzner@unibw.de

ABSTRACT

The paper summarizes numerical and theoretical studies of incompressible, laminar airflow through a single flow passage of a blade-less radial friction turbine. The rotor geometry is based on an optimization of the performance solving simplified, incompressible Navier-Stokes-Equations, presented in Schosser et al. [1]. At first, the influence of dimensionless machine parameters on performance and efficiency with respect to mechanical loads were derived from theoretical analysis. Inflow conditions for maximum performance and efficiency were theoretically determined and later compared to a CFD. In order to quantify the error of the theoretical analysis, the inflow effect on shaft power and flow behavior was examined by CFD. The development of the fully developed axial velocity distribution in the inlet zone is compared to the theoretical, optimum inflow. The influence of Reynolds number and rev speed on the velocity profiles is investigated. Finally, the intended use of the Tesla turbine with its advantages in contrast to conventional turbo machinery is discussed.

Keywords: laminar flow, CFD, friction, blade-less, Tesla turbine

NOMENCLATURE

A	$[m^2]$	inlet area
C	$[-]$	normalized rel. circ. velocity
C_{po}	$[-]$	normalized power coefficient
C_{pt}	$[-]$	economical power coefficient
C_{to}	$[-]$	normalized torque coefficient
F	$[-]$	norm. circ. velocity profile
G	$[-]$	norm. radial velocity profile
M	$[Nm]$	torque
P	$[W]$	shaft power
R	$[-]$	radius ratio
Re	$[-]$	Reynolds number
U	$[-]$	normalized abs. circ. velocity
V	$[-]$	normalized radial velocity
Z	$[-]$	normalized position in gap
c	$[m/s]$	relative circ. velocity
c_p, c_p^*	$[-]$	pressure coefficients
n	$[1/min]$	rev speed
p	$[Pa]$	static pressure
r, d	$[m]$	rotor radius, diameter
s	$[m]$	half of gap width
s_f	$[-]$	safety factor
u	$[m/s]$	absolute circ. velocity
v	$[m/s]$	radial velocity
w	$[m/s]$	resultant velocity
z	$[m]$	cylindrical coordinate
Ω	$[-]$	angular velocity ratio
α	$[°]$	inlet angle
β	$[-]$	friction parameter
η	$[-]$	efficiency
μ	$[Pa \cdot s]$	dynamic viscosity
ν	$[m/s^2]$	kinematic viscosity
ν_p	$[-]$	poisson ratio
ω	$[rad/s]$	angular velocity ratio
ρ	$[kg/m^3]$	density
σ_φ	$[MPa]$	circ. mechanical stress
σ_y	$[MPa]$	yield strength
τ	$[Pa]$	shear stress
φ	$[°]$	circ. direction

Subscripts and Superscripts

1	at the inlet of rotor
2	at the outlet of rotor
is	isentropic
n	normalized
r	radial direction
t	total
v	valid

1. INTRODUCTION

Tesla turbines have been invented by the famous scientist Nikola Tesla [2] at the beginning of the 20th century. They are characterized by their particularly simple and blade-less rotor design and consist of several circular, parallel, flat disks with a central passage in the centre of rotation. All disks are equally

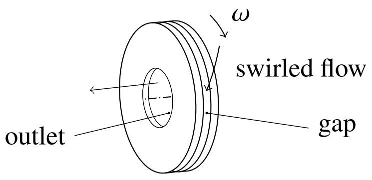

Figure 1. The Tesla turbine principle

spaced with narrow gaps. Any type of fluid can enter the gap at the outer radius of the disks. Driven by a pressure difference, the swirling flow delivered from nozzles or guide vanes follows its spiral path to the rotor outlet at the inner disk radius. Circumferential shear stress induces torque and power. Dependent on fluid, flow parameters and geometry, Tesla turbines are able to work efficiently [3]. Their main advantages are the low-cost design, robustness and competitiveness for small scale turbomachinery, which has recently been discovered by researchers [4], [5]. This paper focuses onto the flow phenomena inside of this turbine. The study is based on rotor dimensions of an existing test rig designed for the determination of velocity profiles inside the Tesla rotor by means of PIV. The test facility and the demonstration of the measurement method has been presented in Schosser et al. [1], [6]. Laminar flow is expected for Re numbers < 400 – 500, which is typical for Tesla turbine operations.

2. THEORETICAL MODEL ANALYSIS

2.1. Incompressible, laminar flow

The steady-state continuity equation, the φ– and r-momentum equations for the bulk flow [1], [7] (Fig. 2)

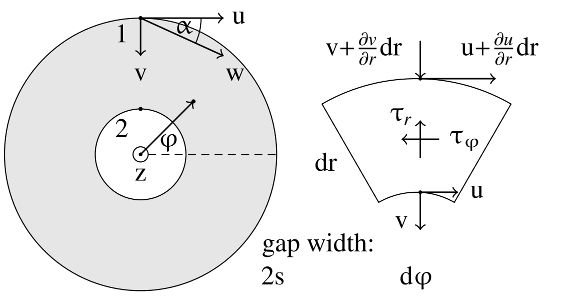

Figure 2. Cyl. coordinatesystem, control volume

can be written as

$$\frac{d\left(\rho\cdot r\cdot v\right)}{dr}=0,\ \rho\cdot v\left[\frac{du}{dr}+\frac{u}{r}\right]-\frac{\mu}{s}\left(\frac{dc}{dz}\right)=0,\quad(1)$$

$$\rho\left[v\frac{dv}{dr}-\frac{u^2}{r}\right]+\frac{dp}{dr}-\frac{\mu}{s}\left(\frac{dv}{dz}\right)=0.\quad(2)$$

Eq. 1, 2 are non-dimensionalized using

$$C\left(R\right)=\frac{c\left(r\right)}{c_1},\quad U\left(R\right)=\frac{u\left(r\right)}{u_1},\quad V\left(R\right)=\frac{v\left(r\right)}{u_1},\quad(3)$$

the dimensionless pressures

$$c_p\left(R\right)=\frac{p\left(r\right)}{\rho u_1^2},\quad c_p^*\left(R\right)=\frac{p\left(r\right)}{p_2}\quad(4)$$

and the dimensionless machine parameters

$$\beta=\frac{3}{2}\frac{r_1}{s}\underbrace{\frac{\nu}{v_1 s}}_{\frac{1}{Re}},\ V_1=\frac{v_1}{u_1},\ \Omega=\frac{r_1\omega}{u_1},\ R=\frac{r}{r_1}.\quad(5)$$

The dimensionless governing equations are

$$\frac{dU\left(R\right)}{dR}+\left(\frac{1}{R}-2\beta R\right)\cdot U\left(R\right)+2\beta\Omega R^2=0,\quad(6)$$

$$\frac{dP}{dR}-V_1^2\cdot\left(\frac{1}{R^3}+\frac{2\beta}{R}\right)-\frac{U\left(R\right)^2}{R}=0.\quad(7)$$

In order to evaluate theoretical and CFD analysis, following coefficients (normalized with their maximum occurring values) are introduced (see [1])

$$C_{to}=\frac{A_1 v_1\rho_1\cdot\left(u_1 r_1-u_2 r_2\right)}{M_{max}},\ C_{po}=\frac{M\cdot\omega}{P_{max}}.\quad(8)$$

The economical power coefficient is defined as

$$C_{pt}=\frac{P_{shaft}}{A_1\cdot\left(p_{1,t}-p_2\right)^{\frac{3}{2}}}.\quad(9)$$

The total isentropic rotor efficency is given by

$$\eta_{is}=\frac{P_{shaft}}{\frac{\dot m}{\rho}\left[\left(p_2+\frac{u_2^2}{2}+\frac{v_2^2}{2}\right)-\left(p_1+\frac{u_1^2}{2}+\frac{v_1^2}{2}\right)\right]}.\quad(10)$$

The fully analytical solutions of Eq. 6 and 7 have already been published in Schosser et. al. [1]. Torque and power are computed by assuming parabolic velocity profiles between the disks and evaluating the resulting circumferential shear stress. The assumed profiles scale with the prevailing bulk velocities in both directions. Development effects at the rotor inlet are neglected. Parameter β describes the flow rate and determines the type of vortex in the gap and is therefore crucial for the generated performance. Other important parameters are the inlet velocity V_1, the radius ratio R and the angular speed Ω, as well as the real axial velocity distribution, which are investigated and validated with CFD.

2.2. Mechanical constraints

A constant rotation of a drilled disk, generates tangential and radial mechanical stress. The stress maximum is at the inner radius r_2 (Dubbel et. al. [8]). Comparing its ratio with the yield strength of the

$$\sigma_\varphi\left(r\right)=\frac{3+\nu_p}{8}\rho\omega^2 r_1^2\Big[1+\left(\frac{r_2}{r_1}\right)^2+\left(\frac{r_1}{r}\right)^2-\frac{1+3\nu_p}{3+\nu_p}\left(\frac{r}{r_1}\right)^2\Big],\quad(11)$$

disk material, determines the mechanical limit of such a rotor. Rewritten into a dimensionless form, the radius ratio R obviously limits the maximum angular velocity Ω for a selected material (see Fig. 4).

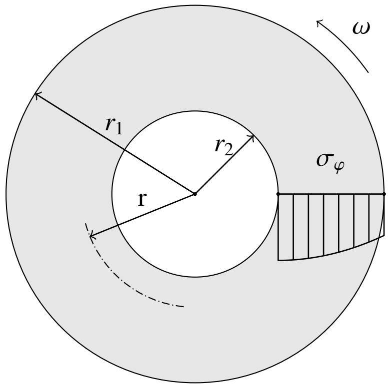

Figure 3. Centrally drilled disk under rotation

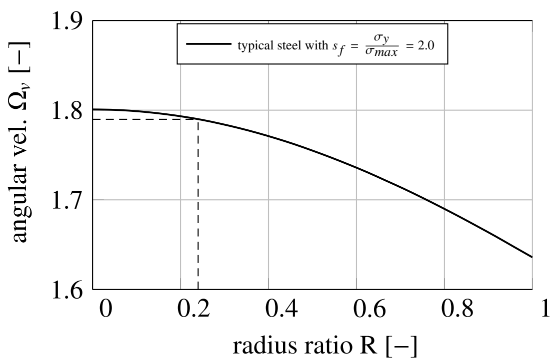

Figure 4. Valid Ω values, limited by material σ_y

The following model analysis and CFD comparison considers these mechanical limits.

3. TURBINE DESIGN PARAMETERS

The design parameters of a Tesla rotor are presented here. The results are derived from the theoretical analysis. They offer the technical limitations of blade-less rotors. To simplify illustrations, Ω is normalized by $u_1 = 100\frac{m}{s}$.

3.1. Dimensionless friction parameter

From Schosser et al. [1] it is known, that β should

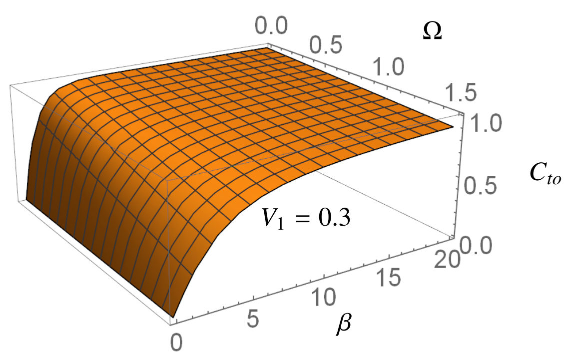

Figure 5. Mapping of torque coefficient C_{to} (β, Ω)

exceed values greater 10 for maximum performance. Fig. 5 shows, that the torque coefficient is almost independent of Ω for β ≥ 10. As β increases with decreasing gap width, the mass flow per gap is restricted. Consequently, more gaps are needed for the same magnitude of power, which increases the price of a Tesla rotor. As a result, an upper limit of β values between 20 to 30 is suggested.

3.2. Dimensionless inlet conditions

Tesla rotors can either be efficient or powerful. The lower V_1, the higher is the isentropic efficiency. On the other hand, a low V_1 and radial mass flow leads to low shaft power per gap. Fig. 6 and 7 show normalized shaft power and efficiency as a function of angular speed. The inlet velocity magnitude w_1 is kept constant, their velocity components instead are varied. This leads to a change of β and influences power and efficiency. Low V_1 corresponds to high β.

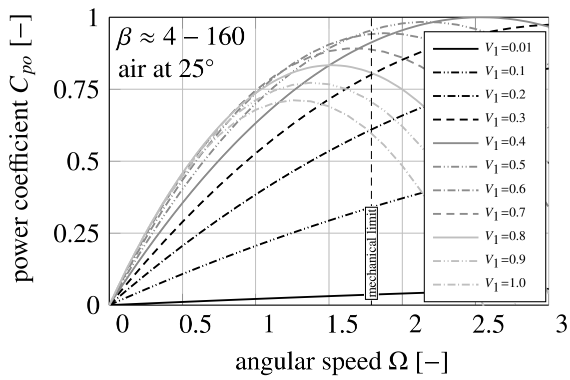

Figure 6. Influence of inlet angles on performance

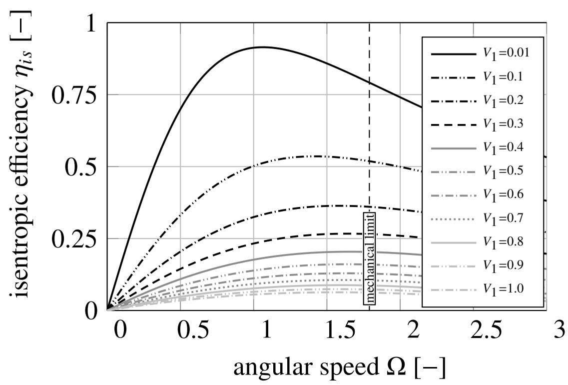

Figure 7. Influence of inlet angles on efficiency

3.3. Dimensionless radius ratio

The influence of the radius ratio $R_2 = r_2/r_1$ is similar to the influence of the inlet condition (Fig. 8, 9). Low R_2 leads to high shaft power per gap. With increasing R_2, the area of the disks inside the turbine's gap, as well as the pressure drop across the rotor is reduced. Low pressure drops lead to highest efficiencies. In this investigation, β and V_1 are constant, the radius ratio R_2 is altered. The higher the radius ratio R, the lower the maximum applicable angular speed.

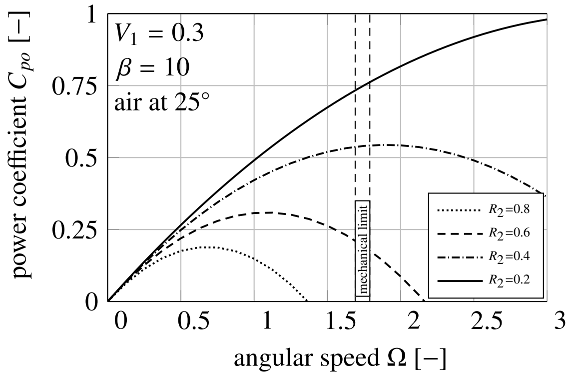

Figure 8. Influence of radius ratio R_2 on perf.

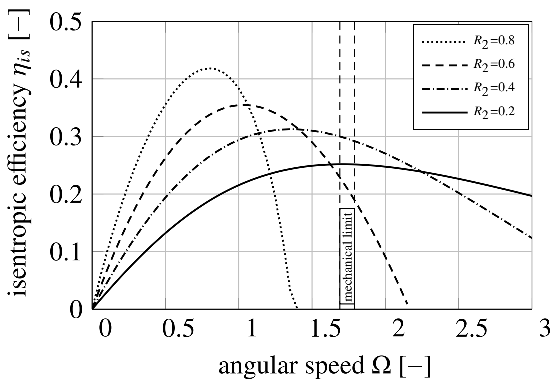

Figure 9. Influence of radius ratio R_2 on efficiency

3.4. Machine parameter relations

The economical power coefficient C_{pt} (Eq. 9) relates shaft power to the total pressure difference between inlet and outlet. When C_{pt} is maximized, the best

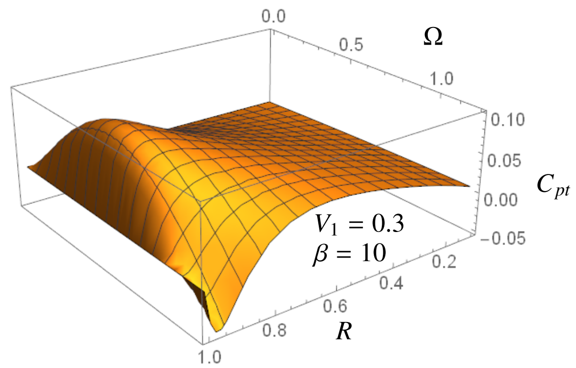

Figure 10. Mapping of power coefficient $C_{pt}\,(R)$

compromise between power per gap and efficiency is found. Fig. 10 introduces the economical power mapping of a Tesla rotor in terms of machine parameters Ω and R for constant and best possible values for inlet velocity ratio V_1 and friction parameter β. During the whole design process it is necessary to consider the upper limit of the angular velocity Ω_v, which is restricted by the mechanical design of the Tesla rotor.

4. CFD MODEL ANALYSIS

In order to analyse the theoretical, incompressible, laminar turbine investigation, various laminar CFD calculations have been performed. The hexa mesh is designed with ICEM 14.5. ANSYS CFX 14.5 is used as a solver. To find a mesh independent solution, the grid has been refined until the outlet velocities had converged. A stationary mesh with co-rotating sidewalls and a rotating mesh show identical results. Rotating domain results are presented here.

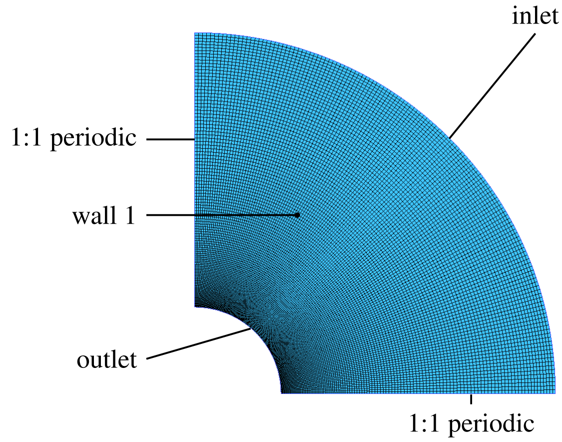

Figure 11. ICEM Mesh, 1/4 disk, gap width 0.2 mm, 756000 nodes, view 1

The applied CFD settings are:

- geometry: r_1=0.125m, r_2=0.03m, 2s=0.2mm
- meshes: 224000, 540000, <u>756000</u>, 1458000, 3400000 nodes (results from underlined mesh)
- rotating domain section (1:1 periodic interface)
- air at 25°C, no turb. model, no heat transfer
- inlet: $w_1 \approx 105\frac{m}{s}$, variable V_1
- outlet: ambient pressure $p_2 = 1bar$
- residual convergence: $1 \cdot 10^{-5}$ rms, $1 \cdot 10^{-3}$ max, auto timescale, double precision
- Ω is made dimensionless with $u_1 = 100\frac{m}{s}$

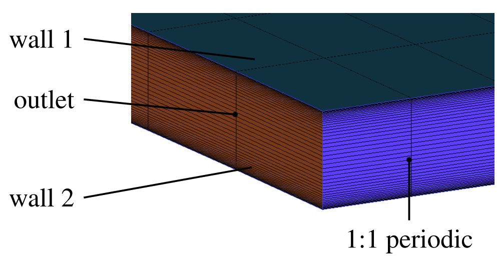

Figure 12. ICEM Mesh, 1/4 disk, gap width 0.2mm, 756000 nodes, view 2

4.1. Inlet conditions

In the laminar CFD, as well as in the theoretical model, the inlet velocity w_1 (Fig. 2) is kept constant. The inlet angle α, hence the velocity components u_1 and v_1 are variable. The significant difference between theory and CFD is, that CFD can simulate the development of the velocity profiles across the rotor. All continuous curves are analytical results, the symbols represent CFD results. The vertically dashed lines in Fig. 13, 14 and 15 denote the mechanical limit of Tesla rotors of that size. Fig. 13 shows the performance map of a Tesla turbine over the whole range of valid angular velocities and investigated inlet conditions. It can be observed, that there is a very good quantitative agreement between laminar CFD and analytical solution at low inlet angles. With increasing α and Ω, the solutions differ more and more from each other. The analytical solution overpredicts shaft power. Same applies to Fig. 14,

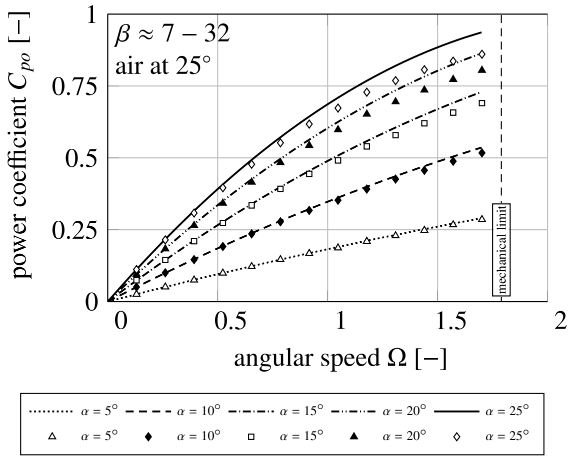

Figure 13. Performance map, CFD comparison

where the torque is plotted. Fig. 15 illustrates the dif-

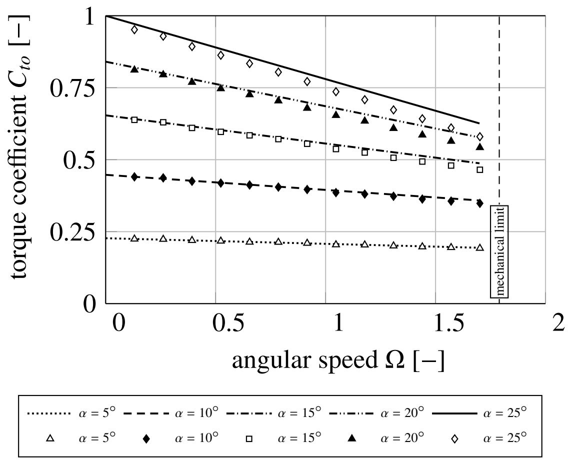

Figure 14. Torque map, CFD comparison

ference between both solutions regarding isentropic efficiency, where the deviation is at its worst. However, the qualitative agreement is satisfactory. To find the reasons for that, the velocity profile is examined in more detail in the next section. Fig. 13 and 15 confirm the theory, that more power per gap leads to lower isentropic efficiencies - or vice versa.

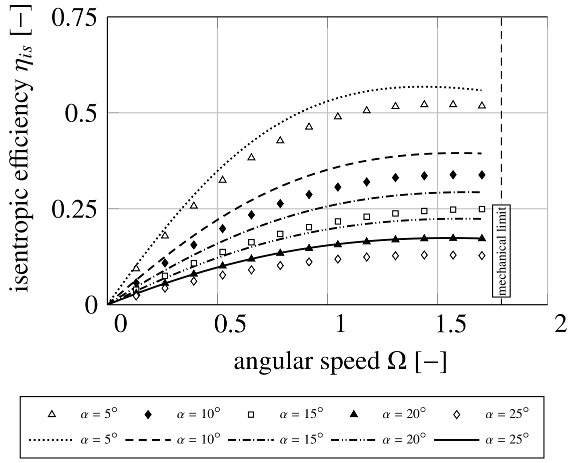

Figure 15. Isentropic efficiency, CFD comparison

4.2. Inflow effect

The inflow effect on turbine performance is investigated by CFD to estimate errors of the theoretical model. In contrast to the expected profile development across the rotor, the model simply scales parabolic z velocity profiles with the bulk velocities $C(R)$, $V(R)$ to compute turbine performance from the resulting circumferential shear stress. In the first CFD setup, "‘block profile"’ approximations are selected at the rotor inlet (see Fig. 1). Due to the gap between stator and rotor, this is expected to happen in real Tesla turbines. To quantify the fully developed flow, velocity profiles $F(R,Z)$ in circumferential and $G(R,Z)$ in radial direction are analysed.

$$C(R,Z) = U(R,Z) - R\Omega = \frac{V_1}{R} \cdot F(R,Z) \tag{12}$$

$$V(R,Z) = -\frac{V_1}{R} \cdot G(R,Z) \tag{13}$$

The continuity equation in radial direction requires

$$\int_0^1 G(R,Z)\,dZ = 1. \tag{14}$$

$F_n(R,Z)$ is normalized by dividing the profile F by its numerical integral

$$F_n(R,Z) = \frac{F(R,Z)}{\int_0^1 F(R,Z)\,dZ}. \tag{15}$$

Moreover, factorized solutions in circumferential

$$F_n(R,Z) = F_n(Z) \cdot C(R) \tag{16}$$

and radial direction

$$G(R,Z) = G(Z) \cdot V(R), \tag{17}$$

are sought. $F_n(Z)$ and $G(Z)$ are fully developed CFD profiles. Numerous CFD calculations were performed. As an example, the development of the velocity profiles in circumferential and radial direction of a typical operating point ($\Omega = 0.92, V_1 = 0.27$) is shown in Fig. 16, 17. The fully developed profiles

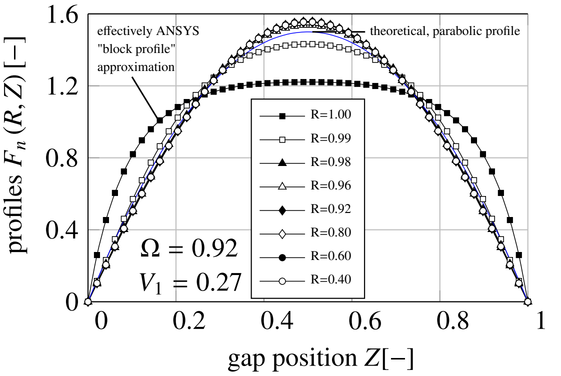

Figure 16. Velocity profiles $F_n(R,Z)$

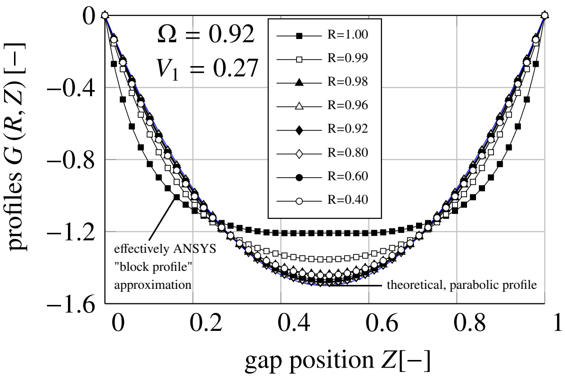

Figure 17. Velocity profiles $G(R,Z)$

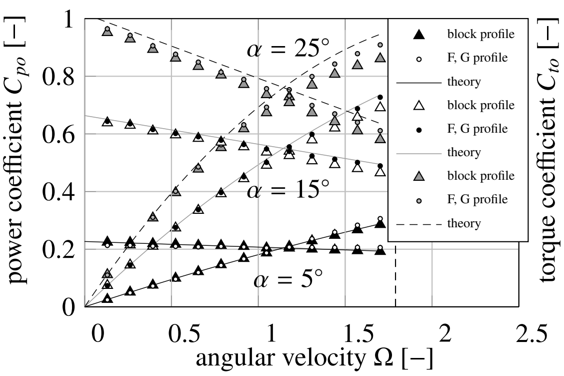

Figure 18. Performance map comparison

$F_n(R,Z)$, $G(R,Z)$ are used as new inlet profiles in a second CFD. The performance and efficiency of both numerical computations and of the theoretical solution are illustrated in Fig. 18 and 19. At small inlet angles the results show very good agreement. With increasing inlet angles, the solutions slightly start to separate from each other. With increasing angular speed, the solutions begin to separate as well. The

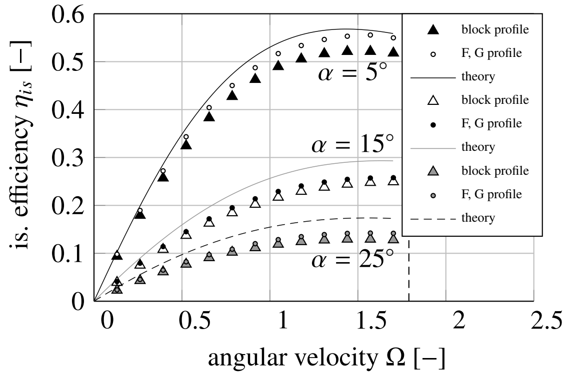

Figure 19. Isentropic efficiency comparison

theory is generally overpredicting torque and power, the first CFD shows the lowest performance. In terms of efficiency, the trends of the presented solutions are similar, but the deviations are a bit higher. Theoretical results are overestimating isentropic efficiency.

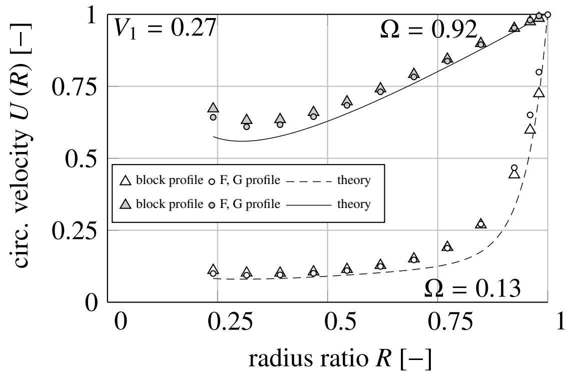

Figure 20. Circ., abs. bulk velocity comparison

The CFD circumferential velocity distributions in Fig. 20 are slightly higher than those from theory and therefore explain the differences in performance results (see Eq. 8). The first CFD shows the highest $U(R)$. The difference is caused by a higher pressure

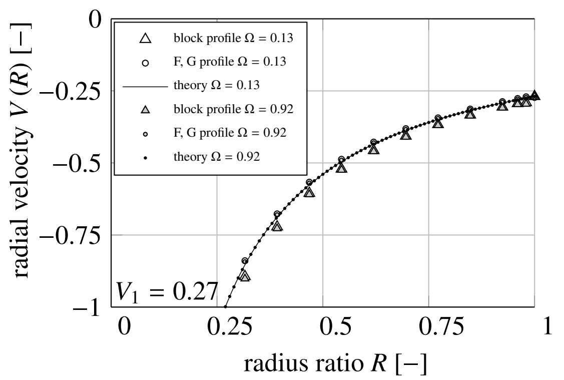

Figure 21. Radial bulk velocity comparison

drop predicted by CFD compared to theoretical results (Fig. 22). The radial velocity distribution instead, show good agreement (Fig. 21). The variations in computed efficiencies originate mainly from slightly different shaft power results.

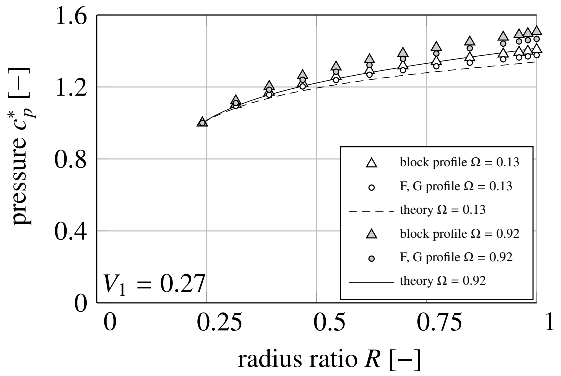

Figure 22. Pressure drop across the rotor

The radial development of the torque coefficient is plotted in Fig. 23. It is interesting to see, that the

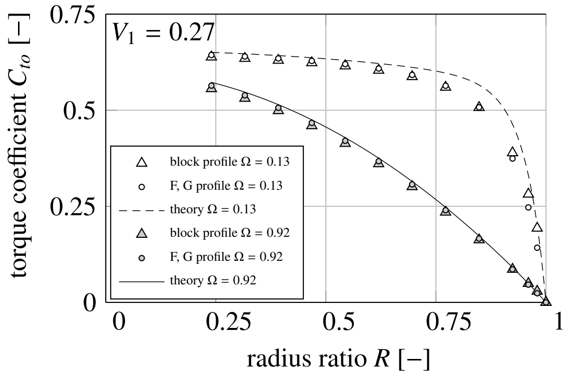

Figure 23. Torque coefficient comparison

block profile simulation generates a little more torque at high radius ratios. This can be explained by a higher circumferential wall shear stress at the inlet zone (see Fig. 16). With decreasing radius ratio, the fully developed inflow simulation is gaining the upper hand again, now producing slightly more torque and power. This is valid for all simulated angular velocities. Obviously, block profiles' higher wall shear stress in radial direction leads to a higher pressure drop. As the outlet pressure is kept constant, the inlet pressure must increase. This makes the flow marginally faster towards the outlet. Hence, the block profiled inflow produces less total torque and power. Dependent on the angular velocity, shaft power differs by up to 5% in this case. The differences in torque and pressure drop between theory and CFD, explain the difference in isentropic efficiency of up to 10% (see Fig. 15, 19). The difference between theoretical analysis and CFD, dependent on V_1 and Ω (see Fig. 16, 19) cannot fully be attributed to the inflow effect.

4.3. Influence of the Reynolds number on the velocity profiles

Fig. 16, 17 showed examples of the development of the axial velocity distribution of a "‘block profile"’ inflow as a function of the radius. The fully developed velocity profiles were fitted by a fourth-order polynomial for the whole range of typical Reynolds numbers. These fits are illustrated in Fig. 24 and 25. Neither in radial, nor in circumferential direc-

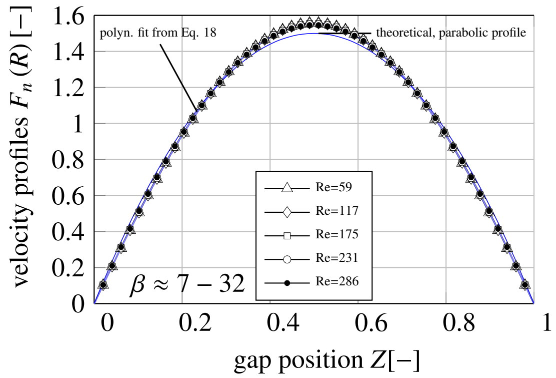

Figure 24. Fully developed velocity profiles $F_n(R)$

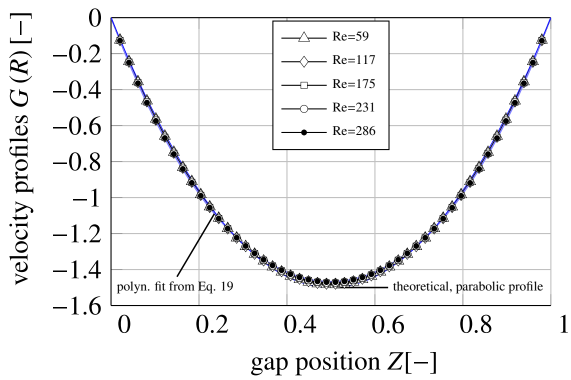

Figure 25. Fully developed velocity profiles $G(R)$

tion, any dependency of the fully developed profile shape on Reynolds number is detectable. The fitting functions for fully developed profiles are

$$F_n(R) = 4.194 \cdot Z^4 - 8.387 \cdot Z^3 - 0.9811 \cdot Z^2 + 5.175 \cdot Z - 0.001824, \tag{18}$$

$$G(R) = 2.703 \cdot Z^4 - 5.405 \cdot Z^3 + 9.254 \cdot Z^2 - 6.551 \cdot Z + 0.001283. \tag{19}$$

4.4. Influence of the revolution speed on the velocity profiles

The fully developed velocity profiles determined from CFD also depend only weakly on revolution speed. The radial velocity profile $G(Z)$ approximates the parabolic profile quite well. Instead, the circumferential velocity distribution $F_n(Z)$ departs from a parabolic velocity profile and definitively influences the predicted shaft power.

5. CONCLUSION

To simplify the design process of Tesla turbines, the flow analysis is coupled with the analytical equation for tangential stress in centrally, drilled and rotating disks, giving the max. applicable angular speed from mechanical integrity considerations.
The influence of dimensionless machine parameters on shaft power and isentropic efficiency are derived. The best compromise between high efficiency and shaft power per gap was found.
Moreover, various analytical results from theory are analysed by laminar CFD. The limitations of the theoretical analysis are exposed. At higher inlet angles, the theoretical solution deviates more and more from the laminar CFD. The qualitative agreement instead, is very promising. In search of reasons for that, an investigation of the development of the velocity profiles and their influence on shaft power and efficiency is performed by means of CFD. Fully developed profiles at the rotor inlet lead to higher predicted shaft power. This and the fact that CFD produces higher pressure drops, explain the deviations in efficiency. Nevertheless, the inflow effect is only a partial explanation. The difference increases with α/V_1 and Ω. The type of velocity distribution between the disks is found for a typical range of Reynolds numbers. The main difference between theory and laminar CFD is, that the CFD profiles in both directions are not fully parabolic and can best be approximated by fourth-order polynomial functions.
Despite certain differences to the CFD, the theoretical model is a very fast tool for dimensioning rotors. In contrast to conventional turbines, Tesla turbines can be scaled easily. With its simple design, low manufacturing costs, the free choice of operating fluid, its possibility to handle droplets and abrasive particles, the Tesla turbine has the ability to find its existence in small scale turbomachinery applications [9], [10], [5], [11].

ACKNOWLEDGEMENTS

This work has been supported by Prof. Dr.-Ing. S. Lecheler and the Faculty of Mechanical Engineering of the University of the Federal Armed Forces of Germany in Munich.

REFERENCES

[1] Schosser, C., Lecheler, S., and Pfitzner, M., 2014, "A Test rig for the investigation of the performance and flow field of Tesla friction turbines", *Proceedings of ASME Turbo Expo 2014*.

[2] Tesla, N., 1913, "Turbine", US Patent 1,061,206, URL `http://www.google.com/patents/US1061206`.

[3] Romanin, V. D., 2012, "Theory and Performance of Tesla Turbines", Ph.D. thesis, University of California,Berkeley.

[4] Romanin, V. D., Krishnan, V. G., Carey, V. P., and Maharbiz, M. M., 2012, "Experimental and analytical study of sub-watt scale Tesla turbine performance", *ASME 2012 International Mechanical Engineering Congress and Exposition*, American Society of Mechanical Engineers, p. 1005Ű1014, URL `http://proceedings.asmedigitalcollection.asme.org/proceeding.aspx?articleid=1751200`.

[5] Krishnan, V. G., Romanin, V., Carey, V. P., and Maharbiz, M. M., 2013, "Design and scaling of microscale Tesla turbines", *Journal of Micromechanics and Microengineering*, Vol. 23 (12), p. 125001.

[6] Schosser, C., Hain, R., Cierpka, C., Lecheler, S., Kähler, C. J., and Pfitzner, M., 2013, "Determination of velocity profiles in small gaps between parallel flat plates by means of tomographic PIV", .

[7] Beans, E. W., 1961, "Performance characteristics of a friction disc turbine", Ph.D. thesis, Pennsylvania State University.

[8] Dubbel, H., Beitz, W., and Kuttner, K.-H., 1994, *Handbook of mechanical engineering*, Springer-Verlag.

[9] Deam, R., Mace, B., Collins, R., and Lemma, E., 2008, "On scaling down turbines to millimeter size", *Journal of Engineering for Gas Turbines and Power*, Vol. 130 (5), p. 052301, URL `http://gasturbinespower.asmedigitalcollection.asme.org/article.aspx?articleid=1426795`.

[10] Krishnan, V. G., Iqbal, Z., and Maharbiz, M. M., 2011, "A micro Tesla turbine for power generation from low pressure heads and evaporation driven flows", *Solid-State Sensors,Actuators and Microsystems Conference (TRANSDUCERS),2011 16th International*, IEEE, p. 1851Ű1854.

[11] Guha, A., and Sengupta, S., 2014, "Similitude and scaling laws for the rotating flow between concentric discs", *Proceedings of the Institution of Mechanical Engineers,Part A: Journal of Power and Energy*, Vol. 228 (4), p. 429Ű439.

Conference on Modelling Fluid Flow (CMFF'15)
The 16th International Conference on Fluid Flow Technologies
Budapest, Hungary, September 1-4, 2015

Correlation of the power coefficients of H-Darrieus Wind Turbines obtained using different turbulence models in CFD computations

László DARÓCZY[1], Gábor JANIGA[2], Dominique THÉVENIN[3]

[1] Corresponding Author. Lab. of Fluid Dynamics and Technical Flows, University of Magdeburg "Otto von Guericke". Universitätsplatz 2, D-39106 Magdeburg, Germany. Tel.: +49 391 67 18194, Fax: +49 391 67 12840, E-mail: laszlo.daroczy@ovgu.de
[2] Lab. of Fluid Dynamics and Technical Flows, University of Magdeburg "Otto von Guericke". E-mail: janiga@ovgu.de
[3] Lab. of Fluid Dynamics and Technical Flows, University of Magdeburg "Otto von Guericke". E-mail: thevenin@ovgu.de

ABSTRACT

Wind energy represents nowadays an increasingly important source of energy as it provides not only an effective solution to reduce the fuel consumption, but reduces the pollutant emission as well. Vertical Axis Wind Turbines or VAWTs were originally considered very promising, but were later superseeded by horizontal axis turbines. There is now a resurgence of interest in VAWTs. Particularly, the H-Darrieus wind turbine appears to be promising not only because of its low cost, but because it is able to operate at low wind speed conditions. However, it suffers from a low efficiency. That is why the optimization of these turbines is a very important field of research.

The flow around the H-Darrieus turbine is highly unsteady with complex physics and dynamic stall. Most turbulence models are not able to capture all these effects correctly. As a result, different models yield different characteristic curves. In an optimization the precise computation of the power coefficient is not so important, as long as the direction of the optimization is correctly predicted.

In the current study a Design-Of-Experiment (DOE) is used to create 40 different asymmetric blade geometries with the in-house optimization software, OPAL++. The power coefficient is evaluated using 2D unsteady CFD computations relying on the commercial software CD-Adapco StarCCM+. Three very popular turbulence models, k-ϵ Realizable, k-ω SST and Spalart-Allmaras are used to model the turbulent flow for the same tip-speed-ratio. Finally, power coefficients are compared. The resulting correlation between the different models is analyzed and conclusions are drawn regarding optimization.

Keywords: computational fluid dynamics, Darrieus turbine, H-rotor, wind energy, turbulence, optimization

NOMENCLATURE

A	$[m^2]$	projected area of the rotor
C_p	$[-]$	power coefficient
C_T	$[-]$	torque coefficient
$C_{x/y}$	$[-]$	force coefficient in coordinate system directions
F	$[N]$	force
H	$[m]$	height of the rotor
N	$[-]$	number of blades
R	$[m]$	radius of the rotor
T	$[Nm]$	torque
y^+	$[-]$	dimensionless wall distance
c	$[m]$	camber
I	$[-]$	turbulence intensity
TVR	$[-]$	turbulent viscosity ratio
u	$[m/s]$	wind speed
β	$[°]$	pitch angle
λ, TSR	$[-]$	tip-speed-ratio
ω	$[rad/s]$	angular velocity
ρ	$[kg/m^3]$	density
φ	$[°]$	phase angle

Subscripts and Superscripts

L, D	lift, drag
th.	theoretical

1. INTRODUCTION

With the world's ever growing hunger for energy the need for clean and reliable energy sources increases as well. Wind energy can be an answer to this need. With each successive evolution of wind turbines the performance and efficiency increase, while operating and installation costs decrease. The gross production of wind energy in the EU27 increased from 80 PJ (2000) to 537 PJ (2010) just over a period of ten years [1], and an increase to 2300 PJ is prognosed for 2030 [2]. Due to this growing significance the efficiency and optimization of wind turbines becomes a more and more crucial area. Several examples of such works can already be found in the scientific literature. For instance, Ribeiro et al. [3]

optimized the airfoil shape of wind turbines. Although horizontal axis wind turbines are mostly found, small vertical axis turbines (Darrieus, Savonius) are interesting as well. Despite the fact that the original patent for Darrieus rotors dates back to 1927, comparatively little research was done compared to HAWTs (i.e., Horizontal Axis Wind Turbines). Recently, a few articles dealt with the analysis and optimization of Darrieus turbines. In particular, Mohamed [4] investigated different airfoils using computational fluid dynamics (CFD) in order to obtain performance improvement of a H-Darrieus rotor.

1.1. Purpose of the study

Due to the increasing importance of wind energy, providing a high performance became more important in the last years. Moreover, since the efficiency of the rotors is already very high, further improvements are only possible with very accurate models. First computational models relied on the highly simplified single streamtube or multiple streamtube [5] models, based on the Glauert actuator disk theory. More recently, URANS (Unsteady Reynolds Averaged Navier Stokes) models were used in CFD. Although LES (Large Eddy Simulations) is expected to be more accurate, they are still computationally too expensive for design optimization.

The goal of the present project is to increase the performance of H-Darrieus rotors by optimizing the airfoil shape. To perform such an optimization, the whole process has to be automatized. For this purpose a module has been derived for our in-house optimization software. In this module the complete CFD workflow has been parameterized, from the geometry creation (number of blades, geometry of the blade, radius of the rotor, etc.), over the meshing (mesh size, size of domain, etc.) to the final CFD setup (choice of CFD software, choice of solver, turbulence model, boundary conditions, etc.). In this way not only the optimization, but also the systematic analysis of the simulations becomes possible.

Moreover, when performing an optimization, one has to keep in mind that the needed time is an essential factor. With an exaggerated temporal or spatial resolution, or when using too complex models, the evaluation of a sufficient number of airfoils becomes impossible. Therefore, it is better to have a lower-accuracy model, as long as this reduced model is indeed able to indicate the *correct direction* of the optimization, i.e.: which design is better or worse?

1.2. Physics of the H-Darrieus Wind Turbine

Wind turbines are usually characterized by their characteristic curve, or TSR-C_p curve. The tip-speed-ratio (TSR, or λ) is the ratio of the tip velocity of the rotating blade compared to the wind speed (u):

$$\text{TSR} = \lambda = \frac{v_{\text{tip}}}{u} = \frac{R\omega}{u}, \tag{1}$$

where R is the radius of the rotor and ω is the angular velocity of the rotor. For the Darrieus rotor the cross-section does not vary with height, i.e., the rotor has the same speed for each cross-section. The cross-section of a Darrieus rotor can be seen in Figure 1, which shows the symbol conventions of the current study. Wind is coming from the right ($\underline{u} = u\underline{e_x}$), and the rotor is rotating with $\underline{\omega} = -\omega\underline{e_z}$ angular speed. The position of the blade is described by the phase angle, φ. The power coefficient, or C_p is the indicator

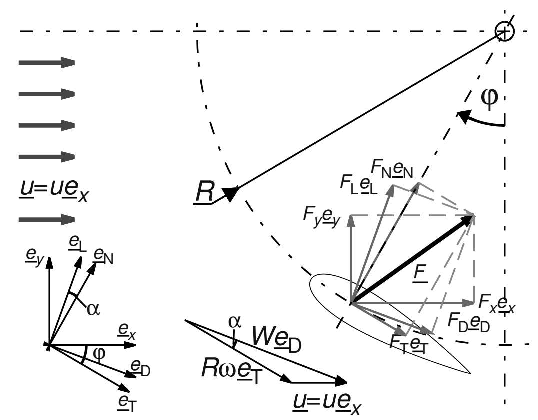

Figure 1. Schematic representation of the H-Darrieus wind turbine (without pitch)

characterizing aerodynamic efficiency. It is the ratio of the power generated by the wind turbine compared to the available energy in the wind:

$$C_p = \frac{P_{\text{mech}}}{P_{\text{total}}} = \frac{T\omega}{\frac{1}{2}\rho u^3 A} = \frac{T\omega}{\frac{1}{2}\rho u^3 2RH}, \tag{2}$$

where A is the projected area of the rotor, ρ is the air density, H is the height of the rotor and T is the (average) torque generated by the rotor (averaged, because the output of the Darrieus turbine is highly transient). This value has a physical threshold, which is known as Betz-limit (59.3%). In reality, even the modern horizontal-axis rotors cannot achieve more than 45-50% efficiency. The power coefficient is related to the torque coefficient, which is computed as

$$C_T = -\frac{T}{\frac{1}{2}\rho u^2 AL} = -\frac{T}{\frac{1}{2}\rho u^2 2R^2 H} = -\lambda C_p\,. \tag{3}$$

By a simple transformation, the drag and lift coefficients of the blades can be determined as well from the global forces (F_x, F_y).

In reality, the characteristic curve is not completely universal and differs slightly when varying rotational speed and wind speed due to the varying Reynolds numbers [6].

The loss of performance at lower tip-speed ratios originates from the stall mechanism: when the angle-of-attack (AOA) of the blade increases (usually above 12 – 13°, [7]), separation occurs and the rotor loses its efficiency. Moreover, in reality, stall also depends on the speed at which the AOA is changing (dynamic stall). .

For higher tip-speed-ratios efficiency loss results mainly from secondary losses: strut losses, wingtip losses, etc. If we assume the wind speed within the rotor to be constant, the theoretical angle of attack can be estimated as

$$\alpha \equiv AOA_{\text{th.}} = \arctan\left(\frac{\sin(\varphi)}{\lambda + \cos(\varphi)}\right) + \beta, \qquad (4)$$

where β is the preset pitch angle. Throughout the turbine rotation, the angle-of-attack is changing, see Fig. 2.

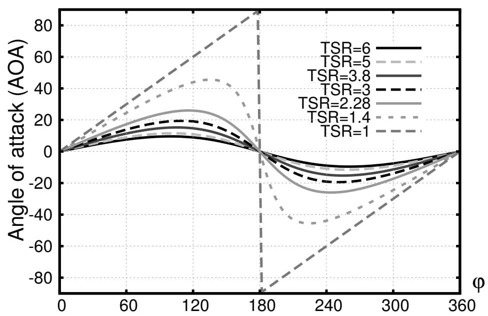

Figure 2. Angle of attack for different tip-speed-ratios

1.3. Advantages and disadvantages

Although Darrieus turbines suffer from several disadvantages (for instance low tip-speed-ratios, inability to self-start and blade fatigue due to oscillating torque), they show many advantages as well. It leads to a comparatively low sound emission and has a quite simple design [4] due to the absence of a yaw system, which decreases the capital investment needed for the construction. It is better suited for an urban environment. Since it is omnidirectional, it is able to operate in very turbulent environments, where the wind direction is constantly changing [8]. Compared to HAWTs it is able to operate at lower wind speeds.

2. AUTOMATIZATION WITH OPAL++

The automatization was implemented in the OPtimization Algorithm Library++ (called simply OPAL++), which is an object-orientated multi-objective optimization and parameterization framework developed at the University of Magdeburg “Otto von Guericke”. Although OPAL++ builds on top of considerable experience with OPAL [9], it is based on a completely new structure. The software has already been successfully applied to many different problems [10, 11] and is strongly focused on CFD-based optimization problems (CFD-O).

2.1. Operating conditions

For the current study a geometry was chosen, which is currently being under development and evaluated in collaboration with industrial partners. The rotor has three blades with $R = 1.5\ m$ radius. The blades have a camber of $c = 160\ mm$ with a rounded trailing edge. The optimal tip-speed ratio is between $3 < \lambda < 4$. For the present study $u = 8.4\ m/s$ was fixed as the wind speed. In the middle of the domain the shaft was taken into account.

3. CFD SIMULATIONS

3.1. Mesh generation

The mesh generation is performed with ANSYS Gambit 2.4.6. The script for mesh generation is executed in a completely automatic way in OPAL++ by a module created specifically for this study. As the flow around a Darrieus rotor is highly transient, the flow has to be fully resolved not only in space, but in time as well. As the rotor is rotating throughout the CFD computation, a moving mesh has to be created using the sliding mesh technique. Therefore, a large rectangular outer domain and a circular rotating inner domain were created, connected by an interface. Both domains are partially structured and involve quadrilateral meshes, see Fig. 3 (unstructured parts are presented with a brick pattern, the density of the pattern indicates the mesh resolution).

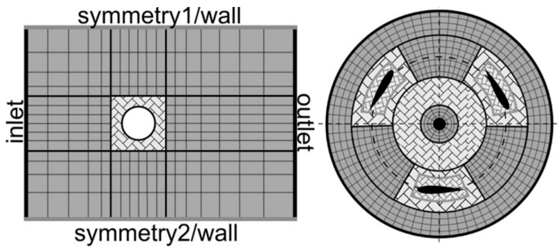

Figure 3. Hybrid mesh structure employed in the study

The mesh size was defined at seven different locations and the C++ module uses size functions to ensure a smooth transition between the different regions. The boundary layer was calibrated using the Schlichting correlation to resolve the flow up to the laminar sublayer. For each evaluated blade $y^+_{\text{mean}} \approx 0.2$, $y^+_{\text{max}} \approx 1$ was true in the present study. After mesh generation the quality is checked to ensure appropriate orthogonality. The mesh near the blade can be seen in Fig. 4.

3.2. Boundary conditions

The four sides of the computational domain are defined as velocity inlet, pressure outlet and symmetry boundaries. Unfortunately, the specification of proper turbulence properties is a very difficult question for wind turbines. Different sources indicate different values and procedures; there are still controversial views concerning this question. The most

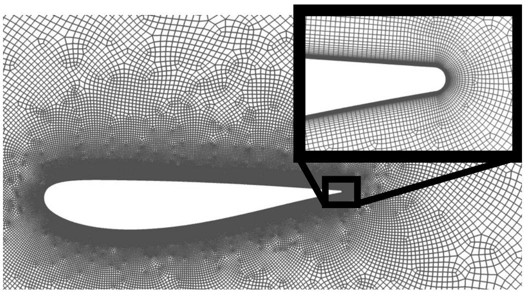

Figure 4. Mesh resolution near the blade

obvious approach would be to use the standard, but the german standard specifies very large intensities based on 10-minute averages. As noted by Spalart and Rumsey [12], in the atmospheric boundary layer the typical length scales are around 100 m and the eddy viscosity can reach 50 m^2/s on windy days (corresponding to $TVR = 3.3 \cdot 10^6$). Moreover, as the rotation speed is quite large with a very small time period ($T < 0.3$ s in the present case), only a part of the turbulent spectra will really interact with the blades in the CFD [13]. Own measurements have confirmed that for a corresponding time-window (2 s) turbulence intensities drop below 2%.

As a consequence, $I = 0.1\%$ and $TVR = 10$ were retained for all configurations of the DOE (Design-Of-Experiment), in agreement with several recommendations from the literature [14, 15].

3.3. CFD setup

Second-order implicit temporal discretization has been systematically applied, together with second-order upwind derivatives. For solving the equation system an incompressible coupled solver was applied. When solving the fluid dynamic equations, there are two possibilities for the pressure-velocity coupling: the segregated approach (SIMPLE, SIMPLEC or PISO in ANSYS Fluent and Segregated or Unsteady PISO in CD-Adapco StarCCM+ [16]), where a predictor-corrector approach is applied, and the Coupled solver (ANSYS Fluent and CD-Adapco StarCCM+ as well), where the momentum and continuity equations are directly coupled. Previous studies in our group indicated that the Coupled solver is able to converge with 24 inner iterations, while segregated solvers require 75-100. This is in agreement with the work of Maitre et al. [7], where 75 inner iterations were necessary for convergence with the SIMPLE method. A further advantage of the Coupled approach is that the required number of iterations is independent of the mesh size [16]. For the solver Courant-number values between 25 and 200 are recommended.

For the temporal resolution a two-level approach was implemented. At first, 10 revolutions were computed with large time steps (72 time-steps per revolution) followed by four detailed one ($\Delta\varphi = 1°$/time step). All computations were performed with CD-Adapco StarCCM+.

3.4. Independency from temporal and spatial discretization

In order to provide appropriate results, mesh independency has to be ensured. The mesh size is very important for turbulence modeling; if the mesh spacing is too coarse, turbulence decay will be grossly underestimated [12]. In order to test mesh independency $I = 0.25\%$, $L = 0.15$ m and solver $CFL = 25$ were applied. The chosen geometry was the airfoil being currently experimentally investigated.

Throughout the studies, a calibration coefficient (c_{calib}) was used to compute the actual mesh sizes ($S_{\mathrm{act,i}}$) from the reference size ($S_{\mathrm{act,i}} = c_{\mathrm{calib}} S_{\mathrm{ref,i}}$; $c_{\mathrm{calib}} = 1$ is the candidate mesh, $S_{\mathrm{ref,i}}$ are the sizes in the candidate mesh). For each turbulence model, five meshes were created with different resolutions. The results are presented in Table 1. The goal was to have $\Delta C_p \leq 0.6\%$ compared to the finest resolution. This was achieved by $c_{\mathrm{calib}} = 1$ at each model. Thus, this mesh setup was retained for further computations. The performance coefficients are not only almost completely identical in the integral sense (average C_T); the $C_T(\varphi)$ curves overlap as well.

Table 1. Mesh independency for the three turbulence models

c_{calib}	C_p (k-ϵ Real.)	C_p (SA)	C_p (k-ω SST)	Mesh size
1.5	40.89	35.17	42.50	225k
1.25	40.99	35.27	42.56	266k
1.0	41.09	35.34	42.82	368k
0.75	41.10	35.36	42.95	546k
0.5	41.44	35.41	43.38	1089k

The effect of the temporal resolution was analyzed as well. When doubling the number of time steps per revolution, the performance coefficients changed to $C_p = 40.20\%$ (k-ϵ Real.), $C_p = 34.50\%$ (Spalart-Allmaras) and $C_p = 42.47\%$ (k-ω SST). Comparing the values to Table 1, one can see that the differences are very small and deemed as acceptable ($\Delta C_p < 1\%$). Thus, $\Delta\varphi = 1°$ was retained for all further computations ($\Delta t \approx 0.82$ ms). One has to keep in mind that the present statement is only valid for the present operating condition. Under stall and deep-stall conditions the number of time steps has to be significantly increased.

3.5. Validation

In case of 2D H-Darrieus Wind Turbine simulations, the direct comparison with experiments is not easy, if possible at all. Although in several articles a full agreement between CFD and experiment is described, such a result does not appear to be realistic, nor possible at all.

Theoretically, CFD can be used to resolve exactly the flow field around a rotating turbine. In practice, several details will be missing due to the shortcomings of different structural and/or physical details. An agreement with an experimental result does not necessarily mean that a mesh-independent solution was found [8], and it is not guaranteed that it will lead to a good agreement for other rotors as well.

The largest differences to be expected between 2D simulations and 3D measurements are the 3D effects, namely strut-losses and wing-tip, vortex-induced losses. The 3D CFD study of Castelli et al. indicated, that for small aspect-ratio rotors, the friction losses due to the arms can lead to more than 20% loss of performance, while the wing-tip can generate up to 25% loss [17]). Additional losses stem from the energy conversion system, e.g., the bearing losses or generator losses. Measurement errors and numerical errors are not negligible either. An additional and significant error is introduced by the turbulence model, which is very difficult to be quantified. As a result, the overestimation of the performance in 2D can be very high, up to 75-95% [8], while underestimations would be difficult to understand.

3.5.1. Comparison with real wind turbine

The present validation is based on the experimental work of Kjellin et al. [18]. In this field test a three-bladed Darrieus rotor with 12 kW rated power output ($u = 12\ m/s$), $H = 5\ m$ height and $D = 6\ m$ diameter was tested and measured for around 350 h. The blades are NACA0021 airfoils, with $c = 0.25\ m$ chord length and tapered end to reduce the wingtip losses. The rotor uses passive stall regulation and has a direct drive (thus, gearbox losses are eliminated). Although the rotor was designed for 127 rpm, the test was conducted at 48 and 57 rpm. The blades are mounted with two struts at 17.6° and have NACA0025 profile with 280-320 *mm* chord length. With the tested constant rotational speeds, the optimal performance of $C_p = 0.29$ was found at $\lambda = 3.30$. The CFD computations were performed with the calibration mesh sizes. The results are presented in Fig. 5. In this figure, the typical be-

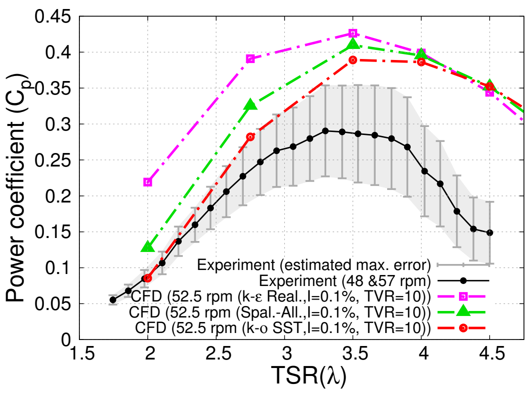

Figure 5. Experimental validation based on [18]

havior of the turbulence models can be seen. The k-ϵ Realizable model is able to predict the shape of the characteristic curves and the location of the maximal performance, but not the exact values. Instead, it shows a constant offset. A similar behavior was experienced by Castelli et al. for a different turbine [17].

In case of the Spalart-Allmaras and k-ω SST models the tendency is completely different. At low tip-speed-ratios the prediction is rather accurate; but, at higher values the differences increase. It is interesting to note, that the difference is cubic in nature ($\propto \lambda^3$). Strut losses have exactly this tendency, but it remains unclear yet if such differences indicate a real physical effect or are the result of a modeling error. The same tendency can be seen, e.g., in [8].

4. PARAMETERIZATION

For the parameterization of the airfoils, 11 variables were used to provide an appropriate flexibility. Eight parameters define the shape of the airfoil in a non-dimensional form, based on an extension of the original NACA4 parameterization [19]. The thickness of the airfoil is defined as

$$t(x) = a_0\sqrt{x} + a_1 x + a_2 x^2 + a_3 x^3 + a_4 x^4. \tag{5}$$

The following criteria are used to compute the coefficients:

$$t(1) = 0, \quad t = (p_t) = t_{max}/2 \tag{6}$$

$$\left.\frac{dt(x)}{dx}\right|_{x=1} = -s_{t,2}\frac{t_{max}}{0.2}; \quad \frac{1}{2}\left(\frac{t_{max}}{0.2}a_0\right)^2 = r_L \tag{7}$$

Thus, the variables of the parameterization are the location and value of the maximal thickness (p_t, t_{max}), the first derivative at the end ($s_{t,2}$) and the leading edge radius (r_L).

The camber-line is defined as:

$$c(x) = \begin{cases} \sum_{i=0}^{3} b_i x^i & \text{if } 0 \le x \le p_c \\ \sum_{i=0}^{3} c_i x^i & \text{if } p_c \le x \le 1. \end{cases} \tag{8}$$

Using the following criteria, the coefficients can be determined:

$$c(0) = 0, \ c(1) = 0, \ c(p_c) = c_{max}, \tag{9}$$

$$\left.\frac{dc(x)}{dx}\right|_{x=0} = s_{c,1}\frac{t_{max}}{0.2}, \ \left.\frac{dc(x)}{dx}\right|_{x=1} = -s_{c,2}\frac{t_{max}}{0.2}. \tag{10}$$

Thus, the parameters needed to define the camber-line are the derivatives at the extremes ($s_{c,1}$, $s_{c,2}$) together with the value and location of the maximal deviation from the axis (p_c, c_{max}). After the camber and the thickness have been defined, the airfoils can be computed using the same transformation as for NACA4 [19].

After the non-dimensional airfoil was defined, it is scaled up to have a trailing edge with r_T radius in order to take into account the manufacturing constraints and a camber length of c. Finally, it is mounted on the radius of the rotor (R) at the mount position $l_m = L_m/c$. Moreover, the blade does not necessarily has to have a perpendicular camber to the radius, thus, the last parameter is the pitch angle (or toe-out angle): β. The pitch angle and the mounting position are not independent (each mounting position is equivalent to a pitch angle), thus for an optimization one of them has to be fixed.

5. RESULTS

5.1. Design-of-Experiment (DOE)

To provide an appropriate sample for the different blade designs, a Design-Of-Experiment was created using 40 individuals. The individuals were generated using a quasi-random low-discrepancy sequence, the SOBOL method.

From the 40 generated airfoils, 37 were valid (further criteria were defined to ensure the $C^{(1)}$ continuity of the airfoil after the transformation). For the Design-Of-Experiment parameter ranges of $0.25 < p_t < 0.35$, $0.17 < t_{max} < 0.25$, $0.01 < s_{t,2} < 0.3$, $0.005 < r_L < 0.08$, $0.25 < p_c < 0.35$, $-0.15 < c_{max} < 0.15$, $0.1 < s_{c,1} < 1.5$, $0.01 < s_{c,2} < 0.2$, $-5° < \beta < 5°$ were used.

5.2. Comparison of turbulence models

The configurations have been evaluated in parallel, using the Linux cluster of the institute. Each single computation took about 2 days with 8 cores. The results are shown in Figure 6. The x and y axes show the performance coefficients obtained with two different turbulence models. Additionally, two blade geometries are presented, which showed large differences between the models. As one can see, the correlation is very strong between the different models, and one can state that a larger performance with one turbulence model will correspond to larger values for another model as well. The k-ϵ Realizable vs. Spalart-Allmaras models have the strongest correlation and the smallest differences.

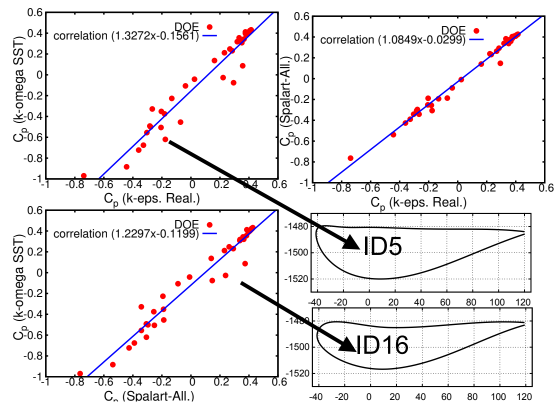

Figure 6. Correlation of performance coefficients with different models

When performing an optimization, however, not the whole domain is of interest; only the configurations with large C_p values should be considered. To analyze these regions, all points were plotted again in Figure 7, where at least one of the turbulence models indicated $C_p > 0.2$. For the computation of the linear trend, points with large discrepancies were removed.

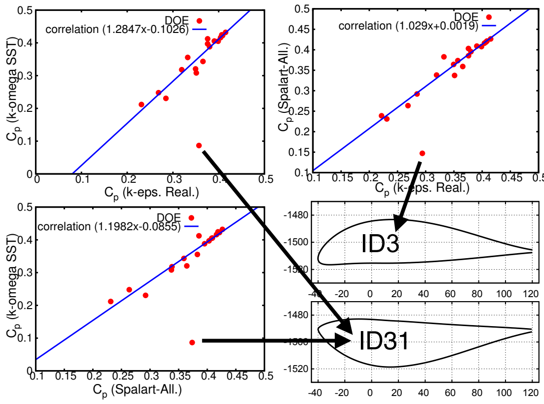

Figure 7. Correlation of performance coefficients with different models (for the linear trend analysis, points showing large discrepancies were removed)

One can see that the agreement between the models is generally very good, especially near the optimum (maximal values). Interestingly, one airfoil was found for each pair of models, which lies very far away from the trend line; this requires further analysis.

5.3. Evolution of coefficients

The evolution of the coefficients for the last rotation have been analyzed for two airfoils. For the first airfoil (ID8), all turbulence models indicated very similar results ($C_p = 38.02\%$, $C_p = 39.54\%$, $C_p = 38.81\%$). However, the performance coefficient is an integral value. Thus, the flow structures do not necessarily have to be identical. Figure 8 shows the hysteresis curves for all turbulence models (based on the theoretical angle of attack) and Figure 9 presents the torque coefficient versus the time for the last simulated revolution. As one can see, the agreement is very good. Small differences are only present at $\phi \approx 270 - 300°$, which corresponds to the largest angle of attack and to the interaction with the Kármán vortex street of the shaft.

Additionally, a second blade (ID3, shown in Fig. 7) was chosen, which shows a large discrepancy in the performance coefficient for the different turbulence models. As one can see in Fig. 11, the torque coefficients have very different shapes, the largest discrepancies being the domain of interaction with the Kármán vortex street and the shaft. As Fig. 10 shows, at higher angle-of-attack the stall effects become very significant, as indicated by the huge peaks. This indicates, that the interaction causes separation and stall. For the computation of the complex vortex structures, more detailed turbulence models would be required, which are incompatible with an optimization.

Finally, a statistical evaluation was performed

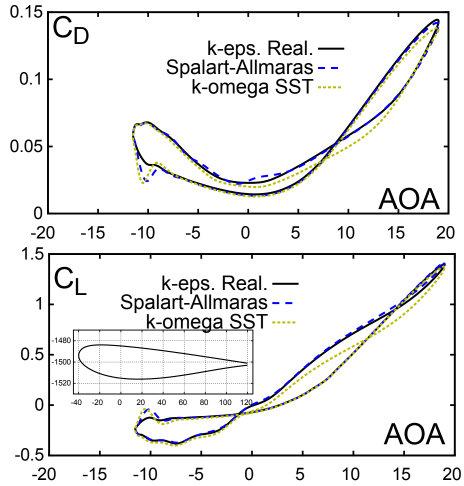

Figure 8. Hysteresis curves for a blade with high performance (ID8)

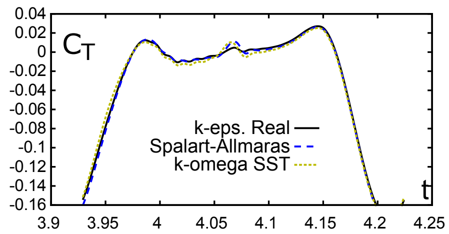

Figure 9. Performance coefficient of a blade with high performance (last revolution)

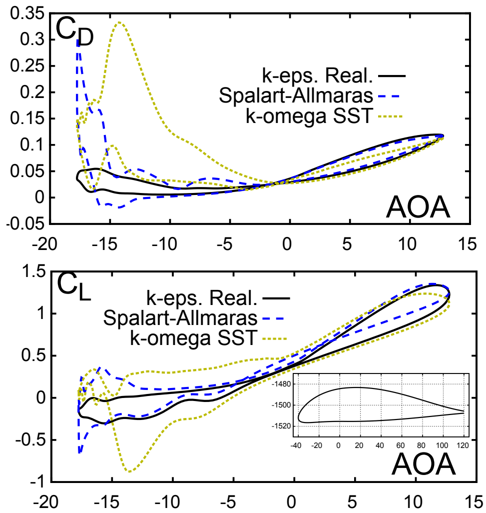

Figure 10. Hysteresis curves for a blade with lower performance (ID3)

with Monte Carlo simulation: choosing randomly two airfoils, if the first airfoil had a better performance coefficient with at least ΔC_p, the probability was computed that the first airfoil was still superior for another turbulence model. The results are presented in Table 2 (E=$k-\epsilon$ Realizable, S=Spalart-Allmaras,

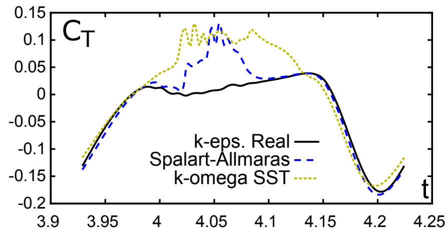

Figure 11. Performance coefficient of a blade with high performance (last revolution, ID3)

O=$k-\omega$ SST). Although the 37 samples are not enough for faithful statistics, the values are still representative. The starred values indicate the statistical evaluation, if only airfoils were taken into account, where $C_p > 0.2$ was true for at least one of the turbulence models. As one can see, the correlation is usually very high. In the domain of interest, it is somewhat lower. This is due to a few outliers; removing only a couple of airfoils, the correlation becomes very high as well. Understanding such outliers will be one subject of our future work.

Table 2. Computed probabilities [%] of improvement for pairs of turbulence models

ΔC_p	E-S	E-O	S-E	S-O	O-E	O-S
0.0	96.1	93.24	96.1	94.4	93.24	94.4
2.0	97.9	95.03	97.9	96.5	94.76	95.4
0.0*	91.58	87.9	91.58	91.23	87.9	91.23
2.0*	96.05	92.76	95.5	94.1	91.14	92.81

6. FUTURE STUDIES

In future studies this comparison will be extended to include other turbulence models (the two most likely candidates are the Reynolds-Stress Models – so that anisotropy can be taken into account –, and the Transitional SST model, which provides an empirical correlation function for the proper simulation of transition effects) and to include additional tip-speed-ratios, focusing especially on the stall domain. Finally, based on further validations and on comparisons with experimental data, an optimization will be carried out using a Genetic Optimization algorithm.

7. SUMMARY

In the present study the performance coefficient was analyzed for 40 different airfoils based on an extended NACA4 parameterization when using three different turbulence models, $k-\epsilon$ Realizable, Spalart-Allmaras and $k-\omega$ SST. The performance coefficient was evaluated based on CFD computations, which were carried out in a completely automatic manner using the OPAL++ parameterization and optimization environment.

The analysis of the results has revealed that the models have a very strong correlation. However, selected airfoils show large discrepancies, which originate from the incorrect modeling of the transitional and stall effect by the turbulence model. When restricting the analysis to the domain of interest ($C_p > 0.2$), the agreement was even better, except for two geometries. This means that getting a high performance is with a high probability independent from the employed turbulence model. With a Monte-Carlo analysis, getting at least 2% improvement in performance will be obtained for all turbulence models with a probability better than 95%. It can be concluded that the URANS method is appropriate for the optimization. Nevertheless, the optimum solution should be checked with several turbulence models. Further tests will be needed to analyze such correlations within the stall domain as well, and to get more accurate estimates for the probabilities.

ACKNOWLEDGEMENTS

The authors gratefully acknowledge the financial support by the BMBF (German Federal Ministry of Education and Research) through the AiF-ZIM project KF2473103WZ3.

REFERENCES

[1] European Commission, 2012, "ENERGY - Country Factsheets V.1.3", .

[2] European Commission - Directorate-General for Energy, 2009, "EU energy trends to 2030", .

[3] Ribeiro, A., Awruch, A., and Gomes, H., 2012, "An airfoil optimization technique for wind turbines", *Applied Mathematical Modelling*, Vol. 36 (10), pp. 4898–4907.

[4] Mohamed, M., 2012, "Performance investigation of H-rotor Darrieus turbine with new airfoil shapes", *Energy*, Vol. 47 (1), pp. 522–530.

[5] Strickland, J. H., 1975, "Darrieus turbine: a performance prediction model using multiple streamtubes", *Tech. rep.*, Sandia National Laboratories.

[6] Genç, M. S., Karasu, I., and Açikel, H. H., 2012, "An experimental study on aerodynamics of NACA2415 aerofoil at low Re numbers", *Experimental Thermal and Fluid Science*, Vol. 39, pp. 252–264.

[7] Maître, T., Amet, E., and Pellone, C., 2013, "Modeling of the flow in a Darrieus water turbine: Wall grid refinement analysis and comparison with experiments", *Renewable Energy*, Vol. 51, pp. 497–512.

[8] Almohammadi, K., Ingham, D., Ma, L., and Pourkashan, M., 2013, "Computational fluid dynamics (CFD) mesh independency techniques for a straight blade vertical axis wind turbine", *Energy*, Vol. 58, pp. 483–493.

[9] Hilbert, R., Janiga, G., Baron, R., and Thévenin, D., 2006, "Multi-objective shape optimization of a heat exchanger using parallel genetic algorithms", *International Journal of Heat and Mass Transfer*, Vol. 49 (15-16), pp. 2567–2577.

[10] Daróczy, L., Janiga, G., and Thévenin, D., 2013, "Systematic analysis of the heat exchanger arrangement problem using multi-objective genetic optimization", *Energy*, Vol. 65, pp. 364–373.

[11] Daróczy, L., Mohamed, M., Janiga, G., and Thévenin, D., 2014, "Analysis of the effect of a slotted flap mechanism on the performance of an H-Darrieus turbine using CFD (GT2014-25250)", *ASME Turbo Expo Conference*, Düsseldorf.

[12] Spalart, P. R., and Rumsey, C. L., 2007, "Effective Inflow Conditions for Turbulence Models in Aerodynamic Calculations", *AIAA Journal*, Vol. 45 (10), pp. 2544–2553.

[13] Kooiman, S., and Tullis, S., 2010, "Response of a Vertical Axis Wind Turbine to Time. Varying Wind Conditions found within the Urban Environment", *Wind Engineering*, Vol. 34 (4), pp. 389–401.

[14] Lanzafame, R., Mauro, S., and Messina, M., 2014, "2D CFD Modeling of H-Darrieus Wind Turbines Using a Transition Turbulence Model", *Energy Procedia*, Vol. 45, pp. 131–140.

[15] Langtry, R. B., 2006, "A Correlation-Based Transition Model using Local Variables for Unstructured Parallelized CFD codes", Ph.D. thesis, Universitaet Stuttgart.

[16] CD-adapco, 2014, *USER Guide Star-CCM+ Version 9.06*, CD-adapco.

[17] Castelli, M. R., Ardizzon, G., Battisti, L., Benini, E., and Pavesi, G., 2010, "Modeling Strategy and Numerical Validation for a Darrieus Vertical Axis Micro-Wind Turbine (IMECE2010-39548)", *ASME 2010 International Mechanical Engineering Congress and Exposition*.

[18] Kjellin, J., Bülow, F., Eriksson, S., Deglaire, P., Leijon, M., and Bernhoff, H., 2011, "Power coefficient measurement on a 12 kW straight bladed vertical axis wind turbine", *Renewable Energy*, Vol. 36 (11), pp. 3050–3053.

[19] Eastman, N., Jacobs, K., Ward, E., and Pinkerton, R. M., 1933, "The Characteristics of 78 Related Airfoil Sections from Tests in the Variable-Density Wind Tunnel", *Tech. rep.*, NACA.

Conference on Modelling Fluid Flow (CMFF'15)
The 16th International Conference on Fluid Flow Technologies
Budapest, Hungary, September 1-4, 2015

A STUDY ON PRESSURE BUILD-UP RESPONSE DUE TO CHECK VALVE CLOSURE USING DYNAMIC MESH

Nam-Seok Kim[1] , Ae-Ju Cheong[2] , Bok-Ki Min[3]

[1] Corresponding Author. Dept. of Reactor System, Korea Institute of Nuclear Safety. 62 Gwahak-ro, Yuseong-gu, Daejeon, Republic of Korea. Tel.: +82 42 868 0845, Fax: +82 42 861 2535, E-mail: nskim@kins.re.kr
[2] Dept. of Nuclear Safety Research, Korea Institute of Nuclear Safety.
[3] Dept. of Reactor System, Korea Institute of Nuclear Safety.

ABSTRACT

In this paper, the dynamic behavior of the flow field within check valve that are installed in pressurized heavy water reactors was investigated by using 3D CFD techniques, and a pressure build-up response to the adjacent equipment due to check valve closure was evaluated. Moving mesh capabilities of ANSYS CFX were used to describe the disc movement of the valve. Two different methods were used: the immersed boundary and the remeshing techniques. These were developed and compared to correctly represent the pressure build-up behavior caused by the compression of the fluid. Finally, an effect on changing the valve closing time was evaluated with the appropriate dynamic mesh technique. Results show that the remeshing method was more suitable to describe a dynamic behavior due to check valve closure, and build-up pressure caused by the compression of the fluid, which has a negative influence on the integrity of the adjacent equipment as short closing time.

Keywords: CFX, check valve, computational fluid dynamics, dynamic mesh, immersed boundary, remeshing

1. INTRODUCTION

Check valves are widely used in industrial hydraulic systems to prevent reverse flow and to protect sensitive components. The check valves that are installed in the nuclear power plants and are used in conducting safety-related functions which include; shutting down a nuclear reactor, maintaining it in a safe-shutdown condition as well as mitigating accidents, shall be exercised or examined in a manner that verifies obturator travel by exercising tests. During exercise tests, a valve disc can suddenly close in accordance with flow acceleration force, disc weights, inertia and the friction of a valve disc. A rapid closure leads to the unexpected pressure transients in the pipeline, and cause damage to the structure, systems and components. Several cases of damaged equipment caused by check valve's sudden closure have been reported. Therefore, because of safety concerns, it is important to represent dynamic characteristics of check valve and evaluate the transient response due to disc movement. Recently, there are several articles that analyze the flow field within check valve using computational fluid dynamics (CFD) technique, and to describe the disc movement using dynamic mesh methods [1~5]. However, due to the difficulty of controlling negative cell volume as deforming mesh, these techniques were not widely applied within the industry as of yet.

The present study aims at representing the dynamic behavior of the flow field within the check valve which is installed in emergency core cooling (ECC) system of pressurized heavy water reactor (PHWR) and evaluating the pressure build-up response to the adjacent equipment due to check valve closure. ANSYS CFX with immersed boundary method and remeshing technique were developed to describe the disc movement, and compared to a correctly represented pressure build-up behaviors of the flow field caused by the compression of the fluid. Finally, an effect on changing the valve closing time was evaluated using an appropriate dynamic mesh technique.

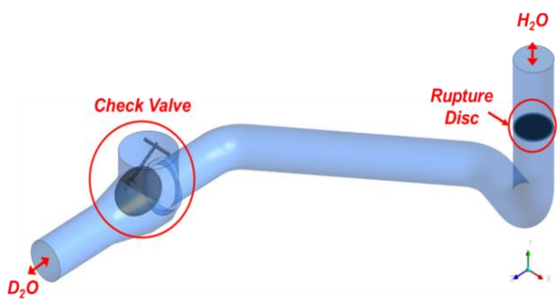

Figure 1. Simple schematic of ECC check valve and rupture disc

2. ANALYSIS AND MODELLING

2.1. ECC System in PHWR

Figure 1 shows a simple schematic of an ECC check valve and a rupture disc which are installed in the ECC injection line of PHWR. The rupture disc was provided in the ECC system to separate the part of the system, which is filled with D2O from the part of the system filled with H2O. The integrity of the rupture disc must be ensured to maintain D2O concentration of the main system. However, the fluid pressure can be increased by closing the valve disc because the pipe length is short (about 12 times the diameter of pipe) enough to compress the fluid between the check valve and the rupture disc.

2.2. Dynamic Mesh Techniques

In ANSYS CFX, there are several moving mesh options available: prescribed surface movement with automatic mesh morphing, explicit 3D mesh movement via multiple mesh files, remeshing with topology change and using immersed solid boundary. In the present study, immersed solid boundary and remeshing with mesh deformation were used to describe the closing motion of the ECC check valve.

2.2.1. Immersed Solid Boundary

It is a way to represent a moving solid without deforming the mesh. The momentum source terms added to the fluid momentum equation can model the bulk behavior of the fluid flow around the rigid solid object. The momentum equation is modified as below:

$$\frac{\partial(\rho U)}{\partial t} + \nabla \cdot (\rho U \times U) = -\nabla p + \nabla \cdot \tau + S_M \qquad (1)$$

where S_M = - $\alpha C(V-V_{IMS})$, C is the momentum source coefficient and α is the momentum force scaling factor.

Figure 2 shows the grid generation for this method. It is shown that the fluid nodes are overlapping with the disc created as an immersed solid.

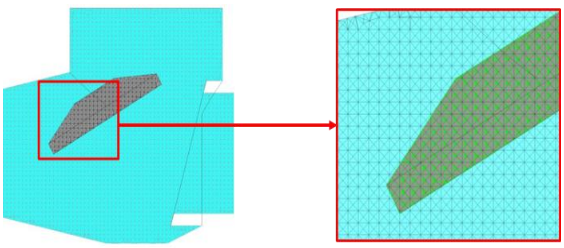

Figure 2. Grid generation for the immersed solid boundary

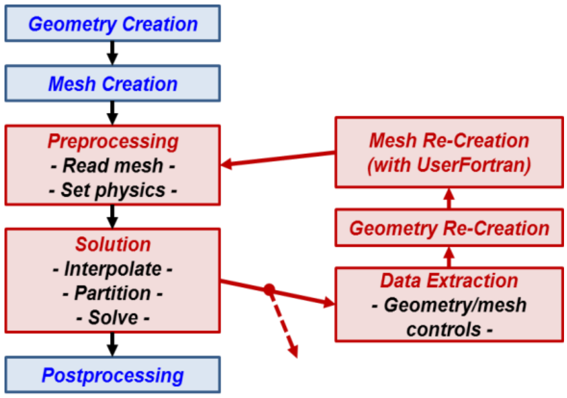

Figure 3. Remeshing scheme for ANSYS CFX with ICEM CFD replay option

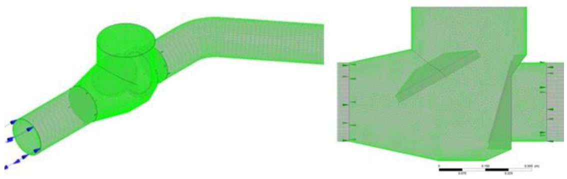

Figure 4. Grid generation

2.2.2. Remeshing

It is a way to generate new mesh on the existed geometry when the large deformation of the grid has occurred. Moving the disc boundary of the check valve is needed to large deformation of the grid, especially, when the disc is almost closed. Therefore, in this study, remeshing with ICEM CFD replay option was applied. Figure 3 shows the remeshing scheme for ANSYS CFX with ICEM CFD.

2.3. Analysis Model

The check valve was simplified and modeled to reduce the number of the grid. The unstructured grids were generated in the check valve region and the structural grids were generated in the pipeline. For the immersed solid boundary, the disc was set to the immersed solid domain. Figure 4 shows the grid generation for analysis.

The inlet condition was set to be opening, which allows flow in both directions. The mesh walls except the surface regions of the disc were set to be stationary wall. The disc was set to be rotated with constant angular velocity. The standard k-e turbulence model was used for turbulence closure. To consider the pressure build-up effect caused by the compression of fluid, the fluid density is defined with the pressure and the bulk modulus of fluid as below.

$$\frac{\partial \rho}{\rho} = \frac{dP}{E_{Fluid}} \quad (2)$$

where ρ is the fluid density, P is the pressure and E_{Fluid} is the fluid modulus of elasticity.

For the remeshing method, as the minimum orthogonality angle is less than 30 degrees, the solver was automatically interrupted to allow ICEM CFD to generate a new mesh on the existed geometry. As for the immersed solid boundary, the momentum force scaling factor of equation (1) was chosen to consider solver convergence and accuracy by sensitivity analysis.

3. RESULTS AND DISCUSSION

3.1. Determination of Dynamic Mesh Techniques

A simulation of the check valve closing transient was initiated by setting the disc position to be fully opened. It is assumed that the initial static pressure of the fluid is the same as atmospheric pressure. Then the disc is closing with constant angular velocity until the disc has reached the fully closed position. The angular velocity is set to 0.61 rad/s, so it takes about 1.275 seconds for the disc to reach the fully closed position. The high resolution and second order backward euler scheme were used for discretization of all governing equations. The residual levels of mass and momentum equations had been reached 10-5 order.

The simulation results of the immersed boundary (left in figures) and the remeshing (right in figures) are shown in figure 5 and 6. Figure 5 represents the velocity and pressure distributions at 70% closure of the disc for the both methods. It shows that the velocity and pressure contours near the disc of the immersed boundary method are similar to the results of remeshing. However, in the case of 98% closure (figure 6), the build-up pressure to the closing direction of the immersed boundary method is lower than the result of remeshing although the velocity distribution looks similar in both results. But taking a closer look between the disc and the seat, as illustrated in figure 7, the local velocity of the remeshing (right in figure 7) is much higher than the result of the immersed boundary method (left in figure 7). It is clearly seen in the velocity profiles at the outlet of the valve due to closing time. The x-axis indicates the velocity, and the y-axis indicates a relative vertical position expressed as divided with the pipe diameter.

The unfilled and filled markers indicate the results of the remeshing and the immersed boundary methods, respectively. It is shown that the velocity profiles at 0.8 and 1.1 seconds are approximately the same in the both results. However, the velocity magnitude of the remeshing at 1.25 seconds (the disc position is 98% closure) is faster than the results of the immersed boundary method and it leads that more fluid can be flowing into the outlet region. As a result, the build-up pressure of the remeshing case caused by compression of the fluid volume is higher than the results of the immersed boundary method.

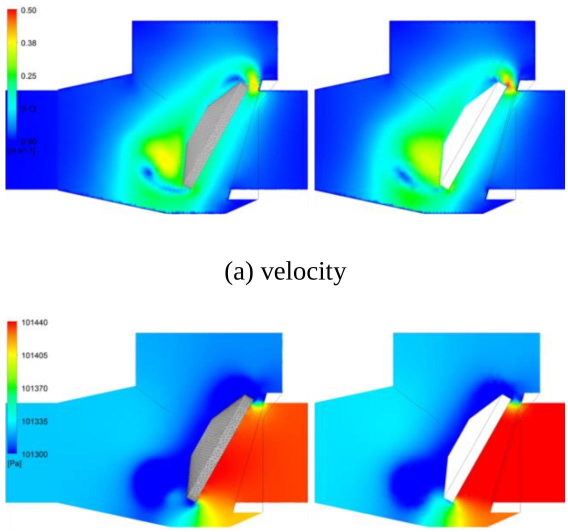

(a) velocity

(b) pressure

Figure 5. Velocity and pressure distribution for immersed boundary(left) and remeshing(right) at 70% closure

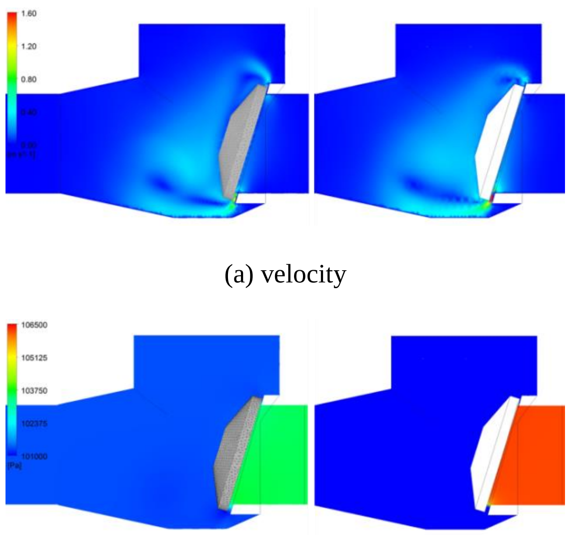

(a) velocity

(b) pressure

Figure 6. Velocity and pressure distribution for immersed boundary(left) and remeshing(right) at 98% closure

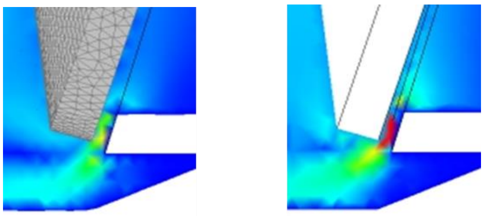

(a) immersed boundary (b) remeshing

Figure 7. Local velocity between the disc and the seat

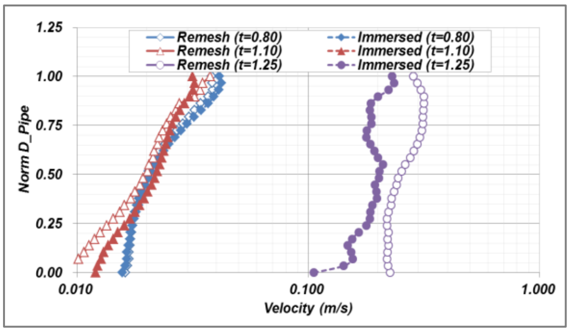

Figure 8. Velocity profiles at the outlet of the valve

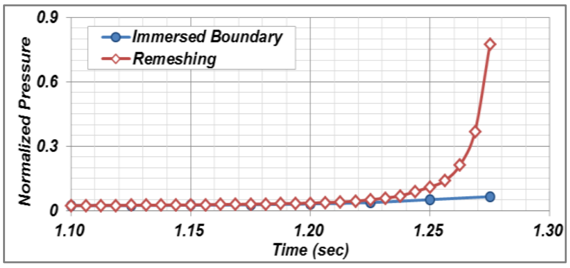

Figure 9. Pressure build-up response due to check valve closure at the outlet side

The reasons why the velocity magnitude for the immersed boundary method is lower than the remeshing are that the immersed solid region doesn't resolve the boundary layer near the disc wall and the viscous on rigid body. Thus, the force produced by closing the disc is not described well. It seems to improve that the fluid mesh around the immersed solid is generated fine enough to allow for effective interpolation of near immersed-boundary-fluid nodes onto the immersed solid and the momentum force scaling factor set to be higher value.

As for these evaluation results, the remeshing method is recommended for analyzing pressure build-up response due to the disc closure.

3.2. Evaluation of Pressure Build-up Response due to Closing Time

As for the aforementioned remeshing method, it was well suited for analyzing dynamic characteristics due to the valve closure. Three cases, which have different disc angular velocity, were generated to evaluate pressure build-up response in accordance with the changing valve closing time. Except the disc angular velocity, all other boundary conditions were the same using the previous calculation. The calculation results are summarized in table 1. When the closing time is 1.020 seconds, which is 80% of 1.275 seconds, the build-up pressure is increasing around 142%. In addition, the build-up pressure is increasing about 172% as the closing time is decreasing about 67%. As for ECC check valve, if the pressure difference at the front and the rear is more than 25 psig, there is the potential for the rupture disc installed the outlet region of ECC check valve to be damaged.

Table 1. Build-up pressure response due to increasing the disc's angular velocity

No	Closing Time	Angular Velocity	Pressure	
	sec	rad/sec	kPa	psi
1	1.275	0.609	102.7	15.1
2	1.020	0.762	146.7	21.5
3	0.850	0.914	177.7	26.0

4. CONCLUSIONS

The present study aims at drawing up recommendations for choosing the appropriate dynamic mesh techniques to describe the dynamic behavior of the flow field within check valve and a pressure build-up response to the adjacent equipment due to check valve closure. The results of calculations made by means of the immersed solid boundary method and remeshing method have been compared. The comparisons of results were similar in the aspect of pressure and velocity distribution during the check valve closure. However, as the valve plate is almost closed, the immersed method can't describe the inflowing behavior of fluid. And the build-up pressure caused by compression of fluid is underestimated.

With these evaluation results, the remeshing method is more suitable to predict an accurate build-up pressure as the check valve is closing. Additionally, the disc's angular velocity dependency was evaluated with appropriate dynamic mesh techniques. Results show that the remeshing method was more accurate to describe the dynamic characteristics of check valve closure, and build-up pressure has a negative influence to the integrity of the adjacent equipment as increasing disc's angular velocity.

ACKNOWLEDGEMENTS

This work was supported by the Nuclear Safety Research Program through the Korea Radiation Safety Foundation(KORSAFe) and the Nuclear

Safety and Security Commission(NSSC), Republic of Korea (Grant No. 1305002)

REFERENCES

[1] Boqvist, E., 2013, "Investigation of a Swing Check Valve using CFD", *Master's Thesis, Linkoping Univ.*

[2] Li, S., Hou, Y. and Li, L., 2013, "Dynamic Characteristics of Swing Check Valve based on Dynamic Mesh and UDF", *Applied Mechanics and Materials*, Vol. 321-324, pp. 86-89.

[3] Provoost, G., 1983, "A Critical Analysis to Determine Dynamic Characteristics of Non-return Valves", *Proc. of 4th Int. Conf. on Pressure Surges*, pp. 275-286.

[4] Thorley, A., 1983, "Dynamic Response of Check Valves", *Proc. of 4th Int. Conf. on Pressure Surges*, pp. 231-242.

[5] Turesson, M., 2011, "Dynamic Simulation of Check Valve using CFD and Evaluation of Check Valve Model in RELAP5", *Master's Thesis, Chalmers Univ. of Tech.*

[6] ANSYS CFX 14.5 Theory Guide, 2014, *Ansys Inc.*

Conference on Modelling Fluid Flow (CMFF'15)
The 16th International Conference on Fluid Flow Technologies
Budapest, Hungary, September 1-4, 2015

AN ALGEBRAIC MODEL FOR THE TURBULENT HEAT FLUXES IN LIQUID METAL FLOWS

Florian TRIMBORN[1], Balázs PRITZ[2], Martin GABI[2]

[1] Corresponding Author. Institute of Fluid Machinery, Karlsruhe Institute of Technology (KIT), Kaiserstraße 12, D-76131 Karlsruhe, Germany. Tel.: +49 721 608 47421, Fax: +49 721 608 43529 , E-mail: trimborn@kit.edu
[2] Institute of Fluid Machinery, Karlsruhe Institute of Technology (KIT)

ABSTRACT

In the framework of this paper a new algebraic model for the turbulent heat flux vector is proposed which is suitable to describe the special behavior of liquid metal flows. As a subproject of the Helmholtz Alliance - Liquid Metal Technologies existing models and new modeling strategies shall be investigated. Liquid metal flows are characterised by a very low molecular Prandtl number which has a huge impact on the transport processes of the turbulent heat fluxes. Due to this special behavior the common technique of modeling the turbulent heat fluxes with a constant turbulent Prandtl number leads to inaccurate results caused by the missing similarity between the velocity and temperature fields. Especially in the case of buoyancy controlled low Prandtl number flows this approach seems to cause huge deficiencies. In order to account for the special behavior of liquid metal flows an algebraic model for the turbulent heat flux vector in conjunction with a second-moment closure for the turbulent Reynolds stresses is proposed here. By derivation from a full second-moment closure and calibration this heat flux model has the potential to offer a new possibility for numerical simulations of heat transfer in liquid metal cooled reactor systems or power conversion systems. The present approach is validated at various Reynolds numbers for a test case within the forced convection regime which neglects the two-way coupling between the temperature and velocity field to simplify the modeling and calibration process.

Keywords: turbulent heat flux model, low molecular Prandtl number, channel flow, forced convection

NOMENCLATURE

BF	$[-]$	Blending factor
d	$[m]$	Distance to the nearest wall
k	$[m^2/s^2]$	Turbulent kinetic energy
n_i	$[-]$	Wall normal vector
y^*	$[-]$	Dimensionless wall distance
y^+	$[-]$	Dimensionless wall distance
$\epsilon_{i\theta}$	$[mK/s^2]$	Dissipation rate of turbulent heat fluxes
$\epsilon_{\theta\theta}$	$[K^2/s]$	Dissipation of temperature variance
ω	$[1/s^2]$	Turbulent frequency
$\overline{\theta'^2}$	$[K^2]$	Temperature variance
Θ^+	$[-]$	Dimensionless temperature

1. INTRODUCTION

The thermal hydraulics of liquid metal flows in applications like liquid metal cooled nuclear reactor systems or so called power conversation systems (PCS), where they allow to operate the process on higher temperatures and thus increasing the overall efficiency, are of wide interest in the research community. In safety reviews of such engineering applications one of the most important concerns is an accurate prediction of the occuring transport processes. As a result of its cooling tasks the liquid metal flow consumes high amounts of thermal energy and needs to be guided to suitable heat exchanger elements. By differences in the temperature field of the liquid metal flow buoyancy effects can occur especially in vertical heated sections of the facility. In order to investigate such phenomena, data from suitable measurement techniques, highly resolved direct numerical simulation (DNS) and numerical simulations based on the Reynolds averaged Navier-Stokes-Equations (RANS), is needed.

In the framework of the LIMTECH-Alliance, supported by the Helmholtz foundation, several project participants investigate new technologies for liquid metal flows in different fields of research. The major task of the present project is the comparison of results from numerical simulations with experimental data of the KASOLA facility (KArlsruher SOdium LAboratory) provided by the Institute for Neutron Physics and Reactor Technology (INR) from the Karlsruhe Institute of Technology (KIT) for a turbulent square duct flow within the free, mixed and forced convection regime.

The special behavior of liquid metal flows, which are characterised by a very low molecular Prandtl number (*Pr*), demands the use of adapted modeling strategies. Common approaches, which are based on a constant turbulent Prandtl number and thus on the so called Reynolds analogy for modeling the turbulent heat fluxes, are widely validated for flows with Prandtl numbers near unity but show great deficiencies in reproducing the correct behavior of liquid metal flows [1, 2, 3]. To obtain more sophisticated and efficient approaches for modeling the turbulent heat fluxes, models based on algebraic truncation or even the solution of full second-moment closures are necessary. Several authors have published algebraic modeling proposals [4, 5, 6]. Their application to buoyancy dominated flows requires the solution of additional equations for the temperature variance and the dissipation rate. In cases of mixed and natural convection the velocity and temperature field are directly coupled through the buoyancy term occuring in the momentum equations. In a full-differential approach this results in the coupled solution of 17 equations. The applicability of algebraic turbulent heat flux models seems to be a reasonable compromise by reducing the overall complexity of the numerical simulation.

In this paper an algebraic approach for the turbulent heat fluxes is derived from a full second-moment closure based on the modeling proposals of Baumann et al. [7], which is used in combination with a second-moment closure for the turbulent Reynolds stresses proposed by Dehoux et al. [8]. For the forced convection regime the DNS data of Abe et al. [9] deliver a possiblity to compare different types of closure approaches for the turbulent heat fluxes in a one-dimensional problem which is one of the main topics illustrated in this paper.

2. ALGEBRAIC TRUNCATION

2.1. Thermal hydraulics of liquid metal flows

For the turbulent velocity field a closure approach of Dehoux [8] is chosen which was validated successfully against DNS data of different flow types. The author derived its second-moment closure for the turbulent Reynolds stresses from a modeling proposal by Manceau and Hanjalić [10]. This type of turbulence model is based on the use of an elliptic blending function for a near-wall model and a homogeneous model of the velocity-pressure gradient correlation terms in the equation of the turbulent Reynolds stress components. The elliptic blending approach demands the solution of an additional Laplace-equation for the blending parameter α_m. The theoretical background for the modeling proposals from Manceau and Hanjalić [10] was a simplification of the second-moment closure published by Durbin [11], which is based on an elliptic relaxation method for modeling the slow and rapid part of the velocity-pressure gradient correlation. The model coefficients and its derivation are published by Manceau and Hanjalić [10] and Dehoux [8].

For a turbulent channel flow within the forced convection regime, the DNS data from Abe et al. [9], [12] delivers the possibility to analyse the special behavior of the turbulent heat fluxes at various molecular Prandtl numbers. The focus of their investigations was the dependency of the turbulent heat transport on Reynolds and Prandtl number effects.

Figures 1 and 2 show the main budget terms in the case of mercury ($Pr = 0.025$) and air ($Pr = 0.71$). By comparing the different budget terms it is clearly visible that in the case of low Prandtl number flows the dominant terms are the production and the dissipation term. The temperature-pressure gradient correlation or so called scrambling term is of less importance. On the other hand in the case of the air flow the latter one becomes the dominant term and it is the main opponent of the production term. This physical behavior in thermal hydraulics has to be considered for the development of modeling approaches in the field of liquid metal flows. Baumann et al. [7] introduced a damping function for the scrambling terms as a function of the molecular Prandtl number. By validating this function against DNS data from Abe et al. [9], [12] for different molecular Prandtl numbers they could correctly reproduce the decreasing importance of this terms [7].

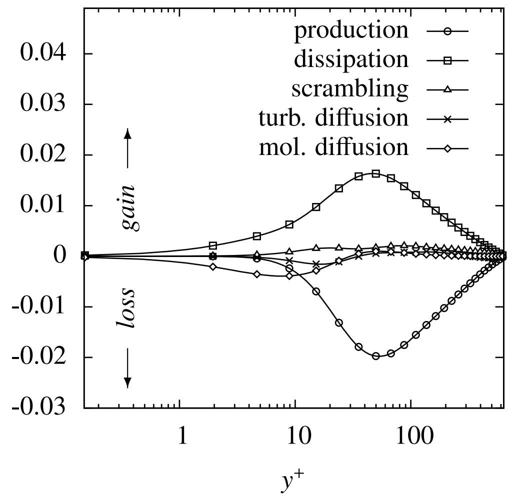

Figure 1. $\overline{v'\theta'}$-budget terms for a Prandtl number of Pr = 0.025 [12]

The common practice to model the dissipation rate of turbulent heat fluxes in flows with Prandtl numbers near unity is to assume an isotropic state given by $\epsilon_{i\theta} = 0$. Due to the increasing importance of this term in liquid metal flows other modeling proposals have to be considered. Wörner et al. [13] published an approach in dependency of the Prandtl number and the time scale ratio $R = \tau_t/\tau_h$ between

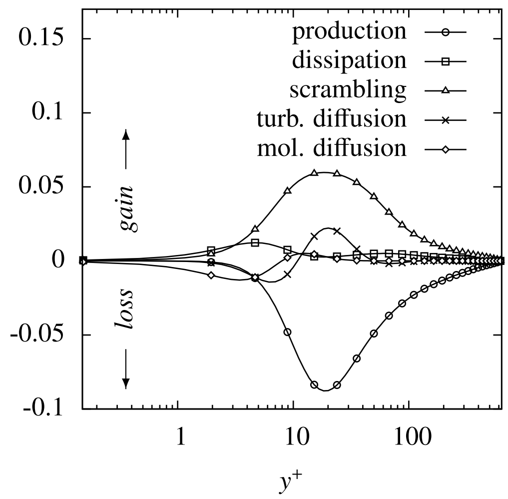

Figure 2. $\overline{v'\theta'}$-budget terms for a Prandtl number of Pr = 0.71 [12]

the thermal time $\tau_t = \overline{\theta'^2}/\epsilon_{\theta\theta}$ and the mechanical time $\tau_m = k/\epsilon$.

Baumann [14] chose an approach by Lai and So [15], which is based on an additional damping in the vicinity of the wall. The damping parameter is determined by the analysis of pipe flows and is characterised as a function of the turbulent Reynolds number:

$$f_{w_{Lai}} = \exp -(Re_t/80)^2. \tag{1}$$

$$Re_t = k^2/(\nu\epsilon) \tag{2}$$

By comparing the results of the modeled dissipation rate and the exact term from the budget analysis, Baumann et al. [7],[14] proposed an additional exponential function based on $y^* = \frac{\sqrt{k}y}{\nu}$, which has nearly similar characteristics then y^+. The use of a maximum function limits the damping function to improve the behavior of the model close to the solid wall. The second-moment closure for the turbulent heat fluxes from Baumann et al. [7, 14] in combination with the $k-\omega$ turbulence model by Hellsten et al. [16] showed a good agreement in comparison with the DNS data from Abe et al. [9, 12] for different molecular Prandtl numbers.

The main reason for deviations in the profiles for the temperature and the turbulent heat fluxes in comparison with the DNS data is mainly the result of a wrongly predicted ratio between the turbulent kinetic energy and the dissipation rate [14]. The ratio between these turbulent quantities is often declared as mechanical time scale τ_m. By choosing a second-moment closure for the velocity field, e.g. [8], as a basis for further modeling, the uncertainty should be reduced and more accurate modeling proposals can be applied, e.g. for modeling the turbulent diffusion terms as proposed by Hanjalić et al. [17]. The coefficients of the second-moment closure for the turbulent heat fluxes by Baumann et al. [7] in combination with a second-moment closure for the momentum equation were slighty recalibrated by in the present work and are specified in Tables 1 and 2. The results of this coupling will be discussed in Section 3.

2.2. Derivation of an algebraic turbulent heat flux model

In the case of a buoyancy dominated flow the full closure of the velocity and temperature equations and the consideration of additional production terms in the Reynolds stress equations demands the solution of overall 17 equations in a three-dimensional test case for the incompressible formulation. The choice of different models for all terms in the equations can be jointly responsible for numerical instabilities. Additionally an enormous number of modeling approaches has to be investigated for each of the unknown terms for different kind of flow types.

With the goal to reduce computational complexity algebraic modeling approaches were already proposed by Launder [4], assuming the three production terms in the heat flux equation to be the most important terms. Dol et al. [18] discussed the theorical basis and justification for the applicability of algebraic flux models in heat transfer applications with natural convection.

The basic steps of deriving an algebraic flux model shall be described in this paper. The equation of the turbulent heat fluxes can be written in its characteristic budget parts as

$$\frac{\mathrm{D}\overline{u_i'\theta'}}{\mathrm{D}t} = P_{i\theta} + \phi_{i\theta} - \epsilon_{i\theta} + D_{i\theta}. \tag{3}$$

Except for the production term $P_{i\theta}$ each term on the right hand side of the equation 3 needs to be modelled. In the present second-moment version of the turbulent heat flux model (SMC) some minor modifications were made in comparison with the differential flux model proposed by Baumann et al. [7, 14].

Instead of using an isotropic approach for the turbulent diffusion an anisotropic approach was implemented in the present second-moment closure for the turbulent heat fluxes, which seems to be the best compromise between accuracy and computational effort and considers the turbulent Reynolds stress tensor instead of the turbulent kinetic energy with a coefficient $C_\theta = 0.22$ as proposed by Jones and Musonge [19]:

$$\begin{aligned} D_{i\theta}{}^t &= \overline{u_i'u_l'\theta'} + \frac{1}{\rho}\overline{p'\theta'} \\ &= \frac{\partial}{\partial x_k}\left(C_\theta \frac{k}{\epsilon}\overline{u_k'u_l'}\frac{\partial\overline{u_i'\theta'}}{\partial x_l}\right). \end{aligned} \tag{4}$$

For the molecular diffusion the diffusion coefficient in the present model is modeled as an average of the kinematic viscosity and the thermal diffusion, as proposed by Baumann [14], which becomes exact for flows with a Prandtl number near unity, see Dol et al. [18]:

$$\begin{aligned} D_{i\theta}{}^{m} &= \frac{\partial}{\partial x_l}\left(\alpha \overline{u_i{}' \frac{\partial \theta'}{\partial x_l}} + \nu \overline{\theta' \frac{\partial u_i{}'}{\partial x_l}}\right) \\ &= \frac{\partial}{\partial x_l}\left(\frac{\alpha+\nu}{2}\frac{\partial \overline{u_i'\theta'}}{\partial x_l}\right). \end{aligned} \tag{5}$$

The error introduced by neglecting the additional terms is rather small which was already investigated in the discussion of the budgets terms of turbulent heat fluxes in Figures 1 and 2.

This present SMC is the starting point for the derivation of an algebraic turbulent heat flux model (AHM) maintaining the main physics of low and high Prandtl number flows.

For deriving an algebraic turbulent heat flux model Dehoux et al. [8] proposed to create a dimensionless vector for the heat fluxes ζ_i based on the work of Rodi [20] for the tensor of anisotropy in the frame of the Reynolds stress modeling:

$$\zeta_i = \frac{\overline{u_i'\theta'}}{\sqrt{k}\sqrt{\overline{\theta'^2}}}. \tag{6}$$

The weak-equilibrium hypothesis implicates that this anisotropic heat flux vector is constant in time and space [18]. A detailed explanation is given by Hanjalić [21], who stated the evolution of turbulence moments is slower than the imposed mean flow, thus the sum of the convective and diffusive transport of turbulent quantities remains correlated. These facts are expressed in consideration of the turbulent heat flux vector by the following equation:

$$\frac{\mathrm{D}\zeta_i}{\mathrm{D}t} - D_{\zeta_i} = 0. \tag{7}$$

The convective and diffusive transport of the turbulent heat fluxes can then be expressed by the transport terms of the turbulent kinetic energy k and the temperature variance $\overline{\theta'^2}$.

$$\begin{aligned} &\frac{1}{\sqrt{k}\sqrt{\overline{\theta'^2}}}\left(\frac{\mathrm{D}\overline{u_i'\theta'}}{\mathrm{D}t} - D_{i\theta}\right) = \\ &\qquad \frac{1}{2}\left[\frac{\overline{u_i'\theta'}}{k^{3/2}\sqrt{\overline{\theta'^2}}}\left(\frac{\mathrm{D}k}{\mathrm{D}t} - D_k\right)\right. \\ &\qquad \left. + \frac{\overline{u_i'\theta'}}{\sqrt{k}\overline{\theta'^2}^{3/2}}\left(\frac{\mathrm{D}\overline{\theta'^2}}{\mathrm{D}t} - D_{\theta\theta}\right)\right]. \end{aligned} \tag{8}$$

The equation for the turbulent heat fluxes can then be written as:

$$\begin{aligned} &P_{i\theta} + D_{i\theta} + \phi_{i\theta} \\ &- \epsilon_{i\theta} - \frac{\overline{u_i{}'\theta'}}{2k}\left(P_k + G_k + D_k - \epsilon\right) \\ &- \frac{\overline{u_i{}'\theta'}}{2\overline{\theta'^2}}\left(P_{\theta\theta} + D_{\theta\theta} - \epsilon_{\theta\theta}\right) = 0, \end{aligned} \tag{9}$$

where $D_{i\theta}$, D_k and $D_{\theta\theta}$ are the total diffusion terms of $\overline{u_i{}'\theta'}$, k and $\overline{\theta'^2}$.

By use of the hypothesis the total diffusion term of turbulent heat fluxes can be expressed as

$$D_{i\theta} = \frac{1}{2}\overline{u_i{}'\theta'}\left(\frac{1}{k}D_k + \frac{1}{\overline{\theta'^2}}D_{\theta\theta}\right). \tag{10}$$

For the scrambling term and the dissipation term models based on the proposals of Baumann et al. [7, 14] were applied

$$\begin{aligned} \phi_{i\theta} = &-f_{pt}C_{T1}\frac{\epsilon}{k}\overline{u_i{}'\theta'} + C_{T2}\overline{u_i{}'\theta'}\frac{\partial u_i}{\partial x_j} \\ &+ C_{T3}\beta g_i\overline{\theta'^2} - f_{pt}C_{T4}\frac{\epsilon}{k}n_i\frac{k^{1.5}}{\epsilon y}, \end{aligned} \tag{11}$$

where

$$f_{pt} = \frac{Pr}{1.2Pr + 0.18} \tag{12}$$

is a damping function expressing the decreasing importance of the scrambling term for low Prandtl number flows. This function is calibrated for different molecular Prandtl numbers with the DNS data provided by Abe et al. [9, 12] for a fully developed turbulent channel flow.

The model for the dissipation term from Baumann et al. [7], which is derived from Lai and So [15], is used for taking into account the increasing dominance of the dissipation in liquid metal flows with heat transfer:

$$\epsilon_{i\theta} = \frac{1}{2}f_{w_{Lai}}\left(1 + \frac{1}{Pr}\right)\frac{\epsilon}{k}\left(\overline{u_i{}'\theta'} + \overline{u_k{}'\theta'}n_k n_i\right), \tag{13}$$

where $f_{w_{Lai}}$ is replaced by f_{w_B}, see Baumann et al. [7]:

$$f_{w_B} = min\left(a\exp\left(by^*\right) + c\exp\left(dy^*\right) + e, 1.0\right). \tag{14}$$

The parameters n_i and y describe the wall-normal direction and wall-normal distance and the coefficients of the model are given in Table 1.

By assuming a local equilibrium state of turbulence between the dissipation and the production of the turbulent kinetic energy and the temperature variance Equation 9 can be rearranged with

$$P_k + G_k = \epsilon, \tag{15}$$

$$P_{\theta\theta} = \epsilon_{\theta\theta}. \tag{16}$$

Finally an algebraic heat flux model is obtained by the authors of this paper containing the main physics of low Prandtl number flows:

$$\begin{aligned} \overline{u_i'\theta'} = &-C^* \left(\frac{k}{\epsilon}\right) \frac{1}{\left(f_{pt}C_{T1} + \frac{1}{2} f_{w_B} \left(1 + \frac{1}{Pr}\right)\right)} \\ &\left[P_{i\theta}^{\Theta} + (1 - C_{T2})\, P_{i\theta}^{U} + (1 - C_{T3})\, G_{i\theta} \right. \\ &- f_{pt} C_{T4} \frac{\epsilon}{k} \overline{u_j'\theta'} n_j n_i \\ &\left. -\frac{1}{2} f_{w_B} \frac{\epsilon}{k} \overline{u_j'\theta'} n_j n_i \right]. \end{aligned} \tag{17}$$

Table 1. Coefficients of the damping functions

model	DFM [7]	SMC	AHM
a	1.35	1.35	1.35
b	0.14	0.14	0.14
c	0.076	0.076	0.076
d	0.016	0.016	0.016
e	0.15	0.13	0.13
f	0.8	1.0	1.0

3. RESULTS OF THE MODELING APPROACH

A two-dimensional forced convection channel flow was chosen as test case for the validation. For this kind of flow several authors published DNS data for the velocity field, e.g. [22] and the temperature field, e.g. Abe et al. [9], for different molecular Prandtl numbers. In this type of flow a one-way coupling between the velocity and the temperature field can be assumed in an incompressible flow in constrast to mixed and natural convection flow regimes and thus the temperature acts as a passive scalar quantity. In general the temperature distribution is controlled by gradients of the streamwise velocity component in the wall-normal direction and thus by convection and diffusive transport processes in forced convection. By choosing a fully developed turbulent flow case only the diffusion terms remains in the equations. For calibration purposes and for the analysis of different budgets and flow physics of the turbulent heat flux equations this test case offers a straightforward reduction of complexity allowing the investigation of a one-dimensional flow problem. Each of the presented models was implemented in the Open Source CFD Software OpenFOAM® [23].

The test case for validation is a two-dimensional channel flow within the forced convection regime. For the streamwise and spanwise directions periodic boundary conditions were used and an identical constant heat flux boundary condition was applied on both solid walls. The Reynolds number based on the friction velocity was fixed to $Re_\tau = 640$ and the dimensional wall distance of the first grid cell for the grid independent solution is $y^+ = 0.57$.

In the following section a comparison between different modeling approaches from literature is made for the two investigated Prandtl numbers $Pr = 0.025$ and $Pr = 0.71$. For the velocity field the turbulence model by Dehoux et al. [8] was chosen, which showed a superior behavior especially in the vicinity of a solid wall. The model maintains the main physics of the so called blocking-effect, the influence of pressure fluctuations and viscous interactions on the Reynolds stresses without using damping functions or parameters based on the wall distance. As stated by several authors the applicability of such approaches shows strong deficiencies especially in complex flow types [8, 10, 11].

Table 2. Coefficients of the different models

model	present AHM	present SMC	Dehoux-DFM [8]	Dehoux-AFM [6]
C_{T1}	3.75	3.75	4.15	3.0
C_{T2}	0.33	0.33	0.3	0.55 ${\alpha_\theta}^3$
C_{T2}	0.55	0.55	0.5	0.55 ${\alpha_\theta}^3$
C_{T4}	0.6	0.6	-	-
C^*	0.98	-	-	3.0
BF	-	-	α_θ	${\alpha_\theta}^3$

In Figures 3, 4, 5 and 6 the results of the present model are compared with different algebraic and differential turbulent heat flux models from literature. Dehoux [6] proposed to use an elliptic blending parameter α_θ for the turbulent heat flux equation which is based on the solution of a second Laplace-equation similiar to the blending parameter α_m for modeling the redistribution term in the Reynolds stress equations. The blending parameter is bounded in the interval $\alpha_\theta \in [0, 1]$. The Laplace-equation for α_θ includes a thermal length scale L_θ, which is a function of the flow properties and flow type. Its derivation and applicability as a function of the mechanical length scale L is discussed extensively in [8]. For more details of the work principle of each of the models the reader is referred to the paper and thesis of Dehoux [8] and Dehoux et al. [6]. For a better understanding of the following figures only each 4th data point of the DNS data provided by Abe et al. [9, 12] is plotted.

As can be seen from the results the present algebraic model based on the modified dissipation rate model for the turbulent heat flux from Baumann et al. [7] and the modifications in combination with a full second-moment closure for the Reynolds stress components show generally a very good agreement

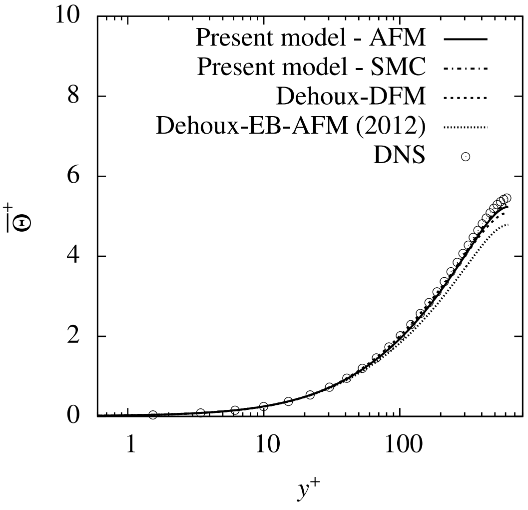

Figure 3. Dimensionless temperature for a Prandtl number of Pr = 0.025

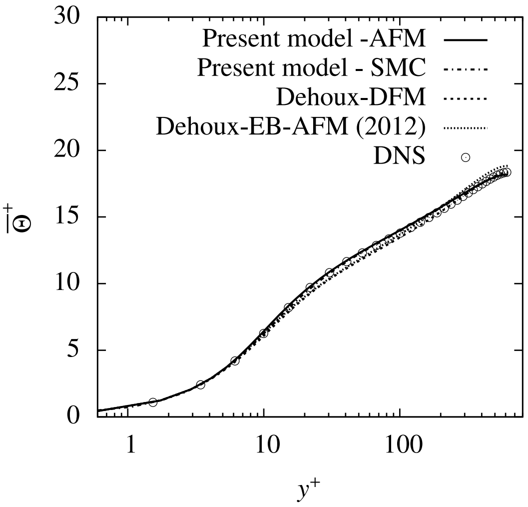

Figure 4. Dimensionless temperature for a Prandtl number of Pr = 0.71

with the DNS data.

In the case of a low molecular Prandtl number flow (Pr = 0.025) there is only a slight underprediction of the dimensionless temperature profile near the centerline of the channel for both versions of the present model, which is caused by a minor overprediction of the turbulent heat fluxes in the wall-normal direction. The present model based on a second-moment closure shows a very good agreement for the wall-normal turbulent heat flux component for the whole channel height, whereas the present algebraic approach is slightly superior in the direct vicinity of a solid wall. The slight deficiencies of the algebraic version of the present model far away from the solid wall is based on the missing of the correct diffusion characteristics and the shortcomings of

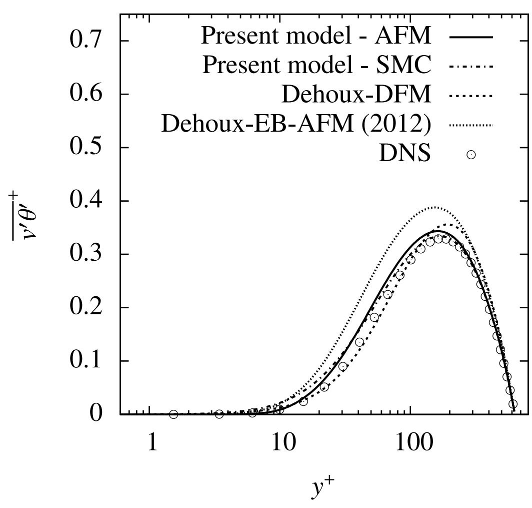

Figure 5. Dimensionless turbulent wall-normal heat flux for a Prandlt number of Pr = 0.025

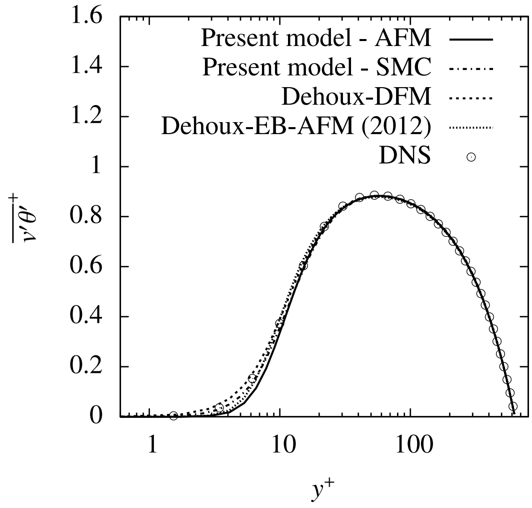

Figure 6. Dimensionless turbulent wall-normal heat flux for a Prandlt number of Pr = 0.71

both assumptions which can be validated by extraction from the DNS data [12].

In the case of a molecular Prandtl number near unity (Pr = 0.71) the present model in both versions shows also a very good agreement with the DNS data. For the wall-normal heat flux the present model based on a second-moment closure shows overall the best agreement with the DNS data especially in the near wall area whereas the algebraic version slightly fails to reproduce the correct turbulent heat flux profile due to the deviation of the equilibrium hypothesis of production and dissipation in the direct vicinity of a solid wall.

Since one of the main goals of deriving an algebraic turbulent heat flux model is to reduce the required computational effort both present models were compared. The present algebraic approach is about 12% faster then the differential version of the present model with a similar convergence behavior of the temperature.

In summary, each of the models reproduces the main physics of the thermal hydraulics in the case of an air flow and for a low Pr number flow the presented models deliver a superior solution compared to models recently found in literature.

4. CONCLUSION

This paper presents a second-moment closure and an algebraic model for the turbulent heat fluxes. They are both suitable to reproduce the physics of the thermal hydraulics in low Prandtl number flows. The present models are based on the proposals and theoretical work of Baumann et al. [7, 14] and use a modified version of the dissipation rate model by Lai and So [15] for the turbulent heat fluxes. A damping function for the so called "scrambling term" incorporates the dependency of this term on the molecular Prandtl number. The present versions of the SMC-model and the algebraic model have been validated for a forced convection channel flow at a Reynolds number of $Re_\tau = 640$ for the molecular Prandtl numbers $Pr = 0.025$ and $Pr = 0.71$. DNS data for this test case are provided by Abe et al. [9, 12]. Both models have been combined with a full second-moment closure of the turbulent Reynolds stresses based on the elliptic-blending approach proposed by Manceau and Hanjalić [10] and improved by Dehoux [8]. This allows the applicability of the model for more complex flow types in further investigations, e.g. heated turbulent square duct flows, and improves the overall accuracy of the results at the expense of numerical stability and computational efficiency. The derivation of an algebraic version based on the present second-moment closure was discussed in detail and the assumptions were verified for this specific test case with the provided DNS data by Abe et al. [9, 12].

As can be seen from the results the present models show a superior behavior for both molecular Prandtl numbers, especially for the wall-normal heat fluxes. The applied assumptions and hypotheses, both outlined in detail by Dol et al. [18] and Dehoux [8], are responsible for minor deficiencies of the present algebraic model in the direct vicinity of the wall. This shortcomings can be explained by the missing of the correct diffusion characteristics and the failure of the latter assumptions, e.g. the existence of an equilibrium between production and dissipation near a solid wall. For the dimensionless temperature in the case of a low molecular Prandtl number flow ($Pr = 0.025$) only minor deviations from the DNS data can be stated for both models. The second-moment closure version performs slighty better then the algebraic model, which is still superior to models recently found in literature. For the prediction of the wall-normal turbulent heat flux component both models cannot fully capture the exact profile in comparison with the DNS data. The best agreement for this heat flux component in low molecular Prandtl number flows is achieved with the differential version of the model with minor advantages over the algebraic model. In the case of a molecular Prandtl number near unity ($Pr = 0.71$) the present model in both versions shows a very good agreement for the dimensionless temperature profile in comparison with the DNS data and is definitely comparable to state-of-the-art models from literature. For the wall-normal turbulent heat flux the present model based on a second-moment closure shows overall the best agreement with the DNS data especially in the near wall area whereas the algebraic version slightly underpredicts the wall-normal turbulent heat flux in the direct vicinity of a solid wall. In summary, each of the models reproduces the main physics of the thermal hydraulics in the case of an air flow but only the modified version of a second-moment closure and a derived algebraic version is able to capture correctly the thermal hydraulics of a low Prandtl number flow. By an algebraic formulation of the turbulent heat fluxes containing the increasing importance of the dissipation term for liquid metal flows, the computational effort was reduced without sacrificing considerably the accuracy in comparison with DNS data.

Further research activities are based on implementing another approach for modeling the dissipation rate of the turbulent heat fluxes by considering a model proposed by Wörner et al. [13], [3] which needs to be calibrated in dependency of the molecular Prandtl number. Also the applicability of an elliptic blending parameter α_θ as described by Dehoux [8] will be investigated.

ACKNOWLEDGEMENTS

The authors would like to thank the Helmholtz Alliance - Liquid Metal Technologies (LIMTECH) for the sponsorship of this investigations.

REFERENCES

[1] Kays, W. M., 1994, "Turbulent Prandtl Number - Where Are We?", *J Heat Transfer*, Vol. 116 (2), pp. 284–295, URL `http://dx.doi.org/10.1115/1.2911398`.

[2] Otić, I., Grötzbach, G., and Wörner, M., 2005, "Analysis and modelling of the temperature variance equation in turbulent natural convection for low-Prandtl-number fluids", *J Fluid Mech*, Vol. 525, pp. 237–261, URL `http://dx.doi.org/10.1017/S0022112004002733`.

[3] Carteciano, L., and Grötzbach, G., 2003, "Validation of turbulence models in the computer code FLUTAN for a free hot sodium jet in different buoyancy flow regimes", *Wissenschaft-*

liche Berichte FZKA 6600, Forschungszentrum Karlsruhe.

[4] Launder, B. E., 1988, "On the Computation of Convective Heat Transfer in Complex Turbulent Flows", *J Heat Transfer*, Vol. 110 (4b), p. 1112, URL http://dx.doi.org/10.1115/1.3250614.

[5] Kenjereš, S., and Hanjalić, K., 2000, "Convective rolls and heat transfer in finite-length Rayleigh-Bénard convection: A two-dimensional numerical study", *PHYSICAL REVIEW E*, Vol. 62 (6), pp. 7987–7998.

[6] Dehoux, F., Lecocq, Y., Benhamadouche, S., Manceau, R., and Brizzi, L.-E., 2012, "Algebraic Modeling of the Turbulent Heat Fluxes Using the Elliptic Blending Approach - Application to Forced and Mixed Convection Regimes", *Flow Turbulence Combust*, Vol. 88 (1-2), pp. 77–100, URL http://dx.doi.org/10.1007/s10494-011-9366-8.

[7] Baumann, T., Oertel jr., H., Stieglitz, R., and Wetzel, T., 2012, "Validation of RANS Models for Turbulent Low Prandtl Number Flows", *The 9th International Topical Meeting on Nuclear Thermal-Hydraulics, Operation and Safety (NUTHOS-9), Kaohsiung, Taiwan*.

[8] Dehoux, F., 2012, "Modélisation statistique des écoulements turbulents en convection forcée, mixte et naturelle", Ph.D. thesis, Université de Poitiers.

[9] Abe, H., Kawamura, H., and Matsuo, Y., 2004, "Surface heat-flux fluctuations in a turbulent channel flow up to $Re_\tau = 1020$ with $Pr = 0.025$ and 0.71", *International Journal of Heat and Fluid Flow*, Vol. 25 (3), pp. 404–419, URL http://dx.doi.org/10.1016/j.ijheatfluidflow.2004.02.010.

[10] Manceau, R., and Hanjalić, K., 2002, "Elliptic blending model: A new near-wall Reynolds-stress turbulence closure", *Physics of Fluids*, Vol. 14 (2), p. 744, URL http://dx.doi.org/10.1063/1.1432693.

[11] Durbin, P. A., 1993, "A Reynolds stress model for near-wall turbulence", *J Fluid Mech*, Vol. 249 (-1), pp. 465–498, URL http://dx.doi.org/10.1017/S0022112093001259.

[12] KawamuraLab, 2014, "DNS Database of Wall Turbulence and Heat Transfer", http://murasun.me.noda.tus.ac.jp/turbulence/, [Online; accessed 14-April-2014].

[13] Wörner, M., Ye, Q.-Y., and Grötzbach, G., "Consistent modelling of fluctuating temperature-gradient-velocity-gradient correlations for natural convection", *Engineering Turbulence Modelling and Experiments 4, ds: W Rodi, D Laurence, Elsevier Science B V*, pp. 165–174.

[14] Baumann, T., 2012, "Turbulenzmodellierung von Strömungen niedriger molekularer Prandtlzahl", Dissertation, Karlsruher Institut für Technologie (KIT).

[15] Lai, Y., and So, R., 1990, "Near-wall modeling of turbulent heat fluxes", *International Journal of Heat and Mass Transfer*, Vol. 33 (7), pp. 1429–1440, URL http://dx.doi.org/10.1016/0017-9310(90)90040-2.

[16] Hellsten, 2004, "A New Two-Equation Turbulence Model for Aerodynamics Applications", Ph.D. thesis, Department of Mechanical Engineering, Helsinki University of Technology (Espoo, Finland).

[17] Hanjalić, K., 1994, "Advanced turbulence closure models: a view of current status and future prospects", *International Journal of Heat and Fluid Flow*, Vol. 15 (3), pp. 178–203, URL http://dx.doi.org/10.1016/0142-727X(94)90038-8.

[18] Dol, H., Hanjalić, K., and Kenjereš, S., 1997, "A comparative assessment of the second-moment differential and algebraic models in turbulent natural convection", *International Journal of Heat and Fluid Flow*, Vol. 18 (1), pp. 4–14, URL http://dx.doi.org/10.1016/S0142-727X(96)00149-X.

[19] Jones, W. P., and Musonge, P., 1988, "Closure of the Reynolds stress and scalar flux equations", *Physics of Fluids*, Vol. 31 (12), pp. 3589–3604, URL http://dx.doi.org/10.1063/1.866876.

[20] Rodi, W., 1976, "A new algebraic relation for calculating the Reynolds stresses", *Zeitschrift für Angewandte Mathematik und Mechanik*, Vol. 65, pp. 219–221.

[21] HanjaliÄĞ, K., 2002, "ONE-POINT CLOSURE MODELS FOR BUOYANCY-DRIVEN TURBULENT FLOWS", *Annual Review of Fluid Mechanics*, Vol. 34 (1), p. 321âĂŞ347, URL http://dx.doi.org/10.1146/annurev.fluid.34.082801.161035.

[22] Kim, J., Moin, P., and Moser, R., 1987, "Turbulence statistics in fully developed channel flow at low Reynolds number", *J Fluid Mech*, Vol. 177, pp. 133–166.

[23] OpenFOAM Foundation, URL http://www.openfoam.org.

Conference on Modelling Fluid Flow (CMFF'15)
The 16th International Conference on Fluid Flow Technologies
Budapest, Hungary, September 1-4, 2015

EVALUATION OF THE REFURBISHMENT POTENTIAL FOR FRANCIS TURBINES USING CFD AND OPTIMISATION TECHNIQUES

Arslan Ömür ÖZCAN[1], Helmut BENIGNI[2], Berk Can DUVA[3], Jürgen SCHIFFER[4], Helmut JABERG[5], Markus MOSSHAMMER[6]

[1] Corresponding Author. TÜBİTAK MAM EE Ankara, İnönü Bulvarı, ODTÜ Yerleşkesi, TR - 06800 Çankaya ANKARA
Tel.:+90 3122101830 1274, E-mail: arslan.ozcan@tubitak.gov.tr
[2] Institute of Hydraulic Fluidmachinery, Graz University of Technology. E-mail: helmut.benigni@hfm.tugraz.at
[3] TÜBİTAK MAM EE Ankara, E-mail: berkcan.duva@tubitak.gov.tr
[4] Institute of Hydraulic Fluidmachinery, Graz University of Technology. E-mail: jürgen.schiffer@tugraz.at
[5] Institute of Hydraulic Fluidmachinery, Graz University of Technology. E-mail: helmut.jaberg@tugraz.at
[6] Institute of Hydraulic Fluidmachinery, Graz University of Technology. E-mail: mosshammer@tugraz.at

ABSTRACT (STYLE: ABSTRACT TITLE)

For a series of 40-year-old Francis turbines an investigation on the refurbishment potential was carried out for the plant operator. Therefore, a comprehensive CFD analysis was performed, starting with the laser scan of the real geometry of runner and guide vane on-site. Based on old drawings of the machines the rest of the units, especially spiral vasing and stay vanes as well as the draft tube, were modelled in a CAD system. An additional inspection of the machines' interior filled lacks regarding unknown geometry sections. After the meshing of all components a mesh study was realised to verify mesh quality and calculation convergence.

Subsequently, a RANS calculation (Reynolds Averaged Navier Stokes) provided information on the overall performance and the losses referring to each component. In a further step, these components were analysed more in detail and a comparison with existing machines was established. The results were also compared to old model and site efficiency tests. Thus, the optimisation potential was figured out and the findings of the simulation were compared to damages e.g. erosion, cavitation and cracks detected during the site inspection. For cavitation analyses the histogram method was used.

Based on an economic study, optimization of the chosen components was carried out in order to improve the overall efficiency and to avoid cavitation zones in the vanned areas. The optimisation was performed by means of two different methods.

Keywords: CFD, Francis, optimisation refurbishment, simulation, turbine

NOMENCLATURE (TITLE: HEADING 1)

A	[m²]	Area
c_m	[m/s]	Meridional velocity
c_u	[m/s]	Circumferential velocity
$D_{nominal}$	[m]	Runner diameter
g	[m/s²]	Gravity
Q	[m³/s]	Discharge
H	[m]	Head
M	[Nm]	Torque
n_q	[rpm]	Specific speed
u	[m/s]	Circumferential velocity
w	[m/s]	Relative velocity
ρ	[kg/m³]	Density
φ	[-]	Flow coefficient
η	[-]	efficiency
ψ	[-]	Pressure number
σ	[-]	Thoman cavition number
ω	[1/s-]	Angular velocity

Subscripts and Superscripts

BEP	Best efficiency point
GV	Guide vane position (angle) in [°]
HWL	Head water level
LE	Leading edge
TE	Trailing edge
TL	Turkish Lira
TWL	Tail water level
Tot-DT-Out	total pressure at draft tube outlet

1. INTRODUCTION (TITLE: HEADING 1)

Hydropower is still an important source of renewal energy. In Turkey every 10 years the electricity demands doubles its size and therefore new power plant go in operation every year. The hydro power plants run then for decades and after this long time operation refurbishment should be done to guarantee the ongoing reliable production. This paper gives an overview of the refurbishment potential of one site. This economic topic was carried out after a detailed analysis of the flow situation within the existing hydraulic followed by an optimisation of the hydraulic to estimate the improvement of production.

In Figure 1, the workflow of the optimisation is given. Based on the geometry and data preparation the whole turbine configuration was recalculated and analysed. At the end of the recalculation the optimisation potential was outlined with a runner improvement concerning efficiency and cavitation behaviour and a guide vane improvement to shift the best efficiency point of the guide vane to lower flow rates. A stay vane improvement at the last 90 degrees of the spiral casing shows later no significant improvement.

The optimisation process was done engineer-based by hand – this means that no automated optimisation routine was used. The optimisation of the components – stay vanes, guide vanes and runner – were carried out in parallel. For the guide vane and stay vane calculation only full model calculations were used, whereas for the runner optimisation the simple setup was used – the best versions were then also calculated in a full model.

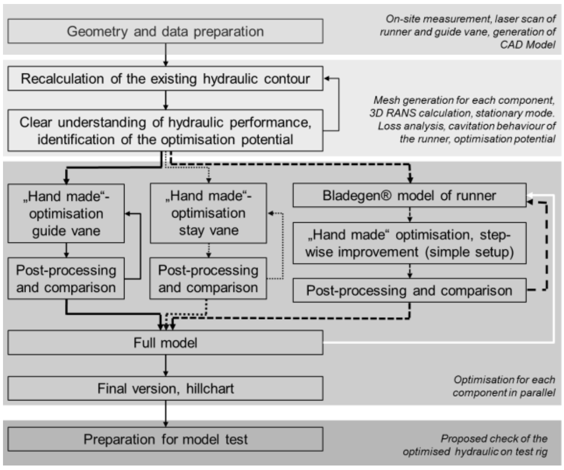

Figure 1. Workflow of the investigation

1.1. Power plant description and history

The hydro power plant was built from 1970 to 1973 and consists of one Francis unit with a nominal power of 56 MW, a nominal diameter of $D_{nominal}$ = 2.58 m for a maximum flow rate of Q = 48 m³/s and a head of H = 132 m. At the end of the horizontal tunnel (6253 m) a surge tank is installed to prevent water hammer, followed by a steel penstock with a length of 345 m. During the last 10 years this hydro power plant provided an average annual production of 184.6 Mio. kWh (minimum 101.6 Mio. kWh, maximum 268.5 Mio. kWh). Specific speed is about n_q=49 rpm.

In April 1974, were after 1200 operation cavitation damages could be detected. At that time, the tail water level (H_{TWL}=58.75m) was lower than expected in part-load operation.

In May 1974 (after preliminary efficiency tests), modifications regarding the “hydraulic shape of the turbine” had to be re-examined. This examination revealed that the nose-plate area of the spiral case due to the narrow cross-section at stay vane 23 (last but one before the nose plate) the flow was substantially retarded. In 1983, a runner change was carried out and cavitation damages were detected during an inspection (see Figure 6b)

Furthermore, an aeration device was mounted downstream the runner to improve turbine performance. Later the aeration device of the standpipe was taken out of operation, however the stand pipe still remained in the draft tube.

The peak efficiency point was measured in 2007 with 91.9% at a flow rate of 35 to 37 m³/s with an ultrasonic flow measurement. A measurement in 1974 was done with the help of current meters and yielded a best efficiency point at a flow rate of about 37 to 40 m³/s. This measurement campaign was measured with about 5% higher head (TWL was 7 m lower than in 2007).

1.2. Geometry model

In April 2014, the spare parts of the hydro power plant were measured on site by means of laser measuring devices. In July 2014 also an inspection inside the unit was realised.

Based on all existing drawings and the information gained during the site visit a CAD model of the unit was prepared which is described in Figure 2a. The draft tube consists of a steel part (Elbow itself) followed by a concrete part. The stay vane before the last stay vane was cut out by the help of a flame cutter. The point of origin of the whole model is set at the intersection of the machine axis with a mid plane, which is exactly the symmetry plane of the spiral and the guide vane. The positive z-axis is located in flow direction into the draft tube (see coordinate system in Figure 2a). The machine rotates counter clockwise around the z-axis. The mass flow enters the spiral in the negative x-direction and leaves the draft tube also in the negative x-direction.

The 0°-position of the guide vane is at fully closed guide vane position.

1.3. CFD Model

The unit was split into components (= domains) for the purposes of CFD-calculation. The calculation starts with the spiral domain in flow direction. This domain also contains the stay vanes. This stay vane region is NOT rotationally periodic (different sizes of stay vanes, cut-out stay vane and cutwater) and thus the integration of the stay vane region into the spiral domain was done. Due to the complex geometry situation as described above, an unstructured grid (see Figure 3) was generated for this component. For the post-processing a cylindrical surface was generated, and later on the losses were split up into spiral and stay vane losses.

After the spiral domain the guide vane domain was connected to the spiral with a general grid interface (GGI [2]). The guide vane mesh passage was generated by means of Turbogrid®, copied into the model 24 times and connected with a 1:1 interface. During the post-processing the single access to the guide vane passage was still possible and used for detailed post-processing.

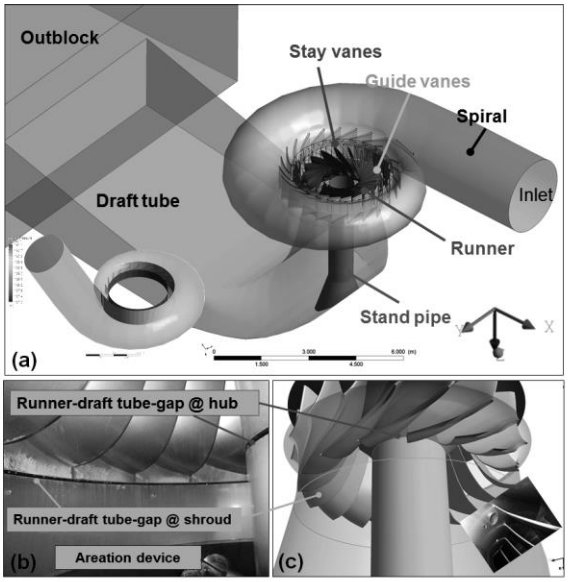

Figure 2. Model of the turbine unit

Between the guide vane and the runner domain the domain interface was set to frozen rotor [2]. The mesh for the passage of the runner domain itself was also generated with Turbogrid® and connected by means of a 1:1 grid interface between the 17 runner blades. The mesh of the runner domain consists of the main passage and an outblock domain (internally connected by a 1:1 interface).

The draft tube domain was then connected with a frozen rotor domain interface. The stand pipe was generated as measured on site, including the conical part at the bottom of the draft tube. The existing, internal aeration device was neglected as this device is out of operation since more than two decades. Downstream of the draft tube an additional component, the so-called outblock, was connected to the draft tube. The function of this component is not exactly representation of the tail water, but to avoid the setting of boundary conditions directly at the draft tube outlet which would influence the draft tube simulation and prescribe the flow situation. In Figure 2a the full model is displayed with different colours for its single components. The position of the interfaces between guide vane with runner and runner with draft tube is displayed in Figure 2(c). As one requirement for grid generation is to have some space behind the trailing edge of the runner, the end point of the rotor – stator interface is a bit more downstream than the runner – draft tube gap in reality. This is shown in Figure 2(b), where the runner– draft tube gap is just behind the trailing edge. On the other side, the gap between runner hub and standpipe was set directly to the intersection between runner hub and standpipe during CFD simulation. In reality, the gap is also a bit more downstream. With reference to the boundary conditions it has to be mentioned that the runner shroud surface in the simulation is a bit longer (and thus larger) than the real one and that the runner hub surface is a bit smaller than the real one. The areation device and the holes for the fastening bolts are neglected (see small photo in Figure 2(c) right).

The interface between guide vane and runner is displayed in Figure 3. The location of Figure 3 is exactly the cut-out stay vane region as mentioned above. In this figure, the stay vane area is coloured grey (unstructured mesh), the guide vane is coloured orange and the runner is visualised in red (both structured meshes).

The stand-alone generated meshes were combined to a complete unit for different guide vane positions. Boundary conditions were set for inlet (green surface in Figure 2a) and outlet pressure, and thus the flow rate resulted. Menter's [1] SST turbulence-model with automatic wall functions was applied, and in order to achieve a satisfying convergence level all sensitive variables and imbalances were monitored. The CFD code utilises a cell-centred control volume with identical nodes for velocity and pressure. A blending factor, which is used for the spatial discretisation method of the convective terms implemented with a hybrid scheme, is computed locally, resulting in a 2nd order accurate scheme.

With the help of the commercial CFD code Ansys CFX V14.5 [2] the Navier-Stokes equations were solved. These Navier-Stokes equations describe the fluid motion in all three dimensions and were used with a Reynolds averaged Navier stokes (RANS) formulation. RANS uses equations where the instantaneous variables are decomposed into mean and fluctuating values with the help of a Reynolds decomposition, whereas these variables are time-averaged. Additionally, a MFR (multiple frame of references) approach was used for the rotating domain (= runner).

1.4. Mesh generation

The mesh generation for guide vane and runner is carried out in Turbogrid ® in a structured way. In order to avoid highly skewed elements at the leading edge of the blade, Turbogrid® mesh-generation was applied in the JHCL mode. The JHCL mode follows a so-called automised block topology depending on the blade metal angle that includes full periodicity and applies an algebraic, semi-isogeometric surface mesh generation procedure.

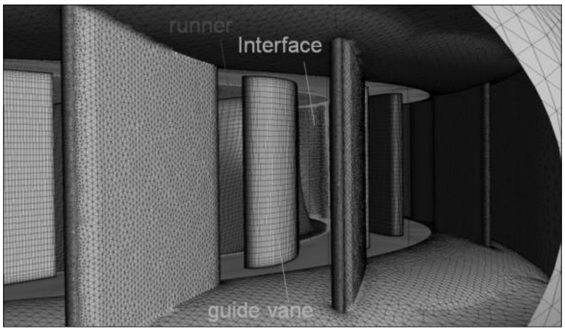

Figure 3. View from spiral downstream to guide vane and runner

The structure of the draft tube is a double butterfly (O-grid) in the cross section whereas this structure is segmented in streamwise direction at every elbow segment. For the stand pipe an additional O-grid must be set around the pipe. The spiral domain was meshed with ICEM® in an unstructured mode and is shown in Figure 3. Finally, the outblock mesh was generated block-structured in ICEM as well. The statistics of the generated meshes for are displayed in Table 1 for different mesh densities, which results in a very fine model with 33 Mio. nodes.

Table 1. Total mesh sizes of full model in Mio. nodes

	Coarse	Medium	Fine	Veryfine
Drafttube	0.95	1.59	4.04	5.68
Guidevane	1.42	2.60	5.19	9.46
Runner	2.04	3.87	6.81	11.59
Spiral	0.93	1.33	2.75	6.39
All Domains	5.33	9.39	18.80	33.13

1.5. Post processing

For the evaluation of the hydraulic performance, the key figures as mentioned in the following are of interest. In general, the net head is the difference between total pressure at the inlet of the spiral and total pressure at the outlet of the draft tube. According to the IEC standard [3], the net head represents the difference between the total pressure at the inlet (inflow of spiral) and the static pressure at the outlet (end of draft tube) where the mean kinetic energy head is added to the outlet pressure. (Eq. 1)

$$H = \frac{p_{Total-Inlet} - p_{Total-Outlet}}{\rho \cdot g} = \frac{p_{Total-Inlet} - \left(p_{Static-Outlet} + \frac{\rho}{2} \cdot \left(Q / A_{Outlet} \right)^2 \right)}{\rho \cdot g} \qquad (1)$$

$$\eta_{Total} = 1 - \frac{\Sigma H_{Loss}}{H} = 1 - \frac{H_{Loss-Intake} + H_{Loss-Guidevane} + H_{Loss-Runner} + H_{Loss-Drafttube}}{H} \qquad (2)$$

$$H_{Loss-Runner} = \frac{p_{Total-Runner-Inlet} - p_{Total-Runner-Outlet}}{\rho \cdot g} - \frac{M_{Runner} \cdot \omega}{\rho \cdot g \cdot Q} \qquad (3)$$

In order to analyse each component separately, a head loss analysis (see Eq. 2) was performed to calculate a cumulative distribution of the total unit. In this case, the total pressure difference between inlet and outlet of each component was set in comparison to the net head. For the runner, the shaft power was also taken into account and subtracted from the losses (Eq. 3). For the determination of the cavitation performance a histogram analysis (for a description of the method see Ref. [4-5]) was performed to evaluate minimum blade pressure. This minimum blade pressure was recalculated to a σ-value (Eq. 4), and then this σ-value was compared to a $\sigma_{plant,allowed-value}$, whereas the local pressure at the blade was set to vapour pressure and the altitude of the machine axis against the tail water was applied(Eq. 5). If $\sigma_{turbine}$ is lower than $\sigma_{plant,allowed}$, cavitation free operation can be stated.

$$\sigma_{turbine,p\_Histogram} = \frac{\frac{p_{Tot-DT-Out} - p_{Histogram}}{\rho \cdot g}}{H} \qquad (4)$$

$$\sigma_{plant,allowed} = \frac{\frac{p_{Tot-DT-Out} - p_{Vapour}}{\rho \cdot g} - \left(H_{TWL} - H_{MachineAxis} \right)}{H} \qquad (5)$$

The net head of the turbine is the difference between the headwater level (HWL) and the tail water level (TWL) minus the losses in the penstock from the water intake to the inflow of the spiral. These losses are system losses and depend on the actual flow rate. The remaining net heads are displayed as measurement points in Figure 5.

1.6. Mesh study

A mesh study was carried out. The main differences occur at the spiral guide vane domains, whereas the runner is almost constant. In Figure 4 the difference of the runner efficiency was analysed for different mesh sizes (see Table 1). Based on this figure it could be stated that the medium grid is sufficient to catch the runner losses in an accurate way.

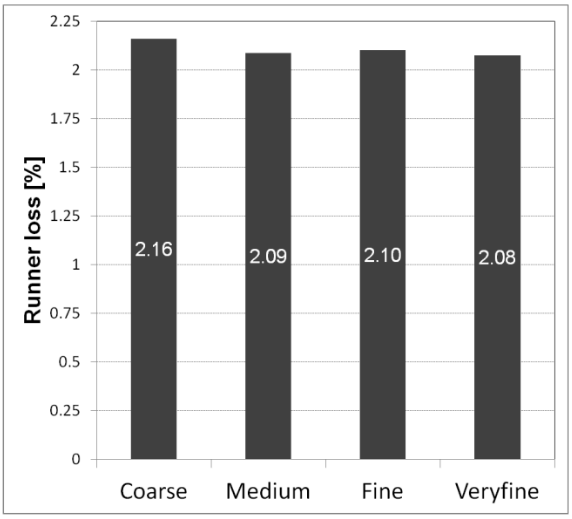

Figure 4. Runner loss during mesh study

2. RESULTS OF THE EXISTING GEOMETRY

The calculations were carried out for different heads. Then, a hill chart was generated which is depicted in Figure 5. The optimum of the machine is reached at a flow rate of 37 m³/s and a head of 124 m. The efficiency is normalised with the best efficiency point.

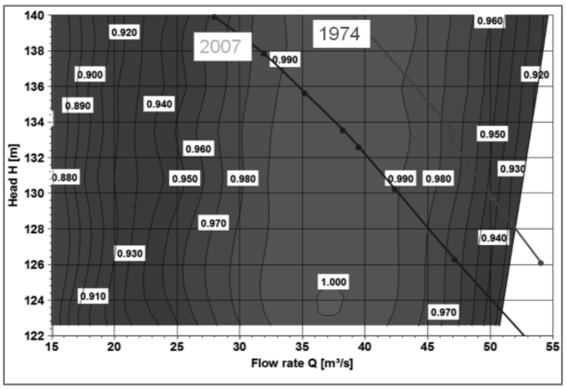

Figure 5. Numerical hill chart of the existing geometry

As far as losses of the measurements are concerned, 3.2% refer to the spiral, stay vane and guide vane. This amount corresponds to the results of the numerical simulation. Guide vane and spiral losses (including stay vanes) are about 3.1%. The losses of the runner are 2.1%. The pressure plot in Figure 6 (a) shows an extremely low pressure zone at the suction side of the blade close to the runner shroud. The stagnation point of the flow at the runner shroud is at the pressure side and the flow circulates around the leading edge from pressure to suction side with high velocities. The stagnation point moves from the pressure side closer to the leading edge for overload operation, but nevertheless this effect becomes stronger.

During the site visit cracks could be found at the leading edge of the runner. These cracks could not only be found on one runner blade but on every single runner blade. Figure 6 (c) shows a photo of the cracks of the runner blades at the leading edge near shroud region. The highest velocities realised in the numerical simulation were found exactly at these locations. The cracks have a length of about 20 to 30 mm and are approx. 5 to 10 mm deep. Figure 6 (b) shows a picture of the inspection report of 1984 where the cavitation damages could also be found at the suction side.

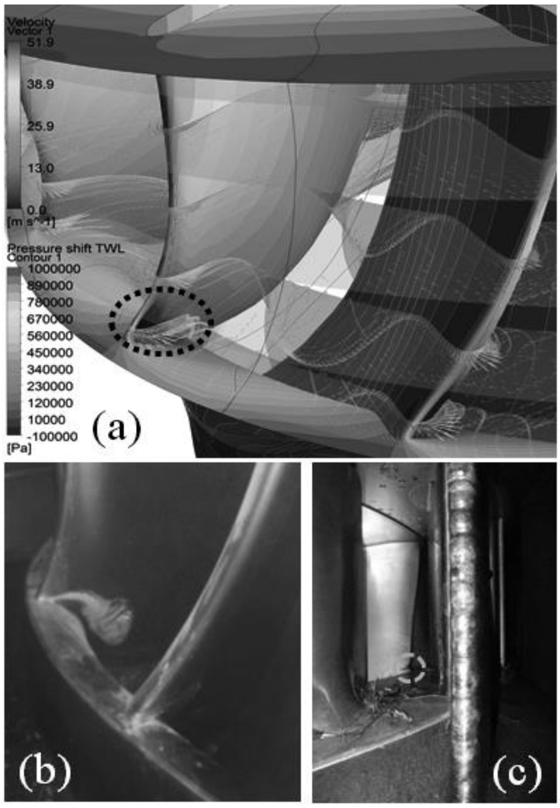

Figure 6. Cavitation damages and cracks on the leading edge

The overall performance is displayed in Figure 7 for the accumulated efficiency and for the cavitation performance. The losses for each component are between the accumulated efficiency curves, which are drawn versus the flow rate. Also, the efficiency curve for the measurement in 2007 is depicted. All of the values are normalized with the best efficiency point of original geometry CFD calculation. Regarding the spiral and the stay vanes, a decrease of the efficiency when increasing the flow rate could be detected. The runner itself has its best efficiency point between 25 and 30 m³/s flow rate with a decreasing efficiency at higher flow rates. For the guide vane the best efficiency point is at full load (maximum power) and the optimum of the draft tube is at a flow rate of about Q = 35 m³/s. The best efficiency is at a flow rate of about 35 to

40 m³/s. At maximum flow rate the power is also increasing. During the measurement campaign the highest flow rate was Q = 52 m³/s.

The cavitation performance is also presented in Figure 7, where the risk for cavitation is visible for flow rates higher than Q = 35 m³/s. There the cavitation coefficient $\sigma_{Turbine}$ is higher than the $\sigma_{plant-value}$. The flow situation through the runner (as a result of the hydraulic contour) leads to a low pressure zone at the leading edge of the runner (at the suction side) and also to low pressure zones at the trailing edge and could be seen in Figure 6(a). This can also be seen in Figure 8 where the blade loading is shown for different span-wise locations. Especially at the shroud region (span=0.95) there is a large zone with low pressure just behind the leading edge. For higher streamwise locations the pressure increases again which means that there is a pump effect. For locations after 60% streamwise the pressure is decreasing again. For a span of 50% and less the hydraulic shape works correctly from a high pressure at the leading edge to a low pressure at the trailing edge. Cavitation could be also detect at the tailing edge pressure side.

3. OPTIMISATION

3.1. Runner

Based on the economic analysis, there is the need for an improvement of the turbine efficiency over the whole range of operation. On the other hand, an improved cavitation performance has to be achieved in order to enable secure operation up to a flow rate of Q = 52 m³/s. To achieve both of these targets, the idea of the so called X-Blade-Design has to be introduced, which was originally developed and patented (US 4479757) by GE Hydro in the beginning of 1982. Later on in 1998, during the development of the Three Gorges Project in China, the technology has been improved to what is now called X-Blade-Technology [6].

Conventional Francis runner designs, like in this case, are susceptible to cavitation damage on the suction side of the blade, particularly at the leading edge. Such cavitation has been known to cause severe damage to the blade, requiring field repair and in some cases blade modifications which are costly and often difficult to perform [6].

In contrast to the conventional Francis runner design the X-Blade-Design comprises a reversed leading edge and a skewed trailing edge. The application of this design philosophy allows for a well-balanced flow field in the passage ways of the runner. Consequently, it results in a more homogeneous pressure distribution on the blade.

Due to the experience gained during the last decade of operation, the improved runner design provides superior peak efficiency, better cavitation performance and a wider range of stable operation [7]. This is shown with the blade loading evaluation in Figure 8. The results of the original and the optimised version refer to the best efficiency point with a guide vane opening of 17.5 degrees.

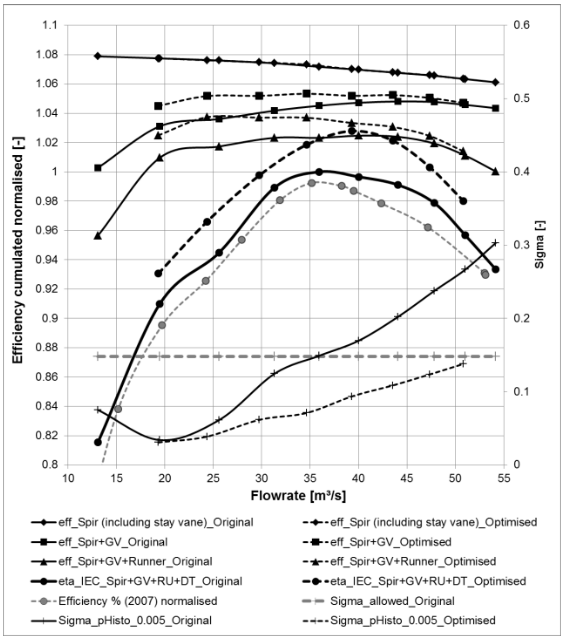

Figure 7. Efficiency splitting and sigma for optimised and original hydraulics, normalised

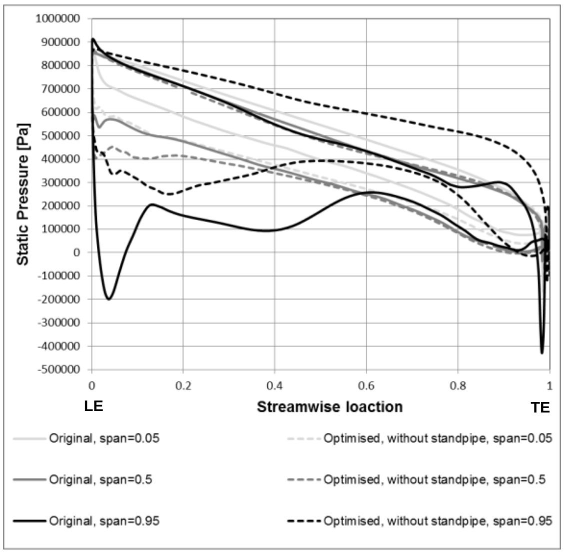

Figure 8. Blade loading for original and optimised version at BEP

A more detailed look into the results of the original runner shows, that the bad flow conditions close to the shroud contour additionally cause zones of separated flow.

The spanwise c_m- and c_u- distribution of the original has to be analysed as well. According to theory, the velocity component c_u should be zero at the outlet of the runner for the best efficiency point of the turbine. Additionally, the c_m-distribution at the outlet of the runner should be as homogeneous as possible. Figure 9 gives an overview of the c_m- and c_u- distribution at the best efficiency point of the original runner obtained in the course of the CFD simulations. As far as it concerns the distribution of the meridional velocity component it turns out that the range between the minimum and maximum c_m-values accounts for 3.5 m/s. The maximum deviation from the average c_m-value which is equal to 9.75 m/s accounts for +/- max. 18%. On the other hand, an analysis of the c_u-distribution shows that the requirement of $c_u = 0$ is fulfilled between 0% and 75% while there is an excessive amount of swirl remaining in the flow between 75% and 100% span. In the latter region there is a lack of energy conversion which definitely needs to be improved.

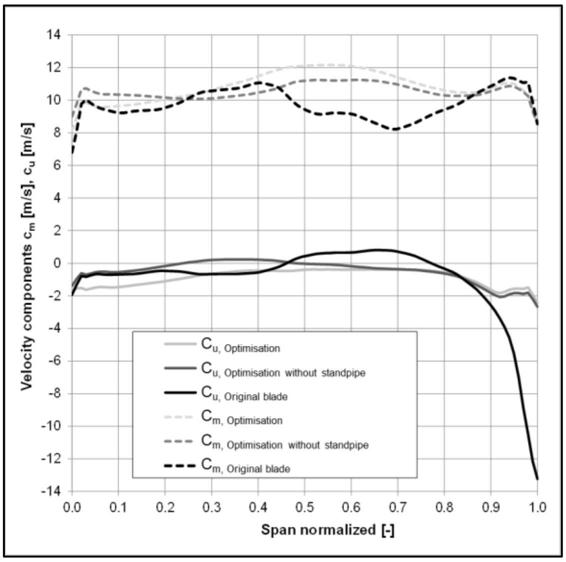

Figure 9. c_m and c_u at runner TE for original and optimised version at BEP

Figure 9 presents also the improvements of the span wise distribution of the c_m- and c_u-velocity components for the optimised runner. Additionally, it turns out that the removal of the standpipe located in the original unit results in more balanced velocity distributions. Due to the removal of the standpipe, the mass flow rate and thus the velocity component c_m is increased while it is decreased in the mid of the runner. Consequently, the increase of the c_m-component close to the hub contour causes a reduction of swirl at the outlet of the runner.

Figure 8 presents the blade loading of the original blade and the optimised version evaluated for a span of 0.05, 0.5 and 0.95 at the best efficiency point. The comparison shows that the use of the X-Blade-Design and the implementation of all the other optimisation measures led exactly to the changes found in [6-7].

The turbine efficiency hill chart of the final optimization version is shown in Figure 10. Compared to the original turbine the best efficiency point in the hill chart (marked with yellow in Figure 10) was shifted from Q = 37 m³/s and H = 124 m to Q = 39.5 m³/s and H = 132m (marked with pink in Figure 10) which ideally fits to the operation range of the turbine (see measurement carried out in the year 2007). The peak efficiency was increased from by 1.7 % relatively.

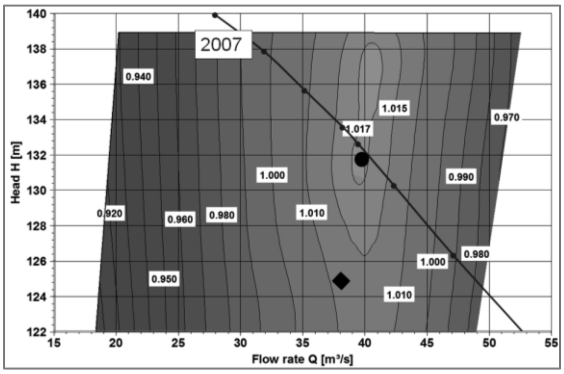

Figure 10. Hill chart of the optimised version, normalised with the efficiency in BEP of the original runner

3.2. Guide vane

The results of the existing guide vane (see Figure 11a) is the basis for the new design of the guide vane. The stagnation point of the existing guide vane for all positions, except the maximum opened position, is not exactly on the leading edge For the new designs it was proposed that the outflow angle remains unchanged. The first design is a symmetrical profile based on a NACA0018 profile and the second is a bended NACA0014 profile. Both profiles are displayed in Figure 11d together with the original profile.

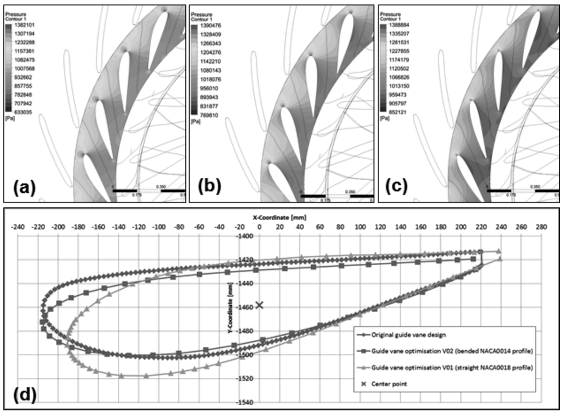

Figure 11. Pressure at mid plane and different guide vane profiles

The flow field with the modified guide vane designs changes at the leading edge. The symmetrical profile (V01) ends with a stagnation point directly on the leading edge of the guide vane.

The stagnation point for V02 is still on the suction side, but significantly better than the original one. V02 shows an improvement of 0.5% over the whole operation range whereas version 1 reaches 1% in the range less than 35m³/s (Figure 7). The maximum flow rate is just above 50m³/s, and thus the annual production will significantly increase with V01. The guide vane adjustment torque is lower than the original version and is always negative.

4. ECONOMIC ASPECT

The stop of the power plant is very expensive because of very high production losses that cannot be compensated as there is no storage capacity available and no parallel installed unit can operate.

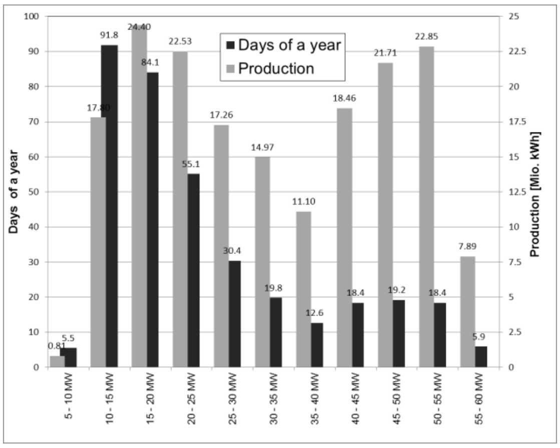

Figure 12. Annual production, averaged (2004-2013)

Additionally to the costs of the runner and the guide vanes the missing energy production has to be taken into account, for which an averaged value is about 0.49 GWh/day (179 million KWh per year, which is the average yearly production of the years 2004-2013, divided by 365 days) and even lower when the assembling / disassembling is shift to a period of low energy production. The price for electricity on the spot market for 2014 was found with an average value of 167 TL and recalculated with an average exchange rate of 2.9 TL/€ to 5.75€-Cent/kWh. With this feed-in tariff consequently 0.49 GWh/day correspond to approx. 27.500 €/day.

To calculate the annual production for both, the existing and the proposed design, a best-fit curve for the efficiency versus the power is generated as a polynomial function and an extrapolation to low as well as to high flow rates was realised with Excel. Then, for every 1 MW the efficiency is calculated and an averaged efficiency is generated for the same power intervals as in Figure 12. With the help of this efficiency the ratio of the improvement for each interval is calculated and accounts to 5.1 GWh /year higher production (287.000 €/year).

5. SUMMARY

The improvements of the runner performance were basically reached by the introduction of a X-Blade design and a smoothed and modified beta-angle distribution. An increase of the beta-angle at the blade inlet close to shroud led to better inflow conditions. A reduction of the beta-angle at the blade outlet close to shroud led to an improved energy conversion of the blade. The symmetrical profile of the guide vanes ends with a stagnation point directly on the leading edge of the guide vane. The improvement reaches 1% within the flow rate range of less than 35m³/s and is still above the level of the existing one up to a flow rate of 50m³/s.

Compared to the original turbine, the best efficiency point in the hill chart was shifted from Q = 37 m³/s and H = 124 m to Q = 39.5 m³/s and H = 132m which ideally fits to the operation range of the turbine. The peak efficiency was increased from by 1.7 % relatively and cavitation-free operation up to a maximum flow rate of more than 50m³/s.

REFERENCES

[1] Menter, F.R., "Two-equation eddy-viscosity turbulence models for engineering applications", AIAA-Journal, 32 (8), 1994.

[2] Ansys CFX, "Program documentation and help", Release 14.5.

[3] IEC 60193: 1999-11, Second Edition, "Hydraulic turbines, storage pumps and pump-turbines – Model acceptance tests".

[4] Benigni, H., Jaberg, H., Schiffer, J.,"Numerical simulation of a Francis runner and comparison with test rig results", Paper 9.09, Proceedings Hydro 2008 – Progressing world hydro development, Ljubljana, October 06-08, 2008.

[5] Gehrer, A., Benigni, H., Köstenberger, M., "Unsteady Simulation of the Flow Through a Horizontal-Shaft Bulb Turbine", Proceedings of the 22nd IAHR Symposium on Hydraulic Maschines and Systems, Stockholm, 2004.

[6] Billdal J. T., "The X-factor", International Water Power And Dam Construction. August 2006.

[7] Demers, A., "Francis Turbine "X-Blade" Technology",. Hydro News, Magazine of Andritz Hydro. No. 15 / 5-2009.

Conference on Modelling Fluid Flow (CMFF'15)
The 16th International Conference on Fluid Flow Technologies
Budapest, Hungary, September 1-4, 2015

THE ANALYSIS OF THE POSSIBILITIES OF USING THE FINITE ELEMENT METHOD TO DETERMINE THE IMPACT OF THE WINGLET APPLICATION ON AERODYNAMIC CHARACTERISTICS OF THE GLIDER WING

Robert SZCZEPANIAK[1], Krzysztof LAMCH[2], Ireneusz SMYKLA[2]

[1] Corresponding Author. Department of Airframe and Engine, Dęblin Air Force Academy. Dywizjonu 303 35, 08-521 Dęblin, Poland. Tel.: +48 855 17 427, E-mail: Robert.szczepaniak@o2.pl
[2] Department of Airframe and Engine, Dęblin Air Force Academy. Dywizjonu 303 35, 08-521 Dęblin, Poland. Tel.: +48 533 505 584, E-mail: krzysztof_lamch@wp.pl
[2] Department of Airframe and Engine, Dęblin Air Force Academy. Dywizjonu 303 35, 08-521 Dęblin, Poland. Tel.: +48 85 517 423, E-mail: smy@op.pl

ABSTRACT

The main purpose of this study was to analyze the possibility of using the finite element method to determine the impact of winglets on the aerodynamic characteristics of the MDM-1 Fox glider wing. The aerodynamic characteristics are a reflection of changing conditions of the flow around the profile (wings) with the changing angle of attack. The 3D design of MDM-1 FOX glider wing, based on the geometry of the wing obtained from the main designer of Margański & Mysłowski Aviation Works, was created in SolidWorks. NACA 641 412 wing profile was used. As for the winglet construction the HQ/Winglet profile was used (due to the fact that the original version of the glider does not have that element). The analysis of the profile pressure distribution was performed in three places. Air was used as a flow factor for numerical computations. The initial conditions of the air were as follows: pressure = 101325 Pa; temperature = 293.2 K; turbulence intensity = 0.1%; flow rate = 30 m/s.

Keywords: glider, induced drag, winglet, wingtip vortices.

NOMENCLATURE (TITLE: HEADING 1)

c	[-]	force coefficient
F	[N]	force
v	[m/s]	absolute velocity vector

Subscripts and Superscripts

z, x	lift, drag

1. INTRODUCTION

In order to increase the lift-to-drag ratio of gliders, as well as airplanes, various studies attempted to create an element which would improve, in economic terms, the flight efficiency of airplanes and the lift-to-drag ratio of gliders. The element, which improved the aerodynamic characteristics of aircraft was undoubtedly a winglet. Research on the optimal winglet was started in the mid-70s by Richard Whitcomb. The first achievements on winglets evoked wide interest among designers which joined the research aiming to find the most effective design for the wing extension. Currently, winglets are being attached to many models of airplanes and gliders. Due to the high costs of the wind-tunnel experiments, it is suggested that simulation studies may be sufficient to verify an acceptable number of designs. However, with the increase of computing capacities of modern computers the numerical analysis of the created geometric model is facilitated, while the computing convergence is the still to be discussed. This work aims at analysis of the possibilities of using the finite element method (simulation studies) to study winglet aerodynamics.

2. REAL MODEL STUDY

MDM-1 FOX (Fig.1) is a two-seat mid-wing high-performance aerobatic glider with a conventional tail unit. The glider's laminate construction is made of glass-fiber epoxy composite and epoxy-carbon fibers composite. [3]

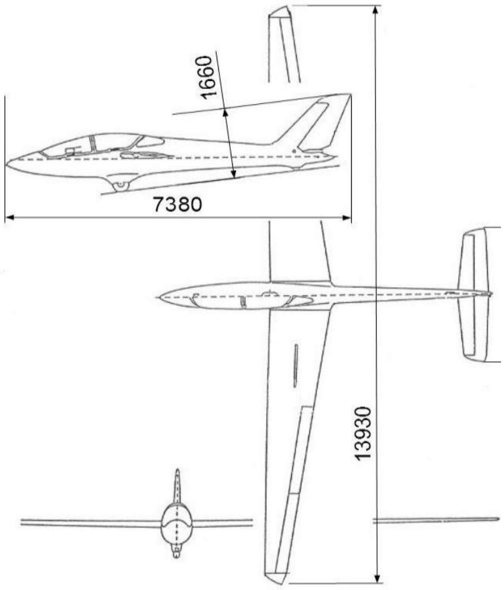

Figure 1. Geometry of a real model [4]

As a result of the growing demand for a two-seat aerobatic glider, in 1992 the design works on MDM-1 FOX aircraft were initiated by Edward Margański, Leszek Dunowski and Jerzy Makula (the name ”MDM” was derived from the last names of the designers). The design of this glider was based on the experiences gathered while developing other gliders, like Kobuz, Jantar and S-1 Swift. The first prototype was tested on the 9th of July 1993 and officially presented during the World Championship in Venlo, in Holland. Jerzy Makula piloted at that time the MDM-1 FOX glider to gold. In the following years FOX proved to be repeatedly successful in international sports events.

A new version, MDM-1 FOX P, which was developed in 1996, was equipped with replacement wingtips increasing the wing span up to 16 meters. In 2001, Solo Fox, a single-seat glider with retractable landing gear, was created. Testing of later versions was performed by Jacek Marszałek and Mariusz Stajewski.

2.1. General characteristics of winglets

The research on winglets for commercial aviation, started by Richard Whitcomb, was based on small and nearly vertical wingtip extensions, KC-135A, which were attached to the aircraft and tested. Whitcomb discovered that winglets can improve the lift-to-drag ratio by up to 7%. Thanks to this discovery winglets started being attached to the most of the new transport aircraft. Many researchers undertook studies on winglet design for commercial and general aviation, as well as for gliders.

Winglet improves the lift-to-drag ratio through reduction of the induced drag caused by wingtip vortices, connected with the side airflow along the edges of wingtips in the direction from lower surface to the upper surface. It is a vertical or diagonal wingtip extension. Winglet improves the lift-to-drag ratio by weakening wingtip vortices and thus diminishes the induced drag (Fig.2). Winglet increases the effective wing area extension without a significant increase in structural load or total weight of the structure.

The choice of a winglet type depends on the necessity and the model of an airplane or a glider. The wingtips can be called a ”dead zone” in relation to the lift-to-drag ratio, as they cause substantial drag force and no significant increase in lift force. Winglet contributes to the acceleration of the airflow on the wingtip by inducing lift force and improving wing load distribution. Furthermore, the angle of attack of this aircraft is diminished in relation to the lift ratio. Consequently, thanks to the application of winglets, the drag force is reduced even with a significant wing area extension.

It is possible to avoid difficulties related to the design of blended winglets by using a special winglet type, raked wingtips, just as it was in the case of the airplane Boeing 767-400. Thanks to the application of winglets, airplanes gain altitude faster and save fuel because of an improved lift profile. Additionally, an airplane can take off using reduced engine power what decreases noise emission and extends the life of an engine.

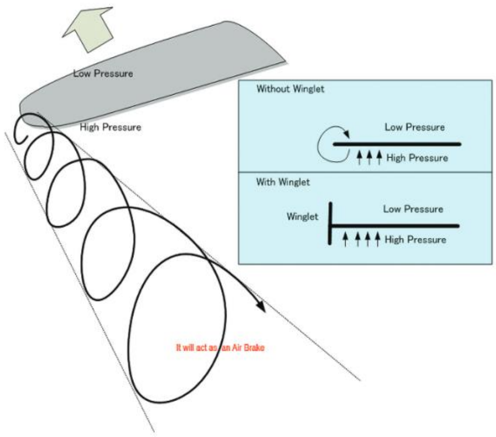

Figure 2. Reduction of wingtip vortex [5]

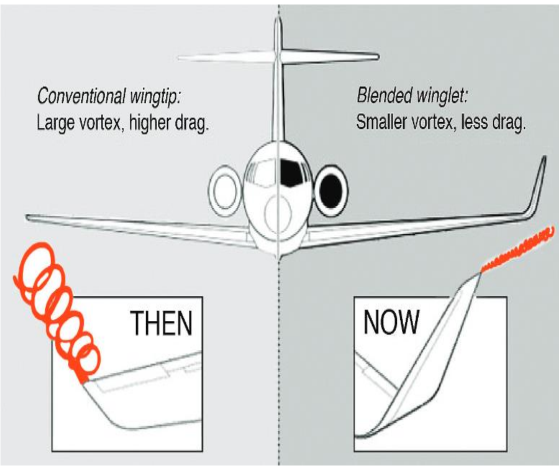

Figure 3. Impact of winglets on modification of the induced drag [6]

2.2. Winglet types

All types of wingtips that are not attached horizontally are classified as winglets. There are three basic types of winglets:

- blended winglets (Fig.4),
- wingtip fences (Fig.5),
- raked wingtips (Fig.6).

2.2.1. Blended winglets

Blended winglet is joined with the wingtip by creating a soft curve instead of an acute angle, what aims at reduction of the drag induced at the wing/winglet junction. An acute angle in this region could interfere with the airflow boundary layer and create turbulence, and thus negate the profits related to the application of a winglet on the wingtip. Blended winglet is used in business jets and gliders, where individual preferences of a purchaser are an important part of the marketing strategy.

Figure 4. Blended winglet [7]

2.2.2. Wingtip fences

They are special winglets that extend the wingtip upwards and downwards. This type is preferred by the European producer of the Airbus aircraft and thus is used in the most of the Airbus models.

Figure 5. Wingtip fences of Airbus A380 [8]

2.2.3. Raked wingtips

It is the newest winglet type (although often classified as a special wing type), where the wingtip is inclined at a larger angle than the rest of the wing. Although they are commonly referred to as winglets, it is recommended to describe them as the integrated wingtip extensions, because they are attached horizontally to the wing, and not vertically as in the case of blended winglets and wingtip fences.

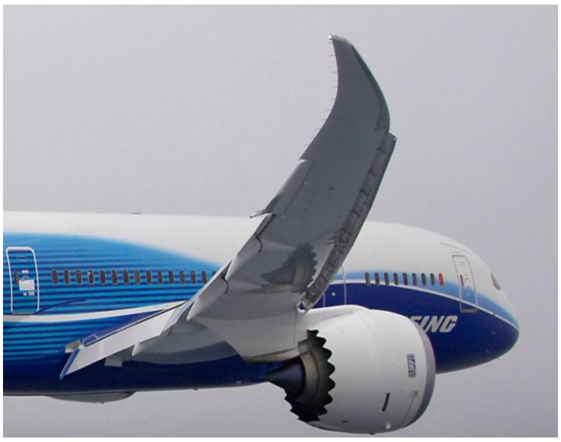

Figure 6. Raked wingtips of Boeing 787 [9]

3. WING MODEL WITH AND WITHOUT A WINGLET

A 3D project of a wing of the MDM-1 FOX glider was created, using SolidWorks software, based on the wing geometry (Fig.7) received from the main designer of the aircraft factory *Margański & Mysłowski S.A.*.

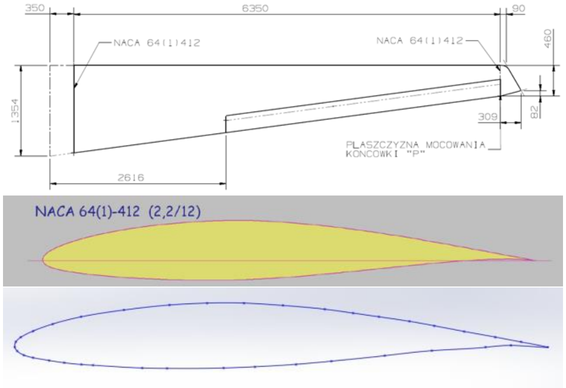

Figure 7. Geometry of the wing and the wing airfoils – real NACA 64(1)-412 [10] and a simulated airfoil

There had not been any winglet created for the MDM-1 FOX glider. Therefore a winglet was designed for this glider, based on available literature, collected observations and conducted experiments, as well as using the airfoil HQ/Winglet (Fig. 8).

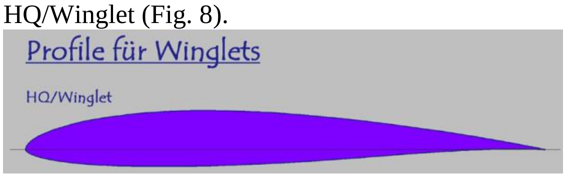

Figure 8. Winglet airfoil HQ/Winglet [11]

The winglet dimensions were chosen in accordance with the classic principles of winglet design:

- leading edge of a winglet should be located around the maximum thickness of the wingtip airfoil,
- maximum thickness of the winglet airfoil should not exceed 8% of the maximum thickness of the wingtip airfoil,
- bend deflection of a winglet should be slightly bigger than the bend deflection of a wingtip,
- ratio between upper and lower chord line should be around 0.3, while the winglet height should be from 0.1 to 0.2 of the half wing span. [7]

4. NUMERICAL ANALYSIS OF THE TESTED WING

Numerical analysis of airflow was performed in following conditions:

- pressure: 101325 Pa
- temperature: 293.2 K
- turbulence intensity: 0.1%.

The wing models were tested for the angle of attack equal to 0°. The analysis of airflow around wings was performed for the speed of 30 m/s. The pressure distribution around the airfoil of wings was defined (Fig. 9):

- AIRFOIL 1: 1 m from the center of symmetry of the wing (Fig.10);
- AIRFOIL 2: 4 m from the center of symmetry of the wing (Fig.11);
- AIRFOIL 3:6.7 m from the center of symmetry of the wing (Fig.12).

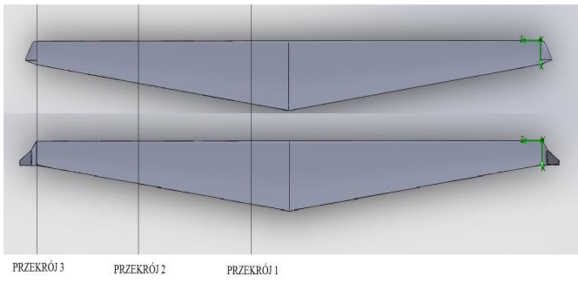

Figure 9. Airfoil around which the numerical analysis was performed

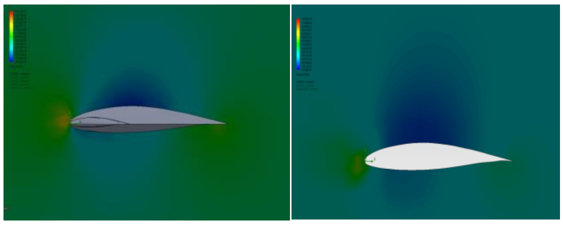

Figure 10. Pressure distribution around airfoil 1 without winglet on the left and on the right

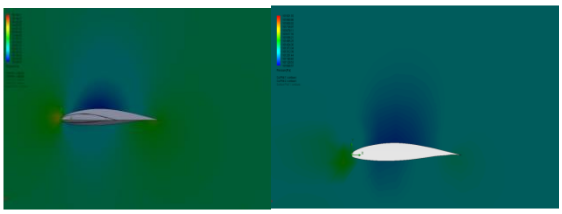

Figure 11. Pressure distribution around airfoil 2 without winglet on the left and on the right

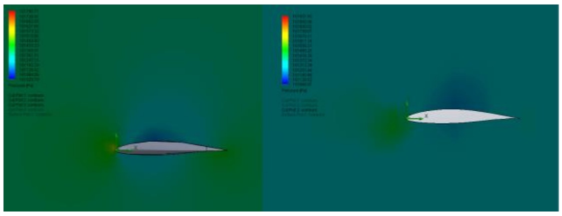

Figure 12. Pressure distribution around airfoil 3 without winglet on the left and on the right

Thanks to the SolidWorks Flow Simulation it was also possible to define the pressure distribution on the wing surface. The analysis of the pressure distribution allows to define the aerodynamic forces on the wings, and consequently, the resultant of these forces, as well as the components of the resultant aerodynamic force: the drag and the lift.

The analysis of pressure on the wingtips indicates a significant pressure difference between the lower and the upper wing surface. This difference causes an additional side airflow from the area of higher pressure (under the wing) to the area of lower pressure (above the wing). This results in creation of wake turbulence, which is the source of the induced drag. Winglet reduces the turbulences occurring on the final chords of a wing, what is depicted in the graphics below.

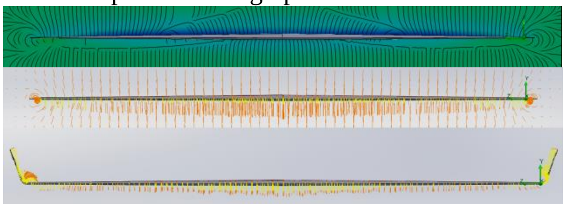

Figure 13. Side airflow of air masses and the velocity distribution of the air streams flowing around the wing without and with a winglet

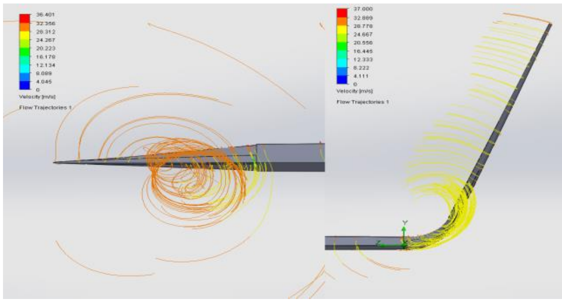

Figure 14. Airflow around the final chords of a wing with and without a winglet, together with generated turbulence

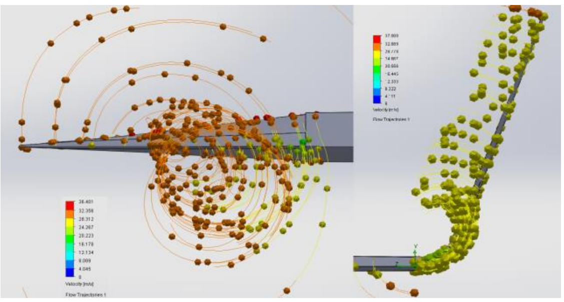

Figure 15. Airflow around the final chords of a wing (distribution of velocity vector field) with and without a winglet

The application of winglets enhances significantly the wing aerodynamics. This occurs through considerably improved coefficients of lift force, presented among others by Abłamowicz [1], and described by the first equation (1), as well as through diminished drag coefficient as shown in the other equation below (2):

$$c_x = \frac{F_x}{S\,(\rho/2)v^2} \tag{1}$$

$$c_z = \frac{F_z}{S\,(\rho/2)v^2} \tag{2}$$

The results of the study are depicted in the graphs below. They demonstrate the impact of the application of winglets on the aerodynamic characteristics for the angles of attack in the range between -10° and 14°. The analysis of the simulation results confirms explicitly that it is possible to use the finite element method to determine the impact of the winglet application on aerodynamic characteristics of the glider MDM-1 Fox.

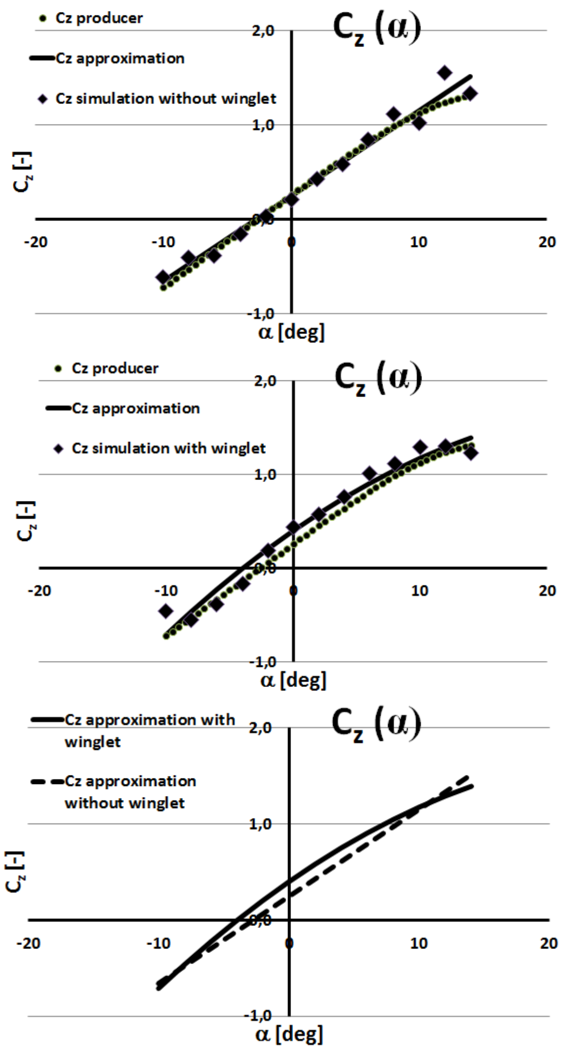

Figure 16. Lift coefficient diagram based on calculation and simulation

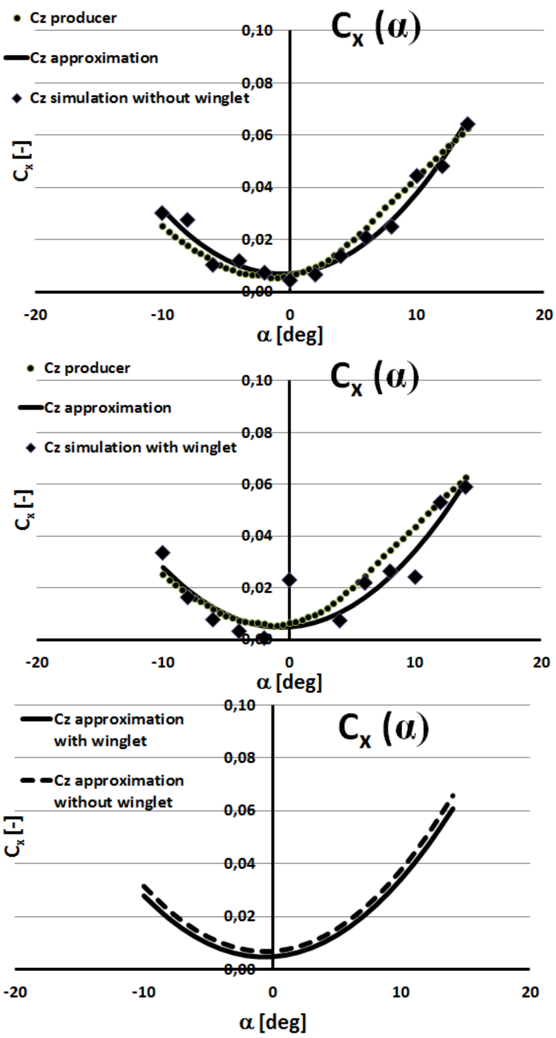

Figure 17. Drag coefficient diagram based on calculation and simulation

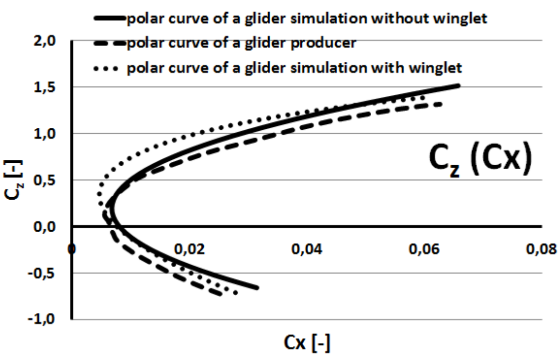

Figure 18. Polar curve of the glider based on the analytic calculations (by the producer) in comparison with the numerical analysis

The graph depicts the lift coefficient (C_Z) in relation to the angle of attack (α) for the wing of the glider Kobuz, which was the inspiration for the design of the glider FOX, in comparison to the values obtained in the numerical simulation of the modelled wing. The characteristic $C_{Lobl}(\alpha)$ presented below was calculated using the lifting-line theory (received from the producer). Illustrated was also the characteristic C_X in relation to the angle of attack of the wing with and without a winglet, in comparison with the calculated values obtained from the analytic calculations. Finally, the polar curve of the analyzed glider was presented.

Based on the numerically defined characteristics of aerodynamic coefficients, their approximation was performed using a polynomial of degree 2, represented by the following expression:

$$c = c_0 + c_1\alpha + c_2\alpha^2 \qquad (3)$$

The physical quantities obtained from the characteristics' approximation are presented in the table 1.

Table 1. The components of the polynomial used for approximation of aerodynamic coefficients, as in the equation (3)

	c_0	c_1	c_2
Cz with winglet	0.4008	0.0943	$-0.0017*10^{-6}$
Cz without winglet	0.2478	0.0905	$6.07*10^{-6}$
Cx with winglet	0.00482	0.00032	0.00026
Cx without winglet	0.0069	0.00032	0.00028

5. SUMMARY

During the analysis of the external airflow around the wing without and with a winglet, the pressure distribution was defined on the wing surface, what confirms that it is possible to specify the aerodynamic characteristics of a wing using the finite element method. The results of simulation studies were compared with the experimental results of a wing of the existing glider, based on the results obtained from the diagrams of aerodynamic characteristics of the given model. These results illustrate the increase of the lift force coefficient and the decrease of the drag force coefficient after the introduction of winglets, which explicitly improve the aerodynamic characteristics of the wing model, and consequently of the glider itself. The diagrams of coefficients, obtained as a result of numerical simulation and the approximation of the results, demonstrate the improved drag coefficient values in the whole range of the angle of attack chosen for this simulation, that is from -10 to +14 degrees, whereas the diagram of the lift coefficient illustrates its increase, apart from the maximum deviation of the angles of attack from the scope of operation of the glider.

Furthermore, the appearance of wake turbulence (in the case of the wing model without a winglet), which is the source of the induced drag, was illustrated, as well as turbulence reduction through the application of a winglet in the given model.

The complex wing model, designed in SolidWorks, will be used, in the form of a 3D printout in the proper scale, as an experimental model for empirical research in a water tunnel. At the same time, a series of numerical simulations in another software will be performed to confirm the results of the study.

REFERENCES

[1] Abłamowicz, A., Nowakowski, W., 1980, „Podstawy aerodynamiki i mechaniki lotu", *Wydawnictwo Komunikacji i Łączności; Warszawa, Poland*.

[2] „Wstępne stadium wpływu wingletów i hamulców aerodynamicznych na zmiany charakterystyk aerodynamicznych modelu samolotu klubowego AS-2" *Praca Instytutu Lotnictwa;* Nr.215/2011; s.29-49.

[3] Margański, E., 1996, „Instrukcja użytkowania w locie szybowca MDM-1 FOX", Wydanie III, *Zakład Remontów i Produkcji Sprzętu Lotniczego*, Bielsko Biała.

[4] http://www.marganski.com.pl/index.php?str=10&idm=14&banner=tak

[5] http://www.aeronautics.nasa.gov/ebooks/downloads/nasa_innovation_in_aeronautics.pdf#page=21

[6] http://www.aeronautics.nasa.gov/ebooks/downloads/nasa_innovation_in_aeronautics.pdf#page=21

[7] http://www.weststaraviation.com/news/west-star-aviation-installs-first-api-blended-winglets-on-falcon-50ex/

[8] http://de.wikipedia.org/wiki/Winglet

[9] http://www.wired.com/2009/12/boeing-787-dreamliner/

[10] http://www.hq-modellflug.de/hqacro-profile.htm

[11] http://www.hq-modellflug.de/hq-winglet-profile.htm

Conference on Modelling Fluid Flow (CMFF'15)
The 16th International Conference on Fluid Flow Technologies
Budapest, Hungary, September 1-4, 2015

NATURAL VENTILATION OF A RESIDENTIAL BUILDING STOREY: AN EXPERIMENTAL AND NUMERICAL STUDY

Walter MEILE[1], Bernd LANGENSTEINER[2], Günter BRENN[2]

[1] Corresponding Author. Institute of Fluid Mechanics and Heat Transfer, Graz University of Technology. Inffeldgasse 25/F, A-8010 Graz, Austria. Tel.: +43 316 873 7343, Fax: +43 316 873 7356, E-mail: meile@fluidmech.tu-graz.ac.at
[2] Institute of Fluid Mechanics and Heat Transfer, Graz University of Technology. E-mail: brenn@fluidmech.tu-graz.ac.at

ABSTRACT

Since many decades, residential buildings have been equipped with mechanical ventilation/air conditioning systems. Due to the energy consumption and the exhaust of green-house gases of such systems, efficient natural ventilation systems are needed as an alternative.

The potential of natural ventilation systems was investigated in the present work by model experiments in wind tunnels and numerical air flow simulations (CFD). Pressure profiles are measured on the facade of a full building model for selected wind directions and velocities. Separated sample storey and single room models in larger scales were applied to measure the air transport through openings under the influence of the external pressure distribution and a temperature difference between the room and the ambient air. The air change rates (*ACH*) were obtained by velocity measurements in the window cross sections and by tracer gas measurements.

The experiments revealed that the wind-driven *ACH* are much larger than the temperature-driven values prescribed in the Austrian standard Ö-NORM B 8110-3. The dependency of the *ACH* on wind direction and speed is modelled. A scaling law for the *ACH* was found. In case of purely thermal effects, a critical temperature difference for the onset of convection was found.

Keywords: Air change rate, natural ventilation, pressure driven flow, thermal effects, wind tunnel experiments

NOMENCLATURE

A	$[m^2]$	area
ACH	$[h^{-1}]$	air change rate
C	[-]	tracer gas mass fraction
D	[-]	door
E	[V]	voltage
H	$[m]$	height
I	[A]	current
Je	[-]	Jensen number
Re	[-]	Reynolds number
R	[-]	room
T	[°]	temperature
U	$[m/s]$	characteristic velocity
V	$[m^3]$	volume
$\dot{V}$	$[m^3/s]$	volumetric flow rate
W	$[m, -]$	width, window
c_P	[-]	static pressure coefficient
c_D	[-]	drag coefficient
l	$[m]$	length
m	[-]	scaling factor
p	$[Pa]$	pressure
u	$[m/s]$	streamwise velocity
t	[s]	time
x, y, z	$[m]$	spatial coordinates
z_0	$[m]$	roughness length
α	[°, -]	angle, power law exponent
ν	$[m^2/s]$	kinematic viscosity
ρ	$[kg/m^3]$	density
Δ	[-]	difference

Subscripts and Superscripts

H	building height
R	roughness, room
crit	critical
eff	effective
el	electrical
g	gradient
i, o	inner, outer
m	model scale
r	real scale
10	10 m height (weather data)
τ	friction
∞	free stream

1. INTRODUCTION

In the planning of buildings, the heating and cooling concepts are developed, with ventilation concepts as an integrated part. Besides mechanical and combined systems, natural ventilation relying on wind-induced pressure or on differences in temperature is the most common form. The air is exchanged through doors, open or tilted windows. For layout purposes it is important to estimate the magnitude of the air change rates correctly. Ventilation through tilted windows is sparsely represented in the literature to date.

The *ACH* strongly depends on the wind direction as well as on the position and size of the openings of the building envelope and on thermal buoyancy in case of temperature differences.

The methods for studying natural ventilation are either full scale experiments in real conditions [1,2], wind tunnel experiments in full or model scale [3,4], and computational fluid dynamics (CFD) simulations. CFD results are compared with analytical results or data from wind tunnel measurements, e.g. in [1,3,5].

In [1] and [2] both wind-driven and thermally induced air exchange were investigated. In these studies, a consistent trend to predict the interaction of the two mechanisms was not found. Three cases under mixed conditions applying local weather data were investigated in [6]. For a single-sided situation they found combined wind and thermally driven natural ventilation to produce *ACH* between 1 and 5 h^{-1}. The impact of the inner topology of buildings on the *ACH* was studied numerically and compared with measurements in [5]. Both simulation and experiment show that the internal geometry does not alter the overall air exchange rate, but is an important factor for the refreshing rate of inner regions. The aforementioned studies incorporated investigations in full scale for single-sided window configurations or for windows on opposite walls. The corresponding literature lacks information on configurations with openings in adjacent walls, and especially on the ventilation through tilted windows.

The thermally driven air exchange with single-sided tilted windows and other special constructions under real meteorological conditions was investigated in [7] at wind velocities below 1.5 m/s. The work [8] accounted for the influence of the window reveal, various rotary and tilting positions, as well as differences in temperature and in wind conditions. A modified model to describe thermally induced ventilation through bottom hung windows for single-sided ventilation was formulated in [9], accounting for embrasures and heating. A combination of interior embrasures and heaters reduce the air exchange potential by approximately 40%. The aforementioned investigations considered only one ventilation opening. A general overview on natural ventilation and appropriate guidelines can be found in the study [10].

The present work investigates natural ventilation concepts for residential buildings with windows (either fully open or tilted) as the usual ventilation openings. The main driving force is the external wind-induced pressure, but thermal effects are also considered. The aim is to quantify flow fields responsible for the air exchange and to identify the magnitude of *ACH* in different rooms of the same storey. This work includes both, single-sided ventilation and cross ventilation for open and tilted windows. The ventilation through tilted windows in adjacent walls is also studied. The main focus is directed to the 3rd and 8th floor exemplarily.

Results without thermal effects are described in more detail in [11,12].

2. BUILDING AND TERRAIN

The building investigated has the dimensions of 14 *m* × 21 *m* and a height of 30 *m*. Within the building, the storeys differ in the height above ground only. The representative storey has a floor plan comprising typical natural ventilation scenarios for rooms with open and tilted windows. Fig. 1 shows the floor plan of the storey, including the notation, and details of the tilted window. Rooms R_1 and R_5 have the same geometry. For special investigations of the situation with tilted windows, a sample single room model with the geometry of room R_5 was developed.

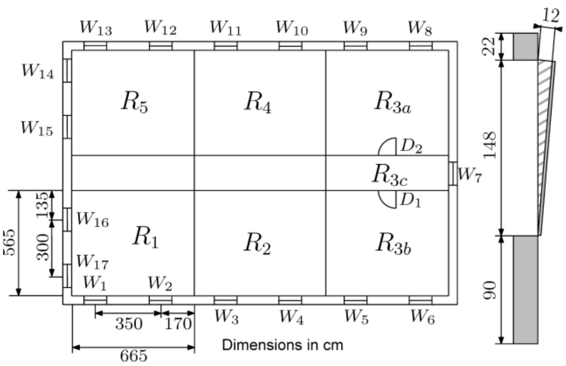

Figure 1. Floor plan of the sample storey, notation, geometry of a tilted window.

In the present study we focus on areas with uniform vegetation and suburban development. Velocities are known at 10 *m* height from weather data: $U(z = 10m) = U_{10}$. The present experiments cover the two wind velocities U_{10} = 2.8 *m/s* and 4.7 *m/s*.

3. EXPERIMENTAL SETUPS AND TECHNIQUES

Three models in different scale were developed and investigated in two different wind tunnels to measure (1) the pressure distribution from the atmospheric boundary layer flow on the full building facade, (2) the *ACH* as derived from air velocities in open window cross sections and in door cross sections in case of tilted windows, (3) the air exchange rate with special account for tilted windows in the single room model, and (4) the influence of thermal buoyancy.

3.1. The models

A model of the complete building was established in 1:75 scale for pressure measurements in a boundary layer wind tunnel. One storey was equipped with pressure holes at appropriate locations on the closed surface and mounted modularly at heights from the 2nd to the 10th floor. Figure 2 is a sketch of this model with the positions of the pressure measurements on the facade.

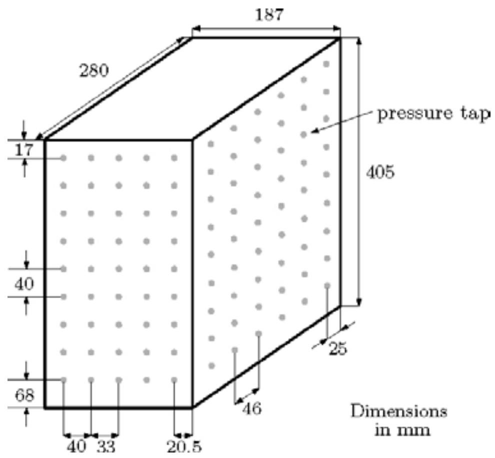

Figure 2. Location of pressure taps.

This small scale does not allow for velocity measurements in tiny openings. These measurements were therefore carried out in a separate sample storey of 1:25 scale (Fig, 3, see also [11]) with the neighbouring storeys below and above as dummies. This configuration was implemented in an aerodynamic wind tunnel where the pressure distribution in different heights above ground was reproduced.

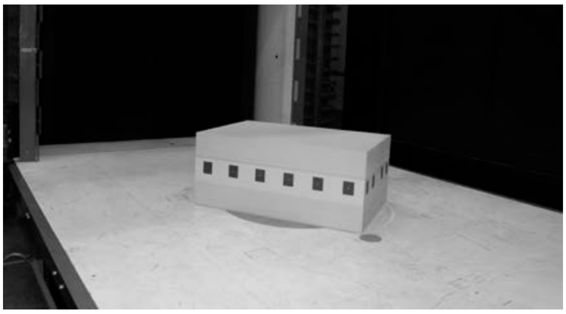

Figure 3. Storey model (1:25) in the test section.

Additionally, for consideration of the situation with tilted windows, a sample single room of again larger scale (1:10) representing the geometry of room R_5 (Fig. 1) was used, likewise with dummy sections.

3.2. Simulation of the atmospheric boundary layer

The boundary layer wind tunnel at Graz University of Technology is Göttingen type with an 8.6 *m* long closed working section. The nozzle exit cross section is 2.0 *m* × 1.0 *m*, and the max. wind speed about 32 *m/s*. A combination of a grid of rods with variable spacing at the nozzle exit, a trip hazard in the form of a saw tooth tread design, and Lego/Duplo blocks as surface roughness elements of various size and spacing on the floor upstream from the test section is used. More details are described in [11, 12].

The velocity profile *U(z)* in the atmospheric wind is described by either the log. law or the more commen power law in the form

$$U(z) = (U_\tau / \kappa) \ln(z/z_0)\,;\; U(z)/U_g = (z/z_g)^\alpha \quad \text{(1a, b)}$$

where z is the height above ground and z_0 is the aerodynamic roughness length. The subscript g refers to the geostrophic values. The velocity profile in the atmospheric boundary layer over suburban terrain is properly described with $z_0 = 0.15$ *m*. In the power law, appropriate parameters are $\alpha = 0.22$ and $z_g = 350$ *m*.

The simulated velocity profile exhibits very good agreement with the log. law between 3 *m* and 40 *m* height in real dimensions, the level of turbulence shows the requested characterstics, and the shear stress is practically constant in the so-called Prandtl layer (cf. [11, 12]). The adaptation of the logarithmic law by regression analysis leads to $z_0 = 0.137/0.126$ *m* (upscaled to real dimensions) for $U_{10} = 4.7/2.8$ *m/s*. An appropriate analysis for the power law yields $\alpha = 0.226$ in both cases which closely matches the desired value.

3.3. Similarity considerations

Reynolds number independence of the pressure distribution at sharp edged bodies is achieved if $Re_H = (u_H \cdot W)/\nu \geq 5 \cdot 10^4$, where u_H denotes the velocity in building height and W the building width perpendicular to the oncoming flow [13].

For the roughness Reynolds number it can be specified that $Re_R = (U_\tau \cdot z_0)/\nu \geq 5$.

Both requirements are fulfilled in the present experiments.

For buildings with a height H much smaller than the thickness of the atmospheric boundary layer the Jensen number $Je = H / z_0$ must be equal in nature ($Je = 200$) and model. In both cases of U_{10} the values of z_0 deduced from the experimental data lead to good agreement.

3.4. Pressure measurements

The pressure distribution on the building surface due to the atmospheric boundary layer flow was measured with low differential pressure sensors of type LBAS100B (SensorTechnics) with a full range of ±100 *Pa*. The 17 pressure sensors were positioned in the centre of the closed rectangular window area of an exchangeable, sensor-equipped storey. The pressure difference on floors 2 to 10 of the building model (scale 1:75) against the ambient pressure of the undisturbed flow was measured for both reference velocities U_{10}. A sketch of the configuration is depicted in Fig. 2 above.

3.5. Velocity measurements

The low-speed aerodynamic wind tunnel at Graz University of Technology (Göttingen type) was used for measuring the air exchange in rooms. The standard nozzle cross section is 2.0 *m* × 1.46 *m*, permitting uniform wind speeds up to 41 *m/s* with a low turbulence intensity of around 0.13%.

The pressure distribution at the closed surface, measured in the boundary layer wind tunnel, was closely reproduced by setting the inflow velocities U_∞ to appropriate values. In particular, the conditions for the 3rd and 8th floor and both reference velocities U_{10} could be achieved with U_∞ = 3.6, 3.8. 5.1, and 5.7 *m/s*.

The velocity measurements were performed with transducer models 8455 and 8465 (TSI Inc.). The range was set from 0.125 to 10.0 *m/s*. The output signals were processed with appropriate DAQ components from National Instruments.

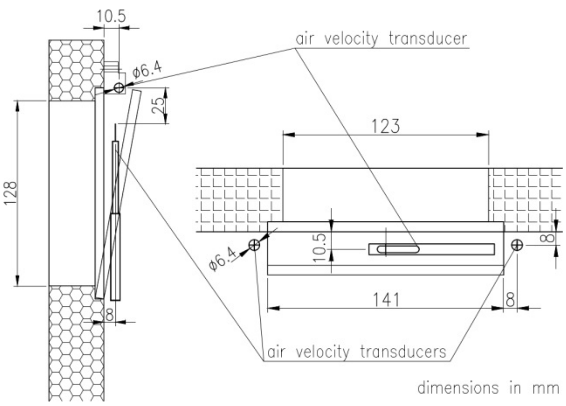

Figure 4. Velocity sensors in the gaps of tilted windows in the single room model (cf. [11])

For fully open windows, the velocity sensors were positioned near the diagonal intersection of the rectangular window, but inside the room (9 *mm* from the inner wall). A similar preocedure was applied for measurements in the doors [see [11]). The effect of the sudden constriction on calculating the flow rate from point-wise velocity data was accounted for by a procedure described in [14].

Measurements in the open gaps of tilted windows were realized in the single room model (1:10), with velocity sensors as shown in Fig. 4.

3.6. Tracer gas measurements

For determining air change processes quantitatively, in particular the *ACH*, the tracer gas method is well established [15]. In the present experiments, the concentration-decay method was used. Carbon dioxide was injected into the model room exposed to the defined external flow field with all windows closed. After formation of a homogeneous mixture of the room air with the CO_2, the windows were tilted pneumatically for a fixed time interval $\Delta t = t_2 - t_1$. The tracer gas concentration was measured at both times t_1 and t_2. by passing the CO_2/air mixture to an infrared Multi Gas Monitor Innova 1316-2 (LumaSense Technologies). This procedure was repeatedly carried out to obtain a time profile of the decaying CO_2 concentration in the room air. Following [15], for constant density the *ACH* can be calculated directly from

$$ACH = (1/\Delta t) \cdot \ln\left(\Delta C(t) / \Delta C(t+\Delta t)\right) \qquad (2)$$

where $\Delta C(t) = C_i(t) - C_o$ and the subscripts denote the internal and external environment.

3.7. Thermal effects

A difference in density between the external and internal air of a building due to temperature differences causes thermal buoyancy which may be an additional driving force. In order to account for this influence flexible heating foils (acting as a floor heating system) were installed in the single room model. To set a constant temperature inside the model, a thyristor TE10 A (Eurotherm) was used as a power controller. The current I_{eff} and voltage E_{eff} were measured by appropriate transducers (Eurotherm, Series E1).

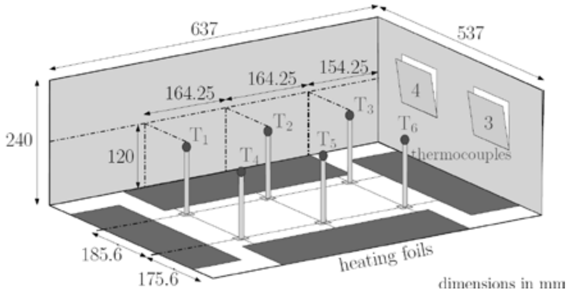

Figure 5. Positions of thermocouples and heating foils inside the single room model

To measure the temperatures within the single room, 6 thermocouples of type K (Eurotherm) were positioned vertically centred as given in Fig. 5. The temperatures were recorded using the Foxboro 2500 Controller (Eurotherm) and controlled by a PID controller of the software package LabView (National Instruments).

The desired room temperature is calculated as the arithmetic mean of the temperatures T_1 to T_6. To quantify the heat losses caused by the heat transfer through the walls, the mean heat flux q of each wall was measured using heat flux sensors of type FQA018CSI (Almemo).

4. NUMERICAL SIMULATIONS

The first phase of the present work was done in the framework of a funded project. During this phase CFD simulations were performed by the Austrian Institute of Technology (AIT). Some cases of experiments (1:25 scale) with fully opened windows and cross ventilation of rooms R_{3a} and R_{3b} (Fig. 1) with tilted windows were considered for comparison. In a further step the numerical domain was upscaled to real dimensions. Details and results are described in [11].

The 1:10 model with tilted windows was simulated in the present study to provide details of the complex flow structure inside the room.

The wind tunnel test section was mapped into the computational domain with overall dimensions of 4×3×1,76*m* in streamwise, spanwise, and vertical directions. A tetrahedral mesh was used to cover walls and the complex geometry around the window openings, while tetrahedral elements were applied in regions of free stream flow in order to reduce the cell number without affecting the accuracy. The overall mesh consisted of around $3 \cdot 10^6$ cells with cell sizes ranging from 10 *mm* (minimum) upwards.

Boundary conditions are defined to match the wind tunnel environment. The upstream (inlet) section is two-part, a solid wall representing the duct and the nozzle exit (2×1.46*m*) defined as a velocity inlet. The lower boundary represents the test section floor and is defined as a solid wall. All other boundaries are defined as pressure outlet with the atmospheric pressure prescribed.

ANSYS Fluent was applied for the simulations applying the steady RANS approach and the realizable k-ε turbulence model. The inflow velocity was set to the experimental conditions with a turbulence intensity of 0.13% and a turbulence viscosity ratio of 10.

In order to investigate possible drawbacks of the relatively coarse grid and the applied model, the computations were repeated on a finer mesh with $\sim 8.6 \cdot 10^6$ cells (2 windows) and $\sim 14 \cdot 10^6$ cells (all windows), where the most critical configurations were considered using both RANS and LES.

5. RESULTS

5.1. The scaling law

The conversion between the *ACH* in real dimensions and in a scaled model is determined by a scaling factor *m*. If the subscripts m and r denote model and real, respectively, the air exchange rate in the different scales is given as

$$ACH_{\mathrm{m}} = \frac{\dot{V}_{\mathrm{m}}}{V_{\mathrm{R,m}}} = \frac{U_{\mathrm{m}} A_{\mathrm{m}}}{V_{\mathrm{R,m}}}; \quad ACH_{\mathrm{r}} = \frac{\dot{V}_{\mathrm{r}}}{V_{\mathrm{R,r}}} = \frac{U_{\mathrm{r}} A_{\mathrm{r}}}{V_{\mathrm{R,m}}} \quad \text{(3a, b)}$$

Using a scale of 1:*m* and for equal velocities in real and model scale, $U_{\mathrm{m}} = U_{\mathrm{r}}$, leads to

$$ACH_{\mathrm{m}} / ACH_{\mathrm{r}} = m \Rightarrow ACH_{\mathrm{r}} = (1/m) \cdot (\dot{V}_{\mathrm{m}} / V_{\mathrm{R,m}}) \quad (4)$$

The length scale *m* enters into the window area *A* and the corresponding volumetric flow rate to the 2nd power but to the 3rd power into the room volume V_{R}. This fact was closely confirmed by the corresponding numerical simulations of AIT mentioned in section 4 (see also [11]).

5.2. Pressure distribution

To validate the pressure measurements, force coefficients were calculated and compared with data from the literature. The pressure distribution measured at the positions shown in Fig. 2 was fitted by a multidimensional function. The mean force coefficients result from integration of the fitting function over the building surfaces and subtracting the results for the windward and leeward side according to the directions. The notation is sketched in Fig. 6. It follows exemplarily for the *x*-direction:

$$F_D = \frac{\rho}{2} U_{\mathrm{H}}^2 \int_A c_{P,\,fitted}\, dA \;\Rightarrow\; c_{D,x} = \frac{F_{D,x}}{(\rho/2) U_{\mathrm{H}}^2 W H} \quad (5)$$

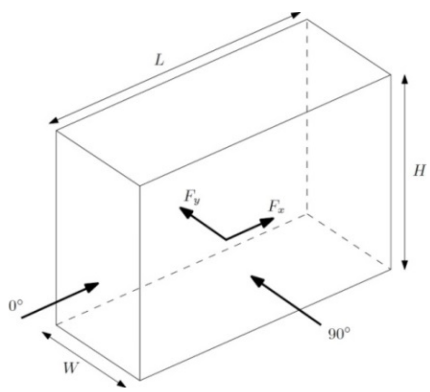

Figure 6. Definition of angles and forces

Following [16] the reference dynamic pressure is calculated with a velocity U_{a} averaged over the building height rather than with the velocity U_{H} in building height. Applying the power law (Eq. (1b)), the conversion factor is given by $U_{\mathrm{H}} / U_{\mathrm{a}} = (1+\alpha)$ which is independent of the building height.

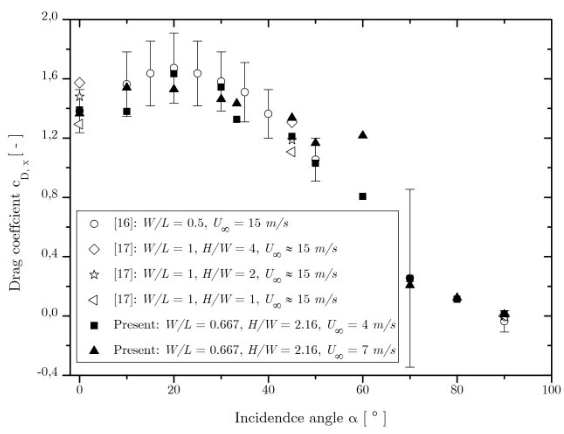

Figure 7. Force coefficients in x-direction.

The force coefficients derived in the present work were compared with data from [16, 17] in Fig. 7. Only the *x*-direction is given here for brevity. The data of [16] are specified with deviation bars to highlight the wide scattering resulting from different boundary layer profiles and geometrical differences.

Fig. 7 shows good agreement of the present data in the given range of experimental scatter, indicating realistic pressure measurements.

5.3. ACH for tilted windows in the single room model, wind driven

The results for the *ACH* obtained with different methods are compared in this section. *ACH* data are upscaled to real dimensions using Eq. (4). The wind directions and the notation of windows are sketched in Fig. 8.

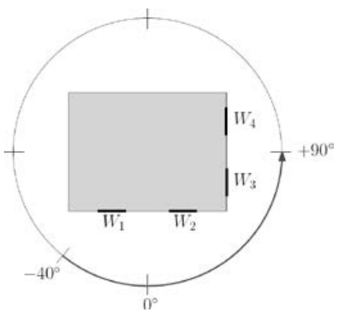

Figure 8. Wind direction, notation of windows

5.3.1. Comparison of methods

Figure 9 compares the *ACH* for two opening configurations resulting from the different methods exemplarily for a velocity U_∞ = 3.6 *m/s* corresponding to the 3rd floor and U_{10} = 2.8 *m/s*.

For cross ventilation with all windows tilted, the sensor readings yield larger *ACH* values than the tracer gas results. Major discrepancies can be observed for angles $\alpha \leq 0°$ which may be ascribed to the very large separation regions near the downstream wall. In contrast, for single-sided ventilation, the sensor readings yield lower values and much smaller discrepancies occurred.

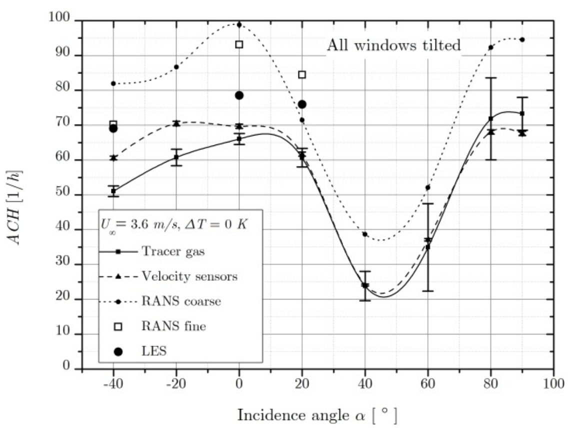

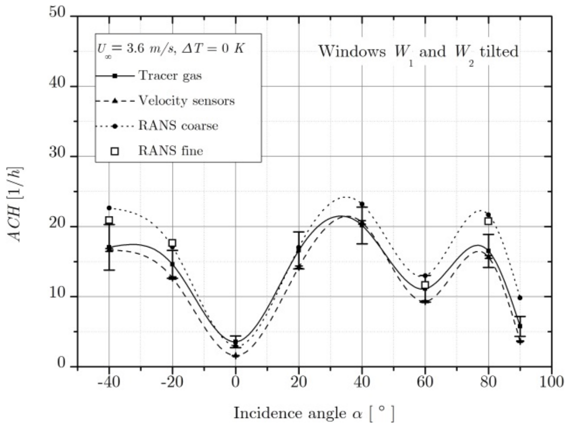

Figure 9. *ACH* with different methods, two opening configurations

Velocity measurements at only 3 locations in a tilted window may provide a plausible estimate of the *ACH*. The accuracy of the representation of the *ACH*, as an integral property of the flow, by local velocities depends strongly on the place of the measurements. In comparison to that, the tracer gas method seems more accurate. The computation of flow fields including vortex shedding with a steady state RANS approach and the k-ε model yielded an overprediction of the turbulent viscosity and a decrease of turbulence in critical regions (wakes). This implied higher flow rates through critical cross sections and an overprediction of the ACH (especially for $\alpha \leq 0°$ and all windows tilted).

5.3.2. Influence of wind velocity and direction on *ACH*

The influence of the wind velocity is depicted in Fig. 10 based on tracer gas measurements only. It is evident that the *ACH* increases with the wind velocity for all incidence angles and all tilting scenarios, which corresponds to the expectation.

With all windows tilted, the largest *ACH* are achieved at angles α = 0°/ 90° because of the flow frontally impinging two openings. The values are nearly equal because of geometrical similarity.

In case of single-sided ventilation, clearly lower values are achieved, with the maximum at α = 40°.

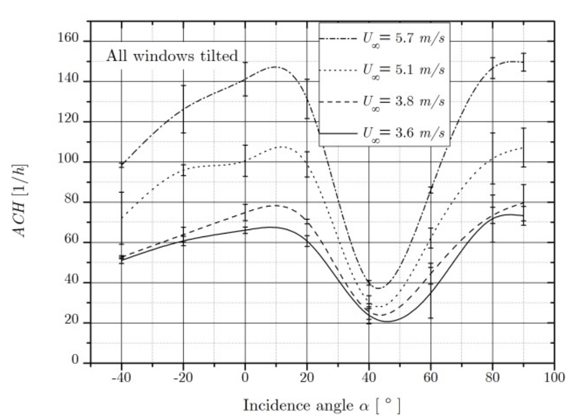

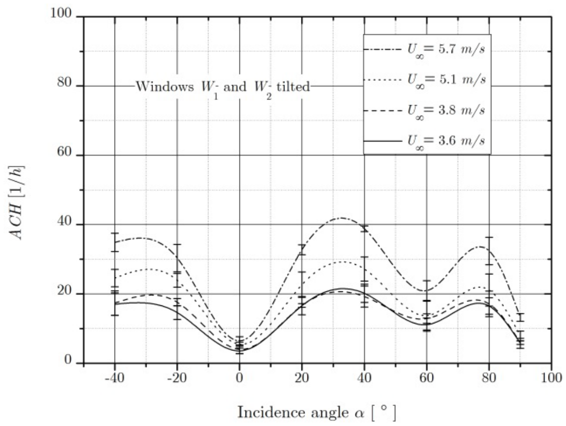

Figure 10. Influence of wind velocity on *ACH*.

In order to find a dependence of the *ACH* on the flow velocity U_∞ and the incidence angle α the air change rate was modelled according to

$$ACH(U_\infty,\alpha) = \underbrace{a_1 + a_2 U_\infty}_{:=A} + \underbrace{\left(b_1 + b_2 U_\infty\right)}_{:=B} \cos^2(2\alpha) \quad (6)$$

where *A* and *B* are the fitting parameters. The excellent fit can be recognized from Fig. 11 for cross ventilation with windows W_1 and W_4 tilted.

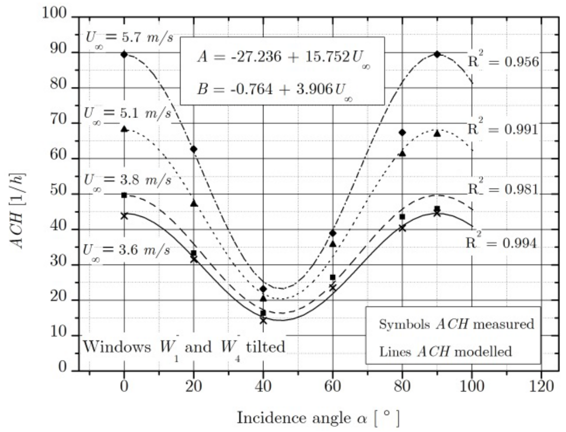

Figure 11. Measured and modelled *ACH*

To depict the influence of the wind velocity on the air exchange, the results from the tracer gas measurements are exemplarily plotted in Fig. 12 for cross ventilation.

It can be recognized that the air exchange rate and, hence, the volumetric air flow rate for angles between 0° and 90° are proportional to the wind velocity. These results are consistent with those of [8, 9], among others. For the depicted scenario of cross ventilation, the proportionalities result in parallel curves for the 0° / 90° and 20° / 80°. For angles 40° / 60° the data show a wider scattering and a lower *ACH* than for the other angles.

The reason may be that the flow is directed along the walls with windows and no distinct stagnation region is formed. Comparable results are obtained for cross ventilation with only W_1 and W_4 tilted, while single-sided ventilation with W_1 and W_2 tilted exhibits a different behaviour.

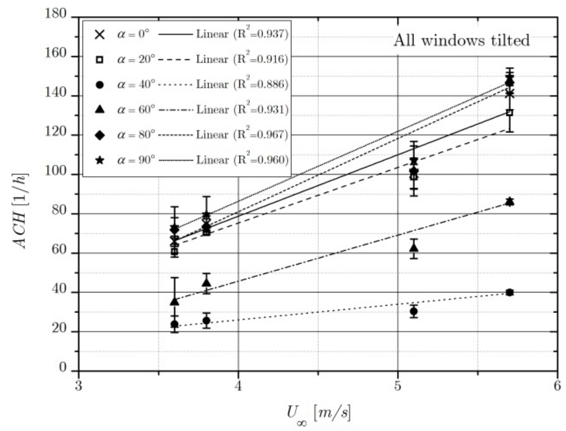

Figure 12. Dependence of *ACH* on velocity

The fitting parameters *A* and *B* in Eq. (6) exhibit a linear proportionality to the wind velocity but different for different opening scenarios. This may be explained by the constant total pressure along a streamline from the undisturbed flow to a point of the room model and applying Bernoulli's equation (see [12]).

5.4. Thermal influence on ACH

For all air velocities studied, the *ACH* increases with the temperature difference ΔT. We show the data for cross ventilation at 3.6 *m/s*. Fig. 13 shows that *ACH* increases by up to 20% due to ΔT=8*K*. The wind and thermal influences are not superimposed linearly. The temperature difference enhances the air exchange mainly for angles $\alpha \leq$ 20°. The difference between the effects of the two different ΔT is not significant. The effect of ΔT on *ACH* decreases with increasing wind velocity.

For single-sided ventilation, the thermal effects on *ACH* are minor for all cases studied here.

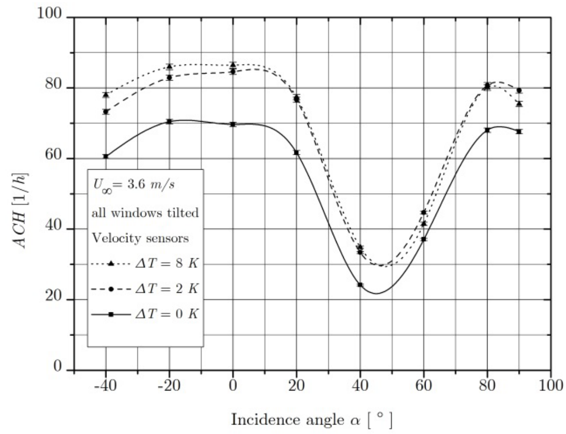

Figure 13. *ACH* with thermal influence

For pure thermally driven air exchange it is well known that the *ACH* is proportional to the square root of ΔT [7, 8]. In the present study it was found that, for inducing an *ACH*, ΔT must exceed a critical value, so that we have a dependency of the form $ACH = A_{th}\,(\Delta T - \Delta T_{crit})^{1/2}$.

The data for all three tilting scenarios yielded critical temperature differences in the range $1.5° \le \Delta T_{crit} \le 1.64°$. A complete derivation is given in [12].

6. SUMMARY

Natural ventilation through tilted windows in residential buildings is investigated by model experiments with different methods and numerical simulations.

In general, the agreement between different experimental results is satisfactory. The numerical data represent qualitatively the *ACH* experimentally measured. The steady RANS approach with the k-ε turbulence model tended to overestimate the ACH, even with the refined grid.

The influence of wind direction and velocity on the *ACH* was described by a model equation. For a given tilting scenario and wind direction, the ACH was found to increase linearly with the wind velocity.

In case of purely thermal effects, a critical temperature difference for the onset of convection was found. The combined effects of wind and temperature differences were quantified.

ACKNOWLEDGEMENTS

The authors acknowledge the funding from the Österreichische Forschungsförderungsgesellschaft mbH - Bridge Project “Native”, Project Number 829657 - during parts of the work.

REFERENCES

[1] Allocca, C., Chen, Q., and Glicksman, L.R., 2003, “Design analysis of single-sided natural ventilation”, *Energy and Buildings*, Vol. 35, pp. 785-795.

[2] Larsen, T.S., and Heiselberg, P., 2008, „Single-sided natural ventilation driven by wind pressure and temperature difference”, *Energy and Buildings*, Vol. 40, pp. 1031-1040.

[3] Lo, L.J., and Novoselac, A., 2012, “Cross ventilation with small openings: measurements in a multi-zone test building”, *Building and Environment*, Vol. 57, pp. 377-386.

[4] Ohba, M., Irie, K., and Karabuchi, T., 2001, „Study on airflow characteristics inside and outside a cross-ventilation model, and ventilation flow rates using wind tunnel experiments”, *Journal of Wind Engineering and Industrial Aerodynamics*, Vol. 89, pp. 1513-124.

[5] Nikas, K.-S., Nikolopoulos, N., and Nikolopoulos, A., 2010, “Numerical study of a naturally cross-ventilated building”, *Energy and Buildings*, Vol. 42, pp. 422-434.

[6] Schulze, T., and Eicker, U., 2013, “Controlled natural ventilation for energy efficient buildings”, *Energy and Buildings*, Vol. 56, pp. 221-232.

[7] Daler, H., Hirsch, E., Haberda, F., Knöbel, U., and Krüger, W., 1984, „Bestandsaufnahme von Einrichtungen zur freien Lüftung im Wohnungsbau“, Forschungsbericht T84-028, Federal Ministry of Research and Technology, Germany, ISSN-0340-7608.

[8] Maas, A., 1995, „Experimentelle Quantifizierung des Luftwechsels bei Fensterlüftung“, *PhD thesis, University of Kassel*.

[9] Hall, M., 2004, „Untersuchungen zum thermisch induzierten Luftwechselpotential von Kippfenstern“, *PhD thesis, University of Kassel*.

[10] ASHRAE, 2009, Handbook of Fundamentals, System International Edition, Chapter 16, American Society of Heating, Refrigerating and Air-Conditioning Engineers, Atlanta.

[11] Teppner, R., Langensteiner, B., Meile, W., Brenn, G., and Kerschbaumer, S., 2014, „Air change rates driven by the flow around and through a building storey with fully open or tilted windows: An experimental and numerical study”, *Energy and Buildings*, Vol. 80, pp. 570-583.

[12] Langensteiner, B., 2014, „Transport processes in ventilated buildings”, *PhD thesis, Graz University of Technology*.

[13] Plate, E., 1982, *Engineering meteorology*, chapter *Wind tunnel modelling of wind effects on structures in engineering*, Elsevier, pp. 573-639.

[14] Sockel, H., 1984, *Aerodynamik der Bauwerke*, Vieweg.

[15] VDI 4300 Part 7, 2001, Indoor Air Pollution Measurement, Measurement of the Indoor Air Change Rate, Verein Deutscher Ingenieure.

[16] Akins, R.E., and Peterka, J.A., 1977, „Mean force and moment coefficients for buildings in turbulent boundary layers”, *Journal of Wind Engineering and Industrial Aerodynamics*, Vol. 2, pp. 195-209.

[17] Kiefer, H., 2003, „Windlasten an quaderförmigen Gebäuden in bebauten Gebieten“, *PhD thesis, University of Karlsruhe*.

Conference on Modelling Fluid Flow (CMFF'15)
The 16th International Conference on Fluid Flow Technologies
Budapest, Hungary, September 1-4, 2015

NUMERICAL DESIGN OF COUNTER-ROTATING TYPE HORIZONTAL-AXIS PROPELLERS INSTALLED IN TIDAL STREAM POWER UNIT

Bin Huang[1], Xue-Song Wei[2], Pin Liu[3], Toshiaki Kanemoto[4] and Jin-Hyuk Kim[5]

[1] Corresponding Author. Faculty of Engineering, Kyushu Institute of Technology. Sensui 1-1, Tobata, Kitakyushu 804-8550, Japan. Tel(Fax) : +81-93-884-3205, Mob: +81-90-9652-7938, E-mail: huang.bin404@mail.kyutech.jp
[2] Faculty of Engineering, Kyushu Institute of Technology; Research student from Zhejiang University, China. E-mail: 13735572905@126.com
[3] Faculty of Engineering, Kyushu Institute of Technology, Japan. E-mail: liu.pin379@mail.kyutech.jp
[4] Faculty of Engineering, Kyushu Institute of Technology, Japan. E-mail: kanemoto.toshiaki886@mail.kyutech.jp
[5] Thermal & Fluid System R&BD Group, Korea Institute of Industrial Technology, Korea. E-mail: jinhyuk@kitech.re.kr

ABSTRACT

Tidal stream is greatly attractive as an extremely reliable, predictable and continuous renewable energy resource. The performance of the power unit plays an important role in converting tidal stream to electric power. First of all, this paper presents a counter-rotating type horizontal-axis propellers, which is installed in a tidal stream power unit equipped with a peculiar generator composed of double rotational armatures, designed based on the traditional blade element momentum theory (BEMT). Subsequently, the Computational Fluid Dynamics (CFD) tool was employed to verify the performance of the designed counter-rotating type horizontal-axis tidal stream power unit, and then the propeller profiles were optimized numerically by CFD analysis. The numerical results indicate that the hydraulic efficiency of the propellers is greatly improved after optimization. The experimental research also provides an evidence of validation of the improvement of the proposed counter-rotating type horizontal-axis propellers.

Keywords: BEMT, CFD, counter-rotating type horizontal-axis propellers, tidal stream

NOMENCLATURE

A	$[m^2]$	propeller area
C_p	[-]	power coefficient
d	$[m]$	propeller diameter
R	$[m]$	blade tip radius
T	$[N{\cdot}m]$	torque
V_{in}	$[m/s]$	inlet speed
Z	[-]	blade number
λ	[-]	tip speed ratio
ρ	$[kg/m^3]$	fluid density
ω	[rad/s]	rotating speed
β	[°]	blade pitch angle

Subscripts and Superscripts

F	front propeller
R	rear propeller
T	tandem propellers

Abbreviation

BEMT	blade element momentum theory
CFD	Computational Fluid Dynamics
EMEC	European Marine Energy Centre
HATST	horizontal-axis tidal stream turbine
MCT	Marine Current Turbines
TSR	tip speed ratio

1. INTRODUCTION

With the rapid growth of oil and gas consumption, there is greatly increasing interest and investigation on the renewable energy in the past decade. Ocean energy as a kind of endless energy resource shows great potential to be harnessed in different ways. The forms of ocean energy can be categorized into tidal, wave, current, thermal gradient and salinity gradient [1]. One such major form of this sustainable energy is the tidal stream energy, which converts the kinetic energy to electric power. The horizontal-axis tidal stream turbine (HATST) has been proposed as a cost-effective turbine to harness energy from the ocean [2].

Over the past decade, both of model test in laboratory and prototype test at offshore sites have been carried out. Bahaj et al. [3-5] performed a series of experimental investigations on the hydrodynamic performance and cavitation performance of an 800mm diameter model tidal turbine in a cavitation tunnel and a towing tank. Their research results provided useful information for the hydrodynamic design of marine current turbine and detailed data for the validation of numerical models. Wang [6] presented an experimental investigation on the cavitation, noise, and slipstream characteristics of an ocean tidal stream turbine. On the other hand, Marine Current Turbines (MCT) Ltd [7] installed a two-bladed turbine capable of generating 300kW off the Devon coast near Lynmouth in May 2003, which is the world's first tidal current turbine in open sea conditions although not grid-connected. And by 2008 they had a 1.2 MW turbine, SeaGen, in Strangford Lough, Northern Ireland which was able to feed electricity into the National Grid. The European Marine Energy Centre (EMEC) Ltd established in Orkney 2003, is the first and only centre of its kind in the world to provide developers of both wave and tidal energy converters, who has finished a lot of tidal turbine tests in its tidal test site: OpenHydro's 250kW open centred turbine in 2006, Tidal Generation Ltd's (TGL, now Alstom) 500kW turbine in 2010, Atlantis Resource Corporation's 1MW horizontal axis turbine AR1000 in 2011, ANDRITZ HYDRO Hammerfest's 1MW pre-commercial tidal turbine in 2012, Voith's 1MW horizontal axis turbine HyTide 1000 in 2013, and so on [8].

Due to the high cost and long period of experimental tests, the Computational Fluid Dynamics (CFD) as an alternative to field measurements has been widely used in the design and optimization of tidal turbines. Macleod et al. [9] provide one of the earliest such studies for a TST, using a k-ε model to model a farm of tidal turbines using an actuator disk approach. Sun [10], Harrison [11] and Batten [12] also applied the actuator disk to simulate the wake characteristics of horizontal axis tidal turbines. O'Doherty [13] investigated the effects of five different RANS turbulence models on the predicted performance of a model horizontal-axis tidal turbine using resolved blade geometry. Fan [14], Mcsherry [15] and Afgan [16] utilized the resolved blade model to validate the performance of a 3-bladed horizontal axis tidal stream turbine designed by Bahaj et al. Malki [17] developed a blade element momentum-computational fluid dynamics (BEM-CFD) model for the prediction of tidal stream turbine performance, and also validate this model with the experimental tow-tank results published by Bahaj et al.

The current study first presents a counter-rotating type horizontal-axis propellers, which is installed in a tidal stream power unit equipped with a peculiar generator composed of double rotational armatures, designed based on the traditional blade element momentum theory. On this basis, the blade profiles were optimized through the results of CFD analysis.

2. DESIGN OF COUNTER-ROTATING TYPE HATST

In this study, a model counter-rotating type tidal stream power unit with the diameter of 500 mm was designed based on the blade element momentum theory (BEMT) as a trade-off between maximizing the Reynolds number and not incurring excessive tunnel blockage correction. The optimal hydrofoil named KIT001 developed from MEL002 with higher lift-drag ratio as shown in Figure1 was selected as the blade elements for both of the front and rear blades. The original blade profiles of the model counter-rotating type HATST designed by BEMT are illustrated in Figure 2. The diameter of the front rotor is d_F = 500mm and the rear rotor is d_R = 420 mm, namely the diameter ratio [$=d_R/d_F$] is 0.84. The number of blades for upstream rotor and downstream rotor is Z_F = 3 and Z_R = 5, respectively. The axial distance between the front and the rear rotors is set to 80mm, and the diameter of the hub is set to 90 mm.

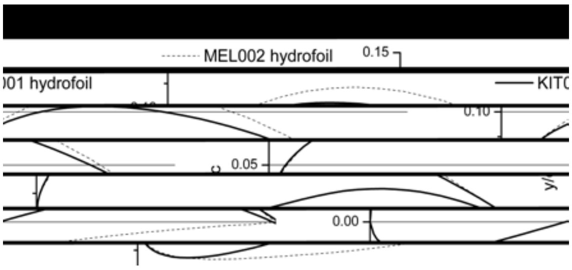

Figure 1. MEL002 hydrofoil and KIT001 hydrofoil

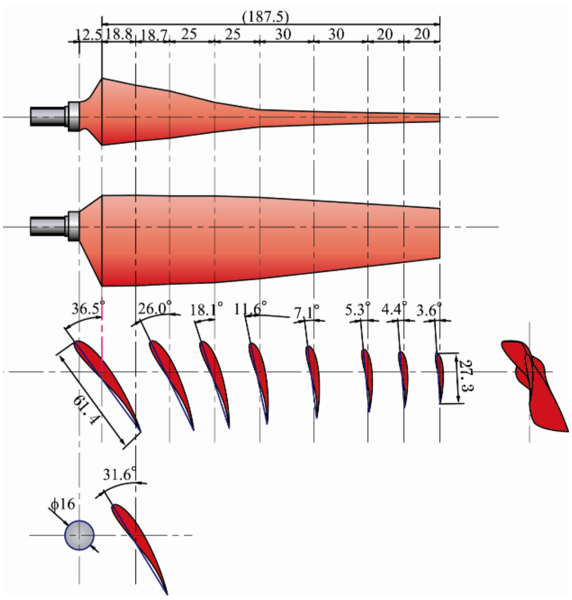

(a) Front blade

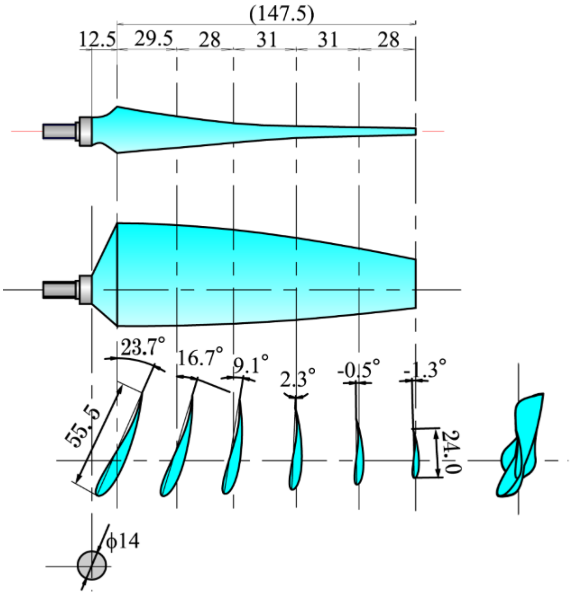

(b) Rear blade

Figure 2. Original blade profiles of the model counter-rotating type HATST

3. CFD MODEL

In order to obtain the performance of the designed counter-rotating type HATST, the k-ω SST (shear stress transport) model in ANSYS CFX 14.0 was used for all calculations in this paper.

The computational domain consists of three parts: the front rotor, the rear rotor and the stator. The length of the stator domain was set to $10d_F$, in which $3d_F$ and $7d_F$ for upstream and downstream of the front blade respectively. The width and depth are 1500mm and 1000mm, respectively. The unit was placed centrally in the domain and the mooring wire or pillar was neglected in calculation. The diameters of the front and rear rotor domains were both set to $1.1d_F$.

A block structured hexahedral grid method in ICEM CFD was employed to generate mesh for all the computational domains. A C-mesh was applied around the blades since it fits well for the hydrofoil shape of the blades. The front rotor block and rear rotor block were built in a 120°segment and 72°segment which both include only one blade as in Figure 3. The refined grids were concentrated in regions of importance such as around the blades and towards and away from the tip. Table 1 presents the mesh statistics of every computational domain.

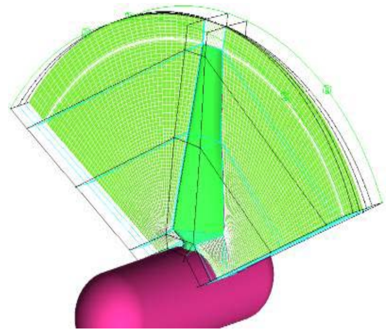

(a) Front rotor

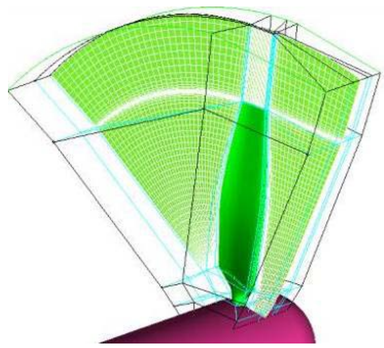

(b) Rear rotor

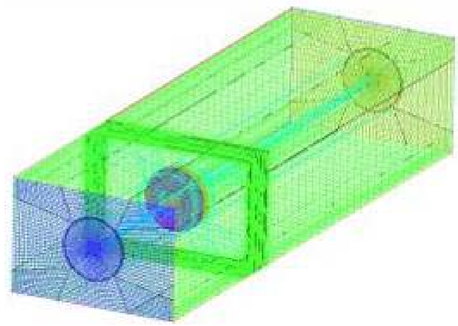

(c) Stator

Figure 3. Blocking strategy and mesh distributions of the computational domains

Table 1. Mesh statistics of the computational domains

Domain	Front rotor	Rear rotor	Stator
Number of elements	605870	792133	613320
Number of nodes	632418	821242	630652
Number of blocks	91	90	175

The k-ω SST model in ANSYS CFX was used in the current study to solve the incompressible Reynolds-average Navier-Stokes equations. The normal velocity and averaged static pressure boundary conditions were prescribed at the inlet and outlet of computational domains, respectively. The no-slip and smooth walls were imposed on solid surfaces. To simplify the simulations and reduce computational cost, only single front blade and single rear blade were calculated assuming rotational periodic interface between the adjacent blades. The stage method which performs a circumferential averaging of the fluxes through the bands on the interface was used for the connection between each computational domain. The convergence criterion was set as the maximum values of the residuals reaching 10^{-4}.

In the counter-rotating type HATST, the radius of the front propeller was selected as reference variable, so the tip speed ratios and power coefficients were defined as follows:

$$\lambda_F = \frac{\omega_F R_F}{V_{in}} \tag{1}$$

$$\lambda_R = \frac{\omega_R R_F}{V_{in}} \tag{2}$$

$$\lambda_T = \lambda_F + \lambda_R \tag{3}$$

$$C_{PF} = \frac{T_F \omega_F}{(1/2)\rho V_{\mathrm{in}}^3 A_F} \tag{4}$$

$$C_{PR} = \frac{T_R \omega_R}{(1/2)\rho V_{\mathrm{in}}^3 A_F} \tag{5}$$

$$C_{PT} = C_{PF} + C_{PR} \tag{6}$$

4. RESULTS AND DISCUSSIONS

The comparison of power coefficients of the original propellers between CFD results obtained from CFD model described previously and experimental data obtained in a water tunnel for a range of TSRs are shown in figure 4. It can be seen that the trend of power coefficients shows good agreement between CFD results and experimental data. However, the experimental values is a little different from the predicted CFD, which can be attributed to the shallow tip-immersion in experimental test due to structural constraints.

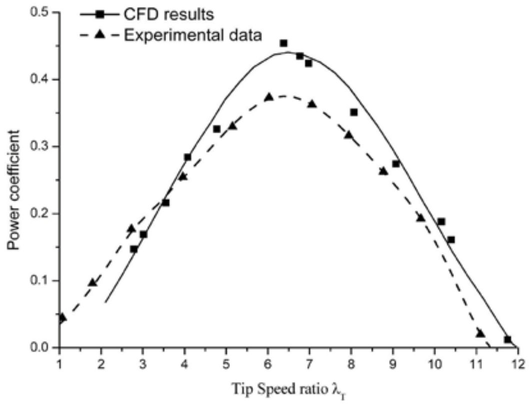

Figure 4. The comparison of power coefficients of the original propellers between CFD results and experimental data

In order to improve the performance of the original propellers, especially the rear propeller as its torque is much lower than that of the front propeller in some range of TSRs, the new blade profiles of the model counter-rotating type HATST were shown in figure 5. The diameter ratio [$=d_R/d_F$] of the new blade profiles was increased to 0.9, and the blade thickness near the hub region was also increased to improve strength.

(a) Front blade

(b) Rear blade

Figure 5. New blade profiles of the model counter-rotating type HATST

Figure 5 compares both of the CFD results and experimental data between the original and new blade profiles. It is clear that the power coefficients of the new propellers have been greatly increased as compared with the original propellers. At the same time, the TRS of the best efficiency point is shifted to the low value, which would account for suppression in cavitation occurrence. Thus it can be seen that the new propellers have increased both of the efficiency and cavitation performance.

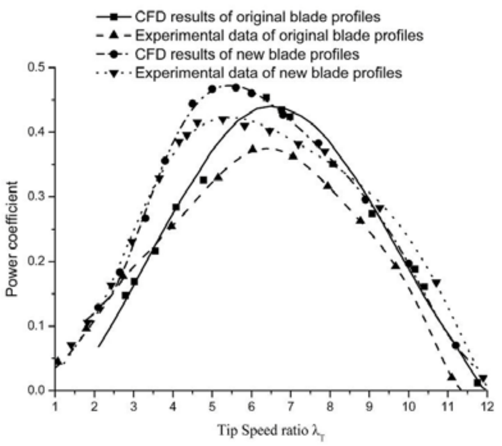

Figure 6. The comparison of power coefficients between the original and new blade profiles

5. CONCLUSIONS

A model counter-rotating type tidal stream power unit with the diameter of 500 mm has been designed based on the BEMT in order to exploit renewable energies form tidal currents. A block structured hexahedral grid and the k-ω SST model in ANSYS CFX 14.0 were employed to predict the hydrodynamic performance of the tidal turbine. Tests in a water tunnel were also carried out to validate the CFD results and optimization results.

The experimental data are consistent in the trend and a little lower in the value as compared with the CFD results, due to the proximity of the free surface in experimental tests. After numerical optimization, both of the efficiency and cavitation performance have been increased obviously.

ACKNOWLEDGEMENTS

The authors wish to thank to Dr. Yuta Usui and Mr. Kohei Takaki who graduated from Kyushu Institute of Technology, in Japan. Some parts of the researches were co-sponsored by the New Energy and Industrial Technology Development Organization in Japan, and Research Project: Grant-in-aid for Science Research (c) (2) in Japan (20Foundation (2012-2014)).

REFERENCES

[1] Bedard, R., Jacobson, P.T., Previsic, M., Musial, W., and Varley, R., 2010, “An overview of ocean renewable energy technologies”, Oceanography, Vol. 23(2), pp.22–31.

[2] Fraenkel, P., 2002, “Power from marine currents”, Proc IMechE Part A: J. Power and Energy, Vol. 216(1), pp.1-14.

[3] Batten, W.M.J., Bahaj, A.S., Molland, A.F., and Chaplin, J.R., 2007, “Experimentally validated numerical method for the hydrodynamic design of horizontal axis tidal turbines”, Ocean Engineering, Vol. 34(7), pp.1013-1020.

[4] Bahaj, A.S., Molland, A.F., Chaplin, J.R., and Batten, W.M.J., 2007, “Power and thrust measurements of marine current turbines under various hydrodynamic flow conditions in a cavitation tunnel and a towing tank”, Renewable Energy, Vol. 32(3), pp.407-426.

[5] Bahaj, A.S., Batten, W.M.J., and McCannb, G., 2007, “Experimental verifications of numerical predictions for the hydrodynamic performance of horizontal axis marine current turbines”, Renewable Energy, Vol. 32(15), pp.2479-2490.

[6] Wang, D., Atlar, M., and Sampson, R., 2007, “An experimental investigation on cavitation, noise, and slipstream characteristics of ocean stream turbines”, Proc IMechE Part A: J. Power and Energy, Vol. 22(2), pp.219-231.

[7] IT Power, Seacore, Gesamthochschule Kassel, and Jahnel-Kesterman, 2005, “SEAFLOW World’s first pilot project for the exploitation of marine currents at a commercial scale”, Final Publishable Report.

[8] http://www.emec.org.uk/.

[9] Macleod, A. J., Barnes, S., and Rados, K. G., 2002, “Wake effects in tidal current turbine farms. Proceedings of MAREC Conference, Newcastle, pp.49-53.

[10] Sun, X., Chick, J. P., and Bryden, I. G., 2008, “Laboratory-scale simulation of energy extraction from tidal currents”. Renewable Energy”, Vol. 33(6), pp.1267-1274.

[11] Harrison, M. E., Batten, W. M. J., Myers, L. E., and Bahaj, A. S., 2009, “A comparison between CFD simulations and experiments for predicting the far wake of horizontal axis tidal turbines”, Proceedings of the 8th European Wave and Tidal Energy Conference, Uppsala, Sweden, pp.566-571.

[12] Batten, W. M. J., Harrison, M. E., and Bahaj, A. S., 2013, “Accuracy of the actuator disc-RANS approach for predicting the performance and wake of tidal turbines”, Philosophical

transactions of the royal society A, mathematical physical and engineering sciences, Vol. 371(1985), pp.20120293.

[13] O'Doherty, T., Mason-Jones, A., O'Doherty, D. M., and Byrne, C. B., 2009, “Experimental and Computational Analysis of a Model Horizontal Axis Tidal Turbine”, Proceedings of the 8th European Wave and Tidal Energy Conference, Uppsala, Sweden, pp.833-841.

[14] Fan, R. J., Chaplin, J. R., and Yang, G. J., 2010, “CFD Investigation of Performance for Marine Current Turbine Based on RANS Simulations”, Key Engineering Materials, Vol. 419-420, pp.309-312.

[15] Mcsherry, R., Grimwade, J., Jones, I., Mathias, S., Wells, A., Mateus, A., and House, E. F., 2011, “3D CFD modelling of tidal turbine performance with validation against laboratory experiments”, Proceedings of the 9th European Wave and Tidal Energy Conference, Southampton, UK.

[16] Afgan, I., McNaughton, J., Rolfo, S., Apsley, D.D., Stallard, T., Stansby, P., 2013, “Turbulent flow and loading on a tidal stream turbine by LES and RANS”, International Journal of Heat and Fluid Flow, Vol.46, pp.96-108.

Conference on Modelling Fluid Flow (CMFF'15)
The 16th International Conference on Fluid Flow Technologies
Budapest, Hungary, September 1-4, 2015

HYDRODYNAMIC MODEL OF NANOSECOND LASER ABLATION OF TUNGSTEN AND BORON

Tomasz MOSCICKI[1], Justyna CHRZANOWSKA[2]

[1] Corresponding Author. Institute of Fundamental Technological Research, Pawinskiego 5B, 02-106 Warsaw, Poland
E-mail: tmosc@ippt.gov.pl
[2] Institute of Fundamental Technological Research. E-mail: jichrzanowska@gmail.com

ABSTRACT

In this paper, the interaction of an Nd-YAG nanosecond laser pulse with a tungsten and boron target and plasma induced during ablation are studied theoretically. Tungsten and boron were chosen due to the significant differences in their chemical and physical properties. Both materials are of great practical importance. The model consists of equations of conservation of mass, momentum and energy, and is solved with use of the commercially available Ansys Fluent software. The calculations show the fundamental differences in ablation of both species. In the case of tungsten, the material evaporation is controlled by the plasma formation, and consequently, the absorption coefficient. The dense plasma plume can block laser radiation and limit energy transfer from the laser beam to the material. In the case of boron, explosive ablation is observed. The calculations also show sharp increase of the plume pressure after plasma formation and a resulting significant increase of the velocity of the plasma plume. The plume velocity obtained from the model is close to that observed in the experiment carried out in similar conditions. Moreover, the effect of laser wavelength on the quality of the deposited boron and tungsten films is discussed on the base of ablation model.

Keywords: ablation mechanism, boron, critical temperature, plasma velocity, pulsed laser deposition, tungsten

NOMENCLATURE

a	$[m^2/s]$	thermal diffusivity
α	$[1/m]$	target absorption coefficient
C	[-]	numerical factor results from normalization
c_p	$[J\ kg^{-1}K^{-1}]$	heat capacity
F	$[J/m^2]$	laser fluence
I_L	$[W/m^2]$	laser intensity
I_0	$[W/m^2]$	peak intensity
k	$[W/m\ K]$	thermal conductivity
κ	$[1/m]$	plasma absorption coefficient
L_v	$[J/kg]$	latent heat of vaporization
λ	$[m]$	laser wavelength
$\vec{n}$	[-]	unit vector perpendicular to the surface
p	$[Pa]$	pressure
R	[-]	reflectivity
r	$[m]$	radial coordinate
ρ	$[kg/m^3]$	mass density
$s1$	$[m]$	Gauss parameter (0.098×10^{-3})
$s2$	$[s]$	Gauss parameter (6.0056×10^{-9})
T	$[K]$	temperature
t	[s]	time
t_0	$[s]$	time offset of the beam maximum
τ	$[s]$	laser pulse duration
$\vec{u}$	$[m/s]$	recession velocity
v	$[m/s]$	velocity
z	$[m]$	axial coordinate

Subscripts and Superscripts

c	critical
L	laser
v	vapour
s	surface
T	target

1. INTRODUCTION

In recent years, growing interest in ultra-incompressible and super-hard materials has been observed. Tungsten triboride WB_3 is one of the most promising inexpensive candidates for ultra-incompressible, super-hard materials [1-2]. Even in the form of thin films, it has super-hard properties [3] and in the future may be an alternative to other hard coatings, such as diamond-like DLC or cubic boron nitride (c-BN). One of the most promising methods of obtaining WB_3 films is pulsed laser deposition (PLD), because it highly suits deposition of hardly meltable metals, such as tungsten [4]. Pulsed laser deposition is a technique where a pulsed laser beam is focused inside a vacuum chamber to strike a target of the material that is to be deposited. This material is ablated from the target, forms a plasma plume and subsequently deposits as a thin film on a substrate. Deposited films may have a thickness from several nanometres to several micrometres. The deposition of high-quality films requires knowledge of the first step of the pulsed laser deposition process, which is laser ablation. The course of target ablation affects plasma plume composition, e.g. vapour to nanoparticle and microparticle ratio.

Besides the deposition of functional films containing boron [3, 5] or tungsten [4], the laser ablation phenomenon is used in applications such as micromachining [6], cleaning [7], and fabrication of microstructures and nanostructures [8]. Tungsten is one of a few possible materials for in-vessel components in forward-looking thermonuclear reactors. Therefore, any investigation of its properties and behaviour is important, and in particular the characterisation of its evaporation processes from the inner wall of a tokamak is needed [9]. Despite numerous applications, the physics of the laser ablation process is not yet thoroughly understood. The physics of the laser ablation process depends not only on the properties of the material, but also laser parameters such as pulse duration, frequency [6], fluence [10] and wavelength [11].

The simple mechanism of ablation consists of three stages. During the interaction of the laser beam with a material, the target is heated to a temperature exceeding its boiling point and sometimes also its critical temperature. In the second stage, material evaporated from the target forms a thin layer of dense plume, consisting of electrons, ions and neutrals. This plasma plume absorbs energy from the laser beam (by means of photoionization and inverse Bremsstrahlung) and its temperature and pressure grow. The resulting pressure gradient accelerates the plume to high velocity perpendicular to the target. At the next time steps, the laser pulse terminates and the plasma plume expands adiabatically [12, 13]. This ablation pattern can be used up to some limit of fluence in which there is no phase explosion yet [10, 13]. It is assumed that the explosive boiling begins when the temperature exceeds 0.9 of the critical temperature [13]. This type of ablation results in the appearance of nanoparticles and microparticles in the plasma plume.

Therefore, detailed knowledge on laser-induced flow dynamics of plasma and understanding of the mechanisms of ablation is necessary for optimizing technological processes and promoting powerful lasers with nanosecond pulse durations for cost-effective use in industries.

In this paper, the theoretical modelling of the target heating and plasma formation during interaction with nanosecond laser pulse is presented. The set of equations consists of the equations of mass, momentum and energy conservation, and are solved with the use of Ansys Fluent software. The main goal of the study is a comparative analysis of the phase transition in the surface layer of a boron and tungsten target induced by nanosecond laser radiation at the wavelengths of 1064 *nm* and 355 *nm* with an intensity of 10^9 *W/cm²* in vacuum. The comparison of the properties of tungsten plasmas for both laser wavelengths is presented. The simple experimental validation of theoretical model is shown.

2. THEORETICAL MODEL

The theoretical model that describes the target heating, formation of the plasma and its expansion, was presented in [14, 15]. The main goal of the present research is a comparative analysis of ablation mechanism of a boron and tungsten target and the impact of this phenomenon on the properties of the plasma for different laser wavelengths. Calculations were made for two wavelengths of an Nd:YAG laser – 355 *nm* and 1064 *nm*. The laser beam with a Gaussian profile (10 ns FWHM) was focused to a spot size of 0.055 mm^2 with a fluence of 10 J/cm^2. It was assumed that the boron or tungsten plume expands to ambient air at a pressure of 10^{-3} *Pa*. In the case of a nanosecond laser, the ablation is thermal; hence, the initial conditions for plume expansion were taken from the theory of the rapid surface vaporization [16]. Therefore, it was assumed the vapour velocity at the end of the Knudsen layer is sonic and the other parameters are $T_v \sim 0.67\, T_s$, $p_v \sim 0.21\, p_s$, $\rho_v \sim 0.31\rho_s$ [16]. In the area with ambient pressure 10^{-3} Pa, the Knudsen number is greater than the threshold value (0.1). However, this is the less important area for calculations of the ablation process. At the place where the laser beam interacts with the target, the pressure suddenly grows and continuum regime is fulfilled. As the laser ablation plume expands into a low-pressure background gas, eventually the density becomes so low that the flow is no longer in a continuum regime. Based on model results, during the first 100 ns the Knudsen number is below 0.1. It is a commonly accepted limiting value above which the mean free path is too long to justify a fluid approximation.

The intensity of laser beam reaching the target surface I_L was used in the form that fits the shape of the laser pulse used in our experiments.

$$I_L(t,r) = \frac{CF}{\tau}\exp\left(-\left(\frac{t-t_0}{s_2}\right)^2\right)\exp\left(-\left(\frac{r}{s_1}\right)^2\right) \times \left(\exp\left(-\int \kappa dz\right)\right) \quad (1)$$

The first part of the equation (1) describes temporal evolution of the laser intensity, the second energy distribution in the laser beam and the last exponential component takes into account the attenuation of the laser beam on its way to the point (r, z) in plasma.

The laser radiation reflected from the surface of target R was included. Due to reflectance, the source component in energy equation is $\kappa I_L(1+R)$ in the case of plasma, and $\alpha I_L(1-R)\exp\left(-\int \alpha dz_T\right)$ for the target. The exponential component takes into account the attenuation of the laser beam on its way to the point (r, z_T) of target.

The presented ablation model consists of two parts. The first part, which is settled with conduction equation [14, 17], was responsible for the determination of the temperature distribution and mass removal in the target. In the second part, the Eulerian system of equations of continuity and the diffusion equation [14, 17] were solved for plasma.

The system of equations was solved iteratively. The target temperature was calculated and then the stream of ablated particles was determined at the end of the Knudsen layer. These conditions were taken as inlet conditions for plume expansion. Next, the absorption of the laser radiation in developing the plasma plume was determined and the target temperature was recalculated according to actual laser intensity at the target surface. The new target temperature was used to determine the conditions at the end of the Knudsen layer, which were subsequently used as inlet conditions for plume expansion. The other boundary conditions for plasma system of equations were as follows. The stream of boron or tungsten vapour was directed perpendicularly to the target surface. At the wall the no-slip boundary and a fixed temperature condition were applied. At the outflow boundary the pressure outlet boundary conditions [17] were used, which required the specification of a static pressure at the outlet boundary. This static pressure value is relative to the operating pressure. The axis boundary conditions were used at the centerline of the axis-symmetric geometry [17].

The boundary condition at the place where the laser beam strikes the surface of the target is

$$-k\frac{\partial T_s}{\partial \vec{n}} = -\rho \vec{u}(t) L_v \qquad (2)$$

where $\vec{u}$ is the recession velocity given by the Hertz-Knudsen equation [10, 14]. Energy losses due to thermal radiation from the surface are small compared to other terms and were neglected. At other boundaries $T = 300\ K$ was assumed.

All the material functions were described in [15] and depend on the temperature in the target and pressure and mass fraction in plasma.

For the plasma, the calculation domain was r = 0.01 m and z = 0.025 m with nonuniform grid with 60 × 200 nodes. The smallest computational cells had dimensions of 50 × 0.1 μm at the vapour inlet. In the case of the target, the calculation domain was r = 0.005 m and $z = 2\times10^{-6}$ m with 130 × 500 nodes, respectively. While the smallest computational cells had dimensions of 12 × 0.004 μm at the target surface. The cell dimensions were fit to appearing gradients after preliminary calculations. Next, it was checked that further decreasing of cell dimensions did not change the results. The time step was adjusted to the smallest cells. Both cases were time-dependent and were solved in axisymmetric geometry. In the case of the plasma, the system of equations was solved by density based (coupled) solver [17] with second order spatial discretization for flow. The default settings [17] were applied for the target.

3. EXPERIMENTAL SETUP

Irradiation of a tungsten and boron target was performed using an Nd:YAG laser (Quantel, 981 E) in a chamber evacuated to a residual pressure of 1×10^{-5} Pa. All ablation parameters were the same as in the theoretical model. Both harmonics were polarized horizontally. The spatial and time profiles of the laser beam were Gaussian. The laser spot diameter defined by I_0/e^2 was determined by registration of the spot size by ICCD camera after attenuation of the laser beam and was 310 μm in the case of 1064 nm and 260 μm in the case of 355 nm wavelength. The incident angle of the laser beam was close to the surface normal. The high-quality targets - boron from Kurt J. Lesker (2.35 g/cm^3 mass density, 99.5% purity) and tungsten from Kurt J. Lesker (19.35 g/cm^3, 99.95% purity) were used. Boron and tungsten thin films were deposited on a silicon (100) polished substrate (Spi Supplies) with ambient temperature. During deposition, the target was rotated to avoid crater formation. The deposition time was 30 minutes (18000 pulses) for each experiment. The laser deposited film surface was subject to inspection under a Scanning Electron Microscope: JEOL, JSM-6010PLUS/LV InTouchScope™. The images of the plasma plume were registered with the use of an ICCD camera. The plasma was imaged on the camera using a 180 cm focal length camera lens. The image intensifier was gated for an exposure time of 5 ns, while the delay time between the laser pulse and the pulse triggering the image intensifier was gradually changed.

4. RESULTS AND DISCUSSION

4.1. Mechanisms of Ablation

During the interaction of the laser beam with a material, the target is heated to a temperature exceeding its boiling point and sometimes its critical temperature [10, 13]. Assuming a constant fluence, the different mechanisms of ablation can occur depending on the critical temperature. In the case where the target temperature is lower than 0.9 T_c mainly evaporation occurs. Explosive boiling begins above this limit. This phenomenon results in nanoparticles and microparticles with target composition present in the plasma plume, besides the expected electrons, ions and neutrals. Both models can be observed during the ablation of tungsten and boron, depending on the laser fluence. Due to the high critical temperature (14778 *K* [18]) and high absorption coefficients 4.4×10^7 and 8.9×10^7 *1/m* [19] respectively, for 1064 *nm* and 355 *nm* laser wavelengths tungsten is a material for which evaporation takes place primarily for the laser intensity below 6×10^{10} W/cm^2 [20]. Figure 1 shows evolution of surface temperature at beam centre r = 0 for laser wavelengths 1064 *nm* and 355 *nm* for tungsten and boron at the laser fluence 10 J/cm^2. For

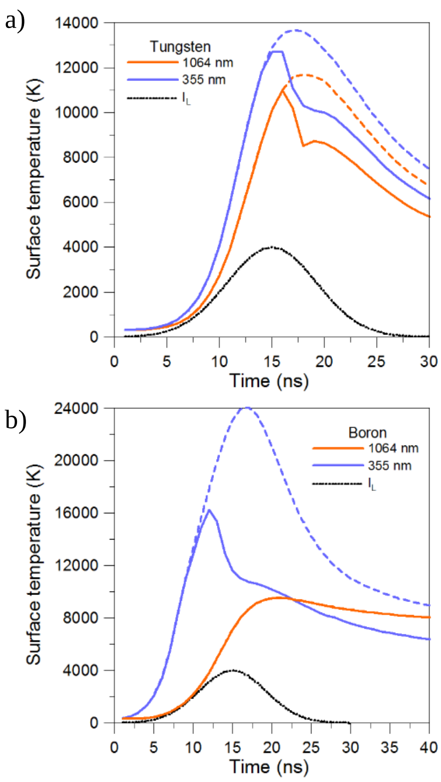

Figure 1. Target surface temperature T_s and laser intensity I_L during first 40 ns (r = 0). a) tungsten target, b) boron target. Broken line denotes case without plasma absorption.

tungsten and the first harmonic of an Nd-YAG laser, the maximum surface temperature is 11700 *K* and for the third 13700 *K* (Fig. 1a). In both cases, the maximum surface temperature is reached in 16 *ns*. At the next time steps the temperature suddenly decreases due to absorption of the laser beam in the plasma.

The laser ablation mechanism is different in the case of boron. For both laser harmonic the maximum temperatures exceed the critical temperature (Fig. 1b), which is about 10000 *K* [18]. In this case, the explosive boiling occurs, which results in a film on which there are different sized irregularly shaped contaminants (Fig. 2a, 2b).

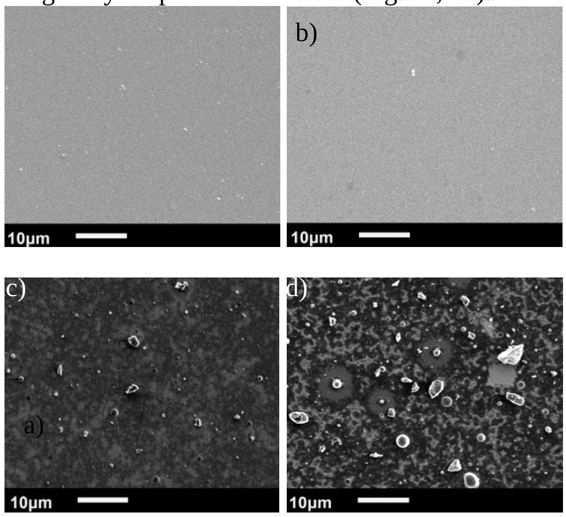

Figure 2. SEM micrograph (×1000) of deposited films: a) boron 355 *nm*, b) boron 1064 *nm* c) tungsten 1064 *nm*, d) tungsten 355 *nm*. *F* = 10 *J/cm2*.

The number and size of debris depends mainly on the optical properties of boron. In the case of λ = 1064 *nm*, the absorption coefficient is 1.3×10^6 m^{-1} [21] and is 23 times lower than for 355 *nm*. The low absorption coefficient results in a much thicker layer of heated material and the critical temperature is exceeded much further (Fig. 3).

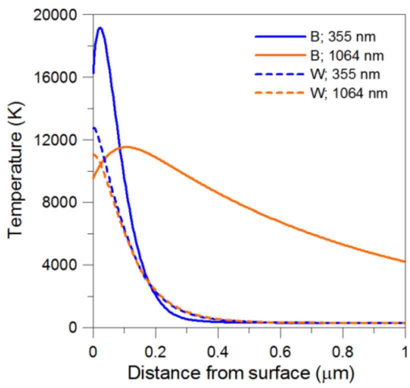

Figure 3. Target temperature T and laser intensity I_L along target axis at the time moments when the surface temperature reaches its maximum value.

The result is an increase in the amount of larger fragments of the target in the deposited film. The maximum temperature for 1064 *nm* is obtained only in 22 *ns*. Due to the small amount of vaporized material, there is practically no plasma absorption. The high maximum temperature ~19000 K is the result of failure of the model neglecting phenomenon of explosive boiling. The rate of temperature equalization with increasing of distance over time is controlled by the coefficient of thermal diffusivity $a = k/(\rho c_p)$. Above the melting point, where it is assumed that the thermal properties and the density does not change, the value of diffusion coefficient is 2.58×10^{-5} and 1.48×10^{-6} m^2/s [15] for tungsten and boron, respectively. The magnitude of this parameter indicates that subsurface overheating of a boron target is equalized much more slowly than in the case of tungsten. Moreover, in the case of tungsten, in connection with larger absorption coefficients, the laser beam penetrates the target to a lower depth.

Both of these phenomena result in the maximum temperature located at the surface and the ablation process mainly by the evaporation of the surface. As a result, the surface of deposited tungsten films is smooth (Fig. 2c, 2d).

This phenomenon is quite different in the case of boron when evaporation from the surface results in maximum of temperature placed at a certain depth. The critical temperature is achieved earlier below surface. The target surface erupts as a result of high stress. In the case of 1064 *nm*, a large amount of energy is accumulated at a depth of about 1 μm. Lower thermal diffusivity of boron causes the increase of target cooling time (Fig. 1b). The studies of ablation of non-metallic materials showed that the process should be carried out with a sufficiently low fluence in order to avoid the phase explosion [10, 11]. However, in the case of boron ablation with the first harmonic, such a procedure could result in temperature decrease below the critical, but simultaneously could cause the lack of ablation.

4.2. Plasma Properties

The first attempt in modelling the expansion of boron and tungsten plasma plume was taken in [15]. The calculated distributions of plasma parameters in the early phase of expansion show that plasma temperatures are higher in the case of tungsten, but the velocities are higher in the case boron [15].

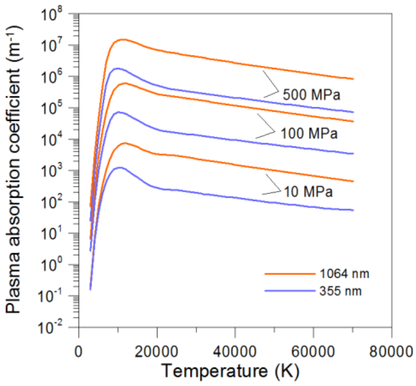

Figure 4. Absorption of 1064 *nm* and 355 *nm* laser radiation in tungsten vapour under pressure 10, 100 and 500 *MPa*.

Differences in the distribution of velocity are logical and based on the weight difference of the two elements. In the case of the temperature distribution, it was necessary to analyse absorption of laser radiation by the plasma of both elements [15]. It was assumed that the ablation process occurs only as a result of evaporation. As shown in the previous section, in modelling of boron the significant approximation was used. Therefore, the effect of the laser wavelength on the behaviour of the plasma is discussed only for tungsten ablation. Figure 4 shows the distribution of the absorption coefficient of tungsten for different temperatures, pressures, and laser wavelength. For the pressure 10^8 *Pa*, the absorption coefficient of 355 *nm* laser radiation is 8.4 times lower than that of 1064 *nm*.

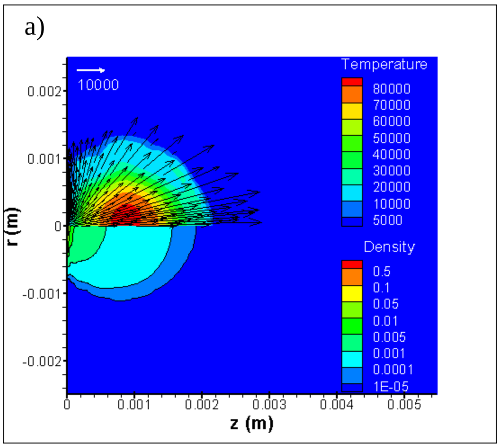

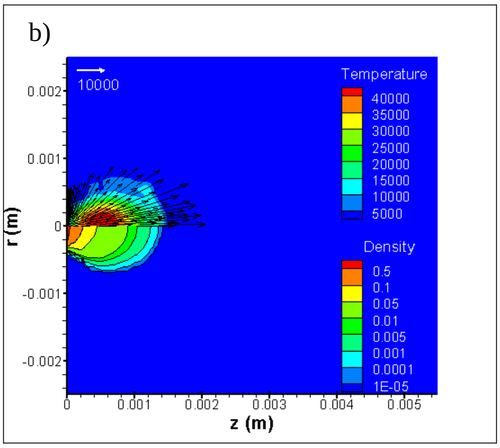

Figure 5. Distribution of density, temperature and velocity in plasma induced during laser ablation of tungsten 100 *ns* after the beginning of the laser pulse for a) 1064 *nm* and b) 355 *nm* laser wavelength.

This affects the plasma ignition timing and its properties. The calculated distributions of plasma temperature and pressure after 100 *ns* of expansion (Fig. 5) show that plasma temperatures are higher in the case of 1064 *nm*, but the pressures and densities are higher in the case of 355 *nm*, which is in agreement with experimental findings [11, 22]. Smaller penetration depth and reflection coefficient *R* in the case of 355 *nm* causes a higher surface temperature of the target; thus, the greater the rate of ablation. The greater ablation rate results in larger mass density of the ablated plume; hence, in higher pressures. An additional consequence of a higher ablation rate is slower expansion and smaller dimensions of the plasma plume. Higher plasma temperature in the case of 1064 *nm* is the result of lower density and stronger plasma absorption. At 100 *ns* after the beginning of the laser pulse, the maximum temperature for the third harmonic is 2 times lower than in the case of the first harmonic of laser irradiation and is about 45000 *K*.

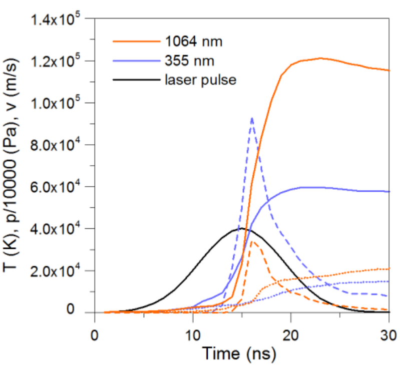

Figure 6. Tungsten plasma parameters during 30 *ns* after the beginning of laser pulse (at *r* = 0) for 1064 *nm* and 355 *nm* laser wavelengths. Dotted line- velocity, broken – pressure, solid – temperature.

The distribution of tungsten plasma parameters during 30th *ns* after the beginning of laser pulse at *r* = 0 is shown in Figure 6. As has been discussed in previous works, the acceleration of the plasma is caused by the hydrodynamic effects [23]. The same is in the case of tungsten. To about 15th *ns*, pressure increases and there is plasma ignition.

Due to the large difference in absorption coefficients depending on the wavelength of the laser, the ignition in the case of 1064 *nm* occurs at a pressure of about 3×10^8 *Pa*, which is three times lower than that for 355 *nm*. In the next time steps, the pressure decreases rapidly, causing the acceleration of the plasma plume. The decrease in density due to the expansion and intensive absorption of energy from the laser beam causes a rapid increase of temperature and velocity. After 30 *ns*, the velocity of the plume ablated by 355 *nm* is 14850 *m/s*, while the velocity of the plume ablated by 1064 *nm* reaches 20750 *m/s* (Fig. 6). For 10 J/cm^2, the total absorption of laser beam is at the level of 6% in the case of 355 *nm* radiation and about 3.5% in the case of 1064 *nm*. As shown in Figure 7a, the decrease in intensity of laser radiation due to laser absorption occurs just before the pulse maximum; e.g., in 13th *ns* in the case of 355 *nm* and 14th *ns* for 1064 *nm*. In both cases, the maximum of absorption is in 17th ns, and is the biggest on the axis of the plasma (Fig. 7b). Greater value of the absorbed energy for third harmonic is due to the earlier ignition and higher absorption coefficient, which strongly grow with increase of plasma pressure (Fig. 4).

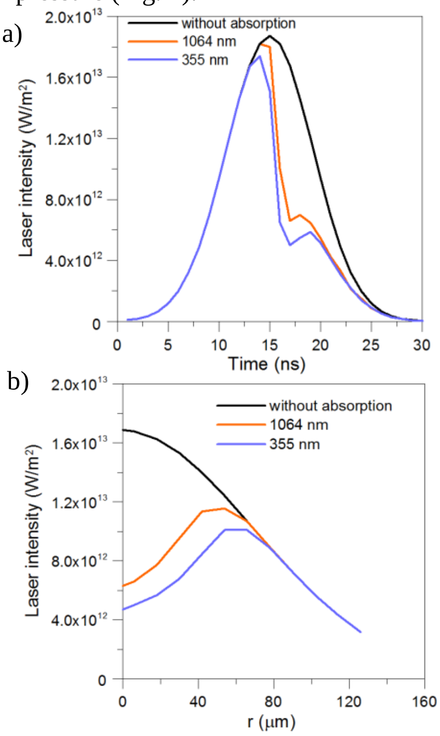

Figure 7. Distribution of laser intensity for 1064 *nm* and 355 *nm* laser wavelengths: a) on the axis during laser pulse, b) radial distribution at *t* = 17 *ns*.

4.3. Experimental Validation

a)

b)

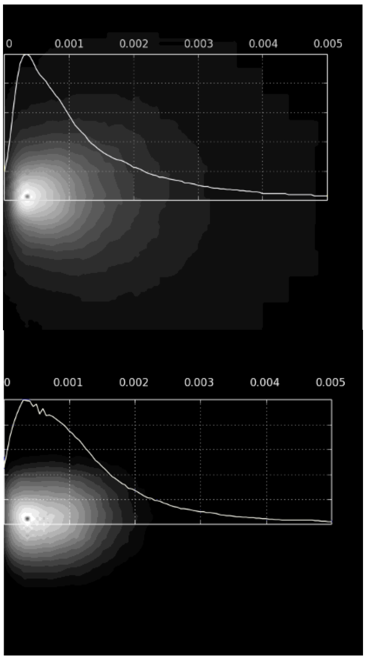

Figure 8. ICCD images of tungsten plasma at delay time 100 ns for a) 1064 *nm* and b) 355 *nm*. Solid line denotes the intensity distribution of plasma radiation on the axis of plasma *r* = 0.

The plasma plume propagation was studied by optical imaging at 80-400 *ns* time delay after the laser shot. The images of tungsten plasma at delay time 100 *ns* for 355 *nm* and 1064 *nm* are presented in Figures 8a and 8b, respectively. For every single image of the plasma plume, the half-Lorentzian plot was fitted to an axis intensity. The Lorentzian plot position is taken as a maximum intensity of the plasma plume, and FWHM is a level of plasma expansion.

a)

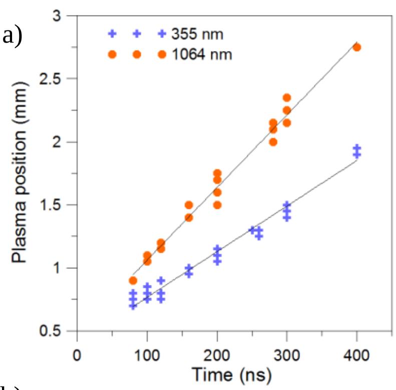

b)

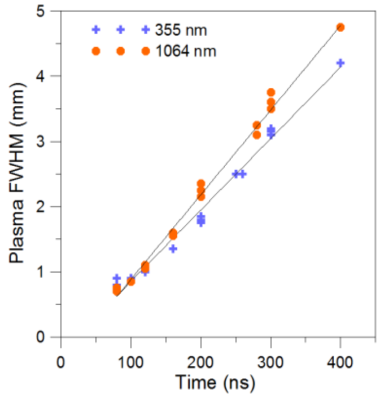

Figure 9. Experimental tungsten plasma plume parameters for 1064 and 355 nm laser wavelengths. a) velocity of plasma propagation, b) velocity of plasma expansion.

Figure 9 presents tungsten plasma position and FWHM of Lorentzian plot fitted to plasma intensity distribution. On the basis of plasma propagation and expansion in time, the plasma displacement and expansion velocity were calculated, respectively. Total velocity of plasma front is defined as a sum of both velocities mentioned above. Results are presented in Table 1.

Table 1. Comparison of tungsten plasma velocity of different wavelengths.

Velocity [*m/s*]	355 *nm*	1064 *nm*
Plasma displacement	3580	5800
Plasma expansion	10545	13000
Total	14125	18800

The quantitative comparison of the experimental plasma shape with the theoretical results is difficult because the images show plasma radiation, which depends both on plasma density and temperature. However, plasma dimensions are similar; e.g., after 100 *ns*, the tungsten plasma diameter is about 2 *mm*. The front velocities obtained from the experimental plasma images are only 10% lower than those calculated in the model.

5. SUMMARY

In this paper, the interaction of an Nd-YAG nanosecond laser beam with a tungsten and boron target induced during ablation plasma are studied theoretically. The calculations show the fundamental differences in ablation of both species. In the case of tungsten, the evaporation of material is controlled by the plasma formation, and consequently, the absorption coefficient. The dense plasma plume can block laser radiation and limit energy transfer from the laser beam to the material. In the case of boron, the explosive ablation is observed. Such behaviour is affected by subsurface heating and transition to super critical state. In the case of 1064 *nm* wavelength, the effect is magnified by the high penetration depth of the laser beam. Therefore, in the ceramics target with a boron excess [1, 24], there may be adverse phenomena which impact the quality of the deposited film.

The calculations show considerable increase of the velocity of the plasma plume due to hydrodynamic effects. In the case of laser ablation of tungsten with 1064 *nm* wavelength, in comparison with 355 *nm*, the plasma plume has a higher energy due to the higher temperature and velocity. At the same time, less material is transported in the plume. Both of these parameters are responsible for the deposition rate of the film and its adhesion. The plume velocity obtained from the model is close to that observed in the experiment carried out in similar conditions.

ACKNOWLEDGEMENTS

This work was supported by the National Science Centre (Poland). Research Project: UMO-2012/05/D/ST8/03052

REFERENCES

[1] Mohammadi, R., Lech, A.T., Xie, M., Weaver, B.E., Yeung, M.T., Tolbert, S.H. and Kaner, R. B., 2011, "Tungsten Tetraboride, an Inexpensive Superhard Material", *Proc Natl Acad Sci* Vol. 108 (27), pp. 10958-10962.

[2] Liang, Y., Fu, Z., Yuan, X., Wang, S., Zhong, Z., and Zhang, W., 2012, "An Unexpected Softening from WB_3 to WB_4", *Europhys Lett*, Vol. 98, pp. 66004.

[3] Rau, J.V., Latini, A., Teghil, R., De Bonis, A., Fosca, M., Caminiti, R., Rossi Albertini, V., 2011, "Superhard Tungsten Tetraboride Films Prepared by Pulsed Laser Deposition Method", *ACS Appl Mater Interfaces*, Vol. 3, pp. 3738–3743.

[4] Dellasega, D., Merlo, G., Conti, C., Bottani C. E., and Passoni, M., 2012, "Nanostructured and Amorphous-like Tungsten Films Grown by Pulsed Laser Deposition", *J Appl Phys*, Vol. 112, pp. 084328

[5] Friedmann, T. A., McCarty, K. F., Klaus, E. J., Barbour, J. C., Clift, W. M., Johnsen, H. A., Medlin, D. L., Mills, M. J., and Ottesen, D. K., 1994, "Pulsed Laser Deposition of BN onto Silicon (100) Substrates at 600˚C", *Thin Solid Films*, Vol. 237, pp. 48-56.

[6] Bulgakova, N.M., Zhukov, V.P., Collins, A.R., Rostohar, D., Derrien, T. J.-Y., and Mocek T., 2015, "How to Optimize Ultrashort Pulse Laser Interaction with Glass Surfacesin Cutting Regimes?", *Appl Surf Sci*, doi:10.1016/j.apsusc.2014.12.142,

[7] Kubkowska, M., Gasior, P., Rosinski, M., Wolowski, J., Sadowski, M.J., Malinowski, K., and Skladnik-Sadowska, E. 2009, "Characterisation of Laser-Produced Tungsten Plasma Using Optical Spectroscopy Method", *Eur Phys J D*, Vol. 54, pp. 463–466.

[9] Jong-Won Yoona, and Kwang Bo Shim, 2011, "Growth of Crystalline Boron Nanowires by Pulsed Laser Ablation", *J Ceram Procces Res*, Vol. 12(2), pp. 199-201.

[8] Afif, M., Girardeau-Montaut, J.P., Tomas, C., Romand M., Charbonnier M., Prakash, N.S., Perez, A., Marest, G., and J.M. Frigerio, 1996, "In Situ Surface Cleaning of Pure and Implanted Tungsten Photocathodes by Pulsed Laser Irradiation", *Appl Surf Sci*,Vol. 96-98, pp. 469-473.

[10] Bulgakova, N.M., and Bulgakov, A.V., 2001, „Pulsed Laser Ablation of Solids: Transition from Normal Vaporization to Phase Explosion", *Appl Phys A*, Vol. 73(2), pp. 199-208

[11] Hoffman, J., Chrzanowska, J., Kucharski, S., Moscicki, T., Mihailescu, I.N., Ristoscu, C., and Szymański, Z., 2014, "The Effect of Laser Wavelength on the Ablation Rate of Carbon", *Appl Phys A*, Vol. 117, pp. 395-400

[12] Singh, R.K., and Narayan, J., 1990, "Pulsed-laser Evaporation Technique for Deposition of Thin Films: Physics and Theoretical Model", *Phys Rev B*, Vol. 41, pp. 8843-8859.

[13] Kelly, R., and Miotello, A., 1996, "Comments on Explosive Mechanisms of Laser Sputtering", *Appl Surf Sci*, Vol. 96-98, pp. 205-215.

[14] Moscicki, T., Hoffman, J., and Szymanski, Z., 2013, "The effect of laser wavelength on laser-induced carbon plasma", *J Appl Phys*,Vol. 114, pp. 083306.

[15] Moscicki, T., 2014, "Expansion of laser-ablated two-component plume with disparate masses", *Phys Scripta*, Vol. T161, pp. 014024.

[16] Knight, C. J., 1979 , "Theoretical Modelling of Rapid Surface Vaporization with Back Pressure", *AIAA Journal*, Vol. 17, pp.519-523.

[17] ANSYS® Academic Research, Release 15.0, Help System, Fluent Documentation, ANSYS, Inc.

[18] Blairs, S., and Abbasi M., H., 2006, "Correlation Between Surface Tension and Critical

Temperatures of Liquid Metals”, *J Colloid Interf Sci,* Vol. 304, pp. 549–553

[19] Rakic, A. D., Djurisic, A. B., Elazar, J. M., and Majewski, M. L., 1998, “Optical Properties of Metallic Films for Vertical-cavity Optoelectronic Devices”, *Appl Opt,* Vol. 37, pp. 5271-5283

[20] Yahiaoui, K., Kerdja, T., and Malek, S., 2010, “Phase Explosion in Tungsten Target under Interaction with Nd : YAG Laser Tripled in Frequency”, *Surf Interface Anal*, Vol. 42, pp. 1299–1302

[21] Morita, N., and Yamamoto, A., 1975,”Optical and Electrical Properties of Boron”, *Jpn J Appl Phys,* Vol. 14, pp. 6

[22] Hussein, A.E., Diwakar, P.K., Harilal, S.S., and Hassanein, A., 2013 ,“The Role of Laser Wavelength on Plasma Generation and Expansion of Ablation Plumes in Air”, *J Appl Phys*, Vol. 113, pp. 143305

[23] Hoffman, J., Moscicki, T., and Szymanski, Z., 2012, “Acceleration and Distribution of Laser-Ablated Carbon Ions Near the Target Surface”, *J Phys D Appl Phys,* Vol. 45, pp. 025201

[24] Moscicki, T., Radziejewska, J., Hoffman, J., Chrzanowska, J., Levintant-Zayonts, N., Garbiec, D., and Szymanski, Z., 2015, “WB_2 to WB_3 phase change during reactive spark plasma sintering and pulsed laser ablation/deposition processes”, *Ceram Int,* Vol. 41 , pp. 8273-8281

Conference on Modelling Fluid Flow (CMFF'15)
The 16th International Conference on Fluid Flow Technologies
Budapest, Hungary, September 1-4, 2015

LOSS COEFFICIENT OF FINITE LENGTH DIVIDING JUNCTIONS

Gergely KRISTÓF[1], András TOMOR[2]

[1] Corresponding Author. Department of Fluid Mechanics, Budapest University of Technology and Economics. Bertalan Lajos u. 4 – 6, H-1111 Budapest, Hungary. Tel.: +36 1 463 4073, E-mail: kristof@ara.bme.hu
[2] Department of Fluid Mechanics, Budapest University of Technology and Economics. E-mail: tomor@ara.bme.hu

ABSTRACT

The subject of this study is the determination of the hydraulic loss coefficient of a bore on a cylindrical pipe with a given diameter and wall thickness, which is the main element of the hydraulic model of fluid distribution systems. In the case of a single-phase flow, the loss coefficient depends on four dimensionless parameters: the Reynolds number in the header, the ratio of the flow velocities in the bore and the header, the diameter ratio and the ratio of the wall thickness and the diameter of the pipe. Due to the large number of cases, it was not possible to investigate this four-dimensional parameter space thoroughly by the methods described in the literature; hence, a novel approach is used for the determination of the loss coefficient by means of the modern three-dimensional computational fluid dynamics methods.

In order to determine the loss coefficient of the bore, more than 1000 three-dimensional simulations were run. The results of these numerical simulations provide an opportunity to elaborate more accurate and simple correlations based on a novel formalism in the most important parameter range for the engineering practice. The accuracy of the new model is proved by comparing its results with literature data.

Keywords: CFD, cylindrical bore, loss coefficient

NOMENCLATURE

A_1	[-]	constant
A_2	[-]	constant
B_1	[-]	constant
B_2	[-]	constant
C	[-]	constant
C_f	[-]	turning loss coefficient
D	[-]	constant
D_1	[m]	inner diameter of the header
D_2	[m]	inner diameter of the bore
L_1	[m]	length of the segment of the pipe
L_2	[m]	wall thickness of the pipe
Re	[-]	Reynolds number
n	[-]	number of simulations for a fitting
p_d	[Pa]	dynamic pressure
p_t	[Pa]	total pressure
p_0	[Pa]	ambient pressure
q_v	[m^3/s]	volume flow rate
v	[m/s]	average velocity
ζ_1	[-]	loss coefficient belongs to the dynamic pressure in the header
ζ_{1t}	[-]	total loss coefficient belongs to the dynamic pressure in header
ζ_2	[-]	loss coefficient belongs to the dynamic pressure in the bore
ζ_{2t}	[-]	total loss coefficient belongs to the dynamic pressure in the bore
ζ_3	[-]	loss coefficient belongs to the dynamic pressure in the bore assuming $\zeta_1 = 1$
ζ_{3t}	[-]	total loss coefficient belongs to the dynamic pressure in the bore assuming $\zeta_1 = 1$
λ	[-]	pipe friction factor

Subscripts and Superscripts

crit	critical value
e	extended value
j	*j*th simulation
1	at the inlet of the investigated segment
2	at the outlet of the bore
~	calculated with power-law formulas
^	obtained by fitting

1. INTRODUCTION

Fluid distribution systems are widely used in industrial processes. Dividing flow manifolds are major elements of these systems, which are applied to the situations where a fluid stream has to be divided into several parallel streams.

This paper focuses on the determination of the hydraulic loss coefficient of a perpendicular, cylindrical bore on a cylindrical pipe with a given diameter and wall thickness. The bore is one of the main elements of the hydraulic model of fluid distribution systems and its hydraulic resistance involves the largest uncertainty.

In the case of a single-phase flow, the loss coefficient depends on four dimensionless parameters: the Reynolds number in the header, the ratio of the flow velocities in the bore and the header, the diameter ratio and the ratio of the wall thickness and the diameter of the pipe. The latter parameter approaches infinity for "T" junctions, which allows for the comparison of new results with known correlations at the high limit of wall thickness to diameter ratio. Experimental investigations [1-3] could not resolve the four-dimensional parameter space in detail and in some cases it is difficult to estimate the model error rising from geometrical differences. Moreover, earlier studies do not investigate the effect of the length of the port, which has a major impact on flow structure, and the port length of dividing-flow manifolds is often small.

A novel approach is used for the determination of the loss coefficient with the help of the modern three-dimensional computational fluid dynamics (CFD) methods, which makes it possible to investigate the mentioned parameter space in more detail. The loss coefficient of the bore is determined for 40 different geometries by using the results of more than 1000 three-dimensional CFD simulations. The results of these numerical simulations provide an opportunity to elaborate more accurate and yet simple correlations based on a novel formalism in the most important parameter range for the engineering practice.

2. RESISTANCE CHARACTERISTICS OF A BORE

2.1. The definition of loss coefficients

A small section of a header pipe with one single bore of normal axis is investigated. The interpretation of geometrical details can be seen in Figure 1. The length of the segment and the wall thickness of the pipe are L_1 and L_2. The inner diameters of the header and the bore are D_1 and D_2, respectively. We assume that $D_2 \leq D_1$.

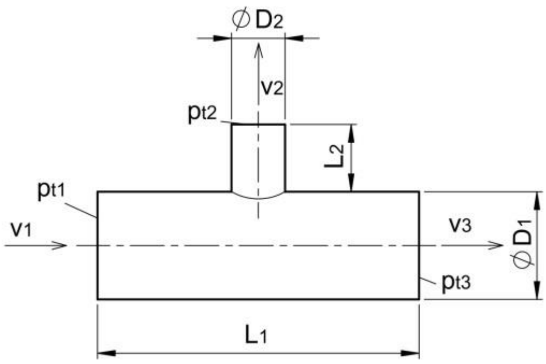

Figure 1. The geometrical model of the bore

In the case, when fluid is discharged through the bore, the flow is divided into two paths. The total pressure loss along each path can be expressed in terms of distinct physical origin. Each term has unique dependence on geometrical and kinematical parameters, which can be expressed by the Bernoulli equation formulated for an incompressible flow. The total pressure drop between the inlet of the investigated section and the outlet of the bore can be written as

$$p_{t1} - p_{t2} = \lambda_1 \frac{L_1}{2D_1} p_{d1} + C_f\, p_{d2} + \lambda_2 \frac{L_2}{D_2} p_{d2} \qquad (1)$$

in which p_d and p_t are dynamic and total pressures in locations indicated by numerical indices. Hydraulic losses are expressed in terms of λ pipe friction factors and C_f turning loss coefficient. The exit loss is modelled according to an isobaric jet model by assuming $p_{t2} - p_0 = p_{d2}$.

In our analysis we reformulate the above expression of turning losses, which is conventionally applied in numerous related studies such as by Wang et al. [4, 5], by introducing, according to Eq. (2), the loss coefficients ζ_1 and ζ_2 which incorporate the dependence of total pressure loss on dynamic pressures in cross-sections 1 and 2. We also assume that ζ_1 and ζ_2 are simpler step functions of the velocity ratio v_2/v_1, having constant values below and above a critical value of the velocity ratio. This assumption, which greatly simplifies the function parameterization, will be validated during the fitting procedure.

$$C_f\, p_{d2} = \zeta_1 p_{d1} + \zeta_2 p_{d2} \qquad (2)$$

Eq. (1) can be written in a more compact form considering the ambient pressure the reference and introducing the total loss coefficients ζ_{1t} and ζ_{2t}:

$$p_{t1} = \zeta_{1t}\, p_{d1} + \zeta_{2t}\, p_{d2}\,, \qquad (3)$$

where

$$\zeta_{1t} = \zeta_1 + \lambda_1 \frac{L_1}{2D_1} \text{ and} \qquad (4)$$

$$\zeta_{2t} = \zeta_2 + \lambda_2 \frac{L_2}{D_2} + 1\,. \qquad (5)$$

2.2. CFD model

Determination of the loss coefficient of a single branch or bore by CFD simulations is a relatively new method. Liu et al. [6], Badar et al. [7] and Ramamurthy et al. [8] have already applied CFD to this purpose; however, their formalisms are different from that of this study. They use the classical loss coefficient approach and express the flow turning loss by only one loss coefficient; moreover, the CFD models are also different and earlier models were not aimed at the exploration of the parameter space.

In this paper, the loss coefficients are determined for 40 different geometries. Due to the large number of cases, it is reasonable to use easily parameterizable geometry designer and meshing programs; hence, geometries are created by ANSYS DesignModeler and meshes are prepared by ANSYS Meshing using ANSYS Workbench 14.5.

The geometry is slightly simplified: only one half of the manifold segment is modelled taking advantage of the symmetry and the outlet of the bore is modelled as a planar surface neglecting the effect of the curved surface of the cylindrical pipe. Hence, the bore is treated as a short branch.

High-quality meshes for the investigation of pipes can be created using the MultiZone method of the ANSYS Meshing program. The created mesh is not structured, but its performance is similar to a well-prepared structured mesh. Tetra cells are used only in the vicinity of the branch and inflation layer is generated near the walls.

The ANSYS FLUENT 14.5 CFD software is applied for the execution of the simulations. The model solves the standard three-dimensional Reynolds-averaged continuity and Navier–Stokes equations for turbulent steady-state flow based on the k-ω SST turbulence model [9]. The investigated fluid is incompressible water; hence, the pressure-based solver is chosen. The pressure-velocity coupling is achieved using the Coupled algorithm. The second order upwind differencing scheme is used for flux formulation.

For the header, at the inlet, velocity inlet boundary condition is used. At this cross-section the input profiles for velocity and turbulent quantities are defined case-by-case from the results of supplementary simulations of flow in infinite cylindrical pipes with the help of periodic boundary conditions. In the case of a manifold with multiple bores this velocity profile is modified by the bores, therefore the results presented herein correspond to a single bore junction; however, it is assumed that this modification has only very small influence on lateral discharge. At the outlet of the header, static overpressure is applied (pressure-outlet). In order to provide realistic outlet conditions even in the presence of recirculating flow, pressure-outlet boundary condition is not prescribed at the outlet of the bore, but on the boundary surfaces of an extended cuboid around it (pressure-outlet-0). Here, the pressure is specified as zero. Wall and symmetry boundary conditions are applied according to the pipe wall and the plane of symmetry, respectively.

All the simulations are run until convergence is achieved. The results of numerical modelling are also checked for mesh independence. According to the mesh independence study, a mesh with a cell number of about 240,000 can be accepted; the mesh was refined two times and all the relative differences between the results obtained on the coarsest and finest meshes were below 2.9%. A typical mesh for the investigated flow manifold segment can be seen in Figure 2. The boundary conditions are also represented.

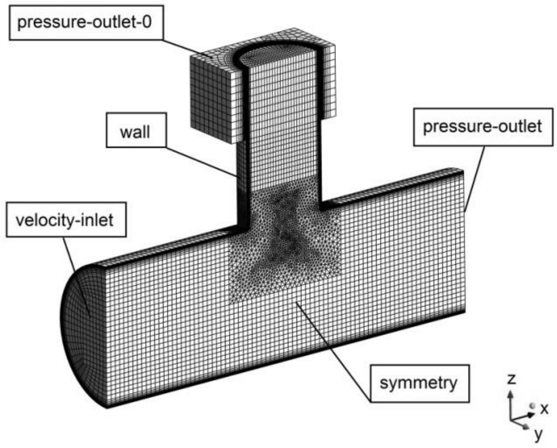

Figure 2. A typical mesh for the investigated section. The boundary conditions are also represented.

2.3. The fitting procedure

According to Eq. (3), the p_{t1} total pressure can be illustrated as a function of the v_2 outlet velocity at a given v_1 inlet velocity and the obtained curve is a parabola. Hence, for a prescribed v_1 velocity the simulation points corresponding to the different v_2 velocities are located along a parabola. If the loss coefficients are functions of geometric parameters and Re_1 only, they can be determined for all geometries by applying a fitting procedure, e.g. the least squares method (LSM). Applying LSM for the determination of the loss coefficients in Eq. (3) one obtains the following two equations:

$$\frac{\partial\left(\sum_{j=1}^{n}\left(p_{t1j}-\hat{p}_{t1j}\right)^2\right)}{\partial\zeta_{1t}}=0 \text{ and} \tag{6}$$

$$\frac{\partial\left(\sum_{j=1}^{n}\left(p_{t1j}-\hat{p}_{t1j}\right)^2\right)}{\partial\zeta_{2t}}=0 \tag{7}$$

where p_{t1j} is the total pressure at the inlet obtained by the jth simulation, n is the number of the simulations used for a given fitting procedure and $\hat{p}_{t1j}$ can be calculated as follows:

$$\hat{p}_{t1j} = \zeta_{1t} p_{d1} + \zeta_{2t} p_{d2j} \tag{8}$$

with p_{d2j} dynamic pressure in the bore obtained by the jth simulation. Substituting Eq. (8) into Eqs. (6) and (7) and performing the derivation the following system of linear equations can be written:

$$\sum_{j=1}^{n} p_{d1}\left(\zeta_{1t} p_{d1} + \zeta_{2t} p_{d2j} - p_{t1j}\right) = 0 \tag{9}$$

$$\sum_{j=1}^{n} p_{d2j}\left(\zeta_{1t} p_{d1} + \zeta_{2t} p_{d2j} - p_{t1j}\right) = 0 \, . \tag{10}$$

The loss coefficients can be determined by solving this system of equations (consists of Eqs. (9) and (10)). The fitting procedure is applicable for different Reynolds numbers and the loss coefficients can be illustrated as a function of Re_1.

If the total pressure in the header is relatively low, it could be necessary to set the value of the ζ_1 loss coefficient to unity in order to avoid negative flow rate through the bore. In this case, the flow turning loss can be calculated with the following formula:

$$C_f p_{d2} = p_{d1} + \zeta_3 p_{d2} \tag{11}$$

and the total loss coefficient ζ_{3t} is defined as follows:

$$\zeta_{3t} = \zeta_3 + \lambda_2 \frac{L_2}{D_2} + 1 \, . \tag{12}$$

If $\zeta_1 = 1$ is assumed, the following one equation has to be solved for the determination of the ζ_{3t} loss coefficient:

$$\sum_{j=1}^{n} p_{d2j}\left(\left(1 + \lambda_1 \frac{L_1}{2D_1}\right) p_{d1} + \zeta_{3t} p_{d2j} - p_{t1j}\right) = 0 \, . \tag{13}$$

The fitting procedure is presented in detail for a particular geometry with $D_2/D_1 = L_2/D_1 = 0.625$. The loss coefficients are determined for nine different Reynolds numbers (from 10,000 to 300,000) and 5-10 simulation points are used for each fitting. The required quantities for the fitting procedure in Eqs. (9), (10) and (13) could be determined by the simulation results. The mass-weighted average of the total pressure at the inlet (p_{t1j}) and the volume flow rate in the bore (q_{v2j}) – from which the v_{2j} velocity is calculated as $v_{2j} = 8q_{v2j}/(D_2^2 \pi)$ – are reported for each simulation. The prescribed inlet velocities (v_1) are known for all simulations. Some representative results of the fitting procedure can be seen in Figure 3.

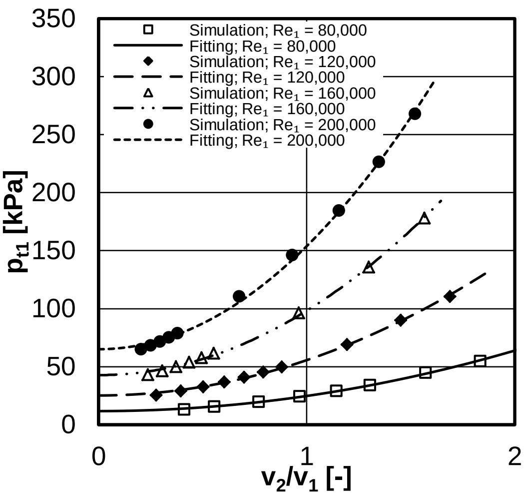

Figure 3. Representative results of the fitting procedure: Total pressure loss as a function of the velocity ratio for fitting both loss coefficients

The total loss coefficients ζ_{1t}, ζ_{2t} and ζ_{3t} can be directly determined by applying this fitting procedure. The ζ_1, ζ_{2e} and ζ_{3e} loss coefficients can be calculated as $\zeta_1 = \zeta_{1t} - \lambda_1 L_1/(2D_1)$, $\zeta_{2e} = \zeta_{2t} - 1$ and $\zeta_{3e} = \zeta_{3t} - 1$, respectively. The value of ζ_{2e} and ζ_{3e} also involves the non-negligible friction loss due to the wall of the bore ($\lambda_2 L_2/D_2$); however, it is reasonable to introduce ζ_{2e} and ζ_{3e} because they can be represented as a function of the Reynolds number in the header (Re_1).

In the case of a smooth pipe, the λ_m friction factor can be calculated with the following well-known formulas:

$$\lambda_m = \frac{64}{Re_m} \text{ for } Re_m < 2320 \, , \tag{14}$$

$$\lambda_m = \frac{0.3164}{Re_m^{0.25}} \text{ for } 2320 \le Re_m \le 10^5 \text{ and} \tag{15}$$

$$\lambda_m = 0.0032 + \left(\frac{0.221}{Re_m^{0.237}}\right) \text{ for } Re_m > 10^5 \tag{16}$$

with $m = 1$ for the header and $m = 2$ for the bore.

According to the nine investigated Reynolds number, the ζ_1, ζ_{2e} and ζ_{3e} loss coefficients can be illustrated as a function of Re_1 (Figure 4).

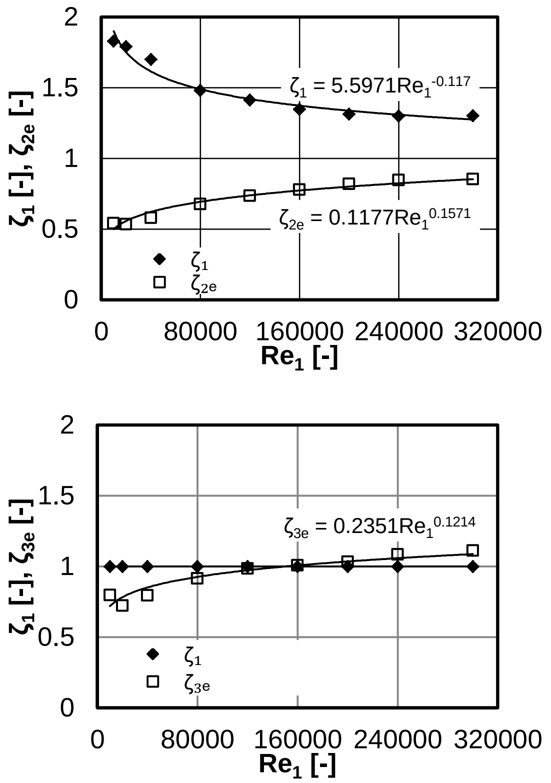

Figure 4. Representative results – loss coefficients as a function of Re_1. Upper: fitting two loss coefficients; Lower: fitting only one loss coefficient (assuming ζ_1 = 1). $D_2/D_1=L_2/D_1$=0.625

As can be seen in Fig. 4, each loss coefficient approximately follows a power-law. Therefore, the loss coefficients can be calculated with the following power-law formulas for all Reynolds numbers:

$$\tilde{\zeta}_1 = A_1\, Re_1^{B_1}\,, \tag{17}$$

$$\tilde{\zeta}_{2\mathrm{e}} = A_2\, Re_1^{B_2} \text{ and} \tag{18}$$

$$\tilde{\zeta}_{3\mathrm{e}} = C\, Re_1^{D}\,, \tag{19}$$

where $\tilde{\zeta}_1$ and $\tilde{\zeta}_{2\mathrm{e}}$ are the approximated loss coefficients obtained by fitting both loss coefficients, $\tilde{\zeta}_{3\mathrm{e}}$ is the approximated loss coefficient assuming ζ_1 = 1, A_1, A_2, B_1, B_2, C and D are constants depend on the geometry.

Analyzing the upper diagram in Fig. 4, it can be clearly seen that the value of the ζ_1 loss coefficient is always larger than unity, and accordingly fitting both loss coefficients provides physically incorrect results for low velocity ratios, because inflow through the bore is made possible for relatively low positive total pressure values in the header – which could be physically meaningless. Therefore, the method with one fitted loss coefficient has to be used for low velocity ratios, and the critical velocity ratio should be determined, above which the effective turning loss coefficient can be determined by fitting two loss coefficients.

The turning loss coefficients for the two different methods can be expressed by the previously introduced loss coefficients as follows:

$$C_{f1} = \zeta_{3\mathrm{e}} + \left(\frac{v_2}{v_1}\right)^{-2} \text{ and} \tag{20}$$

$$C_{f2} = \zeta_{2\mathrm{e}} + \zeta_1\left(\frac{v_2}{v_1}\right)^{-2}. \tag{21}$$

It is important to point out that the C_{f1} and C_{f2} loss coefficients depend directly on the velocity ratio, while ζ_1, $\zeta_{2\mathrm{e}}$ and $\zeta_{3\mathrm{e}}$ depend only on the geometry and Re_1. Hence, C_{f1} and C_{f2} can be illustrated as a function of the velocity ratio. According to the two different approaches, one obtains two different turning loss coefficient curves (Figure 5) and the critical velocity ratio is located at the intersection of the two curves where the following equation is valid:

$$\tilde{\zeta}_{2\mathrm{e}} + \tilde{\zeta}_1\left(\frac{v_2}{v_1}\right)^{-2} = \tilde{\zeta}_{3\mathrm{e}} + \left(\frac{v_2}{v_1}\right)^{-2}. \tag{22}$$

The critical velocity ratio $(v_2/v_1)_{crit}$ can be calculated as:

$$\left(\frac{v_2}{v_1}\right)_{crit} = \sqrt{\frac{\tilde{\zeta}_1 - 1}{\tilde{\zeta}_{3\mathrm{e}} - \tilde{\zeta}_{2\mathrm{e}}}}\,. \tag{23}$$

If $\tilde{\zeta}_1 \geq 1$ and $\tilde{\zeta}_{3\mathrm{e}} > \tilde{\zeta}_{2\mathrm{e}}$, or $\tilde{\zeta}_1 \leq 1$ and $\tilde{\zeta}_{3\mathrm{e}} < \tilde{\zeta}_{2\mathrm{e}}$, then $(v_2/v_1)_{crit}$ exists and can be calculated with Eq. (23).

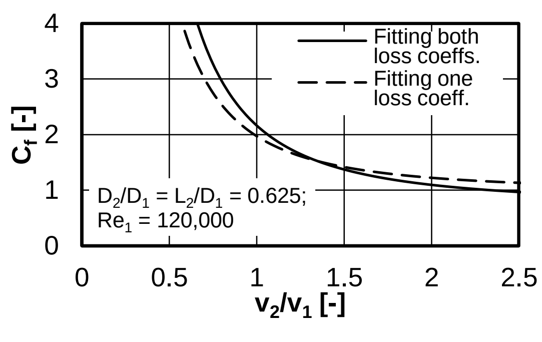

Figure 5. Turning loss coefficients as a function of the velocity ratio for the two different approaches

3. VALIDATION OF THE NEW MODEL

According to a detailed analysis of the model error, all of the fittings are performed by using only three simulation points. 40 different geometries and 9 different Reynolds numbers for each of the geometries are investigated; therefore, 1080 simulations are run. During the simulations, the D_2/D_1 ratio is varied between 0.2 and 1, while a range from 0.1 to 2 is investigated for the L_2/D_1 ratio. The A_1, A_2, B_1, B_2, C, D constants are determined for each of the geometries from the simulation results.

The largest investigated wall thickness (L_2/D_1 = 2) can be considered as a 90-degree “T” junction; therefore, the calculated C_f values can be directly compared with the experimental data provided by Idelchik [10]. It is important to note that the values of ζ_{2e} and ζ_{3e} also involve the non-negligible friction loss due to the wall of the bore; this can moderately increase the calculated turning loss coefficient values and the differences from the reference data [10]. However, Idelchik implies that his loss coefficient values for 90-degree “T” junctions also involve friction losses, which verifies the reasonableness of the introduction of ζ_{2e} and ζ_{3e}.

Figure 6 shows the comparison of the calculated turning loss coefficients with literature data for a diameter ratio of 0.75 and a Reynolds number of 10,000.

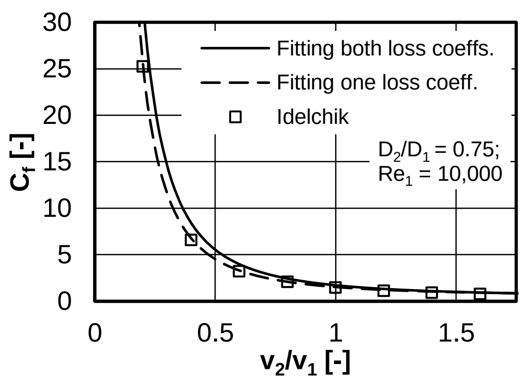

Figure 6. Turning loss coefficients as a function of the velocity ratio – comparison of calculated values with literature data

The calculated turning loss coefficient values approximate the reference data very well. The agreement between the results of fitting one loss coefficient and the data provided by Idelchik is perfect for low velocity ratios; however, there are significant differences between the results of fitting two loss coefficients and the reference data for the low velocity ratio range. The accuracy of the latter method increases with the increase of the velocity ratio and sufficiently accurate results can be obtained for higher velocity ratios.

The small vicinity of the intersection of the two theoretical curves is very important and it is scrutinized with the help of Figure 7.

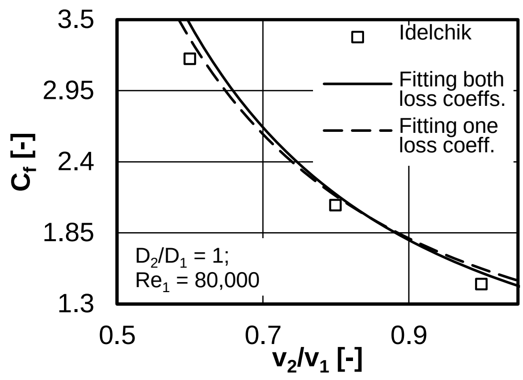

Figure 7. Turning loss coefficients as a function of the velocity ratio – comparison of calculated values with literature data: The small vicinity of the critical velocity ratio

It can be seen in Fig. 7 that below the critical velocity ratio, fitting one loss coefficient gives a better solution for the C_f value; above the critical velocity ratio, the results obtained by fitting two loss coefficients approximate the reference data better.

The calculated turning loss coefficient values are slightly larger than the reference data in all cases. These results agree well with our expectations because the calculated C_f values are moderately increased by an additional friction loss. This friction loss is presumably larger than that in the case of the reference data.

Figure 8 shows the turning loss coefficients as a function of the ratio of the wall thickness and the inner diameter of the pipe for two different diameter and velocity ratios.

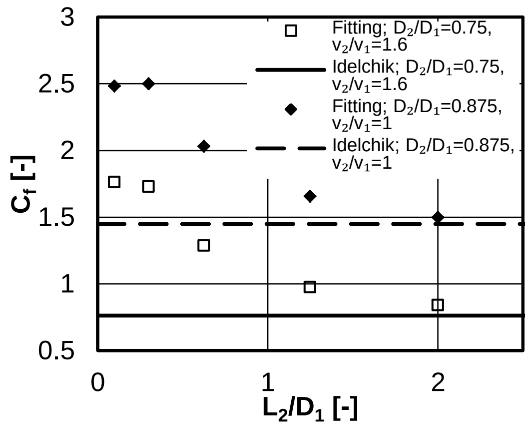

Figure 8. Turning loss coefficient as a function of the ratio of the wall thickness and the inner diameter of the pipe for fitting both loss coefficients – validation of the asymptotic values for large L_2/D_1

The value of the turning loss coefficient decreases with the increase of the wall thickness ratio and approaches the loss coefficient value determined by Idelchik [10] for a 90-degree "T" junction. It can be seen in Fig. 8 that a wall thickness ratio of 2 can be indeed considered as a 90-degree "T" junction.

According to the results of the comparisons, the newly developed fitting procedure is applicable for the determination of the loss coefficients. Below the critical velocity ratio, the turning loss coefficient should be calculated with the approach which uses one loss coefficient; above the critical velocity ratio, this approach can be replaced by the method which uses two loss coefficients. The calculated results approach the available literature data very well; this points to the fact that the investigated four-dimensional parameter space has been accurately resolved.

4. RESULTS AND DISCUSSION

The loss coefficients of the bore are determined for 40 different geometries and 9 different Reynolds numbers for each of the geometries. The loss coefficients as a function of the Reynolds number are approximated by power-law formulas, and the constants of these formulas are determined for all of the geometries. The loss coefficients are calculated with two different approaches in order to achieve the highest accuracy; a flexible method is worked out that properly operates the loss coefficients. The A_1, A_2, B_1, B_2, C and D constants are summarized in Tables (1) and (2) and a guideline is presented for the application of them.

The turning loss coefficient can be calculated as follows:
If

$$\frac{v_2}{v_1} \le \sqrt{\frac{A_1\,Re_1^{B_1}-1}{C\,Re_1^{D}-A_2\,Re_1^{B_2}}}\,, \tag{24}$$

then

$$C_f = C\,Re_1^{D} + \left(\frac{v_2}{v_1}\right)^{-2}, \tag{25}$$

according to fitting one loss coefficient. If

$$\frac{v_2}{v_1} > \sqrt{\frac{A_1\,Re_1^{B_1}-1}{C\,Re_1^{D}-A_2\,Re_1^{B_2}}}\,, \tag{26}$$

then

$$C_f = A_2\,Re_1^{B_2} + A_1\,Re_1^{B_1}\left(\frac{v_2}{v_1}\right)^{-2}, \tag{27}$$

according to fitting both loss coefficients.

Table 1. Constants for the calculation of the loss coefficients – fitting both loss coefficients

D_2/D_1 [-]	L_2/D_1 [-]	A_1 [-]	B_1 [-]	A_2 [-]	B_2 [-]
0.2	0.1	10.083	-0.114	0.8728	0.0313
0.3	0.1	5.8802	-0.087	0.8595	0.0306
0.4	0.1	4.2036	-0.071	0.8274	0.0288
0.5	0.1	3.6174	-0.068	0.7982	0.0302
0.625	0.1	3.4798	-0.075	0.5538	0.0625
0.75	0.1	3.5127	-0.084	0.3438	0.1046
0.875	0.1	2.8319	-0.071	0.3222	0.1122
1	0.1	2.2115	-0.055	0.3855	0.0987
0.2	0.3	3.6332	-0.045	0.8278	0.0087
0.3	0.3	5.8706	-0.087	0.6124	0.0358
0.4	0.3	7.1233	-0.111	0.3742	0.0797
0.5	0.3	4.4354	-0.083	0.401	0.0748
0.625	0.3	5.6771	-0.114	0.1713	0.1489
0.75	0.3	4.2993	-0.099	0.1137	0.1898
0.875	0.3	2.7394	-0.068	0.2005	0.1505
1	0.3	2.8628	-0.078	0.1836	0.1759
0.2	0.625	12.968	-0.168	0.6428	0.0063
0.3	0.625	5.3769	-0.093	0.5567	0.0176
0.4	0.625	5.1465	-0.092	0.4231	0.0421
0.5	0.625	5.1426	-0.099	0.2707	0.0801
0.625	0.625	5.4776	-0.113	0.1331	0.1408
0.75	0.625	3.8547	-0.091	0.1361	0.1422
0.875	0.625	2.3516	-0.056	0.249	0.0993
1	0.625	2.3556	-0.064	0.1674	0.1571
0.2	1.25	23.848	-0.224	0.9259	-0.029
0.3	1.25	6.2569	-0.125	0.7591	-0.017
0.4	1.25	3.2917	-0.074	0.6613	-0.01
0.5	1.25	2.7183	-0.059	0.5255	0.0031
0.625	1.25	2.7805	-0.062	0.3379	0.033
0.75	1.25	2.6523	-0.062	0.1999	0.074
0.875	1.25	2.6878	-0.067	0.1616	0.0898
1	1.25	2.0689	-0.051	0.1502	0.1096
0.2	2	42.031	-0.265	1.291	-0.051
0.3	2	9.7335	-0.165	0.9867	-0.037
0.4	2	3.7704	-0.095	0.8852	-0.035
0.5	2	2.4843	-0.064	0.7852	-0.032
0.625	2	1.5854	-0.025	0.8916	-0.054
0.75	2	1.6507	-0.029	0.6665	-0.039
0.875	2	2.141	-0.053	0.2594	0.0347
1	2	1.4355	-0.025	0.4249	0.0067

Table 2. Constants for the calculation of the loss coefficients – fitting one loss coefficient

D_2/D_1 [-]	L_2/D_1 [-]	C [-]	D [-]
0.2	0.1	0.9385	0.0305
0.3	0.1	0.9503	0.0305
0.4	0.1	0.9419	0.0295
0.5	0.1	0.9644	0.0288
0.625	0.1	0.7926	0.0482
0.75	0.1	0.6455	0.0682
0.875	0.1	0.6293	0.0726
1	0.1	0.7741	0.0566
0.2	0.3	0.8316	0.0129
0.3	0.3	0.6911	0.035
0.4	0.3	0.5352	0.0641
0.5	0.3	0.5505	0.0645
0.625	0.3	0.3766	0.1013
0.75	0.3	0.3129	0.1233
0.875	0.3	0.437	0.1024
1	0.3	0.4808	0.109
0.2	0.625	0.7374	-0.002
0.3	0.625	0.6353	0.0145
0.4	0.625	0.5532	0.0334
0.5	0.625	0.4344	0.0578
0.625	0.625	0.3367	0.0827
0.75	0.625	0.3529	0.0829
0.875	0.625	0.4635	0.0665
1	0.625	0.445	0.0878
0.2	1.25	1.1157	-0.041
0.3	1.25	0.9025	-0.027
0.4	1.25	0.7771	-0.016
0.5	1.25	0.6345	-0.00004
0.625	1.25	0.5011	0.0192
0.75	1.25	0.3897	0.0417
0.875	1.25	0.4194	0.037
1	1.25	0.3785	0.0539
0.2	2	1.6259	-0.067
0.3	2	1.2471	-0.053
0.4	2	1.1091	-0.048
0.5	2	0.9682	-0.043
0.625	2	0.932	-0.046
0.75	2	0.7977	-0.037
0.875	2	0.6103	-0.015
1	2	0.8706	-0.037

5. CONCLUSIONS

The hydraulic loss coefficient of a perpendicular, cylindrical bore on a cylindrical pipe was determined for 40 different geometries; the available experimental database was extended by using the results of modern three-dimensional CFD models. Instead of experimental data, three-dimensional simulation results were used for the fitting of the resistance characteristic of the bore. A four-dimensional parameter space with wide parameter ranges were investigated with a high resolution using the results of more than 1000 three-dimensional simulations.

The total pressure loss was decomposed into two additive parts which are assumed to be proportional to the dynamic pressure in the header and the dynamic pressure in the branch; consequently, two loss coefficients were introduced. These loss coefficients were determined as a function of the Reynolds number at the inlet by applying a fitting procedure. Two different correlations are developed for high and low velocity ratios and the formula for the critical velocity ratio is provided. The results of the novel loss coefficient formula were compared with several known experiments and good correspondence was found. The novel resistance model can be implemented in hydraulic network models.

REFERENCES

[1] Kubo, T. and Ueda, T., 1969, "On the Characteristics of Divided Flow and Confluent Flow in Headers", *Bulletin of JSME*, Vol. 12, No. 52, pp. 802-809.

[2] Zeisser, M. H., 1963, "Summary Report of Single-Tube Branch and Multi-Tube Branch Water Flow Tests conducted by the University of Connecticut", *Pratt and Whitney aircraft division, United aircraft corporation*, Report No PWAC-231 USAEC Contr. AT(11-1)-229

[3] McNown, J. S., 1954, "Mechanics of Manifold Flow", *Transactions of the ASCE*, Vol. 119, No. 1, pp. 1103-1118.

[4] Wang, J., 2011, "Theory of Flow Distribution in Manifolds", *Chemical Engineering Journal*, Vol. 168, Issue 3, pp. 1331-1345.

[5] Wang, J. and Wang, H., 2012, "Discrete Approach for Flow Field Designs of Parallel Channel Configurations in Fuel Cells", *Int J Hydrogen Energy*, Vol. 37, pp. 10881-10897.

[6] Liu, W., Long, Z. and Chen, Q., 2012, "A Procedure for Predicting Pressure Loss Coefficients of Duct Fittings Using Computational Fluid Dynamics (RP-1493)", *HVAC&R RESEARCH*, Vol. 18, pp. 1168-1181.

[7] Badar, A. W., Buchholz, R., Lou, Y. and Ziegler, F., 2012, "CFD Based Analysis of Flow Distribution in a Coaxial Vacuum Tube Solar Collector with Laminar Flow Conditions", *Int J Energy and Environmental Engineering*, Vol. 3, Issue 1, 15 pages

[8] Ramamurthy, A. S., Qu, J., Vo, D. and Zhai, C., 2006, "3-D Simulation of Dividing Flows in 90 deg Rectangular Closed Conduits", *J Fluids Engineering*, Vol. 128, Issue 5, pp. 1126-1129.

[9] Menter, F. R., 1994, "Two-Equation Eddy-Viscosity Turbulence Models for Engineering Applications", *AIAA J*, Vol. 32, pp. 1598-1605.

[10] Idelchik, I. E., 1966, "Handbook of Hydraulic Resistance", *Israel Program for Scientific Translations Ltd.*, Jerusalem

Conference on Modelling Fluid Flow (CMFF'15)
The 16th International Conference on Fluid Flow Technologies
Budapest, Hungary, September 1-4, 2015

Numerical modelling of bypass transition in turbine cascades

Petr LOUDA[1], Jaromír PŘÍHODA[2], Karel KOZEL[3]

[1] Corresponding Author. Dept. of Technical Mathematics, Fac. of Mechanical Engineering, Czech Technical University in Prague, Karlovo nám. 13, 12135 Praha 2, Czech Republic. Tel.: +420 2 2435 7564, Fax: +420 2, E-mail: petr.louda@fs.cvut.cz
[2] Institute of Thermomechanics AS CR v.v.i. E-mail: prihoda@it.cas.cz
[3] Czech Technical University in Prague. E-mail: karel.kozel@fs.cvut.cz

ABSTRACT

The work deals with numerical simulation of turbulent flows in turbine cascades taking into account transition to turbulence. The mathematical model is based on Favre-averaged Navier-Stokes equations closed by a turbulence model. The transition to turbulence is modelled by 2-equation model of Lodefier and Dick (2006) solving equations for intermittency and free-stream factor. In the model, arbitrary transition criteria based on empirical correlations can be used. The turbulence model is the EARSM (explicit algebraic Reynolds stress model). The results are shown for 3D turbine cascade with prismatic geometry and side walls. Fully turbulent and transitional simulations are compared. The implementation of the transition model in the multi-block grids enabling computation of boundary layer thickness and free-stream velocity and turbulence is discussed. The numerical method uses implicit finite volume solver with AUSM-type scheme.

Keywords: 3D turbine cascade, bypass transition model, EARSM turbulence model

1. INTRODUCTION

The mathematical modeling of turbulent flow in turbine cascades serves as design tool as well as improves the understanding of complicated flow patterns typical of these flows. Mathematical models based on the Favre-averaged Navier-Stokes equations present accuracy sufficient in most cases, at acceptable computational cost. However, the accuracy is influenced by turbulence model and its capability to predict bypass transition to turbulence, which occurs at higher free-stream turbulence intensities typically found in turbines, as pointed out by Mayle [1]. Correct prediction of turbulent boundary layer is important for heat exchange between blade and fluid and also can influence the losses e.g. by interaction with shock waves which is different on laminar boundary layer. Common two-equation eddy-viscosity turbulence models usually predict too early start of transition and then the transition is too fast. This problem is further emphasized by overprediction of the turbulent energy production on the leading edge of the blade which has its origin in the eddy-viscosity assumption. Some ad hoc remedies of the later problem has been proposed e.g. by Kato, Launder [2] or Medic, Durbin [3]. Better option is the use of more elaborate constitutive relation for turbulent stress as is the explicit algebraic Reynolds stress model (EARSM), e.g. the variant by Wallin [4] which is used in this work. However the transition still requires explicit triggering. Considering models based on transport equations which seem more general as algebraic ones, the models contain equation for an intermittency variable and also for other auxiliary variable or variables. More recent examples are 3-equation model by Walters and Cokljat [5] or 2-equation model by Menter, Langtry [6]. Also 1-equation model is proposed by Durbin [7]. These models have "local" form enabling easy parallel implementation. However they also share disadvantage of containing transition criteria implicitly. Any non anticipated mechanism of transition requires re-calibration of the model. In this work we apply the γ-ζ model of Lodefier, Dick [8] and Kubacki et al [9] instead. The model contains transition criteria explicitly and any new criterion can be added easily. The downside is that the model distinguishes free-stream and boundary layer and thus is not local. Nevertheless we show for typical 3D cascade geometry that when using multi-block grids the model is block-local and does not require case-specific input under assumption that the whole thickness of boundary layer is contained in one block, at least in region where transition occurs. This can be easily achieved with suitable O-type grid around the blade.

2. MATHEMATICAL MODEL AND NUMERICAL METHOD

The mathematical model of turbulent flow is based on Favre-averaged Navier-Stokes (NS) equations, see e.g. Wilcox [10]. The system consisting of continuity, 3 momentum and energy equation can be written in 3D in Cartesian coordinates

$$\int_V \frac{\partial W}{\partial t} + \oint_{\partial V} F^I d\mathcal{S} = \oint_{\partial V} F^V d\mathcal{S} \tag{1}$$

$$W = \begin{bmatrix} \rho \\ \rho u_1 \\ \rho u_2 \\ \rho u_3 \\ \rho E \end{bmatrix}, \quad F^I = u_c \begin{bmatrix} \rho \\ \rho u_1 \\ \rho u_2 \\ \rho u_3 \\ \rho H \end{bmatrix} + \begin{bmatrix} 0 \\ pn_1 \\ pn_2 \\ pn_3 \\ 0 \end{bmatrix} \tag{2}$$

$$F^V = \begin{bmatrix} 0 \\ t_{i1} + \tau_{i1} \\ t_{i2} + \tau_{i2} \\ t_{i3} + \tau_{i3} \\ (t_{ij} + \tau_{ij})u_j - q_i - q_i^t \end{bmatrix} n_i \tag{3}$$

where V is control volume, n_i outer unit normal vector of its surface, t time, ρ density, u_i velocity vector, E total energy per unit volume, $H = E + p/\rho$ is total enthalpy and p static pressure. The magnitude of normal velocity $u_c = u_i n_i$. Equation of state for perfect gas is prescribed

$$E = \frac{1}{\gamma - 1}\frac{p}{\rho} + \frac{1}{2}(u_1^2 + u_2^2 + u_3^2) + k, \tag{4}$$

with the ratio of specific heats $\gamma = 1.4$ and k is turbulent energy. The molecular stress tensor and heat flux vector respectively are assumed in the form

$$t_{ij} = \mu 2S_{ij}, \quad S_{ij} = \frac{1}{2}\left(\frac{\partial u_i}{\partial x_j} + \frac{\partial u_j}{\partial x_i}\right) - \frac{2}{3}\delta_{ij}\frac{\partial u_k}{\partial x_k}, \tag{5}$$

$$q_i = -\frac{\gamma}{\gamma - 1}\frac{\mu}{Pr}\frac{\partial(p/\rho)}{\partial x_i}, \tag{6}$$

where δ_{ij} is Kronecker delta. The dynamic viscosity μ and Prandtl number

$$\mu = const, \quad Pr = const. \tag{7}$$

The effect of turbulent fluctuations is present by the Reynolds stress tensor τ_{ij} and turbulent heat flux q_i^t, which need to be modeled. An explicit algebraic Reynolds stress model (EARSM) is used here since it is generally superior to eddy viscosity models in 3D. In the EARSM model proposed by Wallin [11], the Reynolds stress is given by

$$\begin{aligned} \tau_{ij} &= a_{ij}\rho k + \frac{2}{3}\rho k \delta_{ij}, \qquad (8)\\ a_{ij} &= \beta_1 \tau S_{ij} \\ &+ \beta_3 \tau^2 (\Omega_{ik}\Omega_{kj} - I\!I_\Omega \delta_{ij}/3) \\ &+ \beta_4 \tau^2 (S_{ik}\Omega_{kj} - \Omega_{ik}S_{kj}) \\ &+ \beta_6 \tau^3 (S_{ik}\Omega_{kl}\Omega_{lj} + \Omega_{ik}\Omega_{kl}S_{lj} - 2IV\delta_{ij}/3) \\ &+ \beta_9 \tau^4 (\Omega_{ik}S_{kl}\Omega_{lm}\Omega_{mj} - \Omega_{ik}\Omega_{kl}S_{lm}\Omega_{mj}), \end{aligned}$$

where τ is turbulent time scale, $\Omega_{ij} = \frac{1}{2}\left(\frac{\partial u_i}{\partial x_j} - \frac{\partial u_j}{\partial x_i}\right)$ rotation rate tensor and $I\!I_\Omega$, IV are invariants formed from S_{ij}, Ω_{ij}. The coefficients β_j are taken from Hellsten [12] where k-ω system is used for turbulent scales prediction.

The k-ω system can be written

$$\int_V \frac{\partial}{\partial t}\begin{bmatrix} \rho k \\ \rho\omega \end{bmatrix} d\mathcal{V} + \oint_{\partial V} u_c \begin{bmatrix} \rho k \\ \rho\omega \end{bmatrix} d\mathcal{S} = \tag{9}$$

$$\oint_{\partial V} \begin{bmatrix} (\mu + \sigma_k \mu_T)\frac{\partial k}{\partial x_i} \\ (\mu + \sigma_\omega \mu_T)\frac{\partial \omega}{\partial x_i} \end{bmatrix} n_i dS + \int_V \begin{bmatrix} P_k - \beta^* \rho\omega k \\ \alpha \frac{\omega}{k} P_k - \beta\rho\omega^2 + CD \end{bmatrix} d\mathcal{V} \tag{10}$$

where the turbulent production $P_k = \tau_{ij}\frac{\partial u_i}{\partial x_j}$, the α, β, β^*, σ_k, σ_ω are model coefficients and CD a cross-diffusion term. The eddy viscosity μ_t is defined as usual from the linear part of Reynolds stress which is dominant. Further the turbulent heat flux is

$$q_i^t = q_i \frac{Pr}{\mu}\frac{\mu_t}{Pr_t} \tag{11}$$

with the turbulent Prandtl number $Pr_t = 0.91$.

In order to model bypass transition to turbulence, the two-equation model of Lodefier and Dick [8] is used. The Reynolds stress is multiplied by turbulence weighting factor

$$\gamma_T = \max[\min(\gamma + \zeta, 1), 0] \tag{12}$$

where γ is near-wall intermittency and ζ free-stream intermittency. The governing equations are

$$\int_V \frac{\partial}{\partial t}\begin{bmatrix} \rho\gamma \\ \rho\zeta \end{bmatrix} d\mathcal{V} + \oint_{\partial V} u_c \begin{bmatrix} \rho\gamma \\ \rho\zeta \end{bmatrix} d\mathcal{S} = \tag{13}$$

$$\oint_{\partial V} \begin{bmatrix} (\mu + \sigma_\gamma \mu_T)\frac{\partial \gamma}{\partial x_i} \\ (\mu + \sigma_\zeta \mu_T)\frac{\partial \zeta}{\partial x_i} \end{bmatrix} n_i dS + \int_V \begin{bmatrix} 2\beta_\gamma(1-\gamma)\sqrt{-\ln(1-\gamma)}\rho U_\gamma F_s \\ -C_2 \mu_\zeta \frac{U}{U_e^2}\frac{\partial U}{\partial n}\frac{\partial \zeta}{\partial n} \end{bmatrix} d\mathcal{V} \tag{14}$$

with boundary conditions in the inlet: $\gamma = 0$, $\zeta = 1$, in the outlet: $\partial\gamma/\partial n = \partial\zeta/\partial n = 0$ and on the wall: $\partial\gamma/\partial n = 0$, $\zeta = 0$.

The ζ is zero in the boundary layer. The γ is zero in laminar flow and starts to increase to 1 in the turbulent boundary layer as soon as the starting function $F_s = 1$. In laminar part $F_s = 0$ and the switch to 1 is triggered by satisfying a transition criterion. The Mayle and Abu-Ghannam, Shaw criteria are used in this work. These express the critical value of the Reynolds number Re_θ from momentum boundary layer thickness θ and free-stram velocity U_e at which the boundary layer starts to be turbulent. If the computed local Re_θ exceeds value from any of the criteria, the F_s is set to 1.

The intermittency γ_T multiplies the turbulent stress. Besides the production terms in k-equation are modified in the transitional part of boundary layer according to:

$$F_G P_k - \min[1.0, \max(\gamma_T, 0.1)]\beta^* \rho\omega k \tag{15}$$

where

$$F_G = B + (1. - B)\gamma_T^{0.75}, \; B = 0.056Tu \tag{16}$$

where Tu [%] is local turbulence intensity.

Solving the above systems of equations, the domain contains 1 period of turbine cascade. Subsonic flow in normal direction is assumed in the inlet as well as in the outlet. Then we prescribe in the inlet: flow angle, total density and total pressure. In the outlet, the mean value of static pressure is fixed which determines the flow regime.

2.1. Numerical solution

For spatial discretization we use a cell centered finite volume method with quadrilateral (in 2D) or hexahedral (in 3D) finite volumes composing a structured grid. The numerical inviscid flux is computed by the AUSMPW+ splitting [13]. The higher order of accuracy is achieved by linear interpolation in the direction of grid lines with e.g. van Leer limiter. The discretization of diffusive flux is central. The approximation of cell face derivatives needed in diffusive terms uses octahedral dual finite volumes constructed over each face of primary volume – the vertices are located at end of primary face and in centers of adjacent primary volumes. For time discretization, the implicit backward Euler scheme is employed where the steady residual at new time level is approximated by linear extrapolation. The Jacobi matrices of the flux are obtained as derivatives of discrete expressions for flux with respect to nodal values from the stencil of implicit operator. We chose 7-point stencil, which leads to block 7-diagonal system of linear equations. The size of a block equals to the number of coupled equations. Numerical solutions of some 3D cases of incompressible flow are given in [14].

2.2. Remarks to the implementation of transition model

The transition model source terms depend on distinction between laminar and turbulent state of boundary layer. Therefore the distinction is needed if the finite volume is located inside a boundary layer and then if a transition criterion is met. The edge of boundary layer is indicated by magnitude of vorticity vector small enough. The threshold is 1 % of maximum value found on the normal to the wall, where maximum is on the wall in attached boundary layer. This distance is then further increased by 30 %.

In 3D geometry with multiple walls, only corners with meeting 2 walls are considered (which is the case in present simulations). Then the evaluation of source terms proceeds in planes perpendicular to the walls. Each finite volume is assigned either to boundary layer or free stream. Near the corner, however, the magnitude of vorticity goes to zero and the algorhitm searching for the free-stream fails. Therefore the still well defined boundary layers on both walls are extrapolated defining an intersection point. All grid points in the corner area are then assigned the free-stream parameters and boundary layer thickness from this intersection point. For simplicity of implementation the terms "normal" or "perpendicular" are understood in terms of grid lines. These are sufficiently normal to the wall and sufficiently straight in considered boundary layers thanks to the use of O-grid around blade.

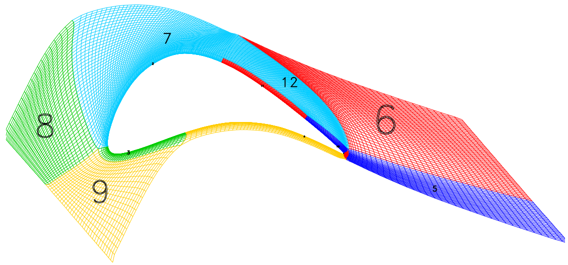

Figure 1. The 12-block finite volume grid in (x, y) plane

For parallel implementation it is desirable that the evaluation of different expressions be local. This is not satisfied when free-stream values or boundary layer thickness are parameters of the model. However the present work uses multi-block grids where it is natural to distribute the work to computing threads block-wise. Then if the whole thickness of the boundary layer is contained within one block, the evaluation is block-local. The finite volume grid is composed of O-grid, consisting of several blocks, around the blade and the thickness of O-grid is chosen large enough to contains the boundary layer.

3. COMPUTATIONAL RESULTS

The computational results are shown for an experimental nozzle guide vane with pitch-to-chord ratio 0.7. The flow regime is transonic with outlet isentropic Mach number $M_{2is} = 0.9$. The Reynolds number $Re_{2is} \approx 8.5 \cdot 10^5$ based on chord length. Ideal gas fluid is assumed with the specific heat ratio $\kappa = 1.4$. The inlet turbulence intensity was set to 5% and ratio of turbulent and laminar viscosity set to 100. For simplicity, uniform inlet data were considered along the whole span. The recovery of boundary layer on side walls is very fast.

The 3D cascade geometry is prismatic with side walls. The span in z-direction equals the chord length b. The grid in (x, y) plane consists of 12 blocks with O-grid around the blade, see Fig. 1, and has approx. 15500 finite volumes. In span-wise direction, 128 finite volumes are used. The total number of finite volumes is thus approximately $2 \cdot 10^6$. The grid is refined along all walls with minimum thickness of finite volume of $5 \cdot 10^{-6} b$, giving wall distance $y^+ < 1$ for cell-centers of first finite volume. The time step for simulation was constant, $\Delta t \approx 0.002 b / \sqrt{p_{01}/\rho_{01}}$. The solution is considered converged if the inflow and outflow rates are equal (with some tolerance) and friction and pressure on the blade no more change.

The Fig. 2 shows 3D view of suction side and one of the side walls in terms of isolines of isentropic

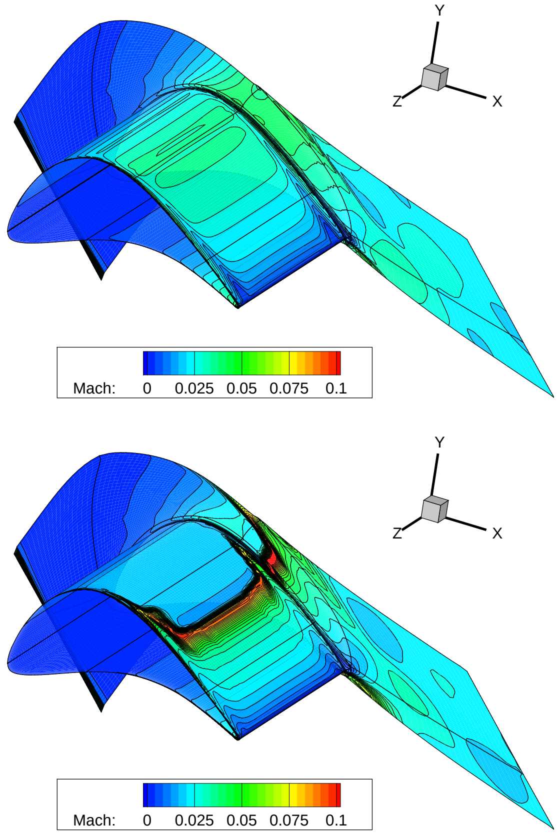

Figure 2. Isolines of Mach number near walls. Above: fully turbulent, below: with transition model

Mach number very near the walls (first off-wall vertices of wall adjacent finite volumes). With transition there is abrupt increase of Mach number where the transition starts on the suction side. The location of transition can be observed on the value of near-wall intermittency γ plotted in Fig. 3. The figure shows γ on the wall, where values near 0 correspond to laminar state and 1 to turbulent state. The transition point in the mid-span agrees with the transition in 2D simulation. In the proximity of the side wall the transition moves upstream. The boundary layer on the pressure side is fully laminar.

Both transition model variables γ and ζ in the mid-plane are shown in Fig. 4. The free-stream factor ζ differs from 1 only very near the wall and in the wake.

The Fig. 5 shows detail of isolines of turbulent energy in the mid-plane mainly in the rear part of suction side where the transition occurs. One can see increase of turbulent energy shortly after start of the transition. Further down-stream the turbulent energy decreases.

The Fig. 6 shows friction on the blade at different span-wise positions. Note that the negative values merely correspond to suction side, there is no separation of the flow (no zero crossing except at leading

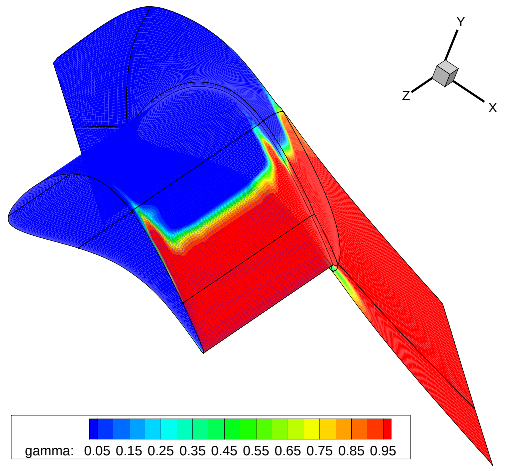

Figure 3. Isolines of intermittency γ near the walls

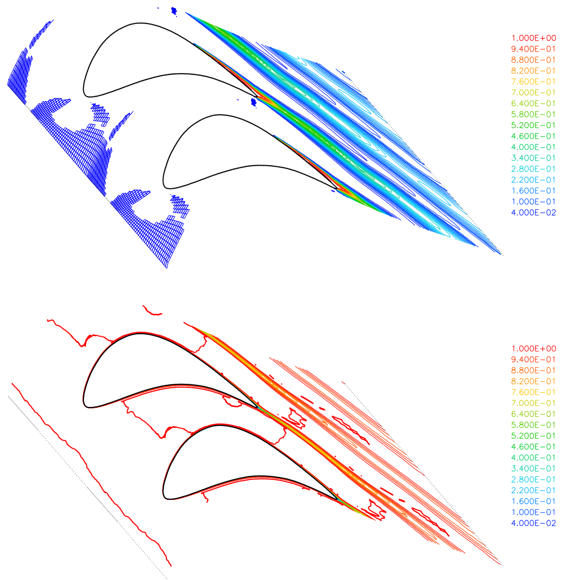

Figure 4. Isolines of near-wall intermittency γ (above) and free-stream intermittency ζ (below) in the mid-plane

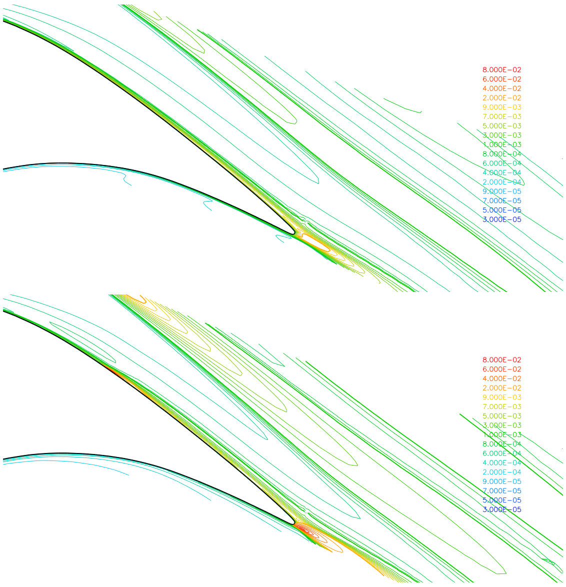

Figure 5. Isolines of turbulent energy in the mid-plane. Above: fully turbulent, below: with transition model

and trailing edge). The value of $z/b = 0$ denotes mid-span plane. Results of fully turbulent and transitional simulation are shown. The shear stress reaches maximum shortly after transition and then decreases to reach nearly same value as in fully turbulent case near the trailing edge. The transition occurs latest in central part of the blade. Approaching side wall, the transition moves forward but very near the side wall ($z/b = 0.49$) is again shifted slightly downstream. However the treatment of corners is not necessarily physical and needs confirmation with experiment. There is some influence of transition on the pressure side too. The friction in transitional case is slightly lower which is expected as the boundary layer is laminar.

The static pressure on the blade in the simulated case is practically independent of transition modeling and span-wise position, see the Fig. 7. The influence very near the wall has been already shown in terms of surface isentropic Mach number.

It is expected that transition may change energy losses in the turbine. The local value of loss coefficient is defined using Laval numbers λ and λ_{is}

$$\xi_l = 1 - \frac{\lambda^2}{\lambda_{is}^2} = \frac{\left[1 - \left(\frac{p_0}{p_{01}}\right)^{\frac{\gamma-1}{\gamma}}\right] \left(\frac{p}{p_0}\right)^{\frac{\gamma-1}{\gamma}}}{1 - \left(\frac{p}{p_{01}}\right)^{\frac{\gamma-1}{\gamma}}} \tag{17}$$

where p_0, p_{01} is local and inlet total pressure respectively and p is local static pressure. The local total pressure is computed from local Mach number and static pressure by isentropic relation. The local coefficient ξ_l is then integrated over 1 period in y-direction giving mean value ξ. The results are shown in Fig. 8 versus span position in several planes

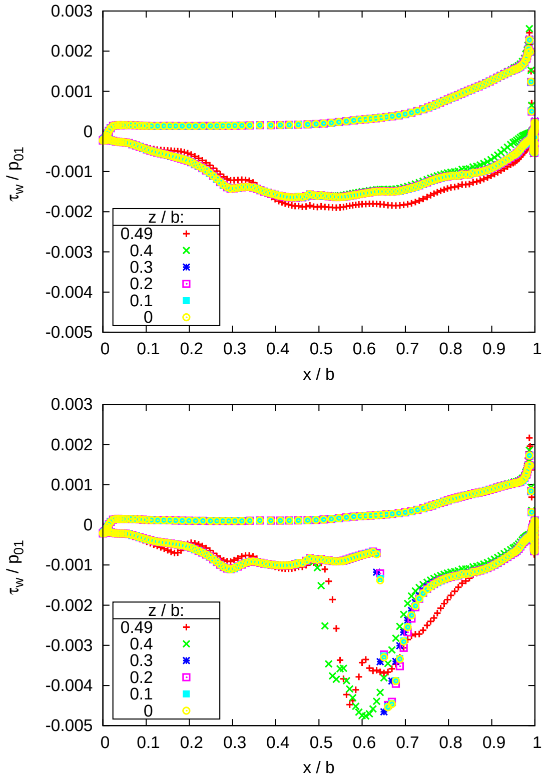

Figure 6. Friction on blade surface at different positions along the span. Above: fully turbulent, below: with transition model. Negative values correspond to suction side

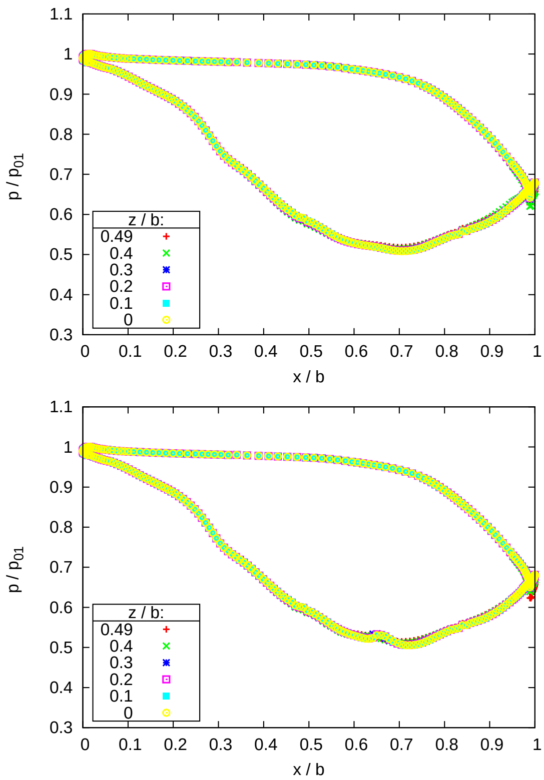

Figure 7. Static pressure on blade surface at different positions along the span. Above: fully turbulent, below: with transition model

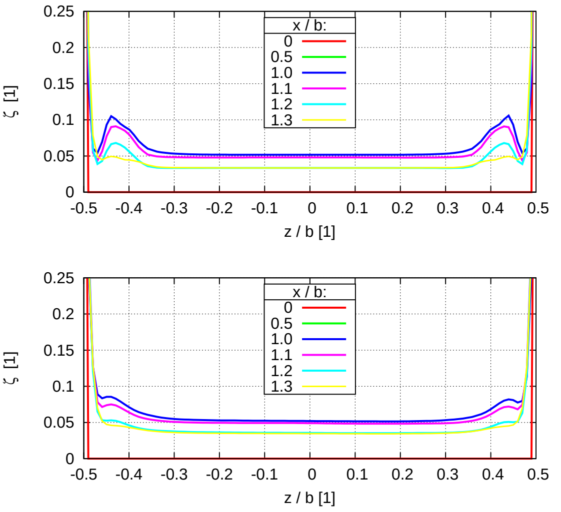

Figure 8. Energy loss coefficient across the span. Above: fully turbulent, below: with transition model

$x = const$. The loss is essentially zero at leading edge ($x/b = 0$) and increases up to the trailing edge ($x/b = 1$). After that it settles on a lower value behind the cascade. The fully turbulent simulation shows clear local maxima next to side walls, whereas with transition model, these maxima are diminished. In general the fully turbulent simulation shows higher loss. However the losses seen in the mid-plane are nearly same in fully turbulent as well as transitional case.

4. CONCLUSIONS

The work presented simulations of 3D turbulent flow through a model turbine cascade with the EARSM turbulence model complemented with the γ-ζ model of transition to turbulence. The mathematical model is solved by implicit AUSM finite volume method on multi-block structured grids. The implementation of transition model does not rely on explicit prescription of boundary layer edge and is adaptive as long as the whole thickness of boundary layer is contained in one block, which is typically O-grid around the blade (consisting of several blocks in tangential direction). Also the treatment of corners is automatic. The physical correctness of transition prediction in the flow in convex corner however still needs to be confirmed by measurement. The results are compared with fully turbulent simulation in terms of pressure and friction on the blade and the flow-field. The energy loss coefficient distribution along the span is also presented. The results exhibit qualitatively correct behavior but quantitatively need to be confirmed by a detailed measurement.

Acknowledgments

This work was supported by the grants P101/12/1271 and 13-00522S of the Czech Science Foundation.

REFERENCES

[1] Mayle, R. E., 1991, “The role of laminar-turbulent transition in gas turbine engines”, *J Turbomachinery*, Vol. 113, pp. 509–537, trans. ASME.

[2] Kato, M., and Launder, B. E., 1993, “The Modelling of turbulent flow around stationary and vibrating square cylinders”, *Ninth Symposium on Turbulent Shear Flows*, Kyoto, Japan.

[3] Medic, G., and Durbin, P., 2002, “Toward improved prediction of heat transfer on turbine blades”, *Journal of Turbomachinery*, Vol. 124, pp. 187–192.

[4] Wallin, S., and Johansson, A. V., 2000, “An explicit algebraic Reynolds stress model for incompressible and compressible turbulent flows”, *J Fluid Mech*, Vol. 403, pp. 89–132.

[5] Walters, D. K., and Cokljat, D., 2008, “A three-equation eddy-viscosity model for Reynolds-averaged Navier-Stokes simulations of transitional flow”, *J of Fluids Engineering*, Vol. 130, pp. 121401–1–121401–14.

[6] Langtry, R. B., and Menter, F. R., 2009, “Correlation-based transition modeling for unstructured parallelized computational fluid dynamics codes”, *AIAA journal*, Vol. 47, pp. 2894–2906.

[7] Durbin, P., 2012, “An intermittency model for bypass transition”, *Int J of Heat and Fluid Flow*, Vol. 36, pp. 1–6.

[8] Lodefier, K., and Dick, E., 2006, “Modelling of unsteady transition in low-pressure turbine blade flows with two dynamic intermittency equations”, *Flow, Turbulence and Combustion*, Vol. 76, pp. 103–132.

[9] Kubacki, S., Lodefier, K., Zarzycki, R., Elsner, W., and Dick, E., 2009, “Further development of a dynamic intermittency model for wake-induced transition”, *Flow, Turbulence and Combustion*, Vol. 83, pp. 539–568.

[10] Wilcox, D. C., 1998, *Turbulence modeling for CFD*, DCW Industries, Inc., California, 2nd edition.

[11] Wallin, S., 2000, “Engineering turbulence modeling for CFD with a focus on explicit algebraic Reynolds stress models”, Ph.D. thesis, Royal Institute of Technology, Stockholm.

[12] Hellsten, A., 2005, “New advanced k-ω turbulence model for high-lift aerodynamics”, *AIAA J*, Vol. 43, pp. 1857–1869.

[13] Kim, K. H., Kim, C., and Rho, O.-H., 2001, “Methods for accurate computations of hypersonic flows I. AUSMPW+ scheme”, *J of Computational Physics*, Vol. 174, pp. 38–80.

[14] Louda, P., 2002, “Numerical solution of 2D and 3D turbulent inpinging jet flow”, Ph.D. thesis, FME CTU, Prague, (in Czech).

Conference on Modelling Fluid Flow (CMFF'15)
The 16th International Conference on Fluid Flow Technologies
Budapest, Hungary, September 1-4, 2015

NUMERICAL INVESTIGATIONS OF RESIDENCE TIME DISTRIBUTION OF AIR IN ELECTRIC MACHINES BASED ON A CANONICAL CONFIGURATION

Toni EGER[1], Dominique THÉVENIN[2], Gábor JANIGA[3], Thomas BOL[4], Rüdiger SCHROTH[5]

[1] Corresponding Author. Laboratory of Fluid Dynamics and Technical Flows, University of Magdeburg "Otto von Guericke". Universitätsplatz 2, D-39106 Magdeburg, Germany. Tel.: +49 391 67 18654 , Fax: +49 391 67 12840, E-mail: toni.eger@ovgu.de
[2] Laboratory of Fluid Dynamics and Technical Flows, University of Magdeburg "Otto von Guericke". E-mail: thevenin@ovgu.de
[3] Laboratory of Fluid Dynamics and Technical Flows, University of Magdeburg "Otto von Guericke". E-mail: gabor.janiga@ovgu.de
[4] Starter Motors and Generators, Robert Bosch GmbH. E-mail: thomas.bol@de.bosch.com
[5] Starter Motors and Generators, Robert Bosch GmbH. E-mail: ruediger.schroth@de.bosch.com

ABSTRACT

Within the last decades, the power density of electrical machines strongly increased. Nevertheless, air as cooling medium is still the cheapest and most reliable choice. In technical flows, the fluid encounters very different flow conditions, which obviously influence enthalpy transport. One of today's challenge is e.g., the identification of indicators to analyze such heat transfer phenomena. Therefore, regions with a high potential for optimization should be located in complex geometries. Considering only these regions, the number of design parameters can be heavily reduced. As final step, Evolutionary Algorithms in combination with Computational Fluid Dynamics (CFD) can be used in order to optimize the flow field (see e.g., [1]). One of such an indicator could be the residence time distribution (RTD), which is commonly used in a wide range of engineering applications and will be analyzed in this work. The fields of RTD are compared to the literature for internal and external flows and finally a numerical study with a „canonical configuration" will be present. The configuration itself represents the flow conditions occurring in an electrical machine. The results show how RTD can be used to quantify flow processes for further applications.

Keywords: External flow, heat transport, internal flow, residence time distribution, transport phenomena

NOMENCLATURE

$\dot{V}$	$[m^3/s]$	Volumetric flow-rate
$A_{Inlet,int}$	$[m^2]$	Area of the inlet interface
D	$[m]$	Cylinder diameter
$E(\theta)$	$[-]$	Differential RTD
$F(\theta)$	$[-]$	Cumulative RTD
Re	$[-]$	Reynolds number
T	$[K]$	Temperature
U	$[m/s]$	Velocity
V	$[m^3]$	Volume
$\dot{q}$	$[W/m^2]$	Heat Flux
r	$[m]$	Radius in polar coordinate system
d_h	$[m]$	Hydraulic diameter
k	$[W/(m.K)]$	Thermal conductivity
p	$[Pa]$	Pressure
r	$[m]$	Radius
u_0	$[m/s]$	Tangential velocity
u_∞	$[m/s]$	Oncoming flow
$x, y, z,$	$[m]$	Coordinate
y	$[m]$	wall-normal
y^+	$[-]$	Dimensionless wall distance
$\bar{\tau}$	$[s]$	Mean residence time
β	$[rad]$	Opening angle
ϵ_a	$[-]$	Air change efficiency
λ	$[-]$	Dimensionless velocity
μ	$[Pa.s]$	Dynamic viscosity
Π	$[-]$	Radius ratio
ρ	$[kg/m^3]$	Density
σ	$[N/m^2]$	Molecular stress tensor
τ	$[s]$	Local mean age of air
θ	$[-]$	Residence time distribution (RTD)
θ_F	$[-]$	First appearance time
Γ	$[Pa.s]$	Diffusivity
φ	$[-]$	Conserved quantity

Subscripts and Superscripts

0	Inner cylinder
1	Outer cylinder
ana	Analytical
crit	Critical
max	Maximum
*	Dimensionless
∞	Ambient

1. INTRODUCTION

Due to higher demands of power density for electric machines, investigations regarding the thermal management are getting more important. This ensures higher reliability and efficiency of the device, to name just two significant aspects. Therefore, enthalpy transport plays an increasing role for the development of electronic devices like, e.g., alternator systems. In turn, the enthalpy transport is strongly influenced by the flow field. Inside an alternator, fan blades generate a pressure gradient by their rotational motion. Air from the engine bay streams through the alternator, flows through the rectifier domain and finally leaves the system in radial direction. In the rectifier domain electronic components are pressed or glued on a heat sink. The design involves openings through the heat sink as well as ribs or pins. Therefore, the fluid encounters different flow conditions that influence enthalpy transport. In most cases, a better cooling is in conflict with other aspects (e.g., costs or aeroacoustic emissions). For instance, a higher volumetric flow-rate increases enthalpy transport. However, the maximum sound pressure level is strictly restricted as well and constrains the available range for the engineer. Due to the complexity of the pathlines and the large quantity of data, the flow field inside an alternator is mainly poorly characterized. To detect local areas where heat transfer to the fluid could be intensified, a first obvious step is to check the temperature on the solid side. However, the temperatures show only the final outcome of the enthalpy transport. They convey no further information about the underlying processes. Looking only at temperatures, it cannot be found what is limiting heat transport and where or why this occurs. In order to solve this issue, the RTD offers a new way to look at heat transport processes inside an alternator. RTD should show the regions where the cooling rate of the fluid undergoes a critical limit and, therefore, limit the heat transport.

In the sequel, we give in section 2 a short introduction for the RTD method, which is typically used in, e.g., building energy industry but also in the chemical industry. In section 3, we introduce the „canonical configuration“ with its geometrical setup. The link between the simple configuration and the complex alternator system will be discussed. In section 4 the physical model as well as the numerical method that are used in this work will be described. In section 5, code validation tests for internal and external flows are discussed by comparing the numerical results with the literature. Section 6 shows the first results from the canonical configuration. A grid-independence test is finally done in section 7 for the results presented in the previous section. In section 8 we present our conclusions.

2. RESIDENCE TIME DISTRIBUTION

The efficiency of heat transfer largely depends on the enthalpy transport and therefore particularly on the flow field. The varying velocity profiles cause fluid elements to spend different times in the alternator system, which results in a wide distribution of RTD in the system. A three dimensional CFD simulation delivers a huge data quantity of e.g., vector arrows, which are difficult to interpret and analyze efficiently. To characterize such complex flow field processes, the chemical industry uses the RTD to study the mixing behavior in e.g., stirred tank reactors. Commonly the local mean age of air (LMA) in seconds is plotted on different planes. From these plots regions where backflow areas or bypassing paths occur are directly visible, which is a huge advantage compared to a confusing vector plot. Liu et al. [2] demonstrated that the moments of age can be computed at only a small fraction of the computing cost required to get the transient concentration solution. The RTD is also widely considered in the building energy industry (e.g., [3, 4, 5]). The residence time distribution θ is defined as:

$$\theta = \frac{\tau}{\bar{\tau}} = \frac{\tau}{V/\dot{V}}. \tag{1}$$

The age of the air is defined with τ and represents the time that a particle spends between entering and leaving the considered system. Analytical formulations are available in the literature to calculate τ for academic problems (see e.g., [6, 7, 8]). Another method is the experimental or numerical calculation of this value, whereby the numerical method is used in this work as described in section 4.2. The mean (hydraulic) residence time is $\bar{\tau}$, the volume is $V = LA$ and the volumetric flow-rate at the inlet is $\dot{V} = A\underline{u}$. Based on the dimensionless form, different studies with with e.g., varying inlet velocities become possible. The American Society of Heating, Refrigerating and Air-Conditioning Engineers (ASHRAE) propose an alternative formulation, called air change efficiency (ACE) factor [4]:

$$\epsilon_a = \frac{V/\dot{V}}{2\tau}. \tag{2}$$

The factor represents the ratio between the shortest possible time needed for replacing the air in the room ($V/\dot{V}$) and the average time for air exchange (2τ). A variety of other indicators are available in the literature as well. For example, Li et al. [9] extended the typical indicators by considering the impact of air delivery processes between airflows with different ages. In addition they consider the mixing of the fresh air entering the system with the recirculating air coming from the system. Commonly, the differential RTD and the cumulative RTD are used to characterize the flow processes:

$$E(\theta) \equiv \tau \cdot E(t) \quad , \quad dF(\theta) = E(\theta)d\theta. \tag{3}$$

Following Fogler [10], the differential RTD $E(\theta)$ describes in a quantitative manner how much time different fluid elements have spent in the reactor. The cumulative distribution function $F(\theta)$ gives the fraction of effluent material that has been in the reactor during a time t or less.

3. CANONICAL CONFIGURATION

A three-dimensional numerical study of an electric alternator delivers a huge quantity of data. Due to the geometrical and physical complexity of the setup a large number of finite volumes have to be used for a simulation (small cells being especially needed in near-wall regions). In most cases, a detailed quantitative analysis of these huge data set is not performed. Looking at the LMA appears as a promising approach. In order to check this point, a simplified but relevant configuration has been first identified, called „canonical configuration" in this work. Eger et al. [11] introduced the concepts underlying this configuration and showed its benefit based on a Nusselt number analysis. Figure 1 explains the choice of the canonical configuration.

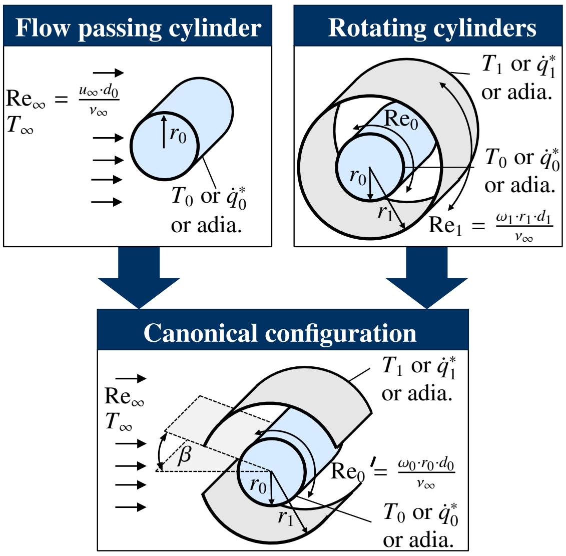

Figure 1. Canonical configuration used for further investigations of transport phenomena and for the development of physically-based indicators of heat transport

Using it, it is possible to investigate fluid processes and heat transport at different scales, controlled either by ambient parameters (global scale) or by near-wall gradients (local scale), alone or in combination, while keeping a single geometrical setup described by a small number of parameters. Thanks to such a simple configuration, the data quantity to analyze is heavily reduced. However, the transport phenomena found in real electric alternator systems are still represented. Thus, the canonical configuration offers the opportunity to investigate physically-based indicators, e.g. residence time distribution for such systems with a high level of generality. Ultimately, a thermal optimization of electric machines regarding fluid and heat transport should become possible. Compared to a single cylinder, two additional design parameters have been added, here β and Π. Table 1 gives an overview about the parameters that have an influence on the flow field locally (within the annuli) as well as globally (in the whole domain). The opening angle β in main flow direction defines the openings on both sides. Its range is obviously defined by $0 \leq \beta \leq \pi/2$. The dimensionless radius ratio Π between the external sleeve (r_1) and the rotating cylinder (r_0) is strictly $\Pi = r_1/r_0 \geq 1$. For increasing opening angle $\beta \to \pi/2$, the canonical configuration converges toward the (external) flow around a cylinder. A decreasing opening angle $\beta \to 0$ leads to the study of the (internal) flow between two concentric rotating cylinders. For the range $0 < \beta < \pi/2$ transport processes involve both aspects.

Table 1. Parameters influencing the flow and temperature field

	Locally	Globally
Dynamic	u_0	u_∞
Heat transfer	$(T_1 - T_0), u_0$	$(T_1 - T_0), u_\infty$
Design	$\Pi = r_1/r_0$	β

4. PHYSICAL MODEL AND NUMERICAL METHOD

In this section the settings for the physical model as well as for the numerical method are presented. The problem described in section 3 is considered as three-dimensional problem. However, the problem can be modeled as two-dimensional, but for achieving a more realistic approach, a three-dimensional model is more appropriate.

4.1. Physical model

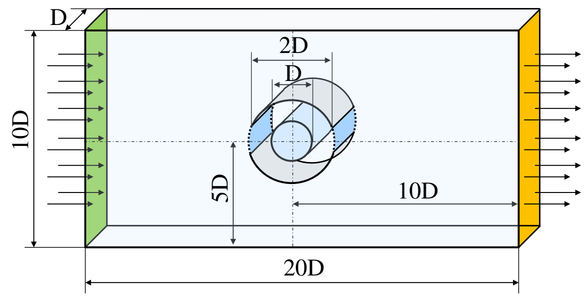

Figure 2. Defined dimensions for the geometrical setup of the canonical configuration

Figure 2 shows the cylinder and surrounding sleeve, which are mounted in a rectangular domain. The area of the interface, where fluid can enters and leave the annuli is defined by:

$$A_{Inlet,int} = \pi \cdot D \cdot \frac{2\beta}{180^\circ} \cdot D. \quad (4)$$

Based on the three-dimensional construction, the walls of the rectangular domain are defined with symmetry boundary conditions. The inlet is typically defined as velocity inlet and we set $\tau = 0$ as boundary condition. Static pressure is defined on the outlet of the rectangular domain. The flow field in all following simulations is considered as steady and incompressible. Ideal gas has been chosen as working fluid (air in this study). Due to the small temperature change in the flow field, the thermo-physical properties such as dynamic viscosity μ and thermal conductivity k are assumed constant.

4.2. Numerical method

The equations of conservation of mass, momentum, and energy are discretized with *ANSYS CFX 15.0*, relying on the Reynolds-Averaged Navier Stokes (RANS) approach. The mean equations are solved as a steady, incompressible Newtonian fluid with variable density [12]:

$$\frac{\partial}{\partial x_j}\left(\rho U_j\right) = 0, \tag{5}$$

$$\frac{\partial}{\partial x_j}\left(\rho U_i U_j\right) = -\frac{\partial p}{\partial x_i} + \frac{\partial}{\partial x_j}\left(\sigma_{ij} - \rho\overline{u_i u_j}\right) + S_M, \tag{6}$$

where ρ is the density, U the velocity, p the pressure, S_M the momentum source and σ_{ij} the molecular stress tensor, defined as:

$$\sigma_{ij} = \mu\left(\frac{\partial u_i}{\partial x_j} + \frac{\partial u_j}{\partial x_i}\right) - \frac{2}{3}\mu\frac{\partial u_k}{\partial x_k}\delta_{ij}. \tag{7}$$

The term $-\rho\overline{u_i u_j}$ is the Reynolds stress tensor resulting from the averaging procedure on the nonlinear convective terms in the momentum equations. The Reynolds averaged energy equation is:

$$\frac{\partial}{\partial x_j}\left(\rho U_j h_{tot}\right) = \frac{\partial}{\partial x_j}\left(\lambda\frac{\partial T}{\partial x_j} - \rho\overline{u_j h}\right) + \frac{\partial}{\partial x_j}\left[U_i\left(\sigma_{ij} - \rho\overline{u_i u_j}\right)\right] + S_E. \tag{8}$$

The viscous work term is expressed by $\frac{\partial}{\partial x_j}\left[U_i\left(\tau_{ij} - \rho\overline{u_i u_j}\right)\right]$, since it is needed for calculations with high velocity gradients. The mean total enthalpy is given by:

$$h_{tot} = h + \frac{1}{2}U_i U_i + k, \tag{9}$$

with the turbulent energy:

$$k = \frac{1}{2}\overline{u_i^2}. \tag{10}$$

The solution of Navier Stokes equation enables to calculate age of particles, based on an additional partial differential equation (PDE). The PDE itself, is derived from the concentration equation and therefore does not interact with the velocity field. Concerning the transport equation for a three dimensional system with turbulent and stationary flow, it is defined as:

$$\frac{\partial}{\partial x_j}\left(\rho U_j\varphi\right) = \frac{\partial}{\partial x_j}\left(\Gamma\frac{\partial\varphi}{\partial x_j} - \rho\overline{u_j\varphi}\right) + S_\varphi, \tag{11}$$

with φ as the conserved quantity which can be e.g., age of air and $\rho\overline{u_j\varphi}$ as the Reynolds flux. The additional variable equation (Eq. 11) are implemented in conjunction with the coverning equations (Eq. 5, 6 and 8) with a defined source term defined as $S_\varphi = \phi$. To calculate the turbulent terms, Menter's Shear Stress Transport turbulence model (SST) is used in this work. The selected advection scheme uses a second-order scheme when possible and blends to a first-order scheme if needed to maintain boundedness. The flow equations are solved sequentially with double precision. For the mesh, hexahedra elements are chosen. In all simulations the mesh verifies $y^+ < 1$, as needed for high accuracy, see [12] for details. The convergence criteria for mass, velocity components, enthalpy and the additional variable τ are set as a factor of 10^{-6}. No difference was observed in the convergence behavior when including the viscous work term.

5. CODE VALIDATION

To validate the implemented system, examples for internal as well as external flows are considered. Our numerical results are compared to analytical formulations or experimental data.

5.1. Internal flow: Hagen-Poiseuille flow

For a diffusion-free laminar pipe flow, several analytical formulations are available in the literature, see [13] for a detailed overview. In their work, Erdogan and Wörner [14] gave analytical formulations for elliptical channels of arbitrary aspect ratio, for a family of moon-shaped channels and for an equilateral triangular channel. They studied the diffusion-free residence time distribution of each geometry and described it by an one dimensional model. As a result, they show that the analytical expression for any elliptical channel is identical with the RTD of a circular channel. The differential RTD E(θ) and cumulative RTD F(θ) function are [13]:

$$\mathrm{E}(\theta) = \frac{1}{2\theta^3} \quad , \quad \mathrm{F}(\theta) = 1 - \frac{1}{4\theta^2} \tag{12}$$

under the consideration of a Hagen-Poiseuille flow. As described in section 2, the residence time distribution θ can be calculated analytically or numerically. The analytical formulation is given by:

$$\theta_{ana} = \frac{\theta_{F,ana}}{\lambda_{ana}} = \frac{u_\infty/u_{max}}{u(r)/u_{max}} \tag{13}$$

with the first appearance time $\theta_{F,ana}$ and the dimensionless velocity λ_{ana}. The fully developed velocity profile $u(r)$ can be found in the literature (e.g. [15]). Numerically, the RTD can be calculated as described in Eq. 1, where τ is the numerically calculated age of air, defined by Eq. 11. The Reynolds number Re_∞ in this study is defined as:

$$\mathrm{Re}_\infty = \frac{d_h u_\infty \rho_\infty}{\mu_\infty} = 512. \tag{14}$$

Figure 3 shows the comparison between the analytical and numerical calculations for $\mathrm{E}(\theta)$ and $\mathrm{F}(\theta)$ plotted against θ. For both functions, the analytical and numerical results are in a very good agreement to each other. However, the results represent one Reynolds number, only. To validate the local age of air for different Reynolds numbers, τ has to be calculated analytically, as well:

$$\tau_{ana} = \frac{L}{u(r)} = \frac{V}{2\dot{V}\left(1-\left(\frac{r}{r_{max}}\right)^2\right)}. \tag{15}$$

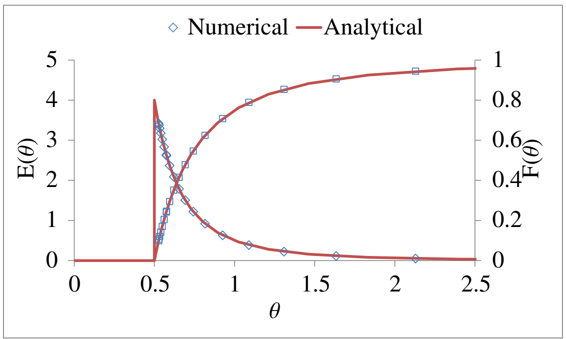

Figure 3. Comparison of $\mathrm{E}(\theta)$ ($\diamond$) and $\mathrm{F}(\theta)$ ($\square$) over θ for a Hagen-Poiseuille flow

Figure 4 shows the comparison of τ (calculated analytically and numerically) for various Reynolds numbers $\mathrm{Re}_{\infty,crit}$. The numerical results are in a very good agreement with the analytical formulation, till the critical Reynolds number of $\mathrm{Re}_{\infty,crit} = 2300$ for laminar flows is reached. In this figure, R is the dimensionless radius, defined as $R = r/r_{max}$. As a whole, the validation for $\mathrm{E}(\theta)$, ($\mathrm{F}(\theta)$) as well as τ is a success for a Hagen-Poiseuille flow.

5.2. Internal flow: Couette flow

As a further validation the age of air in a Couette flow is investigated. The method is similarly to the previous section. Considering one dimensional flow as well, τ_{ana} is defined with the fully developed velocity profile of a Couette flow:

$$\tau_{ana} = \frac{L}{u(r)} = \frac{V}{U\frac{y}{y_{max}}} \tag{16}$$

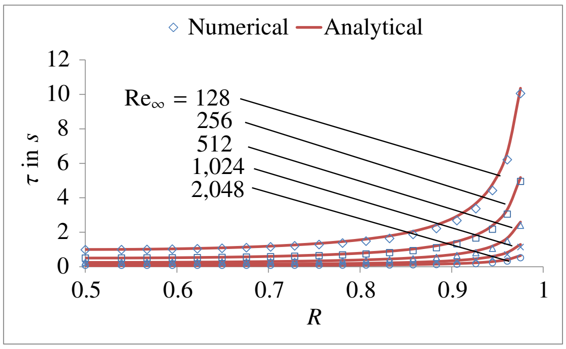

Figure 4. Comparison of τ for various $\mathrm{Re}_{\infty,crit}$ for a Hagen-Poiseuille flow

where U is the velocity of the moving plate and Y the dimensionless distance defined with $Y = y/y_{max}$. In Figure 5 the analytical and numerical values for τ are shown for different Reynolds numbers $\mathrm{Re}_{\infty,crit}$. For the Couette flow the results are in a very good agreement for the range of $128 \leq \mathrm{Re}_\infty \leq 1024$. Following [15], the critical Reynolds number for a laminar Couette flow is $\mathrm{Re}_{\infty,crit} = 1300$. Therefore, the implemented procedure delivers a perfect agreement with the analytical formulation for the two considered examples.

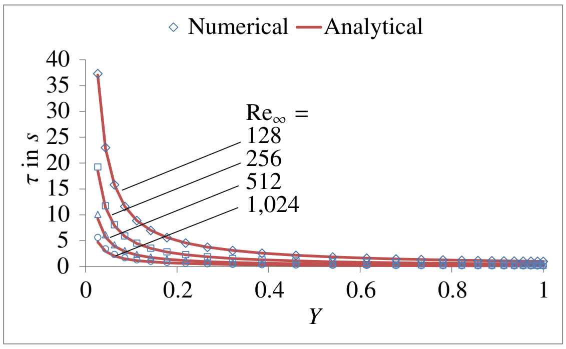

Figure 5. Comparison of τ for various Reynolds numbers for a Couette flow

5.3. External flow: room ventilation

For an overall validation, the RTD for external flows has to be investigated as well. In [16], the authors compared experimental results with their numerical study for a room with a mixing ventilation. The room is modeled as a simple cube with two windows (inlet and outlet, respectively) inside the wall (see [16] for further details of the model). They used the $k-\epsilon$ turbulence model to calculate the turbulence terms in the transport equations. Figure 6 shows the experimental and numerical data from Bartak et al. [16] compared to our numerical results. The values are taken from a plane located in the middle of the room. The magnitudes of all three data are very close to each other. The minimum of θ at $n = 2.25$ is detected in all three cases. The values of our numerical

results are smaller than the numerical results of Bartak et al. [16], but in a good agreement with their experimental results. To explain the differences with their numerical results, one reason could be that we used the more advanced Menter's SST model to calculate the turbulence terms.
This last comparison concludes the validation of our numerical approach regarding internal and external flows. For the tested configurations and parameters, the numerical results are identical or very close to the analytical predictions and experimental observations. However, it was also observed that values of y^+ well below 1 are needed for an accurate analysis of the flow field and of the associated residence time distribution.

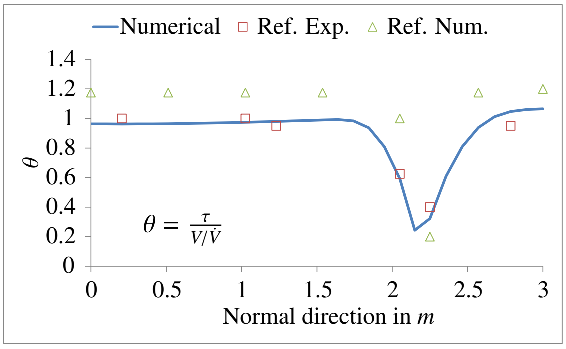

Figure 6. Comparison of θ to the results from Bartak et al. [16] for a ventilated room

6. RESULTS

Using now the canonical configuration for a first study, the dimensionless radius ratio is set to $\Pi = 2$. The opening angle β will change its magnitude in the range of $20° \leq \beta \leq 85°$. For such values the transport processes involve external and internal flows and therefore describe the processes found in a real alternator system. The sleeve is defined as adiabatic and the inner cylinder corresponds to a dimensionless heat flux of:

$$\dot{q}^* = \frac{\dot{q}2r_0}{k_\infty T_\infty} = 0.05. \tag{17}$$

The ambient temperature T_∞, the dynamic viscosity μ_∞ and the thermal conductivity k_∞ are considered as constant with values of 300 K, $1.831 \cdot 10^{-5}$ Pa.s and 0.0261 W/(m.K), respectively. For a first study, the inner cylinder is not in motion, which results in $\mathrm{Re}_0 = 0$ for the local tangential velocity. This ensures that the flow field is not becoming too complex at this early stage. Therefore, only one Reynolds number (Re_∞) influences the flow field together with the varying design parameter β. The range for the simulations is given by $0.5 \leq \mathrm{Re}_\infty \leq 4,096$, changing the values by a factor 2 between two cases. The range for the opening angle is defined with $20° \leq \beta \leq 85°$. For values $\beta \leq 15°$ the residuals are not converging, especially for small Reynolds numbers. Figure 7 shows the volumetric flow-rate for a varying Reynold number Re_∞ and opening angle β in a double logarithmic reference frame. The volumetric flow-rate $\dot{V}$ is analyzed on the interface located at the inlet of the sleeve, where the flow is entering the annuli. With an increasing opening angle β, the area of the inlet interface increases as well (see Eq. 4). Therefore, the volumetric flow-rate $\dot{V}$ increases with the opening angle β.

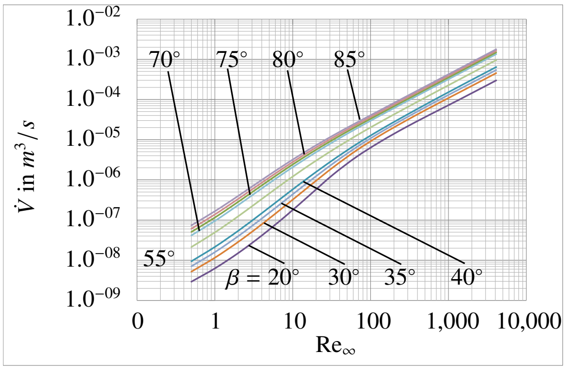

Figure 7. Effect of Re_∞ and β on $\dot{V}$

Figure 8 shows the same analysis with respect to the age of air τ inside the annuli.

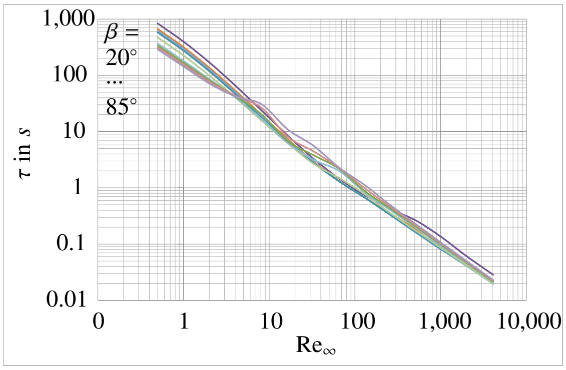

Figure 8. Effect of Re_∞ and β on τ

Both results are in very good agreement to each other. When increasing Reynolds number Re_∞ the volumetric flow-rate increases as well, and the age of air decreases, due to the faster transport of particles. An increasing opening angle β decreases the residence time τ, due to the reduced sleeve surface. For both variables ($\dot{V}$ and τ), the Reynolds number is the dominating parameter. Looking only at the volumetric flow-rate and age of air values, a comparison between the different arrangements is difficult, due to the changing boundary conditions (β and Re_∞). By looking at these results, the surrounding sleeve appears to have only a very small influence on the flow field and, therefore, on the residence time as well. As previously discussed in section 2, it is necessary to consider different volumetric flow-rates $\dot{V}$ and volumes V as well. Therefore, the air change efficiency factor ϵ_a is now considered for the same cases. As previously discussed, this factor quantifies the ability of a system to renew the air and could be helpful as an indicator for heat and flow processes within the annuli. The results are shown in Figure 9. With an increasing opening angle $\beta \to \pi/2$ the air change effectiveness ϵ_a decreases rapidly.

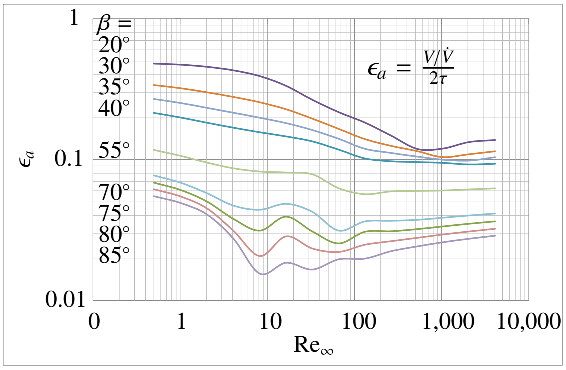

Figure 9. Effect of Re_∞ **and** β **on** θ

Since the total volume V is constant in this case, only $\dot{V}$ and τ change their magnitude. Considering Fig. 7 and Fig. 8, $\dot{V}$ is more strongly influenced by an increasing β compared to τ, due to the increasing area $A_{Inlet,int}$. Therefore, the shortest possible time needed for replacing the air $(V/\dot{V})$ decreases much faster than the average air exchange rate (2τ) with $\beta \to \pi/2$. The setup with the smallest opening angle $\beta = 20°$ is thus the most efficient case when considering the input and output parameter $\dot{V}$ and τ, respectively. There is no advantage connected to a higher $\dot{V}$, due to the small changes of τ obtained when increasing opening angle. For the range $20° \leq \beta \leq 40°$ the behavior of the different opening angles as function of the Reynolds number Re_∞ are qualitatively similar to each other. A minimum in efficiency can be found for each series at a specific, relatively high Reynolds number Re_∞. The opening angle of $\beta = 55°$ can be considered as a transition condition. Above this angle (in the range of $70° \leq \beta \leq 85°$) the curves are again qualitatively similar to each other, but show considerably more complex profiles compared to the small opening angles. Here, different extrema can be detected in the range of $8 \leq \mathrm{Re}_\infty \leq 128$. Note that the air change efficiency of the flow field increases for all cases at high Reynolds numbers, $\mathrm{Re}_\infty \geq 1,024$. In Figure 10 the age of air τ is shown for the cases $\beta = 20°$ and $\mathrm{Re}_\infty = 8$ and 512, respectively.

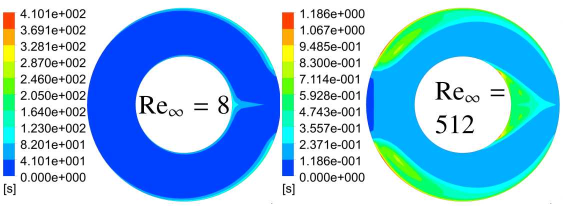

Figure 10. Effect of Re_∞ **for** $\beta = 20°$ **on** τ

It can be seen that the configuration with $\mathrm{Re}_\infty = 512$ results in the lowest air change efficiency ϵ_a due to increasingly large backflow areas. For the case $\mathrm{Re}_\infty = 8$ no backflow exists and, therefore, ϵ_a shows the highest value. The flow passes the whole annuli and heat transfer occurs in a continuous manner. Large backflow areas have been found during post-processing for all cases, where a minimum of the air change efficiency is observed in Fig. 9.

7. GRID-INDEPENDENCE TEST

Since the grid plays a major role for our investigations, a grid-independence test is shown in Figure 11.

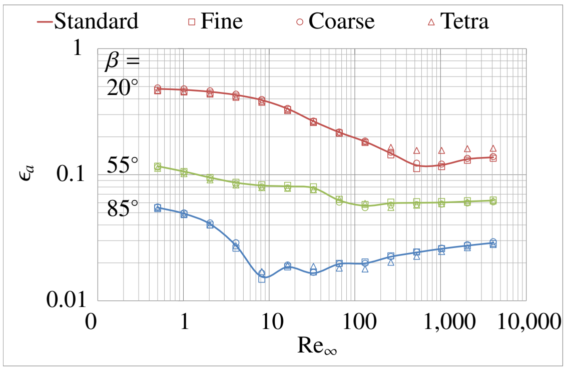

Figure 11. Effect of different grid sizes on ϵ_a

The element size (maximum and first element size) as well as the growing ratio factor were increased by 25% for the coarse and decreased by 25% for the fine mesh. Additionally, a pure tetrahedral mesh is also considered, to quantify possible deviations between a structured and unstructured mesh. The results show, that for different hexahedral element sizes, only small discrepancies occur. The unstructured mesh delivers also results very close to those of the structured mesh as well, except for the limit case $\beta = 20°$. Here, large discrepancies are found for high Reynolds numbers of $256 \leq \mathrm{Re}_\infty \leq 4,096$. Compared to the structured mesh, the minimum is not so clearly visible when using an unstructured tetra mesh. For the other Reynolds numbers, the results are more close to each other. However, a larger number of elements are needed for the unstructured mesh in order to reach the same level of precision. This results in a higher computing time as well as memory requirements. As a whole, these tests show the standard grids employed in this work are sufficient to reach grid-independent results. Small differences are only found for an unstructured mesh for $\beta = 20°$ and at high Reynolds numbers. Even there, the extremal values are still located at the right Reynolds number. Therefore, the discrepancies observed in section 5.3 did not result from the mesh setup. This is in agreement with the results from Bartak et al. [16], who also carried out a grid-independence test and found no big deviation.

Therefore, the better prediction obtained in our case is probably due to the better turbulence model, SST.

8. CONCLUSION

Numerical investigations of residence time distribution relying on a canonical configuration have been done. The developed simulation approach was compared with analytical or experimental results from the literature. Grid-independence tests show that the employed grid is sufficiently fine. A constant wall heat flux along the static cylinder was considered. The oncoming flow u_∞ enters the annuli between static sleeve and cylinder through a varying opening angle $20^\circ \leq \beta \leq 85^\circ$. The age of air τ decreases with an increasing flow rate in the range of $0.5 \leq \mathrm{Re}_\infty \leq 4,096$. However, for a quantitative analysis and a comparison between different arrangements, the dimensionless residence time distribution θ or the air exchange efficiency ϵ_a have to be considered. The results show that with an increasing opening angle β, the efficiency decreases. A minimum can be found for each series at a specific Reynolds number. The lower air change efficiency can be correlated with the existing of large backflow areas, which are visible in the contour plots. The canonical configuration shows, that the residence time distribution can be an efficient way to analyze external and internal flow fields. Therefore, this approach can be used for complex flow fields which can be found in e.g., electrical machines. Based on the air change efficiency ϵ_a an integral analysis can help to compare different alternator systems with each other. High values of ϵ_a can indicate a better performed cooling system. The age of air distribution τ characterizes the complexity of the flow field and shows where the lower heat transport comes from. With this knowledge, promising regions for optimization can be located.

REFERENCES

[1] Thévenin, D., and Janiga, G., 2008, *Optimization and Computational Fluid Dynamics*, Springer-Verlag: Berlin and Heidelberg.

[2] Liu, M., and Tilton, J., 2010, "Spatial distributions of mean age and higher moments in steady continuous flows", *AIChE Journal*, Vol. 56, pp. 2561–2572.

[3] Lin, Z., Chow, T.T., Tsang, C.F., Fong, K.F., and Chan, L.S., 2005, "CFD study on effect of the air supply location on the performance of the displacement ventilation system", *Building and Environment*, Vol. 40, pp. 1051–1067.

[4] ASHRAE, Inc., 2001, *ANSI/ASHRAE Standard 129-1997, Measuring Air-Change Effectiveness*.

[5] Awbi, H., 2000, *Air Distribution in Rooms: Ventilation for Health and Sustainable Environment*, Elsevier.

[6] Pudjiono, P.I., Tavare, N.S., Garside, J., and Nigam, K.D.P., 1992, "Residence time distribution from a continous Couette flow device", *Chemical Engineering Journal*, Vol. 48, pp. 101–110.

[7] Lin, S., 1980 "The residence time distribution for laminar non-newtonian flow in an annulus with negligible diffusion", *Chemical Engineering Science*, Vol. 35, pp. 1477–1480.

[8] Pechoc, V., 1982, "The residence time distribution for laminar flow in an annulus with negligible diffusion", *Chemical Engineering Science*, Vol. 38, pp. 1341–1342.

[9] Li, X., Li, D., Yang, X., and Yang, J., 2003, "Total air age: an extension of the air age concept", *Building and Environment*, Vol. 38, pp. 1263–1269.

[10] Fogler, H., 1986, *Elements of chemical reaction engineering*, Prentice-Hall.

[11] Eger, T., Thévenin, D., Janiga, G., Bol, T., and Schroth, R., 2014, "Identification of a canonical configuration for a quantitative analysis of transport phenomena in electric machines based on entropy generation", *Energy and Sustainability V, WIT Press*, pp. 751–762.

[12] ANSYS, Inc., 2013, *ANSYS CFX-Solver Modeling Guide, Release 15.0*.

[13] Wörner, M., 2015, "General pure convection residence time distribution theory of fully developed laminar flows in straight planar and axisymmetric channels", *Chemical Engineering Journal*, Vol. 122, pp. 555–564.

[14] Erdogan, S., and Wörner, M., 2013, "Influence of channel cross-sectional shape on diffusion-free residence time distribution in fully developed laminar Newtonian flow", *Chemical Engineering Journal*, Vol. 227, pp. 158–165.

[15] Schlichting, H., and Gersten, K., 2000, *Boundary-Layer Theory*. Springer-Verlag: Berlin and Heidelberg.

[16] Bartak, M., Cermak, M., Clarke, J. A., Denev, J., Drkal, F., Lain, M., Macdonald, I. A., Majer, M., and Stankov, P., 2001, "Experimental And Numerical Study Of Local Mean Age Of Air", *Seventh International IBPSA Conference, Rio der Janeiro, Brazil*, pp. 773–779.

Conference on Modelling Fluid Flow (CMFF'15)
The 16th International Conference on Fluid Flow Technologies
Budapest, Hungary, September 1-4, 2015

NUMERICAL STUDY OF THE STAY VANE CHANNEL-FLOW IN A REVERSIBLE PUMP TURBINE AT OFF-DESIGN CONDITIONS

Sandro Erne[1,2], Gernot Edinger[1], Christian Bauer[1]

[1] Institute for Energy Systems and Thermodynamics, Vienna University of Technology, Getreidemarkt 9/302, A-1060 Vienna / Austria
[2] E-mail: sandroerne@gmx.at

ABSTRACT

In this work, the focus is laid on numerical studies of LDV-based flow field measurements in the stay vane channel of a Francis-type pump-turbine model, operating in pump mode. After evaluating the numerical model by means of integral quantities of the pump-turbine, extensive CFD simulations are performed to better resolve the flow characteristics in the stay vane channel. To assess altering flow structures, the computational mesh includes sampling planes, halved into a near-hub and shroud region. Starting at zero discharge, experiments revealed that a further increase of the discharge leads to an flow shifting between shroud and hub of the runner. Close to zero-discharge, three-dimensional flow separation in the stay vane channel is observed, changing to an asymmetric flow in meridional direction when increasing the discharge. Near the best efficiency point, the flow of both hub and shroud side starts getting redistributed uniformly. Numerical investigations in flow characteristics were carried out to allow an examination of onsetting flow disturbances in the distributor. It is found that slightly below the best efficiency point the stay vane channel flow is most affected by unsteady mechanisms. Experimental data of mean flow quantities are fairly well predicted by time-depended flow simulations.

Keywords: transient simulations, OpenFOAM, pump-turbine, rotating stall, stay vane channel

NOMENCLATURE

A/A_{max}	$[-]$	normalized amplitude
C	$[ms^{-1}]$	mean velocity magnitude
C_p	$[-]$	dimensionless pressure coefficient
D_1	$[m]$	impeller inlet diameter
H	$[m]$	net head
K_g	$[-]$	dimensionless torque, $K_g = T/\rho g H b_o t_o^2$
N	$[-]$	cell number
Q	$[m^3 s^{-1}]$	flow rate
Q_{ED}	$[-]$	flow coefficient, $Q_{ED} = Q/\sqrt{gH}D_1^2$
S	$[kgm^2 s^{-2} K^{-1}]$	entropy
T	$[Nm]$	impeller torque
a_o	$[mm]$	gate opening
b_o	$[m]$	distributor height
f	$[-]$	grid study solution
f	$[Hz]$	frequency
f_Ω	$[Hz]$	impeller rotary frequency
f_{RS}	$[Hz]$	rotating stall frequency
h	$[m]$	cell edge length
k	$[m^2 s^{-2}]$	turbulent kinetic energy
m	$[-]$	number of stall cells
n	$[rpm]$	impeller rotational speed
n_q	$[rpm]$	impeller specific speed, $n_q = nQ^{0.5}/H^{0.75}$
p	$[Pa]$	static pressure
q	$[m^3 s^{-1}]$	zonal flow rate
r	$[-]$	grid refinement ratio
t_o	$[m]$	arc length of gate pitch circle
u_1	$[ms^{-1}]$	circumferential velocity, $u_1 = \Omega D_1/2$
η	$[-]$	hydraulic efficiency
μ	$[kgm^{-1} s^{-1}]$	dynamic viscosity
Ω	$[s^{-1}]$	impeller angular speed
ω	$[s^{-1}]$	specific dissipation frequency rate
Φ	$[m^3 s^{-1}]$	face flux
ϕ	$[-]$	scalar or vector quantity
ψ	$[-]$	flux limiter
ε	$[-]$	discretization error
φ	$[-]$	flow coefficient, $\varphi = 8Q/\pi D_1^3\Omega$

Subscripts and Superscripts

cone	draft tube cone
h, l	high, low
hrs	high resolution scheme
i	refinement level
j	face index
lo, up	lower, upper
max	maximum
n	nominal
prim	priming chamber

m, θ, z	streamwise, pitchwise, spanwise
x, y, z	cartesian coordinate

1. INTRODUCTION

Especially when operating a pump-turbine in pump mode, the occurrence of several unsteady flow phenomena upstream of the impeller like rotating stall (RS) or Rotor-Stator-Interaction (RSI) were investigated by many authors in the past.

Only a few studies dealing with the flow in the stay vane channel of a pump-turbine were found, e.g. [1], who merely analyzed the flow between wicket gates and stay vanes. In [2], experimental analysis were performed with a centrifugal pump (n_q = 21rpm) at $Q/Q_n = 0.8$ which revealed a very slow rotating stall in the diffuser channel, rotating at 1% of the impeller rotational speed. Strongly uneven flow in the stay vane channel of a pump-turbine was qualitatively observed by [3] when operating near the best efficiency point at a flow rate $Q/Q_n = 0.8$. The onset of rotating stall phenomena has been investigated by several authors [4, 5], who observed rotating jet flow patterns and blockage in the stay ring at a flow rate $Q/Q_n = 0.8$. A dominant frequency peak at 1 – 2Hz was determined by instationary LDV-measurements in [6] at a part-load flow rate $Q/Q_n = 0.77$. To assess the ability of the computational model to capture transient effects, the work includes a detailed numerical investigation of the specific operating point ($Q/Q_n = 0.74$) at which the onset of rotating stall in the distributor is evident.

As the main purpose of this study was the evaluation of the flow behavior in the stay vane channels, numerical simulations were performed for six "off-design" operating points, ranging from zero-discharge to full load condition. The results obtained from the CFD simulations were compared to data from experiments for each operating point. Experiments were performed with a reduced scale-model pump-turbine which provides accessibility in the spiral case for optical flow measurements using LDV technique. Details about the experimental setup and employed measurement techniques can be found in [7].

2. GRID INDEPENDENCE STUDY

2.1. Computational setup

Transient Reynolds-Averaged-Navier-Stokes (RANS) simulations of discretization order p_i were performed for systematically refined grids G_i with the solutions f_i. Since a reference solution f_{EXP} is known from experiments, only two meshes were considered in this grid study. The reduced computational model consists of the draft tube, impeller and an extended vaneless space domain (see Fig. 2), operating at BEP (Best Efficiency Point) in pumping mode. The cell number N_i of each grid G_i was chosen in a way such that $N_2/N_1 = r^3$. As recommended in [8], the grid refinement ratio r should be at least greater than 1.3, hence $r = h_1/h_2 = \sqrt{2}$ is chosen in the present case. The grid topology of both grids includes hexahedral cell structures only and has been adapted to the usage of wall functions. Grid details can be found in Tab. 1.

The standard two-equation turbulence model k-ω SST was applied to account for the turbulent flow. The case is modeled as a single rotating reference frame and simulated for approximately 30 runner revolutions.

2.2. Discretization Order

A flux-blending discretization scheme is used for all convection terms which yields more numerical robustness for transient simulations of highly turbulent flow. Velocity and turbulence fields are spatially discretized by a blended high resolution TVD (Total Variation Diminishing) scheme, using a flux limiter $\psi(r)$ reading

$$\phi^{hrs} = \phi^l + \psi(r)(\phi^h - \phi^l). \tag{1}$$

A solution of second-order accuracy (central differencing) is given when $\psi(r)$ is close to one, defined by

$$\psi(r) = max\left(min\left(\frac{2}{k}r, 1.0\right), 0.0\right) \tag{2}$$

An upwind differencing scheme of first order is applied when $\psi(r) = 0$. In Eq. 2, k denotes a user defined blending factor, satisfying $0 \le k \le 1$. As in Jasak [9], this limiter function is mainly based on a smoothness parameter r, characterizing the smoothness of the flow region by gradients of the quantity ϕ. As $k < 0.5$ is chosen in the present simulation, the order of accuracy p_i may varies in the flow field of grid G_i. Thus, the formal order of accuracy for grid G_i is obtained from

$$p_i^{hrs} = p_i^l + \overline{\overline{\psi}}_i(p_i^h - p_i^l) \qquad i = 1...2 \tag{3}$$

where $p_i^l = 1.0$ and $p_i^h = 2.0$. In order to take the blending into account, a flux-averaged and time averaged blending factor $\overline{\overline{\psi}}$ is calculated with

$$\overline{\overline{\psi}} = \frac{\sum_{j=0}^{J} \Phi_j \psi_j}{\sum_{j=0}^{J} \Phi_j} \tag{4}$$

where Φ stands for the face flux and J is the total number of faces in the computational domain. Upon evaluation of Eq. 3 and Eq. 4, a formal order of accuracy $p_1^{hrs} = 1.86$ is calculated on the coarse grid and $p_2^{hrs} = 1.90$ on the successively refined grid. The

Table 1. Details of grid study.

grid	N	y^+	$\det_{min}$	$\overline{\overline{\psi}}$	p^{hrs}	$\varepsilon_{h,i}(\hat{p})$
G_1	$4.2E5$	32	0.31	0.85	1.86	0.033
G_2	$1.2E6$	30	0.22	0.90	1.90	0.011

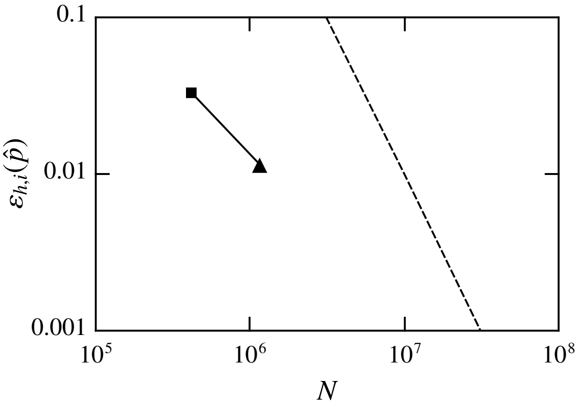

Figure 1. Discretization error: coarse grid G_1 (—■—), fine grid G_2 (—▲—), second-order (- - - -).

observed order of accuracy of the solution reads

$$\hat{p} = \frac{ln\left(\left|\frac{f_{EXP} - f_{i+1}}{f_{i+1} - f_i}\right|\right)}{ln(r)} \tag{5}$$

where i denotes the grid refinement level.

2.3. Results of the grid study

The reference solution f_{EXP} is expressed by the measured static pressure difference between the pressure in the draft tube cone p_{cone} and the pressure in the priming chamber p_{prim}. The positions of the tapered pressure sensors were used for the according wall pressure monitoring during the simulations. The solutions are defined by means of a dimensionless quantity, following

$$f_{G_i} = \frac{8|p_{prim} - p_{cone}|}{\rho D_1^2 \Omega^2} \tag{6}$$

where D_1 denotes the runner inlet diameter and Ω the impeller angular speed. As suggested in [10], the discretization error of the grid G_i is estimated by the common formulation

$$\varepsilon_{h,i}(p) = \frac{|f_{EXP} - f_i|}{r^p - 1}. \tag{7}$$

Grid quality and details of the grid study can be found in Tab. 1. In Fig. 1, it is shown by means of the discretization error estimator that the solutions nearly reach second-order accuracy. For G_1, the observed order of accuracy is slightly greater than the formal order of accuracy, which might be an indicator for non-asymptotic behavior. However, as the order of accuracy p^{hrs} and $\hat{p}$ computed on the refined grid G_2 are almost identically, a grid spacing h_2 was used for all further investigations.

3. NUMERICAL METHOD

For all simulations performed, the open-source CFD software OpenFOAM was used. All grids have been created with the meshing tool ICEM [11] to obtain block-structured grids of high quality. Dimensions and parameters of the scale-model pump-turbine can be found in Tab. 2.

Simulations were carried out for a fully turbulent pump-turbine flow, governed by the incompressible Navier-Stokes equations. A limited 2^{nd}-order scheme was used for all convection and diffusion terms. As shown in Fig. 3, the computational domain consists of fully block-structured grid sub domains which are coupled by mesh interfaces, as shown in Fig. 2-right. The grid has $N = 2.5 \times 10^6$ cells in total and has a constant aspect ratio in normal direction of the walls. The spatial discretization was focused on the stay vane channel where the cell number is in pitchwise direction $N_\theta = 27$, in spanwise direction of the stay vane $N_z = 26$ and in streamwise direction $N_m = 32$. As in the grid study, the widely used k-ω SST turbulence model was used for turbulence modeling, which allows an improved near-wall treatment in ducted flows. For ω-based models, OpenFOAM provides an automatic wall treatment for a better grid

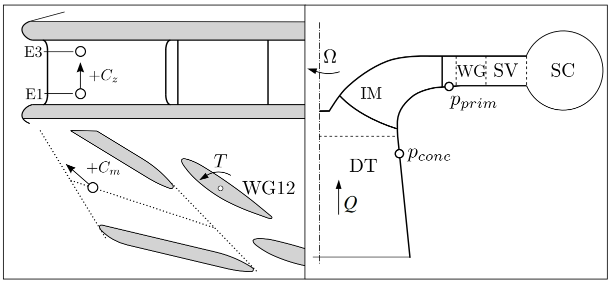

Figure 2. Velocity measurement positions (left), schematic of the computational domain (right) DT draft tube, IM impeller (rotating domain), WG wicket gate, SV stay vane, SC spiral case, (○) wall pressure taps.

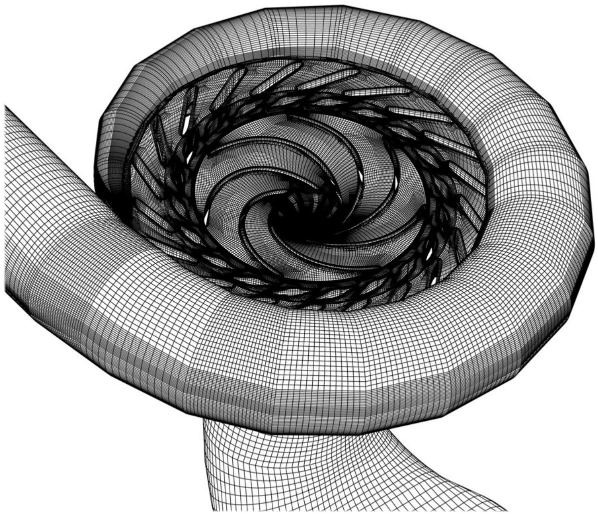

Figure 3. Mesh plot of the complete computational domain.

Table 2. Machine data.

specific speed	n_q	41.5	rpm
inlet diameter	D_1	0.276	m
distributor height	b_o	0.054	m
arc length of gate pitch circle	t_o	0.088	m
number of blades	z_b	7	-
number of guide vanes	z_g	20	-
number of stay vanes	z_s	20	-

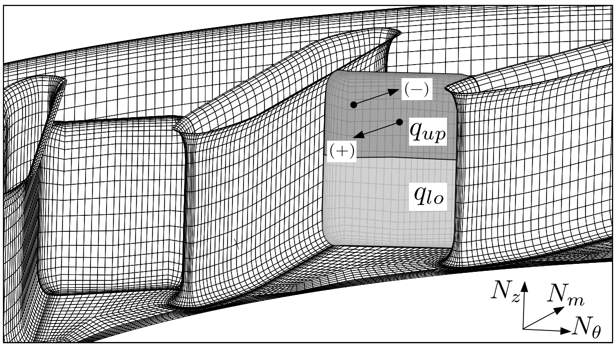

Figure 4. Grid spacing ($N_m \times N_\theta \times N_z$) of domain SV and sampling zones: q_{up} flow rate upper channel zone, q_{lo} flow rate lower channel zone; radial inward (+), outward (−).

refinement in near-wall regions. Depending on the operating point of the pump-turbine, the mean dimensionless wall distance is $y^+ = 20$ on average, but at least beyond the buffer layer ($y^+ > 12$). A constant flow enters at the draft tube inlet with prescribed profiles for the velocity and the turbulent quantities. In order to evaluate the wall-bounded flow regime separately, the inter-blade flow was divided into an upper and lower channel zone, as shown in Fig. 4. For time marching, a 0.96 deg time step was chosen to accurately predict the influence of the wake characteristics of the impeller blades on the wicket gates. Simulations were run about 40 runner revolutions for each operating point. After reaching a quasi steady-state flow solution (>10 runner rev) all quantities of interest were sampled over time for approximately 25 runner revolutions.

4. RESULTS

4.1. Integral Quantities

In what follows, all dimensionless quantities are based on the reference diameter D_1, as recommended in [12]. Besides flow analysis, the hydraulic efficiency of the pump-turbine η_h was assessed by the numerical model and compared to IEC compliant measurements, as can be seen in Fig. 5. Even in deep part load, the hydraulic efficiency is still well

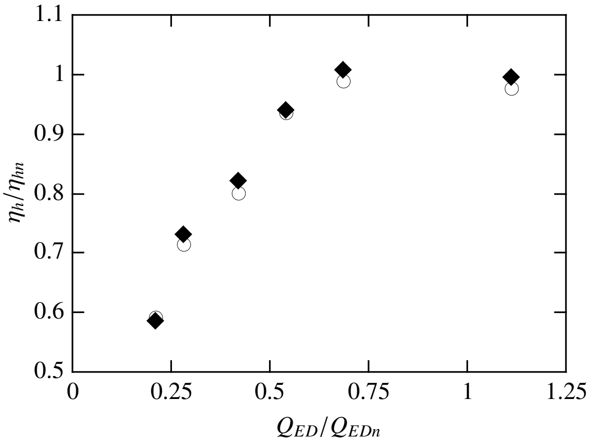

Figure 5. Off-design efficiency at a_o/a_{on} = 0.67: CFD ◆, EXP ○.

predicted by CFD. Even at zero discharge condition, simulation indicates a well agreement with the experimental data from [7]. The average percentage deviation of the simulated values from the model measurements is ±1.2%, which is found to be in an allowable range.

Depending on the wicket gate opening angle and the flow rate of the pump-turbine, the wicket gates tend to either open or close. Opening tendency at small opening angles means that the swirling discharge flow of the impeller has an unfavorable inclination angle at the wicket gates leading edge. This in turn greatly affects the flow in the stay vane channel. Owing to 'off-design'-flow of the pump-turbine, the separation behavior of the wicket gate flow probably has a strong influence on the flow under investigation. Mean flow patterns at the impeller outlet were examined by means of evaluating the torque T of wicket gate no 12 (see Fig. 2-left). As in Fig. 6, model test results and simulation show a reasonable agreement, whereas measurements for $a_o/a_on = 0.67$ were not available. Low flow rates show an opening tendency of the wicket gates. Near Q_{ED}/Q_{EDn} = 0.75, the torque coefficient K_g becomes positive what indicates a closing tendency.

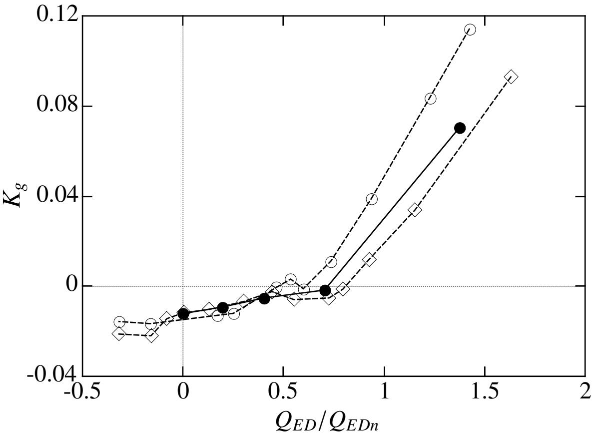

Figure 6. Mean torque coefficient K_g of WG12: CFD a_o/a_{on} = 0.67 —●—, EXP a_o/a_{on} = 0.78 —◇—, EXP a_o/a_{on} = 0.56 —○—.

4.2. Stay vane channel flow patterns

Referring to Fig. 2-left, velocity components C_m and C_z of the guide vane flow were analyzed at 25% (E1) and 75% (E3) of the distributor height, each at 50% in pitchwise direction. In streamwise direction, the two sampling points were located near the channel outlet at 90% of the stay vane length. Figure 7 shows velocity contours and the respective streamlines in the region between runner outlet and spiral case inlet. As can be seen from Fig. 7-a, no net flow enters the spiral case during zero-discharge, but leads to reversal flow in meridional direction in the intervane region due to high circumferential momentum from the runner outlet. As can be seen in Fig. 8, this flow behavior is not revealed by experiments, where a slight flow radially outward can be seen.

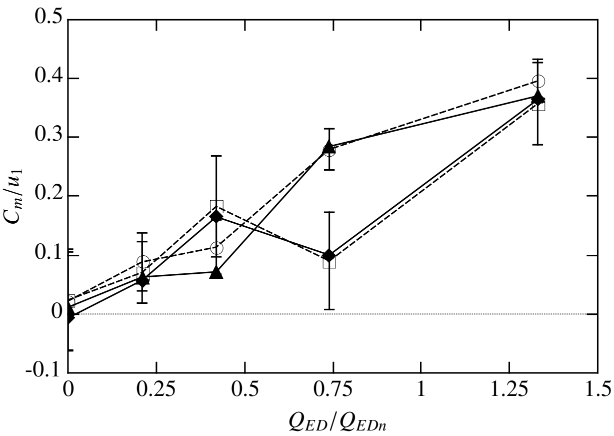

Figure 8. Normalized meridional velocity component C_m in the stay vane channel: CFD E1 —◆—, CFD E3 —▲—, EXP E1 —⊟—, EXP E3 —⊖—.

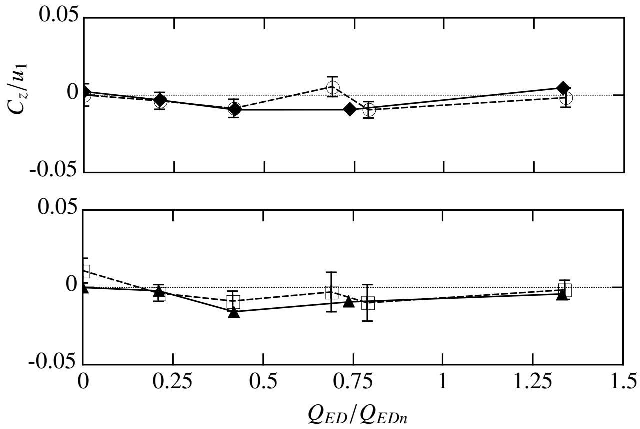

Figure 9. Normalized spanwise velocity component C_z in the stay vane channel: CFD E1 —▲—, CFD E3 —◆—, EXP E1 —⊟—, EXP E3 —⊖—.

Contours of the averaged meridional velocity are shown in Fig. 7-b for $Q_{ED}/Q_{EDn} = 0.21$ and Fig. 7-c for $Q_{ED}/Q_{EDn} = 0.42$. Here, the flow enters the wicket gate section mainly in the upper channel height, possibly due to prerotation at the runner inlet, and gets redistributed throughout the channel height again. In Fig. 7-d at $Q_{ED}/Q_{EDn} = 0.74$, a more less uniform distribution of the mean meridional velocity in the wicket gate section is shown, whereas in the inter-stay vane region a slight downward flow is predicted. Simulations show that for $Q_{ED}/Q_{EDn} = 1.33$ a uniform flow in meridional direction throughout the stay vane and wicket gate channel occurs.

Mean values of the velocity components C_m and C_z in the stay vane channel near the shroud (E1) and hub (E3) are given in Fig. 8 and Fig. 9 respectively. At zero discharge, the simulation revealed reversal flow in the stay vane channel what is not observed by flow velocity measurements, as can be seen in Fig. 8. However, it should be noted that the increased measurement errors bars (representing the standard deviation) in Fig. 8 indicate strong velocity fluctuations. Below the best efficiency point at $Q_{ED}/Q_{EDn} = 0.74$, the uneven flow reaches its maximum and leads to high velocity rates in the upper stay vane channel region. Under full-load conditions, the flow redistributes to a symmetric velocity profile across the channel height, which becomes abundantly clear from Fig. 7-e. In general, the simulations predict comparable changes in flow structure at position E1 and E3 when increasing the flow rate.

Time histories of partial flow rates in the stay vane channel over more than 20 runner revolutions are shown in Fig. 10. In general, when comparing this data with Fig. 8, the flow in the stay vane channel appears to be different at some operating points. This remaining discrepancy may be assigned to the different evaluation procedure of the integral values

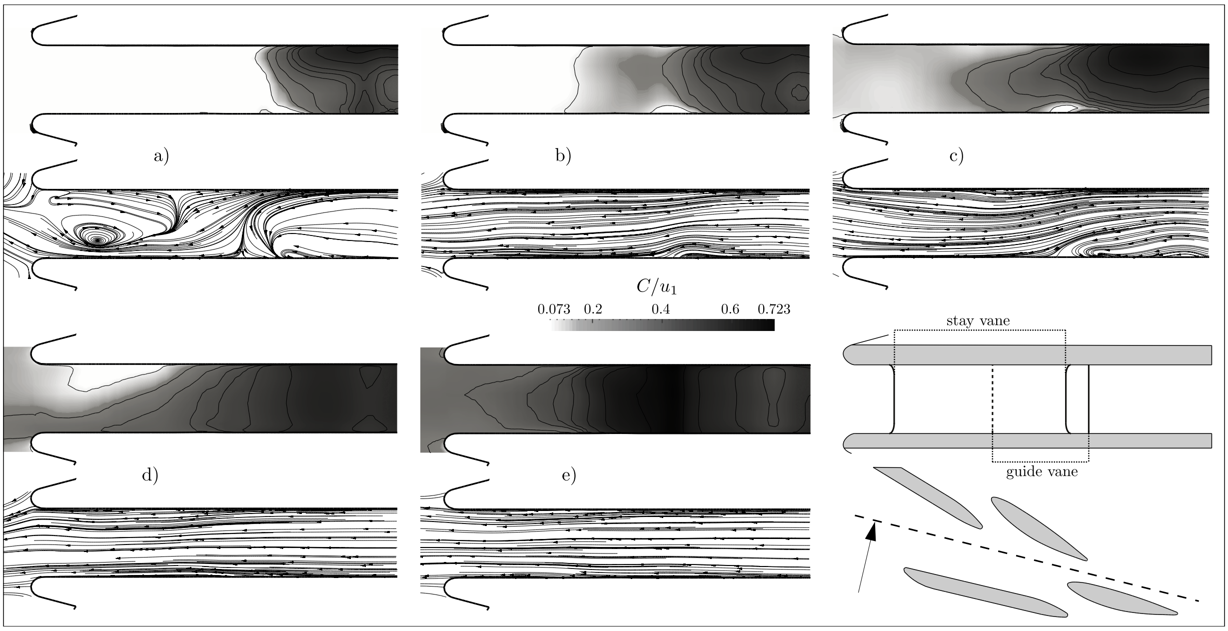

Figure 7. Contour plots and streamlines of the time-averaged meridional velocity C_m in the stay vane channel: a) $Q_{ED}/Q_{EDn} = 0.0$, b) 0.21, c) 0.42, d) 0.74, e) 1.33, sampling plane (– – –).

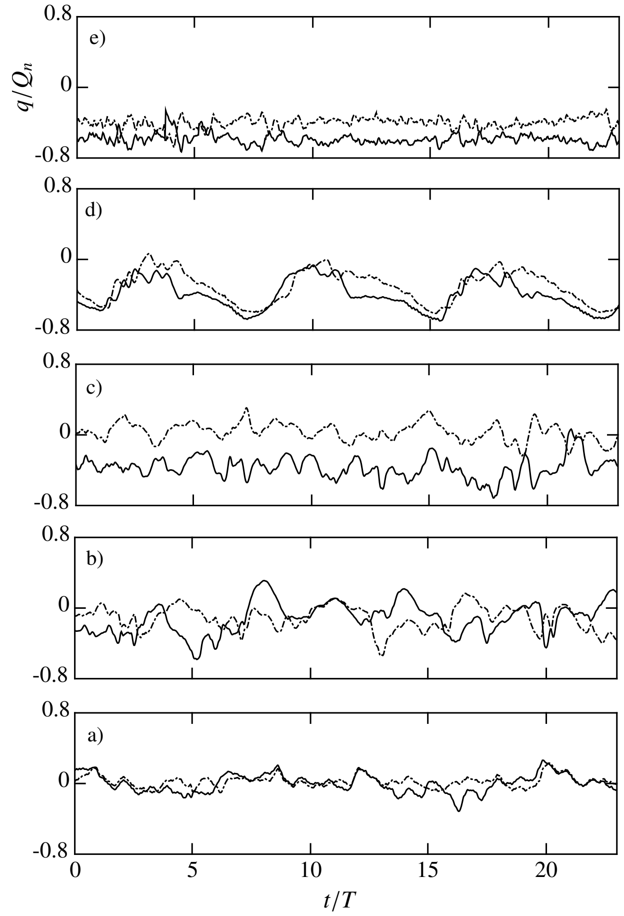

Figure 10. Normalized flow in the stay vane channels: q_{up} upper sampling zone (– · – · –), q_{lo} lower sampling zone (———), a) Q_{ED}/Q_{EDn} = 0.0, b) 0.21, c) 0.42, d) 0.74, e) 1.33.

q_{up} and q_{lo} and the local velocity components C_m (see Fig. 8). The time development of the stay vane channel flow at $Q_{ED}/Q_{EDn} = 0.42$ shows no remarkable periodic fluctuation, but is governed by a non-uniform mean flow field. At $Q_{ED}/Q_{EDn} = 1.33$, the flow rates remain almost constant over time, where q_{up} is predicted to be smaller than q_{lo}. The prediction of both lower and upper flow rate is significant for operating point $Q_{ED}/Q_{EDn} = 0.74$. The simulation shows a periodically appearing jet flow and blocked flow in both upper and lower channel region.

Figure 11 presents power spectra of the stay vane channel flow for various operating points where the amplitudes are normalized by the maximum amplitude calculated. From the waterfall plot, periodic disturbances at $Q_{ED}/Q_{EDn} = 0.74$ are evident. Interestingly, the spectrum for $Q_{ED}/Q_{EDn} = 0.21$ shows a remarkable similarity to this operating point in the low frequency region, at least for the upper flow q_{up}. It must be noted that higher frequencies may not be detected as no sufficient time resolution was provided by CFD, even though the signal in the time domain covered 40 impeller revolutions.

Based on these findings, a detailed study of operating point $Q_{ED}/Q_{EDn} = 0.74$ is presented in order

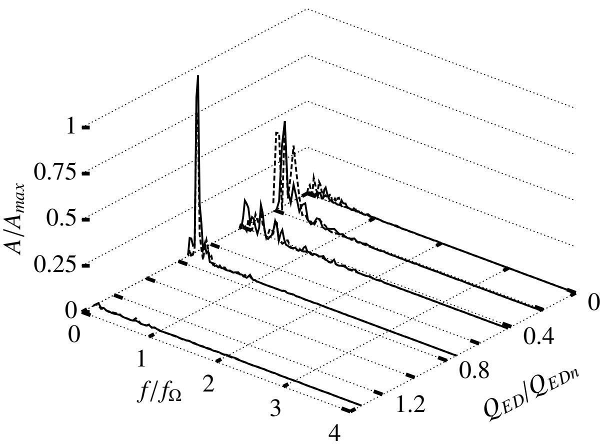

Figure 11. Waterfall plot of power spectra of the stay vane channel flow q_{up} (———) and q_{lo} (– – –).

to verify whether these observations respond with experiments.

4.3. Study of rotating stall in the stay vane channel at $Q_{ED}/Q_{EDn} = 0.74$

To ensure an appropriate identification of low-frequency mechanisms, 40 impeller revolutions were simulated. The instantaneous velocity in the stay vane channel 1 to 20 is presented in Fig. 12 for two different time instants. Velocities were evaluated at 50% in streamwise direction and 50% in spanwise direction of the stay vane channel. The diagram shows an arbitrary impeller position t and the position of the impeller after one quarter revolution of the stalled cells $t + f_{RS}/m$. As shown in the plot, four dominant jets with adjacent blocked cells come apparent in pitchwise direction for $\theta = 0$, $\theta = \pi/2$, $\theta = \pi$ and $\theta = 3\pi/4$ so that four stalled cells $m = 4$ can be easily encountered.

According to Fig. 10-d, time history of both partial flow rates q_{up} and q_{lo} show a significant periodicity. Compared to the lower channel height, however, the flow blockage in the upper channel height appears to be more pronounced and results in reversal flow at short times. This asymmetric distribution is also evident from Fig. 8.

In Fig. 13, a Fourier transform is performed for both experimental and simulated static pressure signal p_{prim}. The frequency is normalized by the impeller rotation frequency f_Ω where the fundamental impeller blade passing frequency and its harmonics are $i\,z_b\,f_\Omega$. The peaks at $f/f_\Omega = 7$, 14, 21 and 28 show a considerable correlation between simulation results and experiments. However, the pressure amplitudes at $f/f_\Omega = 14$ and $f/f_\Omega = 28$ are underestimated by CFD. At $Q_{ED}/Q_{EDn} = 0.74$, a dominant propagation frequency at 1.8Hz of stalling cells is found by simulations, as can be seen from the detail plot in Fig. 13-top.

Considering four spatial modes according to Fig. 12, the rotating stall fundamental frequency is

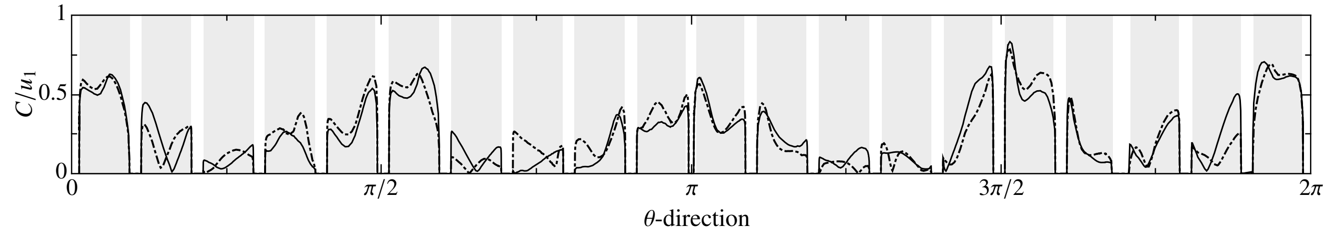

Figure 12. Velocity C in the stay vane channel at $Q_{ED}/Q_{EDn} = 0.74$ for two different time instants: time t (———), time $t + f_{RS}/m$ (– · – · –).

$f_{RS} = 0.135 f_\Omega/4$, which is equal to a propagation speed of 3.4% of the impeller rotational speed. This dominant sub-synchronous frequency modulates the blade passing frequency $7f_\Omega = 93.3$Hz, resulting in remarkable side bands.

Figure 13 below shows a Fourier transform of the measured pressure signal for 40 impeller revolutions with a peak at at 1.77Hz, which is about 25% lower than the simulated peak, as can be see in the detail plot. Furthermore, the frequency analysis of the recorded pressure signal shows symmetric side bands at this rotating stall frequency.

To better visualize the blockage and discharge flow in the distributor, iso-surfaces of the entropy S and velocity magnitude C are introduced. As suggested in [13], the local generation of entropy of a isothermal and incompressible fluid $S = S_D + S'$ can be divided into the part due to mean flow gradients

$$S_D = \frac{\mu}{\overline{T}}\left[2\left(\frac{\partial C_x}{\partial x}\right)^2 + 2\left(\frac{\partial C_y}{\partial y}\right)^2 + 2\left(\frac{\partial C_z}{\partial z}\right)^2 + \left(\frac{\partial C_x}{\partial y} + \frac{\partial C_y}{\partial x}\right)^2 + \left(\frac{\partial C_x}{\partial z} + \frac{\partial C_z}{\partial x}\right)^2 + \left(\frac{\partial C_z}{\partial x} + \frac{\partial C_y}{\partial z}\right)^2\right] \quad (8)$$

and the part resulting from dissipation in the turbulent shear of separating flow [14]

$$S' = \frac{\rho\beta^*\omega k}{\overline{T}} \quad (9)$$

where $\overline{T}$ is the mean fluid temperature and $\beta^* = 0.09$ a model coefficient of the k-ω model. In Fig 14, as expected, four notable regions of strong dissipation are visible, which fully block the channel. These cells of high entropy mainly appear at the stay vane channel inlet and result in a strong stay vane channel flow upstream in direction of the impeller rotation.

Low frequency peaks of the frequency spectrum of various quantities at $Q_{ED}/Q_{EDn} = 0.74$ are summarized in Tab. 3. For the wicket gate torque T, a significant peak arises at 1.83Hz, which is close to the experimental value of p_{prim} (peak at 1.77Hz) and the

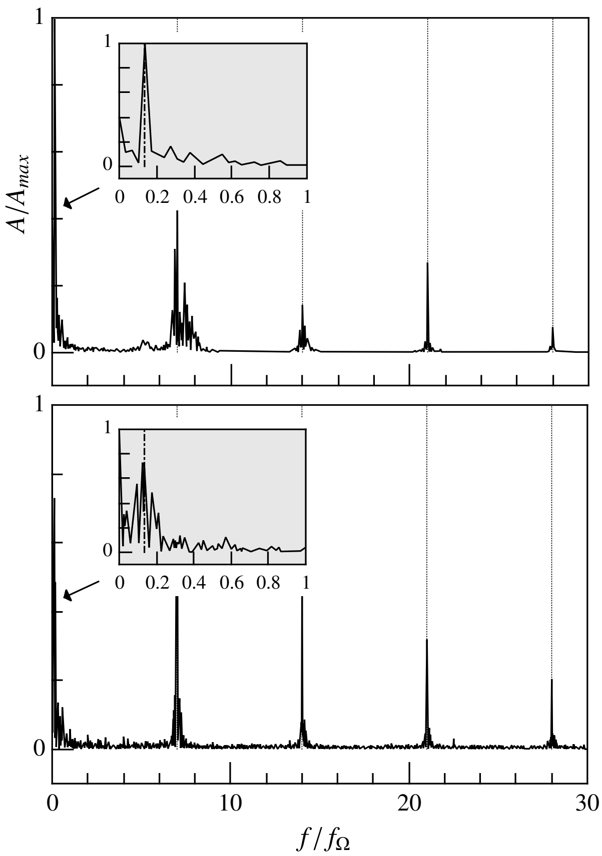

Figure 13. Frequency spectra of the pressure signal p_{prim} at $Q_{ED}/Q_{EDn} = 0.74$: CFD (top), EXP (bottom), (– · – · –) $4 \times f_{RS}$ in the detail plot.

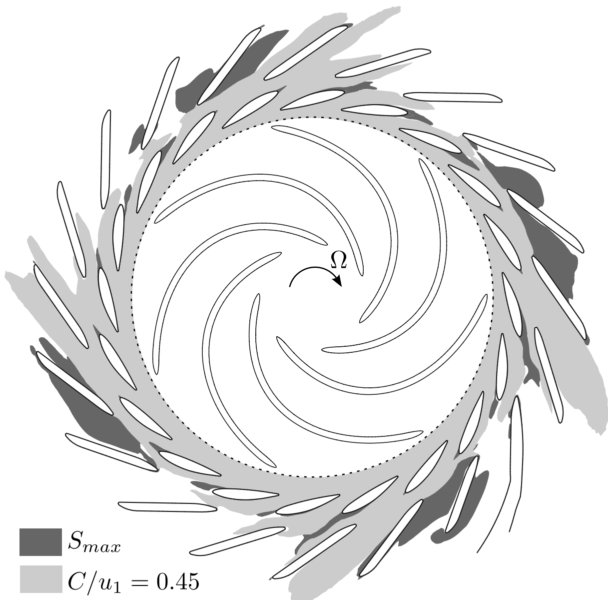

Figure 14. Iso-surfaces of instantaneous velocity magnitude C and entropy S at 50% in spanwise direction, $Q_{ED}/Q_{EDn} = 0.74$.

Table 3. Low frequency peaks (Hz) of frequency response of simulated and measured quantities.

p_{prim} EXP	p_{prim} CFD	$q_{up,lo}$ CFD	T CFD
1.77	1.80	1.87	1.83

value obtained by numerics (peak at 1.80Hz). Compared to experiments, the Fourier transform of both upper flow q_{up} and lower flow q_{lo} shows significant side bands with a discrepancy of $+13\%$ and -7% respectively, caused by the limited frequency resolution and the so called picket-fence effect. Following [15], an interpolation between this peaks yields a frequency of 1.87Hz.

5. CONCLUSION

Besides specific parameters of the pump-turbine, unsteady flow in the stay vane channel was numerically predicted by unsteady RANS-simulations and compared to experimental data. Focusing on the discretization scheme, an extensive grid study gave useful conclusions about resolution and size.

From simulations it was found that the flow structure between the stay vanes is sensitive to inlet flow conditions. At part-load condition, a flow distribution with a maximum near the hub is identified, where at a higher discharge the streamlines of the bulk velocity are slightly deflected towards the shroud. Results from the analysis of the velocities indicated by CFD qualitatively agree with the LDV measurements.

Just 20% below the design flow, four stalling cells traveling at 3.4% of the impeller rotary frequency were encountered. The sub-synchronous peak obtained in the frequency spectrum of the computed pressure corresponds well with measurements and is in agreement with observations of many other authors. This dominant frequency became evident in all transient signal recorded in the distributor for this operating point.

In further studies, the influence of the wicket gate opening on stall flow in the distributor is investigated, as uneven wicket gate flow may gives rise to increase the risk of rotating stall onset.

6. ACKNOWLEDGEMENTS

The financial support of VOITH Hydro is gratefully acknowledged by the authors.

REFERENCES

[1] Mesquita, A. L., and Ciocan, G. D., 1999, "Experimental analysis of the flow between stay and guide vanes of a pump-turbine in pumping mode", *Journal of the Brazilian Society of Mechanical Sciences*, Vol. 21, pp. 580 – 588.

[2] Berten, S., Dupont, P., Fabre, L., Kayal, M., Avellan, F., and Farhat, M., 2009, "Experimental Investigation of Flow Instabilities and Rotating Stall in a High-Energy Centrifugal Pump Stage", *Proceedings of FEDSM 2009*, ASME.

[3] Anciger, D., Jung, A., and Aschenbrenner, T., 2010, "Prediction of rotating stall and cavitation inception in pump turbines", *IOP Conference Series: Earth and Environmental Science*, Vol. 12 (1), p. 012013.

[4] Braun, O., 2009, "Part load flow in radial centrifugal pumps", Ph.D. thesis, École Polytechnique Fédérale de Lausanne.

[5] Xia, L., Cheng, Y., Zhang, X., and Yang, J., 2014, "Numerical analysis of rotating stall instabilities of a pump-turbine in pump mode", *IOP Conference Series: Earth and Environmental Science*, IOP Publishing, Vol. 22, p. 032020.

[6] Zhang, Z., 2010, "Rotating stall mechanism and stability control in the pump flows", *IOP Conference Series: Earth and Environmental Science*, IOP Publishing, Vol. 12, p. 012010.

[7] Edinger, G., 2014, "Experimentelle Untersuchungen zum tiefen Teillastbetrieb von Pumpturbinen", Ph.D. thesis, Vienna University of Technology.

[8] Celik, I. B., Ghia, U., Roache, P. J., and Christopher, 2008, "Procedure for estimation and reporting of uncertainty due to discretization in CFD applications", *Journal of fluids Engineering-Transactions of the ASME*, Vol. 130 (7).

[9] Jasak, H., 1996, "Error analysis and estimation for the finite volume method with applications to fluid flows", Ph.D. thesis, Imperial College London (University of London).

[10] Phillips, T. S., and Roy, C. J., 2014, "Richardson Extrapolation-Based Discretization Uncertainty Estimation for Computational Fluid Dynamics", *Journal of Fluids Engineering*, Vol. 136 (12), p. 121401.

[11] ANSYS Inc., 2010, *ICEM CFD 13.0, Manual*.

[12] IEC 60193 - International Electrotechnical Commision, 1999, *Hydraulic Turbines, Storage Pumps and Pump-Turbines - Model Acceptance Tests*, 2nd edn.

[13] Herwig, H., and Kautz, C. H., 2007, *Technische Thermodynamik*, Pearson Studium.

[14] Kock, F., and Herwig, H., 2004, "Local entropy production in turbulent shear flows: a high-Reynolds number model with wall functions", *International Journal of Heat and Mass Transfer*, Vol. 47 (10-11), pp. 2205–2215.

[15] Kolerus, J., and Wassermann, J., 2011, *Zustandsüberwachung von Maschinen*, Expert-Verlag, Renningen, 5. edn.

Conference on Modelling Fluid Flow (CMFF'15)
The 16th International Conference on Fluid Flow Technologies
Budapest, Hungary, September 1-4, 2015

NUMERICAL INVESTIGATION OF A CENTRIFUGAL COMPRESSOR STAGE WITH IGV INDUCED INLET FLOW DISTORTIONS

Nan Chen[1], Wolfgang Erhard[2]

[1] Corresponding Author. Institute for Flight Propulsion, Technische Universität München. Lehrstuhl für Flugantriebe, Boltzmannstr. 15, 85748 Garching, Germany. Tel.: +49 89289 16186, Fax: +49 89289 16166, E-mail: chen@lfa.mw.tum.de
[2] Institute for Flight Propulsion, Technische Universität München. E-mail: erhard@lfa.mw.tum.de

ABSTRACT

This paper presents the numerical investigation of a single-stage centrifugal compressor stage with focus on the interaction between IGV induced inlet flow conditions and the impeller performance. The inlet flow distortions induced by various IGV types have been applied to different mesh models (single-passage and full-annulus) to perform steady simulations with ANSYS CFX v14.5. The simulation result was validated and compared with previous experimental data. The CFD results show that the flow incidence controlled by the IGV and circumferential flow non-uniformity induced by the IGV are the main factors impacting the impeller performance. Thus the development of new IGV designs with novel geometries, which aim at reducing flow distortions and maintaining moderate preswirls, is demonstrated to be effective in obtaining high stage efficiency over a wide operation range.

Keywords: Centrifugal compressor, CFD, full annulus, IGV, inlet distortion, single passage

NOMENCLATURE

C	$[m/s]$	Velocity
D	$[m]$	Impeller outlet diameter
N	$[rpm]$	Rotational speed
T	$[K]$	Temperature
T_u	[-]	Turbulence intensity
U	$[m/s]$	Impeller tip peripheral speed
c_p	$[J/kgK]$	Specific heat at constant pressure
h	[-]	Head coefficient
$\dot{m}$	$[kg/s]$	Mass flow rate
p	$[Pa]$	Pressure
y^+	[-]	Dimensionless wall distance
Φ	[-]	Flow coefficient
Π_t	[-]	Total pressure ratio
κ	[-]	Isentropic Exponent
η	[-]	Impeller polytropic efficiency
ρ	$[kg/m^3]$	Density
τ	[-]	Impeller work coefficient

Subscripts and Superscripts

abs	Absolute
norm	Normalized
s	Static
t	Total
u	Circumferential

Abbreviations

FA	Full annulus
IGV	Inlet guide vanes
PS, SS	pressure side, suction side
SP	Single passage
Sec	Measurement/model section

1. INTRODUCTION

In modern jet propulsion and the oil & gas industry, improvements in efficiency and operating range are essential to the success of compressor design. If a stable operating range is insufficient, variable inlet guide vanes (IGV) can be introduced to provide preswirls to the inlet flows. A research project was conducted at the Institute for Flight Propulsion, Technische Universität München to experimentally investigate an industrial centrifugal compressor stage (Figure 1) together with different IGV types on a high-speed rotating test rig described in [1]. Typically an IGV stage is used to expand operation range at surge margin [2, 3, 4]. Firstly a symmetrical airfoil with standard symmetric profile (NACA0022) was chosen as the baseline IGV (Type-A). Previous study showed a symmetric profiled IGV works practically with a low setting angle range up to $\pm 30°$ [5]. Therefore, two newly designed IGVs, which are based on uniquely cambered geometries, have been developed to enlarge the operation range especially at low mass

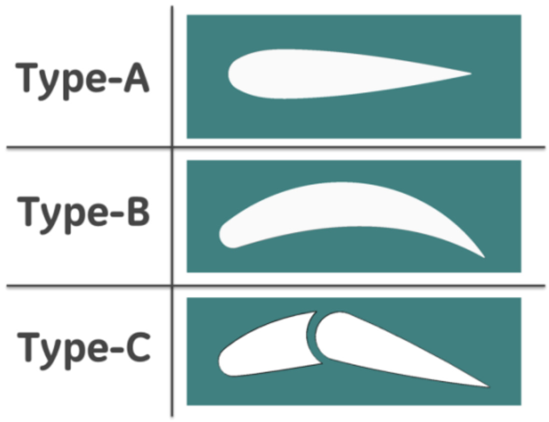

Figure 1. Conceptual sketches of the three IGV types (from [6]).

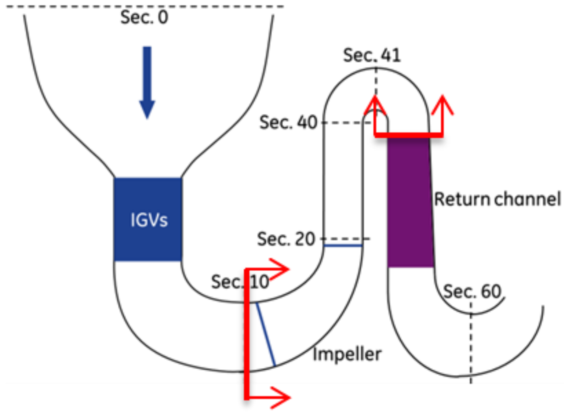

Figure 2. Schematic cross section of compressor stage (mesh domain denoted between red lines).

flow range, and specially treat circumferential flow non-uniformities created by the radial inlet plenum [6]. The first new design has a uniquely cambered airfoil (Type-B), and the second new design features a multi-airfoil consisting of both a uniquely cambered fixed part and a rotating tail (Type-C). This tandem blade design was designed to achieve low incidences at high setting angles by preventing the flow separation on the suction surface [7]. More details on the tandem IGV can be found in [8, 9]. The experimental results show that up to 40% of the pressure losses in the inlet plenum can be reduced by adopting the new circumferentially non-uniform IGV designs, and overall stage efficiency can be increased by 2 points at the stage design point [6]. However, the internal flow mechanisms behind the improved performance with those IGVs still need to be understood fully. As a consequence, this numerical research is an attempt to conduct a systematic analysis to reveal the relationship between the new IGV designs and compressor behaviour.

As indicated in [6], to match the different flow conditions at each vane positions along the circumference of the IGV plenum, the two new IGV concepts adopt individual profiles at each fixing location. Therefore, in practice no periodic symmetry exists in the distribution of IGV airfoils or the flow fields created by them. This feature prevents using single-passage modelling with simplified periodic sidewalls. To deal with the rotor-stator interactions regarding flow non-uniformities and unsteadiness, an entire annulus CFD model may be applied ([10, 11]). To avoid introducing a complete 360° mesh model for the IGV plenum alone, previously measured flow quantities at the impeller inlet section will be applied as inlet boundary conditions. This requires a computation domain starting from Sec10 (Figure 2). In addition, due to the non-uniform inlet distortions, only a full-annulus mesh model for the impeller is able to exactly predict response to inlet distortions.

However, due to time and computation limits in most engineering applications, single-passage models are still regarded as the conventional method to conduct CFD simulations. Therefore, this study employs both single-passage and full-annulus models in the analysis. For the single-passage model, the 1D profiles were calculated by averaging the experimental data along the entire circumference, and then employed at the impeller inlet, while for the full-annulus model the complete inlet flow fields measured were specified as inlet boundary conditions. The measurement result (in [6]) provides full flow fields (p_t, T_t, yaw, p_s, velocities) using 360° measurement of flow mappings, enabling an exact inlet profiles for the CFD simulations.

This numerical study includes two parts as a whole. First a single-passage mesh model is used to conduct steady-state simulations, covering most of the speedlines collected by the previous measurement. Secondly, several steady-state cases are calculated at nominal points with a newly introduced full-annulus model, which is used to further investigate the impact of circumferential non-uniformities existing in the real conditions.

2. COMPUTATION SETUP

2.1. Mesh Domain

The modelling of the compressor stage (depicted in Figure 2) starts from the impeller inlet section (Sec10) up to its outlet (Sec20), follows a vaneless diffuser (Sec20 to Sec40) and a U-bend (Sec42), and ends before the flow reaches the return channel. An artificial contraction is put in place at the domain outlet to prevent backflow during the CFD calculations, similar to the treatment described in [12]. For the single-passage model, while the grids for the impeller were generated by ANSYS TurboGrid, and the grids for the diffuser were generated by ANSYS ICEM. For the full-annulus model, the impeller and diffuser models were

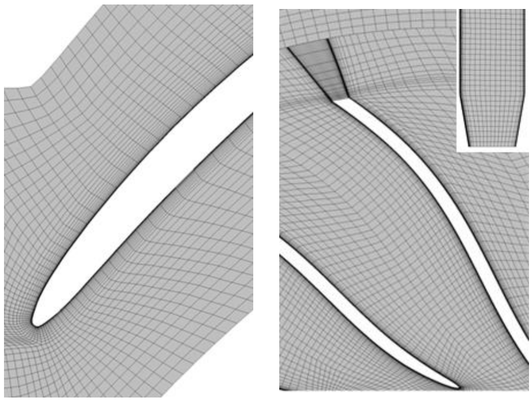

Figure 3. Grid fragments at midspan plane. (Left: single-passage; right: full-annulus; Top right: contraction at diffuser outlet)

coarser per passage to limit the total number of mesh grids, an thus to save on computation resources and memory. All the mesh elements are hexahedron. The statistics of the mesh models applied is summarized in Table 1. A total number of 4.6 million elements were built for the single-passage model, and about 6 million elements for the 360° full model.

Table 1. Summary of mesh statistics (P: Inlet ring; I: impeller; D: diffuser)

Type of Model	Grid size	Min. Orth. Angle [°]	y^+ [-]
Single passage	I: 1.1×10^6 D: 3.5×10^5	I: 27.9 D: 64.1	I: 1.5 D: 25
Full annulus	I: 4.3×10^6 D: 1.6×10^6	I: 33.0 D: 74.1	I: 4.5 D: 25

2.2. Simulation Set-up

2.2.1. Single-passage Case

The modelled impeller is a shrouded impeller designed for the petrochemical industry. For the numerical simulation, the working fluid is set as air ideal gas. The k-ω turbulence model with automatic wall functions was chosen for all the test cases investigated. The frozen-rotor interface was set to connect the impeller to the vaneless diffuser. For the single-passage cases, rotational periodicity was specified at the sidewalls. All the boundary conditions were based on the real experimental data, which was obtained from the rotating test rig as summarized in [6]. Those experimental results were used for setting up the cases extensively, including the combinations of total pressure, total temperature and cylindrical velocity components at the inlet, mass flow rate at the outlet, and impeller rotational speed which varied slightly during the

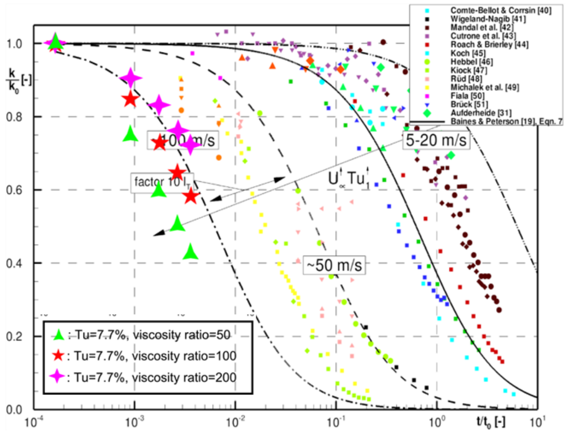

Figure 4. Turbulence decay with T_u=7.7% and different estimated viscosity ratios (50, 100 and 200) at Sec10 together with interpolation curves based on the experimental database from [13].

measurement mass flow rate at the outlet, and impeller rotational to ensure Mach number similitude. For the single-passage cases, p_t, T_t, and yaw angle measured at Sec10 were specified as 1D inlet boundary conditions after averaging along the circumference. Non-slip adiabatic walls were specified at the hub, shroud and blade walls. Moreover, the turbulence intensity was given as 7.7% from earlier CFD results on the IGV plenum alone. The eddy viscosity ratio was estimated as 200, resulting in a turbulence decay curve that remains close to the correct transition at design point (Figure 4 from [13]), when the inflow is approximately equal to 90m/s.

2.2.2. Full-annulus Case

If not otherwise stated, the physical and solver settings are identical for both the single-passage and full-annulus model. Some additional changes for the full-annulus model are as follows:

- The impeller model is a full replica of all single passages. No additional rotational periodicity is defined.
- The data from the measured 360° flow fields of p_t, T_t, and the velocity direction were employed as inlet boundary conditions, without performing a circumferential average.

To evaluate the impact of using the new, coarse full-annulus model, a sensitivity study was conducted with IGV = 0° and 60°. The coarse mesh for the full-annulus simulations tends to decrease impeller efficiency by 0.5-1.0 percent, and thus does not significantly alter the results produced by the full-annulus model.

3. SIMULATION RESULTS

The following section describes the test results and analysis with the two types of modelling. The discussion mainly focuses on the nominal points, which were defined as the middle points along each speedline from surge to stall during the experiment. Table 2 lists the flow coefficients (normalized) for all the nominal points discussed. The nominal points at IGV=0° are actually the design point of the compressor stage.

Table 2. Flow coefficients at the nominal points (normalized with the value with IGV=0°)

IGV angle	0°	20°	40°	60°
Φ_{norm}	1.000	0.944	0.751	0.616

3.1. Steady single-passage test

Before analysing the CFD results in this section, a validation process is performed by extracting the CFD data from a normal slice plane located 2mm downstream from the inlet section. The flow quantities are circumferentially averaged to compare with experimental data specified as 1D profile at Sec10. For example the validation for the three IGV types at 0° is shown in Figure 5. A complete comparison is made for circumferential averaged p_t, T_t, yaw, p_s, T_s, and C_{abs}. (T_s and C_{abs} are not directly measured by the aero probes but calculated using Equations 6 and 7). Fig. 5 shows that most parameters match well with the experimental data. Although small differences (max. 5%) occur in the prediction of velocity, the profile shapes are well-preserved. This validation process was conducted for all simulation points at 0°, 20°, 40° and 60° (not shown), which demonstrates the good quality match between CFD and the experiment. Therefore, the averaged 1D profile is able to mostly represent the inlet flow conditions created by the upstream IGVs.

As the first step of the result analysis, the CFD test cases were extracted from the same locations as previous measurement sections (Sec10, Sec20 and Sec40), through which the performance parameters can be calculated. Since the domain outlet has been changed, the performance parameters discussed here are primarily for the impeller part (from Sec10 to Sec20), including impeller total pressure ratio, work coefficient, impeller polytropic efficiency and head coefficient. The equations for calculating these parameters can be found in the appendix. To save space only the total pressure ratio Π_t and polytropic efficiency η are shown as Figure 6 and 7.

Figure 6 shows the impeller total pressure ratio along each speedline for the three IGV types investigated. The CFD results are plotted together with previously collected experimental data. The steady-state calculations run stable until the last point on the left side near stall, where the CFD

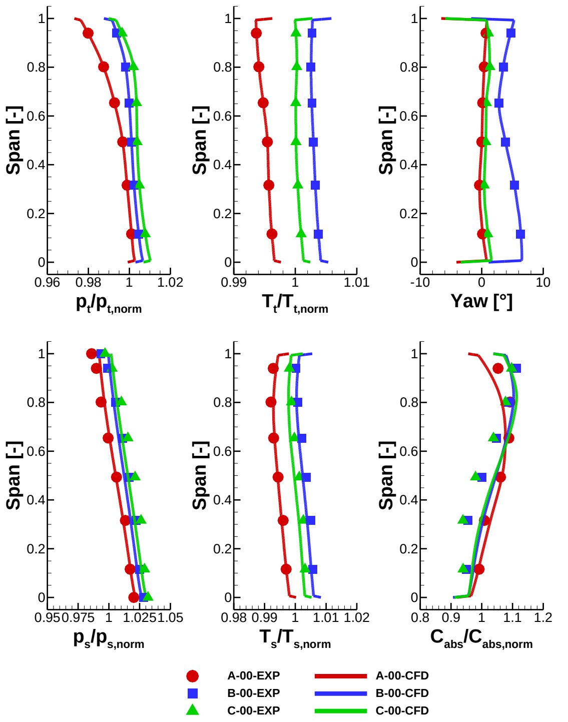

Figure 5. Circumferentially averaged inlet profiles for IGV=0° at nominal points. Shown are measurement data and single-passage CFD result.

failed to converge. Similar problem were experienced when attempting to simulate the speedline with the negative IGV angle (-20°). Therefore, the measurement points at these locations were not covered by the CFD points in Fig. 6. In Fig. 6 a good agreement regarding total pressure prediction was achieved for all IGV types at different settings angles. The relative levels between Type-A, Type-B and Type-C from 0° to 60° were faithfully reproduced by CFD, indicating that this method is appropriate for analysing the relative impacts among different IGV types. In addition, there is a tendency in the CFD data to over-predict the total pressure rise in the impeller. This over-prediction may be due to the fact that the numerical cases are simplified rather than the real cases, which contains local leakage flows due to the cavities and unsteadiness [14]. The amount of over-prediction is highest at the speedlines with IGV=0°. Here all the CFD points are higher than the corresponding measurement points, which suggest that if the incidence angles are in line with the impeller leading edge, then the modelled impeller functions more smoothly than the real impeller. This benefit was cancelled out by the highly over-turned incidence angles with high IGV setting angles, which decreases the level of total pressure ratio, bringing the value back into the measured range. Another discrepancy is found with the baseline type near choke at IGV=60°. Here the

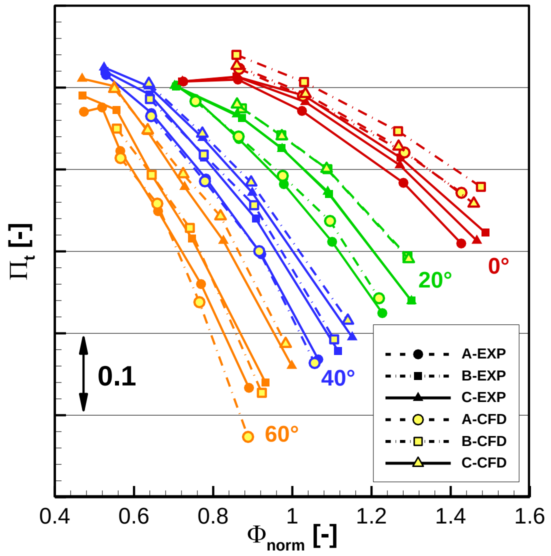

Figure 6. Total pressure ratio (Section10-Section20) as function of normalized flow coefficient. Shown are measurement data and CFD single-passage result.

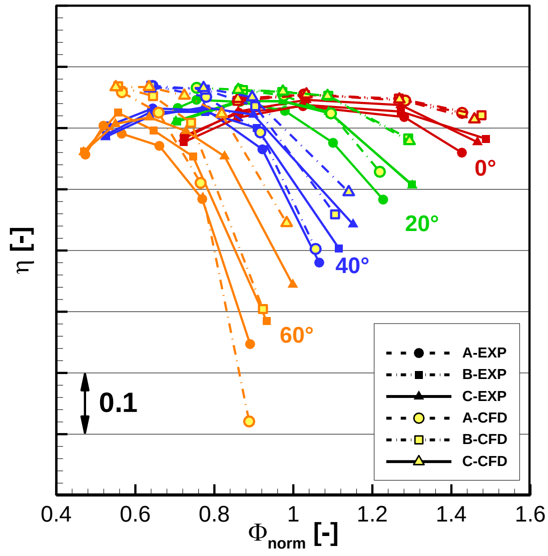

Figure 7. Impeller polytropic efficiency (Sec10-Sec20) as function of normalized flow coefficient. Shown are measurement data and single-passage CFD results.

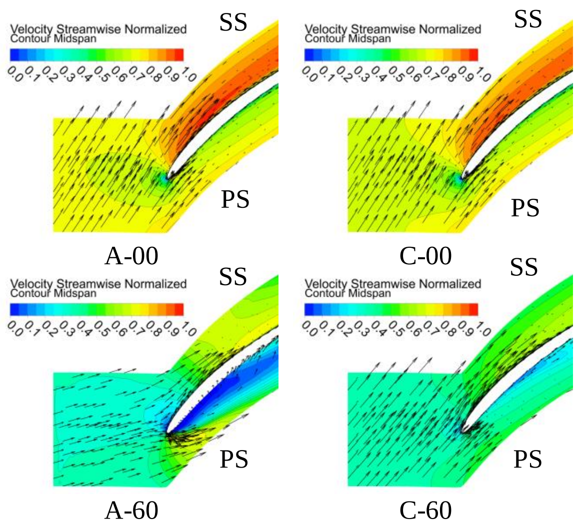

Figure 8. Midspan contours of relative stream velocity at nominal points, IGV setting angles 0° and 60° (above and below) for IGV type-A and type-C, shown together with vector of relative velocity

predicted points are lower than the measured levels of values. It could be that the mass flow rates between CFD and the experiment are not exactly the same, which induces predicted points right to the measured speedline. Thus, a big gap near choke may reflect a relatively small shift in the mass flow.

It should be emphasized that, as discussed in [6], the seemingly massive improvements delivered by the two new IGV types compared to the baseline IGV (e.g at 60°) may be misleading, because at nearly all setting angles tested, the baseline IGV tends to generate stronger preswirls than the other two types. When the preswirl is larger than the setting angle itself, this results in an over-turned incidence angle. This is the case for the Type-A at 60°, when the incidence angle seen by the impeller leading edge is even larger than 60°, as illustrated in Figure 8. Here the test cases for Type-A and Type-C at the nominal points and IGV= 0° and 60° are shown. Type-B has similar velocity conditions as Type-C, and is omitted here. The relative velocities on the midspan plane are plotted as contours from blade-to-blade view. To visualize the velocity direction, the vectors of relative velocities are also presented. It is clear from the dark blue regions for the A-60 case that under this working condition with extremely high turning, the incidence angle generated by the baseline is over-turned in such a way that the flow at the leading edge is driven towards the suction side of the impeller blades. This leads to a recirculated region immediately after the blade's leading edge on the pressure side. Finally, a pressure-side flow separation further downstream becomes inevitable. It may be deduced that when a smaller IGV setting angle for the baseline is chosen which guarantees an exact 60° of preswirl, the operational condition for the baseline might be improved. However since this situation was not part of the experimental test campaign, this feature cannot be supported by experiment data. Additionally, the measured flow fields produced by Type-A always contained more pressure losses at Sec10 than the other types. Thus the new two types of IGV should work still better, even if all three IGV types produce the identical degree of preswirls.

Figure 7 presents the impeller polytropic efficiency for all three IGV types at each simulated speedline. Compared to Fig. 6, more deviations from the experimental results are observed. Although at the nominal point for IGV = 0° the differences are fairly small (~2 percent), large gaps show up as the IGV setting angle becomes larger and as the impeller moves to the off-design regions near-stall (left) and near-choke (right). The reason discrepancy is dependent on the under-predicted total temperature at Sec20 (T_{t20}) predicted by CFD, which results in lower work coefficient values. In other words, under the same given conditions (p_{t10}, T_{t10} and yaw) the simulated cases require less change of total enthalpy transferred from an external energy source than the cases during the experiment. The reasons for this may lie in the heat transfer or the specific work. For the simulation cases all the modelling walls were defined as non-adiabatic walls, while in the real testing environment heat losses always occurred due to the temperature difference between the warm working fluid and the cold environment outside. Without taking into account these heat losses, the CFD should achieve the same compressed total pressure level by transferring less total enthalpy, which could lead to the decreased T_{t20} (Equation 8). Another reason for this discrepancy may be related to the amount of specific work w, which is correlated to the circumferential velocity components, known as the Euler's turbomachinery equation (Equation 9). While U_{20}, U_{10} and C_{u10} values are precisely specified, C_{u20} is associated with the slip factor of the impeller and measurement accuracy of velocity magnitudes and flow angles at the impeller outlet. At this location the traversing probes experienced great unsteadiness produced by the passing blades. Meanwhile, a certain amount of cavity flow leaves the shroud-wall through the labyrinth sealing, which only exists in the real stage. Thus a correct estimation of C_{u20} at Sec20 is difficult. To take into consideration the unsteady effect and secondary flows due to cavities, a dedicated mesh model, as suggested in [6], and transient measurement technique, such as fast-response multi-hole probe, are necessary. This last point goes beyond the scope of this study, and should be examined in the future.

There are also some other parameters of interest such as the impeller work coefficient and the head coefficient, which are not shown here due to space limitations. The results show that CFD tends to predict lower work coefficients because of lower calculated T_{t20}. Together with higher polytropic efficiency, the impeller head coefficient happens to be in line with the experimental results. For an industrial compressor stage, the head coefficient is an important parameter since it combines two factors the compression efficiency on the one hand and the energy cost for the compression on the other. Therefore the alignment between CFD and our experiment may be valuable for judging the compressor performance in the early phases of the design process.

In conclusion, the relative benefits of using different IGV designs can be successfully predicted by CFD, and the absolute values of total pressure ratio predicted by CFD calculations are in most cases accurate. However, for the single-passage model the inlet flow fields have to be averaged as 1D profiles. The simplification creates one source of discrepancy between CFD and the experiment. In order to reproduce the 2D flow fields containing large circumferential non-uniformities, several full-annulus test cases were conducted, which will be discussed in the next section.

3.2. Steady full-annulus test

For the full-annulus model, a similar validation process is conducted in order to evaluate the effects of using 2D inlet flow fields. For example, Figure 9 shows the flow fields simulated by CFD at nominal points for the three IGV types at 0°. The contour maps for the experiment are a little smaller than those for CFD, because the first and the last probe heads were located in the near vicinity of the hub and shroud walls. The CFD results in Fig. 9 were extracted 2mm downstream from the inlet section. From the contour plots in Fig. 9 it is clear that the imposed 2D inlet flow fields comprising of local low-momentum regions passed from the IGV plenum, circumferential non-uniformities as well as extreme flow turning angles, were faithfully reflected by the flow fields generated by the CFD simulations. The validation process was conducted for the other cases at 20°, 40° and 60°, and the quality also proved to be good. Therefore, using a 2D inlet section for is more appropriate than the 1D profile.

Figure 10 compares the total pressure ratio of the simulation results between the single-passage model and the full-annulus model. In total three data groups are shown. The curves denote the experimental results, the points with the same colours are the simulation results from the single-passage model, and the points with the yellow dots are the results from the full-annulus model. The simulation cases for the full-annulus test were conducted only at the nominal points, because in reality the non-nominal points can be replaced by another point with higher efficiency at a better setting angle. To help better orientate the points, the left and right neighbouring points near the nominal points are shown for the experimental and single-passage cases. As expected, for all the IGV types and setting angles, the full-annulus cases predict lower levels of total pressure ratio than the single-passage model. The differences are larger than the

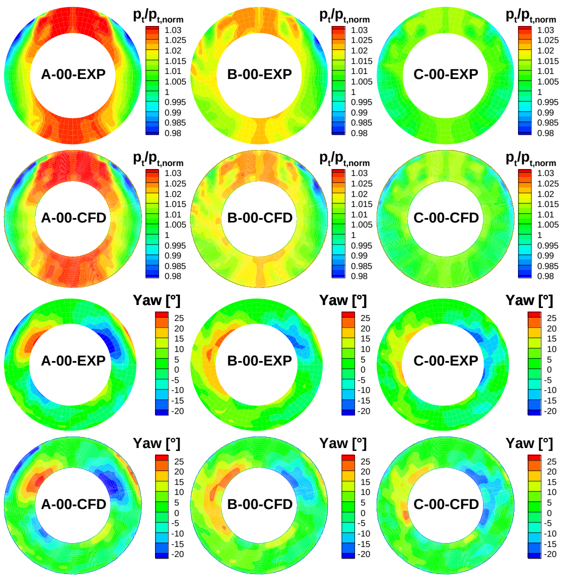

Figure 9. Contours of normalized total pressure and yaw angle at Section10, compared between experimental data and CFD result

changes due to model switching previously discussed, and thus can be regarded as the consequence of introducing extra distortions into the inlet section leading to a total pressure decrease of 0.5 to 1.5 percent. For most cases at 0°, 20°, and 40° where previously CFD predicted higher pressure ratios, the new full-annulus model predicts that the total pressure ratio is within the experimental range. However at 40° and at 60° for all the three types, the total pressure ratio was located even lower than the experimental lines. This difference may suggest that independent of whether a single-passage or a full-annulus model is used, CFD tends to exaggerate the effects of the incidence angle.

Figure 11 shows the polytropic efficiency calculated by the full-annulus model, compared with the experimental data and the single-passage model. Similar to Fig. 10, the full-annulus model predicts lower levels of efficiency, which are nearer to the experimental data. This indicates that by prescribing the 2D flow fields, the additional circumferential non-uniformities caused by the IGVs can be better evaluated using the CFD simulations, especially when the incidence angle created by preswirls is still not large enough to generate more inaccuracy.

In order to quantify the fluctuations along the circumferential direction by introducing flow distortions, the total pressure values were extracted at the trailing edge of the impeller along the circumference. A total of three spanwise circles at the impeller trailing edge (10%, 50% and 90% span from hub to shroud) were chosen to visualize total pressure fluctuations. The result for Type-A at the

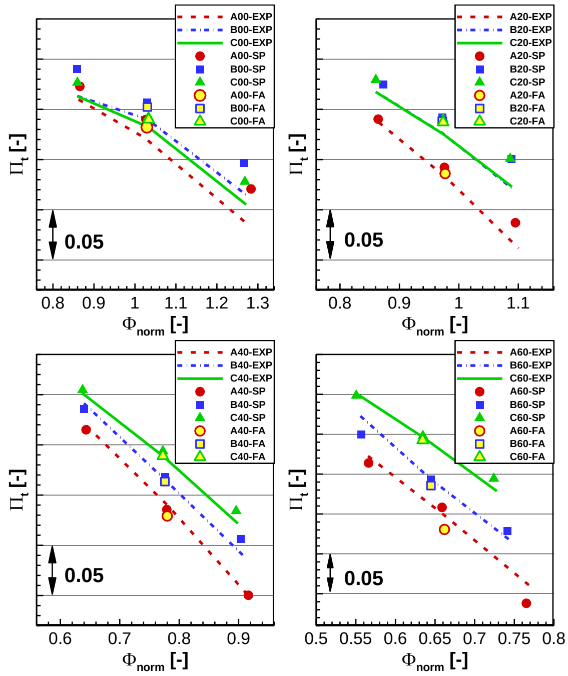

Figure 10. Total pressure ratio as function of normalized flow coefficient. Shown are measurement data, single-passage CFD results and full-passage CFD results.

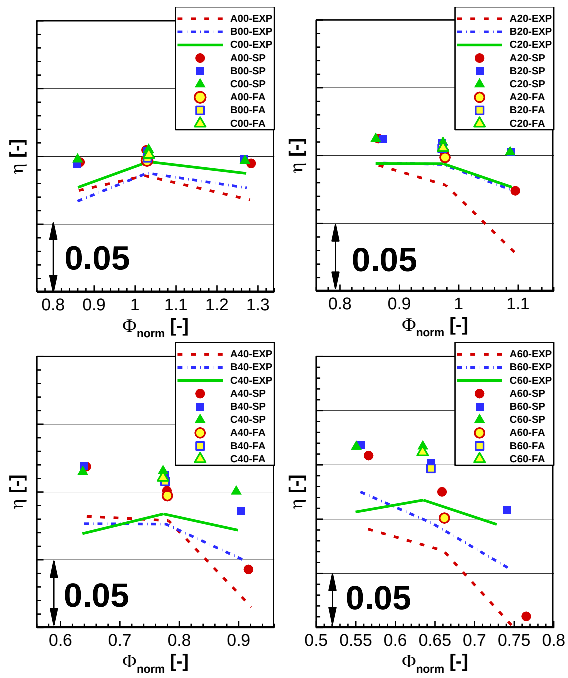

Figure 11. Impeller polytropic efficiency as function of normalized flow coefficient. Shown are measurement data, single-passage CFD results and full-passage CFD results.

nominal point for IGV=60° is plotted in Figure 12. To clearly identify the varying progress of p_t, the predicted data from the full-annulus model (red

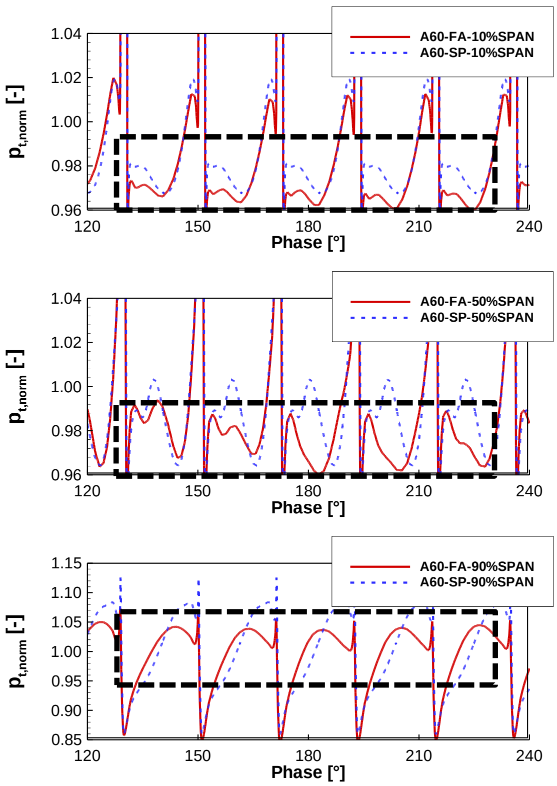

Figure 12. Total pressure (normalized) at impeller outlet varying with the circumference calculated by steady full-annulus CFD, shown are three locations at 10%, 50% and 90% for Type-A with IGV=60°

lines) is shown with the simulation data from the single-passage model, which has been post-processed by repeating p_t across all the blade passages (blue dash lines), with each line normalized by the average value. The 120°-240° range of the whole circumference, where the largest fluctuations occur, is presented. By examining the highlighted regions with the dashed spaces, it is clear that circumferential fluctuations after the impeller are preserved, although they are induced far upstream by the flow uniformities at the inlet. For this specific case, the fluctuations are present mostly near hub (10% spanwise plan) as well as in the core region (50% spanwise plane), and the magnitude of fluctuation reached up to 3 percent. Therefore, using a full-annulus model is useful for taking into account circumferential non-uniformities. For this case with high non-uniformity, the previous experimental data shows that at the inlet, the whole flow field contains 7.8% deviation of average p_t as well as 9.5% deviation of average yaw angle. Started from these inlet conditions, up to 3% fluctuation along the circumference is transmitted throughout the impeller to trailing edge.

4. SUMMARY AND CONCLUSIONS

This numerical study investigates a centrifugal compressor stage with IGV induced flow distortions as inlet boundary conditions. Both single-passage and full-annulus models have been applied to conduct steady simulations on the impeller performance. The numerical results were validated, and then compared with the experimental data. Both model types predict the correct relative levels of performance parameters for the three IGV types. In addition, circumferential non-uniformity was taken into account by using the full-annulus model, which predicts the impeller efficiency closer to the experimental data. While incidence angle is the main contributor shifting the speedlines in the performance map, circumferential non-uniformities further reduce the impeller performance by creating flow fluctuations through the blade passage to the impeller trailing edge. Both maintaining moderate preswirls and reducing circumferential non-uniformities are beneficial for the centrifugal compressor, and thus desirable when adopting new IGV designs.

The future work will concentrate on the transient simulations with the full-annulus model, which takes into consideration the unsteady effects between IGV and impeller. Other work may include adding cavity modelling and using the transient blade row method to substitute for the full-annulus model.

ACKNOWLEDGEMENTS

The author would like to thank GE Global Research for the collaborative research project. Special thanks go to Dr. Christian Aalburg and Dr. Ismail Sezal for their kind suggestions on the project.

APPENDIX

Calculation of impeller performance

- Flow coefficient

$$\Phi = \frac{4\dot{m}}{\rho_{10}\pi D^2 U} \tag{1}$$

- Impeller total pressure ratio

$$\Pi_t = p_{t20}/p_{t10} \tag{2}$$

- Impeller work coefficient

$$\tau = c_p(T_{t20} - T_{t10})/U^2 \tag{3}$$

- Impeller polytropic efficiency

$$\eta = \frac{\kappa-1}{\kappa} \cdot \frac{\ln(p_{t20}/p_{t10})}{\ln(T_{t20}/T_{t10})} \tag{4}$$

- Impeller head coefficient

$$h = \tau \cdot \eta \tag{5}$$

Calculation of T_s and C_{abs} using measured data

- Static temperature

$$T_s = T_t/(\frac{p_t}{p_s})^{\frac{\kappa-1}{\kappa}} \tag{6}$$

- Absolute velocity

$$C_{abs} = \sqrt{2c_p(T_t - T_s)} \quad (7)$$

- Impeller total enthalpy change

$$\Delta h_t = c_p(T_{t20} - T_{t10}) = w + q \quad (8)$$

where: $w = U_{20}C_{u20} - U_{10}C_{u10}$ (9)

REFERENCES

[1] Lang, S., Erhard, W., Kau, H. P. (†), et al., 2014, "Application of Flow Control on a Radial Compressor for Operating Range Extension", in *15th International Symposium of Transport Phenomena and Dynamics of Rotating Machinery*, Honolulu, USA.

[2] Rodgers, C., 1991, "Centrifugal Compressor Inlet Guide Vanes for Increased Surge Margin", *Journal of Turbomachinery*, Volume 113, Issue 4, Pages 696-702.

[3] Whittfield, A., 1998, "*The Performance of a Centrifugal Compressor With High Inlet Prewhirl*", Journal of Turbomachinery, Volume 120, Issue 3, Pages 487-493.

[4] Simon, H., Wallmann, T., and Mönk, T., "Improvement in Performance Characteristics of Single-Stage and Multistage Centrifugal Compressors by Simultaneous Adjustments of Inlet Guide Vanes and Diffuser Vanes", *Journal of Turbomachinery*, Volume 109, Issue 1, Pages 41-47.

[5] Händel D., Niehuis R., Rockstroh U., 2014, "Aerodynamic Investigations of a Variable Inlet Guide Vane With Symmetric Profile", *Proceedings ASME Turbo EXPO, Düsseldorf, Germany*, GT2014-26900.

[6] Sezal, I., Chen, N., et al., 2015, "Introduction of Circumferentially Non-uniform Variable Guide Vanes in the Inlet Plenum of a Centrifugal Compressor for Minimum Losses and Flow Distortions", *Proceedings ASME Turbo EXPO, Montreal, Canada*, GT2015-43467.

[7] Coppinger, M., Swain, E., 2000, "Performance Prediction of an Industrial Centrifugal Compressor Inlet Guide Vane System", *Proceedings of the Institution of Mechanical Engineers Part A - Journal of Power and Energy*, Volume 214, Issue A2, Pages 153-164.

[8] Boehle M, Cagna M., Itter L., 2004, "Compressible Flow in Inlet Guide Vanes With Mechanical Flaps", *Proceedings ASME Turbo EXPO, Vienna, Austria,* GT2004-53191.

[9] Mohseni, A., Goldhahn, E., Van den Braembussche R. A., and Seume, Joerg R., 2012, "Novel IGV Designs for Centrifugal Compressors and Their Interaction With the Impeller", *Journal of Turbomachinery*-, Volume 134, Issue 2, Pages 8.

[10] Simpson A., Aalburg C., Schmitz M., Pannekeet R., Larisch F. and Michelassi V, 2008, "Design, Validation and Application of a Radial Cascade for Centrifugal Compressors", *ASME Turbo EXPO 2008*, Berlin, Germany, GT2008-51262.

[11] Yang, H., Boulanger, J., 2012, "The Whole Annulus Computations of Particulate Flow and Erosion in an Axial Fan", Journal of Turbomachinery, Volume 135, Issue 1, Pages 011040.

[12] Smirnov, P. E, Hansen T., and Menter, F. R., 2007, "Numerical Simulation of Turbulent Flows in Centrifugal Compressor Stages With Different Radial Gaps", *Proceedings ASME Turbo EXPO, Montreal, Canada*, GT2007-27376.

[13] Bode, C., Aufderheide T., Kozulovic, D., and Friedrichs, J. 2014, "The Effect of Turbulence Length Scale on Turbulence and Transition Prediction in Turbomachinery Flows", *Proceedings ASME Turbo EXPO, Düsseldorf, Germany*, GT2014-27026.

[14] Guidotti, E., Naldi, G., Tapinassi L., and Chockalingam, V., 2012, "Cavity Flow Modelling in an Industrial Centrifugal Compressor Stage at Design and Off-Design Conditions", *Proceedings ASME Turbo EXPO, Copenhagen, Denmark*, GT2012-68288.

Conference on Modelling Fluid Flow (CMFF'15)
The 16th International Conference on Fluid Flow Technologies
Budapest, Hungary, September 1-4, 2015

The oscillating drop method for measuring a polymeric time scale

Gregor PLOHL[1], Guenter BRENN,

[1] Corresponding Author. Institute of Fluid Mechanics and Heat Transfer, Graz University of Technology, Inffeldgasse 25/F, 8010 Graz Austria, Tel. +43 316 873-7341, Fax. +43 316 873-7356 Email gregor.plohl@tugraz.at

ABSTRACT

Axisymmetric oscillations of a polymeric liquid drop in a gas are used to measure the deformation retardation time λ_2 of a viscoelastic liquid. The linear theory is applied for describing the oscillatory motion of the drop.

In the experiment, an acoustically levitated individual drop is excited to shape oscillations of the fundamental mode m = 2 by ultrasound modulation. Once the excitation is terminated, the drop performs damped oscillations. The damped oscillatory motion of the levitated drop is recorded as a function of time using a high-speed camera. From the images, the angular frequency and damping rate of the oscillations are determined and used for measuring λ_2.

The basis for the determination of the deformation retardation time from the oscillation data is the characteristic equation for the complex frequency of the drop. A numerical method for determining a pair of liquid properties – the liquid zero-shear dynamic viscosity η_0 and the deformation retardation time λ_2 – from the solution of the characteristic equation is presented. Comparison of the value of η_0 with the result from a rheometric liquid characterisation allows the correct solution to be identified from the manifold of solutions obtained. The results show that the values of λ_2 deviate strongly from the values typically used in simulations of viscoelastic liquid flow.

Keywords: Damped linear drop shape oscillations, polymeric liquid, ultrasonic levitation, polymeric time scales

NOMENCLATURE

A	$[m]$	fitted amplitude
A_1,A_2,B_1	$[-]$	polymer solutions
C_1, C_2	$[]$	integration constants
E	$[-]$	differential operator
P_m	$[-]$	Legendre polynomials
a	$[m]$	equilibrium radius
d	$[1/s]$	damping rate
f	$[Hz]$	oscillation frequency
j_m	$[-]$	spherical Bessel function
m	$[-]$	mode number
p	$[Pa]$	pressure
q	$[1/m]$	complex inverse oscillatory length scale
r, θ, φ	$[m, -, -]$	spherical coordinates
r_i	$[m]$	residuals (fitting error)
r_s	$[m]$	drop shape
t	$[s]$	time
v_r, v_θ, v_φ	$[m/s]$	velocity components
$y(t)$	$[m]$	drop dimensions
y_0	$[m]$	equilibrium drop dimension
α_m	$[1/s]$	complex angular frequency
χ^2	$[m^2]$	test function
ϵ_0	$[m]$	deformation amplitude
η	$[Pa\ s]$	dynamic viscosity
η_0	$[Pa\ s]$	zero-shear viscosity
λ_1, λ_2	$[s]$	polymeric time scales
ν	$[m^2/s]$	kinematic viscosity
ψ	$[m^3/s]$	Stokes stream function
ρ	$[kg/m^3]$	density
σ	$[N/m]$	surface tension
$\underline{\underline{\dot{\gamma}}}$	$[1/s]$	rate of deformation tensor
$\underline{\underline{\tau}}$	$[Pa]$	extra stress tensor
φ_0	$[rad]$	fitted initial phase angle

Subscripts and Superscripts

i	imaginary part
m	mode number
r	real part

1. INTRODUCTION

For their relevance for transport processes, and for scientific interest, oscillations of liquid drops have been under investigation since the time of Lord Rayleigh, who derived the angular frequency $\alpha_{m,0} = \sqrt{m(m-1)(m+2)}\sqrt{\sigma/\rho a^3}$ of linear oscillations for an inviscid drop against the ambient vacuum [1]. Rayleigh's work was extended by Lamb, who included the influence of the viscosity of the drop liquid and obtained the oscillation frequency and the rate of decay of the oscillations in the limits of very high and very low drop viscosity [2]. Lamb also generalized Rayleigh's result by including the influence from a host medium with a non-negligible density ρ_o on the oscillations of an inviscid drop with density ρ_i [3]. He obtained a dependency of the angular frequency of oscillation on a weighted sum of the two densities, $\alpha_m \propto \sqrt{\sigma/(m\rho_o + (m+1)\rho_i)a^3}$. The most general case of an oscillating viscous drop immersed in another liquid with non-negligible density and viscosity was analysed by Miller & Scriven [4]. From their work, the characteristic equation for the oscillating drop emerges in the form of a determinant that must equal zero. For the various special cases of fluid behaviour, the equation reduces to the well known results of previous works.

The characteristic equation of the drop determines the dependencies of the drop shape oscillation frequency and damping rate on physical properties of the drop liquid. These dependencies allow these physical properties to be measured when the oscillation frequency and/or the damping rates are known. This "oscillating drop method" for measuring liquid physical properties has been in use since some decades. The method was applied to measure the interfacial tension between immiscible liquids [5] and the surface tension of the drop liquid against the ambient air [6]. Further to that, the dynamic viscosity of aerodynamically levitated drops of Newtonian liquids was measured [7, 8].

For viscoelastic systems, the oscillating drop method was used for investigating the surface rheology [9, 10]. The materials were surfactant solutions, and the drops were levitated due to the microgravity conditions of the experiment. In a study with crude oil in water, the oscillating pendant drop method was used to determine the dilatational elasticity modulus and the dynamic interfacial tension of the oil [11]. In that method, a drop hanging from the end of a capillary tube performs oscillations under the influence of an excitation. The aim of that study was to quantify the absorption behaviour of crude oil surfactants at oil-water interfaces. A review of oscillating drop and bubble techniques is due to Kovalchuk et al. [12].

In the present study we develop a method for measuring the deformation retardation time of polymeric liquids from damped drop shape oscillations [13]. Polymeric time scales are essential parameters in the modelling of the rheological behaviour of polymeric liquids upon linear deformations by the Jeffreys and other models involving viscoelastic behaviour. Molecular mechanical properties of dissolved polymeric substances are responsible for the time scales, and computational methods are in general unavailable for quantifying them from first principles. This applies in particular because the interaction between the polymer and its solvent plays an important role. A standard method for measuring the deformation retardation time is not established (e.g. [14]). Early work on the measurement of deformation retardation times of large DNA molecules in biosystems is due to Chapman et al. [15]. Another study derives retardation time spectra from rheometric creep data [16]. That method applies to polymer melts rather than solutions.

2. ANALYSIS OF LINEAR DROP SHAPE OSCILLATIONS

Linear viscoelastic drop oscillations are described by the linearised equations of motion for incompressible fluid and a linear viscoelastic material law. The appropriate material law is the Jeffreys model which is obtained as a linear limit of the Oldroyd 8-constant model. The dependency of the motion on time is determined by an exponential function $\exp(-\alpha_m t)$, with the complex angular frequency α_m of mode m. The stress tensor $\underline{\underline{\tau}}$ for this temporal behaviour satisfying the Jeffreys equation reads

$$\underline{\underline{\tau}} = \eta_0 \frac{1 - \alpha_m \lambda_2}{1 - \alpha_m \lambda_1} \underline{\underline{\dot{\gamma}}} = \eta(\alpha_m) \underline{\underline{\dot{\gamma}}} \, . \tag{1}$$

With this material law, the structure of the momentum equation is formally identical to that for a Newtonian fluid, with the only difference that the dynamic viscosity depends on the frequency of the deformations and on the two polymeric time scales λ_1 and λ_2 (correspondence principle).

For analysing the oscillation, the continuity and momentum equations are formulated in spherical coordinates and solved subject to the kinematic boundary condition that the rate of radial displacement of the drop surface $r_s(\theta, t)$ from the spherical equilibrium (Figure 1) equals the radial velocity component at the location of the equilibrium drop radius a, and the dynamic boundary condition that the shear stress at the drop surface, evaluated at $r = a$, is (approximately) zero in the present case of a drop in a gas. The normal-stress boundary condition will finally reveal the characteristic equation of the system.

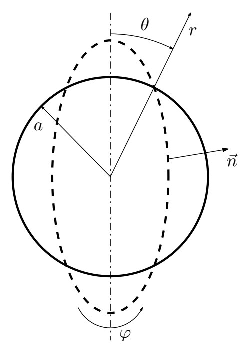

Figure 1. Equilibrium and deformed drop shapes in the spherical coordinate system for $m = 2$. The deformed shape given by the dashed line may be represented as $r_s(\theta, t) = a + \epsilon_0 P_m(\cos\theta) e^{-\alpha_m t}$ [13].

We briefly sketch the derivation of the characteristic equation of the oscillating drop [13]. The oscillation-induced flow in the drop is analysed assuming symmetry in the direction of the azimuthal angle φ. The description of the two-dimensional flow field is based on the Stokesian stream function ψ. Introducing it into the linearised momentum equation by proper definition of the velocity components v_r and v_θ in spherical coordinates, and taking the curl of the resulting equation, we obtain the fourth-order partial differential equation

$$\left(-\frac{1}{\nu(\alpha_m)}\frac{\partial}{\partial t} + E^2\right)\left(E^2\psi\right) = 0 \qquad (2)$$

with the operator [17]

$$E^2 = \frac{\partial^2}{\partial r^2} + \frac{\sin\theta}{r^2}\frac{\partial}{\partial\theta}\left(\frac{1}{\sin\theta}\frac{\partial}{\partial\theta}\right). \qquad (3)$$

The special solution of this equation for the present problem reads

$$\psi = \left[C_{1,m}r^{m+1} + C_{2,m}qr\,j_m(qr)\right]P'_m(\cos\theta)\sin^2\theta e^{-\alpha_m t}, \qquad (4)$$

where j_m is a spherical Bessel function of the first kind of order m. In its argument we have defined

$$q = \sqrt{\alpha_m\rho/\eta(\alpha_m)} = \sqrt{\alpha_m/\nu(\alpha_m)}. \qquad (5)$$

The argument qr represents a non-dimensional viscoelastic length scale. The stream function allows the velocity components v_r and v_θ to be derived. The kinematic and zero shear stress boundary conditions determine the two integration constants $C_{1,m}$ and $C_{2,m}$.

The pressure field is readily obtained with the velocity field known by integration of the momentum equation and reads

$$p = -(m+1)C_{1,m}\rho\alpha_m r^m P_m(\cos\theta)e^{-\alpha_m t}. \qquad (6)$$

The characteristic equation for the complex angular frequency α_m is found from the second dynamic boundary condition stating that the (r, r) component of the total stress tensor vanishes at the drop surface. The characteristic equation reads

$$\frac{\alpha_{m,0}^2}{\alpha_m^2} = \frac{2(m^2-1)}{q^2a^2 - 2qa\,j_{m+1}/j_m} - 1 + \frac{2m(m-1)}{q^2a^2}\left[1 + \frac{2(m+1)j_{m+1}/j_m}{2j_{m+1}/j_m - qa}\right]. \qquad (7)$$

Here the spherical Bessel functions enter at the value qa of their arguments. The equation is formally identical to the results of Lamb [2] and Chandrasekhar [18] obtained for Newtonian liquids. In the present case of a viscoelastic liquid, however, the kinematic viscosity ν involved in the equation is a function of the complex oscillation frequency α_m [19]. In the following section we present an experiment suitable for measuring the complex oscillation frequency α_2 of the drop.

3. EXPERIMENTAL METHOD

For investigating experimentally damped oscillations of individual drops of viscoelastic liquids the technique of acoustic levitation may be used [20]. This technique allows for the positioning of individual drops in the quasi-steady pressure field of a standing ultrasonic wave produced between a vibrating horn and a reflector, as shown in Figure 2. The reflector may have a concave curved surface to enhance the sound pressure level, as in the present apparatus. Oscillations of the levitated object may be excited by amplitude-modulating the ultrasound. Modulation frequencies up to 2 kHz are achievable with the equipment at hand. For further details the reader is referred to [20].

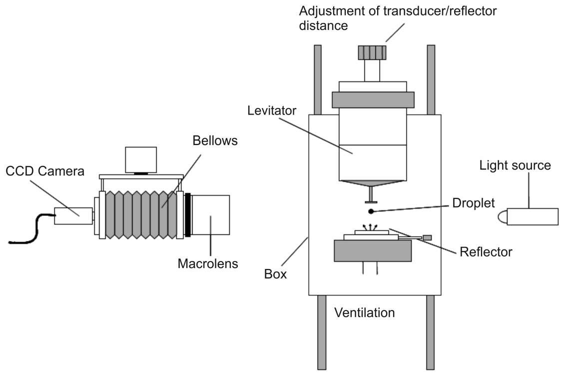

Figure 2. Setup for levitating single drops in an ultrasonic resonator and measuring the drop deformations in forced oscillations by means of image processing [13].

Levitated drops of the test liquids are produced by a syringe with a thin needle to enable the formation of drops with diameters in the range between 1 mm and 3 mm. With the needle tip close to a pressure node of the acoustic levitator, a portion of liquid is pushed out from the syringe to form the droplet. The drop resonance frequency is then determined approximately by a modulation frequency sweep, monitoring the maximum occurring oscillatory drop deformations. The drop is then steadily driven at that resonance frequency, and the modulation is switched off at a time $t = 0$, so that the drop carries out damped oscillations which eventually die out. Note that, when the modulation is switched off, the drop is still kept levitated, since the carrier signal driving the acoustic transducer remains active. The experiment yields both the angular frequency and the damping rate of the free drop oscillations in a linear regime of the motion. These two values form the complex frequency α_m of the drop for the basic oscillation mode $m = 2$. Together with the Rayleigh frequency $\alpha_{m,0}$ of the drop, the left-hand side of the characteristic equation (7) is known. This is the basis for determining two material parameters as solutions of the equation. For a thorough discussion of potentially detrimental influences from the levitation technique, the oblate spheroidal deformed drop shape, the non-linearity of the oscillations and the shear thinning of the liquid the reader is referred to Brenn & Teichtmeister [13].

3.1. Characterisation of the test liquids

Our experiments were carried out with aqueous solutions of the two different polyacrylamides Praestol 2500 and Praestol 2540 from Stockhausen Inc. (Germany). The former is non-ionic with a degree of hydrolysis of 3 - 4 %, while the latter is middle anionic with a degree of hydrolysis of 40 %. The different degrees of hydrolysis of the polymers cause different mechanical flexibilities of the macromolecules. The molar masses are about the same for the two polymers, $15 - 20 \cdot 10^6\ kg/kmol$.

The aqueous solutions were prepared in demineralised water, producing a master solution with a solute mass fraction of 10000 ppm by mass, which was then diluted to achieve the various mass fractions for the experiments. The solutions were stirred over night and then allowed to rest for 24 hours at room temperature in order to achieve a homogeneous solution. The stirring was done with an anchor stirrer at low rotational speed in order to avoid shear-induced degradation of the polymer macromolecules. The shear viscosity of the liquids was measured as a function of shear rate with a rotational rheometer Anton Paar MCR 300. The temperature was kept constant at the value of $20°C \pm 1°C$ in the laboratory where the drop oscillation experiments were carried out. The flow curves of the three liquids are shown in Fig. 3. The densities of the liquids were measured with an oscillating U-tube device with an accuracy of $\pm 0.1 kg/m^3$. They are all in the order of $10^3 kg/m^3$. The surface tension of the liquids against the ambient air was measured with a drop volume tensiometer Lauda TVT 2. The stress relaxation time λ_1 of the liquids was measured with a filament stretching elongational rheometer [21]. A small sample of the liquid with a volume $O(20\mu l)$ is stretched between two plates in a short time $\leq 1ms$ and the diameter relaxation with time of the filament formed by the stretching process is recorded by an optical technique. The diameter evolution is governed by the stress relaxation time λ_1 of the liquid. Measurements repeated 10 times yielded mean values with standard deviations between 6 and 15%. The properties of three aqueous solutions of these polymers investigated in the present study are listed in Table 1.

Table 1. Properties of the three aqueous polymer solutions at 20°C. A_1 and A_2 denote $0.3\ wt\%$ and $0.8\ wt\%$ Praestol 2500 solutions, and B_1 denotes $0.05\ wt\%$ Praestol 2540 solution. The viscosity η_0 was measured with a rotational viscosimeter.

Polymer solution	ρ $[kg/m^3]$	σ $[N/m]$	η_0 $[Pa\ s]$	λ_1 $[s]$
A_1	999.4	0.07315	0.0435	0.078
A_2	1000.9	0.07555	0.7588	0.163
B_1	998.8	0.07651	1.521	0.1377

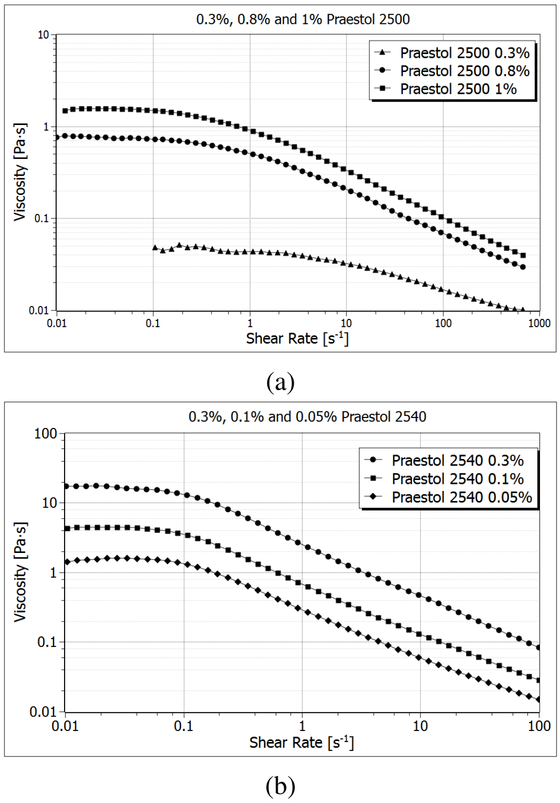

Figure 3. Flow curves of the various solutions of the two polyacrylamides investigated at $20°C$.

3.2. Visualisation of the drop

Images of the levitated drop are recorded by a high-speed camera at a framing rate of 2 kHz under backlight illumination. An uncertainty in the length measurement of $\pm 2\ Pxls$ with the resolution of 167 $Pxls/mm$ results in a sizing uncertainty of $\pm 12\ \mu m$, for a 1.9 mm drop, equivalent to ± 0.6 %. Within at most 10 s after the drop has been placed in the acoustic levitator, one single picture of the drop is taken in order to have its initial shape and volume. This initial state, where the evaporation of the solvent has had no influence on the solution concentration yet, allows the concentration of the polymer in the drop liquid at all later times to be deduced from the volume. The equilibrium radius a is calculated from the recorded instantaneous images. The experiments showed that the maximum decrease of the drop volume observed between the initial state and later states after the frequency sweep is of the order of -15 %, which causes the same increase of the polymer concentration. The related increase of the zero-shear viscosity of the liquid depends on the polymer. For the two polyacrylamides studied in the present experiment we see that η_0 may increase by 25 to 40 % due to the solvent evaporation. The zero-shear viscosity obtained from the experiment is the value corresponding to the concentration of the solution present during the related experiment.

The oscillation shown in Figure 4 was recorded for a Praestol 2500 solution drop with the equilibrium diameter of 1.94 mm. The drop was driven at 120 Hz before the modulation was switched off. From these data, the frequency and damping rate in the last part of the motion were extracted, so that both the linear oscillation behaviour was ensured and the shear-thinning of the polymer solution did not have any influence on the oscillation. The frequency and damping rate are determined using the least-squares method to achieve the best fit of a prescribed function to the damped oscillations measurement data. The damped oscillations, represented by the distance $y(t)$ between the north and south poles of the drop, are modeled by the function

$$y(t) = y_0 + A\cos(2\pi f \cdot t + \varphi_0) \cdot e^{-d(t-t_0)}. \tag{8}$$

The least-squares method was employed to minimize the quantity $\chi^2 = \sum_i r_i^2$, where r_i are residuals giving the difference between each measured data point and its fitted value. The fitting curve for the last part of the oscillation is shown in Fig. 4. The oscillation frequency and the damping rate of this drop, determined by this procedure, are $f = 129.9$ Hz and $d = 36$ s^{-1}. The real and imaginary parts of the complex angular frequency $\alpha_2 = d + i2\pi f$ are therefore known.

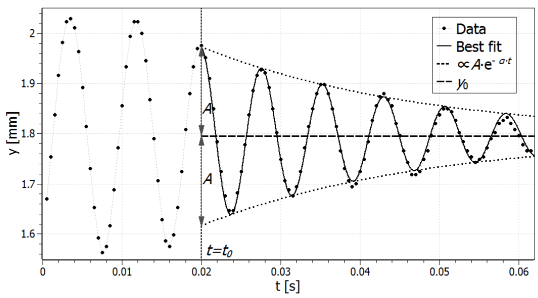

Figure 4. Distance between north and south pole of a levitated 1.94 mm 0.3 $wt\%$ Praestol 2500 solution drop as a function of time in a damped oscillation. Resolution is 167 $Pxls/mm$. The time between two images is 0.5 ms. The fitting curve for the last part of the oscillation is shown.

4. SOLUTION OF THE CHARACTERISTIC EQUATION

The characteristic equation (7) is transcendental in the argument of the spherical Bessel functions involved and must therefore be solved numerically. We present a method for determining η_0 and λ_2 by solving this equation. For the numerical analysis we use the computer algebra software `MATHEMATICA`. As a prerequisite, the complex frequency α_m must be accurately measured in the experiment, and the radius of the drop as well as the density, surface tension and stress relaxation time of the liquid in contact with the ambient air must be known. We address the accuracy requirements to these input parameters in section below.

4.1. Analysis of the characteristic equation

In section 2 we have derived the characteristic equation (7). The equation exibits a complicated set of solutions. We now present an analysis of the characteristic equation. Let us define the complex function $F(qa)$ as per

$$F(qa) = \frac{2\left(m^2-1\right)}{q^2a^2 - 2qa\, j_{m+1}/j_m} - 1 + \frac{2m(m-1)}{q^2a^2}\left[1 + \frac{2(m+1)\, j_{m+1}/j_m}{2j_{m+1}/j_m - qa}\right]. \tag{9}$$

which is the right-hand side of the characteristic equation (7). We examine the behavior of the function in (9) for different values of its argument qa, covering the range of values relevant for our experiments with drops of the viscoelastic liquids in Table 1. In Figure 5(a) the real part of the function $F(qa)$ is shown as a function of the real part of its argument qa, with the imaginary part of qa as a parameter. For large values of the imaginary part of qa, the real part of the function $F(qa)$ is a smooth, piecewise monotonic function. In contrast, for small values of the imaginary part of the argument qa, the real part of the function $F(qa)$ is not monotonic, and for small values of the imaginary part of the argument below 0.1, the function $F(qa)$ exhibits poles. The same behaviour is found by an evaluation of the imaginary part of the function $F(qa)$, as shown in Figure 5 (b).

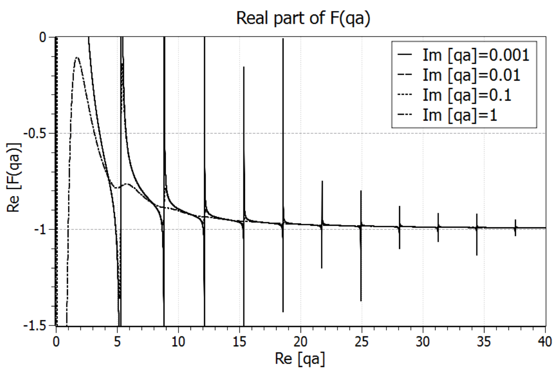

(a)

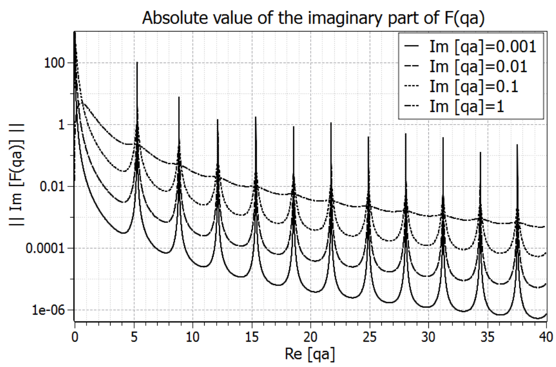

(b)

Figure 5. The function $F(qa)$ for different values of its argument qa in the base mode m=2. (a) The real and (b) the imaginary part.

4.2. Finding the values of the argument qa

The first step is to solve the characteristic equation (7) for the argument qa of the spherical Bessel functions involved in the equation. With the measured complex frequency α_m and the calculated angular frequency $\alpha_{m,0}$ of the fundamental mode $m = 2$, the left-hand side of the equation is known and the argument qa satisfying the characteristic equation can be determined. Due to the influence from the spherical Bessel functions, the equation exhibits a complicated set of solutions. The solutions, which are values of the argument qa satisfying Eq. (7), are searched by scanning the real and imaginary parts of the argument qa of the spherical Bessel functions in the complex qa plane. The scan is carried out with high resolution, so that solutions cannot be missed. Results consist in pairs of the real ($q_r a$) and imaginary ($q_i a$) parts of the argument qa. Figure 6 shows the set of solutions for a 0.3 $wt\%$ Praestol 2500 solution drop with equilibrium radius $a = 0.97$ mm. The liquid drop properties enter the left-hand side of Eq. (7), while the values of qa are still general in this step inasmuch as they may be generated by different combinations of values of η_0, λ_1, λ_2, a and ρ.

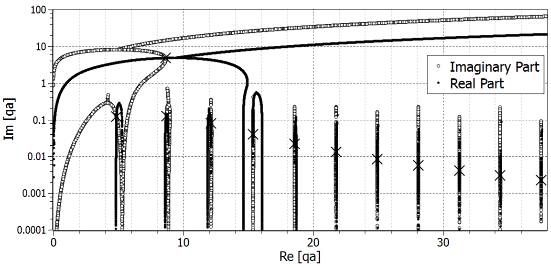

Figure 6. The pairs of real and imaginary parts of the argument qa satisfying the (closed circles) real and (open circles) imaginary parts of the characteristic Eq. (7) for the case of a 0.3 $wt\%$ Praestol 2500 solution drop with equilibrium radius $a = 0.97$ mm. The intersections between the open and closed circles (marked with crosses) are the solutions of the complex Eq. (7).

From the real and imaginary parts of q, q_r and q_i, the pair of material properties (η_0, λ_2) is determined. The relationship between η_0, λ_2 and q given by Eqs. (1) and (5) reads

$$q^2 = \frac{\rho\alpha_2}{\eta_0}\frac{1-\alpha_2\lambda_1}{1-\alpha_2\lambda_2} \,. \tag{10}$$

With the complex frequency $\alpha_2 = d + i2\pi f$ of the drop known, the two liquid properties are readily determined from the real and imaginary parts of Eq. (10).

Identification of the right solution among the calculated pairs follows from comparison of the value of η_0 with the result from measurements with a rotational viscosimeter. The solutions qa of the characteristic equation and corresponding calculated values of zero shear viscosity η_0 and deformation retardation time λ_2 for a 0.3$wt\%$ aqueous Praestol 2500 solution drop with equilibrium radius $a = 0.97$ mm are listed in Table 2. The result for the zero-shear dynamic viscosity η_0 obtained for this liquid is 0.0413 $Pa\ s$, which deviates from the value of η_0 of 0.0435 $Pa\ s$ revealed by rotational viscosimetry by no more than -5%. This agreement is excellent. The corresponding deformation retardation time is $0.899 \cdot 10^{-4}$ s, i.e. of the order of 100 μs. Values of λ_2 commonly used in simulations are $O(\lambda_1/10)$, which is $O(8\ ms)$ for this liquid.

Table 2. Positive roots qa of the characteristic equation (7) and corresponding calculated values of zero shear viscosity η_0 and deformation retardation time λ_2 for a 0.3 $wt\%$ Praestol 2500 solution drop with equilibrium radius $a = 0.97$ mm. The measured oscillation frequency and damping rate are $f = (129.9 \pm 1.3)Hz$ and $d = (36 \pm 3.6)s^{-1}$ respectively.

qa	η_0 [$Pa\ s$]	λ_2 [s]
$4.863 + 0.1211i$	2.0631	$1.508{\cdot}10^{-4}$
$8.658 + 4.792i$	0.2532	$21.37{\cdot}10^{-4}$
$8.733 + 0.1238i$	0.6408	$1.245{\cdot}10^{-4}$
$12.131 + 0.0788i$	0.3324	$1.056{\cdot}10^{-4}$
$15.382 + 0.0404i$	0.2068	$0.962{\cdot}10^{-4}$
$18.583 + 0.022i$	0.1417	$0.926{\cdot}10^{-4}$
$21.764 + 0.0131i$	0.1033	$0.912{\cdot}10^{-4}$
$24.935 + 0.0084i$	0.0787	$0.906{\cdot}10^{-4}$
$28.098 + 0.0057i$	0.06199	$0.902{\cdot}10^{-4}$
$31.257 + 0.0041i$	0.0501	$0.901{\cdot}10^{-4}$
$34.413 + 0.0030i$	0.04133	$0.899{\cdot}10^{-4}$
$37.567 + 0.0023i$	0.03468	$0.899{\cdot}10^{-4}$

An uncertainty and sensitivity analysis of the results shows that the identification of the correct solution qa is reliable and the value of λ_2 depends weakly on the uncertainties of the parameters entering the calculations. More details are given in [22].

The aim of this paper was to develop a reliable method to determine the deformation retardation time λ_2. From the error analysis follows that λ_2 can be accurately determined even if the right solution qa cannot unambiguously be identified. This is due to the weak dependency of λ_2 on the solution qa of the characteristic equation. On the other hand, in order to accurately determine η_0, very accurate measurements of all the input parameters are required. Numerical examples from our experiments are discussed in the next section.

4.3. Results from the experiments

With each of the three polymer solutions sets of 10 measurements were performed. We varied the drop radius and the driving frequency in the experiments. The results are presented in Table 3 and in Figures 7 and 8. Table 3 shows the dynamic viscosities and deformation retardation times of the three aqueous polymer solutions in Table 1.

Figs. 7 and 8 show the results of our measurements achieved with the method presented. In Fig. 7, the zero-shear dynamic viscosities calculated from the oscillating drop measurement data are presented. Fig. 8 shows the measured deformation retardation times λ_2. The results for the three different polymer solutions read as follows:

Table 3. The viscosities η_0 and deformation retardation times λ_2 obtained from oscillating drop measurements.

Polymer	η_0 $[Pa\ s]$	λ_2 $[10^{-4} s]$
A_1	0.043 ± 7.2%	0.98 ± 12.2%
A_2	0.73 ± 11.8%	2.5 ± 16.4%
B_1	1.1 ± 11.6%	1.3 ± 8.8%

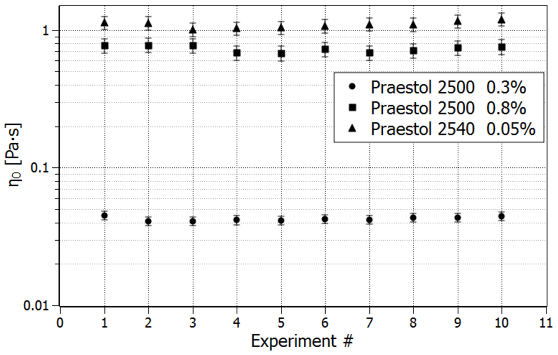

Figure 7. Calculated zero-shear dynamic viscosities η_0 of the investigated polymer solutions for sets of 10 measurements per solution.

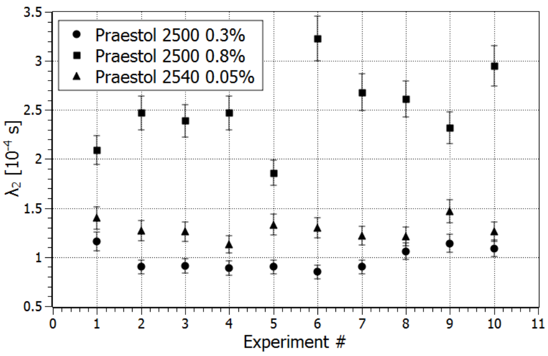

Figure 8. Calculated deformation retardation times λ_2 of the investigated polymer solutions for sets of 10 measurements per solution.

Praestol 2500 0.3 *wt%*
From the experiments with the 0.3*wt%* Praestol 2500 solution drops we obtain $\eta_0 = 0.043\,Pa\,s \pm 7.2\%$ and $\lambda_2 = 0.98 \cdot 10^{-4}\,s \pm 12.2\%$. The value of the zero-shear dynamic viscosity agrees with the value from the shear viscosimetry to within less than −2%. This excellent agreement supports the validity of the data for λ_2.

Praestol 2500 0.8 *wt%*
From the experiments with the 0.8 *wt%* Praestol 2500 solution drops we obtain $\eta_0 = 0.73\,Pa\,s \pm 11.8\%$ and $\lambda_2 = 2.5 \cdot 10^{-4}\,s \pm 16.4\%$. The value of the zero-shear dynamic viscosity agrees with the value from the shear viscosimetry to within −3.8%. This excellent agreement supports the validity of the data for λ_2 for this case also.

Praestol 2540 0.05 *wt%*
From the experiment with the 0.05 *wt%* Praestol 2540 solution drops we obtain $\eta_0 = 1.1\,Pa\,s \pm 11.6\%$ and $\lambda_2 = 1.3 \cdot 10^{-4}\,s \pm 8.8\%$. The value η_0 derived from the oscillation measurement data misses the value $\eta_0 = 1.521\,Pa\,s$ measured by shear viscosimetry by −28%. The value found is rather closer to a value found in an earlier study for the same liquid, which was 1.22 $Pa\,s$ [23]. An explanation for this discrepancy is not readily found. One substantial difference between the above Praestol 2500 and Praestol 2540 is seen in the degree of hydrolysis of the two. While the former are flexible, non-ionic polymers, the latter is a partly hydrolyzed, rigid rod-like molecule producing high dynamic viscosities in aqueous solutions even at low concentration of the polymer.

For these first measured deformation retardation times λ_2 we may conclude that they are more reliable than the data preliminarily presented by [13], with clearly defined confidence intervals. The values are of the order of $100\,\mu s$ for all the solutions investigated so far, with a tendency to increase with the polymer concentration.

5. CONCLUSIONS

In this study we use linear damped shape oscillations of viscoelastic drops for measuring the zero-shear viscosity and the deformation retardation time of polymeric drop liquids. The solution of the linearised equations of change governing the drop shape oscillations yields the characteristic equation for the complex oscillation frequency which is used for determining the material properties. The method for solving the characteristic equation, a basis for applying the present method, further develops the proof-of-concept experiment by [13]. For a given drop, the damping rate and the oscillation frequency are measured in an experiment. Liquid material properties relevant for the oscillations, such as liquid density, surface tension and stress relaxation time, are measured by appropriate standard methods. The zero-shear viscosity and the deformation retardation time of the liquid are obtained as solutions of the characteristic equation of the oscillating drop. Values of the liquid dynamic viscosity are close to those from shear rheometry. They allow the correct solution of the characteristic equation to be identified from a manifold and support the correctness of the deformation retardation times determined. The values of λ_2/λ_1 are found to deviate strongly from the values often used in simulations of viscoelastic liquid flow. Further work will be devoted to investigating the deformation retardation behaviour of various polymers at different concentrations in solvents of different quality.

REFERENCES

[1] Rayleigh, Lord, J. W. S., 1879, “On the capillary phenomena of jets”, *Proc R Soc London A*, Vol. 29, pp. 71–97.

[2] Lamb, H., 1881, “On the oscillations of a viscous spheroid”, *Proc London Math Soc*, Vol. 13, pp. 51–66.

[3] Lamb, H., 1932, *Hydrodynamics, 6th edn*, Cambridge University Press.

[4] Miller, C. A., and Scriven, L. E., 1968, “The oscillations of a fluid droplet immersed in another fluid”, *J Fluid Mech*, Vol. 32, pp. 417–435.

[5] Hsu, C. J., and Apfel, R. E., 1985, “A technique for measuring interfacial tension by quadrupole oscillation of drops”, *J Colloid Interface Sci*, Vol. 107, pp. 467–476.

[6] Hiller, W. J., and Kowalewski, T. A., 1989, “Surface tension measurements by the oscillating droplet method”, *PCH PhysicoChemical Hydrodynamics*, Vol. 11, pp. 103–112.

[7] Egry, I., Lohöfer, G., Seyhan, I., Schneider, S., and Feuerbacher, B., 1998, “Viscosity of the eutectic $Pd_{78}Cu_6Si_{16}$ measured by the oscillating drop technique in microgravity”, *Appl Phys Letters*, Vol. 73, pp. 462–463.

[8] Perez, M., Salvo, L., Suéry, M., Bréchet, Y., and Papoular, M., 2000, “Contactless viscosity measurement by oscillations of gas-levitated drops”, *Phys Rev E*, Vol. 61, pp. 2669–2675.

[9] Tian, Y. R., Holt, R. G., and Apfel, R. E., 1995, “Investigations of liquid surface rheology of surfactant solutions by droplet shape oscillations: Theory”, *Phys Fluids*, Vol. 7, pp. 2938–2949.

[10] Apfel, R. E., Tian, Y. R., Jankovsky, J., Shi, T., Chen, X., Holt, R. G., Trinh, E., Croonquist, A., Thornton, K., Sacco Jr., A., Coleman, C., Leslie, F., and Matthiesen, D., 1997, “Free oscillations and surfactant studies of superdeformed drops in microgravity”, *Phys Rev Letters*, Vol. 78, pp. 1912–1915.

[11] Aske, N., Orr, R., and Sjöblom, J., 2002, “Dilatational elasticity moduli of water-crude oil interfaces using the oscillating pendant drop”, *J Dispersion Sci Technol*, Vol. 23, pp. 809–825.

[12] Kovalchuk, V. I., Krägel, J., Aksenenko, E. V., Loglio, G., and Liggieri, L., 2001, *Novel methods to study interfacial layers*, chap. Oscillating bubble and drop techniques, Elsevier, Amsterdam, pp. 485–516.

[13] Brenn, G., and Teichtmeister, S., 2013, “Linear shape oscillations and polymeric time scales of viscoelastic drops”, *J Fluid Mech*, Vol. 733, pp. 504–527.

[14] Huang, P. Y., Hu, H. H., and Joseph, D. D., 1998, “Direct simulation of the sedimentation of elliptic particles in Oldroyd-B fluids”, *J Fluid Mech*, Vol. 362, pp. 297–325.

[15] Chapman Jr., R. E., Klotz, L. C., Thompson, D., and Zimm, B. H., 1969, “An instrument for measuring retardation times of desoxyribonucleic acid solutions”, *Macromolecules*, Vol. 2, pp. 637–643.

[16] Kaschta, J., and Schwarzl, F., 1994, “Calculation of discrete retardation spectra from creep data”, *Rheologica Acta*, Vol. 33.

[17] Bird, R. B., Stewart, W. E., and Lightfoot, E. N., 1960, *Transport Phenomena*, John Wiley & Sons New York.

[18] Chandrasekhar, S., 1959, “The oscillations of a viscous liquid globe”, *Proc London Math Soc*, Vol. 9, pp. 141–149.

[19] Khismatullin, D. B., and Nadim, A., 2001, “Shape oscillations of a viscoelastic drop”, *Phys Rev E*, Vol. 63, p. 061508.

[20] Yarin, A. L., Brenn, G., Kastner, O., Rensink, D., and Tropea, C., 1999, “Evaporation of acoustically levitated droplets”, *J Fluid Mech*, Vol. 399, pp. 151–204.

[21] Stelter, M., Brenn, G., Yarin, A. L., Singh, R. P., and Durst, F., 2000, “Validation and application of a novel elongational device for polymer solutions”, *J Rheology*, Vol. 44, pp. 595 – 616.

[22] Brenn, G., and Plohl, G., 2014, “The oscillating drop method for measuring the deformation retardation time of viscoelastic liquids”, *J Non-Newtonian Fluid Mech*, submitted.

[23] Pilz, C., and Brenn, G., 2007, “On the critical bubble volume at the rise velocity jump discontinuity in viscoelastic liquids”, *J Non-Newtonian Fluid Mech*, Vol. 145, pp. 124–138.

Conference on Modelling Fluid Flow (CMFF'15)
The 16th International Conference on Fluid Flow Technologies
Budapest, Hungary, September 1-4, 2015

SIMULATION OF MULTIPLE BLUNT-BODY FLOWS WITH A HYBRID VARIATIONAL MULTISCALE MODEL

Emmanuelle Itam[1], Stephen Wornom[2], Bruno Koobus[3], Bruno Sainte-Rose[4], Alain Dervieux[5]

[1] I3M, Université Montpellier 2, Montpellier, France, itamemmanuelle@gmail.com, koobus@math.univ-montp2.fr
[2] LEMMA, 2000 route des Lucioles, Sophia-Antipolis, France, stephen.wornom@inria.fr
[3] I3M, Université Montpellier 2, Montpellier, France, itamemmanuelle@gmail.com, koobus@math.univ-montp2.fr
[4] LEMMA, 11 rue de Carnot F-94270 Le Kremlin-Bicêtre, bruno.sainte-rose@lemma-ing.com
[5] Corresponding Author. INRIA, 2004 Route des lucioles, F-06902 Sophia-Antipolis, Tel.: +33 4 92 38 77 91, E-mail: Alain.Dervieux@inria.fr

ABSTRACT

The present investigation is motivated by the simulation of high-Reynolds number massively separated flows, a challenging problem of prime interest in industry. The turbulence model is based on a hybridization strategy which blends a variational multiscale large-eddy simulation (VMS-LES) equipped with dynamic subgrid scale (SGS) models and a two-equation RANS model. The dynamic procedure (Germano) allows the adaptation of the constant of the SGS model to the spatial and temporal variation of the flow characteristics, while the VMS formulation restricts the SGS model effects to the smallest resolved scales [1]. The hybridization strategy uses a blending parameter, such that a VMS-LES simulation is applied in region where the grid resolution is fine enough to resolve a significant part of the turbulence fluctuations, while a RANS model is acting in the regions of coarse grid resolution [2]. The capability of the proposed hybrid model to accurately predict the aerodynamic forces acting on a circular cylinder in the supercritical regime and on tandem cylinders are investigated.

Keywords: LES, hybrid, dynamic, VMS, blunt body, cylinder, tandem

1. NOMENCLATURE

τ^{LES}	SGS stress tensor
τ^{RANS}	Reynolds stress tensor
μ_{SGS}	SGS viscosity
μ_{RANS}	RANS viscosity
l_{RANS}	RANS characteristic length
Δ	local mesh size
$\bar{C}_d$	Drag
C_l'	Lift rms fluctuations
C_p	Mean pressure coefficient
$\bar{C}_{p_b}$	Mean base pressure coefficient
St	Strouhal number
l_r	Recirculation length
D	Cylindre diameter

2. INTRODUCTION AND MOTIVATIONS

This work takes place in a study of a numerical simulation method suited to industrial problems, equipped with turbulence models adapted to the simulation of turbulent flows with massive separations and vortex shedding. Recent publications concerning this study can be found in [1],[2]. The numerical methods are of low order, applicable on unstructured tetrahedral meshes, and involve numerical dissipation. But this dissipation is made of sixth-order derivatives and very low, and advective accuracy can be as high as fifth order on Cartesian region of the mesh. The main issue which then arises is the choice of turbulence modelling which can combine well with this numerical technology.

In order to address high Reynolds number flows, we have to consider RANS-LES hybridization as in Detached Eddy Simulation (DES) [3, 4]. However DES is not designed for computing subcritical flows for which pure LES is a natural approach. Now, it is important to have a LES mode as accurate as possible. For example, the shear layer between main flow and wake can suffer from the tendancy of a Smagorinsky-like model to reinforce the filtering in these regions. Two techniques are considered to improve the accuracy of the LES component. First, the time-space strength of the filter is controlled by a dynamic process. Second, the width of the filter is numerically controlled by using a variational multiscale formulation.

The present work focuses on the following items:

- The evaluation of dynamic and hybrid VMS-

LES models on the prediction of vortex shedding flows

- The simulation of the flow around circular and square cylinders : these flows involve many features and difficulties encountered in industrial problems and are studied in well documented benchmarks. They are also the first step before the computation of array of cylinders (offshore oil and gas industries, civil engineering, aeronautics)

3. NUMERICAL MODEL

The spatial discretization is based on a mixed finite-volume finite-element formulation, with degrees of freedom located at nodes i of the tetrahedrization. The finite volume part is integrated on a dual mesh built in 2D from median (Figure 1), in 3D from median plans. The diffusive fluxes are evaluated by a finite-element method, whereas a finite-volume method is used for the convective fluxes. The numerical approximation of the convective fluxes at the interface of neighboring cells is based on the Roe scheme [5].

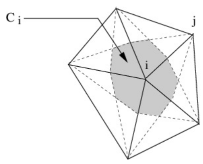

Figure 1. Dual cell in 2D

In order to obtain second-order accuracy in space, the Monotone Upwind Scheme for Conservation Laws reconstruction method (MUSCL) [6] is used, in which the Roe flux is expressed as a function of reconstructed values of the discrete flow variable W_h at each side of the interface between two cells. We refer to [7] for details on the definition of these reconstructed values. We just emphasize that particular attention has been paid to the dissipative properties of the resulting scheme since this is a key point for its successful use in LES. The numerical (spatial) dissipation provided by this scheme is made of sixth-order space derivatives [7] and this is concentrated on a narrow-band of the highest resolved frequencies. This is expected to limit undesirable damping by numerical dissipation of the large scales. Moreover, a parameter γ_S directly controls the amount of introduced viscosity and can be explicitly tuned in order to reduce it to the minimal amount needed to stabilize the simulation.

Time integration uses an implicit second-order backward differencing scheme. In [7], it is shown that when used in combination with moderate time steps, the time dissipation is also quite small.

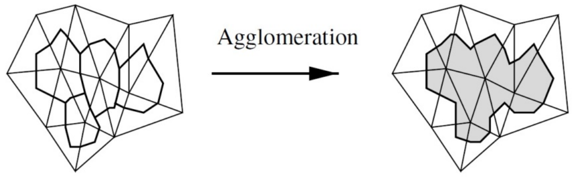

Figure 2. Building the VMS coarse level

4. TURBULENCE MODEL: VMS-LES

The Variational Multiscale (VMS) model for the large eddy simulation (LES) of turbulent flows has been introduced in [8] in combination with spectral methods. In [9], an extension to unstructured finite volumes is defined. That method is adapted in the present work. Let us explain this VMS-LES approach in a *simplified context*. Assume the mesh is made of two embedded meshes, corresponding to a P^1-continuous finite-element approximation space V_h with the usual basis functions Φ_i vanishing on all vertices but vertex i. Let be V_{2h} its embedded coarse subspace V_{2h}. Let V'_h be the complementary space: $V_h = V_{2h} \oplus V'_h$. The space of *small scales* V'_h is spanned by only the fine basis functions Φ'_i related to vertices which are not vertices of V_{2h}. We write the compressible Navier-Stokes equations as follows: $\frac{\partial W}{\partial t} + \nabla \cdot F(W) = 0$ where $W = (\rho, \rho\mathbf{u}, \rho E)$. The VMS-LES discretization writes for $W_h = \sum W_i \Phi_i$:

$$\left(\frac{\partial W_h}{\partial t}, \Phi_i\right) + (\nabla \cdot F(W_h), \Phi_i) = -\left(\tau^{LES}(W_h'), \Phi_i'\right). \quad (1)$$

For a test function related to a vertex of V_{2h}, the RHS vanishes, which limits the action of the LES term to small scales. *In practice*, embedding two unstructured meshes V_h and V_{2h} is a constraint that we want to avoid. The coarse level is then built from the agglomeration of vertices/cells as sketched in Figure 2: It remains to define the model term $\tau^{LES}(W'_h)$. This term represents the SGS stress term, acting only on small scales W'_h, and computed from the small scale component of the flow field by applying either a Smagorinsky or a WALE SGS model, [10], the constants of these models being eventually evaluated by the Germano-Lilly dynamic procedure [11, 12]. The main property of the VMS formulation is that the modeling of the unresolved structures is influencing only the small resolved scales, as described in Figure 3, in contrast with, for example the usual Smagorinsky model. This implies two main properties. First, the backscatter transfer of energy to large scales is not damped by the model. Second, the model is naturally unable to produce an artificial viscous layer at a no-slip boundary, or in shear layers.

5. TURBULENCE MODEL: HYBRID RANS/VMS-LES

The computation of massively separated flows at high Reynolds numbers on unstructured meshes

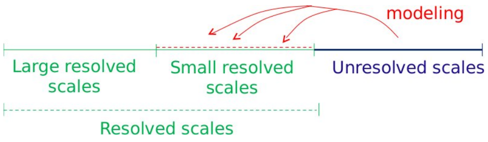

Figure 3. VMS principle

can be addressed with three families of models. Reynolds-Averaged-Navier-Stokes (RANS) is robust but shows accuracy problems in flow regions with massive separation (such as the flow around bluff-bodies). LES, and in particular our VMS-LES is more expensive than RANS, since a very fine resolution -somewhat comparable to DNS- is required in boundary layers at high Reynolds numbers. Hybrid formulations combine RANS and LES in order to exploit the advantages of the two approaches. Our goal is to build and evaluate a hybrid RANS/VMS-LES. The central idea of the proposed hybrid VMS model is to correct the mean flow field obtained with a RANS model by adding fluctuations given by a VMS-LES approach wherever the grid resolution is adequate. Our hybrid model can be shortly derived as follows.

First, let us write the semi-discretization of the RANS equations :

$$\left(\frac{\partial \langle W_h \rangle}{\partial t}, \Phi_i\right) + (\nabla \cdot F(\langle W_h \rangle), \Phi_i) = -\left(\tau^{RANS}(\langle W_h \rangle), \Phi_i\right) \quad (2)$$

in which $\langle W_h \rangle$ denotes the RANS variables.

An equation for the resolved fluctuations $W_h^c = W_h - \langle W_h \rangle$, where W_h denotes the VMS-LES variables that satisfy Eqs. (1), can then be derived by substracting Eqs. (1) and (2) :

$$\left(\frac{\partial {W_h}^c}{\partial t}, \Phi_i\right) + (\nabla \cdot F(W_h), \Phi_i) - (\nabla \cdot F(\langle W_h \rangle), \Phi_i)$$

$$= \left(\tau^{RANS}(\langle W \rangle), \Phi_i\right) - \left(\tau^{LES}({W_h}'), \Phi_i'\right) \quad (3)$$

To identify the regions where the additional fluctuations need to be computed, i.e. the regions where the grid resolution is adequate for VMS-LES, a blending function θ is introduced, which smoothly varies between 0 and 1, and which allows to recover the RANS approach for $\theta = 1$ and the VMS-LES model for $\theta = 0$. Thus Eqs. (3) become

$$\left(\frac{\partial {W_h}^c}{\partial t}, \Phi_i\right) + (\nabla \cdot F(W_h), \Phi_i) - (\nabla \cdot F(\langle W_h \rangle), \Phi_i)$$

$$= (1-\theta)\left[\left(\tau^{RANS}(\langle W \rangle), \Phi_i\right) - \left(\tau^{LES}({W_h}'), \Phi_i'\right)\right] \quad (4)$$

In order to avoid the solution of two systems of equations, Eqs (2) and (4) are recasted together as follows :

$$\left(\frac{\partial W_h}{\partial t}, \Phi_i\right) + (\nabla \cdot F(W_h), \Phi_i) = -\theta\left(\tau^{RANS}(\langle W \rangle), \Phi_i\right) - (1-\theta)\left(\tau^{LES}(W_h'), \Phi_i'\right) \quad (5)$$

where W_h denotes now the hybrid variables. The blending function $\theta = \tanh(\xi^2)$ is defined either by a prescription of the user (zonal option) or from $\xi = \mu_{SGS}/\mu_{RANS}$ or $\xi = \Delta/l_{RANS}$. The RANS component used in the proposed hybrid approach is the $k - \varepsilon$ model proposed by Goldberg and Ota [13]. The hybrid variables then write $W_h = (\rho_h, \rho_h \mathbf{u_h}, \rho_h E_h, \rho_h k_h, \rho_h \varepsilon_h)$.

6. RESULTS

For the simulations presented in this section, characteristic based conditions are used at the inflow and outflow as well as the lateral surface. In the spanwise direction, periodic boundary conditions are applied. No-slip conditions are imposed on the walls for moderate Reynolds numbers and a wall law approach is used for higher Reynolds numbers. The freestream Mach number is set to 0.1 in order to make a sensible comparison with incompressible simulations in the literature. Preconditioning is used to deal with the low-Mach number regime. For all simulations, starting from a uniform flow and once the flow is established, statistics are computed by averaging in time for, at least, 30 vortex-shedding cycles.

6.1. CIRCULAR CYLINDER - SUBCRITICAL

The presented results are compared with other LES computations [14, 15, 16] and with measurements [16, 17, 18]. The flow around a cylinder is strongly dependent on the turbulence which exists in the inflow and the turbulence which is created along the wall boundary layer after the stagnation point. In the case where the inflow involves no turbulence, turbulence is created on the wall at a sufficiently high critical Reynolds number, corresponding to the *drag crisis*. This Reynolds number is between 300, 000 and 500, 000. Under this number, the flow is subcritical and, in short the boundary layer flow is laminar. In this case, we put $\theta = 0$ in our model, which means that the VMS-LES model is combined with a laminar boundary layer, an option which is justified when the turbulence arising is essentially wake turbulence. We consider first a rather low Reynolds of 3900 and analyse in which conditions a better prediction is obtained with a very coarse mesh (290, 000 vertices) and a medium mesh (1, 400, 000 vertices). The WALE SGS is used, and we compare the association of VMS-WALE with dynamic limitation and without. The effect of dynamic limitation results in a global reduction of SGS viscosity, see for example the contours of SGS viscosity obtained at Reynolds 20, 000 which are depicted in Figure 5. Surprisingly, the effect on wake velocity is small in general, but yet rather notable at the limit of wake, see Figures

	Mesh	$\overline{C}_d$	l_r/D	$-\overline{C}_{p_b}$	St
VMS	270K	0.96	1.06	0.94	0.22
VMS dyn.	270K	0.97	1.08	0.93	0.22
VMS	1.4M	0.94	1.47	0.81	0.22
VMS dyn.	1.4M	0.94	1.47	0.85	0.22
LES					
Lee(Min)	7.7M	0.99	1.35	0.89	0.209
Lee(Max)	7.7M	1.04	1.37	0.94	0.212
Kravchenko					
(Min)	0.5	1.04	1.	0.93	0.193
(Max)	2.4M	1.38	1.35	1.23	0.21
Parneaudeau					
(Min)	44M	-	1.56	-	0.207
(Max)	44M	-	1.56	-	0.209
Experiments					
Parneaudeau					
(Min)		-	1.51	-	0.206
(Max)		-	1.51	-	0.210
Norberg					
(Min)		0.94	-	0.83	
(Max)		1.04	-	0.93	
Ong(Min)		-	-	-	0.205
Ong(Max)		-	-	-	0.215

Table 1. Bulk quantities for Re=3900 flow around a cylinder (VMS-WALE vs VMS-WALE dynamic)

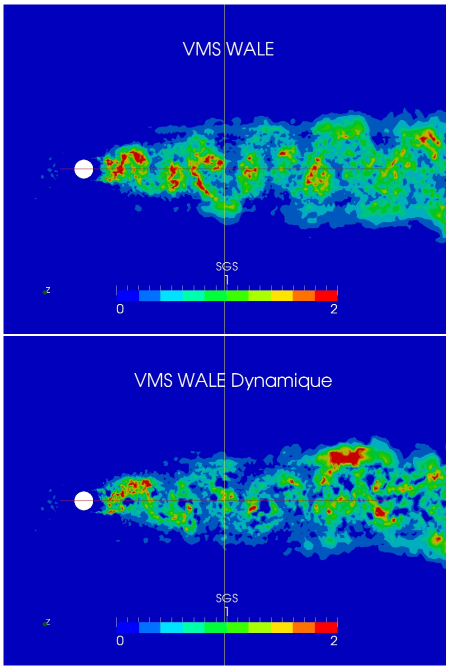

Figure 5. Cylinder, Re=20,000: viscosity ratio μ_{SGS}/μ - non-dynamic VMS versus dynamic VMS

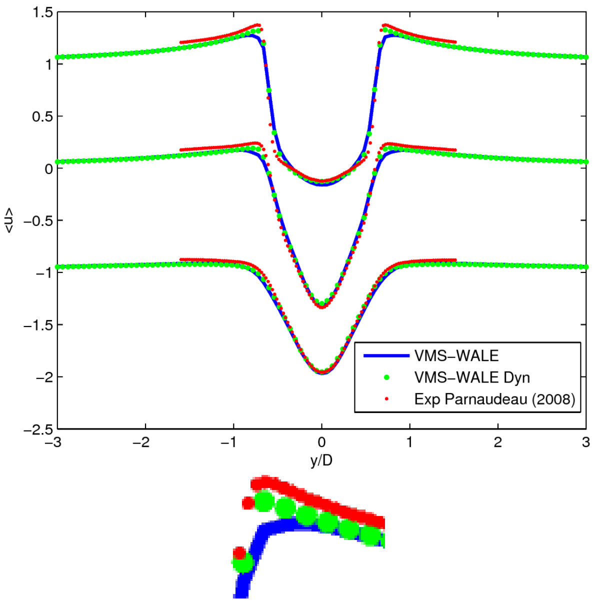

Figure 4. Cylinder, Re=3900: Mean streamwise velocity profiles at x/D = 1.06, 1.54 and 2.02 and a zoom of the x/D = 1.06 cut (finer grid).

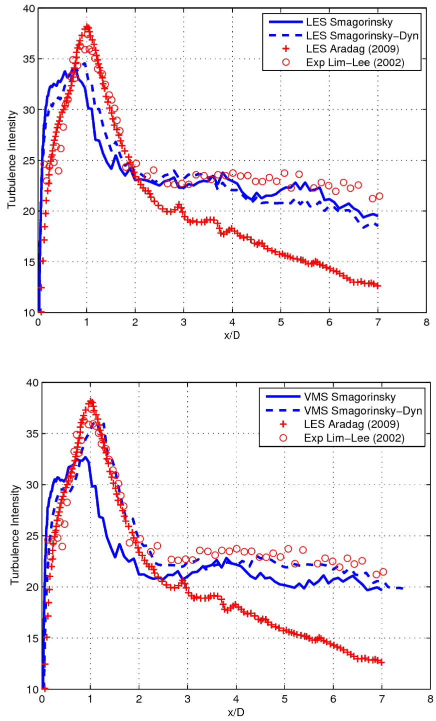

Figure 6. Cylinder, Re=20,000: turbulence intensity in the axis of wake: Dynamic improves LES (top) and strongly improves VMS (bottom).

	Mesh	$\overline{C}_d$	$\frac{l_r}{D}$	St	C'_L	C'_d
VMS:						
	1.2M	2.08	0.74	0.127	1.38	0.25
dyn.	1.2M	2.06	0.82	0.128	1.28	0.24
LES						
(Min)	110K	1.66	0.89	0.07	0.38	0.1
(Max)	3.8M	2.77	2.96	0.15	1.79	0.27
DNS	3.7M	2.1	-	0.133	1.22	0.21
Exp.						
Lyn		2.1	0.88	0.133	-	-
Luo		2.21	-	0.13	1.21	0.18

Table 2. Square cylinder, Re=$22,000$: Bulk coefficients (LES: Rodi ; DNS: Verstappen)

4. Global coefficients are also slightly improved, see Table 1.

A second example is the flow around the circular cylinder with Reynolds number of $20,000$. In Figure 5 we show the rather high variation between the VMS viscosity with and without the dynamic control. The impact of the dynamic procedure on the turbulence intensity along the axis of the wake is important as shown in Figure 6.

6.2. SQUARE CYLINDER

As a second example to show the interest in combining VMS and dynamic control, we computed a classical workshop test case [19]. The incompressible flow around a square cylinder at Reynolds $22,000$ and zero angle of attack is considered. The VMS-LES option is applied on a mesh of 1.2M vertices. The influence of the dynamic procedure on the evaluation of the bulk coefficients is quite small, as shown in Table 2 which also compares the current computation with LES results from [20, 21] and measurements from [22, 23, 24]. Conversely the deviation to measurements of the mean velocity profiles is greatly reduced when the dynamic control is used, see Figures 7,8.

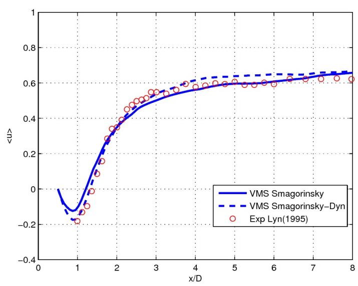

Figure 7. Square cylinder, Re=22K: mean streamwise velocity on the wake center-line.

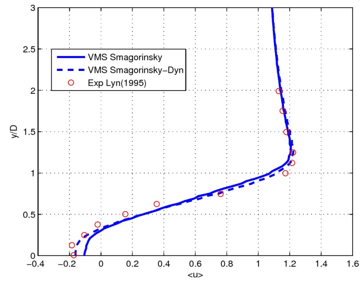

Figure 8. Square cylinder, Re=22K: mean streamwise velocity at $x/D = 1$.

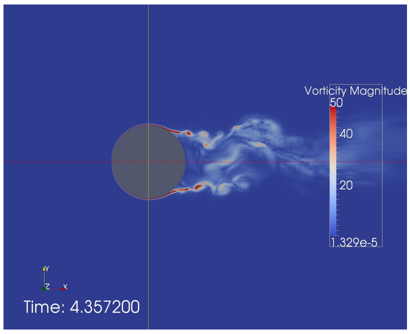

Figure 9. Flow around a circular cylinder at Re=1 million: vorticity field.

6.3. CIRCULAR CYLINDER - SUPERCRITICAL

We now address the flow around a circular cylinder at a Reynolds 1 million, higher than the critical one. We propose to compare the results of three options, (a) $\theta = 0$, that is RANS, (b) $\theta = 1$, that is VMS-WALE, (c) hybrid RANS-VMS-WALE. Moreover, we try to get reasonable results with a medium-sized mesh of 1.2 million vertices. The available experiments are scarce, [22, 23, 24], and show some scatter. Numerical results are found [20, 21]. They present a even higher scatter (Table 3). Among options (a),(b),(c), we observe that the hybrid calculation is in a rather good agreement with the measurements.

6.4. TANDEM CYLINDERS

The last case concerns the flow around two cylinders in tandem, at Re=1.66×10^5. This test case was studied in an AIAA workshop, see [25]. Among the conclusions of the workshop, adressing this case with LES was considered as a too difficult task with existing computers. Results of DES-based computations were much closer to measurements. We have computed the case with a mesh of 2.59M nodes. Two modeling options were considered: (a) RANS and (b) Hybrid VMS-LES-WALE dynamic. An idea of the impact of these options on the resulting flow is proposed in Figure 10. Some comparison of bulk coefficients is given in Table 4 in which the other

	Mesh	$\overline{C}_d$	C'_l	$-\overline{C}_{p_b}$	St
URANS	1.2M	0.24	0.06	0.25	0.46
VMS WALE	1.2M	0.36	0.22	0.22	0.10
Hybrid:					
VMS-WALE	1.2M	0.24	0.17	0.28	0.17
Catalano:					
URANS	2.3M	0.40	-	0.41	0.31
LES	2.3M	0.31	-	0.32	0.35
LES Kim	6.8M	0.27	0.12	0.28	-
Exp.:					
Shih		0.24	-	0.33	-
Gölling		-	-	-	0.10
Zdravkovich:					
(Min)		0.2	0.1	0.2	0.18
(Max)		0.4	0.15	0.34	0.18

Table 3. Flow around a circular cylinder at Rey=1 million: bulk coefficients.

computational figures are taken from [26] and for Lockard and Aybay from [25]. Experimental outputs are taken from [27]. Drag for the first cylinder shows a small scatter with the various hybrid calculations. The simulation around the second cylinder is more challenging as also illustrated by the pressure distributions (Figure 11).

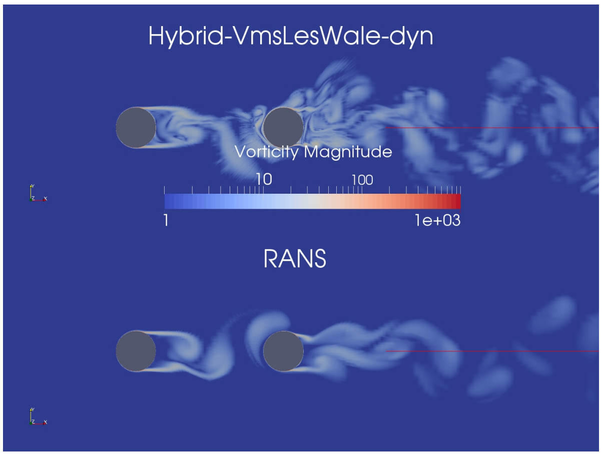

Figure 10. Tandem cylinders: Vorticity magnitude - Hybrid VMS versus RANS.

	Mesh	$\overline{C}_d$ Cyl. 1	$\overline{C}_d$ Cyl. 2
Hybrid VMS dyn.	2.59M	0.64	0.38
Numerical results			
Lockard (2011)	2M-133M	0.33-0.80	0.29-0.52
DES Aybay (2010)	6.7M	0.64	0.44
HRLES Vatsa (2010)	8.7M	0.64	0.45
Experiments		0.64	0.31

Table 4. Tandem cylinders: bulk coefficients (experimental coefficients are computed by integrating experimental pressure of Neuhart).

7. CONCLUSION, PERSPECTIVES

The main effect of dynamic control of SGS viscosity is a significant reduction of the amount of SGS

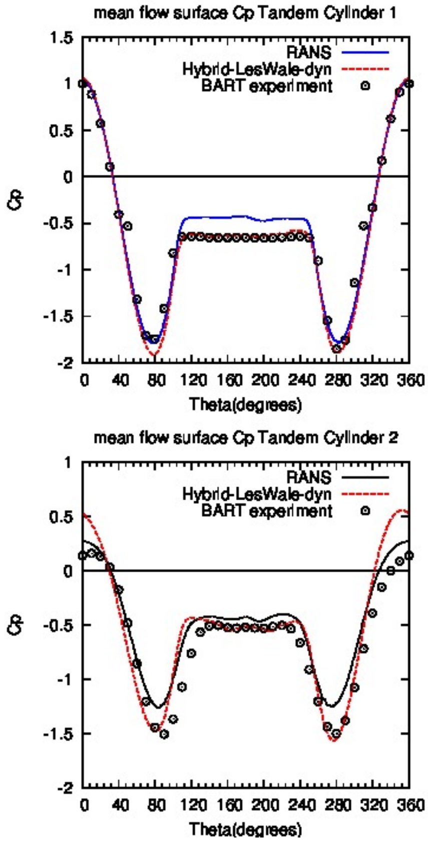

Figure 11. Tandem of cylinders: Mean pressure coefficient distribution and mean C_d.

viscosity in VMS-LES. The impact in VMS-LES is smaller than for pure LES but still non-negligible. In a large part of the tested cases we observe that the dynamic procedure brings a sensible improvement to the agreement with reference data. Then a strategy for blending RANS and VMS-LES is presented. The supercritical flow around a circular cylinder is reasonably well predicted by the proposed VMS hybrid model. The tandem cylinder case shows at the same time some improvement and that further research is necessary.

8. ACKNOWLEDGEMENTS

This work has been supported by French National Research Agency (ANR) through project MAIDESC n^o ANR-13-MONU-0010. HPC resources from GENCI-[CINES] (Grant 2010-x2010026386 and 2010-c2009025067) are also gratefully acknowledged.

REFERENCES

[1] Moussaed, C., Wornom, S., Salvetti, M., Koobus, B., and Dervieux, A., 2014, "Impact of dynamic subgrid-scale modeling in variational multiscale large-eddy simulation of bluff body flows", *Acta Mechanica*, Vol. 1-15.

[2] Moussaed, C., Salvetti, M., Wornom, S., Koobus, B., and Dervieux, A., 2014, "Simu-

lation of the flow past a circular cylinder in the supercritical regime by blending RANS and variational-multiscale LES models", *Journal of Fluids and Structures*, Vol. 47, pp. 114–123.

[3] Spalart, P., Jou, W.-H., Strelets, M., and Allmaras, S., 1997, "Comments on the feasibility of LES for wings, and on a hybrid RANS/LES approach", *Advances in DNS/LES*, pp. 137–147.

[4] Spalart, P., Deck, S., Strelets, M., Shur, M., Travin, A., and Squires, K., 2006, "A new version of detached-eddy simulation, resistant to ambiguous grid densities", *Theor Comput Fluid Dyn*, Vol. 20, pp. 181–195.

[5] Roe, P., 1981, "Approximate Riemann solvers parameters vectors and difference schemes", *J Comp Phys*, Vol. 43, pp. 357–372.

[6] Leer, B. V., 1977, "Towards the ultimate conservative scheme. IV : a new approach to numerical convection", *J Comp Phys*, Vol. 23, pp. 276–299.

[7] Camarri, S., Koobus, B., Salvetti, M., and Dervieux, A., 2004, "A low-diffusion MUSCL scheme for LES on unstructured grids", *Computers and Fluids*, Vol. 33, pp. 1101–1129.

[8] Hughes, T., Mazzei, L., and Jansen, K., 2000, "Large eddy simulation and the variational multiscale method", *Comput Vis Sci*, Vol. 3, pp. 47–59.

[9] Koobus, B., and Farhat, C., 2004, "A variational multiscale method for the large eddy simulation of compressible turbulent flows on unstructured meshes-application to vortex shedding", *Comput Methods Appl Mech Eng*, Vol. 193, pp. 1367–1383.

[10] Nicoud, F., and Ducros, F., 1999, "Subgrid-scale stress modelling based on the square of the velocity gradient tensor", *Flow, Turbulence and Combustion*, Vol. 62, pp. 183–200.

[11] Germano, M., Piomelli, U., Moin, P., and Cabot, W., 1991, "A dynamic subgrid-scale eddy viscosity model", *Phys Fluids A*, Vol. 3 (7), pp. 1760–1765.

[12] Lilly, D., 1992, "A proposed modification of the Germano subgrid-scale closure method", *Phys Fluids*, Vol. A4, p. 633.

[13] Goldberg, U., and Ota, D., 1990, "A $k-\varepsilon$ Near-Wall Formulation for Separated Flows", *Tech. Rep. 91–1482*, AIAA 22nd Fluid Dynamics, Plasma Dynamics & Lasers Conference.

[14] Lee, J., Park, N., Lee, S., and Choi, H., 2006, "A dynamical subgrid-scale eddy viscosity model with a global model coefficient", *Phys Fluids*, Vol. 18 (12).

[15] Kravchenko, A., and Moin, P., 1999, "Numerical studies of flow over a circular cylinder at Re=3900", *Phys Fluids*, Vol. 12 (2), pp. 403–417.

[16] Parneaudeau, P., Carlier, J., Heitz, D., and Lamballais, E., 2008, "Experimental and numerical studies of the flow over a circular cylinder at Reynolds number 3900", *Phys Fluids*, Vol. 20 (085101).

[17] Norberg, C., 1987, "Effects of Reynolds number and low-intensity free-sream turbulence on the flow around a circular cylinder", *Publ No 87/2, Department of Applied Termosc and Fluid Mech, Chalmer University of Technology, Gothenburg, Sweden*.

[18] Ong, L., and Wallace, J., 1996, "The velocity field of the turbulent very near wake of a circular cylinder", *Exp Fluids*, Vol. 20, pp. 441–453.

[19] Rodi, W., Ferziger, J. H., Breuer, M., and Pourquié, M., 1997, "Status of large eddy simulation: results of a Workshop", *ASME J Fluids Eng*, Vol. 119, pp. 248–262.

[20] Wang, M., Catalano, P., and Iaccarino, G., 2001, "Prediction of high Reynolds number the flow over a circular cylinder using LES", *Annual research briefs*, Center for Turbulence Research, Stanford.

[21] Kim, S.-E., and Mohan, L., 2005, "Prediction of unsteady loading on a circular cylinder in high Reynolds number flows using large eddy simulation", *Proceedings of OMAE 2005: 24th International Conference on Offshore Mechanics and Artic Engineering, june 12-16, Halkidiki, Greece, OMAE 2005-67044*.

[22] Shih, W., Wang, C., Coles, D., and Roshko, A., 1993, "Experiments on flow past rough circular cylinders at large Reynolds numbers", *J Wind Eng Indust Aerodyn*, Vol. 49, pp. 351–368.

[23] Goelling, B., 2006, "Experimental investigations of separating boundary-layer flow from circular cylinder at Reynolds numbers from 10^5 up to 10^7; Three-dimensional vortex flow of a circular cylinder", G. Meier, and K. Sreenivasan (eds.), *Proceedings of IUTAM Symposium on One Hundred Years of Bloundary Layer Research*, Springer, The Netherlands, pp. 455–462.

[24] Zdravkovich, M., 1997, *Flow around circular cylinders Vol 1: Fundamentals.*, Oxford University Press.

[25] Lockard, D., 2011, "Summary of the Tandem Cylinder Solutions from the Benchmark Problems for Airframe Noise Computations-I", *Proceedings of Workshop AIAA-2011-353*.

[26] Vatsa, V., and Lockard, D., 2010, "Assessment of Hybrid RANS/LES turbulence models for areoacoustics applications", *AIAA Paper*, Vol. 2010-4001.

[27] Neuhart, D., Jenkins, L., Choudhari, M., and Khorrami, M., 2009, "Measurements of the flowfield interaction between tandem cylinders", *AIAA Paper*, Vol. 2009-3275.

Conference on Modelling Fluid Flow (CMFF'15)
The 16th International Conference on Fluid Flow Technologies
Budapest, Hungary, September 1-4, 2015

MODIFICATION OF A STEAM VALVE DIFFUSER FOR ENHANCED FULL LOAD AND PART LOAD OPERATION USING NUMERICAL METHODS

Clemens Bernhard DOMNICK[1], Friedrich-Karl BENRA[2], Dieter BRILLERT[3], Christian MUSCH[4]

[1] Corresponding Author. Chair of Turbomachinery, University of Duisburg Essen. Lotharstrasse 1, 47057 Duisburg, Germany. Tel.: +49 203 379 3573, Fax: +49 203 379 3038, E-mail: bernhard.domnick@uni-due.de
[2] Chair of Turbomachinery, University of Duisburg Essen. E-mail: friedrich.benra@uni-due.de
[3] Chair of Turbomachinery, University of Duisburg Essen. E-mail: dieter.brillert@uni-due.de
[4] Siemens Energy Sector. E-mail: christian.musch@siemens.com

ABSTRACT

The flow in a steam turbine inlet valve is investigated and improved by numerical methods. From the fluid dynamic point of view two requirements exist: Low pressure losses are desired at the fully opened valve position and dynamic fluid forces acting on the valve plug should be minimized to reduce valve vibration. Usually these undesired dynamic fluid forces occur when the flow is throttled at part load. It is found that these fluid forces are generated by separated jets in the diffuser. The attachment and the separation of the jet are related to the Coanda effect.

By understanding the flow physics a way is found to modify the diffuser design in such a way that the flow separations are reduced. Bell-shaped diffusers are able to reduce the flow losses at full load operation. A diffuser contour that fulfils both requirements is developed.

Keywords: Coanda effect, diffuser flow, steam turbine valve, supersonic wall jet, unsteady CFD, wall jet separation.

NOMENCLATURE

A_{EX}	[-]	area at the exit of the valve gap
A_T	[-]	area at the throat of the valve gap
D_C	[-]	diameter of the contact circle
D_P	[-]	diameter of the valve plug
D_T	[-]	diameter of the valve throat
Ma	[-]	mach number
a	[-]	acceleration
h	[m]	height of the wall jet
p	[bar]	pressure
p_t	[bar]	total pressure
p_1	[bar]	pressure near the wall jet
r	[m]	radius of curvature
u	[m/s]	velocity
y	[m]	wall distance
$y+$	[-]	non dimensional wall distance
Δp_t	[bar]	total pressure loss
α	[°]	angle at contact circle
π_{Co}	[-]	pressure ratio of the coanda jet
π_{Va}	[-]	overall pressure ratio of the valve

Subscripts and Superscripts

att	attachment
bsl	baseline
det	detachment
in	inlet
max	maximum
out	outlet
pre	analytical prediction
ref	reference

Abbreviations

CD	convergent-divergent
OC	operating curve

1. INTRODUCTION

Steam turbine inlet valves are used to control the power output of steam turbines. The design of the valve has to meet several requirements. One criterion is the pressure loss of the valve in open position. It should be as small as possible, as the pressure loss reduces the efficiency of steam turbine installation. Another crucial point is the structural integrity of all valve components. If the valve is operated at part load, a large amount of energy bearing the potential for vibrations is dissipated. Some examples show that at such condition failures of valve components can occur. Tecza et al. [1] and Zhang et al. [2] report of stem fractures. Also surrounding components such as steam pipes can be damaged by valve vibrations. An example for this is given by Michaud et al. [3].

1.1. Literature review

Several investigations show, that the most common causes of valve vibrations are oscillating shocks (Pluviose [4]), jet instabilities (Ziada and Bühlmann [5], Nakano et al. [6]) and jet separations (Stastny [7], Morita [8]). High speed jets are generated at throttled operation when small pressure ratios exist and the flow path is constricted between the valve plug and the valve seat. Especially at large pressure differences jets issuing from the gap formed by the seat and the plug have a large kinetic energy that can be converted to acoustic radiation causing vibrations.

So, the major objective in the aerodynamic design of a steam valve is avoiding shocks and guiding the jet formed between the valve plug and the valve seat in such a way, that it is kept stable and pressure fluctuations are as small as possible. A comparison of different studies shows that an annular wall jet attached to the valve diffuser is the most desired flow topology in terms of pressure fluctuations and vibrations. Stastny et al. [7] show that the desired annular wall jet topology can be obtained by a suitable design of the valve plug. In this study a valve plug with a flat bottom is compared to a convex, valve plug as shown in fig. 1.

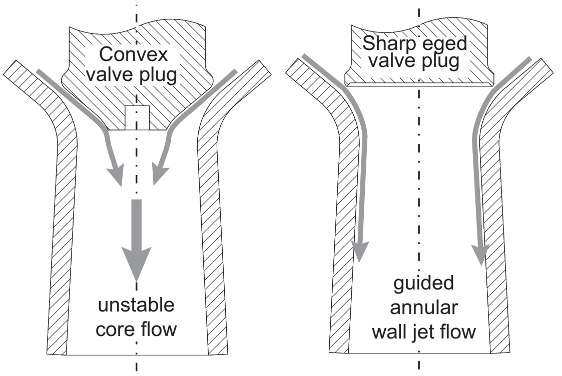

Figure1. Valve plug designs. Sketch by the authors according to Stastny [7]

In case of the convex plug, the flow attaches to the plug guiding it into the centre of the valve diffuser, where an undesired, unstable core flow is formed. In case of the sharp edged valve plug there is no possibility for the flow to attach to the plug. Hence, the flow remains attached to the valve seat and the subsequent valve diffuser and the desired annular flow is formed. In case of this flow topology, the jet is stabilized by the wall and hence the pressure pulsations are reduced significantly.

The CFD analyses of Stastny et al. [7], Schramm et al. [9] and Domnick et al. [10] show that steam valves with sharp edged valve plugs provide the desired core flow at wide operation condition but the undesired core flow can still occur at certain operation conditions. These are large valve lifts and small pressure ratios. Domnick et al. additionally reveal that the attachment of the jet to the wall is related to the Coanda effect. Unsteady CFD calculations by Domnick et al. [11] indicate, that the dynamic fluid forces acting on the valve plug are significantly reduced when the jet attaches.

The knowledge obtained from these studies, shows, that the flow instability and the valve vibrations are reduced when the attached annular wall jet exists in the valve diffuser. In this case the jet is stabilized by the wall and the kinetic energy bearing the potential for pressure fluctuations is gradually dissipated at the wall.

So in this study the contour of a steam valve diffuser is improved to enhance the attachment and hence reduce the vibrations without increasing the pressure loss at the opened valve position.

1.2. Design of the valve diffuser

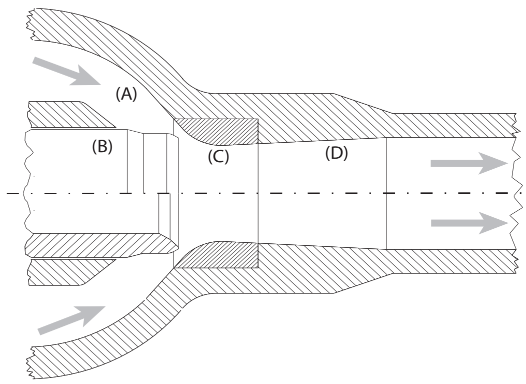

Figure 2. Design of the baseline diffuser

A characteristic design of a steam valve diffuser as installed in large power stations is examined in this study. When a valve of this design is operated in the admissible range of design mass flow, vibrations can be clearly measured, but the vibrational level does not exceed the acceptable level.

The design of the valve diffuser is shown in fig. 2. The flow coming from the valve chest (A) is throttled in the valve gap formed by the valve plug (B) and the curved valve seat (C). Directly downstream of the valve seat the valve diffuser (D) is located. The baseline diffuser design shown here is a simple conical diffuser with a constant opening angle.

1.3. Vibrational characteristic of the valve

The valve shows a typical vibrational characteristic when it is operated at part load. An example is given in fig. 3 showing the vibrational acceleration at the valve stem, the pressure ratio and the valve lift. 100% lift refers to the open position, 0% valve lift corresponds to the closed valve.

At low valve lifts, a high vibrational level can be seen. If the valve is gradually opened, the pressure increases with increasing valve lift due to the swallowing capacity of the turbine connected to the valve. At a certain point, the vibrations suddenly drop to a significant lower level. The pressure ratio of the valve is defined in eq. 1.

$$\pi_{\mathrm{Va}} = \frac{p_{\mathrm{out}}}{p_{\mathrm{t,in}}} \qquad (1)$$

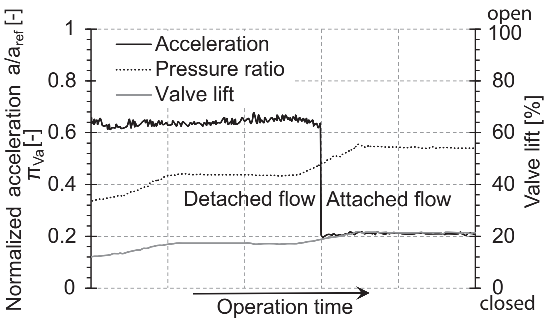

Figure 3. Operational record of a steam valve

The transition point from high vibrations to low vibrations can be reproduced in a single steam turbine installation, but varies among steam turbine installations with different swallowing capacities. In Domnick et al. [10] it is shown that this phenomenon is related to the attachment of the wall jet.

2. NUMERICAL SET UP

The CFD simulations concerning the wall jet separations and the pressure loss are conducted using the commercial CFD solver Ansys-CFX 14. This code employs a fully coupled implicit Navier–Stokes solver. The transient numerical set up finally chosen is second order accurate in space. The thermodynamic and transport properties of the working fluid steam are modeled with the IAPWS real gas model by Wagner et al. [12]. The standard k-ω-SST-turbulence model [13] is applied for the steady state CFD calculation. An automatic near wall treatment provided by the flow solver is used to model the flow close to the wall. This treatment blends automatically the wall value for ω between a wall function for the logarithmic layer and a near wall formulation.

To analyze the jet separations and the pressure loss of the flow in the valve diffuser the valve is investigated at different lift positions. These are summarized in table 1. Different flow domains are used for the investigation on the pressure loss and on the wall jet separations. At full valve lift the geometry of the entire valve diffuser is modeled because asymmetric flow topologies can be relevant to flow separations and hence affect the flow losses. As the flow is not throttled, jet phenomena do not exist at this lift position. The formation of a wall jet is observed at lifts below 70% lift. For the investigation of the jet flow a segment of the diffuser is sufficient according to a previous investigation of the authors [10].

Table1. Different model types

Valve lift	Investigation of	Type of model
100%	Pressure loss	Full model
20%	Wall jet separation	Segment
14%	Wall jet separation	Segment
7%	Wall jet separation	Segment
2%	Wall jet separation	Segment

As the wall friction strongly impacts the flow losses, special attention is paid for the full model to the resolution of the boundary layer. The y+ value is below 10 in the diffuser. As the automatic near wall treatment is used, lage parts of the log-law-region and the buffer region of the boundary are resolved. 40 nodes lie in boundary layer. The near wall velocity profile at the throat of the valve seat is shown in fig. 4. Each dot demarks a computational node.

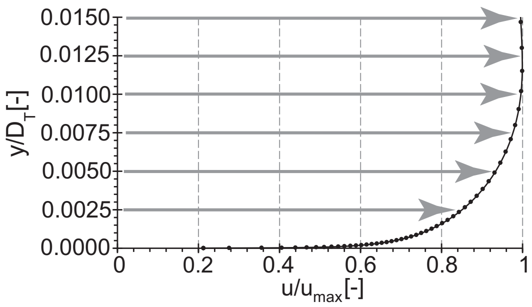

Figure 4. Boundary layer profile

Furthermore, the influence of the discretization outside the boundary layers on the results is analyzed. Three different grids are compared with respect to the total pressure loss. The results are summarized in table 2. The total pressure loss is defined by eq. 2.

$$\Delta p_{\mathrm{t}} = p_{\mathrm{t,in}} - p_{\mathrm{t,out}} \qquad (2)$$

Grid B is chosen for the calculation. A discretization error of 1.2% is estimated for the pressure loss using Richardson extrapolation. The computational domain is shown in fig. 5

Table 2. Grid properties

Grid	Nodes x10^6	$\Delta p_{\mathrm{t}}/\Delta p_{\mathrm{t,max}}$ [−]
A	0.59	1
B	0.95	0.875
C	3.9	0.885

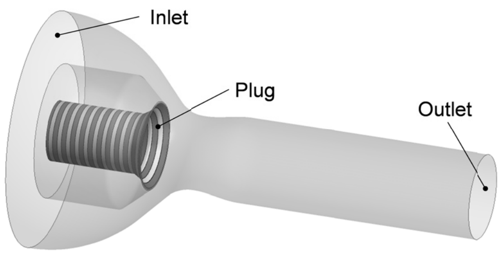

Figure 5. CFD model for flow loss estimation

In case of throttled flow, the investigation is focused on the attachment of the jet. Previous studies conducted by the authors [10] show that attachment characteristics of the wall jet can be obtained by CFD models comprising segments of the axisymmetric diffuser. At typical operation in part load, the flow is chocked and regions with supersonic flow requiring fine block structured hexahedral grids exist. A study on the required spatial resolution for the jet flow can be found in Domnick et al. [10]. The y^+-value in the diffuser is below 30 and the boundary layer is resolved by at least 20 nodes.

Due to the large volume upstream of the small cross sectional area where the flow is chocked, the solution converges slowly. So the use of 60° axisymmetric segments gives a significant reduction of computational time. The flow domain of the 20% lift case is shown in fig. 6.

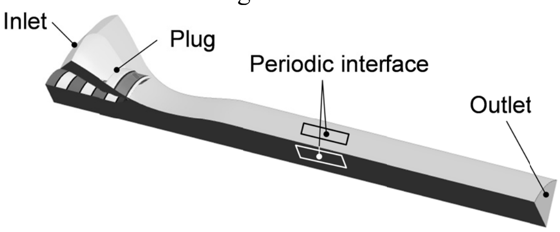

Figure 6. CFD model for wall jet calculations

3. INVESTIGATION ON WALL JET SEPARATION

At first the baseline design of the steam valve is analyzed at low valve lifts for which the vibrations related to the wall jet detachment occur. Two basic flow topologies exist: The detached flow and the attached flow which are both shown in fig. 6. In both cases, the jet is supersonic. At higher pressure ratios the wall jet formed by the valve plug and the valve seat is attached. The attached jet depicted in fig. 7 shows the typical structure of an under expanded supersonic jet comprising expansion and recompression zones (A). With decreasing pressure ratio the strength of the expansion and recompression zones increases. At a certain degree of under expansion an oblique shock (B) occurs downstream the first expansion zone. The flow defection caused by the oblique shock increases with decreasing pressure ratio. When the pressure ratio is sufficiently low, the jet detaches.

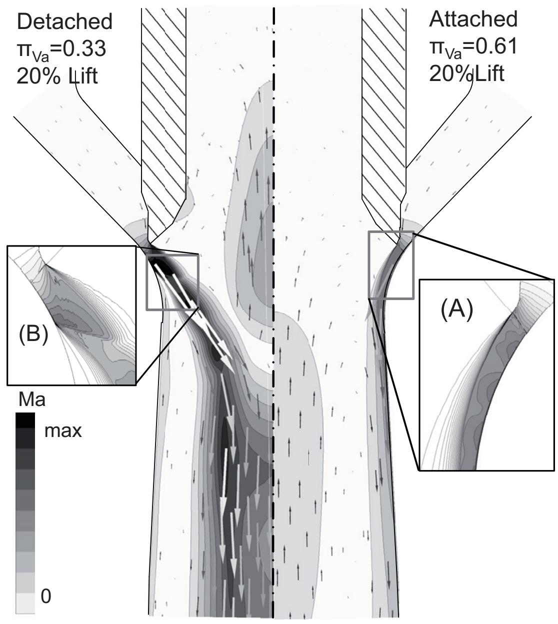

Figure 7. Flow topology in case of the attached and detached flow topology.

The pressure ratio, at which the flow topology changes, is determined for different valve lifts by CFD calculations. Therefore, the outlet pressure is changed gradually at a constant valve lift and a constant inlet pressure. Both increased and decreased outlet pressure is used because hysteresis effects exist.

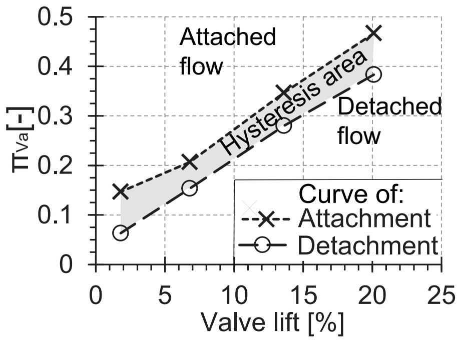

Figure 8. Curve of attachment and detachment for the base line diffuser.

The pressure ratio for which the detached jet attaches is called pressure ratio of attachment, the pressure ratio for which the attached jet detaches is called pressure ratio of detachment. The results are depicted in fig. 8. The pressure ratios of attachment and detachment increase with increasing valve lift.

To figure out the influence of the geometry on the wall jet separations, the numerical results are compared to experimental studies concerning the separation of under expanded Coanda wall jets. These independent experiments are conducted by Gregory-Smith and Gilchrist [14], Matsuo et al. [15] Lowry and Reibe [16] and Sokolova [17].

In these experiments a jet formed in a gap with the height h is accelerated by the pressure ratio π_{Co} and flows along a curved surface with the radius *r*.

According to fig. 9 the same geometric parameters can be taken from the valve geometry. The gap height h depends on the valve lift and r is the radius of curvature at the valve seat. The local pressure π_{Co} determining the wall jet separations is defined in eq. 3.

$$\pi_{\mathrm{Co}} = \frac{p_1}{p_{t,\mathrm{in}}} \tag{3}$$

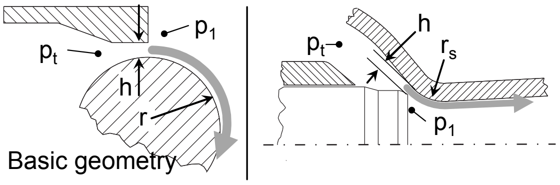

Figure 9. Definition of geometric parameters for the Coanda jet

In fig. 10 the local pressure ratio of attachment π_{Co} from the CFD calculation is drawn versus the radius to height ratio r/h. Obviously, the CFD results match the experimentally obtained results very good. Hence the attachment of the wall jet in the steam valve can be referred to the attachment of the basic Coanda flow.

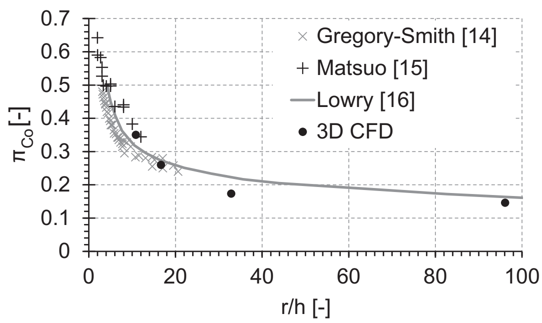

Figure 10. Comparison of the calculated pressure ratio of attachment to experimental data.

Comparing the pressure ratio of detachment to the experimental results in fig. 11 gives a small difference between the numerical and experimental results. Nevertheless, the shape of the trend is reproduced.

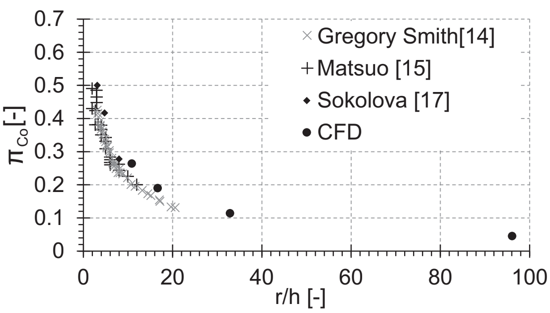

Figure 11. Comparison of the calculated pressure ratio of detachment to experiments

4. MODIFICATION OF THE DIFFUSER SHAPE

The finding, that the pressure ratio of attachment in the steam valve is related to the basic Coanda flow shows a way for the modification of the steam valve diffuser. If the curvature of the valve seat is increased, the geometric r/h-ratio increases as well. Hence, the results of figs.10 and 11 forecast, that the pressure ratio of attachment will decrease for a given valve lift.

4.1. Design constraints for diffuser shape modification

Several constraints arising from the mechanical characteristics of the valve have to be considered during the modification process. The geometric parameters are given in fig. 12.

- The diameter D_P of the valve plug and the outlet diameter D_{Out} must not be changed to avoid a major redesign.
- The position and the diameter (D_C) of the contact circle (Position A in fig. 12) formed by the plug and the seat must not be changed.
- The angle α of the tangent at the contact circle must not be amended to maintain sealing properties and to avoid self-locking effects.

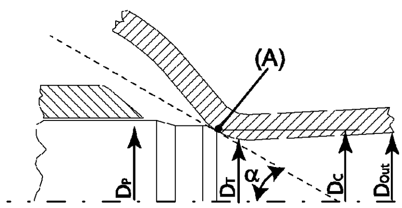

Figure 12. Geometric design constraints

4.2. Impact of seat curvature on wall jet separation at part load

Prior to the CFD investigation a parametric study based on an analytical approach is performed to investigate the effect of the wall curvature on the wall jet separation. This intermediate step is performed as the prediction gives immediately results while the CFD analysis needs at least one week on a modern computer workstation. The analytic approach uses the pressure recovery predicted by the CFD and the pressure ratio of attachment known from the experiments shown in fig. 10. The radius of curvature, defined in fig. 9, is varied according to the geometric constraints given in section 4.1. The results are shown in fig. 13. The radius is normalized by the radius of the baseline design.

It can be seen, that the operational range, in which the flow is attached is extended to lower valve lifts for increased radii. The point of intersection between the operating curve of the valve and the curve of attachment is shifted to lower valve lifts and lower pressure ratios.

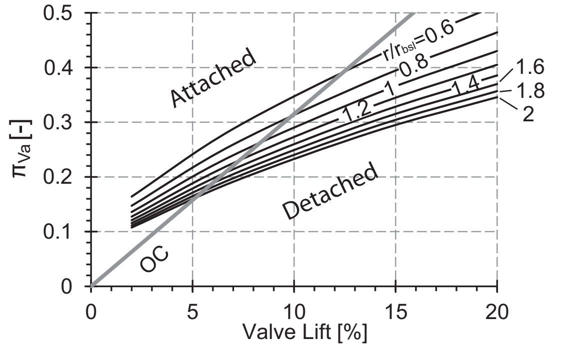

Figure 13. Curves of attachment calculated for different seat radii. (analytical study)

The transition from attached flow to detached flow on the operational curve (OC) versus the radius of curvature is shown in fig. 14. For small radii the enlargement of the radius has a strong effect on the flow transition; for large radii the influence is significantly smaller.

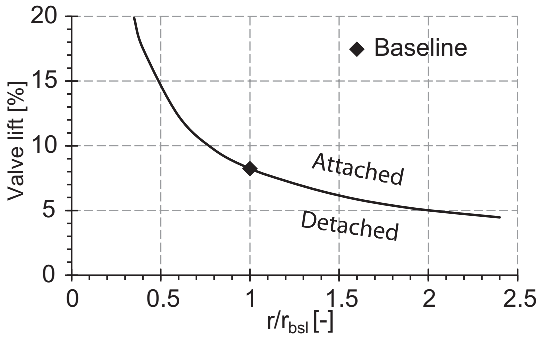

Figure 14. Dependency of the flow transition on the radius of curvature

As the design constrains have to be maintained, the throat diameter D_T becomes smaller when the radius of curvature is increased. Additionally, the length of the diffuser is increased if a classical conical shape is used. This relation is depicted in fig. 15. According to calculations conducted by Biancini [18] the pressure losses at full valve lift are expected to increase if the throat diameter of a valve diffuser is reduced. Hence, this point is investigated in the next section.

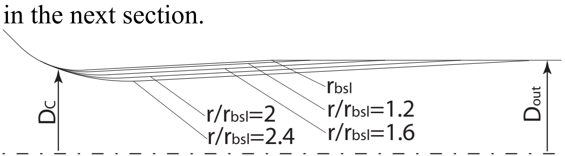

Figure 15. Diffuser contours obtained with different seat radii

4.3. Impact of wall curvature on the pressure loss at full valve lift

The influence of the diffuser design on the pressure losses is analysed. At first the diffuser shape is modified and later in this section the influence of different radii of seat curvature on the pressure loss is investigated using the amended design. As pressure losses are solely relevant at full opened operation of the valve, CFD calculations are performed for this case.

The baseline design of the valve diffuser has a straight, conical diffuser. As the length of the diffuser must not be increased, the pressure losses cannot be reduced by decreasing the opening angle. Hence, the use of a bell shaped curvature is one way to reduce the flow losses under these constraints. An optimal shape of the diffuser design is found by an iterative, manually conducted optimization process. The length of the optimized geometry shown in fig. 16 versus the straight contour of the baseline design does not exceed the length of the baseline geometry for seat radii smaller than 1.6.

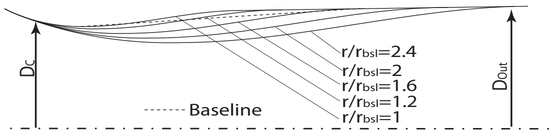

Figure 16. Contours of the curved diffuser for different seat radii

The pressure losses are reduced by 4.5% for the improved curved diffuser with the baseline radius. In the next step the curved diffuser is transferred to valve geometries with an increased seat radius. The influence of the radius of curvature on the pressure loss is depicted in fig. 17 showing the total pressure loss referenced by the total pressure loss of the baseline design. The total pressure losses increase with increasing curvature of the valve seat. As the curved diffuser design has lower losses than the conical diffuser design, the radius of curvature can be increased up to 160% without exceeding the pressure losses of the baseline design. For higher radius ratios the pressure losses increase significantly.

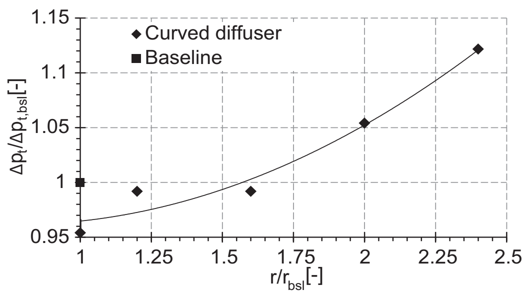

Figure 17. Total pressure loss in dependency of the radius of curvature. (100% valve lift)

4.4. Numerical investigation on the impact of the modified wall curvature

According to the previous results, the radius of curvature at the valve seat can be enlarged by 60% without increasing the pressure loss compared to the baseline design of the diffuser. CFD-calculations are performed to determine the pressure ratio of attachment for this geometry with the enlarged radius. The results are depicted in fig. 18, showing that the operational range without flow separations is increased and the intersection point with the operational curve (OC) is shifted to smaller valve lifts.

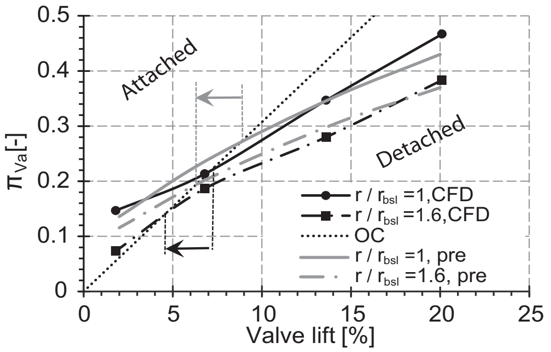

Figure 18. Results of the CFD calculation

This finding basically agrees to the calculation with the analytical 1D-prediction (pre). The absolute value of the transition point from the attached to the detached flow differs between the CFD results and the analytical prediction. But the improvement predicted by both methods agrees well.

5. MODIFICATION OF THE PLUG EDGE

As the detachment of Coanda wall jets is related to the shock caused by the recompression in the under expanded supersonic jet, the attachment of the supersonic jet can be improved by a convergent-divergent gap design (CD-gap). In the divergent part of the gap a controlled expansion occurs. As the controlled expansion reduces the pressure at the outlet of the gap, the expansion and the recompression downstream the gap is weaker. Hence, shocks are less intense and the attachment of the jet is improved. Experimental investigations by Sokolova [17] and Cornelius and Lucius [19] showing that convergent divergent gaps improve the attachment of supersonic wall jets confirm this theoretical consideration.

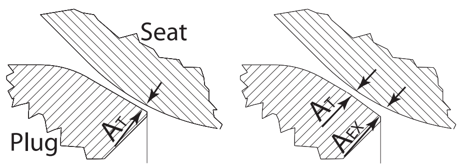

Figure 19. Different valve gaps

A CD-gap can be obtained by reducing the tip diameter of the valve plug according to fig. 19. In the CD design the cross sectional area at the exit A_{EX} is larger than the smallest cross section A_T forming the throat of the gap.

In the baseline design the valve gap has a pure convergent shape. To investigate the effect of the valve gap on the wall jet separation, CFD calculations are performed. The CD gap is obtained by reducing the tip diameter of the valve plug by 0.36%. By this modification a convergent valve gap exist up to 20% valve lift. The tip of the valve plug has to be designed very careful, as convergent divergent gaps with too large divergent sections can produce over expanded jets or even a vertical compression shock in the valve gap. Vertical compression shocks in the valve gap are undesired according to Pluvoise [4] as they can generate strong vibrations. The plug investigated here is designed to avoid these undesired phenomena in the typical operational range. For small lifts at which the pressure ratio is too small to form vertical compression shocks the gap is convergent-divergent. At medium lifts, at which pressure ratios suitable for the formation of a shock exist, the gap is pure convergent. Hence the shock is avoided by this plug design.

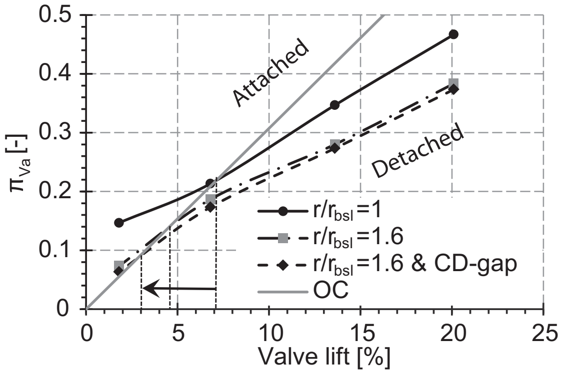

Figure 20. Curve of attachment of the baseline design and the improved designs (CFD)

The results of the CFD calculation depicted in fig. 20 show that the curve of attachment is shifted to lower pressure ratios for small valve lifts. Hence, the intersection with the operating curve (OC) of the valve is moved to lower lifts and pressure ratios, and the operational range in which the separations occur is reduced. As the throat diameter of the valve is not affected, this way to improve the wall attachment does not influence the pressure loss at the open valve position.

5. CONCLUSIONS

The transition from the detached to the attached flow in steam valves is related to the attachment of supersonic Coanda wall jets. In case of the detached flow, the vibrations are higher.

The attachment of the jet can be improved by two methods. The radius of the valve seat can be increased to decrease the pressure ratio of attachment or the attachment can be improved by a convergent-divergent valve gap reducing the strength of the expansion.

The use of curved diffusers can compensate the increased pressure losses and the increased length which come along with increased seat radii. A very large increase of the radius of curvature gives only a small additional improvement of the jet attachment while the pressure losses increase significantly compared to a moderately increased radius.

ACKNOWLEDGEMENTS

This work is conducted as a part of the joint research program COOREFLEX-Turbo in the frame of AG Turbo. The work is supported by the German Federal Ministry for Economic Affairs and Energy under grant number 03ET7020A. The authors gratefully acknowledge Siemens AG for their support and permission to publish this paper. The responsibility for the content lies solely with the authors.

REFERENCES

[1] Tecza J., Chochua, G., Moll, R., 2010, "Analysis of Fluid-Structure interaction in a Steam Turbine Throttle Valve" *Proceedings of ASME Turbo Expo 2010,* GT2010-23788

[2] Zhang, D., Engeda, A., Hardin, J. R., Aungier, R. H., 2004, "Experimental study of steam turbine control valves" *Proceedings of the Institution of Mechanical Engineers, Part C: Journal of Mechanical Engineering Science,* Vol. 218, pp. 493-507

[3] Michaud, S., Ziada, S., Pastorel H., 2001, "Acoustic Fatigue of a Steam Dump Pipe System Excited by Valve Noise", *Journal of Pressure Vessel Technology*, 123, pp. 461-468

[4] Pluviose, M., 1989, "Stabilization of Flow through Steam-Turbine Control Valves", *Journal of Engineering for Gas Turbines and Power*, Vol. 111, pp. 642-646

[5] Ziada, S., Bühlmann E. T., Bolletter, U., 1989, „Flow Impingement as an Excitation Source in Control Valves", Journal of Fluids and Structures, Vol. 3, pp. 529-549

[6] Nakano M., Outa, E., Tajima, K., 1988, "Noise and Vibration Related to the Patterns of Supersonic Annular Flow in a Pressure Reducing Gas Valve", *Journal of Fluids Engineering*, Vol. 110, pp 55 -61

[7] Stastny, M., Bednar, L., Tajc, L., Kolar, P., Martinu, P., Matas, R, 2003, "Pulasting Flows in the Inlet of a Nuclear Steam Turbine", 5th European Conference on Turbomachinery, 17-22.03.2003 Prague, Czech Republic pp. 667-686

[8] Morita, R., Inada, F., Mori, M., Tezuka, K., Tsujimoto, Y., 2005, "Flow Induced Vibration of a Steam Control Valve", Proceedings of PVP2005 ASME Pressure Vessels and Piping Division Conference, pp. 485 -490

[9] Schramm, A., Muller, T., Polklas, T., Brunn, O., Mailach, R., 2014, "Unsteady Flow in Extraction Modules of Industrial Steam Turbines", *Proceedings of ASME Turbo Expo 2014,* June 16-19, Dusseldorf Germany, GT-2014-25394

[10] Domnick, C., Benra, F-K., Dohmen H. J., Musch, C., 2014, "Numerical Investigation on Under Expanded Wall Jet Separation in a Steam Turbine Valve Diffuser", ISROMAC-15, Honolulu, USA, Paper No. TU-305

[11] Domnick, C., Benra, F-K., Dohmen H. J., Musch, C., 2014, Numerical Investigation on the Time-Variant Flow Field and the Dynamic Forces Acting in Steam Turbine Inlet Valves , *Proceedings of ASME Turbo Expo 2014,* June 16-19, Dusseldorf Germany, GT2014-25632

[12] Wagner, W., Cooper, J. R., Dittmann, A., Kijima, J., Kretzschmar, H.-J., Kruse, A., Mares, R., Oguchi, R., Sato, H., Stöcker, I., Sifner, O., Takaishi, Y., Tanishita, I., Trübenbach J., and Willkommen, Th., "The IAPWS Industrial Formulation 1997 for the Thermodynamic Properties of Water and Steam," *ASME J. Eng. Gas Turbines and Power*, Vol. 122, pp. 150-182

[13] Menter, F. R., 1994, "Two-Equation Eddy-Viscosity Turbulence Models for Engineering Applications", *AIAA Journal*, Vol. 32, pp. 1598-1605.

[14] Gregory-Smith, D. G., and Gilchrist, A. R., 1987, "The compressible Coanda wall jet - an experimental study of jet structure and breakaway", *Int. J Heat Fluid Flow*, Vol. 8, pp. 156-164.

[15] Matsuo, S., Setoguchi, T., Kudo, T., Yu, S., 1998, "Study on the Characteristics of Supersonic Coanda jets", *Journal of Thermal Sciences*, Vol. 7, pp. 165-175

[16] Lowry, J G., Reibe, J. M., 1957, "The jet augmented flap" *25th annual meeting of the Institute of the Aeronautical Sciences*. Paper 715

[17] Sokolova, I. N., 1986, "Investigation of Supersonic Coanda Flow", *Fluid Mechanics-Soviet Research*, Vol. 15, pp. 1-6

[18] Bianchini, C., Micio, M., Tarchi, L., Cortese, C., Imparto E., Tampucci, D., 2013, "Numerical Ananlysis of Pressure Losses in Diffuser and Tube Steam Partition Valves", *Proceedings of ASME Turbo Expo 2013,* June 3-7, San Antonio Texas, GT2013-95527

[19] Cornelius, K. C., Lucius G. A., 1994, "Physics of Coanda Jet Detachment at High-Pressure Ratio" *Journal of Aircraft,* Vol.31, pp. 591-596

Conference on Modelling Fluid Flow (CMFF'15)
The 16th International Conference on Fluid Flow Technologies
Budapest, Hungary, September 1-4, 2015

EXTENDED LUBRICATION THEORY FOR GENERALIZED COUETTE FLOW THROUGH CONVERGING GAPS

Helfried STEINER[1], Emil BARIĆ[2], Günter BRENN[3]

[1] Corresponding Author. Institute of Fluid Mechanics and Heat Transfer, Graz University of Technology. Inffeldgasse 25/F, A-8010 Graz, Austria. Tel.: +43 316 873 7344, Fax: +43 316 873 7356, E-mail: steiner@fluidmech.tu-graz.ac.at
[2] Institute of Fluid Mechanics and Heat Transfer, Graz University of Technology. E-mail: baric@fluidmech.tu-graz.ac.at
[3] Institute of Fluid Mechanics and Heat Transfer, Graz University of Technology. E-mail: brenn@fluidmech.tu-graz.ac.at

ABSTRACT

The approximation of the Navier-Stokes equations based on the lubrication theory represents a widely used approach for the computation of viscous flow through narrow gaps. The flow through enamelling dies in the process of the coating of magnet wires with electrical insulation represents a technically highly relevant application. The strongly converging geometries, as typically met in enamelling dies, leading to extremely high axial pressure variations clearly limit the scope of the lubrication theory due to the total neglect of the advective transport. The present work attempts to improve the accuracy of the lubrication theory in predicting such generalized Couette flows, where the shear-driven motion is subject to strong axial pressure gradients, by including the effect of advective transport in terms of a first-order perturbation in both the momentum and energy equations. A comparison of the obtained perturbation solution against CFD results proves the present analytically based perturbation method as a reliable and computationally efficient alternative to the numerical solution of the full set of equations. As such the present approach represents an attractive computational flow model for the development of flow optimized die geometries.

Keywords: Generalized Couette flow, lubrication theory approximation, first-order perturbation

NOMENCLATURE

Ec	[-]	Eckert number
L	$[m]$	axial length of the die
Nu	[-]	Nusselt number
Pr	[-]	Prandtl number
Q	$[m^3/s]$	volumetric flow rate
Re_L	[-]	Reynolds number
T	$[K]$	thermodynamic temperature
U_w	$[m/s]$	velocity of the wire
c_p	$[J/kgK]$	specific heat capacity
h	$[m]$	die exit gap height
n_{geo}	[-]	geometry parameter
k	$[W/m^2K]$	heat transmission coefficient
p	$[Pa]$	pressure
r	$[m]$	radial coordinate
r_w	$[m]$	radius of the wire
r_d	$[m]$	contour of the die
u	$[m/s]$	axial velocity component
v	$[m/s]$	radial velocity component
z	$[m]$	axial coordinate
Δs_d	[m]	wall thickness of the die
α_{out}	$[W/m^2K]$	heat transfer coefficient
δ	$[m]$	difference in gap height between die inlet and outlet
ε	[-]	expansion parameter for velocity
ε_T	[-]	expansion parameter for temperature
η	$[Pas]$	dynamic viscosity
λ	$[W/mK]$	thermal conductivity of the fluid
λ_d	$[W/mK]$	thermal conductivity of the die material
ρ	$[kg/m^3]$	density of the fluid

Subscripts and Superscripts

*	dimensionless quantity
0	zeroth-order solution
1	first-order solution
d	on the inner surface of the die
w	on the surface of the wire
∞	ambient medium

1. INTRODUCTION

The coating of technical surfaces for modifying their superficial properties represents an important step in many industrial applications. In the case of wire enamelling the main goal is to provide a most uniform continuous insulation along the wire surface to avoid any hazard of electrical shorts. The deposition of the fresh enamel is typically controlled by pulling the wire, which has been covered before with fresh enamel in a dip-coating step, through enamelling dies as sketched in Figure 1. The end section of the die characteristically features a converging annular gap. The gap height at the exit finally determines the thickness of the deposited layer. Various studies were carried out in literature on the generalized Couette flow inside the dies, which is characterized by the shear-driven motion caused by a moving wall (wire) and high axial pressure gradients due to the converging geometry. The computational studies among these works often put a particular focus on the effect of non-Newtonian flow behaviour, and they mostly assume the approximation of the lubrication theory. Flumerfelt et al. [1] presented such an analytical solution for planar gaps, while Lin and Hsu [2] analyzed the flow through concentric annuli, considering a power-law fluid. Later, Lin [3] included heat transfer into the computations. Dijksman and Savenije [4] presented an analytical solution of a converging annular gap flow introducing a special toroidal coordinate system. Shah et al. [5] carried out an extensive analytical computation of both flow and heat transfer of power-law fluids inside wire coating dies with constant cross-section.

The neglect of the inertia, i.e. advective transport terms, becomes increasingly questionable in the case of strongly converging cross-sections, which markedly limits the scope of the lubrication theory approximation, when applied to coating dies. Appropriate extensions to the lubrication theory have thus far been proposed only for other flow configurations associated with narrow gaps, like flow in planar journal bearings (Collins et al. [6]), or pressure-driven flow through narrow planar channels with axially varying channel height (Tavakol et al. [7]).

The present work attempts to include the effect of the advective transport in the momentum and heat transfer by perturbing the lubrication theory based solution with corresponding first-order corrections. The possible improvement of the predictions shall be assessed by a validation against CFD results, which are obtained from a numerical simulation of the full set of equations.

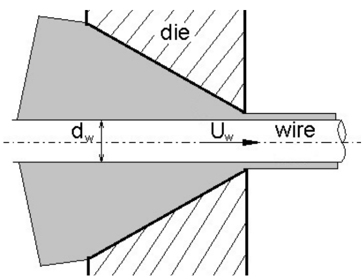

Figure 1. Wire enamelling die operation principle

2. MATHEMATICAL MODEL

The converging flow through the coating die is described in cylindrical coordinates, where the z-direction is aligned with the axis of the moving wire, as seen in Figure 2. The radial (cross-stream) direction r varies between the radius of the wire, $r=r_w$, and the contour of the die, $r=r_d(z)$. L denotes the axial length of the die. The flow is assumed as axisymmetric and steady. The fluid is assumed as Newtonian with constant dynamic viscosity η, thermal conductivity λ, specific heat capacity c_p, and constant density ρ.

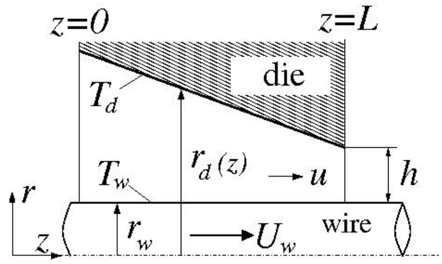

Figure 2. Converging flow domain

The governing equations for axial momentum, radial momentum, and energy read

$$\rho\left(u\frac{\partial u}{\partial z}+v\frac{\partial u}{\partial r}\right)=-\frac{\partial p}{\partial z}+\eta\left[\frac{1}{r}\frac{\partial}{\partial r}\left(r\frac{\partial u}{\partial r}\right)+\frac{\partial^2 u}{\partial z^2}\right] \quad (1)$$

$$\rho\left(u\frac{\partial v}{\partial z}+v\frac{\partial v}{\partial r}\right)=-\frac{\partial p}{\partial r}+\eta\left[\frac{\partial}{\partial r}\left(\frac{1}{r}\frac{\partial(rv)}{\partial r}\right)+\frac{\partial^2 v}{\partial z^2}\right] \quad (2)$$

$$\rho c_p\left(u\frac{\partial T}{\partial z}+v\frac{\partial T}{\partial r}\right)=\lambda\frac{1}{r}\frac{\partial}{\partial r}\left(r\frac{\partial T}{\partial r}\right)+$$
$$2\eta\left[\left(\frac{\partial u}{\partial z}\right)^2+\left(\frac{\partial v}{\partial r}\right)^2+\left(\frac{v}{r}\right)^2\right]+\eta\left(\frac{\partial u}{\partial r}+\frac{\partial v}{\partial z}\right)^2 \quad (3)$$

The conservation of mass is enforced by imposing a constant volumetric flow rate

$$Q=\int_{r_w}^{r_d}2\pi r u\,dr=const. \quad (4)$$

at each cross-section of the die. No-slip conditions are prescribed at the upper and lower radial boundaries:

$$r=r_w:\quad u=U_w,\ v=0, \quad (5)$$
$$r=r_d:\quad u=0,\ v=0. \quad (6)$$

Constant wall temperature and a convective heat loss condition are assumed as thermal boundary conditions, which are written as

$$r = r_w: \quad T = T_w \tag{7}$$

$$r = r_d: \quad \lambda \frac{\partial T}{\partial r} = -k\left(T_d - T_\infty\right) \tag{8}$$

The heat transmission coefficient k connects the conductive heat transfer between the upper wall of the die associated with the wall temperature T_d and the convective heat transfer from the outer surface of the die into the ambience associated with T_∞. It is accordingly defined as the inverse of the sum of the corresponding conductive and convective heat resistances

$$\frac{1}{k} = \frac{\Delta s_d}{\lambda_d} + \frac{1}{\alpha_{out}}, \tag{9}$$

where Δs_d and λ_d are the thickness and the thermal conductivity of the outer wall of the die, respectively, and α_{out} is the heat transfer coefficient for the heat transfer between the surface of the die and the ambient air. Constant ambient pressure is imposed as the axial boundary condition for the pressure:

$$z = 0,\ z = L: \quad p = p_\infty. \tag{10}$$

2.1. Zeroth- and first-order solutions

The lubrication theory approximation and its first-order extension essentially follow from an order-of-magnitude analysis of the non-dimensionalized balances of momentum and heat, where all variables are non-dimensionalized using adequate reference scales to become

$$z^* = \frac{z}{L},\ r^* = \frac{r}{h}$$

$$u^* = \frac{u}{U_w}, \quad v^* = \frac{vL}{hU_w}, \quad p^* = \frac{ph^2}{\mu_0 U_w L},$$

$$T^* = \frac{T}{T_w}, \quad Q^* = \frac{Q}{2\pi h^2 U_w}.$$

Introducing these quantities, the non-dimensional representations of (1)-(4) read

$$\varepsilon\left(u^* \frac{\partial u^*}{\partial z^*} + v^* \frac{\partial u^*}{\partial r^*}\right) = -\frac{\partial p^*}{\partial z^*} + \frac{1}{r^*}\frac{\partial}{\partial r^*}\left(r^* \frac{\partial u^*}{\partial r^*}\right) + \left(\frac{h}{L}\right)^2 \frac{\partial^2 u^*}{\partial z^{*2}} \tag{11}$$

$$\varepsilon\left(\frac{h}{L}\right)^2\left(u^* \frac{\partial v^*}{\partial z^*} + v^* \frac{\partial v^*}{\partial r^*}\right) = -\frac{\partial p^*}{\partial r^*} + \left(\frac{h}{L}\right)^2 \frac{\partial}{\partial r^*}\left(\frac{\partial v^*}{\partial r^*} + \frac{v^*}{r^*}\right) + \left(\frac{h}{L}\right)^4 \frac{\partial^2 u^*}{\partial z^{*2}} \tag{12}$$

$$\varepsilon \Pr\left(u^* \frac{\partial T^*}{\partial z^*} + v^* \frac{\partial T^*}{\partial r^*}\right) = \frac{1}{r^*}\frac{\partial}{\partial r^*}\left(r^* \frac{\partial T^*}{\partial r^*}\right) + 2\Pr \mathrm{Ec}\left(\frac{h}{L}\right)^2\left[\left(\frac{\partial u^*}{\partial z^*}\right)^2 + \left(\frac{\partial v^*}{\partial r^*}\right)^2 + \left(\frac{v^*}{r^*}\right)^2\right] + \Pr \mathrm{Ec}\left[\frac{\partial u^*}{\partial r^*} + \frac{\partial v^*}{\partial z^*}\left(\frac{h}{L}\right)^2\right]^2 \tag{13}$$

$$Q^* = \int_{r_w^*}^{r_d^*} r^* u^* dr^* = const. \tag{14}$$

After this rescaling, the relative magnitude of the individual non-dimensional terms is determined by the multipliers in front of them. The non-dimensional parameter occurring as a prefactor of the advective transport terms on the lhs represents the so called reduced Reynolds number

$$\varepsilon = \mathrm{Re}_L\left(\frac{h}{L}\right)^2 = \frac{\rho U_w L}{\eta}\left(\frac{h}{L}\right)^2. \tag{15}$$

Due to the very small aspect ratio $h/L<<1$ and the fact that the Reynolds number based on the axial length of the die in general strongly exceeds unity (typical values are in the range $\mathrm{Re}_L \approx O(10^3)$, the definition (15) implies

$$\left(\frac{h}{L}\right)^2 << \varepsilon \tag{16}$$

The advective and viscous dissipation terms in the energy equation (13) involve the Prandtl and the Eckert numbers,

$$\Pr = \frac{c_p \eta}{\lambda},\ \mathrm{Ec} = \frac{U_w^2}{c_p T_w},$$

as prefactors, respectively. Analogous to the definition (15) one may define the parameter

$$\varepsilon_T = \varepsilon \Pr = \Pr \mathrm{Re}_L\left(\frac{h}{L}\right)^2. \tag{17}$$

Since $\mathrm{Ec} << \mathrm{Re}_L$, it follows

$$\mathrm{Ec}\Pr\left(\frac{h}{L}\right)^2 \ll \varepsilon_T. \tag{18}$$

The relations (16) and (18) make evident that all the terms in the balances (11)-(13), which are multiplied by $(h/L)^2$, are smaller than order $O(\varepsilon)$, or $O(\varepsilon_T)$.
Introducing the series expansions

$$u^* = u_0^* + \varepsilon u_1^* + \varepsilon^2 u_2^* + \ldots, \tag{19}$$

$$T^* = T_0^* + \varepsilon_T T_1^* + \varepsilon_T{}^2 T_2^* \ldots \tag{20}$$

into the non-dimensionalized equations (11)-(14), and equating the all terms of same order up to the first order, O(ε), or O(ε_T), leads to the following two sets of equations:

zeroth-order ε^0, $\varepsilon_T{}^0$

$$\frac{1}{r^*}\frac{\partial}{\partial r^*}\left(r^*\frac{\partial u_0{}^*}{\partial r^*}\right) = \frac{\partial p_0{}^*}{\partial z^*} \tag{21}$$

$$\frac{\partial p_0{}^*}{\partial r^*} = 0 \tag{22}$$

$$Q_o^* = \int_{r_w^*}^{r_d^*} r^* u_0{}^* dr^* = const. \tag{23}$$

$$-\frac{1}{r^*}\frac{\partial}{\partial r^*}\left(r^*\frac{\partial T_0{}^*}{\partial r^*}\right) = \Pr \mathrm{Ec}\left(\frac{\partial u_0{}^*}{\partial r^*}\right)^2 \tag{24}$$

first-order ε^1, $\varepsilon_T{}^1$

$$\left(u_0{}^*\frac{\partial u_0{}^*}{\partial z^*} + v_0{}^*\frac{\partial u_0{}^*}{\partial r^*}\right) = -\frac{\partial p_1{}^*}{\partial z^*} + \frac{1}{r^*}\frac{\partial}{\partial r^*}\left(r^*\frac{\partial u_1{}^*}{\partial r^*}\right) \tag{25}$$

$$\frac{\partial p_1{}^*}{\partial r^*} = 0 \tag{26}$$

$$Q_1^* = \int_{r_w^*}^{r_d^*} r^* u_1{}^* dr^* = const. \tag{27}$$

$$\frac{1}{r^*}\frac{\partial}{\partial r^*}\left(r^*\frac{\partial T_1^*}{\partial r^*}\right) = -\mathrm{Ec}\left(2\frac{\partial u_0{}^*}{\partial r^*}\frac{\partial u_1{}^*}{\partial r^*}\right) + u_0{}^*\frac{\partial T_0{}^*}{\partial z^*} + v_0{}^*\frac{\partial T_0{}^*}{\partial r^*} \tag{28}$$

The boundary conditions for the zeroth- and first-orders read

$$r^* = r_w^*: \quad \begin{aligned} & u_0^* = 1,\ T_0^* = 1 \\ & u_1^* = 0,\ T_1^* = 0 \end{aligned} \tag{29}$$

$$r^* = r_d^*: \quad \begin{aligned} & u_0^* = 0,\ \frac{\partial T_0^*}{\partial r^*} = -\mathrm{Nu}\left(T_{d,0}^* - T_\infty^*\right) \\ & u_1^* = 0,\ \frac{\partial T_1^*}{\partial r^*} = -\mathrm{Nu}T_{d,1}^* \end{aligned} \tag{30}$$

$$z^* = 0,\ z^* = 1: \quad \begin{aligned} & p_0{}^* = 0 \\ & p_1^* = 0 \end{aligned} \tag{31}$$

respectively, where $Nu = kh/\lambda$ denotes a Nusselt number based on the heat transmission coefficient defined in (9).
The zeroth-order formulation evidently represents the lubrication theory approximation, where all advective transport terms, being of order O(ε), or O(ε_T), are neglected.
The radial integration of Eqs. (21) and (25) yields the zeroth-order and first-order solution for the axial velocity component, written as

$$u_0^* = \frac{\ln\frac{r_d^*}{r^*}}{\ln\frac{r_d^*}{r_w^*}} + \frac{\frac{1}{4}\frac{dp_0{}^*}{dz^*}\left(r^{*2}\ln\frac{r_d^*}{r_w^*} + r_d{}^{*2}\ln\frac{r_w^*}{r^*} + r_w{}^{*2}\ln\frac{r^*}{r_d^*}\right)}{\ln\frac{r_d^*}{r_w^*}}, \tag{32}$$

$$u_1^* = A\left(z^*, r^*\right) - A\left(z^*, r_d^*\right)\frac{\ln\left(r^*/r_w^*\right)}{\ln\left(r_d^*/r_w^*\right)} - \frac{1}{4}\frac{dp_1^*}{dz^*}\left[\left(r_d^{*2} - r_w^{*2}\right)\frac{\ln\left(r^*/r_w^*\right)}{\ln\left(r_d^*/r_w^*\right)} - \left(r^{*2} - r_w^{*2}\right)\right], \tag{33}$$

respectively, with

$$A\left(z^*, r^*\right) = \int_{r_w^*}^{r^*}\frac{1}{r^*}\int_{r_w^*}^{r^*} 2u_0^* r\frac{\partial u_0^*}{\partial z^*}dr^* + \int_{r_w^*}^{r^*} v_0^* u_0^* dr^*. \tag{34}$$

The radial zeroth-order velocity component occurring in Eq. (34) is computed from the continuity equation as

$$v_0^* = -\frac{1}{r^*}\int_{r_w^*}^{r^*}\frac{\partial u_0^*}{\partial z^*}r^* dr^*. \tag{35}$$

The axial variation of the zeroth- and first-order pressure is obtained by substituting the expressions (32) and (33) into the integral mass balances (23) and (27), respectively, and integrating them in the axial direction from z^*=0 to z^*=1.
The radial integration of Eqs. (24) and (28) yields the zeroth- and first-order solution for the temperature written as

$$T_0^* = 1 - \int_{r_w^*}^{r^*}\frac{C\left(z^*, r^*\right)}{r^*}dr^* + \frac{\ln\frac{r^*}{r_w^*}}{G}\left[\mathrm{Nu}\, r_d^*\left(\int_{r_w^*}^{r_d^*}\frac{C\left(z^*, r^*\right)}{r^*}dr^* - 1 + T_{\inf}^*\right) + C\left(z^*, r_d^*\right)\right] \tag{36}$$

and

$$T_1^* = -2\,\mathrm{Ec}\int_{r_w^*}^{r^*} \frac{D\left(z^*,r^*\right)}{r^*}dr^* + \int_{r_w^*}^{r^*} \frac{E\left(z^*,r^*\right)}{r^*}dr^* +$$

$$\frac{\ln\frac{r^*}{r_w^*}}{G}\left(2\,\mathrm{Ec}\,D\left(z^*,r_d^*\right) - E\left(z^*,r_d^*\right)\right) + \tag{37}$$

$$\frac{\mathrm{Nu}\, r_d^* \ln\frac{r^*}{r_w^*}}{G}\left(2\,\mathrm{Ec}\int_{r_w^*}^{r_d^*} \frac{D\left(z^*,r^*\right)}{r^*}dr^* - \int_{r_w^*}^{r_d^*} \frac{E\left(z^*,r^*\right)}{r^*}dr^*\right)$$

respectively, with

$$G = 1 + \mathrm{Nu}\, r_d^* \ln\frac{r_d^*}{r_w^*} \tag{38}$$

$$C\left(z^*,r^*\right) = \int_{r_w^*}^{r^*} r^*\,\mathrm{Pr}\,\mathrm{Ec}\left(\frac{\partial u_0^*}{\partial r^*}\right)^2 dr^*,$$

$$D\left(z^*,r^*\right) = \int_{r_w^*}^{r^*} r^*\left(\frac{\partial u_0^*}{\partial r^*}\frac{\partial u_1^*}{\partial r^*}\right)dr^*, \tag{39}$$

$$E\left(z^*,r^*\right) = \int_{r_w^*}^{r^*} r^* u_0^* \frac{\partial T_0^*}{\partial z^*}dr^* + \int_{r_w^*}^{r^*} r^* v_0^* \frac{\partial T_0^*}{\partial r^*}dr^*.$$

3. NUMERICAL MODEL

Since there are practically no experimental data available on the flow field inside enamelling dies, CFD simulations were carried out as well in order to validate the solutions obtained under the assumptions of the lubrication theory (zeroth-order solution), and to assess the improvement brought about by the inclusion of the advective terms in the first-order extension. The CFD simulations used ANSYS-Fluent 14.2 as the flow solver. Figure 3 shows the computational domain used for the simulations, indicating the individual boundaries. The flow was assumed as steady and axisymmetric. Analogous to the analytical model, the same no-slip dynamic boundary conditions, constant wall temperature and heat flux conditions were imposed at the lower and the upper radial boundaries, as specified in (5)-(8). As can be seen from Figure 3, the computational domain is somewhat extended upstream of z=0 by a short cylindrical section. The attachment of this short cylinder of 10% length of the die allows for some axial development of the Couette-type flow in order to provide flow conditions at z=0, which are well comparable with the inlet conditions of the computations with the analytical model. Uniform ambient pressure $p=p_\infty$ and reference temperature $T=T_w$ were prescribed at the inlet and the outlet of the computational domain, respectively. Even though the temperature is not constant at the exit, imposing a constant value boundary condition does not have any effect on the temperature inside the domain, due to the fact that the flow at the die exit is only directed outwards.

The total size of the computational mesh was roughly 40000 cells in the case used for the present comparison.

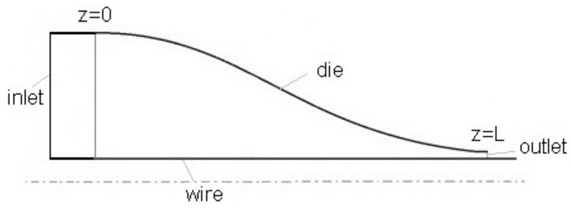

Figure 3. Computational domain and boundaries of the CFD model

4. COMPUTATIONAL RESULTS

The operating conditions considered in the present computations were specified close to real enamelling conditions of thin copper wires. Accordingly, the diameter of the wire was set to $d_w= 2r_w$ =0.15 mm, and the velocity of the wire was set to a value of U_w=22.27 m/s. The length of the die is L=25 mm, and the gap height at the exit is h=5 μm. The difference in gap height between the die inlet and exit was assumed δ=2.4 mm. The material properties of the enamel were assumed as η=0.25 Pas, λ=0.5 W/mK, and c_p =10 J/kgK. The physical parameter setting translates into the Reynolds, Prandtl, and Eckert numbers $\mathrm{Re_L}$=2230, Pr=5, and Ec=0.14.The Nusselt number required by the radially upper thermal boundary condition is set to Nu=1x10^{-4}. Based on their definitions (15) and (17) the expansion parameters used in the first-order contributions in the series expansions (18) and (19) are ε = 8.91x10^{-5} and ε_T = 4.45x10^{-4}, respectively.

The shape of the die was prescribed by assuming the axial contraction as a cosine-type variation of the upper contour written as

$$r_d^* = \frac{r_d}{h} = \frac{r_w}{h} + 1 + \frac{\delta}{2h}\left[1 + \cos\left(\pi\left(\frac{z}{L}\right)^{n_{geo}}\right)\right]. \tag{40}$$

As exemplarily shown in Figure 4, the variation of the geometrical parameter n_{geo} enables to cover a large variety of geometries ranging from completely convex for low values of the parameter n_{geo}, to almost step-like concave geometries for the high values. The functional dependency (40) provides by definition a zero gradient at the exit, which follows from a specific requirement of the real enamelling process. In the following the computational results obtained for the flow and temperature fields are exemplarily discussed for the geometrical parameter n_{geo} set to the value of 2.5, which produces a well representative contour of real die geometries in the application.

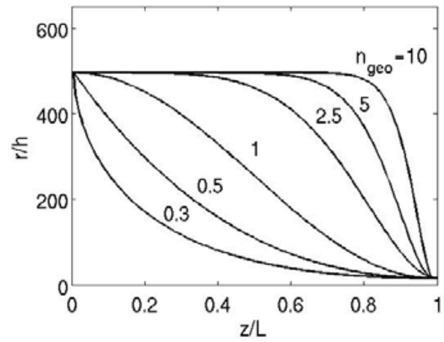

Figure 4. Die contours for different values of the exponent n_{geo}

4.1. Flow field

The contour plot in Figure 5 showing the isotachs of the axial velocity component obtained from the extended lubrication theory solution (zeroth- + first-order solutions) gives a qualitative insight into the typical structure of the converging Couette-type flow. The flow field essentially falls into two sub-regions. In the lower sub-region in the proximity of the wire, the axial velocity has the same direction as the motion of the wire, which indicates the viscous entrainment of the liquid by the wire. The radially upper sub-region exhibits a negative axial velocity. In this region the excess amount of the entrained enamel, which does not leave the die at the exit, is transported backwards and finally ejected outwards at the inlet cross section of the die. Since this reverse flow is essentially dictated by continuity, it is predicted already by the zeroth-order solution. The inclusion of the advective transport in the first-order extension still yields a notable quantitative improvement of the predictions. This is illustrated in Figure 6 showing radial profiles of the axial velocity at four selected cross-sections, located at *z/L*=0.6, *z/L*=0.75, *z/L*=0.85 and *z/L*=0.95, respectively. The neglect of the advective terms in the momentum equation produces evidently a notable deviation from the CFD solution at the cross sections, where the reduction in gap height is very strong, so that the acceleration of the fluid is not negligible any more. As it is also indicated by the steep slope of the radial outer boundary r_d/h in Figure 5, this appears to be particularly the case at the positions *z/L*=0.75 and 0.85. In contrast, at the positions *z/L*=0.6 and *z/L*=0.95, associated with a slower decrease in gap height, the solutions almost collapse.

The observed improvements for the velocity profiles are also reflected in the axial variation of the pressure displayed in Figure 7. The first-order correction brings the analytical solution very close to the CFD results in the region downstream of *z/L*=0.6, where the contour of the die converges fastest.

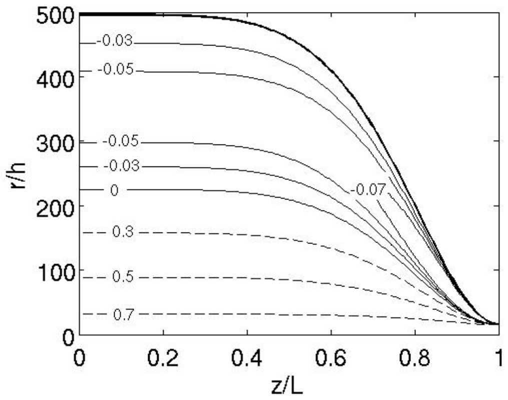

Figure 5. Axial velocity isotachs inside the domain for n_{geo}=2.5, extended lubrication theory

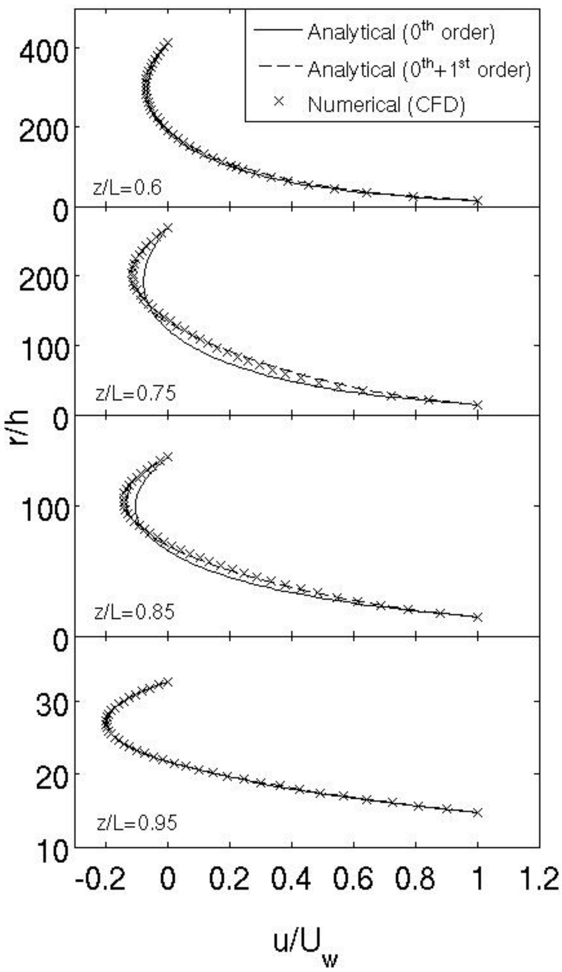

Figure 6. Velocity profiles at selected cross sections

4.2. Heat transfer

Figure 8 shows the radial temperature profiles at the same axial positions considered in the discussion of

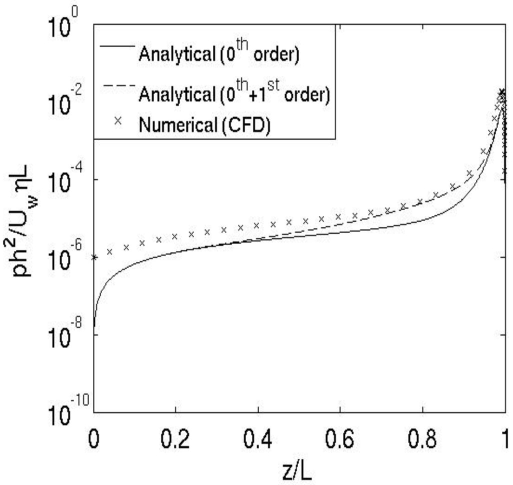

Figure 7. Axial pressure profile

the velocity field above. The neglect of the advective transport in the lubrication theory (zeroth-order solution) leads obviously to markedly stronger deviations from the CFD results than those observed for the axial velocity. Furthermore, including the advective transport in terms of the first-order solution leads to significantly improved predictions, most notably at the positions *z/L*=0.6, 0.75 and 0.85. The gain in accuracy provided by the first-order extension appears to be more pronounced for the transport of heat than for the transport of momentum, which points at a relatively higher relevance of the advective transport in the balance of heat. This may be attributed to the fact that the balance of heat is significantly determined by a strong local source term due to viscous dissipation, which has no counterpart in the momentum balance. Figure 9 shows the spatial variation of the leading-order viscous dissipation in logarithmic scale downstream of *z/L*=0.5. As expected, the viscous heat is mainly generated in the highly sheared region near the moving wire with an increasing tendency towards the exit resulting from the converging geometry of the die. In the zeroth-order solution, the viscous heat can only be transferred by conduction into the radial direction, which leads to higher radial temperature gradients and in consequence markedly higher bulk temperatures as seen in Figure 8. Including the advective transport the first-order extension provides for a further mechanism to transfer the generated viscous heat. Figure 10 shows the radial variations of the advective transport terms, which are included in the first-order solution following equation (28), at the selected cross-section already discussed above. The peaks in the radially inner region near the moving wire clearly indicate a notable advective transport of heat into the horizontal and vertical directions, associated with $u_0^*\left(\partial T_0^*/\partial z^*\right)$, and $v_0^*\left(\partial T_0^*/\partial r^*\right)$, respectively. Based on this transfer mechanism a substantial part of the generated viscous heat is convected downstream, leaving the domain at the exit. In consequence, the temperature radially increases to lower levels as seen in Figure 8 as compared to the zeroth-order solution, which excludes any convective heat transfer and the finally resulting convective heat loss across the exit.

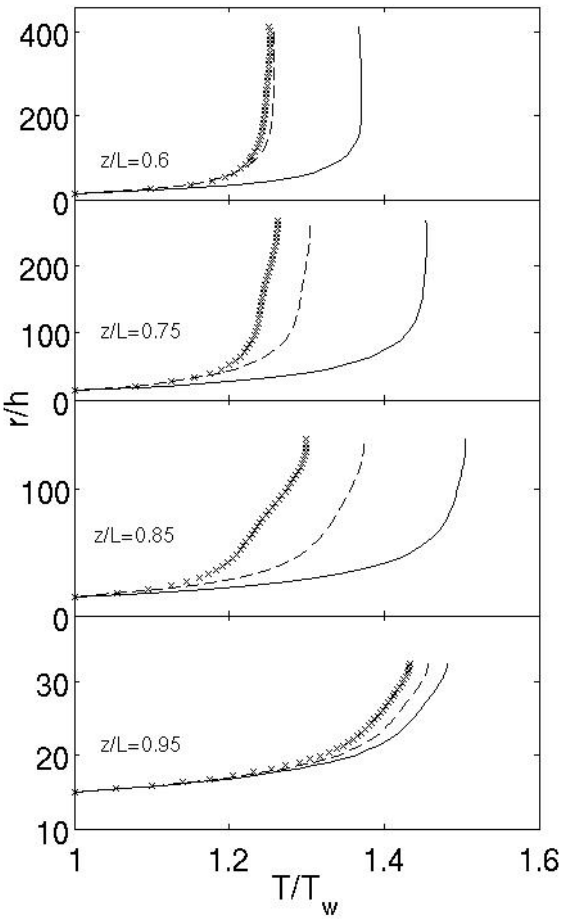

Figure 8. Temperature profiles at selected cross sections (legend from Figure 6.)

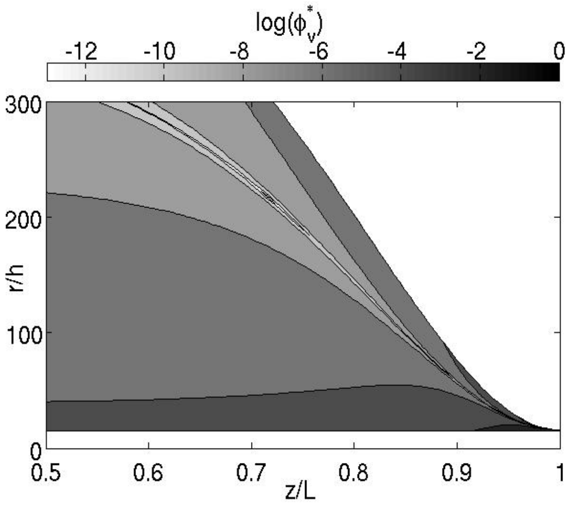

Figure 9. Contours of the leading-order viscous dissipation term $\phi_v^* = \mathrm{Pr}\,\mathrm{Ec}\left(\partial u_0^*/\partial r^*\right)^2$ plotted in logarithmic scale

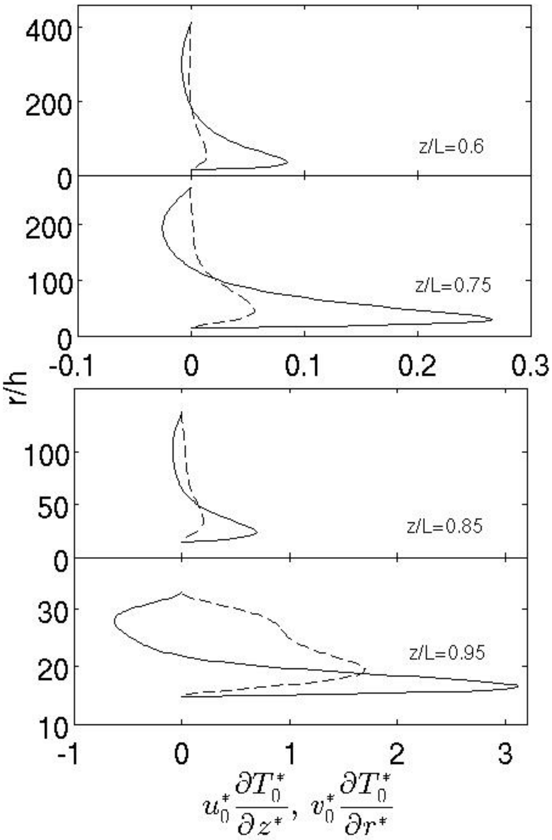

Figure 10. Advective transport terms in the horizontal direction, $u_0^*\left(\partial T_0^*/\partial z^*\right)$ (solid line), and vertical direction, $v_0^*\left(\partial T_0^*/\partial r^*\right)$ (dashed line), at selected cross-sections

5. SUMMARY

The shear dominated flow evolving inside wire enamelling dies is computationally investigated in the framework of the lubrication theory approximation. The viscous generation and transfer of heat are considered as well. The limited scope of the lubrication theory due to the total neglect of the advective transports, especially when applied to strongly converging gap geometries, as typically met in enamelling dies, is extended by including the effect of inertia and convective heat transfer in terms of an appropriate linear first-order perturbation. The predictive capability of the proposed extended analytical approach is assessed in a test case associated with representative operating conditions and die geometry. The comparison of the predictions against CFD results from a numerical simulation of the full set of equations clearly demonstrate the limits of the classical lubrication theory as well as the possible gain in accuracy provided by the proposed first-order extension. The predictions for the radial profiles of the axial velocity and temperature are significantly improved, especially in the region with a fast axial reduction in gap height. The observed improvements provided by the first-order perturbation to account for the advective transport appear to be more pronounced in the transfer of heat than in the transfer of momentum. It is concluded that a reliable description of the redistribution of the generated viscous heat does not allow for a total neglect of the advective transport mechanism. On the other hand, the momentum balance, where no equivalent counterpart for such source term appears, turns out to be less sensitive to this neglect.

Including the proposed first-order perturbation makes the lubrication theory applicable to an extended range of gap geometries, which also suggests this concept as a reliable and computationally efficient tool for the development of novel flow optimized die designs.

ACKNOWLEDGEMENTS

The authors gratefully acknowledge the financial support from the Austrian Research Promotion Agency FFG and the industrial partner MAG Maschinen und Apparatebau AG.

REFERENCES

[1] R. W. Flumerfelt, M.W. Pierick, S. L. Cooper, R. B. Bird, 1969. Generalized plane Couette flow of a non-Newtonian fluid, Ind. Eng. Chem. Fundam. 8(2), 354-357

[2] S. H. Lin, C. C. Hsu, 1980. Generalized Couette flow of a non-Newtonian fluid in annuli, Ind. Eng. Chem. Fundam. , 421-424

[3] S. H. Lin, 1992. Heat transfer to generalized Couette flow on non-Newtonian fluid in annuli with moving outer cylinder, Int. J. Heat Mass Transfer, Vol. 35, 3069-3075

[4] J.F. Dijksman, E. P. W. Savenije, 1985. The flow of Newtonian and non-Newtonian liquids through annular converging regions, Rheologica Acta 24, 105-118

[5] R. A. Shah, S. Islam, A. M. Siddiqui, T. Haroon, 2013. Exact Solutions of a Power Law Fluid Model in Post treatment Analysis of Wire Coating with Linearly Varying Boundary Temperature, Applied Mathematics, Vol. 4, 330-337

[6] D. Collins, M.D. Savage, C.M. Taylor, 1986. The influence of fluid inertia on the stability of a plain journal bearing incorporating a complete oil film, Journal of Fluid Mechanics, vol. 168, 415-430

[7] B. Tavakol, D. P. Holmes, G. Froehlicher, H. A. Stone, 2014. Extended Lubrication Theory: Estimation of Fluid Flow in Channels with Variable Geometry, arXiv: 1403.2343v1 [physics.flu-dyn]

Conference on Modelling Fluid Flow (CMFF'15)
The 16th International Conference on Fluid Flow Technologies
Budapest, Hungary, September 1-4, 2015

NUMERICAL EXPERIMENTS ON THE MUTUAL INTERFERENCE VORTEX FLOW FROM THE PARALLEL ARRANGEMENT TWO CIRCULAR CYLINDERS AT DIFFERENT LOCK-IN MODE

Yoshifumi YOKOI[1,2]

[1] Corresponding Author. Department of Mechanical Engineering, National Defense Academy of Japan. 1-10-20 Hashirimizu, Yokosuka-City, Kanagawa, Japan. Tel.: +81 46 841 3810, Fax: +81 46 844 5900, E-mail: yokoi@nda.ac.jp
[2] Chair of Fluid Dynamics, Hermann-Höttinger-Institut, Techniche Universität Berlin,

ABSTRACT

In this research, the flow characteristic from two circular cylinders which are oscillating by the different mode of vibration was investigated by numerical simulation at the Reynolds number Re = 500, with varied the distance ratio L/d and the amplitude ratio $2a/d$. As a result of the numerical experiments, the flow aspect and change of fluid force which become complicated were shown. In the A-mode oscillation cylinder and the S-mode oscillation cylinder, it was found that the A-mode oscillation cylinder tends to receive mutual interference. In the case of such a complex state, it became clear to completely differ from the result obtained when the aspect and fluid force of the flow are single.

Keywords: circular cylinder, in-line oscillation, lock-in, numerical experiment, separation, vortex

NOMENCLATURE

A	$[m]$	half-amplitude
C_D	[-]	drag coefficient
C_L	[-]	lift coefficient
L	$[m]$	distance between cylinder centres
L/d	[-]	distance ratio
Re	[-]	Reynolds number (= Ud/ν)
St	[-]	Strouhal number (= fd/U)
T	[-]	non-dimensional time
U	$[m/s]$	main flow velocity
a	$[m]$	half-amplitude of oscillation
d	$[m]$	diameter of circular cylinder
f	$[Hz]$	cylinder oscillating frequency
f_K	$[Hz]$	natural Karman vortex frequency
f/f_K	[-]	oscillation frequency ratio
u	$[m/s]$	local moving velocity
u_{max}/U	[-]	velocity ratio
$2a/d$	[-]	oscillation amplitude ratio
ν	$[m^2/s]$	kinematic viscosity of water
π	[-]	pi

Subscripts and Superscripts

AVE	mean value
max	maximum value
RMS	root mean square

1. INTRODUCTION

If a circular cylinder is placed into a steady flow without a time change, vorttices will be discharged alternately. And a Karman vortex street is formed behind the circular cylinder. The Karman vortex is a very stable vortex street, and the vortex corresponding to the flow velocity is formed. That can also be said to be a natural synchronous phenomenon. Many of flows which exist really are what is called unsteady flow to which speed is changed in time. When unsteady, it is thinkable that the characteristics of the phenomenon differ compared with the case of being steady. It is industrially important to grasp the fluid force characteristic and the vortex shedding characteristic of the object put on the unsteady flow field. However, in order to realize an unsteady flow with sufficient accuracy, serious troubles are required in a laboratory. In order to experiment simple, in the laboratory, the object which exercises in the direction of a flow was installed into the steady flow, so the relative unsteady flow is made. If the circular cylinder which is oscillating in a flow is placed, the vortex shedding which synchronized with circular cylinder oscillating frequency will be observed. This phenomenon was called "lock in phenomenon" and, as for this "interference of the flow velocity change", research has been done by many researchers [1-4]. The flow pattern in the lock in state is divided roughly into the "alternate vortex shedding type" and the "simultaneous vortex shedding type". On the other hand, when a structure is in a flow independently, it is rare, and it consists of two or more objects in many cases. Therefore, it is also important to investigate "interference by arrangement". From this, as fundamental research, research on interference of two circular cylinders is done, and the result is also accumulated [5-9].

In recent years, by an author's research consortium, research which combined "interference of the flow velocity change" and "interference by arrangement" is done, and "interference by arrangement" has reported obtaining the result which changes with influences of "interference of the flow velocity change" [10-12]. However, there are many strange portions. Not all the structural rigidity of a structure is the same and differing separately is common. That is, even if it is in the same cross-sectional form, structural rigidity differs, and character frequency also differs. Even if this is placed under the same flow velocity, it can consider causing the lock in where each differs. It is one of the most interesting things in related research. The purpose of this research is to investigate the mutual interference flow characteristic from the circular cylinder in mutually different lock in mode. Research was carried out by numerical simulation.

2. NUMERICAL CALCULATION

2.1. Calculation Apparatus and Method

The numerical experiment apparatus was consisted of simulation software and a notebook type computer (NEC; LaVie LC958/T) as calculation hardware which are on the market. The software which named 'UzuCrise 2D ver.1.1.3 rev.H (College Master Hands Inc., 2006)' is used. This software used the vortex method which is based on the Lagrangian analysis. Since the vortex method is the grid-less method, it is suitable for the unsteady problem of such moving boundary. The vortex method is a direct viscid-inviscid interaction scheme, and the emanation of velocity shear layers due to boundary layer separation is represented by introduction of discrete vortices with viscous core step by step of time. In the present study, the flow was assumed incompressible and two-dimensional flow field. The configuration of circular cylinder was represented 40 vortex panels using a boundary element method. The separating shear layers were represented the discreet vortices, which were introduced at the separation points. The details of calculation technique of vortex method and accuracy of calculation are shown in Kamemoto [13, 14].

2.2. Calculation Conditions, Parameters and Procedure

In the present study, the calculations were performed at the two-dimensional flow field for incompressible and viscous flow. A cylinder diameter d and main flow velocity U were determined as 16 mm and 0.04 m/s so that it could compare with the previous experimental result [10]. Since water is assumed as for test fluid, Reynolds number Re becomes 500. The configuration of circular cylinder was represented 40 vortex panels using a boundary element method. Every calculation continued to until non-dimensional time $T = 200$.

The main parameters of numerical experiment were the existence of oscillation, the oscillation frequency ratio f/f_K, the oscillation amplitude ratio $2a/d$ and the distance ratio L/d. Existence of the oscillation is 2 kinds and they are in the states of cylinder stationary and cylinder oscillation. The oscillating frequency ratio f/f_K is 2 kinds and they are in two typical lock-in states of the single oscillating circular cylinder obtained from the previous experimental result. As for the oscillating frequency ratio, $f/f_K = 1.4$ and $f/f_K = 2.4$ were used. Here the natural Karman vortex shedding frequency was $f_K = 0.6489$ Hz. The oscillation amplitude ratio $2a/d$ is 4 kinds, and they are 0.25, 0.50, 0.75 and 1.00, respectively. The distance ratio L/d is 3 kinds and they are 1.5, 2.5 and 5.5.

The calculation experiment was performed in the following procedures. In the state where it is not oscillating, calculation of a single circular cylinder and parallel two circular cylinders was performed. In the case of single cylinder, the calculation to which the oscillation frequency ratio and the amplitude ratio were varied was performed several times. In the case of parallel two circular cylinders, the calculation to which the oscillation frequency ratio, the amplitude ratio, and the distance ratio were varied was performed several times. Two circular cylinders were individually given a longitudinal sinusoidal oscillation. The arrangement of circular cylinders is shown in Figure 1. Here, in

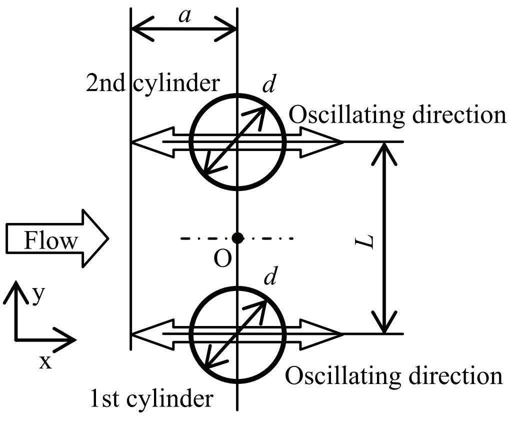

Figure 1. Coordinate system and definition of symbols (O: the coordinate origin)

the case of two circular cylinders, the circular cylinder located in left-hand side toward the flow was called the 1st cylinder, and the circular cylinder located in right-hand side toward the flow was called the 2nd cylinder. The oscillation of f/f_K = 1.4 was given to the 1st cylinder and the oscillation of f/f_K = 2.4 was given to the 2nd cylinder.

3. RESULTS AND DISCUSSIONS

This numerical simulation study was conducted through the following steps. In order to check a numerical computation situation, calculation was performed about the case of a single stationary circular cylinder as the beginning. Next, the state of lock in was checked on oscillating conditions. In order to investigate the influence of a circular cylinder installation interval, the interval of stationary two circular cylinders was varied and calculations were performed. And in the case of parallel two circular cylinders, each circular cylinder was oscillated in different lock-in mode, the distance ratio was varied, and the situation of flow and the fluid force were investigated. The acquired matters are described in the following items.

3.1. In the Case of Single Cylinder

3.1.1. Stationary Case

In order to verify the calculation software to be used, the experimental result and calculation result of a stationary circular cylinder were compared. The time history of the fluid force (a drag component and lift component) of acting on a stationary circular cylinder is shown in Figure 2. The drag oscillation lurking in periodic oscillation and lift oscillation of the lift produced by formation of a Karman vortex street is expressed. The relationship whose oscillation frequency of the drag is twice the oscillation frequency of the lift is shown. The following results were obtained after non-dimension time T = 150. Here, the diagram which defines the quantity about the fluid force is shown in Figure 3. The average value of drag coefficient was C_{DAVE} = 1.08 and the root mean square value of amplitude of drag coefficient was A_{CD} = 0.15. The average value of lift coefficient was C_{LAVE} = 0.00 and the route mean square value of amplitude of lift coefficient was A_{CL} = 0.73. The average Strouhal number for which it determined from the lift oscillating period T was St_{AVE} = 0.26. The Strouhal number is defined by $St = fd/U = d/\Delta tU = 1/T$. When the Reynolds number is Re = 500, it is known that the experimental value of Strouhal number St is about 0.2. Although it seems that this calculation result is highly calculated as compared with an experimental result, it seems that this calculation has obtained the comparatively good calculation result since a two dimensional calculation result

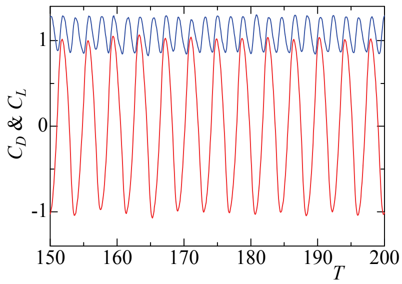

Figure 2. Time histories of drag and lift coefficients, (blue and red lines show drag and lift coefficients, respectievly)

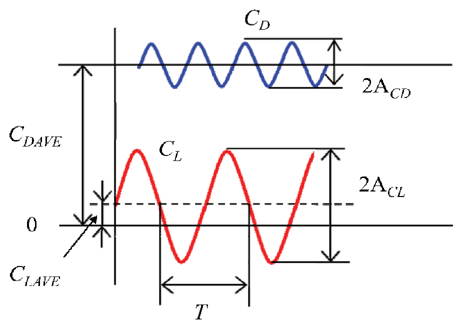

Figure 3. The definition of the magnitude of the drag coefficient or the lift coefficient, and the definition of the oscillating period

becomes higher than an experimental result about 30 to 40%. When the Karman vortex shedding frequency f_K was calculated from the average value of Strouhal number, the Karman vortex shedding frequency was f_K = 0.65 Hz.

3.1.2. Oscillating Case

When forced oscillation of the circular cylinder is carried out, it is one of the most interesting things of this study to investigate how fluid force changes.

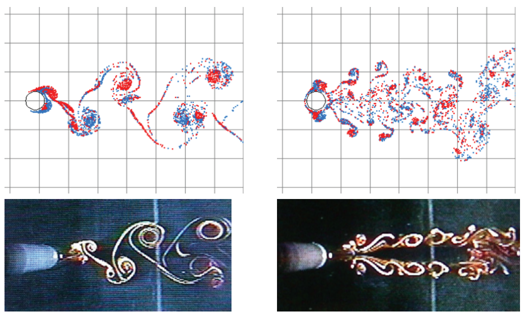

(a) (b)

Figure 4. Two kinds of lock-in flow patterns, (a) shows an alternate vortex shedding type flow pattern (A-mode lock-in), and (b) shows the simultaneous vortex shedding type flow pattern (S-mode lock-in), respectively.

Table 1. The flow pattern of the single oscillating circular cylinder in each oscillating conditions

$2a/d$	f/f_K=1.4 A-mode oscillation	f/f_K=2.4 S-mode oscillation
0.25	A type lock-in	S type lock-in (asymmetry)
0.50	A type lock-in	S type lock-in (symmetry)
0.75	S type lock-in (symmetry)	S type lock-in (asymmetry, mushroom)
1.00	S type lock-in (symmetry, mushroom)	With no vortex formation

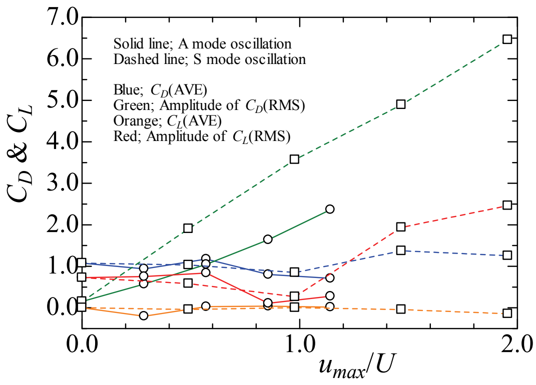

Figure 6. The variation of fluid force component act on single oscillating cylinder, $u_{max}/U = 2a/d \cdot f/f_K \cdot (\pi St)$

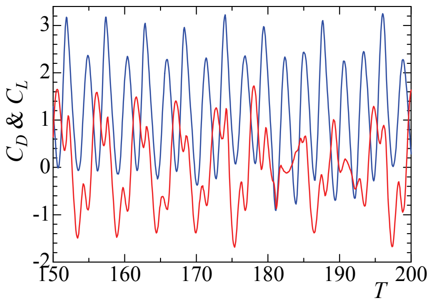

(a)

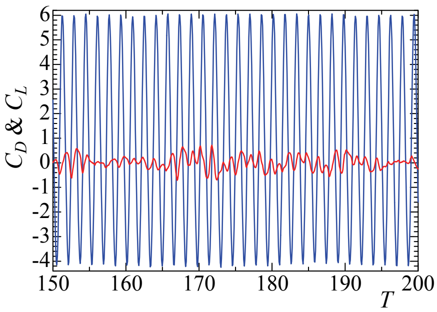

(b)

Figure 5. Time histories of drag and lift coefficients, (blue and red lines show drag and lift coefficients, respectievly) , (a) shows the result in the case of A-mode oscillation and (b) shows the result in the case of S-mode oscillation

The numerical simulation was performed on the oscillating conditions which the alternate vortex shedding lock-in and the simultaneous vortex shedding lock-in generate. One example of the flow patterns obtained by calculation is shown in Figure 4. Here, the flow visualization photographs [10] in the similar experimental condition are shown for comparison. Figure 4(a) is simulating the aspect of alternate vortex shedding lock-in (A-type lock-in). The direction of vortex shedding changes and an aspect that the vortex shedding is performed alternately is shown. An aspect that the vortex discharged from the circular cylinder constitutes a vortex pair which differs in a rotatory direction, respectively, and the vortex street of mushroom shape like the section of a mushroom is formed is expressed well. Figure 4(b) is simulating the aspect of a simultaneous vortex shedding lock-in (S-type lock-in). An aspect that the vortex of mushroom shape is simultaneously discharged from cylinder both sides, and the characteristic aspects of cylinder wake are shown. The result of the flow pattern on other conditions is shown in Table 1. Since the characteristic flow pattern at the time of a lock-in is reproduced well, the credibility of the fluid force required in calculation can consider a high thing.

One example of the time histories of fluid force coefficient obtained by calculation is shown in Figure 5. These figures are in each state of Figure 4. The aspects of a variation of fluid force are shown in Figure 6. An abscissa is the velocity ratio u_{max}/U and an ordinate is each component of fluid force. Here, the velocity ratio defined as $u_{max}/U = 2a/d \cdot f/f_K \cdot (\pi St)$. Since an oscillation frequency ratio f/f_K is constant value, this figure means the variation of the fluid force over the variation of an oscillating amplitude ratio $2a/d$. In the figure, the solid line is in the state of A-mode oscillation, and the dashed line is in the state of S-mode oscillation. In A-mode oscillation, although the value of drag coefficient C_{DAVE} is smaller than a stationary value, the value of a lift coefficient C_{LAVE} scarcely changes to the stationary value. The value of the amplitude of drag coefficient AC_{DRMS} is increasing while the value of amplitude ratio $2a/d$ increases. On the other hand, although the amplitude of lift coefficient AC_{LRMS} scarcely changed the amplitude ratio to $2a/d$ = 0.5, the amplitude of lift coefficient became suddenly small value from amplitude ratio $2a/d$ = 0.75. In S-mode oscillation, the value of drag coefficient

C_{DAVE} and the value of lift coefficient C_{LAVE} scarcely change to the stationary case. The value of amplitude of drag coefficient is large and the value of drag coefficient AC_{DRMS} tends to increase with increase of amplitude ratio $2a/d$. However, the value of amplitude of lift coefficient AC_{LRMS} will become smaller than the value of stationary cylinder case at $2a/d$ = 0.25 and 0.5, the amplitude of lift coefficient became suddenly large value from amplitude ratio $2a/d$ = 0.75.

3.2. In the Case of Two Cylinders

3.2.1. Flow Feature

When circular cylinders were separated enough like distance ratio L/d = 20 or 10, the situation of the flow of the circular cylinder which is oscillating was the same as the case where each circular cylinder exists independently. That is, when the interval of two circular cylinders is separated, it means that there is no interference of mutual lock-in modes. It is known that there is no mutual interference also in two circular cylinders of stationary parallel arrangement. Even if it gave vibration to the circular cylinder, not interfering mutually was checked in such a distance. In two circular cylinders of stationary parallel arrangement, it is known that interference will arise mutually in the distance ratio of L/d = 5.5. So, this systematic numerical simulation was done in the small distance ratio which causes interference mutually. The aspects of the flow at the time of changing an oscillating amplitude ratio for every distance ratio are shown in Figures 7 to 9. In this study, A-mode oscillation is given to the 1st circular cylinder, and S-mode oscillation is given to the 2nd circular cylinder. Figure 7 shows the case of distance ratio L/d = 5.5. Since the vortex shedding from each circular cylinder in each amplitude ratio seems not to be different from the case of each single oscillating circular cylinder, there is still likely to be no interference of lock-in at this distance ratio. However, there is union of two vortex streets after the vortex shedding, and the union position has the tendency to approach circular cylinders, when an amplitude ratio becomes large. Figure 8 shows the case of distance ratio L/d = 2.5. In the cases of amplitude ratio $2a/d$ = 0.25 and 0.5, the vortex shedding from each circular cylinder seems not to be different from the case of each single oscillating circular cylinder. On the other hand, when the amplitude ratio became large, change of its aspect appeared at the 1st circular cylinder. The simultaneous vortex shedding with symmetry changed to the simultaneous vortex shedding without symmetry, and changed into the state where the vortex shedding cannot be presumed. Since the distance ratio L/d narrowed, the union of two vortex streets after the vortex shedding became remarkable, and the aspect of the wake of two circular cylinders

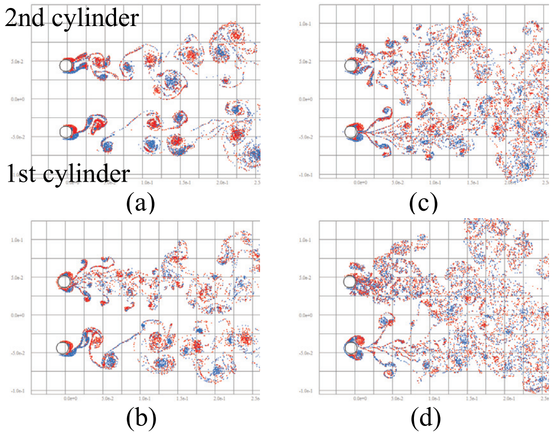

Figure 7. The variation of flow pattern due to change the amplitude ratio 2*a/d* in the case of *L/d* = 5.5, (a) 2*a/d* = 0.25, (b) 2*a/d* = 0.50, (c) 2*a/d* = 0.75, (d) 2*a/d* = 1.00

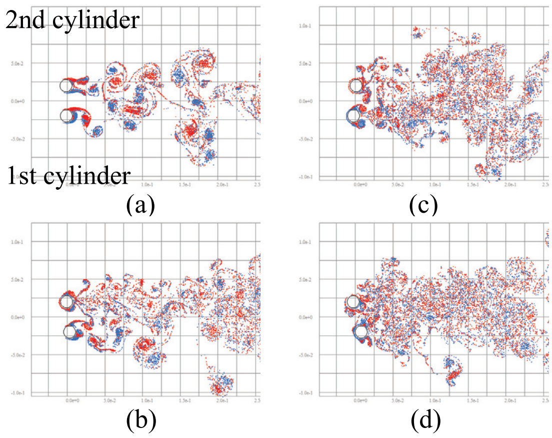

Figure 8. The variation of flow pattern due to change the amplitude ratio 2*a/d* in the case of *L/d* = 2.5, (a) 2*a/d* = 0.25, (b) 2*a/d* = 0.50, (c) 2*a/d* = 0.75, (d) 2*a/d* = 1.00

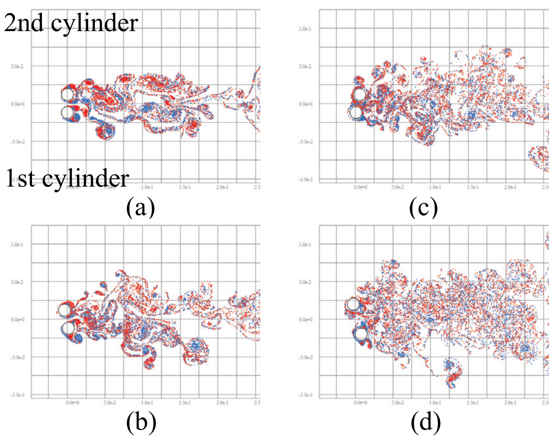

Figure 9. The variation of flow pattern due to change the amplitude ratio 2*a/d* in the case of *L/d* = 1.5, (a) 2*a/d* = 0.25, (b) 2*a/d* = 0.50, (c) 2*a/d* = 0.75, (d) 2*a/d* = 1.00

Table 2. The obtained flow list, symbol A means alternate vortex shedding and symbol S means simultaneous vortex shedding, *L/d* = 0.0 means single cylinder case, and it is shown that a red character differs from the case of a single oscillating circular cylinder

$2a/d$	L/d	1st cylinder	2nd cylinder
0.25	0.0	A (+S)	S (asymmetry)
	20.0	A (+S)	S (asymmetry)
	10.0	A (+S)	S (asymmetry)
	5.5	A (+S)	S (asymmetry)
	2.5	A (+S)	S (asymmetry)
	1.5	S (+A)	S (asymmetry)
0.50	0.0	A	S (symmetry)
	20.0	A	S (symmetry)
	10.0	A	S (symmetry)
	5.5	A	S (symmetry)
	2.5	A	S (symmetry)
	1.5	S (asymmetry)	S (asymmetry)
0.75	0.0	S (symmetry)	S (asymmetry, mushroom)
	5.5	S (symmetry)	S (asymmetry, mushroom)
	2.5	S (asymmetry)	S (asymmetry, mushroom)
	1.5	unknown	unknown
1.00	0.0	S (symmetry, mushroom)	unknown
	5.5	S (symmetry, mushroom)	unknown
	2.5	unknown	unknown
	1.5	unknown	unknown

became complicated, and differed from the case where they are oscillating in the same mode. Figure 9 shows the case of distance ratio L/d = 1.5. In this case, the aspect of vortex shedding changed notably. The flow pattern of an alternate vortex shedding was not seen. Although it is difficult to check in large amplitude ratio, at the 1st circular cylinder, the simultaneous vortex shedding is carried out on condition of all amplitude ratios. The aspect of the wake of two circular cylinders is complicated because of interference of the flow. The result of the obtained flow patterns are shown in Table 2. It was found that the alternate vortex shedding type lock-in receives interference by arrangement.

3.2.2. Characteristics of Fluid Force

It is one of the most interesting things in this study to investigate the variation of the fluid force of two circular cylinders which are oscillating in different lock-in mode. The fluid force is divided into a drag component and a lift component, and those characteristics are evaluated. The changes of each component of the fluid force in each distance

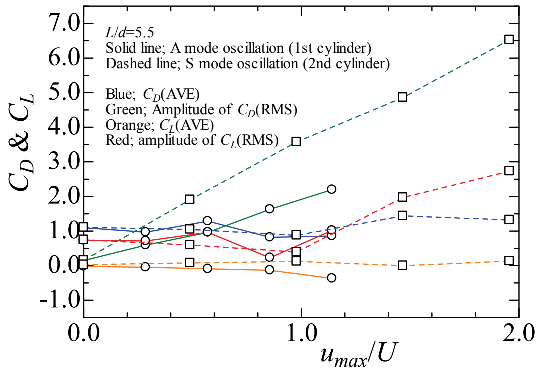

Figure 10. The variation of fluid force component in the case of distance ratio *L/d* = 5.5

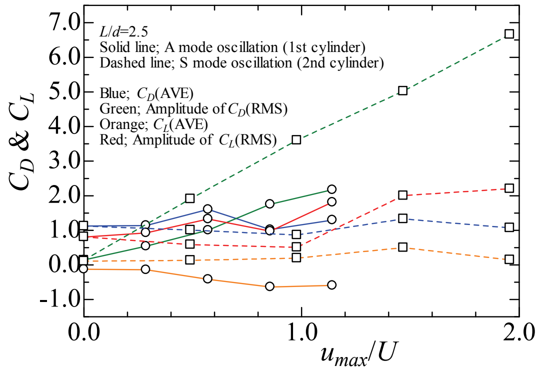

Figure 11. The variation of fluid force component in the case of distance ratio *L/d* = 2.5

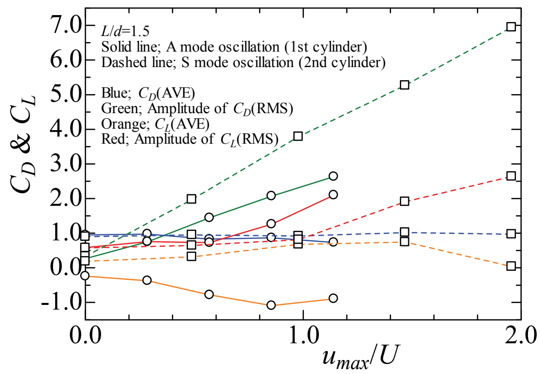

Figure 12. The variation of fluid force component in the case of distance ratio *L/d* = 1.5

ratio L/d are shown in Figures 10 to 12. Here, the average value of drag coefficient and the average value of lift coefficient are arithmetic averages. The values of oscillating amplitude of drag coefficient and lift coefficient are a route mean square to each average value. The data of the fluid force of the range by the non-dimensional time T from 150 to 200 was used for evaluation. In these figures, an abscissa is the velocity ratio u_{max}/U and an ordinate is each component of fluid force. The velocity ratio u_{max}/U = 0 means without cylinder oscillation. Figure 10 shows the result in the case of distance ratio L/d = 5.5. In the drag coefficient, it turns out that there is no great difference as compared with the case where the 1st circular cylinder and the 2nd circular cylinder do not have oscillation, respectively. In the lift coefficient, although most of the 2nd circular cylinder had no variation, with the 1st circular cylinder, the tendency deflected as an amplitude ratio increases was seen. In the amplitude of drag coefficient, the tendency which becomes large was seen as the amplitude ratio increased both circular cylinders. In the amplitude of lift coefficient, the magnitude of the 1st circular cylinder is various by an amplitude ratio, and the 2nd circular cylinder is in the tendency which increases after decreasing. Figure 11 shows the result in the case of distance ratio L/d = 2.5. Although the values of the drag coefficient of the 1st circular cylinder and the 2nd circular cylinder differ from the value at the time of single stationary, the regularity is not found in the variation. In the lift coefficient, although the downward tendency was seen by the increase in an amplitude ratio as for the 1st circular cylinder, the 2nd circular cylinder was almost changeless. In the amplitude of the drag coefficient and the lift coefficient, the same matter as the time of distance ratio L/d = 5.5 was seen. Figure 12 shows the result in the case of distance ratio L/d = 1.5. In both circular cylinders, although the values of those drag coefficients are not so much different from the value at the time of stationary, the values of those lift coefficients tend to become large by the increase in the amplitude ratio. The tendency which becomes large by the increase in an amplitude ratio was the same also about the magnitude of amplitude. In order to investigate the influence of the distance ratio L/d, the calculation result arranged for every amplitude ratio is shown in Figure 13. Here, the restructuring of calculation result was performed on the basis of the case of the circular cylinder which is oscillating independently in each mode in each amplitude ratio. The scale of each figure which constitutes Figure 13 is made into the same scale so that a visual comparison may become easy. By comparing each figure of Figure 13, it is understood that the tendency which differs from the case of a single circular cylinder by increase of an amplitude ratio becomes remarkable. When the value of distance ratio $2a/d$ is small, the large difference can be seen. Especially the thing to describe is remarkable about a lift component. Moreover, in the circular cylinder which is oscillating in A-mode, and the circular cylinder which is oscillating in S-mode, it turned out that the circular cylinder which is oscillating in A-mode tends to be influenced by arrangement. In the case of complex state, it became clear from

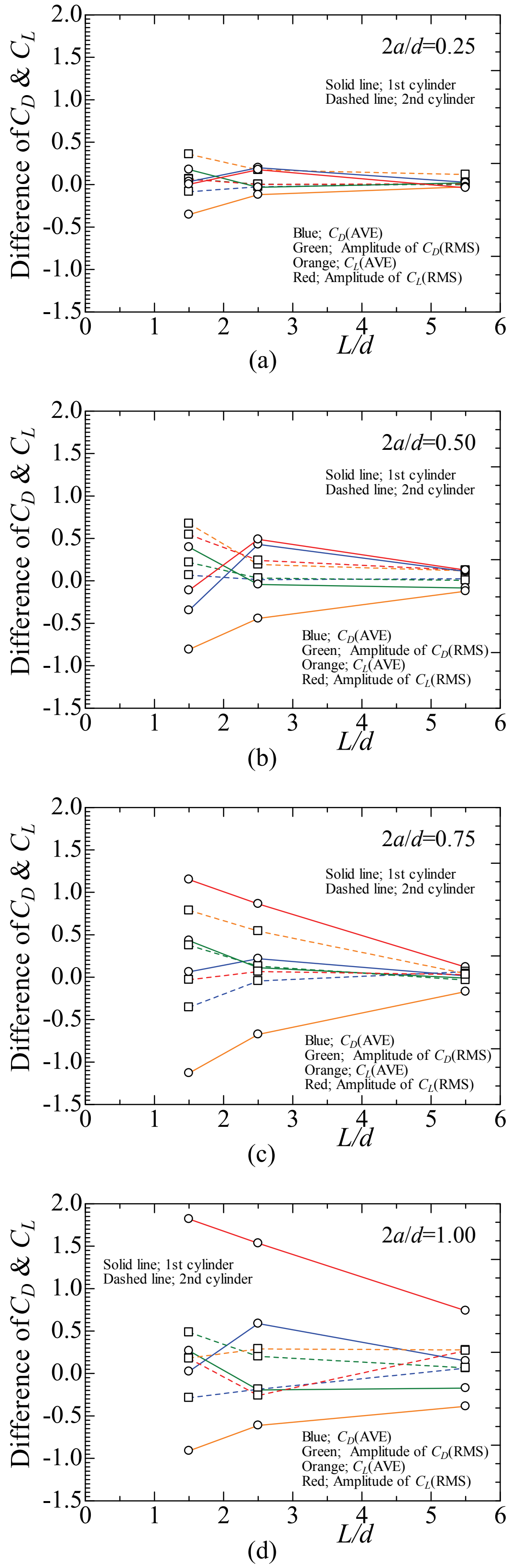

Figure 13. Comparison of the variation of fluid force components by the distance ratio, (a) (b)(c)and (d) show the cases of the amplitude ratio $2a/d$ = 0.25, 0.50, 0.75 and 1.00, respectively

these numerical simulation results to completely differ from the result obtained when the aspect and fluid force of the flow are single. So, in the design of the structures with the small setting interval placed into the flow, the design which expected enough safety ratio beyond the present condition is needed.

4. CONCLUSIONS

Numerical experiments about the vortex flow from two circular cylinders which are oscillating in the different lock-in modes were performed by using the vortex method. The following conclusions were obtained.

(1) When the interval of two circular cylinders is separated, there is no interference of mutual lock-in modes.

(2) If the interval of two circular cylinders is narrow, the vortex streets discharged from each circular cylinder will unite. And the union position has the tendency to approach circular cylinders, when the amplitude ratio becomes large.

(3) It was found that the alternate vortex shedding type lock-in (oscillating in A-mode) receives interference by cylinder arrangement.

(4) In the case of such a complex state, it became clear to completely differ from the result obtained when the aspect and fluid force of the flow are single.

ACKNOWLEDGEMENTS

This study is performed while an author stays in TU-Berlin (Berlin, Germany). Gratitude is expressed to Professor Dr.-Ing. Christian Oliver Paschereit and Dr.-Ing. Christian Navid Nayeri which offered calculation environment. And it is thankful to staff all the persons concerned of the National Defense Academy of Japan which gave the opportunity which can perform research activities in TU-Berlin.

REFERENCES

[1] Griffin, O. M., and Hall, M. S., 1991, "Review-Vortex Shedding Lock-on and Flow Control in Bluff Body Wakes", *Transactions of the ASME*, Vol. 113, pp. 526-537.

[2] King, R., 1997, "A Review of Vortex Shedding Research and its Application", *Ocean Engineers*, Vol. 4, pp. 141-171.

[3] Okajima, A., 1999, "Flow-Induced Vibration of a Bluff Body", *Transaction of the Japan Society of Mechanical Engineers Series B*, Vol. 65 No. 635, pp. 2190-2195.

[4] Okajima, A., 2000, "Vortical Flow and Fluiddynamic Characteristics of an Oscillating Bluff Body", *Transaction of the Japan Society of Mechanical Engineers Series B* , Vol. 66 No. 644, pp. 948-953.

[5] Sarpkaya, T., and Cinar, M., 1980, "Hydrodynamic Interference of Two Cylinders in Harmonic Flow", *Proceeding of Annual Offshore Technology Conference*, Vol. 12 No. 2, pp. 333-340.

[6] Chen, S. S., 1986, "A Review of Flow-Induced Vibration fo Two Circular Cylinders in Crossflow", *Transactions of the ASME J Pressure Vessel Technology*, Vol. 108 No. 4, pp. 382-393.

[7] Sumner, D., Price, S. J., and Paidoussis, M. P., 2000, "Flow-Pattern Identficantion for Two Staggered Circular Cylinder", *Journal of Fluid Mechanics*, Vol. 411, pp. 263-303.

[8] Zdravkovich, M. M., 2003, *Flow Around Circular Cylinder Vol. 2 Applications*, Oxford University Press.

[9] Kim, S., and Sakamoto, H., 2007, "A Study on Characteristics of Flow-Induced Vibrations of Two Circular Cylinders in Staggered Arrangement", *Transactions of Japan Society of Mechanical Engineers Series B*, Vol. 73 No. 725, pp. 139-146.

[10]Yokoi, Y., and Hirao, K., 2008, "Vortex Flow Around an In-Line Forced Oscillating Circular Cylinder", *Transactions of Japan Society of Mechanical Engineers Series B*, Vol. 74 No. 746, pp. 2099-2108.

[11]Yokoi, Y., and Hirao, K., 2014, "The Appearence of Two Lock-in States in the Voltex Flow Around an In-Line Forced Oscillating Circular Cylinder", *EPJ Web Conferences*, Vol. 67, 02131-pp. 1-8.

[12]Yokoi, Y., and Hirao, K., 2014, "The Mutual Interference Vortex Flow from a Pair of In-Line Forced Oscillating Staggered Arranged Circular Cylinders", *Bulletin on the JSME Journal of Fluid Science and Technology*, Vol. 9 No. 3, JFST0057-pp. 1-11.

[13]Kamemoto, K., 1993, "The expandability of the vortex method as a turbulent flow model (the first part: to think a basic of vortex method)", *Computational Fluid Dynamics*, Vol. 2 No. 1, pp. 20-29.

[14]Kamemoto, K., 1994, "The expandability of the vortex method as a turbulent flow model (the latter part: to think a basic of vortex method)", *Computational Fluid Dynamics*, Vol. 2 No. 2, pp. 28-39.

Conference on Modelling Fluid Flow (CMFF'15)
The 16th International Conference on Fluid Flow Technologies
Budapest, Hungary, September 1-4, 2015

INFLUENCE OF THE ADVERSE PRESSURE GRADIENT ON THE SWIRLING FLOW

Sebastian MUNTEAN[1], Constantin TĂNASĂ[2], Romeo F. SUSAN-RESIGA[3], Alin BOSIOC[4]

[1] Corresponding Author. Center of Advanced Research in Engineering Sciences, Romanian Academy-Timisoara Branch. E-mail: seby@acad-tim.tm.edu.ro
[2] Department of Hydraulic Machinery, "Politehnica" University of Timişoara . E-mail: constantin.tanasa@upt.ro
[3] Department of Hydraulic Machinery, "Politehnica" University of Timişoara, Bvd. Mihai Viteazu, No. 1, Timişoara, 300222, Romania. Tel.: +40 256 403692, Fax: +40 256 403692, E-mail: romeo.resiga@upt.ro
[4] Department of Hydraulic Machinery, "Politehnica" University of Timişoara . E-mail: alin.bosioc@upt.ro

ABSTRACT

The flow in the draft tube cone of Francis turbines operated at partial discharge is a complex hydrodynamic phenomenon where an incoming practically steady axi-symmetric swirling flow evolves into a three-dimensional unsteady flow field with precessing helical vortex (also called vortex rope) and associated pressure fluctuations. The paper addresses the influence of the adverse pressure gradient on the swirling flow with vortex breakdown. Consequently, a 2D axi-symmetric model is used to compute the flow. The axi-symmetric swirling flow is computed using available turbulent swirling flow solvers by introducing a stagnant region model (SRM), essentially enforcing a unidirectional circumferentially averaged meridian flow as suggested by the experimental data. Full 3D unsteady flow simulations with same boundary conditions are performed for five cases from a straight pipe up to cone with angle of 25.5°. As a result, the numerical results are compared in order to assess the capabilities of simplified model. The evolution of the quasi-stagnant region is investigated. The vortex sheet angle that separates the quasi-stagnant region and the main flow is evaluated. The energy losses coefficient and kinetic to potential conversion ratio distributions are plotted along to the cone length in order to evaluate the performances. Also, the self-induced instability is quantified based on 3D full unsteady flow simulation.

Keywords: 2D and 3D flow simulation, precessing vortex, swirling flow, self-induced instability, unsteady field analysis

NOMENCLATURE

D_t	$[m]$	reference diameter of throat test section, $D_t = 0.1$
V_z, V_r, V_θ	$[m/s]$	axial, radial, and circumferential velocity components
fv	$[Hz]$	fundamental frequency
Π, K, E	$[W]$	fluxes of potential, kinetic and mechanical energy, respectively
ρ	$[kg/m^3]$	fluid density
μ	$[Pa{\cdot}s]$	dynamic viscosity
ζ	[-]	energy loss coefficient
χ	[-]	kinetic-to-potential energy recovery ratio

1. INTRODUCTION

The variable demand on the energy market, as well as the limited energy storage capabilities, requires a great flexibility in hydraulic turbines operation. As a result, turbines tend to be operated over an extended range of regimes quite far from the best efficiency point. In particular, Francis turbines operated at partial discharge have a high level of residual swirl at the draft tube inlet as a result of the mismatch between the swirl generated by the wicket gates and the angular momentum extracted by the turbine runner [1]. Further downstream, the decelerated swirling flow in the draft tube cone often results in vortex breakdown, Figure 1, which is recognized now as the main cause of severe flow instabilities and pressure fluctuations experienced by hydraulic turbines operated at part load. More than three decades ago Palde [2] concluded that the draft tube surge is a hydrodynamic instability, known as vortex breakdown, occurring in the draft tube as a result of rotation remaining in the fluid as it leaves the turbine runner and enters the draft tube throat.

Figure 1. Helical vortex breakdown in the draft tube cone of Francis turbine at partial discharge.

The main goal of a hydraulic turbine draft tube is to decelerate the flow exiting the runner, thereby converting the excess of kinetic energy into static pressure. The Francis turbines with medium and high specific speeds have compact elbow draft tubes, with rather short discharge cone. Contrary, the Francis turbines with low specific speeds have elbow draft tubes with extended discharge cone and small angle. As a result, the draft tube hydrodynamics is very complex due to the combination of swirling flow deceleration with flow direction change and cross-section shape/area modification. Most of the pressure recovery occurs in the draft tube cone, also called *discharge cone*.

Extensive experimental [3] and numerical [4] investigations have provided a comprehensive understanding of this complex flow phenomenon, with accurate evaluation of the main parameters (precession frequency, amplitude of the wall pressure fluctuations, vortex rope shape), as well as various details of the hydrodynamic field.

Nishi et al. [5] put forward a qualitative model for the precessing vortex rope, based on their experimental investigations. They suggest that the circumferentially averaged velocity profiles in the cone could be satisfactorily represented by a model comprising a dead (quasi-stagnant) water region surrounded by the swirling main flow, Figure 2. This model is also supported by the measured averaged pressure, which remains practically constant within the quasi-stagnation region.

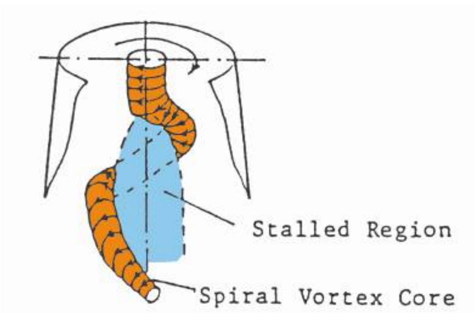

Figure 2. Stagnant region model for the precessing vortex rope, Nishi et al. [5].

All these considerations led to the conclusion that the spiral vortex core observed in the draft tube of a Francis turbine at part load is a rolled-up vortex sheet which originates between the central stalled region and the swirling main flow. Resiga et al. [6] have implemented a stagnant region model within the framework of an incompressible, turbulent, axi-symmetric flow solver. The numerical results for the flow with precessing vortex rope in a Francis turbine discharge cone were in very good agreement with the LDV measured axial and circumferential velocity profiles. Moreover, it was shown that the vortex rope is exactly wrapped around the central stagnant region as computed with an axi-symmetric swirling flow model, Figure 3.

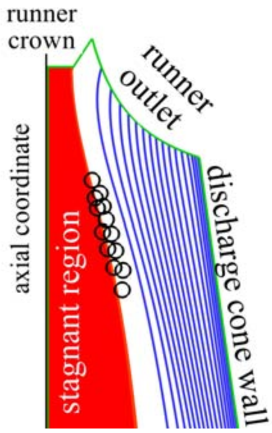

Figure 3. 2D axi-symmetric flow numerical simulation with stagnant region model validated against experimental data, Resiga et al. [6].

A time averaging procedure for the 3D unsteady flow simulation in a swirling flow developed in [7] is used. These numerical results were compared against 2D axi-symmetric swirling flow simulation. It is shown that averaging the flow governing equations provides a reasonable agreement with the three-dimensional averaged results, even when the flow has a strong 3D unsteady character [8]. A full 3D unsteady turbulent flow simulation implies large computing resources. However, the self-induced instability type of the vortex breakdown can be correctly captured with a full 3D unsteady turbulent flow simulation.

In this paper, 2D axi-symmetric turbulent swirling flow and 3D unsteady flow are performed. Numerical results obtained with this model for five cases from a straight pipe up to 25.5° are analyzed for a swirling flow configuration. The evolution of the quasi-stagnant region is visualized plotting the axial velocity map. The angle of the vortex sheet that separates the quasi-stagnant region and the main flow is determined. Next, the energy losses and kinetic-to-potential energy conversion ratio are obtained. Also, the fundamental frequency and maximum amplitude of the unsteady flow field are obtained based on 3D computations. Particularly, the results are useful to develop new control techniques of the swirling flows.

2. NUMERICAL SIMULATIONS

A meridian cross-section of the swirling flow apparatus is shown in Figure 4. The swirling flow apparatus includes a swirl generator and a convergent-divergent test section. The central body ensemble, called swirl generator, includes: leaned struts, guide vanes, free runner and nozzle. This particular setup is aimed at producing a swirling flow at the throat section, similar to the one encountered in Francis turbines operated at partial discharge, [9].

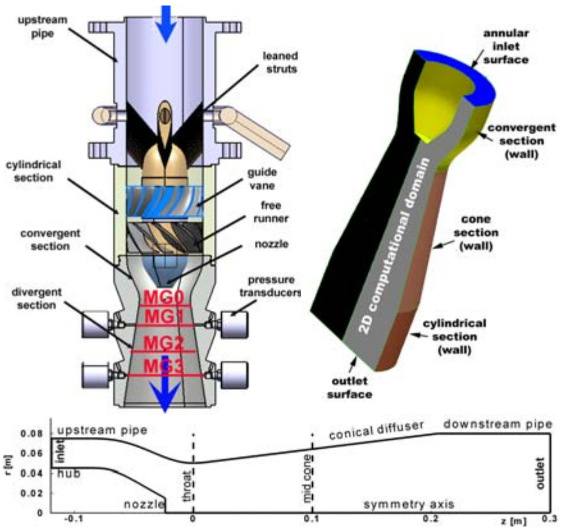

Figure 4. 3D and 2D axi-symmetric computational domains

Although the computational domain is axi-symmetric, Fig. 4, and the inlet boundary conditions are steady and axi-symmetric (radial profiles for axial and circumferential velocity components) [8], the decelerated swirling flow in the conical diffuser develops an instability, with a precessing helical vortex as shown in Fig. 1. Such flow simulations require large computing resources and computing time. As a result, from practical point of view it is preferable to use a more tractable approach to assess the stability properties of the swirling flow, and to estimate to occurrence of unsteady velocity and pressure field.

Since the geometry considered in this study has rotational symmetry, it would be convenient to compute the flow using axi-symmetric governing equations. In doing so, the three-dimensional problem becomes a two-dimensional one, to be solved in the domain shown in Fig. 4. This 2D computational domain is obtained by intersecting the 3D domain from Fig. 4 with a meridian half-plane. From the annular inlet section, the hydraulic passage has a convergent part upstream the throat, followed by a conical diffuser discharging in a downstream pipe. The hub ends with a nozzle. The grids with around 32k quadrilateral cells and boundary layer refinement near the walls (y+ values between 84 and 106) are used. Full 3D unsteady flow simulations are performed on structured grids of approximately 2-2.5M cells walls (y+ values between 207 and 354) together with an unsteady realizable $k-\varepsilon$ turbulence model [10]. It is obvious that the 2D axi-symmetric grid is two orders of magnitude smaller than the one used for the full 3D simulation.

The governing equations for axi-symmetric, turbulent swirling flows of an incompressible fluid are obtained by writing both the continuity and the momentum equations in cylindrical coordinates, then discarding the derivatives with respect to the circumferential coordinate:

i) the continuity equation,

$$\nabla \cdot \underline{V} \equiv \frac{\partial V_z}{\partial z} + \frac{\partial V_r}{\partial r} + \frac{V_r}{r} = 0 \tag{1}$$

ii) axial momentum equation,

$$\begin{aligned}&\frac{\partial V_z}{\partial t} + \frac{1}{r}\frac{\partial}{\partial z}\left(rV_zV_z\right) + \frac{1}{r}\frac{\partial}{\partial r}\left(rV_rV_z\right) = \\ &-\frac{1}{\rho}\frac{\partial p}{\partial z} + \frac{1}{r}\frac{\partial}{\partial z}\left[r\frac{\mu+\mu_T}{\rho}2\frac{\partial V_z}{\partial z}\right] \\ &+\frac{1}{r}\frac{\partial}{\partial r}\left[r\frac{\mu+\mu_T}{\rho}\left(\frac{\partial V_z}{\partial r} + \frac{\partial V_r}{\partial z}\right)\right]\end{aligned} \tag{2}$$

iii) radial momentum equation,

$$\begin{aligned}&\frac{\partial V_r}{\partial t} + \frac{1}{r}\frac{\partial}{\partial z}\left(rV_zV_r\right) + \frac{1}{r}\frac{\partial}{\partial r}\left(rV_rV_r\right) = -\frac{1}{\rho}\frac{\partial p}{\partial r} + \frac{V_\theta^2}{r} \\ &+\frac{1}{r}\frac{\partial}{\partial z}\left[r\frac{\mu+\mu_T}{\rho}\left(\frac{\partial V_r}{\partial z} + \frac{\partial V_z}{\partial r}\right)\right] \\ &+\frac{1}{r}\frac{\partial}{\partial r}\left[r\frac{\mu+\mu_T}{\rho}2\frac{\partial V_r}{\partial r}\right] - 2\frac{\mu+\mu_T}{\rho}\frac{V_r}{r^2}\end{aligned} \tag{3}$$

iv) circumferential momentum equation,

$$\begin{aligned}&\frac{\partial V_\theta}{\partial t} + \frac{1}{r}\frac{\partial}{\partial z}\left(rV_zV_\theta\right) + \frac{1}{r}\frac{\partial}{\partial r}\left(rV_rV_\theta\right) = \\ &-\frac{V_rV_\theta}{r} + \frac{1}{r}\frac{\partial}{\partial z}\left[r\frac{\mu+\mu_T}{\rho}\frac{\partial V_\theta}{\partial z}\right] \\ &+\frac{1}{r^2}\frac{\partial}{\partial r}\left[r^3\frac{\mu+\mu_T}{\rho}\frac{\partial}{\partial r}\left(\frac{V_\theta}{r}\right)\right]\end{aligned} \tag{4}$$

The effective dynamic viscosity is written as the sum of the molecular, μ, and the so-called "turbulent" viscosity, μ_T, the second being computed using various turbulence models. The above axi-symmetric swirling flow model, available in the FLUENT 6.3 code, is used for the present computations together with the realizable $k-\varepsilon$ (RKE) turbulence model. The term "realizable" means that the model satisfies certain mathematical constraints on the Reynolds stresses, consistent with the physics of the flow. When compared with the standard $k-\varepsilon$ and RNG $k-\varepsilon$ models, the RKE model is predicting more accurately the spreading rate of both planar and round jets, [10]. As a result, the RKE turbulence model is chosen for the present investigations.

The radial equilibrium condition used on the outlet section of the computational domain follows from the radial momentum equation (3) for vanishing radial velocity. When setting $V_r = 0$ in Eq. (3), all terms containing the radial velocity disappear. Moreover, the first viscous term becomes negligible if the flow does not evolve anymore in the axial direction, i.e. the axial derivative is vanishing as well. As a result, we obtain the well known condition for the outlet section,

$$\frac{\partial p}{\partial r} = \frac{\rho V_\theta^2}{r} . \quad (5)$$

Note that Eq. (5) does not explicitly specify a pressure profile. Instead, it correlates the radial pressure gradient with the circumferential velocity. When the flow does not have swirl, Eq. (5) reduces to a constant pressure condition on the outlet.

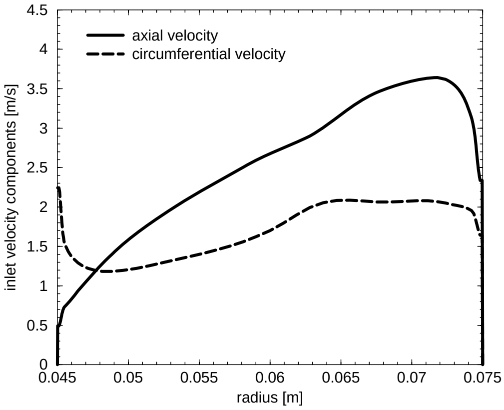

Figure 5. Axial and circumferential velocity profiles on the annular inlet section for both 3D and 2D computational domains.

On the inlet section we prescribe the same axial and circumferential velocity profiles, Figure 5, together with the turbulence quantities obtained based on the numerical simulation [11], as the ones used for the 3D computation [12]. Note that both 3D and 2D axi-symmetric computations have similar boundary conditions and turbulence models. However, it is obvious that the simplified axi-symmetric flow model cannot capture the swirling flow with 3D and unsteady character when the precessing helical vortex is developed as a result of the self-induced instability.

3. NUMERICAL RESULTS

The 2D axi-symmetric turbulent swirling flow with SRM model produces a central stagnant region and the main flow occupying an annular section up to the wall. The cases selected include a straight pipe (with 0°) and four discharge cones (with half-angle from 2.125° to 12.75°). The quasi-stagnant region extension is identified on axial velocity component map for all investigated cases, Figure 6. It is already proved by Resiga el al. [6] that the vortex breakdown (also known as precessing vortex rope) is wrapped on a quasi-stagnant region developed in the axis neighbourhood.

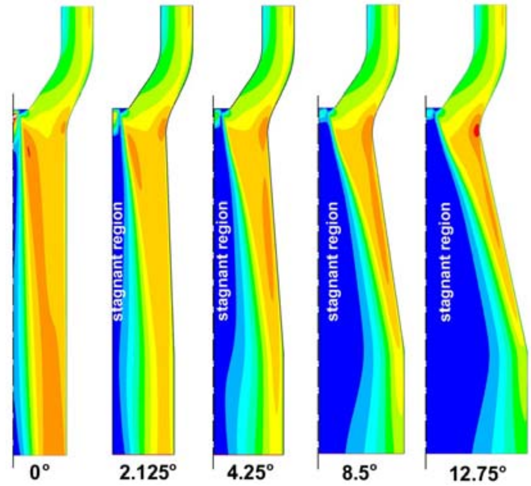

Figure 6. Stagnant region extension identified on the meridian velocity component map from 2D axi-symmetric turbulent swirling flow with SRM model for all investigated cases.

As a result, the vortex sheet generated between the quasi-stagnant region and the main stream is an indicator about self-induced instability. Therefore, the vorticity magnitude map is plotted in Figure 7 selecting the maximum values in the computational domain in order to visualize the vortex sheet.

Clearly, the vortex sheet angle is larger than the discharge cone angle for all cases (Figure 8) being in agreement with experimental data provided by Ciocan and Iliescu [13] for a Francis turbine model. However, the self-induced instability type cannot be indentified based on 2D axi-symmetric numerical analysis.

The main purpose of the cone is to convert as much as possible the kinetic energy into pressure potential energy with minimum energy losses. Therefore, *loss coefficient* ζ and the *kinetic-to-potential energy conversion ratio* χ are defined in order to assess the discharge cone performance.

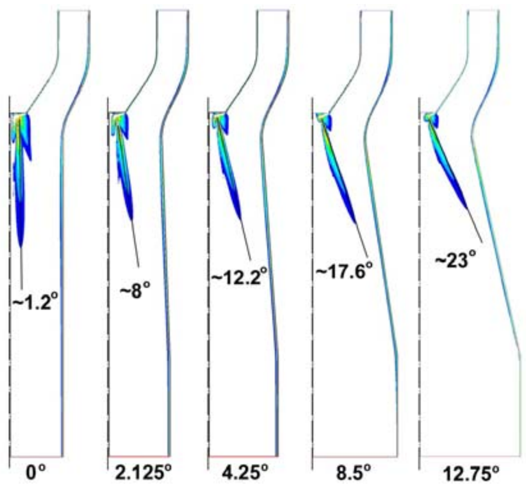

Figure 7. Vortex sheet computed using 2D axi-symmetric turbulent swirling flow with SRM model for all cases.

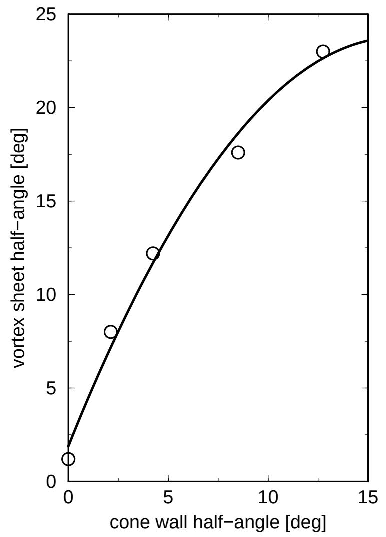

Figure 8. Vortex sheet half-angle computed using 2D axi-symmetric turbulent swirling flow with SRM model for all cases.

The following integral quantities are introduced by Resiga et al. [14] on a generic cross section $S(z)$ at the axial distance z from the inlet section in order to analyze the kinetic-to-potential energy transformation process:

Flux of potential energy

$$\Pi(z) \equiv \int_{S(z)} p(z,r)\, \mathbf{V}\cdot\mathbf{n}\, \mathrm{d}S \quad [W] \tag{6}$$

Flux of kinetic energy

$$\mathrm{K}(z) \equiv \int_{S(z)} \frac{\rho V^2(z,r)}{2}\, \mathbf{V}\cdot\mathbf{n}\, \mathrm{d}S \quad [W] \tag{7}$$

Flux of mechanical energy

$$\mathrm{E}(z) \equiv \Pi(z) + \mathrm{K}(z) \tag{8}$$

For a loss-free flow the flux of total mechanical energy E is constant. However, when energy losses are present E decreases monotonically as the cross section $S(z)$ is moved downstream, i.e. for increasing z in our case.

If we denote $\Pi_0 = \Pi(z=0)$ and $\mathrm{K}_0 = \mathrm{K}(z=0)$, where $z=0$ corresponds to the inlet section (the throat), the total hydraulic power dissipated up to a section $S(z)$ is $\mathrm{E}_0 - \mathrm{E}(z) > 0$, where obviously $\mathrm{E}_0 = \Pi_0 + \mathrm{K}_0$.

The dimensionless *loss coefficient* ζ and the *kinetic-to-potential energy conversion ratio* χ are defined as follow [14]:

$$\zeta(z) \equiv \frac{\mathrm{E}_0 - \mathrm{E}(z)}{\mathrm{K}_0},\quad \chi(z) \equiv \frac{\Pi(z) - \Pi_0}{\mathrm{K}_0 - \mathrm{K}(z)} < 1 \tag{9}$$

The evolution of the energy loss coefficient $\zeta(z)$ in the discharge cone for all five cases using 2D and 3D computation, Figure 9, emphasizes the rapid increase when the adverse pressure gradient is stronger. The loss coefficient is underestimated with 2D axi-symmetric model. The distribution of the energy losses along to the cone with half-angle from 0° to 4.25° seems to be linear. Particularly, the same distribution along to the cone with half-angle of 8.5° is like in the pipe on the first half part while significant energy losses are quantified in the second half part. As a result, a compact discharge cone with half-angle of 8.5° has small energy losses. The energy losses along to the discharge cones with half-angle of 12.75° are significantly larger than other cases. The vortex breakdown phenomenon leads to increased energy losses.

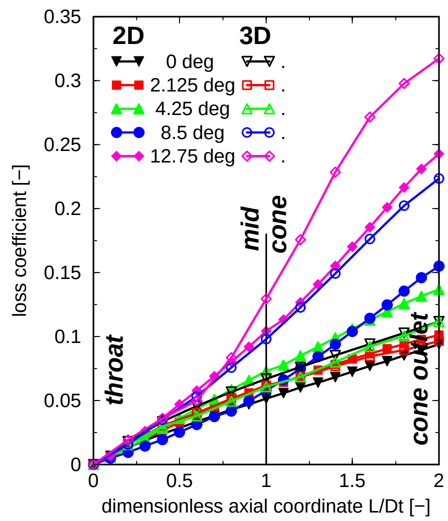

Figure 9. The energy loss coefficient ζ computed with 2D model and 3D for all cases.

Expectedly, the kinetic-to-potential conversion ratio χ is higher for large cone angles while the ratio is almost negligible for small angles, Figure 10. One can observe that the conversion ratio is better in the second part of the cone at lower angles. Contrary, the conversion ratio is better in the first part of the cone at large cone angles.

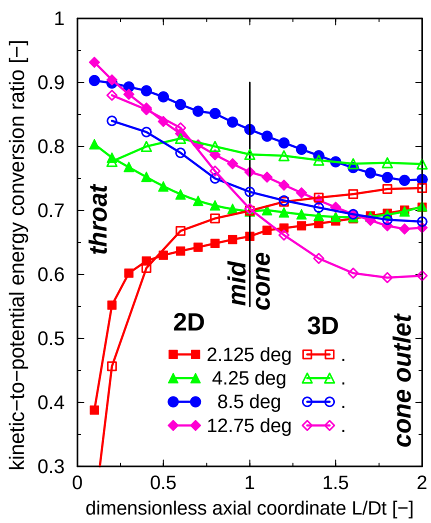

Figure 10. The kinetic-to-potential energy conversion ratio χ computed for all cases.

Bear in mind that this behaviour is yielded for a particular swirling flow configuration. As a result, the appropriate geometry for this particular swirl is the cone with half angle around 4.25° due to the almost constant conversion ratio and reduced energy loss coefficient.

The self-induced instability type developed in the discharge cone is determined based on 3D unsteady numerical simulation, Figure 11. The shape of self-induced instability is visualized using iso-pressure (grey shapes in Fig. 11). Once can observe that the self-induced instability type evolves from an axi-symmetric form in a straight pipe to a helical form in a discharge cone [15]. It is clearly observed that the stagnant region (blue zone in Fig. 11) becomes larger once the adverse pressure gradient is stronger.

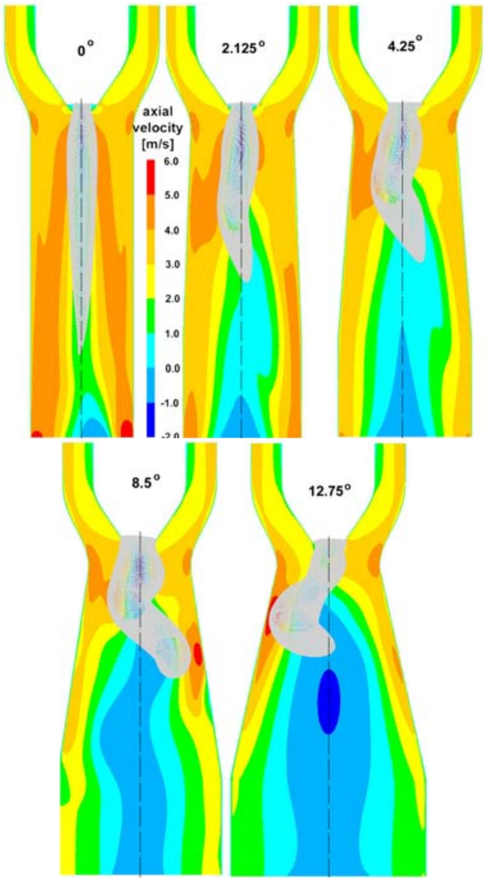

Figure 11. Axial velocity map in a meridian cross-section and self-induced instability type

The pressure pulsations associated to the self-induced instability is recorded on the wall at four levels denoted MG0 (in the throat), MG1, MG2 and MG3 in Fig. 1. Fourier spectra on all levels are obtained using two time steps (1 ms and 0.1 ms), Figure 12. The fundamental frequency (*fv*) associated to the self-induced instability increases once the pressure gradient is weaker suggesting a vortex stretching phenomenon, Figure 13. The discrepancy between values of fundamental frequency computed with 1 ms and 0.1 ms becomes larger toward to stronger adverse pressure gradient, Table 1. The accurate fundamental frequency with respect to experimental data is captured using a time step of 0.1 ms (relative error of 1.3%). The higher harmonics are generated at stronger adverse pressure gradients, Fig. 12.

The maximum amplitude (*Am*) associated to the fundamental frequency is overestimated by computations for both time steps with respect to experimental data, Table 2. However, a more accurate value is computed using a time step of 0.1 ms (relative error of 23.25%). The maximum amplitude associated to the fundamental frequency is directly proportional with the adverse pressure gradient, Figure 14. Moreover, the maximum amplitude associated to the fundamental frequency is moving upstream towards the throat once the adverse pressure gradient is stonger. These results have paved the way toward new control technique of the swirling flows [16, 17].

Table 1. Fundamental frequency (*fv*) of the self-induced instability for all cases

	fv [Hz] (t=1 ms)	*fv* [Hz] (t=0.1ms)	Exp. [Hz]
0 deg.	24.59	25	-
2.125 deg.	15.71	16.74	-
4.25 deg.	13.89	16.2	-
8.5 deg.	10.86	15.8	15.6
12.75 deg.	10.91	15.42	-

Table 2. Maximum amplitude (*Am*) values associated to fundamental frequency for all cases

	Am [Pa] (t=1 ms)	*Am* [Pa] (t=0.1ms)	Exp.	Level
0 deg.	111.8	118.2	-	MG3
2.125 deg.	439.2	530.6	-	MG3
4.25 deg.	1005.6	1274	-	MG2
8.5 deg.	1935.4	1854.9	1505	MG1
12.75 deg.	3559.8	3329.5	-	MG0

4. CONCLUSIONS

The paper addresses the influence of the adverse pressure gradient on the swirling flow. The 2D axi-symmetric swirling flows are computed using available solvers by introducing a stagnant region model (SRM). Also, 3D unsteady computations are performed imposing the same boundary conditions in order to quantify the self-induced instability developed in the cone. Numerical results for five cases from a straight pipe up to cone with angle of 25.5° are analyzed for a particular swirling flow configuration. The evolution of the quasi-stagnant region is quantified plotting the velocity map. The angle of the vortex sheet that separates the quasi-stagnant region and the main flow is quantified. The vortex sheet angle is larger than the discharge cone angle for all cases.

The energy losses and kinetic-to-potential conversion ratio distributions are plotted along to the discharge cone length in order to evaluate it performance.

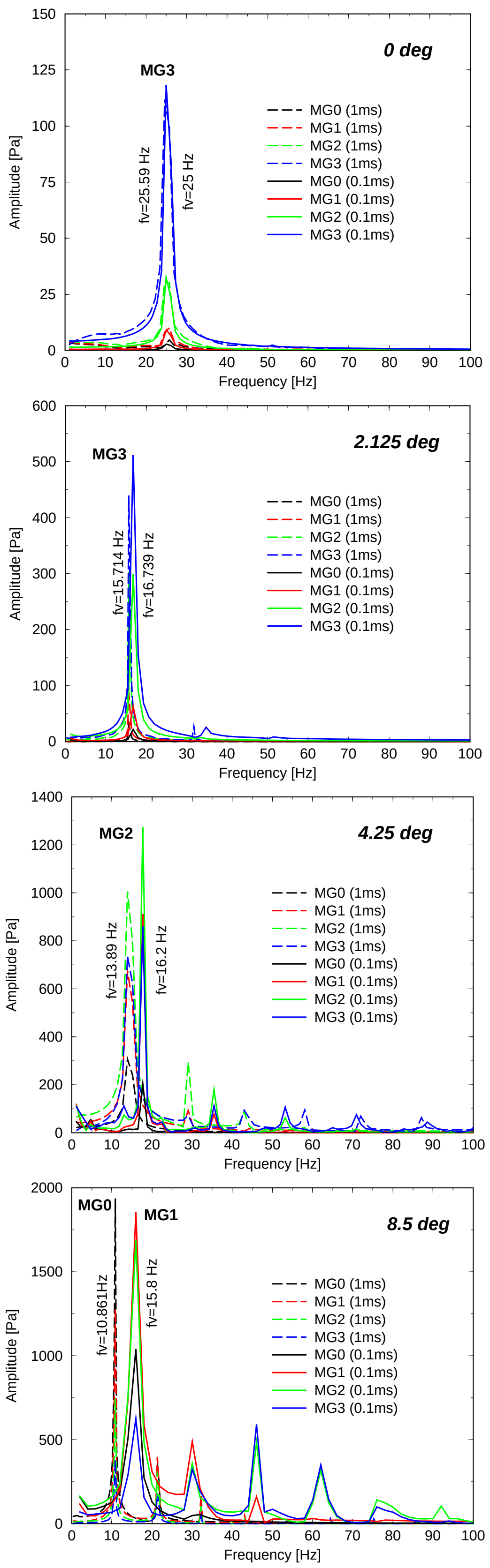

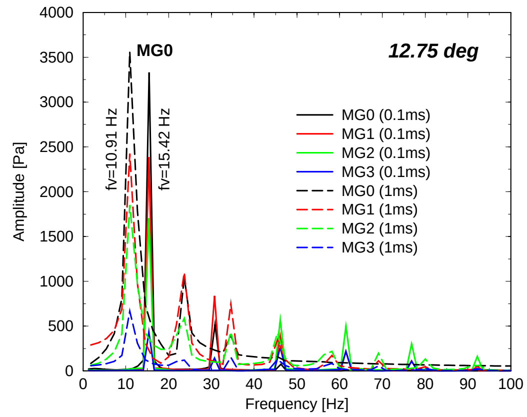

Figure 12. Fourier spectra for unsteady pressure signals in MG0, MG1, MG2 and MG3 computed using two time steps: 1ms (dash line) and 0.1 ms (solid line) for all cases

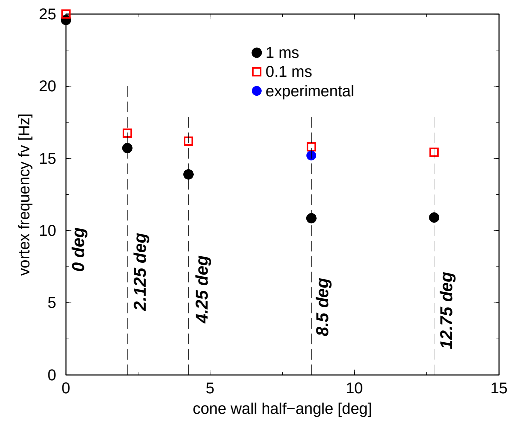

Figure 13. Fundamental frequency of the self-induced instability computed using two time steps: 1ms (●) and 0.1 ms (□) for all cases

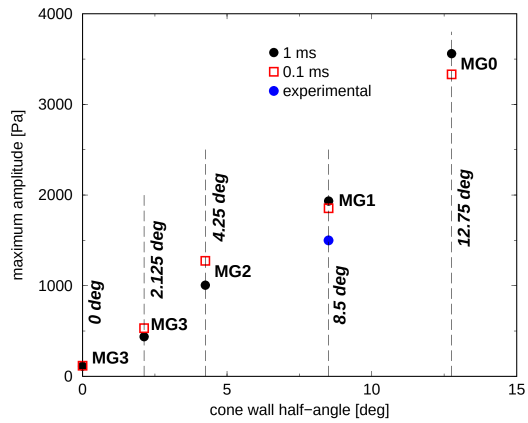

Figure 14. Maximum amplitude associated to the fundamental frequency of self-induced instabilities at two time steps: 1ms (●) and 0.1 ms (□) for all cases

The vortex breakdown phenomenon leads to increased energy losses while the energy conversion is directly proportional with cone angle. The fundamental frequency of the self-induced instability increases once the pressure gradient is weaker suggesting a vortex stretching phenomenon. The maximum amplitude associated to the fundamental frequency is directly proportional with the adverse pressure gradient. The maximum amplitude associated to the fundamental frequency is moving upstream towards the throat once the adverse pressure gradient is stronger. These results have paved the way toward new control technique of the swirling flows [16, 17].

ACKNOWLEDGEMENTS

This work has been supported by Romanian Ministry of National Education, CNCS-UEFISCDI project number PNII–ID-PCE-2012-4-0634. Tanasa C. was supported by the strategic grant POSDRU/159/1.5/S/137070 (2014) of the Ministry of National Education, Romania, co-financed by the European Social Fund – Investing in People, within the Sectoral Operational Programme Human Resources Development 2007-2013.

REFERENCES

[1] Escudier, M., 1987, „Confined Vortices in Flow Machinery", *Annu Rev Fluid Mech*, Vol. 19, pp. 27-52.

[2] Palde U.J., 1972, „Influence of the Draft Tube Shape on Surging Characteristics", *American Society of Civil Engineers National Water Resources Engineering Meeting,* Atlanta, U.S.A.

[3] Ciocan, G. D., Iliescu, M. S., Vu, T. C., Nennemann, B., and Avellan, F., 2007, "Experimental Study and Numerical Simulation of the FLINDT Draft Tube Rotating Vortex", *J Fluids Engineering*, Vol. 129, pp. 146-158.

[4] Stein, P., 2007, "Numerical Simulation and Investigation of Draft Tube Vortex Flow", *PhD Thesis,* Coventry University, U.K.

[5] Nishi, M., Matsunaga, S., Okamoto, M., Uno, M., and Nishitani, K., 1988, "Measurement of three-dimensional periodic flow on a conical draft tube at surging condition", in Rohatgi, U. S., et al., (eds.) *Flows in Non-Rotating Turbomachinery Components*, FED, Vol. 69, pp. 81-88.

[6] Susan-Resiga, R., Muntean S., Stein, P., and Avellan, F., 2009, "Axisymmetric Swirling Flow Simulation of the Draft Tube Vortex in Francis Turbine at Partial Discharge", *Int. J. Fluid Machinery and Systems*, Vol. 2, No. 4, pp. 295-302.

[7] Susan-Resiga, R., Muntean, S., Tanasa, C., and Bosioc, A., 2009, „Three-dimensional versus two-dimensional axisymmetric analysis for decelerated swirling flows", Proc. *Conf. Modelling Fluid Flow CMFF'09*, Budapest, Hungary, pp. 862-870.

[8] Susan-Resiga, R., and Muntean, S., 2008, "Decelerated Swirling Flow Control in the Discharge Cone of Francis Turbines", Proc. *4th Int. Symposium on Fluid Machinery and Fluid Engineering*, Beijing, China, pp. 89-96.

[9] Avellan, F., 2000, "Flow Investigation in a Francis Draft Tube: The FLINDT Project", Proc. *20th IAHR Symposium on Hydraulic Machinery and Systems*, Charlotte, USA, p. DES-11.

[10] Fluent Inc., FLUENT 6.3 User's Guide, 2006.

[11] Susan-Resiga, R., and Muntean, S., 2008, "Decelerated Swirling Flow Control in the Discharge Cone of Francis Turbines", Proc. *4th Int. Symposium on Fluid Machinery and Fluid Engineering*, Beijing, China, pp. 89-96.

[12] Muntean, S., Nilsson, H., and Susan-Resiga, R., 2009, „3D numerical analysis of the unsteady turbulent swirling flow in a conical diffuser using Fluent and OpenFoam", Proc. *3rd IAHR International Meeting of the Workgroup on Cavitation and Dynamic Problems in Hydraulic Machinery and Systems,* Brno, Czech Republic, pp.155-165.

[13] Ciocan G.D. and Iliescu M.S., 2007, „Vortex rope investigation by 3D PIV method", Proc. *2nd IAHR International Meeting of the Workgroup on Cavitation and Dynamic Problems in Hydraulic Machinery and Systems,* Timişoara, Romania, pp. 159 – 172.

[14] Susan-Resiga R, Muntean S, Hasmatuchi V, Anton I and Avellan F., 2010, "Analysis and prevention of vortex breakdown in the simplified discharge cone of a Francis turbine", *J Fluids Engineering*, Vol. 132, No. 5, 051102, pp. 1-15.

[15] Alekseenko, S. V., Kuibin, P.A., and Okulov, V. L., 2007, Theory of concentrated vortices, Springer-Verlag Berlin Heidelberg.

[16] Susan-Resiga, R. F., Tanasa, C., Bosioc, A. I., Ciocan, T., Stuparu, A. and Muntean, S., 2014, "Method and equipment for swirling flow control from conical diffuser of hydraulic turbines", *Patent Application no. A/00621*, Politehnica University, Timisoara, Romania. (in Romanian)

[17] Tanasa, C., Susan-Resiga, R. F., Muntean, S., Stuparu, A., Bosioc, A. I., and Ciocan, T., 2015, "Numerical Assessment of a New Passive Control Method for Mittigating the Precessing Helical Vortex in a Conical Diffuser", Proc. *Conf. Modelling Fluid Flow CMFF'15*, Budapest, Hungary. (submitted)

Conference on Modelling Fluid Flow (CMFF'15)
The 16th International Conference on Fluid Flow Technologies
Budapest, Hungary, September 1-4, 2015

Three-dimensional turbulent Navier-Stokes hydrodynamic analysis and performance assessment of oscillating wings for power generation

Jernej DROFELNIK[1], M.Sergio CAMPOBASSO[2],

[1] University of Glasgow, School of Engineering. James Watt Building South, University Avenue, Glasgow G12 8QQ, United Kingdom. E-mail: j.drofelnik.1@research.gla.ac.uk
[2] Corresponding Author. University of Lancaster, Department of Engineering. Engineering Building, Gillow Avenue, Lancaster LA1 4YW, United Kingdom. Tel.: +44 (0)1524 594673, E-mail: m.s.campobasso@lancaster.ac.uk

ABSTRACT

A wing simultaneously heaving and pitching can extract energy from an oncoming water or air stream. First large-scale commercial demonstrators are being installed and tested. The operating conditions of this device is likely to feature Reynolds numbers in excess of 500,000. Strong finite wing effects spoiling the power generation efficiency are also expected. This paper thoroughly investigates the hydrodynamics of oscillating wings at a Reynolds number of 1,500,000 considering finite wing effects for an aspect ratio 10 wing with either sharp tips or endplates to reduce tip vortex losses. The study of these periodic flows uses three-dimensional time-dependent Navier-Stokes simulations with grids featuring more than 30 million cells. The shear stress transport turbulence model of Menter is used for the turbulence closure. Main contributions include: *a*) the quantification of the efficiency improvement achievable by using wings with endplates rather than bare tips, and *b*) detailed comparisons of the wing hydrodynamics with and without endplates, and the infinite wing.

Keywords: Energy-extracting oscillating wing, Finite wing effects, Turbulent Navier-Stokes CFD

1. INTRODUCTION

Increasing demand for electricity production and stricter environmental policy have greatly contributed to the development of novel alternative renewable devices. A promising concept in the fields of wind turbines and tidal energy systems relies on the use of oscillating wings simultaneously heaving and pitching to extract energy from an oncoming water or air stream. The concept was pioneered by McKinney and DeLaurier [1] in 1981, and further investigated by Jones *et al.* [2]. Several other numerical, experimental and prototype-based studies of the oscillating wing device for power generation followed these pioneering studies. Recently Young *et al.* [3] published a comprehensive review of the analytical, numerical and experimental research work carried out in this field to date. The review focuses on the effects of flapping kinematics and foil geometry on the vortex-structure interaction, a phenomenon that can improve the power generation efficiency for certain laminar and turbulent flow regimes. That article also highlights outstanding questions on the fluid mechanics of the oscillating wing in real installations, characterized by high Reynolds numbers and strong and complex three-dimensional (3D) flow effects.

Kinsey and Dumas [4] performed a thorough parametric computational fluid dynamics (CFD) investigation into the effects of motion parameters (heaving and pitching amplitude and motion frequency) and geometric parameters (foil shape and location of pitching axis) on the power generation efficiency of the oscillating wing. They report that using optimum motion parameters for a laminar flow regime with a Reynolds number based on the foil chord and the freestream velocity of 1100 yields an efficiency of 34%, and also that the main factor controlling the efficiency is the synchronization of heaving motion and unsteady leading edge vortex shedding (LEVS) associated with dynamic stall. These findings were confirmed also in a later study using the compressible Navier-Stokes (NS) research code COSA with a low-speed preconditioner optimized for time-dependent flows [5].

An experimental 2 kW prototype of the oscillating wing for power generation was designed, built and tested by Laval University in water at Lac-Beauport near Quebec City. Measured data confirmed fairly high values of the energy conversion efficiency [6]. Thereafter, Kinsey and Dumas investigated numerically the hydrodynamics of the oscillating wing at a Reynolds number of 0.5 million [7]. Both two-dimensional (2D) and 3D turbulent incompressible FLUENT simulations using the Spalart-Allmaras turbulence model [8] were performed. Cross-comparison of the laminar and turbulent flow simulations using the same wing motion parameters reveals that the efficiency of the energy conversion increases significantly as the Reynolds number increases from low laminar values to fairly high turbulent values [4, 7, 9]. This was reported by the authors of this paper who used COSA to carry out 2D fully laminar [5] and fully turbulent [9] simulations of the oscillating wing using the same wing motion parameters. The comparative analysis of the two regimes reported in [9] revealed that *a*) the power generation efficiency increases at higher Reynolds numbers due to thinner turbulent boundary layers, *b*) LEVS is delayed in the fully turbulent regime due to higher stability of the turbulent bounary layers. Thus the optimal synchronization between wing motion and LEVS achieved in the laminar regime is lost in the high-Reynolds number case. It was assumed that for higher Reynolds numbers further synchronization of wing motion and LEVS could lead to even higher efficiencies than that of 40% obtained for turbulent regime. However, Kinsey and Dumas later showed that high power extraction efficiency at high Reynolds numbers does not necessarily rely on the occurrence of LEVS [10].

Kinsey and Dumas also reported that the power generation loss of the finite wing of aspect ratio (*AR*) 7 with endplates is about 15% of the efficiency of the infinite wing [7]. In a follow-up study, those authors extended their 3D analyses to wings of *AR* 5, 7 and 10 with and without endplates to quantify losses due to finite wing effects and wing tip type. They concluded that, for a finite wing of $AR \geq 10$ with endplates such a loss could be limited to about 10% of the efficiency of infinite span [11].

The interest of the industrial and scientific communities in the oscillating wing device keeps growing, as also highlighted by the installation of the 1.2 MW prototype of Pulse Tidal in the Bristol Channel in 2014 [3]. However, significant uncertainty on the impact of 3D flow effects still exists. This study aims at quantifying the loss of power generation efficiency due to 3D effects making use of time-dependent (TD) finite wing span turbulent flow COSA simulations. Realistic turbulent flow conditions at a Reynolds number of 1.5 million and with nearly optimal wing motion parameters obtained with 2D analyses [9] are used, and the 3D effects are analysed for two different wing end geometries.

The paper starts with the definition of the kinematic and dynamic parameters of the oscillating wing motion. This is followed by the statement of the governing equations and a brief description of the CFD solver. A detailed comparative study of the infinite and finite span wings in turbulent flow conditions is then reported, quantifying and discussing the differences of unsteady hydrodynamic characteristics of the idealised 2D and realistic 3D configurations. A summary of the main findings are provided in the closing section.

2. OSCILLATING WING DEVICE

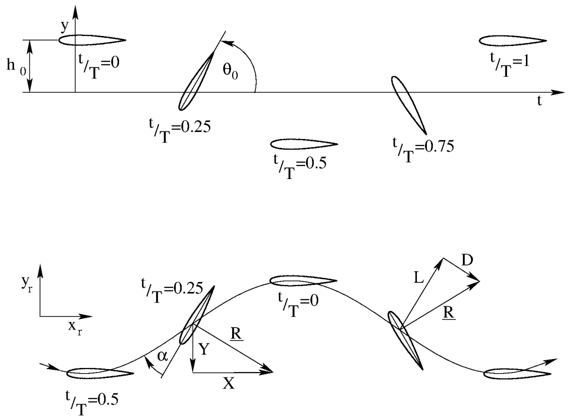

Figure 1. Top: prescribed motion of oscillating wing for power generation. Bottom: foil motion in reference system moving with freestream velocity.

Here an oscillating wing is defined as a foil experiencing simultaneous pitching $\theta(t)$ and heaving $h(t)$ motions. The following mathematical representation of the imposed motion is that adopted in [4]. Taking a pitching axis located on the chord line at position x_p from the leading edge (LE), the foil motion is expressed as:

$$\theta(t) = \theta_0 \sin(\omega t) \qquad \rightarrow \Omega(t) = \theta_0 \omega \cos(\omega t) \tag{1}$$

$$h(t) = h_0 \sin(\omega t + \phi) \rightarrow v_y(t) = h_0 \omega \cos(\omega t + \phi) \tag{2}$$

where θ_0 and h_0 are respectively the pitching and heaving amplitudes, Ω is the pitching velocity, v_y is the heaving velocity, ω is the angular frequency and ϕ is the phase between heaving and pitching. In this study, ϕ is set to 90^o, and the NACA0015 foil is selected. The freestream velocity is denoted by u_∞ and the angular frequency ω is linked to the vibration frequency f by the relationship $\omega = 2\pi f$. The prescribed oscillating motion is depicted in the top sketch of Fig. 1.

An oscillating symmetric foil can operate in two different regimes: propulsive or power-extracting mode. This distinction originates from the sign of the forces that the flow generates on the oscillating foil. Based on the imposed motion and the upstream flow conditions, the foil experiences an effective angle of attack (AoA) α and an effective velocity v_e given respectively by:

$$\alpha(t) = \arctan\left(-v_y(t)/u_\infty\right) - \theta(t) \tag{3}$$

$$v_e(t) = \sqrt{u_\infty^2 + v_y(t)^2} \tag{4}$$

The maximum values of α and v_e have a major impact on the amplitude of the peak forces in the cycle, and also on the occurrence of dynamic stall. The maximum effective AoA reached in the cycle is approximated by the modulus of its quarter-period value, that is $\alpha_{max} \approx |\alpha(T/4)|$. As explained in [4], the power-extracting regime (in a mean sense, over one cycle) occurs when $\alpha(T/4) < 0$. This condition is represented in the bottom sketch of Fig. 1, which provides a time-sequence viewed in a reference frame moving with the farfield flow at u_∞, so that the effective AoA $\alpha(t)$ is made visible from the apparent trajectory of the foil. In this sketch, the resultant force $\underline{R}$ is first constructed from typical lift and drag forces (right-hand side) and then decomposed into X and Y components (left-hand side). One sees that the vertical force component Y is in phase with the vertical velocity component v_y of the foil over the entire cycle. This implies that the wing extracts energy from the fluid as long as no energy transfer associated with the component X of the hydrodynamic force takes place. This is the case since the foil does not move horizontally. The aerodynamic phenomena occurring during the wing oscillation are substantially more complex than the quasi-steady model discussed above. In some cases, for example, the efficiency of the energy extraction was shown to be heavily influenced by the occurrence of unsteady leading edge vortex shedding (LEVS) associated with dynamic stall and the LEVS timing with respect to the foil motion.

Taking a wing span of one unit length, the instantaneous power extracted from the flow is the sum of a heaving contribution $P_y(t) = Y(t)v_y(t)$ and a pitching contribution $P_\theta(t) = M(t)\Omega(t)$, where M is the resulting torque about the pitching center x_p. Denoting by c the foil chord, $C_{P_z} \equiv P_z/(\frac{1}{2}\rho_\infty u_\infty^3 c)$ the power coefficient per wing length at position z, and $C_P = \frac{1}{l}\int_{-l}^{l} C_{P_z} dz$ the power coefficient over the entire wing, where l denotes the semispan, the nondimensional power extracted over one cycle is given by:

$$\overline{C}_P = \overline{C}_{P_y} + \overline{C}_{P_\theta} = \frac{1}{T}\int_0^T \left[C_Y(t)\frac{v_y(t)}{u_\infty} + C_M(t)\frac{\Omega(t)c}{u_\infty} \right] dt$$

where $C_Y(t) = Y(t)/(\frac{1}{2}\rho_\infty u_\infty^2 c)$ and $C_M(t) = M(t)/(\frac{1}{2}\rho_\infty u_\infty^2 c^2)$.

3. NAVIER-STOKES CFD SOLVER

The finite volume structured multi-block compressible Reynolds-averaged NS (RANS) code COSA [5, 9, 12] uses Menter's shear stress transport (SST) turbulence model [13]. Given a moving control volume C with time-dependent boundary $S(t)$, the Arbitrary Lagrangian-Eulerian integral form of the system of the time-dependent RANS and SST equations is:

$$\frac{\partial}{\partial t}\left(\int_{C(t)} \mathbf{U}\, dC\right) + \oint_{S(t)} (\underline{\mathbf{\Phi}}_c - \underline{\mathbf{\Phi}}_d)\cdot d\underline{S} - \int_{C(t)} \mathbf{S}\, dC = 0$$

The array $\mathbf{U}$ of conservative flow variables is defined as: $\mathbf{U} = [\rho \quad \rho\underline{v}^T \quad \rho E \quad \rho k \quad \rho\omega]^T$ where ρ and $\underline{v}$ are respectively the fluid density and velocity vector, and E, k and ω are respectively the total energy, the turbulent kinetic energy and the specific dissipation rate of turbulent kinetic energy, all per unit mass. The perfect gas equation is used to link internal energy, pressure and density. The generalized convective flux vector $\underline{\mathbf{\Phi}}_c$ depends on $\mathbf{U}$ and the velocity of the boundary S. The generalized diffusive flux vector $\underline{\mathbf{\Phi}}_d$ depends primarily on the sum of the molecular stress tensor, proportional to the strain rate tensor $\underline{\underline{s}}$, and the turbulent Reynolds stress tensor. Adopting Boussinesq's approximation, the latter tensor is also proportional to $\underline{\underline{s}}$ through an eddy viscosity μ_T. In the SST model, μ_T depends on ρ, k, ω and the vorticity.

The only nonzero entries of the source term $\mathbf{S}$ are those of the k and ω equations, given respectively by:

$$\begin{aligned} S_k &= \mu_T P_d - \frac{2}{3}(\nabla\cdot\underline{v})\rho k - \beta^*\rho k\omega \\ S_\omega &= \gamma\rho P_d - \frac{2}{3}(\nabla\cdot\underline{v})\frac{\gamma\rho k}{\nu_T} - \beta\rho\omega^2 + CD_\omega \end{aligned}$$

with

$$\begin{aligned} P_d &= 2\left[\underline{\underline{s}} - \frac{1}{3}\nabla\cdot\underline{v}\right]\nabla\underline{v} \\ CD_\omega &= 2(1-F_1)\rho\sigma_{\omega 2}\frac{1}{\omega}\nabla k\cdot\nabla\omega \end{aligned}$$

where $\nu_T = \mu_T/\rho$, $\sigma_{\omega 2}$ is a constant, F_1 is a flow state-dependent function, and σ_k, σ_ω, γ, β^* and β are weighted averages of corresponding constants of the standard $k-\omega$ and $k-\epsilon$ models with weights F_1 and $(1-F_1)$, respectively [13].

COSA is second order accurate in time and space, and uses a very efficient MPI parallelization [14]. The accuracy of the space- and time-discretization has been thoroughly validated by considering a wide set of analytical and experimental test cases [5, 9, 12].

4. RESULTS

Thorough investigations into the 3D hydrodynamics of oscillating wings for power generation are reported herein. Most analyses are based on 3D time-accurate RANS simulations performed with COSA. The physical and computational set-up of all simulations is described first. Thereafter the 3D unsteady flow mechanisms accounting for the variations of the energy capture moving from the ideal scenario of an infinite wing to the realistic case of a finite wing are analyzed. Moreover, the dependence of the 3D flow patterns and, ultimately, of the energy capture efficiency on the wing end geometry is carefully examined.

4.1. physical and numerical set-up

The selected wing profile is the NACA0015 foil. The wing trajectory features a heaving and a pitching motion component defined by Eqs. (1) and (2) respectively. The operating condition characterized by a high efficiency of the energy extraction in the turbulent flow regime described in [9] (case A) is considered. The heaving amplitude h_0 equals one chord and the pitching center is at $x_p = 1/3$ of the chord from the LE. The pitching amplitude θ_0 is 76.33^o and the nondimensionalized frequency $f^* = fc/u_\infty$ is 0.14, where f is the frequency in Hertz. The Reynolds number based on the freestream velocity and the foil chord is $Re = 1.5 \cdot 10^6$, and this value was used for all simulations reported below.

The time-dependent 3D turbulent flow fields past the oscillating wing were computed using structured multi-block non-deforming moving grids. In all simulations the entire grid moved rigidly with the wing. The 3D grid was obtained by extruding the 2D grid past the foil along the spanwise direction. The node coordinates of 2D and 3D grids were nondimensionalized by the foil chord, and the farfield boundary in the foil plane was at about 50 chords from the foil. The required level of refinement of the 3D grid in the 2D plane of the foil was assessed by means of 2D simulations. More specifically, the periodic 2D flow field associated with the motion and flow parameters reported above was computed using a mesh with 98,304 cells (coarse), one with 393,216 cells (medium), and one with 1,575,864 cells (fine) using 256 time-intervals per oscillation cycle. The overall mean power coefficients $\overline{C_P}$ obtained with the coarse and medium grids differed by 2.2%, whereas those obtained with the medium and fine grids differed by 0.4%, pointing to the suitability of the medium grid refinement for this problem. To assess the solution sensitivity to the level of temporal refinement, the selected regime was simulated with the 2D medium-refinement grid using 128, 256, 512 and 1024 time-intervals per oscillation period. The values of $\overline{C_P}$ obtained using 128 and 256 intervals differed by about 1.2%, whereas the difference between the 256-interval and the 512-interval $\overline{C_P}$, and the 512-interval and 1024-interval $\overline{C_P}$ were 0.7% and less than 0.1% respectively. This highlighted that the solution was largely independent of the number of intervals per period when at least 512 time-intervals per period were used. In the light of this outcome and to keep the computational cost of the 3D analyses within the size of the available resources, the level of refinement of the 2D coarse grid was adopted for building the 2D sections of the 3D grid, and 256 time intervals per cycle were used in the 3D simulations analyzed below. It is the authors' view that the use of relatively coarse grids made herein does not significantly affect the main conclusions of the investigations presented below.

The 3D simulations used a symmetry boundary condition at midspan to halve computational costs. The 30,670,848-cell grid was built by stacking a 2D 65,536-cell O-grid in the spanwise direction from the midspan symmetry plane to the lateral farfield boundary which was at 50 chords from the symmetry boundary. The 65,536-cell O-grid had 256 intervals along the foil, and 256 intervals in the normal-like direction. In the foil plane, the farfield boundary was at about 50 chords from the foil, and the distance d_w of the first grid points off the foil surface from the foil itself was about $6 \cdot 10^{-6}$. The AR of the wing was 10. Constant spanwise spacing $\Delta z = 0.02$ was used from midspan to 90 % semispan, and from here the grid was clustered towards the tip achieving a minimum spacing $\Delta z = 0.0003$. The cell size increased again moving from the tip to the lateral farfield boundary. Two wing end topologies were considered, one with sharp tips, the other with endplates. The geometry of the endplate is depicted in Fig. 2. Careful grid design enabled the use of the same grid for both configurations, removing any uncertainty in the comparative analysis of these two configurations arising from using different grid topologies. A view of two 3D grids is provided in Fig. 3.

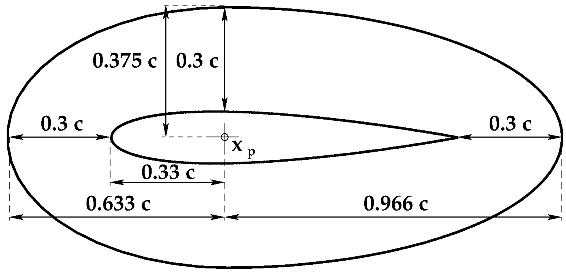

Figure 2. Endplate geometry.

The CFL number of the simulation of the wing with sharp tip and endplate were set to 4 and 3 respectively, and all simulations were run without multigrid. CFL ramping was used for all time steps, and 1,500 iterations were performed to compute the solution of each physical time. With this set-up, the residuals of the NS equations decreased by about 5 orders of magnitude at all physical times and all force and moment components fully converged within 1,000 to 1,100 iterations. All simulations were run until the maximum difference between C_Y over the last two oscillation cycles became less than 0.1% of the maximum C_Y over the last cycle. The number of oscillation cycles typically required to fulfil this requirement varied between four and ten, depending on the spatial and temporal refinement, and also on whether the simulation had been started from a freestream condition or from the solution of a simulation using the same grid but different temporal refinement. It was chosen to monitor the periodicity error of C_Y because the vertical force component gives the highest contribution to the extracted power. For all analyses of the oscillating wing presented in this report, y^+ was found to be smaller than one at all grid points and all times of the periodic flow field.

4.2. aerodynamic analysis

The evolution of the main kinematic parameters of the oscillating wing over one oscillation period is depicted in Fig. 4. The plot shows the time-dependent values of the vertical position h of the wing, its angular position θ, the nondimensionalized

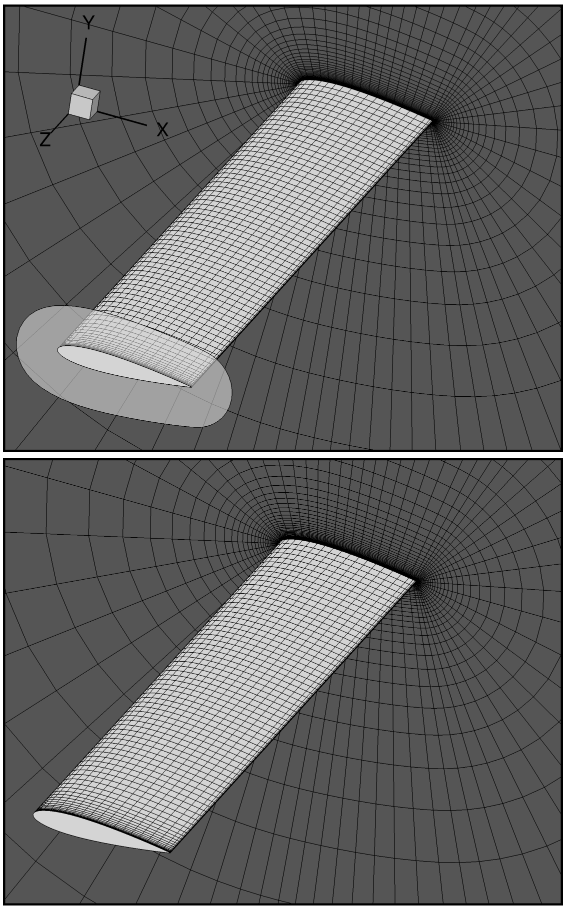

Figure 3. Surface mesh of wing and symmetry boundary (only every fourth grid line in all directions is reported). Top: wing with endplate. Bottom: wing with sharp tip.

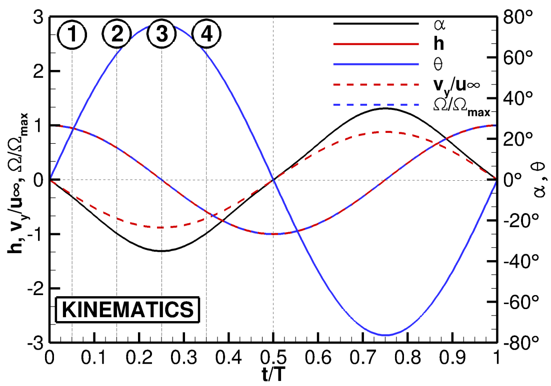

Figure 4. Kinematic parameters.

heaving velocity v_y/u_∞, and the nondimensionalized pitching velocity Ω/Ω_{max}, with Ω_{max} being the maximum pitching velocity of the cycle. The figure also reports the effective AoA α computed with Eq. (3). One notes that the maximum AoA is about 35^o. The four positions labeled 1 – 4 correspond to 5%,15%, 25% and 35% of the period respectively, and are those at which the flow field is examined in greater detail in the following analyses.

Table 1. Mean power coefficients of wing with $AR \to \infty$, AR 10 and endplate (EP), and AR 10 and sharp tip (ST).

AR	$\overline{C}_P$	$\overline{C}_{P_y}$	$\overline{C}_{P_\theta}$
∞	1.004	1.176	-0.172
10 EP	0.941	1.219	-0.278
10 ST	0.882	1.149	-0.267

The mean values of the overall power coefficient $\overline{C}_P$, the heaving power coefficient $\overline{C}_{P_y}$, and the pitching power coefficient $\overline{C}_{P_\theta}$ for the infinite span wing, the AR 10 wing with endplate (EP) and the AR 10 wing with sharp tip (ST) are reported in Table 1. The infinite span analysis was performed with a 2D simulation, whereas the two AR 10 analyses are based on full 3D simulations. One notes that $\overline{C}_P$ of the AR 10 wing with EPs is 6% lower than that of the infinite wing, whereas $\overline{C}_P$ of the AR 10 wing with STs is 12% lower than that of the ideal infinite wing case. The breakdown of the heaving and pitching power components for the three cases highlights that: *a*) the mean negative pitching power (a loss term) of both AR 10 wings increases by a comparable amount with respect to the ideal infinite span case (36% with STs and 38% with EPs), *b*) the heaving power coefficient of the AR 10 wing with STs also decreases (by about 2%) with respect to the ideal case, whereas the heaving power coefficient of the AR 10 wing with EPs increases by about 4%. These observations highlight that 3D flow effects hit the overall energy extraction efficiency of this device in a complex manner, that appears to depend on the geometry of the wing tips.

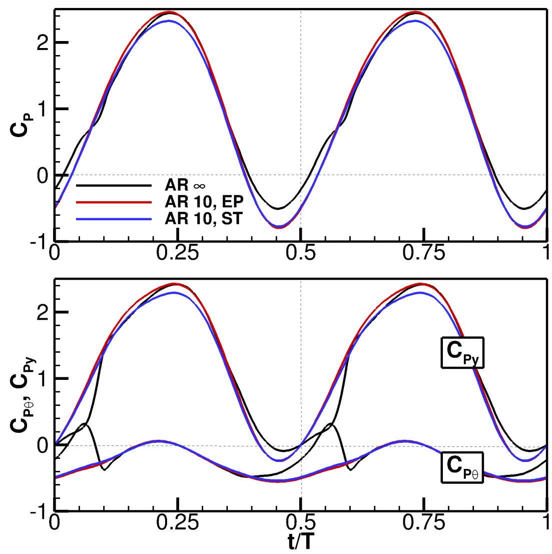

Figure 5. Comparison of overall, heaving and pitching power coefficients.

The two subplots of Fig. 5 report the profiles of C_P, C_{P_y} and C_{P_θ} over the period. In the first 10% and last 15% of both semi-periods, both AR 10 C_P profiles are significantly lower than the AR ∞ configuration (top subplot). This is due to the higher negative pitching power of both finite wings when the wing is at the highest and lowest points of the stroke (bottom subplot). Fig. 5 also highlights that, between about 10% and 35% of both semi-periods, the heaving and overall power coefficients of the wing with EPs are higher than for the ideal wing, whereas those of the wing with STs are lower.

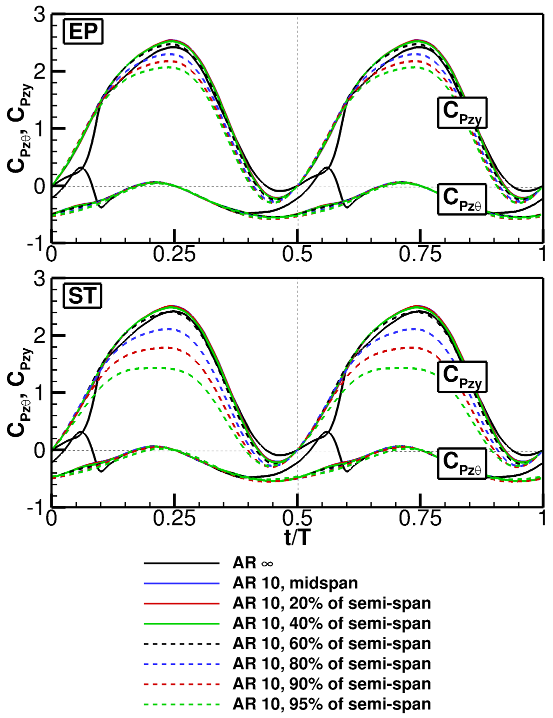

Figure 6. Comparison of heaving and pitching power coefficients per wing length.

To further investigate the dependence of the energy extraction efficiency of the finite span wing on the tip geometry highlighted in Fig. 5, the power coefficient curves per unit length of the AR 10 wings at various spanwise positions are cross compared in Fig. 6, which also reports the AR ∞ profiles for reference. The symbols $C_{P_{zy}}$ and $C_{P_{z\theta}}$ denote respectively the heaving and pitching power coefficients per wing length. One notes that between about 10% and 35% of both semi-periods the reduction of $C_{P_{zy}}$ with respect to the ideal case as one moves from about 80% semispan towards the tip is significantly smaller for the wing with EPs than for the wing with STs. Moreover, in the same portions of the period, the heaving power of the finite span wing is higher with EPs than with STs. These performance differences are due primarily to the existence of a strong tip vortex in the ST configuration, which induces significant downwash lowering the effective AoA with a strength decreasing from tip to midspan. Note also that the largest differences between the heaving power of the two AR 10 wings occur in the period range with maximum nominal AoA. The comparison of the skin friction lines of the two finite span wings at 25 % of the vertical stroke are reported in Fig. 7, which highlights the distortions of the flow path of the wing with STs leading to the formation of the tip vortex. The $C_{P_{z\theta}}$ profiles of Fig. 6 also show that the

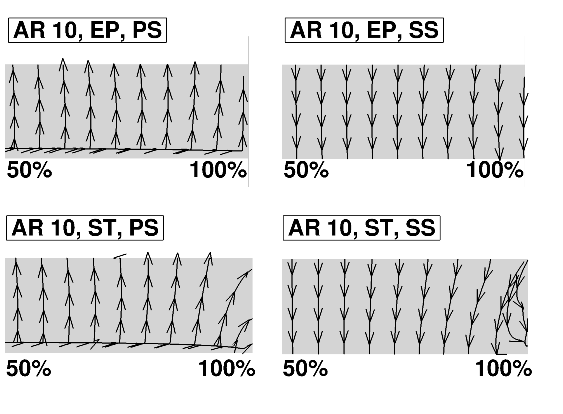

Figure 7. Skin friction lines on pressure side (PS) and suction side (SS) of wing with sharp tips and endplates at 25% of the cycle.

maximum loss-generating increment of the negative pitching power occurs when the finite span wings is close to the highest and lowest positions of the vertical stroke, varies fairly little along the span, and is not significantly affected by the wing tip geometry. As highlighted below, this is due to the absence of LEVS in the 3D flow field of both AR 10 wings.

The two top subplots of Fig. 8 depict the contours of the z-component of the vorticity of the infinite span wing and the midspan section of the AR 10 wing with EPs at 5% of the period (position 1). The bottom subplots refer instead to the 25% point of the period (position 3). The comparison of the top subplots highlights that in the AR 10 configuration, unlike in the infinite span case, there is no LEVS. The low pressure region on the foil side on which the vortex is generated contributes to reduce the energy capture loss due to the negative pitching power. Therefore, the absence of LEVS in the AR 10 case results in higher losses due to the larger (in absolute value) negative pitching power. In the other portions of the period, where LEVS is absent also in the infinite span case, the flow at midspan of the AR 10 wing and that of the wing with no tip effects are nearly identical, as highlighted by the bottom subplots which refer to the position of maximum nominal AoA. These observations also hold for the midspan section of the AR 10 wing with STs, the vorticity contours of which are not reported for brevity. The observations confirm that this loss mechanism arising when dealing with finite span wings is fairly independent of the tip geometry.

The top and bottom subplots of Fig. 9 show the

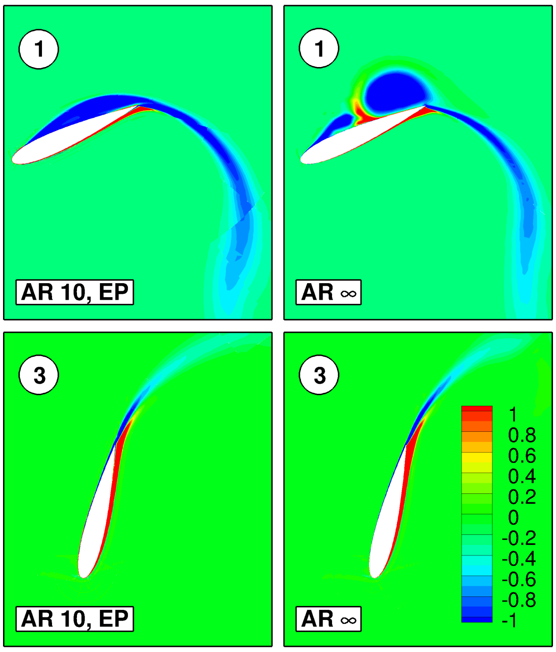

Figure 8. Contours of z component of vorticity of wing with infinite span and at midspan of wing with EPs. Top left: wing with EPs at 5 % of the cycle; top right: infinite wing at 5 % of the cycle; bottom left: wing with EPs at 25 % of the cycle; bottom right: infinite wing at 25 % of the cycle.

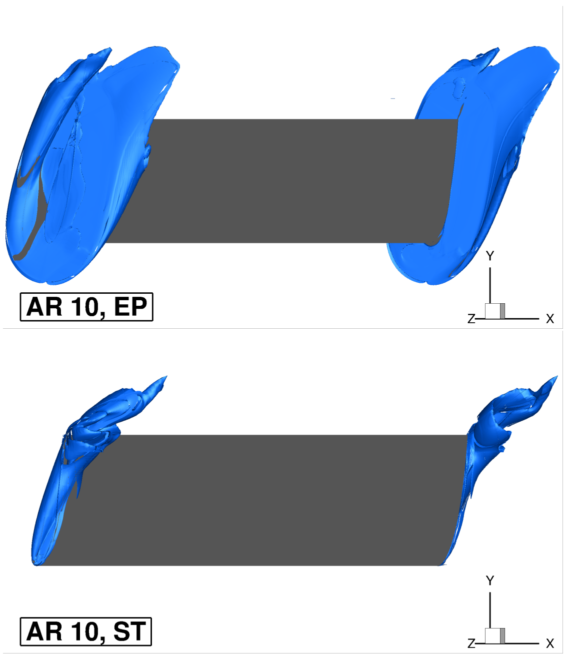

Figure 9. Isosurface of vorticity magnitude (Ω_m = 2) at 25 % of the period. Top: wing with endplates. Bottom: wing with sharp tips.

isosurface of vorticity magnitude ($\Omega_m = 2$) at the tips of the wings with endplates and sharp tips respectively. At the sharp tips vorticity from the pressure side rolls down to the suction side to form a trailing vortex, which causes the downwash effect. The downwash leads to a reduction of the effective AoA to the sections close to the tip, reducing C_{P_y}, as observed in the bottom plot of Fig. 6. The top plot of Fig. 9 shows that a tip vortex exists also for the wing with endplates. This vortex, however, originates at the edge of the endplates and is farther away from the wing than the vortex of the wing with sharp tips, resulting in less pronounced downwash. Moreover the vortex originating at the endplate is smaller than that originating at the sharp tip, because the driving pressure difference is smaller in the former case.

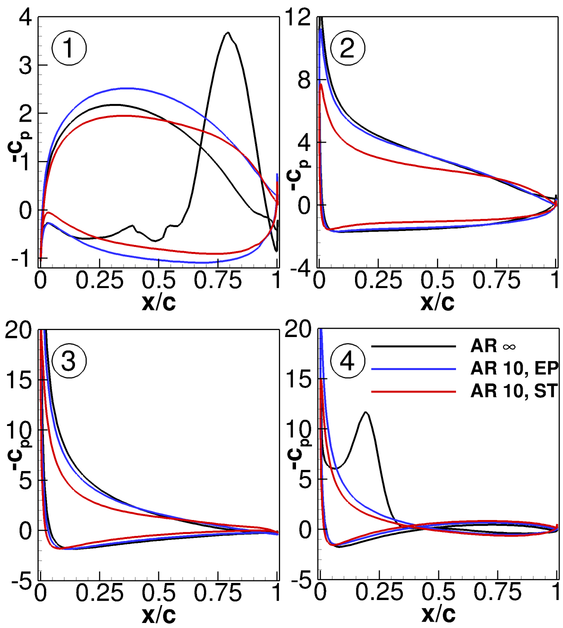

Figure 10. Pressure coefficient c_p of infinite span wing, and *AR* 10 wings with endplates and sharp tips at positions labeled 1-4 in Fig. 4.

The effects of the flow mechanisms discussed above on the static pressure distribution of the wing, which is a measure of the loading, are examined in Fig. 10. Its four subplots compare the static pressure coefficient of the infinite wing, and the 95 % semispan section of the *AR* 10 wings at the positions labeled 1-4 in Fig. 4. All four subplots show that the pressure-based heaving force acting on the wing with endplates is always larger than that on the wing with sharp tips, and this is due to the stronger downwash of the wing with sharp tips, which reduces the effective AoA. At positions 2 and 3, close to maximum nominal AoA, the heaving force per unit length of the infinite span wing is comparable to that of the wing with endplates. At position 1, corresponding to the LE vortex of the infinite wing being close to the trailing edge, the heaving force of the infinite wing is significantly smaller than that of the finite span wings.

5. SUMMARY

A detailed numerical investigation into the impact of flow three-dimensionality on the energy extraction efficiency of oscillating finite span wings was performed. Using the COSA 3D NS code with 30 million-cell grids, the differences of flow patterns and performance parameters between an infinite wing and one with aspect ratio 10 with either sharp tips or endplates were investigated.

The considered wing motion is characterized by a high power generation efficiency of the infinite wing in a turbulent regime at $Re = 1.5 \cdot 10^6$, and this operating condition is characterized by the existence of LEVS. The mean overall power coefficient of the *AR* 10 wing with sharp tips is found to decrease by 12 % with respect to that of the infinite wing. The loss is caused both by the reduction of the effective AoA induced by the downwash associated with the strong tip vortices, and also the LEVS suppression, which yields higher pitching power in the infinite span case. The mean overall power coefficient of the *AR* 10 wing with endplates is found to decrease by only 6 % with respect to the infinite wing. The lower loss with respect to the wing with sharp tips is due to a smaller reduction of the effective AoA due in turn to a weaker downwash achieved by weakening the tip vortices with the endplates.

For the *AR* 10 wing, the reduction of energy capture efficiency due to the LEVS suppression is independent of the tip geometry. A recent optimization study aiming at determining combinations of kinematic parameters (oscillation frequency, heaving and pitching amplitudes) to maximize the energy capture efficiency highlighted that high efficiency levels can be achieved also with kinematic conditions which do not yield LEVS [10]. In the light of the loss associated with the suppression of LEVS when considering finite wing effects, it appears advisable to design these devices avoiding regimes characterized by 2D LEVS, so as to minimize losses due to finite wing effects.

ACKNOWLEDGEMENTS

This work used the ARCHER UK National Supercomputing Service (http://www.archer.ac.uk).

REFERENCES

[1] McKinney, W., and DeLaurier, J., 1981, "The Wingmill: An Oscillating-Wing Windmill", *Journal of Energy*, Vol. 5 (1), pp. 109–115.

[2] Jones, K., Lindsey, K., and Platzer, M., 2003, "An Investigation of the Fluid-Structure Interaction in an Oscillating-Wing Micro-Hydropower Generator", Chakrabarti, Brebbia, Almozza, and Gonzalez-Palma (eds.), *Fluid Structure Interaction 2*, WIT Press, Southampton, United Kingdom, pp. 73–82.

[3] Young, J., Lai, J., and Platzer, M., 2014, "A review of progress and challenges in flapping foil power generation", *Progress in Aerospace Sciences*, Vol. 67, pp. 2–28.

[4] Kinsey, T., and Dumas, G., 2008, "Parametric Study of an Oscillating Airfoil in a Power-Extraction Regime", *AIAA Journal*, Vol. 46 (6), pp. 1318–1330.

[5] Campobasso, M., and Drofelnik, J., 2012, "Compressible Navier-Stokes analysis of an oscillating wing in a power-extraction regime using efficient low-speed preconditioning", *Computers and Fluids*, Vol. 67, pp. 26–40.

[6] Kinsey, T., Dumas, G., Lalande, G., Ruel, J., Mehut, A., Viarogue, P., Lemay, J., , and Jean, Y., 2011, "Prototype testing of a hydrokinetic turbine based on oscillating hydrofoils", *Renwable energy*, Vol. 36, pp. 1710–1718.

[7] Kinsey, T., and Dumas, G., 2012, "Computational Fluid Dynamics Analysis of a Hydrokinetic Turbine Based on Oscillating Hydrofoils", *Journal of Fluids Engineering*, Vol. 134, pp. 021104.1–021104.16.

[8] Spalart, P., and Allmaras, S., 1994, "A one-equation turbulence model for aerodynamic flows", *La Recherche Aerospatiale*, Vol. 1, pp. 5–21.

[9] Campobasso, M., Piskopakis, A., Drofelnik, J., and Jackson, A., 2013, "Turbulent Navier-Stokes Analysis of an Oscillating Wing in a Power-Extraction Regime Using the Shear Stress Transport Turbulence Model", *Computers and Fluids*, Vol. 88, pp. 136–155.

[10] Kinsey, T., and Dumas, G., 2014, "Optimal Operating Parameters for an Oscillating Foil Turbine at Reynolds Number 500,000", *AIAA Journal*, Vol. 52 (9), pp. 1885–1895.

[11] Kinsey, T., and Dumas, G., 2012, "Three-Dimensional Effects on an Oscillating-Foil Hydrokinetic Turbine", *Journal of Fluids Engineering*, Vol. 134, pp. 071105.1–071105.11.

[12] Campobasso, M., Gigante, F., and Drofelnik, J., 2014, "Turbulent Unsteady Flow Analysis of Horizontal Axis Wind Turbine Airfoil Aerodynamics Based on the Harmonic Balance Reynolds-Averaged Navier-Stokes Equations", ASME paper GT2014-25559.

[13] Menter, F., 1994, "Two-Equation Turbulence-Models for Engineering Applications", *AIAA Journal*, Vol. 32 (8), pp. 1598–1605.

[14] Jackson, A., and Campobasso, M., 2011, "Shared-memory, Distributed-memory and Mixed-mode Parallelization of a CFD Simulation Code", *Computer Science Research and Development*, Vol. 26 (3-4), pp. 187–195.

Conference on Modelling Fluid Flow (CMFF'15)
The 16th International Conference on Fluid Flow Technologies
Budapest, Hungary, September 1-4, 2015

CFD-DEM STUDIES OF GRAIN SEGREGATION PATTERNS ON A PILOT SCALE DESTONER

Ananda Subramani KANNAN[1], Michael Adsetts Edberg HANSEN[2], Jens Michael CARSTENSEN[3], Jacob LUND [4] and Srdjan SASIC[5]

[1] Corresponding Author. Department of Applied Mechanics, Chalmers University of Technology, SE 412 96 Gothenburg, Sweden. Tel.: +45 53661689, Fax: +45 4576 1041, E-mail: ananda@chalmers.se
[2] Videometer A/S, DK 2970 Hørsholm, Denmark. E-mail: maeh@videometer.com
[3] Videometer A/S, DK 2970 Hørsholm, Denmark. E-mail: jmc@videometer.com
[4] Westrup A/S, DK 4200 Slagelse, Denmark. E-mail: jacob.lund@westrup.com
[5] Department of Applied Mechanics, Chalmers University of Technology, SE 412 96 Gothenburg, Sweden. E-mail: srdjan@chalmers.se

ABSTRACT

In this paper we study segregation patterns of a bi-dispersed population of grains on a virtual destoner. The numerical setup is implemented in the OpenFOAM® environment using a CFD-DEM framework. We look at different operating points (e.g. deck inclination) in order to characterize the destoner output in terms of degree of segregation between light and heavy material. The entire computational domain is divided into three major zones (i.e. Exit fraction, Inlet/Middling fraction and Pre-Inlet fraction) in order to assess the overall behavior of the inlet feed material over the 'virtual' destoner deck. Our simulations show that the heavy product fraction in the discards stream increases over time with a corresponding accumulation of the 'valuable' light product at the base of the deck, indicating segregation between the stones (heavy product) and the grains (light product). The segregation between these two fractions has also been demonstrated to be sensitive to changes in deck tilt. A deck inclination of 3 degrees is considered optimal while steeper slopes (inclinations of 10 degrees) are deemed unsuitable for segregation and a corresponding 3 fold decrease in the destoner performance is noted. Consequently, the proposed CFD-DEM method provides a valuable framework for studying the underlying phenomena in such segregation of granular material.

Keywords: Bi-dispersed, CFD-DEM, Deck inclination, Destoner,OpenFOAM®, Segregation.

NOMENCLATURE

α	[-]	de Felice coefficient
C_d	[-]	drag coefficient
d	[m]	particle diameter
ε	[-]	local porosity
$\boldsymbol{F}_A$	[N]	fluid particle interaction force
$\boldsymbol{f}_c$	[N]	contact force
$\boldsymbol{f}_d$	[N]	drag force
$\boldsymbol{f}_f$	[N]	fluid-particle interaction force
Φ	[-]	packing fraction
g	[m/s^2]	acceleration due to gravity
I	[$kg.m^2$]	moment of inertia
j	[-]	summation index
k_i	[-]	number of particles
m	[kg]	mass
μ	[$kg/m.s$]	viscosity
N	[-]	number of grains/stones
n	[s]	simulation time
p	[Pa]	static pressure
R_i	[m]	particle diameter
Re_p	[-]	particle reynold's number
ρ	[kg/m^3]	density
t	[s]	time
$\boldsymbol{\tau}$	[$N.m$]	torque
τ	[s]	time
$\boldsymbol{u}$	[m/s]	particle velocity vector
$\boldsymbol{v}$	[m/s]	fluid velocity vector
v	[N]	force
ω	[rad/s]	angular velocity

Subscripts and Superscripts

dis	discards stream
f	fluid
fp	fluid - particle
i	particle i
j	particle j
p	particle
pr	products stream

1. INTRODUCTION

Purity and quality are two important criteria for food production today. Maintenance of the highest standards of quality in production is a challenge that has always been pushing existing technologies. The primordial practice of 'winnowing' has undergone such an incremental transition and is in today's day and age marketed as gravity separators. These equipment work under the fundamental principle of separation of similarly sized entities based on 'specific gravity or density'. The 'destoner' is a typical example of one such gravity separator used in the downstream processing of food grains to remove stone and other heavier contaminants. Sensitivity of the granular material flow to fluctuations in operating conditions (affecting the overall performance) encountered while operating these machinery have further increased the need for a deeper understanding of this phenomenon of gravity separation. The current work aims to investigate the effect of constitutive parameters (such as deck tilt) on the performance of a gravity separator (destoner) set up in an open source computational environment utilizing the Discrete Element Method (CFD-DEM).

The operation of a destoner is thus principally driven by fluidizing air. The constant stream of air in the system (released from the surface of the deck) sorts the grains based on their specific density with grains rising or falling by their relative weight to air. An inclined oscillating deck transports the heavier contaminant (e.g. stones) towards the higher end, while the lighter grain is collected at the base. The operation of a destoner is principally controlled by three main parameters: fluidizing air, reciprocation frequency and deck tilt. Other factors such as stroke length for the throwing action, inlet feed rate and composition and the nature of the deck surface (friction) may also affect the overall performance of the separator. However, for the sake of simplicity it is assumed that these other 'extrinsic' factors are fixed during the period of operation and the performance of the separator is only dependant on the three constitutive parameters.

The limited amount of relevant work on gravity separators (empirical or computational work) can be supplemented by collating results from other closely related applications such as shaking separation of rice and paddy. An empirical basis of granular segregation phenomena can be obtained by examining these related studies on shaking separation of rice. The mechanism of movement of paddy and rice in opposite directions on an oscillating tray separator was first proposed by Das [1]. This mechanism attributed separation to differences in coefficients of friction between paddy and the deck, rice and the deck and paddy and rice respectively. A similar surface contact dominated mechanism could also be applicable to gravity separators. The deck of a destoner has high surface friction to ensure that there is sufficient traction between the particles and the surface to prevent contacting grains from rolling down towards the lower end.

In addition to these empirical efforts, several numerical studies on grain separators have also been reported in literature. The CFD-DEM, a method based on the resolution of inter-particle contact, has been a popular choice for several research groups that investigate agricultural and food processing operations using numerical models. The reported applications of DEM to agricultural and food processing operations is limited to rather simplified case studies (dealing with the behaviour of a few hundred particles) including numerical studies on the separation process of soybeans and mustard seeds by a vibrating screen (Li *et.al. [2]*) and simulation of the shaking separation of paddy and brown rice (Sakaguchi *et.al [3]*). So far, the latter work represents the only validated application of DEM in grain downstream processing. This model was validated against experimental results, with good agreement reported with respect to the wave-like behaviour of the grain assembly and the macroscopic separation behaviour of the rice (Sakaguchi *et.al [3]*).

There is a need for additional CFD-DEM studies of gravity separators that would offer new insights into existing phenomena. Aiming at designing the next generation process. The current work represents such an effort in which a coupled CFD-DEM framework is used to assess relevant system properties as a function of the operating conditions (particularly deck tilt of the destoner). As a first step, the proposed CFD-DEM framework is discussed (along with the relevant constitutive equations) followed by a brief description of the numerical setup (simulation geometry, conditions etc.). Finally, we present the simulation results aiming to quantify the performance of a destoner.

2. THE COMPUTATIONAL METHOD

A coupled particle–fluid model (CFD-DEM) is employed in the current study of granular segregation patterns on a pilot-scale destoner. This would require the integration of the Newton's equation of motion for each particle and the full solution of the Navier–Stokes equations in the computational domain. This section describes the CFD-DEM framework and the corresponding numerical setup used in the current work. The concluding part of this section has a brief description of the metrics adopted to adjudge destoner performance in this work.

2.1. CFD-DEM Framework

In the equation of motion for every individual particle, the gravitational contact, fluid pressure gradient and drag forces are considered as:

$$m_i \frac{dv_i}{dt} = \mathbf{f}_{f,i} + \sum_{j=1}^{k_i} \left(\mathbf{f}_{c,ij} + \mathbf{f}_{d,ij} \right) + m_i \mathbf{g}, \quad (1)$$

The particle forces modelled are: the fluid-particle interaction force (the drag force), $\boldsymbol{f}_{f,i}$, the gravitational force , $m_i\boldsymbol{g}$, and the inter-particle forces which include the contact force, $\boldsymbol{f}_{c,ij}$, and viscous contact damping force $\boldsymbol{f}_{d,ij}$. The drag force is determined at the individual particle level and is hence not only dependent on the relative velocity $(|\boldsymbol{u} - \boldsymbol{v}|)$ between the fluid and particle but also on the presence of the surrounding particles. The formulation suggested by *Di Felice [4]*, which makes use of a voidage function ($f(\varepsilon_f)$) to correct the drag on an isolated particle. This formulation is utilized for estimating fluid-particle drag in this work (Eqs. (2) to (4)) as it co-relates well with fluidized bed applications.

$$\mathbf{f}_{f,i} = \frac{\left\{ f(\varepsilon_f) C_d \pi \rho_f d_p^2 |\mathbf{u}\text{-}\mathbf{v}| (\mathbf{u}\text{-}\mathbf{v}) \right\}}{8} \quad (2)$$

Where,

$$f(\varepsilon_f) = \varepsilon_f^{-(\alpha+1)} \quad (2a)$$

$$\alpha = 3.7\text{-}0.65e\text{^} \left\{ \frac{-\left(1.5\text{-}\log Re_p\right)^2}{2} \right\} \quad (3)$$

$$Re_p = \frac{d_p u \rho_c}{\mu_f} \quad (4)$$

The inter-particle forces act at the contact point between particles (rather than at the centre of mass) generating a torque ($\boldsymbol{\tau}_{ij}$) that causes the particle i to rotate (given as).

$$I_i \frac{d\omega_i}{dt} = \sum_{j=1}^{k_i} \boldsymbol{\tau}_{ij} , \quad (5)$$

I_i is the moment of inertia of the particle i, given as

$$I_i = \frac{2}{5} m_i R_i^2 . \quad (6)$$

The contact force, $\boldsymbol{f}_{c,ij}$, is generally estimated using either the hard-sphere or the soft-sphere approach. The hard-sphere approach is primarily applicable to relatively dilute gas–solid systems as it accounts only for instantaneous and binary collisions. The soft-sphere approach, on the other hand, takes multiple particle contact into consideration and is commonly used to simulate dense gas–particle systems (Crowe *et.al [5])*. Thus, in the current work (as we deal with dense granular flow of grains), the soft-sphere model is employed to calculate the contact forces, including the normal, damping and tangential forces between the particles and between particles and walls. The contact forces are modeled using an analogy with a mechanical system consisting of springs, dashpots and friction sliders. The continuous phase in a CFD-DEM framework is resolved using the standard finite volume methods and the corresponding governing equations are given as:

$$\frac{\partial \varepsilon_f}{\partial \tau} + \nabla.(\varepsilon_f \mathbf{u}_f) = 0, \quad (7)$$

$$\frac{\partial(\rho_f \varepsilon_f \mathbf{u}_f)}{\partial \tau} + \nabla.\ (\rho_f \varepsilon_f \mathbf{u}_f \mathbf{u}_f) = -\varepsilon_f \nabla p - \mathbf{F}_A + \rho_f \varepsilon_f \mathbf{g}, \quad (8)$$

The force $\boldsymbol{F}_A$ is the volumetric fluid-particle interaction force (coupling) calculated on the basis of Newton's third law of motion, i.e., the fluid drag force acting on the individual particles from the fluid phase will react on the individual particles (the fluid-particle drag is summed over a computational cell).

In this work, the coupled CFD-DEM framework is implemented into an Open-source computational platform (OpenFOAM). Prior to implementation of the framework, a validation study of its performance is undertaken. We compare here our results with the measurements made by *Goldschmidt et.al [6]*, on a pseudo two-dimensional, laboratory-scale fluidized bed with corresponding simulations of a pilot scale fluidized bed set-up in the open source framework (*Kannan et.al [7]*).

2.2. Simulation conditions: CFD-DEM framework implementation

The proposed computational framework is applied to describe the segregation phenomena observed in destoners. A schematic of a pilot scale destoner is provided in figure 1. In order to minimize the computational effort, a symmetric transverse section (see Fig. 1) is simulated. The relevant features of the pilot setup such as the vibrating deck and fluidizing air have been accounted for via corresponding vibrational models and continuum treatment of the air (air inlet defined at the table surface) respectively. The reduced computational domain is dimensioned at 40 cm x 30 cm x 24 cm (refer figure 1). The reduced computational domain is dimensioned at 40 cm x 30 cm x 24 cm (Fig. 1 bottom). The simulated feed consists of spherical particles of slightly different sizes (3.0 and 3.15 mm respectively) and stark density differences (in order to mimic stones and food grains) introduced batch-wise. The relevant micro-properties of the feed (e.g. density, Young' modulus, Poisson ration, number etc.) are listed in Table 1.

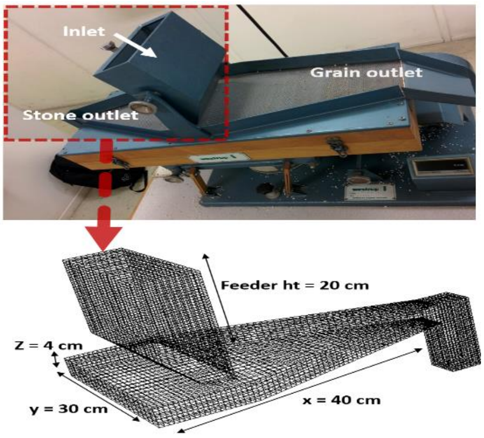

Figure 1. Pilot scale destoner (top) and simulated domain (bottom)

Table 1. Simulation conditions

Particle Micro-properties	
Food grain (modelled on the basis of rapeseed)	
Density (kg m^{-3})*	1100
Young's Modulus (Nm^{-2})*	5.0 * 10^{6}
Poisson ratio (Nm^{-2}) *	0.25
Co-efficient of restitution*	0.6
Coefficient of sliding friction*	0.3
Particle diameter (mm)	3.0
Number of particles	40000
Stone (modelled on the basis of rapeseed)	
Density (kg m^{-3})	2500
Particle diameter (mm) (all other micro-properties are same)	3.15
Number of particles	4000
Continuum properties (air at 20 ºC)	
Viscosity (kg m^{-1} s^{-1})	1.8 * 10^{-5}
Density (kg m^{-3})	1.205
Inlet Air velocity (m s^{-1})	1.5
Time step (s)	2.5 * 10^{-5}
* Micro-properties of Rapeseed adapted from - Transactions of the ASABE Vol. 54 (Boac *et.al* [11])	

Air is introduced into the system by means of a boundary condition that fixes the superficial velocity of air over the deck surface. Additionally, the vibrating action of the deck is approximated to have an amplitude of 1.5 cm/s (estimates from detailed mechanical calculations). The time step used in the numerical simulation is determined from the DEM constraints since the length scales simulated in DEM are much smaller than those of the resolution of the continuous phase.

The destoner removes stones from a given input feed using a combined effect of deck vibration, inclination and fluidization. The inclination of the deck creates the necessary slope needed to convert vertical stratification (achieved by the fluidizing air) into horizontal separation zones along the deck surface. The denser fraction (e.g. stones and other heavier contaminates) stay in contact with the deck and are conveyed to the higher end (by the throwing action of the deck) from where they are eventually removed. The lighter fraction (e.g. grains and other commercially viable material), on the other hand, are fluidized and move towards the lower end of the deck where they are collected. Hence, the right vibrational behavior also needs to be accounted for in the computational framework. In this study, it is assumed that the surface friction of the deck prevents contacting grains from rolling down towards the lower end and furthermore, the implemented vibration model transports them towards the higher end of the deck (i.e. $F_{vibration} > F_{gravity}$ leading to a net upward movement). It is assumed that this motion of the deck has negligible effects on the continuum phase, i.e. it only impacts the particulate phase. Hence, the throwing action of the deck is modelled in a 'static mesh framework' by utilizing non-zero wall boundary conditions based on a constant velocity profile obtained from measurements on a real destoner. This approach reduces the complexity of the corresponding computations, evading dynamic mesh simulations. This motion can be visualized using the schematic in Fig. 2.

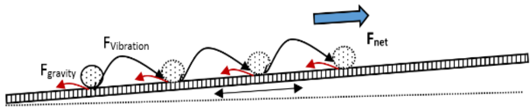

Figure 2. Grain/Stone movement of the deck

2.3. Destoner performance metrics

There are several methods reported in literature that can be used to quantify the performance of grain separators. These methods could be easily extended to describe the performance of a destoner. In the current work, we have chosen to make the performance assessment based on product purity. The purity of the fractions obtained from the outlets of the destoner are estimated on a weight fraction basis, i.e. the weight fraction of stones and alternately grains in the discarded fraction (given as follows)

$$\text{Heavy product fraction} = \frac{N_{stones,dis}}{N_{stones,in}} \quad (9)$$

(Number fraction)

$$\text{Light product fraction} = \frac{N_{grains,dis}}{N_{grains,in}} \quad (10)$$

Ideally, the heavy product fraction should increase in the discards stream from the destoner over time. This would indicate that stones are continually being removed by the apparatus. A limited exodus of ‘valuable’ grain is also tolerable under normal operating conditions. However, in order to ensure the maximum profitability from the process, this removal of valuable grains needs to be kept at the lowest possible level.

For the ease of assessing the data obtained from the simulations, the entire computational domain is divided into three major zones as shown in Fig. 3. The material in the higher end of the deck (collected in the discards trough) is classified as the ‘exit fraction’; the material towards the middle (from x =15 cm to x = 30 cm) of the destoner computational domain is classified as the ‘inlet/middling fraction’ and the material at the lower end (from x =0 cm to x = 15 cm) of the domain is classified as ‘pre-inlet fraction’. This grain number and behavior are individually assessed in each of these zones to objectively quantify the performance of a destoner.

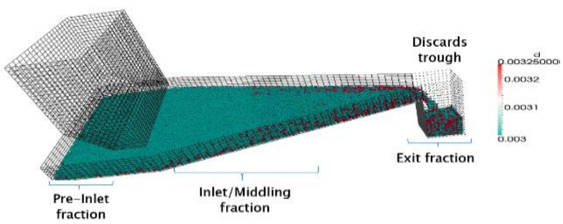

Figure 3. Destoner deck sectioning

3. RESULTS AND DISCUSSION

This section describes some qualitative assesments of the destoner simulations.

3.1. Assessment of the destoner performance (at optimal conditions of operation)

The optimal operating conditions for a destoner are established from data provided by manufacturers. The pilot scale simulation was setup in accordance to these optimal conditions, and the corresponding granular flow of the material over the deck is assessed using the performance metrics described in the earlier sections (Section 2.3). The operating condititons employed in the simulations are detailed in Table 2. The cases are simulated for a total of 5 seconds, after which the corresponding exit, inlet and pre-inlet fractions are assessed. The variation of the number fraction of the heavy and light product in the exit fraction over time is shown in figure 4 (extracted during operation under optimal conditions).

Table 2. Optimal operating conditions (based on data from manufacturers)

Operating parameter	*Set value*
Deck tilt (in degrees)	3
Deck vibration intensity (in terms of velocity)	1.5 cm/s
Inlet air velocity (U.Air)	1.25 m/s

Fig. 4 shows that the fraction of the heavy product rises from around 0.05 to 0.6, while the light product fraction increases from 0.03 to 0.15 after which it begins to level out (over a period of 5 seconds). This is indicative of a continued removal of the heavy product from the lighter (more valuable) product (which is what should be ideally expected).

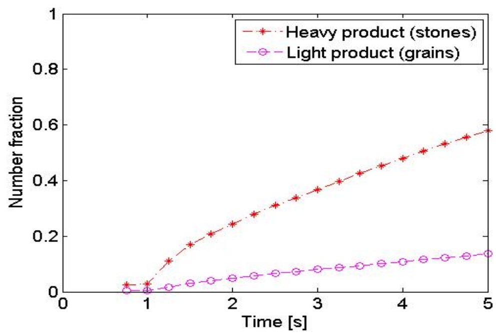

Figure 4. Exit fraction profile for a destoner at a tilt of 3 degrees and U.air of 1.25 m/s

The Fig. 5 shows the inlet/middling fraction profile for the heavy and the light product. Both, the heavy and the light product fraction reduce over time, indicating that there is a net movement of product towards the ‘discards trough’; which is what should be ideally expected. It must however be noted that, along with the heavy product there is also a significant quantity of valuable ‘light’ product being discarded. This is indicative of the fact that there is still a scope for optimizing the operating conditions of the destoners (i.e. the manufacturer supplied values are not the ‘most’ ideal operating conditions).

The pre-inlet fraction profile (Fig. 6) shows a very promising trend in the light and heavy product movement. There is a clear indication of the development of a separation zone in the pre-inlet section, with the number fraction of the heavy product decreasing from 0.15 to 0.03, and the corresponding increase in the number fraction of the light product (from 0.1 to 0.14). This observed trend is indicative of light particle accumulation and consequent exodus of heavy products.

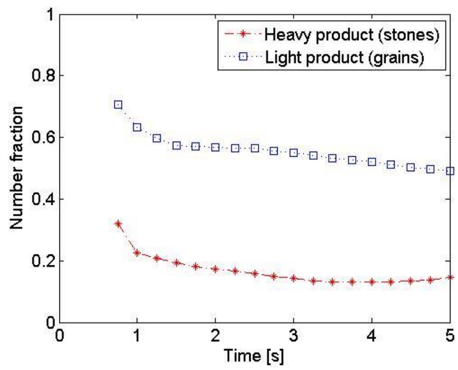

Figure 5. Inlet/Middling fraction profile for a destoner at a tilt of 3 degrees and U.air of 1.25 m/s

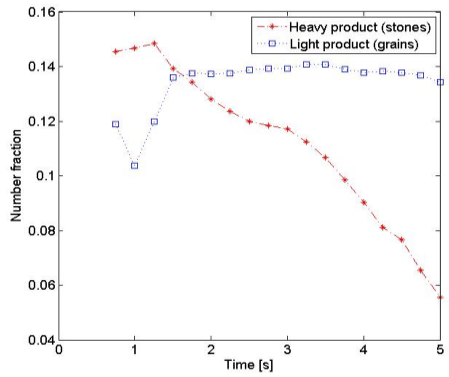

Figure 6. Pre-Inlet fraction profile for a destoner at a tilt of 3 degrees and U.air of 1.25 m/s

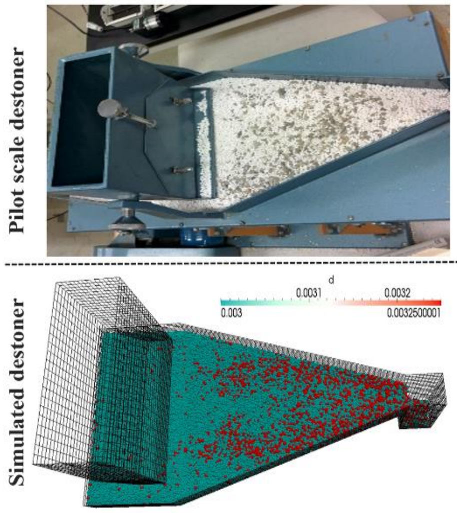

Figure 7. Pilot scale (top) and simulated destoner (bottom) at a deck tilt of 3 degrees (particles colored by diameter) : Snapshot at T = 5 sec)

Additionally, when a snapshot of the destoner simulation is compared with a corresponding snapshot of a pilot scale destoner under operation (see Fig.7), visual similarities are apparent. The general behavioral trends are existent, and these numerical models will form the basis for comprehensive future investigations on destoners.

3.2 Effect of deck tilt on the performance of a destoner

The performance of a destoner is shown to be sensitive to changes in the operating conditions. A slight variation in deck tilt and or any of the other constitutive operating parameters (such as vibration speed, inlet air velocity etc.) could produce drastic changes in the exit, inlet and pre-inlet product profiles. Amongst these constitutive parameters, as a first step, the deck tilt is varied to ~3 times the optimal tilt (i.e. tilt is set to 10 degrees), whilst keeping the vibration intensity and inlet air velocity constant, based on the optimal conditions. The corresponding product fractions (for exit, inlet and pre-inlet zones) are compared with the optimal profiles in order to assess the sensitivity of the destoner performance to deck tilt

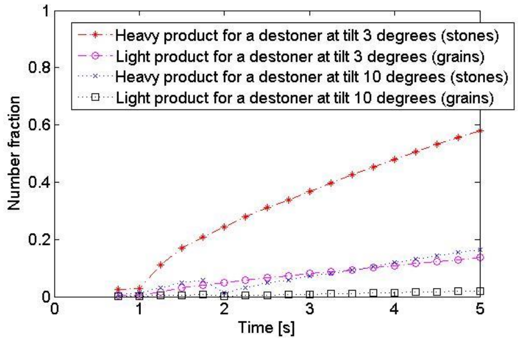

Figure 8. Comparison between the exit profiles of a destoner at optimal (3 degree tilt) and non-optimal operating conditions (10 degree tilt)

The comparison of the exit profiles between the optimal (3 degree tilt) and non-optimal (10 degree tilt) cases show that, on inclining a destoner to 10 degrees, the overall performance is reduced (Fig. 8). The heavy product fraction falls from around 0.6 (for the case with deck tilt of 3 degrees and t = 5 seconds) to around 0.075 (for the destoner at a tilt of 10 degrees). This significant reduction in the 'stone removal capacity' of the destoner is indicative of material clumping at the lower end of the deck. Relating this behavior with the vibration model utilized in this work (Section 2.2), it can be surmised that $F_{vibration} < F_{gravity}$ (i.e. the excessive inclination overpowers the effect of vibration) leading to material clumping (Fig. 9).

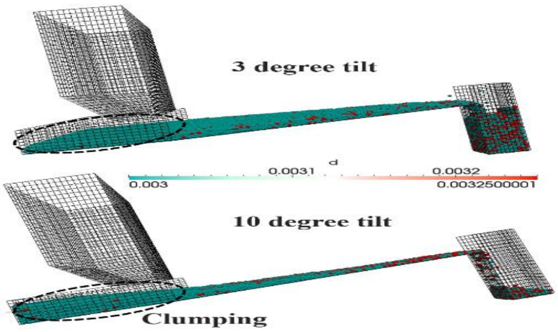

Figure 9. Clumping of material at T = 5 sec (in the destoner operating at 10 degree tilt

The inlet/middling material profiles also reflect the above mentioned clumping. The Fig. 10 shows the middling fraction material profile comparison between the optimal (3 degree tilt) and non-optimal (10 degree tilt) destoner operating conditions. The highlighting trend noticed in this comparison, is the increase in the heavy product fraction (instead of a reduction, which should be ideally noted if material is being transmitted upwards) in the middling section, indicating a net downward movement (towards the lower of the deck) of the same. The heavy product fraction is maintained at around 0.5 for the deck at a 10 degree tilt, while the corresponding fraction for the deck at 3 degrees reduces from 0.3 to 0.15.

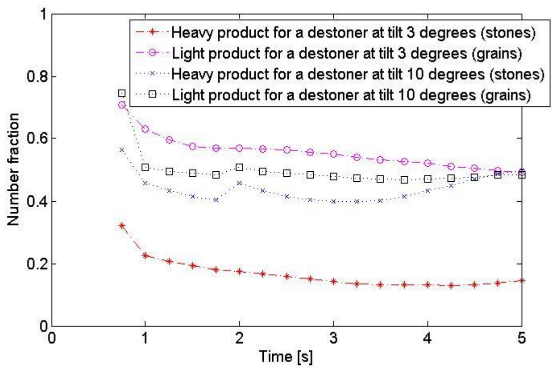

Figure 10. Comparison between the inlet/middling profiles of a destoner at optimal (3 degree tilt) and non-optimal operating conditions (10 degree tilt)

Hence, it can be conclusively stated that increasing the deck tilt by ~3 times of the optimal condition is detrimental to the performance of a pilot scale destoner. The metrics of 'product number fraction' (described in section 2.3) can be represented as percentages (based on the number of light and high fractions). For simplicity, the performance of the destoner can be adjudged using '% of stone removal' given as

$$\% \text{ of stone removal} = (\text{Heavy product fraction}) * 100 \qquad (11)$$

The corresponding performance of the pilot scale destoners is summarized in Table 3. On increasing the deck tilt by ~3 times, a corresponding 3 fold decrease in the destoner performance is noted. This relatively linear relation between deck tilt and % of stone removal is indicative of the sensitivity of the gravity separation process to the operating conditions.

Table 3. Destoner performance assessment

Destoner deck tilt	*% of stone removal*
3 degrees	~ 60 %
10 degrees	~ 20 %

4. CONCLUSION

In the current work, A CFD-DEM based assessment of the performance of a destoner is undertaken. The proposed framework, is set up and implemented in the OpenFOAM® environment. The computational framework individually tracks the motion of every single particle in the domain and couples this with the solution for the continuum flow field, on the basis of Newton's third law of motion. A symmetric cross-section of a pilot scale destoner is simulated first at optimal operating conditions of deck tilt (of 3 degrees) followed by a simulation at ~3 times the optimal tilt. These studies are carried out in order to assess the sensitivity of the destoner operation to the operating conditions.

The virtual destoner (simulated for a period of 5 seconds) under optimal conditions, operates just as a real destoner would do, showing the relevant trends of (specific) gravity separation phenomena. The heavy product fraction in the discards stream increases over time with a corresponding accumulation of the 'valuable' light product at the base of the deck, indicating segregation between the stones (heavy product) and the grains (light product). However, along with the heavy product, there is also a significant quantity of valuable 'light' product being discarded indicating a further scope for process optimization. A detailed validation of the framework (by comparing the numerical results with experimental data from destoners) is warranted before completely acknowledging these results. This would be the immediate research undertaking as a consequence of the results from this work.

The current work aims at describing a simple sensitivity analysis of the destoner operation (to deck tilt) as well. A close to linear relation between deck tilt and % of stone removal (increasing the deck tilt by ~3 times leads to a corresponding 3 fold decrease in the destoner performance) is noted indicative of the sensitivity of the gravity separation process to the operating conditions. These fundamental CFD-DEM studies on a 'pilot-scale' destoner represent a novel method of assessing the performance of gravity separators, opening a wide array of possibilities to design and develop the next generation gravity sorter. Such studies could be used to evaluate novel geometries and structural changes to existing machinery, to ultimately build a sorter that performs with the highest expected efficiency. Granular material of widely varying properties (size, shape and density) could be individually tested in this framework to determine the optimal conditions of operation for the destoner needed to obtain the highest possible degree of segregation between the light (grains) and heavy (contaminant) fractions.

ACKNOWLEDGEMENTS

This project is supported by the SEVENTH FRAMEWORK PROGRAMME of EU, Industry-Academia Partnerships and Pathways (IAPP) - Marie Curie Actions. Grant no.: 324433.

REFERENCES

[1] Das, H., Separation of paddy and rice on an oscillating tray type separator, Journal of Agricultural Engineering Research, Vol. 34, pp. 85-95, 1986.

[2] Li, J., Webb, C., Pandiella, S.S., Campbell, G.M., A Numerical Simulation of Separation of Crop Seeds by Screening - Effect of Particle Bed Depth, Food and Bioproducts Processing , Vol. 80, pp. 109-117, 2002

[3] Sakaguchi, E., Suzuki, M., Favier, J.F., Kawakami, S., PH - Postharvest Technology: Numerical Simulation of the Shaking Separation of Paddy and Brown Rice using the Discrete Element Method, Journal of Agricultural Engineering Research, Vol. 79, pp. 307-315, 2001.

[4] De Felice, R., Tanaka, T., Ishida, T., The voidage function for fluid particle interaction systems, International Journal of Multiphase Flow, Vol. 20 , pp. 153-159, 1994.

[5] Crowe, C.T., Schwarzkopf, J.D., Sommerfeld, M., Tsuji, Y., Multiphase Flows with Droplets and Particles, Second Edition ed., CRC Press : Taylor & Francis Group, pp. 120 - 132, 2012.

[6] Goldschmidt, M.J.V., Link, J.M., Mellema, S., Kuipers, J.A.M., Digital image analysis measurements of bed expansion and segregation dynamics in dense gas-fluidised beds, Powder Technology, Vol. 138, pp. 135-159, 2003.

[7] Kannan, A.S.., Hansen, M.A.E., Carstensen, J.M., Lund, J., Sasic, S. Studies of grain segregation patterns on a destoner using a CFD-DEM approach, 8th International Conference on Computational and Experimental Methods in Multiphase and Complex Flow, WIT press, 2015 (Print).

Conference on Modelling Fluid Flow (CMFF'15)
The 16th International Conference on Fluid Flow Technologies
Budapest, Hungary, September 1-4, 2015

CFD-DEM STUDIES OF GRAIN SEGREGATION PATTERNS ON A CONCEPTUAL DESTONER

Ananda Subramani KANNAN[1], Michael Adsetts Edberg HANSEN[2], Jens Michael CARSTENSEN[3], Jacob LUND [4] and Srdjan SASIC[5]

[1] Corresponding Author. Department of Applied Mechanics, Chalmers University of Technology, SE 412 96 Gothenburg, Sweden. Tel.: +45 53661689, Fax: +45 4576 1041, E-mail: ananda@chalmers.se
[2] Videometer A/S, DK 2970 Hørsholm, Denmark. E-mail: maeh@videometer.com
[3] Videometer A/S, DK 2970 Hørsholm, Denmark. E-mail: jmc@videometer.com
[4] Westrup A/S, DK 4200 Slagelse, Denmark. E-mail: jacob.lund@westrup.com
[4] Department of Applied Mechanics, Chalmers University of Technology, SE 412 96 Gothenburg, Sweden. E-mail: srdjan@chalmers.se

ABSTRACT

Removal of contaminants from 'food grade' quality grains is of great importance in food and grain processing operations. A thorough understanding of the inherent granular segregation profiles on this processing equipment is a pivotal step in the design and development of more efficient processes. One such grain cleaning operation is the 'density-based separation' using a destoner. This process removes stones and other heavy material from lighter food grains using a vibrating deck and fluidizing air. In this paper we formulate a CFD-DEM framework (set up and implemented in the OpenFOAM® environment) to study granular segregation patterns on a destoner. The scheme is first validated by comparing simulations with experimental data using a gas-solid fluidized-bed test case. A good agreement between the experiments and the simulations is noted. This proposed framework is then used to characterize the combined effects of deck inclination and fluidization velocities on the separation profiles generated from a virtual destoner. These profiles have been found to be highly sensitive to changes in fluidization conditions, with the gradual development of segregation zones at velocities close to the minimum fluidization velocity of the heavier component. A deck inclination of 5 degrees and a fluidization velocity of 1.5 m/s is considered optimal while steeper slopes (inclinations of 15 degrees) and lower air velocities (0 m/s) are deemed unsuitable for segregation.

Keywords: CFD-DEM, Destoner, Deck inclination Grain cleaning operation, OpenFOAM®, Fluidization.

NOMENCLATURE

β	$[kg/m^3s]$	interphase-momentum transfer coefficient
C_d	[-]	drag coefficient
d	$[m]$	particle diameter
ε	[-]	local porosity
$\boldsymbol{F}_A$	$[N]$	fluid particle interaction force
$\boldsymbol{f}_c$	$[N]$	contact force
$\boldsymbol{f}_d$	$[N]$	drag force
$\boldsymbol{f}_f$	$[N]$	fluid-particle interaction force
ϕ	[-]	packing fraction
g	$[m/s^2]$	acceleration due to gravity
H_{avg}	$[m]$	average particle bed height
I	$[kg.m^2]$	moment of inertia
j	[-]	summation index
k_i	[-]	number of particles
m	$[kg]$	mass
μ	$[kg/m.s]$	viscosity
n	$[s]$	simulation time
p	$[Pa]$	static pressure
R_i	$[m]$	particle diameter
ρ	$[kg/m^3]$	density
t	$[s]$	time
$\boldsymbol{\tau}$	$[N.m]$	torque
τ	$[s]$	time
$\boldsymbol{u}$	$[m/s]$	particle velocity vector
$\boldsymbol{v}$	$[m/s]$	fluid velocity vector
v	$[N]$	force
ω	$[rad/s]$	angular velocity

Subscripts and Superscripts

f	fluid
i	particle i
j	particle j
p	particle
fp	fluid - particle

1. INTRODUCTION

Ensuring the highest quality of grains meant for large-scale cultivation is an important criterion that should be fulfilled in the current day and age where there is an increasing demand in both the quality and quantity of food. Man has progressively taken steps towards reaching such 'quality' requirements by developing several fundamental cleaning operations. Historically, 'winnowing' has been employed to remove bran and stones from the harvested crop and, over the years, this ancient practice has been refined and developed into modern machinery, which effortlessly clean harvested crops (processing at large volumes). Today, the downstream processing of food grains is achieved by using machinery operating under the fundamental principle of separation of similarly sized entities based on 'specific gravity or density'. The 'destoner' is a typical example of one such equipment used in the downstream processing of food grains to remove stone and other heavier contaminants. Hence, a deeper investigation of the underlying phenomena of granular separation would aid in developing smarter grain cleaning machinery and correspondingly, the purpose of this work is to look at the same using numerical methods.

Destoners employ the difference in a particle's terminal velocity (or "lifting velocity") in a constant stream of air for separation/stratification. An inclined oscillating deck transports the heavier contaminant (e.g. stones) towards the higher end, while the lighter grain is collected at the base. The segregation patterns on the deck of a destoner are principally controlled by three main intrinsic factors: fluidizing air, reciprocation frequency and deck tilt. Other extrinsic (fixed) factors such as stroke length for the throwing action as well as the deck surface friction also affect the behaviour of the grains on the deck. Nevertheless, for the sake of simplicity it is assumed that the performance of the gravity separators are reliant on just the intrinsic factors. The extent of the effect of these intrinsic factors can be gauged by collating results from other closely related applications (to gravity separation) such as shaking separation of rice and paddy.

A fundamental understanding of granular segregation phenomena in a destoner can be obtained by examining these related studies on shaking separation of rice. The movement of paddy and rice in opposite directions on an oscillating tray separator was first described by Das [1] as a result of different coefficients of friction between paddy and the deck, rice and the deck and paddy and rice respectively. A destoner, with separating particles having similarity in shape but differing in specific gravity and surface characteristics, would also function along similar principles. These studies by Das, highlight the fact that shaking separators (such as the destoners) are driven by contact-dominated (dense) granular flows.

Nowadays, with the rapid development in computer technology, there is a noticeable shift towards in-silico description of systems. Such an analysis is generally done by studying the evolution of a dynamic system by solving the fundamental equations of conservation of mass, momentum, energy etc. These assessments can provide novel insights into existing phenomena aiding in designing the next generation process. One such effort - the Discrete Element Method (or DEM), developed by Cundall and Strack (Cundall *et.al* [2]), is a well-established method (based on contact mechanical treatment) that can provide dynamic information, such as trajectories of individual particles and transient forces acting on them. Similar information is exceptionally difficult, if not impossible, to obtain by physical experimentation. Consequently, this method has found increasing application in studying several downstream processing operations.

The application of DEM to agricultural and food processing operations is limited to rather simplified case studies (dealing with the behaviour of a few hundred particles) including numerical studies on the separation process of soybeans and mustard seeds by a vibrating screen (Li *et.al. [3]*) and simulation of the shaking separation of paddy and brown rice (Sakaguchi *et.al [4]*). So far, the work by Sakaguchi et.al represents the only validated application of DEM in grain downstream. This model was validated against experimental results at the macroscopic scale demonstrating the capabilities of DEM as a tool to study granular flow phenomena of food particulates (Sakaguchi *et.al [4]*).

2. SIMULATION METHOD

DEM studies of grain downstream processing are currently limited to describing the flow of a solid particulate bed without examining the influence of the surrounding continuum (air). A coupled particle–fluid model would hence address a wider range of applications and the current work aims to formulate such a CFD-DEM scheme to study granular segregation patterns on a destoner. This section describes the CFD-DEM framework used in the current work.

2.1. CFD-DEM Framework

The DEM is a powerful tool that can provide valuable insights into the bulk 'macro' behaviour of a system by evaluating pertinent 'micro' phenomena. Coupled with CFD, this framework is capable of mapping several pertinent transport fields (such as thermal gradients, concentration profiles, velocity fields etc.) crucial to a wide range of industrial applications. The CFD-DEM approach, was proposed by Tsuji, Tanaka, and Ishida (Tsuji et.al

[5]), and is today one of the most widely used tools in multiphase flow research. In this approach the motion of individual particles is obtained by solving Newton's second law of motion (for both translation and rotation), whereas the continuum flow is resolved by solving the locally averaged Navier-Stokes equations. Thus, the equation governing the translational motion of particle i is given as

$$m_i \frac{dv_i}{dt} = \mathbf{f}_{f,i} + \sum_{j=1}^{k_i} \left(\mathbf{f}_{c,ij} + \mathbf{f}_{d,ij} \right) + m_i \mathbf{g}, \tag{1}$$

The pertinent particle forces modelled are: the fluid-particle interaction force (the drag force), $\boldsymbol{f}_{f,i}$, the gravitational force, $m_i\boldsymbol{g}$, and the inter-particle forces which include the contact force, $\boldsymbol{f}_{c,ij}$, and viscous contact damping force $\boldsymbol{f}_{d,ij}$. The drag force is determined at the individual particle level and is hence not only dependent on the relative velocity ($|\boldsymbol{u} - \boldsymbol{v}|$) between the fluid and particle but also on the presence of the surrounding particles. The empirical Ergun-Wen Yu drag correlation (Eqs. (2) to (4)) is used in the current work with the effect of the presence of other particles considered in terms of local porosity (ε_f).

$$\mathbf{f}_{f,i} = \beta_{pf}(\mathbf{u}-\mathbf{v})/\rho_f \tag{2}$$

For ($\epsilon_f \leq 0.8$)

$$\beta_{pf} = 150 \frac{(1-\varepsilon_f)^2}{\varepsilon_f} \frac{\mu_f}{\left(\phi_p d_p\right)^2} + 1.75(1-\varepsilon_f) \frac{\rho_f}{\left(\phi_p d_p\right)} |\mathbf{u}-\mathbf{v}| \tag{3}$$

For ($\epsilon_f > 0.8$)

$$\beta_{pf} = \frac{3}{4} C_d \frac{|\mathbf{u}-\mathbf{v}|\rho_f(1-\varepsilon_f)}{d_p} \varepsilon_f^{-2.7} \tag{4}$$

The inter-particle forces will generate a torque ($\boldsymbol{\tau}_{ij}$) causing the particle i to rotate.

$$I_i \frac{d\omega_i}{dt} = \sum_{j=1}^{k_i} \boldsymbol{\tau}_{ij}, \tag{5}$$

I_i is the moment of inertia of the particle i, given as

$$I_i = \frac{2}{5} m_i R_i^2. \tag{6}$$

Additionally, there are two widely used approaches to handle particle contact/collisions (the contact force, $\boldsymbol{f}_{c,ij}$): the hard-sphere and the soft-sphere models. The hard-sphere approach accounts only for instantaneous and binary collisions and is hence applicable for relatively dilute gas–solid systems. The soft-sphere model, on the other hand, takes multiple particle contact into consideration and is commonly used to simulate dense gas–particle systems . Thus, in the present work (as we deal with dense granular flow of grains), the soft-sphere model is employed to calculate the contact forces, including the normal, damping and tangential forces between the particles and between particles and walls. The contact forces are modeled using an analogy with a mechanical system consisting of springs, dashpots and friction sliders.

The continuous phase in a CFD-DEM framework is resolved using the standard finite volume methods and the corresponding governing equations are given as:

$$\frac{\partial \varepsilon_f}{\partial \tau} + \nabla.(\varepsilon_f \mathbf{u}_f) = 0, \tag{7}$$

$$\frac{\partial(\rho_f \varepsilon_f \mathbf{u}_f)}{\partial \tau} + \nabla.\,(\rho_f \varepsilon_f \mathbf{u}_f \mathbf{u}_f) = -\varepsilon_f \nabla p - \mathbf{F}_A + \rho_f \varepsilon_f \mathbf{g}, \tag{8}$$

The force $\boldsymbol{F}_A$ is the volumetric fluid-particle interaction force (coupling) calculated on the basis of Newton's third law of motion, i.e., the fluid drag force acting on the individual particles from the fluid phase will react on the fluid phase from the individual particles (the fluid-particle drag is summed over a computational cell). In this work, the coupled CFD-DEM framework is implemented into an Open-source computational platform (OpenFOAM).

2.2. Simulation conditions: CFD-DEM framework implementation

The proposed CFD-DEM framework is applied here to describe the segregation phenomena observed in gravity separators such as destoners (separation of fractions based on their density). Commercial destoners consist of an inclined vibrating deck that is supplied with contaminated granular material. Air is forced through the perforated deck fluidizing the granular material above. The denser fraction (e.g. stones and other heavier contaminates) stay in contact with the deck (are not fluidized) and are conveyed to the higher side (by the throwing action of the deck) from where they are eventually removed. The lighter fraction (e.g. grains and other commercially viable material), on the other hand, are fluidized (do not touch the deck surface) and move towards the lower end of the deck where they are collected. A schematic of the destoner is provided in Fig.1. In order to minimize the computational effort, a symmetric transverse section (as shown in Fig.1) is simulated. As indicated above, this work aims at developing a framework to study granular flow behavior using advanced numerical methods and a scaled-down simulation is a logical first step towards this objective.

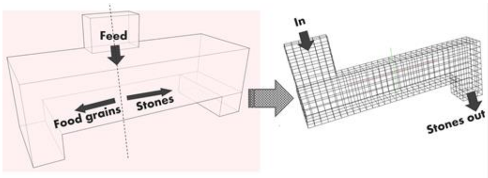

Figure 1. Simulated cross-section

The reduced computational domain is dimensioned at 15 cm x 3 cm x 10 cm. The simulated feed consists of spherical particles of different sizes and densities (to mimic stones and food grains) introduced batch-wise. The relevant micro-properties of the feed (such as Young' modulus, Poisson ration etc.) are listed in table 1.0. Air is introduced into the system by means of a boundary condition that fixes the superficial velocity (of air) over the deck surface. Additionally, the vibrating action of the deck is approximated to have an amplitude of 1.5 cm/s (estimates from detailed mechanical calculations). The time step used in the numerical simulation is determined from the DEM constraints (as the length scales simulated in DEM are much smaller than those of the resolution of the continuous phase).

Table 1. Simulation conditions

Particle Micro-properties	
Food grain (modelled on the basis of rapeseed)	
Density (kg m^{-3})*	1100
Young's Modulus (Nm^{-2})*	$5.0 * 10^6$
Poisson ratio (Nm^{-2}) *	0.25
Co-efficient of restitution*	0.6
Coefficient of sliding friction*	0.3
Particle diameter (mm)	1
Number of particles	4000
Stone (modelled on the basis of rapeseed)	
Density (kg m^{-3})	2500
Particle diameter (mm)	2.5
(all other micro-properties are same)	
Continuum properties (air at 20 ºC)	
Viscosity (kg m^{-1} s^{-1})	$1.8 * 10^{-5}$
Density (kg m^{-3})	1.205
Inlet Air velocity (m s^{-1})	1.5
Time step (s)	$2.5 * 10^{-5}$

* Micro-properties of Rapeseed adapted from - Transactions of the ASABE Vol. 54 (Boac *et.al* [6])

The destoner removes stones from a given input feed using a combined effect of deck vibration, inclination and fluidization. The inclination of the deck creates the necessary slope needed to convert vertical stratification (achieved by the fluidizing air) into horizontal separation zones along the deck surface. Additionally, the right vibrational behavior also needs to be accounted for in the numerical simulations. In this study, it is assumed that the grains that are in contact with the table are 'thrown' towards the higher end of the deck. This motion can be visualized using the schematic in Fig.2.

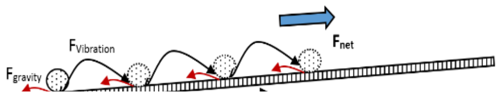

Figure 2. Grain/Stone movement of the deck

The deck of a real destoner is supplemented with a corrugated surface (in order to increase friction) to ensure that there is sufficient traction between the particles and the surface for upward propagation (i.e. for stones $F_{vibration} > F_{gravity}$ leading to a net upward movement). It is assumed that the motion of the deck has negligible effects on the continuum phase, i.e. it only impacts the particulate phase. The throwing action of the deck is modelled in a 'static mesh framework' by utilizing a non-zero wall boundary condition on the deck surface (with a constant velocity obtained from measurements on a real destoner). This approach reduces the complexity of the corresponding computations (evading dynamic mesh simulations).

3. RESULTS AND DISCUSSION

These numerical studies on the destoner have been undertaken in order to better understand the phenomena of gravity seperation and gain a deeper insight into effect of extrinsic factors (such as deck tilt, vibration etc.) on the performance of the gravity separator. This section describes some qualitative assesments of the destoner simulations.

3.1. Validation of the DEM framework

The CFD-DEM framework utilized in this work needs to be validated first (as it is a new code developed in the Open source environment OpenFOAM). This validity has been established by comparing the measurements made by Goldschmidt et.al, on a pseudo two-dimensional, laboratory-scale fluidized bed (with a simple rectangular geometry and well-defined gas inflow conditions) with corresponding simulations of a pilot scale fluidized bed (set-up in the open source framework). Note that the lack of experimental data for destoners has necessitated the use of a fluidized-bed test case for these validation studies.

The simulations were set-up in accordance to the experimental conditions established by Goldschmidt et.al [7], i.e., the domain is dimensioned at 15 cm x 1.5 cm x 70 cm and three fluidization velocities (U_{air}) of 1.56, 1.88 and 2.50 m/s, respectively have been studied individually. Around 24000 particles have been simulated (matching the corresponding number in the experimental studies). The conditions of these benchmark case studies are listed in Table 2.

Table 2. Simulation conditions for the validation studies

Particle Micro-properties (modelled on the basis of Glass Ballotini)	
Density (kg m^{-3})*	2526
Young's Modulus (Nm^{-2})*	1.0 * 10^{8}
Poisson ratio (Nm^{-2}) *	0.35
Co-efficient of restitution*	0.97
Coefficient of sliding friction*	0.09
Particle diameter (mm)	2.5
Number of particles	23,920
Continuum properties (air at 20 ºC)	
Viscosity (kg m^{-1} s^{-1})	1.8 * 10^{-5}
Density (kg m^{-3})	1.205
Inlet Air velocity (m s^{-1})	1.5
Time step (s)	2.5 * 10^{-5}

The cases were simulated for a total of 5 seconds, after which the corresponding average bed heights (H_{avg}) were obtained for each case. This average bed height is then compared with the corresponding experimental measurements by Goldschmidt et.al [7]. The height (H_{avg}) is calculated based on a percentile estimate of the particle *z*-coordinates (representative of height). The percentile estimate used in the current work indicates the maximum height below which 80% of the total particle bed reside.

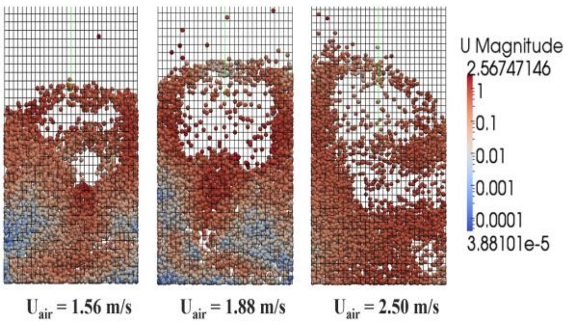

Figure 2. Fluidized bed test cases (t =5 sec) at U_{air} of 1.56, 1.88 and 2.50 m/s (particles colored by magnitude of velocity)

The mean of the 80th percentile of particle *z* position over the time period from 2 (system stabilizes) to 5 seconds (at intervals of 0.25 seconds) is estimated as the average particle bed height <H_{avg}>.

$$\langle H_{avg} \rangle = \frac{\sum_{5}^{t=2} H_{avg}}{n} \qquad (9)$$

Where *n* is the number of time entries between 2 and 5 seconds at intervals of 0.25 seconds (12 entries). This 80th percentile is considered as a reasonable estimate for the average particle bed height (Fig. 4).

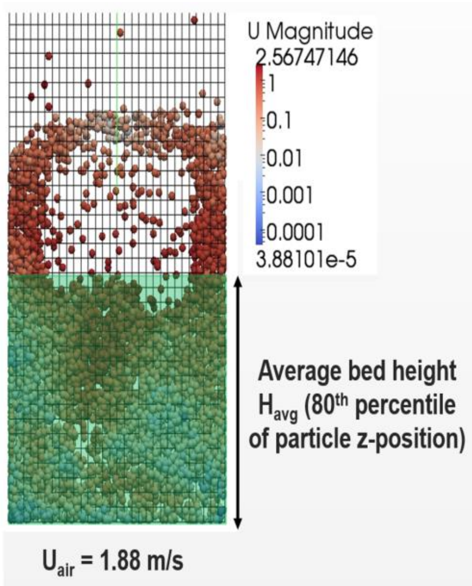

Figure 3. Estimation of average particle bed height <H_{avg}>

The bed expansion dynamics is studied through the variation of <H_{avg}> over increasing fluidization velocities (Fig. 3). Both the experiments and the simulations exhibit a similar trend in <H_{avg}>, with a slight increase followed by stabilization on increasing the fluidization velocity (U_{air}) with the error bars in Fig. 5 representing uncertainties in experimental measurements. The simulations are within these limits with a slight tendency to over predict average particle bed height <H_{avg}>.

This over-estimation indicates that further refinements are needed in the DEM framework particularly with –a) the drag law being used, b) simulated time period (might be too short to obtain statistically significant behavior) or c) the contact mechanical parameters (spring-slider-dashpot model parameters) employed. Nevertheless, the overall performance of the DEM framework, i.e. the stability and accuracy of the code, is deemed acceptable under these restrictions.

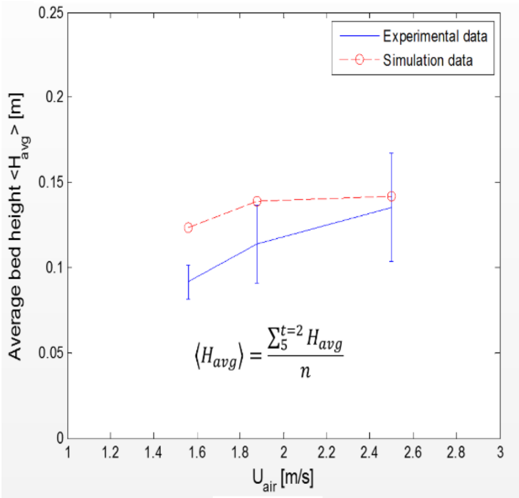

Figure 5. Comparison between average particle bed height <H_{avg}> between simulation and experimental data

3.2. *Pedagogical studies on a conceptual destoner*

As elucidated in the earlier sections, the destoner is an apparatus that removes stones and other heavy material from lighter food grains. This process is essential to ensure crop quality and purity before the subsequent downstream processing of food grains. The underlying physics behind a destoner have seldom been studied using numerical methods such as CFD-DEM and hence a bottom-up approach to understanding the phenomena has been adopted in this work. First, a pedagogic case study was setup (described as the reduced geometry simulations) in order to qualitatively verify (through visual cues) if the physics of gravity separation can be reproduced using a numerical setup. This qualitative assessment is described in the subsequent sections.

3.2.1 Effect of fluidization

Fluidization conditions in the destoner are responsible for segregating the low terminal velocity/ lighter grains (which are lifted up from the deck and slide to the low end of the deck by simple gravitational pull) from the high terminal velocity / heavier contaminants (which stay in contact with the deck and are removed (uphill) by the throwing action of the deck). The effect of fluidizing air velocity (U_f) on the observed segregation patterns on a conceptual destoner are shown in Figs. 6 to 8. The system has been studied over a period of 5 seconds at constant vibrational conditions (amplitude of 1.5 cm/s) and deck inclination (θ = 5 degrees) with and without the effect of fluidization, i.e. at U_f = 0 and 1.5 m/s respectively.

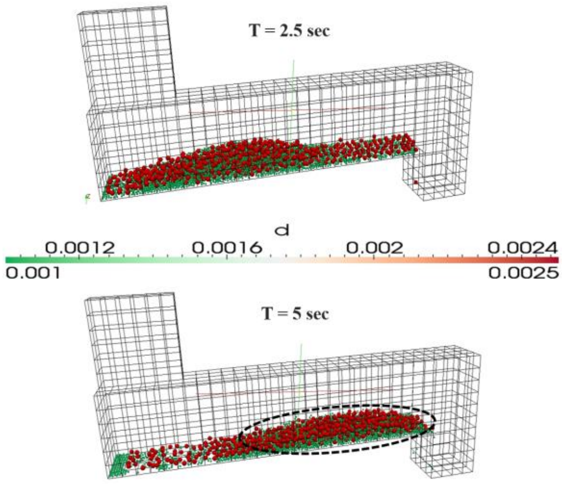

Figure 6. Conceptual Destoner at constant vibrational conditions (amplitude of 1.5 cm) , deck inclination (θ = 5 degrees) and no fluidization (U_f = 0).

A conceptual destoner, when operated in the absence of fluidizing air (U_f = 0) would be unable to segregate between the lighter and the heavier fractions (as depicted in Fig. 6). Due to the inadequacy (or complete absence) of fluidization, both the heavier and lighter fractions are equally impacted by the throwing action of the deck, i.e. there is no segregation of species based on specific gravity, leading to an unsegregated mass of product at the discards outlet (higher end of the deck : the highlighted region in Fig. 6). This pedagogic study clearly identifies the role of air in the segregation process.

The conceptual system is then studied under optimal fluidization conditions (i.e. at U_f = 1.5 m/s). At such superficial velocities (lesser than the minimum fluidization velocity of stones: U_{mf} = 1.6 m/s), the lighter grains (with U_{mf} in the range of 0.65 to 0.75 m/s) would be fluidized (failing to remain in contact with the deck), while the heavier stones would be at the limit of fluidization and stay in contact with the vibrating deck and conveyed upwards. Thus a notable segregation zone between the heavier and lighter fractions is identified, with the heavier fractions predominantly localized at the higher end of the deck (near the discards outlet) and the lighter grain fraction collected at the base. It is also noticed that there is a sizable amount of lighter material at the higher end of the deck (along with the stones). This is explained by the conjoint movement of both heavier material and some of the lighter material entrapped under and/or in between the heavier fractions leading to both heavier and lighter fractions at the discards outlet. This behavior is also witnessed in an actual destoner with a slight exodus of lighter material acceptable to remove the heavier contaminants (see Fig. 7).

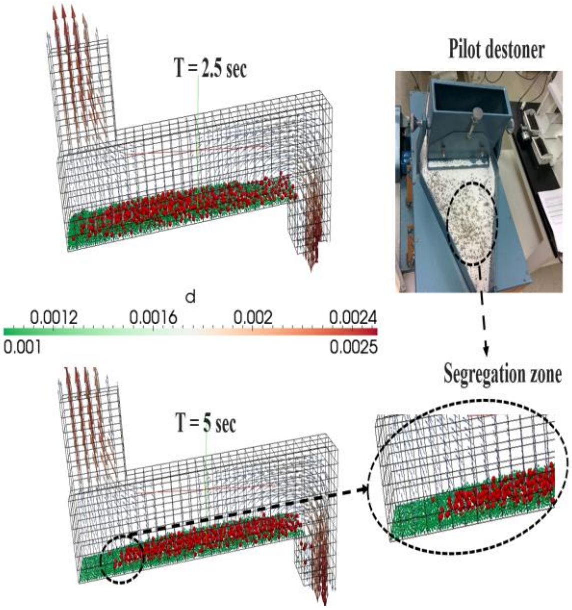

Figure 7. Conceptual Destoner (at constant vibrational conditions of 1.5 cm amplitude , deck inclination 5 degrees and under fluidization conditions of U_f = 1.5 m/s) compared with a pilot destoner (white color section represents the grain) under similar operating conditions (after 5 seconds of operation) : Qualitative assessment.

Hence, a sufficient fluidization velocity is needed in order to generate an optimal separation between the two fractions. Moreover, the numerical simulations were able to successfully reproduce the behavior of a destoner in a conceptual case study.

3.2.2. Effect of deck tilt

The tilt along with the vibration of the deck is responsible for converting the vertical stratification (based on specific gravity) achieved by the fluidizing air into horizontal segregation zones. The effect of deck inclinations (θ = 5 and 15 degrees respectively) on the segregation patterns of a conceptual destoner at constant vibrational (amplitude of 1.5 cm/s) and fluidization conditions (U_f = 1.5 m/s) are shown in Fig. 8. The deck at 5 degrees is considered to be at optimal inclination (based on data from end-users of destoners). The slope provided in this deck is sufficient to enable the lighter grains (that are fluidized) to accumulate at the base, while the heavier stones can be propagated to the higher end and subsequently be removed from the system (i.e. the deck vibrational force component for the heavier fraction can overcome the corresponding gravitational component : $F_{vibration} > F_{gravity}$).

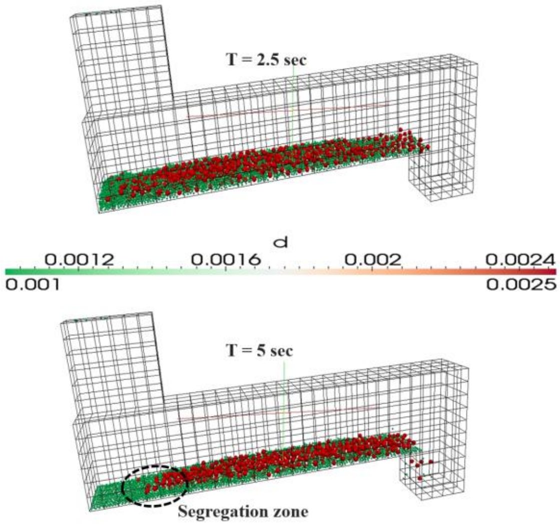

Figure 8. Conceptual Destoner at constant vibrational conditions (amplitude of 1.5 cm) , deck inclination (θ = 5 degrees) and fluidization (U_f = 1.5 m/s).

When increasing the inclination to 15 degrees the observed separation between stones and food grains is poor as clearly indicated by the differences in the granular bed at t = 5 seconds (note the highlighted region in Fig. 9) This deviation from the optimal state can be attributed to the increased gravitational force component (due to increased slope of the deck) experienced by all the particles in the system leading to clumping of both stones and grains at the base of the deck (i.e. the deck vibrational force component (for both stones and grains) cannot overcome the corresponding gravitational component : $F_{vibration} < F_{gravity}$).

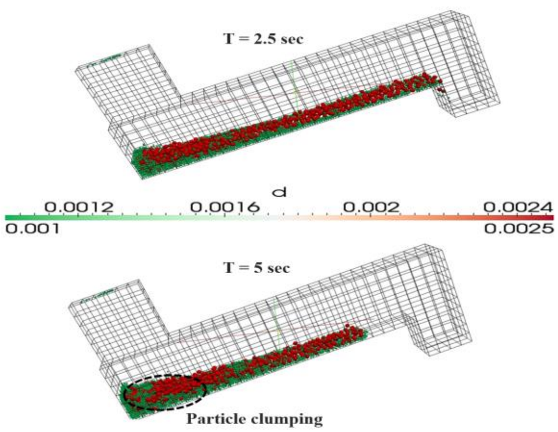

Figure 9. Conceptual Destoner at constant vibrational conditions (amplitude of 1.5 cm) , deck inclination (θ = 15 degrees) and fluidization (U_f = 1.5 m/s).

4. CONCLUSION

A CFD-DEM framework has been proposed in this work in order to reproduce the physics behind gravity separation. In this framework, the time discretized solutions for the instantaneous force balances around individual particles (dispersed phase model) coupled with the Navier-stokes equations (continuum model) are used to describe the overall contact dominated granular flow. The framework is validated using a fluidized-bed test case, with good agreement noted between simulations and experimental data (under suitable restrictions). Furthermore, this fundamental study successfully reproduced the development of a separation zone between stones and grains (modelled based on the micro-properties of rapeseed) on a conceptual destoner. Fluidization and deck inclination are identified as the two critical parameters that affect grain segregation, with fluidization conditions chosen close to the minimum fluidization velocity of stones. At these conditions, the stones are not fluidized and are carried to the steeper end due to the vibrating action of the deck, while the fluidized grains move and collect towards the lower end of the deck. In addition, the degree of inclination of the deck of a destoner is also critical to achieving acceptable segregation on it. A deck inclination of 5 degrees depicts signs of segregation while steeper slopes (inclinations of 15 degrees) are deemed unsuitable for segregation as clumping of both stones and grains is noted at the base of the deck at these conditions. Additionally, a fluidization velocity of 1.5 m/s produced a good separation between the two fractions. These calculated process parameters are akin to the optimal operating parameters of a pilot scale destoner (U_f of 1.45 m/s and 5 degree tilt - data obtained from manufacturers). These fundamental qualitative CFD-DEM studies on a 'conceptual' destoner represent a novel method of assessing the behavior of granular material on gravity separators. These would in turn open a wide array of possibilities to design and develop the next generation gravity sorter. The CFD-DEM framework could be used as a tool to evaluate novel geometries and structural changes to existing machinery, to ultimately build a sorter that performs with the highest expected efficiency. Granular material of widely varying properties (size, shape and density) could be individually tested in this framework to determine the most optimal conditions (of operation for the destoner) needed to obtain the highest possible degree of segregation between the light (grains) and heavy (contaminant) fractions. However, detailed validation (by comparing the numerical results with experimental data from destoners) of this framework is warranted before acknowledging the results from these numerical simulations and would be the immediate research undertaking as a consequence of the results from this work. Nevertheless the general behavioral trends are existent, and these numerical models will form the basis for developing more quantitative approaches to allow further investigations on gravity sorters.

ACKNOWLEDGEMENTS

This project is supported by the SEVENTH FRAMEWORK PROGRAMME of EU, Industry-Academia Partnerships and Pathways (IAPP) - Marie Curie Actions. Grant no.: 324433.

REFERENCES

[1] Das, H., Separation of paddy and rice on an oscillating tray type separator, Journal of Agricultural Engineering Research, Vol. 34, pp. 85-95, 1986.

[2] Cundall, P.A., Strack, O.D.L., A discrete numerical model for granular assemblies, Géotechnique, pp. 47-65, 1979.

[3] Li, J., Webb, C., Pandiella, S.S., Campbell, G.M., A Numerical Simulation of Separation of Crop Seeds by Screening - Effect of Particle Bed Depth, Food and Bioproducts Processing , Vol. 80, pp. 109-117, 2002.

[4] Sakaguchi, E., Suzuki, M., Favier, J.F., Kawakami, S., PH - Postharvest Technology: Numerical Simulation of the Shaking Separation of Paddy and Brown Rice using the Discrete Element Method, Journal of Agricultural Engineering Research, Vol. 79, pp. 307-315, 2001.

[5] Tsuji, Y., Tanaka, T., Ishida, T., Lagrangian numerical simulation of plug flow of cohesionless particles in a horizontal pipe, Powder Technology , Vol. 71 , pp. 239-250, 1992.

[6] Boac, J.M., Casada, M.E., Maghirang, R.G., Harner, J.P., Material and interaction properties of selected grains and oilseeds for modeling discrete particles, Transactions of the ASABE, Vol. 53, pp. 1201-1216, 2010.

[7] Goldschmidt, M.J.V., Link, J.M., Mellema, S., Kuipers, J.A.M., Digital image analysis measurements of bed expansion and segregation dynamics in dense gas-fluidised beds, Powder Technology, Vol. 138, pp. 135-159, 2003.

Conference on Modelling Fluid Flow (CMFF'15)
The 16th International Conference on Fluid Flow Technologies
Budapest, Hungary, September 1-4, 2015

AEROACOUSTIC SIMULATIONS OF THE CAVITY TONE

Péter Tamás NAGY[1], Andreas HÜPPE[2], Manfred KALTENBACHER[3], György PAÁL[4]

[1] Corresponding Author. Department of Hydrodynamic Systems, Budapest University of Technology and Economics. Műegyetem rkp. 3. D building 3rd floor, H-1111 Budapest, Hungary. Tel.: +36 1 463-1442, Fax: +36-1-463-30-91, E-mail: pnagy@hds.bme.hu
[2] Institute of Mechanics and Mechatronics, Vienna University of Technology. E-mail: andreas.hueppe@tuwien.ac.at
[3] Institute of Mechanics and Mechatronics, Vienna University of Technology. E-mail: manfred.kaltenbacher@tuwien.ac.at
[4] Department of Hydrodynamic Systems, Budapest University of Technology and Economics. E-mail: paal@hds.bme.hu

ABSTRACT

The cavity-tone is one of the fundamental aeroacoustic flow configurations. In the past, cavities have been investigated especially at high flow speeds (high subsonic to supersonic) as e.g., occurring in military aircrafts. Nowadays, much research focuses on cavities at low speed as occurring in automobiles and trains.

The investigated cavity is a simple rectangular, open cavity whose length-to-depth ratio is 2 at flow speed of about 0.05 Ma_∞ (Mach number, the ratio of mean flow speed in the farfield and the speed of sound). In this case the so-called hybrid aeroacoustic approach is used. In the first step a CFD (Computational Fluid Dynamics) simulation is carried out applying ANSYS CFX, whereby the effect of compressibility of the fluid is investigated. Based on the CFD results various source term formulations are analysed, and the effect of input variables (velocity, pressure, divergence of Lighthill tensor, Lamb vector, pressure gradient) are investigated. Finally, the acoustic simulations are performed based on the various source term formulations using the in-house code CFS++.

Keywords: cavity-tone, CAA, CFD, source term, low Mach-number

NOMENCLATURE

A	$[m^2]$	nominal size of acoustic load
D	$[m]$	depth of the cavity
L	$[m]$	length of the cavity
Ma	[-]	Mach number
PE	$[dB]$	the pressure level
S	$[Pa/m^2]$	the acoustic load
St	[-]	the Strouhal number
T	$[K]$	the temperature
c_0	$[m/s]$	the speed of sound
e	$[m^2/s^2]$	total energy per unit mass
f	$[Hz]$	the frequency
p	$[Pa]$	pressure
x	$[m]$	coordinates in the mean flow dir.
y	$[m]$	coordinates in the tranversal dir.
λ	$[W/m/K]$	thermal conductivity
γ	[-]	heat capacity ratio
ρ	$[kg/m^3]$	density
$\underline{\omega}$	$[1/s]$	vorticity vector
$\underline{u}$	$[m/s]$	velocity vector
$\underline{\underline{T}}$	$[Pa]$	stress tensor
$\underline{\underline{T}}_{LH}$	$[kg/m^3/s]$	Lighthill tensor
$\underline{\underline{\tau}}$	$[Pa]$	viscous stress tensor
Φ_{cont}	$[kg/m^3/s]$	general mass source
$\underline{\Phi}_{mom}$	$[kg/m^2/s^2]$	general momentum source
$\otimes$		dyadic product

Subscripts and Superscripts

$'$	the fluctuating part of a variable
a	the fluctuating part of an acoustic variable
T	the transpose of a tensor
ic	incompressible
max	maximum of a variable

1. INTRODUCTION

In this paper the cavity tone is investigated, which is one of the fundamental aeroacoustic flow configurations (Figure 1.). The "cavity" is a rectangular cutout in a surface, typically a plane. If there is a flow over the cavity a shear layer is formed, which can lose its stability. The instability wave propagates from the leading edge to the downstream (trailing) edge, while the amplitude of the wave continuously increases. A feedback mechanism develops between the leading and trailing edge. The pressure fluctuation at the trailing edge perturbs the shear layer somehow at the leading edge, where the previously mentioned instability waves are generated. This feedback mechanism leads to oscillations, which are sometimes audible. Apart from the generated sound, this phenomenon usually leads to unwanted mechanical vibrations and also to increased drag force.

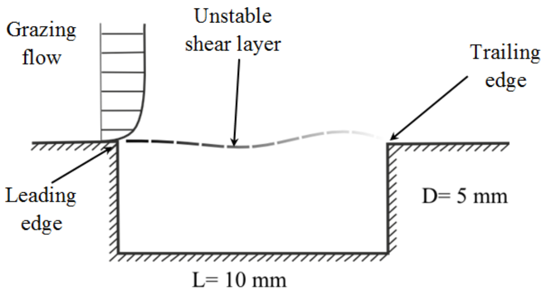

Figure 1. The investigated configuration of cavity-tone

The first studies on cavity noise concerned aeronautic applications in the 1950-1960's [1]. The motivation of research was that the oscillations appeared in the weapon bays of military aircraft. This oscillation can excite the vibrational modes of the aircraft structure, which can quickly lead to structural fatigue issues inside the aircraft [2] and can significantly increase the drag force, too. The speed of the flow was high subsonic to supersonic in these cases. The need to investigate lower velocities appeared in the 1970's mainly because aircraft wheel wells have been seen to be an important source of aerodynamic noise during the landing and take-off of airplanes [3] [4]. In the meantime many other technical applications have been discovered: door gaps and sunroof in automobiles, closed side branches in gas pipelines, slotted flumes, slotted wall wind and water tunnels, bellows-type pipe geometries [5], canal locks, harbour entries, gap between wagons or the pantograph of trains [6].

In this paper a fundamental open cavity, whose length-to-depth ratio is 2, is investigated at flow speed of about 0.05 Ma (Mach number). At such a low Mach number the disparity of scales of acoustic and flow field is significant. The grid of the flow simulation must be fine enough to resolve the boundary layer and small vortices to provide accurate enough results. Usually the desired grid resolution for acoustic computation can be much coarser because the acoustic wavelength is much larger than the vortices or even the cavity. In addition, there are several orders of magnitude differences in the aerodynamic and acoustic variables. E.g. a 1 m/s velocity fluctuation is not extreme in flows, while the amplitude of the acoustic velocity fluctuation at a particle velocity level of 80 dB is only 0.5 mm/s. The human hearing threshold at 1 kHz is around 0 dB sound pressure level, corresponding to 20 μPa in air, which is again several orders of magnitude smaller than an average pressure fluctuation in aerodynamics (10-100 Pa). These orders of magnitude differences between the variables increase the numerical noise, which can pollute the whole acoustic simulation [7]. To reduce these errors one tends to separate the acoustic and the aerodynamic flow fields. The common name for these approaches is hybrid Computational AeroAcoustics (CAA). If the two fields are separated, the crucial point of the computation is to determine the coupling between them. The idea is to derive equations for the acoustic field (model the acoustic field) and then to define acoustic source terms, which are based on the independently solved flow field. The optimal formulation of these equations and source terms is still under research. In this paper various source terms are investigated for the acoustic wave equation. Some of them are valid only for incompressible fluid. The compressibility in our cavity configuration does not play an important role. This fact allows to carry out incompressible flow simulation and to use those coupling formulations that are valid only for incompressible flow. At the same time a compressible flow simulation was carried out to verify the previous statement and investigate the effect of compressibility to the sources.

In Section 2 the governing equations of fluid dynamics are presented briefly and based on them the various formulations of the acoustic source terms are introduced. In Section 3 the CFD simulations are described and their acoustic source fields are compared to each other. In Section 4 the acoustic simulations are presented. Finally, in Section 5 we make some concluding remarks.

2. SOURCE TERM FORMULATION

2.1 The acoustic wave equation with general sources

The basic equations, which describe both the flow and acoustic field, are the Navier-Stokes equations (Eqs. (1) to (2)) with the energy equation, Eq. (3).

$$\frac{\partial \rho}{\partial t} + \nabla \cdot \left(\rho \underline{u} \right) = 0 \qquad (1)$$

$$\frac{\partial \left(\rho \underline{u} \right)}{\partial t} + \nabla \cdot \left(\rho \underline{u} \otimes \underline{u} \right) = \nabla \cdot \underline{\underline{T}} \qquad (2)$$

$$\frac{\partial \rho e}{\partial t} + \nabla \cdot \left(\rho e \underline{u} \right) = \nabla \cdot (-p\underline{u} + \underline{\underline{\tau}}\,\underline{u}) + \nabla \cdot (\lambda \nabla T) \qquad (3)$$

If the fluid is Newtonian (Eq. (4)) and assumed to be an ideal gas (Eq. (5)), the following expressions hold.

$$\underline{\underline{T}} = -\left(p + \frac{2}{3}\mu\nabla\cdot\underline{u}\right)\underline{\underline{I}} + \mu\left(\nabla\otimes\underline{u} + \left(\nabla\otimes\underline{u}\right)^{\mathrm{T}}\right) \quad (4)$$

$$e = \frac{p}{\gamma - 1} + \rho\frac{u^2}{2} \quad (5)$$

Now let us split the variables into mean (time averaged) and fluctuating components as

$$f\left(t,\boldsymbol{x}\right) = \overline{f}\left(\boldsymbol{x}\right) + f^{'}(t,\boldsymbol{x}). \quad (6)$$

and neglect the viscous and non-linear terms, which is usually a good approximation in acoustics. Then the following expression can be obtained

$$\frac{1}{\mathrm{c}_0^2}\frac{\partial p^{'}}{\partial t} + \nabla\cdot\rho\underline{u}^{'} = \Phi_{cont}, \quad (7)$$

$$\frac{\partial\rho\underline{u}^{'}}{\partial t} + \nabla p^{'} = \underline{\Phi}_{mom}. \quad (8)$$

Let us take the time derivative of Eq. (7) and the divergence of Eq. (8). Then the fluctuating velocity can be eliminated and we get the well-known wave equation for the acoustic pressure, Eq. (9), where the sources (S) are on the right hand side

$$\frac{1}{\mathrm{c}_0^2}\frac{\partial^2 p^{'}}{\partial t^2} - \Delta p^{'} = \underbrace{\frac{\partial}{\partial t}\Phi_{cont} - \nabla\cdot\underline{\Phi}_{mom}}_{S}. \quad (9)$$

2.2 The Lighthill analogy

The first, most famous and still widely used analogy is the one proposed by Lighthill in 1951 [8]. The basic idea of Lighthill was that the terms, neglected during the derivation (linearization) of the wave equation, act as sources for the acoustic equation.

$$S = \nabla\cdot\underline{\Phi}_{mom} = \nabla\cdot\nabla\cdot\underline{\underline{T}}_{\mathrm{LH}} \quad (10)$$

The Lighthill tensor is without any assumption:

$$\underline{\underline{T}}_{\mathrm{LH}} = \rho\underline{u}\otimes\underline{u} + p'\underline{\underline{I}} - \underline{\underline{\tau}} - c_0^2\left(\rho - \rho_0\right)\underline{\underline{I}} \quad (11)$$

Lighthill assumed that if the viscous terms are small (the Reynolds number is high), the process is close to isentropic. Therefore, the main sources of sound are vortices. The main acoustic source can be approximated by Eq. (12).

$$\underline{\underline{T}}_{\mathrm{LH}} \approx \rho\underline{u}\otimes\underline{u} \quad (12)$$

This simplification will be used hereafter.

2.2 Approximation of the Lighthill analogy

The following approximations of Lighthill tensor can be found in Ref [9].

2.2.2 The Lamb vector

Let us decompose the velocity field according to Helmholtz, which means that the velocity field can be split into an irrotational and a solenoidal vector field. If we assume that the Lighthill source term is based on incompressible velocity the following relation holds

$$S = \nabla\cdot\nabla\cdot\left(\rho\underline{u}^{\mathrm{ic}}\otimes\underline{u}^{\mathrm{ic}}\right) = \nabla\cdot\left(\rho\underline{\omega}\times\underline{u}^{\mathrm{ic}}\right) - \nabla\cdot\nabla\left(\frac{1}{2}\rho\underline{u}^{\mathrm{ic}}\cdot\underline{u}^{\mathrm{ic}}\right) \quad (13)$$

It can be derived that if the Reynolds-number is high and the Mach-number is low then the main acoustic source will be the first term on the right hand side in Eq. (13) and the second term can be neglected. The expression $\underline{\omega}\times\underline{u}^{\mathrm{ic}}$ is known as Lamb vector.

2.2.3 The Laplacian of the pressure

The Lighthill tensor can be approximated by the incompressible pressure in the following way. Neglecting the viscous terms in Eq. (2) and taking its divergence leads to Eq. (14)

$$\nabla\cdot\left(\frac{\partial\left(\rho\underline{u}\right)}{\partial t}\right) + \nabla\cdot\nabla\cdot\left(\rho\underline{u}\otimes\underline{u}\right) = -\Delta p \quad (14)$$

In an incompressible fluid the first term on the left hand side is zero because of the incompressible continuity equation. The second term on the left hand side is the approximation of the previously mentioned Lighthill tensor.

$$\nabla\cdot\nabla\cdot\underline{\underline{T}}_{\mathrm{LH}} \approx \nabla\cdot\nabla\cdot\left(\rho\underline{u}\otimes\underline{u}\right) \approx -\Delta p \quad (15)$$

The relation (Eq. (15) is valid only if the viscous terms are negligible: the Reynolds number is high.

2.2.3 The time derivative of the pressure

The following source term formulation and its detailed, exact derivation can be found in [7]. Here, only a short, rudimentary derivation is presented.

If a quiescent medium is assumed, (7) is still valid for fluctuating variables. First, let us split the fluctuating pressure (p') into acoustic (p^{a}) and incompressible pressure (p^{ic}). Then, we take the time derivative and rearrange the incompressible pressure to the right hand side. This term can be conceived as source term for the continuity equation. (Eq. (16))

$$\Phi_{cont} = -\frac{1}{c_0^2}\frac{\partial p^{ic}}{\partial t} \tag{16}$$

The source term can be calculated (Eq. (17)) in this case if we substitute into Eq. (9).

$$S = \frac{\partial \Phi_{cont}}{\partial t} = -\frac{1}{c_0^2}\frac{\partial^2 p^{ic}}{\partial t^2} \tag{17}$$

In this case, the solution of the wave equation directly results in the acoustic pressure, (p^a)

3. CFD SIMULATIONS AND ACOUSTIC LOAD

3.1 The CFD simulation domain

In the first step the 2D CFD simulations were performed by ANSYS CFX. The cavity dimensions were the following: L = 10 [mm], D = 5 [mm]. The simulation domain was defined to have a length of 2L before the cavity, a length of 3L after the cavity and 3L above the cavity, as in [13] The length of sponge layer, which is necessary in the compressible simulation to avoid reflection at the boundaries, was 4.5 L in both x and y directions. The mesh was generated by ANSYS ICEM. The finest mesh resolved the cavity by 166x106 cells. The monitor point was placed 0.07D below the corner, which is the most favourable place (experimentally measurable, smaller residuals, larger pressure signal) for investigation ([1], [11]).

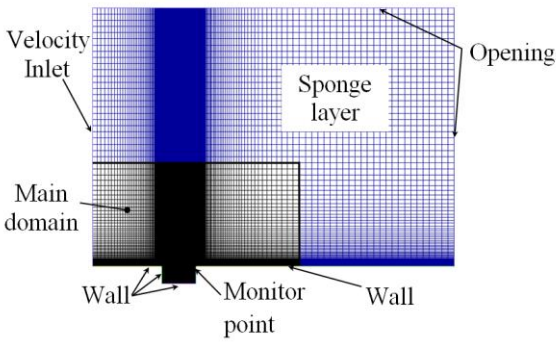

Figure 2. CFD computational grid

The CFD domain with the boundary conditions can be seen in Figure 2. The velocity inlet boundary condition (BC) was a prescribed velocity profile. This velocity profile was calculated by an in-house MatLab code, which generates the Blasius profile. This code provides the prescribed value of boundary layer thickness at the leading edge. It was 1.22 mm in these simulations. The walls at the bottom were modelled as adiabatic "no slip walls". At the outlet and the top of the domain the so-called "opening" boundary condition was used. It prescribes the relative pressure (0 Pa) and the flow direction (normal to the boundary). If the pressure is rigorously constant in a compressible simulation, the acoustic waves are reflected from the boundary. In CFX there is a beta option to turn on acoustic non-reflectivity at the BC but it works well only if the sound waves hit the boundary in the normal direction. (The non-reflective boundary conditions are implemented in most commercial codes based on the 1D wave equation [12].) If the perturbation velocity has also a tangential component at the boundaries, the non-reflective boundary condition can cause instabilities [12] or reflect the acoustic waves [11]. In our case the implicit damping method was implemented in CFX for the continuity equation. Further information can be found in [10].

The mesh investigations in the classical CFD sense have already been carried out by Farkas et al. in [13] on the same configuration. The meshes were also investigated in this work because the resolution of the CFD grid is usually not sufficient for acoustic coupling. The comparison was made based on the original Lighthill source term formulation only. The mesh refinement was applied only close to the trailing edge (the main acoustic source) because in the aerodynamic sense the mesh was appropriate. This method differs from the usual uniform mesh refinement. The main parameters of the investigated meshes can be found in Table 1. The observations are the following: the difference in the results between the coarse and medium mesh is significant. The main acoustic source is not well resolved on the coarse grid. Further improvement is not noticed between the medium and the fine mesh. Based on these results, the medium mesh is selected for further simulations.

Table 1. Mesh parameters of the CFD simulations

Case	Resolution of cavity	Smallest element edge length	Number of elements
Coarse	141x71	20 μm	~104000
Medium	151x91	7 μm	~133000
Fine	166x106	3.5 μm	~174000

3.2 The results of CFD simulations

A Fourier transform was carried out on the pressure signals at the monitor point in the incompressible and the compressible simulations. The results can be seen in Figure 3. The results are qualitatively the same. Here, we have computed the pressure level by $PE = 20\log(p' / p_{ref})$ with p_{ref} = 20 μPa. The fundamental frequency is 1522 Hz with the amplitude of 26.4 Pa (122.4 dB) in the incompressible simulation, while in the compressible simulation the fundamental frequency is 1530Hz and the amplitude was 26.9 Pa (122.6 dB). Although the pressure signal in the compressible simulation was a bit noisier, there was technically no difference between the two simulations. The compressibility of the fluid can be neglected, as expected.

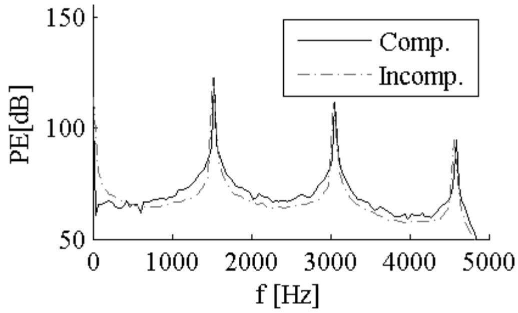

Figure 3. The Fourier transform of the pressure signal at the monitor point

3.3 The comparison of various source term formulations

In a next step the sources are calculated for the acoustic simulation based on the CFD results. The sources, which were introduced in Section 2, are compared with each other. In the first investigation the source field based on the Lighthill tensor was compared to the Laplacian of the pressure in the incompressible case because the previously introduced pressure based formulations are valid only for incompressible flow simulations. The time signal was compared inside the cavity, which can be seen in Figure 4. The monitoring point was placed in the shear layer at equal distances far from the edges of the cavity. To be precise, the monitoring point is at x = L/2, y = 0, where the origin is the leading edge and the x direction is the main flow direction.)

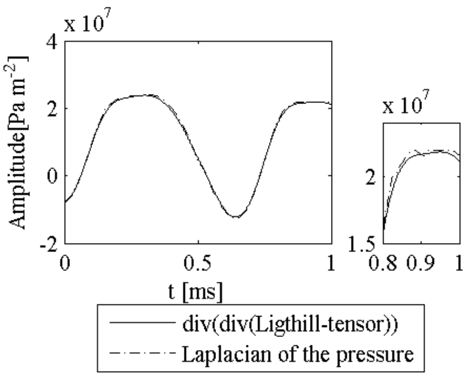

Figure 4. Comparison of the sources calculated based on the Lighthill tensor and the Laplacian of the pressure in the middle of the shear layer

In Fig. 4 it can be clearly seen that the Laplacian of the pressure approximates well the second derivative of the Lighthill tensor, but the signal was noisier in the case of pressure-based-formulation. The reason for this phenomenon can be that the pressure values themselves suffer from higher numerical error, which is further magnified during the calculation of second spatial derivatives. It is difficult to interpret the results because of the lack of knowledge how CFX calculates the pressure.

Table 2. The comparison of source terms defined on the incompressible flow field

Name	$\frac{S_{\text{Mean}}}{S_{\text{1st}}}$	A [m^2]	$S_{\max}$ $\left[\text{Pa / m}^2\right]$
Lighthill	~66 %	2.519e-8	5.6e10
Lamb	~133%	6.116e-7	1.5e11
Time derivative	<1 %	8.072e-4	2.1e4

In a next step Fourier transform is performed on the various sources. Here, the spatial distributions (the shapes) of the sources were compared. The Laplacian of the pressure was excluded from the comparison because significant difference cannot be obtained between Laplacian of the pressure and the double divergence of the Lighthill tensor. Only a small difference was recognized in the compressible computations very close to the edge.

The results of the comparison are summarized in Table 2. for the incompressible simulations. First, the effect of the mean value (S_{Mean}) of the acoustic load is investigated at a probe location close to the edge in all cases. The zero frequency component was compared to the first harmonic component (S_{1st}). It is probable that this value highly depends on the probe location but the tendencies can be roughly estimated based on the monitoring point. This ratio was quite high in the case of velocity based source terms (Lighthill tensor, Lamb vector) and was low in the case, when the source was calculated based on the time derivative of the pressure. The high mean value is non-physical and should be eliminated by the application of filtering. In next step the spatial distribution of the source field is investigated. Let us define the nominal size (A) of the acoustic source as the area, where the acoustic source strength is larger than 1% of the maximum acoustic source strength. This investigation was performed for various ratios of 5%, 10%, 20% and for all cases the tendencies were the same. The nominal size of the acoustic load was the smallest in the case of Lighthill tensor. In the case of Lamb vector formulation the source was larger both in size (A) (30 times) and magnitudes ($S_{\max}$) (2 times). This does not mean unambiguously the usage of Lamb vector produces higher acoustic pressure in the far field, because the phase relationships also influence the final results. This observation could mean that the resolution of the source could be better in the case of Lamb vector formulation and it could be used more effectively on a coarser grid, too. In the case of time derivative of the pressure formulation the size of the acoustic source was much larger (3 orders of magnitude), while its magnitude was much smaller.

Furthermore, it can be stated that the spatial distribution of the sources looked very similar in the compressible and incompressible simulation.

4. ACOUSTIC SIMULATION

4.1 The acoustic simulation domain

The significant advantage of the hybrid approach is that the acoustic simulation domain can be much larger than the CFD domain. The acoustic domain contains three parts in our case. The first one is a small source region where the sound is generated. Here, the acoustic sources were calculated based on the flow simulation data and interpolated to the acoustic source grid. In this case the two meshes (the CFD and acoustic mesh) were identical. The next part is the propagation region where the acoustic waves propagate without any amplification or damping. Within this region, the right hand side of the acoustic wave equation is zero. This region was defined as 1 m before, after and above the cavity. The grid size here was much coarser (5 mm) that is why an interpolation technique described in Ref. [14] was used. The outermost part is the absorption region. This region was a thin layer at the border of simulation domain, where the waves were strongly damped to avoid reflections. Here the so-called perfectly matched layer was defined. Further information about the technique and implementation can be found in Ref. [7].

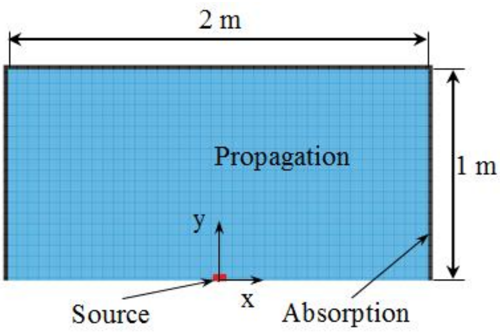

Figure 5. The parts of acoustic simulation domains: the source region, propagation and absorption region; and microphone positions.

4.2 The results of the acoustic simulation domain

The acoustic simulations were carried out by CFS++, which is an in-house software at the TU Wien to solve partial differential equations by finite element method. First, the simulations were carried out, where the sources are defined based on the incompressible flow simulations. A typical acoustic field of the simulation, which was calculated based on the Lighthill tensor can be seen in Figure 6.

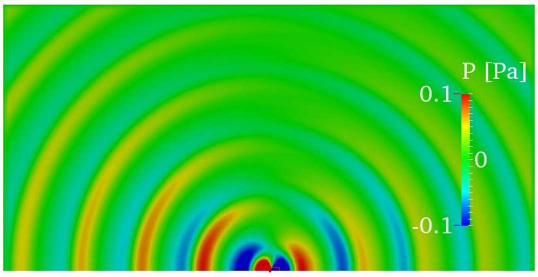

Figure 6. The acoustic pressure field at a given time instance based on Lighthill analogy (incompressible)

The directivity pattern can be clearly associated to a dipole. At the same time the results provided by the second time derivative of the pressure shows an absolutely different radiation pattern, as displayed in Figure 7.

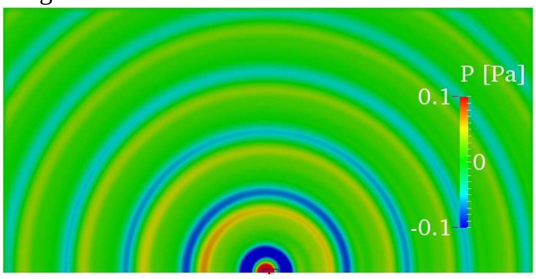

Figure 7. The acoustic pressure field at a given time instance based on second time derivative of the pressure (incompressible)

Howe investigated extensively the cavity tone with the same length-depth ratio at low Mach numbers [15]. He calculated the acoustic field by Green functions. According to his result, the monopole characteristics of the sound appears only at higher frequencies not at the fundamental frequency (which dominates in the time domain) for low Mach numbers. In Figure 8 the directivity patterns were plotted for different Strouhal numbers (*St*). *St* was defined as $St = f\,\mathrm{Ma}_\infty c_0 / L$, where f is the frequency. The monopole part of the sound source plays a significant role only if $St \gtrsim 20$ at Ma = 0.01 as well as for $St \gtrsim 2$ at Ma=0.1 according to Howe. Pure dipole pattern was observed also in [16], where the sound field was calculated based on experimental data. The directivity pattern can indicate the validity of the source term formulations. Fourier transform was performed in all cases on the whole acoustic pressure field (Figure 9). A good qualitative agreement can be seen with the results of Howe (Fig. 8) in Fig. 9.

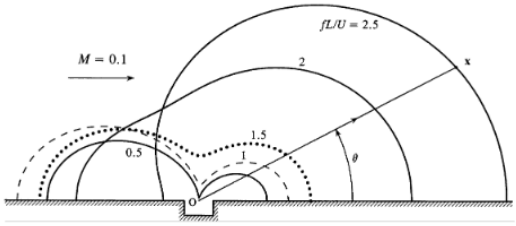

Figure 8. The directivity patterns at Ma=0.1 and *St*={0.5, 1, 1.5, 2,2.5} [15].

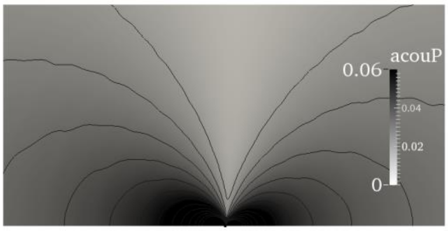

Figure 9. Fourier transform of the acoustic pressure field with contour lines at the first harmonic (*St*=0.88) based on Lighthill analogy (incompressible).

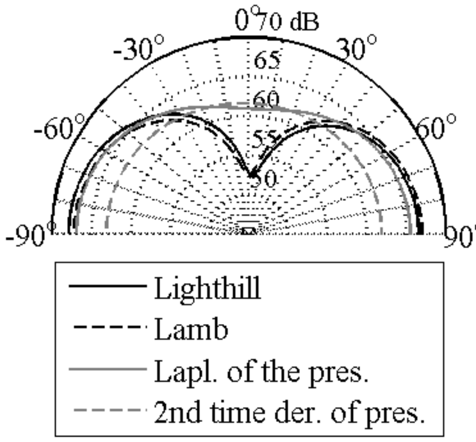

Figure 10. The directivity of the sound field at first harmonic, sources are calculated based on incompressible data

The directivity is evaluated on a circle, with a radius r = 0.4 m around the trailing edge. In Figure 10. it can be seen that the velocity based analogies ("Lighthill tensor", "Lamb vector") reproduce a dipole radiation much better than the pressure-based ones. In the case, when the sources are based on the Laplacian of the pressure or the second time derivative of the pressure, the directivity patterns were much worse if we accept the correctness of the dipole pattern. The worst result was provided by the second time derivative of the pressure. In this case the sound pressure was low in upstream and downstream directions, while it was too strong above the cavity. In the case of Laplacian of the pressure, the results show a weak dipole characteristics which is superposed on a monopole sound characteristics. Here, the amplitudes of the waves were in the right range in both the upstream and downstream directions. The magnitudes differ even a bit between its velocity based results, but this difference was negligible compared to previous cases.

The same investigation was performed on results based on sources calculated from the compressible flow simulation. The acoustic field was very similar to the incompressible cases except for the simulation based on the second time derivative of the pressure. Here a high-frequency noise appeared in the simulation. The radiation pattern looks like a dipole, while in incompressible case it was a monopole. However, it has to be noted that the formulation is only valid for incompressible flows. It is noticeable that there were no visible differences in the source terms based on compressible and incompressible simulations (not shown here). After performing Fourier transform on the results, the directivity patterns were also evaluated along the same circle as before.

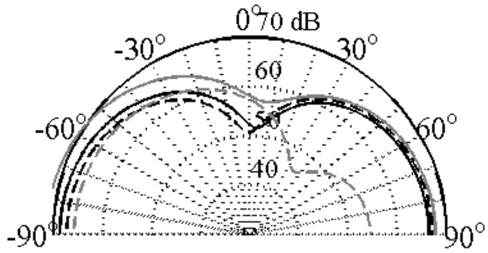

Figure 11. The directivity of the sound field at first harmonic, sources are calculated based on compressible data (notations are same as in Fig. 10.)

In Figure 11, it can be seen that the results were similar to those for the incompressible cases. The main difference appeared in the pressure-based cases which are not valid for compressible flow simulation. Here, the calculations based on the Laplacian of the pressure overpredict the sound pressure, as expected because only the incompressible part of pressure fluctuation induces the acoustic field. At the same time the directivity pattern became more realistic in both pressure-based cases. The reason for this is unclear; maybe the different pressure computation techniques cause this huge difference, especially in the case of the time derivative of the pressure. The pressure signals at various microphone positions obtained for compressible and incompressible simulations were compared. In the case of the velocity-based formulations the differences were negligible. This was expected because these analogies are valid both in compressible and incompressible flows

5. CONCLUSIONS

In this paper various acoustic source term formulations were compared in the case of a rectangular cavity. The load defined by the time derivative of the pressure seemed to be the best based on the comparison of the loads contrary to the final results. The nominal size of the source was much larger, which can mean better resolution and at the same time it had no zero frequency component which could reduce the accuracy. The nominal size of the acoustic load calculated by Lamb vector was larger than the one calculated by Lighthill tensor, but at the same time the zero frequency component was larger, too. A filter was applied in these cases.

Based on the results the following conclusions can be drawn. The velocity-based analogies provide better results than the pressure-based analogies with respect to the directivity patterns. The Laplacian of the pressure calculation method provides quite good results in upstream and downstream directions but strongly overestimates the pressure above the cavity. At the same time no significant difference was noticed close to the trailing edge during the source term investigation in section 2. The second time derivative of the pressure predicts only the sound pressure in the right order of magnitude. The directivity of the sound field is wrong and the method highly overestimates the sound pressure level at the higher harmonics. It must be mentioned that the mesh study was performed only for the Lighthill analogy-based formulation. The authors are sure that such a big difference cannot be caused by a poor resolution of the acoustic sources in the case of pressure-based sources.

The acoustic sources were also calculated for the compressible medium. Here, only the velocity-based analogies are valid, which was confirmed by the results, in spite of the fact that the compressibility does not play a significant role.

To summarize the results, the analogy based on the Lamb vector seems to be the best. It has the best spatial resolution of the source along the velocity-based analogies on a same mesh, while it provides similar results to the original analogy based on Lighthill tensor. The only drawback is the large mean value, but this can be avoided by filtering.

REFERENCES

[1] Healy, G. J., 1974, "Measurements and analysis of aircraft far-field aerodynamic noise," *NASA, Contractor Rep. 2377.*

[2] Rowley, C. W. and Williams, D. R. 2006, "Dynamics and control of high-Reynolds-number flow over open cavities," *Ann. Rev. Fluid Mech.* , vol. 38, pp. 251-276.

[3] Yu, Y. H., 1977, "Measurements of sound radiation from cavities at subsonic speeds," *Journal of Aircraft*, vol. 14, no. 9, pp. 838-843.

[4] Heller, H. H and Dobrzynski, W. M., 1977, "Sound radiation by aircraft wheel well/landing gear configurations," *J. Aircraft*, vol. 14, no. 8, pp. 768-774.

[5] Farkas, B.; Paál, G., and Szabó, K. G. ,2012 , "Descriptive analysis of a mode transition of the flow over an open cavity," *Physics of Fuids*, vol. 24, no. 2.

[6] Gloerfelt, X., 2009*"Cavity noise". Chap. 0, VKI Lectures: Aerodynamic noise from wall-bounded flows*. France: Von Karman Institute.

[7] Hüppe, A., 2014 , *Spectral Finite Elements for Acoustic Field Computation*. Aachen, Germany: Shaker Verlag GmbH.

[8] Lighthill, M. J., 1951, "On sound generated aerodynamically I. General thory," Proceedings of the Royal Society of London, vol. 211, pp. 564-587.

[9] Kaltenbacher, M., 2015, *Numerical Simulation of Mechanic Sensors and Actuators: Finite Elements for mltiphysics*, 3rd ed. Berlin: Springer.

[10]Nagy P., 2014,"Aeroacoustic simulations of the cavity tone" *MSc Diploma-thesis*, Budapest University of Technology and Economics.

[11]Farkas, B., and Paál, G., 2014, "Numerical study on the flow over a simplified vehicle door gap - an old benchmark problem is revisited," *Periodica Polytechnica Civil Engineering*, In Press

[12]Schönrock, O., 2009, "Numerical prediction of flow induced noise in free jets of high Mach numbers," *Thesis of Doctor of Engineering Sciences-University of Stuttgart*.

[13]Farkas, B., and Paál, G., 2009, "Computational investigation on the oscillation frequencies of the shear layer ove an open cavity," in *Conference on Modelling Fluid Flow-The 14th International Conference on Fluid Flow Technologies*. Budapest, Hungary.

[14]Triebenbacher, S.; Kaltenbacher, M.; Flemisch, B., and Wohlmuth, B., 2010, "Applications of the mortar finite element method in vibroacoustics and flow induced noise computations," *Acta Acustica united with Acustica*, vol. 18, pp. 536-553.

[15]Howe, M. S., 2004, "Mechanism of sound generation by low Mach number flow over a wall cavity," *Journal of Sound Vibration*, vol. 273, pp. 103-123.

[16]Koschatzky, V.; Westerweel, J., and Boersma, B. J., 2010, "Comparison of Two Acoustic Analogies Applied to Experimental PIV Data for Cavity Sound Emission Estimation," *16th AIAA/CEAS Aeroacoustic Conference*, no. 2010-3812.

Conference on Modelling Fluid Flow (CMFF'15)
The 16th International Conference on Fluid Flow Technologies
Budapest, Hungary, September 1-4, 2015

ON THE SENSITIVITY OF PLANAR JETS

Péter Tamás NAGY[1], György PAÁL[2]

[1] Corresponding Author. Department of Hydrodynamic Systems, Budapest University of Technology and Economics. Műegyetem rkp. 3. D building 3rd floor, H-1111 Budapest, Hungary. Tel.: +36 1 463-1442, Fax: +36-1-463-30-91, E-mail: pnagy@hds.bme.hu
[2] Department of Hydrodynamic Systems, Budapest University of Technology and Economics. E-mail: paal@hds.bme.hu

ABSTRACT

Planar jets belong to the most researched flows. Many aspects of their instability have been well-known for a long while. One of them is the observation that the jet is more sensitive to disturbances near the orifice exit than elsewhere. Linear stability investigations on various velocity profiles were carried out using the Orr-Sommerfeld (OS) equation to find an explanation. The velocity profiles were provided by analytical approximations and numerical computational fluid dynamics (CFD) simulations.

A special method, the so-called compound matrix method (CMM) was used to solve the OS equation to provide sufficiently accurate results. The adaptation of the method for symmetric jets is derived briefly in this paper. The stability of different velocity profiles was compared based on the local spatial growth rate. The results of the comparison clearly show that velocity profiles near the orifice are more unstable than downstream ones. The local spatial growth rate of disturbance waves was higher close to the orifice. The reason for that was twofold, and these are explained in the paper.

Keywords: Compound matrix method, CMM, Orr-Sommerfeld equation, spatial stability investigation, symmetric planar jet

NOMENCLATURE

b_j	[-]	short notation in the compound matrix
i	[-]	the imaginary unit
n	[-]	arbitrary parameter to define velocity profile
x	[-]	dimensionless coordinate in the mean flow direction
$\hat{x}$	[-]	coordinate in the mean flow direction
y	[-]	dimensionless coordinate in the transversal direction
$\hat{y}$	[-]	coordinate in the mean flow transversal direction
$L(x)$	[m]	the local specific length
$U_{Max}(x)$	[m/s]	the local specific velocity
U_{Mean}	[m/s]	the global specific velocity
$U(y)$	[-]	the non-dimensional velocity profile
$\hat{U}(y)$	[m/s]	the velocity profile
$Re(x)$	[-]	the local Reynolds number
Re_{glob}	[-]	the global Reynolds number
Q	[-]	short notation for one of the characteristic roots of OS equation in the far field
α	[-]	the non-dimensional wavenumber
$\hat{\alpha}$	[rad/m]	the wavenumber
λ_j	[-]	the characteristic roots of OS equation in the far field
ω	[-]	the non-dimensional circular-frequency
$\hat{\omega}$	[rad/s]	the circular frequency
$\Phi(y)$	[-]	the non-dimensional amplitude of perturbation velocity
$\underline{\eta}(y)$	[-]	functions in CMM
$\tilde{\underline{\eta}}(y)$	[-]	the normalized functions in CMM

Subscripts and Superscripts

r	the real part of a variable
i	the imaginary part of a variable

1. INTRODUCTION

The Navier-Stokes equations have only a few analytical solutions. Several of these cannot be usually observed during experiments because they are unstable, as recognised by Reynolds. The stability investigations are still vital in fluid dynamics research.

The basic equation to describe the stability of parallel, incompressible flows is the Orr-Sommerfeld (OS) equation. In this paper planar jets are investigated. The knowledge about their stability behaviour is essential to understand some phenomena (e. g. edge-tone) or even active flow control. It is assumed that the jet is infinitesimally disturbed at the nozzle, a disturbance wave starts, whose amplitude grows in the direction of the mean flow.

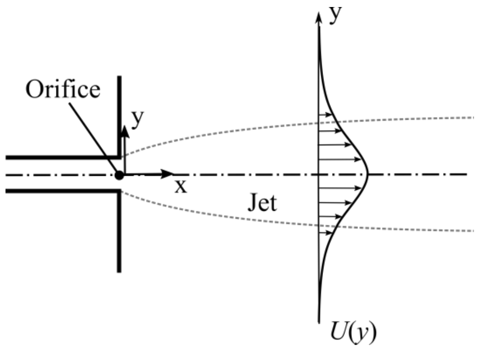

Figure 1. A jet with a (Bickley) velocity profile.

First Tatsumi, Kakutani [1] and Curle [2] investigated the planar jet. They used the OS equation to investigate the Bickley-profile which is the self-similar velocity profile valid far away from the nozzle. They determined the growth rate of disturbances at low Reynolds numbers (defined later) and the critical Reynolds number $Re_{crit} \approx 4$, below which the flow will be stable for any disturbance. Later Nolle [3] calculated the growth rate of disturbances for the same profile in an inviscid flow. The inviscid assumption means in the OS equation theoretically an infinite Reynolds number, practically a large enough number. He validated his calculations by experiments. At the same time Tam [4] investigated the same flow but for the non-parallel case. He stated that "the flow is unstable, regardless of Reynolds number, however defined."

Another observed phenomenon is that the jets are more sensitive to disturbances near the orifice exit [5], than elsewhere. The trivial explanation for this that if the growth of the disturbances is continuous in space then a disturbance which reaches the flow at the nozzle will be amplified along a longer path than the others. As far as the authors know, nobody investigated the growth rates close to the orifice. Only one paper was found [6] where the vicinity of the nozzle was studied. There the jet was modelled as a shear layer, which makes it difficult to compare the results near the orifice to the ones far away, where the Bickley-profile has already developed. The question asked in this paper is, why the jet is more sensitive to disturbances near the nozzle than elsewhere. We are providing an answer based on the stability investigation of various velocity profiles.

The stability investigation was performed using the OS equation in this paper, too. A special method, the so-called compound matrix method (CMM) [7] was used to solve the equation to provide accurate results. Another advantage of this method is that the boundary conditions at infinity can be prescribed simply. The adaptation of the method for symmetric flows is introduced briefly in Section 2. Two sets of velocity profiles were investigated: profiles given by analytical expressions and by CFD-simulations, which describe the flow at the orifice more precisely. They are treated in Section 3. In Section 4 the solution steps and the results of linear stability investigations are presented. Finally, in Section 5 we make some concluding remarks.

2. THE OS EQUATION AND THE COMPOUND MATRIX METHOD

2.1 The OS equation

The OS equation is a fundamental equation to investigate the stability of parallel, incompressible flows. It was derived from the continuity equation and the Navier-Stokes equations. The parallel flow assumption means that the velocity distribution does not change in the flow direction. This assumption is valid globally if the flow has solid, parallel boundaries (developed channel or pipe flow with parallel walls). In some other cases this assumption can be accepted as approximately valid if the flow is investigated locally, as in this paper. During the derivation non-linear terms are neglected and we look for the solution in a complex wave form leading to the well-known OS equation.

$$\begin{aligned}&\Phi^{(iv)} - 2\alpha^2\Phi'' + \alpha^4\Phi = \\ &\mathrm{i}\,Re\left\{\left(\alpha U - \omega\right)\left(\Phi'' - \alpha^2\Phi\right) - \alpha U''\Phi\right\},\end{aligned} \qquad (1)$$

where $\Phi\,(y)$ can be the amplitude of the dimensionless perturbation velocity or the amplitude of the stream function. In this paper the first one was used. $U(y)$ is the non-dimensional velocity profile in the equation. (The specific quantities for non-dimensionalization will be defined in Section 3.3) The dependence on the y variable was not denoted in many equations to keep them clear, but in the nomenclature it was denoted in every case. The definition of the parameters can also be found in the nomenclature.

If we take the limit of Eq. (1) at $Re \to \infty$ then the inviscid case can be obtained. This equation is known as the Rayleigh-equation (Eq. (2)) and it was solved for Bickley profile by Nolle [3].

$$\left(\alpha U - \omega\right)\left[\Phi'' - \alpha^2\Phi\right] - \alpha U''\Phi = 0 \qquad (2)$$

This equation was not used in this paper, but a comparison was made between Nolle's results and our large Reynolds number case.

2.2 The compound matrix method

Usually the solution of the OS equation leads to a boundary value and eigenvalue problem, because boundary conditions are prescribed at two locations. We have to find the *α-ω* parameter pairs, which fulfil the boundary conditions. Another problem is that this fourth order differential equation usually becomes stiff. Let us investigate the solution in the far field, at $y \to \infty$, where $U(y) = U''(y) = 0$ holds for jets. Here, the differential equation (Eq. (1)) can be simplified to (3).

$$\Phi^{iv} - 2\alpha^2\Phi'' + \alpha^4\Phi = \mathrm{i}\, Re\,\omega\left(\Phi'' - \alpha^2\Phi\right) \tag{3}$$

This equation has four different characteristic roots. $\lambda_{1,2} = \mp\alpha$ and $\lambda_{3,4} = \mp Q$ where $Q = \sqrt{\alpha^2 - \mathrm{i}\, Re\,\omega}$. For large Reynolds numbers $\left|\lambda_{3,4}\right| \gg |\lambda_{1,2}|$, which makes the problem stiff. One possibility to solve the problem is the compound matrix method (CMM), which is the best method according to Sengupta [8] for hydrodynamic problems. It provides accurate results and it can be easily implemented. This method was developed for the OS equation by Reid [7]. Later, Sengupta adapted this method for the Blasius profile, where some of the boundary conditions are prescribed at infinity, $y \to \infty$. In this paper his idea is followed during the adaptation of the method for symmetric plane jets.

The general solution of Eq. (1) can be written in the following form:

$$\Phi = a_1\Phi_1 + a_2\Phi_2 + a_3\Phi_3 + a_4\Phi_4 \tag{4}$$

where $\Phi_j(y)$ are the fundamental solutions and

$$\Phi_j(y) \propto e^{\lambda_j y} \text{ as } y \to \infty. \tag{5}$$

In the next step, the boundary conditions have to be prescribed at $y \to \infty$. The fluctuating velocities are assumed to be zero far from the jet, Eq. (6).

$$\Phi\left(y \to \infty\right) = \Phi'\left(y \to \infty\right) = 0 \tag{6}$$

This condition can be fulfilled only if the coefficients of the fundamental solutions, which grow exponentially for $y \to \infty$, have to be zero. This means $a_2(y) = a_4(y) \equiv 0$ because $\lambda_{2,4} > 0$.

Let us introduce six new functions (Eqs. (7) to (12)) and take the derivative with respect to *y* and substitute them to the OS equation (Eq. (1)) which leads to the differential equation system Eq. (13).

$$\eta_1 = \Phi_1\Phi_3' - \Phi_1'\Phi_3 \tag{7}$$

$$\eta_2 = \Phi_1\Phi_3'' - \Phi_1''\Phi_3 \tag{8}$$

$$\eta_3 = \Phi_1\Phi_3''' - \Phi_1'''\Phi_3 \tag{9}$$

$$\eta_4 = \Phi_1'\Phi_3'' - \Phi_1''\Phi_3' \tag{10}$$

$$\eta_5 = \Phi_1'\Phi_3''' - \Phi_1'''\Phi_3' \tag{11}$$

$$\eta_6 = \Phi_1''\Phi_3''' - \Phi_1'''\Phi_3'' \tag{12}$$

$$\underline{\eta}' = \begin{bmatrix} 0 & 1 & 0 & 0 & 0 & 0 \\ 0 & 0 & 1 & 1 & 0 & 0 \\ 0 & \mathrm{b}_1 & 0 & 0 & 1 & 0 \\ 0 & 0 & 0 & 0 & 1 & 0 \\ \mathrm{b}_2 & 0 & 0 & \mathrm{b}_1 & 0 & 1 \\ 0 & \mathrm{b}_2 & 0 & 0 & 0 & 0 \end{bmatrix} \underline{\eta} := \underline{\underline{A}}\underline{\eta}, \tag{13}$$

where $\mathrm{b}_1 := 2\alpha^2 + i\,\mathrm{Re}\left(\alpha\,\mathrm{U} - \omega\right)$ and $\mathrm{b}_2 := \alpha^4 + \alpha^2 i\mathrm{Re}\left(\alpha\mathrm{U} - \omega\right) + i\alpha\mathrm{Re}\,\mathrm{U}''$. In this case all the new functions have the same exponential growth rate for $y \to \infty$ as shown in Eqs. (14) to (19).

$$\eta_{1,\infty} \sim \left(-Q + \alpha\right)e^{-(\alpha+Q)y} \tag{14}$$

$$\eta_{2,\infty} \sim \left(Q^2 + \alpha^2\right)e^{-(\alpha+Q)y} \tag{15}$$

$$\eta_{3,\infty} \sim \left(-Q^3 + \alpha^3\right)e^{-(\alpha+Q)y} \tag{16}$$

$$\eta_{4,\infty} \sim \left(-\alpha Q^2 + \alpha^2 Q\right)e^{-(\alpha+Q)y} \tag{17}$$

$$\eta_{5,\infty} \sim \left(-\alpha Q^3 + \alpha^3 Q\right)e^{-(\alpha+Q)y} \tag{18}$$

$$\eta_{6,\infty} \sim \left(-\alpha^2 Q^3 + \alpha^3 Q^2\right)e^{-(\alpha+Q)y} \tag{19}$$

Let us normalize the $\underline{\eta}$ functions with the limit of the first one as $y \to \infty$ (Eq.(20)). In this case we get the limit at $y \to \infty$ for the normalized function (Eq. (21)), which are the initial conditions at $y \to \infty$. The normalization of the functions modifies the matrix in the differential equation (Eq. (13)) into Eq. (22).

$$\underline{\tilde{\eta}} = \frac{\underline{\eta}}{\eta_{1,\infty}} = \frac{\underline{\eta}}{-Q + \alpha}e^{(\alpha+Q)y} \tag{20}$$

$$\underline{\tilde{\eta}}_\infty = \begin{bmatrix} 1 \\ -(\alpha + Q) \\ \alpha^2 + \alpha Q + Q^2 \\ \alpha Q \\ -\alpha Q(\alpha + Q) \\ \alpha^2 Q^2 \end{bmatrix} \tag{21}$$

$$\underline{\tilde{\eta}} = [\underline{\underline{A}} + \left(\alpha + Q\right)\underline{\underline{I}}]\underline{\tilde{\eta}} \tag{22}$$

If we solve the differential equation system (Eq. (22)) with the initial conditions Eq. (21), it means that the boundary conditions are automatically fulfilled in the far field. Since a fourth order differential equation needs four boundary conditions, the definition of two other boundary conditions is still necessary. For jets two choices are available. The first one is that assuming the perturbation velocity is zero in the far field on the other side of the jet, Eq. (23).

$$\Phi\left(y \to -\infty\right) = \Phi'\left(y \to -\infty\right) = 0 \qquad (23)$$

These boundary conditions can also be implemented, but if we use the symmetry boundary condition the computation cost can be halved. This means the amplitude of perturbation velocity is symmetric to the symmetry line of the jet, Eq. (24). (In the literature this condition is usually called antisymmetric, because the displacement of the jet is antisymmetric.)

$$\Phi'\left(0\right) = \Phi'''\left(0\right) = 0\,. \qquad (24)$$

Substituting Eq. (4) into Eq. (24) leads to Eqs. (25) to (26). This new linear equation system has a non-trivial solution if and only if the determinant of the associated matrix of the system of equations is zero (Eq. (27)). Eq. (27) is identical to the fifth component of $\underline{\eta}$ being 0 at y = 0 (Eq. (28)).

$$a_1\Phi_1'\left(0\right) + a_3\Phi_3'\left(0\right) = 0 \qquad (25)$$

$$a_1\Phi_1'''\left(0\right) + a_3\Phi_3'''\left(0\right) = 0 \qquad (26)$$

$$(\Phi_1'''\Phi_3' + \Phi_1'\Phi_3''')_{y=0} = 0 \qquad (27)$$

$$\eta_5(0) = 0 \text{ and } \tilde{\eta}_5(0) = 0 \qquad (28)$$

The original problem is simplified to an initial value problem, Eq. (22) should be solved with the initial condition Eq. (21) and choose the parameter pairs which fulfil Eq. (28). If these parameters are determined, the eigenvalue problem is solved and the eigenfunctions can be calculated. The original Φ function can be calculated in four different ways, we choose the one (Eq. (29)) presented in [8].

$$\eta_1\Phi'' - \eta_2\Phi' - \eta_4\Phi = 0 \qquad (29)$$

3. ANALYTICAL AND NUMERICAL VELOCITY PROFILES

3.1. Analytical velocity profiles

Schlicting in 1936 [9] and Bickley [10] in 1937 derived a velocity profile for a plane jet if a constant, line momentum source and self-similar flow is assumed. This velocity profile is a good approximation for jets far from the orifice. According to Nolle's experiments [3] this profile can be observed from 8 times the orifice size downstream. The Bickley profile in non-dimensional form is given in Eq (30).

$$U = \mathrm{sech}^2(y) \qquad (30)$$

Two special velocity profiles can be distinguished close to the orifice. The parabolic profile is developed if the nozzle is a long, parallel channel. The other one is “top-hat” profile, in which the boundary layer in the nozzle is very thin. In this case the nozzle is a short, convergent channel. An analytical approximation for the developing velocity profiles is available only in the case of “top-hat” outflow in [3] (Eq. (31)). The velocity profiles, which are closer to the orifice, can be defined by larger n parameters. In this paper the n = {1, 2, 3} cases were investigated, where n = 1 is identical to the original Bickley profile.

$$U = \mathrm{sech}^2(y^n) \qquad (31)$$

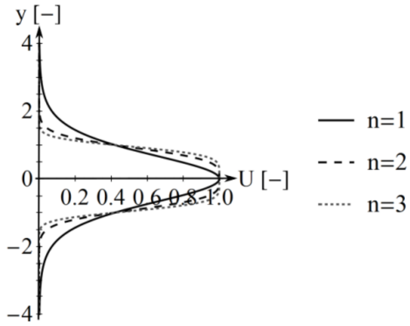

Figure 2. The analytical approximations of the velocity profile close to the orifice ($U = \mathrm{sech}^2(y^n)$).

Table 1. The comparison of the dimensionless flow rates between analytic profiles

Profile	Dimensionless flowrate [-]	The difference from Bickley-p. [%]
Bickley	2	0
$\mathrm{sech}^2(y^2)$	1.9056	-4.7
$\mathrm{sech}^2(y^3)$	1.9138	-4.3
“Top-hat”	2	0

The non-dimensional flowrates were calculated as a basis for the comparison. The result can be seen in Table 1. The maximum difference compared to the Bickley profile was less than 5 %.

3.2. The numerical velocity profiles

It was necessary to carry out CFD simulations because in the case of parabolic velocity profile there are no analytical formulae for the transition profiles between the parabolic and the Bickley profile. In the case of top-hat profile *n* can take only whole numbers and the transitional profiles between cannot be produced analytically. The CFD simulations were carried out on a fine, structured mesh by ANSYS CFX. The size of the orifice was δ = 1 mm, the cell-size was 0.05 mm in the investigated domain, which was 24 mm long. The simulation was carried out at Re_{glob}=100. Re_{glob} is the global Reynolds number in the flow defined by Eq. (32).

$$Re_{glob} = \frac{\delta\, U_{Mean}}{\nu_{air}} \tag{32}$$

where ν_{air} = $1.545\cdot10^{-5}$ m^2/s is the kinematic viscosity of air at 25 °C and U_{Mean} = 1.545 m/s is the mean velocity at the orifice, which can be calculated based on the previous parameters. The global Reynolds number describes the whole flow. In contrast, the local Reynolds number belongs to a given cross-section and describes the local velocity profile. To be consistent with analytical profiles the specific quantities for the local Reynolds number were defined by Eq. (33) as $U_{Max}(\hat{x})$ is maximum velocity in a certain cross-section, $L(\hat{x})$ is the width where the velocity is equal to $0.42\cdot U_{Max}$, coming from the evaluation of Bickley profile at y=1 since $\mathrm{sech}^2(1)\approx0.42$. In this case all the previously defined analytical and numerical profiles are non-dimensionalized on the same way ($1^n = 1$).

$$Re = \frac{L\ U_{Max}}{\nu_{air}} \tag{33}$$

The further non-dimensional quantities were calculated by Eqs (34) to (35).

$$\alpha = \hat{\alpha} L \tag{34}$$

$$\omega = \hat{\omega}\frac{L}{U_{Max}} \tag{35}$$

where $\hat{\square}$ denotes the quantity with dimensions.

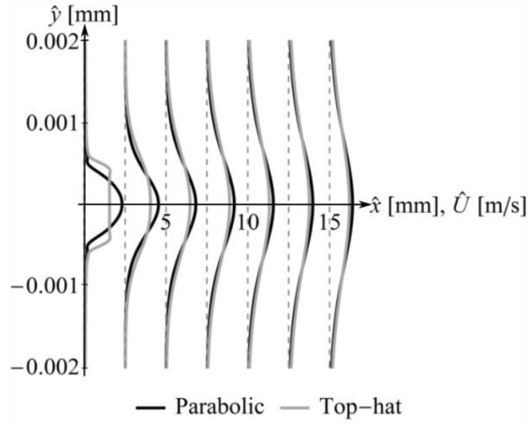

Figure 3. The velocity profiles at various distances from the orifice.

The velocity profiles are exported from CFX at various distances, shown in Figure 3.

The OS equation was used in a non-dimensional form, so that the velocity profiles had to be transformed into the same form. The transformed dimensionless velocity profiles can be seen in Figure 4, where the Bickley profile was also plotted. The velocity profiles turned more rapidly into Bickley profile in the case of parabolic outflow compared to the "top-hat" outflow. The Bickley profile was developed in both cases when $\hat{x} \gtrsim$ 6-8 mm, as it was noted experimentally by Nolle [3], too. Here, the usage of non-dimensional profiles highlights its advantage. If $\hat{x}$ > 8 mm, the stability results for non-dimensional Bickley profile can be used after redimensionalization. If the dimensional form of the stability equations had been be used, the whole solution procedure of the OS equation should have been repeated instead of a simple redimensionalization.

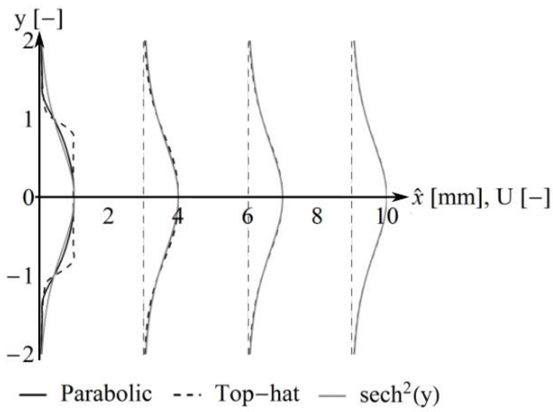

Figure 4. The dimensionless velocity profiles at various distances from the orifice.

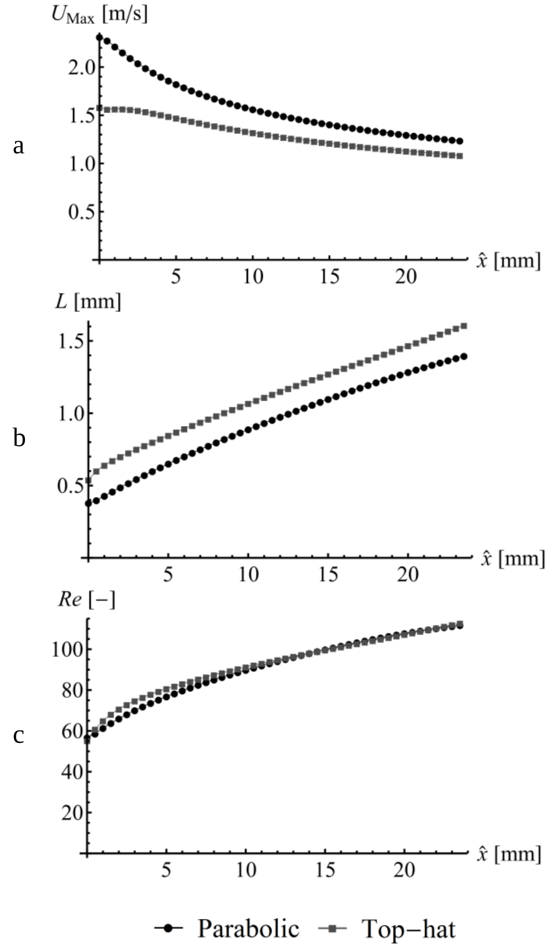

Figure 5. The velocity (a) and the length (b) scales and the local Reynolds number along the mean flow direction ($\hat{x}$).

The various scales were also plotted along the mean flow direction in Figure 5. The following observation can be made based on Figs. 4 to 6 for the dimensional velocity profiles. Although the transformations to the Bickley-profile were rapid in both case, the two flows with different outflows at the orifice (parabolic, "top-hat") are not identical even far from the nozzle. The maximum velocity is always a bit higher in the parabolic case (**a**), while the width of the jet is always a bit larger (**b**) in the "top-hat" case. The continuous increase of the local Reynolds number (**c**) is also observable, which was theoretically also derived far from the orifice [11].

4. THE SOLUTION METHOD AND THE RESULTS

4.1. The solution method

The following parameters should be determined or calculated in the Orr-Sommerfeld equation. The first one is the Reynolds number that could be a specified value (in a real flow, numerical velocity profiles) or an arbitrary parameter (in general, analytic velocity profile). The task is to determine the remaining two parameters, the wave number (α) and circular frequency (ω), which fulfil the condition in Eq. (28). These pairs are the solutions of the eigenvalue problem. Let us define the function D(Re, U, ω, α) (Eq. (36)) then we have to find the roots of this function (D=0).

$$\mathrm{D}\left(Re,\ U,\omega,\ \alpha\right) := \eta_5(y=0)\,|_{Re,U,\omega,\ \alpha} \qquad (36)$$

In the general case the wave both α and ω can be a complex number, but this means innumerable solutions. Here, the spatial stability analysis was used, the amplitude of the wave grows only in space, $\alpha = \alpha_r + \alpha_i$ is a complex number, while ω is real. The spatial growth rate is $\mu_s = -\alpha_i$. In experiments it is possible that the amplitude of the disturbance wave grows both in space and time, but comparison with experiments shows very good agreement with spatial stability analysisin the case of planar jets.

The initial condition Eq. (21) for the differential equation system Eq. (22) is prescribed at $y \to \infty$. A sufficiently large y value has to be chosen such that the boundary conditions are approximately fulfilled and Eq. (5) is true. In the case of analytical profiles y = 12 was chosen where $\mathrm{sech}^2(12) \approx 10^{-10}$. In the case of numerical profiles the velocity in the far field is never zero because of numerical errors. Here a spatial window function, which is one at the centreline of the jet and zero far away from it, was used to avoid this problem. In this case the "infinity" was chosen as the width of the function: $y = 4$.

The critical point during the solution procedure is to determine the first eigenvalue pair. Here, we followed the idea of Sengupta [12]. In the first step the Reynolds number was fixed to 100 in the case of analytic profiles and to the calculated Reynolds number in the case numerical profiles. ω was also fixed at 0.1 in both cases. A fine grid was made in the α-plane $\alpha_r \in [0,2]$ and $\alpha_i \in [-2,1]$ and the differential equation was solved for each α parameter on the grid. The investigation on a larger area is not necessary because a lower α_i means very rapid amplification, which is not observed experimentally. At the same time positive values mean decaying waves that are not interesting from our point of view. After that the $\Re\mathrm{e}(\eta_5(0))=0$ and $\Im\mathrm{m}(\eta_5(0))=0$ contour lines were plotted and the intersection point of these lines is detected. These points are the eigenvalues corresponding to different modes and they are sorted according to ascending α_i values, because lower values mean more rapid growth. It can be assumed that if the Re and ω parameters are changed slightly, the corresponding α values change only slightly. After one point is determined the next point was calculated by modifying slightly the parameters and using the Newton-Raphson method for which the initial guess was the previous solution. With this technique all eigenvalue pairs can be determined for one mode starting from one known intersection point in the α plane. In this paper only the first mode was investigated.

4.2. Results

4.2.1 Results for the analytic profiles

Our results for Bickley the profile are compared to those of Nolle [3] to verify our calculations, for high Reynolds number. The comparison at various Reynolds number can be seen in Figure 6. At Re = 1000 our results were almost identical to the results of Nolle that means the stability properties of the Bickley profile above this number are independent of the Reynolds number.

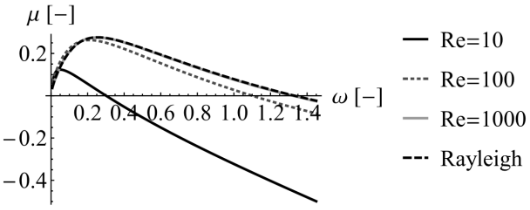

Figure 6. The growth rate of the amplitude of perturbation velocity in the case of Bickley profile for various Reynolds numbers and in the inviscid case (Rayleigh).

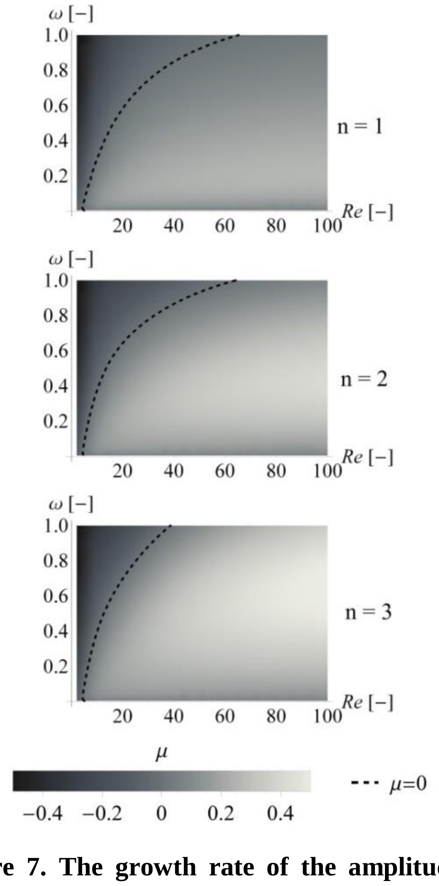

Figure 7. The growth rate of the amplitude of perturbation velocity for various *ω*, *Re* parameters in the case of analytic profiles ($U = \mathrm{sech}^2(y^n)$).

If we reduce the Reynolds number, the non-dimensional growth rate also decreases. The critical Reynolds below which the growth rate is always negative (the perturbation decays) and the flow is stable, is $Re_{\mathrm{crit}} \approx 4.3$. This number was also predicted to be 4.0 in [1] and [2]. This number was the same for all analytic profiles for any $n = \{1, 2, 3\}$ parameters, as shown also in Figure 7. There the dashed line means the neutral stability curve, where the growth rate of perturbation is zero. Another observation is the lower branch of neutral stability curve tends so rapidly to the $\omega = 0$ axis in all cases that it is not visiole in Fig. 7, as calculated in [1] and [2] for the Bickley profile only.

Beside the similarities there is significant difference between the results of the analytical profiles. At a given Reynolds number the growth rates were much higher for large n parameters except at low frequencies. This can be seen in Figure 8. These results show us that the growth of the perturbation velocity wave is more rapid close to the orifice (for large n).

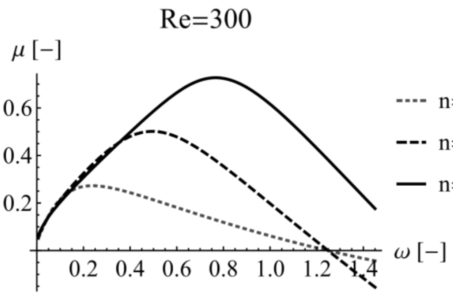

Figure 8. The growth rate of the amplitude of perturbation velocity at *Re* = 300 in the case of analytic profiles ($U = \mathrm{sech}^2(y^n)$)

4.2.2 Results for the numerical profiles

The results were the same in the case of numerical profiles. In Figure 9. the non-dimensional growth rates were plotted at various distances. The growth rates were higher for velocity profiles which are closer to the orifice, except at low frequencies.

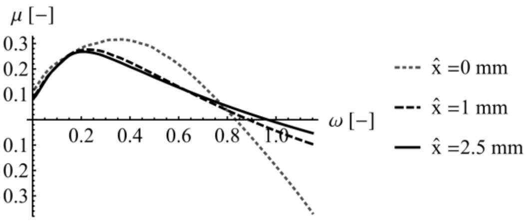

Figure 9. The non-dimensional growth rate of the amplitude of perturbation velocity in the case of numeric profiles at various distances from the orifice.

The non-dimensional results were redimensionalized. The redimensionalized growth-rates were plotted as a function of circular frequency in Figure 10. In this case the differences were more significant, because the local width changes magnify the differences. The dimensional growth rate is inversely proportional to the length scale (Eq. (34)) which is the smaller closer to the orifice than far from it.

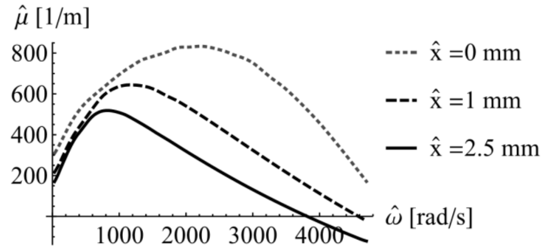

Figure 10. The growth rate of the amplitude of the perturbation velocity in the case of numerical profiles at various distances from the orifice

CONCLUSIONS

In this paper linear stability investigations of various velocity profiles were carried out by the OS equation solved by the CMM. The main goal of the investigation was to give an explanation why the flow at the orifice is more sensitive than elsewhere. The stability results showed that the disturbances grow more rapidly closer to the orifice. These observations were valid to analytical velocity profiles as well as for numerical profiles obtained from CFD. In the case of analytical velocity profiles the critical Reynolds number was the same in all cases $Re_{\mathrm{crit}} \approx 4.3$ and the non-dimensional growth rate is virtually independent of Re if $Re \gtrsim 1000$.

The reason for the higher growth rate close to the orifice was twofold. The first reason was that the velocity profiles, that are closer to the top hat profile, have higher non-dimensional spatial growth rates. These profiles are closer to the orifice. The other one can be explained by the non-dimensional form of stability equations. The local length scale grows continuously from the orifice and the growth rate is inversely proportional to the local length scale for the same non-dimensional velocity profile.

REFERENCES

[1] Tatsumi, T. and Kakutani T., 1958, "The stability of a two-dimensional laminar jet," *J. Fluid Mech.*, vol. 4, no. 3, pp. 261-275.

[2] Curle, N., 1957, "On Hydrodynamic Stability in Unlimited Fields of Viscous Flow," *Proceedings of the Royal Society of London*, vol. 238, no. 1215.

[3] Nolle, A. W., 1998,"Sinuous instability of a planar air jet: Propagation parameters and acoustic excitation," *Acoustical Society of America*, pp. 3690-3705.

[4] Tam, K. K., 1955, "Linear stability of the non-parallel Bickley jet," *Canadian Applied Mathematics Quarterly*, vol. 3, no. 1.

[5] Kerschen, E. J., 1966, "Receptivity theory in compressible flow jet control” AFOSR program final report, Ft. Belvoir Defense Technical Information Center.

[6] Parekh, D. E.; Cain A. B., and Vaporean C: N., 1997, Characterization of Receptivity in jet flow control, UNITED STATES AIR FORCE Air Force Office of Scientific Research

[7] Sengupta, T. K., 2012, *Instabilities of Flows and Transition to Turbulence*, CRC Press.

[8] NG, B. S. and Reid, W. H., 1978, "An initial value method for Eigenvalue Problems Using Compound Matrices," *Journal of Computational Physics*, vol. Physics 30, pp. 125-136.

[9] Schlichting H., 1933, "Laminare Strahlausbreitung," Z. *Angew. Math. Mech.*, vol. 13, pp. 260-263.

[10] Bickley, W., 1937, "The plane jet," *Philos. Mag.*, vol. 23, pp. 727-731, 1937.

[11] White, F. M., 1991, *Viscous fluid flow*, McGraw-Hill.

[12] Sengupta, T. K.; Ballav M. and Nijhawan S., 1994, "Generation of Tollmien-Schlichting waves by harmonic excitation," *Phys. Fluids*, vol. 6, no. 3, pp. 1213-1222.

Conference on Modelling Fluid Flow (CMFF'15)
The 16th International Conference on Fluid Flow Technologies
Budapest, Hungary, September 1-4, 2015

CFD STUDY ON THE EFFECT OF INLET GEOMETRY ON THE CAVITATION PERFORMANCE OF TWO CENTRIFUGAL PUMPS

Gergely Hajgató[1], Csaba Hős[2], László Kullmann[3]

[1] Corresponding Author. Department of Hydrodynamic Systems, Budapest University of Technology and Economics. Műegyetem quay 3., H-1111 Budapest, Hungary. Tel.: +36 1 463 3097, Fax: +36 1 463 3091, E-mail: ghajgato@hds.bme.hu
[2] Department of Hydrodynamic Systems, Budapest University of Technology and Economics. E-mail: hoscsaba@hds.bme.hu
[3] Institute of Hydrodynamic Systems, Budapest University of Technology and Economics. E-mail: kullmann@hds.bme.hu

ABSTRACT

This paper focuses on the study of possible sources of cavitation in a 2.3 MW, 4.7 m^3/s, single-stage, double-suction, welded-casing centrifugal pump, in which the impeller was known to suffer cavitational damage even in normal operating conditions. As the pump operates continuously in a power plant, it was impossible to perform measurements, thus CFD techniques were used to address the problem. Because of the lack of validation data, another pump with slightly different inlet geometry was also analysed by means of CFD, which operates cavitation-free. It was assumed that the cavitation occurs in the former pump due to an improper shape of the pump casing. The analysis concentrates on the inlet region of the pumps and contains only one half of the casings without the pressure side volute and the impeller blades. Both single-phase and multiphase (water+vapour) computations were performed. The results showed that the values of the minimal pressure in the casings are significantly different for the two pumps proving that the cavitation is indeed present in the first pump. It was also found that the effect of the axial gap a between the impeller and the housing is negligible in the range of a/D_1 = 0.0012 to 0.022, with D_1 being the impeller inlet diameter.

Keywords: cavitation, CFD, double-suction centrifugal pump

NOMENCLATURE

A	$[m^2]$	cross-section
H	$[m]$	head of the pump
H_{imp}	$[m]$	head of the impeller
Q	$[m^3/s]$	volumetric flow rate
c	$[m/s]$	fluid mean velocity
d	$[m]$	diameter
d_{m}	$[m]$	mean diameter of a gap
g	$[m/s^2]$	acceleration of gravity
l	$[m]$	gap length
n_{nom}	$[1/s]$	nominal speed of revolution
n_{q}	$[\frac{m^{0.75}}{min\cdot s^{0.5}}]$	specific speed of revolution
p	$[Pa]$	pressure
δ	$[m]$	gap width
η_{v}	$[-]$	volumetric efficiency
λ	$[-]$	gap coefficient
μ	$[-]$	passage number
ν	$[m^2/s]$	kinematic viscosity
ω_{f}	$[rad/s]$	angular speed of the fluid
ω_{imp}	$[rad/s]$	angular speed of the impeller
ϱ	$[kg/m^3]$	fluid density

Subscripts and Superscripts

BEP	best efficiency point
gap	in the gap between the impeller and casing
in, out	at the inlet or outlet of the impeller
1/2	value related to the half of the impeller

1. INTRODUCTION

Cavitation might develop in centrifugal pumps even if sufficient $NPSH$ values are available, see [1, 2, 3]. Unfortunately, *physical cavitation* – i.e. the presence of relatively small cavitating regimes – may cause severe damage yet will not be detected as, unlike *technical cavitation* – the presence of large cavitating regimes and/or blocked flow passages – it does not cause a significant degradation in the hydraulic performance, notable head and/or flow rate drop.

This paper presents a case study on a cooling water pump, which operated at its best efficiency point seemingly without any problem, yet the first regular inspection revealed cavitational erosion on the impeller blades. Once the problem was reported, further on-site investigation could not be performed due to the need of the continuous operation of the power plant. This lead to the idea of using numerical modelling to reveal the origin of cavitation.

To overcome the problem of the unavailable hydraulic parameters – e.g. the value of the $NPSH_a$ or the static pressure in the suction pipe – we decided to perform CFD simulations on a non-cavitating pump with nearly the same design. We shall refer to the original, cavitating pump as 'pump C' while the second, non-cavitating pump as 'pump NC'. Upon comparing the flow patterns in these two pumps, the differences in the pressure distribution along the pump casings reveals the possible reasons of the cavitation.

This paper is organized as follows. Section 2 includes the specifications of the CFD computations (geometry, mesh, boundary conditions, etc.), Section 3 presents the results, while Section 4 gives some possible solutions on improving the hydraulic performance. Finally, Section 5 concludes the study.

2. CFD SIMULATION

2.1. Examined pumps

The subject of the simulations were single-stage, double-suction, welded-casing centrifugal pumps with a semi-axial impeller as seen on the left-hand side of Figure 1. Due to the welded-casing design, a stiffener tongue was built in the suction pipe to improve the rigidity of the pump casing. The spur aimed to reduce the prerotation of the velocity field. These features can be seen on the right-hand side of Figure 1, where the outer casing of the pump had been removed for better visibility. We shall refer to this cavitating pump as 'pump C'.

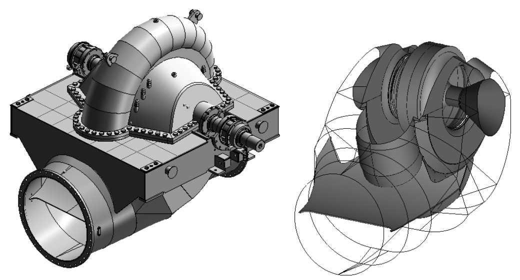

Figure 1. CAD model of the pumps

The other, non-cavitating pump (we shall refer to as 'pump NC') is an earlier design, which operates problem-free in several power plants. Pump C is actually its modified version with a wider and larger diameter impeller, but nearly the same casing. Table 1 contains the hydraulic parameters of the pumps, while Figure 2 shows the inlet of the impeller for pump NC. The contour of the gap ring and the gap ring house was changed in pump C, because the axial length of the gap ring had to be downsized due to the wider impeller. (See Figure 6 and 7 for the difference.) This shape modification was believed to give rise to cavitation, hence great care was devoted to accurate numerical simulation in this regime.

Table 1. Hydraulic parameters of the pumps

	Pump NC	Pump C
$Q_{\mathrm{BEP}}[m^3/s]$	4.725	5.5
$H_{\mathrm{BEP}}[m]$	45	30
$n_{\mathrm{nom}}[1/s]$	8.25	7.05
$n_{\mathrm{q}}[-]$	43.8	54.7

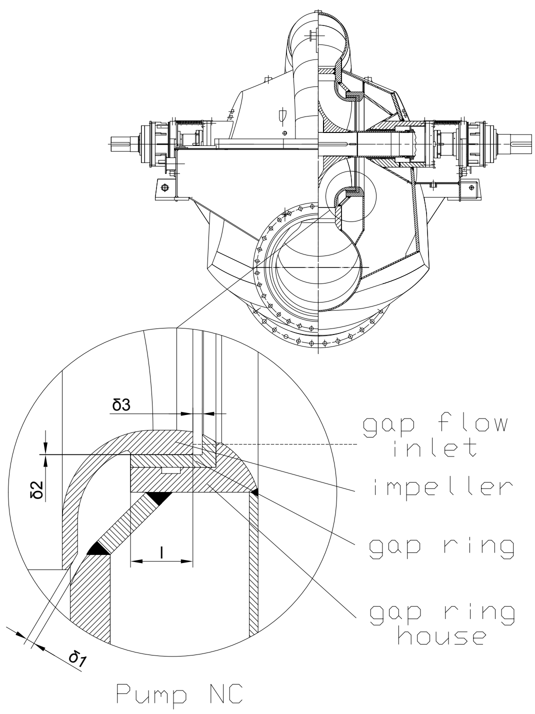

Figure 2. Sectional view of the gap ring and the gap ring house in pump NC

2.2. Numerical models

2.2.1. Physical models

To explore whether the modified gap ring is responsible for the cavitation or not, steady-state simulations were performed on both the original and modified geometries.

Examining the inlet flow in a pump near the BEP usually allows neglecting the upstream effect of the impeller, see e.g. [4, 5, 6]. However, the measurements of Hajdú in [7] did not fully support this statement as he measured slight prerotation even near the BEP. Fáy in [8] explains this effect with the gap flow entering the suction side with a velocity vector with both radial and circumferential component rather than with the moving blades influence.

Considering all these effects, the steady-state flow pattern would not change on the suction side of a pump, if the impeller blades had been removed, but the inlet gap flow had been kept. Furthermore if the pump casing would be split in half along its symmetry plane, the flow patterns would be the same in each half. According to these the simplified physical model contained the half of the pump casing and the half of the impeller only, but without the pressure side volute and the impeller blades.

2.2.2. Estimation of the gap flow

The gap flow is an input parameter of the CFD computations, hence it needs to be estimated for both of the pumps. The calculations presented here are based on the lecture notes of Kullmann [9] and the work of Fűzy [10] and Bohl [11] while the results will be compared to the measurement data collected by Stoffel [12]. Both calculating methods require an initial assumption, that the flow in the gaps is turbulent, thus the hydraulic losses are proportional to the square of the gap fluid velocity.

To estimate the gap flow rate the pressure difference has to be calculated on the sides of the gap first. As seen on 'Figure 2', 3 gaps are presented between the impeller and the casing. The axial gap (marked with δ_2) is one order of magnitude smaller than the others, thus only δ_2 had been considered in the estimation.

The pressure difference can be calculated between the inlet and outlet of the impeller in two ways. 'Eq. (1)' considers the flow passage through the gaps between the impeller and the pump casing, while 'Eq. (2)' considers the flow passage through the impeller. In the former equation the angular speed of the fluid ω_f can be approximated with the half of ω, the angular speed of the impeller.

$$p_\mathrm{out} - p_\mathrm{in} = \Delta p_\mathrm{gap} + \frac{\varrho}{2} \cdot \left[\frac{d_\mathrm{out}^2}{4} - \frac{d_\mathrm{in}^2}{4} \right] \cdot \omega_\mathrm{f}^2 \tag{1}$$

$$p_\mathrm{out} - p_\mathrm{in} = \varrho \cdot g \cdot H_\mathrm{imp} + \frac{\varrho}{2} \cdot (c_\mathrm{in}^2 - c_\mathrm{out}^2) \tag{2}$$

Arranging 'Eq. (1)' and 'Eq. (2)' Δp_{gap} can be calculated. The flow rate through the gap can be estimated using 'Eq. (3)'. The calculation of μ is presented in 'Eq. (4)' according to Fűzy [10].

$$Q_\mathrm{gap,1/2} = \mu \cdot A_\mathrm{gap} \cdot \sqrt{\frac{2 \cdot \Delta p_\mathrm{gap}}{\varrho}} \tag{3}$$

$$\mu = \frac{1}{\sqrt{\frac{\lambda \cdot l}{2 \cdot \delta} + 1.5}} \tag{4}$$

In 'Eq. (4)' λ stays for the gap coefficient, which is a quantity analogue to the wall-friction coefficient. Fűzy [10] publishes a nomogram, from where the value of λ can be read as a function of δ and the l/δ ratio in the range of 0 – 0.3mm and 400 – 800 respectively.

Another way to estimate the volumetric flow rate through a gap is presented in 'Eq. (5)' according to Bohl [11].

$$Q_\mathrm{gap,1/2} = \pi \cdot d_\mathrm{m} \cdot \delta \cdot \sqrt{\frac{\Delta p_\mathrm{gap} \cdot \delta}{2 \cdot l \cdot \varrho}} \cdot \left(3.45 + 5.52 \cdot \log \frac{\delta}{2 \cdot \nu} \cdot \sqrt{\frac{\Delta p_\mathrm{gap} \cdot \delta}{2 \cdot l \cdot \varrho}} \right) \tag{5}$$

Once the gap flow rate is known, the volumetric efficiency of a pump can be calculated by means of 'Eq. (6)'. According to Stoffel [12] the gap-related Reynolds-number can be calculated with 'Eq. (7)' and the volumetric efficiencies can be verified with the aid of 'Figure 3', where different types of efficiency are presented as the function of the specific speed of revolution n_q and which is based on measurement data on real-life pumps.

$$\eta_v = \frac{Q_\mathrm{nom,1/2}}{Q_\mathrm{nom,1/2} + Q_\mathrm{gap,1/2}} \tag{6}$$

$$Re_\mathrm{gap} = \frac{c_{gap} \cdot \delta}{\nu} \tag{7}$$

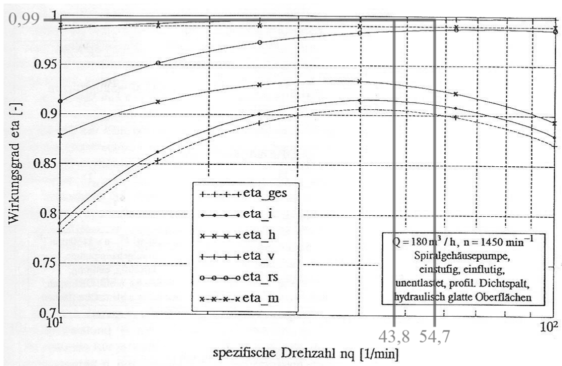

Figure 3. Different types of efficiency in pumps based on measurement data (Originally published by Stoffel [12].)

The methods described above gave a different value for the gap flow rate both in the case of pump C and pump NC. The gap-related Reynolds-number suggested that the flow is turbulent in both cases. Comparing the values with the ones presented on 'Figure 3' the method of Fűzy [10] showed a better approach for the gap flow rate. Thus the results from that calculation had been used by setting up the numerical simulations.

2.2.3. Simulation parameters

The numerical meshing and the simulations was carried out with commercialized codes, namely Ansys ICEM and Ansys CFX. The numerical grid contained tetra elements in the free-stream and prismatic elements near the walls in a total number of approximately 14 million. The prismatic layers had been set up to allow the solver to use wall-functions beside the

SST turbulence model during the computation.

To avoid backflow at the boundaries, the velocity vectors had been prescribed at the gap flow inlet and the outlet of the geometry as seen on 'Figure 4' and the total pressure had been defined at the inlet. The latter value was 1[bar] in each simulation to let the flow patterns comparable in both of the pump casings. The inlet gap flow velocity had both radial and circumferential components, the latter being half of the rotational speed of the impeller, i.e. $\propto \omega_{\text{imp}}/2$. The velocity vectors on the outlet had been prescribed to be perpendicular to the surface of the outlet and the absolute value of the speed had been calculated from adding the half of the nominal volume flow rate of the pump $Q_{\text{nom},1/2}$ and the gap flow $Q_{\text{gap},1/2}$ calculated according to Fűzy [10] divided by the area of the outlet surface.

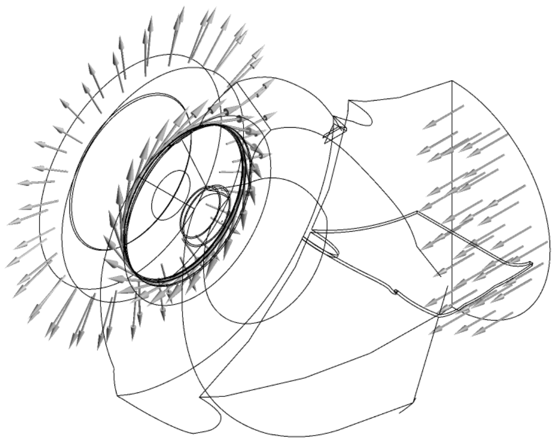

Figure 4. Velocity vectors at the boundaries of the computational geometry

Furthermore, calculations were performed with and without modelling the cavitation. Cavitation was added with the built-in implementation of the Rayleigh–Plesset equation of the Ansys CFX. Several simulations were performed on a modified geometry as well, to study the importance of the axial size of the gap δ_3 (See on 'Figure 2'.) and the flow rate of the pump.

3. RESULTS

3.1. Comparing the numerical values

'Table 2' summarizes the results of the simulations carried out on the model of the non-cavitating and possibly cavitating pump, the latter had been investigated by the flow rate slightly changed and the by the radial gap δ_3 excessively changed.

It is important to mention, that the inlet total pressure had been defined arbitrarily to 1[bar], because the valid pressure value in the suction pipe was not available. With this assumption the flow patterns were even so comparable, but the absolute values of the results are meaningless.

The parameters showed in 'Table 2' are the minimal static pressure in the fluid region $p_{\min}$, the minimal static pressure in the section of the leading edges of the impeller blades $p_{\min,\text{in}}$ and the absolute value of the maximal velocity in the fluid region $v_{\max}$.

Table 2. Results of the simulations (Total pressure at the inlet: $1[bar]$**)**

Pump	$p_{\min}$[]Pa]	$p_{\min,\text{in}}$[Pa]	$v_{\max}$[m/s]
NC	3600	58000	13
C (w/ R–P)	290	39900	15
C	−8500	34700	13.5
C (0.8Q)	30100	51300	12.7
C (1.1Q)	−34700	10100	15
C (0.1δ_3)	n.f.	n.f.	n.f.
C (1.9δ_3)	−7500	36900	13.3

The results of pump NC can be considered as a reference. The results of pump C differs significantly even with the Rayleigh–Plesset-equation taken into consideration (w/ R–P), whether not. As it can be seen, comparing $p_{\min}$ of the latter two, modelling the cavitation describes a lower limit to the static pressure, which would complicate the comparison of the other simulations. Thus these simulations were performed without the Rayleigh–Plesset equation.

Changing the volumetric flow rate causes obvious changes in the minimal pressure and the maximal velocity, but it is noteworthy, that the slight upraise of the flow rate causes excessive drop in the minimal pressure.

Widening the gap δ_3 has marginal effect, as it was expected, but when this gap widens on one side of the impeller, it has to be narrowing on the other. Unfortunately, narrowing this gap resulted in large steps in the size of the mesh elements near the gap flow inlet. This led to converged, but clearly wrong results according numerical failure (n.f.). Thus, the results of this simulation has not been presented here.

3.2. Comparing the flow patterns

Comparing the numerical values could show if the cavitation presented in the fluid domain. To bring the reason of the cavitation to light, the flow patterns have to be examined. According to the numerical results, the flow patterns in pump NC and in pump C (non-modified, Rayleigh–Plesset-equation applied) had been compared.

The distribution of the static pressure on the gap ring house, on the gap ring and in the section of the leading edges of the impeller blades can be seen on 'Figure 5'. The left side shows pump NC, the right side does pump C.

The macro-view of the flow pattern is defined by the pipe-bend-like shape of the pump casing, which is common in the examined pumps. Thus, the minimal pressure point in the section of the leading edge of the impeller blades is at nearly the same place in both of the pumps, but the absolute value of it is smaller in pump C. The overall minimal pressure point lays on the gap ring house in each pump in the vicinity of the excessive bends. It is also visible, that the low-pressure area in pump C is bigger either on the gap ring house and in the emphasized section.

Figure 5. Pressure distribution at the inlet of the impeller. Left side: pump NC, right side: pump C.

The location of the minimal pressure zone is seen also on 'Figure 6' and on 'Figure 7', where the velocity distributions had been visualized in the meridional section of the overall minimal pressure point. These figures clearly show the difference in the geometry as well.

In both of the pumps the gap ring and the gap ring house take the role of a confuser, which conditions the flow before it enters the impeller. In case of pump C ('Figure 7'), this confuser cannot perform fully its task, because the flow separates after the small-radius bend. It is presumable, that this shape feature is in charge for the cavitation occur.

Visualizing the cavitational area in the fluid domain ('Figure 8') verifies the earlier suspicion, vapour are presented only at the gap ring house of pump C at the small-radius bend.

'Figure 9' shows the velocity vectors in the section of the leading edges of the impeller blades in pump C, but they are very similar in pump NC as well. (The spur had been illustrated for better understanding.) Although a prerotation-free velocity field would be beneficial, two counter-rotating zone can be observed yet. One is right behind the spur and one is nearly in the extension of the stiffener tongue. The earlier is more-or-less obvious looking at the shape of the spur, but the latter foreshadows a stagnation zone above or under the stiffener tongue.

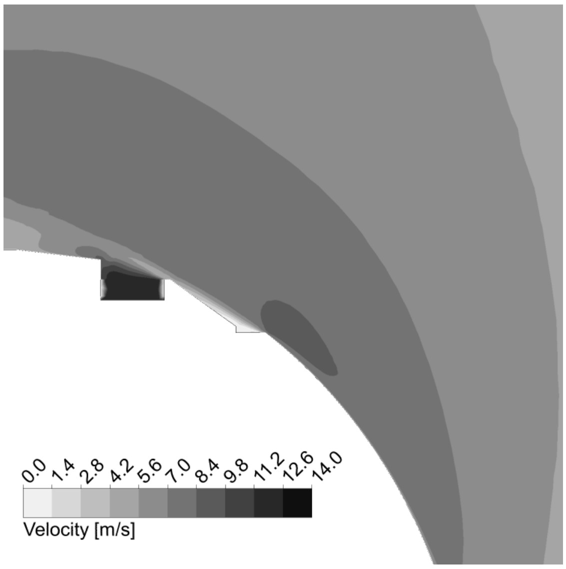

Figure 6. Velocity contours in the meridional section of the minimal pressure - pump NC, flow direction: ←

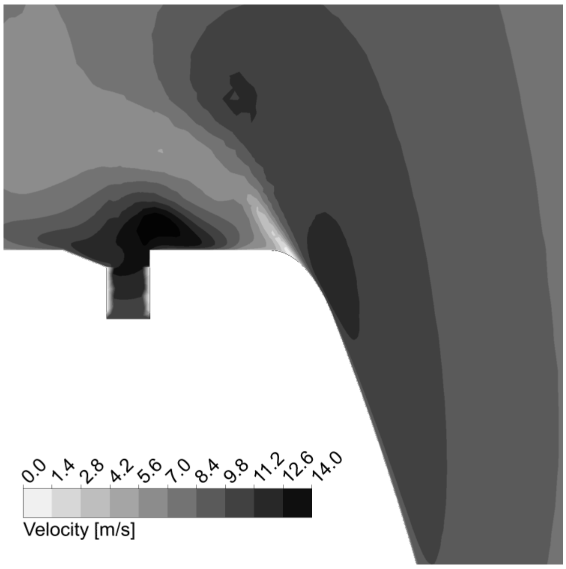

Figure 7. Velocity contours in the meridional section of the minimal pressure - pump C, flow direction: ←

Observing the streamlines shown on 'Figure 10' the latter presumption looks verified, a whirling zone can be seen under the tongue and one can be seen in the upper side of the suction volute as well.

The area of three cross-sections had been calculated under tongue, the results are on 'Figure 11'. According to these, the tongue and the lower part of the pump casing form a diffuser together, which leads to the forming of a stagnation zone in it.

The visualization of the q-criterion had been carried out on 'Figure 12', in which a significant vortex can be seen in the upper side of the suction volute.

Figure 8. Cavitational bubbles on the gap ring house of pump C

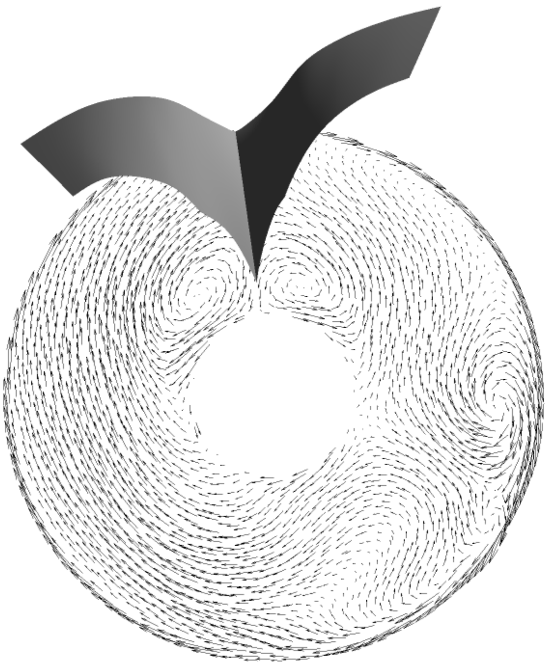

Figure 9. Velocity vectors in the section of the leading edges of the impeller blades - pump C

4. IMPROVING POSSIBILITIES OF THE SUCTION PERFORMANCE

Based on the results described earlier, the initial presume, that the wrong shape feature leads to cavitation in pump C is right. However, looking at the entire flow pattern in the pumps, there are more possibilities to avoid cavitation during operation.

The manifest solution is to redesign the shape of the gap ring house in pump C, even in a similar style as can be found in pump NC. In the latter case the confuser is formed by the gap ring house and the gap ring together before the impeller, while in the earlier

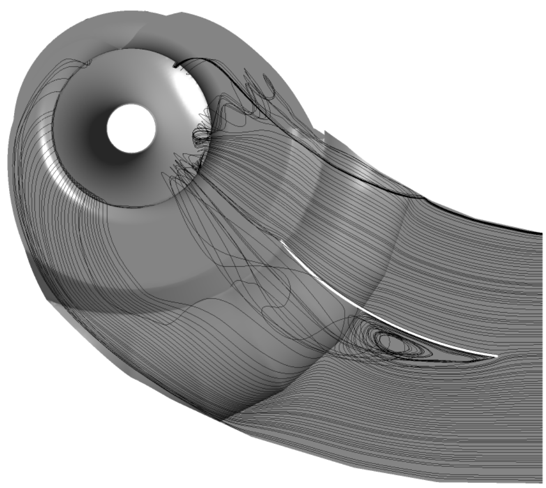

Figure 10. Streamlines started from the inlet in pump C

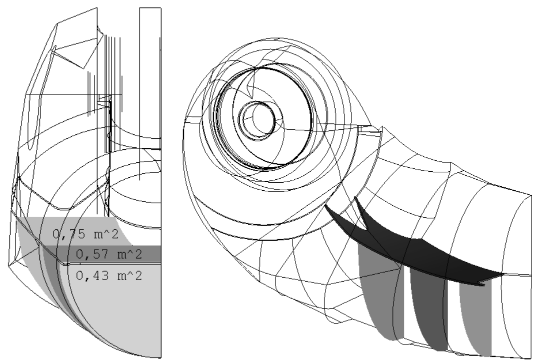

Figure 11. Areas of the cross-sections under the stiffener tongue

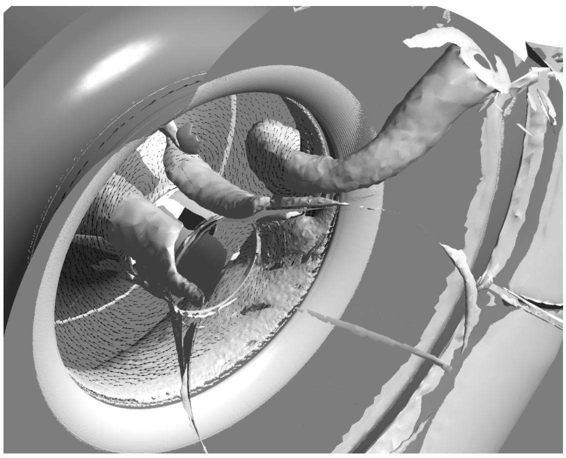

Figure 12. Vortex detected with q-criterion in pump C

case only the gap ring house takes the role of the confuser. It means larger confuser-angle which leads to the separation of the flow right after the smallest-radius bend. This can be the reason of why the cavitation occurs in pump C, but in pump NC not despite of the similar casings.

According to the results of the simulations, the overall suction performance could be upgraded by redesigning the stiffener tongue, or by reconsider its angle of attack at least. The redesigning of the upper side of the suction volute could help the suction performance as well.

5. SUMMARY

The aim of the work described in present paper was to bring the reason of the cavitational damage in a double-suction centrifugal pump to light. To address this problem a non-standard method had been chosen by simulating two similar pump casings and by comparing the results to each other. In the simulation set-up process, the gap flow between the impeller and the pump casing had been estimated according to two different literature.

According to the comparison of the flow patterns in the two, basically similar pump casing, the reason of the cavitational damage is a small-radius bend on the inlet side gap ring house. Although the correction of this shape feature would be satisfactory to avoid cavitation, there are further possibilities to improve the suction performance of the pumps built with this design of pump casing. The most important one is to adjust the angle of attack of the stiffener tongue built in the suction volute.

The results seen in the paper were computed with an arbitrarily chosen suction side pressure, thus the absolute values can be different in the real life pumps, so the size of the cavitational zones shown on 'Figure 8'.

REFERENCES

[1] Shah, S., Jain, S., Patel, R., and Lakhera, V., 2013, "CFD for Centrifugal Pumps: A Review of the State-of-the-Art", *Procedia Engineering*, Vol. 51 (0), pp. 715 – 720, chemical, Civil and Mechanical Engineering Tracks of 3rd Nirma University International Conference on Engineering (NUiCONE2012).

[2] lin LIU, H., xi LIU, D., WANG, Y., fang WU, X., WANG, J., and DU, H., 2013, "Experimental investigation and numerical analysis of unsteady attached sheet cavitating flows in a centrifugal pump", *Journal of Hydrodynamics, Ser B*, Vol. 25 (3), pp. 370 – 378.

[3] ZHU, B., and xun CHEN, H., 2012, "Cavitating suppression of low specific speed centrifugal pump with gap drainage blades", *Journal of Hydrodynamics, Ser B*, Vol. 24 (5), pp. 729 – 736.

[4] Csanády, G. T., 1964, *Theory of Turbomachines*, McGraw-Hill Book Company.

[5] István, J., 2003, *Örvényszivattyúk*, Info-Prod Könyvkiadó.

[6] Breugelmans, F. A. E., and Sen, M., 1982, "Prerotation and fluid recirculation in the suction pipe of centrifugal pumps", *Eleventh Turbomachinery Symposium*, pp. 165 – 180.

[7] Sándor Hajdú, D., 1957, "Elõperdületesen elõreható radiális szivattyú járókerekek", Ph.D. thesis, Magyar Tudományos Akadémia.

[8] Árpád Fáy, D., 2004, "The principle of neglecting upstream reactions", *The sixth International Conference on Hydraulic Machinery and Hydrodynamics*, pp. 85–90.

[9] László Kullmann, D., "Elõadásvázlat az Áramlástechnikai gépek címû, BMEGEVGAG02, BMEGEVGAE01 kódú tárgyakhoz", `www.hds.bme.hu`.

[10] Olivér Fűzy, D., 1978, *Áramlástechnikai Gépek*, Tankönyvkiadó.

[11] Bohl, W., 2005, *Strömungsmaschinen 2*, Vogel Buchverlag.

[12] Stoffel, B., 1994, "Überlegungen zum maximal erreichbaren Wirkungsgrad von Kreiselpumpen", *Strömungsmechanik und Strömungsmaschinen*, pp. 21–32.

Conference on Modelling Fluid Flow (CMFF'15)
The 16th International Conference on Fluid Flow Technologies
Budapest, Hungary, September 1-4, 2015

CALCULATION OF THE PERMEABILITY IN POROUS MEDIA USING THE LATTICE BOLTZMANN METHOD

Amir ESHGHINEJADFARD[1], Gábor JANIGA[2], Dominique THÉVENIN[3]

[1] Corresponding Author. Department of Fluid Mechanics, Institute of Fluid Dynamics and Thermodynamics, University of Magdeburg "Otto von Guericke" 39106, Magdeburg, Germany. Tel.: +49 391 6712324, Fax: +49 391 6712840, Email: amir.eshghinejadfard@st.ovgu.de
[2] Department of Fluid Mechanics, Institute of Fluid Dynamics and Thermodynamics, University of Magdeburg "Otto von Guericke", 39106, Magdeburg, Germany. Email: janiga@ovgu.de
[3] Department of Fluid Mechanics, Institute of Fluid Dynamics and Thermodynamics, University of Magdeburg "Otto von Guericke", 39106, Magdeburg, Germany. Email: thevenin@ovgu.de

ABSTRACT

The Lattice Boltzmann method (LBM) is found highly suitable for complex geometries like flow in porous media due to many advantages. In the current study LBM is used to simulate flow through porous media and to calculate the resulting permeability value. Three different flow configurations are studied: first by manually specifying solid cells in a face centered cube (FCC); then in a body centered cube (BCC); and finally by reading the fluid and solid cells for an arbitrary 3D geometry from a set of 2D computed tomography (CT) images. It was found that the current LBM simulation yields good estimates for the permeability value. It was also observed that higher resolutions lead to more accurate results. The multi relaxation time (MRT) model showed a lower viscosity dependence in comparison with the single relaxation time (SRT) model. At the lowest value for the relaxation time, the Guo-SRT approach showed a better accuracy compared to Shan-Chen and Guo-MRT, while Guo-MRT model is superior at higher relaxation times. The last test case proved that a set of 2D images of an arbitrary geometry can yield the main characteristics of a 3D porous media.

Keywords: lattice Boltzmann method, porous media, permeability

NOMENCLATURE

D	$[m]$	sphere diameter
$\mathbf{F}$	$[N]$	Force vector
$\mathbf{M}$	[-]	Transformation matrix
$\mathbf{S}$	[-]	collision matrix
M	[-]	Mach number
P	$[Pa]$	pressure
U	$[m/s]$	velocity magnitude
Re	[-]	Reynolds number
b	$[N]$	body force
c	$[m/s]$	lattice velocity vector
c_s	$[m/s]$	sound speed
f	[-]	distribution function
k	$[m^2]$	permeability
$\mathbf{u}$	$[m/s]$	macroscopic velocity vector
$\mathbf{v}$	$[m/s]$	shifted velocity vector
$\mathbf{x}$	$[m]$	position vector
Δt	$[s]$	time step
μ	$[Pa.s]$	Dynamic viscosity
ν	$[m^2/s]$	Kinematic viscosity
ζ	$[m/s]$	velocity
ρ	$[kg/m^3]$	density
τ	[-]	relaxation parameter
φ	[-]	porosity
ω	[-]	lattice weight coefficient

Subscripts and Superscripts

f	force
s	sound
eq	equilibrium
−	mean
^	moment space

1. INTRODUCTION

Flow through a porous media is one of the most attracting engineering subjects due to wide practical applications, ranging from catalysts, to mineral rocks, biomedical engineering and filter simulation.

Permeability is perhaps the most important property in the study of a porous media. It is a measure of the ability of a porous media to transmit fluids. Because of costs and time-consuming nature of experimental analysis it is often preferred to determine the permeability by numerical simulations. Standard Navier-Stokes codes fail in many cases to represent flow behavior in porous media, due to poor convergence and instability problems. Additionally, very complex meshing strategies are needed. LBM has emerged in the recent decades as an alternative to the Navier-Stokes equations (NSE) [1, 2]. LBM is based on the mesoscopic physics of Lattice Gas Automata (LGA) [3]. It can be also obtained from the discretized Boltzmann equation. LBM was shown to be equivalent to an explicit, first-order in time, second-order in space finite difference approximation of the NSE [4]. Locality of calculations and easy implementation of no-slip boundary condition in complex geometries and efficient parallelization makes the LBM very efficient for flows with complex geometries [5].

The permeability can be calculated from the Darcy's law [6] in the limit of low Reynolds number and is related to the mean flow velocity and the applied pressure gradient:

$$k = -\frac{\mu \bar{U}}{\left(\frac{dP}{dx}\right)}. \tag{1}$$

In Eq. (1), $\bar{U}$ is the mean velocity in the flow field and $\frac{dP}{dx}$ is applied pressure gradient. In LBM instead of the pressure gradient a uniform body force b_f can be used, which produces the same amount of flow rate as the pressure-driven flow. One should note that the Darcy's law is only valid in the limit of very low Reynolds number (Re), say Re<1. At high Reynolds numbers the contribution of fluid inertia to pressure drop becomes significant and the permeability varies with flow conditions. In such a case, non-Darcy effects must be taken into account.

One of the earliest applications of LBM in porous media simulation can be traced back to the work of Succi et al. [7]. They reported the validity of the lattice-Boltzmann model for flow simulation in complex 3D geometries. Since then many researchers have utilized LBM approach for different cases of single or multi-phase porous media flows. Pan et al. [8] investigated the effect of single or multi relaxation time approaches. They also studied the influence of different bounce-back implementations on accuracy of results for different sets of packs. Degruyter et al. [9] combined X-ray microtomography and LBM to study flow characteristics in samples from different silicic volcanic deposits. Chukwudozie and Tyagi [10] modeled fluid flows in periodic arrays of sphere packs using LBM and different macroscopic flow parameters such as permeability, tortuosity, and β factor were calculated. They also studied the test case of an irregular pack of uniform-diameter spheres constructed from CT images.

This paper is organized as follows. In section 2 a brief description of LBM and relevant equations will be given. Section 3 includes the results which have been obtained for three cases. Permeability values are calculated and the influence of various factors is examined. Finally, conclusions are extracted and given as the last section of this study.

2. LBM

The LBM describes the evolution of a discretized particle distribution function, $f(\mathbf{x}, t, \xi)$, which represents the probability of finding a fictitious particle in a certain location $\mathbf{x}$ with a certain velocity ξ at a certain time t.

A discretization of the Boltzmann equation in time and space, and the conversion of the space of velocities $\{\xi\}$ into a finite set of velocities $\{\mathbf{c}_i\}$ within which the particles are allowed to move in the lattice, leads to the lattice Boltzmann equation:

$$\begin{aligned} &f_i(\mathbf{x}+\mathbf{c}_i\Delta t, t+\Delta t) - f_i(\mathbf{x},\mathrm{t}) = \\ &-\frac{1}{\tau}\left[f_i(\mathbf{x},\mathrm{t}) - f_i^{(eq)}(\mathbf{x},\mathrm{t})\right], \end{aligned} \tag{2}$$

where f_i is the distribution function of particles moving with speed $\mathbf{c}_i$ and the right hand side accounts for the SRT-Bhatnagar, Gross and Krook (BGK) collision term [11] in which the collision operator is based on the SRT approximation to the local equilibrium distribution. Here, τ is the dimensionless mean relaxation time and Δt is the time step. The equilibrium distribution function $f_i^{(eq)}(\mathbf{x},\mathrm{t})$ can be written as:

$$f_i^{eq} = \omega_i \rho \left[1 + \frac{\mathbf{c}_i \cdot \mathbf{u}}{c_s^2} + \frac{(\mathbf{c}_i \cdot \mathbf{u})^2}{2c_s^4} - \frac{u^2}{2c_s^2} \right], \tag{3}$$

where $\mathbf{u}$ is the velcocity vector, u is its magnitude, ω_i is the weight associated with the velocity $\mathbf{c}_i$, and the sound speed c_s is model-dependent. The macroscopic velocity $\mathbf{u}$ in Eq. (3) must satisfy the requirement for low Mach number M, i.e., that $|\mathbf{u}|/c_s = \mathrm{M} \ll 1$.

In the present work, for three-dimensional flows, the nineteen-velocity model (D3Q19) is applied. The D3Q19 model has the velocity vectors $\mathbf{c}_i=\{\mathbf{c}_{ix}, \mathbf{c}_{iy}, \mathbf{c}_{iz}\}$ where $\mathbf{c}_{ix}$= (0, 1, -1, 0, 0, 0, 0, 1, -1, 1, -1, 1, -1, 1, -1, 0, 0, 0, 0), $\mathbf{c}_{iy}$= (0, 0, 0, 1, -1, 0, 0, 1, 1, -1, -1, 0, 0, 0, 0, 1, -1, 1, -1) and $\mathbf{c}_{iz}$= (0, 0, 0, 0, 0, 1, -1, 0, 0, 0, 0, 1, 1, -1, -1, 1, 1, -1, -1). The weight coefficients are: ω_1=1/3, $\omega_2 = \ldots = \omega_7$=1/18, $\omega_8 = \ldots = \omega_{19}$= 1/36. The sound speed in Eq. (3) is then given in non-dimensional form by $c_s = 1/\sqrt{3}$.

Macroscopic quantities including density and velocity are defined by the 0th and 1st moments of the probability distribution function (PDF), respectively:

$$\rho = \sum_i f_i, \tag{4}$$

$$\rho \mathbf{u} = \sum_i \mathbf{c}_i f_i. \tag{5}$$

Conceptually, the SRT-LBM algorithm is implemented in two stages: first, the collision of particles, which controls the relaxation toward equilibrium; and in a second step, the streaming of particles in which distribution functions are shifted to the neighboring lattice cells.

$$\textit{Collision}: \quad f_i'(\mathbf{x},t) = f_i(\mathbf{x},\mathrm{t}) - \frac{\Delta t}{\tau}\left[f_i(\mathbf{x},\mathrm{t}) - f_i^{(eq)}(\mathbf{x},\mathrm{t})\right], \tag{6}$$

$$\textit{Streaming}: \ f_i(\mathbf{x}+\mathbf{c}_i\Delta t, t+\Delta t) = f_i'(\mathbf{x},\mathrm{t}), \tag{7}$$

where the relaxation parameter (τ) in Eq. (6) is related to the kinematic lattice viscosity, ν, through:

$$\nu = \left(\tau - \frac{1}{2}\right) c_s^2 \Delta t. \tag{8}$$

In order to apply the body force into LBM we have used two force schemes: Shan and Chen [12] and Guo et al. [13]. In the former scheme, the equilibrium velocity in Eq. (3) is shifted by using $\mathbf{v}$ instead of $\mathbf{u}$:

$$\mathbf{v} = \mathbf{u} + \frac{\tau}{\rho}\mathbf{F}. \tag{9}$$

Guo et al. [13] proposed the split-forcing LBM, which enables the LBM to recover the NSE (mass and momentum conservation equation) with second-order accuracy. In this model, a force term is first added to the RHS of Eq. (2):

$$f_i'(\mathbf{x},t) = f_i(\mathbf{x},t) - \frac{\Delta t}{\tau}\left[f_i(\mathbf{x},t) - f_i^{eq}(\mathbf{x},t)\right] + F_i(\mathbf{x},t)\Delta t, \tag{10}$$

and momentum is redefined by adding a force term:

$$\rho \mathbf{u} = \sum_i \mathbf{c}_i f_i + \frac{\Delta t}{2}\mathbf{F}. \tag{11}$$

Correspondingly, they used the discrete force distribution function in Eq. (10) as:

$$F_i(\mathbf{x},t) = \left(1 - \frac{1}{2\tau}\right)\omega_i \left[3\frac{\mathbf{c}_i - \mathbf{u}(\mathbf{x},t)}{c^2} + 9\frac{\mathbf{c}_i.\mathbf{u}(\mathbf{x},t)}{c^4}\mathbf{c}_i \right] \cdot \mathbf{F}(\mathbf{x},t). \tag{12}$$

2.1 MRT-LBM

In order to circumvent the limitations of SRT, in particular model instability at low relaxation times, the MRT model was introduced [14].

In the MRT model, different moments of the distribution function relax at different rates, while in SRT model, all moments relax at the same rate. MRT allows defining individual relaxation parameters for all the variables by construction of a collision matrix, providing the maximal number of degrees of freedom to optimize LBM stability. For MRT, the evolution takes place in a moment space instead of velocity space. The MRT-LBM equation with a force term can be written as:

$$\mathbf{f}(\mathbf{x}+\mathbf{c}_i\Delta t, t+\Delta t) = \mathbf{f}(\mathbf{x},\mathrm{t}) - \mathbf{M}^{-1}\left(\mathbf{S}\left[\hat{\mathbf{f}} - \hat{\mathbf{f}}^{eq}\right] - (\mathbf{I} - \frac{1}{2}\mathbf{S})\hat{\mathbf{f}}_F \right) \tag{13}$$

with $\hat{\mathbf{f}}_F = \mathbf{M}\mathbf{f}_F$ and $\mathbf{f}_F = \{F_i\}_{i=0,\cdots,18} = \left(F_0, F_1, \cdots, F_{18}\right)^T$ in D3Q19 model. The forcing term (F_i) has the same form as Eq. (12). Here, $\mathbf{M}$ is 19×19 transformation matrix and $\mathbf{S}$ is a diagonal collision matrix in moment space, and its elements are relaxation times for the respective moments. Further details can be found in [5, 14].

3. RESULTS

In this section the simulation results of an FCC and a BCC cube and an arbitrary porous media (created by a set of CT images) will be presented. The simulations are carried out using the in-house LBM code *Alborz* developed in our group with a D3Q19 stencil.

3.1 CASE A: FCC structure

This part describes the simulation results for an FCC cube. Two node types can be distinguished in the geometry: fluid nodes (1) and solid nodes (0). Solid nodes in this case are manually set in the LBM code using appropriate equations of spheres. Geometry of the test case is shown in Figure 1. The relation of each cube side size with respect to sphere diameter is given in the same figure.

Porosity as defined by the fraction of void space to the total space is φ=0.25952. The permeability in this FCC cube has been previously determined by solving unsteady Stokes equations for the microscopic flow by Chapman and Higdon [15]. They have reported the dimensionless permeability (k^*/D^2) based on the sphere diameter of 1.736×10^{-4}.

Initial conditions for the flow simulations in our study are zero velocity and uniform lattice density of 1.0 throughout the domain. A constant body force is applied along X direction. Boundary condition on solid nodes is the half-way bounce back and periodic boundary condition is applied on all cube faces. The simulation continues until reaching a steady state condition where the permeability value no longer changes.

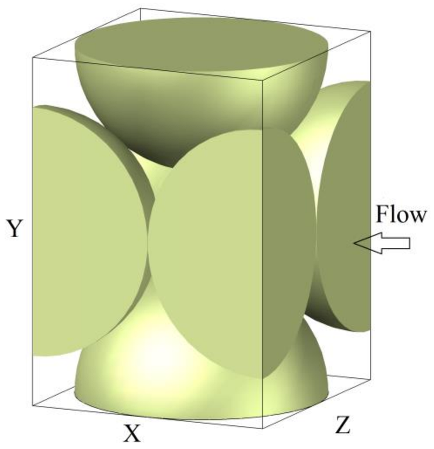

Figure 1. FCC packing (domain: $D\times\sqrt{2}D\times D$)

Table 1 reports the calculated permeability for different sphere diameters, corresponding to different domain resolution using SRT-LBM. The relaxation parameter is τ=0.8 in all cases.

It can be seen from the table that as the domain resolution increases dimensionless permeability gets closer to the reference, 1.736×10^{-4}. The result at the lowest resolution (D=20) is found to be quite far from the expected value. However, the results of D=100, and even more for D=200 are excellent, with less than 2% error. It should be also noticed that to keep the Darcy's law valid for these calculations, small body force values are considered, to ensure low Reynolds number. Reynolds number is calculated based on the mean flow velocity, sphere diameter and kinematic viscosity:

$$\mathrm{Re} = \frac{\bar{U}D}{\nu}. \quad (14)$$

Table 1. FCC packing results for different diameters

Case	D	k/D^2x10^{-4}	Error (%)	Re
1	20	1.360	-21.67	0.0011
2	50	1.821	4.92	0.0228
3	100	1.704	-1.83	0.0017
4	200	1.750	0.83	0.0140

Figure 2 depicts the steady state velocity field for case No. 3 of Table 1 where the velocity distribution on the cube sides can be observed. The reported velocity is in LB units and along X direction.

Figure 3 illustrates the flow field on a 2-D slice at the middle Z-position of Fig. 2. It can be realized that the center of the domain has a much lower velocity compared to the area between the spheres.

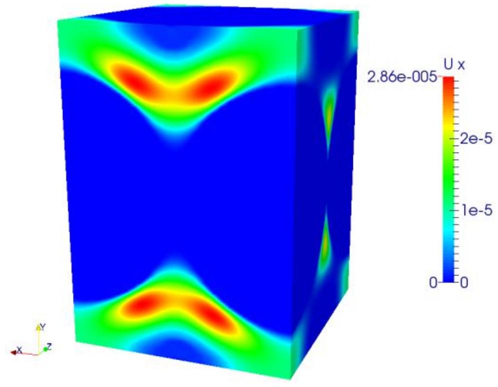

Figure 2. Flow field detail of FCC packing

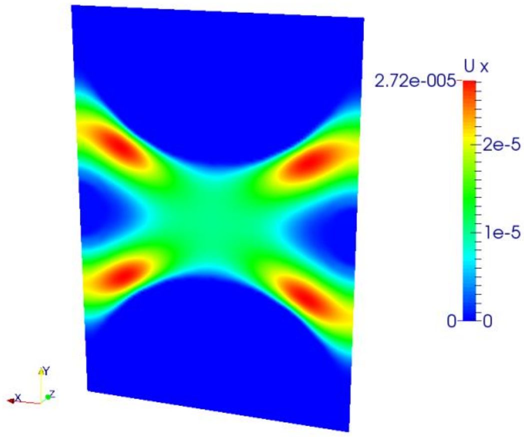

Figure 3. Slice of FCC cube geometry

3.2 CASE B: BCC structure

The second case that is studied here is a BCC structure, as seen in Figure 4. The sphere diameter is D and the cube length in each direction is about 1.1547D which results in a porosity of φ= 0.31982.

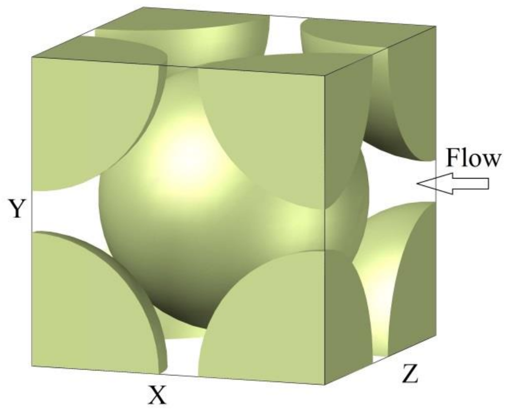

Figure 4. BCC packing ($\frac{2\sqrt{3}}{3}D\times\frac{2\sqrt{3}}{3}D\times\frac{2\sqrt{3}}{3}D$)

Table 2. BCC packing results for different sphere diameters, methods, and relaxation times

Case	D	τ	Method	$k/D^2\times10^{-4}$	Error (%)
1	17.32	0.6	SC-SRT	3.95	-21.30
2	17.32	0.8	SC-SRT	4.71	-6.27
3	17.32	1	SC-SRT	5.28	5.06
4	17.32	0.6	G-SRT	4.57	-9.11
5	17.32	0.8	G-SRT	6.55	30.31
6	17.32	1	G-SRT	8.34	66.03
7	17.32	0.6	G-MRT	4.20	-16.32
8	17.32	0.8	G-MRT	5.52	9.87
9	17.32	1	G-MRT	6.54	30.16
10	43.30	0.6	SC-SRT	4.82	-3.97
11	43.30	0.8	SC-SRT	5.10	1.61
12	43.30	1	SC-SRT	5.29	5.24
13	43.30	0.6	G-SRT	4.92	-2.13
14	43.30	0.8	G-SRT	5.38	7.14
15	43.30	1	G-SRT	5.75	14.44
16	43.30	0.6	G-MRT	4.80	-4.40
17	43.30	0.8	G-MRT	5.10	1.56
18	43.30	1	G-MRT	5.29	5.34
19	86.60	0.6	SC-SRT	4.95	-1.49
20	86.60	0.8	SC-SRT	5.10	1.49
21	86.60	1	SC-SRT	5.18	3.17
22	86.60	0.6	G-SRT	4.97	-1.04
23	86.60	0.8	G-SRT	5.17	2.84
24	86.60	1	G-SRT	5.30	5.43
25	86.60	0.6	G-MRT	4.91	-2.28
26	86.60	0.8	G-MRT	5.03	0.13
27	86.60	1	G-MRT	5.09	1.41
28	173.21	0.6	SC-SRT	4.98	-0.80
29	173.21	0.8	SC-SRT	5.06	0.78
30	173.21	1	SC-SRT	5.10	1.54
31	173.21	0.6	G-SRT	4.99	-0.63
32	173.21	0.8	G-SRT	5.08	1.11
33	173.21	1	G-SRT	5.13	2.10
34	173.21	0.6	G-MRT	4.96	-1.26
35	173.21	0.8	G-MRT	5.01	-0.19
36	173.21	1	G-MRT	5.04	0.31

Initial conditions of flow field are similar to case A and fluid flows through the sphere pack along X direction by means of a body force of 1.0×10^{-7}. Chapman and Higdon [15] reported dimensionless permeability value (k^*/D^2) of 5.023×10^{-4}. Table 2 reports calculated permeability using three approaches: Shan-Chen SRT (SC-SRT), Guo-SRT (G-SRT) and Guo-MRT (G-MRT) for 36 different cases. The results are presented for various relaxation times and domain resolutions.

Figures 5-7 are plotted using the data of Table 2 and represent k/k^* vs. sphere diameter for different relaxation times. One can see immediately that as the domain resolution increases the results get much closer to the reference value. For example the predicted permeability with G-MRT approach for τ=0.8 and D=173.21 shows less than 0.2% error. It is seen from Fig. 5 that for τ=0.6, the G-SRT model has the highest accuracy compared to SC-SRT and G-MRT for all domain resolutions. However, for τ=0.8 and τ=1.0, the G-MRT approach shows its superiority, especially for higher resolutions. It is interesting that for τ=0.8 and τ=1.0, G-SRT shows the poorest results. However, all schemes approach each other and converge toward the reference value as D increases. It can be also observed from Figs. 5-7 that SC-SRT and G-MRT results are very close to each other at D=43.3 for all τ values. Probably it is the limit beyond which G-MRT is superior to SC-SRT at τ=0.8, 1.0 while SC-SRT is superior for τ=0.6. It can be also concluded from Figs. 5 and 7 that all methods underpredict permeability at τ=0.6, while at τ=1.0 all predicted values are higher than the expected value of $k^*/D^2=5.023\times10^{-4}$.

Figures 8-11 represent k/k^* vs. relaxation parameter for different D values. It can be seen that for all D values, G-SRT model shows the highest difference between permeability values of τ=0.6 and τ=1.0. In contrast, G-MRT model shows the lowest sensitivity to this parameter at high resolution. For D=17.32 (the lowest domain resolution considered in this work), SC-SRT is even slightly better.

Generally speaking, when considering only cases with a sufficient domain resolution (Cases 10-36), the G-MRT model shows the best results for τ=0.8 and τ=1.0 while G-SRT is slightly better for τ=0.6.

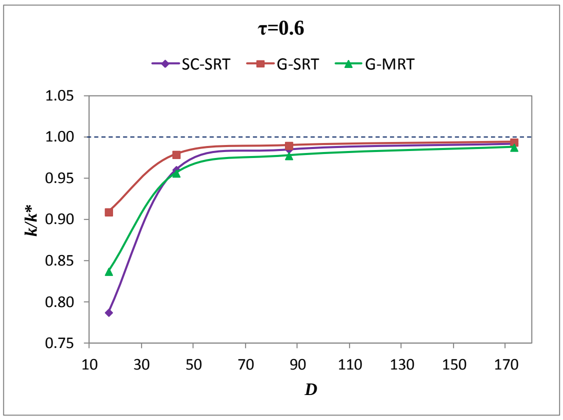

Figure 5. Dimensionless permeability vs. sphere diameter at τ=0.6

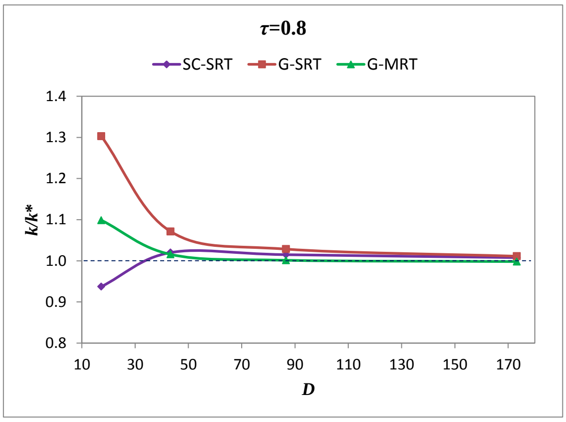

Figure 6. Dimensionless permeability vs. sphere diameter at τ=0.8

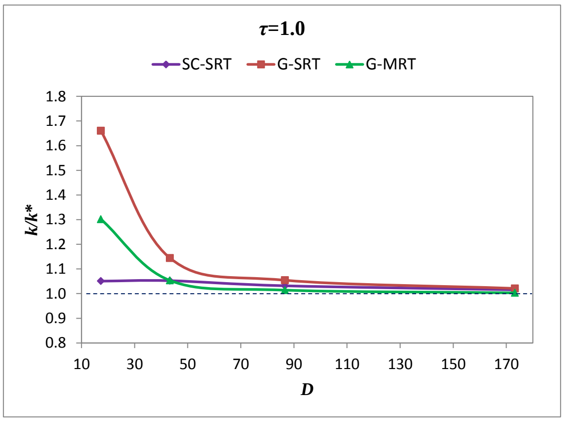

Figure 7. Dimensionless permeability vs. sphere diameter at τ=1.0

It is also interesting to compare the computational efficiency of these methods. For this purpose, the case with D=86.6 and τ=1.0 was selected. Table 3 shows wall clock time for 100 iterations on a standard desktop PC (Core i5, 3.3 GHz CPU, 16 GB RAM). It can be observed that SC-SRT is respectively 25 and 83% faster than G-SRT and G-MRT models, respectively. G-MRT model takes almost 1.47 times longer than G-SRT. The reason behind is that the G-MRT approach includes a force term in the calculations.

Flow field detail is shown in Figure 12 for case 20 of Table 2. Figure 13 depicts streamlines of the same case.

Table 3. Computational time (s) for BCC structure

Method	*D*	Time (s)
SC-SRT	86.6	11.28
G-SRT	86.6	14.12
G-MRT	86.6	20.73

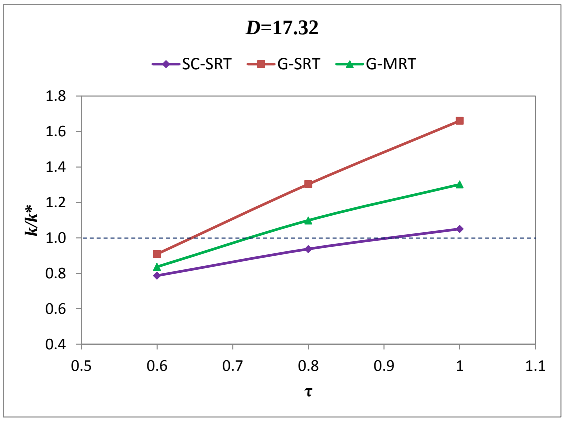

Figure 8. Dimensionless permeability vs. relaxation parameter at D=17.32

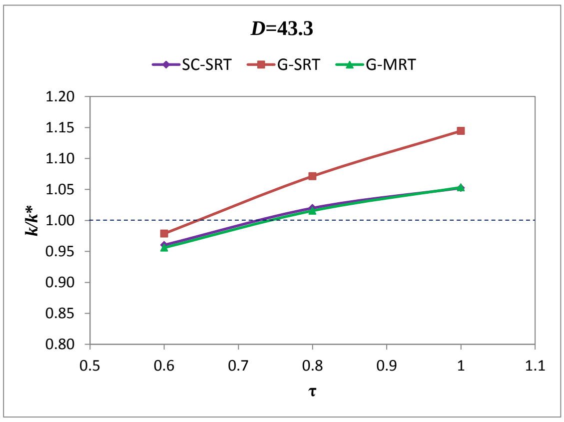

Figure 9. Dimensionless permeability vs. relaxation parameter at D=43.3

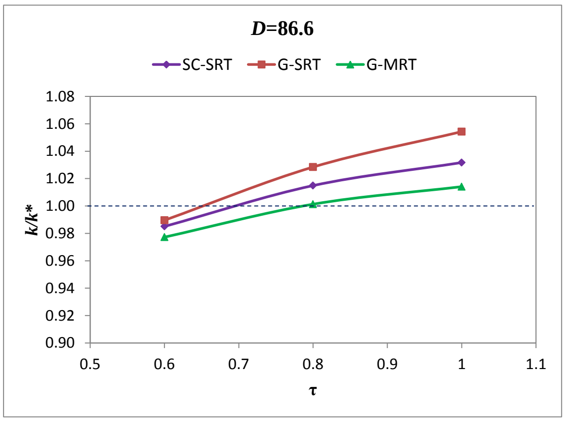

Figure 10. Dimensionless permeability vs. relaxation parameter at D=86.6

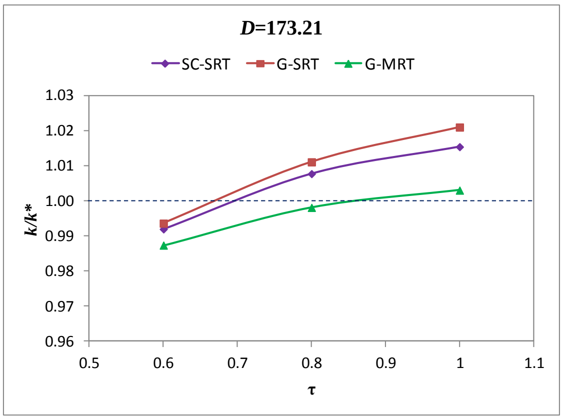

Figure 11. Dimensionless permeability vs. relaxation parameter at *D*=173.21

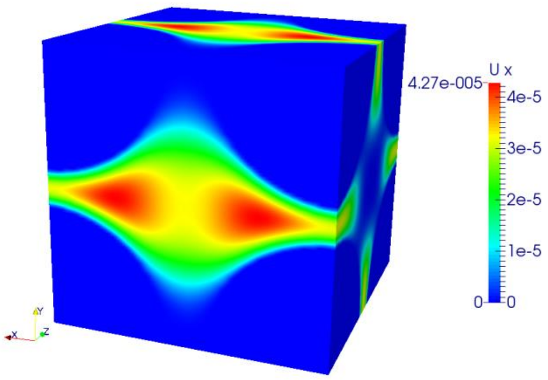

Figure 12. Flow field detail of BCC packing (Case 20)

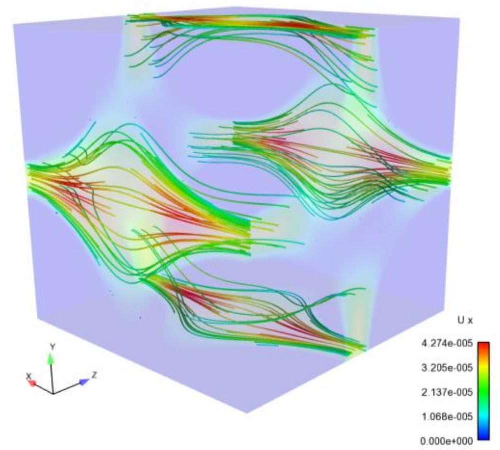

Figure 13. Streamlines of BCC packing (Case 20)

3.3 CASE C

In the last test case the geometry of a 3D porous media is constructed by a set of 2D images. Each image is captured by computed tomography technique. Combining LBM and CT technique allows detailed flow simulation in such complex geometries. However, corresponding simulations may demand powerful computational resources and there is a trade-off between the image resolution and the computational power.

Here, a small section of a porous media has been chosen to investigate the effect of the image resolution on the results. To do so, we compare the calculated permeability at three image resolutions: 1151×1151, 500×500 and 200×200. The number of images for all three cases is 20, which leads to 26.5, 5.0 and 0.8 million grid cells, respectively.

The simulation process is as follows: The CT images are first read by a MATLAB code and a so called geometry file (geometry.txt) is constructed over all images. This text file contains only 0 and 1, where 0 represents solid nodes (black in CT image) and 1 represents pore space (white in CT image). A sample of CT images in high and low resolutions is shown in Figs. 14a. and b. The geometry text file is then read by our LBM code and the computational domain is accordingly created, before starting LBM calculation. Then, LBM proceeds until reaching a steady state condition.

Table 4 shows calculated permeability (in lattice units) and non-dimensional value based on the highest resolution. Relaxation parameter was set to τ=0.8 for all resolutions and Shan-Chen scheme with a constant body force was employed. It can be observed that reducing the image resolution leads as expected to an increasing error, 4.2 and 19 % error for 500×500 and 200×200 image sizes, respectively. Flow field on the same image of Fig. 14 is also shown in Figure 15.

(a)

(b)

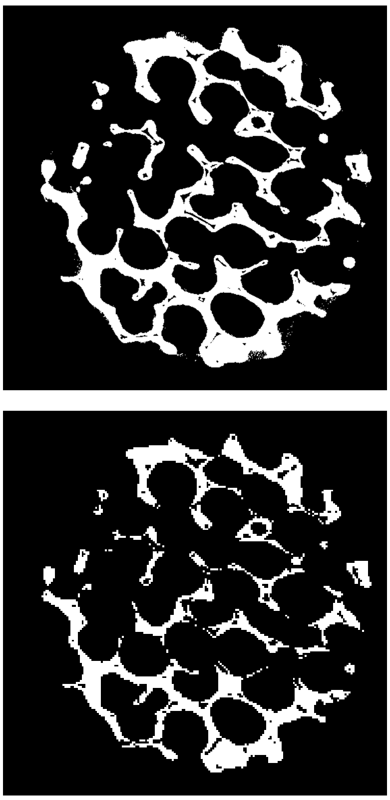

Figure 14. Sample image of porous media simulated. (a): 1151×1151 (b):200×200

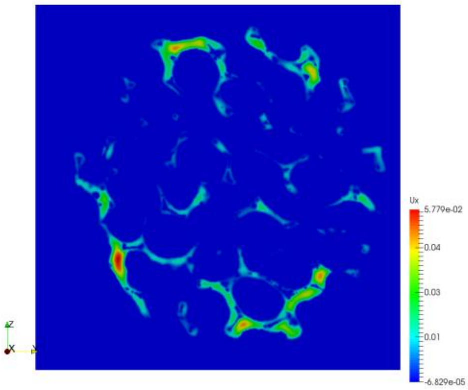

Figure 15. Velocity distribution (Test case C)

Table 4. Calculated permeability in test case C

Domain	Perm. (lu^2)	Dimensionless Perm.	Error (%)
20×1151×1151	6.524	6.524	0.0
20×500×500	1.282	6.795	4.2
20×200×200	0.160	5.286	-19.0

4. CONCLUSIONS

In this paper LBM has been used to simulate fluid flow in porous media. Three different cases were studied. The first two ones are standard FCC and BCC structures. It was found that LBM can compute flow characteristics with high accuracy in such configurations. It was also found that domain resolution has a high influence on the results, since low resolutions may lead to completely misleading results. Furthermore, the influence of the force scheme was examined, comparing Guo-SRT, Guo-MRT and Shan-Chen-SRT. It was shown that at the lowest relaxation time (τ=0.6) Guo-SRT yields the best results for all domain sizes, while Guo-MRT is more accurate at higher relaxation times. It was also observed that at a specific domain size, for all studied approaches, the predicted permeability increases with relaxation time. Comparing Guo-SRT and Guo-MRT proved that Guo-MRT shows a lower dependency on the relaxation parameter and, thus, on viscosity. In the third case considered, geometry is created by a set of CT images and it was observed that a lower resolution leads to rapidly increasing errors compared to the high-resolution LB simulation.

ACKNOWLEDGEMENTS

The financial support of the International Max Planck Research School Magdeburg for Advanced Methods in Process and Systems Engineering (IMPRS ProEng) is gratefully acknowledged. The authors also thank Dr. Michael Schwidder for providing the porous media models and Dr. Stefan Rannabauer for the Micro-CT images.

REFERENCES

[1] Succi, S., 2001, *The Lattice Boltzmann Equation for Fluid Dynamics and Beyond*, Oxford.

[2] McNamara, G. R. and Zanetti, G., 1988, "Use of the Boltzmann equation to simulate lattice-gas automata", *Phys Rev Lett*, Vol. 61, pp. 2332-2335.

[3] Higuera, F. and Jimenez, J., 1989, "Boltzmann approach to lattice gas simulations", *Europhys Lett*, Vol. 9, pp. 663-668.

[4] Junk, M., Klar, A. and Luo, L.-S., 2005, "Asymptotic analysis of the lattice Boltzmann equation", *Journal of Computational Physics*, Vol. 210, pp. 676-704.

[5] Guo, Z. and Shu, C., 2013, *Lattice Boltzmann method and its applications in engineering (advances in computational fluid dynamics)*, World Scientific Publishing Company.

[6] Darcy, H., 1856, *Les fontaines publiques de la ville de Dijon*.

[7] Succi, S., Foti, E. and Higuera, F., 1989, "Three-dimensional flows in complex geometries with the lattice Boltzmann method", *Europhys Lett*, Vol. 10, pp. 433-438.

[8] Pan, C., Luo, L.-S. and Miller, C. T., 2006, "An evaluation of lattice Boltzmann schemes for porous medium flow simulation", *Comput Fluids*, Vol. 35, pp. 898-909.

[9] Degruyter, W., Burgisser, A., Bachmann, O. and Malaspinas, O., 2010, "Synchrotron X-ray microtomography and lattice Boltzmann simulations of gas flow through volcanic pumices", *Geosphere*, Vol. 6, pp. 470-481.

[10] Chukwudozie, C. and Tyagi, M., 2013, "Pore scale inertial flow simulations in 3-D smooth and rough sphere packs using lattice Boltzmann method", *AIChE Journal*, Vol. 59, pp. 4858-4870.

[11] Bhatnagar, P. L., Gross, E. P. and Krook, M., 1954, "A model for collision processes in gases. I. Small amplitude processes in charged and neutral one-component systems", *Phys Rev*, Vol. 94, pp. 511-525.

[12] Shan, X. and Chen, H., 1993, "Lattice Boltzmann model for simulating flows with multiple phases and components", *Phys Rev E*, Vol. 47, pp. 1815-1819.

[13] Guo, Z., Zheng, C. and Shi, B., 2002, "An extrapolation method for boundary conditions in lattice Boltzmann method", *Phys Fluids*, Vol. 14, pp. 2007-2010.

[14] d'Humières, D., 2002, "Multiple–relaxation–time lattice Boltzmann models in three dimensions", *Philos Trans R Soc London, Ser A*, Vol. 360, pp. 437-451.

[15] Chapman, A. and Higdon, J., 1992, "Oscillatory Stokes flow in periodic porous media", *Phys Fluids A*, Vol. 4, pp. 2099-2116.

Conference on Modelling Fluid Flow (CMFF'15)
The 16th International Conference on Fluid Flow Technologies
Budapest, Hungary, September 1-4, 2015

DISCRETE ELEMENT METHOD SIMULATION OF CONTINUOUS BLENDERS

Shahab GOLSHAN[2], Navid MOSTOUFI[1], Reza ZARGHAMI[3], Hamidreza NOROUZI[4]

[1] Corresponding Author. Multiphase Systems Research Lab, School of Chemical Engineering, University of Tehran. 16 Azar Street, Tehran, Iran. Tel.: (+98-21)6696-7797, Fax: (+98-21)6646-1024, E-mail: mostoufi@ut.ac.ir
[2] Multiphase Systems Research Lab, School of Chemical Engineering, University of Tehran. E-mail: shahab_golshan@ut.ac.ir
[3] Multiphase Systems Research Lab, School of Chemical Engineering, University of Tehran. E-mail: rzarghami@ut.ac.ir
[4] Multiphase Systems Research Lab, School of Chemical Engineering, University of Tehran. E-mail: hnorouzi@ut.ac.ir

ABSTRACT

The aim of this work was to study the mixing of granular material in a continuous blender. Two parameters, including impeller rotational speed and number of impeller blades, were studied by means of discrete element method simulations. Three levels were considered for each parameter. Results of this study revealed the details of blending process and illustrated the velocity profile of particles in a blender. Blending quality and dead-zones in a blender were obtained through calculation of velocity fields in the blender. Effect of each parameter on residence time distribution of particles and quality of mixing were studied and discussed separately.

Keywords: blade impeller, continuous blending, DEM, granular flow, powder mixing

NOMENCLATURE

F^N	$[N]$	normal force
F^T	$[N]$	tangential force
I	$[m^4]$	moment of inertia of particle
R	$[m]$	radius of particle
S	$[Pa]$	shear modulus
S^2	[-]	variance
Y	$[Pa]$	Young's modulus
d	$[m]$	particle diameter
g	$[m/s^2]$	acceleration of gravity
k	[-]	stiffness coefficient
m	$[kg]$	mass of particle
p	[-]	proportion of particles in a sample
t	$[s]$	time
v	$[m/s]$	particle velocity
γ	[-]	damping coefficient

Greek letters

δ	$[m]$	displacement
μ_s	[-]	sliding friction
μ_τ	[-]	rolling friction
ρ	$[kg/m^3]$	particle density
σ	[-]	Poisson's ratio
σ_0^2	[-]	upper limit of variance
σ_s^2	[-]	lower limit of variance
ω	[rad/s]	angular velocity

Subscripts and Superscripts

N, T	normal, tangential
i, j	index of particles
–	mean
*	effective

1. INTRODUCTION

Blending is a fundamental operation in various industries involving powders and particles [1-4]. The powder blending is believed to be the most important unit operation in various industries [5]. Consequently, several studies have been performed on modelling the blending process for reaching the optimum operating condition in various types of blenders. For instance, Pernenkil et al. [6] reviewed the most important researches on the blending process, emphasizing continuous operations. The DEM had been utilized as a powerful modelling tool in many powder blending simulations and is proved to be a reliable and applicable technique in various types of modelling [7].

Various types of batch blenders have been widely studied in many research works. Vertical bladed mixers are widely used in laboratory as well as industry for mixing of powders [8, 9]. Many researchers have investigated effect of different operating conditions on blending performance in these types of blenders. Remy et al. [8] simulated the granular flow in a blender equipped with a four-blade impeller using the DEM and reported that the blade orientation has no effect on the speed of mixing and flow pattern of particles. On the other hand, they found that the system frictional specifications extremely affects the granular flow. Similar studies have been carried out using this type of blender, including studying velocity field of particles for different values of particle aspect ratio and bed depth [9], studying particle motion on a rotating flat blade over different blade angles and rotor speed in a similar blender using DEM [10], modelling granular flow of particles in a bladed mixer and studying the kinematics of flow [11, 12] and performance optimization of the blender considering two parameters: blade rake angle and blade gap at the vessel bottom [13]. Chandratilleke et al. [13] utilized the Lacey mixing index as a scale of describing mixing quality, which is also used in this research. Effects of particles size and density on the quality of mixing in a binary mixture were also studied in a vertical bladed mixer [14] and optimum levels of parameters were found in order to reach the highest mixing quality.

Other types of blenders have also attracted much attention. Ploughshare mixer is a prevalent powder blender which can be used in both batch and continuous operations. Early studies on this type of blender include experimental study on the effect of rotation speed and fill level on mixing by means of positron emission particle tracking (PEPT) [15]. Alian et al. [5] simulated ploughshare mixer using DEM and utilized the simulation for investigating the effect of mixer initial loading and impeller rotation speed on the mixing efficiency. Laurent et al. [16] performed a comparative study on ploughshare mixer using DEM and compared the simulation results with experimental data obtained by PEPT. Blending in paddle mixers has been also investigated by different researchers. Hassanpour et al. [17] simulated a paddle mixer using the DEM and studied particle motion in this mixer. They also showed that the DEM can be utilized to forecast particle flow in a mixer. Simulation of the coating process in a paddle mixer was also performed using the DEM and effect of particle size distribution was studied on the dynamics of particle flow and coating uniformity [18]. Another type of industrial blender is horizontal bladed mixer which is geometrically similar to the blender presented in this work, which consists of a horizontal vessel and a bladed impeller operating continuously. Batch operation of this blender was studied by Laurent et al. [19] in which they studied the influence of rotor speed on velocity field of particles and axial dispersion coefficient in a six-bladed horizontal blender.

Despite of its vast industrial application, continuous operation has attracted less attention of researches so far in comparison with batch blenders. The majority of investigations about continuous blenders have been accomplished by Sarkar et al. [20-22]. They studied, using DEM, how the operating conditions, including impeller rotation and fill level, affect the operation of a horizontal bladed continuous mixer [20]. It was shown that Froude number and vessel fill level strongly influence the particle flow pattern in this mixer. In another study, Sarkar et al. [21] investigated the effect of inter-particle cohesion at various impeller speeds and fill levels in a similar continuous blender. Sarkar et al. [22] also accomplished a DEM simulation utilizing periodic slicing approach in a continuous blender and compared its results with their previous works. Markov chains were also utilized for simulating of continuous operation for powder mixing [23]. Combination of Computational fluid dynamics (CFD) and DEM is utilized to study particles mixing patterns in fluidized beds by Norouzi et al. [24, 25].

This work aims to study the effect of impeller rotation speed and number of impeller blades on the particle flow pattern, residence time distribution (RTD) of solids and mixing quality in a paddle blender vessel. For this purpose, a binary mixture of two different powders with different sizes and densities were inserted in a horizontal continuous mixer. By studying the particle flow pattern inside the blender, the dead-zones were also identified. Mean velocity of particles were plotted versus time and RTD analysis was accomplished by entering a pulse tracer flow in the blender and measuring the exit time of these particles. The quality of mixing was measured using Lacey index.

2. MODEL

2.1. DEM

DEM is a numerical method which is mainly used for simulating motion of particles. Cundall et al. [26] developed the DEM for the first time and it is now widely used in various applications for different purposes. The DEM is mainly based on the Newton's second law of motion which implies that the acceleration of a rigid body depends on the sum of all forces acting to it. This technique traces the motion of particles and their position at different time steps is numerically calculated by knowing the net force exerted on them. These forces are mainly gravity and contact forces. Since there are no meaningful effects of air velocity on the motion of particles, the effect of drag force on particles would be negligible. Two basic laws for calculation of particles motion in the DEM are:

$$m_i \frac{dv_i}{dt} = \sum_j (F_{ij}^N + F_{ij}^T) + m_i g \tag{1}$$

$$I_i \frac{d\omega_i}{dt} = \sum_j (R_i \times F_{ij}^T) + \tau_{rij} \tag{2}$$

where m_i, g, v_i, I_i, ω_i and R_i are mass, gravity acceleration, velocity, moment of inertia, angular velocity and radius of particle i, respectively. The contact model in this research was based on the Hertzian contact theory [27] which describes the normal and tangential forces by:

$$F^N = -\tilde{k}_n \delta^{3/2}_n - \tilde{\gamma}_n \dot{\delta}_n \delta_n^{1/4} \tag{3}$$

$$F^T = -\tilde{k}_t \delta_t - \tilde{\gamma}_t \dot{\delta}_t \delta_n^{1/4} \tag{4}$$

in which k, δ and γ show stiffness coefficients, displacements and damping coefficients in normal and tangential directions. Stiffness coefficient is a function of Young's modulus, shear modulus and Poisson's ratio in the form of the following formulas:

$$\tilde{k}_n = \frac{Y\sqrt{2R^*}}{3(1-\sigma^2)} \tag{5}$$

$$\tilde{k}_t = \frac{2\sqrt{2R^* S}}{2-\sigma}\delta_n^{1/2} \tag{6}$$

where Y, R^*, σ and S are Young's modulus, effective radius, Poisson's ratio and shear modulus, respectively. Definition of tangential displacement, Young's and shear modulus, effective radius and damping coefficient could be found elsewhere [27].

As stated before, the quality of mixing in this research is represented by the Lacey index (LI) [28] which is described by:

$$L.I. = \frac{\sigma_0^2 - \sigma^2}{\sigma_0^2 - \sigma_R^2} \tag{7}$$

where σ_0^2 and σ_R^2 are upper (complete segregation) and lower limits (random mixing) of variance in the two-component mixture which are defined by:

$$\sigma_0^2 = p(1-p) \tag{8}$$

$$\sigma_R^2 = \frac{p(1-p)}{n} \tag{9}$$

in which p is the fraction of components and n is the total number of particles in the sample. σ^2 is also defined by:

$$\sigma^2 = \frac{\sum_{i=1}^{N}(y_i - \bar{y})^2}{N-1} \tag{10}$$

and N, $\bar{y}$ are, respectively, number of samples and mean value of y in different samples.

2.2. Blender Geometry

Three geometries with different number of blades (6, 7 and 8 sets of blades) were considered in this work. Figure 1 demonstrates the geometry for 7 sets of impellers. Dimensions of the blender are also specified on this figure.

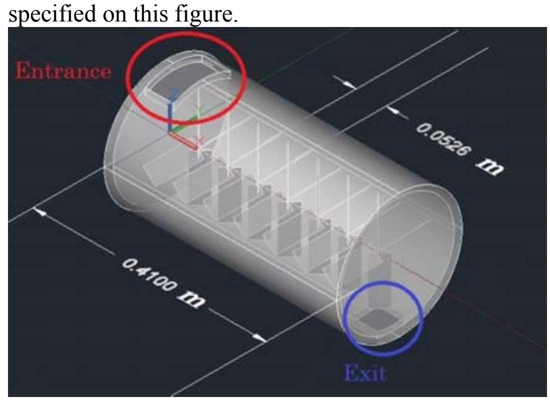

Figure 1. Blender geometry and sizes for 7 bladed impeller. Length of the blender and blade spacing are 41 and 5.26 cm, respectively.

Entrance and exit location of particles are specified in the geometry at the two bottoms of the vessel. The shaft is located at the centre of the vessel. In each set of blades, four blades in the format and dimensions of Figure 2 are placed on the shaft.

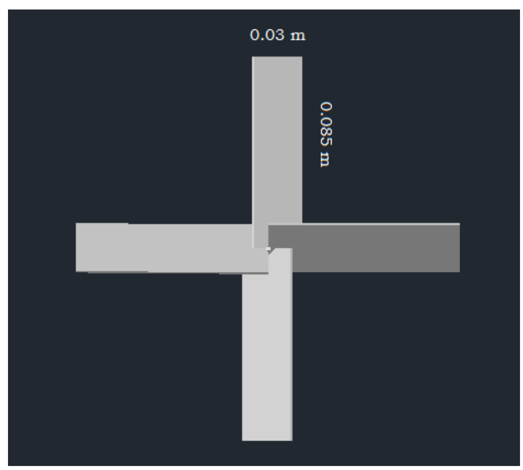

Figure 2. Blade dimensions

2.3. Simulation Parameters

Values of all simulation parameters are listed in Table 1.

Table 1. Simulation parameters

Variable	Symbol	Value
Young's modulus	Y	4×10^7 Pa
Poisson's ratio	σ	0.25
Coefficient of restitution	e	0.5
Rolling friction coefficient	μ_τ	0.05
Sliding friction coefficient	μ_s	0.3
Particle radius	r	1.5 and 2.5 mm
Particle density*	ρ	800 and 100 kg/m^3
Time step	Δt	0.00001 s
Simulation time	-	40 s

* Particles densities are set on 800 and 1000 kg/m^3 for particles with diameters of 3 and 5 mm respectively.

3. RESULT AND DISCUSSION

The time required for reaching the steady state condition in simulations can be determined by plotting the total number of particles inside the blender as a function of time. Figures 3.a and 3.b show how this time varies with changing the rotation speed and number of impellers, respectively.

Fig. 3.a demonstrates that the number of particles in the blender increases with increasing the rotation period (i.e., decreasing the impeller rotation speed). It is also obvious that the system reaches steady state condition after about 10 seconds in all cases. Consequently, for analysis of RTD, the tracers were injected into the vessel after this time and in all cases tracers were inserted at t = 15 s.

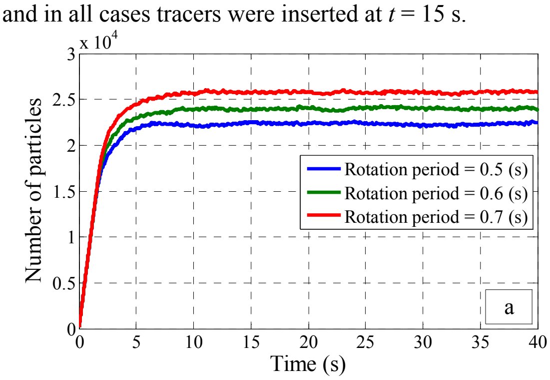

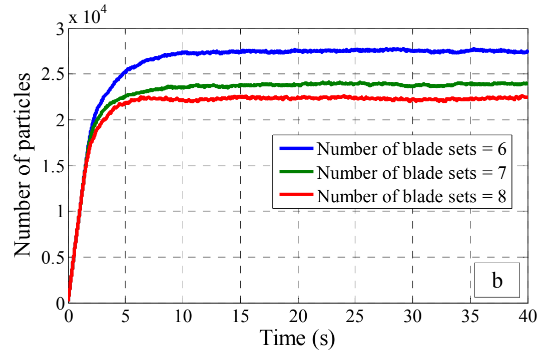

Figure 3. Total number of particles in blender (a) different impeller rotation periods, (b) different number of blade sets.

Fig. 3.b shows that the ultimate number of particles in the blender increases with decreasing the number of blade sets. It should be mentioned that the number of particles directly influences the fill level of the blender.

3.1. Velocity and Distribution Profiles

Figure 4 illustrates that how the particles with different sizes are distributed in the blender after reaching the steady state condition (t = 15 s, in a blender with 8 blade sets and impeller rotation speed of 0.5 s). Radiuses of blue and red particles are 1.5 and 2.5 mm, respectively.

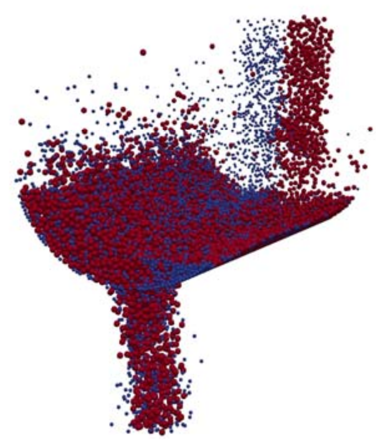

Figure 4. Particles distribution in blender (rotation period = 0.5 and number of blade sets = 8).

Figure 5 shows velocity of particles at the same time (t = 15 s). It can be seen that two separate dead zones exist for the two particle types. Two dead zones are highlighted with two circles in Fig. 5. White and red circles show regions with approximately no motion for fine and coarse particles, respectively.

Average velocity of particles at the above mentioned operating conditions are also plotted in Figures 6.a and 6.b. It can be seen in these figures that increasing the rotation speed (decreasing the rotation period) and increasing the number of blade sets on the impeller leads to greater average velocity.

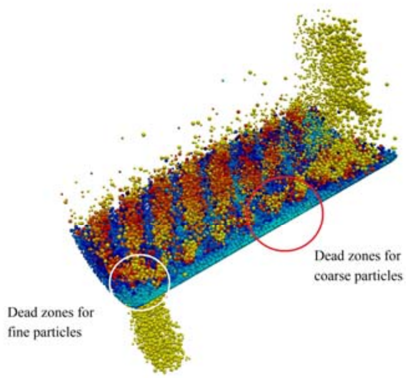

Figure 5. Velocity Distribution of particles in the blender. Two circles in the figure show dead zones for two particle types (rotation period = 0.5 and number of blade sets = 8).

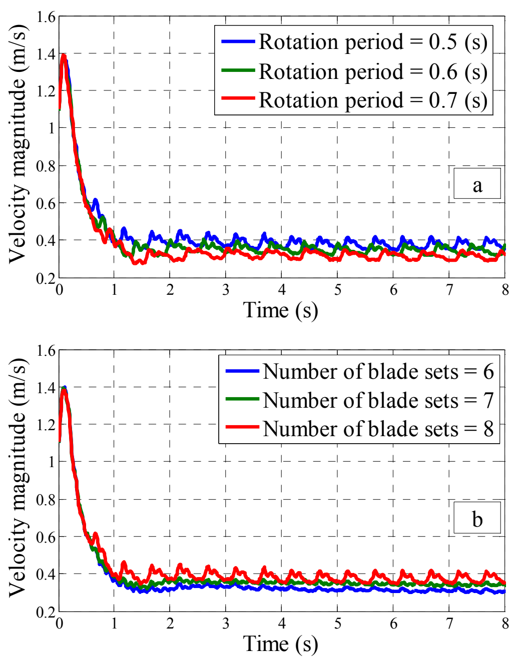

Figure 6. Mean velocity of particles in the blender (a) different rotation periods, (b) different number of impeller blade sets.

3.2. RTD of Particles

RTDs of particles are plotted and compared in the same operating conditions in Figures 7.a to 7.d (constant rotation period = 0.5 or constant number of blade sets = 8). For obtaining the RTD, all particles that are inserted at t = 15 s were considered as the pulse of tracers and residence time of these particles were determined and plotted in each case. In the present work, RTDs are considered separately for fine and coarse particles and are plotted in different plots.

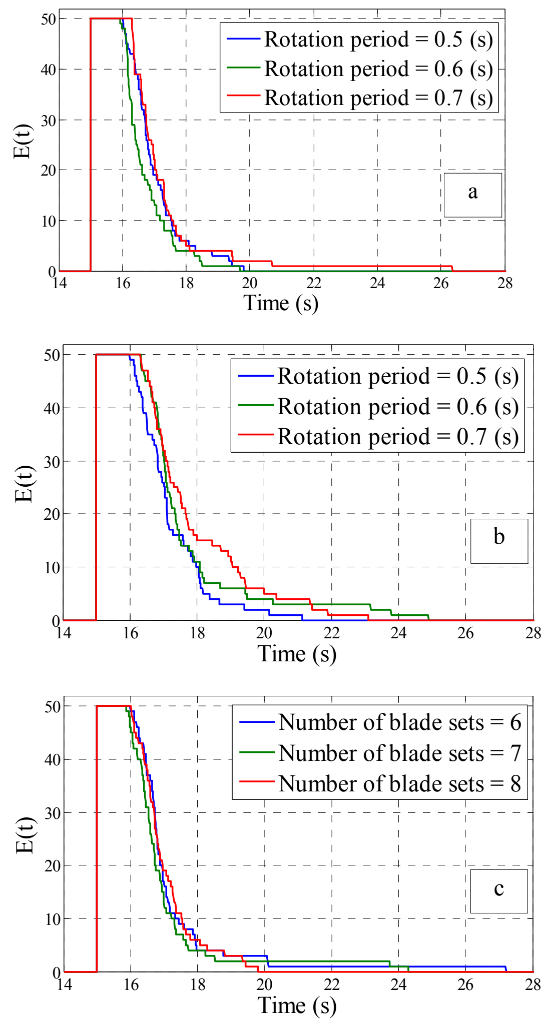

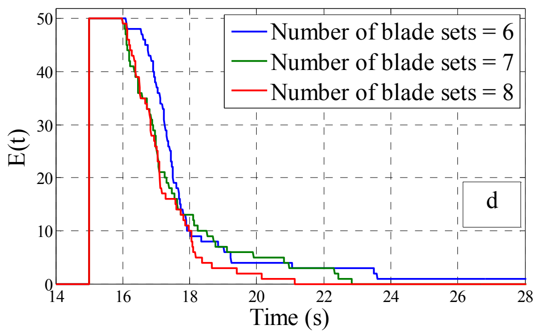

Figure 7. (a) RTD of fine particles at different rotation periods, (b) RTD of coarse particles at different rotation periods, (c) RTD of fine particles at different numbers of impeller blade sets, (d) RTD of coarse particles at different numbers of impeller blade sets.

It can be seen in Figs. 7.a to 7.d that increasing the rotor rotation speed generally makes both fine and coarse particles to exit the blender faster. However, number of blade sets on the impeller has no meaningful effect on the RTD of particles. A comparison between RTD of fine and coarse particles in a similar condition (impeller rotation speed = 0.5 s) is also illustrated in Figure 8 and it can be seen that particles with bigger radius tend to stay longer in the blender.

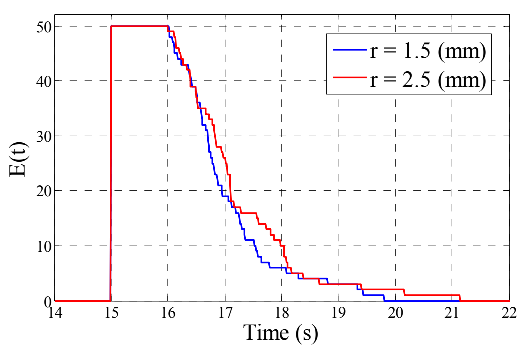

Figure 8. Comparison between RTDs of particles with *d* = 3 and 5 mm.

3.3. Mixing Quality

In the present work, quality of mixing was quantified by means of the Lacey index. For this purpose, four samples were gathered from particles from the discharge of the blender. Figures 9.a and 9.b compare the mixing quality at different operating conditions against time. These figures show the the Lacey index increases with increasing rotation period and number of blade sets.

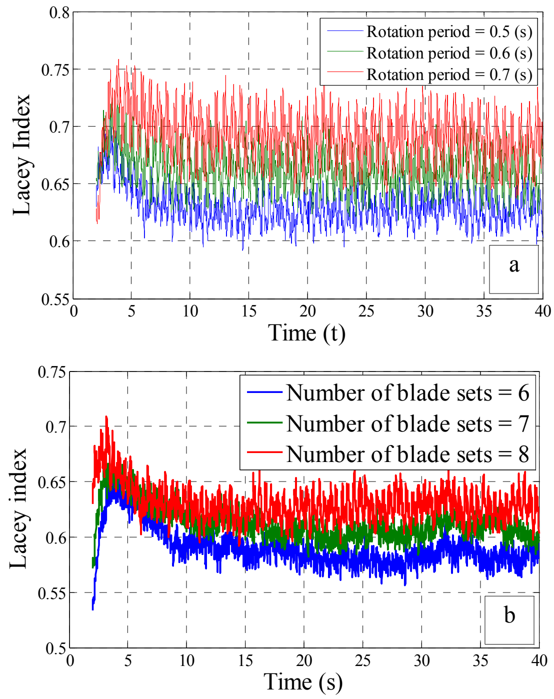

Figure 9. Lacey index (a) as a function of impeller rotation period, (b) as a function of number of blade sets on the impeller.

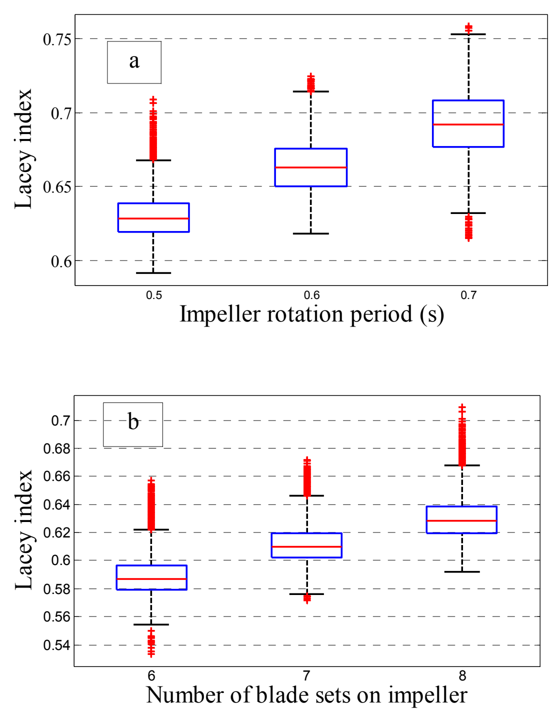

Figure 10. Lacey index (a) as a function of impeller rotation period, (b) as a function of impeller rotation period.

Figures 10.a and 10.b show Lacey index in the same condition in the form of box plots. It can be concluded from Figs. 9 and 10 that Lacey index increases with decreasing the rotation velocity and increasing number of blade sets on the impeller. The main reason for this phenomenon is the fact that with increasing the rotor velocity, particles tend to stay shorter in the blender and mixing index cannot reach higher values. On the other hand, with increasing the number of blade sets, particles encounter more obstacles before exiting the blender and would spend longer time to reach better degrees of mixing. In this case, blade sets act like baffles to stop particles from bypassing.

4. CONCLUSIONS

DEM simulations were used to investigate the effects of impeller rotation speed and number of blade sets of the impeller on the mixing of a binary solid mixture in a continuous blender. Distribution of particles and velocity profiles of particles in the blender were plotted and RTD, velocity magnitude and Lacey index were calculated at three levels of each parameter. Results show two dead zones for particles in the blender and imply that velocity of particles increases when impeller rotation speed or number of blades rises. RTD analysis of fine and coarse particles demonstrated that the impeller rotation speed generally makes particles to exit faster and number of blade sets has no meaningful effect on the RTD. It was also revealed that the Lacey index increases by increasing the impeller rotation period (decreasing impeller rotation speed) and number of blade sets.

REFERENCES

[1] Wightman, C., and Muzzio, F. J., 1998, "Mixing of granular material in a drum mixer undergoing rotational and rocking motions I. Uniform particles", *Powder Technol.*, Vol. 98, pp. 113-124.

[2] Kwan, C. C., Mio, H., Chen, Y. Q., Ding, Y. L., Saito, F., Papadopoulos, D. G., ... and Ghadiri, M., 2005, "Analysis of the milling rate of pharmaceutical powders using the Distinct Element Method (DEM)", *Chem. Eng. Sci.*, Vol. 60, pp. 1441-1448.

[3] Wu, C. Y., 2008, "DEM simulations of die filling during pharmaceutical tabletting", *Particuology*, Vol. 6, pp. 412-418.

[4] Tan, Y., Yang, D., and Sheng, Y., 2009, "Discrete element method (DEM) modeling of fracture and damage in the machining process of polycrystalline SiC", *J. Eur. Ceram. Soc.*, Vol. 29, pp. 1029-1037.

[5] Alian, M., Ein-Mozaffari, F., and Upreti, S. R., 2015, "Analysis of the Mixing of Solid Particles in a Ploughshare Mixer via Discrete Element Method (DEM)", *Powder Technol.*

[6] Pernenkil, L., and Cooney, C. L., 2006, "A review on the continuous blending of powders", *Chem. Eng. Sci.*, Vol. 61, pp. 720-742.

[7] Cleary, P. W., 2009, "Industrial particle flow modelling using discrete element method", *Eng. Computations*, Vol. 26, pp. 698-743.

[8] Remy, B., Khinast, J. G., and Glasser, B. J., 2009, "Discrete element simulation of free flowing grains in a four-bladed mixer", *AIChE J.*, Vol. 55, pp. 2035-2048.

[9] Hua, X., Curtis, J., Hancock, B., Ketterhagen, W., and Wassgren, C., 2013, "The kinematics of non-cohesive, sphero-cylindrical particles in a low-speed, vertical axis mixer", *Chem. Eng. Sci.*, Vol. 101, pp. 144-164.

[10] Chandratilleke, G. R., Yu, A. B., and Bridgwater, J., 2012, "A DEM study of the mixing of particles induced by a flat blade", *Chem. Eng. Sci.*, Vol. 79, pp. 54-74.

[11] Remy, B., Canty, T. M., Khinast, J. G., and Glasser, B. J., 2010, "Experiments and simulations of cohesionless particles with varying roughness in a bladed mixer", *Chem. Eng. Sci.*, Vol. 65, pp. 4557-4571.

[12] Remy, B., Khinast, J. G., and Glasser, B. J., 2011, "Polydisperse granular flows in a bladed mixer: Experiments and simulations of cohesionless spheres", *Chem. Eng. Sci.*, 66, pp. 1811-1824.

[13] Chandratilleke, G. R., Yu, A. B., Stewart, R. L., and Bridgwater, J., 2009, "Effects of blade rake angle and gap on particle mixing in a cylindrical mixer", *Powder Technol.*, Vol. 193, pp. 303-311.

[14] Halidan, M., Chandratilleke, G. R., Chan, S. L. I., Yu, A. B., and Bridgwater, J., 2014, "Prediction of the mixing behaviour of binary mixtures of particles in a bladed mixer", *Chem. Eng. Sci.*, Vol. 120, pp. 37-48.

[15] Jones, J. R., and Bridgwater, J., 1998, "A case study of particle mixing in a ploughshare mixer using Positron Emission Particle Tracking", *Int. J. of Miner. Process.* Vol. 53, pp. 29-38.

[16] Laurent, B. F. C., and Cleary, P. W., 2012, "Comparative study by PEPT and DEM for flow and mixing in a ploughshare mixer", *Powder Technol.*, Vol. 228, pp. 171-186.

[17] Hassanpour, A., Tan, H., Bayly, A., Gopalkrishnan, P., Ng, B., and Ghadiri, M., 2011, "Analysis of particle motion in a paddle mixer using Discrete Element Method (DEM)", *Powder Technol.*, Vol. 206, pp. 189-194.

[18] Li, J., Wassgren, C., and Litster, J. D., 2013, "Multi-scale modeling of a spray coating process in a paddle mixer/coater: the effect of particle size distribution on particle segregation and coating uniformity", *Chem. Eng. Sci.*, Vol. 95, pp. 203-210.

[19] Laurent, B. F. C., and Bridgwater, J., 2002, “Performance of single and six-bladed powder mixers”, *Chem. Eng. Sci.*, Vol. 57, pp. 1695-1709.

[20] Sarkar, A., and Wassgren, C. R., 2009, “Simulation of a continuous granular mixer: Effect of operating conditions on flow and mixing”, *Chem. Eng. Sci.*, Vol. 64, pp. 2672-2682.

[21] Sarkar, A., and Wassgren, C., 2010, “Continuous blending of cohesive granular material”, *Chem. Eng. Sci.*, Vol. 65, pp. 5687-5698.

[22] Dubey, A., Sarkar, A., Ierapetritou, M., Wassgren, C. R., and Muzzio, F. J., 2011, “Computational approaches for studying the granular dynamics of continuous blending processes, 1–DEM based methods”, *Macromol. Mater. Eng*., Vol. 296, pp. 290-307.

[23] Berthiaux, H., Marikh, K., Mizonov, V., Ponomarev, D., and Barantzeva, E., 2004, “Modeling continuous powder mixing by means of the theory of Markov chains”, *Particul. Sci. Technol.,* Vol. 22, pp. 379-389.

[24] Norouzi, H. R., Mostoufi, N., Mansourpour, Z., Sotudeh-Gharebagh, R., and Chaouki, J., 2011, “Characterization of solids mixing patterns in bubbling fluidized beds”, *Chem. Eng. Res. Des.*, Vol. 89, pp. 817-826.

[25] Norouzi, H. R., Mostoufi, N., and Sotudeh-Gharebagh, R., 2012. “Effect of fines on segregation of binary mixtures in gas–solid fluidized beds”, *Powder Technol.*, Vol. 225, pp. 7-20.

[26] Cundall, P. A., and Strack, O. D., 1979, “A discrete numerical model for granular assemblies”, *Geotechnique*, Vol. 29, pp. 47-65.

[27] Tsuji, Y., Tanaka, T., and Ishida, T., 1992, “Lagrangian numerical simulation of plug flow of cohesionless particles in a horizontal pipe”, *Powder Technol.*, Vol. 71, pp. 239-250.

[28] Lacey, P. M. C., 1954, “Developments in the theory of particle mixing”, *J. Appl. Chem.*, Vol. 4, pp. 257-268.

Conference on Modelling Fluid Flow (CMFF'15)
The 16th International Conference on Fluid Flow Technologies
Budapest, Hungary, September 1-4, 2015

NUMERICAL INVESTIGATION OF A PLAIN JET AIR BLAST ATOMISER

Viktor JÓZSA[1]

[1] Corresponding Author. Department of Energy Engineering, Budapest University of Technology and Economics. Műegyetem rkp. 3., H-1111 Budapest, Hungary. Tel.: +36 1 463 2610, Fax: +36 1 463 1762, E-mail: jozsa@energia.bme.hu

ABSTRACT

The air blast atomizers are mainly developed for gas turbine applications. This configuration utilizes high speed auxiliary medium, what tears the fuel jet into droplets. The medium is often compressed air with slightly higher pressure than that of combustion chamber, which is arising from pressure drop of that. In this way the loading of the gas turbine determines the atomizing conditions.

The aim of this paper is to investigate numerically the ring shaped free jet of an air blast atomizer, which flows around the fuel jet. Both of the original air blast and a steam blast configuration were analysed without and with fuel droplets to understand the main characteristics of the flow pattern. The shape of the nozzle was also modified from the original straight type to divergent ones with different angles to give optimal flow pattern at supersonic conditions.

As the final reason of atomisation is to speed up the evaporation and mix the fuel vapour with incoming air, the analysed constructions were also evaluated from firing point of view. To maintain low emission combustion the proper fuel preparation is crucial.

Keywords: gas turbine, air blast atomiser, steam blast atomiser, supersonic free jet

NOMENCLATURE

C_i	[-]	constant
d_0	$[mm]$	diameter of the liquid jet at the root
GLR	[-]	gas to liquid mass ratio
p_g	$[bar]$	atomisation gauge pressure
p_{st}	$[bar]$	static pressure
u	$[m/s]$	relative velocity
SMD	$[\mu m]$	Sauter Mean Diameter
We_{d0}	[-]	Weber number, respective to d_0
ε	[-]	efficiency of energy transfer
ρ_g	$[kg/m^3]$	density of the gas at the nozzle exit
ρ_t	$[kg/m^3]$	density of the gas at the reservoir
σ	$[N/m]$	surface tension

1. INTRODUCTION

Air blast atomisation was developed in the sixties to replace the pressure swirl atomisers mainly in aero propulsion gas turbines. The latter ones can be used only in a narrow range of fuel flow rates, but the full load to idle ratio is commonly 50:1 [1] and even more in state of the art gas turbines. Integrating two different size of pressure swirl atomisers seemed to be good idea, but resulted a complicated system, requiring sophisticated control to meet with the stable burning requirement by increasing the loading from idle, to maximise lifetime and avoid failures [2].

An air blast atomiser can be used in a wide range of loadings, because the required relative velocity is governed by high velocity compressor bleed air, while the velocity of the fuel remains relatively low. As the loading increases, the velocity of air will follow that, resulting an adaptive behaviour. Furthermore this kind of atomiser also used widely in metallurgy for powder production, industrial combustion systems, painting and other coating technologies.

The principle of twin fluid atomisation, including the air blast atomiser, is to transfer kinetic energy from a high-speed gas jet to a liquid stream, which lead to breakup of that to droplets. More transferred energy leads to finer spray.

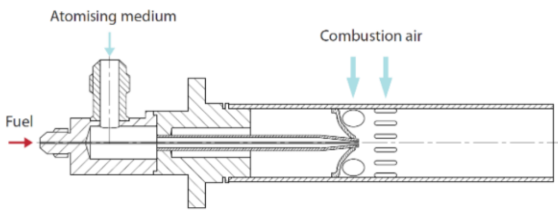

Figure 1. Capstone C-30 burner

To meet the emission standards of today, the fluid fuelled combustion systems apply lean premixed prevaporised (LPP) burner, where the atomised fuel droplets are small enough to evaporate and mix well with the combustion air before the flame front [3]. The subject of this paper is a Computational Fluid Dynamical (CFD) analysis of a Capstone C-30 burner, shown in Figure 1, which was designed to operate with kerosene or diesel fuel, the calculation focused on the latter one.

The atomizing medium is compressed air by design, the available gauge pressure for atomisation is the pressure drop of the internal heat exchanger and the combustion chamber.

The scope of the paper is to virtually decouple the atomizing medium line from the compressor, thus allowing higher atomisation pressure and different medium.

Based on previous burner measurements at atmospheric conditions of A. Kun-Balog et al. [4], it was an interesting conclusion that the transonic and supersonic atomisation resulted more favourable emissions of nitrogen oxides (NO_x), carbon monoxide (CO) and total/unburnt hydrocarbons (THC) overall, compared to subsonic atomisation. The significance of atmospheric analysis is that the burner performance, including atomisation and evaporation will be more, than adequate at higher pressures, therefore air blast atomisers should be designed for the minimum pressure conditions [5].

As a mixing tube is present, detailed measurement of atomisation is challenging, furthermore the mixing tube is glowing red during operation, so making a special glass substitute is not possible. Furthermore R. Sadanandan et al. [6] reported that PIV and simultaneous OH-PLIF measurement of a methane-air flame, which allowed just 100 s for measurement, than the glasses had to be cleaned again. Considering the previous measurement experiences [4] 100 s is not enough for a burner to reach steady state operation.

To speed up the fuel evaporation thus avoid burning droplets in the flame, finer spray is necessary. Considering Figure 1 the larger atomising medium velocity although results smaller drops, the residence time for evaporation in the mixing tube decreases while increasing the velocity of the atomising free jet, the possibility of appearing burning droplets is increasing. Thus the theoretically the best atomising free jet has high momentum, which kinetic energy dissipates fast after the atomisation process complete to maximise the residence time of droplets for evaporation.

Measurement of atomiser characteristics started from magnesium oxide coated plates [7] and high speed photography [8], nowadays Particle Doppler Anemometry (PDA) [9, 10] used extensively for this purpose. Also alternative novel methods can be found in the literature, including infrared thermography [11].

The state of the art numerical approach for modelling particle laden flows is the Large Eddy Simulation (LES) [12–15], if the goal is to calculate the evolution of the turbulent flow field and check the details of the current design. Investigations of atomisation using 2D axisymmetric modelling gives an overview of the system and also a reliable tool, if compared to measurements [16–18] and can be used effectively for design purposes, so the latter method will be used for current analysis.

As it was mentioned above, transonic and supersonic atomisation configurations are favourable from emission point of view based on measurements of A. Kun-Balog et al. [4], which is the only property what the standards demand [19–21]. The designers have free hand, if the operation is under the emission limits.

2. ANALYSED ATOMISER CONFIGURATIONS

From geometry point of view two different configuration was analysed: the original design which contains a convergent nozzle and a straight tube (SN) and a modified version, where the outer pipe wall at the outflow was converted to a 6° divergent nozzle, forming a de Laval nozzle (CD), as shown on Figure 2. Other angle settings than the recommended 6° [22] resulted overexpanded and underexpanded flow, therefore these results are not presented in this paper. If more, than the critical pressure ratio is present, the flow velocity will be supersonic, even with the SN design. The divergent nozzle which is required for further expansion of the gas will be virtual, resulting supersonic flow just after the auxiliary medium outlet, not in the straight part. The expected difference between the SN and CD type nozzle is the smoother flow field with the latter design and [10, 16].

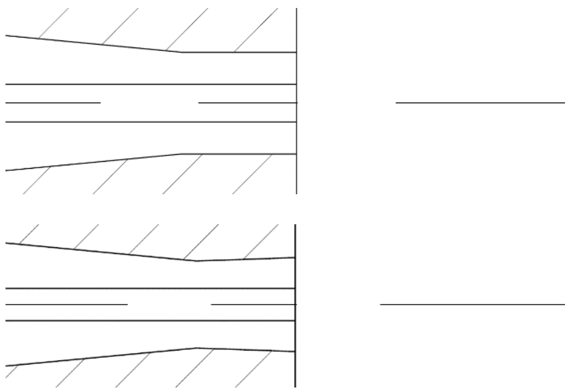

Figure 2. Design of SN type (top) and CD type nozzle (bottom)

The outer diameter of the fuel tube is 0.6 *mm*, which is also the inner diameter of the ring shaped free jet of the SN type nozzle, the outer diameter is 1.6 *mm*. The length of the straight tube is 1.4 *mm*. The outer diameter of the CD type nozzle outlet is 1.75 *mm*.

The main parameter related to droplet breakup is the Weber number, defined for the root of the fuel jet as:

$$We_{d_0} = \frac{\rho_g u^2 d_0}{\sigma} \tag{1}$$

Critical Weber number is a prerequisite of breakup process, which is equal to 12, based on analytical assumptions [3]. In the region of 12 < *We* < 40-100 the breakup is often described with the Taylor Analogy Breakup (TAB) model, developed by P. O'Rourke and A. Amsden [23]. Up to *We* = 800 the process is usually modelled with the Kelvin-Helmholz (KH) breakup, developed by Reitz [24].

The most commonly used describing property of atomisation quality is the volume to surface diameter, also called Sauter Mean Diameter (*SMD*) in the literature. For the first generation of air blast atomisers the most widely used empirical formula was developed by Rizk and Lefebvre [7], which can describe the atomisation process in the 50-120 *m/s* relative velocity region. As for supersonic conditions B. K. Park et al. [10] published a formula based on their PDA measurements, which will be used for validation. First, the energy transfer efficiency should be calculated:

$$\varepsilon = GLR^{-0.773}\left[C_1\left(\frac{1+p_g}{p_{st}}\right)^{3.773} - C_2\left(\frac{1+p_g}{p_{st}}\right)^{2.773} + C_3\left(\frac{1+p_g}{p_{st}}\right)^{1.773}\right] \tag{2}$$

Where the determined constants are the following: C_1=2.374·10^{-6} C_2=3.585·10^{-5} C_3=1.543·10^{-4}.Using (1) and (2) the SMD can be calculated as follows:

$$SMD = \frac{12 d_0}{8 + \{We_{d_0}/[1 + 1/(\varepsilon \cdot GLR)]\}} \tag{3}$$

3. NUMERICAL ANALYSIS

For simulation the Fluent CFD code was applied. Density based solver was chosen for its better handling capability of shockwaves. If one would like to apply further reaction kinetic calculations, the code allow just the volumetric reactions with this solver, where the exact or surrogate kinetics required, which is still a challenging task for chemical engineers. Therefore just the SN and CD nozzle types were analysed without and with droplets. In the first simulation step the realizable *k-ε* model was used with enhanced wall treatment, than the Reynold Stress Model (RSM) was applied to refine the results at rapid changing fields.

The gas flow, which was air and steam, was assumed to be compressible and ideal. Inlet temperature was set to 300 *K*, the outlet pressure was set to 1 *bar*. The computation started with steady analysis of the flow field, than the droplets were subjected to the high speed gas flow at transient conditions to capture the transport process in details and to allow secondary breakup process and collision.

To reduce the required number of cells, the DPM model was applied for adding the droplets to the high speed gas flow. Thus the energy requirement of the primary breakup is neglected, but the secondary breakup with the TAB model and coalescence were allowed. The mass flow rate of standard diesel fuel was 0.35 *g/s*, the location of injection was just above the fuel line, which assumed to be solid, while the detailed atomisation process requires too much CPU time and the current task is to overview many different configurations. The built-in air blast model was used for simulating atomisation. The diameter of the fuel jet was 0.4 *mm*. The relative velocity was set to 300 *m/s*. The Courant-Friedrichs-Lewy (CFL) number of 0.9 and second order schemes were used for flow and turbulence calculations.

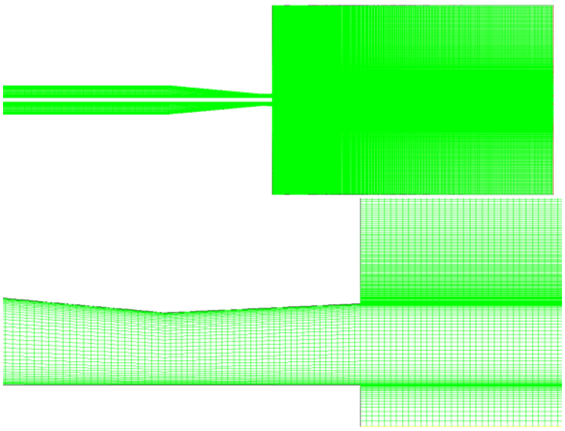

Figure 3. Computational domain of the CD type nozzle (top) and the details of the nozzle outlet (bottom)

As an intensive shear layer arise when the atomising medium exits the nozzle, dense grid was necessary at these regions for the calculations. The number of cells was 187 thousand. Mesh independence analysis was also carried out, helping to finding the optimal resolution of the shear layer.

4. RESULTS AND DISCUSSION

4.1. Analysis of the atomising free jet

The comparison of SN and CD type nozzle at atomisation pressure of 2.5 *bar* shown on Figure 4. Maximum velocity was set to 504 *m/s* in both cases. Latter one shows the shockwaves clearly, while the designed nozzle results smoother flow field. The presence of separation bubble of the SN nozzle at the end of fuel line is considerably smaller, because the CD nozzle was designed to optimum outflow profile, which results parallel streamlines at the exit. As the flow of SN type nozzle immediately expands and there is low pressure inside the separation bubble, the mean direction of the expansion turn towards the axis. After the first compression-expansion fan pair a Mach disk clearly visible.

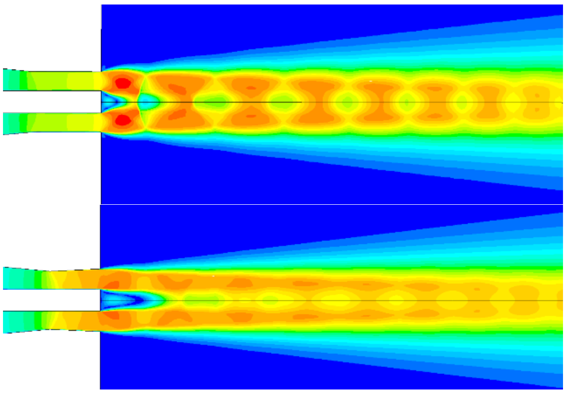

Figure 4. Free jet of SN (top) and CD type nozzle (bottom), p_g = 2.5 *bar*

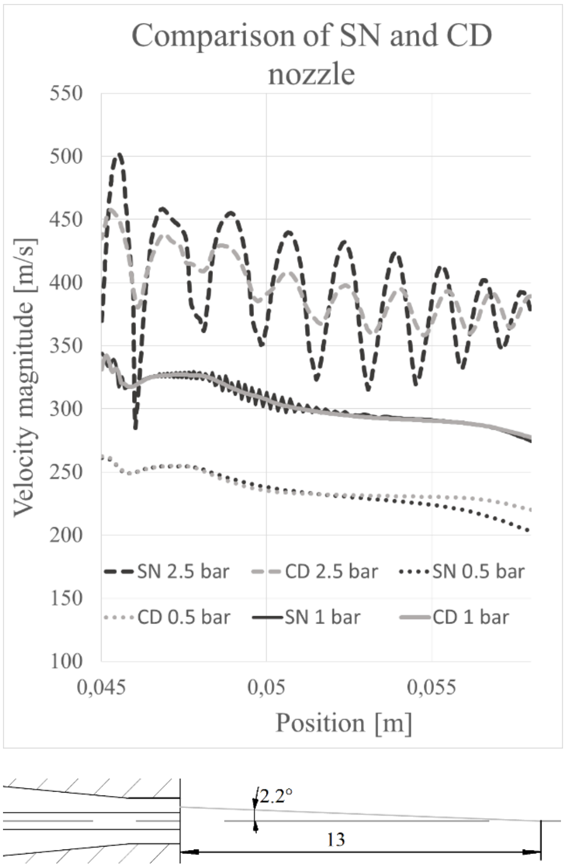

Figure 5. Comparison of SN and CD nozzle at different atomisation gauge pressure levels (top) control line (bottom)

As the second part of the CD nozzle behaves like a diffuser under subsonic conditions, the question is: What extent slows it the free jet down compared to the SN design? Figure 5 contains the comparison of the nozzles at different gauge pressures with the help of a control line, shown at the bottom. 0.5 *bar* atomisation gauge pressure resulted almost the same characteristics in both cases, as well, as 1 *bar*, except the middle of the analysed region. There were small waves present, indicating that the pressure ratio was just above the critical, so the flow just started to turn supersonic. The trends were similar, no significant velocity difference could be observed between the SN and the CD nozzles overall. Atomisation pressure of 2.5 *bar* resulted also similar average velocity and fluctuation periods, but the amplitude is smaller in the CD nozzle outflow. The first period of the SN nozzle velocity profile shows almost halved velocity within 0.4 *mm*, what is also spectacular on Figure 4, indicating the normal shock caused by the Mach disk. As for quantitative summary of the velocity profiles, the average velocity in both cases remain almost the same, just the amplitude of fluctuation varies, which is an important property for combustion chamber designers.

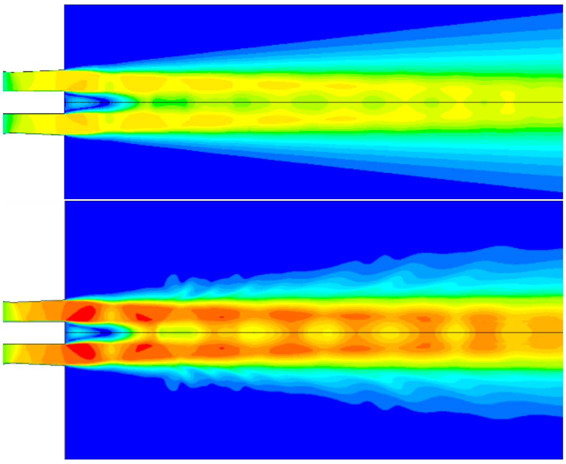

Figure 6. Air (top) and steam free jet (bottom), CD nozzle, p_g = 2.5 *bar*

Figure 6 shows the difference between the flow pattern of air and steam free jet at the same boundary conditions, because of the different thermodynamic properties. The flow field was quite similar, but the average velocity was 30% larger in the case of steam free jet. It can be concluded that the replacement of atomising medium would result remarkable change in the atomisation characteristics and has a much more considerable effect on the process, than fine tuning the nozzle geometry. The similarity of the flow field was also identified in the SN cases as well, the most remarkable difference was also the magnitude of the velocity, the distribution and the fluctuations showed the same trend as the air free jet. The analysis of steam blast atomisation leads far, if the reaction kinetics also involved in the calculation process.

4.2. Introducing droplets

Figure 7 shows the difference in the velocity field when droplets are introduced. The main differences are the absence of periodic fluctuations in the free jet, furthermore the ring shape does not merge when droplets are present. The answer for that is the kinetic energy transfer between the droplets and the inner part of the free jet. As the outer part was not disturbed, the behaviour remained the same. The droplets remained at the core of the computational domain at all simulated cases, when droplets were present. While the other analysed cases resulted similar characteristics, they will not be introduced for flow field evaluation. B. K. Park et al. [10] found that nozzle geometry has low effect on the SMD, therefore just the CD nozzle was analysed at 1, 1.5, 2.5 and 3.5 *bar* atomisation gauge pressures.

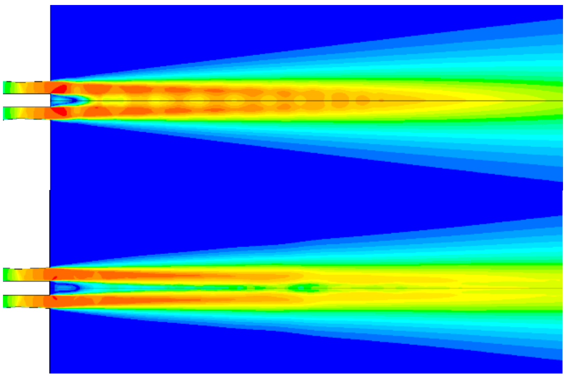

Figure 7. Without droplets (top) and with droplets (bottom), p_g = 2.5 *bar*

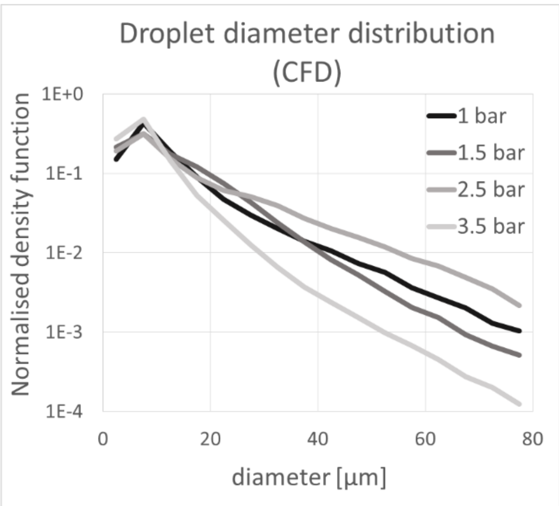

Figure 8. Droplet diameter distribution based on CFD calculations

For calculating We_{d0} B. K. Park et al. [10] recommended to consider $\rho_g = 0.634\ \rho_t$ for SN type, $\rho_g = 0.113\ \rho_t$ for the CD type nozzle.

Table 1. Simulated and calculated SMD based on the literature and CFD

p_g [*bar*]	1	1.5	2.5	3.5
SMD [10]	28.3	13.9	4.91	3.27
SMD (CFD)	10.9	11.6	12.3	8.31

Figure 8 and Table 1 contains the result of SMD of droplets at different atomisation gauge pressure levels with CFD and using Eq. (3). It can be concluded that the two different method show different behaviour. While Eq. (3) shows a continuously decreasing SMD with the increasing atomisation pressure, while CFD based calculations show low dependence on that, this can be seen on Figure 8 and in Table 1 as well. The *We* criterion of TAB was not exceeded during the calculation. Eq. (3) was also evaluated with proper density values of CFD analysis, but the strong fluctuations of density field made hard to determine a clear value of that for input of Eq. (1). Furthermore the calculated SMD was excessively low. Based on the unfavourable results of CFD and empirical formulae, analysis of the much complicated steam blast atomisation was skipped in this paper, the more at that case local condensation of the steam on the surface of the droplets must be considered and makes proper User Defined Functions (UDFs) necessary to implement.

As for summary of CFD analysis of droplets, more accurate modelling of air blast atomisation should be also developed with the help of UDFs for the Fluent CFD code and it should be compared with different measurements on supersonic atomisation.

5. CONCLUSIONS

Numerical analysis of an air blast atomiser was carried out for a plain jet configuration with two different design, namely convergent nozzle with a straight pipe (SN) and a convergent-divergent (CD) nozzle. First, the analysis of the atomising free jet was carried out, than the analysis of atomisation with the built-in air blast atomiser module. The following conclusions could be derived.

1. The velocity field of SN and CD type nozzle were similar in average, the difference between that arise under transonic and supersonic conditions, resulting always larger fluctuation amplitude in the flow properties of SN nozzle compared to CD nozzle. This is important from combustion chamber design point of view.

2. The atomising medium, which was air and steam in this paper, has remarkable effect on the flow field, based on the different thermodynamic properties. Therefore choosing the proper medium is prior to the nozzle design.
3. Droplet diameter calculation of Fluent CFD code not agreed well with the derived SMD empirical formulae based on [10]. Further development of the numerical model of air blast atomisation is necessary.

As for further development proper air blast atomiser model should be developed with the help of User Defined Functions (UDFs), later, a steam blast atomisation model would be also useful to develop, considering the condensation on the surface of the droplets.

ACKNOWLEDGEMENTS

This research was supported by BUTE Department of Energy Engineering relating to the grant TÁMOP-4.2.2.B-10/1--2010-0009.

REFERENCES

[1] A. H. Lefebvre and D. Miller, "The Development of an Air Blast Atomizer for Gas Turbine Application," CoA. Report Aero No. 193 June, 1966.

[2] Y. Huang and V. Yang, "Dynamics and stability of lean-premixed swirl-stabilized combustion," *Prog. Energy Combust. Sci.*, vol. 35, no. 4, pp. 293–364, 2009.

[3] A. Lefebvre and D. R. Ballal, *Gas turbine combustion, third edition*. CRC Press, 2010.

[4] A. K.-B. K. Sztankó, "Reduction of pollutant emissions from a rapeseed oil fired micro gas turbine burner," *Fuel Process. Technol.*, 2015., accepted manuscript

[5] N. a. Chigier, "The atomization and burning of liquid fuel sprays," *Prog. Energy Combust. Sci.*, vol. 2, no. 2, pp. 97–114, Jan. 1976.

[6] R. Sadanandan, M. Stöhr, and W. Meier, "Simultaneous OH-PLIF and PIV measurements in a gas turbine model combustor," *Appl. Phys. B*, vol. 90, no. 3–4, pp. 609–618, Feb. 2008.

[7] A. H. Lefebvre, *Atomization and Sprays*. Taylor & Francis, 1989.

[8] F. L. Dryer, "Water addition to practical combustion systems—Concepts and applications," *Symp. Combust.*, vol. 16, no. 1, pp. 279–295, Jan. 1977.

[9] J. Jedelsky and M. Jicha, "Spatially and Temporally Resolved Distributions of Liquid in an Effervescent Spray," *At. Sprays*, vol. 22, no. 7, pp. 603–626, 2012.

[10] B. K. Park, J. S. Lee, and K. D. Kihm, "Comparative study of twin-fluid atomization using sonic or supersonic gas jets," *At. Sprays*, 1996.

[11] N. K. Akafuah, A. J. Salazar, and K. Saito, "Infrared thermography-based visualization of droplet transport in liquid sprays," *Infrared Phys. Technol.*, vol. 53, no. 3, pp. 218–226, May 2010.

[12] S. V. Apte, K. Mahesh, P. Moin, and J. C. Oefelein, "Large-eddy simulation of swirling particle-laden flows in a coaxial-jet combustor," *Int. J. Multiph. Flow*, vol. 29, no. 8, pp. 1311–1331, Aug. 2003.

[13] S. V. Apte, M. Gorokhovski, and P. Moin, "LES of atomizing spray with stochastic modeling of secondary breakup," *Int. J. Multiph. Flow*, vol. 29, no. 9, pp. 1503–1522, Sep. 2003.

[14] D. Caraeni, C. Bergström, and L. Fuchs, "Modeling of Liquid Fuel Injection , Evaporation and Mixing in a Gas Turbine Burner Using Large Eddy Simulations," pp. 223–244, 2001.

[15] W. P. Jones, S. Lyra, and S. Navarro-Martinez, "Large Eddy Simulation of Turbulent Confined Highly Swirling Annular Flows," *Flow, Turbul. Combust.*, vol. 89, no. 3, pp. 361–384, Jul. 2012.

[16] N. Zeoli and S. Gu, "Computational validation of an isentropic plug nozzle design for gas atomisation," *Comput. Mater. Sci.*, vol. 42, no. 2, pp. 245–258, Apr. 2008.

[17] A. Belhadef, A. Vallet, M. Amielh, and F. Anselmet, "Pressure-swirl atomization: Modeling and experimental approaches," *Int. J. Multiph. Flow*, vol. 39, pp. 13–20, Mar. 2012.

[18] U. Fritsching, "Droplets and particles in sprays: tailoring particle properties within spray processes," *China Particuology*, vol. 3, no. 1–2, pp. 125–133, Apr. 2005.

[19] A. F. Sarofim and R. C. Flagan, "NOx control for stationary combustion sources," *Prog. Energy Combust. Sci.*, vol. 2, pp. 1–25, 1976.

[20] C. H. Cho, G. M. Baek, C. H. Sohn, J. H. Cho, and H. S. Kim, "A numerical approach to reduction of NOx emission from swirl premix burner in a gas turbine combustor," *Appl. Therm. Eng.*, vol. 59, no. 1–2, pp. 454–463, Sep. 2013.

[21] Y. Ohkubo, "Low-NOx Combustion Technology," vol. 41, no. 1, pp. 12–23.

[22] T. Lajos, *Az áramlástan alapjai*, 4th ed. Budapest, 2008.

[23] P. O'Rourke and A. Amsden, "The TAB Method for Numerical Calculation of Spray Droplet Breakup," *SAE Tech. Pap.*, p. 872089, 1987.

[24] R. D. Reitz, "Modeling Atomization Processes in High-Pressure Vaporizing Sprays," *At. Sprays*, vol. 3, pp. 309–337, 1987.

Conference on Modelling Fluid Flow (CMFF'15)
The 16th International Conference on Fluid Flow Technologies
Budapest, Hungary, September 1-4, 2015

EFFECT OF ORIENTATION OF FORCED MOTION ON THE FLOW PAST A CIRCULAR CYLINDER FOLLOWING A FIGURE-8 PATH

László BARANYI[1]

[1] Corresponding Author. Department of Fluid and Heat Engineering, University of Miskolc, 3515 Miskolc-Egyetemváros, Hungary. Tel.: +36 46 565 154, Fax: +36 46 565 471, E-mail: arambl@uni-miskolc.hu

ABSTRACT

This numerical study investigates the low-Reynolds-number flow past a circular cylinder placed in a uniform stream following a slender figure-8 path, using a thoroughly tested two-dimensional computational method based on the finite difference method. This type of two-degree-of-freedom motion have often been observed in practice. The combined effects of transverse oscillation amplitude, frequency ratio (0.9, 1.0 and 1.1), amplitude ratio (0.0, 0.1, 0.2, 0.3 and 0.4) and direction of cylinder orbit (clockwise (CW) and anticlockwise (ACW) in the upper loop of figure-8) were investigated at Reynolds number 150 on the mechanical energy transfer and the time-mean values of lift and drag. Results differ substantially depending on the direction of orientation. Mechanical energy transfer between fluid and cylinder was positive (potential danger of vortex-induced vibration) over a much larger parameter domain for ACW direction compared to CW. On the other hand, the CW case is much more prone to the occurrence of vortex switches.

Keywords: circular cylinder, drag and lift coefficients, figure-8 path, mechanical energy transfer, Reynolds number, Strouhal number

NOMENCLATURE

A_x, A_y	[-]	oscillation amplitude in x and y directions, non-dimensionalised by d
C_D	[-]	drag coefficient, $2D/(\rho U^2 d)$
C_L	[-]	lift coefficient, $2L/(\rho U^2 d)$
D	[N/m]	drag force per unit length
E	[-]	mechanical energy transfer
FR	[-]	frequency ratio, f_y/St_0
L	[N/m]	lift force per unit length
Re	[-]	Reynolds number, Ud/ν
St	[-]	Strouhal number, $f_v d/U$
T	[-]	cycle period, non-dimensionalised by d/U
U	[m/s]	free stream velocity
a_{0x}, a_{0y}	[-]	cylinder acceleration in x and y directions, non-dimensionalised by U^2/d
d	[m]	cylinder diameter, length scale
f_x, f_y	[-]	oscillation frequency in x and y directions, non-dimensionalised by U/d
f_v	[s^{-1}]	vortex shedding frequency
x,y	[-]	Cartesian co-ordinates, non-dimensionalised by d
Δt	[-]	time step, non-dimensionalised by d/U
ν	[m^2/s]	kinematic viscosity
ρ	[kg/m^3]	fluid density
Θ	[-]	phase angle between cylinder motions in x and y directions

Subscripts and Superscripts

D	drag
fb	fixed body
L	lift
v	vortex
x, y	components in x and y directions

1. INTRODUCTION

Several engineering structures exhibit vibration problems caused by vortex shedding. Some examples of these in real life are the vibration of silos, smokestacks, underwater pipes or risers or the tube bundles of heat exchangers. When vortices are shed from the body a periodic force is generated which can cause fatigue of or damage to the structure, especially if the vortex shedding frequency is near the natural frequency of the structure and the damping is small. The noisy operation of a device can be another result of vortex-induced vibration (VIV). Due to its practical importance many researchers have dealt with one-degree-of-freedom (1-DoF) motion, most frequently cylinder oscillation transverse to the main stream (see, e.g. [1-3]). The other type of 1-DoF motion is in-line with the main stream (see e.g. [4, 5]).

In most cases, however, vibration occurs in both transverse and in-line (streamwise) directions, leading to a two-degree-of-freedom (2-DoF) motion. Relatively few studies deal with either free or forced 2-DoF motions, two types of which have been observed in practice: (a) when the oscillation frequencies in the two directions are identical (f_x=f_y=f), resulting in an elliptical path (e.g. [6, 7]), (b) when the frequency of cylinder oscillation in the streamwise direction is approximately double that of the transverse direction (f_x=2f_y), yielding a figure-8 path (see e.g. the experimental studies [8-12]). [8, 9] have shown that when the cylinder is also free to oscillate in-line with the flow (2-DoF), the hydrodynamic forces can be very different than those observed for a cylinder oscillating only in the crossflow direction (1-DoF). The phase angle difference Θ between in-line and transverse motions of the cylinder results in not only different cylindrical paths (figure-eight, distorted figure-eight and crescent shape) but even different orientations along the path (clockwise and anticlockwise orbit on the upper loop of figure-eight), [10, 11]. It was shown in [10] that the value of Θ can alter the reduced velocity for which a transition between 2S and 2P (see [1]) shedding occurs. During the forced cylinder motion experiments in [12] the effect of phase angle Θ on lift was investigated.

In a 2-DoF free vibration numerical study [13] figure-eight and crescent shape paths were obtained, just like in the experimental studies [10, 11]. In the numerical study [14] flow around a mechanically oscillated cylinder following a figure-eight path was investigated in at Reynolds number Re=400, frequency ratios f_y/St$_0$=0.9, 1.0 and 1.1 and at two different A_x/A_y ratio values while varying the transverse amplitude of oscillation. They also carried out computations for both directions of orbit and found that an anticlockwise orbit in the upper loop resulted in a positive power coefficient, meaning an increased chance of VIV for a cylinder in free vibration.

The present author in [15] numerically investigated the time-mean of force coefficients and the mechanical energy transfer E between a cylinder placed in a uniform stream and forced to follow a figure-eight path and the fluid at Re=200, 250 and 300 at a fixed amplitude ratio A_x/A_y=0.14 against the frequency ratio in the lock-in domain for both clockwise (CW) and anticlockwise (ACW) directions of orbit on the upper loop of figure-eight. It was found that the flow features and the energy transfer depend strongly on the direction of orbit. For the CW orbit the value of E was negative (energy is extracted from the cylinder) in the whole parameter domain investigated, meaning that in this case there is no danger of VIV. For the ACW case, however, the opposite was obtained, indicating a potential risk of VIV in the case of an elastically supported cylinder.

The main objective of this paper is to investigate the effect of amplitude ratio (limited to slender cylinder paths in the transverse direction) and frequency ratio (ratio of cylinder oscillation frequency in transverse direction and the frequency of vortex shedding from a stationary cylinder at the same Reynolds number) on the time-mean of force coefficients, focusing on the positive mechanical energy transfer between the fluid and the cylinder.

2. COMPUTATIONAL METHOD

A non-inertial system fixed to the accelerating cylinder is used for the computation of the two-dimensional (2D), constant property, low-Reynolds number incompressible fluid flow around a circular cylinder placed in a uniform stream. The governing equations are the non-dimensional Navier-Stokes equations in a non-inertial system fixed to the moving cylinder, the equation of continuity and a Poisson equation for pressure. A no-slip boundary condition is used for the velocity and a Neumann type boundary condition for the pressure is used on the cylinder surface. At the far region potential flow is assumed.

The physical domain, which is bounded by two concentric circles with radii R_1 and R_2, is transformed into a rectangular computational domain with equidistant spacing. This mapping ensures a fine grid scale near the cylinder and a coarse grid in the far field. The transformed governing equations and boundary conditions are solved by the finite difference method. For further details see [7]. The code developed by the author has been extensively tested against experimental and computational results and good agreement was found (see [7]). In this study the dimensionless time step is 0.0005, the computational domain is characterised by R_2/R_1=160 and the grid size is 361x292.

The layout of the cylinder path is shown in Figure 1. Here U is the free stream velocity (velocity scale), d=2R_1 is the cylinder diameter (length scale), and A_x and A_y are the dimensionless amplitudes in x and y directions, respectively. Every quantity is made dimensionless by the combination of U and d. The dimensionless displacements of the forced cylinder motion x_0, y_0 in x and y directions are given by

$$x_0(t) = A_x \sin(2\pi\, f_x\, t + \Theta)\,, \tag{1}$$

$$y_0(t) = A_y \sin(2\pi\, f_y\, t)\,, \tag{2}$$

where f_x and f_y are the cylinder oscillation frequencies in x and y directions non-dimensionalised by U/d. Equations (1) and (2) ensures a figure-eight or distorted figure-eight path if f_x = 2f_y. Depending on the phase angle Θ between cylinder motions in x and y directions, clockwise (CW) or anticlockwise

(ACW) orbit can be obtained at the upper loop of figure eight:

$$f_x = 2 f_y;\ \ \Theta = \pi,\ \ \text{(for CW)}, \tag{3}$$

$$f_x = 2 f_y;\ \ \Theta = 0,\ \ \text{(for ACW)}. \tag{4}$$

Equations (3) and (4) ensure a regular figure-eight path (see Fig. 1).

The following notations are used for the amplitude ratio ε and frequency ratio FR:

$$\varepsilon = A_x / A_y, \tag{5}$$

$$\mathrm{FR} = f_y / \mathrm{St}_0. \tag{6}$$

In Eqs. (5) and (6) A_x and A_y are the dimensionless oscillation amplitudes in x and y directions, and St_0 is the dimensionless vortex shedding frequency for a stationary cylinder at that Reynolds number. The St_0 value St_0=0.18366 for Re=150 is from [16].

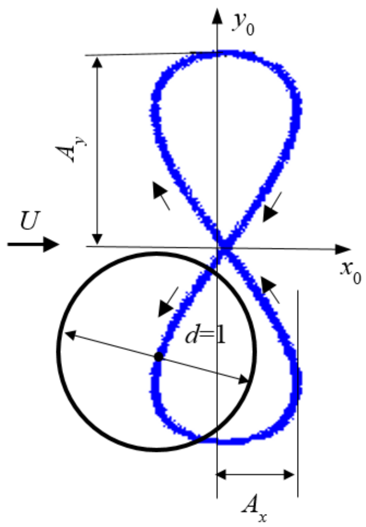

Figure 1. Layout for the figure-eight path, CW

Throughout this paper the lift (C_L) and drag (C_D) coefficients used do not contain the inertial forces originating from the non-inertial system fixed to the moving cylinder. These coefficients are often termed 'fixed body' coefficients (see [2]). The two sets of coefficients can be written as

$$C_L = C_{Lfb} + \frac{\pi}{2} a_{0y},\ C_D = C_{Dfb} + \frac{\pi}{2} a_{0x}, \tag{7}$$

where subscript *fb* stands for fixed body (understood in an inertial system) [17]. In Eq. (7) a_{0x} and a_{0y} accelerations are the second time derivatives of cylinder displacements x_0, y_0 given in Eqs. (1) and (2). Since a_{0x} and a_{0y} are T-periodic functions their time-mean (TM) values vanishes, resulting in identical TM values for lift and drag in the two systems.

The non-dimensional mechanical energy transfer E originally introduced in [3] for a transversely oscillating cylinder is extended for a general 2-DoF motion of the cylinder in [7]:

$$E = \frac{2}{\rho U^2 d^2} \int_0^T \mathbf{F} \cdot \mathbf{v}_0 \mathrm{d}\, t = \int_0^T \left(C_D\, v_{0x} + C_L\, v_{0y} \right) \mathrm{d}\, t\,. \tag{8}$$

Since the frequencies in the two directions are different (see Eqs. (3) and (4)) the larger period of T=T_y=1/f_y is chosen for the investigation. In Eq. (8) $\mathbf{F}$ is the force vector per unit length of cylinder, $\mathbf{v_0}$=(v_{0x},v_{0y}) are the velocity vector of the cylinder.

3. RESULTS AND DISCUSSION

During the systematic investigations the value of amplitude ratio ε is kept constant at 0, 0.1, 0.2, 0.3 and 0.4 at Re=150 and at frequency ratios of FR=0.9, 1.0 and 1.1 for both clockwise (CW) and anticlockwise (ACW) orbit on the upper lobe of figure-eight, while the transverse oscillation amplitude A_y varied. Only locked-in cases are considered in this paper. Larger ε values mean a “thicker” figure-eight path but even the largest ε value investigated ensures a relatively slender path. First the effects of flow parameters on the TM values of lift (C_L) and drag (C_D) coefficients will be shown, then effects of the mechanical energy transfer E, and finally the vicinity of a jump (due to a switch in the vortex structure) is investigated. Pre- and post-jump analysis in the vicinity of a jump was also carried out.

The FR=1.1 case, also investigated, is not shown here, as it provides little new information. At FR=1.1 there is a wider no-lock-in domain than at the lower FR values.

3.1. Effect of flow parameters on time-mean of force coefficients

The time-mean (TM) and root-mean square (rms) values of lift, drag, base pressure and torque coefficients were investigated but due to lack of space only TM of lift and drag will be shown here. The scales on the axes for each pair of figures (CW and ACW) are kept the same for ease of comparison.

Figure 2 shows the TM of lift for FR=0.9 for different amplitude ratios (ε) against the transverse oscillation amplitude A_y. The value ε=A_x/A_y=0 (eps=0 in the figure) means pure transverse oscillation. The top figure shows the case when the cylinder orbit on the upper loop of figure-eight is clockwise (CW) and for the bottom figure the orbit is anticlockwise (ACW). The difference for the two directions of orbit is conspicuous. For the CW case the TM of lift is zero at small A_y values. It represents 2S shedding, which means that two single vortices are shed in a vortex shedding period [1]. This is the Kármán vortex street typical for low-Re-number flow past a stationary circular cylinder placed in a uniform stream. By increasing A_y, at some critical A_y value depending on

ε, the symmetry in the flow is broken by an instability, a pitchfork bifurcation [18] starts and the TM of lift ceases to be zero any more.

This phenomenon is similar to that of the buckling rod. There are two possible solutions but only one of them are realised. There are two attractors in this non-linear system (periodic orbits in this case), each has a 'basin of attraction' in the initial condition space, and the solution is attracted to one or the other, depending on the initial conditions. By changing initial conditions a basin boundary may be crossed. As a result the solution would switch from one to the other [18]. This bifurcation starts at smaller A_y values for higher ε values: it starts at around A_y =0.3 for ε =0.4 and at around A_y =0.8 for pure transverse oscillation (ε =0). It can also be seen in the top figure that for ε =0.3 and 0.4 the solutions are first attracted to one attractor and then abruptly switch to the other, and thus jumps can be observed in the TM of lift at around A_y =0.45. For smaller ε values such switches do not occur in the parameter domain investigated.

In the bottom figure in Fig. 2 (ACW orbit) almost all TM values are zero in the investigated A_y domain. The ε =0 case shows a similar tendency to its CW counterpart but near A_y =0.8 it bifurcates to negative TM of lift values. For the thickest figure-eight path case, i.e. for ε =0.4, the TM value is zero up to around A_y =0.61, where there is a jump to a negative TM value, and remains negative as A_y increases. At this point 2S shedding ceases to exist.

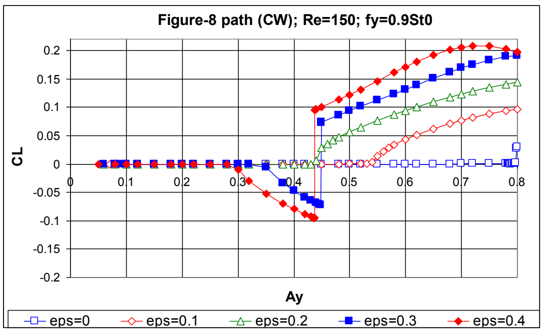

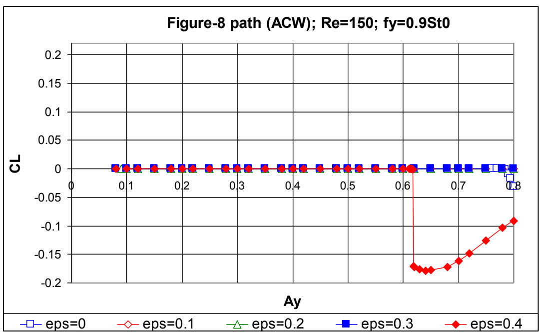

Figure 2. Time-mean value of lift against A_y at FR=0.9: top – CW; bottom – ACW

Figure 3 shows the TM of drag coefficients against A_y for FR=0.9 for different amplitude ratios ε.

In the CW case, the TM of drag increases with A_y for all ε, as expected. Interestingly, TM values are lowest for the ε=0.1 and curves for ε=0 and 0.2 almost coincide. Between ε=0.2 and 0.4 the TM values increase monotonically with ε. The phenomenon that causes jumps in the TM of lift (see Fig. 2 top) has no visible effect on the TM of drag.

In the ACW orbit (Fig. 3 bottom) similar trends can be observed with some differences. One difference is that the TM values are higher for the ACW case. Another is the TM of drag is a monotonic function of amplitude ratio ε. The third is that for ε=0.4 a jump can be detected at around A_y=0.61, just like in the TM of lift curve in Fig. 2.

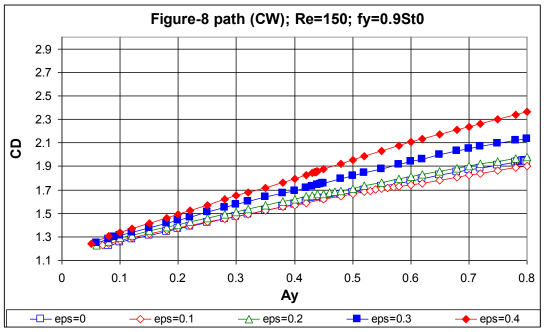

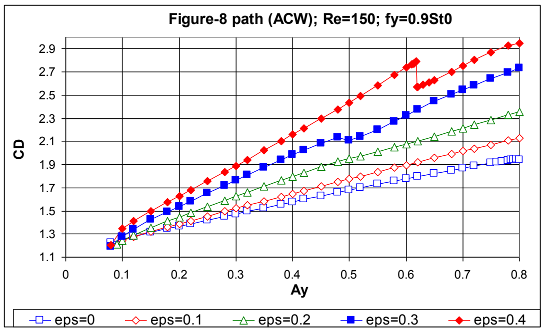

Figure 3. Time-mean value of drag against A_y at FR=0.9: top – CW; bottom – ACW

Figures 4 and 5 show the TM of lift and drag for frequency ratio FR=1.0 for both CW and ACW directions of orbit. The TM of lift for CW is shown against A_y in the top figure of Fig. 4. The similarity to the case of FR=0.9 (see Fig. 2 top) is striking. The ACW case (Fig. 4 bottom) is partly similar to its FR=0.9 counterpart (see Fig. 2 bottom) but here the TM of lift for the ε=0.3 case is not zero, there are sudden switches or jumps in both ε=0.3 and 0.4 curves and the absolute value of lift is larger than in the FR=0.9 case.

Figure 5 shows the TM of drag versus A_y. The CW case is similar to the FR=0.9 case (see Fig. 3 top) but the values are somewhat higher for the case of FR=1.0 and there are small jumps in the ε=0.3 and 0.4 curves at around A_y=0.24. As for the ACW case, comparing it to the curves for FR=0.9, one can say that the main trends are similar in the two figures, but for the ACW case for ε=0.2 there is a jump and even a discontinuity at around A_y=0.35. As was mentioned earlier, only locked-in cases are considered in this study. Here the discontinuity means that at some A_y values the flow is not locked-in (the flow is not synchronised with the cylinder motion). For ε=0.4 two jumps are found in the curve.

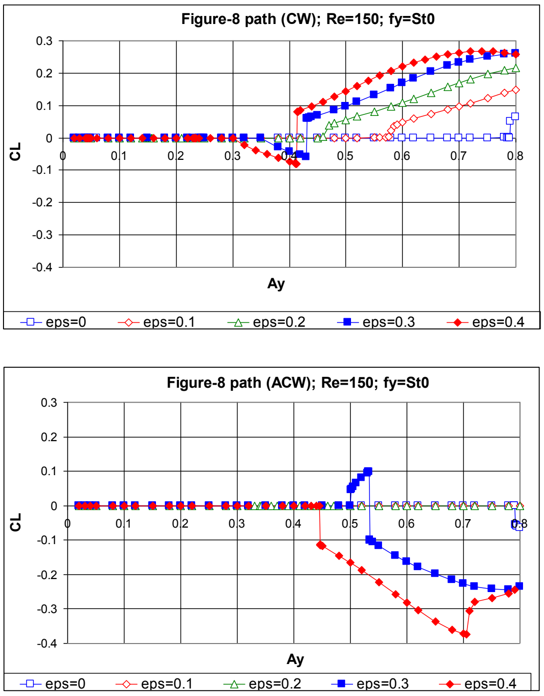

Figure 4. Time-mean value of lift against A_y at FR=1.0: top – CW; bottom – ACW

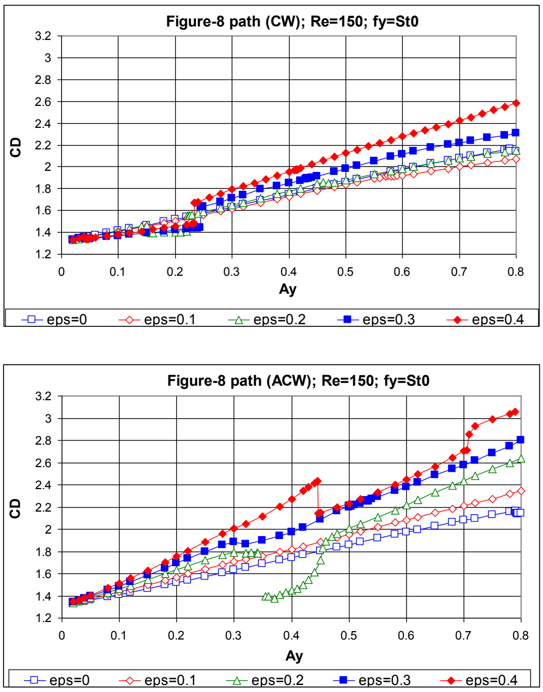

Figure 5. Time-mean value of drag against A_y at FR=1.0: top – CW; bottom – ACW

3.2. Effect of flow parameters on the mechanical energy transfer

Let us see now how the mechanical energy transfer E, defined by Eq. (8), depends on the following parameters: direction of orbit (CW or ACW), frequency ratio FR=f_y/St$_0$, amplitude ratio $\varepsilon=A_x/A_y$, and transverse cylinder oscillation amplitude A_y. Again, the scales on the axes for each pair of figures (CW and ACW) are kept the same for ease of comparison. Figure 6 shows E against A_y for FR=0.9 and ε=0, 0.1, 0.2, 0.3 and 0.4 for the CW orbit (top figure). It can be seen that E is decreasing with ε and that E is negative for the largest part of the parameter domain for the CW orbit. Negative E means that energy is extracted from the cylinder by the fluid. In this case the flow is acting to dampen the cylinder motion. Positive E values, however, can be dangerous for a freely vibrating (or elastically supported) cylinder because positive E amplifies the cylinder motion, since in this case the cylinder obtains energy from the flow. The bottom figure in Fig. 6 zooms in on positive E values. As can be seen, positive E values can only be found for ε=0 and 0.1. In the case of ε=0 (transverse oscillation) E is positive in the interval of $0.08 < A_y < 0.48$ and the peak value in E is around 0.17, found at A_y=0.32. For ε=0.1 the value of E is even smaller ($E > 0$ if $0.09 < A_y < 0.28$ and E_{max} is around 0.04 and at A_y=0.2). For ε=0.2, 0.3 and 0.4 no positive E values can be found in the whole investigated A_y domain for FR=0.9 and CW orbit.

Figure 7 shows E against A_y for FR=0.9 and ε=0, 0.1, 0.2, 0.3 and 0.4 for the ACW (top figure) orbit. A direct comparison of this figure with its CW counterpart (Fig. 6 top) shows that for the ACW case the absolute value of the negative E values at large A_y values is much smaller than for the CW orbit and the order of the curves belonging to different ε values is different. Hence the flow has a lower dampening effect on the vibration of an elastically supported cylinder when the orbit is ACW. The bottom figure of Fig. 7 zooms in on positive E values. As can be seen, positive E values occur for all five ε values in this case. For each curve E has a maximum and the smallest peak E values occur at ε=0, and E basically increases with increasing ε values (in contrast with the CW case; see Fig. 6 bottom). The maximum value of E is around unity, and positive E values occur for almost all of the investigated A_y domain. Comparing this figure with its CW counterpart reveals that the positive E values are much larger for the ACW case. Hence this orbit is much more dangerous in the case of a freely vibrating cylinder than the cylinder with a CW orbit.

This investigation was repeated for frequency ratio FR=1.0. The relevant computational results for E for both the CW and ACW orbits are shown in Figures 8 and 9. The CW orbit (Fig. 8 top) shows similar tendencies to its FR=0.9 counterpart (Fig. 6 top). When zooming in on the positive E values it can be seen that positive values now occur at three ε

values of 0, 0.1 and 0.2. The tendency is similar to the case of FR=0.9 (see Fig. 6 bottom) but the largest E value is about 0.4 this time. Also, jumps occur in the curve for ε=0.2.

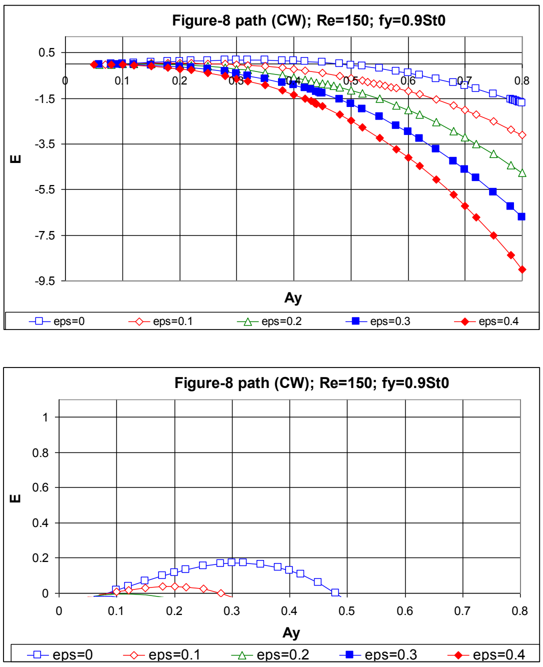

Figure 6. E against A_y at FR=0.9 and CW orbit (top); zoom in on positive E (bottom)

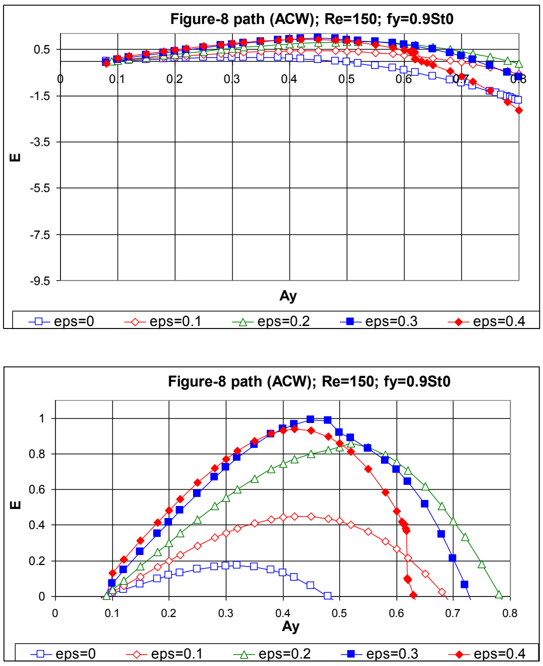

Figure 7. E against A_y at FR=0.9 and ACW orbit (top); zoom in on positive E (bottom)

Figure 9 shows the ACW case for FR=1. The top figure is very similar to its FR=0.9 counterpart (see top figures in Figs. 7 and 9). The bottom figure in Fig. 9 is also similar to the zoomed in figure for FR=0.9 for ACW orbit (see Fig. 7 bottom) with the small difference that the FR=1.0 case contains not only jumps but also non-locked in sections (see the case of ε=0.2). The peak value in E is also quite high: E=0.832 at A_y=0.4 for ε=0.4.

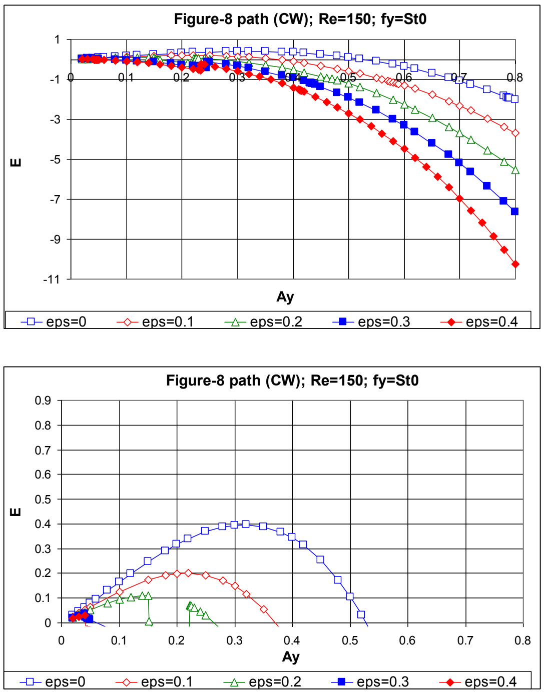

Figure 8. E against A_y at FR=1.0 and CW orbit (top); zoom in on positive E (bottom)

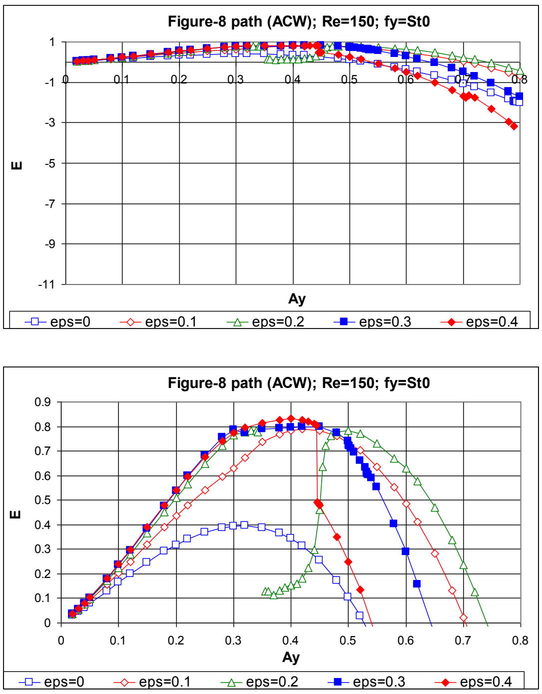

Figure 9. E against A_y at FR=1.0 and ACW orbit (top); zoom in on positive E (bottom)

3.3. Pre- and post-jump analysis

The vicinity of a jump in the TM of lift is investigated by different means, but due to lack of space only two will be shown here: a drag-lift limit cycle curve and vorticity contours before (-) and after (+) a jump. The data for the jump shown here are FR=0.9, ε=0.4, CW orbit; A_{y-}=0.4374, A_{y+}=0.4375; the jump can be seen clearly on the top figure in Fig. 2. By eliminating the time from the periodic fixed body lift and drag coefficients, the limit cycles can be obtained. The top figure in Figure 10 shows limit cycles (C_{Dfb},C_{Lfb}) for A_{y-} (thick line) and A_{y+} (thin line). Although there is just a tiny difference between oscillation amplitudes, still the limit cycle curves differ from each other quite a lot. While not obvious at first sight, these curves are mirror images to each other (flipping along the line of C_{Lfb}=0), as can also be seen in the bottom figure of Fig. 10, where the post-jump C_{Lfb} is replaced by (-C_{Lfb}). The two curves coincide with each other very well (this time both curves are plotted as thin lines).

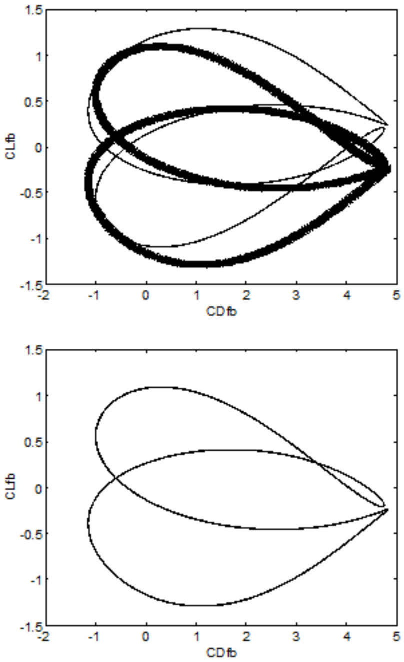

Figure 10. Limit cycle curves (FR=0.9, ε =0.4, CW), A_{y-}=0.4374 (thick line); A_{y+}=0.4375 (thin line), (C_{Dfb},C_{Lfb}) (top); (C_{Dfb},-C_{Lfb}) (bottom)

Computed vorticity contours are shown in Figure 11 for A_{y-} (top) and A_{y+} (bottom) amplitude values. The grey colour indicates negative vorticity values (rotating clockwise), and the black is positive (anticlockwise). The pre- and post-jump vorticity contours are taken at the instants of t=66T=399.2885 and t=66.5T=402.3135 (shifted by half a period), respectively. As can be seen in the two figures the vorticity contours are almost perfectly mirror images of each other, as was also found for the limit cycles. The vortex shedding mode is P+S, meaning that a pair (P) of vortices and a single (S) vortex are shed in one period [1]. Before the jump the pair of vortices are in the lower row, after the jump they switch to the upper row. The pre- and post jump time-history curves also show that they are not a mere reflection of each other; they are reflected and translated by half a period (T/2) with respect to each other. That is why the vorticity contour snapshots are also taken shifted by T/2.

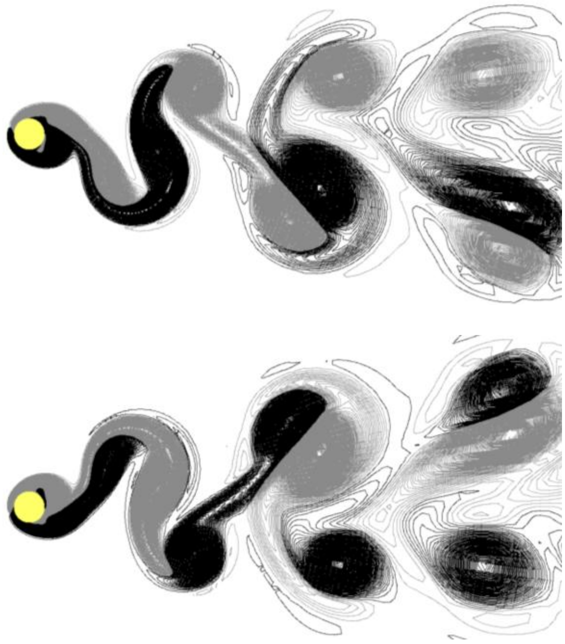

Figure 11. Vorticity contours: top pre-jump (A_{y-}=0.4374); bottom post-jump (A_{y+}=0.4375)

4. CONCLUSIONS

Flow around a circular cylinder forced to follow a slender figure-eight path is investigated numerically at frequency ratios FR=0.9, 1.0 and 1.1, Re=150, and amplitude ratios ε=A_x/A_y=0, 0.1, 0.2, 0.3 and 0.4 in the lock-in domain. Mechanical energy transfer E and time history of lift and drag are plotted against transverse oscillation amplitude A_y while other parameters are kept constant. Both clockwise (CW) and anticlockwise (ACW) orbits on the upper loop of a figure-eight path are investigated.

From the results it can be stated that

- Time-mean of lift is very sensitive to the direction of cylinder orbit;
- Energy transfer E for the CW case: E is negative in the largest part of the parameter domain, and positive E values are confined to moderate A_y values (A_y < 0.53). There are small positive E peaks for the smaller ε values (the maximum value of positive E peaks belongs to ε =0); for larger ε values there are no positive E values at all.
- Energy transfer E for the ACW case: E is positive in the largest part of the parameter domain (amplifying vibration effect). There are large positive E peaks, and the value of the

peaks increases with ε (unlike in the CW case). This situation represents a potencial risk for vortex-induced vibration VIV for free vibration cases, and can lead to fatigue of the structure.

- The pre- and post-jump analysis around a switch or jump in the value of TM of lift shows that both the drag-lift limit cycle curves and vortex contours belonging to pre- and post-jump amplitude values are mirror images of each other.

Future investigations could include computations at further Reynolds numbers or frequency ratios.

ACKNOWLEDGEMENTS

The work was carried out as part of the TÁMOP-4.2.1.B-10/2/KONV-2010-0001 project in the framework of the New Hungarian Development Plan. The realization of this project is supported by the European Union, co-financed by the European Social Fund. The author would like to thank Mr. L. Daróczy for designing the flow visualization software used in Fig. 11.

REFERENCES

[1] Williamson, C.H.K., 1988, "Vortex formation in the wake of an oscillating cylinder", *Journal of Fluids and Structures*, Vol. 2, pp. 355–381.

[2] Lu, X.Y., and Dalton, C., 1996, "Calculation of the timing of vortex formation from an oscillating cylinder", *Journal of Fluids and Structures*, Vol. 10, pp. 527–541.

[3] Blackburn, H.M., and Henderson, R.D., 1999, "A study of two-dimensional flow past an oscillating cylinder", *Journal of Fluid Mechanics*, Vol. 385, pp. 255–286.

[4] Wootton, L.R., 1972, *Resume on Full-scale Tests on Oscillation of Piles in Marine Structures*, Construction Industry Research & Information Association (CIRIA), London

[5] Al-Mdallal, Q.M., Lawrence, K.P., and Kocabiyik, S., 2007, "Forced streamwise oscillations of a circular cylinder: Locked-on modes and resulting fluid forces", *Journal of Fluids and Structures*, Vol. 23, pp. 681–701.

[6] Didier, E., and Borges, A.R.J., 2007, "Numerical predictions of low Reynolds number flow over an oscillating circular cylinder", *Journal of Computational and Applied Mechanics*, Vol. 8(1), pp. 39–55.

[7] Baranyi, L., 2008, "Numerical simulation of flow around an orbiting cylinder at different ellipticity values", *Journal of Fluids and Structures*, Vol. 24, pp. 883–906.

[8] Jauvtis, N., and Williamson, C.H.K., 2004, "The effect of two degrees of freedom on vortex-induced vibration and at low mass and damping", *Journal of Fluid Mechanics*, Vol. 509, pp. 23–62.

[9] Dahl, J.M., Hover, F.S., and Triantafyllou, M.S., 2006, "Two-degree-of-freedom vortex-induced vibrations using a force assisted apparatus", *Journal of Fluids and Structures*, Vol. 22, pp. 807–818.

[10] Jeon, D., and Gharib, M., 2001, "On circular cylinders undergoing two-degree-of-freedom forced motions", *Journal of Fluids and Structures*, Vol. 15, pp. 533–541.

[11] Sanchis, A., Sælevik, G., and Grue, J., 2008, "Two-degree-of-freedom vortex-induced vibrations of a spring-mounted rigid cylinder with low mass ratio", *Journal of Fluids and Structures*, Vol. 24, pp. 907–919.

[12] Dahl, J.M., Hover, F.S., and Triantafyllou, M.S., 2008, "Third harmonic lift forces from phase variation in forced crossflow and in-line cylinder motions", Proc. *9th International Conference on Flow-Induced Vibrations*, Prague, pp. 799–804.

[13] Prasanth, T.K., and Mittal, S., 2009, "Flow-induced oscillation of two circular cylinders in tandem arrangement at low Re", *Journal of Fluids and Structures*, Vol. 25, pp. 1029–1048.

[14] Peppa, S., Kaiktsis, L., and Triantafyllou, G.S., 2010, "The effect of in-line oscillation on the forces of a cylinder vibrating in a steady flow", *American Society of Mechanical Engineers, Fluids Engineering Division (Publication) FEDSM*, 3 (PARTS A and B), pp. 21–28.

[15] Baranyi, L., 2012, "Simulation of a low-Reynolds number flow around a cylinder following a figure-8-path", *International Review of Applied Sciences and Engineering*, Vol. 3(2), pp. 133–146.

[16] Posdziech, O., and Grundmann, R., 2007, "A systematic approach to the numerical calculation of fundamental quantities of the two-dimensional flow over a circular cylinder", *Journal of Fluids and Structures*, Vol. 23, pp. 479–499.

[17] Baranyi, L., 2005, "Lift and drag evaluation in translating and rotating non-inertial systems", *Journal of Fluids and Structures*, Vol. 20(1), pp. 25–34.

[18] Strogatz, S.H., 1994, *Nonlinear Dynamics and Chaos*. Westview Press, Cambridge MA.

Conference on Modelling Fluid Flow (CMFF'15)
The 16th International Conference on Fluid Flow Technologies
Budapest, Hungary, September 1-4, 2015

STATISTICAL MODELLING OF SPRAY BREAKUP PROCESSES IN INDUSTRIAL GAS-LIQUID FLOWS

Henrik STRÖM[1], Srdjan SASIC[2]

[1] Corresponding Author. Division of Fluid Dynamics/Division of Energy Technology, Chalmers University of Technology, SE-412 96 Gothenburg, Sweden. Tel.: + 46 (0) 31 772 13 60, E-mail: henrik.strom@chalmers.se
[2] Division of Fluid Dynamics, Chalmers University of Technology, SE-412 96 Gothenburg, Sweden. E-mail: srdjan@chalmers.se

ABSTRACT

Sprays are used in industrial applications where high heat and mass transfer rates and good mixing are of primary importance. Today, there is no single mathematical framework available to predict the entire spray breakup process at an acceptable computational cost for a typical problem of industrial size. In this work, we develop a volume-of-fluid (VOF) framework that is combined with Lagrangian particle tracking (LPT) to take advantage of the respective strengths of these two approaches in the dense and dilute regions of the spray. A statistical model is constructed that makes the transition from the VOF to the LPT formulation possible using input data about the primary breakup process obtained from detailed VOF simulations. A novel void-handling scheme is used to make volume conservation possible for the two approaches combined on a single computational mesh. Some examples of the procedure in which the statistical model is tuned are shown and results from the combined framework are presented.

Keywords: LPT, multiphase flow, numerical methods, spray breakup, statistical modelling, VOF

NOMENCLATURE

C_D	[-]	drag coefficient
$\underline{F}$	$[N/m^3]$	momentum source term
d	$[m]$	diameter
$\underline{g}$	$[m/s^2]$	gravitational acceleration vector
M	$[kg/m^3]$	mass source term
m	$[kg]$	mass
P	$[Pa]$	pressure
Re	[-]	Reynolds number
t	$[s]$	time
$\underline{u}$	$[m/s]$	velocity vector
$\underline{x}$	$[m]$	position vector
α	[-]	volume fraction in the VOF representation occupied by the liquid phase
β	[-]	volume fraction available to VOF phase
$\underline{\underline{\tau}}$	$[Pa]$	molecular stress tensor
$\underline{\underline{\tau_t}}$	$[Pa]$	turbulent stress tensor
ρ	$[kg/m^3]$	density
μ	$[Pa,s]$	viscosity
ξ	[-]	location parameter
σ	[-]	scale parameter

Subscripts and Superscripts

LPT	Lagrangian particle tracking
p	parcel
r	relative

1. INTRODUCTION

The high heat and mass transfer rates obtainable in sprays are of great importance in a wide range of industrial applications (e.g., combustion, drying, and gas-liquid mixing). Due to the difficulties involved in experimental investigations of dense two-phase flows, numerical simulations are indispensable when investigating their behaviour. The atomization of a liquid in a gas-liquid flow can be described by a volume-of-fluid (VOF) model [1], where a single set of balance equations is solved and where the volume fraction field of the phases is tracked throughout the domain. This approach allows all the temporal and spatial scales relevant to the fluid dynamics to be resolved, but is extremely computationally expensive for industrial systems. A more appropriate technique is then to use Lagrangian particle tracking (LPT) [2], where computational parcels representing droplets are tracked through the gas. Unfortunately, LPT is only applicable to dispersed flows and thus cannot be used to predict the primary breakup process.

In this work, a VOF model is developed that is coupled to an LPT solver. The VOF model is solved together with a two-equation turbulence model in the parts of the domain where the flow is clearly separated. A switching scheme is developed that enables the transfer of mass from the VOF description to the LPT description and vice versa. The switching scheme enables implicit handling of the primary breakup by the VOF formulation via a statistical model, whereas the resulting droplet flow and its secondary breakup are handled by the LPT formulation, thus taking advantage of the respective strengths of the two approaches. A supporting void-handling scheme has been devised to make volume conservation possible, which is otherwise impossible unless different computational grids are used for the mentioned techniques. The switching scheme is based on a statistical model that is constructed via regression modelling using data obtained from highly resolved VOF simulations. The versatility of the combined VOF-LPT framework is illustrated and promising results are presented.

2. MODELLING

The model developed in the present work is a combined VOF-LPT model applied to a gas-liquid system. Since it is the liquid that is atomized and undergoes the transition from continuous to dispersed (and potentially back again), the gas phase is chosen to be the continuous phase in the model formulation. Consequently, the gas is only present in the VOF formulation, whereas the liquid can theoretically be simultaneously present in both the VOF and the LPT formulation. Later, we will introduce the switching scheme that transfers mass between the two formulations. In the terminology related to the switching between the two frameworks, we denote the liquid as the *switching phase* and the gas as the *non-switching phase*. In addition to the switching scheme, a void handling scheme is also necessary to prevent local overpacking of LPT parcels. Finally, the switching scheme is built around a statistical model that enables a mapping of VOF properties to LPT properties. This model and its two supporting schemes are also described in the following.

2.1. VOF model

In the VOF part of the framework, a shared set of equations is used for both phases. The pressure and velocity fields are determined from shared continuity and momentum balance equations, assuming that the velocity of the two phases is continuous across the interface:

$$\frac{\partial(\beta\rho)}{\partial t} + \nabla\cdot(\beta\rho\underline{u}) = M_{\mathrm{LPT}} \qquad (1)$$

$$\frac{\partial(\beta\rho\underline{u})}{\partial t} + \nabla\cdot(\beta\rho\underline{u}\underline{u}) = -\beta\nabla P + \nabla\cdot\left[\beta\left(\underline{\underline{\tau}} + \underline{\underline{\tau}}_{\mathrm{t}}\right)\right] + \beta\rho\underline{g} + \underline{F}_{\mathrm{LPT}} \qquad (2)$$

Note that this formulation differs with respect to a conventional VOF model by accounting for the fact that a fraction (1 - β) of a computational cell is occupied by the LPT representation. The local physical properties (density and viscosity) are obtained by weighing together the contributions from the gas and liquid in proportion to their presence in each cell. This presence is monitored by solving a continuity equation for the volume fraction of liquid, α, according to:

$$\frac{\partial(\beta\alpha)}{\partial t} + \nabla\cdot(\beta\alpha\underline{u}) = 0 \qquad (3)$$

Here, it should be emphasized that α is the volume a fraction of liquid in the fraction β of the computational cell available to the VOF formulation.

The turbulent stress tensor in Eq. (2) is obtained from the SST k-ω model [3], implying that the VOF model is a so-called *filtered* VOF model. The resolved interface is therefore to be interpreted as having been filtered with the same filter as the velocity and pressure fields in the derivation of the Reynolds-Averaged Navier-Stokes (RANS) equations. In the detailed VOF simulations used to tune the statistical model (see Section 2.4), the effects of surface tension are modelled via the continuum surface force model [4].

Eqs. (1) and (2) are discretized on a co-located grid using the second-order upwind scheme for the convective terms, second-order central differencing for the diffusion terms and first-order implicit discretization for the transient terms. The pressure-velocity coupling algorithm is PISO, and PRESTO! is used as the pressure interpolation scheme. Eq. (3) is discretized using a first-order explicit formulation for the transient term, and geometric reconstruction is used for the face flux interpolation. The β-field is calculated from a loop over all LPT parcels and is thus known during the solution of the Eulerian equations. Conservative forms of the governing equations in integral form are used to ensure mass conservation also in the presence of heterogeneities in the β-field [5].

2.2. LPT model

The LPT part of the framework is used to track the drop fragments created in the primary atomization process. These fragments are represented by computational parcels that represent a number of such fragments. The positions and velocities of the fragments are updated by applying Newton's second law:

$$\frac{d\underline{x}_{\mathrm{p}}}{dt} = \underline{u}_{\mathrm{p}} \tag{4}$$

$$m_{\mathrm{p}}\frac{d\underline{u}_{\mathrm{p}}}{dt} = 3\pi\mu d_{\mathrm{p}}\frac{C_D Re}{24}\left(\underline{u}-\underline{u}_{\mathrm{p}}\right)+ \frac{\pi d_{\mathrm{p}}^3}{6}\left(\rho_{\mathrm{p}}-\rho\right)\underline{g} \tag{5}$$

In the formulation of Eq. (5), it has been assumed that the net force acting on a computational parcel can be approximated by the sum of the drag force and the buoyancy force. It has furthermore also been assumed that these forces can be obtained with acceptable accuracy by neglecting the intricate details of the shape of a fragment by simply considering its sphere-equivalent diameter. The drag correlation used is that of Morsi and Alexander [6], secondary breakup of the LPT parcels into smaller fragments is handled by the Wave model [7], and turbulent dispersion is modelled with an eddy-interaction model [8].

2.3. Switching scheme

Any combination of a VOF and an LPT framework must have a switching scheme that lays down the rules for how and when to move mass from the VOF framework to the LPT one, and vice versa. In general, the case of switching from LPT to VOF is the easier task. If an LPT parcel enters a computational cell where the fraction β that is occupied by the VOF phases has a volume fraction α of the switching phase equal to one, the LPT parcel is removed and the mass and momentum goes into the VOF description. In such a switch, mass and momentum are conserved, both globally and locally.

Going from a VOF to an LPT description is not as straightforward, however, and there exist a number of suggestions for how to do this. One approach is based on a direct, one-to-one identification of fragments smaller than some threshold level that are then removed from the VOF description to appear in the LPT description [9, 10]. Here, we refer to this as *direct switching*. The main disadvantage associated with this technique is that the primary breakup has to be resolved, which is still extremely computationally demanding. The main advantage is that all information (positions, mass, momentum, and even some description of shape) may be preserved in the switching between the two models. However, this preservation can only happen at the cost of having to use separate computational meshes for the different techniques, since the theoretical assumptions underlying the derivation of the LPT model relies on that the size of an LPT parcel is significantly smaller than the computational cell in which it is currently residing. Multigrid techniques may be used to overcome these limitations [11], but they require additional computational overhead and also development of new techniques for switching from LPT to VOF. Such additional complications are not in line with the aim of the current work, which is to derive a robust and computationally efficient method for industrial applications.

Grosshans et al. [12] developed a combined statistical VOF-LPT technique in which it is assumed that the LPT parcels do not occupy any volume in the VOF description. This assumption is adequate when the LPT formalism is used in the dilute regions of a spray, but does not allow volume conservation (and hence not mass conservation) of the non-switching phase. Note that this inconsistency will affect both the switching from VOF to LPT as well as that from LPT to VOF. Consequently, such an approach is useful to study the fluid dynamics in situations where the continuous phase density is very low in comparison to the dispersed phase density, but is not generally well suited to applications where species transport and chemical kinetics in the non-switching phase are of interest as well. In the latter cases, failure to conserve the mass of the non-switching phase may have too severe implications for the overall accuracy of the computation.

In the present work, we have developed a switching scheme that is active in one or more pre-defined regions of the computational domain. We call such a region a *switching zone*. The switching zones are to be located in the regions of the domain where the liquid is atomized, and they should be defined in such a way that they cover the entire length from where continuous liquid enters to where the fragments created in the primary atomization process exits.

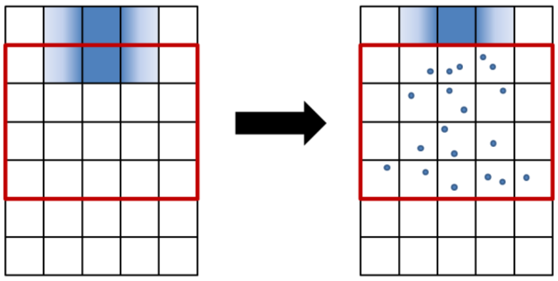

Figure 1. Conceptual illustration of the switching scheme developed in the current work

The red square in Figure 1 illustrates a switching zone in a flow situation where a gas-liquid two-phase flow moves downwards in the figure. As mass belonging to the switching phase enters the switching zone (left part of Fig. 1), it is transferred into the LPT description at the end of the time step by the switching scheme. It is however to be expected that one or several cells in the switching zone will be occupied with so much of the switching phase that a direct switching cannot be carried out on the mesh without resulting in local overpacking. At the same time, as the LPT fragments are to represent the outcome of the primary atomization, they are not necessarily to appear in the same computational cells as where the VOF mass was taken from. Instead, a statistical model is invoked that uses the variables (average volume fraction and phase-averaged velocities) on the inlet of the switching zone to sample appropriate LPT parcel properties from statistical distributions representing the outcome of the primary atomization process (right part of Fig. 1). As a direct consequence, conservation of the solution variables (mass and momentum) is guaranteed on a per-zone basis for the switching zone, and not necessarily on a per-cell basis.

2.4. Statistical model

The properties (size, position and velocity) of each LPT parcel inserted into the switching zone are sampled from statistical distributions using a statistical model. This model takes the area-averaged volume fraction and the phase-averaged velocities on the inlet to the switching zone is its input variables and uses uniformly distributed random numbers to sample a set of cumulative distribution functions (CDFs) for the LPT properties. These CDFs are obtained *a priori* from highly-resolved simulations of the atomization region using only the VOF model. A structure identification algorithm has been developed that identifies all isolated VOF structures in a given α-field and retrieves their properties (size, position and velocity). A great number of such snapshot data sets are obtained for a long time series of VOF simulation data. These data sets are then filtered to remove information pertaining to the liquid core or any possible fragments smaller than some lower threshold (e.g. four computational cells) related to what can be resolved on the employed mesh. The filtered data is thereafter inspected and functional forms for the distributions of the aforementioned properties are chosen. Next, the distribution functions are fitted to the available data. This process produces a detailed statistical model, but one that is only valid for the inlet conditions to the switching zone used in the detailed VOF simulations (in terms of α and $|\underline{u}_r|$) . Therefore, linear regression models are constructed for all parameters in the statistical distributions. Depending on the distribution function chosen, 2-6 parameters are needed to describe the distribution of each variable (size, position and velocity). Each parameter is determined by a regression model with three coefficients. Constructed in this way, the complete statistical model can hence approximate the CDFs of all variables in the complete [α, $|\underline{u}_r|$]-space.

The significance of the statistical model is that it uses data from only four detailed VOF time series to predict the CDFs. This number of cases has to be kept low in order not to lose computational efficiency. However, since four cases are not enough to allow regression of non-linear models, we have to assume that the variation of the properties among the parcels is uncorrelated. Previous experience tells us that the case-to-case variations over large spans in [α, $|\underline{u}_r|$]-space are significantly larger than e.g. size-dependence of properties such as the velocities, which supports the current approach. At the same time, it should be stressed that if the data snapshots obtained from the detailed VOF simulations should be subdivided into sub-classes based on one variable (e.g. size) to allow a size-dependence to captured by the statistical model, this would at the same time decrease the number of data points available in the fitting procedures, which would be detrimental to the predictive qualities of the model as a whole.

2.5. Void handling scheme

In a conventional LPT framework for dilute flows, the handling of the void created in each computational cell due to the presence of the Lagrangian parcels (denoted (1 - β) in the current work) is rather straightforward. Theoretical problems arise, however, in the limit of very low values of β. When the presence of the LPT fragments approaches the packing limit, some method must be invoked to prevent overpacking, which would otherwise yield unphysical results and risk crashing the solver. In detailed simulations of dense suspensions, it could be worthwhile to model actual particle collisions – an approach known as four-way coupling [13]. When particle collisions cannot be resolved (because of a too high computational cost), another option is to prevent overpacking by introducing a particle pressure [14]. In the current work, we aim at simulating systems of industrial size and where the dynamics of fragment collisions are not well known. The focus thus has to be primarily on computational efficiency and robustness, and we have therefore developed a novel void handling scheme that harmonizes with the statistical description of the atomization process adopted in the design of the switching scheme.

The void handling scheme first determines the local values of (1 - β) by summarizing the presence of LPT parcels in each computational cell. In the event that the value of (1 - β) calculated in this way should exceed the value corresponding to a randomized close packing of spheres, it is limited to this value and the remaining void is distributed to the cell neighbours. In that way, the fulfilment of all conservation laws is again guaranteed globally, whereas it is not necessarily maintained on a per-cell basis.

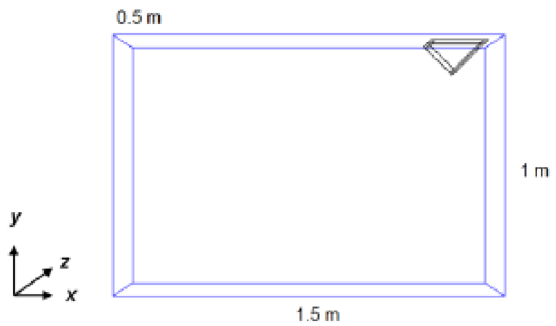

Figure 2. Illustration of the computational domain

3. RESULTS

All computations are performed for the domain illustrated in Figure 2. The inlet is located in the square duct entering from the upper right corner. The top plane is a no-slip wall, the bottom plane is a pressure outlet and the sides have periodic boundary conditions. The mesh contains more than 4.5 million hexahedral cells.

In order to generate data to tune the statistical model, we start with a small number of detailed VOF simulations (see Table 1). The incoming flow is assumed to be fully separated, so that the listed values of α can be interpreted both as the average volume fraction of liquid as well as the location of the liquid surface expressed as a fraction of the inlet height. The liquid velocity is fixed and the variation of the relative velocity is accomplished by varying the gas velocity. The liquid-to-gas density and viscosity ratios are approximately 12 and 4.5, respectively. Taking the side of the inlet duct as the characteristic length, both the gas and liquid Ohnesorge numbers are small while the Weber and Reynolds numbers are large. Consequently, inertial forces are more important than viscous and surface tension forces, and breakup of the incoming liquid jet is to be expected.

First, the detailed VOF simulations produce the data needed to tune the statistical model. A snapshot from Case #2 is shown in Figure 3. Very fine spatial and temporal resolutions are needed to resolve the breakup into these fragments, and the computational cost of simulating this breakup process in its entirety with dynamically changing boundary conditions is an insurmountable task for applications of industrial scale. The aim of the current work is to show how the properties of these fragments can be relatively well approximated by a statistical model that is fitted to the behaviour observed in the four detailed cases, which are chosen to adequately span the relevant property space. In order to facilitate the discussion, we will limit ourselves to the u-component of the velocity of the liquid fragments for the following discussion, but the same principle is valid for all the variables predicted by the statistical model. The performance of the VOF-LPT code developed here is finally assessed by applying it in the same computational domain but at a significantly lower mesh resolution (less than 750,000 cells).

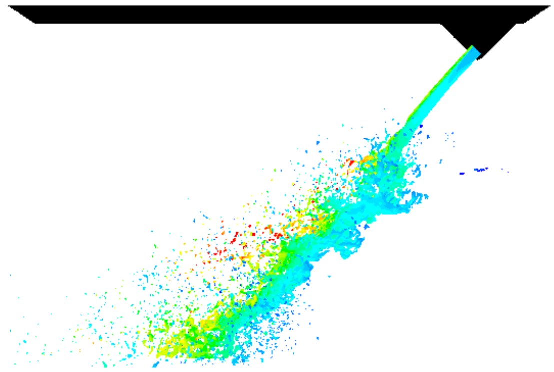

Figure 3. Snapshot from one of the detailed VOF cases (Case #2) showing contours of velocity magnitude on the gas-liquid interface

The probability distribution functions (PDFs) for the u-velocity obtained from the raw, filtered data are shown as histograms in Figure 4. It is emphasized here that although the four cases represent significant changes to the variables of primary interest in the atomization process (cf. Table 1), the distributions have striking similarities. For this particular variable (the u-velocity), an extreme value distribution was chosen as the most appropriate functional form.

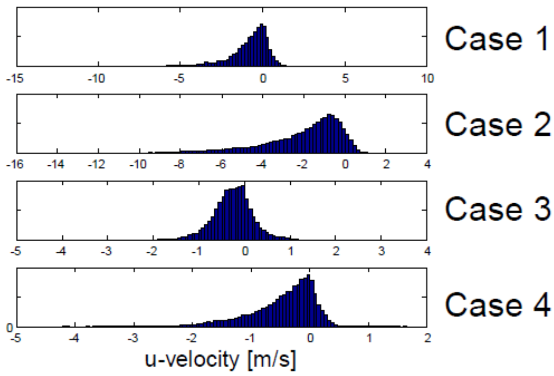

Figure 4. The raw, filtered probability distribution functions for the u-velocity of the liquid fragments produced in the detailed VOF cases

Table 1. Case specifications for the detailed VOF simulations

Case	α	$\lvert \underline{u}_r \rvert$
1	0.75	10 m/s
2	0.25	10 m/s
3	0.75	1.5 m/s
4	0.25	1.5 m/s

An extreme value distribution is characterized by two parameters, the location parameter ξ and the scale parameter σ. The probability distribution function is given by:

$$PDF\left(u_{\mathrm{p}};\xi,\sigma\right)=\frac{1}{\sigma}\exp\left[\frac{u_{\mathrm{p}}-\xi}{\sigma}\right]\exp\left[-\exp\left(\frac{u_{\mathrm{p}}-\xi}{\sigma}\right)\right] \quad (6)$$

It is thus possible to fit appropriate values of ξ and σ for each of the four detailed VOF cases. Such a fitting procedure for the u-velocity data produces the graphs shown in Figure 5, which agree well with the distribution of the raw data in Fig. 4. This observation allows us to propose that a reasonable approximation of the distribution of a property in a given point in [α, $|\underline{u}_{\mathrm{r}}|$]-space can be obtained as long as the distribution is known and its parameters can be determined. The distribution is chosen in the fitting procedure, and is hence already known, so the remaining task is to determine the parameters.

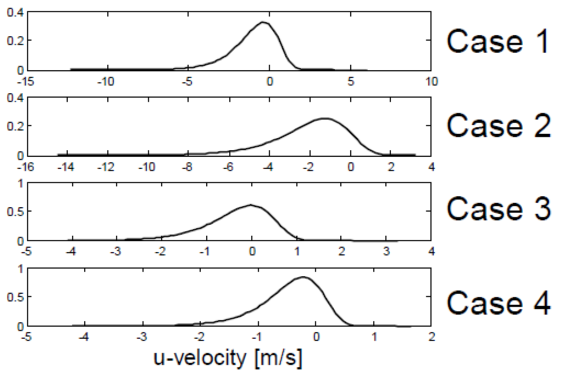

Figure 5. The four probability distribution functions for the u-velocity in the detailed VOF cases fitted to four extreme value distributions

To determine the parameters of each distribution for an arbitrary point in [α, $|\underline{u}_{\mathrm{r}}|$]-space, a linear regression model is fitted to the available data in the four points covered by the detailed VOF simulations. For example, the regression models for the u-velocity distribution become:

$$\xi=\chi_1+\chi_2\alpha+\chi_3|\underline{u}_{\mathrm{r}}| \quad (7)$$

$$\sigma=\chi_4+\chi_5\alpha+\chi_6|\underline{u}_{\mathrm{r}}| \quad (8)$$

In other words, six coefficients (χ_1-χ_6) are fitted in the linear regression and thereafter form the basis for describing how ξ and σ vary in the entire [α, $|\underline{u}_{\mathrm{r}}|$]-space. In this way, the statistical model is able to compute the PDFs and the CDFs for the u-velocity of the fragments formed in the primary atomization in the detailed VOF simulations. Figure 6 illustrates what the CDF from which the u-velocity is sampled looks like for the four detailed VOF cases.

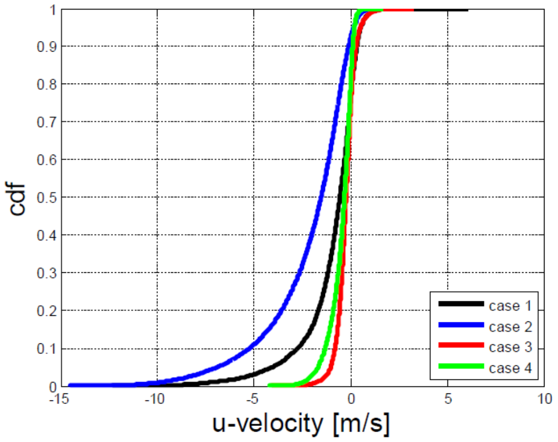

Figure 6. Cumulative distribution functions for the u-velocity of liquid fragments produced in the detailed VOF cases

The process is then repeated for every property (size, position and velocity) that the statistical model needs to predict, and the result is a set of seven different distribution functions with 28 parameters and 84 coefficients, all of which can be obtained from the detailed VOF data via the structure identification algorithm and the fitting procedures.

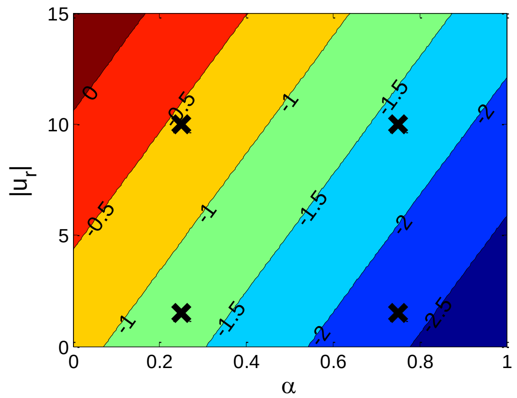

Figure 7. Visualization of the mean expected u-velocity when sampling from the 2-parameter statistical distribution using a 6-coefficient linear regression model (the points for the four detailed VOF cases are illustrated by black crosses)

Visualization of the PDF or CDF for every point in [α, $|\underline{u}_{\mathrm{r}}|$]-space would require four dimensions, so we choose to visualize how the mean of the PDF varies instead (Figure 7). It is important to note that although certain inferences related to the physics of the atomization process seemingly can be made directly from Fig. 7 (related to the relationship between the velocity of the fragments and the volume fraction and relative velocity), certain important features, such as the spread in the distribution – visible in Fig. 6, is not reflected in Fig. 7. We therefore stress the fact that the statistical model always samples LPT properties from the complete CDFs.

Finally, the complete combined VOF-LPT framework is used to simulate Case #2 again (Figure 8), but now on a mesh that contains less than 750,000 cells. The statistical distributions of the LPT parcel properties have been analysed and agree well with those of the detailed VOF simulation. Also the overall characteristics of the spray agree well between the combined VOF-LPT framework and the detailed VOF simulation. These promising results illustrates the potential of the proposed modelling framework to enable simulations of dynamic spray breakup processes in industrial gas-liquid flows at only a fraction of the computational cost of a fully resolved VOF simulation.

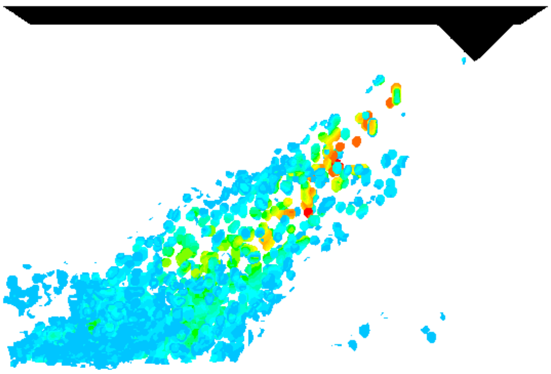

Figure 8. Snapshot from the combined VOF-LPT simulation of Case #2 showing contours of velocity magnitude on iso-surfaces of the LPT parcel concentration

5. SUMMARY

In this work, a coupled VOF-LPT framework is developed to enable numerical simulations of industrial processes involving transient spray breakup processes of two immiscible fluids (either gas-liquid or liquid-liquid). The VOF model is solved together with a two-equation turbulence model in the parts of the domain where the flow is clearly separated. A switching scheme is developed that enables the transfer of mass from the VOF description to the LPT description and vice versa. The switching scheme enables implicit handling of the primary breakup by the VOF formulation via a statistical model, whereas the resulting droplet flow and its secondary breakup are handled by the LPT formulation, thus taking advantage of the respective strengths of the two approaches. A special focus has been to make volume conservation possible on a single computational grid. The switching scheme is based on a statistical model that is constructed via regression modelling using data obtained from highly resolved VOF simulations. All of the steps included in the development and construction of the statistical model are outlined, and examples from a spray simulation in a domain of industrial size are included. The combined VOF-LPT framework outlined here has the potential to serve as a valuable numerical tool in present and future endeavours to predict the macroscopic behaviour in industrial spray breakup processes.

ACKNOWLEDGEMENTS

The computations were partly performed on resources at Chalmers Centre for Computational Science and Engineering (C3SE) provided by the Swedish National Infrastructure for Computing (SNIC).

REFERENCES

[1] Hirt, C. W., and Nichols, B. D., 1981, ”Volume of fluid (VOF) method for the dynamics of free boundaries”, *J Comput Phys*, Vol. 39, pp. 201-225.

[2] Subramaniam, S., 2013, ”Lagrangian-Eulerian methods for multiphase flows”, *Progr Energy Comb Sci*, Vol. 39, pp. 215-245.

[3] Menter, F. R., 1994, ”Two-Equation Eddy-Viscosity Turbulence Models for Engineering Applications”, *AIAA J*, Vol. 32, pp. 1598-1605.

[4] Brackbill, J. U., Kothe, D. B., and Zemach, C., 1992, ”A continuum method for modeling surface tension”, *J Comput Phys*, Vol. 100, pp. 335-354.

[5] Wu, C. L., Nandakumar, N., Berrouk, A. S., and Kruggel-Emden, H., 2011, ”Enforcing mass conservation in DPM-CFD models of dense particulate flows”, *Chem Eng J*, Vol. 174, pp. 475-481.

[6] Morsi, S. A., and Alexander, A. J., 1972, ”An investigation of particle trajectories in two-phase flow systems”, *J Fluid Mech*, Vol. 55, pp. 193-208.

[7] Reitz, R. D., 1987, ”Mechanisms of atomization processes in high-pressure vaporizing sprays”, *Atomization Spray Tech*, Vol. 3, pp. 309-337.

[8] Gosman, A. D., and Ioannides, E., 1983, ”Aspects of computer simulation of liquid-fuelled combustors”, *J Energy*, Vol. 7, pp. 482-490.

[9] Herrmann, M., 2010, ”A parallel Eulerian interface tracking/Lagrangian point particle

multi-scale coupling procedure", *J Comput Phys*, Vol. 229, pp. 745-759.

[10] Vallier, A., 2013, "Simulations of cavitation from the large vapour structures to the small bubble dynamics", *PhD thesis, Lund University, Division of Fluid Mechanics*.

[11] Farzaneh, M., Sasic, S., Almstedt, A.-E., Johnsson, F., and Pallarès, D., 2011, "A novel multigrid technique for Lagrangian modeling of fuel mixing in fluidized beds", *Chem Eng Sci*, Vol. 66, pp. 5628-5637.

[12] Grosshans, H., Szász, R.-Z., and Fuchs, L., 2014, "Development of an efficient statistical volumes of fluid-Lagrangian particle tracking coupling method", *Int J Num Methods Fluids*, Vol. 74, pp. 898-918.

[13] Laín, S., Sommerfeld, M., and Kussin, J., 2002, "Experimental studies and modelling of four-way coupling in particle-laden horizontal channel flow", *Int J Heat Fluid Flow*, Vol. 23, pp. 647-656.

[14] Snider, D. M., 2001, "An incompressible three-dimensional multiphase particle-in-cell model for dense particle flows", *J Comput Phys*, Vol. 170, pp. 523-549.

23Conference on Modelling Fluid Flow (CMFF'15)
The 16th International Conference on Fluid Flow Technologies
Budapest, Hungary, September 1-4, 2015

REVIEW OF NUMERICAL MODELS OF CAVITATING FLOWS WITH THE USE OF THE HOMOGENEOUS APPROACH

Agnieszka NIEDŹWIEDZKA[1], Wojciech SOBIESKI[2]

[1] Corresponding Author. Faculty of Technical Sciences, University of Warmia and Mazury in Olsztyn. ul. M. Oczapowskiego 11, 10-957 Olsztyn, Tel.: +48 89 523-35-63, Fax: +48 89 523-32-55, E-mail: agnieszka.niedzwiedzka@uwm.edu.pl
[2] Faculty of Technical Sciences, University of Warmia and Mazury in Olsztyn. E-mail: wojciech.sobieski@uwm.edu.pl

ABSTRACT

The focus of research works on cavitation has changed since the 1960s; the behaviour of a single bubble is no more the area of interest for most scientists. Its place took the cavitating flow considered as a whole. Many numerical models of cavitating flows came into being within the space of the last fifty years. They can be divided into two groups: multi-fluid and homogeneous (i.e. single-fluid) models. The group of homogenous models contains two subgroups *r*: models based on transport equation and pressure based models. Several works (Senocak and Shyy, Goel and Frikha) tried to order particular approaches and presented short reviews of selected studies. However, these classifications are too rough to be treated as sufficiently accurate. The aim of this paper is presentation of the development paths of numerical investigations of cavitating flows with the use of the homogeneous approach in order of publication year and with relatively detailed description. This review focuses not only on the list of the most significant existing models, but also on presentation their advantages and disadvantages as well as the reasons that inspired us to look for the new ways of numerical predictions of accuracy and dimensions of cavitation. The article includes also the division of source terms of presented models based on the transport equation with the use of standardized symbols that could be directly implemented in the universal udf (i.e. user defined function) located in the appendix. This udf is intended to use in Fluent (ANSYS software).

Keywords: CFD, cavitation, homogeneous approach

NOMENCLATURE

A	$[m^2]$	interfacial area concentration
A_0	$[s]$	oscillation amplitude
C	[-]	model constant
C_μ	[-]	empirical turbulent viscosity constant
$\overleftrightarrow{I}$	[-]	unit tensor
L	$[m]$	length scale
R	$[m]$	bubble radius
R_1	$[J/(mol\cdot K)]$	universal gas constant
T	$[K]$	temperature
T_s	$[K]$	saturation temperature
U	$[m/s]$	velocity magnitude
V	$[m^3]$	volume
Y	[-]	mass fraction
c	$[m/s]$	speed of sound in the mixture
c_{wallis}	$[m/s]$	propagation of acoustic waves without mass transfer
d	$[m]$	body diameter
f	$[Hz]$	oscillation frequency
k	$[m^2/s^2]$	turbulence kinetic energy
k_p	[-]	scaling constant
k_v	[-]	scaling constant
$\dot{m}$	$[\mathrm{kg/m^3 \cdot s}]$	mass source
n_0	$[nuclei/m^3]$	nuclei concentration per unit volume
p	$[Pa]$	local fluid pressure
p_{sat}	$[Pa]$	saturated liquid pressure
$\overleftrightarrow{q}^m$	$[kg/ms^2]$	molecular heat flux
$\overleftrightarrow{q}^R$	$[kg/ms^2]$	turbulent heat flux
r	$[m]$	radius
$\vec{s}_b$	$[\mathrm{N}/m^3]$	source of mass forces
$\vec{s}_e$	$[\mathrm{J}/(m^3/s)]$	source of energy
t	$[s]$	time
t_∞	$[s]$	time scale of free stream value
u	$[m/s]$	velocity
$u_{l,n}$	$[m/s]$	interfacial velocity
$u_{l,n}^{net}$	$[m/s]$	interface velocity relative to local flow field
$u_{v,n}$	$[m/s]$	vapor phase normal velocity
α	[-]	volume fraction
$\bar{\alpha}_{(w,z)}$	[-]	average value of the appearance or disappearance coefficient
ε	$[m^2/s^3]$	dissipation density
μ	$[Pa\cdot s]$	dynamic viscosity

μ_{tm}	$[Pa{\cdot}s]$	the eddy viscosity
ρ	$[kg/m^3]$	density
σ	$[N/m]$	surface tension
$\overleftrightarrow{\tau}^m$	$[kg/ms^2]$	viscous molecular stress tensor
$\overleftrightarrow{\tau}^R$	$[kg/ms^2]$	turbulent Reynolds stress tensor

Subscripts

K	Kubota model
S	Schnerr and Sauer model
d	evaporation term
g	gas
l	liquid
m	mixture
p	condensation term
ref	reference
v	vapor
nuc	nucleation site
∞	free stream value

1. INTRODUCTION

The cavitation history dates back to 1894. The first description of an occurrence of vapour bubbles in water appeared in Reynolds' paper, but it should be emphasized that throughout this document there is no such expression like "cavitation" [1]. Thorneycroft and Barnaby to describe the unknown phaenomenon that was responsible for the wear of the surface of a screw propeller used this expression not until one year later [2]. Twenty-two years went by before Rayleigh published the first mathematical model of cavitation in an incompressible fluid [3]. The awareness of weak points of the first model such neglecting of surface tension and liquid viscosity caused a long scientific discussion that went on sixty years. The finally form of bubble dynamic equation was presented in 1977 by Plesset and Prosperetti [4]. Until today, the well-known form of the mathematical model of bubble dynamic is called until today the Rayleigh-Plesset equation – Eq. (1).

$$R\frac{d^2R}{dt^2}+\frac{3}{2}\left(\frac{dR}{dt}\right)^2=\frac{p_{sat}-p}{\rho_l}-\frac{2\sigma}{\rho_l R}-4\frac{\mu_l}{\rho_l R}\frac{dR}{dt} \qquad (1)$$

The Rayleigh-Plesset equation was the basis for pioneering works in the area of numerical investigations, which covered the analyses of behaviour of a single bubble under the influence of the variable pressure of the surrounding liquid [5]. In the course of time, the focus of research works on cavitation has changed. The place of the analyses of the behaviour of a single bubble took the cavitating flow considered as a whole. All numerical simulations of the cavitating flow, regardless of the used approach (multi-fluid or homogeneous), require to solve the appropriate set of governing equations, that can include mass, momentum or energy equations – Eqs. (2) to (4) [6].

$$\frac{\partial\rho}{\partial t}+div\left(\rho\vec{u}\right)=0 \qquad (2)$$

$$\frac{\partial}{\partial t}\left(\rho\vec{u}\right)+div\left(\rho\vec{u}\otimes\vec{u}\right)=div\left(-p\overleftrightarrow{I}+\overleftrightarrow{\tau}^m+\overleftrightarrow{\tau}^R\right)+\rho\vec{s}_b \qquad (3)$$

$$\begin{aligned}&\frac{\partial}{\partial t}(\rho e)+div\left(\rho e\vec{u}+\rho\vec{u}\right)=\\&div\left[\left(\overleftrightarrow{\tau}^m+\overleftrightarrow{\tau}^R\right)\vec{u}+\overleftrightarrow{q}^m+\overleftrightarrow{q}^R\right]+\rho\vec{s}_e\end{aligned} \qquad (4)$$

In the case of multi-fluid approach, the number of sets of governing equations is dependent on number of considered phases. In the homogeneous approach, one set of governing equations is solved for all phases. One way that enables to take the change of vapour fraction into consideration, is introduction of an additional transport equation – Eq. (5) that in the most of cases bases on the above mentioned Rayleigh-Plesset equation.

$$\frac{\partial\rho_v\alpha_v}{\partial t}+div\left(\rho_v\alpha_v\vec{u}\right)=\Delta\dot{m} \qquad (5)$$

This homogeneous models are called models based on transport equation. The transport equation is expressed in form of mass transfer rates (called source terms) that have different forms for condensation ($\dot{m}^+$), when the local fluid pressure increases above the saturated liquid pressure and evaporation ($\dot{m}^-$), when the local fluid pressure drops below the saturated liquid pressure – Eq. (6).

$$\dot{m}=\begin{cases}\dot{m}^+ & if\ p>p_{sat}\\ \dot{m}^- & if\ p<p_{sat}\end{cases} \qquad (6)$$

Until today several works [7-11] tried to order particular approaches and presented short reviews of selected studies. This review aims to order and make complete all works up to now.

2. THE DEVELOPMENT PATHS OF NUMERICAL INVESTIGATIONS OF CAVITATING FLOWS WITH THE USE OF THE HOMOGENEOUS APPROACH

Kubota proposed the first homogeneous model based on transport equation, which gained the international fame, in 1992 [12]. Until today, many researches [13, 14] use the model as a reference point in their investigations. Kubota formulated the local homogeneous model (*LHM*) equation of motion – Eqs. (7) on the basis of the exact nonlinear Rayleigh-Plesset equation.

$$\begin{aligned}&\left(1+2\pi\Delta r^2 n_0 R\right)R\frac{D^2R}{Dt}+\left(\frac{3}{2}+4\pi\Delta r^2 n_0 R\right)\left(\frac{DR}{Dt}\right)^2+\\&2\pi\Delta r^2\frac{Dn_0}{Dt}R^2\frac{DR}{Dt}=\frac{p_{sat}-p}{\rho_l}\end{aligned} \qquad (7)$$

In the first analyses the initial value of bubble radius R was set to $1 \cdot 10^{-6}$ m. Unfortunately, the nonlinear character of the model led to instability.

Many researches tried to identify the weak points of the Kubota model and suggested their own solutions of the pointed problems. Merkle et al. [12, 15-17] presented in 1998 their own version of source terms – Eqs. (8) and (9). Unlike the source terms proposed by Kubota, their variant does not refer to the bubble radius, but to the change of the liquid density, which is proportional to the dynamic pressure – Eq. (10). The parameter κ has a value between 0.2 and 0.5. Changes of fluid volume caused by changes of its density allow considering the fluid as compressible. Merkle et al. took also the characteristic time scale of fluid motion t_∞ into account, through the formulation of the source terms. The characteristic time scale of fluid motion – Eq. (11) allowed expressing the time necessary to transition from one phase to other in the condensation and evaporation source terms.

$$\dot{m}^{+} = \frac{C_p \rho_l \alpha_v (p - p_{sat})}{(0.5 \rho_l U_\infty^2) t_\infty} \qquad p > p_{sat} \qquad (8)$$

$$\dot{m}^{-} = -\frac{C_d \rho_l \rho_l (1-\alpha_v)(p_{sat} - p)}{(0.5 \rho_l U_\infty^2) \rho_v t_\infty} \qquad p < p_{sat} \qquad (9)$$

$$\Delta p = \frac{\kappa \rho_\infty U_\infty^2}{2} \qquad (10)$$

$$t_\infty = \frac{d}{U_\infty} \qquad (11)$$

Kunz et al. [18-20], in 1999, presented the other solution of source terms – Eqs. (12) and (13). The authors used the approach based on the Ginzburg-Landau potential. Hohenberg and Alperin [21] emphasized usefulness of this theory for dynamic phenomena emphasized in 1977. In the numerical analyses was implemented k–ε turbulence model.

$$\dot{m}^{+} = \frac{C_p \rho_l \alpha_l^2 (1-\alpha_l)}{t_\infty} \qquad p > p_{sat} \qquad (12)$$

$$\dot{m}^{-} = -\frac{C_d \rho_l \alpha_l (p_{sat} - p)}{(0.5 \rho_l U_\infty^2) t_\infty} \qquad p < p_{sat} \qquad (13)$$

In 2001 appeared many transport based cavitation models. Schnerr and Sauer [22] presented the first transport based cavitation model which source terms do not need any empirical constants – Eqs. (14) and (15). The transport equation requires only quantitative values of the physical parameters. The model avoids any non-physical parameter. The value of bubble radius R was set to $3 \cdot 10^{-5}$ m. The source terms – Eqs. (14) and (15) include a part which describes the dynamic of bubble growth. This expression – Eq. (16) is a simplified form of the Rayleigh-Plesset equation which became the base for many subsequent models of transport equation.

$$\dot{m}^{+} = \frac{\rho_v \rho_l}{\rho_m} \alpha_v (1-\alpha_v) \frac{3}{R} \sqrt{\frac{2}{3} \frac{(p - p_{sat})}{\rho_l}} \qquad p > p_{sat} \qquad (14)$$

$$\dot{m}^{-} = -\frac{\rho_v \rho_l}{\rho_m} \alpha_v (1-\alpha_v) \frac{3}{R} \sqrt{\frac{2}{3} \frac{(p_{sat} - p)}{\rho_l}} \qquad (15)$$

$$p < p_{sat}$$

$$\dot{R} = \frac{dR}{dt} = \sqrt{\frac{2}{3} \frac{(p - p_{sat})}{\rho_l}} \qquad (16)$$

Senocack and Shyy [23] suggested coupling of source terms with a pressure-based algorithm. The pressure-based algorithm consists of a pressure-velocity-density coupling scheme that use an upwinded density interpolation. The applied source terms – Eqs. (17) and (18) approximate in form to the source terms presented by Kunz in 1999. The presented model is called Interfacial Dynamics Cavitation Model (IDM). In numerical simulations, the authors applied the k–ε turbulence model.

$$\dot{m}^{+} = \frac{(1-\alpha_l)(p - p_{sat})}{(u_{v,n} - u_{I,n})^2 (\rho_l - \rho_v) t_\infty} \qquad p > p_{sat} \qquad (17)$$

$$\dot{m}^{-} = -\frac{\rho_l \alpha_l (p_{sat} - p)}{\rho_v (u_{v,n} - u_{I,n})^2 (\rho_l - \rho_v) t_\infty} \qquad p < p_{sat} \qquad (18)$$

Iben [24] based the form of the evaporation and condensation rates of his model – Eqs. (19) and (20) on the Rayleigh-Plesset equation. The main feature that distinguish the presented formulation from the above listed source terms is using of the empirical model constant only in the condensation rate. This procedure is aimed at considering the slower tempo of the condensation process. The value of bubble radius R was set to $0.5 \cdot 10^{-5}$ m.

$$\dot{m}^{+} = C_p \rho_v \frac{6\alpha_v}{2R} \sqrt{\frac{2}{3} \frac{(p - p_{sat})}{\rho_l}} \qquad p > p_{sat} \qquad (19)$$

$$\dot{m}^{-} = -\rho_l \frac{6\alpha_v}{2R} \sqrt{\frac{2}{3} \frac{(p_{sat} - p)}{\rho_l}} \qquad p < p_{sat} \qquad (20)$$

In 2002 appeared the first commercial used model called Full Cavitation Model [25] which was formulated by Singhal et al. The form of the defined source terms – Eqs. (21) and (22) is similar to the forms that were presented by Schnerr and Sauer [22] or Iben [24]. All mentioned equations (both condensation and evaporation terms) contain the square root of the quotient, which numerator is the difference between the local pressure and vapor pressure, and denominator is the liquid density. One feature distinguishes the source terms of Singhal model from all solutions of the time: source terms express not only the changes of bubble dimensions (the Rayleigh-Plesset equation as the starting point through formulating of the transport expressions), but also the local turbulent kinetic energy ($\sqrt{k}$), the surface tension (σ = 0.0717 N/m) and the content of noncondensible gases (NCG) in the liquid ($f_g \approx 10$ ppm). The vapour mass fraction is calculated based on Eq. (23). The name of the model – Full Cavitation Model derives from taking into consideration such many factors by formulating of the source terms.

$$\dot{m}^{+} = C_p \frac{\sqrt{k}}{\sigma} \rho_l \rho_l \sqrt{\frac{2}{3}\frac{(p - p_{sat})}{\rho_l}} Y_v \qquad p > p_{sat} \quad (21)$$

$$\dot{m}^{-} = -C_d \frac{\sqrt{k}}{\sigma} \rho_l \rho_v \sqrt{\frac{2}{3}\frac{(p_{sat} - p)}{\rho_l}} \left(1 - Y_v - Y_g\right) \qquad p < p_{sat} \quad (22)$$

$$Y_v = \frac{\alpha_v}{\rho_m} \quad (23)$$

In 2003 appeared also few models of cavitating flow based on transport equation that are worth mentioning and describing. The first of them is Frobenius model [26]. For this model characteristic is the specific form of the source terms – Eqs. (24) and (25), which express no more the change of the liquid mass, but the change of the vapour volume fraction. The change of the vapour volume fraction is calculated based on Eqs. (26), which describes the vapor fraction in the liquid, and Eq. (16), which describes the dynamic of the bubble growth. Frobenius set the value of nuclei concentration n_0 to $1 \cdot 10^8$ nuclei/m^3 and the value of bubble radius R to $30 \cdot 10^{-6}$ m.

$$\frac{d\alpha_v}{dt} = C_p \frac{n_0}{1 + 4/3 n_0 \pi R^3} 4\pi R^2 \sqrt{\frac{2}{3}\frac{(p_{sat} - p)}{\rho_l}} \qquad p < p_{sat} \quad (24)$$

$$\frac{d\alpha_v}{dt} = -C_d \frac{n_0}{1 + 4/3 n_0 \pi R^3} 4\pi R^2 \sqrt{\frac{2}{3}\frac{(p - p_{sat})}{\rho_l}} \qquad p > p_{sat} \quad (25)$$

$$\frac{d\alpha_v}{dt} = \frac{n_0}{1 + 4/3 n_0 \pi R^3} \cdot \frac{d}{dt}\left(\frac{4}{3}\pi R^3\right) \quad (26)$$

The next model that appeared in 2003 was Saito one [27]. A new variable A, expressing the interfacial area concentration in the vapour-liquid mixture – Eq. (27) is characteristic in this model For both mass transfer rates – Eqs. (28) and (29). The authors do not give the answer about the values of the model constants used. The only tip is a mutual relationship between all constant expressed in Eq. (30). The value of empirical model constant C was set in the numerical simulations of Saito et al. [27] to 0.1 m^{-1}.

$$A = C_a \alpha_v (1 - \alpha_v) \quad (27)$$

$$\dot{m}^{+} = C_p A \alpha_v (1 - \alpha_v) \frac{(p - p_{sat})}{\sqrt{2\pi R_1 T_S}} \qquad p > p_{sat} \quad (28)$$

$$\dot{m}^{-} = -C_d A \alpha_v (1 - \alpha_v) \left(\frac{\rho_l}{\rho_v}\right) \frac{(p_{sat} - p)}{\sqrt{2\pi R_1 T_S}} \qquad p < p_{sat} \quad (29)$$

$$C = C_p C_a = C_d C_a \quad (30)$$

The source terms of the model proposed by Zwart et al. in 2004 [28] – Eqs. (31) and (32) have a similar form as in Iben model – Eqs. (17) and (18), but the vapor volume fraction α_v in the condensation rate was replaced by the product of the nucleation site of volume fraction α_{nuc} and the remaining fluid volume fraction $(1\text{-}\alpha_v)$. Zwart et al. use the standard k–ε model with modified expression for the eddy viscosity – Eq. (33). The mixture density from the original expression was replaced with the density function described in Eq. (34). The value of the bubble radius R, just as in Kubota model, was set to $1 \cdot 10^{-6}$ m and the value of the nucleation site of volume fraction α_{nuc} to $5 \cdot 10^{-4}$ [28].

$$\dot{m}^{+} = C_p \frac{3\alpha_v \rho_v}{R} \sqrt{\frac{2}{3}\frac{(p - p_{sat})}{\rho_l}} \qquad p > p_{sat} \quad (31)$$

$$\dot{m}^{-} = -C_d \frac{3\rho_v (1 - \alpha_v)\alpha_{nuc}}{R} \sqrt{\frac{2}{3}\frac{(p_{sat} - p)}{\rho_l}} \qquad p < p_{sat} \quad (32)$$

$$\mu_{tm} = f(\rho) C_\mu \frac{k^2}{\varepsilon} \quad (33)$$

$$f(\rho) = \rho_v + \left(\frac{p_v - \rho_m}{p_v - \rho_l}\right)^n (p_l - \rho_v) \quad (34)$$

The starting point in the development of a new transport equation for Wu et al. [29] was the model proposed by Senocack and Shyy [17] in 2001.– Eqs. (15) and (16). Wu et al. estimated the interfacial velocity by applying an approximate procedure. Additionally, they used correlations between the net interface velocity – $u_{I,n}^{net}$ and the mass transfer $\Delta\dot{m}$ – Eq. (35) and correlation between the net interface velocity $u_{I,n}^{net}$ and the flow field local velocity $u_{I,n}^{Local}$ – Eq. (36) to achieve the final form of their form of mass transfer rates – Eqs. (37) and (38). The value of the flow field local velocity $u_{I,n}^{Local}$ is equal the value of the vapor phase normal velocity $u_{v,n}$.

$$u_{I,n}^{net} A = \Delta \dot{m} \tag{35}$$

$$\left(u_{v,n} - u_{I,n}\right)^2 = \left[u_{v,n} - \left(u_{I,n}^{net} + u_{I,n}^{Local}\right)\right]^2 = u_{I,n}^{net2} \tag{36}$$

$$\dot{m}^+ = \frac{(1-\alpha_l)(p - p_{sat})}{\left(u_{I,n}^{net}\right)^2 (\rho_l - \rho_v) t_\infty} \qquad p > p_{sat} \tag{37}$$

$$\dot{m}^- = -\frac{\rho_l \alpha_l (p_{sat} - p)}{\rho_v \left(u_{I,n}^{net}\right)^2 (\rho_l - \rho_v) t_\infty} \qquad p < p_{sat} \tag{38}$$

In 2006 Merkle et al. [30 and 31] presented a new homogeneous model which mass transfer rates are defined in Eqs. (39) and (40). The form is distinguished from the all above mentioned models through appearance of two scaling constants k_v, k_l and k_p – an as small as possible factor. The values were set in numerical calculations [31] as follow: $k_v = 100.0$, $k_v / k_l = 15.0$ and $k_p = 0.02$.

$$\dot{m}^+ = k_l \frac{\rho_v \alpha_l}{t_\infty} \left(\frac{p - p_{sat}}{k_p p_v}\right) \qquad p > p_{sat} \tag{39}$$

$$\dot{m}^- = -k_v \frac{\rho_v \alpha_l}{t_\infty} \left(\frac{p_{sat} - p}{k_p p_v}\right) \qquad p < p_{sat} \tag{40}$$

Sobieski [32] presented the condensation and evaporation rates – Eqs. (41) and (42) as distinct from all above mentioned works through applying of the oscillation equation. This approach is connected with periodic character of cavitation.

$$\dot{m}^+ = \overline{\alpha}_{(w,z)} C \left(1 + A_0 \sin(ft)(p - p_{sat}) \frac{u^2}{2} f(Y_g)\right) \qquad p > p_{sat} \tag{41}$$

$$\dot{m}^- = -\overline{\alpha}_{(w,z)} C \left(1 + A_0 \sin(ft)(p_{sat} - p) \frac{u^2}{2} f(Y_g)\right) \qquad p < p_{sat} \tag{42}$$

Sobieski [32] additionally inserted a function relating mass source intensity to the mass fraction of gas – Eq. (43) in the transport equation.

$$f(Y_g) = \begin{cases} \sqrt{Y_g^{\lim it} Y_g} & \rightarrow Y_g \le Y_g^{\lim it} \\ Y_g^{\lim it} & \rightarrow Y_g \ge Y_g^{\lim it} \end{cases} \tag{43}$$

Dauby et al. [33] presented a really simple form of transport equation – Eqs. (44) and (45) which consists only of empirical coefficient C_p and C_d, liquid volume fraction α_l and pressure difference.

$$\dot{m}^+ = C_p (1 - \alpha_l)(p - p_{sat}) \qquad p > p_{sat} \tag{44}$$

$$\dot{m}^- = -C_d \alpha_l (p_{sat} - p) \qquad p < p_{sat} \tag{45}$$

Since 2011 researches have been looking for new ways to solve the problem of an insufficient capability of cavitation prediction. Their research area are no more only equations of bubble dynamic or well-known physical relationships between vapour and liquid fraction in fluid. Scientists wish to find the solution of problems with prediction of cavitation through connecting this phenomenon with e. g. the propagation of acoustic waves or complex mathematical formulae.

Huang and Wang [34] in 2011 described a new innovative solution of mass transfer rates – Eqs. (46) and (47).

$$\dot{m}^+ = \chi(\rho_m / \rho_l) \dot{m}_K^+ + (1 - \chi(\rho_m / \rho_l)) \dot{m}_S^+ \qquad p > p_{sat} \tag{46}$$

$$\dot{m}^- = \chi(\rho_m / \rho_l) \dot{m}_K^- + (1 - \chi(\rho_m / \rho_l)) \dot{m}_S^- \qquad p < p_{sat} \tag{47}$$

Their approach to formulate the transport equation consists of using of a blending function $\chi(\rho_m/\rho_l)$ – Eq. (48).

$$\chi\left(\frac{\rho_m}{\rho_l}\right) = 0.5 + \frac{\tanh\left[\dfrac{C_1\left(\dfrac{0.6\rho_m}{\rho_l} - C_2\right)}{0.2(1 - 2C_2) + C_2}\right]}{[2\tanh(C_1)]} \tag{48}$$

The authors additionally combined the blending function with the expressions of source terms of Kubota $\dot{m}_k^-$, $\dot{m}_k^+$ [13] and Schnerr and Sauer $\dot{m}_S^-$, $\dot{m}_S^+$ [22]. The values of the model constants C_1 and C_2 are set to 4 and 0.2.

Goncalves [35] presented in 2014 the first version of transport equation which form includes two quantities not used before: the speed of sound c and the propagation of acoustic waves without mass transfer c_{wallis} – Eq. (49).

$$\frac{1}{\rho c_{wallis}^2} = \frac{\alpha}{\rho_v c_v^2} + \frac{1 - \alpha}{\rho_l c_l^2} \tag{49}$$

The use of correlation between the sound speed and the thermodynamic equilibrium was a good idea, but the proposed form of transport equation required the introduction of changes. In 2014 Goncalves and Charrière [11] showed the modified version of mass transfer – Eqs. (50) and (51).

$$\dot{m}^+ = C_p \frac{\rho_v}{\rho_l} \alpha_l \frac{(p - p_{sat})}{0.5 \rho_{ref} u_{fer}^2} \qquad p > p_{sat} \tag{50}$$

$$\dot{m}^- = \frac{\rho_l \rho_v}{\rho_l - \rho_v}\left(1 - \frac{c^2}{c_{wallis}^2}\right) div\bar{u} \qquad p < p_{sat} \qquad (51)$$

In 2015 the scientists came back to the Rayleigh-Plesset equation (Eq. 16) and tried to formulate a new equation which on the one hand describes the bubble dynamic with more precision and on the other hand hasn't any negative influence on the calculations stability. The team of Russian researches [36] emphasized the relationship between the bubble radius and the Reynolds number, what bears fruit in a new form of the dynamic component of transport equation (Eq. 52)

$$\frac{dR}{dt} = \sqrt{\frac{2}{3}} tgh\left(1.221\left(\frac{R_0\sqrt{\Delta p \cdot \rho}}{4\mu}\right)^{0.35}\right)\sqrt{\frac{2}{3}\frac{(p_{sat} - p)}{\rho_l}} \quad (52)$$

Konstantinov et al. [36] combined the new dynamic component with the static component from the mass transfer rates proposed by Zwart et al. [28] and achieved new source terms (Eqs. 53 and 54).

$$\dot{m}^+ = C_p \frac{3\alpha_v \rho_v}{R} \cdot \sqrt{\frac{2}{3}} tgh\left(1.221\left(\frac{R_0\sqrt{\Delta p \cdot \rho}}{4\mu}\right)^{0.35}\right) \cdot \sqrt{\frac{2}{3}\frac{(p_{sat} - p)}{\rho_l}} \qquad p > p_{sat} \qquad (53)$$

$$\dot{m}^- = -C_d \frac{3\rho_v(1-\alpha_v)\alpha_{nuc}}{R} \cdot \sqrt{\frac{2}{3}} tgh \left(1.221\left(\frac{R_0\sqrt{\Delta p \cdot \rho}}{4\mu}\right)^{0.35}\right) \cdot \sqrt{\frac{2}{3}\frac{(p_{sat} - p)}{\rho_l}} \qquad p < p_{sat} \qquad (54)$$

5. SUMMARY

This article presents an exhaustive overview of the homogeneous models of cavitating flows since 1992 until today. The focus of research works has changed since 1960s, but the aim is still the same – the correct prediction of cavitation occurrence. The main starting point for the transport based homogeneous models was the Rayleigh-Plesset equation, which considers the dynamic of a single bubble. The actual research ways to predict the behaviour of the whole cavitating flow go far beyond the basic equation. They consider e. g. the influence of the sound speed or introduce a blending function in transport equation. The descriptions of each model accompany essential equations and values of quantities used by the authors in their calculations. A possibility to implementation of transport based homogeneous models has Fluent – ANSYS software. The users should pay attention, that the tool to udf implementation has changed. It is no more macro DEFINE CAVITATION RATE but DEFINE MASS TRANSFER, what results in the way to make the udf. The appendix contains an example udf for simulating of cavitating flows and the table of empirical coefficients used in the chosen transport equation based cavitation models. It should be emphasized that the value of empirical coefficient can change for specific terms and the nuclei concentration n_0 and the initial bubble radius R are also no fixed values, but depend on many conditions.

APPENDICES

Table 1. List of empirical coefficient used in the chosen transport equation based cavitation models.

Lp.	Name of the first author	C_{prod}	C_{dest}
1.	Kubota (1992)	50	0.01
2.	Merkle (1998)	1	80
3.	Kunz (1999)	0.2	0.2
4.	Iben (2000)	>1	>1
5.	Schnerr and Sauer (2001)	-	-
6.	Senocack and Shyy (2001)	X	X
7.	Singhal (2002)	0.02	0.01
8.	Frobenius (2003)	50	0.02
10.	Saito (2003)	X	X
9.	Zwart (2004)	50	0.01
11.	Wu (2005)	-	-
12.	Merkle (2006)	-	-
13.	Sobieski (2006)	-	-
14.	Dauby (2007)	1	80
15.	Huang and Wang (2011)	-	-
16.	Goncalves (2014)	-	X
17.	Konstantinov (2015)	50	0.01

X – no sufficient data

UDF DEFINE MASS TRANSFER

```
#include "udf.h"
DEFINE_MASS_TRANSFER(test,cell,thread,from_index,from_species_index,to_index,to_species_index)

{
Thread *gas = THREAD_SUB_THREAD(thread, from_index);
Thread *liq = THREAD_SUB_THREAD(thread, to_index);

real f_l;          /*liquid mass fraction [-]*/
real f_v;          /*vapour mass fraction [-]*/
real p_vapor;      /*saturated pressure [Pa]*/
real p_m;          /*mixture pressure [Pa]*/
real ro_l;         /*liquid density [kg/m^3]*/
real ro_m;         /*mixture density [kg/m^3]*/
real k_m;          /*kinetic energy*[m^2/s^2]/
real ro_v;         /*vapour density [kg/m^3]*/
real void_l        /*liquid volume fraction [-]*/
real void_v        /*vapour volume fraction [-]*/
```

```
real f_g;            /*gas mass fraction [-]*/
real dp;             /*pressure difference [Pa]*/
real T_l;            /*liquid temperature [K]*/
real T_v;            /*vapour temperature [K]*/
real T_SAT;          /*saturation temperature [K]*/
real source;         /*vapour mass source*/
real sigma;          /*surface tension [N/m]*/
real Ce;             /*evaporation constant [-]*/
real Cc;             /*condensation constant [-]*/

p_m = ABS_P(C_P(cell,thread),op_pres);
ro_m = C_R(cell,thread);
ro_v = C_R(cell,gas);
ro_l = C_R(cell,liq);
void_l = C_VOF(cell,liq);
void_v = C_VOF(cell,gas);
f_v = void_v*ro_v/ro_m;
f_l = 1.0 - f_v - f_g;
T_l = C_T(cell, liq);
T_v = C_T(cell, gas);
T_SAT = 373.15;
source = 0.0;
sigma = 0.073;
f_g = 1.5e-05;
k_m = C_K(cell,thread);
Ce = 0.02;
Cc = 0.01;

if ( T_l >= T_SAT)
   { /* Evaporating */
source = -Ce*sqrt(k_m)*ro_l*ro_v/sigma*
((2*(p_vapor-p_m)/3/ro_l)*(1/2))*(1-f_v-f_g);
   }
else if (T_v < T_SAT)
 { /* Condensing */
   source = Cc*sqrt(k_m)*ro_l*ro_l/sigma*
((2*(p_vapor-p_m)/3/ro_l)*(1/2))*f_v;
   }
  return (source);
   }
```

REFERENCES

[1] Reynolds, O., 1894, “Experiments Showing the Boiling of Water in an Open Tube at Ordinary Temperatures”, *Scientific Papers on Mechanical and Physical Subject*, Vol. II, Cambridge University Press, Cambridge, 1900-1903, pp. 578-587.

[2] Thorneycroft, J., and Barnaby, S. W., 1895, “Torpedo-Boat Destroyers”, *Institution of Civil Engineers*, Vol. 122, pp. 51-55.

[3] Rayleigh, L., 1917, “On the Pressure Developed in a Liquid during the Collapse of a Spherical Cavity”, *Philosophical Magazine*, Vol. 34, pp. 94-98.

[4] Plesset, M. S., and Prosperetti, A., 1977, “Bubble Dynamics and Cavitation”, Annual Review of Fluids Mechanics, Vol. 9, pp. 145-185.

[5] Ivany, R. D., and Hammit, F. G., 1965, “Cavitation Bubble Collapse in Viscous Compressible Liquids – Numerical Analysis”, *Journal of Basic Engineering*, Vol. 87, pp. 977-985.

[6] Sobieski, W., 2011, “The Basic Equations of Fluid Mechanics in FormFcharacteristic of the Finite Volume Method”, *Technical Sciences*, Vol. 14, pp. 299-313.

[7] Senocack, I., and Shyy, W., 2001, “Numerical Simulation of Turbulent Flows with Sheet Cavitation”, Proc. *4th International Symposium on Cavitation (CAV2001)*, Pasadena, USA.

[8] Žnidarčič, A., Mettin, R., and Dular, M., 2015, “Modelling Cavitation in a Rapidly Changing Pressure Field – Apllication to a Small Ultrasonic Horn”, *Ultrasonic Sonochemistry*, Vol. 22, pp. 482-492.

[9] Frikha S., Coutier-Delgosha, O., and Astolfi, J. A., 2008, “Influence of the Cavitation Model on the Simulation of Cloud Cavitation on 2D Foil Section”, *International Journal of Rotating Maschinery*, Vol. 2008, 12 pages.

[10] Goel, T., Thakur, S., Haftka, R., Shyy, W., and Zhao, J., 2008, “Surrogate Model-Based Strategy for Cryogenic Cavitation Model Validation and Sensitivity Evaluation”, *International Journal for Numerical Methods in Fluids*, Vol. 58, pp. 969-1007.

[11] Goncalves, E., Charrière, B., 2014, “Modeling for Isothermal Cavitation with a Four-Equation Model”, *International Journal of Multiphase Flow*, Vol. 59, pp. 54-72.

[12] Kubota, A., Kato, H., and Yamaguchi, H., 1992, “A New Modeling of Cavitating Flows: a Numerical Study of Unsteady Cavitation on a Hydrofoil Section”, *Journal of Fluid Mechanics*, Vol. 240, pp. 59-96.

[13] Ducoin, A., Huang, B. and Young, Y. L., 2012, “Numerical modeling of unsteady cavitating flows around a stationery hydrofoil”, *International Journal of Rotating Maschinery*, Vol. 2012.

[14] Shi, S., Wang, G., and Hu, Ch., 2014, “A Rayleigh-Plesset Based Transport Model for Cryogenic Fluid Cavitating Flow Computations”, *Science China Physics, Mechanics and Astronomy*, Vol. 57, pp. 764-773.

[15] Hejranfar, K., and Hesary, K. F., 2009, “Assessment of a Central Difference Finite Volume Scheme for Modeling of Cavitating Flows Using Preconditioned Multiphase Euler

Equation", Proc. *7th International Symposium on Cavitation (CAV2009)*, Ann Arbor, USA.

[16]Huang, B., Ducoin, A., and Young, Y. L., 2013, "Physical and Numerical Investigation of Cavitating Flows Around a Pitching Hydrofoil", *Physics of Fluids*, Vol. 25.

[17]Merkle, C. L., Feng, J., and Buelow, P. E. O., 1998, "Computational Modeling of the Dynamics of Sheet Cavitations", Proc. *3rd International Symposium on Cavitation*, Grenoble, France.

[18]Kunz, R. F., Boger, D. A., Chyczewski, T. S., Stinebring, D. R., and GibelingH. J., 1999, "Multi-phase CFD Analysis of Natural and Ventilated Cavitation about Submerged Bodies", Proc. *FEDSM*, Vol. 99.

[19]Morgut, M. and Nobile, E., 2012, "Numerical predictions of cavitating flow around model scale propellers by CFD and advanced model calibration", *International Journal of Rotating Machinery*, Vol. 2012.

[20]Morgut, M., Nobile, E., and Biluš, I., 2011, "Comparison of Mass Transfer Model for the Numerical Prediction of Sheet Cavitation around a Hydrofoil", *International Journal of Multiphase Flow*, Vol. 37, pp. 620-626.

[21]Hohenberg, P. C., and Halperin, B. I., 1977, "Theory of Dynamic Critical Phenomena," *Reviews of Modern Physics*, Vol. 49, pp. 435-479.

[22]Schnerr, G. H., and Sauer, J., 2001, "Physical and Numerical Modeling of Unsteady Cavitation Dynamics", Proc. *4th International Conference on Multiphase Flow (ICMF'01)*, New Orleans, USA.

[23] Senocak, I., and Shyy, W., 2001, "Numerical simulation of turbulent flows with sheet cavitation", Proc. *4th International Symposium on Cavitation (CAV2001)*, Pasadena, USA.

[24]Iben, U., 2002, "Modeling of Cavitation", *Systems Analysis Modeling Simulations*, Vol. 42, pp. 1283-1307.

[25]Singhal, A. K., Athavale, M. M., Li, H., and Jiang, Y., 2002, "Mathematical Basis and Validation of the Full cavitation Model", *Journal of Fluids Engineering*, Vol. 124, pp. 617-624.

[26]Frobenius, M., Schilling, R., Bachert, R., Stoffel, B., and Ludwig, G., 2003, "Three-Dimensional, Unsteady Cavitation Effects on a Single Hydrofoil and in a Radial Pump – Measurements and Numerical Simulations, Part Two: Numerical Simulation", Proc. *5th International Symposium on Cavitation (CAV2003)*, Osaka, Japan.

[27]Saito, Y., Nakamori, I., and Ikohagi, T., 2003, "Numerical Analysis of Unsteady Vaporous Cavitating Flow around a Hydrofoil", Proc. *5th International Symposium on Cavitation (CAV2003)*, Osaka, Japan.

[28] Zwart, P. J., Gerber, G., and Belamri, T., 2004, „A Two-Phase Flow Model for Prediction Cavitation Dynamics." Proc. *ICMF 2004 International Conference on Multiphase Flow*, Yokohama, Japan.

[29] Wu, J., Wang, G., and Shyy, W., 2005, "Time-Dependent Turbulent Cavitating Flow Computations with Interfacial Transport and Filter-Based Models", *International Journal for Numerical Methods in Fluids*, Vol. 49, pp. 739-761.

[30] Merkle, C. L., Li, D., and Venkateswaran, S., 2006, "Multi-Disciplinary Computational Analysis in Propulsion", *AIAA Journal*, Paper 4575.

[31]Park, W.; Ha, C.; Merkle, C. L., 2009, „Multiphase Flow Analysis of Cylinder Using a New Cavitation Model", Proc. *7th International Symposium on Cavitation (CAV2009)*, Ann Arbor, USA.

[32]Sobieski, W., 2006, "Mass Exchange Model in Flows with Cavitation", *Task Quarterly*, Vol. 10, pp. 401-416.

[33]Dauby, D., Leroyer, A., and Vissonneau, M., 2007, "Computation of 2D Cavitating Flows and Tip-Vortex Flows with an Unstructured Ranse Solver".

[34]Huang, B., and Wang, G. Y., 2011, "A Modified Density Based Cavitation Model for Time Dependent Turbulent Cavitating Flow Computations", *Chinese Science Bulletin*, Vol. 56, pp. 1985-1992.

[35]Goncalves, E., 2013, "Numerical Study of Expansion Tube Problems: Towards the Simulation of Cavitation", *Computer & Fluids*, Vol. 72, pp. 1-19.

[36]Konstantinov, S. Y., Tselischev, D. V., and Tselischev, V. A., 2015, "Numerical Cavitation Model for Simulation of Mass Flow Stabilization Effect in ANSYS CFX", *Modern Applied Sciences*, Vol. 9, pp. 21-31.

Conference on Modelling Fluid Flow (CMFF'15)
The 16th International Conference on Fluid Flow Technologies
Budapest, Hungary, September 1-4, 2015

FLOW STRUCTURE OF RECIRCULATION ZONE BEHIND BACKWARD FACING STEP IN A NARROW CHANNEL

Václav URUBA

Corresponding Author. Department of Fluid Mechanics, Institute of Thermomechanics Academy of Sciences of the Czech Republic, Dolejškova 5, 182 00 Praha, Czech Republic. Tel.: +420 266 053 414, Fax: +420 286 584 695, E-mail: uruba@it.cas.cz

ABSTRACT

Structure of the flow-field behind a backward-facing step in a narrow channel is studied experimentally using time-resolved PIV technique. The channel width is 4 step heights, Reynolds number based on the step height was about 12 thousands. The flow-field behind the step is strongly dynamical in nature. Instability of the free shear layer of Kelvin-Helmholtz (K–H) type is studied in details using simple averaging, Proper Orthogonal Decomposition (POD), and Oscillation Pattern Decomposition (OPD) methods. Typical time-mean as well as dynamical structures are to be presented being in the form of systems of vortex trains.

Keywords: Backward facing step, Channel flow, Kelvin-Helmholtz instability, Narrow channel, Oscillation Pattern Decomposition, Proper Orthogonal Decomposition, Time-resolved PIV.

NOMENCLATURE

e	[-]	base of natural logarithm
f	[1/s]	frequency
h	[m]	step height
p	[-]	periodicity
Re	[-]	Reynolds number
r_{uv}	[-]	correlation coefficient
s	[m]	spacing
Sr	[-]	Strouhal number
T	[s]	period
τ_e	[s]	e-folding time
$\underline{U_{in}}$	[m/s]	input velocity
U,V	[m/s]	mean velocity components
v	[m/s]	speed of structures

Subscripts and Superscripts

i	number of mode
x, y, z	Cartesian coordinates

1. INTRODUCTION

The flow behind a backward facing step is one of canonical cases, generating highly dynamical flow field, including backflow regions. To study such type of flow case, which is characterized by spatio-temporal dynamics, proper methods have to be used. Currently, measurement data from advanced methods, as time-resolved PIV, are available. The measured time-resolved data set inherently contains a large quantity of useful information, and adequate methods of analysis are necessary to extract it in a form useable for further conclusions and use in follow-up engineering calculations, e.g. aeroelasticity and aeroacoustics. Unfortunately, classical statistical approach is not sufficient for the job. Therefore, more sophisticated alternative processing methods are required.

Two advanced processing methods (POD and OPD), are to be used for evaluation of the given case.

The Kelvin–Helmholtz (K-H) instability can occur in presence of a free shear layer. Such flow is generated in the low-field forming behind the backward-facing step. The flow over the backward facing step is considered to be 2D in sense of statistical characteristics as a rule, meaning that the ratio of the step height and channel width is very high. In our case we have a narrow channel meaning that the channel with is 4 step heights only.

2. EXPERIMENTAL SETUP

The blow-down facility has been used for the experiments. The wind tunnel had rectangular cross-section with filled corners within the contraction (to suppress corner vortices), honeycomb, and a system of damping screens followed by contraction with contraction ratio 16. The area of the test section input was 0.25 m high and 0.1 m wide. The time mean velocity differed from homogeneity in planes perpendicular to the tunnel axis in the order of tenths of percent. The channel downstream the backward facing step was 1 m long. The step was placed close to the channel inlet.

In the channel inlet, the boundary layer thickness on the walls in the step position was about 3 mm, the step height was h = 25 mm. Velocity in the inlet on the step was U_{in} = 7.5 m/s and natural turbulence level was about 0.1 % in the working section input. The Reynolds number defined using the step height was Re = 12 400. All presented dimensions are related to the step height h and velocities to the inlet velocity U_{in}.

Schematic view of the experimental setup and measurement areas is given in Figure 1.

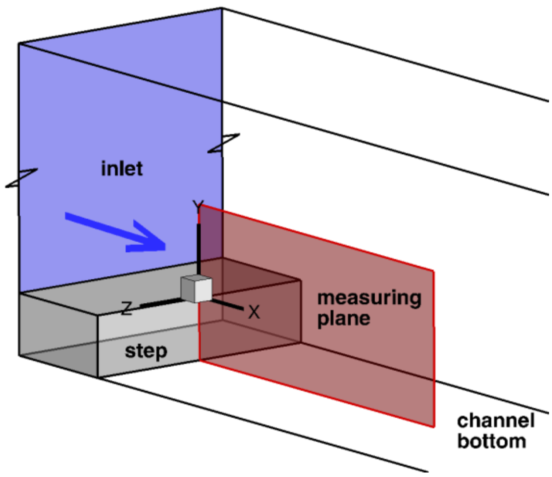

Figure 1. Experimental setup

The Time-Resolved PIV measurement method was used in the experiments. Measuring system Dantec Dynamics used a double-pulse laser New Wave Pegasus Nd:YLF @ 525 nm, maximum double-pulse frequency was 10 kHz, pulse energy 2 x 10 mJ @ 1 kHz (average laser power 10 W per head), with standard Dantec light sheet optics Series 80. Fast CMOS camera Phantom V611 had maximum resolution 1280 x 800 pixels and full-resolution frame rate 6 000 fps (corresponding to maximum measurement frequency 3 000 double snaps per second). SAFEX fog generator has been used for seeding. Standard-issue Dantec Dynamics software DynamicStudio (DS) Version 4.1 was used for all measurement evaluations. The presented experiments were intended to cover low-frequency dynamics and offering good statistics. For all measurements, the acquisition frequency 1 kHz and record length 5 000 double-snaps in sequence has been used. This corresponded to record length of 5 seconds. According to Nyquist theorem, such frequency and record length allowed for dynamical analysis of frequencies up to 500 Hz.

More details on measurement set-up are given in references [3] and [4].

3. METHODS OF ANALYSIS

The time resolved PIV method provides time evolution of instantaneous velocity fields within the measuring plane, i.e. spatio-temporal data.

The mean velocity field has been evaluated first to obtain the flow statistics and remove the mean. Evaluation of first and second order statistics (mean and variance or covariance) is a classical approach to evaluation of turbulent data.

The two approaches to flow-field dynamics analysis are to be applied on the obtained data: Proper Orthogonal Decomposition (POD) and Oscillation Pattern Decomposition (OPD).

The POD method has been widely used in studies of turbulence. Historically, it was introduced in the context of turbulence by Lumley [2] as an objective definition of what was previously called big eddies, and which is now widely known as “coherent structures”.

Extraction of deterministic (non-random) features from a random, fine grained turbulent flow, is a challenging problem. The POD provides an unbiased technique for identifying such structures. The mathematical background of POD is sufficiently described in [8].

Results of POD are represented by spatial “POD modes”, which depict patterns of flow field, carrying maximum turbulent kinetic energy.

The extension of POD method is Bi-Orthogonal Decomposition (BOD). While POD analyses data in spatial domain only, BOD performs spatiotemporal decomposition. As a result, if BOD is calculated from time-resolved data, both spatial (topos) and temporal (chronos) modes can be evaluated. Each chronos represents evolution of given mode amplitude in time, its topology is defined by the corresponding topos.

The second approach to spaciotemporal data analysis used in the presented study is the OPD method, which is described in details in [7] and [8].

The OPD method evaluates the basis representing oscillating modes of the extended dynamical system. Each OPD mode is characterized by a single frequency f and damping representing underlying cyclostationary elementary processes involved in the phenomenon notwithstanding that hidden. Damping is quantified using the e-folding time τ_e representing the time delay of reducing the mode amplitude by e. The topology of a given OPD mode is defined by complex maps (real and imaginary parts). OPD modes nature is typically a wave or travelling structures propagating in space, or pulsating pattern represented by complex vector field.

Historically, OPD predecessor methods were introduced in climatology to model temporal and spatial evolution of meteorological data. These methods are called Principal Interaction Patterns (PIP) and Principal Oscillation Patterns (POPs) – see [1].

The stability concept used in rating of the OPD modes is based on evaluation of tendency of a given pattern appearing in the flow-field. It evaluates the flow-field ability to transfer energy into or from the pattern. Lyapunov stability concept suggests exponential time-evolution of a pattern magnitude resulting in exponential growth to infinity of exponential decay to zero.

More details on the OPD method could be find e.g. in [1, 7, 8].

In general all OPD modes should be more or less damped (e-folding time is positive) in statistical sense described above. The growing feature (negative e-folding time) cannot be observed if statistics is performed properly.

4. RESULTS

The velocity distribution in the measuring plane (plane of symmetry) time evolution is subjected to detailed analysis.

4.1. Raw Data

Flow field behind the step strongly fluctuates. To demonstrate the data dynamics, an example of few randomly selected snapshots are shown in Figure 2. The color denotes vorticity, blue is negative (clockwise) and red is positive. Streamlines are added arbitrarily, to clarify the instantaneous flow field structure.

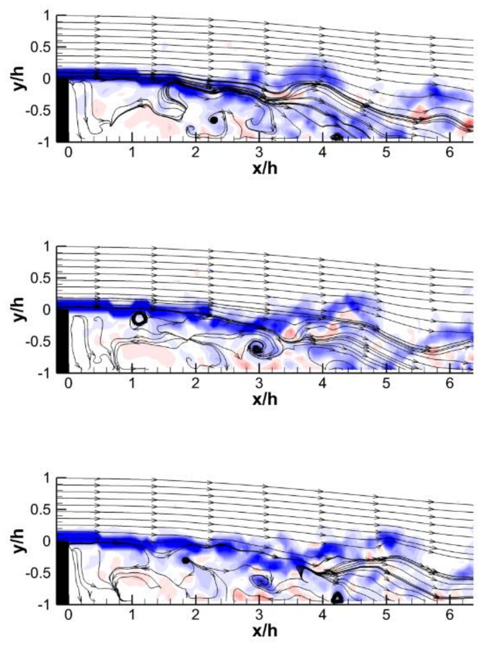

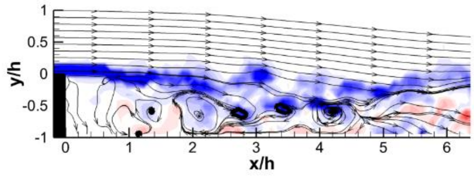

Figure 2. Snapshots of vorticity distribution

Vorticity distributions in Fig. 2 show free shear layer with negative (clockwise) vorticity. Behind the step, within the so called zone of recirculation, presence of large amount of small vortical structures is visible, with both positive and negative orientations. The topology of this zone is very complex and dynamical in nature. Such behavior is typical for strongly turbulent flow.

4.2. Statistical Analysis

In Figure 3, the distribution of mean vorticity is shown, representing mean velocity field of 5 000 snapshots (compare with instantaneous snapshots in Fig. 2).

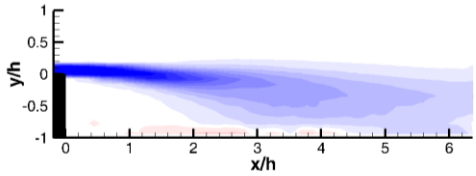

Figure 3. Mean vorticity field

Negative vorticity within the free shear layer is visible in Fig. 3, however, the fine-grained dynamical structure of the recirculation zone (see Fig. 2) has been lost.

Mean velocity vector field is shown in Figure 4, together with vectorlines. The recirculating zone is clearly visible with the vortex center located in position [2.8; -0.5], creating back flow close to the channel bottom. Small secondary vortex with opposite orientation (anticlockwise) appears in [0.4; 0.9] position. Please note that this time-mean picture never exists in the instantaneous level, in any particular time moment.

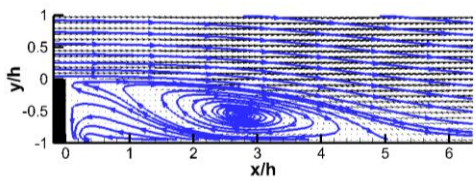

Figure 4. Mean velocity field vectorlines

The generally accepted definition of backflow region is based on presence of negative value of streamwise (x-direction) mean velocity component

U. The back-flow region is clearly visible in Figure 5, where only mean streamwise velocity component is plotted. Back-flow region of negative streamwise velocity is depicted in blue.

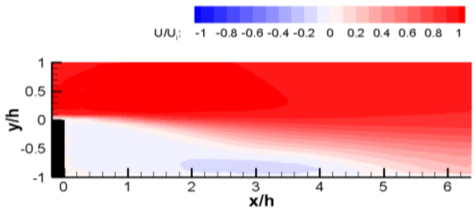

Figure 5. Streamwise mean velocity component distribution

The vertical spanwise (*y*-direction) mean velocity component *V* distribution in Figure 6 indicates falling (negative) region in blue and rising (positive) in red.

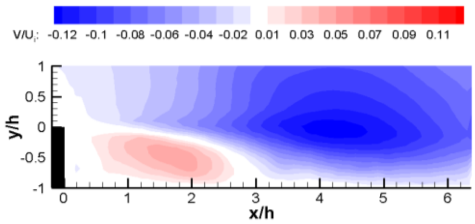

Figure 6. Spanwise mean velocity component distribution

The flow dynamics can be indicated by velocity variance. In Figure 7, distribution of streamwise and spanwise velocity component sum (indicator of turbulent kinetic energy) is shown. Maximum of variance is located close to the free shear layer.

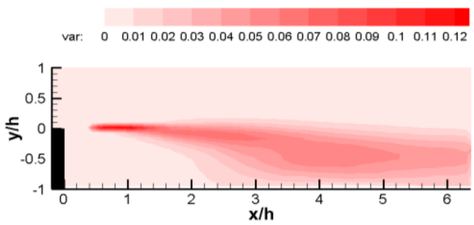

Figure 7. In-plane velocity variance distribution

The other indicator of flow dynamical activity is correlation coefficient. The presence of negative correlation coefficient is an indicator of turbulence production. Its distribution in the measured flow field is given in Figure 8. Negative value (blue) indicates production of turbulence.

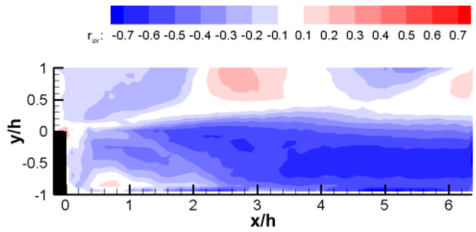

Figure 8. Correlation coefficient distribution

The results of statistical analysis clearly show the size and shape of the recirculation zone in classical sense, capturing its border. However, no information on its structure and dynamics is provided.

4.3. POD Analysis

The POD modes of the velocity data have been performed. The first four spatial modes (toposes) with the biggest energy are shown in Figures 9a–d.

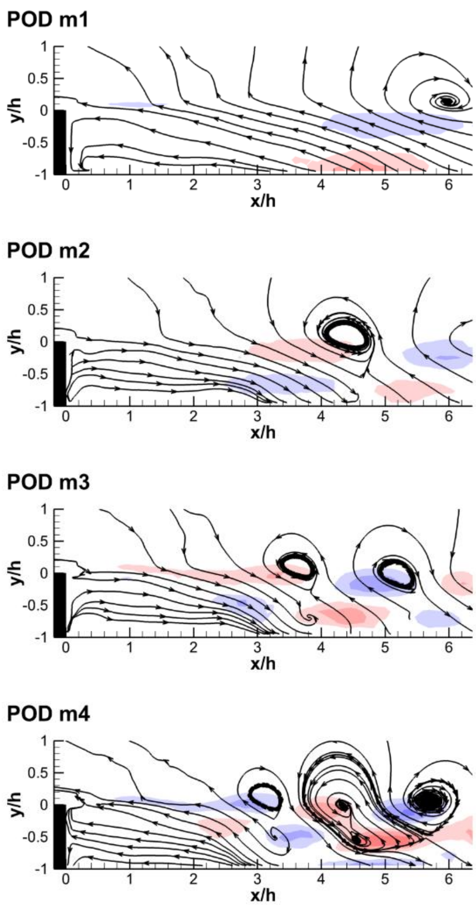

Figures 9.a–d First four POD spatial modes (toposes)

The toposes are velocity vector fields, which are depicted by vorticity distribution with arbitrarily added vectorlines. This representation clearly shows the deterministic structures, basically vortices, randomly appearing in the flow field. The first four modes cover about 27 % of the total kinetic turbulent energy of the flow field. The topology of toposes suggests presence of vortical structures close to the free shear layer formed along the border between the flow over the step and recirculation region.

The dynamics of the POD modes is represented by corresponding chronoses. In Figure 10 the chronoses for first four POD modes are shown forming complementary information to the toposes in Fig. 9. However, only a small part (0.05 s) from overall record length (5 s) is shown to demonstrate the signal structure.

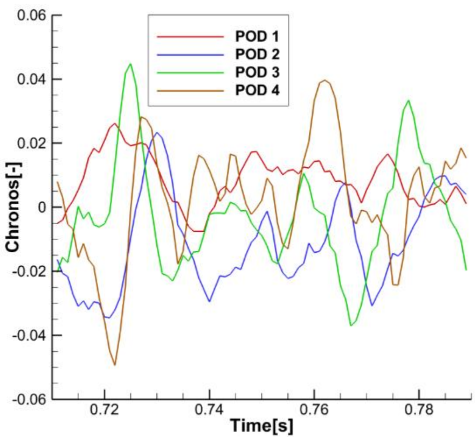

Figure 10. Evolution of the four POD modes in time

As mean value of each mode is zero, it is clear, that the signals are representing dynamics of the modes. The evolution in time of each mode is apparently random, each mode involves dense (continuous, non-discrete) spectrum of fluctuations, characterized by many frequencies present in the spectrum.

The main advantage of POD/BOD method is that it reduces the amount of measured data very efficiently, without losing information on flow field dynamics. However the POD/BOD method fails very often in clear dynamic analysis of the flow field as the individual modes could not be linked to a single frequency. Furthermore, the dynamics of structures represented by BOD is of pulsating nature only (amplitude changes, shape remains), while most turbulent structures are traveling in space ("waves").

4.4 OPD Analysis

The Oscillating Pattern Decomposition (OPD) method provides clear insight into the flow-field dynamics. It is based on stability analysis of coherent structures physically present in the flow, but hidden in chaos and not distinguishable by averaging and/or POD/BOD.

OPD evaluates individual oscillating modes (structures) appearing in the flow. Each mode is characterized by its topology in the flow, by its evolution/movement in the flow, by its single discrete frequency, and by its damping/decay of its amplitude. Note that in comparison with POD, the OPD mode unambiguously defines the frequency and dynamical changes of the structure pattern during one period of cyclostationary process (i.e. periodical with decaying amplitude).

In the OPD implementation, the BOD method is used for reduction of amount of data and filtering of statistical noise. On these data, the OPD method is applied. For details see [8]. (In the described case, the BOD modes were approved for the OPD analysis with chronos autocorrelation bigger than 0.4 only.)

To evaluate the individual OPD mode significance, the periodicity could be used besides the e-folding time. Periodicity p of a given mode is defined as e-folding time τ_e and oscillation period T ratio:

$$p = \tau_e / T = \tau_e \; f \; . \tag{1}$$

The OPD modes are oscillating by definition. If $p = 1$ means the mode amplitude decay by e during a period. Then $p = 0.343$ corresponds to situation, when the mode amplitude decays by factor 10. Periodicity value bigger than 0.343 indicates true oscillating process. (The value of 0.343 means that during one oscillation period the amplitude of oscillations is reduced to 10 %). If decay is faster than 0.343, then such modes are called decaying modes.

The OPD spectrum as frequency vs. e-folding time is given in Figure 11, while periodicity is shown in Figure 12.

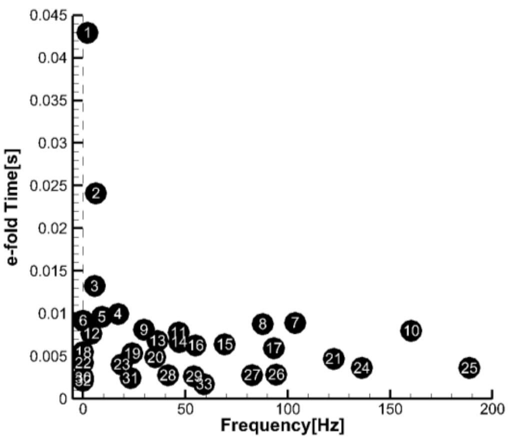

Figure 11. OPD spectrum – e-folding time vs. frequency

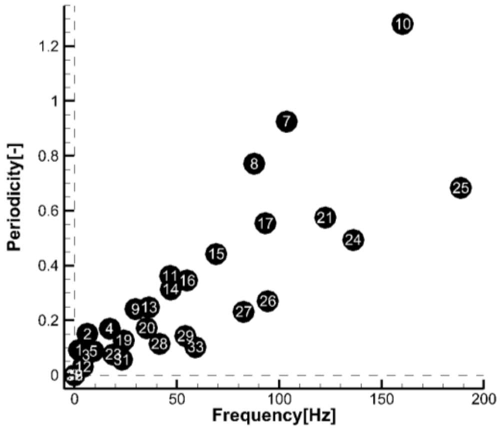

Fig. 12 – Periodicity of OPD modes

In Figs. 11 and 12, numbering of OPD modes is added; the numbers are assigned according to the e-folding time (numbering starts from longest times/ minimum damping).

Spatial OPD modes consist of real and imaginary parts respectively, forming complex form. Regarding structures complexity, two basic types of modes exist. If the real part of the given mode is dominant while imaginary is very weak or even vanishing, the structure dynamics is of pulsating character (see e.g. recirculation area in a wake, where mean velocity is close to zero). For traveling modes both real and imaginary parts are very similar, with distinct structures, however, shifted in space. The shift represents their positions in different phases of the cyclostationary decaying process (phase shift $\pi/2$). (An example of traveling structures is e.g. von Karman vortex street.)). The speed v of traveling structures could be estimated:

$$v = s/T = s\ f\ , \qquad (2)$$

where s is structures spacing and T is period.

The OPD spatial modes, representing the K–H instability, are presented bellow. For the K–H instability, the train of vortices moving along the free-shear layer is typical. All those modes are of traveling character and oscillating. However other modes of pulsating and/or decaying character are present in the flow as well, but, for simplification, are not presented here.

The OPD mode with the most pronounced structure typical for the K–H instability is mode No. 10, shown in Figure 13. Both real and imaginary parts are depicted, in form of vectorlines and vorticity distribution (blue/red, as above). The imaginary part represents the same configuration of vortices as the real part, only shifted in space and time by a quarter of period.

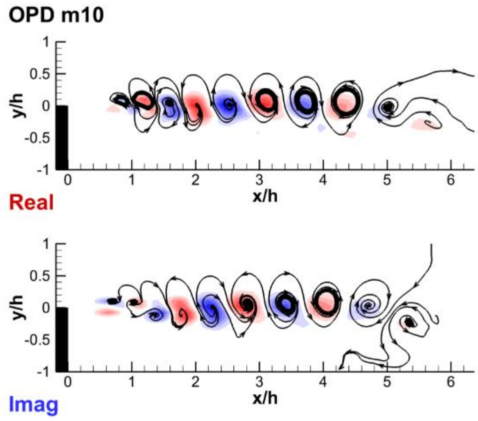

Figure 13. OPD mode 10, real and imaginary parts

In our case, the OPD 10 mode is characterized by its frequency, e-folding time, and periodicity respectively: f_{10} = 160.30 Hz, τ_{e10} = 7.992 ms, p_{10} = 1.281. Velocity of vortical structure train v_{10} is approx. 0.59 U_{in}.

The other modes with vortex trains involved are numbers 7, 8, 21, and 24. Real parts of those modes are shown in Figs. 14 to 17.

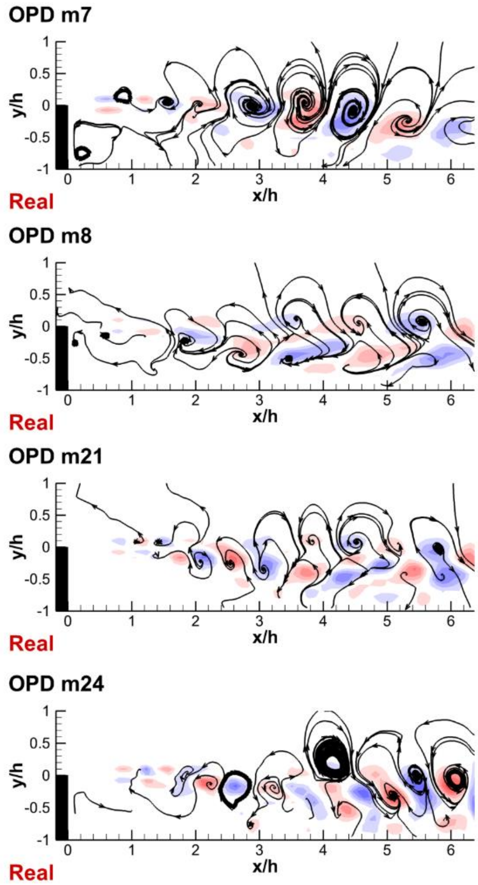

Figures 14.a-d OPD modes 7, 8, 21 and 24 respectively, real parts

The Strouhal number Sr shown in Table 1 is defined by using inlet velocity and step height for the OPD mode no. i:

$$\mathrm{Sr}_i = \frac{f_i\ h}{U_i}\,. \tag{3}$$

All the OPD modes presented above are true oscillating modes with travelling nature, representing dynamical behavior of the shear layer behind the backward-facing step in the plane of symmetry. This behavior connected with Kelvin-Helmholtz instability is characterized by various topologies of vortical structures, objectively present simultaneously in the flow. The modes 10 and 7 represents single train of vortices arranged in a single line with alternating orientation – positive and negative vorticity. The OPD modes 8 and 21 are not so coherent and they are characterized by the double-train topology. The two parallel trains of vortices with checkered arrangement could be distinguished. The last OPD mode presented here no. 24 is even less chaotic in nature, but suggesting similar structure with maximum dynamical activity located to the recirculation region border.

5. CONCLUSIONS

Flow field behind a backward-facing step in a narrow channel has been studied experimentally using time-resolved PIV technique in the plane of symmetry in the streamwise direction. Dynamics of the flow-field has been analyzed by several methods, and results were compared and interpreted.

As a basic case, the classical statistical analysis has been used. This kind of analysis provides information on extent of dynamic region in space, and estimates overall energy of the dynamic process. Nevertheless, no information on fine-grained spatial structure as well as on time/ frequency characteristics can be provided.

The POD method provides topology of the most energetic dynamical structures present in the flow field. However, analysis of dynamical behavior of those structures, suggested by the POD method, or by its extension BOD method, is very limited. Each POD mode is generally characterized by dense spectrum in time, and no information about movement in space and topology changes of the structures forming the POD modes can be provided. POD/BOD does not offer any specific frequency information. The topology of the most energetic structures resulting from the POD method is characterized by vortical structures localized in the interface between fluid flowing over the step and so called recirculation region behind the step.

OPD method represents the flow dynamics in the most complex and detailed way. OPD decomposes the flow field dynamics into several important modes, each mode being characterized by unique frequency, damping and topology, and represent an underlying cyclostationary process hidden in random pseudoperiodical behavior of the turbulent flow field. Typically, travelling structures as vortex trains form the OPD modes. The OPD modes presented here suggest the dynamical structures in the form of vortices trains in simple or double line configuration with alternative orientation and moving in the streamwise direction with velocity slightly above a half of the inlet velocity.

Table 1. Selected OPD modes with vortex trains related to the K–H instability

OPD mode i	f_i [Hz]	τ_{ei} [ms]	p_i [1]	Sr_i [1]	v_i/U_{in} [1]
7	103.64	8.938	0.926	0.345	0.52
8	87.77	8.786	0.771	0.293	0.59
10	160.30	7.992	1.281	0.534	0.59
21	122.34	4.698	0.575	0.408	0.61
24	136.11	3.631	0.494	0.454	0.50

ACKNOWLEDGEMENTS

This work was supported by the Grant Agency of the Czech Republic, project GAP101/12/1271.

REFERENCES

[1] Hasselmann, K., 1988, "PIPs and POPs: The Reduction of Complex Dynamical Systems Using Principal Interaction and Oscillation Patterns", *Journal of Geophysical Research*, 93, D9, 11.015-11.021.

[2] Lumley, J.L., 1967, "The structure of inhomogeneous turbulent flows", *Atm.Turb. and Radio Wave Prop*., Yaglom and Tatarsky eds., Nauka, Moskva, pp.166-178.

[3] Uruba, V., 2014, "Dynamics of Reattachment of the Flow behind Backward-Facing Step in a Narrow Channel", *AIP Conference Proceedings*, Vol. 1608, pp. 253-256.

[4] Uruba, V., 2014, "Study on Flow behind Backward-Facing Step in a Narrow Channel", *Journal of Physics Conference Series*, Vol. 530, Article Number: UNSP 012024

[5] Uruba, V., 2014, "Dynamics of secondary flow behind backward-facing step in a narrow channel", *EPJ Web of Conferences*, Vol. 67, Article Number: 02120.

[6] Uruba, V., 2013, "Dynamics of flow behind backward-facing step in a narrow channel", *EPJ Web of Conferences*, Vol. 45, Article Number: UNSP 01108.

[7] Uruba, V., 2012. "Methods of spatio-temporal data analysis", Proc. *XX Fluid Mechanics Conference*, Gliwice, Institute of Power Engineering and Turbomachinery, (Chmielniak, T.; Wróblewski, W.), pp. 152-153.

[8] Uruba, V., 2012, "Decomposition Methods in Turbulence Research", *EPJ Web of Conferences*, Vol. 25, Article Number: 01095.

[9] Uruba, V., Jonas, P., Mazur, O., 2007, "Control of a channel-flow behind a backward-facing step by suction/blowing", *International Journal of Heat and Fluid Flow*, Vol. 28, No. 4, pp. 665-672.

Conference on Modelling Fluid Flow (CMFF'15)
The 16th International Conference on Fluid Flow Technologies
Budapest, Hungary, September 1-4, 2015

EFFECT OF DROPLET DEFORMATION PLACED ON A VIBRATING PLATE ON THE MEASUREMENT OF DYNAMIC SURFACE TENSION

Satoko YAMAUCHI [2], Shuichi IWATA [1], Ryo NAGUMO [3],
Hideki MORI[4] and Yumiko YOSHITAKE[5]

[1] Corresponding Author. Department of Materials Science and Engineering, Graduate School of Engineering, Nagoya Institute of Technology. Gokiso-cho, Showa-ku, Nagoya, 466-8555, Japan. Tel.: +81-52-735-5256, Fax: +81-52-735-5255, E-mail: iwa@nitech.ac.jp
[2] Dept. of Materials Sci. and Eng., Graduate School of Eng., Nagoya Inst. of Tech., E-mail: yamauchi.satoko@chemeng.nitech.ac.jp
[3] Dept. of Materials Sci. and Eng., Graduate School of Eng., Nagoya Inst. of Tech., E-mail: nagumo.ryo@nitech.ac.jp
[4] Dept. of Materials Sci. and Eng., Graduate School of Eng., Nagoya Inst. of Tech., E-mail: mori.hideki@nitech.ac.jp
[5] Department of Mechanical Engineering, Nagaoka University of Technology, E-mail: yoshitake@nagaokaut.ac.jp

ABSTRACT

Dynamic surface tension is one of the most important physical properties for interfacial phenomena of many applications. Iwata *et al.* proposed a measurement method of dynamic surface tension, which can be determined by comparing a theoretical droplet shape and a droplet shape of small amount sample liquid on the vibrating plate. It was found that dynamic surface tension increases with the increase in the vibration frequency. However, due to a size of droplet, local flow inside the droplet cannot be identified clearly experimentally. Therefore, we investigated the deformation of shell liquid of the droplet on the vibrating plate using 2D finite element method in this study. The gas-liquid droplet surface area is calculated locally in each section of radial angle under given apparent gravity. At the maximum apparent gravity, lower and upper part of the droplet surface can expand and shrink, respectively. Alternately, at the minimum apparent gravity, it reproduces the reverse phenomenon. However, the total surface area is almost constant during one period. Considering the deformation of shell liquid of the droplet, we could also identify a type of deformation. We found that the local droplet deformation at the interface can be related to the measurement of dynamic surface tension.

Keywords: deformation, dynamic surface tension, finite element method

NOMENCLATURE

A	$[m]$	amplitude of vibration
D	$[m]$	characteristic length
S	$[m^2]$	surface area
T	$[s]$	period
a	$[m]$	radius of three phase contact circle
b	$[m]$	droplet height
f	$[s^{-1}]$	vibration frequency
g	$[m/s^2]$	gravity acceleration
g^*	$[m/s^2]$	maximum apparent gravity acceleration
i	[-]	time step
p	$[Pa]$	pressure
t	$[s]$	time
u	$[m/s]$	characteristic velocity
v	$[m/s]$	velocity in r direction
w	$[m/s]$	velocity in z direction
$\lambda_1,\lambda_2,\lambda_3$	[-]	eigenvalues of deformation rate tensor
μ	$[Pa\cdot s]$	viscosity
π	[-]	circular constant
θ	$[^\circ]$	radial angle
ρ	$[kg/m^3]$	density
σ	$[mN/m]$	surface tension
$\underline{\underline{S}}$	[-]	rate of deformation tensor
$\underline{e_z}$	[-]	unit vector in z direction
$\underline{g}'$	$[m/s^2]$	apparent gravity acceleration
$\underline{n}$	[-]	unit normal vector
$\underline{v}$	$[m/s]$	velocity vector
$\underline{\underline{\delta}}$	[-]	unit tensor
$\underline{\underline{\tau}}$	$[N/m^2]$	total stress tensor
$2H$	$[m^{-1}]$	mean curvature

Subscripts and Superscripts

G, L	gas and liquid phase
g_{max},g_{min}	maximum and minimum apparent gravity force
m, M	smallest, largest
r, ϕ, z	direction

1. INTRODUCTION

Liquid atomization is an attractive phenomenon in many applications, such as spray coating, ink-jet printing, fuel injection equipment, spray cooling, and pesticide spraying [1-4]. Liquid atomization in these applications can enhance the heat or mass transfer on droplet surface, coating or distribution area, and the momentum exchange between the fine particles and surrounding fluids. In the liquid atomization, deformation of the liquid and droplet size are very important. As droplet size is affected by surface tension so deformation of the liquid can be controlled by surface tension and viscous force [5, 6]. As the size of droplet is finer, surface tension becomes very important physical property. Surface tension depends on concentration of local components on the liquid interface and temperature. If a unit local interface is spreading in a short time, the interfacial components may be varied with diffusion and adsorption rate of substances. In other words, surface tension is varied with the time of interface formation (surface age). It is called dynamic surface tension. Generally, dynamic surface tension can be measured by the maximum bubble pressure method [7, 8], the pendant-drop method [9-11], and the jet reaction method [12]. These methods measure additional forces to produce the new interface. Such spreading interfacial area can be affected by the dynamic surface tension according to the rate of diffusion of surfactant molecules to the interface and the adsorption rate of the molecules on the interface [13, 14]. However, these methods mentioned above require some quantity of liquid volume (at least a cup of samples) and would be difficult to measure newly-synthesised materials and valuable materials. Therefore, it is desirable to develop a dynamic surface tension measurement method that uses only a small amount of sample.

Iwata *et al.* proposed a measurement method of dynamic surface tension, which uses shape of small amounts of droplet on the vertically vibrating plate [15]. This method consists of two stages; measuring a shape of a small droplet placed on the vibrating plate experimentally and numerical analysis in the following process. The apparent surface tension (dynamic surface tension) can be determined by optimizing parameters used in numerical analysis until the theoretical droplet shape and the experimental droplet shape agrees well within a given tolerance. Droplet can be deformed by apparent gravity produced by vibration of the vertically vibrating plate and the amplitude. With an increase in vibration frequency, droplet deformation can get bigger. The concentration gradients of surfactants on new interface can be formed. Therefore, dynamic surface tension can be increased. They showed frequency dependence of the dynamic surface tension of soluble surfactants solution [15]. Driving force of this phenomenon is considered to be the limited diffusion and adsorption rate of surfactants to the new interface. In this method, interfacial area can be renewed by deformation. However, it is difficult to clarify the change in local area on the droplet surface. In this study, we investigated the deformation type of a droplet on the vibrating plate using 2D finite element method.

2. SIMULATION MODEL

We simulated droplet deformation on the vibrating plate by using commercial software, the COMSOL Multiphysics combined with the CFD module and the micro fluidics module. This software uses the finite element method in spatially and method of line in time progressing. The calculation domain consists of cross sectional of a droplet with an axis symmetrical geometry. Figure 1 shows an initial calculation domain, which is a quarter of a circle with radius a=1.0 *mm*. Cylindrical coordinate system is applied and droplet is symmetrical around the z-axis. Effect of gas phase is assumed to be negligible. Therefore, problems regarding liquid phase was calculated by this model.

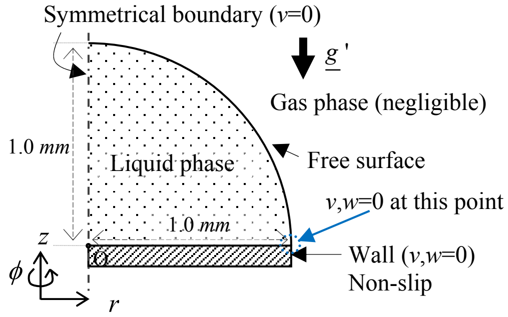

Figure 1. Initial calculation domain

2.1. Basic Equations

We used biquadratic mesh with biquadratic interpolation for velocity and bilinear interpolation for pressure. Apparent gravity force which has been applied to the droplet due to vibration can be expressed as volumetric force of the droplet.

We assume incompressible laminar flow. The governing equations are equation of continuity and momentum equation as follows.

$$\nabla \cdot \underline{v} = 0 \tag{1}$$

$$\rho\left(\frac{\partial v}{\partial t} + \underline{v} \cdot \nabla \underline{v}\right) = \nabla \cdot \underline{\underline{\tau}} + \rho \underline{g}' \tag{2}$$

where $\underline{\underline{\tau}}$ is the total stress tensor expressed as following equation,

$$\underline{\underline{\tau}} = -p\underline{\underline{\delta}} + 2\eta \underline{\underline{S}} \tag{3}$$

The apparent gravity acceleration vector *g'* is defined as: ,

$$\underline{g}' = \left(-g - A(2\pi f)^2 \sin(2\pi f t)\right)\underline{e_z} \tag{4}$$

The apparent gravity can be oscillated with time *t*.

2.2. Boundary conditions

No slip condition is applied on the solid surface. The axis symmetrical condition is applied along z axis. As for the free surface, the interface-tracking method is applied to determine the moving boundary [16]. Here, a nodal point on the three phase contact line is fixed at (r, z)=(a, 0). The force balance equation, which takes into account the pressure force, stress and surface tension, is considered along the interface,

$$p_G \underline{n} + \underline{\underline{\tau}} \cdot \underline{n} + 2H\sigma \underline{n} = \underline{0} \qquad (5),$$

where p_G is gas phase pressure and $\underline{n}$ is normal vector on the surface pointing outward.

2.3. Parameters

We use following two parameters to clarify the deformation of the droplet on the vibrating plate, Reynolds number and Weber number. A characteristic length D is a radius of three phase contact circle a (=1.0 mm), and characteristic velocity u is defined as the following equation,

$$u = \sqrt{Ag^*} = \sqrt{A\left(A(2\pi f)^2 + g\right)} \qquad (6),$$

where g^* is the maximum of apparent gravity. Reynolds number and Weber number can be expressed as follows.

$$Re = \frac{Du\rho}{\mu} = \frac{a\rho\sqrt{A\left(A(2\pi f)^2 + g\right)}}{\mu} \qquad (7)$$

$$We = \frac{\rho u^2 D}{\sigma} = \frac{a\rho A\left(A(2\pi f)^2 + g\right)}{\sigma} \qquad (8)$$

In this study, we assumed that surface tension value as constant through a period of vibration, even if local surface area was changed. This indicates that the given surface tension is equivalent to the averaged surface tension value throughout that period. In addition, the local flow driven by surface tension gradient has been neglected. As we calculated a droplet of dilute aqueous solution, density and viscosity were almost same as water. Therefore, density and viscosity were defined as ρ=1000 kg/m^3 and μ=1.0 $mPa{\cdot}s$. Amplitude A of vibrating plate was set at 1.0 mm as a constant.

3. RESULTS AND DISCUSSION

3.1. Variation of the droplet surface

Droplet is deformed as changes in the apparent gravity force. Figure 2 shows cross sectional shapes of water droplet at maximum and minimum apparent gravity force at constant Reynolds number of 200. We assume temperature is 25 °C, so surface tension of water is 71.99 mN/m [17].

It can be seen from Fig. 2 that, surface area at the gas-liquid interface is varied between maximum and minimum apparent gravity force. On the other hand, interfacial area at solid (wall)-liquid interface is kept constant because of the fixed three phase contact line (v,w=0).

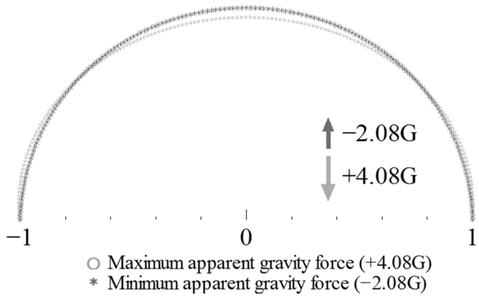

Figure 2. Water droplet shape at maximum and minimum apparent gravity at *Re*=200 (σ=71.99 *mN/m*).

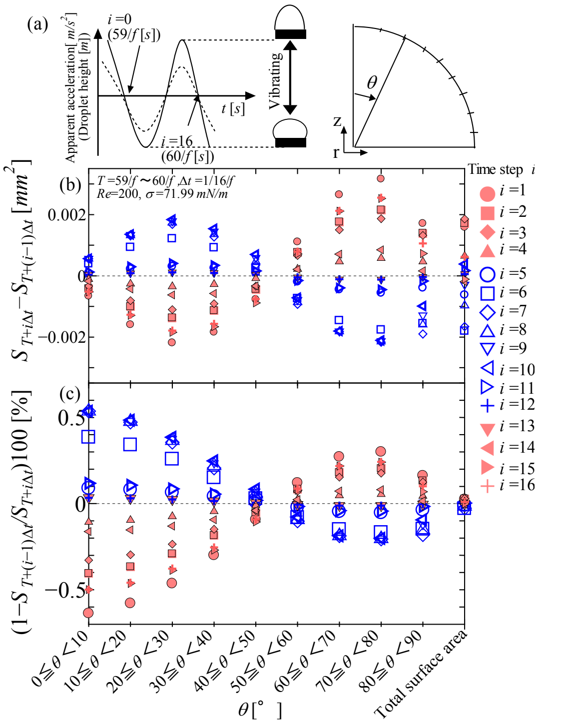

Figure 3. Time series plots of increased local surface area and its corresponding increasing ratio for each of local position over a period between 59th cycles and 60th cycles at *Re*=200 (σ=71.99 *mN/m*).

So to clarify the change in local surface area of the droplet, we plot time series of local surface with an increasing ratio during 1/16 of the cycle time (=T/16) over a period between 59th and 60th calculation cycles in Fig. 3. The droplet surface is divided into 9 local surfaces at a radial angle of 10 degrees. The apparent gravity varies with time step i. When the vibration plate is moving downward and the plate position is just at the center of vibration, we set the time step i as 0. When time step i is ranged $1 \le i \le 3$ and $13 \le i \le 16$, the vibrating plate is moving downward. When time step i is ranged $5 \le i \le 11$, the vibrating plate is moving downward.

At i=4 and 12 are expressed as a maximum and minimum volumetric force point, respectively. As it can be seen in Fig.3, section of increasing in the surface area is dependent on the direction of increasing in the volumetric force. When apparent acceleration is increasing to the direction of -z, for example i=1, surface area is decreasing at 5 sections of θ between 0 and 50 degrees. At the same time, at the other 4 sections of θ between 50 and 90 degrees, surface area is increasing. On the other hand, when apparent acceleration is increasing to the direction of z, for example i=6, surface area is decreasing at 4 sections of θ between 50 and 90 degrees. Simultaneously the other 5 sections of θ between 0 and 50 degrees, surface area is increasing. This tendency means that surface area is increased or decreased at the specific section until volumetric force is respectively maximum or minimum. Therefore, renewal surface area during half period is expressed by the integral of surface variation between maximum and minimum volumetric forces. Surface area of droplet in each section is varied with radial angle θ. Difference of results can occur between variation amount and variation ratio of surface area.

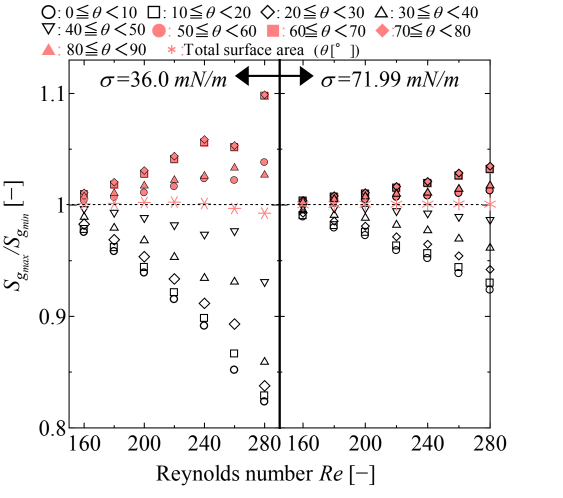

Figure 4. Effect of Reynolds number on the variation of surface area at surface tension σ=71.99 *mN/m* and 36.0 *mN/m* (reference in Fig.3(a))

In addition, ratio of surface area depends on Reynolds number and Weber number as shown in Figures 4 and 5. In Figs. 4 and 5, ratio of surface area (renewal surface area during half period) between the maximum and the minimum apparent gravity forces are shown at each section. Variation of Reynolds number means difference in the vibration frequency in this case, as it has been shown in equation (7). Time results show the actual one period depends on the Reynolds number.

In Fig.4 it is shown that, tendency of the section of surface area can be considered as variation ratio of surface area which may become bigger with higher Reynolds number. In addition, big variation ratio of surface area may be made within a short time because higher Reynolds number indicates shorter period. In terms of the measurement of dynamic surface tension, the higher vibration frequency can be made not only faster formation of interface but also formation of bigger renewal surface area. Therefore, to utilize the higher vibration frequency is effective to consider the faster interfacial formation phenomena. This may also cause the phenomena at which dynamic surface tension of soluble surfactants solution depend on the vibration frequency by limited rate of mass transfer in the previous study [15]. However, the total surface area is varied little and variation ratio of surface area is different in each section. Therefore, we can consider that the deformation at the interface can be characterised on each part (As you can see in detail in the section 3.2).

In Fig.5, we found that ratio of surface area depends on the Weber number at constant Reynolds number, similarly. However, in this case, we don't consider the “dynamic” surface tension in the droplet deformation. We don't know whether the phenomenon is consistent with the actual phenomena now. Here, we considered that effect of the deformation types of droplet on the measurement of dynamic surface tension, and we found which can be independent of Reynolds number and Weber number at later chapter. In this paper, we take attention to the deformation types. The "dynamic" surface tension will be assumed at this simulation in near future.

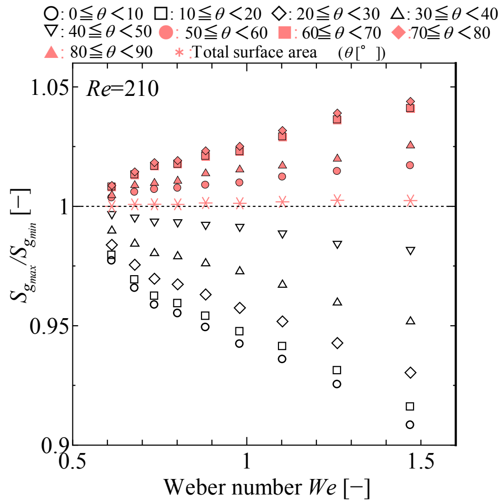

Figure 5. Effect of Weber number on the variation of surface area at *Re*=210 (reference in Fig.3(a))

3.2. Deformation of the droplet

Nakayama *et al.* presented the quantification of the deformation type of melting polymer by use of deformation rate tensor [18]. Largest and smallest eigenvalues of deformation rate tensor can be expressed by λ_M and λ_m. According to Nakayama *et al.* [18] indicates that $\lambda_M>0$, $\lambda_m<0$, and the range of λ_m/λ_M is between -2 and -0.5 for incompressible fluids. For pure uniaxial and biaxial elongational flows, λ_m/λ_M is -0.5 and λ_m/λ_M is -2, respectively. For pure planar shear flow, λ_m/λ_M is -1. Therefore, we observed deformation types at the interface by this method.

We calculated eigenvalues of deformation rate tensor by using the rule of Sarrus and Cardano's formula for cubic equation. Typical examples of the results are shown in Figure 6. We considered that history of local deformation on the droplet surface can be important. It is shown that the ratio of largest and smallest eigenvalues every $1/16/f$ [s] between $59/f$ and $60/f$ [s] except T_{gmax} and T_{gmin} [s]. Increasing direction of volumetric force is expressed by different tone. Tendency of eigenvalues ratio can be depended on the plate moving direction.

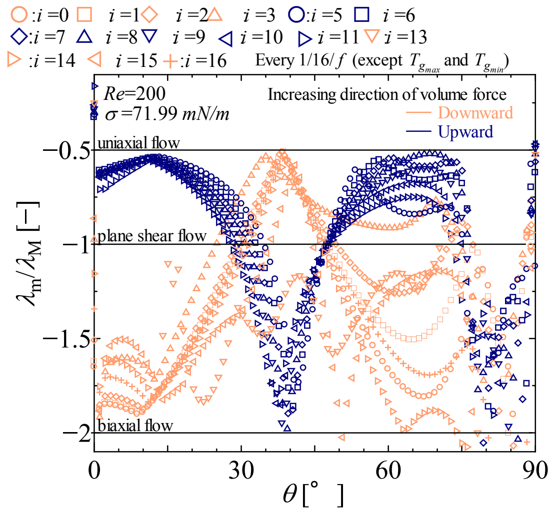

Figure 6. Ratio of largest and smallest eigenvalues at the gas-liquid interface at *Re*=200 (reference in Fig.3(a))

Commonly, planer shear flow (i.e., the ratio of eigenvalues approaching to nearly -1) occur at θ of 30 degrees and 47 - 50 degrees. When the moving direction is downward, biaxial flow (i.e., the ratio of eigenvalues approaching to nearly -2) occurs at θ of 8 - 15 degrees, uniaxial flow (i.e., the ratio of eigenvalues approaching to nearly -0.5) occurs at θ

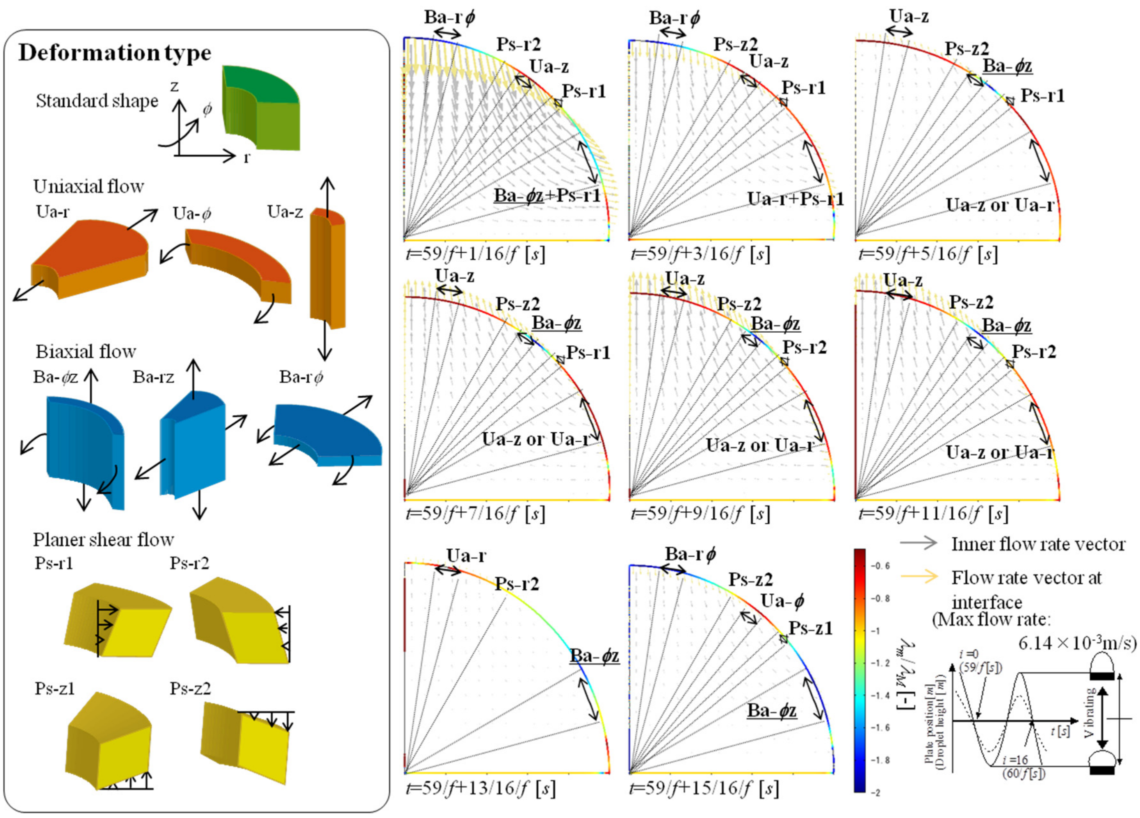

Figure 7. Consideration of deformation types of droplet shell (color variation of shell and sign correspond to the deformation type) at *Re*=200 and σ=71.99 *mN/m* every 1/8/*f* [*s*] over a period between 59th and 60th calculation cycles (*t*=59/*f* + *i*/16/*f*, when *i*=1, 3, 5, 7, 9, 11, 13, 15)

of 35 - 40 degrees, and planer shear flow occurs at θ of 60 - 75 degrees. On the other hand, when the moving direction is upward, biaxial flow occurs at θ of 35 - 40 degrees, uniaxial flow occurs at θ of 8 - 15 degrees and 60 - 75 degrees. Similar behavior can be seen at the other Reynolds number, *Re* and the other surface tension σ (or Weber number, *We*). Therefore, the ratio of eigenvalues is independent of the *Re* and σ (or *We*).

We assumed the deformation types of droplet shell at the above radial angles (8 to 15 degrees, 30 degrees, 35 to 40 degrees, 47 to 50 degrees, and 60 to 75 degrees) by using the ratio of eigenvalues and flow vectors on the domain as shown in Figure 7. On the left side of the Fig.7, basic deformations of a control volume are presented. We discuss type of local extensional deformations on the droplet surface. Flow rate vectors are proportional to the flow rate. Maximum flow rate is 6.14×10^{-3} *m/s*. Underlined legends indicate that the local surface area extended apparently. In terms of increment in local surface area, biaxial flow can be the best deformation. In principle, droplet surface area can be strongly affected by biaxial extensional flow in ϕ, z directions (except top of the droplet surface). These biaxial extensional flows occur around θ=60-75 degrees and θ=35-40 degrees for moving plate in –z and z direction, respectively. On the other hand, the other deformation types can produce a little surface area or decreasing surface area or not changing surface area in some cases. Considering these behaviors mentioned above, the increasing in the local surface area can be produced by biaxial deformation.

Let's consider the droplet deformation when the surfactant molecules are adsorbed on the droplet surface. As described above, increase amount in local surface area due to droplet deformation can be varied with *Re* or *We* or σ, however, deformation type cannot be varied with them. When deformation is occurred at the local surface, surfactants can be moved or adsorbed or desorbed. These behaviors are summarized in Figure 8. In the case of planer shear flow, the amount of surface area can be almost the same, and surfactants adsorbed at the interface may be moving along the surface. In uniaxial and biaxial flow, surface area can be increasing or decreasing dependent on the deformation. In case of decreasing surface area, density of adsorbed surfactant molecules at the interface can be increased and surface tension can be decreased until the surface concentration reaches up to c.m.c. In a short time, surface tension can alternately come back to the static condition due to desorption and diffusion of surfactants from the interface to the bulk liquid. On the other hand, in case of increasing surface area, density of surfactant molecules at the interface can be decreased and surface tension can be increased temporary. In a short time, surface tension can approaches to the static condition due to diffusion of surfactants to the interface and adsorption of surfactants on the interface. This temporary variation of surface tension can be expressed by dynamic surface tension. For factor of determining dynamic surface tension, mass transfer rate and adsorption rate is very important [13]. Sakai *et al.* mentioned that diffusion rate of sodium myristic acid is faster than adsorption rate, which was measured by sodium myristic acid solution at 0.05 *mol/m³* and 0.1 *mol/m³* [14]. In this case, dynamic surface tension is controlled by diffusion rate of substance.

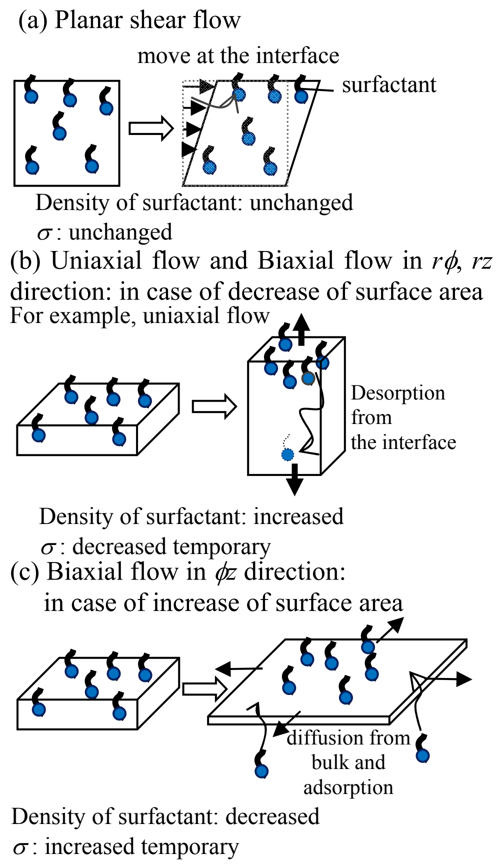

Figure 8. Image of the deformation of droplet including surfactants

In this study, increase and decrease in local surface area occurred simultaneously. Therefore, surface tension can be varied temporarily with each local surface. In addition, at higher *Re*, limited rate of diffusion and adsorption may have an effect on dynamic surface tension due to shorter formation time of droplet interface and bigger amount of new surface area. We found that understanding of deformation types at the interface can be important to study the local surface tension on the measurement of dynamic surface tension.

4. CONCLUSIONS

Firstly, we found the amount of increase or decrease in local surface area depends on the moving direction of plate, *Re*, *We*, and σ. Droplet surface area on the vibrating plate can be increasing and decreasing simultaneously at the different θ.

Secondly, we also found that deformation type depends on the moving direction of plate and θ, and independent on *Re*, *We*, and σ. Deformation type is important in terms of increasing surface area and measurement of dynamic surface tension.

REFERENCES

[1] Arthur H.Lefebvre,1980,"Airblast Atomization", *Prog. Energy Combust. Sci.*, Vol.6, pp.233-261.

[2] Su Han Park, Hyung Jun Kim, Hyun Kyu Suh, Chang Sik Lee, 2009, "Atomization and spray characteristics of bioethanol and bioethanol blended gasoline fuel injected through a direct injection gasoline injector", *Int. J. Heat Fluid Fl.*, Vol.30, pp.1183-1192.

[3] M. Ghodbane and J. P. Holman, 1991,"Experimental study of spray cooling with Freon-113", *Int. J. Heat Mass Transfer*, Vol.34, pp.1163-1174.

[4] Wiliam M. Grissom and F.A.Wierum, 1981, "Liquid Spray Cooling of a Heated Surface", *Int. J. Heat Mass Transfer*, Vol.24, pp.261-271.

[5] Xiaoguang Zhang and Osman A.Basaran, 1997, "Dynamic Surface Tension Effects in Impact of a Drop with a Solid Surface", *J. Colloid Interf. Sci.*, Vol.187, pp. 166-178.

[6] Martin Rein, 1993, "Phenomena of liquid drop impact on solid and liquid surfaces", Fluid Dynamics Research, Vol.12, pp.61-93.

[7] Sugden, S., 1922, "XCVII.-The Determination of Surface Tension from the Maximum Pressure in Bubbles", *J. Chem. Soc*., Vol. 121, pp. 858-866.

[8] Mysels, K. J., 1990, "The Maximum Bubble Pressure Method of Measuring Surface Tension, Revisited", *Colloids and Surfaces*, Vol. 43, pp. 241-262.

[9] Ferguson, A., 1923, "On the measurement of the surface tension of a small quantity of liquid", *Proceedings of the Physical Society of London*, Vol. 36, pp. 37-44.

[10] Garanet, J. P., Vinet, B. and Gros, P., 1994, "Considerations on the Pendant Drop Method: A New Look at Tate's Law and Harkins' Correction Factor", *J. Colloid and Interface Sci.*, Vol. 165, pp. 351-354.

[11] del Rio, O., I. and Neumann, A. W., 1997 "Axisymmetric Drop Shape Analysis: Computational Methods for the Measurement of Interfacial Properties from the Shape and Dimensions of Pendant and Sessile Drops", *J. Colloid and Interface Sci*., Vol. 196, pp. 136-147.

[12] T. Hasegawa, , H. Asama, and T. Narumi, 2003, "A Simple Method for Measuring Elastic Stresses by Jet Thrust and Some Characteristics of Tube Flows", *J. Soc. Rheology*, *Japan*, Vol. 31(4), pp. 243-252.

[13] Kalpak P. Gatne, Milind A.Jog, and Raj M. Manglik, 2009, "Surfactant-Induced Modification of Low Weber Number Droplet Impact Dynamics", Landmuir, Vol.25(14), pp.8122-8130.

[14] K. Sakai, H. Honda, and Y. Hiraoka, 2005," Rapid ripplon spectroscopy with ms time resolution", *REVIEW OF SCIENTIFIC INSTRUMENTS* , 76, 063908

[15] S. Iwata, S. Yamauchi, Y. Yoshitake, R. Nagumo, H. Mori, "Effect of vibration frequency on dynamic surface tension", *Soft matter*, in preparation.

[16] Ruo Ki, Tao Tang, and Pingwen Zhang, 2002, "A Moving Mesh Finite Element Algolithm for Singular Problems in Two and Three Space Dimensions", *J. Comptational physics*,Vol.177, pp.365-293.

[17] N. B. Vargaftik, B. N. Volkov, and L. D. Vojak, 1983, "International Tables of the Surface Tension of Water", *J. Phys. Chem. Ref. Data*, Vol. 12, No. 3

[18] Y. Nakayama, E. Takeda, T. Shigeishi, H. Tomiyama, T. Kajiwara, 2011, "Melt-mixing by novel pitched-tip kneading disk in a co-rotating twin-screw extruder", *Chemical Engineering Science*, Vol.66, pp.103-110.

Conference on Modelling Fluid Flow (CMFF'15)
The 16th International Conference on Fluid Flow Technologies
Budapest, Hungary, September 1-4, 2015

EFFECT OF PRESSURE-OSCILLATION ON BUBBLE SHAPE AND BIREFRINGENCE PROFILE OF CMC LIQUID AROUND A TINY BUBBLE

Hikaru HORIUCHI[2], Shuichi IWATA[1], Ayaka MIZUKOSHI[3], Md Walid Bin Quashem[4], Ryo NAGUMO[5], Hideki MORI[6], Tsutomu TAKAHSHI[7] and Takashi ONUMA[8]

[1] Corresponding Author. Department of Materials Science and Engineering, Graduate School of Engineering, Nagoya Institute of Technology, Gokiso-cho, Showa-ku, Nagoya, Aichi 466-8555, Japan. Tel: +81-52-735-5256, Fax: +81-52-735-5255, E-mail: iwa@nitech.ac.jp
[2] Dept. Materials Sci. and Eng., Graduate School of Eng., Nagoya Inst. of Tech., E-mail: horiuchi.hikaru@chemeng.nitech.ac.jp
[3] Dept. Materials Sci. and Eng., Graduate School of Eng., Nagoya Inst. of Tech., E-mail: mizukoshi.ayaka@chemeng.nitech.ac.jp
[4] Dept. Materials Sci. and Eng., Graduate School of Eng., Nagoya Inst. of Tech., E-mail: justsaikat@gmail.com
[5] Dept. Materials Sci. and Eng., Graduate School of Eng., Nagoya Inst. of Tech., E-mail: nagumo.ryo@nitech.ac.jp
[6] Dept. Materials Sci. and Eng., Graduate School of Eng., Nagoya Inst. of Tech., E-mail: mori.hideki@nitech.ac.jp
[7] Department of Mechanical Engineering, Nagaoka University of Technology, E-mail: ttaka@nagaokaut.ac.jp
[8] Optical Measurement Division, PHOTRON LIMITED, E-mail: oonuma@photron.co.jp

ABSTRACT

Removing tiny bubbles from highly viscoelastic fluids has been a significant challenge. We propose a new method, named Pressure Oscillating Defoaming (POD), where the rising velocity of bubbles is increased by application of oscillating pressure. In general, tiny bubble in the viscoelastic fluid exhibits a spherical shape. However, unusual shapes were observed under pressure oscillating field.

In this study, we observed the motion of a 1μL air bubble in 5.0 wt% CMC (Carboxyl Methyl Cellulose) aqueous solution under a pressure-oscillating field. With increasing pressure-oscillation, the bubble shape changes from spherical to vertically aligned oblate ellipsoid, where the symmetrical axis remains stable in the horizontal direction. This results in the unique finding that the bubble shape is along the symmetrical axis in the vertical direction. Furthermore, 2D retardation distributions were measured by the high speed polarization camera. A pair of strong oriented regions was observed in both sides of the oblate ellipsoid bubble during the contraction phase. There was a complicated flow pattern in the vicinity of the bubble surface where a bubble can be predicted in the form of a cusp along the direction of circumference with negative wake.

Keywords: Flow Birefringence Measurement, Negative Wake, Pressure-oscillation, Viscoelastic Fluid

NOMENCLATURE

a	$[m]$	horizontal diameter
b	$[m]$	longitudinal diameter
C	$[Pa^{-1}]$	stress optical coefficient
D	$[m]$	bubble diameter
I	$[-]$	light intensity
N_1	$[Pa]$	first normal stress difference
t	$[s]$	time
δ'	$[nm]$	retardation
$\Delta n'$	$[-]$	birefringence
$\dot{\gamma}$	$[s^{-1}]$	shear rate
η	$[Pa \cdot s]$	viscosity
η_0	$[Pa \cdot s]$	zero-shear viscosity
λ	$[m]$	wave length
σ	$[Pa]$	stress
ξ	$[m]$	distance from bubble surface
ζ	$[m]$	light pass length

Subscripts and Superscripts

eq	equivalent
H	horizontal direction
L	lower bubble
min	minimum
max	maximum
U	upper bubble
V	vertical direction

1. INTRODUCTION

There have been many studies focusing on the motion of a gas bubble because of its fundamental and practical importance to many industrial processes. For the case of Newtonian fluids, the discussions in understanding the characteristics can be found in many studies. However, for the case of non-Newtonian fluids, the characteristics have not been fully investigated. In the case of viscoelastic fluid, the bubble shape varies depending on the size and rheological properties in viscoelastic solution.

DeKee, D and Chhabra [1] observed free rising bubble in 1 wt% CMC solution and PAAm (Poly Acrylic Amyde) solution. They reported four major shapes; spherical, prolate teardrop, oblate cusped and spherical cap. Prolate bubbles appear in highly concentrated viscous CMC aqueous solutions while small bubbles rise in such fluid. Generally, in these cases, the normal stress acts on the side of the bubble, leading to a bubble shape changes to prolate.

Hassagar [2] applied laser Doppler anemometry and reported the presence of backflow in the wake region in a solution of polyacrylamide in glycerol, and he termed it a "negative wake". He also revealed that the shape of the bubble at the rear pole is not similar to that of a cusp but that of a knife edge. The knife edge was exhibited by all bubbles with a volume larger than about 50 mm^3. Bubbles in the volume range 20-50 mm^3 showed a weak cusp, and bubbles smaller than about 20 mm^3 had a perfectly rounded rear pole.

To investigate the structure of a negative wake, Herrera-Velarde [3] analysed the flow around bubbles in aqueous polyacrylamide (PAAm) solutions, using particle image velocimetry (PIV) for bubbles with a volume close to the critical volume at which the discontinuous change in rise velocity occurs. They reported that when the bubble volume is smaller than the critical volume, the flow resembles that of a bubble rising in a Newtonian fluid. Therefore, the velocity in the wake of the rising bubble is positive. For bubbles with volumes greater than the critical volume, markedly modified velocity distribution and a negative wake were observed.

S.B.Pillapakkam and P.Singh [4] investigated the reason for the negative wake using direct numerical simulations (DNS). In the case of a viscoelastic fluid, at the top of the bubble the velocity is directed upwards, while the fluid velocity at the bottom, a negative wake is present, which is directed downwards. In other words, an upper vortex ring and a lower voltex ring are present around the bubble. Therefore the net momentum flux contribution to the bubble from the top and bottom surfaces is guaranteed to be positive. However, bubble shape and negative wake structure are obtained only when the bubble column is larger.

Removing tiny bubbles from highly viscoelastic fluids has been a significant challenge and has been researched for a long time. S. Iwata [5] proposed a new method, named Pressure Oscillating Defoaming (POD), where the rising velocity of bubbles is increased by application of oscillating pressure. When the pressure was released, the bubble size increased and again there was some local flow around the bubble. The local flow may produce local shear in the vicinity of the bubble. Thus, for shear-thinning fluids, the oscillating pressure acts to depress the apparent shear viscosity of the fluid surrounding the bubble, resulting in an enhancement in the tiny bubble rising velocity.

We observed the shape of a 1μL bubble in 5 wt% CMC under pressure-oscillating field. Images of the bubble were taken by high-speed cameras from two directions; front and side. As pressure-oscillation increased, the shape of the bubble changed from spherical to vertically aligned oblate spheroid in which the symmetrical axis was stable horizontally and the axis rotated slowly as shown in Figure1. The shape of bubble indicated that the symmetrical axis was in the vertical direction. This result introduces a new finding towards the future research to determine the shape of tiny bubbles under elastic effect and variable pressure oscillating field.

In this study, we focus on the stress near a tiny bubble under pressure-oscillating field with the help of high-speed polarization camera. This approach is an optical technique that can be measured without contact.

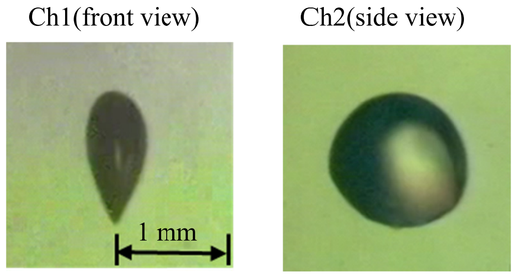

Figure 1. Bubble shape at contraction phase under pressure-oscillation in 5.0 wt% CMC

2. EXPERIMENTS

2.1 TEST FLUID

The rheological property of two different types of highly viscous liquids a 5.0 wt% aqueous CMC solution (Wako Chemical) and a 0.8 wt% aqueous SPA solution (Wako Chemical)) are shown in Figure 2. The rheological properties are measured by a Rheometer (Haake Co. RS-600) system with the cone-plate flow geometry. Both liquids were stirred for 10 days at 25°C. And all experiments were performed at 25°C.

The rheological properties of the SPA *aq.* was re-plotted from Iwata et al [5]. In this report, we used 5.0 wt% CMC *aq.* for test fluid. As can be seen in Fig. 2, the zero-shear viscosity of the test fluid is about 100 $Pa \cdot s$, which is approximately equal to that of the SPA *aq*. The CMC *aq.* shows weaker shear-thinning behavior than the SPA *aq*. Fig. 2 also indicates that, CMC shows higher normal stress difference; N_1 value. At a high shear field, the CMC *aq*. shows stronger elastic behavior than the SPA aq.

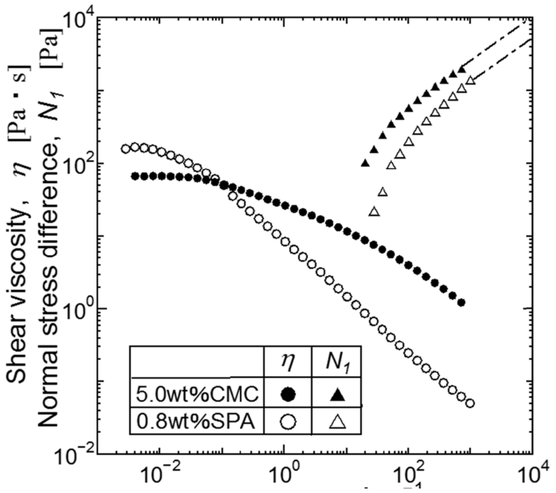

Figure 2. Rheological behavior of 5.0 wt% CMC*aq*. and 0.8 wt% SPA *aq*.

2.2 EXPERIMENTAL APPARATUS

Figure 3 shows the schematic diagram of our experimental apparatus. The test section comprises a quartz cell (40 mm× 10 mm× 10 mm) with a special lid made of a rubber diaphragm and a screw cap. First, the cell is filled with the sample liquid and a tiny air bubble (1 mm^3) which is injected into the liquid using a microsyringe. The cell is sealed airtight with the special lid and turned upside down.

Secondly, we carefully set the test cell at a suitable height so that the rubber sheet of the cell cap remains in contact with the top end of the vibrating piston. The liquid pressure inside the fixed cell can be controlled by mechanical vibration with the piston attached to the vibrating platform. The vibrating platform can be controlled by a sine-wave generator boosted with a power amplifier system (Wavemaker APA-050FAGO Asahi seisakusho Co. Ltd). When the liquid pressure is increased inside the cell the bubble becomes smaller and there are some local flows around the bubble.

2.3 BIREFRINGENCE MEASUREMENT

The bubble was recorded by a high-speed polarization measurement camera (CRYSTA PI-1P, PHOTRON LIMITED) for two-dimensional retardation distribution. We set up a camera with resolution 512 X 512 (Maximum resolution of image sensor is 1024 X 1024), frame rate 6000 fps, shutter speed 1/6000 s. Fig. 3 shows a schematic view of the apparatus.

Green light of 532 nm wavelength emitted from the light source is aligned with the circular polarized light by passing it through the circular polarized film. When the light pass through a sample, the retardation that is integral of change in polarization state due to orientation of photo elastic material in the flow field occurs, and a polarization state changes. The camera captures the polarization state.

The camera is embedded with a high-speed polarization sensor with pixelated micro-polarizer. The transmitted light can be captured by the high-speed polarization image sensor, which consists of 1024 X 1024 polarization array as shown in Figure 4. The image sensor is composed of four pair linear polarizers, which has strainght line polarizer of differnet direction by 45 degrees to adjacent for pixels. The retardation δ' is calculated from each light intensity ; $I_{1,2,3,4}$ which was detected by image sensor. (Eqs.(1) and (2)).

Assuming validity of the stress-optical rule for the local flows around the bubble let us consider a component of the deviatoric part of stress tensor is correlated by birefringence $\Delta n'$ and inverse of the stress-optical coefficient C expressing by equation (3). Furthermore, birefringence $\Delta n'$ is given as equation (4). Where δ' is the retardation and ζ is the light pass length of the sample. When it supposes light path length to be uniformity, the stress σ is proportional to the retardation δ'. It means that it calculate stress distribution to calculate retardation distribution.

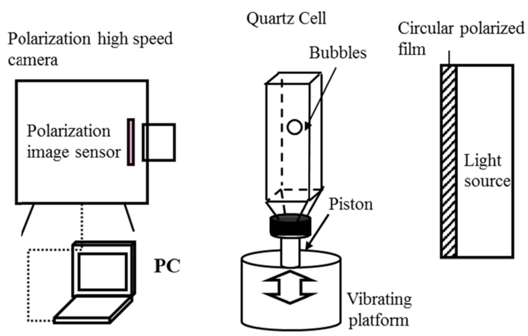

Figure 3. Schematic view of flow birefringence measurement

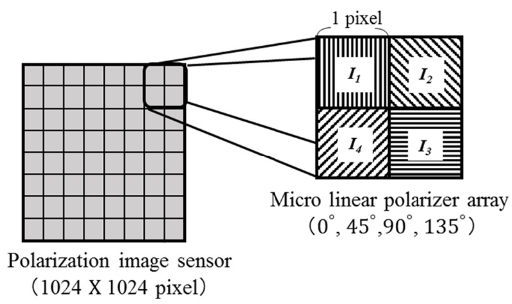

Figure 4. Polarization image sensor

$$\delta' = \sin^{-1}\frac{\sqrt{(I_3 - I_1)^2 + (I_2 - I_4)^2}}{I_0} \quad (1)$$

$$I_0 = \frac{I_1 + I_2 + I_3 + I_4}{2} \quad (2)$$

$$\sigma = \frac{1}{C}\Delta n' \quad (3)$$

$$\Delta n' = \frac{\lambda\delta'}{2\pi\zeta} \quad (4)$$

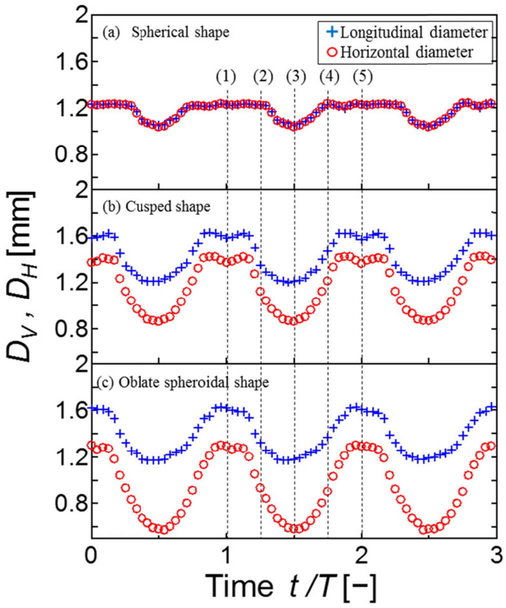

Figure 5. Periodic change in longitudinal and horizontal bubble diameters

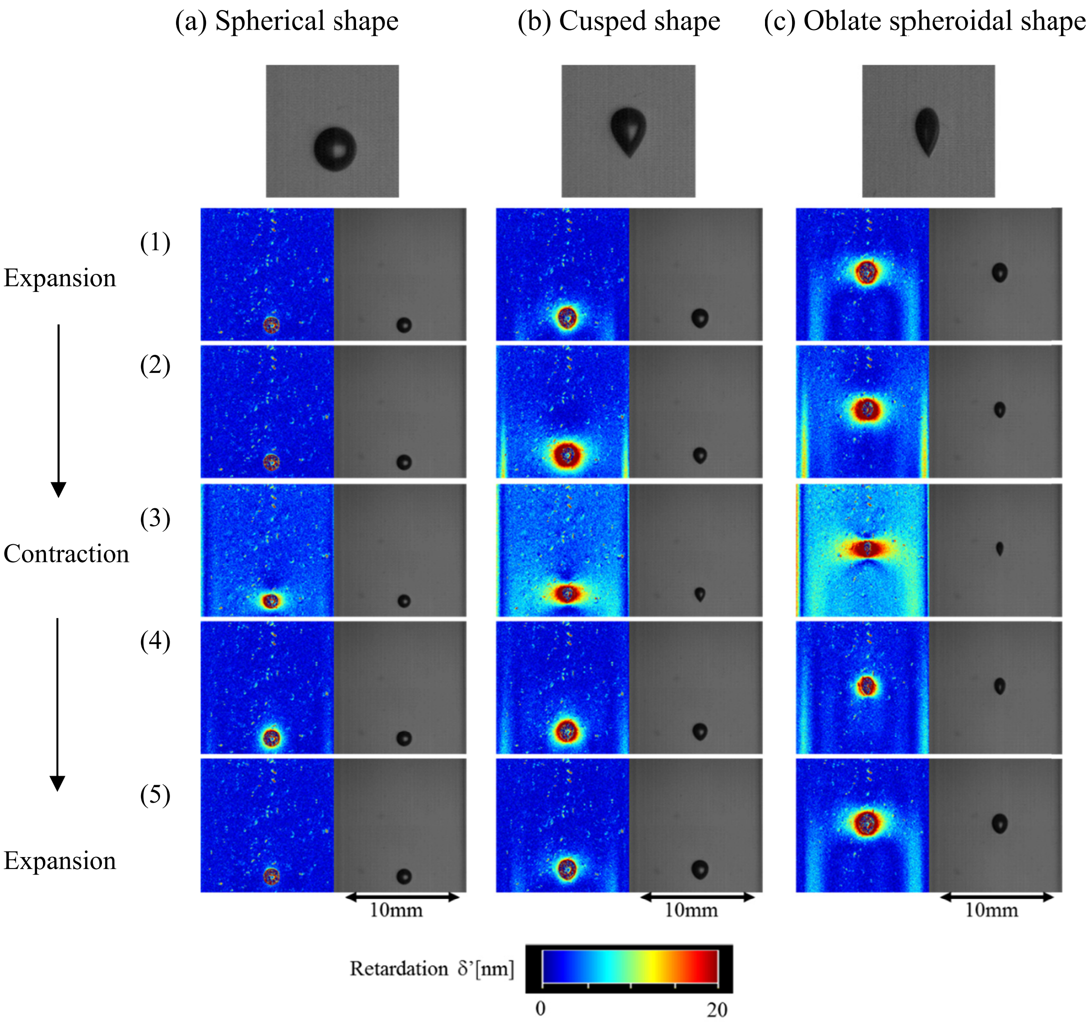

Figure 6. Retardation profile sround the bubble

3. RESULT AND DISCUSSION

3.1 RETARDATION DISTRIBUTION

We applied 250 Hz pressure oscillation to a bubble, in contrast with 6000 fps shutter frame rate. Therefore, 24 frames capture one period of bubble expansion and contraction. Figure 5 shows typical three types of shape during a period; (a) spherical shape (b) cusped shape (c) vertical aligned oblate spheroid shape. Fig. 5 illustrates the horizontal and longitudinal bubble diameters (D_H and D_L, respectively) under oscillating pressure. The numbers on the plots correspond to the frame numbers of the images in Figure 6, respectively.

The pressure becomes stronger in the order of (a), (b), (c). The left side of the color map is retardation distribution map around the bubble, and each gray original image is shown beside it. Both sides of the retardation map is cell walls. The color map has scale of 0 or 20nm retardation. The range indicates that a strong retardation can been seen in both sides of a bubble. It indicates that there should be strong stress range in the side of the bubbles at contraction phase.

If we focus on the relationship of the bubble shape and change in retardation distribution in the detailed retardation map then we will find an oblate spheroid shape. In both phases of expansion and contraction, the retardation appears around the bubble. Firstly, in the contraction phase, the horizontal diameter becomes shorter with small-shrinking vertical diameter. On the other hand, retardation spreads in the horizontal direction. The largest retardation distribution can be seen at the time of maximum contraction phase. Secondly, in the expansion process, the horizontal diameter becomes longer with small-expanding vertical diameter. In this phase, the retardation distribution spreads in the concentric direction.

3.2 RATE OF DEFORMATION AROUND THE BUBBLE

When a spherical air bubble expands and contracts, it is possible to evaluate the shear rate of the fluid near the surface of the bubble by the spherical model [5]. In this study, we calculated the shear rate of the vicinity fluid of the flat ellipsoid bubble by modifying the spherical model. We define the radius of the minor axis direction as a and the long axis direction as b. We calculated the volume of the flat ellipsoidal bubble from Eq.(5). Then, the volume; V is converted to a sphere with the same volume and the average of sphere radius; D_{eq} is an equivalent diameter calculated by Eq.(6). From these, we calculated the shear rate by using a spherical model.

$$V = \frac{4}{3}\pi a b^2 \tag{5}$$

$$D_{eq} = \sqrt[3]{ab^2} \tag{6}$$

As a result, under pressure-oscillating field, when the bubble remained spherical shape (a), shear rate on the bubble surface was 325 s^{-1}. When the shape changes to cusped shape (b) and ellipsoidal oblate shape (c), the shear rates were 1060 s^{-1} and 1250 s^{-1}. Furthermore the normal stress difference, N_1 value, indicating the elasticiy is high in the case of (b) and (c) as shown in Fig. 1. It is expected that the fluid around the bubble shows strong elasticity. In nature, surface tension makes the bubble spherical shape. The strong elastic effect appeared in the vicinity of the bubble might overcome the effect of surface tension, and the bubble may change to the vertically aligned oblate spheroid shape.

3.3 STRESS FIELD AROUND THE BUBBLE

We performed the evaluation based on the retardation value on both sides of a bubble. ξ/D_{eq} is a non-dimensional distance, the distance from bubble surface ξ normalized by average of sphere radius D_{eq}. ξ/D_{eq} is zero at the bubble surface.

Firstly, we focus on the horizontal direction. The retardation value in the horizontal direction is plotted depending on the non-dimensional distance ξ/D_{eq} in Figure 7. The retardation value indicates the highest value in the vicinity of the bubble surface; around ξ/D_{eq}=0. It indicates that a strong stress is generated on the bubble surface, and is attenuated with distance. In other words, the retardation value increases exponentially closing to the bubble surface.

Comparing three types of the bubble shape, the oblate spheroid shape produces the strongest retardation, followed by cusped shape and spherical shape. Each result is a reflection of the degree of deformation. Moreover, in comparing the contraction and expansion phase, it can be seen that the distribution of strong retardation range widely.

Secondly, we focus on the vertical direction (Figure 8). It shows the strongest retardation value in the vicinity of the bubble surface like horizontal direction . However the value is rapidly attenuated as ξ/D_{eq} is increasing, unlike the result of the horizontal direction. Especially for oblate shape in contraction phase, the attenuation is remarkable. These results correspond to local flow structure around the bubble. The details are discussed in the next section.

(a) contraction phase

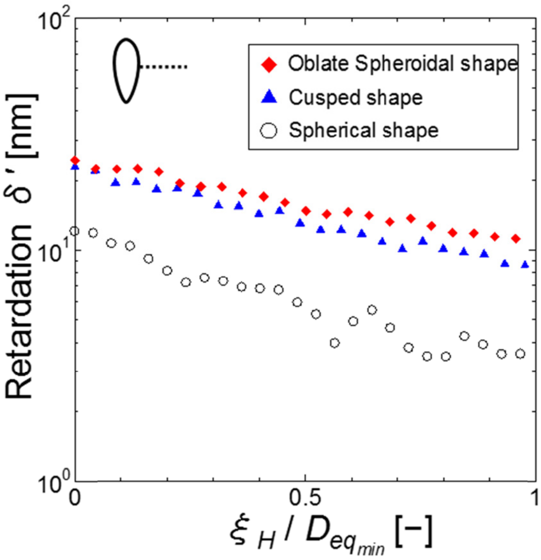

(b) expansion phase

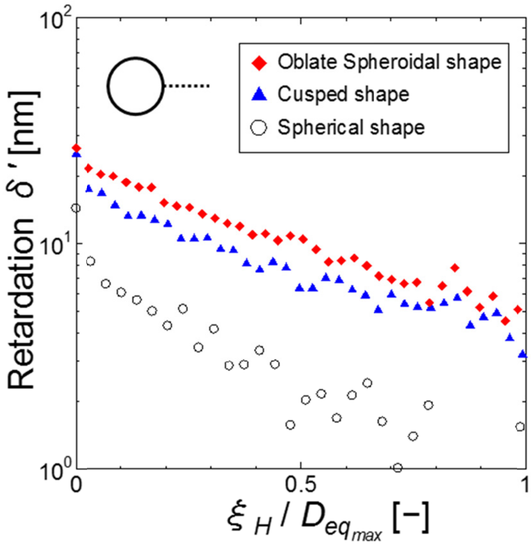

Figure 7. Effect of non-dimensional distance on horizontal retardation at (a)contraction phase, (b)expansion phase.

(a) contraction phase

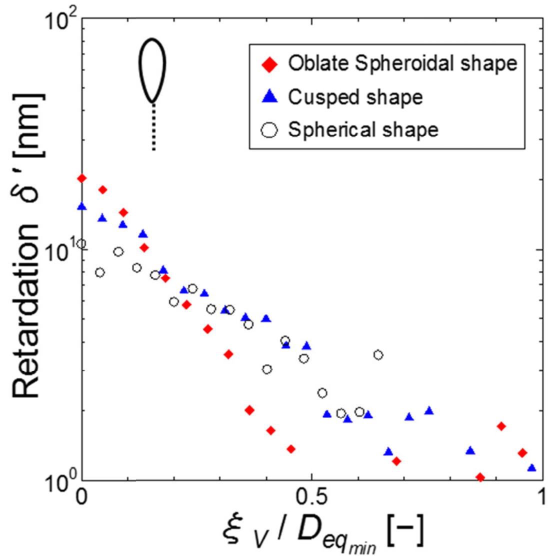

(b) expansion phase

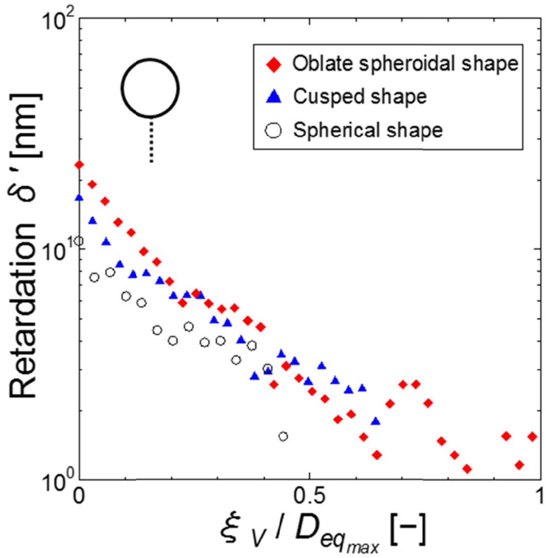

Figure 8. Effect of non-dimensional distance on vertical retardation at (a)contraction phase, (b)expansion phase.

3.4 LOCAL FLOW MODEL

Generally, the bubble keeps sphereical shape in itself due to the surface tension. While applying a weak pressure, the bubble also keeps sphere because the bubble is pressured isotropically (Figure6 (a)). However, we apply instantaneous deformation of expansion and contraction to a bubble in the viscoelastic solution using a pressure oscilattion. In this case, local flow occurs around the bubble, moreover effect of elasticity is greater than the restoring force dut to surface tension. We consider the local flow structure of each shape.

Firstly, we focus on the cusped shape (Figure6 (b)). When the bubble changes to contraction from expansion, the bubble volume decreases. Then the fluid flows into the vacant space to fill. We refer to this supplying flow as inflow. Figure 9 shows flow structure of cusped shape in the contraction phase. In contraction phase, inflow surrounding the bubble concentrate in the lower part. Then it starts to flow in the lower direction. Here hoop stress occurs along the bubble edge. Therefore, the bubble exhibit a cusped shape.

Secondly, we focus on the oblate spheroidal shape (Figure6 (c)). In this case, inflow is located on either side of the bubble and starts to flow along the circumferential direction. This flow structure can image a ball which is sandwiched between two sheets as shown in Figure 10 (a). Assuming that we pull the two sheets in all directions, the ball is crushed and it deforms to the oblate shape. At the same time, the luquid between sheets and a ball is discharged to outside. Because of this both sided outflow, the bubble makes the edge circular. In other words, it constitutes of negative wake in the circumferential direction. Furthermore, hoop stress is generated along the bubble edge as shown in Figure 10 (b). Hoop stress is caused by the elasticity of the liquid.

We compare both of flow structure and the retardation distribution. In case of cusped shape, outflow is concentrated, it makes a local uniaxial

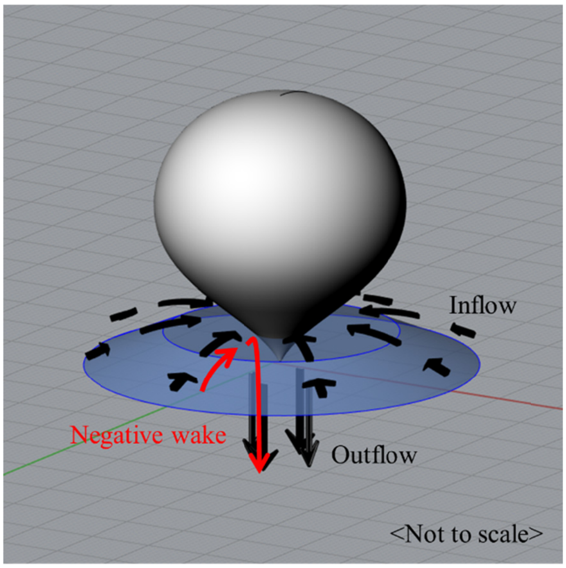

Figure 9. Flow structure around the cusped bubble in the contraction phase

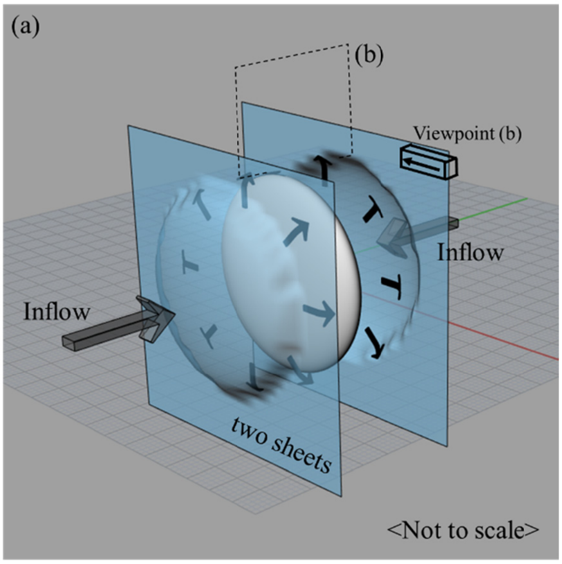

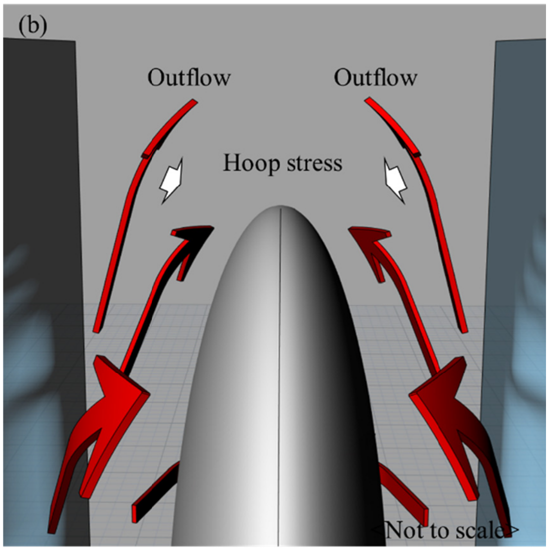

Figure 10. (a) Flow structure around the oblate spheroidal bubble in the contraction phase (b) Outflow with circumferential bubble edge

elongational flow. In contrast, outflow of oblate spheroicdal shape is spreaded flow. Therefore, it is a weak flow while taking in any cross-section. The reason of different tendency of oblate shape in Figure8 (a) is here.

4. CONCLUSIONS

In this study, we discussed about bubble shape and the birefringence profile around the bubble under pressure oscillation. Three types of bubble shape appear under pressure-oscillating field in CMC solution. The shapes are spherical, cuspidal and oblate spheroidal. They appear in accordance with the shear rate, which is calculated by the spherical model (in the chapter 3.2). In addition, we measured the stress distribution of each bubble shape with 2D polarization high speed camera. As a result, we found that, firstly, strong stress field is generated in the vicinity of the bubble surface and finally, stress field is different for each shape, and it is influenced by the elasticity. Furthermore from this result, each flow structure is modelled as shown in figure 9 and 10.

5. ACKNOWLEDGEMENTS

Part of this work was supported by JSPS KAKENHI Grant Numbers (C)23560195 and (C)26420107.

6. LITERATURE CITED

[1] D. De Kee and R.P.Chhabra, “*A photographic study of shapes of bubbles and coalescence in Non-newtonian polymer solutions*”, 1988, Rheol Acta 27:656-660

[2] Hassager O, “*Negative wake behind bubbles in non-newtonian liquids*”, 1979, Nature Vol.279

[3] J.R. Herrera-Velarde, R. Zenit, D. Chehata, and B. Mena, "*The flow of non-Newtonian fluids around bubbles and its connection to the jump discontinuity*", 2003, J. Non-Newtonian Fluid Mech. 111, 199

[4] Shriram B. Pillapakkam, Pushpendra Singh, Denis Blackmore and Nadine Aubry, "*Transient and steady state of a rising bubble in a viscoelastic fluid*", 2007, J. Fluid Mech. Vol. 589, pp215-252

[5] S. Iwata, *et al*., "*Pressure Oscillation Defoaming for Viscoelastic Fluid*", *J. Non-Newtonian Fluid Mech.*, 151, 30-37 (2008)

[6] Barnett, S. M., Humphery, A.E., and Litt, M., 1966, "*Bubble Motion and Mass Transfer in Non-Newtonian Fluids*", AIChE J, 12(2), pp. 253-259

[7] G.Astarita and G.APuzzo, 1965, "*Motion of Gas Bubbles in Non-Newtonian Liquids*", Vol.11 NO.5 pp. 815-820

[8] D. FUnfschilling and H. Z. LI, "*Effects of the Injection Period on the Rise Velocity and Shape of a Bubble in a Non Newtonian Fluid*", 2006, Chemical Engineering Research and Design, 84(A10): 875-883

[9] Y. J. Liu, T. Y. Liao and D. D. Joseph, "*A two-dimensional cusp at the trailing edge of an air bubble rising in a viscoelastic liquid*", Journal of Fluid Mechanics ,Vol. 304 / December 1995, pp 321- 342

Conference on Modelling Fluid Flow (CMFF'15)
The 16th International Conference on Fluid Flow Technologies
Budapest, Hungary, September 1-4, 2015

NUMERICAL INVESTIGATION OF THE EFFECT OF HEMATOCRIT ON BLOOD FLOW CHARACTERISTICS IN A STENOSED VESSEL

Kun Hyuk SUNG[1], Kyoungchul RO[2], Hong Sun RYOU[3]

[1] Department of Mechanical Engineering, Chung-Ang University, Seoul, Korea. Tel.: +82 2 813 3669, E-mail: ilmarekhs@cau.ac.kr.
[2] Department of Railroad Vehicle Engineering, Dongyang University, Korea. E-mail: kcro@dyu.ac.kr
[3] Corresponding Author. Department of Mechanical Engineering, Chung-Ang University, Seoul, Korea. Tel.: +82 2 820 5280, E-mail: cfdmec@cau.ac.kr.

ABSTRACT

Recently, pathogenesis and diagnosis of vessel disease have numerically investigated based on wall shear stress (WSS) related index and flow fractional reserve (FFR). Thus, it is important to understand the hemorheology characteristics and the behavior of red blood cells (RBCs) has a significant influence on shear viscosity of blood. However, almost previous researches have used a single phase blood (SPB) model which is unable to consider a change in local distribution of RBCs.

This study is focused on the effect of hematocrit on blood flow characteristics in a stenosed vessel. The migration and segregation of RBCs are simulated with the multi-phase blood (MPB) model which considers two phases of RBCs and plasma by using the Eulerian-Eulerian method.

Compared with the MPB model, the pressure drop cross the stenosis and the maximum WSS decrease 7% and 60%, respectively. On the contrary, the length of recirculating flow regions after the stenosis increases 15% in the SPB model. This is because the SPB model overpredicts the shear viscosity of blood in disturbed flow region. Consequently, it is necessary to consider the change in local hematocrit to more accurately obtain the blood flow characteristics in a stenosed vessel.

Keywords: multi-phase blood model, stenosis, pressure drop, wall shear stress, CFD.

NOMENCLATURE

ρ	$[kg/m^3]$	density
$\vec{v}$	$[m/s]$	velocity vector
μ	$[Pa \cdot s]$	shear viscosity
κ	$[Pa \cdot s]$	bulk viscosity
p	$[Pa]$	pressure
r_o	$[m]$	radius of vessel
R	$[m]$	radius of vessel in stenosed region
z_o	$[m]$	axial length of stenosis region
ε	[-]	volume fraction

Subscripts and Superscripts

i	any one of RBC and plasma phase
RBC	RBC phase
plasma	plasma phase

1. INTRODUCTION

Atherosclerosis, which is a major factor of stenosis, is caused by a complex interaction between blood elements and the physiological state of the endothelium at the sites of disturbed flow. The stenosis is caused by a narrowing or blocking of the arteries due to plaque which restricts blood flow, and reduces the amount of oxygen to the heart. Several studies have investigated a correlation of hemo-dynamic characteristics with atherosclerotic plaque sites located at curvatures and branches [1, 2].

Blood consists mainly of a dense suspension of red blood cells (RBCs) in plasma, and the interaction between RBCs and plasma is a key factor on the non-Newtonian behavior of blood. Most of total hemodynamic force, i.e., wall shear stress, is caused by behavior of RBCs such as aggregation and adhesion [3]. In a decade, multi-phase models have investigated to simulate the behavior of blood cells [4, 5]. However, almost of the numerical studies have assumed that blood is a single-phase fluid by using viscoelastic models such as Carreau, Casson, Power-law and etc [6]. The single-phase models are impossible to consider the behavior of RBCs.

Recently, FFR-CT technique has being investigated to determine the severity of coronary stenosis. Fractional flow reserve (FFR) is an invasive method using a pressure probe. On contrary, FFR-CT analysis is a non-invasive method numerically analysing blood flow in a 3D model of the coronary tree created from CT-data. Thus, more accurate CFD model is essential to consider a variety of physiological flow conditions and rheological conditions.

This study is focused to investigate the effect of hematocrit on blood flow. To achieve the purpose, blood is modelled by the single-phase blood (SPB) model and the multi-phase blood (MPB) model and the results of both models are compared to each other regarding hemodynamic factors such as pressure drop across the stenosis, wall shear stress and reattachment point.

2. METHODS

Blood is modelled by the SPB model and the MPB model. Non-Newtonian viscosity model is used to consider a hemorheological behavior for each blood model and numerical cases are presented in Table 1.

Table 1. Non-Newtonian model for blood models

Case	Non-Newtonian viscosity model
SPB	Carreau model
MPB	Two-phase model

2.1. Modelling and grid generation

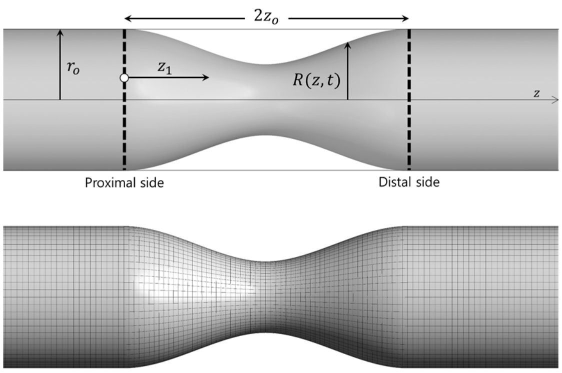

Figure 1. Stenosed blood vessel model and grid

As shown in Figure 1, the diameter of vessel in the stenosis region is modelled by using Eq. (1) suggest by Young [7].

$$R(z)=\left[r_o-a\cdot r_o\left[1+\cos\pi\left(\frac{z-z_1}{z_o}\right)\right]\right] \tag{1}$$

Axial length of the stenosed region is 16 mm and the diameter of vessel except the stenosed region is 8mm constantly. Rate of stenosis is 50% with no eccentricity, i.e., a is 0.5.

The grid for numerical analysis comprises 570,840 hexahedra cells, and the number of cells is selected by a grid independent test.

2.2. Governing equations

2.2.1. Single-Phase Model

For a single phase flow, general conservation equations for mass and momentum are respectively presented as Eqs. (2) to (3).

$$\nabla\cdot\left(\rho\vec{\upsilon}\right)=0 \tag{2}$$

$$\nabla\cdot\left(\rho\vec{\upsilon}\vec{\upsilon}\right)=-\nabla p\delta+\nabla\cdot\left(\mu\dot{\gamma}\right) \tag{3}$$

where, blood density is 1,090 kg/m^3 [8].

In the single-phase model, the cells suspended in blood are simplified as a continuous viscous fluid by using non-Newtonian fluid models. In our study, Carreau model is used to simulate the shear thinning behavior of blood. Eq. (4) is used for constitutive relation between the shear viscosity of blood and the rate of shear strain. In Eq. (4), constants such as $\mu_0, \mu_\infty, \lambda$ and n are selected to consider blood rheology characteristics [9].

$$\mu=\mu_\infty+\left(\mu_0-\mu_\infty\right)\left[1+\left(\lambda\dot{\gamma}\right)^2\right]^{\frac{(n-1)}{2}} \tag{4}$$

2.2.2. Multi-Phase Model

In our study, the Eulerian-Eulerian multiphase model is used to simulate the behavior of the cells suspended in blood. The continuous phase is plasma which is the Newtonian fluid, and the dispersed phase is red blood cells (RBCs). In our study, white blood cells and platelets are neglected because almost of the total hemodynamic force is caused by the RBCs [3]. Consequently, blood flow is considered as a two-phase flow including plasma and RBCs. The phasic volume fraction model is used for computing the volume occupied by each phase at all of local positions. The summation of volume fraction of each phase is equal to one as shown in Eq. (5).

$$\varepsilon_{\text{plasma}}+\varepsilon_{\text{RBC}}=1 \tag{5}$$

The continuity equation for each phase is given by Eq. (6).

$$\nabla\cdot\left(\rho_i\varepsilon_i\vec{\upsilon}_i\right)=0 \tag{6}$$

where, *i* represents any one phase of both phases. Densities of RBCs and plasma are 1,020 kg/m^3 and 1,100 kg/m^3, respectively. The momentum equation for each phase is given by Eq. (7).

$$\nabla\cdot\left(\rho_i\vec{\upsilon}_i\vec{\upsilon}_i\right)=-\varepsilon_i\nabla p\delta+\nabla\cdot\left(\bar{\bar{\tau}}_i\right)+\sum_{i=RBC}\beta\left(\vec{\upsilon}_{\text{RBC}}-\vec{\upsilon}_{\text{Plasma}}\right) \tag{7}$$

$$\overline{\overline{\tau}}_i = \varepsilon_i \left(\mu_i \dot{\gamma}_i \right) + \varepsilon_i \left(\kappa - \frac{2}{3} \mu_i \right) \nabla \cdot \vec{\upsilon}_i \overline{\overline{I}} \quad (8)$$

where, plasma viscosity, μ_{Plasma}, is 0.001 Pa·s and coefficient, β, is referred from Schiller and Naumann model [3, 10]. The constitutive equation, Eq. (8), for stress tensor of each phase is used to solve Eqs. (5) to (7). Also, μ_{RBC} must be determined to solve Eq. (8). For calculating the shear viscosity of RBC phase, we use the two-phase blood model suggested by Jung et al. [4], which is applicable to a wide physiological range of hematocrit and the shear rate [11]. In addition, the effect of the behavior of RBCs is considered with a function of the volume fraction of RBCs and the shear rate.

2.3. Numerical details

Three dimensional incompressible Navier-Stokes equations are solved by ANSYS FLUENT V14 based on the finite volume method with the pressure-based coupled solver. The flow regime is laminar because mean Reynolds number is below 200 in all cases at the cross-sectional plane of the center of stenosis. For the pressure-velocity coupling, the SIMPLE algorithm and the phase coupled SIMPLE algorithm are used in the SPB case and the MPB case, respectively. Residual criteria for all variables is below 1E-3.

2.3.1 Boundary conditions

The velocity-inlet boundary condition is applied to the inlet of the vessel. The inlet velocity is 0.1 m/s which is an average velocity of pulsatile flow at the common carotid artery [12]. The pressure-outlet with static pressure 0 Pa condition is applied to the outlet of the vessel. The wall of the vessel is rigid with no-slip condition. In the MPB case, the volume fraction of RBCs is fixed to 45% at the inlet of the vessel.

3. RESULTS

3.1. Pressure drop across the stenosis

The pressure drop across the stenosis is defined as a mean pressure difference between the proximal and distal plane as described in Figure 2. The distal plane is located far enough from Z=0 to not include reverse flows.

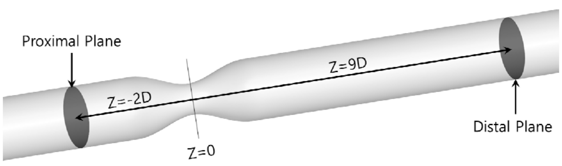

Figure 2. Two planes for averaging pressure

Compared with the MPB case, the pressure drop increases by 7.5% in the SPB case as base on values in Table 2. This result is related to the viscous effect near wall.

Table 2. Pressure drop across the stenosis

Case	Proximal [Pa]	Distal [Pa]	ΔP [Pa]
SPB	88.1	11.9	76.2
MPB	81.8	2.3	70.5

3.2. Wall Shear Stress

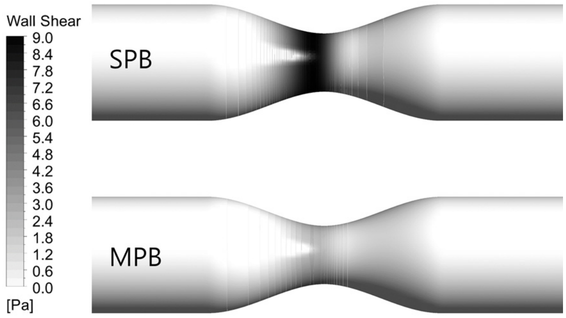

Figure 3. Wall shear stress distribution

Figure 3 shows wall shear stress (WSS) distribution of all cases. The maximum WSS in the SPB case and the MPB case is 9.1 Pa and 3.7 Pa, respectively. Compared with the SPB case, WSS and shear viscosity of the MPB case decreases respectively by 64% and 35% as presented in Table 3.

Table 3. Properties averaged on circumferential line at the center of stenosis (Z=0)

Case	WSS [Pa]	Shear viscosity [Pa · s]
SPB	7.55	3.66E-3
MPB	2.70	2.38E-3

In the MPB case, the shear viscosity is closer to the viscosity of plasma due to a decrease in RBCs phase near the wall of the stenosis region, where the minimum volume fraction of RBCs is 41.8%. It implies that the two-phase model of the MPB case realistically traces the mechanisms for the exchange of momentum and mass between RBCs and plasma.

3.3. Reattachment point

Compared with the SPB case, flow recirculating region occurs after the stenosis in the MPB case. Figure 4 shows axial velocity vector and reverse flow regions where the axial velocity is negative.

Reattachment point is defined as the end of the reverse flow region in Fig. 4. The reattachment point of the MPB case is further way from the stenosis. This is because the shear viscosity decreases as mentioned earlier in Section 3.2, that is, the viscous effect decreases near wall as compared with the SPB case.

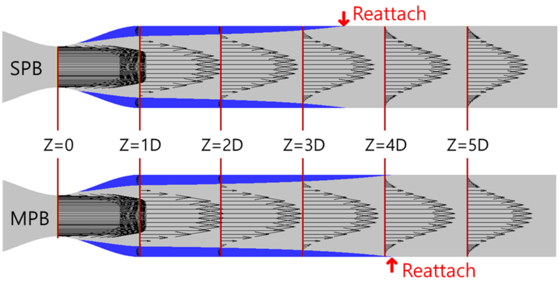

Figure 4. Axial velocity vector from each line and reverse flow region

4. DISCUSSION

Methodologically, the FFR depends only on the distal to proximal pressure difference in the coronary artery. Measurements are taken by placing a probe across the stenosis during hyperaemia, and thereby it allows the physician to determine the stenosis severity. The index, which is defined as Eq. (9), is relatively independent on heart rate and blood pressure [13].

$$\mathrm{FFR} = \frac{P_{\mathrm{proximal}} - P_{\mathrm{distal}}}{P_{\mathrm{proximal}}} \tag{9}$$

In the result of our study, pressure drop across stenosis varies with the blood model by 7.5 percentage point. On the contrary, the FFRs of all cases are 0.86 as based on values in Table 2. This is because the FFR is relative index related to the proximal pressure and the pressure drop across the stenosis. Thus it is not affected by the blood model.

On the other hand, the blood model has a significant influence on local blood flow mechanics such as local WSS and flow recirculating region. In general, the physiological magnitude of WSS, i.e., baseline WSS, ranges approximately from 1.5 to 2.5 Pa [14]. The leukocytes adhesion is activated as WSS is over 7.5 Pa, thereby leading to atherosclerosis or hyperplasia [15]. The maximum WSS difference between both cases is 5.4 Pa which is a significant value by comparison to the baseline WSS. In addition, disturbed flow conditions play a role in platelet activation, atherosclerotic plaque cap rupture.

Compared with the SPB case, disturbed region after the stenosis increases in the MPB case due to a decrease in the viscous effect near wall and the distal pressure.

5. CONCLUSION

In order to investigate the effect of hematocrit on blood flow, blood is modelled by the single-phase blood (SPB) model and the multi-phase blood (MPB) model. The results are as follows.

- Compared with the SPB case, WSS and shear viscosity of the MPB case decreases respectively by 64% and 35%.
- Compared with the MPB case, the pressure drop increases by 7.5% in the SPB case.
- FFR is constant regardless of the blood model.
- The reattachment point of the MPB case is further way from the stenosis.

Consequently, it is necessary to consider the change in local hematocrit to more accurately obtain the blood flow characteristics in a stenosed vessel. On the contrary, SPB model is more effective for calculating FFR with respect to a reduction of computing time although it over-predicts viscous effect near wall.

ACKNOWLEDGEMENTS

This research was supported by Basic Science Research Program through the National Research Foundation of Korea(NRF) funded by the Ministry of Education(2014R1A1A2055996).

REFERENCES

[1] Caro, C. G., Fitz-Gerald, J. M. and Schroter, R. C., 1971, "Atheroma and arterial wall shear. Observation, correlation and proposal of a shear dependent mass transfer mechanism for atherogenesis", *Proc R Soc Lond B Biol Sci*, Vol. 177, pp. 109-59.

[2] Malek, A. M., Alper, S. L. and Izumo, S., 1999, "Hemodynamic shear stress and its role in atherosclerosis", *JAMA : the journal of the American Medical Association*, Vol. 282, pp. 2035-2042.

[3] Jung, J., Lyczkowski, R. W., Panchal, C. B. and Hassanein, A., 2006, "Multiphase hemodynamic simulation of pulsatile flow in a coronary artery", *J Biomech*, Vol. 39, pp. 2064-73.

[4] Jung, J. and Hassanein, A., 2008, "Three-phase CFD analytical modeling of blood flow", *Medical Engineering & Physics*, Vol. 30, pp. 91-103.

[5] Yilmaz, F. and Gundogdu, M. Y., 2009, "Analysis of conventional drag and lift models for multiphase CFD modeling of blood flow", *Korea-Australia Rheology Journal*, Vol. 21, pp. 161-173.

[6] Pereira, J. M. C., Serra e Moura, J. P., Ervilha, A. R. and Pereira, J. C. F., 2013, "On the uncertainty quantification of blood flow viscosity models", *Chemical Engineering Science*, Vol. 101, pp. 253-265.

[7] Young, D. F., 1968, "Effect of a Time-Dependent Stenosis on Flow Through a Tube", *Journal of Manufacturing Science and Engineering*, Vol. 90, pp. 248-254.

[8] Van Tricht, I., De Wachter, D. S., Tordoir, J. H. and Verdonck, P. R., 2005, "Does the Dialysis Needle Design Affect the Hemodynamics in the Vascular Access?", *ASAIO Journal*, Vol. 51, pp. 58A.

[9] Cho, Y. I. and Kensey, K. R., 1991, "Effects of the non-Newtonian viscosity of blood on flows in a diseased arterial vessel. Part 1: Steady flows", *Biorheology*, Vol. 28, pp. 241-262.

[10] Jung, J., Hassanein, A. and Lyczkowski, R. W., 2006, "Hemodynamic computation using multiphase flow dynamics in a right coronary artery", *Ann Biomed Eng*, Vol. 34, pp. 393-407.

[11] Brooks, D. E., Goodwin, J. W. and Seaman, G. V., 1970, "Interactions among erythrocytes under shear", *J Appl Physiol*, Vol. 28, pp. 172-7.

[12] Gijsen, F. J., van de Vosse, F. N. and Janssen, J. D., 1999, "The influence of the non-Newtonian properties of blood on the flow in large arteries: steady flow in a carotid bifurcation model", *J Biomech*, Vol. 32, pp. 601-8.

[13] de Bruyne, B., Bartunek, J., Sys, S. U., Pijls, N. H., Heyndrickx, G. R. and Wijns, W., 1996, "Simultaneous coronary pressure and flow velocity measurements in humans. Feasibility, reproducibility, and hemodynamic dependence of coronary flow velocity reserve, hyperemic flow versus pressure slope index, and fractional flow reserve", *Circulation*, Vol. 94, pp. 1842-9.

[14] Ku, D. N., Giddens, D. P., Zarins, C. K. and Glagov, S., 1985, "Pulsatile flow and atherosclerosis in the human carotid bifurcation. Positive correlation between plaque location and low oscillating shear stress", *Arteriosclerosis*, Vol. 5, pp. 293-302.

[15] Kleinstreuer, C., Hyun, S., Buchanan, J. R., Jr., Longest, P. W., Archie, J. P., Jr. and Truskey, G. A., 2001, "Hemodynamic parameters and early intimal thickening in branching blood vessels", *Crit Rev Biomed Eng*, Vol. 29, pp. 1-64.

Conference on Modelling Fluid Flow (CMFF'15)
The 16th International Conference on Fluid Flow Technologies
Budapest, Hungary, September 1-4, 2015

USING 3D SHAPE OPTIMIZATION TO REDUCE TURBULENT MIXING LOSSES INSIDE THE ROTOR CAVITY OF A PITOT-TUBE-JET-PUMP FOR FLUID-FLUID SEPARATION

Jan MEYER[1], László DARÓCZY[2], Gábor JANIGA[3], Dominique THÉVENIN[4]

[1] Corresponding Author. Laboratory of Fluid Dynamics and Technical Flows, Institute of Fluid Dynamics and Thermodynamics, University of Magdeburg "Otto von Guericke". Universitaetsplatz 2, 39106 Magdeburg, Germany. Tel.: +49 391 67 18194, Fax: +49 391 67 12840, E-mail: jan.meyer@ovgu.de
[2] Laboratory of Fluid Dynamics and Technical Flows, Institute of Fluid Dynamics and Thermodynamics, University of Magdeburg "Otto von Guericke". E-mail: laszlo.daroczy@ovgu.de
[3] Laboratory of Fluid Dynamics and Technical Flows, Institute of Fluid Dynamics and Thermodynamics, University of Magdeburg "Otto von Guericke". E-mail: janiga@ovgu.de
[4] Laboratory of Fluid Dynamics and Technical Flows, Institute of Fluid Dynamics and Thermodynamics, University of Magdeburg "Otto von Guericke". E-mail: thevenin@ovgu.de

ABSTRACT

An unconventional radial pump is considered in this work for low-specific speed applications: the Pitot-Tube-Jet-Pump (PTJ pump). Using an optimized diffusor channel from a previous study, the external geometry of the pick-up tube placed within the rotor cavity is investigated in the present study. The main goal is to check if the highly efficient diffusor design can be considered as superior as well for fluid-fluid separation application, or if the classical design is more advantageous because it leads to less back-mixing.

Computational Fluid Dynamics (CFD) simulations are used together with a genetic optimization algorithm to find an improved surface design. The objective is to minimize the turbulent kinetic energy within the rotor cavity while taking into account all relevant manufacturing constraints.

Keywords: CFD, low specific speed, optimization, pump, turbomachinery, turbulence reduction

1. INTRODUCTION

To classify the impeller design in turbomachinery, the non-dimensional specific speed n_S is used, which is defined as:

$$n_S = \omega \cdot \frac{\sqrt{Q}}{(g \cdot H)^{3/4}}, \tag{1}$$

where ω is the rotational speed, Q is the volumetric flow rate, g is the gravitational acceleration, H is the total head. Pumping fluid in low specific speed ranges (, i.e., $n_S < 0.03$) is in general done by rotary displacement pumps, as they have better hydraulic efficiency compared to radial pumps. However, there is an increasing demand for centrifugal pumps working at low-specific speed, due to decreased noise and vibration, very compact design and higher speed.

The key factor for the adverse radial pump performance is caused by the disc friction losses inside the impeller, being dominant at this operation point [1]. A possible solution for this problem can be found in the unconventional design of the so-called Pitot-Tube-Jet pump (PTJ pump), where the impeller has no disc friction loss due to closed impeller channels. It operates at $n_S \approx 0.015$ and delivers a better performance for a given diameter and speed compared to conventional pumps. However, the design of this pump has not been improved since the first patents, decades ago (see, e.g., [2]).

2. WORKING PRINCIPLE OF PTJ PUMP

One of the main advantages of the PTJ pump is its simple and very robust design. There are just 3 key components: the rotor, the impeller and the stationary pick-up tube (or Pitot-tube) sketched in Fig. 1. Fluid transport and elevation is achieved in the PTJ pump due to a rotodynamic principle where fluid enters the pump's suction line and is passed through various closed rectangular impeller channels, which continuously increase the fluid's kinetic energy and static pressure in radial direction. For a standard radial pump, the fluid would now exit the impeller outward into a volute or spiral casing. Instead, in a PTJ pump, the fluid is gathered in a rotating chamber and rotates close to the rotor wall with nearly the same velocity. Inside the rotor the fluid is gathered by a stationary pick-up tube. The diffusor channel is comparable in its function to a volute. The kinetic energy of the fluid is partly transformed into pressure energy

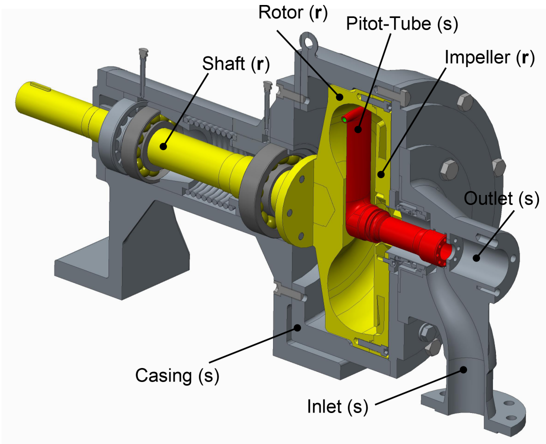

Figure 1. Cut representation of a classical Pitot-Tube-Jet-Pump (PTJ pump). The CAD model shows rotating (r, in yellow) and static (s, in red) parts

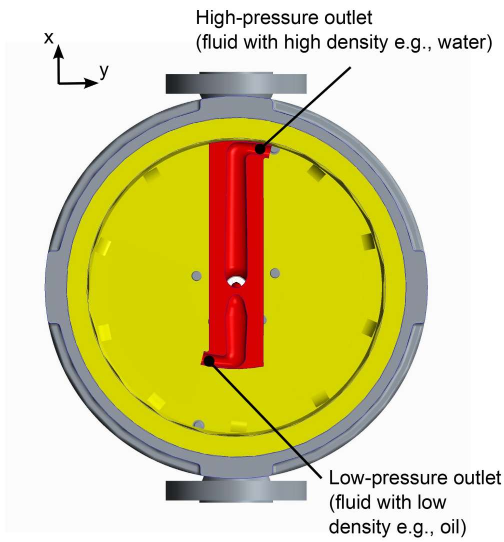

Figure 2. Application of the PTJ pump for fluid-fluid separation using two-wing pick-up tube with separate outlets at different radial positions

due to the diffusor passage inside the pick-up tube. Overall relative velocities between fluid and solid are small except for the stationary parts (, i.e., the pick-up tube). Polishing the surface and choosing a suitable geometrical design help minimizing the losses. According to [3] it is possible with a PTJ pump to generate shut-off heads up to 2000 m and flow-rates at best efficiency point up to 100 m^3/h. Due to the vanishing disc friction loss in the impeller and the efficient transformation of kinetic energy inside the rotor cavity, the PTJ pump is able to generate up to 1.6 times the head of a comparable centrifugal pump [4].

The adaption of the PTJ pump for liquid-liquid separation can be achieved using a double-wing pick-up tube with two separate outlets (Fig. 2). The fluid mixture inside the cavity experiences centrifugal forces, as a result the lighter liquid forms a bulk region close to the axis (, i.e., low-pressure outlet), while the heavier liquid is gathered at the outer peripheral of the rotor (, i.e., high-pressure outlet). This is why the pick-up tube inlets are placed at different radial positions with respect to the axis of rotation. Considering for instance an oil/water system and assuming a steady liquid-liquid interface inside the cavity, we can discharge clarified oil close to the axis and purified water at the periphery of the rotor. However, the oil-water interface in-between is very sensitive towards turbulent mixing, as caused by the blockage of the pick-up tube and associated wake. Since the residence time of the fluid mixture is limited, such back-mixing effects need to be minimized, which is done now with shape optimization.

3. REVIEW

Recent studies using CFD to improve the impeller design for the PTJ pump have been described in [5, 6, 7]. Also, experiments were discussed in [8] to study the impact of the external Pitot-tube geometry on pump performances. However, the geometry changes were done manually, with a heuristic approach. In a previous investigation [9], the authors already reduced the total pressure loss inside the diffusor channel by 70% with help of CFD-based optimization combined with a mesh morphing technique, compared to the standard configuration. This shows the high potential for improving the classical design towards better efficiency when using appropriate numerical simulations and optimization methods.

However, the previous study considered only the flow within the diffusor channel. No external contour is available so far for the Pitot-tube. A well-suited design is needed as well for the external geometry, since it will impact directly the flow within the rotor. This is important to reduce corresponding pressure losses, but even more when using simultaneously the PTJ pump for liquid-liquid separation, since back-mixing of the two liquid phases must be avoided by all means.

According to the classical Kutta-Joukowski theorem for a two-dimensional, incompressible flow the streamlines around the pick-up tube can only close-in at leading and trailing edge for a non-viscous flow. In reality viscous effects are obviously encountered, which lead to flow separation and a vortex street in the wake. The energy for these vortices must to compensated by the pump engine, decreasing the overall efficiency. For a conventional pick-up tube, a wing-shaped external body already leads to more favorable conditions, reducing the losses (Fig. 3).

Nevertheless, as shown in [9] the 90-degree bends inside the classical diffusor lead to strong recirculation and energy losses. This study checks the possibility of finding a favorable external contour of the diffusor channel, so that both (i) total pressure losses inside the diffusor and (ii) external mixing losses in the rotor cavity are simultaneously minimized. This is done in a fully automatic approach, the

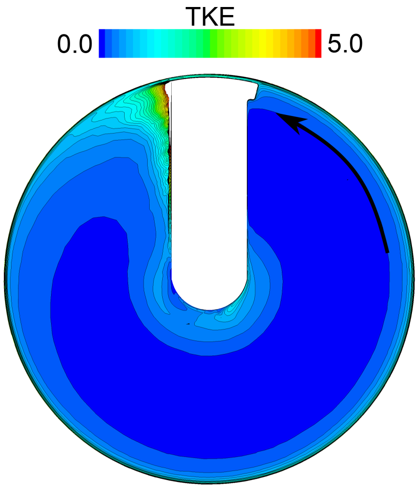

Figure 3. Contour plot of turbulent kinetic energy for a classical pick-up tube in rotating cavity (n = 3000 *rpm*); arrow indicates direction of rotation

whole computations being carried out without human interaction.

The turbulent losses induced by the external contour are crucial to improve performance and need to be strongly reduced in order to open a new field of applications for PTJ pumps: liquid-liquid separation with simultaneous transport. The principle application of the PTJ pump for multiphase separation has already been patented in the 1970's [10] but, to the best of our knowledge, only fluid-solid separation has been considered up to now [11].

The driving force in centrifugal separation is the density difference $\Delta\rho$ between the species in the mixture. The density difference for fluid-fluid applications is much smaller than for fluid-solid configurations, which makes the development of a robust and efficient in-line, liquid-liquid centrifugal separator highly challenging. However, the design of the PTJ pump shows some favorable properties for this application, and a proper system optimization should lead to a successful design.

4. SETUP

The analysis of the external geometry of the Pitot-tube inside the rotor cavity is carried out in a fully-automatic manner, where the optimization work-flow is outlined in Fig. 4. Several steps and software products are required for the robust and efficient generation, simulation and evaluation of the flow phenomena. The objective function is the turbulent kinetic energy k, which is defined as the root-mean-square caused by the velocity fluctuations $\underline{u}'$.

$$k = \frac{1}{2}\sum_{i=1}^{3}\underline{u}_i'^2 \tag{2}$$

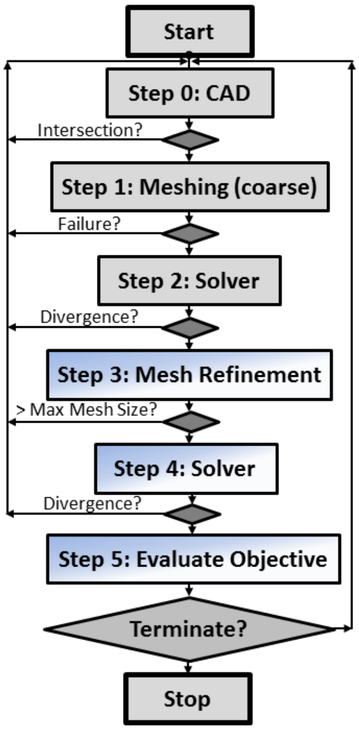

Figure 4. Workflow for shape optimization using OPAL++

In order to reduce losses and back-mixing effects coming from the pick-up tube, the global volume-weighted average of $\bar{k}$ (or TKE) inside the rotor cavity must be minimized.

$$TKE = \bar{k} = \frac{1}{V}\int k\, dV = \frac{\sum_{\mathrm{i}} k_{\mathrm{i}} V_{\mathrm{i}}}{\sum_{\mathrm{i}} V_{\mathrm{i}}} \tag{3}$$

A short description of the computational setup is given below.

4.1. CAD

A CAD (computer-aided design) model is first generated by *CREO Parametric*. The model is created in 3D in full-scale for a PTJ pump with 400 mm diameter. The design parameters are shown in Fig. 5. The internal diffusor passage (green channel in Fig. 5) is generated with a NURBS-spline (Non-Uniform Rational B-spline) connected by 4 variable design points (, i.e, P1 to P4). The respective positions are defined in the $x - y$ plane by radius R and angle φ. The radius and angle for the pick-up tube inlet P0 is fixed for a better compatibility with a conventional pick-up design. The inlet diameter has a circular cross-section and is fixed to $d_0 = 12.7\ mm$. The design of the diffusor passage (inner) is based on a pre-study for $Q = 16\ m^3/h$ with the help of a parametrized CAD model. In this previous study the total pressure losses were minimized by varying the position of the design points P1 to P4 and the respective cross-section width and length. The resulting diffusor channel is kept in this study as a design constraint. A trivial approach for the external pick-up tube contour (see orange geometry in Fig. 5) would be to extrude a wall thickness to the diffusor channel. However it is well-known from airfoil aerodynamics that using instead a streamlined contour reduces flow separation. Therefore an appropriate width W and length L must be found, as pressure gradients due to curvature changes are strongly coupled with flow separation. Four cross-sections are defined in the control points P1 to P4 to allow flexible design changes in radial direction, as we have a radial velocity profile inside the rotating cavity. Imagining no pick-up tube inside the cavity would lead to rigid body motion. Due to the presence of the pick-up tube the velocity profile is distorted and the external cross-sections need to be adapted by shape-optimization to reduce turbulent mixing losses. The positions for the control points P1 to P4 are fixed and only the width W and the length L are varied. The cross-sections are defined to be normal to the NURBS-spline. In total 8 design variables are needed. The allowed ranges for the optimization are listed in Tab. 1, where $S1$ to $S4$ represent the respective cross-section with the control points. These are set relative to the inlet diameter of the pick-up tube (d_0). Trailing and leading edge of the cross-sections are sharp. At P0 a constant circular cross-section is defined with a diameter of 16 mm.

Table 1. Parameter ranges for the design

Design-Parameter	Min [-]	Max [-]
S1W/d_0	1.181	1.575
S1L/d_0	1.575	2.362
S2W/d_0	1.575	3.622
S2L/d_0	1.969	4.882
S3W/d_0	1.969	3.622
S3L/d_0	2.362	4.882
S4W/d_0	3.150	3.622
S4L/d_0	3.228	4.882

4.2. Numerical Simulation

The commercial software package *CD-adapco STAR-CCM+* is used to discretize the flow domain and solve the governing equations using a cell-based finite-volume approach. The steady state simulations are performed in 3D using a coupled flow solver. With the present values of the rotational speed $\omega = 314\ rad/s$ and water kinematic viscosity $\nu = 10^{-6}\ m^2/s$ the Reynolds number is Re $= \frac{\omega r^2}{\nu} = 1.26 \cdot 10^{07}$. This means that the flow is highly turbulent and a turbulence model is needed to close the additional Reynolds stress term in the Navier-Stokes equation. In this study we use the $k-\omega\ SST$ model [12] as it provides the benefits of a $k-\epsilon$ model in the far-field and the $k-\omega$ model near

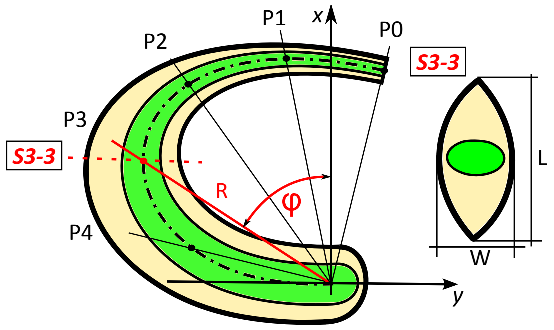

Figure 5. Parametrization of the external geometry (orange) for optimization, the internal diffusor passage being kept from previous study (green); note that this figure does not represent the optimum geometry due to confidentiality issues

the wall. The wall has a no-slip condition and rotates with $\omega = 314\ rad/s$. There are no other boundary conditions necessary as it is a closed cavity.

Meshing was executed in *CD-adapco STAR-CCM+* in a *Parts-Based* approach. This meshing strategy is very useful for shape optimizations as it provides great repeatability. Design changes only need to be done for the input part (, i.e., pick-up tube) and are directly propagated through the pipeline to the volume mesh without user interaction. The mesh consists of polyhedral cell shapes in the core flow and prismatic cells in the wall-bounded flow regime to reduce numerical diffusion and improve accuracy and convergence (here: 10 prismatic cells for all walls). The first cell height is adapted for wall-function, which means that there is no need to resolve the complete boundary layer. Instead, a modeling approach can be used (, i.e., All-y+ Wall treatment). This is a cost-effective approach that enables the simulation and evaluation of many design individuals; a complete resolution of the boundary layer would require larger cell numbers and even more computational time. The automatic surface meshing uses local refinement based on curvature and surface proximity without user interaction. Leading and trailing edge as well as surface areas of the pick-up tube with high surface curvature can be captured accurately in a robust way during the shape optimization. The polyhedral volume mesh is automatically created from the underlying tetrahedral mesh. Global mesh density properties are implied to specify the transition between surface and volume mesh cells (here: mesh density: 1.4; growth rate: 0.6).

As shown in Fig. 4 the meshing procedure consists of two steps - a low-fidelity solution (Step 2) and a high-fidelity solution (Step 4). Optimization of an objective function for complex geometries is time-consuming and requires vast computational efforts. The more design variables and constrains, the more complex is the relation between shape deformation and objective function. As it is not necessary to calculate in detail all flow phenomena for unfavorable configurations, it is much more straightforward to start with a coarse design and use first affordable, low-fidelity simulations (for example coarse mesh, 2D-Euler solvers or vortex lattice methods). Then, the best resulting designs can be used as an initial input for more faithful, but also more time-consuming, simulations. In this study the term low-fidelity work-flow is used for the numerical steps 1 and 2, while the high-fidelity work-flow consists of all steps between Step 1 and 4. Using such a multi-fidelity optimization the efficiency can be greatly enhanced.

The coarse mesh in Step 1 consists of approx. 170 000 cells and is used for the simulation of the key flow features in the rotor cavity. Convergence for the objective function is achieved after 2000 iterations with residuals below 10^{-06}. In Step 3 and Step 4 the mesh is refined based on the flow properties of the low-fidelity solution and additional 1500 iterations are calculated. Mesh refinement is done based on a threshold for the objective function (here: TKE threshold 2 m^2/s^2), which means that each cell in the flow domain is evaluated by StarCCM+ according to the threshold. The threshold has been adapted and tested in first manual studies regarding accuracy and computational time.

```
IF (Cell[TKE] > 2 m^2/s^2)
     MeshSize = 1 mm;
END;
```

This dynamic refinement is capable of improving only flow regions with high TKE (here, cell size reduced to 1 mm). With the improved spatial mesh resolution further simulation time is dedicated to Step 4 in order to improve simulation accuracy. The overall mesh size varies due to this adaptive meshing from $300,000$ up to 2.7 Million cells. For the simulation it means between 2 to 13 times lager computational times compared to the coarse mesh. In order to check that the multi-fidelity work-flow delivers the same trend, the resulting volume-weighted average TKE values for 30 design individuals are plotted in Fig. 6. A linear trend $f(y) = bx$ is observed, starting at the point of origin, which supports the reliability of the low-fidelity work-flow to identify optimized design individuals. A very high coefficient of determination of $R^2 = 0.9876$ is achieved. To calculate a mesh independent TKE value, an even finer grid resolution is necessary. However this is not economic for an optimization, as computational time increases up to a week per individual. The strong correlation between low- and high-fidelity in Fig. 6 confirms that optimized individuals within a low-fidelity approach are also superior with higher resolution. For the final design, which is chosen by the industrial partner for manufacturing, a mesh-independent simulation is running. Due to confidential issues no further details can be given in this paper.

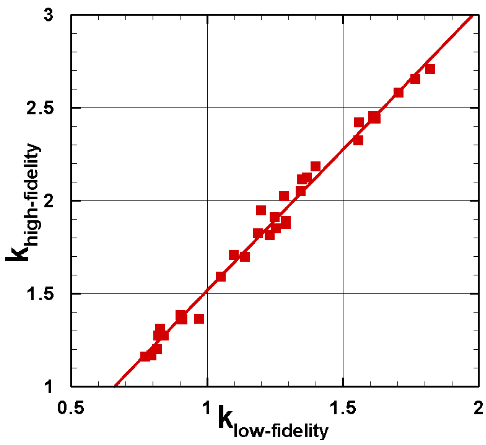

Figure 6. Correlation of turbulent kinetic energy (k) between low- and high-fidelity model for 30 different individuals, x-axis represents the results with low-, y-axis the results with high-fidelity model

4.3. Optimization

The analysis and the optimization of the different configurations have been carried out using the OPtimization Algorithm Library++ (called simply OPAL++). OPAL++ is an object-orientated multi-objective optimization and parametrization framework developed at the University of Magdeburg "Otto von Guericke", [13]. OPAL++ builds on top of our considerable experience with OPAL (see for instance [14]), but it is based on a completely new structure. The software has already been successfully applied to many different problems [13]. The software supports parallel execution, both at the evaluation and at the CFD level, contains several optimization algorithms (NSGA-II, OMOPSO, SPEA2, etc.), Response Surface Methods (Ordinary Kriging with Detrending, Radial Basis Functions, etc.), Design-of-Experiment methods (Near Orthogonal Latin Hypercube Sampling, SOBOL, etc.) and Non-Intrusive Polynomial Chaos (NIPC)) as well.

5. RESULTS

5.1. Low-Fidelity Results

The shape optimization is based on an evolutionary approach using a single-objective genetic algorithm initialized with a Near Orthogonal Latin Hypercube Sampling, which ensures an appropriate exploration. All variables are real-coded. SBX crossover and mutation operators are applied. The algorithm uses a very strong elitism for an aggressive exploitation. Reproduction is based on a tournament. Each generation consists of 40 individuals, the fitness function is the TKE. Default values are used for mutation, cross-over and cross-over coefficients according to [15]. A total of 16 generations have been analyzed (, i.e., 640 individuals), whilst each individual is calculated on a single workstation (Intel Xeon E3-1230 3.30 GHz, 32 GB memory) within 0.5 h. The individual is only valid as long as the numerical solution converges and as long as the outer geometry does not intersect the inner diffuser channel or the rotor. Setting smaller parameter ranges would decrease the variations in the population. However, an increased parameter range contains many individuals with intersection and renders a large portion of the population invalid, making the comparison of their fitness impossible. Note that the term invalid means in this study unfeasible with infinite constrain violation. The investigated parameter range leads overall to 541 valid designs after 16 generations (, i.e., 85 % validity). The results corresponding to all valid designs are plotted in Fig. 7. It can be seen that the wide TKE scatter at the beginning ($\Delta TKE = 1.276\ m^2/s^2$) narrows as the optimization proceeds and a (hopefully global) minimum is approached. In the 16th generation the absolute values for TKE differ only by $\Delta TKE = 0.028\ m^2/s^2$. This uniformity is expected as the optimal solution is approached. To see if the small variation in TKE is coupled with various design possibilities, the standard deviation σ is calculated for each design parameter x_i for the best 40 valid individuals.

$$\sigma_i = \sqrt{(x_i - \bar{x}_i)^2} \tag{4}$$

The higher the deviation for a single parameter, the more the external geometries deviate from each other even after 16 generations. The resulting deviations are listed in Tab. 2. Most variations can be found in the length in section 2 ($S2L/d_0$) with about ± 13 %. Multi-modality is checked for the best 40 individuals but all design values are close to a single value. This means a robust design can be expected after even more generations.

The parallel coordinate plot (short: PCP) in Fig. 8 is a common visualization tool to show high-dimensional correlations. Here 8 design parameters and 1 objective function are presented, leading to a 9-dimensional space. The best individual with minimized TKE is plotted in blue. The respective parameter values are listed in Tab. 2.

It is evident, that the axes are normalized to enable the proper representation of all dimension. Except section 4, the optimal value is always well within the range. The reason is that further decreasing the cross-section width $S4W/d_0$ leads to unavoidable intersection between the fixed diffusor channel and the external cross-section. Previous studies indicated that this lower limit is still manufacturable for the present diffusor channel. The maximum value for the cross-section length $S4L/d_0$ is limited by the diameter of the discharge body of the pick-up tube in axis direction.

This is why for both parameters the standard deviation in Tab. 2 is so small, the optimum lies close to the outside of the parameter domain - it cannot be further improved due to design constraints. Adapting the parametric CAD-model can lead to a more flexible and intensive shape optimization in this area. Nevertheless, the kinetic energy of the flow close to the axis is quite low.

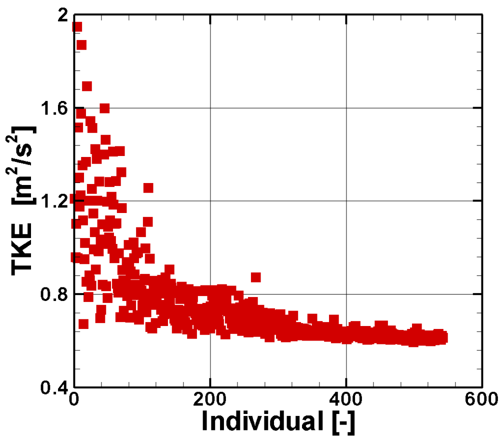

Figure 7. Minimizing turbulent kinetic energy in low-fidelity approach with genetic algorithm (single-objective)

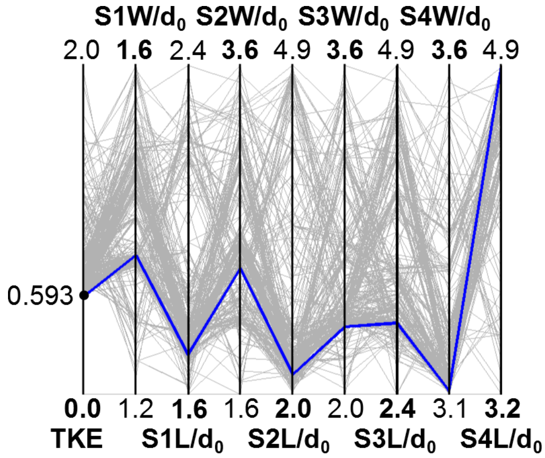

Figure 8. 9-dimensional parallel coordinate plot (PCP) for all individuals during low-fidelity approach. Non-dimensional ranges for design parameters according to Tab. 1. The best individual is marked with blue

This is why the authors rather recommend to pay attention to the outer sections of the pick-up tube with high kinetic energy. Also, for the purpose of liquid-liquid separation, the use of a multiple wing pick-up tube would be necessary as already shown in Fig. 2. Here, a re-design of the CAD model needs to be done close to the axis in order to join the double-wing Pitot-tube in an aerodynamically friendly way.

5.2. High-Fidelity Solution

As already shown in the pre-study in Fig. 6, the mesh refinement approach in the wake of the pick-up tube is showing different quantitative values, but the same trend as the low-fidelity solution. This means

Table 2. Optimum design values for external geometry and maximum standard deviation σ (in percentage) to quantify variation in design parameters over best 40 valid individuals

Design-Parameter	Optimum-Value [-]	σ [%]
$S1W/d_0$	1.347	± 7.15 %
$S1L/d_0$	1.669	± 6.27 %
$S2W/d_0$	2.356	± 5.24 %
$S2L/d_0$	2.136	± 13.47 %
$S3W/d_0$	2.307	± 6.72 %
$S3L/d_0$	2.905	± 5.17 %
$S4W/d_0$	3.153	± 0.39 %
$S4L/d_0$	4.881	± 0.60 %

that optimization with the help of the low-fidelity model can predict the appropriate trends. However, in order to compute the exact values, the high-fidelity model has to be applied. To properly resolve the turbulence in the wake the threshold for the TKE refinement is reduced to 0.5 m^2/s^2.

If starting with this threshold at the beginning of the optimization, meshes of about 10 million cells would be obtained for unfavorable designs with high mixing losses. Using the last 20 individuals of the low-fidelity approach as initialization we can now simulate with an averaged mesh size of only 3.5 Million cells. The parameter range in Tab. 1 is not changed for the high-fidelity solution.

Additional 3 generations (20 individuals per generation) are calculated using the high-fidelity approach. Each individual is calculated on a single workstation (Intel Xeon E3-1230 3.30 GHz, 32 GB memory) within 10 h. In the end the volume averaged TKE is reduced by 1.2 % compared to the best individual from the first generation. It delivers a final value of TKE = 1.448 m^2/s^2.

Comparing the volume-averaged turbulent kinetic energy for a classical wing-shaped pick-up tube using the same wake refinement threshold and boundary conditions leads to TKE = 0.262 m^2/s^2. This shows clearly that, specifically for fluid-fluid separation, using a classical pick-up tube is more favorable, even though it suffers from higher energy losses inside the diffusor.

5.3. Energy Losses

Comparing the optimized design regarding energy consumption is done by integrating the shear stress τ_{Wall} tangential to the rotor wall surface with respect to the axis of origin. This leads to a torque generated by shear stress. Due to the axisymmetric rotor casing there are no pressure moments in the current setup. For a complete PTJ pump this is not true: pressure moments act inside the impeller due to 3D blade curvature. As only the rotor cavity is simulated, these effects inside the impeller are not captured.

First simulations of a complete PTJ pump show that pressure moments inside the impeller do not vary for different pick-up tubes. This is completely different to conventional radial pumps at higher specific speed with a volute. Here, the interaction between impeller and volute tongue is quite sensitive to geometric variations. Further studies need to be performed for a PTJ pump to analyze the flow structures inside the impeller channels for different pick-up tubes.

The value P_{rot} in Eq. 5 represents the power, which is needed to keep the fluid body rotating against the resistance of the pick-up tube inside the rotor cavity and must be delivered by the engine. If the impeller performance is unaffected (, i.e., same pressure head for each pick-up tube), the change in overall efficiency in Eq. 6 can be assumed to be caused (i) by the variation of the external pick-up tube surface (, i.e., disc friction losses) and (ii) the diffusor performance. As mentioned previously the energy losses in the diffusor were optimized in a previous study. A classical diffusor with two 90-degree bends has more than double pressure losses $\Delta p_{\text{l,tot}}$ compared to the optimized diffusor (Tab. 3).

Nevertheless, the shape optimization of the external surface in the present study has shown that mixing losses inside the rotor cavity are more favorable for the classical design. To achieve a global maximum for the overall efficiency, a complete pump optimization thus needs to be performed, where the impact of internal diffusor and external surface are taken into account simultaneously. This will be done in the near future. A first test is presented in Table 3, where the pressure losses $\Delta p_{\text{l,tot}}$ inside the diffusor are compared for an operating point of Q = 16 m^3/h.

A constant total pressure at the pick-up tube inlet is assumed for both configurations ($\Delta p_{\text{tot}} = 15\ bar$). It is shown that even though the necessary power input for the optimized pick-up tube is larger due to increased secondary flow inside the rotor, an efficiency improvement of about 9 % can be achieved, using

$$P_{\text{rot}} = M \cdot \omega = \int_A r \cdot \omega \cdot \tau_{\text{Wall}}\, dA \tag{5}$$

and

$$\eta = \frac{Q \cdot (\Delta p_{\text{tot}} - \Delta p_{\text{l,tot}})}{M \cdot \omega}. \tag{6}$$

This is due to the fact that the diffusor improvement dominates over the additional mixing losses. However, this comparison is achieved by using data from decoupled simulations and needs to be validated with complete pump simulations.

6. CONCLUSIONS

The optimized diffusor channel for the pick-up tube should be shielded with an aerodynamically optimized external contour in order to minimize mixing losses and back-mixing. A single-objective genetic algorithm has been used to perform CFD-based op-

Table 3. Estimation of the the pump performance following the optimization of the external diffusor contour. Results are compared to the respective classical pick-tube. Values are calculated in a rotating cavity without inlet or outlet (rigid body rotation). For pressure losses $\Delta p_{\mathrm{l,tot}}$ an operating point of Q = 16 m^3/h is assumed inside the diffusor

Quantity	Optimized	Standard
M [Nm]	46.45	37.44
ω [rad/s]	314.16	314.16
P_{rot} [kW]	14.59	11.76
Δp_{tot} [bar]	15.00	15.00
$\Delta p_{\mathrm{l,tot}}$ [bar]	2.56	7.41
η [%]	37.60	28.46

timization using 3D steady simulations. The optimization loop has been presented and discussed and a dedicated multi-fidelity approach has been introduced. After evaluating more than 720 design configurations within more than 870 h of simulation time, the volume-averaged turbulent kinetic energy could be reduced by 12 % compared to the starting setup. However, compared to the classical pick-up tube, the mixing losses are still larger. Further recommendations are then given to further improve this design design based on the parametrized CAD-model for liquid-liquid separation applications. As long as a better solution has not been identified, it is recommended to use a classical wing-shaped pick-up tube.

However, when using the PTJ pump only for fluid pumping, a higher efficiency can be reached with the improved diffusor design as long as the increased disc-friction losses do not annihilate the obtained improvement inside the diffusor channel. Further studies will reveal if a compromise between inner diffusor design and external contour might be obtained. This question can only be solved with a full 3D pump optimization, taking into account the complete model of the PTJ pump.

REFERENCES

[1] Stepanoff, A. J., 1993, *Centrifugal and Axial Flow Pumps: Theory, Design, and Application*, Krieger Publishing Company, 2. ed.

[2] Erickson, J. W., and Williams, C. P., 1974, "Pitot Pump with Means for Excluding Leakage from Bearings", US Patent 3838939.

[3] Gülich, J. F., 2010, *Kreiselpumpen: Handbuch für Entwicklung, Anlagenplanung und Betrieb*, Springer, Berlin.

[4] Osborn, S., 1996, "The Roto-Jet Pump: 25 Years New", *World Pumps*, Vol. 1996 (363), pp. 32–36.

[5] Wang, C. L., Zhao, C. L., Zhang, T. F., and Liu, D., 2012, "The Numerical Simulation of Full Flow Field of Roto-Jet Pump and Analysis of Energy Losses", *Advanced Materials Research*, Vol. 562-564, pp. 1369–1372.

[6] Zhu, F. N., Liu, D., Yang, X. Y., and Wang, C. L., 2013, "Numerical Simulation of the Three-Dimensional Turbulent Flow in Roto-Jet Pump", *Applied Mechanics and Materials*, Vol. 341-342, pp. 375–378.

[7] Zang, W., Li, X. C., Chen, Y., and Luo, Y. T., 2014, "Numerical Study of the inside Flow Field and the Rectangle Channel Impeller of Roto-Jet Pump", *Applied Mechanics and Materials*, Vol. 529, pp. 164–168.

[8] Komaki, K., 2012, "Performances and Rotating Flows of Rotary Jet Pump", *Open Journal of Fluid Dynamics*, Vol. 2 (4), pp. 375–379.

[9] Meyer, J., Daróczy, L., and Thévenin, D., 2014, "New Design Approach for Pitot-Tube Jet Pump", *Proceedings of ASME Turbo Expo 2014: Turbine Technical Conference and Exposition*, GT2014-25310.

[10] Erickson, J. W., and Budrys, V., 1974, "Pitot Pump with Centrifugal Separator", US Patent 3817446.

[11] Marshek, K. M., Naji, M. R., and Andries, G. C., 1982, "An Experimental Study of Rotor-Filter Pump Performance", *Journal of Energy Resources Technology*, Vol. 104 (3), pp. 259–268.

[12] Menter, F. R., 1994, "Two-Equation Eddy-Viscosity Turbulence Models for Engineering Applications", *AIAA Journal*, Vol. 32 (8), pp. 1598–1605.

[13] Daróczy, L., Janiga, G., and Thévenin, D., 2014, "Systematic Analysis of the Heat Exchanger Arrangement Problem using Multi-Objective Genetic Optimization", *Energy*, Vol. 65, pp. 364–373.

[14] Hilbert, R., Janiga, G., Baron, R., and Thévenin, D., 2006, "Multi-Objective Shape Optimization of a Heat exchanger using Parallel Genetic Algorithms", *International Journal of Heat and Mass Transfer*, Vol. 49 (15-16), pp. 2567–2577.

[15] Daróczy, L., Janiga, G., and Thévenin, D., "OPAL++ Manual v.2.4.06", *Otto-von-Guericke-University Magdeburg (LSS)*.

Conference on Modelling Fluid Flow (CMFF'15)
The 16th International Conference on Fluid Flow Technologies
Budapest, Hungary, September 1-4, 2015

DIFFERENT REGIMES OF THE FLOW AROUND A U-BEAM AND THEIR IMPORTANCE FOR FLUTTER VIBRATIONS

Johannes Strecha[4], Sergey Kuznetsov[2], Stanislav Pospíšil[3], Herbert Steinrück[1]

[1] Corresponding Author. Institute of Fluid Mechanics and Heat Transfer, Vienna University of Technology. Getreidemarkt 9, 1060 Vienna, Austria. Tel.: +43 1 58801 32231, Fax: +43 1 58801 932231, E-mail: herbert.steinrueck@tuwien.ac.at
[2] Institute of Theoretical and Applied Mechanics, Academy of Sciences of the Czech Republic. E-mail: kuznetsov@itam.cas.cz
[3] Institute of Theoretical and Applied Mechanics, Academy of Sciences of the Czech Republic. E-mail: pospisil@itam.cas.cz
[4] Institute of Fluid Mechanics and Heat Transfer, Vienna University of Technology. E-mail: johannes.strecha@tuwien.ac.at

ABSTRACT

Vibrations of a slender U-profile in turbulent cross-flow are studied with the aid of 2D-CFD simulations and wind tunnel experiments. The simulations indicate that there are two different patterns of the flow around the stationary U-profile. Vortices form either towards the leeward flange of the profile, or behind its windward flange. The latter vortices move through the cavity of the profile and lead to large fluctuations of the aerodynamic forces. Thus, the flow patterns determine the vibration response of the U-profile. By comparison with wind tunnel experiments it is shown that aspects of either flow pattern are present in the real flow field. Contrary to simulation results the real flow appears to change between either flow pattern. At zero inclination neither flow pattern prevails. Inclining the profile favours one or the other flow pattern. The importance of the inclination angle and the flow pattern becomes apparent when studying free vibrations of a tensioned belt with U-shaped cross section. Positive inclination of the belt leads to more pronounced vibrations than negative inclination.

Keywords: Vortex induced vibrations, Particle Image Velocimetry, CFD Simulations, Free vibrations

NOMENCLATURE

B	[m]	U-profile length
H	[m]	U-profile height
I	[−]	Turbulence intensity
U^*	[−]	Reduced velocity
c_D	[−]	Drag coefficient
c_L	[−]	Lift coefficient
c_M	[−]	Moment coefficient
f_{vs}	[Hz]	Vortex shedding frequency
f_0	[Hz]	Eigenfrequency
s_v	[m/s]	Flow velocity standard deviation
t	[s]	Flow-time
u_∞	[m/s]	Far-field flow velocity
y	[m]	(Vertical) displacement
y^+	[−]	Wall distance (CFD)
δ	[−]	Logarithmic decrement
ν	[m^2/s]	Kinematic viscosity (air)
ρ	[−]	Air density
φ	[°]	Rotation angle
Re	[−]	Reynolds number
St	[−]	Strouhal number

Subscripts and Superscripts

(P)	Quantity obtained by experiment
(R)	Quantity under the U-flow pattern
(U)	Quantity under the U-flow pattern
max	Maximum of a (field) quantity
0	Constant value
$\ddot{}$	Second time derivative
$\hat{}$	Peak amplitude
$\tilde{}$	Dimensionless quantity

1. INTRODUCTION

Bluff bodies in cross-flow can be excited to vibrations through various mechanisms relevant in different parameter regimes. Among those, vortex induced vibrations can be particularly challenging to study. Vortex formation and decay, a very complex process on its own, interacts with the motion of the body. The intriguing complexity of the flow field can be revealed by Computational Fluid Dynamics (CFD) simulations. Yet, the accuracy of such simulations, especially when studying turbulent flows, has to be questioned and verified by experiments. The author's research focus is to study cross-flow induced vibrations of bluff bodies through CFD simulations. Specifically, vibrations of a prismatic structure with U-shaped cross section with the aspect ratio $B/H = 4.65$ (see Figure 1) are investigated. Such structures are relevant in many industrial applications.

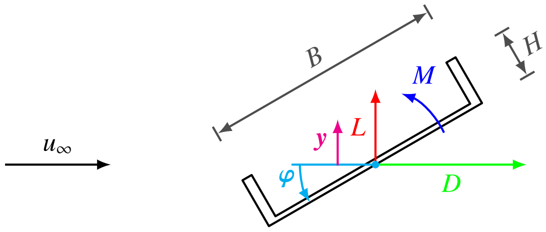

Figure 1. Sketch of the U-profile

Previous two-dimensional (2D) CFD studies of the flow around a statically inclined U-shaped profile lead to the conclusion that there exist two distinct, time-periodic patterns of the flow [1], called U-flow pattern and R-flow pattern. Depending on the inclination angle of the structure different vortex formation patterns would occur. At some inclinations both patterns could be observed through preparation of the initial conditions. Both flow-pattern were metastable in the sense that no spontaneous change of the pattern would occur. Given the complexity of the turbulent flow-field and the restrictive modelling assumptions in the simulation methods a thorough verification of these findings by experiments is required.

The results of this verification are presented in this paper. The investigation relies on the results of 2D-CFD simulations, Particle Image Velocimetry wind tunnel experiments and free vibration experiments involving a tensioned belt with U-shaped cross section. These approaches are detailed in section 2. Comparison between simulated and measured flow fields is given in section 3, wherein the profile is considered to be statically inclined, φ = const. It will be shown that there are indeed different patterns of the flow around the profile, and that the simulations represent a simplified version of the real flow field. The importance of the flow patterns is highlighted in section 4 on the basis of free vibration tests of a tensioned belt at different angles of inclination.

2. METHODS

The experiments were carried out at the Centre of Excellence Telč in the Czech Republic. It has a closed-loop wind tunnel with two closed test-sections, the "aerodynamic" section and the "climatic" section. The former has a cross-section of 1.9 m × 1.8 m and is equipped with honeycombs to reduce the turbulence intensity to about $I = 1\%$. The latter has a cross-section of 2.5 m × 3.9 m but is not equipped with honeycombs [2].

2.1. Particle Image Velocimetry (PIV)

The model for the PIV experiments was made of 5 mm thick perspex and had the dimensions B = 300 mm and H = 60 mm. Its length was 600 mm. It was mounted horizontally in cantilever fashion on an auxiliary plate. The free end was open to not impede the camera's view of the flow-field. A vertical section of the flow field, distanced 300 mm from the auxiliary plate, was illuminated by a LASER from above. Special care was taken to reduce light reflections to a minimum.

The flow field was recorded by a *Dantec Flow Sense EO* camera with a resolution of 2048 × 2048 pixels and analysed with the *Dantec DynamicStudio* version *3.31*. Data presented in this paper was obtained by applying the *Adaptive Correlation* method with a final interrogation area size of 64 px × 64 px overlap 0.5, followed by a 3 × 3 spatial moving average filter. The camera's optical axis was pointing towards the center of the horizontal plate of the model. In the sample image in Figure 2 the model's cross-section is indicated (red). The regions indicated by the blue rectangles contain shadows cast by the glued edges of the model. Contrast there is low and the results are inaccurate. The blue rectangles are shown in every figure showing a flow-field obtained by PIV.

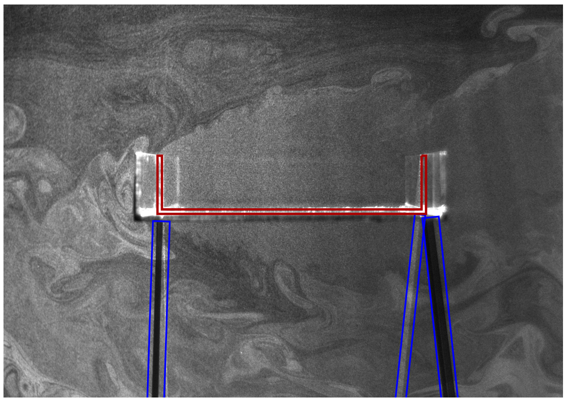

Figure 2. Sample image acquired during the PIV experiments.

Additionally the wake was studied with the help of a CTA probe. The flow velocity magnitude was several locations at the distance B behind the model. These measurements were used to obtain the vortex shedding frequency f_{vs} which is in turn used to calculate the Strouhal number $\mathrm{St} = f_{vs}H/u_\infty$.

2.2. Deformable belt

The experiments involving the tensioned belt were carried out in the "climatic" section of the wind tunnel because of its larger cross-sectional area. The model was made of a rubber band, reinforced with 22 steel cables (diameter 2.9 mm). They were tensioned with a hydraulic cylinder. The sidewalls of the belt were made of non-reinforced rubber. The cross-section of the belt had the same dimensions as the PIV model (B = 300 mm, H = 65 mm). The belt was 2.25 m long. The mass and torsional moment of inertia per unit length were 5.43 kg/m and 0.190 kg m^2/m, respectively. The equilibrium angle of inclination could be adjusted by rotating the belt's fixation on the frame. The acceleration of the belt was recorded by two capacitive, uni-axial accelerometers. They were placed at the half height on either side of the model (see Figure 3). The acceleration signals $\ddot{y}_1$ and $\ddot{y}_2$ were integrated twice in

Fourier space to obtain the belt displacement y_1 and y_2. Due to the non-existent honeycombs in the "climatic" section of the wind tunnel, the turbulence intensity reached levels of about $I = 10\,\%$.

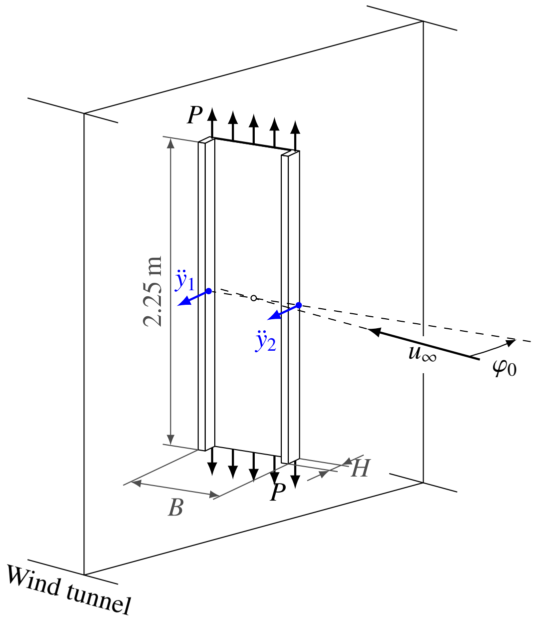

Figure 3. Sketch of the tensioned belt experiment

When the tensioning force 14.2 kN was applied, the lowest eigenfrequencies of the belt were $f_{0,y} = 11.4\,\text{Hz}$ and $f_{0,\varphi} = 10.8\,\text{Hz}$ (pertaining to mode-1 heave and pitch motion). With this tensioning force the logarithmic decrements pertaining to the heave and pitch mode were $\delta_y = 0.021$ and $\delta_\varphi = 0.029$, respectively. The flow conditions in the experiment will be characterised by the dimensionless, so-called reduced velocity. It is the far-field flow velocity u_∞ scaled with the product of the profile height H and the pitch eigenfrequency $f_{0,\varphi}$: $U^* = u_\infty / H f_{0,\varphi}$.

2.3. CFD Simulations

The 2D-CFD simulations were performed using the commercial CFD software package *Ansys Fluent*, version *14.5*. The flow-field was calculated in a rectangular, two-dimensional computational domain and unsteady RANS (URANS) models were used (specifically: the $k\omega$-SST model). The calculation mesh contained approximately $57 \cdot 10^3$ quadrilateral cells, $22.8 \cdot 10^3$ of which are in a region of diameter $2.2B$ centered around the profile. The velocity inlet was placed at a distance $7.7B$ upstream of the profile, the outflow boundary $16.9B$ downstream. Either symmetry boundary at the top and bottom of the domain had a vertical distance of $9.2B$ to the profile. In the wall regions $y^+ \sim 1$ was achieved, implying that low-Reynolds formulations of the wall functions were used. Only second order discretisations were used. At the inlet boundary a free-stream turbulence intensity of $I = 1\,\%$ and an eddy viscosity ratio of 1 were specified.

3. FLOW PATTERNS

The flow fields obtained by simulation will be compared with PIV results. The simulations were carried out at a Reynolds number $\text{Re} = u_\infty B/\nu = 2.45 \cdot 10^5$. In the PIV experiments $\text{Re} = 4.3 \cdot 10^4$ could be reached. The turbulence intensity of the oncoming flow was $I = 1\,\%$ in both cases. Neither the PIV nor the simulations fully resolve the turbulent fluctuations of the flow. In the simulation most fluctuations are modelled through their contribution to the turbulent kinetic energy. The PIV method does not resolve structures smaller than the size of an interrogation area.

The available data consists of the time-periodic flow-fields under either flow patterns obtained by 2D-CFD simulation, and flow-field snapshots obtained by PIV. Meaningful comparison of this data requires a careful approach and will be made in two steps. First, the time-averaged flow fields will be compared. Then snapshots of the flow field will be discussed. Finally the influence of the inclination angle is discussed. The structure is at rest throughout this section, $y \equiv 0$ and $\varphi = \text{const.}$

3.1. Time-averaged flow fields

As a first step the statistics of the flow-field are analysed, i.e. the time-average and standard deviation of the flow velocity. The flow fields obtained by PIV experiments and 2D-CFD simulations are compared. Flow field statistics from PIV data were obtained using one complete series of captured flow field snapshots, which includes estimated 9.5 flow periods, i.e. the sampling time was 9.5 times the vortex shedding frequency under the R-flow pattern, $t_s = 9.5/f_{vs}$. Statistics from simulations were calculated using only one flow period, since the simulated flow is time-periodic.

In Figure 4 the flow-field is visualised by arrows oriented in the direction of the time-averaged flow velocity and scaled by the local velocity magnitude. Additionally, an iso-line of the velocity magnitude standard deviation at the value $0.5\, s_{v,\max}$ is marked (red), where $s_{v,\max}$ is the maximal standard deviation in the field. Areas of large velocity standard deviation indicate regions where the flow is strongly time-dependent. Also note the regions in Fig. 4 where the PIV result is inaccurate (blue rectangles). In the time-averaged flow-field in Fig. 4 a single vortical structure rotating clockwise can be seen above the leeward half of the cavity. However, this region is also characterised by a large velocity standard deviation, indicating a time-dependent and flow field. Below, these regions will be further discussed by snapshots. Furthermore the evolution of the free shear layer separating from the bottom windward corner of the profile is strongly time-dependent and, naturally, the wake behind the profile. The maximal value of the flow velocity standard deviation, scaled with the far-field flow velocity u_∞ was $s^{(P)}_{v,\max}/u_\infty = 0.46$.

Simulation results of either flow pattern are

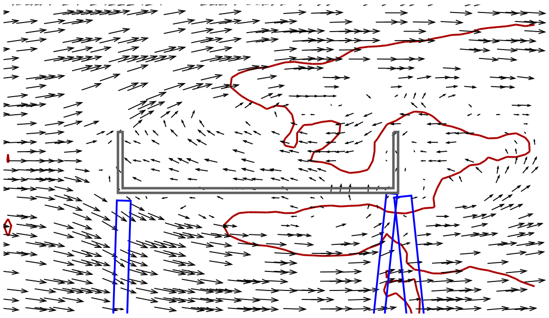

Figure 4. Time-averaged flow field (arrows) with an isoline of the velocity magnitude standard deviation (red), obtained by PIV.

shown in Figure 5. The time-averaged flow-field of the U-flow pattern is characterised by a single, large vortical structure in the cavity of the profile (Fig. 5a), rotating clock-wise. This structure is part of a time-dependent region of the flow-field, as indicated by the red standard deviation contour at $0.5s^{(U)}_{v,\max}$. In fact, it encompasses the whole cavity, as well as the wake of the profile. The maximal, non-dimensional standard deviation was $s^{(U)}_{v,\max}/u_\infty = 0.94$, including the contribution from the turbulent kinetic energy.

Unlike the previously discussed flow fields the time-averaged R-flow field (Fig. 5b) is characterised by two vortical structures in the cavity of the profile. One vortex in the leeward half of the cavity is rotating in clockwise direction while the other vortex in the windward half of the cavity is rotating in counter-clockwise direction. Note that the standard-deviation iso-line at $0.5s^{(R)}_{v,\max}$ (where $s^{(R)}_{v,\max}/u_\infty = 0.57$), which already includes the contribution from the turbulent kinetic energy, encompasses only the wake of the profile and a small region in the free shear layer above the cavity and not the two vortical structures.

No conclusive evidence for either flow pattern can be obtained by comparing the time-averaged flow fields. The standard deviations as seen in the PIV data indicate that the flow-field becomes instationary well before the leeward corners of the profile (Fig. 4). Yet, the instationary regions of the U-flow field begins right after the windward flange of the profile. The instationary regions of the R-flow field encompass mainly the wake and it appears that the flow in the cavity and above is almost stationary. The next section discusses snapshots of the flow-field in the light of the already gained insights.

3.2. Flow-field snapshots

First, snapshots of the R-flow pattern are discussed. Investigation of all snapshots during a flow period shows that the two vortices in the cavity are indeed stationary. The topology of the flow field in the cavity does not change. Hence the temporal statistics previously discussed show a very small flow velocity standard deviation. A snapshot of the flow-field under the U-flow pattern is shown in Figure 6. Observe the similarity of the flow-field in the cavity between this figure and Fig. 5b. Yet, the profiles of the horizontal flow velocity component suggest that the free shear layer is sensitive to small perturbations by. Especially the local velocity profile at $x = -0.32B$ (blue, left profile in Fig. 6) resembles that of the shear layer in a Kelvin-Helmholtz scenario. Indeed, the large values of the turbulence intensity I (estimated from the turbulent kinetic energy, magenta line) indicate that many eddies are formed in the free shear layer. These eddies are not resolved in space and time, but accounted for through the turbulent kinetic energy. Larger vortices, present in the wake of the profile are resolved in space and time. The clear distinction between the resolved and modelled timescales is an implicit assumption of URANS models. Critics of URANS methods argue that the evolution of free shear layers may depend sensitively on small eddies and that the implied separation of timescales is not given in bluff body flows [3].

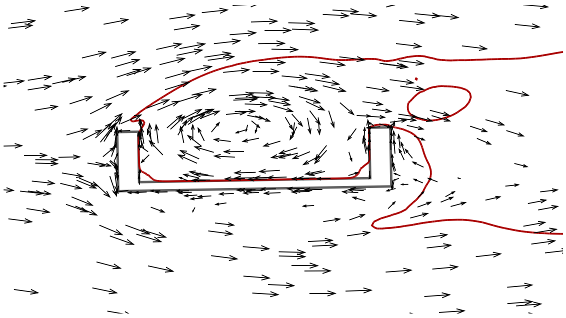

(a) U-flow pattern

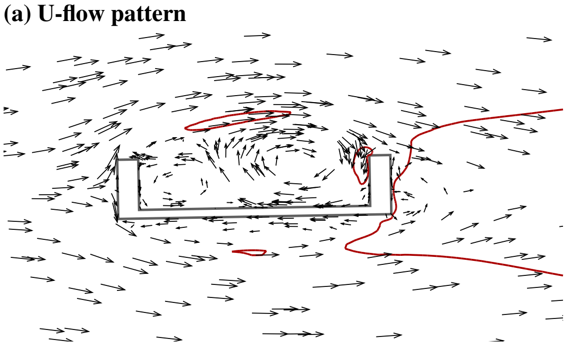

(b) R-flow pattern

Figure 5. Time-averaged flow field (arrows) with an isoline of the velocity magnitude standard deviation (red), obtained by CFD Simulation.

Recall, that the U-flow pattern revealed a strongly time-dependent flow-field in the cavity (Fig. 5a). Indeed, a snapshot of the flow-field shows that unlike under the R-flow pattern, the average flow-field has very little in common with a snapshot (Figure 7). By the velocity profile (blue) it can be seen that the free shear layer rolled up right behind the windward flange of the profile to form a vortex rotating in clockwise direction (the "cavity vortex"). Inspection of flow field snapshots shows that this vortex is not stationary. It grows, detaches from the windward flange, travels through the cavity, and is swept over the leeward flange into the wake. The

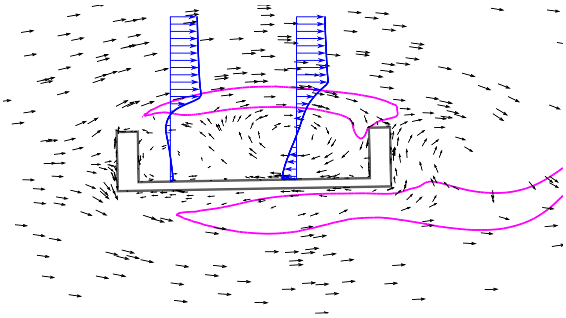

Figure 6. Snapshot of the simulated flow-field (R-flow pattern) with two u-velocity profiles and a turbulence intensity isoline, I = 15 %.

green arrow in Fig. 7 shows the approximate path of the vortex core. The vortex at the tip of the arrow was formed behind the windward flange (where the green arrow begins) during the previous flow period and has travelled towards the leeward flange. The turbulence intensity is low where the cavity vortex forms but large between the two vortical structures, and also around the shear layer below the profile.

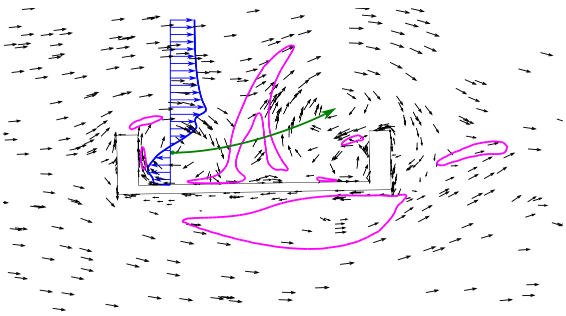

Figure 7. Snapshot of the simulated flow-field (U-flow pattern) with a u-velocity profile and a turbulence intensity isoline, I = 15 %.

Another often stated criticism of URANS methods, especially in two-dimensional computational domains, is the slow decay of vortical structures as they travel through the computational domain. The large turbulence intensities around the second vortex in Fig. 7 suggest that the (three-dimensional) decay of the cavity vortex may be important in reality. Before the influence of the cavity vortices on the aerodynamic forces is discussed, a comparison with snapshots of the flow field obtained by the PIV experiments is given, where evidence for the cavity vortices will be given.

Some snapshots of the flow-field resemble the aforementioned R-flow patterns in a way (see Figure 8). The shear-layer is curved weakly and reaches over the cavity of the profile (green arrows). Vortices can be seen in the wake behind the profile. The flow in the cavity itself does not resemble the R-flow pattern. Instead, the orientation of the arrows suggest a three-dimensional flow-field. Despite this, the velocity profile (blue) is similar to the profile shown in Fig. 6, locally resembling a Kelvin-Helmholtz Scenario. In parallel shear-flows such a velocity profile could be unstable by Fjørtoft's criterion [4]. Indeed, a vortex of considerable size can be seen in this snapshot to the right of the velocity profile (green arrows). These vortices were modelled as a contribution to the turbulent kinetic energy in the simulations under the R-flow pattern (see Fig. 6). The question is whether these vortices can take on the role of the cavity vortex, which is observed in 2D-CFD simulations under the U-flow pattern.

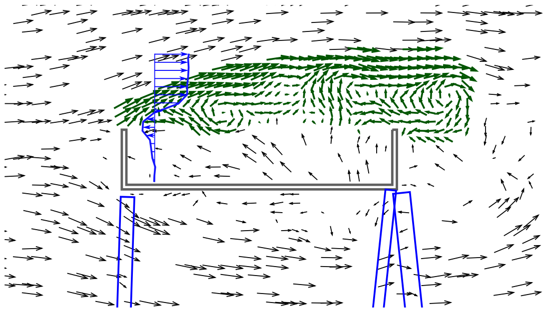

Figure 8. Snapshot of the flow-field (PIV), visualised by arrows and a u-velocity profile. The shear layer is curved weakly.

There is evidence that vortices can form right behind the windward flange of the profile (see Figure 9, green arrows). By the u-velocity profile (blue) it can be seen that a clockwise-rotating vortex is located at this position. Under the R-flow pattern a counter-clockwise rotating vortex would be present. This vortex is not stationary, but travels through the cavity towards the leeward flange. Also in Fig. 9 a second vortex rotating in clockwise direction can be seen at this position (green arrows). Subsequent snapshots show the left vortex detaching from the windward flange and travelling towards the leeward flange [5]. Furthermore it can be observed that many vortical structures are located below the profile. These were also modelled as a contribution to the turbulent kinetic energy in the simulations.

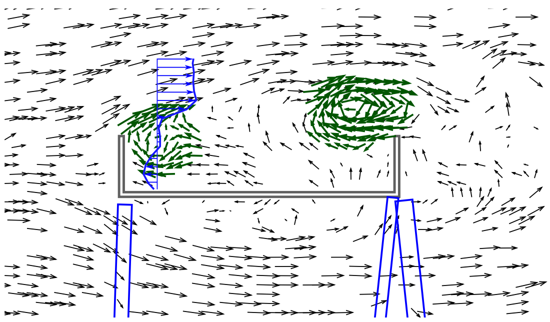

Figure 9. Snapshot of the flow-field (PIV), visualised by arrows and a u-velocity profile. A cavity-vortex has formed.

Thus, aspects of both flow patterns were observed at the same angle of inclination in the PIV experiments. The Figs 8 and 9 show only two out of 44 recorded flow-field snapshots. These snapshots were analysed how closely they resemble either the U-flow or the R-flow pattern. It was chosen to count snapshots where vortices rotated in counter-clockwise direction in the windward half of the cavity as “R-flow frame”. Frames where clockwise rotating vortices were located in the cavity of the profile were considered an “U-flow frame”. All other frames were counted as “undecidable”. Of 44 frames spanning 19 flow periods, 13 frames resembled the U-flow pattern by the above described criteria. Only one was considered to represent the R-flow pattern. The remaining 30 frames were deemed “undecidable”. These frames are mainly characterised by small vortices forming in the free shear layer and a possibly three-dimensional flow in the cavity (similar to Fig. 8). The two almost stationary vortices seen in 2D-CFD simulations under the R-flow pattern (Fig. 5b) could be unstable in three dimensions. Thus, the “undecidable” frames may resemble the R-flow pattern. Then, the flow switches between two bi-stable states corresponding to the flow patterns observed in 2D-CFD simulations. The simulations show no intermittent change between the flow patterns. Change between flow patterns from U-flow to R-flow and back again could only be achieved by substantially varying the inclination angle during a simulation run.

3.3. Aerodynamic forces

In this section the aerodynamic forces acting on the U-profile will be discussed on the basis of simulation results. The drag and lift force and torsional moment per unit length are given by $c_{\mathrm{D|L}}\frac{1}{2}\rho u_\infty^2 H$ and $c_\mathrm{M}\frac{1}{2}\rho u_\infty^2 HB$, respectively. They were obtained from simulations at the same Reynolds-Number $\mathrm{Re} = 2.45 \cdot 10^5$ as in the flow-field snapshots above. Since the flow is turbulent and considered to be periodic, a time-series of aerodynamic forces obtained by URANS simulation can be thought of as the so-called *phase average*. Note that the time-periodicity of the flow is contradicted by the PIV experiments and that the following figures are used to illustrate the influence of the cavity vortices only.

The time-series of the aerodynamic forces under the R-flow pattern are almost sinusoidal (Figure 10). The oscillation frequency equals the vortex shedding frequency. Vortices are formed in the wake of the profile (Fig. 6) and do not impinge upon any part of the profile. The lift coefficient is always positive and the coefficient of torsional moment oscillates with an amplitude of $\hat{c}_\mathrm{M} = 0.13$.

The aerodynamic forces under the U-flow pattern show much more features (Figure 11). Most importantly, the U-flow pattern leads to a different fundamental frequency of the aerodynamic forces than under the R-flow pattern (note the scale of the time-axis in Figs. 10 and 11). Under the U-flow pattern, the influence of the vortex formation in the wake is much less important than the influence of the cavity vortex. Inspection of snapshots of the flow-field

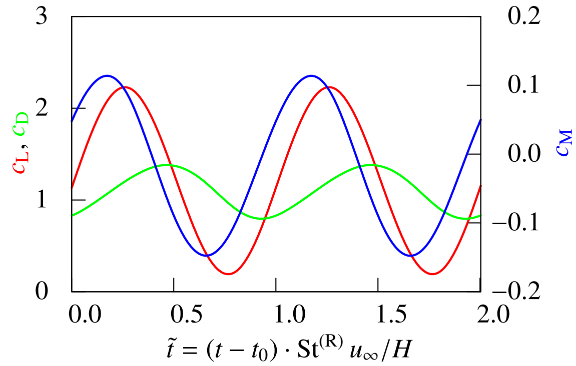

Figure 10. Time-series of the aerodynamic force coefficients under the R-flow pattern (simulation at $\varphi = 0°$)

leads to the following conclusions: The drag coefficient is the greatest when a cavity vortex is swept into the wake ($\tilde{t} \approx 0.25$). At the same time, the lift coefficient is negative and almost assumes its minimal value. The coefficient of torsional moment also assumes its minimum then. Maximum lift occurs when the cavity vortex has detached from the windward flange and is in the middle of the cavity ($1.1 \lesssim \tilde{t} \lesssim 1.7$). The coefficient of torsional moment is large in this interval and assumes its maximum shortly before the cavity is swept into the wake. It oscillates with an amplitude of $\hat{c}_\mathrm{M} = 0.63$.

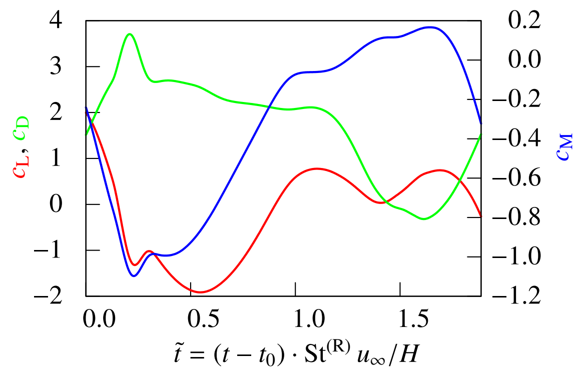

Figure 11. Time-series of the aerodynamic force coefficients under the U-flow pattern (simulation at $\varphi = 0°$)

Thus, the fundamental frequency of the aerodynamic forces is given by the speed at which the vortex travels through the cavity of the profile. In the simulations this travelling speed is rather slow so that the flow period under the U-flow pattern is almost twice as large as under the R-flow pattern, $\mathrm{St}^{(\mathrm{R})} \approx 2\mathrm{St}^{(\mathrm{U})}$. Inspection of the PIV snapshots yields that this timing is almost correct. In one instance $\mathrm{St}^{(\mathrm{P,U})} = 1.95^{(\mathrm{P,R})}$ was obtained: $\mathrm{St}^{(\mathrm{P,U})}$ was determined from three successive frames showing cavity vortices. $\mathrm{St}^{(\mathrm{P,R})}$ was obtained from the frequency spectrum of the velocity magnitude measured behind the profile with a CTA probe. At this inclination, $\mathrm{St}^{(\mathrm{P,U})}$ could not be determined reliably from CTA data. Cavity vortices form irregularly and are subject to three-dimensional decay.

3.4. Influence of the angle of inclination

The flow around statically inclined U-profiles was also investigated by means of PIV measurements. First, let the U-profile be positively inclined, $\varphi_0 = 5°$. Application of the criteria described above lead to the following results: Of 44 available snapshots none resembled the R-flow pattern but 26 showed features of the U-flow pattern. The remaining 18 snapshots were deemed undecidable. When positively inclined, the leeward flange of the profile is closer to the free shear layer and influences the formation of cavity vortices such that they appear more often. Inspection of the flow velocities in the wake behind the U-profile by means of a CTA probe showed that there is a band of frequencies present, yielding $0.065 \leq \mathrm{St}^{(\mathrm{P,U})} \leq 0.083$. These frequencies correspond to the formation of cavity vortices. They are lower than the Strouhal number attributed to the "classical" vortex shedding $\mathrm{St}^{(\mathrm{P})} = 0.133$, obtained at $\varphi_0 = 0°$, and also lower than the Strouhal numbers others observed in the flow around a rectangular prisms with similar aspect ratio [6].

When the U-profile is negatively inclined, $\varphi_0 = -5°$ none of the 44 available snapshots resemble either U-flow or R-flow pattern. Instead, every frame is "undecidable" by the above described criteria. The snapshots are characterised by a very complex flow in the cavity which appears to be non-periodic and highly three-dimensional. The shear layer separating from the top windward corner of the profile is still easily perturbed and forms vortices. Yet they move above the leeward flange and do not influence the flow in the cavity much. Inspection of the flow velocities in the wake yield a Strouhal number $\mathrm{St}^{(\mathrm{P})} = 0.133$ which is numerically equal to the value of St obtained at zero inclination $\varphi_0 = 0°$.

Changing the angle of inclination in the simulations leads to similar results. At a positive inclination $\varphi_0 = 5°$ or negative inclination $\varphi_0 = -5°$ vortices form according to the U-flow pattern or the R-flow pattern, respectively. The topology and character of the flow at either angle is equal to the corresponding pattern at zero inclination.

4. FLOW INDUCED VIBRATIONS

In this section the relevance and influence of the cavity vortices for flow induced vibrations will be shown by discussing the influence of the angle of inclination on the vibration amplitudes. The vibration amplitudes in Figure 12 are given as the minimal and maximal average peak amplitude: The values of ten consecutive local maxima of the displacement signal were averaged to obtain one average peak amplitude. With an overlap of five consecutive maxima the next portion of the signal, again containing ten consecutive local maxima, was analysed. The minimal and maximal average peak amplitude was stored and used to plot the bars in the figure. The experiments described here were carried out with a single belt eigenfrequency of $f_{0,\varphi} = 11.4\,\mathrm{Hz}$. The reduced velocity U^* was varied by changing the far-field flow velocity u_∞. The Reynolds number range was $2.0 \cdot 10^5 < \mathrm{Re} < 4.5 \cdot 10^5$ in these experiments.

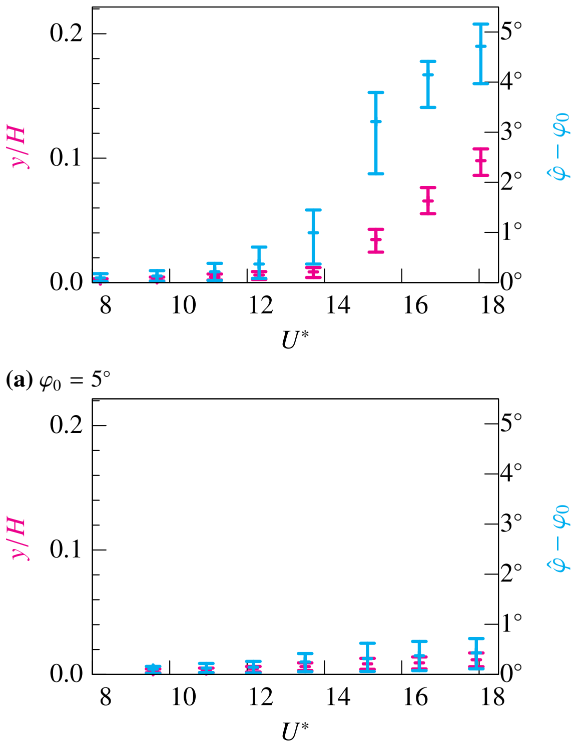

(a) $\varphi_0 = 5°$

(b) $\varphi_0 = -5°$

Figure 12. Dimensionless heave and pitch motion at several reduced velocities and two base inclinations φ_0.

At positive inclination $\varphi_0 = 5°$ (Fig. 12a) vibration amplitudes stay small for reduced velocities up to $U^* = 12$. From there on the pitch amplitude increases to values up to $\hat{\varphi} - \varphi_0 \approx 5°$. The heave amplitudes also increase, but appear to be less important than the pitch motion. Recall, that the peak amplitude of the coefficient of torsional moment was almost five times larger under the U-flow pattern than under the R-flow pattern. The reduced velocity from which on vibration amplitudes increase, $U^* = 14$, corresponds to the formation frequency of cavity vortices observed in the simulations under the U-flow pattern. Taking the inverse of the Strouhal numbers at the constant, positive inclination $\varphi = 5°$ leads to an estimate of the critical velocity $12.0 \leq U^* \leq 15.4$. Since vibration amplitudes increase until the largest achieved reduced velocity, $U^* \approx 18$, the lock-in range of the cavity vortices appears to be rather large, or another instability mechanism is in effect.

At negative inclination $\varphi_0 = -5°$ (Fig. 12b) vibration amplitudes stay small for all investigated reduced velocities, $\hat{\varphi} - \varphi_0 < 1°$. If there were vortex induced vibrations at $U^* \approx 7.5$, the corresponding lock-in range has to be rather small since vibration amplitudes at $U^* \approx 9.5$ are minimal.

5. CONCLUSIONS AND OUTLOOK

Two time-periodic flow pattern were observed in 2D-CFD simulations of the flow around a profile with U-shaped cross-section. By thorough comparison with data obtained by PIV experiments it was confirmed that aspects of both flow patterns are present in the flow-field. The intermittent change of flow patterns, observed in the experiments, is not unique to the flow around a U-profile. Such phenomena are also reported by Tamura and Itoh in their study of the flow around a short rectangular prism [7]. There, the flow patterns are related to the either weak or strong roll-up of a shear layer behind a short rectangular prism with $B/H = 0.2$. In the present case the shear layer roll-up is also relevant, but it is the formation of cavity vortices brought on by the strong shear layer roll-up that is thought to be the defining aspect of the U-flow pattern. It was shown that these cavity vortices have a tremendous influence on the aerodynamic forces acting on the profile. Such cavity vortices (or "surface travelling vortices") were observed by Kubo et al in their experimental study of the flow around an H-shaped prism with an aspect ratio of $B/H = 10$, [8]. Kubo et al also indicated that the formation of cavity vortices can be influenced by forcing the profile to move. This further underlines the importance for vibration excitation by the cavity vortices since it confirms that the vortex formation synchronises to the profile motion. Furthermore, the velocity spectra obtained by CTA measurements of the wake behind the statically inclined profile show that the formation of cavity vortices does not take place at a single, well defined frequency but rather in an interval of frequencies. This also indicates that the formation frequency is not a given constant but that it can change.

As a way to investigate the importance of the cavity vortices for flow induced vibrations, vibrations of a tensioned belt at different base inclinations were studied. At negative base inclination vibration amplitudes were very low in general. At positive inclination vibrations set in at a reduced velocity which is be related to the cavity vortex formation frequency. The importance of such vortices for flow induced vibrations is also highlighted by others [8, 9].

Comparison of simulated and calculated (PIV) flow fields shows that the simulation methods need more attention in future research. While the applied URANS methods are computationally feasible, they yield "simplified" results. The flow patterns are time-periodic and the intermittent change cannot be predicted. Due to [3] there is considerable doubt that extending the computational domain to three dimensions but using the same turbulence model would lead to more accurate results. An estimate for the computational cost of an LES simulation of the present case, based on grid resolutions in [6], leads to the conclusion that pure LES is prohibitively expensive. Scale Adaptive Simulations are considered as option.

ACKNOWLEDGEMENTS

The support of the Czech-Taiwan research project GAČR No. 13-24405J and NSC101WFD0400131 as well as the support of LO1219 - Sustainable advanced development of CET and RVO 68378297 is gratefully acknowledged.

REFERENCES

[1] Strecha, J., and Steinrück, H., 2014, "Dependence of the aeroelastic stability of a slender U-beam on the realized flow pattern", *PAMM*, Vol. 14 (1), pp. 497–498.

[2] "Climatic Wind Engineering Laboratory | Centre of Excellence Telč", URL `http://cet.arcchip.cz/wind-laboratory-en`, Accessed on 2015-02-18.

[3] Fröhlich, J., and von Terzi, D., 2008, "Hybrid LES/RANS methods for the simulation of turbulent flows", *Progress in Aerospace Sciences*, Vol. 44 (5), pp. 349–377.

[4] Drazin, P. G., 2002, *Introduction to Hydrodynamic Stability*, Cambridge University Press, ISBN 978-0-52-100965-2.

[5] Strecha, J., In preparation, "Flow induced vibrations of a slender U-beam (working title)", Ph.D. thesis, Vienna University of Technology, supervisor: Prof. Herbert SteinrÃijck. Second Examiner: Stanislav Pospíšil.

[6] Mannini, C., Šoda, A., and Schewe, G., 2011, "Numerical investigation on the three-dimensional unsteady flow past a 5:1 rectangular cylinder", *Journal of Wind Engineering and Industrial Aerodynamics*, Vol. 99 (4), pp. 469–482.

[7] Tamura, T., and Itoh, Y., 1999, "Unstable aerodynamic phenomena of a rectangular cylinder with critical section", *Journal of Wind Engineering and Industrial Aerodynamics*, Vol. 83 (1–3), pp. 121–133.

[8] Kubo, Y., Hirata, K., and Mikawa, K., 1992, "Mechanism of aerodynamic vibrations of shallow bridge girder sections", *Journal of Wind Engineering and Industrial Aerodynamics*, Vol. 42 (1–3), pp. 1297–1308.

[9] Matsumoto, M., Shirato, H., Yagi, T., Shijo, R., Eguchi, A., and Tamaki, H., 2003, "Effects of aerodynamic interferences between heaving and torsional vibration of bridge decks: the case of Tacoma Narrows Bridge", *Journal of Wind Engineering and Industrial Aerodynamics*, Vol. 91 (12–15), pp. 1547–1557.

FUEL MIXING IN BUBBLING FLUIDIZED BEDS: AN EXPERIMENTAL AND NUMERICAL STUDY

Srdjan SASIC[1], Meisam FARZANEH[2] and Henrik STRÖM[3]

[1] Corresponding Author. Department of Applied Mechanics, Chalmers University of Technology, SE-412 96 Gothenburg, Sweden. Tel.: + 46 (0) 31 772 52 38, E-mail: srdjan@chalmers.se
[2] Department of Applied Mechanics, Chalmers University of Technology, Gothenburg, Sweden. E-mail: meisam.farzaneh@chalmers.se
[3] Department of Applied Mechanics, Chalmers University of Technology, Gothenburg, Sweden. E-mail: henrik.strom@chalmers.se

ABSTRACT

In this paper we study experimentally and numerically the behaviour of inert and fuel particles in a bubbling gas-solid fluidized bed. We use the Particle Image Velocimetry (PIV) technique to obtain detailed information on the dynamics of the inert particles. Furthermore, a digital image analysis technique is applied to track an illuminated tracer particle in the bed, in an attempt to reproduce the behaviour of the fuel particles. The results of the experimental work are presented in the form of the averaged velocity vectors of the inert and tracer particles. In addition, a numerical investigation is carried out where the inert bulk phase is modelled within the Eulerian-Eulerian framework and large fuel particles are tracked in a Lagrangian frame of reference. The stresses in an inert phase are modelled using the visco-plastic constitutive law (the so-called μ-rheology approach). The assumption that the inert particulate phase behaves as a visco-plastic fluid leads to a correct prediction of the movement of the fuel particles in the bed.

Keywords: Fluidization, Fuel mixing, Numerical Simulation, Particle Image Velocimetry (PIV)

NOMENCLATURE

Note that only the most important symbols are given here. All other symbols are explained as they appear in the manuscript.

H	[m]	bed height
I	[-]	inertial number
	[s^{-1}]	shear rate
S	[s^{-1}]	strain rate tensor
U_t	[$m\ s^{-1}$]	terminal velocity
U_{mf}	[$m\ s^{-1}$]	minimum fluidization velocity
U_f	[$m\ s^{-1}$]	fluidization velocity
V	[m^3]	volume (of a fuel particle)
v	[$m\ s^{-1}$]	velocity
ε	[-]	volume fraction
τ	[N/m^2]	stress tensor
μ	[Pa.s]	viscosity

1. INTRODUCTION

Biomass pyrolysis, gasification and combustion have become extensively used technologies in recent times in our demands for renewable energy sources. In comparison with some other traditional combustion techniques (e.g. burning pulverized coal), combustion in fluidized beds has a number of advantages, such as a more stable combustion environment, lower temperature combustion and lower pollutant production. Fluidized-bed combustors typically involve multiple particulate phases: a low mass fraction (<5%) of large and light fuel particles in a bed of finer and heavier particles (e.g. sand, fuel ash and limestone). The fuel particles are typically large (1.0 cm or larger) and they occupy only a small fraction of the bed material. On the other hand, the bulk phase consists of small (less than 1.0 mm) inert particles. The differences in size and density between the two types of particles lead to distinctive circulation patterns for the fuel particles in the bed. To be able to understand the process of combustion of fuel particles in a fluidized bed, one first needs to obtain detailed information on their motion.

When it comes to experimental work, in [1] the authors used a digital image analysis technique to track a single tracer particle in a 0.4 m wide two-dimensional bed. The properties of the tracer particle were similar to those of the fuel particles. The study resulted in the preferential positions, the averaged velocity vectors and the horizontal and vertical dispersion coefficients of the tracer particle.

Furthermore, the authors looked at the effect of the air-distributor pressure drop on the motion of the tracer particle. Their results indicated that a reduction of the air-distributor pressure drop leads to formation of high-through flow regions and consequently to less solid mixing in the bed.

We use the results from [1] in this work to validate our numerical results. In addition, we carry out an additional experimental study on the behaviour of the inert particles in a bed and, for that purpose, we use Particle Image Velocimetry (PIV).

In the numerical part of our work, we propose a combined tracking technique that we term here the Eulerian-Eulerian-Lagrangian (E-E-L) technique. The inert phase is composed of a large number of sand-like small particles and is treated as a continuous phase. The Eulerian-Eulerian (E-E) part treats the carrying phase (the gas) and the inert solid particles as interpenetrating continua. It results in the velocity and pressure fields of the inert solid and gas phases that are used for calculation of the forces acting on a fuel particle, e.g. the drag and buoyancy. A limited number of large fuel particles are tracked using a Lagrangian particle tracking method. Since the fuel particles occupy only a small fraction of the bed material, it is reasonable to assume that the movement of the fuel particles is entirely governed by the dynamics of the bulk and gas phases and that the fuel particles do not influence the flow of the inert solids. Therefore, an accurate modelling of the inert particulate phase is crucial in order to correctly describe the behaviour of the fuel particles.

The E-E approach typically applies the kinetic theory of granular flow (KTGF) to model the stresses of the solid phase [2]. The theory can be applied for rapid-flow regimes, which are sufficiently dilute so that inter-particle collisions can be assumed instantaneous and binary. However, in both moderately and highly dense regimes, such as those that may be encountered in bubbling fluidized beds, the behaviour of the particulate phase is dominated by enduring frictional contacts of multiple neighbouring particles. In such a regime the fundamental assumptions of the KTGF are violated and the theory will fail to predict the accurate behaviour of the system. To overcome this problem, several models, mostly derived from the critical state theory of soil mechanics, were proposed for modelling frictional stresses of dense packed particles [3]. The classical soil mechanics describes the mechanical behaviour of a system as a rate-independent plastic regime characterized by a constant friction coefficient. The models developed from soil mechanics, starting from the Coulomb frictional law, have been widely applied in fluidized-bed simulations. This is typically done by dividing the solid stresses into two parts: the kinetic-collisional part, handled by the KTGF, and the frictional part, modelled by incorporating a frictional stress theory. The frictional stress models are activated above a certain threshold value of the solids volume fraction. As an alternative to the latter approach, different constitutive laws can be proposed [4] by identifying similarities between the behaviour of granular materials and that of visco-plastic fluids. Here, an important assumption is the local nature of rheological behaviour, namely that the shear stress is a function of the local shear rate. One of the goals of the present work is thus to compare the results obtained by using the visco-plastic approach with those obtained from the traditionally-used models [e.g. 3]. In that sense, note that regarding the constitutive models for the simulations, the only model that is different in the computational cases treated here is the representation of the frictional stresses.

2. MODELLING

We apply our numerical framework in an open-source code MFIX [5]. The details on the implementation of the KTGF in that code can be found in [5].

2.1. Models for frictional stresses

In [3] the authors developed a frictional stress model that accounts for compressibility of dense granular flows.

$$\boldsymbol{\tau}_{\mathrm{f}} = -P_{\mathrm{f}}\mathbf{I} + 2\mu_{\mathrm{f}}\boldsymbol{S_s} \tag{1}$$

where P_f is frictional pressure and $\boldsymbol{S_S}$ the solid-phase strain rate tensor. The frictional viscosity is given by:

$$\mu_{\mathrm{f}} = \frac{\sqrt{2}P_{\mathrm{f}}\sin(\phi)}{\sqrt{\mathbf{S}_{\mathrm{s}}:\mathbf{S}_{\mathrm{s}} + \Theta/d_{\mathrm{s}}^2}}\left\{n - (n-1)\left(\frac{P_{\mathrm{f}}}{P_{\mathrm{c}}}\right)^{1/(n-1)}\right\} \tag{2}$$

with P_c being the critical pressure (for details, see [3]), d_s diameter of solid particles and n is an exponent that determines the shape of the yield surface [3]. It is interesting to note that this model accounts for the dilatation ($\nabla\cdot\mathbf{v}_s > 0$ and $P_f < P_c$) and compaction ($\nabla\cdot\mathbf{v}_s < 0$ and $P_f > P_c$) of the particulate flow. Here, $\mathbf{v}_s$ is the velocity of the solid phase. Note that the condition $\nabla\cdot\mathbf{v}_s = 0$ is valid only for the critical state, in which there is a change of volume due to the deformation of the particulate phase. In such a case $P_f = P_c$.

On the other hand, in [4] granular materials are considered as visco-plastic fluids. Here, the shear stress $\boldsymbol{\tau_f}$ is a function of the shear rate $\dot{\Gamma}$, the isotropic pressure *Piso* and the inertial number *I*. The latter is a dimensionless number representing the ratio between the macroscopic deformation timescale $1/\dot{\Gamma}$ and the microscopic inertial timescale $(d_{\mathrm{s}}^2\rho_{\mathrm{s}}/P_{\mathrm{iso}})^{0.5}$. The friction coefficient is then an increasing function of the inertial number starting at the value μ_1 at $I = 0$ (the quasi-static flow) up to the value μ_2 at large I (the kinetic regime). The frictional stress then takes the following form:

$$\boldsymbol{\tau}_{\mathrm{f}} = \begin{cases} -P_{\mathrm{iso}}\mathbf{I} + \mu(I)P_{\mathrm{iso}}\dfrac{\dot{\boldsymbol{\Gamma}}}{|\dot{\boldsymbol{\Gamma}}|} & \varepsilon_{\mathrm{s}} > \varepsilon_{\mathrm{s}}^{\min} \\ 0 & \varepsilon_{\mathrm{s}} < \varepsilon_{\mathrm{s}}^{\min} \end{cases} \quad (3)$$

with ε_{s} being the volume fraction of the solid phase. The friction coefficient will be:

$$\mu(I) = \mu_1 + \frac{(\mu_2 - \mu_1)}{(\frac{I_0}{I} + 1)} \quad (4)$$

with the shear rate

$$\dot{\boldsymbol{\Gamma}} = \nabla \underline{\mathrm{v}_{\mathrm{s}}} + \left(\nabla \underline{\mathrm{v}_{\mathrm{s}}}\right)^T \quad (5)$$

and the inertial number:

$$I = \frac{d_{\mathrm{s}}|\dot{\boldsymbol{\Gamma}}|}{(P_{\mathrm{iso}}/\rho_{\mathrm{s}})^{0.5}} \quad (6)$$

where

$$I_0 = 0.279,\ \mu_1 = \tan(20.9),\ \mu_2 = \tan(32.76),\ |\dot{\boldsymbol{\Gamma}}| = (\dot{\boldsymbol{\Gamma}}:\dot{\boldsymbol{\Gamma}})^{0.5}. \quad (7)$$

2.2. Tracking technique

The equation of motion of the fuel particles is written as:

$$m_{\mathrm{p}}\frac{d\mathbf{v}_{\mathrm{p}}}{dt} = 3d_{\mathrm{p}}\mu_{\mathrm{g}}f_{\mathrm{g}}(\mathbf{v}_{\mathrm{g}} - \mathbf{v}_{\mathrm{p}}) + 3d_{\mathrm{p}}\mu_{\mathrm{s}}f_{\mathrm{s0}}(\mathbf{v}_{\mathrm{s}} - \mathbf{v}_{\mathrm{p}}) + m_{\mathrm{p}}\underline{\mathrm{g}} - \rho_{\mathrm{mix}}\underline{\mathrm{g}}V_{\mathrm{p}} + \frac{1}{2}\rho_{\mathrm{mix}}V_{\mathrm{p}}\left(\frac{D\mathbf{v}_{\mathrm{mix}}}{Dt} - \frac{d\mathbf{v}_{\mathrm{p}}}{dt}\right) \quad (8)$$

where $\mathbf{v}_p$, m_p, d_p and V_p are the velocity, mass, diameter and volume of a fuel particle, respectively, and $\mathbf{v}_g$ is the velocity of the gas phase. We calculate the drag force on the fuel particle from the other two phases in an independent manner. In Equation (8), the first and second terms on the r.h.s represent the drag forces on the fuel particles exerted by the gas and the inert solids phase, respectively. The third term is the weight of the fuel particle and the fourth and fifth terms are respectively the buoyancy force and the added mass force exerted by the mixture (gas and inert solids). Note that we keep the added mass force in our equation of motion, even if that force is typically omitted when tracking solid particles. In our case, the fuel particles are suspended in a medium of relatively similar density (i.e. the mixture of the inert-phase particles and the carrying fluid).

The density and velocity of the mixture of gas and inert solids are calculated as follows:

$$\rho_{\mathrm{mix}} = \varepsilon_{\mathrm{s}}\rho_{\mathrm{s}} + \varepsilon_{\mathrm{g}}\rho_{\mathrm{g}}, \quad (9)$$

$$\mathbf{v}_{\mathrm{mix}} = \varepsilon_{\mathrm{s}}\mathbf{v}_{\mathrm{s}} + \varepsilon_{\mathrm{g}}\mathbf{v}_{\mathrm{g}}. \quad (10)$$

The drag factor on a fuel particle exerted by the gas phase is expressed by the correlation proposed in [5], which takes into account the effects of the local volume fraction of the gas phase: $f_{\mathrm{g}} = \varepsilon_{\mathrm{g}}^{-3.7}f_{\mathrm{g0}}$. The drag factors on an isolated fuel particle exerted by the inert and gas phases, f_{s0} and f_{g0} , are also calculated according to [5]. Note that this work assumes the so-called enhanced buoyancy effect (an enhanced buoyancy effect of fuel particles due to endogenous bubbles generated by the release of volatile matter) to be of little or negligible importance for the fuel mixing process.

2.3. Statistical procedure

The statistical analysis includes obtaining a probability density function (PDF) of the presence of fuel particles in different regions of the bed, which in essence gives their preferential positions in the bed. This is done by counting the number of times that the fuel particles enter each statistical cell (not to be confused with the spatial resolution of the movement of the phases in the bed). The horizontal dispersion coefficient of the fuel particles in each statistical cell is calculated by the Einstein's expression:

$$D_{\mathrm{cell}} = \frac{1}{N_P}\sum_{n=1}^{N_P}\frac{(\Delta l_n)^2}{2\Delta t_n} \quad (11)$$

This equation represents an analogy between the diffusion of gas molecules in a continuous isotropic medium and the mixing of fuel particles in fluidized beds. In (11) Δt_n is the time interval between two snapshots and Δl_n the displacement of the fuel particles during Δt_n. Finally, N_P is the number of times that the fuel particles are present in the cell under consideration during the operation.

2.4. Computational cases and numerical procedure

We assume that, due to the wall effects that influence the dynamics of bubbles in two-dimensional geometries, only qualitative results can be obtained from these studies. Yet, such units have also been shown to be of great value for understanding of large-scale fluidized-bed systems, provided they are operated according to certain criteria [1]. We simulate here 20 fuel particles in order to get sufficient data for statistical analysis. We have designed two computational cases to portray the results of our simulations: Case 1 (the initial bed height (H_0) of 0.4 m and a fluidization velocity (U_f) of 0.4 m/s) and Case 2 (the initial bed height of 0.4 m and a fluidization velocity of 0.95 m/s).

The computational domain is discretized by a structural mesh of 72000 (120 × 600) quadrilateral cells. To check grid independency of the solution, the simulations are performed using a number of grid sizes and no sensitivity of the solutions was observed for the grids with more than 72000 cells. Superbee, which is a second-order accurate scheme, is used for discretizing the convection terms. In addition, to speed up the simulations, MFIX applies an automatic time-step adjustment. The pressure and velocity are coupled by the SIMPLE algorithm [5] and the interphase interaction term is treated through the Partial Elimination Algorithm [5].

To accurately formulate the inlet boundary condition, the plenum is included in the computational domain and the air distributor is modeled as a porous zone with a specified resistance. Note that the uniform velocity inlet, which is a common choice in most numerical studies of fluidized beds, represents high pressure-drop distributors. However, in industrial-size beds, low pressure-drop distributors are typically used, which leads to a non-uniform flow condition at the distributor and a significantly different flow pattern.

According to the tracking technique explained above, the flow of the inert solids and the gas phase are first resolved. Then, a number of fuel particles, which are initially randomly positioned in the bed, are tracked.

3. EXPERIMENTS

The experimental apparatus used in the present study is a pseudo two-dimensional fluidized bed (0.4m × 2.15m × 0.015m) with a Plexiglas front wall. A schematic view of the setup is shown in Figure 1. The fluidizing air enters the bed through a distributor made of a perforated plate having 2 mm in diameter holes and the total hole areas of 2%. Glass beads are used as inert particles (ρ_s = 2600 kg/m^3 and d_s = 330 μm). The properties of such particles are similar to those of sand particles typically used as the inert bed material in fluidized beds. The particles have a minimum fluidization velocity (U_{mf}) of 0.12 m/s and a terminal velocity (U_t) of 1.76 m/s.

As for the PIV, in this work we assume that the bed is two-dimensional and that the flow patterns are measured in the front-wall plane. The use of a conventional laser for illumination of bed particles is not possible because of speckles and the high density of bed particles. Instead of a pulsed laser, light from a continuous source is applied. The PIV system consists of two Imager ProX 4M cameras, having 2048×2048 resolution, 8×500 W lamps as the light source, a synchronizing device, a computer, and DaVis software from LaVision company, to collect and process images. We have taken special care to minimize the displacement field. This means that any non-coincidence field is captured before each measurement and subtracted from the velocity fields obtained.

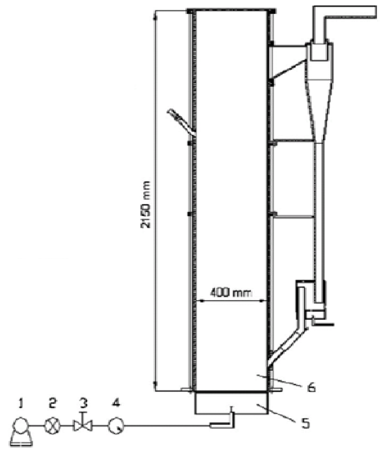

Figure 1: Schematic of the fluidized bed setup: 1) compressor, 2) stop valve, 3) control valve, 4) rotameter 5) plenum, 6) riser

Exposure is set in such a way that blurred appearance of the particles is avoided in the high-speed regions. In PIV, the recorded images are pre-processed by subtracting sliding background of 10 pixel scale and applying the particle intensity normalization (available in DaVis software). To extract velocity fields, a decrease from 128×128 pix (2 passes) to 64×64 pix (3 passes) interrogation window with 50% overlapping is used in multi-pass mode. A masking routine is used to exclude bubble areas, to avoid the effects of the velocity field created by the inert particles inside the bubbles. The masks are black-and-white images with black areas corresponding to bubbles and the white areas to solids.

4. RESULTS AND DISCUSSION

To examine the performance of the frictional stresses (and thus the overall stress tensor for the particulate phase) used here, we analyse the motion of a single fuel particle in the bed by looking at the experimental and numerical results for its position and velocity.

Figure 2 (top) shows the horizontal position of the fuel particle for a period of 100 seconds of operation, as obtained by the experiments. We see that the fuel particle moves in a cyclic pattern. It moves downwards at the regions near the walls. Then, close to the distributor, it starts moving upwards with the upcoming bubbles and returns to the surface, which is indicated by quick jumps in the vertical position of the fuel particle. As seen here, the fuel particle spends most of the time in the sinking (descending) phase, whereas the rising (ascending) one takes a much shorter time.

Fig. 2 (middle) shows the motion of the fuel particle simulated using the frictional model proposed in [3].

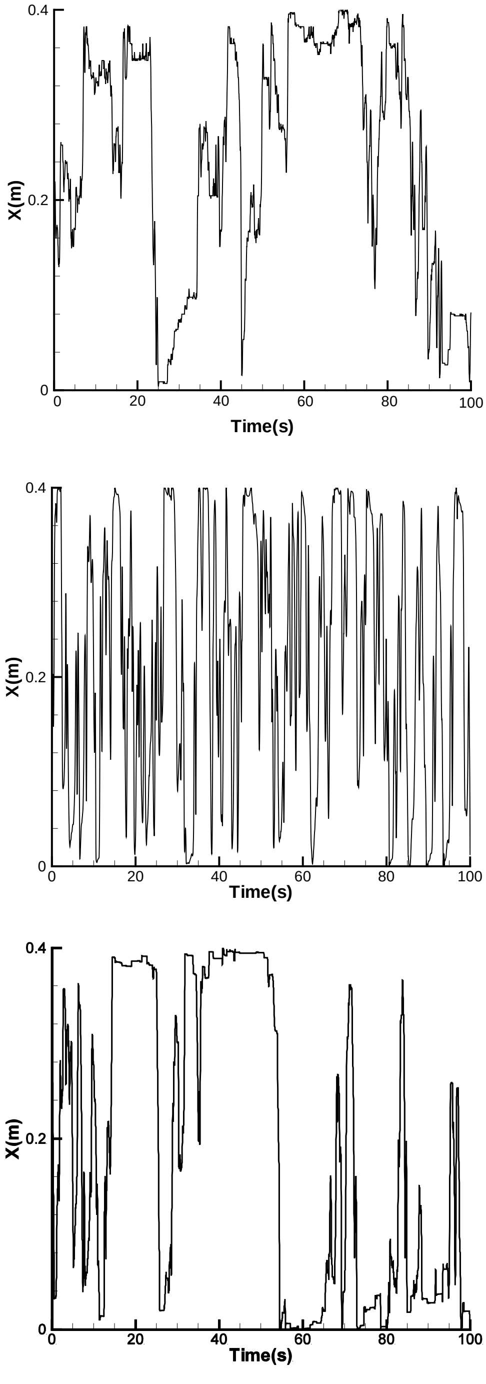

Figure 2. The horizontal position of the fuel particle in the bed: top: experiments; middle: frictional model, expressions (1) and (2); bottom: frictional model: expressions (3)-(7). Case 1.

This model captures the circulation of the fuel particle, but it clearly predicts much shorter cycles. On the other hand, employing the visco-plastic model [4] (Fig. 2 (bottom)) results in a circulation pattern for the fuel particle that is more similar to the experimental results. Here, the fuel particle sinks rather slowly at the wall. These slow-moving periods represent situations in which the fuel particle is surrounded by the inert particles and therefore, it totally follows the motion of the inert phase. The better prediction obtained by the visco-plastic model can be explained by the fact that it gives higher solids viscosity, and consequently, lower solids velocity at the wall where the particulate flow is dense and involves few bubbles. In such dense locations, the frictional stresses play a major role. The obtained conclusions remain when we look at the vertical position of the fuel particle (Figure 3).

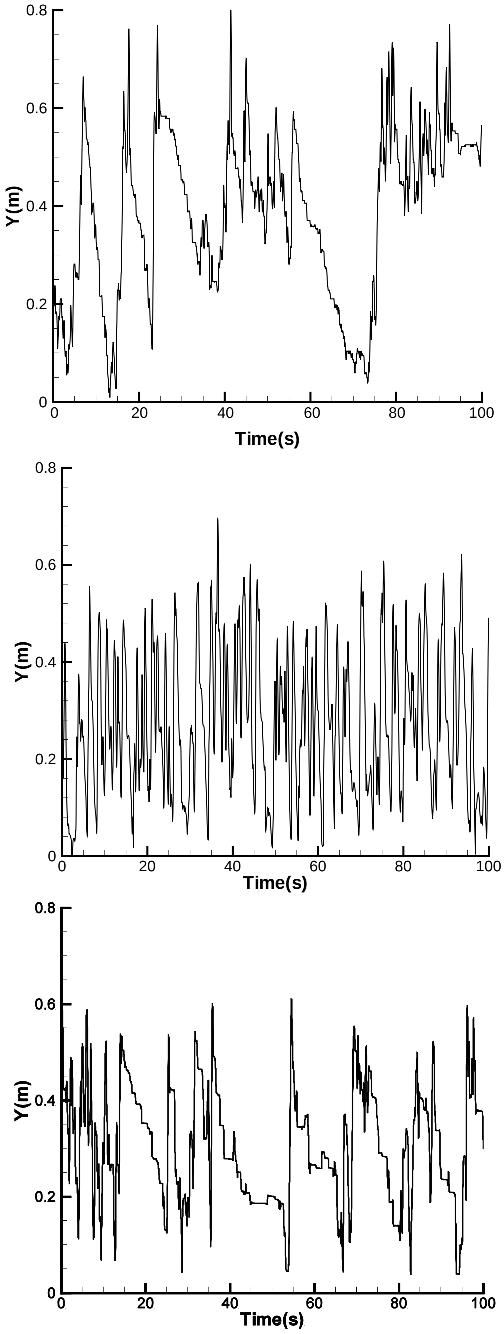

Figure 3. The vertical position of the fuel particle in the bed: top: experiments; middle: frictional

model, expressions (1) and (2); bottom: frictional model: expressions (3)-(7). Case 1.

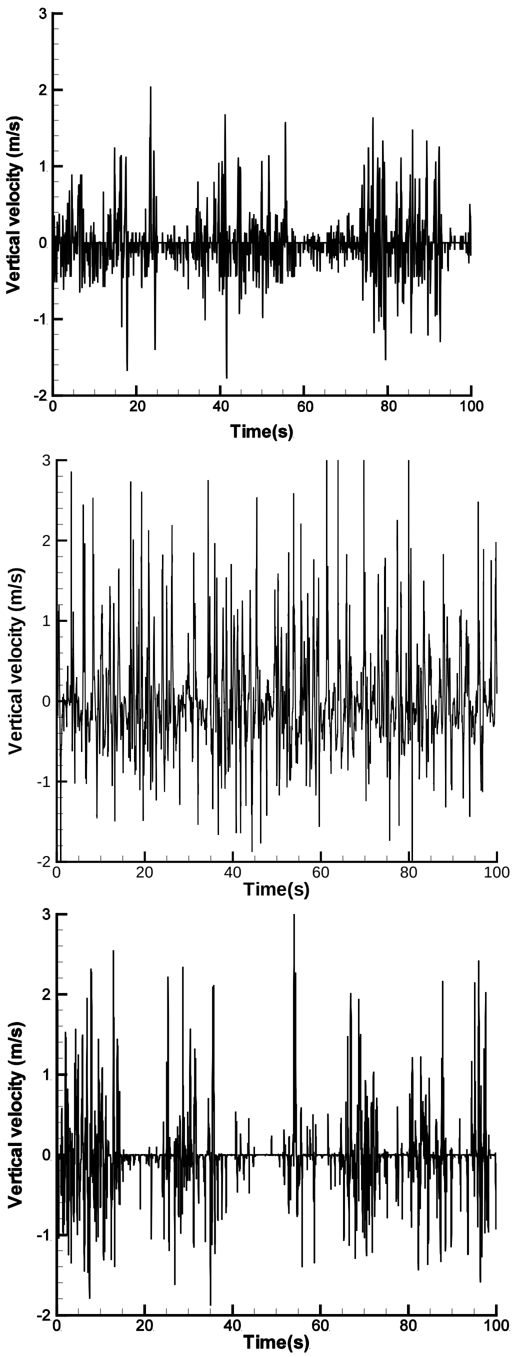

Figure 4. The vertical velocity of the fuel particle in the bed: top: experiments, middle: frictional model, expressions (1) and (2), bottom: frictional model: expressions (3)-(7). Case 1.

We now focus on the velocity of the fuel particle. As seen in the experimental results, the horizontal and vertical velocities of the fuel particle fluctuate around zero. The movement of the fuel particle is represented by an intermittent signal in which the high-frequency activity comes in bursts separated by relatively long quiescent periods (low amplitude fluctuations). Note that a typical example of such a signal is the one obtained (after being high-pass filtered) by a hot-wire anemometer in a turbulent single-phase flow. Such a pattern is observed in both the horizontal (not shown here) and vertical directions. The vertical component (Figure 4 (top)) is of greater importance, since it is associated with the bubble movement in the bed. The positive values of the vertical velocity reflect the presence of rising bubbles. After a number of small jumps, a large bubble carries up the fuel particle to the surface of the bed and then throws the particle to the freeboard zone. The prominent jumps in the velocity signal of the fuel particle are therefore representative of a quick movement of the fuel particle by vigorous bubbles. The significant negative values of the velocity represent the fall of the fuel particle in locations in which the latter is less hindered by the inert particles. In addition, there are many instances when the velocity of the fuel particle is considerably low, illustrating occasions in which the inert particles, due to high inter-particle friction, do not move at all or move at a very low speed. If the fuel particle is trapped in such a dense zone, it has to follow the bulk phase.

Numerical results for the velocity of the fuel particle are presented in Fig. 4 (middle and bottom). Using the model proposed in [3] leads to a velocity signal that is fluctuating vigorously. Even though the magnitude of the velocity, both horizontal and vertical, is comparable to the experimental results, the intermittent pattern, as identified before, is not observed. This means that, according to this representation of the slid-phase stress tensor, the emulsion phase is constantly moving and that the model underestimates the frictional stresses within the phase representing the inert particles. Fig. 4 (bottom) shows the velocities of the fuel particle for the simulations employing the visco-plastic model. The use of this model leads to a significant change when compared to the previous model. Here, the velocity profiles, both horizontal (not shown here) and vertical appear more like the experimental ones. The zero-valued zones are now clearly visible suggesting that the visco-plastic model can better estimate the frictional component of the stress tensor of the inert particles. The results imply that there are occasions when the particles cannot slide over each other due to high friction.

Similar observations can be made for the case with a higher fluidization velocity (Case 2). A circulation pattern is also observed in which the fuel particle sinks to the bottom of the bed and then rises up by the upcoming bubbles. Compared to Case 1, the circulation is significantly faster. This can be explained by the fact that increasing the fluidization velocity, while retaining the amount of the bed material, leads to a lower bulk density. Thus, the fuel particle is somewhat less affected by the inert particles and it can move downwards more freely.

Now we look at the preferential positions and the velocity vectors of the fuel particles in the bed. As seen in Figure 5 (top), the experimental findings reveal two preferred regions for the fuel particles (illustrated by the dark colour), which are located close to the walls. These regions represent the locations where the fuel particles spend most of the time during operation. In addition, the average motion of the fuel particles forms two vortices in which the fuel particle descends at the wall and ascends at the centre. The fuel particles, which are submerged in the emulsion phase, move slowly downwards in the near-wall regions. Then, they are carried up by the upcoming bubbles in the middle of the bed. Numerical simulations using the model suggested in [3] (not shown here) fail to reproduce the observed behaviour of the fuel particles.

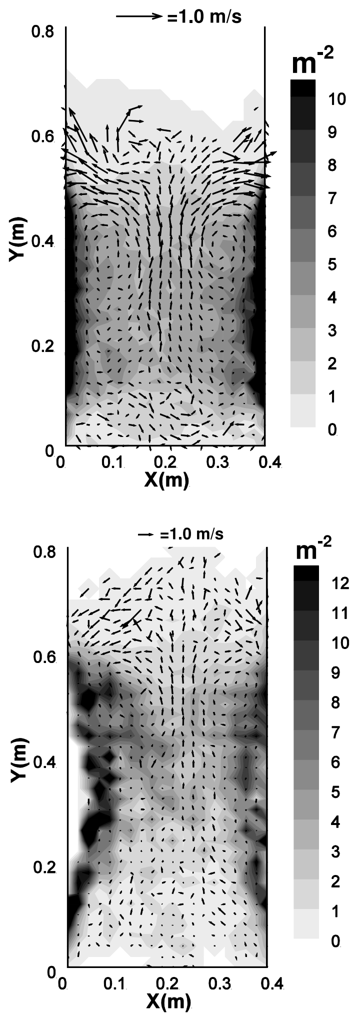

Figure 5. Experimental (top) and numerical (bottom) results for the fuel particle velocity vectors (indicated by arrows) and the PDF of the presence of fuel particles. In the simulations the frictional model is expressed by (3)-(7). Case 1.

From Fig. 5 (bottom) we see that the two preferred zones at the walls and the two vortices are successfully predicted by the simulations. Still, there exist some differences between the simulations and experiments in terms of the magnitude of the velocity of the fuel particles.

Finally, we are interested here on the detailed information of the behaviour of the solid inert phase, as obtained by PIV measurements. In particular, we look at the bubble fraction and the averaged velocity vectors of the inert particles.

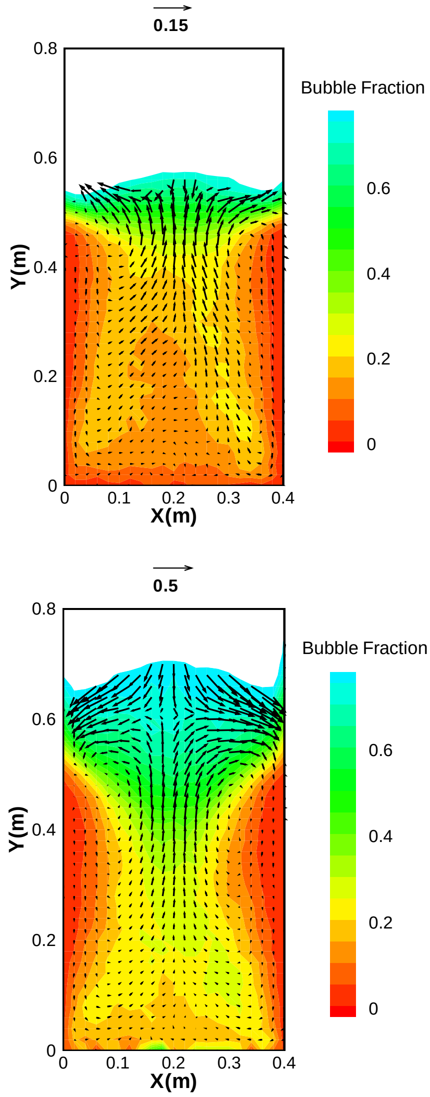

Figure 6. Bubble fracton and the average circlation pattern of inert solid particles, as obtained by PIV measurements. Top: Case 1; bottom: Case 2.

Figure 6 (top) shows the averaged velocity vectors of the inert particles for the Case 1. There are two main bubble paths visible is the dense bottom bed (H < 0.3 m). The two bubbles formed at the bottom corners rise and merge at the centre and form a large bubble at the height of 0.3 m above the distributor. An increase in the fluidization velocity (Case 2) leads to a higher bed expansion and a larger velocity for the solid particles (Fig. 6 (bottom). Even though increasing the fluidization velocity maintains the same general pattern, the bubble merging height for the latter case is shorter than that for the case with a lower fluidization velocity.

We now shift our attention to the motion of the fuel particles in the bed. The aim is to understand how their behaviour is influenced by the dynamics of the inert and gas phases.

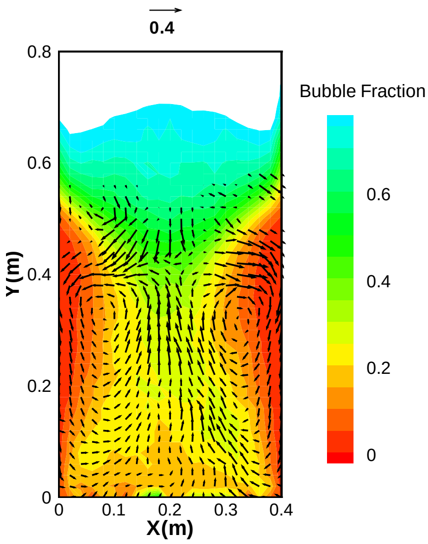

Figure 7. Bubble fracton and average circlation pattern of the fuel particles, as obtained by PIV measurements. Case 2.

As observed in Figure 7, the two bubbles created at the walls carry upwards the fuel particle, while moving towards the middle of the bed. Then, the two bubbles coalesce. The fuel particle, after a ride on the large bubble at the centre is thrown towards the wall. At the wall it descends with the emulsion phase until it is picked up again by the bubbles.

5. CONCLUSIONS

We look in this paper at different formulations of the stresses of the particulate phase when carrying out continuum modelling of dense regions of gas-solid fluidized beds. We focus on the problem of fuel mixing by tracking a number of fuel particles in a bulk of inert particles. The inert solid phase and the fluidizing air are resolved within the Eulerian framework and the fuel particles are tracked by a Lagrangian particle tracking technique. The position and velocity of a fuel particle are obtained and compared with experimental results.

The movement of the inert solids in a two-dimensional fluidized bed is investigated using Particle Image Velocimetry (PIV) measurements. It is concluded that the motion of the fuel particles in the bed is predominantly governed by the bubble flow pattern in the bubble-rich zones. In these zones, the inert particles drift down in the wake of the bubbles and their upwards velocity is lower than that of the fuel particles. On the other hand, within the dense particulate zones, where the fuel is submerged in the inert particle phase, the fuel particle follows the emulsion phase. The experimental results also indicate that the fuel particles move in a circulatory pattern, ascending in the centre of the bed and descending at the walls.

Our simulations show that this complex pattern cannot be captured by the commonly-used frictional models originating from soil mechanics. Such models are found to underestimate the frictional stresses, leading to erratic ascending and descending movements for the fuel particles. Instead, we have found that assuming the inert particulate phase to behave as a visco-plastic fluid leads to a more correct prediction of the movement of the fuel particles in the bed.

REFERENCES

[1] Pallarès, D., Johnsson, F., 2006, "A novel technique for particle tracking in cold 2-dimensional fluidized beds-simulating fuel dispersion", Chemical Engineering Science, 61, 2710-2720.

[2] Lun, C. K. K., Savage, S. B., Jeffrey, D. J., Chepurniy, N., 1984, "Kinetic theories for granular flow: inelastic particles in Couette flow and slightly inelastic particles in a flow field". Journal of Fluid Mechanics, 140, 233-256.

[3] Srivastava, A., Sundaresan, S., 2003, "Analysis of a frictional–kinetic model for gas–particle flow". Powder Technology, 129 (1–3), 72–85.

[4] Jop, P., Forterre, Y., Pouliquen, O., 2005, "Crucial role of side walls for granular surface flows: consequences for the rheology". Journal of Fluid Mechanics, 541, 167-192.

[5] Benyahia, S., Syamlal,M., O'Brien,T.J., Summary of MFIX Equations. (2012), https://mfix.netl.doe.gov/documentation/MFIXEquations2012-1.pdf.

Conference on Modelling Fluid Flow (CMFF'15)
The 16th International Conference on Fluid Flow Technologies
Budapest, Hungary, September 1-4, 2015

FLUIDDYNAMICAL CHARACTERIZATION OF A BUBBLE COLUMN FOR INVESTIGATION OF MASS-TRANSFER

Péter KOVÁTS[1], Dominique THÉVENIN[2], Katharina ZÄHRINGER[3]

[1] Laboratory of Fluid Dynamics and Technical Flows, Otto-von-Guericke-Universität Magdeburg. Universitätsplatz 2., D-39106 Magdeburg, Germany. Tel.: +49 391 - 67 18654, Fax: +49 391 - 67 12840, E-mail: peter.kovats@ovgu.de
[2] Laboratory of Fluid Dynamics and Technical Flows, Otto-von-Guericke- Universität Magdeburg. E-mail: dominique.thevenin@ovgu.de
[3] Laboratory of Fluid Dynamics and Technical Flows, Otto-von-Guericke- Universität Magdeburg. E-mail: katharina.zaehringer@ovgu.de

ABSTRACT

Bubble column reactors are multiphase reactors that are used in many process engineering applications. In these reactors a gas phase comes into reaction with a fluid phase and transport processes from the gas to the liquid phase are often the limiting factors. Their characterization is therefore interesting for the optimization of multiphase reactors.

For a better understanding of the transfer mechanisms and chemical reactions, a laboratory scale bubble reactor was investigated. In this reactor, the mass transfer between the two phases can be followed by the help of 2-tracer laser induced fluorescence (2T-LIF). To characterize the flow field in the reactor, two different methods have been applied. First, the shadowgraphy technique is used, which is based on particle recognition with backlight illumination, combined with particle tracking velocimetry (PTV). With this approach, the characteristics of the bubbles, such as bubble diameter, velocity, shape or position are obtained for various process conditions. The bubble trajectories in the column can be obtained in this manner. Secondly, the liquid phase flow can be determined by particle image velocimetry (PIV). The combination of both methods, for bubbles and liquid, leads to a complete characterization of the reactor.

The results of these measurements will be presented together with an analysis of the important parameters that influence the mass transfer.

Keywords: bubble column reactor, CO_2, PIV, shadowgraphy, two-phase flow, two-tracer-LIF

NOMENCLATURE

d_e	[mm]	equivalent diameter

1. INTRODUCTION

Bubble columns are widely used in the industry, for example in bioprocesses or in water treatment. These columns are sometimes employed just to mix the liquid with the help of gas bubbles or they are employed for a chemical process, where the dispersed gas comes into reaction with the liquid phase through gas-liquid mass transfer. Often these transport processes are the limiting factor in the reaction rate so their characterization is interesting for the optimization of these reactors. Gas-liquid mass transfer is influenced by the flow in the column and it is necessary to investigate the bubble column in this context.

Although bubble motion and behaviour have been widely studied, most of these studies considered the behaviour of a single bubble [1-5]. Some experiments were made in bubble swarms, but the bubbles were not uniform [6, 7] or just one inlet nozzle was applied [8-10]. In these experiments the bubble columns were usually rectangular.

In the present study almost uniform bubble swarms, generated with four small nozzles, were investigated in a cylindrical tank.

In a first step, the relationship between bubble diameter and bubble velocity in our column has been verified for several water qualities and compared to the literature (terminal velocity of air bubbles in water at 20°C from Clift et al. [11]). The bubble trajectories were determined. Then the liquid flow was characterized through PIV measurements, covering the whole bubble column. Since these fluid dynamical measurements aim at characterizing the mass transfer from the gas to the liquid, the method for determining gas concentrations in the liquid is presented first. Another objective of these experimental measurements is the supply of experimental data for the validation of numerical models.

2. 2T-LIF TECHNIQUE

To investigate these columns and processes a laboratory scale bubble reactor was built in our institute. The description of the experimental setup can be found in a previous study [12]. The first reaction investigated in this reactor is the mass transfer from CO_2 bubbles into a basic (pH=9) water-NaOH phase.

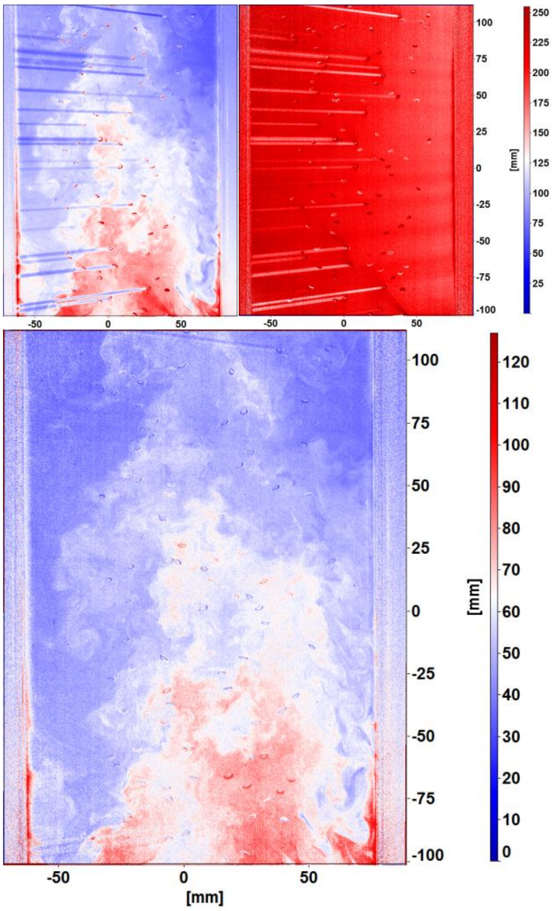

Figure 1. Upper left: raw image from 1st camera with 550nm filter for Uranin; Upper right: raw image from 2nd camera with 705nm filter for Pyridine 2; Bottom: overlapped images

During this reaction the pH value is decreasing. In order to track the pH, the two tracer laser induced fluorescence technique (2T-LIF) is used. In this experiment, the reactor was filled up with de-ionised water and CO_2 gas was led into the liquid at the bottom of the reactor through small nozzles. In the liquid, two fluorescence dyes were dissolved. One of these dyes is changing its fluorescence intensity with the pH (uranine), the other stays passive (pyridine 2). With the help of this second dye, reflections on the bubble surface, bubble shadows and the laser sheet inhomogeneity could be reduced drastically (Figure 1).

For a better understanding of the transport mechanisms, conditioning the reaction, a complete characterization of the flow within the bubble column is necessary. It is important to know, what are the limiting factors and what are the properties of the bubbles.

3. EXPERIMENTAL SETUP

Two types of experiments were carried out to characterize completely the fluid dynamics within the bubble column (Figures 2 and 3). For the CO_2 bubble phase the shadowgraphy technique combined with Particle Tracking Velocimetry (PTV) was used to recognize the bubbles and identify the bubble characteristics, like average diameter, shape, position, velocity and trajectories. For the liquid phase Particle Image Velocimetry (PIV) was used to examine the surrounding hydrodynamics.

Bubble column reactor

The same bubble column with a diameter of 0.14m and a height of 0.8m was employed for both experiments (number 4 in Figs. 2 and 3). This bubble column was made from acrylic glass with a thickness of 4mm and was surrounded by a rectangular acrylic box. This box contained de-ionized water for a better refractive index matching. Preliminary experiments have prooved, that this gives better results, than to match the index of acrylic glass. The bottom of the bubble column can be changed from a single nozzle gas outlet to a bottom with 4 in-line nozzles, which are spaced by 2.2cm. The nozzles are stainless steel capillaries with an inner diameter of 0.25mm. Through these nozzles bubbles with a diameter of about 2.5-3 mm are produced. In all cases – except for filling height and water quality measurements – the column was filled up with 11.5l de-ionised water. The CO_2 gas

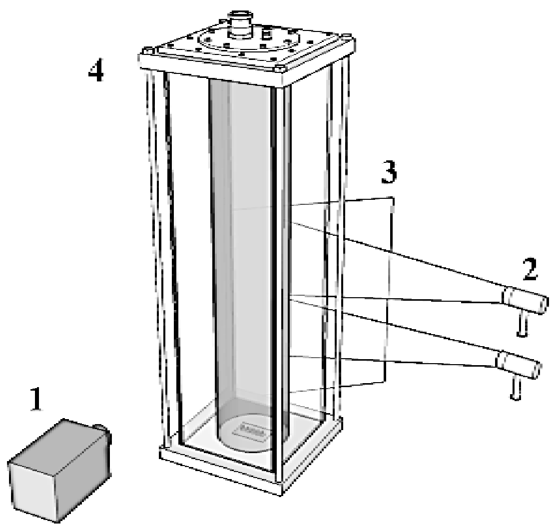

Figure 2. Experimental setup for shadowgrapy

was supplied from a pressurised bottle. All the measurements were made at atmospheric pressure and room temperature.

Shadowgraphy setup

For the shadowgraphy measurements an Imager pro HS 4M CCD camera (number 1. in Fig. 2) was applied with a 2016 x 2016 pixel resolution and 150 kHz maximal frame rate. The camera was equipped with a Carl-Zeiss Makro Planar T*2/50mm ZF-I lens. To illuminate the investigation area and bubbles two Dedocool CoolH halogen lights were used (number 2 in Fig. 2). To avoid damage of the CCD, because of the high illumination intensity, the light was diffused on a white background (number 3 in Fig. 2). The images were taken with a frame rate of 0.1 kHz in the lower 0.3 m in the bubble column. The experimental images were acquired and processed with DaVis software (LaVision). With this method the influence of different parameters (gas flow rate, water quality, pH and fill height) was investigated on the bubble flow.

PIV setup

For the PIV measurements one Imager Intense CCD camera (number 1 in Fig. 3) was applied with a 1376x1040 pixel resolution and 10Hz maximal frame rate. The camera was equipped with a Nikon AF Micro Nikkor 60mm f/2.8D lens. As tracer particles polymethyl methacrylate (PMMA) Rhodamin B particles were used with a diameter of 1-20 µm.

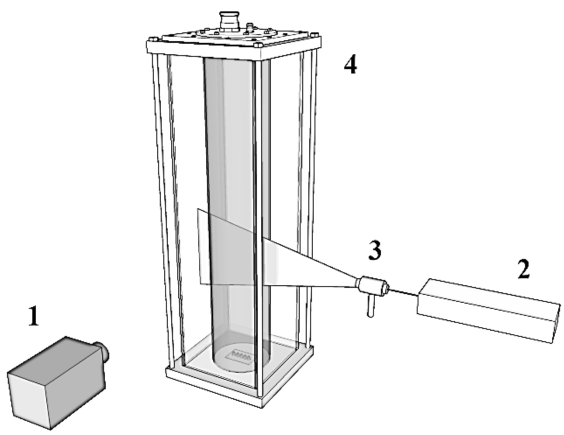

Figure 3. Experimental setup for PIV

The particles were excited by a double-pulsed Nd:YAG laser (Spectra Physics) with 532nm laser light (number 2 in Fig. 3). The produced laser beam was expanded by a light sheet optics (number 3 in Fig. 3). To supress the laser light and reflections on the bubbles surfaces a 537nm longpass filter was mounted onto the camera lens. The geometrical positions were calibrated with a 3D calibration target. The experimental images were acquired with 6.6Hz in double frame mode. The delay time between the two frames was 5 ms. The flow rate of the CO_2 gas was set up through a variable area flow meter to 8l/h. For postprocessing of the raw images DaVis 8.2 (LaVision) has been used. For the vector calculation a cross-correlation (multi-pass, decreasing size) PIV algorithm was used with an interrogation window size from 64x64 pixels to 32x32 pixels. To remove false vectors and refine the vector field, especially in the vicinity and shadows of the bubbles vector postprocessing was necessary, as described later in detail.

4. RESULTS

Shadowgraphy

During the measurement four series of 250 images were taken. Preliminary experiments showed, that 250 images are enough for a statistical result. Thus four measurement series were acquired for each parameter.

For the bubble size detection, a previously recorded background was first removed. Then, the program was able to recognize each bubble and its diameter was calculated, as well as coordinates and centricity parameters.

For the bubble velocity detection a double frame recording was made from the time series. In the second step a sliding background was removed. Then, the program recognized the bubbles and with a PTV algorithm it followed in the second frame the movement of the bubbles that, have been recognised in the first frame. The produced vector shows the movement of each bubble and according to this, the bubble velocity. With the help of these vectors, a trajectory can be drawn for each bubble (Figure 4).

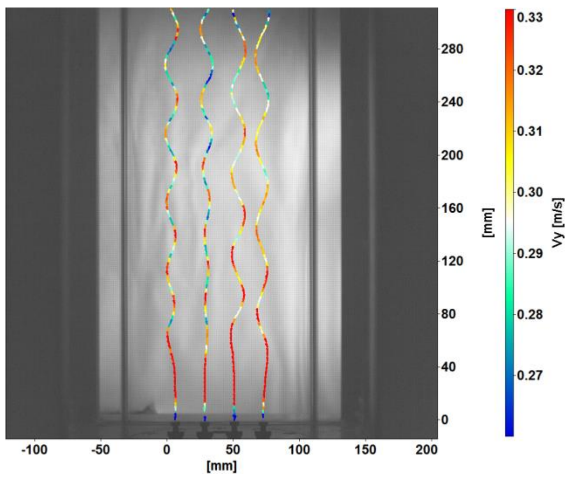

Figure 4. Bubble trajectories, coloured with vertical velocity component

Mendelson [13] has divided the bubble regime into four regions as follows:

Region 1: d_e < 0.7 mm; region 2: 0.7 < d_e < 1.4 mm; region 3: 1.4 < d_e < 6 mm; region 4: d_e > 6 mm.

The produced bubbles are in the third region with an average diameter of 2.2-3mm (Table 1).

In this region the bubbles are no longer spherical and they follow a helical/zigzag path, like it is indeed the case in our bubble column (Figures 4 and 5). The movement of the bubbles is in fact three dimensional as it can be seen from the two views in Figure 5.

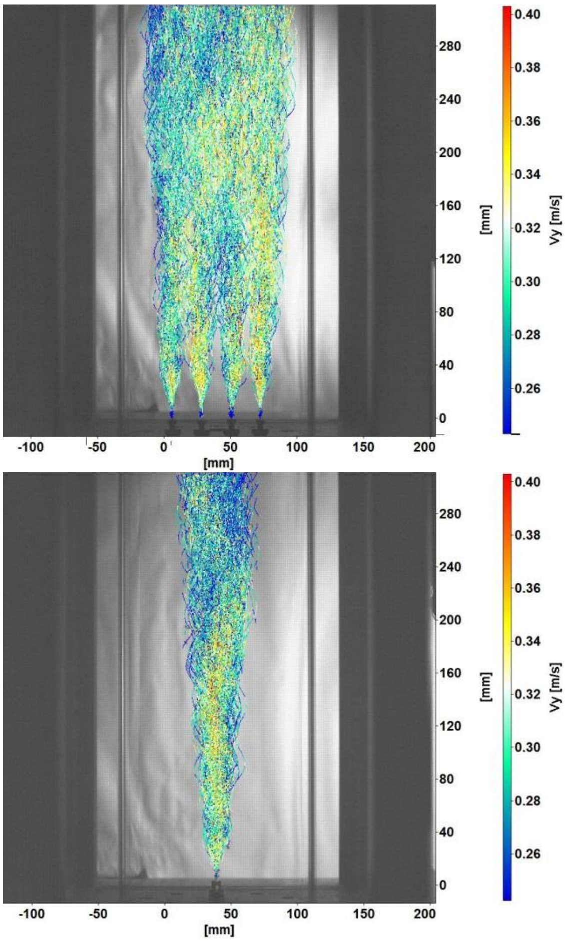

Figure 5. Bubble trajectories in front (upper) and side (lower) view, coloured with vertical velocity component

Firstly, the influence of the fill height on bubble diameter and velocity was determined. The images were taken for five different fill volumes of 3, 5, 7, 9 and 11.72 l (maximum fill volume). No noticeable differences could be remarked between the five cases. The average bubble diameter was 2.4mm and the average velocity was 0.33 m/s.

Then, the influence of water quality was investigated. The applied water was always clear, not contaminated but in different qualities, namely tap water, de-ionised water, distilled water and bi-distilled water. The results showed, that the water quality did not influence the bubble behaviour. The average diameter and velocity were the same as measured for the different fill heights.

The next investigated parameter was the pH. An acidic, a nearly neutral and a basic water solution were tested. As expected, the CO_2 dissolved best in the basic liquid, so at pH 12.5 the measured average bubble diameter was only 2.3mm, compared to 2.4 and 2.5mm in the other cases. In contrast to the diameter, the average velocity showed no measurable differences. This result is confirmed by the diagram in [11], where the difference in the average velocity for bubble sizes between 2 and 2.5mm is very slight.

The last parameter varied was the gas flow rate. The different values were set by a variable area flow meter (Yokogawa). The lowest investigated flow rate was 3.5 l/h, because this is the lowest flow rate, where all the four nozzles produced bubbles. Figure 6 shows that the higher the flow rate, the higher is the bubble diameter, but also the broader is the bubble size distribution (BSD).

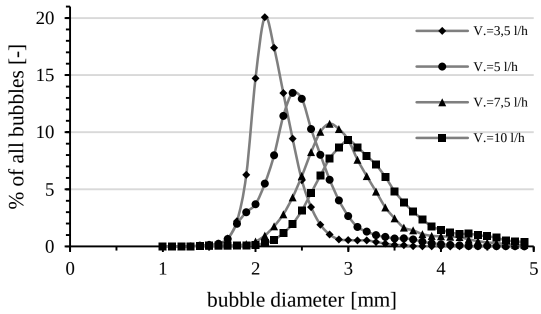

Figure 6. Bubble diameters at different flow rates

For the average velocity the effect is inverse. The smaller bubbles at low flow rate have higher velocities (Figure 7) with a narrower distribution.

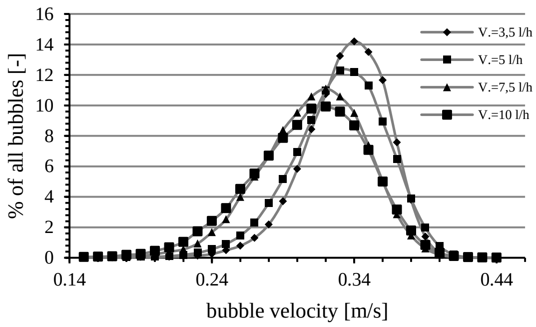

Figure 7. Bubble velocities at different flow rates

In the light of these results we can say, that only the gas flow rate has a pronounced influence on the average velocity and average bubble size in the investigated bubble column. Just in one case, at high pH (over 12) shrinking of the bubbles is noticeable in the investigation area. In all other cases the bubble size stays almost constant throughout the investigated area (Table 1).

Table 1. Results of mean bubble diameters (mm) and vertical velocities (m/s)

		Average bubble diameter	Rounded values	Average vertical velocities
Fill volume (l)	**11.72**	2.4225	**2.4**	**0.334**
	9	2.3225	**2.3**	**0.331**
	7	2.375	**2.4**	**0.331**
	5	2.3775	**2.4**	**0.335**
	3	2.2725	**2.3**	**0.335**
pH Value	**12.48 with NaOH**	2.3325	**2.3**	**0.334**
	6	2.3	**2.3**	**0.333**
	3.8 with HCl	2.4075	**2.4**	**0.330**
	4 with CO2	2.535	**2.5**	**0.325**
Different flow rate (l/h)	**3.5**	2.245	**2.2**	**0.334**
	5	2.445	**2.4**	**0.329**
	7.5	2.855	**2.9**	**0.311**
	10	3.055	**3.1**	**0.308**
Water quality	**1x dest.**	2.3875	**2.4**	**0.312**
	2x dest.	2.33	**2.3**	**0.329**
	de-ion.	2.325	**2.3**	**0.331**
	tap water	2.2775	**2.3**	**0.329**

Liquid dynamics

Since the field of view of the camera covers only about one fourth of the bubble column height, four measurement locations were chosen along the column axis. 1000 double images were taken at each location to form 1000 individual snap-shot velocity fields.

After the first processing step, the bubbles and their shadows are clearly visible, due to a wealth of spurious vectors (Figure 8 upper left, red and blue regions). The raw image with the visible bubbles is superimposed on this image, for clarity. In these regions there are either no tracer particles (within the bubbles) or laser light illumination is very weak (in the shadows). Thus, these regions are not processed appropriately through a simple cross-correlation. To get rid of these imperfections, it is necessary to use refined post processing steps.

During postprocessing, first an allowable vector range filter was employed according to the generated *Vx/Vy* scatter plot. Then, with the help of a median filter and taking into account the 8 neighbouring interrogation areas, the highest (here wrong) correlation peak, was replaced by the second, third or fourth highest correlation peak, until the given filter criteria was fulfilled. The vector position was disabled if none of the peaks fulfilled the criteria. These few disabled areas were replaced with an interpolated value from the 8 neighbours.

This result can be seen in Fig. 8 upper right, once more with the superimposed raw image to locate the bubbles and shadows.

For a better readability, the same velocity field is presented with a different colour scale (now adapted to the real maximum and minimum values) on the bottom of Fig. 8.

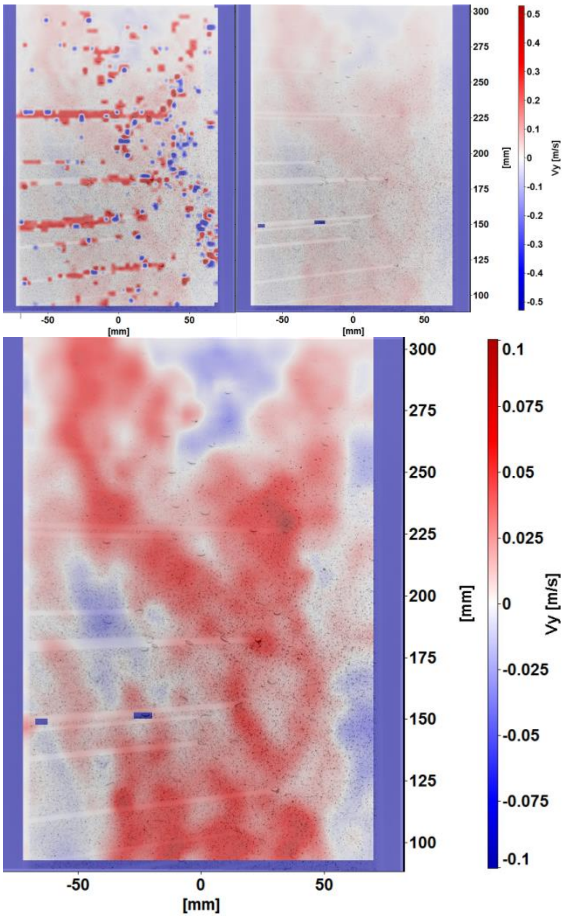

Figure 8. Vertical velocity component (m/s) for one snapshot without vector postprocessing (upper left), with postprocessing (upper right) and with an adapted colour scale (bottom).The raw particle image is used as background for the location of the bubbles and shadows. These velocity fields have been obtained at the second measurement position

The snap-shot vertical velocity component is represented here for the second measurement section (from 90mm to 300mm over the bubble outlet). Regions with maximum velocities of about 9cm/s can be recognized in the centre part of the column. Near the wall, regions with negative velocity appear, which are part of a descending flow, discussed later.

To obtain an average flow field 1000 post processed individual velocity fields were averaged for each position (Figure 9).

As expected, the averaged images show an almost symmetric velocity field in the bubble column with an ascending centre part and a thin descending zone near the column wall.

With the results of all four measurement sections a full height flow field could be created (Figure 10). At the bottom of the image, the four bubble nozzles are visible. In the first 0.3m, the vertical centre velocity is around 0.055 m/s, because the bubble swarm is still concentrated. Above 0.3m, bubbles are spreading sideways and start to occupy the whole thickness of the column; thus, the velocity is decreasing. In the top section, a recognizable backflow exists on both sides, because of the liquid surface (Figure 11). This leads to the mentionned downward flow along the walls of the whole column (Fig. 10).

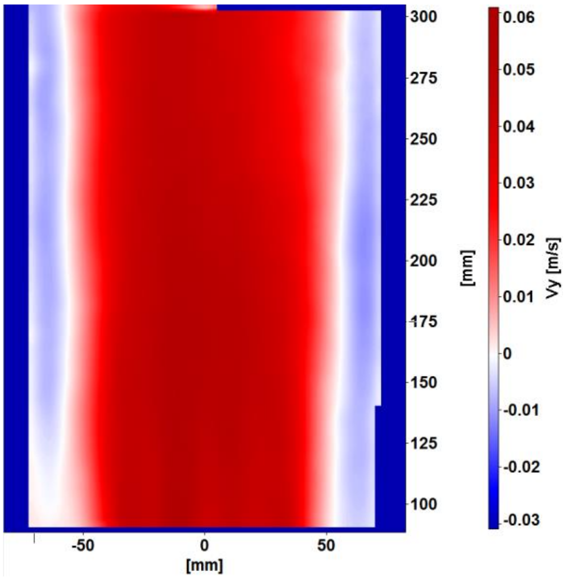

Figure 9. Averaged vertical velocity component at the second measurement position

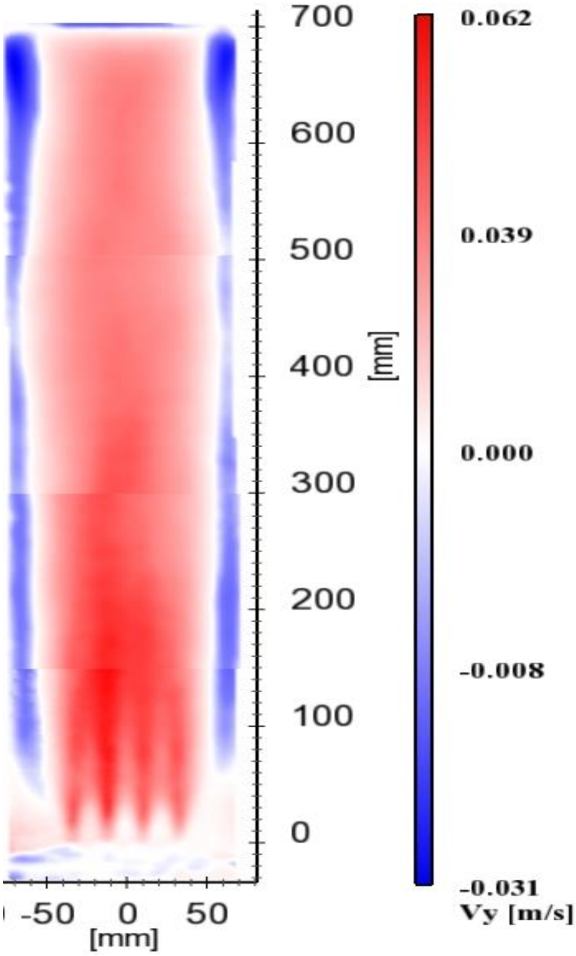

Figure 10. Mean vertical velocity component (m/s) for the full height of the volumn

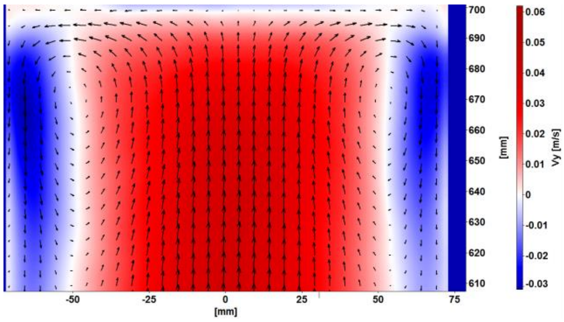

Figure 11. Flow field near the surface

5. CONCLUSIONS

In this paper two combined methods for characterizing the fluid dynamics of a bubble column reactor have been used. The shadowgraphy technique combined with PTV was used to investigate the bubble behaviour, while the PIV technique was applied to characterize the liquid flow.

The bubble behaviour has been examined as a function of different parameters. Only the gas flow rate induced significant changes in bubble size and velocity. With a higher flow rate, more gas could be dissolved from the bubbles into the liquid and the higher bubble flow can enhance mixing in the reactor, thus influencing the mass transfer in the column. Because of the three dimensional motion of the bubbles, planar shadowgraphy cannot resolve the exact bubble movement. To avoid this problem, a stereo-shadowgraphy setup with two cameras will be used in the future.

With PIV the flow field in the bubble reactor could be investigated adequately considering a few lines of bubble swarms. With this rather small amount of bubbles, the problem of bubble shadows can be solved. In a bigger volume occupied by bubbles, more shadows appear. In this case, the laser sheet may not sufficiently excite the fluorescent tracer particles behind the bubbles. To solve this problem it might be necessary to apply another laser sheet from the other side, to get counter propagating sheets. In the future PIV measurements with different flow rates will be carried out, to investigate also the mixing process in the column. A further aim is the detailed investigation of the flow field around individual bubbles. For this and for a time-resolved analysis of the liquid flow field high-speed PIV will be used.

ACKNOWLEDGEMENTS

This work has been financially supported by the German research foundation (DFG) in the framework of the SPP 1740 "Reactive Bubbly Flows" under project number ZA-527/1-1.

The authors would also like to thank the students Niklas Brandt and Tim André Kulbeik for their help in doing the experiments. The help of C. Kisow and S. Herbst for building the bubble column are gratefully acknowledged.

REFERENCES

[1] Wegener, M., Paul, N. , Kraume, M., 2014, „Fluid dynamics and mass transfer at single droplets in liquid/liquid systems", *International Journal of Heat and Mass Transfer*, Vol. 71, pp. 475–495.

[2] Nagami, Y., Saito, T., 2013, „Measurement of modulation induced by interaction between bubble motion and liquid-phase motion in the decaying turbulence formed by an oscillating-grid", *Particuology*, Vol. 11,pp. 158-169.

[3] Saito, T., Toriu, M., 2015, Effects of a bubble and the surrounding liquid motions on the instantaneous mass transfer across the gas-liquid interface., *Chemical Engineering Journal*, Vol. 265, pp. 164-175.

[4] Bozzano, G., Dente, M., 2001, "Shape and terminal velocity of single bubble motion: a novel approach", *Computational Chemical Engineering*, Vol. 25(4-6), pp. 571-576.

[5] Rollbusch, P.; Bothe, M.; Becker, M.; Ludwig, M.; Grünewald, M.; Schlüter, M.; Franke, R., 2015, "Bubble columns operated under industrially relevant conditions – Current understanding of design parameters", *Chemical Engineering Science*, Vol. 126, pp. 660–678.

[6] Sathe, M.J., Thaker, I.H., Strand, T.E., Joshi, J.B., 2010, „Advanced PIV/LIF and shadowgraphy system to visualize flow structure in two-phase bubbly flows", *Chemical Engineering Science*, Vol. 65, pp. 2431–2442.

[7] Sathe, M.J., Mathpati, C.S., Deshpande, S.S, Khan, Z., Ekambara, K., Joshi. J.B., 2011, „Investigation of flow structures and transport phenomena in bubble columns using particle image velocimetry and miniature pressure sensors", *Chemical Engineering Science*, Vol. 66, pp. 3087–3107.

[8] Sathe, M., Joshi, J., Evans, G., 2013, „Characterization of turbulence in rectangular bubble column", *Chemical Engineering Science*, Vol. 100, pp. 52–68.

[8] Liu, Z., Zheng, Y., Jia, L., Zhang, Q., 2005, „Study of bubble induced flow structure using PIV", *Chemical Engineering Science*, Vol. 60, pp. 3537-3552.

[10] Besbes, S., El Hajem, M., Ben Aissia, H. , Champagne, J.Y., Jay, J., 2015, „PIV measurements and Eulerian–Lagrangian simulations of the unsteady gas–liquid flow in a needle sparger rectangular bubble column", *Chemical Engineering Science,Vol.* 126, pp. 560-572.

[11] Clift, R., Grace, J.R., and Weber, M.E., 1978, *Bubbles, drops and particles*, Academic Press, New York.

[12] Zähringer, K., Wagner, L.-M., Kováts, P. Thévenin, D., 2014, „Experimental characterization of the mass transfer from gas to liquids in a two-phase bubble column", *7th International Workshop on Transport Phenomena with Moving Boundaries*, Berlin, Germany.

[13] Mendelson, H. D, 1967, "The Prediction of Bubble Terminal Velocities from Wave Theory", *A.I.Ch.E. Journal*, Vol. 13 (No. 2), pp. 250-253.

Conference on Modelling Fluid Flow (CMFF'15)
The 16th International Conference on Fluid Flow Technologies
Budapest, Hungary, September 1-4, 2015

FORMULATION OF STRESSES IN DRY GRANULAR FLOWS

Adam JARETEG[1], Klas JARETEG[2] and Srdjan SASIC[3]

[1] Department of Applied Mechanics, Chalmers University of Technology. E-mail: adam.jareteg@chalmers.se
[2] Department of Applied Physics, Chalmers University of Technology. E-mail: klas.jareteg@chalmers.se
[3] Corresponding Author. Department of Applied Mechanics, Chalmers University of Technology, SE 412 96 Gothenburg, Sweden. E-mail: srdjan@chalmers.se

ABSTRACT

We employ in this paper a Discrete Element Modelling (DEM) method to characterize rheology of dry, dense granular flows. We particularly look at the formulation of macroscopic system stresses based on the forces acting on individual particles. In addition, we study the possible coexistence in a domain of interest of different regimes of granular flow. The modelling framework is implemented in an open-source computational framework (OpenFOAM) in order to simulate dry granular flow in a Couette shear cell. The system is dense with particle volume fractions close to the maximum packing of particles. To accurately describe the contact forces on the particles, a soft-sphere model is used.

Our simulations identify the following trends in the behaviour of granular material: increasing the values of the solid volume fraction, shear rate or friction, respectively, unambiguously leads to both higher stresses and their different distribution in the system. Finally, tendencies on the ratio between shear and normal stresses are investigated as a function of the volume fraction.

Keywords: DEM, formulation of stresses, granular flow, OpenFOAM

NOMENCLATURE

Note that only main properties are given here. All other parameters are explained as they appear in the paper.

$\boldsymbol{F}$	[N]	force (in general)
I	[$kg.m^2$]	moment of inertia
d	[m]	particle diameter
$\boldsymbol{f}_c$	[N]	contact force
$\boldsymbol{g}$	[m/s^2]	gravity acceleration
k	[-]	spring coefficient
m	[kg]	mass
α	[-]	solid volume fraction
η	[-]	dashpot coefficient
μ	[-]	coefficient of friction
$\boldsymbol{\sigma}$	[N/m^2]	stress (in general)
	[$1/s$]	shear rate
ξ	[-]	overlap
ω_i	[rad/s]	angular velocity of a cell

Subscripts and Superscripts

D	deviatoric
T	trace
n	normal (appearing with force)
t	tangential (appearing with force)

1. INTRODUCTION

Granular flows are present in many large-scale industrial processes where particles and powders are transported or mixed. At present, a quantitative depiction of the latter processes typically relies on a continuum framework. However, the inherent complexity of such flows makes it exceptionally challenging to formulate general macroscopic governing relations.

A particular feature of granular flows is that granular matter can, under certain circumstances, behave like a solid, liquid or gas (if, for example, there is strong agitation present in the system). Currently, there exists no comprehensive theory that can, under a single modelling framework, describe those three regimes and predict the transition between them.

The present paper is a part of an ongoing effort to study the mentioned regimes of granular flow, and in particular, the conditions under which the transitional (or liquid-like) behaviour takes place. Studies [1] show that, in the latter regime, there is simultaneous presence of enduring contacts between particles (characterizing a solid-like behaviour) in the system and those that occur through a shorter period of time (illustrating the behaving of a system as a liquid).

We have chosen a DEM simulation framework in this paper since it enables us to look in the same time at the influence of both microscopic (particle-related) and macroscopic properties of the system of interest. To be more specific, the main particle properties are the particle friction coefficient and inelasticity, while the macroscopic ones are related to the solid volume fraction and properties such as the shear rate. In addition, we discuss some specific features when employing the DEM framework for simulating granular flows, such as the influence of initial placement of particles, ways of defining stresses and the consequences of carrying out two-dimensional simulations.

2. SIMULATION METHOD AND GEOMETRY

Discrete Element Modelling (DEM) framework is a powerful tool that can provide valuable insights into the macroscopic behaviour of a granular flow system by tracking individual particles present in the system [2]. The motion of particles is obtained by solving the Newton's second law of motion (for both translation and rotation). The equation governing the translational motion of a particle i reads:

$$m_i \frac{dv_i}{dt} = \boldsymbol{f}_{f,i} + \sum_{j=1}^{k_i} \boldsymbol{f}_{c,ij} + m_i \boldsymbol{g} \tag{1}$$

with m_i and v_i being the mass and velocity of the particle, respectively. The forces acting on particles are typically: the fluid-particle interaction force $\boldsymbol{f}_{f,i}$ (the drag force, not present in our work since we look at dry granular flow), the gravitational force $m_i\boldsymbol{g}$, and the inter-particle contact forces $\boldsymbol{f}_{c,ij}$.

The inter-particle forces will generate a torque ($\boldsymbol{T}_{ij}$) causing the particle i to rotate with an angular velocity ω_i:

$$I_i \frac{d\omega_i}{dt} = \sum_{j=1}^{k_i} \boldsymbol{T}_{ij} \tag{2}$$

with I_i being the moment of inertia of the particle i.

There are two widely used approaches to handle particle contacts [3]: the hard-sphere and the soft-sphere models. The former approach accounts for instantaneous and binary collisions and it is hence applicable for relatively dilute systems. The soft-sphere model [4], on the other hand, takes multiple particle contacts into consideration and is commonly used to simulate dense gas–particle systems. Thus, in the present work (as we deal with dense granular flow), the soft-sphere model is employed to calculate the contact forces, including the normal, damping and tangential forces between the particles and between particles and walls. The contact forces are modelled using an analogy with a mechanical system consisting of springs, dashpots and friction sliders. The normal force between two particles is formulated as:

$$F_n = k_n \xi^{3/2} - \eta_n u \tag{3}$$

where ξ is the normal overlap between the particles, k_n is a spring coefficient related to the material properties of the particles, η_n is a dashpot coefficient controlling energy dissipation and u is the relative velocity between the particles. The first part of the r.h.s of the equation (3) is the Hertzian model [7] for colliding spheres, whereas the second part is a dashpot representation for the inelasticity of the contact and it represents the energy loss in a collision. Note that the dashpot term also introduces a certain amount of energy dissipation into the system making the simulations more stable. The representation of tangential forces depends on whether sliding between particles is present or not:

$$F_t = \begin{cases} -\mu|F_n|, & for \;\; k_t\xi_t > \mu|F_n| \\ -k_t\xi_t - \eta_n u_{slip}, & else \end{cases} \tag{4}$$

with ξ_t being the tangential overlap defined as the product of the slip velocity (u_{slip}) and the time step for the soft sphere model. Constituent parts of the soft sphere model for particles A and B are summarized in Table 1.

Table 1: Variables used in the soft sphere model

Coefficient	Formulation
Normal spring constant	$k_n = 4/3\sqrt{R_{eff}}E^*$
Tang. spring constant	$k_t = 8\sqrt{R_{eff}\xi_t}G^*$
Dashpot constant	$\eta_n = \alpha\sqrt{M_{eff}k_n}\xi^{1/4}$
ScaledYoung's modulus	$E^* = E/2\left(1-\sqrt{\nu}\right)$
Scaled shear modulus	$G^* = G/2(2-\nu)$
Shear modulus	$G = E/2(1+\nu)$
Effective mass	$M_{eff} = M_A M_B/(M_A + M_B)$
Effective radius	$R_{eff} = d_A d_B/(d_A + d_B)$

Choice of a time step is essential when applying the soft sphere model. If it is too large, the overlaps may behave likewise, something that results in the forces becoming unphysically large. In this work we calculate the collision time using the following expression:

$$t_n = 1.1\,\pi^{7/5} R \left(\frac{\rho}{E^* \sqrt{|u|}}\right)^{2/5} \tag{5}$$

with E^* as the scaled Young's modulus, as given in Table 1.

A Couette shear cell is a standard geometry used in numerous studies [e.g. 1] dealing with modelling of granular flow. In the present work, it is particularly suitable since it allows for the co-existence of different regimes of granular flow (i.e. from a solid-like to a gas-like behaviour).

The numerical framework is implemented into an open-source computational platform (OpenFOAM). Note that the code itself requires the use of a mesh, even if the latter is not required in a general DEM methodology. Each cell in the mesh stores a list with the particles present in that cell, but also a list of neighbouring cells, identifying possible collisional partners for the particles residing in the cell of interest. The solution procedure uses two time steps: the collisional time step as defined by expression (5) and the so-called global time step Δt_g that governs the resolution of other forces (e.g. gravitational force or drag if an interstitial fluid is present). Each global time step is then divided into a number of sub time steps to make sure that even a fastest collision is still resolved in sufficient detail. We do it here by first calculating the shortest collisional time ($t_{min,coll}$) possible, with n_{res} as the number of steps to resolve the collision: $t_{min,coll} = {t_n}/{n_{res}}$ and then each sub time step is chosen according to: $\Delta t_{sub} = min(\Delta t_g, t_{min,coll})$. Now, within each sub time step, the corresponding sub iteration begins with all the forces on the particles *not* originating from collisions to be calculated and the particle positions updated accordingly. When the update is complete, the collisional forces are calculated. For any tracked particle, the particles in the possible neighbouring list are located first. Then, an overlap check is performed. If the overlap is detected, the corresponding force is calculated using expressions (3) and (4). The particle-wall collisions are evaluated in the same manner.

Finally, it is of interest to look at the effect on the results of the initial distribution of particles in the cell. This distribution determines the solid fraction of particles that is achievable in the simulations while making the solutions independent of the initial lattice (the particles have to be able to break out of the initial lattice). This problem is often forgotten in DEM simulations and its origin is in the existence of rather different governing time scales in different regions of a Couette cell. For example, it has been shown in [6] that the scales that govern the outer regions are relatively long. This could imply that the long simulation times are needed or that the problem may in essence be dependent on the initial configuration. An undesired consequence is that initialization of the particle field might in fact be a simulation parameter. To have a closer look at this problem, two different methods for placing the particles have been used (Figure 1):

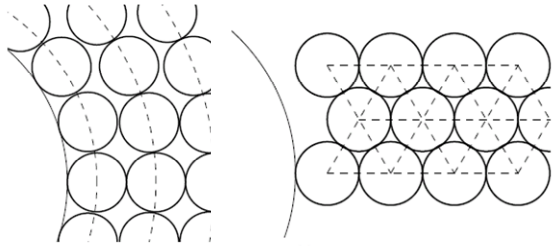

Figure 1: Initial placement patterns of particles: left) circular, right) triangular.

A triangular lattice is the closest packing achievable when packing circles and would theoretically reach solid fractions $\alpha_{max} \approx 0.9069$. Note that this is not possible in the simulated geometry since placing particles close to the wall is restricted, rendering it impossible to perfectly fit the lattice to the circular shape of the geometry. The maximum packing reachable for the cases tried in this work is $\alpha_{max} \approx 0.85$. On the other hand, a circular placement pattern reaches solid fractions of $\alpha_{max} \approx 0.78$. This limit is somewhat lower than in other studies [5, 6] that operate with solid fractions of up to 0.82. The benefit of placing particles according to Fig. 1 (left) is that the structure is not as rigid as the triangular one. Both types of initial placement are based on that the inner and outer rings of a Couette cell are perfect circles. Although the shape in the simulation closely resembles the desired one, it is not exactly circular. When the geometry is discretized into a mesh, the walls are constituted of many straight lines instead of a smooth arc. This generally has a minor influence on the simulations but it does make a difference in the beginning. Due to the straight edges, some particles will be placed partly inside the walls. The solution algorithm will interpret this as an overlap between the wall and the particle and it will result in an added force in accordance with the soft-sphere model. This introduces artificial forces during the initial period of a simulation and it is important not to use the data from such a period for any statistical analysis.

3. CALCULATION OF STRESSES

To calculate the stresses in a granular flow, a method is required to transform the forces in contacts between particles into a global field of stresses. We use here the method proposed in [5] where

$$\sigma = \frac{1}{V} \int_V dV' \sigma' \tag{6}$$

where σ is the stress for an arbitrary volume V and $\sigma' = \sigma'(\boldsymbol{x})$ is the arbitrary local stress in that volume. In DEM, this local stress can be understood as the stress of a particle at the position x, σ^p $(\boldsymbol{x})$. The integration then reduces to a sum over the particles belonging to the volume:

$$\sigma = \frac{1}{V} \int_{p \in V} V^p \sigma^p \tag{7}$$

Here, we assume that the contact force (f_c) acting on a particle at a contact point c is constant over the contact surface. Then the mean particle stress can be calculated as:

$$\sigma^p = \frac{1}{V^p} \sum_{contacts\ c} f_c \otimes l_c^p \tag{8}$$

where l_c^p is the vector from the centre of the particle p to the point of contact c.

The stress σ is a tensor but its scalar quantification may significantly simplify the analysis. Here, we follow [5] and quantify the deviatoric part of the stress tensor by taking a square root of its second invariant:

$$\sigma_D = \frac{\sqrt{(\sigma_1 - \sigma_3)^2 + (\sigma_1 - \sigma_2)^2 + (\sigma_2 - \sigma_3)^2}}{\sqrt{6}} \tag{9}$$

where σ_{1-3} are the principle stresses. Another important measure of the stress tensor is its trace $\sigma_T = \sum_{k=1}^{3} \sigma_{kk}$ and it illustrates the magnitude of the stresses.

Finally, the shear rate has to be defined since it will help us in distinguishing the prevailing type of behaviour in the system (solid-like, gas-like or intermediate). According to [5], the shear rate $\dot{\gamma}$ in a Couette geometry is:

$$\dot{\gamma} = \frac{1}{2} \sqrt{\left(\frac{\partial u_\varphi}{\partial r} - \frac{u_\varphi}{r}\right)^2 + \left(\frac{\partial u_\varphi}{\partial z}\right)^2} \tag{10}$$

Here, u_φ is the velocity in the tangential direction in a cylindrical coordinate system. This formulation is difficult to use for the shear rate calculation, due to the fact that u_φ is a system property that first needs to be estimated from the particles motion. Instead, we use (as in [1]):

$$\dot{\gamma} = \frac{\omega R}{H} \tag{11}$$

where ω is the angular frequency applied to the system, R is the inner ring radius and H is the gap width of the geometry.

To calculate the stresses as defined by expression (7), the Couette device is discretized into a number of radial bins as shown in Figure 2. In each bin, an average stress value represents the stresses of the particles in that bin. This results in a discretized radial stress profile in the geometry. When averaging the stresses in a bin, a particle weighting factor is introduced to compensate for the event that a particle may not be entirely within the bin domain. This is done in order to reduce the influence of the averaging volume. Compared to another common averaging technique, where an entire particle is assigned to a bin based on its centre, introducing particle weights allows for using narrower bins and, as a consequence, a higher resolution [5]. In this work we calculate the weight factor as $w^p = A_b^p / A^p$, with A_b^p being the area projection of particle p onto the plane of the bin b and is calculated as

$$A_b^p = R^2\big(\pi - \phi_b + \sin\phi_b \cos\phi_b - \phi_{b+1} + \sin\phi_{b+1} \cos\phi_{b+1}\big) \tag{12}$$

The weight is calculated assuming that a ring intersects a particle with straight lines (Figure 3), where the different angles are defined as $\phi_b = arccos\left(\left(r_p - r_b\right)/R\right)$ and $\phi_{b+1} = arccos\left(\left(r_{b+1} - r_p\right)/R\right)$.

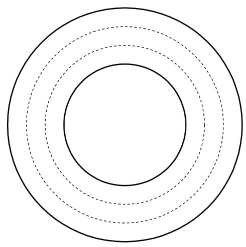

Figure 2: Example of discretization into bins. In this case, three bins are used.

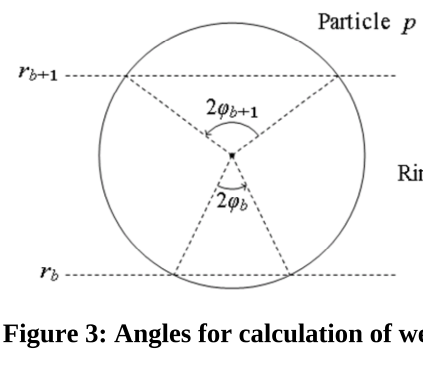

Figure 3: Angles for calculation of weights

The stress of a single bin then becomes

$$\sigma_b = \frac{1}{V_b} \sum_{p \in V} w_b^p \sigma^p \tag{13}$$

4. RESULTS AND DISCUSSION

Table 2 summarizes the standard setup for the simulations. All other tests introduce variations of individual parameters in relation to the standard case.

Table 2: Settings of the standard case

Property	Value
Simulation time (*s*)	10
Particle density ($kg\ m^{-3}$)	964
Young's Modulus (*MPa*)	600
Poisson ratio	0.25
Particle friction	0.8
Annular frequency of inner ring (*rad/s*)	10
Particle diameter (*mm*)	10
Collision resolution	$n_{res} = 12$

We start with comparing the deviatoric fraction (σ_D/σ_T) for the two types of initial placement of particles as mentioned above.

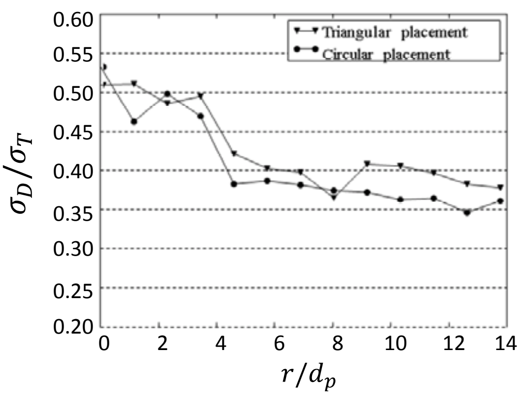

Figure 4: The deviatoric fractions as a function of initial particle placement

Differences are observed (Figure 4) with the triangular lattice giving slightly higher both deviatoric fractions and the trace (not shown here). This means that, when the influence of other parameters is to be investigated, the same initialization of particles is required to be able to compare the results.

Now we look at the influence of solid fraction and the particle friction on the stresses. Note that each data point in the graphs represents the averaged stress for a bin. For the following plots 13 bins have been used. The gap width in the Couette cell is $H \approx 15d_p$ and with 13 bins each bin is larger than the size of the particles. In [5] it is shown that using bins lager than the particle size is preferred in order to avoid the dependence of the averaging volume on the results. The x-axis coordinates have been normalized with the particle diameter (d_p) and translated in such a way that $x = 0$ is at the inner ring.

From Figure 5 it is seen that the deviatoric fraction, or the shear stress, shows a tendency to increase relative to the trace for decreasing solid fractions. The higher the solid fraction, the quicker the data tend to a limit of 0.3, indicating that the shear stresses are absorbed faster by denser systems. The reason for the increase in deviation from a mean curve with decreasing solid fractions is attributed to an increase of importance for high contact forces in rare circumstances. Around 80 samples are used for these curves and for dense systems; each sample is likely to have a great number of particle contacts occurring with significant forces involved. The more dilute the systems become, the less frequent particles contacts become. But there might still be occasions where, for example, some particles lock close to the rotating ring and the forces thereby introduced will be so large that a significant impact on the averages will be made.

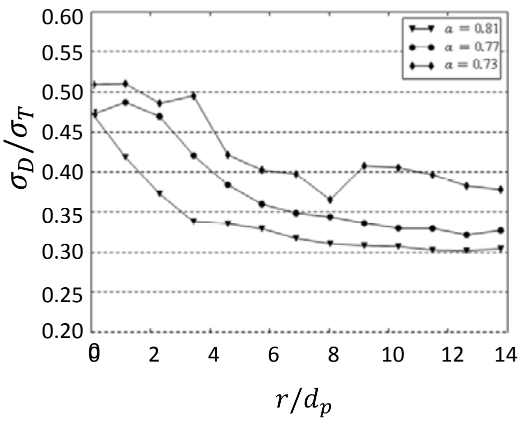

Figure 5: The deviatoric fractions for different solid fractions

Figure 6 illustrates that the trace of the stress tensor behaves similarly in a cell irrespective of the solid fraction, but with a rather different magnitude. For each solid fraction, σ_T is fairly constant through the entire domain, possibly decreasing somewhat towards the outer part, but it differs two orders of magnitude between the highest and the lowest solid fractions. This increase in magnitude for higher α is attributed to the fact that the trace is a measure of the mean of the normal forces between the particles. Denser systems yield more contacts and more force is required to shear such a system. This then in turn yields higher stresses.

We now turn our attention to the influence of the coefficient of friction on the stresses. It is clear that the lower the friction, the easier the particles slide over each other and the transfer of forces between them will decrease.

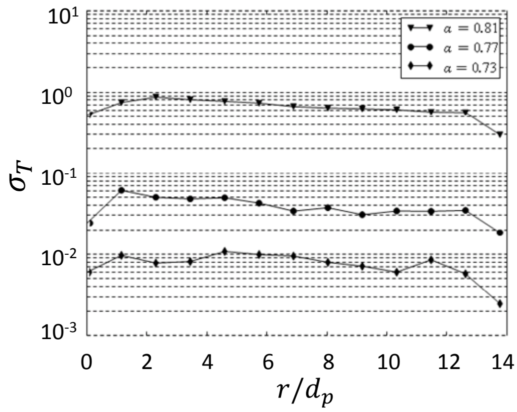

Figure 6: The trace of stresses for different solid fractions

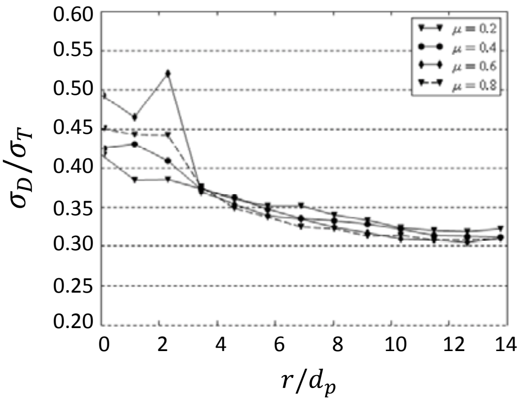

Figure 7: The deviatoric fractions for different coefficients of friction

Figure 7 shows that, for increasing friction, there will be slightly higher stresses close to the inner wall and that they will decay farther out in the geometry. This trend is not strong and it indicates that the particle friction might not significantly influence the character of the stresses. This result is maybe somewhat against expectations. It is straightforward that when the particles transfer less tangential forces, the shear stresses will decrease.

From studying the trace (Figure 8) it is clear that the particle friction has a big impact on the stress magnitude. For μ = 0.6 and μ = 0.8 the friction seems high enough that the same forces are transferred in the inner region of the geometry. But they are to a lesser degree transferred through the system for μ = 0.6. For μ = 0.4 even less forces seem to propagate through the system, including the inner region, but the cases seem qualitatively similar. The lowest friction, μ = 0.2, does no longer resemble the other cases. It is believed that the friction is now so low that the particles easily slide over each other and that the force cannot be transferred into the domain.

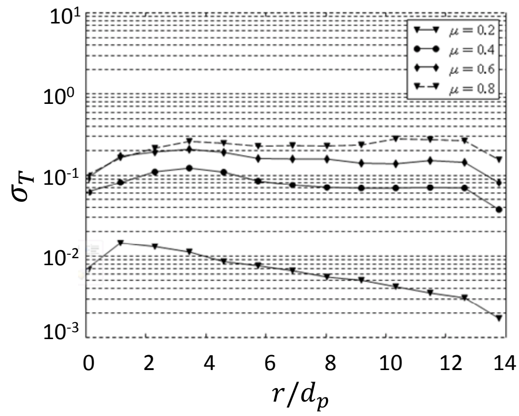

Figure 8: The trace of the stresses for different coefficients of friction

Another interesting effect that we have observed in our simulations is the appearance of regions in the cell that barely move (formation of "crystal" structures). We have chosen here to use two types of particles (with different sizes) to see the persistence of the described effect in relation to the case when the monosized particles are used.

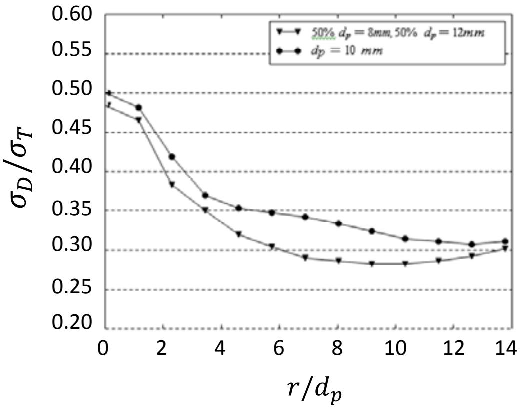

Figure 9: The deviatoric fractions for different particle size distributions

The deviatoric fractions for both cases (Figure 9) seem to agree fairly well close to the outer ring and they are only slightly lower close to the inner ring for the bimodal distribution. Note that deviatoric fraction decreases more rapidly in the middle region of the system for the case with two particle sizes. A possible explanation is that in this case the particles can move more freely due to the absence of a rigid lattice structure. An easier movement between particles means that less shearing forces would be transferred into the system.

The trace of the stress tensors for both cases (Figure 10) agrees well in the inner regions of the system. In the middle part, a difference appears where the trace is higher for the case with two types of particles. It is difficult to know whether this observation is not just an artefact from the simulations. Namely, a probable source of error is the two-dimensional assumption made to evaluate the stress (expression 13). Such an assumption works well for equally-sized particles since the point of contact will be at the same height for all particles. But for those of different size (and having in mind that we deal with spherical particles), the point of contact between a small and a large particle will be at a different height than that of two equally sized ones. This allows the larger particles to climb above the smaller ones and the smaller particles to even stack on each other (Figure 11(top)). To mitigate this problem in the simulations, an artificial force is introduced in the third direction to glue the particles in that direction. This effectively forces all particles to lie on a plane (Fig. 11(bottom)), but the problem of some particle overlap due to the different sizes still remains. Another uncertainty is whether such an artificial force affects the simulations. To clarify the latter dilemma, two simulations with the same settings except for the added force are presented in Figures 12 and 13. The deviatoric fractions in the two cases agree well, supporting the results shown in Fig. 9 as being physical. The trace is a bit smaller for the case with the artificial force, but the curves otherwise follow each other relatively closely (not shown here).

Finally, we want to see how our simulation framework can predict the regimes (and the transition between them) of granular flow in a Couette cell. Figure 13 shows the average shear stress as a function of the dimensionless shear rate. Each data point represents a full 10s simulation with the corresponding setup (a certain α and a certain rotational frequency). Theoretically [1], there should be, for low shear rates, no dependence between the stress and the shear rate. For high shear rates, the slope n of the stress/shear rate curve should be around $n = 2$ in the log-log diagram.

When analysing results from such a graph, care has to be taken regarding the detail of information available. Trends can most likely be trusted, while exact relations probably require more data to ensure the statistics. For higher shear rates, both simulations for solid fractions α = 0.73 and α = 0.77 show a dependence such that n ≈ 2, according to expectations. The data points for the higher end of the shear rates all collapse fairly well on the same line for both solid fractions which increases the credibility of the trend.

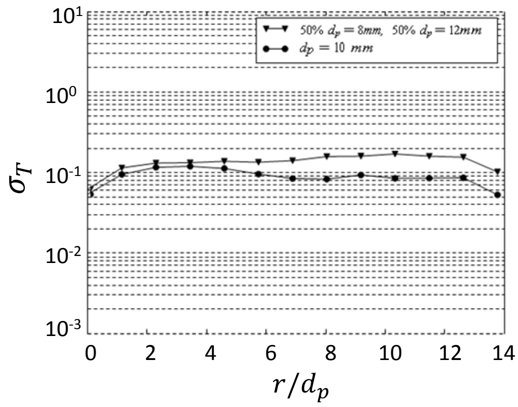

Figure 10: The trace of stresses for different particle size distributions

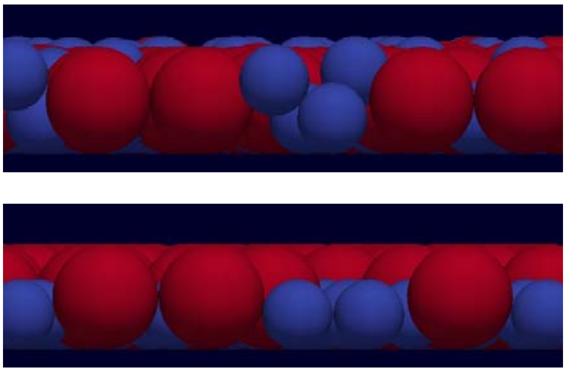

Figure 11: Comparison of particle placement when two types of particles are used: top – without artificial force; bottom – with artificial force

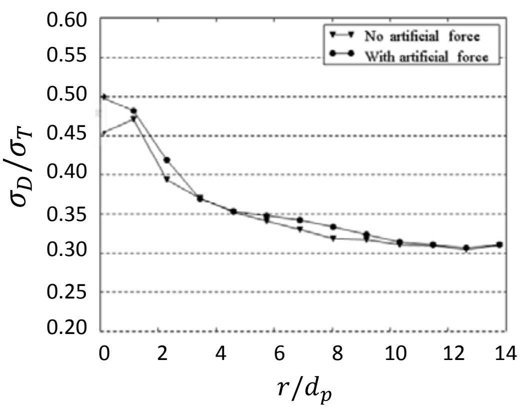

Figure 12: The deviatoric fractions with and without artificial force added

When the shear rate decreases, different trends are observed. For the lowest solid fraction α = 0.73, the curve flattens significantly and for the lower shear rates the stress seem to be almost independent of the rate. The accuracy of the data is likely to be smaller than that for the higher shear rates. For α = 0.77, a clear decrease in dependence seen for the lowest solid fraction is no longer present. For the case with the highest solid fraction, the dependence for the high shear rates is slightly weaker than for the other solid fractions and tends to $n \approx 1 - 1.5$. This dependence seems to persist or slightly decrease when the shear rates go down, to the point where the results become inconsistent. It is believed that, for the highest solid fraction, $\alpha = 0.81$, the lattice structure that the particles form is difficult to escape, which causes roughly the same behaviour independent of the shear rate applied. For the highest shear rate applied, a visual inspection shows that the entire mass of particles behaves like a rigid body. The high shear rate engages the particles to a degree where the friction of the outer wall is not enough to keep the outer layer still. This is possible since the crystal-like structure created by the particles stretches through almost the entire domain. For the lower solid fractions in the high shear rates region, the inner region of particles is strongly engaged and the outer region is still in a lattice structure but it does not cover as much of the domain. In such a case, there is obviously a band allowing an existence of an intermediate region.

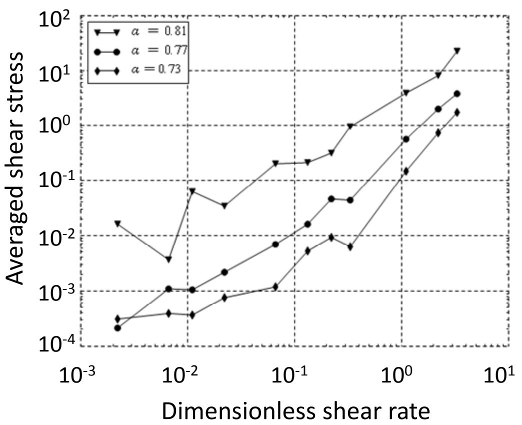

Figure 13: Shear stress as a function of shear rate

4. CONCLUSIONS

We investigate in this work how stresses in a dense dry granular flow are influenced by fundamental microscopic (i.e. particle-related) and macroscopic properties of a system. We have seen that care should be taken when an initial placement of particles is made for the simulations. For example, a triangular lattice yields high solid fractions but also a stiff structure. Either long simulation times or the use of different particle sizes (or both), are preferred in order to ensure independence of the initial setup.

When evaluating the response of the stresses to different characteristic system properties, it is concluded that:

- The solid fraction has a large impact on the magnitude of the stresses with a difference of several orders of magnitude for solid fractions spanning from $\alpha = 0.73$ to $\alpha = 0.81$.
- The magnitude of the stresses is strongly dependent on the friction where the biggest difference between the highest and lowest frictions is roughly two orders of magnitude. It is noticeable that for the lowest friction the trace of the stress tensor is no longer constant but decreasing.
- For lower solid fractions, there is a more clear transition between different regimes in the system. We are thus able to clearly distinguish solid-like, intermediate and gas-like behaviours in a dense, dry granular flow system.

REFERENCES

[1] Tardos, G.I., McNamara, S. and Talu, I., Slow and intermediate flow of a frictional bulk powder in the Couette geometry. Powder Technology, 131, 23–39, 2003.

[2] Zhu, H.P., Zhou, Z.Y., Yang, R.Y., Yu, A.B., Discrete particle simulation of particulate systems. Chemical Engineering Science, Vol. 62, 3378-3396, 2007.

[3] Crowe, C.T., Schwarzkopf, J.D., Sommerfeld, M., Tsuji, Y., Multiphase Flows with Droplets and Particles, Taylor & Francis Group, 2012.

[4] Silbert, L., Ertas, D., Grest, G., Halsey, T., Levine, D., Plimpton, S.J., Granular flow down an inclined plane: Bagnnold scaling and rheology, Physical Review E, 64, 0513021, 2001.

[5] Lätzel, M., Luding, S. and Herrmann, H.J., Macroscopic material properties from quasi-static, microscopic simulations of a two-dimensional shear-cell. Granular Matter, 2, 123–135, 2000.

[6] Veje, C.T., Howell, D.W. and Behringer, R.P., Kinematics of a two-dimensional granular Couette experiment at the transition to shearing. Physical Review E, 59, 739–745, 1999.

[7] Dintea, E., Tijskens, E. and Ramon, H., On the accuracy of the Hertz model to describe the normal contact of soft elastic spheres, Granular matter, 10, 209-221, 2008.

Conference on Modelling Fluid Flow (CMFF'15)
The 16th International Conference on Fluid Flow Technologies
Budapest, Hungary, September 1-4, 2015

INVESTIGATING THE ACCURACY OF DIFFERENT FIDELITY NUMERICAL METHODS FOR MODELLING THE AERODYNAMICS OF A BOX-WING AIRCRAFT

Csaba JÉGER[1], Dániel KUTROVICH[2], László NAGY[3]

[1] Department of Aeronautics, Naval Architecture and Railway Vehicles, Budapest University of Technology and Economics.
E-mail: csaba.jeger@gmail.com
[2] Department of Aeronautics, Naval Architecture and Railway Vehicles, Budapest University of Technology and Economics.
E-mail: k.dani1992@gmail.com
[3] Corresponding Author, Department of Fluid Mechanics, Budapest University of Technology and Economics. Bertalan Lajos u. 4 – 6, H-1111 Budapest, Hungary. Tel: (+36-1)-463-3465 Fax: (+36-1)-463-3464 E-mail: nagy@ara.bme.hu

ABSTRACT

This paper deals with the aerodynamics of a box-wing (a type of closed-wing) aircraft. As demand for long-endurance long-range unmanned aircraft is still rising rapidly, closed-wing designs could provide a cheaper, smaller and more efficient solution. Current literature on the topic mostly omits the deeper aerodynamic analysis, and instead opts for low-fidelity methods. Research of this unconventional wing shape is important to design, build and maintain aircraft for higher range, endurance and lower price. Computational Fluid Dynamics (CFD) analysis with high resolution methods is carried out on a small test aircraft. The investigation starts from Reynolds-Averaged Navier–Stokes (RANS) simulations with Shear Stress Transport (SST) turbulence model, and continued with higher accuracy Large Eddy Simulation (LES) and Detached Eddy Simulation (DES) models. Adaptive meshing is used for increased accuracy and performance. Numerical results are then compared to wind tunnel tests. The lift coefficients calculated and measured were particularly well matched. Pressure and shear stress distributions around the wings produced very similar profiles with every model.

Keywords: RANS, DES, LES, box-wing, nonplanar wing, UAV

NOMENCLATURE

Symbols

b	[mm]	wingspan
c	[mm]	chord length
c_L	[-]	lift coefficient
c_D	[-]	drag coefficient
I	[%]	turbulence intensity
m	[g]	mass
l	[mm]	length
u	[m/s]	flow velocity
S	[m^2]	wing area projected to the xy plane
t	[%]	airfoil thickness
γ	[°]	wing sweep angle
ψ	[°]	vertical connector sweep angle

Subscripts and Superscripts

ref	reference
L, D	lift, drag

Abbreviations

CFD	Computational Fluid Dynamics
SST	Shear Stress Transport
RANS	Reynolds Averaged Navier-Stokes
LES	Large Eddy Simulation
DES	Detached Eddy Simulation
VLM	Vortex Lattice Method
UAV	Unmanned Aerial Vehicle
AOA	Angle of Attack
GIS	Grid Induced Separation
IDDES	Improved Delayed Detached Eddy Simulation
CG	Centre of Gravity
RMS	Root Mean Square
FTN	Flow-Through Number

1. INTRODUCTION

The box-wing configuration is an unconventional nonplanar aircraft wing layout with several attractive properties. Theoretically it has the highest span efficiency due to the reduced induced drag and structural loads are also favourable compared to an equivalent planar wing. The wings form a closed loop and are connected to the fuselage on the front and rear of the vehicle.

A small test aircraft with a box-wing layout was designed and built along with a reduced-size model for wind tunnel measurements. The polar diagram of the aircraft was acquired for a fixed airspeed using multiple CFD methods and compared to data from subscale tests. Figure 1 shows the constructed aircraft during a test flight.

Figure 1. Small box-wing UAV in flight.

There is a well-developed literature available on the preliminary and conceptual design of nonplanar aircraft particularly box-wing configurations, for example in [1] and [2]. Low-fidelity Vortex Lattice Method (VLM) codes are employed in a number of recent works to enhance the accuracy of concentrated-parameter calculations, such as in [3]. Frediani et al. [4] [5] used the ANSYS Fluent solver for the RANS simulations of a proposed box-wing passenger aircraft.

It was suggested by Spalart et al. [6] that Detached Eddy Simulations are specifically effective on wing flow problems given that RANS simulations are not accurate enough and LES simulations have higher computational cost.

2. PROBLEM DESCRIPTION

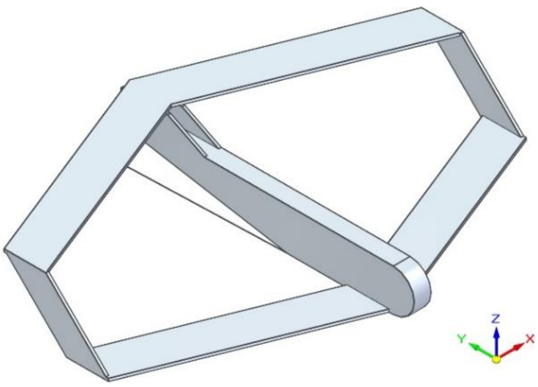

Figure 3. Test aircraft geometry.

For the ease of construction the aircraft has a very simple geometry which can be seen on Figure 2. It is powered by a small electric pusher engine which is omitted from both the CFD model and the wind tunnel mock-up. The wings are constant chord, 6% flat-plate profile along with the inverted vertical stabilisers and the rear wing mount. The forward and rear wing segments have inverted sweep angles, forming a rhomboidal (diamond) shape. The rear wing segments are offset from the forward segments along the vertical axis. The aircraft was made primarily from 6 mm depron sheet which is a commonly used material for models of this size. Principal dimensions and data are summarised in Table 1.

Table 1. Aircraft data

m [g]	b [mm]	l [mm]	S [m^2]
298.0	1000.0	650	0.2

γ [°]	ψ [°]	c [mm]	t [%]
68,20	45	100	6

The investigation is carried out on a fixed airspeed of 5.1 m/s and between the angle of attack (AOA) range of -1 and 6 degrees in the wind axes for the RANS simulations with 1 degree increments and in the 0° and 6° points for the DES and LES simulations.

3. NUMERICAL METHOD

The CFD model is the half of a parabola revolved around the Y axis with half of the aircraft imprinted in it as the problem is considered symmetric in the XZ plane. With this shape the angle of attack could be changed without mesh modifications.

Mesh generation was done in the ANSYS ICEM 14.5 commercial meshing software. An

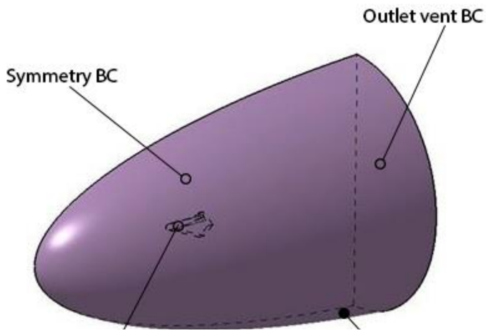

Figure 2. Flowfield with the boundary conditions.

unstructured tetrahedral mesh was used which was refined in the wake region of the wing and around the aircraft. The CFD simulations were carried out using the ANSYS Fluent 14.5 commercial software.

For the computations, hexahedral cells in a 15-layer thick boundary layer were used to ensure well-resolved wall modelling. The y+ value on the surface was below 1 in every instance.

The pressure-based SIMPLE scheme was used with second order discretisation. RANS simulations used the standard two-equation Menter SST turbulence model, without the energy equation.

Mesh sensitivity studies were conducted with 3 meshes with 7.9, 8.5 and 11.2 cells. For the RANS and DES simulations, the second mesh (8.5 million cells) was used, LES simulations ran on the third mesh (11.2 million cells).

3.1. Large Eddy Simulations

For LES computation the literature usually suggests the use of high accuracy schemes [7] [8]. The need for them can be understood considering the properties of low order numerical schemes. Writing the partial differential equation modified by the numerical scheme, it can be found that for the case the scheme has accuracy less than 2^{nd} order a dissipative term is appearing. This term can be also called viscous term with numerical viscosity, because the effect is similar to the viscous dissipation. This viscosity is scaling with the square of the cell size, which means has a very similar form to the turbulent viscosity of the Smagorinsky model [9]. This fact explains why it is important to avoid the presence of such term in the solution. Using dissipative scheme it is impossible to distinguish between by the model and by the scheme produced dissipation. And the judgement of the result becomes difficult.

Other important requirement is for numerical schemes, that they should be stable, in the meaning that they do not amplify numerical errors. This requirement is usually in contradictory with the previous requirement especially for unstructured solvers [10] [11] [12].

The LES simulations used the incompressible implicit second-order finite volume method with a collocated grid arrangement implemented.

3.2. Detached Eddy Simulations

The Detached Eddy Simulation was originally developed for massively separated and high Reynolds number flows [13] for this reason it was a feasible candidate for this work. DES is a hybrid method where the near-wall regions are resolved with a RANS approach while the rest of the flow is treated with a LES method. DES was formulated with a number of the turbulence models and for this work the two-equation Menter SST model was used. The original formulation (often referred to as DES97) produced a premature and unphysical separation in certain cases, which is called Grid Induced Separation (GIS). The effect affects problems with thick boundary layers and shallow-angle separations and is caused by the DES limiter switching to LES mode which produces a stress depletion which in turn lowers skin friction, causing the separation. To combat GIS the modified model called Improved Delayed Detached Eddy Simulation (IDDES) was used which modifies the DES length scale (d) to preserve the RANS mode in the boundary layer. The coupled RANS model was the SST k-ω model.

4. WIND TUNNEL MEASUREMENTS

Measurements were carried out for comparison with the numerical results in the Blackbird 1 wind tunnel of the Department of Fluid Mechanics at the Kármán Tódor Fluid Dynamics Laboratory. The M=1:4 scaled-down model was 3D printed and surface-treated to create a smooth and accurate test article. Model dimensions can be found in Table 2.

Table 2. Scale model data

b [mm]	c [mm]	l [mm]	S [m^2]
250.0	25	177	0.0125

This small blower-type wind tunnel has interchangeable test sections in sizes of 0.35×0.35 m, 0.4×0.5 m and 0.15×1 m cross section which could be closed or opened (from to the laboratory atmosphere). The 0.15x 1 m cross section allows the testing of two-dimensional flow phenomena. Wind tunnel data is summarised in Table 2. The flow field evaluation confirmed that the tunnel is suitable not only for educational, but also for certain scientific measurements [14].

The investigation was done in the smallest opened test section (0.35x0.35m) designated as "high speed". (According to Figure 4 the platform labelled as 12. was used instead of number 11. which is the closed test section).

The turbulence intensity (I) defined in (1) is 0.8% in the test section.

$$I = \frac{\sqrt{\overline{(u-\overline{u})^2}}}{|u|} \tag{1}$$

Where the numerator is the RMS (Root Mean Square) of the velocity and $\overline{u}$ is the mean velocity. The parameters are summarised in Table 3.

Table 3. Blackbird 1 wind tunnel parameters

	Size (WxHxL) [m]	Contraction ratio [-]	Max. test section velocity [m/s]
A	0.35×0.35×1	8.16	24
B	0.15×1×1	6.67	19.5
C	0.5×0.4×1	5	15

To maintain the Reynolds number of 33,750 the tests were conducted with 20.4 m/s velocity (measured dynamic pressure 250 Pa). The acting forces were measured with a two-component load cell. A Labview program was used to execute the measurements with the load cell connected to a PC through an NI PCI 6036E A/D converter. The dynamic pressure of the wind velocity was measured with a static Pitot tube connected to a digital manometer (absolute error: 2 Pa). Angle of attack was controlled with a small servo actuator. The measurement setup can be seen on Figure 5.

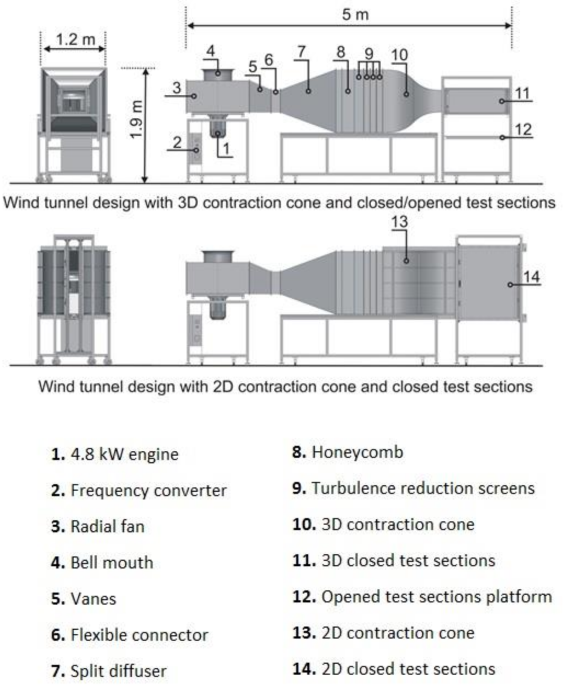

Figure 4. Wind tunnel layout and components. Top: with 0.35×0.35m test section. Bottom: with 1×0.15 m (2D) test section. Image courtesy of Gulyás et al. **[14]**.

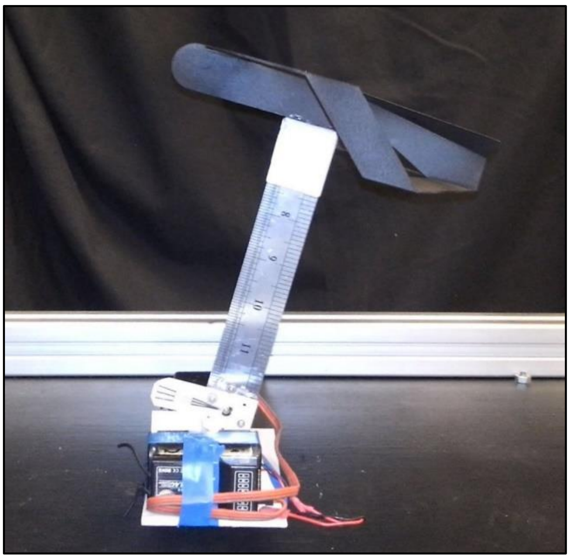

Figure 5. Test setup with the wind tunnel mock-up mounted upside down.

The measured forces were the lift (L) and drag (D) components of the aerodynamic force. The constant error of the load cell was derived from the calibration data along with the effect of the moving CG (Centre of Gravity) as function of the AOA.

Reynolds number is based on the chord (c), inlet reference velocity (u_{ref}). The velocity of the flow, used as reference velocity, was derived from pressure measurements on the calibrated inlet confusor. The blockage ratio at 6° angle of attack was 7.5% in the test section. The Mach number during the measurement was 0.03.

5. RESULTS

The DES and LES simulations were assessed after reaching 6 Flow-Through Number (FTN). Coefficients were time-averaged (example shown on Figure 6.) to be comparable with RANS and experimental data.

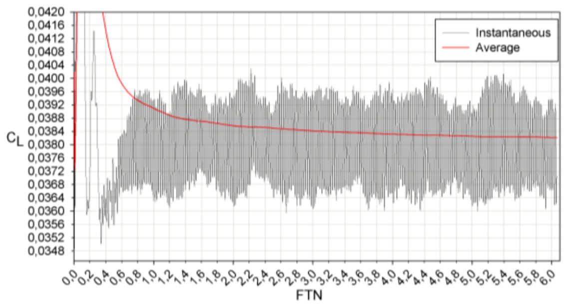

Figure 6. Convergence of the lift coefficient ($\boldsymbol{c_L}$) for the half-aircraft in the 6° AOA DES simulation with the time-averaged coefficient (red), as a function of FTN.

Two series of measurements were conducted with 5-second and 10-second sampling times respectively. The results are summarised in Figure 7. This data is shown along with the simulation results in Figure 8 and Figure 9.

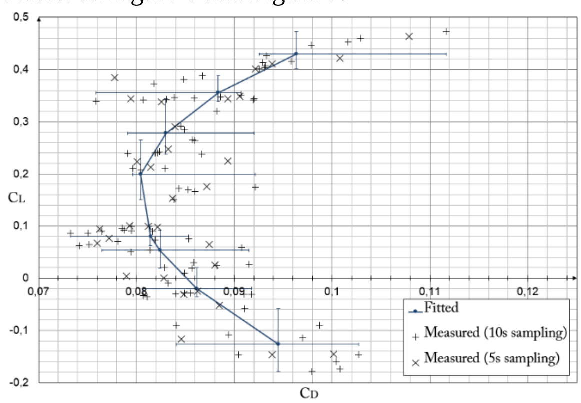

Figure 7. Measured polar diagram of the aircraft.

It can be seen on Figure 8 and Figure 9 that the LES and DES data obtained for 0° and 6° AOA are very close to each other with the difference in both parameters less than 0.6%.

The calculated lift coefficient and the experimental results are in good agreement, the drag coefficient, however does not match well the numerical results and the difference steadily increases with the AOA. In the -1 +1° AOA range, the calculated and measured parameters are within the error range of the study.

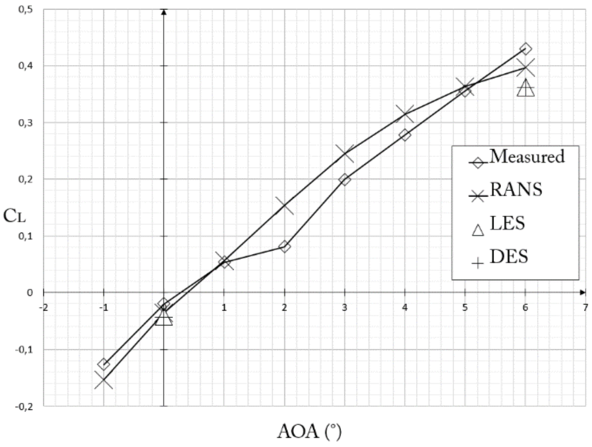

Figure 8. Lift coefficients as a function of the angle of attack (calculated and measured).

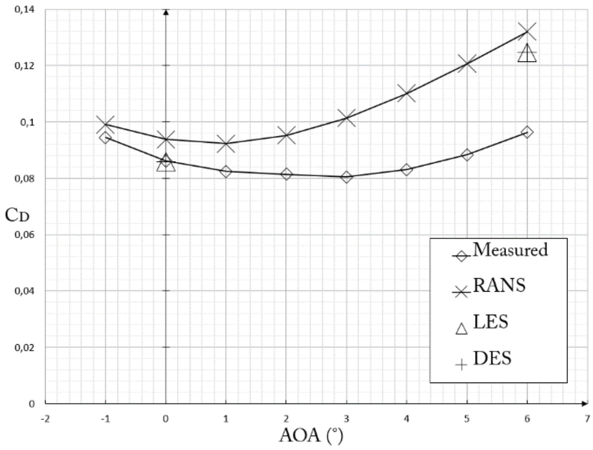

Figure 9. Drag coefficients as a function of the angle of attack (calculated and measured).

The pressure distribution on the wings are similar in each simulations case. The DES and LES methods show a negative pressure region near the trailing edge of the forward wing. The plots of pressure around the middle sections of both the forward and rearward wings are shown on Figure 10 and Figure 11 respectively.

The shear stress distributions reveal the well-resolved separation bubble downstream the leading edge, shown on Figure 12 and Figure 13.

The difference between results is further shown on Figure 14 and Figure 15 where the vortex system is visualised with isosurfaces of Q-criterion [15], colour-coded with the magnitudes of velocity. The comparison is at 0° and 6° AOA respectively and both the RANS results and the high-fidelity results are compared. The interaction between the lower- and upper wings can be observed in Figure 15.

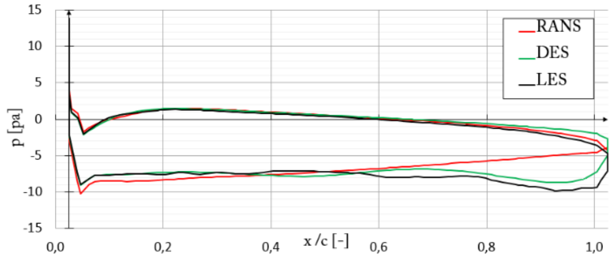

Figure 10. Pressure distribution around the profile at 6° AOA, mid-span, forward wing. The coordinates are relative to the chord length.

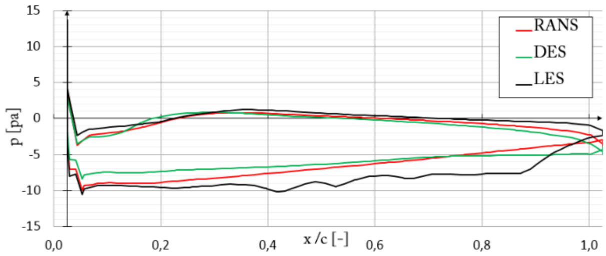

Figure 11. Pressure distribution around the profile at 6° AOA, mid-span, rear wing. The coordinates are relative to the chord length.

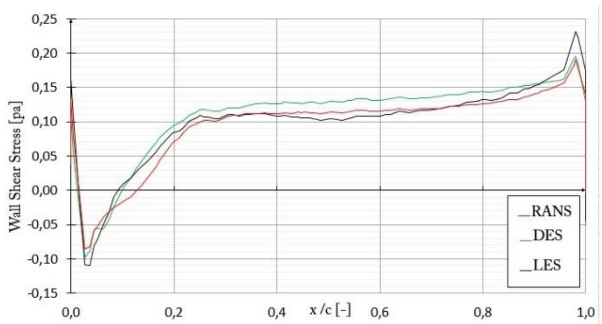

Figure 12. Shear stress distribution at 6° AOA, mid-span, forward wing. The coordinates are relative to the chord length.

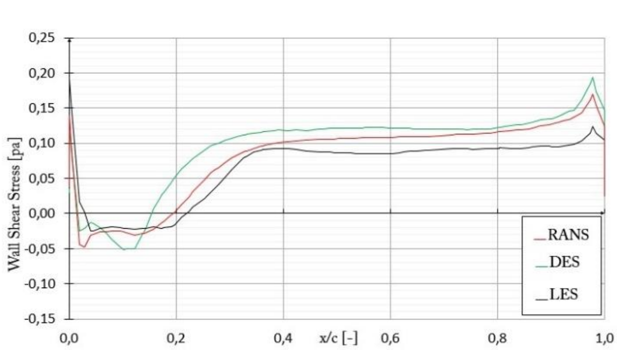

Figure 13. Shear stress distribution at 6° AOA, mid-span, rearward wing. The coordinates are relative to the chord length.

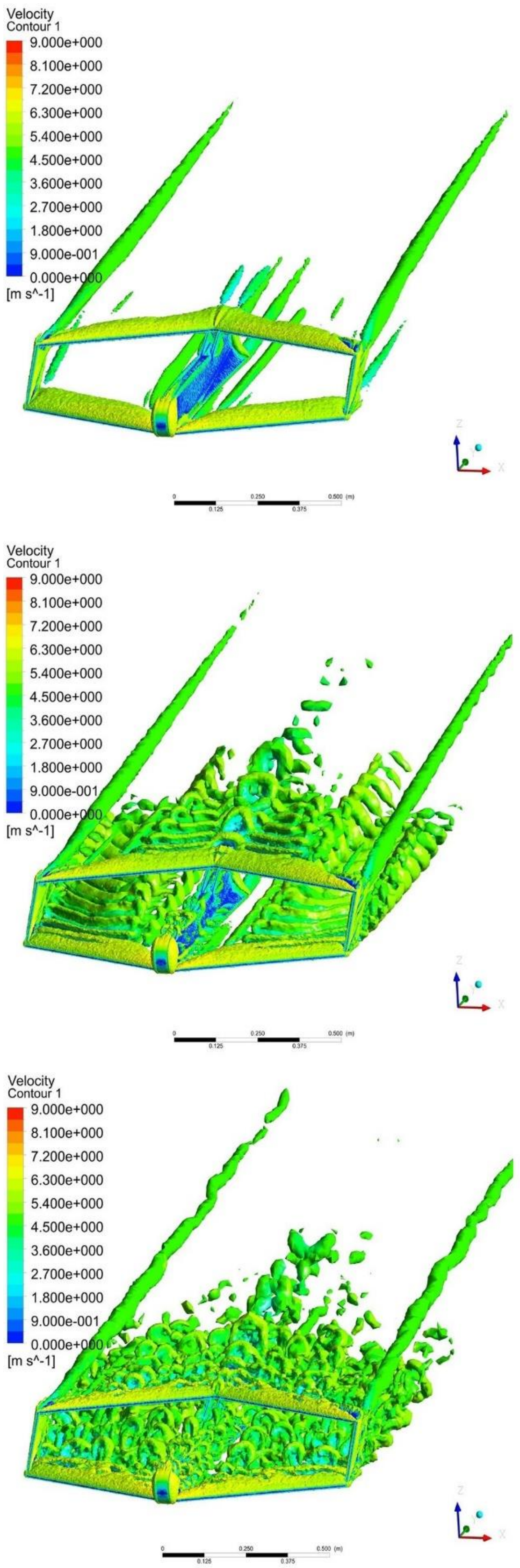

Figure 14. Q-criteria isosurfaces (Q=0.0014) with the contours of velocity magnitude for the RANS (top) DES (middle) and LES (bottom) simulations at 6° AOA.

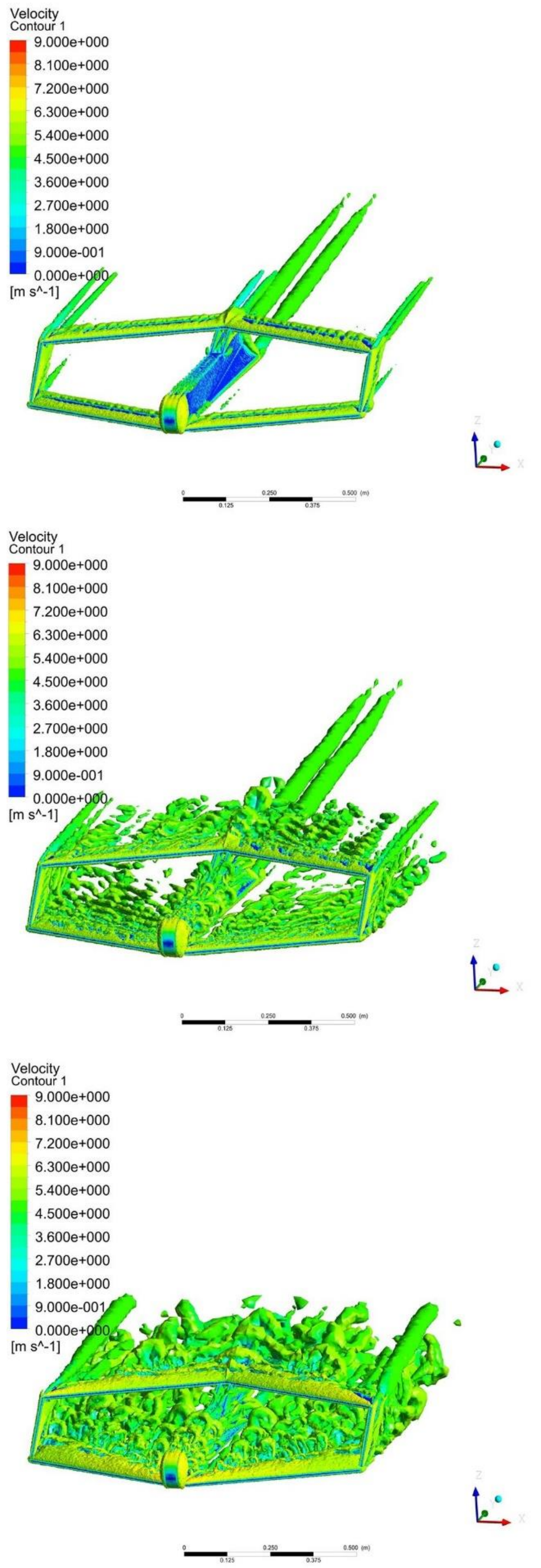

Figure 15. Q-criteria isosurfaces (Q=0.0014) with the contours of velocity magnitude for the RANS (top) DES (middle) and LES (bottom) simulations at 0° AOA.

6. CONCLUSIONS

In the present study, the CFD analysis of a box-wing aircraft using high fidelity numerical codes was presented.

Using an unstructured tetrahedral mesh a comparison between RANS, DES and LES models was made. While all of the models resolved the tip vortexes on the stabilisers and the vortexes originating from the ends of the wing connectors, the additional resolution of the DES and LES model yielded refined results comparable with the wind tunnel results at the lower AOA range.

The test aircraft used in this study is a rough prototype used to test out construction techniques and stability. A refined version is under development with proper airfoils and geometry using the experience acquired with the current vehicle.

The further evaluation of DES and LES techniques in this case is pending. The mesh sensitivity of the problem using structured hexahedral, polyhedral or hybrid meshed should also be studied. It is concluded that the computational requirements of this problem are moderate enough to be affordable for industrial application.

ACKNOWLEDGEMENTS

The authors would like to thank András Gulyás for his invaluable help with the wind tunnel measurements, Péter Rimóczi and Varinex co. ltd. for manufacturing the mock-up, and the Department of Fluid Mechanics for providing the computational power and wind tunnel time for this study.

The work relates to the scientific program of the project "Development of quality-oriented and harmonized R+D+I strategy and the functional model at BME", supported by the New Hungary Development Plan (Project ID: TÁMOP-4.2.1/B-09/1/KMR-2010-0002). It is also supported by the project "Talent care and cultivation in the scientific workshops of BME" project (Project ID: TÁMOP-4.2.2/B-10/1-2010-0009).

REFERENCES

1] P. Jemitola és J. P. Fielding, „Box Wing Aircraft Conceptual Design," in *28th International Council of the Aeronautical Sciences*, Brisbane, 2012.

2] D. Schiktanz és D. Scholz, „Box Wing Fundamentals - an Aircraft Design Perspective," in *Deutscher Luft- und Raumfahrtkongress,* Bremen, 2011.

3] F. A. Khan, Preliminary Aerodynamic Investigation of Box-Wing Configurations using Low Fidelity Codes, MSc. Thesis, Kiruna: Lulea University of Technology, 2010.

4] A. Frediani, "The Prandtl Wing," *VKI lecture series: "Innovative Configurations and Advanced Concepts for Future Civil Transport Aircraft",* 2005.

5] A. Frediani, M. Gasperini, G. Saporito és A. Rimondi, „Development of a Prandtl plane aircraft configuration," in *Proceedings of the 17th AIDAA Congress,* Roma, 2003.

6] P. R. Spalart, W. H. Jou, M. Strelets és S. R. Allmaras, „Comments on the feasibility of LES for wings, and on a hybrid RANS/LES approach," *Advances in DNS/LES,* %1. kötet1, pp. 4-8, 1997.

7] M. Lesieur, O. Metais és P. Comte, „Large-eddy simulations of turbulence," *Cambridge university press,* 2005.

8] P. Sagaut, „Large Eddy Simulation for Incompressible Flows," *Springer,* 2004.

9] M. Germano, U. Piomelli, P. Moin és W. Cabot, „A Dynamic Subgrid-Scale Eddy Viscosity Model," *Physics of Fluids A: Fluid Dynamics,* %1. kötet3, %1. szám7, pp. 1760-1765, 1991.

10] I. Celik, Z. Cehreli és I. Yavuz, „Index of resolution quality for Large Eddy Simulation," *Journal of Fluids Enfineering,* %1. kötet127, %1. szám5, pp. 949-958, 2005.

11] L. Nagy, T. Régert és M. Lohász, „Large-Eddy Simulation in the vicinity of the RAF-6E airfoil in a reduced domain," in *In: XIX Polish National Fluid Dynamics Conference, KKMP2010*, Poznań, Poland, 5-9 September 2010, 2010.

12] B. Geurts, Elements of direct and large eddy simulation, R.T. Edwards, 2004.

13] P. R. Spalart, „Detached-eddy simulation.," *Annual Review of Fluid Mechanics 41,* pp. 181-202, 2009.

14] A. Gulyás és M. Balczó, „Development of a Small Blower-type Wind Tunnel for Educational Purposes," in *28th microCAD International Multidisciplinary Scientific Conference,* Miskolc, 2014.

15] G. Haller, „An objective definition of a vortex," *Journal of Fluid Mechanics,* %1. kötet525, pp. 1-26, 2005.

16] M. Shur, P. R. Spalart, M. Strelets és A. Travin, „Detached-eddy simulation of an airfoil at high angle of attack," *Engineering turbulence modelling and experiments,* %1. kötet4, pp. 669-678, 1999.

Conference on Modelling Fluid Flow (CMFF'15)
The 16th International Conference on Fluid Flow Technologies
Budapest, Hungary, September 1-4, 2015

A NUMERICAL STUDY ON THE EFFECT OF HYDRAULIC DIAMETER OF SHAFT ON THE PLUG HOLING PHENOMENA IN THE SHALLOW UNDERGROUND TUNNEL

D. B. Baek[1], S. Bae[2], H. S. Ryou[3]

[1] Department of Mechanical Engineering, Chung-Ang University. E-mail: baekda@cau.ac.kr
[2] Department of Mechanical Engineering, Chung-Ang University. E-mail: sybzzang@cau.ac.kr
[3] Corresponding Author. Department of Mechanical Engineering, Chung-Ang University. E-mail: cfdmec@cau.ac.kr

ABSTRACT

When the plug holing phenomena occurs, the actual exhausting smoke flow rate could not be able to satisfy the design criteria of the smoke ventilation. The plug holing phenomena is influenced by heat release rate, shaft's height, width, area, etc., but has not yet suggested accurate criteria for the plug holing. Because the hydraulic diameter is an important factor affecting tunnel smoke analysis (the back-layering distance, the critical velocity, etc.), hydraulic diameter effect should be considered for plug holing criteria. In this study, we performed the numerical study for considering the hydraulic diameter effect of vertical shaft on the plug holing phenomena. Size of the subject tunnel, 1/6th geometrically scaled, is 7m long, 1.2m wide and 1.1m high. The factors such as the heat release rate, the shaft height and the shaft area have been held as a constant, 40.0 kW, 0.5 m and 0.16m^2, respectively. We then change hydraulic diameter of shaft, in order to analyze the hydraulic diameter effect. According to the numerical result, plug holing is occurred when the hydraulic diameter of the shaft is over than 0.375 m. For considering this hydraulic diameter effect on the plug holing phenomenon, we suggest the new Fr number based on hydraulic diameter. Also, the plug holing is occurred when the new Froude number is lower than 0.96

Keywords: Hydraulic diameter, Natural ventilation, Plug holing, Shallow underground tunnel

NOMENCLATURE

ρ_0	$[kg/m^3]$	ambient air density
ρ_s	$[kg/m^3]$	smoke density
δ_s	$[m]$	smoke layer thickness
P	$[Pa]$	pressure
g	$[m/s^2]$	gravity acceleration
V	$[m/s]$	average of smoke velocity
A_{HD}	$[m^2]$	smoke vent area
D_{HD}	$[m]$	smoke vent hydraulic diameter
h	$[m]$	smoke vent height
w	$[m]$	width of tunnel
L	$[m]$	length of tunnel
ΔP	$[pa]$	pressure gradient of shaft

Subscripts and Superscripts

s	smoke
a	air
x, y, s	axial (along the wind tunnel axis), transversal, span wise (coordinate)

1. INTRODUCTION

A shallow tunnel is defined as the tunnel located below the ground about 10m [1]. In the shallow tunnel, natural ventilation system is used for ventilating the smoke and air conditioning. If the shafts are improperly designed, the smoke exhaust with flesh air due to the flow characteristic under the shaft in the fire situation. This phenomenon is defined as the plug holing [2]. To improve the natural ventilation system, various researches were performed for analyzing the effect of height, area, and shape of shaft and heat release rate of fire on plug holing. Hinkley [2] studied the plug holing with natural ventilation system. Also the criterion using Froude number was proposed to estimate the plug holing. However, the effect of height of shaft was not considered, therefore the stack effect was not considered in that criterion. Spratt [3] proposed the relationship between plug holing and shape, location of shaft through experimental work. However, he used for the mechanical ventilation systems. Therefore, these results are not proper to apply natural ventilation system. Recently, Ji [4] studied the effects of shaft height and heat release rate on the plug holing using the reduced tunnel experiment. He proposed modified Richardson number to estimate the plug holing occurrence. After that, Ji [5] studied the effect of aspect ratio of shaft on the plug holing using numerical analysis. However, in those two studies, hydraulic diameter, an important factor of smoke movement, was not considered. From previous researches for smoke movement in tunnel fires [6-16], it was verified that the hydraulic diameter of tunnel affects the back layering distance and the critical velocity. Therefore, the plug holing which occurred in the shaft of natural ventilation should be also influenced by the hydraulic diameter of the shaft.

The numerical study is performed for analyzing the effect of hydraulic diameter of the shaft on the plug holing. To validate numerical method, the numerical result of tunnel fire has been compared with experiment. After that, various numerical simulations are performed with conditions used in validation case. Finally, we propose modified criterion Fr including the hydraulic diameter effect.

2. EXPERIMENT

To represent the actual phenomenon by using the reduced model, it is necessary to analyse the similarity between the full-scale model and the reduced model. Smoke flow in the tunnel is governed by buoyancy and the ceiling jet flow. The relationship between the two forces is represented by Fr number and preservation of the Froude number can be expressed as follow. [17].

$$Fr = \frac{V_{EXP}^2}{gL_{EXP}} = \frac{V_{FULL}^2}{gL_{FULL}} \tag{1}$$

, where L_M is characteristic length of experiment and L_{FULL} is characteristic length of full scale. V_{EXP} is characteristic velocity of experiment and V_{FULL} is characteristic velocity of full scale.

The tunnel used for experiment is scaled by a factor of 1/7. As shown in Fig 1, which represents the schematic and picture of the tunnel, the tunnel is 7m long and cross-sections of tunnel is rectangular shape (1.1m height, 1.2m width).

The tunnel wall is made by concrete with a thickness of 0.2m. For estimating the smoke layer height, a thermocouple tree is installed at 1.5 m apart from right side. Also, the thermocouple tree consists of 15 K-type thermocouples (chromel-alumel, temperature range -200 – 1260 ^{o}C) with vertically 4cm interval. The square pool with length of 0.25 m is located at 1 m apart from left side. N-heptane is used for fuel of fire.

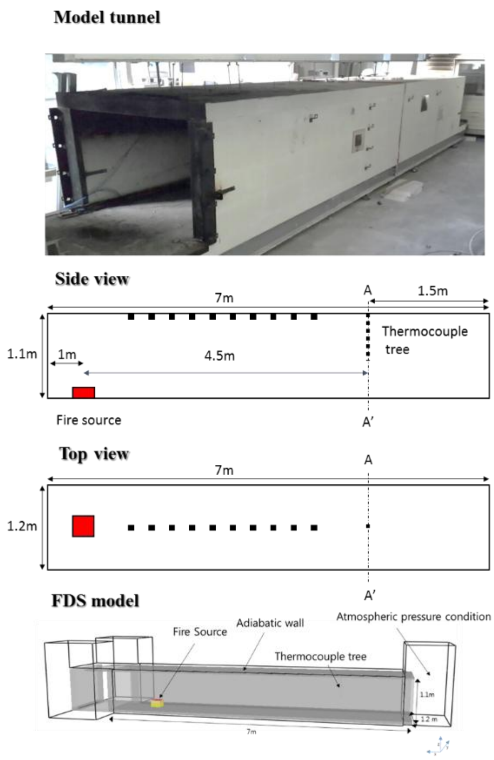

Figure 1. Geometry of experimental and numerical tunnel

For calculating the heat release rate, the mass loss is measured by the load cell (load cell CAS BC-5AS, indicator CAS CI-5010A). Using to the mass loss data, burning rate and HRR can be estimated by the following formulas [18].

$$\dot{m}_{EXP}'' = \frac{\Delta W_f}{\Delta t \cdot A_f} \tag{2}$$

$$\dot{Q}_{EXP} = \dot{m}_{EXP}'' \cdot A_f \cdot \Delta H_c \tag{3}$$

Where m_{EXP}'' is burning rate and ΔW_f is mass loss of fuel during the Δt, ΔA_f is the area of pool ΔH_c is the heat of combustion and $\dot{Q}_{EXP}$ is the HRR in experiment.

Fig. 2 represents the variation of mass of the fuel as time elapsed measured by the load cell. The variation of mass is divided into three regions such

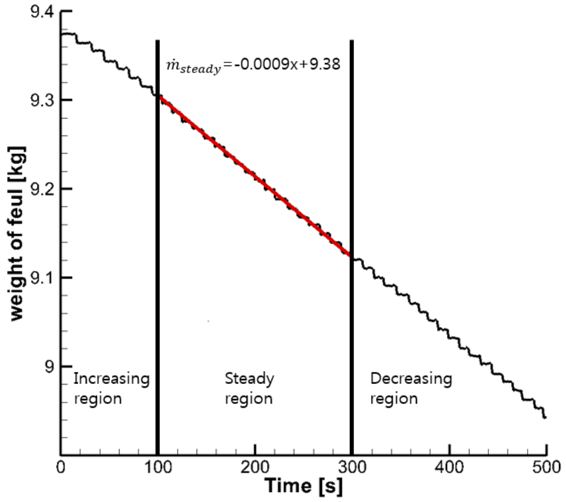

Figure 2. variation of mass of the fuel as time elapsed

as increasing region, decreasing region and steady region. As shown in fig 2, mass loss rate (0.0009kg/s) of the steady region is used for calculating the burning rate of fuel. Then, using equation (2), the burning rate is calculated as 0.0144kg/s·m^2. After that, by using to equation (3) with ΔH_c of N-heptane (44600 kJ/g), Q̇ is calculated as 40.14 kW.

3. NUMERICAL SIMULATION

3.1. Simulation Model

In this study, FDS (Fire Dynamic Simulation version 6.1.2) developed by NIST is used for simulating to effect of hydraulic diameter of the shaft on plug holing. FDS simulates the heat flow with Low Mach Number based on Navier – Stokes equation. The combustion model is used to Mixture Fraction model. The turbulence model is applied with LES eddy-viscosity model of Smagorinsky. Also, the mass conservation, momentum conservation, energy equation and ideal gas equation, which are used in FDS, are as follow. [19, 20]

$$\frac{\partial \rho}{\partial t} + \nabla \rho \vec{u} = 0 \tag{4}$$

$$\frac{\partial (\rho \vec{u})}{\partial t} + \nabla \rho \vec{u}\vec{u} + \nabla \mathrm{p} = \rho \vec{f} + \nabla \tau_{ij} \tag{5}$$

$$\frac{\partial (\rho h)}{\partial t} + \nabla \rho h \vec{u} = \frac{D\rho}{Dt} + q'' - \nabla \vec{q} + \Phi \tag{6}$$

$$\rho = \frac{\rho RT}{M} \tag{7}$$

3.2. Validation

In this study, to validate numerical method, the temperature of smoke layer has been compared with experiment. HRR in simulation is assumed as

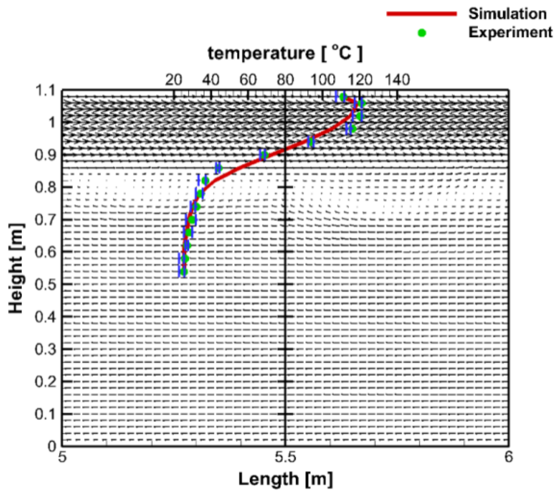

Figure 3. averaged vector velocity contour and the temperature profile both experiment and simulation during 120 to 180

constant, 40.14kW, for comparing with the result of steady region. As shown in Fig 5, the tunnel geometry is set as same with experimental tunnel, and outer concrete wall is assumed to adiabatic condition. The computational domain of both exit is extended since the smoke flow is affected by boundary of the each end of tunnel. All boundary of the computational domain is set to atmosphere pressure. The optimum grid resolution was selected in a natural ventilation tunnel fire test by grid independent tests. It was determined grid size of 0.04m. In this case, the number of the lattice is about 199,000.

To validate numerical method, the temperature of smoke layer has been compared with experiment. HRR in simulation is assumed as constant, 40.14kW, for comparing with the result of steady region.

As shown in Fig 1 – (d), the tunnel geometry is set as same with experimental tunnel, and outer concrete wall is assumed to adiabatic condition. The computational domain of both exit is extended since the smoke flow is affected by boundary of the each end of tunnel. All boundary of the computational domain is set to atmosphere pressure.

Fig. 3 represents the averaged vector contour during 120s to 180s and the temperature profile of experiment and simulation. Temperature profile is located at thermocouple tree in experiment and velocity vector field represents the flow around the thermocouple tree. As shown in Fig 3, simulation results are in good agreement with experimental results within about 5 ºC.

Generally, smoke flows out to the end of tunnel beneath the ceiling surface, and the fresh airflows into the fire under the smoke layer [21-23]. Therefore, in this study, the boundary of the smoke layer is assumed as velocity with 0 m/s of the averaged velocity as shown in Fig 3. From this, the upper smoke layer thickness is estimated as 30 cm from the ceiling. Also, temperature at the boundary of smoke layer is estimated as 36°C.

3.3. Simulation Conditions

Based on the validated result, the plug holing is analysed to hydraulic diameter of the shaft. The tunnel geometry is set as same, and the vertical shaft with height of 1.5 m is located over the thermocouple tree. When the smoke discharge from the shaft, it assume that the heat transfer by mixing smoke and fresh air is little. It is assumed that criterion of the smoke layer boundary is estimated as 35.5 °C around the thermocouple tree, and the criterion of the plug holing occurrence is defined by the smoke layer boundary appear in shaft. After that, various hydraulic diameter of shafts are selected as shown in

Table 1. Classification of the numerical studies case

	Length [*m*]	Width [*m*]	Area [m^2]	Hydraulic diameter [*m*]
Case1	0.4	0.4	0.160	0.4
Case2	0.36	0.44	0.159	0.397
Case3	0.32	0.5	0.160	0.39
Case4	0.28	0.57	0.159	0.375
Case5	0.24	0.66	0.159	0.352

Table 1. The area set as constant as possible in grid size 4cm, and hydraulic diameters are changed from 0.4m to 0.352m.

4. RESULTS AND DISCUSSTION

4.1. Plug holing occurrence due to hydraulic diameter

Fig 4 represents the temperature contour around the shaft in x-plane at center of tunnel. The range of temperature is from 36 °C to 100 °C, and the smoke layer boundary is defined as 36 °C due to the assumption of the smoke layer boundary in previous section 3.2. To observe the fresh air clearly, temperature under 36 °C is colored in deep grey on the contour. Sunken area is defined as the partially rising smoke layer beneath the shaft due to buoyancy. Also, the size and location of the sunken area is related with the emission of fresh air.

As shown in Fig 4, as the hydraulic diameter of the shaft decreases, sunken area moves to the downstream of the shaft. Also, in case 5, fresh air does not flow into the shaft, because the sunken area is located at the down-stream end of shaft Therefore, discharge of smoke can be maximized by change of the hydraulic diameter in same area. Also, quality of the discharge can be estimated by the temperature of downstream. That is, in the case 5, the temperature of downstream is relatively lower than other cases, because the discharge of smoke is increased.

The sunken area for cases 1-4 are located under center of the shaft. From this result, plug holing can

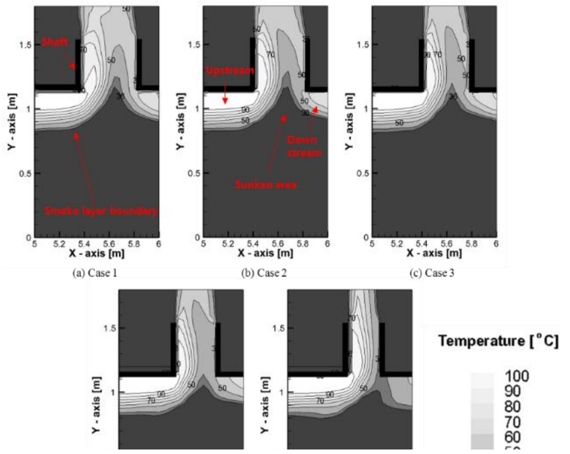

Figure 4. The temperature contour and velocity vector plot around the shaft in the z-plane (z=1.1)

be occurred in case 1-4. In order to visualize the occurrence of plug holing, the temperature contour and velocity vector plot around the shaft in the z-plane (z=1.1) are represented in Fig 5. The black box in the figures indicates the boundary of shaft.

In fig 5 – (a) and (b), the fresh air under the temperature of 36 °C is observed within the shaft. The amount of discharging smoke should be decreased by the fresh air through the shaft in cases 1 and 2. In fig 5 – (c) and (d), the fresh air under the temperature of 36 °C is not observed within the shaft although location and shape of the sunken area in cases 3 and 4 are similar with cases 1 and 2. From this result, it is confirmed that the decrease of the hydraulic diameter affect to the discharge characteristic of the smoke.

The velocity vector plot represents the characteristic of the gas flow in shaft. The smoke is gathered in the lower temperature region and discharge through the shaft. Moreover, the backflow defined as the flow of the opposite to the usual is occurred. That is, the smoke of downstream is discharged through the shaft, because the buoyancy

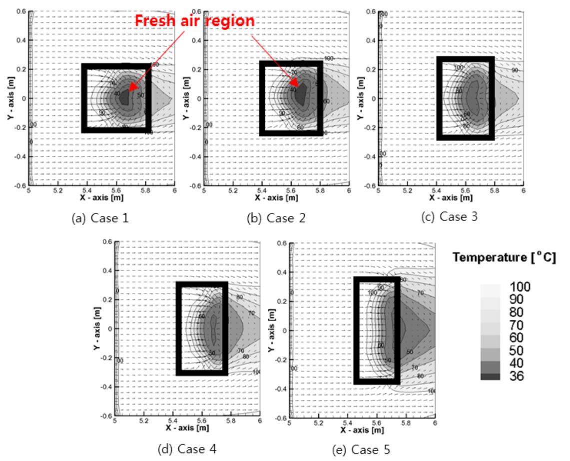

Figure 5. The temperature contour around the shaft in x-plane at center of tunnel.

is increased by the increment of hydraulic diameter. Also the increase of the buoyancy force cause the discharge of the fresh air and occurrence of plug holing. Therefore, the effect of hydraulic diameter of shaft have to be considered for defining the occurrence of plug holing.

4.2. New Modified Fr'

Two criteria were proposed for defining the criterion for estimated occurrence of plug holing.

One of these, a new Froude number was proposed by Hinkley and represents as fallow.

$$Fr = \frac{u_e A}{(g\Delta T/T_0)^{1/2} d^{5/2}} \tag{8}$$

where, u_e is the smoke emission velocity, A is area of the shaft, d is the thickness of smoke layer, ΔT is the average temperature of the smoke layer and T_0 is ambient temperature.

The critical value of new Fr number is 1.8, and plug holing is occurred as the value is lower than the $F_{critical}$. However, the effect of shape factor of the shaft is not considered in new Froude number

$$F_{inertia} = \frac{1}{2}\rho_s V^2 \delta_s D_{HD} \tag{10}$$

For considering the shape factor of shaft, a modified Richardson number was proposed by Ji et al. and represent as fallow.

$$Ri' = \frac{\Delta\rho g h A}{\rho_{s0} v^2 d w} \tag{9}$$

where, $\Delta\rho$ is density difference between smoke and air, A is area of shaft, ρ_{s0} is the density of smoke, v is the velocity of smoke below vent without smoke exhaust and w is width of shaft.

The critical value of modified Ri is 1.4 and plug holing is occurred when the value is upper than the $Ri_{critical}$. However, the effect of the hydraulic diameter of the shaft is not considered in these criteria, although plug holing is affected by hydraulic diameter, as discussed in previous section.

Therefore, the criterion for considering the effect of hydraulic diameter is necessary. In this study, a new criterion with consideration of effect of hydraulic diameter is proposed for estimating the occurrence of plug holing.

As discussed in section 4.1, the plug holing is affected by the inertia and buoyancy of the smoke. That is, when the smoke is discharged in natural ventilation system, smoke is affected by ceiling jet flow and stack effect; inertia force and buoyancy force. Therefore, Fr number is used for applying the criterion, because the physical definition of the Fr number is the relative ratio between the inertia and gravity force.

Hence, inertia force is estimated by the magnitude of force on the ceiling jet flow in the shaft. To measure the inertia force, the average velocity of smoke is used. As shown in fig 6, the average

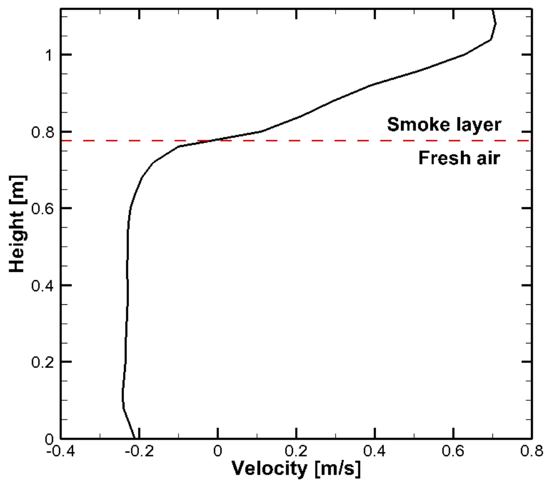

Figure 6. Velociry plot in the tunnel

velocity is calculated by the velocity in smoke layer which is height of 1.1 m to 0.78 m. As a result, average velocity is calculated as 0.46 m/s. Also, hydraulic diameter of the shaft is used for estimating the acting area of the inertia force, because inertia force of plug holing have to be limited to the shaft area. Then, the $F_{inertia}$ equation are as follow

where, δ_s is the thickness of the smoke, $D_{H.D.}$ is the hydraulic diameter of the shaft and V is the average velocity of the smoke movement.

Gravity force is considered by the buoyancy force in the shaft. In natural ventilation system, the governing force is the buoyancy force. The magnitude of stack effect is shown as Eq. (11) . Therefore, gravity force $F_{gravity}$ is represented as multiplying magnitude of stack effect by area of shaft. For applying the effect of hydraulic diameter, area of the shaft is calculated by the hydraulic diameter. Then, the $F_{gravity}$ equation are as follow

$$\Delta P = (\rho_s - \rho_a) g h \tag{11}$$

$$F_{gravity} = (\rho_s - \rho_o) g h A_{HD} \tag{12}$$

where, ρ_s is density of smoke, ρ_a is density of air and $A_{H.D.}$ is the area of the shaft using to the hydraulic diameter ($A_{HD} = \pi \cdot {D_{HD}}^2/4$).

Finally, inertial and gravitational forces considering the hydraulic diameter are used for modifying the Fr number. Thus, the modified Fr number (Fr') is represented as follow.

$$Fr' = \frac{\frac{1}{2}\rho_s V^2 \delta_s D_{HD}}{(\rho_s - \rho_o) g h A_{HD}} = 0.393 \frac{\rho_s V^2 \delta_s}{(\rho_s - \rho_a) g h D_{HD}} \tag{13}$$

Table 2 lists the comparing between the modified Fraude number and the results from the previous researches. As listed in table 2, new Fr number and modified Ri number are not changed with the variation of hydraulic diameter. Also, the new Fr number estimates that the plug holing would be occurred for all case, and modified Ri number estimates that the plug holing would not be occurred for all case. However, the modifed Fr number estimate that the plug holing would be occurred in case 1,2 because hydraulic diameter is considered in modified Fr number. From this result, the critical value of modified Fr number is about 0.96, because the occurrence of the plug holing is different between case 2 (0.397 m in hydraulic diameter) and 3 (0.39 m in hydraulic diameter). From this result, the criteria proposed in this study, modified Fr number, is more accurate for classifying the occurrance of plug holing.

Table 2. Calculating the criteria and occurrence of plug holing

	Plug holing occurrence	New Fr	Modified Ri	Fr'
Case1	O	1.006	0.139	0.943
Case2	O	0.996	0.138	0.952
Case3	X	1.006	0.139	0.966
Case4	X	1.003	0.139	1.004
Case5	X	0.996	0.138	1.071

5. CONCLUSION

In this study, the numerical study is performed for analyzing the effect of hydraulic diameter of the shaft on the plug holing in the underground tunnel. The conclusions are summarized as follows.

1. Result show that the hydraulic diameter of the shaft affects the smoke emissivity and the occurrence of plug holing.

2. In this study, the range of the hydraulic diameter of the shaft is from 0.4 m to 0.35 m. As the hydraulic diameter is 0.39 m, the plug holing is occurred. From this result, Modified Fr number is proposed.

3. The critical value of modified Fr number is estimated as 0.96. The modified Fr is less than 0.96, plug holing is occurred. Therefore, a modified Fr can be used to design a shape of shaft on the natural ventilation system.

ACKWLEDGEMENTS

This research was supported by the Next Generation Fire Protection & Safety Core Technology Development Program funded by the Ministry of Public Safety and Security ("Grant No. NEMA-NG-2014-52")

REFERENCES

[1] S. Kwon, 2011 "Initial thermal conditions around an underground research tunnel at shallow depth", *International Journal of Rock Mechanics and Mining Sciences*, Vol. 48, pp. 86–94

[2] P. L. Hinkley, 1970, "The flow of hot gases along an enclosed shopping", *Fire Reasherch Station*. Note no.807.

[3] Spratt, Heslden, 1974, "Efficient Extraction of Smoke from a Thin Layer under a Ceiling", *Fire Research Note* No 1001.

[4] Ji Ji., Z.H. Gao, C.G. Fan, W. Zhong. J.H. Sun, 2012, "A study of the effect of plug-holing and boundary layer separation on natural ventilation with vertical shaft in urban road tunnel fires", *International Journal of Heat and Mass Transfer* 55, pp. 6032−6041.

[5] Ji Ji., J.Y. Han, C.G. Fan, Z.H. Gao, J.H. Sun, 2013, "Influence of cross-sectional area and aspect ratio of shaft on natural ventilation in urban road tunnel", *Internatinal Journal of Heat and Mass Transfer* 67, pp. 420- 431.

[6] Sung Ryong Lee, Hong Sun Ryou, 2006, "A numerical study on smoke movement in longitudinal ventilation", *Building and Environment* Vol. 41, pp. 719 – 725.

[7] Danziger NH, Kennedy WD. 1982, "Longitudinal ventilation analysis for the Glenwood canyon tunnels." *the Fourth International Symposium Aerodynamics and Ventilation of Vehicle Tunnels*, pp. 169-186.

[8] Wu, Y., Bakar, M.Z., 2000, "Control of smoke flow in tunnel fires using longitudinal ventilation systems – a study of the critical velocity", *Fire Safety Journal* 35, pp. 363–390.

[9] Sung Ryong Lee, Hong Sun Ryou, 2005, "An Experimenta l Study of the Effect of the Aspect Ratio on the Critical Velocity in Longitudinal Ventilation" *Journal of Fire Sciences*, Vol. 23, pp. 119 – 138.

[10] C.C. Hwang, J.C. Edwards, 2005, "The critical ventilation velocity in tunnel fires – a computer simulation", Fire Saf. J., pp. 213–244.

[11] J. Kunsch, 1998 "Critical velocity and range of a fire-gas plume in a ventilated tunnel", *Atmos. Environ*. 33 (1) pp. 13–24.

[12] J.S. Roh, H.S. Ryou, D.H. Kim, W.S. Jung, Y.J. Jang, 2007, "Critical velocity and burning rate in pool fire during longitudinal ventilation", *Tunnelling Underground Space Technol*. 22 (3), pp. 262–271.

[13] K. Van Maele, B. Merci, 2008, "Application of RANS and LES field simulations to predict the critical ventilation velocity in longitudinally ventilated horizontal tunnels", *Fire Saf. J*. 43, pp. 598–609.

[14] K.C. Tsai, H.H. Chen, S.K. Lee, 2010, "Critical ventilation velocity for multi-source tunnel fires", *J. Wind Eng. Ind. Aerodn*. 98 pp. 650–660.

[15] Y. Hui, J. Li, Y. Lixin, 2009, "Numerical analysis of tunnel thermal plume control using longitudinal ventilation", *Fire Saf*. J. 44, pp. 1067–1077.

[16] Weng, M et al. 2015. "Prediction of Back-layering Length and Critical Velocity in Metro Tunnel Fires." *Tunnelling and Underground Space Technology* Vol 47, pp. 64–72.

[17] Quintiere, J.G., 1989, "Scaling Applications in Frie Research, Fire Safety journal, Vol. 15, pp. 3 – 29.

[18] Quintiere, J.P. 1997, "Principles of Fire Behaviour", Delmar Publishers.

[19] K. Van Maele, B. Merci, 2008, "Application of RANS and LES field simulations to predict the critical ventilation velocity in longitudinally ventilated horizontal tunnels", *Fire Saf. J*. 43, pp. 598–609.

[20] McGrattan, K., 2009, "Fire Dynamics Simulator (Version 5) User's Guide." National Institute of Standards and Technology.

[21] L.Y. Cooper, M. Harkleroad, J. Quintiere, W. Rinkinen, 1982, "An experimental study of upper hot layer stratification in full-scale multiroom fire scenarios", *Journal of Heat Transfer* Vol 104, pp. 741–749.

[22] Barenblatt, G.I., 1996. "Scaling, self-similarity, and intermediate asymptotics: dimensional analysis and intermediate asymptotics", *Cambridge University Press*

[23] Li, Y.Z., Lei, B., Ingason, H., 2010. "Study of critical velocity and backlayering length in longitudinally ventilated tunnel fires" *Fire Saf. J. 45*, pp. 361–370

Conference on Modelling Fluid Flow (CMFF'15)
The 16th International Conference on Fluid Flow Technologies
Budapest, Hungary, September 1-4, 2015

A Two-Fluid/DQMOM Methodology for Condensation in Bubbly Flow

Klas JARETEG[1], Srdjan SASIC[2], Paolo VINAI[3], Christophe DEMAZÍERE[3]

[1] Corresponding Author. Department of Applied Physics, Chalmers University of Technology. Fysikgården 4, SE-41296 Gothenburg, Sweden. Tel.: 46 31 772 3077, Fax: Fax +46 31 772 3079, E-mail: klas.jareteg@chalmers.se
[2] Department of Applied Mechanics, Chalmers University of Technology. E-mail: srdjan@chalmers.se
[3] Department of Applied Physics, Chalmers University of Technology. E-mail: vinai@chalmers.se, demaz@chalmers.se

ABSTRACT

In this paper a two-fluid framework for simulating two-phase bubbly flow in heated vertical channels is proposed. The aim is to simulate the two-phase flow and heat transfer of the liquid phase and the vapour phase under subcooled conditions in nuclear reactors where light water serves as coolant, namely Light Water Reactors (LWRs). The framework couples a two-fluid solver and a population balance equation (PBE) solver. A formulation of the PBE including condensation of vapour bubbles is outlined and implemented for the direct quadrature method of moments (DQMOM). Furthermore a wall boiling condition is formulated and expressed in terms of a boundary condition that allows the bubble distribution at the wall to be specified. The formulated system is applied to a system with condensation vapour bubbles in a subcooled liquid entering at the inlet and to a system with wall boiling, i.e emergence of vapour bubbles due to a superheated wall. The proposed DQMOM method is compared to the multiple size-group (MUSIG) method, and it is shown to capture the space dependence of the bubble size distribution with a low number of abscissas and in a computationally efficient manner.

Keywords: DQMOM, Light Water Reactors, PBE, Two-fluid solver, Wall boiling

NOMENCLATURE

$\mathbf{J}$	$[N/m^3]$	Momentum transfer due to phase change
$\mathbf{M}$	$[N/m^3]$	Momentum transfer due interfacial forces
$\mathbf{U}$	$[m/s]$	Phase velocity
C	$[m/s]$	Condensation rate
$H_{g\to l}$	$[J/kg]$	Latent heat for condensation
Nu	$[-]$	Nusselt number
P	$[Pa]$	Pressure
$\mathbf{q}$	$[W/m^2]$	Conduction heat flux
$\mathbf{q}^t$	$[W/m^2]$	Turbulent heat flux
$\mathbf{r}$	$[-]$	Spacial position
$\mathbf{x}$	$[-]$	Internal phase space coordinate for the PBE
$\mathbf{g}$	$[m/s^2]$	Gravitational acceleration
d_s	$[m]$	Sauter mean diameter
h	$[J/kg]$	Specific enthalpy
k	$[m^2/s^2]$	Turbulent kinetic energy
n	$[1/m^3]$	Bubble number density
w	$[1/m^3]$	Weight
α	$[-]$	Void fraction
β	$[-]$	Liquid fraction
ϵ	$[m^2/s^3]$	Turbulent kinetic energy dissipation
Γ	$[kg/m^3.s]$	Mass transfer rate
ξ	$[m]$	Abscissa (bubble size)
$\mathbf{\Lambda}$	$[kg/m^3.s]$	Enthalpy transfer due to phase change
$\bar{\bar{\tau}}$	$[Pa]$	Stress tensor
$\bar{\bar{\tau}}^t$	$[Pa]$	Turbulent stress tensor
λ	$[W/m.K]$	Thermal heat conductivity
ν	$[m^2/s]$	Kinetic viscosity
ν^t	$[m^2/s]$	Turbulent kinetic viscosity
ρ	$[kg/m^3]$	Density

Subscripts and Superscripts

g	vapour phase
i	phase
j	bubble size index
l	liquid phase
t	turbulent quantity

1. INTRODUCTION

Boiling of water is a crucial process in many different applications. One example is nuclear reactors that employ light water as coolant, i.e. the so-called Light Water Reactors. In such a case the coolant enters the nuclear reactor core from the bottom, flows upwards along vertical channels and remove the heat generated via nuclear fission reactions in the fuel pins. On the other hand, the water properties also have an impact on the rate of fission reactions. Therefore accurate simulations of the fluid dynamics and heat transfer are needed to design and operate nuclear reactors in an efficient and safe manner.

Since nuclear reactor cores are relatively large systems with complex geometries, development of methods that can describe and capture the behaviour of the coolant at different scales are of capital importance [1]. In standard two-fluid approaches for the simulation of two-phase flow, quantities are calculated over relatively coarse meshes and/or with averaged correlations, so that the heterogeneous size distribution of bubbles is lost. However, the details of this distribution may have a strong influence in different parameters, such as the condensation rate and the drag coefficient.

As an attempt to retrieve the bubble size information, a PBE might be coupled to the two-fluid solver (e.g. [2]). The PBE can be used to model the convection and diffusion of the bubbles as well as the aggregation and breakage of the same. The MUSIG method is based on discretizing the contiguous bubble size distribution in a set of fixed ranges (classes), resulting in one vapour fraction equation for each size. For subcooled boiling, a PBE has previously been solved using different MUSIG approaches (e.g. [2, 3]). In order to capture the large range of bubble sizes in real reactor systems, a prohibitively large number of fixed sizes might be necessary.

In the current project the DQMOM algorithm is used for the PBE. In contrast to the MUSIG approach, the DQMOM is based on a quadrature expansion of the bubble size distribution. By solving for the quadrature weights and abscissas, the distribution is dynamically captured in space and time, avoiding the issue of a large number of classes. For a full description of DQMOM see the work of Marchisio and Fox [4]. Whereas DQMOM has been applied to various conditions of adiabatic two-phase flows, the application to subcooled boiling conditions, i.e. including condensation in the formulation, is less used.

As part of an ongoing effort to develop a fine-mesh computational framework for two-phase flow and conjugate heat transfer simulations in nuclear reactors, the present paper focuses on the modeling of condensation. This process is relevant in the early stage of boiling, i.e. in the so-called sub-cooled boiling heat transfer regime. In these conditions bubbles are formed at the superheated wall and can detach, although the liquid bulk is still below saturation. The bubbles are thus transported in the sub-cooled liquid bulk and they can condense.

In view of this, a model for condensation is added to the DQMOM, and is tested for an upward subcooled liquid flow with bubbles, in a two-dimensional vertical channel. Two cases with different distributions of the bubbles are discussed: first, a prescribed bubble distribution is given at the inlet; second, a size distribution of bubbles is specified at the wall as a wall boiling condition, resembling the bubble generation in sub-cooled boiling mode. The results along with the computational efficiency of the algorithm are compared to the ones obtained with a MUSIG formulation.

2. METHODOLOGY

In order to describe the PBE approach proposed, the utilized two-fluid framework is also outlined. It should be noted that the PBE and the two-fluid model are coupled in both directions. The total vapour fraction is calculated by the PBE and used in the two-fluid equations. In addition, the size distribution will influence the constitutive laws (e.g. drag) used in the momentum conservation equations. Furthermore, the thermophysical state, as calculated by the energy conservation equation in the two-fluid framework, is necessary to determine the condensation rate for the bubbles. Finally, the vapour velocity calculated from momentum conservation equations is needed for the convective term in the PBE.

2.1. Two-fluid framework

The two-fluid framework is based on the conservation of mass

$$\frac{\partial \alpha_i \rho_i}{\partial t} + \nabla \cdot (\alpha_i \rho_i \mathbf{U}_i) = \Gamma_i, \tag{1}$$

momentum

$$\frac{\partial \alpha_i \rho_i \mathbf{U}_i}{\partial t} + \nabla \cdot (\alpha_i \rho_i \mathbf{U}_i \otimes \mathbf{U}_i) = -\nabla \cdot \left(\alpha_i (\bar{\bar{\tau}}_i + \bar{\bar{\tau}}_i^t)\right) - \nabla(\alpha_i P) + \alpha_i \rho_i \mathbf{g} + \mathbf{M}_i + \mathbf{J}_i, \tag{2}$$

and enthalpy

$$\frac{\partial \alpha_i \rho_i h_i}{\partial t} + \nabla \cdot (\alpha_i \rho_i h_i \mathbf{U}_i) = -\nabla \cdot \alpha_i (\mathbf{q} + \mathbf{q}^t) + \frac{D(\alpha_k P)}{Dt} - \mathbf{U}_i \cdot \nabla \cdot (\alpha_i \bar{\bar{\tau}}_i^t) + \alpha_i \bar{\bar{\tau}}_i : \nabla \mathbf{U}_i + \mathbf{\Lambda}_i. \tag{3}$$

As a result of the inclusion of the PBE, the phase fraction equation, Eq. (1), is not directly solved to compute the vapour fraction. However, in order to formulate a pressure relation, Eqs. (1) and (2) are combined to a pressure equation shared between the phases [5]. The combined equation can be seen as a generalization to two phases of a typical Schur complement to the mass and momentum equations [6]. It should be noted that in the derivation of the pressure equation, the right hand side (RHS) of Eq. (1) must be included in order to get a consistent mass flux from the resulting velocity. This is not necessary in the case of adiabatic flow where the mean velocity is divergence free (i.e. $\nabla \cdot (\alpha_g \mathbf{U}_g + \alpha_l \mathbf{U}_l) = 0$).

The momentum conservation equations are solved in a phase-intensive form, where the time derivatives and convective terms are split (for details see [5]). This has the advantage of allowing the momentum equations to be solved also in regions where the vapour phase disappears, which is potentially the situation when modelling the subcooled boiling regime. The enthalpy equation, Eq. (3), is solved in the same phase-intensive manner, in order to reach a consistent use of the facial mass fluxes arising in the discretization process.

The turbulence of the liquid phase is modelled using the Standard $k-\epsilon$ equations, for which the turbulent kinetic energy is calculated as

$$\begin{aligned}\frac{\partial \beta k}{\partial t} + \nabla\cdot(\beta k \mathbf{U}_l) = \nabla\cdot\beta\left(\nu_l + \frac{\nu_l^t}{\sigma_k}\right)\nabla k + \\ \beta\nu_l^t(\nabla\otimes\mathbf{U}_l) : (\nabla\otimes\mathbf{U}_l + (\nabla\otimes\mathbf{U}_l)^T) - \beta\epsilon_l,\end{aligned} \tag{4}$$

where σ_k is a model constant, and with the turbulent dissipation calculated by

$$\begin{aligned}\frac{\partial \beta\epsilon}{\partial t} + \nabla\cdot(\beta\epsilon\mathbf{U}) = \nabla\cdot\beta\left(\nu + \frac{\nu_t}{\sigma_\epsilon}\right)\nabla\epsilon + \\ \beta C_{1\epsilon}\frac{\epsilon}{k}\nu_t(\nabla\otimes\mathbf{U}) : (\nabla\otimes\mathbf{U} + (\nabla\otimes\mathbf{U})^T) - \beta C_{2\epsilon}\frac{\epsilon^2}{k},\end{aligned} \tag{5}$$

where σ_ϵ, $C_{1\epsilon}$ and $C_{2\epsilon}$ are model constants (see e.g. [7]). The turbulent viscosity of the vapour phase is modelled as a constant function of the liquid turbulent viscosity and turbulent quantities $\mathbf{q}^t$ and $\bar{\bar{\tau}}^t$ are computed according to the turbulent phase viscosities (ν^t). Both phases are assumed to be Newtonian fluids.

The momentum interfacial forces included are drag, virtual mass, lift forces and turbulent dispersion. For the drag, the Schiller-Naumann correlation is used [8]. For the lift and virtual mass forces, size-independent constants (C_l and C_{vm}) are used (for details see e.g. [9]). The turbulent dispersion is modelled by the Bertodano model [10]. For the size dependent drag correlation, the total force is computed as the sum of the drag associated with each separate bubble size. Whereas the constitutive relations for the forces are of importance for accurate modelling of the two-phase system, as the current work is focused on the PBE methods, the interfacial forces are not further investigated in the current paper.

2.2. Population balance methodology

A general population balance equation can be written as

$$\begin{aligned}\frac{\partial n(\mathbf{x},\mathbf{r},t)}{\partial t} + \nabla_{\mathbf{x}}\cdot\left(\frac{\partial\mathbf{x}(\mathbf{x},\mathbf{r},t)}{\partial t}n(\mathbf{x},\mathbf{r},t)\right) \\ +\nabla_{\mathbf{r}}\cdot(\mathbf{U}(\mathbf{x},\mathbf{r},t)n(\mathbf{x},\mathbf{r},t)) = S(\mathbf{x},\mathbf{r},t)\end{aligned} \tag{6}$$

where $\mathbf{x}$ corresponds to the internal phase space, in this case the bubble size, and n is interpreted as the number density of bubbles [11]. The source term, $S(\mathbf{x},\mathbf{r},t)$, will in the general case include the birth and death due to aggregation and breakage, which is not covered in the present paper. For the purpose of simulating subcooled boiling with DQMOM, the internal phase space convection (second term on the left hand side in Eq. (6)) is used to represent the bubble condensation. For the MUSIG the condensation is instead modelled as a source term.

2.2.1. MUSIG

In order to differentiate the proposed DQMOM formulation from the earlier proposed MUSIG formulation, a brief description of the latter is included. For MUSIG the internal phase space is split in a set of N bubble sizes, with one vapour fraction equation per class j

$$\frac{\partial\alpha_{g,j}\rho_g}{\partial t} + \nabla\cdot(\alpha_{g,j}j\rho_g\mathbf{U}_g) = S_j. \tag{7}$$

In Eq. (7), the source term S_j will account for the birth and death of bubbles of size j due to aggregation and breakage processes, and for the condensation of bubbles from other sizes [12]. Due to the fixed bubble size the condensation only occurs as an exchange of bubbles (or void) between neighbour classes. No change in the bubbles classes is accounted for, and the current size distribution is thus only expressed in terms of the a priori determined bubble sizes.

2.2.2. DQMOM

In contrast to the MUSIG approach, for DQMOM the sizes are not a priori determined. Instead the distribution is written as a quadrature approximation in terms of weights (w) and abscissas (ξ)

$$n(\xi;\mathbf{x},t) \approx \sum_{i=0}^{N-1} w_j(\mathbf{x},t)\delta(\xi - \xi_j(\mathbf{x},t)) \tag{8}$$

which are all solved for. The system of equations is closed by taking $2N$ moments of the PBE and inserting the quadrature approximation (Eq. (8)). As a result, a set of transport equations for the weights and weights times abscissas is retrieved and solved in space and time using a standard CFD approach. Thus the weights as well as the abscissas are dynamic in space and time. This generally allows for fewer sizes than in the MUSIG approach.

In order to include the effect of condensation, the internal phase space convection is related to the condensation rate according to

$$\frac{\partial\xi(\mathbf{r},t)}{\partial t} = C(\xi,\mathbf{r},t). \tag{9}$$

This allows for a contiguous decrease in the bubble size, which, in the absence of aggregation and breakage, makes the bubble size distribution directly follow the size dependent condensation rate.

In the current work, the condensation rate is modelled as

$$C(\xi) = -2\frac{Nu\lambda_l\left(T_g - T_l\right)}{\xi H_{g\to l}}, \tag{10}$$

where the Nusselt number implicitly depends on the flow properties [13]. Due to the dependence on the phase velocities and the thermophysical state, the condensation rate will, as already mentioned, couple the PBE to the rest of the two-fluid framework.

2.3. Wall boiling

In order to capture the growth of bubbles at the superheated walls of the fuel pins, a wall boiling boundary condition is required. The bubble sizes at the wall is typically calculated according to an empirical model (for an overview see e.g. [14]). In the general case, the wall condition should allow an arbitrary distribution of bubbles to be born from evaporation at the wall.

For DQMOM, all source terms are described in terms of the local sizes ξ_j in the current computational cell (see e.g. aggregation and breakage source terms [15]). Given that an arbitrary distribution is required, the current size distribution in the cell closest to the wall is not necessarily accurately representing the required bubble sizes. Instead a wall flux condition based on the desired sizes is formulated. The condition makes use of a fictitious wall flux at the boiling wall, introducing the required sizes of vapour bubbles. By adding the flux only when solving the transport equations for DQMOM, no additional momentum is induced. A distribution of weights and abscissas is computed to represent the desired bubbles at the wall.

This should be compared to the MUSIG model where the bubbles from the wall are added, according to the desired distribution, to one of the static bubble classes. Even though not dynamically representing the wall distribution, the static distribution will cover all sizes and the proposed flux condition can thus be used also for the MUSIG approach.

2.4. Implementation

The two-fluid framework as well as the PBE solvers (MUSIG and DQMOM) are implemented in foam-extend-3.1 (previously the extension track of OpenFOAM®-1.6-ext) [16]. The existing framework was extended with solvers and libraries for condensation models, fluid properties and the PBE solvers. The two-fluid framework is in part based on the existing two-phase flow adiabatic solver.

3. RESULTS

The two-fluid equations are combined with the DQMOM approach for two cases of subcooled flow. In the first system, a flow of subcooled liquid with a prescribed distribution of vapour bubbles at the inlet is simulated. This case is followed by a domain with a wall boiling condition applied as proposed above. In both cases, the calculated vapour concentrations and bubble distributions are compared between DQMOM and MUSIG, where the latter is applied with $N = 30$ as typically used elsewhere [17]. Finally, the computational performance is outlined and analyzed in terms of relative CPU-time. The geometry of the two-dimensional simulated domain and the accompanying boundary conditions are displayed in Figure 1.

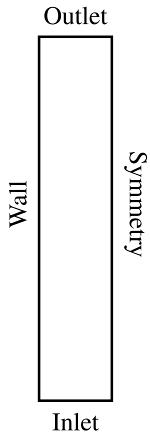

- Domain size: 50 cm × 10 cm
- Mesh size: 50 × 15 cells

Inlet conditions:
- $\mathbf{U}_{g,\max} = (0, 0, 0.3)$ -parabolic profile
- $\mathbf{U}_{l,\max} = (0, 0, 0.1)$ -parabolic profile
- $k = 10^{-3}$,
- $\epsilon = 10^{-3}$

Wall conditions:
- $\mathbf{U}_g$: slip
- $\mathbf{U}_l$: noslip
- k: zero gradient
- ϵ: zero gradient

Figure 1. System description and boundary conditions for the simulated domain.

3.1. Vapor inlet condition

In the first case vapour is introduced at the inlet of the system, without boiling at the wall. The bubbles enter 3 K subcooled and the bubbles at the inlet follow a normal distribution in size around the mean diameter 7 mm and with a total void fraction of 5%. The thermophysical properties correspond to water at a pressure of 0.1 MPa. The DQMOM inlet and initial sizes are chosen according to the same bubbles size distribution, whereas 30 uniform size intervals are chosen for MUSIG. For DQMOM, two to five abscissas are used in the simulations.

As seen from the resulting void distribution in Figure 2, the total vapour fraction quickly decreases over the axial direction. In comparison to the MUSIG results, the void fraction as computed by DQMOM decreases faster. This is explained by the average bubble size shown in Figure 3. As indicated, the average size decreases more rapidly for DQMOM than MUSIG. Considering that fixed, evenly spaced, size intervals are applied for MUSIG the resolution in size quickly diminishes as the bubbles become very small. Due to an inverse dependence with size in the condensation rate, as seen in Eq. (9), the bubble shrinkage accelerates over the displayed axial direction. As the bubbles become smaller, the dynamic sizes of DQMOM can still follow the distribution whereas the resolution of the static distribution in MUSIG results in a slower decrease in size.

From Fig. 2 it is also evident that solutions from DQMOM converge, and that three abscissas differ from five abscissas first at $z = 0.1$. This indicates that DQMOM quickly converges as further abscissas are added. Further, it is seen that the void fraction for DQMOM reaches a constant level approximately at $z = 0.13$. This is a result of the numerical method used to compute the abscissas in relation to the condensation rate. As the abscissas are contiguously decreasing in size and in addition the condensation rate increases with the inverse of the bubble size, the

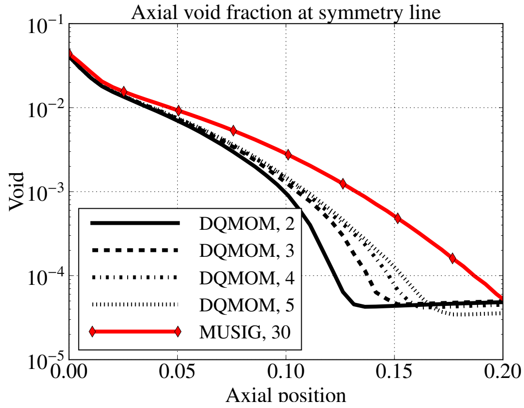

Figure 2. Axial void fraction at symmetry line at t=5 s for z = 0.0 to z = 0.20.

system needs to be dampened. Such implementation will not notably influence the physics of the problem as the vapour fraction in the described region is very small and is neither affecting the flow of the liquid nor the heat transfer.

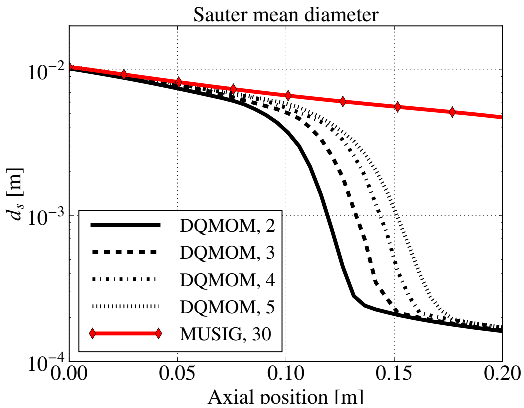

Figure 3. Axial Sauter mean diameter at symmetry line at t=5 s for z = 0.0 to z = 0.20.

3.2. Subcooled wall boiling condition

In the second case the outlined wall boiling condition is applied at the left boundary ("Wall" in Fig. 1). At the wall, the same distribution of bubble sizes is used as in the previous case. The distribution would in general need to be computed according to an applied boiling model, depending on the local thermophysical state. However, for the purpose of demonstrating the method and compare it to MUSIG, an a priori size distribution is applied at the wall.

Figure 4 displays the horizontal void fraction at mid-elevation. As seen from the figure, the void fraction first increases slightly along the horizontal direction from the wall up to x = 0.01 and then decreases rapidly. DQMOM and MUSIG predict a similar void profile along the horizontal direction. However, the results obtained with DQMOM show a more rapid decrease in the bubble sizes. In the current case the difference between the number of abscissa for DQMOM is less pronounced and seemingly DQMOM converges already for three abscissas.

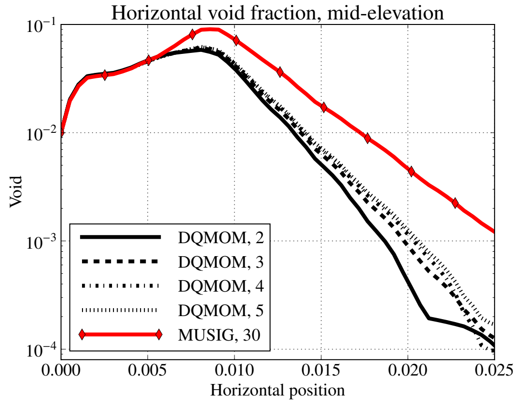

Figure 4. Horizontal void fraction at mid-elevation (t=5 s).

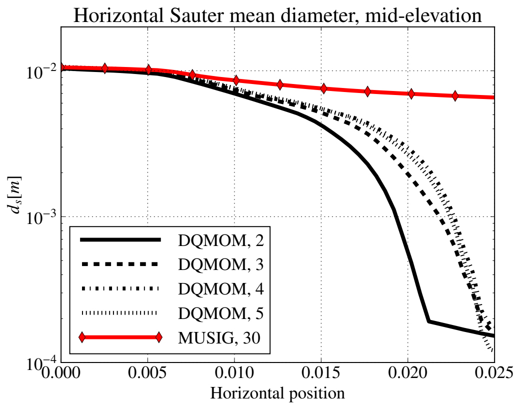

Figure 5. Horizontal Sauter mean diameter at mid-elevation (t=5 s).

3.3. Computational performance

Table 1 gives the relative computational time for the different number of abscissas and in comparison to MUSIG. Due to the complexity of the DQMOM method, five abscissas is more expensive than MUSIG with 30 classes. On the other hand, as previously discussed, it is not required for all simulations to use five abscissas. Since DQMOM with only three abscissas gives a reasonable agreement with five abscissas, the results in Tab. 1 suggest that DQMOM is approximately five times cheaper than MUSIG. The results are to be considered as indicative and the computational performance could be increased or lowered for both MUSIG and DQMOM on including different physics or when applied to different geometries. For a more definite conclusion further comparisons are required.

Table 1. Performance comparison for inlet vapour distribution

Solver	N	Time [a.u.]
DQMOM	2	1.0
DQMOM	3	1.3
DQMOM	4	3.8
DQMOM	5	8.8
MUSIG	30	6.8

4. SUMMARY

In the current paper a framework for a two-fluid/DQMOM methodology was proposed. The solver has the capability to take in account condensation in subcooled boiling conditions with bubbles introduced as a wall boiling condition. The evolution of the vapour phase in a two-dimensional vertical channel was simulated, and a comparison was performed with the results obtained with the MUSIG method. The presented axial and horizontal vapour fractions and bubble size distributions suggest that DQMOM gives similar results as MUSIG for regions with large bubbles, whereas a higher resolution of small bubbles is allowed due to the dynamic abscissas. The computational times indicates that DQMOM can capture larger bubble ranges than MUSIG with a smaller computational cost. Further studies on the stability and performance of condensation with DQMOM needs to be performed and also compared to a larger range of MUSIG simulations. In addition, aggregation and breakage of bubbles should be studied in combination with condensation.

ACKNOWLEDGEMENTS

The project was carried out within DREAM (Deterministic REActor Modelling), a multi-disciplinary task force at Chalmers University of Technology aimed at developing next-generation high-fidelity modelling techniques for nuclear reactors. This project has been supported by SKC Swedish Center for Nuclear Technology. The computations were performed on resources at Chalmers Centre for Computational Science and Engineering (C3SE) provided by the Swedish National Infrastructure for Computing (SNIC).

REFERENCES

[1] Yadigaroglu, G., 2005, "Computational Fluid Dynamics for nuclear applications: from {CFD} to multi-scale {CMFD}", *Nuclear Engineering and Design*, Vol. 235 (2âĂŞ4), pp. 153 – 164.

[2] Yeoh, G., and Tu, J., 2006, "Two-fluid and population balance models for subcooled boiling flow", *Applied Mathematical Modelling*, Vol. 30, pp. 1370–1391.

[3] Krepper, E., Beyer, M., Lucas, D., and Schmidtke, M., 2011, "A population balance approach considering heat and mass transfer - Experiments and CFD simulations", *Nuclear Engineering and Design*, Vol. 241, pp. 2889–2897.

[4] Marchisio, D., and Fox, R., 2005, "Solution of population balance equations using the direct quadrature method of moments", *Aerosol Science*, Vol. 36, pp. 43–73.

[5] Weller, H., 2005, "Derivation, Modeling and Solution of the Conditionally Averaged Two-Phase Flow Equations", *Tech. rep.*, OpenCFD.

[6] Elman, H., 2005, "Preconditioning Strategies for Models of Incompressible Flow", *Journal of Scientific Computing*, Vol. 25 (1), pp. 347–366.

[7] Ferziger, J., and Peric, M., 2002, *Computational Methods for Fluid Dynamics*, Springer.

[8] Schiller, L., and Naumann, Z., 1935, "A drag coefficient correlation", *Zeitschrift des Vereines Deutscher Ingenieure*.

[9] Prosperetti, A., and Tryggvason, G., 2007, *Computational Methods for Multiphase Flow*, Cambridge University Press, Cambridge, United Kingdom and New York, NY, USA.

[10] Lopez de Bertodano, M., 1991, "Turbulent Bubbly Flow in a Triangular Duct", Ph.D. thesis, Rensselaer Polytechnic Institute, Troy, New York.

[11] Ramkrishna, D., 2000, *Population balances: Theory and applications to particulate systems in engineering*, Academic Press.

[12] Lucas, D., Beyer, M., Frank, T., Zwart, P., and Burns, A., 2009, "Condensation of steam bubbles injected into sub-cooled water", *The 13th International Topical Meeting on Nuclear Reactor Thermal Hydraulics (NURETH-13), Kanazawa, Japan*.

[13] Issa, S. A., Weisensee, P., and MaciÃąn-Juan, R., 2014, "Experimental investigation of steam bubble condensation in vertical large diameter geometry under atmospheric pressure and different flow conditions", *International Journal of Heat and Mass Transfer*, Vol. 70 (0), pp. 918 – 929.

[14] Yeoh, G., and Tu, J., 2010, *Computational Techniques for Multiphase Flows*, Elsevier Ltd.

[15] Marchisio, D., Vigil, R., and Fox, R., 2003, "Quadrature method of moments for aggregation-breakage processes", *Journal of Colloid and Interface Science*, Vol. 258 (2), pp. 322 – 334.

[16] Wikki, 2015, "foam-extend-3.1", URL `http://wikki.gridcore.se/foam-extend/foam-extend-3-1-zagreb`, (last visited February 16, 2015).

[17] Krepper, E., Lucas, D., Frank, T., Prasser, H.-M., and Zwart, P. J., 2008, "The inhomogeneous MUSIG model for the simulation of polydispersed flows", *Nuclear Engineering and Design*, Vol. 238 (7), pp. 1690 – 1702.

Conference on Modelling Fluid Flow (CMFF'15)
The 16th International Conference on Fluid Flow Technologies
Budapest, Hungary, September 1-4, 2015

ON THE TRACK OF THE BORDA-CARNOT LOSS

Eszter LUKÁCS[1], János VAD [2]

[1] Corresponding Author. Department of Fluid Mechanics, Budapest University of Technology and Economics. Bertalan Lajos u. 4 – 6, H-1111 Budapest, Hungary. Tel.: +36 1 463 2546, Fax: +36 1 463 3464, E-mail: lukacs@ara.bme.hu
[2] Department of Fluid Mechanics, Budapest University of Technology and Economics. E-mail: vad@ara.bme.hu

ABSTRACT

Based on previous experiments carried by the authors, a simple and effective way was found to reduce the pressure loss of a Borda-Carnot sudden expansion. The method consisted of so called mini-flaps, which were placed on the step of the sudden expansion, forming a mini-diffuser. This article targets a detailed theoretical investigation of the flow in a sudden expansion for better comprehension of the underlying physics, serving as a basis for optimization of the mini-flap method. As a start, an ideal modelling case in a sudden expansion without mini-flaps was examined, and the average pressure along the transitional area was derived with the help of the momentum equation. Then a viscous flow was investigated. Using boundary layer equations in the free shear layer, the pressure distribution in the separation bubble after the sudden expansion was determined, leading to the classical Borda-Carnot loss equation. Finally, the effects of friction on the pressure loss were further examined with the help of the momentum equation, defined on several different control surfaces. This investigation has led to understanding the flow behavior when using mini-flaps, showing that there exists an optimal angle of the mini-flaps for maximum pressure loss reduction.

Keywords: sudden expansion, pressure loss reduction, theory

NOMENCLATURE

A	*[m]*	surface magnitude
F_τ	*[N]*	force resulting from shear stress
P	*[N]*	force caused by pressure
n	*[m]*	normal coordinate
p	*[Pa]*	static pressure
s	*[m]*	streamwise coordinate
v	*[m/s]*	velocity magnitude
x	*[m]*	main flow direction
β	*[rad]*	angle of the free shear layer
ρ	$[kg/m^3]$	density
τ	*[Pa]*	shear stress
$\Delta p'_{BC}$	*[Pa]*	Borda-Carnot loss

Subscripts and Superscripts

1	at the inlet of the flow
2	at the outlet of the flow
2id	at the outlet of the flow in the ideal case
1,2id	average of parameters at the inlet and outlet in the ideal case
A_2-A_1	surface of the step of the sudden expansion
S	superficies of stream-surface in the viscous case
SS	stream-surface in the ideal case
-	space average

1. INTRODUCTION

The Borda-Carnot sudden expansion has always been of great interest in research, both from theoretical and practical point of view. Its theoretical popularity is due the fact, that in spite of a fairly simple geometry, it presents numerous interesting flow features. From the practical side, the Borda-Carnot element (also mentioned as BC element later on) is frequently used in pipe systems, wherever static pressure increase or velocity reduction is needed, but there is no sufficient space for a high-efficiency diffuser. As energy savings is an issue of primary importance nowadays, the pressure loss reduction of the sudden expansion is indicated, in order to reduce the allover pressure loss of the pipe system.

The flow features and the pressure loss of the Borda-Carnot sudden expansion is widely discussed, and often included in hydraulic hand- and textbooks. Idelchik [1] gives a thorough overview about the pressure loss for different area ratios, sudden expansion geometries, upstream velocity profiles, etc., however the underlying theory is not addressed. A more detailed derivation of the pressure loss of a BC element is presented in Lajos [2], by means of using former measurement results of the pressure distribution inside the sudden expansion. An axisymmetric sudden expansion has been examined by means of computational fluid dynamics (CFD) in Oliviera et. al [3,4], and a general correlation for the loss coefficient has been set up for laminar, Newtonian flows. Laminar flows in abrupt circular expansions has also been studied experimentally by Back and Roschke [5,6], discussing the reattachment length and its dependence on the state of the upstream flow. As for turbulent flows in sudden expansions, a great variety of cases have been extensively researched, both experimentally and numerically, such as the effect of inlet turbulence on the reattachment length [7], precession in sudden expansions with low inlet swirl [8], behavior of non-Newtonian flows [9] and separating and reattaching flow structures in suddenly expanding rectangular ducts [10].

Concerning energy conservation, several research studies have been dedicated to reduce the pressure loss of a sudden expansion. Lukács and Régert [11] – focusing on rectangular cross-sectioned air ducts - have carried out experiments in a BC element with rectangular cross-section for the turbulent flow regime. The authors have proposed an effective and easily manufactured device to reduce the pressure loss, in the form of small flow control elements - so called mini-flaps - placed at the step of the sudden expansion, forming basically a very short diffuser. An optimal angle of the mini-flaps has been found to reach maximum possible pressure loss reduction. A similar idea has been put forward by Bae and Kim [12,13], who has targeted the pressure loss reduction of an axisymmetric sudden expansion by chamfering the edges of the BC element. In their work, a new correlation to estimate the pressure loss has been proposed, based on CFD calculations.

Findings of Lukács and Régert [11] served as a basis for the present article. The objectives of the authors include generating a theoretical support for the formerly carried out experiments on order to find whether there exits an optimal set-up (including angle and length) of the mini-flaps. The obtained formulae are also expected to be of use in refining the measurement set-up by highlighting the relevant parameters to be measured.

2. CASE OF AN IDEAL FLOW

As stated before, the experiments [11] - intended to reduce the pressure loss of a Borda-Carnot sudden expansion - were carried out in a three-dimensional, viscous system. However, the settlement of basic theoretical considerations is to be started in a more simple way, and only then one can proceed towards a more complex and more realistic model. Therefore a two-dimensional, ideal flow is to be examined first (see Figure.1), which is going to give us an idea about the static pressure distribution inside the BC element, and how the different pressures relate to each other. The results can take us one step closer to determine the limits of a possible pressure loss reduction.

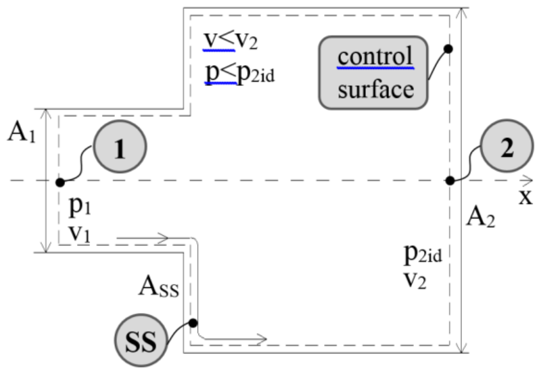

Figure 1. Ideal flow in the Borda-Carnot sudden expansion and basic notations

The static pressure in the larger cross section is given by the frictionless Bernoulli equation Eq. (1). The pressure increase is ideal.

$$p_{2id} = p_1 + \frac{\rho}{2}(v_1^2 - v_2^2) \tag{1}$$

The flow – being ideal – follows the wall of the sudden expansion without separation. The surface at the transitional area of the sudden expansion is a stream surface, denoted by A_{ss} henceforward (see Fig.1).

So what is the average pressure ($\overline{p}_{ss}$) forming on this stream surface A_{ss}? In order to derive the magnitude of $\overline{p}_{ss}$ the momentum equation inside the BC element is set up on the control surface, denoted by a dashed line in Fig.1. Locations 1 and 2 are sufficiently far from the sudden expansion so that the streamlines become parallel. Figure 2 shows a magnified streamline in the vicinity of A_{ss}, and the notations, necessary to formulate the momentum equation.

$$-\rho v_1^2 A_1 + \rho v_2^2 A_2 =$$
$$p_1 A_1 - p_{2id} A_2 + \int p_{ss}\, dA_{ss} \sin\beta \tag{2}$$

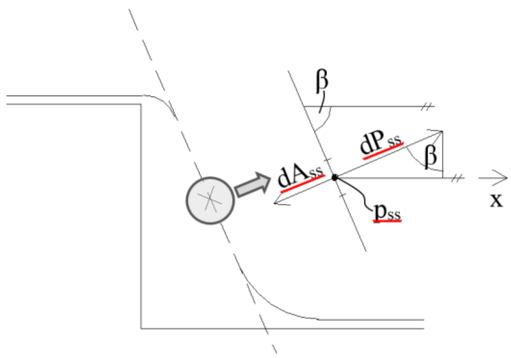

Figure 2. Elementary section of a streamline in the ideal case

After certain simplifications of Eq. (2), and substituting Eq. (1) and the continuity equation: Eq. (3), one can get three other expressions: Eqs. (4 to 6), which gives us an idea about the magnitude of the average pressure along the wall of the transitional area.

$$v_1 A_1 = v_2 A_2 \quad (3)$$

$$\overline{p}_{ss} = p_{2id} - \frac{\rho}{2}(v_1 - v_2)v_2 \quad (4)$$

$$\overline{p}_{ss} = p_1 + \frac{\rho}{2}(v_1 - v_2)v_1 \quad (5)$$

$$\overline{p}_{ss} = \overline{p}_{1,2id} + \frac{1}{2}\left[\frac{\rho}{2}(v_1 - v_2)^2\right] = \overline{p}_{1,2id} + \frac{\rho}{2}(v_1 - v_2)\frac{v_1 - v_2}{2} \quad (6)$$

, where $\overline{p}_{1,2id} = \frac{p_1 + p_{2id}}{2}$.

3. CASE OF A VISCOUS FLOW

Taking one step further from the ideal but closer to reality, viscosity is added into the investigated scheme. Referring back to an ideal case (Fig.1), the loss of the momentum flux of the fluid is: $[\rho v_1^2 A_1 - \rho v_2^2 A_2]$. This loss can be attributed the decelerating effect of the force $p_{2id}A_2$, against the accelerating forces $p_1 A_1$ and $\overline{p}_{ss}(A_1 - A_2)$. The loss of the momentum flux in case of a viscous flow is the same as in the case of an ideal flow: $[\rho v_1^2 A_1 - \rho v_2^2 A_2]$, as continuity still holds. However, because of the frictional losses, the pressure $\overline{p}_{A_2-A_1}$ building up on the surface at the transitional area $(A_2 - A_1)$ is smaller than $\overline{p}_{ss}$ in the ideal case. As a result of this, the $\overline{p}_{A_2-A_1}(A_2 - A_1)$ accelerating force is smaller, therefore the decelerating force at the outlet is also smaller: $p_2 A_2 < p_{2id}A_2$. This means that the outlet pressure in the viscous case is less than in the ideal case: $p_2 < p_{2id}$. The Borda-Carnot loss is defined by Eq. (7).

$$p_{2id} - p_2 \mathrel{\widehat{=}} \Delta p'_{BC} \quad (7)$$

Investigating the magnitude of the pressure $\overline{p}_{A_2-A_1}$ is crucial in calculating the losses. So let us take a closer look at what happens with the fluid after leaving the edge of the sudden expansion. The path of the viscous flow and the relevant notations are shown in Figure 3. As the fluid leaving the small tunnel cannot follow the abrupt change in the cross-section of the tunnel, the boundary layer separates and a separation bubble is created right at the foot of the sudden expansion. The separation bubble is separated from the flow by a free shear layer, across which the velocity changes rapidly perpendicular to the streamlines [2]. According to Newton's viscosity law, this rapid change in velocity causes significant shear stress in the free shear layer, also supported by measurements of Lukács and Régert [11]. Although the free shear layer is not a strictly defined surface, an abstraction is made and therefore it can be considered as kind of an average stream surface, in which significant shear stress is present in spite of absence of wall friction. As a free shear layer and a boundary layer shares several common features, a free shear layer equation can be created based on the generally known boundary layer equation.

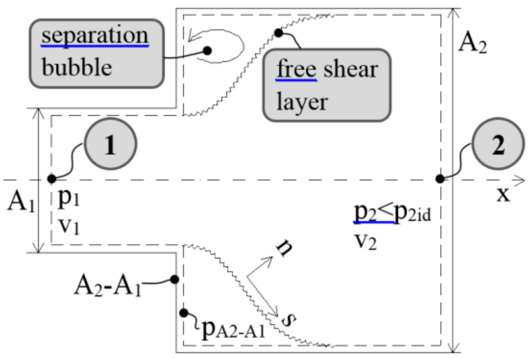

Figure 3. Viscous flow in the Borda-Carnot sudden expansion and basic notations

In order to create the shear layer equation, the following considerations are made based on [2]: (1) the flow is planar, (2) the streamwise (s) component of the velocity is significantly bigger than the normal (n) component: $v_n \ll v_s$, (3) changes in the normal direction are significantly bigger than changes in the streamwise direction $\frac{\partial()}{\partial s} \ll \frac{\partial()}{\partial n}$, (4) the flow is stationary, (5) gravity is neglected. Applying these considerations to the Navier-Stokes equation, the result is shown in Eq. (8):

$$\frac{\partial p}{\partial n} \approx 0 \quad (8)$$

, which means that the static pressure is nearly constant perpendicularly to the shear layer, therefore the pressure in the shear layer equals the pressure in the free stream flow (see Figure 4).

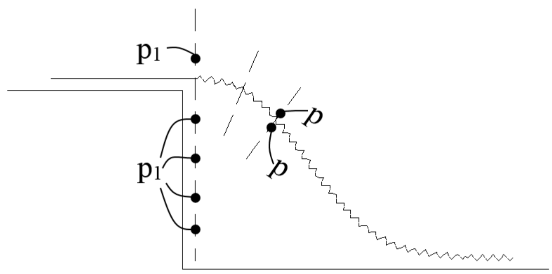

Figure 4. Static pressure distribution across the free shear layer

Eq. (8) allows us to draw the following conclusions, regarding the pressure distribution inside the Borda-Carnot sudden expansion: (1) on the surface $(A_1 - A_2)$ the pressure is constant, and it equals the upstream pressure p_1. This conclusion is supported by measurement results and is generally used when deriving the Borda-Carnot loss [2]. It also supports the approach, according to which the pressure in a separation bubble is nearly constant, and it equals to the pressure on the surface of an imaginary body, replacing the separation bubble [2], therefore $\overline{p}_{A_2-A_1} = p_1$. (2) On a given $s = const.$ coordinate the pressure is constant and it is equal to the pressure in the free stream flow. This knowledge results to be useful when improving the measurement system of the mini-flaps [11], as simple wall pressure measurements will let us estimate the static pressure distribution inside the main flow as well.

Based on all of the above concluded, the momentum equation (Eq. (9)) is set up on the control surface shown in Fig. 1, which is the most commonly used in the derivation of the Borda-Carnot pressure loss. The effect of wall friction is neglected. This supposition is supported by measurement results of Lukács and Régert [11].

$$-\rho v_1^2 A_1 + \rho v_2^2 A_2 = p_1 A_1 + \overline{p}_{A_2-A_1}(A_2 - A_1) - p_2 A_2 \qquad (9)$$

After certain simplifications and substitution of the continuity equation, the resulting momentum equation (Eq. (10)) reads as:

$$p_2 - p_1 = \rho v_2 (v_1 - v_2) \qquad (10)$$

If Eq.1 and Eq.10 are substituted into Eq. (7), the well-known Borda-Carnot pressure loss can be expressed as shown in Eq. (11):

$$\Delta p'_{BC} = \frac{\rho}{2}(v_1 - v_2)^2 \qquad (11)$$

4. FRICTION AS CAUSE OF THE PRESSURE LOSS

It has been shown that viscosity is responsible for the Borda-Carnot loss ($\Delta p'_{BC}$), but by what means does it generates the pressure loss in the sudden expansion? The following approach is applied: frictional losses in the flow are caused by the shear stress emerging in the free shear layer, which can be closely related to viscosity. Wall friction is neglected so far. The free shear layer is considered to be a stream surface, bounding the free stream flow. The momentum theorem is then applied to a segment of the flow bounded by the stream surface, as shown in Figure 5.

The slowly moving fluid in the separation bubble retains the free stream flow, therefore the *x*-component of the elementary force coming from the shear stress on the superficies of the control surface ($d\underline{F}_\tau$) is negative. Considering an axisymmetric case, for a given *x*-coordinate and a representative β angle, the momentum equation in the *x*-direction is given by Eq. (12):

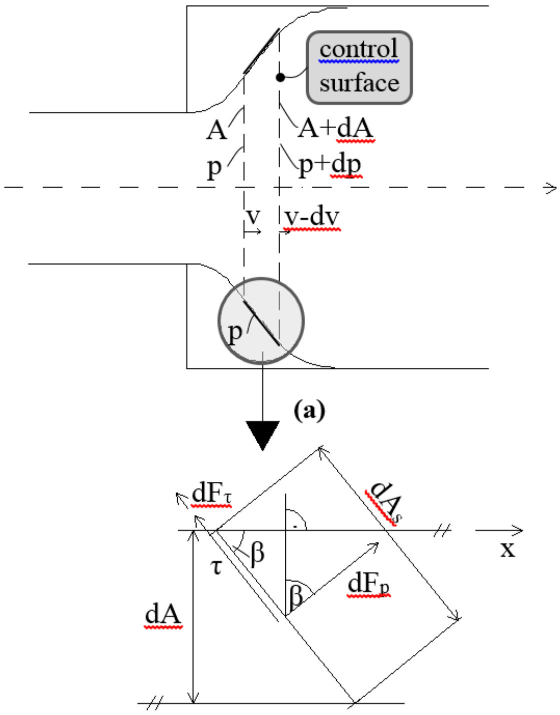

Figure 5. (a) Control surface in case of a viscous flow (b) Magnified section of the free shear layer and notations

$$-\rho v^2 A + \rho(v - dv)^2 (A + dA) = pA - (p + dp)(A + dA) + p dA_s \sin\beta - \tau dA_s \cos\beta \qquad (12)$$

After simplification the equation reads as shown in Eq. (13):

$$\rho v^2 A - \rho 2 v dv A = -dpA - \tau dA \frac{1}{\tan\beta} \qquad (13)$$

Substituting a simplified form of the continuity equation (Eq. (14)) into Eq. (13), gives us Eq. (15):

$$v dA = dv A \qquad (14)$$

$$\rho v dv A = dpA + \tau dA \frac{1}{\tan\beta} \qquad (15)$$

The change of pressure is defined as the difference between the ideal pressure drop and the pressure loss, as shown in Eq. (16):

$$dp = dp_{id} - d(\Delta p') \qquad (16)$$

The ideal pressure drop is given by the Euler-equation [2], as shown in Eq. (17):

$$v \frac{\partial v}{\partial s} = -\frac{1}{\rho}\frac{\partial p}{\partial s} \qquad (17)$$

In one-dimensional approach Eq. (17) can be rearranged to Eq. (18):

$$dp_{id} = \rho v dv \quad (18)$$

Substituting Eqs. (16) and (18) into Eq. (15) gives us Eq. (19):

$$d(\Delta p') = \tau \frac{dA}{A} \frac{1}{\tan\beta} \quad (19)$$

Although Eq. (19) clearly demonstrates that the pressure loss is generated by the shear stress arising in the free shear layer, by further exploitations of the momentum theory one can get a more clear-cut idea about the possibilities of the pressure loss reduction in the Borda-Carnot element. Two momentum equations are going to be set up: one is on the control surface "A", which is the classical approach, and the other is on the control surface "B", along the shear layer considered as a stream surface. The control surfaces are shown in Figure 6.

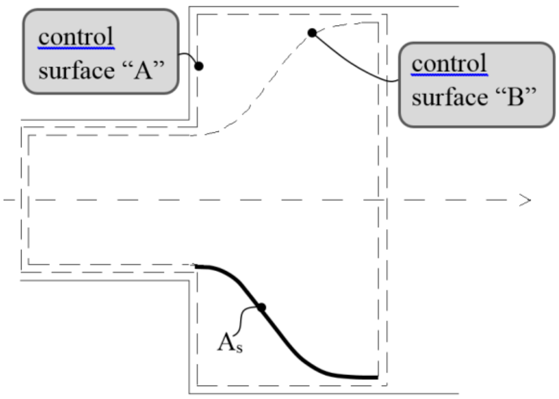

Figure 6. Control surfaces "A" and "B" inside the BC element

The momentum equation for control surface "A" has been already given in Eq. (9). Combining this equation with Eq. (7) and rearranging the formula, the pressure loss of the BC element can be expressed as shown in Eq. (20):

$$\Delta p'_{BC} = \frac{1}{A_2}\left\{p_{2id}A_2 + \rho v_2^2 A_2 - \rho v_1^2 A_2 - p_1 A_1 - \overline{p}_{A_2-A_1}(A_2 - A_1)\right\} \quad (20)$$

From Eq. (20) it can be concluded that the only theoretical way (according to this approach) to reduce the pressure loss of a BC element is to increase the pressure $\overline{p}_{A_2-A_1}$. All other terms are defined by the inlet pressure, mass flow rate and geometry of the BC element.

The momentum equation written on control surface "B" is given by Eq. (21):

$$-\rho v_1^2 A_1 + \rho v_2^2 A_2 = p_1 A_1 + \int p dA_s \sin\beta - \int \tau\, dA_s \cos\beta - p_2 A_2 \quad (21)$$

Rearranging Eq. (21) the pressure loss of the BC element can be expressed as shown in Eq. (22):

$$\Delta p'_{BC} = \frac{1}{A_2}\{p_{2id}A_2 + \rho v_2^2 A_2 - \rho v_1^2 A_2 - p_1 A_1 - \int p dA_s \sin\beta + \int \tau\, dA_s \cos\beta\} \quad (22)$$

According to Eq. (22) there are two possible ways to reduce the pressure loss in the BC element: (1) if $\int p dA_s \sin\beta$ is increased, where the augmentation of p is actually a consequence of the pressure loss reduction or (2) if $\int \tau\, dA_s \cos\beta$ is decreased.

Let us concentrate on how the frictional losses (see Eq. (23)) of the "free shear layer diffuser" can be reduced by reducing the friction forces. As for a simpler approach, the free shear layer between the separation and reattachment points is considered to be a straight line, and is characterized by an average β angle: $\bar{\beta}$. Our goal is to find the optimal $\bar{\beta}$ angle, for which the friction losses are minimal.

$$S = \int (\tau \cos\beta) dA_s \quad (23)$$

According to Eq. (23), if $\bar{\beta}$ is small, $\cos\bar{\beta}\, dA_s$ – which is basically the length of the separation bubble - will be large, and if $\bar{\beta}$ is increased, $\cos\bar{\beta}\, dA_s$ will be reduced. Ergo, increasing $\bar{\beta}$ results in decreased frictional losses, while decreasing $\bar{\beta}$ the frictional losses will be increased. This observation is also supported by Guo et al [14], according to whom the larger the separation bubble downstream the step is, the higher the pressure loss will be. A possible method of changing the magnitude of angle $\bar{\beta}$ is installing the formerly mentioned mini-flaps placed into the BC element [11]. Due to the Coanda effect the flow stays attached to the surface of the mini-flaps, thus $\bar{\beta}$ can be increased, therefore the length of the separation bubble and the pressure loss coefficient can be reduced. However, there is a limit in increasing $\bar{\beta}$, as for angles too large the pressure gradient will be increased, which leads to an early boundary layer separation [2] and the mini-flaps will not be able to influence the pressure loss. The optimal $\bar{\beta}$ angle is therefore the largest possible angle of the mini-flaps, where flow separation does not occur yet.

5. SUMMARY

In this article the theoretical background of the causes of the pressure loss in a Borda-Carnot sudden expansion has been investigated. A general method to reveal the underlying physics was to use the momentum equation for different control surfaces in different flow cases. First, the case of an ideal flow was examined, which gave us a general idea about how the representative static pressures relate to each other, with special emphasis on the average pressure at the step of the sudden expansion. Then viscosity was taken into consideration which involved the formation of a separation bubble and a free shear layer creating a boundary between the free stream flow and the separation bubble. A free shear layer equation was created based on the well-known boundary layer equation, which gave a theoretical support to that the pressure along the wall at the step of a sudden expansion is equal to the pressure inside the free stream flow. This allowed the authors to express the Borda-Carnot loss in its most frequently used form. Finally, friction emerging in the free shear layer was examined, being the main cause of the pressure loss. A general relationship between the pressure loss, the shear stress and the angle of the free shear layer was derived. Based on this relationship, the existence of an optimal average β angle of the free shear layer was concluded, in order to reach maximum pressure loss reduction.

As for future plans, in order to verify that the above described concept is proper, the following parameters are to be measured: (1) pressure distribution in different cross-sections at various locations along the axis of the flow, (2) the average shear stress and angle of the free shear layer, (3) velocity distribution, and (4) the form of the so-called free shear layer diffuser. Combining the theory, derived in this article and the results of the future measurements, a half-empirical model can be set up to describe the working mechanism and optimal use of the mini-flap method.

ACKNOWLEDGEMENTS

This work has been supported by the Hungarian National Fund for Science and Research under contract No. OTKA K 112277.

REFERENCES

[1] Idelchik, I. E., 2001, “Handbook of hydraulic resistance”, edition 3, (Begell House Publishers, New York).

[2] Lajos, T., 2008, “Az áramlástan alapjai”, edition 4, (Budapest)

[3] Oliveira, P. J. and Pinho, F. T., 1997, “Pressure drop coefficient of laminar Newtonian flow in axisymmetric sudden expansions”, *International Journal of Heat and Fluid Flow*, Vol. 19, pp. 655-660.

[4] Oliveira, P. J., Pinho, F. T and Schulte A., 1998, “A general correlation for the local loss coefficient in Newtonian axisymmetric sudden expansions”, *International Journal of Heat and Fluid Flow*, Vol. 18, pp. 518-529.

[5] Back, L. H. and Roschke, L. J., 1972, “Shear-layer flow regimes and wave instabilities and reattachment lengths downstream of an abrupt circular expansion”, *Journal of Applied Mechanics*, Vol. 39, pp. 677-681.

[6] Back, L. H. and Roschke, L. J., 1976, “The influence of upstream conditions on flow reattachment lengths downstream of an abrupt circular channel expansion”, *Journal of Biomechanics*, Vol. 9, pp. 481-483.

[7] Mandal, A. and Majumder, S., 2014, “Effects of inlet centre line turbulence on the turbulent flow through an axi-symmetric sudden expansion”, *Procedia Engineering*, Vol. 90, pp. 275-281.

[8] Guo, B., Langrish, T. A. G. and Fletcher, D. F., 2002, “CFD simulation of precession in sudden pipe expansion flows with low inlet swirl”, *Applied Mathematical Modelling*, Vol. 26, pp.1-15.

[9] Poole, R. J. and Escudier, M. P., 2004, “Turbulent flow of viscoelastic liquids through an axisymmetric sudden expansion”, *Journal of Non-Newtonian Fluid Mechanics*, Vol. 117, pp. 25-46.

[10] Papapodoulos, G. and Otugen, M. V., 1995, “Separating and reattaching flow structure in a suddenly expanding rectangular duct”, *ASME Journal of Fluids Engineering*, Vol. 117, pp. 17-23.

[11] Lukács, E. and Régert, T., 2012, “Pressure loss of a Borda-Carnot sudden expansion applying a passive flow control method”, *Journal of Power and Energy*, Vol. 226, pp. 182-191.

[12] Bae, Y. and Kim, Y. I., 2014, “Prediction of local pressure drop for turbulent flow in axisymmetric expansions with chamfered edge”, *Chemical Engineering Research and Design*, Vol. 92, pp. 229-239.

[13] Bae, Y. and Kim, Y. I., 2014, “Prediction of local pressure drop for turbulent flow in axisymmetric expansions with chamfered edge: Effect of Reynolds number”, *Annals of Nuclear Energy*, Vol. 73, pp. 33-38.

[14] Guo, B. Y., Hou, Q. F., Yu, A. B., Li, L. F. and Gou, J., 2013, “Numerical modelling of the gas flow through perforated plates”, *Chemical Engineering Research and Design*, Vol. 91, pp. 403-408.

Conference on Modelling Fluid Flow (CMFF'15)
The 16th International Conference on Fluid Flow Technologies
Budapest, Hungary, September 1-4, 2015

INFLUENCE OF ICE ACCRETION ON THE NOISE GENERATED BY AN AIRFOIL SECTION

Róbert SZÁSZ[1], Matilda RONNFORS[2], Johan REVSTEDT[3]

[1] Corresponding Author. Department of Energy Sciences, Lund University, PO.Box. 118, 22100, Lund, Sweden. Tel.: +46 46 222 0480, Fax: +46 46 222 4717, E-mail: robert-zoltan.szasz@energy.lth.se
[2] Department of Energy Sciences, Lund University. E-mail: matilda.ronnfors@energy.lth.se
[3] Department of Energy Sciences, Lund University. E-mail: johan.revstedt@energy.lth.se

ABSTRACT

We investigate the noise generated by an airfoil section. Three cases are considered, one with a clean airfoil and two cases with airfoils with ice accretion. The amount of ice is the same in the two cases with ice accretion, but the surface of the accreted ice layer is smoother in one of them. The noise is computed using a hybrid approach. First the flow and the acoustic sources are computed. Second, the noise propagation is predicted by solving an inhomogeneous wave equation. The results indicate that in this case the accreted ice layer leads to a decrease of the radiated noise levels, especially in the lower frequency range.

Keywords: acoustics, airfoil, CFD, Immersed Boundary, LES, wave equation

NOMENCLATURE

$\underline{\underline{T}}$	$[-]$	Lighthill stress tensor
H	$[-]$	Heaviside function
Re	$[-]$	Reynolds number
S	$[-]$	airfoil surface
St	$[-]$	Strouhal number
V_{rel}	$[m/s]$	Relative speed
$\underline{u}$	$[m/s]$	flow velocity
c	$[m/s]$	sound speed
p'	$[Pa]$	acoustic pressure
t	$[s]$	time
x	$[m]$	coordinate
ρ	$[kg/m^3]$	fluid density

Subscripts and Superscripts

i, j index

1. INTRODUCTION

With the increasing number of installed wind turbines, there are less and less available areas for the installation of new turbines. As a consequence, new turbines are often built in cold climate areas (Nordic regions or high altitudes). A recent review of the status of wind energy in cold climate is presented in [1]. Even if the available wind resources in such areas are often superior to the ones available at warmer climate, icing is a severe issue having several negative effects.

Beside the changes in the aerodynamic shape of the blade (directly influencing the blade performance), the extra added mass causing vibrations of the structure, and ice throw, changes in the radiated noise is an issue which gathers more and more focus [1]. Even wind turbines with clean airfoils may emit noise levels which cause annoyance for people living in nearby residential or recreational areas (see e.g. [2, 3]). As a result, several countries introduced strict limits on the maximum allowed noise emission levels of a wind turbine. For wind turbines, the major part of the radiated noise is generated aerodynamically. In the presence of ice accretion not only the aerodynamic performance but also the radiated noise pattern is changed. An improved understanding of these changes is important to avoid the radiated noise levels exceeding the prescribed limits. Furthermore, such knowledge has the potential to be included in ice detection algorithms.

There are a large number of experimental measurements of the noise emitted by wind turbines. Fujii et al. [4] measured the noise emitted by wind turbines having different tower leg cross sectional shapes. The results showed that a slender elliptic cross-section would be the quietest for the operating parameters considered. Björkman [5] carried out long-time noise measurements in the vicinity of existing wind-turbines showing an increase in the high-frequency range with increasing wind speed. Recently, Oerlemans et al. [6] used a microphone array to identify the virtual location of the noise sources. The conclusion was that, except a small contribution of the hub, the noise is mainly generated by the rotor blades and practically all noise emitted towards the ground is produced during the downward motion. Another conclusion is that broadband trailing edge noise is the dominant one for the studied wind turbine. Extensive measurements were carried out around the NREL Phase VI turbine [7, 8] providing a database for comparison with numerical computations (see e.g.Johansen et al.[9], Schmitz and Chattot [10]).

Experimental measurements, however, have several drawbacks. Due to varying atmospheric conditions the experiments are not repeatable and have to be carried out over a long time period. It is difficult to isolate the contribution of the wind turbine, or the contribution of different components. Although wind tunnel testing is possible and gives control over the boundary conditions, this approach is very expensive and the scaling of the results is not straightforward.

Numerical methods supplement the experimental measurements and with the increase of the computational power the detail of the results grew substantially during recent years. Due to the similarity of wind turbines to helicopter rotors, early computations were based on methods used in aviation. A thorough review of different computational methods is presented in Hansen et al.[11] .

There are several numerical methods to determine the sound generated by turbulent flow fields. Solution of the compressible Navier-Stokes equations by Direct Numerical Simulations (DNS) or Large Eddy Simulations (LES) would predict both the flow and the acoustic fluctuations and their propagation. This approach, however, is not efficient for low-Mach number flows, such as the one around a wind turbine, and where noise propagation to long distances is of importance. The first numerical predictions were based on semi-empirical methods, however, these methods turned out to be very sensitive to model parameters. Glegg et al. [12] showed that the assumption of right turbulence length scales is crucial for accurate predictions.

Hybrid approaches are based on the assumption that, for low Mach number flows, the acoustic perturbations are small and the flow variables can be decomposed in a hydrodynamic and an acoustic part. Using hybrid approaches, the acoustic noise will be determined in two steps. First, the incompressible set of Navier-Stokes equations are solved which provides the turbulent flow field. Second, based on the turbulent flow field, the acoustic sources are determined and the acoustic field is resolved. Such approaches provide the possibility to use dedicated solvers for the flow and acoustic governing equations, with the possibility of using different timesteps, domain sizes and mesh resolutions. Although there have been attempts to account for turbulence using Reynolds Averaged Navier-Stokes (RANS) based models in the flow solvers (see e.g. Page et al.[13], Bailly et al.[14]), LES (or DNS) is more appropriate to capture the dynamics of the acoustic sources. Ewert and Schröder [15] applied a hybrid method based on LES of compressible flow and acoustic perturbation equations to predict trailing edge noise.

The goal of this paper is to analyse the effect of the accreted ice layer on the flow-field and on the noise emitted from an airfoil section. This geometry was chosen since a full wind turbine simulation would require exhaustive computational resources. Furthermore, the noise generated by the airfoil section can give insight into some of the mechanisms influencing noise generation in the full scale wind turbine as well. A hybrid approach (described in Section 2) is used to achieve this goal. Three cases are presented. The reference case is a configuration with a clean airfoil. This case is compared to two cases with ice accretion, matching one of the icing events recorded in [16]. The amount of accreted ice in the two cases is the same, the difference being only that in the last case the shape of the ice layer is smoothed. The results indicate that the shape/roughness of the accreted ice layer has a noticeable effect on the radiated noise.

2. METHODS

A hybrid approach is used to determine the radiated noise. The flow variables are decomposed in a semi-compressible (the density is depending on the temperature only, but not the pressure) part and an acoustic part. Consequently, there is a flow solver resolving the semi-compressible Navier-Stokes equations and an acoustic solver solving an inhomogeneous wave equation for the perturbation density. Both solvers are nondimensionalized, using the chord length as a lengthscale and the inlet velocity magnitude as velocity scale.

2.1. Flow solver

The flow solver handles the turbulence by using LES. Finite differences on a cartesian grid are applied for discretization. The geometry of the airfoil is accounted here by the Immersed Boundary Method (IBM) c.f. Salewski et al. [17, 18]. The approach is implemented in our in-house LES well validated solver c.f. Olsson and Fuchs[19], Gullbrand et al.[20]. The code is parallelised using the MPI library. The LES flow solver provides the acoustic sources. An analysis of the acoustic sources revealed that the quadrupole sources were significantly larger than the dipole and monopole sources. As a consequence, in the acoustic computations only the quadrupole sources are used.

2.2. Acoustic solver

The noise propagation is predicted by solving an inhomogeneous wave equation for the acoustic pressure (Eq. 1).

$$\frac{1}{c^2}\frac{\partial^2 p'}{\partial t^2} - \nabla^2 p' = \frac{\partial}{\partial x_i x_j}\left(\underline{\underline{T}}_{ij} H(S)\right) \quad (1)$$

For isothermal flows the entropy and viscous effects can be neglected, thus the Lighthill stress tensor is having the form:

$$\underline{T}_{ij} = \rho \underline{u}_i \underline{u}_j. \tag{2}$$

Equation 1 is integrated in time using an explicit second order method, the spatial discretization is also second order accurate. The acoustic sources being not necessarily saved with the frequency matching the timestep of the acoustic solver, the acoustic sources are interpolated linearly between to consecutive data sets.

3. PROBLEM SET-UP

To our knowledge, no experimental measurements of noise emissions from airfoils subject to ice accretion is publicly available. The lack of such data is probably due to difficulties of acoustic measurements in refrigerated wind tunnels. Here, the 'In-fog icing event 2' presented in [16] has been selected as a testcase. Since no acoustic measurements are available, the computations presented herein should be treated as qualitative indications of expected tendencies. This set-up was chosen because it corresponds to rime-ice formation conditions when all droplets impacting on the surface freeze instantaneously and is easier to model than glaze-ice conditions, when a fraction of the water runs along the profile. In [16] several cases have been tested, simulating different radial positions of a real wind turbine blade. Here, the case corresponding to the lowest radial position was chosen, its parameters being summarised in Table 1.

Table 1. Main parameters of the icing phenomenon

Profile	NACA 63415
Angle of attack	3^o
LWC	0.37 g/m^3
MVD	27.6 μm
Vrel	18.7 m/s
Re	2.49×10^5
time	10.6 *min*
Mass of accreted ice	24 ± 1.75 g

The sketch of the computational domain is shown in Figure 1. The flow solver being non-dimensional, all length have been normalised with the chord length (0.2 m). For the velocity scale the inlet velocity magnitude was chosen. The transversal cross section of the domain is smaller than in the experiments (WxH=1.0x2.5 instead of 2.5x3.0) to reduce the computational effort, however, it is considered still large enough to consider the flow three-dimensional.

A constant, top-hat velocity profile is imposed at the inlet of the domain, while at the outlet flux-conserving zero gradient conditions are applied. Slip

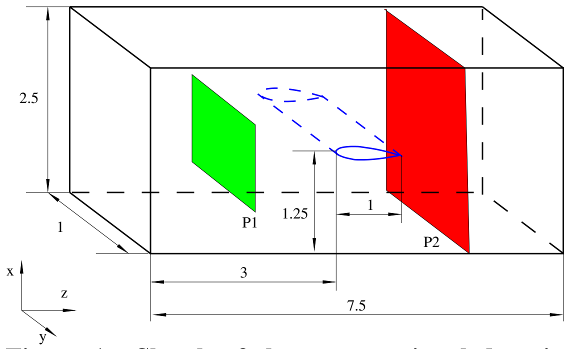

Figure 1. Sketch of the computational domain used in the flow solver and the coordinate system

conditions are used on the side walls. The immersed boundary method forces no-slip conditions at the blade surface.

Droplets of equal size, matching the Liquid Water Content (LWC) and median Volume Diameter (MVD) listed in Table 1, are released upstream the blade, in the plane marked P1 in Figure 1. Those droplets which did not accrete on the blade surface are removed from the simulations when passing the axial position marked P2 in the figure.

Three cases are presented, one computed around the clean airfoil (denoted by Base in the followings) and two cases with airfoil shapes adjusted to account for ice accretion, one of them being smoothed less (denoted case Ice1) and one where stronger smoothing is applied (case Ice2). The three airfoils used in the computations are shown in Figure 2.

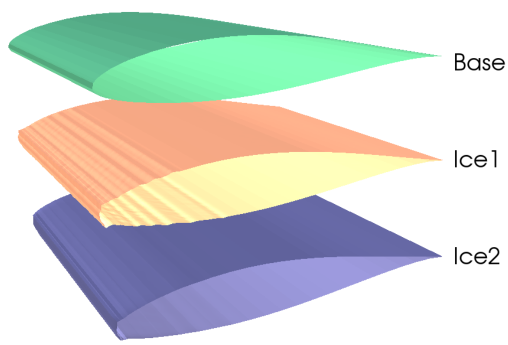

Figure 2. Airfoil profiles used in the three evaluated cases.

The acoustic domain covers a larger volume than the flow domain, its size is 10, 1 and 20 chord lengths in *x*,*y* and *z* directions, respectively. Figure 3 shows a cross section of the acoustic domain where the position of the monitoring points are marked as well. In all computations reflecting boundary conditions have been applied on the airfoil surface and non-reflecting boundary conditions on all sides of the computational domain. The mach number resulting from the experimental conditions is very low, $M = 0.06$. The computations have been carried out in two stages. First, 5 time units (based on the convection velocity and chord length) have been computed to develop the acoustic field. Second, statistics have been collected for 10 time units (more than 8 'wave-through' times).

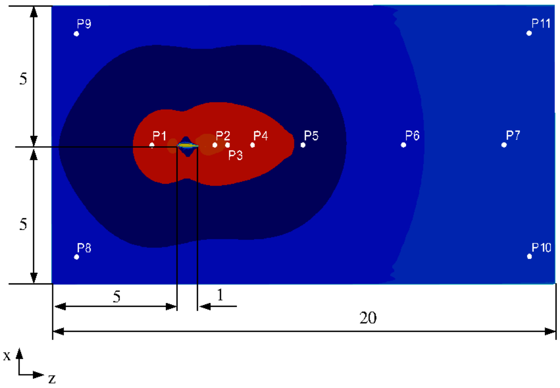

Figure 3. Sketch of the acoustic computational domain and the position of monitoring points

4. RESULTS

4.1. Flow field

This work is a continuation of [21], the set-ups for the flow computations match the cases reported therein. Therefore, here we present only the flow features relevant for the acoustic computations. Velocity fluctuations were found to be the major sound sources. Figure 4 shows the RMS of the streamwise velocity component for the three cases. The largest fluctuation levels are found in all three cases downstream the trailing edge region where slight separation occurred. A comparison of the base case with a clean airfoil (top) and the case with rough ice surface (middle) reveals that the maximum velocity fluctuation levels are amplified towards the leading edge of the airfoil due to the presence of the ice. In contrary, in the trailing edge region lower fluctuation levels are noticed. In the case with smoother ice layer (bottom picture in Figure 4) one can still observe an increase of the fluctuations in the boundary layers around the airfoil, whereas in the trailing edge region the fluctuations are of the same order of magnitude as in the clean airfoil case.

To understand the reason of decreased velocity RMS levels in the second case, instantaneous snapshots of the vortical structures are visualised for the Base and Ice1 cases in Figure 5 using the λ_2 method. For the case with ice accretion one can observe perturbations already in the leading edge region. Further downstream, small vortices, generated by the corrugated shape of the accreted ice layer, are seen on the pressure side of the airfoil. At the trailing edge region very long structures are seen on the suction side of the clear airfoil. Analogous structures are seen in

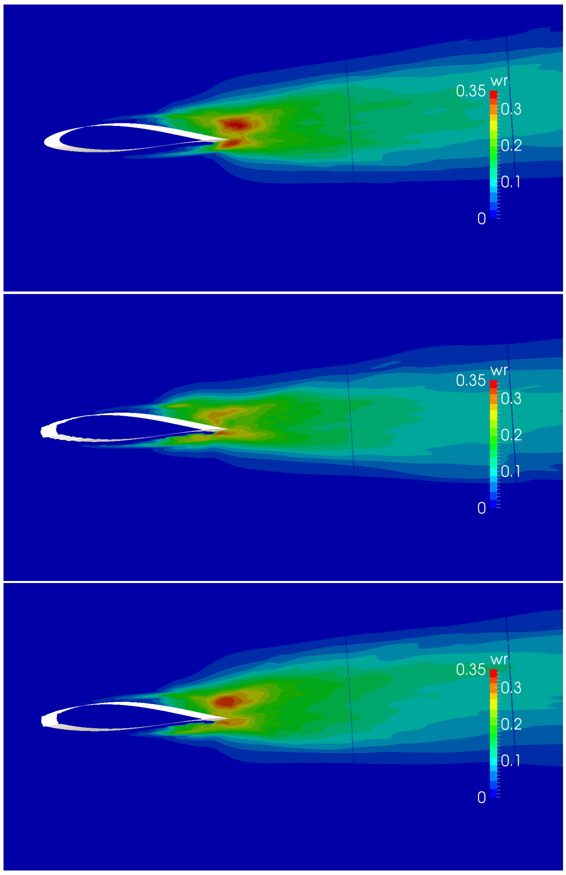

Figure 4. RMS of the streamwise velocity component: Base case (top), Ice1 (middle), Ice2 (bottom)

the case with ice accretion as well, however, these structures are more wrinkled than in the case of the clean airfoil, due to upstream disturbances. Thus, the reduction of the velocity fluctuations in the trailing edge region is due to the faster breakup of the shedded vortices as a result of the amplified perturbations generated by the accreted ice. In case Ice2 the ice layer being smoother, these perturbations are weaker and, as a consequence, their effect on the trailing edge vortices is also smaller and result in larger fluctuation levels than in the case with more corrugated ice layer.

4.2. Acoustic sources

Since not the magnitude, but the variation of the acoustic sources is more important for the generation of noise, the rms of the acoustic sources are plotted in Figure 6 for the three studied cases. In all cases the dominant noise generation region is downstream the trailing edge, in the separation region. Comparing the case with the clean airfoil (top) with the ones with ice accretion, no significant effect is seen on the extent of the dominant source region. The most noticeable influence is the increase of the source fluctuations on the pressure side, close to the trailing edge. This is the region where small vortices are generated by the upstream ice layer (see the bottom picture in

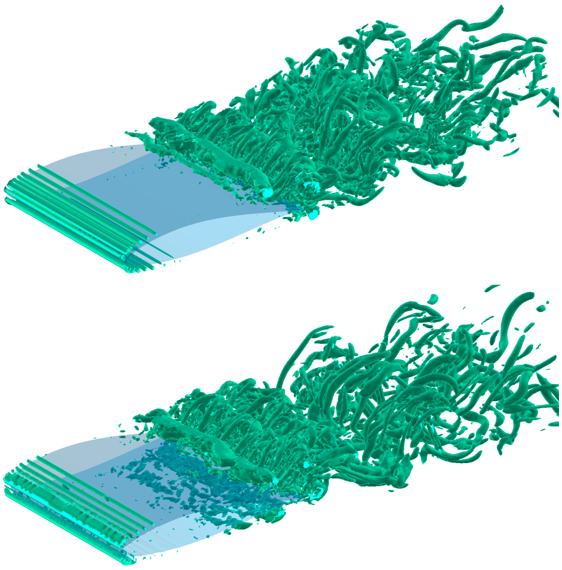

Figure 5. Instantaneous snapshots of the vortical structures: Base case (top), Ice1 (middle)

Figure 5). This increase in noise source magnitude is stronger in case Ice1, compared to case Ice2.

4.3. Acoustic field

4.3.1. Grid sensitivity

To assess the influence of grid resolution, the sound generated by the clean airfoil has been simulated using four different meshes, with nondimensional cell sizes 2.0e-2, 2.5e-2, 3.33e-2 and 5.0e-2, the number of cells used for discretization ranging from 1.6 to 25 million cells.

Figure 7 shows the spectra of the acoustic pressure fluctuations in three monitoring points. To reduce the congestion of the plots, the coarsest case has been omitted. At the monitoring point located immediately upstream the airfoil, P1 (top), all three spectra are generally overimposed each other, discrepancies begin to be visible at Strouhal numbers larger than ca. 50. In this region there are no significant acoustic sources, the acoustic pressure fluctuations are propagating from the airfoil region. The second monitoring point presented, P2 (middle), is located immediately downstream the airfoil. The three spectra match very well, with slightly larger peaks for the coarsest case at two frequencies (St approximately 6 and 20). In this region the imposed acoustic sources dominate and significantly larger levels are observed than at point P1. The last monitoring point presented in Figure 7 is located far from the airfoil (bottom, P7). At this position the spectra are overimposed until ca St=50, for larger frequencies rather significant discrepancies are visible. The low-frequency end of the spectra is smooth due to the lack of the imposed sources coming from the flow field. As a conclusion, the predicted spectra are reliable until a highest frequency of ca, St=50. This limitation is deemed acceptable, since lower frequencies propagate to larger distances in the nature and are more important to be predicted accurately.

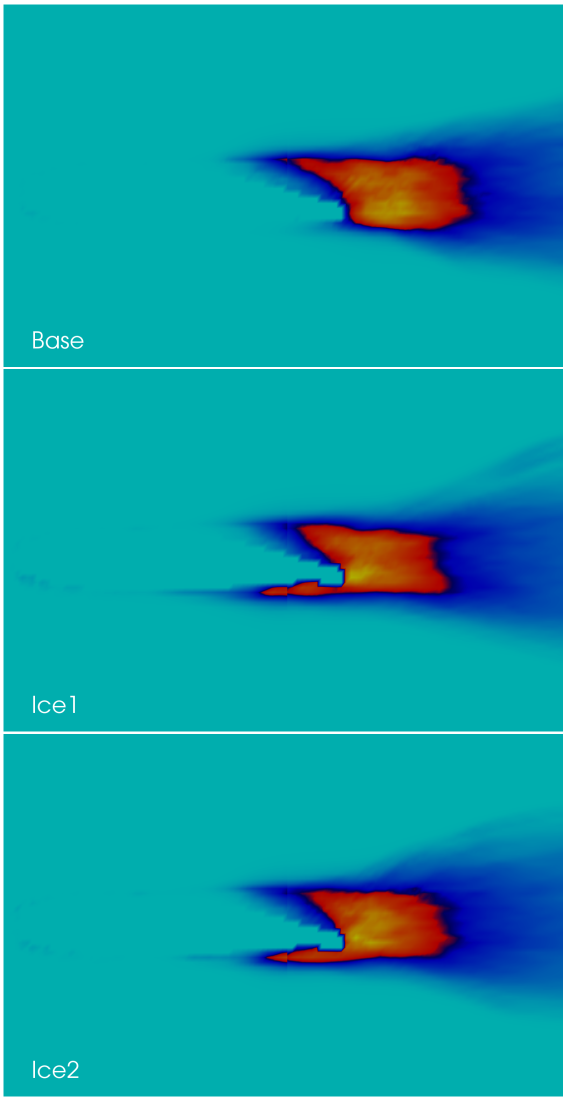

Figure 6. RMS of the quadrupole acoustic sources: Base case (top), Ice1 (middle) and Ice2 (bottom)

4.3.2. Acoustic pressure field

To visualise the directivity of the radiated acoustic noise, the base 10 logarithm of the rms acoustic pressure is shown in Figure 8. This quantity is directly proportional to the emitted sound pressure levels. Although the isocontours are similar for the three cases, minor differences can be observed. The strongest radiated noise is observed for the base case, whereas the weakest noise is seen for the case with smoothed ice layer (Ice2). Considering that the noise sources occupy slightly larger volume (on the pressure side) in case Ice2 compared to the base case, the lower emitted noise levels are explicable by the fact that not only the magnitude of the acoustic sources is important but their time evolutions as well. Further-

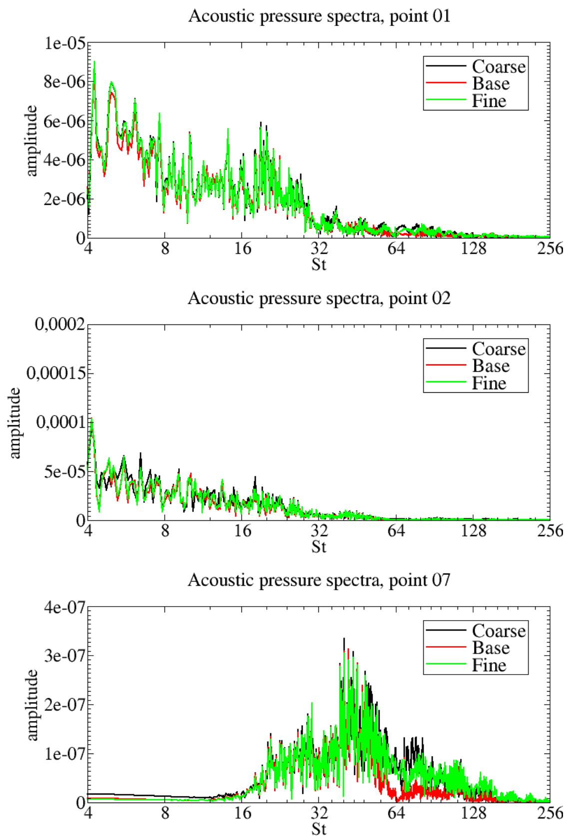

Figure 7. Spectra of the acoustic pressure fluctuations for three meshes, from top to bottom Points 1, 2 and 7 (see Figure 3 for the position of the monitoring points).

more, the amplitude of the noise sources in the vortex shedding region is slightly lower in case Ice2. In case Ice1 the emitted noise levels are intermediate to those in cases Base and Ice2. In this case the sources are strongest on the pressure side of the airfoil, however, the large scale vortical structures in the trailing edge region are broken down by the upstream disturbances faster than in the case of a clean airfoil.

The spectra of the radiated noise is shown for three monitoring points in Figure 9 (see Figure 3 for the positions of the monitoring points). At the monitoring point located close to the trailing edge (Point 2, top picture) the acoustic sources dominate and large amplitudes are seen in the lower frequency range. However, not all of these frequencies are actually propagated as sound, as it can be clearly seen in the middle picture, showing the spectra at a monitoring point located further downstream in the wake of the airfoil (Point 6). At this point one can observe that the peak at approximately $St = 20$ from the base case is damped in both cases with ice accretion, whereas a slight increase at $St = 42$ is seen for case Ice1. The third monitoring point, P8, shown in Fig. 9 is located in front of the airfoil on the pressure side. At this location a strong amplification of the

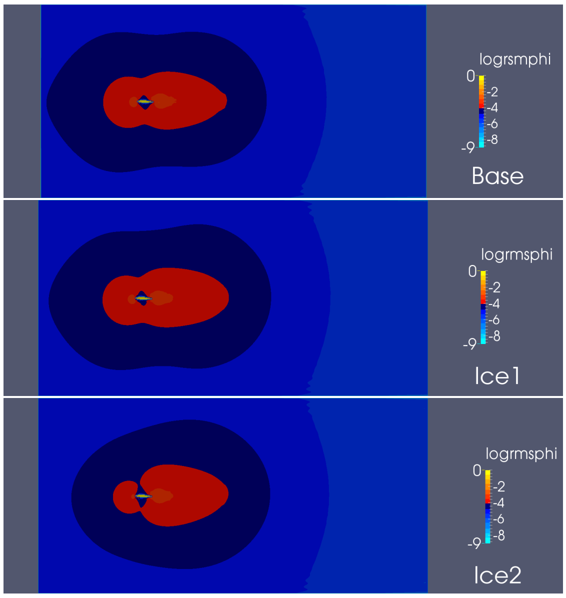

Figure 8. Isolevels of the logarithm of the RMS pressure fluctuations: Base case (top), Ice1 (middle) and Ice2 (bottom).

$St = 22$ amplitude is observed for the case with corrugated ice layer, probably due to the stronger acoustic sources on the pressure side of the airfoil.

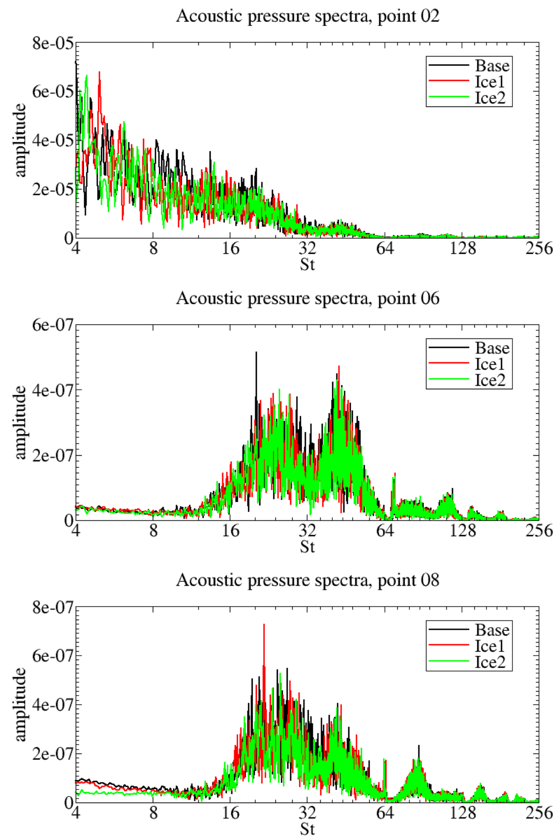

Figure 9. Spectra of the acoustic pressure fluctuations

For an easier comparison of the emitted noise levels Figure 10 shows filtered spectra at the same monitoring points. The filtering is achieved by applying running averaging based on 40 consecutive points. One can observe a clear reduction of noise levels around $St = 10$ and $St = 20$ in the vicinity of the trailing edge for the cases with accreted ice (top plot). At the point located further downstream (middle plot), the noise levels are damped by the ice layer between $St = 19$ and $St = 22$, whereas for $St = 22-25$ are slightly amplified. For $St = 26-41$ the levels in case Ice2 are significantly lower than in the base case, the levels in case Ice1 being damped only for $St > 29$. At the monitoring point located upstream reduced noise levels are observed between $St = 20-40$, the case with smooth ice layer showing lower values.

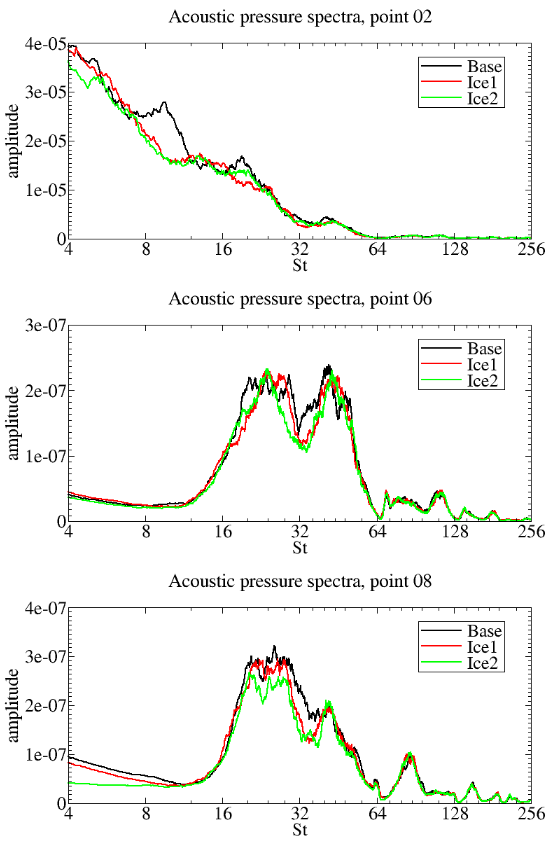

Figure 10. Filtered spectra of the acoustic pressure fluctuations

5. CONCLUSION

The noise emitted by airfoil sections have been computed using a hybrid approach. The flow solver is based on LES to account for turbulence and the immersed boundary method to describe complex geometries on the cartesian grid. The flow solver provides the acoustic sources used in the second stage of the computations where an inhomogeneous wave equation is solved to predict the noise propagation.

Three cases have been considered, one with a clean airfoil and two with airfoils subject to ice accretion. In these later cases the amount of accreted ice was the same but the smoothness of the accreted ice surface differed.

The computations revealed that in this specific case the noise levels decreased when ice accreted on the airfoils, the reduction of noise levels being stronger for the case with smoother ice surface. This reduction is attributed to the fact that in the base case separation was observed in the trailing edge region and the accreted ice layer generated perturbations which lead to a faster break-up of the vortices shed in the trailing edge region, thereby resulting in lower emitted noise levels.

The analysis of the radiated noise spectra indicates that indeed certain peaks are strongly damped by the presence of ice; nevertheless, there are positions where the opposite phenomenon occurs. The damping of the lower frequency amplitudes in the presence of ice (as long as no significant contribution is generated in the high frequency part) is beneficial, since the low frequency components propagate to longer distances in nature. One should emphasise however, that these results are not general, in cases where no shedding noise is observed for the clean airfoils the emitted noise with ice accretion is expected to be stronger.

ACKNOWLEDGEMENTS

This work has been supported by the Swedish Energy Agency within the framework of the Cold Climate project *Wind Turbines in Cold Climates: Fluid Mechanics, Ice Accretion and Terrain Effects*. The authors would like to acknowledge as well the computational resources provided within the SNIC framework by the Center for Scientific and Technical Computing at Lund University, LUNARC.

REFERENCES

[1] Laakso, T., Baring-Gould, I., Durstewitz, M., Horbaty, R., Lacroix, A., Peltola, E., Ronsten, G., Tallhaug, L., and Wallenius, T., 2010, "State-of-the-art of wind energy in cold climates", URL `http://www.vtt.fi/publications/index.jsp`.

[2] Pedersen, E., 2003, "Noise annoyance from wind turbines - a review", *Naturvårdsverket*, Vol. Report 5308.

[3] Pedersen, E., 2007, "Human response to wind turbine noise. Perception, annoyance and moderating factors", Ph.D. thesis, The Sahlgrenska Academy, Göteborg University, Göteborg, Sweden.

[4] Fujii, S., Takeda, K., and Nishiwaki, H., 1984, "A note on tower wake/blade interaction noise of a wind turbine", *J Sound and Vibration*, Vol. 97 (2), pp. 333–336.

[5] Björkman, M., 2004, "Long time measurements of noise from wind turbines", *J Sound and Vibration*, Vol. 277, pp. 567–572.

[6] Oerlemans, S., Sijtsma, A. P., and Lopez, B. M., 2007, "Location and quantification of noise sources on a wind turbine", *J Sound and Vibration*, Vol. 299, pp. 869–883.

[7] Hand, M., Simms, D., Fingersh, L., Jager, D., Cotrell, J., Schreck, S., and Larwood, S., 2001, "Unsteady Aerodynamics Experiment Phase VI: Wind Tunnel Test Configurations and Available Data Campaigns", *Tech. Rep. NREL/TP-500-29955*, National Renewable Energy Laboratory.

[8] Schreck, S., and Robinson, M., 2004, "Tip Speed Ratio Influences on Rotationally Augmented Boundary Layer Topology and Aerodynamic Force Generation", *Journal of Solar Energy Engineering*, Vol. 126, pp. 1025–1033.

[9] Johansen, J., Sørensen, N. N., Michelsen, J. A., and Schreck, S., 2002, "Detached-Eddy Simulation of Flow Around the NREL Phase VI Blade", *Wind Energy*, Vol. 5, pp. 185–197.

[10] Schmitz, S., and Chattot, J.-J., 2006, "Characterization of Three- Dimensional Effects for the Rotating and Parked NREL Phase VI Wind Turbine", *Journal of Solar Energy Engineering*, Vol. 128, pp. 445–454.

[11] Hansen, M., Sørensen, J., Voutsinas, S., Sørensen, N., and Madsen, H., 2007, "State of the art in wind turbine aerodynamics and aeroelasticity", *Progr Aerospace Sciences*, Vol. 42, pp. 285–330.

[12] Glegg, S., Baxter, S., and Glendinning, A., 1987, "The prediction of broadband noise from wind turbines", *J Sound and Vibration*, Vol. 118 (2), pp. 217–239.

[13] Page, G., McGuirk, J., Hossain, M., Self, R., and Bassetti, A., 2003, "A CFD coupled acoustic approach for coaxial jet noise", *AIAA paper*, Vol. AIAA 2003-3286.

[14] Bailly, C., Candel, S., and Lafon, P., 1996, "Prediction of supersonic jet noise from a statistical acoustic model and a compressible turbulence closure", *J Sound and Vibration*, Vol. 194 (2), pp. 219–242.

[15] Ewert, R., and Schröder, W., 2004, "On the simulation of trailing edge noise with a hybrid LES/APE method", *J Sound and Vibration*, Vol. 270, pp. 509–524.

[16] Hochart, C., Fortin, G., Perron, J., and Ilinca, A., 2008, "Wind turbine performance under icing conditions", *Wind Energy*, Vol. 11 (4), pp. 319–333, URL `http://doi.wiley.com/10.1002/we.258`.

[17] Salewski, M., Duwig, C., Milosavljevic, V., and Fuchs, L., 2007, "LES of Spray Dispersion and Mixing in a Swirl Stabilized GT Combustor", *AIAA paper*, Vol. AIAA-2007-0924.

[18] Salewski, M., Duwig, C., Milosavljevic, V., and Fuchs, L., 2007, "Large Eddy Simulation of Spray Combustion in a Swirl-Stabilized Gas Turbine Burner", *AIAA paper*, Vol. AIAA-2007-5634.

[19] Olsson, M., and Fuchs, L., 1996, "Large Eddy Simulation of the Proximal Region of a Spatially Developing Circular Jet", *Phys Fluids*, Vol. 8 (8), pp. 2125–2137.

[20] Gullbrand, J., Bai, X.-S., and Fuchs, L., 2001, "High-order cartesian grid method for calculation of incompressible turbulent flows", *Int J Numerical Methods in Fluids*, Vol. 36, pp. 687–709.

[21] Szasz, R., and Fuchs, L., 2013, "The effect of icing on airfoil wake structures", *4th International Conference on Jets, Wakes and Separated Flows, ICJWSF2013*, ICJWSF?1072.

Conference on Modelling Fluid Flow (CMFF'15)
The 16th International Conference on Fluid Flow Technologies
Budapest, Hungary, September 1-4, 2015

NUMERICAL SOLUTION OF FLUIDS FLOW THROUGH CHANNEL WITH T-JUNCTION

Radka KESLEROVÁ[1], Karel KOZEL[2], David TRDLIČKA[2]

[1] Corresponding Author. Department of Technical Mathematics, Czech Technical University in Prague. Karlovo nám. 13, 121 35 Prague, Czech Republic. E-mail: keslerov@marian.fsik.cvut.cz
[2] Department of Technical Mathematics, Czech Technical University in Prague. E-mail: Karel.Kozel@fs.cvut.cz, David.Trdlicka@fs.cvut.cz

ABSTRACT

This work deals with the numerical simulation of steady flows of laminar incompressible viscous and viscoelastic fluids through the channel with T-junction. The fundamental system of equations is the system of generalized Navier-Stokes equations for incompressible fluids. This system is based on the system of balance laws of mass and momentum for incompressible fluids. For the different choice of fluids model the different model of the stress tensor is used, Newtonian and Oldroyd-B models.

Numerical tests are performed on three dimensional geometry, a branched channel with one entrance and two outlet parts. Numerical solution of the described models is based on cell-centered finite volume method using explicit Runge-Kutta time integration.

Keywords: finite volume method, generalized Newtonian fluids flow, generalized Oldroyd-B fluids flow, multistage Runge-Kutta method, system of Navier-Stokes equation

NOMENCLATURE

$\underline{\underline{D}}$	[-]	symmetric part of velocity gradient
$\underline{F}, \underline{G}, \underline{H}$	[-]	numerical fluxes
L_0	$[m]$	reference radius
P	[-]	kinematic pressure
$\underline{\underline{R}}, \underline{\underline{R_\beta}}$	[-]	diagonal matrices
S	[-]	source term
U_0	$[m.s^{-1}]$	reference velocity
$\underline{\underline{T}}$	[-]	stress tensor
$\underline{\underline{T_e}}$	[-]	Newtonian part of stress tensor
$\underline{\underline{T_s}}$	[-]	elastic part of stress tensor
$\underline{\underline{W}}$	[-]	antisymmetric part of velocity gradient
$\underline{W}$	[-]	vector of conservative variables
a, b	[-]	parameters for cross model
p	$[Pa]$	pressure
t	$[s]$	time
$t_1, \ldots, t_6$	[-]	components of the stress tensor
u, v, w	$[m.s^{-1}]$	velocity components
$\underline{u}$	$[m.s^{-1}]$	velocity vector
x, y, z	$[m]$	Cartesian coordinates
β	$[m.s^{-1}]$	artificial compressibility coefficient
λ	$[s]$	parameter for cross model
λ_1	$[s]$	relaxation time
λ_2	$[s]$	retardation time
μ	$[Pa.s]$	dynamic viscosity
μ_e	$[Pa.s]$	viscoelastic dynamic viscosity
μ_s	$[Pa.s]$	Newtonian dynamic viscosity
μ_0	$[Pa.s]$	dynamic viscosity for cross-model
ρ	$[kg.m^{-3}]$	density

Subscripts and Superscripts

0	reference value
c	convective part
v	viscous part
δ	symbol for upper covective derivative

1. INTRODUCTION

Branching of pipes occurs in many technical or biological applications. In biomedical applications, it is the complex branching system of blood vessels in human body. The blood can be characterized by shear-thinning viscoelastic property and the blood flow can be described by generalized Oldroyd-B model, see [1] and [2]. In prewious work we studied the numerical simulation of generalized Newtonian and Oldroyd-B fluids flow in 2D branching channel, [3], [4], [5]. In this article this problem will be extended to the study of generalized Newtonian and Oldroyd-B fluids flow in 3D branching channel with T-junction.

2. MATHEMATICAL MODEL

The governing system of equations is the system of generalized Navier-Stokes equations, see [6]. This system consists of the continuity equation

$$\text{div}\ \underline{u} = 0 \tag{1}$$

and the momentum equation

$$\rho\frac{\partial \underline{u}}{\partial t} + \rho(\underline{u}.\nabla)\underline{u} = -\nabla P + \text{div}\ \underline{\underline{T}}, \tag{2}$$

where P is the pressure, ρ is the constant density, $\underline{u}$ is the velocity vector. The symbol $\underline{\underline{T}}$ represents the general stress tensor

$$\underline{\underline{T}} = \begin{pmatrix} t_1 & t_2 & t_3 \\ t_2 & t_4 & t_5 \\ t_3 & t_5 & t_6 \end{pmatrix}. \tag{3}$$

In this work three different definitions of the stress tensor are considered. For the viscous fluids the Newtonian mathematical model is used, denote $\underline{\underline{T}} = \underline{\underline{T_s}}$, (see e.g. [2], [7])

$$\underline{\underline{T_s}} = 2\mu_s\underline{\underline{D}}, \tag{4}$$

where μ_s is the dynamic Newtonian viscosity and tensor $\underline{\underline{D}}$ is the symmetric part of the velocity gradient, $\underline{\underline{D}} = \frac{1}{2}(\nabla\underline{u} + \nabla\underline{u}^T)$.

In the case of viscoelastic fluids, the simplest viscoelastic model (Maxwell model) can be used, denote $\underline{\underline{T}} = \underline{\underline{T_e}}$,

$$\underline{\underline{T_e}} + \lambda_1\frac{\delta\underline{\underline{T_e}}}{\delta t} = 2\mu_e\underline{\underline{D}}, \tag{5}$$

where λ_1 is the relaxation time and μ_e is the viscoelastic dynamic viscosity. The symbol $\frac{\delta}{\delta t}$ represents the upper convected derivative, see eq.(9).

By combination of these two models (Newtonian and Maxwell) the behaviour of mixture of viscous and viscoelastic fluids can be described. This model is called Oldroyd-B and it has the form

$$\underline{\underline{T}} + \lambda_1\frac{\delta\underline{\underline{T}}}{\delta t} = 2\mu\left(\underline{\underline{D}} + \lambda_2\frac{\delta\underline{\underline{D}}}{\delta t}\right), \tag{6}$$

where symbols λ_1 and λ_2 are the relaxation and the retardation time (with dimension of time).

The stress tensor $\underline{\underline{T}}$ in the system of equations (1) and (2) can be decomposed to the viscous $\underline{\underline{T_s}}$ and viscoelastic part $\underline{\underline{T_e}}$. Both tensors are defined by corresponding rheological models, Newtonian (4) and Maxwell (5)

$$\underline{\underline{T_s}} = 2\mu_s\underline{\underline{D}}, \qquad \underline{\underline{T_e}} + \lambda_1\frac{\delta\underline{\underline{T_e}}}{\delta t} = 2\mu_e\underline{\underline{D}}, \tag{7}$$

where

$$\frac{\lambda_2}{\lambda_1} = \frac{\mu_s}{\mu_s + \mu_e}, \qquad \mu = \mu_s + \mu_e. \tag{8}$$

The upper convected derivative $\frac{\delta}{\delta t}$ used in the viscoelastic part of the stress tensor is defined by the relation, for more details see [2], [8],

$$\frac{\delta\underline{\underline{T_e}}}{\delta t} = \frac{\partial\underline{\underline{T_e}}}{\partial t} + (\underline{u}.\nabla)\underline{\underline{T_e}} - (\underline{\underline{W}}\,\underline{\underline{T_e}} - \underline{\underline{T_e}}\,\underline{\underline{W}}) - (\underline{\underline{D}}\,\underline{\underline{T_e}} + \underline{\underline{T_e}}\,\underline{\underline{D}}), \tag{9}$$

where $\underline{\underline{D}}$ is symmetric part and $\underline{\underline{W}}$ is antisymmetric part of the velocity gradient, $\underline{\underline{D}} = \frac{1}{2}(\nabla\underline{u} + \nabla\underline{u}^T)$, $\underline{\underline{W}} = \frac{1}{2}(\nabla\underline{u} - \nabla\underline{u}^T)$.

For the numerical modelling of the generalized Newtonian and Oldroyd-B fluids flow it is necessary to generalize the mathematical models. In this case the viscosity function is defined by cross model (for more details see [9], [10])

$$\mu(\dot\gamma) = \mu_s + \frac{\mu_0 - \mu_s}{(1 + (\lambda\dot\gamma)^b)^a}, \tag{10}$$

$$\dot\gamma = 2\sqrt{\frac{1}{2}\text{tr}\ \underline{\underline{D}}^2}, \tag{11}$$

with special parameters $\mu_0 = 1.6\cdot 10^{-1}Pa.s, \mu_s = 3.6\cdot 10^{-3}Pa.s, a = 1.23, b = 0.64, \lambda = 8.2s$. For Newtonian and Oldroyd-B flow, the viscosity is kept constant and equal to μ_s.

Let's summarize our system of equations. First, continuity equation and momentum equation

$$\text{div}\ \underline{u} = 0 \tag{12}$$

and the momentum equation

$$\rho\frac{\partial \underline{u}}{\partial t} + \rho(\underline{u}.\nabla)\underline{u} = -\nabla P + 2\mu(\dot\gamma)\text{div}\ \underline{\underline{D}} + \text{div}\ \underline{\underline{T_e}} \tag{13}$$

and the equation for the viscoelastic stress tensor $\underline{\underline{T_e}}$

$$\frac{\partial\underline{\underline{T_e}}}{\partial t} + (\underline{u}.\nabla)\underline{\underline{T_e}} = \frac{2\mu_e}{\lambda_1}\underline{\underline{D}} - \frac{1}{\lambda_1}\underline{\underline{T_e}} + \\ + (\underline{\underline{W}}\,\underline{\underline{T_e}} - \underline{\underline{T_e}}\,\underline{\underline{W}}) + (\underline{\underline{D}}\,\underline{\underline{T_e}} + \underline{\underline{T_e}}\,\underline{\underline{D}}). \tag{14}$$

For types of fluids with following parameters are tested in the considered domain

Newtonian	$\mu_s(\dot\gamma) = \mu_s$	$\underline{\underline{T_e}} \equiv 0$
generalized Newtonian	$\mu_s(\dot\gamma)$	$\underline{\underline{T_e}} \equiv 0$
Oldroyd-B	$\mu_s(\dot\gamma) = \mu_s$	$\underline{\underline{T_e}}$
generalized Oldroyd-B	$\mu_s(\dot\gamma)$	$\underline{\underline{T_e}}$

3. NUMERICAL SOLUTION

The mathematical models described above are solved numericaly the artificial compressibility approach combined with the finite-volume discretization. The artificial compressibility method [11], [3], [12] is used to obtain equation for pressure. It means that the continuity equation is completed by a pressure time derivative term $\frac{1}{\beta^2}\frac{\partial p}{\partial t}$, where β is positive parameter, making the inviscid part of the system of equations hyperbolic

$$\frac{1}{\beta^2}\frac{\partial p}{\partial t} + \mathrm{div}\ \underline{u} = 0, \quad (15)$$

the parameter β in this work is chosen equal to the maximum inlet velocity. This value ensures good convergence to steady state but is not large enough to make the transient solution accurate in time. Therefore it is suitable for steady flows only. The discretization is done by a cell-centered finite volume method with hexahedral finite volumes. The system including the modified continuity equation and the momentum equations can be written in conservative form

$$\underline{\underline{\tilde{R}_\beta}}\underline{W}_t + \underline{F}^c_x + \underline{G}^c_y + \underline{H}^c_z = \underline{F}^v_x + \underline{G}^v_y + \underline{H}^v_z + \underline{S}, \quad (16)$$

$$\underline{\underline{\tilde{R}_\beta}} = \mathrm{diag}(\frac{1}{\beta^2}, 1, \dots, 1),$$

where $\underline{W}$ is vector of unknowns, $\underline{W} = (p, u, v, w, t_{e1}, \dots, t_{e6})$, by superscripts c and v the inviscid and the viscous fluxes are denoted. The symbol $\underline{S}$ denotes the source term

$$\underline{W} = \begin{pmatrix} p \\ u \\ v \\ w \\ t_1 \\ \vdots \\ t_6 \end{pmatrix}, \quad \underline{F}^c = \begin{pmatrix} u \\ u^2+p \\ uv \\ uw \\ ut_{e1} \\ \vdots \\ ut_{e6} \end{pmatrix}, \quad (17)$$

$$\underline{G}^c = \begin{pmatrix} v \\ uv \\ v^2+p \\ vw \\ vt_{e1} \\ \vdots \\ vt_{e6} \end{pmatrix}, \quad \underline{H}^c = \begin{pmatrix} w \\ uw \\ vw \\ w^2+p \\ wt_{e1} \\ \vdots \\ wt_{e6} \end{pmatrix}, \quad (18)$$

$$\underline{F}^v = \begin{pmatrix} 0 \\ 2\mu(\dot\gamma)u_x \\ \mu(\dot\gamma)(u_y+v_x) \\ \mu(\dot\gamma)(u_z+w_x) \\ 0 \\ \vdots \\ 0 \end{pmatrix}, \underline{G}^v = \begin{pmatrix} 0 \\ \mu(\dot\gamma)(u_y+v_x) \\ 2\mu(\dot\gamma)v_y \\ \mu(\dot\gamma)(v_z+w_y) \\ 0 \\ \vdots \\ 0 \end{pmatrix}, \quad (19)$$

$$\underline{H}^v = \begin{pmatrix} 0 \\ \mu(\dot\gamma)(u_z+w_x) \\ \mu(\dot\gamma)(v_z+w_y) \\ 2\mu(\dot\gamma)w_z \\ 0 \\ \vdots \\ 0 \end{pmatrix}, \quad (20)$$

$$\underline{S} = \begin{pmatrix} 0 \\ (t_{e1x}+t_{e2y}+t_{e3z})/\rho \\ (t_{e2x}+t_{e4y}+t_{e5z})/\rho \\ (t_{e3x}+t_{e5y}+t_{e6z})/\rho \\ 2\frac{\mu_e}{\lambda_1}u_x - \frac{t_{e1}}{\lambda_1} + 2u_x t_{e1} + \\ +(u_y+v_x)t_{e2} + (u_z+w_x)t_{e3} \\ \frac{\mu_e}{\lambda_1}(u_y+v_x) - \frac{t_{e2}}{\lambda_1} + u_y t_{e4} + \\ +u_z t_{e5} + u_y t_{e1} + w_y t_{e3} + u_x t_{e2} + v_y t_{e2} \\ \frac{\mu_e}{\lambda_1}(u_z+w_x) - \frac{t_{e3}}{\lambda_1} + u_y t_{e5} \\ + + u_z t_{e6} + u_z t_{e1} + v_z t_{e2} + u_x t_{e3} + w_z t_{e3} \\ 2\frac{\mu_e}{\lambda_1}v_y - \frac{t_{e4}}{\lambda_1} + \\ +(u_y+v_x)t_{e2} + 2v_y t_{e4} + (v_z+w_y)t_{e5} \\ \frac{\mu_e}{\lambda_1}(v_z+w_y) - \frac{t_{e5}}{\lambda_1} + v_x t_{e3} + \\ +v_z t_{e6} + u_z t_{e2} + v_z t_{e4} + v_y t_{e5} + w_z t_{e5} \\ 2\frac{\mu_e}{\lambda_1}w_z - \frac{t_{e6}}{\lambda_1} + \\ +(u_z+w_x)t_{e3} + (v_z+w_y)t_{e5} + 2w_z t_{e6} \end{pmatrix}, \quad (21)$$

where symbols $t_1, \dots, t_6$ denote the coefficients of the symmetric stress tensor $\underline{\underline{T_e}}$.

Eq. (16) is discretized in space by the finite volume method and the arising system of ODEs is integrated in time by the explicit multistage Runge–Kutta scheme ([3], [4], [13], [14]).

The flow is modelled in a bounded computational domain where a boundary is divided into three mutually disjoint parts: a solid wall, an outlet and an inlet. At the inlet Dirichlet boundary condition for velocity vector and for the stress tensor is used and for the pressure homogeneous Neumann boundary condition is used. At the outlet parts the pressure value is prescribed and for the velocity vector and the stress tensor homogeneous Neumann boundary condition is used. The no-slip boundary condition for the velocity vector is used on the wall. For the pressure and stress tensor homogeneous Neumann boundary condition is considered.

4. NUMERICAL RESULTS

This section deals with the comparison of the numerical results of generalized Newtonian and generalized Oldroyd-B fluids flow. Numerical tests are performed in an idealized branched channel with the square cross-section. Fig. 1 shows the shape of the tested domain. The computational domain is discretized using a structured, wall fitted mesh with hexahedral cells. The domain is divided to 4 blocks with 153 000 cells.

As initial condition the following model parameters are used: $L_0 = 0.0031\ m$, $\mu_e = 0.0004 Pa.s$, $\mu_s = 0.0036 Pa.s$, $\lambda_1 = 0.06 s$, $U_0 = 0.0615\ m.s^{-1}$, $\rho = 1050 kg.m^{-3}$.

At the inlet the Dirichlet boundary conditions for velocity are used, the parabolic profile with maximum velocity value U_0. At the outlet the constant pressure values are prescribed (0.0005 Pa (main channel) and 0.00025 Pa (branch)). In Fig. 2 the axial velocity profile for tested types of fluids close

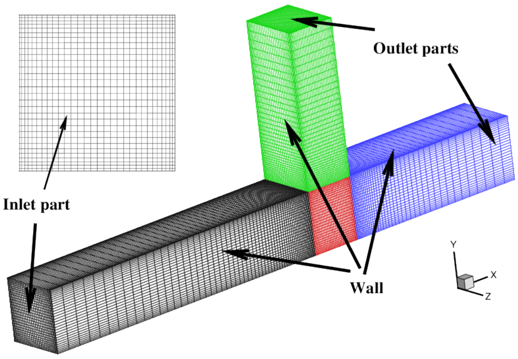

Figure 1. Structure of the tested domain.

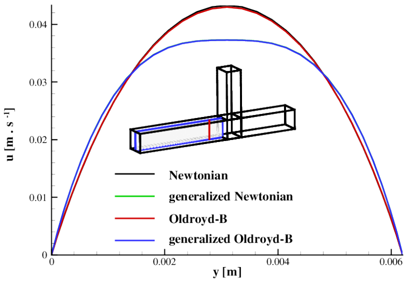

Figure 2. Axial velocity profile of tested fluids.

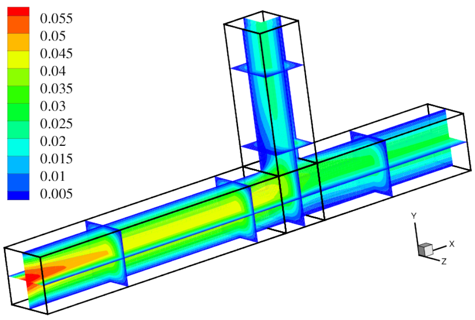

Figure 3. Velocity isolines of steady flows for Newtonian fluids.

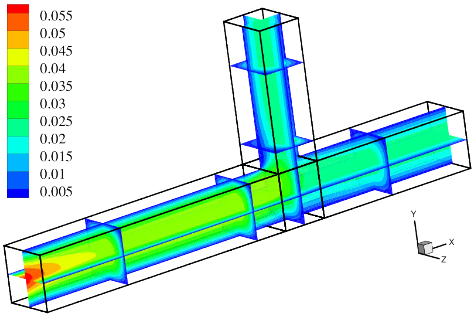

Figure 4. Velocity isolines of steady flows for generalized Newtonian fluids.

to the branching is shown. The lines for Newtonian and Oldroyd-B fluids are similar to the parabolic line, as was assumed. From this velocity profile is clear that the shear thinning fluids attain lower maximum velocity in the central part of the channel (close to the axis of symmetry) which is compensated by the increase of local velocity in the boundary layer close to the wall.

In Figs. 3, 4, 5 and 6 the velocity isolines and the cuts through the main channel and the small branch are shown.

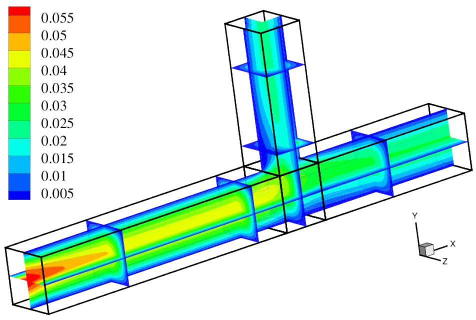

Figure 5. Velocity isolines of steady flows for Oldroyd-B fluids.

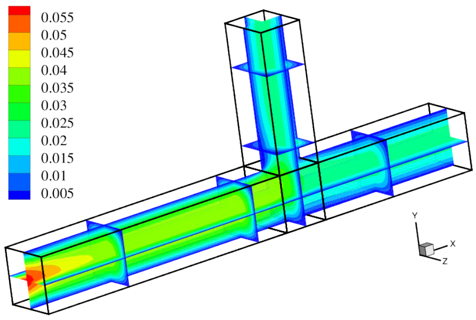

Figure 6. Velocity isolines of steady flows for generalized Oldroyd-B fluids.

The axial velocity isolines in the center-plane area for Newtonian and generalized Newtonian fluids are shown in the Figs. 7 and 8. For Oldroyd-B and generalized Oldroyd-B fluids these are shown in the Figs. 9 and 10.

It can be observed from these that the size of separation region for generalized Newtonian and generalized Oldroyd-B fluids is smaller than for Newtonian and Oldroyd-B fluids, see in detail Figs. 11 - 14.

5. CONCLUSION

In this paper a finite volume solver for incompressible laminar viscous and viscoelastic flows in the branching channel with T-junction and circle cross section was described. Newtonian and Oldroyd-B fluids models were generalized by the

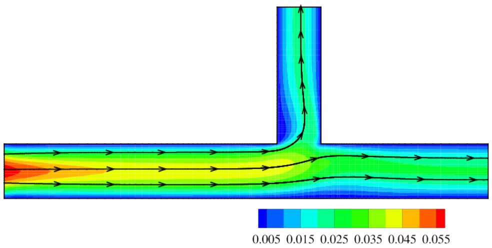

Figure 7. Axial velocity isolines in the center-plane area for Newtonian fluids.

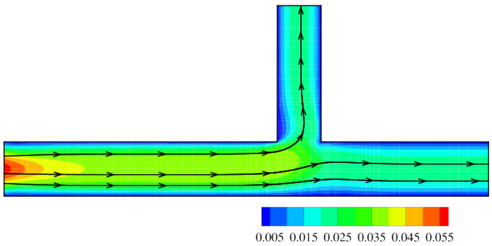

Figure 8. Axial velocity isolines in the center-plane area for generalized Newtonian fluids.

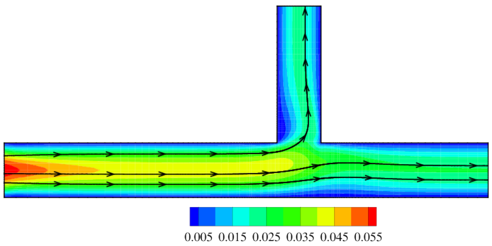

Figure 9. Axial velocity isolines in the center-plane area for Oldroyd-B fluids.

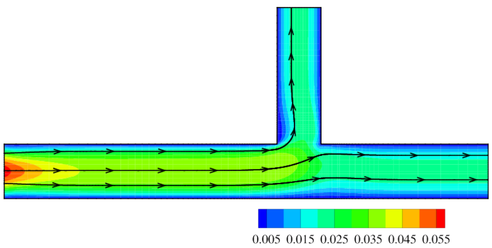

Figure 10. Axial velocity isolines in the center-plane area for generalized Oldroyd-B fluids.

cross model for numerical solution of generalized Newtonian and Oldroyd-B fluids flow. The explicit Runge-Kutta method was considered for time integrating. The numerical results obtained by this method were presented.

Numerical results were compared. It has been shown that in this type of the channel the numerical results for Newtonian and Oldroyd-B fluids are similar. From the presented velocity profile is clear that

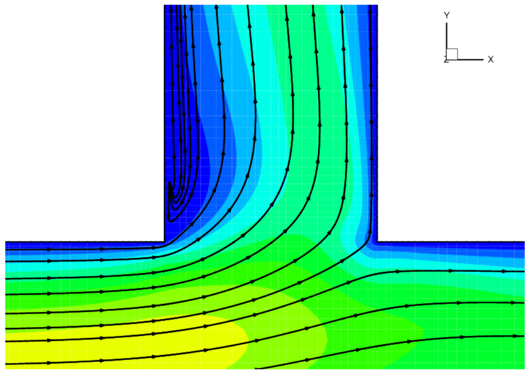

Figure 11. Axial velocity isolines in the center-plane area in the separation region for Newtonian fluids.

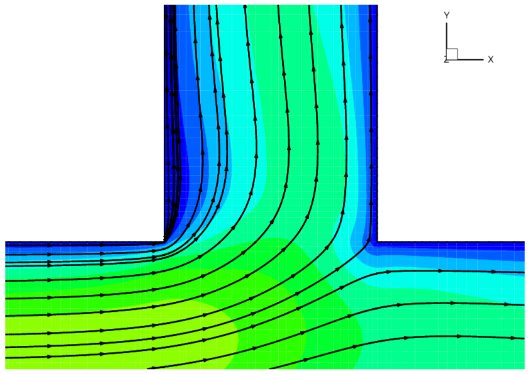

Figure 12. Axial velocity isolines in the center-plane area in the separation region for generalized Newtonian fluids.

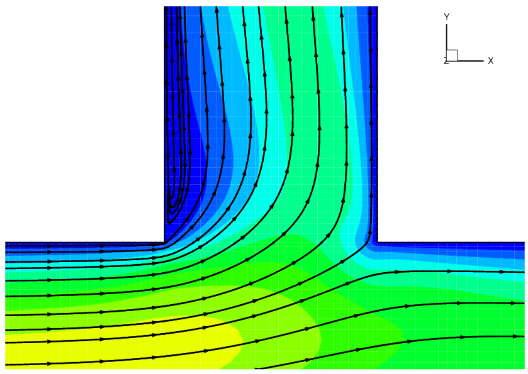

Figure 13. Axial velocity isolines in the center-plane area in the separation region for Oldroyd-B fluids.

the shear thinning fluids (generalized Newtonian and Oldroyd-B fluids) attain lower maximum velocity in the central part of the channel (close to the axis of symmetry) which is compensated by the increase of local velocity in the boundary layer close to the wall.

The future work will be occupy with the numerical simulation of viscous and viscoelastic fluids flow in the branching channel with circle cross-section

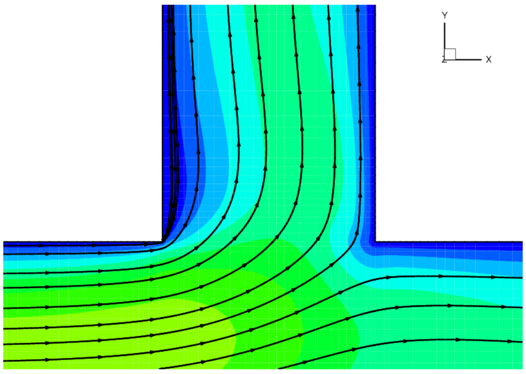

Figure 14. Axial velocity isolines in the center-plane area in the separation region for generalized Oldroyd-B fluids.

and with the comparison numerical results of both type of channels.

ACKNOWLEDGEMENTS

This work was supported by grant SGS13/174/OHK2/3T/12 of the Czech Science Foundation.

REFERENCES

[1] Anand, M., Kwack, J., and Masud, A., 2013, “A new generalized Oldroyd-B model for blood flow in complex geometries”, *Journal of Engineering Science*, Vol. 72, pp. 78–88.

[2] Bodnar, T., Sequeira, A., and Prosi, M., 2010, “On the shear-thinning and viscoelastic effects of blood flow under various flow rates”, *Applied Mathematics and Computation*, Vol. 217, pp. 5055–5067.

[3] Keslerová, R., and Kozel, K., 2010, “Numerical modelling of incompressible flows for Newtonian and non-Newtonian fluids”, *Mathematics and Computers in Simulation*, Vol. 80, pp. 1783–1794.

[4] Keslerová, R., and Kozel, K., 2012, “Numerical simulation of generalized Newtonian and Oldroyd-B fluids flow”, *Proceedings of the 16th Seminar on Programs and Algorithms of Numerical Mathematics*.

[5] Keslerová, R., and Kozel, K., 2011, “Numerical Simulation of Viscous and Viscoelastic Fluids Flow by Finite Volume Method”, *Proceedings of the 6th International Symposium on Finite Volumes for Complex Applications*.

[6] Beneš, L., Louda, P., Kozel, K., Keslerová, R., and Štigler, J., 2013, “Numerical simulations of flow through channels with T-junction”, *Applied Mathematics and Computation*, Vol. 219, pp. 7225–7235.

[7] Bodnar, T., and Sequeira, A., 2010, “Numerical study of the significance of the non-Newtonian nature of blood in steady flow through stenosed vessel”, *Advances in Mathematical Fluid Mechanics*, pp. 83–104.

[8] Bodnar, T., Sequeira, A., and Pirkl, L., 2009, “Numerical simulations of blood flow in a stenosed vessel under different flow rates using a generalized Oldroyd-B model”, *Numerical Analysis and Applied Mathematics*, Vol. 2, p. 645âĂŞ648.

[9] Rabby, M., Razzak, A., and Molla, M., 2013, “Pulsatile Non-Newtonian Blood Flow through a Model of Arterial Stenosis”, *Procedia Engineering*, Vol. 56, pp. 225–231.

[10] Vimmr, J., and Jonášová, A., 2010, “Non-Newtonian effects of blood flow in complete coronary and femoral bypasses”, *Mathematics and Computers in Simulation*, Vol. 80, pp. 1324–1336.

[11] Chorin, A., 1967, “A numerical method for solving incompressible viscous flow problem”, *Journal of Computational Physics*, Vol. 135, pp. 118–125.

[12] Louda, P., Příhoda, J., Kozel, K., and Sváček, P., 2013, “Numerical simulation of flows over 2D and 3D backward-facing inclined steps”, *International Journal of Heat and Fluid Flow*, Vol. 43, pp. 268–276.

[13] LeVeque, R., 2004, *Finite-Volume Methods for Hyperbolic Problems*, Cambridge University Press.

[14] Jameson, A., Schmidt, W., and Turkel, E., 1981, “Numerical solution of the Euler equations by finite volume methods using Runge-Kutta time-stepping schemes”, *AIAA 14th Fluid and Plasma Dynamic Conference California*.

Conference on Modelling Fluid Flow (CMFF'15)
The 16th International Conference on Fluid Flow Technologies
Budapest, Hungary, September 1-4, 2015

EXPERIMENTAL AND NUMERICAL INVESTIGATION ON FLUID-STRUCTURE-INTERACTION OF AUTO-ADAPTIVE FLEXIBLE FOILS

Matthias VOSS[1,2], Paul Uwe THAMSEN[1], Hans-Dieter KLEINSCHRODT[2], Michael DIENST[2]

[1] Corresponding Author. Department of Fluid System Dynamics. Berlin University of Technology. Straße des 17. Juni 135, 10623 Berlin, Germany. Tel.: +49 314 27832, Fax: +49 314 21472, E-mail: info@fsd.tu-berlin.de
[2] Department of Department VIII Mechanical Engineering, Process and Environmental Technology. Beuth University of Applied Sciences Berlin. E-mail: kleinsch@beuth-hochschule.de

ABSTRACT

The aim of the presented research is the examination of nature-inspired flexible and internally structured foils by conducting practical and numerical experiments. By imitating natural methods of propulsion and by studying mechanical systems from fishes (fin rays), the so called fin-ray-effect is used to create an auto-adaptive foil.

Depending on the inner structure for a given symmetrical profile (NACA0016), the resulting outline of the flow adaptive profile is detected and compared by means of numerical simulation covering the strongly coupled fluid-structure-interaction. By varying the mean stream velocity and angle of attack, several configurations are examined. The numerical simulations are capable of reproducing the main effects of the fin-ray system and reveal some general rules of concept when equipping flexible sheets in a foil-like manner with structural elements to create a suction-/pressure-side interaction. Future work needs to focus on the mechanical system used to approximate the prototype, as well as the three-dimensional behaviour of the foil.

Keywords: adaptive flexible foils, CFD, FEM, FSI, fin ray

NOMENCLATURE

U [m] deformation
E [Pa] modulus of elasticity
F [N] force
OpenCV [-] free library for "Computer Vision"

c [-] chord length
$c*$ [-] flexible length
d [m] diameter of pipe DN400
$\underline{v}$ [m/s] absolute velocity vector
y^+ [-] dimensionless wall distance
ν [-] Poisson's ratio
ρ [kg/m^3] density
ω [-] relaxation factor

Subscripts and Superscripts

I-IV marker positions
inlet at the inlet of the test section
PS, SS pressure side, suction side
f fluid domain
s solid domain
x, y, z axial (along the water tunnel axis), transversal, spanwise (coordinate)
^ chordwise averaged
− temporal mean
* flexible section

1 INTRODUCTION

Living nature inspires scientists, engineers and developers to create new types of products and processes. There are two separate bionic approaches either aiming at a functional design by reproducing certain aspects of the system, which are being analysed starting with an application (e.g. shape, material, structure, drag, efficiency) – or at an aesthetic design-proposal (e.g. shapes that appear smart, act in analogy to man crafted solutions or create certain reactions to a customer) [1], [2]. We will focus on the first principle. The task of bionics is therefore to transfer the biological methods into engineering designs and to develop new technologies.

Since controlling the flow around a body or locomotion against resistance depends on very complex interactions (e.g. turbulence, friction, temperature or overall size) and is one of the main tasks in e.g. aviation, pumping, fluidic transportation - reducing the amount of energy needed for propulsion with the best system available creates the need to develop advanced techniques to meet every aspect of the task – this is where the wide variety of locomotory solutions of ray-finned fishes provide the best answers nature can give and therefore it has been the subject of recent research. Especially ray-finned fishes are of interest when searching for solutions, since they represent more than half of all vertebrates [3]. Actinopterygii or „ray-finned“ fishes are a very successful class of “bony fish” (Osteichthyes) – the body shapes, materials and skeleton structures have been under evolutionary pressure and developed advanced techniques for swimming, feeding and manoeuvring as a result of nearly 500 million years of evolutionary changes [4]. Most of the fins consist out of segmented bony elements (rays) connected by a collagenous and flexible membrane, which create a balanced system of stiffness and flexibility in order to facilitate the fish to establish a fluid-structure-interaction in its aquatic environment. The mechanical system equips the fish to shape the curvature of every single ray resulting in a complex shape of the fins [5].

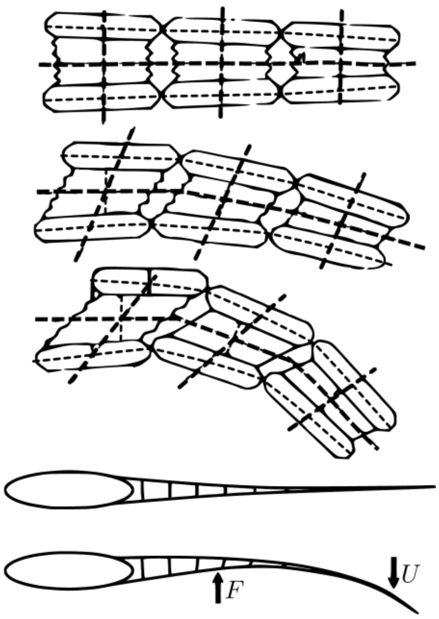

Figure 1. A mechanical system for the link chain in fin rays as proposed by Videler and Geerlink, original illustration from [6] **(top), non-orthodox behaviour with tip deformation U against direction of impact F (bottom).**

When analysing the mechanical system and keeping in mind to develop a flexible foil one can conclude: a) at least one fin ray is needed, b) every fin ray is made out of the same components and c) ideally the ray is under tension. The latter is due to the fact that it is easier to shape a body to withstand tension rather than compression since compression can always lead to buckling which needs a lot more material/energy to be damped and will therefore be avoided.

2 EXPERIMENTAL SETUP

2.1 Test Section

The experiments were carried out at the “Collaborative Test Centre 1029” at the Institute of Fluid Dynamics and Technical Acoustics (ISTA). The rectangular testing chamber section is 0,063 m^2 (0.3 x 0.21 *m*, *length* 0.55 *m*), with velocities ranging from 2 to 6 *m/s* at atmospheric pressure. The foil is mounted on both sides at the vertical walls and fixed by groove and tongue on a stainless shaft (x/c=0.1), with a radial bearing on one side and a guided pin at the opposite. An external fixed clamp is used to prevent the shaft from rotating freely; the angle of the foil is adjustable from outside the chamber (+/-0.1°). The gap between the mounted foil and the vertical wall is about 2mm. Three sides of the chamber are visually accessible for LDA and PIV measurements.

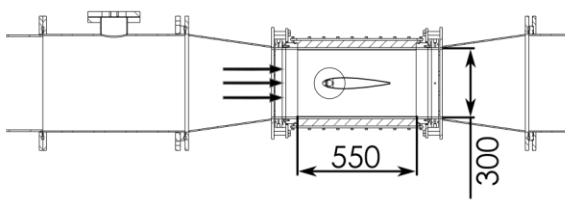

Figure 2. Test chamber with flexible foil mounted on a fixed shaft (x/c=0.1) allowing rotation +/-20° AoA and visual accessibility

2.2 Shape, Material and Mechanical Interior of the Foil

The undeformed shape has a symmetrical section (NACA0016, chord c =0.3 *m*, span b =0.21 *m*), with three positions (I-III) to set the turn-buckles representing the fin rays, as shown in Figure 3. The foil is composed of polycarbonate (PC) sheet material (thickness 3 *mm* (FoilA) and 2 *mm* (FoilB-I)) for the top and bottom side and several CNC- machined parts for the nose-segment. Angled cuts in the nose segment and pre-bended polycarbonate sheets create a very strong bond to prevent the foil from tearing when being deformed. The whole system is glued together, rough surfaces are smoothed out. For the tip-section FORMEROL F.10 was used in order to close the shape up to a sharp trailing edge. This silicone elastomer shows excellent bonding to polycarbonate and can be moulded easily.

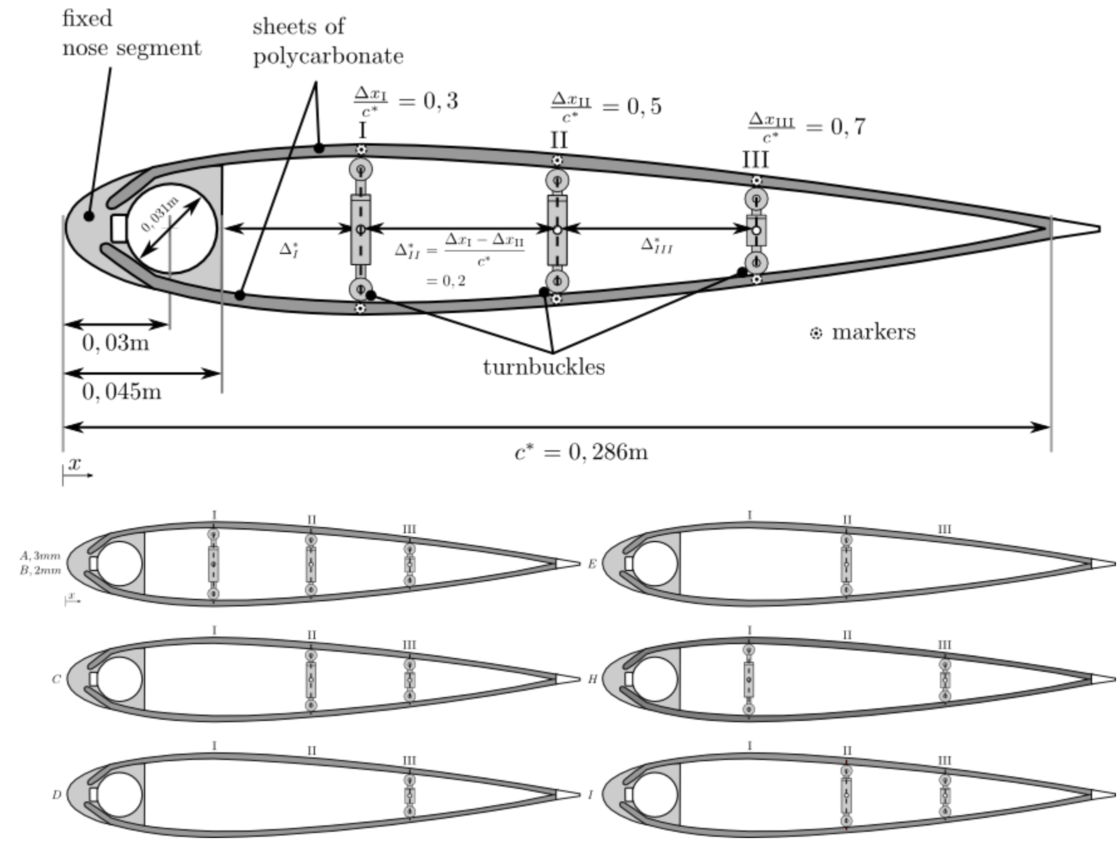

Figure 3. Markers and dimensions of the flexible foil with fixed nose segment and evenly spaced fin ray positions I-III (∆I,II,III=0,2·c*) along the chord length c* (top); Variations A-I of the mechanical components forming the fin rays (bottom)

The fin rays are represented by adjustable turnbuckles which are held in place by a steel shaft (diameter 1.4 *mm*) which in turn is held by 8 eye-bolts per ray, threaded and glued into the sheet material before bending the sheets to shape. The mounting is needed for tilting the rays against the surfaces when being in "deformed configuration", see Figure 1 (top). The final symmetrical foil shape was established by adjusting each turn-buckle and is secured by counter nuts at each turn-buckle. For this study the rays are evenly spaced along the flexible section in the available void between the upper and lower part, starting at 0.066·c, due to the fixed nose segment with sufficient wall thickness for gluing and enough space in-between the sheets at the tip region to place the third ray-section. Since there needed to be at least 3 ray positions to test several setups, the spacing between the rays was chosen to be $0.2 \cdot c^*$. Since the polycarbonate sheets did not meet in a sharp trailing edge, the flexible section was set to $c^*=0.286$ *m* starting at x/c=0.

The modulus of elasticity *E* for the polycarbonate sheets was validated against cantilever beam experiments (see Figure 6) and static load test (see Figure 7) and was found to show good agreements between numerical and tested setup for a value of *2.1 GPa*.

2.3 Deformation Detection

The deformation of the foil is measured photometrically by taking a series of high definition pictures (resolution: 4200 *x* 2000 *px*) and by tracking the marker positions I-III along the pressure-/suction side of the foil, as shown in Figure 3. The tracking uses a modified Hough transform for grayscale images ("HoughCircles" method) from [7], which is part of the OpenCV-Library (Open Source Computer Vision) - wrapped for the programming language Processing 2.0 in version "OpenCV for Processing 0.4.5" [8], [9].

Depending on the camera position and focus, the average resolution calculates to *18,1 px/mm*. The real picture for detecting is not only grayscale, but shows very bright, coloured markers to separate the detected points at each side of the foil, see Figure 5. Every picture is converted to the HSV-colour space (hue, saturation, value) and decomposed into different grayscale-pictures by selecting the appropriate hue values for the markers (e.g. for very strong red and green).

Due to small perturbations in the flow the foil is heaving slightly and a series of pictures (duration 10 s, 3 pictures per second) is recorded, resulting in a median value for the displacement U for the different markers at each position.

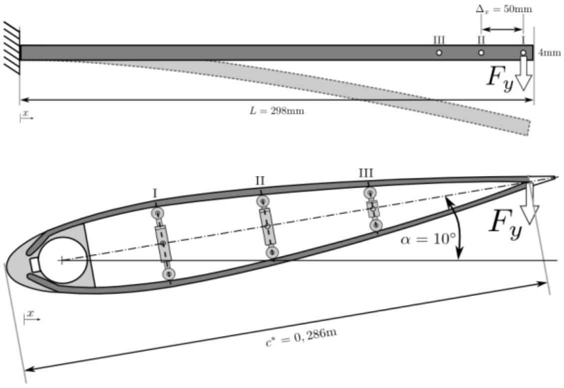

Figure 4. Beam test setup, polycarbonate sheet 298x4x40 *mm* (top)- Static load test setup, Foil B, AoA 10° (bottom)

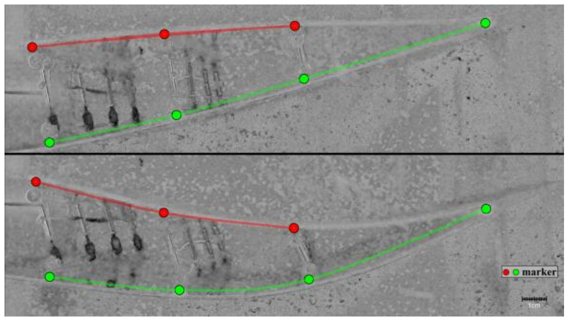

Figure 5. Example of detected points along pressure- and suction side, the lines indicate the shape of the foil as detected on the gray-scale image, FoilB, AoA 10°

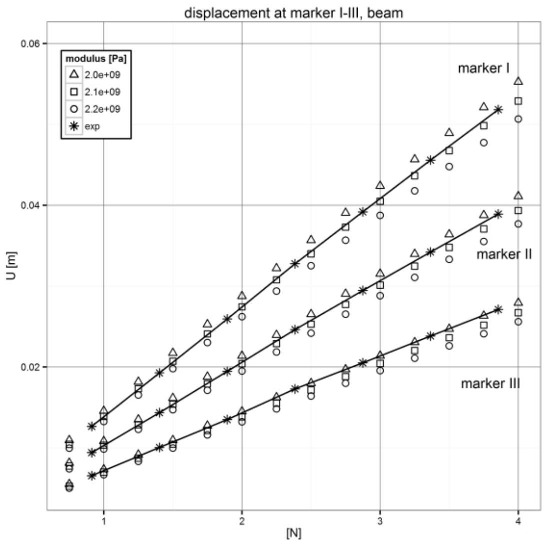

Figure 6. Comparison between the numerical and the experimental beam case for displacement; with varying modi for polycarbonate

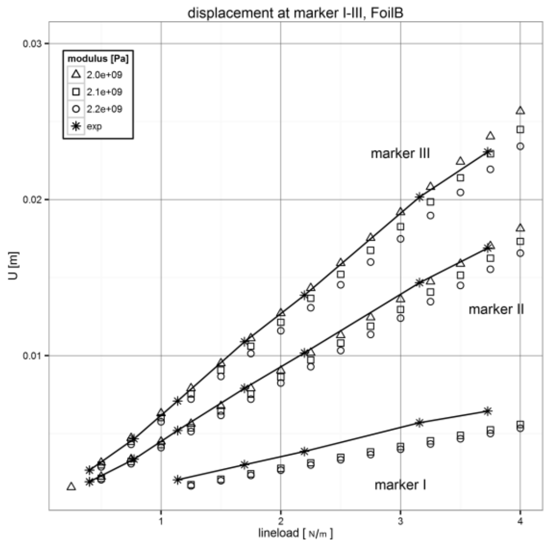

Figure 7. Comparison of static load test; FoilB; only marker positions for upper side are shown

The deformation detection is calibrated for every camera setup by measuring the well-known sheet thickness, resulting in a conversion factor for every setup. The conversion factor is used to transform the pixel information into the reported deformation values (Figure 6,Figure 7 and Figure 11).

3 NUMERICAL SETUP

The fluid-structure interaction is simulated using the system-coupling capability of the commercial software system ANSYS Workbench (R15.0) by transferring the interface quantities (forces/pressure *p(x,y,z)* and deformation *U(x,y,z)*) between the CFD solver (ANSYS CFX) and the FEM solver (ANSYS) in a fully coupled, portioned manner [10]. Testing the setup from [10]–[12] proved the capability of the chosen software package to be capable of solving the benchmark case of Turek and Hron. The interface consists of the wetted area of the foil (upper and lower side) neglecting the inner part. Since both domains show a strong interaction, a 2-way-FSI setup is used to determine the transient effects. A brief overview of the models and settings is given below.

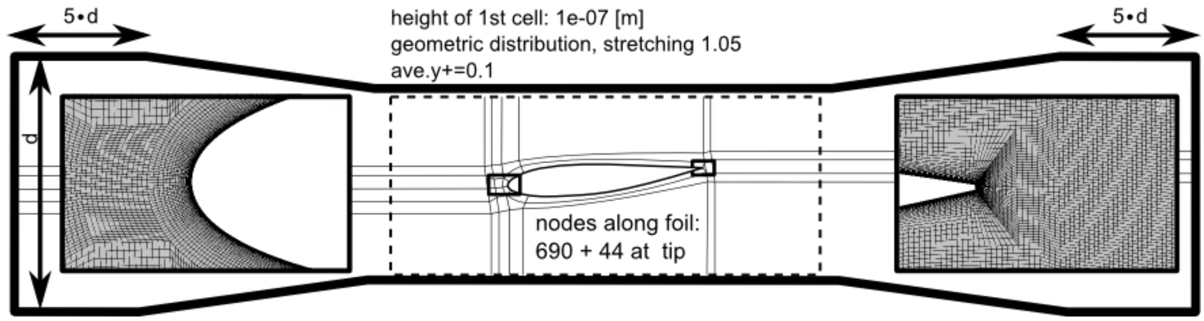

Figure 8. numerical fluid domain with block structured hexahedral mesh, ~730.000 nodes

3.1 Fluid Model

The fluid domain is simulated by assuming a incompressible flow of a Newtonian fluid (Water 20°C). The *k-ω SST* turbulence model is used, as it is capable of accurately capturing transitional effects and separation-induced transition when coupled with the γ-Re_{θ}transition model, see [13]–[15]. After a smooth start-up period (3*s*) up to the maximum inlet velocity, the transient simulations have a total simulation time of *T*=5*s* with a fixed timestep (Δt_f=$10^{-2}s$), resulting in a steady solution for every tested configuration at the end of each calculation. The convergence is set to be fulfilled when reaching $\varepsilon = 10^{-5}$ for mass and momentum. The start-up procedure has shown to be the best approach for creating a system with very large deflections and very thin structural parts.

In a very similar test scenario (section of chamber, Re-number, symmetrical NACA foil [15], [16]) it was found that 80-90% of the flow can be considered to be 2D flow, therefore a 2D-model with approximately 730.000 computational nodes is used, see 8. The overall node amount and their distribution along the foil were found as the result of a mesh sensitivity study. The computational domain is extended by 5*d (diameter of circular section, d = 400 *mm*) for the up- and downstream direction, starting after the diffusor/nozzle, to match the inflow and outflow boundary conditions. It must be noted, that applying a 2D simplification in this case is not taking into account the diverging/converging sections behind the diffusor/nozzle. Applying the pressure/free-stream area-corrected dimensions to the up- and downstream region ($d_{2D/corrected}$ = 598 *mm*) showed no significant change in the pressure distribution around the foil.

3.2 Solid Model

The solid model consists out of hexahedral volume elements (20node 3D quadratic, SOLID186, mechanical properties in Table 1) for the flexible foil, and 1D beam elements for the rays (relevant properties in Table 2), defined by pointwise connected points at the upper and lower part of the foil (d= $5 * 10^{-4}$m). The structural mechanics are solved at the beginning of every timestep (Δt_s=$10^{-2}s$) and iterate until structural convergence is achieved (relative force and momentum convergence 10^{-2}).

3.3 Mesh deformation and Coupling

Mesh quality is maintained during the simulation-runs by applying an additional variable to solve for a diffusive transport equation to calculate the ratio at which the mesh is allowed to translate in relation to the distance to the foil. Therefore the mesh around the foil remains almost the same for all configurations when being deformed and it showed excellent performance regarding to skewness, min.angle and orthogonality.

Constant under-relaxation $\omega_{relax} = 0.25$ for the deformation and no relaxation for the loads are considered. The y-direction of both the transferred displacement and forces is set to meet a convergence criterion of 10^{-4} at the interface. The remaining interface values are set to 10^{-2} for the L2-norm of the load-vector [17].

Table 1. Mechanical properties of foil (polycarbonate) and tip-section (Formerol F10)

	E [MPa]	ρ [kg/m^3]	ν [-]
polycarbonate	2100	1200	0.49
Formerol F10	5.59	1380	0.49

Table 2. Mechanical and geometrical properties of beam elements

properties	value
E [GPa]	210
ρ [kg/m^3]	7850
ν[-]	0.49
r [mm]	0.25

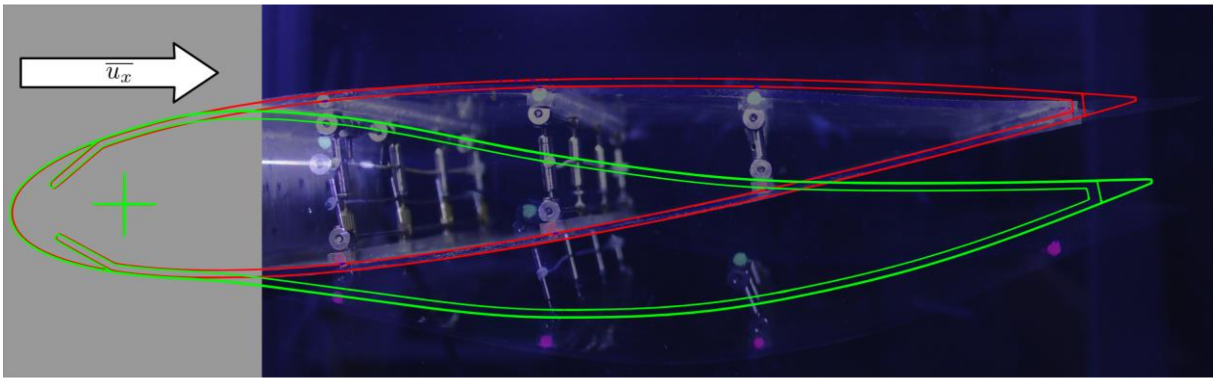

Figure 9. Qualitative comparison between experiment and numerical results, superimposed pictures of deformed foil from experiment and contour from FSI simulations, Foil B AoA 6°

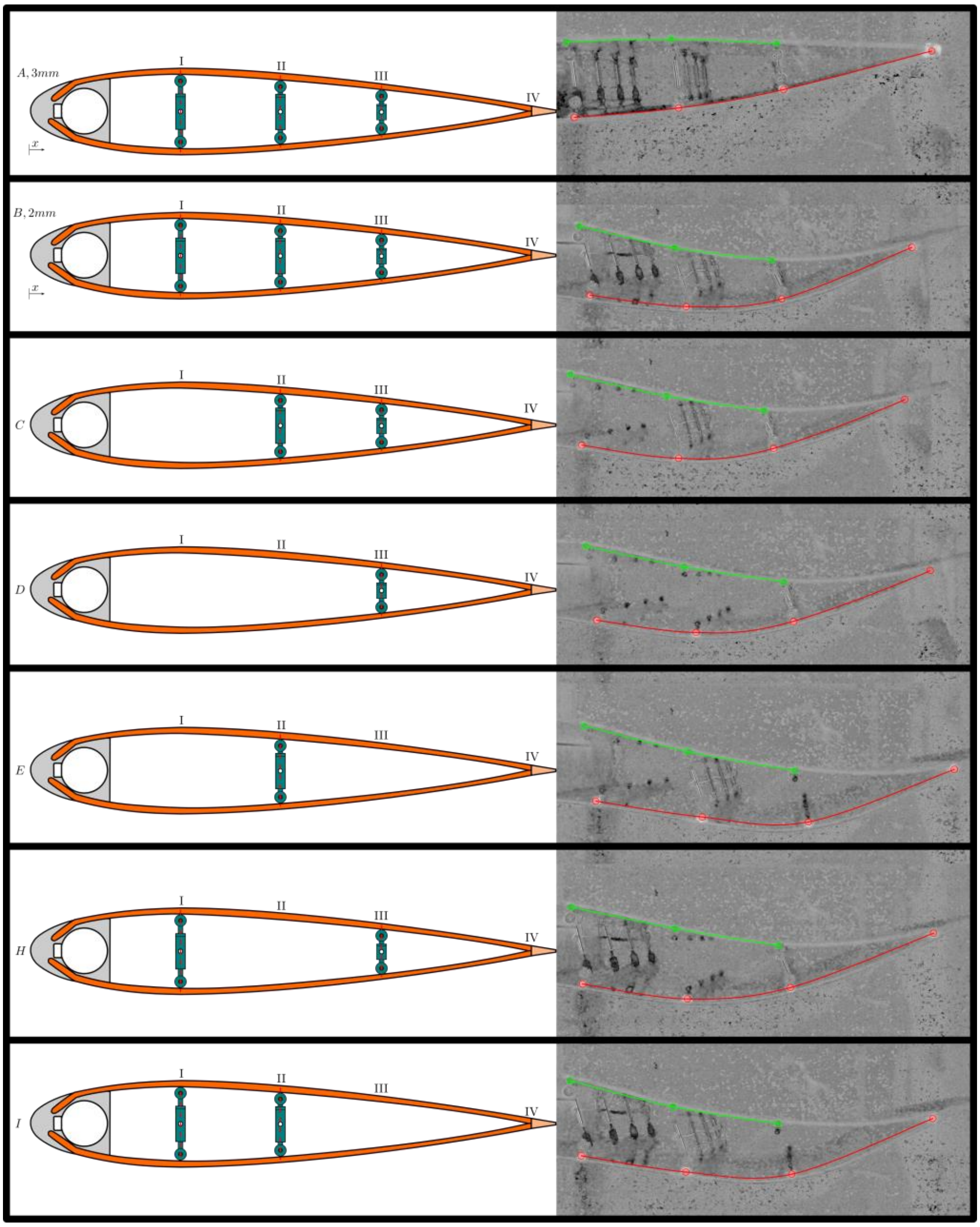

Figure 10. deformed contours for variations on the internal structures, FoilA-I, AoA 6°, $\overline{u_x} \cong 2\ ^{m}/_{s}$

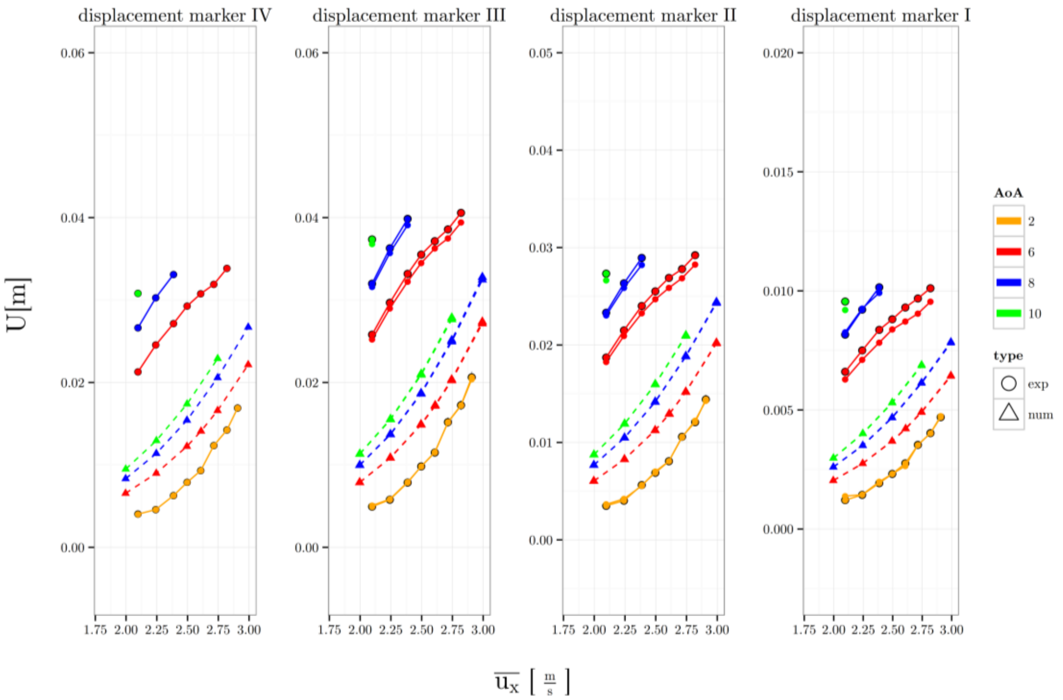

Figure 11. Quantitative comparison between experiment and numerical results for FoilB, displacement U at markers for ranging inlet velocities $\overline{u_x}$ at different AoA (6°,8°,10°), upper side (circles with black border) and down side shown for markers I-IV

4 RESULTS AND COMPARISSON

For the sake of simplicity only FoilB will be compared in detail since it has been found to represent the fin-ray effect as expected. As can be seen in Figure 9 the general behaviour of the fin-ray-system can be modelled as mentioned above. The deformations regarding FoilA, which has the same internal structures as FoilB, show the same relative movement between the markers, as well as the shape of the deflected foil, but with much less deformation (<0.5*cm*) and will not be discussed therefore. When changing the sheet thickness from 3*mm* (FoilA) to 2*mm* (FoilB) the relative deformations at the marker-positions increase severely, even for small AoA at moderate inflow velocities, e.g. for 2° AoA (see Figure 11).

Despite the fact that the quantitative comparison reveals a large mismatch, the foil shows the supposed s-shaped contour (see Figure 1,bottom) when being deformed, both in the numerical and the experimental setup. The tip-section (marker IV) shows lower displacement values over the whole measuring range compared to ray-position III, resulting in the convex/concave curvature.

There is a clear difference between the displacement for pressure- and suction side at a certain marker position (Figure 11,marker III). The relative displacement between the markers shows the asymmetric behaviour for pressure- and suction side of the flexible foil. Especially for higher AoA the angular displacement or inclination of the rays against the centre plane of the undeformed foil is apparently visible. For the same foil setup this behaviour is less visible regarding the numerical results, where no significant relative displacement can be found when comparing the pressure- and suction-side for FoilB.

Changing the internal rays results in a differently shaped contour for the same flow conditions (FoilB-I, Figure 10). Regarding the ray position I there is no evidence that changes at this position causes major changes in the behaviour of the foil (FoilB, FoilC). At this position and for the given modulus the influence of the fixation remains dominant. When comparing changes at ray position II (FoilD, FoilH), a lower curvature for both the pressure- and the suction side of the foil is visible, as well as bulging due to the absent of the ray. The same is even more striking when changing the fixation at ray position III (FoilE, FoilI), where a very strong bulging changes the curvature especially for the suction-side.

Exceedingly strong is the influence of bulging at position III if the fixation at position I is free at the same time. This combination results in a strong thinning out (FoilE). Compared to the situation when solely removing position III (FoilI), the curvature at the downside is equally strong influenced, but less thinning out occurs since the additional stabilisation at positions I yields additional spacing to the overall trend in curvature at the downside.

It is assumed that the angular fixation at the tip-region contributes to the change in curvature as well, especially to the curvature trend at the section between ray position III and the tip, but was not designed to be modifiable in the tested prototype. Experiments with a similar foil setup showed major influence at position III, when applying a joint at the tip region instead of an angular fixation.

The numerical simulations show the main features regarding displacement and change in displacement when changing the inflow conditions or AoA. Future studies will focus on comparing the numerical simulations in greater detail.

5 SUMMARY

The proposed mechanical system is capable of reproducing the fin-ray-effect and was tested for varying AoA and inflow velocities. The suggested prototype showed differences in curvature and displacement when changing the internal topology of the fin rays.

For the same setup numerical experiments were carried out in order to validate the numerical procedure. It has been found that the numerical setup is capable of reproducing major trends of the interaction between the proposed system and the surrounding flow field, but reveals differences when being checked against local deformations.

ACKNOWLEDGEMENTS

The presented work has been carried out within the framework of the research project “CRC 1029 - TurbIn” funded by the German Research Foundation (DFG). This work has also been supported by the doctoral grant of the Beuth University of Applied Sciences. The authors would like to thank their project partners for the great collaboration.

REFERENCES

[1] Fu, L. M., and Yu, H. Y., 2014 , “Intention Bionic Principle of Automotive Body Shape Design,” *Appl. Mech. Mater.*, Vol. 496–500, pp. 2638–2642.

[2] Coelho, D. A., and Versos, C. A. M., 2011 , “A comparative analysis of six bionic design methods,” *Int. J. Des. Eng.*, Vol. 4, no. 2, p. 114.

[3] Lauder, G. V., and Drucker, E. G., 2004 , “Morphology and Experimental Hydrodynamics of Fish Fin Control Surfaces,” *IEEE J. Ocean. Eng.*, Vol. 29, no. 3, pp. 556–571.

[4] Lauder, G. V., Madden, P. G. A., Tangorra, J. L., Anderson, E., and Baker, T. V, 2011 , “Bioinspiration from fish for smart material design and function,” *Smart Mater. Struct.*, Vol. 20, no. 9, p. 094014.

[5] Lauder, G. V., and Madden, P. G. A., 2007 , “Fish locomotion: kinematics and hydrodynamics of flexible foil-like fins,” *Exp. Fluids*, Vol. 43, no. 5, pp. 641–653.

[6] Videler, J. J., and Geerlink, P. J., 1986 , “The Relation Between Structure and Bending Properties of Teleost Fin Rays,” *Netherlands J. Zool.*, Vol. 37, no. 1, pp. 59–80.

[7] Yuen, H. K., Princen, J., Illingworth, J., and Kittler, J., 1990 , “Comparative study of Hough Transform methods for circle finding,” *Image Vis. Comput.*, Vol. 8, no. 1, pp. 71–77.

[8] Borenstein, G., 2013 , “opencv-processing,” *GitHub Repos.*

[9] Bradski, G., 2000 , “The OpenCV Library,” *Dr Dobbs J. Softw. Tools*, Vol. 25, pp. 120–125.

[10] Turek, S., Hron, J., Razzaq, M., Wobker, H., and Schäfer, M., “*Fluid Structure Interaction II*,” Vol. 73. Berlin, Heidelberg: Springer Berlin Heidelberg, 2010, pp. 413–424.

[11] Hron, J., and Turek, S., “Proposal for numerical benchmarking of fluid-structure interaction between an elastic object and laminar incompressible flow,” in *Fluid-Structure Interaction*, Vol. 53, Bungartz and Schäfer, Eds. Berlin: Springer, 2006, pp. 371–385.

[12] Breuer, M., De Nayer, G., Münsch, M., Gallinger, T., and Wüchner, R., 2012 , “Fluid–structure interaction using a partitioned semi-implicit predictor–corrector coupling scheme for the application of large-eddy simulation,” *J. Fluids Struct.*, Vol. 29, pp. 107–130.

[13] Menter, F. R., “Two-equation eddy-viscosity turbulence models for engineering applications,” *AIAA Journal*, Vol. 32. pp. 1598–1605, 1994.

[14] Ducoin, A., and Young, Y. L., 2013 , “Hydroelastic response and stability of a hydrofoil in viscous flow,” *J. Fluids Struct.*, Vol. 38, pp. 40–57.

[15] Ducoin, A., Astolfi, J. A., Deniset, F., and Sigrist, J.-F., 2009 , “Computational and experimental investigation of flow over a transient pitching hydrofoil,” *Eur. J. Mech. - B/Fluids*, Vol. 28, no. 6, pp. 728–743.

[16] Leroux, J.-B., Astolfi, J. A., and Billard, J. Y., 2004 , “An Experimental Study of Unsteady Partial Cavitation,” *J. Fluids Eng.*, Vol. 126, no. 1, p. 94.

[17] ANSYS® Academic Research, “ANSYS Mechanical APDL Coupled-Field Analysis Guide,” Vol. 3304, no. October. ANSYS Inc., pp. 724–746, 2012.

Conference on Modelling Fluid Flow (CMFF'15)
The 16th International Conference on Fluid Flow Technologies
Budapest, Hungary, September 1-4, 2015

Finite element method application for turbulent and transitional flows

P. SVÁČEK[1],

[1] Corresponding Author. Department of Technical Mathematics, Faculty of Mechanical Engineering, Czech Technical University in Prague. Tel.: +4202 2435 7413, Fax: +4202 2435 7413, E-mail: petr.svacek@fs.cvut.cz

ABSTRACT

This paper is interested in numerical simulations of the interaction of the fluid flow with an airfoil. Particularly, the problem of the turbulent flow around a flexibly supported airfoil. The paper consider the laminar - turbulence transition of the flow on the airfoil surface. The transitional model is based on the two equation $k-\omega$ turbulence model, where the additional two equations for the intermittency and transitional onset Reynolds number are included. The motion of the computational domain is treated with the aid of the arbitrary Lagrangian-Eulerian method. The attention is paid mainly to the numerical approximation of the complex nonlinear coupled problem. The numerical results are shown.

Keywords: aeroelasticity, finite element method, 2D RANS equations, sudden gust

NOMENCLATURE

α		airfoil torsion
EA		elastic axis of the airfoil
h	[m]	airfoil bending
I_α	[kg m^2]	inertia moment of the airfoil
k	$[m^2 s^{-2}]$	turbulent kinetic energy
k_h	$[N/m]$	bending stiffness
k_α	$[N\,m\,]$	torsion stiffness
$L(t)$	$[N]$	aerodynamical lift force
m	$[kg]$	mass of the airfoil,
$M(t)$	$[Nm]$	aerodynamical torsional moment
ν	$[m^2 s]$	fluid kinematic viscosity
ν_T	$[m^2 s]$	turbulent kinematic viscosity
p	$[Pa]$	mean pressure
ρ	$[kgm^{-3}]$	fluid density
$Re_{\theta t}$		momentum thickness Reynolds number
S_α	[kg m]	static moment of the airfoil
S_{ij}		components of $\boldsymbol{S}(\boldsymbol{u}) = \frac{1}{2}(\nabla \boldsymbol{u} + (\nabla \boldsymbol{u})^T)$
$\boldsymbol{u}$	$[m/s]$	mean flow velocity $\boldsymbol{u} = (u_1, u_2)$
ω	$[s^{-1}]$	turbulent specific dissipation rate
γ		intermittency coefficient

1. INTRODUCTION

The fluid-structure interaction (FSI) problems are important in various technical problems in civil, aerospace and mechanical engineering (see e.g. [1], [2]) but also e.g. in biomechanics (see e.g. [3]). Recently, the development of the numerical methods in a combination with the fast progress of computers allows to numerically simulate much more complex phenomenas of fluid flows as turbulence and structure deformation, where the material and geometrical nonlinearities can be taken into account.

In this paper we focus on the numerical simulation of the mutual interactions of the turbulent flow with vibrating airfoils. The large vibration amplitudes and the nonlinear forces are taken into account. The similar problems were also considered in the previous papers, the paper [4] dealt with the numerical simulation of the interaction of two-dimensional (2D) incompressible viscous flow with the airfoil, whose motion is described by three degrees of freedom (3-DOF). The further extension was published in [5], where the finite element (FE) solution of the Reynolds averaged Navier-Stokes (RANS) equations combined with Spalart-Allmaras or k-ω turbulence models was used for the approximation of the turbulent flow. The flow model was coupled with a system of nonlinear equations of motion of the airfoil.

The flow was also modeled by the RANS equations combined with the $k-\omega$ turbulence model in the paper [6], where the developed in-house FE code was applied to the numerical simulation of the aeroelastic interaction of flexibly supported 2-DOF airfoil with the 2D incompressible viscous turbulent flow subjected to a sudden gust. The developed method was successfully tested comparing the results with the study published in [7], [8], where the airfoil response to the gust was computed by a commercial CFD program code. The same FSI problem was studied in [9], where the aeroelastic response of the airfoil to the gust computed for the turbulent airflow was compared with the solution considering the laminar flow.

In this case, the appearance of the flow separation on the upper surface of the profile can significantly influence the aeroelastic response. The application of the turbulent model on the other hand consider the boundary layer to be turbulent on the whole surface of the airfoil. In reality the transition from laminar to turbulent flow exists on the surface of the airfoil.

There are several transition models being used for approximation of the transitional flow, see, e.g., [10], [11], [12] or [13]. One of the most popular approaches is the use of the equation for the intermittency coefficient, cf. [14]. In this case, the empirical correlations needs to be applied, where some non-local operations needs to be used (e.g. determination of the boundary layer thickness). Such operations are not well suited for the use on non-structured grids. In order to get rid of these non-local operations, the intermittency equation can be coupled to the additional modelled variable, the modelled transitional onset momentum-thickness Reynolds number, see [15], [16]. The empirical correlations for the onset criteria can be than related to this new local variable.

In the present paper this model is described and applied for numerical simulation of 2D viscous incompressible flow past a moving airfoil. The structure of the paper is as follows, first the mathematical model of the considered problem is described. Further, its numerical approximation is explained and the numerical results are presented.

2. MATHEMATICAL DESCRIPTION

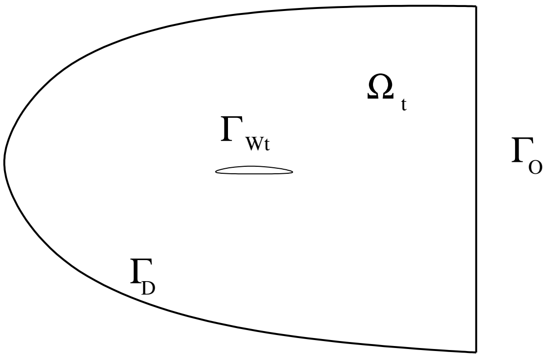

Figure 1. Sketch of the computational domain Ω_t and the parts of the boundary $\partial\Omega_t$.

2.1. Mathematical model

The mathematical formulation of the problem consists of the flow model, the structure model and the interface conditions. We consider the two-dimensional time dependent computational domain $\Omega_t \subset \mathbb{R}^2$ with the Lipschitz continuous boundary $\partial\Omega_t$, see Figure 1. The fluid motion in the domain Ω_t is modelled using the Reynolds averaged Navier-Stokes system of equations in Ω_t

$$\begin{aligned} \frac{\partial u_i}{\partial t} + \frac{\partial}{\partial x_j}(u_i u_j - 2\nu_{\text{eff}} S_{ij}) + \frac{\partial p}{\partial x_i} &= 0, \\ \nabla \cdot \boldsymbol{u} = 0, \end{aligned} \tag{1}$$

where $\boldsymbol{u} = (u_1, u_2)$ is the mean part of the fluid velocity vector, $S_{ij} = \frac{1}{2}(\frac{\partial u_i}{\partial x_j} + \frac{\partial u_j}{\partial x_i})$ are the components of $\boldsymbol{S} = \boldsymbol{S}(\boldsymbol{u})$ the symmetric part of the gradient of $\boldsymbol{u}$, p is the mean part of the kinematic pressure (i.e., the pressure divided by the constant fluid density ρ), $\nu_{\text{eff}} = \nu + \nu_T$, ν is the kinematic viscosity of the fluid (i.e. the viscosity divided by the density ρ), ν_T is a turbulent viscosity (obtained by an additional model), see e.g. [17], [18].

The system (1) is equipped with boundary conditions prescribed on the mutually disjoint parts of the boundary $\partial\Omega = \Gamma_D \cup \Gamma_O \cup \Gamma_{Wt}$:

$$\begin{aligned} &\text{a)} \quad \boldsymbol{u} = \boldsymbol{u}_D \qquad \text{on } \Gamma_D, \\ &\text{b)} \quad \boldsymbol{u} = \boldsymbol{w}_D \qquad \text{on } \Gamma_{Wt}, \\ &\text{c)} \quad -2\nu_{\text{eff}}\boldsymbol{S}(\boldsymbol{u})\boldsymbol{n} + p\boldsymbol{n} = 0 \qquad \text{on } \Gamma_O, \end{aligned} \tag{2}$$

where $\boldsymbol{w}_D$ is the velocity of the boundary Γ_{Wt}. For the sake of simplicity, let us set $p_{\text{ref}} = 0$. Further, the system (1) is equipped with an initial condition $\boldsymbol{u}(x, 0) = \boldsymbol{u}_0(x)$ for $x \in \Omega_0$.

2.2. SST turbulence model

In order to enclose the system (1) the turbulent viscosity is modelled with the aid of SST $k - \omega$ turbulence model, see [19]. In order to predict the transition the $\gamma - \overline{Re}_{\theta t}$ model is used, see [15]. The SST turbulence model is a modification of the $k - \omega$ turbulence model for which the turbulent viscosity is given by $\nu_T = \frac{k}{\omega}$ Here, the turbulent kinetic energy $k = k(x, t)$ and the turbulent specific dissipation rate $\omega = \omega(x, t)$ are modelled by

$$\begin{aligned} \frac{\partial k}{\partial t} + \boldsymbol{u} \cdot \nabla k &= \gamma_{\text{eff}} P_k - \beta^* \omega k \overline{\gamma_{\text{eff}}} + \nabla \cdot (\varepsilon_k \nabla k), \\ \frac{\partial \omega}{\partial t} + \boldsymbol{u} \cdot \nabla \omega &= P_\omega - \beta\omega^2 + \nabla \cdot (\varepsilon_\omega \nabla \omega) + C_D, \end{aligned} \tag{3}$$

where the production and the destruction terms are modified due in the first equation using the effective intermittency coefficient γ_{eff} and $\overline{\gamma}_{\text{eff}} = \max(\min(\gamma_{\text{eff}}, 1), 0.1)$. Further, the viscosity coefficients are given by $\varepsilon_k = \nu + \sigma_k \nu_T$ and $\varepsilon_\omega = \nu + \sigma_\omega \nu_T$ and the source terms P_k and C_D are defined by

$$P_k = \nu_T \mathbf{S}(\boldsymbol{u}) : \mathbf{S}(\boldsymbol{u}), \quad C_D = \frac{\sigma_D}{\omega}(\nabla k \cdot \nabla \omega)^+,$$

and $P_\omega = \frac{\alpha_\omega \omega}{k} P_k$. The closure coefficients $\beta, \beta^*, \sigma_k, \sigma_\omega, \alpha_\omega, \sigma_D$ are chosen, by [19]. See also [20] or [17].

The SST $k{-}\omega$ model is equipped with the boundary conditions

$$\begin{array}{llll} \text{a)} & k = k_\infty, & \omega = \omega_\infty & \text{on } \Gamma_D, \\ \text{b)} & k = 0, & \omega = \omega_{\text{wall}} & \text{on } \Gamma_{Wt}, \\ \text{c)} & \dfrac{\partial k}{\partial \boldsymbol{n}} = 0, & \dfrac{\partial \omega}{\partial \boldsymbol{n}} = 0, & \text{on } \Gamma_O. \end{array} \tag{4}$$

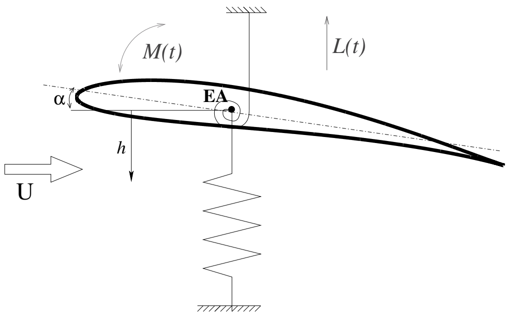

Figure 2. The flexibly supported airfoil model.

2.3. Transition model

The transition from laminar to turbulence regimes is modelled with the aid of the Menter's γ–$\overline{Re}_{\theta t}$ model, see [15], where the equation for the intermittency coefficient γ is written in the ALE form as

$$\frac{\partial \gamma}{\partial t} + \boldsymbol{u} \cdot \nabla\gamma = P_\gamma - E_\gamma + \nabla \cdot ((\nu + \frac{\nu_T}{\sigma_f})\nabla\gamma), \tag{5}$$

where $P_\gamma = P_{\gamma,1} - c_{e1}\gamma P_{\gamma,1}$ and $E_\gamma = c_{e2}\gamma E_{\gamma,1} - E_{\gamma,1}$ are the transition source and destruction terms with $P_{\gamma,1} = F_{\text{length}} c_{a1} S \sqrt{\gamma F_{\text{onset}}}$, $E_{\gamma,1} = c_{a2}\Omega\gamma F_{\text{turb}}$. Here, S and Ω are the strain rate and vorticity magnitudes and the transition onset is modelled by $F_{\text{onset}} = (F_{\text{onset2}} - F_{\text{onset3}})^+$, where $F_{\text{onset2}} = \min\left(\max\left(F_{\text{onset1}}, F^4_{\text{onset1}}\right), 2\right)$, $F_{\text{onset1}} = \frac{Re_V}{2.193 Re_{\theta c}}$, $Re_V = \frac{y^2 S}{\nu}$, $F_{\text{onset3}} = \max\left(1 - \left(\frac{R_T}{2.5}\right)^3, 0\right)$, $R_T = \frac{k}{\nu\omega}$, $F_{\text{turb}} = e^{-(R_T/4)^4}$, where y denotes the wall distance, and $Re_{\theta t}$ is the transition Reynolds number. The following constants for the intermittency equation were used $c_{e1} = 1$, $c_{a1} = 2$, $c_{e2} = 50$, $c_{a2} = 0.06$, $\sigma_f = 1$. Further, $Re_{\theta c}$ is the critical Reynolds number given by an empirical correlation, and another empirical correlation is used for the function F_{length}, which controls the length of the transition region. The correlations are based on newly defined transported unknown $\overline{Re}_{\theta t}$ governed by the ALE form of the equation

$$\frac{\partial \overline{Re}_{\theta t}}{\partial t} + \boldsymbol{u} \cdot \nabla\overline{Re}_{\theta t} = P_{\theta t} + \nabla \cdot (\sigma_{\theta t}\nu_{\text{eff}}\nabla\overline{Re}_{\theta t}), \tag{6}$$

where the source term $P_{\theta t}$ is given by

$$P_{\theta t} = c_{\theta t}\frac{\rho}{t_\infty}\left(Re_{\theta t} - \overline{Re}_{\theta t}\right)(1 - F_{\theta t}),$$

$c_{\theta t} = 0.03$, $\sigma_{\theta t} = 2$, $t_\infty = 500\nu/U^2$ is the time scale, U is the local magnitude of the velocity $U = \|\boldsymbol{u}\|_2$ and the blending function $F_{\theta t}$ is defined as

$$F_{\theta t} = \min\left(1, \max\left(F_{\text{wake}} e^{-(y/\delta)^4}, 1 - \left(\frac{\gamma - 1/c_{e2}}{1 - 1/c_{e2}}\right)\right)\right),$$

$$\delta = \frac{375\Omega y}{U}\theta,\ \theta = \frac{\overline{Re}_{\theta t}\nu}{U},\ F_{\text{wake}} = e^{-(Re_\omega/10^5)^2},$$

and $Re_\omega = \frac{\omega y^2}{\nu}$. The source term $P_{\theta t}$ on the right hand side of equation (6) includes also the Reynolds number $Re_{\theta t}$ given by an empirical correlations.

The transition model (5) and (6) is equipped with the boundary conditions

$$\begin{array}{llll} \text{a)} & \gamma = 1, & \overline{Re}_{\theta t} = \overline{Re}_{\theta t\infty} & \text{on } \Gamma_D, \\ \text{b)} & \dfrac{\partial \gamma}{\partial \boldsymbol{n}} = 0, & \dfrac{\partial \overline{Re}_{\theta t}}{\partial \boldsymbol{n}} = 0 & \text{on } \Gamma_{Wt}, \\ \text{c)} & \dfrac{\partial \gamma}{\partial \boldsymbol{n}} = 0, & \dfrac{\partial \overline{Re}_{\theta t}}{\partial \boldsymbol{n}} = 0 & \text{on } \Gamma_O. \end{array}$$

Empirical correlations. In order to enclose the model, the empirical correlations published in [21] are used. First, the length of the transition is controlled by $F_{\text{length}} = F_{\text{length}}(\overline{Re}_{\theta t})$. Further, the transitional onset momentum thickness Reynolds number $Re_{\theta t}$ is correlated to pressure gradient λ_θ and to turbulence intensity Tu. Further, the correlation for $Re_{\theta t}$ and for the critical Reynolds number are specified, cf. [21] or [12].

2.4. ALE formulation

In order to practically treat the motion of the domain Ω_t, the Arbitrary Lagrangian-Eulerian (ALE) method is used, see [22]. The ALE mapping $\mathcal{A} : \Omega_0^{ref} \mapsto \Omega_t$, $\mathcal{A} = \mathcal{A}(\xi, t) = \mathcal{A}_t(\xi)$ defined for all $t \in (0, T)$ and $\xi \in \Omega_0^{ref} = \Omega_0$ is assumed to be smooth and to have smooth bounded Jacobian $\mathcal{J}(x, t)$ Furthermore, by $D^{\mathcal{A}}/Dt$ the ALE derivative is denoted (i.e. the derivative with respect to the reference configuration) and $\boldsymbol{w_D}$ denotes the domain velocity. The ALE derivative is then related to the time derivative by (see also [23], [22])

$$\frac{D^{\mathcal{A}} f}{Dt}(x, t) = \frac{\partial f}{\partial t}(x, t) + \boldsymbol{w}_D(x, t) \cdot \nabla f(x, t), \tag{7}$$

where $\boldsymbol{w_D}$ denotes the ALE domain velocity defined by

$$\boldsymbol{w}_D(x, t) = \frac{\partial \mathcal{A}(\xi, t)}{\partial t}, \qquad x = \mathcal{A}(\xi, t). \tag{8}$$

In order to approximate the equations on time dependent domains, the time derivative in equations (1), (3), (5) and (6) are replaced by the ALE time derivative using the formula (7), which also modifies the convection term. In the practical computation this is not complicated and thus, for the sake of brevity, we do not focus on the ALE formulations.

2.5. Structure model

The flow model is coupled with the structure model representing the flexibly supported airfoil (see Figure 2). The airfoil can be vertically displaced by h (downwards positive) and rotated by angle α (clockwise positive). The nonlinear equations of motion then read (see [23])

$$m\ddot{h} + S_\alpha\,\ddot{\alpha}\,\cos\alpha - S_\alpha\dot{\alpha}^2\sin\alpha + k_h h = -L(t), \quad (9)$$
$$S_\alpha\ddot{h}\cos\alpha + I_\alpha\ddot{\alpha} + k_\alpha\alpha = M(t).$$

where m is the mass of the airfoil, S_α is the static moment around the elastic axis (EA), and I_α is the inertia moment around EA. The parameters k_h and k_α denote the stiffness coefficients. On the right-hand side the aerodynamical lift force $L(t)$ and aerodynamical torsional moment $M(t)$ are involved, which satisfy

$$L = -l\int_{\Gamma_{Wt}} \sigma_{2j}n_j\,dS,$$
$$M = l\int_{\Gamma_{Wt}} \sigma_{ij}n_j r_i^{\text{ort}}\,dS, \quad (10)$$

where

$$\sigma_{ij} = \rho\left[-p\delta_{ij} + 2\nu S_{ij}\right], \quad (11)$$

where $r_1^{\text{ort}} = -(x_2 - x_2^{\text{EA}})$, $r_2^{\text{ort}} = x_1 - x_1^{\text{EA}}$ and l denotes the depth of the airfoil section, $x^{\text{EA}}e = (x_1^{\text{EA}}, x_2^{\text{EA}})$ is the position of EA of the airfoil at the time instant t, see Figure 2.

3. NUMERICAL APPROXIMATION

In this section, the approximation of the presented mathematical model, consisting of the Reynolds averaged Navier-Stokes equations, the modified k-ω turbulence model and the $\gamma - \overline{Re}_{\theta t}$ turbulence model, is presented. First, the time discretization is described based on the backward difference formula. Further, the finite element method is used for the approximation of the ALE conservative formulation of the RANS equations and stabilized using the SUPG/PSPG method together with the div-div stabilization, see [23]. Further, the four equations of the transition model are discretized in time, linearized and stabilized using the SUPG method. Let us moreover mention, that in the computations for the $k - \omega$ equations the crosswind diffusion is also applied, see [5]. For the sake of brevity it is omitted here, see also [24].

3.1. Time discretization

We consider the equidistant partition $t_j = j\Delta t$ of the time interval I with a time step $\Delta t > 0$, and denote the approximations $\boldsymbol{u}^j \approx \boldsymbol{u}(\cdot, t_j)$, $p^j \approx p(\cdot, t_j)$ and similarly $k^j = k(\cdot, t_j)$, $\omega^j = \omega(\cdot, t_j)$, $\gamma^j = \gamma(\cdot, t_j)$, $\overline{Re}_{\theta t}^{\,j} = \overline{Re}_{\theta t}(\cdot, t_j)$. Moreover, we approximate the domain velocity $\boldsymbol{w}_D$ at time level t_j by $\boldsymbol{w}_D^j$. We shall focus on the description of the discretization at a time instant t_{n+1}, which is kept fixed throughout this section. For the sake of simplicity the subscript t_{n+1} shall be omitted, i.e. $\Omega = \Omega_{t_{n+1}}$ and we shall denote by $Q = L^2(\Omega)$ the Lebesgue space and by $\boldsymbol{W} = \boldsymbol{H}^1(\Omega)$ the Sobolev space. Further, by $\boldsymbol{X}$ the space of the test functions shall be denoted

$$\boldsymbol{X} = \left\{z \in \boldsymbol{W} :\ z|_{\Gamma_D \cup \Gamma_{W t_{n+1}}} = 0\right\}.$$

Then the time derivative in the weak formulation of (1) is approximated at the time $t = t_{n+1}$ by the second order backward difference formula, i.e.

$$\left.\frac{\partial\varphi}{\partial t}\right|_{t_{n+1}} \approx \frac{3\varphi^{n+1} - 4\varphi^n + \varphi^{n-1}}{2\Delta t}. \quad (12)$$

3.2. Spatial discretization of flow model

The weak formulation of the time discretized Reynolds averaged Navier-Stokes equations is obtained by the multiplication the equations (1) by a test function $z \in \boldsymbol{X}$, integration over the domain Ω_t, application of the Green's theorem and using approximation (12). The (spatial) weak formulation reads: Find $U^{n+1} = (\boldsymbol{u}^{n+1}, p^{n+1}) \in \boldsymbol{W} \times Q$ such that $\boldsymbol{u}$ approximately satisfies the boundary conditions (2a,b) and

$$a(U^{n+1}, V) = L(V). \quad (13)$$

holds for all $V = (z, q) \in \boldsymbol{X} \times Q$. The forms $a(\cdot,\cdot,\cdot)$ and $L(\cdot)$ defined for any $U = (\boldsymbol{u}, p) \in \boldsymbol{W} \times Q$, $U^* = (\boldsymbol{u}^*, p) \in \boldsymbol{W} \times Q$ and $V = (z, q) \in \boldsymbol{X} \times Q$,

$$a(U, V) = \frac{3}{2\Delta t}\Big(\boldsymbol{u}, z\Big)_\Omega + \Big((\overline{\boldsymbol{w}} \cdot \nabla)\boldsymbol{u}, z\Big)_{\Omega_t}$$
$$+ (\nu_{\text{eff}}\boldsymbol{S}(\boldsymbol{u}), \boldsymbol{S}(z))_\Omega + (\nabla \cdot \boldsymbol{u}, q)_\Omega - \Big(p, \nabla \cdot z\Big)_\Omega,$$
$$L(V) = \frac{4}{2\Delta t}(\boldsymbol{u}^n, z^n)_{\Omega_{t_n}} - \frac{1}{2\Delta t}\Big(\boldsymbol{u}^{n-1}, z^{n-1}\Big)_{\Omega_{t_{n-1}}}.$$

In order to approximate the problem (13), the spaces $\boldsymbol{X}, \boldsymbol{W}$ and Q are approximated by finite element subspaces $\boldsymbol{X}_\Delta, \boldsymbol{W}_\Delta$ and Q_Δ, respectively.

The spaces $\boldsymbol{X}_\Delta, \boldsymbol{W}_\Delta$ and Q_Δ are . Here, the Taylor-Hood family of finite elements are used, defined over an admissible triangulation $\mathcal{T}_\Delta$ of the computational domain $\Omega = \Omega_{t_{n+1}}$. In order to stabilize the method the fully stabilized scheme (see [25]) is used, which consists of streamline-upwind/Petrov-Galerkin(SUPG) and pressure-stabilizing/Petrov-Galerkin(PSPG) stabilization combined with the div-div stabilization, see [25].

The stabilized discrete problem reads: Find $U = (\boldsymbol{u}_\Delta^{n+1}, p_\Delta^{n+1}) \in \boldsymbol{W}_\Delta \times Q_\Delta$ such that $\boldsymbol{u}^{n+1}$ satisfies approximately the Dirichlet boundary conditions (2,a,b) and

$$a(U; U, V) + \mathcal{L}(U, V) + \mathcal{P}(U, V) = L(V) + \mathcal{F}(V),$$

holds for all $V = (z, q) \in \boldsymbol{X}_\Delta \times Q_\Delta$, where the terms $\mathcal{L}$ and $\mathcal{F}$ are the SUPG/PSPG terms defined by

$$\mathcal{L}(U, V) = \sum_{K \in \mathcal{T}_\Delta} \delta_K\Big(\frac{3\boldsymbol{u}}{2\Delta t} - \nu\triangle\boldsymbol{u} + (\boldsymbol{v} \cdot \nabla)\boldsymbol{u} + \nabla p, \Psi\Big)_K,$$
$$\mathcal{F}(V) = \sum_{K \in \mathcal{T}_\Delta} \delta_K\Big(\frac{1}{2\Delta t}(4\tilde{\boldsymbol{u}}^n - \tilde{\boldsymbol{u}}^{n-1}), \Psi\Big)_K,$$

where the function $\overline{\boldsymbol{w}}^{n+1} = \boldsymbol{u}^* - \boldsymbol{w}_D^{n+1}$ stands for the transport velocity, $\Psi = (\overline{\boldsymbol{w}}^{n+1} \cdot \nabla)z + \nabla q$ and $\tilde{\boldsymbol{u}}^k = \boldsymbol{u}^k \circ \mathcal{A}_{t_k} \circ \mathcal{A}_{t_{n+1}}^{-1}$. The div-div stabilizing terms $\mathcal{P}(U, V)$ read

$$\mathcal{P}(U, V) = \sum_{K \in \mathcal{T}_\Delta} \tau_K (\nabla \cdot \boldsymbol{u}, \nabla \cdot z)_K. \tag{14}$$

Here, the following choice of the stabilizing parameters τ_K and δ_K based on the local element length h_K is used for the Taylor-Hood family of finite elements, $\tau_K = \max_{x \in \Omega} \|\boldsymbol{u}(x)\|_2$, $\delta_K = h_K^2 / \tau_K$.

3.3. Spatial discretization of the turbulence/transitional model

Furthermore, the complete transition model consisting of equations (3), (5), (6) is step-by-step time discretized, weakly formulated and stabilized formulation is introduced. The time derivatives in equations (3), (5) and (6) are approximated using the 2nd order backward difference formula (12), the equations for k, ω, γ and $\overline{Re}_{\theta t}$ are multiplicated by φ_k, φ_ω, φ_γ and $\varphi_{\overline{Re}_{\theta t}}$, respectively, integrated over Ω_t, and the Green's theorem is applied. The function spaces are then approximated by their finite element counterparts consisting of piecewise linear functions defined over the triangulation $\mathcal{T}_\Delta$. The stabilized formulation is obtained using a linearization of the non-linear terms and an application of the SUPG stabilization procedure.

4. NUMERICAL RESULTS

The developed numerical method was applied on numerical approximation of flow a flexibly supported airfoil subject to the change of flow conditions, see [8]. The results are compared with the previous study of the authors [6], where turbulent and non-turbulent flows were considered without modelling of the turbulent-laminar flow transition. The considered airfoil shape is given by

$$z = \frac{k_{\mathrm{KT}}(c_{\mathrm{KT}} - 1)}{((Z-1)/(Z-c_{\mathrm{KT}}))^{k_{\mathrm{KT}}} - 1}, \qquad k_{\mathrm{KT}} = \frac{360 - \alpha_T}{180}$$

where $Z = X + iY$ and $z = x + iy$ are complex variables describing the unit circle and the airfoil shape in $X-Y$ and $x-y$ complex planes, respectively. The constants $c_{\mathrm{KT}} = -0.89 - 0.11i$ and $\alpha_T = 2\,\mathrm{deg}$ determine the airfoil shape (A1), see Fig. 2. The following values were used $m = 2 \times 10^{-4}\,\mathrm{kg}$, $I_\alpha = 1.2 \times 10^{-7}\,\mathrm{kg\ m^2}$ and $S_\alpha = 2 \times 10^{-6}\,\mathrm{kg\ m}$. The airfoil chord was $c = 0.1m$, the elastic axis was located at 30 % of the chord, and the depth of the airfoil section was $l = 0.03\,\mathrm{m}$. The stiffness coefficients of the springs were $k_h = 26\,\mathrm{N/m}$, $k_\alpha = 0.29\,\mathrm{N\ m/rad}$.

The air density was $\rho = 1.225\,\mathrm{kg\,m^{-3}}$ and the air kinematic viscosity was $\nu = 1.453 \times 10^{-5}\,\mathrm{m^2/s}$. The inlet turbulence intensity was 1% ($k = 1.5 \times 10^{-4}\, U_\infty^2$, $\omega = 10\,\mathrm{s^{-1}}$ on Γ_I). The finite element triangular mesh was used, anisotropically refined nearby the boundary in order to well capture the turbulent boundary layer, wake and also the separation region. The described stabilized finite element method was used, and the computations were performed on the coarse and the fine mesh. A vertical gust of 1 s duration was considered as a sudden perturbation of the aeroelastic system for $t \in [t_0, t_0 + 1]$

$$V_g(t) = \frac{V_G}{2}\left(1 + \cos(\pi(t - t_0))\right),$$

where $V_G = 1.5\,\mathrm{m\,s^{-1}}$ and $V_G = 5\,\mathrm{m\,s^{-1}}$ were considered for the light and heavy gusts, respectively.

The aeroelastic airfoil responses $h(t)$ and $\alpha(t)$ numerically simulated in the time domain for the light gust ($V_G = 1.5\,\mathrm{m\,s^{-1}}$) are shown in Fig. 3. The numerically simulated airfoil responses $h(t)$ and $\alpha(t)$ for the heavy gust ($V_G = 5\,\mathrm{m\,s^{-1}}$) are shown in Fig. 4. The results for the transitional flow model are close to the simulations using the turbulence model, but before the gust starts and also when it dissappers, the fluid flow becomes almost laminar on the airfoil surface. See also turbulent kinetic energy pattern around the airfoil shown in Fig. 6, where the most of the turbulent kinetic energy is in a far wake and almost zero turbulent kinetic energy is at the airfoil surface.

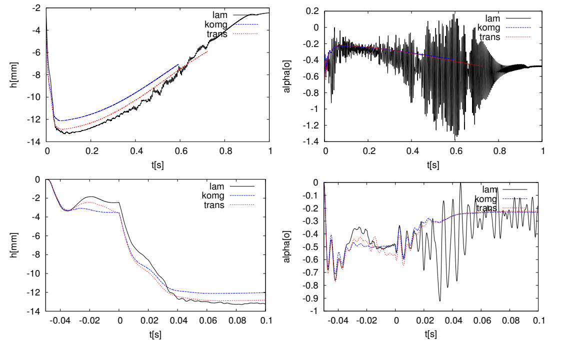

Figure 3. Aeroelastic response to the light gust: Comparison of results computed by laminar, turbulent and transitional models.

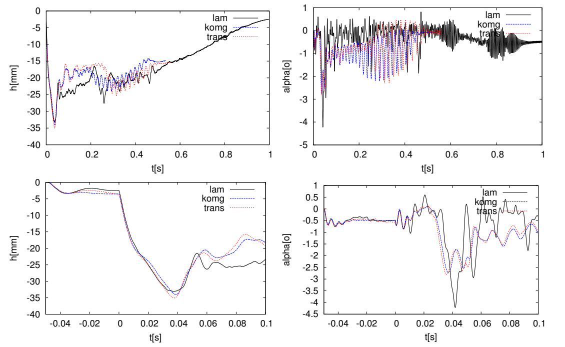

Figure 4. Aeroelastic response to the heavy gust: Comparison of results computed by laminar, turbulent and transitional models.

5. CONCLUSION

The new original FE method taking into account transition of the laminar to turbulent flow was developed and successfully applied on the FSI problem of flow induced vibrations when the 2-DOF air-

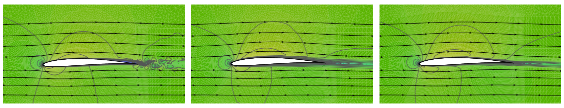

Figure 5. Comparison of velocity flow patterns for the laminar(left), turbulent(middle) and transitional(right) models just before the gust starts.

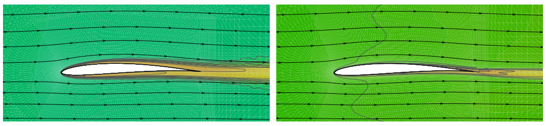

Figure 6. Comparison of the turbulent kinetic energy k distribution for the turbulent(left) and transitional(right) models just before the gust starts.

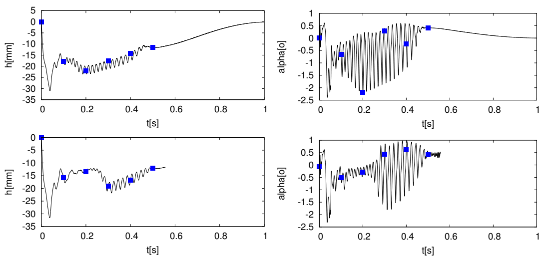

Figure 7. Comparison of the aeroelastic response computed by turbulent (top) and transitional model (bottom). The marked time instants. corresponds to the flow patterns shown in Fig. 8.

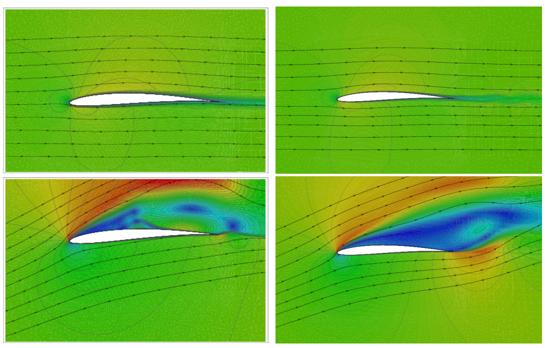

Figure 8. Heavy gust aeroelastic response: comparison of flow velocity patterns for turbulent (left) and transitional (right) models at two time instants

foil was loaded by a sudden gust. The preliminary results computed by the developed in-house software demonstrated usability of the method in solution of a practical FSI problem. The method was partially verified by comparison with the previous results of the authors when only laminar or turbulence model were implemented into the numerical method. In addition to implementation of the laminar-turbulent flow transition, some new ingredients into the developed method were added. The transitional model was shown to better "switch" between the laminar/turbulent model. On the other hand its application for the time dependent problems seems to require a further modification. This is particularly due to the fact, that the original model for the separated regions predicts too high intermittency coefficient.

ACKNOWLEDGEMENTS

This work was supported by the project No. P101/12/1271 of the Czech Science Foundation.

REFERENCES

[1] Clark, R., Cox, D., Curtiss, H., Edwards, J., Hall, K., Peters, D., R., S., Simiu, E., Sisto, F., and Strganac, Th.W., D. E. e., 2004, *A modern course in aeroelasticity*, Kluwer Academic Publishers, Springer, 4th rev. and enlarged ed edn.

[2] Paidoussis, M., 2013, *Fluid-Structure Interactions. Slender structures and axial flow*, Academic Press, Elsevier, 2nd Edition.

[3] Bodnár, T., Galdi, G. P., and Nečasová, v. (eds.), 2014, *Fluid-Structure Interaction and Biomedical Applications*, Birkhäuser Basel.

[4] Feistauer, M., Horáček, J., Ružička, M., and Sváček, P., 2011, "Numerical analysis of flow-induced nonlinear vibrations of an airfoil with three degrees of freedom", *Computers & Fluids*, Vol. 49 (1), pp. 110 – 127.

[5] Feistauer, M., Horáček, J., and Sváček, P., 2014, "Numerical simulation of vibrations of an airfoil with three degrees of freedom induced by turbulent flow", *Commun Comput Phys*, p. 43 pp., accepted.

[6] Sváček, P., and Horáček, J., 2015, "On mathematical modeling of fluid–structure interactions with nonlinear effects: Finite element approximations of gust response", *Journal of Computational and Applied Mathematics*, Vol. 273 (0), pp. 394 – 403.

[7] Berci, M., Gaskell, P. H., Hewson, R., and Toropov, V., 2013, "A semi-analytical model for the combined aeroelastic behaviour and gust response of a flexible aerofoil", *J Fluids Struct*, Vol. 38, pp. 3–21.

[8] Berci, M., Mascetti, S., Incognito, A., Gaskell, P. H., and Toropov, V. V., 2010, "Gust response of a typical section via CFD and analytical solutions", J. C. F. Pereira, and A. Sequeira (eds.), *ECCOMAS CFD 2010, V. European Conference on Computational Fluid Dynamics*, p. 10 pp.

[9] Horáček, J., and Sváček, P., 2014, "Finite element simulation of a gust response of an ultralight 2-DOF airfoil", *Proceedings of the ASME 2014 Pressure Vessels & Piping Conference*, Anaheim, California, USA, PVP2014-28390, p. 10.

[10] Craft, T., Launder, B., and Suga, K., 1997, "Prediction of turbulent transitional phenomena with a nonlinear eddy-viscosity model", *Int Jour Heat and Fluid Flow*, Vol. 18, pp. 15–28.

[11] Walters, D. K., and Cokljat, D., 2008, "A three-equation eddy-viscosity model for Reynolds-averaged Navier-Stokes simulations of transitional flow", *Journal of Fluids Engineering*, Vol. 130 (12), p. 121401.

[12] Suluksna, K., and Juntasaro, E., 2008, "Assessment of intermittency transport equations for modeling transition in boundary layers subjected to freestream turbulence", *International Journal of Heat and Fluid Flow*, Vol. 29 (1), pp. 48 – 61.

[13] Příhoda, J., 1992, "Modelling of transition domain for computation of boundary layer", *Strojnícky časopis*, Vol. 43 (5), pp. 428–441, in czech.

[14] Suzen, Y. B., Huang, P., Hultgren, L. S., and Ashpis, D. E., "Predictions of separated and transitional boundary layers under low-pressure turbine airfoil conditions using an intermittency transport equation", .

[15] Menter, F., Langtry, R., and Völker, S., 2006, "Transition modelling for general purpose CFD codes", *Flow, Turbulence and Combustion*, Vol. 77 (1-4), pp. 277–303.

[16] Suzen, Y., Huang, P., Hultgren, L. S., and Ashpis, D. E., 2003, "Predictions of separated and transitional boundary layers under low-pressure turbine airfoil conditions using an intermittency transport equation", *Journal of turbomachinery*, Vol. 125 (3), pp. 455–464.

[17] Wilcox, D. C., 1993, *Turbulence Modeling for CFD*, DCW Industries.

[18] Pope, S. B., 2000, *Turbulent Flows*, Cambridge University Press, Cambridge.

[19] Menter, F. R., 1994, "Two-Equations Eddy-Viscosity Turbulence Models for Engineering Applications", *AIAA Journal*, Vol. 32 (8), pp. 1598–1605.

[20] Kok, J. C., 1999, "Resolving the dependence on free-stream values for the k-omega turbulence model", *Tech. rep.*, National Aerospace Laboratory NLR.

[21] Langtry, R. B., and Menter, F. R., 2009, "Correlation-Based Transition Modeling for Unstructured Parallelized Computational Fluid Dynamics Codes", *AIAA JOURNAL*, Vol. 47 (12), pp. 2894–2906.

[22] Nobile, F., 2001, "Numerical approximation of fluid-structure interaction problems with application to haemodynamics", Ph.D. thesis, Ecole Polytechnique Federale de Lausanne.

[23] Sváček, P., Feistauer, M., and Horáček, J., 2007, "Numerical simulation of flow induced airfoil vibrations with large amplitudes", *Journal of Fluids and Structures*, Vol. 23 (3), pp. 391–411.

[24] Codina, R., 1993, "A discontinuity capturing crosswind-dissipation for the finite element solution of the convection diffusion equation", *Computational Methods in Applied Mechanical Engineering*, Vol. 110, pp. 325–342.

[25] Gelhard, T., Lube, G., Olshanskii, M. A., and Starcke, J.-H., 2005, "Stabilized finite element schemes with LBB-stable elements for incompressible flows", *Journal of Computational and Applied Mathematics*, Vol. 177, pp. 243–267.

[26] Braack, M., and Mucha, P. B., 2014, "DIRECTIONAL DO-NOTHING CONDITION FOR THE NAVIER-STOKES EQUATIONS", *Journal of Computational Mathematics*, Vol. 32 (5), pp. 507–521.

Conference on Modelling Fluid Flow (CMFF'15)
The 16th International Conference on Fluid Flow Technologies
Budapest, Hungary, September 1-4, 2015

Numerical Investigation of the Interaction of a Finite-Size Particle with a Tangentially Moving Boundary

Francesco ROMANÒ[1], Hendrik C. KUHLMANN[2],

[1] Corresponding Author. Department of Fluid Mechanics and Heat Transfer, Vienna University of Technology, Tower BA/E322, Getreidemarkt 9, 1060 Vienna, E-mail: francesco.romano@tuwien.ac.at
[2] Department of Fluid Mechanics and Heat Transfer, Vienna University of Technology, Tower BA/E322, Getreidemarkt 9, 1060 Vienna, E-mail: h.kuhlmann@tuwien.ac.at

ABSTRACT

The motion of a finite-size particle in steady two-dimensional lid- and shear-driven square-cavity flows is investigated. The coupled equations are solved numerically using a DG-FEM method combined with the so-called smoothed-profile method (SPM) [X. Luo, M. R. Maxey, G. E. Karniadakis, J. Comput. Phys. 228 (2009), 1750–1769]. The spectral convergence enables an accurate and efficient computation of particle trajectories without moving grids. Fully resolved particle trajectories are compared with streamlines and trajectories from one-way coupling. In the shear-driven square cavity with convex streamlines finite-size particles suffer a significant displacement effect when passing the moving boundary closely. While inertia displaces the particle towards outer streamlines, the finite size effect alone displaces the particle towards inner streamlines. For weakly inertial particles the latter displacement effect is qualitatively similar to the displacement modelled by inelastic collision in a one-way-coupling approach.

Keywords: DG–FEM, finite-size particle, free-surface flow, particle-laden flow, SPM, wall effect

1. INTRODUCTION

Two-phase flows arise in many natural phenomena and are of great interest for industrial processes ([1]). Therefore, it is of crucial importance to understand the basic mechanisms involved in such flows in order to predict and control their behavior.

Among multiphase flows, particle-laden flows are made of a continuously connected fluid phase and an immiscible dispersed phase consisting of particles. Typically, the particles are very small compared to the reference length of the fluid domain in which they are immersed. Therefore, the particulate phase is often approximated by point-wise elements. This approximation dramatically simplifies the numerical treatment of multiphase flows. It is justified if the Stokes numbers governing the particle motion are sufficiently small, i.e. St $< 10^{-4} \div 10^{-5}$.

The assumption of point-wise particles leads to a one-way coupling between the fluid and the particle phase. While point-particles are transported by the flow, the particles do not affect the fluid motion within the one-way-coupling approximation. It becomes more accurate the more dilute the particles are. The one-way-coupling approximation breaks down when the particles move very close to boundaries of the domain, e.g. walls or free-surfaces. In the near-boundary regions finite-particle-size effects can play an important role in the evolution of the particulate phase and a proper description of the finite-size-particle motion has to deal, in particular, with the lubrication gap between particle and boundary.

As demonstrated by [2] and [3], particle-boundary interactions can be of crucial importance in modelling physical phenomena like particle-accumulation structures (PAS) in a thermocapillary liquid bridge [4]. While PAS can be qualitatively predicted by the collision model of [2] (called particle–free-surface interaction (PSI) model by [3]), there is no physics-based particle–boundary interaction model available to date which could describe the rapid de-mixing phenomenon leading to PAS. The aim of the present investigation, therefore, is to study the effect of tangentially moving walls and free-surfaces on the trajectories of finite-size particles immersed in an incompressible fluid flow. The need for a dedicated model becomes apparent considering the trajectories of point particles near the boundaries in one-way-coupling approximation: when the minimum distance of a particle trajectory and a boundary becomes less than the radius of the particle it would have to physically penetrate this boundary. As this is not realistic for solid walls as well as for capillary surfaces with high surface tension the finite-size effect clearly plays an important role in determining the real particle trajectory. To remedy this inconsistency of the one-way-coupling approach a dedicated modelling of the particle motion near boundaries is required for a proper description of the evolution of the particulate phase.

We tackle this problem by a two-way-coupling approach in which all relevant scales are resolved numerically. The current problem is mathematically formulated in section 2. Section 3 describes the discretization method using DG–FEM and SPM, including some benchmarks to verify the correct implementation of the numerical solver developed. Section 4 gathers the results of a parametric investigation of inertia and initial velocity-mismatch effects for particle–wall as well as particle–free-surface interactions. Moreover, a comparison with the discontinuous PSI model introduced in [5] and [2] is presented. Finally, in section 5, conclusions will be drawn and prospects for future investigations are outlined.

2. FORMULATION OF THE PROBLEM

We consider the transport of solid particles in an incompressible Newtonian fluid. For simplicity we neglect buoyancy forces. The governing equations are

$$\nabla \cdot \boldsymbol{u} = 0, \tag{1a}$$

$$\frac{\partial \boldsymbol{u}}{\partial t} + \boldsymbol{u} \cdot \nabla \boldsymbol{u} = -\frac{1}{\rho_\mathrm{f}} \nabla p + \nu \nabla^2 \boldsymbol{u}, \tag{1b}$$

$$\frac{\partial T}{\partial t} + \boldsymbol{u} \cdot \nabla T = \kappa \nabla^2 T. \tag{1c}$$

The equations of motion for the i-th particle moving in the fluid are

$$\boldsymbol{F}_i = M_i \dot{\boldsymbol{V}}_i, \tag{2a}$$

$$\boldsymbol{R}_i = \mathsf{I}_i \cdot \dot{\boldsymbol{\Omega}}_i, \tag{2b}$$

where ρ_f is the fluid density, $\boldsymbol{u}$, p and T are the flow velocity, pressure and temperature field, respectively, ν is the kinematic viscosity, κ the thermal diffusivity, and $\boldsymbol{F}$, $\boldsymbol{R}$, $\boldsymbol{V}$, $\boldsymbol{\Omega}$, M and I are the particles' forces, torques, translational and rotational velocities, mass and inertia tensor, respectively. The coupling between the two phases results from the no-slip condition on the particles' surfaces.

While the equations of motion have been presented in a dimensional form, the flow simulation employs a non-dimensionalization. Since we shall consider the pure mechanical lid-driven cavity and also a thermocapillary-driven cavity we apply different scalings depending on the particular case. For the lid-driven cavity we use the convective scaling

$$\boldsymbol{u} = \hat{\boldsymbol{u}} U \ , \ \ \boldsymbol{x} = \hat{\boldsymbol{x}} L, \ \ t = \hat{t}\frac{L}{U} \ , \ \ p = \hat{p} \rho_\mathrm{f} U^2, \tag{3}$$

where U is the velocity of the lid, L a characteristic length, and the superscript ^ indicates non-dimensional quantities. For the thermocapillary-driven cavity we use the viscous scaling

$$\boldsymbol{u} = \hat{\boldsymbol{u}} \frac{\nu}{L}, \ \boldsymbol{x} = \hat{\boldsymbol{x}} L, \ t = \hat{t} \frac{L^2}{\nu}, \ p = \hat{p} \frac{\rho_\mathrm{f} \nu^2}{L^2}, \ T = \hat{T} \Delta T, \tag{4}$$

where ΔT is a characteristic temperature difference.

3. NUMERICAL METHODS AND CODE VALIDATION

The numerical treatment of two-phase problems can be roughly classified into two main categories. In the Lagrangian description of the particle motion a computational mesh is co-moving with the particle (e.g. the ALE method [6]). In the Eulerian representation of the particle motion all governing equations are solved on a stationary grid (DLM, FCM, IMB and IIM, see e.g. [7] and [8]).

In the present investigation, an Eulerian approach is adopted implementing a *smoothed-profile method* (SPM). It includes the effect of the particles on the flow in a smooth body-force fashion instead of explicitly enforcing the no-slip boundary condition on the particles' surfaces. The computational grid for the flow simulation includes both phases. A thin interface layer across each particle's surface is used to smoothly pass from fluid-dynamics to rigid-body equations of motion.

To calculate the velocities of the particles we use the penalty-body-force approach as discussed in [9] and [10]. This method guarantees the rigidity of the particle and implicitly applies the no-slip boundary condition responsible for coupling the two-phases. To distinguish between the solid domain of particle i and the surrounding fluid domain we use the concentration function

$$\phi_i(\boldsymbol{x}, t) = \frac{1}{2}\left[\tanh\left(\frac{a_i - |\boldsymbol{x} - \boldsymbol{P}_i|}{\xi_i}\right) + 1\right], \tag{5}$$

where $\boldsymbol{P}_i$ and ξ_i are, respectively, the centroid position and the interface thickness of the i-th particle and a_i is the radius of the particle assumed to be circular (in 2D) or spherical (in 3D). The function ϕ is called the *smoothed profile* and equals to one inside the particles, whereas it is zero in the fluid phase. For temporal discretization the second-order stiffly-stable splitting scheme of [11] is employed, including a semi-implicit treatment of the particle-phase. For the spatial discretization we use a discrete-Galerkin finite-element method (DG–FEM). Within this approach the algorithm used for simulating the particle-laden flow (1) and (2) reads (see [9] for details):

$$\boldsymbol{P}_i^{n+1} = \boldsymbol{P}_i^n + \Delta t \sum_{k=0}^{K} a_k \boldsymbol{V}_i^{n-k},$$

$$\frac{\delta_0 \tilde{\boldsymbol{u}} - \alpha_0 \boldsymbol{u}^n - \alpha_1 \boldsymbol{u}^{n-1}}{\Delta t} = -\beta_0 \boldsymbol{N}(\boldsymbol{u}^n, \boldsymbol{u}^n) - \beta_1 \boldsymbol{N}(\boldsymbol{u}^{n-1}, \boldsymbol{u}^{n-1}),$$

$$
\begin{aligned}
\frac{\delta_0 \tilde{T} - \alpha_0 T^n - \alpha_1 T^{n-1}}{\Delta t} &= -\beta_0 N(\boldsymbol{u}^n, T^n) \\
&\quad - \beta_1 N(\boldsymbol{u}^{n-1}, T^{n-1}), \\
\nabla^2 p^* &= \frac{\delta_0}{\Delta t} \nabla \cdot \tilde{\boldsymbol{u}}, \\
\frac{\partial p^*}{\partial \hat{\boldsymbol{n}}} &= -\beta_0 \hat{\boldsymbol{n}} \cdot \left(\frac{D\boldsymbol{u}^n}{Dt} + \nu \nabla \times \boldsymbol{\omega}^n \right) \\
&\quad - \beta_1 \hat{\boldsymbol{n}} \cdot \left(\frac{D\boldsymbol{u}^{n-1}}{Dt} + \nu \nabla \times \boldsymbol{\omega}^{n-1} \right), \\
-\nabla^2 \boldsymbol{u}^* + \frac{\delta_0}{\nu \Delta t} \boldsymbol{u}^* &= \frac{\delta_0}{\nu \Delta t} \tilde{\boldsymbol{u}} - \frac{1}{\nu} \nabla p^*, \\
-\nabla^2 T^{n+1} + \frac{\delta_0}{k \Delta t} T^{n+1} &= \frac{\delta_0}{k \Delta t} \tilde{T}, \\
\boldsymbol{F}_i^n &= \frac{1}{\Delta t} \int_\Omega \rho_{\mathrm{f}} \phi_i^{n+1} \left(\boldsymbol{u}^* - \boldsymbol{u}_{\mathrm{p}}^n \right) \mathrm{d}\boldsymbol{x}, \\
\boldsymbol{R}_i^n &= \frac{1}{\Delta t} \int_\Omega \boldsymbol{r}_i^{n+1} \times \left[\rho_{\mathrm{f}} \phi_i^{n+1} \left(\boldsymbol{u}^* - \boldsymbol{u}_{\mathrm{p}}^n \right) \right] \mathrm{d}\boldsymbol{x}, \\
\boldsymbol{V}_i^{n+1} &= \boldsymbol{V}_i^n + M_i^{-1} \Delta t \sum_{k=0}^{K} a_k \boldsymbol{F}_i^{n-k}, \\
\boldsymbol{\Omega}_i^{n+1} &= \boldsymbol{\Omega}_i^n + I_i^{-1} \Delta t \sum_{k=0}^{K} a_k \boldsymbol{R}_i^{n-k}, \\
\phi^{n+1} \boldsymbol{u}_{\mathrm{p}}^{n+1} &= \sum_{i=1}^{N_{\mathrm{p}}} \phi_i^{n+1} \left[\boldsymbol{V}_i^{n+1} + \boldsymbol{\Omega}_i^{n+1} \times \left(\boldsymbol{x} - \boldsymbol{P}_i^{n+1} \right) \right], \\
\nabla^2 p_p &= \delta_0 \nabla \cdot \left[\frac{\phi^{n+1} \left(\boldsymbol{u}_{\mathrm{p}}^{n+1} - \boldsymbol{u}^* \right)}{\Delta t} \right], \\
\frac{\partial p_p}{\partial \hat{\boldsymbol{n}}} &= \frac{\delta_0}{\Delta t} \left(\phi^{n+1} \left(\boldsymbol{u}_{\mathrm{p}}^{n+1} - \boldsymbol{u}^* \right) \right) \cdot \hat{\boldsymbol{n}}, \\
\frac{\delta_0 \boldsymbol{u}^{n+1} - \delta_0 \boldsymbol{u}^*}{\Delta t} &= \frac{\delta_0 \phi^{n+1} \left(\boldsymbol{u}_{\mathrm{p}}^{n+1} - \boldsymbol{u}^* \right)}{\Delta t} - \nabla p_{\mathrm{p}}, \qquad (6)
\end{aligned}
$$

where $N(\boldsymbol{u}, \cdot)$ represents the non-linear term written in a conservative form as follows

$$
N(\boldsymbol{u}, \cdot) = \frac{\partial (u \cdot)}{\partial x} + \frac{\partial (v \cdot)}{\partial y} + \frac{\partial (w \cdot)}{\partial z}. \qquad (7)
$$

The superscript $*$ refers to the flow field obtained without updating the perturbation caused by the particles, e.g., $p^{n+1} = p^* + p_{\mathrm{p}}$, where the subscript p indicates the field due to the particles perturbation. The coefficients a_k originate from the BDF scheme which is adopted for integrating the particle positions and velocities. The position vector from the i-th particle center is denoted $\boldsymbol{r}_i$ and the coefficients δ_0, $\alpha_0, \alpha_1, \beta_0, \beta_1$ are tabulated in [11].

In order to clearly identify the particle-boundary interaction only a single particle will be simulated in the flow. However, SPM would be very efficient for simulating several particles, even of complex shapes. Finally, for the spatial discretization an Interior Penalty Discontinuous Galerkin (IPDG) method is employed.

The present investigation will be limited to two–dimensional flows and circular particles. To verify the correct implementation of the solver four different benchmarks are considered. Two for testing the fluid part of the splitting algorithm and two different ones for the particle part.

As a first check we consider the lid-driven flow in a square cavity using the dimensionless boundary conditions

$$
\begin{aligned}
&\hat{\boldsymbol{u}}\,(\hat{x} = -1/2) = (0, 0), \quad \hat{\boldsymbol{u}}\,(\hat{x} = +1/2) = (0, 0), \\
&\hat{\boldsymbol{u}}\,(\hat{y} = -1/2) = (0, 0), \quad \hat{\boldsymbol{u}}\,(\hat{y} = +1/2) = (1, 0).
\end{aligned} \qquad (8)
$$

We use an evenly-spaced distribution of vertices of a triangular computational mesh. Table 1 shows the grid convergence obtained by our DG-FEM using 5th-order polynomials and N nodes per each space dimension of the cavity. The monitored quantities are streamfunction and vorticity $\hat{\psi}$ and $\hat{\omega}$, respectively. The computed data in Table 1 shows a good agreement with literature data. This favourable comparison proves the correct implementation of the mass and momentum balances in the algorithm (6).

Table 1. Lid-driven cavity benchmark: Re = 1000.

Grid/Ref.	$\min(\hat{\psi})$	$\hat{\omega}_{\min(\hat{\psi})}$	$\hat{x}_{\min(\hat{\psi})}$	$\hat{y}_{\min(\hat{\psi})}$
[12]	−0.119	−2.068	0.031	0.065
[13]	−0.118	−2.050	0.031	0.063
[14]	−0.119	−2.066	0.034	0.064
$N = 10$	−0.114	−1.975	0.033	0.067
$N = 20$	−0.117	−2.023	0.032	0.063
$N = 30$	−0.118	−2.039	0.031	0.065
$N = 40$	−0.118	−2.040	0.031	0.064
$N = 50$	−0.118	−2.045	0.031	0.065

To extend the verification to the energy equation a thermocapillary-driven cavity is considered. Following [15] the free-surface of the cavity is assumed non-deformable, i.e. we consider the asymptotic limit of a large mean surface tension and assume that the free-surface is adiabatic. The non-dimensional boundary conditions are

$$
\begin{aligned}
\hat{x} = -1/2 &: \hat{u} = 0, \quad \hat{v} = 0, \quad \hat{T} = -1/2, \\
\hat{x} = +1/2 &: \hat{u} = 0, \quad \hat{v} = 0, \quad \hat{T} = +1/2, \\
\hat{y} = -1/2 &: \hat{u} = 0, \quad \hat{v} = 0, \quad \partial_{\hat{y}} \hat{T} = 0, \\
\hat{y} = +1/2 &: \partial_{\hat{y}} \hat{u} = -\mathrm{Re} \partial_{\hat{x}} \hat{T}, \quad \hat{v} = 0, \quad \partial_{\hat{y}} \hat{T} = 0,
\end{aligned} \qquad (9)
$$

where the thermocapillary Reynolds number is $\mathrm{Re} = \gamma \Delta T d / (\rho_{\mathrm{f}} \nu^2)$ with surface tension coefficient γ and the imposed temperature difference ΔT between the side walls. Due to the characteristic features of thermocapillary flows, the finite elements must be refined near the hot and cold corners of the free-surface. Considering 5th-order polynomials the grid refinement is controlled only by the size parameter h. Table 2 lists some key parameters for this problem. The superscript 'fs' refers to the free-surface, the subscripts 'left', 'middle' and 'right' stand for $\hat{x} = -1/2$, $\hat{x} = 0$ and $\hat{x} = 1/2$, respectively, and Nu is the Nusselt number

$$\mathrm{Nu} = \int_{-\frac{1}{2}}^{+\frac{1}{2}} \left(\hat{u}\hat{T} - \frac{\partial \hat{T}}{\partial \hat{x}} \right) \mathrm{d}\hat{y}. \tag{10}$$

We find grid convergence. The good agreement with literature data again confirms correct implementation of (6).

Table 2. Thermocapillary-driven cavity benchmark: Re = 10000, Pr = 1.

Grid/Ref.	$\min(\hat{\psi})$	$\hat{\omega}_{\min(\hat{\psi})}$	$\hat{x}_{\min(\hat{\psi})}$	$\hat{y}_{\min(\hat{\psi})}$
[16]	32.3	697	−0.08	0.12
[17]	32.1	701	−0.07	0.13
[18]	32.4	729	–	–
[15]	32.2	702	−0.07	0.13
h = .07	32.225	704.9	−0.075	0.130
h = .06	32.228	705.0	−0.074	0.130
h = .05	32.222	703.0	−0.074	0.131
h = .04	32.232	704.1	−0.073	0.130
h = .03	32.231	705.5	−0.072	0.128

Grid/Ref.	$\mathrm{Nu}_{\mathrm{left}}$	$\mathrm{Nu}_{\mathrm{middle}}$	$\mathrm{Nu}_{\mathrm{right}}$
[16]	4.33	4.40	4.36
[17]	4.36	–	4.36
[18]	4.44	4.36	4.30
[15]	4.36	4.36	4.36
h = .07	4.392	4.374	4.337
h = .06	4.383	4.397	4.336
h = .05	4.377	4.352	4.365
h = .04	4.374	4.352	4.366
h = .03	4.370	4.357	4.366

Grid/Ref.	$\hat{u}^{\mathrm{fs}}_{\mathrm{middle}}$	$\max(\hat{u}^{\mathrm{fs}})$	$\hat{x}_{\max(\hat{u}^{\mathrm{fs}})}$
[16]	−296	–	–
[17]	−305	–	–
[18]	−306	–	–
[15]	−304	−712	−0.496
h = .07	−304.6	−680.8	−0.4964
h = .06	−304.5	−678.8	−0.4962
h = .05	−304.7	−690.9	−0.4956
h = .04	−304.8	−691.1	−0.4955
h = .03	−304.8	−688.8	−0.4959

Finally, in order to test the correct implementation of the splitting algorithm in dealing with the perturbation field due to the particle, two more benchmarks are presented. In both the cases a circular cylinder is immersed in a fluid at rest. The cylinder axis is located in the center of a square computational domain, the linear dimension of which is 100 diameters of the cylinder. To avoid effects from the domain boundary far-field conditions have been imposed on the domain boundaries. The scaling is based on the dynamic pressure as in (3).

In the first case, the x position of the cylinder with diameter D is forced to oscillate harmonically with frequency f according to $x(t) = -A\sin(2\pi f t)$. The non-dimensional groups of interest are the cylinder's Reynolds number and the Keulegan–Carpenter number

$$\mathrm{Re} = \frac{U_{\max} D}{\nu}, \quad \mathrm{KC} = \frac{U_{\max}}{fD}, \tag{11}$$

where $U_{\max}$ is the maximum oscillation velocity. The resulting drag coefficient is compared with experimental and numerical data [19] for nine periods of oscillation for Re = 100 and KC = 5. From the very good agreement between computed and literature data for the drag coefficient shown in Fig. 1 we consider the code verified regarding the forces on the particle.

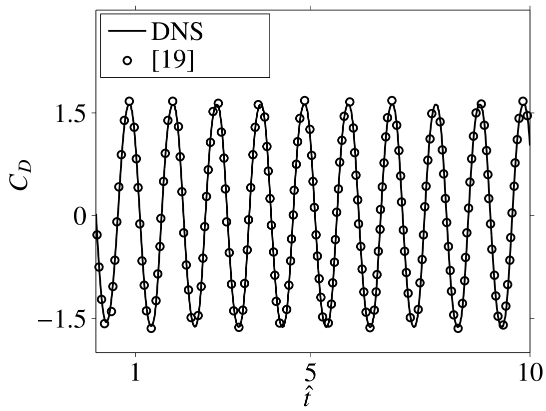

Figure 1. Drag coefficient $C_D = F_x/\rho_f U^2_{\max} D$ for in-line oscillating cylinder benchmark: Re = 100, KC = 5.

In the final benchmark, the cylinder is forced to rotate periodically according to

$$\Omega(t) = A\sin(2\pi f t). \tag{12}$$

The resulting torque coefficient is compared with numerical data of [20] for five periods of oscillation. For Re = 300 and non-dimensional frequency f = 0.2 we find a very good agreement with the data of [20] (Fig. 2). This successful comparison concludes the validation of our code.

4. RESULTS

Two main effects on the particle motion of the two-way coupling will be investigated. At first, the initialization transient is considered for a particle immersed in a lid-driven cavity flow for Re = 100. Thereafter, the inertial effect is investigated for particles heavier than the fluid moving in a thermocapillary-driven cavity for Re = 1000 in the limit Pr → 0.

The latter simulations are then compared with the PSI model [2, 3] applied to one-way coupled finite-size perfect tracers. In order to briefly present the basic assumption of such an approach, the reader is referred to Fig. 3: due to its finite-size the distance between the particle's trajectory (trajectory of the center of a non-deformable spherical/circular

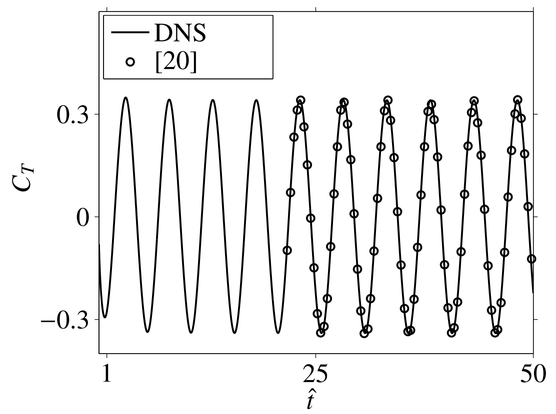

Figure 2. Torque coefficient $C_T = R/\frac{1}{2}\rho_f U_{max}^2 D^2$ for rotational oscillating cylinder benchmark: Re = 300, f = 0.2.

particle) and a non-deformable boundary must always remain larger than the particle radius a. If this condition is violated within the one-way coupling approach, the particle is assumed to experience a perfectly inelastic impact upon making contact with the boundary leading to a sliding motion along the boundary as long as the wall-normal velocity is directed out of the fluid domain.

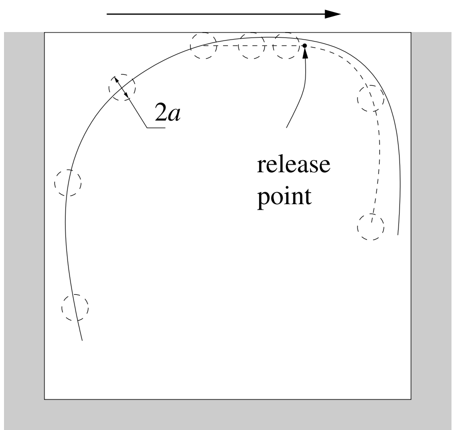

Figure 3. Schematic representation of the PSI model effects on particle trajectories.

4.1. *Initialization Effect for a Particle in a Lid-Driven Cavity Flow*

The initial conditions for a particle placed in flow at $t = 0$ influence its trajectory for $t > 0$. This is particularly true, since the perturbation of the flow caused by the presence of a finite-size particle are typically unknown. Therefore, we investigate the initial behavior for a range of initial conditions.

We consider two different initial conditions for a finite-size particle initiated at the same position. In the first simulation the centroid velocity and the rotation rate of the particle are initially matched to that of the flow. In the second simulation the initial translation and rotation rates of the particle are set to zero. The particle radius is $a = 0.03L$, i.e. 3% of the length of the cavity, and the particle-to-fluid density ratio is $\varrho = \rho_p/\rho_f = 2$.

In Fig. 4 the unperturbed streamlines and the two trajectories are depicted. Obviously, the influence of the initial conditions of the particle can be neglected on the trajectories shown. This is due to the short time scale τ_p of the particle as compared to the time scale of the flow τ_f as given by the Stokes number

$$\mathrm{St} = \frac{\tau_p}{\tau_f} = \frac{2\rho_p a^2}{9\rho_f L^2}\mathrm{Re}. \tag{13}$$

For $a/L = 0.03$, Re = 100 and $\rho_p/\rho_f = 2$, St = 4×10^{-2} the relaxation time of the particle is nearly two orders of magnitude smaller than the time scale of the flow. Hence, the discontinuous initial conditions will rapidly smooth out. The simulations show no visible effect of the initial conditions on the trajectories.

In Fig. 4 the particles are initiated at $(\hat{x}_{in}, \hat{y}_{in}) = (-0.420, 0.30)$. The simulation time covered by the figure is $\hat{t} = 5$ and the particles take $\hat{t}_* = 2.39$ to cross the whole cavity length and arrive near $(\hat{x}_*, \hat{y}_*) = (0.440, 0.30)$. Considering this as a conservative estimation for the convective time along the trajectory of the particle, the relaxation time would be $\tau_p = 0.04$. The relative particle position would then be $\left(\hat{x}_p, \hat{y}_p\right) \approx (-0.424, 0.32)$. It implies that the travelled distance is smaller than the particle radius, illustrating the rapid particle relaxation process.

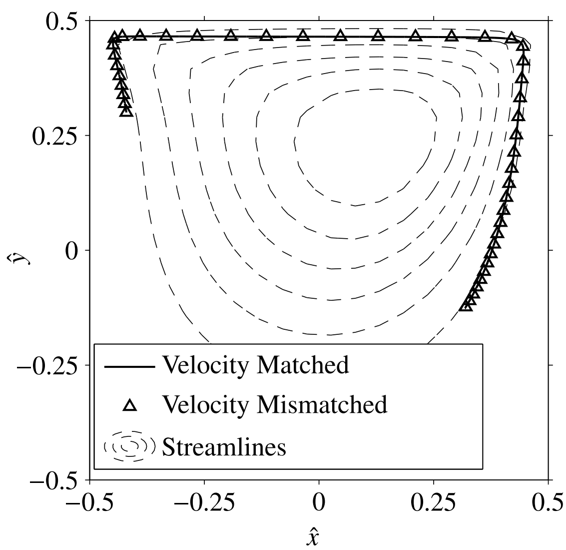

Figure 4. Effect of different initial conditions on particle trajectories initialized at the same point.

The robustness of the particle trajectories with respect to the initial conditions also applies to the initial position along a given particle trajectory. This is demonstrated in Fig. 5 where the trajectories of three particles are considered which were initialized with zero velocity and zero rotation rate. Two of these particles were initiated at different y locations on the trajectory of the first particle (reference trajectory, full line). There is not visible difference among the three trajectories shown.

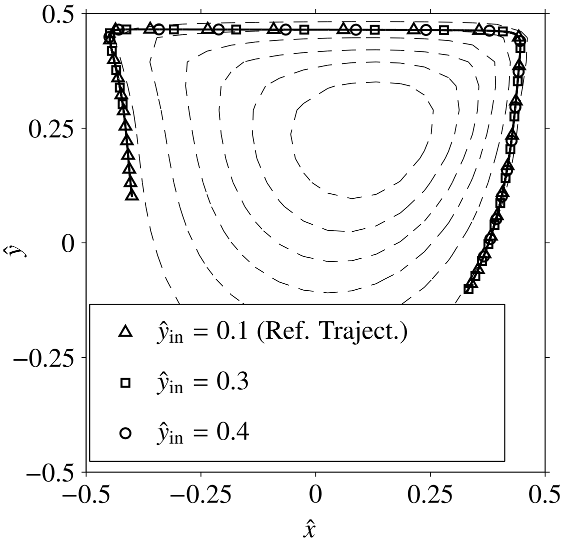

Figure 5. Effect of the different initial conditions for particles initialized along the same reference trajectory (see text for details).

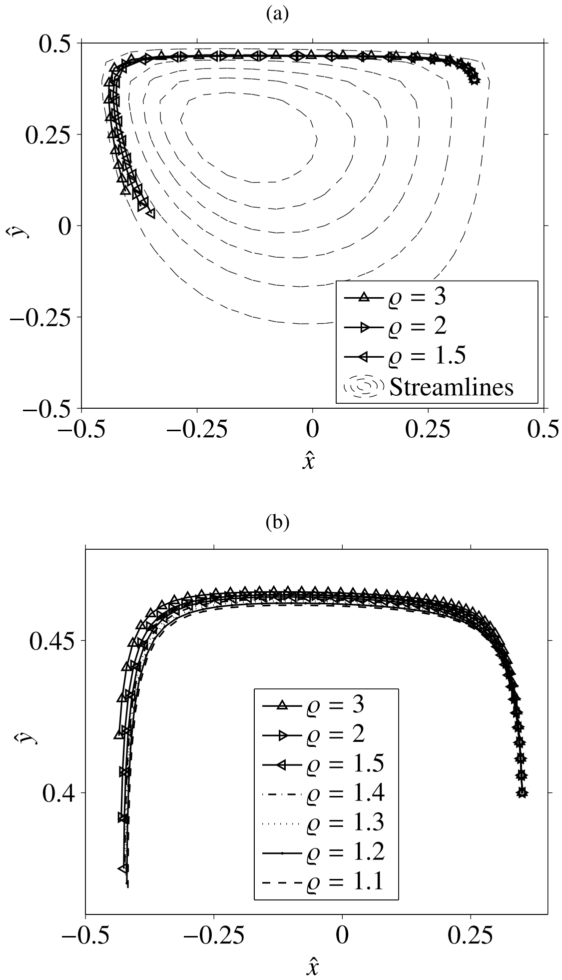

Figure 6. Trajectories for heavy particles with $a = 0.03L$ initialized at the same reference point. (a) Comparison with unperturbed flow streamlines. (b) Comparison among 7 different density ratios ϱ. Note the different scaling of the axes.

4.2. Particle–Free-Surface Interaction

The motion of finite-size particles near thermocapillary free-surfaces is of particular interest, because streamlines can strongly gather near the free-surface [21]. Moreover, the free-surface is locally expanding or contracting [22]. Both effects are related to each other and promote a significant amount of suspended particles to be transported close to the free-surface.

We consider a differentially-heated square cavity in the limit Pr $\rightarrow$ 0 for Re $= 10^3$ such that the free-surface temperature varies linearly. Thus the flow is driven by a constant shear stress along the free-surface. We are interested in the effect of inertia for heavy particles ($\varrho > 1$) moving close to the free-surface. Furthermore, a comparison will be made between particle trajectories obtained by two-way and one-way coupling with the PSI model (see Fig. 3) being applied to the latter. Trajectories for point and finite-size density-matched particles (one-way coupled) will be compared with those for finite-size, heavy particles (two-way coupled). To isolate the finite-size effect from the inertia effect we extrapolate the trajectories for $\varrho \neq 1$ to $\varrho = 1$ and compare the result with the trajectory obtained by one-way coupling in conjunction with the PSI model.

To investigate the effect of the density ratio ϱ on the motion of finite-size particles with $a = 0.03L$ the initialization position of the particles is kept constant. Figure 6a shows trajectories for different values of ϱ together with streamlines of the unperturbed flow. The motion of the particles nearly parallel to the interface is not significantly affected by inertia effect. Inertia is important in the turning regions of high flow acceleration.

A close-up shown in Fig. 6b reveals that the trajectories sensibly differ from the streamlines (trajectories of perfect tracers). This is due to two main contributions: particle-boundary interaction and inertia. Due to the inertial centrifugal acceleration heavier particles tend to move closer to the boundaries. This conclusion is not obvious, however, because the two contributions mentioned cannot easily be separated. The stronger the centrifugal forces the stronger are the finite-size and boundaries effects. Clearly, finite-size effects oppose the inertial centrifugal one. Moreover, the trajectory cannot simply be represented by a linear superposition of both effects. As a result, the trajectories deviate from each other near the cold (upper left) corner of the cavity, but finally approach each other again. Yet, the trajectories remain significantly different from each other.

Since the trajectories depend smoothly on ϱ we

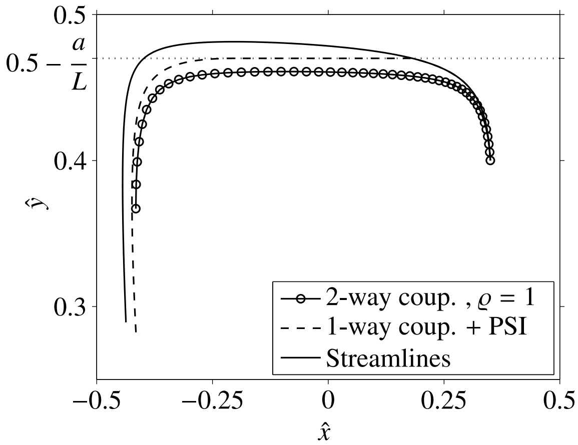

Figure 7. Comparison between 2-way coupled simulation and 1-way coupled PSI model for trajectories integrated for $\Delta\hat{t} = 0.02$, $a = 0.03L$.

can extrapolate the results obtained to the trajectory of a density-matched particle ($\varrho = 1$). In this limit centrifugal effects are absent and the trajectory is determined by the finite-size effect only. In Fig. 7 the resulting trajectory is compared with streamlines and the trajectory for one-way-coupling using the inelastic PSI model [2, 3, 23]. In the one-way-coupled motion the density-matched particle moves on streamlines (full line and dashed line) as long as the streamline distance from the boundary is larger than the particle radius. Thus the PSI can be interpreted as a *streamline hopping* [3]. During the approach to the free-surface the two-way-coupled trajectory (circles), initially coinciding with a streamline, deviates from the streamline towards its concave side. Thus it differs from the one-way coupling trajectory as a result of the close-by boundaries. Moreover, the trajectory from two-way coupling stays away from the free-surface by a distance significantly larger than the particle radius a. This is interpreted to be due to viscous effects in the gap between the particle and the free-surface (thin viscous film). Finally, during the departure from the free-surface, the trajectory deviates towards the convex side of the streamlines. This deviation does not fully compensate, however, the deviation from the original streamline during the approach phase. As a result, the two-way coupled particle trajectory for the density-matched particle moves much closer to the trajectory predicted by the PSI model than to the streamline from which it originated before interacting with the free-surface.

This result is significant, since the rapid particle accumulation (PAS) in liquid bridges has been traced back to the transfer between streamlines of density-matched particles [2, 3, 23]. Figure 7 shows that the streamline transfer predicted by the two-way coupling simulation is even stronger, for the present parameters, than the one assumed by the PSI model and one-way coupling. The similarity of the amount of streamline hopping for both trajectories (PSI and two-way coupling) seems to indicate that the simple PSI model can, indeed, qualitatively predict the real particle clustering by particle–boundary interaction.

5. CONCLUSION

A DG-FEM has been implemented for simulating non-isothermal incompressible Navier–Stokes flows. In combination with an SPM the motion of finite-size particles has been computed in two-way-coupling manner. The two-dimensional version of the code was verified by considering different benchmarks involving moving bodies. As expected, for small Stokes numbers the initialization of a finite-size particle in a developed flow has a negligible influence on the motion of two-dimensional particles for times of the order of the characteristic time of the flow.

Considering the steady flow with convex streamlines in a lid-driven square cavity (Dirichlet boundary conditions) and in a stress-driven square cavity (Neumann boundary conditions) finite-size particle trajectories near the tangentially moving boundary have been computed by fully resolving the flow around the particle. Significant deviations of the particle trajectory from the streamlines are caused by particle–boundary interaction and, for heavy particles, by inertia. Inertia-induced centrifugal forces displace the particle to the *outer* streamlines in the regions of high streamline curvature. For density-matched particles the particle–boundary interaction alone displaces the particle to *inner* streamlines when they pass the moving boundary in a close distance. For the parameters studied the displacement effect due to the particle–boundary interaction is even stronger than the streamline hopping predicted by the inelastic collision model (PSI model) of [2, 3]. Since the rapid particle accumulation [24, 4] found in thermocapillary liquid bridges can be reproduced by the inelastic collision model (PSI) [23, 3] by which a particle is displaced to *inner* streamlines of the flow, the present result confirms this mechanism from first principles. The particle displacement towards inner streamlines is counteracted by centrifugal forces for heavy particles. This could explain the measurements of [4] according to which the formation time for particle accumulation structures (PAS) increases with particle density and size.

It remains to be shown that the displacement effect found in two dimensions for circular particles is also acting in three-dimensional lid- and shear-driven flows seeded with finite-size spherical particles. The analysis can also be extended to study particle–particle interaction. These open problems are beyond the scope of the present paper and will be subject to future investigations.

REFERENCES

[1] Crowe, C. T., Schwarzkopf, J. D., Sommerfeld, M., and Tsuji, Y., 2011, *Multiphase flows with*

droplets and particles, CRC press.

[2] Hofmann, E., and Kuhlmann, H. C., 2011, "Particle accumulation on periodic orbits by repeated free surface collisions", *Physics of Fluids (1994-present)*, Vol. 23 (7), p. 072106.

[3] Mukin, R., and Kuhlmann, H. C., 2013, "Topology of hydrothermal waves in liquid bridges and dissipative structures of transported particles", *Phys Rev* E, Vol. 88, p. 053016.

[4] Schwabe, D., Mizev, A. I., Udhayasankar, M., and Tanaka, S., 2007, "Formation of dynamic particle accumulation structures in oscillatory thermocapillary flow in liquid bridges", *Phys Fluids*, Vol. 19, p. 072102.

[5] Kuhlmann, H., and Hofmann, E., 2011, "The mechanics of particle accumulation structures in thermocapillary flows", *The European Physical Journal Special Topics*, Vol. 192 (1), pp. 3–12.

[6] Duarte, F., Gormaz, R., and Natesan, S., 2004, "Arbitrary Lagrangian-Eulerian method for Navier–Stokes equations with moving boundaries", *Computer Methods in Applied Mechanics and Engineering*, Vol. 193 (45–47), pp. 4819–4836.

[7] Lomholt, S., and Maxey, M. R., 2003, "Force-coupling method for particulate two-phase flow: Stokes flow", *Journal of Computational Physics*, Vol. 184 (2), pp. 381–405.

[8] Peskin, C. S., 2002, "The immersed boundary method", *Acta Numerica*, Vol. 11, pp. 479–517.

[9] Luo, X., Maxey, M. R., and Karniadakis, G. E., 2009, "Smoothed profile method for particulate flows: Error analysis and simulations", *Journal of Computational Physics*, Vol. 228 (5), pp. 1750–1769.

[10] Nakayama, Y., and Yamamoto, R., 2005, "Simulation method to resolve hydrodynamic interactions in colloidal dispersions", *Phys Rev E*, Vol. 71, p. 036707.

[11] Karniadakis, G. E., Israeli, M., and Orszag, S. A., 1991, "High-order splitting methods for the incompressible Navier-Stokes equations", *Journal of Computational Physics*, Vol. 97 (2), pp. 414–443.

[12] Botella, O., and Peyret, R., 1998, "Benchmark spectral results on the lid-driven cavity flow", *Computers and Fluids*, Vol. 27 (4), pp. 421–433.

[13] Ghia, U., Ghia, K., and Shin, C., 1982, "High-Re solutions for incompressible flow using the Navier-Stokes equations and a multigrid method", *Journal of Computational Physics*, Vol. 48 (3), pp. 387–411.

[14] Sahin, M., and Owens, R. G., 2003, "A novel fully implicit finite volume method applied to the lid-driven cavity problem – Part I: High Reynolds number flow calculations", *International Journal for Numerical Methods in Fluids*, Vol. 42 (1), pp. 57–77.

[15] Kuhlmann, H. C., and Albensoeder, S., 2008, "Three-dimensional flow instabilities in a thermocapillary-driven cavity", *Phys Rev E*, Vol. 77, p. 036303.

[16] Carpenter, B. M., and Homsy, G. M., 1990, "High Marangoni number convection in a square cavity, part II", *Phys Fluids A*, Vol. 2, p. 137.

[17] Xu, J., and Zebib, A., 1998, "Oscillatory two- and three-dimensional thermocapillary convection", *Journal of Fluid Mechanics*, Vol. 364, pp. 187–209.

[18] Peltier, L. J., and Biringen, S., 1993, "Time-dependent thermocapillary convection in a rectangular cavity: numerical results for a moderate Prandtl number fluid", *Journal of Fluid Mechanics*, Vol. 257, pp. 339–357.

[19] Dütsch, H., Durst, F., Becker, S., and Lienhart, H., 1998, "Low-Reynolds-number flow around an oscillating circular cylinder at low Keulegan-Carpenter numbers", *Journal of Fluid Mechanics*, Vol. 360, pp. 249–271.

[20] Kim, D., and Choi, H., 2006, "Immersed boundary method for flow around an arbitrarily moving body", *Journal of Computational Physics*, Vol. 212 (2), pp. 662–680.

[21] Zebib, A., Homsy, G. M., and Meiburg, E., 1985, "High Marangoni number convection in a square cavity", *Phys Fluids*, Vol. 28, pp. 3467–3476.

[22] Kuhlmann, H. C., Mukin, R. V., Sano, T., and Ueno, I., 2014, "Structure and dynamics of particle-accumulation in thermocapillary liquid bridges", *Fluid Dynamics Research*, Vol. 46 (4), p. 041421.

[23] Muldoon, F. H., and Kuhlmann, H. C., 2013, "Coherent particulate structures by boundary interaction of small particles in confined periodic flows", *Physica D*, Vol. 253, pp. 40–65.

[24] Tanaka, S., Kawamura, H., Ueno, I., and Schwabe, D., 2006, "Flow structure and dynamic particle accumulation in thermocapillary convection in a liquid bridge", *Phys Fluids*, Vol. 18, p. 067103.

Conference on Modelling Fluid Flow (CMFF'15)
The 16th International Conference on Fluid Flow Technologies
Budapest, Hungary, September 1-4, 2015

NUMERICAL AND EXPERIMENTAL INVESTIGATION OF THE EJECTOR EFFECT APPLICABLE TO LOW HEAD VERTICAL KAPLAN TURBINES

Jürgen SCHIFFER[1], Helmut BENIGNI[2], Helmut JABERG[3]
Rudolf FRITSCH[4], Joan GOMEZ[5]

[1] Corresponding Author. Institute of Hydraulic Fluidmachinery, Graz University of Technology. Kopernikusgasse 14/IV, A-8010 Graz, Austria. Tel.: +43 316 873 7573, Fax: +43 316 873 7577, E-mail: juergen.schiffer@tugraz.at
[2] Institute of Hydraulic Fluidmachinery, Graz University of Technology. E-mail: helmut.benigni@tugraz.at
[3] Institute of Hydraulic Fluidmachinery, Graz University of Technology. E-mail: helmut.jaberg@tugraz.at
[4] ZT Fritsch GmbH. E-mail: office@zt-fritsch.at
[5] The City College Of New York. E-mail: jgomezp000@citymail.cuny.edu

ABSTRACT

In order to contribute to the global transition from fossil to renewable energy sources several countries all over the world are now focusing also more strongly on power generation from small-scale hydropower plants. A very important aspect in this context is how to maximize the exploitation of the hydraulic power available at a new power plant site.

One possibility for the maximization of the power output is the technical utilization of the ejector effect, which can reasonably be used for low head applications. The ejector effect is reached by conscious merging of the draft tube flow with the high energy excess water flow via combination of a bent draft tube with an ejector chute. In case of surplus water, a hydraulic power increase of up to 25 % can be reached compared to a conventional power plant design. Although the ejector effect can only be used in case of flood water, the annual energy production can be significantly increased.

In order to get a more scientific insight into the idea of the energetic use of the excess water, as well as to improve the planning security of future water power projects, a model test rig was created at the Institute for Hydraulic Fluidmachinery at Graz University of Technology. Additionally, the experimental programme was accompanied by numerical simulations.

The comparison of numerical results with the measurement data acquired on the test rig shows that both approaches match well, however, it also highlights some shortcomings of the numerical model. Nevertheless, it was proven that the numerical simulation is an appropriate approach for a realistic investigation of the ejector effect taking into account all its negative and positive aspects.

Keywords:
Low head hydro power; Vertical Kaplan turbine; Ejector effect; Open channel flow; VOF method; Two-phase simulation;

NOMENCLATURE

Fr	[-]	Froude number
H_{HW}	[m]	Headwater level
H_{TW}	[m]	Tail water level
H	[m]	Gross head
H_{Tot}	[m]	Total head
H_{Tu}	[m]	Turbine head
M	[-]	Model scale
$P_{hydr.}$	[W]	Hydraulic power available
Q	[m³/s]	Flow rate
g	[m/s²]	Gravitation constant
ρ	[kg/m³]	Density of water

Subscripts and Superscripts

DTout	Draft tube outlet
Ej	Ejector
HW	Headwater
Model	Model test rig
PT	Prototype
Tot	Total
Tu	Turbine
TW	Tail water

1. INTRODUCTION

The problem of utilizing at least a part of the energy inherent in flood discharges that is usually lost in case of run-of-river water power plants arose around 1900 where different power plant concepts were studied and even taken into operation. [1]

Later on, in the 1950-ies, Slisskii [2] published refinements of the methods for the calculation of

„head increasers". According to his design recommendations a few power plants utilizing the ejector effect were built in Russia.

The common physical principle underlying all the concepts is to mix the excess water flow with the flow leaving the draft tube, and thus to transmit a part of the kinetic energy inherent in the added high velocity flow to the rather slow flow leaving the turbine. This effect – also called "ejector effect" - is accompanied by a corresponding reduction in the pressure level at the draft tube outlet which can be considered equivalent to lowering the tail water level. Consequently, an increased effective turbine head can be reached.

Mosonyi [1] states that the economical utilization of the ejector effect is limited to a comparatively low gross head of around H = 2 - 10 m.

However, it turned out that the concepts investigated between 1900 and 1950 have fallen into oblivion afterwards. Several years ago the idea was taken up again for the construction of some new small-scale hydro power projects in Austria.

On the basis of two reference projects (Power Plants MÜHLTALWEHR [3] and WAIDHOFEN [4]) it was shown, that the integration of the ejector principle led to a significant increase of production in case of surplus water.

In order to get a more scientific insight into the idea of the energetic use of the excess water as well as to evaluate the most significant factors that influence the ejector effect a research project was initiated. On the one hand a model test rig was built at the Institute for Hydraulic Fluidmachinery at Graz University of Technology. On the other hand the model tests were accompanied by comprehensive two phase numerical flow simulations in order to allow a much easier and faster investigation of different design parameters of an ejector power plant in near future.

The project results and derived conclusions make an important contribution to a better understanding of the ejector effect and to improve the planning security of future water power projects.

2. THE EXPERIMENTAL MODEL AND THE USED TESTING FACILITY

In order to achieve an experimental investigation close to reality the substantial parts of the reference power plant WAIDHOFEN were designed using a model scale of M = 1:10.

The amount of water as well as the water levels adjusted in course of the experiments was converted from the prototype to the model using the Froude number *Fr*, which is the crucial non-dimensional number for free surface open channel flows. Thus the following conversion rules have to be taken into account in order to convert the flow rate and the water levels from the prototype to the model:

$$Q_{\mathrm{Model}} = Q = Q_{\mathrm{PT}} \cdot \mathrm{M}^{5/2}$$
$$H_{\mathrm{HW-Model}} = H_{\mathrm{HW}} = H_{\mathrm{HW-PT}} \cdot \mathrm{M}$$
$$H_{\mathrm{TW-Model}} = H_{\mathrm{TW}} = H_{\mathrm{TW-PT}} \cdot \mathrm{M}$$

To simulate the flow phenomena occuring at the nominal turbine flow rate at the reference power plant ($Q_{\mathrm{Tu\text{-}Max}}$ = 30 m³/s) in course of the model tests a turbine flow rate of Q_{Tu} = 94.8 l/s has to be adjusted. The water levels to be adjusted at the test rig have to be linearly scaled down. Thus, a gross head H of 0.5 m to 0.7 m has to be adjusted to simulate a gross head of H = 5 – 7 m available at the prototype.

Compared to the reference power plant two simplifications were made in course of the construction of the model test rig. On the one hand it was not possible to model the full width of the headwater basin due to space constraints in the laboratory. Instead an open headwater tank with maximally possible width was used. On the other hand the model tests were carried out without using any model turbine. The power output would have been just around a few 100 W and the verification of the positive impact of the ejector would have become more difficult. Instead the turbine was replaced by a pipe section which was placed between the headwater tank and the draft tube of the turbine. In order to provide evidence of the positive impact of the ejector the increased hydraulic power available for the turbine was measured.

The three dimensional CAD-model of the designed test rig is shown in Figure 1 and Figure 2. The water delivered by the main pump of the test rig enters the open headwater tank (2) via the inlet pipe (1). With the help of the turbine pipe section (3) a part of the water Q_{Tu} is directed to the draft tube of the turbine (4). The other part of the water flow Q_{Ej} passes the ejector chute (5).

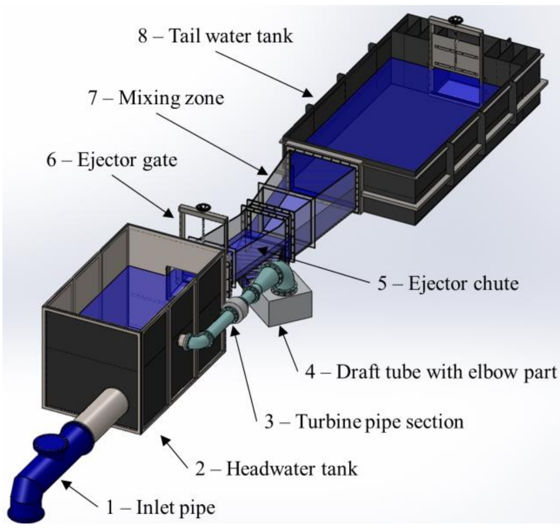

Figure 1. Three-dimensional view onto the CAD-model of the ejector test rig

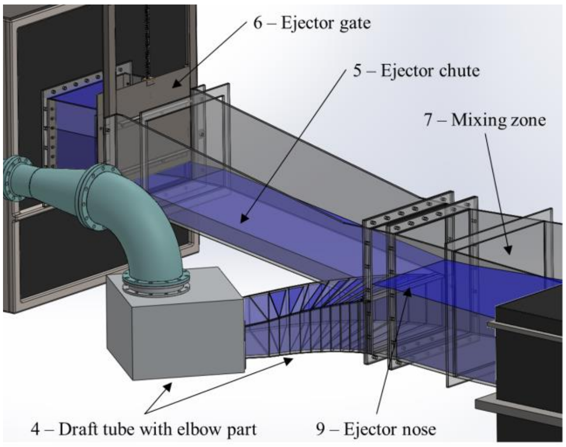

Figure 2. Detail view onto the CAD-model showing the ejector chute and the draft tube

With the help of the ejector gate (6) the ejector flow Q_{Ej} as well as the water level in the headwater tank is regulated. Furthermore, the edge connecting the ejector chute with the outlet of the draft tube is called ejector nose (9). Within the mixing zone (7) the turbine flow Q_{Tu} and the ejector flow Q_{Ej} are joined and consequently directed into the open tail water tank (8). At the very end of the tail water tank the water escapes through a rectangular hole in vertical direction into the test loop.

The most important physical quantities to be measured are the total flow rate Q, the turbine flow rate Q_{Tu}, the absolute pressure measured at the outlet of the draft tube, the headwater level $\mathrm{H_{HW}}$ (measured at the inlet tank) and the tail water level $\mathrm{H_{TW}}$ (measured at the end of the tail water tank). In this context it has to be pointed out that the level of the headwater and tail water are referred to the level of the ejector nose.

Additionally the figures previously discussed show that the substantial components of the model – like the ejector chute, the bent part of the draft tube and the mixing zone of draft tube and ejector flow – were manufactured from acrylic glass to additionally allow a visual observation of the occurring flow phenomena.

The procedure used in course of the experimental programme is summarized as follows: While the ejector gate was closed the main pump of the test rig was started and the headwater and tail water tanks were filled until a head water level of H_{HW} = 0.70 m was reached. Via variation of the vertical position of a weir panel located in the tail water tank, the tail water level had to be adjusted to a value of H_{TW} = 0.00 m. At this initial operation point a turbine flow rate of around Q_{Tu} = 90 l/s is obtained. Starting from this point the ejector gate was opened and thus the ejector activated. The total flowrate $Q = Q_{\mathrm{Tu}} + Q_{\mathrm{Ej}}$ was increased step by step by an increased speed of the feed pump of the test loop and subsequently measurement points were taken. For all adjusted operation points the headwater level was kept constant. After reaching a total flow rate which was at least four times higher than the initial flow rate the just outlined was repeated again with following four initial tail water levels with respect to the level of the ejector nose: H_{TW} = - 0.03 m / + 0.04 m / + 0.06 m / + 0.08 m

3. EXPERIMENTAL RESULTS AS BASIS FOR THE NUMERICAL SIMULATION

As initially mentioned the hydraulic power available for the turbine was measured to verify the positive impact of the ejector. The hydraulic power measured on the test rig is defined as:

$$P_{\mathrm{hydr.}} = \rho \cdot g \cdot Q_{\mathrm{Tu}} \cdot H_{\mathrm{Tu}}$$

While the turbine flow rate $\mathrm{Q_{Tu}}$ is directly measured with an inductive flow meter the turbine head $\mathrm{H_{Tu}}$ is calculated as total head difference between headwater and the draft tube outlet:

$$H_{\mathrm{Tu}} = H_{\mathrm{Tot-HW}} - H_{\mathrm{Tot-DTout}}$$

The experimental results acquired in course of the measurement programme are exemplarily presented with Figure 3 referring to an initial tail water level of H_{TW} = 0.00 m and a head water level of H_{HW} = 0.70 m which was kept constant in course of the measurements. The diagram shows the water levels $\mathrm{H_{HW}}$ and $\mathrm{H_{TW}}$ as well as the hydraulic power P_{hydr} available at the turbine plotted against the total flow rate Q. The data points marked with an unfilled circle refer to the hydraulic power that is measured if a traditional weir would be used instead of the ejector. Due to the fact that the tail water level H_{TW} increases with increasing total flow rate it is obvious that the hydraulic power WITHOUT ejector decreases. On the other hand the hydraulic power is even increased, followed by a slight descend when the ejector chute is used for the draining of the excessive water. At the operation point with the highest flow rate the hydraulic power available for the turbine is still around 18 % higher than compared to the situation without ejector.

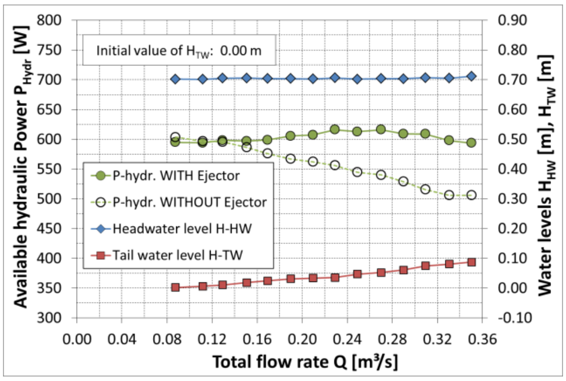

Figure 3. Increase of the available hydraulic power due to the ejector effect deteced in course of the measurement programme

In order to verify whether the increase of the available hydraulic power is reached by an increased turbine head and/or an increased turbine flow rate Figure 4 provides a more detailed analysis of the measurement results. The diagram presents the turbine flow rate Q_{Tu} and the turbine head H_{TU} plotted against the total flowrate Q for the situation with and without ejector. It turns out that the ejector effect does not only cause an increase of the turbine head H_{Tu} but also of the turbine flow rate Q_{Tu} which is – though decreasing – higher than the „normal" turbine flow rate. This is due to a suction effect which is closely connected with the reduction of the tail water level at the draft tube outlet. This finding can be observed up to a total flow rate of Q = 0.34 m³/s. At higher flow rate a decrease of the turbine flow rate due to the ecjector effect can be expected.

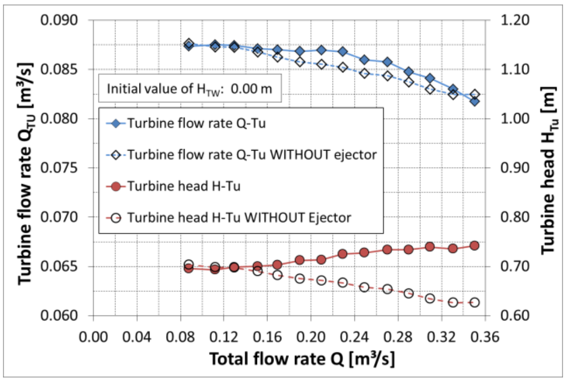

Figure 4. Turbine flow rate and turbine head measured with and without ejector

Moreover, Figure 5 shows a visual evaluation of the occurring flow phenomena. Referring to a total flow rate of Q = 0.21 m³/s the presented picture shows that the highly energetic flow in the ejector chute results in a locally decreased tail water level at the turbine outlet. The dimensions given in Figure 5 were recorded in course of the measurements and were used for a comparison between measurement and CFD results.

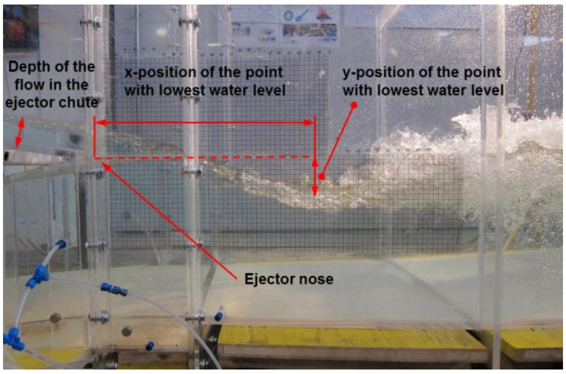

Figure 5. Picture taken of the locally reduced water level at the outlet of the draft tube due to the ejector effect

4. CFD-SIMULATION OF THE EJECTOR EFFECT APPLICAPLE TO LOW HEAD VERTICAL KAPLAN TURBINES

The numerical simulation of the flow phenomena connected with the ejector effect requires the use of an appropriate multi-phase CFD-model in order to accurately calculate the phase interface between water and air.

In the field of hydraulic fluidmachinery such multi-phase simulations are rather uncommon due to their high computational effort. An exception is made in case of the occurence of unfavourable flow patterns in the intake or tailrace structures of low head hydropower applications that may have a negative impact on the performance of the turbine/s. Weissenberger et al. [5] for example presented a qualitative comparison of test and simulation results of a complete scale model which was tested for the "Lower Saint Anthony Falls" StrafloMatrix™ project. A full bay model with a scale of 1:15 was used to investigate the approaching flow conditions for the turbine units in the laboratory. In parallel extensive two-phase CFD simulations of the headwater region were carried out in order to check the applicability to predict the resulting flow fields at the inlet of the turbines.

More common is the use of multi-phase models in course of hydraulic engineering studies like published by Andersson et al. [6] who carried out an investigation of the free surface flow during spilling of a reservoir in a down scale model. It was found that the used CFD approach enables a realistic prediction of separation zones and local reductions of the water level around the guide walls of the investigated structure.

A very detailed evaluation of CFD-simulations dealing with intake flow problems of low head hydro power plants was presented by Aigner et al. [7]. The authors compared the achieved simulation results with PIV-measurements carried out at a model of a run-off-river power plant manufactured from acrylic glass. The published studies were basically aimed at the detection of vortex formations occurring at the intake structure of a Kaplan turbine. It was proven that the two-phase CFD-model is capable of predicting the location as well as the intensity of the occurring vortex structures with astonishing accuracy.

Based on the good experience with the multi-phase free surface CFD-models presented in the discussed reference cases, a similar approach was used for the numerical simulation of the ejector model. The commercial software package ANSYS-Workbench V15.0 was used for the generation of meshes, the setup of the two-phase CFD-model and the evaluation of CFD-results.

4.1. Description of the CFD-mesh

Using the ANSYS Workbench meshing tool one single CFD-mesh without any interfaces inside was created. The experience gained with multi-phase-simulations using ANSYS-CFX shows that an improved stability of simulations can be reached in this way.

While tetrahedron elements were used for the main flow regions, prism layers were placed on the walls of the ejector model to appropriately resolve the boundary layer. Additionally mesh refinement was used in the expected regions of phase separation between water and air. Figure 6 and Figure 7 present a visualization of the created CFD meshes. While Figure 6 shows a 3D-view onto the unstructured mesh of the headwater tank, the turbine pipe section, the mixing zone and a part of the tail water region, Figure 7 presents a detail view of the mesh created in the region where the ejector flow mixes with the flow leaving the draft tube. The recess represents the previously described ejector nose. It is clearly visible that a mesh refinement was applied in the region where the interface between water and air is expected.

Figure 6. 3D-view onto the unstructured mesh generated for the ejector model

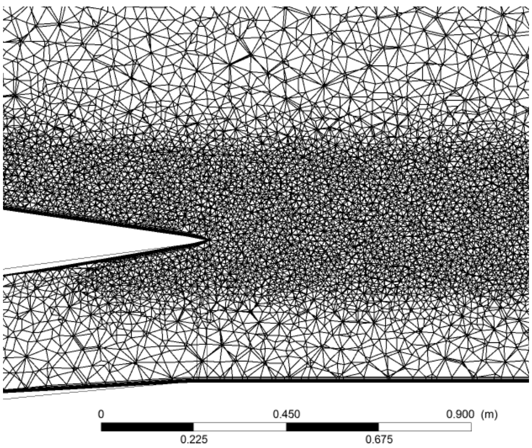

Figure 7. Detail view of the mesh created in the region where the excess water flow is mixed with the flow leaving the draft tube

4.2. Description of the CFD-model

In the field of CFD various numerical models are capable to describe and predict the physics of multiphase flow. An overview of the most common models with a description of the theoretical background and the range of possible applications is given by E. Stenmark [8].

For the exceptional case of a free surface flow where the fluids (commonly water and air) are separated by a distinct resolvable interface, experience shows that the Volume-Of-Fluid (VOF) method is an appropriate approach to capture all physical effects connected with the multi-phase problem ([5], [6], [7]). Recommendations to use this method to describe free-surface flows were also published by ANSYS [9].

The VOF method is a modelling technique for tracking and locating the free surface in a domain where at least two phases appear in parallel. The first journal-publication of this method was presented by Hirt et al. [10] in 1981. Nowadays this method is implemented in several commercial CFD software packages.

Within the ANSYS-CFX graphical user interface (GUI) the VOF-method is implemented as so called homogeneous multiphase model [11]. To use this model the whole flow domain needs to be represented with a fixed mesh. All fluids share a common velocity and turbulence field and the motion of the phases is calculated along with the shape of the interface between the phases. Furthermore a phase indicator function is used to track the interface between two or more phases. The indicator function has a value of “1” or “0” when a control volume is entirely filled with one of the phases and a value between “1” and “0” if an interface is present in the control volume.

Due to the published recommendations regarding the numerical simulation of free surface problems the homogeneous multiphase model incorporated in ANSYS-CFX was used to perform stationary CFD-simulations to investigate the ejector effect. As recommended for multiphase problems in the ANSYS CFX-Solver Modeling Guide [11] the k-ε model with scalable wall functions was used to model the turbulence.

Furthermore the High Resolution advection scheme was applied for the spatial discretization of the Reynolds Averaged Navier Stokes equations. The High Resolution scheme uses a close to second order solution in flow regions with low variable gradients. In regions with higher gradients the solution will approach a first order scheme, in order to prevent over- and undershoots and to maintain robustness. The convergence criterion for the root mean square residuals of pressure, velocity and the mass of water and air was set to 10^{-4}.

An overview of the CFD-model established in ANSYS-CFX is shown with Figure 8. The inlet boundary condition (see very left side in Figure 8) was set as a constant mass flow rate of water. In course of the CFD-study 5 different operation points each with a flow rate of Q_1 = 87.5 l/s, Q_2 = 130 l/s, Q_3 = 170 l/s, Q_4 = 210 l/s and Q_5 = 250 l/s were investigated. While the flow rate of Q_1 was applied to the case with closed ejector ramp, the flow rate values of Q_2 to Q_5 were used for the simulations with activated ejector ramp. At the outlet of the ejector model (see very right side in Figure 8) a constant average pressure of 0.03 bar representing a water level of H = 0.30 m above the outlet surface was defined.

At the top of the headwater and tail water tank (see up and down arrows in Figure 8) an absolute pressure of 0 bar was set and an opening was defined enabling only a circulation of air. The vertical position of the weir panel located in the tail water tank was adjusted in a way to reach an initial tailwater level of H_{TW} = + 0.04 m.

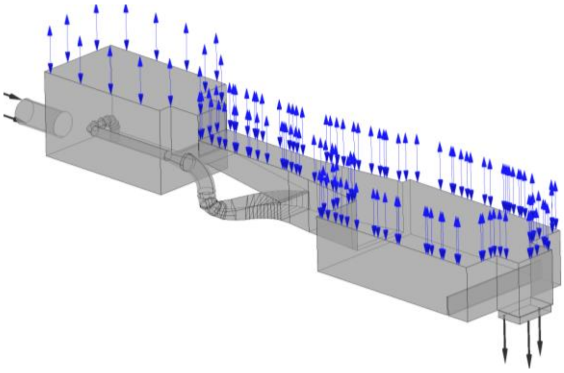

Figure 8. Overview of the CFD-model established in ANSYS-CFX

An important prerequisite for stable simulations was the definition of initial values for the water volume fraction. The initial condition for the water surface level in the headwater tank and in the tail water tank was defined by giving an initial water depth close to the water depth measured in the physical model. The free surface was then allowed to adjust itself during the simulation.

It turned out that the combination of the described boundary conditions and the initialisation of the flow field led to a satisfying convergence history. Nevertheless it took several thousand iterations to reach CFD-results with stable headwater and tail water levels and thus flow conditions that show no dependence on the simulation progress.

All simulations were performed on a workstation with an Intel XEON 3.40 GHz processor (16 cores) providing a memory of 64 GB RAM and Windows 7 / 64 Bit operation system.

4.3. Evaluation of CFD-results and comparison with measurements

The experimental results presented in this paper refer to a headwater level of H_{HW} = 0.70 m which was kept constant in course of one measurement series. The combination of total flow rate Q and the opening of the ejector gate required to reach this level was transferred to the simulation settings. Thus, it could be expected that the increase of flow rate from Q_1 = 87.5 l/s to Q_5 = 250 l/s would result in a constant water level in the headwater tank as well, while a local reduction of the tail water level at the draft tube outlet is reached.

This presumption is exemplarily confirmed with visualizations of the water volume fraction shown with following figures. Figure 9 presents a three dimensional view onto the ejector model with the free water surface as ISO-surface and contours of the water volume fraction plotted on a cross sectional area for a total flow rate of Q_3 = 170 l/s. It is clearly visible that a rather plane water surface adjusts in the headwater tank while distinct water waves appear in the tail water especially in the region around the draft tube outlet.

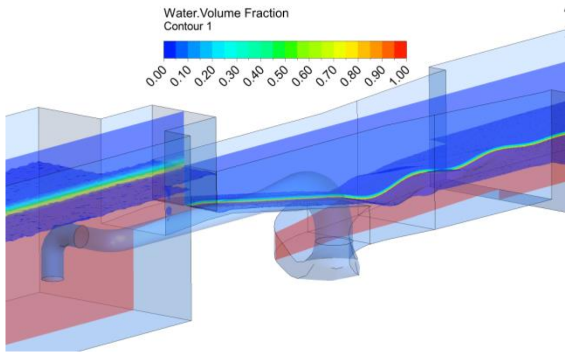

Figure 9. Free Water Surface and Water Volume Fraction plotted on a cross sectional area for the operation point Q_3 = 170 l/s

Furthermore the flow rate dependent change of the wave structure in the tail water is presented by Figure 10. While it is obvious that the increase of the total flow rate Q causes a significantly decreased water level at the draft tube outlet, the octahedrons mark the position of the lowest water level at the draft tube outlet measured in course of the experiments. At first glance it turns out that there is quite a good accordance between measurement and simulation.

However, the evaluation of CFD-results also showed that a constant head water level of H_{HW} = 0.70 m was only reached for the operation points with a flow rate of Q_2 = 130 l/s, Q_3 = 170 l/s and Q_4 = 210 l/s. At the other two operation points the head water level was slightly higher and lower, respectively.

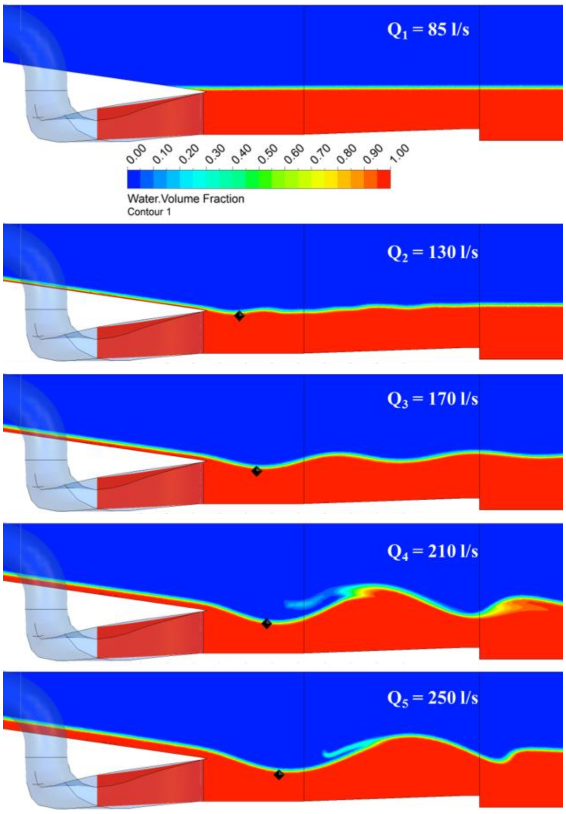

Figure 10. Water Volume Fraction plotted on a cross sectional area for Q_1 = 87.5 to Q_5 = 250 l/s

Another view onto the results is presented with Figure 11, showing velocity contours on several planes in the tail water region of the ejector model. It can be seen that a homogenization of the tail water flow is only reached at the transition to the tail water tank at the very right end of the picture. Within the mixing zone of the ejector model a clear differentiation of ejector and draft tube flow can be observed.

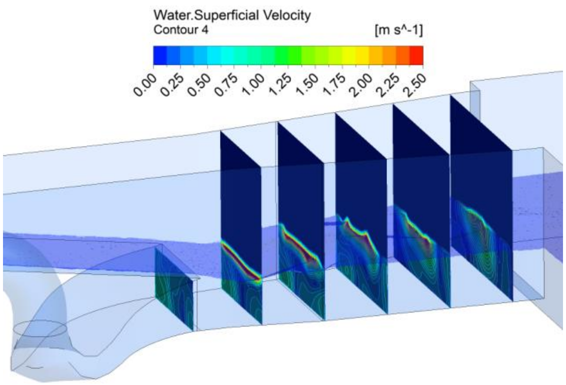

Figure 11. Contour plots of the water velocity in the tail water region of the ejector model for a flow rate of Q_3 = 170 l/s

Finally, a quantitative comparison of CFD- and measurement results is presented with Figure 12 showing a contour plot of the percentage of the increased power output due to the ejector effect. The diagram summarizes the measurement results (exemplarily presented with Figure 3) achieved in course of all the measurement series, each with an initial tail water level of H_{TW} = -0.03 m / 0.00 m / + 0.04 m / + 0.06 m / + 0.08 m.

On the one hand it turns out that the ejector is capable of increasing the hydraulic power available at the turbine by a maximum of 18 %. On the other hand an analysis of the presented data shows that the positive effect of the ejector does not only depend on the ejector flow rate but also on the tail water level with respect to the level of the ejector nose. If the tail water level is too high even a comparably high ejector flow rate does not cause an increase of the power output.

The filled circles present the increased power output calculated by means of CFD for the operation points with a total flow rate of Q_2 = 130 l/s, Q_3 = 170 l/s and Q_4 = 210 l/s. The turbine flow rate Q_{Tu}, the absolute pressure measured at the outlet of the draft tube, the headwater level H_{HW} and the tail water level H_{TW} required to calculated the hydraulic power available at the turbine were evaluated at the same positions as on the test rig.

It turns out that the experiment and the CFD-simulation show the same trend for the prediction of the percentage of the increased power output. The deviation of the presented percentage rates is negligibly small.

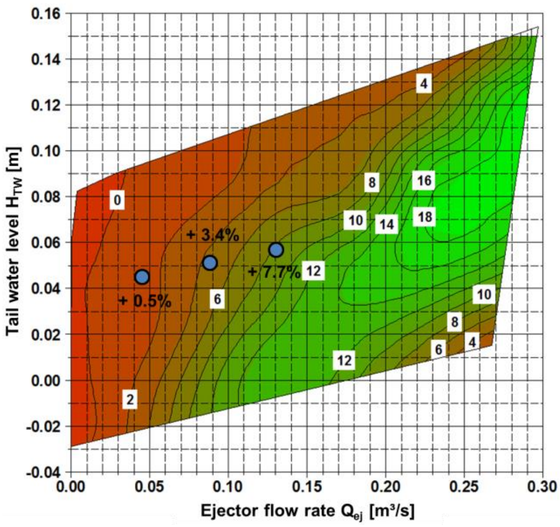

Figure 12. Contour plot of the percentage of the increased power output due to the ejector effect valid for H_{HW} = 0.70 m = const.

6. CONCLUSIONS

The results presented in this paper show that the experimental programme as well as the numerical simulation give evidence of the positive impact of the ejector principle on the hydraulic power available at the turbine of a low head hydropower plant. Concerning the prediction of the positive impact of the ejector both approaches independently show a significant sensitivity to the ejector flow rate and the tail water level. The deviations between CFD- and measurement results obtained at the same operation points are negligibly small.

Consequently, it was proven that the numerical simulation is an appropriate approach for a realistic investigation of the ejector effect and for the prediction of its positive impact. Based on this finding it is now possible to carry out further numerical investigations with changed design parameters of the ejector model, in order to find out the ideal parameters for the inclination of the chute, the transition of the draft tube to the tail water and so on.

Thus, the presented results make an important contribution to improve the planning security of future water power projects using the ejector principle.

ACKNOWLEDGEMENTS

This work was carried out in cooperation with the engineering company ZT Fritsch GmbH and has been financially supported by the Austrian Research Promotion Agency (FFG) under the Energy Mission AUSTRIA programme.

REFERENCES

[1] Mosonyi E.: Low-Head Power Plants. 3. Auflage. Budapest: Akademiai Kiado, 1987.

[2] Slisskii S.M.: Ejection into tailraces of hydropower plants. 1. Auflage. Moskau: Gosudarstvennoe Energeticheskoe Izdatel’stvo, 1953.

[3] Drack K.: Effizienzsteigerung bei Klein-wasserkraftwerken durch Nutzung der „Ejektorwirkung“ am Beispiel Mühltalwehr. Firmenschrift der K. u. F. Drack GmbH & Co. KG. Scharnstein, 2007.

[4] Gruber R.: Ejektor Kraftwerk macht Standort an der Ybbs wirtschaftlich. In: ZEK-Hydro 5/2013. S. 14-17.

[5] Weissenberger S., Steinmassl J., Grafenberger P.: Free surface simulations of intakes for low head machines. ASIA 2010.

[6] Andersson A.G., Andreasson P., Lundström T.S.: CFD-Modelling and Validation of Free Surface Flow During Spilling of Reservoir in Down-Scale Model, Engineering Applications of Computational Fluid Mechanics, 7:1, 159-167. 2013.

[7] Aigner, D.; Lichtneger, P.: Ein Beitrag zur Strömungsoptimierung an Wasserkraftanlagen am Beispiel eines Buchtenkraftwerkes. 13. Int. Anwenderforum Kleinwasserkraftwerke. 23./24.September 2010, Kempten, Allgäu

[8] Stenmark, E.: On Multiphase Flow Models in ANSYS CFD Software. Master’s Thesis in Applied Mechanics, CHALMERS UNIVERSITY OF TECHNOLOGY. Göteborg, Sweden 2013.

[9] Bakker, A.: Extensive Multiphase Flow Capabilities. ANSYS Advantage ,Volume II, Issue 4, 2008.

[10] Hirt, C.W.; Nichols, B.D.: Volume of Fluid (VOF) Method for the Dynamics of Free Boundaries. JOURNAL OF COMPUTATIONAL PHYSICS 39, 201-225 (1981).

[11] ANSYS CFX-Solver Modeling Guide. ANSYS, Inc. Release 15.0, Southpointe November 2013.

Conference on Modelling Fluid Flow (CMFF'15)
The 16th International Conference on Fluid Flow Technologies
Budapest, Hungary, September 1-4, 2015

OPTIMISATION OF A VARIABLE PITCH MIXED FLOW DIFFUSER PUMP WITH NUMERICAL METHODS AND TEST RIG VERIFICATION

Stefan HÖLLER[1], Helmut BENIGNI[2], Helmut JABERG[3]

[1] Corresponding Author. Institute for Hydraulic Fluidmachinery, Graz University of Technology. Kopernikusgasse 24/IV, A-8010 Graz, Austria. Tel.: +43 316 873 7574, Fax: +43 316 873 107574, E-mail: hoeller-litzlhammer@tugraz.at
[2] Institute for Hydraulic Fluidmachinery, Graz University of Technology. E-mail: helmut.benigni@tugraz.at
[3] Institute for Hydraulic Fluidmachinery, Graz University of Technology. E-mail: helmut.jaberg@tugraz.at

ABSTRACT

Mixed flow pumps with impeller blades which are adjustable during operation are often used in cooling applications and therefore they are mostly installed in pump sumps. This type of installation necessitates a pump design with lowest net positive suction head required ($NPSH_R$) as well as high heads at overload operation. Furthermore, a wide operation range down to low flow rates is mandatory. Apart from such requirements, many of these pumps suffer from two instabilities in part load operation, which have to be considered during the design process. One instability results from recirculation from the impeller into the suction region and the other one from rotor-stator interactions between impeller and diffuser – referred to as diffuser instability. The present paper describes the design of a pump geometry consisting of the suction region (bell mouth), the impeller with adjustable blades and the diffuser for a pump with a specific speed of n_q=95rpm. Starting with a theoretical 1D design for the meridional contour, it is demonstrated that in the course of the design development most of the challenges can already be predicted by means of 3D computational fluid dynamics (CFD). Thus, high reliability on such CFD results without the use of (time-consuming and expensive) prototypes is possible. Furthermore, a multi-objective optimisation of the suction region and the diffusor were realised. Finally, the results achieved for the optimized pump were validated on the test rig providing which a nearly perfect match – not only with regard to efficiency and pump characteristic but also as far as prediction of part load instability is concerned.

Keywords:
CFD, Comparison of measurement and simulation, Multi-objective genetic optimisation (MOGA), Part load instability, Transient calculations;

NOMENCLATURE

A	[m²]	Area
D	[m]	Diameter
H	[m]	Pump head
$NPSH$	[m]	Net pressure suction head
NSS	[rpm]	Suction specific speed
Q	[m³/s]	Flow rate
Re	[-]	Reynolds number
T	[Nm]	Torque
c_m	[m/s]	Meridional velocity
g	[m/s²]	Gravity
n	[rpm]	Rotational speed
n_q	[rpm]	Specific speed
m	[-]	Mode number
p	[Pa]	Pressure
u	[m/s]	Circumferential speed
z	[-]	Number of blades
φ	[-]	Flow coefficient
η	[-]	Efficiency
λ	[-]	Power number
ν	[-]	Multiplier
ρ	[kg/m³]	Density
ω	[1/s-]	Angular velocity
ψ	[-]	Pressure number

Subscripts and Superscripts

3	3% head drop, used for NPSH and NSS
BEP	Best efficiency point
Design	Design point of the pump
i	incipient
R	required
Ref	Reference
r, d	runner, diffuser
stat	static
v	vapour

1. INTRODUCTION

Most mixed flow pumps, also with variable pitch blades, may suffer from two instabilities in part load operation. Though these instabilities are due to physical reasons and well known for decades [1, 2], the correct numerical prediction is still a problem/challenge in the development of a new hydraulic design. To comprehend how difficult it is to predict correct part load behaviour, it is vital to understand the origin of the two main instabilities [3].

1.1. Instability

The diffuser instability is based on the rotor-stator interactions between impeller and diffusor. At part load a backflow out of the diffuser channel at the diffuser inlet may occur. This phenomenon is caused by a distorted impeller outflow at part load and may cause instability in the head curve.

A further decrease of the flowrate causes a pre-rotation of the fluid in the inlet region of the pump. Due to a decreasing relative velocity and therefore a flatter flow angle, flow separation, recirculation (rotating stall) and part load vortices (pre-swirl) occur. These effects cause recirculation from the impeller into the suction region which results in recirculation instability.

Further experimental investigations [4-6] have also shown a strong connection between backflow effects and diffusor instability. Though all those phenomena can be visualized by means of tests, it is still challenging to show them in numerical simulations. Early investigations by Muggli [7] have provided good correlation between CFD simulation and measurements. Nowadays, results of numerical simulations show excellent accordance with test results at and near the best efficiency point (BEP) (see for example [8]). Around the BEP the incident flow to the impeller and diffusor is almost undisturbed. At part load operation, flow separation due to inaccurate incident flow begins, and this is the main problem of a reliable numerical simulation. To predict flow separation exactly – especially in turbomachines – transient models [9-11] with adequate turbulence resolving/modelling are required. Although the progress in CFD during the last decades was tremendous, it is still not possible to fully resolve all necessary aspects. Especially at an early stage of the design process, complex and expensive simulations like Hybrid-LES models – which are the most reliable – are still not affordable. Though these simulations are meanwhile capable of predicting many flow phenomena correctly, the ratio between the effort required and the additional benefit is unsatisfying.

1.2. Variable pitch versus fixed blade

The concept of a variable pitch pump is much more complicated in terms of the mechanical adjustment of the blade. The benefit is clearly visible in Figure 1 – the envelope of the efficiency as well as the best efficiency points of each head curve for different blade position are shown. Such pumps are very often used together with systems in which the system curve has a strong increase at higher flow rates (system curves with low or zero static head component, but high dynamic head component). For a fixed blade pump the available head strongly decreases with increasing flow rates. For a variable pitch pump the blade could be opened for higher flow rates and thus the head does not drop down. Towards part load this appears vice versa. The zero flow rate is lower for a more closed position, and so also the power consumption is lower.

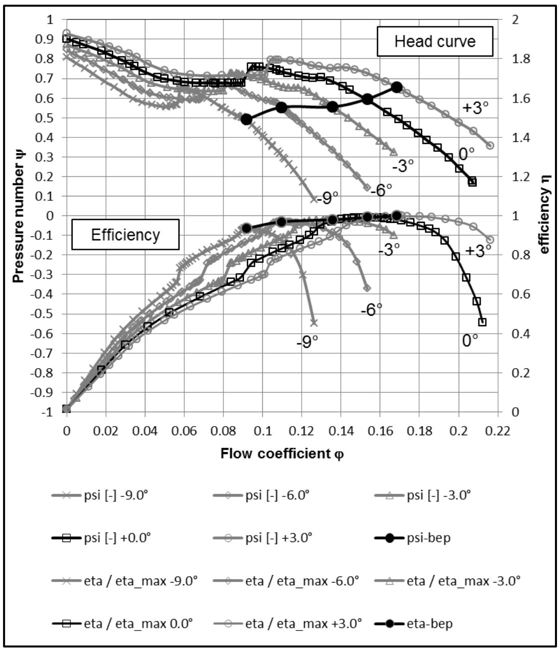

Figure 1. Head curves and efficiencies for variable pitch pump

A further advantage is the efficiency in part load and overload which is significantly better with a variable pitch pump. In this case, the envelope of the efficiency must be compared to one efficiency curve of a chosen blade position (see Figure 1).

The present paper presents a design approach with respect to a mixed flow pump regarding special demands to suction and part load behaviour by means of numerical simulations. The methodology applied, which includes a simple theoretical design, manual as well as fully automated optimisation and the validation with a model test is described in detail and proves the success of this approach.

2. HYDRAULIC DESIGN

The pump presented in this paper is designed for a specific speed of n_q=95rpm as a variable pitch pump. As of cavitation performance $NSS_R \geq$ 1600rpm at 100% Q_{Design} and $NSS_R \geq$ 1500rpm at 130% Q_{Design} were required (Definition by the NSS, see chapter 3.2). So, the overload cavitation point is the challenging target.

Figure 2 presents the workflow used to develop the hydraulic design of the presented pump. Starting with a literature study and a 1D design on several streamlines, a first 3D model of the hydraulic design was generated with Ansys BladeGen®.

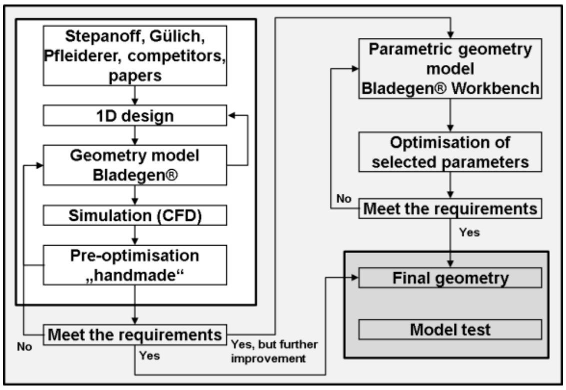

Figure 2. Workflow of hydraulic design

Once achieving a smooth geometry, already at this early development stage CFD calculations were carried out and post-processed. In a further development stage parametric models for the diffuser and the inlet section were generated in order to be able to perform automated optimisation. The final geometry was tested on the test rig to validate the simulation results.

2.1. Runner

Starting with the design of the meridional shape – based on design approaches and guidelines by Stepanoff [1] and Gülich [2] – and a 1D design on various streamlines, the first focus regarding the impeller design was to meet the cavitation targets required in part load, at the best efficiency point (BEP) and under overload conditions. Apart from velocity triangles, the meridional shape was a key part during the design process. The meridional shapes of the runner and diffusor are shown in Figure 3 for the newly designed hydraulic. A six blade impeller with variable blades is the result together with a diffusor with 11 vanes. The hub and shroud contour around the impeller blade must be spherical to ensure the blade adjustment with a constant tip clearance.

$$m = \left| v_2 \cdot z_r - v_3 \cdot z_d \right| \quad (1)$$

Gülich [2] and Karassik [12] present a formula how to choose the right number of blades in order to avoid pressure pulsations. This formula is presented in Eq. 1 whereas v_2 and v_3 are multipliers from 1 to 3 which are used to calculate the value m. In the hydraulic turbine industry m=0 is often used, however for pumps it is most important to avoid this with respect to pumps, especially radial pumps and multistage pumps. Only m=1 and m=2 are of interest, however they are not as critical for axial or semi-axial flow pumps.

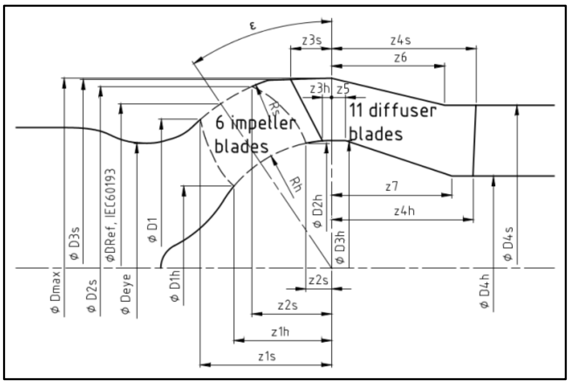

Figure 3. Meridional design

In Table 1 a calculation for different impeller and diffuser blade numbers is depicted, whereas 11 or 13 diffusor blades show the best results for 6 runner blades as low numbers (1 or 2) only occur once in a row.

Table 1. Impeller diffusor blade combinations

z_r		5	5	5	5	5	6	6	6	6	6	7	7	7	7	7
z_d		9	10	11	12	13	9	10	11	12	13	9	10	11	12	13
v_2	v_3															
1	1	4	5	6	7	8	3	4	5	6	7	2	3	4	5	6
1	2	13	15	17	19	21	12	14	16	18	20	11	13	15	17	19
1	3	22	25	28	31	34	21	24	27	30	33	20	23	26	29	32
2	1	1	0	1	2	3	3	2	1	0	1	5	4	3	2	1
2	2	8	10	12	14	16	6	8	10	12	14	4	6	8	10	12
2	3	17	20	23	26	29	15	18	21	24	27	13	16	19	22	25
3	1	6	5	4	3	2	9	8	7	6	5	12	11	10	9	8
3	2	3	5	7	9	11	0	2	4	6	8	3	1	1	3	5
3	3	12	15	18	21	24	9	12	15	18	21	6	9	12	15	18

The head coefficient realised was chosen rather high in comparison to Gülich [2]. The head coefficient does not only influence the efficiency, its effect on the cavitation behaviour is even more pronounced as the head coefficient is a measure for the blade loading. Nowadays, the tools (e.g. CFD) and experiences are much better and one can go to higher blade loadings. The then smaller blade has a smaller wetted surface and thus lower friction losses.

2.2. Diffusor

As mentioned above, Stepanoff [1], Gülich [2], and also Pfleiderer [13] facilitate the generation of a suitable meridional shape of the impeller, whereas for the diffusor there is only few information available. Though Gülich [2] gives clues for the design of a straight diffusor without any deflection, like the area ratio as a function of the diffusor length, these are not or only partly suitable for a mixed flow pump. The main challenge in designing a good diffusor is a smooth flow deceleration in combination with minimal flow separation. An additional problem lies in the induced secondary flows by flow deflection from radial to axial direction in combination with the blading.

So, the first designs were simple 1D approaches considering the problems mentioned. After validation with the use of numerical simulation, a complex diffusor model was created for optimisation purposes. Due to the large number of input (geometry) and output parameters, a multi-objective genetic algorithm (MOGA inside ANSYS Workbench) was chosen for optimisation. The overall pump length must be as short as possible because of fabrication costs. As a result of the optimisation process, the meridional section and the blading were generated in compliance with minimal losses and only a small characteristic curve dip.

The meridional design of the whole pump is shown in Figure 3 whereas dashed lines indicate a "hand-made" hydraulic geometry and continuous lines represent a geometry which was generated by the automated optimisation process. The hub and shroud contour of the diffusor were generated with straight lines to lower fabrication costs.

3. NUMERICAL SIMULATION

3.1. Numerical models

Different models were generated and analysed before optimisation started. Model A consists of a 1 out of 6 section of the suction bell (i.e. a 60° circular segment). The inner part of the inflow was neglected (see Figure 4a) as the axis of the pump is a singular point having only very limited influence on the hydraulic characteristics. But, this modification enormously speeded up mesh generation. In Model A the rotor consists of 1 out of 6 passages for the impeller domain (i.e. one out of the six runner blades). Finally, the diffusor consists of 1 out of 11 passages and the mesh generation for diffuser and impeller was done with Turbogrid®).

Model B (see Figure 4b) consists of a suction bell as stator with a full 360° model whereas this mesh was generated with ICEM®. The rotor consists of 1 out of 6 passages for the impeller domain. For the diffusor 1 out of 11 passages was modelled. Model C (see Figure 4c) is the same as Model B, however in this case one runner passage was connected to two diffuser passages. This model was used to investigate the interference between runner and diffusor in detail.

Finally, Model D represents the full model with the suction bell (stator) as a full 360° model. The rotor now consists of 6 out of 6 passages for the impeller domain. The diffusor consists of 11 out of 11 passages for the stator domain. The periodic faces of the impeller and diffusor domains have 1-to-1 interfaces.

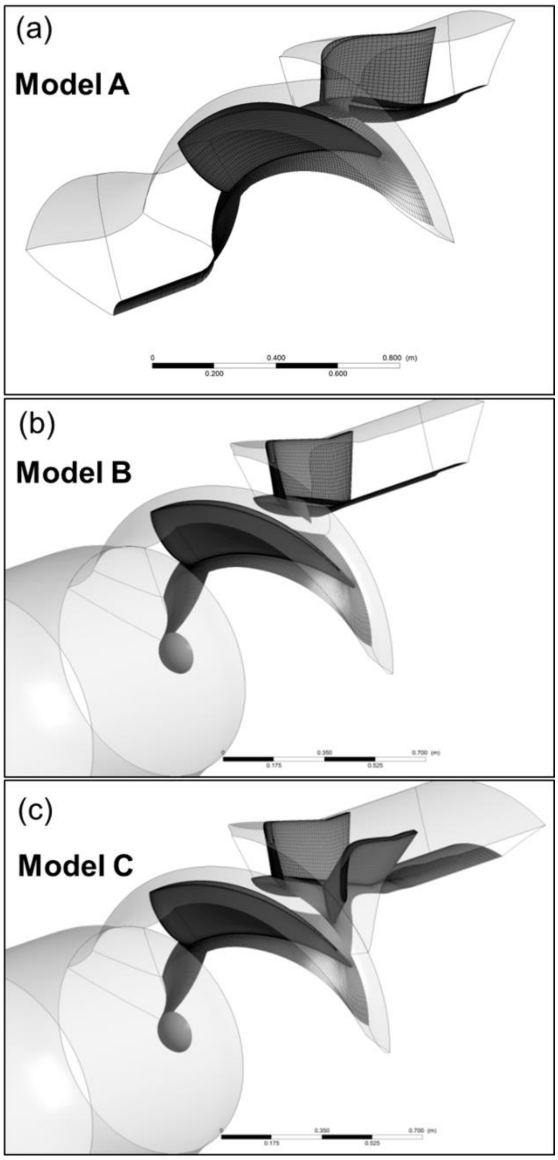

Figure 4. Models for CFD calculation

Table 2. Statistics of the numerical models

Values in 1000	Model	A	B				C		D	
	Runner		25 K	200 K	500 K	600 K	250 K	600 K	HJCL	ATM
Nodes										
Domain	passages									
Inflow		27	56	56	56	56	56	140	140	140
Runner	all	142	25	226	538	636	279	636	3817	3942
	one	142	25	226	538	636	279	636	636	657
Stator	all	100	22	136	231	231	199	457	2541	2541
	one	100	22	136	231	231	99.5	229	231	231
All Domains	all	270	103	419	826	924	535	1233	6498	6623
Elements										
Domain	passages									
Inflow	all	25	53	53	53	53	53	132	132	132
Runner	all	132	22	212	511	605	261	605	3632	3753
Stator	all	92	19	125	215	215	184	429	2360	2360
All Domains	all	248	94	390	778	873	497	1167	6124	6245

All important combinations are listed in Table 2 with their overall mesh sizes. The results of the mesh study are summarised in Figure 5. For head, efficiency and *NSS* there is no more difference between the models 500K and 600K, so the results were grid-independent.

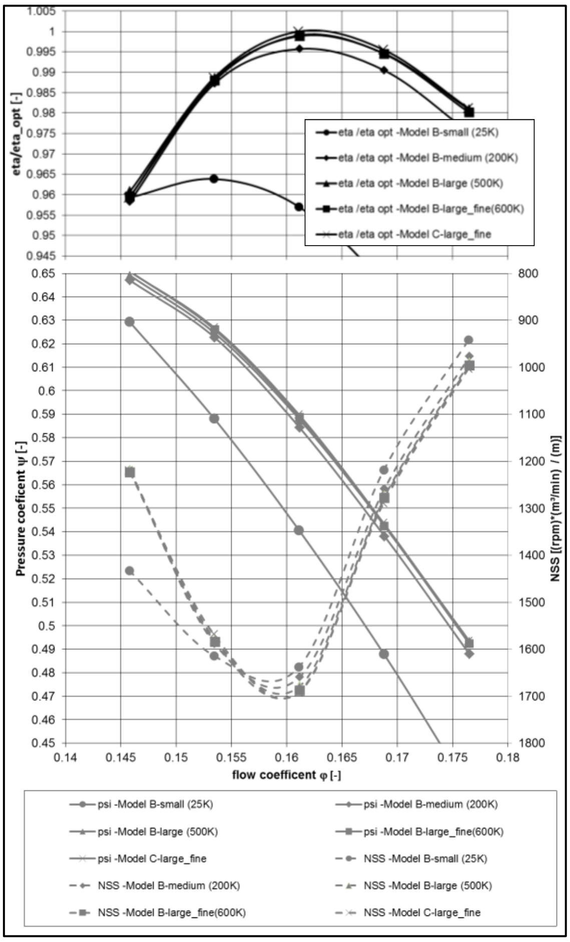

Figure 5. Impeller blade mesh topology

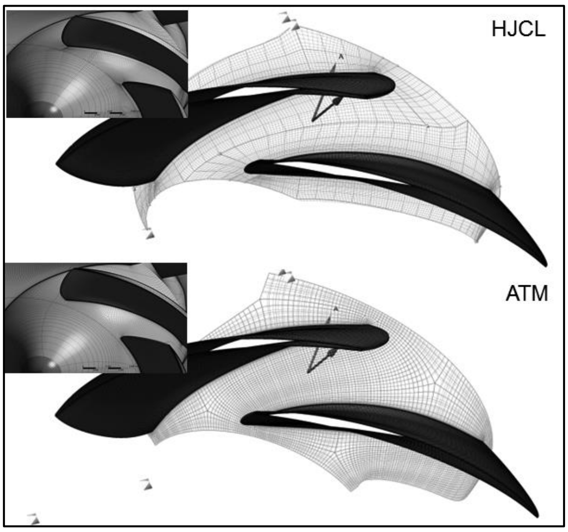

Figure 6. Impeller blade mesh topology

Model C with two instead of one diffusor passage showed exactly the same values for head and *NPSH*, but with a slightly better efficiency (see also Figure 5).

The HJCL mode of Turbogrid® follows an automated block topology depending on the blade metal angle, including full periodicy, and applies an algebraic, semi-isogeometric surface mesh generation procedure. As we intend to simulate the pump operation down to deep part load operation, extremely closed runner positions are required. The HJCL template of the mesh program does not support such closed runner positions. Therefore, the new ATM-mode was used. In Figure 6, the grid topology is shown together with the realised mesh for the final geometry – top for the HJCL template and bottom for the ATM template. The simulations were carried out with Ansys-CFX – for the general settings see Table 3.

Table 3. General CFD settings

Option	Design Process	Evaluation	Transient
	Model C	Model D	Model D
Inlet	Mass Flow Rate	Mass Flow Rate	Mass Flow Rate
Outlet	Average Static Pressure	Average Static Pressure	Average Static Pressure
Turbulence Model	SST [14]	SST [14]	SAS-SST [15]
Timescale	iter. 1 to 25: $1/(\omega * z_r * z_d)$	iter. 1 to 25: $1/(\omega * z_r * z_d)$	-
	iter. 26 to 50: $1/(\omega * z_r)$	iter. 26 to 100: $1/(\omega * z_r)$	-
	iter. 51 to 150: $1/\omega$	iter. 101 to 500: $1/\omega$	-
Time Step	-	-	revolution 1: $12/360*2\pi/\omega$
			revolution 2 to 6: $1/360*2\pi/\omega$
Coefficient Loops	-	-	10

3.2. Post-processing

For the evaluation of the hydraulic performance, the key figures as mentioned in the following are of interest. In general, the net head is the difference between total pressure at the outlet and total pressure at the inlet. According to standard ISO 9906 [16], the net head represents the difference between the static pressure at the outlet and the inlet – where the mean kinetic energy head difference is added to the head (geodetic head difference neglected, see Eq. 2). The pressure is measured on the test rig on 4 pressure measuring taps which were displaced by 90° angle distance of each other. The locations were set 2D away from the flange (Figure 7). The post-processing of the CFD results was then carried out in a similar way (Eq. 3)

$$H = \frac{1}{\rho g}\left[\left(\frac{1}{4}\sum_{i=1}^{4} p_i + \frac{\rho}{2}\left(\frac{Q}{A}\right)^2\right)\Bigg|_{Outlet} - \left(\frac{1}{4}\sum_{i=1}^{4} p_i + \frac{\rho}{2}\left(\frac{Q}{A}\right)^2\right)\Bigg|_{Inlet}\right] \tag{2}$$

$$H = \frac{1}{\rho g}\left[\frac{1}{A_{Outlet}}\left(\int p_{stat}\cdot dA\right)\Big|_{Outlet} - \frac{1}{A_{Inlet}}\left(\int p_{stat}\cdot dA\right)\Big|_{Inlet}\right] + \frac{\left(\frac{Q_{Outlet}}{A_{Outlet}}\right)^2 - \left(\frac{Q_{Inlet}}{A_{Inlet}}\right)^2}{2g} \tag{3}$$

The *NPSH* evaluation was carried out by means of histogram analysis. Nor was the CFX cavitation module used, neither any other cavitation model.

This method was cross-checked several times [17, 18]. The pressure $p_{Histogram}$ is the value, when the pressure at a certain percentage of the blade surface exhibits pressures lower than $p_{Histogram}$. The idea is, that a single value for the minimum pressure is not real but happens in a numerical simulation. With this pressure we calculate the *NPSH* value in the conventional way in a single phase calculation without a cavitation model. The point is that one must know how big the area percentage representative for the pump type under investigation is. This percentage changes for different types of pumps and must be known. It can only be found by comparing a sufficiently large number of experimental and numerical results for different pump types. By reducing the area percentage one shifts the calculated *NPSH* value towards $NPSH_i$, by increasing it towards $NPSH_3$.

Head was analysed with the normalised pressure coefficient ψ (see Eq. 4), the flowrate is expressed by the normalized flow coefficient φ (see Eq. 5), and for the cavitation the suction specific speed is used, whereas the flow rate is used in m³/min, *NPSH* in m and the rotational speed in rpm. Therefore, the $NPSH_3$ (Eq. 6), is recalculated to NSS_3 (Eq. 7). The efficiency is benefit versus expenditure and described in Eq. 8. The power is normalised to λ with Eq. 9.

$$\psi = \frac{Y}{\frac{u_2^2}{2}} = \frac{2 * g * H}{{u_2}^2} \tag{4}$$

$$\varphi = \frac{c_m}{u} = \frac{Q}{A * u} \tag{5}$$

$$NPSH = \frac{p_{tot,s} - p_v}{\rho \cdot g} \tag{6}$$

$$NSS_3 = n * \frac{\sqrt{Q}}{{NPSH_3}^{0.75}} \tag{7}$$

$$\eta = \frac{H \cdot Q \cdot \rho \cdot g}{T \cdot \omega} \tag{8}$$

$$\lambda = \frac{\varphi \cdot \psi}{\eta} \tag{9}$$

4. EXPERIMENTAL SETUP

There is no preferred diameter for the model pump defined in the ISO 9906 [16], but a few requirements by the IEC 60193 standard [19] for the model test. First of all, the Reynolds number should be higher than Re = 4 x 10^6: The reference diameter D_{Ref} (see Figure 3) has to be larger than 0.3 m. To fulfill these requirements a model of the scale 1:3.6 (model : prototype) based on the results of the numerical simulation is chosen. The reference diameter is D_{Ref}=322.4 mm. The model pump was manufactured and installed on the closed circuit 4-quadrant test rig at Graz University of Technology (Figure 7). The speed-regulated model, consisting of a runner with 6 blades and a diffuser with 11 guide vanes, was equipped with a 90 kW speed regulated motor/generator. The impeller consists of a turned and milled hub and 6 separate, turned and milled impeller blades. After the assembly of the impeller blades the shroud contour is turned spherically and the impeller is balanced.

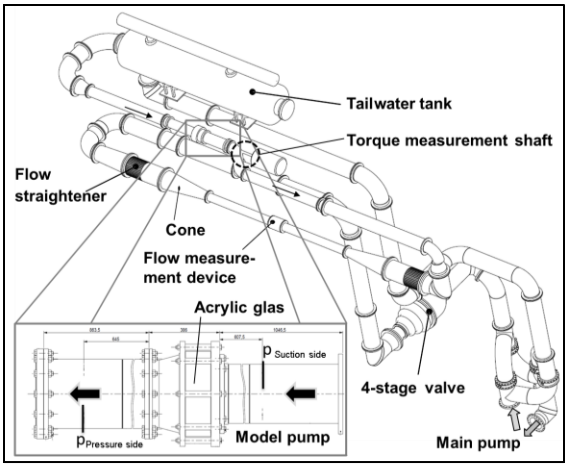

Figure 7. 4 -quadrant test rig

The diffusor is CNC milled from the solid and will be welded into the turned shroud contour by spot weld through holes in the shroud. For visual investigations (especially with respect to cavitation) an acrylic glass shroud casing was mounted (see Figure 7). The experimental setup and the measurement instruments were based on the IEC60193 standard [19] providing measurement accuracy of 0.2%. The measurement itself is realised according to ISO 9906 [16]

5 NUMERICALS AND MEASUREMENT RESULTS

In Figure 8 the head curves (normalised pressure number ψ) for different blade positions are shown versus the flow rate (normalized flow coefficient) for both CFD and test rig. A good correlation over the whole range could be detected. Zone A indicates the main instability zone of the pump for different blade positions. The pump normally could be operated only on the right side of each curve and this is generally indicated as operation limit in pump data sheets. The second Zone B indicates the diffuser instability and is from minor level. This zone is not an unstable head curve according to [20], where a stable curve is described as a curve with continuously increasing head while the flow rate is decreasing. This zone could be eliminated with diffuser modifications (eg. reduction of diffuser blade numbers and diffuser inlet and outlet angles) only by a shift of the best efficiency point to lower flow rates. The dotted lines indicate the CFD calculations in stationary mode and especially in the optimum provide good predictions of the head. Zone A is also well predicted whereas Zone B could not be found in the CFD results.

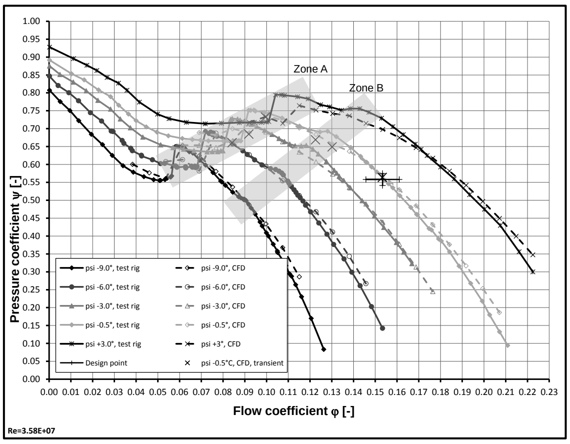

Figure 8. Head curves for different blade positions, CFD vs. test rig

In addition to the stationary calculations transient calculations were carried out. These calculations are marked with crosses for the -0.5° blade position. Especially the head drop in Zone A is captured well with these transient calculations, where after 3 revolutions the calculations were transient in time and the next 3 revolutions were averaged for the result. In Figure 9, for one blade position also the efficiency and the cavitation values are compared between test rig and CFD calculation. The efficiency is normalized with the best efficiency value of the test rig.

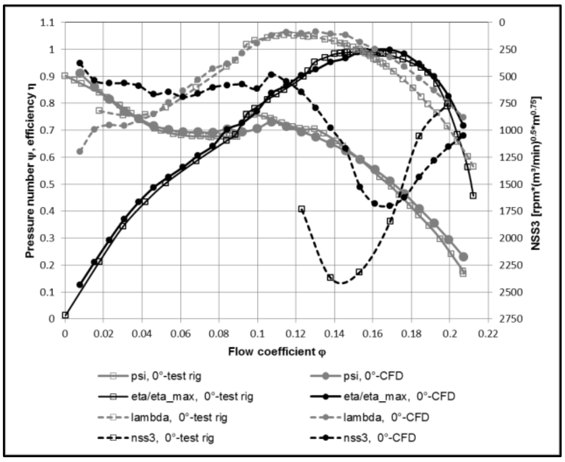

Figure 9. Blade position 0 degree, CFD vs. test rig

It can be clearly seen that the BEP point is shifted to slightly higher flow rates as the design target. This must be realised to catch the overload cavitation target together with an overall good pump performance. For the comparison between CFD test rig results the *NSS* value shows larger differences at lower flow rates. In the diagram the *NSS* value is drawn with a changed axis direction from highest values on the bottom to lowest values at the top. This was done to use this normalised specific value in the same way as pump charts with *NPSH*.

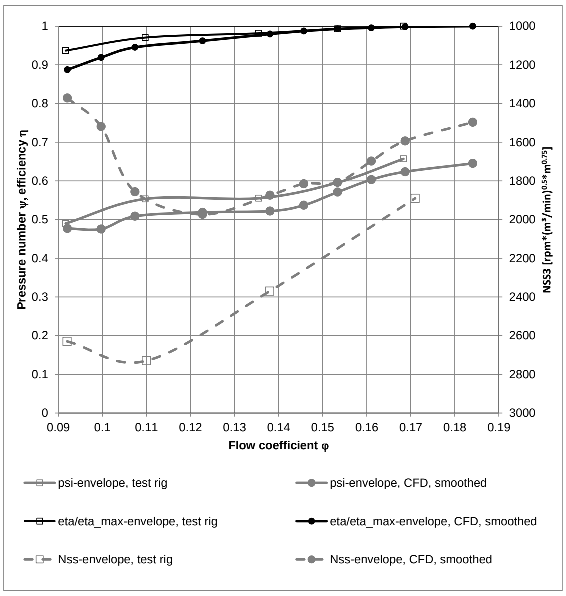

Figure 10. Envelope, CFD vs. test rig

The difference between CFD and test rig could be explained with the histogram method itself, which is conservative and indicates the *NPSH*$_i$ value at these flow rates instead of the *NPSH*$_3$ value. Additionally, the power is marked in the diagram with the normalized λ value. For this blade position the highest power consumption is at 75% flow rate. For both, part load as well as overload, the power consumption is lower. Finally, in Figure 10 the envelope is shown for different blade positions. The highest efficiency is realised at fully opened blade, but on a significantly high level at the nominal design flow rate. Instead of a decreasing head curve the envelope of the designed mixed flow pump leads to a slightly increasing head curve while the flow rate is increasing. This happens when the blade is always adjusted to its best position. Now, the pump is a single regulated device at constant speed or for variable speed a double-regulated aggregate. In comparison to the test rig, the CFD results are slightly shifted to higher flow rates and therefore the envelope for *NSS*, efficiency and the head (pressure coefficient ψ) are shifted by 5%. The *NSS* values of the CFD are lower (higher *NPSH*) than the test rig results, but especially at overload close together – this was the crucial point during the design process and could be kept with the actual design. For $\varphi = 0.2$ (130% of the nominal operation point) the *NSS* is higher than the requested *NSS*.

6. CONCLUSION

This paper presents the overall design process of a high performance mixed flow variable pitch pump from the scratch with the help of CFD. The workflow presented shows the steps up to the model test. The meridional design based on available formulas was optimised in two steps. First, a runner was realised, more or less by means of a "hand-made" stepwise optimisation, and together with this runner design the rest of the pump was developed. Therefore, a MOGA and further optimisation steps were used to attain not only the requested performance in BEP but also the overload cavitation target. With the help of stationary simulations good correlation was found, and together with transient simulations the main stability could be calculated in a correct way as well. The diffuser instability could not be calculated in a correct way with the help of numerical methods – however, this region is not of great interest as the head curve is still stable within this operation range.

REFERENCES

[1] Stepanoff, A. J., 1959, Radial- und Axialpumpen, Springer.

[2] Gülich, J. F., 2004, Kreiselpumpen, Springer.

[3] Hergt, P., Starke, J., 1985, „Flow patterns causing instabilities in the performance curves of centrifugal pumps with vaned diffusers", 2nd International Pump Symposium, Houston.

[4] Sinha, M., Pinarbasi, A., Katz, J., 2001, "The flow structure during onset and developed states of rotating stall within a vaned diffuser of a centrifugal pump", ASME Journal of Fluids Engineering, vol. 123, pp. 490–499.

[5] Wuibaut, G., Bois, G., Dupont, P., et al., 2001 "PIV measurements in the impeller and vaneless diffuser of radial flow pump in design and off-design operation condition" ASME Journal of Fluids Engineering, vol. 124, pp. 791–797.

[6] Miyabe, M., Furukawa, A., Maeda, H., Umeki, I., Jittani, Y., 2008, „On Improvement of Characteristic Instability and Internal Flow in Mixed Flow Pumps", Journal of Fluid Science and Technology, vol. 3, pp. 732-743.

[7] Muggli, F. A., Holbein, P., Dupont, P., 2002, "CFD calculation of a mixed flow pump characteristic from shutoff to maximum flow", ASME Journal of Fluids Engineering, vol. 124, pp. 798–802.

[8] Oh, H.W, Yoon, E. S., 2008, "Hydrodynamically detailed performance analysis of a mixed-flow waterjet pump using computational fluid dynamics", Proc. IMechE Vol. 222, Part C: J. Mechanical Engineering Science.

[9] A. Lucius, G. Brenner, 2010, "Unsteady CFD simulations of a pump in part load conditions using scale-adaptive simulation", International Journal of Heat and Fluid Flow. Volume 31, Issue 6, December 2010, pp 1113–1118,

[10] Zhang, W., Yunchao, Y., Hongxun, C., 2009, "Numerical Simulation of Unsteady Flow in Centrifugal Pump Impeller at Off-Design condition by Hybrid RANS/LES Approaches", High Performance Computing and Applications, 2nd International conference, Shnghai, China, pp. 571-578.

[11] Yamade, Y., Kato, C., Shimizu, H., Nagahara, T., 2009, "Large Eddy simulation of internal flow of a mixed-flow pump", Proceedings of the ASME 2009 Fluids Engineering Division Summer Meeting, Vail, Colorado, USA.

[12] Karassik, I, Messina, J. P., Cooper, P., Heald, C.C., "Pump Handbook", third edition, ISBN 0-07-0304032-3, MrGraw-Hill, 2001.

[13] Pfleiderer, C., Petermann, H., 2005, "Strömungsmaschinen", 7th edition, ISBN 3-540-22173-5, Springer.

[14] Menter, F. R., 1994, "Two-equation eddy-viscosity turbulence models for engineering applications", *AIAA journal*, vol. 32, pp.1598–1605.

[15] Menter, F. R., Egorov, Y., 2005, "A Scale-Adaptive Simulation Model Using Two-Equation Models", *AIAA journal*., pp. 271–283.

[16] International Standard ISO 9906:2012, *Rotodynamic pumps – Hydraulic performance acceptance tests – Grades 1, 2 and 3*.

[17] Gehrer, A., Benigni, H., Penninger, G., 2004, "Dimensioning and Simulation of Pro-cess Pumps," *Karlsruhe Pump Users Technical Forum*, Karlsruhe, Germany.

[18] Benigni, H., Jaberg, H., Yeung, H., Salisbury, T., Berry, O., 2012, „Numerical Simulation of Low Specific Speed API Pumps in Part-Load Operation and Comparison with Test Rig Results", in: Journal of Fluids Engineering 134 (2012) 2, pp. 024501-024501.

[19] IEC60193, 1999, Hydraulic turbines, storage pumps and pump-turbines, Model acceptance tests, Second edition 11-1999.

[20] International standard ISO 13709: First edition, "Centrifugal pumps for petroleum, petrochemical and natural gas industries", equal to API 610, 11th edition.

Large Eddy Simulation of Flow Around a Slender Body at High Angles of Attack

Ibraheem AlQadi[1], Eltayeb ElJack[2], Salah Hafez[2], Khalid Juhany[2]

[1] Corresponding Author. Aeronautical Engineering Department, King Abdulaziz University, P.O. Box 80204, Jeddah, 21589, Saudi Arabia. E-mail: ialqadi@kau.edu.sa
[2] Aeronautical Engineering Department, King Abdulaziz University, P.O. Box 80204, Jeddah, 21589, Saudi Arabia.

ABSTRACT

Large eddy simulation of the flow field around an Ogive-cylinder body at high angles of attack is presented. Three simulations were carried out for Reynolds number of $10,000$ at three angles of attack 45°, 55°, and 65°. The asymmetric wake-vortex phenomenon was observed at angles of attack 55° and 65°. The phenomenon is captured in the absence of artificial geometrical asymmetries of forced flow irregularities. The results suggest that wake-vortex asymmetry is due to an absolute hydrodynamic instability. An investigation of the unsteady flow field was carried out using dynamic mode decomposition. The analysis identified two dominant unsteady modes; unsteady wake and unsteady shear layer. At 45° the wake is much more coherent and dominant than the shear layer, whereas at 55° and 65° the shear layer is most dominant. Near the nose, the shear layer mode is dominant for all angles of attack. However, as we move downstream the wake mode become dominant for angle of attack 45° while the shear layer mode continue to be dominant for angles of attack 55° and 65°.

A synchronization was observed between the location of dominant mode switching and location of vortex breakdown.

Keywords: Dynamic mode decomposition, High angle of attack aerodynamics, Slender body aerodynamics, wake-vortex

1. INTRODUCTION

Flow over slender bodies at an angle of attack exhibits the development of symmetric and asymmetric wake-vortex flow modes. The symmetric mode develops at small angles of attack. At higher angles, an asymmetry develops in the wake-vortex system. The asymmetric wake-vortex poses a control problem for aircraft and missiles at high angles of attack due to the resulting yawing moments. If the complex behavior of the wake-vortex system is identified then it might be possible to devise an active control system at higher angles of attack when traditional control surfaces become ineffective.

Zilliac et al. [1] carried out measurements on an ogive-cylinder model. The tests revealed four angle-of-attack regimes that categorize the type of vortex behavior to be expected on pointed bodies of revolution. The regimes are symmetric leeward-side flow ($\alpha < 30°$), intermediate range ($30° < \alpha < 50°$) of steady asymmetric flow, nearly bistable range ($50° < \alpha < 65°$), and vortex shedding ($\alpha > 65°$).

Early experimental studies have shown that high angles of attack flow field is affected by Reynolds number, Mach number, fineness ratio, and the nose bluntness. Additionally it was found that the flow field is highly sensitive to small changes in testing conditions as well as geometrical irregularities due in imperfections in model constriction. The flow visualization study of Gowen et al [2] investigated the effects of nose shape, shape bluntness, and Reynolds number on the onset of asymmetric wake-vortex system. It was found that the asymmetry onset angle of attack is increased by reducing the fineness ratio or increasing the nose bluntness. Reynolds number was found to be relevant only for high fineness ratio in which increasing the Reynolds number decreases the asymmetry onset angle of attack. Wardlaw and Morrison [3] investigated several sets of data collected form fifteen different sources. A linear regression analysis was performed to extract flow field trends. The analysis emphasized some of the finding by Forrest et al such as the effect of fineness ratio and nose bluntness. However, the investigation also concluded that the asymmetry onset angle of attack decreases with increasing model length and the maximum side force decreases with increasing Mach number.

Zilliac et al. [1] observed a strong dependency of the leeward-side flow field orientation on tip geometry. Leu et al. [4] carried out experimental investigations on the flow field around a conventional sharp-nose ogive cylinder and an elliptic-tip ogive cylinder. The results showed that changes in the direction of the side force are related to changes in the asymmetry of the pressure distribution along the body. They found that the variation of the side force with the roll angle for the elliptic tip is more predictable than that for the sharp ogive tip. Flow visualization studies showed that, when the angle of attack increases, the locations of vortex asymmetry, vortex breakaway, and vortex breakdown propagate upstream toward the tip. In addition, it is found that, at $\alpha = 45°$ and $50°$, the changes in the vortex structure with the roll angle occur in a more gradual manner; i.e., one can see a nearly symmetric flow pattern occurring between the two opposite asymmetric flow patterns. On the other hand, at $\alpha = 60°$, changes in the flow pattern with the roll angle are more abrupt, leading to the formation of a bi-stable state.

Banks et al. [**?**] carried out detailed wind tunnel and flight investigations on F/A-18 configuration to investigate the causes of various high angle of attack phenomena. It was found that fixing forebody cross flow transition on model provided data that accurately match flow fields and aerodynamic characteristics of flight at high angles of attack. Wind tunnel results showed that small geometry differences especially nose boom can have a pronounced effect at high angles of attack. These differences must be modeled in sub-scale tests in order to obtain accurate correlation with flight data.

Bridges [5], in a review paper suggested two causes for high angles of attack vortex asymmetry; inviscid hydrodynamic instability of symmetrically separated vortices or asymmetric boundary layer separation on each side of the body. Stahl and Asghar [6] experimentally studied the asymmetric vortex system on two circular cones with different sizes at high angles of attack to determine the onset angle of attack of asymmetric vortex as a function of free stream Reynolds number. The two cone models have the same fineness ratio of 3.6 and the same semi apex angle of 4 degree. The Reynolds numbers are $Re_D = 0.005 \times 10^6$ and 0.202×10^6 based on the bottom diameter of the cones respectively. The vortex asymmetry was determined by a smoke flow and laser-light sheet. The results showed that the onset angle of attack of asymmetric vortex decreased with increasing Reynolds numbers. Liu and Deng [7] carried out aerodynamic force measurements and wake flow visualizations over slender bodies (cone cylinder, elliptic-nose cylinder). The experimental results showed that at angles of attack $(30° - 40°)$, the flow is unsteady and the signal of side forces contains wide ranges of amplitudes and frequencies. The unsteadiness phenomena include low-frequency three-dimensional effects, asymmetry related vortex flipping, moderate frequency von Karman vortex shedding and higher shear layer fluctuations.

The challenge of controlling the wake-vortex system stems from the highly unstable and perceptive nature of the flow field. Leu, et al [4] used micro fabricated balloon actuators for side force control on a slender body. The Balloon actuators can be packaged on curve surfaces of a cone-cylinder slender body and actuated at different roll angles. Aerodynamic force measurement results indicate the effects of micro balloon actuators vary at different actuation locations on the cone-cylinder slender body. Micro balloon actuators change nose shapes of the slender body which determines adverse-pressure-gradient values and directly influence the origin of the separation lines and characteristics of the separated vortices over the leeside surface. Xueying and Yankui [8] tested various active and passive forebody vortex flow control techniques such as forebody strakes, helical trips, unsteady bleed, and micro blowing. However, theses techniques were not sufficiently effective.

From a numerical prospective, massively separated flow around slender bodies at high angles of attack presents a number of challenges to current CFD methods and techniques. The wake-vortex flow behind the body is a complex unsteady viscous flow where nonlinear effects are dominant. The wake exhibits extremely complex flow patterns with separation and attachment regions, vortex interaction, and vortex breakdown. Simulation of such flows entails accurate computation of all of these unsteady complex physical phenomena. Cummings et al. [9] pointed out that flows at high angles of attack are more difficult to predict due to the nonlinear effects that takes place in the early stages of forming shear layers that will eventually develops into the vortex wake system. Various factors contribute to the computational difficulties such as the proper modeling of turbulence and transition for vortical and separated flow, use of suitable numerical algorithm that can accommodates flow asymmetry and employing grids that allow for accurate prediction of the flow field. Thin-Layer RANS have been used to simulate steady slender body flow at low to moderate angle of attack with symmetric wake-vortex. Dejani and Levy [10], Dejani *et al.* [11] and Murman [12] used Thin-Layer RANS to demonstrate the necessity of perturbation at the body nose for asymmetric wake-vortex. However, at high angles of attack Thin-Layer RANS assumption breaks down since the wake is highly unsteady with large-scale turbulent structures and therefore the full unsteady Navier-Stokes equations have to be solved instead [13].

Although an extensive number of studies were carried out to investigate the behavior of the wake-vortex system the mechanism responsible for the development of asymmetric wake-vortex flow at high angles of attack is still not well defined. The present study investigates the onset of vortex asymmetry with increasing angle of attack using LES. The objective is to accurately resolve the unsteady flow field especially the three dimensional boundary-layer developing over the nose cone, the formation of the vortex sheets, and the spatial/temporal evolution of the wake-vortex system. Dynamic Mode Decomposition (DMD) is applied to the resulting numerical database to study the dynamical behavior of this flow and shed some light on the root causes of the asymmetric wake-vortex phenomenon.

2. COMPUTATIONAL METHODOLOGY

2.1. Mathematical Model

As stated in the introduction, RANS is not suitable since the problem in hand is highly unsteady. Since DNS is not feasible due to extreme grid requirements, LES is a suitable approach for the flow field under consideration. In LES the spatially filtered three-dimensional time-dependent Navier-Stokes equations are solved numerically for all motions with a scale larger than the mesh size of the chosen numerical grid, while the small-scale, mainly dissipative motion is simulated by a sub-grid scale (SGS) model. The filtered equations are given by:

$$\frac{\partial \bar{u}_i}{\partial x_i} = 0 \tag{1}$$

$$\frac{\partial \bar{u}_i}{\partial t} + \frac{\partial \bar{u}_i \bar{u}_j}{\partial x_j} = -\frac{1}{\rho}\frac{\partial \bar{p}}{\partial x_i} + \frac{\partial\left(2\nu \bar{S}_{ij}\right)}{\partial x_j} - \frac{\partial \tau_{ij}}{\partial x_j} \tag{2}$$

The equations are written using the compact index-notation form where i and j vary from 1 to 3. u_i are the velocity vector components, p is the pressure, ρ is the fluid density and ν is the kinematic molecular viscosity. The overbar denotes spatially filtered quantities. The last term in the momentum equation is the divergence of the sub-grid-scale stresses $\tau_{ij} = \overline{u_i u_j} - \bar{u}_i \bar{u}_j$. The sub-grid-scale stresses are modeled using the eddy-viscosity concept:

$$\tau_{ij} = 2\upsilon_t \bar{S}_{ij} + \frac{1}{3}\delta_{ij}\tau_{kk} \tag{3}$$

$$\bar{S}_{ij} = \frac{1}{2}\left(\frac{\partial \bar{u}_i}{\partial x_j} + \frac{\partial \bar{u}_j}{\partial x_i}\right) \tag{4}$$

The sub-grid-scale eddy viscosity ν_t is computed using the dynamic Smagorinsky model of Germano *et al.* [14] as modified by Lilly [15]:

$$\nu_t = C_S \Delta^2 \left|\bar{S}\right| \text{ where } \bar{S} = \sqrt{2\bar{S}_{ij}\bar{S}_{ij}} \text{ and}$$
$$\Delta = (\Delta x \Delta y \Delta z)^{\frac{1}{3}}$$

The coefficient C_s is computed dynamically by applying a second filter with filter width twice the filter width Δ based on the grid spacing. The computed value of C_s is clipped to the range $(0.0 < C_s < 0.23)$.

2.2. Solution Method

The computations were carried out using the Ansys–Fluent V14.5 CFD software [16]. A pressure-based solver is used to solve the above equations. The solver uses the SIMPLE scheme for pressure-velocity coupling and green-gauss node-based approach for gradients evaluation. The unsteady LES runs employ a second-order bounded central spatial discretization scheme and an implicit second-order time marching scheme. The time step is equal to 0.0001 seconds, with a maximum of 50 error-reduction sub-iterations per time-step.

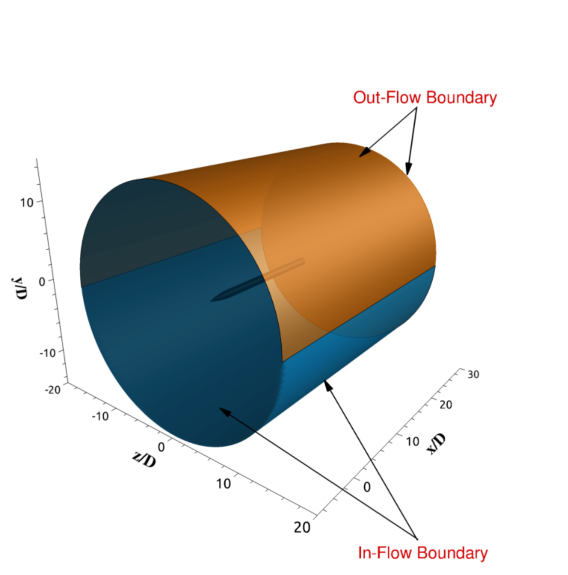

Figure 1. Computational domain

2.3. Computational Domain and Operating Conditions

The geometry used in the current computation is an ogive-cylinder with a diameter of $D = 3.5cm$. The model length is $L = 18.5D$ with slenderness ratio of 3.5 and 15 for the ogive and the cylinder respectively. The computational domain is constructed such that the domain boundaries are $6.5D$ upstream of the model nose, $10D$ downstream of the model base, and $15D$ away from the model surface in the radial direction. Velocity component were specified at in-flow boundary while extrapolation was used at the out-flow boundary. No-slip condition was applied at the model surface. The free-stream conditions are selected to yield Reynolds number of $10,000$. Three angles of attack were considered: 45°, 55°, and 65°.

2.4. Computational Grid

The quality of the computational grid has a major effect on the computed results. Inadequate grid density and sudden changes in grid point distribution bring about errors in spatial development of vortical structures while discontinuity and non-smoothness in grid line slopes give rise to numerical instabilities due to abrupt variations in grid metrics. Therefore, good quality grid with adequate density is necessary for a successful simulation. The reported results are obtained on a composite O-type grid of size 16.7 million grid points (16.6 million hexahedral cells). There are 510 grid points along the model alone with 201 grid points in the direction normal to the surface

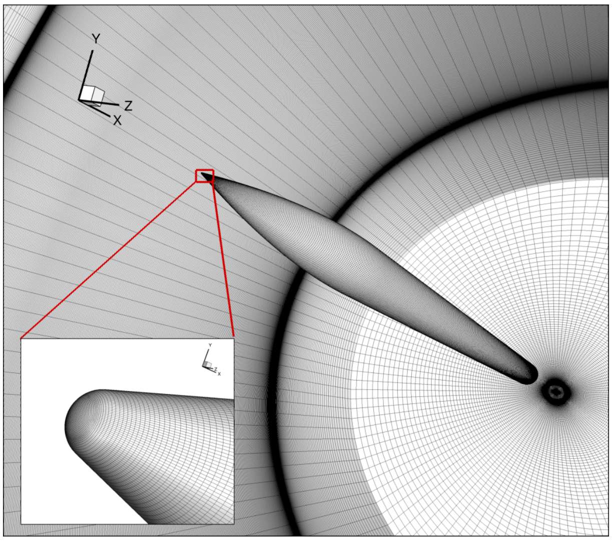

Figure 2. Computational grid

and 121 grid points in the azimuthal direction. Figures 1 and 2 show the computational domain and the employed grid. The grid is generated as a structured grid, using Pointwise, to produce a smooth and orthogonal mesh. This is essential for the current study as unsteady vortex dominated flow is sensitive to grid quality.

For near-wall regions LES requires stream-wise and azimuthal mesh resolutions of Δx^+ and $\Delta\theta^+ \leq 50$. The superscript $^+$ indicates non-dimensionalization with u^* and ν (*i.e.* $\Delta x^+ = \Delta x u^*/\nu$). For the current simulation the mesh resolution in the stream-wise direction ranges from $\Delta x^+ = 1/5$, near the nose, to a maximum of 50, 11 diameters downstream from the nose. The resolution in the azimuthal direction is $\Delta\theta^+ = 19$. In the direction normal to the wall, well-resolved LES requires a much finer spacing, $\Delta n^+ \leq 1$. For the current calculation, the first grid point is located at $\Delta n^+ \approx 0.35$. Given the the operating Reynolds number, the grid resolution is more than sufficient.

2.5. Dynamic Mode Analysis

Higher order statistical methods that optimally decompose the flow field have many shortcomings that limit its implementation to turbulent flows. In the last 30 years the most used method is Proper Orthogonal Decomposition (POD) [17] and [18]. Despite the usefulness of POD in analyzing wall bounded and free shear flows, it has many drawbacks. Firstly, the most energetic mode as identified by POD is not always the most important mode in the flow field. Secondly, POD method is based on an ensemble averaged two-point correlation tensor, therefore, all phase information are lost in the averaging process. Thirdly, the method being based on an ensemble averaged correlation tensor means that it is very expensive to calculate and the statistical error depends on the number of snapshots, *i.e.*, the more snapshots the better the accuracy of the method.

Dynamic Mode Decomposition method, [19] and [20], does not require any ordering of the data in space or in a form of a matrix, all that matters is a sequence of snapshots in time $V(:,t)$ regardless how they are ordered in space. Hence, DMD method considers a two dimensional matrix for any given flow field whether full three dimensional or plane two dimensional. The first matrix dimension is space and the second is time. Consider a set of data consisting of n snapshots, sampled experimentally or numerically, and ordered in time with a constant time step Δt:

$$\mathbf{V}_1^n = \{v_1, v_2, v_3, \ldots, v_n\} \tag{5}$$

The snapshots are assumed to be linearly correlated, *i.e.*, v_j is linearly correlated with v_{j+1} or $v_{j+1} = \mathbf{A}v_j$, and this linear mapping can be implemented to the whole data set $\mathbf{V}_1^n$ to obtain a set of the following form:

$$\{v, \mathbf{A}v, \mathbf{A}^2 v, \ldots \mathbf{A}^{n-1} v\} \tag{6}$$

or

$$\mathbf{V}_2^{n+1} = \mathbf{A}\mathbf{V}_1^n \tag{7}$$

For sufficiently large sequence, one can assume linear relation between snapshots and construct the n^{th} snapshot by a linear combination of the preceding $(n+1)$ snapshots, that is:

$$\mathbf{V}_2^{n+1} = \mathbf{A}\mathbf{V}_1^n \approx \mathbf{V}_1^n \mathbf{S} \tag{8}$$

$\mathbf{S}$ is a companion matrix that contains the coefficients of the linear mapping. The problem now becomes a least-square problem to find $\mathbf{S}$ that approximate the linear mapping with a minimum error.

$$[\mathbf{Q}, \mathbf{R}] = qr(\mathbf{V}_1^{n-1}) \tag{9}$$

$$\mathbf{S} = \mathbf{R}^{-1}\mathbf{Q}^H \mathbf{V}_2^n \tag{10}$$

Once the companion matrix is calculated one can solve the following eigenvalue problem:

$$\mathbf{S\Phi} = \mathbf{\Gamma\Phi} \tag{11}$$

The eigenvalues of $\mathbf{S}$ contain the growth rates and phase velocities of the modes, while the eigenvectors represent the shape of the dynamic modes.

$$\lambda_j = \frac{\log(\mathbf{\Gamma}_{jj})}{\Delta t} \tag{12}$$

The real parts of λ represent the growth rates, while the imaginary parts represent the corresponding phase velocities. The dynamic modes are then reconstructed by projecting the original snapshots onto the eigenvectors as follows:

$$DM(j) = \mathbf{V}_1^{n-1}(:,:)\mathbf{\Phi}(:,j) \tag{13}$$

3. RESULTS

The calculations were carried out for 25 flow-through times to allow for flow field development. Then a set of 1024 snapshots were collected at ten

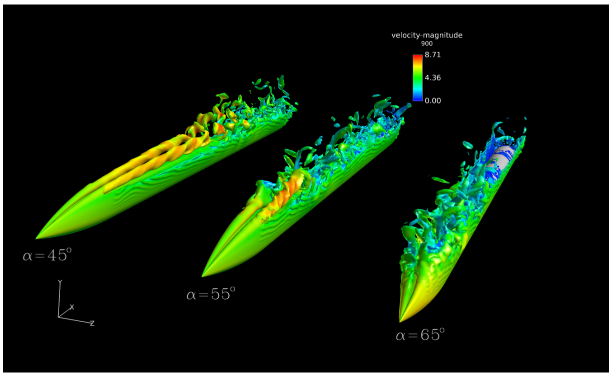

Figure 3. instantanous iso-vorticity colored by velocity magnitude

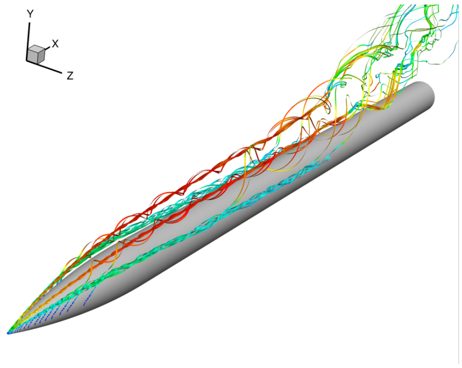

Figure 4. Instantaneous pathlines at $\alpha = 45°$

stream-wise stations. It should be emphasized that no artificial asymmetry was introduced in the computations. The computational domain and the grid are symmetric with only double precession roundoff errors. The spatial numerical scheme is a central-difference scheme and the computations were performed using double precession accuracy.

Figure 3 shows the instantaneous iso-vorticity magnitude colored by velocity magnitude. At $\alpha = 45°$ the wake-vortex is almost symmetric with simultaneous vortex breakdown further downstream. At $\alpha = 55°$ the flow becomes asymmetric. At $\alpha = 65°$ the flow is highly asymmetric with asymmetric vortex separation and breakdown starting closer to the nose. Figures 4, 5 and 6 display instantaneous pathlines at different angles of attack. The figures show an initially symmetric attached wake-vortex at $\alpha = 45°$. As the angle of attack is increased to$\alpha = 55°$, vortex shedding becomes asymmetric and the wake-vortex starting to separate and breaks down. At higher angle, $\alpha = 65°$, the locations of vortex-separation and vortex-breakdown propagate upstream and the flow over the body becomes very complex and unsteady. Although the flow in all cases is initially laminar it goes through transition to turbulence in the separated shear-layer and at the location where the wake-vortex system breaks down. The results shows that flow asymmetry occurs in the absence of geometrical imperfections and is most probably due to an absolute instability.

Dynamic Mode Decomposition was applied to the numerical databases that have been generated using large eddy simulation at 10 stream-wise planes normal to the slender body at different stream-wise locations ($x/d = 0.3$ to 15 as shown in figure 7), and at angles of attacks 45° , 55°, and 65°. For all 30 planes the plots of real part of the eigenvalues versus imaginary part resulted in a unit circle suggesting that the pressure signals are quasi-periodic.

DMD analysis identified two dominant unsteady modes; unsteady wake and unsteady shear layer. An extensive search process for the dominant shear layer and dominant wake modes in each down-stream plane was carried out. It was found that the domin-

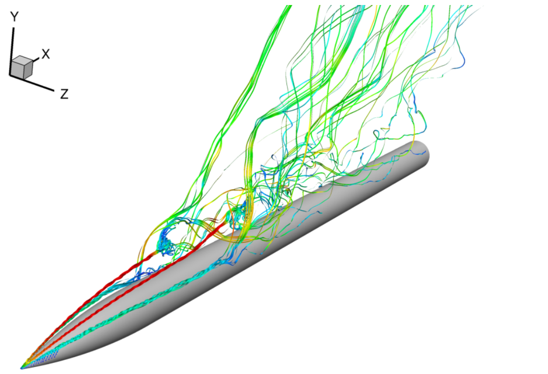

Figure 5. Instantaneous pathlines at $\alpha = 55°$

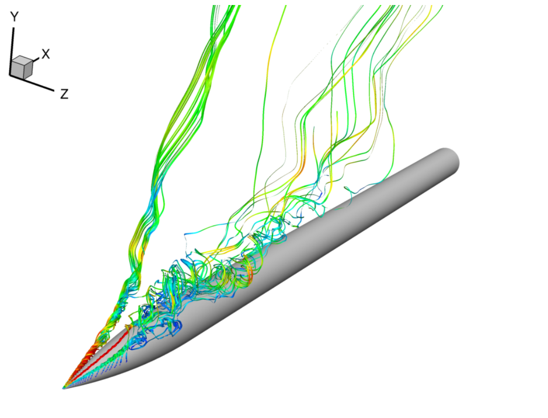

Figure 6. Instantaneous pathlines at $\alpha = 65°$

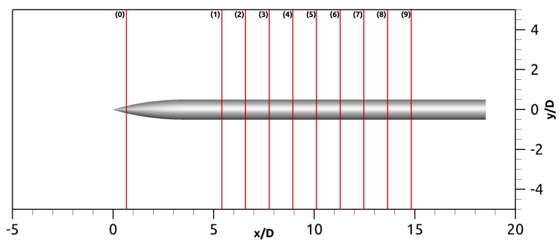

Figure 7. streamwise locations where timeseries data was collected

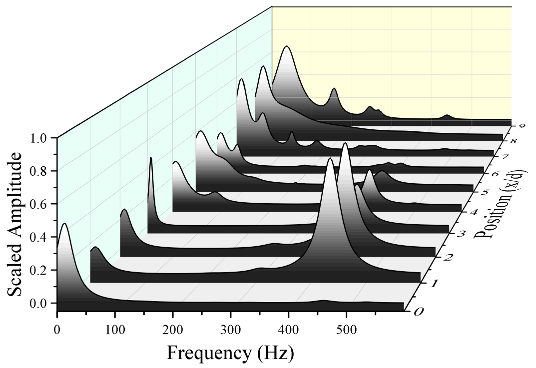

Figure 8. DMD spectrum for α = 45° at 10 different downstream planes

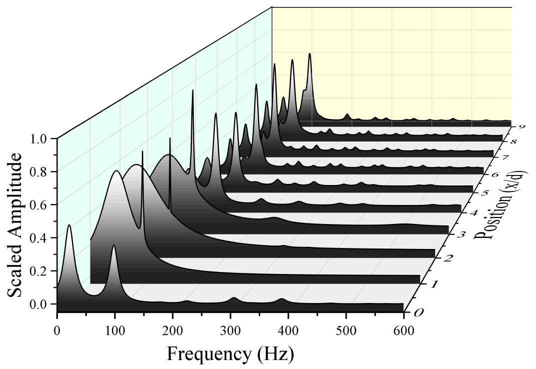

Figure 9. DMD spectrum for α = 55° at 10 different downstream planes

ant shear layer frequency for all three angles of attack and all down-stream stations lies between $75-100Hz$ as shown in figures [spectrum 1, 2, and 3], whereas the wake dominant frequencies range between $4-7Hz$ as shown in the same figures. It is noted that the dominant shear layers at 55° and 65° have too many higher sub-harmonic modes than the dominant shear layers at 45°, indicating the break-down of vortical structures at these angles of attack. It is also noted that at 45° the wake is much more coherent and dominant than the shear layer, whereas at 55° and 65° the shear layer is most dominant. It was also observed that near the nose, the shear layer mode is dominant for all angles of attack. However, as we move downstream the wake mode become dominant for angle of attack 45° while the shear layer mode continue to be dominant for angles of attack 55° and 65°.

4. SUMMARY

LES of the flow around an Ogive-cylinder body at high angles of attack have been presented. The asymmetric wake-vortex phenomenon was observed at angles of attack of α = 55° and α = 65°. The results also showed that the phenomenon is present in the absence of artificial geometrical or flow asymmetry. An investigation of the unsteady flow field

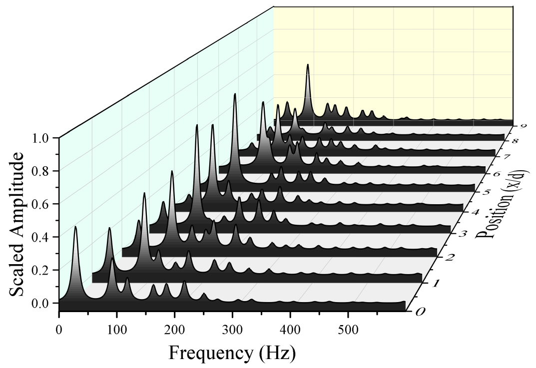

Figure 10. DMD spectrum for α = 65° at 10 different downstream planes

was carried out using dynamic mode decomposition. The analysis identified two dominant unsteady modes; unsteady wake and unsteady shear layer. At α = 45° the wake is much more coherent and dominant than the shear layer, whereas at α = 55° and α = 65° the shear layer is most dominant. Near the nose, the shear layer mode is dominant for all angles of attack. However, as we move downstream the wake mode become dominant for angle of attack α = 45° while the shear layer mode continue to be dominant for angles of attack α = 55° and α = 65°.

ACKNOWLEDGEMENTS

This work was supported by King Abdulaziz City for Science and Technology (KACST) under the NSTIP strategic technologies program - Project. No. (8-SPA135-3). The authors would like to acknowledge the support provided by Science and Technology Unit at King Abdulaziz University. Computational resources were provided by King Abdulaziz University HPC facilities.

REFERENCES

[1] Zilliac, G., Degani, D., and Tobak, M., 1991, “Asymmetric vortices on a slender body of revolution”, *AIAA journal*, Vol. 29 (5), pp. 667–675.

[2] Gowen, F. E., and Perkins, E. W., 1953, “A Study of the Effects of Body Shape on the Vortex Wakes of Inclined Bodies at a Mach Number of 2”, *Tech. Rep. NACA-RM-A53I17*, NACA.

[3] Wardlaw, A., and Morrison, A. M., 1976, “Induced side forces at high angles of attack”, *Journal of Spacecraft and Rockets*, Vol. 13 (10), pp. 589–593.

[4] Leu, T.-S., Chang, J.-R., and Lu, P.-J., 2005, “Experimental investigation of side force control on cone-cylinder slender bodies with flexible micro balloon actuators”, *Experimental*

thermal and fluid science, Vol. 29 (8), pp. 909–918.

[5] Bridges, D. H., 2006, "The asymmetric vortex wake problemâĂŤasking the right question", *The 36th AIAA Fluid Dynamics Conference*, AIAA 2006-3553, pp. 1737–1765.

[6] Stahl, W., and Asghar, A., 1996, "Dependence on Reynolds number of onset of vortex asymmetry behind circular cone", *AIAA paper*, Vol. 64.

[7] Liu, P., and Deng, X., 2003, "Experimental investigation of aerodynamic characteristics on slender bodies at high angles of attack", *Canadian aeronautics and space journal*, Vol. 49 (1), pp. 31–40.

[8] Xueying, D., and Yankui, W., 2004, "Asymmetric vortices flow over slender body and its active control at high angle of attack", *Acta Mechanica Sinica*, Vol. 20 (6), pp. 567–579.

[9] Cummings, R. M., Forsythe, J. R., Morton, S. A., and Squires, K. D., 2003, "Computational challenges in high angle of attack flow prediction", *Progress in Aerospace Sciences*, Vol. 39 (5), pp. 369–384.

[10] Degani, D., and Levy, Y., 1992, "Asymmetric turbulent vortical flows over slender bodies", *AIAA journal*, Vol. 30 (9), pp. 2267–2273.

[11] Levy, Y., Hesselnik, L., and Degani, D., 1996, "Systematic study of the correlation between geometrical disturbances and flow asymmetries", *AIAA journal*, Vol. 34 (4), pp. 772–777.

[12] Murman, S. M., 2000, "Geometric perturbations and asymmetric vortex shedding about slender pointed bodies", *AIAA Journal*, pp. 2000–4103.

[13] Degani, D., and Marcus, S., 1997, "Thin vs full Navier-Stokes computation for high-angle-of-attack aerodynamics", *AIAA journal*, Vol. 35 (3), pp. 565–567.

[14] Germano, M., Piomelli, U., Moin, P., and Cabot, W. H., 1991, "A dynamic subgrid-scale eddy viscosity model", *Phys Fluids A-Fluid*, Vol. 3 (7), pp. 1760–1765.

[15] Lilly, D., 1992, "A proposed modification of the Germano subgrid-scale closure method", *Phys Fluids A-Fluid*, Vol. 4 (3), pp. 633–635.

[16] ANSYS, Inc, Canonsburg, PA, USA, 2012, *ANSYS–FLUENT 14.5 Manual*, 14.5 edn.

[17] Lumley, J. L., 1967, "The Structure of Inhomogeneous Turbulent Flows", *In Atmospheric Turbulence and Radio Wave Propagation*, Moscow, pp. 166–178.

[18] Holmes, P., and Lumley, J. L.and Berkooz, G., 1996, *Turbulence, Coherent Structures, Dynamical Systems and Symmetry*, Cambridge University Press.

[19] Rowley, C. W., Mezic, I., Bagheri, S., Schlatter, P., and Henningson, D. S., 2009, "Spectral analysis of nonlinear flows", *Journal of Fluid Mechanics*, Vol. 641, p. 115âĂŞ127.

[20] Schmid, P. J., 2010, "Dynamic mode decomposition of numerical and experimental data", *Journal of Fluid Mechanics*, Vol. 656, p. 5âĂŞ28.

A COMPARATIVE STUDY OF TURBULENCE MODELS FOR THE FLOW IN A RIB-ROUGHENED, INTERNAL TURBINE BLADE COOLING CHANNEL

Sebastian SCHOLL[1], Stefano VAGNOLI[2], Tom VERSTRAETE[3],

[1] Corresponding Author. Department of Turbomachinery and Propulsion, Von Karman Institute for Fluid Dynamics. Chausee de Waterloo 72, 1640 Rhode-St-Genese, Belgium. Tel.: +32 2 359 9611, Fax:+32 2 359 96 00, E-mail: sebastian.scholl@vki.ac.be
[2] Department of Turbomachinery and Propulsion, Von Karman Institute for Fluid Dynamics. Chausee de Waterloo 72, 1640 Rhode-St-Genese, Belgium. E-mail: stefano.vagnoli@vki.ac.be
[3] Department of Turbomachinery and Propulsion, Von Karman Institute for Fluid Dynamics. Chausee de Waterloo 72, 1640 Rhode-St-Genese, Belgium. E-mail: tom.verstraete@vki.ac.be

ABSTRACT

The present contribution focuses on the aerodynamic predictive capabilities of Reynolds-Averaged Navier-Stokes (RANS) simulations and Large Eddy Simulations (LES) for internal gas turbine cooling channels. Rib-roughened surfaces are employed for such kind of applications to promote turbulence and to increase the heat transfer between the wall and the coolant. The numerical results for a cooling channel with a blockage ratio of 0.3 and a Reynolds number of 40,000 are compared with experimental data obtained at the Von Karman Institute for Fluid Dynamics (VKI). Different turbulence model approaches have been tested, and their predictive capabilities are evaluated: the results clearly show the inferiority of RANS simulations, both based on the Boussinesq eddy viscosity assumption and on Reynolds-stress modeling, in comparison with the performed LES in predicting the flow behavior.

Keywords: CFD, Internal rib-roughened cooling channels, LES, RANS, Turbomachinery, Turbine blade cooling

NOMENCLATURE

C_μ	[]	model constant (0.09)
D_h	$[m]$	hydraulic Diameter
H	$[m]$	rib height
L	$[m]$	channel length
Ma	[]	Mach number
P	$[m]$	pitch length
Re	[]	Reynolds number
U	$[m/s]$	Velocity magnitude
k	$[m^2/s^2]$	turbulence kinetic energy
u, v, w	$[m/s]$	velocity components
$y+$	[]	dimensionless wall distance
c	$[m/s]$	Speed of sound
$\underline{\underline{F}}$	[]	flux tensor
$\underline{\underline{S}}_{ij}$	$[m/s]$	mean strain rate tensor
$\underline{W}$	[]	conservative variable vector
$\overline{\overline{\theta}}$	[]	filtered quantity
δ_{ij}	[]	Kronecker delta
ϵ	$[m^2/s^3]$	dissipation rate of the turbulence kinetic energy
ν_t	$[m^2/s]$	turbulent viscosity
$\overline{\theta}$	[]	time-averaged quantity
ρ	$[kg/m^3]$	density
τ_{ij}	$[m^2/s^2]$	Reynolds stress components
θ'	[]	fluctuating quantity
ν_{SGS}	$[m^2/s]$	subgrid-scale turbulent viscosity

1. INTRODUCTION

With the rising use of energy and the claims for environmental awareness, the turbomachinery industry tries to improve the gas turbine efficiency by several means, one of which consists in increasing the turbine inlet temperature to increase the turbine cycle efficiency. In modern engines, the turbine inlet temperature exceeds the metal melting temperature such that internal and external cooling techniques need to be applied and developed. For the internal cooling of turbine blades, a common technique to increase the heat transfer in the blade is to use roughened surfaces or turbulators, which promote higher turbulence levels in the flow.
Since the life of a turbine blade is reduced by half with an increased turbine solid temperature of only 30 Kelvin [1], the prediction of local heat transfer coefficients and temperatures is a crucial step towards the design of high pressure turbine blades and vanes.
Until now, it remains a difficult task to experimentally or numerically predict the complex flow structures inside such channels. The major objective of this contribution is an evaluation of different numerical techniques comparing their aerodynamic predictions and validating them against experimental data.

The following section introduces the governing equations and the used solvers. Thereupon, the test case of a high blockage ratio channel and its computational setup is introduced. Finally, the results for different turbulence models and simulation approaches is presented.

2. NUMERICAL METHODS

2.1. Governing equations

The governing equations for the present computations are the Navier-Stokes equations and the filtered LES equations describing the conservation of mass and momentum as described as follows in conservative form:

$$\frac{\partial \underline{W}}{\partial t} + \nabla \cdot \underline{\underline{F}} = 0, \tag{1}$$

with the conservative variables $\underline{W} = (\rho, \rho u, \rho v, \rho w)$, the flux tensor $\underline{\underline{F}}$, the density ρ and the velocity components (u, v, w). For the conducted steady simulations the time derivative disappears and for the incompressible computations, the density ρ is constant. For the LES, the fluid follows filtered equations leading to the following LES equations:

$$\frac{\partial \underline{\bar{W}}}{\partial t} + \nabla \cdot \underline{\underline{\bar{F}}} = 0, \tag{2}$$

with the conservative variables $\bar{W} = (\bar{\rho}, \bar{\rho}\tilde{u}, \bar{\rho}\tilde{v}, \bar{\rho}\tilde{w})$, the flux tensor $\bar{F}$, the density $\bar{\rho}$ and the velocity components $(\tilde{u}, \tilde{v}, \tilde{w})$.

2.2. RANS approach and solver

The RANS formulation is based on the Reynolds averaging [2] with each dependent quantity split into an averaged and a fluctuating component: $\Theta = \overline{\theta} + \theta'$ with the overline denoting a Reynolds averaged quantity and the prime denoting a fluctuating quantity. Including the splitted quantities into the Navier-Stokes equations results in the appearance of a new term in the momentum equation, the Reynolds stresses: $\tau_{ij} = -\overline{u_i' v_j'}$, which needs to be modeled.

Two basic principles exist and are employed in the present study to model the Reynolds stresses: First, the so-called Reynolds-stress model considers each term of the Reynolds stress tensor individually, solving a transport equation for each component. Second, with the Boussinesq eddy viscosity assumption [3], the Reynolds stresses are approximated with:

$$-\overline{\underline{u}'\underline{v}'} = 2\nu_t \underline{S}_{ij} - \frac{2}{3} k \delta_{ij}, \tag{3}$$

with the mean strain rate tensor $\underline{S}_{ij} = \frac{1}{2}\left(\frac{\partial u_i}{\partial x_j} + \frac{\partial u_j}{\partial x_i}\right)$, the turbulence kinetic energy k, the Kronecker delta δ_{ij} and the turbulent viscosity ν_t, which the Boussinesq eddy viscosity assumption introduces as a new quantity that needs modeling.

The first RANS model that has been used, the $k - \epsilon$ model [4, 5], computes the turbulent viscosity from $\nu_t = C_\mu k^2/\epsilon$, with the model constant C_μ the turbulence kinetic energy k and its dissipation rate ϵ. For the turbulence kinetic energy and its dissipation rate two model transport equations are solved.

The second used RANS model was the Launder Reece Rodi (LRR) Reynolds-stress model, which solves transport equations for each of the Reynolds-stress tensor components.[6, 7]

For the RANS computation, a solver based on the Open source Field Operation and Manipulation C++ libraries (OpenFOAM®) was used to solve the incompressible steady state equations with a SIMPLE algorithm. The equations were discretized with a finite volume method [8] and a second order central scheme in space was employed for the Navier-Stokes and continuity equations, whilst the turbulence equations were discretized by an upwind scheme.

2.3. LES approach and solver

After the filtering operation, the unknowns appearing in the LES equations, i.e., the subgrid-scale (SGS) quantities, need to be modeled. The Boussinesq eddy viscosity assumption is applied for which a subgrid-scale turbulent viscosity ν_{SGS} is introduced. Two different LES approaches with two different solvers have been applied: First, a compressible LES solver, AVBP, developed at CERFACS (Schönfeld and Poinsot[9]; Mendez and Nicoud [10]) has been applied. Second, the LES solver from OpenFOAM® framework has been used for comparison.

The solver AVBP models the SGS quantities via the Wall-adapting local Eddy-viscosity (WALE) model (Nicoud and Ducros [11]). The equations are discretized by centered spatial schemes and explicit time schemes with a Finite-Element based two step Taylor-Galerkin (TTGC) scheme for the convection in a cell-vertex formulation (Colin and Rudgyard [12], and Donea and Huerta [13]). This explicit scheme is of third order accuracy in space (on hybrid meshes) and time, providing low dissipation, especially suitable for LES. The diffusion term is discretized with a vertex-centered operator closely following the Galerkin method and is of second order, having a $\Delta 2$ stencil (Colin et al. [14], and Donea and Huerta[13]).

The solver used from the OpenFOAM® platform is an incompressible solver. The pressure-velocity coupling was treated with the PISO algorithm, which uses a momentum predictor and a correction loop in which the pressure equation is solved and the momentum equation corrected based on the pressure change. The flow equations are discretized with an explicit Euler scheme in time and a second order central finite-volume discretization scheme in space, introducing a small amount of upwinding for the advection terms to increase the stability. The Smagorinsky model was used to compute the subgrid-scale turbulent viscosity, including the van Driest formulation to model the small non-isotropic turbulent scales close to the wall.

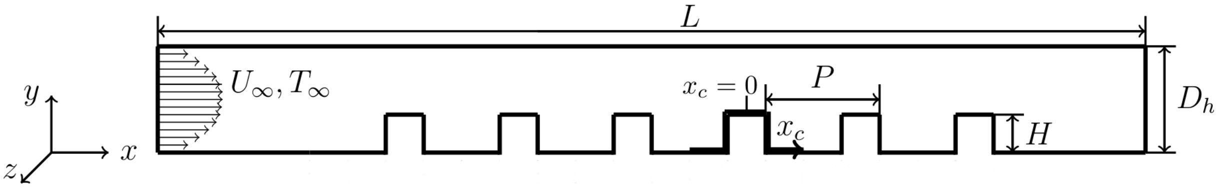

Figure 1. Channel configuration

3. TEST CASE AND COMPUTATIONAL SETUP

3.1. The experimental configuration

The applied configuration models the experimental facility of Cakan [15], Cukurel [16], Cukurel and Arts [17], which was a simplified model of an internal rib-roughened aircraft gas turbine blade cooling passage with a pitch to rib ratio of 10 and a blockage ratio of 0.3 (Table 1 summarizes the dimensions). The cooling passage was scaled up by a factor of 15 with respect to real engine conditions. The scaling ratios for the experiments resulted from a compromise between the need for high measurement resolution and limiting electrical power supply ([15]).
The experimental facility consisted of three sections: an inlet, a test and an outlet section from which the test section with its six ribs was fully represented by the configuration for the numerical simulations (Fig. 1). The cross section dimensions were 75x75 mm and the test section length was 1260 mm.

Table 1. Channel and flow characteristics (Cukurel 2012).

Parameter	abbr.	Value
Reynolds number	Re_{D_h}	40,000
number of ribs		6
length	L	1597.5 mm
hydraulic diameter	D_h	75 mm
rib height	H	22.5 mm
pitch to rib ratio	P/H	10
blockage ratio	H/D_h	0.3

3.2. The numerical model

Although the rib of the cooling channel repeats itself periodically as described in the previous paragraph, the total number of six ribs was kept similar to the experimental model to avoid possible arbitrary effects of periodic boundary conditions that occur as Fransen et al. [18] have shown.
The applied Reynolds number for all simulations was 40,000 as in the experimental campaigns. No-slip conditions were applied at all walls. The inlet and outlet boundaries were positioned far from the actual part of interest, avoiding major influences on the flow around the ribs. Adiabatic conditions were applied on the walls.

Keylock et al. [19] demonstrated on a single rib with a lower blockage ratio (0.15) than in the present study that the rib has such a strong effect on the flow that the precise nature of the inlet condition, with regards to the turbulent fluctuations and length scales, is forgotten and only small differences for the flow separation and reattachment may appear.
The reattachment lengths and many flow quantities will be preserved reasonably well, regardless of the inlet profile. Due to the even larger blockage ratio used in this study, a turbulent mean profile without fluctuations for the flow was applied as inlet condition for the LES.
Two different scalings were used for the two different solvers, as explained as follows:
To simulate the exact flow conditions with the small Mach number of the experimental campaign of Cukurel (2012) at Ma = 0.02 the computational time (using AVBP, a compressible solver with explicit time integration for the LES) would have been unjustifiably long. Hence, the Mach number was increased to Ma = 0.2, keeping the same Reynolds number, based on the bulk velocity and the hydraulic diameter D_h, at 40,000. This scaling granted a decrease of the computational cost and a re-scaling to more real engine conditions, while maintaining the similarity with the experimental data and keeping the simulated Mach number small enough to avoid compressibility effects. The time step is controlled via the Courant-Friedrich-Lewy (CFL) condition for compressible flows: $CFL = \frac{(U+c)\Delta t}{\Delta x} \simeq 0.7$, with the smallest grid cell size Δx and the minimal Δt in the whole domain, Und $c$eing the local flow and sound speeds. The Navier-Stokes Characteristic Boundary Conditions (NSCBC) of Poinsot and Lele [20], were applied at the inlet and the outlet for AVBP.
Since the OpenFOAM® computations were done with an incompressible solver, the same dimensions as in the experiments were kept, again, at a Reynolds number of 40,000. For the outlet, the static pressure was fixed for both LES and RANS and a zero gradient condition was applied at the inlet and the walls. The velocity profile was set at the inlet, set to a zero gradient condition at the outlet and set to no-slip conditions at the walls.

3.3. Description of used meshes

After a mesh convergence study, two different meshes have been used for the two different solvers. Table 2 summarizes their properties and the following sections detail the applied mesh creation strategies.

Table 2. Used meshes.

	mesh $M_{OpenFOAM^{®}}$	mesh M_{AVBP}
# of cells	3.2 million	20.3 million
mean y+	2.6	3.4

3.3.1. Mesh for LES computations with AVBP

With the present wall-resolved approach for the numerical simulations and the ubiquitous presence of walls in the internal cooling passage, the mesh requirements are high, leading to demanding and costly computations.
The unstructured LES solver AVBP was designed to deal with hybrid meshes. Therefore, a hybrid mesh (consisting of tetrahedra within the channel and prismatic elements at the walls) has been used for the current application. Figure 2 shows the tetrahedra of the used mesh around two ribs of the channel in the symmetry plane.
For reliable results, the closest grid point needs to be within the viscous sublayer, leading to small grid cells at the wall. A prismatic layer in the wall-normal direction provides a good orthogonality and needs less elements for the same resolution than a tetrahedral layer. Fransen [21] recently observed that using one prism layer results in the best mesh quality for a hybrid mesh in such a ribbed geometry, which has been done for the present computations. Increasing the amount of prism layers penalized the quality in the rib to bottom wall corners.

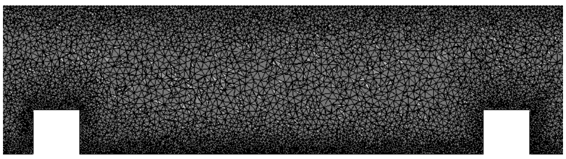

Figure 2. Mesh around two ribs for LES computation with AVBP.

3.3.2. Mesh for RANS and LES computations with OpenFOAM®

Figure 3 shows the mesh used for the computations with OpenFOAM®. A structured mesh consisting of hexahedra has been used. The y+ value of this mesh was slightly lower than the y+ value of the AVBP mesh, but the order of the spatial numerical scheme one order smaller. Most distances of the first grid cell to the wall remain lower than 5, remaining within the viscous sub-layer. The y+ distribution is penalized by the grid cells at the corners, where a boundary layer is not existent.

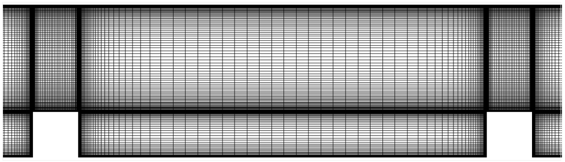

Figure 3. Mesh around two ribs for LES and RANS computation with OpenFOAM®.

4. RESULTS

This section compares the results for all simulations with each other and with the available experimental data. Even though the flow field is three-dimensional and highly unsteady, the quantity of interest is the flow field in the statistically steady sense. The RANS simulations are steady-state themselves, while the experimental data obtained with Particle Image Velocimetry (PIV) by Casarsa [22] and the LES were time averaged.

4.1. Primary recirculation zones

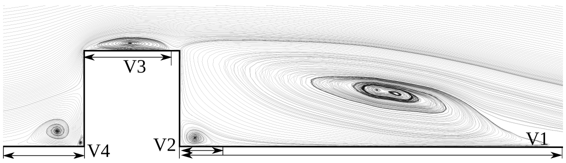

Figure 4. Streamlines on center-plane with LES using AVBP.

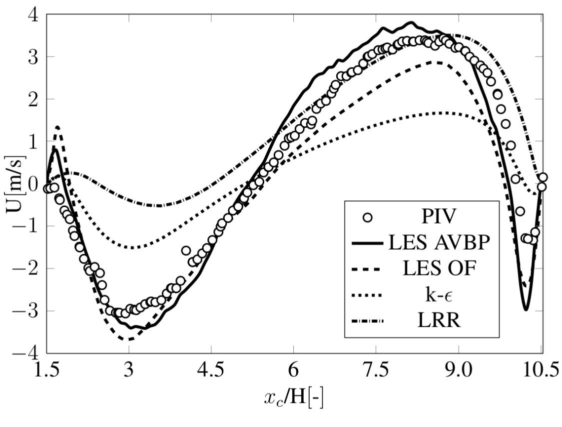

Figure 5. Streamwise velocity comparisons: between experimental and numerical data along the symmetry plane at y/H = 0.05 and between the two LES cases and the RANS cases. Results for experiments by Casarsa [22]. Note: values for the AVBP LES results have been divided by the scaling factor for comparison.

Figure 4 shows the main recirculation zones in streamwise direction obtained from the LES with AVBP. Four major recirculation zones exist: the largest recirculation zone after the rib (V1), a small

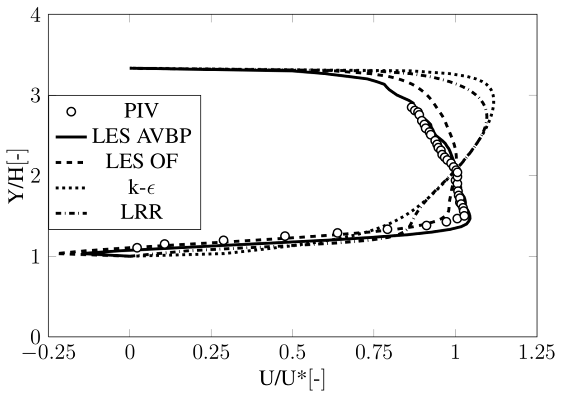

Figure 6. Streamwise velocity comparisons at $x_c/H = 0$, forU*=U(y/H=2.06). PIV by [22].

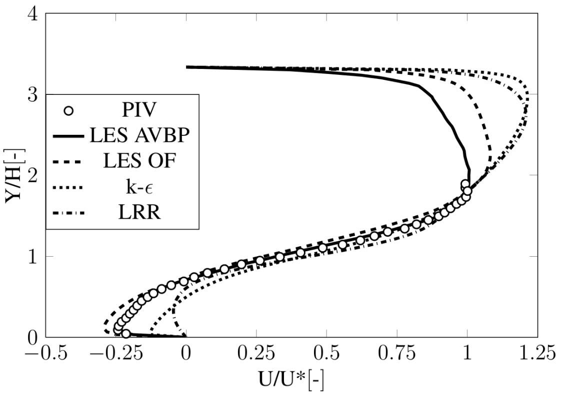

Figure 7. Streamwise velocity comparisons at $x_c/H = 2.5$, for U*=U(y/H=1.78). PIV by [22].

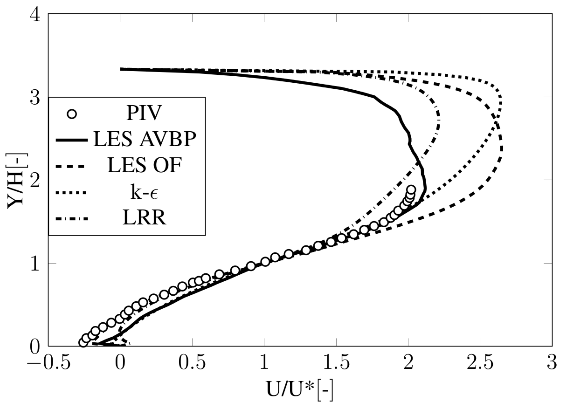

Figure 8. Streamwise velocity comparisons at $x_c/H = 4.5$, for U*=U(y/H=1). PIV by [22].

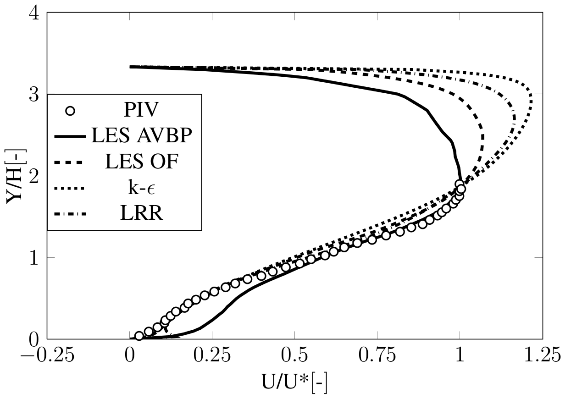

Figure 9. Streamwise velocity comparisons at $x_c/H = 5.5$, for U*=U(y/H=1.88). PIV by [22].

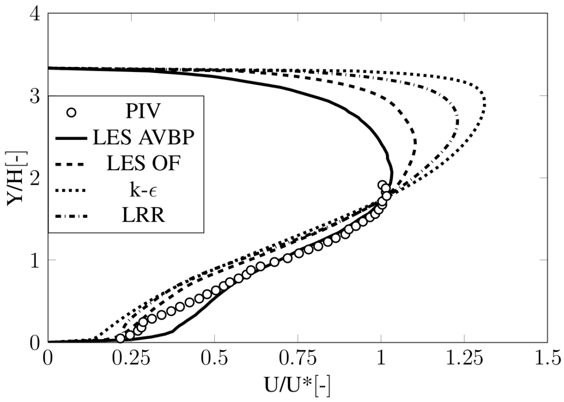

Figure 10. Streamwise velocity comparisons at $x_c/H = 6.5$, for U*=U(y/H=1.72). PIV by [22].

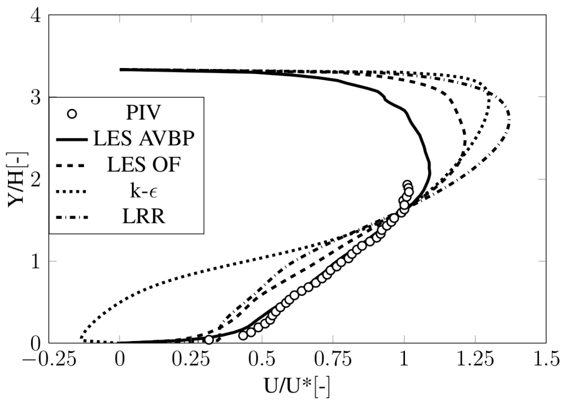

Figure 11. Streamwise velocity comparisons at $x_c/H = 8.5$, for U*=U(y/H=1.63). PIV by [22].

recirculation zone directly behind the rib (V2), a recirculation zone on the rib top (V3) and another recirculation zone in front of the rib (V4). Figure 5 shows the streamwise velocity at the height of the measurement taken to evaluate the recirculation point. The experiment resulted in a value of $x/H = 5.3$ for the reattachment location. Both LES are in good accordance with this value, with $x/H = 5.2$ for the AVBP LES and $x/H = 5.4$ for the OpenFOAM® LES. The RANS underpredict the reattachment location. Downstream of the reattachment location the LRR Reynolds-stress model is still in satisfactory agreement with the experiment, even though it does not predict the recirculation zone directly in front of the rib (V4).

Upstream of the reattachment point the LRR Reyn-

olds stress model is in a bad agreement with the PIV data. The $k-\epsilon$ does neither predict the front rib recirculation zone (V4), nor predict the streamwise velocity upstream and downstream of the reattachment point well.
Both LES, on the other hand, give good predictions of the streamwise velocity and also capture all recirculation zones.
Figures 6-11 show the streamwise velocity profile evolution starting on top of the rib 6 proceeding to the pitch in-between two ribs until the front of the subsequent rib. The velocity profiles are continuously better predicted by the LES.
Table 3 shows the sizes for the recirculation zones V1 and V3 of all simulations compared with the available experimental data. The zone sizes are measured in the symmetry plane of the channel and expressed in multiples of the rib height H. The reattachment lengths were measured at a small distance above the wall with a negative streamwise velocity for V1 at $y/H = 0.05$ and for V3 at $y/H = 0.01$.
Both LES show a good agreement with the PIV data, being within or close to the uncertainty of the experiments.
The RANS simulations, however, both the $k-\epsilon$ model and the LRR Reynolds-stress model fail to predict realistic sizes of the recirculation zones. The major zone V1 is under predicted by both models, even more by the Reynolds-stress model. The $k-\epsilon$ model, however, completely fails to predict the recirculation zone on the rib top, while it is still by far under predicted by the Reynolds-stress model.

Table 3. Recirculation zone sizes

	V1	V3
exp. Casarsa [22]	3.76H-3.84H	0.6H-0.9H
LES, AVBP	3.7H	0.86H
LES, OF	3.93H	0.91H
RANS, $k-\epsilon$	3.51H	-
RANS, LRR	2.87H	0.49H

4.2. Secondary flow structures

Figures 12 shows the streamlines for the PIV measurement on the rib top at the mid-section of the rib. Figure 13 demonstrates that the three-dimensional flow field is not reproduced by the $k-epsilon$ model and that it provides only two-dimensional results. Figure 14 shows the streamlines for the LRR Reynolds-stress model, which is known to be capable of reproducing secondary flow structures. This model also fails, in the present case, to correctly reproduce the flow field.
Figure 15 shows the streamlines for the LES of the OpenFOAM® computations. The secondary flow structures are well-visible and in a good agreement with the experimental data. Only the center of the secondary flow structure is positioned higher in the channel than in the experiment. In the top corners of the channel, above the rib, another, smaller secondary flow structure is visible. It is counter-rotating opposite to the main circulation zones over the rib. Figure 16 shows the streamlines on top of the rib for the LES with AVBP. Again, as for the OpenFOAM® LES, the secondary flow is well reproduced. The agreement with the experiment is very good, also for the position of the circulation zone center and for the magnitude of the circulation. As for the LES with OpenFOAM® and opposed to the experimentally shown streamlines, small counter-rotating circulation zones are visible, even smaller as in the OpenFOAM® case.
To summarize the results for the secondary flow structures, only the LES, in particular obtained with AVBP show a good agreement with the experiment.

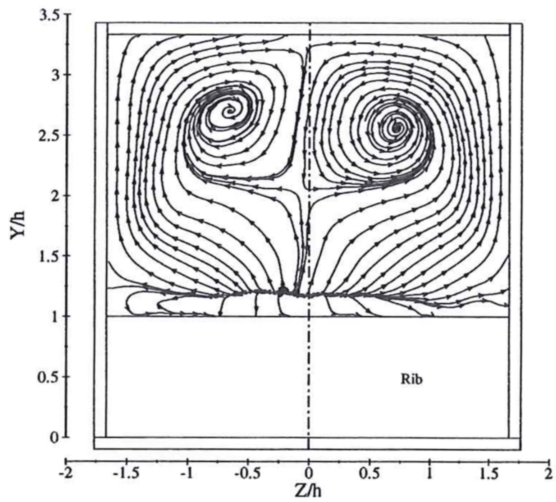

Figure 12. Streamlines on rib top from experimental measurements (PIV) by Casarsa [22].

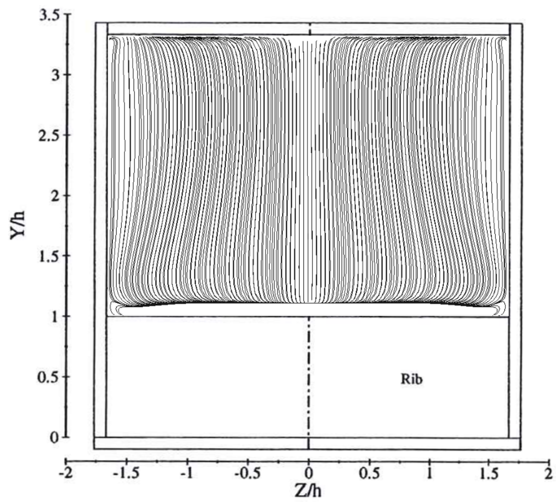

Figure 13. Streamlines on rib top with $k\epsilon$ turbulence model.

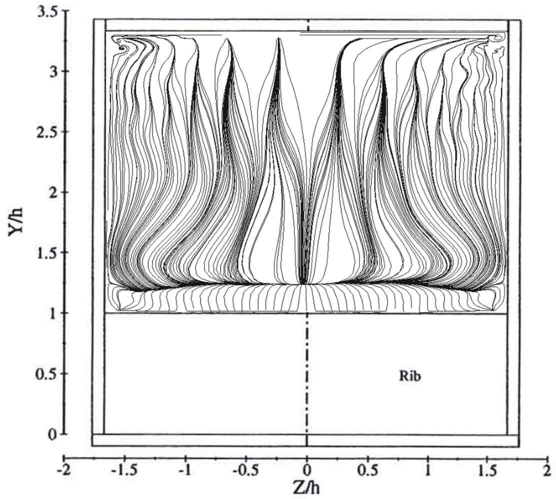

Figure 14. Streamlines on rib top with LRR turbulence model.

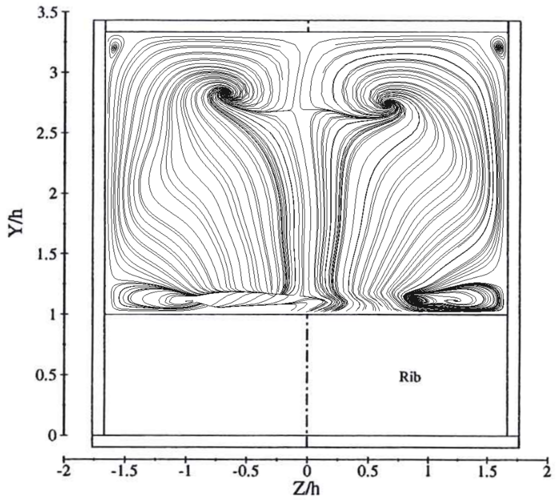

Figure 15. Streamlines on rib top with LES using OpenFOAM®.

5. CONCLUSION

A rib-roughened internal turbine blade cooling channel was simulated with different approaches for the turbulence modeling. Simulations with turbulence modeling based on the Boussinesq eddy viscosity assumption were compared with Reynolds-stress model simulations and finally with two different Large Eddy Simulation approaches. The results have been compared with and validated against existing existing data obtained from the Von Karman Institute for Fluid Dynamics. This study demonstrates: (1) Secondary flow structures present in the flow are not reproduced by the tested RANS turbulence models. (2) Even the primary recirculation zones are poorly predicted by the turbulence models. (3) LES are well-suitable to reproduce all mean-flow structures present in the complex flow field.

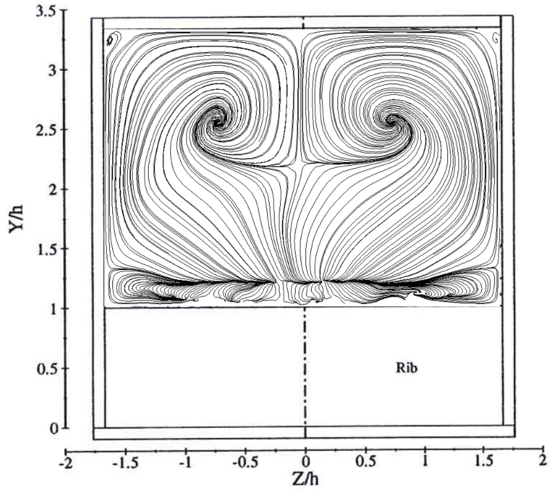

Figure 16. Streamlines on rib top with LES using AVBP.

ACKNOWLEDGMENTS

The research leading to these results has received funding from the European Community's Seventh Framework Programme (FP7, 2007-2013), PEOPLE programme, under the grant agreement No FP7-290042(COPAGT project).
The authors further greatly acknowledge the valuable help for the AVBP computations by Dimitrios Papadogiannis, Florent Duchaine and Laurent Gicquel.

REFERENCES

[1] Han, J., Dutta, S., and Ekkad, S., 2000, *Gas Turbine Heat Transfer and Cooling Technology*, Taylor & Francis.

[2] Reynolds, O., 1895, "On the dynamical theory of incompressible viscous fluids and the de-termination of the Criterion", *Philosophical Transactions of the Royal Society of London*.

[3] Boussinesq, J., 1877, "Essai sur la theorie des eaux courantes", *Memoires presentes par divers savants a l'Academie des Sciences 23 (1): 1-680.*

[4] Spalding, B. L. L., 1972, "Leclayer in Mathematical Models of Turbulence", *Academic Press London*.

[5] Launder, B., and Sharma, B., 1974, "Application of the energy dissipation model of turbulence to the calculation of flow near a spinning disc", *Letters in Heat and Mass Transfer*.

[6] Launder, B., Reece, G., and Rodi, W., 1975, "Progress in the development of a Reynolds-stress turbulence closure", *Journal of Fluid Mechanics*.

[7] Gibson, M., and Launder, B., 1978, "Ground effects on pressure fluctuations in the atmospheric boundary layer", *Journal of Fluid Mechanics*.

[8] Weller, H. G., Tabor, G., Jasak, H., and Fureby, C. ., 1998, "A tensorial approach to computational continuum mechanics using object-oriented techniques.", *Computers in Physics 12,6,620-631*.

[9] Schönfeld, T., and Poinsot, T., 1999, "Influence of boundary conditions in LES of premixed combustion instabilities", *Annual Research Briefs Center for Turbulence Research, NASA Ames and Stanford University, pp 73-84*.

[10] Mendez, S., and Nicoud, F., 2008, "Large eddy simulation of a bi-periodic turbulent flow with effusion", *Journal of Fluid Mechanics, 598, pp 27-65*.

[11] Nicoud, F., and Ducros, F., 1999, "Subgrid-scale stress modelling based on the square of the velocity gradient.", *Flow Turb Combust*, Vol. 62, pp. 183–200.

[12] Colin, O., and Rudgyard, M., 2000, "Development of high-order taylor-galerkin schemes for unsteady calculations", *Journal of Computational Physics 162(2), pp338-371*.

[13] Donea, J., and Huerta, A., 2003, *Finite Element Methods for Flow Problems,*, John Wiley and Sons, Ltd, Chichester, UK,.

[14] Colin, O., Benkenida, A., and Angelberger, C., 2003, "3D modeling of mixing, ignition and combustion phenomena in highly stratified gasoline engine", *Oil and Gas Science Tech 58, 1 , 47-62, 111*.

[15] Cakan, M., 2000, "Aero-Thermal Investigation of Fixed Rib-Roughened Cooling Passages", Ph.D. thesis, Universite Catholique de Louvain and Von Karman Instititue for Fluid Dynamics.

[16] Cukurel, B., 2012, "Conjugate Heat Transfer Investigation of a Fixed Rib Roughened Cooling Passage.", Ph.D. thesis, Purdue University and Von Karman Institute for Fluid Dynamics.

[17] Cukurel, B., and Arts, T., 2013, "Local Heat Transfer Dependency on Thermal Boundary Condition in Ribbed Cooling Channel Geometries", *ASME Journal of Heat Transfer*, Vol. 135, pp. 101001–1–101001–11.

[18] Fransen, R., Gourdain, N., and Gicquel, L., 2012, "Steady and Unsteady Modeling for Heat Transfer Predictions of High Pressure Turbine Blade Internal Cooling", *Proceedings of ASME Turbo Expo*.

[19] Keylock, C. J., Tokyay, T. E., and Constantinescu, G., 2012, "A method for characterizing the sensitivity of turbulent flow fields to the structure of inlet turbulence.", *Journal of Turbulence*.

[20] Poinsot, T., and Lele, S., 1992, "Boundary Conditions for Direct Simulations of Compressible Viscous Flows", *J Comput Phys, 101(1), pp 104-129*.

[21] Fransen, R., 2013, "- Simulation aux Grandes Echelles pour la modélisation aérothermique des aubages de turbines refroidies", Ph.D. thesis, Université de Toulouse - MeGeP - Dynamique des Fluides.

[22] Casarsa, L., 2003, "Aerodynamic Performance Investigation of a Fixed Rib-Roughened Internal Cooling Passage", Ph.D. thesis, Universita Degli Studi Udine and Von Karman Instititue for Fluid Dynamics.

Conference on Modelling Fluid Flow (CMFF'15)
The 16th International Conference on Fluid Flow Technologies
Budapest, Hungary, September 1-4, 2015

FLOW INVESTIGATION OF A ZIGZAG AIR CLASSIFIER

Christoph Roloff[1], Hannes Mann[2], Jürgen Tomas[2] and Dominique Thévenin[3]

[1] Corresponding Author. Institute of Fluid Dynamics and Thermodynamics, Otto-von-Guericke-University Magdeburg. Universitaetsplatz 2, 39112 Magdeburg, Germany. Tel.: +49 391 6712336, Fax: +49 391 6712840, E-mail: christoph.roloff@ovgu.de
[2] Institute of Process Engineering, Otto-von-Guericke-University Magdeburg, Universitaetsplatz 2, 39106 Magdeburg, Germany
[3] Institute of Fluid Dynamics and Thermodynamics, Otto-von-Guericke-University Magdeburg, Germany

ABSTRACT

Particle separation is a very common requirement in processing industries. For a separation by particle size sieving is widely used technique, particularly for moderate to big particles. For particle diameters below a few millimetres, air classifiers are valuable alternatives and can be found in applications related to waste treatment, recycling or preparation of agricultural material. The particulate material is fed into the channel and, depending on the operating conditions, heavy particles fall down while light particles are entrained upwards into a cyclone where they are separated from the air.

Although the zigzag air classifier is a well-established apparatus, still many unknowns exist when describing the process dynamics and trying to optimize overall performance with respect to purity and efficiency.

In order to foster understanding of the involved mechanisms, the current work investigates experimentally the flow inside a pilot scale zigzag classifier under different operating conditions. Pressure, temperature and humidity sensor data as well as laser Doppler velocimetry (LDV) measurements are presented and processed to estimate the volumetric flow rate inside the channel, which can be used as boundary condition in future numerical simulations. Furthermore, the particle image velocimetry (PIV) technique applied in a single separation segment is introduced and derived flow fields are presented delivering a valuable database for validation of simulations.

Keywords: air classifier, zigzag channel, particle separation, LDV, PIV

NOMENCLATURE

Δp	[Pa]	pressure loss
h	[mm]	channel width
r	[mm]	radial distance
R	[mm]	pipe radius
Re	[ ]	Reynolds number
rpm	[$1/min$]	fan speed
T	[°C]	temperature
U	[m/s]	velocity magnitude
$\dot{V}$	[m^3/s]	volumetric flow rate

Subscripts and Superscripts

max	maximum value
fit	refers to the fit function
–	temporal average

Abbreviations

CFD	computational fluid dynamics
DEHS	Di-Ethyl-Hexyl-Sebacat
fps	frames per second
LDV	laser Doppler velocimetry
PIV	particle image velocimetry
SMD	sauter mean diameter

1. INTRODUCTION

A zigzag air classifier is an apparatus used for separation of a solid dispersed particle phase into its fine and coarse fraction. It mainly consists of a vertical channel through which a certain amount of air is blown. From a side opening the good to be separated is fed into the channel and, depending on the parameters set, the coarse fraction falls downwards while the fine fraction is lifted with the airstream to the adjacent cyclone. The characteristic settling velocity determined by parameters such as size, density and shape of each particle thereby acts as separation property. The term "zigzag" refers to the geometrical pattern used to cascade the single duct elements in this apparatus, where a change of direction of the main flow under a certain angle and a repeated cross flow separation in these elbow elements is achieved. The multistage approach affects the quality of the separation in a beneficial manner: Each particle is exposed to a separation stage several times during its flight through the apparatus. Thus, the overall separation sharpness can be considered high whereas the amount of particles assigned to the incorrect fraction is small.

Air classifiers are typically used to separate particles in the range of 200 µm to a few millimetres and can realize high volume and mass throughputs. Applications can be found in the recycling, building and food industries, for example to separate scrap cables, shredded plastic bottles or tea stalks and leaves.

Although, the principle of the apparatus is well known for several decades, up to now, predictive and physically motivated models to describe the performance of the separator a priori hardly exist. Modelling approaches have been attempted for instance by Senden [1], Rosenbrand [2], Schubert [3] and Tomas and Gröger [4].

In order to converge to the final aim of deriving a more reasonable modelling approach, better understanding of the process dynamics, involved process parameters and underlying fluid dynamical relations is highly desirable. Therefore, computational fluid dynamics (CFD) and state-of-the-art measurement techniques have been applied to a pilot scale apparatus of a zigzag air classifier.

The CFD environment offers the opportunity to account for the most relevant phenomena involved in the desired resolution, i.e. in particular the turbulence inside the channel and the dispersed phase flow during separation. Moreover, it allows to easily modify boundary conditions, such as mass flow rates of fluid and solids but also the geometrical constraints of the zigzag channel. This enables to cover a quite reasonable amount of process parameters which could be subject to process optimisation and simplified apparatus model derivation.

The fluid dynamical measurements are however indispensable, as the numerical solutions may depend on different constraints of the modelling approach such as spatial discretisation (computational grid), turbulence model and discrete phase treatment. Hence, validation data from experiments under realistic conditions are required in order to help judging which modelling approach is the most reasonable to carry out reliable CFD simulations. Moreover, the CFD relies on appropriate boundary conditions which have to be derived from measurements as well.

In the following, the pilot scale zigzag classifier will be introduced and details on estimating the inflow boundary conditions (volume flow rate) for numerical studies using particularly the laser Doppler velocimetry (LDV) technique will be discussed. Furthermore, the particle image velocimetry (PIV) setup covering a part of a separation stage and the derived flow field results will be presented.

2. EXPERIMENTAL SETUP

The following chapter describes the pilot scale zigzag apparatus and the involved measurement techniques, i.e. LDV and PIV setups.

2.1. Pilot Scale Zigzag Classifier

The pilot scale air classifier consists of the zigzag channel featuring seven single separation stages aligned vertically as can be understood from Figure 1 (3). Air is blown by controllable fan (7) in a closed circuit through the apparatus, i.e. it goes through zigzag channel, through an aero-cyclone (5), a filter (8) and re-enters the blower. Particles are fed to the facility through a small duct at mid height of the zigzag channel by means of a screw feeder (2) connected to a silo (1). The separated material is collected in two containers, one for the coarse fraction falling down into (4) and one for the fine fraction lifted with and separated from the airstream into (6).

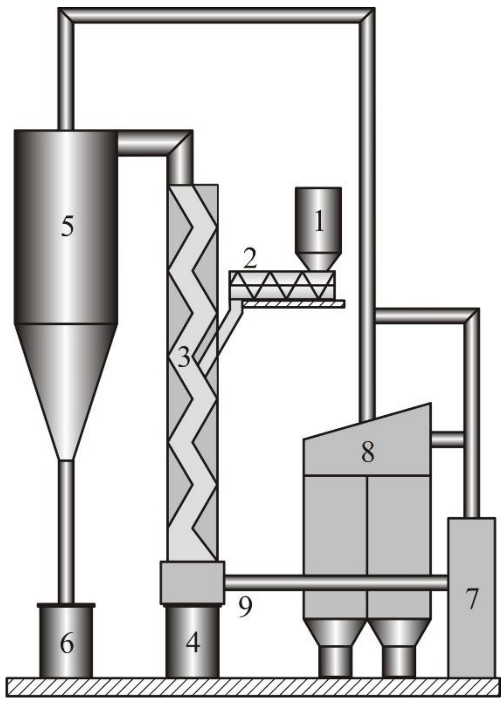

Figure 1. Principle sketch of the investigated pilot scale zigzag air classifier with (1) silo, (2) screw feeder, (3) zigzag channel, (4) container for coarse fraction, (5) aero-cyclone, (6) container for fine fraction, (7) fan, (8) filter, (9) inflow pipe

Each zigzag segment of the channel is approx. 400 mm long and features a cross section of 200 x 170 mm². The inclination angle between neighbouring ducts is 120°. The front side of the zigzag channel consists of 8 mm thick glass plates enabling optical access. The overall height of the facility of about 4 m reveals its huge dimension and the associated difficulties for measurement equipment to be positioned appropriately.

The apparatus is equipped with basic sensor technique for capturing temperature, humidity and absolute pressure data inside the horizontal inflow pipe (depicted as (9) in Figure 1). This pipe furthermore contains a Prandtl tube for providing velocity data in mid-axial position. Finally, the pressure loss through the zigzag channel is monitored by a differential pressure sensor which is connected to two pressures drillings: the first one placed at the backside of the entrance plane of the zigzag channel, the second one placed shortly after the 90° twisted duct above the zigzag channel. Monitoring of the pressure loss is mainly intended to act as simple validation source for future CFD simulations.

All sensor data were sampled with 1 Hz and processed using LabView 13.0.

2.2. Laser Doppler Velocimetry

For reliable CFD simulations boundary conditions are required that should meet the real conditions of the pilot scale apparatus as close as possible. Of particular importance for the zigzag classifier is the inflow rate. It determines the flow conditions inside the channel and thus is directly coupled to the separation process and its quality. As estimating the flow rate merely from the Prandtl tube velocity data in the inflow pipe seemed to be too vague, a laser Doppler velocimetry setup was constructed to cover two different cross sectional planes at different heights close to the entrance of the zigzag channel. Figure 2 depicts the LDV setup. A three-axis traverse was positioned in front of the apparatus. The LDV probe (1D backscatter probe, 532 nm laser wavelength, 150 mW laser power) was mounted to the traverse such that it could be positioned automatically at different in-plane positions at fixed height and measure the z- or the x-component of the flow velocity.

Seeding for LDV as well as for PIV was provided by a high volume liquid atomiser connected to the coarse fraction container beneath the zigzag channel entrance. It generates droplets of DEHS with a sauter mean diameter (SMD) between 2 – 5 µm according to the manufacturer. LDV data was processed using the ILA flowPOINT software.

2.3. Particle Image Velocimetry

To obtain quantitative insight into the flow field inside the zigzag channel, the particle image velocimetry technique was applied. Therefore, the channel had to be modified slightly in order to generate a further optical access perpendicular to the front glass. Hence, a glass window frame was constructed and fit into the left side wall of the third separation stage (see Figure 3). It was designed to be detachable for cleaning purposes and for the option to position a calibration target in the appropriate measuring plane.

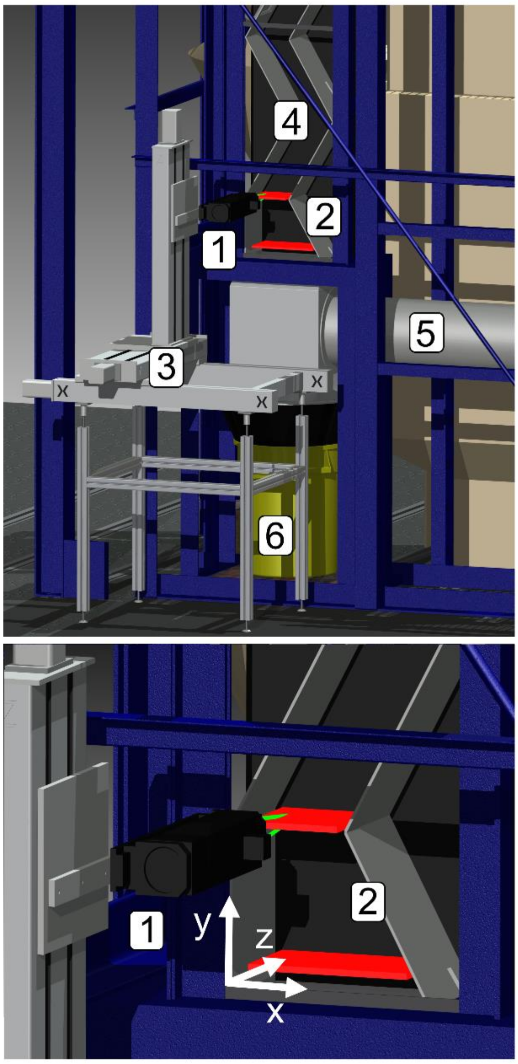

Figure 2. Setup of the LDV system with (1) LDV probe, (2) LDV measurement planes, (3) traverse, (4) zigzag channel, (5) inflow pipe, (6) container for coarse fraction (seeding injection) and LDV coordinate system (white arrows)

The PIV system itself consisted of a highspeed camera (1100 fps with 2016 x 2016 pixel resolution) equipped with a 50 mm macro lens. The camera was arranged such that its viewing direction was perpendicular to the x-z-plane of the channel. Additional tilting of 60° allowed for correct alignment with the channel stage. The local coordinate system was defined to have its origin in the deflection edge of the channel (not within the field of view of the camera), the x-axis along the lower channel wall of the segment and the new y-axis normal to that wall.

A double cavity high speed laser (527 nm wavelength, 2 x 30 mJ per pulse at 1000 Hz) was used as illumination. Its beam was mirrored four times to reach the investigated measurement stage and formed to a light sheet just before the glass window (see again Figure 3). For triggering, recording and processing of the PIV images Davis 8.2 was used.

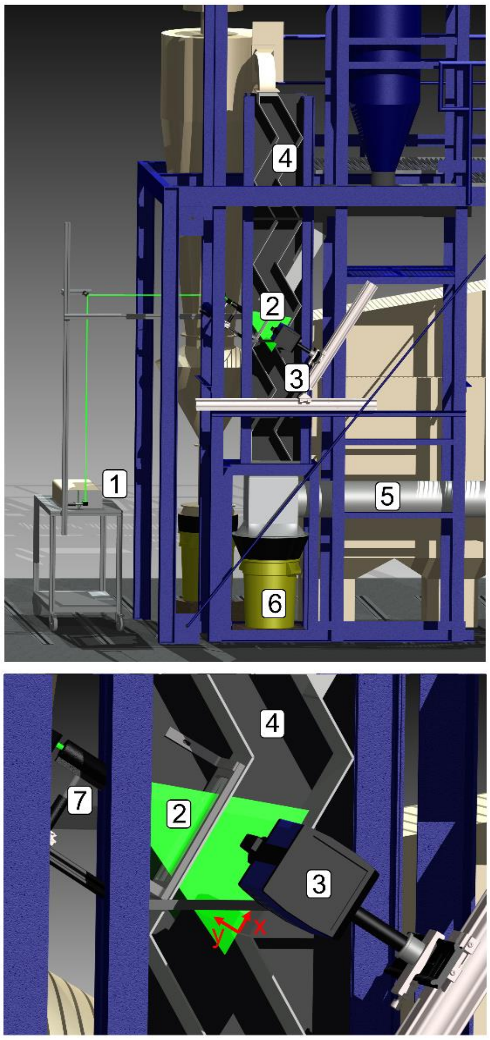

Figure 3. Setup of the PIV system with (1) PIV laser, (2) PIV light sheet, (3) PIV camera, (4) zigzag channel, (5) inflow pipe, (6) container for coarse fraction (seeding injection), (7) light sheet optics and PIV coordinate system (red arrows)

3. APPARATUS PERFORMANCE

The performance of the air classifier in single phase operation (without a solid phase to be separated but in case of LDV/PIV with droplet seeding) was evaluated using the obtained measurement data.

3.1. Repeatability

First it was checked how repeatable the adjustments of the fan speed controlled the velocity in the channel. As the closed circuit design of the classifier also leads to significant heat generation during operation over time, different channel temperatures were tested with respect to changes in flow rate. 25,000 LDV samples of the z-velocity component were recorded at mid position of the lower cross sectional plane and time averaged to obtain Figure 4. The frequency converter setting to control the fan speed was kept constant for all measurements.

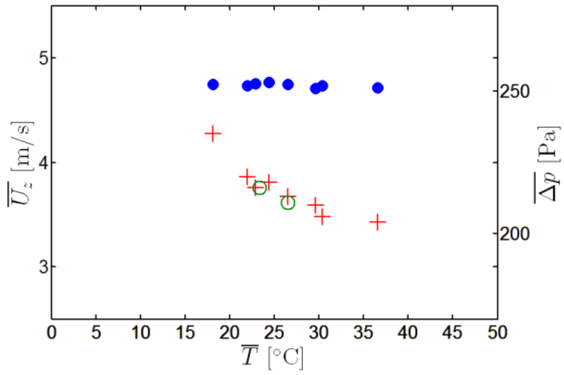

Figure 4. Dependency of z-velocity component $\overline{U}_z$ (blue filled circles) and pressure loss through the channel $\overline{\Delta p}$ (red crosses during LDV measurement, green circles without seeding) with temperature $\overline{T}$.

No significant change of velocity (blue filled circles) can be observed indicating a constant flow rate without temperature dependency. Evaluation of the pressure loss recordings (red crosses) however reveals a clear influence of the channel temperature. With increasing temperature the pressure loss decreases. Pressure loss readings without active LDV seeding generation (green circles) indicate that the impact of seeding injection can be considered negligible.

3.2. Flow Rate

To provide a reasonable estimate of the flow rate inside the zigzag channel, the Prandtl tube and the LDV data was evaluated.

The differential pressure readings from the Prandtl tube were used to compute the velocity in mid-axial position of the inflow pipe by applying Bernoulli's law. The required value for the air density was estimated using the measured temperature and humidity values and by assuming the humid air to be a mixture of ideal gases, namely dry air and water vapour. The flow rate was then estimated by integrating the radial velocity distribution for a turbulent pipe flow [5]:

$$U = U_{max} \cdot \left(1 - \frac{r}{R}\right)^n \qquad (1)$$

with

$$n = \sqrt{(100 \cdot Re)^{-\frac{1}{4}}} \qquad (2)$$

over the cross sectional area, which is valid for $Re < 10^5$ and hence applicable for the considered fan speeds. It has to be noted, however, that the inflow pipe length is too short to allow the flow to be fully developed.

The LDV measurements were conducted in two different cross sectional planes: the first very close to the entrance of the zigzag channel (height: 47 mm) with a resolution of 12 x 7 measurement points; the second at 260 mm height at the first deflection of the channel with 13 x 11 points. Figure 5 exemplarily displays the time averaged z-velocity component at each sampling point in the two planes for the fan speed of 0.25 rpm/rpm_{max}.

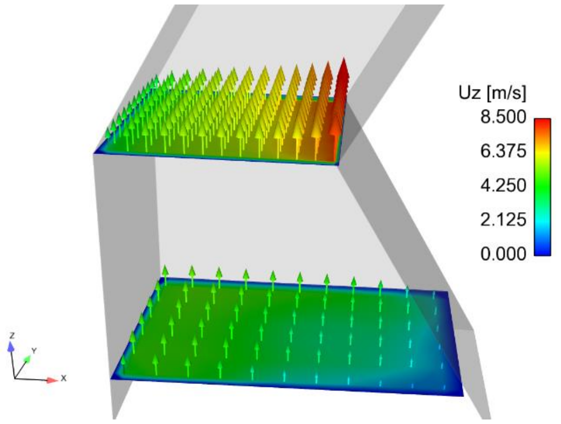

Figure 5. LDV measurement planes with vector arrows indicating the magnitude of the z-velocity component at the sampling points

At the lower plane, z-velocities decrease with the x-coordinate, finding maxima at the left side of the channel of about 4.6 m/s. In the upper plane, the z-velocity distribution is reversed. Increasing velocities with the x-coordinate can be found with maxima close to the deflection edge of the channel of about 8.5 m/s. Due to the smaller cross sectional area of the upper plane, a higher overall level of z-velocity magnitude can be observed. Only minor changes of velocity with the y-coordinate are apparent.

Integrating the velocity distribution over the cross sectional area delivers the flow rate through the planes. A linear scheme was chosen to interpolate the velocity in between the sampling points of the LDV. Close to the walls two different approaches were followed: the first is a linear interpolation to zero velocity directly at the wall (no slip); the second is a linear extrapolation of the two measurements points closest to the wall (extrapolation). This leads to a lower and an upper bound estimate for the flow rate, respectively. Figure 6 depicts the computed flow rates from the Prandtl tube readings and the LDV measurements.

While the differences between the estimates from the two different planes are very small, the different wall treatment approaches deliver more diverging results. The flow rate from the Prandtl tube is somewhat in between but features a nonlinear slope with increasing fan speed. This can be attributed to changing entrance lengths with fan speed, i.e. Reynolds number, leading to differently developed radial velocity profiles.

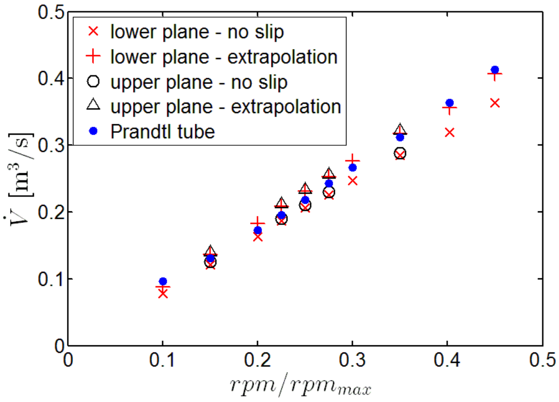

Figure 6. Dependency of the computed flow rate with fan speed.

A more detailed inspection of the different flow rates can be realized with Figure 7. It shows deviations of all computations relative to a fit of both upper plane approaches.

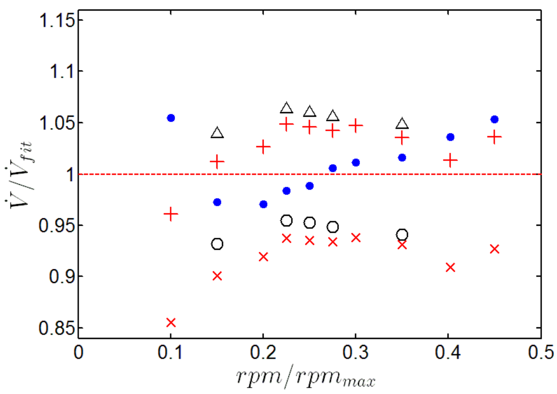

Figure 7. Deviations of the different flow rate estimates from a linear fit of both upper plane approaches with fan speed.

It confirms that differences occurring between the different planes are in the order of 1 – 3% while the wall interpolation approaches lead to deviations of up to 12%. Obviously, the ratio between Prandtl tube flow rate and fit flow rate tends to deliver higher values with increasing fan speed, which confirms the assumption of not fully developed turbulent flow with varying entrance length in the inflow pipe.

4. PIV RESULTS

PIV recordings were taken at different fan speeds (between 0.05 to 0.4 rpm/rpm$_{max}$) in the third separation stage of the zigzag channel (see again Figure 3). The field of view ranged from about 46 to 208 mm in x-direction and the entire channel width of 173 mm in y-direction (note that due to the tilted camera the x-axis is aligned with the channel stage with its origin at the deflection edge, see PIV coordinate system in Figure 3). 1000 double-frame images separated by different inter-frame delays according to the found velocities were recorded at 5 Hz to ensure independent snapshots of the flow. These images were evaluated in an adaptive multi-pass cross correlation scheme with a final interrogation window size of 32 x 32 pixels. Figure 8 displays exemplarily the vector fields obtained from a single double-frame image and the time average of the entire recorded sequence for a fan speed of 0.15 rpm/rpm$_{max}$.

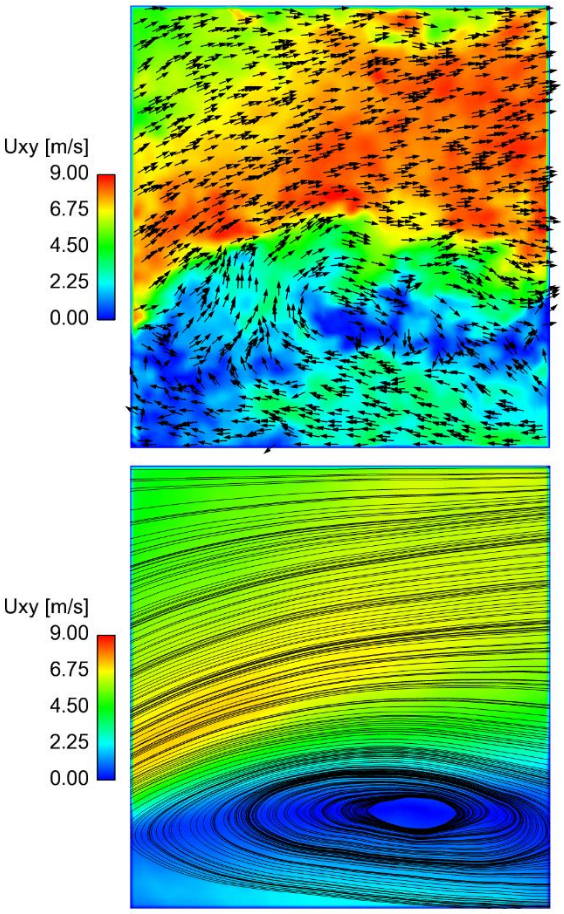

Figure 8. Instantaneous PIV snapshot (upper illustration) and time averaged velocity field including streamlines (lower illustration) for fan speed 0.15 rpm/rpm$_{max}$.

It becomes clear that a huge separation zone is created by the deflection edge leading to strong vortex formation at the lower channel region. The velocity field features local minima particularly in the separation zone while in the main stream in the upper channel region velocities up to 9 m/s can be found. The time averaged data show a narrower velocity range with a maximum of about 7 m/s. The overlaid streamlines once again indicate the separation zone with reversed flow in the lower channel region and the main stream region above. Comparison of both graphics confirms the strong transient character of the flow inside the stage featuring intense turbulent velocity fluctuations.

The flow field at a higher fan speed of 0.35 rpm/rpm$_{max}$, as depicted exemplarily in Figure 9, shows a quite similar behaviour but with somewhat finer scales in the vortical structures. Of course, higher velocities can be identified ranging up to 22 m/s. The time averaged data almost features identical streamlines with maximum velocities inside the main stream of 16 m/s.

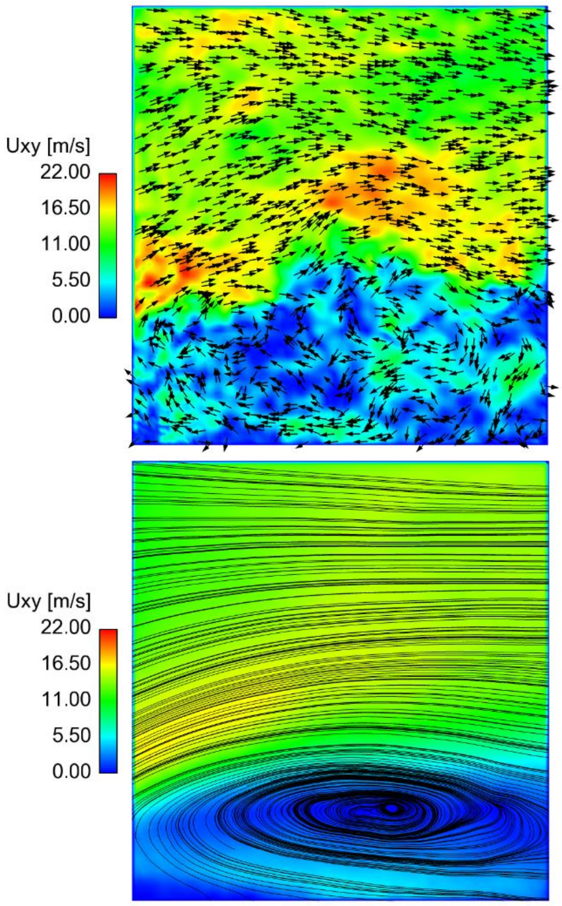

Figure 9. Instantaneous PIV snapshot (upper illustration) and time averaged velocity field including streamlines (lower illustration) for fan speed 0.35 rpm/rpm$_{max}$.

To inspect the velocity distribution inside the channel more detailed, profiles of the x-velocity component at different x-positions were extracted from the time-averaged PIV data. Figure 10 displays the profiles of four different fan speeds of the apparatus, 60 mm after the deflection edge of the PIV segment. The profiles clearly indicate the separation zone at lower channel width where reversed flow and strong velocity gradients towards the main stream flow can be recognised. With increasing channel width velocities feature a maximum and decrease until the upper channel wall. Figure 11, which shows the same velocity profiles normalised by their respective maximum values, reveals that the shape of the profiles is rather independent of the fan speed. Especially, the points of the maximum velocities can be found all over at 0.38 channel width. The slopes through the separation zone match remarkably well, except for the region very close to the lower wall.

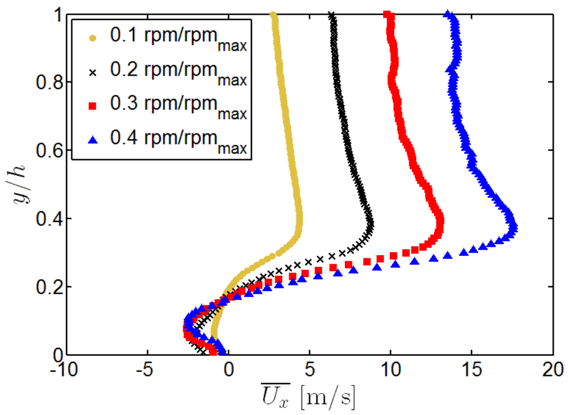

Figure 10. Profiles of the x-velocity component with channel width *y/h* at *x* = 60 mm (after the deflection edge) for different fan speeds

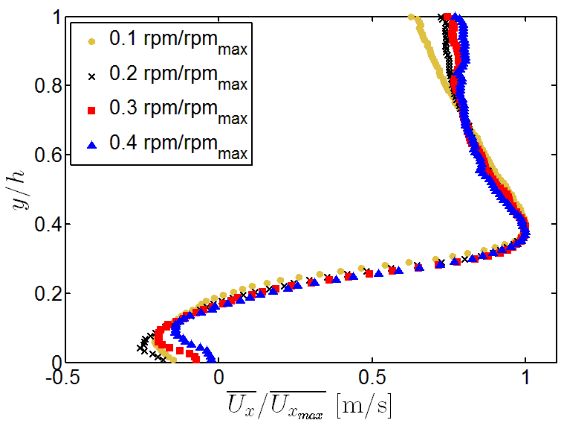

Figure 11. Profiles of the x-velocity component normalized by its maximum value with channel width y/*h* at *x* = 60 mm (after the deflection edge) for different fan speeds

From Figure 11, the same profiles at an x-position farther downstream (180 mm after the deflection edge) can be observed. The profiles do not feature such a distinct point of maximum velocities such as the previous ones. The upper part shows quite constant velocities which then decrease inside the separation zone. Again, the normalised profiles appear very similar. The point of maximum velocities can be found at increased width of 0.6 indicating the more dominant separation zone.

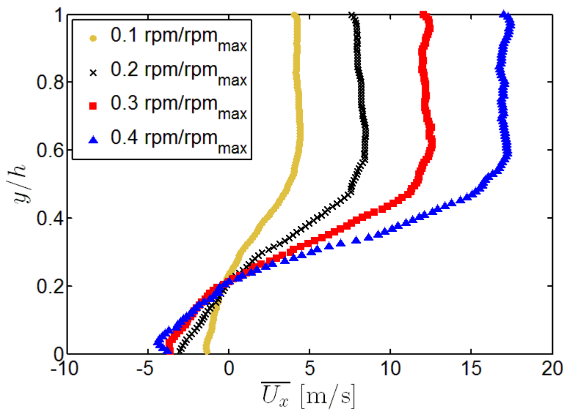

Figure 12. Profiles of the x-velocity component with channel width y/*h* at *x* = 180 mm (after the deflection edge) for different fan speeds

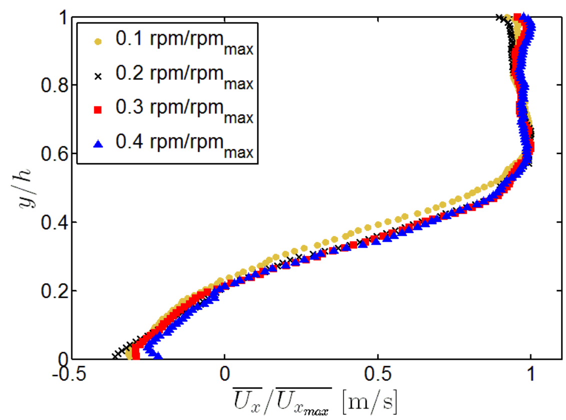

Figure 13. Profiles of the x-velocity component normalized with its maximum value with channel width y/*h* at *x* = 180 mm (after the deflection edge) for different fan speeds

5. SUMMARY

The present work introduces comprising measurement results undertaken at a pilot scale zigzag air classifier to characterize the single phase flow inside its separation channel. Classical sensor readings as well as laser Doppler velocimetry data have been used to estimate a volumetric flow rate for different fan speeds of the apparatus. These data are particularly valuable to be used as inflow boundary condition for future numerical simulations. Furthermore, particle image velocimetry measurements have been carried out in a segment of the zigzag channel. Derived velocity fields and profiles are presented revealing the strong transient character of the flow and the huge separation zone after the deflection stage including quantitative measures for the velocity magnitude. As a consequence, it can be assumed that numerical simulations necessarily have to be carried out in a transient manner in order to reliable capture the relevant flow features inside the zigzag channel. The experimental database can then be used as validation source for identifying appropriate models and their parameters.

ACKNOWLEDGEMENTS

This work is part of the priority program SPP 1679 „Dynamische Simulation vernetzter Feststoff-prozesse“ and is supported financially by the Deutsche Forschungsgemeinschaft (DFG).

The supporting work of Mr. Eduard Lukas is greatly acknowledged.

REFERENCES

[1] Senden, M. M. G., 1979, „Stochastic models for individual particle behavior in straight and zig zag air classifiers”, *Dissertation, Technical University of Eindhoven, Eindhoven*.

[2] Rosenbrand, G. G., 1986, „The separation performance and capacity of zigzag air classifiers at high particle feed rates”, *Dissertation, Technische Technical University of Eindhoven, Eindhoven*.

[3] Schubert, H., Böhme, S., Neeße, T., Espig, D., 1986, „Klassieren in turbulenten Zwei-Phasen-Strömungen”, Aufbereitungs-Technik 27 (6), pp. 295-306.

[4] Tomas, J., Gröger, T., 1999, „Mehrstufige turbulente Aerosortierung von Bauschutt”, Aufbereitungs-Technik 40 (8), pp. 379-386.

[5] Truckenbrodt, E., 1996, *Fluidmechanik, Bd 1*, Springer, Berlin.

Conference on Modelling Fluid Flow (CMFF'15)
The 16th International Conference on Fluid Flow Technologies
Budapest, Hungary, September 1-4, 2015

COMPLEX STRUCTURES BEHIND PLASMA DBD ACTUATOR IN A NARROW CHANNEL

Pavel PROCHÁZKA[1], Václav URUBA[2]

[1] Corresponding Author. Institute of Thermomechanics, Czech Academy of Sciences. Dolejškova 5, 18200 Prague 8, Czech Republic. Tel.: +420 266 053 313, E-mail: prochap@it.cas.cz
[2] Institute of Thermomechanics, Czech Academy of Sciences.

ABSTRACT

There was tested a wire dielectric barrier discharge (DBD) actuator recently and it was shown that it can produce sufficient ionic wind to influence the boundary layer by generation vortical structures. This article will describe the image of complex flow behind the actuator. The boundary layer developed inside a channel react with the plasma ionic wind which can be generated in steady or in unsteady regime. The flow field will be investigated in experimental way by Particle Image Velocimetry (PIV). The main investigated plane is perpendicular to the bottom of the channel and in longitudinal direction. More, stereoscopic PIV will be used to study the cross-section plane. To depict the flow properties, the statistical approach will be utilized as well as dynamical analysis, e.g. Oscillating Pattern Decomposition.

Keywords: boundary layer, DBD, PIV, plasma actuation, POD

NOMENCLATURE

F^+	[-]	reduced frequency
$S_{h\theta}$	[-]	Strouhal number
U_θ	$[m \cdot s^{-1}]$	velocity
U_∞	$[m \cdot s^{-1}]$	free velocity
X_{te}	$[m]$	separation length
f	$[Hz]$	frequency
$\underline{\theta}$	$[m]$	momentum thickness

1. INTRODUCTION

The active methods of flow control still remain in the center of interest for many research groups in academic or in industrial research as it can allow to modify properties of the flow only if there is a need unlike the passive flow control methods. Each machine should work in working regime with maximal efficiency. However, there are broad groups of machines which have to work in non-proposal conditions (including start of the process). The active methods as synthetic jets or promising non-thermal plasma are very suitable to use them during those conditions while they are not disturbing elements in working regime. Plasma actuation has many advantages in comparison with synthetic jets (SJ). Mainly, they have no mechanical moving parts and convert electrical energy into fluidic motion directly. Thus they are very reliable, their weight is law and they are easy to fix on the surface, they are not source of vibration and noise. Concerning electrical properties, their response time is very short and they allow to use any modulation of the power signal. Plasma is then very useful for flow control in any parameters. [1]

This research is devoted to investigation of a plasma actuator influence to naturally developed boundary layer with goal to develop suitable actuator and control method for using in Glaubert-Goldschmiedt body (so-called Hump). There are some non-dimensional numbers using to determine the most effective control frequency in the theory of control (e.g. [2]) by SJ. Strouhal number defined as

$$Sh_\theta = \frac{f \cdot \theta}{U_\theta} \tag{1}$$

where θ is momentum thickness in the point of separation and U_θ is the velocity magnitude. This parameter corresponds to the convective instability (Kelvin-Helmholtz instability) which is related to the shear layer defects (the origin and grow of crosswise vortical structures). It is possible the effectively modify the flow by changing the character of these vertical structures. The use of reduced frequency (non-dimensional) is more practical approach [3].

$$F^+ = \frac{f \cdot X_{te}}{U_\infty} \tag{2}$$

This equation is derived from (1) and is more relevant, hence it uses the separation length (bubble) X_{te} and the velocity outside of the boundary layer. The reduced frequency is given in the literature between 0,8 and 1,6 in dependency on used aerodynamic model [2,3]. Using equation (2) should help to tune plasma actuator on optimal modulation frequency and enhance their effectivity.

Above mentioned has led to investigation of unsteady regime of plasma actuator. During this regime, plasma-induced ionic wind is not generated continuously (as in steady regime) but series of vortices are created which properties are a function of modulation parameters (mainly the modulation frequency; f in equation (2)). Previously, the influence of spanwise oriented actuator on boundary layer was investigated. This article will deal with actuator oriented in streamwise configuration and flow field behind the actuator in statistical as well as in dynamical aspects.

2. EXPERIMENTAL SETUP

2.1. Plasma actuator

Wire type of plasma Dielectric Barrier Discharge (DBD) actuator [4] is adjusted version of simple DBD actuator. It consists of just two electrodes which are separated by a dielectric layer. The upper and powered electrode is actually thin wire (40 μm) used for HA anemometry and it is preloaded by spiral torsion spring. The lower electrode is thin layer of gold glaze and is grounded and encapsulated. The horizontal distance of these electrodes is 2 *mm*. The material of dielectric is silica glass (it has good dielectric strength and thermal extension) and its thickness is only 1 *mm*. The platform of actuator has dimension 150 x 100 *mm* (figure 1). This kind of actuator is able to produced ionic wind very close to the surface in horizontal meaning with velocities approximately 2 $m \cdot s^{-1}$ (the magnitude of velocity is strongly dependent on many electrical and geometrical parameters, mainly on voltage magnitude).

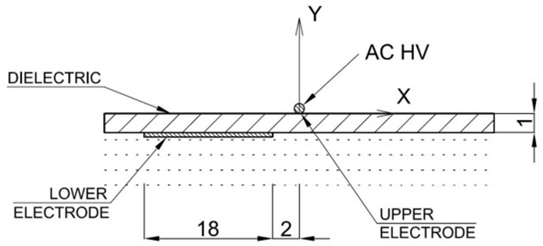

Figure 1. Scheme of plasma DBD actuator – wire type

The actuator was totally rebuilt to be able to produce the ionic wind perpendicular to main flow inside a channel. Now, both electrodes extend along the actuator and are parallel to channel walls (fig. 2). The position of wire electrode was at one third of platform width while the position of wire electrode was just in the middle of platform length in the previous spanwise type. The holders of the wire and the spring were replaced to the lower side of the actuator to not affect the flow at all. Previous type had the holder of wire at the upper side and they were located at the corners of rectangular channel. A comparison of boundary layer velocity profiles between spanwise and streamwise oriented actuator was conducted and no changes were shown.

2.2. Power source

Power source was introduced in study [5]. Briefly, it was designed and fabricated in the Institute of Thermomechanics. This source was developed to produce high-voltage high-frequency waveform for alternating supply. It has so-called shut-down function which allows to incorporate amplitude (rectangular) modulation. The maximal voltage is approx. 12 *kV* and frequency is adjustable but for this experiment was set to 16 *kHz*. During these conditions, a wall-jet-like flow is produced via plasma discharge. The application of modulation results in occurrence of vortical structures inside the jet. The vortex diameter, distance of each other and other parameter are strongly dependent on modulation frequency (which is in order of units of Hertz or tens of Hertz) and duty cycle. Duty cycle inversely expresses what rate of one period the plasma discharge is on. Duty cycle of 30*%* means that 70*%* of one period the plasma is on and ionic wind is blowing.

2.3. Experimental layout

The investigated boundary layer was developed inside rectangular Perspex channel with length of 3000 *mm* (fig. 2). The cross-section dimensions were 250 x 100 *mm* and the actuator was a part of bottom wall of the channel so there was no edge or step which could influence free flow. The middle of that actuator was 2275 *mm* downstream from the inlet to the channel which was connected to the blow-down wind tunnel.

The wall of the channel and of the tunnel contraction was without any turbulizators so the parameter of zero-pressure gradient boundary layer was changed just by varying velocities in the outlet of the tunnel. The velocities were 5, 10 and 20 $m \cdot s^{-1}$ which corresponds to conventional boundary layer thickness (at the place of the plasma discharge) of 54, 51 and 41 *mm*, respectively. Then Reynolds number was defined according to the conventional thickness of boundary layer or according to the length to channel inlet (see table 1). The main investigated plane is perpendicular to the bottom of the channel and in longitudinal direction. The CCD camera was placed so that the plasma-induce flow was oriented toward the objective. There were three different positions of camera traversing downstream the actuator to record longer view than one image setting offers. These position were related with three distinct positions of velocity profiles that were investigated in distance L = 60, 150 and 250 *mm*.

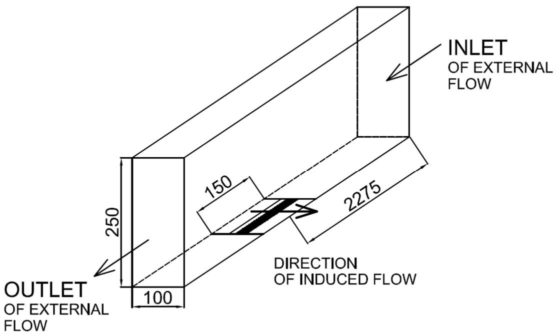

Figure 2. Experimental layout, actuator placed in streamwise position

The base case, where the plasma actuator was off all the time, was used as a reference case. The steady regime where the continuous wall-jet-like flow was produced was second case and the most investigating case was unsteady regime, where the modulation frequencies were varying from 10 to 50 *Hz* and duty cycle was set to 30*%*.

2.4. Measurement technique

The time-resolved Particle Image Velocimetry (PIV) was used as a main anemometry method. There was utilized laser New Wave Pegasus Nd:YLF with double head and with cylindrical optics. The wavelength is just 527 *nm*. Maximal laser frequency is 10 *kHz* and shot energy of one pulse is 10 *mJ* (for 1 *kHz* frequency). The used CCD camera is Phantom V711 and has maximal spatial resolution 1280 x 800 pixels which can be reduced resulting in higher possible frequency. However, standard acquisition frequency is 6 *kHz* and total memory of camera is 8 GB of double images.

This research has statistical point of view as well as dynamical one. Both require different approach concerning acquisition frequency and length. To fulfill the Nyquist criterion, the acquisition frequency was set to 2 *kHz* to not miss all fast dynamical processes in the moving fluid. On the other hand, to obtain good statistical quantities, it is desirable to perform longer measurement, at least 10 second was captured. Then the frequency was set to 100 *Hz* as sufficient value.

The total accuracy of PIV method is up to 1-2*%* if several assumptions are fulfilled, e.g.: proper particle image size, using windows matching, image density, etc. [6]

3. RESULTS

3.1. Statistical approach

The main flow field was computed from instantaneous images taken during time of at least ten seconds. The effect of plasma actuation on boundary layer can be seen very well from velocity profiles. The profiles are normalized with respect to the external flow to be able to compare different cases. Every figure of velocity profile contains blue solid line (steady regime - actuation on), red dashed line (base case – actuation off) and green dotted one (unsteady case with modulation). Most figures will be plotted in second position of camera, where the velocity profile is investigated 150 *mm* downstream from the center of the actuator platform.

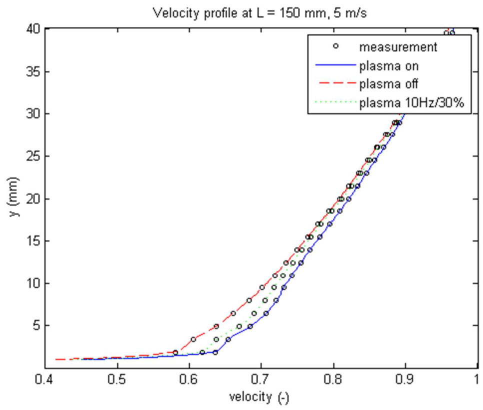

Figure 3. Velocity profile improvement in second position by 5 $m{\cdot}s^{-1}$

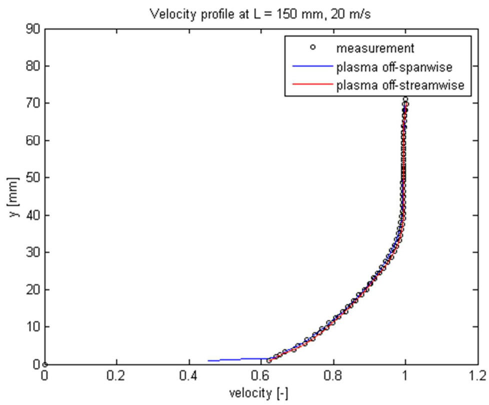

Figure 4. Comparison of base cases – spanwise and streamwise orientation

There is velocity profile improvement for the case of spanwise actuation (plasma-induced ionic with dispose the same direction as the main flow inside the channel) in the figure 3. The maximum velocity gain was 8 *%* for boundary layer developer under 5 $m{\cdot}s^{-1}$, however it became much weaker for 20 $m{\cdot}s^{-1}$. All other results will be devoted to perpendicular ionic wind where longitudinal vortex structures should be present in the wake.

The figure 4 shows the comparison of freely developed boundary layer over streamwise and spanwise oriented actuator. Profiles demonstrate perfect agreement which proves that the actuators do not affect by themselves the flow in any case. The cross section of plasma streaks is visible in the figure 5 which shows visualization of the flow in the vicinity of powered wire. There are at least eleven streaks along the wire (the entire length of wire is not captured) and it seems that each plasma streak generates one small jet (black areas) perpendicular to the channel longitudinal axes. These jets with effect of main flow create longitudinal vortices.

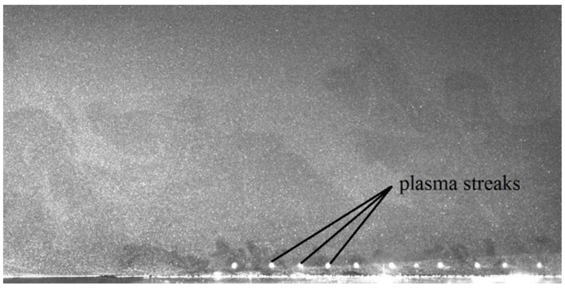

Figure 5. Visualization of plasma streaks and perpendicular ionic wind

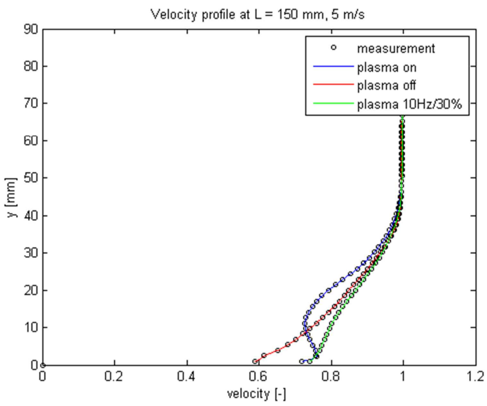

Figure 6a. Velocity profiles for second position and 5 $m{\cdot}s^{-1}$

The figure 6a shows the comparison of velocity profiles gained in the second position for velocity of 5 $m{\cdot}s^{-1}$ and for all three regimes. The effect of plasma steady actuation seems to be very helpful if the acceleration of fluid near to the wall is desirable (e.g. to modify skin friction). On the other hand, there is a strong decrease of velocities about 10 *%* in logarithmic region of boundary layer. The added momentum generated by plasma deflects the main flow a little bit but at the same time it enhances strongly the velocities close to the surface, since the plasma ionic wind occurs up to 1 *mm* above the surface. Consequently rotating vortex influences by its upper half the boundary layer by strongly deceleration. The effect of unsteady actuation does not demonstrate this behavior at all. The reason might be shorter time of plasma discharge (duty cycle of 30 *%*). To answer these questions, there is a need to perform stereoscopic PIV measurement of cross-section planes. The figures 6b and 6c are plotted for main velocities of 10 and 20 $m{\cdot}s^{-1}$.

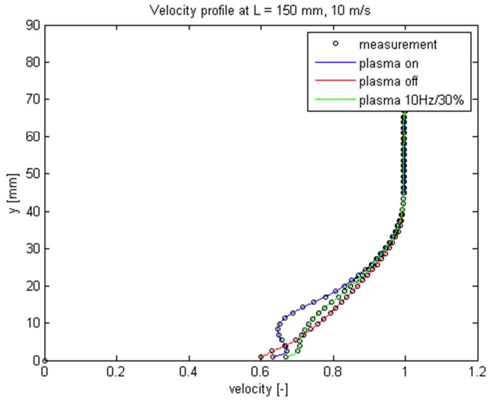

Figure 6b. Velocity profiles for second position and 10 $m{\cdot}s^{-1}$

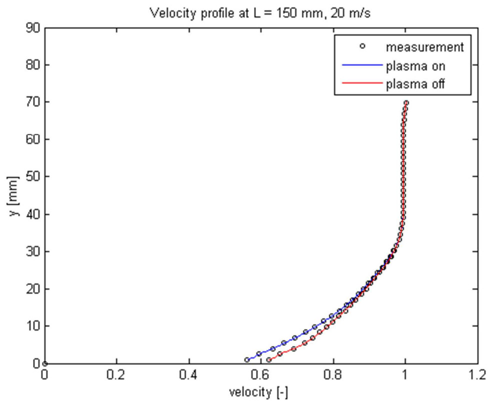

Figure 6c. Velocity profiles for second position and 20 $m{\cdot}s^{-1}$

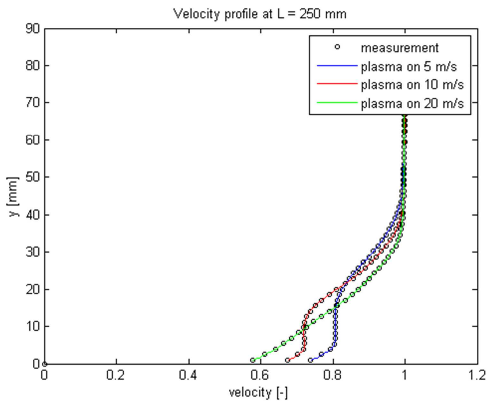

Figure 7. Comparison of all three velocities in third position

There is a comparison of different velocities in the third position in the figure 7. This figure shows that velocity of 20 $m \cdot s^{-1}$ is almost resistant to plasma actuation. The same conclusion was made for spanwise oriented actuator. Very interesting result was gained when various modulation frequencies were investigated. Unlike spanwise oriented actuator, now there is almost no effect of changing frequency. This phenomenon appears for all velocities and it seems that duty cycle could have a crucial role. However all measurement was performed for one value of DC.

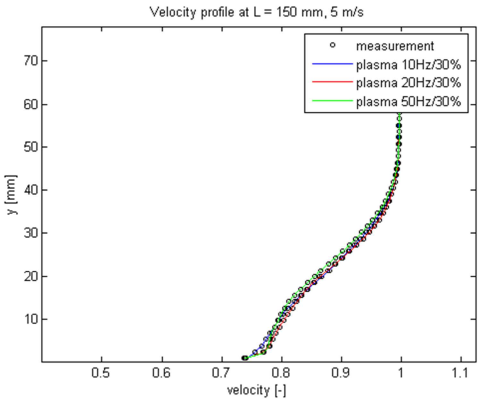

Figure 8. Comparison of three modulation frequencies

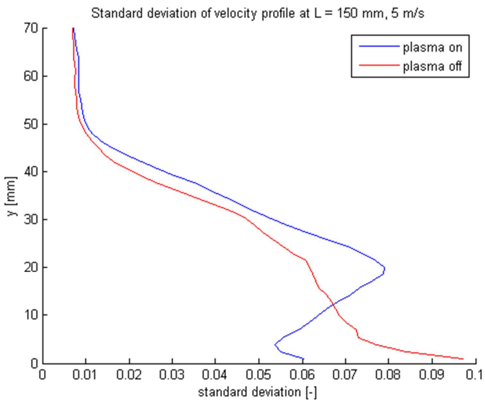

Figure 9a. Standard deviation in second position for 5 $m \cdot s^{-1}$

Standard deviation of velocity profiles (velocity variance) was computed from mean flow filed. The figure 9a shows that the flow is more stable in the vicinity of the wall (where the velocities were accelerated by plasma) and there is more oscillating flow above this region which corresponds very well with figures 6.

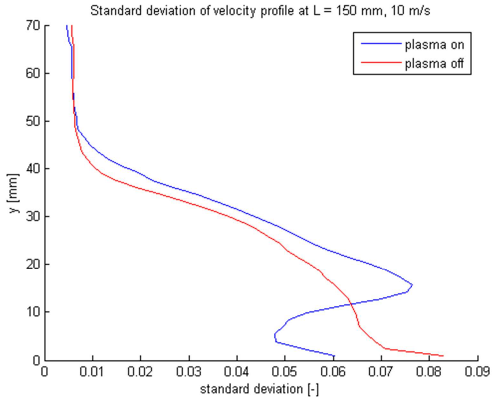

Figure 9b. Standard deviation in second position for 10 $m \cdot s^{-1}$

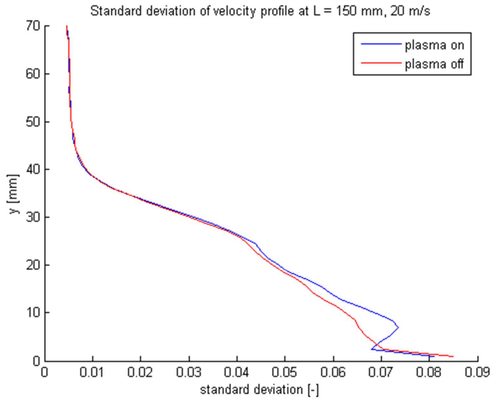

Figure 9c. Standard deviation in second position for 20 $m \cdot s^{-1}$

3.2. Dynamical approach

To describe systematically dynamical phenomena behind the actuator, there is a need to capture three-component measurement in cross plane, for all that Proper Orthogonal Decomposition (POD) was applied to velocity field in first position measured under unsteady case – modulation frequency was 10 *Hz*. Table 1 shows kinetic energy distribution of first ten modes.

Table 1. Kinetic energy of modes

No.	1	2	3	4	5
En. [%]	19,19	11,46	5,9	4,15	2,54
No.	6	7	8	9	10
En. [%]	2,42	2,08	1,91	1,51	1,36

The third mode is plotted in the figure 10. This mode was chosen as the most important mode with cyclical vertical structures Mode is polled using streamlines to make visible all structures. Notice, that the direction of streamlines is not important because the analysis is coming out from fluctuation velocity components. From these very preliminary results, it seems that this mode could be related to added momentum coming from plasma actuation.

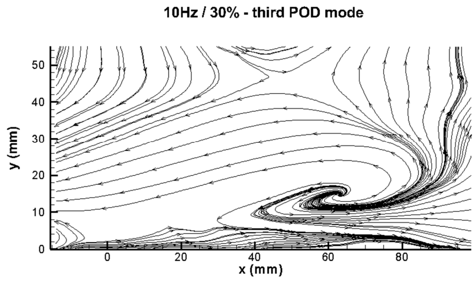

Figure 10. Unsteady case by 10 *Hz*, third mode, plotted using streamlines

4. CONCLUSION

Since the investigation of spanwise oriented plasma DBD actuator was performed previously, this article has dealt with the effect of streamwise oriented plasma actuator on freely developed boundary layer inside rectangular channel. The main part of this work was dedicated to description of boundary layer under actuation of plasma both during steady condition and during unsteady actuation. From velocity profiles gained from mean flow field, it was found out that the added momentum impact the viscous sublayer by strong acceleration. On the other hand, rotating vortex structure causes that the velocity gradient (shear velocity) is negative further the surface.

Most surprising was the fact that the effect of modulation frequency on resulting flow field was almost negligible. To confirm this attribute, a complex stereoscopic measurement in cross-section planes will have to be done. The dynamical analysis using POD is not as suitable as Oscillation Pattern Decomposition (OPD) method as it can reveal not only certain mode with related kinetic energy, but also a frequency connected with each mode. Also the future work will include the OPD analysis of both longitudinal and cross planes to be able to fully express the complexity of the flow.

ACKNOWLEDGEMENTS

The authors gratefully acknowledge financial support of the Grant Agency of the Czech Republic, No. GP14-25354P.

APPENDICES

Table 1. Reynold numbers based on horizontal distance or on conventional BL thickness

	Re_x	Re_δ
5 $m{\cdot}s^{-1}$	$750{\cdot}10^3$	$18{\cdot}10^3$
10 $m{\cdot}s^{-1}$	$1500{\cdot}10^3$	$34{\cdot}10^3$
20 $m{\cdot}s^{-1}$	$3000{\cdot}10^3$	$55{\cdot}10^3$

REFERENCES

[1] Moreau, E., 2007, “Airflow control by non-thermal plasma actuators”, *Journal of Physics D: Applied Physics*, Vol. 40, pp. 605-636.

[2] Hasan, M. A., 1992, “The Flow over a Backward-Facing Step under Controlled Perturbation: Laminar Separation”, *Journal of Fluid Mechanics*, Vol. 238, pp. 73-96.

[3] Matějka, M., 2013, “Shear and Boundary Layer Control – Synthetic Jet”, *Habilitation, Czech Technical University in Prague, Faculty of Mechanical Engineering*.

[4] Procházka, P., Uruba, V., 2013, “Physical Principle Dealing with Development of Vortices Formed by DBD Actuator”, Proc. *Experimental Fluid Mechanics*, Kutná Hora, Czech republic, pp. 594-598.

[5] Procházka, P., Uruba, V., 2011, “Generation of the Vortex Train Using Plasma Barrier Discharge Actuator”, *Proc. In Applied Mathematics and Mechanics*, Graz, Austria, pp. 667-668.

[6] Raffel, M., Willert, C., Wereley, S., Kompenhans, J., 2007, “Particle image velocimetry”, Springer-Verlag, Berlin Heidelberg.

Conference on Modelling Fluid Flow (CMFF'15)
The 16th International Conference on Fluid Flow Technologies
Budapest, Hungary, September 1-4, 2015

MASS TRANSFER ANALYSIS OF AN ISOTHERM SYSTEM ON A SIEVE TRAY USING COMPUTATIONAL FLUID DYNAMICS

Gabriel JUSTI[1], Conrado ZANUTTO[2], Gabriela LOPES[3], José GONÇALVES[4]

[1] PostGraduate Program in Chemical Engineering, Federal University of São Carlos. Via Washington Luiz, km 235, São Carlos-SP, Brazil. Tel.: +55 16 3351 8045, E-mail: gabrielhjusti@yahoo.com.br
[2] PostGraduate Program in Chemical Engineering, Federal University of São Carlos. E-mail: conradozanutto@gmail.com
[3] Department of Chemical Engineering, Federal University of São Carlos. E-mail: gclopes@ufscar.br
[4] PostGraduate Program in Chemical Engineering, Federal University of São Carlos. E-mail: jasgon@ufscar.br

ABSTRACT

Distillation is one of the most important industrial separation techniques. It requires high quantity of energy, corresponding to around 40% of the total energy consumption of chemical industries. Computational fluid dynamics (CFD) techniques allow a microscopic description of the physical characteristics of the fluid motion. The main purpose of this study was to develop a computational fluid dynamics model for vapor-liquid flows that was able to predict the mass transfer on a sieve tray from a non-ideal perspective. A two-phase, three-dimensional and transient model, in an Eulerian-Eulerian approach was proposed for ethanol/water system at 1 atm. The continuity, momentum and chemical species equations were used to describe the vapor and liquid phases. The sieve tray geometry that was simulated was based on experimental work[1]. The variables which were predicted in this work were volume fractions, mass fraction profiles and separation efficiency. The mass transfer model predictions were compared with experimental and numerical data and presented good agreement. This study shows that CFD can be used as a powerful tool for sieve tray design and optimization.

Keywords: CFD, distillation, efficiency, multiphase flow, sieve tray

NOMENCLATURE

A_B	$[m^2]$	active bubbling area
A_{CL}	$[m^2]$	liquid inlet area
$A_{H,i}$	$[m^2]$	hole area
N_H	$[-]$	total holes number
Q_L	$[m^3/s]$	liquid volumetric flow rate
T	$[K]$	temperature
U	$[m/s]$	x-component of velocity
U_S	$[m/s]$	vapor superficial velocity
V	$[m/s]$	y-component of velocity
X_A	$[-]$	mass fraction of A in liquid phase
Y_A	$[-]$	mass fraction of A in vapor phase
μ	$[Pa\ s]$	dynamic viscosity

Subscripts and Superscripts

inlet — at the inlet region

1. INTRODUCTION

Separation processes are techniques which consume a great quantity of energy. Among these processes, distillation columns are one of the most important and utilized techniques. Distillation is a physical process of separation based on the difference of volatility of the components in a mixture, and that kind of technique involves heat, mass and momentum transfer. A better understanding of the mechanisms that occur in industrial scale processes is important in order to improve equipment design and process development[2, 3, 4].

Continuous improvements in computer technology and numerical methods have allowed the possibility to deal with phenomena from its fundamental equations and on a microscopic scale, through techniques of Computational Fluid Dynamics (CFD). In this way, an appreciable amount of computational studies have been done in the last years with sieve trays. Some of these studies were focused on the comprehension of hydrodynamics phenomena that occurs on sieve trays, making possible the analysis of important factors, such as: velocity distribution, liquid and vapor volume fractions profiles along the tray, regions of intense turbulence and regions of liquid accumulation[5, 6, 7, 8, 9, 10, 11, 12].

In recent studies[13, 14], the mass and energy transfer along the stage has been analyzed simultaneously. Both authors proposed a three-dimensional and multiphase flow, in an Eulerian-Eulerian framework. Rahimi et al.[13] carried out their model in a stationary approach, and Noriler et al.[14] in a transient approach. Thus, the continuity, momentum, energy and chemical species equations were applied for both fluids, for predictions of efficiency and temperature and concentration fields.

In this way, this study aimed to deepen the analysis of mass transfer that occurs on sieve trays. An ethanol/water system at 1 atm was used.

2. MATHEMATICAL MODELING

The model was based on a three-dimensional, transient and multiphase flow. An Eulerian-Eulerian approach was used to model the liquid and vapor phases. Thus, each phase was treated as an interpenetrating continuum phase having separate transport equations. Therefore, the Reynolds averaged Navier-Stokes equations (RANS) for continuity, momentum and chemical species transfer were numerically solved for each phase. Since the pressure and temperature gradients are very little over a same distillation stage, the system was considered isothermal and at 1 atm, where both phases have their own temperatures over the stage.

2.1. Model Assumptions

The following assumptions were imposed on the model proposed: a two-phase system was considered in the simulation; the gas phase is the dispersed phase and the liquid phase is the continuous phase; the binary system ethanol-water was used in this simulation; the net rate of the mass transfer between the phases is considered to be so small that it can be neglected; and no turbulence models was used for dispersed phase.

2.2. Closure Equations

In order to numerically solve the proposed model, additional equations are required. In this way, some terms were modeled, such as turbulence, interphase momentum transfer and interphase chemical species transfer.

2.2.1. Turbulence

The Shear Stress Transport (SST) turbulence model was used to describe the turbulence on the sieve tray. This turbulence model combines the advantages of the k-ϵ model and k-ω model, with a possibility to describe accurately regions that are near of the wall. Remembering that only the liquid phase was considered in the turbulence model, while the gas phase was considered as laminar. The SST model is well discussed in the literature[15, 16].

2.2.2. Drag Coefficient

The interphase momentum transfer term was considered, in this work, only due to the drag force. The drag coeficient was estimated using the correlation of Krishna et al.[17], which was proposed for the rising of a swarm of large bubbles in the churn turbulent regime.

2.2.3. Higbie Theory

For interphase mass transfer, the Higbie penetration theory[18] was used to calculate the liquid and gas mass transfer coefficients. The proposed theory has been widely used to calculate the gas and liquid mass transfer coefficient in distillation stages. As mentioned by Rahimi et al.[13] and Rahimi et al.[19], this model assumes that the composition of the film does not stay stagnant as considered in the film model and the exposure time is determined by the hydrodynamic properties of the system.

3. NUMERICAL METHODOLOGY

3.1. Geometry and Numerical Grid

A three-dimensional and full geometry, based on the experimental work[1], was used in the simulation and was built using the software ANSYS Design Modeler. The geometry details of the sieve tray and the boundary conditions are presented in Table 1 and Figure 1.

Table 1. Operational conditions based on work[1]

Tray diameter	1.213	*m*
Tray spacing	0.61	*m*
Weir lenght	0.925	*m*
Weir height	0.05	*m*
Downcomer lenght	0.572	*m*
Hole diameter and pitch	1.27×5	*cm*
% Bubbling area (over total area)	76	%
% Hole area (over bubbling area)	5	%

The numerical grid used in the simulation was developed using the software ANSYS Meshing, and consists in a hybrid grid with tetrahedral meshing elements in the hole region (height of 0.01 *m*) and hexahedral meshing elements in the other regions (height of 0.60 *m*). Figure 2 shows the details of the numerical mesh.

The total cell number used was 1856032 cells and 1564249 nodes. As can be seen in Fig. 2, there are a more density of meshing elements in the regions near to the hole region in relation to the top region, and it is important to attain accurate representation of vapor-liquid interaction occurring in the regions near to the base of the tray.

3.2. Boundary and Initial Conditions

The initial and boundary conditions are essential for closing the model and allow the resolution of numerical equations involved in the simulation. Figure 1 illustrates the boundary regions of the sieve tray.

3.2.1. Liquid Inlet

At the liquid inlet in the Figure 1, only liquid was considered entering through this region and was adopted a velocity condition by assuming a uniform

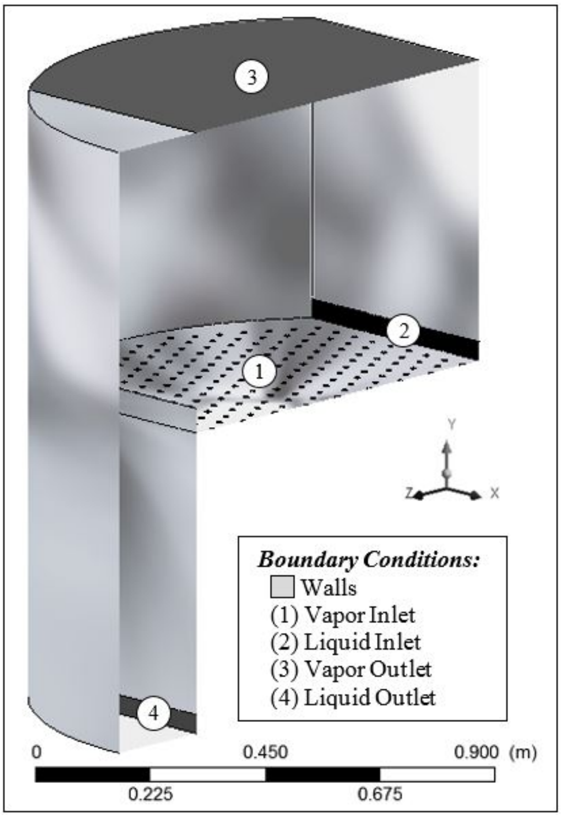

Figure 1. Flow geometry and boundary conditions

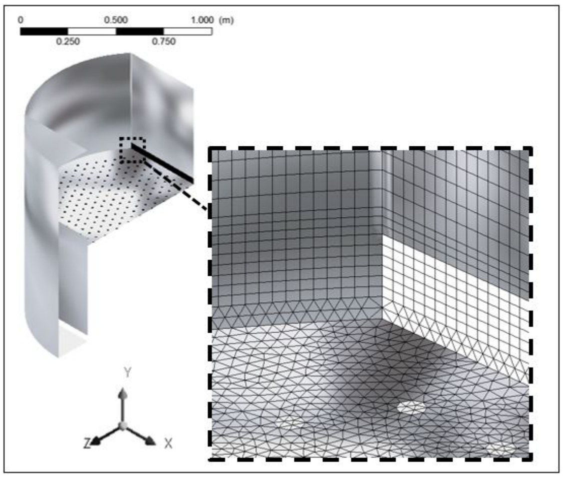

Figure 2. Details of the mesh used

velocity profile according to Equation 1:

$$U_{\mathrm{L,inlet}} = \frac{Q_{\mathrm{L}}}{A_{\mathrm{CL}}} \quad (1)$$

It was considered that only liquid phase enters this region, because the amount of dragged vapor by the liquid is negligible. Additionally, an ethanol mass fraction of 0.785 was specified.

3.2.2. Vapor Inlet

It was considered that the vapor mass flow rate entering through the holes of the tray is the same in each hole. Thus, the vapor velocity that flows through the holes was calculated according to Equation 2:

$$V_{\mathrm{L,inlet}} = \frac{U_{\mathrm{S}}\, A_{\mathrm{B}}}{N_{\mathrm{H}}\, A_{\mathrm{H},i}} \quad (2)$$

It was considered that only gas phase enters this region, because the amount of dragged liquid by the vapor is negligible. Additionally, an ethanol mass fraction of 0.812 was specified.

3.2.3. Liquid and Vapor Outlets

At the liquid outlet region, a pressure condition was adopted and it was used in order to simulate a resistance in the liquid outlet, which actually exists due to the lower tray. This resistance involves the emergence of a liquid buildup in the outlet downcomer. In this study it was considered a column of accumulated liquid of 50% of the downcomer length.

At the vapor outlet region it was also used a pressure condition by specifying a relative pressure of zero, that is, an absolute pressure of 1 atm.

3.2.4. Walls

A non-slip wall boundary condition was specified for both phases. The sieve tray was simulated in its entirety.

3.2.5. Domain Initialization

The initial condition applied in the simulation consisted of the domain filled only with gas. Thus, it was possible to observe the tray filling by the liquid phase.

3.3. Simulation Settings

The simulation was carried out using the software CFX-Pre 14.5. The operation conditions used for the liquid and gas in the simulation were a liquid volumetric flow rate equal to $Q_{\mathrm{L}} = 6.94 \times 10^{-3}\ m^3/s$, and a factor $F_{\mathrm{S}} = 1.015\ m/s\ (kg/m^3)^{0.5}$, respectively. The F_{S} factor is defined as a function of vapor superficial velocity and vapor density, i.e.,

$$F_{\mathrm{S}} = U_{\mathrm{S}} \sqrt{\rho_{\mathrm{V}}} \quad (3)$$

Physical properties of liquid and vapor phases used in the simulation are presented in the Table 2.

For continuity, momentum and chemical species transfer equations, the Upwind interpolation scheme was used for the advective terms and the first order backward euler scheme was employed for the transient terms. For the equations related to turbulence, the high resolution scheme was used. The coupled solution method was used to solve the model, with all the equations solved simultaneously as a single system.

Table 2. Physical properties of liquid and vapor phases

	Ethanol Water Mixture		
	Liquid	Vapor	Units
T_{inlet}	354.8	356.9	K
$X_{\text{A,inlet}}$	0.785	-	-
$Y_{\text{A,inlet}}$	-	0.812	-
ρ	820	1.255	kg/m^3
μ	0.403×10^{-3}	1.010×10^{-5}	$Pa\ s$
D_{A}	6.201×10^{-9}	1.689×10^{-5}	m^2/s

The simulation was conducted using thirty processors AMD Opteron 2.40 GHz (30x2.40) running in parallel to simulate 40 seconds of multiphase and multicomponent flow on a sieve tray. The simulation was carried out for 40 s in the chemical species transfer analysis, where fixed time steps that varied from $5.0{\times}10^{-4}$ to $2.5{\times}10^{-3}$ s were used.

4. RESULTS AND DISCUSSION

4.1. Grid Sensitivity Tests

Figures 3 and 4 show the grid sensitivity tests, which were used to confirm the independence of the results in relation to the grid size, where the numerical results should not change significantly as the grid size is further decreased. The grids 1, 2, 3, and 4, we have, respectively, a number of nodes of 951620, 1102116, 1564249, and 1940384. The maximum values of aspect ratio are, respectively, 14.986, 13.386, 12.555, and 11.875. The average values of aspect ratio are, respectively, 2.503, 2.854, 2.205, and 1.873. The average values of skewness are, respectively, 0.209, 0.169, 0.151, and 0.147. The average values of element quality are, respectively, 0.667, 0.598, 0.724, and 0.805.

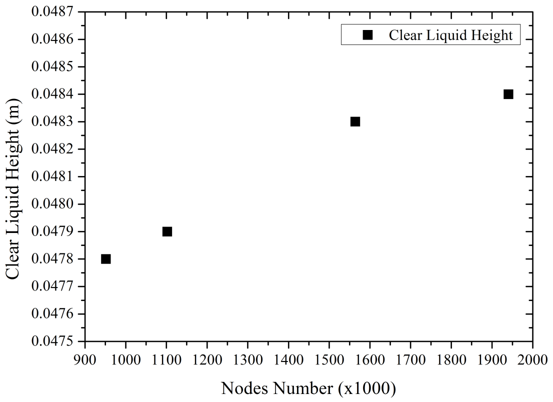

Figure 3. Clear liquid height as a function of the number of nodes for each grid.

To evaluate the stability of the numerical grid, the clear liquid height as global variable and the w component of the liquid velocity as local variable were chosen. Aiming to verify the w component of the liquid velocity, 7 lines were used along the tray (at elevation of 0.038 m above the tray floor), in which a great quantity of monitor points were used along the lines. In Figure 4, the measuring lines are presented in terms of a dimensionless coordinate (x/R) which was obtained by the ratio of the x coordinate belonging to each line of analysis and the radius of the tray (R = 0.6065 m).

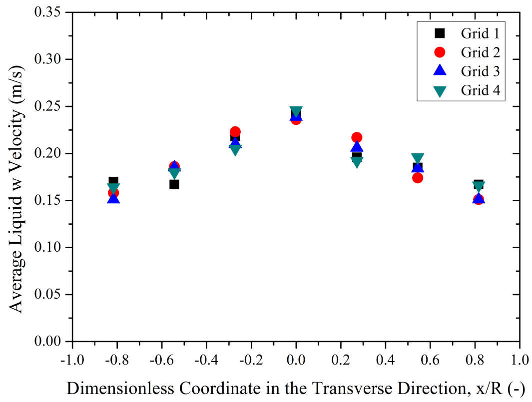

Figure 4. Liquid velocity profile as a function of dimensionless coordinate (x/R) in the upstream region, evaluated in a ZX plane (y = 0.038 m) for each grid

As shown in 3, it can be noted that the value of clear liquid height tends to assume an approximately constant value after a certain level of refinement. Similarly, Figure 4 shows a low influence of each grid refinement on measured velocities. In this work Grid 3 was used, with 1856032 cells and 1564249 nodes.

4.2. Mass Fraction Profiles

Figure 5 shows the ethanol mass fraction in the liquid phase over the tray in an YZ plane located at the center of the tray (x = 0 m) and in a ZX plane located at a height of 0.038 m above the base of the tray (y = 0.038 m) for the instant of 40 s.

From Figure 5a, it can be observed that the liquid enters the tray with a greater fraction of ethanol and as it flows towards the weir, a decrease in the concentration of ethanol can be observed, which in this case is the most volatile, while having an increase in the water mass fraction, which in this case is less volatile component, and it is due to the chemical species transfer between with vapor phase. Figure 5b, which presents the ethanol mass fractions field in the liquid phase over the tray in a ZX plane located at a height of 0.038 m above the base of the tray (y = 0.038 m) for the instant of 40 s. As can be seen, the liquid mixture has mass fractions variations over its inventory.

Figure 6a presents the ethanol mass fraction field in the vapor phase over the tray in the YZ plane located at the center of the tray (x = 0 m) for the instant of 40 s. The mass fraction of ethanol in the vapor increases with the vapor flowing over the tray in an upward direction, that is, the vapor becomes more

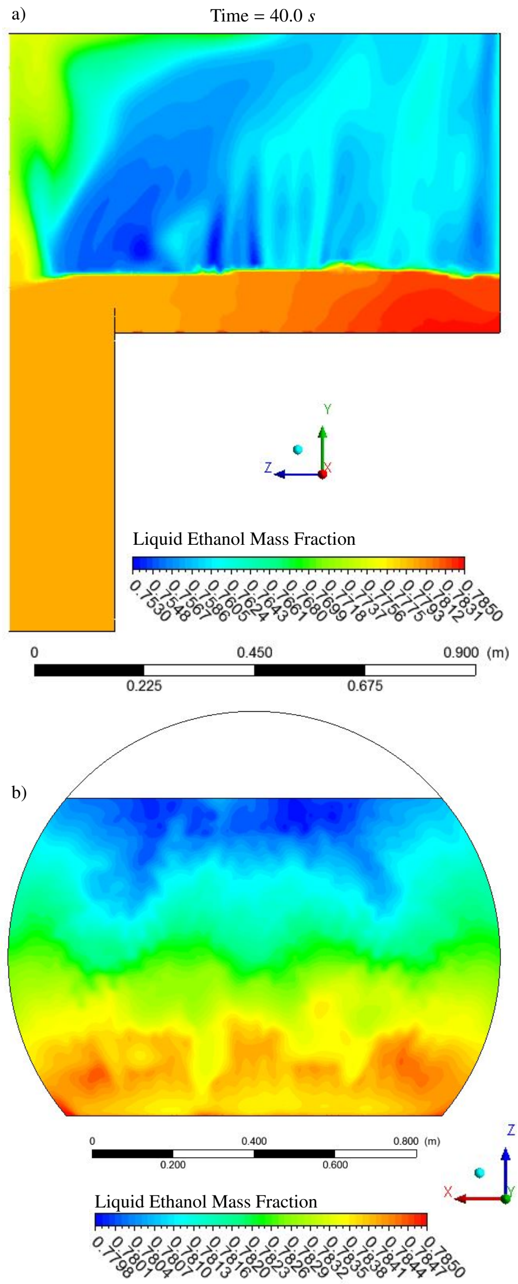

Figure 5. Ethanol mass fraction profile for the liquid phase for: (a) YZ plane x = 0 m; and (b) ZX plane at 0.038 m above the base of the tray

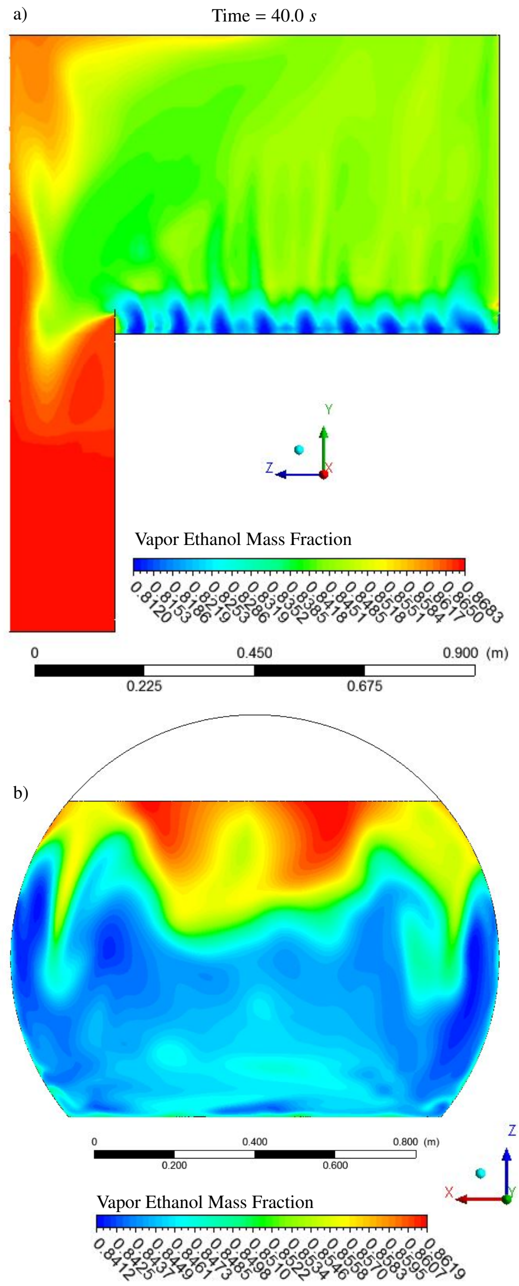

Figure 6. Ethanol mass fraction profile for the vapor phase for: (a) an YZ plane at the tray center; and (b) ZX plane at the vapor outlet region

concentrated in the more volatile component, while the mass fraction of water decreases. Figure 6b also shows the ethanol mass fraction in the vapor at the vapor outlet region, that is, at the top of the tray, for the final time of 40 s. It can be seen that the profile is non-uniform. Furthermore, Figure 5b shows the non-uniformity of the mass fraction profile over the liquid mixture inventory. Thus, these non-uniformities imply different efficiencies over the same stage, making it important to analyze point efficiencies. Point efficiency allows showing in which regions the mass transfer is more pronounced.

The average (based on the outlet area) of ethanol mass fractions in the vapor and liquid outlet regions as a function of time are shown in Figures 7 and 8, respectively, in a range between 25 to 40 seconds. The dotted lines represent the average (based on time) mass fraction of ethanol and were calculated in a time interval in which the flow had reached the "quasi-stationary" state, in this case between 25 to 40 seconds.

It is observed that the ethanol compositions in the vapor and liquid phases have a random behavior, which shows once again the complexity of the flow

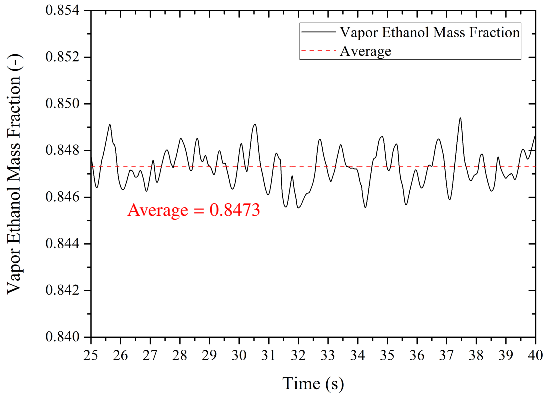

Figure 7. Ethanol mass fraction evaluated at the vapor outlet for a range of 25 to 40 *s*

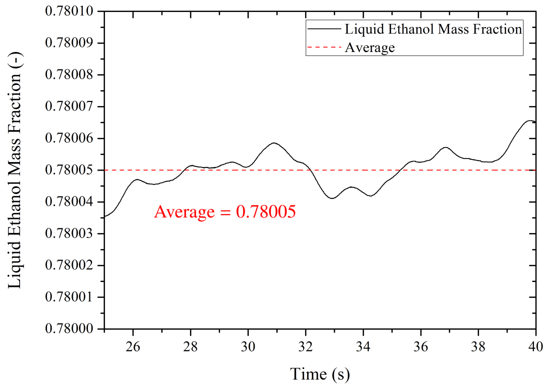

Figure 8. Ethanol mass fraction evaluated at the liquid outlet for a range of 25 to 40 *s*

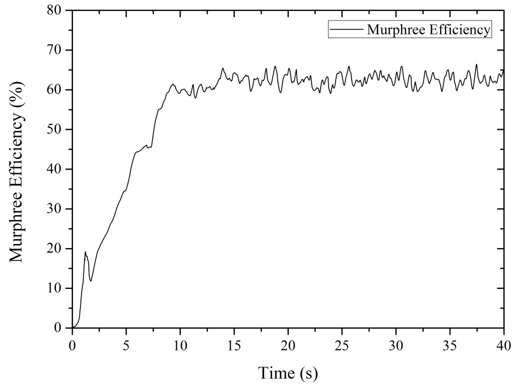

Figure 9. Murphree Efficiency as a function of time

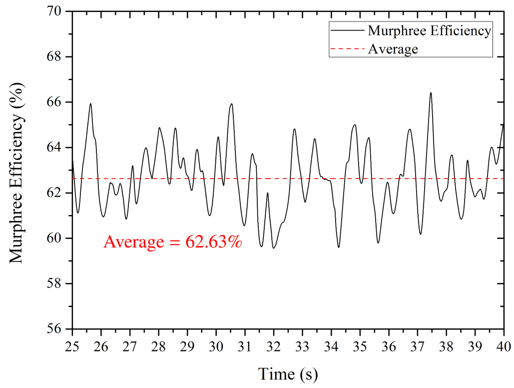

Figure 10. Murphree Efficiency as a function of time for a range of 25 to 40 *s*

on sieve trays. Note that the oscillation is random, and not periodic.

4.3. Murphree Efficiency

The global tray efficiency can be calculated based on the Murphree[20] efficiency. In the Murphree efficiency, the mass fraction of ethanol in the vapor inlet and outlet are related to the mass fraction of ethanol in vapor that would leave the tray if the vapor were in equilibrium with the liquid leaving the tray. The Murphree efficiency values are shown in Figure 9.

Figure 10 shows the variation of the Murphree tray efficiencies for a range of 25 to 40 s for the vapor phase, and the dotted lines represent the average (based on time) of the Murphree efficiency, calculated between the interval of 25 to 40 s.

As mentioned by Wankat[21], the distillation column design calculations are generally based on the equilibrium stage concept, which states that streams leaving a stage are in equilibrium. However, aiming the optimization of sieve trays, the first step is to know how non-ideal the flow on these devices is. As shown in the results previously, both phases have changes in ethanol mass fraction over its inventory and, consequently, the mixture cannot be considered as an ideal mixture and the chemical potential equilibrium is not achieved.

4.4. Point Efficiency

As suggested by West[22], by dividing the tray in different regions, the Murphree efficiency concept can be applied for each region and the point efficiency is calculated. Figure 11 presents the profile of ethanol mass fractions in the vapor and liquid phases as a function of the position on the tray, and also show the ethanol mass fraction in the vapor phase that would be in equilibrium with the liquid phase leaving the tray, for the instant of 40s. In Figure 11, $z = 0$ m represents the liquid inlet region and $z = 0.785$ m represents the weir region. An important result by analyzing Figure 11 is that the ethanol mass fraction in the vapor phase which would be in equilibrium with the liquid phase leaving the tray, always has a higher ethanol fraction than in vapor which leave the tray in a real flow. That is an indication that the real mass transfer occurring over the tray is far from the mass transfer which would occur in an ideal stage.

In this way, from the evaluation of the ethanol mass fractions in the phases as a function of the position occupied, it is possible to estimate the point efficiency values over the tray. The calculated val-

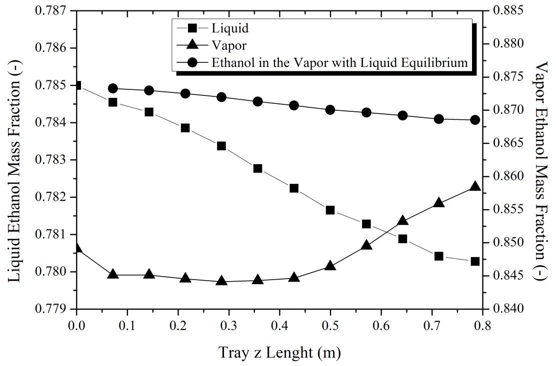

Figure 11. Ethanol mass fraction profile in the liquid and vapor phases, and in the vapor that would be in equilibrium with the liquid phase leaving the tray, as a function of the tray position (point)

ues are shown in Figure 12, showing the variation in point efficiencies along the tray. The dotted line represents the average value of the tray Murphree efficiencies. In Figure 12, subdomain 1 comprises the liquid inlet region and the subdomain 11 comprises the downcomer region.

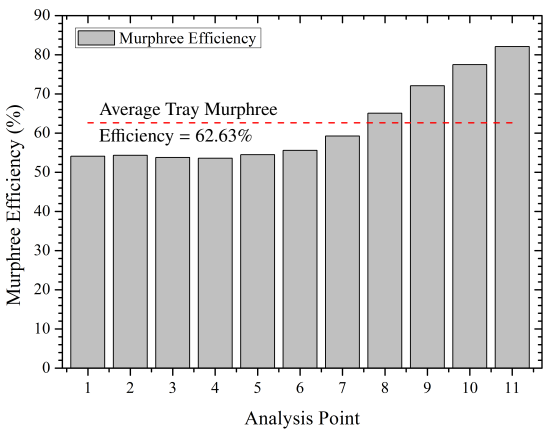

Figure 12. Point efficiencies evaluated over the subdomains and the average tray efficiency

From Figure 12, it is noted that the efficiency increases towards the weir. An explanation for this gradual increase when the liquid approximates the weir is based on residence time concept. Thus, the liquid near its inlet has a smaller residence time than the liquid phase near the weir. Since the mass transfer is strongly influenced by the liquid-vapor contact time, it can be concluded that the liquid near the weir has performed a greater mass transfer. Another factor to be considered is the tendency that the liquid has to return towards the center of the tray due to contact with the weir. The same trend of point efficiency variation was found by Noriler et al.[14] and Rahimi et al.[19].

4.5. Models Comparation

After the results obtained by numerical simulation, it is important to compare and discuss some factors related to the model used. Figure 13 compares the tray efficiencies of the model used in this study, as well as the tray efficiencies obtained by two CFD studies, and an efficiency value obtained by MacFarland et al.[23] correlation, all for ethanol/water system. The CFD study carried out by Noriler et al.[14] was from a sieve tray with a diameter of 0.3 m and 180 rectangular holes, and the Zuiderweg correlation was used for the mass transfer coeficient. The CFD study conducted by Oliveira[24] was based on a sieve tray with the same geometry of this study.

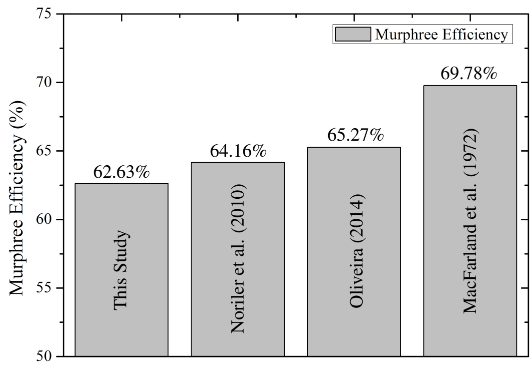

Figure 13. Murphree efficiencies comparison

As shown in Figure 13, the average tray efficiency obtained in this study are situated in the same range of values (60-70%) that the efficiencies obtained by Noriler et al.[14], Oliveira[24] and the predicted plate efficiency by correlation MacFarland et al.[23]. The studies carried out by Noriler et al.[14] and Oliveira[24] are very similar to the study in this paper, which are the application of CFD techniques to the liquid-vapor flow on sieve trays. As seen in Figure 13, the efficiency obtained by Oliveira[24] was greater when compared with the simulation of this study for the same computational domain. This difference is due to the physical property values used by Oliveira[24] who were withdrawn from the study Noriler et al.[14]. In this study the physical properties were calculated using an average temperature of 355.85 K.

5. CONCLUSIONS

The methodology proposed in this study was found to be adequate to describe the separation efficiency of a gas-liquid flow on a sieve tray of a distillation column. It was possible to calculate the stage efficiency based on models that consider the spatial and temporal variations over the computational domain. This is important in terms of design and optimization of distillation sieve trays. Finally, CFD techniques can be used to optimize trays designs and their operating conditions for distillation processes.

ACKNOWLEDGEMENTS

The authors acknowledge FAPESP, CNPq, CAPES and PostGraduate Program in Chemical Engineering of the Federal University of São Carlos.

REFERENCES

[1] Solari, R. B., and Bell, R. L., 1986, "Fluid Flow Patterns and Velocity Distribution on Commercial-Scale Sieve Tray", *AIChE Journal*, Vol. 32, pp. 640–648.

[2] Kister, H. Z., 1992, *Distillation Design*, Boston: McGraw-Hill.

[3] Henley, E. J., and Seader, J. D., 1981, *Equilibrium-stage Separation Operations in Chemical Engineering*, Wiley: New York.

[4] Krishnamurthy, R., and Taylor, R., 1985, "A Nonequilibrium Stage Model of Multicomponent Separation Processes. Part II: comparison with experiment", *AIChE Journal*, Vol. 31 (3), pp. 456–465.

[5] Mehta, B., Chuang, K. T., and Nandakumar, K., 1998, "Model for Liquid Phase Flow on Sieve Trays", *Transactions IChemE*, Vol. 76, pp. 843–848.

[6] Fischer, C. H., and Quarini, G. L., 1998, "Three-dimensional Heterogeneous Modeling of Distillation Tray Hydraulics", *AIChE Annual Meeting*, pp. 15–20.

[7] Krishna, R., Van Baten, J. M., Ellenberger, J., Higler, A. P., and Taylor, R., 1999, "CFD Simulations of Sieve Tray Hydrodynamics", *Transactions IChemE*, Vol. 77, pp. 639–646.

[8] Yu, K. T., Yuan, X. G., You, X. Y., and Liu, C. J., 1999, "Computational Fluid-dynamics and Experimental Verification of Two-phase Two-dimensional Flow on a Sieve Column Tray", *Chemical Engineering Research and Design*, Vol. 77 (6), pp. 554–560.

[9] Van Baten, J. M., and Krishna, R., 2000, "Modelling Sieve Tray Hydraulics Using Computational Fluid Dynamics", *Chemical Engineering Journal*, Vol. 77, pp. 143–151.

[10] Liu, C., Yuan, X. G., Yu, K. T., and J., Z. X., 2000, "A Fluid-dynamic Model for Flow Pattern on a Distillation Tray", *Chemical Engineering Science*, Vol. 55, pp. 2287–2294.

[11] Gesit, G., Nandakumar, K., and Chuang, K. T., 2003, "CFD Modeling of Flow Patterns and Hydraulics of Commercial-scale Sieve Trays", *AIChE Journal*, Vol. 49, pp. 910–924.

[12] Teleken, J. G., Werle, L. O., Marangoni, C., Quadri, M. B., and Machado, R. A. F., 2009, "CFD Simulation of Multiphase Flow in a Sieve Sray of a Distillation Column", *Brazilian Journal of Petroleum and Gas*, Vol. 3 (3).

[13] Rahimi, R., Rahimi, M. R., Shahraki, F., and Zivdar, M., 2006, "Efficiencies of Sieve Tray Distillation Columns by CFD Simulation", *Chemical Engineering Technology*, Vol. 29, pp. 326–335.

[14] Noriler, D., Barros, A. A. C., Maciel, M. R. W., and Meier, H. F., 2010, "Simultaneous Momentum, Mass, and Energy Transfer Analysis of a Distillation Sieve Tray Using CFD Techniques: prediction of efficiencies", *Industrial & Engineering Chemistry Research*, Vol. 49, pp. 6599–6611.

[15] Menter, F. R., 1994, "Two-equation Eddy-viscosity Turbulence Models for Engineering Applications", *American Institute of Aeronautics and Astronautics*, Vol. 32, pp. 1598–1605.

[16] Wilcox, D. C., 2004, *Turbulence Modeling for CFD*, California: DCW Industries.

[17] Krishna, R., Urseanu, M. I., Van Baten, J. M., and Ellenberger, J., 1999, "Rise Velocity of a Swarm of Large Gas Bubbles in Liquids", *Chemical Engineering Science*, Vol. 54, pp. 171–183.

[18] Higbie, R., 1935, "The Rate of Absorption of a Pure Gas into a Still Liquid During Short Periods of Exposure", *Transactions of the American Institute of Chemical Engineers*, Vol. 35, pp. 365–389.

[19] Rahimi, R., Sotoodeh, M. M., and Bahramifar, E., 2012, "The Effect of Tray Geometry on the Sieve Tray Efficiency", *Chemical Engineering Science*, Vol. 76, pp. 90–98.

[20] Murphree, E. V., 1925, "Rectifying Column Calculations: with particular reference to n component mixtures.", *Industrial and Engineering Chemistry*, Vol. 17, pp. 747–750.

[21] Wankat, P. C., 2007, *Separation Process Engineering*, Upper Saddle River: Prentice Hall.

[22] West, F. B., Gilbert, W. D., and Shimizu, T., 1952, "Mechanism of Mass Transfer on Bubble Plates: plate efficiencies", *Industrial and Engineering Chemistry*, Vol. 44, pp. 2470–2478.

[23] MacFarland, S. A., Sigmund, P. M., and Van Winkle, M., 1972, "Predict Distillation Efficiency", *Hydrocarbon Processing*, Vol. 51, pp. 111–114.

[24] Oliveira, G. C., 2014, "Aplicação de Técnicas de CFD na Melhoria da Eficiência de Estágio em Colunas de Destilação para Produção de Etanol", Ph.D. thesis, Universidade Federal de São Carlos.

***Conference on Modelling Fluid Flow (CMFF'15)**
The 16th International Conference on Fluid Flow Technologies
Budapest, Hungary, September 1-4, 2015*

INVESTIGATION OF CAVITATING FLOW OVER A HYDROFOIL USING DIFFERENT MATHEMATICAL CAVITATION MODELS

Dorota HOMA[1], Włodzimierz WRÓBLEWSKI[2]

[1] Corresponding Author. Institute of Power Engineering and Turbomachinery, Silesian University of Technology. Konarskiego street 18, 44-100 Gliwice, Poland. Tel.: +48 32 237 1546, E-mail: dorota.homa@polsl.pl
[2] Institute of Power Engineering and Turbomachinery, Silesian University of Technology. E-mail: wlodzimierz.wroblewski@polsl.pl

ABSTRACT

Cavitation can occur in flow when local pressure drops below the saturation pressure. It includes both vaporization and condensation of vapour bubbles. As this is a multiphase flow and quite complicated phenomenon, there are a few mathematical models describing it. Aim of this paper is to verify their utility in case of different type of cavitation. The investigated case included flow over a hydrofoil. The grid independence study was performed assuming one phase fluid model and setting boundary condition that excluded developed cavitation. The investigated hydrofoil was Clark-Y. For different cavitation numbers the vapour areas appearance and their changes in time were observed. Also the pressure and vapour volume fraction distribution was described. The cavitation numbers were chosen in a way that enabled to observe different types of cavitation: incipient and sheet cavitation. The isothermal two-phase fluid model was assumed. The calculations were performed using OpenFOAM. The obtained results were compared to the available measurements data.

Keywords: cavitating flow, cavitation models, CFD, flow over hydrofoil, multiphase flow.

NOMENCLATURE

C	[-]	empirical coefficient
F	[-]	coefficient
R	[kg/m^3s]	source term
S	[N/m]	surface tension
c	[m]	chord length
n	[-]	number per volume of liquid
p	[Pa]	pressure
r	[m]	radius
t	[s]	time
u	[m/s]	velocity
α	[-]	vapour volume fraction
ρ	[kg/m^3]	density
σ	[-]	cavitation number

Subscripts

B	bubble
c	condensation
e	evaporation
l	liquid
m	mixture
v	vapour
s	saturation
∞	free stream

1. INTRODUCTION

Cavitation phenomenon is one of the most important issue when designing and exploiting pumps' systems. As the working under cavitating condition can lead to serious damage of the blades and walls of the rotor, it is useful to provide simulations which can assess the risk of cavitation appearance at defined flow condition. The crucial concern is to use the cavitation model which can provide the results as close to the experimental data as possible.

This paper includes comparison of two popular cavitation models – Schnerr & Sauer and Kunz model. The case is the flow over a Clarky-Y hydrofoil.

2. DESCRIPTION OF MODELS

Cavitation modelling can be gathered into two main groups: one-fluid and two-fluid models. In one-fluid models the flow is threated as the mixture of two phases and the conservation equations (mass and momentum) for the mixture are solved. In this simulation no slip between the phases was assumed. To calculate fraction of gaseous phase mass conservation equation of vapour is solved [1].

$$\frac{\partial \alpha \rho_v}{\partial t} + \nabla(\alpha \rho_v u) = R_e - R_c \tag{1}$$

The difference between used models is definition of source terms R_e and R_c. In Kunz model they are defined empirically. Kunz used free stream velocity and time (derived from free stream velocity and characteristic length) The formulas are as follows [2-4]:

$$R_e = \frac{C_e \rho_v \alpha \min(0, p - p_s)}{0.5 \rho_l u_\infty^2 t_\infty} \tag{2}$$

$$R_c = \frac{C_c \rho_v \alpha^2 (1-\alpha)}{t_\infty} \tag{3}$$

The coefficient Ce and Cc are assumed according to the case. In Schnerr & Sauer model the source terms are derived from Rayleigh-Plesset (RP) equation, which describes the dynamics of vapour bubbles. The RP equation is simplified, no surface tension is assumed, as in formula below [5]:

$$\frac{Dr_B}{Dt} = \sqrt{\frac{2}{3}\frac{p_B - p}{\rho_l}} \tag{4}$$

The final formulas for source terms [6]:

$$R_e = \frac{\rho_l \rho_v}{\rho} \alpha (1-\alpha) \frac{3}{r_B} \sqrt{\frac{2}{3}\frac{p_s - p}{\rho_l}} \tag{5}$$

$$R_c = \frac{\rho_l \rho_v}{\rho} \alpha (1-\alpha) \frac{3}{r_B} \sqrt{\frac{2}{3}\frac{p - p_s}{\rho_l}} \tag{6}$$

The radius of bubble r_B is derived from vapour volume fraction and number of bubbles per volume of liquid, as shown in equation 7 [6]:

$$r_B = \left(\frac{\alpha}{1-\alpha} \frac{3}{4\pi} \frac{1}{n_B} \right)^{\frac{1}{3}} \tag{7}$$

3. SIMULATION SET-UP

The simulation concerns flow over a ClarkY hydrofoil. The overview of the geometry is shown in Figure 1.

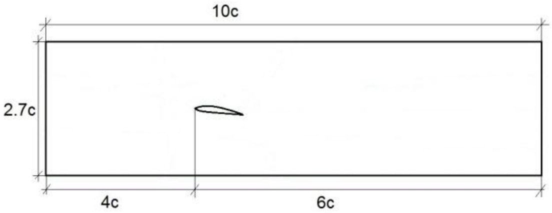

Figure 1. Overview of geometry

The foil is placed in distance of 4c from the inlet and 6c from the outlet. The height of the channel is set to 2.7c. Chord of the foil is equal to 70 mm. The simulation is performed at constant inlet velocity. The pressure at the outlet is consequently lowered. The calculations were performed in OpenFOAM open source code with the solver interPhaseChangeFoam, which captures the dynamics of the cavitating flow [7]. The simulation set up is based on other investigations [8,9], the turbulence model was chosen after analysing others articles dedicated to hydrofoil cavitation modelling [10-13]. The simulation set up is shown in table 1.

Table 1. Simulation set up (bc – boundary conditions)

Chord length	70 mm
Angle of attack	8°
Heat transfer model	isothermal
Flow temperature	20°C
Turbulence model	k-ω SST
Side walls bc	symmetry
Upper/lower wall bc	wall
Outlet bc	static pressure case dependent
Inlet velocity	10 m/s
Turbulence intensity at inlet	5%
Reynolds number	700 000

Table 2. Models parameters

Kunz		Schnerr & Sauer	
C_e	20000 [4]	n_B	$1.6x10^{13}$
C_c	1000 [4]	r_B	10^{-6}

4. GRID INDEPENDENCE STUDY

To ensure that the results of the simulation do not depend on the grid size the grid independence study was performed. Four different hexahedra grids were examined. They were all 2D surface meshes extruded in perpendicular direction by 10 layers of 1 mm thickness. Around the foil the C-grid was used. The number of cells varied from 281 to 427 thousands. The grids with symbols S2 and S3 have similar number of cells, but they had different cells distribution on upper and lower side of the foil. For observing the cavitating structures the distribution of nodes on edges of the foil is very important. The cells number in each grid and C-grid layers number are described in table 3. The distribution of cells along the edges is placed in table 4. The blocking used in meshes with location of three parts of foil edge is shown in Figure 2.

Table 3. Grid cells and C-grid layers numbers

Grid symbol	Number of cells	C-grid layers
S1	281820	50
S2	313260	50
S3	387420	75
S4	472272	90

Table 4. Cell distribution on foil edges

Grid symbol	US	LS	LEA
S1	100	70	25
S2	120	85	30
S3	100	70	25
S2	100	70	25

US – upper side
LS –lower side
LEA – leading edge area

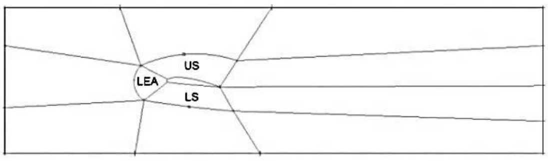

Figure 2. Mesh blocking

All the grids were used during calculation with outlet pressure equal to 100 kPa. This setting disabled developed cavitation structures to occur. After calculations pressure distribution for different grids were compared. In Figure 3. pressure distribution over the foil is shown.

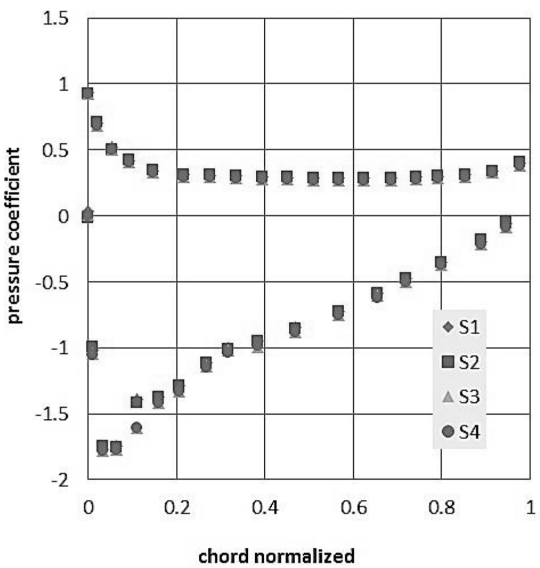

Figure 3. Pressure distribution for different grids

For grid S1, with the lowest number of cells, on the upper side of the foil near the leading edge the increase of pressure is observed. There is no such rise of pressure in case of meshes S3 and S4. The mesh with symbol S2 has similar number of cells as the mesh S3, but has different cells distribution. For this grid, the different pressure distribution occurs comparing to grids S3 and S4. To perform further simulation, the grid S3 was chosen. In the figure 4. the overview of grid is shown and in the figure 5. zoom of the o-grid is presented.

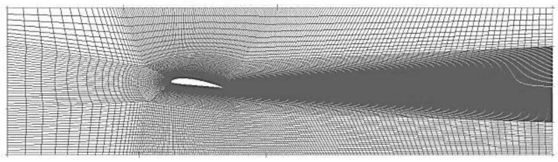

Figure 4. Overview of the grid

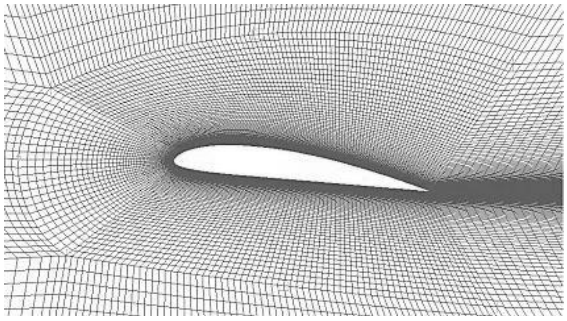

Figure 5. Zoom of the C-grid

5. RESULTS INCIPIENT CAVITATION

The characteristic value that describes the cavitating flow is called cavitation number. It is defined as [14]:

$$\sigma = \frac{p - p_s}{0.5\rho u_\infty^2} \tag{8}$$

Cavitation flow regimes depend on cavitation number calculated from velocity and pressure of free stream flow. In case of flow over a hydrofoil, four different flow regimes can be distinguished: incipient, sheet, cloud and super cavitation [8,14]. Incipient cavitation is a first stage of cavitation over a foil. Cavitation number is about 1.6, which refers to the outlet pressure 82180 Pa. According to [8] the growth cavitation structure of hairpin (or horseshoe) shape is observed. Growing and collapsing of bubbles occur with frequency of about 265 Hz (3.78 ms per period).

In Figures 6. and 7. comparisons of time-averaged pressure and time-averaged vapour volume fraction in monitor point located on the foil are presented. As it can be observed, the distributions on the lower side of the foil are almost the same (the difference does not exceed 3%). For upper side of the foil, within the chord normalized from 0 to 0.2 the pressure distributions obtained by both models are almost the same. Form chord 0.2 to 0.4 the pressure distribution obtained by Kunz model surpasses the one obtained from Schnerr & Sauer model. Within chord 0.4 to 1 the pressure distributions coincide, except from chord between 0.6 and 0.8.

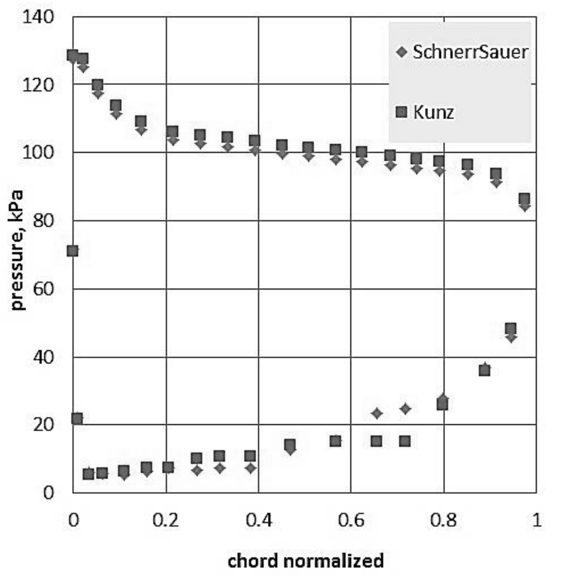

Figure 6. Time-averaged pressure distribution for different models. Incipient cavitation

The distributions of vapour volume fraction around the hydrofoil differ for both models (Fig.7.).

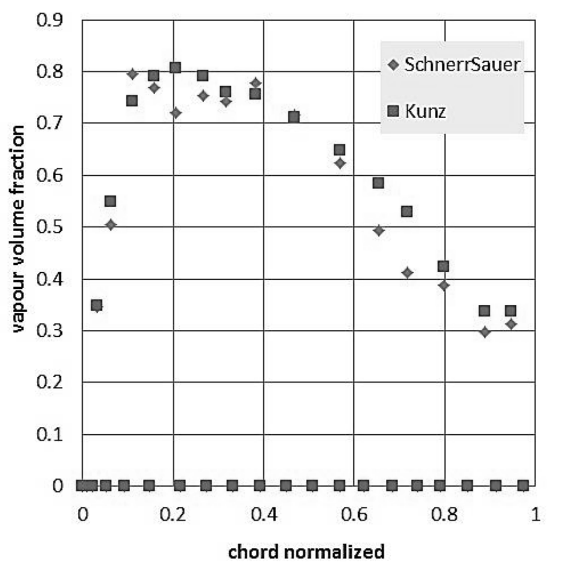

Figure 7. Time-averaged vapour volume fraction distribution for different models. Incipient cavitation

For Schnerr & Sauer model after the growth to about 0.79 at chord 0.15, the inclination to the value of 0.72 at chord 0.2 is observed. It can be explained by analysing the picture of the period in Figure 8., where one cycle of incipient cavitation obtained by Schnerr & Sauer model is shown. The cavitation bubble is attached very close to the leading edge but the area of higher pressure before the main cavitation structure is observed (Fig.8. g-j). After the drop, the vapour volume fraction rises to the value of 0.78 at chord 0.4. From chord 0.4 to 1.0 the vapour volume fraction consequently lowers. For Kunz model the values of vapour volume fraction are generally higher than for Schnerr & Sauer model, expect from chord length 0.1and 0.4. At this chords the values obtained by Kunz model are slightly lower. When using Kunz model there is no pit like in Schnerr & Sauer model, the distribution is also more smooth. At chord from 0.1 to 0.25 and from 0.55 to 0.8 the biggest difference between both of the models is noticed.

5.1. Schnerr & Sauer model incipient cavitation period

The bubbles start to form near the leading edge (Fig.8. a and b). Then they grow until 11 ms (Fig.8 d-e), the cavitation occupies all the upper side of the foil. Next the structures break in parts from rear region to leading edge. (Fig.8. e–h). Highly unsteady flow near the trailing edge is observed. When water breaks up to the foil and clings to it, the bubbles are pushed off the wall and they disappear (Fig.8. i-l). The new cavitation structure is formed. The period is equal to about 30 ms. That is longer than it was observed during the experiment [8].

5.2. Kunz model incipient cavitation period

As in case of calculation with Schnerr & Sauer model the bubbles of vapour start to form from leading edge of the foil. Then they grow but in different way than in previous case. The unsteady region on the upper side of the foil can be observed (Fig.9. b-c). The oval shape structure is attached to the upper wall of the foil (Fig.9. d). The structure changes the shape to sharp, then it detach from the foil (Fig.9. g). The vapour bubbles eventually collapse outside the foil (Fig.9. h-j). The new cavitation form is growing (Fig.9. l). The period is about 28 ms.

6. RESULTS SHEET CAVITATION

After lowering pressure to 72000 Pa the cavitation number drops to 1.4. The different flow regime is distinguished, which is called sheet cavitation. More cavitating vortex pairs appear and number of bubbles in vortex increase [8]. The

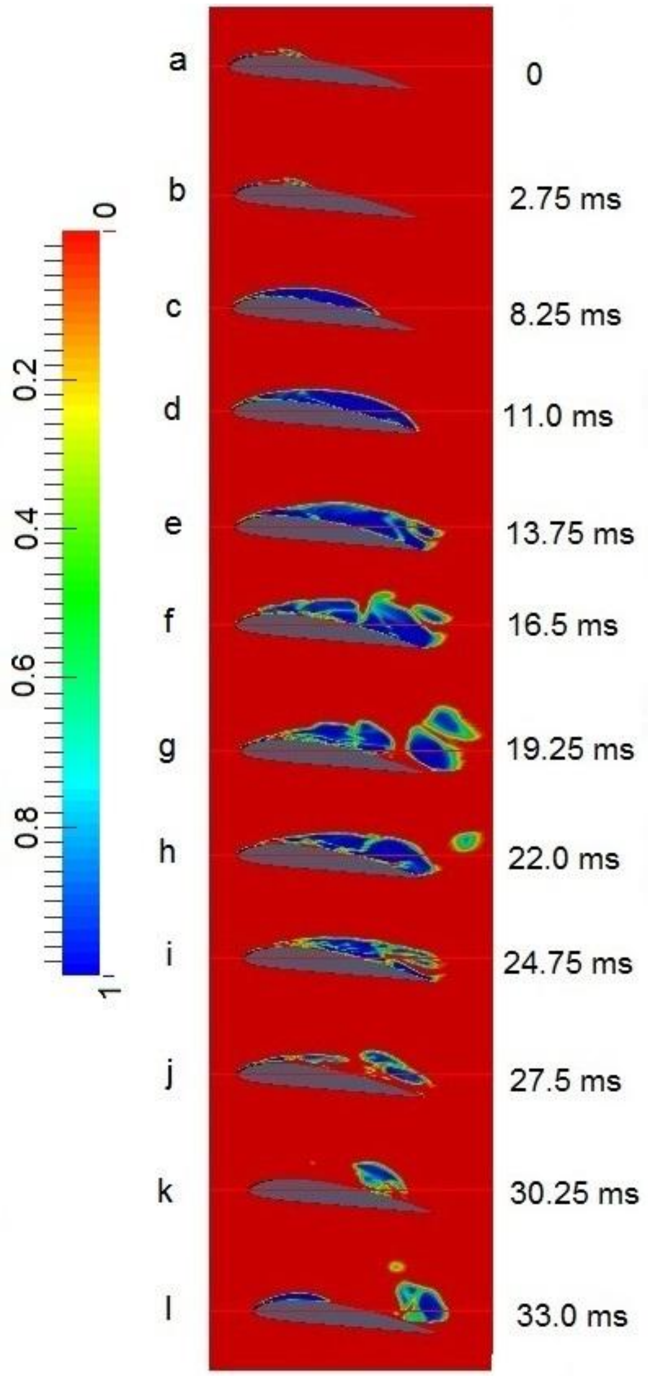

Figure 8. One period of incipient cavitation, Schnerr & Sauer model

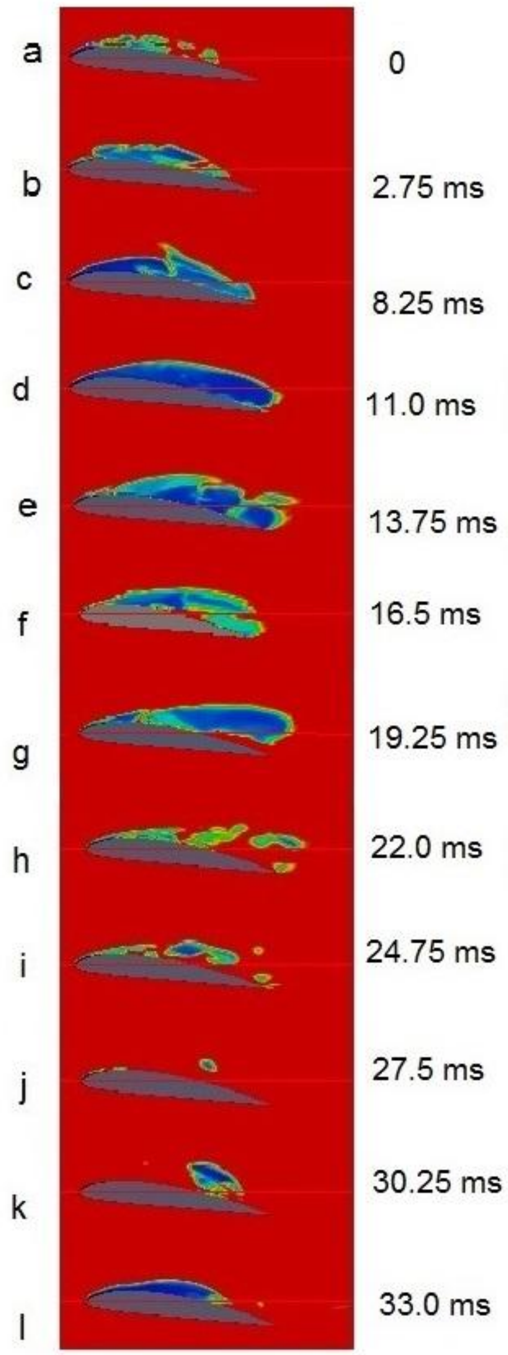

Figure 9. One period of incipient cavitation, Kunz model

frequency of changes is about 200 Hz (period 5 ms). In Figures 10. and 11. the time – averaged pressure distributions and time – averaged vapour volume fraction distributions are compared for both models.

As in case of incipient cavitation the pressure on the lower side of the foil is the same for Kunz model and for Schnerr & Sauer model. For all of the upper side of the foil pressure obtained from Schnerr & Sauer model exceeds the one obtained from Kunz model. For Kunz model the pressure distribution can be divided into two stages: the one from beginning of the foil to chord equal to 0.4 and the other from chord 0.4 to the end of the foil. For the first one the pressure is very low and does not change a lot. For second one, the pressure rises roughly. It can be explained on basis of Figure 13., where one period of sheet cavitation obtained from Kunz model is shown. In fig.13i the remarkable split into two cavitation structure can be noticed.

The location of the split correspond with the change of pressure distribution trend.

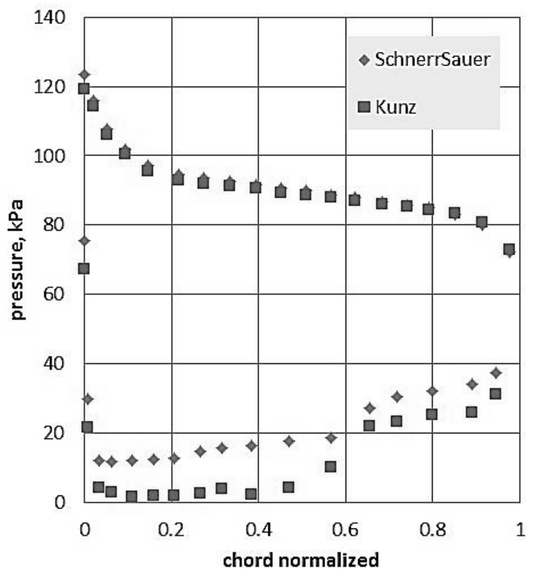

Figure 10. Time-averaged pressure distribution for different models. Sheet cavitation

The distribution of vapour volume fraction for Schnerr & Sauer model for upper side of the flow grows from chord 0 to chord about 0.15, where it reaches the maximum equal to 0.8.

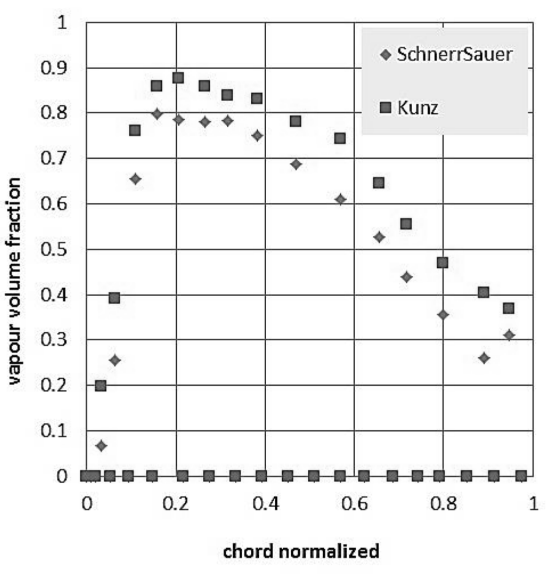

Figure 11. Time-averaged vapour volume fraction distribution for different models. Sheet cavitation

Then the vapour structures shrinks and the vapour volume fraction lowers consequently until the end of the foil. The distribution of vapour volume fraction for Kunz is higher than for Schnerr & Sauer model. The maximum value of vapour volume fraction is noticed at chord 0.2 and it is equal to 0.88. That is remarkably higher than in case of incipient cavitation. From this chord until the end of the foil the value of vapour volume fraction lowers. Both distributions have shape of a hill. At the end of the foil the pressure obtained from two models coincide.

6.1. Schnerr & Sauer model sheet cavitation period

The period of sheet cavitation calculated with Schnerr & Sauer model is placed in Figure 12. The cavitation forms as in incipient cavitation, near the leading edge of the foil (Fig.12 c). Then it grows consequently to about ¾ of chord length (Fig.12. e). Simultaneously, the cavitation bubble near the trailing edge forms and eventually collapse (Fig.12. b–e). The cavitation bubble attached to the upper side of the foil shrinks (Fig.12. f-h) to about half of the chord. Then it enlarges again and occupied whole of the upper side of the foil (Fig.12. j). The unsteady rear region is noticed, the break of cavity structure occurs there (Fig.12. l-o). The water starts to move upwards the foil, and occupies most of the upper side of the foil (Fig.12 p). Finally the cavitation bubbles collapse and disappear, the cycle starts all over again (Fig.12. r). The period of changes is equal to about 40 ms, which is much more than during the experiment [8].

6.2. Kunz model sheet cavitation period

In case of Kunz model the process of creating and growing the cavitation bubble occurs in much more unsteady way. The period of changes is shown in Fig.13. The end of previous cycle is captured in Fig.13. a. The cavitation bubbles form near the leading edge (Fig.13. b) and they grow until 11 ms (Fig.13. e), reaching the ¾ of the chord length. Then structure starts to decompose, first the number of bubbles reduces from about half of the chord (Fig.13. f), then unsteady region near the trailing edge is noticed. Eventually the cavitation structure splits into two (Fig.13. i) smaller cavitation clouds. The one closer to leading edge shrinks remarkably within 5.5 ms (Fig.13. j-l), the other one attached to the rear region of the foil gets smaller more slowly and within next 11 ms disappear (Fig.13. m). At the same time the new structure is forming near the leading edge. The period of changes in this case is about 33 ms, which is less than in case of Schnerr & Sauer model, but still remarkably more than during the experiment [8].

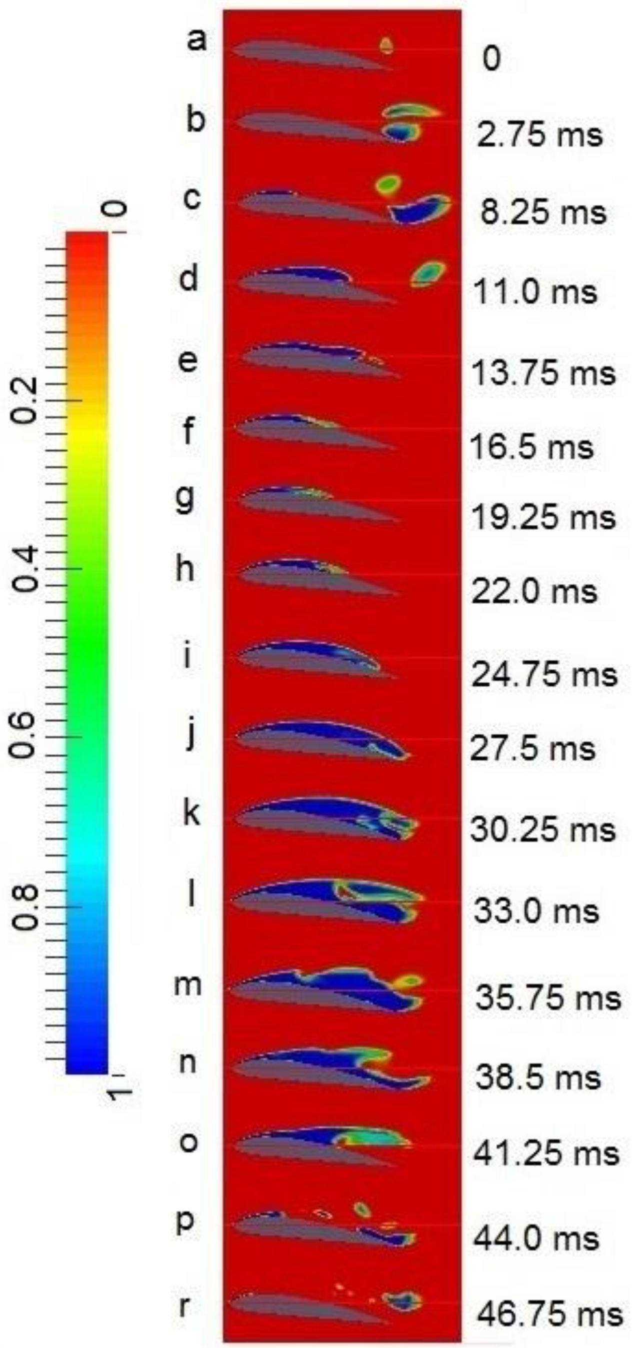

Figure 12. One period of sheet cavitation, Schnerr & Sauer model

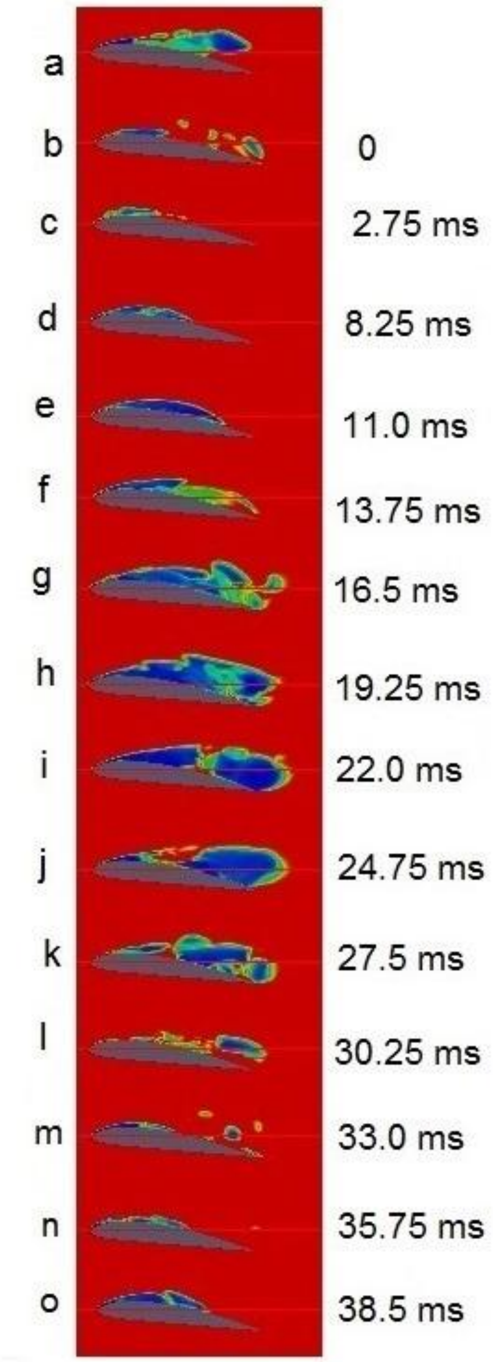

Figure 13. One period of sheet cavitation, Kunz model

7. SUMMARY

In article the two popular models of cavitation were investigated: namely Kunz and Schnerr & Sauer. For both models calculations were performed using interPhaseChangeFoam solver of OpenFOAM code. At first the grid independence study was performed. The grids varied from each other by number of grid cells as well as cells distribution on the upper side of the foil, where major changes of cavitation structures take place. The grid independence study was done at boundary condition which refers to cavitation number equal to 2. This enabled developing cavitation clouds. After choosing the grid, the calculations started. The investigated flow regimes were incipient and sheet cavitation, which are characterized by cavitation number 1.6 and 1.4. For both models the cyclic changes of cavitation structures were observed.

They are different for both models. In case of incipient cavitation the time – averaged pressure distributions on the lower side of the foil are similar for both models, but the time – averaged vapour volume fraction distributions show that in case of Kunz model the values of this parameters are higher than in case of Schnerr & Sauer model. When lowering pressure to corresponding cavitation number equal to 1.4, the sheet cavitation flow regime was observed. For this case, the time – averaged pressure distributions show differences comparing two models. For Kunz model the pressure is lower and has different tendency. It can be noticed that for this model the division of the cavitation structure occurs. The time – averaged vapour volume fraction distributions for Schnerr & Sauer model and for Kunz model have shape of a hill – they grow, reach the maximum and then evenly slides. Comparing the changes of cavitation structures, in case of Shnerr & Sauer model, the growth of vapour bubbles and break of cavitation structure near the trailing edge are well noticeable. In case of Kunz model the dynamics is slightly different. The cavitation structure split into two parts, and both cavitation bubbles collapse separately.

After the calculation it can be state that interPhaseChangeFoam solver captures the dynamics of cavitating flow sufficiently. The investigation shows that there are discernible differences between the results obtained when using different models of cavitation. For both models the period of changes was over predicted in case of incipient, as well as in case of sheet cavitation. For Kunz model the period was generally shorter than for the Schnerr & Sauer model. The cause of this will be further investigated in the future. The investigation indicates that there still are some improvements of the model that are needed to implement, so that the mathematical model corresponds to the experiment data as good as possible. The further research, including next cavitation flow regimes and comparison of such parameters as drag and lift force are planned.

REFERENCES

[1] Puffary, B., 2006, “Numerical Modelling of Cavitation”, *Design and Analysis of High Speed Pumps*

[2] Kunz, R., 2000, “A preconditioned Navier-Stokes method for two-phase flows with application to cavitation prediction”, *Computers & Fluid* Vol 29 p. 849-875

[3] Roohi, E., Zahiri, A. P. and Pasandideh-Fard, M., 2012, “Numerical Simulation of Cavitation around a Two – Dimensional Hydrofoil Using VOF Method and LES Turbulence”, *Proceedings of the Eight International Symposium on Cavitation (CAV 2012)*

[4] Bensow, R. E., Bark, G., 2010, “Simulating cavitating flows with LES in OpenFOAM”, *5th European Conference On Computational Fluid Dynamics*

[5] Brennen, C. E., 1995, *Cavitation and Bubble Dynamics*, Oxford University Press

[6] Schnerr, G. H., Sauer, J., 2001, “Physical and Numerical Modelling of Unsteady Cavitation Dynamics”, *Fourth International Conference on Multiphase Flow*, New Orleans, Louisiana

[7] Gosset, A., Diaz Casas, V. and Lopez Pena, F., 2010, “Evaluation of the CavitatingFoam Solver for Low Mach Number Flow around a 2D Hydrofoil”, *Fifth OpenFOAM Workshop*, Gothenburg, Sweden

[8] Wang, G., Senocak, I., Shyy, W., Ikohago, T., and Cao, S., 2001, *Dynamics of attached turbulent cavitating flows*, Progress in Aerospace Sciences 37 p. 551 - 581

[9] Wang, G., Zhang, B., Huang, B. And Zhang, M., 2009, “Unsteady Dynamics of Cloud Cavitating Flows around a Hydrofoil”, *Proceedings of the Seventh International Symposium on Cavitation CAV2009*, Ann Arbor, Michigan, USA.

[10] Li, Z., Pourquie, M., Van Terwisga, T., 2010, “A numerical study of steady and unsteady cavitation on a 2D hydrofoil”, *9th International Conference on Hydrodynamics*, Shanghai, China, *Journal of Hydrodynamics*, vol.22(5), supplement:770-777

[11] Li, D. Q., Grekula, M., Lindell, P., 2009, “A modified SST k-ω Turbulence Model to Predict the Steady and Unsteady Sheet Cavitation on 2D and 3D Hydrofoils”, *Proceedings of the Seventh International Symposium on Cavitation CAV2009*, Ann Arbor, Michigan, USA.

[12] Huang, B., Wang, G., 2011, “Partially averaged Navier-Stokes methods for time-dependent turbulent cavitating flows”, *Journal of Hydrodynamics*, Vol.23(1):26-33

[13] Li, D. Q., Grekula, M., Lindell, P., 2010, “Towards numerical prediction of unsteady sheet cavitation on hydrofoils”, *9th International Conference on Hydrodynamics*, Shanghai, China, *Journal of Hydrodynamics*, vol.22(5), supplement:741-746

[14] Arndt, E. A., 2012, “Some Remarks on Hydrofoil Cavitation”, *Journal of Hydrodynamics*, Vol(24)3: 305-314

Conference on Modelling Fluid Flow (CMFF'15)
The 16th International Conference on Fluid Flow Technologies
Budapest, Hungary, September 1-4, 2015

BLOOD FLOW ANALYSIS IN A RUPTURED INTRACRANIAL ANEURYSM: A LONG TERM STUDY

Philipp BERG[1], Oliver BEUING[2], Gábor JANIGA[3]

[1] Corresponding Author. Lab. of Fluid Dynamics and Technical Flows, University of Magdeburg "Otto von Guericke", Universitaetsplatz 2, Magdeburg D-39106, Germany, Tel.: +49 391 67 181 95, Fax: +49 391 67 128 40, E-mail: berg@ovgu.de
[2] Institute for Neuroradiology, University Hospital Magdeburg, E-mail: oliver.beuing@med.ovgu.de
[3] Lab. of Fluid Dynamics and Technical Flows, University of Magdeburg "Otto von Guericke", E-mail: janiga@ovgu.de

ABSTRACT

Intracranial aneurysms are dilatations of the arterial vessel wall, which are prone to rupture and can lead to sudden death or strong disabilities. Unfortunately, reliable criteria explaining growth and rupture have not been identified yet.
To improve our knowledge regarding these mechanisms, the blood flow in a patient-specific ruptured intracranial aneurysm is analysed based on three image sequences that were acquired within 41 months. The 3D-reconstructions allow a longitudinal quantification of the volumetric growth and the assessment of areas with highest morphological change. Afterwards, computational fluid dynamics were used to characterise flow parameters, which are known to induce pathophysiological processes in cerebral vessel walls.
The numerical computations identified areas of abnormally low wall shear stress in regions of highest volume increase. Additionally, elevated oscillatory shear was found at the suspected rupture site, confirming findings of previous studies. However, the analysis of the pressure distribution revealed no significant impact on growth or rupture of the aneurysm. This longitudinal investigation demonstrates how the hemodynamics within an intracranial aneurysm change after more than three years of morphological adjustment. Therefore, this deeper understanding helps to improve the computational approach and strengthens the methodology towards a better reliability of the numerical results in the future.

Keywords: Cerebral aneurysm, rupture, blood flow, long-term follow-up

NOMENCLATURE

$AWSS$	$[Pa]$	averaged wall shear stress
OSI	$[-]$	oscillatory shear index
p	$[mmHg]$	pressure
WSS	$[Pa]$	wall shear stress

Subscripts and Superscripts

CFD	computational fluid dynamics
DSA	digital subtraction angiography
ICA	internal carotid artery
PICA	posterior inferior cerebellar artery
PC-MRI	phase-contrast magnetic resonance imaging

1. INTRODUCTION

Intracranial aneurysms are dilatations of the arterial vessel wall and are estimated to occur in 2-6% of the western population [1]. Approximately 0.1% of these people experience the catastrophic event of a rupture leading to a subarachnoid hemorrhage. Up to 50% of the patients die within 30 days after rupture of an aneurysm, and approximately 1/3 of those who survive exhibit severe, irreversible disabilities. Therefore, a patient-specific treatment is required, but unfortunately, the process of vessel wall remodelling is yet little understood. In particular, reliable rupture criteria are essential but have not been identified until now.

In order to investigate the haemodynamics in the human vasculature, well established numerical methods were applied. Especially computational fluid dynamics (CFD) was used to describe the blood flow in intracranial aneurysms and the number of related publications increased enormously during the last two decades.

The most extensive studies were carried out by Xiang et al. [2] and Cebral et al. [3], whereby partly contradicting conclusions have been drawn. The first study analysing 119 aneurysms significantly correlated the event of a rupture with low wall shear stress (WSS) as well as high oscillatory shear (OSI). In contrast, the evaluation of the other database (210 aneurysms) revealed that high WSS in combination with a concentrated inflow jet might have caused rupture. Only the presence of a complex flow structure in ruptured aneurysms was found in both studies. Other computational studies containing much smaller numbers of aneurysms either confirmed the previous findings or identified other flow-based parameters, which are supposed to be responsible for vessel wall remodelling [4].

Since in all computational studies numerous assumptions are still needed to describe the flow with a reasonable temporal and computational effort and since the parameters causing rupture are still controversial, the acceptance of CFD is still rather limited among physicians [5]. Hence, more reliable analyses are required containing additional information regarding the progression of the disease.

In contrast to these cross-sectional studies, longitudinal investigations are extremely rare since aneurysms usually remain undetected or are getting treated soon after detection. Acevedo-Bolton et al. [6] observed the growth of an intracranial aneurysm over four years. Using CFD they concluded that aneurysm growth likely occurs in regions of abnormally low wall shear stress. However, the image data were acquired using phase-contrast magnetic resonance imaging (PC-MRI), which may introduce optical artifacts or blurred images due to the limited resolution. Another study that compared aneurysm growth of seven patient-specific aneurysms based on MRI sequences confirmed the previous findings [7]. Low WSS was also correlated with regions of strongest aneurysm growth.

To improve our knowledge regarding aneurysm development, growth and rupture, the blood flow in a ruptured patient-specific intracranial aneurysm is analysed in the present work based on three different image sequences. The time span of 41 months documents the growing process and the attending physician detected the rupture site after the final imaging.

Three-dimensional reconstructions allow the quantification of the volumetric growth and in particular the assessment of areas with highest morphological change. Afterwards, a fine spatial and temporal discretization of the reconstructions enables the computation of characteristic flow parameters using CFD. Hence, the effect on pathophysiological processes in cerebral vessel walls can be investigated and possible triggers may be identified that caused the growth and finally the rupture of this cerebral malformation.

2. MATERIALS AND METHODS

2.1. Case description

A 61-year-old female underwent routine follow-up MRIs after subarachnoid haemorrhage and clipping of two middle cerebral artery aneurysms in 1993. In February 2011 two de-novo aneurysms at the right posterior inferior cerebellar artery (PICA) and the left internal carotid artery (ICA) were detected. The PICA-aneurysm was treated with coil embolization. The second aneurysm was not suited for endovascular coiling, as the posterior communicating artery developed from the aneurysm sac with a broad base and the circle of Willis was incomplete with absence of a P1-segment on the left side. Surgery was recommended, but not performed. A control DSA (Digital Subtraction Angiography) 5 months later showed no changes in size or shape of the untreated aneurysm. The patient was lost to further follow-up, until she presented with acute subarachnoid haemorrhage due to rupture of the untreated ICA-aneurysm in July 2014. Emergency DSA demonstrated a significant growth of the aneurysm, which was treated with surgical clipping afterwards. The patient recovered well with no neurologic sequelae. Figure 1 illustrates two representative DSA images of the first (2011) and the last (2014) scan, respectively.

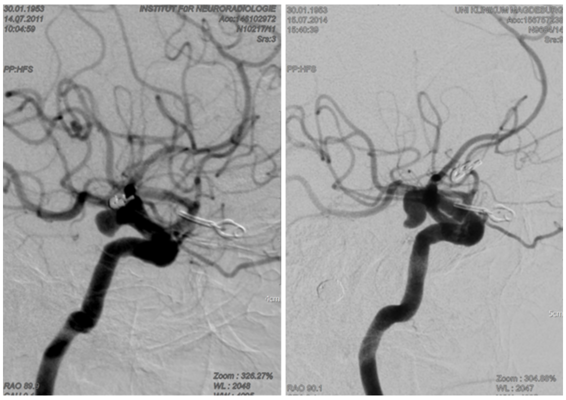

Figure 1. Initial (left) and third (right) digital subtraction angiography of the investigated intracranial aneurysm. The time span between both acquisitions is 41 months and the growth of the dilation is clearly visible in the 2D projection

2.2. Vascular reconstruction

The image acquisition was carried out using 3D-DSA with a Siemens scanning device. The segmentation as well as the reconstruction of the investigated aneurysm models was performed with MeVisLab 2.3 (MeVis Medical Solutions AG, Bremen, Germany). In this context, the three-dimensional surface models were obtained by applying a seeded region-growth algorithm. Afterwards, visual artifacts such as melted arteries or small holes in the geometry were manually corrected using Blender 2.68a (Stichting Blender Foundation, Amsterdam, The Netherlands). Finally, Taubin-smoothing was applied on the discrete surface meshes to ensure a more realistic representation [8, 9]. To guarantee plausible results of the reconstructed aneurysm models, the virtual geometries were reviewed by a local neuroradiologist. Figure 2 illustrates the investigated cases, which represent the stage at initial presentation of the patient in the hospital (1), a 5 months follow-up scan (2) as well as the image acquisition after rupture (3).

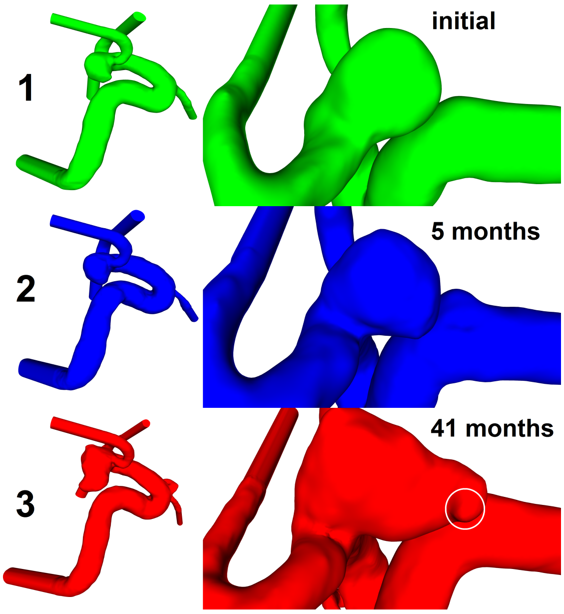

Figure 2. Three-dimensional reconstructions of the patient-specific aneurysm model for three different stages: 1) initial presentation in the hospital, 2) 5 months follow-up, 3) rupture of the aneurysm after 41 months (the white circle indicates the presumed rupture site)

2.3. Spatial discretization

The reconstructed aneurysm surfaces were spatially discretized using ANSYS ICEM-CFD 14.5 (Ansys Inc., Canonsburg, PA, USA). Tetrahedral as well as prismatic elements were generated and local refinement was applied in regions of high curvature, e.g., the aneurysm neck. In order to resolve the velocity gradients close to the arterial wall, four prism layers were inserted in each case with an initial height of 0.1 mm and a growth ratio of 1.2 was defined. The resulting meshes that were finally used for the hemodynamic simulations consisted of approximately 2.1 million elements for case 1, 2.2 million for case 2 and 1.9 million elements for case 3, respectively. Previous studies showed that mesh-independent solutions are achieved at this level of refinement [10, 11].

2.4. Haemodynamic simulation

For the haemodynamic simulations the integral formulation of the governing equations for continuity and momentum conservation were solved with the commercial software package ANSYS Fluent 14.5 (Ansys Inc., Canonsburg, PA, USA). Blood was considered to be an isothermal, incompressible (ρ = $1055 kg/m^3$) and Newtonian ($\eta = 4 \cdot 10^{-3}\ Pa \cdot s$) fluid. Although blood is a representative of non-Newtonian fluids and the viscosity can show a strong shear-dependency, a comparison with the typically used Carreau-Yasuda model showed no significant difference in the velocity profiles for the present range of vessel diameters.

Due to the lack of case-specific boundary conditions, time-dependent flow rates extracted from a PC-MRI measurement at the left internal carotid artery were implemented. The corresponding Reynolds numbers varied between 304 and 548 with an average of Re = 432. The time-dependent values of the PC-MRI measurement were extracted from the raw image data using EnSight 9.2 (CEI Inc., Apex, NC, USA) and a post-processing tool developed by Stalder et al. [12]. Figure 3 contains the corresponding flow curve that was used for the haemodynamic simulations of the three cases. To ensure a fully-developed velocity profile within the investigated fluid domains, each inlet has been extruded by five times of the corresponding mean diameter in advance [13].

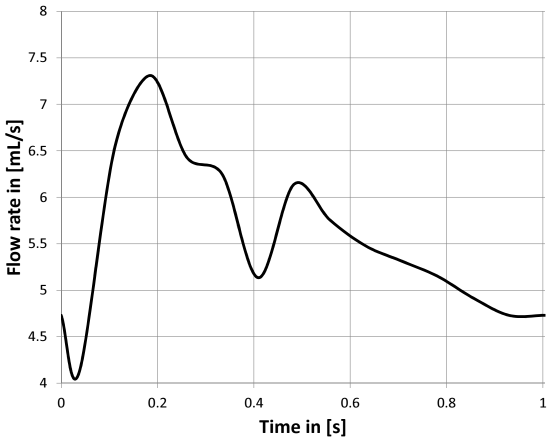

Figure 3. Measured PC-MRI flow rate curve that was applied to the inlet section of each reconstruction of the internal carotid artery

Although intracranial vessel walls consist of flexible soft tissue, the vessel walls were assumed to be rigid for every case and no-slip boundary conditions were defined. This assumption is caused by the lack of appropriate vessel wall properties. If fluid-structure interactions (FSI) are considered in future studies, accurate wall properties must become measurable [14].

For all outlets an area-dependent mass flow weighting was defined throughout the cardiac cycle. This approach was chosen due to the lack of knowledge regarding the pressure variation in the different vessel branches.

In order to calculate the existing velocity fields within the domains, a pressure-implicit algorithm (PISO) was used for all transient simulations. A constant time step size was chosen as $1 \cdot 10^{-4}$ s leading to approximately 10 000 time steps per cardiac cycle (period time T = 1.01 s). Three cardiac cycles were simulated for each case. Only the last was finally analysed discarding the first two. The accuracy of the spatial as well as the temporal discretization was defined to be second order. Convergence was obtained when the scaled residuals decreased below a value of 10^{-5} within each time step. Due to the high number of elements and the small time steps the computational domains have been decomposed in advance in order to simulate in parallel. All simulations were carried out on 8 CPUs.

2.5. Analysis

The analysis of the investigated cases is divided into morphological as well as haemodynamical changes.

2.5.1. Morphological change

To characterize the growth of the vascular dilatation the aneurysm was dissected from the parent vessel in each stage. Afterwards, the corresponding surfaces as well as the volumes were calculated and compared with each other.

2.5.2. Haemodynamic parameters

For the analyses of blood flow effects, common haemodynamic parameters that are known to influence the inner surface of the cerebral vessels are computed. As introduced in 'Eq. (1)' WSS is temporally averaged over one cardiac cycle (AWSS).

$$AWSS = \frac{1}{T}\int_0^T |WSS| \cdot dt \tag{1}$$

Additionally, the temporal changes of the wall shear stress directions are considered using the oscillator shear index (OSI). 'Eq. (2)' introduces the corresponding computation [15].

$$OSI = \frac{1}{2}\left(1 - \frac{|\int_0^T WSS \cdot dt|}{\int_0^T |WSS| \cdot dt}\right) \tag{2}$$

Finally, the relative pressure distribution averaged over one heartbeat is analysed to identify possible regions of increased load on the vessel wall. Here, the reference pressure was set to zero at one outlet the calculate the relative values on the whole vessel surface.

3. RESULTS

3.1. Morphological change

Figure 4 contains the direct comparison of the three-dimensional reconstructions. To improve the visibility opaque as well as transparent representations were chosen. Additionally, the morphological change between two stages and between all three stages is considered, respectively.

The first two sequences reveal that almost no spatial differences are present. The scan after five months (blue) shows only a marginal change in the width of the aneurysm compared to the initial imaging (green). Simultaneously, the distance between the ostium (interface between the aneurysm sack and the healthy parent artery) and its opposite area decreases leading to a smaller height of the dilation. However, the calculation of the morphologically relevant parameters such as aneurysm surface area and volume (see Table 1) reveals no clear difference. Both parameters are approximately identical indicating no growth of the intracranial aneurysm.

The comparison between stages 2 and 3 that represents a time span of three years shows a different behaviour. Clear morphological changes are visible and a considerable growth of the malformation can be noticed. The surface area almost doubles and the volume of the corresponding reconstruction scales by a factor of more than two. Interestingly, the height of the aneurysm remains nearly the same compared to both previous sequences and the aneurysm sack is growing mostly in width. Additionally, a small blister-like region develops at the highest distance to ostium. Such a bleb formation was often observed at intracranial aneurysms and is known to be prone to rupture due to their extra thin wall thickness [16].

Table 1. Morphological parameters of the aneurysm at three stages

Case	Area [mm^2]	Volume [mm^3]
1	128	120
2	130	121
3	247	243

3.2. Haemodynamic parameters

Due to the morphological change between the investigated stages the haemodynamical flow experiences deviations as well. This leads to different flow situations and in consequence to different loads on the corresponding inner wall of the aneurysm.

Figure 5 shows the time-averaged wall shear stress AWSS for the three cases as representatives of the analysed cardiac cycle. As commonly known, normal as well as high shear values are mostly present at the parent vessel proximal and distal to the aneurysm. Additionally, elevations can be noticed at the dome area of the aneurysm opposite to the ostium. Here, the entering blood flow impinges on the inner vessel wall and gets directed along the spherical shape. In contrast to these observations, the lowest AWSS values are present proximal to the siphon of the internal carotid artery and, most interestingly, along the sides of the aneurysm. These areas were previously identified as zones of strongest growth.

The computation of the oscillatory shear index is illustrated in Figure 6. Only a few areas exhibit high

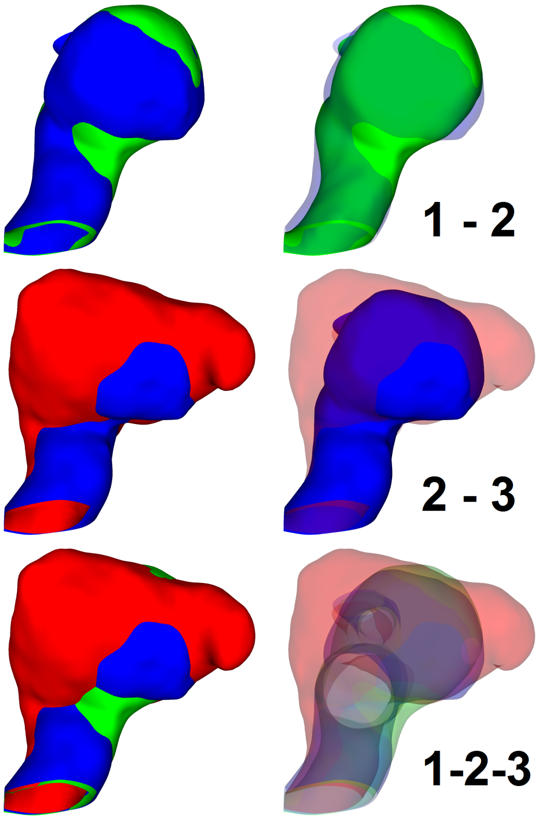

Figure 4. Morphological change of the aneurysm surface between the stages 1 (green), 2 (blue) and 3 (red): opaque (left), transparent (right)

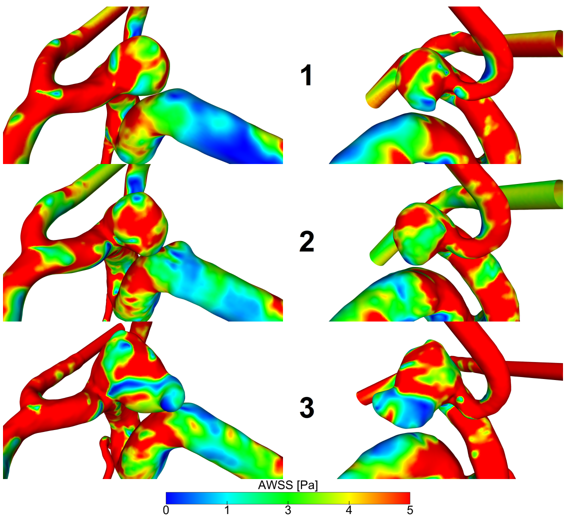

Figure 5. Cycle-averaged wall shear stress (AWSS) of the three stages from two different perspectives

values indicating elevated changes of the wall shear stress directions.

The initial stage of the aneurysm shows increased values along the parent internal carotid artery and some minor spots distributed distal to aneurysm. Furthermore, a slightly higher OSI can be noticed at the tip of the aneurysm.

In contrast, nearly no signs of an increased OSI are present for stage 2 and due to the spherical shape the aneurysm shows nearly no oscillatory shear.

However, the third stage exhibits high OSI values along the part of the aneurysm that grew within the intermediate three years. These high values are caused by the irregular shape of the dilatation and are located at the possible rupture site.

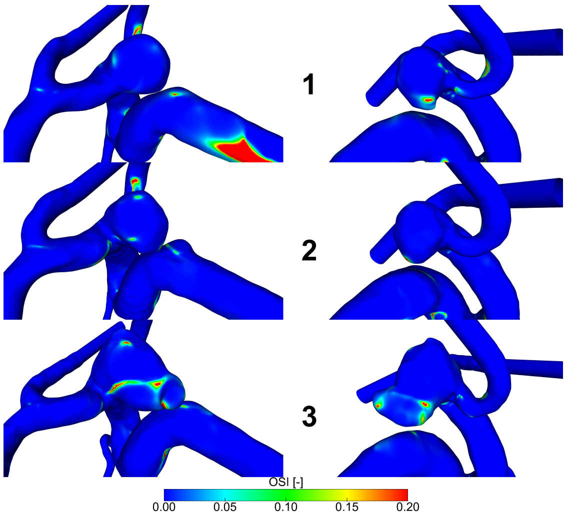

Figure 6. Oscillatory shear index (OSI) for the three stages from two different perspectives

In addition to the velocity-based haemodynamic parameters, the pressure distribution on the considered vessel region was analysed (see Figure 7). The illustrated relative pressure was averaged for one cardiac cycle and represents the temporal mean load on the inner vessel surface.

As previously described, the blood flow enters the aneurysm with a concentrating inflow jet that impinges on the opposite side of the ostium. In this region, increased pressure is visible and the area of elevated load even increases from case to case. In contrast, smaller pressure values are present in regions where the biggest volume increase was identified. However, the considered range of the relative pressure difference is very small indicating that only minor pressure differences exist throughout the whole aneurysm surfaces.

4. DISCUSSION

The number of computational studies that investigate the haemodynamics in intracranial aneurysms increased drastically within the last two decades. Unfortunately, the enthusiasm in the beginning turned into a slight depression since the essential mechanisms such as initiation, growth and rupture of this vascular disease are still poorly understood. Reasons for that trend are numerous assumptions, which are required for the simulations, and the absence of

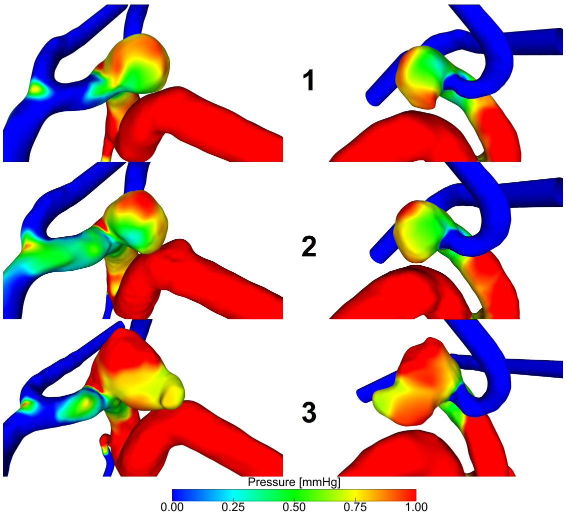

Figure 7. Cycle-averaged relative pressure of the three stages from two different perspectives

precise in vivo measurements of the patient-specific morphological and haemodynamical situation.

Additionally, global conclusions and responsible parameters are drawn from only single aneurysm studies and partly the numerical methods are ironically described as 'Colour For Doctors' or 'Confounding Factor Dissemination' [5]. In order to overcome these doubts and to strengthen the capability of numerical methods related to vascular diseases, this study contributes a valuable analysis to the community. Due to its longitudinal character, including three different stages of an aneurysm development, more reliable conclusion can be derived compared to single stage investigations. The analysis of the volume increase revealed that the growth mostly occurred along the sides of the aneurysm and not, as one could expect, at the impingement zone of the entering inflow jet. This observation confirms the suspicion that a vessel wall experiencing a certain load strengthens in order to resist against this force. In contrast, regions of the dilatation beside the impingement area remodelled, which leads to the assumption that a certain load on the inner vessel surface is required in order to maintain stability. Consequently, computational methods might be used in the future to evaluate the growing risk of a certain aneurysm based on the level of wall shear stress. However, further quantifications are required to identify concrete absolute or relative values. Furthermore, other longitudinal studies need to be carried out including a higher number of cases and the consideration of local wall properties.

The same improvements of the computational models are required for the rupture risk assessment. Although increased oscillatory shear was detected at the suspected rupture site, one cannot argue that this haemodynamic parameter is capable of predicting rupture. However, beside this evaluation, an extensive study by Xiang et al. [15] as well as the International Rupture-Challenge 2013 [17] identified indications that correlate the event of a rupture with OSI.

The pressure analysis also shows clear differences on the aneurysm surface, but since the absolute deviations are very small compared to those along the parent artery, conclusions regarding the effect of pressure should not be drawn. Nevertheless, this study contributes to the improvement of knowledge regarding the question, why intracranial aneurysms grow and in which direction this growth is oriented. With increasing accuracy of the numerical models, a standardisation of the computations as well as an easier applicability, using automated methods, CFD can become a valuable tool with clinical relevance. Especially, due to the risk-free analyses, physicians can evaluate the status of a detected aneurysm and hence be supported during the patient-specific therapy planning.

Although the haemodynamic simulations consider patient-specific reconstructions of the intracranial aneurysm, several assumptions are required in order to handle the computational and temporal effort and receive numerical results in a reasonable time.

Firstly, the three-dimensional reconstructions are carried out with a threshold-based segmentation method. Hence, minor deviations to the real geometry are possible, which may also be caused by optical artefacts of the different imaging data. However, the same experienced person carried out all three reconstructions, which decreases the subjective error.

Secondly, the walls are assumed to be rigid and no flexibility is taken into account. Although the local wall thickness is expected to have a significant impact on the rupture probability, numerical modelling of the corresponding regions without the presence of reliable and precise measurements is expected to be needless. Different studies already considered fluid-structure-interactions in intracranial aneurysms but mostly constant wall thicknesses and an isotropic material behaviour were assumed [18, 19, 20].

Thirdly, patient-specific inflow boundary conditions that represent the flow situation during the image acquisition were not available. Therefore, highly resolved time-dependent flow rates, which were measured using a 7 Tesla PC-MRI, were applied to the corresponding inflow cross-section at the internal carotid artery [21].

5. CONCLUSIONS

This study analysed the morphological as well as the haemodynamical change of a ruptured intracranial aneurysm and its blood flow, respectively. Based on three image datasets that were acquired within a time frame of 41 months, possible causes of the wall remodelling and the rupture could be identified.

Especially in regions that experience abnormally low wall shear stress a volumetric increase was observed. This confirms previous findings and demonstrates that CFD methods can be used to predict endangered areas on the aneurysm surface. Furthermore, oscillatory shear was present at the suspected rupture site showing the possible relevance concluded by other groups.

Further analyses that characterize the internal haemodynamical flow behaviour will be carried out in the future. Therefore, unstable flow structures might be identified that were previously correlated with the event of a rupture.

ACKNOWLEDGEMENTS

This research is supported by a research grant of the "International Max Planck Research School (IMPRS) for Advanced Methods in Process and System Engineering (Magdeburg) ".

Additionally, the work of this paper is partly funded by the Federal Ministry of Education and Research within the Forschungscampus STIMULATE under grant number 13GW0095A.

The authors warmly acknowledge Timo Oster (University of Magdeburg) for his assistance regarding the registration of the three reconstructed datasets.

REFERENCES

[1] Bonneville, F., Sourour, N., and Biondi, A., 2006, “Intracranial aneurysms: an overview”, *Neuroimaging Clin N Am*, Vol. 16 (3), pp. 371–382.

[2] Xiang, J., Natarajan, S. K., Tremmel, M., Ma, D., Mocco, J., Hopkins, L. N., Siddiqui, A. H., Levy, E. I., and Meng, H., 2011, “Hemodynamic-morphologic discriminants for intracranial aneurysm rupture”, *Stroke*, Vol. 42 (1), pp. 144–52.

[3] Cebral, J. R., Mut, F., Weir, J., and Putman, C. M., 2011, “Association of Hemodynamic Characteristics and Cerebral Aneurysm Rupture”, *American Journal of Neuroradiology*, Vol. 32 (2), pp. 264–270.

[4] Chung, B., and Cebral, J. R., 2015, “CFD for Evaluation and Treatment Planning of Aneurysms: Review of Proposed Clinical Uses and Their Challenges”, *Ann Biomed Eng*, Vol. 43 (1), pp. 122–138.

[5] Kallmes, D. F., 2012, “Point: CFD-Computational Fluid Dynamics or Confounding Factor Dissemination”, *Am J Neuroradiol*, Vol. 33 (3), pp. 395–396.

[6] Acevedo-Bolton, G., Jou, L. D., Dispensa, B. P., Lawton, M. T., Higashida, R. T., Martin, A. J., Young, W. L., and Saloner, D., 2006, “Estimating the hemodynamic impact of interventional treatments of aneurysms: numerical simulation with experimental validation: technical case report”, *Neurosurgery*, Vol. 59 (2), pp. E429–30; author reply E429–30.

[7] Boussel, L., Rayz, V., McCulloch, C., Martin, A., Acevedo-Bolton, G., Lawton, M., Higashida, R., Smith, W. S., Young, W. L., and Saloner, D., 2008, “Aneurysm growth occurs at region of low wall shear stress: patient-specific correlation of hemodynamics and growth in a longitudinal study”, *Stroke*, Vol. 39 (11), pp. 2997–3002.

[8] Moench, T., Gasteiger, R., Janiga, G., Theisel, H., and Preirn, B., 2011, “Context-aware mesh smoothing for biomedical applications”, *Computers & Graphics-Uk*, Vol. 35 (4), pp. 755–767.

[9] Neugebauer, M., Lawonn, K., Beuing, O., and Preim, B., 2013, “Automatic generation of anatomic characteristics from cerebral aneurysm surface models”, *Int J Comput Assist Radiol Surg*, Vol. 8 (2), pp. 279–289.

[10] Berg, P., Janiga, G., and ThÃl’venin, D., 2012, “Detailed Comparison Of Numerical Flow Predictions In Cerebral Aneurysms Using Different CFD Software”, J. Vad (ed.), *15th Conference on Modelling Fluid Flow*, ISBN 978-963-08-4588-5, pp. 128–135.

[11] Janiga, G., Berg, P., Beuing, O., Neugebauer, M., Gasteiger, R., Preim, B., Rose, G., Skalej, M., and Thevenin, D., 2013, “Recommendations for accurate numerical blood flow simulations of stented intracranial aneurysms”, *Biomed Tech*, Vol. 58 (3), pp. 303–314.

[12] Stalder, A. F., Russe, M. F., Frydrychowicz, A., Bock, J., Hennig, J., and Markl, M., 2008, “Quantitative 2D and 3D Phase Contrast MRI: Optimized Analysis of Blood Flow and Vessel Wall Parameters”, *Magnet Reson Med*, Vol. 60 (5), pp. 1218–1231.

[13] Pereira, V. M., Brina, O., Gonzales, A. M., Narata, A. P., Bijlenga, P., Schaller, K., Lovblad, K. O., and Ouared, R., 2013, “Evaluation of the influence of inlet boundary conditions on computational fluid dynamics for intracranial aneurysms: A virtual experiment”, *J Biomech*, Vol. 46 (9), pp. 1531–1539.

[14] Alastruey, J., Parker, K. H., Peiro, J., Byrd, S. M., and Sherwin, S. J., 2007, “Modelling the circle of Willis to assess the effects of anatomical variations and occlusions on cerebral flows”, *J Biomech*, Vol. 40 (8), pp. 1794–805.

[15] Xiang, J., Tutino, V. M., Snyder, K. V., and Meng, H., 2014, “CFD: Computational Fluid

Dynamics or Confounding Factor Dissemination? The Role of Hemodynamics in Intracranial Aneurysm Rupture Risk Assessment", *Am J Neuroradiol*, Vol. 35 (10), pp. 1849–1857.

[16] Meng, H., Tutino, V. M., Xiang, J., and Siddiqui, A., 2014, "High WSS or Low WSS? Complex Interactions of Hemodynamics with Intracranial Aneurysm Initiation, Growth, and Rupture: Toward a Unifying Hypothesis", *Am J Neuroradiol*, Vol. 35 (7), pp. 1254–1262.

[17] Janiga, G., Berg, P., Sugiyama, S., Kono, K., and Steinman, D. A., 2014, "The Computational Fluid Dynamics Rupture Challenge 2013-Phase I: Prediction of Rupture Status in Intracranial Aneurysms", *Am J Neuroradiol*.

[18] Bazilevs, Y., Hsu, M. C., Zhang, Y., Wang, W., Liang, X., Kvamsdal, T., Brekken, R., and Isaksen, J. G., 2010, "A fully-coupled fluid-structure interaction simulation of cerebral aneurysms", *Comput Mech*, Vol. 46 (1), pp. 3–16.

[19] Lee, C. J., Zhang, Y., Takao, H., Murayama, Y., and Qian, Y., 2013, "A fluid-structure interaction study using patient-specific ruptured and unruptured aneurysm: The effect of aneurysm morphology, hypertension and elasticity", *J Biomech*, Vol. 46 (14), pp. 2402–2410.

[20] Valencia, A., Burdiles, P., Ignat, M., Mura, J., Bravo, E., Rivera, R., and Sordo, J., 2013, "Fluid Structural Analysis of Human Cerebral Aneurysm Using Their Own Wall Mechanical Properties", *Comput Math Methods Med*, article ID 293128, 18 pages.

[21] Berg, P., Stucht, D., Janiga, G., Beuing, O., Speck, O., and Thevenin, D., 2014, "Cerebral Blood Flow in a Healthy Circle of Willis and Two Intracranial Aneurysms: Computational Fluid Dynamics Versus Four-Dimensional Phase-Contrast Magnetic Resonance Imaging", *J Biomech Eng*, Vol. 136 (4).

Conference on Modelling Fluid Flow (CMFF'15)
The 16th International Conference on Fluid Flow Technologies
Budapest, Hungary, September 1-4, 2015

CFD Simulation on the Dynamics of a Direct Spring Operated Pressure Relief Valve

István Tamás ERDŐDI[1], Csaba HŐS[2],

[1] PhD student, Department of Hydrodynamic Systems, Budapest University of Technology and Economics. E-mail: ierdodi@hds.bme.hu
[2] Associate professor, Corresponding Author. Department of Hydrodynamic Systems, Budapest University of Technology and Economics. Műegyetem rkp. 3, H-1111 Budapest, Hungary. Tel.: +36 1 463 2216, Fax: +36 1463 3091, E-mail: hoscsaba@hds.bme.hu

ABSTRACT

This paper focuses on the estimation of the fluid force acting on the disc of a direct spring operated pressure relief valve (DSOPRV) under static and dynamic conditions. One possibility of modelling is to assume that the total fluid force can be computed by multiplying the static pressure difference between the upstream and downstream side of the valve with the so-called effective area function, which depends only on the valve opening. The advantage of this method is its simplicity and that the effective area function can be easily measured, however, it does not take into account transient effects. Another approach is to use an unsteady CFD model with rigid body dynamics included (this also assumes the use of deforming mesh/automatic remeshing technology), which resolves transient effects but is computationally expensive. The goal of this paper is to compare these two approaches. Results from the quasy-static computations show a good correspondence with the CFD runs, indicating that the simplifications behind the effective area concept are reasonable.

Keywords: CFD, fluid-structure interaction, linear stability, nonlinear vibrations, pressure relief valve

NOMENCLATURE

A_{eff}	$[m^2]$	effective area
A_{pipe}	$[m^2]$	cross-sectional area of the pipe
A_{ref}	$[m^2]$	reference area
C_D	$[-]$	discharge coefficient
D_{pipe}	$[m]$	diameter of the pipe
F	$[N]$	force
Re	$[-]$	Reynolds number
$\bar{e}$	$[-]$	relative opening
$\dot{m}$	$[kg/s]$	mass flow rate
e	$[J/kg]$	specific energy
k	$[Ns/m]$	damping coefficient
m	$[kg]$	reduced mass
p	$[Pa]$	static pressure
p_{set}	$[Pa]$	set pressure
s	$[N/m]$	spring stiffness
t	$[s]$	time
v	$[m/s]$	velocity
x	$[m]$	valve displacement
x_0	$[m]$	pre-compression of the spring
ω_0	$[Hz]$	natural frequency
κ	$[-]$	ratio of specific heats
ξ	$[-]$	damping ratio
ζ	$[m]$	deviation from the equilibrium opening
λ	$[-]$	Darcy friction factor
ρ	$[kg/m^3]$	density

Subscripts and Superscripts

CFD	CFD related variable
0	ambient
eq	at an equilibrium point
e	at the pipe end

1. INTRODUCTION

Pressure relief valves (PRVs) are used as the last line of defence against overpressure in industrial environments. There are two main parameters of these valves regarding their operation: the *set pressure* (p_{set}), which is the minimum pressure at which the valve opens, and the *capacity*, that is (by definition) the flow rate through the valve at full lift and at 110% of the set pressure. The latter describes how fast the overpressure can be reduced to the desired level and as such maintaining it is critical from a safety point of view. It is possible that under certain circumstances instabilities arise which reduce the capacity, endangering the whole system. The goal of this paper is to investigate the behaviour of a direct spring operated PRV in gas service with a focus on stability. This configuration consists of a disc pressed against the seat at the pipe end by a pre-compressed spring. The advantage of this simple design is that the set pressure can be easily adjusted through the pre-compression of the spring and the probability of mechanical failure can be kept at a minimal level due to the low number of moving parts. In order to avoid exceeding the time available for blowdown, adding any kind of artificial damping is forbidden by the current industrial standards [1].

Based on this, the valve disc can be modelled as a 1 DoF oscillator, which — due to the force acting on it— is described by a non-linear differential equation. This means that dynamic instabilities must be taken into account. The RP520 standard of the American Petroleum Institute distincts three different kinds of instabilities for the direct spring operated PRVs. The first one is the so-called *cycling*, during which the set pressure slowly builds up again and again after closing the valve, resulting in small frequency (< 1 Hz) vibrations. Contrary to this, both *flutter* and *chatter* are large frequency (> 10 Hz) self-excited vibrations — the difference between them is that during chatter the amplitude is so large that the disc usually impinges on the seat and upper stopper, resulting in not only a decrease in capacity but mechanical damage as well. Cycling is well-understood and means to avoid it are already included in the standards. However, the reasons behind flutter and chatter are not completely clear according to API, but it is mentioned that these are due to the acoustic coupling of the valve disc and the pipe end. Ongoing research activities aim to gain a better understanding of these phenomena [2, 3].

The goal of this paper is (a) to provide a steady-state CFD model for the evaluation of the force acting on the valve disc and the capacity, (b) to study the transient valve response by a deforming mesh CFD model and (c) to compare the results of unsteady CFD runs against simplified ODE (ordinary differential equation) model including quasy-steady fluid force characteristics.

2. THEORETICAL BACKGROUND

The system under analysis consists of a straight pipe section and the valve itself. The governing equations describing the behaviour of these components are derived in this section.

2.1. The valve disc dynamics

As stated before, the valve disc can be modelled as an oscillator:

$$m\ddot{x} + k\dot{x} + s(x + x_0) = F_{\mathrm{total}}(x, p_{\mathrm{e}}), \tag{1}$$

that can also be written as

$$\ddot{x} + 2\xi\omega_0\dot{x} + \omega_0^2(x + x_0) = \frac{F_{\mathrm{total}}(x, p_{\mathrm{e}})}{m}. \tag{2}$$

As of now both the damping and the total force are unknown. Here x_0 stands for the pre-compression of the springs, which is a constant parameter.

2.1.1. Modelling the force

The total force can be traced back to two physical phenomena — force acts both because of the pressure distribution on the disc and due to the change in the momentum of the out-flowing gas:

$$F_{\mathrm{total}} = F_{\mathrm{pres}} + F_{\mathrm{mom}}, \tag{3}$$

where the force from the pressure distribution is

$$F_{\mathrm{pres}} = A_{\mathrm{pipe}}(p_{\mathrm{e}} - p_0). \tag{4}$$

Unfortunately, F_{mom} cannot be calculated analytically as neither the velocity nor the direction of the outflow jet is known. A solution to this is to introduce the effective area, which supposes that the total force can be evaluated as a multiplication of the static pressure difference and an area function [2]:

$$F_{\mathrm{total}}(x, p_v) = A_{\mathrm{eff}}(x)(p_{\mathrm{e}} - p_0), \tag{5}$$

As there is no flow when the valve is seated (i.e. $x = 0$), the effective area for that position equals the cross-sectional area of the pipe, that is

$$A_{\mathrm{eff}}(x = 0) = A_{\mathrm{pipe}}. \tag{6}$$

Substituting the effective area into Eq. (2) gives

$$\ddot{x} + 2\xi\omega_0\dot{x} + \omega_0^2(x + x_0) = \frac{A_{\mathrm{eff}}(x)}{m}(p_{\mathrm{e}} - p_0). \tag{7}$$

It can be seen that this equation is indeed a non-linear ordinary differential equation. One of the goals of the stationary mesh CFD simulations presented later is to obtain the $A_{\mathrm{eff}}(x)$ function for the given PRV.

2.1.2. Stability of the linearized system

The first step in the linear stability analysis is finding the equilibria x_{eq} from Eq. (7), taking into account that $\dot{x}_{\mathrm{eq}} \equiv 0$ and $\ddot{x}_{\mathrm{eq}} \equiv 0$:

$$x_{\mathrm{eq}} = \frac{A_{\mathrm{eff}}(x)}{m\omega_0^2}(p_{\mathrm{e}} - p_0) - x_0. \tag{8}$$

Linearizing the effective area around this point results in

$$A_{\mathrm{eff}}(x) \approx A_{\mathrm{eff}}(x_{\mathrm{eq}}) + \left.\frac{\mathrm{d}A_{\mathrm{eff}}(x)}{\mathrm{d}x}\right|_{x=x_{\mathrm{eq}}}(x - x_{\mathrm{eq}}), \tag{9}$$

which can be substituted back into Eq. (7) to get

$$\ddot{x} + 2\xi\omega_0\dot{x} + \omega_0^2[(x - x_{\mathrm{eq}}) + x_{\mathrm{eq}} + x_0] = \frac{A_{\mathrm{eff}}(x_{\mathrm{eq}}) + \left.\frac{\mathrm{d}A_{\mathrm{eff}}(x)}{\mathrm{d}x}\right|_{x=x_{\mathrm{eq}}}(x - x_{\mathrm{eq}})}{m}(p_{\mathrm{e}} - p_0). \tag{10}$$

Utilizing that x_{eq} is an equilibrium solution and introducing $\zeta = x - x_{\mathrm{eq}}$ gives

$$\ddot{\zeta} + 2\xi\omega_0\dot{\zeta} + \omega_0^2\zeta = \frac{\left.\frac{\mathrm{d}A_{\mathrm{eff}}}{\mathrm{d}x}\right|_{x=x_{\mathrm{eq}}}\zeta}{m}(p_{\mathrm{e}} - p_0), \tag{11}$$

which after reorganization is

$$\ddot{\zeta} + 2\xi\omega_0\dot{\zeta} + \left(\omega_0^2 - \frac{\left.\frac{\mathrm{d}A_{\mathrm{eff}}}{\mathrm{d}x}\right|_{x=x_{\mathrm{eq}}}}{m}(p_{\mathrm{e}} - p_0)\right)\zeta = 0. \tag{12}$$

The resultant differential equation is linear, and this way of writing shows the physical effect of the effective area: the linearized force decreases the coefficient of the displacement, i.e. the spring stiffness. The term in the brackets can be regarded as an "effective spring stiffness", therefore loss of stability is reached when it becomes negative, i.e.

$$\omega_0^2 - \frac{\left.\frac{\mathrm{d}A_{\mathrm{eff}}}{\mathrm{d}x}\right|_{x=x_{\mathrm{eq}}}}{m}(p_{\mathrm{e}} - p_0) < 0, \tag{13}$$

and after reorganization for the derivative of the effective area:

$$\left.\frac{\mathrm{d}A_{\mathrm{eff}}}{\mathrm{d}x}\right|_{x=x_{\mathrm{eq}}} > \frac{\omega_0^2 m}{p_{\mathrm{e}} - p_0} = \frac{s}{p_{\mathrm{e}} - p_0}. \tag{14}$$

Therefore the stability of an equilibrium solution for a given pressure difference and spring stiffness can be determined from the derivative of the effective area at the equilibrium displacement, meaning that knowing the $A_{\mathrm{eff}}(x)$ function is crucial from the point of stability as well.

2.2. Mass flow rate through the valve

As stated before, the mass flow rate through the valve is one of the most important parameters. There are two ways to obtain it based on the ratio of the pressure at the pipe end and the ambient pressure.

2.2.1. Chocked flow

The flow is said to be chocked if this ratio is above the critical pressure ratio [4], which for air ($\kappa = 1.4$) is

$$\left(\frac{p_{\mathrm{e}}}{p_0}\right)_{\mathrm{critical}} = \left(\frac{\kappa + 1}{2}\right)^{\frac{\kappa}{\kappa - 1}} = 1.8929, \tag{15}$$

the formula for the mass flow rate [4] is

$$\dot{m}_{\mathrm{out}} = C_{\mathrm{D}} A_{\mathrm{ref}} \sqrt{\kappa \rho_{\mathrm{e}} p_{\mathrm{e}} \left(\frac{2}{\kappa - 1}\right)^{\frac{\kappa+1}{\kappa-1}}}, \tag{16}$$

where the reference area equals

$$A_{\mathrm{ref}} = D_{\mathrm{pipe}} \pi x. \tag{17}$$

The most problematic part of Eq. (16) is the discharge coefficient: the other main goal of the stationary mesh CFD simulations is to investigate its values at various valve lifts and pipe end pressures.

2.2.2. Non-chocked flow

The equation for the mass flow rate for compressible non-chocked flows [5] is

$$\dot{m}_{\mathrm{out}} = C_{\mathrm{D}} A_{\mathrm{ref}} \sqrt{2 \rho_{\mathrm{e}} p_{\mathrm{e}} \left(\frac{\kappa}{\kappa - 1}\right) \left[\left(\frac{p_0}{p_{\mathrm{e}}}\right)^{\frac{2}{\kappa}} - \left(\frac{p_0}{p_{\mathrm{e}}}\right)^{\frac{\kappa+1}{\kappa}}\right]}. \tag{18}$$

2.3. Interaction between the valve and the pipe end

There is also the possibility of the valve disc hitting the end of the pipe, which phenomenon is not covered by the above derived equations. This event can have two outcomes: either the disc bounces back with a set loss of kinetic energy or it sticks to the pipe end. As these are not covered by the deforming mesh simulations, their modelling can be omitted if the sole goal of the 1D model is to produce a comparable output to the CFD results.

2.4. The pipe

The flow in the pipe can be regarded as a one-dimensional, unsteady, subsonic, compressible gas flow with wall friction, which is described by the following system of partial differential equations [6]. The continuity is

$$\frac{\partial \rho}{\partial t} + \frac{\partial \rho v}{\partial x} = 0, \tag{19}$$

the 1D equation of motion with pipe friction looks like

$$\frac{\partial \rho v}{\partial t} + \frac{\partial \left(\rho v^2 + p\right)}{\partial x} = \frac{\lambda(v)\rho}{2 D_{\mathrm{pipe}}} v|v|, \tag{20}$$

and the adiabatic energy equation is

$$\frac{\partial \rho e}{\partial t} + \frac{\partial (\rho v e + p v)}{\partial x} = 0. \tag{21}$$

The Darcy friction factor was defined as a function of the velocity, using Blasius' approximation for turbulent flows [7]:

$$\lambda(v) = 1.264 \, (Re(v))^{-0.25} = 1.264 \left(\frac{v D_{\mathrm{pipe}}}{\nu}\right)^{-0.25} \tag{22}$$

2.5. Numerical solution of the system

All of the above equations were implemented into the 1D model. Eq. (7) was solved using a 4th/5th order Runge-Kutte solver, while the Lax-Wendroff method [8] was applied to Eqs. (19) to (21). A constant total pressure reservoir boundary condition was defined for one end of the pipe, while the other was coupled with the valve. The compressible method of characteristics was used for both [6].

3. STEADY-STATE CFD SIMULATIONS

The goal of the stationary mesh CFD simulations is to investigate the flow properties at various *fixed* openings and reservoir pressures. With these information it will also be possible to obtain the $A_{\mathrm{eff}}(x)$ and C_{D} values required for the 1D model. However, it must be noted that this method of approach assumes that even though these parameters refer to dynamic processes, they can be approximated from steady-state solutions. All the CFD simulations were done using ANSYS-CFX.

Both [9] and [10] investigate the general flow parameters of valves, while [11] uses an approach similar to this work, as it also approximates the dynamic properties from results of fixed opening solutions.

An advanced version of this method can be seen in [12]: the authors generated individual meshes for a large number of openings and their solver chooses from them based on the calculated displacement values. Its advantage is that the process more or less retains its dynamic nature, however, the valve openings can only be discrete values and its resolution depends on the number of prepared meshes.

During the modelling the axisymmetry of both the geometry and the boundary conditions were taken into account, therefore only a wedge shaped domain was generated with a central angle of 5°. This also means that all of the results had to be rescaled for the full 360° geometry with a multiplication.

The dimensions of the modelled valve correspond to the measuring equipment located in the laboratory of the Department of Hydrodynamic Systems in order to ease the comparison of the calculated and the measured results in the future. This includes a pipe with an inner diameter of 40.2 mm (corresponding to 1 1/2″ nominal) and a valve disc diameter of 55.7 mm. The length of the pipe was set to be $10D_{\mathrm{pipe}}$.

3.1. Simulation settings

Due to the axisymmetry, a wedge shaped domain with one cell in the radial direction was sufficient for the modelling of the problem. The block structured mesh was created using ICEM and consists of 90787 nodes. The domain, the boundary conditions and the element numbers are illustrated in Fig. 1. The thinner lines denote the edges of the blocks. A mesh dependency study was also carried out, which is presented at the end of this section.

The opening pressure was set to be 1 bar (absolute), while the temperatures at both the inlet and the opening were 293 K. The inlet total pressure was varied between 1–6 bar and the valve opening range of 0.05–$0.35D_{\mathrm{pipe}}$ was resolved with a step size of $0.05D_{\mathrm{pipe}}$. To ease the notation, relative values for the opening will be used from now on:

$$\bar{x} = x/D_{\mathrm{pipe}}. \tag{23}$$

As the steady-state solver only produced converging residuals at very low pressure ratios, a transient one was used in most cases. In these the simulations were stopped after both the force acting on the valve and the inlet mass flow rate had converged. The medium was set to be air with the ideal gas assumption. High Resolution and Second Order Backward Euler schemes were used for the advection and the time stepping, respectably. The k-ε model was chosen for turbulence, because its scalable wall function supposedly provides reasonable accuracy for the boundary layer even without its full numerical resolution [13]. A turbulence model dependency study was also concluded, which is presented at the end of this section. The time step is variable and is automatically adjusted by the solver to maintain a set number (between 5 and 9) of inner loop iterations.

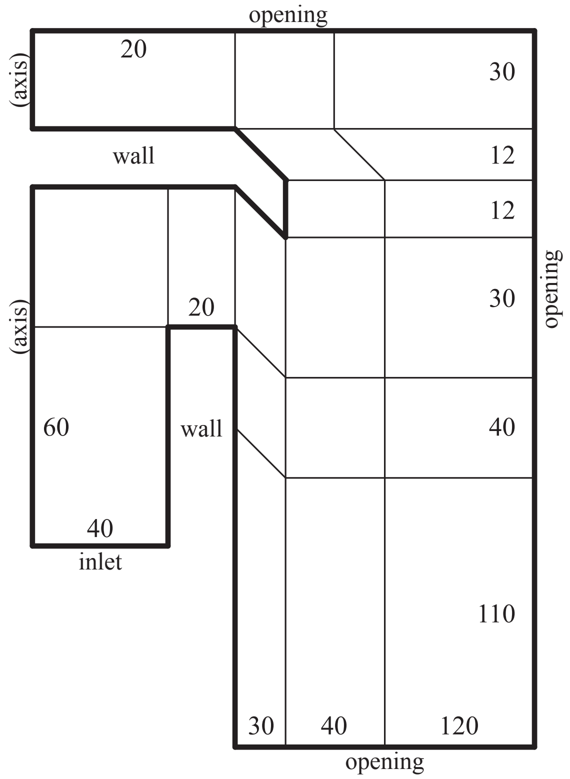

Figure 1. The domain, the boundary conditions and the element numbers (not a proportional illustration).

3.2. Results for the discharge coefficient

The discharge coefficient can be calculated from Eq. (16) by substituting the mass flow rate obtained from the CFD simulations ($\dot{m}_{\mathrm{out}} = \dot{m}_{\mathrm{out,CFD}}$), which is

$$C_{\mathrm{D}} = \frac{\dot{m}_{\mathrm{out,CFD}}}{A_{\mathrm{ref}}\sqrt{\kappa\rho_{\mathrm{v}}p_{\mathrm{v,CFD}}\left(\frac{2}{\kappa-1}\right)^{\frac{\kappa+1}{\kappa-1}}}}. \tag{24}$$

The pipe end pressures were also taken from the CFD simulations, while the densities were calculated from the inlet temperature as experience showed that the variations in it along the pipe are negligible.

The discharge coefficients can be seen in Fig. 2. Note that the above formula for the mass flow rate is only valid for chocked flows, i.e. when the pressure ratio at the valve is below critical, therefore in this case C_{D} is not expected to be constant in the non-chocked range. After averaging the results in the chocked range, a value of $C_{\mathrm{D}} = 0.8778$ was obtained for the discharge coefficient.

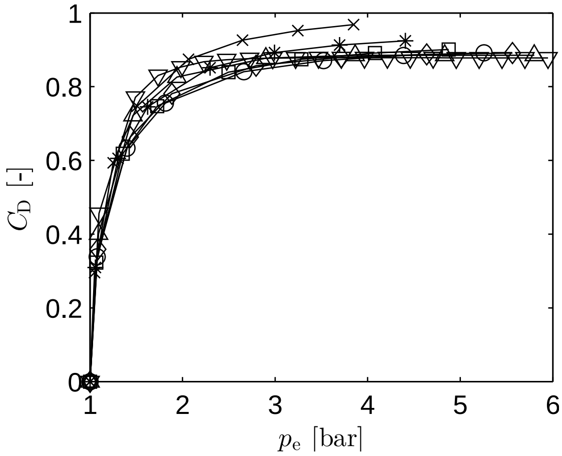

Figure 2. The discharge coefficients at various openings (▽: $\bar{x}$ = 0.05, △: $\bar{x}$ = 0.10, ◇: $\bar{x}$ = 0.15, ○: $\bar{x}$ = 0.20, □: $\bar{x}$ = 0.25, ∗: $\bar{x}$ = 0.30, ×: $\bar{x}$ = 0.35).

3.3. Results for the effective area

The effective area was calculated from Eq. (5) by substituting the force acting on the valve and the static pressure from the results of the CFD simulations:

$$A_{\mathrm{eff}} = \frac{F_{\mathrm{total,CFD}}}{p_{\mathrm{e,CFD}} - p_0}. \tag{25}$$

The ambient pressure (p_0) is known from the boundary condition, therefore the effective area can be obtained. The ratio of the effective area and the cross-sectional area of the pipe is shown in Fig. 3.

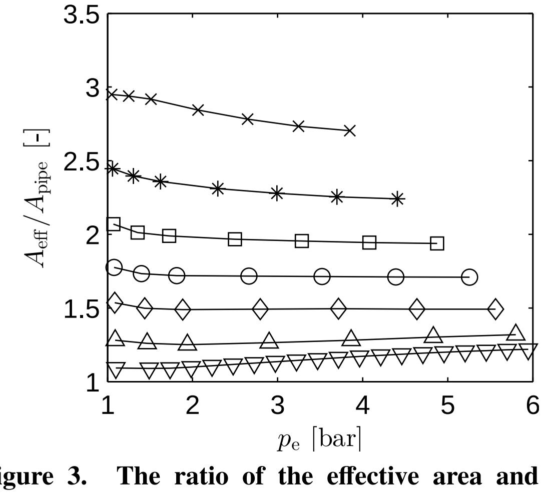

Figure 3. The ratio of the effective area and the cross-sectional area of the pipe at various openings (▽: $\bar{x}$ = 0.05, △: $\bar{x}$ = 0.10, ◇: $\bar{x}$ = 0.15, ○: $\bar{x}$ = 0.20, □: $\bar{x}$ = 0.25, ∗: $\bar{x}$ = 0.30, ×: $\bar{x}$ = 0.35).

Results show that it is reasonable to assume that the effective area depends only on the opening, as it does not significantly vary with the pressure. The $A_{\mathrm{eff}}(x)$ function can be calculated by averaging the values corresponding to the same openings. The result can be seen in Fig. 4, which also includes the piecewise cubic interpolation of the function.

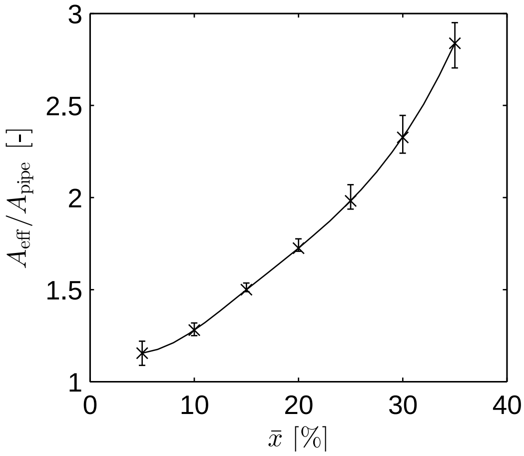

Figure 4. The mean effective area versus the opening (×: CFD results, –: piecewise cubic interpolation) with the maximum and minimum values (errorbars)

3.4. Equilibrium and stability

First, the equilibrium points must be calculated from Eq. (7):

$$s(x_{\mathrm{eq}} + x_0) = A_{\mathrm{eff}}(x_{\mathrm{eq}})(p_{\mathrm{e,eq}} - p_0). \tag{26}$$

The pre-compression can be expressed from the set pressure by substituting $x_{\mathrm{eq}} = 0$ and utilizing that $A_{\mathrm{eff}}(0) = A_{\mathrm{pipe}}$:

$$x_0 = \frac{A_{\mathrm{pipe}}(p_{\mathrm{set}} - p_0)}{s} \tag{27}$$

The characteristic curves, i.e. the $p_{\mathrm{e,eq}}(x_{\mathrm{eq}})$ functions corresponding to various set pressures can be formulated using Eqs. (26) and (27). The stability of the points on the $p_{\mathrm{e}} - x$ plane was obtained from Eq. (14). The equilibrium curves for different set pressures and the boundary of stability (b.o.s.) are shown in Fig. 5. The equilibria to the left of the b.o.s. are unstable. All of these calculations were made with a spring stiffness of s = 12500 N/m.

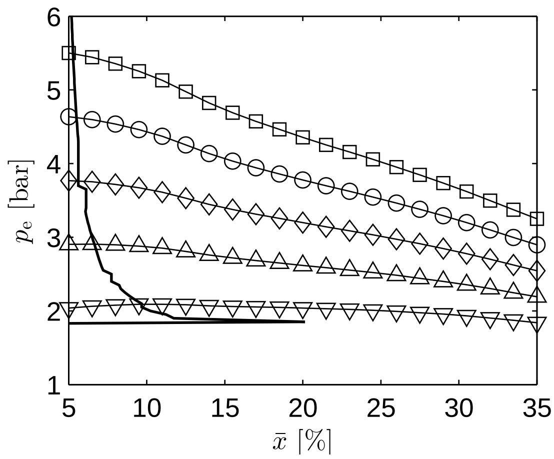

Figure 5. The equilibrium curves (▽: p_{set} = 2 bar, △: p_{set} = 3 bar, ◇: p_{set} = 4 bar, ○: p_{set} = 5 bar, □: p_{set} = 6 bar) and the b.o.s. (–).

3.5. Mesh and turbulence model dependency study

To reduce computational time, both the mesh and the turbulence model dependency studies were only concluded at around the corner points of the investigated inlet total pressure and valve opening domain, i.e. at $p_{t,min} = 1.5$ bar and $p_{t,max} = 6.0$ bar, and at $x_{min} = 0.05D_{pipe}$ and $x_{max} = 0.35D_{pipe}$.

For the mesh dependency study a mesh was generated with two times as many elements on all edges. The relative differences in both the forces acting on the valve and the inlet mass flow rates were under 0.5%, indicating that the domain had been sufficiently resolved by the original mesh.

The effect of turbulence modelling was investigated by repeating the simulations in the aforementioned corner points with both the baseline k-ω and the k-ω SST and compared their results to those from the original simulations, where k-ε had been used. The largest relative differences were 3.67% for the force and 5.40% for the mass flow rate, both of which are sufficiently small.

4. DEFORMING MESH CFD SIMULATIONS

During the calculations of the previous section a method of determining the equilibria and their stability for a direct spring operated pressure relief valve was shown, but it involved the major assumption that the effective area function can be obtained from steady-state fixed valve positions. To investigate the effect of the unsteadiness of a real process another model was assembled in which the valve disc is free to move in the direction of the pipe axis.

4.1. Modelling of the spring

The effect of the spring is taken into account through the *Rigid Body* option of CFX with its built-in *spring* feature. The spring stiffness and the mass of the moving body had to be defined. As the simulated domain has a centre angle of 5° (instead of the full 360°), both of them had to be rescaled appropriately, i.e. multiplied by 5°/360°. The unloaded position of the spring must also be set. It can be calculated from the pre-compression (x_0) and the initial position ($x(0)$):

$$x_{CFD,unloaded} = -(x(0) + x_0). \tag{28}$$

4.2. Mesh deformation and dynamic remeshing

The movement of the valve disc results in a change in the fluid domain, which is handled by allowing the deformation of the mesh. The *Mesh Stiffness* was set in a way that the larger the cell volume, the less it deforms in order to preserve the mesh quality at the critical regions (at the walls, in the free jet) as much as possible. The chosen value for the stiffness is

$$s_{mesh} = \frac{1}{V_{cell}} \left[\frac{m^5}{s}\right]. \tag{29}$$

Even though this setting permits a significant displacement from the initial position of the valve, during testing it turned out to be less than satisfactory as the mesh still suffers a significant loss of quality to the point that sometimes negative cell volumes would occur. To prevent this, the ICEM CFD replay script based remeshing feature was used, which is covered in detail in [14], only its basics will be summarized here.

First of all, a condition for the remeshing has to be defined through an *Interrupt Condition* — when this expression becomes *true*, the solver stops. In these simulations it happens when the area average of the *Total Mesh Displacement* at the valve reaches 1 mm. It proved to be a good quantity to monitor as its value resets to zero after every remeshing.

The remeshing itself is set in a *Configuration*, which is triggered by the *Interrupt Condition*. Its *ICEM CFD Replay* option requires the geometry file (*.tin) of the initial position, a replay script for the meshing (*.rpl), the mapping of the moving part between ICEM and CFX, and a monitor for the total displacement. The area average of the *Total Centroid Displacement* at the valve was used for the latter (it is not reset during the remeshing). The unit conversion between ICEM and CFX (i.e. from millimetres to metres) is handled by the *ICEM CFD Geometry Scale*, which was set to be 0.001. A remeshing step goes as follows:

1. The *Interrupt Condition* is fulfilled.
2. The solvers stops and ICEM is called.
3. The geometry file is loaded into ICEM and is shifted with the value of the corresponding monitor.
4. The meshing replay script is run on the modified geometry.
5. A new simulation — with the new mesh — is initialized with the results of the stopped one.

This way the required mesh quality can be maintained even for extremely large deformations, as long as no change occurs in the topology. An example for the latter would be the seating of the valve, which is not covered by this model.

A similar approach, albeit without remeshing, can be found in [15]. The calculations listed there are quite similar in nature to these, except that in their case the reservoir was also implemented in the CFD model.

5. COMPARISON OF THE 1D AND THE DEFORMING MESH RESULTS

To check whether the steady-state assumption of the effective area was correct, 1D simulations based on the model described in the first section

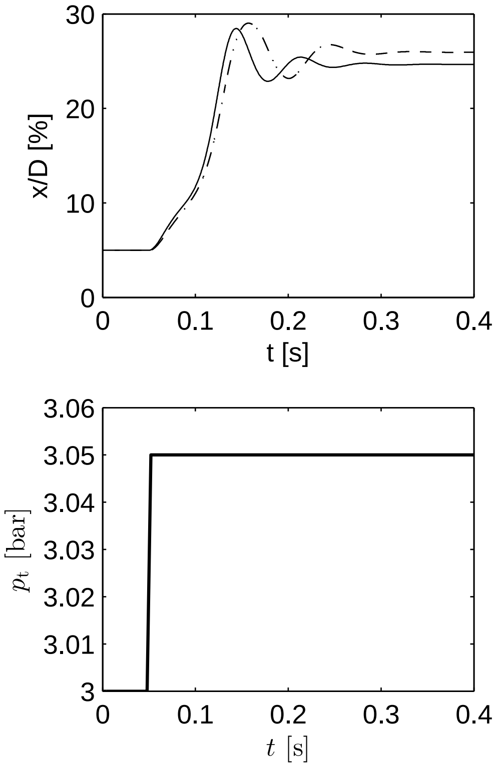

Figure 6. Valve responses of the deforming mesh CFD (cont. line) and the 1D (dash-dot line) models in the case of a sudden pressure jump

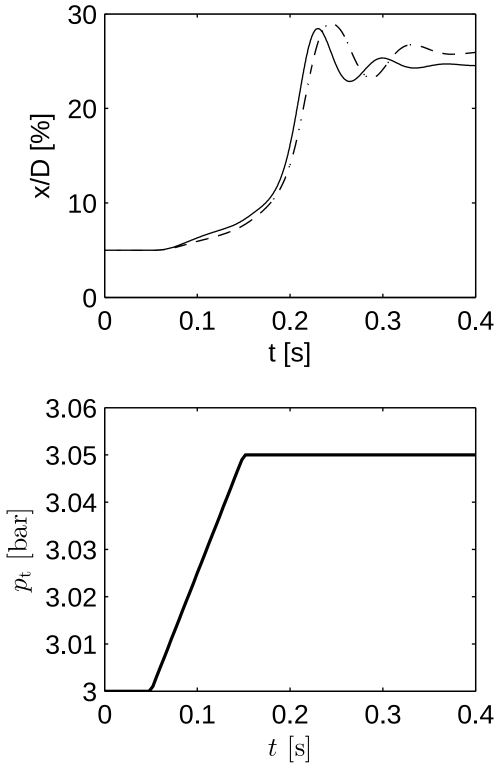

Figure 7. Valve responses of the deforming mesh CFD (cont. line) and the 1D (dash-dot line) models in the case of a slow pressure jump

were compared to the results of the deforming mesh CFD method. The spring stiffness was set to 12500 N/m and its pre-compression was defined such that the valve was in an equilibrium position at the start. The discharge coefficient was also set according to the steady-state simulations ($C_D = 0.8778$), while the damping ratio was approximated as $\xi = 5\%$. Two cases were simulated with the same inlet total pressure jump but with different jump durations. The valve responses and the pressure profiles are illustrated in Figs. 6 and 7. The correspondence is satisfactory as the displacements in the 1D model closely follows those of the deforming mesh solution, even though a minor difference can be observed in the new equilibria.

As the most important modelled parameter is the effective area, it is beneficial to compare the piecewise cubic interpolation of its steady-state result to those from the two deforming mesh simulations. The various effective areas can be seen in Fig. 8. The difference between the two deforming mesh cases are negligible, indicating that the rate of change in the pressure had no effect on the effective area in this parameter range. Since the steady-state curve also runs close to them, it means that the results for both the displacements versus time and the effective areas strongly imply that the basic assumption, i.e. the independence of the effective area from the pipe end pressure was correct.

6. CONCLUSIONS

The stationary mesh simulations proved to be computationally cost-effective in mapping a large segment of the $p_t - \bar{x}$ plane both in terms of the effective area and the discharge coefficient. These also made possible the linear stability analyses of various equilibrium solutions. The piecewise cubic interpolation of the effective area and the averaged value of the discharge coefficient were also useful for the 1D model.
The deforming mesh CFD results confirmed that the approximation of the effective area from the steady-state flow fields is indeed accurate enough that it can be used for the modelling of pressure jump scenarios.

The 1D model is an effective and fast tool for transient calculations, albeit strongly depending on the aforementioned input parameters. This behaviour also gives it a lot of flexibility, i.e. it can be easily modified to simulate the response of other PRVs if these parameters are known from either CFD simulations or measurements.

As always, there is a wide horizon for improvements. One of the authors' future goals is to implement the reservoir dynamics in the CFD model, either by meshing the vessel — as seen in [15] —

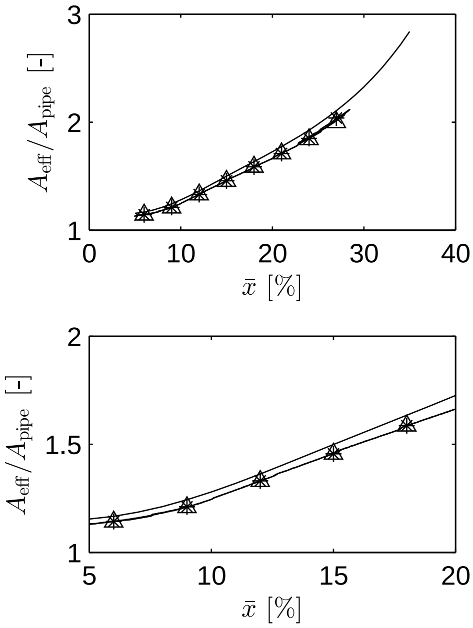

Figure 8. Comparison of the effective areas (–: interpolated steady-state, △: sudden pressure jump, ∗: slow pressure jump).

or by solving the corresponding ordinary differential equation on the pipe inlet boundary. The other is the solution to the seating of the valve, which involves a topological change in the mesh, but no investigations has been made in this direction yet.

REFERENCES

[1] API, 2013, "Sizing, Selection, and Installation of Pressure-Relieving Devices in Refineries", *API RP520 Part II, Sixth Edition*, American Petroleum Institute, Washington, USA.

[2] Hős, C., Champneys, A., Paul, K., and McNeely, M., 2014, "Dynamic behavior of direct spring loaded pressure relief valves in gas service: Model development, measurements and instability mechanisms", *Journal of Loss Prevention in the Process Industries*, Vol. 31, pp. 70–81.

[3] Bazsó, C., and Hős, C., 2013, "An experimental study on the stability of a direct spring loaded poppet relief valve", *Journal of Fluids and Structures*, Vol. 42, pp. 456–465.

[4] Zucker, R. D., and Biblarz, O., 2002, *Fundamentals of Gas Dynamics*, John Wiley & Sons, 2 edn.

[5] Ooosthuizen, P. H., and Carscallen, W. E., 2013, *Introduction to Compressible Fluid Flow*, Taylor & Francis Group, 2 edn.

[6] Zucrow, M. J., and Hoffman, J. D., 1976, *Gas Dynamics*, Vol. 1, John Wiley & Sons.

[7] Blasius, H., 1913, "Das Aehnlichkeitsgesetz bei Reibungsvorgängen in Flüssigkeiten", *Mitteilungen über Forschungsarbeiten auf dem Gebiete des Ingenieurwesens*, Vol. 131.

[8] Lax, P., and Wendroff, B., 1960, "Systems of conservation laws", *Communications on Pure and Applied Mathematics*, Vol. 13, pp. 217–237.

[9] Dossena, V., Marinoni, F., Bassi, F., Franchina, N., and Savini, M., 2013, "Numerical and experimental investigation on the performance of safety valves operating with different gases", *International Journal of Pressure Vessels and Piping*, Vol. 104, pp. 21–29.

[10] Dempster, W., and Elmayyah, W., 2013, "Two phase discharge flow prediction in safety valves", *International Journal of Pressure Vessels and Piping*, Vol. 110, pp. 61–65.

[11] Song, X.-G., Park, Y.-C., and Park, J.-H., 2013, "Blowdown prediction of a conventional pressure relief valve with a simplified dynamic model", *Mathematical and Computer Modelling*, Vol. 57, pp. 279–288.

[12] Beune, A., Kuerten, J., and van Heumen, M., 2012, "CFD analysis with fluid–structure interaction of opening high-pressure safety valves", *Computers & Fluids*, Vol. 64, pp. 108–116.

[13] ANSYS, 2012, "ANSYS CFX-Solver Theory Guide", Release 14.5.

[14] ANSYS, 2012, "ANSYS CFX Reference Guide", Release 14.5.

[15] Song, X., Cui, L., Cao, M., Cao, W., Park, Y., and Dempster, W. M., 2014, "A CFD analysis of the dynamics of a direct-operated safety relief valve mounted on a pressure vessel", *Energy Conversion and Management*, Vol. 81, pp. 407–419.

Conference on Modelling Fluid Flow (CMFF'15)
The 16th International Conference on Fluid Flow Technologies
Budapest, Hungary, September 1-4, 2015

EFFECT OF CYCLING MOTION ON HUMAN ARTERIAL BLOOD FLOW

Viktor SZABÓ[1], Gábor HALÁSZ[2]

[1] Corresponding Author. Department of Hydrodynamic Systems, Budapest University of Technology and Economics. Műegyetem rkp. 3, H-1111 Budapest, Hungary. Tel.: +36 1 463 2542, Fax: +36 1 463 3091, E-mail: vszabo@hds.bme.hu
[2] Department of Hydrodynamic Systems, Budapest University of Technology and Economics. E-mail: halasz@hds.bme.hu

ABSTRACT

This paper is a further development on a previous paper [1] on the 1D modelling of the arterial blood flow in a stationary human body. Here the effect of movement, specifically of cycling motion on the arterial blood flow is investigated. It seems that if the legs move the volumetric flow rate increases in all the arteries leading to the legs, while the blood flow remains unchanged in other branches. The interaction of medical and mechanical aspects are considered in detail.

Keywords: Artery system, momentum equation, blood flow, numerical simulation, method of characteristics, body acceleration.

NOMENCLATURE

D	$[m]$	diameter
E_1	$[N/m^2]$	elastic modulus
E_2	$[N/m^2]$	elastic modulus
R	$[Pa/m^3s]$	resistance
Q	$[m^3/s]$	volumetric flow rate
a	$[m/s]$	wave propagation speed
f	$[m/s^2]$	body acceleration
g	$[m/s^2]$	acceleration of gravity (9.81 m/s^2)
h	$[m]$	elevation
p	$[Pa]$	transmural pressure
t	$[s]$	time
v	$[m/s]$	axial velocity
x	$[m]$	length
β	[-]	constant
δ_0	$[m]$	wall thickness
ε_1	$[m]$	elastic deformation
ε_2	$[m]$	viscoelastic deformation
ε	$[m]$	total deformation
η_2	$[Ns/m^2]$	damping factor
ν	$[m^2/s]$	kinematic viscosity
ρ	$[kg/m^3]$	density of the blood (1050 kg/m^3).
ω	$[rad/s]$	angular velocity
Δ	[-]	difference between two time steps

Subscripts and Superscripts

0	initial value
e	value from the previous time step
x	parallel component

1. INTRODUCTION

Simulating blood flow in a mobile arterial system is a highly complex task. First of all, the specific parameters (e.g. vascular diameter or length) can be different for each person. In addition to this, these parameters are effected by several factors during physical exercises. Moreover, blood flow measurement in an in vivo human subject is a challenging task. In case of blood pressure, one of the requirements of making correct measurements is to keep the arm immobile [2] [3]. Numerical modelling of human arterial system help us to understand the effects of motion on blood flow.

In the past, several 1 dimensional models have been introduced for the simulating of blood flow in the static human arterial system. Some used lumped parameter methods like impedance method [4] [5], while others used distributed models like the method of characteristics (MOC) [6] [7] or the two-step Lax-Wendroff method [8]. However, most models that took the effect of externally-imposed periodic body accelerations on blood flow into account restricted their study on single arteries [9] or stenosed arteries [10] [11].

We previously published a model for the simulation of blood flow in a static human arterial network using the MOC where blood was modelled as a Newtonian-fluid [1]. In this paper we use the same model except that we include the body acceleration caused by the inertial force in the momentum equation which enables us to extend the application of the model to mobile networks too.

Using this model, we study the effect of cycling motion on blood flow.

2. MODELS AND METHODS

The detailed description of the model can be found in [1]. In this paper only a summarized description is provided.

The arterial tree consists of 45 branches and is adapted from Avolio [4] (see Figure 1). In the model, blood is treated as a Newtonian-fluid and the so called Stuart model is used for the modelling of viscoelastic vascular wall-properties. In this model, the total deformation of the vessel (ε) is described as the sum of the elastic deformation (ε_1) and the viscoelastic deformation (ε_2) represented by the Kelvin-Voigt element (see Figure 2).

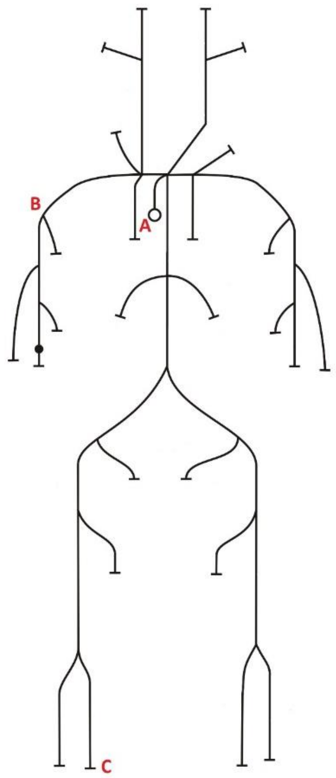

Figure 1. Schematic diagram of the arterial system (adapted from [1])

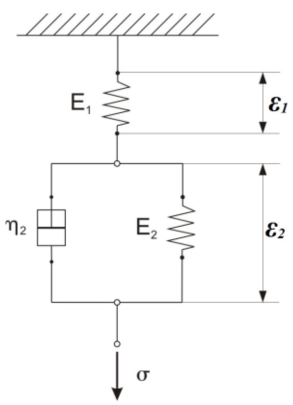

Figure 2. Schematic diagram of the Stuart model (retrieved from [1])

In the model, the following equations are solved simultaneously using the MOC as described in [12] and [13]:

1. Momentum equation:

$$\frac{\partial v}{\partial t} + v\frac{\partial v}{\partial x} + \frac{1}{\rho}\frac{\partial p}{\partial x} + \mathrm{g}\frac{dh}{dx} + \frac{32\nu}{D^2}v = 0 \quad (1)$$

2. Modified continuity equation:

$$2\frac{\partial \varepsilon}{\partial t} + 2v\frac{\partial \varepsilon}{\partial x} + (2\varepsilon + 1)\frac{\partial v}{\partial x} = 0 \quad (2)$$

3. Equations of the Stuart model:

$$\frac{pD_0}{2\delta_0}(2\varepsilon + 1) = E_1\varepsilon_1 \quad (3)$$

$$\frac{pD_0}{2\delta_0}(2\varepsilon + 1) = E_2\varepsilon_2 + \eta_2\dot{\varepsilon}_2 \quad (4)$$

$$\varepsilon = \varepsilon_1 + \varepsilon_2 \quad (5)$$

where D_0 and D are the initial and instantaneous diameters, p is the transmural pressure, v is the axial velocity, h is the elevation, δ_0 is the wall thickness, ν is the kinematic viscosity, g is the acceleration of gravity (9,81 m/s^2) and ρ is the density of the blood (1050 kg/m^3).

The values of E_1, E_2 and η_2 in the Stuart model were calculated on an empirical way because of the significant computational demands of using generic algorithm for the fine tuning of these parameters.

Wave-propagation speed (a), diameter and strain are calculated using the Stuart model:

$$\varepsilon_2 = \varepsilon_{2e}e^{-\frac{E_2}{\eta_2}\Delta t} + \frac{p_e D}{2\delta_0 E_2}(2\varepsilon_e + 1)\left(1 - e^{-\frac{E_2}{\eta_2}\Delta t}\right) \quad (6)$$

$$\varepsilon = \varepsilon_2 + \frac{p_e D}{2\delta_0 E_1}\,(2\varepsilon_e + 1) \quad (7)$$

$$a = \sqrt{\frac{E_1\delta_0}{\rho\, D_0}}(\varepsilon + 1)^{\frac{\beta}{2}} \quad (8)$$

$$D = D_0(\varepsilon + 1) \quad (9)$$

where ε_{2e} and ε_e are the viscoelastic and total deformation from the previous time step, p_e refers to the transmural pressure from the previous time step, and Δt is the time step.

In equation (8) the exponent β is chosen to be equal to 2 to establish is a linear correlation between the wave-speed (a) and the wall deformation (ε) which is in accordance with the observations of Anliker et al [14].

The boundary condition in the arterioles and the capillaries are given by the following equation:

$$\Delta p = R \cdot Q \quad (10)$$

where R and Q denotes the resistance and volume flow rate, respectively.

Heart was considered as a cyclic pressure generator producing periodic pressure pulses shown in Figure 3.

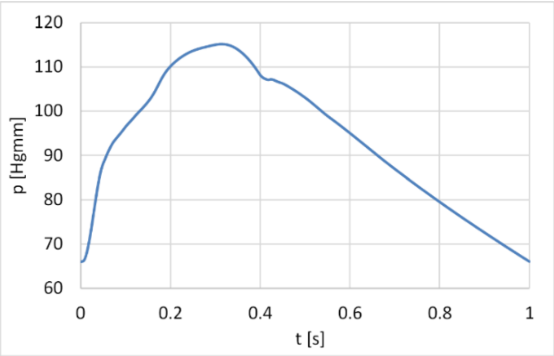

Figure 3. Blood pressure at the heart

At the beginning of the simulation zero velocity, zero deformation and constant pressure was set as an initial value for every arteries. After starting the calculation the quasi-steady state is achieved within a few heart cycles.

Since the force appearing the momentum equation can be any function of position and time and the state of motion of the liquid [15], the application of the previously described model can be extended from static to mobile systems by including the body acceleration caused by the inertial force into equation (1). After applying these changes, the modified version of the momentum equation takes the following form:

$$\frac{\partial v}{\partial t} + v\frac{\partial v}{\partial x} + \frac{1}{\rho}\frac{\partial p}{\partial x} + g\frac{dh}{dx} + f_x + \frac{32\nu}{D^2}v = 0 \qquad (11)$$

where f_x is the parallel component of the body acceleration caused by the inertial force and depends on the time and the actual position of the artery.

First, the modified model was used to calculate the pressure distribution in simple networks (e.g. single rotating and accelerating tube). The results of the simulation matched well with the analytical solutions.

Next, the model was used to study the effect of cycling motion on the arterial system. The exercise was performed at different levels of angular velocity (ω). In each time step the parallel component of the gravitational and body acceleration was calculated for each branch based on its actual position. Using the MOC, pressure and velocity were calculated by solving the equations defined previously.

Finally, average blood flow was calculated in the ascending aorta, the arteria axillaris and the tibialis posterior (points denoted by A, B, C in Figure 1, respectively).

3. RESULTS

The results can be seen in Table 1. The blood flow rate increased in the ascending aorta and the tibialis posterior with the increase of ω. The results were similar in all the vessels located between the ascending aorta and the tibialis posterior. However, the average blood flow did not change significantly in the arteria axillaris.

Table 1. Average blood flow rates [l/min] in the ascending aorta (A), the arteria axillaris (B) and the tibialis posterior (C)

ω	A	B	C
0.0	5.0948	0.3259	0.0735
0.5	5.1011	0.3259	0.0779
1.0	5.1369	0.3259	0.0806
1.5	5.1415	0.3259	0.0845
2.0	5.1906	0.3260	0.0866

4. DISCUSSION

In our model, the length and elastic modulus of the blood vessels were constant. The heart pressure as well as the peripheral resistances are assumed to be the same throughout the simulation, although it is well-known that resistance decreases in working skeleton muscles.

In case of most parameters, it is difficult to make measurements in a mobile arterial system and thus validate our results against in vivo data. On the other hand, by assuming parameters to be constant, the effect of motion can be separated by that of other factors. Therefore, despite of the limitations of the model, the results can help us understand the effects of motion on a mobile arterial system.

5. CONCLUSION

In this paper an attempt was made to study the effect of cycling motion on the arterial blood flow. Our previously published one-dimensional model [1] was modified by including the body acceleration caused by the inertial force into the momentum equation.

Results show an increase in the average blood flow with the intensity of the exercise which is in accordance with previous studies that examined the effect of body acceleration on single arteries [16] [17]. Because of the limitations of the model, further studies need to be carried out to support this result.

6. REFERENCES

[1] G. Bárdossy and G. Halász, “Modeling blood flow in the arterial system,” *Period. Polytech. Mech. Eng.*, vol. 55, no. 1, p. 49, May 2011.

[2] B. P. McGrath, “Ambulatory blood pressure monitoring.,” *Med. J. Aust.*, vol. 176, no. 12, pp. 588–92, Jun. 2002.

[3] M. Mitka, “Many physician practices fall short on accurate blood pressure

measurement.," *JAMA*, vol. 299, no. 24, pp. 2842–4, Jun. 2008.

[4] A. P. Avolio, "Multi-branched model of the human arterial system.," *Med. Biol. Eng. Comput.*, vol. 18, no. 6, pp. 709–718, 1980.

[5] N. Stergiopulos, D. F. Young, and T. R. Rogge, "Computer simulation of arterial flow with applications to arterial and aortic stenoses," *J. Biomech.*, vol. 25, no. 12, pp. 1477–1488, Dec. 1992.

[6] R. L. Rockwell, M. Anliker, and J. Elsner, "Model studies of the pressure and flow pulses in a viscoelastic arterial conduit," *J. Franklin Inst.*, vol. 297, no. 5, pp. 405–427, May 1974.

[7] J. C. Stettler, P. Niederer, and M. Anliker, "Theoretical analysis of arterial hemodynamics including the influence of bifurcations. Part I: mathematical models and prediction of normal pulse patterns.," *Ann. Biomed. Eng.*, vol. 9, no. 2, pp. 145–64, Jan. 1981.

[8] K. Azer and C. S. Peskin, "A one-dimensional model of blood flow in arteries with friction and convection based on the Womersley velocity profile.," *Cardiovasc. Eng.*, vol. 7, no. 2, pp. 51–73, Jun. 2007.

[9] V. Sud and G. Sekhon, "Arterial flow under periodic body acceleration," *Bull. Math. Biol.*, vol. 47, no. 1, pp. 35–52, 1985.

[10] N. K. Verma, S. U. Siddiqui, and R. S. Gupta, "Pulsatile flow of blood in mild stenosis," *e-Journal Sci. Technol.*, vol. 6, no. 5, pp. 61–76, Feb. 2011.

[11] D. S. Sankar and U. Lee, "Nonlinear mathematical analysis for blood flow in a constricted artery under periodic body acceleration," *Commun. Nonlinear Sci. Numer. Simul.*, vol. 16, no. 11, pp. 4390–4402, Nov. 2011.

[12] V. L. Streeter and E. B. Wylie, *Hydraulic Transients*. New York, NY, USA: McGraw-Hill Book Company, 1967.

[13] J. Alastruey, K. H. Parker, J. Peiró, and S. J. Sherwin, "Analysing the pattern of pulse waves in arterial networks: a time-domain study," *J. Eng. Math.*, vol. 64, no. 4, pp. 331–351, Feb. 2009.

[14] M. Anliker, M. K. Wells, and E. Ogden, "The Transmission Characteristics of Large and Small Pressure Waves in the Abdominal vena Cava," *IEEE Trans. Biomed. Eng.*, vol. BME-16, no. 4, pp. 262–273, Oct. 1969.

[15] J. Serrin, *Mathematical principles of classical fluid mechanics*, vol. VIII. 1959.

[16] P. Nagarani and G. Sarojamma, "Effect of body acceleration on pulsatile flow of Casson fluid through a mild stenosed artery," *Korea-Australia Rheol. J.*, vol. 20, no. 4, pp. 189–196, 2008.

[17] M. El-Shahed, "Pulsatile flow of blood through a stenosed porous medium under periodic body acceleration," *Appl. Math. Comput.*, vol. 138, no. 2–3, pp. 479–488, Jun. 2003.

Conference on Modelling Fluid Flow (CMFF'15)
The 16th International Conference on Fluid Flow Technologies
Budapest, Hungary, September 1-4, 2015

THE REDISTRIBUTIONS OF PRESSURE ON THE SURFACES OF IMPINGING AND SAID WALL IN THE REVERSE CHAMBER

Jarosław BARTOSZEWICZ[1], Leon BOGUSŁAWSKI[1], Robert KŁOSOWIAK[1], Rafał URBANIAK[1]

[1] Corresponding Author. Poznan University of Technology, Faculty of Machines and Transportation, Chair of Thermal Engineering, ul.Piotrowo 3, 60-965 Poznań, Poland. Tel.: +48 61 6652212, Fax: +48 61 665 2281, E-mail: jaroslaw.bartoszewicz@put.poznan.pl

ABSTRACT

Different kinds of analyses of free jets and impinging jets have been described in world literature for years. This is the consequence of very high demand for solutions in this class of flows. The problem occurs in a situation when the authors try to use the results obtained for free unstimulated jets to describe other flow of similar classes. This kinds flow geometry influence on momentum, mass and energy transport inside thermal flow machines. In such situations, despite of the frequently apparent likeness to free jets, we deal with different class flows, the restricted flows. One of the elements of this paper is the indication of differences between the mentioned flow geometries.

This paper will presents measurements results of static pressure distribution and pressure fluctuation on the inner surfaces of the reverse chamber. The test results described the distribution of pressure on the impinged wall and the reverse chamber wall. The results describing pressure changes and fluctuations for various inflow velocities and various distances between the pipe outlet and the impinged surface have been presented. Characteristics of turbulent flow in chamber were measured by used constant temperature anemometer. The purpose of the paper is to indicate the differences between different flows: the axis-symmetrical free jet outflowing to the stationary surroundings, a jet impinging a stationary flat surface, and a jet flow impinged flat surface in round close chamber which generated axis-symmetrical return flow.

Keywords: impinging jet, reverse chamber, circulating jet, axis-symmetrical jet, turbulence.

Nomenclature:

D	[m]	diameter of internal pipe
k	[m^2/s^2]	kinetic energy of flow turbulence
p	[Pa]	static pressure
p'	[Pa]	fluctuation of static pressure
R	[m]	radius of reverse chamber
Tu	[%]	turbulence intensity
U	[m/s]	axial component of velocity
u'	[m/s]	fluctuation of axial component of velocity
y	[m]	radial coordinate
z	[m]	axial coordinate

Subscripts and Superscripts

max maximal value

1. INTRODUCTION

The tests on free and impinging jets have their beginnings in the 1960's when papers describing the phenomena occurring in flat jets [4] and impinging jets [11] were presented. In both cases, the papers were devoted to description of mass, momentum and energy transport in the jet and between the jet and solid surface. The tools necessary for such analysis in those years were based on hot wire anemometric techniques [13]. However, only the 1970's saw a significant growth of papers on free jets and contributed to the precise description of the phenomena occurring in free and impinging jets. Such papers as [8, 10, 12, 23] provided the understanding of the structure of such jets. Further authors began the laborious work of testing the processes and their correlations within the jets [5, 7, 18, 22]. Late 1980's brought a dynamic growth of papers related to the numerical modeling of free jets and the description of turbulence within the jets, in particular [16]. Ever since then and until present, every year we see more and more works on free jets and the descriptions of their interaction with solids. The issues the authors try to solve, however, are much more complex than those occurring in the past. Relevant from the point of view of free and restricted jets are the following test results: evolution of free jet flowing out of ventilation and being transformed into a wall jet [6], the natural convection effect on the heat exchange processes near the impinged surface [15], the effect of large temperature gradients on the transport processes on the impinged surface [20]. A separate group of papers are those describing the transport processes between free jets and rotating surfaces [19], descriptions of the correlations between the stresses on the impinged walls, appearing as a result of free jet inflow and helpful with corrosion reduction [9], descriptions of free jet deformation due to the action of transverse jets in the outlet nozzle [21], transverse flame deformation under external influence [14], or finally the tests on velocity distribution in the fluidal deposit the gas jet flows through [17]. The papers referred in the last paragraph indicate the wide use of free and impinging jets in technology especially in thermal-flow machines. The authors shows the analysis of the flow structure in a jet at variable geometry of the reverse chamber in the paper [1] and free and impinging jet in the papers [2, 3].

2. GEOMETRIC MODEL AND TEST METHODS

The main part of the tests is the axis-symmetrical reverse chamber shown in figure 1. The main flow direction changes twice in the reverse chambers. The jets flowing out of the internal pipe, at beginning, is of free jet nature, then it impinges the flat surface of the chamber bottom, where the flow direction first time changes by 90°. Within the inflowing jet's axis, at the so-called stagnation point, the maximum pressure occurs. Such flow can be given as a simplified definition of the impinging jet. Upon change of direction, the wall jet get the radial direction. Before it reaches the side wall, it separates from the impinged surface and thus the second stagnation point is located on the side wall near the reverse chamber corner. Next, the jet changes its flow direction by the 90° angle again. From this point, as the counter-flow jet in relation to the basic jet, flowing out of the internal pipe, flows towards the reverse chamber outlet. The internal channel is built of a steel sharp-edged pipe of internal diameter of D = 0.04 m and 1.2 m length. The external chamber casing was made of plexi of internal diameter of R = 0.39 m and length 0.7 m. A photo of the test chamber is presented in figure 2 with pressure measuring points on the impinged wall and on the side wall. The points are distributed unevenly. The position of the measuring points was based on the results of the numerical calculations made earlier with the use of the Phoenic's code. A sliding ring with ten radial supports bracing the chamber is visible on the right side, enabling its sliding along the internal pipe and achievement of coaxiality of the chamber in relation to the internal pipe. It enables the change of distance between the internal pipe outlet and impinged surface.

The measurement set is built of two independent measurement circuits. The first is adapted to measure static pressures on the walls of the reverse chamber. The principal part is the pressure difference converter FCO14 manufactured by Farness Control Limited with measuring range from 0 to 10 kPa and average readout accuracy 0.4%. In case of measuring fluctuations of pressure in the measuring points, a microphone connected to a signal transducer was installed on the chamber walls. The set marked ICP Signal Conditioner SC-3000 manufactured by Energocontrol enables recording pressure fluctuations in two variants with two upper and lower pass filters (100-50000 Hz and 1000-100000 Hz). In addition, the microphone characteristics were verified based on the measure of signal from the CTA anemometer with the use of a single wire sensor. Figure 3 presents the correlation between both recorded signals.

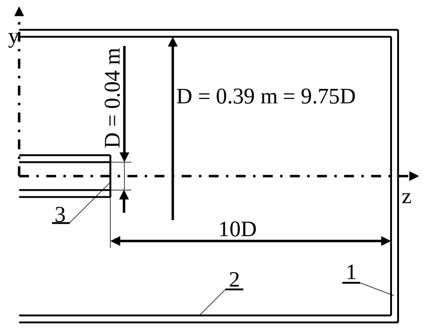

Figure 1. The schema of reverse chamber: 1 – impinging wall, 2 – side wall, 3 – outlet of pipe

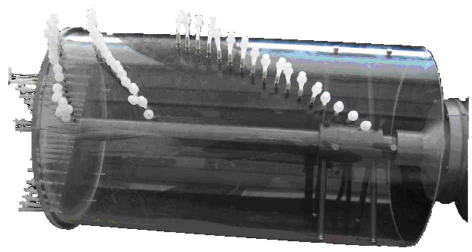

Figure 2. Photo of reverse chamber

The measurement of velocity and its fluctuation was carried out independently of pressure measurements based on the TSI-1050 Constant Temperature Anemometer (CTA). The standard X probe TSI-1241 was used to measure the two components of velocity. The position of the jet axis was indicated by the laser beam. The CTA signal was recorded by a IOtech ADC488/8SA A/D converter which was controlled by TurboLab. The auto trigger option was selected. Subsequently, the recorded signal was processed and analysed by means of the same program.

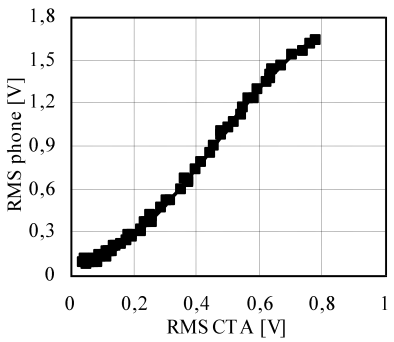

Figure 3. The characteristic of phone

3. BOUNDARY CONDITIONS

The measurements were made on an axis-symmetrical jet, not swirled and unstimulated flowing out from the sharp-edged round channel diameter of 0.04 m to the reverse chamber of 0.39 m diameter. The geometrical conditions corresponded to the pipe outlet position in relation to the impinged surface, varying from *z/D* = 10 to *z/D* = 0.2. The measurements were made for three velocities at pipe outlet: 10, 30 and 50 m/s, which corresponds to the Reynolds numbers: 26000, 78000 and 130000, respectively. The air temperature was maintained on the level of 20^{o}C. The measurements of mean values in time: pressure, axial component and their fluctuations was carried out.

4. RESULTS

In figure 4 standardized radial profiles of static pressure for three initial velocities of the jet are presented and for the varying distance between the internal pipe outlet and the impinged surface. Compared to the free impinging jets, differences in the profiles are noticed. The overpressure value (fig. 3) disappears at the distance about 1*D* from the stagnation point. In case of the test results, a shift of the crossing point of the abscissa axis from *z/D* = 1.8 to *z/D* = 0.0 was observed in the function of varying distance between the jet outlet and the impinged surface. The most significant difference appears on the impinged wall after zero of velocity has been reached. The static pressure continues to decrease making an underpressure zone. The maximum underpressure values drop along the decrease of jet outlet distance from the impinged surface, but increasing their size on the impinged wall. Such effect is the consequence of change of the main flow direction near the outflow wall where the static pressure grows until it reaches positive values.

In case of static pressure fluctuation changes, the distributions obtained for different velocities as shown in figure 5, shows significant diversity. The highest values are obtained for the lowest inflow velocity, i.e. for the lowest pressure value at the stagnation point. This means that the pressure fluctuation level is not a function of pressure in the stagnation point, but a consequence of energy and momentum transport from velocity fluctuation to pressure fluctuation during the turbulent motion.

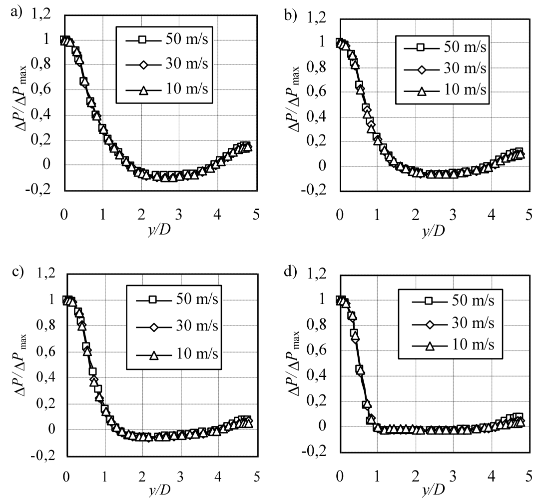

Figure 4. The radial distribution of static pressure on the impinging wall: *z/D* = 10, b) *z/D* = 8, c) *z/D* = 6, d) *z/D* = 1

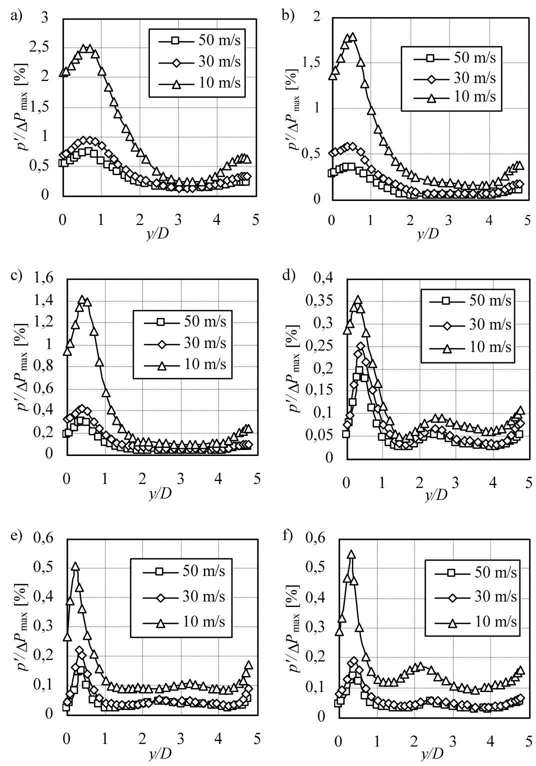

Figure 5. The radial distribution of fluctuation of static pressure on the impinging wall: a) *z/D* = 10, b) *z/D* = 8, c) *z/D* = 6, d) *z/D* = 4, e) *z/D* = 2, f) *z/D* = 1

The pressure fluctuation distribution corresponds to the results obtained for free jets impinging with local maximum at the distance *y/D* ≈ 0.5, afterwards dropping to zero or ambient level. In case of the reverse chamber, another pressure fluctuation growth on the impinged wall was recorded, corresponding to the location of the second stagnation point on the side wall.

Figure 6 shows static pressure distributions on the outflow wall. In the under-pressure zone on the side wall the distributions are characterized with slight differences for large distances between the jet outflow and the impinged surface. The differences increase along with the outlet approaching the impinged wall, particularly for high outflow velocities. The largest differences appear near the corner where the second stagnation point is located. The rule that the faster the jet flows on the impinged surface the higher is the static pressure value on the outflow surface and its maximum is located nearer the reverse chamber. Figure 6 presents a slight growth of the static pressure value from the corner and then its drop to the under-pressure value. The pressure reach the value to zero at the distance *z/D* ≈ 9 from the pipe outlet and the value of the maximum under-pressure at the distance *z/D* ≈ 7.5. The differences in the causes of the functions obtained for various velocities are negligible. Slight differences in the results in the under-pressure zone are comparable to the measurement precision, which impedes explicit interpretation of them.

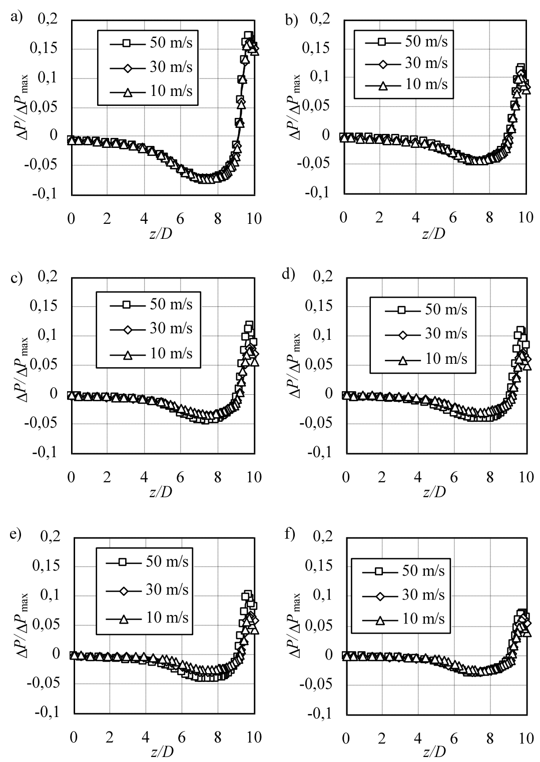

Figure 6. The axial distribution of static pressure on the side wall: a) *z/D* = 10, b) *z/D* = 8, c) *z/D* = 6, d) *z/D* = 4, e) *z/D* = 2, f) *z/D* = 1

As the chamber is axis-symmetrical and the inflow near the corner of the reverse chamber has a radial direction, we should consider that we have a stagnation line located on the side wall. The pressure fluctuation distribution on the side wall, in all the three cases, has a similar shape with local maximum at the distance *z/D* ≈ 9.6 from the pipe outlet and local minimum at the distance *z/D* = 8-9. From this point to the distance *z/D* ≈ 6 the pressure fluctuation grows and next permanently drops to the pipe outlet of the reverse chamber. Figure 7 presents the axial distribution of fluctuation of static pressure on the said wall. At the distance *z/D* ≈ 6 (fig. 7) the existence of area of jet detachment from the side wall should be expected responsible for this local fluctuation growth. The accurate indication of the detachment point based on pressure fluctuation measurements is impossible as their maxi mum does not fall on the stagnation point, as shown in fig. 12. The values of pressure fluctuation drop when reduction of the distance between the outlet of pipe and the impinged wall accrue.

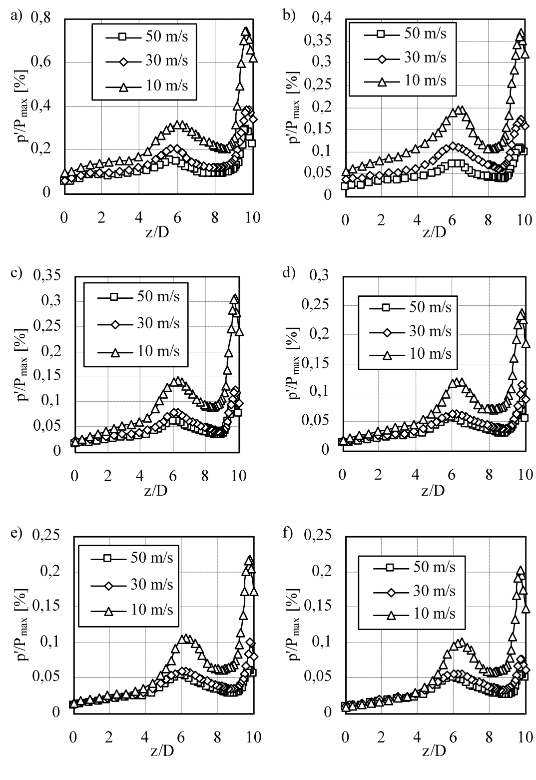

Figure 7. The axial distribution of fluctuation of static pressure on the said wall: a) *z/D* = 10, *z/D* = 8, *z/D* = 6, *z/D* = 4, *z/D* = 2, *z/D* = 1

5. SUMMARY

As a result of the measurements a number of differences between the free impinging jet and the jet flowing in the reverse chamber can be indicated. The most important ones include:

- increase to about z/D = 6 of the potential core length in the axis of the outflow jet, potential core is longer than in free jets,
- decrease of the jet mixing zone on the side of the outflow axis and its asymmetry caused by the counter-flow jet effect,
- diversified distribution of velocities in the jet flowing out of the chamber, depending on the jet flow velocity from the internal pipe,
- unlike the free jets, with maximum velocity fluctuation shifts away from the axis, we observe a local shift towards the axis caused by the counter-flow effect,
- the increase of the stagnation area, compared to the impinging free jet and its decrease along with decrease of the distance between the internal pipe outlet and the impinged surface of the reverse chamber,
- the occurrence of under-pressure on the impinged wall and its expansion along with decrease of the distance between the emitter's outlet and the impinged wall,
- no significant effect of the side velocity on distributions of mean static pressure values excluding the zone of maximum underpressure on the outflow wall and overpressure in the second stagnation point with the value and location depending on the initial jet velocity.

The impact of the jet outflow velocity and the change of distance between the outflow and the impinged surface observed on the distributions of pressure fluctuation on both walls is really significant.

REFERENCES

[1] Bartoszewicz J., Kłosowiak R., Bogusławski L., 2012, The analysis of the flow structure in a jet at variable geometry of the reverse chamber, *International Journal of Heat and Mass Transfer*, 55, pp. 3239–3245.

[2] Bartoszewicz J., 2006, Numerical analysis of fluid flow in heat exchanger with non-standard inlet sections, *17th International Congress of Chemical and Process Engineering, CHISA, T. 3 Hydrodynamic Processes*, pp. 807.

[3] Bartoszewicz J., Bogusławski L., 2010, The effectivity of two-equation turbulence model in an impinging jet in a short nozzle to surface distance, *International Journal of Theoretical and Applied Mechanics*, 14, No 2, pp. 337-347.

[4] Bradbury L.J.S., 1965, The structure of a self-preserving turbulent planar jet, *Journal of Fluid Mechanics*, 23, pp. 31–64.

[5] Brown F.K., Roshko A., 1974, On the density effects and large structure in turbulent mixing layers, *Journal of Fluid Mechanics*, 64, pp. 775–816.

[6] Cho Y. et al., 2008, Theoretical and experimental investigation of wall confluent jets ventilation and comparison with wall displacement ventilation, *Building and Environment*, 43, pp. 1091–1100.

[7] Cohen, J., Wygnanski, I., 1987, The evolution of instabilities in the axisymmetric jet. Part 1. The linear growth of disturbances near the nozzle. *Journal of Fluid Mechanics*, 176, pp. 191–219.

[8] Crow S.C., Champagne F.M., 1970, Orderly structure in jet turbulence, *Journal of Fluid Mechanics*, 48, pp. 547–591.

[9] Demoz A., Dabros T., 2008, Relationship between shear stress on the walls of a pipe and an impinging jet, *Corrosion Science*, 50, pp. 3241–3246.

[10] Deo R.C. et al., 2007, Comparison of turbulent jets issuing from rectangular nozzles with and without sidewalls, *Experimental Thermal and Fluid Science*, 32, pp. 596–606.

[11] Gardon R., Akfirat J.C., 1965, The role of turbulence in determining the heat transfer characteristics of impinging jets, *International Journal of Heat and Mass Transfer*, 8, pp. 1261–1272.

[12] Gutmark E., Wygnanski I., 1976, The planar turbulent jet, *Journal of Fluid Mechanics*, 73, pp. 465–495.

[13] Heskestad G., 1965, Hot-wire measurements in a plane turbulent jet, *Trans. ASME, Journal of Applied Mechanics*, 32, pp. 721–734.

[14] Hourri A., AngersB., Be´nard P., 2009, Surface effects on flammable extent of hydrogen and methane jets, *International Journal of Hydrogen Energy*, 34, pp. 1569-1577.

[15] Koseoglu M.F., Baskaya S., 2009, Experimental and numerical investigation of natural convection effects on confined impinging jet heat transfer, *International Journal of Heat and Mass Transfer*, 52, pp. 1326–1336.

[16] Launder BE, Rodi W., 1983, The turbulent wall jet - measurement and modeling. *Annual Review of Fluid Mechanics*, 15, pp. 429–459.

[17] Ounnar A. et al., 2009, Hydrodynamic behavior of upflowing jet in fluidized bed: Velocity profiles of sand particles, *Chemical Engineering and Processing*, 48, pp. 617–622.

[18] Popiel Cz.O., Buguslawski L., 1986, Mass or heat transfer in impinging single, round jets

emitted by a bell-shaped nozzle and sharp-ended orifice, *Proceeding of the 8th International Heat Transfer Conference*, 3, pp. 1187–1192.

[19] Şara O.N. et al., 2008, Electrochemical mass transfer between an impinging jet and a rotating disk in a confined system, *International Communications in Heat and Mass Transfer*, 35, pp. 289–298.

[20] Shi Y., Mujumdar A.S., Ray M.B., 2004, Effect of large temperature difference on impingement heat transfer under a round turbulent jet, *International Communication of Heat Mass Transfer*, 31, pp. 251–260.

[21] Tamburello D.A., Amitay M., 2008, Active control of a free jet using a synthetic jet, International *Journal of Heat and Fluid Flow*, 29, pp. 967–984.

[22] Winant C.D., Browand F.K., 1974, Vortex pairing-the mechanism of turbulent mixing layer growth at moderate *Reynolds number, Journal of Fluid Mechanics*, 63, pp. 237–255.

[23] Wygnanski I., Peterson R.A., 1974, Coherent motion in excited free shear flows, *AIAA Journal*, 25, pp.201–213.

Conference on Modelling Fluid Flow (CMFF'15)
The 16th International Conference on Fluid Flow Technologies
Budapest, Hungary, September 1-4, 2015

TOWARDS A BETTER UNDERSTANDING OF TURBOMACHINERY BEAMFORM MAPS

Csaba Horváth[1], Bence Tóth[2]

[1] Corresponding Author. Department of Fluid Mechanics, Faculty of Mechanical Engineering, Budapest University of Technology and Economics. Bertalan Lajos u. 4 – 6, H-1111 Budapest, Hungary. Tel.: +36 1 463 2635, Fax: +36 1 463 3464, E-mail: horvath@ara.bme.hu
[2] Department of Fluid Mechanics, Faculty of Mechanical Engineering, Budapest University of Technology and Economics. E-mail: tothbence@ara.bme.hu

ABSTRACT

Beamforming processes developed specifically for rotating sources have provided a nonintrusive means by which turbomachinery noise sources can be localized. Investigations by Horváth et al. have shown that for unducted rotating coherent noise sources beamforming will localize the noise sources to their Mach radii rather than their true noise source positions. As a further step, Horváth et al. have shown that beamforming investigations utilizing beamforming processes developed specifically for the investigation of rotating noise sources in an absolute as well as a rotating reference frame need to take noise sources appearing on the hub into consideration in order to accurately identify all noise sources. The investigations showed that for certain frequencies this noise source can result from a combination of motor noise which is truly located on the hub, rotor-stator interaction noise radiating from along the rotor blade span, and even rotor-stator interaction noise radiating from along the span of the stationary guide vanes. The present investigation continues this study by investigating certain parameters and providing further guidelines for separating the beamform peak which is localized to the hub into its true noise source components, which are located on the axis as well as along the span of the rotor and the stator, making it possible to better understand turbomachinery beamform maps.

Keywords: axial flow turbomachinery, beamforming, Mach radius, tonal noise sources

NOMENCLATURE

B	[-]	blade count
L_B	[dB]	beamforming peak level
L_p	[dB]	sound pressure level
M_t	[-]	blade tip Mach number
M_x	[-]	flow Mach number
n	[-]	harmonic index
p	[Pa]	sound pressure
p_a, p_b	[Pa]	sound pressures of coherent noise sources
p_{ref}	[Pa]	reference sound pressure
p_t	[Pa]	total sound pressure
x	[-]	number of equal strength coherent in phase noise sources
y, z	[m]	coordinates in the plane of the fan
z^*	[-]	Mach radius
α	[°]	phase angle
Θ	[°]	angle of the viewer

Subscripts and Superscripts

one	contribution form one source
1	acoustic harmonic
2	loading harmonic

1. INTRODUCTION

As legislations and regulations have become more stringent along with the expectations of customers, the amount of research in the field of turbomachinery aeroacoustics has progressively increased. As a result of this, turbomachinery design requirements are continuously evolving, often pushing the limits of design practices. The drive to further increase efficiency and reduce noise levels is also pushing technology to develop at a fast pace. Design, simulation, and measurement technologies are therefore being refined and even radically reformed in the process. With regard to acoustic measurement technology, microphone technology has been improved, measurement techniques have been developed, and a combination of the two has helped us gain more information from the recorded acoustic data than ever before possible.

Traditionally, microphones have been set up and recorded individually, with the spectrum of the individual microphone signals providing a vast amount of information regarding the radiated noise field of the investigated phenomena. The development of phased array microphone beamforming technology has made it possible to extend these capabilities, simultaneously recording multiple microphone signals and then processing the results in order to learn more about the noise sources which are being investigated. Beamforming processes developed specifically for rotating sources have provided a nonintrusive means by which the noise sources of turbomachinery can be localized [1-3]. Utilizing phased array microphones and these advanced beamforming algorithms we are able to collect data for identifying turbomachinery noise sources, which is becoming a common practice [1-5]. On the other hand, the results are not so easily understood. Most beamforming algorithms assume that the noise is generated by compact incoherent noise sources, in most cases resulting in beamform maps which localize the noise sources to their true locations. If the investigated noise sources are coherent, the beamforming algorithms often have a hard time distinguishing one source from the other, resulting in the noise sources being incorrectly located on the beamform maps. This publication is one in a series that aims at understanding the beamform maps of various unducted turbomachinery applications. The goal is to first understand these beamform maps and then use the newly gained knowledge for developing methods of evaluating them, while in the long run taking this a step further and developing new beamforming methodologies specifically for the investigation of rotating noise sources. Questions which are addressed in this investigation are: If a noise source which is localized to the axis by beamforming is looked at in an absolute or rotating reference frame, will the source strength be the same? When we have multiple coherent noise sources which are localized to the same Mach radius position, how can we determine the individual contributions? With regard to the second question, only a few specific cases are looked at here, since there are many possibilities which need to be investigated.

The publications of Horváth et al. regarding unducted rotating coherent noise sources have shown that the noise sources are pinpointed to their respective Mach radii rather than their true locations by beamforming methodologies [6]. The name “Mach radius” or “sonic radius” refers to the mode phase speed, the speed at which the lobes of a given mode rotate around the axis, having a Mach number of 1 at the Mach radius (z^*, a normalized radius, where $z^* = 1$ refers to the blade tip) when examined from the viewpoint of the observer [7]. See Eq. (1). Based on these findings, Horváth et al. have explained the beamform maps of rotating coherent noise sources with regard to counter-rotating open rotors that are investigated from the sideline [8] as well as explaining why certain noise sources are localized to the axis in the case of a generic unducted axial flow fan test case which is investigated from the axial direction [9].

The investigation of a generic unducted axial flow fan test case by Horváth et al. focused on the noise sources appearing on the axis of the fan [9]. In many similar investigations, noise sources located on the axis have been associated with motor noise with no further investigations being considered [1, 5]. Taking into account what is known from [6] regarding unducted rotating coherent noise sources appearing at their respective Mach radii, it was shown that the noise sources appearing on the hub can for certain frequencies be resulting from noise sources located along the span of the rotor or the guide vane. This occurs when the wave fronts of coherent noise sources experience constructive and destructive interference, interacting with the phased array in the same manner as the wave front of a single monopole noise source located at the Mach radius of the given instance would. In the test case described in [9] the Mach radius is zero and therefore the noise source is localized to the axis. The Mach radius is calculated using Eq. (1), with n being the harmonic index, B being the blade count or guide vane count, M_t being the blade tip Mach number, M_x being the flow Mach number, and Θ being the angle of the viewer with regard to the axis (upstream direction referring to 0°), with subscripts 1 and 2 referring to the rotor or guide vane of the acoustic harmonic and loading harmonic, respectively. The equation is formulated for a turbomachinery system consisting of two rotors or one rotor and one guide vane which are moving relative to one another. Acoustic harmonic refers to the rotor or guide vane which is radiating noise while being loaded by the potential field and/or the viscous wake of the other, which is referred to as the loading harmonic. Both rows of rotors or guide vanes need to be considered as acoustic as well as loading harmonics in order to receive a complete and accurate sound field, since each blade row loads the other blade row and also radiates sound simultaneously [7].

$$z^* = \frac{(n_1 B_1 - n_2 B_2)}{\left(n_1 B_1 M_{\mathrm{t},1} + n_2 B_2 M_{\mathrm{t},2}\right)} \frac{(1 - M_x \cos\Theta)}{\sin\Theta} \quad (1)$$

The results presented in [9] therefore provide an explanation as to why the investigated noise sources appear on the axis. Three tonal components of unducted axial flow turbomachinery noise were investigated: motor noise, interaction noise radiating from the guide vanes as they interact with the rotors, and interaction noise radiating from the rotors as they interact with the guide vanes. The present report makes a further contribution to these results, providing information regarding how to distinguish between the contribution of the motor, each rotor, and each stator to the level of the apparent noise source appearing on the axis. This is done by individually investigating the effect of each of these noise sources on the beamform peak which is localized to the axis. In this way further guidelines are provided which will help in separating the noise source appearing on the axis into its components.

This investigation is motivated by a desire to better understand the beamform maps of unducted axial flow turbomachinery, which is necessary in order to accurately process the results of rotating coherent as well as incoherent noise sources which are processed using currently available beamforming methods, and which will provide the basis of a new beamforming investigation method designed specifically for the investigation of unducted rotating coherent noise sources.

2. TURBOMACHINERY NOISE SOURCES

In categorizing turbomachinery noise sources, they can be split into two main groups, tonal and broadband noise sources. Tonal noise sources are characterized by a discrete frequency, and are associated with the regular cyclic motion of the rotor blades with respect to a stationary observer and with the interaction of the rotors with adjacent structures [10]. These are referred to as Blade Passing Frequency (BPF) tones and interaction tones, respectively. With respect to the present investigation, the coherence of the noise sources also needs to be taken into consideration. Coherent noise sources are characterized by a time invariant phase relationship. While in most cases broadband noise sources are not coherent, many tonal turbomachinery noise sources often are. Broadband noise sources are characterized by a wide frequency range, and are associated with the turbulent flow in the inlet stream, boundary layer, and wake [10].

3. AXIAL FLOW FAN TEST CASE

In this investigation a synthetic axial flow fan test case is presented. The synthetic fan is used instead of a real fan in order to provide a means by which multiple noise sources can individually be investigated while easily manipulating certain variables. Figure 1 provides a schematic of the fan test case which is synthesized herein. An axial flow fan having a variable number of rotor blades (5 are pictured in the figure) and downstream guide vanes (1 is pictured in the figure) is investigated by a microphone phased array located 0.3 *m* in the upstream axial direction. The fan has a diameter of 0.4 *m*. The diameter of the phased array is 1m. The microphones of the array are arranged along a logarithmic spiral, based on the design used in the OptiNav Inc. Array 24: Microphone Phased Array System.

The following three components of turbomachinery noise are investigated: motor noise, guide vane noise radiating from the guide vanes as they interact with the rotors, and rotor noise radiating from the rotors as they interact with the guide vanes. The motor is represented by 1 stationary monopole noise source located on the axis. The guide vanes are represented by stationary coherent monopole noise sources located at the blade tips, and the rotors are represented by coherent rotating monopole noise sources located at the blade tips. Figure 2 shows a schematic of the monopole noise sources which replace the true noise sources. They are represented by small spheres in the figure.

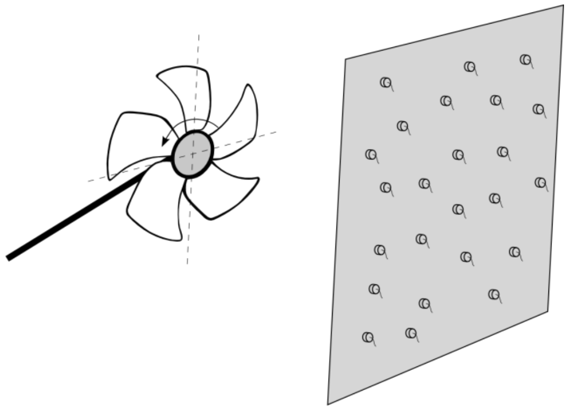

Figure 1. Schematic of the fan test case which is synthesized in the investigation.

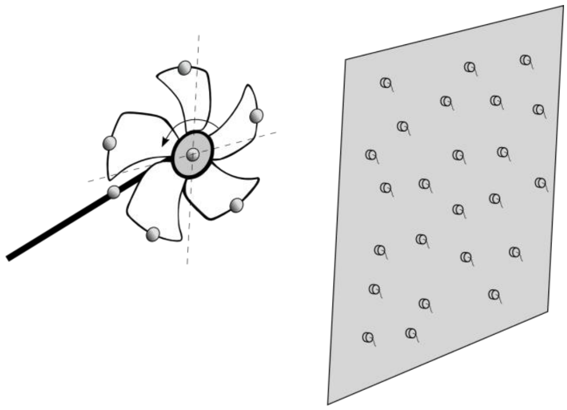

Figure 2. Synthetic fan test case, with monopole noise sources replacing the rotors, guide vanes and motor.

Only simulations of the synthetic test cases are presented in this investigation, but it should be mentioned that [9] showed that the simulations correctly localize the noise sources to their Mach radii and therefore these simulations can be used in further investigating other parameters. In order to account for the limited resolution of the finite aperture array, the investigated frequency is chosen as 3000 *Hz* for all test cases, and therefore the results provide beamform maps which clearly depict the investigated noise sources. Being a synthetic case, the sound pressure amplitude is defined at each noise source position instead of the sound power and whenever possible defined as having a sound pressure value which would be equivalent to a sound pressure level of 60 *dB* if measured at the source position. This investigation does not investigate the effect of phase difference at the source location, and therefore the phase of each noise source was set equal. The stationary monopole noise source located on the axis and representing the motor radiates at the investigated frequency, and should be considered as a harmonic of the motor noise. The stationary monopole noise sources representing the guide vanes also radiate at the same investigated frequency, as a result of the potential field and/or the viscous wake of the rotor blades rotating at a given RPM and interacting with the guide vanes or a harmonic of this tone. The coherent rotating monopole noise sources located at the blade tips and representing the rotors radiate at the same investigated frequency, which is resulting from the potential field and/or viscous wake of the guide vanes interacting with the rotor blades or one of its harmonics.

4. BEAMFORMING

For the simulations presented herein, in-house virtual noise source generation and propagation software is used for creating virtual microphone signals at the microphone positions. The in-house code is able to produce noise sources which are moving at subsonic speeds, while taking into account sound intensity attenuation with distance and the Doppler Effect. The simulation data is processed by versatile in-house beamforming software. Two types of algorithms are used: the classical frequency-domain based Delay & Sum (DS) method [11], which can localize incoherent stationary sources in an absolute reference frame, and the Rotating Source Identifier (ROSI) method [1], which can localize the incoherent sources which are stationary in a rotating reference frame. The results provide beamform maps, which display the magnitudes and the positions of the strongest sources located in the investigated plane for a given frequency range. The magnitudes of the beamform map sources are presented as levels which are calculated from sound pressure squared values which have been corrected for sound intensity attenuation with regard to distance. The values are therefore given with regard to the source position. The reference value used in the calculation of the levels is $2*10^{-5}$ *Pa*. Using these two algorithms, the sound sources originating from both the stationary and rotating elements of the fan can be localized.

Beamforming utilizes the phase differences measured between the microphone signals to determine the direction of arrival of the wave fronts. By adjusting the phase shifts (time delays) of the microphone signals relative to each other, a maximum correlation can be obtained between them. The corresponding phase shifts give information as to the direction of arrival of the wave fronts and hence the locations of the noise sources. This forms the basis of the DS beamforming method [11]. The method can be considered as forming a sensitivity curve, called mainlobe that is directed toward possible compact monopole noise source positions by phase adjustments. These possible source positions are defined by the user, providing focus points for the beamforming methodology, and the beamform maps display the strengths of the investigated sources.

The ROSI beamforming method is an extension of the DS method for rotating source models [1]. The main difference between the two methods is that the ROSI method applies a so called deDopplerization step in order to place the rotating noise sources into a rotating reference frame and hence make them stationary. The positions and velocities of the possible noise sources are accounted for by correcting the time difference and amplitude data with regard to each receiver position. The corrected source signals are then processed with a beamforming method that corresponds with the DS method. For a more detailed description of the ROSI method, see reference [1]. A more detailed description of the phased array microphone system and of the beamforming algorithms applied in the in-house code is available in [5].

In processing the test data the following parameters are applied. A sampling rate of 44100 *Hz* is used and 2 seconds worth of data are processed. A Hanning window is applied with a windowing size of 2048, which is applied with a 50% overlap. The narrowband beamform peak data is presented in the beamform maps and diagrams. It should be mentioned that the rotor noise sources were modelled in a rotating reference frame and when needed transferred into an absolute reference frame (making them rotating sources) by processing the data with the ROSI method. Vice versa, the stator noise sources were modelled in an absolute reference frame and when needed transferred into a rotating reference frame (rotating the stationary sources) by processing the data with the ROSI method.

5. RESULTS

As stated in the introduction, this paper further investigates turbomachinery noise sources which are localized to the axis by beamforming. The goal is to understand the effect of rotor blade number, stator blade number, and noise source amplitude on the resulting apparent noise source located on the axis, in order to help determine the contribution of each individual noise source.

The first test investigates the effect of motor noise source level on the level of the noise source located on the beamform map. The test examines changing the level of a single tonal noise source which is physically located on the axis and beamforming the results in both an absolute as well as rotating reference frame using the DS and ROSI beamforming methods. Figure 3 presents a diagram which compares the sound pressure level of the defined amplitude at the source location to the calculated beamform peak value, which is also calculated with regard to the source location. It can be seen that the values coincide well for the absolute and rotating reference frame results, having a constant difference of approximately 0.1 *dB*. This shows that the magnitude of the noise source which is physically located on the axis is independent from the coordinate system in which the noise source is investigated. Looking at Fig. 3, it can also be seen that with regard to the magnitude of the noise source there is a linear relationship between the source magnitude and the beamforming peak value. This suggests, as is customary in the beamforming literature, that for tonal sources physically located on the axis, the array can be calibrated with the help of a known source, after which the integral of the beamform map can be used in order to quantify results [11].

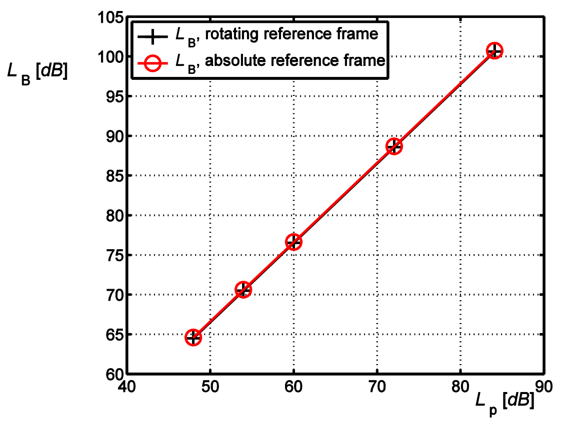

Figure 3. Relationship between the beamform peak level and the sound pressure level of the motor noise calculated with respect to the source.

The second test case investigates the effect of blade number on the level of the apparent noise source located on the axis. Multiple coherent in phase noise sources were evenly distributed around the axis. The noise sources were investigated in an absolute as well as rotating reference frame in order to investigate the effects of stationary sources (stators) in an absolute as well as rotating reference frame. (This is the same as investigating rotating sources (rotors) in a rotating and stationary reference frame, respectively, and therefore only one set of data is presented.) The number of sources was varied while keeping the frequency the same and therefore the rpm of the rotor was varied accordingly for each case. Source numbers ranging from 15-20 were investigated. Since this investigation does not look at the effect of phase difference between the sources, the number of rotors and stators is always kept equal and therefore the noise sources are always in phase.

Regarding coherent noise sources, it is known from classical acoustics that Eq. (2) can be used to determine the sound pressure level, L_p, of a single microphone measurement, where p_{ref} is the reference sound pressure and p_t is the total sound pressure, which can be determined according to Eq. (3) [12]. Here p_a and p_b refer to the sound pressures of two coherent noise source signals and α refers to the phase angle between them. The equation can be extended to take into account multiple sources. With regard to beamforming maps and superimposed apparent noise sources the authors have no information which can help in determining the contribution of each individual coherent noise source. This test is designed to give us a better understanding of these contributions.

$$L_p = 10 \log_{10}\left(\frac{{p_t}^2}{{p_{ref}}^2}\right) \quad (2)$$

$$ {p_t}^2 = {p_a}^2 + {p_b}^2 + 2 p_a p_b \cos\alpha \quad (3)$$

Typical beamform maps from this multiple noise source test can be seen in Figures 4 and 5. The fan is viewed from the upstream direction, as depicted in Fig. 1, with the axis passing through the 0,0 position. Fig. 4 shows the beamform map of 15 equal strength rotating coherent in phase noise sources (stationary noise sources which have been processed using ROSI). Fig. 5 depicts the beamform map of 15 equal strength stationary coherent in phase noise sources (stationary noise sources processed using DS). As expected from the earlier investigations of Horváth et al. [9], the noise sources are always localized to the axis by beamforming. A summary of the coherent in phase noise source results can be seen in Figure 6, which depicts the beamform peak level of the apparent noise source which is localized to the axis for both the rotating as well as stationary coherent in phase noise sources as a function of source number.

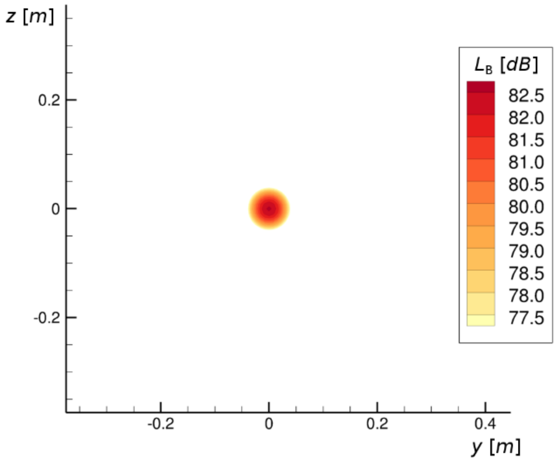

Figure 4. Beamform map of 15 stationary, coherent, in phase noise sources investigated in the rotating reference frame.

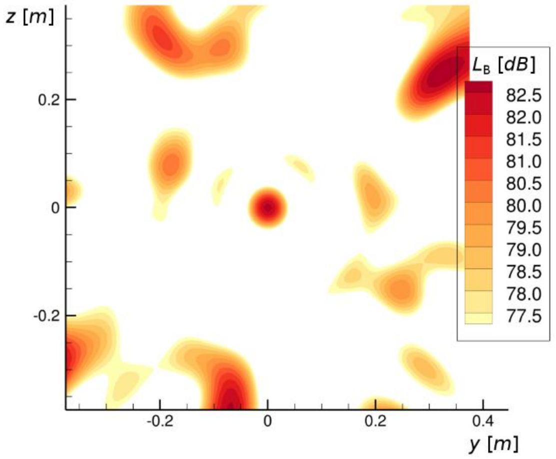

Figure 5. Beamform map of 15 stationary, coherent, in phase noise sources investigated in the absolute reference frame.

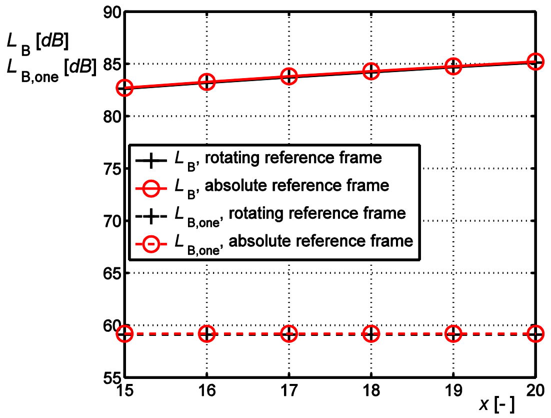

Figure 6. Beamform peak level of the equal strength coherent in phase apparent noise source as a function of source number.

In this investigation it is assumed that all of the coherent noise sources are of equal strength, which is known to be true in this case and generally true for axisymmetric turbomachinery noise sources. It is also known that the wave fronts of coherent noise sources experience constructive and destructive interference as they propagate, resulting in modes. In this test case a planar wave mode is traveling along the axis of the fan, the Mach radius of which is zero. Since the microphones used in the investigation are all relatively close to the axis and far enough away from the noise source for the planar wave mode to have already developed, it is expected that the contributions from each of the noise sources should be in the same phase at the in plane microphone positions as at the source positions. If this hypothesis is true, and the noise sources have the same phase difference at the microphones as they do at their source locations, then an equation which is analogous to Eq. (2) will describe the increase of beamform peak level at the Mach radius as a function of number of coherent in phase noise sources. According to the hypothesis, in this test case $\cos(\alpha)$ is equal to 1 since the phase of each noise source is the same, and Eq. (2) can be rewritten for the beamform peak level, L_B, of x coherent in phase noise sources of equal strength, as seen in Eq. (4). Here p_one refers to what would be the pressure amplitude of the beamform peak which could be calculated back from the beamforming results for one of the equal strength coherent in phase noise sources at the apparent source location. The equation can be rewritten for levels, as seen in Eq. (5). $L_\mathrm{B,one}$ refers to the beamform peak level contribution from one of the equal strength coherent in phase noise sources at the apparent source location (Mach radius). Rearranging Eq. (5), one can solve for $L_\mathrm{B,one}$, which should be equal for each instance investigated here, if the hypothesis is correct.

$$L_\mathrm{B} = 10\log_{10}\left(\frac{{p_\mathrm{one}}^2}{{p_\mathrm{ref}}^2}\right) + 10\log_{10}\left(\frac{x^2}{{p_\mathrm{ref}}^2}\right) \tag{4}$$

$$L_\mathrm{B} = L_\mathrm{B,one} + 20\log_{10}(x) \tag{5}$$

The values for $L_\mathrm{B,one}$ are also plotted in Fig. 6 as a function of number of sources, where it can be seen that they are equal. It can therefore be concluded that though the noise sources are not physically located at the Mach radius position, the levels can be added using equations which are customarily used for the addition of coherent sound pressure levels. Taking advantage of this, one can determine the beamform peak amplitude contribution of one of the equal strength coherent in phase noise sources to the apparent noise source located at the Mach radius position.

The investigation is conducted in both the absolute as well as rotating reference frame with the help of the DS and ROSI methods, as can be seen in Fig. 6. Similar to the results for the noise source which is physically located on the axis, the difference between $L_{B,one}$ for DS and ROSI is approximately 0.1 *dB*. This shows that the results are independent of reference frame in which they are investigated, as was also the case for the noise source physically located on the axis.

Since the amplitudes of the noise sources used in the second test are defined as having a sound pressure level of 60 *dB* at the source position, they can be compared to the one case in the first test which also has a magnitude of 60 *dB*. The values of the beamform map peaks do not agree as can be seen in comparing Figs 3 and 6. Though beyond the scope of this investigation, further tests will investigate the relationship between the beamform peak level of one noise source which is physically located on the axis to the contribution from one of the noise sources which contributes to the apparent noise source which is located at the Mach radius.

6. CONCLUSIONS

This investigation is one in a series which looks at the beamforming results of coherent rotating noise sources through a turbomachinery fan test case. The goal is to better understand the beamforming results of currently available beamforming methods and to provide preliminary information which is needed in the development of a new beamforming method designed specifically for rotating coherent noise sources.

While earlier investigations provided information as to the localization of the rotating coherent noise sources to the Mach radius, which is the axis in this particular case, this investigation takes this a step further. The first test case investigates whether the level of a noise source which is physically located on the axis is affected by the choice of reference frame. The results show that the results are the same for the DS and ROSI investigations. The results also suggest that the results can be quantified by integrating the beamform maps, as is customary in beamforming investigations, though this is beyond the scope of the present investigation.

A second test investigates the contribution from equal strength coherent in phase noise sources to the magnitude of the apparent noise source located at the Mach radius. The noise sources are investigated in a rotating as well as absolute reference frame. The results show that the equations used in acoustics for adding levels can be applied in determining the contributions from equal strength coherent in phase noise sources to the apparent noise source located at the Mach radius. The results show that the same levels can be calculated for one test case independent of reference frame in which it is investigated. On the other hand, the beamforming peak level is dependent on whether the noise source is physically located at the given position or just an apparent noise source.

Though beyond the scope of this present report, further tests will investigate the relationship between the beamform peak level of one noise source which is physically located on the axis to that of the contribution from one of the noise sources which contributes to the apparent noise source which is located on the axis.

ACKNOWLEDGEMENTS

This work has been supported by the Hungarian National Fund for Science and Research under contract K 112277 and relates to the scientific program of the projects "Development of quality-oriented and harmonized R+D+I strategy and the functional model at BME" and "Talent care and cultivation in the scientific workshops of BME" under grants TÁMOP-4.2.1/B-09/1/KMR-2010-0002 and TÁMOP-4.2.2/B-10/1-2010-0009, respectively.

REFERENCES

[1] Sijtsma, P., Oerlemans, S., and Holthusen, H., 2001, "Location of Rotating Sources by Phased Array Measurements", *National Aerospace Lab. Technical Report* Paper NLR-TP-2001-135.

[2] Pannert, W., and Maier, C., 2014, "Rotating Beamforming – Motion-Compensation in the Frequency Domain and Application of High-Resolution Beamforming Algorithms", *Journal of Sound and Vibration*, Vol. 333, Issue 7, pp. 1899-1912.

[3] Herold, G., and Sarradj, E., 2015, "Microphone Array Method for the Characterization of Rotating Sound Sources in Axial Fans", Proc. *International Conference on Fan Noise, Technology and Numerical Methods*, Lyon, France, paper 026.

[4] Kennedy, J., Eret, P., Bennett, G., Sopranzetti, F., Chiariotti, P., Castellinni, P., Finez, A., and Picard, C., 2013, "The Application of Advanced Beamforming Techniques for the Noise Characterization of Installed Counter Rotating Open Rotors" Proc. *19th AIAA/CEAS Aeroacoustics Conference*, Berlin, Germany, Paper AIAA 2013-2093.

[5] Benedek, T., and Tóth, P., 2013, "Beamforming Measurements of an Axial Fan in an Industrial Environment", *Periodica Polytechnica Mechanical Engineering*, Vol. 57, No. 2, pp. 37-46.

[6] Horváth, Cs., Envia, E., and Podboy, G. G., 2014, "Limitations of Phased Array Beamforming in Open Rotor Noise Source Imaging", *AIAA Journal*, Vol. 52, No. 8, pp. 1810-1817.

[7] Parry, A. B., and Crighton, D. G., 1989, "Prediction of Counter-Rotation Propeller Noise", Proc. *AIAA 12th Aeroacoustics*

Conference, San Antonio, Texas, AIAA-89-1141.

[8] Horváth, Cs., 2015, "Beamforming Investigation of Dominant Counter-Rotating Open Rotor Tonal and Broadband Noise Sources", *AIAA Journal*, Vol. 53, No. 6, pp. 1602-1611.

[9] Horváth, Cs., Tóth, B., Tóth, P., Benedek, T., and Vad, J., 2015, "Reevaluating Noise Source Appearing on the Axis for Beamform Maps of Rotating Sources", Proc. *International Conference on Fan Noise, Technology and Numerical Methods*, Lyon, France, paper 013.

[10] Smith, M. J. T., 1989, *Aircraft noise*, Cambridge University Press.

[11] Mueller, T., Allen, C., Blake, W. K., Dougherty, R. P., Lynch, D., Soderman, P., and Underbrink, J., 2002, *Aeroacoustic Measurements: Chapter 3.*, Springer.

[12] Norton, M., and Karczub, D., 2003, *Fundamentals of Noise and Vibration Analysis for Engineers*, Cambridge University Press.

Conference on Modelling Fluid Flow (CMFF'15)
The 16th International Conference on Fluid Flow Technologies
Budapest, Hungary, September 1-4, 2015

CASE-SPECIFIC SEMI-EMPIRICAL GUIDELINES FOR SIMULTANEOUS REDUCTION OF LOSS AND EMITTED NOISE IN AN AXIAL FLOW FAN

Tamás BENEDEK[1], János VAD[2]

[1] Corresponding Author. Department of Fluid Mechanics, Faculty of Mechanical Engineering, Budapest University of Technology and Economics. Bertalan Lajos u. 4 – 6, H-1111 Budapest, Hungary. Tel.: +36 1 463 2464, Fax: +36 1 463 3464, E-mail: benedek@ara.bme.hu
[2] Department of Fluid Mechanics, Faculty of Mechanical Engineering, Budapest University of Technology and Economics. E-mail: vad@ara.bme.hu

ABSTRACT

The paper presents the semi-empirical investigation on the effect of the inlet axial velocity profile on the total efficiency and the upstream-radiated noise of an industrial axial flow fan rotor, installed in a free-inlet, free-exhaust setup. As a preliminary empirical diagnostics step, the emitted noise of the fan was measured by means of a Phased Array Microphone system, and the inlet axial velocity profile was taken with use of a vane anemometer. Supported by the measurements, the spanwise distribution of the emitted noise was estimated on the basis of the momentum thickness of the blade suction side boundary layer, being considered also as a loss indicator of the fan blading. The spanwise distribution of the momentum thickness was calculated with use of 2D empirical cascade correlations. The appropriateness of the applied rotor through-flow model was assessed by means of CFD simulation. Based on the semi-empirical model, the paper presents the method for surveying the dependence of the total efficiency and average sound pressure level for various inlet axial velocity profiles. Such method forms a basis for simultaneously reducing the loss and the emitted noise, while retaining the global aerodynamic performance of the fan.

Keywords: axial flow fan, efficiency, inlet velocity profile, noise, phased array microphone

NOMENCLATURE

A	[dB]	parameter in Eq. 4
d_t	[mm]	tip diameter
k	[-]	exponent in Eq. 5
L_P	[dB]	area-averaged SPL
$L_{P\Theta*}$	[dB]	Θ*-based approximation of SPL
$L_{\Theta*}$	[dB]	momentum thickness level
n	[RPM]	rotor speed
P	[Pa]	sound pressure
R	[-]	dimensionless radius
α	[°]	flow angle (from axial direction)
Φ	[-]	global flow coefficient
φ	[-]	local axial flow coefficient
η_t	[-]	total efficiency
ν	[-]	hub to tip ratio
ψ_{is}	[-]	local isentropic total pressure rise coefficient
ψ'_{sw}	[-]	local swirl loss coefficient
$\Theta*$	[-]	momentum thickness parameter
ω	[-]	local friction loss coefficient

Subscripts

1	rotor inlet
2	rotor outlet

Abbreviations

CFD	Computational Fluid Dynamics
PAM	Phased Array Microphone
ROSI	Rotating Source Identifier
SPL	sound pressure level
SST	Shear Stress Transport
2D	two-dimensional

1. INTRODUCTION

The inlet condition of an axial flow fan installed in an industrial environment often differs from the condition assumed in fan design or realized during the laboratory measurements forming the basis of fan catalogue data. The alteration in the inlet velocity profile influences the flow incidence to the blades, and has a major effect on the development of the boundary layer on the suction side of the fan blades. As noted in [1], the suction side boundary layer plays a key role in the generation of the aerodynamic loss over the blade surface. The boundary layer thickness can be used as an indicator of total pressure loss [2]. The suction side boundary layer is also one of the major aero-acoustic noise sources of the fan [3]. As reported in [4], the emitted noise relates to the boundary layer thickness. These findings can be summarized as follows. a) The inlet axial velocity profile substantially influences the condition of the blade boundary layer, *via* the angle of flow incidence to the blade sections. b) As such, it has a significant effect on the aerodynamic performance and noise of the fan. c) While retaining the global aerodynamic performance of the fan (flow rate, total pressure rise), the inlet axial velocity profile may be suitably tuned for simultaneously reducing the emitted noise and the total pressure loss (i.e. improving the total efficiency). Tuning the inlet axial velocity can be carried out by means of aerodynamically profiled rotor entry sections. For example, the ISO standard [5] prescribes the use of a bellmouth entry upstream of the fan in certain measurement installations – regardless of what type of inlet condition was assumed in the design of the rotor under consideration. The bellmouth entry aims at ensuring that the flow is uniform over the entire rotor intake section. Therefore, it is a means for realizing the "uniform axial inlet condition", often used in axial fan design as an idealized condition.

In the papers [6-8], Benedek and Vad presented a diagnostics method for discovering case-specific semi-empirical correlations between the spatial distribution of the aerodynamic properties and the noise sources of the fan blading. The diagnostic method, adaptable to on-site studies of industrial fans, is based on the following experimentation: a) measurement of the rotor inlet axial velocity profile, b) Phased Array Microphone (PAM) experiments. For the case study in [7-8], it was reported that the emitted sound pressure is proportional to the momentum thickness of the blade wake in the third-octave frequency bands that are the most important from the viewpoint of human audition.

In the present paper, the evaluation method related to the case study detailed in [7-8] is further developed, enabling the case-specific semi-empirical investigation on the effect of the inlet axial velocity profile on the aerodynamic loss and the emitted noise.

This paper is considered as a Technical note for the Workshop "Beamforming for Turbomachinery Applications" organized at CMFF'15. The paper aims at provoking a discussion on the topics outlined in the Summary.

2. THE FAN OF CASE STUDY, MEASUREMENT SETUP

The fan of case study is a ventilating fan with tip diameter d_t = 300 *mm*, hub-to-tip ratio ν = 0.3, tip clearance 6.6% relative to the span, and n = 1430 *RPM* rotor speed. The fan has 5 forward skewed blades and has no guide vanes. The fan was built in a short duct, in a free-inlet, free-exhaust setup (zero static pressure rise). The fan is equipped with a short, rounded inlet rim (photograph in [6]).

The inlet axial velocity profile was measured with use of a vane anemometer along two diameters being perpendicular to each other. The PAM measurement was performed from the upstream direction with use of an OptiNav Inc. Array24 microphone array. The distance between the PAM and the fan was 1.83 d_t, the PAM plate was set perpendicular to the axis of rotation, and the centre of the array coincided with the rotor axis. A more detailed description of the fan, the measurements and their evaluation can be found in [7-8].

3. SEMI-EMPIRICAL CALCULATION OF THE RADIAL DISTRIBUTION OF THE AERODYNAMIC PROPERTIES

3.1 The "simplified" through-flow model

In the papers [6-8], the aerodynamic properties were calculated along the span from the measured inlet axial velocity profile and from the geometrical data of the blading, using a two-dimensional (2D) cascade approach. In the aforementioned papers, the authors used the straightforward through-flow model inspired by reference [3] that the radial velocity component is *fully neglected* inside the rotor, i.e. the circumferentially averaged inlet and outlet axial velocity profiles are identical. This through-flow model is labelled herein as "***simplified" model***.

The "simplified" model enables the easiest treatment of through-flow in rotor analysis, and is directly consistent with the 2D cascade approach. Furthermore, it enables that the realistic angles of flow incidence to the blade sections are considered in the rotor analysis, determined directly from the measurement of the inlet axial velocity profile. Its obvious limitation is the inability to represent *any* rearrangement of the axial velocity profile through the rotor.

In the present paper, the "simplified" model is competed with a more sophisticated through-flow model, labelled herein as "***radial equilibrium" model***, and outlined in what follows.

3.2 The "radial equilibrium" model

In the case of axial flow rotors, the well-known radial equilibrium equation makes a connection between the outlet axial velocity profile and the radial distribution of total pressure rise of the blading. For further details, e.g. [3] is referred to. The dimensionless form of the radial equilibrium equation is the following:

$$\left(\eta_t - \frac{\psi_{is}(R)}{2 \cdot R^2}\right)\frac{d}{dR}\psi_{is}(R) = \frac{d}{dR}\varphi_2^2(R) \qquad (1)$$

The equation was implemented in the former calculation method [6] *via* an iteration algorithm. In the first step, the radial distributions of the aerodynamic properties were computed with use of the inlet axial velocity profile. Then, the outlet axial velocity profile was recalculated from the resulting isentropic pressure rise distribution using the continuity equation, and the radial equilibrium equation (1). In the following steps, the aerodynamic properties were calculated with the *average* of the inlet and the new outlet axial velocity profiles, to be consistent with the 2D cascade approach. The computation was continued until the relative difference between the outlet axial velocities derived from the last two iteration steps stayed below 1%.

The benefit of the "radial equilibrium" model is some (restricted) capability to represent the rearrangement of the axial velocity profile through the rotor, being of significance in certain axial fans. Its main limitations are as follows. a) By principle, the radial equilibrium equation is strictly valid only farther away from the blade row. Therefore, its applicability is theoretically doubtful for a short-ducted fan, such as the one in the present case study. b) The model allows for the presence of minor radial flow velocities, associated with the rearrangement of the axial velocity profile through the rotor. However, the radial velocity is neglected in Eq. (1). c) The annulus wall boundary layers are neglected further on, such as in the "Simplified" model. d) To be consistent with the 2D cascade analysis, an obligate modelling step is the averaging of the inlet and outlet axial velocity profiles. This tends to introduce unrealistic angles of flow incidence to the blade sections, being unfavourable in predicting the aerodynamic as well as acoustic behaviour of the rotor, especially near the leading edge. For example, flow separation may be presumed near the leading-edge – due to an erroneously predicted, extreme incidence angle –, that does not occur in reality.

A judgement is to be made whether the "simplified" or the "radial equilibrium" through-flow model is more realistic in the case study under discussion. As a reference case, approximating the realistic aerodynamic behaviour of the rotor, a Computational Fluid Dynamics (CFD) simulation was carried out.

3.3 CFD technique

A steady state CFD simulation was carried out for the fan with use of the Ansys FLUENT 15 software. In the model, the supporting struts were neglected, as a reasonable modelling simplification (in preliminary studies, the aerodynamic effect of the narrow downstream struts was found negligible). With this simplification, the geometry became rotationally periodic. Therefore, only one blade passage was modelled. The computational domain was distributed to three parts: the inlet and the outlet zones were steady, and the middle zone (the short duct including the rotor) was considered as a rotating zone. During the calculations, the frozen rotor method was used. The size of the inlet and the outlet zones was 5 times the rotor radius both in the axial and radial direction. On the inlet and outlet boundaries, identical and constant pressure was prescribed, according to the measurement setup. The turbulent phenomena were modelled with use of Menter's Shear Stress Transport (SST) model [9], which is widely used in the CFD simulations of turbomachinery [10-13]. The numerical mesh was a fully structured hexamesh, containing ~2.5 million elements in such a way that two-thirds of the cells were in the rotating zone. The appropriateness of the spatial resolution of the numerical mesh was checked with a grid sensitivity study.

Corresponding to the limitations in the aerodynamic measurement data available for the industrial fan setup, the validation of the CFD technique was confined to comparing the computational results with the following measurement-based data. a) The flow coefficient, Φ, representing globally the aerodynamic operation of the elemental rotor blade cascades. b) The inlet axial velocity profile, playing a key role in tailoring the aerodynamic as well as acoustic behaviour of the individual blade cascades along the radius [8][14-15].

The Φ data derived a) from preliminary fan performance curve measurements, b) from the vane anemometer measurements on the inlet axial velocity profile, and c) from CFD modelling as an output, are presented in **Table 1**. The CFD-based global flow coefficient is in good agreement with the experimental data. The discrepancy between the CFD- and measurement-based data is within the estimated range of experimental uncertainty of ± 4 % [6]. Therefore, it is concluded that the simulation accurately represents the aerodynamic co-operation of the individual rotor blade sections.

Table 1. The global flow coefficient for 0 *Pa* static pressure rise

	Φ
Performance curve meas.	0.313
Inlet axial velocity profile meas.	0.316
CFD	0.307

The inlet axial velocity profiles, measured by means of the vane anemometer, as well as those derived from the CFD computation, are presented in **Figure 1**. The measurement uncertainty is indicated using error bars. As demonstrated in the figure, the computation fairly well resolves the spanwise gradient of the inlet axial velocity (inlet axial velocity increasing along the radius), being of significance in developing the non-free vortex behaviour of the rotor [6]. The agreement between the computed and measured inlet axial velocity data is fair farther away from the annulus walls, i.e. in the spanwise region of R = 0.45÷0.85. Therefore, it is concluded that the simulation represents well the inlet condition of the individual blade sections in this region.

Based on the above, the CFD technique outlined herein is considered as a validated tool for representing the realistic behaviour of the rotor blade sections, with special regard to the spanwise region of R = 0.45÷0.85.

As Fig. 1 shows at R > 0.85, the simulation overpredicts the velocity deficit dedicated to flow separation anticipated at the periphery of the fan inlet section. As qualitative (wool tuft) experiments confirmed, the separation zone is considerably smaller than that predicted by the simulation.

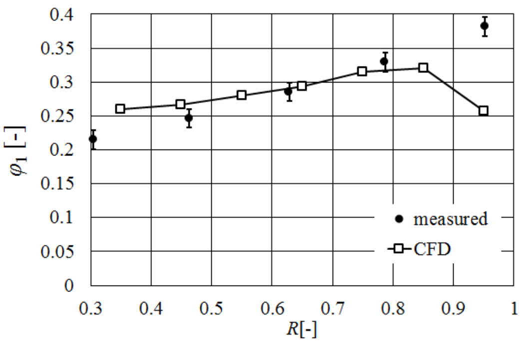

Figure 1. Inlet axial velocity profiles

3.4 Comparison between the through-flow models

In the classical 2D cascade analysis incorporated in the diagnostics method in [6-8], the inlet and outlet flow angles play a key role. In [7-8], the authors presented the correlation between the momentum thickness and the circumferentially averaged sound pressure. The wake momentum thickness is calculated in a 2D cascade approach, with use of the Lieblein diffusion factor [1], being the function of the inlet and outlet flow angles.

Therefore, the inlet and outlet flow angles are considered herein as the key indicators in investigating the appropriateness of the "simplified" and the "radial equilibrium" through-flow models.

Figures 2 to 3 present the spanwise distribution of the inlet and outlet flow angles, respectively, obtained with use of the "simplified" as well as the "radial equilibirum" model, in comparison with the CFD-based data. The semi-empirically modelled distributions obtained with use of the various through-flow models are equipped with error bars. These error bars represent the propagation of the measurement error of the axial inlet velocity – indicated in Fig. 1 –, as well as propagation of the measurement error of data on the blade geometry, in the semi-empirically modelled results.

Fig. 2 demonstrates that the "simplified" model better approximates the CFD-based inlet flow angle distribution. Taking the error bars into account, the quantitative agreement is fair in the region of R = 0.45÷0.85. The "radial equilibrium" model does not provide such a quantitative agreement over the entire region R = 0.45÷0.85.

As suggested by Fig. 3, the "radial equilibrium" model provides a better agreement with the CFD-based outlet flow angles away from the endwalls. However, investigating the region R = 0.45÷0.85, and considering the error bars as well, it is stated that the quantitative agreement between the "simplified" model and the CFD results is still satisfactory.

Based on the above observations, the following conclusion is made. Since a *single* throughflow-model is to be chosen that fairly well represents *both* the inlet and the outlet flow angle distributions, *the "simplified" model is better for the present case study*. Therefore, the "simplified" model, already applied in references [6-8], is utilised further on.

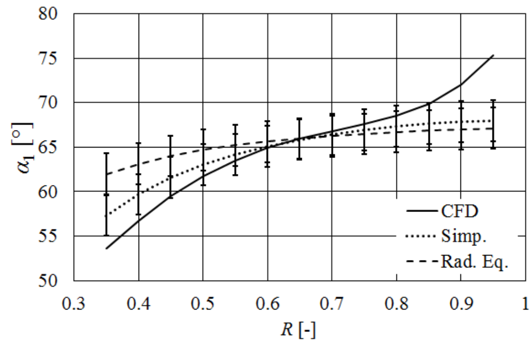

Figure 2. Inlet flow angle distributions

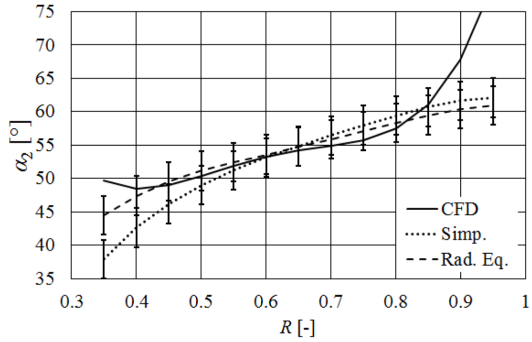

Figure 3. Outlet flow angle distributions

It is noted that a) none of the through-flow models are capable for treating the near-endwall phenomena, such as near-endwall blockage, b) the validity of the CFD tool is limited in the near-endwall region. Therefore, according to the expectations, the discrepancy between the CFD-based and semi-empirical data is increased near the annulus walls, for both the inlet (Fig. 2) and outlet (Fig. 3) flow angles.

4. CORRELATION BETWEEN THE NOISE AND THE AERODYNAMIC LOSS

The levels on a beamforming map represent the sound pressure level distribution in the investigation plane. [16] Based on that in the papers [6-8], the circumferentially averaged sound pressure level was calculated from the beamforming maps, with a third-octave band frequency resolution. At first, the noise source maps were calculated for each investigated frequency band using the Rotating Source Identifier (ROSI) [17] algorithm. Then the sound pressure values of the noise source maps in the rotor area were interpolated to an equidistant mesh. The mesh size was 100 cells both in radial and in circumferential direction. The sound pressure values were area-averaged along the circumference on this mesh, and the sound pressure level (SPL) at each radial location was calculated from the averaged sound pressure values. An example of the noise source map and the resultant SPL distribution is shown in **Figure 4**. The dashed-dotted line represents the hub radius. The circle in the upper-left corner of the map represents the estimated spatial resolution.

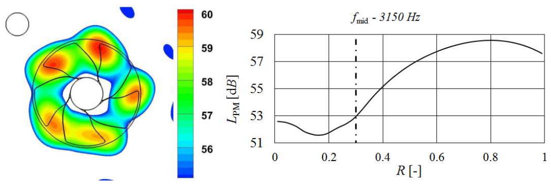

Figure 4. The noise source map, and the related averaged spanwise SPL distribution, for the frequency band of mid-frequency of 3150 *Hz*

In the papers [7] and [8], the following correlation was presented between the emitted noise and the momentum thickness of the blade wake:

$$P \propto \theta^* \qquad (2)$$

By introducing the momentum thickness level

$$L_{\theta^*} = \log_{10}\left(\theta^*\right) \qquad (3)$$

, the sound pressure level can be calculated using the following formula:

$$L_{P\theta^*} = A + 20 \cdot L_{\theta^*} \qquad (4)$$

The spanwise distribution of the momentum thickness level is calculated. Afterwards, by best-fitting the trend functions of Eq. (4) to the PAM-based spanwise SPL distributions, the A values can be estimated for every third-octave bands for which the suction side boundary layer is the dominant noise source. In the present case, the third-octave bands of middle frequencies of 2000, 2500 and 3150 [*Hz*] were found as such frequency intervals. The A values for these frequency bands are presented in **Table 2**.

Table 2. The estimated *A* parameters

f_{mid} [*Hz*]	A [d*B*]
2000	106.3
2500	105
3150	98.2

5. EFFECT OF THE INLET VELOCITY PROFILE ON THE LOSS AND THE NOISE

The alteration of the inlet axial velocity profile modifies the aerodynamic behaviour of the individual blade sections. This is manifested in the alteration of the spanwise distribution of the momentum thickness. This represents the alteration of the global total pressure loss, and, *via* the trend in relationship (2), the alteration of the emitted noise as well.

In the following investigation, the global operational point of the fan is kept constant. This operating point, valid for the previous studies [6-8] as well, is characterised as follows. a) The flow rate, representing the user demand, is prescribed at Φ = 0.316. b) The static pressure rise is zero (free-inlet, free-exhaust). c) The useful total pressure rise is the dynamic pressure calculated with the mean axial velocity corresponding to the constant Φ.

It is investigated herein how the modification of the inlet axial velocity profile influences the global loss and noise of the fan. Since the operational point is prescribed, only *moderate changes* are assumed in the aerodynamic as well as acoustic behaviour of the individual blade sections. In mathematical sense, such *moderate changes* allow for the following assumptions. a) For each frequency band, the proportionality represented by the relationship (2) is valid further on, with unchanged factors of proportionality (linearization for moderate changes). b) This means that the A values presented in Table 2 are to be used further on in predicting the sound pressure level for the various bands *Via* Eq. (4), for altered momentum thickness values.

The inlet axial velocity profile is prescribed approximately as a power function of the radius:

$$\varphi_1(R) = \varphi_1(\nu)\left(\frac{R}{\nu}\right)^k \qquad (5)$$

The shape of the velocity profile is tuned by modifying the value of the k exponent. The axial velocity at the hub, represented by $\varphi_1(\nu)$ in Eq. (5), is set in accordance with the integral condition of the prescribed Φ value.

As already noted, the “simplified” through-flow model was applied in the study reported below. The global total efficiency and the average sound pressure level were investigated as functions of k for the interval $k = 0 \div 1$, as demonstrated in **Figures 5 to 6**. $k = 0$ and $k = 1$ represent a uniform axial inlet condition, and a spanwise linearly increasing inlet axial velocity, respectively.

The global total efficiency (Fig. 5) is the mass-average of the local total efficiency over the span. The local total efficiency was calculated as presented in Eq. (6). It considers the blade friction loss (ω), calculated from the momentum thickness [1]; and the swirl loss (ψ'_{sw}), being equal to the mass-averaged dynamic pressure corresponding to the outlet swirl velocity.

$$\eta_t = \frac{\psi_{is} - \omega - \psi'_{sw}}{\psi_{is}} \qquad (6)$$

The average sound pressure level (Fig. 6) was calculated as follows. The spanwise-resolved sound pressure distributions were estimated using the Eq. (4). Then the sound pressure values were area-averaged over the annulus area for the individual frequency bands. The resultant average sound pressure has been presented in a logarithmic level form in Fig. 6.

The measured inlet velocity profile, presented in Fig. 1, and corresponding to the studies carried out so far [6-8], can be approximated using Eq. (5) with a substitution of $k = 0.45$. The results corresponding to this exponent – in what follows, referred to as "measured case" – are indicated in Figs 5 to 6 using dashed lines.

As Fig. 5 shows, the total efficiency increases with k. The main reason is the moderation of the swirl loss, being the dominant loss in Eq. (6), with increasing k values. With reference to the measured case, an efficiency deterioration of 1 % and an efficiency gain of 0.7% are predicted at $k = 0$ and $k = 1$, respectively.

In the literature [18], the classic formula by Regenscheit is proposed for estimating the emitted noise of the fan from the global aerodynamic properties. Considering that the global operational point is fixed in the present case study, the alteration of global efficiency, according to Fig. 5, is the only factor that influences the noise emission *via* the formula in [18]. Considering the efficiency deterioration of 1 %, the formula in [18] predicts an increase of noise of only ≈ 0.4 dB for the $k = 0$ case, relative to the measured case. This prediction is optimistic, in comparison with the results in Fig. 6, as discussed below.

The average SPL in Fig. 6 reaches its minimum at $k = 0.6$, being close to the measured case. The maximum SPL value can be found at $k = 0$, for which the increase of noise is ≈ 2 dB compared to the measured case – more than predicted on the basis of [18].

The above observations suggest that the fan in this case study exhibits favourable aerodynamic and acoustic features when the measured non-uniform axial inlet velocity profile ($k = 0.45$) is realized. The efficiency is at the middle of the investigated efficiency range of 81 ± 1 %, and the emitted noise is practically at the minimum.

Equipping the fan with an aerodynamically designed bellmouth entry, as proposed in [5], would approximate the uniform axial inlet condition of $k = 0$. Contrary to the expectations, the bellmouth entry is predicted herein to deteriorate the total efficiency by 1 %, and to increase the boundary layer related noise by 2 dB. These undesired changes are minor from a quantitative point of view, but draw the attention to the unwanted tendencies that may be more significant in other cases. The "myth" that the bellmouth entry contributes to the minimization of loss – and, as such, to the minimization of noise [18] – is to be replaced by a more systematic, tuned design of the rotor + its inlet section, for simultaneous reduction of loss and noise.

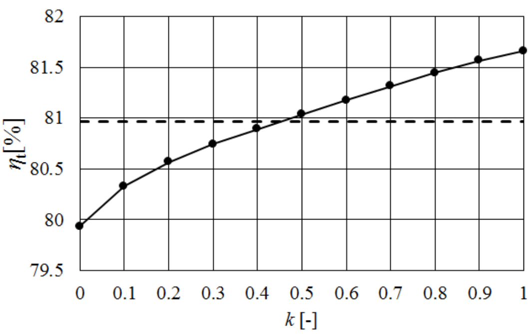

Figure 5. The total efficiency as a function of *k*

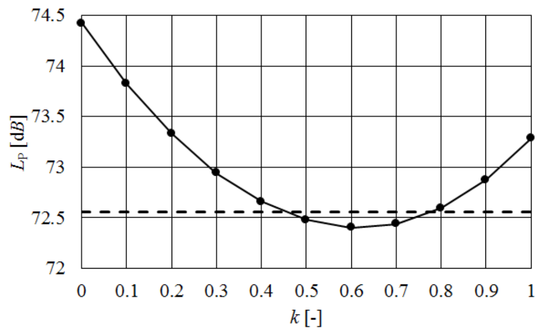

Figure 6. The average SPL as a function of *k*

CONCLUSION AND FUTURE REMARKS

In the paper, as continuation of research reported in [6-8], the effect of the inlet axial velocity profile on the total efficiency and on the upstream-radiated noise of an axial flow fan have been investigated, by means of a concerted aerodynamic-acoustic diagnostics method, incorporating PAM measurements. The results are summarized as follows, and some remarks are made for the continuation of the research programme.

1) The appropriateness of the “simplified” and the “radial equilibrium” through-flow models was investigated by comparing the modelled inlet and outlet flow angle distributions to computational results obtained by means of an experimentally validated CFD tool. In the present study, the “simplified” model, prescribing identical rotor-inlet and -outlet axial velocity profiles, was judged as being more realistic than the “radial equilibrium” model. Therefore, the “simplified” model has been used in the present case study. One important, generally valid advantage of the “simplified” model is that the realistic angles of flow incidence to the blade sections are considered in the rotor analysis, determined directly from the measurement of the inlet axial velocity profile. The proper modelling of inlet flow angles is essential in the concerted aerodynamic-acoustic analysis.

2) Based on semi-empirical correlations obtained in the previous research steps, a methodology was elaborated for a systematic investigation of the effect of the altered inlet velocity profile on the global total efficiency and the upstream-radiated average SPL. The inlet axial velocity profile was modelled by means of a power function, and the shape of the velocity profile was controlled by means of altering the power exponent k. Cases extending from the uniform axial inlet condition (k = 0) to spanwise linearly increasing axial inlet velocity (k = 1) were studied.

3) It has been found that the measured non-uniform inlet axial velocity profile provides a favourable aerodynamic and acoustic operation for the fan: the efficiency is at the middle of the investigated efficiency range of 81 ± 1 %, and the emitted noise is practically at the minimum.

4) Equipping the fan with an aerodynamically designed bellmouth entry would approximate the uniform axial inlet condition of k = 0. The bellmouth entry was predicted to deteriorate the total efficiency by 1 %, and to increase the emitted noise by 2 d*B*. This underlines the importance of systematic, tuned design of the rotor + its inlet section, for simultaneous reduction of loss and noise.

5) In the future, the predictions are to be confirmed by experiments. For this purpose, a bellmouth entry is to be designed and manufactured for realization of uniform axial velocity profile. The bellmouth entry is to be installed to the inlet of the case study fan, instead of the presently available short, rounded inlet rim. The aerodynamic and acoustic measurements are to be repeated for confirmation of the trends outlined in the previous point.

ACKNOWLEDGEMENTS

This work has been supported by the Hungarian National Fund for Science and Research under contract No. OTKA K 112277.

Gratitude is expressed to Ms. Anna Ilona Sipos for her help in programing, to Ms. Anna Tóth for the CFD simulations, and to Dr. Csaba Horváth and Mr. Bence Tóth for their useful comments.

The work relates to the scientific programs "Development of quality-oriented and harmonized R+D+I strategy and the functional model at BME" (Project ID: TÁMOP-4.2.1/B-09/1/KMR-2010-0002) and "Talent care and cultivation in the scientific workshops of BME" (Project ID: TÁMOP-4.2.2/B-10/1-2010-0009).

REFERENCES

[1] Vad, J., 2011, “Correlation of Flow Path Length to Total Pressure Loss in Diffuser Flows”, *Proceedings IMechE, Part A - J Power Energy*, Vol. 225, pp. 481-496.

[2] Lieblein, S., 1965, *Experimental Flow in Two-Dimensional Cascades, Chapter VI in Aerodynamic Design of Axial-Flow Compressors*, NASA SP-36, Washington D.C.

[3] Carolus, T., 2003, *Ventilatoren*, Teubner Verlag.

[4] De Gennaro, M., and Kuehnelt, H., 2012, “Broadband Noise Modelling and Prediction for Axial Fans,” Proc. *International Conference on Fan Noise, Technology and Numerical Methods (FAN2012)*, Senlis, France, ISBN 978-0-9572374-1-4.

[5] EN ISO 5801:2008 (E), “*Industrial Fans. Performance testing using standardized airways*”.

[6] Benedek, T., and Vad, J., 2014, “Concerted Aerodynamic and Acoustic Diagnostics of an Axial Flow Industrial Fan, Involving the Phased Array Microphone Technique,” *ASME Paper* GT2014-25916.

[7] Benedek, T., and Vad, J., 2015, ”Spatially Resolved Acoustic and Aerodynamic Studies Upstream and Downstream of an Industrial Axial Fan with Involvement of the Phased Array Microphone Technique,” Proc. *11th European Conference on Turbomachinery Fluid Dynamics and Thermodynamics*, Madrid, Spain, Paper # 128.

[8] Benedek T., and Vad J., 2015, “An industrial on-site methodology for combined acoustic-aerodynamic diagnostics of axial fans, involving the Phased Array Microphone technique”, *Int. J Aeroacoustics* (accepted)

[9] Menter, F.-R., 1993, "Zonal two equations k–ω turbulence models for aerodynamic flows", AIAA paper 93-2906.

[10] Reese, H., Carolus, T., and Kato, C., 2007, "Numerical prediction of the aeroacoustic sound sources in a low pressure fan with inflow distortion", Proc. *International Conference on Fan Noise, Technology and Numerical Methods (FAN2007),* Lyon, France.

[11] Younsi, M., Bakir, F., Kouidri, S., and Rey, R., 2007, "Numerical and experimental study of unsteady flow in a centrifugal fan", *Proceedings IMechE, Part A - J Power Energy*, Vol. 221, pp. 1025-1036.

[12] Bamberger, K., and Carolus, T., 2012, "Optimization of axial fans with highly swept blades with respect to losses and noise reduction", Proc. *International Conference on Fan Noise, Technology and Numerical Methods (FAN2012)*, Senlis, France.

[13] Guédeney, T., and Moreau, S., 2015, "Unsteady RANS simulations of a low speed fan for analytical tonal noise prediction", Proc. *11th European Conference on Turbomachinery Fluid Dynamics and Thermodynamics*, Madrid, Spain, Paper # 123.

[14] Sharland, I. J., 1964, "Sources of noise in axial flow fans", *J Sound Vib*, Vol. 3, pp. 302-322.

[15] Carolus, T., Schneider, M., and Reese, H., 2007, "Axial fan broadband noise and prediction", *J Sound Vib*, Vol. 300, pp. 50-70.

[16] Koop, L., 2006, "Beamforming Methods in Microphone Array Measurements: Theory, Practice and Limitations," *VKI Lecture Series 2007/01: Experimental Aeroacoustics*, Rhode Saint-Genése, Belgium

[17] Sijtsma, P., Oerlemans, S., and Holthusen, H., 2001, "Location of Rotating Sources by Phased Array Measurements", AIAA Paper 2001-2167.

[18] VDI 3731 Blatt 2, 1990, "*Emissionkennwerte technischer Schallquellen. Ventilatoren.*"

Conference on Modelling Fluid Flow (CMFF'15)
The 16th International Conference on Fluid Flow Technologies
Budapest, Hungary, September 1-4, 2015

INTERPOLATION-ANALYTICAL APPROXIMATION OF THE MBWR32 EQUATION OF STATE TO ACCOUNT FOR THE PROPERTIES OF REAL WORKING FLUIDS IN THREE-DIMENSIONAL CALCULATIONS

Andrii RUSANOV[1], Roman RUSANOV[2], Piotr LAMPART[3],

[1] Department of the Hydro Power Machines, A.N. Podgorny Institute of Problems of Mechanical Engineering of NAS of Ukraine. E-mail: rusanov@ipmach.kharkov.ua
[2] Corresponding Author. Department of Turbines, The Szewalski Institute of Fluid-Flow Machinery, Polish Academy of Sciences. 14 Fiszera st., 80-231 Gdansk, Poland. Tel.: +48 58 699 52 48, Fax: +48 58 341 61 44, E-mail: rrusanov@imp.gda.pl
[3] Department of Turbines, The Szewalski Institute of Fluid-Flow Machinery, Polish Academy of Sciences. E-mail: lampart@imp.gda.pl

ABSTRACT

The paper describes a modified form of the Benedict-Webb-Rubin thermal equation of state with 32 members received on the basis of its thermodynamic functions. The developed method of interpolation-analytical approximation of the modified Benedict-Webb-Rubin equation of state accounts for the real properties of working medium in 3D calculations. Constants of the equation of state are selected on the basis of available thermodynamic property tables. On the one hand, it allows for sufficient accuracy, and on the other - does not require a significant increase in computational cost.

The proposed method is validated using a sample working fluid – MDM (silica oil), which is used in ORC cycles of low-power cogeneration plants. It is shown that the mBWR32 equation with the obtained constants provides a good accuracy in the whole range of variation of thermodynamic values in the gaseous state and on the saturation line.

Keywords: Benedict-Webb-Rubin equation of state, interpolation-analytical approximation, the free Helmholtz energy

NOMENCLATURE

a	$[m/s]$	sonic speed
C_p	$[J/(kg*K)]$	isobaric heat capacity
C_v	$[J/(kg*K)]$	isochoric heat capacity
f	$[J/kg]$	Helmholtz free energy
$G(i)$	[-]	constant of mBWR32 equation
h	$[J/kg]$	enthalpy
N	[W]	power
P	$[Pa]$	pressure
P_o	$[Pa]$	constant for Tamman equation
R	$[J/(kg*K)]$	gas constant
S	$[J/(kg*K)]$	entropy
T	$[K]$	temperature
u	$[J/kg]$	internal energy
γ	[-]	adiabatic index
η	[%]	efficiency
v	$[m^3/kg]$	specific volume
ρ	$[kg/m^3]$	density

1. INTRODUCTION

In modeling of spatial gas dynamic processes on the basis of numerical integration of the Reynolds-averaged Navier-Stokes equations, it is necessary to establish the relation between the thermodynamic quantities in the form of a state equation. Currently, the most common equations of state used in the three-dimensional computations are equations of perfect gas, Tammann and Van der Waals equations [1]. Unfortunately, in many cases, these equations do not provide the required accuracy of the results. A remedy could be the equation of Benedict-Webb-Rubin, which is one of the most universal and reliable equations of state. A direct use of this equation in three-dimensional calculations is currently not possible, because in that case the computing time is increased by 1.5 - 2 orders of magnitude.

The paper presents a modified form of the Benedict-Webb-Rubin thermal equation of state with 32 members (mBWR32). A method for the determination of constants of the modified Benedict-Webb-Rubin equation is proposed on the basis of the available tables of thermodynamic quantities. The quadruple precision of calculations (32 significant digits in floating point operations) is used for the determination of the constants as well as for the calculation of thermodynamic parameters. The proposed method is validated on a sample working fluid – MDM, which is used in ORC cycles of low-power cogeneration plants.

2. MODIFIED BENEDICT-WEBB-RUBIN EQUATION OF STATE. BASIC THERMODYNAMIC FUNCTIONS

The thermally modified Benedict-Webb-Rubin equation of state of with 32 members [2] has the form:

$$
\begin{aligned}
P &= \rho RT + \rho^2\left[G(1)T + G(2)T^{1/2} + G(3) + \frac{G(4)}{T} + \frac{G(5)}{T^2}\right] \\
&+ \rho^3\left[G(6)T + G(7) + \frac{G(8)}{T} + \frac{G(9)}{T^2}\right] + \\
&+ \rho^4\left[G(10)T + G(11) + \frac{G(12)}{T}\right] + \rho^5[G(13)] + \\
&+ \rho^6\left[\frac{G(14)}{T} + \frac{G(15)}{T^2}\right] + \rho^7\left[\frac{G(16)}{T}\right] + \\
&+ \rho^8\left[\frac{G(17)}{T} + \frac{G(18)}{T^2}\right] + \rho^9\left[\frac{G(19)}{T^2}\right] + \\
&+ \rho^3\left[\frac{G(20)}{T^2} + \frac{G(21)}{T^3}\right]\exp(\gamma\rho^2) + \\
&+ \rho^5\left[\frac{G(22)}{T^2} + \frac{G(23)}{T^4}\right]\exp(\gamma\rho^2) + \\
&+ \rho^7\left[\frac{G(24)}{T^2} + \frac{G(25)}{T^3}\right]\exp(\gamma\rho^2) + \\
&+ \rho^9\left[\frac{G(26)}{T^2} + \frac{G(27)}{T^4}\right]\exp(\gamma\rho^2) + \\
&+ \rho^{11}\left[\frac{G(28)}{T^2} + \frac{G(29)}{T^3}\right]\exp(\gamma\rho^2) + \\
&+ \rho^{13}\left[\frac{G(30)}{T^2} + \frac{G(31)}{T^3} + \frac{G(32)}{T^4}\right]\exp(\gamma\rho^2)
\end{aligned} \tag{1}
$$

For the simulation of spatial viscous flows it is necessary to know thermodynamic dependencies for the following values: u; $h=u+P/\rho$; C_v; C_p; S; a. To determine these dependencies, differential equations of thermodynamics [1], equation (1) and a dependence for the Helmholtz free energy f are used. The Helmholtz free energy can be introduced into equation (1) using the expression:

$$P = \rho^2\left(\frac{\partial f}{\partial \rho}\right)_T \tag{2}$$

Equation (2) allows us to express the Helmholz free energy f in the form of an arbitrary polynomial with respect to T. In this paper, the expression for the Helmholtz free energy taken in the form:

$$f = f_i + f_v \tag{3}$$

where

$$
\begin{aligned}
f_i &= RTln(\rho) + \\
&+ \rho\left[G(1)T + G(2)\sqrt{T} + G(3) + \frac{G(4)}{T} + \frac{G(5)}{T^2}\right] + \\
&+ \frac{\rho^2}{2}\left[G(6)T + G(7) + \frac{G(8)}{T} + \frac{G(9)}{T^2}\right] + \\
&+ \frac{\rho^3}{3}\left[G(10)T + G(11) + \frac{G(12)}{T}\right] + \frac{\rho^4}{4}G(13) + \\
&+ \frac{\rho^5}{5}\left[\frac{G(14)}{T} + \frac{G(15)}{T^2}\right] + \frac{\rho^6}{6}\frac{G(16)}{T} + \\
&+ \frac{\rho^7}{7}\left[\frac{G(17)}{T} + \frac{G(18)}{T^2}\right] + \frac{\rho^8}{8}\frac{G(19)}{T^2} + \\
&+ \frac{G(33)}{T} + G(34)T + G(35)T^2 + G(36)Tln(T) + \\
&+ G(37);
\end{aligned}
$$

$$
\begin{aligned}
f_V &= I_1\left[\frac{G(20)}{T^2} + \frac{G(21)}{T^3}\right] + I_2\left[\frac{G(22)}{T^2} + \frac{G(23)}{T^4}\right] + \\
&+ I_3\left[\frac{G(24)}{T^2} + \frac{G(25)}{T^3}\right] + I_4\left[\frac{G(26)}{T^2} + \frac{G(27)}{T^4}\right] + \\
&+ I_5\left[\frac{G(28)}{T^2} + \frac{G(29)}{T^3}\right] + \\
&+ I_6\left[\frac{G(30)}{T^2} + \frac{G(31)}{T^3} + \frac{G(32)}{T^4}\right];
\end{aligned}
$$

$$I_1 = \int \rho \exp(\gamma\rho^2)d\rho = \frac{1}{2\gamma}\exp(\gamma\rho^2);$$

$$I_2 = \int \rho^3 \exp(\gamma\rho^2)d\rho = \frac{\gamma\rho^2 - 1}{2\gamma^2}\exp(\gamma\rho^2);$$

$$I_3 = \int \rho^5 \exp(\gamma\rho^2)d\rho = \frac{\gamma^2\rho^4 - 2\gamma\rho^2 + 2}{2\gamma^3}\exp(\gamma\rho^2);$$

$$I_4 = \int \rho^7 \exp(\gamma\rho^2)d\rho = \frac{\gamma^3\rho^6 - 3\gamma^2\rho^4 + 6\gamma\rho^2 - 6}{2\gamma^4}\exp(\gamma\rho^2);$$

$$I_5 = \int \rho^9 \exp(\gamma\rho^2)d\rho = \frac{\gamma^4\rho^8 - 4\gamma^3\rho^6 + 12\gamma^2\rho^4 - 24\gamma\rho^2 + 24}{2\gamma^5}\exp(\gamma\rho^2);$$

$$I_6 = \int \rho^{11} \exp(\gamma\rho^2)d\rho = \begin{pmatrix}\gamma^5\rho^{10} - 5\gamma^4\rho^8 + 20\gamma^3\rho^6 - \\ -60\gamma^2\rho^4 + 120\gamma\rho^2 - 120\end{pmatrix}\frac{\exp(\gamma\rho^2)}{2\gamma^6}$$

An additional polynomial comprising five members is supplemented to equation (3), which leads to an increase in the number of constants G from 32 to 37. This polynomial yields zero value to equation (1). In view of (1) and (3) the required thermodynamic functions take the form as below:

The internal energy:

$$u = f - T\left(\frac{\partial f}{\partial T}\right)_\rho \tag{4}$$

where $\left(\frac{\partial f}{\partial T}\right)_\rho = \left(\frac{\partial f_i}{\partial T}\right)_\rho + \left(\frac{\partial f_V}{\partial T}\right)_\rho$;

$$\left(\frac{\partial f_i}{\partial T}\right)_\rho = R ln(\rho) +$$
$$+\rho\left[G(1) + \frac{1}{2}\frac{G(2)}{\sqrt{T}} - \frac{G(4)}{T^2} - 2\frac{G(5)}{T^3}\right] +$$
$$+\frac{\rho^2}{2}\left[G(6) - \frac{G(8)}{T^2} - 2\frac{G(9)}{T^3}\right] +$$
$$+\frac{\rho^3}{3}\left[G(10) - \frac{G(12)}{T^2}\right] + \frac{\rho^5}{5}\left[-\frac{G(14)}{T^2} - 2\frac{G(15)}{T^3}\right] -$$
$$-\frac{\rho^6}{6}\frac{G(16)}{T^2} + \frac{\rho^7}{7}\left[-\frac{G(17)}{T^2} - 2\frac{G(18)}{T^3}\right] -$$
$$-\frac{\rho^8}{4}\frac{G(19)}{T^3} - \frac{G(33)}{T^2} + G(34) +$$
$$+2G(35)T + G(36) + G(36) ln(T);$$

$$\left(\frac{\partial f_v}{\partial T}\right)_\rho = I_1\left[-2\frac{G(20)}{T^3} - 3\frac{G(21)}{T^4}\right] +$$
$$+I_2\left[-2\frac{G(22)}{T^3} - 4\frac{G(23)}{T^5}\right] +$$
$$+I_3\left[-2\frac{G(24)}{T^3} - 3\frac{G(25)}{T^4}\right] +$$
$$+I_4\left[-2\frac{G(26)}{T^3} - 4\frac{G(27)}{T^5}\right] +$$
$$+I_5\left[-2\frac{G(28)}{T^3} - 3\frac{G(29)}{T^4}\right] +$$
$$+I_6\left[-2\frac{G(30)}{T^3} - 3\frac{G(31)}{T^4} - 4\frac{G(32)}{T^5}\right].$$

Isochoric heat capacity:

$$c_V = \left(\frac{\partial u}{\partial T}\right)_\rho = \left(\frac{\partial f}{\partial T}\right)_\rho - \left(\frac{\partial f}{\partial T}\right)_\rho -$$
$$-T\left(\frac{\partial^2 f}{\partial T^2}\right)_\rho = -T\left(\frac{\partial^2 f}{\partial T^2}\right)_\rho \tag{5}$$

where $\left(\frac{\partial^2 f}{\partial T^2}\right)_\rho = \left(\frac{\partial^2 f_i}{\partial T^2}\right)_\rho + \left(\frac{\partial^2 f_V}{\partial T^2}\right)_\rho$;

$$\left(\frac{\partial^2 f_i}{\partial T^2}\right)_\rho = \rho\left[-\frac{1}{4}\frac{G(2)}{T^{\frac{3}{2}}} + 2\frac{G(4)}{T^3} + 6\frac{G(5)}{T^4}\right] +$$
$$+\frac{\rho^2}{2}\left[2\frac{G(8)}{T^3} + 6\frac{G(9)}{T^4}\right] + \frac{2}{3}\rho^3\frac{G(12)}{T^3} +$$
$$+\frac{\rho^5}{5}\left[2\frac{G(14)}{T^3} + 6\frac{G(15)}{T^4}\right] + \frac{\rho^6}{3}\frac{G(16)}{T^3} +$$
$$+\frac{\rho^7}{7}\left[2\frac{G(17)}{T^3} + 6\frac{G(18)}{T^4}\right] + \frac{3}{4}\rho^8\frac{G(19)}{T^4} +$$
$$+2\frac{G(33)}{T^3} + 2G(35) + \frac{G(36)}{T};$$

$$\left(\frac{\partial^2 f_V}{\partial T^2}\right)_\rho = I_1\left[6\frac{G(20)}{T^4} + 12\frac{G(21)}{T^5}\right] +$$
$$+I_2\left[6\frac{G(22)}{T^4} + 20\frac{G(23)}{T^6}\right] +$$
$$+I_3\left[6\frac{G(24)}{T^4} + 12\frac{G(25)}{T^5}\right] +$$
$$+I_4\left[6\frac{G(26)}{T^4} + 20\frac{G(27)}{T^6}\right] +$$
$$+I_5\left[6\frac{G(28)}{T^4} + 12\frac{G(29)}{T^5}\right] +$$
$$+I_6\left[6\frac{G(30)}{T^4} + 12\frac{G(31)}{T^5} + 20\frac{G(32)}{T^6}\right]$$

Isobaric heat capacity:

$$c_P = \left(\frac{\partial h}{\partial T}\right)_P = \left[\frac{\partial}{\partial T}\left(u + \frac{P}{\rho}\right)\right]_P = \left(\frac{\partial u}{\partial T}\right)_P -$$
$$-\frac{P}{\rho^2}\left(\frac{\partial \rho}{\partial T}\right)_P = \left(\frac{\partial f}{\partial T}\right)_P - \left(\frac{\partial f}{\partial T}\right)_\rho - T\left[\frac{\partial\left(\frac{\partial f}{\partial T}\right)_\rho}{\partial T}\right]_P -$$
$$-\frac{P}{\rho^2}\left(\frac{\partial \rho}{\partial T}\right)_P = -T\left[\frac{\partial\left(\frac{\partial f}{\partial T}\right)_\rho}{\partial T}\right]_P =$$
$$= -T\left[\left(\frac{\partial^2 f}{\partial T^2}\right)_\rho + \frac{A}{\rho^2}\left(\frac{\partial \rho}{\partial T}\right)_P\right] =$$
$$= -T\left[\left(\frac{\partial^2 f}{\partial T^2}\right)_\rho - \frac{A^2}{\rho^2 B}\right] = c_V + \frac{A^2 T}{\rho^2 B} \tag{6}$$

where

$$A = \rho R + \rho^2\left[G(1) + \frac{1}{2}\frac{G(2)}{\sqrt{T}} - \frac{G(4)}{T^2} - 2\frac{G(5)}{T^3}\right]$$
$$+\rho^3\left[G(6) - \frac{G(8)}{T^2} - 2\frac{G(9)}{T^3}\right] +$$
$$+\rho^4\left[G(10) - \frac{G(12)}{T^2}\right] +$$
$$+\rho^6\left[-\frac{G(14)}{T^2} - 2\frac{G(15)}{T^3}\right] - \rho^7\left[\frac{G(16)}{T^2}\right] +$$
$$+\rho^8\left[-\frac{G(17)}{T^2} - 2\frac{G(18)}{T^3}\right] - 2\rho^9\left[\frac{G(19)}{T^3}\right] +$$
$$+\rho^3\left[-2\frac{G(20)}{T^3} - 3\frac{G(21)}{T^4}\right]\exp(\gamma\rho^2) +$$
$$+\rho^5\left[-2\frac{G(22)}{T^3} - 4\frac{G(23)}{T^5}\right]\exp(\gamma\rho^2) +$$

$$+\rho^7\left[-2\frac{G(24)}{T^3}-3\frac{G(25)}{T^4}\right]\exp(\gamma\rho^2)+$$
$$+\rho^9\left[-2\frac{G(26)}{T^3}-4\frac{G(27)}{T^5}\right]\exp(\gamma\rho^2)+$$
$$+\rho^{11}\left[-2\frac{G(28)}{T^3}-3\frac{G(29)}{T^4}\right]\exp(\gamma\rho^2)+$$
$$+\rho^{13}\left[-2\frac{G(30)}{T^3}-3\frac{G(31)}{T^4}-4\frac{G(32)}{T^5}\right]\exp(\gamma\rho^2);$$

$$B=RT+2\rho\left[G(1)T+G(2)\sqrt{T}+G(3)+\frac{G(4)}{T}+\frac{G(5)}{T^2}\right]+$$
$$+3\rho^2\left[G(6)T+G(7)+\frac{G(8)}{T}+\frac{G(9)}{T^2}\right]+$$
$$+4\rho^3\left[G(10)T+G(11)+\frac{G(12)}{T}\right]+$$
$$+5\rho^4[G(13)]+6\rho^5\left[\frac{G(14)}{T}+\frac{G(15)}{T^2}\right]+$$
$$+7\rho^6\left[\frac{G(16)}{T}\right]+8\rho^7\left[\frac{G(17)}{T}+\frac{G(18)}{T^2}\right]+$$
$$+9\rho^8\left[\frac{G(19)}{T}\right]+\left(3\rho^2+2\gamma\rho^4\right)\left[\frac{G(20)}{T^2}+\frac{G(21)}{T^3}\right]*$$
$$*\exp(\gamma\rho^2)+\left(5\rho^4+2\gamma\rho^6\right)*\left[\frac{G(22)}{T^2}+\frac{G(23)}{T^4}\right]\exp(\gamma\rho^2)+$$
$$+\left(7\rho^6+2\gamma\rho^8\right)\left[\frac{G(24)}{T^2}+\frac{G(25)}{T^3}\right]\exp(\gamma\rho^2)+$$
$$+\left(9\rho^8+2\gamma\rho^{10}\right)\left[\frac{G(26)}{T^2}+\frac{G(27)}{T^4}\right]\exp(\gamma\rho^2)+$$
$$+\left(11\rho^{10}+2\gamma\rho^{12}\right)\left[\frac{G(28)}{T^2}+\frac{G(29)}{T^3}\right]\exp(\gamma\rho^2)$$
$$+(13\rho^{12}+2\gamma\rho^{14})\left[\frac{G(30)}{T^2}+\frac{G(31)}{T^3}+\frac{G(32)}{T^4}\right]\exp(\gamma\rho^2)\cdot$$

Entropy:

$$S=-\left(\frac{\partial f}{\partial T}\right)_\rho \tag{7}$$

Sonic speed:

$$a^2=\left(\frac{\partial P}{\partial\rho}\right)_S=\frac{T\left(\frac{\partial P}{\partial T}\right)_\rho+c_V\left(\frac{\partial T}{\partial v}\right)_P}{\rho^2 c_V\left(\frac{\partial T}{\partial P}\right)_\rho}=$$
$$=\frac{T\left(\frac{\partial P}{\partial T}\right)_\rho+c_V\rho^2\left(\frac{\partial T}{\partial\rho}\right)_P}{\rho^2 c_V\left(\frac{\partial T}{\partial P}\right)_\rho}=B+\frac{TA^2}{c_V\rho^2} \tag{8}$$

3. METHOD OF INTERPOLATION-ANALYTICAL APPROXIMATION OF THE THERMODYNAMIC FUNCTIONS

For the first time, this method was applied in the three-dimensional calculation to account for the thermodynamic properties of water and steam based on the equation of state IAPWS-95 [3, 4]. Under this approach, the required thermodynamic functions were determined by the dependencies:

$$T=\frac{p}{\rho R z\_t(\rho,p)};\ \rho=\frac{p}{h}z\_\rho(h,p);$$
$$u=\frac{p}{\rho}\frac{z\_u(\rho,p)}{z\_t(\rho,p)};\ p=\rho\cdot u\cdot z\_p(\rho,u);$$
$$a=\sqrt{\frac{p}{\rho}\frac{z\_a(\rho,p)}{z\_t(\rho,p)}};\ h=\frac{p}{\rho}\left(1+\frac{z\_u(\rho,p)}{z\_t(\rho,p)}\right);$$
$$C_V=R\cdot z\_C_V(\rho,p);\ S=R\cdot z\_S(\rho,p);$$
$$u_p=\frac{z\_u(\rho,p)}{\rho\cdot z\_t(\rho,p)};\ u_\rho=-\frac{p}{\rho}\frac{z\_u(\rho,p)}{z\_t(\rho,p)};$$
$$S_p=\frac{C_V}{p};\ S_\rho=-\frac{C_p}{\rho};\ T_p=\frac{1}{\rho R\cdot z\_t(\rho,p)};$$
$$T_\rho=-\frac{p}{\rho^2 R\cdot z\_t(\rho,p)} \tag{9}$$

where $z\_t(\rho,p)$, $z\_\rho(h,p)$, $z\_u(\rho,p)$, $z\_p(\rho,u)$, $z\_C_v(\rho,p)$, $z\_C_p(\rho,p)$ $z\_S(\rho,p)$ – the dimensionless compressibility coefficients for the corresponding thermodynamic functions determined by interpolation from a pre-calculated arrays of the base points. To reduce the dimension of the array without a loss of accuracy, independent variables - the pressure and density - are considered in a logarithmic scale.

Values of the dimensionless compressibility coefficients are defined in the base points as:

$$z\_t=\frac{p}{\rho RT};\ z\_u=\frac{u}{RT};\ z\_\rho=\frac{h\rho}{p};$$
$$z\_p=\frac{p}{\rho\cdot u};\ z\_a=\frac{a^2}{RT};\ z\_C_V=\frac{C_V}{R};$$
$$z\_C_p=\frac{C_p}{R};\ z\_S=\frac{S}{R}, \tag{10}$$

where corresponding values p, ρ, T, u, h, a, C_p, C_v and S are calculated using the thermodynamic relations (1, 4-8).

4. DETERMINATION OF CONSTANTS FOR THE EQUATION OF STATE

Usually, constants for equations of state are determined based on the experimental data. In the literature, one can find information about values of the constants of simple equations of state for various types of working media [2]. Open information about values of constants for the modified Benedict-Webb-Rubin equation of state with 32 members is available only for a few working media [1]. However, there are various software packages that allow us to calculate the array of fields of thermodynamic functions for any working medium. Theoretically, these arrays can be directly used in the determination of the coefficients (10). Using the existing software, it is usually possible to obtain arrays of a few hundred points only. However, to maintain the high accuracy of three-dimensional gas dynamics calculations, the dimension of arrays should typically be as high as a few million. Therefore, in the described method the obtained arrays of thermodynamic function values are used to determine the necessary constants of the Benedict-Webb-Rubin equation of state, and then new arrays of the required dimension are calculated with the help of equations (1, 4-8).

The gas constant R is determined as a ratio of the universal gas constant to the molecular weight of the considered working medium. The remaining constants γ, G are determined using the least squares method [5, 6] to assure the smallest square deviation of the dimensionless unknown function from the array base point values:

$$\sum_{i=1}^{n}\left(\frac{f_i - y_i}{y_i}\right)^2 \to \min \tag{11}$$

where f_i – the required thermodynamic function of the modified Benedict-Webb-Rubin equation of state at point i of the array; y_i – value of the thermodynamic function at point i; n – dimension of the base points array. The problem (11) can be solved in the following way. If γ is assumed as known and constant, then the conditon (11) can be replaced by the condition (12):

$$\sum_{i=1}^{n}\sum_{j=1}^{37}\left(\frac{f_i - y_i}{y_i^2}\frac{\partial f_i}{\partial G_j}\right) = 0 \tag{12}$$

where j is the number of constants G. The expression (12) is a system of 37 linear equations with respect to 37 unknowns G for the thermodynamic functions: the pressure, Helmholtz free energy, entropy and the partial derivative of pressure with respect to density at constant temperature. The linear system of equations (12) is solved by the Gauss method with dominant diagonal terms [5, 6]. The accuracy of calculations is set at quadruple precision with 32 characters. Such a large mantissa is needed to maintain the required high accuracy. The global search for the problem (11) is carried out by varying γ in the range:

$$-100\rho_*^2 \le \gamma \le 100\rho_*^2 \tag{13}$$

where ρ_* is the value of the density at the critical point. Constants are found for the simultaneous fulfillment of condition (11) for the following thermodynamic functions: pressure, the Helmholtz free energy, entropy, and the partial derivative of pressure with respect to density at constant temperature.

5. APPROBATION OF THE PROPOSED METHOD

To validate the functionality of the method, sample detailed numerical investigations were carried out for the expansion line of four last stages (stages 4-7) of a 100 kW ORC cogeneration turbine operating on MDM as a working medium [7, 8]. The meridional section of the turbine flow part is presented in Figue 1, whereas stator and rotor profiles of the investigated stages 4-7 are illustrated in Figure 2. The calculations were performed with the following boundary conditions:

- inlet parameters upstream of stage 4:
  - pressure: 2.76 *bar*;
  - temperature: 530.4 *K*;
- outlet parameters:
  - pressure: 0.17 *bar*;
- rotational speed: 9000 *rev/min*.

3D numerical investigations of flow were made with the help of the software complex *IPMFlow*, which is the development of the software systems *FlowER* and *FlowER-U*. It implements the following elements of the mathematical model: the unsteady Reynolds-averaged Navier-Stokes equations, SST Menter differential two-equation turbulence model, implicit quasi-monotone high-order ENO-scheme [9, 10].

A base point array of values of thermodynamic functions was obtained with the help of the program REFPROP [11] in 735 points within the entire range of pressure and temperature available for this medium in REFPROP. The following values of constants were obtained:

R= 0.3515168000E+02;
γ=-0.26227017080742012151357373739971D-04
G(01)= 0.30220786811127874006041159254D+00
G(02)= -0.495233944170545289062576542307D+01
G(03)= -0.225501201197491314642998011829D+03
G(04)= 0.107906234213802120996678810443D+06
G(05)= -0.372657132543797518687633762851D+08
G(06)= -0.627320725108084212417049028312D-03
G(07)= 0.215743936748432144179678929724D+01
G(08)= -0.192205460461420765746900736543D+04
G(09)= 0.517361137204233382712063500157D+06
G(10)= 0.766264823125748039322791551715D-06
G(11)= -0.434353699956369187362735134447D-02
G(12)= 0.161657815774704243989178292974D+01
G(13)= 0.288814234808349750753865171475D-05
G(14)= 0.227250568997175780038146727298D-04
G(15)= -0.652886158820518451942746541068D-02
G(16)= -0.456739733049471206918455720386D-07
G(17)= 0.231242587293920118661113372857D-10
G(18)= 0.186380264921967994590840358405D-07
G(19)= -0.126528342901003631469807144831D-10
G(20)= 0.347527618252179836075855868907D+06
G(21)= -0.160950582611693360862236427413D+09

G(22)= 0.693289101786031245959518372491D+01
G(23)= -0.953438468030805490987102326088D+06
G(24)= 0.297824147414970198157551618564D-03
G(25)= -0.2305342355531245981576803850333D+00
G(26)= -0.213236230412490644485878013528D-08
G(27)= 0.167631613366536556924666638381D-02
G(28)= 0.904911503767510905693979818203D-13
G(29)= -0.704815505181047779157572048773D-10
G(30)= -0.501394975086843725544491118562D-18
G(31)= 0.454671117815342747169810491557D-15
G(32)= -0.539871248063102930246035212608D-13
G(33)= 0.117126880134545422586004289266D+09
G(34)= 0.140470196549871558017639577219D+05
G(35)= -0.469999084243383589981287193248D+00
G(36)= -0.193705173670445390344105907111D+04
G(37)= -0.116961966600901591984328215895D+07.

(14)

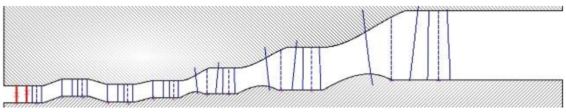

Figure 1. The meridional section of the flow part.

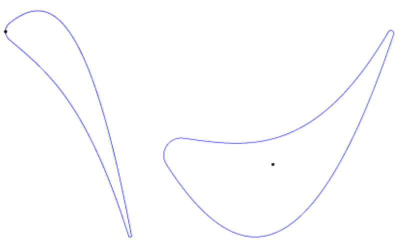

Stator and rotor of stage 4

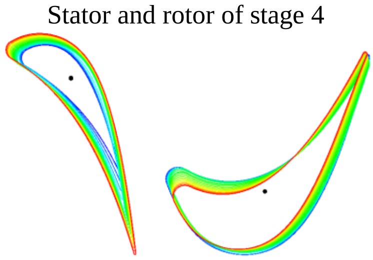

Stator and rotor of stage 5

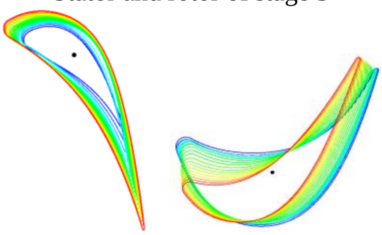

Stator and rotor of stage 6

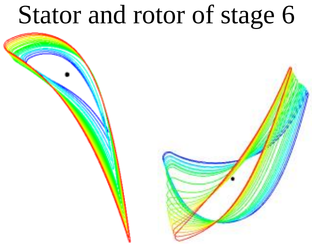

Stator and rotor of stage 7

Figure 2. Hub-to-tip profile sections for stage 4-7

With the above constants (14), the mean square deviation of values of thermodynamic functions (1, 4-8) from the array base point values is equal to 0.02%, whereas the maximum square deviation does not exceed 0.17%.

The calculations were performed for the h-type grid with the total number of cells in one stage more than 1 million (about 500 thousand cells in one blade), where y+ is less than 5. 1 CPU was used for 3D calculations of 1 stage. The computational time needed for the calculation of one turbine stage using the Tammann equation of state is equal to about 12 hours. Using tables of state (mBWR32 equation of state), it takes near 14 hours of computations for a one stage.

Figure 3 shows sample visualisation of flow patterns in the investigated turbine stages obtained from 3D calculations with the modified Benedict-Webb-Rubin equation of state. The pictures of velocity vectors exhibit regular flow patterns and a relatively high flow efficiency.

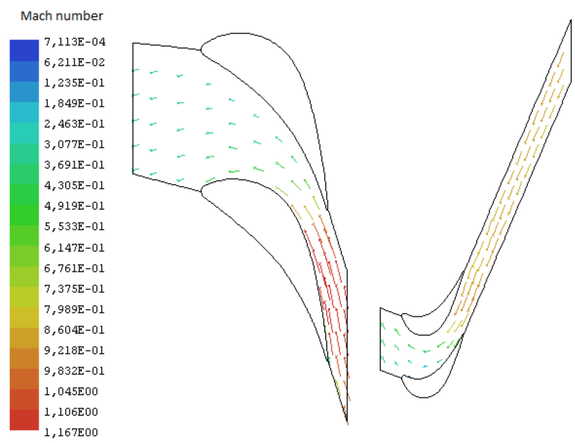

Figure 3. Velocity vectors in the last stage at the average blade-to-blade section (50% of blade height)

The calculations using the methodology of interpolation-analytical approximation of the modified Benedict-Webb-Rubin equation of state with 32 members are compared with those of the Tammann equation of state:

$$p+p_0=R\rho T \qquad (15)$$

Constants for the Tammann equation were evaluated from static inlet parameters and isentropic outlet parameters of the working medium:

γ=1.019;
c_p=1689.8 $J/(kg*K)$;
R=31.64 $J/(kg*K)$;
P_o=-1613.07 Pa;

(16)

Tables 1 and 2 show the comparison of results obtained from the two considered state equations. The comparison of flow parameters in the axial gaps downstream of subsequent stages and enthalpy drops in subsequent stages is given in Table 1, whereas integral characteristics of the stages and stage group are gathered and compared in Table 2.

The calculations using the modified Benedict-Webb-Rubin equation of state exhibit slightly larger drops of pressure, temperature and enthalpy in subsequent stages and predict higher flow efficiency in the calculated turbine stages. In the presented case, the differences between the results shown in Tables 1-2 are not that significant. This is due to the fact that in this flow part, the absolute values of pressure, temperature and enthalpy drops are not that high and, most important, because MDM belongs to the class of dry fluids. The differences are expected to be much higher for wet medium with phase transitions within the expansion range. More investigations will be carried for both dry and wet medium, including water vapour, and they will soon be validated by experimental data.

Table 1. Comparative characteristics of steam parameters in the axial gaps

Stage №	Equation of state	P_{out}, *bar*	*T, K*	Δh, *J/kg*
4	Tammann	1.53	525.3	8431
	mBWR32	1.54	524.6	8597
5	Tammann	0.8	519.7	9609
	mBWR32	0.79	518.7	9943
6	Tammann	0.4	513.7	10126
	mBWR32	0.39	512.8	10650
7	Tammann	0.17	505.9	13208
	mBWR32	0.17	505.7	13310

Table 2. Comparative characteristics of integral characteristics

stage №	Equation of state	η, %	*N, kW*
4	Tammann	83.94	12.8
	mBWR32	87.12	13.2
5	Tammann	87.33	15.75
	mBWR32	86.92	16.1
6	Tammann	87.97	17.35
	mBWR32	87.36	18.1
7	Tammann	90.94	21.8
	mBWR32	90.75	21.55
4-7	Tammann	87.99	67.7
	mBWR32	88.32	69.1

6. CONCLUSION

A method of interpolation-analytical approximation of the modified Benedict-Webb-Rubin equation of state was developed to account for real properties of working medium in three-dimensional flow calculations. Constants of the modified Benedict-Webb-Rubin equation of state with 32 members were determined on the basis of the available arrays of thermodynamic functions, values. The method allows us on the one hand to provide a sufficient accuracy, and on the other hand does not require a significant increase in computational cost. Test calculations of the last 4 stages of a 100 kW ORC turbine with MDM as a working medium are presented. It is shown that the proposed method of determination of the state equation constants yields the standard deviation of 0.02% and the maximum deviation of 0.17% from the array values. Differences in evaluation of flow parameters using the modified Benedict-Webb-Rubin equation of state and Tammann equation in the axial gaps downstream of the subsequent stages are also described. These results will soon be validated by experimental data.

REFERENCES

1. Nashchokin, V. V., 1980, Technical Thermodynamics and Heat Transfer, 496 p. (in Russian).

2. Younglove, B. A. and Ely, J. F., 1987, “Thermophysical Properties of Fluids II Methane, Ethane, Propane, Isobutane, and normal Butane”, Journal of Physical and Chemical Reference, Data 16, 577 p.

3. IAPWS, Revised Release on the IAPWS Formulation 1995 for the Thermodynamic Properties of Ordinary Water Substance for General and Scientific Use.

4. Rusanov, A.V., 2013, “Interpolation-analytical method of accounting for real properties of gases and liquids”, East European Journal of advanced technologies, Vol. 3/10 (63), pp. 53−57, ISSN 1729-3774 (in Russian)

5. Samarskij, A .A. and Gukin, A. V., 1989, Numerical methods, 432 p. (in Russian)

6. Volkov, E. A., 1987, Numerical methods, 248 p. (in Russian)

7. Rusanov, A. V., Lampart, P., Rusanov, R. A., Szymaniak, M., 2013, “ Development of the flow part of the turbine for cogeneration plant that uses low-boiling working body”, Vestnik of engine building, Vol. 2, pp. 35 – 44. (in Russian)

8. Rusanov, A., Lampart, P., Rusanov, R., Bykuc, S., 2013, “Elaboration of the flow system for a cogeneration ORC turbine”, Proc 12th Conf on Power System Engineering, Thermodynamics & Fluid Flow, Pilzen, Czech Republic, 10 p. (on CD)

9. Yershov, S.V. and Rusanov, A.V., 1996, Copyright certificate of complex three-dimensional calculation programs of gas flows in multistage turbomachines «FlowER». (in Ukrainian)

10. Rusanov, A.V. and Yershov, S.V., 2008 “Mathematical modeling of unsteady gasdynamic processes in the setting of turbomachines”, Kharkov: IPMash NAS of Ukraine, 275p. (in Russian)

11. REFPROP, National Institute of Standards and Technology Standard Reference Database Number 23.

Conference on Modelling Fluid Flow (CMFF'15)
The 16th International Conference on Fluid Flow Technologies
Budapest, Hungary, September 1-4, 2015

Transient numerical solutions of an extended Korteweg-De Vries equation describing solitary waves in open-channel flow

Richard JURISITS[1]

[1] Corresponding Author. Institute of Mechanics, University of Leoben, Franz-Josef-Strasse 18, A-8700 Leoben, Austria. Tel.: +43 3842 402 4018, Fax: +43 3842 46048, E-mail: richard.jurisits@unileoben.ac.at

ABSTRACT

A solitary wave in two-dimensional, incompressible, turbulent free-surface flow over a plane bottom with small, constant slope is considered. The flow is assumed to be slightly supercritical with Froude numbers close to 1. If the flow far upstream and far downstream is fully developed, a simple argument based on the law of momentum shows that for a solitary wave to exist, the bottom friction cannot be constant all along the channel bed. In [1] the situation was considered where the bottom roughness of the channel is constant over some distance and slightly higher than in the rest of the channel bed, giving rise to a higher bottom friction coefficient. In an asymptotic analysis in [1] an extended Korteweg-De Vries (KdV) equation was derived to describe the surface elevation of the fluid. Adopting this equation, we solved it numerically by posing an coupled boundary-value eigenvalue problem and obtained results for stationary and transient wave solutions as well as for the eigenvalue, which corresponds to distinct values of the bottom friction coefficient. While the numerical solutions as compared to the asymptotic solutions agree qualitatively in the stationary case, there were major differences found in case of the transient solutions.

Keywords: extended Korteweg-De Vries equation, free-surface flow, solitary wave, turbulent flow

NOMENCLATURE

H_1	$[-]$	dimensionless perturbation of fluid surface elevation
L	$[-]$	dimensionless length of region of enlarged bottom roughness
T	$[-]$	dimensionless time
V	$[-]$	dimensionless wave speed
X	$[-]$	dimensionless coordinate in main flow direction
X_0	$[-]$	initial position of transient asymptotic solution
Fr	$[-]$	Froude number
Re	$[-]$	Reynolds number
h	$[m]$	fluid surface elevation
k	$[-]$	root describing wave decay behaviour
t	$[s]$	time
u	$[m/s]$	flow velocity in main flow direction
x	$[m]$	coordinate in main flow direction
y	$[m]$	coordinate normal to main flow direction
$\vec{g}$	$[m/s^2]$	gravity acceleration vector
α	$[-]$	slope of channel bottom
β	$[-]$	expansion parameter
δ	$[-]$	auxiliary parameter
Γ	$[-]$	function characterizing region of enhanced bottom friction
λ	$[-]$	eigenvalue
ε	$[m/s^2]$	expansion parameter
φ	$[-]$	step function
ΔT	$[-]$	numerical time step
ΔX	$[-]$	numerical space step
ℓ	$[m]$	length of region of enlarged bottom roughness

Subscripts and Superscripts

T	time derivative
X	space derivative
m	maximum (crest) value
r	reference position far upstream
$\overline{abc}$	ensemble average
(0)	lowest order in asymptotic expansion
+	unstable
−	stable

1. INTRODUCTION

A solitary wave in two-dimensional, incompressible, turbulent free-surface flow over a plane bottom with small, constant slope α is considered, see Figure 1. If the flow far upstream and far downstream is fully developed, a simple argument based on the law of momentum shows that for a solitary wave to exist, the bottom friction cannot be constant

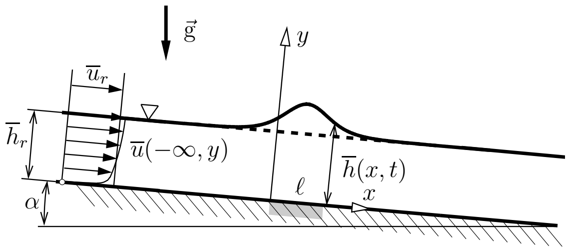

Figure 1. A solitary wave in open-channel flow. The nomenclature was taken from [1], with overbars indicating ensemble-averaged quantities of the velocity $u(x, y, t)$ in direction x parallel to the channel bottom and the surface elevation $h(x, t)$. The subscript r denotes some reference position very far upstream where the flow is fully developed. The shaded region of length ℓ indicates a region with increased bottom roughness.

all along the channel bed. Since the momentum flow rate far upsteam and far downstream is the same, the forces acting on a control volume of fluid must balance. Forces arising from the hydrostatic pressure cancel, too. If surface tension and surface shear forces are neglected, the increased weight of the fluid under the solitary wave must therefore be balanced by increased bottom friction forces.

Following that argument, a situation as in Fig. 1 is considered, where the bottom roughness of the channel is assumed to be constant over some distance ℓ and slightly higher than in the rest of the channel bed, giving rise to a higher bottom friction coefficient. The flow is assumed to be slightly supercritical with Froude numbers close to 1.

In an analysis given by Schneider [1], a coupled asymptotic expansion of the Reynolds-averaged Navier-Stokes equations was performed for differences of the Froude number to 1, $(\mathrm{Fr} - 1) \equiv \varepsilon \to 0$, the Reynolds number $\mathrm{Re} \to \infty$, and the slope of the channel bottom $\alpha \to 0$, with the remarkable feature that any recourse to turbulence modelling was avoided. $\overline{h}_r$ and $\overline{u}_r$ were defined to denote the reference quantities of Reynolds-averaged fluid elevation and volumetric mean velocity, respectively, in fully developed flow. The main result of the asymptotic analysis was an extended KdV equation describing the surface elevation $\overline{h} = (1 + \varepsilon H_1)\overline{h}_r$ of the fluid in terms of the dimensionless coordinate $X = 3\sqrt{\varepsilon}x/\overline{h}_r$ and dimensionless time $T = (9/2)\varepsilon^{3/2}(\overline{u}_r/\overline{h}_r)t$ and reads as follows:

$$H_{1,T} = H_{1,XXX} + (H_1 - 1)\, H_{1,X} - \beta\, [H_1 - \Gamma(X)]\,. \qquad (1)$$

The term extending the classical KdV equation includes a parameter β, which is small within the assumptions of the asymptotic expansion and which characterizes the effect of turbulent dissipation. The function $\Gamma(X)$ describes the increased bottom friction due to the increased roughness over the bottom length ℓ and was assumed to be given as

$$\Gamma(X) = \lambda\varphi(X) \qquad (2)$$

with

$$\varphi(X) \equiv 1 \text{ for } 0 < X < L,$$
$$\text{and } \varphi(X) \equiv 0 \text{ for all other values of } X, \qquad (3)$$

where $L = 3\sqrt{\varepsilon}\ell/\overline{h}_r$ was taken to be 1 in [1]. The eigenvalue λ determines the amount of increase in bottom roughness as necessary for the fluid to fulfill the conditions of the law of momentum. Eq. (1), together with the obvious boundary conditions for a solitary wave

$$X \to \pm\infty : H_1 \to 0, \qquad (4)$$

was solved in [1] again by asymptotic methods for small values of β.

2. STATIONARY SOLUTIONS

First, the stationary form of the extended KdV, Eq. (1) with $H_{1,T} \equiv 0$ was considered. The results for this case were already presented in a previous work, see [2].

For the friction-free case $\beta = 0$ and $\Gamma \equiv 0$, a well-known analytical solution of Eq. (1) is the solitary wave solution

$$H_1^{(0)} = 3\,\mathrm{sech}^2[(X - X_m^{(0)})/2], \qquad (5)$$

with its crest located at the undetermined position $X_m^{(0)}$.

From the asymptotic theory in [1] it follows that to lowest order in the expansion parameter β the solution of Eq. (1) is given by $H_1 = H_1^{(0)}$, with $X_m^{(0)} = \left\{X_m^{(0)-} = -0.8164, X_m^{(0)+} = 1.8164\right\}$ and $\lambda = \lambda^{(0)} = 12$. The two eigensolutions $H_1^{(0)-}$ and $H_1^{(0)+}$ termed stable and unstable in [1], corresponding to positions of the wave crests $X_m^{(0)} = X_m^{(0)-}$ and $X_m^{(0)} = X_m^{(0)+}$, respectively, refer to the classical notion whether (full time-dependent) solutions of Eq. (1) starting close to the corresponding stationary solution will stay close to or rather diverge, respectively, from the stable or unstable stationary solution in the limit of large times.

Numerical solutions of Eq. (1) may be obtained by formulating a coupled boundary-value eigenvalue problem with respect to the space variable X. In addition to the two boundary conditions in Eq. (4), Eq. (1) needs to be supplemented by two further boundary conditions, which may be posed as to obtain the correct decay behaviour of H_1 for $X \to \pm\infty$. Assuming H_1 to decay as $H_1 \sim \exp(kX)$, Eq. (1) gives

$$k^3 - k - \beta = 0, \qquad (6)$$

with three roots which are real for $\beta \leq \beta_{max} \approx 0.383$. For small values of β these roots are

$$\begin{aligned} k_1 &= -1 + \tfrac{1}{2}\beta + O(\beta^2), \\ k_2 &= -\beta + O(\beta^2), \\ k_3 &= 1 + \tfrac{1}{2}\beta + O(\beta^2). \end{aligned} \tag{7}$$

In the numerical solutions presented in the following, the two additional boundary conditions used were

$$X \to -\infty : H_{1,X} \to k_3, \tag{8}$$

$$X \to +\infty : H_{1,X} \to k_1, \tag{9}$$

with the corresponding exact solutions of Eq. (6). The choice of k_1 instead of k_2 in Eq. (9) for $X \to +\infty$ gives a "fast" decay behaviour as compared to the choice of k_2 and was motivated by the results of the numerical integration, which was carried out for both choices and revealed rather large gradients close to the right end of the integration domain in case of the choice of k_2, which was therefore dropped in the following considerations. The numerical solutions of the full Eq. (1) for the stationary case were obtained with the package MATLAB R2010A using the BVP4c integrator. Typical values chosen were for the stepsize $\Delta X \approx 2 \cdot 10^{-3}$ and relative error tolerances of 10^{-9}. The discontinuous function $\varphi(X)$ defined in Eq. (3) was replaced by the approximating function $\frac{1}{4}(1 + \tanh(X/\delta))(1 - \tanh((X - L)/\delta))$ with $\delta = 0.01$ in order to avoid difficulties in determining numerical derivatives.

3. TRANSIENT SOLUTIONS

In [1], a method originally due to Scott [3] was applied to obtain an asymptotic solution for transient values of the crest heights $H_{1m}(T)$ for $L = 1$, and a first-order ordinary differential equation valid for small values of β and slowly varying wave speeds V of the solitary wave was obtained:

$$\begin{aligned} \frac{3}{\beta}\frac{\mathrm{d}V}{\mathrm{d}T} &= 4(1-V) \\ -12\Big\{&\tanh\left[\tfrac{1}{2}(1 - X_0 - VT)\sqrt{1-V}\right] \\ &+ \tanh\left[\tfrac{1}{2}(X_0 + VT)\sqrt{1-V}\right]\Big\}. \end{aligned} \tag{10}$$

The transient asymptotic solution thereby is still of the form of a sech^2 function, with its amplitude given by $3(1 - V)$ and its crest being located at $X_m^{(0)} = X_0 + VT$. For the special case of $V \equiv 0$, Eq. 10 gives just an algebraic condition with the asymptotic values for the stationary crest positions $X_m^{(0)-}$ and $X_m^{(0)+}$ as solutions, which were obtained earlier in the asymptotic analysis.

In solving Schneider's full time dependent extended KdV Eq. (1) numerically, transient solitary wave solutions were obtained and compared to the asymptotic transient solutions following from Eq. (10). For the case of the numerical transient solutions of the full Eq. (1), the stationary solution obtained from the eigenvalue problem of the stationary form of Eq. (1) was shifted in X direction by values of $-\beta$ and $+\beta$, respectively, and posed as initial solution of the full time dependent problem. While the time integration was performed by a forward difference scheme, the space integration was performed by fixing the value of λ to the eigenvalue of the respective stationary solution. Since the space integration procedure then reduces to a simple boundary value problem not involving the determination of an eigenvalue, one of the four boundary conditions used in the stationary problem had to be dropped, which was chosen to be the condition (8). The other boundary conditions for the spacewise integration as well as the remaining conditions for the numerical integration were kept the same as in the stationary problem, in particular a fast decay behaviour of the solutions was assumed. The numerical solutions of the full Eq. (1) were again obtained with the package MATLAB R2010A using the BVP4c integrator in space and a forward difference scheme in time. Typically, a time step size of $\Delta T \approx 1 \cdot 10^{-1}$ was used, yielding Courant numbers of about 0.4 or less.

For the case of the asymptotic transient solutions, transient values of the crest heights $H_{1m}^{(0)}(T)$ were obtained from Eq. (10) by solving an initial value problem, in which the initial position $X_m^{(0)-}$ of the asymptotic stable stationary solution $H_{1m}^{(0)-}$ and $X_m^{(0)+}$ of the asymptotic unstable stationary solution $H_{1m}^{(0)+}$, respectively, were shifted in X direction by $-\beta$ and $+\beta$, respectively.

In accordance between the numerical and the asymptotic analysis of Eq. (1), the transient numerical solutions show that solitary waves starting close to also converge to the stable stationary solution, whereas no convergence to an unstable stationary solution follows. Figure 2 shows this result for $\beta = 0.1$ and $L = 1$.

For the case of stable solutions, shown as solid black lines, the height of crests initially located at $X_m = X_m^- - \beta$ or $X_m = X_m^- + \beta$ converge to the stable stationary position $X_m = X_m^-$ with the stationary crest height H_{1m}^-, shown with a black "+" symbol in Fig. 2, thereby justifying the identification of these solutions as a stable solutions. Although with different absolute values as compared to the numerical solutions, the same is true for the transient asymptotic solutions, shown as solid grey lines. The height of crests initially located at $X_m = X_m^{(0)-} - \beta$ or $X_m = X_m^{(0)-} + \beta$ converge to the stable stationary position $X_m = X_m^{(0)-}$ with the asymptotic value of the stationary crest height $H_{1m}^{(0)-} = 3$, shown with a grey "+" symbol in Fig. 2. In contrast to the numerical solutions, the convergence of the asymptotic solutions is different and shows no spiralling behaviour. This is a consequence of the asymptotic expansion performed to "lowest order" in β, leading to Eq. (10) valid for slowly varying wave speeds, which cannot describe the oscillatory fast time behaviour of the wave crest heights seen in the numerical solutions.

For the case of unstable transient numerical solutions

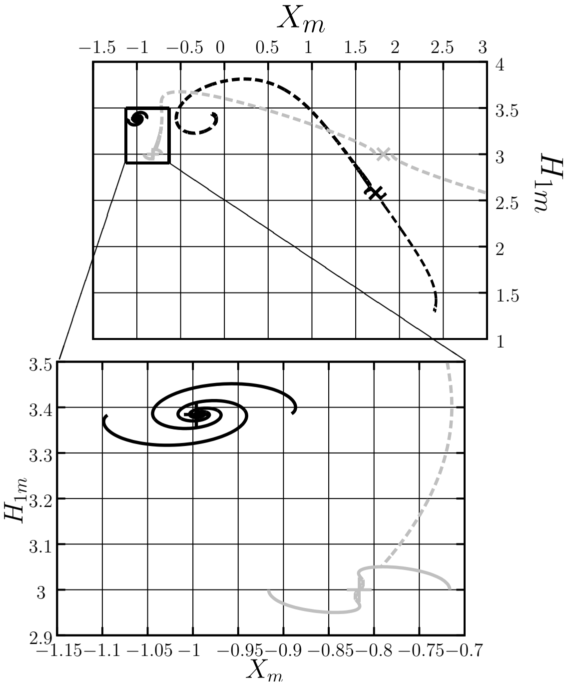

Figure 2. Crest heights $H_{1\,m}$ of the transient numerical solutions of Eq. (1) (in black) in comparison to the asymptotic solutions (in grey) as function of their dimensionless position X_m, with $\beta = 0.1$, $L = 1$ and fixed values of λ. The solid lines represent stable transient solutions in the sense that they converge to the stable stationary solution with crest heights $H^-_{1\,m}$ and $H^{(0)-}_{1\,m}$, respectively, shown as "+" symbol in black and grey, respectively, which were found in the corresponding coupled boundary-value eigenvalue problem of the stationary form of Eq. (1) and in the asymptotic analysis in [1], respectively. The dashed lines represent unstable transient solutions in the sense that they diverge away from the unstable stationary solution with crest heights $H^+_{1\,m}$ and $H^{(0)+}_{1\,m}$, respectively, shown as "x" symbol in black and grey, respectively. Numerical integration domain in space: $X \in [-30, 50]$.

of Eq. (1), shown as dashed black lines in Fig. 2, the height of crests initially located at $X_m = X^+_m - \beta$ or $X_m = X^+_m + \beta$ diverge away from the unstable stationary position $X_m = X^+_m$ with the stationary crest height $H^+_{1\,m}$, shown with a black "x" symbol. Again with different absolute values as compared to the numerical solutions, the same is true for the transient asymptotic solutions, shown as dashed grey lines. The height of crests initially located at $X_m = X^{(0)+}_m - \beta$ or $X_m = X^{(0)+}_m + \beta$ diverge away from the unstable stationary position $X_m = X^{(0)+}_m$ with the asymptotic value of the stationary crest height $H^{(0)+}_{1\,m} = 3$, shown with a grey "x" symbol in Fig. 2. While the unstable asymptotic solution for the solitary wave initially shifted to the right by the value $+\beta$ decays in the limit of large times, the corresponding numerical solution converges to a different stationary solution, with its values for the crest height and position seen as the lower terminating point of the black dashed line in Fig. 2. An analogon to this novel stationary solution is not present in the asymptotic analysis in [1]. The unstable asymptotic solution for the solitary wave initially shifted to the left by the value $-\beta$ finally converges back to the stable stationary solution. The corresponding numerical solution converges to a stationary solution again different to all the precedingly determined stationary solutions, where the convergence at the left side of the black dashed line takes place in a spiralling manner, with its limiting values for large times missing in Fig. 2. This stationary solution is different from the stable stationary solution determined previously, which is obvious since the value of λ is different, but it is remarkable in the sense that it represents a different eigensolution with a different eigenvalue to the stationary eigenvalue problem subject to the same boundary conditions as compared to the previously determined stable stationary eigensolution H^-_1. Also to this novel stationary solution there is no analogon in the asymptotic analysis considered here. This leads to the conclusion that the eigenvalue problem is degenerate and naturally raises the questions of how many eigensolutions exist and which of them will actually be realized.

Figure 3 shows the shapes of the numerical solutions of Eq. (1) for $\beta = 0.1$, $L = 1$. The line marked $T = 200$ represents the solution resulting from perturbing the stable stationary solution H^-_1 obtained from the original eigenvalue problem from its original position $X_m = X^-_m$ to the left by the amount $-\beta$ after a time $T = 200$. This solution is almost identical with the stable stationary solution. The line marked H^+_1 represents the unstable stationary solution obtained from the original eigenvalue problem. The line marked $T = 300$ represents the novel stationary solution resulting from perturbing H^+_1 from its original position $X_m = X^+_m$ to the right by the amount $+\beta$, the crest of which had appeared as the the lower terminating point of the black dashed line in Fig. 2. The line marked $T = 68$ represents the solution which crest was seen as the the terminating point on the left end of the black dashed line in Fig. 2, resulting from perturbing H^+_1 from its original position $X_m = X^+_m$ to the left by the amount $-\beta$. This solution may give an idea of how the novel stationary solution it is approaching to will be looking like. At least in the case of the solution marked $T = 300$, this makes clear why an analogon to this solution is not accessible via an asymptotic expansion to lowest order at the current stage, since the considerable differences to the solitary wave may not be seen as a small perturbation in terms of the parameter β.

4. CONCLUSION

Solitary waves in turbulent open-cannel flow are governed by an extended KdV equation which was

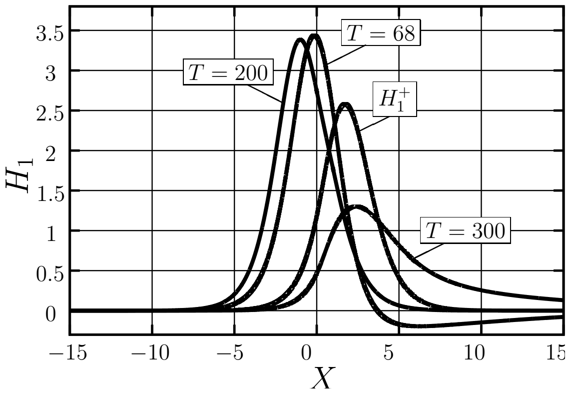

Figure 3. Shapes of the numerical solutions of Eq. (1) for β = 0.1, L = 1. The line marked T = 200 represents the resulting solution of H_1^- being initially shifted by $-\beta$ after a time T = 200. H_1^+ represents the unstable stationary solution. The line marked T = 300 represents the resulting solution of H_1^+ being initially shifted by $+\beta$ after a time T = 300, and the line marked T = 68 represents the resulting solution of H_1^+ being initially shifted by $-\beta$ after a time T = 68.

derived in [1] without any recourse to turbulence modelling. The problem of finding stationary solitary waves for a piecewise constant enhanced bottom roughness in the cannel may be formulated as a coupled boundary-value eigenvalue problem, with the eigenvalue determining the necessary amount of increase in bottom roughness for the wave to comply with the law of momentum. For given values of the parameters, two eigensolutions were found corresponding to a stable and an unstable stationary wave in the channel. This is in accord with an asymptotic analysis of the stationary problem, given in [1]. In determining transient solutions, waves starting close to also converge to the stable stationary solution, whereas no convergence to an unstable solution follows. Instead, the solutions starting close to the unstable stationary solution converge to novel stationary solutions, a feature not being present in the asymptotic analysis. This reveals the problem that multiple solutions to the eigenvalue problem exist, with solutions differing considerably from the classical soliton solution.

ACKNOWLEDGEMENTS

The author is deeply indebted to the ideas of professor W. Schneider and the fruiful ongoing collaboration on the subject. Thanks go also to Dr C. Buchner, who developed the first version of the MATLAB code on which the current version is based, leading to the results in this paper. Finally, the financial support by Androsch International Management GmbH is gratefully acknowledged.

REFERENCES

[1] Schneider, W., 2013, “Solitary Waves in Turbulent Open-channel Flow”, *JFM*, Vol. 726, pp. 137–159.

[2] Jurisits, R., 2014, “Numerical Solutions of an Extended Korteweg-de Vries Equation Describing Solitary Waves in Turbulent Open-channel Flow”, *Proc. Appl. Math. Mech.*, Vol. 14, pp. 701–702.

[3] Scott, A., 2003, *Nonlinear Science*, Oxford University Press.

Conference on Modelling Fluid Flow (CMFF'15)
The 16th International Conference on Fluid Flow Technologies
Budapest, Hungary, September 1-4, 2015

WINDAGE POWER LOSSES IN HIGH SPEED ROTATING MACHINES FOR DIFFERENT GAP RATIOS NOT HAVING AXIAL FLOW: A GENERALLY VALID ESTIMATION AND LITERATURE OVERVIEW

Sebastian FLEDER[1], Bjoern GWIASDA[2], Thomas REVIOL[3], Martin BOEHLE[4]

[1] Corresponding Author. Faculty of Mechanical and Process Engineering, Institute of Fluid Mechanics and Fluid Machinery, University of Kaierslautern, Gottlieb-Daimler-Strasse, 67663 Kaiserslautern, Tel. +49 631/205-5556, Fax +49 631/205-3909. Email: sebastian.fleder@mv.uni-kl.de
[2] Faculty of Mechanical and Process Engineering, Institute of Fluid Mechanics and Fluid Machinery, University of Kaierslautern. Email: gwiasda@mv.uni-kl.de
[3] Faculty of Mechanical and Process Engineering, Institute of Fluid Mechanics and Fluid Machinery, University of Kaierslautern. Email: reviol@mv.uni-kl.de
[4] Faculty of Mechanical and Process Engineering, Institute of Fluid Mechanics and Fluid Machinery, University of Kaierslautern. Email: martin.boehle@mv.uni-kl.de

ABSTRACT

In past studies, many approaches to predict windage losses in gaps between concentric cylinders have been performed. Especially the case of a rotating inner cylinder was the object of many investigations. When applying the results of the latter investigations to predict the power loss in a rotor-stator system, large variations are discovered in the resulting data. This effort illustrates an attempt to predict these losses with a more general model, having a larger scope of application. For this, a dimensional analysis is used to show the main influences on a Rotor-Stator System. A test setting is presented, which allows the modification of some of the identified parameters. All experiments are performed with water and include amongst others, large ranges of Reynolds number and gap size. Using numerical investigations, the findings of the experiments will be supported and improved and the torque needed to actuate the rotor is validated with measured values. Experimental and numerical results are combined to create a new, one-dimensional prediction of windage losses depending on geometry and Reynolds number. The investigations are based on an electrical engine, used to actuate turbomachinery. It is also used as a hybrid engine device in other forms of industrial application, but the results can also be applied to journal bearings and similar problems.

Keywords: dimensionless torque, friction losses, wall bounded flow, windage losses

ρ	density	$\frac{kg}{m^3}$
ν	kinematic viscosity	$Pa\ s$
μ	dynamic viscosity	$Pa\ s$
T	temperature	K
M	torque	Nm
s_1	axial gap between Rotor and Stator side 1	mm
s_2	axial gap between Rotor and stator side 2	mm
h	gap size	mm
r_A	stator radius	mm
r_i	rotor radius	mm
l	rotor length	mm
G	dimensionless torque	–
$\frac{r_i}{r_a}$	gap ratio	–
Re_{gap}	gap Reynolds number	–
Re_{ax}	axial Reynolds number	–
Re_{rad}	radial Reynolds number	–
Re_{circ}	circumferential Reynolds number	–

NOMENCLATURE

1. INTRODUCTION

In times of increasing importance of high efficiency devices and improvement in energy usage, many research topics deal with the subject of increasing power density, especially in electrical drives. One of many approaches for electrical motors is to increase the rotational speed to lift the output power. An electrical drive is often built with a small gap between a rotating part and a stationary part. With increasing superficial velocity of rotating parts in small gaps, friction losses can increase up to values that highly influence the efficiency of the device. Many theoretical and experimental approaches to determine the losses in electrical motors and other quickly rotating machinery have been made without leading to a generally valid formulation to predict the power losses. The goal of this effort is to simplify the electrical engine as a rotor-stator system like a Taylor-Couette flow and formulate a generally valid law, based on theoretical approaches and numerical and experimental investigations. A one-dimensional method to predict the losses due to fluid friction (windage losses) in gaps between a rotating inner cylinder and a stationary outer cylinder will be provided. An overview of historical and more recent work shows the inaccuracy of the existing formulations for some sort of applications. Even in newer publications, the references used to predict performance is based on methods developed in the late 60s, who neglect the influence of important parameters on the power loss, because they are formulated for a very specific point of use. Therefore they are not suitable for the prediction of windage losses in a large range of geometrical parameters or state of flow. An overview is given, a variety of geometries are simulated using CFD, a test bench is used to validate the numerical results and a new formulation is presented.

2. OVERVIEW

A large number of theoretical and experimental investigations have been made in the field of windage losses. For a better overview, the different publications are split up in two groups, experimental models and analytical or theoretical models. Most of the models define the power loss by a dimensionless friction factor which has to be calculated through an implicit formula. The authors that developed a new formulation for windage losses are depicted in table 1, together with the boundary conditions of the investigations, represented by fluid, gap size and gap ratio (definition see chapter 3: Dimensional Analysis and Pi-Theorem), the gap Reynolds number and the factors, used to predict the windage losses according to the formula presented in chapter 2.3: Summary of Investigations and Problems.

2.1. Experimental models

The first experimental investigations with Water have been made by Yamada [1]; [2] in 1960 and 1961. His experimental setup consisted of two concentric, smooth cylinders, the inner one rotating. The power loss is determined by measuring the torque on the stationary part. Additional experiments tried to describe the influence of grooves in the surface of both, rotating and stationary part. In 1967, Mack [3] published his thesis covering air friction in small sized electrical motors running under ambient pressure in air. In 1968, Vrancik [4] tested an electrical motor running under an atmosphere of Argon and Freon-12 under different pressures from 0.3 to 2.75 bara. In addition to his experimental investigations, he analytically determined a formula to predict the power loss. The experiments are performed with smooth rotors and with macroscopic grooves. Gorland et Al. [5] investigated a smooth Rotor in air under ambient pressure in 1970. In 1992 , Lathrop et Al. [6] investigated a fixed gap containing water and water-glycol-mixture. Later that year, they slightly extended the range of the Reynolds-Number without formulating a new law [7]. Later on, in 2009 and 2010, Bruckner [8] and Wright [9] conducted the first experiments under high-pressure CO_2 and even in supercritical CO_2. Bruckner also performed experiments in He and N_2 under different pressures up to 20 bara. His experimental values were partly in good accordance to the results of Vrancik. Raymond et Al. [10] tested a smooth Rotor supported by magnetic bearings and compared the results with different models by Kasarda [11], [12] and White [13]. Saari [14] is analysing high-speed induction machines and the power losses in them. He refers to Vrancik, Mack and Yamada.

In the last few years, the topic of windage losses rose in importance. Most of the recent investigations only tried to predict windage loss in a very specific context, like an electric drive or a high-speed gearbox. Kiohey et Al. [15] used the correlation by Vrancik to estimate the power losses in a 60kW electrical drive for the use in hybrid energy vehicles. Iversen [16] refers to the measurements of Bruckner [8], Vrancik [4] and Schlichting [17] to predict the windage losses of a turbo-compressor for use in a supercritical CO_2-Brayton-cycle. Kus and Neksa [18] tried to develop a model for initial design of turbo compressors for CO_2, using the correlations used by Vrancik [4] and White [9]. In the same Year, the same formula is used in their second publication [19].

In addition to the static-state investigations, Yamada [1]; [2] and Gazley [20] investigated the influence of an axial flow through the gap. The axial flow will not be investigated in this paper.

2.2. Analytical and theoretical models

The first theoretical approaches by observing boundary layer time and curved streamlines in rotor-stator-systems was made by Schlichting and Gertsen [17]. Recent theoretical work was published by Pirro and Quadrio in 2006 [21]. They were the first to analyze influence of a dimensionless factor of gap size and rotor diameter. They analyzed the investigations of different researchers like Lewis and Swinney [22]. The formulated law expresses the power loss as a function of fluid, geometry, von-Karman-constant and two different constants, dependent on gap size. No own experiments have been made. The same proceeding is done by Eckgart [23] in 2007. They use the same experimental values as Pirro and Quadrio, except for another value for the von-Karman-constant. Due to this constant, their formula is slightly different from Pirro which leads to a different prediction of the power loss. None of the

Figure 1. Comparison of different predictions for the same boundary conditions

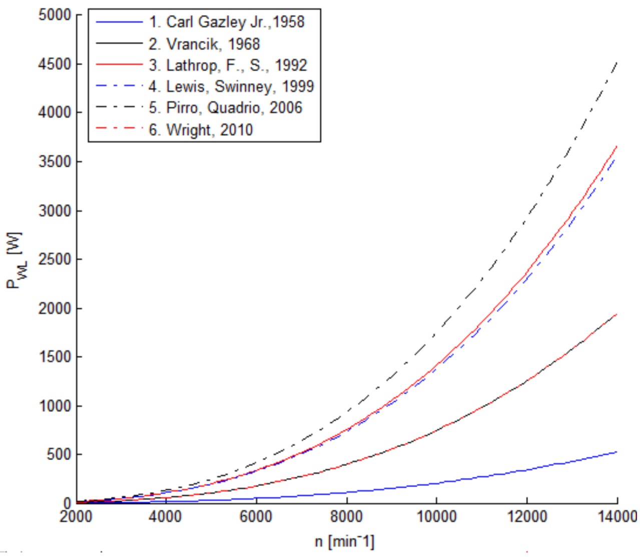

above verified their assumptions by own experiments or simulations.

2.3. Summary of Investigations and Problems

In table 1, the different investigations are listed, together with the gap size, the gap ratio, the gap Reynolds number and the two constants a and b for the friction coefficient used in the following equation. All investigations describe the power losses by introducing a friction factor C_f. C_f can be determined by iteratively solving the following equation

$$\frac{1}{\sqrt{c_f}} = a + b \cdot ln\left(Re \cdot \sqrt{c_f}\right) \qquad (1)$$

The constants a and b are provided by every author. As a and b are specified by a curve fit through the gained data, none of the authors took into account the influence of the gap ratio. Only Pirro [10] collected data from other publications to provide a first approach in this idea, without validating his results by a new experiment.

Figure 1 shows the predicted windage losses according to the different publications for a fictional test-case which lies within the validated bounds of the laws. Depending on the source, the losses vary a lot. Between the smallest and the largest prediction, a factor of 9 can be found. This is expected to be aresult of the assumption that the losses only depend on the Reynolds number. Different Geometries or different states of flow with the same Reynolds number predict the same losses, which is not correct.

3. DIMENSIONAL ANALYSIS AND PI-THEOREM

To examine the fundamental influences on power loss and friction, the different dimensions in a rotor-stator system like the present one are analyzed. The Buckingham PI-theorem is applied to the system and the dimensionless factors are investigated. In general, the system can be visualized as follows in Figure 2. The inner cylinder, called rotor (depicted in dark gray) is rotating within a stationary cylinder (shaded in the right illustration), called stator. The space between the two cylinders (height h) is filled with a coolant, e.g. water or another process fluid. The full length of the rotor is marked with l. Due to mechanical requirements, small gaps between the front surfaces of the rotor and the front surfaces of the stator exist (s_1 and s_2). These small gaps lead to so called front-surface influences, who have an influence on the flow structure in the gap. In addition to the depicted geometrical and material properties, three velocity components are used to describe the state of flow.

A large variety of geometrical parameters can be set, describing the entire system explicitly. One of the main dimensions of this system is the diameter of the rotating part. All other dimensions can be expressed based on this dimension.

$$\Pi_{s_1} = \frac{s_1}{r_i}; \Pi_{s_2} = \frac{s_2}{r_i}; \Pi_{r_a} = \lambda = \frac{r_a}{r_i}; \Pi_h = \frac{h}{r_i}; \Pi_l = \frac{l}{r_i} \qquad (2)$$

The flow state can be expressed by three Reynolds numbers, based on the three velocity components. For the present case, a cylindrical coordinate system with axial, radial and circumferential velocity components can be used.

$$\Pi_{Re_{ax}} = \frac{\rho h c_{ax}}{\nu}; \Pi_{Re_{rad}} = \frac{\rho h c_{rad}}{\nu}; \Pi_{Re_{circ}} = \frac{\rho h c_{circ}}{\nu} \qquad (3)$$

For the upcoming results, the circumferential gap Reynolds number, built with circumferential surface velocity of the rotor and the gap size h, will be used. In the present investigations, the general parameter defining the geometry and the flow state in the system are the circumferential and the gap-Reynolds-number Re_{circ} and Re_{gap}, the gap-ratio and the length-to-radius ratio of the rotor r_a/r_i and l/r_i. The power loss can be expressed in accordance to [21] and [22] by the dimensionless torque G, which follows directly out of the dimension analysis.

$$\Pi_G = G = \frac{M}{l \rho \nu^2} \qquad (4)$$

None of the authors listed above varied the gap ratio (see Table 1) in a wide range, therefore no generally valid law could be formulated. The goal of the

Table 1. Summary of other authors

Author	Medium	Gap size / ratio	Re_{gap}	a	b
Yamada [1]	Water	0.431 3.315 / 0.897 - 0.986	$0 - 3 \cdot 10^4$	2.04	1.786
Gazley [9]	Air	0.43 mm / unknown	$10^2 - 10^6$	2.04	1.786
Vrancik [4]	Argon. Freon-12	6.00 mm / unknown 1.02 mm / 0.9848	10^6	2.04	1.786
Lathrop [6]	Water-Glycerol-Mixture	60.6 mm / 0.7253	$10^3 - 10^6$	-1.63	1.52
Lathrop [7]	Water-Glycerol-Mixture	60.85 mm/ 0.7246	$800 - 1.23 \cdot 10^6$	-1.63	1.52
Lewis [22]	Water-Glycerol-Mixture. Water-Ethylen-Mixture	60.86 mm / 0.724	$2 \cdot 10^3 - 10^6$	- 1.83	1.56
Pirro [21]	No values given : Theoretical approach			$\frac{\sqrt(\pi)*\eta}{(1-\eta)} \cdot \left[N + M \cdot \ln\left(\frac{\sqrt(\pi)\cdot\eta}{1-\eta}\right)\right]$ M = 1.56. N = -1.83	$\frac{\sqrt(\pi)\cdot\eta}{(1-\eta)} \cdot M$ M = 1.56
Eckhardt [23]	See [6]. [7]. [22]	60.86 mm / 0.724	$2 \cdot 10^3 - 10^6$	No friction factor	
Bruckner [8]	CO2. N2. Air	0.47 4.572*mm* / 0.79 0.97	$10^3 - 5 \cdot 10^6$	none	None
Wright [9]	CO2	3.175 mm / 0.888	unknown	See [4]	See [4]

Table 2. Overview over considerated parameters

Author	Reynolds number	Gap ratio	Length ratio	experimental validation
Yamada [1]	●	○	○	●
Gazley [20]	●	○	○	●
Vrancik [4]	●	○	○	●
Lathrop [6]	●	○	○	●
Lathrop [7]	●	○	○	●
Lewis [22]	●	○	○	●
Pirro [21]	●	●	○	○
Eckhardt [23]	●	○	○	●
Bruckner [8]	●	○	○	●
Wright [9]	●	○	○	●

Figure 2. Schematics of a Rotor-Stator-Device

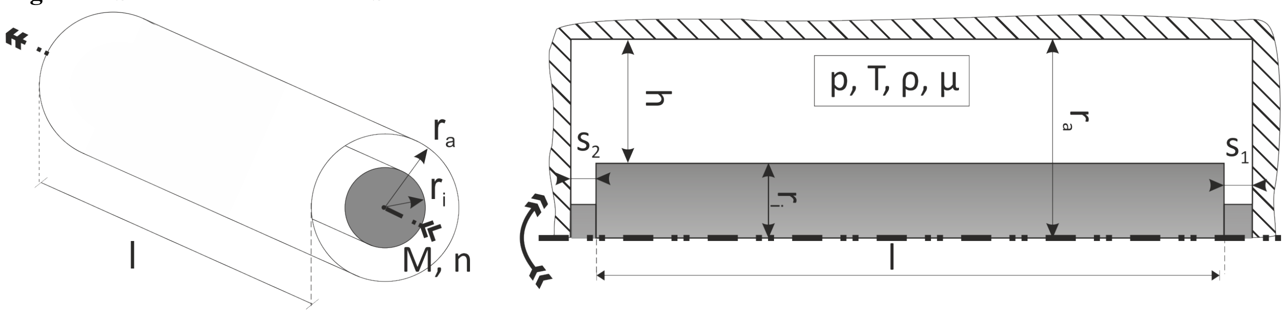

present paper is to identify a dependency between dimensionless torque, Reynolds number and gap ratio in the form of:

$$G = m \cdot Re^{\alpha} \quad (5)$$

Where m and α are both functions of $\frac{r_a}{r_i}$. This approach contains the advantage, that the power loss is not only a function of Reynolds but a function of Reynolds and geometry. Table 2 gives an overview whether or not the above-named authors considered Reynolds number, gap ratio or length ratio in their laws.

4. EXPERIMENTAL AND NUMERICAL INVESTIGATIONS

4.1. Experimental Setup

The water test rig is built in acrylic glass to allow optical access to the rotating parts. A schematic picture of the test bench is depicted in figure 3. Between the outer cylinder and the inner one several different cylinders can be mounted to vary the gap size and gap size ratio. As depicted in table 3, the present test rig can extend the range of validated research to smaller gap ratios (which means larger gaps).

A rotating shaft is suspended in two alloy lids. One end of the shaft exits the wet area to be connected to a clutch. An electrical Motor with a maximum rotation speed of 10,000 RPM is powering the system. The driving-torque and rotation speed is determined by a torque transducer with a measuring range corresponding to the expected values. Motor, torque transducer and shaft are coupled by metal bellow couplings. The rotating shaft is covered with three cylinders, each 27mm in radius. The middle one is fixed on the shaft and rotates with the same speed. The two smaller outer ones are suspended on the shaft by ball bearings. They rotate with a lower rotation speed, only driven by friction of the bearings on the inside and the fluid on the outer surface. The two outer cylinders are assembled to reduce the effect of the front surfaces on the flow and allow an estimation of the torque on the shell of the cylinder without the torque provided by the front faces. Due to the power loss inside of the test bench, the temperature of the water rises. As the kinematic viscosity of water reduces with rising temperature, this effect allows to test in a wider range of Reynolds number than with constant temperature. Therefore, the temperature is measured using a PT100 probe. All measurement data is acquired over a period of 10 seconds and averaged over that time span to avoid statistical influence on the measured data. To ensure statistical independence, every working point is tested several times in independent series.

As the radius of the shaft and the rotation speed of the two outer cylinders are small compared to the middle cylinder, the effect on the torque and the losses can be seen as small. Numerical investigations will prove that estimation to be accurate. In table 3, the gap ratios used from other authors is depicted in comparison to the present test rig.

4.2. Numerical Setup

The numerical investigations are performed with ANSYS CFX 14.0 To verify the validity of the measurement, the exact geometry of the test bench with the material properties of Water at 25° are simulated. All geometries consist of two concentric cylinders, the inner one rotating. The geometry of the outer cylinder is varied to set different gap sizes and gap ratios. For every rotor-stator-combination, a variation of rotational speed is examined, to vary the Reynolds number. Only a cutout of 45° is simulated with periodic boundary condition on the cut planes. Calculations with larger cut angles are done to verify the values. The meshes are created using ANSYS ICEM CFD with a structured blocking, using only hexahedral elements. Near wall refinement is applied. The meshes contain 1.2 million elements. The gap is meshed with at least 55 elements in height, 400 in length and resolved in steps of 1° in circumferential direction. The surface mesh on one periodic surface and a magnification of a near wall region is depicted in figure 4. The fluid is modeled by isothermal water. The temperature rise in the test rig is neglected in the simulations. By simulating the same range of rotational speed, the maximum Reynolds number reached is about 20 % lower than in the experiment. All walls are set as smooth walls with no slip boundary condition. As all rotating parts are rotational symmetric, the wall velocity can be set to rotating wall and calculations can be performed in a stationary reference frame. The convergence is monitored and a residual target of 10^{-5} for mass and momentum residuals is reached for almost all of the simulations. A minimum of 1500 steps with an automatic time step is calculated. To validate the convergence, the torque on the rotating part is monitored as a target criterion. After the 1500 steps, all calculations reached a minimal oscillation of the target value of under 3 % of the value.

The numerics are performed in steady state simulations and using a specified blend factor of one for the advection scheme and a second order scheme for turbulence. The turbulence models have been varied, using $k - \epsilon$, $k - \omega$ and SST model. The mesh sizes are varied from smaller to larger meshes to prove mesh-independent target values. The best accordance is reached with SST model and a near wall refinement to y+-values of under 10. A finer wall treatment only leads to longer calculation times without improving the result.

5. RESULTS OF THE EXPERIMENTAL AND NUMERICAL INVESTIGATIONS

5.1. Discussion of the numerical results

The numerically calculated dimensionless torque G as defined in chapter 3 as a function of the gap Reynolds number $Re_{gap} = \frac{r_{rotor} \cdot \omega_{rotor} \cdot \rho}{\mu}$

Figure 3. Cut view of the test Bench

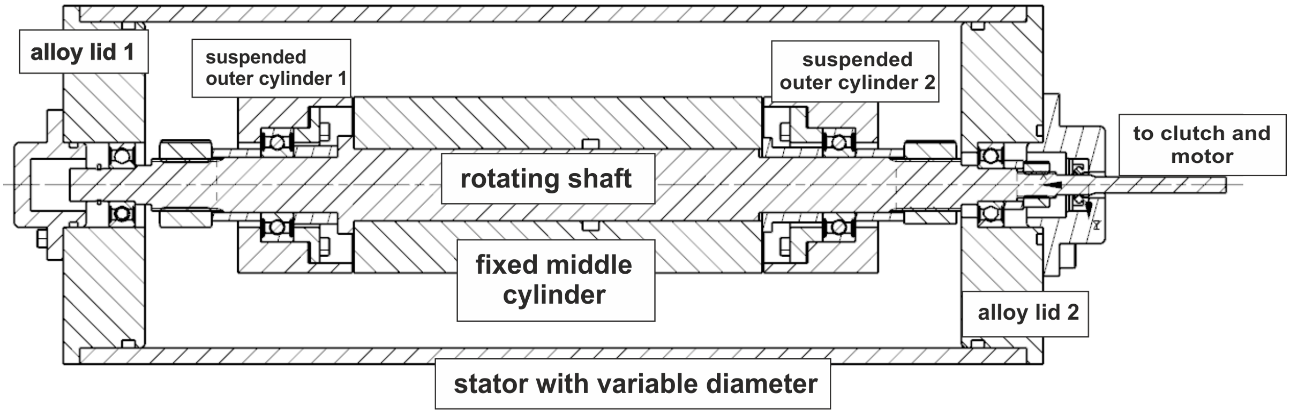

Figure 4. Mesh and magnification of near wall treatment

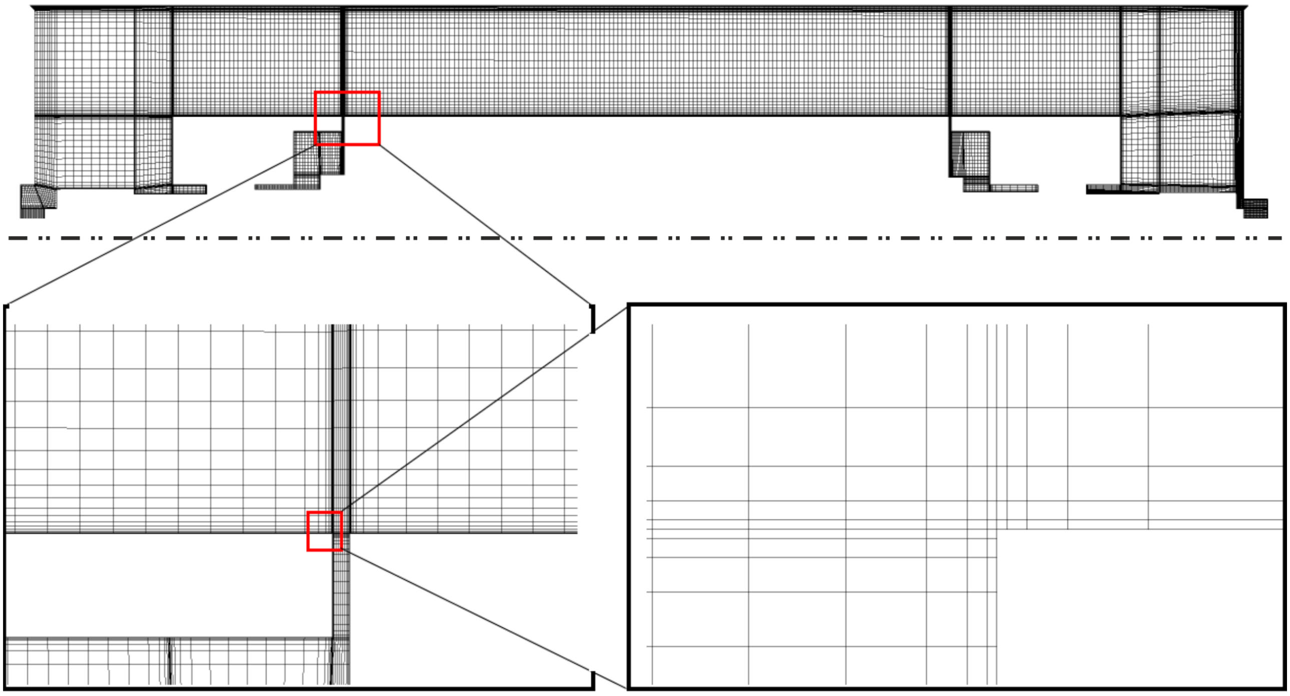

Table 3. Comparison of gap ratio determined in this paper to other authors

Present gap ratios analysis done by	0.5 - 0.6 none	0.6 - 0.7 none	0.7 - 0.8 Lathrop [6],[7], Lewis [22], Eckhardt [23]	0.8 - 0.9 Wright [9], using the equation of Vrancik [4], Bruckner [8]	0.9 - 0.98 Yamada [1], Vrancik [4], Bruckner [8]

Figure 5. Numerical results

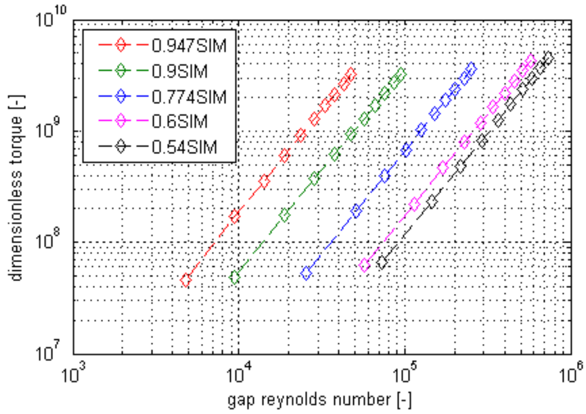

for different gap ratios is shown in figure 5. Five different curves are depicted. Every curve displays the dimensionless torque for one specific gap ratio λ. It consists of several data points, obtained by varying the rotational speed from 1,000 to 10,000 RPM in steps of 1,000 RPM. The curves are depicted in a double-logarithmic manner. The legend shows the gap ratio and the source of the data points (SIM for simulation). The range of Re is from 5,000 to about 75,000. They all show a similar gradient and are shifted laterally. With increasing gap size (decreasing gap ratio), the curve has a lateral offset to higher Reynolds numbers. This shows, that the losses must not be a function of Reynolds number only, but also of geometry.

Knowing this fact, one can observe a local minimum in the losses, when varying the gap ratio without changing the rotation speed. When calculating the losses with a friction factor, with decreasing Re_{gap} and constant Re_{circ}, material data and length ratio, the losses increase. The fact that there is a local minimum at a specific gap ratio could not be reproduced. Experiment and numerical data both show this behavior. The numerically calculated losses in the test rig for different gap sizes with water at 20°C at a rotational speed of 7000 RPM in dependency of the gap ratio are depicted in figure 6. With decreasing gap ratio, the losses decrease until reaching a turning point at a gap ratio of about 0.93, from which on the losses increase slightly.

5.2. Discussion of the experimental results

A test run with air is done to validate the bearing and friction torque of the sealing. The results are depicted in figure 7. This amount of torque is used as an offset to calibrate the loss calculation. At maximum rotation speed, the torque offset is about 0.5 percent of the losses.

To ensure reproducible and statistically valid results, every data point consisting of gap ratio and rotational speed is tested ten times for a total of ten seconds. As the water temperature rises during the

Figure 6. Local minimum in power loss distribution

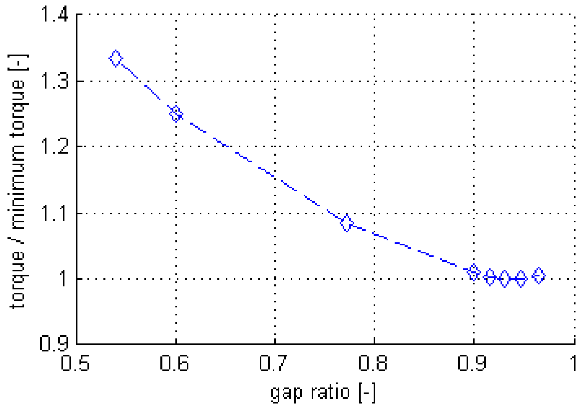

Figure 7. Torque of test run in air

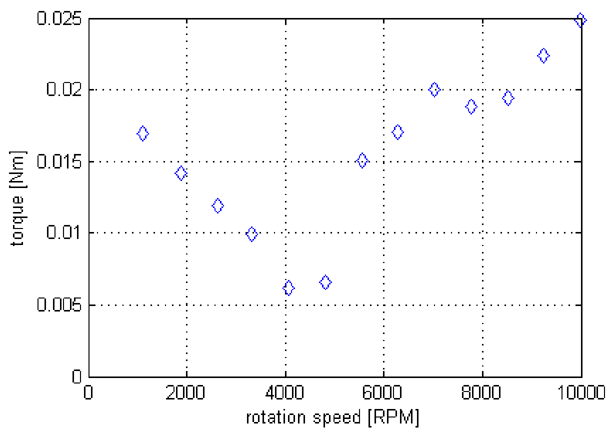

Figure 8. Experimental results

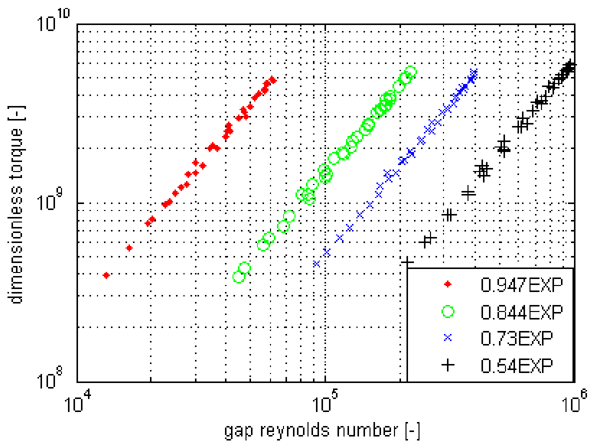

Figure 9. Comparison of experimental and numerical results

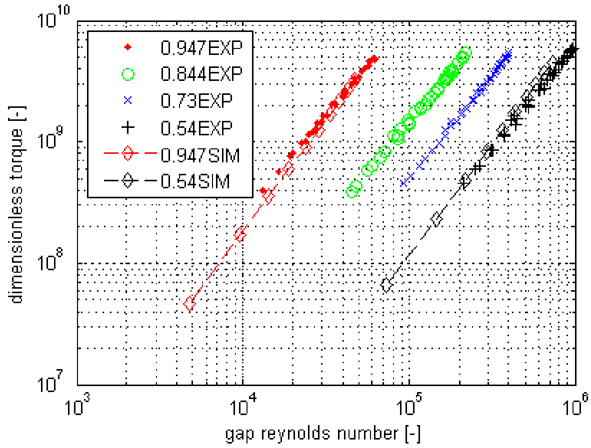

measurement, the water is changed regularly. Like this, it can be assured that the results are independent from each other. To reduce a dependency of the previous state of flow, the test rig is randomly stopped and the different rotational speeds are not tested in the same order.

The dimensionless torque for different gap ratios is depicted in a double-logarithmic diagram in figure 8. The dimensionless torque rises with rising Reynolds number in a potential manner for every gap ratio. The slope of the curves is very similar, but reduces slightly with decreasing gap size (increasing gap ratio). With decreasing gap ratio, the curves have a lateral offset to higher Reynolds numbers. The data points of each gap ratio are in very good accordance to each other and repeatable.

5.3. Comparison of the results

The numerical and experimental results show a similar behavior. With increasing gap ratio, the dimensionless torque experiences an offset in horizontal direction. A comparison for two numerical and four experimental curves is depicted in figure 9.

When comparing the numerical and experimental data, it can be observed, that the numerical data has a slightly steeper curve than the experimental one. When fitting a potential function in form of

$$G = m * Re^{\alpha} \quad (6)$$

through the data, the characteristic form of the curves are represented by the numerics and experiment, but the absolute values differ from the experimental ones. When describing the factor m and exponent α only as function of the gap ratio, the characteristics is reproduced quite well. Figure 10 shows the trend of m and α as function of gap ratio. To predict the power loss in a certain system, factor and exponent for the corresponding gap ratio can be deducted

Figure 10. Factor and exponent for prediction of power loss

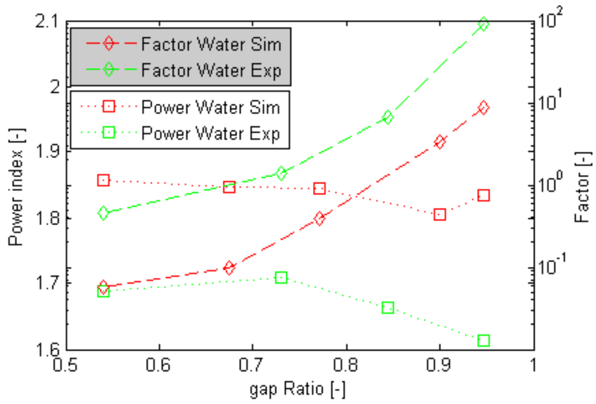

Figure 11. Curve fit data for factor and exponent

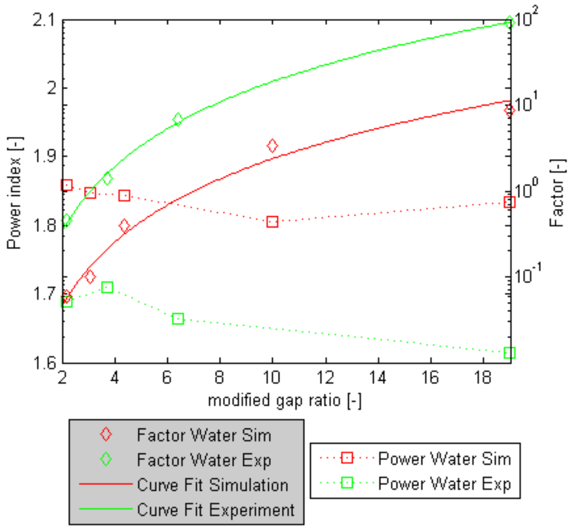

from the graph. To formulate a mathematical law to directly calculate the windage losses, the dependency of the geometry can be calculated by a least squares curve fit through the data points which represents the characteristics of the curve. The best fit seems to be a model with the following assumptions:

$G = m \cdot Re^{\alpha}$

where m is a function of the geometry and α is nearly constant. m can be expressed by two constant coefficients c_1 and c_2 to fit in the function $m = c_1 \cdot \left[\frac{1}{1-\lambda}\right]^{c_2}$

$\alpha = constant$; $\alpha_{sim} = 1.83$ and $\alpha_{exp} = 1.65$

and

$c_{1sim} = 0.0087$ and $c_{2sim} = 2.4335$

$c_{1exp} = 0.0622$ and $c_{2sim} = 2.479$

The curves for m and α as a function of the modified gap ratio $\lambda_{mod} = \frac{1}{1-\lambda}$ are shown in figure 11.

The experimental and numerical results show clearly, that a dependency of dimensionless torque

Figure 12. Comparison of Losses for Simulation Data and the analytical formulas obtained by Experimental and numerical Data set

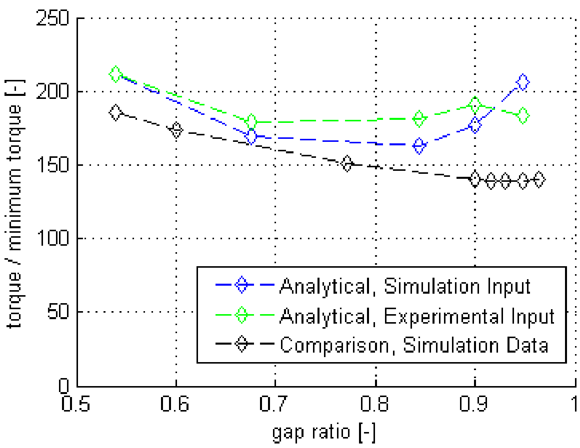

and therefore power losses from Reynolds and geometry exists. A discrete formula for the prediction of lateral displacement and slope of dimensionless torque as function of geometry has been shown and increased the accuracy of windage loss prediction for a large range of gap ratio and Reynolds number. A Comparison for the test rig with a gap ratio of 0.54 filled with water at 42°C and a rotational speed of 7000 RPM is shown in figure 12. A very good agreement between the analytical models and the numerical data over a large range of gap ratio can be observed.

5.4. *Uncertainities in the experimental investigations*

The flow structures in the system are highly turbulent, which leads to oscillating values for the torque. A temperature rise in the system ca be measured during the tests. By measuring torque, temperature and rotational speed over a longer period of time, the oscillation of the values is averaged to a mean value. The temperature measurement by PT100 probe is a delayed and punctual measurement. Especially when rotating at high speeds, the losses rise up to values that heat up the entire test bench. A non-uniform temperature distribution in the test bench can lead to false values and falsify the calculation of Reynolds-number and dimensionless torque. The torqe transducer has a non-linearity and a general uncertainity of 0.2% of the measuring range.

6. CONCLUSION

A study of the existing predictions for windage losses has shown that many formulations are only valid in a small range of gap ratio λ or Re_{gap}. A test rig for water has been described and the experimental results are shown as well as the simulations of the test rig. A dependency of the power loss in the system on Re_{gap} and λ has been proven for simulation and experiment. Based on both data sets, a new formulation for the losses is presented.

Further experiments with different test rigs and further numerical investigations will improve accuracy of the given formula and extend the range of Re_{gap} and gap ratio λ. Both, numerical and experimental investigations have been conducted using smooth rotor and stator geometries. The influence of surface roughness (e.g. technical/manufactured roughness or sand grain roughness) may be investigated in further studies. Possible effects of compressibility of the fluid may also be investigated in other tests.

ACKNOWLEDGEMENTS

The numerical investigations have been done on the High-Performance Cluster Elwetritsch on the technical University Kaiserslautern. We appreciate for the possibility to use these resources.

REFERENCES

[1] Yamada, Y., 1960, "Resistance of a Flow Through an Annulus with an inner Rotating Cylinder", *Bulletin of the Japan Society of Mechanical Engineers*.

[2] Yamada, Y., 1961, "Torque Resistance of a Flow between Rotating Co-Axial Cylinders, having Axial Flow", *Bulletin of the Japan Society of Mechanical Engineers*.

[3] Mack, M., 1967, "Luftreibungsverluste bei elektrischen Maschinen kleiner BaugrÃűÃ§e", *Dissertation der UniversitÃd't Stuttgart*.

[4] Vrancik, J. E., 1968, "Prediction of Windage Power Loss in Alternators", *NASA Technical Note*.

[5] et Al., H. G., 1970, "Experimental Windage Losses for close Clearance Rotating Cylinders in the turbulent Flow Regime", *NASA Technical Memorandium*.

[6] Lathrop, D. P., Fineberg, J., and Swinney, H. L., 1992, "Turbulent Flow between Concentric Rotating Cylinders at large Reynolds Number", *Physical Review Letters*.

[7] Lathrop, D. P., Fineberg, J., and Swinney, H. L., 1992, "Transition to Shear-driven Turbulence in Couette-Taylor Flow", *Physical Review Letters*.

[8] Bruckner, R. J., 2009, "Windage Power Loss in Gas Foil Bearings ant the Rotor-Stator Clearance of High Speed Generators in High Pressure Environments", *NASA Technical Memorandium*.

[9] Wright, S., Radel, R. F., Vernon, M. E., Rochau, G. E., and Pickard, P. S., 2010, "Operation and Analysis of a Supercritical CO2 Brayton Cycle", *SANDIA National Laboratories*.

[10] Raymond, M. S., Kasarda, M., and Allarie, P., 2008, “Windage Power loss modelling of a smooth Rotor supported by homopolar Actice Magnetiv Bearings”, *Journal of Tribology*, (130).

[11] Kasarda, M., 1998, “Experimentally Determined Rotor Power Loss in Homopolar and Heteropolar Magnetic Bearings”, *Proceedings of the international Gas Turbine and Aeroengine Congress and Exhibition*.

[12] Raymond, M. S., Kasarda, M., and Allarie, P., “Comparison of measured Rotor Power Losses in Homopolar and Heteropolar Magnetic Bearings”, *Proceedings of MAG*.

[13] White, F. M., 2005, *Viscous Fluid Flow*, McGraw-Hill.

[14] Saari, J., 1998, “Thermal analysis of high-speed induction machines”, *Helsinki University of Technology*.

[15] Kiyota, K., Kakishima, T., and Chiba, A., 2014, “Estimation and Comparison of the Windage Loss of a 60 kW Switched Reluctance Motor for Hybrid Electric Vehicles”, *International Power electronics Concerence*.

[16] Iverson, B. D., Conboy, T. M., Pasch, J. J., and Kruizenga, A. M., 2013, “Supercritical CO2 Brayton Cycle for Solar Thermal Energy”, *Journal of applied Energy*, (111).

[17] Schlichting, H., Gersten, K., and Krause, E., 2000, “Boundary Layer Theory”, *8th edition*.

[18] Kus, B., and Neksa, P., 2013, “Development of a one-dimensional model for initial design and evaluation of oil-free CO2 turbo-compressor”, *Interantional Journal of Refrigeration*, (36).

[19] Kus, B., and Neksa, P., 2013, “Novel Partial admission radial compressor for CO2-applications”, *Interantional Journal of Refrigeration*, (36).

[20] Gazley, C., 1959, “Heat Transfer Characteristics of the Rotationaland Axial Flow between Concentric Cylinders”, *Transactions of the American Society of MEchanical Engineering*.

[21] Pirro, D., and Quadrio, M., 2006, “Turbulent Skin Friction Law for the turbulent Taylor-Couette flow”, *Scientific Report*.

[22] Lewis, G. S., and Swinney, H. L., 1999, “Velocity Structure Functions, scaling and transitions in high reynolds number taylor-Couette-Flow”, *Physical Review Letters*.

[23] Eckgart, B., Grossmann, S., and Lohse, D., 2007, “Torque Scaling in turbulent Taylor-Couette Flow between independantly rotating Cylinders”, *Journal of Fluid Mechanics*, Vol. 581.

Conference on Modelling Fluid Flow (CMFF'15)
The 16th International Conference on Fluid Flow Technologies
Budapest, Hungary, September 1-4, 2015

NUMERICAL ASSESSMENT OF A NEW PASSIVE CONTROL METHOD FOR MITIGATING THE PRECESSING HELICAL VORTEX IN A CONICAL DIFFUSER

Constantin TANASA[1], Romeo SUSAN-RESIGA[2], Sebastian MUNTEAN[3], Adrian STUPARU[4], Alin BOSIOC[5], Tiberiu CIOCAN[6]

[1] Corresponding Author. Department of Hydraulic Machinery, "Politehnica" University Timisoara. Bv. Mihai Viteazu, No.1, Tel.: +40 256403692, E-mail: constantin.tanasa@upt.ro
[2] Department of Hydraulic Machinery, "Politehnica" University Timisoara, E-mail: romeo.resiga@upt.ro
[3] Romanian Academy – Timisoara Branch, E-mail: sebastian.muntean@upt.ro
[4] Department of Hydraulic Machinery, "Politehnica" University Timisoara, E-mail: adrain.stuparu@upt.ro
[5] Department of Hydraulic Machinery, "Politehnica" University Timisoara, E-mail: alin.bosioc@upt.ro
[6] Department of Hydraulic Machinery, "Politehnica" University Timisoara, E-mail: tiberiu.ciocan@student.upt.ro

ABSTRACT

Decelerated swirling flows in conical diffusers (e.g. discharge cone of hydraulic turbines), can develop self-induced instabilities for some configurations of incoming flow. An upstream steady and axis-symmetrical flow becomes unsteady and three-dimensional. As a result, a characteristic precessing helical vortex and associated pressure fluctuations that hinder the operation of hydraulic turbines. This paper introduces a novel approach for mitigating the swirling flow instabilities using a diaphragm into the cone. Consequently, the severe flow deceleration and corresponding central quasi-stagnant region are diminished, with an efficient mitigation of the precessing helical vortex and its associated pressure fluctuations. Five cases (one without and four with diaphragm) are numerically investigated. It is shown that the diaphragm can mitigate the unsteadiness. Moreover, the dynamic-to-static pressure recovery and hydraulic losses in the conical diffuser are computed.

Keyword: conical diffuser, diaphragm, numerical study, precessing helical vortex

NOMENCLATURE

A	[-]	equivalent amplitude
C_{KR}, C_{PR}	[-]	kinetic and potential recovery coefficients, respectively
A_d	[m^2]	diaphragm interior area
A_o	[m^2]	test section outlet area
A_r	[m^2]	areas ratio
D_t	[m]	reference diameter from the throat of the convergent-divergent test section, $D_t = 0.1$
L_{VK}	[-]	von Karman length scale
Sh	[-]	Strouhal number
V_t	[m/s]	reference velocity from the throat of convergent-divergent test section
d	[m]	diaphragm interior diameter
f	[Hz]	dominant frequency
p_{RMS}	[Pa]	random mean square of the pressure signal
Π, K, E	[W]	potential, kinetic and mechanical energy fluxes, respectively
ρ	[kg/m^3]	density
ζ	[-]	energy loss coefficient
χ	[-]	kinetic-to-potential energy recovery ratio

1. INTRODUCTION

In last three decades the development of energy systems imposes new requirements in operating of hydraulic turbines due to energy market. In particular, their operation on a wide range, far away from the best efficiency point. Such requirements have emerged on the need to maintain some balance between production and consumption to the inclusion of fluctuating energy sources (e.g. wind energy, photovoltaic), and on the other hand, from economic considerations related to market fluctuations of electricity prices. Although e.g. Francis turbines are designed to operate at best efficiency point or close to, they get to be operated at part load. The fact that the runner blades are not adjustable lead to unwanted hydrodynamic phenomena leading to a rapid growth of hydraulic losses reflected in turbine efficiency. Moreover, the hydrodynamic instabilities generate severe pressure fluctuations in the draft tube cone.

These phenomena are known for a long time, but their effects are felt more acutely today.

The software and hardware development in the recent years make 3D turbulent and unsteady swirling flow simulations possible. Ruprecht et al. [1] have used the finite element software product called FENFLOSS developed at Stuttgart University to determine the 3D swirling unsteady-flow with precession characteristics. Zhang et al. [2] has studied the origin of the pressure fluctuations on the Francis turbine operating at part load operation. These fluctuations are responsible for structural turbine damages and even power plant damages. Muntean et al. [3] have performed a 3D numerical analysis of the swirling flow in simplified test section geometry. The computed vortex rope using numerical simulation has a similar configuration with that observed on experimental test rig. A comparison between experimental results and 2D axis-symmetric numerical simulation was performed by Susan-Resiga et al. [4]. This work proved that a 2D axis-symmetric simulation is able to capture very well the measured velocity profiles at different levels along to the draft tube cone. Also, it was demonstrated that a 2D axis-symmetric simulation is able to capture the steady field similar to a 3D numerical simulation. However, it is obviously that the unsteady pressure filed cannot be computed based on 2D axis-symmetric simulation. Consequently, 3D numerical simulation is used in order to assess the new control method.

Several groups have used the test case developed at Politehnica University Timisoara (UPT) called “Timisoara swirl generator” to validate numerical results against experimental data [5]. Petit et al. [6] have used OpenFoam code for numerical analysis of swirling flow generator along with convergent-divergent test section. A numerical calculation, which involved comparing and validating the results of the FLUENT code, was analysis by Ojima et al. [7]. The conclusion of these investigations was that different numerical codes were able to capture the numerical results of the experimental data very well. The drawback of this study is that the time of three-dimensional calculation is large, so it is difficult to calculate a number of operating regimes in a short time. In order to eliminate or to mitigate the instabilities from the draft tube cone different techniques have been implemented in hydraulic turbines [8-13]. These methods lead to reducing the pressure pulsations over a narrow regime but they are not effective or even increase the unwanted effects.

The fundamental problem addressed in this paper is studying from numerical point of view, a new passive control method of the decelerated swirling flow with helical vortex breakdown. The new method involves the use of a diaphragm installed into the conical diffuser [14].

The second section presents the problem setup for numerical analysis, including the computational domain and boundary conditions. Section 3 analyzes the flow field quantifying the hydraulic losses and kinetic-to-potential energy conversion. Also, the unsteady pressure field analysis is performed for the cases with the diaphragm with respect to the case without it. The conclusions are summarized in last section.

2. COMPUTATIONAL DOMAIN AND BOUNDARY CONDITIONS

The computational domain corresponds to convergent-divergent part of the swirling flow apparatus developed at Politehnica University Timisoara (UPT) [15]. The convergent section is bordered by the annular inlet section and the throat (Fig. 1). The annular inlet section is considered just downstream to the runner blades. The divergent section includes a discharge cone with semi-angle of 8.5° similar to FLINDT project [16] and a pipe. Four values of the diaphragm interior diameter of d = 0.134, 0.113, 0.1, 0.88 m are considered in this numerical study. The diaphragm is located at the cone outlet. Table 1, shows the areas ratio between diaphragm interior area and outlet test section area.

Table 1.

Diaphragm interior diameter *d* [m]	Diaphragm interior area A_d [m^2]	Test section outlet area A_o [m^2]	Areas ratio A_r [%]
0.134	0.014	0.02	70
0.113	0.01	0.02	50
0.1	0.0078	0.02	40
0.088	0.006	0.02	30

The computational domain with diaphragm is presented in Fig. 1. A structured mesh with 2.7M cells is generated on each computational domain (with and without diaphragm).

Boundary conditions imposed for each case uses a velocity profile at the inlet, and average pressure on the outlet of the section. The inflow boundary conditions are obtained computing the flow upstream. As a result, the inlet velocity profile (axial, radial and circumferential velocity components) as well as the turbulent quantities (kinetic energy and turbulence dissipation rate) corresponding to a runner speed of 1000 rpm are imposed on annular inlet section. Figure 2a, b, shows the velocity profiles from the inlet test section. 3D unsteady numerical simulations with and without diaphragm were performed using the FLUENT code in order to assess the new approach.

For the numerical setup it was used SAS turbulence model. SAS modelling is an approach for simulating unsteady turbulent flows.

SAS can be applied in combination with most ω-based URANS turbulence models [17, 18].

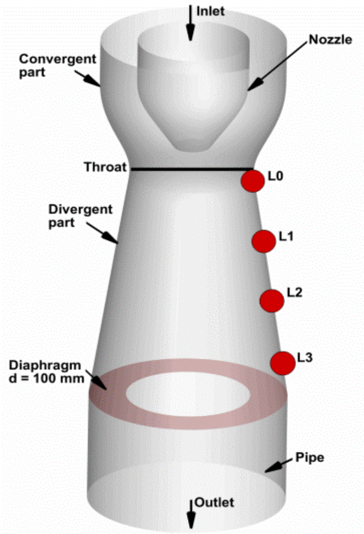

Figure 1. 3D computational domain of the case with diaphragm.

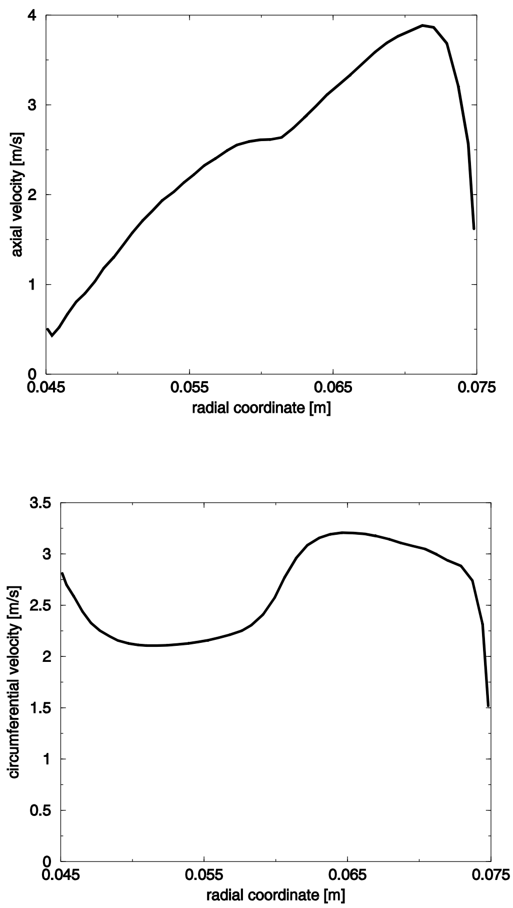

Figure 2. Velocity profiles from the inlet test section

The original SAS model was formulated as a two-equation model, with the variable $\Phi = \sqrt{k}L_t$ for the scale equation:

$$\frac{\partial(\rho k)}{\partial t} + \frac{\partial(\rho \bar{U}_j k)}{\partial x_j} = P_k - c_\mu^{3/4}\rho\frac{k}{\Phi^2} + \frac{\partial}{\partial x_j}\left(\frac{\mu_t}{\sigma_t}\frac{\partial k}{\partial x_j}\right) \quad (1)$$

$$\frac{\partial(\rho\Phi)}{\partial t} + \frac{\partial\left(\rho\bar{U}_j\Phi\right)}{\partial x_j} = \frac{\Phi}{k}P_k\left(\zeta_1 - \zeta_2\left(\frac{L_t}{L_{vk}}\right)^2\right) - \quad (2)$$
$$-\zeta_3\rho k + \frac{\partial}{\partial x_j}\left(\frac{\mu_t}{\sigma_\Phi}\frac{\partial\Phi}{\partial x_j}\right)$$

$$\mu_t = c_\mu^{1/4}\rho\Phi \quad (3)$$

$$L_{vK} = K\left|\frac{\bar{U}'}{\bar{U}''}\right|; \qquad \bar{U}' = S = \sqrt{2S_{ij}S_{ij}};$$
$$\bar{U}'' = \sqrt{\frac{\partial^2\bar{U}_i}{\partial x\partial j}\frac{\partial^2\bar{U}_i}{\partial x_k\partial x_k}}; \quad S_{ij} = \frac{1}{2}\left(\frac{\partial\bar{U}_i}{\partial x_j} + \frac{\partial\bar{U}_j}{\partial x_i}\right); \quad (4)$$
$$L_t = \frac{\Phi}{\sqrt{k}}$$

The main new term is the one including the von Karman length scale L_{vK},, which does not appear in any standard RANS model. The second velocity derivative allows the model to adjust its length scale to these structures already resolved in the flow. This functionality is not present in standard RANS models. The term L_{vK} can be transformed and implemented into any other scale-defining equation resulting in SAS capabilities as in the case of the SAS-SST model. For the SAS-SST model, the additional term in the ω-equation resulting from the transformation has been designed to have no effect on the SST model's RANS performance for wall boundary layers. It can have a moderate effect on free shear flows. The SAS model will remain in steady RANS mode for wall bounded flows and can switch to SRS mode in flows with large and unstable separation zones.

The time step for the numerical simulations in both cases was t = 0.56 ms. All numerical solutions were converged down to residuals as low as 10^{-3}. Pressure monitors denoted L0…L3 have been achieved on 4 levels. The axial distance between two consecutive pressure taps located on the cone wall is 50 mm.

3. NUMERICAL RESULTS

3.1. Unsteady pressure analysis

Numerical simulations for turbulent swirling flow in the test section from UPT, have been performed for 4 cases of the adjustable diaphragm and for the case without diaphragm. Figures 3a to 3e, shows a first set of numerical results of Q-criterion iso-surface for each case. Q criterion is defined as follow: $Q = 1/2(\Omega^2\text{-}S^2)$ where S is strain rate and Ω vorticity rate [17, 18], respectively. One can clearly observe that the helical vortex structure evolves into a straight vortex structure for cases with diaphragms, from d = 0.113 m to d = 0.088 m. As a result, the pressure pulsations associated to the straight vortex are mitigated due to the eccentricity is significantly reduced. The above statement is supported by unsteady analysis of pressure signals from the pressure monitors of the domain.

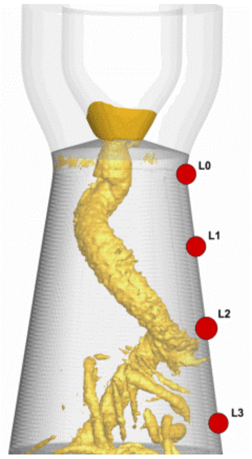

Figure 3. a) Q criterion iso-surface of 1e^5 for the case without diaphragm.

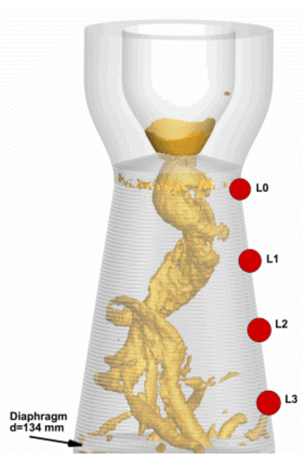

b) Q criterion iso-surface of 1e^5 for the case with diaphragm diameter of d = 0. 134 m.

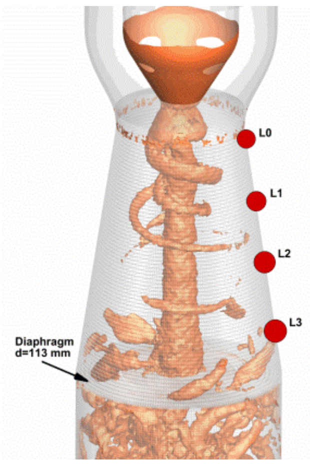

c) Q criterion iso-surface of 1e^4 for the case with diaphragm diameter of d = 0.113 m.

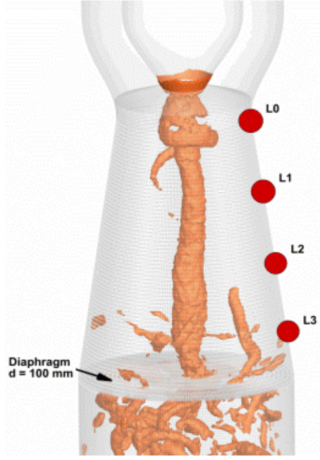

d) Q criterion iso-surface of 1e^4 for the case with diaphragm diameter of d = 0.1 m.

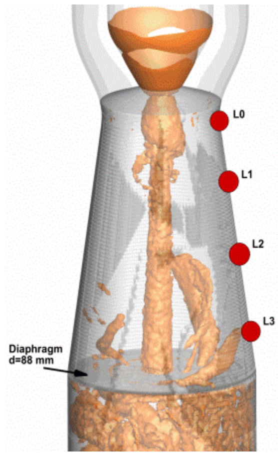

e) Q criterion iso-surface of 1e^4 for the case with diaphragm diameter of d = 0.088 m.

Since the unsteady part of the pressure signal is periodic, we characterize it using the helical vortex precessing frequency, *f* (Hz), and the equivalent amplitude computed using Parceval's theorem [19]. In dimensionless form, the precessing frequency is expressed using the Strouhal number, (eq. 5) and the pressure pulsation amplitude (eq. 6). Note, that according to Parseval's theorem, the equivalent pressure fluctuation amplitude is $\sqrt{2}p_{RMS}$, whereas p_{RMS} in the random mean square of the fluctuating part of the pressure signal.

$$Sh = f\,\frac{D_t}{V_t} \qquad (5)$$

$$A \equiv \frac{\sqrt{2}p_{RMS}}{\rho V_t^2/2} \qquad (6)$$

Figure 4a,b, recalls the decrease in both amplitude and frequency of the pressure fluctuation measured by Bosioc et al. [12] and Tanasa et al. [13] at the L0-L3 levels of the conical diffuser, with the increase in the relative control jet method and flow-feedback. For the investigated method, in this paper, it is obviously that the adjustable diaphragm provides a significant drop in both amplitude and frequency. The diaphragms with interior diameter d = 0.1 and 0.113 m provides the largest amplitude reduction (up to 65%), while the Strouhal number decreases up to 80%.

We conclude, that the passive method presented in this paper, has the potential to effectively mitigate the pressure fluctuations in decelerated swirling flow with precessing helical vortex.

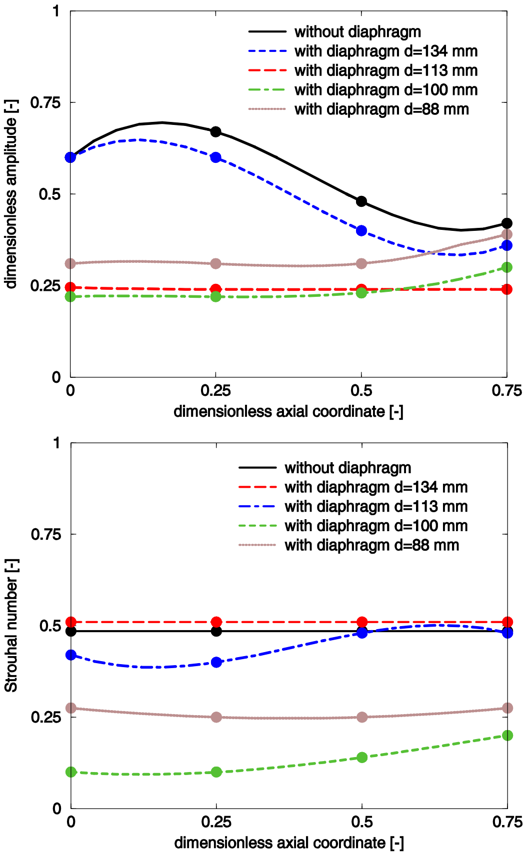

Figure 4. Equivalent amplitudes corresponding to pressure taps from the test section domain a) and Strouhal number b), versus axial coordinate.

3.2. Mean pressure analysis

The main purpose of the hydraulic turbine draft tube is to convert as much as possible the kinetic energy at the runner outlet into pressure potential energy with minimum hydraulic losses. We introduce the following integral quantities in order to analyze the kinetic-to-potential energy transformation process, as well as its efficiency:

Flux of potential energy

$$\Pi(x) \equiv \int_{S(x)} p(x,y) V \cdot n dS \ [\mathrm{W}] \tag{7}$$

Flux of kinetic energy

$$K(x) \equiv \int_{s(x)} \frac{\rho V^2(x,y)}{2} V \cdot n dS \ [\mathrm{W}] \tag{8}$$

Flux of mechanical energy

$$E(x) \equiv \Pi(x) + K(x) \ [\mathrm{W}] \tag{9}$$

A dimensionless loss coefficient ζ is usually defined as:

$$\zeta(x) \equiv \frac{E_0 - E(x)}{K_0} = \left(1 - \frac{K(x)}{K_0}\right) - \frac{\Pi(x) - \Pi_0}{K_0} \tag{10}$$

where, $\left(1 - \frac{K(x)}{K_0}\right)$ = $C_{KR}(x)$, is the kinetic energy recovery coefficient and $\frac{\Pi(x) - \Pi_0}{K_0}$ = $C_{PR}(x)$, is potential energy recovery coefficient. The kinetic-to-potential energy conversion ratio can be quantified as:

$$\chi(x) \equiv \frac{\Pi(x) - \Pi_0}{K_0 - k(x)} < 1 \tag{11}$$

Figure 5a,b, shows that both C_{KR} and C_{PR} has an improvement of the energy recovery until the outlet of the test section where exist an decrease, because of diaphragm which is implemented here and introduce recirculation zones. The hydraulic loss coefficient ζ, Figure 6, and the kinetic-to potential energy conversion ratio χ, Figure 7, also have a small improvement for the cases with diaphragm, while in the last part of test section it decreases.

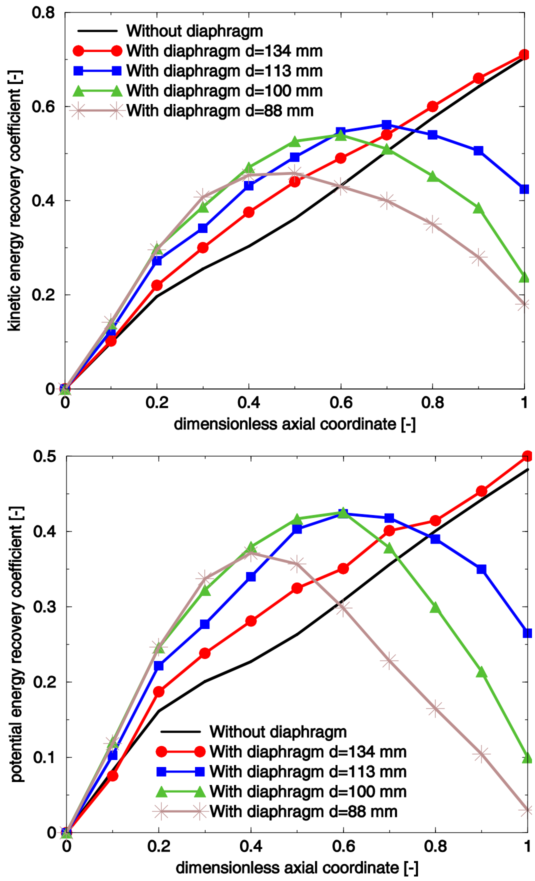

Figure 5. Potential CPR (a) and CKR (b) energy recovery coefficients versus axial coordinate.

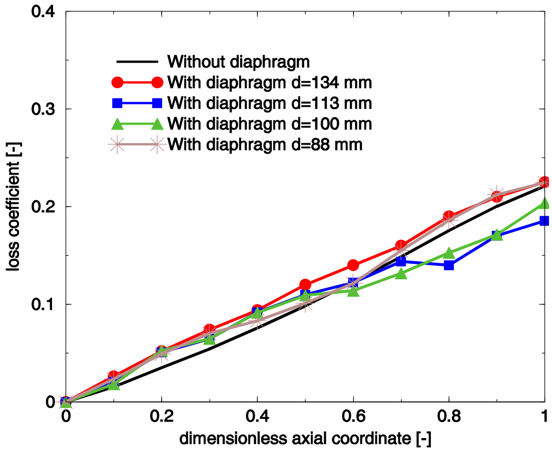

Figure 6. Energy loss coefficient ζ distribution along to versus axial coordinate.

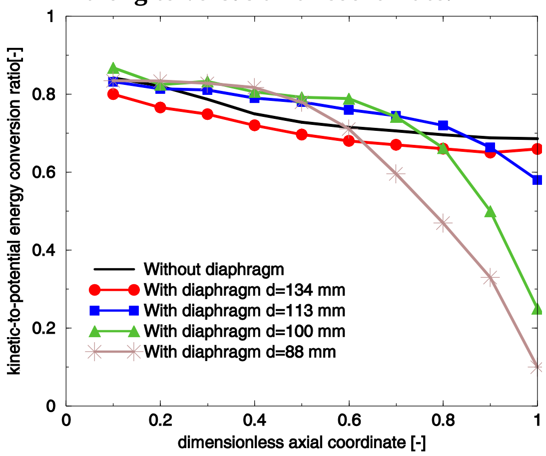

Figure 7. Kinetic-to-potential energy conversion ratio χ in the test section versus axial coordinate.

4. CONCLUSIONS

The paper introduces a new concept for mitigating the swirling flow with helical vortex. The pressure pulsations associated to the helical vortex are mitigated introducing a adjustable diaphragm in the cone. Full 3D unsteady numerical simulations with and without diaphragm were performed in order to assess the dynamic and kinetic-to-potential energy recovery performances of the concept. The numerical results clearly show that the helical vortex evolves in a straight vortex structure when the diaphragm is switched on. As a result, the unsteady pressure signals associated to the helical vortex are mitigated up to 65% in the amplitude and 80% in frequency when the straight vortex is developed. Also, the improvement of pressure recovery is important while hydraulic losses are diminished, especially in first part of the test section. This novel concept paves the way towards a new passive control technique in turbomachinery.

ACKNOWLEDGEMENTS

Dr. Tanasa and Dr. Ciocan, were partially supported by the strategic grant POSDRU/159/1.5/S/137070 (2014) of the Ministry of National Education, Romania, co-financed by the European Social Fund – Investing in People, within the Sectoral Operational Programme Human Resources Development 2007-2013". Dr. Muntean S. was supported by Romanian Academy program.

REFERENCES

[1] Ruprecht, A., Helmrich, Th., Aschenbrenner, Th., and Scherer, T, 2002, “Simulation of the Vortex Rope in a Turbine Draft Tube”, Proc. *21st IAHR Symposium on Hydraulic Machinery and Systems*, pp 259-276.

[2] Zhang, R., Mao, F., Wu, J., Chen, S., Wu, Y., and Liu, S., 2009 “Characteristics and Control of the Draft-Tube Flow in Part-Load Francis Turbine”, *J. Fluids Eng. – Trans. ASME*, **131**(2), 021101, pp. 1-13, doi: 10.1115/1.3002318.

[3] Muntean, S., Nilsson, H., and Susan-Resiga, R., 2009, „3D numerical analysis of the unsteady turbulent swirling flow in a conical diffuser using Fluent and OpenFoam”, *In*: *Proceedings of the 3rd IAHR International Meeting of the Workgroup on Cavitation and Dynamic Problems in Hydraulic Machinery and Systems*. Brno, Czech Republic, pp.155-165.

[4] Susan-Resiga, R., Muntean, S., Tanasa, C., and Bosioc, A., 2009, „Three-dimensional versus two-dimensional axisymmetric analysis for decelerated swirling flows”, *In*: *The 14th International Conference on Fluid Flow Technologies*. Budapest, Hungary.

[5] OpenFOAM test case available at: http://openfoamwiki.net/index.php/Sig_Turbomachinery_/_Timisoara_Swirl_Generator

[6] Petit, O., Bosioc, A., Nilsson, H., Muntean, S., and Susan-Resiga, R., 2011, „Unsteady simulations of the flow in a swirl generator using OpenFoam”, *IJFMS*, **4**(1).

[7] Ojima, A., and Kamemoto, K., 2010, „Vortex method simulation of 3D and unsteady vortices in a swirling flow apparatus experimented in "Politehnica" University of Timisoara”, *In*: *25th IAHR Symposium on Hydraulic Machinery and Systems, Online at: IOP Conf. Series: Earth and Environmental Science*. Timisoara, Romania.

[8] Thike, R.H., 1981, „Practical solutions for draft tube insatbility”, *Water Power and Dam Construction*, **33**(2), pp.31-37.

[9] Pappilon, B., Sabourin, M., Couston, M., and Deschenes, C., 2002, "Methods for air admission in hydro turbines", *Proceedings of the 21st IAHR Symposium on Hydraulic Machinery and Systems*, Lausanne, Switzerland, pp. 1-6.

[10] Kjeldsen, M., Olsen, K., Nielsen, T., and Dahlhaug, O., 2006, "Water injection for the mitigation of draft tube pressure pulsations", *IAHR International Meeting of W.G. on Cavitation and Dynamic Problems in Hydraulic Machinery and Systems*, Barcelona, Spain.

[11] Nishi, M., Wang, X. M., Yoshida, K., Takahashi, T., and Tsukamoto, T., 1996, "An Experimental Study on Fins, Their Role in Control of the Draft Tube Surging", *Hydraulic Machinery and Cavitation, in Cabrera, E., et al., eds., Kluwer Academic Publishers*, Dordrecht, The Netherlands, pp. 905-914.

[12] Bosioc, A., Susan-Resiga, R., Muntean, S. and Tanasa, C., 2012, "Unsteady Pressure Analysis of a Swirling Flow with Vortex Rope and Axial Water Injection in a Discharge Cone", *J. Fluids Eng. – Trans. ASME,* **134**(8), 081104, pp. 1-11.

[13] Tanasa, C., Susan-Resiga, R. F., Muntean, S., and Bosioc, A. I., 2013, "Flow-Feedback Method for Mitigating the Vortex Rope in Decelerated Swirling Flows", *J. of Fluids Eng*., **135**(6).

[14] Susan-Resiga, R. F., Tanasa, C., Bosioc, A. I., Ciocan, T., Stuparu, A. and Muntean, S., "Method and equipment for swirling flow control from conical diffuser of hydraulic turbines", (in Romanian), *Patent Application no. A/00621, 13.08.2014,* Applicant: Politehnica University, Timisoara, Romania.

[15] Susan-Resiga, R., Muntean, S., Hasmatuchi, V., Anton, I., and Avellan, F., 2010, "Analysis and Prevention of Vortex Breakdown in the Simplified Discharge Cone of a Francis Turbine", *J. Fluids Eng. – Trans. ASME*, **132**(5), pp. 1-15.

[16] Avellan, F., 2000, "Flow Investigation in a Francis Draft Tube: The FLINDT Project", *Proc. Of the 20th IAHR Symposium on Hydraulic Machinery and Systems*, Charlotte, USA, p. DES-11.

[17] Menter, F. R., 1993, "Zonal Two Equation k-ω Turbulence Models for Aerodynamic Flows", *AIAA Journal*, p. 93-2906.

[18] Menter F.R., 1994, "Two-Equation Eddy-Viscosity Turbulence Models for Engineering Applications", *AIAA Journal*, **32**(8), pp. 1598-1605.

[19] Riley, K. F., Hobson, M. P., and Bence, S. J., 2002, "Mathematical Methods for Physics and Engineering", *Cambridge University Press*, Cambridge, United Kingdom, Chap. 12.8.

Conference on Modelling Fluid Flow (CMFF'15)
The 16th International Conference on Fluid Flow Technologies
Budapest, Hungary, September 1-4, 2015

BIFURCATION STRUCTURE OF A PERIODICALLY DRIVEN BUBBLE OSCILLATOR NEAR BLAKE'S CRITICAL THRESHOLD

Ferenc HEGEDŰS[1], Roxána VARGA[2], Kálmán KLAPCSIK[3]

[1] Corresponding Author. Department of Hydrodynamics Systems, Budapest University of Technology and Economics, Faculty of Mechanical Engineering. Műegyetem rkp. 3, H-1111 Budapest, Hungary. Tel.: +36-1-463-1680, Fax: +36-1-463-3091, E-mail: hegedusf@hds.bme.hu
[2] Department of Hydrodynamics Systems, Budapest University of Technology and Economics. E-mail: rvarga@hds.bme.hu
[3] Department of Hydrodynamics Systems, Budapest University of Technology and Economics. E-mail: kklapcsik@hds.bme.hu

ABSTRACT

It is well-known that gas/vapour bubbles in liquids growth indefinitely if the ambient pressure exceeds Blake's critical threshold. For several decades of investigations, researchers tried to find numerical evidence for the stabilization of such bubbles by applying a harmonically varying pressure field on the liquid domain (ultrasonic irradiation) in this regime, with only partial success. Since, the applied linearization on the bubble models restricted the findings only for small amplitude radial oscillations. Therefore, the present paper intends to reveal the particularly complex dynamics of a harmonically excited bubble near, but still below Blake's threshold. The computed solutions with a variety of periodicity, e.g., from period 1 up to period 9, form a well-organised structure with respect to the pressure amplitude of the excitation, provided that the applied frequency is higher than the first subharmonic resonance frequency of the bubble. This predictable behaviour provides a good basis for further investigation to find the relevant stable oscillations beyond Blake's threshold. Although, the investigated model is the very simple Rayleigh—Plesset equation, the applied numerical technique is free of the restriction of low amplitude oscillations.

Keywords: bubble dynamics, bifurcation structure, nonlinear analysis, Rayleigh—Plesset equation, ultrasonic stabilization, transient chaos

NOMENCLATURE

t	$[s]$	time
R	$[m]$	bubble radius
p	$[\mathrm{Pa}]$	pressure
P	$[\mathrm{Pa}]$	ambient pressure
T	$[\mathrm{K}]$	ambient temperature
ρ	$[\mathrm{kg/m^3}]$	density
μ	$[\mathrm{kg/(m\cdot s)}]$	dynamic viscosity
ω	$[\mathrm{rad/s}]$	angular frequency
σ	$[\mathrm{Nm}]$	surface tension
κ		ratio of the specific heats

Subscripts and Superscripts

$\cdot$	time derivative
L	liquid
∞	far away from the bubble
A	amplitude
G	gas
V	vapour
C	critical condition
R	relative quantity
ref	reference quantity

1. INTRODUCTION

Irradiating a liquid with high frequency high intensity ultrasound, bubbles and bubble clusters are formed, called acoustic cavitation [1]. During the oscillations of the bubbles, their wall velocities can exceed thousands of $\mathrm{m/s}$ due to the inertia of the liquid domain. This phenomenon is usually called as collapse phase, and often referred to as inertial cavitation [2]. At the collapse sites, the generated extreme conditions, such as the high temperature and pressure or the induced shock wave, are exploited by various ultrasonic technological applications.

In sonochemistry, for instance, the utilization of ultrasound can increase the efficiency of various chemical reactions [3-5]. This novel technology has been spread in food and other inorganic industrial applications, in which the keen interest is to produce homogeneous mixtures from immiscible liquids, alteration of the viscosity of many food systems, increase the efficiency of heterogeneous catalysis, wastewater treatment or pasteurisation etc., see e.g. [6, 7]. Moreover, the application of ultrasound can be a new, novel and promising technology in cancer therapy via the tissue erosion effect of acoustic cavitation [8].

Although the ultrasonic irradiation generates bubble ensembles, the study of a single spherical bubble is an important building block in both the theoretical and numerical understanding of the fundamentals of the applications. Therefore, many researchers have investigated the dynamics of a single bubble with sophisticated numerical analysis and with an increasing complexity of the physical modelling. The accumulated numerical results are summarised in many books, reviews and papers [1-2, 9-19].

The majority of the studies usually deal with liquid water at room conditions, that is, at $25\,^{o}\mathrm{C}$ ambient temperature and at $1\ \mathrm{bar}$ ambient pressure. In this case, stable bubble oscillation is ensured because of the strictly dissipative nature of physical system. At very low ambient pressure, however, such behaviour cannot be guaranteed. By lowering the pressure below the well-known Blake's critical threshold [20] the bubbles tend to grow indefinitely (without ultrasonic irradiation). This phenomenon is known as the classic cavitation.

For several decades of investigations, researchers tried to find numerical evidence for the stabilization of the bubbles by applying a harmonically varying pressure field on the liquid domain (ultrasonic irradiation) in this regime with only partial success. Since, the applied linearization on the bubble models restricted the findings only for small amplitude radial oscillations. The first significant advancement is obtained by Hegedűs [12] who could prove the existence of stably oscillating bubbles beyond Blake's threshold without any restriction in the nonlinearities. Although his result is a notable milestone, the stable solutions found correspond only to a special kind of bubble behaviour, called period 1 oscillations.

The main aim of the present paper is to reveal the complex dynamics of a harmonically excited spherical air/vapour bubble placed in water near, but still below Blake's threshold. The found solutions show a variety of periodicity, e.g., from period 1 up to period 9, which form a well-organised structure with respect to the pressure amplitude of the excitation, provided that the applied frequency is higher than the first subharmonic resonance frequency of the bubble. This predictable behaviour provides a good basis to extend the already acquired understanding by Hegedűs [12] from period 1 solutions to oscillations with arbitrary periodicity beyond the critical threshold. Although the applied model is the simple Rayleigh—Plesset equation, the employed numerical technique does not involve linearization or other reduced order modelling. Therefore, the presented technique can be easily extended for more complex models with high amplitude oscillations.

2. THE BUBBLE MODEL

The bubble model governing the evolution of the bubble radius is the simple well-known Rayleigh—Plesset equation [9] written as

$$R\ddot{R} + \frac{3}{2}\dot{R}^2 = \frac{1}{\rho_L}(p_L - p_\infty), \qquad (1)$$

where the dot stands for the derivative with respect to time, $R(t)$ is the time dependent bubble radius, ρ_L is the density of the liquid water. The pressure at the bubble wall in the liquid side is p_L and far away from the bubble

$$p_\infty(t) = P_\infty + p_A\, sin(\omega t) \qquad (2)$$

is a sum of the static ambient pressure P_∞ and the harmonic driving with pressure amplitude p_A and angular frequency ω. The relationship between the pressure inside and outside the bubble at its wall is defined by the mechanical balance:

$$p_G + p_V = p_L + \frac{2\sigma}{R} - 4\mu_L\frac{\dot{R}}{R}. \qquad (3)$$

Here, the total pressure inside the bubble is the sum of the non-condensable gas pressure p_G and vapour pressure p_V. The vapour pressure was constant during the simulations, but it depended on the constant ambient temperature. The surface tension is σ and the liquid kinematic viscosity is μ_L. The air inside the bubble follows a simple adiabatic state of change written in the form according to [12]:

$$p_G = \left(\frac{2\sigma}{3\kappa R_C}\right)\left(\frac{R_C}{R}\right)^{3\kappa}, \qquad (4)$$

where R_C is the equilibrium bubble radius of the unexcited system ($p_A = 0$) at Blake's threshold (see the detailed explanation below) and $\kappa = 1.4$ is the ratio of the specific heats for diatomic gas content.

In the bubble model, we assume that the water contains some amount of dissolved gas. The seeds or nuclei-sites, which can be pre-existing gas micro bubbles, are the week points of the liquid where the acoustic cavitation can be initiated. The mass of gas inside the bubble than can grow by rectified diffusion forming larger gas/vapour bubbles [21]. The process of rectified diffusion has orders of magnitude larger time scale than the period of the acoustic forcing.

It is important to emphasize that the constant vapour pressure and adiabatic state of change for the gas content is a severe assumption [22]. In the present study, however, the main aim is to reveal the topology of the stable periodic solutions rather than the precise physical description. This simple model allows to perform detailed parameter studies, which were essential in the understanding of the topology. Moreover, many other oscillators in different branches of science have the same/similar topological description implying that the found structure is universal in harmonically excited systems. Therefore, we expect the same qualitative behaviour for more complex bubble models, as well.

1.1. Equilibrium radius of the unexcited system

The equilibrium bubble radius curve of the unexcited system ($p_A = 0\ Pa$) is presented in Fig. 1 at ambient temperature $T_\infty = 37\ ^oC$, and computed by means of Eqs. (1) to (4) by setting all the time derivatives to zero. The stable R_E^s and the unstable R_E^u equilibrium radii are represented by the black and red curves, respectively. The two kinds of long-term behaviour are separated by the Blake's critical conditions marked by the dot in Fig. 1, where the curve turns back and tends to infinity as the tension approaches to zero.

According to [12], the critical condition can be characterised by its critical equilibrium radius set to be $R_C = 0.1\ mm$, which is the upper limit of the typical nuclei size in water [9]. Then, the critical tension can be formulated as

$$p_V - P_C = \frac{2\sigma}{R_C}\frac{3\kappa - 1}{\kappa} = 1067\ Pa. \tag{5}$$

By defining a dimensionless relative pressure as

$$P_R = \frac{p_V - P_\infty}{p_V - P_C}, \tag{6}$$

three main region can be distinguished in the horizontal axis. If $P_R < 0$ there is only one stable equilibrium radius, the system is strictly dissipative and all the trajectories tend to this sole stable behaviour. In case of $0 < P_R < 1$, an unstable fix point appears beside the stable one. In spite of the existence of stable long-term behaviour, stable oscillations cannot be guaranteed in this parameter domain, and bubbles may grow to infinity for a given set of initial conditions. Above $P_R = 1$ (beyond Blake's threshold), equilibrium radii are completely absent. Regardless of the initial conditions, it is impossible to obtain stable oscillation. Again, this region was the keen interest by many researchers to find evidence for the stabilization mechanism of harmonic forcing discussed in more detail in the Introduction.

Although Hegedűs [12] have already find the evidence for the existence of stable solutions, it is restricted only to period 1 oscillations. In his work, the crucial starting point was the exploration of all the stable period 1 solutions in the pressure amplitude p_A – frequency ω parameter plane at relative pressure $P_R = 0.9$.

Therefore, the main aim of the present study is to reveal and explore the structure and organization of the periodic solutions at the same relative pressure (0.9) marked by the blue vertical line in Fig. 1. This means that the ambient pressure is $P_\infty = 5458\ Pa$. The obtained topological description is an important progress toward the extension of the numerical results beyond Blake's threshold from period 1 solution to arbitrary periodicity.

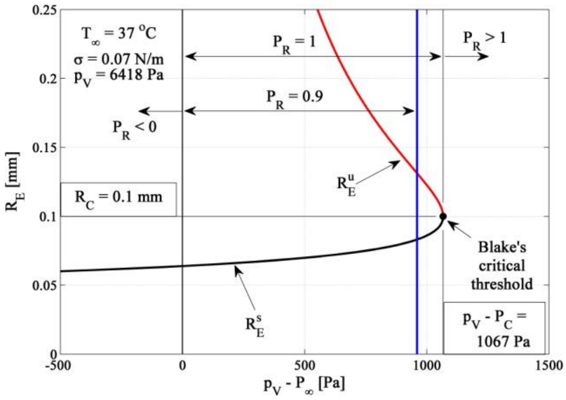

Figure 1. Equilibrium bubble radius curve as a function of the tension $p_V - P_\infty$ at ambient temperature $T_\infty = 37\ ^oC$. The solid black and red curves are the stable and unstable equilibrium radii, respectively. The black dot denotes Blake's critical threshold.

1.2. Dimensionless quantities and parameter values

Throughout the paper, dimensionless quantities were used for better numerical behaviour, such as, dimensionless time:

$$\tau = \frac{\omega t}{(2\pi)}. \tag{7}$$

Observe that in the dimensionless system the period of the excitation becomes unity $\tau_o = 1$. The dimensionless bubble radius and wall velocity are

$$y_1 = \frac{R}{R_C} \tag{8}$$

and

$$y_2 = \frac{2\pi\dot{R}}{R_C\omega}, \tag{9}$$

respectively. Finally, the relative frequency is defined as

$$\omega_R = \frac{\omega}{\omega_{ref}}, \tag{10}$$

where the reference frequency, according to [12], is

$$\omega_{ref} = \sqrt{\frac{4\sigma}{\rho_L R_C^3}} = 16793\frac{rad}{s}. \tag{11}$$

The values of the applied parameters and material properties are summarized in Table 1. The liquid properties are calculated from the Haar—Galagher—Kell equation of state [23] with $P_\infty = 5458\ Pa$. and with $T_\infty = 37\ ^oC$.

Table 1. Values of the applied parameters and material properties

Property	Value
Ambient pressure P_∞	5458.3 Pa
Ambient temperature T_∞	$37\ ^oC$
Surface tension σ	$0.07\ N/m$
Liquid density ρ_L	$993.13\ kg/m^3$

Liquid dyn. viscosity μ_L	$6.858 \cdot 10^{-4}\ \frac{kg}{m \cdot s}$
Vapor pressure p_V	$6418.8\ Pa$
Bubble size R_C	$0.1\ mm$
Relative pressure P_R	0.9
Pressure amplitude p_A	$0\ kPa - 10\ kPa$
Excitation frequency ω_R	$0.1 - 5$

2. RESULTS AND DISCUSSION

The simplest and still widely used method to find stable oscillations is to take an initial value problem solver and integrate system (1) to (4) forward in time by applying suitable initial conditions $y_1(0)$ and $y_2(0)$. After the convergence to a stable solution (attractor), some characteristic properties of the found solution are recorded. For instance, the points of the Poincaré map (see the detailed description later), the maximum bubble radius and wall velocity of the bubble oscillation, the largest Lyapunov exponent to reveal the existence of chaotic attractor or the periodicity in case of periodic orbits. In the following, with this simple method, the stable solutions will systematically be explored as a function of the pressure amplitude p_A and excitation frequency ω.

1.2. Unique features of the oscillations

Due to the non-strictly dissipative nature of the system, the hunting for stable oscillations is not trivial. Figure 2 shows two examples for a stable (black curve) and for an unstable (red curve) transient trajectory by applying relatively close initial conditions. Keep in mind that the period of the excitation of the dimensionless system τ_o is unity, therefore, the integer values of the horizontal axis represents integer number of acoustic cycles. Consequently, after surviving approximately 8 cycles, the unstable solution starts to diverge exponentially from the stable one, and tends to grow infinitely.

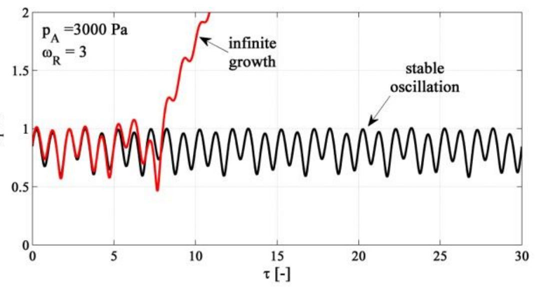

Figure 2. Dimensionless bubble radius vs. time curves for a stable bubble oscillation (black curve) and for an unstable transient solution (red curve).

The technique to overcome this difficulty is to apply several randomized initial conditions. The more the number of the initial conditions the greater the probability to find stable orbits. During the numerical calculations, 20 initial conditions were used at a given parameter combination. As a by-product, this method is capable to explore the co-existence of the different kind of attractors. Figure 3 represents three kind of stable periodic solutions at pressure amplitude $p_A = 2556\ Pa$ and at relative frequency $\omega = 5$. Observe that the periods of the oscillations are equal to (black), 7 times (blue) and 21 times (red) the period of driving. In the language of nonlinear dynamics, these solutions are called period 1, 7 and 21 attractors, respectively. Such co-existence is a clear evidence for the non-linear nature of the bubble oscillator.

The periodic orbits in the state space, y_1-y_2 plane, form closed curves, see the lower panel of Fig. 3. Because of the time dependent harmonic forcing, the trajectories in this plane can intersect themselves demonstrated by the blue curve corresponding to the period 7 orbit. Therefore, in the forthcoming diagrams, only the points of the Poincaré section will be presented, which are obtained by sampling the continuous solutions with the period of the driving. This technique is very common in periodically driven non-linear systems [24]. Observe that the trajectory of the period 21 solution is omitted, and only the 21 number of red Poincaré points are depicted in order to avoid overcrowding of the figure.

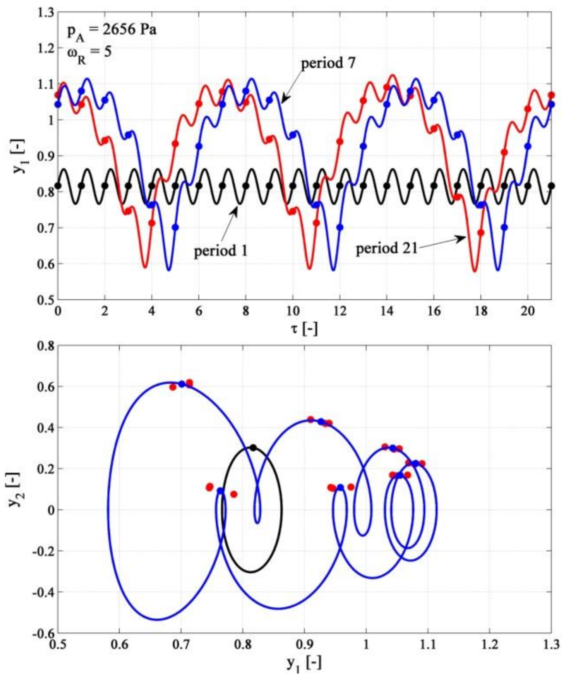

Figure 3. Co-existing stable period 1 (black), period 7 (blue) and period 21 (red) attractors. Upper panel: dimensionless bubble radius vs. times curves. Lower panel: trajectories in the state space. The dots are the points of the Poincaré section.

Another interesting feature of the system is the presence of transient chaos [25], which further complicates the finding of stable bubble motions. Such oscillations are chaotic, but they are unstable in nature. Therefore, they are extremely difficult to find. Integrating the system backward in time cannot solve the problem either, as they are usually related to chaotic saddles. The appearances of solutions with a relatively long seemingly stable behaviour which finally become unstable as the time tends to infinity are good indicators for the existence of a chaotic saddle. An example for such transient bubble oscillation is presented in Fig. 4, where the solution seems to be stable up to 80 acoustic cycles.

The determination of some characteristic properties, such as the largest Lyapunov exponent, fractal dimension etc., of the transient chaos needs huge number of numerical computations. A typical technique, for instance, is to measure the escape rate of several trajectories, initiated randomly [25]. Although the method is relatively simple, for sufficient precision, the application of millions of initial conditions is usually required.

During the numerical computations, the maximum number of allowed acoustic cycles were 1500. After this, the solution was regarded as stable chaos provided that its Lyapunov exponent was positive. If the Lyapunov exponent is negative and the solution does not converged until 1500 cycles, then the solution was discarded.

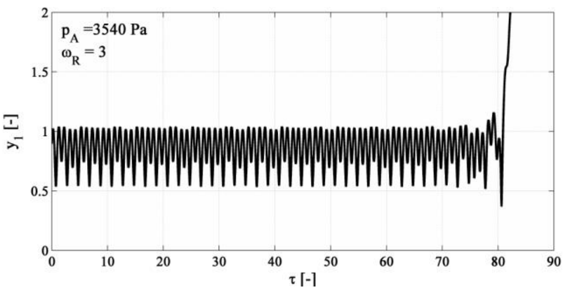

Figure 4. Unstable solutions with a very long seemingly stable behaviour indicating the presence of transient chaos.

1.2. Topological structure of the periodic attractors

A more condensed representation of the behaviour of the bubble is the bifurcation diagram, where a particular property of the found attractors, e.g. the maximum of the bubble radius or a single component of the Poincaré section, is presented as a function of a parameter. In Fig. 5. the first co-ordinate of the Poincaré section $P(y_1)$ is plotted against the pressure amplitude p_A at $\omega_R = 1$. The periodicities of the found attractors are marked by arabic numbers.

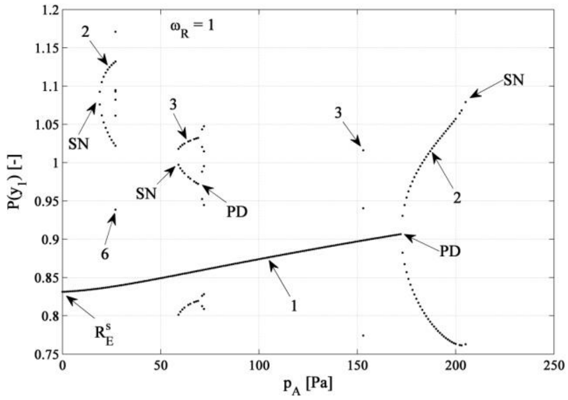

Figure 5. Example for a bifurcation diagram, that is, the first component of the Poincaré section is presented as a function of the pressure amplitude p_A as control parameter at relative frequency $\omega_R = 1$.

From the stable equilibrium radius R_E^s of the unexcited system, a stable period 1 solution emerges as the pressure amplitude is started to increase from $p_A = 0\ Pa$. It becomes unstable at $p_A = 172\ Pa$ and a new period 2 attractor comes to existence through a period doubling (PD) bifurcation. This period doubled solution turns back and become unstable at approximately $p_A = 205\ Pa$ via a saddle-node (SN) bifurcation. The unstable branch (computed in [13] for a similar structure) turns back again via an SN bifurcation at $p_A = 19\ Pa$ establishing a period 2 attractor co-existing with the former period 1 stable solution.

Observe that in a relatively wide parameter range a period 3 attractor emerges via an SN bifurcation and go through a PD bifurcation. Such co-existence of the attractors is a common feature of non-linear systems.

In order to get a global picture about the relevant periodic attractors in the pressure amplitude p_A - relative frequency ω_R parameter plane, a series of bifurcation diagrams were computed and presented in Fig. 6, similar to that of demonstrated in Fig. 5. As the relative frequency is increased from 2 to 5 a remarkably complex and intriguing structure is being evolved.

At relative frequency $\omega_R = 2$ (Fig. 6A), the main bifurcation structure is formed by the period 1, 2, 3, 4 and 5 solutions. Their organisation seems to follow a simple rule, namely, between the appearance of two solutions with period X and Y, there is another one with period $X + Y$. Observe, for instance, that between the period 3 and 2 attractors there is a period 5 stable solution, as well. Further increasing the relative frequency, the obtained results strongly supports this structural description, see Fig. 6B to Fig. 6D. Gradually, more and more attractors, up to period 9, emerge through SN bifurcations towards the negative pressure amplitudes, whose periodicities obey the aforementioned simple rule.

This topological description in terms of the periodicity is summarised by a pictogram in Fig. 7 up to level four. In the literature, this organisation is called as Farey-ordering, and it seems to a universal rule describing the topology of the stable solutions in many dynamical systems [26-30].

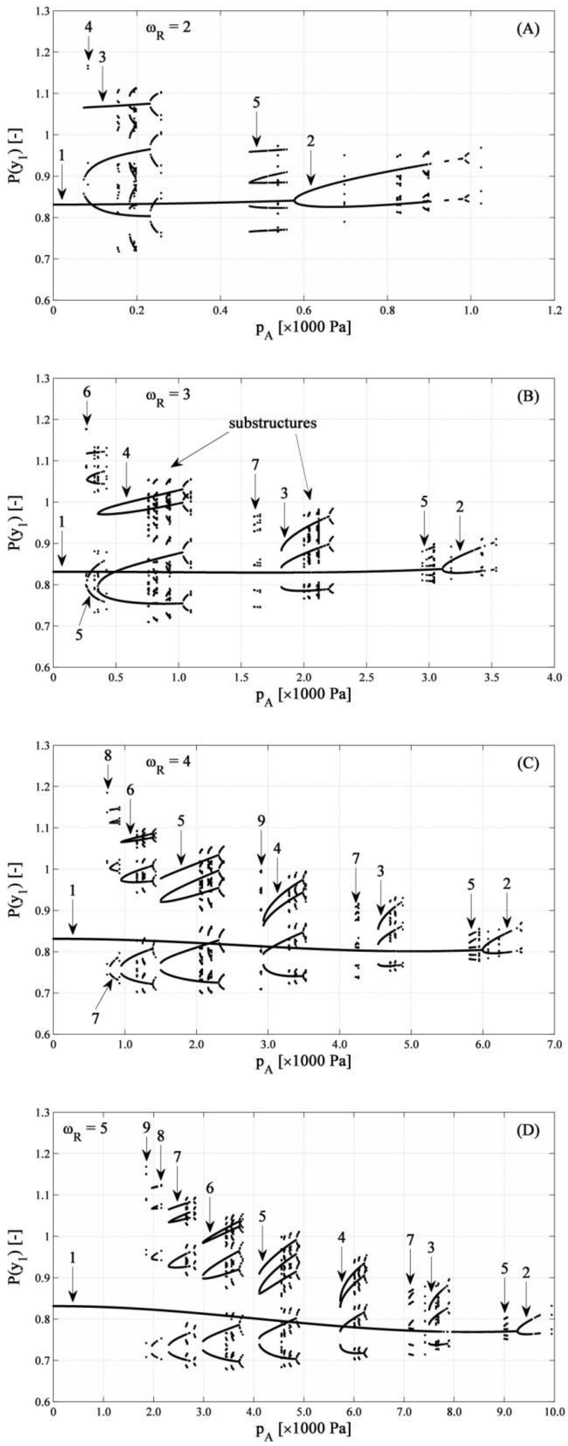

Figure 6. Series of bifurcation diagrams with the pressure amplitude p_A as control parameter at different relative frequencies ω_R.

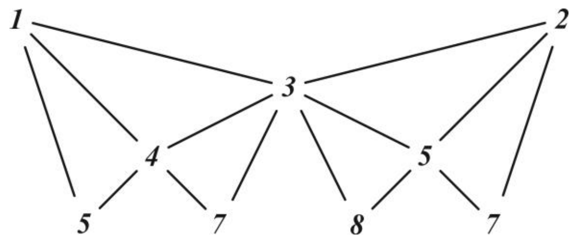

Figure 7. Organisation structure of the periodic attractors as a function of the pressure amplitude p_A as control parameter in terms of periodicity above relative frequency $\omega_R > 2$.

It should be noted, that a fine co-existing substructure exists for each periodic attractor, see e.g. the stable solutions with very high periodicities in the range of period 4 and 3 solutions in Fig. 6.B. The analysis of these attractors is out of the scope of the present investigation.

5. SUMMARY

In case of a spherical gas/vapour bubble, at constant, but sufficiently low ambient pressure (beyond Blake's critical threshold) equilibrium radius does not exist and the bubble tends to grown indefinitely. In this parameter region, Hegedűs [12] could find evidence for stable bubble oscillation by applying harmonically varying pressure filed on the liquid domain, however, only for a special, period 1 solutions. In order to extend this knowledge to arbitrary periodicity, this paper focuses on the topological description of the stable solutions at low, but still above the critical threshold. The results show that organisation of the attractors follows a simple rule characterised by the well-known Farey-ordering. This finding is vital and necessary to leap forward, and obtain a good theoretical understanding for the stabilization mechanism for ambient pressures beyond Blake's critical threshold.

The mathematical model was the simple Rayleigh—Plesset equation, which is a second order non-linear ordinary differential equation. The size of the applied bubble was 0.1 mm placed in liquid water.

ACKNOWLEDGEMENTS

This work has been supported by the Hungarian National Fund for Science and Research under contract No. OTKA K81621.

REFERENCES

[1] Leighton, T. G., 1994, *The Acoustic Bubble*, Academic, London.

[2] Young, F. R., 1989, *Cavitation*, McGraw-Hill, London.

[3] Merouani, S., Hamdaoui, O., Rezgui, Y., and Guemini, M., 2013, "Effects of ultrasound frequency and acoustic amplitude on the size of

sonochemically active bubbles – Theoretical study”, *Ultrason Sonochem*, Vol. 20, pp. 815-819.

[4] Brotchie, A., Mettin, R., and Grieser, F., 2009, “Cavitation activation by dual-frequency ultrasound and shock waves”, *Phys Chem Chem Phys*, Vol. 11, pp. 10029-10034.

[5] Prabhu, A. V., Gogate, P. R., and Pandit, A. B., 2004, “Optimization of multiple-frequency sonochemical reactors”, *Phys Chem Eng Sci*, Vol. 59, pp. 4991-4998.

[6] Knorr, D., Zenker, M., Heinz, V. and Lee, D.-U., 2004, “Applications and potential of ultrasonics in food processing”, *Trends Food Sci Tech*, Vol. 15, pp. 261-266.

[7] Patist, A., and Bates, D., 2008, “Ultrasonic innovations in the food industry: From the laboratory to commercial production”, *Innov Food Sci Emerg Technol*, Vol. 9, pp. 147-154.

[8] Kennedy, J. E., Haar, G. R. and Cranston, D., 2014, “High intensity focused ultrasound: surgery of the future?”, *Brit J Radiol*, Vol. 76, pp. 590-599.

[9] Brennen, C. E., 1995, *Cavitation and Bubble Dynamics*, University Press, Oxford.

[10] Feng, Z. C., and Leal, L. G., 1997, “Nonlinear bubble dynamics”, *Annu Rev Fluid Mech*, Vol. 29, pp. 201-243.

[11] Lauterborn, W., and Kurz, T., 2010, “Physics of bubble oscillations”, *Rep Prog Phys*, Vol. 73, pp. 106501.

[12] Hegedűs, F., 2014, “Stable bubble oscillations beyond Blake’s critical threshold”, *Ultrasonics*, Vol. 54, pp. 1113-1121.

[13] Hegedűs, F., Hős, C., and Kullmann, L., 2013, “Stable period 1, 2 and 3 structures of the harmonically excited Rayleigh—Plesset equation applying low ambient pressure”, *IMA J Appl Math*, Vol. 78, pp. 1179-1195.

[13] Hegedűs, F., and Kullmann, L., 2012, “Basin of attraction in a harmonically excited bubble model”, *Period. Polytech Mech Eng*, Vol. 56, pp. 125-132.

[14] Sojahrood, A. J., and Kolios, M. C., 2012, “Classification of the nonlinear dynamics and bifurcation structure of ultrasound contrast agents excited at higher multiples of their resonance frequency”, *Phys Lett A*, Vol. 376, pp. 2222-2229.

[15] Behnia, S., Sojahrood, A. J., Soltanpoor, W., and Jahanbakhsh, O., 2009, “Nonlinear transitions of a spherical cavitation bubble”, *Chaos Soliton Fract*, Vol. 41, pp. 818-828.

[16] Behnia, S., Sojahrood, A. J., Soltanpoor, W., and Jahanbakhsh, O., 2009, “Nonlinear transitions of a spherical cavitation bubble”, *Chaos Soliton Fract*, Vol. 41, pp. 818-828.

[17] Behnia, S., Sojahrood, A. J., Soltanpoor, W., and Sarkhosh, L., 2009, “Towards classification of the bifurcation structure of a spherical cavitation bubble”, *Ultrasonics*, Vol. 49, pp. 605-610.

[18] Behnia, S., Sojahrood, A. J., Soltanpoor, W., and Jahanbakhsh, O., 2009, “Suppressing chaotic oscillations of a spherical cavitation bubble through applying a periodic perturbation”, *Ultrason Sonochem*, Vol. 16, pp. 502-511.

[19] Parlitz, U., Englisch, V., Scheffczyk, C., and Lauterborn, W., 1990, “Bifurcation structure of bubble oscillators”, *J Acoust Soc Am*, Vol. 88, pp. 1061-1077.

[20] Blake, F. G., 1949, “The onset of cavitation in liquids: I.”, *Acoustic Res Lab, Harvard Univ Tech Memo*, No. 12.

[21] Fyrillas, M.M., Szeri, A. J., 1994, “Dissolution or growth of soluble spherical oscillating bubbles”, *J Fluid Mech*, Vol. 277, pp. 381-407.

[22] Plesset, M.S., Prosperetti, A., 1977, “Bubble dynamics and cavitation”, *Ann Rev Fliud Mech*, Vol. 9, pp. 145-185.

[23] Haar, L., Gallagher, J. S., and Kell, G. S., 1988, *NBS/NRC Wasserdampftafeln*, Springer, Berlin.

[24] Kuznetsov, Y. A., 2004, *Elements of Applied Bifurcation Theory*, Springer, New York.

[25] Lai, Y.-C., and Tél, T., 2010, *Transient Chaos: Complex Dynamics on Finite-Time Scales*, Springer, New York.

[26] Gilmore, R., and McCallum, J. W. L., 1995, “Structure in the bifurcation diagram of the Duffing oscillator”, *Phys Rev E*, Vol. 51, pp. 935-956.

[27] Goswami, B. K., 1998, “Self-similarity in the bifurcation structure involving period tripling, and a suggested generalization to period *n*-tupling”, *Phys Lett A*, Vol. 245, pp. 97-109.

[28] Gilmore, R., 1998, “Topological analysis of chaotic dynamical systems”, *Rev Mod Phys*, Vol. 70, pp. 1455-1529.

[29] Cvitanović, P., and Myrheim, J., 1983, “Universality for period n-tuplings in complex mappings”, *Phys Lett A*, Vol. 94, pp. 329-333.

[30] Englisch, V., and Lauterborn, W., 1994, “The winding-number limit of period-doubling

cascades derived as Farey-fraction", *Int J Bifurcat Chaos*, Vol. 4, pp. 999-1002.

Conference on Modelling Fluid Flow (CMFF'15)
The 16th International Conference on Fluid Flow Technologies
Budapest, Hungary, September 1-4, 2015

TWO-PARAMETER BIFURCATION ANALYSIS FOR THE SEEKING OF HIGH AMPLITUDE OSCILLATION OF A PERIODICALLY DRIVEN GAS BUBBLE IN GLYCERINE

Kálmán KLAPCSIK[1], Ferenc HEGEDŰS[2]

[1] Corresponding Author. Department of Hydrodynamic Systems, Budapest University of Technology and Economics. P.O. Box 91, 1521 Budapest, Hungary. Tel.: +36 1 463 1680, Fax: +36 1 463 3091, E-mail: kklapcsik@hds.bme.hu
[2] Department of Hydrodynamic Systems, Budapest University of Technology and Economics. E-mail: hegedusf@hds.bme.hu

ABSTRACT

The dynamics of a harmonically driven spherical gas/vapour bubble has been studied intensely in the last decades. The collapse of a bubble induce extreme conditions, such as high pressure and temperature or even shock waves. The ultrasonic technology exploit these conditions in various fields of industry, for example, ultrasonic pasteurization, alteration of the viscosity of thixotropic fluids, production of new kind of copolymers, or in cancer therapy. The present study intends to aid the applications through the numerical investigation of a harmonically excited spherical gas bubble placed in the highly viscous glycerine. We seek parameter regions where the bubble wall velocities as high as possible, perhaps even higher than the sound speed in the liquid domain. Such kind of high amplitude, collapse-like radial oscillations are difficult to find due to the very high viscosity, which is approximately three orders of magnitude greater than of water. The two investigated parameters were the pressure amplitude and the frequency of the harmonic forcing. The applied model was the Keller—Miksis equation, which is a second order nonlinear ordinary differential equation, describing the bubble wall motion and taking into account liquid compressibility as a first order approximation.

Keywords: Bubble dynamics, bifurcation structure, non-linear analysis, Keller-Miksis equation, glycerine, chaos

NOMENCLATURE

M	[-]	Mach number
P_∞	$[bar]$	ambient pressure
R	$[mm]$	bubble radius
R_0	$[mm]$	reference bubble radius
R_E	$[mm]$	equilibrium radius
$\dot{R}$	$[m/s]$	bubble wall velocity
$\ddot{R}$	$[m/s^2]$	bubble wall acceleration
T_∞	$[°C]$	ambient temperature
c	$[m/s]$	sound velocity
f	$[Hz]$	frequency of the bubble oscillation
f_0	$[Hz]$	linear eigenfrequency of the undamped bubble oscillation
m_G	$[g]$	mass of the gas inside the bubble
p_{G0}	$[Pa]$	reference gas pressure
p	$[Pa]$	pressure
p_A	$[bar]$	pressure amplitude
p_∞	$[bar]$	pressure away from bubble
t	$[s]$	time
t_0	$[s]$	period of driving time
κ	[-]	ratio of specific heats
μ	$[Pa{\cdot}s]$	dynamic viscosity
ν	$[Hz]$	driving frequency
ρ	$[kg/m^3]$	density
σ	$[N/m]$	surface tension
τ	[-]	dimensionless time
τ_0	[-]	dimensionless period of driving
ω	$[rad/s]$	angular frequency of excitation
ω_0	$[rad/s]$	linear angular eigenfrequency of undamped system
ω_R	[-]	relative frequency

Subscripts and Superscripts

G, L, V	gas, liquid, vapour
Max	maximal
ref	reference quantity

1. INTRODUCTION

Cavitation causes serious damage in common engineering application, such as in turbomachinery and in hydraulic systems. In most cases, cavitation occurs as sheet cavitation or bubble swarm, thus the applicability of numerical results on a single spherical bubble is limited. However, there are special applications in which the spherical geometry is a proper assumption, such as in case of microbubbles [1], since the surface tension contract the bubble as small and as spherical as possible.

Although the spherical geometry is rather simple, the dynamics of the bubble can be very complicated. The excited bubble behave as an oscillatory system. During its oscillation, the bubble wall velocity can be extremely high due to the inertia of the liquid domain, resulting in many orders of magnitude smaller bubble size than the equilibrium state. This process is called as collapse phase. At the minimum bubble radius, the pressure and the temperature can reach 1000 *bar* and 8000 *K* [2]. Due to the high temperature, chemical reactions can take place, producing free radicals such as H', H_2, O', OH', HO_2' HO', H_2O_2, [3, 4], which are the keen interest of a special field of chemistry, called sonochemistry. Taleyarkhan et al. [5] and Lahey et al. [6] observe neutron emission in deuterated acetone, indicating the presence of fusion. Taleyarkhan et al. [5] numerically revealed that the temperature inside a highly compressed bubble can reach 10^6 to 10^7 *K*, supporting the experimental observation.

In the last decades, many industrial applications, related to the ultrasonic technology, have emerged. The main aim is to enhance the mass, heat and momentum transfer between various phases by exploiting the physical effects of the collapse of gas/vapour bubbles. For instance, a promising process in food preservation is the ultrasonic pasteurization. At moderate temperature, approximately at 50 *°C*, the membrane of the bacterial weakens and become less resistant against cavitation damage. Knorr et al. [7] successfully reduce the amount of E. Coli bacteria in whole eggs. Ultrasound used widely in polymer research. A number of studies reported that, the molecular weight and the chain length can be reduced during high intensity ultrasound irradiation [8]. The ultrasonic technology can be used in cancer therapy as well [9-11]. The collapse of the bubble damage the solid tumours aiding the transport of genes and medicines through the cell.

The main motivation to support the applications through the numerical investigation of a harmonically excited spherical gas bubble placed in the highly viscous glycerine. We seek parameter regions where the bubble wall velocities as high as possible, even higher than the sound speed in the liquid domain. The viscosity of the glycerine is approximately three times larger than that of water, therefore the system has a high damping effect, which makes the hunting for high amplitude collapse-like bubble oscillation difficult. The applied bubble model is the Keller—Miksis equation [12], which is a second order nonlinear ordinary differential equation describing the bubble wall motion and taking into account liquid compressibility as a first order approximation. According to the ultrasonic technology, the two investigated parameters are the pressure amplitude p_A and the frequency ν of the harmonic excitation.

2. MATHEMATICAL MODEL

During the numerical investigation, the well-known Keller—Miksis equation was used with some minor modification according to Lauterborn and Kurz [13]:

$$\left(1-\frac{\dot{R}}{c_L}\right)R\ddot{R}+\left(1-\frac{\dot{R}}{3c_L}\right)\frac{3}{2}\dot{R}^2 = \left(1+\frac{\dot{R}}{c_L}+\frac{R}{\rho_L c_L}\frac{d}{dt}\right)\frac{(p_L-p_\infty)}{\rho_L}. \quad (1)$$

It is a second order, nonlinear ordinary differential equation describing the variation of the bubble radius $R(t)$ in time, where c_L sound velocity in the liquid domain, ρ_L liquid density, p_L pressure at the bubble wall. The material properties depend on the ambient temperature T_∞ of the liquid domain. The pressure far away from the bubble $p_\infty(t)$ consist of a static and a periodic component, according to the ultrasonic irradiation:

$$p_\infty(t) = P_\infty + p_A \cdot sin(\omega t), \quad (2)$$

there P_∞ is the ambient pressure in the liquid domain, p_A and $\omega = 2\pi\nu$ are the pressure amplitude and angular frequency of the harmonic excitation. The bubble content assumed to be a mixture of non-condensable diatomic ideal gas, and glycerine vapour. Therefore the pressure inside the bubble is the sum of the partial pressures of the gas (air) p_G and vapour p_V. The pressure of gas content was approximated by an adiabatic relationship:

$$p_G = p_{G0}\left(\frac{R_0}{R}\right)^{3\kappa}. \quad (3)$$

The ratio of specific heats is $\kappa = 1.4$. The mass of the gas inside the bubble are determined by the reference pressure p_{G0}, and the reference bubble radius R_0:

$$m_G = \frac{4p_{G0}R_0^3\pi}{3\Re T_\infty}, \quad (4)$$

where $\Re$ is the specific gas constant. The connection between the pressures in the liquid and the gas/vapour domain at the bubble wall, is described by the mechanical balance:

$$p_G + p_V = p_L + \frac{2\sigma}{R} + 4\mu_L\frac{\dot{R}}{R}, \quad (5)$$

where σ is the surface tension and μ_L is the dynamic viscosity of the glycerine, both depend on the ambient temperature T_∞. The material properties were taken from the results of The Dow Chemical Company [14].

2.1 Reducing the number of parameters

In Eqs. (1) to (5) all parameters can be determined with five quantities [15]. The ambient pressure P_∞ and the ambient temperature T_∞ specify the material properties of a pure substances. In our special case, all material properties of glycerine depend on only the ambient temperature T_∞, the dependence of P_∞ is neglected. The equilibrium radius of the bubble was prescribed, $R_E = 0.1\ mm$, to determine the size of the bubble. For unexcited system ($p_A = 0$), and all time derivates are zeros, thus Eq. (5) can be rewritten:

$$0 = p_V - P_\infty + p_{G0}\left(\frac{R_0}{R_E}\right)^{3\kappa} - \frac{2\sigma}{R_E}. \tag{6}$$

Since the mass of the bubble depend on the product of $(p_{G0}R_0^3)$, either the reference pressure p_{G0} or the reference bubble radius R_0 can be chosen arbitrarily. In our case, the reference bubble radius was chosen to be equal to equilibrium radius $R_0=R_E$, thus from Eq. (6) the reference gas pressure can be calculated:

$$p_{G0} = \frac{2\sigma}{R_E} - (p_V - P_\infty). \tag{7}$$

The remaining two parameters are the pressure amplitude p_A and the angular frequency ω of the excitation, see Eq. (2). The angular frequency can vary between several orders of magnitude, therefore it was normalized with the linear eigenfrequency of the undamped system [2]:

$$\omega_0 = \sqrt{\frac{3\kappa(P_\infty - p_V)}{\rho_L R_E^2} + \frac{2(3\kappa - 1)\sigma}{\rho_L R_E^3}}. \tag{8}$$

The dimensionless relative frequency, which was used during the computations is defined as:

$$\omega_R = \frac{\omega}{\omega_0}. \tag{9}$$

The Mach number corresponding to the bubble wall velocity:

$$M = \frac{\dot{R}}{c_L}. \tag{10}$$

During the simulation, the bubble radius, the bubble wall velocity and the time was normalized with reference quantities. The reference bubble radius was the equilibrium radius $R_{ref} = R_E$, the reference velocity defined as $v_{ref} = R_E/t_{ref}$, where $t_{ref} = \omega/2\pi$.

3. PROPERTIES OF THE BUBBLE OSCILLATOR

3.1. Computation of stable solutions

The Keller—Miksis model can be viewed as a two dimensional nonlinear oscillator. Closed analytic solutions are not known, except for empty bubble [13], however, numerical solutions are easily obtained. The simplest method is to use an initial value problem solver with suitable initial conditions for the radius of the bubble $R(0)$ and for the velocity of the bubble wall $\dot{R}(0)$, then integrate the system forward in time. After some transient period, the trajectory progressively converges to a stable state, called attractor.

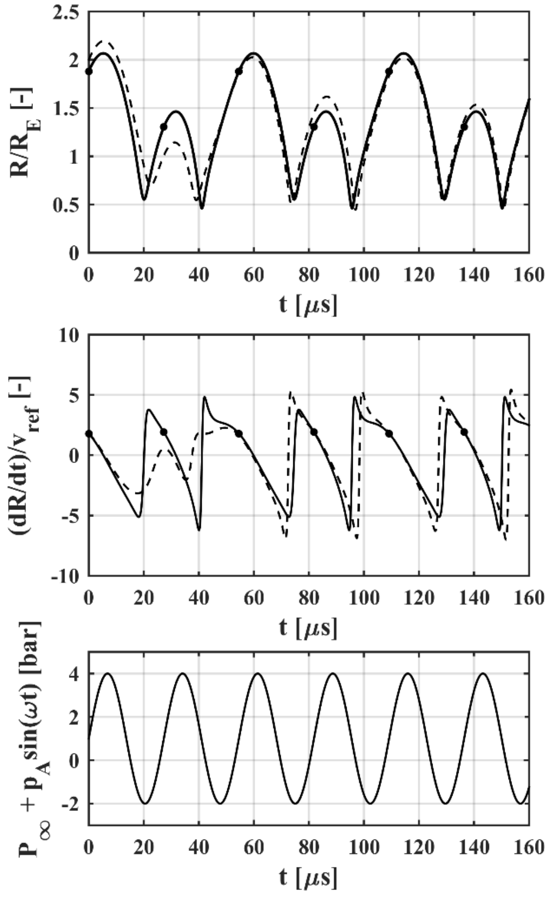

Figure 1. Dimensionless bubble radius and bubble wall velocity vs. time curves at $p_A = 4\ bar$ and $\omega_R = 1.25$. The solid line denotes the attractor, the dashed line denotes the transient solution. The lower graph represent the pressure excitation in time. The black dots are the points of the Poincaré sections.

A typical example of solution is presented in Figure 1 at $p_A = 4bar$ and $\omega_R = 1.25$. On the upper, chart, the dimensionless bubble radius R/R_E, on the middle chart the dimensionless bubble wall velocity

$\dot{R}/v_{ref}$ are presented as a function of time. The solid line denotes the attractor, and the dashed line denotes the transient solutions. The lower graph represent the harmonic pressure excitation (see Eq. (2)).

The solution can be represented in the $(R,\dot{R})$ phase plane. In the simplest case, the trajectory of an attractor construct a closed curve on the phase plane. Figure 2 shows the attractor of the solutions apparent in Fig. 1, in the phase plane. The transient trajectory (dashed curve) starts from the initial condition (denoted by empty circle) and converges to the steady state (solid cure).

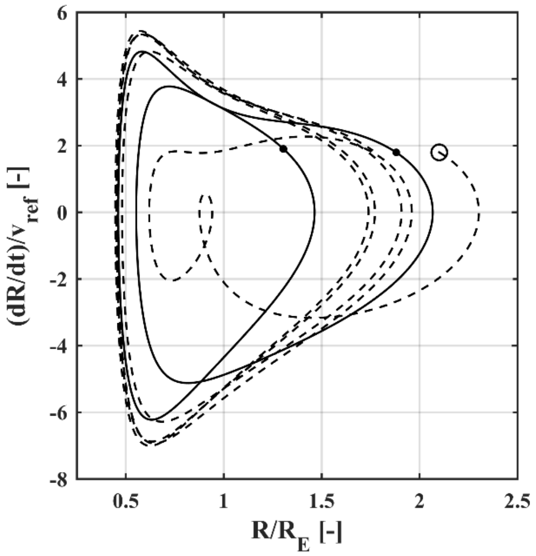

Figure 2. The normalized bubble radius–bubble wall velocity phase plane. Dots are the points of Poincaré sections, and the round denotes the initial conditions.

The trajectories of the complex solution may intersect themselves, making the representation of the results difficult. To avoid this difficulty, one can represent only the Poincaré map, obtained by sampling the continuous trajectory at every integer multiple of the period of driving time t_0. The dots in Fig. 1 and Fig. 2 are the points of Poincaré sections.

During our investigation, the whole trajectories was not recorded, only the Poincaré maps and the maximum values of bubble radius and wall velocity. With these quantities, the main characteristics of the oscillation can be described without the representation of the trajectories. The employed software was Matlab, and the numerical method was a 4th order Runge—Kutta scheme with 5th order embedded error estimation.

3.2. The different types of stable solution

Besides the the simplest solution with period t_0, sub-harmonic oscillations may occur, which only repeat after 2, 3 or more period of excitation, hence the attractor returns exactly to the starting value after 2, 3, or more acoustic cycles. If the solution return to themselves after N period of excitation, where N is integer, the solution called period N solution.

Since the solution is sampled every integer multiple of t_0 in the phase plane, the period N solutions are represented by N dots. In Figure 3, period 1 (solid line), 2 (dashed line) and 3 (dotted line) solutions are demonstrated. On the upper panel, the normalized bubble radius R/R_E as a function of normalized time $\tau = t/t_{ref}$, on the lower panel the periodic attractors in the dimensionless phase plane are represented, respectively. Observe that the solution demonstrated on Fig. 1 and Fig 2 was 2 period solution.

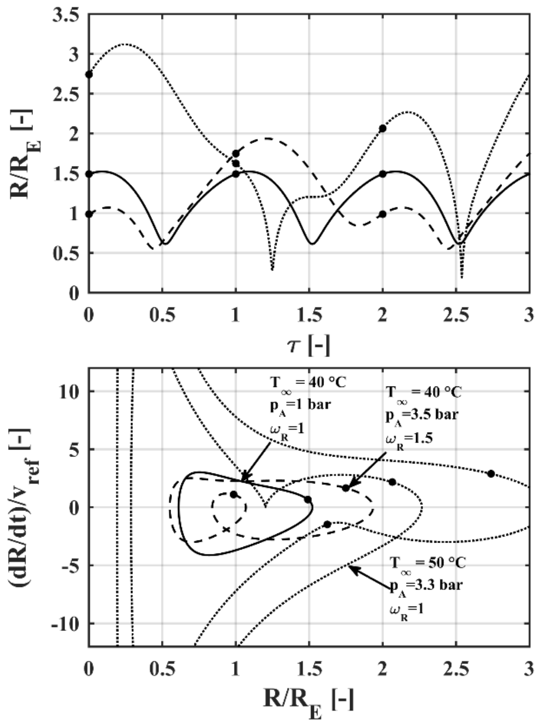

Figure 3. Examples of different periodic attractors: period 1, 2 and 3 solutions are denoted by solid, dashed and dotted lines.

The period may even go to infinity to yield never repeating bubble oscillations. In this case, trajectories never closing. This type of solution is called chaotic attractor.

An example for chaotic solution is demonstrated in Figure 4. On the phase plane (lower panel), trajectories are not plotted, only the points of Poincaré points are represented, to avoid overbidding the figure.

In Figure 5 the spectrum of the period 1, 2, 3 and chaotic solutions, which were demonstrated in Fig. 3 and Fig. 4 are represented. The frequency of the bubble oscillation f was normalized with the driving frequency ν. On subplot a) (period 1 solution), the fundamental frequency is same as the frequency of the excitation, there are peaks at $f/\nu = 1$ and at its harmonics. The spectrum on subplot b) belongs to the period 2 solution. It shows that a sub-harmonic frequency appeared at $f/\nu = 1/2$, therefore, the bubble oscillation repeat after two acoustic cycles.

On subplot c), sub-harmonics appearing at $f/\nu = 1/3$ and $f/\nu = 2/3$. This spectrum belongs to the period 3 solution. The spectrum of the chaotic solution subplot d) is continuous, where a broad band noise is superimposed on the fundamental frequency, but it's from a deterministic system.

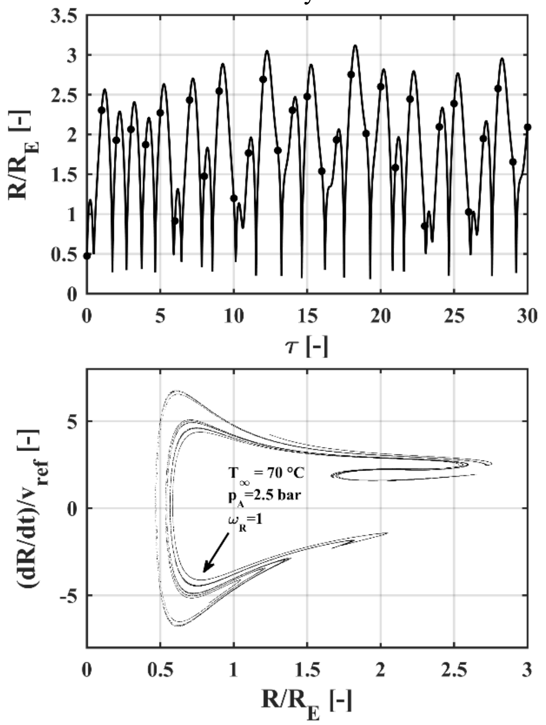

Figure 4. Example of chaotic attractor.

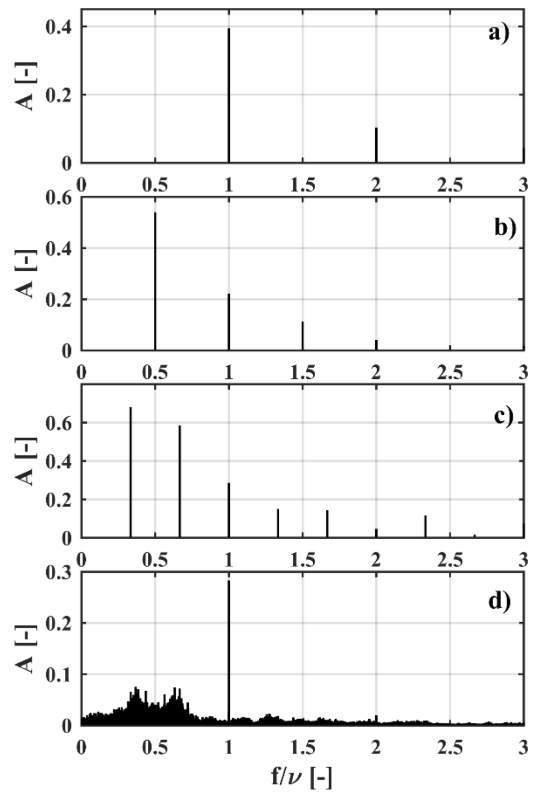

Figure 5. The spectrum of the different types of solution.

4. BIFURCATION DIAGRAMS

A usual way to investigate a periodically driven dynamic system, is to present the bifurcation diagrams. In a bifurcation diagram, only one coordinate of the Poincaré section is plotted as a function of a parameter, called "control parameter". In Figure 6, the upper chart is a pressure amplitude bifurcation diagram, in which the normalized bubble radius of the points of the Poincaré section (R_P/R_E) were plotted as a function of the pressure amplitude p_A at constant $\omega_R = 1.25$ driving frequency. During the computation, the pressure amplitude was increased by 0.01 bar from 0.01 to 5 bar. At each parameter, 5 randomly generated initial conditions were applied in the simulations to reveal the coexisting stable solutions. The period N solutions generate N points on the bifurcation diagram. If the solution was chaotic, 512 points were plotted, which appear in a scattered way along a vertical line bounded by the size of the attractor.

A period 1 solution is bifurcated from the equilibrium state of the unexcited system ($p_A = 0\ bar$ and $R_P/R_E = 1$). As the pressure amplitude increasing, the solution undergoes a period doubling sequence, then approximately at pressure amplitude $p_A = 4\ bar$ the bubble oscillation became chaotic. After a short chaotic segment, simple periodic and chaotic windows alternate. The relevant periodic solutions are marked by numbers on the diagram.

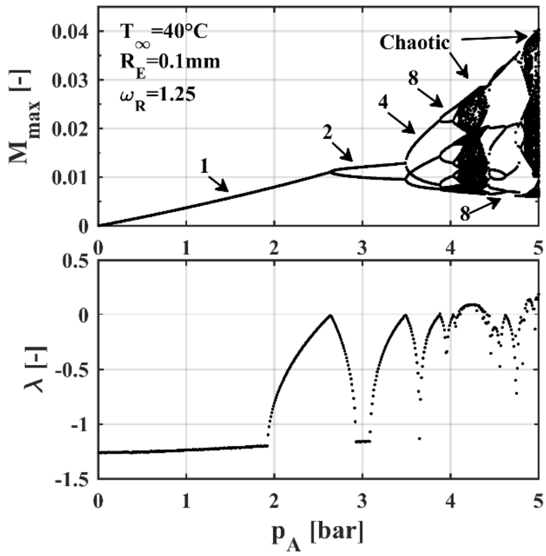

Figure 6. Pressure amplitude bifurcation diagram and Lyapunov exponent at $\omega_R = 1.25$ driving frequency

On the lower panel, the Lyapunov exponent λ (see [13], [16-17]), was plotted as a function of the pressure amplitude p_A. The Lyapunov exponent lower than zero for periodic oscillation. When the oscillation approaches a period doubling point, the Lyapunov exponent approaches zero. For chaotic solutions the Lyapunov exponent gets positive value.

Figure 7 shows similar bifurcation diagrams, but the control parameter was the relative frequency ω_R.

It increased from 0.01 to 3 with the increment of 0.01, and again 5 random initial conditions were applied to reveal the coexisting stable attractors. In this case, the pressure amplitude was chosen constant during the simulation ($p_A = 4\ bar$).

On the upper panel, the normalized bubble radius R_P/R_E versus relative frequency ω_R was plotted. The Arabic numbers mark the periodic solutions. The figure shows that there is a saddle-node bifurcation [15] at $\omega_R = 0.25$, then the period 1 solutions undergoes a period doubling sequence. Near to $\omega_R = 1$ (the frequency of the excitation equal with the eigenfrequency of the undamped system, $\nu = f_0 = 29{,}3\ kHz$) a chaotic window appeared. After the chaotic window, period halving processes can be observable. On the lower graph, the Lyapunov exponent as the function of the relative frequency was plotted, which aids to distinguish the simple periodic and chaotic solutions.

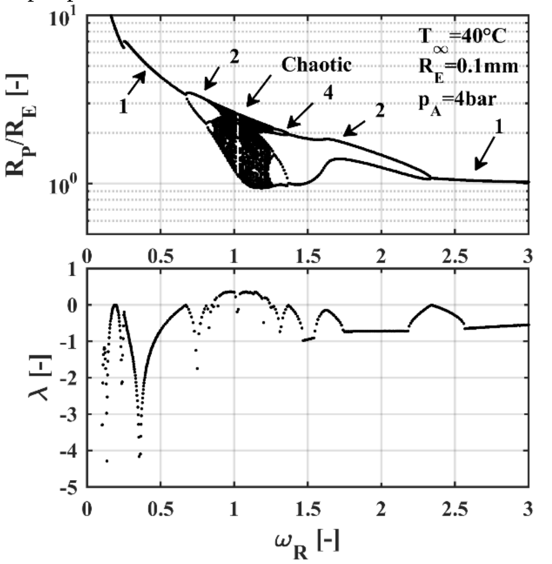

Figure 7. Frequency response curves and Lyapunov exponent at $p_A = 4\ bar$ pressure amplitude.

5. DETAILED PARAMETER STUDY

It was mentioned earlier that the oscillation of bubble depends only on five parameters. In the present investigation, the effect of the pressure amplitude p_A and the frequency ω_R were studied in detail. Further pressure amplitude bifurcation diagrams, and frequency response curves were calculated at different relative frequencies ω_R, and at different pressure amplitudes p_A. The ambient temperature $T_\infty = 40\ °C$, the ambient pressure $P_\infty = 1\ bar$ and the equilibrium radius $R_E = 0.1\ mm$ was constant during each simulation. The parameter set, which was used in the present research is summarized in Table 1.

Table 1. Parameter set during numerical computation

Equilibrium radius	R_E	0,1 [mm]
Ambient pressure	P_∞	1 [bar]
Ambient temperature	T_∞	40 [$°C$]
Relative frequency	ω_R	0-3 [-]
Pressure amplitude	p_A	0-5 [bar]

After the convergence of the solutions, the points of the Poincaré section, the maximum values (radius and wall velocity) of the oscillation, and the Lyapunov exponent were recorded. The results of the computation can be summarized on two dimensional contour plots.

Fig. 6 and Fig. 7 showed that the Lyapunov exponent helps to distinguish the simple periodic and chaotic oscillations. Figure 8 represents the values of the Lyapunov exponent λ as a function of the pressure amplitude p_A and the relative frequency ω. The diagram helps to identify the chaotic region, where the Lyapunov exponent bigger than zero (black area). It shows that the oscillation become chaotic between $\omega_R = 0.75 - 1.5$ and above $p_A = 3.5\ bar$. The white colour corresponding to the zero values of the Lyapunov exponent, where the period doubling bifurcations or the transition of periodic to chaotic solution takes place. If the Lyapunov exponent smaller than zero (grey area) the solution converges to a simple periodic attractor. The driving frequency ν is denoted on the secondary (top) x axes.

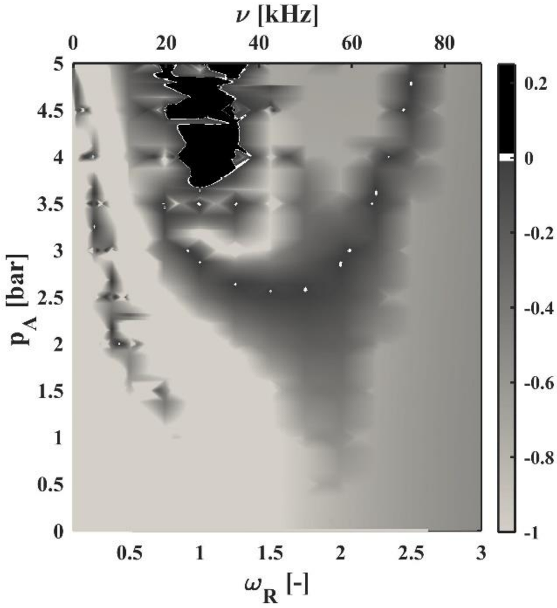

Figure 8. Lyapunov exponent λ as a function of the pressure amplitude p_A and frequency ν (or relative frequency ω_R) of excitation.

Behnia et al. [18] emphasize the importance of chaos control in medical application such as drug delivery. The oscillation of the bubble generate local turbulence and liquid microcirculation. It can be exploited in application such as micromixing and microstreaming [19-20]. These application may operate efficiently in the chaotic region.

In order to investigate the strength of the collapse, the maximal bubble wall velocity $\dot{R}_{Max}$, rescaled to the Mach number M_{Max}, plotted on logarithmic scale in the $p_A - \omega$ parameter plane, shown in Figure 9. It shows that the at lower relative frequency, lower than $\omega_R = 0.5$, and at higher pressure amplitude, higher than $p_A = 1\,bar$, the bubble wall velocity increase rapidly (dark grey are), and reach the speed of sound, where $M_{Max} = 1$. The boundary of $M_{Max} = 1$ is marked with white colour on the contour plot. According to [13], such small frequency domain is called as "Giant response region". As the frequency is increasing and the pressure amplitude is decreasing, the available maximal Mach number is decreasing (light grey area) as well. The frequency of irradiation ν is represented on the secondary x axis as well.

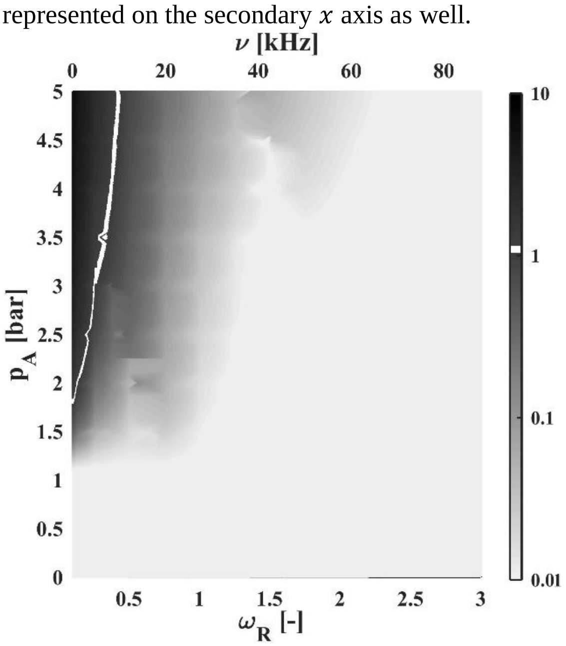

Figure 9. The maximal Mach number M_{max} on logarithmic scale as a function of the pressure amplitude p_A and relative frequency ω_R of excitation.

More violent collapse of the bubble can be reached, when the frequency of the excitation is below the main resonance. The applications may operate in an efficient way in this regions.

At higher frequencies the bubble oscillate softly, but there are application such as micromixing and microstreaming [19-20], where the oscillation of the bubble, generate local turbulence and liquid micro-circulation, which enhance the rate of the transport processes.

6. SUMMARY

The excited spherical gas/vapour bubbles behave like a nonlinear oscillator. During the oscillation of the bubble, at the collapse-phase, extreme conditions are generated such as high temperature, pressure and shock waves. These conditions are exploited in many fields of industry by the rapidly developing ultrasonic technology. This is the main motivation to investigate a spherical excited bubble placed into the highly viscous glycerine.

We seek parameter regions, where the bubble wall velocities as high as possible, may be even higher than the sound speed in the liquid domain. The high viscosity of the glycerine means high damping rate, which weakens the strength of the collapse. The applied bubble model was the modified Keller—Miksis equation, which takes into account the liquid compressibility. The two investigated parameter was the pressure amplitude p_A and the angular frequency ω of the harmonic excitation, according to the ultrasonic irradiation. The other parameters were constant during the investigation.

The results showed that at lower relative frequencies below $\omega_R = 0.5$ and higher pressure amplitude than $p_A = 1\,bar$ the bubble wall velocity reaches the sound velocity or even higher, resulting in supersonic bubble wall velocity. This region called as the giant response region. The application could operate efficiently in this parameter region.

For higher frequencies and smaller pressure amplitudes the bubble wall velocity does not reach extreme values. This domain can be important in cases, when the strong bubble collapse not a strict requirement, for example in micromixing or microstreaming.

ACKNOWLEDGEMENTS

This research has been supported by the Hungarian Scientific Research Fund – OTKA, from the grant no. K81621.

REFERENCES

[1] Koch, P., Kurz, T., Parlitz, U., Lauterborn, W., 2011, "Bubble dynamics in a standing sound field: The bubble habitat", Acoust. Soc. Am. Vol. 130, pp. 3370-3378.

[2] Brennen, C.E., 1995, "Cavitation and bubble dynamics", Oxford University Press, New York.

[3] Storey, B.D., Szeri, A.J., 2000, "Water vapour, sonaluminescence and sonochemistry", Proc. R. Soc. Lond. Vol. 456, pp. 1685-1709.

[4] Kanthale, P., Ashokkumar, M., Grieser, F., 2009, "Sonoluminescence, sonochemistry (H_2O_2 yield) and bubble dynamics: Frequency and power effects." Ultrason. Sonochem. Vol. 15, pp. 143-150.

[5] Taleyarkhan, R.P., West, C.D., Cho, J.S., Lahey, Jr.R.T., Nightmatulin, R.I., Block, R.C., 2002. "Evidence for nuclear emissions during acoustic cavitation." Science Vol. 295, pp. 1868-1873.

[6] Lahey, Jr.R.T., Taleyarkhan, R.P., Nigmatulin, R.I., 2007. “Sonofusion technology revisited.” Eng. Des. Vol. 237, pp. 1571-1585.

[7] Knorr, D., Zenker, M., Heinz, V., Lee, D-U., 2004, “Application and potential of ultrasonics in food processing.” Trends Food Sci. Tech. Vol. 15, pp. 261-266.

[8] Konaganti, V.K., Madras, G., 2010, “Ultrasonic degradation of poly(methyl metharcrylate-co-alkyl acrylate) copolymers.” Ultrason. Sonochem, Vol. 17, pp. 403-408.

[9] Rosenthal, I., Sostaric, J.Z., Riesz, P., 2004, “Sonodynamic therapy – a review of the synergistic effects of drugs and ultrasound.” Ultrason. Sonochem. Vol. 11, pp. 349-363.

[10]Hernot, S., Klibanov, A.L., 2008, ‘Microbubbles in ultrasound-triggered drug and gene delivery.” Adv. Drug. Deliv. Rev. Vol. 60, pp. 1153-1166.

[11]Yu, T., Wang, Z., Mason, T.J., 2004, “A review of research into the uses of low level ultrasound in cancer therapy.” Ultrason. Sonochem. Vol. 11, pp. 95-103.

[12]Keller, J.B., Miksis., 1980, “Bifurcation structure of the classical Morse oscillator.” J. Chem. Phys. Vol. 93, pp. 3950-3957.

[13]Lauterborn, W., Kurz, T., 2010, “Physics of bubble oscillations of gas bubbles in liquids.” J. Acoust. Soc. Am. Vol. 59, pp. 283-293.

[14]Dow Chemical Company, http://www.dow.com/

[15]Hegedűs, F., 2014, “Stable bubble oscillations beyond Blakes critical threshold.” Ultrasonics Vol. 54, pp. 1113-1121.

[16]Lauterborn, W., Parlitz, U., 1988, “Methods of chaos physics and their application to acoustics.”, J. Acoust. Soc. Am. Vol. 84, pp. 1975-1993.

[17]Parlitz, U., Englisch, V., Scheffcyk, C., Lauterbor, W., 1990, “J.Acoust. Soc. Am. Vol. 88, pp. 1061-1077.

[18]Behnia, S., Sojahrood, A. J., Soltanpoor, W., Jahanbakhsk O., 2009, “Suppressing chaotic oscillations of a spherical cavitation bubble through applying a periodic perturbation.”, Ultrason. Sonochem. Vol. 16, pp. 502-511.

[19]Nyborg, W. L., 1958, “Acoustic streaming near a boundary.” J. Acoust. Soc. Am. Vol. 30, pp. 329-339.

[20]Lighthill, S. J., 1978, “Acoustic streaming.” J. Sound Vib. Vol. 61, pp. 391-418.

Conference on Modelling Fluid Flow (CMFF'15)

The 16th International Conference on Fluid Flow Technologies
Budapest, Hungary, September 1-4, 2015

Theoretical and Experimental Study of High Speed Submerged Cavitating Jets: Strouhal Number, Shedding Frequencies of Cavitation, Bubble Collapse Energy, and Micro-Nano Water Hammer

Ezddin Hutli[1], Milos Nedeljkovic[2], Attila Bonyár[3]

[1]Department of Thermohydraulics, Centre for Energy Research, Hungarian Academy of Sciences, Budapest-Hungary, E-mail: ezddinhutli@yahoo.co
[2]Corresponding Author. University of Belgrade, Faculty of Mechanical Engineering, 16 Kraljice Marije, Beograd, Serbia, Telph.: +381 11 3302 401, Fax: +381 11 3370 364, E-mail: mnedeljkovic@mas.bg.ac.rs
[3] Department of Electronics Technology, Budapest University of Technology and Economics, Budapest-Hungary, E-mail: attila.bonyar@gmail.com

ABSTRACT

The characteristics of the cavitation phenomenon in high speed submerged water jets was investigated based on both experimental and theoretical bases, in order to improve their performance. Experimentally certain metal specimens were attacked by a high speed cavitating jet under certain working conditions. The obtained images of the target samples using atomic force microscope (AFM) and a white light interferometer showed that the plastic deformation is caused by the cavitation collapse on or near to the target surface. The force generated by jet cavitation is employed to modify the surface roughness in the order of nano and micro scales. The geometrical shape of the pits and hills on the surface demonstrate the characteristics of nano and micro jets. The theoretical relation between Strouhal number and cavitation shedding frequency is presented. The nozzle geometry and injection pressure has a big influence on the shedding frequency of the cavitation rings, and on the Strouhal number. Mathematical expressions are derived to estimate the energy of bubble collapse and to estimate the nano and micro water hammer.

Keywords: cavitation energy, microjet-water hammer, plastic deformation, shedding frequency,

NOMENCLATURE

V_J	[m/s]	Exit jet velocity
P_1	[bar]	Upstream pressure
v	[m/s]	Jet impact speed
St	[-]	Strouhal number
x/d_{out}	[-]	Non-dimensional standoff distance
d_{in}, d_{out}	[mm]	Inlet, outlet nozzle diameter
$f_{R.shedding}$	[Hz]	Vortex-ring shedd. frequency
$f_{C.shedding} = f_{cloud}$	[Hz]	Cavitation cloud shed. frequency
$I_{C.cav}, I_{R.cav}$	[Watt]	Intensity of cavitation cloud, vortex ring
$E_{C.cav} = E_{Could-Collapse}$	[J]	Cavitation energy
$P_{amb} = P_2$	[bar]	Ambient pressure = downstream pressure
L_C	[mm]	Average cavity cloud length
c_1, c_2	[-]	Correction factors
$R_{Average}$	[mm]	Average cavity or ring radius
ε	[-]	Non-dimensional aspect ratio
Q	[m^3/s]	Flow rate from nozzle
P_{WH}	[Pa]	Jet water hammer
ρ_L	[kg/m^3]	Liquid density
C_L	[m/s]	Sound speed in liquid
P_j	[Pa]	Micro-jet pressure

F_{cloud}	[N]	Cloud force
F_{th}	[N]	Threshold force
P_i	[Pa]	Pressure of micro jet (i)
A_i	[μm^2]	Damaged area by micro jet (i)
Q_{MJ}	[mm^3/s]	Micro-jet flow rate
$v_{MJ} = v_L$	[m/s]	Micro-jet velocity
$P_{MJ\ -\ power}$	[watt]	Micro-jet power
p_{WH-MJ}	[Pa]	Micro-jet water hammer
P_{load}	[Pa]	Peak load
p_{dy-MJ}	[Pa]	Micro-jet dynamic pressure

1. INTRODUCTION

Over the past few years, cavitating fluid jets have received a considerable attention, primarily with laboratory experiments, to understand their behavior and to determine the feasibility of their use in a variety of situations. Recently, these testing and evaluation efforts have proven certain applications of the cavitating jet, which include: cleaning paint and rust from metal surfaces; underwater removal of marine fouling; removing of high explosives from munitions; augmenting the action of deep-hole mechanical bits used to drill for petroleum or geothermal energy resources; widely use in cutting, penning flushing, and modification of surface characterization. Thus the cavitating fluid jet method is indeed commercially attractive since long time ago [1-3]. As can be determined from the published literature, not much is known about the unsteady behaviour of the cavitating jet and the development as well as the collapse of the cavitation clouds on the impinging surface. If the unsteady behaviour and the jet structure are clarified in detail, it is expected that, the jet working capacity can be drastically improved. Many researchers has focused on this subject and they found that, the cavitation clouds in general behave stochastically in both time and space, with a very rapid change within μs [1-5]. Other researchers showed that, the phenomenon is periodical and it depends on the working conditions [6, 7].

The aim of this work was primarily to investigate theoretically and experimentally the behaviour of cavitation as clouds and rings and roughly to determine the initiating mechanism at the start of the cavitation damage and the erosion process in FCC materials (Al-alloy as a tested material). The protocol of using a cavitating jet generator as test rig is presented in our previous publication [7]. The test rig uses two types of nozzles, convergent and divergent. Since the cavitation effect is greatly depending on the nozzle type and geometry, their properties are illustrated in Figure 1.

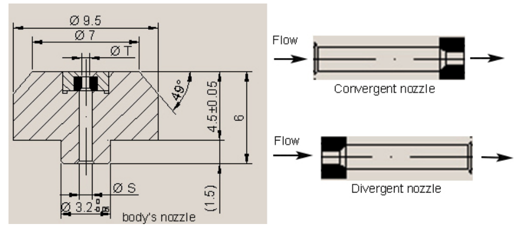

Figure 1. Schematic illustration of the convergent and divergent nozzles. The values are in mm.

2. CAVITATION CLOUD DYNAMIC AND STROUHAL NUMBER CALCULATION

As it is well known, the cavitating flow is a two-phase flow, which consists of a continuous liquid phase and a dispersed gaseous phase in the form of bubbles in cavity clouds. In this kind of flow a relative motion exists between the bubbles and the surrounding fluid. In many cases, the transfer of mass and/or heat usually is of great importance. Cavity flows behave very differently from single-phase flows. The presence of a second phase with significantly different density, viscosity and elasticity considerably alters the effective properties of such a mixture. The interfaces between the liquid and the gas phase are deformable and unsteady. Encounters between bubbles can lead to bouncing or coalescence. Bubbles may accelerate, deform, execute shape or volume oscillations or even break up (collapse) [8]. Since in our case a continuous jet is used, the vortex ring does not appear clearly, and also the oscillation and collapse of the individual bubbles cannot be seen. We can follow only the shedding and discharging of the cavity clouds (macro level). As it is already shown in pervious publications, the characteristic unsteady motion of cavitation clouds can be discerned with the observation of the cavitating area using a high-speed video camera (100,000 f/s). It was noted that the shedding pattern has a periodic character, although it does not stay regular for a long time and it can change with the variation of the working conditions as could be seen in Fig. 2 and Fig. 3. The imperfect shedding pattern could be the result of the incompatibility between the test equipment (nozzles, feed pumps, test chamber, and recording system) [7]. In general as it appears, the cloud expands to almost middle of the trajectory; this distance depends on the working conditions. The leading part of the main cavitating jet moves gradually toward the target and then the jet shows a shrinking motion in the diameter close to the exit of the nozzle, as can be clearly seen in the case of convergent nozzle in Fig. 3.

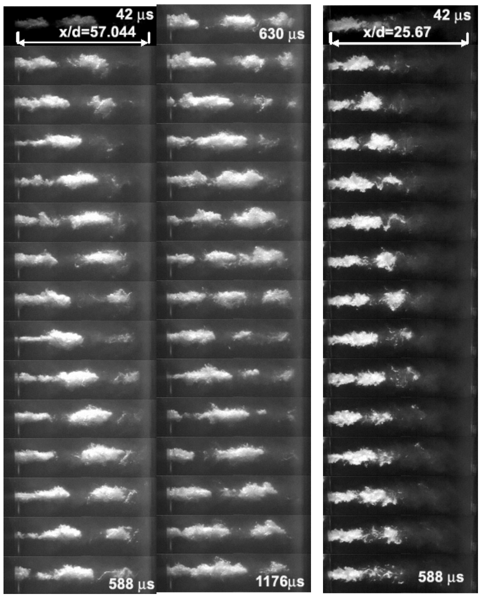

Figure 2. High-speed camera images (24000 f/s, 512*128) of the shedding patterns. Left two columns: Convergent nozzle ($P_1 = 105$ bar, $P_2 = 2.06$ bar, $V_J = 124$ m/s, $\sigma = 0.02568$, $T = 18.5\ ^oC$). Right column: divergent nozzle ($P_2 = 1.89$ bar, $V_J = 18.2$ m/s, $\sigma = 1.142$, $T = 20\ ^oC$). The flow is from left to right.

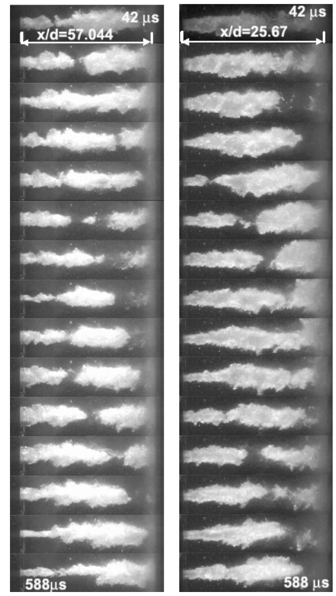

Figure 3. High-speed camera images (24000 f/s, 512*128) of the shedding patterns. Left- column: Convergent nozzle ($P_1 = 177$ bar, $P_2 = 2.06$ bar, $V_J = 162$ m/s, $\sigma = 0.0155$, $T = 18.5\ ^oC$). Right column: divergent nozzle ($P_1 = 267$ bar, $P_2 = 1.89$ bar, $V_J = 31.5$ m/s, $\sigma = 0.37$, $T = 20\ ^oC$).

This shrinking motion in the diameter does not appear clearly in the case of a divergent nozzle, while for a convergent nozzle this phenomenon usually could be observed. This cloud shrinking motion moves toward the upstream direction. At the same time some downstream clouds, which have already shrunk, change to a growing stage and translate toward the downstream direction. This reentrant motion reaches the nozzle exit and then changes to a new shedding motion of a cavitation cloud in the reverse direction. As it appears in some images, there are discontinuous parts of the cavitation clouds, which are caused by the arrival of the reentrant motion at the nozzle exit (see Fig. 2 and Fig. 3). The leading part a of new cavitating cloud, defined at this point of discontinuity, moves downstream with a certain speed depending on the working conditions. Two consecutive frames were used (42 µs time difference) to estimate the speed of the leading edge of the cavity clouds (for convergent nozzle $V \approx 79$ m/s for $P_1 = 105$ bar and $V \approx 104$ m/s for $P_1 = 177$ bar, while for divergent nozzle $V \approx 52$ m/s for $P_1 = 90.5$ bar, and $V \approx 119$ m/s for $P_1 = 267$ bar). However, this speed does not represent the real speed of the clouds.

The analysis of long recordings (600 frames obtained with a shutter time of 20 µs) revealed that the cavitation phenomenon appears to have a chain-reaction behavior, i.e. the cloud shrinking or disappearance might be related to the propagation of a pressure wave as a result of the collapse process. A starting mechanism (reaction of the cloud with the surroundings and with itself) may be the existence of a high-pressure distribution due to the rapid enlargement after the nozzle exit. As a result, the new cavitating jet grows and develops in a coalescing manner with some already existing clouds and then moves downstream from the exit of the nozzle. The translational speed of the leading part of cavitating jet remains constant in the beginning, then acceleration and de-acceleration processes take place. As a result a new pressure distribution map is formed, as can be seen in the curves of Fig. 4. In fact these curves do not represent the real speed of the cavity clouds, as we can see the speed is increasing, decreasing, and it is constant for only short periods. Also it could be noticed from Fig. 2 and Fig. 3 that the cavity clouds do not keep their shape, there are changes which are related to the forces acting on the clouds. In general the total force acting on the bubble or on the cavity cloud is composed of separate and uncoupled contributions from pressure gradient, drag, lift due to vorticity, virtual mass, hydrodynamic interactions force (hydrodynamic interactions between adjacent bubbles) and gravity [8]. Therefore, as the object is subjected to static and dynamic forces, the volume and the area are changing, thus the calculated speed (V) does not exactly represent the jet speed (V_j).

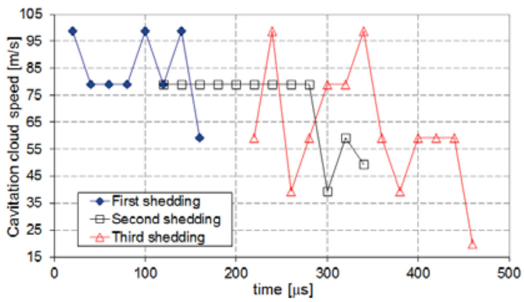

Figure 4. Cavitation cloud speed calculated from consecutive jet images (50000 f/s, 256*64) with the following conditions: Convergent nozzle (D_{out} = 0.45 mm), P_1 = 105 bar, P_2 = 2.06 bar, V_J = 124 m/s, σ = 0.02568, T = 18.5 °C, X/d = 57.044.

As it was presented in a previous publication, the periodicity of the cloud-like cavity shedding shows different values for convergent and divergent nozzles (which have different (L_m / d_o)), though it varies with the inlet and outlet diameter [7]. The differences in nozzle geometry lead to a big difference in exit jet velocity and in addition to a big difference in the cavitation number. The difference in jet exit velocity for the two cases leads to a big difference in the intensity of the produced cavitation; when the other parameters are assumed to be constant (see Fig. 2 and Fig. 3). Sato K and Saito Y [3] calculated that the Strouhal number (S_t), which is depending on the time-average cavity length L_m, is approximately 0.3-0.4, which qualitatively agrees with the previous results (e.g. Le et al. (1993)) [9]. Their used nozzle diameter was 22 mm with a velocity range of 9.65 - 10.4 m/s (circular-cylindrical nozzle). In our present work, the Strouhal number is calculated by the same manner based on the average jet velocity at nozzle exit (V_J) and by using the $f_{C.shedding}$ average shedding frequency. The results are presented in Table 1. Please note, that the jet velocity (V_j) is differ from the cavitation cloud speed (V). V_j was calculated by the mentioned method using the flow rate and pressure values. $f_{C.shedding}$ was calculated from the obtained recordings. The relation between the shedding frequency and the Strouhal number will be discussed in Chapter 3. From Table 1 we can see that at low pressures in both of the cases (convergent and divergent nozzles), smaller Strouhal numbers are obtained because of the shorter length of cavitating cloud which also lead to the instability of the cavitating jet.

Table.1 Strouhal number calculation

Parameter	Convergent X/d = 57.044		Divergent X/d = 25.67	
P_1 (bar)	105	177	90.5	267
V_J (m/s)	124	162	18.2	31.5
$f_{C.shedding}$ (Hz)	6335	4880	7140	4170
L_m (mm)	10.96	24.2	8.01	24.47
St (-)	0.56	0.73	3.14	3.24

The comparison between the convergent and divergent nozzles, shows that, the Strouhal number is larger for the divergent nozzle. This is due to the big difference in the velocities between the two cases. The deviation between our results and that presented by Sato K and Saito Y [3] is related to the differences in the working conditions (geometrical and hydro-dynamical). Please note that the presented shedding frequencies are average values and their determination has limits, which have different reasons for convergent and divergent nozzles. In the case of divergent nozzle with low injection pressure the unclear shedding of cloud-like cavity may be depending on the weakening of vortex formation and the increase of three-dimensional disturbance on the separated shear layer [3]. But in the case of high injection pressure for both cases (convergent and divergent), the reason for unclear distinguishing between both shedding and discharging processes is related to a strong vortex formation, the inherent compact behavior of the shear layer and the length of cavitating area, and in addition to the fast formation of vortex cavitation and their interaction with each other. Based on this result it should be noted that the shedding frequency at low pressure and the influence of nozzle geometry remains to be further examined from the point of view of vortex behavior on the shear layer.

3. RELATION BETWEEN THE SHEDDING FREQUENCY OF CAVITATION CLOUDS AND THE RINGS

As it was found by Yamauchi Y. et al [10], the vortex ring cavitation takes place periodically in the region of free jet, and its frequency is given by Eq. 1.

$$f_{R.shedding} = \left(\frac{St}{x}\right) \bullet V_J \tag{1}$$

Where x is equal to L_m (the time-averaged cavity length). Based on that, the cavitating jet and its cloud structure can be considered as a succession of vortex bubble rings with diameters related to the nozzle diameter d_o. The cavitation intensity per unit time, $I_{c.cav}$ can be expressed as the number of cavitation events per unit time, ($f_{C.shedding}$), and the collapse energy of each cavitation event, $E_{C.cav}$ can be expressed as in Eq. 2.

$$I_{C.cav} = f_{C.shedding} \bullet E_{C.cav} \tag{2}$$

The potential energy of the cavity $E_{c.cav}$ can be expressed as in Eq. 3. It is the product of its maximum volume and the pressure difference between the surrounding liquid and the cavity contents, which we will approximated as the P_{amb} (ambient pressure):

$$E_{C.cav} = \frac{1}{4}\pi \bullet d_o^2 \bullet L_C \bullet c_1 \bullet P_{amb} \tag{3}$$

Where L_C is the cavity length, and c_1 is a correction factor. As it is known, the cloud is a group of rings connected with each other. Based on the ring cavities hypotheses, the cavitation ring potential energy $E_{R.cav}$ can be expressed with Eq.4, where $R_{Average}$ is the average radius of an otherwise not perfectly symmetric ring (Fig. 5), and taking into consideration the assumption that the vapor pressure in the cavity ring (P_V) is much less than P_{amb}. The image of a real cavitation ring and the illustration of an ideal ring can be seen in Fig. 5.

$$E_{R.cav} = \pi^2 \bullet c_2 \bullet d_o \bullet R^2_{Average} \bullet P_{amb} \tag{4}$$

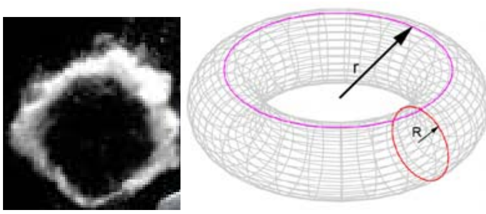

(a) (b)

Figure 5. (a) Cavitation ring (b) An ideal ring is the product of two circles; in this case the red circle is swept around the axis defined by the pink circle (spread angle). $r = f(d_o)$ is the radius of the pink circle, *R* is the radius of the red one.

The ring intensity with defined by $f_{R.emission}$ and $I_{R.cav}$ is given by Eq.5

$$I_{R.cav} = f_{R.emission} \bullet E_{R.cav} \tag{5}$$

Using the product of the pressure and flow rate for getting the hydraulic power of the cavitating jet, therefore, the energy conversion efficiency (η) can be written as in Eq.6.

$$\eta = \frac{f_{R.emission} \bullet E_{R.cav}}{0.5\rho V_j^2 Q} = \varepsilon^2 2\pi \left(\frac{St \bullet P_{amb}}{\rho V_j^2} \right) = 2\pi\varepsilon^2 St\sigma \tag{6}$$

Where ε and the jet Strouhal number St in terms of ring cavities are defined by Eq.7 and Eq.8, respectively,

$$\varepsilon = \frac{2R_{\max}}{d_o} \tag{7}$$

$$St = n\frac{f_{C.shedding} \bullet d_o}{V_j} \tag{8}$$

Where *n* is the number of rings which produce one cloud. Both parameters, $f_{C.shedding}$ and a $f_{R.emission}$ are depending on the geometrical and hydrodynamic working conditions, and they are connected as defined by Eq.9

$$f_{C.shedding} = \frac{f_{R.emission}}{n} \tag{9}$$

Where n is the number of vortex rings gathered to create one cloud $(n \geq 1)$.

4. FORCE AND ENERGY EMITTED BY THE CAVITY COLLAPSE

The shock wave is usually emitted by a high speed velocity jet of liquid created during the end of collapse period (closure of cavity). The amplitude of the pressure pulse is the greatest near the center of emitted wave and during the first moments of the emission. Thus the effective damage of collapse depends strongly on the position of the collapse center and the solid surface [11]. The total energy of bubble collapse is divided into two essential parts: one part represents the energy of thr shock waves and the other represents the energy of the micro-jet. The part which belongs to the micro-jet is divided also into another two parts: one represents the kinetic energy of the micro-jet and the rest represents the impacting energy which is transferred to the target material. This behavior resembles a water hammer, which will damage the target material as a result of the energy transfer (see Fig. 6, Fig. 7, and Fig. 8). The formula given by Eq. 10 might be used to determine the water hammer produced by the micro-jet, where the subscripts (*L*) refer to the liquid [12].

$$P_{WH} = \rho_L C_L v \tag{10}$$

Experiments by Hancox L. and Brunton H. (1966) show that multiple impacts by water at a speed of 90 m/s can erode even stainless steel [12]. If the micro-jet velocity is higher than 433 m/s, the pressure caused by the water hammer effect is

650 MPa, which is considered to damage the steel surface [13, 14]. According to the results presented by Soyama H. et al. [15] the force that leads to surface damage (pits) can be estimated by using the P_{WH} (water hammer pressure) that creates one pit damage, which is equal to P_j (micro jet pressure), therefore the force of one micro-jet is presented by Eq. 11.

$$F_j = P_{WH} / A_{pit} \tag{11}$$

Under this assumption, every single bubble will collapse and create only one micro-jet. As the cloud contains n-number of bubbles and all generate micro-jets is hitting the target the cloud force can be calculated by using Eq.12.

$$F_{cloud} = \sum_{i=1}^{n} P_i / A_i \tag{12}$$

Where n is the number of pits, and the number of micro jets. A_{pit} is equal to the cross-section area of the micro jet head. The total force acting on the target surface for a certain time *t* (exposure time) and in one point (one pit) are defined by Eq.13 and Eq.14 respectively,

$$F_{total} \cong F_{cloud} * f_{cloud} * t \tag{13}$$

$$F_{total-point} \cong F_{mj} * f_{micro-jet} * t \tag{14}$$

Since the decay time of the jet is very small (for a jet with 2 to 3 mm in diameter the decay time is 1 or 2 μs [11]) we can assume that, after a given exposure time (*t*) which is less or equal to the incubation time, the total force which is acting on the target surface ($F_{total-point}$) can be even higher than F_{th} (threshold force) but neither plastic deformation or erosion will occur as a result of cavitating jet impact. The time needed to establish the stage of a plastic deformation is related to the mechanical properties of the material, mainly to its ability to absorb the energy of the shock loading without macroscopic deformation (which is related to the stacking fault energy).

If the exposure time passes beyond the incubation time period the damage will start, regardless of the relation between $F_{total-point}$ and F_{th}, which latter is determined by the mechanical properties of the target material.

The impacting energy of the cavitating jet (cloud) is defined by Eq.15

$$E_{Could-Collapsed} = F_{total} * A_{damaged} * Q \tag{15}$$

The micro-jet flow rate Q_{MJ} could be estimated by using Eq.16, after calculating the micro-jet velocity by using Eq. 10. Using the same manner we can estimate the total power of the emitted micro-jet which contains two parts (dynamic and impact power) as defined in Eq.17.

$$Q_{MJ} = A_{pit} * v_{MJ} \tag{16}$$

$$P_{MJ-power} = Q_{MJ} * p_{WH-MJ} + Q_{MJ} * p_{dy-MJ} \tag{17}$$

5. MICRO-JET AND DAMAGE MECHANISM

We could obtain some information on the damage mechanism by comparing the micro-jet impact pressure in the case when the jet is just capable to deform the surface of the target. The water hammer pressure of a jet with a flat tip is as in Eq.18. [12].

$$P_{WH} = \rho_L C_L v_L \tag{18}$$

The impact pressure can be up to three times higher when the jet tip is round or conical (Lesser MB & Field JE 1983) [16]. The duration of the water hammer pressure is given by the time required for the relaxation wave to travel from the periphery to the center of the jet. It amounts to only 10 ns for a jet diameter of 30 μm. Afterwards, the specimen is affected by the dynamic pressure (Eq.19). The peak load P_{load} will occur immediately as given by Eq.20

$$P_{dyn.} = 0.5 \rho_L v_L^2 \tag{19}$$

$$P_{load.} = c \rho_L v_L A \tag{20}$$

where A is the cross section of the micro jet head which is assumed to be equal to the pit cross-section area (A_{pit}). The load starts to decay as soon as the sideways flow begins. The decay time from peak load will be the time needed for the waves to move into the center of impact from the boundary of the jet [12]. It is a known fact that the strength of materials as well as their elastic modulus rise with increasing strain rate (Kolsky H 1949) [17], so the strain rates involved in the impact of a jet with a velocity of 80 ms^{-1} are in the order of $\dot{\varepsilon}$ ≈ 105 s^{-1}. Besides the strain rate dependence of the yield strength, the short duration (10 ns) of the water hammer pressure may be another reason why a high value of the impact pressure is required to damage the sample. The obtained results suggest that the water hammer pressure produced by the micro-jet, which lead to a macroscopically visible plastic deformation in the specimens surface (Al-Mg-alloy) was greater than the threshold value which represent the ultimate stress (the dynamic yield strength) of these specimens. In the macro level, the obtained cavitation damage is a result of repetition of collapses of cavitation clouds on/near target surface. The number of collapses i.e. the number of impacts can be roughly calculated by multiplying the shedding/ collapsing clouds frequency with the exposure time. The frequency (f [s^{-1}]) is calculated by using the formula in a previous publication. [7].

The damage on the specimen surface is concentrated within the ring formed by the cavitation bubbles, usually observed as a cloud of bubbles. This feature is regulated by the nozzle geometry [7]. The observed lesser cavitation damage within the ring as well as away from it is due to the much lower density of collapsing bubbles, i.e. in these areas the damage process is shifted to much longer times. At the beginning of the cavitation attack, the virgin specimen is assumed to have a smooth surface (in our case the scratches are shallower than 0.5 μm). Also, the used Al alloy was able to absorb a large part of the impact energy due to good ductility. This energy caused the plastic deformation of the whole specimen to be localized in the ring.

The cavitation ring collapses at the moment of its impact on the surface of the specimen and micro-jets are produced. The velocity of the micro/nano-jets is the function of the position of bubble collapse. In some literature it can be found that maximum jet velocities are between 50 and 100 m/s, while others report 950 m/s [12]. Due to the varying size of the bubbles, the formed "micro-jets" will hit the specimen at angle other than 90^o, introducing the shear stress component on the surface. Reported values of the micro-jets induced local material stress are between 100 MPa up to over 1000 MPa [10]. This shear component seems to be sufficient to start plastic deformation on the surface of the specimen, leading to more or less pronounced roughness (Fig. 6, and Fig. 7). After this initial step, further micro jets hit the roughened surface (instead of the smooth and polished one), which leads to the rupture and erosion of the surface (Fig. 8). The surface erosion is assumed to be analogous with the crack initiation step. Further erosion is followed by the wave-guide model for acceleration of surface damage. The plastic deformation takes place when the maximum stress applied on the material target is higher than the yield stress. The time while the material is under this stage is called the "incubation time", in which plastic deformation occurs on the attacked surface without mass loss. This time is a function of the mechanical properties of the material subjected to this stress (cavitation) when the other parameters are kept constant. It should be noted that, in the investigation the cavitation damage, the possible influence of temperature, which increases during the cavitation bubble collapse, should be taken into account [12]. The result in Fig. 6 and Fig. 7 illustrate the possibility of using the cavitation phenomenon as a tool to modify the surface characteristic in the nano- and micro level.

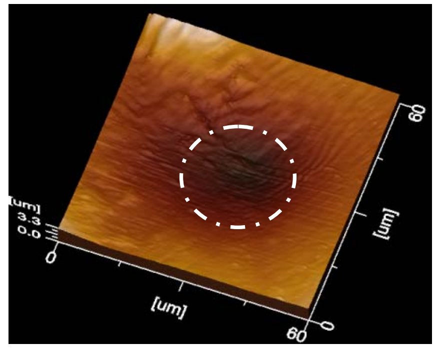

Figure 6. 3D topography AFM images of the investigated Al sample after 30 s test, (R_a = 0.518 μm).

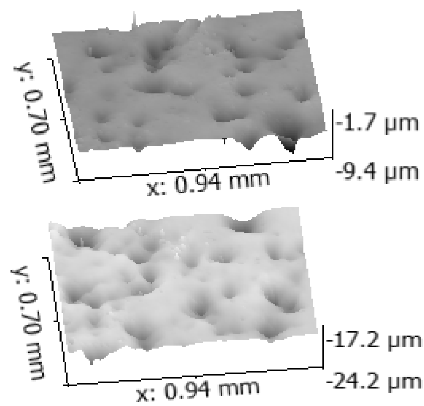

Figure 7. Surface topography of the Al-alloy sample after short time exposure (15 and 20 s) respectively, at 3 mm away from the center of jet impact (10x magnification) with the same working conditions.

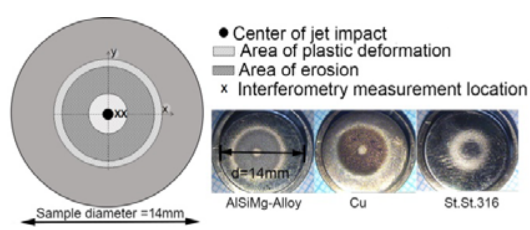

Figure 8. Illustration of the cavitation damage pattern (center of jet impact, plastic deformation and erosion stage). The presented digital images were obtained after long term exposure (1800s).

CONCLUSIONS

In this work an experimental and theoretical study was presented to investigate the characteristics of cavitating water jets. The results show that, a periodic shedding of cavitation cloud is the main characteristic of the phenomenon in cavitating jets caused by the reentrant motion towards the nozzle exit. The reentrant motion starts around the exit region of the nozzle and can be related to a propagation of cloud shrinking and enlargement or disappearance along the jet. Theoretical formula connected to the shedding frequency of clouds and rings is presented and the influence of geometrical and hydrodynamic conditions on the calculation of the Strouhal number was investigated. The FCC material damaged by cavitating jet was investigated with white light interferometry and atomic force microscopy. The interaction between the micro jet and the sample surface was discussed. The energies and force emitted by cavitation clouds and rings (micro jet water hammer) were presented in mathematical forms. Therefore, according to these obtained results, there is a possibility to improve the performance of the cavitating jet for such application in the nano- and micro scale.

REFERENCES

[1] Soyama, H., et al, 1994, "High-Speed Cavitation Cloud Observations Around HighSpeed Submerge Water Jets", 2nd Int. Symposium on Cavitation, Tokyo Japan, pp. 225-230.

[2] Vijay, M., et al, 1991, "A Study of the Characteristics of Cavitating Water Jets by Photography and Erosion", Elsever Science Publishers L td, Jet Cutting Technology, Proceeding of the 10th Int. Conference, pp. 37-67.

[3] Sato, K., and Yasuhiro, S., 2003, "Unstable Cavitation Behavior in a Circular Cylindrical Orifice Flow", JSEM, international journal series B, Vol.,45, pp.638-645.

[4] Toyoda, K., et al, 1999, "Visualization of theVortical Structure of a Circular Jet Excited by Axial and Azimuthal Perturbation", Jou. of Visualization, Vol. 2, pp.17-24

[5] Ganippa, L.C., 2001, "Comparison of Cavitation Phenomena in Transparent Scaled-Up Single-Hole Diesel Nozzles", Fourth International Symposium on Cavitation, California Institute of Technology, Pasadena,CA, USA ,CAV 200, http://cav2001.library.caltech.edu/162/00/Ganippa.pdf

[6] Soyama, H., 2005, High-Speed Observation of a Cavitating Jet in Air, Journal of Fluids Engineering, Transactions of the ASME, Vol. 127, pp. 1095-1101.

[7] Hutli, E. and Nedeljkovic, M., 2008, Frequency in Shedding / Discharging Cavitation Clouds Determined by Visualization of a Submerged Cavitating Jet, Journal of Fluids Engineering, Transaction of the ASME, Vol. 130, pp. 561–568.

[8] Sridhar, G. and Katz, J., 1995, Drag and Lift Forces on Microscopic Bubbles Entrained by a Vortex, The Physics of Fluids,Vol. 7, pp.389-399.

[9] Le, Q., Franc, J.P.,1993, Michel, J.M. Partial Cavities: Global Behavior and Mean Pressure Distribution, Journal of Fluids Engineering, Vol. 115, pp. 243-248.

[10] Yamauchi, Y., et al., 1996, "Formation of Process of Vortex Ring Cavitation in High Speed Submerged Water Jet", Transactions of JSME, series B, Vol. 62, pp.72-78.

[11] Karimi, A., and Martin, J.L., 1986, "Cavitation Erosion of Materials", International Metals Reviews, Vol. 31, pp. 1-26.

[12] Hancox, N. L. & Brunton, J.H., 1966, "High Speed Liquid Impact", Philosophical Transactions of the Royal Society of London, Series A, Mathematical and Physical Sciences, the Royal Society, pp79-85.

[13] Emil, A.B., et al., 2001, "Dynamics of Laser-Induced Cavitation Bubbles near an Elastic Boundary", Journal of Fluid Mechanics. Vol.433, pp. 251-281.

[14] Chen, H.S., et al., 2008, "Effect of Hydro-dynamic Pressures near Solid Surfaces in the Incubation Stage of Cavitation Erosion", Journal of Engineering Tribology, Vol. 222, pp. 523-531.

[15] Soyama, H., et al., 2001, "A New Parameter to Predict Cavitation Erosion", 4th International Symposium on Cavitation, California Institute of Technology, Pasadena, CA USA. http://cav2001.library.caltech.edu/313/00/syama2.pdf

[16] Lesser, M. B., Field, J. E. 1983, The Impact of compressible liquids. Annual Review of Fluid Mechanics, Vol.15, pp. 97-122.

[17] Kolsky, H., 1949, An Investigation of the Mechanical Properties of Materials at Very High Rates of Loading, Proc. Phys. Soc. London, B62:676-700.

Conference on Modelling Fluid Flow (CMFF'15)
The 16th International Conference on Fluid Flow Technologies
Budapest, Hungary, September 1-4, 2015

COMPARISON OF TURBULENT UNSTEADY FLOWS IN A REVERSING CHAMBER

Robert KŁOSOWIAK[1], Jarosław BARTOSZEWICZ[2],Rafał URBANIAK[3],

[1] Corresponding Author. Poznan University of Technology, Chair of Thermal Engineering, Piotrowo 3, PL-60965 Poznan, Poland
Tel.: +48 61 6652209, Fax: +48 61 6652281, E-mail: robert.klosowiak@put.poznan.pl
[2] Poznan University of Technology, Chair of Thermal Engineering. E-mail: jaroslaw.bartoszewicz @.put.poznan.pl
[3] Poznan University of Technology, Chair of Thermal Engineering. E-mail: rafal.urbaniak@put.poznan.pl

ABSTRACT

This paper presents the results of numerical simulation on gas flow inside a cylindrical vessel. Reversing chamber is a vessel which changes twice the direction of gas flow. A jet exiting in the chamber meets the incoming stream from the opposite direction. Investigated phenomena include the flow interacting with the walls, and therefore present characteristics of free and confined flows. The results obtained were juxtaposed with the results obtained for free jets and impinging jets. In the areas of high-pressure gradients intense turbulence occur and intensify the events occurring there with a change in the Reynolds number. The calculations were performed for the undisturbed gas stream flowing out of the nozzles at varying Reynolds numbers 25000, 75000 and 125000. The simulation results show the distribution of velocity, pressure and shear stress on the impinging wall. Also included are the pressure and velocity distributions in the cross-section of the reversing chamber. Selected results will be compared with a fixed flow and results of the experiment.

Keywords: turbulent flow, unsteady, transient, CFD, reversing chamber, combustion chamber

1. INTRODUCTION

Studies related to free streams are carried out on a large scale. These are both, basic research and applied research as having different applicability. During this study modern tools were used to do research with greater precision, on a larger scale, observing multiple parameters since the flow turbulence is extremely important because of its uniqueness. Research related to turbulent flow is focused on the observation of phenomena specific to transport: of momentum, mass and energy. In the literature we can find a number of publications on the flowing streams and their influence on the flow around bodies. At the same time, the analysis of experimental studies and numerical studies in this field is conducted. Among the limited flow analyses a plane impinging jet should be distinguished due to its great importance. Research is carried out on several levels of knowledge. A large group of publications focuses of research on fluid mechanics, particularly on identification phenomena in the flow, validation of experimental results and numerical calculations. This group of analyses demonstrates more signs of basic research. Another group of publications comprises articles focused on research related to heat transfer. The next group of works can be classified to some extent, as applied research involving applicability. Most often, they discuss the intensification of cooling systems or heating surface with a plane. In this respect, we can cite many works, such as Martin, supported Downs and James[1], Popier[2], Jambunathan[3], Viskanta[4], Zuckerman and Lior[5]. S. Roux[6] in his work presents the analysis of temperature fluctuations caused by the presence of vortices on the surface of the walls being impinged. Tests included unsteady analysis of temperature on the surface of the wall. The results indicated a number of important factors that may affect the temperature fluctuation, but clearly do not correspond. Similar work has been taken by Yue Tzu-Yang[7]; however, to analyse the temperature distribution on the surface of the impinged wall numerical methods were used. Simulations were carried out for small Reynolds numbers and signs of laminar flow were observed. Apart from the Reynolds number for turbulence, the author applied an additional criterion, i.e. the distance of the nozzle from the impact surface. For a simulated laminar flow from the nozzle and a small distance from the wall, stationary vortices were obtained on the wall surface. In the article he presents the essence of the Reynolds number and the information that this parameter is not sufficient to determine the flow turbulence. During simulated laminar flow from the nozzle both, the laminar and turbulent flow, were obtained at the impact surface. Moreover, a specific parameter was developed, i.e. the ratio of the nozzle diameter to the distance from the wall being impinged. Applying two parameters (Re and H / W) enable to predict the nature of the flow. The study has once again confirmed the intensification of heat transfer in turbulent flow and has been verified by experimental data from the literature. Tests are carried out not only using air as the working medium. In industry lotions are also widely used as refrigerants, especially there, where intensification of heat exchange must be the highest. M.Y. Abdelsalam[8] suggests in one article to use water as a coolant. Apart from measurements of temperature and heat flux on the wall being impinged, the authors also deal with the analysis of phenomena occurring between the jet and the wall. Observations and conclusions of these studies were confirmed by studies presented in this work.

Most of the above cited works were dedicated to heat exchange in the steady and transient state. In the next step of analyzing the results obtained from investigation of this phenomenon, the authors attempt to describe turbulent phenomena occurring on the surface of the wall. Authors of other articles focused on analyzing the flow and phenomena occurring from the outflow from the nozzle to the reaction with the wall. The publication of Zdeněk Trávníček[9] discusses an interesting case of the annular flow jet hitting on the wall. Researchers analyse the velocity field and the pressure within the walls being impinged. Also the study of Kłosowiak and Bogusławski[10] analyses conducted tests related to typical impinging jet. The purpose of the study was to obtain the greatest shear stress on the wall surface. The work was undertaken to provide information about the highest angle of attack of a jet. Analyzing the results of the study, the three, Zdeněk Trávníček and Kłosowiak and Bogusławski obtained a similar pattern of distribution of the local heat flux and shear stress on the wall being impinged. A large number of papers that have been published around the world is dedicated to studies on free and impinging jets. These jets are widely applied in engineering. Papers [11][12][13] provide descriptions of free jets' structure, which was supplemented in subsequent years by the study of processes occurring in the jets. In recent years, more complex phenomena occurring in the free and confined jets, have been investigated. In paper [14], the authors present the results concerning the effect of natural convection on the heat transfer in the impinged area. To date, two papers related to the description of phenomena occurring in the reverse chambers have been described. Apart from paper [15], paper [16] presents some results of the jet flowing through a reverse chamber made of porous materials. The observed results differed from those obtained for the impinging jets and, similarly to paper [17], indicated the necessity of a thorough research on jets flowing in reverse chambers. Preliminary results indicate significant differences between the free and impinging jets and the flows in reverse chambers.

2. TURBULENCE MODEL

SST turbulence model combines the advantages of both, the standard model of the k-ε and k-ω model. As compared to the equations in the model k-ω, turbulence model SST changes the concept of turbulence arising in the equation for kinetic energy turbulence. From the equation

– equation of kinetic energy turbulence:

$$g_x \frac{\partial T}{\partial x} + g_{\square\downarrow} \qquad (1)$$

– equation of energy dissipation rate

$$\partial\rho\omega/\partial t + (\partial\rho c_{\downarrow}x\ \omega)/\partial x + (\partial\rho c_{\downarrow}y\ \omega)/\partial y + (\partial\rho c_{\downarrow}z\ \omega)/\partial z = \qquad (2)$$

From the equation of kinetic energy turbulence (1), the equation if energy dissipation rate (2) is obtained

$$P_t = \mu_t \Phi \qquad (3)$$

The SST model may be developed as follows

$$P_t = \min(\mu_t \Phi, C_{lmt}\varepsilon) \qquad (4)$$

SST model also introduces a new source of energy dissipation

$$\frac{(1-F_1)2\rho\sigma_{\omega 2}}{\omega}\left[\frac{\partial k}{\partial x}\frac{\partial \omega}{\partial x}+\frac{\partial k}{\partial y}\frac{\partial \omega}{\partial y}+\frac{\partial k}{\partial z}\frac{\partial \omega}{\partial z}\right] \qquad (5)$$

New member of the equation is indicated by F1, which is a function of linking the two models. In the vicinity of the wall, the value of one is assumed, and on the outside of the trim in an open stream reaches the value of zero. Some publications present the application of this model and its description. Another publication informs on a model automatically switching to the calculations function on the wall, and when it is solved, the flow model away from the wall runs the k-ε model. The coefficients used in the model are calculated taking the value of F1 into account.

$$\varphi = F_1\varphi_1 + (1-F_1)\varphi_2 \qquad (6)$$

The coefficient φ (σ_ω, σ_k, γ, β ^ ') is characteristic for the SST model and coefficients φ_1 and φ_2 in the models represent the k-ω and k-ε, respectively. The core values of the various constants in the SST model are described in the Table 1.

Table 1. Values of constants characteristic of the SST model

	C_{lmt}	γ_1	β'_1	σ_{k1}	$\sigma_{\omega 1}$	σ_{k2}	$\sigma_{\omega 2}$	γ_2	β'_2
SST	10^{15}	0,5532	0,075	1,176	2	1,0	1,168	0,4403	0,0828

3. GEOMETRIC MODEL AND TEST METHODS

An object of tests is the axisymmetrical reverse chamber, shown in fig. 1, where the direction of the main flow changes twice. Jet flowing out from the internal pipe, in its initial run, is a free jet, then it impinges the flat surface of the chamber bottom, where the flow direction changes for the first time by 90 degrees. On the inflowing jet's axis, at the so-called stagnation point, the pressure reaches its maximum value. Such flow can be treated as a simplified definition of the impinging jet. Upon changing the direction, the wall jet is headed towards into the radial direction. However, before it reaches the flow wall, it separates from the impinged wall and thus the second stagnation point is located on the side wall near the corner of the reverse chamber. The jet changes again its flow direction by the angle of 90 degrees. From this point, as a counter-flow jet in relation to the basic jet flowing out from the internal pipe, it flow towards the outlet of the reverse chamber. As the distance from the outlet to the impinging wall increas, the wall jet may separate from the flow wall. This point is depending by the jet kinetic energy. The test chamber reflecting the nature of such flow is built of a steel sharp-edged pipe of internal diameter D = 0.04 m and of 0.005 m thickness. The chamber casing of internal diameter R = 0.475 m and the length of 0.7 m was made of Plexiglass. The test chamber was mounted on an open aerodynamic tunnel shown in Fig. 2. The air movement in the tunnel is forced through a fan connected to the tunnel by two elastic couplers. A filter, reducing particles contaminating the air, was installed in the initial section, while the straightened vanes unify the velocity and turbulence fields in the channel. Laser, situated behind the impinged surface, positioned the entire reverse chamber with the internal pipe.

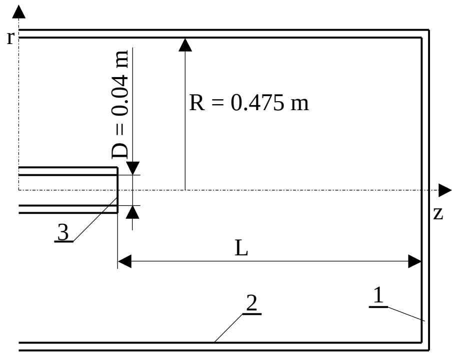

Fig. 1. Diagram of reverse chamber

1 – impinging wall, 2 – side wall, 3 – outlet of pipe

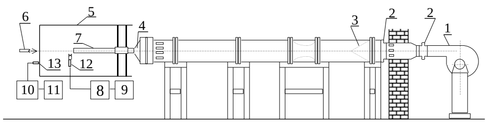

Fig. 2. Diagram of measurement stand: 1 – fan, 2 – elastic coupler, 3 – filter, 4 – nozzle, 5 – reverse chamber, 6 – laser for calibration, 7 – steel pipe, 8 – CTA module, 9 – computer, 10 – digitizer of pressure and its fluctuations, 11 – millimeter, 12 – CTA probes, 13 - phone

The measurement of velocity and its fluctuations were made using the CTA anemometer. The standard X probe TSI-1241 was used to measure two components of velocity. The laser beam indicated the position of the jet axis. Probes were connected to the TSI-1050 constant temperature anemometer bridge. CTA signal was recorded using IOtech ADC488/8SA A/D converter which was controlled by TurboLab 4.0. The auto trigger option was selected. Subsequently, the recorded signal was processed and analyzed by means of the same program.

4. BOUNDARY CONDITIONS

Measurements were made in an axisymmetrical jet, not swirled and unstimulated, flowing out from the sharp-edged ring channel of 0.04 m in diameter to the reverse chamber of 0.475 m in diameter. The position of pipe outlet, in relation to the impinged surface, was varying from z/D=10 to z/D=2. The boundary conditions used for measurements comprised the changes in air outflow velocity from the internal pipe in the reverse chamber. Measurements were made for three velocities in the pipe outlet: 10, 20 and 50 m/s, which corresponded to the Reynolds numbers from 26000 to 78000, respectively. The air temperature was maintained on the level of 20°C. The tests included measurements of average values in time: axial and radial components of velocity and their fluctuations.

The numerical calculations were based on the geometry of the actual property described in the boundary conditions for the experiment being carried out. Numerical calculations were performed for many different variants of velocity and distance of the nozzle from the bottom of the reverse chamber. Velocities in the pipe outlet varied from 2 to 50 m/s and the turbulence intensity was 4%.

5. EXPERIMENT RESULTS

Normalized radial profiles of the axial component of velocity and its fluctuation for three different flow velocities in the inner pipe have been presented in figures 3 a), b), and c). The shape of the graph describing the jet flowing from the pipe is in line with the actual impinging jet [17]. With respect to the impinging jet, the area under the positive part of the curve is slightly larger, which means that the flowing jet is rapidly spreading in the chamber. Unlike the free jets, where the core potential reaches the distance r/D=4 in the reverse chamberbetween distances from z/D=6 to z/D=7in the axis of the pipe is observed. A different situation is observed in the region of the wall flow, where significant differences in the velocity waveform profiles for different flow velocities are visible. Between distances from z/D=7 to z/D=10radial velocity profiles are similar and the jet behaves in the same way. From a distance of r/D=6, a noticeable difference in the structure and character of the flow velocity equal to 10m/s was observed.

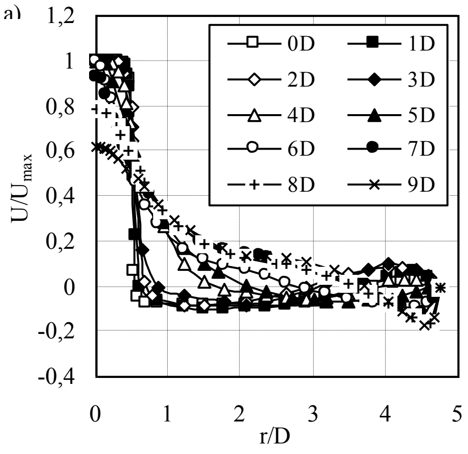

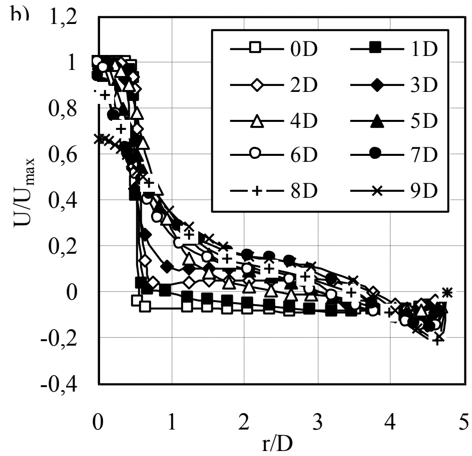

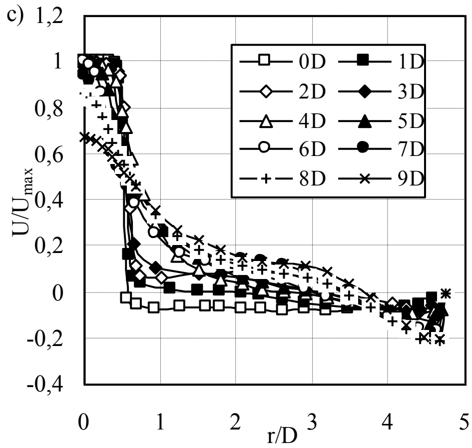

Figure 3. Distributions of the axial component of velocity at: a – 10[m/s], b – 30[m/s], c – 50 [m/s]

At the distance of r/D ~ 5, the flow separates from the trailing wall. The backward jet directs the medium flowing through the central part of the chamber to the outlet. A jet flowing in the direction of the outflow pipe appears on the wall. It represents positive values of velocity as is shown in those figures. In the case of velocity 30 m/s and 50 m/s, the jet behaves as the boundary [co?], moves towards the outlet and gradually increases towards a jet from the wall flow to the axis flow. We may observe a shift of the intersection of the x-axis profiles of about r/D=3 and y/D=2. At cross section r/D=0 the jet fills the whole cross-section of the reverse chamber between the inner pipe and the wall flow. For these two velocities, in the middle of the reverse chamber a vortex lying at a distance of r/D=2 is formed; it represents local maximums in the figures. Comparing figure 3a with figures 3b and 3c, for a velocity of 10 m/s, the differences are negligible in terms of the distribution, which should be associated with the different nature of the flow at the wall flow.

6. NUMERICAL ANALYSIS

The results of numerical simulations for all measurements made for each velocity tested during experimental research were analyzed. They are related to transient flow. The duration of the simulation depended on the measurement section and geometrical conditions. In general, time within which the flow achieved the set conditions varied between 1 and 2s. The results of simulations are presented in the form of velocity map.

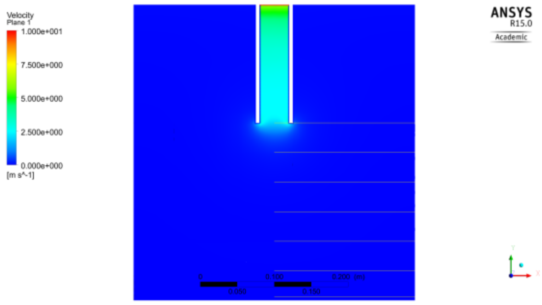

Fig. 3. Distribution of velocity for a distance of 6D, velocity 10m/s, time of simulation: 0.05 [s]

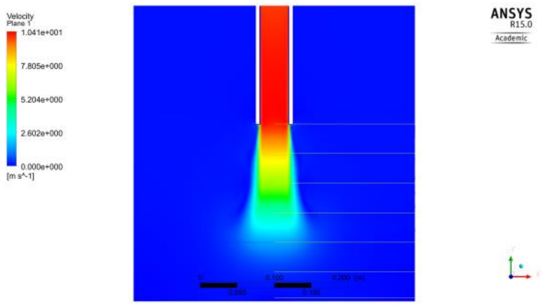

Fig. 4. Distribution of velocity for a distance of 6D, velocity 10m/s, time of simulation: 0.035 [s]

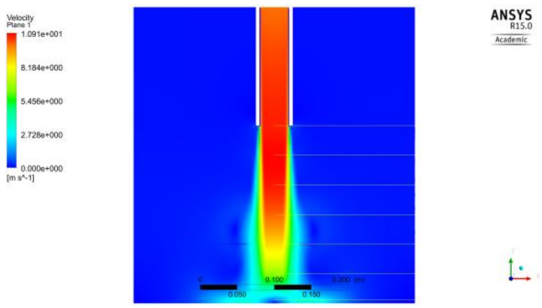

Fig. 5. Distribution of velocity for a distance of 6D, velocity 10m/s, time of simulation: 0.065 [s]

Figures from 3 to 9 present the velocity distribution in the entire volume of the reversing chamber. Only selected time steps are presented here. From the graphs we can read in the chamber promoting velocity [?]. An important aspect of 3D visualization is the ability to observe changes in the parameters of the entire volume of the reversing chamber. During the simulation is possible to observe propagation asymmetry of the jet.

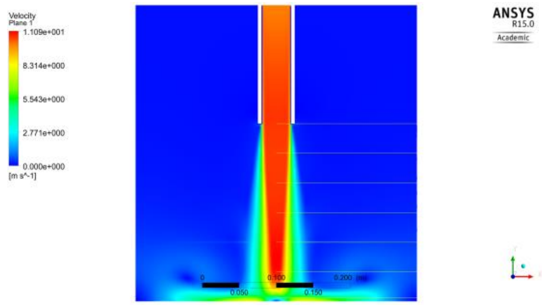

Fig. 6. Distribution of velocity for a distance of 6D, velocity 10m/s, time of simulation: 0.155 [s]

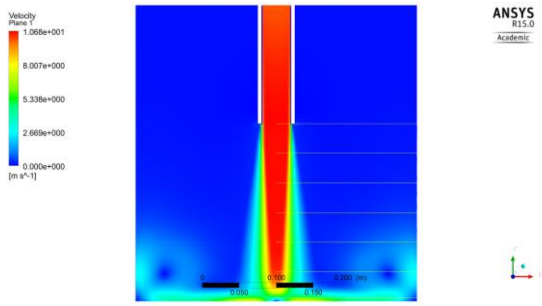

Fig. 7. Distribution of velocity for a distance of 6D, velocity 10m/s, time of simulation: 0.215 [s]

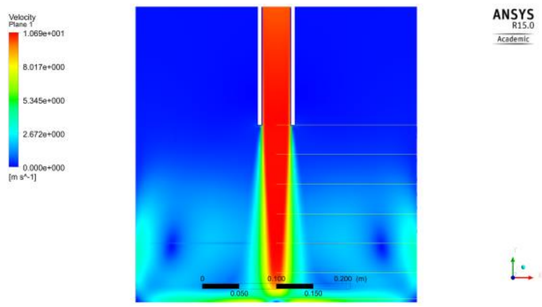

Fig. 8. Distribution of velocity for a distance of 6D, velocity 10m/s, time of simulation: 0.575 [s]

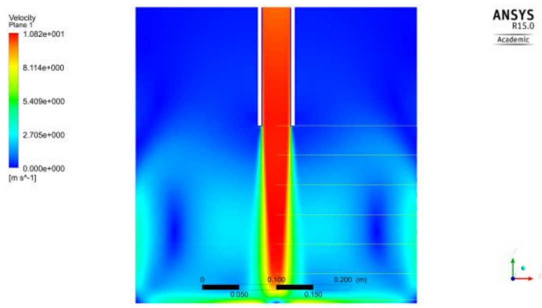

Fig. 9. Distribution of velocity for a distance of 6D, velocity 10m/s, time of simulation: 1.075 [s]

In the subsequent time steps, we can observe the formation of specific areas for jet limited by the plate. Figure 5 shows the moment of impingement on the wall, the formation of the stagnation region and the first change of the fluid flow direction. This figure, at the height of 2D, presents the characteristic of such an area. It could be caused by water beating the bottom of the reversing chamber.

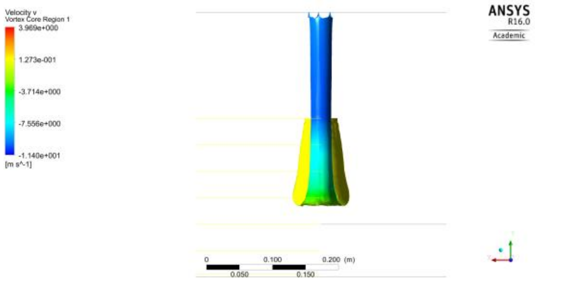

Fig. 10. Distribution of vortex core for the distance of 6D, velocity 10m/s, time of simulation: 0.35 [s]

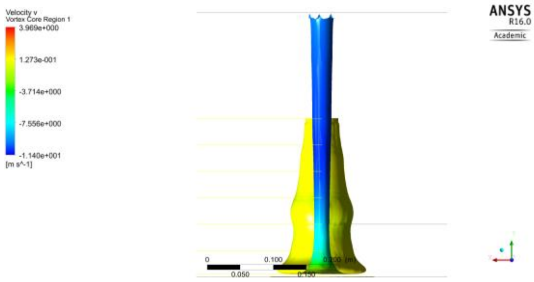

Fig. 11. Distribution of vortex core for the distance of 6D, velocity 10m/s, time of simulation: 0.065 [s]

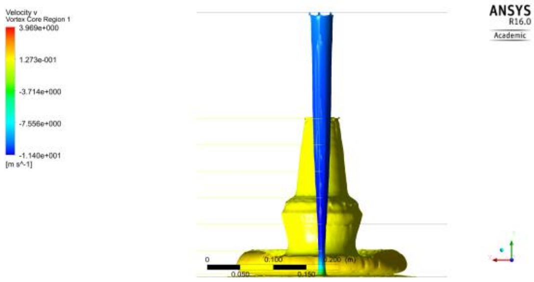

Fig. 12. Distribution of vortex core for the distance of 6D, velocity 10m/s, time of simulation: 0.095 [s]

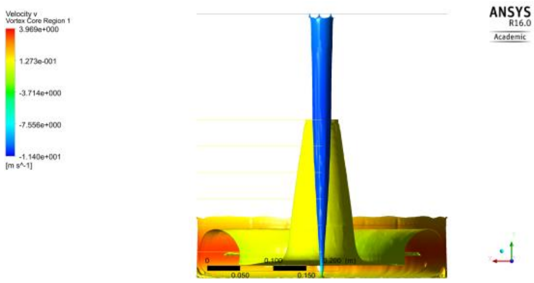

Fig. 13. Distribution of vortex core for the distance of 6D, velocity 10m/s, time of simulation: 0.215 [s]

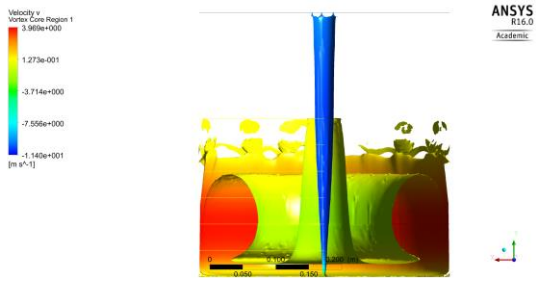

Fig. 14. Distribution of vortex core for the distance of 6D, velocity 10m/s, time of simulation: 0.775 [s]

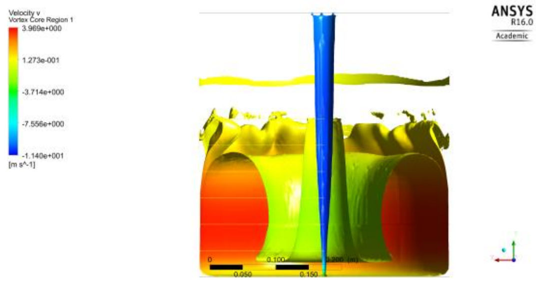

Fig. 15. Distribution of vortex core for the distance of 6D, velocity 10m/s, time of simulation: 1.075 [s]

A similar effect for the vortex core formation is presented in figures 11 and 12. Figures from 10 to 15 present the formation of the vortex core in the reversing chamber. Those figures have added new data to the analysis of the velocity fields as they indicated the formation of additional space vortices. The turbulence generated in the reversing chamber can be observed in the jet outflow from the nozzle. The impingement region is created with vortices of a small diameter formed and propagated to the sidewalls of the reversing chamber. Then the vortex increases and is heading towards the outlet of the reversing chamber. The diameter of the vortex increases up to stabilize conditions in the entire space of the chamber. Figure 15 shows this situation, stabilized in accordance with the conditions of steady flow simulation and experimental results.

7. CONCLUSION

Modeling the flow in the reversing chamber brings interesting results. The ability to simulate unsteady flow brings new information on the flow inside the chamber. Steady flow simulations do not have the opportunity to present the formation of vortices of different frequencies. In the simulations, we can presume established formation of turbulence by observing the velocity fields. However, in the case of the walls, gradient of the impingement velocity does not suggest the formation of such a thick layer of vortices. Unsteady flow modeling allows demonstrating a mechanism of vortices formation. Moreover, it enables determining the construction of the vortex metrology and analysis. Such data are essential in order to determine the number of Strouhal simultaneity.

The simulation results are consistent with transient flow in steady flow simulations and experiments.

REFERENCES

[1] Downs, S.J. & James, E.H. (1987). Jet Impingement Heat Transfer – A Literature Survey, ASME National Heat Transfer Conference, No.87-H-35, ASME, New York

[2] Popiel, C., Trass, O., 1991. Visualization of a free and impinging round jet. Exp. Therm. Fluid Sci. 4, 253–264.

[3] Jambunathan, K., Lai, E., Moss, M.,& Button, B.,1992 A review of heat transfer data for single circular jet impingement, Int. J. Heat and Fluid Flow 13 (106-115)

[4] Viskanta, R. (1993). Heat Transfer to Impinging Isothermal Gas and Flame Jets, Experimental Thermanl and Fluid Science, Vol.6, No. 2, (February 1993), pp. 111-134, ISSN 0894-1777

[5] Zuckerman N. and LIOR N., Jet Impingement Heat Transfer: Physics, Correlations, and Numerical Modeling, advances in heat transfer vol. 39 (565-631), 2006

[6] S. Roux a,⇑, M. Fénot b, G. Lalizel b, L.-E. Brizzi c, E. Dorignac Evidence of flow vortex signatures on wall fluctuating temperature using unsteady infrared thermography for an acoustically forced impinging jet, International Journal of Heat and Fluid Flow, 2014

[7] Yue-Tzu Yang, Shing-Cheng Chang ⇑, Chu-Shiang Chiou, Lattice Boltzmann method and large-eddy simulation for turbulent impinging jet cooling, International Journal of Heat and Mass Transfer, 543-553, 2013.

[8] M. Y. Abdelsalam, M. M. Kamal, and M. Aboelnasr, Flat Surface Heat Transfer Enhancement By An Impinging Circular Free Water Jet, Experimental Heat Transfer, 27:276–295, 2014

[9] Zdeněk Trávníček a , Václav Tesař a , Zuzana Broučková a & Kazimierz Peszyński, Annular Impinging Jet Controlled by Radial Synthetic Jets, Taylor & Francis, Heat Transfer Engineering, 35(16–17):1450–1461, 2014

[10] Kłosowiak R., Bogusławski L., Shear stress distribution on flat surface impinged by jets, 21st International Congress of Chemical and Process Engineering CHISA 23-27 August 2014 Prague

[11] Crow S.C., Champagne F.M., Orderly structure in jet turbulence, Journal of Fluid Mechanics, 48, 547–591, 1970.

[12] Wygnanski I., Peterson R.A., Coherent motion in excited free shear flows, AIAA Journal, 25, 201–213, 1974.

[13] Gutmark E., Wygnanski I., The planar turbulent jet, Journal of Fluid Mechanics, 73, 465–495, 1976.

[14] Koseoglu M.F., Baskaya S., Experimental and numerical investigation of natural convection effects on confined impinging jet heat transfer, International Journal of Heat and Mass Transfer, 52, 2009, 1326–1336.

[15] Bartoszewicz J., Kłosowiak R., Bogusławski L., The analysis of the flow structure in a jet at variable geometry of the reverse chamber, International Journal of Heat and Mass Transfer, 55, 2012, 3239-3245.

[16] Deo R.C. et al., Comparison of turbulent jets issuing from rectangular nozzles with and without sidewalls, Experimental Thermal and Fluid Science, 32, 2007, 596–606.

[17] Yeh Y.-L. et al., Vertical structure evolutions and spreading characteristics of a plane jet flow under anti-symmetric long-wave excitation, Experimental Thermal and Fluid Science, 33, 2009, 630–641.

[18] F. R. Menter. “Two-Equation Eddy-Viscosity Turbulence Models for Engineering Applications”. AIAA Journal. Vol. 32. 1598–1605. 1994.

Conference on Modelling Fluid Flow (CMFF'15)
The 16th International Conference on Fluid Flow Technologies
Budapest, Hungary, September 1-4, 2015

ON THE INVESTIGATION OF TWO-DIMENSIONAL BIFURCATION STRUCTURE OF AN ACOUSTICALLY EXCITED GAS BUBBLE

Roxána VARGA[1], Ferenc HEGEDŰS[2],

[1] Corresponding Author. Department of Hydrodynamic Systems, Faculty of Mechanical Engineering, Budapest University of Technology and Economics. H-1111 Budapest, Hungary, Müegyetem rkp. 3. E-mail: rvarga@hds.bme.hu
[2] Department of Hydrodynamic Systems, Budapest University of Technology and Economics. E-mail: hegedusf@hds.bme.hu

ABSTRACT

The peculiar dynamics of harmonically excited spherical gas bubbles via acoustic irradiation has been extensively studied in the last decades. During the radial oscillations of the bubbles, their wall velocities can reach several hundreds or even thousands of m/s resulting in high pressure and temperature, and shock wave emission into the liquid domain. This collapse-like behaviour is exploited by the rapidly developing ultrasonic technology, where these extreme conditions can be used in several fields of polymer industry, food technology, medicine and many others. In this study, the radial oscillation of a single gas bubble placed in water was studied by applying the Keller-Miksis equation, a second order non-linear differential equation describing the evolution of the bubble radius in time. Numerical computations were carried out using the tools of bifurcation theory to investigate the bubble dynamics. The two main parameters were the pressure amplitude of the excitation and the bubble size, while the excitation frequency was kept constant at the resonant frequency of the bubble. The main aim was to reveal the domains of the collapse-like oscillations in the two-dimensional parameter space. As a by-product, the chaotic domains found can help to avoid unpredictable behaviour, which can be crucial in medical applications.

Keywords: Acoustic cavitation, chaos, bifurcation structure, bubble dynamics, Keller-Miksis equation, non-linear analysis.

NOMENCLATURE

f_0	$[Hz]$	resonance frequency of the bubble
Ma	$[-]$	Mach number
N	$[-]$	period of a solution
P_∞	$[Pa]$	ambient pressure
R	$[m]$	bubble radius
R_E	$[m]$	equilibrium radius of the unexcited system
T_∞	$[^oC]$	ambient temperature
c_L	$[m/s]$	liquid sound speed
n	$[-]$	polytropic index
p_L	$[Pa]$	pressure at the bubble wall
p_∞	$[Pa]$	pressure far away from the bubble
p_A	$[bar]$	pressure amplitude of the excitation
p_G	$[Pa]$	non-condensable gas content of the bubble
p_V	$[Pa]$	vapour pressure
t	$[s]$	time
y_1	$[-]$	dimensionless bubble radius
y_2	$[-]$	dimensionless bubble wall velocity
λ	$[-]$	Lyapunov exponent
μ_L	$[kg/ms]$	liquid kinematic viscosity
ω	$[rad/s]$	angular frequency of the excitation
ω_0	$[rad/s]$	eigenfrequency of the unexcited system without damping
ρ_L	$[kg/m^3]$	liquid density
σ	$[N/m]$	surface tension
τ	$[-]$	dimensionless time
τ_0	$[-]$	dimensionless period time of the excitation
τ_p	$[-]$	dimensionless period time of a solution

Subscripts and Superscripts

A	amplitude
E	equilibrium
G	gas
L	liquid
V	vapour
ac	acoustic
max	maximum value
p	period value
0	reference value
∞	far away from the bubble

1. INTRODUCTION

In various fields of modern science, ultrasound is a promising and emerging technology. When a liquid medium is exposed to high intensity and high frequency ultrasound, gas bubbles can be generated which then begin to oscillate radially [1]. During this oscillation, the bubble may shrink so violently that its wall velocity reaches several hundreds or thousands of m/s, resulting in extreme conditions around itself. This phase of the oscillation is called the collapse phase, in which the pressure and the temperature can be as high as $1000\,bar$ and $8000\,K$ [2], respectively. The high pressure can result in the launch of a strong pressure wave or shock wave [3, 4]. These effects can cause physical or chemical changes at the collapse site. Therefore, ultrasonic technology is used in several fields of polymer industry, food technology, medicine and many others. For example, the generated shock waves can reduce a polymer's chain length in solution [5]. Or in medicine, a commonly used method to break up kidney stones is the generation of shock waves via ultrasound [6]. In food industry, ultrasound is a successful method for preservation: only a moderately high temperature weakens the bacterial cell membrane which then are less resistant to cavitational damage [7].

The oscillation of a harmonically excited gas bubble is known to be strongly nonlinear [8]. Depending on the parameters of the excitation and on the liquid or the equilibrium radius of the bubble, it may oscillate significantly differently. This leads to the importance to investigate numerically the dynamics of a single spherical gas bubble placed in water. In this paper the model used to describe the radial oscillation of the bubble in time is the Keller-Miksis equation, a second order strongly nonlinear ordinary differential equation. The changing parameters are the pressure amplitude of the excitation and the equilibrium radius of the bubble. To detect the stable periodic and chaotic coexisting solutions, the equation was solved with 5 random initial conditions for every parameter combination. The used solver was a 4^{th} order Runge–Kutta cheme with a 5^{th} order embedded error estimation.

2. THE MATHEMATICAL MODEL

During the oscillation of a harmonically excited gas bubble, it's wall velocity can reach several thousands of m/s. This large amplitude, collapse-like oscillation is strongly affected by the compressibility of the liquid [9], [10]. Therefore, for the numerical simulations the modified form [11] of the Keller-Miksis equation [12] was used to take into account the compressibility of the liquid:

$$\left(1-\frac{\dot{R}}{c_L}\right)R\ddot{R}+\left(1-\frac{\dot{R}}{3c_L}\right)\frac{3}{2}\dot{R}^2=\frac{1}{\rho_L}\left(1+\frac{\dot{R}}{c_L}\right)(p_L-p_\infty(t))+\frac{R}{\rho_L c_L}\frac{d\left(p_L-p_\infty(t)\right)}{dt}. \tag{1}$$

Equation 1 is a second order, strongly nonlinear ordinary differential equation. $R = R(t)$ is the bubble radius, and the dot stands for the derivative with respect of time t. ρ_L and c_L are the density and sound speed in the liquid domain, respectively. The pressure at the bubble wall is p_L, and the pressure far away from the bubble is

$$p_\infty = P_\infty + p_A \sin(\omega t), \tag{2}$$

where P_∞ is the static or ambient pressure, p_A is the pressure amplitude and ω is the angular frequency of the periodic excitation. The relationship between the pressures inside and outside the bubble at the bubble wall can be written as

$$p_G + p_V = p_L + \frac{2\sigma}{R} + 4\mu_L\frac{\dot{R}}{R}, \tag{3}$$

where the total pressure inside the bubble is the sum of the partial pressures of the non-condensable gas content p_G and the vapour pressure p_V. The surface tension is σ and the liquid kinematic viscosity is μ_L. The gas inside the bubble obeys a simple polytropic relationship [11]:

$$p_G = \left(\frac{2\sigma}{R_E} - (p_V - P_\infty)\right)\left(\frac{R_E}{R}\right)^{3n}, \tag{4}$$

where R_E is the equilibrium radius of the unexcited system and $n = 1.4$ is the polytropic exponent.

For the numerical simulations, equations 1-4 were rewritten into a first order dimensionless ordinary differential equation system. The dimensionless time was chosen to be $\tau = t\omega/2\pi$, hence every integer value N_{ac} of τ means N_{ac} numbers of acoustic cycle of the excitation. The dimensionless bubble radius and bubble wall velocity are defined as $y_1 = R/R_E$ and $y_2 = R2\pi/R_E\omega$, respectively.

The liquid properties were calculated from the Haar–Galagher–Kell equation of state [13] with $T_\infty = 25\,^oC$ and $P_\infty = 1\,bar$. The pressure amplitude of the excitation was varied between 1 and 5 bar, and the frequency was kept constant at the resonant frequency of the bubble, that is, the eigenfrequency of the unexcited system without damping, which is according to Brennen:

$$\omega_0 = \sqrt{\frac{3n(P_\infty - p_V)}{\rho_L R_E^2} + \frac{2(3n-1)\sigma}{\rho_L R_E}}. \tag{5}$$

Table 1 shows the exact values of the parameters used during the computations.

2.1. Numerical tools

Since equation system 1-4 is highly nonlinear, the solutions of the dimensionless system describing the time evolution of the bubble radius are strongly dependent on the parameters. Even a slight change in one of them may result in a qualitatively different behaviour, and periodic and chaotic attractors can coexist. A solution with period τ_p is called a period N solution if $N = \tau_p/\tau_0$, where τ_0 is the period of the excitation. A chaotic, aperiodic solution, however, has infinite periodicity. At fix parameter combination periodic and chaotic attractors may coexist.

Table 1. Liquid properties calculated from the Haar–Gelegher–Kell equation of state with $T_\infty = 25\,^oC$ and $P_\infty = 1\,bar$, and the values of the changing parameters of the computations.

liquid sound speed c_L	$1497\,m/s$
vapour pressure p_V	$3166.8\,Pa$
liquid dynamic viscosity μ_L	$0.00089\,kg/ms$
liquid density ρ_L	$997\,kg/m^3$
surface tension σ	$0.072\,N/m$
equilibrium radius R_E	$1\,\mu m - 0.1\,mm$
pressure amplitude p_A	$1 - 5\,bar$
frequency of the excitation ω	ω_0

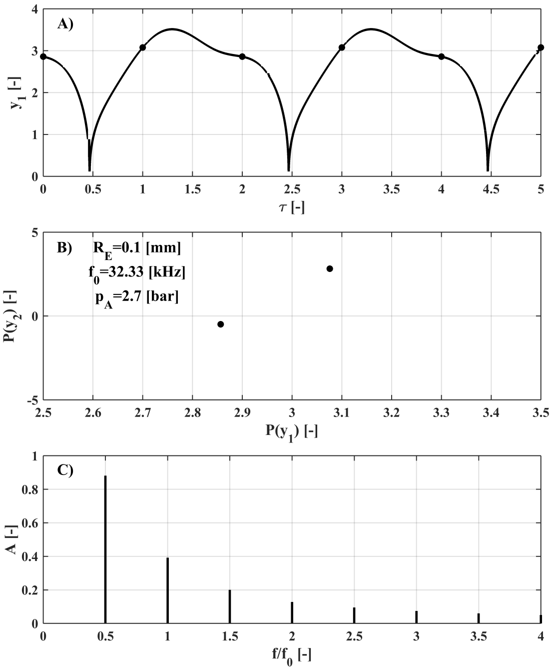

Figure 1. A) Time evolution, B) Poincare section, C) amplitude spectrum of a periodic solution.

A usual way to represent a solution is the time evolution of one of its coordinate, or its Poincaré map, where the trajectory of the solution is sampled at every integer multiple time of τ_0. While a period N solution is represented with N dots in the Poincaré map, a chaotic solution is represented with as many points as many time cycles were simulated. An other common method is to create the amplitude (power) spectrum of the nonlinear oscillation. The power spectra is discrete in the case of periodic oscillation and continuous in the case of chaotic oscillation. The spectra of a period N solution show lines at the driving frequency ω and at $k\omega/N$ for $k = 1, 2, \ldots, N-1$.

Figures 1 and 2 give the time evolution A), the Poincaré map B) and the amplitude spectrum C) of a period 2 and a chaotic solution, respectively. The simulations were carried out for a bubble of $R_E = 0.1\,mm$ equilibrium radius driven at its resonance frequency, which is $f_0 = \omega_0/2\pi = 32.33\,kHz$. The pressure amplitude was $p_A = 2.7\,bar$ for the periodic, and $p_A = 2.6\,bar$ for the chaotic oscillation. In diagrams A) the dots on the curves mark the integer cycles of the excitation. While for the periodic oscillation the trajectory repeats itself at every second acoustic cycle, the trajectory of the chaotic solution never repeats itself. Since the Poncaré map in Fig. 1B) contains only two dots, this is a period 2 solution. In Fig. 2B), the trajectory was simulated for 10000 cycles, hence the map contains the same amount of points. This specific structure of the chaotic solution is called a strange attractor. The power spectra of the periodic trajectory (Fig. 1C)) has a line at half the driving frequency, and at its harmonics. The spectra of the chaotic solution is indeed continuous (Fig. 2C)).

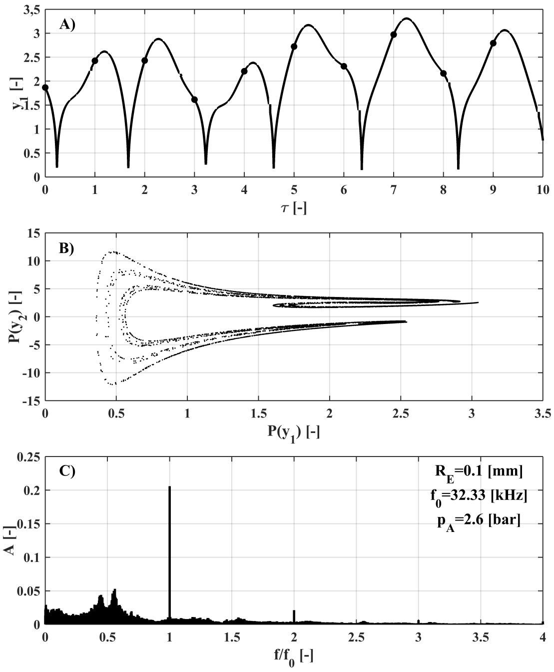

Figure 2. A) Time evolution, B) Poincare section, C) amplitude spectrum of a chaotic solution.

A typical measure for the chaoticity of the oscillation is the Lyapunov exponent λ, a number that describes the exponential divergence of two trajectories initiated from slightly different initial conditions. The maximum Lyapunov exponent λ_{max} is negative in the case of periodic oscillation, positive for chaotic solutions. When period doubling bifurcation occurs (when a period 2^k, $k \geq 0$ solution becomes unstable and a period 2^{k+1} attractor emerges) λ_{max} is zero.

To explore the qualitative change of the solutions as a function of a parameter, one can create bifurcation diagrams. Here one coordinate of the Poincaré map of the solutions are plotted versus the changing (control) parameter. Figure 3 shows the dimensionless bubble radius y_1 response to the pressure amplitude A) and the Lyapunov exponent spectra B) when the bubble radius at rest is $50\,\mu m$. The Lyapunov exponent is indeed positive when the oscillation is chaotic, and zero when period doubling bifurcations occur (see the vertical lines).

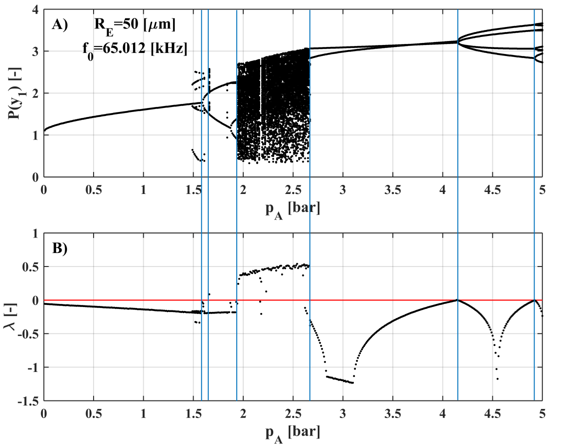

Figure 3. A) Bifurcation diagram and B) Lyapunov exponent spectra.

To compute a stable solution, the most common way is to solve an initial value problem, and calculate the trajectory of the transient solution until it converges to an attractor. In this paper, for every parameter combination 5 random initial conditions were used to detect the relevant coexisting attractors. After the convergence, in case of a period N solution N points of its Poincare map were recorded, and 128 points in case of a chaotic solution. For every solution the Lyapunov exponent was also calculated. The solver was a 4^{th} order Runge–Kutta scheme with a 5^{th} order embedded error estimation, used in Matlab environment.

3. RESULTS AND DISCUSSION

To detect the parameter combinations for collapse-like oscillations, several 1-dimensional and a 2-dimensional bifurcation diagrams were computed with the pressure amplitude of the excitation and the equilibrium radius of the bubble as control parameters. For the computations, the pressure amplitude was varied between 0 and 5 bar with 0.01 bar increment. The equilibrium radius was varied between 1 μm and 0.1 mm with 0.5 μm increment. The biggest bubble radius was chosen to be 0.1 mm, since, according to Brennen [1], this is the possible largest nucleus size in water. The frequency of the excitation was chosen to be the resonance frequency of the bubble ω_0. All the remaining parameters were kept constant, their exact values are given in Table 1. In order to compare the bubble wall velocity with the liquid sound speed c_L, the maximum Mach number Ma_{max} was also calculated with Eq. 6:

$$Ma_{max} = \frac{R_E \omega_0 y_{2,max}}{2\pi c_L}, \tag{6}$$

where $y_{2,max} = |y_2(i \le \tau \le i+1|$, where $i = 1, 2, \ldots, N$, where N is the period of the oscillation or 128 in the case of chaotic solution.

3.1. Pressure amplitude as control parameter

To get a comprehensive picture about the effect of the pressure amplitude on the bubble oscillation, six bifurcation diagrams were computed with three different equilibrium radii. Figure 4 shows the dimensionless bubble radius response, and Fig. 5 the maximum Mach number response as a function of the pressure amplitude.

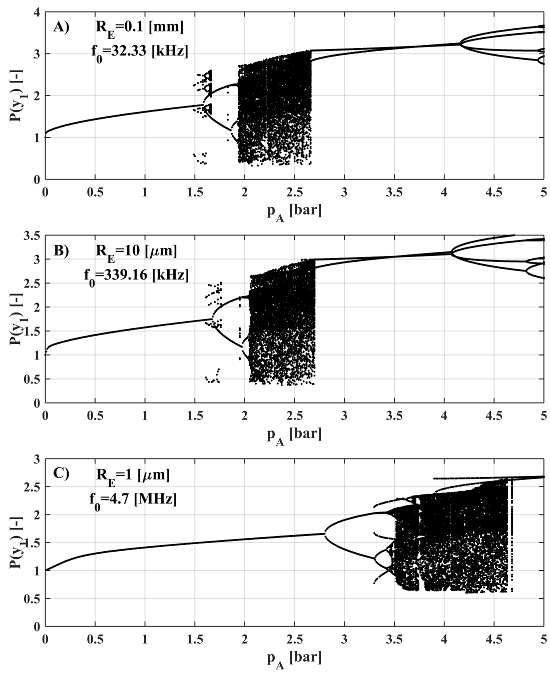

Figure 4. Bifurcation diagrams of the dimensionless bubble radius with the pressure amplitude as the control parameter.

Figure 4A) shows the bifurcation structure of a bubble with 0.1 mm radius at rest, and at driving frequency $f_0 = 32.33\,kHz$. Between 0 and 1.49 bar pressure amplitude only a period one solution exist. At 1.57 bar it becomes unstable and through a period doubling bifurcation, a period 2 attractor emerges. At 1.84 bar a period doubling cascade (a series of period doubling bifurcations) starts and becomes chaotic at 1.98 bar. Between 1.49 and 1.66 bar pressure amplitude two other stable period 3 attractors coexist with the previously existing solution. The wide chaotic regime that exists between 1.98 and 2.66 bar emerges through a global bifurcation before the accumulation point of the period doubling cascade of the period 1 solution. After this chaotic oscillation a period 2 stable orbit emerges and at 4.16 bar pressure amplitude it starts its period doubling cascade.

For a 10 times smaller bubble radius (Fig. 4B)) the bifurcation structure does not change significantly. The bifurcation points and the chaotic regime exist almost at the same values of the pressure amplitude. For an even smaller bubble, with $1\,\mu m$ equilibrium radius (Fig. 4) the bifurcations shift towards higher pressure amplitudes compared to the larger bubbles. The first period 1 oscillation does not go through any bifurcations until $2.79\,bar$ pressure amplitude. The attractors, which exist for a small period of pressure amplitude for bigger bubble radius, merge into the chaotic regime which exist between 3.52 and $4.63\,bar$. The chaotic oscillation loses its stability at about $4.7\,bar$ from where only a period 2 solution exists.

For all the three examined bubble structure, the radial oscillation of the bubbles are higher after the chaotic attractors lose their stability. While the period 1 solutions before the chaotic regimes oscillate at a 1.5 times bigger bubble radii than the equilibrium radii, after the chaotic oscillation this radii is 3 times the equilibrium radii.

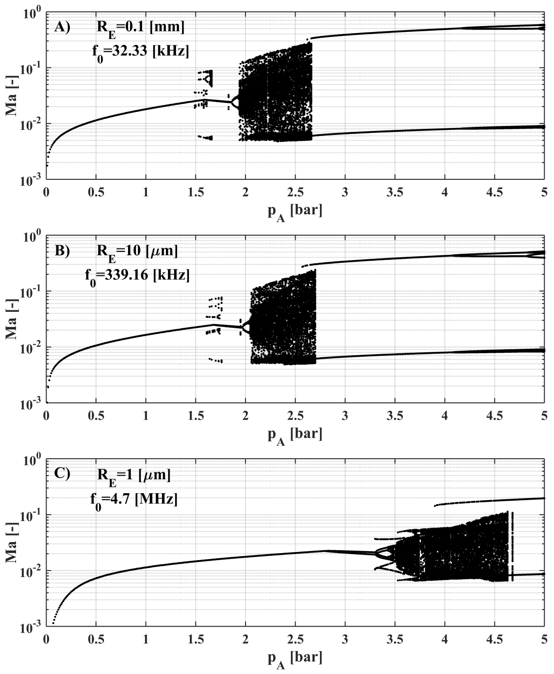

Figure 5. Bifurcation diagrams of the maximum Mach number with the pressure amplitude as the control parameter.

Figure 5 shows the evolution of the Mach number for the same bubble sizes as those of presented in Fig. 4. For all three bubbles the maximum Mach number significantly increases between the two sides of the chaotic oscillation. Figure 5A) and B) shows that for bigger bubble radii, when high bubble wall velocities are desired, it is recommended to excite the bubble at higher pressure amplitudes than $2\,bar$, and when chaotic oscillation is not desired, above $2.7\,bar$. While before the chaotic regime the maximum bubble wall velocity that can be reached is approximately $36\,m/s$, after it, it is almost 10 times higher with about $330\,m/s$. In the case of such small bubbles, as shown in Fig. 5C), up to $3.3\,bar$ pressure amplitude the maximum Mach number does not grow rapidly neither. For bubbles with $10\,\mu m$, before the chaotic regime the maximum bubble wall velocity is about $30\,m/s$, and after it, it gets as high as $201\,m/s$.

3.2. Equilibrium radius as control parameter

In the previous subsection, a qualitative change in the bifurcation structure of the bubble oscillation was shown only when the bubble is as small as $1\,\mu m$. Consequently it is an important question that at what bubble size this structure changes so significantly. For the answer, several more bifurcation diagrams were calculated with the equilibrium radius as control parameter, see Fig. 6.

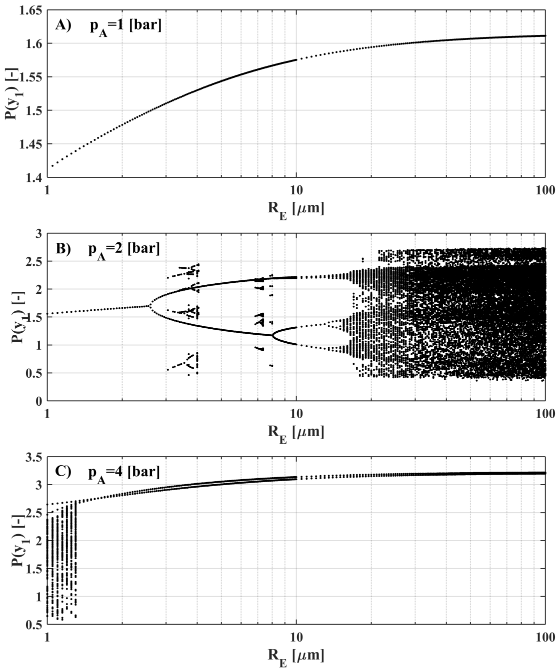

Figure 6. Dimensionless bubble radius response curves with the equilibrium radius as the control parameter.

Figure 6A) shows the structure when the pressure amplitude of the excitation is 1 bar. For the investigated bubble sizes, only a period 1 stable attractor exist. As the equilibrium radius increases, the magnitude of the radial oscillation increases as well.

For 2 bar pressure amplitude, the oscillation of the bubble is substantially changes with increasing equilibrium radius. Up to $2.5\,\mu m$ radius only a period 1 stable solution exists, when a period doubling bifurcation occurs. The period doubling cascade, initiating at about $16.5\,\mu m$, results in the chaotic attractor which exists up until the end of the simulation. Between 3 and $4\,\mu m$ equilibrium radius two period 3 solutions coexist with the period 2 oscillation. An other period 6 coexisting attractor was found between 6.8 and 8 μm.

Finally, at 4 bar pressure amplitude chaotic oscillation only exists for bubbles whit equilibrium radii smaller than 1.3 μm. For bigger bubbles, the oscillation is a period 2 oscillation around an almost 3 times bigger bubble radii than their radii at rest.

3.3. 2-dimensional bifurcation structure

For a more condensed representation of the collapse-like behaviour, bi-parametric plots are effective tools. With colormap representation, the parameter combinations where desired behaviour may occur are easily seen. Figures 7 to 9 show the contour plot of the maximum Lyapunov exponent λ_{max}, the maximum Mach number Ma_{max} and the period in the $R_E - p_A$ plane, respectively. In case of coexisting solutions the largest values were depicted.

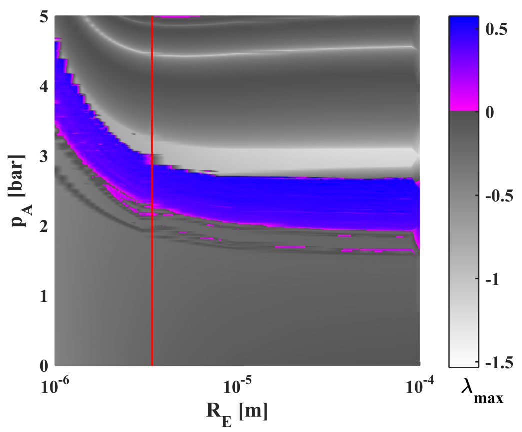

Figure 7. Bi-parametric map of the maximum Lyapunov exponent λ_{max} as the function of the equilibrium radius R_E of the bubble and the pressure amplitude p_A of the excitation.

The maps are scaled together. It is interesting how the chaotic oscillation shifts upwards when the equilibrium radius decreases to a critical value (see the coloured band in Fig. 7). This shift in the structure can also be observed in both of the maximum Mach number in Fig. 8 and the period in Fig. 9. In Figure 9 the colourful areas are where periodic solutions exist with a period lower than 8, chaotic oscillations and period doubling bifurcations are the black areas. The critical equilibrium radius is approximately $R_{E,crit} = 3.4\,\mu m$, where the red line is in all three diagrams. $R_{E,crit}$ was calculated from Eq. 5, at this bubble radius $\omega_0 = 0$, and the oscillation is overdamped. Above this value the equilibrium radius R_E has only a minor effect on the bifurcation structure. Below this threshold, however, the structure rapidly changes with decreasing radius. High Mach numbers can be reached when the pressure amplitude is higher than 2.6 bar and the equilibrium radius is larger than

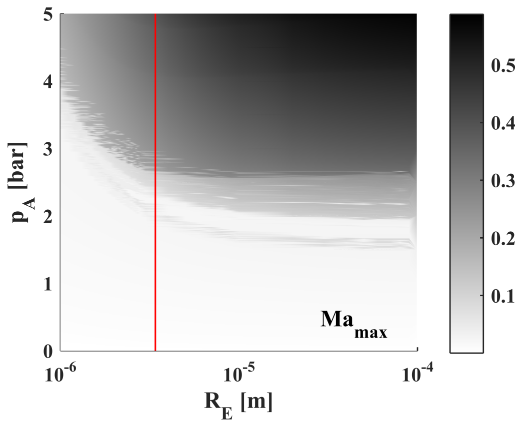

Figure 8. Bi-parametric map of Ma_{max} as the function of the equilibrium radius R_E of the bubble and the pressure amplitude p_A of the excitation.

the critical value $R_{E,crit}$ (8). As the bubble radius gets smaller, higher pressure amplitudes are needed in order to generate higher Mach numbers.

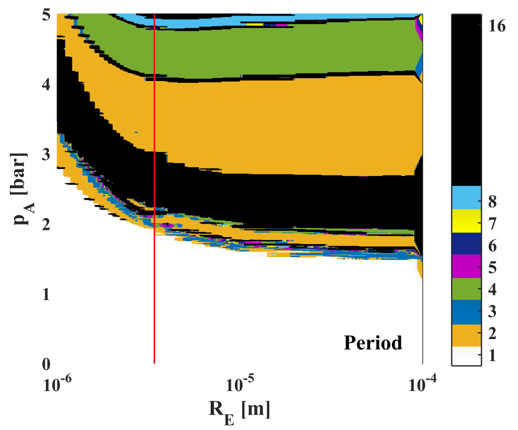

Figure 9. Bi-parametric map of the maximum period of the solutions as the function of the equilibrium radius R_E of the bubble and the pressure amplitude p_A of the excitation.

Comparing Fig. 8 with Fig. 7 and 9 a connection between higher Mach numbers and the chaotic zone can be observed. Before the chaotic oscillation (grey area below the pink-blue band in Fig. 7) when only period 1 solution exists (white area in Fig. 9), the Mach numbers are lower than 0.01. In the chaotic band there is an increase in the Mach number, it can be as high as 0.13. After the vanish of the chaotic oscillations, and a period 2 solution emerge, the bubble oscillates with a significantly higher maximum wall velocity, the Mach number can reach 0.5.

4. SUMMARY

The nonlinear dynamics of an acoustically excited single spherical gas bubble in water have been investigated. The effect of the pressure amplitude and the bubble size at rest on the oscillation structure was studied numerically. The regions of periodic and chaotic oscillations were detected by means of the maximum Lyapunov exponent. To measure the strength of the collapse the bubble wall velocities rescaled to Mach numbers were also computed. Results show that above $3.4\,\mu m$ equilibrium radius the oscillation structure does not change significantly when the pressure amplitude is in between 0 and 5 *bar*. For bubbles with smaller than $3.4\,\mu m$ bubble radius, a change in the oscillation occur, the chaotic oscillations only occur for higher pressure amplitudes. The highest Mach number solutions exist beyond approximately $p_A = 2.6\,bar$ pressure amplitude, after the chaotic oscillations vanish, for above $R_{E,crit} = 3.4\mu m$ equilibrium radii in the investigated range.

ACKNOWLEDGEMENTS

This research has been supported by the Hungarian Scientific Research Fund — OTKA, under grant no. K81621.

REFERENCES

[1] Brennen, C. E., 2013, *Cavitation and bubble dynamics*, Cambridge University Press.

[2] Suslick, K. S., and Flannigan, D. J., 2008, "Inside a collapsing bubble: sonoluminescence and the conditions during cavitation", *Annu Rev Phys Chem*, Vol. 59, pp. 659–683.

[3] Pecha, R., and Gompf, B., 2000, "Microimplosions: cavitation collapse and shock wave emission on a nanosecond time scale", *Physical review letters*, Vol. 84 (6), p. 1328.

[4] Koch, S., Garen, W., Hegedüs, F., Neu, W., Reuter, R., and Teubner, U., 2012, "Time-resolved measurements of shock-induced cavitation bubbles in liquids", *Applied Physics B*, Vol. 108 (2), pp. 345–351.

[5] Suslick, K. S., and Price, G. J., 1999, "Applications of ultrasound to materials chemistry", *Annual Review of Materials Science*, Vol. 29 (1), pp. 295–326.

[6] Chaussy, C., Brendel, W., and Schmiedt, E., 1980, "Extracorporeally induced destruction of kidney stones by shock waves", *The Lancet*, Vol. 316 (8207), pp. 1265–1268.

[7] Knorr, D., Zenker, M., Heinz, V., and Lee, D.-U., 2004, "Applications and potential of ultrasonics in food processing", *Trends in Food Science & Technology*, Vol. 15 (5), pp. 261–266.

[8] Lauterborn, W., 1976, "Numerical investigation of nonlinear oscillations of gas bubbles in liquids", *The Journal of the Acoustical Society of America*, Vol. 59 (2), pp. 283–293.

[9] Hickling, R., and Plesset, M. S., 1964, "Collapse and rebound of a spherical bubble in water", *Physics of Fluids (1958-1988)*, Vol. 7 (1), pp. 7–14.

[10] Prosperetti, A., and Lezzi, A., 1986, "Bubble dynamics in a compressible liquid. Part 1. First-order theory", *Journal of Fluid Mechanics*, Vol. 168, pp. 457–478.

[11] Lauterborn, W., and Kurz, T., 2010, "Physics of bubble oscillations", *Reports on Progress in Physics*, Vol. 73 (10), p. 106501.

[12] Keller, J. B., and Miksis, M., 1980, "Bubble oscillations of large amplitude", *The Journal of the Acoustical Society of America*, Vol. 68 (2), pp. 628–633.

[13] Haar, L., Gallagher, J. S., Kell, G. S., and Grigull, U., 1988, *NBS/NRC Wasserdampftafeln*, Springer Berlin et al.

Conference on Modelling Fluid Flow (CMFF'15)
The 16th International Conference on Fluid Flow Technologies
Budapest, Hungary, September 1-4, 2015

INVESTIGATION OF DREDGE HOSE EROSION BY CFD DRIVEN METHODOLOGY

Péter TÓTH[1], Gergely KRISTÓF[2], Attila CSOBÁN[3] István GRÉPÁLY[4] Tibor NAGY[5]

[1] Corresponding Author. CFD.HU Ltd., Budapest Medve u. 24., H-1027 Budapest, Hungary. Tel.: +36 1 209 9025, Fax: +36 1 209 9026, E-mail: toth@cfd.hu
[2] Department of Fluid Mechanics, Faculty of Mechanical Engineering, Budapest University of Technology and Economics. E-mail: kristof@ara.bme.hu
[3] Department of Machine and Product Design, Faculty of Mechanical Engineering, Budapest University of Technology and Economics. E-mail: csoban.attila@gt3.bme.hu
[4] ContiTech Rubber Industrial Kft. E-mail: Istvan.Grepaly@fluid.contitech.hu
[5] Rubber-Consult Kft. E-mail: Tibor.Nagy-EXT@fluid.contitech.hu

ABSTRACT

Dredge hoses are of great importance to the mining and transportation industry. One of the aims of the hose design is to extend the operational lifetime. The lifetime can be increased by carefully choosing the pipe lining material. Development of such lining requires good knowledge of the particle-surface impact characteristics inside the transport pipe and also requires a fast laboratory testing tools for erosion resistant material. The present study uses Discrete Phase Modelling (DPM) with Computational Fluid Dynamics (CFD) to investigate the sensitivity of erosion rate in a pipe bend in terms of typical flow conditions and particle impact parameters. The results shows that for accurate prediction of the erosion rate the particle impact properties and material behaviour is need to be known at less than 5° of impact angles. A measurement at this low impact angle is not common in the literature; therefore usual testing methodology is not readily applicable. The study discusses a laboratory measurement technique supported by CFD and Discrete Element Method with which low impact angle erosion can be investigated. The erosion rate and particle impact parameters can be determined leading to a parameterization of the erosion process which can be used in full scale pipe erosion prediction.

Keywords: CFD, DEM, erosion, particle laden flow, dredge hose

NOMENCLATURE

ΔP	$[kgms^{-1}]$	Impulse change
A_f	$[m^2]$	facet area of the surface where the particle caused erosion
D	$[m]$	inner diameter of the hose
D_s	$[m]$	diameter of the sample
N_p	$[-]$	number of particles contacted the wall
R_er	$[ms^{-1}]$	erosion rate (velocity)
Y_d	$[-]$	particle mass fraction
$\bar{d}$	$[m]$	the average diameter of the distribution
$\dot{m}_p$	$[kgs^{-1}]$	mass flow rate of particle p
b	$[-]$	velocity exponent
g	$[ms^{-2}]$	gravitational acceleration
k	$[N^{-1}]$	spring constant
m_p	$[kg]$	mass of particle p
n	$[-]$	the spread parameter of the distribution
p_1	$[-]$	erosion model parameter
p_2	$[-]$	erosion model parameter
p_3	$[-]$	erosion model parameter
t_c	$[s]$	contact time of particle with surface
v_p	$[ms^{-1}]$	velocity of particle p
v_s	$[ms^{-1}]$	sample velocity
v_in	$[ms^{-1}]$	inlet velocity
α_p	$[°]$	impact angle of particle p
α_conn	$[-]$	erosion model parameter
δ	$[m]$	overlap between particle and material surface
η_n	$[-]$	normal restitution coefficient
μ	$[-]$	Coulomb friction coefficient
ρ_w	$[kgm^{-3}]$	the densitiy of wall lining material
ρ_p	$[kgm^{-3}]$	particle material density
ξ	$[-]$	damping coefficient
$C()$	$[-]$	erosion particle diameter function
$f()$	$[-]$	erosion impact angel function

Subscripts and Superscripts

1n	impact normal
n	surface normal direction

1. INTRODUCTION

The erosion behaviour of materials is studied from many aspects over the past decades. In spite of the tremendous effort to understand the details of the erosion mechanisms and quantitatively predict the amount of removed material, one can find that the literature does not present a universal, quantitative model for describing the erosion/abrasion process in real life conditions [1]. This is especially true for rubber lining materials for pipes. The erosion process of pipes is affected by parameters of the contact materials as well as the parameters of the particle impacts [2], [3]. In case of a dredge hose the time needed to have an observable amount of erosion can be months [4]. This leads to an experimental challenge for separating and measuring the importance of the different erosion parameters. In addition the laboratory measurements often cannot reproduce accurately the erosion conditions in the real life application [5]. It is also difficult to use pure simulation driven technique to predict the erosion behaviour of materials.

A key concept for successful simulations of erosion of pipelines is a macroscopic erosion model characterising individual particle effects[1, 6, 7]. The investigations in the literature agree [8, 3] that there is a distinction between the type of material removal and erosion when the particles are hitting the surface from normal or from an oblique angle. Considering pipe flows it is clear that oblique angles are dominant [5]. Possibly one of the first erosion model used at oblique angles was derived by Finnie [9]. The important parameters of such a single impact particle erosion model are the particle diameter, velocity magnitude, impact angle and mass flow rate of the particles. The model does not give insight how the material erosion parameters are related to the mechanical material strength parameters.

The erosion parameters of this type of model are valid for one surface material particle shape pairs, although for a certain extent the shape factor of the particles can be taken into account [1].

In the present work based on a coupled Computational Fluid Dynamics (CFD) and particle simulation (DPM) technique we show the importance of the low angle particle impacts in the pipe flow.

The parameters related to the material are usually determined from experimental data. An overview of the different laboratory testing methods and models can be found in [2, 5, 10]. The time needed for laboratory parameter measurement has to be shortened in order to be able to investigate the effect of the parameters and different materials. This is hard to achieve without changing the erosion conditions and leads to an inaccuracy in model parameters derived from the tests. Such a speed-up can be achieved by increasing the velocity of the particles, assuming that the velocity exponent of the model is not strongly velocity dependent, which is often not the case [5]. Another method is to increase the concentration of particles. In this paper we introduce an experimental-numerical hybrid testing methodology in order to determine the erosion parameters of the sample material. In order to decrease the time of the measurement dense slurry was used in the test bed and in the corresponding simulation. We propose an equivalence model, which is based on the invariance of momentum transfer, contact time and impact angle. Using this equivalence model the calculated collision statistics can be fitted to the measured erosion rates using a single particle erosion model. The model is applied to a pipe bend in a slurry transport pipe.

2. EROSION MODELLING

The two basics goals of erosion modelling of slurry pipes are:

a.) Determination of pipe life. Only wear type of failure mechanism is investigated, sudden failures are not accounted for.

b.) The increase of erosion resistance of the transport pipe. This includes the development of simplified testing methods for lining materials supporting the development of erosion resistant compounds as well as the construction for more erosion resistant pipe routing.

As it is suggested in the introduction the experimental or the numerical simulation procedures alone are hardly appropriate to achieve these goals. In this paper the erosion model for the lining material written in a general form as follows [11]:

$$R_{\mathrm{er}} = \sum_{p=1}^{N_{\mathrm{p}}} \frac{\dot{m}_p C(d_p) f(\alpha_p)(v_p/v_0)^{b(v_p)}}{A_{\mathrm{f}}\rho_w} \tag{1}$$

The erosion rate R_{er} depends on the flow rate of the particles hitting the wall $\dot{m}_p$, on the particle diameter function $C(d_p)$, on the impact velocity angle $f(\alpha_p)$ and on the velocity function $v_p^{b(v_p)}$. Generally the exponent of the velocity dependence function $b(v_p)$ can be also dependent on the velocity. The reference velocity $v_0 = 1$ is for providing dimensional homogeneity. The model predicts the average erosion rate of the A_f surface of the wall having a density of ρ_w. If the impact parameters d_p, α_p, v_p are computed with a particle simulation, along with the pipe flow computation and the model functions ($C(d_p)$, $f(_p)$ $b(v_p)$) are known then the fluid mechanics model can predict the erosion rate of the pipe geometry. This model then used to calculate the pipe lifetime, and can be used to identify critical point of the design for further refinements. The model does not contain all parameters affecting the erosion therefore the conditions in which the model functions are determined should be similar to the real case. The erosion parameters are determined for a given surface-abrasion material pair.

3. DREDGE HOSE SIMULATION

In order to investigate the erosion rate of the dredge hose a Discrete Phase Model (DPM) is used with a coupled CFD simulation. In a DPM particle model it is assumed that the particles are forming a dilute phase and not affecting each other significantly; therefore interaction between the particles are not accounted for. When the particles are impacting the wall they remove material according to Eq. (1), however the geometry of the pipe is not deformed as the result of the erosion. The restitution coefficient in the wall normal direction is prescribed as a typical value for the lining material $\eta_n = 0.3$ and considered independent of the impact angle and the velocity. The restitution coefficient in the tangential direction depends on the impact angle of the particle and it is prescribed according to [12] (Fig. 7), using a curve fit for the different materials. The experience shows that a critical element of a hose system can be a 90° bend with minimum bending radius (10D) in the vertical plane and flow direction up to down. This is chosen for the simulation. The geometry and the CFD mesh is illustrated in Fig. 1. The diameter of the hose $D = 0.254$ *m*. The model contains about 220000 cell volumes. The k-ϵ turbulence model is used. The outlet boundary condition was a pressure boundary condition. The simulation is performed by the commercial CFD software ANSYS Fluent 15.0.

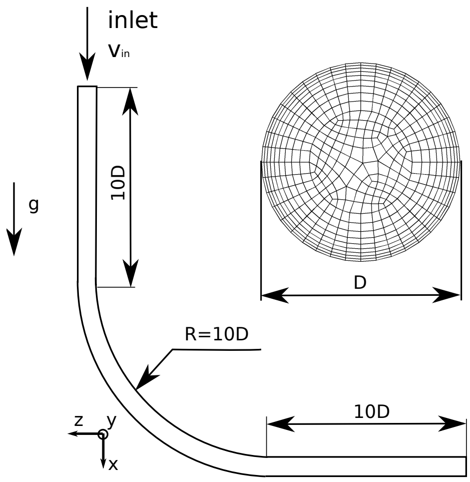

Figure 1. Hose bend simulation geometry and mesh

3.1. Inlet boundary condition

The inlet volume flow rate, particle concentration and distribution is representing an industrial case. At the inlet uniform velocity profile with $v_{in} = 4.73\ ms^{-1}$ is prescribed with turbulent intensity of 5% and hydraulic diameter of 0.2 *m*. The volume fraction of the particles at the inlet is 12 $\%v/v$ leading to a particle mass flow rate of $\dot{M}_p = 94.9\ kgs^{-1}$ with average particle density of 3300 kgm^{-3}. The inlet distribution of the particle size can be approximated by a Rosin-Rammler distribution.

$$Y_d = e^{-\left(d_p/\bar{d}\right)^n} \qquad (2)$$

where Y_d is the particle mass fraction, which is the total mass of the particles having a diameter greater than d_p. The parameters of the model are the average particle diameter $\bar{d}$ and the spread parameter n. The particle distribution with the known points and fitted Rosin-Rammler distribution is depicted in Fig. 1.

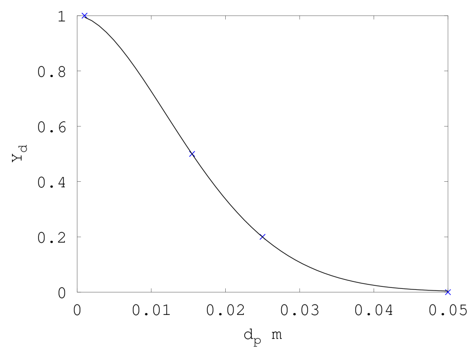

Figure 2. Particle distribution according to Rosin-Rammler model fitted on the known distribution points

The model parameters are well approximated by $d_p = 0.019$ *m* and $n = 1.765$. The distribution is modelled by 10 different particle size bins split evenly between particle diameters of 1 and 50 *mm*.

3.2. Time averaged impact parameters of particles

The number of surface strikes during the simulation can be seen in Fig. 3. There are small number of impacts in the vertical part of the tube. The impact count is gradually increasing along the bottom of the pipe bend and it reaches its maximum at about 60° of bend angle measured from the horizontal z axis. Then it is slightly decreasing. The other two distinct parts at the bottom of the pipe where impact number is high possibly caused by the bouncing of particles at the bottom of the pipe. The time averaged impact particle diameter can be seen in Fig. 4. The average diameter of the particles where the most of the particle impacts occur is higher than about 20 *mm*. It can be also seen that the largest average diameter can be found at the bottom of the horizontal pipe. The contour plot of the time average impact angle can be seen in Fig. 5. The vertical part of the tube shows uneven distribution of the particle impact angel which is party because of the developing flow region close to the inlet boundary. It possibly also show signs of not perfect statistics convergence. The regions where erosion could be prominent is where the impact number is high and the impacting particles have large diameter. However in this region the average impact angle is very small, typically below 3°. This is an important observation because it implies high sensitivity of the erosion behaviour on the impact angle function of the erosion model.

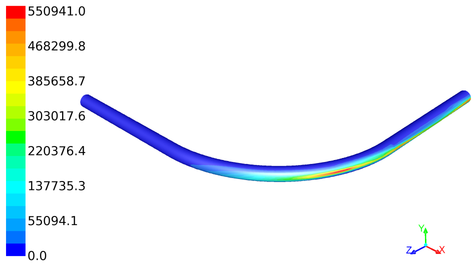

Figure 3. The number of surface particle impacts during the averaging of impact statistics.

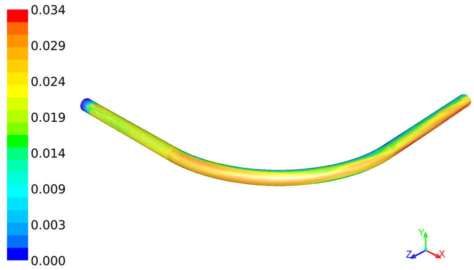

Figure 4. Contour plot of the time averaged diameter of the particle impacted the pipe wall. Unit: [m].

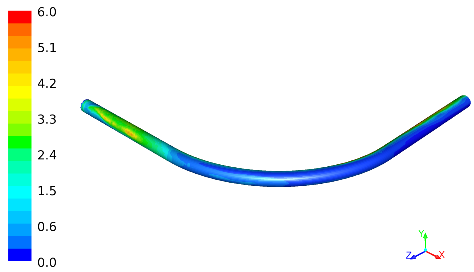

Figure 5. Contour plot of the time averaged impact angle of the particles on the pipe wall. Unit: [°].

4. EROSION MODEL SENSITIVITY TO THE ANGEL FUNCTION

In order to investigate the expected erosion pattern on the pipe surface the erosion model is parametrized based on a finally fitted model (See Sec. 5.2). The diameter function based on the literature [3] has been chosen to be a linear function with a constant coefficient $C(d_p) \equiv c$. Since the velocity is not changing significantly the velocity exponent also considered to be constant $b(v_p) \equiv b$. The most complex and most sensitive part of the erosion model is the angle function. For the angle function a convex function is chosen in the range of shallow angles. This is decided based on the theory presented in the work of [3]. In the present study an inverse gamma distribution is used, because it qualitatively better fits the higher angle data than the function proposed by [3]. The parameters of this inverse gamma function is determined according to final test results. In order to investigate the sensitivity of the erosion pattern below impact angle of 3° a linear approximation of this function is applied in the range of low angles. This linear function in combination with the normalized inverse gamma function can be described as follows:

$$f(\alpha_p) = \begin{cases} \dfrac{\alpha_{\mathrm{conn}}^{g_2} \mathrm{e}^{-\frac{p_1}{\alpha_{\mathrm{conn}}}} - p_3 g_1^{g_2} \mathrm{e}^{g_2}}{g_1^{g_2} \mathrm{e}^{g_2} \alpha_{\mathrm{conn}}} \alpha + p_3 & \text{if } \alpha \le \alpha_{\mathrm{conn}} \\ \alpha^{g_2} \mathrm{e}^{-\frac{p_1}{\alpha}} & \text{if } \alpha > \alpha_{\mathrm{conn}} \end{cases} \tag{3}$$

where $g_1 = \frac{p_1}{p_1+1}$ and $g_2 = -p_2 - 1$, the parameters of the angle function is p_1, p_2, p_3, α_{conn}. The sensitivity of the angle function is performed by changing the value of α_{conn} while keeping all other parameters of the erosion model unchanged. The fixed parameters of the erosion function was: $c = 1.71e-8$, $b = 1.63$, $p_1 = 3.19$, $p_2 = 1.49$, $p_3 = 0$, based on final results Sec. 5.2. The angle function α_{conn} is varied as $15°, 9°, 7°, 5°$. The corresponding maximum erosion rates was 120, 40, 13 and 10 $mm/year$ showing that it is indeed very important to measure the erosion angle function accurately at the low impact angle range. The result showed that not only the maximum rate of the erosion but also the erosion pattern qualitatively changed in the simulations.

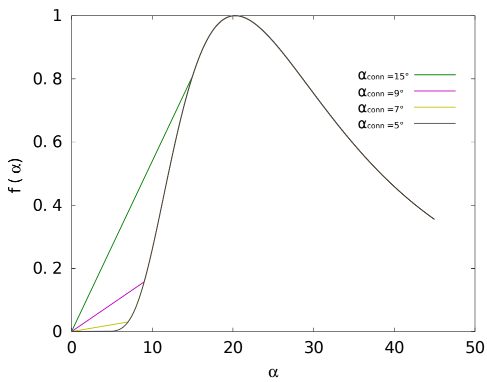

Figure 6. Angle function with $\alpha_{\mathrm{conn}} = 15°, 9°, 7°, 5°$ parameter values for erosion sensitivity test with DPM pipe model.

4.1. *Measurement methodology of the erosion angle function*

The erosion angle function is measured by several authors in the literature [5, 8]. The measurement requires the knowledge of particle impact angle and the erosion rate while keeping all other erosion parameters constant such as particle diameter, particle mass flux, particle impact velocity. The typical erosion measurement device where such a parameter isolation can be done are the sand blasting testing types or the centripetal accelerator or slurry pot tester. The sand blasting method is working with relatively high velocities in the range of about 20 to 100 m/s. The centripetal accelerator and slurry pot tester can be used at smaller velocity. By checking the literature for example: [5, 8] one can observe that there is no measurement data at low angles below about 5°-10°. The reason for the missing data is possibly that the impact angle is derived from the configuration of the measurement apparatus and it is not measured directly at the impact surface, therefore the uncertainty of the angle can be high. The usual methods are not appropriate to perform measurements at low angles. It is also assumed that it is not feasible to build a test rig where the impact parameters of the individual particles such as velocity, impact angle particle size, impact position can be sampled locally at the surface without affecting the flow. Therefore in the following section a new hybrid methodology is suggested.

5. PROPOSAL FOR NEW MEASUREMENT METHODOLOGY

In order to obtain low impact angle data for the erosion model, it is proposed to use a methodology where the particle impact parameters are obtained with a detailed numerical simulation of the measurement device, therefore the impact angle at the material surface can be registered as well as the other impact parameters. The requirements of such a measurement technique is summarized as follows:

i.) Erosion conditions similar to the hydraulic transport pipes.

ii.) The laboratory method must speed up the erosion process found in a real pipe.

iii.) Numerical simulation of the test should be feasible and economically viable.

iv.) The methodology should provide accurate enough data for the erosion model.

Requirement i.) implies, that the impact angle, impact velocity, type of contact materials transporting fluid is similar in the model and in the real case. The second requirement can be satisfied by increasing the erosion rate by increasing the number of impacts per unit area of the sample surface. Due to the increased stream of particles the description of their interaction becomes of a prime interest in parametrizing contacts. Because the erosion model Eq. 1 assumes individual particle impact the impact parameters of the simulation has to be transformed into individual contact parameters. Such an equivalence model is discussed in Sec. 5.1 The iii.) requirement can be satisfied if the test bench contains relatively low number of particles and the flow Reynolds number kept as small as possible. The accuracy (iv.)) can be provided by careful and repeated measurements and simulation where sensitivity analysis in terms of uncertain input variables is done.

Based on these requirements the proposed measurement configuration is a slurry pot type erosion tester similar to the one found in [8]. In this erosion tester the samples are attached to a rotating arm and immersed in a dense multiphase abrasive fluid. The sketch of the top view of the erosion tester is depicted in Fig. 7. In the presented case the two samples are rotated with tangential velocity of $v_s = 0.69\ ms^{-1}$. The drag force on the samples can be derived from the torque measured on the pot.

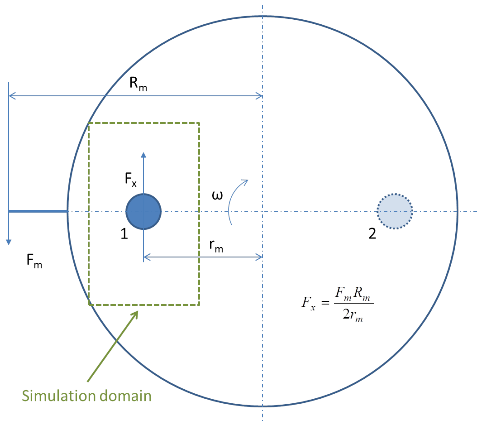

Figure 7. Sketch of the erosion tester (top view, the figure is not drawn to scale).

For our investigations the erosion tester was build without the bottom impeller [8] and the samples are prepared as cylindrical pieces $D_s = 23\ mm$ in diameter and their height are 100 mm. The base of the domain where the DEM simulation is performed also illustrated in Fig. 7. The simulation domain does not account for the curved flow because of the limitations of the modelling technique (momentum source terms for the particles are not prescribed in the model). The boundary conditions and flow conditions are defined for a coupled CFD-DEM (Discrete Element Method) simulation technique in ANSYS Fluent. The three dimensional computational domain and boundary conditions are depicted in Fig. 8. Every time step one sheet of DEM particles are enter the domain with zero slip velocity. The other boundary conditions are defined to mimic the conditions in the slurry pot. The water air phase surface is not modelled in the simulation, the simulation domain was filled with water completely

In this setup the required computational resources can be controlled by the particle loading of the fluid which is also measurement parameter. The DEM simulation uses spherical particle model while in our measurement setup the used abrasive particles were 2mm corundum particles with irregular shape.

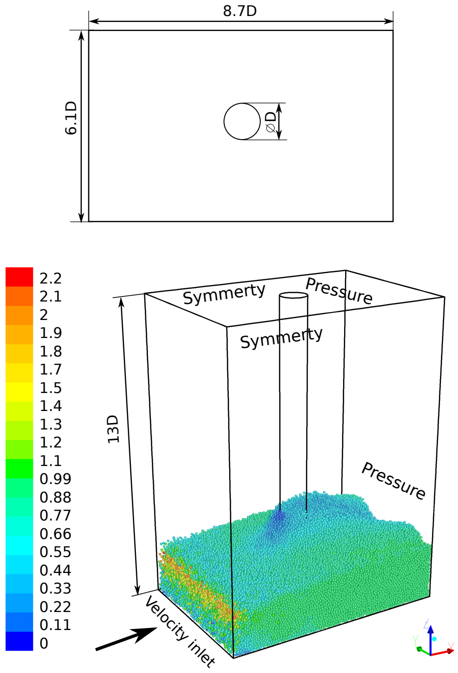

Figure 8. The DEM simulation model of the erosion tester. Particle velocity is shown in contour plot.

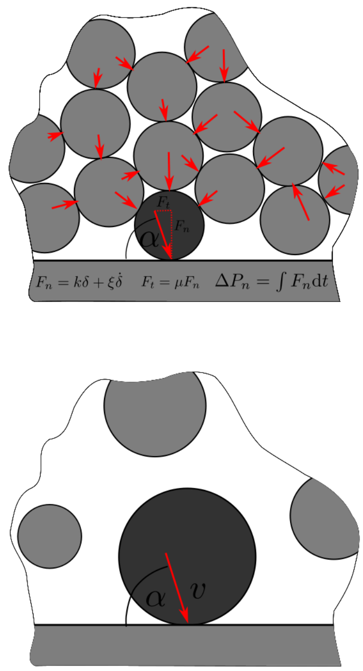

Figure 9. The dense multiphase particles with the illustration of contact chain (above), the dilute multiphase particles used in the erosion model (below)

For this reason the particle diameter and density in the DEM model has to be determined based on mass flux, impact number (particle volume) equivalence. Without the detailed derivation of this equivalence it has been found that the simulation has to be performed with particles having a diameter of 2.3 mm and density of 3133 kgm^{-3} which is about 20% less than the density of corundum. The impact model between the particles in the normal contact direction is a spring-dashpot model with spring constant of 8000 Nm^{-1} and restitution coefficient of 0.5. In the tangential direction a Coulomb friction model is used. Based on the matching of drag force of the sample piece in the measurement and in the simulation, we found that the friction coefficient between the spherical particles has to be 0.15.

The measurement can provide the erosion profile at different slurry depths along the sample surface. The DEM simulation provides the impact behaviour of the particles in dense slurry. However, the erosion model Eq. 1 assumes individual particle impact on the material surface. Therefore a calculation methodology to obtain particle impact parameters for the erosion model must be established in order to be able to fit the erosion model to the measured erosion rate data.

5.1. The impact equivalence model

The typical contact behaviour of the dense multiphase flow present in the erosion tester is a multibody contact. This contact behaviour leads to a contact chain between particles and test piece. This is illustrated in Fig. 9.

Due to this contact chain the momentum difference of the contacting particle between the time of surface impact and release does not represents the energy transferred to the material surface. The momentum change has to be computed by the integral of the contact force over the time of contact. This is the impulse given to the surface by the particles. Using the impulse and contact model an equivalent case for the dilute particle flow can be defined where only one particle impact is resulting in the same energy transfer. In this way the dilute phase erosion model can be parametrized by utilizing the dense phase DEM simulation and measurement.

The mathematical description for such an equivalence can be formulated as follows. The wall contact model of the DEM simulation is a spring dashpot model in the normal direction having two parameters: the spring constant k, and the damping coefficient ξ. In the tangential direction the Coulomb friction model is used with friction coefficient μ. The normal and tangential forces can be computed as follows:

$$F_n = k\delta + \xi\dot{\delta} \tag{4}$$

$$F_t = \mu F_n \tag{5}$$

The damping coefficient can be computed form the measured restitution coefficient of the material:

$$\xi = \frac{-2\sqrt{m_p k}\ln \eta_n}{\sqrt{\pi^2 + \ln^2 \eta_n}} \tag{6}$$

By solving the well known differential equation for the damped oscillator the contact time can be expressed for the spring dashpot model:

$$t_c = \sqrt{\frac{m_p}{k}\left(\pi^2 + \ln^2 \eta_n\right)} \tag{7}$$

Assuming spherical particles with density ρ_p the dilute flow equivalent particle diameter can be expressed as follows:

$$d_p = \sqrt[3]{\frac{3kt_c^2}{4\pi\rho_p\left(\pi^2 + \ln^2 \eta_n\right)}} \tag{8}$$

The contact time is obtained from the DEM simulation for each particle wall impact. The particle wall contact spring constant k, and normal restitution coefficient η_n obtained from testing the sample material. It is possible to use realistic k values for the particle rubber surface contact. (For the particle-particle contact the k values are decreased due to numerical reasons [5])

The dilute phase erosion model requires also the impact velocity vector. The surface normal component of the impact velocity can be computed from the impulse change of the contact particle in the normal direction which is computed by the DEM simulation.

$$v_{\mathbf{1n}} = \frac{3\Delta P_{\mathbf{n}}}{4\pi\rho_p d_p^3 (1 + \eta_n)} \tag{9}$$

The tangential component of the velocity cannot be determined from the tangential impulse change because the Coulomb contact model the tangential impulse change is independent of the tangential velocity (the friction coefficient is assumed to be independent of the velocity) Instead of the tangential velocity we determine the impact angle from the assumption that the impact angle depends on the flow around the test piece. In steady state flow there is a typical impact angle at a given surface position. (The flow has very small RMS fluctuations close to the front stagnation point of the test piece.) A good approximation of the impact angle is therefore extracted from the DEM simulation by averaging the angle of the velocity vector of the particles at impact. This impact angle is considered as the same in case of the dense and dilute multiphase flow. Using the impact angle the magnitude of the velocity vector for the dilute flow can be computed.

5.2. Results from the DEM simulation

The simulation result using the equivalence model is shown in the form of contour plots in Figs. 10. The larger equivalent particle diameters can be found at the highest sludge depth. This means that the contact time of the particles with the wall is higher when their concentration is higher and moving slowly close to a stagnation line at the sample surface. The impact angle values above the highest impact angle of about 71° are clipped because no impact situations are depicted as 90° on the contour plot. Most of the sample surface is strike by particles at angle below 30°. Low impact angle contact is typical at the side of the sample.

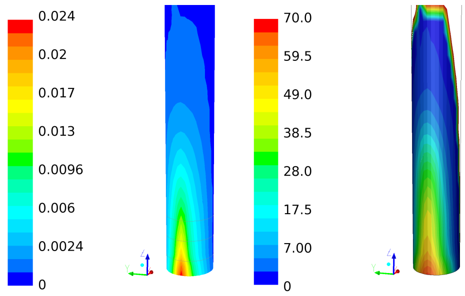

Figure 10. The equivalent particle diameter d_e (left) and impact angle α (right)

The equivalent normal contact velocity is depicted in Fig. 11 left. The highest equivalent contact velocities found around the bottom of the sample, which is possible because the equivalent velocity measures not the individual particles velocity (which is relatively small at the bottom of the pot), but the combined effect of the particles in chain contact.

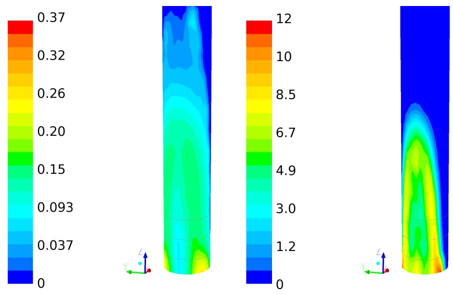

Figure 11. The equivalent impact normal velocity v_{1n} (left) and the predicted erosion rate using material parameters based on [3] (right)

In order to visualise the typical erosion pattern on the sample the erosion model parameters are obtained from by a parameter fit with the inverse gamma angle function (the parameters $p_3 = 0$, $\alpha_{conn} = 0°$ is kept fixed during the fit.) The results of the simultaneous parameter fit of the erosion profiles with the measurement gave $c = 1.71 \times 10^{-8}$, $b = 1.63$, $p_1 = 3.19$, $p_2 = 1.48$. The material of the rubber sample is the same as in [4].

The erosion pattern on the front of the test sample can be seen in Fig. 10 right. The highest erosion rate found not at the movement direction (x direction) but sideways and at greater sludge depth.

The figure also shows 3 profile position where the measurement data is obtained and fitted with the equivalent model in order to determine the parameters of the material.

The erosion pattern in the dredge hose bend is depicted in Fig. 12 The highest erosion rate is about 10 $mm/year$.

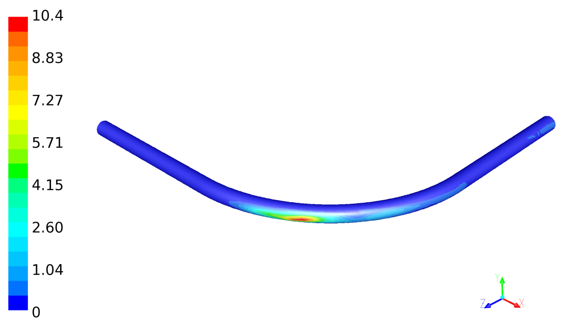

Figure 12. Contour plot of the erosion pattern with the fitted erosion model. The erosion values are in [mm/year].

6. CONCLUSIONS

In this paper we presented an analysis of the erosion process of pipe bends focusing on the requirements of particle impact angle modelling. The numerical simulation of a pipe bend with 12 % v/v of particle concentration shows that the typical impact angle of particles in a pipe bend in the area of critical erosion pattern is less than a few degrees. The investigation with a general formulation of an erosion model showed that the predicted maximal value as well as the pattern of the erosion is strongly depends on the slope of the erosion angle function. The literature shows that usual erosion testing methods like the sand blast or centripetal erosion tester do not provide accurate erosion data at erosion angles important for the pipe bend. To overcome this deficiency a hybrid testing methodology is proposed where the parameters of the erosion model is determined by the parameter fitting of the measured erosion rate and the erosion model where impact parameters are obtained by a CFD-DEM simulation. We proposed a methodology for computing the impact parameters for the individual particle erosion from the dense multiphase flow simulation based on the particle contact time, impulse change and average impact angle close to the surface.

ACKNOWLEDGEMENTS

The authors would like to thank ContiTech Rubber Industrial Kft. for the research initiative and financial support of the project as well as the support for the publication of the results. This work was supported by New Széchenyi Plan (GOP-1.1.1-11-2011-0062).

REFERENCES

[1] Chen, X., McLaury, B. S., and Shirazi, S. A., 2004, "Application and experimental validation of a computational fluid dynamics (CFD)-based erosion prediction model in elbows and plugged tees", *Computers & Fluids*, Vol. 33 (10), pp. 1251 – 1272.

[2] Lyczkowski, R. W., and Bouillard, J. X., 2002, "State-of-the-art review of erosion modeling in fluid/solids systems", *Progress in Energy and Combustion Science*, Vol. 28 (6), pp. 543 – 602.

[3] Arnold, J. C., and Hutchings, I. M., 1992, "A model for the erosive wear of rubber at oblique impact angles", *Journal of Physics D: Applied Physics*, Vol. 25 (1A), p. A222.

[4] Katona, T., and Nagy, T., 2014, "Full Scale Wear Test with Different Hose Liners", *Kautschuk Gummi Kunststoffe*, Vol. 1, pp. 22–26.

[5] Burnett, A. J., 1996, "The use of laboratory erosion tests for the prediction of wear in pneumatic conveyor bends", Ph.D. thesis, University of Greenwich, uk.bl.ethos.320600.

[6] Tan, Y., Zhang, H., Yang, D., Jiang, S., Song, J., and Sheng, Y., 2012, "Numerical simulation of concrete pumping process and investigation of wear mechanism of the piping wall", *Tribology International*, Vol. 46 (1), pp. 137 – 144, 37th Leeds-Lyon Symposium on Tribology Special issue: Tribology for Sustainability: Economic, Environmental, and Quality of Life.

[7] Varga, M., Goniva, C., Adam, K., and Badisch, E., 2013, "Combined experimental and numerical approach for wear prediction in feed pipes", *Tribology International*, Vol. 65, pp. 200 – 206.

[8] Desale, G. R., Gandhi, B. K., and Jain, S. C., 2011, "Development of Correlations for Predicting the Slurry Erosion of Ductile Materials", *Journal of Tribology*, Vol. 133 (3), pp. 031603–1 – 031603–10.

[9] Finnie, I., 1960, "Erosion of surfaces by solid particles", *Wear*, Vol. 3 (2), pp. 87 – 103.

[10] Spero, C., Hargreaves, D., Kirkcaldie, R., and Flitt, H., 1991, "Review of test methods for abrasive wear in ore grinding", *Wear*, Vol. 146 (2), pp. 389 – 408.

[11] SAS IP, Inc, *ANSYS Fluent 15.0 Theory Guide*, ANSYS Inc.

[12] Mueller, P., Antonyuk, S., Stasiak, M., Tomas, J., and Heinrich, S., 2011, "The normal and oblique impact of three types of wet granules", *Granular Matter*, Vol. 13 (4), pp. 455–463.

Conference on Modelling Fluid Flow (CMFF'15)
The 16th International Conference on Fluid Flow Technologies
Budapest, Hungary, September 1-4, 2015

SOME ASPECTS OF DISINTEGRATION OF ANNULAR LIQUID SHEET IN PRESSURE-SWIRL ATOMIZATION

Jan JEDELSKÝ[1], Milan MALÝ[2], Martin HOLUB[2], Miroslav JÍCHA[2]

[1] Corresponding Author. Faculty of Mechanical Engineering, Brno University of Technology. Technická 2896/2, Brno 61669, Czech Republic. Tel.: +420 541143266, Fax: +420 541143365, E-mail: jedelsky@fme.vutbr.cz
[2] Faculty of Mechanical Engineering, Brno University of Technology. E-mail: milanmaly@email.com, mholub@centrum.cz, jicha@fme.vutbr.cz

ABSTRACT

In pressure-swirl (PS) atomization, the internal flow structure and the formation of a liquid film are closely linked to the quality of the resulting spray. The flow, as a subject to several disturbing sources, contain unsteadiness that can harm the atomization. In this paper, imaging is used to study discharge, near nozzle flow and primary breakup for small PS atomizer. The atomizer performance is characterised in terms of discharge coefficient, liquid sheet thickness, breakup distance, and nozzle efficiency. The breakup length according to near nozzle visualization and sheet breakup analysis was found much smaller than the length predicted using the inviscid model and both external and internal sources were identified as possible reasons. External flow instability sources were found by means of pressure fluctuation sensing upstream the nozzle. Phase-Doppler anemometry was used to document the mean structure of the developed spray and to characterise spray fluctuations. The findings are used to propose possible changes in the atomizer design for improvement of its performance.

Keywords: flow unsteadiness, liquid sheet, pressure-swirl atomizer, primary breakup

NOMENCLATURE

A	$[mm^2]$	area
C_D	[-]	discharge coefficient
D_{32}	$[\mu m]$	Sauter mean diameter
ID_{32}	$[\mu m]$	overall Sauter mean diameter
L	$[mm]$	length
R	$[mm]$	radial distance
Re_W	[-]	Reynolds number acc. Walzel
SCA	$[deg]$	spray cone angle
We	[-]	Weber number
X	[-]	air core area to final orifice area ratio
Z	$[mm]$	axial distance
b	$[mm]$	width
d	$[mm]$	diameter
f	$[Hz]$	frequency
h	$[mm]$	height
$\dot{m}$	$[kg/h]$	mass flow rate
r	[-]	relative radial distance
t	$[\mu m]$	thickness
w	$[m/s]$	velocity
Δp	$[MPa]$	pressure drop at the nozzle
μ	$[kg/(m{\cdot}s)]$	dynamic viscosity
η_a	[-]	atomization efficiency
η_n	[-]	nozzle efficiency
ρ	$[kg/m^3]$	density
σ	$[kg/s^2]$	liquid/gas surface tension

Subscripts and Superscripts

b	in the breakup distance
c	critical
g	gas (air)
l	atomized liquid
o	exit orifice
p	swirl ports
s	swirl chamber

1. INTRODUCTION

Pressure-swirl (PS) atomizers are abound type of spraying devices in industrial, domestic, agricultural and other applications. For decades, attention has been paid to improve their atomization characteristics with a number of parametric studies for the optimization of their design [1-4] and others. Any improvement in the spraying performance results in significant economic savings due to an increase of an atomization efficacy and consequent processes. To obtain such improvements deep insight into the processes accompanying the atomization process is required.

PS atomizers convert the pressure energy of pumped liquid into internal swirl motion under which the liquid leaves the discharge orifice and spreads as a conical liquid film outside the nozzle.

The film breaks up due to aerodynamic forces between the liquid and stagnant surrounding air. There is a strong link between the internal flow, discharge, formation of the liquid film and parameters of the resulting spray [5]. The flow, as a subject to several disturbing sources, shows unsteadiness that can harm the atomization process.

Donjat et al. [6] observed oscillations on the air core/liquid interface as the main evidence of the unsteady character of the internal flow structure of a pressure swirl atomizer. Kim et al. [7] with a high-speed camera examined the variations and stability of the air core in the swirl chamber and by accurate measurement detected the fluctuations of the external liquid film thickness. Their study confirms that air core shape and liquid film thickness are directly related. Marchione et al. [8] analyzed the fluctuating behavior of the spray with a fast imaging technique. They found two oscillation modes, around 100 and 1800 Hz, which negatively affect the flame stability and the resulting combustion efficiency. Lavante and Maatje [9] observed highly three−dimensional character of the internal flow using numerical simulations. They confirmed two phenomena (spiraling disturbances on the air core surface and periodical contractions/expansions of its elliptical cross-section) observed previously experimentally by Cooper and Yule [10].

In this paper, we focus on a PS atomizer used to deliver sprayed fuel into the combustion chamber of turbojet aircraft engines, where fine droplets and stable spray are crucial requirements. We inspect the originally designed nozzle using advanced measurement techniques in combination with available data with aim to find its weak points for potential improvements and propose/discuss possible design changes (keeping the concept of PS nozzle) to improve its performance. The work is based on a study of primary breakup, liquid sheet stability, breakup distance, and nozzle efficiency. The structure of developed spray is detailed using Phase-Doppler anemometry.

2. EXPERIMENTAL SETUP

Experiments were performed at a specially designed facility for spray generation under controlled conditions in the Spray laboratory at the Brno University of Technology. The experimental apparatus includes an atomizer under test, cold test bench with fluid supply system, phase-Doppler analyzer (PDA), digital camera and equipment for pressure fluctuation sensing in front of the atomizer.

2.1 Cold test bench

A schematic layout of the test bench is shown in Figure 1. It consists of a gear feed pump (3) that supplies fuel from a main tank (1) through filters (2), flow meter (4) and control valve (7) into the atomizer (8). The spray falls into a collector and then it is returned to the main supply tank. The flow rate is regulated by a bypass needle valve (9).

Flow rate in fuel line is metered by Siemens Mass 2100 Di3 Coriolis mass flow meter fitted with a Mass 6000 transmitter. Flow rate uncertainty is 0.2% of its actual value. The feeding line is also equipped with pressure (5) and temperature readings (6). Uncertainty of pressure sensor (BD Senzor DMP 331i) is 0.35% of actual value. Error of temperature sensor Omega PR-13 is 0.2 °C.

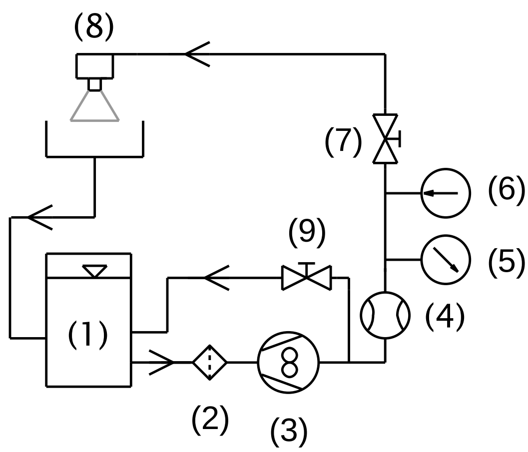

Figure 1. Liquid circuit with control and measuring items

2.2 Atomizer description

Small PS atomizer developed for an aircraft engine was investigated on a cold test bench. Its internal dimensions correspond to Figure 2. The nozzle was placed on a body and gripped to 3D computer controlled support. Alignment accuracy is 0.2 mm against PDA zero point.

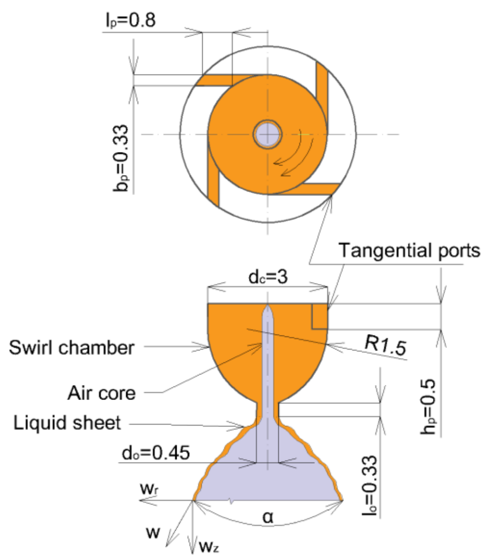

Figure 2. Atomizer; top section (above) and side section (bottom)

Kerosene jet A-1 was used as testing liquid. Physical properties of jet A-1 at room temperature are: $\sigma = 0.029$ kg/s^2, $\mu_l = 0.0016$ kg/(m·s), $\rho_l = 795$ kg/m^3. All tests were done with one batch at 20 °C.

Operation regimes of the atomizer were controlled by setting the inlet pressure to three values: $\Delta p = 0.5$, 1 and 1.5 MPa.

2.3 Phase-Doppler analyzer

Characteristics of the sprayed droplets (time-resolved droplet size and velocity) were probed using two-component Fiber PDA Dantec dynamics. Basic system parameters are given in Table 1 and its configuration with coordinate system is shown in Figure 3.

PDA measurements were made in six radial sections of the spray at axial distances of $Z = 2.5$, 5, 12.5, 25, 37.5 and 50 mm from nozzle exit orifice. Two perpendicular axes with 25 positions each were measured. In every position, 100,000 samples or 60 seconds were taken.

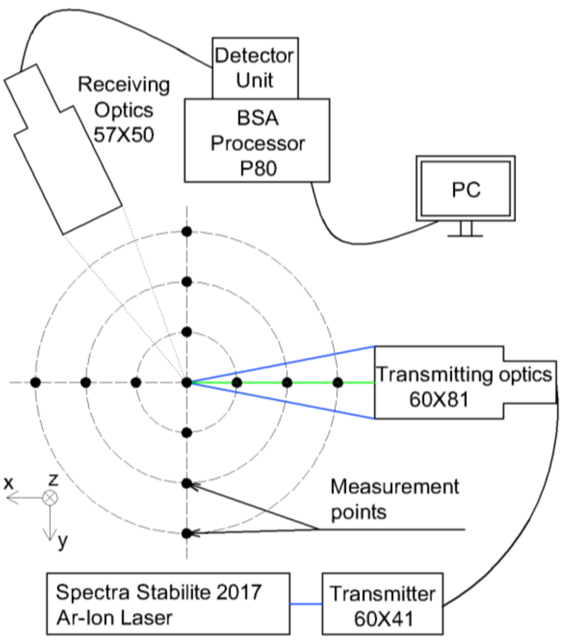

Figure 3. Arrangement of the PDA measurement

2.4 Setup for photographic documentation

Detailed spray image was taken using camera Canon EOS D300 with Canon EF 100 mm f/2.8 UMS Macro lens. The spray was illuminated from the side by Nd:YAG NewWave Research Gemini laser with a pulse duration of 5 ns and energy of pulse of 50 mJ.

2.5 Pressure fluctuation measurement

Time-resolved measurement of pressure fluctuations in the atomizer feeding line was taken using piezoelectric sensor Kistler 601A connected to Kistler 5015A charge meter. The signal was recorded into NI LabVIEW 2013 software at a sampling rate of 2 kHz. The piezoelectric sensor was mounted in the fuel supply line close to the nozzle inlet.

Table 1. Main parameters of the PDA setup

Parameter	Value	
Laser power output	1 W	
Wavelength	488 nm and 514.5 nm	
Front focal length of transmitting optics	310 mm	
Front focal length of receiving optics	500 mm	
Scattering angle	70°	
Mask	B	
Spatial filter	0.200 mm	
Velocity	Axial	Radial, Tangential
Velocity center	8 m/s	0 m/s
Velocity span	32 m/s	30 m/s
Sensitivity	800 V	1000 V
SNR	0	3
Signal gain	20 dB	20 dB
Level validation ratio	8	2

3. RESULTS AND DISCUSSION

The first part focuses to near nozzle flow and the second one deals with the developed spray.

3.1. Discharge, sheet formation, and primary breakup

The character of the internal flow strongly influences the spray. The atomizer is too small for internal flow visualizations, so the character of the flow inside the swirl chamber was estimated using external findings.

3.1.1. Internal flow and discharge

The internal flow during our experiments covered a range of Walzel Reynolds number $\mathrm{Re}_W = \sqrt{2\rho_l \Delta p}\, d_o / \mu_l = 7930 - 13735$ (see Table 3) which exceeds the critical value for turbulent transition $\mathrm{Re}_{Wc} = 5000$ proposed by Walzel [11] and suggests the flow to be fully turbulent.

Table 2. Basic characteristics of the flow

Δp	$\dot{m}_l$	C_D	η_n	Z_b	t_0
MPa	kg/h	–	–	mm	μm
0.5	5.4	0.334	41	4.1	59
1.0	7.3	0.320	34	3.6	62
1.5	9.0	0.322	34	3.0	63

The discharge coefficient of the flow through the exit orifice, C_D, is roughly independent of the pressure drop (see Table 2) and in relatively good agreement with prediction of Rizk and Lefebvre [12]:

$$C_D = 0.35\left(\frac{A_p}{d_s d_o}\right)^{0,5}\left(\frac{d_s}{d_o}\right)^{0,25} \tag{1}$$

which gives $C_D = 0.39$. The pressure range allows the nozzle to operate in the region of sheet formation, where the discharged liquid forms a conical sheet (see Figure 4); its thickness at the nozzle orifice is, as common for low viscosity liquids, almost constant over the pressure range studied as well: t_0 = 59–63 µm (Table 2). It roughly fits to the prediction of Giffen and Muraszew [13] for nonviscous fluids (73 µm) and to Lefebvre and Suyari [14]:

$$0.735 C_D^2 = \frac{(1-X)^3}{1+X} \tag{2}$$

where the ratio of the area of the air core to the area of the final discharge orifice $X = (d_o - 2t_o)^2 / d_o^2$. Eq. (2) results into t_0 = 74 µm while other, more complex, equations give much worse agreement.

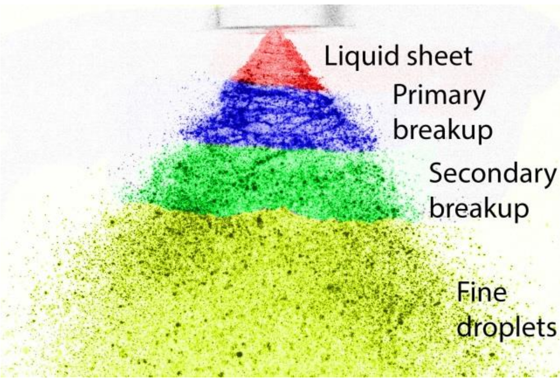

Figure 4. Near nozzle spray structure

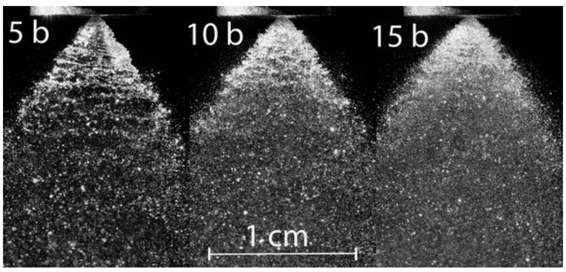

Figure 5. Spray structure at Δp = 0.5 MPa

3.1.2. Nozzle efficiency

The efficiency of energy conversion (of inlet potential energy into kinetic energy at the nozzle exit) inside the atomizer is characterised by the nozzle efficiency $\eta_n = \rho_l w_o^2 / 2\Delta p$. The nozzle efficiency was estimated approximating of our PDA data for velocity of the liquid phase in the near nozzle positions to the velocity at exit orifice. In our case η_n = 0.41–0.34 (Table 2). For comparison we in [15] found η_n = 0.53–0.59 for larger PS atomizer, where η_n moderately decreases with Δp. Other authors [16, 17] report lower values as η_n = 0.1–0.4 while Horvay and Leuckel [18, 19] found η_n = 0.42–0.66 depending on the shape of the convergent part of the swirl chamber and Yule with Chinn [20] reported for large PS atomizers η_n = 0.73–0.86. The main role of the swirl chamber is to provide a thin liquid film imposed with high velocity into still ambient air. The comparison with other authors indicates a potential to increase the nozzle efficiency (and so the discharge velocity) and reduce the drop size; the work should focus on the geometry the convergent part of the swirl chamber [18, 19].

Table 3. Characteristics of the flow and spray

Δp	SCA*	ID_{32}**	η_a	We_g	Re_W
MPa	deg	µm	–	–	–
0.5	75	53	0.65	0.62	7930
1.0	79	42	0.42	1.08	11215
1.5	82	38	0.31	1.62	13735

* based on photography
** calculated for Z = 50 mm

3.1.3. Liquid sheet formation

The conical liquid sheet attenuates with distance from the orifice, Z. The sheet also deforms due to interaction with the ambient gas (the Kelvin-Helmholtz type of instability) together with turbulent fluctuations imposed during internal flow.

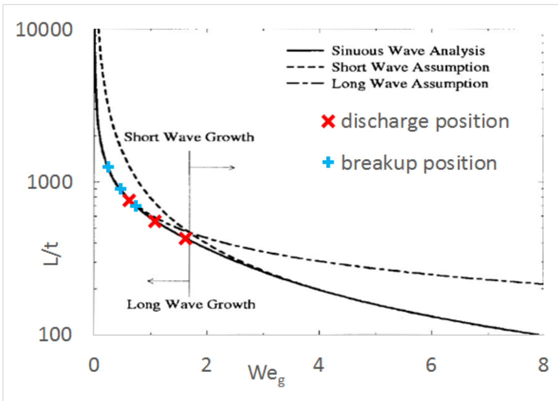

Figure 6. Dimensionless breakup length as a function of We_g for the general, inviscid sinuous, long wave and short wave modes with present data

The actual gas Weber number at the discharge orifice position of $We_g = \rho_g w_{lo}^2 t_o / 2\sigma = 0.6 - 1.6$ (see Table 3) in comparison with a critical Weber number $We_{gc} = 27/16$ [21] (below which long waves dominate and above which short waves dominate, Figure 6) shows that the atomizer operation points are placed just below the transition from long to short wave growth and the sheet breaks up namely due to long-wave instability of sinuous mode (Figure 4 and 5). The varicose mode, typical for density ratios ρ_g/ρ_l near unity, does not participate in our case as also confirmed with the near nozzle vizualizations (Figure 5 and other images not shown here). The long wave sheet instabilities are well seen in Figure 5 for the regime Δp = 0.5 MPa, while for the other two regimes with increased pressure and Weber number also short-wave instabilities are present and support the sheet breakup.

The sheet oscillations are amplified and finally cause the sheet to disrupt or tear into fragments as shown in Figure 4 at $Z_b \sim 3$–4 mm (see Table 2) with the breakup thickness $t_b \sim 27$ µm. The breakup length $L_b \sim 4$–5 mm is much smaller than the length predicted using the inviscid model for our data at both the discharge and the breakup positions (for the discharge conditions e.g. $L_b \sim 13.5$–22.4 mm). Larger breakup length would allow the liquid sheet to attenuate more prior to breakup and would result in smaller droplets. The model assumes a spectrum of infinitesimal disturbances imposed on the initially steady motion of the liquid film. Such instabilities produce fluctuating velocities and pressures. In a real case these disturbances have a finite value and, especially if their frequency corresponds to the frequency of the most unstable mode, these could significantly reduce the breakup length. This issue will be addressed in the next chapter.

The detached sheet fragments pack into irregularly shaped filaments (detectable in Figure 5 (regime 0.5 MPa) as thin horizontal threads in the primary breakup zone) which, due to the capillary instability, later on resolve to single droplets.

The relative importance of internal viscous and surface tension forces during the sheet disintegration can be judged by the ratio of the liquid phase Weber and Reynolds numbers at the nozzle exit [22] $We_l/\mathrm{Re}_o = w_{lo}\mu_l/\sigma$ which increases from 1.3 at Δp = 0.5 MPa to 2 at Δp = 1.5 MPa. It suggests for the moderately higher importance of viscosity at this spray formation stage.

3.1.4. Internal flow fluctuations

Several possible phenomena could contribute here: unsteadiness imposed externally (pump, valves), air core instabilities and complexities of the vortical internal flow.

Two methods have been used to detect the sources of internal flow fluctuations. Pressure fluctuation measurement was taken in the atomizer feeding line (see Chapter 2.5) and PDA was used for near nozzle measurement of the liquid flow characteristics at Z = 12.5 mm.

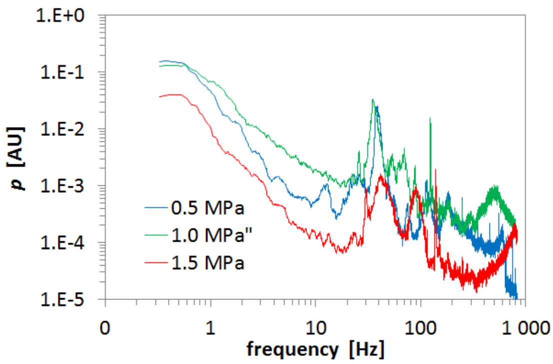

Figure 7. Frequency spectra of the pressure fluctuations in the feeding line

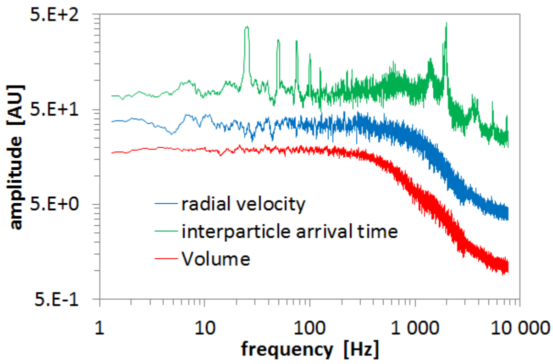

Figure 8. Frequency spectra of radial velocity, droplet volume and interparticle arrival time; the amplitudes are normalised to allow comparison, Δp = 1 MPa, r = 0.5, z = 12.5 mm

The fluctuations are strong for small frequencies (probably unsteadiness in the liquid delivery) and at frequencies around 40 Hz and 130 Hz that corresponds to pump and tooth frequencies.

Isolated peaks at such frequencies, if these fluctuations propagate through the atomizer chamber, should be present in the frequency spectra of the discharged liquid. We assume that pressure fluctuations should convert to fluctuations of liquid velocity. Similarly, fluctuations in internal flow or air core disturbances should lead to deformations of the liquid sheet and disrupt its homogeneity causing fluctuation peaks in the frequency response of some spray characteristics. Frequency spectra of droplet velocity, interparticle arrival time, droplet diameter and volume were analysed for this reason. Figure 8 (only data for Δp = 1 MPa are given for conciseness) shows very flat frequency response of the droplet volume and also of the radial velocity (see also similar character of axial velocity spectra in Figure 9). The frequency response of interparticle arrival time contains several isolated peaks that could be attributed to pump frequency and probably to air core fluctuations as well. Note that similar way to detect characteristic breakup frequencies used Leboucher et al. [23]. These findings support the suspicion that internal instabilities are responsible for such short breakup distance.

3.1.5. Discussion on sheet thickness

The spray size D_{32} for simplex nozzles depends on the initial liquid sheet thickness as $D_{32} \propto t_o^{0.4}$ [24]. Eqs. (1) and (2) show the relation between geometrical parameters of the atomizer and t_0 so their suitable variation should reduce the droplet size. These factors, however, also affect other important spray parameters such as SCA and flow rate so their certain combination must be kept. This can be solved using the expression obtained for SCA by Ballester and Dopazo [25]:

$$2SCA = 16.2\left(\frac{A_p}{d_s d_o}\right)^{-0,39} d_o^{1,13} \mu_l^{-0,9} \Delta p^{0.39} \qquad (3)$$

and keeping the condition for constant flow rate: $C_D d_o^2 = const$. Using Eqs. (1–3) a prediction of 1% improvement in D_{32} requires the key nozzle dimensions (d_o, d_s, port size) to change by ~10% while required SCA and flow rate kept precisely or 2% improvement in D_{32} requires the main nozzle dimensions to change by ~5% while keeping required SCA and flow rate within 5% tolerance. Simple scaling down should lead to comparable results as $D_{32} \propto \dot{m}_l^{0.25}$ [5] and considering that internal flow character would not change yields $\dot{m}_l \propto d_o^2$ so finally $D_{32} \propto d_o^{0.5}$. This analysis suggests that tuning of the key nozzle dimensions offers only very limited space for spray optimization. A confirmation that the liquid sheet already performs well results from the comparison of the actual sheet thickness with slightly overestimated values from predictions [13, 14].

3.2. Spray structure

The developed spray results from upstream conditions of the internal flow and interaction with surrounding air.

3.2.1. Mean spray structure

The radial distribution of mean droplet velocity well corresponds to other observations of hollow cone sprays. It is qualitatively similar amongst all three pressure regimes and amongst all the four studied axial positions (see Figure 9). Axial velocity reaches a local maximum near the positions of the maximum liquid flux, which corresponds to $r = R/Z \sim 0.5$. It gradually decreases both to outer spray border and to spray centreline due to the deceleration of droplets in the air. The centreline position, however, shows some unexpected increase in the velocity magnitude compared to the velocity in maximum liquid flux positions with axial distance from the nozzle. This effect is more distinct with the pressure increase. It was already explained for similar nozzle as cloud formation of the central droplets that "keep their momentum while the main-stream droplet structure expand with downstream distance and its interaction with surrounding air increases" [26].

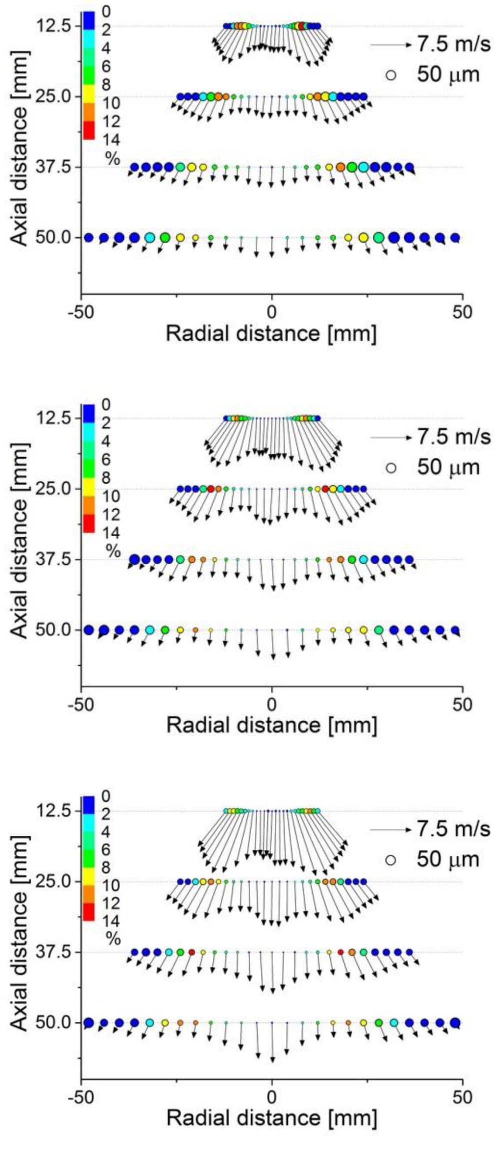

Figure 9. Droplet size (circles), velocity (axial and radial mean components, vectors) and liquid flux (colour) in four radial spray sections, from top to bottom 0.5, 1 and 1.5 MPa

Radial velocity increases with r from near-zero values at spray centre to $r \sim 0.6$ and then slowly decreases in the outer spray. The maximum value is roughly one-half of that one for axial velocity.

Tangential velocity reaches its maximum at $r \sim 0.2$ and its magnitude is one order lower than the other two components so it can be neglected in further considerations, and it was also not displayed in Figure 9 due to difficulties with its scale.

The mean spray structure (spatially resolved mean velocity, drop size and mass flux) was found to well extrapolate the mean characteristics of the conical liquid sheet with the effect of the interaction of droplets with surrounding air.

3.2.2. Spray fluctuations

Spectral content of fluctuations of droplet velocity was estimated with the aim to document the effect of interaction of droplets with surrounding air and to possibly detect relics of internal instabilities.

The results in radial positions of maximum flux at all four inspected axial distances from discharge orifice are depicted in Figure 10. Each frequency spectra can be divided into three bands: low-frequency part (below 10 Hz), middle range, and upper range above 1 kHz. The first part contains fluctuations with an amplitude increasing towards low frequencies that can be related to fluctuations in the liquid feeding line (compare the spectra with the one in Figure 7) or in surrounding air. Their energy content is very low (see Figure 11). The middle range fluctuations vary moderately with frequency and do not show any significant systematic peaks. A gradual decrease in the intensity with axial distance is due to energy transfer from droplets to surrounding air.

The last band shows a uniform decay of the fluctuations with frequency as $\propto f^{-1.18}$ above a cut-off frequency of 0.5–1 kHz depending on the axial position.

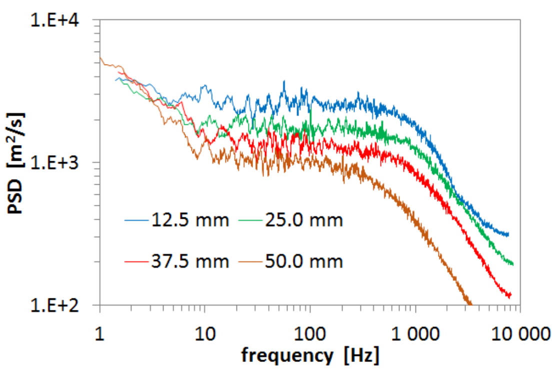

Figure 10. PSD of fluctuations of axial droplet velocity, Δp = 1 MPa, r = 0.5

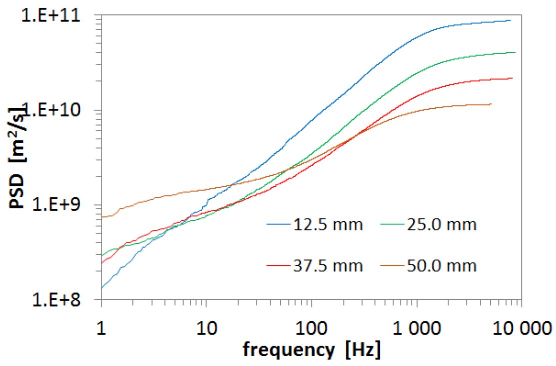

Figure 11. Cumulative PSD of droplet velocity fluctuations, Δp = 1 MPa, r = 0.5

4. SUMMARY

The study of PS atomizer was focused on discharge, near nozzle flow with liquid breakup and fully developed spray. Internal flow was found to be fully turbulent with discharge coefficient of the flow through the exit orifice roughly independent of the pressure drop. A conical liquid sheet was formed at the nozzle exit for the whole range of operational pressures. Near nozzle visualization and analysis of the sheet breakup using linear stability theory indicated operation of the atomizer just below the transition from long to short wave growth and the sheet break up namely due to long-wave instability of sinuous mode.

The actual breakup length was much smaller than the length predicted using the inviscid model that opened a question of internal nozzle instabilities. Using pressure fluctuation measurement upstream the nozzle and PDA measurement in the spray both external (gear pump) as well as internal (air core instabilities or complexities of the vortical internal flow) sources were detected as possible reason for the short breakup distance. Analysis of relations between geometrical parameters of the atomizer and liquid sheet thickness suggests that tuning of the key nozzle dimensions for our nozzle gives only very limited space for spray optimization.

The estimated nozzle efficiency shown here has a rather low value (0.41–0.34) in comparison with published data indicates a potential to increase the discharge velocity and reduce spray size focusing on modification of the geometry of the swirl chamber.

The spray structure was described based on spatially resolved velocity, drop size and mass flux. Radial profiles of these mean values were found to extrapolate well the characteristics of the conical liquid sheet with the effect of the interaction of droplets with surrounding air. Moreover, frequency spectra of fluctuations of droplet velocity in the positions of maximum flux were analysed.

ACKNOWLEDGEMENTS

This work has been supported by the project No. GA15-09040S funded by the Czech Science Foundation and the project LO1202 NETME CENTRE PLUS with the financial support from the Ministry of Education, Youth and Sports of the Czech Republic under the "National Sustainability Programme I".

REFERENCES

[1] Jones, A., 1982, "Design optimization of a large pressure-jet atomizer for power plant", Proc. Proceedings of the Second International Conference on Liquid Atomization and Spray Systems, p. 181.

[2] Xue, J., Jog, M. A., Jeng, S. M., Steinthorsson, E., and Benjamin, M. A., 2004, "Effect of geometric parameters on simplex atomizer performance", Aiaa Journal, 42(12), pp. 2408-2415.

[3] Elkotb, M. M., Rafat, N. M., and A., H. M., 1978, "The Influence of Swirl Atomizer Geometry on the Atomization Performance", Proceedings of the first ICLASS Tokyo, pp. 109 – 115.

[4] Tratnig, A., and Brenn, G., 2010, "Drop size spectra in sprays from pressure-swirl atomizers", International Journal of Multiphase Flow, 36(5), pp. 349-363.

[5] Lefebvre, A. H., and Ballal, D. R., 2010, "Gas turbine combustion alternative fuels and emissions", Taylor & Francis,, Boca Raton, pp. 1 online resource (xix, 537 p.).

[6] Donjat, D., Estivalezes, J., and Michau, M., 2002, "A description of the pressure swirl atomizer internal flow", ASME.

[7] Kim, S., Khil, T., Kim, D., and Yoon, Y., 2009, "Effect of geometric parameters on the liquid film thickness and air core formation in a swirl injector", Measurement Science and Technology, 20(1), p. 015403.

[8] Marchione, T., Allouis, C., Amoresano, A., and Beretta, F., 2007, "Experimental investigation of a pressure swirl atomizer spray", Journal of Propulsion and Power, 23(5), pp. 1096-1101.

[9] Von Lavante, E., and Maatje, U., 2002, "Investigation of unsteady effects in pressure swirl atomizers", ICLASS Zaragoza, 9, p. 11.

[10] Cooper, D., and Yule, A., 2001, "Waves on the air core/liquid interface of a pressure swirl atomizer", Proc. Proc. ILASS-Europe.

[11] Walzel, P., 1993, "Liquid atomization", Journal Name: International Chemical Engineering (A Quarterly Journal of Translations from Russia, Eastern Europe and Asia); (United States); Journal Volume: 33:1, pp. Medium: X; Size: Pages: 46-60.

[12] Rizk, N. K., and Lefebvre, A. H., 1985, "Internal flow characteristics of simplex swirl atomizers", Journal of Propulsion and Power, 1(3), pp. 193-199.

[13] Giffen, E., and Muraszew, A., 1953, *The Atomization of Liquid Fuels*, Chapman & Hall Ltd., London.

[14] Lefebvre, A., and Suyari, M., 1986, "Film thickness measurements in a simplex swirl atomizer", Journal of propulsion and Power, 2(6), pp. 528-533.

[15] Jedelsky, J., and Jicha, M., 2014, "Energy considerations in spraying process of a spill-return pressure-swirl atomizer", Applied Energy, 132(0), pp. 485-495.

[16] Rizk, N., and Lefebvre, A., 1987, "Prediction of velocity coefficient and spray cone angle for simplex swirl atomizers", International Journal of Turbo and Jet Engines, 4(1-2), pp. 65-74.

[17] Loffler-Mang, M., and Leuckel, W., 1991, "Atomization with Spill-Controled Swirl Pressure-Jet Nozzles", ICLASS-91, Gaithersburg, MD, USA, pp. 431-440.

[18] Horvay, M., and Leuckel, W., 1985, "LDA-measurements of liquid swirl flow in converging swirl chambers with tangential inlets", Proc. 2nd International Symposium on Applications of Laser Anemometry to Fluid Mechanics, p. 11.

[19] Horvay, M., and Leuckel, W., 1986, "Experimental and theoretical investigation of swirl nozzles for pressure-jet atomization", German chemical engineering, 9(5), pp. 276-283.

[20] Yule, A., and Chinn, J., 2000, "The internal flow and exit conditions of pressure swirl atomizers", Atomization and Sprays, 10(2), pp. 121-146.

[21] Senecal, P. K., Schmidt, D. P., Rutland, C.J., Reitz, R. D. and Corradini, M. L, 1999, "Modeling high-speed viscous liquid sheet atomization", International Journal of Multiphase Flow, 25(6–7), pp. 1073–1097.

[22] Yule, A. J., and Dunkley, J. J., 1984, Atomization of Melts: For Powder Production and Spray Deposition, Oxford University Press, USA.

[23] Leboucher, N., Roger, F., and Carreau, J. L., 2014, "Atomization characteristics of an annular liquid sheet with inner and outer gas flows", 24(12), pp. 1065-1088.

[24] Simmons, H. C., and Harding, C. F., 1981, "Some effects of using water as a test fluid in fuel nozzle spray analysis", Journal of Engineering for Power-Transactions of the Asme, 103(1), pp. 118-123.

[25] Ballester, J., and Dopazo, C., 1994, "Discharge coefficient and spray angle measurements for small pressure-swirl nozzles", Atomization and sprays, 4(3).

[26] Durdina, L., Jedelsky, J., and Jicha, M., 2014, "Investigation and comparison of spray characteristics of pressure-swirl atomizers for a small-sized aircraft turbine engine", International Journal of Heat and Mass Transfer, 78(0), pp. 892-900.

Conference on Modelling Fluid Flow (CMFF'15)
The 16th International Conference on Fluid Flow Technologies
Budapest, Hungary, September 1-4, 2015

A LATTICE-BOLTZMANN METHOD-BASED FLUID-STRUCTURE INTERACTION SOLVER FOR A FLAPPING MOTION SIMULATION

Rafał DALEWSKI[1], Mariusz RUTKOWSKI[2], Konrad GUMOWSKI[3], Łukasz ŁANIEWSKI-WOŁK[4]

[1] Corresponding Author. Department of Aerodynamics, Institute of Aeronautics and Applied Mechanics, Faculty of Power and Aeronautical Engineering, Warsaw University of Technology. ul. Nowowiejska 24, 00-665 Warsaw, Poland. Tel.: +48 22 234 6006, Fax: +48 22 234 6006, E-mail: rdalewski@meil.pw.edu.pl
[2] Department of Aerodynamics, Institute of Aeronautics and Applied Mechanics, Faculty of Power and Aeronautical Engineering, Warsaw University of Technology. ul. Nowowiejska 24, 00-665 Warsaw, Poland. Tel.: +48 22 234 1521, Fax: +48 22 234 6006, E-mail: mrutkowski@meil.pw.edu.pl
[3] Department of Aerodynamics, Institute of Aeronautics and Applied Mechanics, Faculty of Power and Aeronautical Engineering, Warsaw University of Technology. ul. Nowowiejska 24, 00-665 Warsaw, Poland. Tel.: +48 22 234 7767, Fax: +48 22 234 6006, E-mail: kgumowski@meil.pw.edu.pl
[4] Department of Aerodynamics, Institute of Aeronautics and Applied Mechanics, Faculty of Power and Aeronautical Engineering, Warsaw University of Technology. ul. Nowowiejska 24, 00-665 Warsaw, Poland. Tel.: +48 22 234 7767, Fax: +48 22 234 6006, E-mail: llaniewski@meil.pw.edu.pl

ABSTRACT

The aim of this research was to verify a concept for an efficient and reliable numerical Fluid-Structure Interaction method for viscid flow over rigid and deformable geometries flapping motion simulations. High frequencies of flapping and relatively small dimensions, thus low Reynolds numbers, consume significant amount of time and produce difficulties hard to solve.

The research was conducted in two stages. The first was numerical with the usage of the novel approach, and the second was experimental, conducted for a flapping mechanism in a controlled isolated volume. PIV was used for visualization and quantification of the flow. The experimental part was validating the numerical stage. Simulations enhanced the detailed observation of the phenomena.

Tested object, a bar in flapping motion placed in a rectangular domain, was simplified to observe precisely a correlation between methods. This 2D numerical case was compared to quasi-2D case of the flow in rectangular box. This is an initial stage for broader research programme aiming at implementation of Lattice-Boltzmann method to simulate full insects flapping motion taking into account wing deformation and object dynamics.

Keywords: Lattice-Boltzmann, Flapping, PIV, Experiment, PIV.

NOMENCLATURE

M,m	[*N/m*]	Moment
u	[*m/s*]	Velocity
T	[s]	Relaxation time
f	[*m/s*]	Density
F	[N]	Force

Subscripts and Superscripts

neq	non-equilibrium
eq	equilibrium

1. INTRODUCTION

The Lattice-Boltzmann method is one of the most promising methods for rapid CFD calculations. Its adoption to FSI problems has a great potential worth overcoming initial difficulties. Such an adoption is presented in a very simple test solved both numerically and experimentally.

The numerical setup consists of a square domain in the middle of which a rectangle rotates in a flapping motion mode. This setup is presented in Figure 1.

Implementation and validation of modules responsible for computational fluid dynamics (CFD) and deformation of proposed geometry was conducted. A highly efficient Lattice Boltzmann Method solver (CLB) designed for multiple-GPU architecture was employed with a Multiple Relaxation Time (MRT) collision model for two- and three-dimensional lattices implemented.

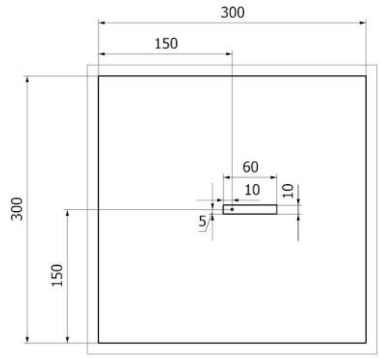

Figure 1. Lattice-Boltzmann problem setup.

For higher Reynolds number flows, LES turbulence modelling was used (Smagorinsky model). Immerse boundary technique was employed for a moving boundary, where forces were discretized with Exact Difference Method. Simplified cases of flapping motion was simulated and validated against the experimental data. Non-linear displacement model of a body deformation was implemented.

This research was planned as a validation of novel numerical simulation technique to be implemented in flapping motion research. Next steps will focus on flapping motion mechanism development, control and modification. Usage of this fast and efficient simulation environment enables dynamic control model building and almost real-time testing, enabling efficient motion control even for very small objects.

2. CFD MODEL

Numerical simulations were conducted using Lattice Boltzmann Method (LBM). In recent years this method gained wide recognition as a reliable method for complex flows. For an introdution of LBM the reader is referred to the book by Succi [1]. LBM used in combination with immersed boundary method is used in many flow problems, where boundaries are moving or deforming [2]. These methods can also provide accurate values of forces acting on the moving boundaries, as showed by Li et al [2].

We used Multiple-Relaxation-Time (MRT) LBM proposed by d'Humi`eres et al [3]. This method provides superior stability compared to single relaxation time methods and also has faster rates of decay for non-physical modes of the LMB dynamics. These two properties make this method a good candidate for calculating flow around quickly moving objects. To further stabilize the flow solution, turbulence modelling was used. We used Large Eddy Simulation (LES) with a simple Smagorinski model, derived by Krafczyk et al [4], tuned for our specific implementation of MRT LBM. Combination of LES with MRT provide stable solutions for a wide range of Reynolds numbers keeping high performance (and high locality) of LBM method.

For immerse boundary a forcing scheme was used. The moving boundary was modelled as an external force field acting on fluid. It was calculated so that the flow velocity at the boundary is equal to the velocity of the rigid body. Many methods can be used to implement external forces in LBM. We chose Exact Difference Method introduced for two-phase flows by Kupershtokh et al [5], as it provides good stability for a wide range of parameters. Because of the forcing method used, no artificial smoothing of the force field had to be used (which is a part of many immerse boundary methods).

For a set of densities $f_{i,}$ final collision operator of the method consist of these steps (for the basics of LBM method we refer the reader to [1]):

1. calculate moments from the densities

$$m = Mf \tag{1}$$

2. extract velocity u and density d from m.
3. calculate the non-equilibrium moments

$$M^{neq} = M - M^{eq}(d,u) \tag{2}$$

4. calculate S tensor from non-equilibrium moments.
5. calculate turbulence viscosity and relaxation time T (same as Krafczyk et al [4]) from S
6. relax the moments (using MRT):

$$M^{neq} = M^{neq}\,(1-T) \tag{3}$$

7. modify velocity by the momentum introduced by the force in the time step:

$$u = u + Fdt \tag{4}$$

8. calculate post-collision moments:

$$M = M^{neq} + M^{eq}(d,u) \tag{5}$$

9. calculate densities:

$$f = M - 1m \tag{6}$$

Resulting method is very compact and local, making is perfect for highly-efficient parallel implementation. The numeric scheme was executed in the framework of a multi-GPU implementation of LBM method called CLB. The code was used by the authors in earlier work using LBM for porous media flows, two-phase flows and topology optimization with adjoint method. The code is highly customizable and can easily accommodate for a wide range of LBM models.

The plate was modelled as a rigid moving rectangle with the position and angle prescribed by the user (consistent with the experimental data). External boundaries of the flow domain were set as no-slip wall conditions implemented with a simple Bounce Back boundary condition [1].

3. TEST RIG

A reliable verification was quite a challenging task. Case study requirement was to meet two assumptions: quasi-two-dimensionality and flapping motion of an object.

The simplest geometry to analysis was a rigid and rotating rectangle inside of measuring space in shape of a square. Rectangle's rotation axis was in some distance from its end and was concentric with respect to the geometric center of mentioned measuring space as shown in Figure 1. Experimental stand consisted of a longitudinal rotating plate and the measuring chamber in the shape of a prism. Analyzed cross-section lied between upper and lower wall of the prism (Figure 3)

3.1. Experimental stand

Designed experimental stand was made entirely of Poly(methyl methacrylate). Motion was realized by bipolar stepped motor attached to one of the bases. Motor performed a dedicated control program. Figure 3 and 4 present the rig.

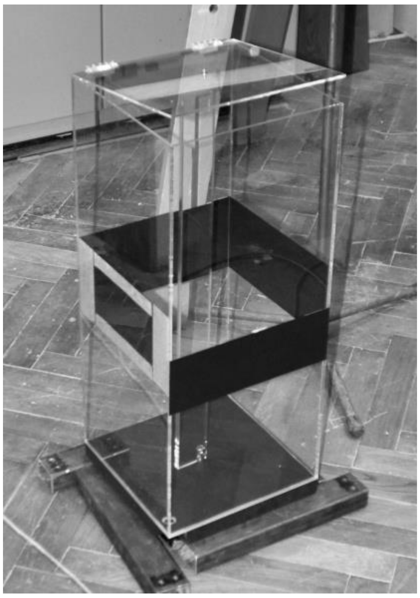

Figure 3. The stand (700 mm height), black elements were used to improve PIV experiment

3.2. PIV measurement stand.

Figure 5 presents final setup for PIV analysis on the basis of the oil droplets. As shown in Fig. 5, laser light was pointed in half the height of the stand and images were shoot from above. Black surfaces helped to eliminate the influence of the background.

During PIV measurement, imiges were made with 15 Hz frequency. The experiment was carried out more than 10 times for the same setting. Between each measurement, there was a two-minute delay, to ensure that the fluid velocity and vorticity are low, in comparison to an average velocity during a movement of the plate.

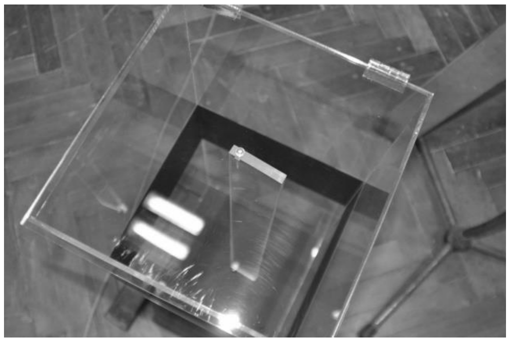

Figure 4. Experimental stand from above

Figure 5. PIV measurement setup

4. .EXPERIMENTAL RESULTS

Figures 6 to 8 are examples of results. Both figures represents one movement – plate is on one of two maximum rotation positions (Figure 8 presents plate in second maximum position). Background (grey scale) in Fig. 6 represents velocity and in Fig. 7 represents vorticity. Vectors on both Figures represents velocity.

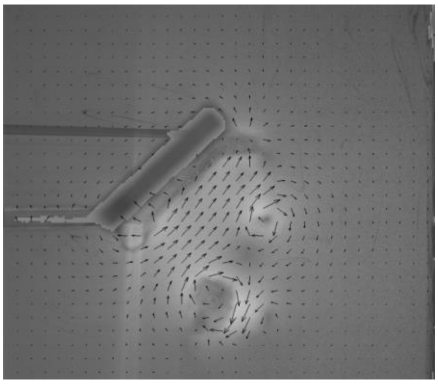

Figure 6. PIV image. Plate during motion. Vectors and grey scale represents velocity. The longest vector represents $0,6\ \left[\frac{m}{s}\right]$

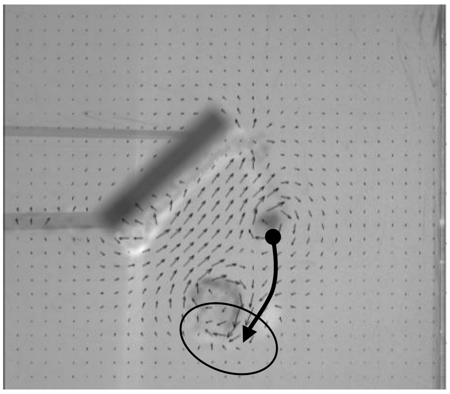

Figure 7. Plate during motion. Vectors represents velocity and grey scale represents vorticity. The brightest color represents $125\ \left[\frac{1}{s}\right]$, darkest color represents $-125\ \left[\frac{1}{s}\right]$. Black line shows place of creation and path of highlighted contra-rotating structure.

For the number of experiments conducted, a certain pattern for this specific case, was noted. It is described below.

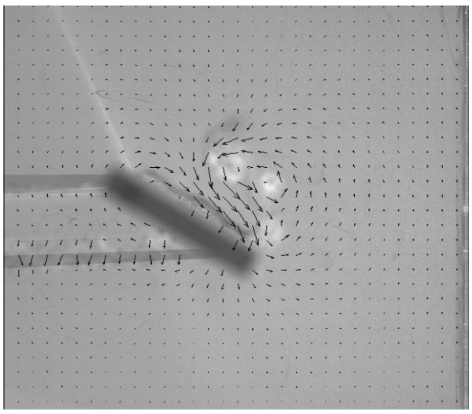

Figure 8. Behavior of vortices.

3 similar patterns were observed:

1. Surrounding vortices - When plate reach one of two maximum positions and is changing direction. One or two vortices are thrown from edge of the plate by flow parallel to plate (this flow is visible on Figs. 6-8 on the one side of plate). After plate change its direction, those vortices are moving on the other side of the plate behind newly created ones. Fig 8. shows negative vortices from previous movement among positive vortices.

2. Asymmetric beginning – This phenomena occurs during flow development, that is first 3 periods of motion. Actually created formations have too low energy in comparison to vortices created in forthcoming motion. Those vortices, when thrown on the other side of plate, have low rotation to enclose all the negative structures. This explains formation, visible on Figs. 6 and 7, moving towards top wall. Two counter rotating vorticity structures escape the proximity of plate. Those “low energy” formations grow in strength with time that is why path of first escaping structure is strongly curved and next one is straighter.

3. 3 periods – After two structures containing positive and negative vortices, which move towards the top wall, motion of the plate become “symmetric” – same amount of vortices with positive and negative rotation. From now on case is fully developed and analysis became very unsteady. Similarities with “asymmetric beginning” are still visible but random and non-2D factor is dominant. Although vorticity becomes very chaotic, velocity of fluid in close proximity smoothed, which is shown in Figure 9.

Those three similarities, repeated in number of experiments, should appear in simulation as well.

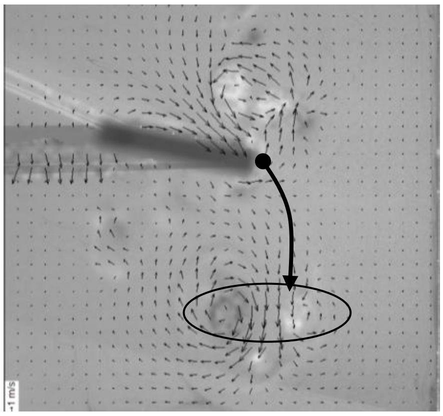

Figure 9. Double contra-rotating vortex structure escaping proximity of the plate. Within whole motions there are only a few structures during development of the flow

5. SIMULATIONS

Geometry for simulation was accordingly to the geometry presented in Fig. 1. This method requires the assumption of two physical constants. Those are: viscosity of fluid and maximum predicted velocity value. Those two values were chosen empirically. It is important to mention that resolution of simulation was 711 x 711. For proposed CFD method it gives 523292 mesh size.

6. RESULTS DISCUSSION

In this chapter both analyzes were compared. As it was mentioned in chapter 4, comparison will show common parts between them.

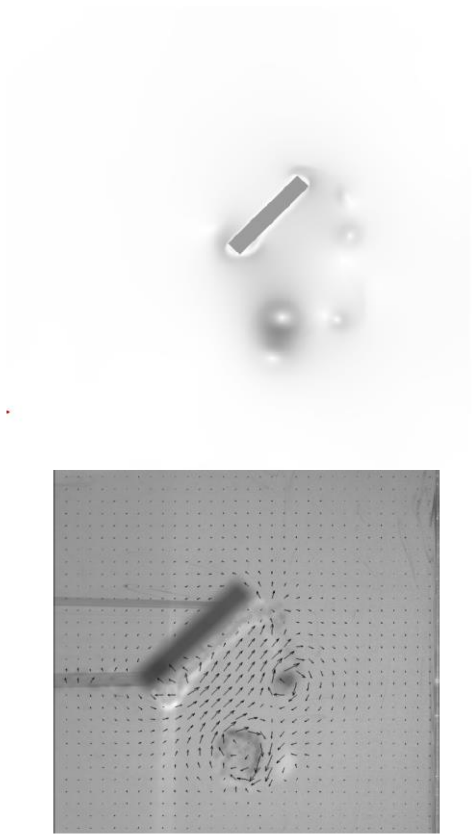

Figure 10. Comparison of first “escaping structure”

Figures 10 and 11 present comparison of escaping structures. Behavior is comparable with that observed in PIV measurements. Similarities can be observed e.g. for vortices with high vorticity. With a decreament of vorticity, similarity decreases as well. Those differences can be due to low resolution in the analysis of PIV.

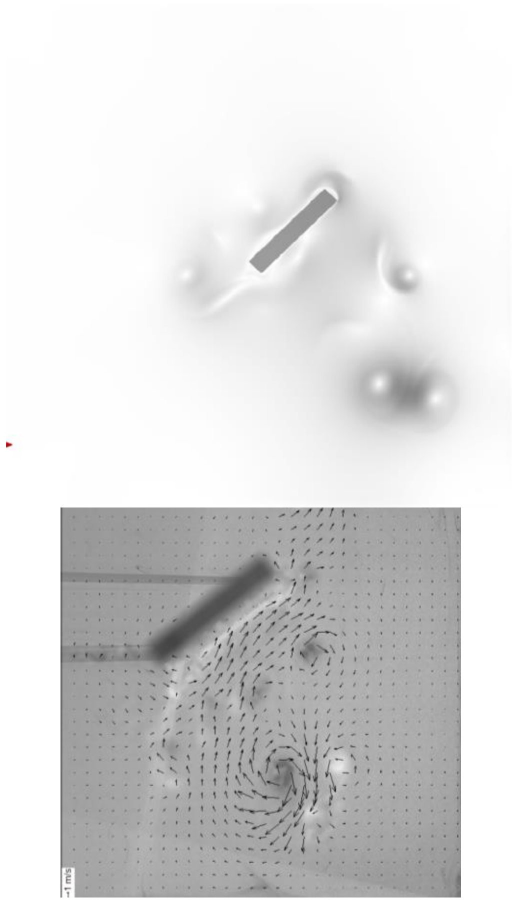

Figure 11. Comparison of second “escaping” structure

Figure 12 presents velocity distribution in close proximity to the plate. As one can see taking both experimental and simulation data on an “active” side, that is where vortices are actually created, the velocity distribution is even. Although, cascade of vortices is in enough distance from plate to let the stream develop, is so close enough to affect and accelerate it. On the passive side, flow is more chaotic. This is due vortices previously made by active side of that phase. Plate is moving towards those vortices. During that movement structures are forced to transfer energy to the stream, also in few cases stream eject mentioned vortices towards the plate according to the vector of the stream.

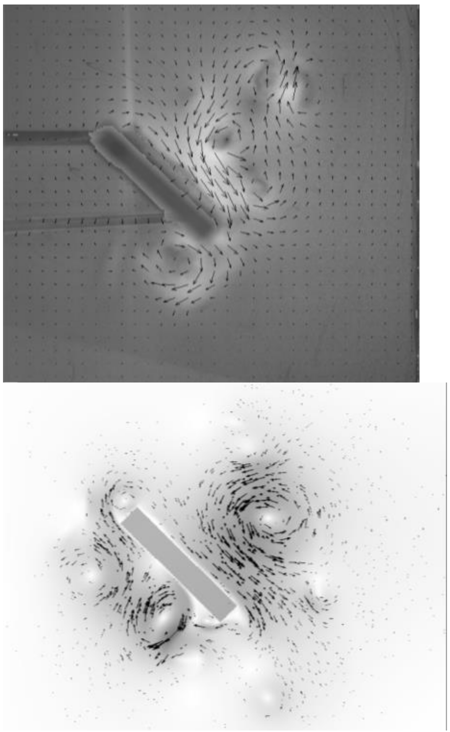

Figure 12. Comparison of velocity distribution.

7. SUMMARY

CFD model for Fluid-structure interaction as well as verification case was proposed. Initial observations lead to a conclusion of a good correlation between experiment and computation. This approach seems to have a great potential especially in flapping motion simulations. The results of the numerical analysis in most cases coincide with the experiment.

Future plans related to the issue presented assume further development of both experimental data gathering (specific two-dimensional cases of unsteady flapping motion) and numerical method implementation, especially a three-dimensional code.

ACKNOWLEDGEMENTS

This work has been supported by the Polish National Centre for Research and Development, Lider III Programme under contract No. 143/.

REFERENCES

[1] S. Succi, *The lattice Boltzmann equation: for fluid dynamics and beyond*, Oxford university press, 2001.

[2] Fang-Bao Tian, Hu Dai, Haoxiang Luo, J. F. Doyle, B. Rousseau, *Fluid – structure interaction involving large deformations: 3D simulations and applications to biological systems*, Jurnal of Computational Physics 258 (2014) 451-469

[2] Li, Huabing and Lu, Xiaoyan and Fang, Haiping and Qian, Yuehong, *Force evaluations in lattice Boltzmann simulations with moving boundaries in two dimensions,* Phys. Rev. E, 2004

[3] D. d'Humi`eres, *Multiple–relaxation–time lattice boltzmann models in three dimensions*, Philosophical Transactions of the Royal Society of London. Series A: Mathematical, Physical and Engineering Sciences 360 (1792) (2002) 437–451.

[4] Krafczyk, Manfred, Jonas Tölke, and Li-Shi Luo. *Large-eddy simulations with a multiple-relaxation-time LBE model.* International Journal of Modern Physics B 17.01n02 (2003): 33-39.

[5] A. L. Kupershtokh, D. A. Medvedev, D. I. Karpov, *On equations of state in a lattice boltzmann method*, Computers & Mathematics with Applications 58 (5) (2009) 965 – 974

Conference on Modelling Fluid Flow (CMFF'15)
The 16th International Conference on Fluid Flow Technologies
Budapest, Hungary, September 1-4, 2015

EXPERIMENTAL TESTING AND NUMERICAL SIMULATIONS OF A DUCTED COUNTER-ROTATING MAV PROPELLING SYSTEM AEROACOUSTICS

Rafał DALEWSKI[1], Witold KRUSZ[2], Konrad GUMOWSKI[3]

[1] Corresponding Author. Department of Aerodynamics, Institute of Aeronautics and Applied Mechanics, Faculty of Power and Aeronautical Engineering, Warsaw University of Technology. ul. Nowowiejska 24, 00-665 Warsaw, Poland. Tel.: +48 22 234 6006, Fax: +48 22 234 6006, E-mail: rdalewski@meil.pw.edu.pl
[2] Department of Aerodynamics, Institute of Aeronautics and Applied Mechanics, Faculty of Power and Aeronautical Engineering, Warsaw University of Technology. ul. Nowowiejska 24, 00-665 Warsaw, Poland. Tel.: +48 22 234 1521, Fax: +48 22 234 6006, E-mail: wkrusz@meil.pw.edu.pl
[3] Department of Aerodynamics, Institute of Aeronautics and Applied Mechanics, Faculty of Power and Aeronautical Engineering, Warsaw University of Technology. ul. Nowowiejska 24, 00-665 Warsaw, Poland. Tel.: +48 22 234 7767, Fax: +48 22 234 6006, E-mail: kgumowski@meil.pw.edu.pl

ABSTRACT

In the presented research a ducted propelling system for a MAV was investigated taking into account its aeroacoustic properties. The propulsion system consist of a duct (inner diameter 55 mm), with two counter-rotating propellers. The combination of relatively small dimensions and high rotational velocities imposes both difficult and interesting flow condition also in terms of aeroacoustics.

The proposed research was conducted in experimental and simulation stage. The main purpose was to identify main noise sources and identify methods of noise mitigation.

The results combined with further research will serve to develop a methodology for noise mitigation in a small propelling system. Identification of laminar separation occurrence in a flow by means of acoustic measurement may also be implemented as an assembly and production quality verification of MAVs.

Keywords: Aeroacoustics, Experiment, Noise, CAA/CFD, Ducted propulsion systems, MAV Design.

NOMENCLATURE

$\tilde{u}_n$	[m/s]	wave vector amplitude
ψ_n	[-]	wave vector phase
$\vec{\sigma}_n$	[-]	wave vector direction
u	[m/s]	velocity component
p	[Pa]	pressure

1. INTRODUCTION

Micro Air Vehicles propulsion system under investigation is an efficient but also a noisy one. The scope of presented research was to experimentally quantify acoustic field and simulate it to analyse sources and potential of noise reduction. The other aim was to investigate potential flow quality assessment on the basis of noise signal analysis.

Therefore a test setup was designed and manufactured allowing for 360deg. observation of sound power and identification of dominating frequencies. Tests were performed to investigate best relative setting of rotors and inlet taking into account noisiness.

A tested model, presented in Figure 1 was a MAV propulsion system comprising two counter-rotating propellers driven by one BLDC motor each. An inlet was formed by a contracted duct. The three elements are set along common axis and can be relatively translated.

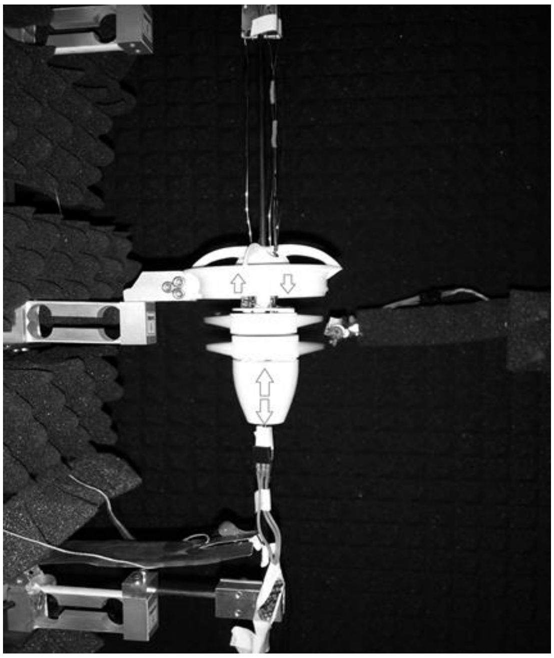

Figure 1. The tested model

To investigate and quantify the most interesting cases a numerical model was built and solved using Ansys/CFD tools (Fluent 15). This analysis was used predominantly for sound sources power and placement identification and quantification.

Finally data was set and compared. Results were discussed.

2. TEST RIG

An experimental part was conducted using a setup comprising following elements:

- an anechoic chamber 1000x1000x1000mm (in Figure 2),
- a stand allowing for relative translation of the inlet duct, upper and lower rotor,
- a microphone positioning mechanism, allowing for microphone rotation around the tested objects with various radii (in Figure 3),
- calibrated microphone with data acquisition and analyse system,
- a control setup for rotational velocity regulation.

In the experiment a calibrated microphone setup was used. Signal was processed using fast Fourier transform method (FFT) and analysed with regard to various rotors velocities and inlet positions (those three elements can be set in different relative position, moving along a common axis).

A special configuration without rotors blades comprising only the rotating elements working in similar conditions to identify the engine and remaining parts noise was tested. Results were analysed in frequency domain taking into account short and long period sampling for identification of different working condition and modes. The influence of surface roughness was taken into consideration. Results are presented in chapter 5.

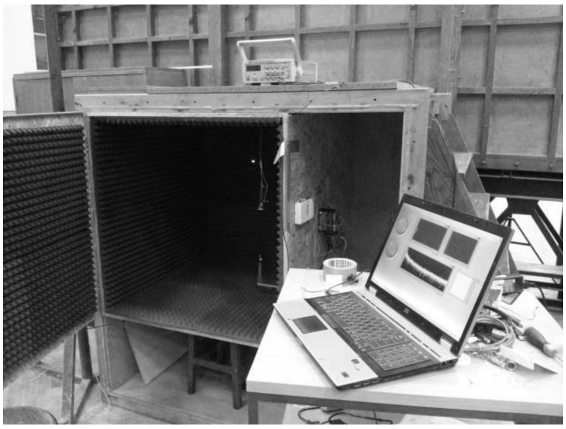

Figure 2. Testing chamber setup

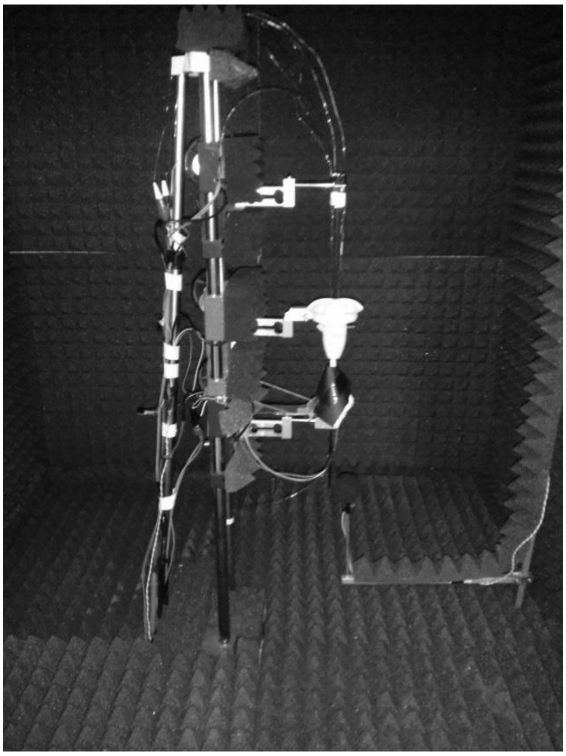

Figure 3. Test model setup

3. CFD MODEL

Numerical calculations used to determine the source of sound in the tested object were carried out using the RANS methods implemented in a commercial package Fluent 15.

A computational model was built, consisting of a domain divided into the inlet part with the inlet pressure boundary condition, domains containing the geometry of the inlet duct and the outlet part with the pressure outlet boundary, as well as two rotary domains containing the geometry of the upstream and downstream rotor.

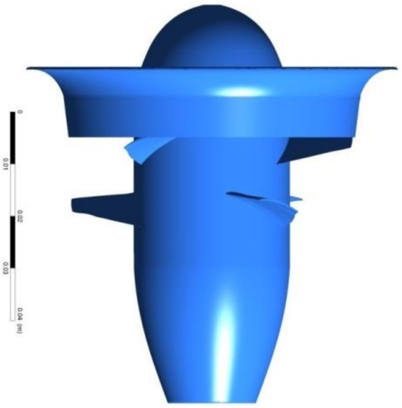

Figure 4. CFD model of two counter-rotating propellers and a duct

The domain was meshed using unstructured mesh method with 16 million nodes, with the possibility of parametric modifications associated with the movements of the lower rotor and the inlet duct.

Turbulence was modeled using a 4-equations Transition SST model which allows for modeling of the laminar-turbulent transition. Y+ parameter in near wall region was below 1.

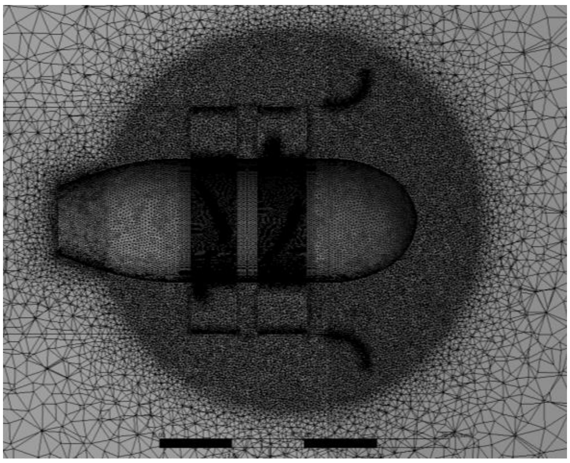

Figure 5. Cross section of CFD mesh.

Calculations were carried out in the following manner: at the beginning of a simulation it was done with a use of an option “Moving reference frame”, after obtaining a satisfactory degree of convergence and after the forming of intake velocity field, calculations were switched to transient mode using a “Moving mesh” option. The calculations were modeled on equal rotational speeds on the upstream and downstream rotor amounting to 2304 rad/s (app. 360 Hz). Aeroacoustics phenomena were modeled using a broadband noise model. Sources of sound were identified using the linearized Euler equations (LEE). Those equations can be derived from the Navier-Stokes equation by decomposing flow variables on average acoustic and turbulent components, assuming that the acoustic components are significantly smaller than the average flow and turbulence components. The result is a linearized Euler equation (1) on the acoustic velocity components. Index "a" relates to the respective acoustic indexes, and " ' " relates to turbulent components.

$$\frac{\partial u_{ai}}{\partial t} + U_j \frac{\partial u_{ai}}{\partial x_j} + u_{aj}\frac{\partial U_i}{\partial x_j} + \frac{1}{\bar{\rho}}\frac{\partial p_a}{\partial x_i} - \frac{\rho_a}{\bar{\rho}^2}\frac{\partial P}{\partial x_i} = -U_j \frac{\partial u_i'}{\partial x_j} - u_j'\frac{\partial U_i}{\partial x_j} - u_j'\frac{\partial u_i'}{\partial x_j} - \frac{1}{\bar{\rho}}\frac{\partial p'}{\partial x_i} - \frac{\partial u_i'}{\partial t} + \frac{\partial}{\partial x_j}\overline{u_j' u_i'} \qquad (1)$$

The right side of equation (1) is a part responsible for sound generation. First two components of the right side of the equation are referred to as "shear-noise" source terms, as are associated with tangential stress. The third component is referred to as "self-noise" source term, because it involves only turbulent velocity components.

$$\vec{u}(\vec{x},t) = 2\sum_{n=1}^{N} \tilde{u}_n \cos\left(\vec{k}_n \cdot \vec{x} + \psi_n\right)\vec{\sigma}_n \qquad (2)$$

A turbulent flow field essential for the calculation of source conditions LEE is obtained by a method of random generating of noise and radiation. In this method, the turbulent velocity field and its derivatives are calculated from the sum of N Fourier modes (2).

4. CFD RESULTS

The main task of the part related to numerical calculations was to determine the source of sound in the test model of a flying microrobot.

Validation of CFD results were performed using stand equipped with three tensometers . There were tested two rotors configuration printed using SLS method (Solid Laser Sintering). Two sets of rotors were tested: a rough configuration, with higher roughness and a smooth - hand polished. For design point, thrust components of inlet, upstream and downstream rotor were measured. Comparisons of experimental results confirmed correctness of CFD model.

Table 1. Comparision of total thrust for propulsion system presented in publication. Force in G (Gram).

	Total thrust
CFD	54,6@22W
SLS rough	59@20W
SLS polished	48@17W

The used LEE model allowed to define noise-generating points on the surfaces of blades. View from the top on the rotor blades (Figure 5) shows a significant noise emission surface on the upstream surface of the downsteam rotor, with a visible part of noise-wiping by vortices generated in the upper rotor. As shown in the attached contours, the lower rotor is the main source of aeroacoustic noise.

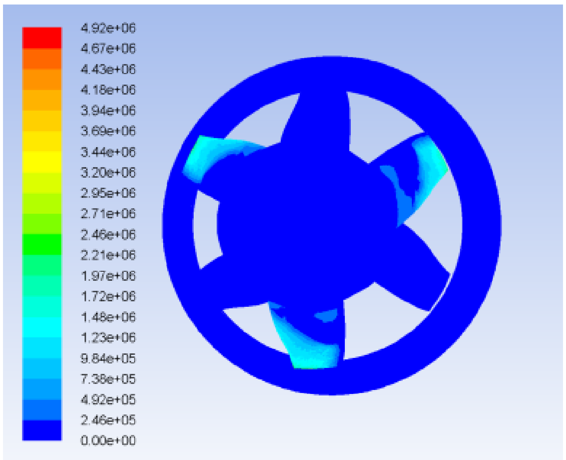

Figure 6. LEE Self Noise X-source (m/s2), view from outlet side

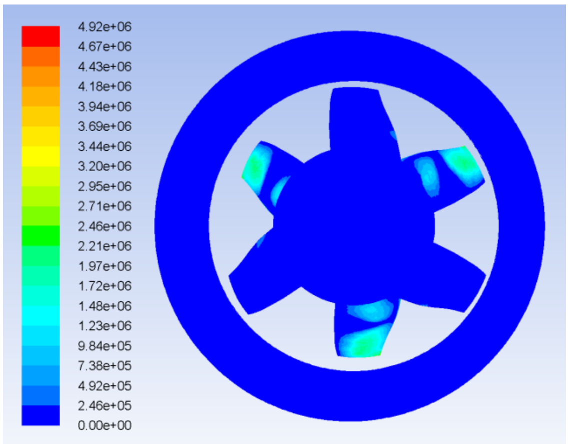

Figure 7. LEE Self Noise X-source (m/s2), view from inlet side

The downstream rotor (Figure 6), due to working in turbulent wake conditions in the slipstream behind the upstream rotor, is working in different conditions. In fact, entire lower and upper surfaces of its blades are sources of sound emission. An upstream rotor is much better dampened due to working in a quiet, undisturbed air flow from the intake.

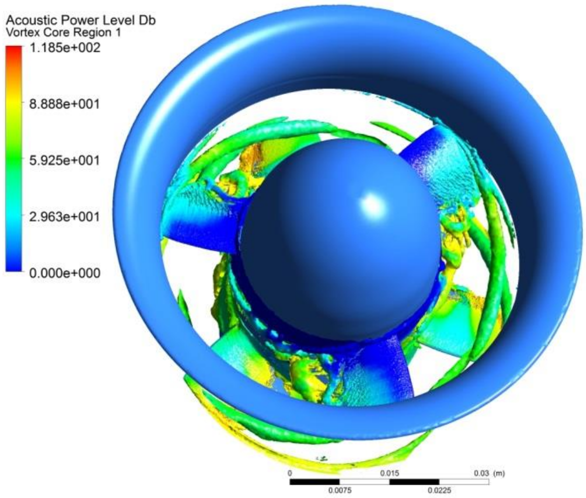

Figure 8. Acoustic Power Level (dB) on upstream rotor. Contours presented on vorticity isosurfaces.

Curle's Integral formulation [6] based on acoustic analogy were used to approximate local contribution from the body surface turbulent layer to the total acoustic power. The Boundary Layer Noise Source Model was used for Acoustic Power calculations.

In the picture above (fig. 7) contours of an Acoustic Power Level in (dB) are presented on the vorticity isosurfaces. Similarly, by analysing the distribution of values, a significant generation of acoustic energy on a lower blade can be observed (Figure 8).

Experimental tests have performed to validate this phenomenon. With the differential speed setting, the lower rotor always emits sound of greater intensity.

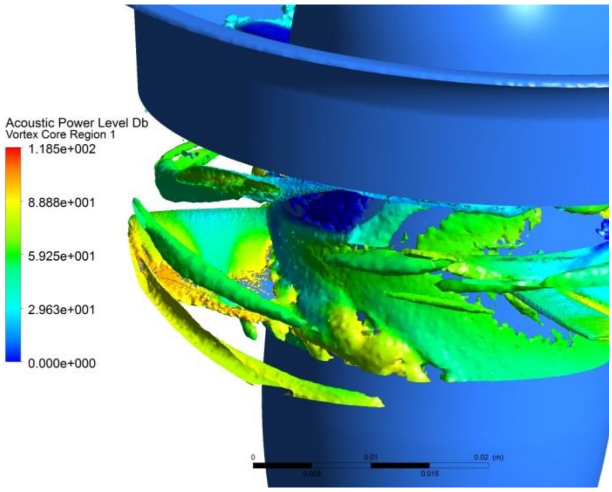

Figure 9. Acoustic Power Level (dB) on downstream rotor. Contours presented on vorticity isosurfaces.

5. EXPERIMENTAL RESULTS

As a result of fast Fourier transformation signal analysis folowing results (Figure 9,10 and 11) were presented. The first (fig. 9) one depicts result taken from a wake behind the propulsion system (radius 100 mm from the point on axis of rotation and the top of upper rotor). Rotor speed 330Hz (app. 20 kRPM – kilo rotations-per-minute).

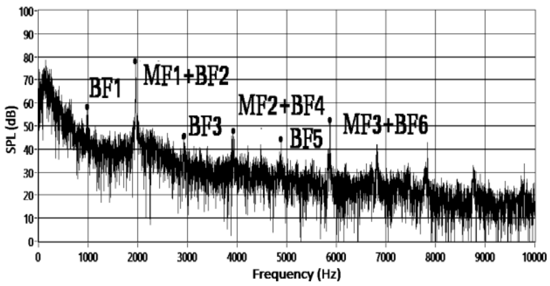

Figure 10. Frequency spectrum of a signal recorded from a wake; BF-Blade Frequency mode, MF-Motor Frequency mode

For the position of the microphone at a distance of 100 mm from the test object, a strong noise of high intensity up to 2kHz was registered. For frequencies 330, 660 and 990Hz there is a single peak equal to the rotor speed and 2nd and 3rd mode, and for about 2 kHz peak relevant to the sum of the sounds generated by the engines and blades. Up to 1 kHz a broadband noise is observed.

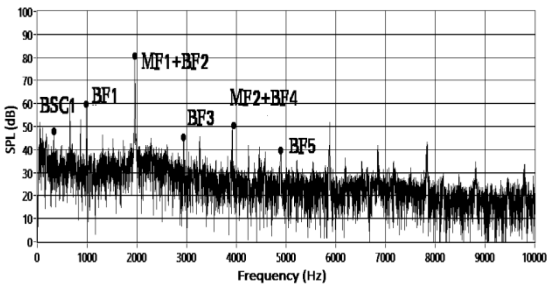

Figure 11. Frequency spectrum of a signal recorded outside the wake (10°, 100mm); BF-Blade Frequency mode, MF-Motor Frequency mode, BSC- Brushless engine controler 330Hz

For the angle more then 10 degrees from the axis (100 mm radius), an impact of the wake is not registered (Figure 10). A far less noisy signal spectrum is recorded. The component with the highest amplitude of 80 dB is the peek for frequencies corresponding to the work of a 6-poles brushless motor. This is its first mode of 1,98kHz frequency. A more distinct peak is the one related to the work of the blades for 990 Hz (rotor radial velocity 3rd mode). The remaining peaks correspond to the subsequent modes related to propellers' speeds multiplications of basic rotor frequencies 330, 660 and 990Hz and basic engines frequency 1,98kHz. Spectral components below the value connected to the rotational speed of the blades correspond most probably to vibrations of the robot's support construction.

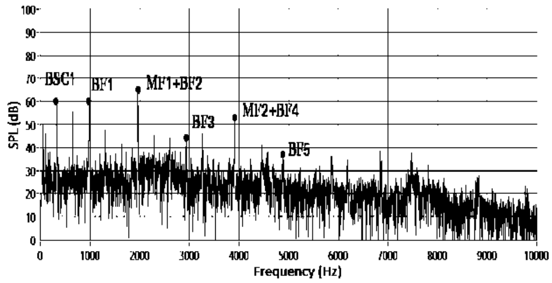

Figure 12. Frequency spectrum of a signal recorded outside the wake (90°, 100mm); BF-Blade Frequency mode, MF-Motor Frequency mode, BSC- Brushless engine controler 330Hz

Acoustic spectrum for the probe angle of 90 degrees to the axis of rotation is characterized by a decreased volume for the frequency component connected to the work of engines and by an increased sound correlated with the first and second frequency mode related to the rotational speed of the blades (Figure 11). Lower sound power app. 65 dB is observed.

Following two pictures (Figure 12 and 13) present graphs of the sound power level for selected frequencies as a function of the measurement beam angle rotation for the basic configuration at the speed of 330Hz. The sound sensor was positioned 100 mm from the tested object. The charts show the dependence of amplitude on essential aeroacoustic data. F1 corresponds to the frequency of the rotor drive system, F2 is a frequency connected with the work of a 6-pole brushless motor summed with the other mode of blades, F3 and F4 are the subsequent frequency modes.

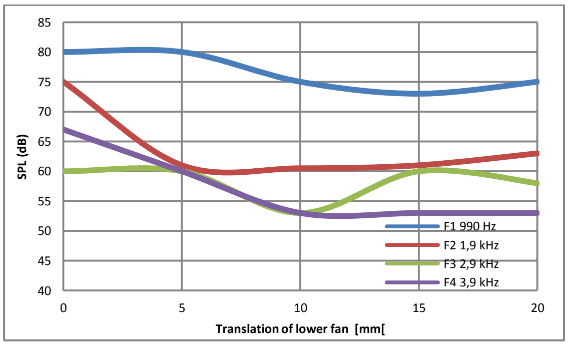

Figure 13. Sound Pressure Level (SPL) observed 100 mm 10° from the top of upstream rotor and the axis when the downstream rotor is separated from the inlet-upper lower block.

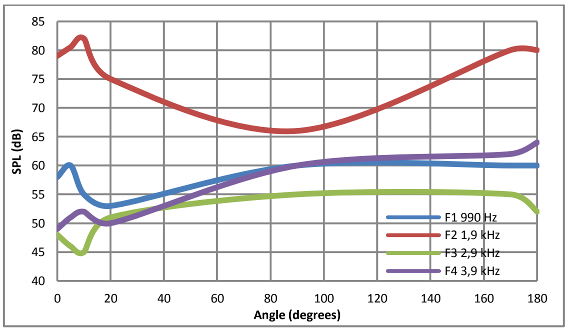

Figure 14. Sound Pressure Level (SPL)observed around the tested object for selected frequencies

The biggest changes in the sound levels occur during the passage through the wake stream (Figure 13). In the area outside the stream, the changes are minimal and difficult to notice. For the beam angle of 90 degrees, a minimum sound level is achieved for the frequency related to the work of motors, which is an effect of shielding of the drive through the duct. For the same conditions, for a blade-related frequency, a maximum level is achieved. In the given configuration, the measurement directed at the downstream rotor is recorded, which is the main source of aeroacoustic sound according to CFD calculations.

Another measurement concerned measuring four dominant frequencies in the sound spectrum. Frequency levels were recorded connected with blade velocity F1 (990Hz) and F3 (2,97kHz) and an accumulated frequency of blades and engine F2 (1,98kHz) and F4 (3,96kHz) as a function of moving away the upper rotor from the downstream rotor (Figure 12). A 360 degree characteristics of an overall sound power level is presented in Figure 14.

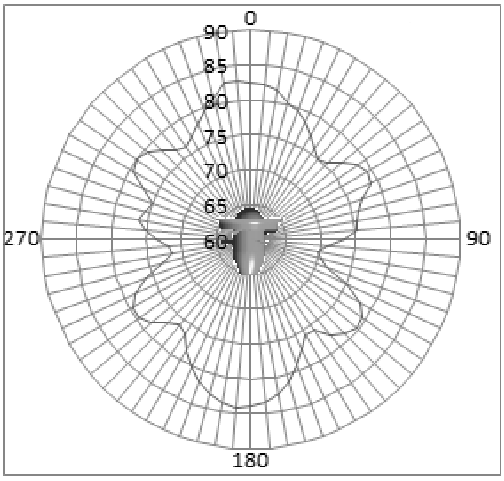

Figure 15. Circular acoustic characteristic of propulsion system. Values of Sound Pressure Level SPL (dB), microphone position 100mm. from target, upstream and downstream rotor rotates with 2304 rad/s.

6. RESULTS DISCUSSION

Presented results allow for preliminary study of this MAV aeroacoustics characterization.

As initially assumed, basic frequencies are related to rotors rotational velocities (330, 660 and 990 Hz). The following most intense peaks (1,98 Hz, 2,97Hz, etc.) are related to the third mode of blade rotation originated sound. Those could be intensified by two effects: - interaction (cutting) of vortices and – BLDC motor noise. An increment in separation of the downstream rotor seems also beneficial regarding noise reduction. A small (10 mm) separation of rotors should allow for 1,98 kHz frequency reduction by 15 dB, and 5 dB overall which seems to be a promising direction.

An overall noisiness of the propulsion system is accepted (app. 80 dB, 100 mm form the object), although in close spaces it may by to loud, a 10-20 dB decrement will be a perfect target. This can be obtained by rotors sheltering, but also what more challenging by source intensity reduction. These studies will be further conducted varying rotors velocities to identify more clearly the origins of certain sound sources and frequencies and what follow, further sound power level decrement.

ACKNOWLEDGEMENTS

This work has been supported by the Polish National Centre for Research and Development, Lider III Programme under contract No. LIDER/04/143/L-3/11/NCBR/2012.

REFERENCES

[1] Malecki, I., 1964, Teoria Fal i Układów Akustycznych, PWN (in Polish)

[2] Groenweg, J., F., Aeroacoustics of Advanced Propellers *NASA Technical Memorandum 103137*

[3] Hubbard, H., H., et al., 1991, Aeroacoustics of Flight Vehicles, *NASA Reference Publications 1258, Vol. 1 WRDC Technical Report*.

[4] McAlpine, A., Kingan, M., J., 2012, Far-field sound radiation due to an installed open rotor, *International Journal of Aeroacoustic, 11, (2), 213-234*

[5] Marinus, B., G., Roger M., 2010, Aeroacoustic and Aerodynamic Optimization of Aircraft Propeller Blades, *16th AIAA/CEAS Aeroacoustics Conference, June 2010, Stockholm*

[6] N. Curle, The Influence of Solid Boundaries upon Aerodynamic Sound, *Proceedings of the Royal Society of London. Series A, Mathematical and Physical Sciences*, 231:505-514, 1955.

Conference on Modelling Fluid Flow (CMFF'15)
The 16th International Conference on Fluid Flow Technologies
Budapest, Hungary, September 1-4, 2015

EXPERIMENTAL AND NUMERICAL MAV PROPULSION SYSTEM DESIGN AND PERFORMANCE TESTING

Rafał DALEWSKI[1], Konrad GUMOWSKI[2], Tomasz BARCZAK[3], Jan GODEK[4]

[1] Corresponding Author. Department of Aerodynamics, Institute of Aeronautics and Applied Mechanics, Faculty of Power and Aeronautical Engineering, Warsaw University of Technology. ul. Nowowiejska 24, 00-665 Warsaw, Poland. Tel.: +48 22 234 6006, Fax: +48 22 234 6006, E-mail: rdalewski@meil.pw.edu.pl
[2] Department of Aerodynamics, Institute of Aeronautics and Applied Mechanics, Faculty of Power and Aeronautical Engineering, Warsaw University of Technology. ul. Nowowiejska 24, 00-665 Warsaw, Poland. Tel.: +48 22 234 7767, Fax: +48 22 234 6006, E-mail: kgumowski@meil.pw.edu.pl
[3] Department of Theory of Machines and Robots, Institute of Aeronautics and Applied Mechanics, Faculty of Power and Aeronautical Engineering, Warsaw University of Technology. ul. Nowowiejska 24, 00-665 Warsaw, Poland. Tel.: +48 22 234 1546, Fax: +48 22 234 7513, E-mail: tbarczak@meil.pw.edu.pl
[4] Department of Welding Engineering, Institute of Manufacturing Processes, Faculty of Production Engineering, Warsaw University of Technology. ul. Narbutta 85, 02-524 Warsaw, Poland. Tel.: +48 22 8499797, Fax: +48 22 8499797, E-mail: jangodek@gmail.com

ABSTRACT

The counter-rotating propelling system for a Micro Air Vehicle (MAV) with a contraction inlet was tested experimentally and simulated in ANSYS/Fluent 15 environment.

The propulsion system was manufactured by means of Selective Laser Sintering (SLS), a rapid prototyping method, of polyamide (PA) with additional finishing made of polished coatings. A correlation between various setting of the mechanism (relative position of rotors and inlet, with and without presence of a duct) and loads was investigated. Results were compared for a ducted and non-ducted configuration and in two finishing – rough and polished.

Chosen configurations were also simulated in ANSYS/Fluent 15 environment with the usage of RANS capabilities to measure the impact of upper rotor vortex interaction with the boundary layer of the lower rotor and mutual interaction of vortices. The results were validated against experimental results.

Keywords: Counter-rotating propellers, Ducted propulsion systems, MAV Design, PIV.

1. INTRODUCTION

Micro Air Vehicles require efficient propulsion system. It stays in contradiction with their small dimensions and inefficient low Reynolds flow regime. An interesting option is a ducted propulsion system.

This kind of drive was used to build a flying robot, designated to move in indoor and bushy scenario. Apart of aerodynamic advantages it provides also safe operation for fast rotating propellers in difficult environment.

Rotors were designed basing on hybrid BEM/Actuating disc theory with corrections. The main configuration was tested and described in authors' previous publications [2]. The current configuration was designed to work without the main section of the duct.

The scope of this work was to investigate further properties of the modified system without a complete duct (significant decrease of mass), but with a contracted inlet.

Therefore a test setup was designed and manufactured allowing for independent measurements of forces on inlet elements, upper rotor and lower rotor plus nacelle. Two propertiess were quantified – thrust force and power consumed. As in the previous research [2] samples were tested polished and unpolished. Resulting surface roughness is presented in Table 1.

Table 1. Roughness measurements result [2]

Sample	Ra (μm)
SLS rough	16.53 (+8.93/-4.78)
SLS finished upper/lower	0.39 (+0.04/-0.06)

Tests were performed to investigate best relative setting of rotors and inlet.

2. TEST RIG

The experimental setup presented in Figure 1 provided measurements of axial loads of each particular element of the system (upper rotor, lower rotor, inlet duct). Elements were placed in the test rig allowing for spacing adjustment in the axis of rotation. A strain gauge was dedicated to each element of the system thus allowing for independent measurements of elements' loads contribution to the system.

Data acquisition system was built basing on NI cards, and an control and acquisition system was developed with Labview software.

Data were gathered for a matrix with two variables i.e. elements relative positions (inlet – upper rotor, upper – lower rotor). Dimensions were changed by 2 mm.

Two rotors (the same geometry) designed for a ducted system were used – in first data series rough (app. 16 μm roughness), in the second smoothed after surface treatment. Propelling system was externally powered, electrical conditions (current, voltage and power consumed) were measured. Rotors were dynamically balanced.

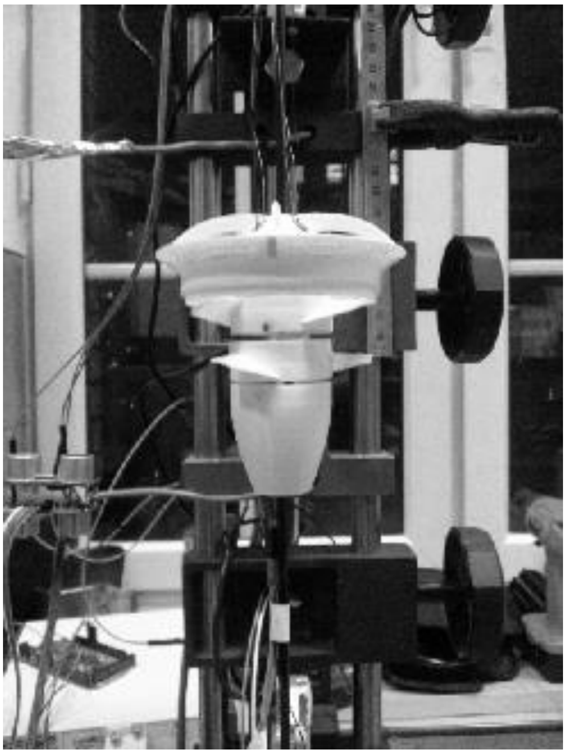

Figure 1. The tested model

The important factor was to compare a ducted and non-ducted system, where in the open configuration (with contracted intake duct) propeller spacing was adjusted to observe the effect of spacing on the minimization of the effects of induced drag. PIV measurements were performed for tip vortices visualization and quantification of field properties for a single rotor. Additionally the aim of PIV measurement was to observe vortex appearance and interactions in the helical wake to identify the conditions for strong and weak vortex formation in the upper and lower rotor.

3. CFD MODEL

Simulations were performed in Fluent 15 CFD environment. A model presented in Figure 2 was employed. Mesh consisting of 18 M cells was created. Calculations were performed using RANS model with k-ω SST turbulence model with transition modelling ability. Model allowed for propellers rotation (mesh sliding).

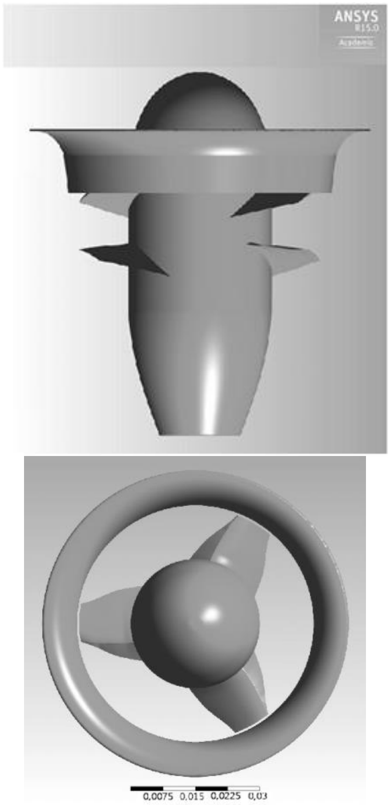

Figure 2. Model used for simulations.

4. EXPERIMENTAL RESULTS

The aim of experimental testing was to observe force and power consumption variation generated by the set of elements and its individual elements in the partially ducted CRP system. Variation of forces was observed in function of three different variables – two types of spacing (inlet translation against upper and lower rotor, lower rotor translation against lower-upper rotor block) and different rotational velocities. Forces were given in grams (of force, sensors were scaled in grams). Distance d0 is a reference value equal to rotor diameter 54 mm. Rotational velocity was given in rotations per minute (RPM).

In Figure 3 we can observe an effect of inlet separation from the upper and lower rotor block (they remain in initial position). What can be clearly seen is the loss of total thrust when separation increases. It is due to the loss observed for the inlet, partially compensated by increment of thrust on the upper rotor. It is however not that beneficial and final thrust loss is equal to 9%.

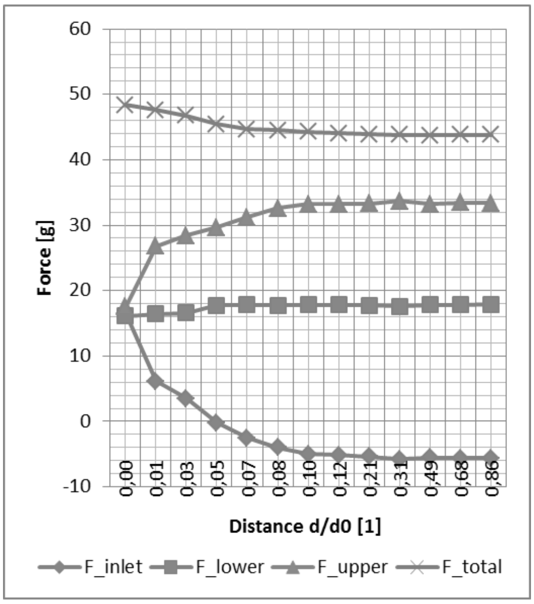

Figure 3. Influence of inlet separation from rotors block (19800 RPM, both rotors).

In the following Figure 4 an influence of lower rotor separation from the inlet-upper rotor block may be observed. Its influence is far less critical then the inlet separation, although for rotational velocity equal to 19,8 kRPM it is 3,2%. Although individual rotors thrusts variation can by observed up to 1,5 characteristic dimension, the total remains untouched from separation equal to 0,5 d0.

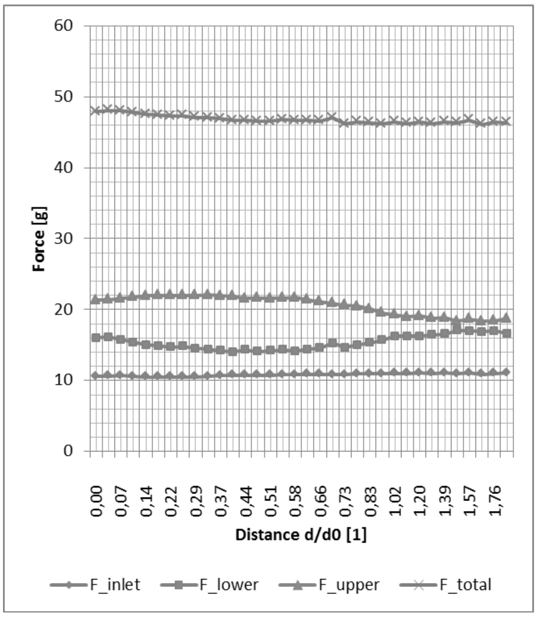

Figure 4. Influence of lower rotor separation from inlet-upper rotor (19800 RPM, both rotors).

Finally in Figure 5 we can observe a variation in total and individual thrusts in case where rotational velocities are not equal. With higher lower rotor velocity it appears that bigger separation (+10% for 21/19,8 velocities ratio) becomes beneficial for total thrust.

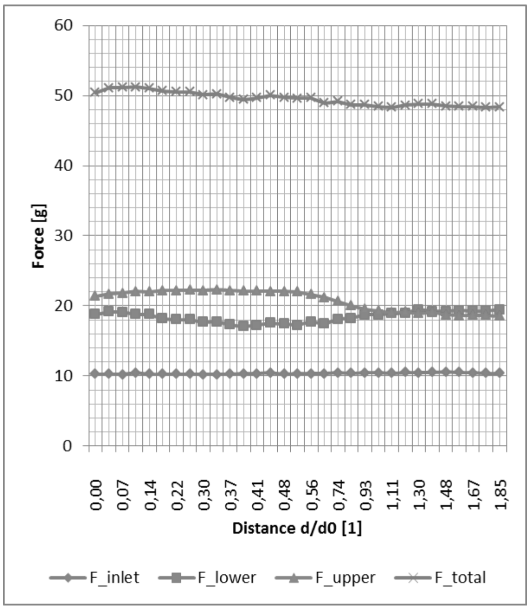

Fig. 5. Influence of lower rotor separation from inlet-upper rotor (19800 RPM, upper rotor, 21000 RPM lower rotor).

Two main observations may be formed on the basis of above fig 3-5. Firstly inlet separation influences total force produced significantly even with relatively small separation, secondly the lower rotor movement influence is less significant, and for a long distance almost unchanged. We can also observe that for uneven rotors velocities the closest upper to lower rotor distance is not the most beneficial.

Further extracted results were set in table 2 and 3 presenting total force difference for closest and furthest position obtained by propelling system when inlet is translated (table 2), lower rotor is translated (table 3). In table 4 results are gathered when different rotational velocities are indicated for upper and lower rotor by different positions of lower rotor.

Table 2. Difference in total force produced by propelling system for maximum and minimum separation of inlet, for different rotational velocities (RPM).

RPM	18000	19800	21600
ΔFtot [%]	10,4	9	8,3

Table 3. Difference in total force produced by propelling system for maximum and minimum separation of lower rotor, for different rotational velocities (RPM).

RPM	19800	21600
ΔFtot [%]	3,2	4,7

Table 4. Maximum force produced, maximum to force produced for minimum separation force, position for which maximum force was obtained, for different rotational velocities.

Upper RPM	18600	19800	19800	19800
Lower RPM	19800	19800	20400	21000
Ftot max	42,27	48,08	51,23	52,06
F0/Ftotmax	1	0,995	0,983	0,998
d/d0	0	0,037	0,1	0,07

The last table extract observation regarding optimal position of lower rotor for different rotational velocities for upper and lower rotor. Table 2 and 3 show that opposite tendency occurs – for greater rotational velocities inlet separation is less influencing, where for lower rotor separation – more.

5. REULTS OF SIMULATIONS

Results of simulations are presented in Figure 6 to 9. In the first (fig. 6) one can observe velocity induced by the propulsion system. For 19800 rotations per minute (RPM) it is equal to mean 16 m/s for a wake stream. Its turbulence intensity is on the mean level of 5-6%.

In the second picture (figure 7) a pressure distribution over the upper rotor upper surface can be observed. It shows good surface loading due to the in-duct blade tip working conditions.

On the other hand in figure 8 a lower rotor upper surface pressure distribution can be observed. It shows uneven loading with conditions for strong helical wake formation, which can be observed e.g. in figure 9 and PIV measurements for individual rotor. In the same picture (fig. 9) we can observe that the lower rotor forms a stronger tip vortex then the upper. The upper produce its vortex due to not perfect sheltering effect of the duct, which covers only a part of the blade.

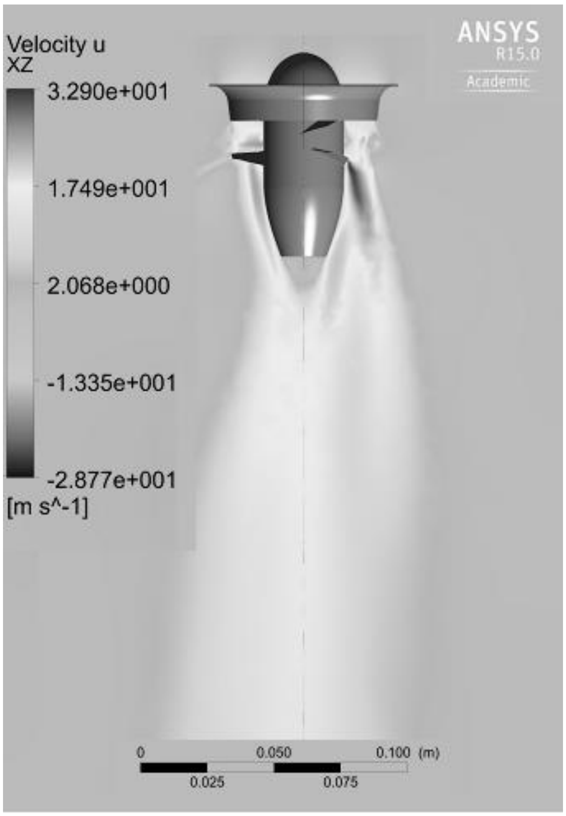

Figure 6. Velocity distribution for both rotors and in the wake (19800 RPM, both rotors, initial position)

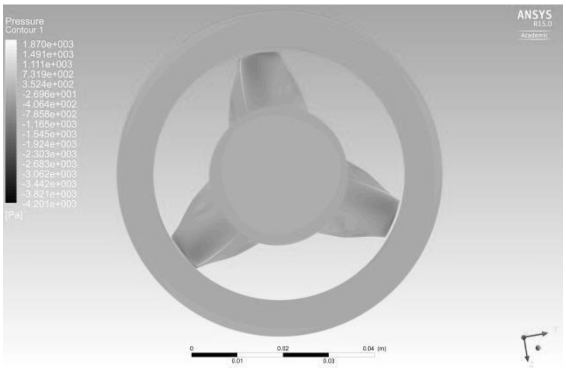

Figure 7. Pressure distribution over the upper rotor upper surface (19800 RPM, both rotors, no separation)

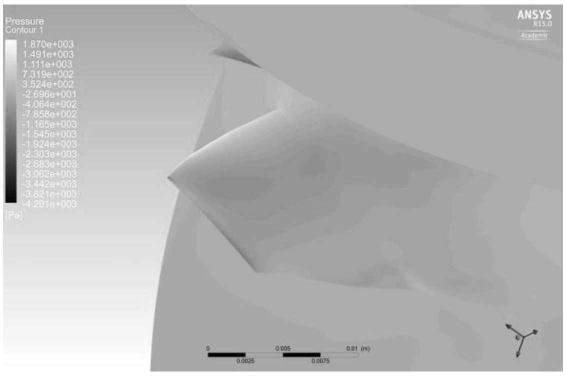

Fig. 8 Pressure distribution over the upper rotor upper surface (19800 RPM, both rotors, no separation)

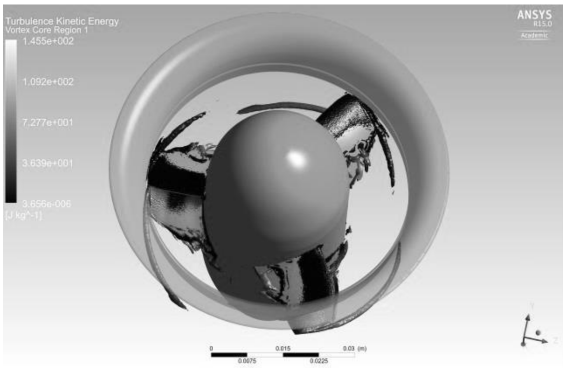

Fig. 9 Influence of lower rotor separation from inlet-upper rotor (19800 RPM, both rotors).

6. PARTICLE IMAGE VELOCIMETRY (PIV)

To identify and quantify tip vortex formation a PIV measurements were additionally performed. It shows a strong but unstable due to wake high turbulence intensity formation. As one can observe in figure 10 and 11 three blades vertices can be observed lasting for a single rotation and further mixed into the wake stream.

PIV confirmed also high turbulence intensity is on the mean level in the close wake of 5-6%. It has to be stressed out that this constitutes a completely different working conditions for the lower rotor, what can be clearly seen in fig. 3 – 5.

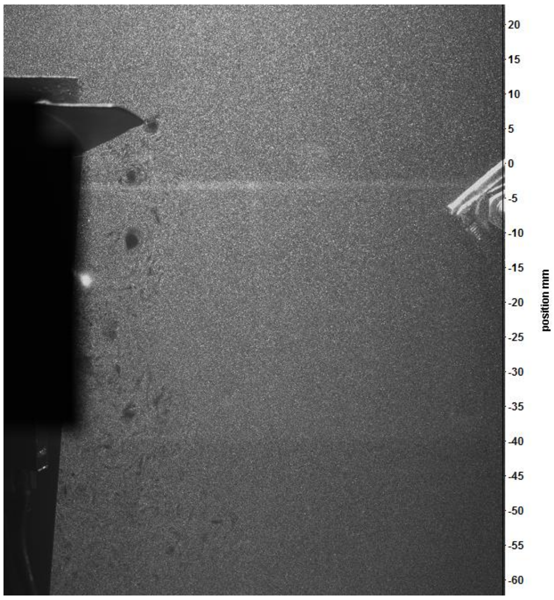

Figure 10. Picture taken from PIV system showing tip vortices formation (single rotor, 22000 RPM, both rotors)

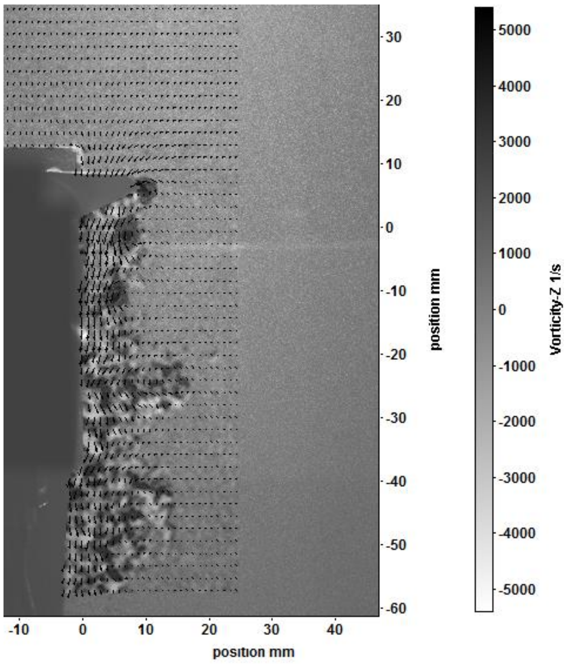

Figure 11. Vorticity field from PIV system showing tip vortices formation and a turbulent wake (single rotor, 22000 RPM, both rotors)

6. RESULTS DISCUSSION

Three groups of observations can be discussed in presented results summary. The first group relates directly to experimental results and pure separation effect influence, the second relates to flow properties and the third describes comparison with previously measured ducted (long duct) propulsion system properties.

Going to the first group we can formulate following observation – ducted inlet presence is beneficial and its position is of great importance for total thrust production. Lower rotor should be adjusted to different working conditions (higher turbulence), but low Reynolds number with high turbulence will still decrease its efficiency. When different rotational velocities are expected (which due to unequal moment production and autorotation balance is usually the case) increased separation may positively influence total thrust production.

High loading of the blades is not beneficial for blades working outside the duct. Because blades were designed for in-duct conditions its open rotor performance is not very impressive. Therefore a strong helical wake is produced (PIV), and a very turbulent wake is present. On the other hand, however fig. 4 shows that for significantly wide separation both rotors produce almost equal portion of thrust.

Finally in the table 5 and 6 results for tested propulsion system and a fully ducted (both rotor sheltered) are set.

First observation in this group depicts a strange correlation between rough rotors of the model described in this paper and its ducted ancestor. Also in the comparison to the finished surface results obtained for the configuration presented it is unexpected and needs to be further tested. Namely results obtained for rough configuration are 1) higher than for the polished ones an 2) they are higher than for rough ducted results. This needs to be retested.

Taking into account only polished configurations – ducted drive is more efficient, produces more lift at less power consumed (app. 10% more lift at 8% less power required). Fluent made computation are in relatively good correlation to the experimental results what confirms assumed method of testing (turbulence and transition models).

Those type of drives seem to be most promising for small propulsion system of MAV. Its current efficiency (3 gram of 1 Watt) for this flow regime is relatively promising but further testing of roughness influence may lead to increment of current efficiency.

Table 5. Thrust force in gram (@power-supplied) results. Force in G (gram) for a ducted drive [2].

	19 kRPM	21 kRPM	22.5 kRPM
SLS rough	28@12W	36@14.7W	40.7@16.9W
SLS finished	42@13W	53@15.5W	60.5@17.6W
Fluent	42@14W	-	58@18.5W

Table 6. Thrust force in gram (@power-supplied) results. Force in G (gram) for a propulsion system presented in this publication.

	19800 RPM	21600 RPM	19800 RPM d/d0 = 86%
SLS rough	48@16W	59@20W	43@16.8W
SLS finished	37@16W	48@17W	-
Fluent	-	54,6@22W	-

ACKNOWLEDGEMENTS

This work has been supported by the Polish National Centre for Research and Development, Lider III Programme under contract No. LIDER/04/143/L-3/11/NCBR/2012.

REFERENCES

[1] Drela, M., 1989, XFOIL: an Analysis and Design System for Low Re *Airfoils Springler-Verlag Lec. Notes in Eng. 54*

[2] Dalewski, R., T., Gumowski, K., Barczak, T., Godek J., 2014, "Performance of a Micro-UAV lifting system built with the usage of rapid prototyping methods", *Journal of Physics Conference Series 08/2014*. DOI: 10.1088/1742-6596/530/1/012027

[3] Schafroth, D., M., 2010, Aerodynamics, Modelling and Control of an Autonomous Micro Helicopter, *DISS. ETH NO. 18901*, Zürich

[4] Kunz, P., J., 2003, Aerodynamics and Design for Ultra-Low Reynolds Number Flight, *PhD Dissertation*, Standford

[5] Kunz, P., J., Kroo, I., 2001, Analysis and Design of Airfoils for Use at Ultra-Low Reynolds Numbers, Fixed and Flapping Wing Aerodynamics for Micro Air Vehicle Applications, edited by T. J. Mueller, Vol. 195, *Progress in Aeronautics and Astronautics, AIAA*, Reston, VA, 2001, Chap. 3.

[6] Glauert, H., 1948, The Elements of Aerofoil and Airscrew Theory, *Cambridge University Press*, London.

[7] McCormick, Barnes, W., 1999, Aerodynamics of V/STOL Flight *Dover Publications Inc.*, New York.

Conference on Modelling Fluid Flow (CMFF'15)
The 16th International Conference on Fluid Flow Technologies
Budapest, Hungary, September 1-4, 2015

EFFECT OF GROOVES SHAPE ON AERODYNAMIC CHARACTERISTICS OF SQUARE AND CIRCULAR CYLINDER IN 2 DIMENSIONAL FLOW

Tengku Fikri[1], Hiroo Okanaga[2],

[1] Corresponding Author. Department of Mechanical Engineering, Tokai University. 259-1292, 4-1-1 Kitakaname, Hiratsuka-shi, Kanagawa, Japan. Tel.: +81 4 63(58) 1211, Fax: +81 4 63(59) 2207, E-mail: tengkufikri@gmail.com
[2] Department of Fluid Mechanics, Tokai University. E-mail: okanaga@tokai-u.jp

ABSTRACT

The fluid flow characteristics and drag reduction of square and circular cylinder with grooves are investigated. The grooves, which are linear to the flow direction and applied to bluff bodies' surface, have three shapes (arc, rectangular and triangular shape). The drag coefficient is measured from wind tunnel experiment and the flow around square and circular cylinder are visualized from the spark tracing method and the suspension method. Results from wind tunnel experiment showed that, in the case of square cylinder, the square cylinders with rectangular grooves have optimum drag coefficient than that of arc and triangular grooves. Moreover, the reduction of circular cylinder's drag coefficient is higher than that of square cylinders. From the flow visualization experiments, the tendency of flow patterns of grooved square and circular cylinders are similar to their drag coefficient reduction pattern.

Keywords : grooves, square cylinder, circular cylinder, drag reduction, drag coefficient

NOMENCLATURE

C_D	[-]	drag coefficient
D	[N]	drag force
ρ	[kg/m^3]	density
A	[m^2]	frontal projected area
U	[m/s]	velocity (wind tunnel)
w	[mm]	grooves' width
i	[mm]	grooves' intervals
b	[mm]	grooves' depth
d	[mm]	length/diameter of test models
w/d	[-]	width ratio
i/d	[-]	interval ratio
b/d	[-]	depth ratio
Re	[-]	Reynolds number
R	[-]	Reduction rate (%)
C_{Do}	[-]	S0's drag coefficient
C_{Dx}	[-]	grooved models' drag coefficient
u	[mm/s]	inlet velocity along X-axis (water tunnel)
u_0	[mm/s]	inlet average velocity (water tunnel)
$\lvert u/u_o \rvert$	[-]	absolute velocity (water tunnel)
M	[mm]	separation width
X, Y		coordinates (water tunnel)

1. INTRODUCTION

Drag reduction on bluff bodies has been studied for past few years. It is understood that drag coefficient of bluff bodies is influenced by bluff bodies' shapes and surface structure.

Naudascher [1] carried out experimental analysis on controlling the flow separation of square cylinders with the various corners shapes. In Japan, Mizota and Okajima [2] investigated the relationship between the aspect ratio of the rectangular cylinder and drag coefficient. They indicated that the maximum drag coefficient C_D is 3.0 when aspect ratio is at 0.62.

Sushanta Dutta [3] studied the flow past a square cylinder at an angle of incident at low Reynolds number. At Re 410, a minimum of drag coefficient is observed at 22.5°. This effect attributes are caused by wake asymmetry originating from shear layers of unequal lengths on each side of the cylinder. When the wake area loss its symmetry, the transverse velocity and the base pressure increases making the drag force lower.

T.TAMURA [4] studied the effect of corner shape (chamfered and rounded) and its presence to aerodynamic characteristics of a square cylinder. From the experiment result, drag coefficient of square cylinder with corner shape is lower than normal square cylinder. The drag coefficient of chamfered and rounded square cylinder decreased compared with the drag coefficient of normal square cylinder because the separated shear stress at side of square cylinder becomes closer and reduces the drag force.

M. KOIDE [5] studied the effect of grooves to the aerodynamic characteristics around square cylinder. The grooves represent the balcony of tall buildings. Furthermore, B.AFIQ[6] focused on the effect of grooves width and interval to the aerodynamic characteristics of square cylinder. From the experiment, the drag coefficient of square cylinder with grooves is lower than normal square cylinder. In addition, the drag coefficient becomes lower as the grooves interval is larger.

Y.WAKAI and S.TAKAYAMA[7] studied the effect of grooves shape(arc, rectangular and triangular) to the flow characteristics and the drag reduction of circular cylinder. The grooves are applied along the axial direction on the surface of the circular cylinder. Their experiment results showed that circular cylinder with triangular grooves has lower drag coefficient than other grooves shape because the boundary layer flow over triangular grooves is thinner than arc and rectangular grooves, and also has higher transverse velocity which resulted low drag force for the circular cylinder.

These literature reviews indicates that studies of aerodynamic characteristics around bluff bodies are important for its application in various industrial uses. It is known that drag coefficient can be reduced by changing the bluff bodies' shape and grooves implementation on its surface. However, there are only few researches that discussed about the effect of grooves shape to drag coefficient of bluff bodies and the overall effects remain unknown. Therefore, this paper reports the aerodynamic characteristics of bluff bodies with various grooves' shapes. The objective of this study is to clarify the optimum grooves' shape and the groove's interval whose drag coefficient is the lowest. 13 square and 7 circular cylinder as bluff bodies with three different grooves shapes which are rectangular, arc and triangular are used in this experiment. Drag coefficient is measured by wind tunnel experiment. Furthermore, flow visualization around square and circular cylinder is carried out by spark tracing method and water suspension method.

2. INSTRUMENTAL APPARATUS

2.1. Model Configuration

The test model which served as the basic structure for experiment is shown in figure 1. It is consisted of ABS synthetic resin with 40 *mm* length (d) and 100 *mm* height (h). Moreover, 20 types of grooved square and circular cylinder with different sizes of grooves' interval ratio (i/d) and width ratio (w/d) had been used in the experiment as shown in table 1. The groove depth (b), is set to 2 *mm* in all square and circular cylinder except for triangular grooves which have 1.5 *mm* and 2 *mm* depth.

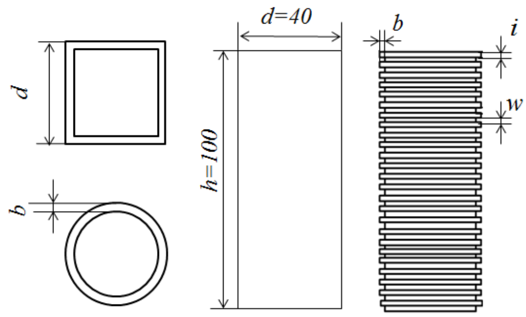

(a) Cross section of test models

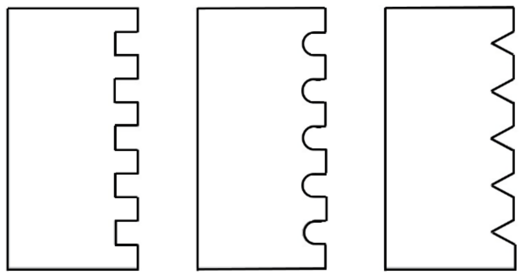

(1)Rectangular[R] (2)Arc[A] (3)Triangular[T]
(b) Grooves shape
Figure 1. Test model Configuration

Table 1. Models Configuration

Type	Grooves Ratio		A [mm^2]
	i/d	b/d	
S0	0	0	0.004000
SR22	0.05	0.05	0.003800
SR32	0.075	0.05	0.003840
SR52	0.125	0.05	0.003888
SA22	0.05	0.05	0.003821
SA32	0.075	0.05	0.003857
SA52	0.125	0.05	0.003900
ST21	0.05	0.0375	0.003950
ST31	0.075	0.0375	0.003960
ST51	0.125	0.0375	0.003972
ST22	0.05	0.05	0.003900
ST32	0.075	0.05	0.003920
ST52	0.125	0.05	0.003944
C0	0	0	0.004000
CR22	0.05	0.05	0.003800
CR32	0.075	0.05	0.003840
CR52	0.125	0.05	0.003888
CA22	0.05	0.05	0.003821
CA32	0.075	0.05	0.003857
CA52	0.125	0.05	0.003900

The implementation of grooves onto the surface of square and circular cylinder along the flow direction also effected the size of frontal projection area (A). The frontal projection area (A) for grooved bluff bodies is calculated by omitting the grooves area as shown in table 1.

2.2. Drag Measurement

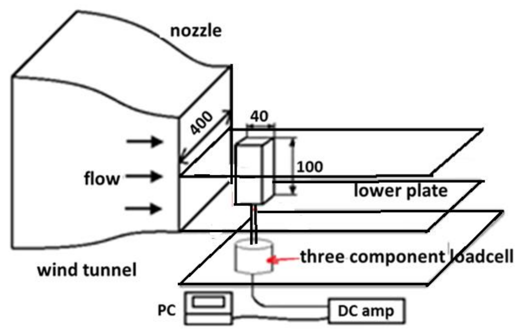

Figure 2. Apparatus for drag coefficient measurement

Figure 2 shows the experimental apparatus used for drag coefficient measurement and flow visualization around the square cylinder. The wind tunnel have a test section of 400 *mm* × 400 *mm* and the flow velocity used for this experiment was 30 *m/s* (Re =8.0 × 10^4). The turbulence intensity in this velocity range of this wind tunnel is 0.3%. The test model is placed at the center of the test section to minimize blockage effects. The distance between the upper plate and the test model is approximately 0.5 *mm*. The test model is attached to a three component load cell to measure the drag, lift and yawing moment. Equation for drag coefficient is shown in eq. (1).

$$C_D = \frac{2D}{\rho A U^2} \tag{1}$$

Where D is the drag force which are measured from the component load cell, ρ is the density of air, A is the frontal projection area and U is the flow velocity.

2.3. Flow Visualization by Suspension Method

Figure 3 shows the schematic view of the visualization experiment and figure 4 the definition of coordinates for the absolute velocity distribution measurement point. The visualization experiment using a laser light sheet and a high speed camera (HAS-500 KATOKOKEN CO, LTD). The tracer particles for this experiment are Orgasol (average diameter = 50 μm, relative density = 1.03). By using a laser and high speed camera, the movements of the tracers are taken to observe the flow characteristic around the square and circular cylinder. The experiment is carried out as follows; shutter speed 1/200 Sec and Re=8000. All image of the experiment are analyzed by using a PIV analysis software. (FlowExpert - KATOKOKEN CO, LTD)

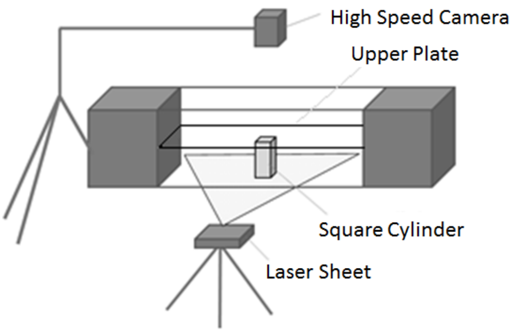

Figure 3. Apparatus for water tunnel experiment

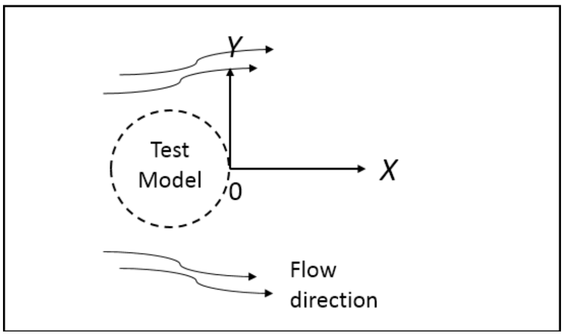

Figure 4. Definition of coordinates

2.4. Flow Visualization by Spark Tracing Method

Figure 5 shows the experimental apparatus of the spark tracing method. The power source for this experiment is a high-voltage/high frequency pulse generator. The applied voltage is 250 *kV*, the pulse interval is 150 μs and the number of pulse is 150. The electricity is stored in a pulse drive unit and then passed through a pulse transformer and two fixed electrodes. The electrode material is tungsten, and has a diameter of the electrode is 0.3 *mm*. The first electric spark from the pulse wave arcs to another electrode and the air is ionized. This ionized air moves together with the flow. The second electric spark from the pulse wave passes through this ionized air because the electric resistance of the ionized air is low, and the second electric spark again produces ionized air. The ionized air from the second electric spark moves together with the flow and the third electric spark moves through the ionized air from the second electric spark. The flow pattern around the test model can be visualized by repeating this process. The Reynolds number of this experiment is the same to drag coefficient measurement which is Re =8.0 × 10^{4}.

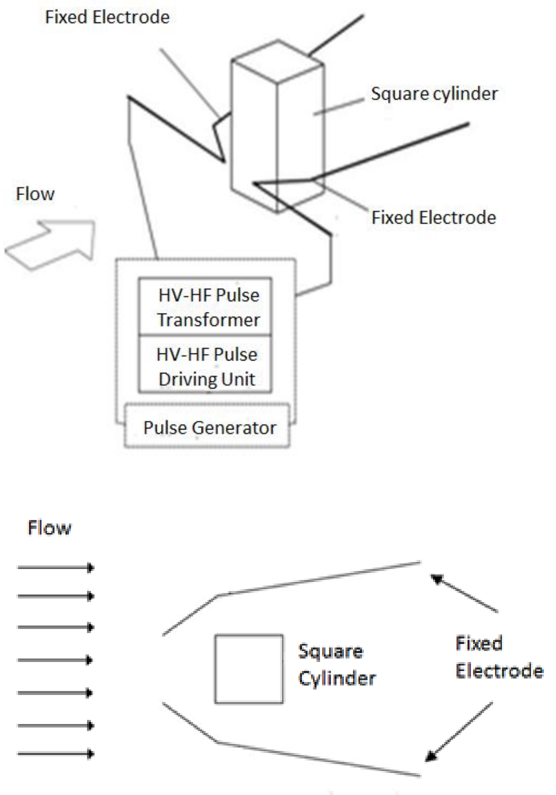

Figure 5. Apparatus for spark tracing method

3. EXPERIMENT RESULT

3.1. Drag Measurement

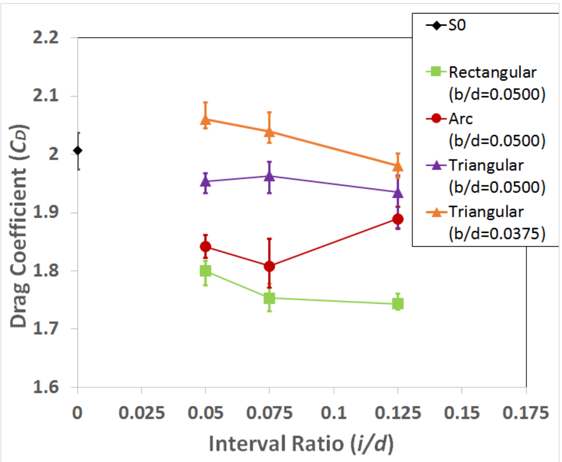

Figure 6. Drag Coefficient of Square Cylinder

Figure 6 shows the relationship between drag coefficient and grooves interval ratio for square cylinder with different grooves shape. From the result, the drag coefficient of normal square cylinder is approximately 2.0, which is similar to the result from past researches. Therefore, this result considered to be reliable. The drag coefficient of grooved square cylinder is lower than the normal square cylinder. Furthermore, the square cylinder with rectangular grooves has the lowest drag coefficient followed by arc and triangular grooves. In the case of increasing grooves' interval ratio(i/d) from 0.05 to 0.125, the drag coefficient of square cylinder with rectangular grooves shows decreasing pattern. Meanwhile, the drag coefficient for arc grooves decreased from i/d=0.05 to 0.075, and increased after i/d=0.075. The drag coefficient of square cylinders with triangular grooves with depth ratio of 0.0375 and 0.05 is higher than the normal square cylinder and its trendline showed irregular pattern where drag coefficient of trianglular grooves with depth ratio of 0.0375 decreased from i/d=0.05 to i/d=0.125 while depth ratio of 0.05 shows no significant changes. Therefore, the square cylinder with rectangular grooves with an interval ratio of 0.125 is the best model for the effect of drag reduction in the case of square cylinders.

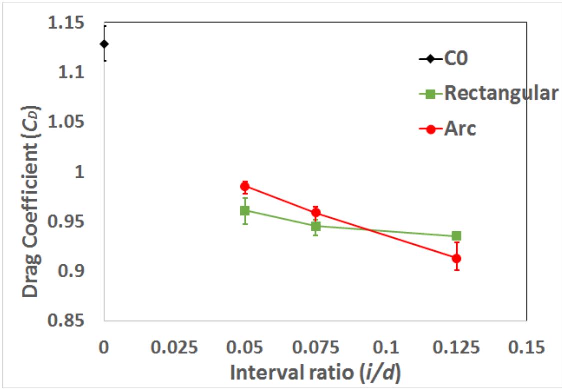

Figure 7. Drag Coefficient of Circular Cylinder

Figure 7 shows the effect of grooves shape to drag coefficient in circular cylinder. From the result, the value of drag coefficient of circular cylinder is close to 1.2, thus this result is reliable. Furthermore, it is clarified that the effect of grooves to drag coefficient of circular cylinder is similar to the square cylinder which its drag coefficient decreases as grooves are applied onto its surface. In the case of increasing grooves' interval ratio for circular cylinder, circular cylinder with rectangular grooves has lower drag coefficient than arc grooves.

Figure 8 and 9 shows the graphs of reduction rate of drag coefficient for square and circular cylinder. The reduction rate of drag coefficient is calculated from eq. (2).

$$R(\%) = \frac{C_{D0} - C_{Dx}}{C_{D0}} \times 100 \qquad (2)$$

Where R is the percentage of reduction rate of drag coefficient, C_{D0} is drag coefficient of S0 and C0 and C_{Dx} is drag coefficient of 18 types of grooved square and circular cylinders. From figure 8, square cylinder SR52 has the highest reduction rate of drag coefficient at 13.12%. In the case of circular cylinder as shown in figure 9, circular cyinder with arc grooves CA52 has the highest reduction rate at

19.1%. Thus, the reduction of circular cylinder's drag coefficient is higher than that of square cylinders

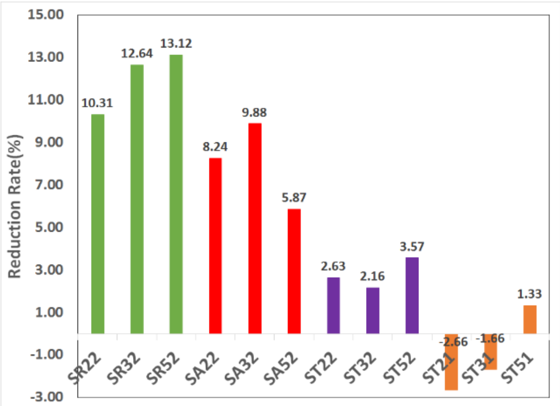

Figure 8. Reduction rate (%) of drag coefficient in square cylinder

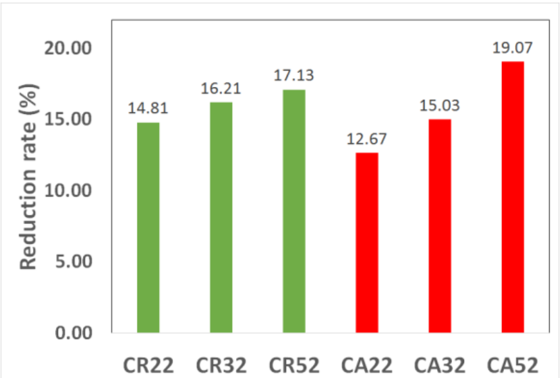

Figure 9. Reduction Rate (%) of drag coefficient in circular cylinder

3.2. Flow visualizations by spark tracing method

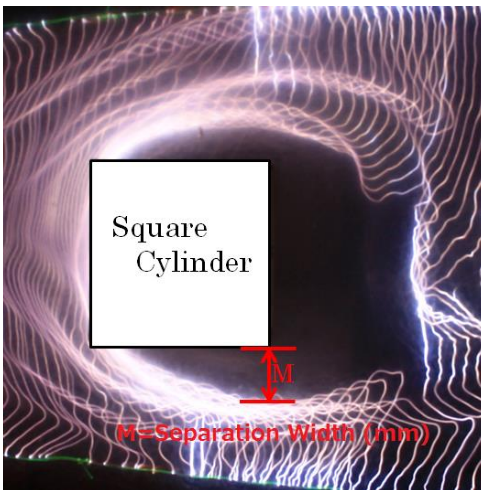

Figure 10. Flow visualization of spark tracing method

Figure 10 shows the picture taken from Spark Tracing Method experiment and the definition of M. 50 pictures of flow around each square cylinder were taken due to the unsteady flow and the separation width (M) for each 50 images is measured and the average value of separation width for each square cylinder is shown in figure 11. From the result, it is clarified that the separation width decreases as the drag coefficient decreases because of higher transverse velocity across grooved square cylinder surface. Furthermore, rectangular grooves has the lowest separation width followed by arc and triangular grooves, thus justified the drag coefficient result in figure 6.

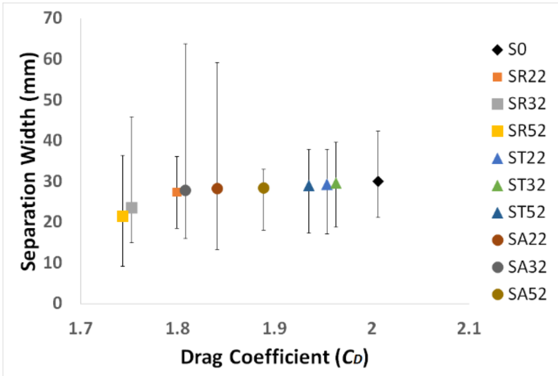

Figure 11. Relationship between separation width and drag coefficient of square cylinder (Spark tracing method)

3.2. Flow visualizations by water tunnel experiment

In figure 13(a), the letter M indicates the size of separation width.and figure 13(b) and 13(c) shows the colour-contra images of average of absolute velocity around the square cylinder, which are analysed from video with a duration of 10 seconds taken by a high speed camera of 200 fps, by using a PIV analysis software.

Figure 13(b) and 13(c) show images of absolute velocity around S0 and SR52. It is observed that the low velocity region (dark blue colour region) of SR52 is narrower than S0 because of SR52 has lower drag coefficient than S0 that lead to the flow velocity around S52 faster than S0.

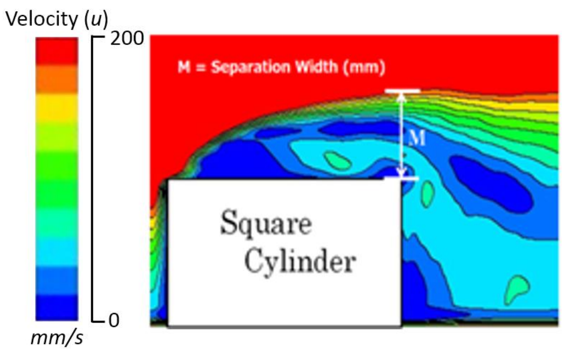

(a). Definition of separation width (M)

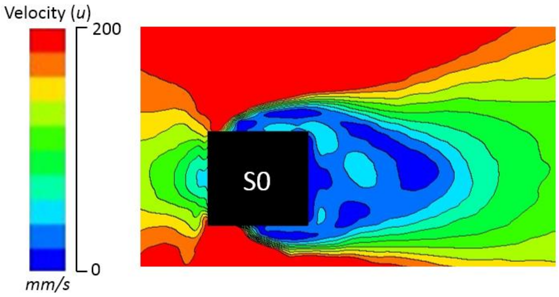

(b) Average of absolute velocity around square cylinder S0

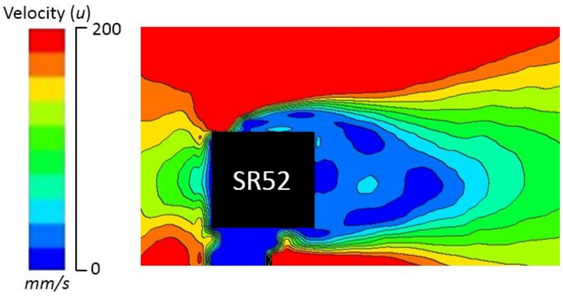

(c) Average of absolute velocity around SR52 (*i*/*d*=0.125)

Figure 13. Differences of low velocity region between S0 and SR52

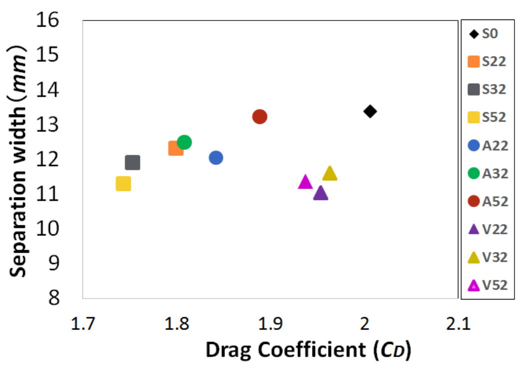

Figure 14. Separation width in square cylinder (Water Tunnel Experiment)

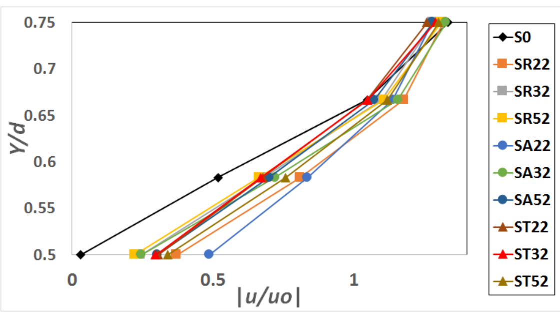

Figure 15. |*u/uo*| distribution at *X/d*=0, *Y/d*=0.5~0.75

Figure 14 shows the relationship between size of separation width and drag coefficient for square cylinder. S0 has the highest separation width because it has the highest drag coefficient than the grooved square cylinders. This result shows that separation width decreases as drag coefficient decreases which is similar with the result obtained from spark tracing method as shown in figure 11. However, triangular grooves showed an irregular pattern, thus more experiments are needed to clarify these phenomenas.

Figure 15 shows the absolute velocity distribution result for square cylinders from *Y/*d=0.5 to 0.75 at *X/d*=0. From the result, grooved square cylinders have higher velocity than the normal square cylinder S0 that causes the low velocity region to become narrower.

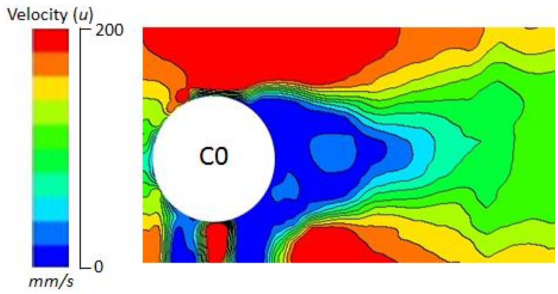

(a) Average absolute velocity around C0

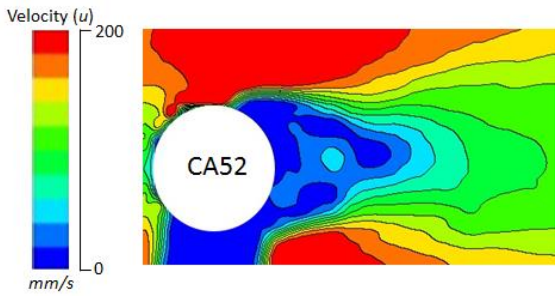

(b) Average absolute velocity around CA52 (*i*/*d*=0.125)

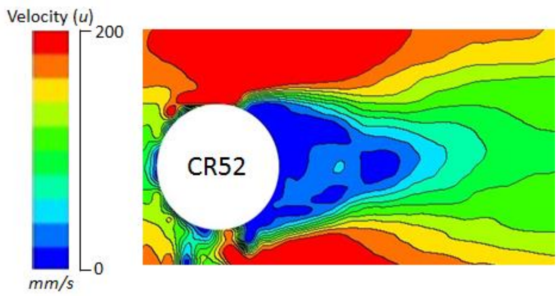

(c) Average absolute velocity around CR52 (*i*/*d*=0.125)

Figure 16. Differences of low velocity region between C0, CA52 and CR52

Figure 16 shows images of different size of low velocity region for circular cylinders. It is observed that there is no difference of flow pattern between normal circular cylinder C0, CR52 and CA52 except that the separation point for C0 precedes more than CR52 and CA52.

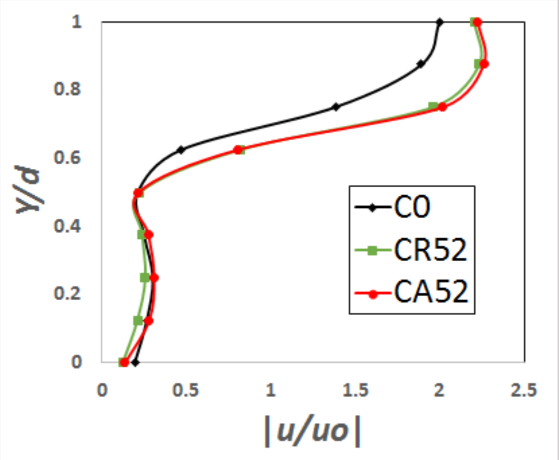

Figure 17. Absolute velocity distribution results at measurement point of *X/d*=0

Figure 17 shows the absolute velocity distribution ($|u/u_o|$) results calculated at *X/d*=0 for circular cylinder. The circular cylinder with grooves has higher flow velocity than circular without grooves. As a result, it is clarified that implementation of grooves onto the circular cylinder surface increases the flow velocity of X-direction around circular cylinder resulted in lowering its drag coefficient. Furthermore, the flow velocity for each circular cylinder gradually increases as it flows further away from circular cylinder in Y-direction.

4. CONCLUSIONS

In this study the influence of various groove shape and body shape to the aerodynamic characteristics around square cylinder is investigated by wind tunnel experiment and flow visualization. Furthermore, flow around the square and circular cylinder can be concluded as follows;

(a) Conclusion for square cylinder;

1. The lowest drag coefficient for grooved square cylinders occurs when the square cylinder has rectangular grooves and has an interval ratio *i/d* of 0.125 (SR52).
2. The square cylinder with triangular grooves with depth of 1.5 *mm* (*b/d*=0.0375) has higher drag coefficient than other square cylinders.
3. Separation width of square cylinder decreases when the drag coefficient decreases

(b) Conclusion for circular cylinder;

1. The trendline of drag coefficient for circular and square cylinder with rectangular grooves is similar.

(c) Conclusion for both square and circular cylinder is as follows;

1. Test models with low drag coefficient possesses flow with a high velocity.
2. The reduction rate of drag coefficient of circular cylinder is bigger than square cylinder.

REFERENCES

[1] E. Naudascher, J.R. Weske and B. Fey, „Exploratory study on damping of galloping vibrations", *Journal of Wind Engineering and Industrial Aerodynamics*, Vol. 8, Issues 1–2, 1981, pp211–222.

[2] T MIZOTA, A OKAJIMA, „Experimental studies of time mean flows around rectangular prismas", *Journal of JSCE*, No.312, 1981, pp 39-47.

[3] Sushanta Dutta, P. K. Panigrahi and K. Muralidhar, "Experimental Investigation of Flow Past a Square Cylinder at an Angle of Incidence," *Journal of Engineering Mechanics*, Vol. 134, Issue 9, 2008, pp. 778-803.

[4] T. TAMURA and T. MIYAGI, 1999, "The effects of turbulence on aerodynamic forces on a square cylinder with various corner shapes," *Journal of Wind Engineering and Industrial Aerodynamics*, Vol. 83, Issues 1-3, pp. 135-145

[5] M.KOIDE, H.OKANAGA and K.AOKI, 2006, "Effect of grooves on the aerodynamics around corner cut square cylinder", *Proceeding of The School of Engineering of Tokai University*, Vol. 46, No. 2, pp. 79-84 (in Japanese).

[6] B.AFIQ and H.OKANAGA, 2012, "Aerodynamic characteristics of square cylinder with grooves (Effect of width and interval of grooves)", *Proceedings of The School of Engineering of Tokai University*, Vol. 37, pp. 29-34.

[7] Y.WAKAI, S.TAKAYAMA and K.AOKI, 2004, "Flow characteristics and drag reduction mechanism on the groove shape of circular cylinder with grooves", *Proceedings of The School of Engineering of Tokai University*, Vol. 44, No.2, pp. 61-65.

Conference on Modelling Fluid Flow (CMFF'15)
The 16th International Conference on Fluid Flow Technologies
Budapest, Hungary, September 1-4, 2015

THE EFFECT OF SURFACE STRUCTURES TO THE AERODYNAMIC CHARACTERISTICS OF SOCCER BALL WITH OR WITHOUT ROTATION

Takuto Mizusawa[1], Mohad Eqkhmal[2], Gou Yagi[3]
Hiroo Okanaga[4], Katsumi Aoki[5]

[1] Department of Mechanical Engineering, Tokai University. 4-1-1 Kitakaname, Hiratsuka-shi, Kanagawa, 259-1292 Japan. Tel.: +81-463-58-1211, E-mail: 1bem2239@mail.tokai-u.jp
[2] Department of Mechanical Engineering, Tokai University. E-mail: eqkhmalrazak@gmail.com
[3] Mechanical Engineering, Graduate school of Engineering, Tokai University. E-mail: 3bmkm055@mail.tokai-u.jp
[4] Corresponding Author. Department of Mechanical Engineering, Tokai University. E-mail: okanaga@tokai-u.jp
[5] Department of Mechanical Engineering, Tokai University. E-mail: katsumi@keyaki.cc.u-tokai.ac.jp

ABSTRACT

Nowadays various types of balls are used in sports. For example, many types of soccer balls show different air flow characteristics that impact the outcome of the game. Mach research on the aerodynamic characteristics of type of soccer balls have been done. However, the effects of surface to the aerodynamic characteristics are still unkown. In this paper, the effects of surface structure of balls with or without rotation on the aerodynamic characteristics of balls are investigated by using a wind tunnel experiment. Seven types of model balls made by 3D printer are used in this experiment. For the aerodynamic characteristics, a wind tunnel was used to measure the drag of the balls and for the flow visualization in an oil film method was used to measure the angle between stagnation point and separating point on the balls. In the results, for balls without rotation, the critical Reynolds number for balls with few panels is higher than that of the balls with many panels. In visualization, the separating angle becomes a high angle as the Reynolds number becomes higher. In addition, the effect of the various kinds of surface structures of balls with rotation is also investigated.

Keywords: Aerodynamic characteristics, Ball with rotation, Model ball, Soccer ball, Various surface structure

NOMENCLATURE

C_D	[-]	drag coefficient
C_L	[-]	lift coefficient
A	[m^2]	area
ρ	[kg/m^3]	density
U	[m/s]	velocity
θ	[°]	separation angle

Subscripts and Superscripts

L, D	lift, drag

1. INTRODUCTION

Nowadays various types of moving balls are used in sports. Some ball games, for example football or baseball, are some of the most popular sports. The surface structures of balls in these sports are different. For example, in football games, many non-rotating curved balls have been used recently. Jabulani was used in the 2010 soccer World Cup. The aero characteristics of this ball is interesting because the number of panels is lower and the movement in a knuckle shot is greater than that of previous balls.

There has been a lot of research on the aerodynamic characteristics of various moving balls. For example, Ito studied the effect that a soccer ball's surface roughness has on its aerodynamic characteristics. The results of the visualization and wind tunnel experiments show almost identical results for rough and smooth soccer balls [1]. In addition, Asai carried out a visualization experiment for non-rotating soccer balls. From the results of the visualization, ring-shaped vortexes were produced behind the ball [2]. Moreover, we studied the relationship between the surface structure and aerodynamics of soccer balls. Our results show that an increasing number of panels for a non-rotating ball made the Reynolds number of the critical region decrease [3] [4]. Furthermore, Seo carried out an experiment regarding drag coefficients of 8 kinds of soccer balls. His study shows that total seam length influences the drag coefficient [5]. However, the flow characteristics of various kinds of soccer balls are still unknown. In this paper, the effect of the surface structure of soccer balls on the aerodynamic characteristics of the ball is investigated by using model balls made by a 3D printer that changed the number of panels and the shape of the panel. The experimental method used wind tunnel experiments and an oil film method for the flow visualization.

2. EXPERIMENTAL APPARATUS

2.1. Wind tunnel

A blow-down type wind tunnel made for the test soccer balls was used for the aerodynamic measurements and flow visualization. The size of test section is 400*mm* × 400*mm*. In this experiment, the flow velocity is changed from about 15 to 60 *m/s*. The turbulence intensity in this flow velocity range is within 0.3%. A rectangular frame of 500*mm*×500*mm* is placed at 175*mm* from the outlet of the wind tunnel as shown in Figure 1. The test ball is fixed at the center of the frame using a piano wire, giving tension at both the fixed ends. The diameter of the piano wire is 2.6*mm*. The ratio (d_p /d) of the piano wire diameter (d_p) to the sphere diameter (d) is 0.037 or less, so the effect of the piano wire is assumed to be negligible [6]. In this study, d_p/d was 0.024. Furthermore, the blockage ratio in this wind tunnel test is 5.9%.

The drag D and lift L acting on the test balls are measured by taking the mean value of 2000 data at every 1.0×10^{-3} intervals, using the three component load cells with the attached strain gauge. The Reynolds number of this experiment is between 0.6×10^5 and 2.8×10^5.

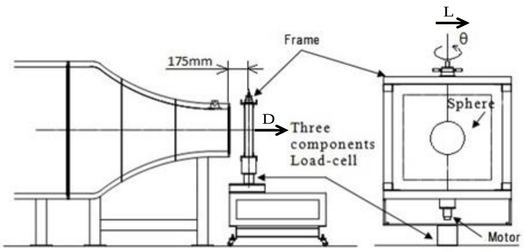

Figure 1. Schematic diagram of wind tunnel

2.2. Measurement of Drag and Lift

The drag coefficient C_D and lift coefficient C_L are calculated with the following equations (1).

$$D, L = C_{D,L}\frac{\rho A U^2}{2} \tag{1}$$

2.3. Flow visualization

The oil film was made by oleic acid, titanium dioxide, liquid paraffin, and linseed oil. Oleic acid was added to prevent the oil film from drying. In addition, titanium dioxide was used for white coloring. The mixing rate is oleic acid: 1*ml*, titanium dioxide: 2*g*, liquid paraffin: 5*ml*, linseed oil: 1*ml*. The moisture, the dust, and so on on the surface of the balls were removed. Moreover, the oil film was spreaded thinly and uniformly all over the surface of the balls.

2.4. Experimental balls

Figure 2 shows the front surface of the Smooth ball and model balls, which are shown from the front surface of the wind tunnel. The size of the Smooth ball is 220*mm*, and the model balls are at 1/2 scale, 110*mm*. These model balls were made with the 3D printer; the material is Polylactic acid. Model 0 is the model ball which have no groove. Model 1 is the model ball of a 32 panel soccer ball in general use. Models 2 to 6 have differing numbers of ball panels in order to reseach the effect of panel numbers. Model 2 has 32 panels, Model 3 has 20, Model 4 has 14 panels, Model 5 has 12 panels, and Model 6 has 8 panels. The depth of the grooves of these balls are all 0.8*mm*. In this study, we define 0° as the aspect that becomes axial symmetry.

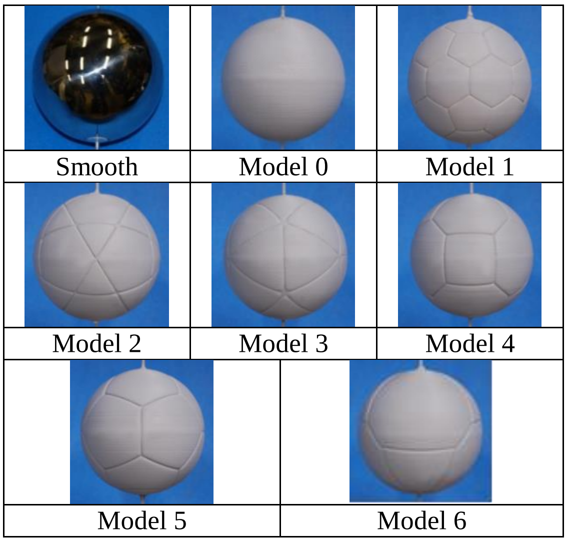

Figure 2. Experimental balls (0°)

Figure 3 and 4 show the surface at 45° and 90° of the model balls. The changing angle was made by a left turn when we saw the top of the balls.

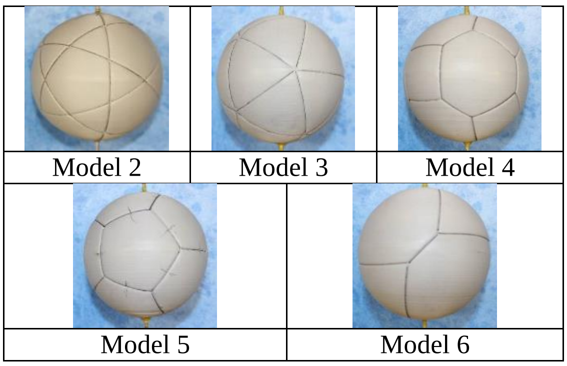

Figure 3. Experimental balls (45°)

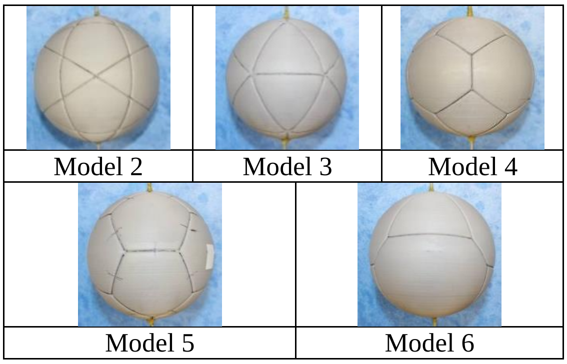

Figure 4. Experimental balls (90°)

3. EXPERIMENTAL RESULTS

3.1. Drag and Lift coefficient measurement (0°)

Figure 5 shows the drag coefficients at 0° for Smooth and Model 0 to 6.

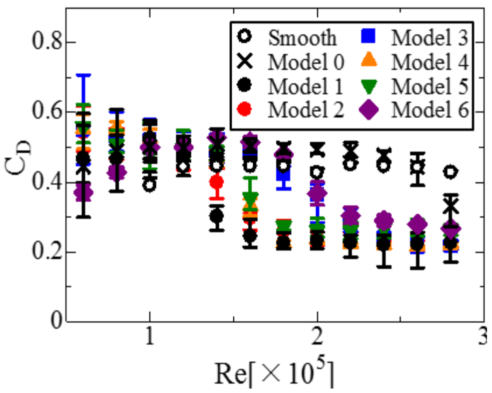

Figure 5. The drag coefficient measurement (0°)

It is known that the C_D value for smooth sphere is largely independent (C_D≒0.45) of the Reynolds numbers in the sub-critical region (Re≦2.0×10^5) [7]. In this experiment, the C_D value is as same as that value in the sub-critical region. The tendency of Model 0 is as same as Smooth in this experiment region. The critical Reynolds number for each balls are Model 1: Re=1.0×10^5~1.6×10^5; Model 2: Re=1.0×10^5~1.8×10^5; Model 3: Re=1.6×10^5~2.4×10^5; Models 4 and 5: Re=1.4×10^5~1.8×10^5; Model 6: Re=1.6×10^5~2.2×10^5. From these results, the critical region of Models 1 to 6 sift to low Reynolds number than that of smooth sphere. This is caused by surface structure. Models 4 and 5 which have nearly equal numbers of panels have the same critical Reynolds number. In addition, the critical Reynolds number of Model 2 which has the most number of panels of all model balls is the lowest of all balls. It is said that the critical Reynolds number increase as the number of panels decreases, in other words, the surface of the balls becomes smoother [8]. However, Model 3 shows a different tendency and the critical Reynolds number of this model is equal to that of Model 6.

Figure 6 shows the lift coefficients at 0° for Models 1 to 6. From this result, the region of Reynolds number of lift coefficient changing is the same as the critical Reynolds number of the drag coefficient.

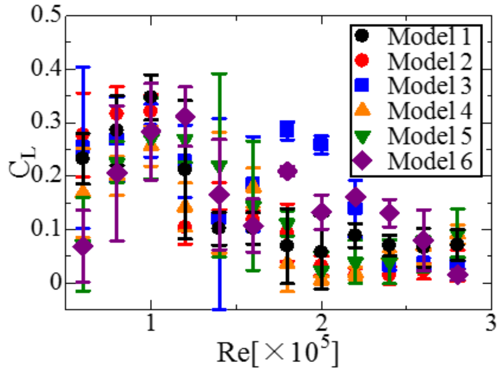

Figure 6. The lift coefficient measurement (0°)

Figure 7 shows the relationship between the number of panels and the critical Reynolds number at 0°. We define the critical region where the drag coefficient suddenly changes as shown in Figure 5. In Figure 7, plots indicate the middle of the critical region, as the critical Reynolds number and the error bar shows uppest and lowest Reynolds number of critical region. The critical region of these balls changes from a high Reynolds number to a low Reynolds number as the number of panels increases. However, the critical Reynolds number of Model 3 is higher than balls with fewer panels.

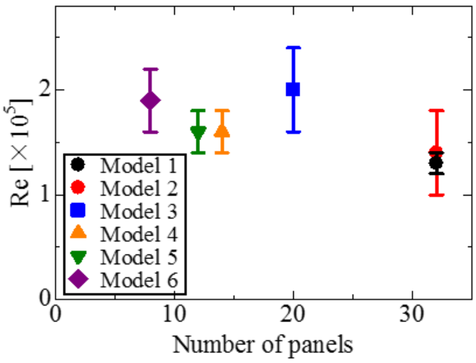

Figure 7. Relationship of number of panels and critical Reynolds number (0°)

Figure 8 shows the relationship between total groove length and critical Reynolds number at 0°. The critical Reynolds numbers for Models 1 and 2 (total groove length is over 2000*mm*) are lower than the other balls. Moreover, the critical Reynolds number becomes lower, as the total seam length becomes longer. However, the critical Reynolds number of Model 3 is higher than balls with shorter total seam lengths. This tendency is the same as the relationship between the number of panels and the critical Reynolds number.

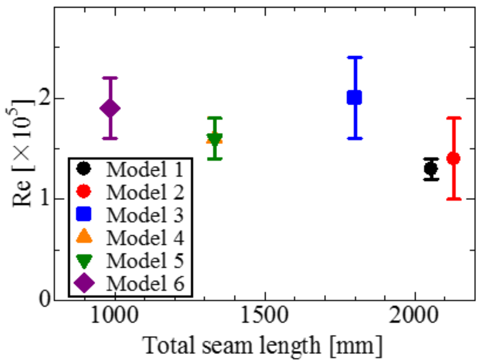

Figure 8. Relationship of total seam length and critical Reynolds number (0°)

3.2. Drag and Lift coefficient measurement (45°)

Figure 9 shows the drag coefficients at 45°. The drag coefficient of all balls in the sub-critical region and super critical region are the same as that at 0°.

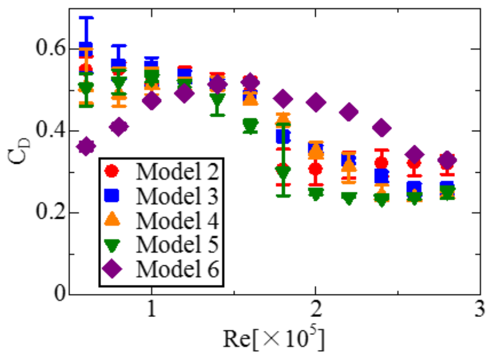

Figure 9. The drag coefficient measurement (45°)

Figure 10 shows the relationship between the number of panels and the critical Reynolds number at 45°.

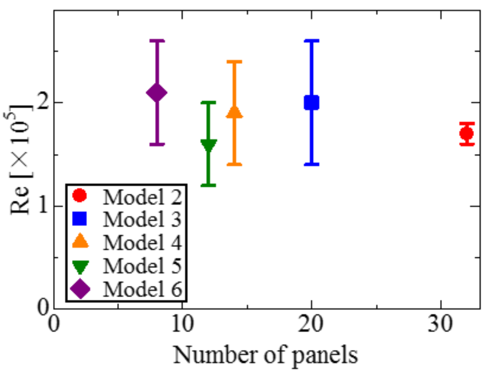

Figure 10. Relationship of number of panels and critical Reynolds number (45°)

The critical Reynolds number of Models 2, 4 and 6 is higher than that at 0°. However, the critical Reynolds numbers of the other balls are the same as those at 0°. In addition, the critical region of Model 2 became narrower than that at 0°, but the critical region of Models 3 to 6 became broader than at 0°.

Figure 11 shows the relationship between total groove length and critical Reynolds number at 45°. The critical Reynolds number becomes lower as the total seams length becomes longer. The critical Reynolds numbers in Models 2, 4 and 6 are higher than at 0°. These tendencies are the same as the relationship of panels and critical Reynolds number at 45°.

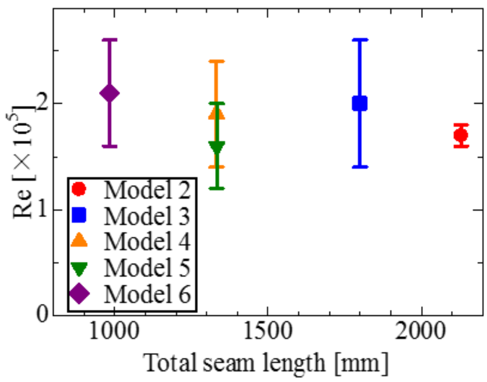

Figure 11. Relationship of total seam length and critical Reynolds number (45°)

3.3. Drag and Lift coefficient measurement (90°)

Figure 12 shows the drag coefficients at 90°. In the sub-critical region, it is higher than that at 0° and 45° of Model 6. On the other hand, it is lower than that at 0° and 45° of the other balls.

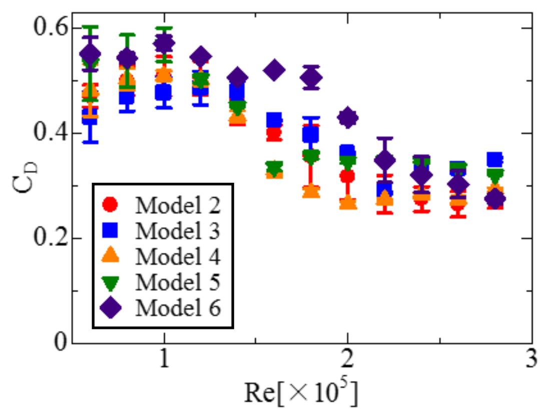

Figure 12. The drag coefficient measurement (90°)

Figure 13 shows the relationship between the number of panels and the critical Reynolds number at 90°. The tendency at 90° is the same as that at 45°. However, the critical Reynolds number at 90°

in Models 2 and 5 are lower than at 0°. On the other hand, Models 3 and 6 are higher than at 0°. The critical region of Model 2 became broader than that of the other angles. In Model 3, the critical region is swifter to lower its Reynolds number than the other angles. In Model 4, the critical region at 90° is the same as that at 45°, but the region is broader than that at 45°. In Model 5, the critical Reynolds number shifts about Re=0.2 $\times$ 10^5 to a lower Reynolds number compared with the other angles. Last, in Model 6, the critical region at 90° is the same as that at 45°, and this region is higher than that at 0°.

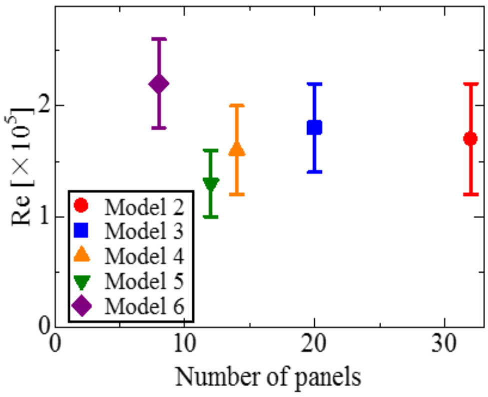

Figure 13. Relationship of number of panels and critical Reynolds number (90°)

Figure 14 shows the relationship between total groove length and critical Reynolds number at 90°. The critical Reynolds number becomes lower as the total seams length becomes longer. This tendency is the same as the relationship of panels and critical Reynolds number at 90°. However, the critical Reynolds number in Model 4 and 5 don't show this tendency.

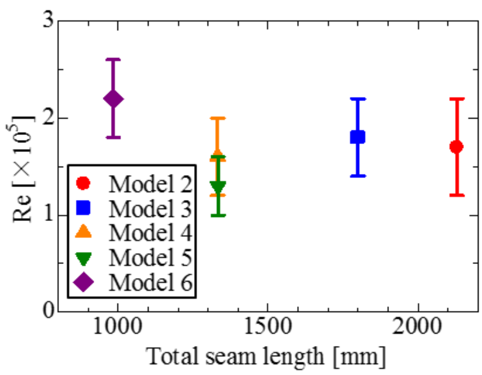

Figure 14. Relationship of total seam length and critical Reynolds number (90°)

3.4. Flow visualization(0°)

Figure 15 shows the result of the oil film method for smooth spheres in each region. These images were taken from the left side of the ball by a still camera. The wind velocity of the sub-critical region is 11[*m/s*]; of the critical region is 22[*m/s*]; and of the super critical region is 33[*m/s*]. Flow visualization was carried out 5 times at each region. Furthermore, we define the separation angle which is measured between the stagnation point and separation point, and the average angle was measured from these images.

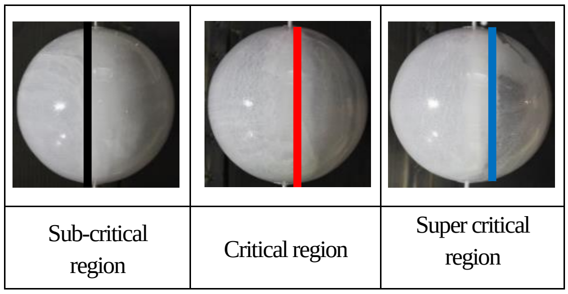

Figure 15. The results of flow visualization of smooth sphere in each region

Figure 16 shows the relationship between each region and the separation angle for a smooth sphere. The separation angle of the sub-critical region is the lowest of the three regions and the super critical region is the highest. From these results, the separation angle becomes rear side as Reynolds number becomes higher. Moreover, the separation angle is about 80° in the sub-critical region. This result is an agreement with the separation angle of smooth sphere [8].

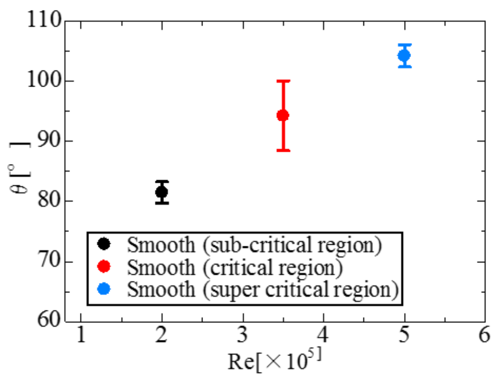

Figure 16. The relationship between each regions and separation angle of smooth sphere(0°)

Figures 17 to 19 show the relationship between the number of panels and separation angle in sub-critical region, in critical region and the super critical region. The separation angle become rear side as the wind velocity is higher compared with that of a smooth sphere.

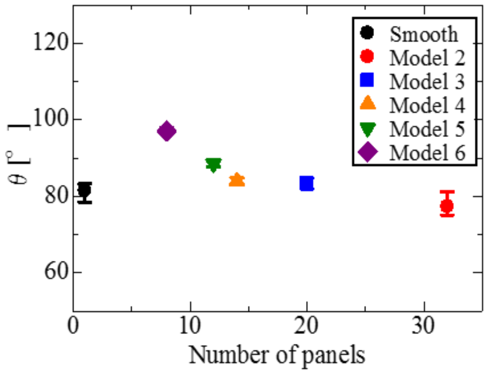

Figure 17. The relationship between number of panels and separation angle (sub-critical region)

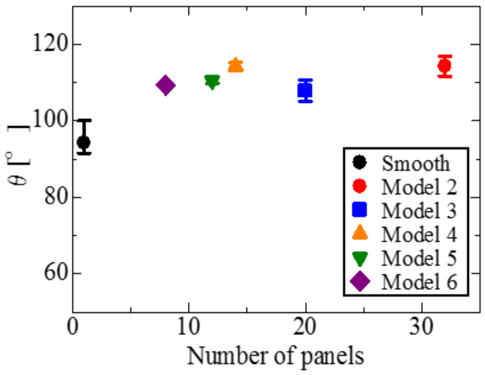

Figure 18. The relationship between number of panels and separation angle (critical region)

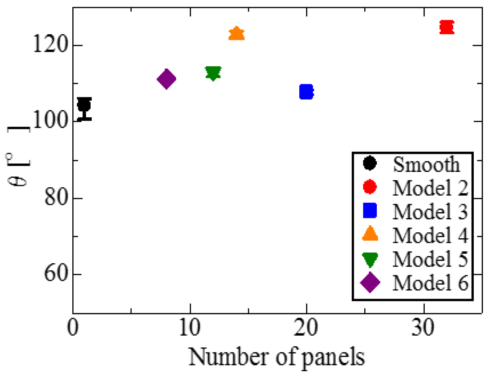

Figure 19. The relationship between number of panels and separation angle (super critical region)

3.5. Flow visualization(45°)

Figure 20 shows the differences of the separation point from the right side and left side at 45°. Therefore, measurements of the separation angle were carried out on two sides.

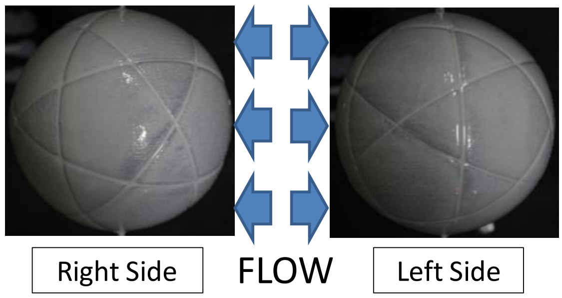

Figure 20. The differences between the right side and left side at 45°

Figure 21 shows the relationship between the number of panels and separation angle in the sub-critical region on the two sides. The separation angles are different from the right sides and left side of Model 3 and 4. In particular, the difference of Model 3 and 4 was bigger than the other balls. On the other hand, the relationship between the separation angle and the lift coefficient was not shown.

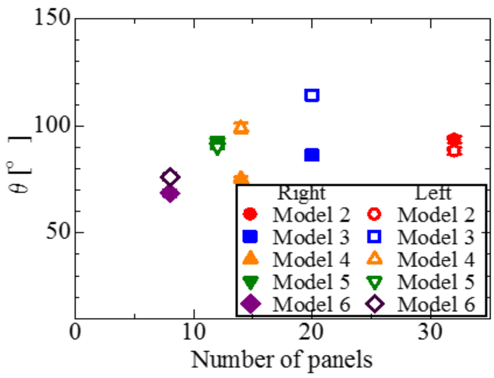

Figure 21. The relationship between the number of panels and separation angle in the sub-critical region

Figure 22 shows the relationship between the number of panels and separation angle in the critical region on the two sides.

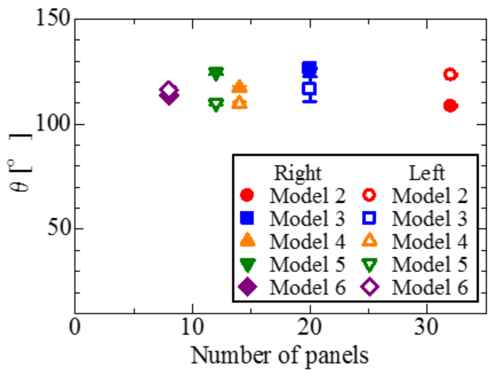

Figure 22. The relationship between number of panels and separation angle in critical region

The differences of separation angles are smaller than those in the sub-critical region. Moreover, the lift coefficient is lower than that of the other region, and it is almost 0.

Figure 23 shows the relationship between the number of panels and separation angle in the super critical region at two aspects. The tendency is the same as in the critical region.

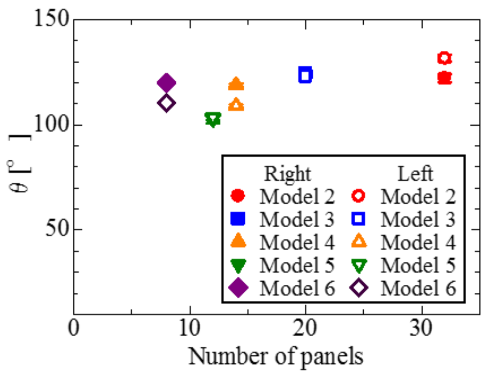

Figure 23. The relationship between number of panels and separation angle in super critical region

3.6. Flow visualization(90°)

Figures 24 to 26 show the relationship between the number of panels and separation angle in the sub-critical region, in the critical region and the super critical region. The separation angle become rear side as the wind velocity is higher. This tendency is the same as that of 0°. However, the separation angle of Model 6 in the critical region is different from the other balls in the same region.

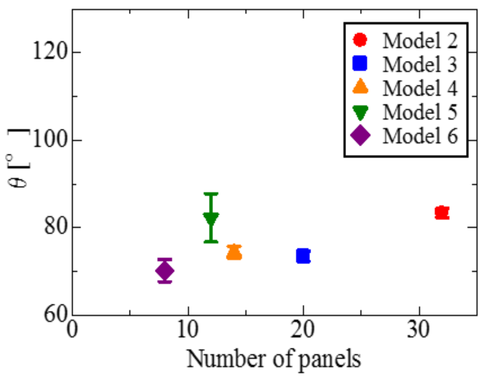

Figure 24. The relationship between number of panels and separation angle (sub-critical region)

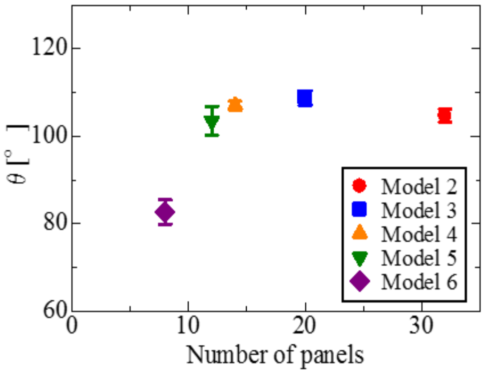

Figure 25. The relationship between number of panels and separation angle (critical region)

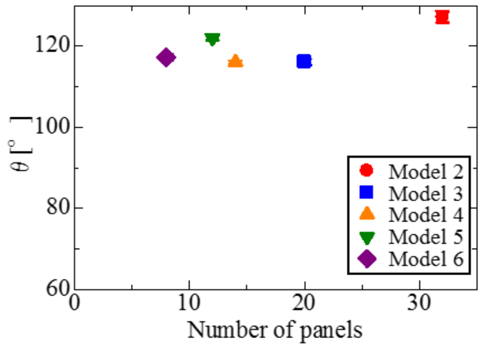

Figure 26. The relationship between number of panels and separation angle (super critical region)

3.7. Drag and Lift coefficient measurement (with rotation)

Figure 27 shows the drag coefficients of rotating balls of Models 2 to 6. The number of revolutions is 1000[*rpm*].

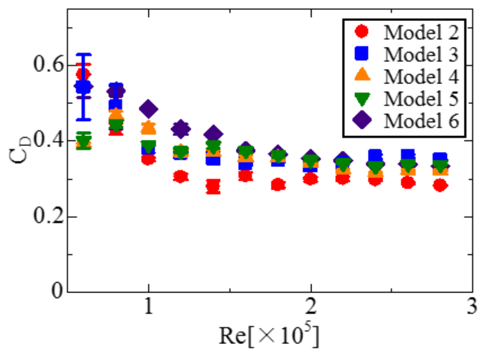

Figure 27. The drag coefficient measurement of rotating balls

As Reynolds number higher, the drag coefficient are lower. Over than Re=1.6×10^5, drag coefficient are fixed amount. In Model 2, the lowest drag coefficient is after Re=1.0×10^5. Moreover, the drag coefficient of Model 6 is higher than that of

Models 3, 4 and 5 from Re=1.0×10^5 to Re=1.8×10^5.

Figure 28 shows the lift coefficients of rotating balls for Models 2 to 6. The lift coefficient value of Model 2 is higher than that of the other balls in all Reynolds numbers.

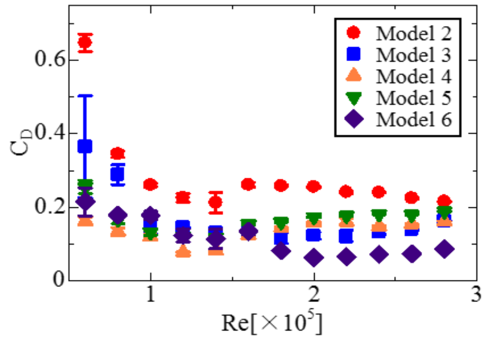

Figure 28. The lift coefficient measurement of rotating balls

Figure 29 shows the Relationship of number of panels with drag coefficient and lift coefficient at Re=2.0 × 10^5. This Reynolds number in this equipment is the super critical region. The more panel numbers, the lower the drag coefficient of each balls. However, as the number of panels increase, the lift coefficient increase.

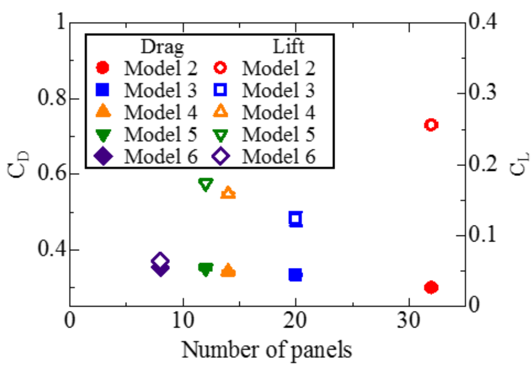

Figure 29. Relationship of number of panels with drag coefficient and lift coefficient at Re=2.0×10^5

CONCLUSION

In this study, the flow characteristics and flow visualization of a model balls are investigated. Drag and lift coefficient are measured. Flow visualization, by using the oil film method is carried out, and the following conclusions can be made about flow around the balls

Non rotation:

・Critical region of Model 2-Model 6 changes to a low Reynolds number as the number of panels at 0°, 45°, and 90°.

・The drag coefficient is the lowest and the lift coefficient is the highest in Model 2 with rotation.

・The separation angle moves to the rear side as to the Reynolds number becomes higher.

・Differences of the separation angle are seen between the left side and right side at 45° in the sub-critical region. However, the differences are smaller as the Reynolds number becomes higher.

・The effect of the surface structure on aerodynamic characteristics is bigger when the panel number is 20 or less.

With rotation (1000[*rpm*]):

・As Reynolds number higher, the drag coefficient and lift coefficient are lower. Besides, more than Re=1.6×10^5, these values are fixed amount.

・As the number of panels at the super critical region increase, the drag coefficient is lower.

REFERENCES

[1] Ito S, Asai T and Seo K. Comparison of Aerodynamics Performance on Soccer balls (In Japanese). Proc JSME annual meeting 2009. Morioka city in Japan, pp279-280, 2009.

[2] Asai T, Nakayama M, Hong S, Naito K, Sakamoto K and Suda S. Nonstationarity on Knuckling effect ball in soccer (In Japanese). Proc of the JSME Symposium: Sports and Human Dynamics 2009. Fukuoka city, pp82-87, 2009.

[3] Yagi G, Okanaga H and Kimura T. The Relationship between Surface Structure and Aerodynamic of Soccer ball (In Japanese). Proc of JSME annual meeting 2013. Okayama city in Japan.

[4] Yagi G, Okanaga H and Aoki K. The effect of surface structure on the frow characteristics of ball. Proc of 16th International Symposium on Flow Visualization. Okinawa in japan

[5] Seo K, Yorita D, Nagai H, Asai K, Asai T and Ito S. Aerodynamic behavior of a soccer ball (In Japanese). Transactions of Visualization Society of Japan Vol. 32 Suppl. No.1, pp345-348,2012.

[6] Smits A.J. and Smith D.R. A New Aerodynamic Model of a Golf Ball in Flight. Science and Golf Ⅱ, pp.340-347, 1994.

[7] Mizota T. Kuba H. and Okajima A. Erratic Behaviourf Knuckleball : (1) Quasi-Steady Flutter Analysis and Experiment. Journal of wind engineering (62), 3-13, 1995-01-31

[8] Aoki K, Muto K, Okanaga H. Mechanism of Drag Reduction by Dimple Structures on a Sphere (Fluids Engineering). Transactions of the JSME Vol.76 No.770 pp.1473-1480, 2010

Conference on Modelling Fluid Flow (CMFF'15)
The 16th International Conference on Fluid Flow Technologies
Budapest, Hungary, September 1-4, 2015

DEVELOPMENT OF A CFD MODELLING METHODOLOGY FOR ENVIRONMENTAL GAS DISPERSION OVER COMPLEX TERRAIN

Valérie Eveloy[1], Peter Rodgers[2], Katharina Defung[2], Jordan Armitage[2]

[1] Corresponding Author. Department of Mechanical Engineering, The Petroleum Institute. PO Box 2533 Abu Dhabi, United Arab Emirates. Tel.: +974 2 607 5533, E-mail: veveloy@pi.ac.ae
[2] Department of Mechanical Engineering, The Petroleum Institute. PO Box 2533 Abu Dhabi, United Arab Emirates.

ABSTRACT

In this study a computational fluid dynamics (CFD) modelling methodology to predict airflow and gas dispersion in hydrocarbon production fields having complex terrain is developed and validated. Three series of published experimental and numerical studies are selected to serve as benchmark data. These configurations permit modelling complexity to be incremented in controlled steps, in terms of terrain geometry, physics solved, and boundary conditions. Overall, CFD predictions are found to be in good agreement with corresponding published data. Instances of prediction discrepancies are discussed in the context of experimental uncertainty, modelling parameters and spatial discretization.

Keywords: atmospheric, computational fluid dynamics, gas dispersion, terrain, topology.

1. INTRODUCTION

Chemical and petrochemical process plants seek to control their environmental impact, including hydrocarbon, acid gas and greenhouse gas emissions. In addition to raising environmental and economic concerns, these emissions can also induce significant safety hazards for the plant personnel and nearby communities. Sour hydrocarbon reserves contain high concentrations of acid gases (e.g., carbon dioxide (CO_2), hydrogen sulphide (H_2S), sulphur dioxide (SO_2)), the toxicity of which is well documented, even at low concentrations [1]. To develop emergency and environmental response plans to accidental or planned gas releases, the chemical and hydrocarbon process industry typically relies on simple, computationally economical gas dispersion models, such as integral models. Such models solve simple differential equations that represent the dispersion phenomena as a whole [2], rather than solving for the three-dimensional, time-dependant velocity, pressure and concentration fields. Their limited accuracy has been extensively documented, particularly in the presence of complex terrain or building topologies, or in situations where the release characteristics and/or meteorological conditions depart from the conditions for which the models were initially developed [2,3]. These shortcomings, combined with advances in computational resources, have led the research community to recommend the use of computational fluid dynamics (CFD) [3]. Although sophisticated computational techniques (e.g., large eddy simulation, direct numerical simulation) can provide accurate solutions, their computational cost and user skill requirements, combined with uncertainties in meteorological conditions and the number of possible gas release scenarios that need to be evaluated, are considered prohibitive for application in industry. Reynolds Average Navier Stokes (RANS)-based models have the potential to bridge the gap between sophisticated and integral gas dispersion models, in terms of accuracy and computational cost.

The objective of this work is to develop and evaluate a RANS-based CFD modelling methodology implemented in a commercially-available, general purpose CFD code [4], to predict gas flow and dispersion in hydrocarbon fields having complex terrain. Based on a review of the literature on the modelling of atmospheric boundary layers and gas dispersion, three series of experimental/numerical studies are identified for model validation. These cases provide both extensive experimental and CFD modelling data, and permit modelling complexity to be incremented in controlled stages, in terms of the physics solved (i.e., fluid flow only, versus both fluid flow and gas concentration), terrain complexity (i.e., idealized versus actual topology), and characterization environment (i.e., wind tunnel versus fielded conditions). The configurations consist of wind tunnel airflow over an idealized axisymmetric hill [5], and two actual isolated hills; Askervein hill in Scotland [6], which provides airflow data only, and the Cinder Cone Butte in Idaho, U.S.A. [7], which provides both airflow and gas concentration data.

2. NUMERICAL MODELS

The modelling methodology is based on that presented by Persson et al. [8], Castro et al. [9], and Apsley and co-workers [10,11] for the axisymmetric hill, Askervein hill, and Cinder Cone Butte cases using high-Reynolds number k-ε turbulent flow models. Therefore, the modelling methodology is essentially summarized here, with emphasis on instances of departure from these studies.

The axisymmetric hill geometry was constructed using SolidWorks, a standard CAD software. For Askervein hill and the Cinder Cone Butte, MicroDEM, Thrimble SketchUp 8, and SolidWorks, were used to import and process actual terrain geometry from digital geographical databases into ANSYS Version 15.0 DesignModeler. The geometry was spatially discretized using ANSYS Meshing, with the governing equations solved using Fluent.

All models were solved as steady-state, with unsteady flow modelling also investigated for the Askervein case. The computational method, given in [4], is based on a cell-centered, unstructured finite volume discretization and a SIMPLE-type [12] segregated solution procedure. All computations were performed using second-order upwind scheme for the convective terms and central differencing for the diffusive terms. Given the industry's preference towards computationally robust, economical models, that permit the evaluation of a large set of possible release scenarios with reasonable accuracy, the standard high-Reynolds number k-ε flow model [13], which has been widely used for the modelling of atmospheric boundary layer flows, was applied as a starting point for all three cases, in conjunction with a standard wall function formulation [14]. As previous studies have reported improvements in prediction accuracy using other formulations of the k-ε model (i.e., Renormalization group (RNG) and Realizable k-ε), these models were also investigated here for certain cases. The fluid flow, thermal and species transport boundary conditions applied for the respective cases are based on those modelled in [8-11]. All solutions were verified to be computational domain size and mesh independent, with comparison made to previous numerical studies [8-11]. Cell orthogonal quality typically ranged from 0.30 to 0.95 (average, 0.9); skewness from 8 x 10^{-5} to 0.8 (average, 0.20); and cell aspect ratio from 1.1 to 15 (average, 4.5).

2.1. Axisymmetric Hill

The experimental configuration of Simpson and co-workers [5,15,16] consists of a three dimensional axisymmetric hill with a circular base, mounted on the centre floor of a wind tunnel having a length of 7.62 m, width of 0.91 m and height of 0.25 m. The hill is 78 cm high and has a base radius equal to twice the hill height, with the hill surface coordinate defined in Simpson et al. [5]. Despite the simplicity of the hill geometry, the airflow reported by Simpson and co-workers [5,15,16] is complex and highly three-dimensional. The flow accelerates and the pressure decreases over the top of the hill. The flow decelerates downstream due to the adverse pressure gradient. On the lee side, flow separation takes place due to the streamwise flow meeting the backflow induced by flow originating from the sides of the hill.

Given the symmetry of the experimentally observed flow phenomena, half geometry model was constructed. The computational domain shown in Figure 1 extended 12, 10 and 3.205 times the hill height in the streamwise, spanwise, and cross-stream directions respectively. The computed streamwise, spanwise, and cross-stream velocity profiles are to be compared to the experimental and numerical data at five cross-stream rakes in plane z/h = 3.69, the locations of which are shown in Figure 1. At the domain inlet, that is at a distance of 3.4 times hill height upstream of the hill centre, a normal power law airflow velocity profile was prescribed [8]:

$$v_x = \begin{cases} U(\frac{y}{\delta})^{1/n} & y < \delta \\ U & y \geq \delta \end{cases} \tag{1}$$

where U refers to the free-stream velocity, 27.5 m/s, δ refers to the boundary layer thickness, x and y are the stream-wise and transverse coordinates, and

$$n = \log\ (Re) = 7.1 \tag{2}$$

The Reynolds number, Re, in Equation (2) is based on the distance between the wind tunnel test section

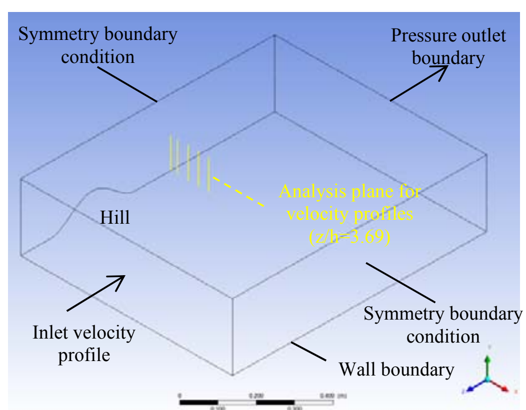

Note: Butte dimensions, height h = 78 mm, base radius, Ø = 2 h. Domain dimensions, 12h x 10h x 3.205h (streamwise x spanwise x transverse free-stream flow directions).

Figure 1. Computational domain for the axisymmetric hill model, showing locations of analysis plane for velocity profile predictions.

inlet and the computational domain inlet. Default software settings were applied at the domain inlet for turbulent intensity, *TI* (i.e., 5%) and turbulent viscosity ratio, *TVR* (i.e., 10). At the domain outlet, which was positioned at a distance of 8.6 times hill height downstream of the hill centre, a Dirichlet condition for pressure (i.e., uniform pressure) and homogeneous Neumann conditions for all other dependent variables were applied. Symmetry boundary conditions were applied along the domain spanwise planes. No-slip boundary conditions were imposed along the top and bottom domain horizontal boundaries, with homogeneous Neumann conditions for all other variables.

The computational domain was discretized using a hybrid prism-tetrahedral mesh having 4.4 million cells, which is over twice the grid density applied in [8].

2.2. Askervein Hill

Askervein hill is an isolated elliptical-like shaped hill, with 2 km- and 1 km-long major and minor axes, respectively, and a height of 116 m. The data set selected here, case TU03-B [6], was collected on October 3, 1983 from 14:00 to 17:00, which was characterised by a moderate wind from the southwest, with an upstream average velocity of 8.9 m/s and average direction of 210° from North, as well as rain from 10:00 to 11:00 a.m. followed by occasional sunny intervals. Wind velocity and direction, and turbulence data were collected using 48 nos. hill surface-mounted towers (10 – 50 m height) equipped with a range of anemometer types. The location of the measurement towers is depicted in Figure 2. Both the measured non-dimensional speed-up factor, ΔS, and non-dimensional turbulent kinetic energy, k^*, profiles along analysis Planes A and AA (Figure 2) [6], are to be used as metrics to assess predictive accuracy.

The computational domain inlet was aligned perpendicularly to the upstream wind direction. The domain dimensions were set at 6 km x 4 km x 0.5 km in the streamwise, spanwise and transverse flow directions (Figure 3), respectively.

A normal power law velocity profile [17] defined by Equation (3) was prescribed at the domain inlet, i.e. 1.2 km upstream of hill centre:

$$u(y) = 5.8323(y + y_0)^{0.1783} \qquad (3)$$

where y_0 refers to the surface roughness length. This profile was found to fit the measured velocity profile more accurately than logarithmic law profiles applied in e.g. [9,18]. Turbulent kinetic energy (k) and turbulent dissipation rate (ε) profiles were specified at the domain inlet, following the approach of [19]. A Dirichelt (i.e., zero gauge) pressure boundary condition was applied at the domain outlet, positioned 4.8 km downstream of the hill trailing edge. A no-slip boundary condition was imposed along the domain bottom horizontal wall.

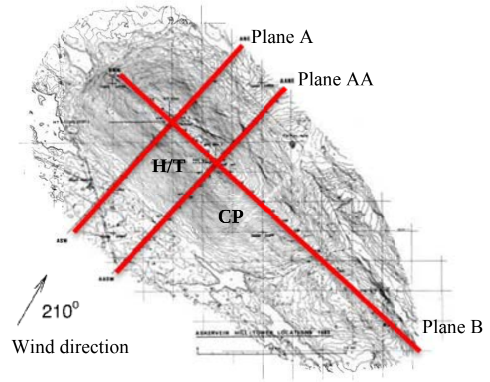

Note: Lines refer to locations of flow measurement towers.

Figure 2. Topographic map of Askervein hill, showing the locations of the measurement towers, based on [6].

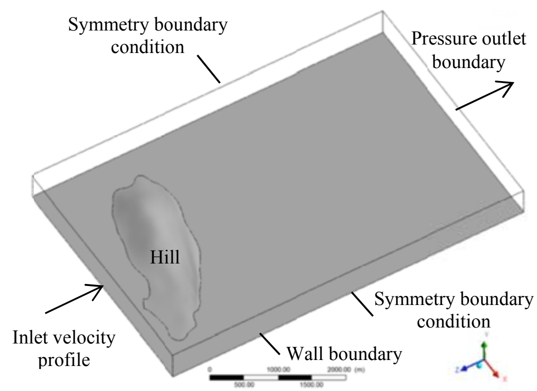

Note: Hill dimensions, height h = 116 m, elliptical-like major and minor axes, 2 km- and 1 km-long respectively. Domain dimensions, 6 km x 4 km x 0.5 km (streamwise x spanwise x transverse flow directions).

Figure 3. Computational domain for Askervein hill model.

The effect of the ground cover of the hill and surrounding terrain, which essentially consisted of heather, grass, low scrub and some flat rocks [20] was modelled using a surface roughness length of 0.03 m based on Mickle et al.'s [21] analysis of the experimental data, with parametric analyses undertaken to assess prediction sensitivity to this variable within the range of 0.03 to 0.2 m. Symmetry boundary conditions were applied along the domain spanwise planes, located 1.25 km and 2.75 km from the hill centre, and along the upper horizontal boundary.

In addition to the standard k-ε model, the RNG k-ε and realizable k-ε models were also applied to seek potential improvements in prediction accuracy. In addition, both steady state and unsteady flow modelling were investigated.

Computational domain sizes ranging from 6.0 x 4.0 x 0.5 km to 8.0 x 6.0 x 0.7 km were constructed, in conjunction with hexahedral and hybrid prism-tetrahedral meshes ranging from 2 to 15 million cells. Based on prediction sensitivity analyses, the final computational domain size was set at 6 km x 4 km x 0.5 km, and was discretized using a hybrid mesh having 15.1 million cells, which exceeds the grid densities applied in [9,17,22].

2.3. Cinder Cone Butte

The Cinder Cone Butte is a two-peaked almost axisymmetric, isolated 105 m high hill. The base of the hill is nearly circular and approximately 1 km in diameter. Phase II experiments focused on simultaneous SF_6 and $CBrF_3$ tracer concentration measurements, with smoke plume releases [7]. Concentration data was supplemented by wind speed and ambient air temperature measurements at fixed sites, Laser Interferometry Detection and Ranging (LIDAR), and photographic observations of plume behaviour. The airflow data was recorded using six meteorological towers. Air samples were collected by automatic bag samplers on the hill surface and analysed by gas chromatography to determine hourly average surface concentrations. In comparison with the extensive ground concentration data set, the corresponding flow field data set is limited.

Case 206, 0500-0600 local time, was selected for the present study. The hourly average wind speed and direction were 2 m/s and 127° (i.e., from South East by East, SEbE), respectively. SF_6 was released continuously for one hour at a rate of 0.062 g/s from a source located 595 m from the hill centre at an orientation of 123.5°, and 35 m above the ground. This case is characterized by very stable atmospheric conditions, with a release source located at, or very near, the dividing-streamline height, defined in [10].

The computational domain (Figure 4) extended 11 x 5 x 1.2 km in the streamwise, spanwise and cross-stream directions, respectively. At the domain inlet, positioned 5 km upstream of the hill

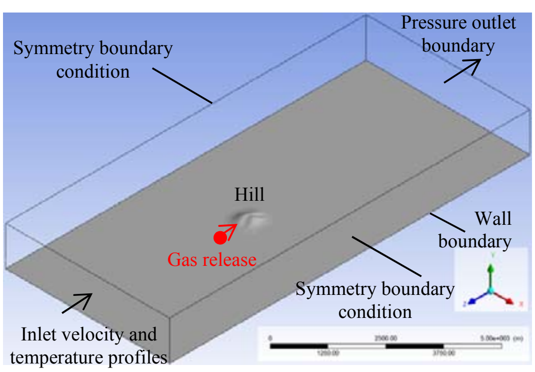

Note: Hill dimensions, height h = 100 m, nearly circular base diameter, approximately 1 km. Domain dimensions, 11 x 5 x 1.2 km (streamwise x spanwise x transverse flow directions).

Figure 4. Computational domain for the Cinder Cone Butte model.

centre, a power-law velocity profile [10] that models the experimental profile measured up to 150 m altitude [7], was imposed:

$$U(y) = \begin{cases} U_0 (y/150)^n & y < 150\,m \\ U_0 & y \geq 150\,m \end{cases} \qquad (4)$$

where U_0 = 9.14 m/s and n = 0.9. This profile leaded to unrealistic velocities at the upper boundary of the domain. A second profile, defined as in Equation (4) for $y \leq 150$ m, but with a uniform free-stream velocity for $y > 150$ m, was therefore also assessed. The potential temperature (θ) profile prescribed at the domain inlet follows [10]:

$$\theta\,(y) = \theta_0 + \left(\frac{d\theta}{dy}\right)_\infty \left[y + \frac{L_{MO}}{5} \ln\left(\frac{z}{y_0}\right)\right] \qquad (5)$$

where θ_0 = -2.16°C, $(d\theta/dy)_\infty = 2.98 \times 10^{-2}$ K/m is the measured hourly-average potential temperature gradient, and the Monin-Obukhov length, L_{MO} = 33 m. Similarly to the inlet velocity profile, to avoiding unrealistic temperature values in the upper region of the domain as per Equation (5), a modified form of the above potential temperature profile was also investigated, having constant values of potential temperature for $y > 150$ m. Uniform turbulent intensity and turbulent viscosity ratio were prescribed at the domain inlet, with three uniform turbulent intensity values (i.e., 1%, 5%, and 10%) tested to assess prediction sensitivity to this variable. In addition, the profiles of turbulent kinetic energy (k) and its dissipation rate (ε) derived from [23,24] were also tested. A uniform pressure boundary condition was applied 6 km downstream of the hill centre. Symmetry boundary conditions were applied at the domain upper boundary, and ±2.5 km from the hill centre in the spanwise flow direction. A no-slip boundary condition was imposed along the lower horizontal wall, with a surface roughness length of 0.1 m [10]. A roughness length of 0.3 m was also evaluated. Two values of heat flux on the ground surface were investigated, $Q_H = 0$ and $Q_H = 20$ W/m^2, with the latter value employed by [10]. The emission source was modelled as a point source.

A hybrid prism-hexahedral mesh was employed. The mesh density, 4.67 million cells, exceeds that employed in [10], i.e. 0.15 million cells for a domain size of 13 x 5 x 2 km.

3. COMPARISON OF NUMERICAL PREDICTIONS WITH PUBLISHED DATA

For each case, the predicted main flow and/or dispersion features are described and compared with corresponding experimental and numerical data. Due to space constraints, a representative data sample is presented for each case. The impacts of boundary conditions, turbulence model, and spatial discretization are discussed.

3.1. Axisymmetric Hill

The predicted time-averaged streamwise, spanwise and cross-stream, velocity profiles at five cross-stream rakes in plane z/h = 3.69 (Figure 1), are compared with corresponding experimental [5] and numerical [8] data in Figure 5.

In Figure 5a, the predicted streamwise velocity profiles are in good agreement with experimental and numerical reference data at *x*/*h* values of 0.33, 0.81, 1.3 and 1.79, as well as with numerical reference data at *x*/*h* = 0 (centre plane). However in the centre rake (*x*/*h* = 0), both sets of numerical data underpredict the streamwise velocity component up to an elevation *y*/*h* = 0.8, relative to measurements.

Both predicted spanwise velocity profiles in Figure 5b are very similar, and in reasonable agreement with measurement, but are underpredicted at *x*/*h* = 0.33. In Figure 5c, good agreement is obtained at all analysis rakes, except in the centre rake (*x*/*h* = 0), where the cross-stream velocity component is overpredicted. To summarise, the predictions display reasonable agreement with the experimental data, except near the central plane, where RANS does not capture the complex flow phenomena. Improved prediction accuracy in this region was obtained using LES by Persson et al. [8], which is consistent with other numerical studies for similar cases.

3.2. Askervein Hill

In Figure 6, the predicted speed-up factor profile along Plane A (Figure 2) at an altitude of 10 m above the ground, *ΔS*, is overall in good agreement with both measurement and the numerical data of Castro et al. [9]. Although not shown due to space constraints, similar agreement was obtained along Plane AA (Figure 2). The localized discrepancies observed at *x* = ± 500 m are attributable to digital terrain data truncation on the periphery of the hill base.

The non-dimensional turbulent kinetic energy (*k**) profile along Plane A is overall qualitatively captured in Figure 7, but the computed profile is underestimated relative to measurement. The profile predicted by [9] is overestimated by a similar magnitude. This may be partly attributable to the alignment error for gill anemometers reported by [6]. Similar trends were obtained for Plane AA.

Prediction sensitivity to turbulent flow model, steady versus unsteady flow treatment, and surface roughness length were assessed. The predicted speed-up factor was found to display minimal sensitivity to turbulent flow model for the standard, RNG and Realizable variants of the high-Reynolds number *k*-*ε* model. The recirculation region observed experimentally on the leeside of Plane A [6] was found to be captured only using unsteady flow treatment. Zero and 0.2 surface roughness lengths were considered as lower and upper limits

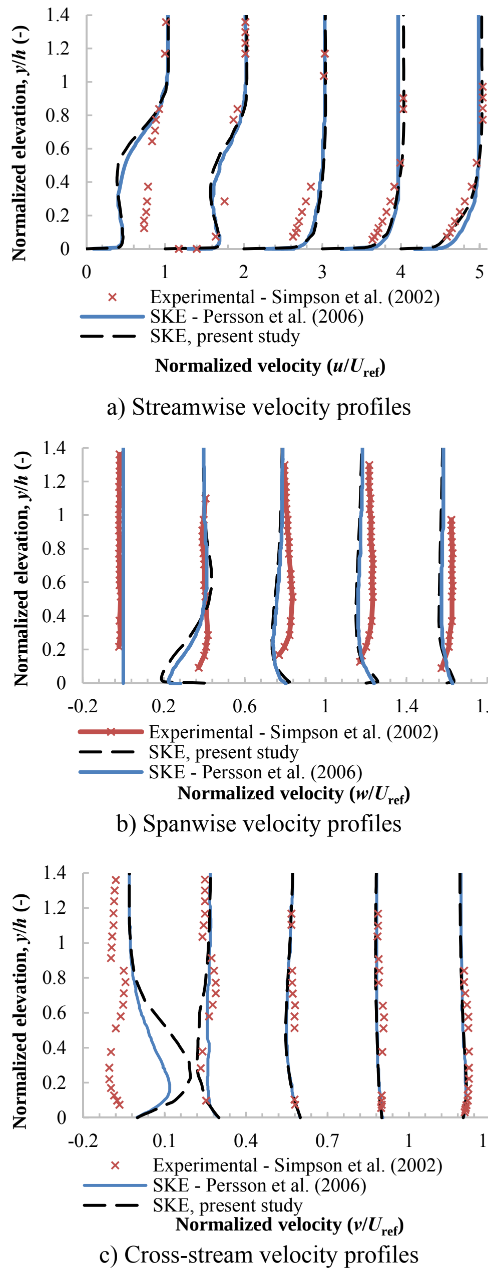

Figure 5. Comparison of predicted and measured velocity profiles downstream of the axisymmetric hill at analysis rakes defined by z/h=3.69 and *x*/*h* values of 0, 0.33, 0.81, 1.3 and 1.79, from left to right (Figure 1). SKE refers to the *k*-*ε* model.

for prediction sensitivity analysis in the present case. As surface roughness length increased, the predicted speed-up factor at a given measurement location significantly decreased. The default roughness length of 0.03 m was found to yield good agreement between predictions and measurements in Figures 6 and 7.

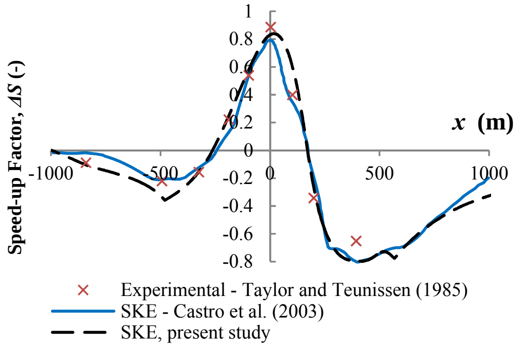

Note: x = 0 represents the location of H/T in Figure 2. Computational mesh size of 15.1 million cells.

Figure 6. Comparison of predicted and measured speed-up profiles in Plane A at an altitude of 10 m above Askervein hill's surface.

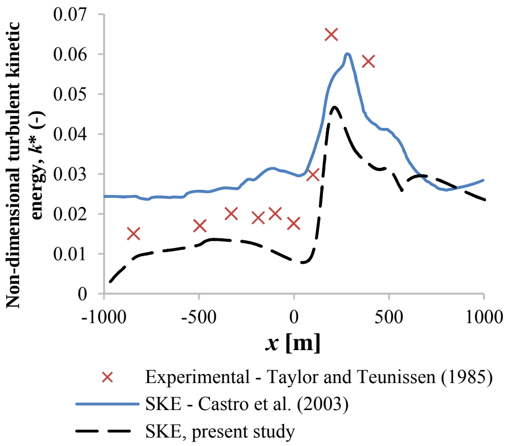

Note: x = 0 represents the location of H/T in Figure 2. Computational mesh size of 15.1 million cells.

Figure 7. Comparison of predicted and measured non-dimensional turbulent kinetic energy profiles in Plane A at an altitude of 10 m above Askervein hill's surface.

3.3. Cinder Cone Butte

Fluid flow and SF_6 concentration predictions are compared to both the measurements of [7] and numerical predictions of Apsley and co-workers [10,11]. As previously noted, the available experimental flow field data for this case is limited, in comparison with the concentration data, which may not permit sources of gas dispersion prediction discrepancies to be fully isolated.

The predicted wind velocity profile at meteorological Tower A, which is located approximately 2 km away from the hill centre, is underpredicted at low altitudes (i.e., up to 60 m) relative to the measured data of Strimaitis et al. [25], as indicated in Figure 8. Alteration of the prescribed boundary conditions, as described in Section 2.3, was not found to yield a better match

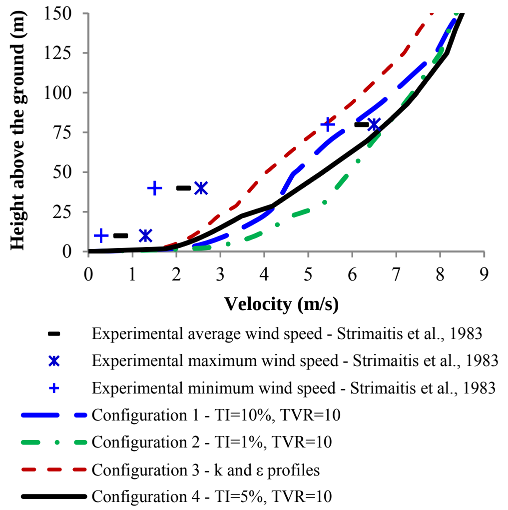

Note: Configurations 1 to 4 represent sensitivity analyses to turbulent boundary conditions at the domain inlet. Configuration 1 corresponds to default predictions. TI and TVR refer to turbulence intensity level and turbulent viscosity ratio applied at the computational domain inlet.

Figure 8. Comparison of predicted and measured [25] wind velocity profiles over Cinder Cone Butte at Tower A.

between the shapes of the predicted and measured velocity profiles. Analysis of the velocity profile at Tower A is not reported in Apsley and co-workers [10,11].

Although not shown due to space constraints, the predicted flow streamlines in a horizontal plane 25 m above the ground suggest that the present model predicts less lateral flow divergence at that altitude than Apsley's [10] model. In addition, unlike in [10], no recirculating flow region is found on the lee side of the butte at 20-25 m altitude. More pronounced flow lateral divergence as well as flow recirculation are however predicted at lower altitudes (i.e., < 10 m) in the present model.

The maximum SF_6 ground level concentration predicted by the present model in Figure 9a is in good agreement with Lavery et al.'s [7] experimental data (Figure 9b). However, discrepancies in measured and predicted distributions of SF_6 ground level concentration are evident, which may be related to discrepancies between the measured and predicted velocity profiles in Figure 8, and underestimation of lateral flow divergence. The predicted dispersion cloud is narrower than Apsley's [10] predictions, and essentially covers the central part of the Butte, whereas Apsley's [10] plume covered much of the Butte's north-east face. Apsley [10] related the crosswind spread of their plume to the downwind separation of streamlines initially close together, which is not significant in the present study.

Several factors may contribute to discrepancies between the present predictions, corresponding

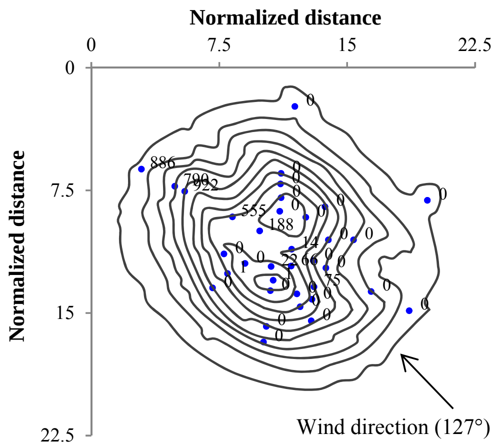

a) Present predictions

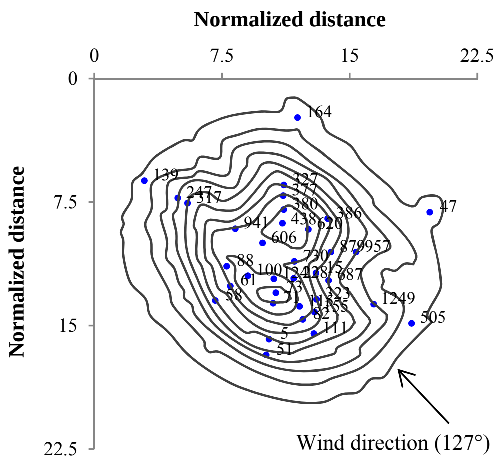

b) Experimental [7]

Note: Height contours presented at 10 m intervals, beginning with the 5 m height contour. Concentration in ppt.

Figure 9. Comparison of predicted and measured SF_6 ground level concentrations over Cinder Cone Butte.

measurements [7] and Apsley and co-workers' modelling [10,11]. Considering experimental measurements:

- Uncertainties exist in the temperature and velocity profiles above 150 m altitude.
- Experimental wind velocity, temperature, and concentration data are hourly averaged. The wind velocity and direction fluctuated during the experiment, which may have impacted the concentration field [7,10,11].

Considering comparison with Apsley and co-Workers' predictions [10,11]:

- The predictions reported in [10] were obtained using a form of the standard high-Reynolds number k-ε flow model, that intended to limit the computed turbulent length scale by a specified maximum scale. This modification aimed at overcoming the excessively diffusive nature of the standard k-ε model, which otherwise eroded the approach-flow temperature profile encountering the hill.
- To reduce computational expenses, an analytically calculated concentration field was prescribed in the vicinity of the emission source in [10], rather than explicitly solving for this concentration field using CFD.
- Computational mesh size and distribution differ, with approximately ten times larger mesh size employed in the present study relative to [10,11].
- The geometry modelled in [10] was digitized manually from the height contours in the EPA Milestone Report [7] and mapped onto a rectangular grid using a local weighting method.
- A local equilibrium thermal boundary condition (zero normal flux derivative) was imposed on the ground surface in [10].

The sensitivity analyses undertaken here indicate prediction sensitivity to these variables.

4. SUMMARY

Three sets of published studies having both experimental and numerical data for environmental airflow and gas dispersion over isolated hills were identified to develop and evaluate a CFD modeling methodology for atmospheric pollutant dispersion. For the axisymmetric and Askervein hill cases, good prediction accuracy was obtained relative to both measurements and previously published numerical data, suggesting that airflow over actual isolated hills is reasonably well captured in this study. For the Cinder Cone Butte case, despite good agreement in the magnitude of the predicted maximum ground level gas concentration, discrepancies in the concentration distribution were observed, which may be related to flow field prediction discrepancies. Potential sources of prediction discrepancies include experimental measurement uncertainty, which is compounded by limited flow field data, uncertainties in boundary conditions, and turbulent flow model. An additional benchmark for gas dispersion could be considered.

To permit the prediction of pollutant flow and dispersion in hydrocarbon fields, the present modelling work needs to be extended to i) terrain with more complex topographies, including multiple hills, ii) facility building topologies, and iii) the full range of local environmental conditions (seasonal, day/night), which would result in different atmospheric stability conditions.

ACKNOWLEDGEMENTS

The financial support of ADNOC Research & Development Gas Sub-Committee is gratefully acknowledged.

REFERENCES

[1] Skrtic, L, 2006, “Hydrogen Sulfide, Oil and Gas, and People’s Health,” Master’s of Science Thesis, University of California, Berkeley, USA.

[2] Mannan, M.S. (Editor), 2012, Chapter 15: Emission and Dispersion, *in* Lees' Loss Prevention in the Process Industries (Fourth Edition), Butterworth-Heinemann, UK, pp. 752-1074.

[3] Zhang, B. and Chen G.M., 2010, “Quantitative risk analysis of toxic gas release caused poisoning - A CFD and dose–response model combined approach,” Process Safety and Environmental Protection, Vol. 88, pp. 253–262.

[4] Fluent Inc., 2014, Fluent 15.0, Fluent Inc., Lebanon, New Hampshire, USA.

[5] Simpson, R. L., Long, C. H., & Byun, G., 2002, “Study of Vortical Separation from an Axisymmetric Hill,” International Journal of Heat and Fluid Flow, Vol. 23, pp. 582-591.

[6] Taylor, P. A. and Teunissen, H. W., 1985, “The Askervein Hill Project: Report on the Sept./Oct. 193, Main Field Experiment,” Research Report MSRB-84-6, Meteortological Services Research Branch, Atmospheric Environment Service, 4905 Dufferin Street, Downview, ON, Canada M3H 5T4.

[7] Lavery, T.F., Bass, A., Strimaitis, D.G., Venkatram, A., Green, B.R., Drivas, P.J., 1982, “EPA complex terrain model development: First milestone report,” US EPA Report EPA-600/3-82-036.

[8] Persson, T., Liefvendahl, M., Bensow, R. E., and Fureby, C., 2006 “Numerical Investigation of the Flow over an Axisymmetric Hill using LES, DES and RANS,” Journal of Turbulence, Vol. 7, No. 4.

[9] Castro, F., Palma, J., and Lopes, A. S., 2003, “Simulation of the Askervein Flow, Part 1: Reynolds Averaged Navier–Stokes Equations (k−ε Turbulence Model),” Boundary-Layer Meteorology, Vol. 107, pp. 501-530.

[10] Apsley D. D., 1995, “Numerical Modelling of Neutral and Stably Stratified Flow and Dispersion in Complex Terrain,” Ph.D. Thesis, University of Surrey.

[11] Apsley, D. D. and Castro, I.P., 1997, “Numerical Modelling of Flow and Dispersion around Cinder Cone Butte,” Atmospheric Environment, Vol. 31, pp. 1059-1071.

[12] Patankar, S. V., 1980, Numerical Heat Transfer and Fluid Flow, Hemisphere Publishing Corp.

[13] Launder, B. E., and Spalding, D. B., 1972, Lectures in Mathematical Models of Turbulence, Academic Press, London, England.

[14] Launder, B. E. and Sharma, B. I., 1974, "Application of the Energy-Dissipation Model of Turbulence to the Calculation of Flow Near a Spinning Disc," Letters in Heat and Mass Transfer, Vol. 1, No. 2, pp. 131-138.

[15] Ma, R. and Simpson, R. L., 2005, “Characterization of Turbulent Flow Downstream of a Three-Dimensional Axisymmetric Bump,” In Proceedings of 4 th International Symposium on Turbulence and Shear Flow Phenomena, Williamsburg, VA, USA, pp. 1171-1176.

[16] Byun, G. and Simpson, R. L., 2006, “Structure of Three-Dimensional Separated Flow on an Axisymmetric Bump,” American Institute of Aeronautics and Astronautics (AIAA) Journal, Vol. 44, No. 5, pp. 999-1008.

[17] Moreira, G. A., Santos, A. A., Nascimento, C. A., and Valle, R. M., 2012, “Numerical Study of the Neutral Atmospheric Boundary Layer over Complex Terrain,” Boundary-Layer Meteorology, Vol. 143, No. 2, pp. 393-407.

[18] Zhang, X., 2009, “CFD simulation of neutral ABL flows,” Risø National Laboratory for Sustainable Energy, Technical University of Denmark, Roskilde, Denmark, Report No. Risø-R-1688(EN).

[19] Richards, P., and Hoxey, R., 1993, “Appropriate Boundary Conditions for Computational Wind Engineering Models using the k-ϵ Turbulence Model,” Journal of Wind Engineering and Industrial Aerodynamics, Vol. 46-47, pp. 145-153.

[20] Taylor, P. A. and Teunissen, H. W., 1987, “The Askervein Hill Project: Overview and Background Data,” Boundary-Layer Meteorology, Vol. 39, pp. 15-39.

[21] Mickle, R. E., Cook, N. J., Hoff, A. M., Jensen, N. O., Salmon, J. R., and Taylor, P. A., 1988, “The Askervein Hill Project: Vertical Profiles of Wind and Turbulence,” Boundary-Layer Meteorology, Vol. 43, No. 1-2, pp. 143-169.

[22] Gobbi, M. F. and Dorweiler, R. P., 2012, “Simulation of Wind over a Relatively Complex Topography: Application to the Askervein Hill,” Journal of the Brazilian Society of Mechanical Sciences and Engineering, Vol. 34, No. 4, pp. 492-500.

[23] Boçon, F. T., 1998a, “Modelagem Matemática do Escoamento e da Dispersão de Poluentes na Microescala Atmosférica”, Tese de Doutorado (Ph.D. Thesis), Universidade Federal de Santa Catarina, Florianópolis, Brazil.

[24] Boçon, F. T. and Maliska, C. R., 1998b, “Application of a Non Isotropic Model to Stable Atmospheric Flows Over 3D Topography”, In Proceedings of the 7th Brazilian Congress of Engineering and Thermal Sciences, Rio de Janeiro, Brazil, vol. 2, pp. 1334-1339.

[25] Strimaitis D. G., Venkatram A., Greene B. R., Hanna S., Heisler S., Lavery T. F., Bass A. and Egan B. A., 1983, EPA complex Terrain Model Development: Second Milestone Report, 1982m EPA-600/3-83-015, U.S. Environmental Protection Agency, Research Triangle Park, NC.

Conference on Modelling Fluid Flow (CMFF'15)
The 16th International Conference on Fluid Flow Technologies
Budapest, Hungary, September 1-4, 2015

DYNAMIC MESHING STRATEGIES TO MODEL FLUID FLOW IN ROLLING PISTON COMPRESSORS

Balázs Farkas[1], Viktor Szente[2], Jenő Miklós Suda[3]

[1] Corresponding Author. Department of Fluid Mechanics, Budapest University of Technology and Economics. Bertalan Lajos u. 4 - 6, H-1111 Budapest, Hungary. Tel.: +36 1 463 2464, Fax: +36 1 463 3464, E-mail: farkas@ara.bme.hu
[2] Department of Fluid Mechanics, Budapest University of Technology and Economics. E-mail: szente@ara.bme.hu
[3] Department of Fluid Mechanics, Budapest University of Technology and Economics. E-mail: suda@ara.bme.hu

ABSTRACT

By the nature of their working process, the clearances within the volumetric compressors are subjected to complex deformations. Therefore, deforming mesh has to be used to simulate transient effects with CFD codes. Using dynamic meshing makes the simulation of essential phenomena such as leakage flows and heat transfer effects quite challenging because the desired mesh quality close to the boundaries and within the narrow seal cavities is not easily maintainable in every instant as a result of deforming numerical domain. To achieve the desired mesh quality several methods are available. ANSYS Fluent has inbuilt smoothing and re-meshing options which give relatively limited control to the user. To overcome this issue predefined meshes can be used which can assure appropriate resolution at certain positions of the rolling cylinder which can help to keep the mesh quality within acceptable limit for the whole cycle. For more elaborate solution the mesh can be also fully controlled by using user defined functions which allows for creating unique meshing algorithm for the given problem. The aim of this study is to compare the accessible models within ANSYS Fluent and find a proper meshing method which allows to provide accurate prediction about the performance of a rolling piston compressor in the early stage of the design process.

Keywords: CFD, dynamic meshing, rolling piston compressor

1. INTRODUCTION

Because of the urgent need to use environmentally friendly energy resources, many new progressive solutions have been developed or are under ongoing development in recent years. Part of these solutions extract electric power from geothermal sources which can be an efficient way when easily accessible high thermal energy sources are available. However recently further efforts have been made to extract electric power from low enthalpy heat sources. Same sources are already widely used for air conditioning and heating purposes mainly for small individual households. Nevertheless, power generation using low enthalpy heat sources is more challenging since the low temperature ratio already restricts the thermal efficiency of the applied thermodynamic cycle. Therefore, the efficiency of the individual components used to realize the thermodynamic cycle has to be as high as possible to provide a cost efficient solution, even if waste amount of heat is available from the source. In case of conventional solutions the compressor and the expander are key elements of the system. To get the highest efficiency, choice of the construction type for the given purpose is as important as the careful design and manufacturing is. Here the traditional rolling piston type compressor design was used as a platform and was further improved as it is shown in Figure 1 to achieve sufficiently high performance. The vane

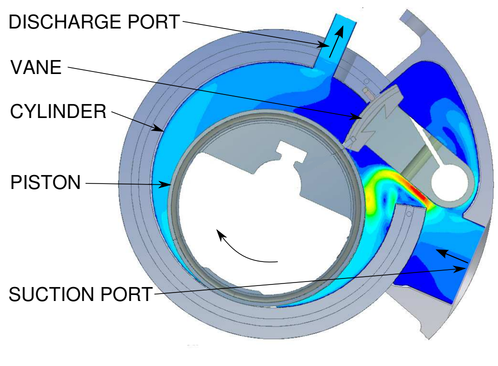

Figure 1. Velocity distribution within the rotating piston compressor designed by Magai [1]

which separates the high and low pressure chambers was redesigned and it is directly driven from the crankshaft of the piston which provides constant gap between the vane and piston, regardless the rotation speed without using extensive constrictive force and increasing the friction induced losses. The piston is solidly mounted on the crankshaft and does not roll along the inner surface of the cylinder. This design makes it similar to the trochoidal compressors, which do not require extremely small and expensive manufacturing tolerances because of the closed sealing border of the compression space and neither do they need oil for sealing [2].

To verify the theory, Computational Fluid Dynamics (CFD) tool was chosen to estimate the performance of this new design. Although CFD is known to be a very economical tool during evolutionary design process [3], most of the positive displacement compressor related studies are focused on developing and using concentrated parameter models since these components were considered as mainly thermodynamic devices. But within the past decade the havoc caused by fluid dynamics in destroying the efficiency has started gaining attention due to the pressing need for making these machines more energy efficient and reliable.

In 2004 two papers were presented at the International Compressor Engineering Conference in Purdue by the same company introducing a parametric CFD study related to the effect of the design of the notch [4] and suction piping [5] in meaning of noise and efficiency in case of a given double discharge compressor architecture. In both cases STAR-CD, a general CFD software was used for the simulations. The applied meshing techniques were not discussed in details but figures presented in [4] show a quadratic mesh within the cylinder with extended region of highly skewed elements around piston-cylinder gap and close to the vane. Despite these anomalies, the results resembled well the theory. In [5] where experimental tests were also conducted, the numerically predicted efficiency was also aligned well with the test results to verify the theory. More importantly, the trends in the change of performance parameters caused by geometry modifications, were predicted in good fashion.

In a study from 2010 by Liang et al. [6] two different kind of rolling piston compressors were investigated which were implemented with pressure activated discharge valves. The same solvers for the solution and governing the motion of the deforming mesh were used as in the above mentioned studies, but no further details were enclosed either. The predictions were also compared with experimental results. The error of the cooling capacity and power with the simulation and experiment test were less then 7%. The pressure rise vs. cranckshaft angle diagram of the simulation result is also claimed to be very close to the experiment test, although evident discrepancies can be observed on the presented graphs. Hui Ding et al. [7] from 2014 presented a new approach for simulating the applied discharge reed valve. For the simulations the PumpLinx CFD package were used which is specially targeted for simulating volumetric machines. According to the figures the applied meshing and re-meshing algorithms result in a good quality mesh within the whole computational domain where no highly distorted elements could been picked up. Here no further details about the applied meshing methods were enclosed either. Impressively, a whole revolution was claimed to be simulated within five hours on a general purpose quad-core Intel Xeon CPU at 2.67GHz machine. The predictions seemed to be aligned well with the theory, but obtained results were not compared to experimental test results.

Although deforming meshing seems to be ineludible, in the study of Brancher & Deschamps [8] the effect of the rotating rolling piston on the suction and discharge losses was estimated by steady 3D CFD solutions at different crankshaft angles. The predicted effective flow area and effective force area coefficients were implemented into a lumped parameter model. As a result significant improvement in the performance estimation were confirmed by experimental data.

2. SIMULATION MODEL

3D representation of the of the numerical domain resembling the Magai design compressor is presented on Figure 2(a). Since in this case the model

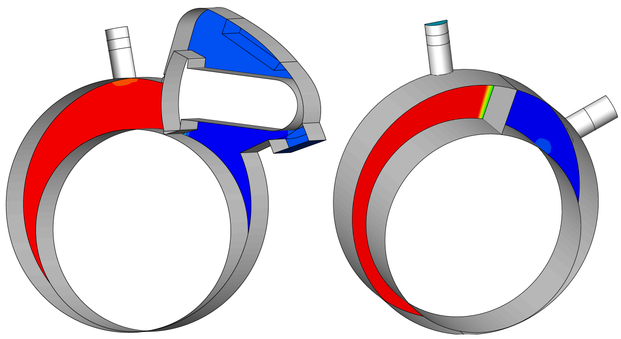

(a) (b)

Figure 2. Comparison between original Magai type compressor geometry (a) and the redesigned model compressor geometry (b)

compressor is symmetrical, the numerical domain was divided into two and only one half of it was modeled and it was completed by using symmetry boundary condition at the symmetry plane. The initial mesh was created using ANSYS Workbench but during the simulation the mesh was controlled by Fluent's dynamic mesh models [9]. The domain was meshed by triangular elements on the frontal faces which were then extruded to the axial direction parallel to the crankshaft creating wedge type elements as it is shown on Figure 3(a). During the transient computation the mesh was only regenerated on the frontal base mesh and this frontal mesh was than projected to the parallel mesh surfaces similarly as the base mesh was initially created. In ANSYS fluent terminology it is referred as 2.5D approach. The node points on the cylinder remained station-

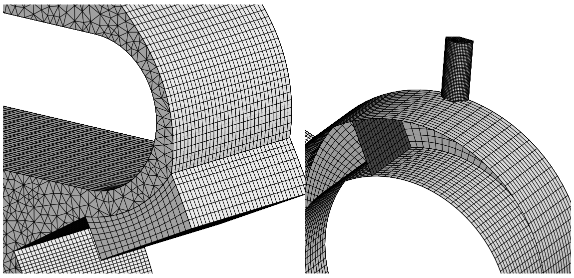

(a) (b)

Figure 3. Comparison of the numerical mesh for original Magai type compressor geometry (a) and for the redesigned model geometry (b)

ary and the nodes on the piston and vane surfaces followed rigid body like motion, which means that they kept their position respect to each other meanwhile the piston and the vane were rotated along their axes. To control the node points on the base surface spring/Laplace based smoothing and re-meshing algorithms were used. Both algorithms are part of the Fluent's dynamic mesh models. As the distortion of the cells increases by the large scale movements, ANSYS Fluent agglomerates cells that violate the initially defined skewness or size criteria and locally re-meshes the agglomerated cells or faces. If the new cells or faces satisfy the skewness criterion, the mesh is locally updated with the new cells with the solution interpolated from the old cells. Otherwise, the new cells are discarded and the old cells are retained [9]. This solution results in relatively easy model setup since only the rigid body motion of the moving parts has to be predefined by the user by external User Defined Functions (UDF's) and the rest is taken care by the Fluent's inbuilt algorithms. The maximum size of the cells in the tangential direction on the surfaces were limited by the gap between the moving elements to gain appropriate mesh quality within the small clearances. The deforming grid has to provide a connected domain of constant area which means that no parts of the flow domain can be isolated from the rest, therefore even in the smallest gap a one cell high layer has to be remained. Rest of the base surface is discretized with constant size elements which resulted in unreasonable resolution outside the boundary regions. Several attempts were made to preserve the initial mesh quality but in every case after the first revolution of the piston the computational domain got overlayed with homogeneous size distribution elements. This method resulted in eminently time consuming simulations. The simulation for one revolution took almost five days on a quad-core i7 k2600 processor when the mesh counted $2 \cdot 10^5$ cells in average, and the simulation was parallelized for all four cores available in one processor. The idea to use predefined meshes at given crankshaft angles were dropped when attempts to model the check valve were implemented. This is because unlike in case of a piston which rotates at a constant speed the position of the check or reed valve at a given crankshaft angle cannot be predicted in advance [10].

2.1. Redesigned model and new re-meshing approach

Because of the unexpectedly long solution time, the old model was replaced and the new computational domain is shown in Figure 2 (b). Here the vane was replaced by an impermeable blade with infinitesimal thickness which significantly reduces the complexity of the original geometry. The new discretization is presented in Figure 3 (b) in comparison with the original mesh. The mesh contains only hexaghedral elements. The position of the mesh nodes within the cylinder were fully controlled by an external UDF using designated macros provided by ANSYS Fluent. The re-meshing process is illustrated in Figures 4 (a) and (b). During the rotation of the piston the axial position of the nodes do not change, which means that the nodes do not move parallel to the direction of the crankshaft. The motion of the nodes on the piston resembles a rigid body like motion, where the point *P*, which is the center of the piston, point *V*, which is the bottom point of the vane on the piston, and point *A*, which is an arbitrary node point on the piston surface, retain their position in respect to each other at each instant of the cylinder motion. This rigid body motion is described by the motion of the imaginary *O-V* rod which is part of the simple *O-P-V* crank mechanism where point *O* is the center of the cylinder and also defines the position of the axis of the crankshaft. The crankshaft angle is defined by the angular position of the *O-P* section which rotates around point *O*. The movement of point *V* is restricted to the vertical direction which also means that the blade keeps its vertical position during the rotation of the cylinder. This motion resembles the motion of a piston in a hinged vane compressor [11]. The position of an arbitrary *A'* node point on the cylinder surface is than defined as the projection of point *A* from the piston surface along the straight *O-A-A'* line. The rest of the points

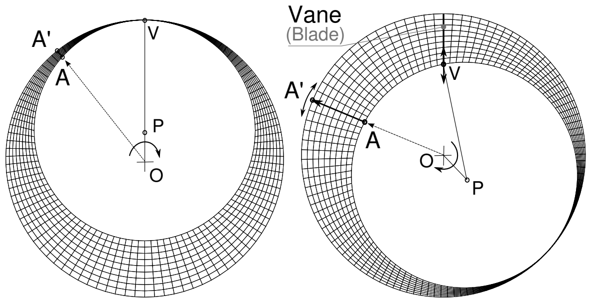

(a) (b)

Figure 4. Illustration of the new meshing process by two meshes taken at (a) 0^o **and (b)** 135^o **crankshaft angles**

between *A* and *A'* are distributed equally within the straight *A-A'* section. This equal distribution is optional and not restricted by the method. Also, the method can be adapted to different blade thicknesses. Using the same settings discussed in the following section the simulation of one revolution took approximately twelve hours on the same architecture using just one core of the quad-core processor. The mesh holds constant number of $2 \cdot 10^4$ cells. At this point, parallelization was not implemented in the prewritten UDF code, since the achieved simulation time was already acceptable. Also, by running different cases in parallel, the available computational capacity was suitably utilized by the simultaneously running serial processes.

3. COMPARISON BETWEEN THE DIFFERENT MODELS

For performance estimations, the compressor was throttled back by adding a porous layer upstream from the exit of the outlet pipe. The porous media was modeled by the addition of the Darcy-Forchheimer type source term to the standard fluid flow equations. For both models, the outlet pipe was connected across a non-conformal mesh interface [9] to the cylinder and the geometry of the outlet pipe was identical in both cases. In case of the simplified model the inlet pipe was also connected in the same way to the cylinder. The inlet and outlet pipe tangential position for the simplified model was defined so that compression process would have the same extension as it is in the case of the original model. The solver was used with the standard settings. To model turbulent quantities, realizable k-ϵ turbulence model was used, both at the inlet and the outlet the ambient temperature and pressure was imposed as boundary conditions. For the preliminary computations the walls were considered to be adiabatic. The working fluid was taken as ideal compressible air.

Because of the meshing considerations, the moving elements are not connected directly to their counterparts at the sealings, therefore here the flow is restricted by a porous domain defined within a narrow area limited to couple of cells within a given radius around the theoretical contact points. Here the porous resistance was also defined by Darcy-Forchheimer source term. In both cases, the viscous resistance was set to the maximum allowed value, for which the stability of the solution is ensured.

The models were tested at two distinct throttling configuration. The predicted variation of the pressure at the cylinder exit just upstream the porous zone is shown in Figures 5 (a) and (b). The results align relatively well in both low and high throttling cases. Although, despite that the same loading was imposed for both models, the predicted pressure ratio reached higher values in case of the redesigned and simplified model compressor (Fig. 2 (b)) than in case of the original design resembling the exact geometry of the Magai compressor (Fig. 2 (a)). Hence, the gradient of the curves representing the actual pressure rise in the model compressor is slightly higher, both in Fig. 5 (a) and (b).

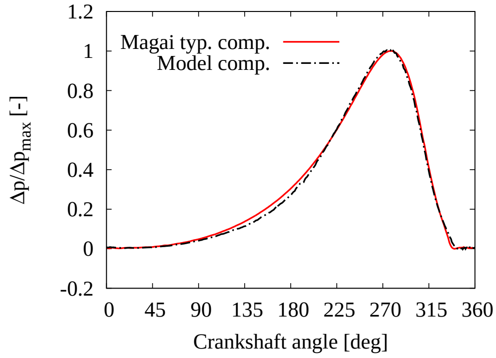

(a)

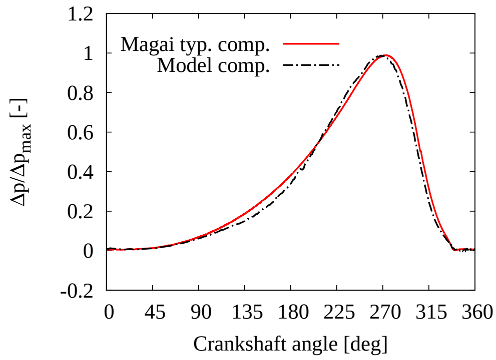

(b)

Figure 5. Pressure difference between the inlet and the outlet normalized with the maximum value at (a) high and (b) low throttling conditions, predicted by the original model resembling the Magai type compressor geometry and the simplified model compressor

In case of the model compressor, the predicted volumetric efficiency was 93% at lower throttling and 90% at higher throttling. On the other hand, the same values are consecutively 88% and 84% in case of the original Magai type compressor model. The discrepancies are the result of the higher leakage flow predicted by the original model. In the original geometry there are two extra sealings connected to the vane which were not taken into the account in the simplified model. However, the leakage flow can be adjusted by changing the viscous resistance of the porous zone at the sealing contact positions, and part of the vane blade can be turned to be permeable to simulate the leakage across the vane. Still, there is not much chance to significantly improve the predictions before relevant measurement data are available for appropriate tuning.

4. COMPRESSOR AND DISCHARGE VALVE

Rolling piston compressors are usually implemented with a discharge valve to prevent back flow when the discharge port is connected to a high pressure reservoir. The applied valves are usually simple reed valves made of high-grade steel. However, the Magai type compressor was planned to be coupled with a commercially available pneumatic check valve for the duration of the first test period because of practical reasons. The numerical model is presented in Figure 6.

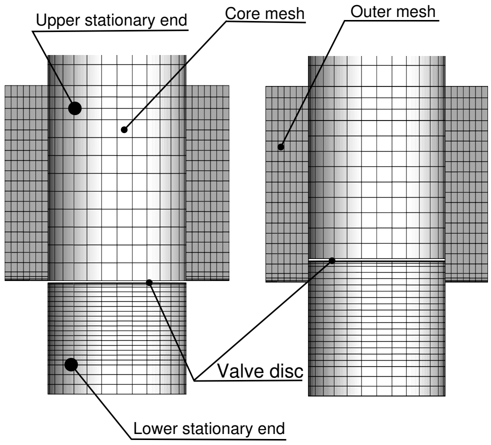

Figure 6. The numerical model of the discharge valve in closed and fully opened position

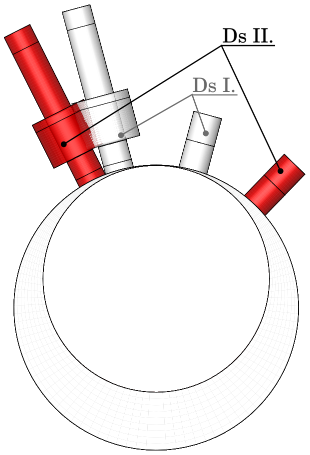

Figure 7. Representation of the different setups

The core and the outer part of the mesh is connected across a non-conformal mesh interface. The core part between the upper and lower stationary end is dynamic and follows the movement of the pressure activated valve disc. The position of the node points within this dynamic region is controlled by ANSYS Fluent's smoothing algorithm and no re-meshing was applied. This solution can be only used with the simplified compressor model, since the smoothing algorithm is not accessible when the 2.5D model is active. Because of the vane design of the Magai type compressor, the tangential distance between inlet and the outlet ports is relatively high compared to the traditional rolling piston type compressor architectures. This can result in decreased volumetric efficiency,

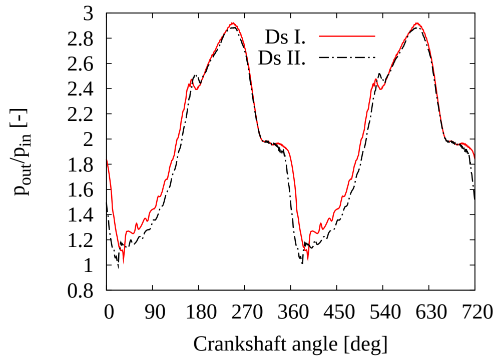

Figure 8. Ratio between the inlet and the cylinder outlet pressure in function of the Crankshaft angle in case Ds I. and Ds II.

since the effective compressed volume is reduced. To investigate the effect of the tangential separation of the inlet and outlet ports, two distinct designs were tested as it is shown in Figure 7. In both cases loading was imposed by the increased pressure at the outlet boundary, which resembles a scenario when the outlet port is connected to a pressurized system. This ratio was set to be relatively low and the pressure at the outlet boundary is twice as high as the inlet pressure. Figure 8 show the variation of the pressure ratio between the cylinder outlet pressure upstream the discharge valve and the inlet ambient pressure. There is no significant difference between the two curves. However, in case of DsI., when the in-take and the discharge ports are closer to each other, the pressurization starts earlier and the discharge process takes longer. There is a distinct overshoot in maximum pressure compared to the outlet pressure at the outlet boundary, which is the result of the throttling imposed by the sudden area change between the cylinder and the discharge pipe, and also of the additional throttling imposed by the discharge valve itself. The

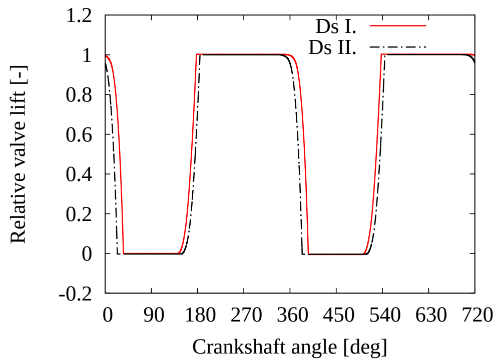

Figure 9. The relative valve lift in function of the Crankshaft angle in case Ds I. and Ds II.

relative valve lift is presented in Figure 9. The area ratio between the outlet port and free surface of the opened valve is 0.95. The variation of the valve lift also confirms the longer discharge process in case of Ds I., although no significant difference can be observed. However the predicted volumetric efficiency is dropped from 94% to 86% as the angular distance was increased between the inlet and outlet ports from Ds I. to Ds II..

5. CONCLUSION

To improve the performance of the traditional rolling piston type compressors, a new design was introduced. To verify the expectations regarding the redesigned system the CFD model of the new geometry was prepared and tested.

To increase the computational efficiency and reduce computational, original model was simplified and a new 3D moving mesh approach was introduced.

The new method was compared to the original algorithm which was provided by the ANSYS Fluent solver.

Despite some marginal discrepancies, the viability of the new method was proven although no final conclusion can be withdrawn before sufficient experimental data will be available.

The new moving mesh approach has proved the potential for further development and the possibility to adapt it for more complex geometries. Finally, a more complex compressor model coupled with a discharge valve was introduced to investigate the effect of the increased angular separation between the suction and the discharge port.

It was estimated that it has moderate effect on the overall performance at low pressure ratios. If these trends can be experimentally confirmed than a future parametric study can be conducted with a new model to find an optimal design.

6. ACKNOWLEDGEMENT

This research has been supported by the New Széchenyi Plan under contract No. KMR_12-1-2012-0199.

REFERENCES

[1] I. Magai, "http:// www.magaimotor.magai.eu," 2014.

[2] ASHRAE, *Compressors*. 2000 ASHRAE Systems and Equipment Handbook, 2000.

[3] B. G. Prasad, "Cfd for positive displacement compressors," in *International Compressor Engineering Conference*, (Purdue University), July 12-15 2004.

[4] W. Geng, C. H. Liu, and Y. Z. Wang, "The performance optimization of rolling piston compressors based on cfd simulation," in *International Compressor Engineering Conference*, (Purdue University), July 12-15 2004.

[5] C. H. Liu and W. Geng, "Research on suction performance of two-cylinder rolling piston type rotary compressors based on cfd simulation," in *International Compressor Engineering Conference at Purdue*, (Purdue University), July 12-15 2004.

[6] S. Liang, S. Xia, X. Kang, P. Zhou, Q. Liu, and Y. Hu, "Investigation of refrigerant flow simulation and experiment of rolling piston," in *International Compressor Engineering Conference at Purdue*, (Purdue University), July 12-15 2010.

[7] H. Ding and H. Gao, "3-D transient cfd model for rolling piston compressor with dynamic reed valve," in *International Compressor Engineering Conference at Purdue*, (Purdue University), July 14-17 2014.

[8] R. D. Brancher and C. J. Deschamps, "Modeling of rolling-piston compressors with special attention to the suction and discharge processes," in *International Compressor Engineering Conference at Purdue*, July 14-17 2014.

[9] *ANSYS Fluent documentation., v14.5, http://www.ansys.com*, 2012.

[10] B. Farkas, V. Szente, and J. M. Suda, "A simplified modeling approach for rolling piston compressors," *Period. Polytech. Mech. Eng.*, vol. 59, no. 2, pp. 94–101, 2015.

[11] M. Okur and I. S. Akmandor, "Experimental investigation of hinged and spring loaded rolling piston compressors pertaining to a turbo rotary engine," *Applied Thermal Engineering*, vol. 31, no. 6-7, pp. 1031–1038, 2011.

Conference on Modelling Fluid Flow (CMFF'15)
The 16th International Conference on Fluid Flow Technologies
Budapest, Hungary, September 1-4, 2015

INFLUENCE OF BOUNDARY CONDITIONS ON THE STRATIFIED FLUID FLOW IN ATMOSPHERIC BOUNDARY LAYER

Hynek ŘEZNÍČEK[1], Luděk BENEŠ[2]

[1] Corresponding Author. Department of Technical Mathematics, Faculty of Mechanical Engineering-Czech Technical University in Prague. Technická 4, 166 07 Praha 6 - Dejvice, Czech Republic. Tel.: +420-22435-7538, E-mail: hynek.reznicek@fs.cvut.cz
[2] Department of Technical Mathematics, Faculty of Mechanical Engineering-Czech Technical University in Prague. Technická 4, 166 07 Praha 6 - Dejvice, Czech Republic. E-mail: ludek.benes@fs.cvut.cz

ABSTRACT

The mathematical model of 2D flow of viscous incompressible stratified fluid is presented in this paper. The flow over the cosine-shaped hill was calculated in the Atmospheric Boundary Layer (ABL). The influence of different boundary conditions on stationarity of the flow and generation of turbulent eddies was studied. Navier – Stokes equations of fluid flow in Boussinesq approximation were solved by finite volume method on structured non-orthogonal grid. The AUSM method with MUSCL reconstruction was used. The integration in time was approximated by BDF formula, the artificial compressibility was used in dual time. Further numerical experiments are presented with different boundary conditions. In order to eliminate the interaction between the original and reflected lee waves from upper boundary, the boundary domain method was added. The influence of boundary domain damping functions was studied.

Keywords: atmospheric boundary layer, boundary conditions, boundary domain, finite volume method, CFD, stratified fluid flow

NOMENCLATURE

g	$[m/s^2]$	gravity acceleration
p	$[Pa]$	pressure
F_{ext}	$[-]$	external fluxes
H	$[-]$	inviscid fluxes
R	$[-]$	inviscid fluxes
τ	$[s]$	artificial time
G	$[ms^{-2}]$	volume acceleration vector
H^p	$[-]$	artificial pressure diffusion flux
n	$[-]$	outer normal to the cell
u	$[m/s]$	velocity
W	$[-]$	vector of unknowns
Z	$[-]$	Difference between time steps
Δ	$[m$ resp. $s]$	step size
δ	$[-]$	Kronecker delta
μ	$[Pa.s]$	dynamic viscosity
ν	$[m^2/s]$	kinematic viscosity
ρ	$[m^3/s]$	density
ξ	$[-]$	damping function

Subscripts and Superscripts

$*$	average variable in domain
$,t$	time derivative
$,x_i$	space derivatives
0	background variable
bd	boundary domain values
i, j	vector coordinates ($\in \{1, 2\}$)
n	time index
$'$	perturbation
$+/-$	AUSM upstream index

1. INTRODUCTION

The pollution in the ABL is increasing these days and its different effects on human life are more investigated. The numerical modelling can help us to predict the transmission of the pollution and to understand its behaviour. However there are a lot of models for concentration, the core of this problem lies in an accurate fluid flow modelling. Dangerous areas can be easily identified from exact simulation of the velocity field and density distribution. Examined problems cover the research field of micrometeorology [1].

The computational fluid dynamics has its own specifics, which differ from another problems arise from measurement in real atmosphere or in wind tunnels. Even for simple mathematical model, the solution depends strongly on boundary conditions. In our case the flow is described by 2D Navier–Stokes equations for incompressible stratified fluid. The Coriolis terms are neglected due to the micro-scale [2]. The additional transport equation for density (its perturbation) is coupled to the momentum equations through a buoyancy term. Consequently this buoyancy terms generate lee waves behind an obstacle such as cosine-shape hill, which propagate on long distance. These waves are affected by the artificial boundaries of the computed domain.

The similar geometric arrangement of the computer domain as in article [3] is selected as reference. Three experiments with different boundary conditions take place in this study. First, the homogeneous Neumann boundary condition for the perturbation of density on bottom boundary was changed to homogeneous Dirichlet condition and the influence on stationarity of the flow were evaluated. Second, the input profile was changed because undeveloped input current creating unphysical waves near the input boundary, the effects on these unphysical waves were studied. Third, the boundary domain on the top boundary was added and it was expected, that its influence on the wave reflection from the top boundary would be observed.

Goal of this scope lies in creating (and implementing) new stable 2D model for fluid flow in ABL. This Basis should serve for future model of pollution concentration transport (near highway) in ABL.

2. MATHEMATICAL MODEL

This section describes in detail development and simplification of the mathematical model for incompressible fluid flow with variable density. Necessary assumptions and approximations are introduced.

2.1. Simple incompressible model

The fully incompressible fluid with negligible heat transmission is assumed. This assumption is similar to consideration of the fluid with infinite Prandtl number, therefore the equation for conservation of heat is not needed.

The assumption of fluid incompressibility is justified because the velocity in ABL is low. Incompressible fluid flow has to satisfy the divergence-free constraint:

$$\frac{\partial u_j}{\partial x_j} = 0, \tag{1}$$

where index $j = \{1, 2\}$ indicates 2D vector components and Einstein's summation convention is used. The flow of this fluid is described with conservations laws. The conservation of mass is given by the continuity equation with variable density ρ

$$\frac{\partial \rho}{\partial t} + \frac{\partial \rho u_j}{\partial x_j} = 0. \tag{2}$$

Using the eq. (1) and the chain rule of differentiation this equation leads to the transport equation for density in a form:

$$\frac{\partial \rho}{\partial t} + u_j \frac{\partial \rho}{\partial x_j} = 0. \tag{3}$$

The conservation of momentum is described by Navier – Stokes equation:

$$\frac{\partial \rho u_i}{\partial t} + \frac{\partial \rho u_j u_i}{\partial x_j} = -\frac{\partial p}{\partial x_i} + \mu \frac{\partial^2 u_i}{\partial x_j^2} + \rho G_i, \tag{4}$$

where u_i is the velocity vector, p denotes the pressure , μ is kinematic viscosity and G_i denotes the vector of volume acceleration. Using chain rule of differentiation for the left side of this equation together with eq. (3) leads to:

$$\frac{\partial u_i}{\partial t} + \frac{\partial u_j u_i}{\partial x_j} = -\frac{1}{\rho}\frac{\partial p}{\partial x_i} + \nu \left(\frac{\partial^2 u_i}{\partial x_j^2} \right) + G_i. \tag{5}$$

Expressing further the gravity force $G_i = -g\delta_{i2}$ leads to the following set of equations :

$$\begin{aligned} \frac{\partial u_j}{\partial x_j} &= 0, \\ \frac{\partial \rho}{\partial t} + u_j \frac{\partial \rho}{\partial x_j} &= 0, \\ \frac{\partial u_i}{\partial t} + \frac{\partial u_j u_i}{\partial x_j} &= -\frac{1}{\rho}\frac{\partial p}{\partial x_i} + \nu \left(\frac{\partial^2 u_i}{\partial x_j^2} \right) - g\delta_{i2}. \end{aligned} \tag{6}$$

2.2. Boussinesq approximation

We assumed that pressure and density fields are perturbation of hydrostatic equilibrium state:

$$\begin{aligned} p(t, x_1, x_2) &= p_0(x_2) + p'(t, x_1, x_2), \\ \rho(t, x_1, x_2) &= \rho_0(x_2) + \rho'(t, x_1, x_2). \end{aligned} \tag{7}$$

The background density and pressure fields are linked via the hydrostatic relation:

$$\frac{\partial p_0}{\partial x_2} = -\rho_0 g. \tag{8}$$

It is common to use the Boussinesq approximation for these premises for simulations in the ABL. The transport equation for density (3) can be rewritten (using divergence-free constraint (1)):

$$\frac{\partial \rho_0}{\partial t} + \frac{\partial \rho'}{\partial t} + u_j \frac{\partial \rho_0}{\partial x_j} + u_j \frac{\partial \rho'}{\partial x_j} = 0. \tag{9}$$

Since background density depends only on the vertical coordinate ($\rho_0 = \rho_0(x_2)$) it leads:

$$\frac{\partial \rho'}{\partial t} + u_j \frac{\partial \rho'}{\partial x_j} = -u_j \frac{\partial \rho_0}{\partial y} \delta_{j2}. \tag{10}$$

The vertical hydrostatic pressure in eq. (5) is replaced by eq. (8). The newly formed term is given together with gravitational force term and according to eq. (7) the horizontal part of the background pressure gradient is equal to zero. It leads to:

$$-\frac{1}{\rho}\frac{\partial p}{\partial x_i} - g\delta_{i2} = -\frac{1}{\rho}\frac{\partial p'}{\partial x_i} - \frac{\rho'}{\rho} g\delta_{i2}. \tag{11}$$

At the end density is approximated by average density in computing area ρ_*

. The system of equations in Boussinesq approximation is then:

$$\begin{aligned}
\frac{\partial u_j}{\partial x_j} &= 0, \\
\frac{\partial \rho'}{\partial t} + \frac{\partial u_j \rho'}{\partial x_j} &= u_2 \frac{\partial \rho_0}{\partial x_2}, \qquad (12) \\
\frac{\partial u_i}{\partial t} + \frac{\partial u_j u_i}{\partial x_j} &= -\frac{1}{\rho_*}\frac{\partial p'}{\partial x_i} + \nu\left(\frac{\partial^2 u_i}{\partial x_j^2}\right) - \frac{\rho'}{\rho_*} g \delta_{i2},
\end{aligned}$$

where the second equation in (12) was modified using (1), to obtain the conservative form of the equations. These are integrated in space and the Gauss-Ostrogradsky theorem can be used.

2.3. Vector form of equations

The whole system (12) can be rewritten into a vector 2D conservative form:

$$PW_{,t} + H(W)^{(i)}_{,x_i} - \nu(R(W)^{(i)}_{,x_i}) = F_{ext}, \qquad (13)$$

where the $W = [p', \rho', u_1, u_2]^T$ is vector of unknowns, matrix $P = diag[0,1,1,1]^T$, symbol $(.)_{,x_i}$

or $(.)_{,t}$

denotes derivatives, matrices Hcontain the inviscid fluxes:

$$\begin{aligned}
H^{(1)} &= [u_1, u_1\rho', u_1^2 + p'/\rho_*, u_1 u_2]^T, \\
H^{(2)} &= [u_2, u_2\rho', u_1 u_2, u_2^2 + p'/\rho_*]^T. \qquad (14)
\end{aligned}$$

Matrices R are the viscous fluxes

$$\begin{aligned}
R^{(1)} &= [0, 0, u_{1,x_1}, u_{2,x_1}]^T \\
R^{(2)} &= [0, 0, u_{1,x_2}, u_{2,x_2}]^T \qquad (15)
\end{aligned}$$

and vector F_{ext} is the source term

$$F_{ext} = [0, -u_2 \frac{\partial \rho_0}{\partial x_2}, 0, -\frac{\rho'}{\rho_*} g]^T \qquad (16)$$

3. NUMERICAL APPROXIMATION

The high resolution finite volume method was used. Discretization was done by the methods of lines.

3.1. Spatial discretization

The AUSM scheme was used for space discretization of inviscid fluxes:

$$\int_{\partial\Omega} [H^{(1)} n_1 + H^{(2)} n_2] ds \approx$$

$$\approx \sum_{l=1}^{4} \left[\begin{pmatrix} 1 \\ \rho \\ u_{1+/-} \\ u_{2+/-} \end{pmatrix} u_n + \frac{p}{\rho_*}\begin{pmatrix} 0 \\ 0 \\ n_1 \\ n_2 \end{pmatrix}\right] s_l, \qquad (17)$$

where quantities p and ρ on the cell face are approximated by the central formula from neighbouring cells. Velocities on the cell face are computed using MUSCL reconstruction according to van Leer [4]:

$$u_+ = u_{k+1} - \frac{1}{2}\delta_+, \quad \text{resp.} \quad u_- = u_k + \frac{1}{2}\delta_- \qquad (18)$$

with the Hemker-Koren slope limiter function:

$$\delta_{+/-} = \frac{a_{+/-}(b^2_{+/-} + 2) + b_{+/-}(a^2_{+/-} + 1)}{2a^2_{+/-} + 2b^2_{+/-} - a_{+/-} b_{+/-} + 3},$$

$$\begin{aligned}
a_+ &= u_{P+1} - u_P;\ a_- = u_{L+1} - u_L, \\
b_+ &= u_P - u_{P-1};\ b_- = u_L - u_{L-1}. \qquad (19)
\end{aligned}$$

The numbers $P, L \in \mathbb{Z}$ denote index values of the velocities (e.g. face between cells (k) and $(k+1)$ i.e $P = k+1$ (index by u_+) a $L = k$ (index by u_-)). Since the pressure is approximated by central difference, the scheme is stabilised by the artificial pressure diffusion introduced in [5]. The discrete version of the additional flux i.e. for face between cells (k) and $(k+1)$ is given by:

$$H^{(p)} = [\frac{p_{k+1} - p_k}{\beta_p}, 0, 0, 0]^T, \qquad (20)$$

where $\beta_p = U_{max} + \frac{2\nu}{\Delta}$, Δ is the step size of grid. The viscous fluxes are discretized in the central way on dual (diamond type) mesh. This scheme is of the second order in space. See details in [6].

3.2. Time integration

The artificial compressibility method with dual time was used in time discretization. The resulting system of ODEs was integrated in physical time. Suitable Runge–Kutta multistage scheme was used in dual time

After the space discretization the time derivative is approximated by the robust second order BDF formula:

$$W_{,t} \approx \frac{3W^{n+1} - 4W^n + W^{n-1}}{2\Delta t}. \qquad (21)$$

The time step Δt can be chosen according to the problem. If we define the reziduum as:

$$\begin{aligned}
\mathrm{Rez}(W^{n+1}) := P\frac{3W^{n+1} - 4W^n + W^{n-1}}{2\Delta t} + \\
+ H(W^{n+1}) + R(W^{n+1}) - F_{ext}(W^{n+1}), \qquad (22)
\end{aligned}$$

then the following system of equations has to be rewritten for the time step $n+1$:

$$\mathrm{Rez}(W^{n+1}) = 0. \qquad (23)$$

This equation is solved by principle of artificial compressibility method in an artificial (dual) time τ. The dual time derivative of pressure is added to the continuity equation. The stationary solution of the following system is sought:

$$\tilde{P} W_{,\tau} + \mathrm{Rez}(W^{n+1}) = 0, \qquad (24)$$

where $\tilde{P} = [1,1,1,1]^T$. The system of ODEs is solved by an explicit 3-stage Runge-Kutta method.

4. THE NUMERICAL EXPERIMENTS

The numerical experiments were computed in the 2D computational domain 90×30 m large, with the cosine shaped hill with hight $h = 1$ m. The whole situation is shown in the Fig. 1. The structured, non-orthogonal grid with 233×117 points was used. The smallest vertical step was $\Delta_{x_2} = 0.03$ m. This domain is based on the model suggested in [3] for the purpose of easy validation.

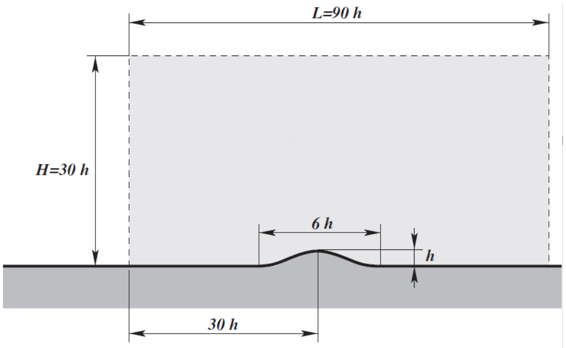

Figure 1. *Base computational domain*

4.1. Set up of parameters

These physical parameters where used in our computations. The average density was $\rho_* = 1 \frac{\text{kg}}{\text{m}^3}$ and the gradient of background density was set for all experiments to the same value $\frac{\partial \rho_0}{\partial x_2} = -0.01 \frac{\text{kg}}{\text{m}^4}$. The stratification of fluid is given by the Brunt-Väisälä frequency

$$N^2 = -\frac{g}{\rho_*}\frac{\partial \rho_0}{\partial x_2}. \tag{25}$$

We have calculated several cases under the different stratification, which can be achieved by the different gravity acceleration $g = -5, -10, -20, -50 \frac{\text{m}}{\text{s}^2}$. The propagation of lee waves depends on stratification.

The same kinematic viscosity as in [3] was chosen $\nu = 10^{-3} \frac{\text{m}^2}{\text{s}}$. This set up ensure lower influence of turbulence, because the Reynolds number is approximately $Re = 1000$. The greater Reynolds number should be used for real atmosphere, but the turbulence model would be required in this case. Characteristic velocity was $U_0 = U_{max} = 1 \frac{\text{m}}{\text{s}}$. Physical time step was chosen to $\Delta_t = 0.1$ s.

4.2. Boundary conditions

The boundary conditions for validation are introduced here. Different settings are mentioned directly in description of the each experiment. The boundary conditions are realised by ghost cells method. The values of the unknowns are calculated through the linear extrapolation to obtain the right values on the boundaries.

Inlet: The horizontal velocity component is prescribed by power law wind profile $u_1 = U_{max}(\frac{x_2}{h})^{1/40}$. The homogeneous Dirichlet condition was prescribe for other variables as mentioned in [7], only the pressure was extrapolated.

Outlet and top: Homogeneous Neumann condition was prescribed for all variables.

Bottom: The pressure was extrapolated. The no-slip (homogeneous Dirichlet) condition for velocity components was prescribed and the homogeneous Neumann condition for the density (its perturbation) was given.

5. VALIDATION

The wavelength of lee waves was compared to the theoretical values and the profiles of vertical velocity on sectional line were compared to the ones within the original article [3], for validation of the numerical model results. The shape and character of waves was quite similar. Small differences in the wavelength was probably caused by different evaluation time. The article do not provide the time of evaluation.

5.1. Wavelength

The theoretical values of wavelength were computed from the Brunt-Väisälä frequency for each stratification. Than the wavelength was measured by two methods: the distances of the wave maxima were determined and the wavelengths in section line perpendicular to the direction of waves propagation were plotted. The results are shown in Table 1. Considering the errors in measurement (approx. 1 m), the values are in a good agreement.

Table 1. The comparison of theoretical and measured values of wavelength

	Theory	Measure	
		Distance	Section line
$\lvert g \rvert$ $\left[\frac{\text{m}}{\text{s}^2}\right]$	wavelength [m]		
5	31	33	33
10	22	23	17
20	15	17	12
50	10	10	7

5.2. Vertical velocity profile

The values of vertical velocity were plotted along the sectional line started in the middle of the hill and the inclination was 45 degrees. The plotting was done for each stratification and it was compared to vertical velocities profile from [3]. The amplitudes and the shape of results in Fig. 2 are similar to the original ones in Fig. 3.

The lee waves are observed in both figures, there are more waves for higher gravity acceleration in the original figure. It can be caused by a little bit different time of evaluation. Even if there is declared to have the final (stationary) flow in the original figure, the flow is changing a little bit all time and the waves are slightly moving.

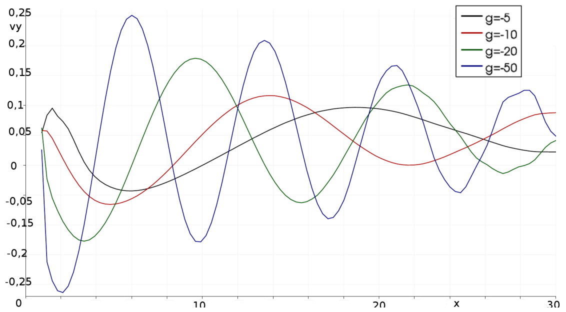

Figure 2. *Vertical velocities profiles*

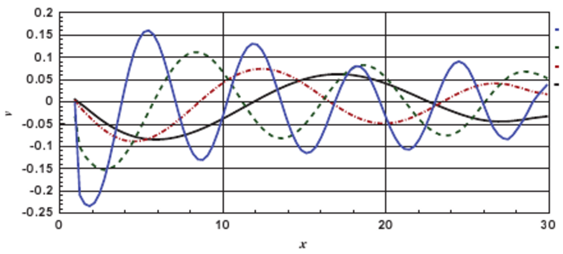

Figure 3. *Vertical velocities profile from [3]*

6. DIFFERENT BOUNDARY CONDITIONS

Three changes of boundary conditions are described in this section and the result are presented. First, the boundary condition for the density (its perturbation) at the bottom was changed to homogeneous Dirichlet condition. Second, the wind profile on input was changed to reduce the waves occuring at the entrance. The boundary domain was added on the upper boundary and the behaviour of the flow was studied in the third numerical experiment.

6.1. Boundary condition for the density

If the homogeneous Neumann condition for density perturbation is prescribed on the bottom boundary, some non-stationary behaviour of the flow occures in the vicinity of the hill. This fact is disturbing, so the homogeneous Dirichlet condition was tried. The new condition has stronger restrictions on the flow.

The differences between two consecutive physical time steps were calculated as:

$$Z(W) := \sqrt{\frac{1}{N}\sum_j (W_j^{n+1})^2 - (W_j^n)^2}. \qquad (26)$$

he pressure component of the this differences was observed. Figs. 4 and 5 show this differences plotted in dependence on iterations of physical time. The first one is more stationary then the second one, because the stronger restriction prevents the formation of vortices. The plots are from the experiment with $g = -50\ \frac{\mathrm{m}}{\mathrm{s}^2}$, because the effect is most visible there.

The effect is more obvious, when the vertical velocity profile on the horizontal section line is plotted.

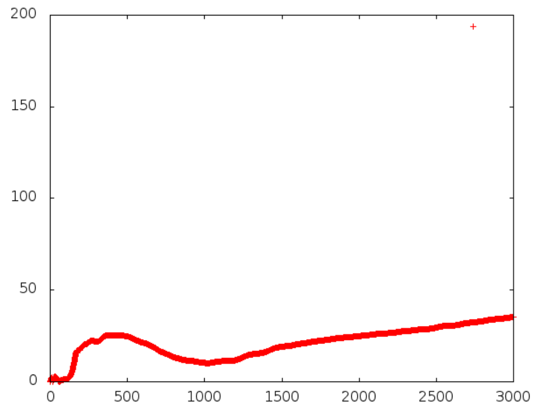

Figure 4. *Differences Z for Dirichlet boundary cond.*

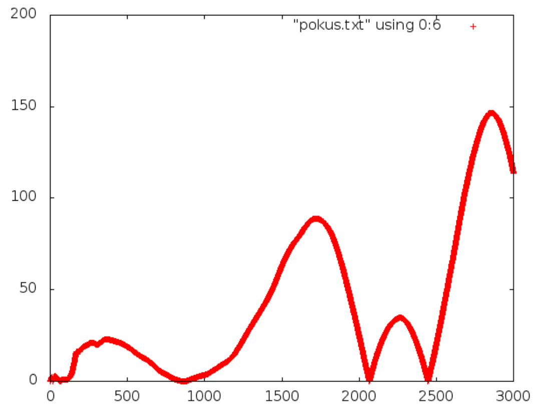

Figure 5. *Differences Z for Neumann boundary cond.*

The section line was in $h = 1$ m above surface (tangent to the top of the hill). Fig. 6 shows this profile for $g = -10\ \frac{\mathrm{m}}{\mathrm{s}^2}$. The original experiments from previous section are marked in blue ("val"), it shows the situation with homog. Neumann condition for density perturbation. This condition produced vortexes behind the hill, unlike homog. Dirichlet condition. The figure also shows situation, when the slope limiter from eq. (19) is omitted (mark "lam") - in this case the flow is much more damped, and the effect is not noticeable.

The physical explanation of the numerical experiment lies in the thermal influence of the ground. If the density perturbation is not constant (homogeneous Neumann condition), the air could be heated from the ground. However no heat transfer is still assumed in the fluid. The heating from the ground is neglected in the case of homogeneous Dirichlet condition - the corresponding situation in real ABL can be found in a very stable stratification when the sun does not heat the ground properly. The stable stratification terms are very important for modelling the pollution transport, because the pollution is most transported in a lower part of atmosphere where it is

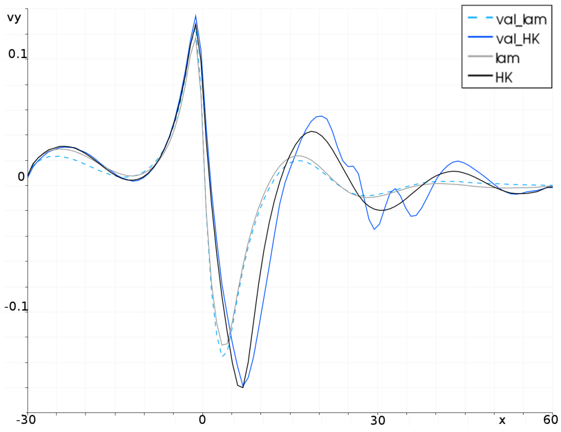

Figure 6. *Horizontal profile of vertical velocities*

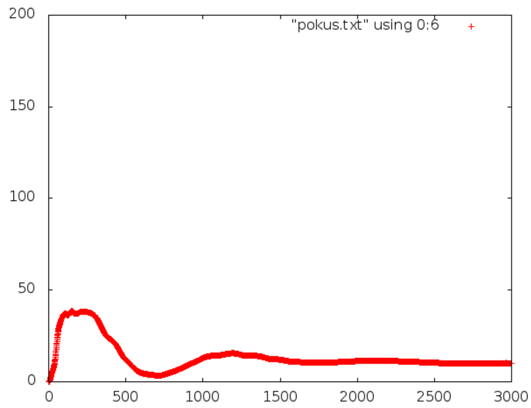

Figure 8. *Differences Z for the other input profile*

most dangerous.

6.2. Input velocity profile

The wind profile for the input horizontal velocity was changed. The flow was allowed to developed into the 10 m periodic channel (with the same top and bottom boundary conditions as in computational domain). After 100 cycles the wind profile at the output of the channel was prescribed to the input of computational domain. The Fig. 7 shows the result for $g = -50\ \frac{\mathrm{m}}{\mathrm{s}^2}$, which can by compared with figures in Appendix (validation).

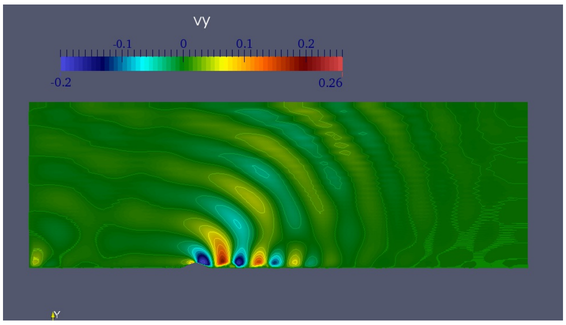

Figure 7. *The field of vertical velocities for other input profile*

The waves occuring at the entrance are smaller, but the amplitudes of vertical velocities in the domain are not the same as in the validation experiments. It can be caused by the different mass flow rate, although the maximum velocity of the input profile was the same.

This change on the input boundary condition has got influence on the stationarity as well, as it is illustrated in Fig. 8 (in comparison to Fig.5), where the differences Z in dependence on iterations of physical time were again plotted for $g = -50\ \frac{\mathrm{m}}{\mathrm{s}^2}$.

6.3. Boundary domain

The technique of boundary domain (bd) was adopted for the top boundary. It means the domain in which all waves were damped was added to the boundary. The new variables in domain are computed as follows:

$$W_{bd} = \overline{W} + \xi(y_{bd})(W - \overline{W}), \tag{27}$$

where $\overline{W}$ is the average of values over the whole bd , and damping function ξepends on vertical coordinate of domain:

$$y_{bd} = \frac{x_2 - (x_{top} - h_{bd})}{h_{bd}}, \tag{28}$$

where h_{bd} is the thickness of the boundary domain and $x_{top} = max(x_2)$. The damping function has to fulfill the following conditions, according to [8]:

$$\begin{aligned} \xi(0) &= 1, \qquad & \frac{\partial \xi}{\partial y_{bd}}(y_{bd}) &\leq 0, \\ \xi(1) &= 0, \qquad & \frac{\partial \xi}{\partial y_{bd}}(0) &= 0. \end{aligned} \tag{29}$$

The pressure has to be omitted from the damping, because prescribe pressure value on the boundary is disabled (see [7]).

The numerical experiment was performed for $g = -50\ \frac{\mathrm{m}}{\mathrm{s}^2}$, because the lee waves are shorter, and the bd could be small. The hight of the bd was chosen to $h_{bd} = 10$ m because the waves with wavelength approximately 10 m have to be dampened (see Table 1). The simple damping function fulfilling (29) was computed $\xi(y_{bd}) = 1 - y_{bd}^2$. The situation is well documented in Figs. 9 and 10. The waves were reflected from both boundaries - the top boundary and the bottom of the bd. The results are shown in figure 9 .

The vertical velocities were plotted in the same section line as in Fig. 2. The validation values are marked by the blue dashes line ("val_bd" for the whole domain and "val" for the original domain). The bd method deforms whole field of the velocity (near the boundary of bd at 30 m) as it can be seen in Fig. 11.

It is difficult to achieve the good results with simple damping function and small domain. Large bd could produced the desired effect, unfortunately

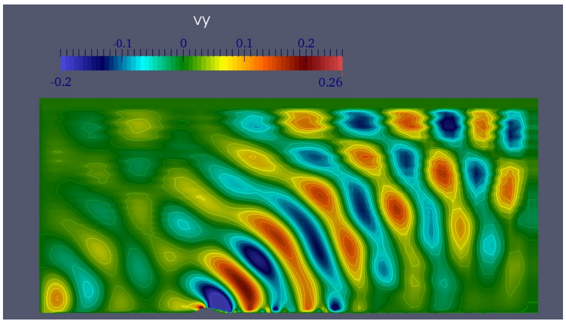

Figure 9. *Vertical velocity field in experiment with bigger domain including bd*

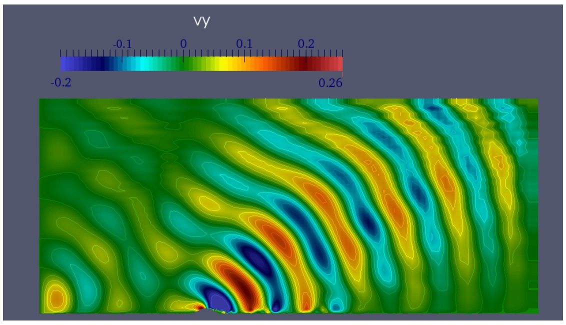

Figure 10. *Vertical velocity field in the same domain without damping*

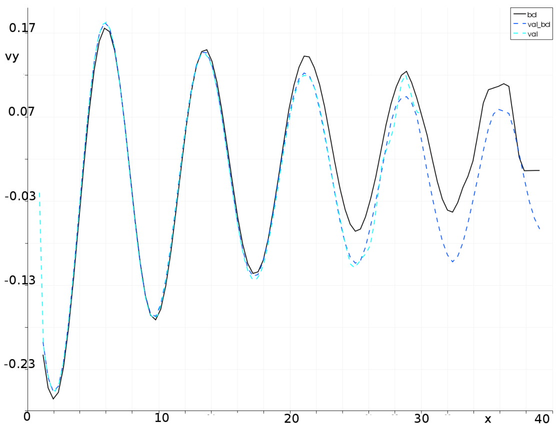

Figure 11. *Vertical velocity plotted to the section line*

the larger bd would extend the computational time (because of the added grids). It is better to try another approach to the non-reflecting boundaries.

7. SUMMARY

The three experiments with boundary condition were presented. The bottom boundary condition for the density perturbation and the input profile have the positive influence on the stationarity of the flow.

The boundary domain method with simple damping function was presented. Unfortunately this setting does not give sufficient results.

ACKNOWLEDGEMENTS

This work was supported by grant SGS13/174/OHK2/3T/12 of the Czech Science Foundation.

REFERENCES

[1] Arya, P.S., 2001, *Introduction to Micrometeorology* , Academic press

[2] Holton, J. R., 2004, *An introduction to Dynamic Meteorology*,Elsevier academic press (4th edition)

[3] Bodnar, T., et. al, 2011, "Application of Compact Finite-Difference Schemes to Simulations of Stable Stratified Fluid Flows", *J of Applied Matematics and Computation*, Vol. 08, pp 58ĺ

[4] Van Leer, B., 1979, "Towards the Ultimate Conservative Difference Scheme. V. A Second-order Sequel to Godunov's Method",*J. of Computational Physics*, Vol. 32

[5] Dick, E., Vierendeels, J., Riemslagh, K., 1999, "A Multigrid Semi-implicit Line-method for Viscous Incompressible and Low-Mach-number Flows on High Aspects Ratio Grids, *J. of Comp. Physics*, Vol. 154

[6] Ferziger, J. H., Peric, M., 1997, *Computational Methods for Fluid Dynamics*, Springer (2nd edition)

[7] Feistauer, M., Felcman, J., Straškraba, I., 2003 *Mathematical and Computational Methods for Compressible Flow*, Oxford University Press

[8] Wasistho, B., 1997, "Spatial Direct Numerical Simulation of Compressible Boundary Layer Flow", *Universiteit Twente*

APPENDIX

The validations vertical velocity plots for every stratification.

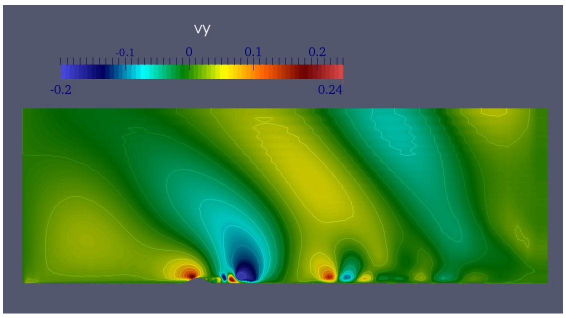

Figure 12. *Field of vertical velocity for $g = -5\ \frac{\mathrm{m}}{\mathrm{s}^2}$*

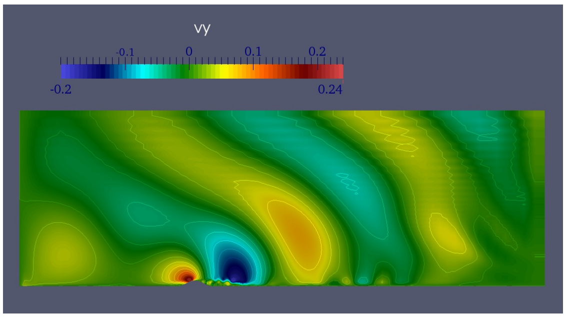

Figure 13. *Field of vertical velocity for* $g = -10\ \frac{\mathrm{m}}{\mathrm{s}^2}$

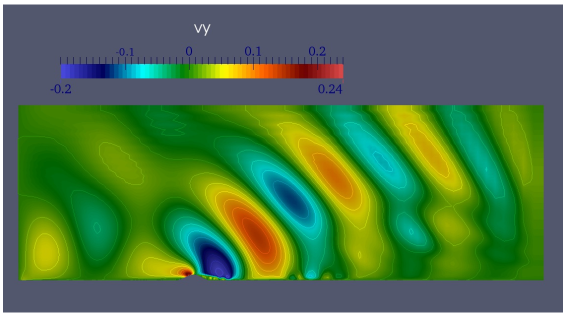

Figure 14. *Field of vertical velocity for* $g = -20\ \frac{\mathrm{m}}{\mathrm{s}^2}$

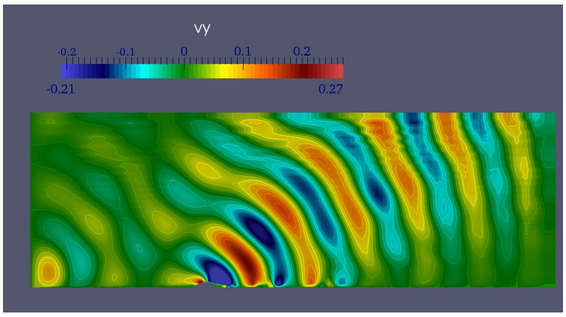

Figure 15. *Field of vertical velocity for* $g = -50\ \frac{\mathrm{m}}{\mathrm{s}^2}$

Conference on Modelling Fluid Flow (CMFF'15)
The 16th International Conference on Fluid Flow Technologies
Budapest, Hungary, September 1-4, 2015

PREDICTION OF FIBER DISPERSION FOR GLASS FIBER REINFORCED PLASTICS IN A TWIN-SCREW EXTRUDER USING FLOW SIMULATION

Kunihiro HIRATA[1], Hiroshi ISHIDA[2], Motohiro HIRAGORI[2], Yasuya NAKAYAMA[3] and Toshihisa KAJIWARA[3]

[1]Technical Solution Center, Polyplastics Co., Ltd., Japan
[2] Production Department, Polyplastics Co., Ltd., Japan
[3] Department of Chemical Engineering, Kyushu University, Japan. E-mail : kajiwara@chem-eng.kyushu-u.ac.jp

ABSTRACT

We study a basic mechanism of glass fiber dispersion in a twin-screw extruder with backward-mixing screw (BMS) and forward kneading disk (FKD) elements using the computational fluid dynamics (CFD). The result of CFD for BMS and FKD elements reveals that the melt mixing by a BMS is highly effective to act the required stress on overall polymer. We propose the time-integrated stress as evaluation index of glass fiber dispersion and can obtain a good correlation between the incidence probability of undispersed glass-fiber bundles measured experimentally and the minimum value of the time-integrated stress distribution obtained from the flow simulation.

Keywords: Melt mixing, Twin-screw extruder, Mixing element, Dispersion, Glass fiber

1. INTRODUCTION

Twin-screw extruders (TSEs) are widely used in compounding process of polymer composites because of their high operability and high kneading performance. Uniform kneading of various fillers within the molten polymer is required for molding process and product designs from the viewpoint of functional expression of fillers. The glass-fiber-reinforced plastic (GFRP) is a representative polymer composite and dispersion techniques for GFRP can be mainly classified into two categories: glass fiber fracture techniques in which fibers are broken to a target length and glass-fiber bundle dispersion techniques that dissociate glass-fiber bundles into individual fibers. The present study discusses to quantitatively elucidate the mechanism about the effectiveness of a backward-mixing screw (BMS) for glass-fiber bundles dispersion using three-dimensional flow analysis. We also establish the evaluation index for glass-fiber bundles dispersion by the simulation.

2. EXPARIMENT

We used a polybutylene terephthalate (PBT, polyplastics Co., Ltd., Tokyo, Japan) as a matrix resin. To facilitate the observation of dispersion failure of glass fiber bundles, black PBT pellets, which were prepared with carbon black (CB) by a master batch process, were added. For the glass fiber, we used E-glass (Nippon Electric Glass Co., Ltd., Otsu, Japan) which is 13 μm in average diameter and 3 mm in average length. Each glass fiber bundle contained several thousand fiber combined with a binder. The TSE employed was a TEX44αII (screw diameter = 47mm, screw length = 2,800 mm, Japan Steel Works, Ltd.). The PBT pellets are completely melted in the melting section before the glass fiber bundles are added through the feeder and dispersed in the mixing section. The screw configuration in the mixing section consisted of two types of screw element forms, i.e., a forward kneading disk (FDK) and a backward mixing screw (BMS) as shown in Fig.1. Five screw configurations were utilized in the mixing section: FKD with L/D = 1.0 and 2.0, and BMS with L/D = 1.0, 2.0 and 2.5. To quantify the degree of dispersion of the glass fiber bundles, we counted the number of undispersed pellets per 10 kg (approximately 700,000 pellets) by the direct observation of a white substance on the pellet cross section using a loupe on plastic sheet.

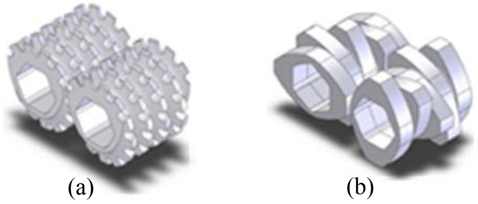

(a) (b)

Figure 1. Configuration of Mixing Element for (a) Backward Mixing Screw (BMS) and (b) Forward Kneading Disk (FDK) .

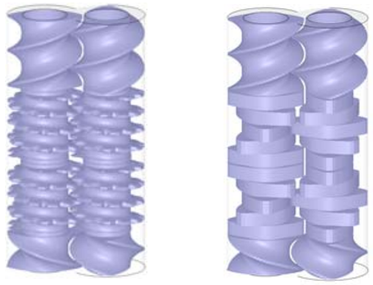

(a) (b)

Figure 2. Analysis Domain for (a) BMS and (b) FKD.

3. NUMERICAL SIMULATION

A three-dimensional flow simulation was performed to clarify the dynamics in a TSE using the commercial software Screwflow-Multi (R-flow, Japan) based on the finite volume method. Figure 2 shows the analysis domains used. We analyzed the non-isothermal flow under the following conditions: 1) material is fully filled in the analysis region, 2) inertia effect is negligible and 3) fluid is purely-viscous and has a shear-thinning viscosity. Boundary conditions are as follows: 1) no-slip and 220 ºC on barrel surface, 2) experimental condition of velocity and natural condition of temperature on screw surface, 3) constant velocity and temperature corresponding to experimental values on inlet section and 4) natural conditions of velocity and temperature on outlet section. Particle tracer analysis was also performed, using about 7,000 tracer particles which were uniformly distributed in the cross section near the inlet at initial state, to discuss the flow patterns and obtain the physical properties locally along particle tracer trajectories.

4. RESULTS AND DISCUSSION

Figure 3 shows the experimental result for probability of undispersed glass-fiber bundle. The experimental results demonstrate that number of pellets containing undispersed glass-fiber bundles for BSM was much less th an for FKD. However, it is increased with hroughput, i.e. rotational speed of screws, even though the local stress increases with screw rotation speed.

To understand the basic mechanism of flow and mixing for BMS and FKD elements, we carried out the flow simulation of one screw rotation and calculated the maximum stress acting on tracer particles for one screw rotation. The result is shown in Fig.4. We classified into three ranges of maximum stress, i.e. low (0-100kPa), mid (100-200kPa) and high (lager than 200kPa) stress ranges. We can see some probability in low stress range for FKD but not for BMS. On the other hand, all the tracer particles pass through the middle or high stress region during one rotation for the BMS. From the experimental result that the incident probability

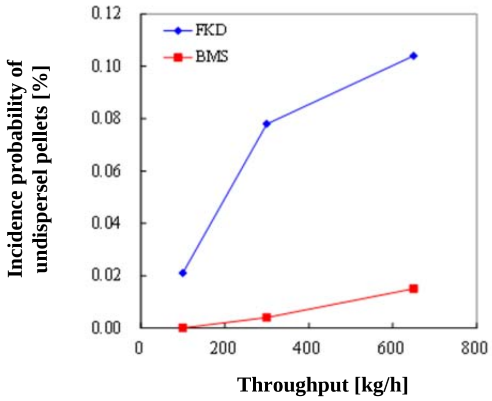

Figure 3. Incident Probability of Pellets Containing Undispersed Glass Fiber Bundles for *L*/*D*=1.0.

of undispersed glass-fiber bundle increases with throughput, the probability is related to both the stress magnitude and residence time. We consider the time-integrated stress along the trajectory of tracer as following equation:

$$\sum_i = \int_0^{T_i} dt \int dx\,\delta\left(x - X_i(t)\right)\,\tau(x,t)$$

where t is time, x is coordinate, τ is stress invariant, and X_i and T_i are position and residence time of the i-th tracer, respectively.

Figure 5 shows the probability distribution of the time-integrated stress at Q=300 kg/h and Ns=300 rpm for different mixing elements. We first tried to take a correlation between incident probability of pellets containing undispersed glass fiber-bundles and the average values of probability distribution of time-integrated stress, but good correlation could be obtained. Then we consider the minimum value of probability distribution of time-integrated stress is more suitable because the probability of undispersed fiber-bundle is very low. It is thought that stress over a certain value is required to dissolute glass–fiber bundles in melt section. The result is shown in Fig. 6 and we can

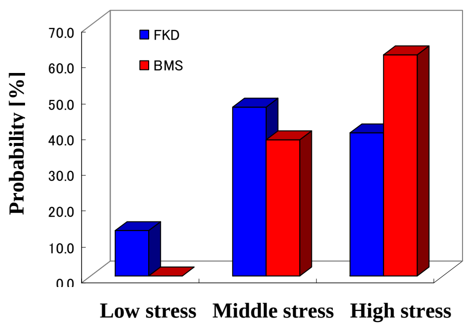

Figure 4. Probability of Maximum Stress Acting on Tracer Particle during One Screw Rotation. Low: 0-100kPa, Middle: 100-200kPa, High: >200kPa

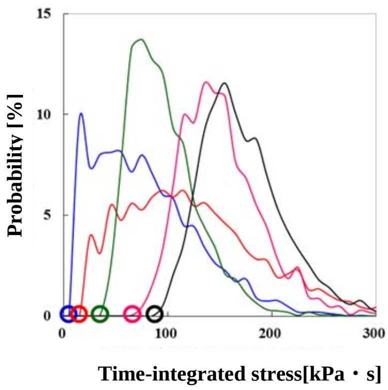

Figure 5. Probability of Time-Integrated Stress.

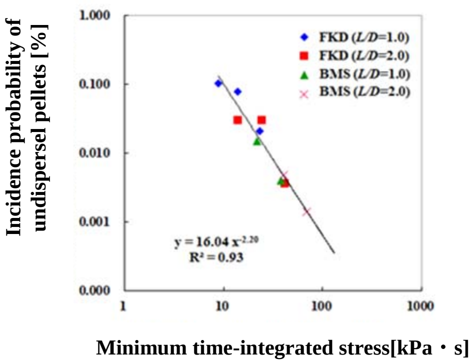

Figure 6. Correlation between Minimum Time-Integrated Stress and Incident Probability of Undispersed Pellet.

obtain good correlation even though configurations of mixing elements and operation conditions are different.

If the time-integrated stress is increased by the extruder operating conditions or screw element configuration, the temperature increases greatly due to viscous heating of the resin melt and thermal degradation of the resin will be concerned. We obtained the limitation of throughput at which the minimum value of time-integrated stress is less than 75 kPa·s from the Fig.6. This means that incident probability of pellets containing undispersed glass fiber-bundles is less than 0.002%. We obtained another limitation of throughput at which the temperature in outlet section is less than 290 ºC by the numerical simulation because PBT decomposes thermally at 300 ºC. Figure 7 shows the operation window for throughput and length of mixing region, considered both the incident probability of pellets containing undispersed glass fiber-bundles and thermal degradation. The intersection point denotes the optimal condition.

5. CONCLUSIONS

We carried out the three-dimensional flow simulation and tracer particle analysis for dispersion of glass-fiber bundles in the melt-mixing region within a twin screw extruder. The result of flow simulation for a BMS and FKD reveals that the melt mixing by a BMS is highly effective to act the required stress on overall materials. In addition, we can obtain a good correlation between the incidence probability of undispersed pellets measured experimentally and the minimum value of distribution of the time-integrated stress calculated numerically.

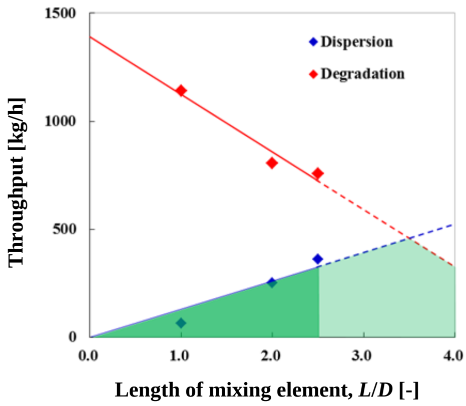

Figure 7. Window for Predicting the Operation Conditions in which Incidence Probability of Undispersed Glass-Fiber Bundle and Thermal Degradation.

REFERENCES

[1] K. Hirata, H. Ishida, M. Hiragohri, Y. Nakayama and T. Kajiwara, 2013, *Intern. Polym. Processing*, XXVIII, 368-375.

[2] K. Hirata, H. Ishida, M. Hiragohri, Y. Nakayama and T. Kajiwara,2013, *Polym. Eng. Sci.*, DOI 10.1002/pen.

Conference on Modelling Fluid Flow (CMFF'15)
The 16th International Conference on Fluid Flow Technologies
Budapest, Hungary, September 1-4, 2015

NUMERICAL ANALYSIS OF NATURAL-, BIO- AND SYNGAS FLAMES IN GAS TURBINE COMBUSTOR MODEL USING FLAMELET METHOD

Sohail IQBAL[1], Ali Cemal BENIM[1], Franz JOOS[2], Alexander WIEDERMANN[3]

[1] Düsseldorf University of Applied Sciences, Department of Mechanical and Process Engineering, CFD Lab., Josef-Gockeln-Str. 9, D-40474 Düsseldorf, Germany Tel.: +49 (0) 211 43 51 410, Fax: +49 (0) 211 43 51 403, E-mail: sohail.iqbal@fh-duesseldorf.de
[2] Helmut Schmidt University, Laboratory of Turbomachinery, Holstenhofweg 85, D-22008 Hamburg, Germany. Tel: +49 (0) 406 541 27 25, Fax: +49 (0) 406 541 24 36, E-mail: joos@hsu-hh.de
[3] MAN Diesel and Turbo SE, Engineering Gas Turbines, Steinbrinkstr. 1, D-46145 Oberhausen, Germany. T: +49 (0) 208 692 22 38, F: +49 (0) 208 692 91 18, Email: alexander.wiedermann@man.eu

ABSTRACT

Turbulent reacting flows in model combustor are investigated both numerically and experimentally. The main purpose is the validation of the experimental data against the numerical results. For numerical simulation of the reacting flow, a flamelet model based on the progress variable approach is used with presumed PDF for the mixture fraction and progress variable. Numerical simulation were performed with URANS $k-\omega$ SST turbulence model. The numerical results showed good agreement with the experimental data. The numerical study is extended with the consideration of alternative fuels (bio- and syngas) flames and compared with the natural gas flame within the URANS context. The peak temperature obtained with the syngas and biogas fuels was nealy equal but considerably less that natural gas flame.

Keywords: biogas, flamelet progress variable method, SST, syngas

NOMENCLATURE

C	$[-]$	Progress variable
C_p	$[Jkg^{-1}K^{-1}]$	Specific heat capacity at constant pressure
Q	$[Jm^{-3}s^{-1}]$	Volumetric heat release
Re	$[-]$	Reynolds number
T	$[K]$	Temperature
U	$[ms^{-1}]$	Velocity
Y	$[-]$	Mass fraction
Z	$[-]$	Mixture fraction
Z''^2	$[-]$	Variance of mixture fraction
k	$[m^2s^{-2}]$	Turbulence kinetic energy
p	$[kgm^{-1}s^{-2}]$	Pressure
β	$[-]$	Probability density function
χ	$[s^{-1}]$	Scalar dissipation rate
ϵ	$[m^2s^{-3}]$	Turbulence dissipation rate
λ	$[-]$	Progress parameter
μ	$[kgm^{-1}s^{-1}]$	viscosity
ω	$[s^{-1}]$	Turbulence eddy frequency
ϕ	$[-]$	Vector of Y, T and θ_C
σ	[-]	Schmidt number
θ_C	$[kgm^{-3}s^{-1}]$	Source term for progress variable equation

Subscripts and Superscripts

i	Species index
t	Turbulent value
u, b	Unburned and burned state
$\bar{}$	Mean value
$\tilde{}$	Favre averaged

1. INTRODUCTION

Flue gas recirculation (FGR) is a promising technology to improve the combustion efficiency of the gas turbines and reduce the CO_x emissions. CO_x produced by the combustion of fossil fuels is one of the major contributor to the climate change. However, FGR technology changes the operation of the gas turbines by effecting the combustion behaviour. The main idea of this technology is to capture some of the exhaust gas of combustion and add it to incoming fresh air. The effect of the varying FGR ratios was discussed in [1] for different fuels. The goal of the present paper is to numerical investigate this phenomenon and validate with the experimental data.

Numerical investigation of isothermal swirling flows was performed in [2, 3, 4] for flows with relatively low Re (5000-7000). These conditions do not represent the typical gas turbine where the Re are very high (>50,000). Swirling flows with high turbulence (Re >50,000) were investigated in [5, 6]. The effect of the various turbulence modeling approaches based on URANS and LES procedures was investigated in detail in [6]. The effect of grid independency for LES was shown for swirling flow. However, this was only for isothermal flows without chemical reactions.

The goal of the present paper is twofold. Firstly, a validation study is performed for the methane-air flame with small amount of FGR to the inlet air. The numerical results are validated with the experimental data. Secondly, the validated combustion model is then applied to other fuels (biogas and syngas) and the numerical results are compared with methane-air flame. However in this part, the simulations were performed without FGR to analyze the combustion characteristics only.

2. EXPERIMENTAL SETUP

The CAD model of the combustor[1] is shown in Fig. 1 where a single swirler with 12 channels is used to induce the swirl to the inlet air. The experiments were performed at Helmut Schmidt University, Laboratory of Turbomachinery, Hamburg. Fuel is injected to the combustor nozzles connected to the swirler channel vanes. After passing through the swirler vanes both the fuel and air streams enter the burner nozzle and into the main combustion chamber of hexahedral crossection. A converging exhaust gas nozzle is attached to the burner outlet to avoid the reverse flow.

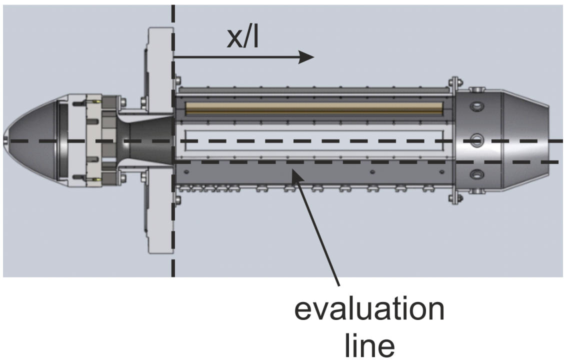

Figure 1. Experimental combustor setup.

3. NUMERICAL MODELING

3.1. Geometry, case setup and boundary conditions

A block structured mesh was used for all the simulations as shown in Fig. 2 with nearly 1.2 million cell elements. The inlet boundary condition was imposed on the swirler channed inlet with the given mass flow rate and the zero gradient was considered at the outlet for velocity. The pressure at the outlet was taken as the atmospheric pressure. The mass flow rate of fuel and air stream was 0.0009217 kg/s and 0.03575 kg/s respectively. The composition of the oxidizer stream(FGR20) is given in Table 1 and the fuel used is natural gas (NG) with the composition given in Table 2.

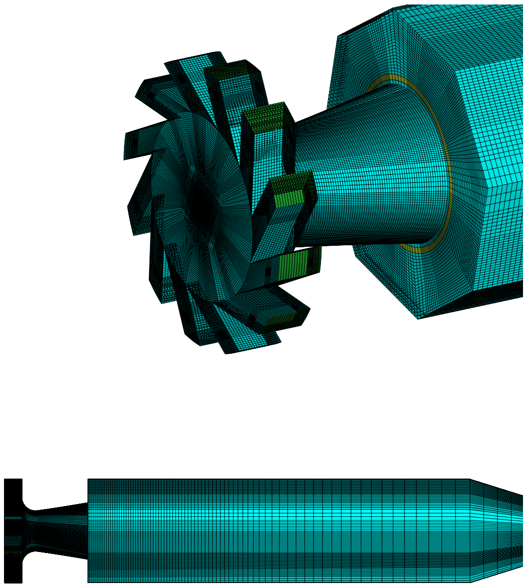

Figure 2. Combustor geometry and mesh

Table 1. Composition (vol-%) of oxidizer stream.

	O_2	H_2O	CO_2	Ar	N_2
FGR0	20.6	1	-	0.9	77.5
FGR20	17.9	2.3	2.2	0.9	76.7

3.2. Governing equations

The continuity and momentum equations for transient compressible flow are given in Eq. (1) and (2).

$$\frac{\partial \bar{\rho}}{\partial t} + \frac{(\partial \bar{\rho} \widetilde{U}_j)}{\partial x_j} = 0 \qquad (1)$$

$$\frac{\partial(\bar{\rho}\widetilde{U}_i)}{\partial t} + \frac{\partial(\bar{\rho}\widetilde{U}_j\widetilde{U}_i)}{\partial x_j} = -\frac{\partial \bar{p}}{\partial x_i} + \frac{\partial \tau_{ji}}{\partial x_j} + \frac{\partial}{\partial x_j}\left[\mu_t\left(\frac{\partial \widetilde{U}_i}{\partial x_j} + \frac{\partial \widetilde{U}_j}{\partial x_i}\right) - \frac{2}{3}\bar{\rho}k\right] \qquad (2)$$

For computational investigation, opensource CFD program OpenFOAM[7] was used. For modeling μ_t a two equation $k-\omega$ SST model [8] was used within unsteady RANS context. A second order upwind scheme was used to discretize the convective terms in the transport equations for all the variables. A first order Euler scheme was used for time stepping with the time step size corresponding to a Courant number of less than 1.

3.3. Turbulence-chemistry Interaction

In this paper, the steady laminar flamelet model developed at our institute based on the progress variable appoach [9] is used. The steady laminar flamelet

Table 2. Composition (vol-%) of fuel stream.

	CH_4	C_3H_8	CO_2	CO	H_2	O_2	N_2
NG	92.5	5.2	1.3	-	-	-	1
BG	49.5	-	36	-	10	1.8	2.7
SG	10	22	4	22	40	-	2

equations are given in Eq. (3).

$$\rho \frac{\chi}{2} \frac{\partial^2 Y_i}{\partial Z^2} - \dot{m}_i = 0 \qquad \chi = 2 D_Z (\nabla Z)^2 \tag{3}$$

The assumption of unique functional dependence of χ on Z leads to the state relation given by Eq. (3),

$$\phi = \phi(Z, \chi_{st}) \tag{4}$$

The solution of the flamelet equations results in a so called S-shaped curve shown in Fig. 3. The upper branch represents the stable burning flamelets till the turning point which corresponds to the quenching limit. After the quenching limit the curve continues to decreasing scalar dissipation rate and describes the unstable flamelets whereas the lower branch corresponds to non-burning flamelets. Pierce and Moin [9] parametrized the flamelets based on a new flamelet parameter λ by projecting the flame states horizontlly along the S-shaped curve. The parameter λ for this study is defined through progress variable C given by Eq. (5).

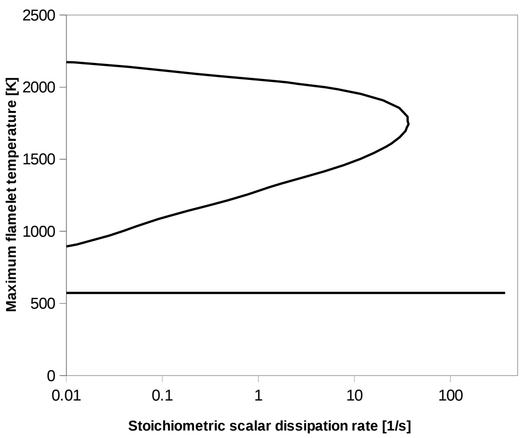

Figure 3. S-shaped curve for NG-FGR20 flame.

$$C = \frac{T - T_u}{T_b - T_u} \qquad \lambda = max(C) \qquad \theta_C = \frac{Q}{C_p (T_b - T_u)} \tag{5}$$

Hence, the solution of Eq. (3) can then be represented as,

$$\phi = \phi(Z, \lambda) \tag{6}$$

Assuming that Z and λ are independent, the mean value of the scalar ϕ is given by Eq. (7). The mean values of the scalars ϕ are stored in the form of 3D lookup-tables of the form $(\widetilde{Z}, \widetilde{Z''^2}, \widetilde{\lambda})$.

$$\widetilde{\phi} = \int_0^\infty \int_0^1 \phi(Z,\lambda) \beta(\widetilde{Z}, \widetilde{Z''^2}) \delta(\lambda - \widetilde{\lambda}) dZ d\lambda \tag{7}$$

The conversion of the lookup tables from $\widetilde{\lambda}$ space to $\widetilde{C}$ is done by the remapping technique of Ravikanti[10]. Once the tables are converted to $\widetilde{C}$ space, a transport equation for each of $\widetilde{Z}$,$\widetilde{Z''^2}$ and $\widetilde{C}$ given in Eq. (8) and (9) respectively is solved along with momentum equations. The species mass fraction and temperature are then calculated by using Eq. (7).

$$\frac{\partial(\bar{\rho}\widetilde{Z})}{\partial t} + \frac{\partial(\bar{\rho}\widetilde{U}_j\widetilde{Z})}{\partial x_j} = \frac{\partial}{\partial x_j}\left[\left(\frac{\mu}{\sigma} + \frac{\mu_t}{\sigma_t}\right)\frac{\partial \widetilde{Z}}{\partial x_j}\right]$$
$$\frac{\partial(\bar{\rho}\widetilde{Z''^2})}{\partial t} + \frac{\partial(\bar{\rho}\widetilde{U}_j\widetilde{Z''^2})}{\partial x_j} = \frac{\partial}{\partial x_j}\left[\mu_t \frac{\partial \widetilde{Z''^2}}{\partial x_j}\right] + 2\frac{\mu_t}{\sigma_t}\frac{\partial \widetilde{Z}}{\partial x_j}\frac{\partial \widetilde{Z}}{\partial x_j} - c\bar{\rho}\frac{\epsilon}{k}\widetilde{Z''^2} \tag{8}$$

$$\frac{\partial(\bar{\rho}\widetilde{C})}{\partial t} + \frac{\partial(\bar{\rho}\widetilde{U}_j\widetilde{C})}{\partial x_j} = \frac{\partial}{\partial x_j}\left[\left(\frac{\mu}{\sigma} + \frac{\mu_t}{\sigma_t}\right)\frac{\partial \widetilde{C}}{\partial x_j}\right] + \bar{\rho}\widetilde{\theta}_C \tag{9}$$

The steady laminar flamelet solutions were obtained using FlameMaster code [11]. The chemical mechanism used for the combustion of NG-FGR20 flame is GRI 3.0 with unity Lewis number for all the species and the assumption of adiabatic flame.

3.4. Results and Discussion

Time-averaged results of NG-FGR20 flame using the flamelet progress variable model are shown in Fig. 4. The numerical simulation was performed for a period 2τ for the flow field to develop in the whole combustor, where τ is time required for an arbitrary particle of fluid to travel the whole length of the combustor. After the flow field was developed in the combustor, time-averaging was performed for a duration of 4τ. The inner- and outer-recirculation zones which help in stabilization of the flame are clealy visible in the streamline plot of Fig. 4a. The temperature field obtained for the flame is shown in Fig. 4b with a peak value of nearly 1550K. The position of the flame is at the exit of the inlet nozzle and inside the main combustion chamber which is important for the integrity of the experimental setup. The evolution of the CO mass fraction is presented in Fig. 4c where its peak value of 0.025 occurs in the reaction zone and is consumed when the reaction is complete. The validation of the numerical results with the experimental data is shown Fig. 5 along the axis of symmetry of the combustion chamber. In Fig. 5a temperature is compared with the experimental data and the qualitative

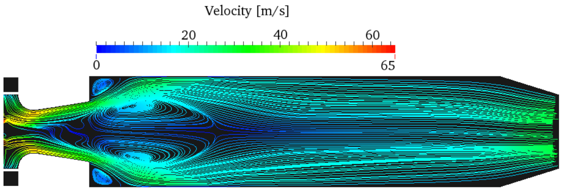

(a) Velocity Streamlines

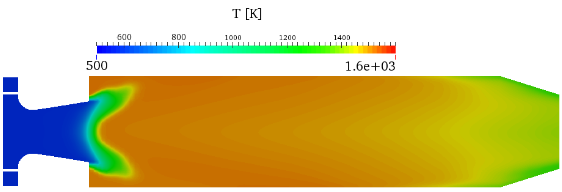

(b) Temperature

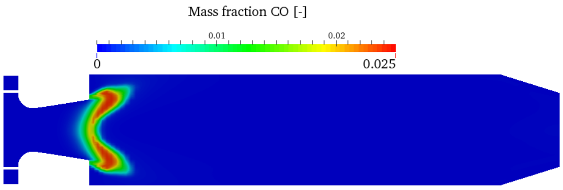

(c) Mass fraction of ***CO***

Figure 4. Numerical results of NG-FGR20 flame

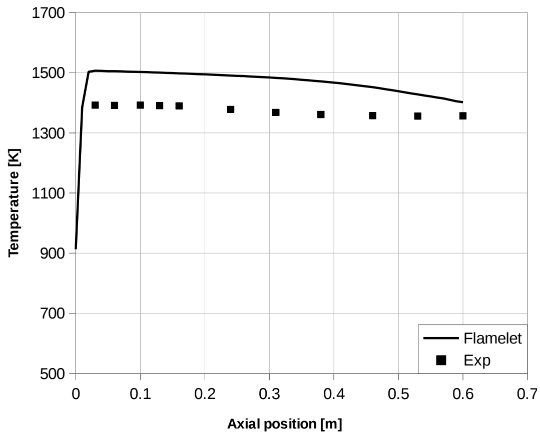

(a)

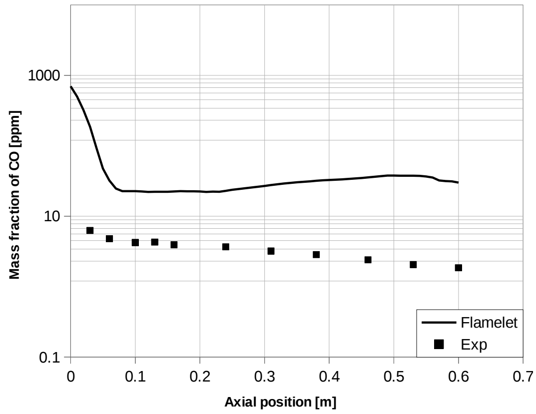

(b)

Figure 5. A comparison of numerical and experimental results.

agreement between the experimental and numerical results is good. The peak value of the temperature is slightly higher for the numerical result as compared to experimental data. This can be due to the fact that the flame was assumed to be adiabatic without heat loss.

The comparison of the CO mass fraction between numerical results and experimental data is presented in Fig. 5b and shows similar trend which was noticed for the temperature field. The value is slightly higher for the numerical results. However qualitative agreement is still good.

4. ALTERNATIVE FUEL GASES

In this part of the paper, the above study is extended using different fuel compositions and with similar mass flow rate of fuel and air streams. Three different fuels were investigated i.e. natural gas(NG), biogas (BG) and syngas (SG) with the compositions given in Table 2. The oxidizer composition was kept the same corresponding to FGR0 in Table 1.

4.1. Results and Discussion

The time-averaged simulation results for the three fuels are shown in Fig. 6 for the temperature field. A brief look at the results shows that the peak temperature obtained for BG and SG was 950K. However the temperature in the combustor was considerably less than that for the NG flame where the peak value was 1570K.

The reaction zone for BG was extended inside the combustor and is larger compared to NG. In case of SG, flashback occured where the flame propagated upstream into the inlet nozzle and stabilized as shown in Fig. 6c. There are several mechanisms that can trigger a flashback [12]. In the present case, flashback due to combustion instabilites can be ruled out, as implied by calculations and experiments. Flashback due to Combustion Induced Vortex Breakdown is less likely to be the cause, since the expansion ratio, which is observed to correlate to this phenomenon [12] is even smaller for SG (where the flashback occurs) compared to the other cases. Thus, it likely that the flashback is due to flame propagation in the core or in the boundary layers due to increased laminar flame speed by the higher hydrogen content of SG.

The results of the numerical simulation for CO mass fraction are shown in Fig. 7. The peak value of the CO mass fraction for BG and SG considerably smaller that the NG with a value of 0.025. The effect of the flashback in the case of SG can be seen in Fig. 7c where a large amount of CO in the fuel stream

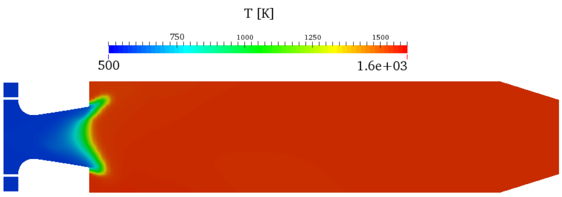

(a) NG

(b) BG

(c) SG

Figure 6. Contour plot of temperature field.

is present till the reaction commences.

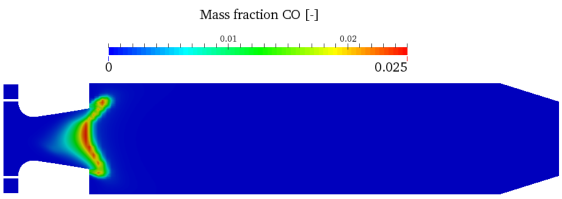

(a) NG

(b) BG

(c) SG

Figure 7. Contour plot of *CO* mass fraction field.

The effect of the FGR for NG flames can be seen by comparison of Fig. 6a and Fig. 4b corresponding to FGR0 and FGR20. The peak temperature is nearly equal for both cases. However, the temperature at the outlet is significantly less in case of FGR20.

5. CONCLUSION

Turbulent reacting flows in model combustor are investigated both numerically and experimentally. The main purpose is the validation of the experimental data against the numerical results. For numerical simulation of the reacting flow, a flamelet model based on the progress variable approach is used with presumed PDF for the mixture fraction and progress variable. Numerical simulation were performed with URANS $k-\omega$ SST turbulence model. The numerical results showed good agreement with the experimental data. The of the adiabatic flame showed slight overprediction of temperature and mass fraction of CO. The numerical study is extended with the consideration of alternative fuels (biogas and syngas) and compared with the natural gas flame results within the URANS context. The peak temperature obtained with the syngas and biogas fuels was nearly equal but considerably less than natural gas flame. In the case of syngas, the flame exhibited flashback by igniting in the nozzle which should be avoided for the safety of the combustion chamber.

FUTURE WORK

In the present paper, the effect of the adiabatic flame assumption showed sligt over prediction of the numerical results. This effect is more prominent in the prediction of NO_x emmissions and hence the heat loss effects should be taken into consideration which will be investigated in the future studies. Also, the effect of the FGR for the biogas and syngas fuels will be investigated further.

ACKNOWLEDGEMENTS

The authors are grateful to the Ministry of Innovation Science and Research of the German State of North Rhine-Westphalia (MIWF NRW) and the European Union for the financial support for this work.

REFERENCES

[1] Fischer, S., Kluss, D., and Joos, F. 2014 “Experimental investigation of a fuel flexible generic gas turbine combustor with external flue gas recirculation”. *Proceedings of ASME Turbo Expo 2014, Power for Land, Sea and Air, Dusseldorf, Germany*.

[2] Benim, A. C., Nahavandi, A., and Syed, K. 2005 “URANS and LES Analysis of Turbulent Swirling Flows”. *Progress in Computational Fluid Dynamics*, Vol. 5, pp. 444–454.

[3] Benim, A. C., Escudier, M. P., Nahavandi, A., Nickson, K., and Syed, K. 2008 “DES Analysis of Confined Turbulent Swirling Flows in the Sub-Crirtical Regimes”. *Advances in Hybrid RANS-LES Modelling*, Vol. 5, pp. 171–182.

[4] Benim, A. C., Escudier, M. P., Nahavandi, A., Nickson, K., and Syed, K. 2010 “Experimental

and Numerical Investigation of Incompressible Turbulent Flow in an Idealized Swirl Combustor". *International Journal of Heat and Fluid Flow*, Vol. 20, pp. 348–371.

[5] Benim, A. C., Cagna, C., Joos, F., Nahavandi, A., , and Wiedermann, A. 2014 "Computational Analysis of Turbulent Swirling Flow in Water Model of a Gas Turbine Combustor". *Proceedings of the 6th International Conference on Computational Heat and Mass Transfer, South China University of Technology, Guangzhou, China*, pp. 338–346.

[6] Benim, A. C., Iqbal, S., Nahavandi, A., Meier, W., Wiedermann, A., and Joos, F. 2014 "Analysis of turbulent swirling flow in an isothermal Gas Turbine combustor model". *Proceedings of ASME Turbo Expo 2014, Power for Land, Sea and Air, Dusseldorf, Germany*.

[7] OpenFOAM 2013 *OpenCFD Ltd. (ESI Group), Bracknell, UK*, `http://www.openfoam.com`.

[8] Menter, F. R., Kuntz, M., and Langtry, R. 2003 "Ten Years of Industrial Experience with the SST Turbulence Model". *Turbulence, Heat and Mass Transfer*, Vol. 4, pp. 625–632.

[9] Pierce, C. D. and Moin, P. 2004 "Progress-variable approach for large eddy simulation of non-premixed turbulent combustion". *Journal of Fluid Mechanics*, Vol. 504, pp. 73–97.

[10] Ravikanti, V. V. S. M. 2008 "Advanced Flamelet Modeling of Turbulent Non-Premixed and Partially Premixed Combustion". *PhD Thesis, Loughborough University, UK*.

[11] Pitsch, H. 1998 "A C++ Computer Program for 0-D and 1-D Laminar Flamelet Calculations". *RWTH Aachen*.

[12] Benim, A. C. and Syed, K. 2015 *Flashback Mechanisms in Lean Premixed Gas Turbine Combustion, 1st Edition*. Elsevier Academic Press.

Conference on Modelling Fluid Flow (CMFF'15)
The 16th International Conference on Fluid Flow Technologies
Budapest, Hungary, September 1-4, 2015

COMPARISON OF SGS MODELS IN LARGE-EDDY SIMULATION FOR TRANSITION TO TURBULENCE IN TAYLOR-GREEN FLOW

Ilyas YILMAZ[1], Lars DAVIDSON[2]

[1] Corresponding Author. Department of Mechanical Engineering, Faculty of Engineering, Istanbul Aydin University. Florya, 34295, Istanbul, Turkey. Tel.: +90 212 444 1 428, Fax: +90 212 425 57 59, E-mail: ilyasyilmaz@aydin.edu.tr [1]
[2] Division of Fluid Dynamics, Department of Applied Mechanics, Chalmers University of Technology. SE-412 96 Gothenburg, Sweden. Tel. +46 31 772 14 04, Fax. +46 31 18 09 76, E-mail: lada@chalmers.se

ABSTRACT

A study was done to observe and to analyze the behavior of various Sub-Grid Scale (SGS) models in Large-Eddy Simulation (LES) for the flow where laminar, transitional and turbulent regimes are found during the evolution. Taylor-Green Vortex (TGV) flow which shows the fundamental mechanisms of vortex stretching and breakdown, transition to turbulence and turbulent decay was selected as a challenging test case for this study. It is initially laminar at early times. However, the effects of viscous interactions result in vortex breakdown and disordering of initially well-organized structures and the flow undergoes transition to turbulence and decays in time. From this point of view, it may serve as a prototype for industrial flows where the flow regimes can change rapidly. The tested SGS models are the Smagorinsky, the dynamic Smagorinsky, the Vreman model, the WALE model and the one-equation model. All the models tested capture the overall physics of TGV flow. However, differences are observed mainly during transition. It is under- or over-predicted slightly, depending on the grid resolution. The SGS models capable of scaling their inherent dissipations produced better results when comparable with the reference DNS solutions.

Keywords: Large-Eddy Simulation, Sub-Grid Scale modeling, Taylor-Green Vortex flow, Transition to turbulence

NOMENCLATURE

DNS	Direct Numerical Simulation
LES	Large-Eddy Simulation
RANS	Reynolds-Averaged Navier-Stokes
SGS	Sub-Grid Scale
TGV	Taylor-Green Vortex
WALE	Wall-Adapting Local Eddy-Viscosity
K	Mean resolved kinetic energy
L	Domain length
Q	Vortex detection criterion based on the 2nd invariant of the velocity gradient tensor
$S(n)$	High-order velocity-derivative moments, skewness (n=3) and flatness (n=4)
U	Characteristic velocity
$-\frac{dK}{dt}$	Dissipation of resolved kinetic energy
$C_s, C_W, C_k, C_\epsilon$	Constants in SGS models
$P_{k_{sgs}}$	Production term
Re	Reynolds number
Re_λ	Taylor micro-scale Reynolds number
S_{ij}	Strain-rate tensor tensor
Δ	Grid size
δ_{ij}	Kronecker delta
λ	Taylor micro-scale
$\mathbf{u}$	velocity vector
∇	Nabla operator
ν	Kinematic viscosity
ν_{sgs}	Sub-grid scale kinematic viscosity
ω	Vorticity
ω^2	Enstrophy
ρ, ρ_0	Density, Initial density
τ	Non-dimensional time
τ_{ij}	Sub-grid scale stress tensor
g_{ij}	Velocity gradient tensor
k	Wave number
k_{sgs}	Sub-grid scale kinetic energy
p, p_0, p_∞	Pressure, initial pressure, ref. pressure
t	Time
u_0, v_0, w_0	Initial velocity field
u_i	Velocity component
x_i	Space component

Subscripts and Superscripts

$< >$	Space averaged
$\bar{\ }$	Grid filtered
$\tilde{\ }$	Test filtered
rms	Root mean square

[1]Present address: Division of Fluid Dynamics, Department of Applied Mechanics, Chalmers University of Technology, 412 96, Gothenburg, Sweden, E-mail:ilyasy@chalmers.se

1. INTRODUCTION

Most of industrial and engineering flows are inherently turbulent. They may also be transitional, i.e., subject to rapid changes in their flow regimes in both time and space due to structural necessities, instabilities in their origins, surface porosity, heat effects, etc. Their transitional/turbulent behaviors must be predicted accurately to prevent high costs and to make the flows feasible as well. Numerically, the most direct way on ensuring this is Direct Numerical Simulation (DNS). In DNS, all the scales of turbulent are resolved properly. However, due to its excessive grid resolution and time-step requirements, it is only available for relatively low Reynolds number flows in simple geometries. The Reynolds-Averaged Navier-Stokes (RANS) approach, which models all the scales, has been used for many years with a reduced accuracy and limited capability. Nowadays, RANS is not accomplishing current demands of engineering. As a result, Large-Eddy Simulation (LES), where most of the scales are resolved by grid and the contributions coming from the Sub-Grid Scales (SGS) are modeled, is becoming a natural choice.

LES is attractive method since it has a balance among accuracy, capability, numerical cost and industrial/engineering demands. The major drawback of LES is lacking of a universal SGS model which is equally applicable to all kinds of flows including curvature, separation-reattachment, buoyancy, heat transfer, etc. Because of this reason, LES research mainly focuses on developing efficient SGS models and its applications. Since choosing appropriate models can not directly be known a priori, analyzing the behavior of models and comparing them are always useful for many purposes, as it has been done by many researchers for various flows.

In this study, we perform LES of Taylor-Green Vortex (TGV) flow with five different SGS models. TGV is the simplest fundamental flow that represents vortex stretching and energy cascade processes that lead to turbulence[1]. Initially, it is well-organized and laminar. At later times, the viscous diffusion plays an important role in dynamics and distorted structures are formed. The decay rate of the kinetic energy reaches its peak after a couple of *eddy-turnover time*, around $\approx$ 9. Then the flow structures die out due to the viscosity, following approximately the power-law spectrum. This transitional behavior is entirely determined by the viscosity. For Reynolds number, $Re \geq 1000$, this picture becomes very clear[2]. Numerically, the kinetic energy should be preserved during the inviscid simulations, due to the lack of the viscous effects.

TGV basically represents the mechanism of transition to turbulence and its decay. From this point of view, it can be regarded as a canonical example to some industrial/engineering flows and serve as an appropriate test case for especially turbulence modeling approaches.

The outline of the paper is as follows. Section 2 briefly describes the governing equation in LES, SGS models used in this study and the solver as well. Section 3 provides information about the numerical setup of TGV flow. Section 4 presents the results with detailed analyses and discussions.

2. SIMULATION METHODOLOGY

The central differencing finite-volume method was used to discretize the governing equations on a collocated grid. Second-order Crank-Nicolson scheme was employed for time advancement[3]. The numerical procedure is based on an implicit fractional step technique combined with an efficient multi-grid pressure Poisson solver [4].

The grid-filtered incompressible Navier-Stokes equations in LES read

$$\begin{aligned} \frac{\partial \bar{u}_i}{\partial x_i} &= 0 \\ \frac{\partial \bar{u}_i}{\partial t} + \frac{\partial}{\partial x_j}(\bar{u}_i\bar{u}_j) &= -\frac{1}{\rho}\frac{\partial \bar{p}}{\partial x_i} + \nu\frac{\partial^2 \bar{u}_i}{\partial x_j \partial x_j} - \frac{\partial \tau_{ij}}{\partial x_j} \end{aligned} \qquad (1)$$

Here, τ_{ij} are the SGS stresses given as $\overline{u_i u_j} - \bar{u}_i\bar{u}_j$.

Most SGS models are eddy-viscosity models of the form ,

$$\tau_{ij} - \frac{\delta_{ij}}{3}\tau_{kk} = -2\nu_{sgs}\bar{S}_{ij} \qquad (2)$$

which relates the SGS stresses to the large-scale strain rate tensor, $\bar{S}_{ij}$,

$$\bar{S}_{ij} = \frac{1}{2}\left(\frac{\partial \bar{u}_i}{\partial x_j} + \frac{\partial \bar{u}_j}{\partial x_i}\right) \qquad (3)$$

The SGS models used in this study are the Smagorinsky, the dynamic Smagorinsky, the Wale model, the Vreman model and the one-equation model of Yoshizawa. While the first four models compute ν_{sgs} only using algebraic relations, the Yoshizawa one-equation model solves an additional equation for SGS kinetic energy, k_{sgs}.

For the Smagorinsky model[5], ν_{sgs} is obtained via

$$\nu_{sgs} = (C_s\Delta)^2|\bar{S}| \qquad (4)$$

where $|\bar{S}| = \sqrt{2\bar{S}_{ij}\bar{S}_{ij}}$. The Smagorinsky constant, C_s, is set to 0.1 and Δ is equal to grid size.

The dynamic Smagorinsky model tested here is the one proposed in [6]. It uses the same analogy with the Smagorinsky model. However, C_s in Eq.4 is not constant anymore. Instead, it is computed dynamically using a test filter as

$$C_s = \frac{1}{2} = \frac{D_{ij}P_{ij}}{P_{ij}P_{ij}} \qquad (5)$$

Here,

$$D_{ij} = T_{ij} - \tilde{\tau}_{ij}$$

$$T_{ij} - \frac{\delta_{ij}}{3} T_{kk} = -2C_s^2 \tilde{\Delta}^2 |\tilde{\bar{S}}| \tilde{\bar{S}}_{ij} \tag{6}$$

$$P_{ij} = \Delta^2 \widetilde{|\bar{S}|\bar{S}_{ij}} - \tilde{\Delta}^2 |\tilde{\bar{S}}| \tilde{\bar{S}}_{ij}$$

where (˜) denotes the test filter usually taken as twice the grid filter and T_{ij} is the SGS stresses on the test filter. This model allows *backscattering*, i.e., negative C_s from the small scales to the resolved flow.

The Wall-Adapting Local Eddy-Viscosity (WALE) model[7] employs the traceless symmetric part of the square of the velocity gradient tensor which is

$$S_{ij}^d = \frac{1}{2}(\bar{g}_{ij}^2 + \bar{g}_{ji}^2) - \frac{1}{3}\delta_{ij}\bar{g}_{kk}^2 \tag{7}$$

and calculates ν_{sgs} using

$$\nu_{sgs} = (C_W \Delta)^2 \frac{(S_{ij}^d S_{ij}^d)^{3/2}}{(\bar{S}_{ij}\bar{S}_{ij})^{5/2} + (S_{ij}^d S_{ij}^d)^{5/4}} \tag{8}$$

with $C_W = 0.33$.

The Vreman model[8] is also an eddy-viscosity model that has the following algebraic relation

$$\nu_{sgs} = 2.5 {C_s}^2 \sqrt{\frac{B_\beta}{\alpha_{ij}\alpha_{ij}}} \tag{9}$$

with

$$\alpha_{ij} = \frac{\partial \bar{u}_j}{\partial x_i}$$

$$\beta_{ij} = \Delta_m^2 \alpha_{mi}\alpha_{mj}$$

$$B_\beta = \beta_{11}\beta_{12} - \beta_{12}^2 + \beta_{11}\beta_{33} - \beta_{13}^2 + \beta_{22}\beta_{33} - \beta_{23}^2 \tag{10}$$

The last model introduced here is the one-equation model by Yoshizawa[9]. The SGS kinetic energy equation solved by the model reads

$$\frac{\partial k_{sgs}}{\partial t} + \frac{\partial}{\partial x_j}(\bar{u}_j k_{sgs}) = \frac{\partial}{\partial x_j}\left[(\nu + \nu_{sgs})\frac{\partial k_{sgs}}{\partial x_j}\right] + P_{k_{sgs}} - C_\epsilon \frac{{k_{sgs}}^{3/2}}{\Delta} \tag{11}$$

with $P_{k_{sgs}} = 2\nu_{sgs}\bar{S}_{ij}\bar{S}_{ij}$, $\nu_{sgs} = C_k \Delta {k_{sgs}}^{1/2}$, $C_k = 0.07$ and $C_\epsilon = 1.05$.

Due to the formulations, the SGS models presented here, except the constant Smagorinsky model, theoretically have capability to detect flow regions including transitional, laminar, shear, wall and to scale or vanish their SGS dissipations properly.

3. FLOW SETUP

The initial velocity field is given by

$$u_0 = U \sin(kx)\cos(ky)\cos(kz)$$
$$v_0 = -U \cos(kx)\sin(ky)\cos(kz) \tag{12}$$
$$w_0 = 0$$

and the initial pressure field provided by the solution of the Poisson equation is

$$p_0 = p_\infty + (\rho_0 U^2/16)(2+\cos(2kz))(\cos(2kx)\cos(2ky)) \tag{13}$$

where k is the wave number, $\frac{2\pi}{L}$. L is the domain length 2π.

Boundaries are triply-periodic. Since the characteristic velocity is bounded by the unity and the characteristic length is set to 1, the Reynolds number is defined as the inverse of the kinematic viscosity, $1/\nu$ and set to 1600 . This also leads to an *eddy-turnover time* of order unity. The Taylor micro-scale Re number (Re_λ) can be defined as $\sqrt{2Re}$, giving an initial value of 55. Simulations were performed on uniform 64^3 and 128^3 grids and followed up to 15 non-dimensional time-units with a time-step of 2.5×10^{-2}.

4. RESULTS AND DISCUSSION

Fig.1 shows how the initially well-organized structures lose their symmetries in time due to the energy cascade and the vortex stretching and start to break into smaller ones.

Fig.2 compares various flow diagnostics such as evolution of the mean resolved kinetic energy (K), skewness, flatness and Taylor micro-scale λ computed by each model. K, which is computed as $K = \frac{1}{2}\langle\bar{u}_i\rangle^2$, decreases due to increase in dynamic, viscous interactions. Skewness ($n = 3$) and flatness ($n = 4$) are the high-order velocity-derivative moments (structure functions) given by

$$S(n) = \frac{1}{3}\sum S_i(n) \tag{14}$$

where

$$S_i(n) = (-1)^n \frac{\langle\left(\frac{\partial \bar{u}_i}{\partial x_i}\right)^n\rangle}{\langle\left(\frac{\partial \bar{u}_i}{\partial x_i}\right)^2\rangle^{\frac{n}{2}}} \quad \text{(no summation on i)} \tag{15}$$

The skewness characterizes the rate at which enstrophy increases by vortex stretching. Whereas, the flatness is a measure of the intermittency of the vorticity field driven by vortex stretching and folding. Their average values given in the literature change from 0.2 to 0.7 for skewness, and from 3 to 40 for flatness [10]. All the models produce similar results which are in the given range and show the same behavior. The largest discrepancies between model results and the reference solution are observed in skewness, both around $t/\tau \approx 4$ and around transition time. The same discrepancy was also observed by Hahn[11].

The Taylor micro-scale averaged over the three homogeneous spatial directions is given as,

$$\lambda = \frac{1}{3}\sum \lambda_i \tag{16}$$

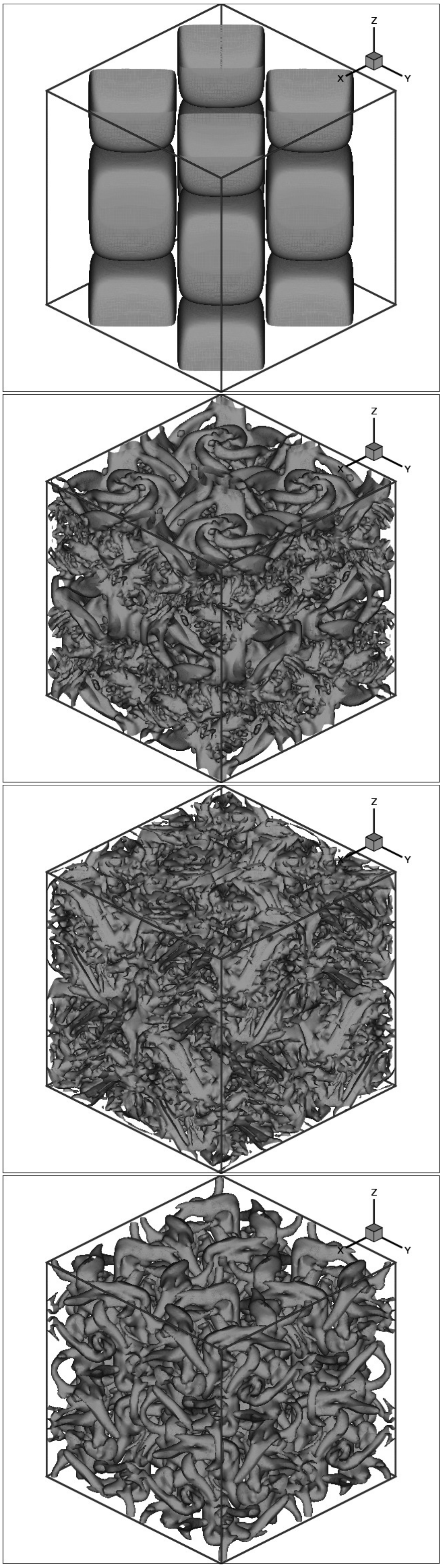

Figure 1. $Q = -\frac{1}{2}\frac{\partial u_i}{\partial x_j}\frac{\partial u_j}{\partial x_i}$ **iso-surfaces at** $\tau = 0, 10, 20, 50$ **from top to bottom respectively.** ($Q = 0.019$)

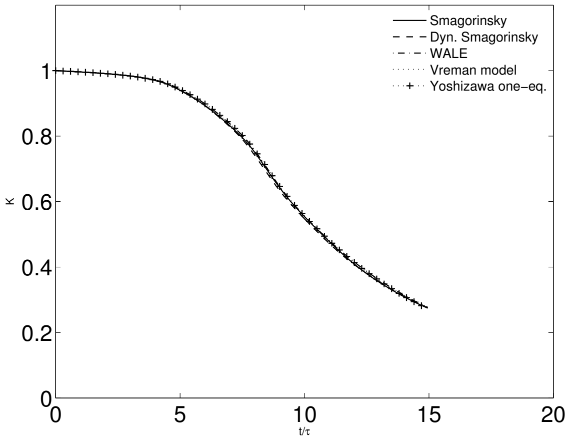

(a) Mean resolved kinetic energy

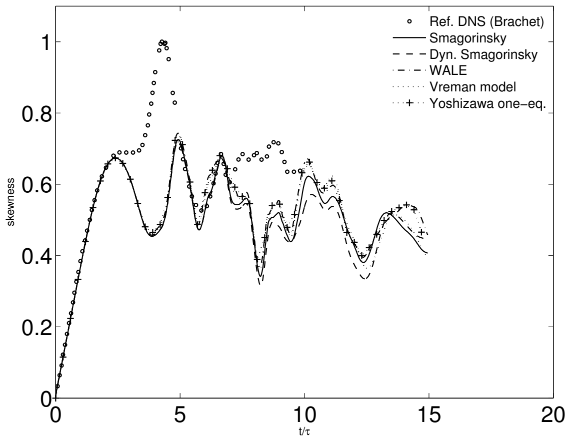

(b) Skewness

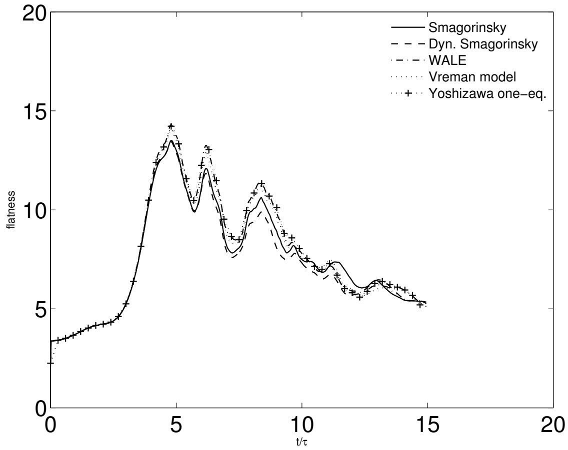

(c) Flatness

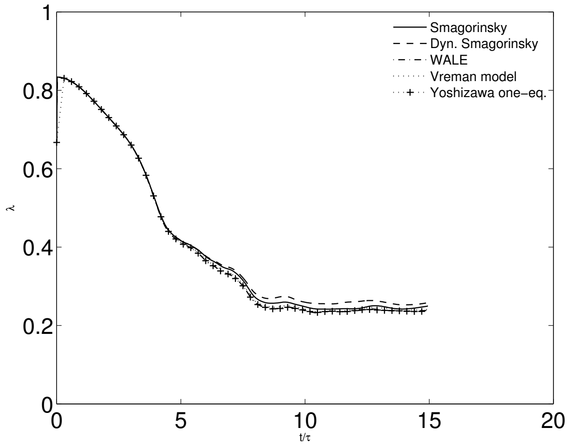

(d) λ

Figure 2. Evolution of various flow diagnostics in time on fine grid

where

$$\lambda_i = \sqrt{\frac{\langle (u_i)^2_{rms} \rangle}{\langle (\frac{\partial \bar{u}_i}{\partial x_i})^2 \rangle}} \qquad \text{(no summation on i)} \qquad (17)$$

The Taylor micro-scale is a length scale which was first introduced by Taylor[12]. It does not have an exact physical meaning [13]. However, it is often used to define a Reynolds number that characterizes grid turbulence [14]. It is an intermediate length scale between integral and Kolmogorov's length scales. It is roughly assumed that, below the Taylor micro-scale, fluid viscosity significantly affects the dynamics of turbulent eddies in the flow, the turbulent motions are subject to strong viscous forces, and kinetic energy is dissipated into heat [15].

In Fig.3, the dissipation of mean resolved kinetic energies, $-dK/dt$, are plotted for different resolutions. Zoomed view of the transition peaks are also provided. It seems that all the SGS models included here are having difficulties in handling transition to turbulence in time. Regardless of the grid resolution, the transition time is predicted slightly earlier ($t/\tau_{sim} \approx 8.2$) by the models than the reference DNS solution ($t/\tau_{DNS} \approx 9$). This behavior corresponds to over dissipative nature of the SGS models for transition. Additionally, while the value of the transition peak is higher than the reference on the fine grid, on the coarse grid, it is vice versa. It points out an increasing dissipation of mean resolved kinetic energy with an increasing resolution. All the models also have different peak structures. The Smagorinsky and the dynamic Smagorinsky models show the most noticeable differences among the models.

The mean enstrophy is given as the square of vorticity(ω),

$$\langle \bar{\omega}^2 \rangle = \langle |\nabla \times \bar{\mathbf{u}}|^2 \rangle \qquad (18)$$

Enstrophy is the resolving power of a numerical scheme that is a measure of its ability to represent the flow physics accurately on a finite number of grid cells [16]. As seen in Fig. 4, it follows a path similar to the mean kinetic energy dissipation. Its value predicted by the models increases with increasing grid resolution which points out high resolution requirement of models. The Yoshizawa one-equation model, the Vreman model and the WALE model show noticeably better performance, as it should be because of their advanced differential operators in finding C_s and computing ν_{sgs}.

The SGS viscosities plotted in Fig. 5a and 5b are one of the most important quantities to make some assessment when doing LES. First of all, no backscattering is predicted by the models. The Smagorinsky and the Dynamic Smagorinsky models behave completely different than the others. Their computed ν_{sgs} values are strongly depend on the grid resolution. The Yoshizawa one-equation model have a very smooth path in time, while evolution of the others are relatively fluctuating in time.

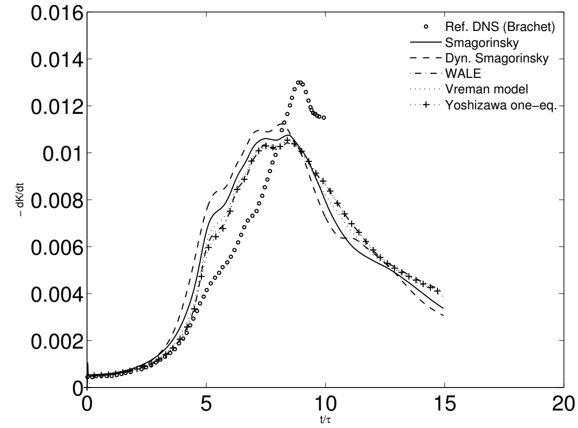

(a) Coarse grid (64^3)

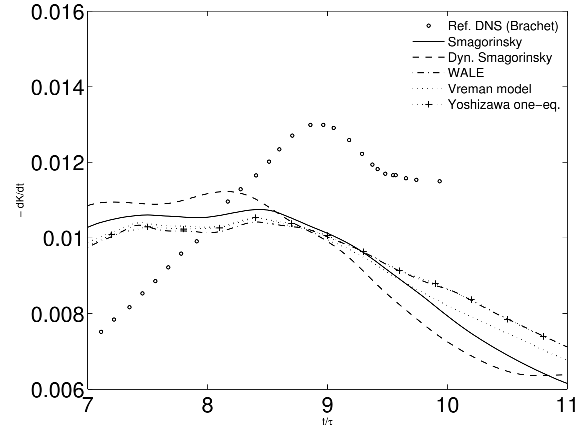

(b) Zoom to transition peak (64^3)

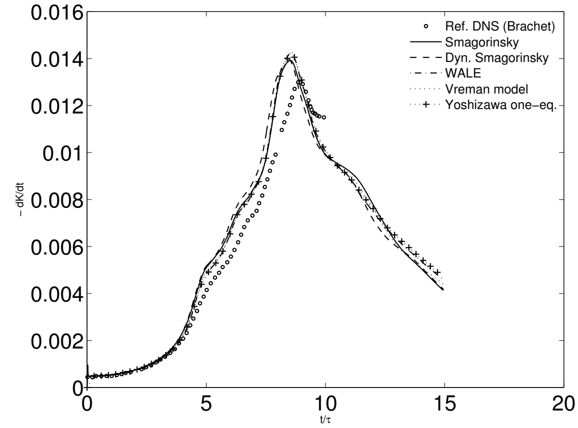

(c) Fine grid (128^3)

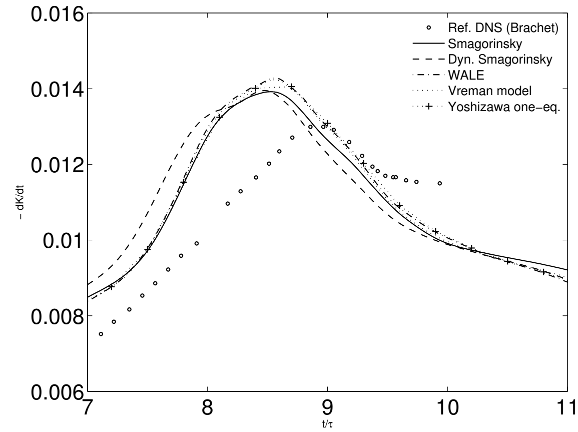

(d) Zoom to transition peak (128^3)

Figure 3. Dissipation of mean resolv. kin. energy

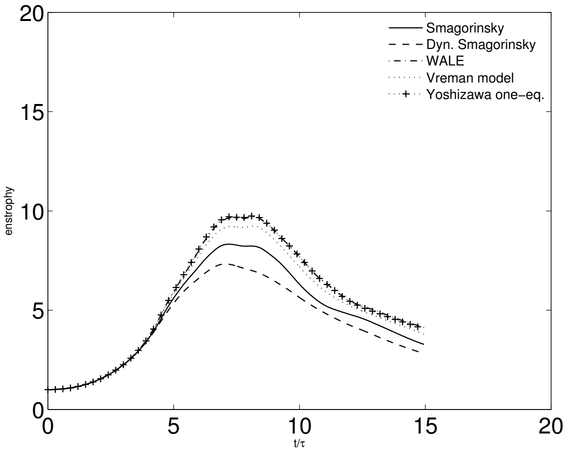

(a) Coarse grid (64^3)

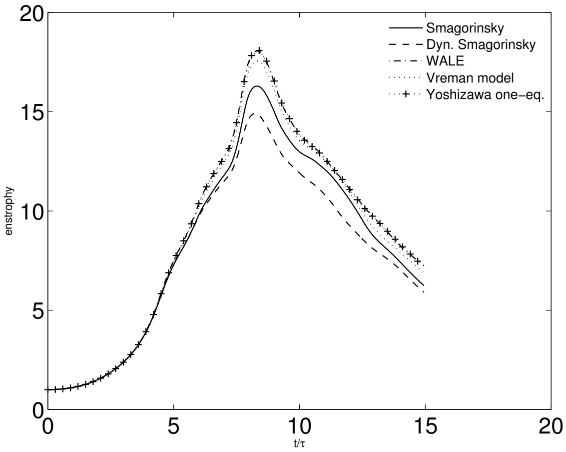

(b) Fine grid (128^3)

Figure 4. Evolution of enstrophy in time

Production term, $P_{k_{sgs}} = 2\nu_{sgs}\bar{S}_{ij}\bar{S}_{ij}$ in Fig.5c and 5d computed by the models on the coarse grid is wider than the fine grid solution which is narrow and accumulated around the transition time. The minimum values are given by the WALE model and the Yoshizawa one-equation model. The largest values are computed by the Smagorinsky and the Dynamic Smagorinsky models. Unlike the SGS viscosities, the production is almost independent of the grid resolution.

In order to observe the distribution of turbulent kinetic energy among the wave numbers, the energy spectrum is also computed at time $t/\tau = 8.2$ when the dissipation reaches its peak and plotted in Fig.6. Kolmogorov's $k^{-5/3}$ line in the inertial sub-range is also plotted for comparison. There is no noticeable difference among them in the inertial sub-range. However, at high wave numbers or smaller scales where the viscous dissipation dominates the flow (i.e., dissipation range), there is an observable difference between the Dynamic Smagorinsky and the Yoshizawa one-equation model. The Dynamic Smagorinsky model is the most dissipative in this range due to the largest contribution of μ_{sgs} to the total dynamic viscosity.

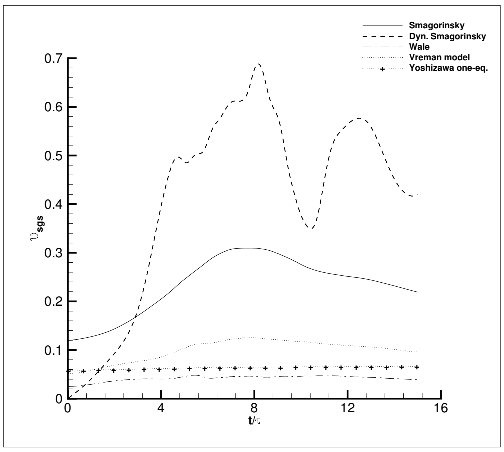

(a) Coarse grid (64^3)

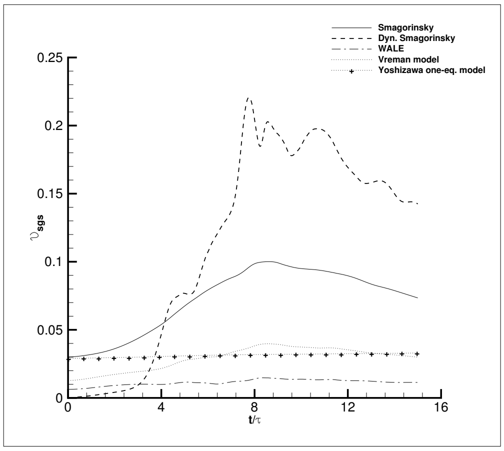

(b) Fine grid (128^3)

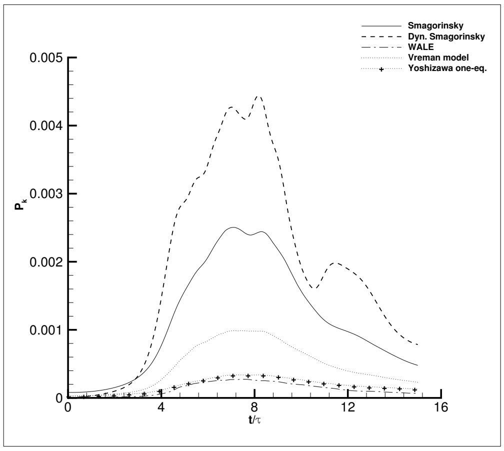

(c) Coarse grid (64^3)

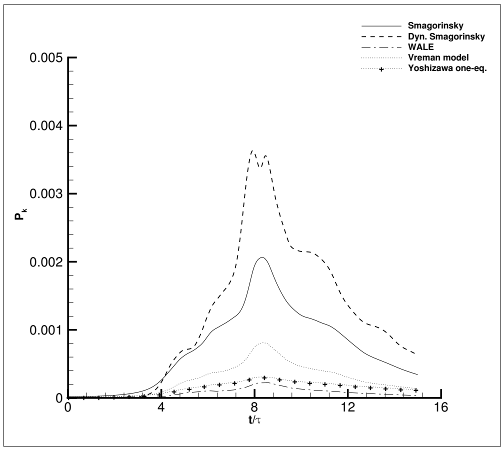

(d) Fine grid (128^3)

Figure 5. Evolution of $P_{k_{sgs}}$ term and ν_{sgs} in time

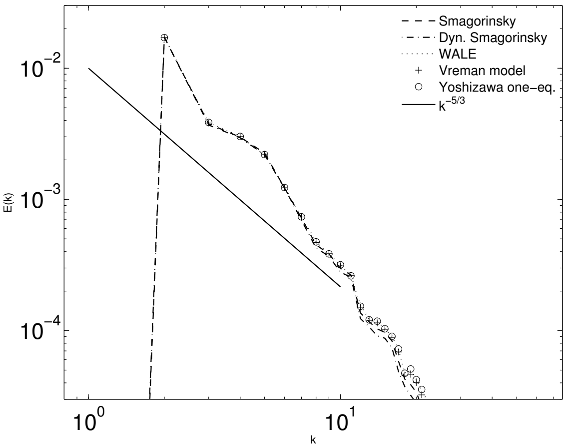

Figure 6. Turbulent kinetic energy ($E(k)$) .vs. wave number (k)

This study shows that SGS models constructed with advanced mathematical operators, which are able to describe the flow structures and their interactions in a physically correct way, produce results close to DNS by adaptively scaling their inherent dissipations. Further tests must be done for the flows including other complex features such as spatial transition and separation-reattachment regions, for better understanding of the behavior of SGS models.

ACKNOWLEDGEMENTS

IY thanks to The Scientific and Technological Research Council of Turkey (TUBITAK) for supporting his research stay in Sweden. The financial support of SNIC (Swedish National Infrastructure for Comp.) for computer time at C3SE (Chalmers Center for Comp. Sci. and Eng.) under the Project C3SE 2015/1-11 is also gratefully acknowledged.

REFERENCES

[1] Taylor, G., and Green, A., 1937, "Mechanism of the Production of Small Eddies from Large Ones", *Roy Soc London Proc Series A*, Vol. 158, pp. 499–521.

[2] Brachet, M., Meiron, D., Orszag, S.A.and Nickel, B., Morf, R., and Frisch, U., 1983, "Small Scale Structure of the Taylor-Green Vortex", *J Fluid Mechanics*, Vol. 130, pp. 411–452.

[3] Davidson, L., and Peng, S. H., 2003, "Hybrid LES-RANS modelling: A One-equation SGS Model Combined with a k-ω Model for Predicting Recirculating Flows", *Int J for Num Meth in Fluids*, Vol. 43 (9), pp. 1003–1018.

[4] Emvin, P., 1997, "The Full Multigrid Method Applied to Turbulent Flow in Ventilated Enclosures Using Structured and Unstructured Grids", Ph.D. thesis, Dept. of Thermo and Fluid Dynamics, Chalmers University of Technology.

[5] Smagorinsky, J., 1963, "General Circulation Experiments with the Primitive Equations", *Monthly Weather Review*, Vol. 91, p. 99.

[6] Yang, K., and Ferziger, J., 1993, "Large-Eddy Simulation of Turbulent Obstacle Flow Using a Dynamic Subgrid-Scale Model", *AIAA Journal*, Vol. 31 (8), pp. 1406–1413.

[7] Nicoud, F., and Ducros, F., 1999, "Subgrid-Scale Stress Modelling Based on the Square of the Velocity Gradient Tensor", *Flow, Turbulence and Combustion*, Vol. 62 (3), pp. 183–200.

[8] Vreman, A. W., 2004, "An eddy-viscosity subgrid-scale model for turbulent shear flow: Algebraic theory and applications", *Physics of Fluids (1994-present)*, Vol. 16 (10), pp. 3670–3681.

[9] Yoshizawa, A., 1986, "Statistical theory for compressible turbulent shear flows, with the application to subgrid modeling", *Physics of Fluids (1958-1988)*, Vol. 29 (7), pp. 2152–2164.

[10] Sreenivasan, K. R., and Antonia, R. A., 1997, "The Phenomenology of small-scale turbulence", *Annual Review of Fluid Mechanics*, Vol. 29, pp. 435–472.

[11] Hahn, M., 2008, "Implicit Large-Eddy Simulation of Low-Speed Separated Flows Using High-Resolution Methods", Ph.D. thesis, Cranfield University, School of Engineering, Department of Aerospace Sciences.

[12] Taylor, G., 1935, "Statistical theory of turbulence", *Proceedings of the Royal Society of London Series A, Mathematical and Physical Sciences*, Vol. 151 (873), pp. 421–444.

[13] Pope, S., 2000, *Turbulent Flows*, Cambridge University Press.

[14] Tennekes, H., and Lumley, J., 1972, *A First Course in Turbulence*, The MIT Press.

[15] Landahl, T., and Mollo-Christensen, E., 1992, *Turbulence and Random Processes in Fluid Mechanics*, Cambridge University Press.

[16] Shu, C.-W., Don, W.-S., Gottlieb, D., Schilling, O., and Jameson, L., 2005, "Numerical Convergence Study of Nearly Incompressible, Inviscid Taylor–Green Vortex Flow", *Journal of Scientific Computing*, Vol. 24, pp. 1–27.

Conference on Modelling Fluid Flow (CMFF'15)
The 16th International Conference on Fluid Flow Technologies
Budapest, Hungary, September 1-4, 2015

CFD CALCULATION OF NEW LP STAGE BEFORE THE EXTRACTION POINT IN A 225 MW TURBINE

Mariusz SZYMANIAK[1], Andrzej GARDZILEWICZ[2]

[1] Corresponding Author. Turbine Department, Institute of Fluid Flow Machinery Polish Academy of Sciences. Fiszera 14, 80-231 Gdansk, Poland. Tel.: +48 58 6995 106, Fax: +48 58 4116 144, E-mail: masz@imp.gda.pl
[2] Turbine Department, Institute of Fluid Flow Machinery, Polish Academy of Sciences. E-mail: gar@imp.gda.pl

ABSTRACT

A new design of steam turbine stage before the extraction point is presented. In this solution a special ring leads the steam leakage flow directly to the heat exchanger. The performed experiments and calculations confirmed operating and efficiency advantages of the new design, which has been applied, so far, in 30 old turbines with Baumann stages and, more recently, in the modernised LP exit parts of 225 MW turbines in the Polaniec, Kozienice, and Laziska power plants. In total, in recent 25 years the new solution has been applied in fifteen 225 MW turbines with new last stages of ND37 and ND41 type.

Keywords: turbine stages, leakages, extraction point, axial flow turbomachinery

NOMENCLATURE

N	[MW-]	power
C_m	[m/s]	axial velocity
p_t	[bar]	total pressure
p	[kPa]	static pressure
H	[mm]	height of blade
t	[degC]	temperature
q_k	[kJ/kWh]	specific heat consumption

1. INTRODUCTION

For operating reasons, steam turbine stages should have clearances over the rotor blades. The steam flow through these clearances has higher energy than the main flow; also its direction is different. Consequently, it is a source of kinetic energy losses in this turbine part, mainly resulting from the formation of separation zones, intensive mixing processes, and blockage of the flow to regenerative heat exchangers. In particular, extremely intensive dissipative processes are observed in the area above the unshrouded rotor blades of LP turbine last stages, where the steam flow leaving the clearance accelerates to transonic velocities. These anomalies have been confirmed experimentally on 200 MW turbines [1, 2]. The measuring instruments used in those experiments are shown in Figure 1.

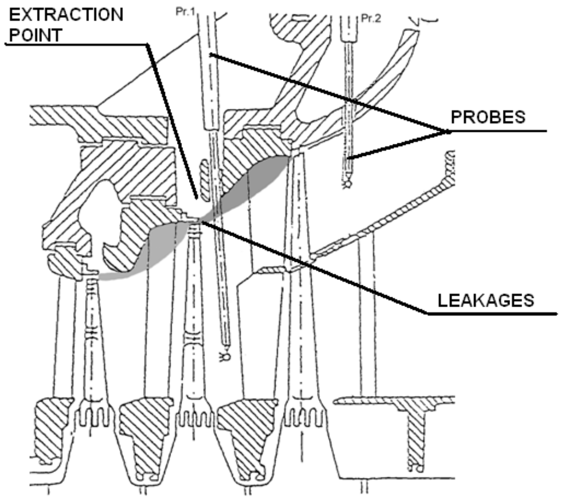

Figure 1. Thermal measurement equipment used in the LP section of 200 MW turbine with Bauman stage; zones of influence of the tip leakage flow are shadowed grey.

Plate probes inserted into the flow path enabled to measure pressure, temperature, and velocity distributions with high accuracy. Based on the analysis of the recorded data, a new very efficient solution has been proposed, patented and practically applied [3]. A concept of the new solution of steam turbine stage before the regenerative extraction point is shown in Figure 2.

A properly shaped ring installed in the tip clearance area of the unshrouded rotor blade directs the leakage flow to the extraction chamber. Leaving aside details of the patent, its advantages mainly consist in eliminating the swirl zone in the flow, as the ring removes a so-called aerodynamic curtain generated by the transonic steam flow behind the tip clearance.

a)

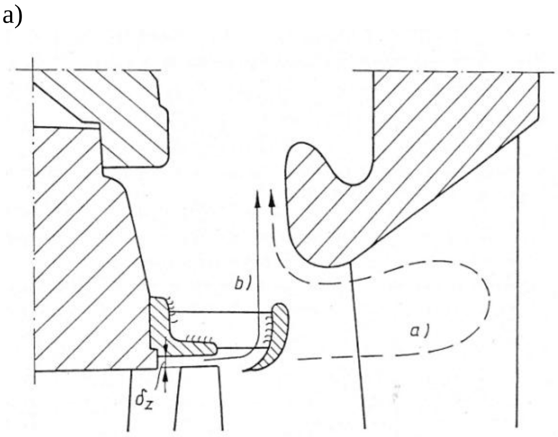

b)

Figure 2. New design of the stage before the extraction point (a). Ring inside the turbine flow path [3] (b).

Simultaneously, the steam flow capacity of the stage behind the extraction point is significantly increased by:

- eliminating the mixing between the tip leakage flow and the main flow, as the leakage flow goes directly to the extraction chamber;
- additional thermal loading of the first regenerative exchanger, which is usually underheated, by the high-energy leakage flow from the extraction chamber. It is noteworthy that the mass flow rate of the leakage flow is comparable to that of the extraction flow;
- eliminating the liquid phase from the flow, since the ring operates as a separator of secondary water droplets existing in that part of steam turbine.

The results of pressure measurements performed on an older 200 MW turbine before and after its modernisation are shown in Figure 3 [2]. For reference purposes, the diagrams in the figure also include calculated velocity distributions. The presented results of measurements and calculations confirm the advantages of the new solution.

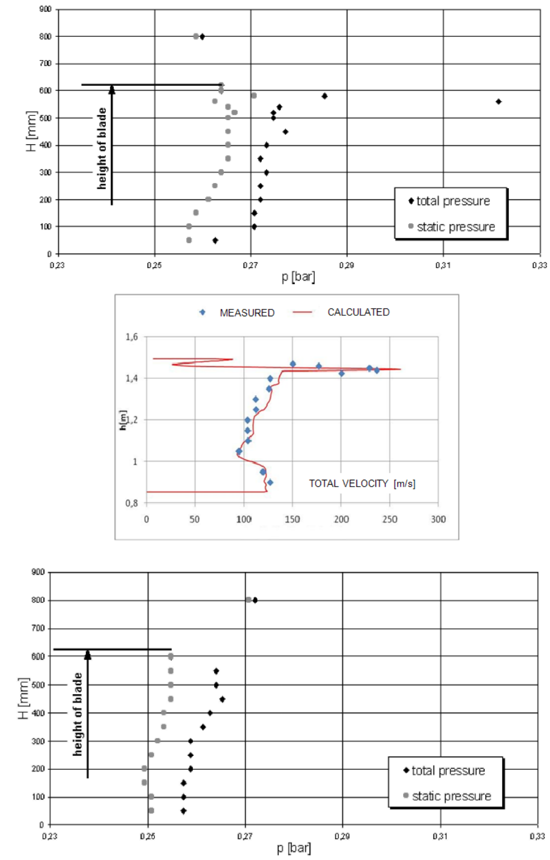

Figure 3. Distribution of total and static pressure along the measuring line before modernisation (upper diagram) and after ring introduction behind the 2-nd LP turbine stage (lower diagram) [2].

Quantitative benefits resulting from the use of the patent were evaluated for 400 - 800 kW, depending on operating conditions. Over the period of 1991 – 2015, the new solution has been applied in fifteen 225 MW turbines, with no operating trouble recorded [4].

2. PROPOSAL OF STAGE MODERNISATION IN APPLICATION TO 225 MW LP TURBINE

Possible applications of the patent in the low-pressure parts of the 225 MW turbines, which were modernised in Poland, were presented in 2002 [5]. A general concept of stage modernisation is shown in Fig. 4. It was developed based on experimental investigations performed in a real steam turbine with ND 37 exit, produced by Alstom. A schematic diagram of the measurement system is shown in Fig. 4. The performed measurements enabled to detect the presence of a jet downstream the tips of the unshrouded rotor blades in the last-but-one stage. Like in older constructions, this jet disturbed the flow structure by blocking the steam admission to the regenerative extraction system.

These results of the measurements were confirmed by complementary computer simulations, selected results of which are shown in Fig. 5. The figure compares total pressure distributions in the stage before and after ring introduction.

The presence of the jet flow and the blockage was confirmed by distributions of salt deposits observed on the surfaces of the last stage stator blades in the real turbine [6]. In fact, this jet was not only the source of energy losses, but also provoked untypical erosion damages of the last stage blade system (see Fig. 6).

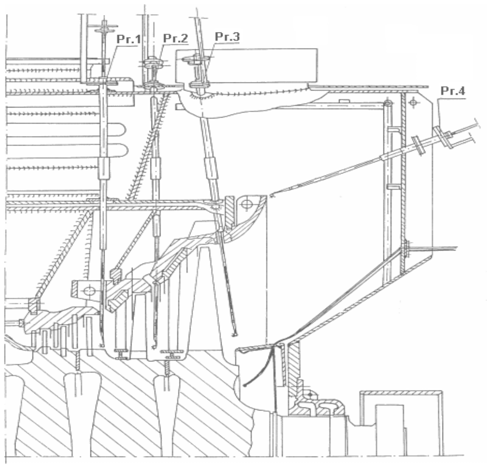

Figure 4. Measuring system in the new LP part of 225 MW turbine.

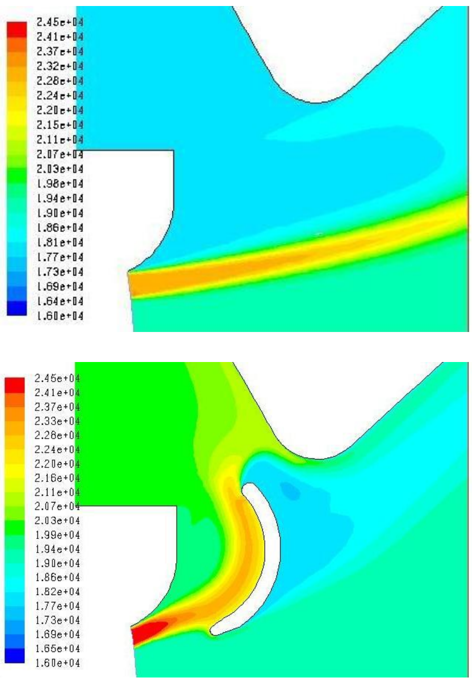

Figure 5 Graphic presentations of pressure and streamline patterns in the gap between 225 MW turbine stages 3 and 4 [5].

Intensified damages of the leading edges in their tip sections were mainly caused by large water droplets, recorded in the steam flow, which were not disintegrated in the blockage area. Minor damages observed in the remaining part of the leading edge were generated by smaller droplets splashed by the leakage flow. In particular, the erosion defects situated in the blade area beyond the hardened zone, see arrow in Fig. 6, are very dangerous for the structure of turbine blades. The water droplets which reach this area have highly acidic nature (pH<5), which can be a source of dangerous cracks in the erosion zone [7].

Fig. 6. Leading edge damage patterns observed in the 225 MW turbine last stage stator blade system.

To eliminate those unfavourable phenomena, a decision was made to install a ring in the blade system in the modernised 225 MW turbine with exit ND41A [8]. A design of the new solution is shown in Fig. 7.

To estimate benefits and check the new solution, the experimental investigation [9] and the CFD technique were employed [10]. Due to the fact that the installed ring better organised the flow in the blade system and removed the effects of swirl, mixing and blockage, certain benefits of its installation were acquired. In this case the layout of the ring in the flow path was optimised numerically.

When the ring is installed too high, it does not fully eliminate the blockage, but divides the flow into two parts. It does not separate water droplets collecting behind the last-but-one stage either (see Fig. 8a). On the other hand, when the ring is too low, it increases the swirl zone in the aerodynamic wake of the flow and unfavourably decreases the pressure in the extraction chamber.

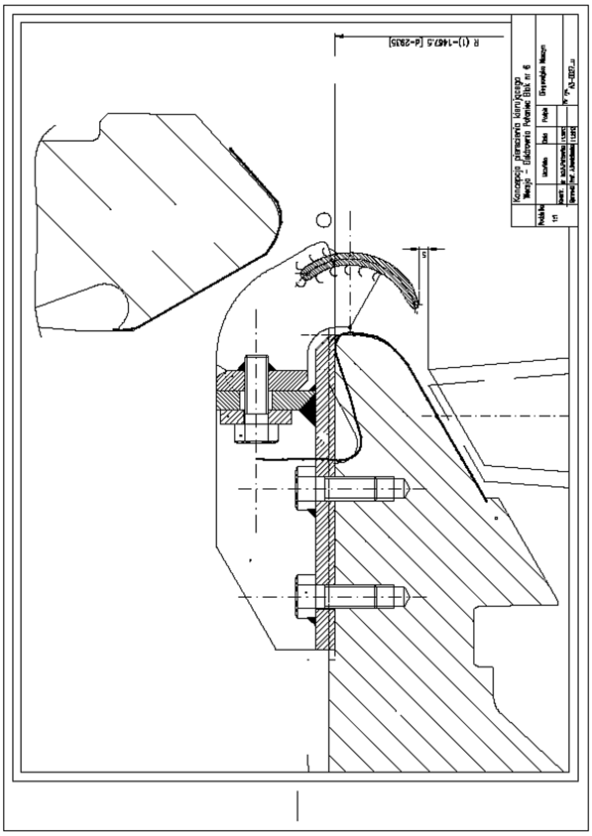

Fig. 7. Design of patent based ring assembly in the modernized exhaust ND 41A [8].

When the ring was too short, it rapidly stopped the leakage flow on the limiting wall, thus generating energy losses and possible erosion of the stator grip (Fig. 8b). And when it was too long, it undesirably intensified swirls in the extraction chamber (Fig. 8c).

The streamline pattern for the optimal ring position and dimension, in efficiency terms, is shown in Fig. 9 and compared to the pattern before modernisation.

For this ring position, and for the thermodynamic data corresponding to nominal conditions of turbine operation, the pressure increase calculated in the extraction chamber was equal to 2-3 kPa, which is equivalent to 3-4 deg C rise of the feedwater temperature after the first exchanger.

The numerical calculations also revealed that after the modernisation the efficiency of the last stage increased by about 1%, assuming the unchanged efficiency levels in the remaining stages. This efficiency increase results mainly from more uniform velocity distribution at inlet to the last stage stator after the modernisation. The gains are not impressive but worth noticing if we take into account that the nominal power of the last stages in both LP turbines exceeds 20 MW.

a)

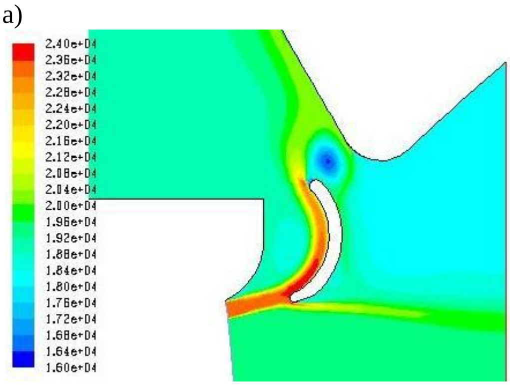

b)

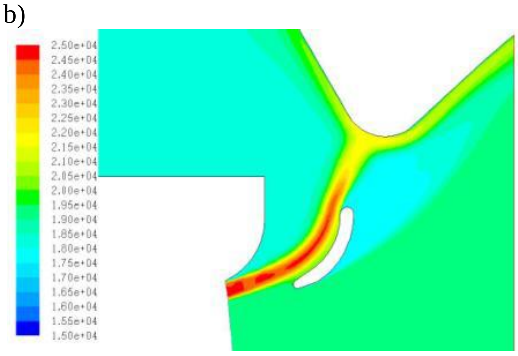

c)

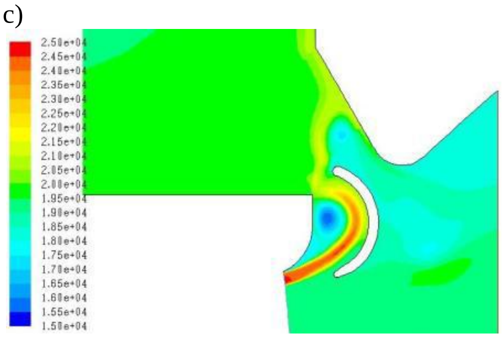

Fig. 8 Total pressure distribution after the last-but-one stage for different ring installations in the turbine flow (a) ring too high, (b) ring too short, (c) ring too long.

The presented data, referring both to efficiency and pressure changes in the extraction chamber, were used to calculate gains resulting from the use of the patent, based on the thermal cycle balance of the entire turbine. The calculations made use of the in-home code DIAGAR, tuned to the turbine operation parameters measured in the power plant [11].

Figure 10 shows turbine power increase as a function of load and condenser pressure, for the same thermal parameters at turbine inlet and exit before and after modernisation.

For the turbine load ranging within 120-225 MW and the condenser pressure equal to 3-6 kPa we can expect the turbine power increase by 150-420 kW, which corresponds to the reduction of the specific heat consumption by 10-15kJ/kWh.

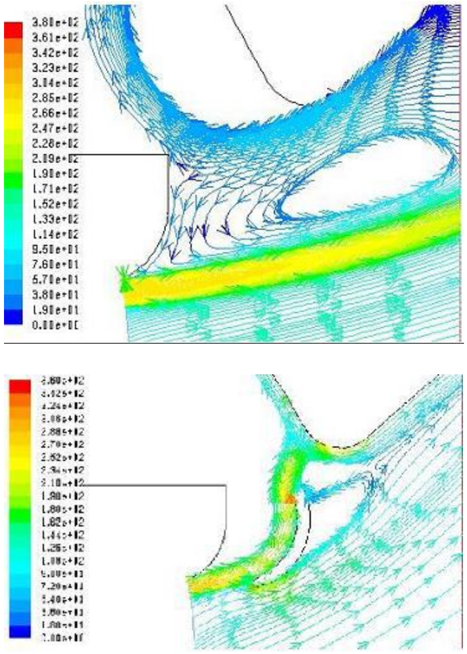

Fig. 9. Comparing streamline patterns behind stage 3 before and after modernisation

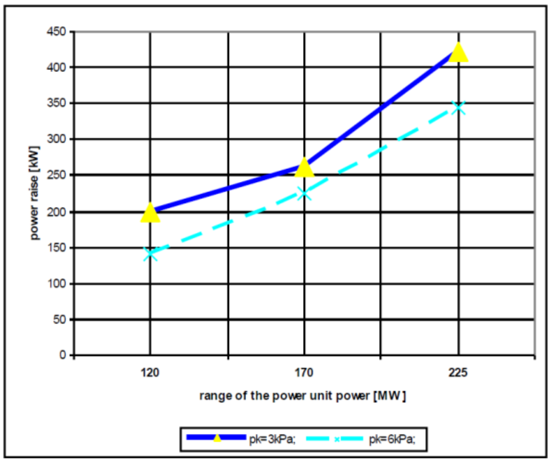

Figure 10. Power gain in the 225 MW turbine after patent application.

The adopted design solution was carefully analysed in strength and dynamic aspects. The structure of the ring turned out safe and reliable. The performed calculations took into account different operating conditions, including start-ups and shut-downs [12].

The technology of manufacturing and assembly has been carefully elaborated [13]. It takes into account specific conditions of steam turbine operation. The ring installed in the turbine is shown in Fig.11.

Fig. 11. Photos of the ring installed in stator grips in 225 MW turbine.

Visual inspections, done after 2 years of turbine operation with the installed rings, did not reveal any increase of erosion threat.

CONCLUSIONS

1. The application of a new stage design before the extraction point in the LP part with the ND41A exit of the 225MW turbine leads to power gains exceeding 400 kW, which is equivalent to the reduction of the specific heat consumption by 15 kJ/kWh. These gains result from higher load of the

first exchanger and improved flow efficiency of the last stage.

2. Introducing the ring in the diffuser behind stage 3 not only removes the steam leakage, but also eliminates water droplets separated in this turbine part, because the ring mounted inside the flow path operates as an ejector. This should reduce damages of the last-stage stator blade leading edges, especially in their unhardened sections.

3. The new construction turned out relatively easy to assembly and safe in operation. The rings are to be precisely fixed in the turbine with respect to the stator grips, taking into account not only machining tolerances but also relative movements of the moving and stationary turbine parts during turbine start-ups and shut-downs.

4. The planned final verification of the obtained gains will base on more precise thermodynamic measurements, and detailed inspection of the blade surfaces to assess erosion progress.

REFERENCES

[1] Gardzilewicz A, Marcinkowski S, 1995 *Diagnosis of LP Steam Turbine prospects of Measuring Technique*, PWR Vol. 28 1995, Joint Power Generation Vol. 3 ASME 1995, pp. 349-358,

[2] Gardzilewicz A, 1995 *Analysis of Regenerative Extractions of Turbine Based on Thermal Measurements in Power Plants,* VDI Berichte 1186, 1995 Erlangen, pp. 427-443, 8

[3] Gardzilewicz A and Marcinkowski S, 1997 *Stage of Steam Turbine*, Patent No 160-805, Warsaw, Poland (in Polish),

[4] Gardzilewicz A, Marcinkowski S, Sobera H. and Józefowicz Z 1994 *Experimental Experience of Patent No. 160-805 Application in 200 MW Turbines*, Energetyka *(No. 3), pp. 73-78*, (in Polish),

[5] Gardzilewicz A, Marcinkowski S, Karcz M., Bielecki M., Badur J., Banaszkiewicz M. and Malec A.,2002, *Proposal of Modernisation of System Turbine Stage*, Task Quarterly 6 *(No. 4), pp577-581,*

[6] Gardzilewicz A, Marcinkowski S, Szymaniak M., 2009, *Surveys and Erosion Threat Analysis of Lasts Stages of 225 MW Turbine (Power Unit 3) in Kozienice Power Station*, Diagnostyka Maszyn Ltd. Report No. 6/09, (in Polish),

[7] Gardzilewicz A, Marcinkowski S., 2004, *Corrosive-Erosive Threat to the LP Stages of Steam Turbines*, Proc. XVIII Workshop on Turbomachinery, Plzen 2004,

[8] Gardzilewicz A, Palzewicz A., Szymaniak M., Gluch J., Gronert J., Graczyk P., 2009, *Application of new Solution for LP Stages in the Power Unit No. 3 in Polaniec Power Station*, Diagnostyka Maszyn Ltd. Report No. 26/10, (in Polish),

[9] Gardzilewicz A, Marcinkowski S, 1993, *Investigations of steam flow in the LP part of 225 MW Modernised Turbine (Power Unit 4) in Polaniec Power Station*, Diagnostyka Maszyn Ltd. Report No. 6/93, (in Polish),

[10] Szymaniak M., Gardzilewicz A, 2009, *CFD Technique Applied for the Modernisation of a Steam Turbine Construction in the Regenerative Extraction Area*, Proc. IX ISAIF, Gyeongju (Korea) 2009,

[11] Gardzilewicz A., Gluch J., Bogulicz M., Uzieblo W., 2002, *DIAGAR Program Version 2002*, Diagnostyka Maszyn Ltd. Report No. 28/02, (in Polish),

[12] Badur J., Slawinski D., 2008, *Strength and Dynamic Calculation for the Patent No. P160-805*, Diagnostyka Maszyn Ltd. Report No. 05/08.

[13] Graczyk P., Graczyk T., Gronert J., 2014, *Technology of manufacturing and assembly of ring in the steam turbine*, Posteor Ltd. Report No. 07/15, (in Polish).

Conference on Modelling Fluid Flow (CMFF'15)
The 16th International Conference on Fluid Flow Technologies
Budapest, Hungary, September 1-4, 2015

NUMERICAL STUDY OF SEPARATION PHENOMENA IN THE DAM-BREAK FLOW INTERACTING WITH A TRIANGULAR OBSTACLE

Alexander KHRABRY[1], Evgueni SMIRNOV[1], Dmitry ZAYTSEV[1], Valery GORYACHEV[2]

[1] Department of Aerodynamics, St.-Petersburg State Polytechnic University. E-mail: aero@phmf.spbstu.ru
[2] Corresponding Author. Department of Mathematics, Tver State Technical University. 170026, Tver, emb. A. Nikitina, 22, Russia. Tel.: +7 4822 311510, E-mail: valery@tversu.ru

ABSTRACT

Dam-break turbulent flow interacting with obstacles is simulated with the VOF method implemented in an in-house unstructured-grid finite-volume Navier-Stokes code. A special attention is paid to prediction of separation phenomena using low-Re computational grids that provide full resolution of viscous sublayers on the bottom and side confining walls, if any. Some original developments aimed at improvement of the VOF method robustness for such kind of flows are presented. The test case considered is interaction of the dam-break induced water stream with a triangular obstacle. Computations under conditions of experiments by Soares-Frazao (2007) have been carried out on the base of 2D and 3D formulations. It is shown that action of the bottom wall friction leads to formation of one or two separation "bubbles", depending on the flow development phase, and to occurrence of associated hills at the free surface, which are observed in experimental photos as well. Taking into account presence of side walls of the experimental channel results in solutions with a considerably 3D shape of the computed free surface, and its side view much better agrees with the experimental photos than that given by 2D solutions. Moreover, local-in-time separation of the flow from the side walls is predicted with the 3D formulation.

Keywords: CFD, dam-break flow, flow-obstacle interaction, viscosity induced separation, VOF method

NOMENCLATURE

$\underline{v}$	$[m/s]$	velocity vector
p	$[Pa]$	pressure
C	[-]	marker function
t	$[s]$	time
$\underline{g}$	$[m/s^2]$	gravitational acceleration vector
ρ	$[kg/m^3]$	density
μ	$[Pa{\cdot}s]$	dynamic molecular viscosity
F	$[m^3/s]$	volumetric flux
V	$[m^3]$	computational cell volume
$\underline{S}$	$[m^2]$	computational cell face area vector

Subscripts and Superscripts

l, g	liquid, gas
i, j	current and previous time layers
P	center of a computational cell
f	center of a computational cell face

1. INTRODUCTION

Dam-break flows or other impact single-wave flows may cause damage of civil and industrial buildings and constructions. For the sake of the damage mitigation or minimization such kind of flows must be well studied including all the aspects of their interaction with different obstacles.

To date experimental data is available for several model dam-break flows that interact with obstacles having different shape (triangular – [1, 2], trapezoidal – [3, 4], vertical wall – [5, 6] and others). As a rule, experimental works provide a set of photos showing free surface configuration for different time instants.

Currently experimental studies are being displaced more and more by numerical simulation applicable to a wide variety of flows. Different numerical models have different computational costs and areas of applicability. According to this trend, experiment is increasingly used as a data source for validation of mathematical models and computational tools. Sure, this statement is completely applicable to the problems attributed to the dam-break flows.

Traditionally numerical modeling of a single wave propagation and its interaction with different obstacles is performed using a method of shallow water equations (SWE) (see for example [1, 7-10]), which provides a proper prediction of unsteady areas of water raise before the obstacles (positions of these areas and their height). However, the SWE method is not capable to reproduce details of wave-obstacle interaction, such as overturning (breaking) of a negative wave, which appears when a stream is fully or partly reflected by an obstacle, and fails to predict accurately pressure distribution over walls of the obstacle (especially in case of bluff obstacles). As well, as pointed in some of the aforementioned contributions, the SWE method does not predict accurately propagation speed of the main intensive wave and reflected waves, and does not reproduce details of their free surface shape.

Alternative to the SWE approach is solving the full 3D or 2D (in case of flow uniformity in the spanwise direction) Navier-Stokes (NS) equations, or the Reynolds Averaged Navier-Stokes equations, (RANS), if turbulence is considered as a significant factor. Capabilities of the SWE and NS approaches are compared, in particular, in [3] and [11]. Computational results obtained via solving the Navier-Stokes equations for dam-break flow interacting with different obstacles can be found in [2-5, 12, 13].

Separation zone may occur at front side of an obstacle. Such a zone can be seen, in particular, in the 2D velocity field computed with code Flow-3D for a model dam-break flow interacting with a trapezoidal obstacle [3]. Apparently, appearance of this zone is caused by an adverse pressure gradient occurring when the flow goes up at a front side of the obstacle.

Application of numerical methods for analysis of such a complicated flow like the intensive single-wave interaction with an obstacle requires a justified assurance that no scheme factors are affecting considerably a solution. This requirement is related to both the schemes used for prediction of free surface evolution and to the approaches employed for near-wall layer treatment.

Typically, the flows under consideration are characterized by high Reynolds numbers, and are often (in most cases) modeled with usage of one or another turbulence model. Here it should be noted that majority of previous computations of free surface flow developing over a wall were performed with application of the standard wall function technique (using so-called high-Re computational grids) to satisfy no-slip condition on the solid wall or even with prescribing slip condition. It is well known however that the standard wall functions do not perform well in case of boundary layer separation caused by adverse pressure gradient.

Nowadays the most popular approach for free surface tracking is the Volume-of-Fluid (VOF) method [14]. It allows performing computations in cases of strong deformation of free surface including the case of wave breaking. In this method free surface position is determined by space distribution of so-called marker function presenting volume fraction of fluid. Marker function is governed by a convective transport equation, and the quality of numerical schemes used for approximation of this equation affects directly the free surface artificial smearing or/and deformation.

It is well known that application of conventional schemes for convective flux evaluation is not suitable for solution of the marker-function equation as it leads to smearing of a transitional area, where the fluid volume fraction must vary rapidly from zero to unity, over plenty computational cells. There are several specialized (so-called “compressive”) numerical schemes proposed in literature for approximation of this equation, for example HRIC [15], CICSAM [16] and M-CICSAM scheme [17].

The present work is aimed to development and application of 3D numerical techniques for modeling of dam-break turbulent flow interacting with an obstacle. Some original developments aimed at improvement of the VOF method robustness for such kind of flows are presented. A special attention is paid to prediction of separation phenomena using low-Re computational grids that provide full resolution of viscous sublayers on the bottom and confining side walls. Results of 2D and 3D computations performed for a test configuration with a triangular obstacle are presented and discussed.

2. COMPUTATIONAL METHOD

Present developments and computations are based on using an in-house unstructured-grid finite-volume Navier-Stokes code called Flag-S. In this code the VOF method is used for free surface tracking, and the SIMPLEC algorithm is used for pressure-velocity coupling in computations of incompressible fluid motion. Note also that all computational results presented below were obtained without taking into account effects of surface tension on the gas-liquid interface.

2.1. VOF method

As mentioned in Introduction, in the framework of the VOF method [14] free surface position is determined by spatial distribution of so-called marker-function C, which in fact is volume fraction of fluid in a computational grid cell: C=1 – cell contains only liquid, C=0 – cell contains only gas. It is assumed that the free surface coincides with an isosurface C=0.5. Herewith, liquid and gas can be treated as a single fluid having variable material properties defined as follows (this approach is called one fluid formulation):

$$\rho = C\rho_{l} + (1-C)\rho_{g} \qquad (1)$$

$$\mu = C\mu_l + (1 - C)\mu_g \quad (2)$$

Governing equations for this effective fluid motion are solved throughout the entire computational domain and no boundary conditions at the gas-liquid interface are needed.

To apply the finite-volume method, the governing equations are written in a conservative form. Conservative form of the momentum equation is given by:

$$\frac{\partial \rho \underline{v}}{\partial t} + \nabla \cdot (\rho \underline{v}\underline{v}) = -\nabla p + \nabla \cdot (\mu \nabla \underline{v}) + \rho \underline{g} \quad (3)$$

The equation governing convective transport of the volume fluid fraction can be also transformed to a conservative form (4) using continuity equation (5) applicable for incompressible liquid and gas.

$$\frac{\partial C}{\partial t} + \nabla \cdot (C\underline{v}) = 0 \quad (4)$$

$$\nabla \cdot \underline{v} = 0 \quad (5)$$

According to the finite-volume technique, discretized forms of these equations are as follows (summation is performed over all faces of a control volume being a computational cell):

$$V \frac{C_P^i - C_P^j}{t^i - t^j} = \sum_f \beta (C_f F_f)^i + (1 - \beta)(C_f F_f)^j \quad (6)$$

$$\sum_f F_f = 0 \quad (7)$$

Here F_f is volumetric flux defined as $F_f = \underline{S}_f \cdot \underline{v}_f$. Different values of parameter β correspond to different time-discretization schemes. Note that form (6) ensures conservation of the marker-function total amount in the computational domain, i.e. ensures liquid and gas global conservation.

As seen from (6), values of the marker-function at computational cell faces, C_f, are required. They should be evaluated via interpolation of C-values from neighboring cells. It is known that conventional upwind schemes most commonly used for discretization of convective terms (in momentum equation, for example) are inappropriate for equation (6) as they lead to smearing of the gas-liquid interface over many computational cells.

In the literature, several specialized (so-called “compressive”) numerical schemes are proposed for approximation of C_f. A detailed comparative study of performance of two popular schemes HRIC [15] and CICSAM [16], and also a promising modification of CICSAM scheme, M-CICSAM [17] was conducted in work [18]. The latter one has demonstrated its superiority over the other schemes examined: less dependence on quality of computational grid and time step size. According to these findings, the M-CICSAM scheme was chosen for the computations presented below. It was found also that the Crank-Nicolson scheme (corresponding to β=0.5) is preferable when solving equation (6) [18].

In case of taking into account turbulence effects, the set of above-given governing equations is added by transport equations of turbulence parameters that define the eddy viscosity, and the latter is simply added to the molecular one. For the present computations, two-equation SST turbulence model developed by Menter [19] was used, and the transport equations of this model were solved throughout the computational domain, i.e. with no boundary conditions at the gas-liquid interface.

2.2. Approximation of convective part of the momentum equation

Convective flux of momentum at a cell face is evaluated via application of an interpolation procedure using density and velocity values from neighbouring cells. At that, a specific issue arises when treating the area corresponding to the gas-liquid interface since fluid density in this area changes rapidly by several orders. As a result of this rapid change, density approximation method has a dramatic effect on the cell-face momentum flux evaluated. As pointed in [20], writing momentum equation in the above given conservative form (3) implies that at the stage of their discretization the density interpolation procedure must provide those density values at cell faces that (together with the applied time approximation scheme) ensure fulfilment of discretized conservative form of non-stationary continuity equation for the effective fluid. This requirement may be satisfied by using same time approximation for the momentum equation and for equation (4), and evaluating cell-face density values directly using C_f values that are computed at solving equation (6) [20].

However, the above described approach prevents implementation of special numerical “tricks” that can improve effectiveness and robustness of the VOF method and quality of the computed marker-function field. One of such “tricks”, aimed at extra sharpening of the gas-liquid interface, is reported in [21]. Another motivation for rejection of the approach elaborated in [20] is due to difficulties with its implementation in the framework of fractional step strategy, which is rather efficient and implies that several time steps are done at solving equation (6) within one time step at solving the fluid dynamics governing equations.

To avoid the necessity of usage of fully consistent discrete approximations for equations (3) and (4) one could, in particular, employ the momentum equation written in the conventional non-conservative form (8a), as it was done, for instance, in [22], or in the “partially” conservative formulation (8b) used in [23]:

$$\rho \frac{\partial \underline{v}}{\partial t} + \rho \underline{v} \cdot \nabla \underline{v} = RHS \tag{8a}$$

$$\rho \frac{\partial \underline{v}}{\partial t} + \rho \nabla \cdot (\underline{v}\underline{v}) = RHS \tag{8b}$$

Discretized forms of these equations given by (9a) and (9b) illustrate that no density face values are needed:

$$V \rho_{\mathrm{P}} \frac{\partial \underline{v}}{\partial t} + \rho_{\mathrm{P}} \underline{v}_{\mathrm{P}} \sum_{\mathrm{f}} F_{\mathrm{f}} = RHS \tag{9a}$$

$$V \rho_{\mathrm{P}} \frac{\partial \underline{v}}{\partial t} + \rho_{\mathrm{P}} \sum_{\mathrm{f}} F_{\mathrm{f}} \underline{v}_{\mathrm{f}} = RHS \tag{9b}$$

These two variants were tried at implementation of the VOF method in code Flag-S (note that for time discretization of momentum equation the Crank-Nicolson scheme was used for all the computations presented below). It has been established, however, that both schemes (9) result in dramatic false deformation of gas-liquid interface even in relatively simple cases. As an example, Fig.1 depicts results of 2D test computations carried out with schemes (9a) and (9b) for case of gravity-induced free falling of a circular liquid cylinder, diameter 0.04 m, surrounded by air (the latter remains at rest far from the cylinder). Obviously, that at very short times (when the cylinder velocity is small and liquid-air interaction is insignificant) the shape of the cylinder has to remain practically the same as at the initial instant. Fig. 1 shows, however, that both schemes (9) produce large deformations of the cylinder shape even for a time interval of 0.07 s that is sufficiently small (the cylinder passes less than one diameter).

To overcome this issue, it is suggested to rewrite the momentum equation in novel form (10) and to use its discrete analog (11). This form provides a proper reduction of errors originated from numerical violation of mass balance in computational cells.

$$\rho \frac{\partial \underline{v}}{\partial t} + \nabla \cdot (\rho \underline{v}\underline{v}) - \underline{v} \nabla \cdot (\rho \underline{v}) = RHS \tag{10}$$

$$V \rho_{\mathrm{P}} \frac{\partial \underline{v}}{\partial t} + \sum_{\mathrm{f}} \rho_{\mathrm{f}} F_{\mathrm{f}} \underline{v}_{\mathrm{f}} - \underline{v}_{\mathrm{P}} \sum_{\mathrm{f}} \rho_{\mathrm{f}} F_{\mathrm{f}} = RHS \tag{11}$$

For the test case with falling liquid cylinder, results of computations preformed with scheme (11) are also shown in Fig. 1. One can see a radical improvement of the prediction quality, as compared with the case of using schemes (9a) and (9b).

Note that a form analogous to (11) was used for discretization of convective term in transport equations of turbulence model.

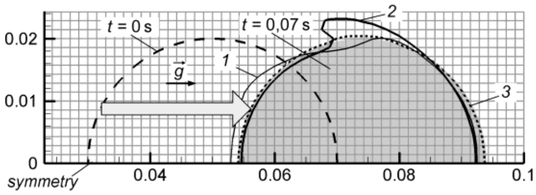

Figure 1. Effect of momentum convective term numerical approximation on the shape of free falling liquid cylinder: 1 – approximation based on using scheme (9a), 2 – (9б), 3 – (11)

2.3. Approximation of pressure gradient

The finite-volume discretization for pressure gradient in momentum equation (3) is given by:

$$(\nabla p)_{\mathrm{P}} = \frac{1}{V} \sum_{f} p_{\mathrm{f}} \, \underline{S}_{\mathrm{f}} \tag{12}$$

Here again pressure values p_{f} at cell face centers should be evaluated via interpolation of pressure values from neighboring cells. Unfortunately, conventional linear interpolation technique (13) works incorrectly in case of resting liquid and gas, which is characterized by discontinuity in pressure gradient. For the sake of clarity, consider a case where a mesh face coincides with a free surface (see Figure 2). In this case, usage of correct pressure values at centers of neighboring cells 1 and 2 will produce an overestimated pressure value at the face. As a result, for cells 1 and 2 application of (12) gives a pressure gradient value that is not balanced with the gravity force. Consequently, momentum equation will be not satisfied in case of zero fluid velocities (as it should be), and non-physical, increasing in time local oscillations of velocity and pressure fields will arise.

$$p_{\mathrm{f\,lin}} = \frac{p_1 d_2 + p_2 d_1}{d_1 + d_2} \tag{13}$$

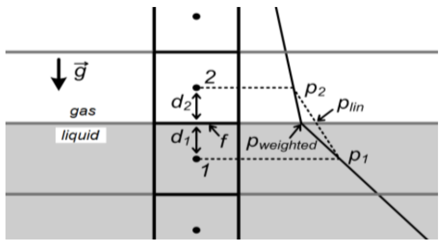

Figure 2. Scheme of pressure distribution in the vicinity of gas-liquid interface for case of resting liquid and gas, and interpolated pressure values at a mesh face coinciding with the interface

It can be easily obtained that a correct face pressure value is generated when using a density-weighted interpolation given by:

$$p_{\text{f weighted}} = \frac{p_1 \rho_2 d_2 + p_2 \rho_1 d_1}{\rho_1 d_1 + \rho_2 d_2} \quad (14)$$

It has been established, however, that usage of scheme (14) in case of liquid and gas motion leads to occurrence of intensive even-odd pressure oscillations near the gas-liquid interface, in particular, in the above presented case of a free falling liquid cylinder. To overcome this issue, a combination of schemes (13) and (14) is proposed where the weight ξ is dependent on value of the angle α between normal to a grid face and the gravity vector:

$$p_{\text{f}} = \xi \cdot p_{\text{f weighted}} + (1-\xi)\, p_{\text{f lin}}, \quad \xi = cos^2(\alpha) \quad (15)$$

Test computations performed in the present work with scheme (15) have shown that it works correctly in both the cases of resting and free falling liquid.

2.4. Problems of accurate resolution of viscous near-bottom layer in case of liquid spreading along a dry wall

As mentioned above, free surface flows, and in particular dam-break flows, are most commonly modeled using high-Re computational grids and standard wall-function technique for determination of wall friction. However, accurate prediction of flows with occurrence of near-bottom separation zones requires accurate resolution of near-wall viscous layer that implies using a low-Re grid strongly clustered near the wall (with normalized distance, Y^+, of the first computational point to the wall less or about unity). First our attempts to use such a grid for simulation of dam-break flow developing along a dry bottom have highlighted a serious issue.

Consider the simplest 2D dam-break test case, where after sudden removal of the retaining wall the fluid floods the dry horizontal wall due to gravity (see Figure 3, a). The computations with a low-Re grid have shown that the air initially located in computational cells in vicinity of the dry bottom can not be properly displaced by the spreading fluid because velocity values in these cells are very low. As a result, a thin elongated non-physical air layer occurs at the bottom (Fig. 3, b).

To make sure that this artefact is not caused by any mistakes in code Flag-S, a computational run for this test case was also performed with commercial CFD code ANSYS Fluent-14.0 using the same grid, and results are shown in Fig. 3, c. One can see that in the solution using Fluent a non-physical near-bottom air layer is observed as well (the reason of spatial oscillations seen in the Fluent solution remains unclear).

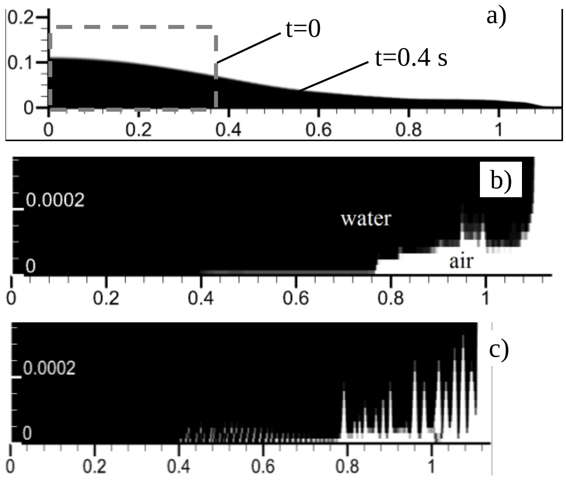

Figure 3. Occurrence of non-physical near-bottom air layer in computations of water flow spreading along a dry wall: (a) general view, (b,c) view of near-bottom zone (stretched in the vertical direction) from results obtained with (b) code Flag-S and (c) ANSYS Fluent

Obviously that this non-physical air layer leads to a radical under-estimation of wall friction. As a result, boundary layer separation phenomenon can not be predicted accurately. So a special numerical technique should be introduced to overcome this issue. In the present work, an artificial diffusion term acting in a thin near-wall region was added to the marker-function transport equation as follows:

$$\frac{\partial C}{\partial t} + \nabla \cdot (C\, \underline{v}) = max(\nabla \cdot (\chi \nabla C), 0) \quad (16)$$

$$\chi = \begin{cases} 0 & , d > d_{\text{cell}} \\ \chi_{\max} \dfrac{d_{\text{cell}} - d}{d_{\text{cell}}} & , d \le d_{\text{cell}} \end{cases} \quad (17)$$

Here $\chi_{\max}$ and d_{cell} are user defined parameters, and d_{cell} defines distance from the wall within which the diffusion term is active. Typically, it can be set to one half of computational cell size in the flow core. With such a choice, d_{cell} is sufficiently large to cover the area of the non-physical effect under consideration and at the same time it is sufficiently small to avoid noticeable influence on the flow field prediction. $\chi_{\max}$ is a diffusion coefficient. For the present computations it was set to $0.0001(gH^3)^{1/2}$, where H is the initial height of the water. This relatively small value was sufficient to completely avoid occurrence of the non-physical air layer.

3. RESULTS OF COMPUTATIONS FOR A TRIANGULAR OBSTACLE

3.1. 2D computations

Experimental study of dam-break water flow interaction with a triangular obstacle was conducted in [1] under geometrical and initial conditions defined in Figure 4. In the experiments, the flow was treated as nominally two-dimensional. Confining side walls were transparent, and the free-surface shape at various time instants was fixed with a photo camera.

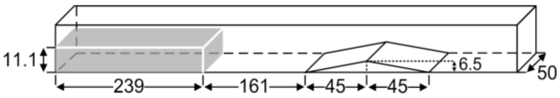

Figure 4. Experimental conditions in [1]. All dimensions are given in centimetres

Basic two-dimensional computations were performed with no-slip conditions on the initially dry bottom of the channel and the obstacle surface. The computational grid had 25 000 quadrangle cells and was clustered near the wall so that Y^+-values were less than unity. Additional run was done using slip conditions, both on the bottom and the obstacle surface. For this run, the grid had 16 000 cells, with no clustering near the wall. For both the runs, the SST turbulence model [19] was employed.

Free surface shapes computed with two types of wall boundary conditions are compared in Figure 5. The computational results are superposed onto experimental photos given in [1] for two time instants counted from the instant of sudden removal of retaining partition. One can see that the free surface shape predicted with the slip condition (Fig. 5 a, c) disagrees with experimental observations dramatically. An accurate resolution of near wall viscous effects results in a considerable improvement of the flow prediction quality. The most important difference between the solutions is attributed to manifestation of separation phenomena in the case of no-slip conditions. Fig. 5 shows that firstly one (at t=3.0s) and then two (t=3.7s) relatively large separation zones occur in front of and at the obstacle. Occurrence of these zones leads to formation of «hills» on the free surface, visible in the experimental photos as well.

Two more runs with accurate resolution of viscous sublayer were performed reducing the molecular viscosity by 10 and 100 times, and keeping the sizes of the channel as in the experiments [1]. Note that after rescaling of the problem according to the similarity theory, one can easily conclude that these runs are equivalent to cases of real-viscosity water flow developing after the dam breaks with initial water level of 55 cm and 240 cm correspondingly. Despite a considerable increase of the Reynolds number, in both the solutions the separation effects remain significant, and the separation zone size is reduced less than two times even in the case of the largest Reynolds number.

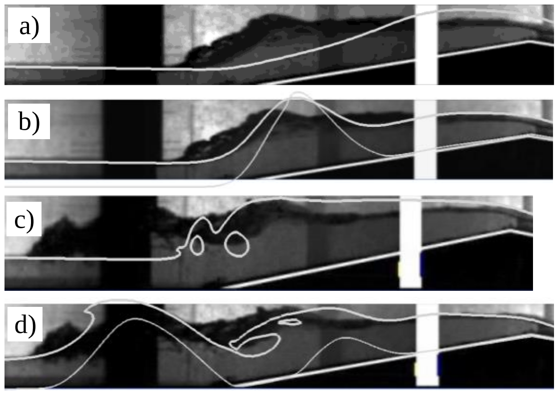

Figure 5. Effect of bottom friction on the free-surface shape computed: (a,c) – slip condition, (b,d) – no-slip (separation zone is shown as well). Simulation results are superposed on the experimental photos given in [1] for (a,b) t=3.0 s and (c,d) t=3.7 s

3.2. 3D computations

Three-dimensional computations were performed to analyse the effect of the side walls confining the experimental channel in the spanwise direction (see Fig. 4). Due to the symmetry of the experimental configuration with respect to the middle plane, the computational domain covers only a half of the channel. The computational grid used had one million hexahedral cells and was clustered both near the bottom and near the side wall, with the same evaluation of Y^+-value as in the 2D runs. As previously, the SST turbulence model was used to introduce the eddy viscosity effects.

Figure 6 illustrates 3D free surface shape computed for the same time instants as in the experiments and 2D computations. A considerable deviation of developing waves from a 2D form takes place in the area covering more that one third of the channel. 3D effects are even more pronounced when considering the separation zones. For instance, vorticity lines originated from the middle-plane core of the separation zone(s) deviate from a straight line (that would be in a 2D flow) in the major part of the flow domain.

For the time instant of t=3.0 s, Figure 7 shows patterns of computed fluid velocity vectors projected on the 3D free surface and on the symmetry plane. One can see that a rather large recirculation occurs by this time near the side wall, namely at the area where the water starts to interact with the obstacle. This “local-in-time” recirculation zone evolves with time considerably.

Figure 8 presents a comparison of side view of computed 3D free surface with the experimental photos from [1]. Due to 3D shape of the free surface, this view is not a line as in the 2D case, but looks like a complicated band. Notably that such a "band" is seen in the experimental photos as well: at each photo one can clearly see a dark area along the free surface. Comparing Figs. 5 and 8, one can conclude that a much better agreement with the experiments is achieved on the base of 3D formulation taking into account viscosity effects near the side walls.

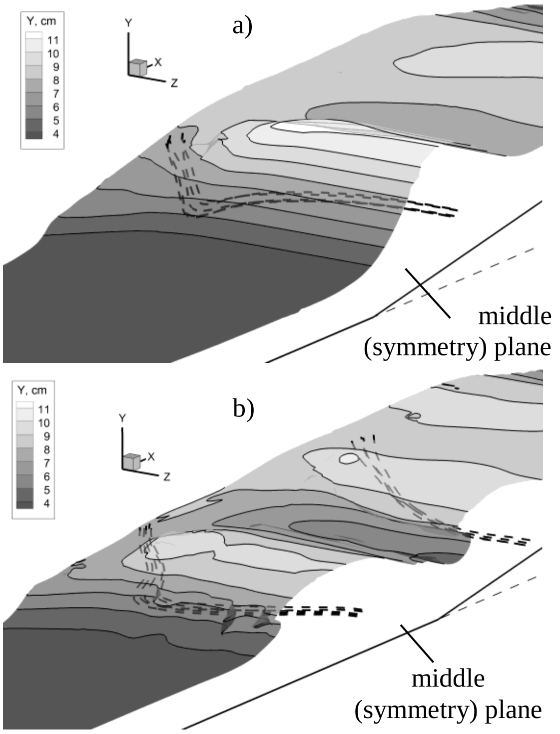

Figure 6. 3D free surface shape computed at (a) t=3.0 s and (b) t=3.7 s for flow over the triangular obstacle under conditions of experiments [1]. Vorticity lines originated from the middle-plane core of the separation zone(s) are shown as well (dashed lines)

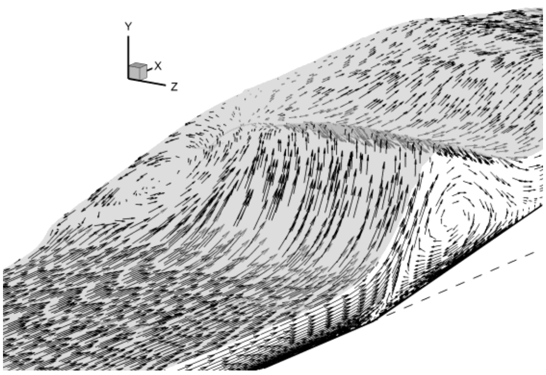

Figure 7. Patterns of computed fluid velocity vectors on the 3D free surface and in the symmetry plane, t=3.0 s

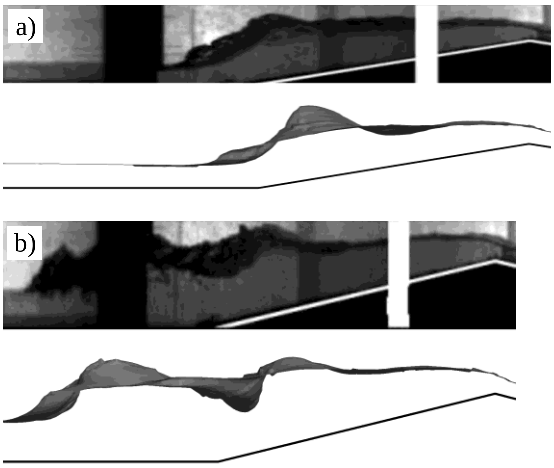

Figure 8. Comparison of side views of 3D free surface computed at (a) t=3.0 s and (b) t=3.7 s with experimental photos from [1]

4. CONCLUSIONS

On the base of VOF method, 3D computational techniques have been developed providing accurate treatment of both the free surface evolution and viscous near-bottom layer in the flow developing after a dam break and interacting with obstacles. Computations under conditions of experiments with a triangular obstacle have been carried out on the base of 2D and 3D formulations. Action of the bottom wall friction leads to formation of one or two separation "bubbles", depending on the flow development phase, and to occurrence of associated hills at the free surface. Taking into account presence of the experimental channel side walls gives a solution with a considerably 3D shape of the computed free surface, and its side view much better agrees with the experimental photos than that given by 2D solutions. As well, local-in-time separation of the flow from the side walls is predicted with the 3D formulation.

ACKNOWLEDGEMENTS

The work was partially supported by the Russian Foundation of Basic Research (grant No. 14-07-00065).

REFERENCES

[1]. Soares-Frazao, S., 2007, "Experiments of dam-break wave over a triangular bottom sill", *J Hydraul Res*, Vol. 45, extra issue, pp. 19-26.

[2] Kocaman, S., Ozmen-Cagatay, H., 2012, "The effect of lateral channel contraction on dam break flows: Laboratory experiment", *J Hydrol*, Vol. 432-433, pp. 145-153.

[3] Ozmen-Cagatay, H., Kocaman, S., 2011, "Dam-break flow in the presence of obstacle:

experiment and CFD simulation", *Eng Appl Comp Fluid Mech*, Vol. 5, pp. 541-552.

[4] Ozmen-Cagatay, H., Kocaman, S., 2012, "Investigation of Dam-Break Flow Over Abruptly Contracting Channel With Trapezoidal-Shaped Lateral Obstacles", *ASME J. Fluids Eng*, Vol. 134, pp.081204-1-081204-7.

[5] Hu, C., Sueyoshi, M., 2010, "Numerical Simulation and Experiment on Dam Break Problem", *J Mar Sci Appl* Vol. 9, pp.109-114.

[6] Lobovsky, L., Botia-Vera, E., Castellana, F., Mas-Soler, J., Souto-Iglesias, A., 2014, "Experimental investigation of dynamic pressure loads during dam break" *J Fluids Struct*, Vol. 48, pp. 407-434.

[7] Liang, D., Falconer, R.A., Lin, B., 2006, "Comparison between TVD-MacCormack and ADI-type solvers of the shallow water equations", *Advances in Water Resources*, Vol. 29(12), pp. 1833-1845.

[8] Liang, Q, Borthwick, A.G.L., 2009, "Adaptive quadtree simulation of shallow flows with wet-dry fronts over complex topography", *Computers and Fluids*, Vol. 38(2), pp. 221-234.

[9] Bellos, V., Hrissanthou, V., 2011, "Numerical simulation of a dam-break flood wave", *European Water*, Vol. 33, pp. 45-53.

[10] Singh, J., Altinakar, M.S., Ding, Y., 2011, "Two-dimensional numerical modeling of dam-break flows over natural terrain using a central explicit scheme", *Advances in Water Resources*, Vol. 34, pp. 1366-1375.

[11] Biscarini, C., Di Francesco, S., Manciola, P., 2010, "CFD modelling approach for dam break flow studies", *Hydrology and Earth System Sciences*, Vol. 14, pp. 705-718.

[12] Park, I.R., Kim, K.S., Kim, J., Van, S.H., 2009. "A volume-of-fluid method for incompressible free surface flows". *Int J Numer Meth Fluids*, Vol. 61, pp. 1331–1362.

[13] Marsooli, R., Wu, W., 2014. "3-D finite-volume model of dam-break flow over uneven beds based on VOF method", *Advances in Water Resources*, Vol. 70, pp. 104-117.

[14] Hirt, C.W., Nichols, B.D., 1981, "Volume of fluid (VOF) method for the dynamics of free boundaries", *J Comp Phys*, Vol. 39, pp. 201-226.

[15] Muzaferija, S., Peric, M., Sames, P., Schelin, T., 1998, "A two-fluid Navier-Stokes solver to simulate water entry", Proc. *22 Symposium on Naval Hydrodyn.*, Washington DC, pp. 638-651.

[16] Ubbink, O., Issa, I., 1999, "A method for capturing sharp fluid interfaces on arbitrary meshes", *J Comput Phys*, Vol. 153, pp. 26-50.

[17] Waclawczyk, T., Koronowicz, T., 2008, "Remarks on prediction of wave drag using VOF method with interface capturing approach", *Arch Civ Mech Eng*, Vol. 8, pp. 5-14.

[18] Khrabry, A.I., Smirnov, E.M., Zaytsev, D.K., 2010, "Solving the Convective Transport Equation with Several High-Resolution Finite Volume Schemes: Test Computations", Proc. *International Conf. on Comput. Fluid Dyn. (ICCFD-6)*, St Petersburg, Russia, pp. 535-540.

[19] Menter, F.R., 1994, "Two equation eddy-viscosity turbulence models for engineering applications", *AIAA J*, Vol. 32. pp. 1598-1605.

[20] Ubbink, O., 1997, "Numerical predictions of two fluid systems with sharp interfaces", PhD Thesis, Imperial College, University of London.

[21] Khrabry, A.I., Smirnov, E.M., Zaytsev, D.K., "Free surface flow computations using the M-CICSAM scheme added with a sharpening procedure", Proc. *European Congr. on Comput. Methods in Applied Sciences and Engineering (ECCOMAS 2012)*, Vienna, Austria, CD-ROM, ISBN: 978-3-9502481-9-7, 2 p.

[22] Wemmenhove, R., 2008, "Numerical simulation of two-phase flow in offshore environments", *PhD thesis, University of Groningen*, 141 p.

[23] Hogg, P.W., Emerson, D.R., 2006, "An implicit algorithm for capturing sharp fluid interfaces in the volume of fluid advection method", *Technical Report* DL-TR-2006-001, 26 p.

Conference on Modelling Fluid Flow (CMFF'15)
The 16th International Conference on Fluid Flow Technologies
Budapest, Hungary, September 1-4, 2015

CFD SIMULATION OF A CONNECTED EXPANDER - COMPRESSOR SYSTEM

Péter FÜLE[1], Viktor SZENTE[2]

[1] Corresponding Author. Department of Fluid Mechanics, Budapest University of Technology and Economics. Bertalan Lajos u. 4 – 6, H-1111 Budapest, Hungary. Tel.: +36 1 463 2546, Fax: +36 1 463 3464, E-mail: fule@ara.bme.hu
[2] Department of Fluid Mechanics, Budapest University of Technology and Economics. E-mail: szente@ara.bme.hu

ABSTRACT

In the current study a connected expander – compressor system is investigated. The system is a novel development of such systems to extract mechanical energy from low enthalpy sources, e.g. thermal water, geothermal sources. The system consists of an expander in which warm air expands and flows toward a compressor stage. The connection between the devices has a heat exchanger, thus cooled air is introduced to the compressor. After compression the flow exits the compressor at around atmospheric conditions. During the investigation the Computational Fluid Dynamics (CFD) model of this system is built. The heat exchange in the connecting duct is modelled as an idealised heat exchanger with no pressure loss and perfect efficiency. The aim of the investigation is to find out the flow related parameters and efficiency of the whole connected system with the help of CFD simulations.

Keywords: CFD, low enthalpy heat source, rotary piston compressor, rotary piston expander, thermodynamic cycle

NOMENCLATURE

D_p	$[m]$	piston diameter
L	$[m]$	length
M	$[Nm]$	moment
P	$[W]$	power
Q	$[J]$	heat energy
R	$[J/kg/K]$	specific gas constant
S_h	$[W/m^3]$	energy source term
T	$[K]$	temperature
V	$[m^3]$	volume
c_p	$[J/kg/K]$	specific heat capacity
e_0	$[J]$	total energy
f_{rotor}	$[Hz]$	rotor frequency
k	$[m^2/s^2]$	turbulence kinetic energy
m	$[kg]$	mass
$\dot{m}$	$[kg/s]$	mass flux
p	$[Pa]$	pressure
q	$[W]$	heat flux
s_{out}	$[m]$	distance to heat exchanger outlet
t	$[s]$	time
u	$[m/s]$	velocity
x	$[m]$	coordinate
δ_{ij}	[-]	Kronecker delta
ε	$[m^2/s^3]$	turbulence dissipation rate
η	[-]	efficiency
ρ	$[kg/m^3]$	density
τ_{ij}	$[Pa]$	viscous stress tensor
ω_{rotor}	$[rad/s]$	rotor angular velocity

Subscripts and Superscripts

D	desired (temperature at compressor inlet)
c	channel
cell	value at computational cell
current	at current time step
he	heat exchanger
i,j	i-th or j-th component
mech	mechanical
tot	total value for whole system
*	non-dimensional quantity

1. INTRODUCTION

Rotary compressors are widely used in air conditioning systems, cooling systems, e.g. refrigerators [1, 2]. Some advantages of rotary compressors are compact size, low weight, reliability, silent operation, relatively high specific performance and low cost. However these advantages can only be achieved by careful design, optimisation and assembling. [3-5]

There are different ways to separate the low and high pressure chambers of a compressor. The two most common types are spring loaded vane and hinged vane separations. Schematic drawings of these types can be seen in Figure 1. The problem with the spring loaded type is that at high speeds of revolution the vane can separate from the piston surface due to high acceleration. This leads to temporary leakage and also wears down the components. This problem does not occur with hinged vanes, but the construction becomes more complex. [6]

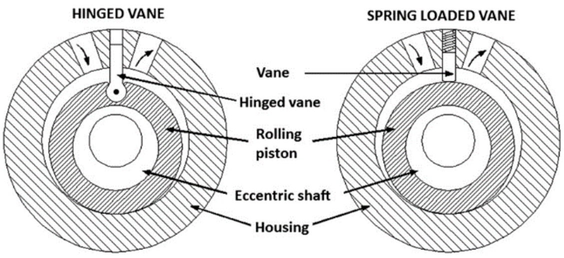

Figure 1. Schematic figure of spring loaded vane and hinged vane type compressors [6]

To avoid the problems mentioned with spring loaded vanes, more solutions are developed. For hinged vane separation there is another special way, when the housing of the compressor is also rotating. This solution is called revolving vane or synchronal rotating compressor. [7-9]

Another method is the sliding vane separation. In this case multiple vanes are mounted in the piston which rotates eccentrically in the housing or concentrically in an oval shaped housing. [10, 11]

Another special solution is the rotating spool compressor, which is similar to the sliding vane concept, but there is only one vane mounted across the whole cross section of the piston. [12, 13]

In the current study the compressor chambers are separated in a way, that the vane is connected mechanically to the driving shaft, this way the connection between the piston and the vane is always ensured. Another difference compared to conventional compressors is that the piston is not rolling along the surface of the compressor chamber's house, but it is solidly mounted on the driving shaft. [14, 15]

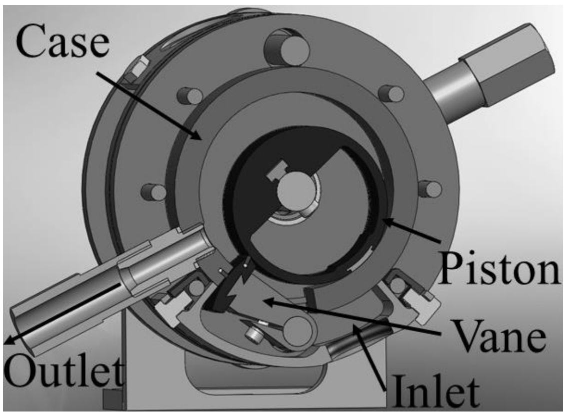

Figure 2. 3 dimensional model of the compressor [14]

Figure 2 shows the assembled model of the compressor showing the most important parts.

The study is focused on a connected system, where the formerly described compressor is connected after an expander (the operation of the compressor is reversed). The point of this concept is to build an inverse engine [14]. Figure 3 shows the schematic drawing of the connected system. The letters “E” and “C” mean expander and compressor respectively. “Q” and “q” describe heat exchange in “H” and “h” heat exchangers. V_f is the feeder valve of the expander and V_o is the outlet valve of the compressor.

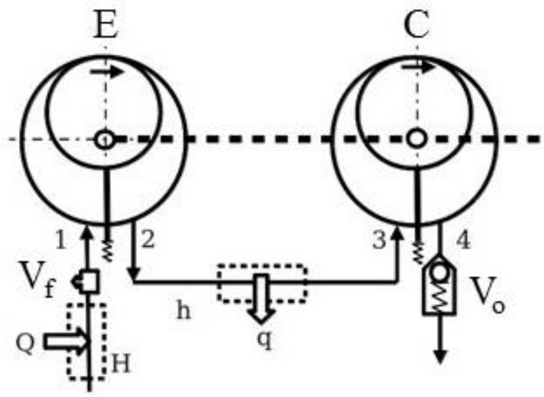

Figure 3. Schematic drawing of the connected expander – compressor system [14]

The expander and the compressor is connected through a heat exchanger which is modelled in the current study as an idealised heat sink.

The working principle is the following: hot air at atmospheric pressure, e.g. from geothermal sources, enters the expander through the feeder valve. As the air fills up the chamber of the expander it performs work on the driving shaft. After closing the feeder valve the air expands as the compressor starts the suction. After a revolution of the piston the air flows through the heat exchanger and it is cooled down to a desired temperature. After that the compressor compresses the cooled air to around atmospheric pressure before it exits to the atmosphere through the output valve. As the air loses heat in the heat exchanger its volume decreases compared to point 1 (assuming equal mass flow rate). Therefore it requires less work to push the air out of the compressor (volumetric and compression work) than the amount it introduced during intake and expansion. This way positive moment can be extracted on the shaft.

The pressure – volume diagram can be seen in Figure 4 and 5 showing the basic thermodynamic processes described above in the expander, exchanger and the compressor. In case of this example – just as for the simulations – the losses are neglected in the system. [14]

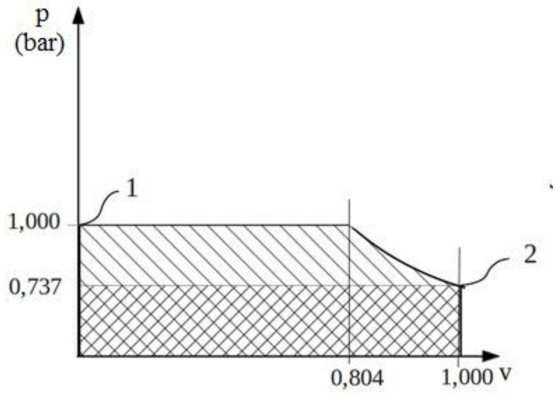

Figure 4. Pressure – volume diagram of expander. Volume is normalised by the maximum chamber volume. [14]

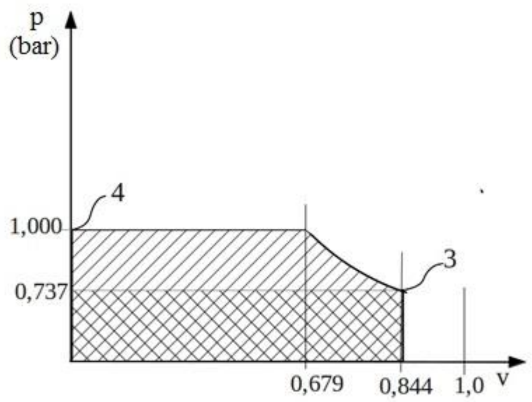

Figure 5. Pressure – volume diagram of compressor. Volume is normalised by the maximum chamber volume. [14]

The system is analysed in various operating states (different rotor frequencies and compressor inlet temperatures) with different connecting channel lengths. The different channel lengths are investigated to find out its impact on the results in order to use as few computational cells as possible. The main goal is to find out the efficiency of the system at various operating conditions.

2. METHODOLOGY

2.1. Governing equations

The simulations are done in ANSYS FLUENT version 14.5. In the simulations the flow is considered compressible and ideal gas law is used. Therefore the governing equations of the flow are the continuity and Navier-Stokes equations for compressible flows, the energy equation and the equation of state of ideal gases (Eqs. (1) to (4)).

$$\frac{\partial \rho}{\partial t} + \frac{\partial}{\partial x_\mathrm{i}}(\rho u_\mathrm{i}) = 0 \tag{1}$$

$$\frac{\partial(\rho u_\mathrm{i})}{\partial t} + \frac{\partial}{\partial x_\mathrm{j}}\left[\rho u_\mathrm{i} u_\mathrm{j} + p\delta_\mathrm{ij} - \tau_\mathrm{ij}\right] = 0 \tag{2}$$

$$\frac{\partial(\rho e_0)}{\partial t} + \frac{\partial}{\partial x_\mathrm{j}}\left[\rho u_\mathrm{j} e_0 + u_\mathrm{j} p + q_\mathrm{j} - u_\mathrm{i}\tau_\mathrm{ij}\right] = 0 \tag{3}$$

$$p = \rho R T \tag{4}$$

The turbulence is modelled by the realizable $k-\varepsilon$ model [16] with enhanced wall treatment.

2.2. Modelling the heat exchanger

One of the goals of the investigation is to model the heat exchanger in the connecting channel between the expander and the compressor. The real life system has a long section of heat exchanger with a relatively complex geometry which would be a long time to model and would take up too many computational cells, thus increasing the computational costs. Therefore simplification of the heat exchanger is needed.

The geometry is simplified to a single channel connecting the expander and the compressor. The geometry can be seen in Figure 6.

This channel has a zone in it, which acts like a heat sink by introducing negative source term into the energy equation. The heat exchanger's fluid dynamic and other losses are neglected, no pressure loss is induced in the current model, but in later models it will be taken into account. The value of the needed source term is computed according to Eqs. (5) to (8) via FLUENT user defined function (UDF). The UDF loops over all cells in the selected zone and calculates the source term value for every cell.

$$Q = c_p m (T_\mathrm{D} - T_\mathrm{cell}) \tag{5}$$

$$t_\mathrm{current} = \frac{s_\mathrm{out}}{u_\mathrm{cell}} \tag{6}$$

$$P = \frac{Q}{t_\mathrm{current}} \tag{7}$$

$$S_\mathrm{h} = \frac{P}{V_\mathrm{cell}} \tag{8}$$

The calculations are based on simple thermodynamic relations. Eq. (5) describes the needed heat energy for a given mass of fluid to achieve the desired temperature, T_D. The mass is computed by the instantaneous density at the current time and the volume of the computational cell. The time needed is approximated by the x component of the velocity at the current time and the length in x direction to the end of the heat exchanger zone (Eq.

(6)). The cooling (or heating) power is then computed according to Eq. (7). The value of the source term needs to be normalized to unit volume $[W/m^3]$, thus applying Eq. (8) in the end.

It can be seen, that the sign of the source term value depends on the direction of the *x* component of the velocity. To avoid undesirable positive source term values, i.e. heating, for cells with backward flow, the source term value is set to zero for these cells until the *x* velocity becomes positive again.

2.3. Geometry and numerical mesh

The geometry of the connected system can be seen in Figure 6. The compressor is upside down to make the connecting channel as simple as possible. The single straight channel is the least disturbing to the flow and the simplest way to connect the expander and compressor. The results are not influenced by this placement of the compressor, because gravity is not taken into consideration.

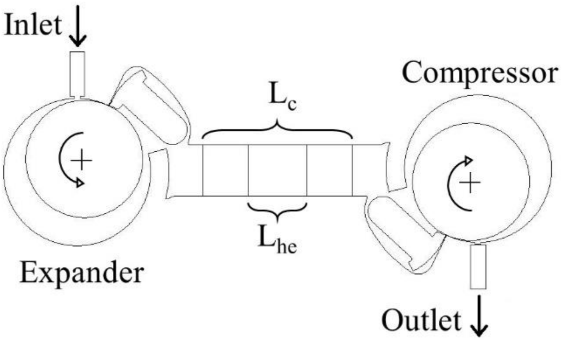

Figure 6. Geometry of the connected system. The channel length is measured from the expander outlet to the compressor inlet.

A non-dimensional channel length, L_c^*, is introduced. It is made non-dimensional by the piston diameter, as seen in Eq. (9).

$$L_c^* = \frac{L_c}{D_p} \tag{9}$$

Three channel lengths are investigated, the base length is $L_c^* = 1.27$, the other two lengths are $L_c^* = 2.54$ and $L_c^* = 3.81$.

The numerical meshes initially contain around 30 000 computational cells depending on the channel length, but this varies as re-meshing is utilized. The pistons are rotating during the simulations and the vanes are also moving with the pistons, thus deforming mesh and re-meshing is used in these zones. These zones are meshed with triangular elements. The non-deforming zones are meshed with quadratic elements. There is a check valve modelled at the outlet section of the compressor. The zone where the valve can move is meshed also with quadratic elements and mesh layering is used. Figure 7 shows the close vicinity of the valve. The two walls which represent the valve can move up and down opening or closing the outlet section. The outlet section is connected to the valve section with mesh interfaces.

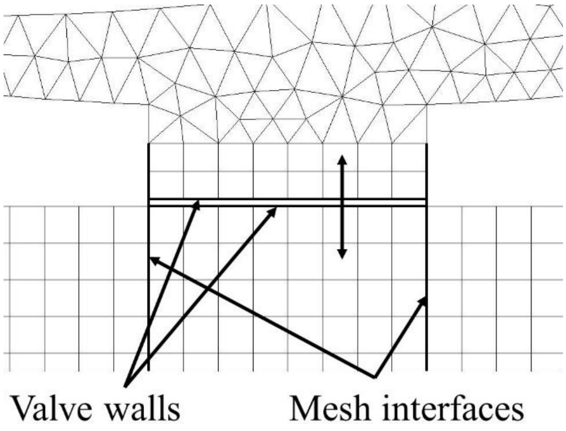

Figure 7. Compressor outlet valve model with the numerical mesh in its vicinity. Triangular cells belong to the compressor's dynamic zone.

In Fig. 7 a part of the triangular mesh of the compressor's dynamic zone can also be seen. The valve walls are moving up and down and the layering process makes sure to insert or collapse cells based on cell size ratios.

2.4. Simulated operating points

Table 1 shows the simulated operating condition values.

Table 1. Simulated operating points

f_{rotor} $[Hz]$	L_c^* [-]	T_D $[K]$
20, 30, 50	1.27, 2.54, 3.81	275
20, 30, 50	1.27	293, 303

The impact of the channel length is investigated with $T_D = 275$ $[K]$ and for all the rotor frequencies. Further simulations are carried out only with the shortest channel length, this decision is explained in section 3.1.

The inlet and outlet pressures are set to atmospheric pressure. The inlet temperature is set to 353 $[K]$, the outlet ambient temperature is set to 300 $[K]$.

3. RESULTS

In this section the results are shown from different aspects. First the impact of the channel length is discussed, then the heat exchanger model is analysed and finally the efficiencies are shown.

3.1. Channel length

Table 2 shows the difference in the mean mass flow rate at the inlet between the base channel length and the two longer channels.

Table 2. Inlet mean mass flow rate differences

		L_c^* [−]	
		2.54	**3.81**
$f_{rotor}[Hz]$	**20**	0.8%	3.3%
	30	2.1%	1.8%
	50	2.4%	0.2%

It can be seen that the length of the channel does not influence the inlet mass flow rate significantly. In Table 3 the differences of the total mean moment can be seen. The total mean moment is calculated by summing the mean moment of the expander and the compressor.

Table 3. Total mean moment differences

		L_c^* [−]	
		2.54	**3.81**
$f_{rotor}[Hz]$	**20**	3.1%	5.4%
	30	10.7%	2%
	50	11.8%	4.8%

These differences are somewhat higher than the inlet mean mass flow rate differences, but looking at Figures 8 to 9 it can be said, that the differences are in an acceptable range to say that they do not influence the main trends significantly. Therefore it is sufficient to investigate the further cases with only the shortest channel length saving computational time. Figures 8 to 9 show the inlet mass flow rate and compressor moment for 50 [*Hz*] frequency and the last two simulated revolutions. Aside from the initial transients, the differences in the results are close to within line width, especially for the inlet mean mass flow rate. The characteristics are similar to these on the other two rotor frequencies as Tables 2 to 3 suggest.

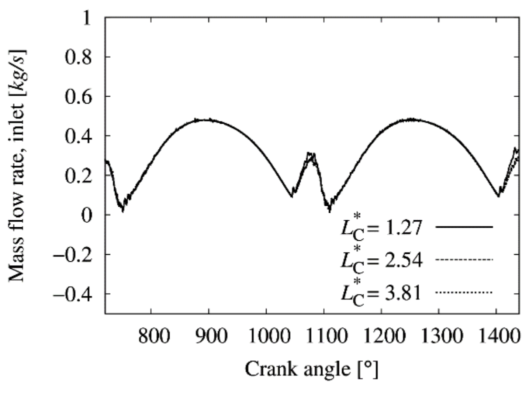

Figure 8. Inlet mass flow rate for the second two revolutions, $f_{rotor} = 50\ [Hz]$

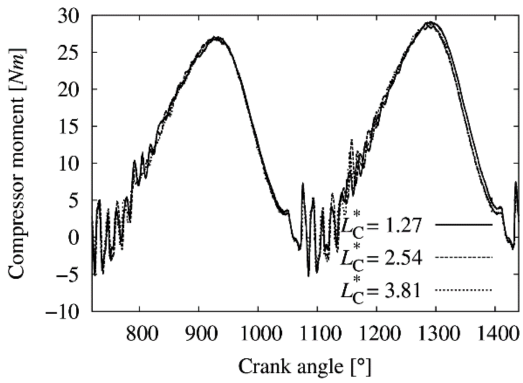

Figure 9. Compressor moment for the second two revolutions, $f_{rotor} = 50\ [Hz]$

Also a mesh dependency investigation is carried out with the chosen shortest channel length. The mesh of the compressor and expander is not changed as they are dense enough – based on former experiences [17] – and it would slow down the simulations very significantly, but the mesh of the channel is halved and doubled compared to the base, which has been used before. The mass flow rate and temperature is monitored at the compressor inlet after the channel. These two quantities are important in terms of the heat flux and also can affect the mechanical power - and therefore the efficiency - in the compressor, thus they are chosen for the comparison. The differences compared to the base meshes can be seen in Tables 4 and 5.

Table 4. Mean mass flow rate difference at compressor inlet

		Mesh density	
		half	**double**
$f_{rotor}[Hz]$	**20**	0.1%	2.7%
	30	3.0%	4.9%
	50	0.8%	0.5%

Table 5. Mean temperature difference at compressor inlet

		Mesh density	
		half	**double**
$f_{rotor}[Hz]$	**20**	0.8%	1.3%
	30	0.6%	0.4%
	50	0.1%	0.1%

It can be seen, that the base mesh is appropriate for the preliminary investigations of the system, the differences are under 5% for every case.

3.2. Heat exchanger

The heat exchanger is used in this study to cool the air to a desired temperature before it enters into the compressor. In this study three desired temperature values are tested, namely 275 [*K*], 293

[K] and 303 [K]. Figures 10 to 12 show the temperature at the compressor inlet for all three frequencies.

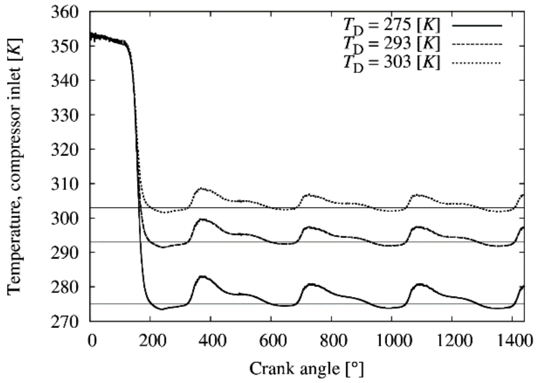

Figure 10. Compressor inlet temperatures for the first four piston revolutions, $f_{\text{rotor}} = 20\ [Hz]$

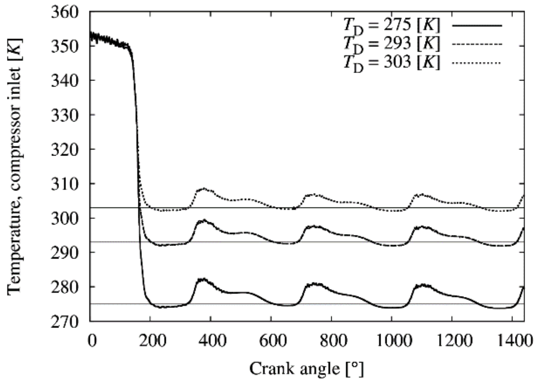

Figure 11. Compressor inlet temperatures for the first four piston revolutions, $f_{\text{rotor}} = 30\ [Hz]$

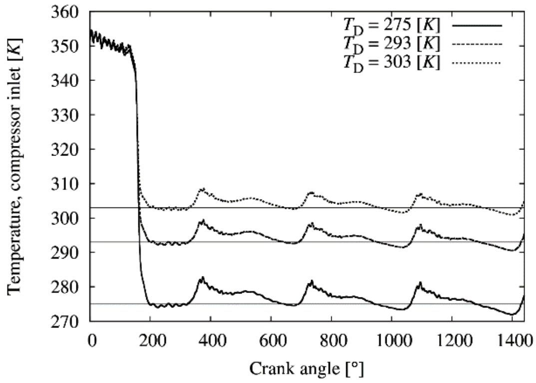

Figure 12. Compressor inlet temperatures for the first four piston revolutions, $f_{\text{rotor}} = 50\ [Hz]$

It can be seen, that the heat exchanger model is not able to hold a constant temperature but the results are acceptable, the temperatures alternate around the desired values within an acceptable interval, thus the model can be used for the preliminary studies.

3.3. Efficiency

The efficiency is calculated by mechanical energy and total heat flux. Mechanical energy comes from the total moment of the expander and compressor and the angular velocity (Eq. (10)).

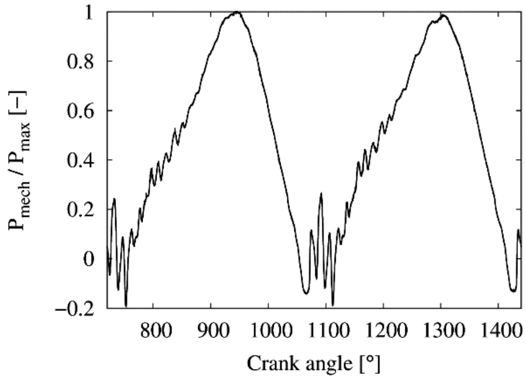

Figure 13. Total power output of expander and compressor, last two simulated revolutions, $f_{rotor} = 50\ [Hz]$

In Figure 13 the total power output of the expander and compressor can be seen normalised by the maximum value of the output.

Heat flux is calculated for the expander, heat exchanger and compressor and then it is summed (Eq. (11)). In Figure 14 the heat flux of the heat exchanger can be seen. It is also normalised by its maximum value.

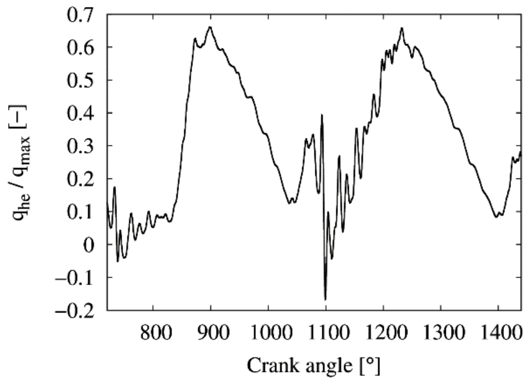

Figure 14. Heat flux of the heat exchanger, last two simulated revolutions, $f_{rotor} = 50\ [Hz]$

$$P_{\text{mech}} = M_{\text{tot}}\omega_{\text{rotor}} \tag{10}$$

$$q = c_p\dot{m}\Delta T \tag{11}$$

The ratio of these quantities gives the efficiency of the system (Eq. (12)). First a mean value is calculated for the mechanical power and the heat fluxes, then the ratio can be calculated.

$$\eta = \frac{P_{\mathrm{mech}}}{q_{\mathrm{tot}}} \tag{12}$$

Table 6 shows the calculated efficiencies for the various frequencies and compressor inlet temperatures.

Table 6. Efficiency for various operation points

		$T_{\mathrm{D}}[K]$		
		275	**293**	**303**
$f_{\mathrm{rotor}}[Hz]$	**20**	7%	6.9%	5.2%
	30	9.9%	9.1%	7.7%
	50	19.5%	16.7%	15.8%

It can be seen, that the efficiency is increasing with increasing the rotor frequency and for lower compressor inlet temperatures. From 5.2% the efficiency can go up to almost 20% by increasing the frequency from 20 to 50 [*Hz*] and cooling the compressor inlet air to around 275 [*K*] instead of 303 [*K*]. Referring to [14], where preliminary theoretical calculations can be found for the inverse motor, the obtained efficiency values seem realistic. However these results are obtained by neglecting the heat exchanger's fluid dynamic and other losses and also the losses of the expander and compressor (e.g. leakage losses). By taking this into consideration, the efficiency values will decrease, especially at higher rotor frequencies. The results are to be compared to measurement data in the future.

4. SUMMARY

CFD simulation of a connected expander – compressor system was carried out for various operation points. The system is intended to be used as an inverse motor, extracting energy from low enthalpy heat sources. This work was a preliminary study to identify the effects of certain system characteristics with help of CFD simulations. During the work an idealised heat exchanger was modelled and tested with different temperatures and connecting channel lengths. The simulations showed that the channel length was not impacting the results significantly, thus the shortest channel was sufficient to use, therefore lowering computational costs. The efficiency depending on the operation point parameters was around 5% to 20%. The validation with measurement data and further development of the model is subject of future studies.

ACKNOWLEDGEMENTS

This research has been supported by the New Széchenyi Plan under contract No. KMR_12-1-2012-0199.

REFERENCES

[1] Ooi, K. T., Wong, T., 1997, "A computer simulation of a rotary compressor for household refrigerators", *Applied Thermal Engineering*, Vol. 17, No. 1, pp. 65-78.

[2] Ooi, K. T., 2005, "Design optimization of a rolling piston compressor for refrigerators", *Applied Thermal Engineering*, Vol. 25, No. 5-6, pp. 813-829.

[3] Yanagisawa, T., Shimizu, T., 1985, "Leakage losses with a rolling piston type rotary compressor. I. Radial clearance on the rolling piston", *International Journal of Refrigeration*, Vol. 8, No. 2, pp. 75-84.

[4] Yanagisawa, T., Shimizu, T., 1985, "Leakage losses with a rolling piston type rotary compressor. II. Leakage losses through clearances on rolling piston faces", *International Journal of Refrigeration*, Vol. 8, No. 3, pp. 152-158.

[5] Yanagisawa, T., Shimizu, T., 1985, "Leakage losses with a rolling piston type rotary compressor. III", *International Journal of Refrigeration*, Vol. 8, No. 3, pp. 159-165.

[6] Okur, M., Akmandor, I. S., 2011, "Experimental investigation of hinged and spring loaded rolling piston compressors pertaining to a turbo rotary engine", *Applied Thermal Engineering*, Vol. 31, pp. 1031-1038.

[7] The, Y., Ooi, K. T., 2009, "Experimental study of the Revolving Vane (RV) compressor", *Applied Thermal Engineering*, Vol. 29, pp. 3235-3245.

[8] Yang, H., Qu, Z., Zhou, H., Yu, B., 2011, "Study on leakage via the radial clearance in a novel synchronal rotary refrigeration compressor", *International Journal of Refrigeration*, Vol. 34, No. 1, pp. 84-93.

[9] Tan, K. M., Ooi, K. T., 2011, "Heat transfer in compression chamber of a revolving vane (RV) compressor", *Applied Thermal Engineering*, Vol. 31, pp. 1519-1526.

[10] Bianchi, G., Cipollone, R., 2015, "Theoretical modelling and experimental investigations for the improvement of the mechanical efficiency in sliding vane rotary compressors", *Applied Energy*, Vol. 142, pp. 95-107.

[11] Al-Hawaj, O., "Theoretical modeling of sliding vane compressor with leakage", 2009, *International Journal of Refrigeration*, Vol. 32, pp. 1555-1562.

[12] Kemp, G., Garrett, N., Groll, E., 2008, "Novel Rotary Spool Compressor Design and Preliminary Prototype Performance", *Proceeddings of the International Compressor Engineering Conference*, Purdue University, West Lafayette, IN USA, No. 1328

[13]Kemp, G., Elwood, L., Groll, E., 2010, "Evaluation of a Prototype Rotating Spool Compressor in Liquid Flooded Operation", *Proceeddings of the International Compressor Engineering Conference*, Purdue University, West Lafayette, IN USA, No. 1389

[14]Magai, I., 2014, "http://magaimotor.magai.eu/"

[15]Farkas, B., 2014, "CFD simulation of a new type rolling piston compressor designed for heat pumps", *GÉP*, Vol. 65, No. 5, pp. 37-40.

[16]Shih, T.-H., Liou, W. W., Shabbir, A., Yang, Z., Zhu, J., 1994, "A New $k-\varepsilon$ Eddy Viscosity Model for High Reynolds Number Turbulent Flows – Model Development and Validation", NASA Technical Memorandum

[17]Farkas, B., Szente, V., Suda, J. M., 2015, "A Simplified Modeling Approach for Rolling Piston Compressors", *Period. Polytech. Mech. Eng.*, Vol. 59, No. 2, pp. 94-101.

Conference on Modelling Fluid Flow (CMFF'15)
The 16th International Conference on Fluid Flow Technologies
Budapest, Hungary, September 1-4, 2015

ASSESSING THE ACCURACY OF THE NUMERICAL PREDICTION OF AIR ENTRAINMENT INTO PUMP SUMP

Raja ABOU ACKL[1], Andreas SWIENTY[1], Paul Uwe THAMSEN[1]

[1] Corresponding Author. Department of Fluid Mechanics, Berlin Institute of Technology. Straße des 17. Juni 135, 10623 Berlin, Germany. Tel.: +49 -314 79741, Fax: +49 314 21472, E-mail: raja.abouackl@fsd.tu-berlin.de

ABSTRACT

In this study the qualitative prediction of the air entrainment into a wet pit pumping station by means of numerical simulation was assessed. The research was based on the use of physical and numerical models to reproduce the flow conditions inside the wet pit as well as the air entrainment to the pump. In this context experiments were conducted on a model of a circular wet pit pumping station. The air entrainment was evaluated by measuring the depth, the width and the length of the bubbled region caused by a plunging water jet and by observing the air bubbles in the outlet pipe of the pump. Furthermore the same experiments were reproduced by numerical simulations using the VOF multiphase model to simulate the interaction of the liquid water phase and the gaseous air phase.
The results of the experiments and the numerical simulations were compared in order to assess the accuracy of the numerical results. It was found that the numerical simulation yields results that match the experimental observations very well.

Keywords: Air entrainment, CFD, pumping station, wet pit.

NOMENCLATURE

$\mathbf{g}$	acceleration of gravity, m s²
$\mathbf{F}$	force, N
Fr	Froude number
k	turbulent kinetic energy, m^2 s^{-2}
L	characteristic length, m
T	temperature
$\mathbf{u}$	velocity, ms−1
V	characteristic velocity, m s−1
VOF	Volume of Fluid

Greek letters

α_A	Volume fraction of air
α_W	volume fraction of water
ε	turbulent energy dissipation rate, m^2 s^{-3}
ρ	density of the fluid, kg m^{-3}
μ	dynamic viscosity kg m^{-1} s^{-1}

Subscripts

A	Air
avg	average
W	Water

1. INTRODUCTION

The circular wet pit design is one of the simplest design of pumping stations and the most popular one due to its relative simple construction techniques and smaller footprint for a given sump volume [1]. In this case the submersible pumps are located directly in the wastewater collection pit. Therefore it is important that the individual components do not affect each other. Special attention shall be paid by positioning the inlets in the pumping station, in order to assure good working conditions for the pumps and avoid air entrainment to them.
The aim of this article is to evaluate a numerical simulation method predicting the air entrainment to the pump in order to be used during the pumping station design phase or during the improvement of already existing ones.

2. AIR ENTRAINMENT IN WET PIT PUMPING STATIONS

Due to the 'intermittently' working conditions of the wet pit pumping stations the height between the inlet pipe and the free liquid surface in the pit changes constantly. Which means that the waste water forms a free jet falling on to the sump waste water surface (Fig.1). Depending on the velocity and the height of the falling jet air bubbles may be entrained beneath the surface by the plunging jet, [2-4].

The air entrainment by a plunging jet takes place when the jet impact velocity exceeds a critical value, which is a function of the inflow conditions, [2, and 3]. The maximum penetration depth of the air bubbles depends on many parameters such as the impact diameter of the jet, the velocity at the water surface, the jet instability and the free surface deformation [4-6]. Entrained air caused by an impacting jet has an influence on the liquid flow field and on the debris transport in the sump [5].

Moreover the performance of the pump will be affected if this depth is big enough and the flow conditions are suitable to let the air bubbles enter it. In general, centrifugal pumps can pump water with up to 5-10% gas content [7]. Yet, lower amounts of gas already influence the pumping system operation, changing the power consumption and hydraulic head reducing the efficiency of the system. Furthermore vibrations could arise which would damage the bearings. Thus, air entrainment of all amounts should be avoided and be considered during the design process.

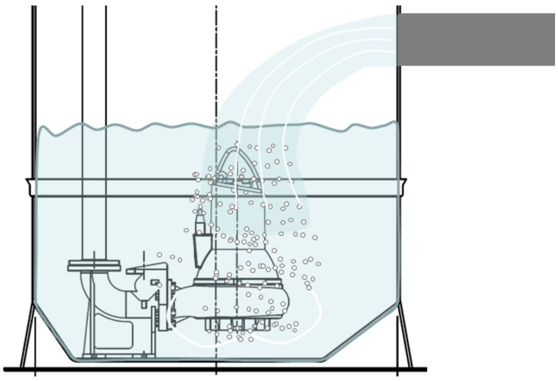

Figure 1. Air entrainment in wet well pumping station

Many researches tried to analyse the mechanism of air entrainment and the penetration depth of a plunging jet, for example [6] [16-18]. However most of the studies are based on experimental investigations for jets from nozzles falling into a receiving reservoir or for a velocity that is not applicable in the waste water system. Moreover the flow inside the pump sumps is irregular and very complicated with three dimensional patterns, due to the flow induced by the suction effect of the working pumps, in addition to the interaction between the ‘tight’ space and the flow conditions in the sump.

Thus the conclusions and the formulas derived from these studies are not, or at least partly, applicable in the case of an impinging jet into a wet pit pumping station.

3. METHODOLOGY

The ability to predict the flow conditions and the air entrainment in the sump is very important during the design process in order to improve the design and avoid the air entrainment to the pump. The physical laboratory study is a precious tool that helps to describe hydraulic phenomenon and predict very complicated flow conditions. However it is common to use a scaled physical model in the laboratory due to economical and space demands.

Due to hygienic reasons water is used to imitate the waste water in this stage of research.

3.1 The scale effect

A physical model is a geometrically reduced or sometimes enlarged reproduction of a real-world prototype [12], and is used as research tool for finding the technically and economically optimal solution of engineering problems [9]. In free-surface flows, which this case is, gravity plays an important role and thus Froude similitude should be used in order to fulfil the geometric similarity of the water surface [9]. This similarity means that the Froude number, as shown in Eq. (1), is kept identical both in the model and the prototype.

$$\mathrm{Fr} = (\text{inertial force/gravity force})^{0.5} = \frac{V}{(gL)^{0.5}} \tag{1}$$

The entrainment of air bubbles by a plunging jet is governed by the surface tension and the flow turbulence, implying the use of Weber similitude and Reynolds similarity respectively. Thus the air entrainment in the small model based upon Froude similitude could be affected, due the underestimating of the flow turbulence and the overestimating of the surface tension. There are many countermeasures to minimize scale effects in Froude models such as the calibration, the replacement of fluid, the using of scale series and the use of limiting criteria concerning the force ratios [9, 11].

On the contrary the numerical models represent the real problem with no need of scaling. Hereof the idea arises to use the numerical simulation to predict the air entrainment in such complicated situations. But on the other hand the simplifications in the numerical solution lead to some deviations between the model and the prototype. Therefore there is a need to calibrate and assess the accuracy of the numerical simulation with experimental investigations.

3.2 Qualitative evaluation of the air entrainment

After Bin [6] the bubbles resulting from plunging liquid jet will dispersed beneath the liquid surface and form two regions classified according to the size of the bubbles:

- The biphasic conical region containing bubbles that reach maximum depth where the buoyancy forces balance the momentum of the jet.
- The region of bigger rising bubbles

The predicting of the bubble size is difficult. In addition the accurate calculation and the measuring of the air flow rate that enters the water is very complicated. However as already mentioned above, air entrainment of all amounts should be avoided, and consequently it is irrelevant to measure and find the exact amount of air entrained to the sump but rather to find the operation and flow conditions that led to air entrainment into the pump.

In this research two methods are used to evaluate the air entrainment in the pumping station.

1. Measuring the dimension of the bubble cloud (Fig.2) i.e. the region occupied with the bubbles, which represents a qualitative evaluation of the air entrainment in the sump
2. Observing the air bubbles in the outlet pipe of the pump. This gives an indicator of the air entrainment to the pump, which is the most important one.

In this sense a physical model that fulfils the demands of these methods is designed.

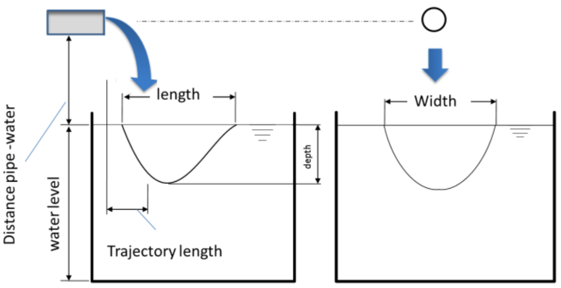

Figure 2. Sketch of the 'entrained bubble cloud'

3.3 The physical test model.

The physical model is designed upon Froude similarity. The scale 1:3.2 is chosen to simulate a typical market standard sump of a 1600 mm diameter with a standard acrylic cylinder of 500 mm. The height of the model is 750 mm and the inflow pipes are mounted at a height of 450 mm above the bottom of the tank, reproducing the height of 1440 mm in original full-scale design.

A simplified model has been used to represent the most important features of the duplex circular wet pit pumping station. The Representative Model consists of: coupling systems, guide bars, pressure pipe and dummy pumps. The need of reference geometry implies the use of a simple tank with flat floor, called the 'baseline geometry'. The inflow direction relatively to the pumps centreline position as well as the water level can be changed in the model (Fig. 3).

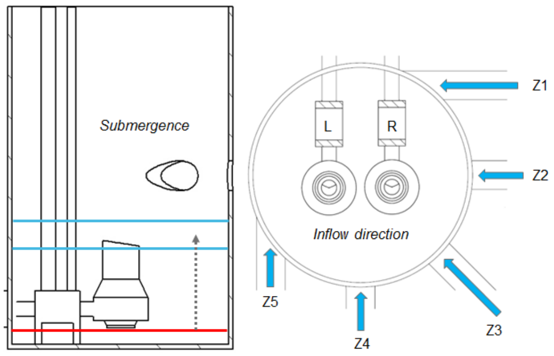

Figure 3. The adaptable parameters of the model

The implemented test rig of the physical model is made of acrylic (Fig. 4) to enable the observation of the aerated region inside the sump and the bubbles entering the dummy pump at various operating conditions. It is possible to conduct the experiments in two working conditions:

1. Varied water level to reproduce pumping cycles.
2. Constant water level to enable the conduction of the test for long time constant inflow.

Figure 4. Test stand

3.4 The numerical test model.

There are many numerical simulation studies concerning the air entrainment, for example [4] presents 2D simulation results of round vertical liquid jet plunging into bath with focus on bubbles size and the influence of the jet velocity using smoothed volume of flow technique. [20] studied the formation of the air cavities generated by translating plunging jet into pool, whereas [5] researched the influence of the air entrainment on fibber transportation in the sump.

In our study the Volume of Fluid (VOF) method was used to simulate the air entrainment and the air bubbles formation. The water and the air are assumed to be incompressible and Newtonian fluids. In this method a phase q_A of the multiphase fluid consisting of the phases q_W (water) and q_A (air) is described by its volume fraction (α_A) in a computational cell. For α_A the following three states apply:

$\alpha_A = 0$, the cell is empty of the q_A phase,
$\alpha_A = 1$, the cell is full of the q_A phase,
$0 < \alpha_A < 1$, the cell contains the interface between the q_W and the q_A phase.

In the absence of sources of mass and momentum, the continuity equation for the volume fraction of the phase q_A is written as

$$\frac{\partial}{\partial t}\left(\alpha_q \rho_A\right) + \nabla\left(\alpha_q \rho_A \boldsymbol{u}\right) = 0. \quad (2)$$

Thereupon the q_W phase volume fraction is computed from the relation: $\alpha_W + \alpha_A = 1$. The momentum equation depends on the volume fractions of the phases through the properties ρ and μ.

$$\frac{\partial(\rho \boldsymbol{u})}{\partial t} + \nabla(\rho \boldsymbol{u}\boldsymbol{u}) = -\nabla p + \nabla[\mu(\nabla \boldsymbol{u} + \nabla \boldsymbol{u}^T)] + \rho \boldsymbol{g} + \boldsymbol{F} \quad (3)$$

In this equation **u** is the velocity vector, ρ is the density, p is the pressure, **g** is acceleration of gravity and **F** is the equivalent volume force due to the surface tension. When modelling the free

A transport equation is solved for the water phase to model the surface between water and air in the absence of any inter-phase mass transfer

$$\frac{\partial}{\partial t}(\alpha_w) + \nabla(\alpha_w u) = 0. \quad (4)$$

In this two-phase system the volume fraction of the air phase is being tracked, the density in each cell is given by

$$\rho = \alpha_A \rho_A + (1 - \alpha_A)\rho_W \,. \quad (5)$$

The viscosity μ is computed in the same manner:

$$\mu = \alpha_A \mu_A + (1 - \alpha_A)\mu_W \,. \quad (6)$$

Furthermore k-e turbulence model were used with wall functions.

3.4.1 Computational domain and boundary conditions.

Unsteady CFD calculations applying the CFD code ANSYS/Fluent were performed. Figure 5 shows the 3D computational domain. It is discretised into 4.9 10^6 tetrahedral cells with max 3mm length in each direction , and partitioned into 14 subdomains, every domain calculated with one processors. The assessment of the independence of the results on the computational grid was checked by further calculations applying a finer grid to capture the smallest air bubbles, and the suitable mesh where selected, not presented here.

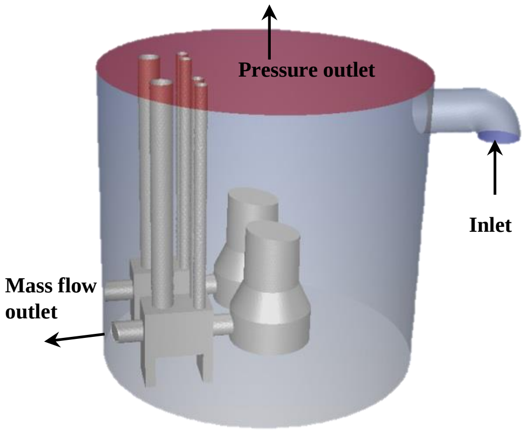

Figure 5. Numerical setup

The calculations were made with the densities and viscosities of air and water at 15°C. The simulations were performed with a water-air surface tension set at 0.073 N/m. The PISO algorithm was used for pressure–velocity coupling. The interface between fluids was represented with Geometric Reconstruction Scheme. At the inlet, a velocity profile is specified for the velocity. The open top of the pit has a pressure outlet boundary condition, and the outlet of the simulation geometry has a mass flow boundary condition. With this combination the water level in the pit remains constant. Computations were continued till the global residuals reached 10^{-5}. During the unsteady calculation an adaptive time-stepping method was used to ensure a Courant-Friedrichs-Levy number less than 1. At the initial time, the domain is filled up to a certain level with water. The remaining region consists of air.

4. RESULTS AND COMPARISON

The experimental investigations were systemically conducted by choosing an inflow direction and carrying out the experiments at various water levels and flow rates. During every experiment the bubbles zone was monitored using video recording, moreover the acrylic outlet pipes of the dummy pumps were observed for air bubbles (Fig. 6). Depending on the records the depth, the width and the length of the cloud were determined.

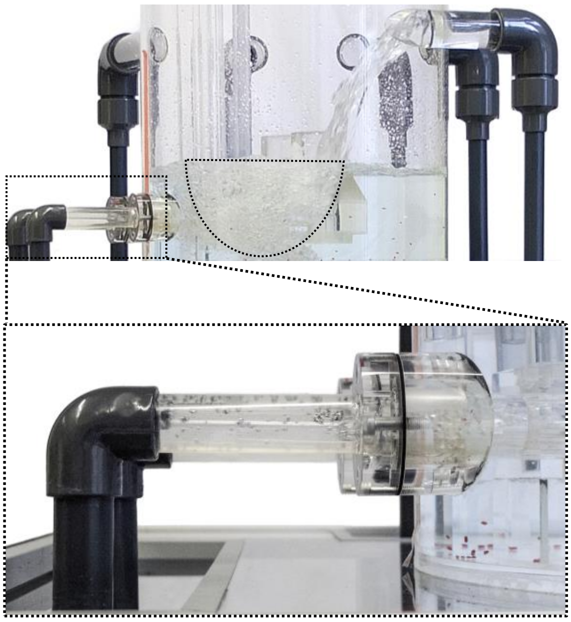

Figure 6. Bubble cloud and the air entrainment to the pump

A series of computations were started with boundary conditions that represent the experimental flow conditions. The simulated time was 30 s. After that a video was generated and the same procedure of the experimental investigation was applied concerning the dimensions of the bubbled region (Fig. 7).

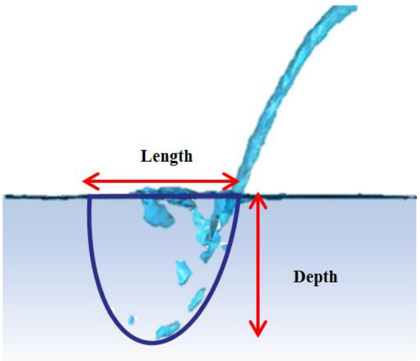

Figure 7. Measured variables of the air entrainment

The air entrainment to the pump was analysed by checking the appearance of the air phase using a control surface positioned on the suction side of the pump.
The number of the executed experimental test series was very large, as a result of the diversity of the working combinations for five chosen water levels (Fig. 8).

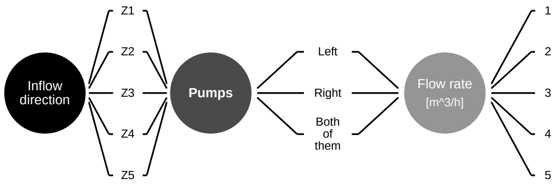

Figure 8. Possible working combinations

Thus only 8 cases were simulated in the numerical model, namely the inflow direction Z2 at two water level and four flow rates as shown in the table 1

Table 1. Summary of the numerical cases

Water level [m]	0.2	0.32
Flow Rate [m³/ h]	1 2 3 4	1 2 3 4

Both experimental and numerical results are presented. The experimental observations were used to validate the simulation results regarding the dimensions of the bubbles cloud and the (yes/no) indicator of the air entrainment to the pump

4.1 Dimensions of the bubbles cloud.

From Fig. 9, it can be seen that the simulation results and the experimental values are relatively in good agreement. The behaviour is captured and the results reveal that the model and the interface tracking are able to capture the bubble cloud generated from an impinging jet.

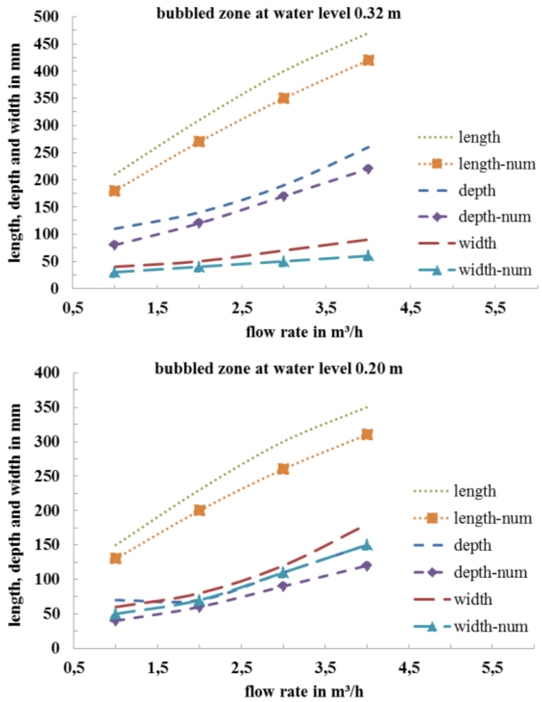

Figure 9. Experimental and numerical dimensions of the bubbles cloud

The results show that the numerical model underestimates the phenomena. The deviation can be explained by the uncertainties of the numerical model and the inaccuracy of the measurements in the experimental setup.
At the inlet the turbulence is neglected which means that the jet instability and the free surface deformation are not sufficiently reproduced. The air entrainment is highly affected by the turbulence in the jet and the free surface of the receiving pool.
Furthermore the measurements of the flow rate, the dimensions of the bubble zone as well as the water level contain some inaccuracy, leading to a mismatch between the boundary conditions in both setups and to deviations in the results.

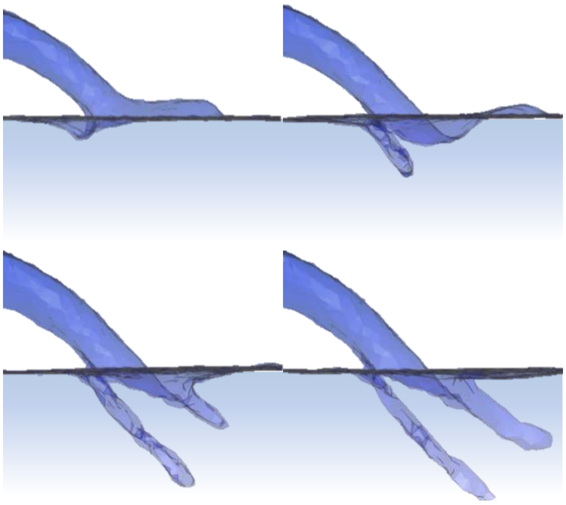

Figure 10. Cavities development from the impinging jet (32cm water level and for 2 m^3/h flowrate)

The Fig. 10 shows that an air cavity develops as the water jet penetrates the water and surrounds its surface. This mechanism should be evaluated in the next step of the researches using high speed video monitoring.

4.2 Air entrainment to the pump

The air entrainment to the pump depends on the balance of various forces that act on the bubbles depending on their volume, namely the buoyancy forces, the momentum of the moving bubbles and the effect of the flow induced from the working pump. Considering the difficulty to capture all the small bubbles, the dimensions of the bubble cloud are underestimated. In this sense it can be justified that the numerical model succeeded to predict the air entrainment to the pump in 5 of the 8 cases.
However the calculations of the rest of the cases are planned, which will give a better indicator on the accurate of the numerical simulation.

5. SUMMARY

The presented paper described the research of experimental and simulation investigations to assess the numerical simulation accuracy of modelling a plunging water jet on a free surface of a wet pit pumping station. The three-dimensional numerical model was applied to reproduce the experimental setup to predict the air entrainment and the flow characteristics at several flow conditions. The air entrainment was qualitatively evaluated by defining the dimensions of the bubbles cloud and observing the air bubbles entering the suction side of the pump. The numerical VOF model proved to give relatively acceptable results compared to the experimental data. The dimensions of the cloud in the numerical approach had the same behaviour of the experimental model, but with some underestimations. Assessing the use of CFD as tool in the scale series is planned as future works to define the scale effect on the air entrainment and evaluate the transferability of the model results to the original prototype.

REFERENCES

[1] American National Standards Institute ANSI/HI 9.8, 2012, American National Standard for Pump Intake Design.

[2] Zhu, Y., Oguz H. N., & Prosperetti A., 2000. “On the mechanism of air entrainment by liquid jets at a free surface”, *Journel of Fluid Mech.. Vol .401*, p.151-177.

[3] Kiger K. T., Duncan J. H., 2011 “Air-Entrainment Mechanisms in Plunging Jets and Breaking Waves” *Annual Review of Fluid Mechanics* Vol. 44: 563-596 .

[4] Qu. X.L., et al., 2011. “Characterization of plunging liquid jets: A combined experimental and numerical investigation”, *International Journal of Multiphase Flow* 37, 722–731.

[5] Krepper, E., et al., 2011. “Influence of air entrainment on the liquid flow field caused by a plunging jet and consequences for fibre deposition”, *Nuclear Engineering and Design* 241, 1047–1054

[6] Bin, A. K., 1993. “Gas entrainment by plunging liquid jets”, *Chemical Engineering Science*, Vol.48, p.3585-3630.

[7] Gülich, J., 2008 „Kreiselpumpen: Handbuch für Entwicklung, Anlagenplanung und Betrieb: Ein Handbuch für Entwicklung, Anlagenplanung und Betrieb“ , *Springer*.

[8] Chanson, H., et al., 2002, “Similitude of Air Entrainment at Vertical Circular Plunging Jets”. *Proceedings of ASME FEDSM’02.*

[9] Heller, V., 2011. “Scale effects in physical hydraulic engineering models” *Journal of Hydraulic Research* Vol. 49, No. 3, pp. 293–306.

[10] Weismann, D., Gutzeit, T., 2006. “Kommunale Abwasser-pumpwerke“. *Vulkan Verlag*.

[11] Bollrich, D., 1989. „Technische Hydromechanik. 2. spezielle Probleme“. *Verl. für Bauwesen*.
[12] Kobus, H., 1984. „Wasserbauliches Versuchswesen. DVWK Schriften 39. Spezielle Probleme”. *Verl. Paul Parey*.
[13] Kawakita, K. et.al. 2012, ”Experimental study on the similarity of flow in pump sump models”, *26th IAHR Symposium on Hydraulic Machinery and Systems*.
[14] Padamabhan, M., et.al., 1984. “Scale Effects in Pump Sump Models”, *Journal of Hydraulic Engineering*, Vol.110: 1540-1556.
[15] Chanson H, Aoki S, Hoque A., 2006, “Bubble entrainment and dispersion in plunging jet flows: freshwater versus seawater”, *J Coastal* Res 22(3):664–677
[16] Chanson H 2008, “Turbulent air–water flows in hydraulic structures: dynamic similarity and scale effects”, *Environ Fluid Mech* 9(2):125–142
[17] Nakasone, H.,1987, “Study of Aeration at Weirs and Cascades”. *Journal of Environmental Engineering*, Vol.113, No.1, p.64-81.
[18] Yamagiwa, K., Mashima, T., Kadota, S. and Ohkawa, A.,1993 “Effect of liquid properties on gas entrainment behavior in a plunging liquid jet aeration system using inclined nozzles”. *Journal of Chemical Engineering of Japan*, 26, No.3, p.333-336
[19] Sande, E. van der, Smith, J.M., Eintragen von Luft in eine Flussigkeit durch einen Wasserstrahl, *Chemie-Ing.-Techn*. 44.Jahrg. 1972/Nr.20
[20] Denis Brouilliot, Pierre Lubin, 20013, “Numerical simulations of air entrainment in a plunging jet of liquid”, *Journal of Fluids and Structures* Volume 43, November 2013, Pages 428–440
[21]

Conference on Modelling Fluid Flow (CMFF'15)
The 16th International Conference on Fluid Flow Technologies
Budapest, Hungary, September 1-4, 2015

ASSESSING THE ACCURACY OF TURBULENCE MODELS FOR RESOLVING SHEAR AND SWIRL FLOWS IN PIPES

Andreas SWIENTY[1],Raja ABOU ACKL[1], Paul Uwe THAMSEN[1]

[1] Corresponding Author. Department of Fluid Mechanics, Berlin Institute of Technology. Straße des 17. Juni 135, 10623 Berlin, Germany. Tel.: +49 314 27832, Fax: +49 314 21472, E-mail: andreas_swienty@tu-berlin.de

ABSTRACT

An accurate prediction of flows using CFD depends on a large number of factors. In addition to discretizing the flow region, the correct definition of boundary or initial conditions and the choice of suitable numerical methods, the applied turbulence model influences the results of the flow simulation to a great extent. Therefore a validation of the results with the experimental data is of great importance for a correct selection of a turbulence model.

It is the scope of this paper to assess different turbulence models for the simulation of pipe flows. The calculation results of pipe flows through a combination of 90° elbows and a 1/3 segmental orifice are compared with experimental measurement results. This has the advantage that the suitability of the turbulence models for simulating both shear and swirl flows can be investigated. Thus, the k-ω, k-ε model and the Launder Reece Rodi Reynolds stress model are compared with each other and experimental results. Furthermore, this investigation is extended through including a much more c detached-eddy simulation. This model provides better prediction of the flow by resolving the large eddies and modelling the small ones. The experimental results originate from LDV measurements over the entire pipe cross-section. This measuring method provides velocity vectors over the measured surface

Keywords: CFD, turbulence models, k-ε, k-ω, LRR, DES

NOMENCLATURE

c	[]	turbulence parameter
D	[m]	diameter of the pipe
DES		detached eddy simulation
F	[N]	force
g	[m s²]	acceleration of gravity
k	[$m^2\ s^{-2}$]	turbulent kinetic energy
LES		large eddy simulation
LDV		laser doppler velocimetry
LRR		Launder Reece Rodi
p	[Pa]	pressure
PIV		particle image velocimetry
R,r	[m]	radius
(U)RANS		(unsteady) Reynolds-averaged Navier–Stokes
t	[s]	time
u	[$m\ s^{-1}$]	velocity
w	[$m^3\ s^{-1}$]	flow rate

Greek letters

ε	[, $m^2\ s^{-3}$]	turbulent energy dissipation rate
η	[$m^2\ s^{-1}$]	dynamic viscosity
ρ	[$kg\ m^{-3}$]	density of the fluid
σ	[]	turbulence parameter
ω	[s^{-1}]	specific rate of dissipation

Subscripts and Superscripts

vol volumetric

1 INTRODUCTION

In order to perform a reliable simulation of a flow problem with CFD, an understanding of the procedures and methods used is strongly needed. Apart from creating an incorrect mesh for the simulation model and a false indication of numerical methods, the choice of the turbulence model affects the outcome enormous. In addition, it is essential to validate the simulation results with measurements. The aim of this work is to investigate different turbulence models of the open source CFD program OpenFOAM for capturing pipe flows, which are disturbed by a segmental orifice and a combination of elbows based on measurement results. Elbow and segmental orifice fittings are the most common problems in pipes. Furthermore, these installations generate swirl and shear flows which require high demands on the turbulence model. The data used for comparison are measured on a test stand for investigating pipe flows by means of LDA. LDA measurements just as

PIV measurements [1], are well suited for the study of highly vortical flows. Furthermore, these methods allow the capturing of large-scale as well as small-scale flow structures. Takamura [2] investigated the complex turbulent flow in a short elbow pipe under high Reynolds number conditions. In addition, Tanaka [3] carried out some URANS simulations of unsteady eddy motion in pipe flows at high Reynolds numbers conditions. Weissenbrunner [4] investigated the flow field after a 7 % segmental orifice by means of PIV measurements and transient detached eddy simulation as well as a stationary simulation with a RANS turbulence model. Vijiapurapu [5] considered the influence of different turbulence models for flows through rough pipes. With this work, an overview will be provided on how different turbulence models represent disturbed pipe flows.

2 EXPERIMENTAL SETUP

In order to validate the simulation data, the described pipe fittings were examined on a test rig (figure 1). From a 4 m³ big tank water is pumped in a closed circuit by a centrifugal pump. The piping, with a diameter D=53.6 mm, is made primarily from Poly-Vinyl-Chloride (PVC). This allows a high flexibility of the test rig. The working fluid is tap water at 20 °C. A wide range of Reynolds numbers can be examined, since the pump generates a maximum flow rate of 42 m³/h. In this study a Reynolds number of 50000 was used. In front of the measurement site a 100 D long straight pipe ensures a fully developed flow. In addition, this is supported by the installation of a plurality of perforated plates and a tube bundle rectifier at the beginning of this pipe section. At the measuring section a flow profile over the entire tube cross-section can be measured with Laser Doppler Velocimetry. The disturbance of the flow is directly induced by the installed fitting before the measuring section.

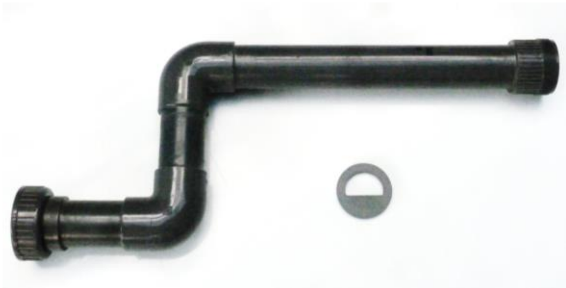

Figure 2. The 1/3 segmental orifice and the 90 ° elbow combination made of PVC for the experiments on the test rig

A 1/3 segmental orifice with a thickness of 7 mm was investigated. In a segmental orifice a region of the tube cross section is closed by a segment. In this way a partially closed valve in pipelines can be imitated. The second examined geometry consists of two consecutive 90° elbows (figure 2). The main function of an elbow is to redirect a pipe flow in a desired direction. At the interior side of an elbow the flow separates. This cause a complex flow field and vortices shedding downstream.

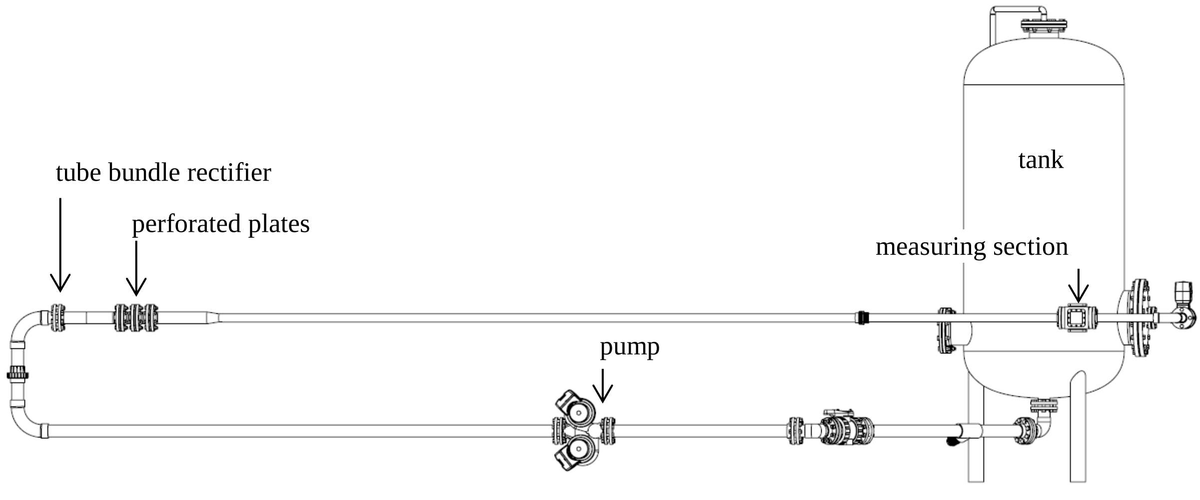

Figure 1. Representation of the test stand for the investigation of flow profiles of pipe flows

3 NUMERICAL SETUP

The swirling flow after the elbow and the shear flow after the segmental orifice are simulated with the same element size as well as boundary layers for the simulation grid and settings of the numerical method with the k-omega and the k-epsilon turbulence model and the LRR turbulence model (RANS model). In addition, these studies are extended by a computational-intensive detached eddy simulation. For this purpose the computational grid and the numerical methods were adapted to the requirements of the DES.

For an incompressible flow, the following continuity equation applies:

$$\nabla \boldsymbol{u} = 0\,. \tag{1}$$

Furthermore, the following can be written for the momentum equation:

$$\rho \frac{\partial \boldsymbol{u}}{\partial t} = -\rho \boldsymbol{u} \nabla \boldsymbol{u} + \eta \nabla^2 \boldsymbol{u} - \nabla p + \rho \boldsymbol{g}\,. \tag{2}$$

The k-ε turbulence model is the workhorse of practical engineering flow calculations to simulate mean flow characteristics for turbulent flow conditions [6]. It is a two equations model which gives a general description of turbulence by means of two transport equations. This approach consists of the two values k and ε. The equation k, the turbulent kinetic energy, and ε, the rate of dissipation of the turbulent kinetic energy, have the following form:

$$\frac{\partial \rho k}{\partial t} + \nabla(\rho k \boldsymbol{u}) = \nabla\left(\frac{\eta_t}{\sigma_k} \nabla k\right) + \hat{P} - \rho \varepsilon \tag{3}$$

and

$$\frac{\partial \rho \varepsilon}{\partial t} + \nabla(\rho \varepsilon \boldsymbol{u}) = \nabla\left(\frac{\eta_t}{\sigma_\varepsilon} \nabla \varepsilon\right) + C_{\varepsilon 1} \frac{\varepsilon}{k} \hat{P} - C_{\varepsilon 1} \rho \frac{\varepsilon^2}{k}\,. \tag{4}$$

In the k-ω turbulence model, the turbulent kinetic energy is calculated after

$$\frac{\partial \rho k}{\partial t} + \nabla(\rho k \boldsymbol{u}) = \hat{P} - \beta^* \rho \omega k + \nabla\left[\left(\eta + \frac{\eta_t}{\sigma_k}\right) \nabla k\right] \tag{5}$$

and the specific rate of dissipation is calculated after

$$\frac{\partial \rho \omega}{\partial t} + \nabla(\rho \omega \boldsymbol{u}) = \alpha \frac{\omega}{k} \hat{P} - \beta^* \rho \omega^2 + \nabla\left[\left(\eta + \frac{\eta_t}{\sigma_\omega}\right) \nabla \omega\right]. \tag{6}$$

The equations contain some adjustable constants. The values of these constants originate from numerous iterations of data fitting for a wide range of turbulent flows. Through these two modeling approaches for the turbulence the required computational effort and resources are reduced. The Reynolds stress model [7 and 8] involves calculations of the individual Reynolds stresses using differential transport equations. Detached-eddy simulation (DES) is an example of a new kind of methods that seek to bridge the gap existing between the just introduced RANS approaches and large-eddy simulation (LES) concerning computational cost and predictive accuracy. In the regions next to walls RANS models can represent the flow very well at minimal computational cost, however they exhibit significant deficiencies in massively-separated flows. On the contrary LES delivers more accurate predictions due to the limitation of modelling empiricism to the smallest turbulent structures. However the numerical cost for wall-bounded flows is enormous and increases strongly with Reynolds number.

In Figure 3, the simulation model of the segmental orifice and the elbow combination is shown. For the segmental orifice the data were evaluated at 7 D and for the elbow combination 10 D downstream of the disturbance.

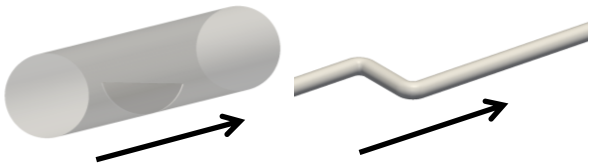

Figure 3. Representation of the simulation geometry of the segmental orifice (l) and the elbow combination (r)

For the stationary calculations with the k-ε, k-ω and LRR turbulence model a structured mesh with boundary layers was created with a total of 6.2 million elements. For the transient DES this mesh was further refined, up to 13 million elements. Mostly, the element number was increased in the axial direction. A representation of the two meshes is shown in Figure 4. The assessment of the independence of the results on the computational grid was checked by further calculations applying a general finer grid, here not presented.

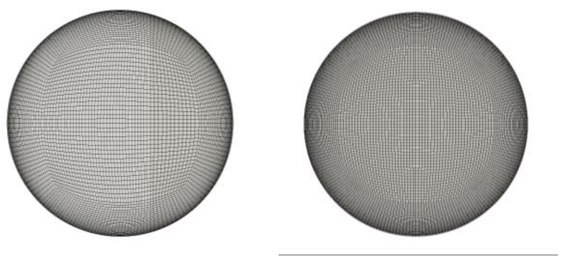

Figure 4. Computational mesh for the segmental orifice (l) and the elbow combination (r)

At the inlet a fully developed velocity profile was calculated with a periodic boundary condition. In this method the fully developed velocity profile is created by using a periodic boundary condition starting with an uniform velocity profile (cp figure. 5). This was applied to the cases with the DES and

RANS turbulence models. For the simulation, a kinematic viscosity of 1,004 x 10^{-6} m² s^{-1} was selected for the property of the fluid.

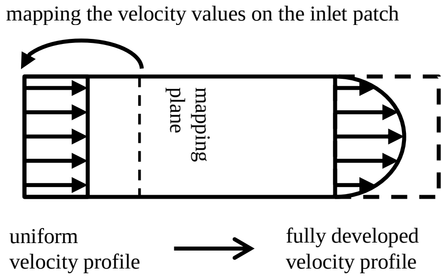

Figure 5. The cycling mapped boundary condition

4 RESULTS AND COMPARISSON

The results of the calculations of the 1/3 segmental orifice are shown in the following figures 6-8. It is easy to see that the detached eddy simulation resolves more small structures than the simulations with the RANS turbulence model. In general, the simulations show a velocity profile, as it is expected downstream of a segmental orifice.

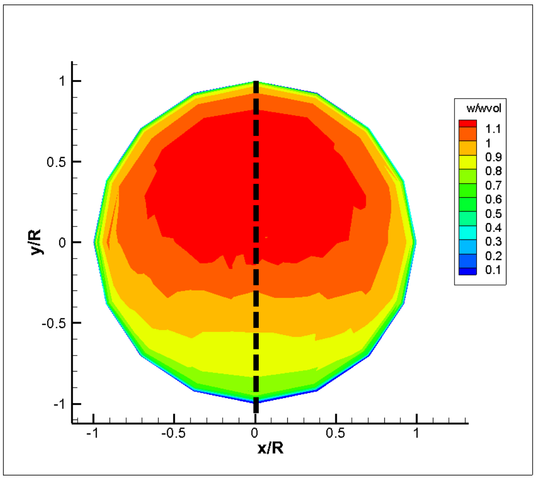

Figure 6. Measurement result with LDV of the segmental orifice

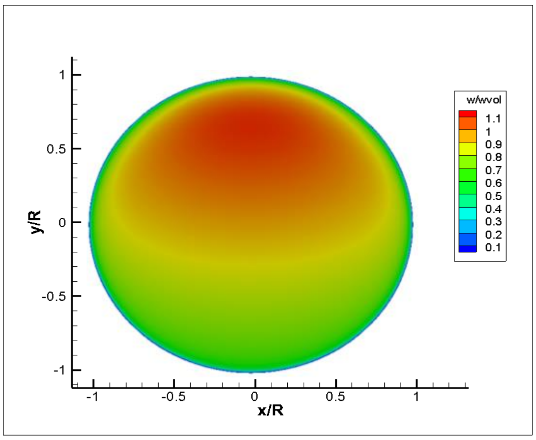

Figure 7. Simulation result with the k-ω turbulence model of the segmental orifice

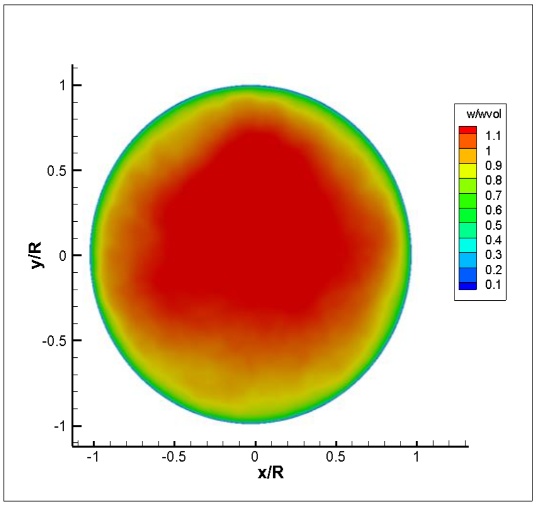

Figure 8. Detached eddy simulation result of the segmental orifice

In addition, the data is evaluated along the axis of symmetry (cp. figure 6). The velocity profiles along this axis are shown in figure 8.

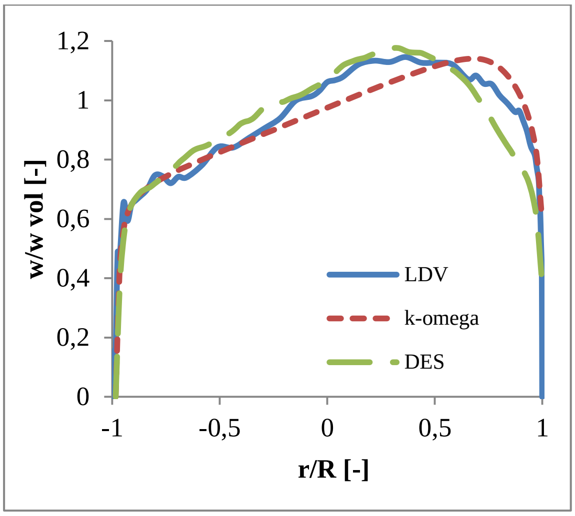

Figure 8. Comparison of velocity profiles from different turbulence models of the segmental orifice

The simulation results of the elbow combination are evaluated in the same manner. The figures 10-14 show the velocity profiles.

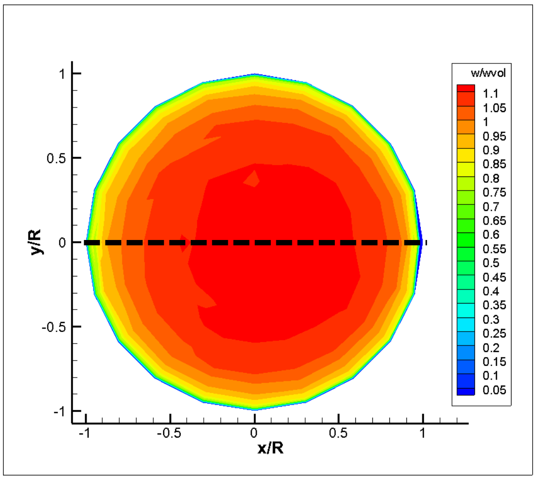

Figure 10. Measurement result with LDV of the elbow combination

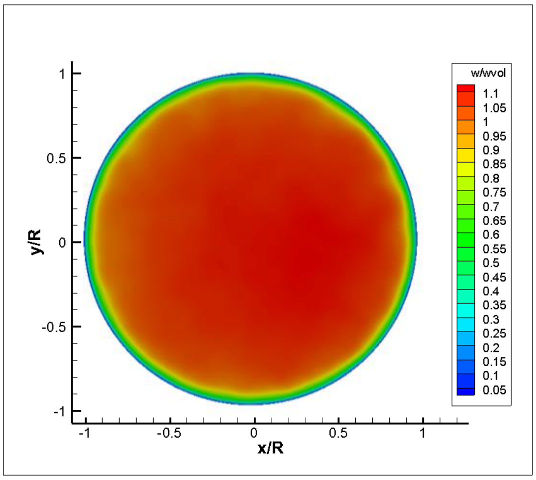

Figure 11. Detached eddy simulation result of the elbow combination

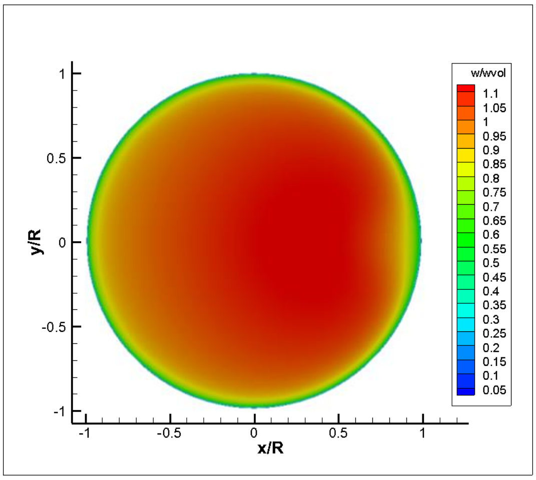

Figure 2. Simulation result with the k-ω turbulence model of the elbow combination

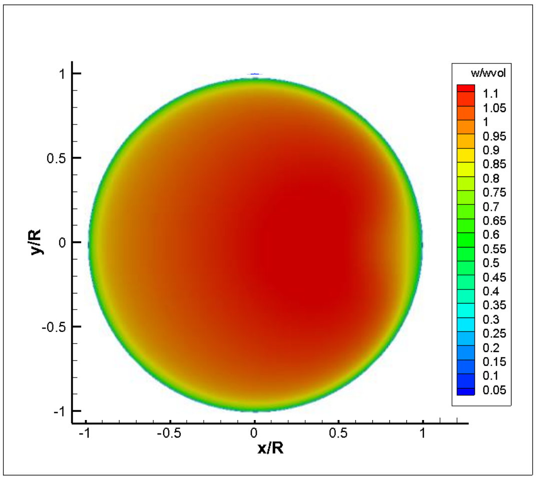

Figure 3. Simulation result with the k-ε turbulence model of the elbow combination

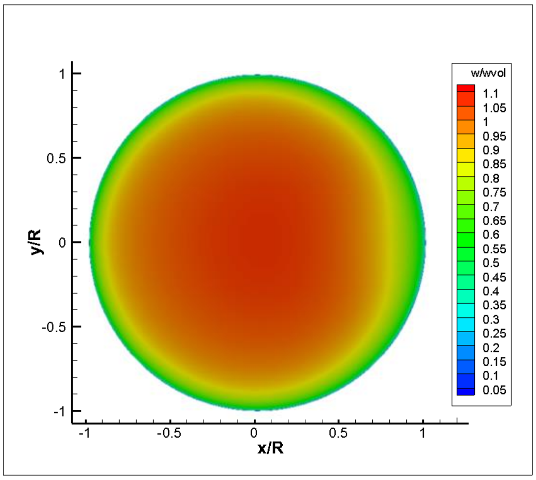

Figure 4. Simulation result with the LLR turbulence model of the elbow combination

In the elbow combination, all turbulence models were compared along one path (cp. figure 10), too. The following chart shows the different velocity profiles.

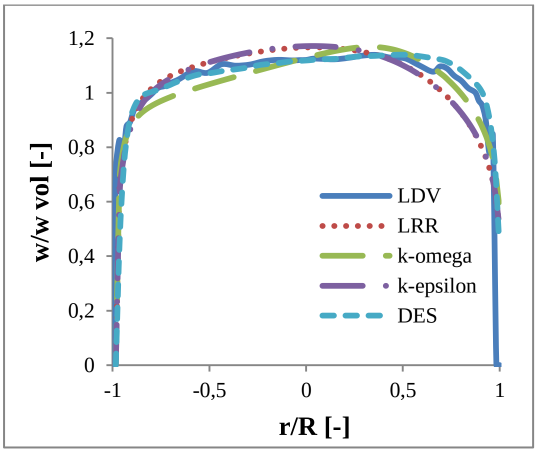

Figure 5. Comparison of velocity profiles from different turbulence models of the elbow com

5 SUMMARY AND CONCLUSION

The aim of this study was to investigate various turbulence models for the simulation of shear and swirl flows. In order to validate the simulation results measurements were performed on a 1/3 segmental orifice and a combination of 90° elbows on a test rig for investigating pipe flows. The velocity profiles over the entire pipe cross section were measured by means of LDV. In a further step, the simulation models of the described disturbances were created. The k-omega, the k-epsilon, the LRR and the detached eddy simulation turbulence models were examined in this study for capturing the flow conditions.

The comparison of the simulation results showed that the computationally expensive detached eddy simulation resolves the flow very well both in the segmental orifice and in the elbow combination. Nevertheless in the case with the segmental orifice this model shows some inaccuracy in the regions near to the wall. This can be lead back to the resolution of the mesh in this area.

Regarding the RANS turbulence models, the k-ω model showed a good correlation with the measurements. Concerning the elbow combination the LRR model performed just as poorly as the k-ε model. However the LRR model is suitable for resolving flows with high vortex intensity, therefore, it can be reasonably concluded that the exciting vortices after the elbow combination are not strong enough to use the benefits of this turbulence model.

REFERENCES

[1] Sharp, K.V., Adrian, R.J., 2001. PIV study of small-scale flow structure around a Rushton turbine. A.I.Ch.E. Journal 47 (4), 766–778.

[2] Takamura, H., Ebara, S., Hashizume, H., Aizawa, K., Yamano, H., 2012. Flow visualisation and frequency fluctuations of complex turbulebt flow in a short elbow piping under high Reynolds number condition. Journal of Fluids Engineering Vol. 134, pp. 101201-1-101201-8, 2012.

[3] Tanaka, M., Ohshima, H., Yamano, H., Aizawa, K., and Fujisaki, T., 2010. U-RANS simulation of unsteady eddy motion in pipe elbow at high Reynolds number condition. Proc. 2010 International Congress on Advances in Nuclear Power Plants (CD-ROM), pp 1699-1708.

[4] Weissenbrunner, A., Eichler, T., and Lederer, T., 2014. CFD simulation of a flow disturber in a pipe and comparison with PIV-Measurement. Fachtagung "Lasermethoden in der Strömungsmesstechnik" 2014. pp 22-1-22-8.

[5] Vijiapurapu, S. and Cui, J., Performance of turbulence models for flows through rough pipes. Applied Mathematical Modelling Vol. 34, pp. 1458–1466, 2010.

[6] ANSYS, I., 2009. ANSYS Fluent 12 Users Guide, April 2009.

[7] Launder, B.E., Reece, G.J., Rodi, W., Progress in the development of a Reynolds-stress turbulence closure, J. Fluid Mech. 68 (3) (1975) 537–566.

[8] Fu, S., Launder, B.E., and Leschziner, M.A., Modeling strongly swirling recirculating jet flow with Reynolds-stress transport closures, in: Sixth Symposium on Turbulent Shear Flows, Toulouse, France, 1987.

Conference on Modelling Fluid Flow (CMFF'15)
The 16th International Conference on Fluid Flow Technologies
Budapest, Hungary, September 1-4, 2015

LES-CMC of oxy-combustion of hydrogen jet

Agnieszka ROSIAK[1], Artur TYLISZCZAK[2], Andrzej BOGUSLAWSKI[3]

[1] Institute of Thermal Machinery, Czestochowa University of Technology. Armii Krajowej 21, 42-201 Czestochowa, Poland.
Tel.: +48 34 3250 507, Fax: +48 34 3250 555, E-mail: rosiaka@imc.pcz.czest.pl
[2] Institute of Thermal Machinery, Czestochowa University of Technology. E-mail: atyl@imc.pcz.czest.pl
[3] Institute of Thermal Machinery, Czestochowa University of Technology. E-mail: abogus@imc.pcz.czest.pl

ABSTRACT

Large Eddy Simulation / Conditional Moment Closure (LES-CMC) simulations of non-premixed turbulent hydrogen jet in oxy-combustion regimes are performed. The fuel is pure hydrogen and the oxidiser is a mixture O_2/H_2O with mass fraction of water in the range $Y_{H_2O} = 0.1 - 0.7$. The fuel issues into a hot oxidiser stream at $1045K$, auto-ignites and the flame propagates through the domain. The problem analysed offers new challenges to combustion modelling as depending on O_2 content in the oxidiser stream the combustion process may be strongly unsteady and on the border of stability and flammability limits. It is shown that LES-CMC is well suited for such studies. We analyse the auto-ignition and forced ignition processes followed by a flame propagation and stabilisation phases. The obtained results show that for low content of water in oxidiser the auto-ignition time is a linear function of Y_{H_2O}. The axial locations of auto-ignition spots increase with H_2O content in oxidiser, whereas the auto-ignition scenario is basically the same. It is found that for $Y_{H_2O} <$ 0.6 the flame attaches to the nozzle whereas for the cases $Y_{H_2O} = 0.6$ and $Y_{H_2O} = 0.7$ the flames remain lifted but they lift-off heights are smaller than the nozzle diameter.

Keywords: CMC, hydrogen, LES, non-premixed combustion, oxy-combustion, turbulent jet

NOMENCLATURE

Sc	$[-]$	Schmidt number
D	$[m]$	nozzle diameter
D_ξ	$[m^2/s]$	molecular diffusivity
N	$[s^{-1}]$	scalar dissipation rate
T	$[K]$	temperature
U	$[m/s]$	velocity
Y_k	$[-]$	reactive scalar
p	$[Pa]$	pressure
t	$[s]$	time
u_i	$[m/s]$	velocity component
x_i	$[-]$	axis coordinate
$\dot{\omega}_k$	$[mol/m^3\ s]$	reaction rate
η	$[-]$	sample space variable for ξ
μ	$[Pa\ s]$	molecular viscosity
ρ	$[kg/m^3]$	density
ξ	$[-]$	mixture fraction

Subscripts and Superscripts

cf	related to co-flow
fuel	related to fuel
ign	related to auto-ignition
MR	most-reactive
sgs, t	related to subgrid or turbulent
ST	stoichiometric
i, j, k	indices of the coordinate axis, species

1. INTRODUCTION

Oxy-combustion technology is a promising option to reduce the emission of greenhouse gases to the atmosphere. The oxy-combustion technology has been proposed almost simultaneously by Horn and Steinberg [1] and by Abraham et al. [2] in 80s. During the oxy-fuel combustion the oxygen (with purity of more than 95%) and recycled flue gas are mixed and used to carry out the combustion process. By removing the nitrogen from the oxidiser the oxy-combustion process allows to eliminate the oxides of nitrogen. The nitrogen is usually replaced by the carbon dioxide and therefore the oxy-combustion process is often combined with carbon capture technology which minimises emission of the carbon dioxide [3, 4].

Combustion process carried out in oxygen atmosphere differs from conventional air combustion. Generally, the primary effects of oxy-combustion process are higher flame temperature and burning velocity whereas the ignition temperature is lower. The oxy-combustion technology is still on early level of development and many questions related to combustion characteristics, ignition, flame stability or optimal oxidiser composition remain unanswered. In general, in the field of combustion an experimental analysis constitutes difficult and expensive task as it requires a dedicated apparatus and sophisticated measurements techniques. Experimental research in oxy-combustion problems are additionally complicated by very high temperatures and unsteadiness, if we consider ignition and flame propagation processes. Hence, further development of oxy-fuel combustion technology can be supported by numerical methods within the framework of Computational Fluid Dynamics (CFD). The present literature in the field of modelling of oxy-combustion processes is mainly focused on oxy-coal and oxy-natural gas combustion as they are the most abundant fuels [5, 6].

In the present work Large Eddy Simulation (LES) method is combined with one of the most advanced and accurate combustion model, i.e., Conditional Moment Closure (CMC) model for modelling of non-premixed oxy-combustion of turbulent hydrogen jet. The LES-CMC approach enables to capture very complex combustion phenomena such as local extinctions [7], auto-ignition [8] and forced ignition [9]. In the field of oxy-combustion the LES-CMC approach was used by Garmory and Mastorakos [10] for modelling combustion of CH_4/H_2 in O_2/CO_2 atmosphere. In the present study we consider combustion of pure hydrogen in O_2/H_2O mixture, thus we study a perfectly clean combustion with water as the final product. We will concentrate on the analysis of auto- and forced ignition processes and flame stability for a wide range of oxidiser composition and velocity. The research will also aim to determine flammability range, flame stability and distribution of temperature and species mass fractions as functions of co-flow parameters.

2. MODELLING

2.1. LES formulation

In LES the large scales in the turbulent flow are directly resolved on a given numerical mesh, while the smaller scale (subgrid scale) effects must be modelled. Applying the filtering procedure to the continuity equation, the Navier-Stokes equations and the transport equation for the mixture fraction gives

$$\frac{\partial \bar{\rho}}{\partial t} + \frac{\partial \bar{\rho}\tilde{u}_j}{\partial x_j} = 0 \tag{1}$$

$$\frac{\partial \bar{\rho}\tilde{u}_i}{\partial t} + \frac{\partial \bar{\rho}\tilde{u}_i\tilde{u}_j}{\partial x_j} = -\frac{\partial \bar{p}}{\partial x_i} + \frac{\partial \tau_{ij}}{\partial x_j} + \frac{\partial \tau_{ij}^{\mathrm{sgs}}}{\partial x_j} \tag{2}$$

$$\frac{\partial \bar{\rho}\tilde{\xi}}{\partial t} + \frac{\partial \bar{\rho}\tilde{u}_i\tilde{\xi}}{\partial x_i} = \frac{\partial}{\partial x_i}\left(\bar{\rho}D_\xi \frac{\partial \tilde{\xi}}{\partial x_i}\right) + \frac{\partial J_{\mathrm{sgs}}}{\partial x_i} \tag{3}$$

where the overbar symbol stands for LES filtering applied to density and pressure. The wide tilde symbol stands for the Favre filtering applied to the velocity field $\tilde{u}_i = \overline{\rho u_i}/\bar{\rho}$ and mixture fraction $\tilde{\xi} = \overline{\rho\xi}/\bar{\rho}$. The term $D_\xi = \mu/\bar{\rho}\mathrm{Sc}$ is the molecular diffusivity, $\mathrm{Sc} = 0.7$ is the Schmidt number, and τ_{ij} represents the stress tensor of the resolved field. Unresolved subgrid stress tensors τ_{ij}^{sgs} and J_{sgs} are modelled by the eddy-viscosity type model defined as

$$\tau_{ij}^{\mathrm{sgs}} = 2\mu_{\mathrm{sgs}}S_{ij} - \frac{1}{3}\tau_{kk}\delta_{ij} \qquad J_{\mathrm{sgs}} = \bar{\rho}D_{\mathrm{t}}\frac{\partial \tilde{\xi}}{\partial x_i} \tag{4}$$

where $S_{ij} = 1/2\left(\partial\tilde{u}_i/\partial x_j + \partial\tilde{u}_j/\partial x_i\right)$ is the rate of the strain tensor of the resolved field. The subgrid (or turbulent) viscosity μ_{t} is computed according to the model proposed by Vreman [11]. The subgrid diffusivity is defined as $D_{\mathrm{t}} = \mu_{\mathrm{t}}/\bar{\rho}\mathrm{Sc}_{\mathrm{t}}$ where the turbulent Schmidt number is assumed constant $\mathrm{Sc}_{\mathrm{t}} = 0.4$ [12].

2.2. CMC formulation

The CMC model has been formulated by Klimenko and Bilger [13] in the 90s. The LES-CMC model was presented by Navarro-Martinez et al. [14] approximately ten years later where it was derived applying the density-weighted conditional filtering operation to the transport equations for the reactive scalar (Y_k) (species mass fraction and total enthalpy). The CMC equations in the LES context are given as [12, 14]:

$$\frac{\partial Q_k}{\partial t} + \widetilde{u_i|\eta}\frac{\partial Q_k}{\partial x_i} = \widetilde{N|\eta}\frac{\partial^2 Q_k}{\partial \eta^2} + \widetilde{\dot{\omega}_k|\eta} + e_{Y,k} \tag{5}$$

where $k = 1, \ldots, n$ is the index of n reacting species and $k = n+1$ stands for enthalpy. The operator $(\cdot|\eta) = (\cdot|\ \xi = \eta)$ is the conditional filtering operator with conditioning being done on the mixture fraction [14]. The symbol $Q_k = \widetilde{Y_k|\eta}$ represents the conditionally filtered reactive scalar, $\widetilde{u_i|\eta}$ - velocity, $\widetilde{N|\eta}$ -scalar dissipation rate, $\widetilde{\dot{\omega}_k|\eta}$ -reaction rate. The symbol $e_{Y,k} = \frac{\partial}{\partial x_i}\left(\widetilde{D_{\mathrm{t}}|\eta}\frac{\partial Q_k}{\partial x_i}\right)$ represents the subgrid interactions [12]. The conditionally filtered velocity $\widetilde{u_i|\eta}$ and subgrid diffusivity $\widetilde{D_{\mathrm{t}}|\eta}$ are usually expressed directly by the filtered values [7, 12, 14], i.e., $\widetilde{u_i|\eta} \approx \tilde{u}_i$, $\widetilde{D_{\mathrm{t}}|\eta} \approx D_{\mathrm{t}}$ whereas the conditionally filtered scalar dissipation rate is usually computed with the Amplitude Mapping Closure (AMC) model [12, 14]. The conditionally filtered reaction rate is evaluated with the 1st order closure [13] where the subgrid conditional fluctuations are neglected, i.e., $\widetilde{\dot{\omega}_k|\eta} \approx \dot{\omega}_k\left(Q_1, Q_2, ..., Q_n, Q_{n+1}\right)$.

2.3. Numerical methods

The computations have been performed using an in-house LES solver (SAILOR) [15] based on the low Mach number approach [16] and spatial discretisation performed by the 6th order half-staggered compact difference method [15, 17] for the Navier-Stokes and continuity equations and with 5th order WENO scheme [18] for the mixture fraction. The time integration is performed with a predictor-corrector method with the help of the 2nd order Adams-Bashforth and Adams-Moulton methods. The SAILOR code was verified in previous LES studies concentrating on gaseous flows, multiphase flows and flames [8, 19, 20, 21].

The CMC equations are solved applying the operator splitting approach where the transport in physical space, transport in mixture fraction space and chemistry are solved separately. In physical space, the conditional variables are smoother than the filtered ones and therefore the CMC equations are discretised using only the 2nd order finite difference method. The convective terms are computed using 2nd order TVD (Total Variation Diminishing) method with van Leer limiters. The diffusive terms are discretised using the central finite difference scheme. The chemical kinetics is modelled using detailed mechanism with 9 species and 19 reactions [22] and the source terms are calculated using CHEMKIN interpreter. VODPK package is employed to solve the CMC equations in mixture fraction space.

3. COMPUTATIONAL CONFIGURATION

To the best authors knowledge there are no experimental data available for combustion of pure H_2 jet in the mixture of O_2/H_2O. Hence, configuration used by Cabra et al. [23] for auto-ignition studies of turbulent H_2/N_2 jet in a co-flow of lean H_2/air combustion products was adapted in the present work. Motivation of this choice is the fact that for this test case many LES-CMC calculations were performed and they were in good agreement with experimental findings.

In the present case the fuel jet consists of the pure hydrogen, it is injected into a heated mixture of oxygen and water through a nozzle with the internal diameter $D = 0.00457m$ at the ambient pressure. The temperature of the fuel jet is equal to $T_{\text{fuel}} = 305K$ and the co-flowing stream temperature is $T_{\text{cf}} = 1045K$. The analysis is performed for various oxidiser compositions with the mass fraction of water Y_{H_2O} varying in the range of $0.1 - 0.7$. The co-flow velocity depends on Y_{H_2O} such that the excess of O_2 relative to H_2 mass flow rate is constant and equal to 30%. This leads to the co-flow velocities in the range $U_{\text{cf}} = 1.161m/s - 4.990m/s$. The fuel velocity equals to $107m/s$.

The computational domain is a rectangular box with dimensions $14D \times 30D \times 14D$. The LES-CMC calculations are extremely expensive from the computational point of view. A common simplifying approach is to use two separate meshes in physical space: one for the solution of the flow field (CFD mesh) and another one, much coarser for the CMC equations (CMC mesh). Methodology of data exchange between CFD and CMC mesh may be found in [12]. In the present case we found that the CFD mesh with $128 \times 160 \times 128$ nodes stretched radially and axially towards the jet region and the uniform CMC mesh with $15 \times 80 \times 15$ nodes, provide nearly grid independent results. Influence of mesh density was examined in previous study related to the original Cabra flame configuration [8]. It was found that minor differences had quantitative character and were visible in the time-averaged data only. For instance the maximum temperature values on two

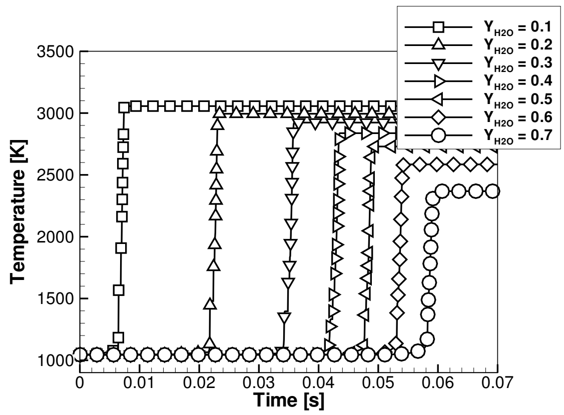

Figure 1. Evolution of maximum temperature in auto-ignition phase. Results for 0D-CMC calculations.

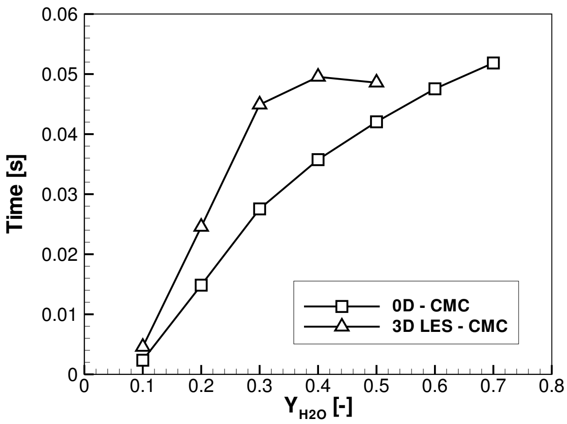

Figure 2. Dependence of auto-ignition time on oxidiser composition for 0D-CMC and 3D LES-CMC calculations.

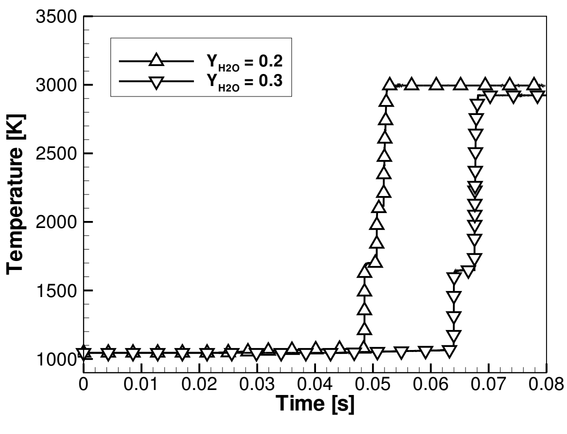

Figure 3. Evolution of maximum temperature in auto-ignition phase. Results for 3D LES-CMC calculations.

meshes was less than 1% . Similarity of the solutions obtained on different meshes was attributed to the high-order discretisation method, which is assumed to yield the grid independent results at relatively small number of the nodes.

4. RESULTS

4.1. Analysis of auto-ignition time

The procedure of auto-ignition simulation consists of two subsequent steps. In the first part, in every node of the CFD mesh the solution is initialised within mixture fraction space assuming a linear distribution of species and enthalpy between the oxidiser composition ($\xi = 0$) and the fuel composition ($\xi = 1$). Next, the flow evolves in physical and mixture fraction spaces. If the temperature is sufficiently large auto-ignition spots appear somewhere in the flow domain. Then, the second simulation step begins which consists of propagation of the flame which eventually stabilises as a lifted or attached, depending on the flow conditions.

Before depicted above LES-CMC computations a preliminary analysis was performed using the so-called 0D-CMC approach. In such a 0D-CMC method the simulations are performed only in mixture fraction space and the obtained solutions give insight on how the oxidiser composition affects the maximum temperature, auto-ignition time and distributions of species mass fractions. The ignition time t_{ign} is assumed here as the time from the beginning of the simulations to the time instant when the temperature rises 1K over T_{cf}. In the calculations the maximum value of the scalar dissipation rate used in AMC model is $N = 1s^{-1}$. Figure 1 shows temperature evolution and auto-ignition time for $Y_{H_2O} = 0.1 - 0.7$. It is seen that for low values of Y_{H_2O} the temperature is very large (above 3000K for $Y_{H_2O} = 0.1$) and decreases for increasing Y_{H_2O} (below 2500K for $Y_{H_2O} = 0.7$). Apart from that increasing content of H_2O in oxidiser significantly affects delaying of the auto-ignition. Dependence of auto-ignition time on oxidiser composition can be seen in the Figure 2 . In the range $Y_{H_2O} = 0.1 - 0.3$ the values of t_{ign} exhibit linear behaviour expressed as $t_{\text{ign}} = 0.126 Y_{H_2O} - 0.010$ which is characterized by a line inclined 7.2°. For the other cases ($Y_{H_2O} = 0.4 - 0.7$) the ignition time varies non-linearly. Full 3D LES-CMC simulations were performed according to the procedure depicted at the beginning of this section. They allowed to determine analogical dependence $t_{\text{ign}}(Y_{H_2O})$ for the cases with ($Y_{H_2O} = 0.1 - 0.5$). For other two investigated cases ($Y_{H_2O} = 0.6$, $Y_{H_2O} = 0.7$) the auto-ignition process has not occurred and therefore the combustion process has been successfully initialised by a spark which is discussed later. As in 0D-CMC computations it is found that for $Y_{H_2O} = 0.1 - 0.3$ the values of t_{ign} obtained from LES-CMC behave linearly. However, this time the relation is given as $t_{\text{ign}} = 0.201 Y_{H_2O} - 0.015$ and the inclination is equal to 11.4°. The differences in the line inclination and t_{ign} values with LES-CMC and 0D-CMC calculations can be observed in the Fig. 2. The fact that $t_{\text{ign}}(Y_{H_2O})$ behave linearly indicates that for low content of H_2O in co-flowing stream the auto-ignition time is mainly affected by the chemical process and solution in mixture fraction space, whereas the impact of the convective and diffusive transport in physical space seems negligible. It becomes more important only for cases with $Y_{H_2O} > 0.3$. In Fig. 2 this manifests by a shorter ignition time for $Y_{H_2O} = 0.5$ than for $Y_{H_2O} = 0.4$. Hence, for $Y_{H_2O} > 0.3$ the auto-ignition process is a combined effect of interaction between chemistry and turbulence. Sample evolutions of the maximum temperature in auto-ignition phase obtained from 3D LES-CMC computations for $Y_{H_2O} = 0.2$ and $Y_{H_2O} = 0.3$ are presented in the Fig-

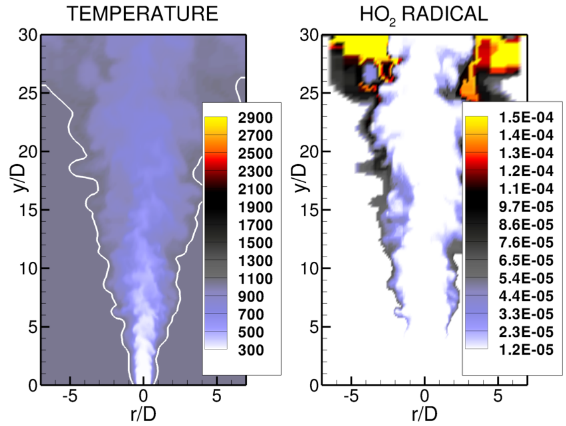

(a) **(b)**

Figure 4. Contours of temperature (a) and HO_2 mass fraction (b) at the time instant $t = 4.87 \times 10^{-2} s$ – beginning of the auto-ignition. The white lines in figure (a) denotes locations of the most reactive mixture fraction $\xi_{\text{MR}} = 0.0007$. Results for $Y_{H_2O} = 0.2$.

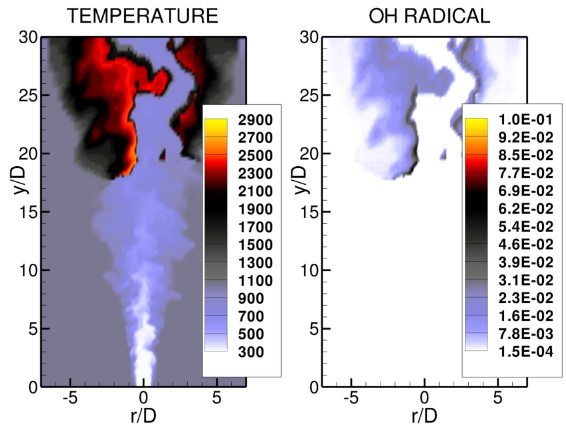

(a) **(b)**

Figure 5. Contours of temperature (a) and OH mass fraction (b) at the time instant $t = 5.21 \times 10^{-2} s$ – propagation of the flame. Results for $Y_{H_2O} = 0.2$.

ure 3. As in these cases the ignition process is mostly dependent on chemistry the evolution of temperature is reminiscent of solutions presented in Fig. 1. Additionally in Fig. 3 shortly after auto-ignition a temperature stagnation on certain level for some short time can be observed. Very similar behaviour was also observed for 0D-CMC calculations, however, it occurred at lesser extent than in 3D LES-CMC computations. Appearing of such plateaux is most likely caused by numerical artifacts, which at the present time we are not able to univocally explain.

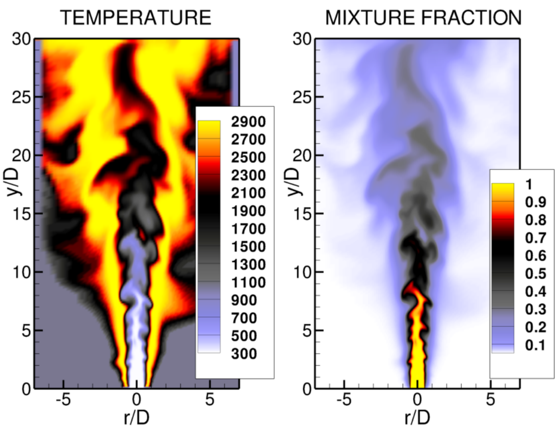

(a) (b)

Figure 6. Contours of temperature (a) and mixture fraction (b) – fully developed flame. Results for $Y_{H_2O} = 0.2$.

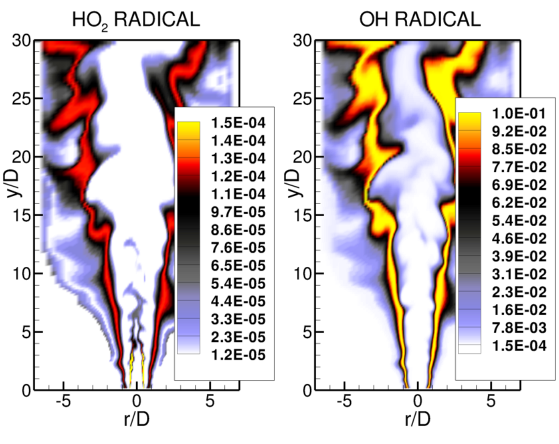

(a) (b)

Figure 7. Contours of HO_2 mass fraction (a) and OH mass fraction (b) – fully developed flame. Results for $Y_{H_2O} = 0.2$.

4.2. 3D LES-CMC results

Sample results obtained from full 3D LES-CMC computations are shown in the Figures 4 to 11. In the performed simulations two cases corresponding to $Y_{H_2O} = 0.1$ and $Y_{H_2O} = 0.5$ turned out unstable. Shortly after ignition, when the flame started to develop in the domain, very large temperature gradients appeared and destabilised the solution procedure. In effect the solution diverged. As this may be understood for $Y_{H_2O} = 0.1$ where the temperature is very large, such unstable behaviour for $Y_{H_2O} = 0.5$ seems strange. Mostly because for the cases $Y_{H_2O} = 0.2, 0.3, 0.4$ the solution was stable and the results were obtained without difficulties. At the present time we are not able to find out what are the reasons of this instability. Hence, the cases for $Y_{H_2O} = 0.1$ and $Y_{H_2O} = 0.5$ are analysed only partially.

4.2.1. Auto-ignition

The obtained results for case with $Y_{H_2O} = 0.1 - 0.5$ show that after the occurrence of auto-ignition the flame propagates rapidly towards the nozzle and remains nearly attached to the nozzle. In the present simulations the flame never fully attaches to the inflow plane because of assumed inert boundary condition at the inlet. The evolution of the flame for $Y_{H_2O} = 0.2$ starting from auto-ignition phase, up to the developed flame, is shown in Figures 4 to 7. The presented contours show the temperature, HO_2 and OH radicals, and mixture fraction for subsequent time instances, respectively, starting from $t = 4.87{\times}10^{-2}s$ which correspond to $0.024s$ after t_{ign}. The auto-ignition begins at the distance of approximately $15D$ from the inlet. The white line in the Figure 4a corresponds to the most reactive mixture fraction, i.e., where the auto-ignition occurs first. For the case with $Y_{H_2O} = 0.2$ the most reactive mixture fraction is very small and equals to $\xi_{\text{MR}} = 0.0007$. At the time instant $t = 4.87 \times 10^{-2}s$ the maximum temperature is only slightly higher than T_{cf} and therefore it is not visible in the contours, however, the first signs of the auto-ignition are already seen. They manifest by a rise of the mass fractions of the so-called pre-ignition species, HO_2, shown in the Figure 4b. In the next time steps, at $t = 5.21 \times 10^{-2}s$, an intense production of OH radical is visible at the distance of approximately $20D$, the temperature increases rapidly and the flame starts to propagate downstream (Figure 5). Eventually, the flame stabilises and attaches to the inlet in the first CMC cells. This is visualised in Figure 6 which shows also that high temperature regions are in the mixing layer and the maximal temperature is at the level of approximately $3000K$. Figure 7 presents typical distributions of HO_2 and OH radicals in the fully developed flame. For the rest of the cases, except two unstable simulations discussed before, the auto-ignition and flame propagation scenarios are basically the same and they end similarly resulting in the attached flames.

4.2.2. Spark ignition

In cases in which the co-flow temperature was to small to cause auto-ignition the flame was initiated by a spark modelled by a locally introduced

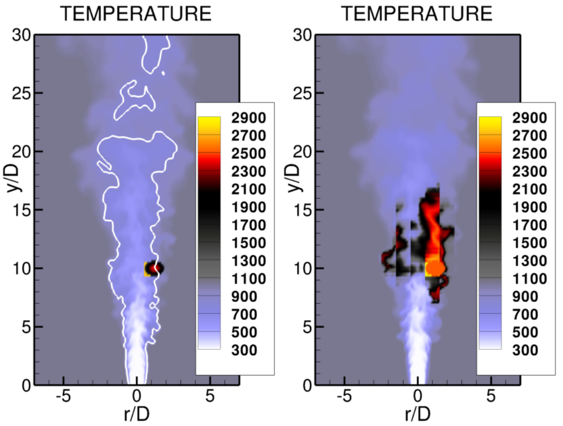

(a) (b)

Figure 8. Contours of temperature at the time instant $t = 7.27 \times 10^{-2} s$ (a) and at the time instant $t = 7.29 \times 10^{-2} s$ (b) – initialising of the spark ignition. The white lines in figure (a) denotes locations of the stoichiometric mixture fraction $\xi_{\mathrm{ST}} = 0.048$. Results for $Y_{H_2O} = 0.6$.

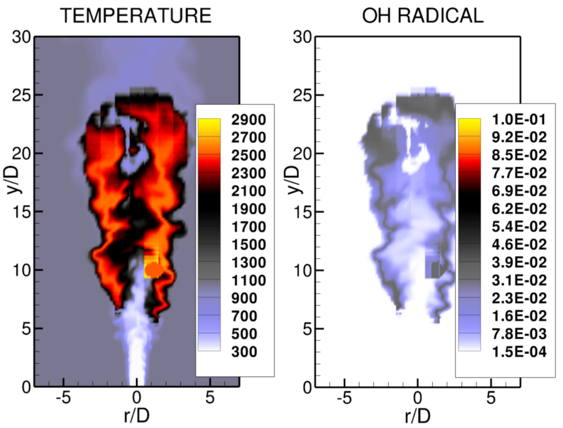

(a) (b)

Figure 9. Contours of temperature (a) and OH mass fraction (b) at the time instant $t = 7.30 \times 10^{-2} s$ – the final stage of the spark ignition, production of OH. Results for $Y_{H_2O} = 0.6$.

flame kernel. Such an ignition process relies on two steps: (i) 0D-CMC simulations are performed which provide "burning" solution in mixture fraction space; (ii) the obtained solution is prescribed in selected CMC cells and kept for some time (duration of the spark). In present studies we are not intended to analyse methods of spark initiation or dependence of successful attempt of ignition on a spark size or its intensity. In this work the spark is used just to initiate the combustion process, hence, we use relatively strong spark with the 0D-CMC simulations performed with arbitrarily assumed scalar dissipation rate $N_0 = 1 s^{-1}$. The spark was embedded on

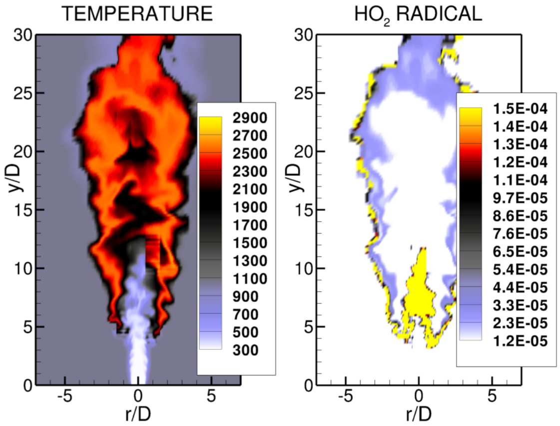

(a) (b)

Figure 10. Contours of temperature (a) and HO_2 mass fraction (b) at the time instant $t = 7.32 \times 10^{-2} s$ – soon after the spark has been switched-off, destruction of HO_2. Results for $Y_{H_2O} = 0.6$.

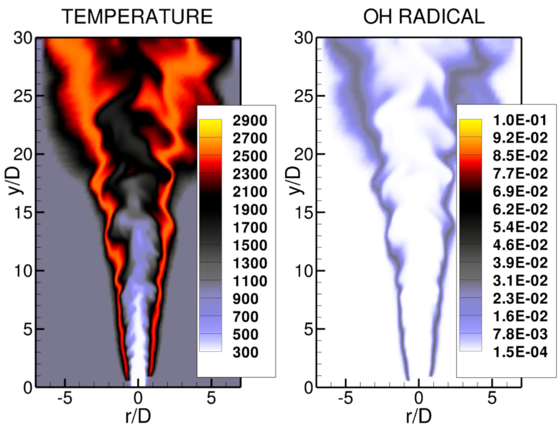

(a) (b)

Figure 11. Contours of temperature (a) and OH mass fraction (b) at the time instant $t = 8.75 \times 10^{-2} s$ – developed flame. Results for $Y_{H_2O} = 0.6$.

CMC cells lying at the distance $10D$ from the inlet in the shear layer between the fuel and oxidiser in the region close to the stoichiometric mixture fraction. This point was selected as suitable for successful ignition. The spark was modelled as a sphere with dimension $6 \times 10^{-3} m$ and its duration was assumed equal to $0.05 \times 10^{-2} s$.

Figures 8 to 11 present sample flame evolution obtained with $Y_{H_2O} = 0.6$ starting from initialisation of the spark, up to the developed flame. The spark was 'switched on' at the time instant $t = 7.27 \times 10^{-2} s$. In Figure 8a the spark is seen as a spherical region of high temperature. The white line corresponds to the stoichiometric mixture fraction $\xi_{\mathrm{MR}} = 0.048$. Shortly after the spark initialisation an expansion of high temperature area is observed (see Figure 8b).

The time instant $t = 7.30 \times 10^{-2} s$ corresponds to the final stage of the spark duration in which the production of OH radical is visible already upstream, i.e., at the distance $y/D \approx 5$. The temperature increases rapidly and the flame starts to propagate (Figure 9). The subsequent phase of flame propagation is shown in the Figure 10 corresponding to a time soon after the spark has been switched-off. The species HO_2 extends over the border of the flame and the flame propagates towards the inlet. Finally, it stabilises nearly the inflow plane in the second CMC cell and achieves maximum temperature at the level of approximately $2600K$ (Figure 11).

5. CONCLUSIONS

The LES-CMC approach was used for combustion modelling of pure hydrogen jet in oxygen-water atmosphere. To the best author knowledge these research constitutes one of the first attempts in the field of LES-CMC modelling of perfectly clean combustion process.

LES-CMC simulations were preceded by the so-called 0D-CMC calculations performed only in mixture fraction space. It was shown that for cases corresponding to low content of water in oxidiser stream, $Y_{H_2O} = 0.1 - 0.3$, the auto-ignition time varies linearly. The results of 3D LES-CMC simulations allowed to determine similar linear trend, though the absolute auto-ignition times were significantly longer compared to 0D-CMC results. Moreover, 3D LES-CMC computations showed that for $Y_{H_2O} > 0.3$ the auto-ignition process is affected by the interaction of chemistry and turbulence, and $Y_{H_2O} = 0.6$ is the critical value above which the auto-ignition does not occur, at least in the analysed simulation time. The subsequent research was focused on the analysis of influence of the oxidiser composition on auto-ignition process. It was found that the axial locations of auto-ignition spots increase with H_2O content in the oxidiser. However, the auto-ignition scenario turned out to be basically the same for all of cases except two unstable simulations ($Y_{H_2O} = 0.1$ and $Y_{H_2O} = 0.5$) which were analysed only partially. In cases in which the auto-ignition has not appeared, the combustion process was initialised by a spark modelled by a locally introduced flame kernel. The flame evolutions for auto-ignition case ($Y_{H_2O} = 0.2$) and spark ignition case ($Y_{H_2O} = 0.6$) were presented and analysed. Results obtained from 3D LES-CMC computations showed that the maximum temperature achieved in a fully developed flame decreases for increasing content of H_2O in the co-flowing stream. The obtained values of maximum temperature are in the range $2370K - 3000K$. The radial size of the flame turned out to be indirectly sensitive to Y_{H_2O} content as it was used to adjust the co-flow velocity. This aspect was not discussed in details in the paper. However, from the presented figures it could be observed that for smaller Y_{H_2O} content, and thus smaller co-flow velocity, the flame was wider. The performed simulations showed that the lift-off height of the flame is slightly dependent on the co-flow parameters. For the cases with $Y_{H_2O} = 0.6$ and $Y_{H_2O} = 0.7$ the flames stabilised very close to the inlet in the second and the third CMC cell which corresponds to the distance smaller than one nozzle diameter. For smaller Y_{H_2O} content we observed attached flames.

REFERENCES

[1] Horn, F., and Steinberg, M., 1982, “Control of carbon dioxide emissions from a power plant (and use in enhanced oil recovery)”, *Fuel*, Vol. 61 (5), pp. 415–422.

[2] Abraham, B., Asbury, J., Lynch, E., and Teotia, A., 1982, “Coal-oxygen process provides CO2 for enhanced recovery”, *Oil Gas J*, Vol. 80 (11), pp. 415–422.

[3] Toftegaard, M., Brix, J., Jensen, P., Glarborg, P., and Jensen, A., 2010, “Oxy-fuel combustion of solid fuels”, *Prog Energy Combust Sci*, Vol. 36 (5), pp. 581–625.

[4] Scheffknecht, G., Al-Makhadmeh, L., Schnell, U., and Maier, J., 2011, “Oxy-fuel coal combustion-A review of the current state-of-the-art”, *Int J Greenh Gas Control*, Vol. 5, pp. 16–35.

[5] Warzecha, P., and Bogusławski, A., 2014, “LES and RANS modeling of pulverized coal combustion in swirl burner for air and oxy-combustion technologies”, *Energy*, Vol. 66, pp. 732–743.

[6] Warzecha, P., and Bogusławski, A., 2014, “Simulations of pulverized coal oxy-combustion in swirl burner using RANS and LES methods”, *Fuel Process Technol*, Vol. 119, pp. 130–135.

[7] Garmory, A., and Mastorakos, E., 2011, “Capturing localised extinction in Sandia Flame F with LES–CMC”, *Proc Combust Inst*, Vol. 33 (1), pp. 1673–1680.

[8] Tyliszczak, A., 2013, “Assessment of implementation variants of conditional scalar dissipation rate in LES-CMC simulation of auto-ignition of hydrogen jet”, *Arch Mech*, Vol. 65, pp. 97–129.

[9] Triantafyllidis, A., Mastorakos, E., and Eggels, R., 2009, “Large Eddy Simulations of forced ignition of a non-premixed bluff-body methane flame with Conditional Moment Closure”, *Combust Flame*, Vol. 156 (12), pp. 2328–2345.

[10] Garmory, A., and Mastorakos, E., 2015, “Numerical simulation of oxy-fuel jet flames using unstructured LES–CMC”, *Proc Combust Inst*, Vol. 35, pp. 1207–1214.

[11] Vreman, A., 2004, "An eddy-viscosity subgrid-scale model for turbulent shear flow: Algebraic theory and applications", *Phys Fluids*, Vol. 16 (10), pp. 3670–3681.

[12] Triantafyllidis, A., and Mastorakos, E., 2010, "Implementation issues of the Conditional Moment Closure model in Large Eddy Simulations", *Flow Turbul Combust*, Vol. 84 (3), pp. 481–512.

[13] Klimenko, A., and Bilger, R., 1999, "Conditional moment closure for turbulent combustion", *Prog Energy Combust Sci*, Vol. 25 (6), pp. 595 – 687.

[14] Navarro-Martinez, S., Kronenburg, A., and Di Mare, F., 2005, "Conditional Moment Closure for Large Eddy Simulations", *Flow Turbul Combust*, Vol. 75 (1-4), pp. 245–274.

[15] Tyliszczak, A., 2014, "A high-order compact difference algorithm for half-staggered grids for laminar and turbulent incompressible flows", *J Comput Phys*, Vol. 276, pp. 438–467.

[16] Cook, A. W., and Riley, J. J., 1996, "Direct numerical simulation of a turbulent reactive plume on a parallel computer", *J Comput Phys*, Vol. 129 (2), pp. 263–283.

[17] Lele, S. K., 1992, "Compact finite difference schemes with spectral-like resolution", *J Comput Phys*, Vol. 103 (1), pp. 16–42.

[18] Shu, C.-W., 2003, "High-order finite difference and finite volume WENO schemes and discontinuous Galerkin methods for CFD", *Int J Comput Fluid Dyn*, Vol. 17 (2), pp. 107–118.

[19] Tyliszczak, A., 2013, "LES-CMC and LES-Flamelet simulation of non-premixed methane flame (Sandia F)", *J Th App Mech*, Vol. 51 (4), pp. 859–871.

[20] Aniszewski, W., Bogusławski, A., Marek, M., and Tyliszczak, A., 2012, "A new approach to sub-grid surface tension for LES of two-phase flows", *J Comput Phys*, Vol. 231 (21), pp. 7368–7397.

[21] Tyliszczak, A., Bogusławski, A., and Drobniak, S., 2008, "Quality of LES predictions of isothermal and hot round jet", *Quality and Reliability of Large-Eddy Simulations*, Springer, pp. 259–270.

[22] Mueller, M., Kim, T., Yetter, R., and Dryer, F., 1999, "Flow reactor studies and kinetic modeling of the H2/O2 reaction", *Int J Chem Kinetics*, Vol. 31 (2), pp. 113–125.

[23] Cabra, R., Myhrvold, T., Chen, J., Dibble, R., Karpetis, A., and Barlow, R., 2002, "Simultaneous laser Raman-Rayleigh-LIF measurements and numerical modeling results of a lifted turbulent H2/N2 jet flame in a vitiated coflow", *Proc Combust Inst*, Vol. 29 (2), pp. 1881–1888.

Conference on Modelling Fluid Flow (CMFF'15)
The 16th International Conference on Fluid Flow Technologies
Budapest, Hungary, September 1-4, 2015

FLUID-STRUCTURE-ACOUSTIC COUPLING

Matthias Springer[1], Christoph Scheit[2], Stefan Becker[3]

[1] Corresponding Author. Institute of Process Machinery and Systems Engineering, University Erlangen-Nuremberg. E-mail:sp@ipat.uni-erlangen.de
[2] Institute of Process Machinery and Systems Engineering, University Erlangen-Nuremberg. E-mail:sh@ipat.uni-erlangen.de
[3] Institute of Process Machinery and Systems Engineering, University Erlangen-Nuremberg. E-mail:sb@ipat.uni-erlangen.de

ABSTRACT

The present work deals with the aeroacoustic sound radiated by a forward–backward facing step in combination with a flexible wall behind the step. A numerical flow computation with coupled aeroacoustic and vibroacoustic simulation was carried out. The structural deformations of the oscillating plate like structure in the wake of the forward–backward facing step were considered to be small and therefore not affecting the flow field. The presented approach enables a separate consideration for the aeroacoustic as well as the structural borne noise. The influence of the interactions of the acoustic medium with the flexible structure on the vibroacoustic sound radiation is investigated. Additional to the simulations, aeroacoustic measurements in an acoustic wind tunnel were performed for validation purposes.

Keywords: aeroacoustics, LES, vibroacoustics

NOMENCLATURE

Δ	$[m]$	spanwise extension of flow geometry
$\hat{q}$	$[kg/s^2]$	spanwise averaged acoustic source term
μ	$[Ns/m^2]$	dynamic viscosity
ρ'	$[kg/m^3]$	acoustic density
ρ_0	$[kg/m^3]$	fluid density
σ_n	$[N/m^2]$	normal stresses due to acoustic pressure
τ_{ij}	$[N/m^2]$	viscous stress tensor
$\tilde{q}$	$[kg/ms^2]$	3D acoustic source term
ξ_i	$[m]$	mechanical displacement
c_0	$[m/s]$	speed of sound
D	$[m]$	dimension of forward–backward facing step
E	$[N/m^2]$	modulus of elasticity
L	$[m]$	width of windtunnel nozzle
n_i	$[-]$	vector in wall–normal direction
p	$[Pa]$	static pressure
p'	$[Pa]$	acoustic pressure
R	$[m]$	distance between step and microphone point
t	$[s]$	time
T_{ij}	$[kg/ms^2]$	Lighthill stress tensor
u_i	$[m/s]$	fluid velocity
v'_i	$[m/s]$	acoustic particle velocity
x_i	$[m]$	cartesian coordinates

1. INTRODUCTION

Flow induced noise is very important regarding many technical applications. As an example, the aeroacoustic as well as the vibroacoustic noise induced by the turbulent flow field around cars or planes has an unfavorable influence on the comfort for passengers and therefore, on the quality of the vehicle. In order to predict the acoustic behavior of technical products during the design process, the usage of numerical simulation software is a valuable measure to prevent unfavorable acoustic effects. Aeroacoustic noise is induced by turbulent pressure fluctuations e.g in turbulent shear layers or recirculation areas. Vibroacoustic noise is generated by the interaction of turbulent wall bounded flows with flexible surfaces. The turbulent pressure and wall shear stress fluctuations excite the flexible structure to vibrate in their characteristic eigenmodes. According to the eigenfrequencies, sound is radiated from the flexible structures surface. Previous studies dealing with fluid–structure–acoustic interaction are shown in [1]. A large eddy simulation (LES) of a forward–backward facing step flow in the context of fluid–structure–acoustic interaction was conducted. The feasibility of a strong fluid–structure coupling producing aeroacoustic and vibroacoustic noise is demonstrated. A comparison to experimental data shows that noise radiation is overpredicted. The influence of the backcoupling of the acoustic medium on the flexible surface and therefore on the vibroacoustic sound radiation is not taken into account. Investigations on a comparable setup with application for vehicle interior noise are published in [2]. In this study, a turbulent flow interacts with the flexible cover of a cavity. This work is focused on the noise radiation into the cavity. The influence of the structural deformations on the flow field, as well as the interaction of the acoustic field with the flexible structure are considered. However, no investigations of the influence of this interaction between structure and acoustic medium are shown. Besides the above mentioned numerical approaches, were physical fields are computed and coupled to each other in time domain, much effort has been put into the development of analytical approaches for modeling the interactions of turbulent boundary layers with elastic surfaces and the associated vibroacoustic sound radiation. Fundamental information can be found in [3]. Current work on vibroacoustics excited by turbulent boundary layers is documented in [4].

The goal of the current work is to compute the aeroacoustic, as well as the vibroaocustic sound radiation by the combination of a turbulent flow field behind a forward–backward facing step and a flexible plate with turbulent fluid load. In computing the physical domains by numerically solving the physical basic equations (fluid dynamics, structural dynamics and linear acoustics), the presented approach overcomes the disadvantages of the analytical approaches regarding the analysis of complex geometries. By neglecting the modification of the flow due to structural displacements, the high computational costs of a strong fluid–structure coupling can be saved and the sufficient resolution of the turbulent flow field can be focused on. The coupling between flow field and acoustic field is realized by calculating aeroacoustic source terms from the velocity field at simulation time. In a post–processing step, the acoustic field is computed on the basis of the acoustic source terms. The vibroacoustic sound radiation is based on the surface velocity of the flexible structure. To show the influence of the interaction between structure and acoustic medium, one–sided and two–sided coupled vibroacoustic simulations were carried out and compared to each other. In case of a one–sided coupling, the computation of the transient mechanic deformation of the flexible plate and the vibroacoustic field were carried out subsequently. In the two–sided coupled case, a coupled system of acoustic and mechanic equations was solved to allow for the interactions between the two systems. Besides the numerical investigations, microphone measurements of the sound radiated by the forward–backward facing step were carried out in a low–noise wind tunnel. A comparison between numerical and experimental results will be given and discussed.

2. NUMERICAL SETUP

2.1. Fluid mechanical Setup

The three–dimensional flow field generated by the forward–backward facing step was computed by means of LES. The flow computation was carried out using the software FASTEST-3D [5]. This code solves the transient, incompressible Navier–Stokes equations on structured grids:

$$\frac{\partial u_i}{\partial x_i} = 0 \tag{1}$$

$$\rho_0 \left(\frac{\partial u_j}{\partial t} + \frac{\partial \left(u_i u_j \right)}{\partial x_i} \right) = -\frac{\partial p}{\partial x_j} - \frac{\partial \tau_{ij}}{\partial x_i} \tag{2}$$

with

$$\tau_{ij} = \mu \left(\frac{\partial u_i}{\partial x_j} + \frac{\partial u_j}{\partial x_i} \right) \tag{3}$$

The equations were discretised using the finite volume method (FVM). The influence of the unresolved flow scales was modeled with a Smagorinsky subgrid scale model. The Smagorinsky constant was set to 0.1. Time discretisation was performed with a 4th–order Runge-Kutta Scheme. For the calculation of the convective fluxes, a central difference scheme was used. The velocity-pressure coupling is conducted with the predictor–corrector algorithm.

The forward–backward facing step was a quadratic obstacle attached to a flat plate with edge length of $D = 0.02\,\mathrm{m}$. The spanwise extend of the geometry was chosen to be $10\,D$. In spanwise direction, periodic boundary conditions were applied. The height of the computational domain was $20\,D$. At the outflow boundary a convective boundary condition was used. At the inflow boundary, a laminar boundary layer profile was set. This boundary layer profile origins from LDA–measurements during previous performed experimental investigations [1] of the current geometry. The velocity at the boundary layer edge was 20 m/s. This yields a Reynolds number of 26.000, based on inflow velocity and step height D. The grid size was chosen to obtain a wall normal resolution of $y^+ < 1$ (Fig. 2). The streamwise and spanwise resolution in the wake region of the step was $x^+ < 40$ (Fig. 1) and $z^+ < 20$ (Fig. 3), respectively. The overall number of hexahedron control volumes was 91.6 Millions. To get a CFL-number below 1, the time step size was chosen to be $4 \cdot 10^{-7}$ s.

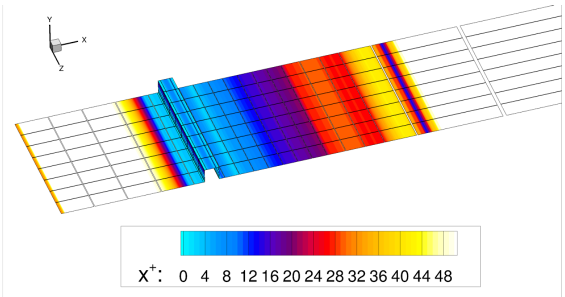

Figure 1. Time averaged x^+ - distribution

2.2. Aeroacoustic Setup

Aeroacoustic source terms were computed at simulation time from the incompressible flow vari-

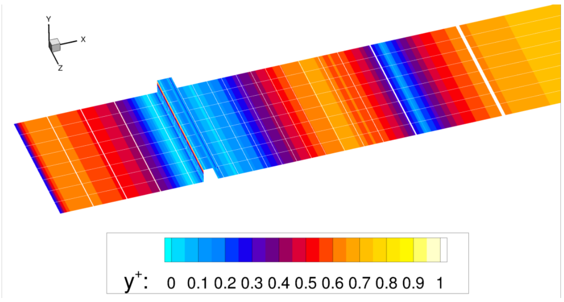

Figure 2. Time averaged y^+ - distribution

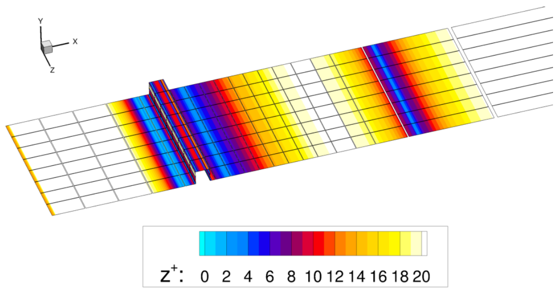

Figure 3. Time averaged z^+ - distribution

ables. Based on these acoustic source terms, the radiation of sound was computed using the software CFS++ [6]. This solver uses the finite–element method (FEM) to solve the Lighthill equation.

$$\frac{\partial^2 \rho'}{\partial t^2} - {c_0}^2 \frac{\partial^2 \rho'}{\partial {x_i}^2} = \frac{\partial^2 T_{ij}}{\partial x_i \partial x_j} \tag{4}$$

with the Lighthill Tensor being approximated as:

$$T_{ij} = \rho_0 u_i u_j \tag{5}$$

In the present work, an alternative source term formulation, which is equivalent to the original formulation, was used. The divergence of Eq. (2) results in:

$$\frac{\partial^2 \left(\rho_0 u_i u_j\right)}{\partial x_i \partial x_j} = -\frac{\partial^2 p}{\partial {x_i}^2} \tag{6}$$

The acoustic sound radiation of the 3D source term distribution was computed in a 2D acoustic simulation. Therefore, a spanwise averaging over the flow geometry with width Δ of the 3D acoustic source terms $\tilde{q}$ was performed:

$$\hat{q} = \int_{\Delta/2}^{\Delta/2} \tilde{q} \mathrm{d}z \tag{7}$$

The acoustic pressure is computed for a 2D region shown in Fig. 4. Except the walls of the fluid domain, which are modeled as acoustically hard walls, the whole acoustic domain is surrounded by a perfectly matched layer (PML [7]) in order to damp the acoustic pressure to zero towards the outer faces of the domain. Thereby, reflections of acoustic waves at the domain boundaries can be prevented. Acoustic

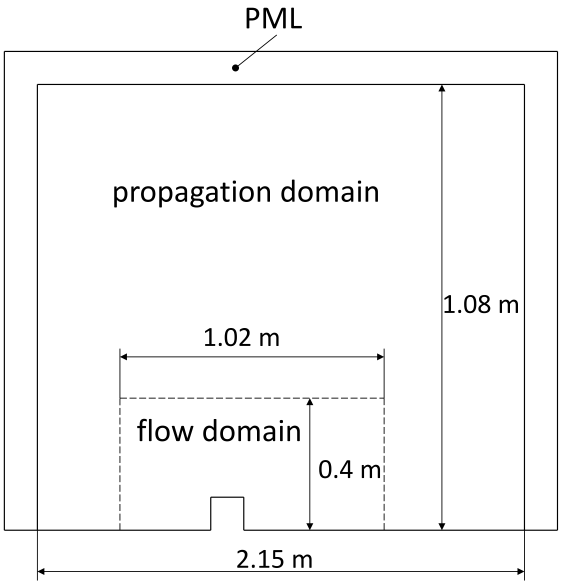

Figure 4. Acoustic domain

source terms are calculated at simulation time during flow computation [8]. The source terms are stored on the CFD grid. The acoustic computation is performed on a grid which is much coarser than the CFD grid. Therefore, a conservative interpolation of the acoustic sources between the fine CFD grid and the much coarser CAA grid has to be done [9]. The CAA grid is an equidistant, orthogonal, quadrilateral grid with a grid size of 2.5 mm in streamwise and wall-normal direction. Due to this grid size, acoustic waves below approximately 6800 Hz are resolved spatially with 20 computational points per wavelength. The output interval for acoustic source terms is $1 \cdot 10^{-5}$ s (sampling rate 100 kHz). Acoustic waves with frequency up to 5000 Hz are resolved with 20 points per period. A physical time period of 0.133 s was realized.

2.3. Vibroacoustic Setup

The vibration of the plate was induced by the turbulent wall pressure and wall shear fluctuations (Fig. 5). Due to these excitations, the plate vibrated in its characteristic eigenmodes. The surrounding fluid was not modified by the plates displacement. The sound radiation of the plate was described by the linear wave equation. Therefore, the surrounding fluid was assumed to be at rest. The wall–normal velocity of the plate surface must coincide with the wall–normal component of the acoustic particle velocity. Thus, the following relation holds on the plate surface :

$$\frac{\partial \xi_i}{\partial t} n_i = v_i' n_i \tag{8}$$

By writing Eq. 2 for the acoustic properties and neglecting the viscous term, after linearising, the momentum equation for acoustic is obtained. Hence, with Eq. (8) we obtain the coupling relation for the mechanical displacement and the acoustic pressure:

$$\frac{\partial^2 \xi_i}{\partial t^2} n_i = \frac{1}{\rho'} \frac{\partial p'}{\partial n_i} \tag{9}$$

In case of considering the interaction between structure and acoustic medium, the normal stresses due to the acoustic pressure have to be taken into account:

$$\sigma_n = -n_i p' \tag{10}$$

For the calculation of the plates vibration, the plate was modeled as a aluminium plate with a thickness of 3 mm, a density of 2700 kg/m^3 and a modulus of elasticity of E = $70 \cdot 10^9$ N/m^2. The spanwise and streamwise extension of the plate amounted to 170 mm × 170 mm. The plate was joined on a rigid baffle over a length of 10 mm at the four edges by fixing the corresponding nodes of the mechanical grid. This resulted in an effective flexible area of 150 mm × 150 mm.

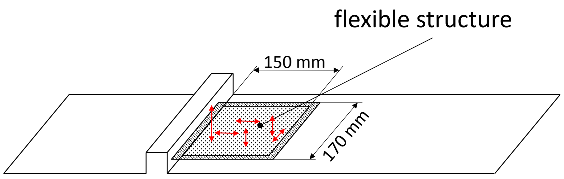

Figure 5. Flexible structure loaded by pressure force F_p and shear force F_τ

The transient mechanical computation of the plate was carried out with the code CFS++. The load vector from the flow simulation which was composed of pressure and wall shear force is interpolated on the mechanical grid. Because of the different grid sizes (fluid grid finer than mechanical grid), the interpolation had to be carried out conservatively. The mechanical grid consisted of 19200 hexahedral cells with second order basis functions. The timestep size was $1 \cdot 10^{-5}$ s which is equal to the timestep size of the aeroacoustic simulation.

The propagation of the vibroacoustic sound was computed on a similar domain like the aeroacoustic sound (Fig. 6). The computation was carried out using the code CFS++. The grid consists of orthogonal, hexahedric cells with first order basis functions. The domain near the flexible plate has a finer discretisation than the rest of the propagation region. The two domains with different grid sizes are connected via a non-matching grid interface ([10]). The whole acoustic domain is surrounded by a PML to prevent reflections from the domain boundaries.

3. EXPERIMENTAL SETUP

The acoustic measurements were performed in the acoustic wind tunnel of the University of Erlangen–Nuremberg, which is equipped with sound absorbers (anechoic chamber conditions). A description of the wind tunnel is given in [11]. The square cylinder obstacle with edge length of $D = 0.02$ m

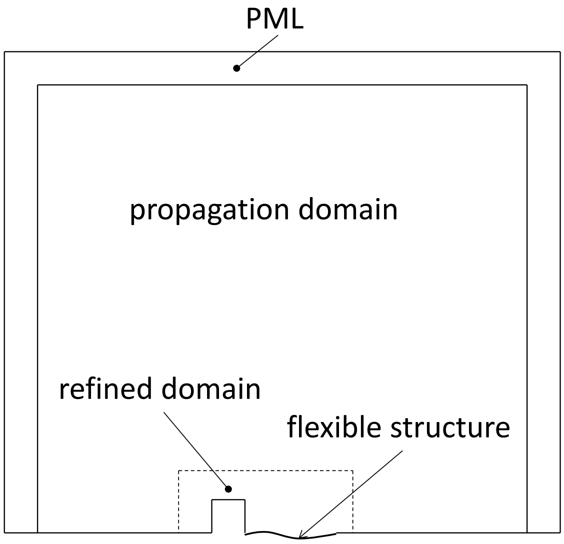

Figure 6. Vibro–acoustic domain

was attached on a flat plate. The spanwise extent of the obstacle was 35 D. The measurements were carried out at a wind speed of 20 m/s to realize the same Reynolds number as in the simulation. The simulated results show that the laminar boundary layer of the inflow became rapidly turbulent because a turbulent boundary layer profile starts to develop at 0.5D after the inlet. Therefore a boundary layer tripping was installed right after the wind tunnel's nozzle to ensure comparable boundary conditions between measurement and simulation. A microphone was installed directly above the step with a distance of 1 m. The setup is illustrated in Fig. 7. The microphone measurements were performed for 30 s with a sampling rate of 48 kHz. The microphones used where 1/2 – inch free–field microphones from Bruel & Kjaer of the type 4189 – L – 001.

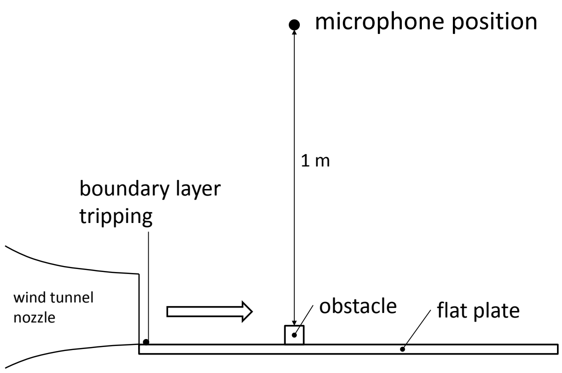

Figure 7. Experimental setup

4. RESULTS

4.1. Flow field

The time-averaged flow field generated by the forward–backward facing step is shown in Fig. 8. The velocity is normalized with the inflow velocity of 20 m/s. The flow is characterized basically by two recirculation areas. The first recirculation area develops in front of the obstacle due to pressure induced boundary layer separation. Its length is 1.6D. The second recirculation area is formed by the wake of the obstacle. It has a length of 13.5D. In Fig. 9 the time–averaged distribution of the turbulent kinetic energy normalized with the kinetic energy of the inflow is shown. Turbulence develops mainly in the shear layers between the main flow and the recirculation areas. Due to the large velocity gradients in the shear layer of the rear recirculation area, especially behind the obstacle's windward edge, the maxima of the turbulent kinetic energy are located there.

LDA measurements [1] show comparable size of

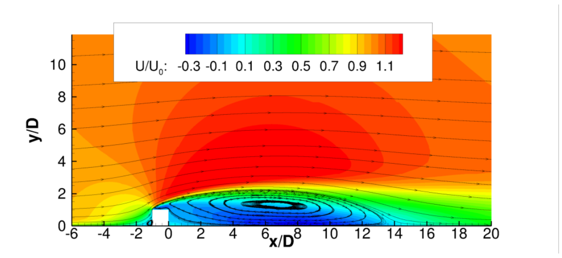

Figure 8. Time-averaged velocity field in main flow direction

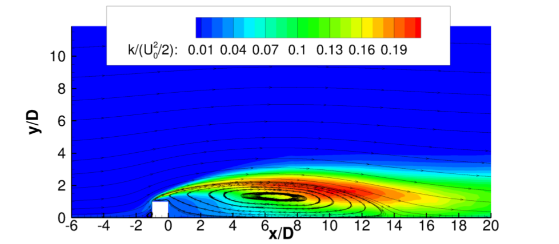

Figure 9. Time-averaged velocity field and distribution of turbulent kinetic energy k

the front recirculation area, but a much shorter detachment length of the rear recirculation area. The measured detachment length is 10.5D. One reason can be differences in the oncoming flow in measurement and simulation because the recirculation length depends on the ratio of the boundary layer thickness of the approaching flow to the obstacle height [12]. Nevertheless, profiles of the turbulent kinetic energy (Fig. 10 and Fig. 11) are comparable to the LDA measurements. The shape, as well as the peak values are similar. Due to the larger extent of the rear recirculation area in case of the simulation, the location of the maximum of the turbulent kinetic energy is above the maximum of the measured values. In Fig. 12 the distribution of the pressure fluctuations at an arbitrary timestep is shown. Due to the turbulent eddies developing in the shear layer of the rear recirculation area, pressure fluctuations occur in the shear layer and in the wake region of the step.

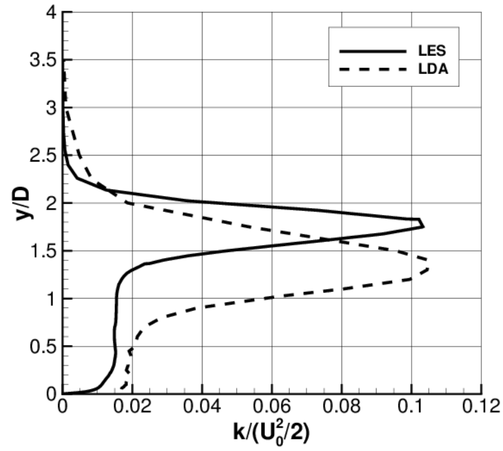

Figure 10. k–profiles at $x = 1D$ behind step

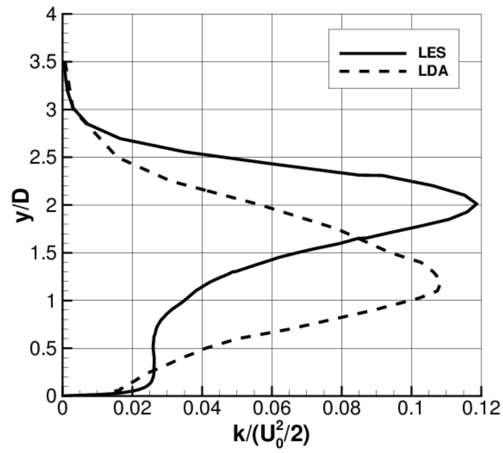

Figure 11. k–profiles at $x = 3D$ behind step

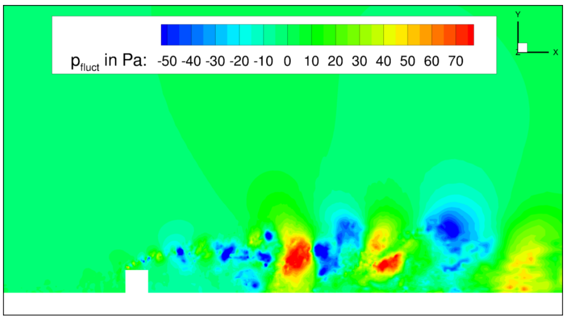

Figure 12. Distribution of pressure fluctuations at arbitrary time step

4.2. Acoustic results

4.2.1. Aeroacoustic

The aeroacoustic computation using Lighthill's acoustic analogy is based on the acoustic source term distribution. In Fig. 13 the distribution of the source term density at a distinct time step on the fine CFD grid is shown. The dominant acoustic sources are located in the shear layer of the obstacle's recirculation area. This is the flow region with the largest turbulent fluctuations, which can be seen in the distribution of turbulent kinetic energy (Fig. 9). The

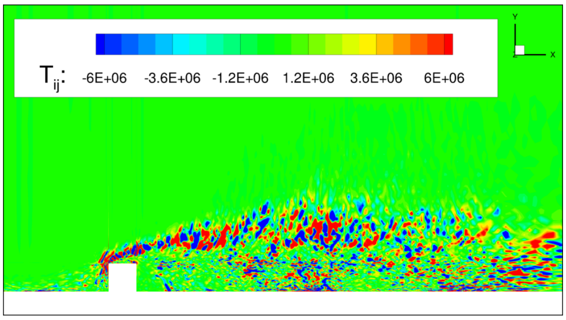

Figure 13. Acoustic source term distribution on fine CFD grid

distribution of the acoustic pressure is illustrated in Fig. 14. Here, it has to be considered that Lighthill's acoustic analogy is not valid in the source region. Only for the propagation region where no source terms are present, pure wave propagation is computed. The power spectral density of the computed

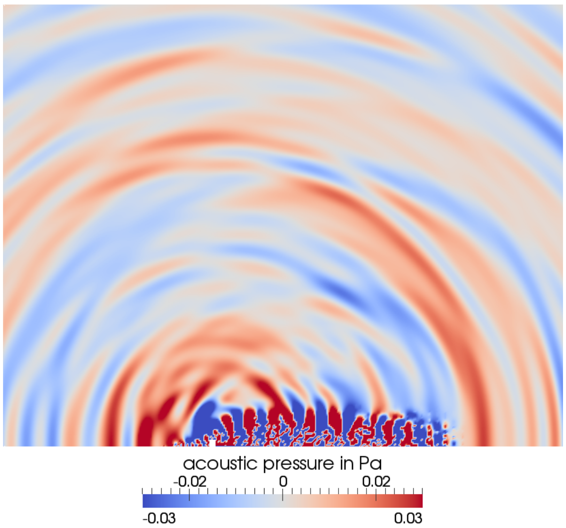

Figure 14. Distribution of acoustic pressure

acoustic sound pressure level (SPL) at the monitor point 1 m above the obstacle and the comparison with experimental results is plotted in Fig. 15. The comparison is performed with the averaged experimentally determined spectrum as well as with a superposition of experimentally determined spectra evaluated equally to the computed spectrum. To compare the results of the 2D aeroacoustic simulation with experimentally obtained data, a sound pressure correction from 2D to 3D had to be performed. According to [13] the relation between the 3D–corrected sound pressure level $SPL_{3D,\Delta}$ radiated by a slice of the width of the step geometry ($\Delta = 10D$) and the sound pressure level of the 2D aeroacoustic simulation SPL_{2D} is:

$$SPL_{3D,\Delta} = SPL_{2D} + 10\log\left(\frac{f\Delta^2}{Rc_0}\right) \tag{11}$$

The distance to the microphone point is donated by R and the speed of sound by c_0. To compare with the results of the windtunnel measurements, where a nozzle of the width $L = 0.2496\,\text{m}$ was used, an additional correction has to be performed:

$$SPL_{3D,L} = SPL_{3D,\Delta} + 10\log\left(\frac{L}{\Delta}\right) \tag{12}$$

The comparisons show that the numerical results are located within the region of the equivalent evaluated measurements. Between 500 Hz and 1500 Hz there are only minor differences. Below and above this region, the averaged numerical results are located approx. 5 – 10 dB below repectively above the averaged measurements within the region of equivalent evaluated measurements. The flattening of the experimentally results above 1000 Hz due to the influence of the recirculation area is also visible in the numerical data. The decay in the frequency region towards 10000 Hz agrees good between simulation and measurement.

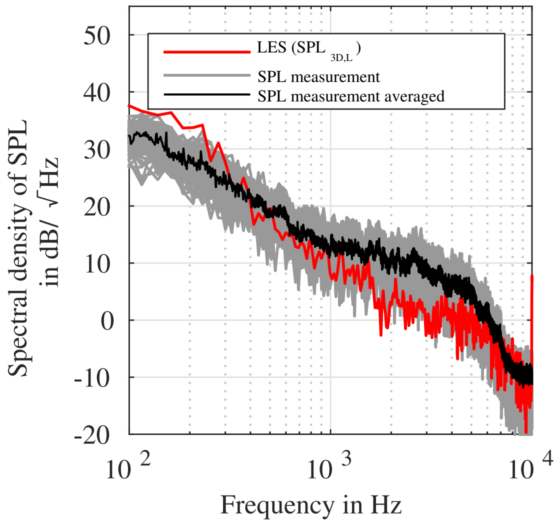

Figure 15. Power spectral density of sound pressure level (Monitor point 1 m above obstacle) – Comparison between measurement and simulation

4.2.2. Vibroacoustic

The vibroacoustic simulations were carried out as one–sided as well as two–sided coupled simulations. By comparing the results, the influence of the interaction between the structure and the acoustic medium becomes obvious. The wall normal displacement of the center point of the plate is shown in Fig. 16. The plate movement is driven by a load vector composed of pressure force and wall shear force extracted from the turbulent flow field. These loads are imprinted on the surface of the plate during the one–sided or two–sided coupled simulations. Due to the pressure decrease in the wake region of the obstacle the mean deflection of the plate is in upward direction. The frequency of the dominant oscillation is approx. 1160 Hz which is the first eigenfrequency of the plate. Due to the two–sided coupling obvious damping effects can be observed. The amplitude of the displacement at the plate center point is reduced from approx. $3 \cdot 10^{-7}$ m to approx. $1 \cdot 10^{-7}$ m. In Table 1, the first five eigenfrequencies according

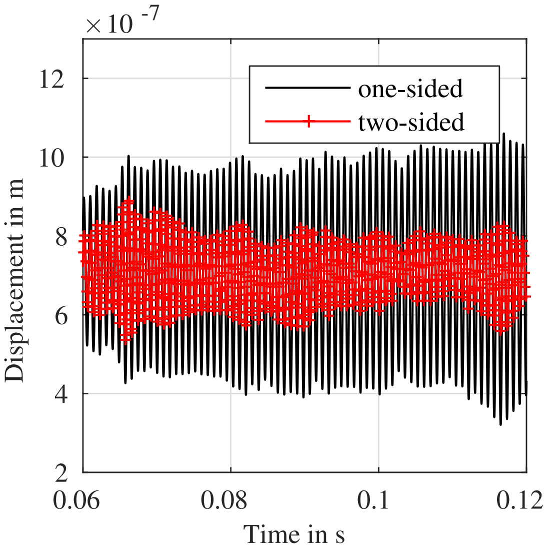

Figure 16. Displacement at the plate center – comparison between two–sided and one–sided simulation

to the boundary conditions mentioned in section 2.3 are listed. The spectral density of the plate velocity

Table 1. First five computed eigenfrequencies in Hz

1st	2nd	3rd	4th	5th
1160	2359	3469	4209	4232

at the center point is shown in Fig. 17. The dominant modes are the first eigenmode as well as the forth eigenmode. The effect of the two–sided coupling is visible in a reduction of the spectral density of the velocity for the excited eigenmodes. In case of the first eigenmode a reduction from approx. $2 \cdot 10^{-3}$ m/(s $\sqrt{Hz}$) to approx. $1 \cdot 10^{-4}$ m/(s $\sqrt{Hz}$) is visible. The higher eigenmodes show similar behavior. The acoustic spectrum due to the plate vibration is shown in Fig. 18. It is the result of the evaluation of the acoustic pressure time signal at the microphone point. Due to the two–sided coupling, the sound pressure level reduces from 41.1 dB to 34.7 dB in case of the first eigenmode. The behavior for the higher eigenmodes is comparable.

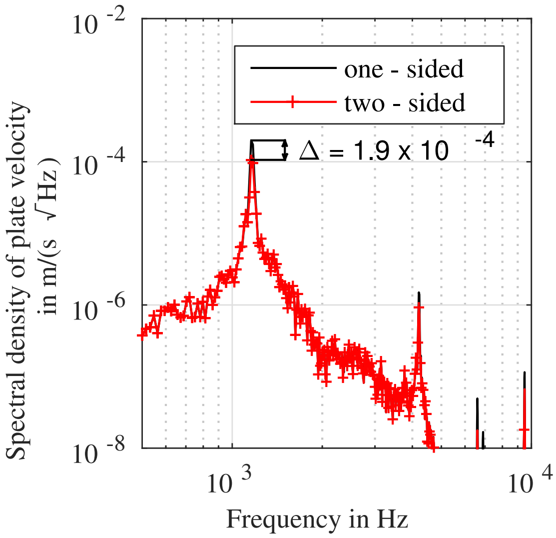

Figure 17. Spectral density of vibration velocity at plate center – comparison between two–sided and one–sided simulation

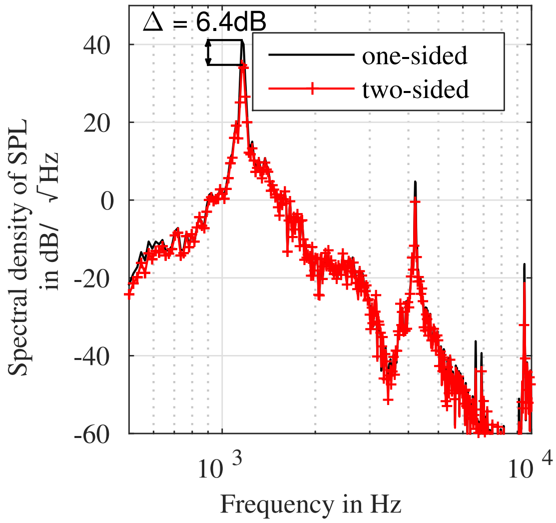

Figure 18. Vibroacoustic sound at microphone point – comparison between two–sided and one–sided simulation

5. CONCLUSION

The flow simulation of the turbulent flow over a forward–backward facing step with coupled aeroacoustic and vibroacoustic simulation was presented. The results of the aeroacoustic simulation were compared with aeroacoustic measurements. Good comparability over a wide frequency range was observed. The vibroacoustic simulations were carried out as one–sided, as well as two–sided coupled simulations to investigate the influence of the interaction between structural vibration and acoustic medium. As a result of these simulations, vibroacoustic sound radiation was based on the temporal displacement of a flexible plate located in the wake region of the step, loaded with turbulent pressure and shear stress forces. The vibroacoustic analysis showed the plate being excited mainly in its first and forth eigenfrequency. Hence, the sound radiation was dominated by these frequencies. The comparison of the one–sided and the two–sided coupled simulations showed a strong influence of the interaction between structural deformation and acoustic medium. Due to the acoustic medium, considerable damping effects on the structural deformation and therefore on the sound radiation can be observed. Conclusively, the presented work showed the feasibility to capture the fluid–structure–acoustic interaction for complex turbulent flows. In addition to measurements, the simulative approach allows for detailed insight into the mechanisms of noise generation and enables the separation of aeroacoustic and vibroacoustic noise.

REFERENCES

[1] Schäfer, F., Müller, S., Uffinger, T., Becker, S., and Grabinger, J., 2010, "Fluid-Structure-Acoustics Interaction of the Flow Past a Thin Flexible Structure", *AIAA Journal*, Vol. 48, pp. 738–748.

[2] Vergne, S., J.-M., A., G'Styr, N., and Perie, F., 2002-03, "Simulation of Cavity Aero-Elastic Noise Induced by an External Turbulent Flow Perturbed by a Small Ruler", *Proceedings of the International Workshop on "LES for Acoustics"*, German Aerospace Center,DLR,Göttingen, Vol. DGLR-Report.

[3] Blake, W., 1986, *Mechanics of Flow–Induced Sound and Vibration*, Academic Press, Inc.

[4] Ichou, N., Bareille, O., Troclet, B., Hiverneau, B., Rochambeau, M., and Chronopoulos, D., 2013, "Vibroacoustics under Aerodynamic Excitation", *Flinovia – Flow Induced Noise and Vibration Issues and Aspects*, Consiglio Nazionale Ricerce, Rome, pp. 227–248.

[5] Durst, F., and Schäfer, F., 1996, "A Parallel Block/Structured Multigrid Method for the Prediction of Incompressible Flows", *International Journal of Numerical Methods in Fluids*, Vol. 22, pp. 249–565.

[6] Kaltenbacher, M., 2010, "Advanced simulation tool for the design of sensors and actuators", *Procedia Engineering*, Vol. 5, pp. 597–600.

[7] Hüppe, A., 2012, "Spectral Finite Elements for Acoustic Field Computation, Dissertation", Ph.D. thesis, Vienna University of Technology.

[8] Scheit, C., Esmaeili, A., and Becker, S., 2013, "Direct Numerical Simulation of a Flow Over a Forward–Facing Step – Flow Structures and Aeroacoustic Source Regions", *International Journal of Heat and Fluid Flow*, Vol. 43, pp. 184–193.

[9] Kaltenbacher, M., Escobar, M., Becker, S., and Ali, I., 2008, "Computational Aeroacoustics Based on Lighthills Acoustic Analogy", *Computational Acoustics of Noise Propagation in Fluids*, Vol. 4, pp. 115–142.

[10] Triebenbacher, S., 2012, "Nonmatching Grids for the Numerical Simulation of Problems from Aeroacoustics and Vibroacoustics, Dissertation", Ph.D. thesis, Vienna University of Technology.

[11] Hahn, C., Becker, S., Ali, I., Escobar, M., and Kaltenbacher, M., 2007, "Investigation of Flow Induced Sound Radiated by a Forward Facing Step", *New Results in Numerical and Experimental Fluid Mechanics*, Vol. 6, pp. 438–445.

[12] Bergeles, G., and Athanassiadis, N., 1983, "The Flow Past a Surface–Mounted Obstacle", *ASME Journal of Fluids Engineering*, Vol. 105, pp. 461–463.

[13] Oberei, A., Roknaldin, F., and Hughes, T., 2002, "Trailing–Edge Noise Due to Turbulent Flows", *Tech. rep.*, Boston University, Report No. 02–002.

FLOW ANALYSIS OF A SIDE BRANCH ARTERY COVERED BY A FLOW DIVERTER DEVICE

Gábor ZÁVODSZKY[1], Benjámin CSIPPA[2], György PAÁL[3]

[1] Corresponding Author. Department of Hydrodynamics Systems, Faculty of Mechanical Engineering, Budapest University of Technology and Economy, Műegyetem rakpart 3., 1111 Budapest, Hungary. Tel.: +36 1 463 1111/5798, E-mail: zavodszky@hds.bme.hu
[2] Department of Hydrodynamics Systems, Budapest University of Technology and Economics. E-mail: bcsippa@hds.bme.hu
[3] Department of Hydrodynamics Systems, Budapest University of Technology and Economics. E-mail: paal@hds.bme.hu

ABSTRACT

Abdominal aneurysms are pathological lesions on our largest artery, the abdominal aorta. These malformations, amongst other unfavourable physiological effects, carry a severe risk of rupture. Applying stent grafts in these arteries as part of the medical treatment is a common practice to exclude weakened arterial wall sections from the blood flow. However, it might lead to undesired side-effects in several cases. When the treated vessel section encompasses side branches, the stent graft placed inside the vessel might cover some of its smaller side branches, thus significantly modifying or even blocking the blood flow in them. The usual solution is either cutting new openings on the surface of the stent graft at the location of the vessel side branches and pull smaller stent grafts through them, hence creating "arms", or not implanting stent grafts at all. In the current work, an alternative solution was investigated in two dimensions: instead of a stent graft, a simple stent, i.e., a flow diverter device is implanted which covers the two large side-branches, namely the renal arteries. The volume flow of these two covered side-branches was investigated as a function of varying stent resistances. It was found that the proper selection of stent resistance can significantly reduce the velocities inside the lesion, thus reducing the mechanical stresses on the dilated wall section while still allowing enough blood flow through the side-arteries to ensure proper renal functions. The present analysis also covers the regions where potential thrombus formations might occur in the future due to reduced flow velocities.

Keywords: aneurysm, CFD, flow diverter, lattice Boltzmann

NOMENCLATURE

p	$[Pa]$	pressure
κ	$[m^2]$	permeability
κ_1	$[m^{-1}]$	inertial permeability
μ	$[Pa\ s]$	dynamic viscosity
$\vec{v}$	$[m/s]$	velocity
c_0	$[kg/m^3 s]$	linear permeability coefficient
c_1	$[kg/m^4]$	quadratic permeability coefficient

1. INTRODUCTION

Cardiovascular diseases represent the leading cause of death in Europe [1] in the working population (bellow the age of 65). These diseases can manifest themselves in several different ways. One particular form usually found along arteries is called an aneurysm. They are lesions on the vessel wall forming berry-like sacs (saccular form aneurysms) or radial enlargements of the section (fusiform aneurysms). The latter is the usual one on our largest artery, the abdominal aorta. The presence of this malformation poses a high risk for the patient in the form of a possible rupture. Such a severe event carries a high rate of morbidity of approximately 90% [2]. The treatment method is usually based on the implantation of a stent-graft inside the concerned aortic section [3]. That is, a metallic stent-tube covered with densely woven polyester textile is inserted inside the vessel that excludes the enlarged sections of the vessel from the main flow. There are cases, however, when this solution is not satisfactory. The extent of the abdominal aneurysm can be such that it incorporates the branching points for the renal arteries. These arteries carry around 1.1 l of blood per minute in an average 70 kg male towards the kidneys. If the blood supply is reduced to as low as 0.25 l per minute, it is considered to be a life-threatening state, requiring immediate medical intervention [4]. It follows that the usage of stent-grafts in the case of affected renal arteries is not directly possible since covering these artery branches would be a life-endangering act. One of the alternative solutions to this problem is to employ flow diverters such as those utilised in cerebral aneurysms. They are essentially similar to stent-grafts without the densely woven texture, therefore they permit the blood to flow through their surface while imposing some hydrodynamic resistance upon this flow. For a successful treatment, a densely woven stent should be used in order to reduce the flow sufficiently next to the diseased vessel wall to prevent its rupture. However, another problem emerges at this point: the flow inside the covered side branch is reduced as well. In case of the renal artery, the continuous blood flow is of vital importance for maintaining proper kidney functions, as outlined above. Therefore, the medical practitioner has to balance the hydrodynamic resistance value of the flow diverter to reduce the risk of the aneurysmal rupture to a sufficiently low level while permitting enough blood to reach the kidney. The blood flow of an aortic section was simulated using a series of stents, each having a different hydrodynamic resistance, placed inside the parent vessel of the renal arteries to investigate how the available blood supply of one of the covered side branches is changing. The expected effect is that they permit enough blood flow for the kidneys to remain healthy and functional while decreasing the flow velocity inside the aneurysmal sac to the point where blood might come to a stasis. According to the works of [5, 6], the desired hydrodynamic resistance in abdominal aneurysms can be achieved by implanting multiple stents concentrically. The resulting resistance of this multi-layer stent is statistically equal to the sum of the distinct resistances of the implanted stents [7] with some variance caused by the fact that the different layers might overlap in a different way. The emerging flow field inside a two-dimensional projection of a real abdominal aneurysm geometry was investigated in the current work . The volumetric outflow parameters of the covered renal arteries were inspected in the bare geometry and in the presence of several stents, each representing a different hydrodynamic resistance.

2. METHODS

The chosen numerical solution method was the lattice Boltzmann method (LBM), which has been shown to be capable of producing highly accurate results for transient blood flow simulations [8]. The Bhatnagar-Gross-Krook (BGK) collision model [9] was used for the dynamics of the fluid numerical cells on a regular D2Q9 lattice. The walls were considered to be no-slip surfaces, implemented using a simple bounce-back numerical scheme. The geometry originates from a computer tomography (CT) angiography record. The stent itself has a rather complex geometry, thus in our simulation it is represented as a layer of porous material, neglecting the actual positions of the struts inside the net of the stent. The main idea of the usage of porous media instead of the exact stent geometry is to reduce the simulation complexity by approximating the actual effect of the stent by homogenous resistance. This can be a viable simplification as the medical practitioner has little control over the axial angle of the stent when implanting it. Therefore, the accurate position and angle of the struts inside the vessel are unknown before the implantation.

For porous media, it is known that the pressure drop is nearly linearly proportional to the flow velocity in case of low velocities [10]. For higher velocities, the pressure drop exceeds the one predicted by this linear approximation. To account for this effect, one can extend the linear model with a quadratic term called Forcheimer's term [11]. Several successful numerical simulations were carried out in the past using this formalism [12, 13].

$$\triangledown p = -\frac{\mu}{\kappa}\vec{v} - \frac{\rho}{\kappa_1}|\vec{v}|\vec{v} \tag{1}$$

Since density and viscosity do not change during the simulations, the two constant multipliers of the linear and quadratic velocity terms can be denoted as $c_0 = \mu/\kappa$ and $c_1 = \rho/\kappa_1$, respectively.

Acquiring a proper value for c_0 and c_1 is not an easy task. In the present work they were recovered from measurements. Though the accurate description of the experimental configuration would exceed the boundaries of this paper, the main ideas are briefly outlined below. The method is based on measuring the pressure drop between the two sides of the stent under steady flow conditions. The pressure drop values corresponding to different volume flow rates form a second order polynomial curve (with some variance caused by measurement errors). Fitting a second order polynomial yields the required constant values. Naturally, the different types and brands of flow diverting devices display a wide spectrum of resistance values. For our investigation a low-resistance Pipeline product was chosen to define a realistic base hydrodynamic resistance. Please note that the current question is whether a resistance value exists at which the flow velocities inside the sac are strongly reduced while the volume flow through the side-arteries is still adequate for the healthy operation of the kidneys. Determining the exact resistance values and porosity constants at which this happens shall require a three-dimensional study.

The effect of this resistance is imposed upon the fluid in the form of an external force. Guo's forcing term [14] was used in order to implement this external force accurately in the LBM simulation.

2.1. Simulation setup

The geometry is shown in Fig. 1. The inlet is the opening located at the top while the other three openings are outlets. For all the simulation runs, the regions denoted by light grey colour are considered as fluid regions except for the last simulation where they represent thrombosed blood, therefore they are considered to be solid.

The Reynolds number was set to 1500 at the inlet at the highest flow rate instant (at the systolic peak), which at the cardiac cycle length of 1 s happens around $t = 0.32$ s. This setting led to a time-averaged

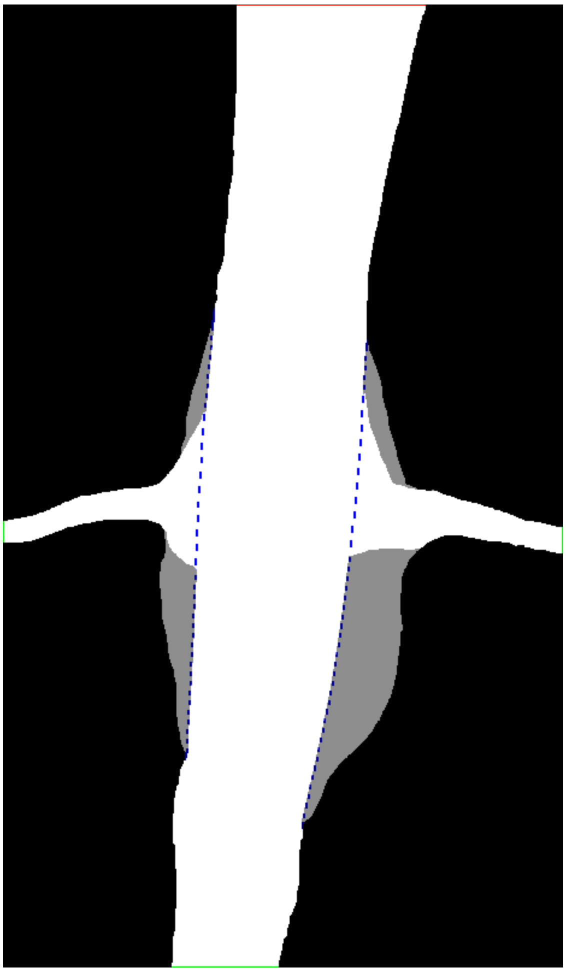

Figure 1. The geometry of the abdominal aneurysm. The black region represents the solid numeric cells. The dashed lines denote the location of the implanted stent while the light grey region denotes the locations for thrombotised blood.

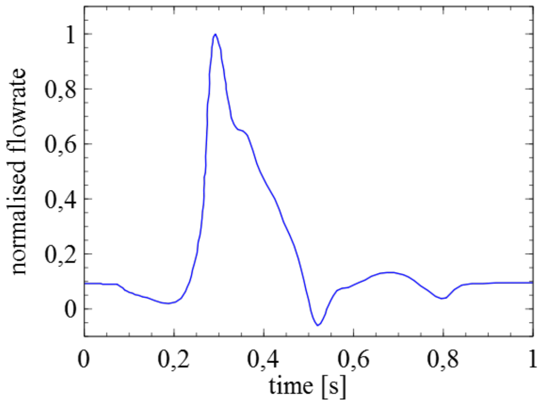

Figure 2. Normalised flow rate at the inlet during a cardiac cycle $(1\ s)$ **[15].**

Reynolds number of 491.7. The inflow had a parabolic velocity distribution along the inlet line with a time-varying amplitude depicted in Fig. 2. This volumetric flow rate bears the characteristics of that of one observable during a real cardiac cycle. The given Reynolds number belongs to the lower regions of the physiological values observable in a human aorta. At the higher end of the possible Reynolds values turbulent behaviour can be expected which would question the apparent resistance of the stent since the measurements are carried out under laminar flow conditions. Using these inlet values, however, the flow is assumed to remain laminar throughout the cardiac cycle. The outlets were defined to be at a constant pressure level. This approach is motivated by the fact that the onward vessel network presents an approximately constant pressure resistance.

The permeability constants were basically set to the default values of $c_0 = 2.9 \times 10^5 \frac{kg}{m^3\ s}$ and $c_1 = 9 \times 10^7 \frac{kg}{m^4}$. These values represent the experimentally acquired hydrodynamic resistance of a typical stent intended for smaller cerebral arteries. The stents designed for abdominal implantation use wider struts and a denser net, henceforth are expected to display higher resistances (though their exact hydrodynamic resistance values are not available for public use). The stent resistance was gradually increased from $c_0 = 0$ and $c_1 = 0$ to $c_0 = 6.9 \times 10^6 \frac{kg}{m^3\ s}$, $c_1 = 2.16 \times 10^9 \frac{kg}{m^4}$ (48 times the resistance of the basic one) in our simulations.

3. RESULTS

The simulation result of the case with no stent is shown in Fig. 3. This, as well as the following velocity magnitude figures, presents values normalised with the highest velocity magnitude value occurring at the inlet (which value is naturally the same for all the simulations).

Figure 4 presents the results for the simulation with an implanted stent using the default porous material values. The velocities (as expected from the low basic resistance values) are barely decreased regarding both the renal arteries and the enlarged regions of the aneurysm.

Figure 5 shows the velocity magnitudes for the stent with the highest resistance. The flow inside the sac is strongly dampened while the renal flow is only slightly decreased. This behaviour might be the result of the significant difference between the linear and quadric terms of the porous material representing the stent. For the radial part of the flow with typically smaller velocity components, the smaller linear term dominates while the higher resistance caused by the larger quadric term quickly increases for the larger axial components of the flow. This leaves the slower radial components of the flow nearly intact while reducing the axial components strongly, thus creating the possibility of thrombosis formation inside the enlarged portions of the vessel.

The time-averaged outflow through the renal arteries was measured during the simulations. Figure 6 presents the normalised outflow values for the left

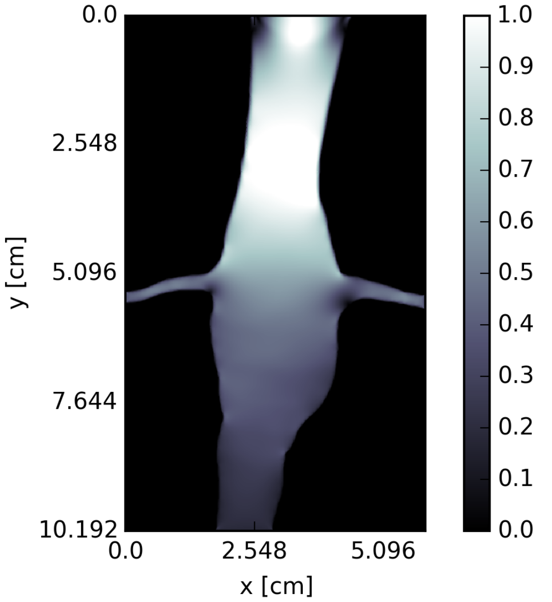

Figure 3. Normalised velocity magnitudes with no stent inside the geometry at the time of the systolic peak.

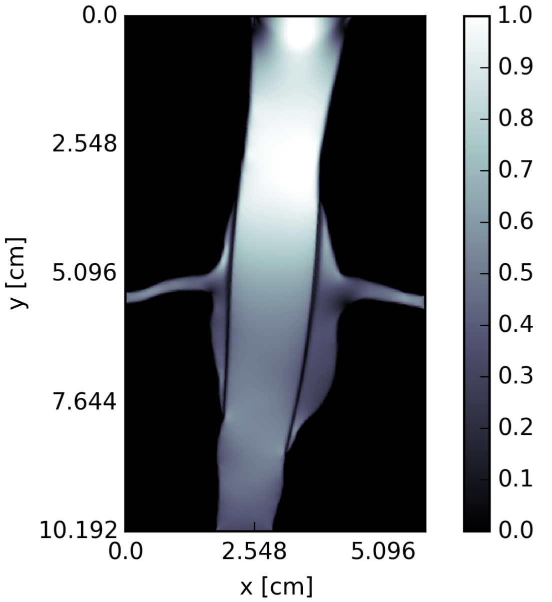

Figure 4. Normalised velocity magnitudes with a stent ($c_0 = 2.9 \times 10^5 \frac{kg}{m^3\ s}$, $c_1 = 9 \times 10^7 \frac{kg}{m^4}$) inside the geometry at the time of the systolic peak.

artery (the right one only slightly differs). The values are normalised with the time-averaged outflow of the arteries when no stent is inserted. The results show that even with the highest stent resistance when there is practically no flow in most regions inside the sac, the arteries can maintain most of their volumetric outflow, around 95%. This value is well above the medically critical limit of about 25 – 30%. The

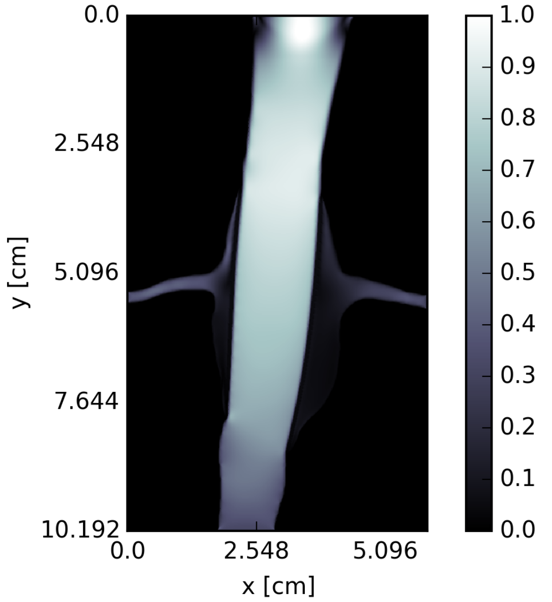

Figure 5. Normalised velocity magnitudes with a stent ($c_0 = 6.9 \times 10^6 \frac{kg}{m^3\ s}$, $c_1 = 2.16 \times 10^9 \frac{kg}{m^4}$) inside the geometry at the time of the systolic peak.

question of longer term effects arises here since if the flow velocities are sufficiently decreased (as the case seems to be with the highest resistance stent), the arteries might receive enough flow with these lower velocities due to the large surface of the stent. However, there might be issues when the thrombotisation of the stagnant or slow-current regions begin since they decrease the permeable surface area and the remaining surface might not be sufficient to sustain enough flow. To investigate the question, a second geometry was created where all the regions possibly prone to thrombosis are represented as solid cells (light grey region in Fig. 1), thus allowing only for a reduced surface for the parent artery to supply the side branches.

Figure 7 shows the results for the thrombotised geometry using the stent with the highest resistance. The flow velocities are visibly reduced (particularly at the instant around the systolic peak), however, the side branches still manage to maintain 85% of their original blood flow.

4. CONCLUSIONS

The results seem to support the idea of using stents (or rather multilayer stents) to treat abdominal aneurysms where stent-grafts do not present a viable option due to side branch occlusion. A carefully selected stent with a high hydrodynamic resistance value might hamper the flow in the enlarged aortic regions, thus reducing the mechanical load on the corresponding diseased vessel walls. Furthermore, this flow reduction seems to have a major effect only on the larger axial components in the given geometry. This is favourable for maintaining the

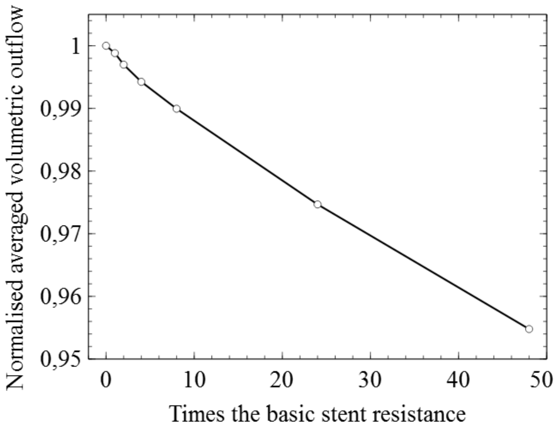

Figure 6. Normalised volumetric flow rate at the left renal artery outlet with the different stent resistances.

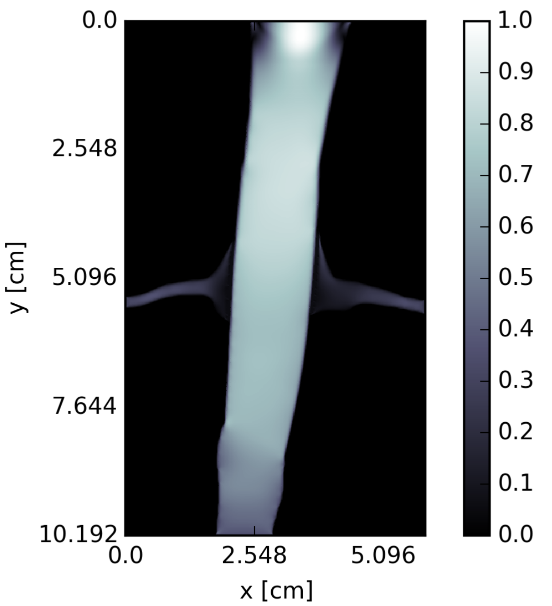

Figure 7. Normalised velocity magnitudes with a stent ($c_0 = 6.9 \times 10^6\ \frac{kg}{m^3\ s}$, $c_1 = 2.16 \times 10^9\ \frac{kg}{m^4}$) inside the geometry of the thrombotised aneurysm at the time of the systolic peak.

healthy volume flow for the kidneys since the radial components are barely reduced. Even if the desired thrombosis occludes large parts of the stent surface, the volumetric outflow of the side branches remains sufficient. However, there are several approximations in our simulations that should be pointed out. On one hand, the real abdominal aneurysm flows are inherently three-dimensional phenomena, henceforth a two-dimensional model might not properly capture all the processes. On the other hand, the homogenous porous material approximation of the stent geometries might produce a different behaviour in some cases (e.g., a too dense real stent might get covered with endothelial cells after a while, thus further reducing its permeability). Still, the treatment of an abdominal aneurysm using a stent with an appropriately chosen resistance value seems to be possible and further investigations in this direction are encouraged by the results.

REFERENCES

[1] Allender, S., Scarborough, P., Peto, V., Rayner, M., Leal, J., Luengo-Fernandez, R., and Gray, A. 2008 *European cardiovascular disease statistics*. European Heart Network.

[2] Egelhoff, C., Budwig, R., Elger, D., Khraishi, T., and Johansen, K. 1999 “Model studies of the flow in abdominal aortic aneurysms during resting and exercise conditions”. *Journal of Biomechanics*, Vol. 32, No. 12, pp. 1319–1329.

[3] Kato, N., Dake, M., Miller, D. C., Semba, C., Mitchell, R. S., Razavi, M., and Kee, S. 1997 “Traumatic thoracic aortic aneurysm: treatment with endovascular stent-grafts.”. *Radiology*, Vol. 205, No. 3, pp. 657–662.

[4] Prowle, J. R., Ishikawa, K., May, C. N., and Bellomo, R. 2008 “Renal blood flow during acute renal failure in man.”. *Blood Purification*, Vol. 28, No. 3, pp. 216–225.

[5] Henry, M., et al. 2008 “Treatment of renal artery aneurysm with the multilayer stent”. *Journal of Endovascular Therapy*, Vol. 15, No. 2, pp. 231–236.

[6] Polydorou, A., et al. 2010 “Endovascular Treatment of Aneurysm With Side Branches-A Simple Method. Myth or Reality?”. *Hospital Chronicles*, Vol. 5, No. 2.

[7] Ugron, Á., Szikora, I., and Paál, G. 2014 “Measurement of flow diverter hydraulic resistance to model flow modification in and around intracranial aneurysms”. *Interventional Medicine and Applied Science*, Vol. 6, No. 2, pp. 61–68.

[8] Závodszky, G. and Paál, G. 2013 “Validation of a lattice Boltzmann method implementation for a 3D transient fluid flow in an intracranial aneurysm geometry”. *International Journal of Heat and Fluid Flow*, Vol. 44, pp. 276 – 283.

[9] Bhatnagar, P. L., Gross, E. P., and Krook, M. 1954 “A model for collision processes in gases. I. Small amplitude processes in charged and neutral one-component systems”. *Physical Review*, Vol. 94, No. 3, p. 511.

[10] Ergun, S. 1952 “Fluid flow through packed columns”. *Chemical Engineering Progress*, Vol. 48.

[11] Ruth, D. and Ma, H. 1992 "On the derivation of the Forchheimer equation by means of the averaging theorem". *Transport in Porous Media*, Vol. 7, No. 3, pp. 255–264.

[12] Thauvin, F. and Mohanty, K. 1998 "Network modeling of non-Darcy flow through porous media". *Transport in Porous Media*, Vol. 31, No. 1, pp. 19–37.

[13] Rochette, D. and Clain, S. 2003 "Numerical simulation of Darcy and Forchheimer force distribution in a HBC fuse". *Transport in Porous Media*, Vol. 53, No. 1, pp. 25–37.

[14] Guo, Z., Zheng, C., and Shi, B. 2002 "Discrete lattice effects on the forcing term in the lattice Boltzmann method". *Physical Review E*, Vol. 65, No. 4, p. 046308.

[15] Finol, E. A. and Amon, C. H. 2001 "Blood flow in abdominal aortic aneurysms: pulsatile flow hemodynamics". *Journal of Biomechanical Engineering*, Vol. 123, No. 5, pp. 474–484.

Conference on Modelling Fluid Flow (CMFF'15)
The 16th International Conference on Fluid Flow Technologies
Budapest, Hungary, September 1-4, 2015

Damping and Resonant Break-up Mechanisms of the Gas Bubble Subjected to an Acoustic Wave in Liquid

Vladimir VANOVSKIY[12], Alexander PETROV[21]

[1] Corresponding Author. Department of Theoretical Mechanics, Moscow Institute of Physics and Technology. 9 Institusky Per. 141701, Dolgoprudny, Russia. Tel.: +7 916 724-40-52, E-mail: vovici@gmail.com
[2] Mechanics of Systems Laboratory, Institute for Problems in Mechanics of the Russian Academy of Sciences. E-mail: petrovipmech@gmail.com

ABSTRACT

The linear theory of bubble oscillations damping in liquid is constructed in the case of free and forced radial oscillations. All the dissipation mechanisms are considered: thermal, viscous and acoustic. The main assumption made is the pressure uniformity inside the bubble. The concept of averaging over volume helps to obtain the response function in clear and easy-to-use form. The constructed theory is used to describe bubble oscillations near the resonance and in conditions of frequencies resonance of radial and arbitrary axially symmetric deformation mode 2:1. The asymptotic behaviour and mode magnitudes are obtained using the efficient Krylov-Bogolyubov averaging technique. The enormous growth of the deformation mode can be attributed as a sign of bubble break-up and is one of the mechanisms of subharmonics appearance in the bubble emission spectrum. The estimative criterion of bubble break-up is obtained for the cases of the slow and fast acoustic wave start.

Keywords: break-up criterion, resonance 2:1, driven oscillations, bubble break-up, subharmonics, bubble damping

NOMENCLATURE

F	$[-]$	acoustic wave magintude
P_n	$[-]$	nth Legendre polynomial
T	$[K]$	gas temperature
T_∞	$[K]$	liquid temperature
a	$[m]$	bubble radius
a_0	$[m]$	bubble equilibrium radius
c_p	$[J/(kg \cdot K)]$	gas heat capacity
k	$[m^2/s]$	gas thermal diffusivity
p	$[Pa]$	gas pressure
p_{ext}	$[Pa]$	pressure in fluid at the bubble boundary
p_∞	$[Pa]$	external pressure in fluid
$\underline{v}$	$[m/s]$	gas velocity vector
γ	$[-]$	gas heat capacity ratio
c	[m/s]	sound speed in fluid
$\lambda = \rho c_p k$	$[W/(m \cdot K)]$	gas thermal conductivity
μ	$[Pa \cdot s]$	fluid viscosity
ρ	$[kg/m^3]$	fluid density
ρ_g	$[kg/m^3]$	gas density
σ	$[N/m]$	surface tension
ω_ξ	$[1/s]$	resonant mode frequency

INTRODUCTION

The bubble break-up problem has applications in medicine, oceanology and in all fields related to cavitation and sonoluminescence. The break-up mechanism could help in opening the blood-brain-barrier and delivering drugs into brain [1], for example. The mechanism of break-up is not yet fully understood and has gained much interest in the present science. The damping mechanisms of oscillating gas bubble in liquid are explored much better in many profound works on this topic. The problem of damping in bubbly liquid has many civil and military applications as the bubbles can strongly influence the propagation of sound in fluid.

There is much evidence that the bubbles in acoustic field emit subharmonic sound at frequency being integer part of the driving frequency [2]. This fact can be attributed to existence of nonspherical bubble harmonics resonant to driving frequency. There exist many experimental works that prove the possibility of bubble break-up because of its nonspherical shape oscillations [3]. The theory on this topic usually consider the nonlinear interaction between oscillation modes and there were many works done for freely oscillating bubble that predicted the amplified energy transfer at frequency resonance 2:1 [4, 5]. The possibility of break-up was mentioned in the latest works on this topic [6, 7] that dealt with the problem of resonant energy transfer from radial oscillations mode to any deformation mode in case of free oscillations. In the latter two works the period of energy transfer and asymptotic trajectories were obtained and the enormous growth of deformation mode was attributed as a sign of break-up possibility. The main disadvantage of these works is that the damping was not considered at all and the case considered in these works could be somehow attributed to the shock wave bubble excitation although the dependence of excitation magnitude on shock wave parameters would be not the most easy problem to solve. In this work a bubble in an acoustic wave is considered and for the purpose of this paper the case of axially symmetric deformation oscillations are considered (as shown in [7] the axially symmetric mode will be the most dangerous for the break-up phenomenon).The problem is solved in a Hamiltonian approach by an effective Krylov-Bogolyubov averaging method [8]. In order to obtain radial bubble oscillation magnitude in linear case in an acoustic wave of known frequency and magnitude the different bubble damping mechanisms are considered in the linear approach.

Thus, the first part of this work is devoted to a clear and easy-to-use procedure of obtaining the magnitude of the linear oscillations of gas bubble in liquid. The results are obtained with the help of the key concept of averaging over volume. The problem is strongly linked to the problem of the free bubble oscillations in liquid and the damping constant and frequency of the free oscillations are obtained in implicit form.

The first description of radial bubble oscillations was made by Minnaert in 1933 [9]. Adiabatic gas behavior was assumed and the dissipation and surface tension were neglected.The first linear theories of damping were incomplete and used rather rough assumptions [10, 11]. The next works [12, 13] were made without the key assumption of pressure uniformity inside the bubble that can strongly simplify the system of equations. Without this assumption the system of equations can't be solved analytically even in implicit form and only some approximating solutions can be proposed. The idea of pressure uniformity inside the bubble was firstly proposed by [11] and was developed in [14]. In one of the latest works [15] all the damping mechanisms are considered and the key assumption of pressure uniformity is made but the solution of equations is very hard to trace. The answer is not given in clear and easy-to-use form. The first part of this work is an attempt to obtain the most simple and clear solution using the key concept of averaging over volume [16]. The main assumptions made are: 1. The density of gas is much less than of liquid (pressure uniformity inside the bubble). 2. The thermal conductivity of gas is much less than of liquid (temperature uniformity outside the bubble). 3. The gas is close to ideal (state equation). 4. The viscosity and acoustic radiation may be considered small effects. 5. The liquid is far from its boiling point and the phase transitions effects can be neglected.

1. DISSIPATION MECHANISMS OF THE OSCILLATING BUBBLE IN FLUID

A gas bubble subjected to an acoustic wave in liquid is considered. We assume the bubble volume $r \le a(t)$ to be filled with ideal gas and no phase transitions to occur on its boundary. The outside area is filled with liquid. The density of gas is much less than of liquid and the pressure in the bubble $p(t)$ is considered to be uniform. The thermal conductivity of liquid is much higher than of the bubble and the liquid temperature T_∞ is considered constant. Precise gas dynamics equations are used for the thermal effects inside the bubble. Viscous dissipation is considered as an additional pressure inside the bubble. Acoustic dissipation is considered by using the more general Keller equation [17] instead of Rayleigh-Plesset equation to link interior and exterior of the bubble. All the equations are linearised and solved with the help of the concept of averaging over volume.

1.1. General Equations

The equation of state for the gas inside the bubble:

$$\frac{p}{\rho_{\rm g} T} = Const \tag{1}$$

The equation of thermal conduction in the volume of the bubble ($r \le a(t)$):

$$\lambda\left(\frac{\partial^2 T}{\partial r^2} + \frac{2}{r}\frac{\partial T}{\partial r}\right) = \rho_{\rm g}\, c_p \frac{dT}{dt} - \frac{dp(t)}{dt} \tag{2}$$

The key assumption is made that the gas pressure $p = p(t)$ is independent on spatial variables. This assumption is substantiated by the smallness of gas density and velocity $\nabla p = \rho_{\rm g} d\underline{v}/dt$.

The density can be excluded from Eq. (2) by deriving it on $c_p\, \rho_{\rm g}\, T = \gamma p(t)/(\gamma - 1)$

$$\frac{k}{T}\left(\frac{\partial^2 T}{\partial r^2} + \frac{2}{r}\frac{\partial T}{\partial r}\right) = \frac{d}{dt}\ln T - \frac{\gamma - 1}{\gamma}\frac{d}{dt}\ln p \tag{3}$$

The first boundary condition links the pressure in gas and fluid at the bubble boundary and accounts for the surface tension and viscosity:

$$p = p_{\rm ext} + 2\sigma/a + 4\mu\dot{a}/a \tag{4}$$

And two more boundary conditions are needed for the temperature behavior. These conditions are the absence of the heat flow in the center of the bubble and the equality of temperature in the bubble and in liquid at the boundary:

$$\left.\frac{\partial T}{\partial r}\right|_{r=0} = 0, \quad T(t, a) = T_\infty \tag{5}$$

In order to link the pressure at the bubble boundary in the fluid with the external driving pressure $p_\infty(1 + S(t))$ the Keller equation [17] can be used in the form given by [15]. This equation approximately accounts for the liquid compressibility:

$$\left(1-\frac{\dot{a}}{c}\right)a\ddot{a}+\frac{3}{2}\left(1-\frac{\dot{a}}{3c}\right)\dot{a}^2= \\ \frac{1}{\rho}\left(1-\frac{\dot{a}}{c}+\frac{a}{c}\frac{d}{dt}\right)(p_{\text{ext}}-p_\infty(1+S(t))) \tag{6}$$

1.2. Linear Approximation

The small bubble oscillations are considered and the cases of free and driven oscillations are considered together. In order to obtain the linear response the external driving pressure is considered to be

$$p_\infty(1+S(t))=p_\infty(1+F\,e^{i\Omega t}) \tag{7}$$

The solution is sought in the form of real parts of complex functions

$$\begin{gathered} a=a_0(1+Ae^{i\Omega t}),\quad p_{\text{ext}}=p_\infty(1+Pe^{i\Omega t}) \\ T=T_\infty(1+\theta(r)e^{i\Omega t}),\ \rho_{\text{g}}=\rho_{\text{g}0}(1+\rho'_{\text{g}}(r)e^{i\Omega t}) \end{gathered} \tag{8}$$

Here $A \ll 1$ and $P \ll 1$ are constants and $\theta(r)$, $\rho'_{\text{g}}(r)$ depend only on r. Substituting Eq. (8) in Eqs. (3) to (5) and leaving only linear terms a linear equation with boundary conditions is obtained:

$$\begin{gathered} k\left(\theta''(r)+\frac{2}{r}\theta'(r)\right)-i\Omega\theta(r)=-i\Omega\frac{\gamma-1}{\gamma}\tilde{P}, \\ \tilde{P}=P-\frac{2\sigma}{a_0p_\infty}A+4i\frac{\mu\Omega}{p_\infty}A \end{gathered} \tag{9}$$

$$\theta'(0)=0,\quad \theta(a_0)=0 \tag{10}$$

The same straightforward linearization procedure is applied to (6):

$$\frac{\rho a_0^2\Omega^2}{p_\infty}A+\left(1+i\frac{a_0\Omega}{c}\right)(P-F)=0 \tag{11}$$

The general solution of (9) is written in the form:

$$\theta=\frac{\gamma-1}{\gamma}\tilde{P}(1+\frac{C_1}{r}\sinh(r\sqrt{i\Omega/k})+\frac{C_2}{r}\cosh(r\sqrt{i\Omega/k})$$

From (10) values $C_1=-a_0/\sinh(a_0\sqrt{i\Omega/k})$, $C_2=0$ re obtained. The solution is

$$\theta=\frac{\gamma-1}{\gamma}\tilde{P}\left(1-\frac{\sinh(xZ)}{x\sinh(Z)}\right),\ Z=a_0\sqrt{\frac{i\Omega}{k}},\ x=\frac{r}{a_0} \tag{12}$$

The next step is averaging over volume values of gas physical parameters:

$$\overline{p}=p_\infty(1+Pe^{i\Omega t})+2\frac{\sigma}{a}+4\mu\frac{\dot{a}}{a}=p_\infty(1+\tilde{P}e^{i\Omega t})+2\frac{\sigma}{a_0}$$

$\overline{\rho_{\text{g}}}a^3=const \Rightarrow \overline{\rho'_{\text{g}}}=1-3A$ - mass conservation law

$$\overline{\theta}=3\int_0^1\theta(x)x^2dx=\frac{\gamma-1}{\gamma}\tilde{P}(1-3G(Z)),$$

where $G(Z)=\frac{1}{\sinh Z}\int_0^1\sinh(xZ)x\,dx=\frac{Z\coth Z-1}{Z^2}$. Using (1) one obtains:

$$\overline{\theta}=\frac{\gamma-1}{\gamma}\tilde{P}(1-3G(Z))=\frac{\tilde{P}}{1+\frac{2\sigma}{a_0p_\infty}}+3A$$

Taking into account (11) and substituting $\tilde{P}$ from (9) a linear system of equations is obtained:

$$\left.\begin{aligned} P-F+\frac{\rho a_0^2\Omega^2}{p_\infty}\left(1+i\frac{a_0\Omega}{c_l}\right)^{-1}A=0 \\ (P-\frac{2\sigma}{a_0p_\infty}A+4i\frac{\mu\Omega}{p_\infty}A)\Big[(1+\frac{2\sigma}{a_0p_\infty})^{-1}- \\ -\frac{\gamma-1}{\gamma}(1-3G(Z))\Big]+3A=0 \end{aligned}\right\} \tag{13}$$

The further procedure depends on the case considered. The only difference between free and driven oscillations is that in the first case $F=0$ and the complex frequency is obtained from the condition of the system (13) degeneracy (the complex frequency Ω will enable us to obtain bubble own frequency $\Omega_0=\text{Re}\Omega$ and the dimensionless damping constant $\delta=\frac{2\pi\text{Im}\,\Omega}{\text{Re}\,\Omega}$). In the forced oscillations case frequency Ω is known and the response function $A(\Omega)/F$ can be easily obtained from the system (13).

1.3. Linear response

We introduce the dimensionless numbers describing the corresponding effects:
$Ma=\frac{a_0\Omega}{c}$ - Mach number, the significance of acoustic radiation;
$Vis=\frac{4\mu\Omega}{p_\infty}$ - the ratio of the viscous pressure to the external pressure;
$St=\frac{2\sigma}{a_0p_\infty}$ - the ratio of the Laplace pressure to the external pressure;
$Pe=\frac{a_0^2\Omega}{k}$ - Peclet number $\approx$ squared ratio of bubble radius to oscillatory thermal length;
$Dy=\frac{\rho a_0^2\Omega^2}{p_\infty}$ - the ratio of the dynamic pressure to the external pressure.
Usually Ma, Vis, St are much less than 1. The linear response on driving force F is obtained anyway by solving the system (13):

$$Resp(\Omega)=\frac{A(\Omega)}{F}=\Big(\frac{Dy}{1+i\,Ma}+St-i\,Vis- \\ -\frac{3}{\frac{1}{1+St}-\frac{\gamma-1}{\gamma}(1-3G(\sqrt{i\,Pe}))}\Big)^{-1} \tag{14}$$

It is worth mentioning that the obtained magnitude near the resonance strongly depends on the small Ma, Vis and St parameters, although the effect of thermal dissipation associated with Pe number dominates for not very small bubbles.

In Figure 1 one can observe that resonant response is not too big and is decreasing with bubble size decrease. The resonant curves from left to right show the response as function of frequency for an air bubble of a certain size (1 mm, 100 μm, 10 μm and 1 μm in water at atmospheric pressure $p_\infty=10^5$ Pa.

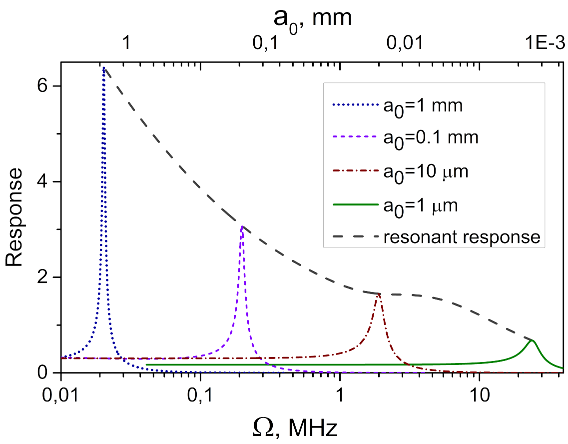

Figure 1. Response curves for different bubble radii in resonant and nonresonant case

The curve enveloping the resonant peaks is depicted by a black dashed line. The thermal dissipation is the main damping effect for not very small bubbles with radii $a_0 > 10\mu m$ and viscosity is more important for smaller ones. For the frequencies greater than resonant the response function quickly falls to zero because of Dy quadratic dependency on frequency (liquid has much inertia at these frequencies). The interesting feature of obtained dependencies is that the response tends to a nonzero constant for all frequencies less than resonant (obviously it should tend to -1/3 at $\Omega \to 0$ because of the gas mass conservation law). The effect of the nonuniformity of liquid temperature on response was estimated and the response have changed to less than 0.5 % for the air bubbles in water even at resonance.

2. THE RESONANT MECHANISM OF BUBBLE BREAK-UP

A Hamiltonian approach is used to investigate the possibility of bubble break-up in the case of resonance of radial and arbitrary axially symmetric deformation mode 2:1. The acoustic wave is considered to be in resonance with the radial mode and the magnitude of the radial bubble oscillations in the linear case is obtained from the previous part. Thus, the damping effects of the radial mode can be considered precisely and the only assumption made is that the damping of the deformation mode is negligibly small (corroborated by smallness of volume change in case of deformation bubble oscillations and smallness of the viscosity effects at not too small bubble sizes). The equations describing the energy transfer between the modes are used in the form provided in [6]. It is shown that the energy transfer between the modes can lead to a huge increase of the deformation mode magnitude which can be attributed as sign of possible bubble break-up.

2.1. Bubble equations

Following the work [6] the axially symmetric bubble with two degrees of freedom is considered and its surface is described by:

$$r(\theta,\tau) = a_0\left(1 + x(\tau) + \xi(\tau)P_n(\eta)\right),\ \eta = \cos(\theta) \tag{15}$$

Here $x(\tau)$ and $\xi(\tau)$ stand for small magnitudes of radial and deformation oscillations. We follow the same straightforward procedure as in the cited work (the procedure consists of obtaining velocity potential up to the second degree of smallness by $x(\tau)$ and $\xi(\tau)$, kinetic and potential energies and the Lagrangian function up to third degree of smallness by $x(\tau)$ and $\xi(\tau)$ and obtaining Hamiltonian function by making variables substitution and considering the resonance condition). The Hamiltonian written in terms of dimensionless time $t = \omega_\xi \tau$ ($\omega_\xi = \sqrt{\frac{\sigma(n-1)(n+1)(n+2)}{\rho a_0^3}}$ is resonant mode frequency) and substituted variable $\xi = y\sqrt{(n+1)(2n+1)}$ and including only the resonant terms in case of the resonance 2:1 could be written in the form

$$H = \frac{1}{2}(u^2+v^2+4x^2+y^2)-\frac{3}{2}xv^2-(n+3)uyv+4(n+1)xy^2 \tag{16}$$

Variables u and v stand for moments associated with x and y. The condition of resonance of the modes is:

$$a_0 = \left(\frac{2(n-1)(n+1)(n+2)+1}{3\gamma} - 1\right)\frac{2\sigma}{p_\infty} \tag{17}$$

As for the driven oscillations with damping one should add the term responsible for driving acoustic wave magnitude in Hamiltonian and add damping in the Hamilton equations of the bubble. Thus, (16) will be modified to:

$$H = H_2 + F_1, H_2 = \frac{1}{2}(u^2 + v^2 + 4x^2 + y^2),$$
$$F_1 = 4(n+1)xy^2 - \frac{3}{2}xv^2 - (n+3)uyv + \alpha x\cos 2t \tag{18}$$

and Hamilton equations will look like

$$\begin{aligned} \dot{x} - u &= -(n+3)yv \\ \dot{u} + 4x &= (3/2)v^2 - 4(n+1)y^2 - \alpha\cos 2t - \beta u \\ \dot{y} - v &= -(n+3)yu - 3xv \\ \dot{v} + y &= (n+3)uv - 8(n+1)xy \end{aligned} \tag{19}$$

The introduced constants α and β are responsible for driving force and damping and can be linked with the previous part. Firstly, if the pressure outside the bubble will increase by F percent the bubble volume in low-frequency limit will decrease by the same percent number. Thus, the x will decrease by $F/3$ percent. In our case the stationary point of linear equation is $x = -\alpha/4$. One can conclude that

$$\alpha = (4/3)F \tag{20}$$

The β-term responsible for damping will be found from a linear system solution obtained in previous part of our work by equating our system linear response at resonance (the solution is simply $u = (-\alpha/\beta)\cos 2t,\ x = (-\alpha/(2\beta))\sin 2t$) and the resonant response from (14):

$$\left|\frac{A(\Omega)}{F}\right| = Resp(\Omega) = \frac{|x|}{F} = \frac{2}{3\beta}$$

Thus the expression for β is

$$\beta = \frac{2}{3\,Resp(\Omega)} \tag{21}$$

2.2. Averaging procedure

Considering the driving force relatively small we introduce a small parameter $\epsilon = \sqrt{\alpha}$. The dissipation is considered small too $\beta = \epsilon\beta_1$. The system solution is sought in the form:

$$x = \epsilon^2(\tilde{x} - x_0),\ u = \epsilon^2(\tilde{u} + (n+3)\frac{\Lambda^2}{2}\sin 2t)$$
$$y = \epsilon\Lambda\sin t + \epsilon^2\tilde{y},\ v = \epsilon\Lambda\cos t + \epsilon^2\tilde{v} \tag{22}$$
$$\Lambda = \pm\frac{2}{\sqrt{4n-1}},\quad x_0 = \frac{8n+5}{4(4n-1)}$$

Substituting (22) into (19 we obtain the system:

$$\begin{aligned}
&\dot{\tilde{x}} - \tilde{u} = \epsilon A_1,\ \dot{\tilde{u}} + 4\tilde{x} = \epsilon A_2\\
&\dot{\tilde{y}} - \tilde{v} = \epsilon A_3,\ \dot{\tilde{v}} + \tilde{y} = \epsilon A_4\\
&A_1 = -(n+3)\Lambda(\tilde{y}\cos t + \tilde{v}\sin t)\\
&A_2 = -8(n+1)\Lambda\tilde{y}\sin t + 3\Lambda\tilde{v}\cos t-\\
&-\beta_1(\tilde{u} + (n+3)(\Lambda^2/2)\sin 2t)\\
&A_3 = -3\Lambda\cos t(\tilde{x} - x_0)-\\
&-(n+3)\Lambda\sin t(\tilde{u} + (n+3)(\Lambda^2/2)\sin 2t)\\
&A_4 = -8(n+1)\Lambda\sin t(\tilde{x} - x_0)+\\
&+(n+3)\Lambda\cos t(\tilde{u} + (n+3)(\Lambda^2/2)\sin 2t)
\end{aligned} \tag{23}$$

As one can observe the coefficients Λ and x_0 were chosen in such a way as to eliminate all terms of the order $O(1)$ from the right part of (23). The asymptotic solution is obtained by the technique described in [18]. In the absence of the right parts the system (23) has the solution:

$$\begin{aligned}
&\tilde{x} = X\cos 2t + (U/2)\sin 2t,\ \tilde{u} = U\cos 2t - 2X\sin 2t\\
&\tilde{y} = Y\cos t + V\sin t,\quad \tilde{v} = V\cos t - Y\sin t
\end{aligned} \tag{24}$$

When the right parts are considered X,U,Y,V start depending on time. Substituting (24) into (23) and taking into account the dependence of X,U,Y,V on time we obtain a system:

$$\begin{pmatrix} \cos 2t & \sin 2t \\ -\sin 2t & \cos 2t \end{pmatrix}\begin{pmatrix} \dot{X} \\ \dot{U}/2 \end{pmatrix} = \epsilon\begin{pmatrix} A_1 \\ A_2/2 \end{pmatrix}$$
$$\begin{pmatrix} \cos t & \sin t \\ -\sin t & \cos t \end{pmatrix}\begin{pmatrix} \dot{Y} \\ \dot{V} \end{pmatrix} = \epsilon\begin{pmatrix} A_3 \\ A_4 \end{pmatrix} \tag{25}$$

By grouping the $\dot{X}$,$\dot{U}$,$\dot{Y}$,$\dot{V}$ in the left part the system is reduced to the standard form for the Krylov-Bogolyubov averaging technique application:

$$\begin{aligned}
\dot{X} &= \epsilon(A_1\cos 2t - (A_2/2)\sin 2t)\\
\dot{U} &= \epsilon(2A_1\sin 2t + A_2\cos 2t)\\
\dot{Y} &= \epsilon(A_3\cos t - A_4\sin t)\\
\dot{V} &= \epsilon(A_4\sin t + A_3\cos t)
\end{aligned} \tag{26}$$

The next step is substituting in A_1-A_4 from (23) (24) and averaging (26) over time:

$$\begin{aligned}
\frac{dX}{d(\epsilon t)} &= -\frac{\beta_1}{2}X + \frac{(4n-1)\Lambda}{8}Y + \frac{(n+3)\Lambda^2}{8}\beta_1\\
\frac{dU}{d(\epsilon t)} &= -\frac{\beta_1}{2}U + \frac{(4n-1)\Lambda}{4}V\\
\frac{dY}{d(\epsilon t)} &= -\frac{4n-1}{4}\Lambda X - \frac{8n+5}{2}\Lambda x_0 - \frac{(n+3)^2\Lambda^3}{4}\\
\frac{dV}{d(\epsilon t)} &= -\frac{(4n-1)\Lambda}{8}U
\end{aligned} \tag{27}$$

One can easily verify that all the system (27) eigenvalues have negative real part

$$\lambda_{1,2,3,4} = -\frac{\beta_1}{4} \pm \sqrt{\left(\frac{\beta_1}{4}\right)^2 - \frac{4n-1}{8}}$$

and therefore the solution exponentially quickly ($\sim \exp(-\epsilon\beta_1 t/4)$) approaches to its stationary point:

$$\begin{aligned}
X_0 &= -\frac{8n(9n+16)+97}{(4n-1)^2},\quad U = 0\\
Y_0 &= \mp\frac{10n(8n+15)+91}{(4n-1)^{5/2}}\beta_1,\quad V = 0
\end{aligned} \tag{28}$$

It is worth noting that this stationary point is stable by the second Bogolyubov theorem on averaging [8]. The constructed asymptotic solution is:

$$\begin{aligned}
&x(t) = \alpha(X_0\cos 2t - x_0)+\\
&+\alpha(X(\sqrt{\alpha}t)\cos 2t + U(\sqrt{\alpha}t)\sin 2t)\\
&y(t) = \pm\frac{2\sqrt{\alpha}}{\sqrt{4n-1}}\sin t + \alpha Y_0\cos t+\\
&+\alpha(Y(\sqrt{\alpha}t)\cos t + V(\sqrt{\alpha}t)\sin t)
\end{aligned} \tag{29}$$

The solution consists of quickly oscillating or constant first two terms and a slowly decreasing by magnitude third term depending on "slow time" $\tilde{t} = \sqrt{\alpha}t$. All the functions describing the third term can be found from (27) combined with the initial conditions:

$$\omega = \frac{\sqrt{2(4n-1)-\beta_1^2}}{4}, \; \psi = \arctan\frac{\beta_1}{4\omega}$$
$$X = (C_1\cos\omega\tilde{t} + C_2\sin\omega\tilde{t})e^{-\beta_1\tilde{t}/4}$$
$$Y = \sqrt{2}(C_2\cos(\omega\tilde{t}-\psi) - C_1\sin(\omega\tilde{t}-\psi))e^{-\beta_1\tilde{t}/4}$$
$$U = -\sqrt{2}(C_4\cos(\omega\tilde{t}+\psi) - C_3\sin(\omega\tilde{t}+\psi))e^{-\beta_1\tilde{t}/4}$$
$$V = (C_3\cos\omega\tilde{t} + C_4\sin\omega\tilde{t})e^{-\beta_1\tilde{t}/4}$$
$$x(0) = \alpha(X_0 - x_0 + C_1)$$
$$y(0) = \alpha(Y_0 + \sqrt{2}(C_2\cos\psi + C_1\sin\psi))$$
$$u(0) = -\alpha\sqrt{2}(C_4\cos\psi - C_3\sin\psi)$$
$$v(0) = \alpha(\pm\frac{2}{\sqrt{\alpha}\sqrt{4n-1}} + C_3) \tag{30}$$

For the complete problem consideration one should prove that the obvious solution $y = v = 0$ is unstable. The proof is rather simple and the instability was proven analytically and by numerical modeling.

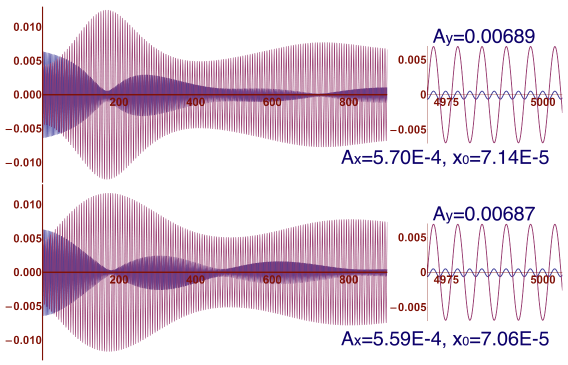

Figure 2. Comparison of the precise numerical simulation results and the exact solution

On the Figure 2 the obtained analytical solution is compared with the numerical simulation of the initial system (19) with the same initial conditions. Functions $x(t)$ and $y(t)$ are plotted with blue and red color (or one can observe that $y(t)$ is bigger than $x(t)$ on both parts of the plot. In the top part there is plotted numerical solution and in the bottom the analytical one. Left part is devoted to the $t < 900$ and the right part to $9970 < t < 10000$. The initial conditions for simulation were: $\alpha = 0.0001$, $\beta_1 = 1$, $n = 19/8$, $x(0) = -0.004$, $u(0) = -0.01$, $y(0) = -0.002$, $v(0) = 0.004$. The obtained analytical formulas describe the qualitative behaviour of the system at first moment and are very precise in describing the steady oscillations. These oscillations magnitude practically doesn't change when we slightly modify the driving frequency and damping coefficient. Numerical simulations have shown that the possible frequency mismatch is proportional to $\sqrt{\alpha}$.

2.3. The break-up criterion

Now one should consider at which moment the bubble will be in the most danger of break-up. Two possibilities arise:

1. The acoustic wave slowly gains its magnitude. In this case the maximal deformation mode magnitude will be observed in the end of process where all oscillations are stable. The maximal magnitude is:

$$y_{max} \approx \frac{2\sqrt{\alpha}}{\sqrt{4n-1}}$$

2. The maximal value of deformation mode magnitude is observed during the transient process. This is the case of quickly starting acoustic wave. As to consider the second case one can make an assumption that initial value of oscillations magnitude is very small and all the initial values of x,y,u,v are practically zero. As one may observe from (30) these conditions lead to big value of C_3 and possibly big value of C_4. Solving the equations for initial conditions equal to zero we obtain:

$$C_3 = \mp\frac{2}{\sqrt{\alpha}\sqrt{4n-1}}, \; C_4 = C_3\tan\psi$$

If damping coefficient $\beta_1 < 4n-1$ than C_4 is smaller than C_3. Another option is investigated numerically and gives no interesting features in the system behaviour because of very big damping. Thus, one may consider C_3 as main term provoking big deformation oscillations in the transient process. Taking into account only the greatest terms by $\sqrt{\alpha}$ one can obtain the deformation mode behaviour:

$$y(t) \approx \pm\frac{2\sqrt{\alpha}}{\sqrt{4n-1}}(1 - e^{-\beta_1\tilde{t}/4}\cos\omega\tilde{t})\sin t$$

This function has maximum at $\omega\tilde{t} \approx \pi$ and its maximal magnitude will be

$$y_{max} \approx \frac{2\sqrt{\alpha}}{\sqrt{4n-1}}(1 + e^{-\beta_1\pi/(4\omega)})$$

Considering both cases together one can write

$$y_{max} \approx \frac{2\sqrt{\alpha}}{\sqrt{4n-1}}(1+K), \tag{31}$$

$K = 0$ for a slowly starting acoustic wave and $K = \exp(-\beta\pi/(4\omega\sqrt{\alpha}))$ for a sudden acoustic wave start, if dissipation is small ($\beta \ll \sqrt{\alpha}$) the K-coefficient approaches to its maximal value of 1 and the maximal magnitude is twice the stationary.

One may observe that $y \sim (1/\sqrt{\alpha})x$ is much greater than x for little driving forces. However, its absolute value is rather small because of its proportionality to $\sqrt{\alpha}$. A question arise how the magnitude y is linked to the absolute value of deformation. Turning back to $\xi = y\sqrt{(n+1)(2n+1)}$ and considering only deformation terms the bubble surface equation (15 will look like:

$$\frac{r(\theta,\tau)}{a_0} = 1+\xi_{max}P_n(\cos\theta)\sin\omega_\xi\tau$$
$$\xi_{max} = 2\sqrt{\frac{\alpha(n+1)(2n+1)}{4n-1}}(1+K) \tag{32}$$

From intuitive considerations the critical value of

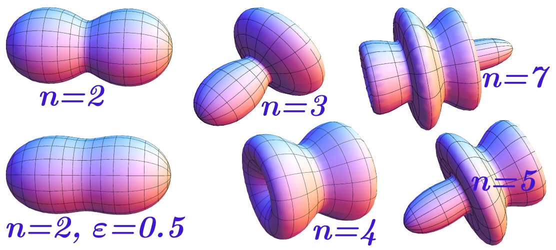

Figure 3. Some "dangerous" deformation modes

ξ_{max} for break-up is $\sim$ 1. Some modes associated with different Legendre polynomial indices n are shown on the Figure 3. All the pictures except the bottom left one are drawn for $\xi\approx 1$. Numerical simulations show that a neck separating parts of the bubble appears around $\xi_{max}=0.5$. Thus, we obtain the estimative criterion for break-up:

$$\alpha > \frac{4n-1}{8(1+K)^2(n+1)(2n+1)} \tag{33}$$

The most interesting case for bubble break-up to occur is $K=1$. The question is how to define quick or slow acoustic wave start. One may think that the time scale is $4/\beta$. But as we consider $\beta_1^2 < 4n-1$ the more important is the time scale of transient oscillations. Going to the initial time we obtain the condition of a quick process in terms of the acoustic wave appearance time τ_{start}:

$$\tau_{\text{start}} \ll \frac{\pi}{\sqrt{\alpha\omega\omega_\xi}} \approx \frac{2\sqrt{2}\pi}{\sqrt{4n-1}\sqrt{\alpha}\omega_\xi}$$

The condition for K to be approximately 1 is the damping smallness $\beta_1\pi/(4\omega) << 1$. Using (20),(21) and the resonance condition $\Omega/\omega_\xi = 2$ and considering both cases a) and b) the criterion (4) is transformed to

$$\left.\begin{array}{l} \text{if} \quad \tau_{\text{start}} \ll \frac{30}{\Omega},\ Resp(\Omega) > \frac{4}{3} \\ \text{then} \quad F > \frac{3(4n-1)}{32(n+1)(2n+1)(1+K)^2} \\ \text{else,} \quad F > \frac{3(4n-1)}{32(n+1)(2n+1)} \approx \frac{1}{5n} \end{array}\right] \tag{34}$$
$$K = e^{-\frac{\pi}{\sqrt{6(4n-1)Resp^2(\Omega)F-1}}}$$

For the case of nonzero K the inequality starts being implicit, although is solved or estimated easily. For $Resp(\Omega) > 8$ one may consider $K\approx 1$. For example, for the deformation mode with $n=7$ from (17) the bubble radius $a_0\approx 290\mu m$ is obtained. The response function (14) for such bubble radius is $Resp(\Omega)\approx 4.41$, $\Omega\approx 70.7\ Khz$. The condition for the fast acoustic wave appearance is $\tau_{\text{start}} \ll 0.44\ ms$. In this case the break-up acoustic wave magnitude should $F > 0.0088$ or the pressure in the wave should be ΔP >900 Pa if the surrounding water is at atmospheric pressure. In the case of slowly appearing acoustic wave the break-up magnitude should be 2100 Pa. The K and F for quick processes were found by a simple iterative method after 5 iterations.

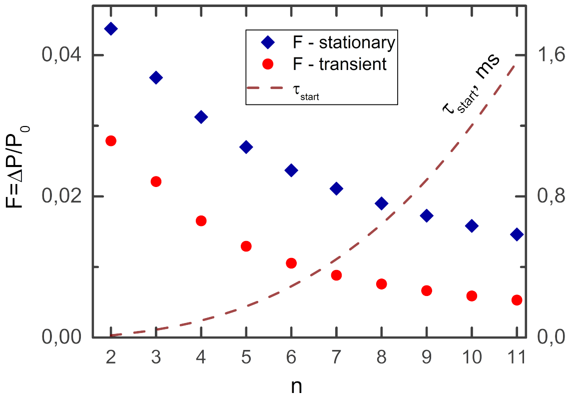

Figure 4. Break-up magnitude

On the Figure 4 the break-up magnitudes are plotted as functions of deformation mode Legendre polynomial indices in the case of slow (diamonds) and sudden (circles) acoustic wave start. Dashed line corresponds to the calculated time of the fast acoustic wave start τ_{start} (right scale). For small n the required magnitude may be difficult to achieve at atmospheric pressure and bubble resonant frequency (which is $\sim 1/n^3$). As for the big n-modes the magnitudes seem rather accessible especially for the case of sudden acoustic wave start. As was mentioned before the possible mismatch in frequency or in the bubble size in order the effect to occur $\sim\sqrt{F}$.

3. SUMMARY

The damping mechanisms of gas bubble in liquid are mostly interesting by their applications in the other problems of cavitation. Because of that the easiness of use is very important for the damping constants obtained in this article. The concept of averaging over volume strongly simplified the solution and gave the possibility to obtain new results. The results are precise with assumptions made which are valid practically for all real bubbles.

The possibility of break-up for a gas bubble placed in an acoustic wave in liquid was investigated using an efficient Krylov-Bogolyubov averaging method. A huge growth of deformation oscillations magnitude for the resonance between the modes 2:1 can lead to break-up for bubbles of resonant radii. The two cases were considered: when the acoustic wave slowly appears in liquid and when it appears suddenly. The difference between these two cases is that in the second one the maximal deformation will occur during the transient process and can achieve as high as two times the stationary deformation oscillations magnitude. The estimative criterion of break-up acoustic wave magnitude was proposed for both cases. The obtained magnitude is experimentally accessible for rather big bubbles corresponding to not too high acoustic frequencies and big deformation mode Legendre polynomial numbers.

In the work is demonstrated the deformation mode to be excited even at small driving wave magnitudes. The magnitude of deformation oscillations can reach very large values for bubbles with resonant size compared with radial oscillations magnitude. These results can help one understand the appearance of multiple subharmonics in emission spectrum of bubbly liquid in an acoustic wave.

The main drawbacks of the proposed solution are:
1. The break-up is strongly nonlinear effect and the used linear theory can give only estimative break-up criterion. As for the precise criterion the bubble motion should be simulated numerically up to the point the break-up occurs
2. The Hamiltonian in the second part is constructed under the assumptions of the adiabatic bubble behaviour. The behaviour at resonance may be considered close to adiabatic and the assumption made can introduce some errors in Hamilton function coefficients but not in the general system behaviour.
3. Phase transitions were not considered. This point may be important for bubbles in hot liquid near the liquid boiling point or for the vapour bubbles.

ACKNOWLEDGEMENTS

The work was supported by the Russian Science Foundation, project No 14-19-01633.

REFERENCES

[1] Choi, J. J., e. a., 2007, “Spatio-temporal analysis of molecular delivery through the bloodâĂŞbrain barrier using focused ultrasound”, *Phys Med Biol*, Vol. 52, pp. 5509–5530.

[2] Neppiras, E. M., 1980, “Acoustic cavitation”, *Phys Rep*, Vol. 61, pp. 159–251.

[3] Leighton, T. G., 1988, “Image intensifier studies of sonoluminiscence, with applications to the safe use of medical ultrasound”, Ph.D. thesis, Cambridge University.

[4] Longuet-Higgins, M. S., 1991, “Resonance in nonlinear bubble oscillations”, *Journal of Fluid Mechanics*, Vol. 224, pp. 531–549.

[5] Ffowcs Williams, J. E., and Guo, Y. P., 1991, “On resonant nonlinear bubble oscillations”, *Journal of Fluid Mechanics*, Vol. 224, pp. 507–529.

[6] Vanovskii, V. V., and Petrov, A. G., 2011, “Oscillations of gas bubbles in liquid at resonance of frequencies 2:1 of radial and arbitrary axisymmetrical modes”, *Doklady Physics*, Vol. 56, pp. 194–198.

[7] Vanovskii, V. V., and Petrov, A. G., 2012, “The resonant mechanism of subdivision of a gas bubble in a fluid”, *Doklady Physics*, Vol. 57, pp. 238–242.

[8] Bogolyubov, N. N., and Mitropol’skii, Y. A., 1961, *Asymptotic methods in the theory of non-linear oscillations*, Gordon & Breach, Delhi.

[9] Minnaert, M., 1933, “On Musical Air-Bubbles and the Sounds of Running Water”, *Phil Mag*, Vol. 16, pp. 235–248.

[10] Pfriem, H., 1940, “Zur thermischen DÃď’mpfung in Kugelsymmetrische schwingenden Gasblasen”, *Akustische Zeitschrift*, Vol. 5, pp. 202–207.

[11] Devin, C., 1959, *Survey of Thermal, Radiation, and Viscous Damping of Pulsating Air Bubbles in Water*, Report: David W. Taylor Model Basin, Navy Department, David Taylor Model Basin.

[12] Chapman, R. B., and Plesset, M. S., 1971, “Thermal Effects in the Free Oscillations of Gas Bubbles”, *J Basic Eng*, pp. 373–376.

[13] Prosperetti, A., 1977, “Thermal Effects and Damping Mechanisms in the Forced Radial Oscillations of Gas Bubbles in Liquids”, *J Acoust Soc Am*, Vol. 61, pp. 17–27.

[14] Nigmatulin, R. I., and Khabeev, N. S., 1974, “Heat exchange between a gas bubble and a liquid”, *Fluid Dynamics*, Vol. 9 (5), pp. 759–764.

[15] Prosperetti, A., 1991, “The thermal behaviour of oscillating gas bubbles”, *Journal of Fluid Mechanics*, Vol. 222 (1), pp. 587–616.

[16] Petrov, A. G., 2009, *Analytical Hydrodynamics*, Fizmatlit, Moscow.

[17] Keller, J. B., and Kolodner, I. I., 1956, “Damping of underwater explosion bubble oscillations”, *Journal of Applied physics*, Vol. 27 (10), pp. 1152–1161.

[18] Zhuravlev, V. P., 1997, “A controlled Foucault pendulum as a model of a class of free gyros”, *Izv AN MTT [Mechanics of Solids]*, (6), pp. 27–35.

Solution of Navier-Stokes Equations in Squeezing Flow between Parallel Plates in Two-dimensional Case

Alexander G. PETROV[1,2], Irina S. KHARLAMOVA[2,3]

[1] Corresponding Author. Department of Theoretical Mechanics, Moscow Institute of Physics and Technology. 9 Institusky Per. 141701, Dolgoprudny, Russia. Tel.: +7 916 079-61-58, E-mail: petrovipmech@gmail.com
[2] Laboratory of Mechanics of Systems, Institute for Problems in Mechanics RAS, pr. Vernadskogo 101-1, 119526 Moscow, Russia. E-mail: petrovipmech@gmail.com
[3] Department of Mechanics of Fluids and Disperse Systems, Institute of Hydrodynamics ASCR, Pod Pat'ankou 30/5, 166 12 Prague 6, Czech Republic. E-mail: kharlamova@ih.cas.cz

ABSTRACT

The velocity profile in a layer of a two-dimensional viscous Newtonian fluid between two parallel plates, where one plate is immobile and other is either moving away or moving to the first one, is studied. The distance between plates changes in time according to arbitrary power-law: $h \sim |t|^s$. The unsteady Navier-Stokes equations in three independent variables with some special substitutions were reduced to a system of ordinary differential equations. As result, a new boundary value problem of the third order with two variables was found. Precise solutions of the Navier-Stokes equations are constructed as series in powers of Reynolds number. The cases of motion with $s = 0.5,\ 1,\ 2$ are studied in detail. In the case $s = 0.5$ the series is convergent and the self-similar, one-parametric solution can be obtained; in other cases the series is asymptotic. For some Reynolds numbers greater than critical, the velocity of flow near the boundaries has opposite direction to the average velocity; it is the counterflow phenomenon. The critical Reynolds numbers corresponding to the appearance of counterflow for all three cases were determined.

Keywords: closed form solution, counterflow, Navier-Stokes equations, squeezing flow between plates, two-dimensional viscous flow

1. NOMENCLATURE

NOMENCLATURE

ν	$[m^2/s]$	coefficient of kinematic viscosity
ρ	$[kg/m^3]$	fluid density
a	$[-]$	coefficient in the power-law, $1/s$
b	$[-]$	pressure coefficient
c	$[-]$	pressure coefficient, $1 + a + b$
$h(t)$	$[m]$	distance between the plates
k	$[m/s]$	amplitude of velocity of the upper plate
P	$[-]$	pressure caused by fluid flow
s	$[-]$	coefficient in the power-law
t	$[s]$	time
u, v	$[-]$	components of fluid velocity between the plates
v_x, v_y	$[m/s]$	components of fluid velocity between the plates
x, y	$[m]$	axial coordinates, along and perpendicular the plates
Y	$[-]$	vertical coordinate, perpendicular the plates, $Y \ni [-1, 1]$
$\dot{h}$	$[m/s]$	velocity of the upper plate
p	$[Pa \cdot m^3/kg]$	total pressure between the plates
p_0	$[Pa \cdot m^3/kg]$	initial pressure between the plates
$Re(t)$	$[-]$	Reynolds number, $h\dot{h}/\nu$
Re_*	$[-]$	Reynolds number, convergence radius
Re_{back}	$[-]$	critical Reynolds number at wich counterflow appears

2. INTRODUCTION

Exact solutions of the Stokes or the Navier-Stokes equations are of great importance in theoretical hydrodynamics. Their solution is quoted in many textbooks and treatises on hydrodynamics in both classical works [1, 2, 3] and contemporary [4, 5]. The closest to the present solution is a set of exact solutions by Hiemenz [6], described in detail in review by Wang [7] and treatises [3]. Solution of Hiemenz describes flow of fluid from infinity towards a plane with a sticking boundary condition on the plane. A similar solution was constructed by Howarth [8]. A steady state flow between two parallel planes was examined in Brandy's work [9]. An exact solution was found in Brandy's work [9] for the flow with zero

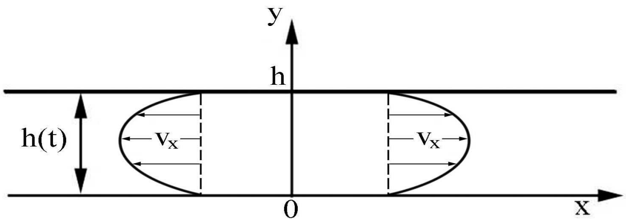

Figure 1. Scheme of fluid flow between the two parallel plates

velocity condition on one plane and velocity proportional to the longitudinal coordinate on the other.

There are a lot of contemporary works about squeezing flow between two parallel plates or disks with the distance changing in time like $h \sim t^{1/2}$ and among them: [10], [11] [12], [13], [14], in which the flow of non-Newtonian fluids in a two- or three-dimensional case is studied.

Similar problem was examined, for example, in the works of Thorpe [15] and Wang [16], however only for the case $h \sim \sqrt{t}$. More particularly the problem of squeezing two-dimensional viscous flow between parallel plates was covered in the work [17].

The present paper offes a mathematical method allowing solution of the phisical problem formulted for a more general law of motion of the plates.

3. FORMULATION OF BOUNDARY VALUE PROBLEM

A two-dimensional viscous flow with velocity components $v_x(t,x,y)$, $v_y(t,x,y)$ and pressure $p(t,x,y)$ in a two-dimensional fluid layer $0 < y < h$, $-\infty < x < \infty$ between parallel plates is considered here. The plate at $y = 0$ is immobile, the second plate moves with $h(t)$ law, see Fig. 1; both cases $\dot{h}(t) > 0$ and $\dot{h}(t) < 0$ are possible. The inflow/outflow at infinity is defined by the continuity condition and by the form of the sought solution, which will be given in further.

The boundary value problem with sticking condition on the plates is formulated as follows

$$
\begin{aligned}
&\frac{\partial v_x}{\partial x} + \frac{\partial v_y}{\partial y} = 0,\\
&\frac{\partial v_x}{\partial t} + v_x\frac{\partial v_x}{\partial x} + v_y\frac{\partial v_x}{\partial y} + \frac{\partial p}{\partial x} = \nu\left(\frac{\partial^2 v_x}{\partial x^2} + \frac{\partial^2 v_x}{\partial y^2}\right),\\
&\frac{\partial v_y}{\partial t} + v_x\frac{\partial v_y}{\partial x} + v_y\frac{\partial v_y}{\partial y} + \frac{\partial p}{\partial y} = \nu\left(\frac{\partial^2 v_y}{\partial x^2} + \frac{\partial^2 v_y}{\partial y^2}\right),\\
&v_x(t,x,0) = v_x(t,x,h) = 0,\\
&v_y(t,x,0) = 0, \quad v_y(t,x,h) = \dot{h},
\end{aligned} \tag{1}
$$

where ν is coefficient of kinematic viscosity, the fluid density without loss of generality is set to unity ($\rho =$ 1). Solution of the problem (1) is sought in the form

$$
\begin{aligned}
&v_x = \frac{\dot{h}}{h}x(u(Y,Re) - 1),\\
&v_y = \frac{\dot{h}}{2}(v(Y,Re) + 1 + Y),\\
&p = \dot{h}^2\left[b\frac{x^2}{2h^2} + P(t,Y)\right] + p_0(t),\\
&Y = \frac{2y}{h} - 1, \quad Y \in [-1,1].
\end{aligned} \tag{2}
$$

New functions $u(Y)$ and $v(Y)$ are presented the dimensionless components of fluid velocity between the plates; they are depending on new vertical coordinate Y, where the points $Y = \pm 1$ are the boundaries. For the predefined law of motion $h(t)$ lets denote value $h\dot{h}/\nu$ as Re, which absolute value is the Reynolds number and sign coincides with that of $\dot{h}$. In the remaining text we will call it just Reynolds number. Note that this value depends on time. This dependence should be taken into account when calculating partial time derivatives in Eq. (1).

After substitution of (2) in the first two Navier-Stokes Eqs. (1) we arrive at the following boundary value problem for system of ordinary differential equations with new functions:

$$
\begin{aligned}
&u + v' = 0,\\
&vu' + u^2 - (2+a)u + 1 + a + b - 4\frac{1}{Re}u'' +\\
&+(2-a)Re\frac{\partial u}{\partial Re} = 0,\\
&u(-1) = u(1) = 1, \quad v(-1) = v(1) = 0.
\end{aligned} \tag{3}
$$

The prime here denotes derivative with respect to Y. Parameter a implies a power law time dependence of the distance between plates with arbitrary power s:

$$
\begin{aligned}
&h = k|t - t_0|^s, \quad a = 1/s,\\
&Re(t) = \frac{1}{\nu}sk^2|t - t_0|^{2s-1}\operatorname{sign}(t - t_0),
\end{aligned} \tag{4}
$$

where k is an amplitude of velocity of the upper plate. The system of Eqs. (3) is a system of partial differential equations of the third order; together with defined law of plates motion $h(t)$ it allows determination of functions $u(Y)$ and $v(Y)$ and parameter b determining the pressure $p(t,Y,Re)$. The case $Re > 0$ corresponds to increasing gap between the plates, $Re < 0$ - to decreasing. Formulation of new boundary value problem (3) must include also the initial condition defined for some Re. The resulting initial-boundary value problem is not considered here. Our aim is construction of a family of particular solutions of Eqs. (3) in form of series in powers of Reynolds number.

4. EXPANSION IN POWERS OF REYNOLDS NUMBER

The boundary value problem (3) can be represent as one equation for $v(Y,Re)$ with boundary conditions:

$$
\begin{aligned}
&-vv'' + (v')^2 + (2+a)v' + c + \frac{4}{Re}v'''+ \\
&+(a-2)Re\frac{\partial v'}{\partial Re} = 0, \qquad (5)\\
&v(-1) = v(1) = 0, \quad v'(-1) = v'(1) = -1,
\end{aligned}
$$

where $c = 1 + a + b$. For small Reynolds number the solution of this boundary value problem can be found as series in Reynolds number with coefficients in the expansion being functions of Y. Though the Reynolds number is dependent on time, the time itself is included into equation (5) parametrically and Y and Re can be considered as independent variables.

$$
\begin{aligned}
&c = 1 + a + b = \frac{c_{-1}}{Re} + c_0 + c_1 Re + ..., \qquad (6)\\
&v = v_0 + v_1 Re + v_2 Re^2 + ...
\end{aligned}
$$

For the leading term the solution of the following boundary value problem is

$$
c_{-1} = 12, \quad v_0(Y) = \frac{1}{2}Y\left(1-Y^2\right). \qquad (7)
$$

The solution for the second order approximation is

$$
\begin{aligned}
&c_0 = -\frac{1}{5}a - \frac{5}{7}, \qquad (8)\\
&v_1(Y) = \frac{Y\left(Y^2-1\right)^2}{1120}\left(-Y^2 + 7a + 12\right).
\end{aligned}
$$

The coefficient of pressure $b = c - 1 - a$ is found as series in Reynolds number

$$
b = \frac{12}{Re} + b_0 + b_1 Re + b_2 Re^2 + ... \qquad (9)
$$

with $b_{-1} = c_{-1}$, $b_0 = c_0 - a - 1$, $b_1 = c_1$ and so on. Every coefficient $b_n(a)$ or $c_n(a)$ is a polynomial of power $n+1$ in parameter a with rational coefficients. The leading term $b = 12/Re$ of the expansion was found yet by Reynolds [18] with help of his celebrated lubrication layer approximation.

The most interesting cases of upper plate motion are those with parameter a accepting the following values: $a = 2$ - corresponds to gap changing with law $h = k\sqrt{|t|}$; $a = 1$ - corresponds to steady change of the gap $h = k|t|$; $a = 1/2$ - describes uniformly accelerated change $h = kt^2$.

5. CASE $A = 2$. GAP BETWEEN PLATES CHANGES ACCORDING TO THE LAW $H = K\sqrt{|T|}$.

In case of distance between plates changing as $h = k\sqrt{|t|}$, $a = 2$ the partial derivative with respect to Reynolds number in Eq. (5) is equal to zero. Thus we come to a boundary value problem for ordinary differential equation, which is readily solved numerically:

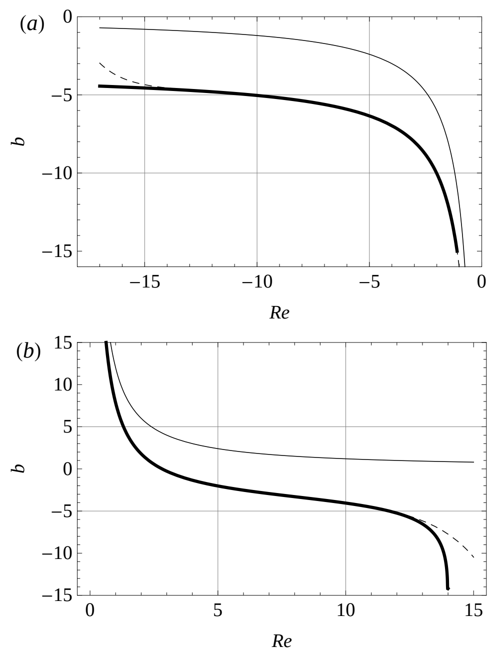

Figure 2. Dependence $b(Re)$ at $a = 2$ for $Re < 0$ and $Re > 0$: solid thick line - numerical solution by the shooting method, dashed line - solution in series $b(Re, a)$ of 15 terms, solid thin line - the leading term $b = 12/Re$ of the expansion.

$$
\begin{aligned}
&-vv'' + (v')^2 + 4v' + c + \frac{4}{Re}v''' = 0, \quad c = 3 + b\\
&v(-1) = v(1) = 0, \quad v'(-1) = v'(1) = -1.
\end{aligned}
\qquad (10)
$$

This problem can be solved numerically by the shooting method. For given Re the method allows determination of parameter c or $b = c - 3$ and function $v(Y)$. Fig. 2 shows dependences $b(Re)$, calculated numerically by the shooting method and approximately with help of partial sum of 15 terms from series (9), and asymptotic solution of Reynolds – $b = 12/Re$, $|Re| \ll 1$.

The coefficients of the series $b(Re)$ at $a = 2$ decrease as geometric series. Its radius of convergence can be approximately estimated by the d'Alembert's ratio test as $Re_* \approx a_n/a_{n+1}$, where instead of limit $n \to \infty$ a large enough n is taken: for $n = 50$ radius of convergence of series b is $Re_* \approx 14$. As was shown in work [19], at the interval $Re < Re_*$ there exists a set of exact solutions of (10); also at $Re > Re_{*2} \approx 39$ and at $Re > Re_{*3} \approx 89$ another families of exact solutions exist. So, for each n-th set the value Re_{*n}, a countable set of continuous families of exact solutions of (10) can be found.

From graphical comparison on Fig. 2 one can see that numerical solution and solution in series disagree at $|Re|$ near Re_*. On the plot the disagreement starts appearing at $|Re| \approx 13$, and at point $|Re| \approx 14$ the difference is significant.

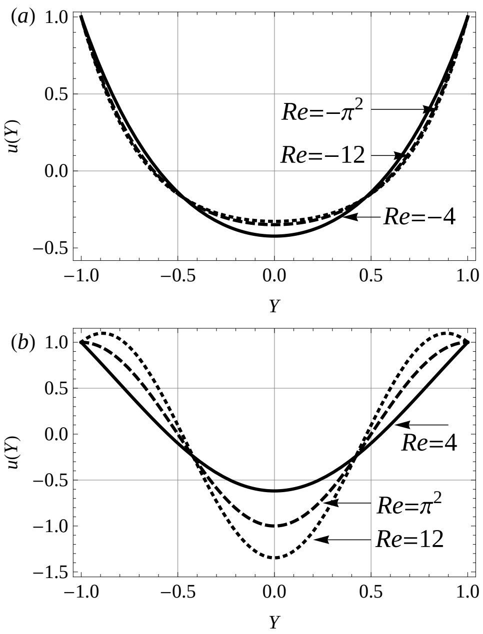

Figure 3. Flow diagrams $u(Y)$, $a = 2$: for decreasing $Re = -4, -\pi^2, -12$ and increasing $Re = 4, \pi^2, 12$ gap between the plates.

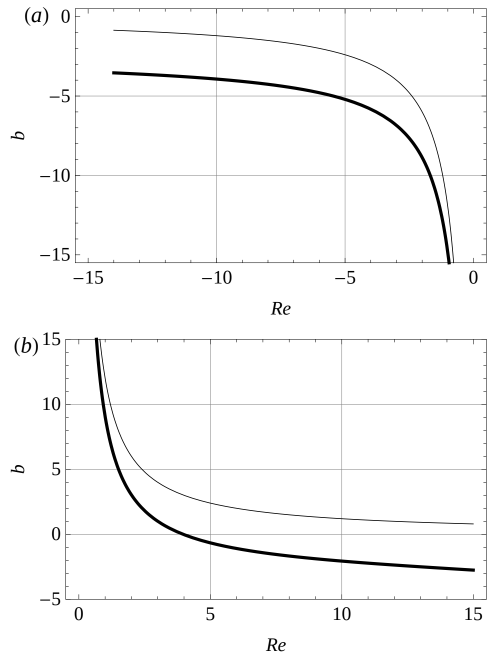

Figure 4. Dependence $b(Re)$ for $a = 1$, for $Re < 0$ and $Re > 0$: thick solid line - the series solution $b(Re, a)$ with 10 terms, thin solid line - the leading term $b = 12/Re$.

5.1. Closed form solution. Counterflow

In the case of plates moving apart ($Re > 0$) at $a = 2$ in work [19] a closed form solutions of the problem (10) were found at points $Re = n^2\pi^2$, n - natural number, as

$$u = (-1)^n \cos n\pi Y, \quad v = \frac{(-1)^n}{n\pi} \sin n\pi Y, \quad b = -4. \tag{11}$$

One of the interesting solutions is a solution $Re = \pi^2 \approx 10$; it separates the family of functions $u(Re, Y)$ into two physically different cases. In the first case ($Re < \pi^2$) the fluid between the plates flows in one direction. In the second case ($Re > \pi^2$) the fluid near the plates flows in opposite direction. Let us call this phenomenon a counterflow, and the value Re_{back}, above which it is observable - a critical Reynolds number. The counterflow is illustrated in Fig. 3. The case $a = 2$ is unique in that a closed form solution of the boundary value problem was found at point $Re = \pi^2$ that in turn is critical for the counterflow appearance, i.e. $Re_{back} = \pi^2$. For more information, how to find a critical Reynolds numbers Re_{back} for arbitrary value of a see the work [17].

Fig. 3 shows velocity profiles $u(Y)$, calculated with help of the series solution $\sum_{n=0}^{15} u_n(Y, a)Re^n$ of 15 terms for Reynolds numbers corresponding to decreasing ($Re < 0$) and increasing ($Re > 0$) gap between the plates. Also one can see on the figure that at Reynolds numbers greater than critical ($Re = 12$) velocity $u(Y)$ near the boundaries $Y = \pm 1$ has opposite direction to the average velocity (the counterflow phenomenon).

6. CASE $A = 1$. STEADY CHANGE OF THE GAP BETWEEN THE PLATES, $H = K|T|$.

In case $a = 1$ Eqs. (5) and their series solutions (6) correspond to change of the gap with are divergent, however they are an asymptotic. It means that an estimation of these series by an analytical function it is still possible. For the best approximation of asymptotic series by function, one needs to take N terms of its expansion in series, where N is the number of the minimal in absolute value term. The error of the approximation will be of the same order as the next to the minimal term. For instance, the value $b(a = 1, Re = 10)$ is approximated by partial sum of 10 terms with error 10^{-8}.

Fig. 4 shows the dependences $b(Re)$ at $Re > 0$ and $Re < 0$ in range $|Re| < 20$, defined by the sum of 10 terms, together with the leading term.

Velocity profiles $u(Y)$ at some Reynolds numbers are shown in Fig. 5. The critical Reynolds number was found as $Re_{back} = 16.5$. The plot distinctly shows the counterflow at $Re = 25 > Re_{back}$. The asymptotic series of 9 terms were used for plotting dependence $u(Y)$, as at this number the terms of the series $u'_n(Y = 1, a = 1)$ achieve their minimal value on $15 < |Re| < 30$. The plots do not change if the number of terms used in calculation would change by four ($N = 9 \pm 4$), even though the minimal term of the series $u'_n(Y = 1, a = 1)$ at $Re = 1$ is achieved at $N > 35$.

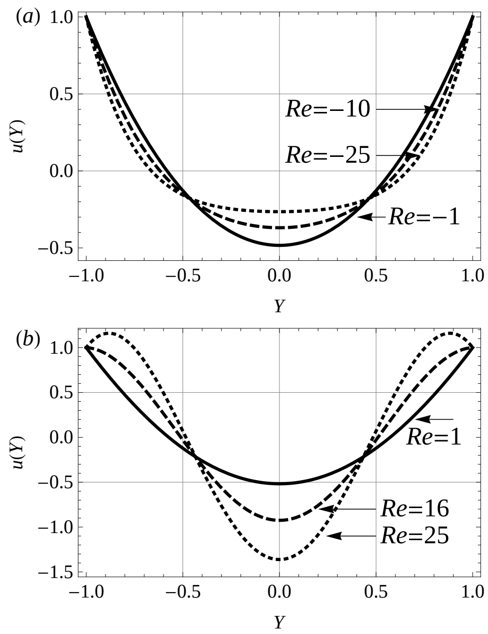

Figure 5. Flow diagrams $u(Y, a = 1)$, for decreasing $Re = -1$ -10, -25 and increasing $Re = 1$, 16, 25 gap between the plates, constructed with use of the series solution with 9 terms.

7. CASE $A = 0.5$. UNIFORMLY ACCELERATED CHANGE OF THE GAP BETWEEN THE PLATES, $H = KT^2$.

At $a = 0.5$ Eqs. (5) and their series solutions (6) correspond to the uniformly accelerated motion of the upper plate $h = kt^2$. This case is analogous to the case $a = 1$. Solution in series form also diverges. The dependence $b(Re)$ at $Re > 0$ and $Re < 0$ on segment $|Re| < 20$, defined by a partial sum of 5 terms, see Fig. 6.

Velocity profiles $u(Y)$ for some Reynolds numbers are shown in Fig. 7. The critical Reynolds number was found as $Re_{back} \approx 22.7$. It is seen that for Reynolds numbers greater than critical $Re = 30 > Re_{back}$ the counterflow has appeared.

8. CONCLUSIONS

The present notice considers a two-dimensional problem of viscous flow between two parallel plates. One plate is immobile, the other approaches or moves apart from it, so that the distance between the plates changes as a power law $h \sim t^s$.

The boundary value problem with conditions of fluid sticking on the plates was formulated for this. By a change of variables the initial Navier-Stokes equations were reduced to a partial differential equation of third order and two variables, which together with boundary conditions form a new initial-boundary problem. As result a velocity profiles and pressure between the plates were found.

In the case $s = 1/2$ the problem is reduced to an ordinary differential equation; and it can be easily analysed by numerical methods. In that case a self-

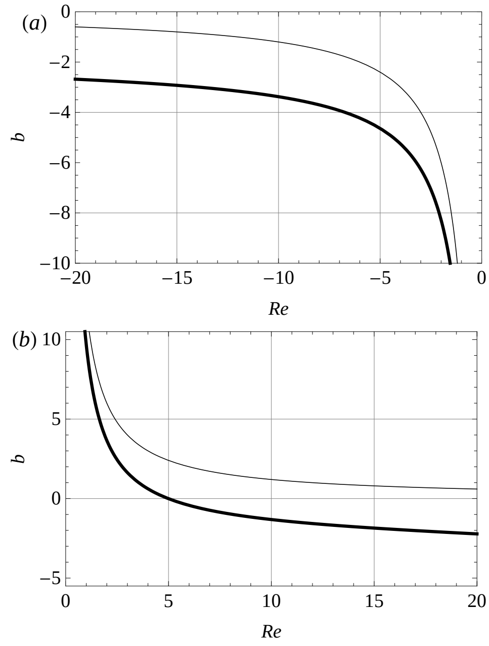

Figure 6. Dependence $b(Re)$ for $a = 0.5$, for $Re < 0$ and $Re > 0$: thick solid line - solution in series $b(Re, a)$ consisting of 5 terms, thin solid line - the leading term $b = 12/Re$.

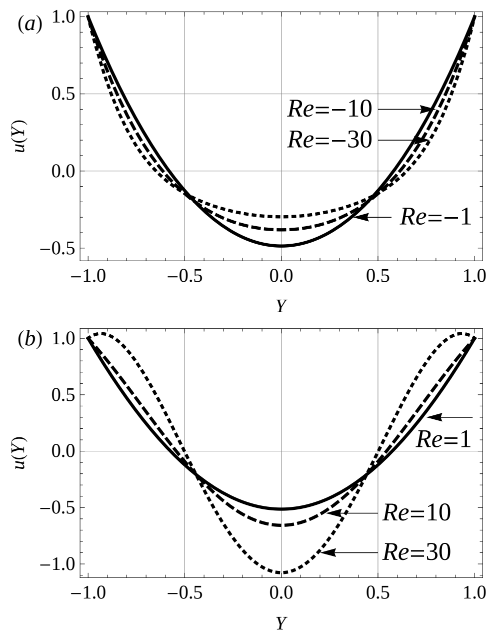

Figure 7. Velocity profiles $u(Y)$, for $a = 0.5$ for approaching ($Re = -1, -10, -25$) and moving apart ($Re = 1, 10, 25$) plates, plotted from the series solution of 5 terms.

similar solution exists - the velocity field between the plates is expressed through elementary trigonometric functions if Reynolds number equals $Re = n^2\pi^2$.

For arbitrary exponent s a set of particular solutions in form of series in powers of Reynolds number were constructed. For $s = 1/2$ the series is convergent with radius $Re_* \approx 14$. For other exponents the series is asymptotic. The best approximation of the solutions were found as partial sums of the asymptotic series.

Here was shown that if plates move apart with velocity such that Reynolds number becomes greater than some critical, Re_{back}, a counterflow arises between the plates, i.e. the fluid near the boundaries flows in the opposite direction relative to the average flow. In case $a = 2 - Re_{back} = \pi^2$, if $a = 1 - Re_{back} \approx 16.5$ and if $a = 1/2 - Re_{back} \approx 22.7$.

9. ACKNOWLEDGEMENTS

The work was supported by the Russian Science Foundation, project No 14-19-01633.

REFERENCES

[1] Kochin, N. E., Kibel, I. A., and Roze, N. V., 1964, *Theoretical Hydromechanics*, New York, Interscience Publishers.

[2] Landau, L. D., and Lifshitz, E. M., 1959, *Fluid Mechanics*, London, Pergamon Press.

[3] Batchelor, G. K., 1973, *An Introduction to Fluid Dynamics*, Cambridge University Press.

[4] Ayaz, F., and Pedley, T. J., 1999, “Flow through and particle interception by an infinite array of closely-spaced circular cylinders”, *Eur J Mech B/Fluids*, Vol. 18, pp. 173–196.

[5] Keh, H. J., and Wang, L. R., 2008, “Slow motions of a circular cylinder experiencing slip near a plane wall”, *J Fluids Structs*, Vol. 24, pp. 651–663.

[6] Hiemenz, K., 1911, “Die Grenzschicht an einem in den gleichformigen Flussigkeitsstrom eingetauchten geraden Kreiszylinder”, *Dingler’s Polytech J*, Vol. 326, pp. 321–410.

[7] Wang, C. Y., 1991, “Exact solution of the steady Navier-Stokes equations”, *Annu Rev Fluid Mech*, Vol. 23, pp. 159–177.

[8] Howarth, L., 1936, “On the calculation of the velocity and temperature distributions for flow along a flat plate”, *Proc Royal Soc of London*, Vol. A 154, pp. 364–377.

[9] Brady, J. F., and Acrivos, A., 1981, “Steady flow in a channel or tube with an accelerating surface velocity. An exact solution to the Navier-Stokes equations with reverse flow”, *J Fluid Mech*, Vol. 112, pp. 127–150.

[10] Siddiqui, A. M., Rana, M. A., Qamar, R., Irum, S., and Ansari, A. R., 2012, “On the Numerical Solution of Unsteady Squeezing MHD Flow of a Second Grade Fluid Between Parallel Plates”, *Adv Studies Theor Phys*, Vol. 6, pp. 27 – 36.

[11] Zwick, K. J., Ayyaswamy, P. S., and Cohen, I. M., 1997, “Oscillatory enhancement of the squeezing flow of yield stress fluids: a novel experimental result”, *J Fluid Mech*, Vol. 339, pp. 77–87.

[12] Qayyum, A., Awais, M., Alsaedi, A., and Hayat, T., 2012, “Unsteady Squeezing Flow of Jeffery Fluid between Two Parallel Disks”, *Chin Phys Lett*, Vol. 29, p. 034701.

[13] Hashmi, M. M., Hayat, T., and Alsaedi, A., 2012, “On the analytic solutions for squeezing flow of nanofluid between parallel disks”, *Nonlinear Analysis: Modelling and Control*, Vol. 17, pp. 418–430.

[14] Mustafa, M., Hayat, T., and Obaidat, S., 2012, “On heat and mass transfer in the unsteady squeezing flow between parallel plates”, *Meccanica*, Vol. 47, pp. 1581 – 1589.

[15] Thorpe, J. F., 1967, “Further Investigation of Squeezing Flow Between Parallel Plates”, *Develop in Theor and Appl Mech*, Vol. 3, pp. 635–648.

[16] Wang, C. Y., 1976, “The squeezing of a fluid between two plates”, *J of Appl Mech*, Vol. 43, pp. 579–583.

[17] Petrov, A. G., and Kharlamova, I. S., 2014, “The solutions of Navier-Stokes equations in squeezing flow between parallel plates”, *Europ J of Mechanics B-Fluids*, Vol. 48, pp. 40–48.

[18] Reynolds, O., 1886, “On the Theory of Lubrication and Its Application to Mr. Beauchamp Tower’s Experiments, Including an Experimental Determination of the Viscosity of Olive Oil”, *Phil Trans of the Royal Soc of London*, Vol. 177, pp. 157–234.

[19] Petrov, A. G., 2012, “Exact solution of the Navier-Stokes equations in a fluid layer between the moving parallel plates”, *J Appl Mech and Tech Physics*, Vol. 53, pp. 642–646.

Conference on Modelling Fluid Flow (CMFF'15)
The 16th International Conference on Fluid Flow Technologies
Budapest, Hungary, September 1-4, 2015

The Motion of a Solid Particle in an Acoustic Standing Wave

Alexander G. Petrov[12], Mariana S. Lopushanski[12]

[1] Moscow Institute of Physics and Technology, Institutskiy per. 9, Dolgoprudny, Moscow Region, 141700, Russian Federation, E-mail: petrovipmech@gmail.com
[2] Institute for Problems in Mechanics of the Russian Academy of Science, prosp. Vernadskogo 101, block 1, Moscow, 119526 Russian Federation, E-mail: masha.alexandra@gmail.com

ABSTRACT

The nonlinear integro-differential movement equation of a solid spherical particle in the field of a standing wave in compressible liquid is studied. The velocity and density of fluid are expressed in terms of harmonic functions depending on time and coordinate. A modification of the averaging method is used. The modification used in this paper proposes expansion by the parameter squared, and therefore it requires only one approximation. The modification proposed allowed to obtain the averaged equation for the nonlinear integro-differential equation. It is shown that the averaged solution of the integro-differential equation depends only on time and two similarity parameters. The first one is the ratio of the particle density and fluid density and the second one is a combination of vibration parameters and some characteristics of the fluid and particle. It is shown that one may neglect the Basset force only at small values of the second similarity parameter. It is shown that the influence of the Basset force must be taken into account with the help of developed theories when considering the movement of particles of micro and nano dimensions in the ultrasonic diapason of the vibration frequency, in other words, for the modes used in contemporary technologies.

Keywords: averaging method, Basset-Bossinesq-Ossen equation, Basset history force, particle in a standing wave, sedimentation, viscous fluid

NOMENCLATURE

Re	$[-]$	Reynolds number
μ	$[Pa \cdot s]$	dynamic viscosity
ν	$[m^2/s]$	kinematic viscosity
ω	$[rad/s]$	wave angular frequency
ρ	$[kg/m^3]$	fluid density
ρ_s	$[kg/m^3]$	particle density
τ	$[-]$	dimensionless time
A	$[m]$	wave amplitude
a	$[m]$	particle radius
c	$[m/s]$	sound velocity in fluid
f_B	$[-]$	dimensionless Basset history force
g	$[m/s^2]$	Earth's standard acceleration due to gravity
q	$[-]$	dimensionless coordinate
t	$[s]$	time
U_∞	$[m/s]$	terminal speed
v	$[m/s]$	wave velocity
w	$[m/s^2]$	acceleration of the particle

1. INTRODUCTION

In this paper the movement of a spherical particle in a viscous fluid in a vessel with a vibrating bottom (laminar case, Re $\ll 1$) is studied.

Forces caused by gravitation (the gravitational force and the Archimedes force) and the hydrodynamic forces act on the solid particle, whose size is significantly smaller than the wavelength. The hydrodynamic forces divide into inertial forces and viscous forces. The viscous forces are found by solving the linear Navier-Stokes equations (Stokes approximation). In case of stationary motion of a particle in a high-viscosity fluid at rest the solution was offered by Stokes. In this case the force is proportional to the velocity of the particle. In case of an arbitrary dependence of velocity on time, the force that acts on the particle was found by Boussinesq and Basset in [1, 2]. It equals the sum of the Stokes force and the force, expressed through a linear integral operator from the relative acceleration of the particle (Basset force). The Basset force depends on the whole prehistory of the motion. Without the consideration of the Basset force, the motion equation of the particle is differential and is easy to study using analytical or numerical methods. If taking into consideration the Basset force, the equation becomes integro-differential (IDE) and in literature it is called the Basset-Boussinesq-Oseen equation. In an incompressible fluid the equation is linear and there are many works devoted to the construction of its solution.

In the absence of vibration the Basset-

Boussinesq-Oseen equation describes the sedimentation of the particle due to the forces, caused by gravitation. In [3] the IDE is transformed into an ordinary differential equation (ODE) of second order. The ODE describes the forced oscillations of a linear oscillator with the resistance force being proportional to velocity. The particular solution of the ODE that satisfies the corresponding initial solution is also a solution for the IDE. In many subsequent works (see, for example, [4]) it was pointed out that the ODE, when solved numerically, is less time consuming and requires less memory than IDE. However, when the ratio of the fluid density and particle density is $k = \rho/\rho_s < 4/7$, the resistance force from the ODE changes sign and becomes thrust, this making the numerical construction of the particular solution of ODE impossible due to the exponential growth of small perturbations. In light of this, the corresponding phase density range was studied in [5], based on the numerical solution of the initial IDE earlier suggested in [4] method.

The difficulties in building a numerical solution when $k < 4/7$ stimulate the attempts of building a particular analytical solution convinient for use, which corresponds to the solution of the particle at rest sedimentation problem. In [6, 7, 8] the formal solutions, obtained with the help of the Laplace transformation, are given. The most compact form of the solution is given in [6]

$$u(\tau) = \frac{\sqrt{k_1}}{\alpha-\beta}\left[\frac{e^{\alpha\tau}\mathrm{Erfc}\sqrt{\alpha\tau}}{\sqrt{\alpha}} - \frac{e^{\beta\tau}\mathrm{Erfc}\sqrt{\beta\tau}}{\sqrt{\beta}}\right],$$
$$k_1 = \frac{9k}{2+k}, \quad k = \frac{\rho}{\rho_s},$$

where α and β are the roots of the equation $x^2 + (2 - k_1)x + 1 = 0$, ρ is the density of the fluid, ρ_s is the density of the particle and $u(\tau)$ is a dimensionless particle velocity function. But these roots may be either negative or complex. And it was not pointed out how to extract from a formally complex solution the real function. Therefore, it is impossible to use such a solution directly to construct, for example, the plot $u(\tau)$.

In the comments to the solution given in [7], it is suggested to mark out the real branch of the solution with the help of Maple and build the asymptotic for big time values. But these results are not presented.

In [9] a simplified algorithm of reducing the IDE to ODE is presented and the precise solution of the motion equation in explicit form for all the parameters is obtained. Using these results, the asymptotic expansion for the dependence of the coordinate X and the velocity U on time is obtained. From the solution of this problem it follows that the terminal speed U_∞

$$U = U_\infty(1 + a/\sqrt{\pi\nu t} + O(1/t))$$

is establishing slowly, inversely proportional to the square root of time, which is substantially different from the sedimentation of the particle by Stokes law (the establishment of terminal speed is exponential in this case).

In [9] an experimental verification of the obtained particle sedimentation law is made. Therefore, the experiment proves that the consideration of the Basset force is crucial for the measurement of the viscosity coefficient by the sedimentation of a ball, as the ball must make a long way for the establishment of constant speed. With the help of the asymptotic obtained the way the ball must make for the establishment of constant speed is calculated.

According to multiple experiments the sedimentation of heavy solid particles stops in a vessel whose bottom is exhibited to high-frequency vibration. Due to the vibration the particles stop depositing and concentrate in horizontal planes, through a distance of half wavelength. The problem describing this effect theoretically is formulated like this in [10, 11, 12].

In [13] the sedimentation of a solid spherical particle from quiescence in an incompressible fluid in a vessel with a vibrating bottom is studied. Taking into consideration the Basset force, the problem is reduced to solving the Cauchy problem for a linear integro-differential equation. The exact solution of this problem and simple asymptotic formulas are obtained, a thorough analysis of the influence of Basset force on the oscillation and sedimentation processes of the particle is made. It is shown that the consideration of the Basset force makes a substantial amendment to the classical dependence of the amplitude on frequency, diminishing its value and substantially slowing down the achievement of its constant value.

Under the influence of the vibration on fluid a standing wave is formed. The velocity v and the density ρ in it depend on the coordinate x and the time t by the following law

$$v(t,x) = -A\omega\sin\tau\cos q,$$
$$\rho = \rho_0\left(1 + \frac{A\omega}{c}\cos\tau\sin q\right),$$

Here A and ω are the wave amplitude and frequency, c is the sound velocity in fluid.

The motion equation of the particle is

$$(\rho + 2\rho_s)\ddot{x} = 3\rho w - 2(\rho_s - \rho)g - \frac{9\mu}{a^2}\left(\frac{dx}{dt} - v\right) -$$
$$-\frac{9}{\pi a}\sqrt{\pi\rho\mu}\int_0^t\left(\frac{d^2x}{dt'^2} - \frac{\partial v}{\partial t'}\right)\frac{dt'}{\sqrt{t-t'}},$$
$$w = \partial v/\partial t + v\partial v/\partial x, \quad b = A\omega/c.$$

Let us introduce the following dimensionless quantities $q(\tau) = (\omega/c)x$, $\tau = \omega t$,. Then the velocity and the acceleration of the particle are expressed through the following derivatives $\dot{q}$ and $\ddot{q}$ and

$$\frac{dx}{dt} = c\dot{q}, \frac{d^2x}{dt^2} = \omega c\ddot{q}.$$

Let us express the particle motion equation as follows

$$\frac{d^2q}{d\tau^2} + 3K\varepsilon^2\frac{dq}{d\tau} + \varepsilon^2\cos\tau\cos q +$$
$$\varepsilon^4\frac{4s+1}{12}\sin 2q = f_B$$
$$s = \frac{\rho_s}{\rho}, \quad K = \frac{\nu c}{Aa^2\omega^2}, \quad \varepsilon = \sqrt{\frac{3A\omega}{c(1+2s)}} \tag{1}$$

Here f_B is the Basset history force, and

$$f_B = -3\varepsilon\sqrt{\frac{3sK}{\pi(1+2s)}}I(\tau),$$
$$I(\tau) = \int\limits_0^\tau \frac{\frac{d^2q}{d\xi^2} + \frac{1}{3}\varepsilon^2(1+2s)\cos\xi\cos q}{\sqrt{\tau-\xi}}d\xi.$$

Without the consideration of the Basset force this equation is studied in the monograph [10] and more precisely in the monographs [11] and [12]. In [11] the asymptotic solution is built with the help of the third approximation of the averaging over the small parameter ε method. The same result is easier obtained with the help of the first improved approximation by the expansion in parameter ε^2. In order to simplify the problem, the gravitation force in Eq. (1) is neglected. Its influence is negligible providing that $g/(\omega c) \ll \varepsilon^2$ [11, 12]. This usually holds at high-frequencies. The analysis considering the gravitational force, but without taking into consideration the Basset force, is presented in [11, 12].

In this paper the averaging method to study the nonlinear problem of the movement of the particle in an acoustic wave in compressible fluid is used. The Bogoliubov theorems can be found in ([14]).

2. AVERAGING METHOD WITHOUT THE BASSET FORCE CONSIDERATION

In this section use of the Bogoliubov theorem will be made. Let us remember it. Consider two Cauchy problems

$$\frac{dx}{dt} = \varepsilon X(t,x,\varepsilon), \quad x(0) = x_0 \tag{2}$$

and

$$\frac{du}{dt} = \varepsilon X_0(u,\varepsilon), \quad u(0) = x_0, \tag{3}$$

where the right member of Eq. (2) is defined by x on $D \subset R^n$ – an open connected set, $0 \le t < +\infty$, $0 \le \varepsilon \le \varepsilon_1$ and the function $X(t,x,\varepsilon)$ is periodical by t with period T. Then, under some supplementary assumptions, $\|x(t) - u(t)\|$ is of order ε.

Now let us define the improved first approximation. Here only a short explanation is provided, for more details see, for example, [14]. Consider the system Eq. (2) where $X(t,x,\varepsilon)$ is a periodical function with period T. We may rewrite the system as follows

$$\frac{dx}{dt} = \varepsilon X_0(x,\varepsilon) + \varepsilon\tilde{X}(t,x,\varepsilon), \tag{4}$$

where $X_0(x,\varepsilon)$ is the average over time of $X(t,x,\varepsilon)$ and the average value of $\tilde{X}(t,x,\varepsilon)$ over the period is 0. Let us make the following variable change

$$x = u + \int \varepsilon\tilde{X}(t,u,\varepsilon)dt = u + \varepsilon U_1(t,u) + O(\varepsilon^2). \tag{5}$$

Then the new system will be

$$\frac{du}{dt} = \varepsilon X_0(u,\varepsilon) + \varepsilon^2 X_1(u,\varepsilon) + \varepsilon^2\tilde{X}_1(t,u,\varepsilon), \tag{6}$$

where $X_1(u,\varepsilon)$ does not depend on time and the average of $\tilde{X}_1(t,u,\varepsilon)$ over the period is 0. If only the first term in the right side of Eq. (6) is kept, Eq. (3) from the Bogoliubov theorem is obtained. So its solution $u = \bar{u}(t)$ is the first approximation of system Eq. (2). Considering Eq. (5), the first improved approximation $x = \bar{u}(t) + \varepsilon X_1(t,\bar{u}(t))$ is obtained.

Let us first provide the solution of Eq. (1) using the averaging method without taking into account the Basset force. We write Eq. (1) in form of a system of equations

$$\frac{dp}{d\tau} = -3\varepsilon^2 Kp - \varepsilon^2\frac{4s+1}{12}\sin 2q - \cos\tau\cos q$$
$$\frac{dq}{d\tau} = \varepsilon^2 p. \tag{7}$$

As one may see the system is not in its standard form, but it can be easily brought to it by a change of variables

$$q = Q + \varepsilon^2\cos\tau\cos Q, \quad p = P - \sin\tau\cos Q. \tag{8}$$

The equations for Q and P have a standard form

$$\frac{dQ}{d\tau} = \varepsilon^2 P,$$
$$\frac{dP}{d\tau} = \varepsilon^2(-3KP - \frac{2s-1}{6}\sin 2Q +$$
$$+(3K\cos Q - P\sin Q)\sin\tau + \frac{1}{4}\cos 2\tau\sin 2Q). \tag{9}$$

Here the terms of order ε^4 are discarded.

Averaging the right sides over τ, the system of first approximation is obtained

$$\frac{dQ}{d\tau} = \varepsilon^2 P$$
$$\frac{dP}{d\tau} = \varepsilon^2\left(-3KP - \frac{2s-1}{6}\sin 2Q\right). \tag{10}$$

The system of equations may be written in the form of the equation of the oscillations of a mathematical pendulum with friction by making the substitution $\tau_1 = \varepsilon^2\tau$

$$\frac{d^2(2\bar{Q})}{d\tau_1^2} + 3K\frac{d(2\bar{Q})}{d\tau_1} +$$
$$\frac{2s-1}{3}\sin(2\bar{Q}) = 0, \quad \bar{Q}(\tau_1) = Q(\frac{\tau_1}{\varepsilon^2}). \tag{11}$$

This equation may be presented in the form of energy variation

$$\frac{d}{d\tau_1}\left(2\left(\frac{d\bar{Q}}{d\tau_1}\right)^2 + \Pi(\bar{Q})\right) = -12K\left(\frac{d\bar{Q}}{d\tau_1}\right)^2,$$

$$\Pi(\bar{Q}) = -\frac{2s-1}{3}\cos(2\bar{Q}).$$

By the Lyapunov theorem the points of minimum of the function $\Pi(\bar{Q})$

$$s > 1/2 : \bar{Q}_0 = n\pi,$$
$$s < 1/2 : \bar{Q}_0 = (1/2+n)\pi,\ n = 0, \pm1, \pm2, ... \quad (12)$$

are the points of stable equilibrium to which, by the second theorem of Bogolyubov, correspond stable periodical solutions. Let us calculate them with precision ε^4 using the substitution Eq. (8)

$$q = \bar{Q}_0 + \varepsilon^2 \cos\tau \cos\bar{Q}_0 + O(\varepsilon^4).$$

With the help of the substitution $\bar{Q} = \bar{Q}_0 + \tilde{Q}$ Eq. (2) in the neighbourhood of point $\bar{Q}_0$ found in Eq. (2) is linearised

$$\frac{d^2\tilde{Q}}{d\tau_1^2} + 3K\frac{d\tilde{Q}}{d\tau_1} + \left|\frac{2s-1}{3}\right|\tilde{Q} = 0$$

With the initial conditions $\tilde{Q}(0) = a,\ \dot{\tilde{Q}}(0) = 0,\ a \ll 1$, the solution is close to the solution of the linearised equation. When $r^2 = 27K^2 - 4|2s-1| > 0$ the solution is

$$\tilde{Q}(\tau_1) = \frac{a}{r}e^{-(3/2)K\tau_1}\times$$
$$\times\left[3\sqrt{3}\,K\sinh\frac{r\tau_1}{2\sqrt{3}} + r\cosh\frac{r\tau_1}{2\sqrt{3}}\right]. \quad (13)$$

When $r^2 = 4|2s-1| - K^2 > 0$ the solution is

$$\tilde{Q}(\tau_1) = \frac{a}{r}e^{-(3/2)K\tau_1}\times$$
$$\times\left[3\sqrt{3}\,K\sin\frac{r\tau_1}{2\sqrt{3}} + r\cos\frac{r\tau_1}{2\sqrt{3}}\right]. \quad (14)$$

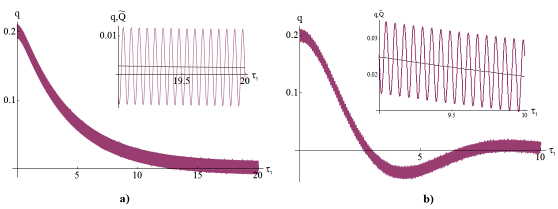

Figure 1. The solution of the first and the improved first approximation of the equation of motion of a solid particle: a) $K = 1,\ s = 1.5,\ \varepsilon = 0.1$**; b)** $K = 0.25,\ s = 1.5,\ \varepsilon = 0.1$**.**

In Figures 1 and 2 the numerical and asymptotic solutions in the neighborhood of point of stable equilibrium $\bar{Q}_0 = 0$ are considered, chosen from the series points (2).

In Fig. 1 the solutions of the first improved approximation $q = \tilde{Q}(\tau_1) + \varepsilon^2\cos\left(\frac{\tau_1}{\varepsilon^2}\right)\cos(\tilde{Q}(\tau_1))$ for two cases are presented:

a) $s = 1.5,\ K = 1,\ \varepsilon = 0.1$. The function $\tilde{Q}(\tau_1)$ is defined as in Eq. (2). The argument of the function varies between $\tau_1 \in (0, 20)$. Next to it is shown a fragment of the solution of the first and improved first approximation on the interval $\tau_1 \in (19, 20)$. b) $s = 1.5,\ K = 0.25,\ \varepsilon = 0.1$. The function $\tilde{Q}(\tau_1)$ is defined as in Eq. (2).The argument of the function varies between $\tau_1 \in (0, 10)$. Next to it is shown a fragment of the solution of the first and improved first approximation on the interval $\tau_1 \in (9, 10)$.

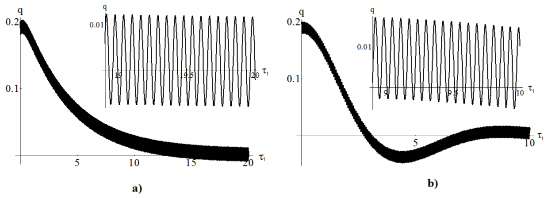

Figure 2. The numerical solutions of the exact solid particle motion equations: a) $K = 1,\ s = 1.5,\ \varepsilon = 0.1$**; b)** $K = 0.25,\ s = 1.5,\ \varepsilon = 0.1$**.**

In Fig. 2 the numerical solutions for the initial Eq. (2) for the following two cases are shown: a) $s = 1.5,\ K = 1,\ \varepsilon = 0.1$ and b) $s = 1.5,\ K = 0.25,\ \varepsilon = 0.1$. Next to them fragments in the intervals $\tau_1 \in (19, 20)$ and $\tau_1 \in (9, 10)$ are shown.

The comparison of Figures 1 and 2 shows that the numerical solutions of the initial equation are practically identical to their asymptotic solutions.

3. THE AVERAGING METHOD WITH THE CONSIDERATION OF THE BASSET FORCE

We will now solve the particle motion equation Eq. (1) considering the Basset force. The particle motion equation Eq. (1) may be rewritten as follows

$$\frac{d^2q}{d\tau^2} + 3K\varepsilon^2\frac{dq}{d\tau} + \varepsilon^2\cos\tau\cos q +$$
$$+\varepsilon^4\frac{4s+1}{12}\sin 2q = f_B$$
$$f_B = -3\varepsilon\sqrt{\frac{3sK}{1+2s}}\,I(\Phi(\tau)),$$
$$I(\Phi(\tau)) = \frac{1}{\sqrt{\pi}}\int_0^\tau \frac{\Phi(\xi)}{\sqrt{\tau-\xi}}d\xi,$$
$$\Phi(\tau) = \frac{d^2q}{d\tau^2} + \varepsilon^2\frac{1+2s}{3}\cos\tau\cos q. \quad (15)$$

Here I is the integral operator. The equation becomes integro-differential. The Basset force depends on the whole rather difficult particle motion trajectory. It must be retained in the computer memory during the numerical calculations of the Basset force, which makes solving the integro-differential equation more complicated.

Considering the Basset force, the initial dimensionless equation Eq. (1) may be expressed as follows

$$\frac{dq}{d\tau} = \varepsilon^2 p,$$
$$\frac{dp}{d\tau} = -3\varepsilon^2 Kp - \varepsilon^2 \frac{4s+1}{12} \sin 2q -$$
$$\cos\tau\cos q + f_B/\varepsilon^2 \qquad (16)$$

Let us formulate the motion trajectory research problem near the stable equilibrium point $q = n\pi$ when $s > 1/2$. Instead of Eq. (8) following substitution is used

$$q = n\pi + Q + (-1)^n(\varepsilon^2\cos\tau\cos Q +$$
$$+\varepsilon^3 C\cos(\tau - \pi/4)),$$
$$p = P - (-1)^n\left(\sin\tau\cos Q + \varepsilon C\sin(\tau - \pi/4)\right),$$
$$C = 2(s-1)\sqrt{\frac{3sK}{1+2s}}. \qquad (17)$$

This substitution, as well as the substitution Eq. (8) nullifies the term $\cos\tau\cos q$. The term with the multiplier C is introduced to compensate the oscillatory term of the Basset force. From Eq. (2)it is denoted that Q and P are small of order ε^2.

After the substitution Eq. (3) in the equation Eq. (3) (therefore, $\cos q = (-1)^n - \varepsilon^2 Q\cos\tau + O(\varepsilon^4)$ and $\varepsilon^2\sin 2Q = 2\varepsilon^2 Q + O(\varepsilon^4)$) and the neglection of terms of order ε^4 the following system of differential equations in variables Q, P is obtained

$$\frac{dP}{d\tau} = \varepsilon^2\left(-3KP + 3(-1)^n K\sin\tau - \frac{4s+1}{6}Q\right) +$$
$$+(-1)^n\varepsilon C\cos(\tau - \pi/4) + \frac{f_B}{\varepsilon^2},$$
$$\frac{dQ}{d\tau} = \varepsilon^2 P. \qquad (18)$$

The subintegral function from the Basset force can be written as

$$\Phi(\tau) = \varepsilon^2\left(\frac{dP}{d\tau} + (-1)^n\frac{2}{3}(s-1)\cos\tau\right) - \varepsilon^4\frac{1+2s}{3}Q(\cos^2\tau).$$

In [13] was proved the following asymptotic expansion

$$I(\cos\tau) = \cos(\tau - \pi/4) - \frac{1}{2\sqrt{\pi}\tau^{3/2}} + O(\tau^{-5/2}).$$

Using it for the Basset force, it is obtained that

$$f_B = f_B' - \varepsilon^3 C\cos(\tau - \pi/4),$$
$$f_B' = -3\varepsilon\sqrt{\frac{3sK}{1+2s}}\left(I\left(\varepsilon^2\frac{dP}{d\tau} - \varepsilon^4\frac{1+2s}{6}Q\right)\right)$$

After substituting this expression in Eq. (3) and averaging the right side the following equations for Q and P are obtained

$$\frac{dQ}{d\tau} = \varepsilon^2 P$$
$$\frac{dP}{d\tau} = \varepsilon^2\left(-3KP - \frac{2s-1}{3}Q\right) - 3\varepsilon\sqrt{\frac{3sK}{1+2s}}\times$$
$$\times\left(I\left(\frac{dP}{d\tau}\right) - \varepsilon^2\frac{1+2s}{6}I(Q)\right)$$

Let us simplify the integrals with the help of transformations $\tau_1 = \varepsilon^2\tau,\ \xi_1 = \varepsilon^2\xi$

$$\sqrt{\pi}I\left(\frac{dP}{d\tau}\right) = \int_0^\tau \frac{dP/d\xi d\xi}{\sqrt{\tau - \xi}} = \varepsilon\int_0^{\tau_1}\frac{d\bar{P}/d\xi_1 d\xi_1}{\sqrt{\tau_1 - \xi_1}} =$$
$$= \varepsilon\sqrt{\pi}I\left(\frac{d\bar{P}}{d\tau_1}\right), \quad \bar{P}(\tau_1) = P(\frac{\tau_1}{\varepsilon^2}),$$

$$\varepsilon^2\sqrt{\pi}I\left(Q(\tau)\right) = \int_0^\tau\frac{Q(\xi)d\varepsilon^2\xi}{\sqrt{\tau - \xi}} = \varepsilon\int_0^{\tau_1}\frac{\bar{Q}(\xi_1)d\xi_1}{\sqrt{\tau_1 - \xi_1}} =$$
$$= \varepsilon\sqrt{\pi}I\left(\bar{Q}(\tau_1)\right), \quad \bar{Q}(\tau_1) = Q(\frac{\tau_1}{\varepsilon^2}).$$

One may denote that when passing to the dimensionless time variable τ_1 the system does not depend on the parameter ε

$$\frac{d\bar{P}}{d\tau_1} = \left(-3K\bar{P} - \frac{2s-1}{3}\bar{Q}\right) - 3\sqrt{\frac{3sK}{1+2s}}\times$$
$$\times\left(I\left(\frac{d\bar{P}}{d\tau_1}\right) - \frac{1+2s}{6}I(\bar{Q}(\tau_1))\right),$$
$$\frac{d\bar{Q}}{d\tau_1} = \bar{P}.$$

The periodical solution that corresponds to the stationary point $\bar{Q} = 0,\ \bar{P} = 0$ of the averaged equation is

$$q = \frac{\omega}{c}x = n\pi + (-1)^n\left(\varepsilon^2\cos\omega t + \varepsilon^3 C\cos(\omega t - \pi/4)\right)$$

We denote that at the maximums and minimums of the standing wave speed $v(t, x)$ the solid particles oscillate in opposite directions. The main term of the oscillation amplitude of order ε^2 is determined by the solution of the problem without the Basset force consideration. The Basset force makes a correction of the amplitude of order $\varepsilon^3 C$.

The obtained averaged system may be written as one integro-differential equation

$$\frac{d^2\bar{Q}}{d\tau_1^2} + 3K\frac{d\bar{Q}}{d\tau_1} + \frac{2s-1}{3}\bar{Q} + 3\sqrt{\frac{3sK}{1+2s}}\times$$
$$\times\left(I\left(\frac{d^2\bar{Q}}{d\tau_1^2}\right) - \frac{1+2s}{6}I(\bar{Q}(\tau_1))\right) = 0, \qquad (19)$$

where $\tau_1 = \varepsilon^2\tau$. The time $t = 1/(\varepsilon^2\omega)$ corresponds to the value $\tau_1 = 1$. If this time is divided by the vibration period $\Delta t = 2\pi/\omega$, the number of periods is obtained

$$N_1 = 1/(2\pi\varepsilon^2) \qquad (20)$$

The averaged motion of the solid particle is fully determined by two parameters: the density ration s and the dimensionless parameter $K = \frac{\nu c}{A a^2 \omega^2}$.

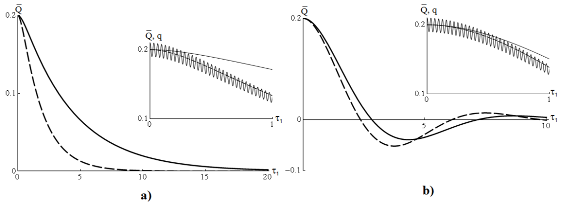

Figure 3. The solution of the first approximation of the solid particle motion equation considering the Basset force (dashed line) and without considering it (firm line):
a) $K = 1,\ s = 1.5,\ \varepsilon = 0.1$**; b)** $K = 0.25,\ s = 1.5,\ \varepsilon = 0.1$**.**

In the Figure 3 are shown the solutions of the averaged equation Eq. (2) without the Basset force consideration (by a firm line) and the solution of the averaged equation Eq. (3) considering the Basset force (by a dashed line) for two cases: a) $s = 1.5,\ K = 1,\ \varepsilon = 0.1$. The argument of the function $\bar{Q}(\tau_1)$ changes between $\tau_1 \in (0, 20)$.

b) $s = 1.5,\ K = 0.25,\ \varepsilon = 0.1$. The argument of the function $\bar{Q}(\tau_1)$ changes between $\tau_1 \in (0, 10)$.

The wavy lines represent the direct calculation of the initial equation Eq. (3).

When the dimensionless parameters are $s = 1.5, K = 1, \varepsilon = 0.01$ the parameters in CGS are $s = 1.5,\ c = 1.5 \times 10^5\, cm/s,\ \nu = 0.01,\ \omega = 2\pi \times 10^5,\ A = 3.18 \times 10^{-6}\, cm,\ a = 0.00345$.

As one may denote from the graph in Fig. 3a), the stable periodical particle motion without the Basset force consideration is established in $\tau_1 \approx 20$, where τ_1 is the dimensionless time variable, and, if the Basset force is considered, in $\tau_1 \approx 10$. With the help of Eq. (20) one may find the number of oscillatory motion periods during this time $N = 10N_1 = 1.5 \times 10^4$. To calculate the Basset force integral Eq. (3) it is necessary to choose the integration step of order 1/10 of the oscillation period. Totally, there will be $100N_1 = 1.5 \times 10^5$ steps. The number of computations for the direct numerical solution of the integro-differential equation Eq. (1) is proportional to $(100N_1)^2 \approx 2.25 \times 10^{10}$. Such computations are practically impossible and this is the reason the application of the averaging method is crucial.

As the averaged trajectory does not depend on the parameter ε^2, then for the numerical solution of the equations Eq. (1), Eq. (3) the parameters are changed as follows $A = 10^{-5},\ a = 0.3$. The parameter ε^2 increases by 1000 times, and the similarity parameters s and K remain unchanged. Then the computation time decreases by 10^6 times. The result of this computation is presented in Fig. 3a). But even in this case the computation of the initial equation is performed only until the time $\tau_1 = 1$, as the number of operations required at each step increases with time. If the computations until the value of time $\tau_1 = 1$ require 30 minutes, then for $\tau_1 = 10$ they require about 3000 minutes. From the figure one may denote that denote that there exists an essential difference between the particle motion trajectory with and without the Basset force consideration. This difference increases as the parameter K increases.

When $s = 3/2,\ K = 1/4$ the comparison of the curves $q(t)$ is given in Fig. 3 b). From all the parameters given only the radius of the particle is different from the previous case and $a = 0.007$. Here the trajectories with and without the Basset force consideration are rather close. The difference between them decreases as the parameter K decreases.

4. CONCLUSION

We used the averaging method to obtain the first improved approximation of the solution of the nonlinear particle motion equation in compressible fluid without considering the Basset force. We also provide the results for some numerical experiments of the initial equation (not averaged), and compare them. We note that they are practically indistinguishable, meaning that the averaging method gives a good approximation of the exact solution. We then use the averaging method for the equations considering the Basset force. We denote that if we try to calculate directly the solution, it requires too much machine time. The differences between the trajectory calculated without the Basset force consideration and the one with the Basset force consideration are substantial for $K > 0.25$. For example, if the frequency is about 10^6 Hz, kinematic viscosity is of order 0.01 and the amplitude is about 10^{-5}, then the Basset force may be neglected for particles whose radii are greater than 10^{-2} cm. This means that if one wants to calculate the trajectories of micro and nano particles, the Basset force must be considered. The trajectory of the particle may be found by solving equation Eq. (3) with the help of the numerical scheme proposed in [9]. Because the averaged function changes smoothly, it is sufficient to use a grid of no more than 100 elements, which requires 10000 computations.

ACKNOWLEDGEMENTS

The work was supported by the Russian Science Foundation, project No 14-19-01633.

REFERENCES

[1] Boussinesq, J., 1885, “Sur la resistance que oppose un liquide indefini en repos, sans pesanteur, au mouvement varie dŠune sphere solide quŠil mouille sur toute sa surface, quand les vitesses restent bien continues et assez faibles pour que leurs carres et produits soient negligeables.”, *Compt Rend Acad Sci Paris*, Vol. 100, pp. 935–937.

[2] Basset, A. B., 1888, “On the motion of a sphere in a viscous liquid.”, *Phil Trans R Soc Lond*, Vol. A 179, pp. 43–63.

[3] Villat, H., 1943, “On the motion of a sphere in a viscous liquid.”, Paris: Gauthier-Villars., p. 540.

[4] Michaelides, E. E., 1992, “A novel way of computing the Basset term in unsteady multiphase flow computations.”, *Phys of Fluids*, Vol. A4, pp. 1579–1582.

[5] Nevskii, Y. A., and Osiptsov, A. N., 2008, “On the role of the ŞhereditaryŤ forces in the gravitational convection of suspensions problems.”, *The Moscow University Herald Ser 1 Mathematics, mechanics*, Vol. 4, pp. 37–40.

[6] Belmonte, A., Jacobsen, J., and Jayaraman, A., 2001, “Monotone solutions of a nonautonomous differential equation for a sedimenting sphere.”, *Electronic J Different Equat*, Vol. 62, pp. 1–17.

[7] Coimbra, C. F. M., and Rangel, R. H., 1998, “General solution of the particle momentum equation in unsteady Stokes flows”, *J Fluid Mech*, Vol. 370, pp. 53–72.

[8] Sobral, Y. D., Oliveira, T. F., and Cunha, F. R., 2007, “On the unsteady forces during the motion of a sedimenting particle”, *Powder Technology*, Vol. 178:2, pp. 129–141.

[9] Petrov, A. G., Vodop’yanov, I. S., and Shunderyuk, M. M., 2010, “Unsteady Sedimentation of a Spherical Solid Particle in a Viscous Fluid”, *Fluid Dynamics*, Vol. 45:2, pp. 254–263.

[10] Ganiev, R. F., and Ukrainskiy, L. E., 1975, *The Dynamics of Particles under the Influence of Vibrations [in Russian].*, Kiev: Nauk. Dumka, p. 168.

[11] Nigmatulin, R. I., 1990, *Dynamics of Multiphase Media*, Vol. 1, CRC Press.

[12] Petrov, A. G., 2009, *Analytical Hydrodynamics [in Russian].*, Moscow: Fizmatlit, p. 520.

[13] Visitskii, Y., Petrov, A. G., and Shunderyuk, M. M., 2009, “The motion of a particle in a viscous fluid under gravity, vibration and Basset’s force”, *J Appl Math Mech*, Vol. 73:5, pp. 548–557.

[14] Zhuravlev, V. P., and Klimov, D. M., 1988, *Applied Methods in Vibrations Theory [in Russian].*, Moscow:Nauka.

Conference on Modelling Fluid Flow (CMFF'15)
The 16th International Conference on Fluid Flow Technologies
Budapest, Hungary, September 1-4, 2015

Solution of Navier-Stokes Equations in Squeezing Flow between Parallel Plates in Axisymmetric Case

Alexander G. PETROV[1,2], Irina S. KHARLAMOVA[2,3]

[1] Corresponding Author. Department of Theoretical Mechanics, Moscow Institute of Physics and Technology. 9 Institusky Per. 141701, Dolgoprudny, Russia. Tel.: +7 916 079-61-58, E-mail: petrovipmech@gmail.com
[2] Laboratory of Mechanics of Systems, Institute for Problems in Mechanics RAS, pr. Vernadskogo 101-1, 119526 Moscow, Russia. E-mail: petrovipmech@gmail.com
[3] Department of Mechanics of Fluids and Disperse Systems, Institute of Hydrodynamics ASCR, Pod Pat'ankou 30/5, 166 12 Prague 6, Czech Republic. E-mail: kharlamova@ih.cas.cz

ABSTRACT

The velocity profile in a layer of viscous Newtonian fluid between two parallel plates (disks), where one plate is immobile and other is either moving away or moving to the first one, in axisymmetric case, is studied. The distance between plates changes in time according to arbitrary power-law: $h \sim |t|^s$. The unsteady Navier-Stokes equations in three independent variables with some special substitutions were reduced to a system of ordinary differential equations. As result, a new boundary value problem of the third order with two new variables was found. Precise solutions of the Navier-Stokes equations are constructed as series in powers of Reynolds number. The cases of motion with $s = 0.5$, $h \sim \sqrt{|t|}$; uniform motion with $s = 1$, $h \sim |t|$; and uniformly accelerated motion with $s = 2$, $h \sim t^2$ of the plates are studied in detail. For the case $h \sim \sqrt{|t|}$ the self-similar, one-parametric, continuous in Reynolds number solution in series was resulted; for other cases the series is asymptotic. For some Reynolds numbers greater than critical, the velocity of flow near the boundaries has opposite direction to the average velocity; it is the counterflow phenomenon. The critical Reynolds numbers corresponding to the appearance of counterflow for all three cases were determined.

Keywords: axisymmetric viscous flow, closed form solution, counterflow, Navier-Stokes equations, squeezing flow between plates

1. NOMENCLATURE

NOMENCLATURE

ν	$[m^2/s]$	coefficient of kinematic viscosity
ρ	$[kg/m^3]$	fluid density
a	$[-]$	coefficient in the power-law, $1/s$
b	$[-]$	pressure coefficient
c	$[-]$	pressure coefficient, $1/2 + a + 2b$
$h(t)$	$[m]$	distance between the plates
k	$[m/s]$	amplitude of velocity of the upper plate
P	$[-]$	pressure caused by fluid flow
r, z	$[m]$	cilindrical coordinates, along and perpendicular the plates
s	$[-]$	coefficient in the power-law
t	$[s]$	time
u, v	$[-]$	components of fluid velocity between the plates
v_r, v_z	$[m/s]$	components of fluid velocity between the plates
Y	$[-]$	vertical coordinate, perpendicular the plates, $Y \ni [-1, 1]$
$\dot{h}$	$[m/s]$	velocity of the upper plate
p	$[Pa \cdot m^3/kg]$	total pressure between the plates
p_0	$[Pa \cdot m^3/kg]$	initial pressure between the plates
$Re(t)$	$[-]$	Reynolds number, $h\dot{h}/\nu$
Re_*	$[-]$	Reynolds number, convergence radius
Re_{back}	$[-]$	critical Reynolds number at wich counterflow appears

2. INTRODUCTION

The present paper discusses a problem of a squeezing axisymmetric flow of viscous Newtonian fluid between two parallel plates (disks). It is a natural continuation of paper [1], where the boundary value problem for a two-dimensional squeezing flow was solved. The unsteady Navier-Stokes equations with some special substitutions were reduced to a system of ordinary differential equations and solutions of them are constructed as series in powers of Reynolds number.

Similar problem was examined in works of Thorpe [2], Wang [3], Wang [4]. Thorpe in the work

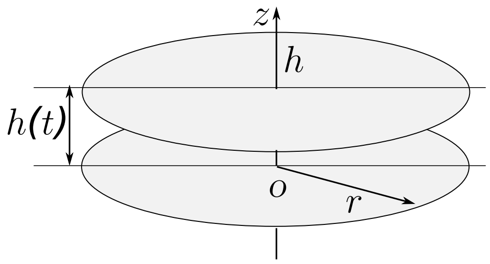

Figure 1. Scheme of axisymmetric fluid flow between two plates (disks). Lower plate is immobile and upper is moving either away or towards the first one according to an arbitrary power law $h \sim |t|^s$.

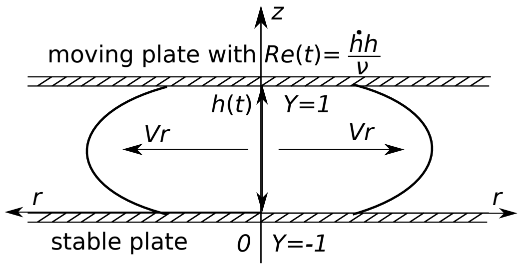

Figure 2. Schematic visualization of flow between two plates.

[2] gives only statement of boundary value problem for axisymmetric case, as a one differential equation of 4^{th} order wihout solution. Also, in the work of Wang [3], the main equation can be restored, if we will differentiate our main equation. Its solution coincides with the solution presented here for the case $a = 2$. However, the boundary value problem derived here is of the third order. A short review of these exact solutions can be found in the book [5].

Also, the counterflow phenomenon between parallel plates at their motion apart was already observed by Thorpe citeThorpe and Wang [3]. Thorpe noted that velocity gradient at walls became zero, if plates move according to a special law of motion with some specific Reynolds numbers. Wang noted an existence of reversal flow near the plates' walls, if plates move with some negative squeezing numbers (analogue to Reynolds number). In contrast to the previous works, in the present work was noted that the counterflow occurs when Reynolds number is exceeding its critical value. The critical Reynolds numbers were determined for different regimes of upper plate motion. So, in the present investigation the authors have broadened a branch of possible observation of this phenomenon and shown the procedure of calculating a critical Reynolds number, that can be helpful for standing experiments.

3. FORMULATION OF BOUNDARY VALUE PROBLEM

Here is considered an axisymmetric viscous flow with velocity components $v_r(t, r, z)$, $v_z(t, r, z)$ and pressure $p(t, r, z)$ in fluid layer $0 < z < h$, $0 < r < \infty$ between two parallel plates. The lower plate at $z = 0$ is immobile, while the second plate moves with $h(t)$ law, see Fig. 1. Upper plate can move away or move to the first one, so the cases $\dot{h}(t) > 0$ and $\dot{h}(t) < 0$ are both possible ($\dot{h} = dh/dt$).

The Navier-Stokes equations in cylindrical coordinate system for axisymmetric flow with no-slip condition on the plates are formulated as follows

$$
\begin{aligned}
&\frac{v_r}{r} + \frac{\partial v_r}{\partial r} + \frac{\partial v_z}{\partial z} = 0,\\
&\frac{\partial v_r}{\partial t} + v_r\frac{\partial v_r}{\partial r} + v_z\frac{\partial v_r}{\partial z} + \frac{\partial p}{\partial r} =\\
&= \nu\left(\frac{\partial^2 v_r}{\partial r^2} + \frac{1}{r}\frac{\partial v_r}{\partial r} + \frac{\partial^2 v_r}{\partial z^2} - \frac{v_r}{r^2}\right),\\
&\frac{\partial v_z}{\partial t} + v_r\frac{\partial v_z}{\partial r} + v_z\frac{\partial v_z}{\partial z} + \frac{\partial p}{\partial z} =\\
&= \nu\left(\frac{\partial^2 v_z}{\partial r^2} + \frac{1}{r}\frac{\partial v_z}{\partial r} + \frac{\partial^2 v_z}{\partial z^2}\right),\\
&v_r(t, r, 0) = v_r(t, r, h) = 0,\\
&v_z(t, r, 0) = 0, \quad v_z(t, r, h) = \dot{h},
\end{aligned}
\tag{1}
$$

where ν is coefficient of kinematic viscosity; the fluid density without loss of generality is set to unity ($\rho = 1$). The solution of problem (1) is sought in the form

$$
\begin{aligned}
&v_r = \frac{\dot{h}}{h} r(u(Y, Re) - \frac{1}{2}),\\
&v_z = \frac{\dot{h}}{2}(v(Y, Re) + 1 + Y),\\
&p = \dot{h}^2\left[b\frac{r^2}{2h^2} + P(t, Y)\right] + p_0(t),\\
&Y = \frac{2z}{h} - 1, \quad Y \in [-1, 1].
\end{aligned}
\tag{2}
$$

With substitutions (2) the Navier-Stokes Eqs. (1) will be reduced to a new form. New functions $u(Y)$ and $v(Y)$ are presented the dimensionless components of fluid velocity between the plates; they are depending on new vertical coordinate Y, where the points $Y = \pm 1$ are the boundaries. For the predefined law of motion $h(t)$ the Reynolds number depends on time $Re(t) = h\dot{h}/\nu$; this dependence should be taken into account when calculating partial time derivatives in Eq. (1).

After substitution of (2) in the first two Navier-Stokes Eqs. (1) we arrive at the following boundary value problem for system of ordinary differential equations with new functions:

$$
\begin{aligned}
&2u + v' = 0,\\
&vu' + u^2 - (1+a)u + \frac{1}{4} + \frac{a}{2} + b -\\
&-\frac{4u''}{Re} + (2-a)Re\frac{\partial u}{\partial Re} = 0 \qquad (3)\\
&u(-1) = u(1) = \frac{1}{2},\\
&v(-1) = v(1) = 0.
\end{aligned}
$$

The prime here denotes derivative with respect to Y. Parameter a implies a power law time dependence of the distance between plates with arbitrary power s:

$$
\begin{aligned}
&h = k|t-t_0|^s, \quad a = 1/s,\\
&Re(t) = \frac{1}{\nu} sk^2|t-t_0|^{2s-1}\operatorname{sign}(t-t_0),
\end{aligned} \qquad (4)
$$

where k is an amplitude of velocity of the upper plate. The system of Eqs. (3) is a system of partial differential equations of the third order; together with defined law of plates motion $h(t)$ it allows determination of functions $u(Y)$ and $v(Y)$ and parameter b determining the pressure $p(t, Y, Re)$. The case $Re > 0$ corresponds to increasing gap between the plates, $Re < 0$ - to decreasing. Formulation of new boundary value problem (3) must include also the initial condition defined for some Re.

4. EXPANSION IN POWERS OF REYNOLDS NUMBER

Let us formulate the boundary value problem (3) as one equation for $v(Y, Re)$ with boundary conditions:

$$
\begin{aligned}
&-vv'' + \frac{(v')^2}{2} + (1+a)v' + c +\\
&+\frac{4v'''}{Re} + (a-2)Re\frac{\partial v'}{\partial Re} = 0, \qquad (5)\\
&v(-1) = v(1) = 0,\\
&v'(-1) = v'(1) = -1.
\end{aligned}
$$

where $c = 1/2 + a + 2b$. For small Reynolds number the solution of this boundary value problem can be found as series in Reynolds number:

$$
\begin{aligned}
&c = \frac{c_{-1}}{Re} + c_0 + c_1 Re + ...,\\
&v = v_0 + v_1 Re + v_2 Re^2 + ...
\end{aligned} \qquad (6)
$$

For the leading term the solution of the following boundary value problem is

$$
c_{-1} = 12, \quad v_0(Y) = \frac{1}{2}Y(1-Y^2). \qquad (7)
$$

The solution for the second order approximation is

$$
\begin{aligned}
&c_0 = -\frac{(-31-14a)}{70},\\
&v_1(Y) = -\frac{Y(Y^2-1)^2}{2\,240}(9 + 14a + Y^2).
\end{aligned} \qquad (8)
$$

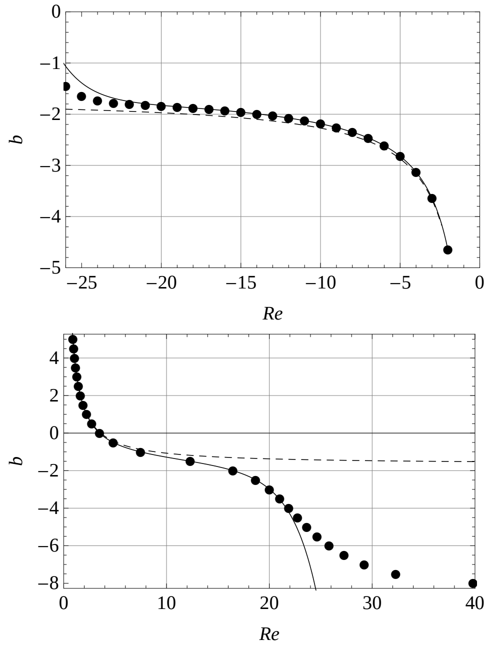

Figure 3. Dependence of the coefficient of pressure $b(Re, a)$ in (2) in case $a = 2$ for $Re < 0$ and $Re > 0$: dots - numerical solution by the shooting method, solid line - solution in series $b = \sum_{n=-1}^{N} b_n Re^n$ of 17 terms ($N = 15$), dashed line - the first two terms $b = 6/Re - 117/70$ of the expansion.

The coefficient of pressure $b = 1/2(c - a - 1/2)$ is found as series in Reynolds number

$$
b = \frac{12}{Re} + b_0 + b_1 Re + b_2 Re^2 + ... \qquad (9)
$$

with $b_{-1} = c_{-1}$, $b_0 = 1/2(c_0 - a - 1/2)$, $b_1 = c_1$ and so on. Every coefficient $b_n(a)$ or $c_n(a)$ is a polynomial of power $n+1$ in parameter a with rational coefficients.

The Reynolds number in Eq. (5) varies in time, thus its solution depends on time only through the Reynolds number. Eq. (5) does not accept any initial velocity profiles, but only those that can be achieved by partial solution (6) for some values of a, k, $t - t_0$, see (4).

The most interesting cases of upper plate motion are those with parameter a accepting the following values: $a = 2$ - corresponds to gap changing according to the law $h = k\sqrt{|t|}$; $a = 1$ - corresponds to steady change of the gap $h = k|t|$; $a = 1/2$ - describes uniformly accelerated change $h = kt^2$.

5. CASE $A = 2$. GAP BETWEEN PLATES CHANGES ACCORDING TO THE LAW $H = K\sqrt{|T|}$.

In the case $a = 2$ the distance between plates changes as $h = k\sqrt{|t-t_0|}$; note that if $Re < 0$, then $t < t_0$. The partial derivative with respect to Reynolds number in Eq. (5) is zero. Thus we come to a boundary value problem for ordinary differential equation,

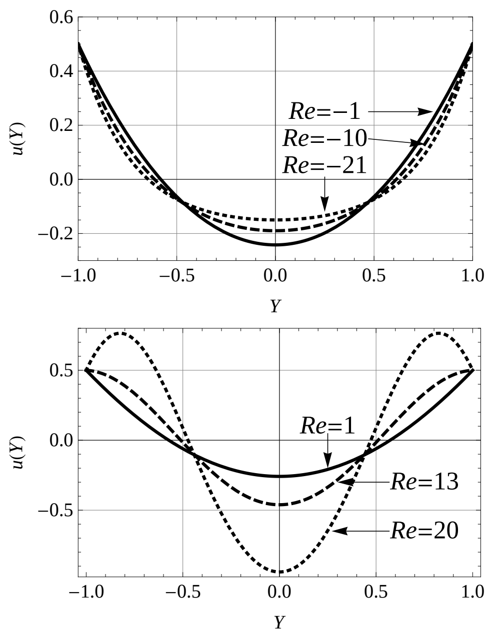

Figure 4. Flow diagrams $u(Y) = \sum_{n=0}^{15} u_n Re^n$ **associated with** v_r **(2),** $a = 2$**: for decreasing** $Re = -1, -10, -21$ **and increasing** $Re = 1, 13, 20$ **gap between the plates.**

which is readily solved numerically:

$$\begin{aligned}
&-vv'' + \frac{(v')^2}{2} + 3v' + c + \frac{4}{Re}v''' = 0,\\
&c = 2.5 + 2b\\
&v(-1) = v(1) = 0,\\
&v'(-1) = v'(1) = -1.
\end{aligned} \tag{10}$$

The problem (10) can be solved numerically by the shooting method. For given Re the method allows determination of parameter c and function $v(Y)$, later the function $u(Y) = -1/2dv(Y)/dY$ can be found. Fig. 3 shows dependences $b(Re)$, calculated numerically by the shooting method and approximately with help of partial sum of 17 terms from series (9), and asymptotic solution $b = 6/Re - 117/70$. The series solution is valid only till $Re = \pm 21$; at $|Re| > 21$ series solution is divergent from numerical solution and becomes invalid. The asymptotic solution is close to the exact solution till $Re = \pm 10$. The radius of convergence of series b (9) is infinite.

For counterflow phenomenon [1], the critical Reynolds numbers (Re_{back}) can be found as roots of the equation:

$$\left.\frac{\partial u}{\partial Y}\right|_{Y=1,\, Re=Re_{back}} = 0, \tag{11}$$

where $\partial u/\partial Y$ can be determined from the first of Eqs. (3) and the second of Eqs. (6) as $u' = -1/2 \sum_{n=0}^{N} v_n'' Re^n$. Thus the calculated roots Re depend on the considered number N of terms of the series. The sequence of positive roots converges to 13.37; it means that the critical Reynolds numbers from which the counterflow phenomenon already can be observed is $Re_{back} = 13.37$. The counterflow for the critical Reynolds number and for the numbers larger than the critical is illustrated in Fig. 4.

Fig. 4 shows velocity profiles $u(Y)$, calculated with help of the series solution $\sum_{n=0}^{N} u_n(Y, a)Re^n$ of 16 terms ($N = 15$), for Reynolds numbers corresponding to decreasing ($Re < 0$) and increasing ($Re > 0$) gap between the plates. On the figure, one can see that for positive Reynolds numbers greater than critical ($Re = 20 > Re_{back}$), velocity $u(Y)$ near the boundaries $Y = \pm 1$ has opposite direction relative to the average velocity. This is an example of a counterflow phenomenon. However, for a large negative Reynolds number ($Re = -21$), flow has the original direction; the counterflow is not observed. So, we can conclude that the counterflow appear only for plate motion with positive Reynolds numbers, in other words, only for increasing gap between the plates.

Note that in the considered case ($a = 2, s = 1/2$), the absolute value of Reynolds number does not depend on time: $Re = k^2/2\nu\, sign(t - t_0)$; i.e. the velocity profile will keep its shape during the entire time of plates motion; and it demonstrates that the solution has a self-similar character. Thus, the velocity profiles illustrated in Fig. 4 correspond to the different values of k.

For obtaining the dimension velocity profile v_r and v_z the formulae Eq. (2) are used. Fig. 2 shows the schematic visualization the flow between the plates.

6. CASE $A = 1$. STEADY CHANGE OF THE GAP BETWEEN THE PLATES, $H = K|T|$.

In the case $a = 1$ Eqs. (5) and their series solutions (6) correspond to the change of the gap between the plates according to the law $h = k|t|$. This case differs from the previous one: the Navier-Stokes equations can not be reduced to an ordinary differential equation, as it was done in previous case, and the self-similar solutions of this problem does not exist. The series $b(Re)$ at $a = 1$ is divergent, but it is an asymptotic, see [1]. Dependences $b(Re)$ for positive and negative Reynolds numbers are shown in Fig. 5.

For the best approximation of asymptotic function one needs to take N terms of its expansion in series, where N is the number of the minimal in absolute value term $b_N\, Re^N$, but the number of the term N depends on Reynolds number. For example, sor the case considered here ($a = 1$), for the series $b(Re)$ the number of the minimal in absolute value term N for $Re = 10$ equals 9; for $Re = 20$, $N = 8$; for $Re = 30$, $N = 7$. For asymptotic series the error of the approximation of partial sum is of the same order as the term next to the minimal, i.e. $b = \sum_{n=-1}^{N} b_n Re^n \pm b_{N+1}\, Re^{N+1}$.

The critical Reynolds number Re_{back} obtained from Eq. (11) is about $Re_{back} \approx 26.5$ ($N = 11$).

The asymptotic series with $N = 15$, 6, and 6

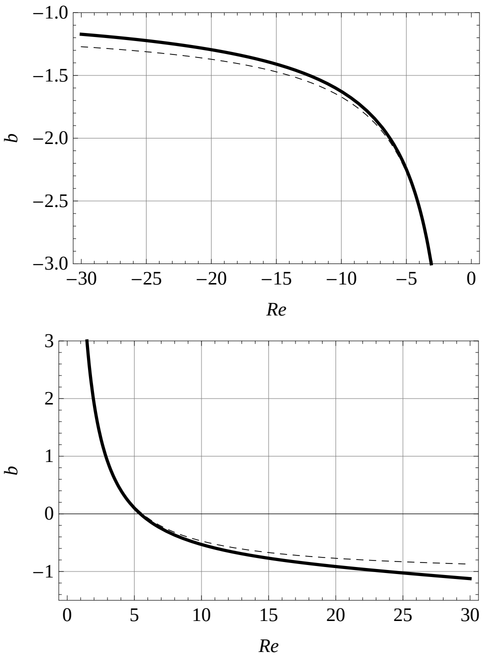

Figure 5. Dependences $b(Re)$ **for** $a = 1$**:** $Re < 0$ **and** $Re > 0$**: solid line - the series solution** $b(Re, a)$ **with 11 terms (**$N = 9$**), dashed line - the first two terms** $b = 6/Re - 15/14$**.**

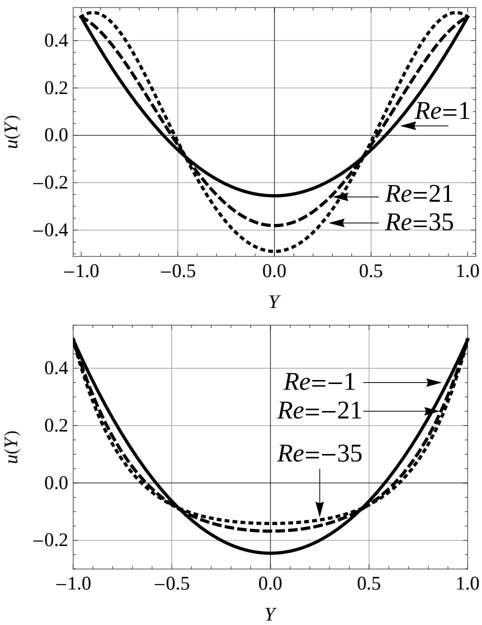

Figure 6. Flow diagrams $u(Y) = \sum_{n=0}^{N} u_n Re^n$ **(**$N =$ 15**, 6, 6) associated with** v_r **(2),** $a = 1$**: for decreasing** $Re = -1,\ -21,\ -35$ **and increasing** $Re =$ $1,\ 21,\ 35$ **gap between the plates.**

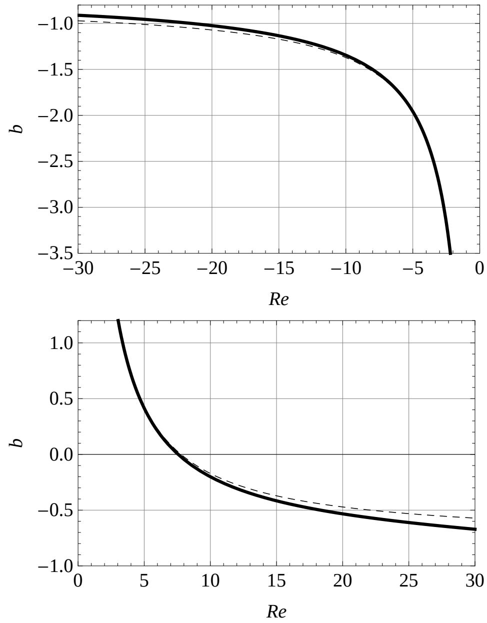

Figure 7. Dependence $b(Re)$ **for** $a = 0.5$ **for** $Re < 0$ **and** $Re > 0$**: solid line - solution in series** $b(Re, a)$ **consisting of** 7 **terms (**$N = 5$**), dashed line - the first two terms** $b = 6/Re - 27/35$**.**

terms used for plotting velocity profiles $u(Y)$ at Reynolds numbers -1, -21, -35, 1, 21 and 35; they are shown in Fig. 6. The plot distinctly shows the existence of the counterflow at $Re = 35 > Re_{back}$. The plots would not change if the number of terms used in calculation changes by 2 ($N \pm 2$); indeed, the error of the calculation in this case is less than 1% for $Re > 30$. (The error of the calculation is estimated as a term relation: u_{N+1}/u_0).

The profiles and the corresponding Reynolds numbers, shown in Fig. 6 are consequently achieved during a steady in time motion of the upper plate according $h = k|t|$ with the same k value. In other words, the curves in Fig. 6 are an evolution in time of velocity profile.

7. CASE $A = 0.5$. UNIFORMLY ACCELERATED CHANGE OF THE GAP BETWEEN THE PLATES, $H = KT^2$.

At $a = 0.5$ Eqs. (5) and their series solutions (6) correspond to the uniformly accelerated motion of the upper plate $h = kt^2$. This case is analogous to the case $a = 1$: the series b_n also diverges. The dependences $b(Re)$ at positive and negative Reynolds numbers are shown in Fig. 7.

The critical Reynolds number Re_{back} was found from the Eq. (11) for 6 terms ($N = 5$) as $Re_{back} \approx$ 43.5.

Velocity profiles $u(Y)$ for some Reynolds numbers are shown in Fig. 8. It is seen that for Reynolds numbers greater than critical $Re = 48 > Re_{back}$ the counterflow has appeared. The error in the calculation of velocity profile for $Re = 48$, u_4/u_0, is much

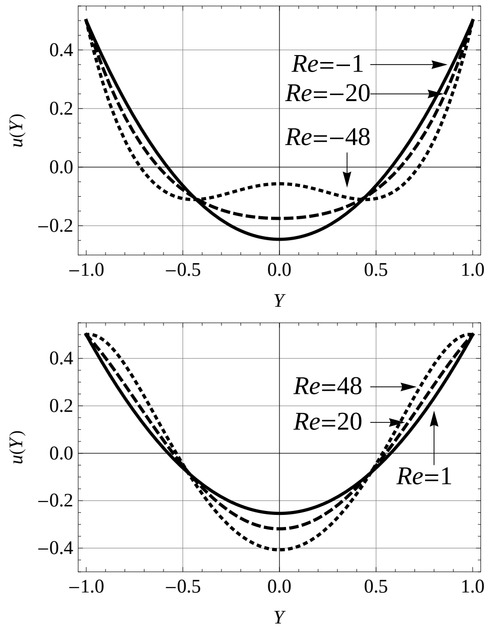

Figure 8. Velocity profiles $u(Y) = \sum_{n=0}^{N} u_n Re^n$ ($N = 14$, 3, 3) associated with v_r (2) for $a = 0.5$: for approaching ($Re = -1, -20, -48$) and moving apart ($Re = 1, 20, 48$) plates.

less then 1%.

8. CONCLUSIONS

The paper considers a problem of viscous squeezing flow between two parallel plates (disks) in axisymmetric case. One plate is immobile, the other approaches or moves apart from it, so that the distance between the plates changes according to the power law $h \sim t^s$.

A boundary value problem with no-slip conditions on the plates was formulated for this. By a change of variables the initial Navier-Stokes equations were reduced to a partial differential equation of third order with two variables, which together with boundary conditions form a new boundary value problem. A set of particular solutions in form of series in powers of Reynolds number were constructed. The flow and pressure between the plates were determined.

At the case $s = 1/2$ the initial Navier-Stokes equations were reduced to one ordinary differential equation that allowed easy determination of the solution by numerical methods. In this case, the solution as the series in powers of Reynolds number converge with infinite radius of convergence. For other examined exponents ($s = 1, 2$) the series were asymptotic. For the best approximation of the series in these cases the partial sums of the asymptotic series with certain numbers of terms were proposed.

In the constructed solution an effect of counterflow has been marked: at plates moving apart the flow velocity in vicinity of their surface was directed opposite to the average velocity between the plates. The counterflow occured when Reynolds number was exceeding its critical value $Re \geqslant Re_{back}$. The theoretical Reynolds numbers Re_{back} was determined for different regimes of upper plate motion: for $s = 1/2$, $Re_{back} \approx 13.4$, for $s = 1$, $Re_{back} \approx 26.5$, and for $s = 2$, $Re_{back} \approx 43.5$.

In spite of the fact that for axisymmetric squeezing flow and for plane squeezing flow the similar solution technique was used, the solutions differ qualitatively. In the case of the plane flow, the several continual family of solutions exist (several curves $b(Re)$ satisfying to the initial equations). In this case, only one family of solutions exists (one curve $b(Re)$ satisfying to the initial equations).

9. ACKNOWLEDGEMENTS

The work was supported by the Russian Science Foundation, project No 14-19-01633.

REFERENCES

[1] Petrov, A. G., and Kharlamova, I. S., 2014, "The solutions of Navier-Stokes equations in squeezing flow between parallel plates", *Europ J of Mechanics B-Fluids*, Vol. 48, pp. 40–48.

[2] Thorpe, J. F., 1967, "Further Investigation of Squeezing Flow Between Parallel Plates", *Develop in Theor and Appl Mech*, Vol. 3, pp. 635–648.

[3] Wang, C. Y., 1976, "The Squeezing of a Fluid Between Two Plates", *J Appl Mech*, Vol. 43, pp. 579–582.

[4] Wang, C. Y., and Watson, L. T., 1979, "Squeezing of a viscous fluid between elliptic plates", *Appl Sicentific Res*, Vol. 45, pp. 195–207.

[5] Drazin, P., and Riley, N., 2006, *The Navier-Stokes Equations: A Classification of Flows and Exact Solutions*, Cambridge.

Conference on Modelling Fluid Flow (CMFF'15)
The 16th International Conference on Fluid Flow Technologies
Budapest, Hungary, September 1-4, 2015

STRUCTURE CHANGE OF SHEAR-BANDS OF CTAB/NASAL WORMLIKE MICELLAR SOLUTIONS IN A CONCENTRIC CYLINDER FLOW CELL

Tsutomu TAKAHASHI[1], Masatoshi ITO[2], Takafumi MIZUKAMI[3], YumikoYOSHITAKE[4]

[1] Corresponding Author. Department of Mechanical Engineering, Nagaoka University of Technology, 1603-1 Kamitomioka, Nagaoka, Niigata, 940-2188 Japan. Tel.: +81 258 47 9728, Fax: +81 258 47 9770, E-mail: ttaka@nagaokaut.ac.jp
[2] Department of Mechanical Engineering, Nagaoka University of Technology, E-mail: fluor@stn.nagaokaut.ac.jp
[3] Department of Mechanical Engineering, Nagaoka University of Technology, E-mail: s091068@stn.nagaokaut.ac.jp
[4] Department of Mechanical Engineering, Nagaoka University of Technology, E-mail: yoshitake@nagaokaut.ac.jp

ABSTRACT

The generation and growing process of the shear bands in a wormlike micelles solution are visualized and evaluated quantitatively using the flow-birefringence method and the image analysis. A concentric cylinder flow cell is used to visualize flow birefringence and a stress control rheometer is used as a test plat form. Two linear polarizers are set on it with the cross Nicole arrangement to observe the flow birefringence. The transmitted light is changed its color by the retardation of the birefringence on the light transmitted pass. The degree of the phase difference caused by the flow-birefringence is evaluated by reference to Michel-Levy Interference Color Chart. The orientation angle of each shear band is evaluated by the extinction position. The stress-optic coefficient $\boldsymbol{C}$ is calculated from the distribution of the flow birefringence and the orientation angle along to the radial direction. Using the accelerated shear flow with low shear acceleration rate, the shear bands are growing steadily until a critical shear rate that is in the unstable flow region for the step shear. The banding profile is constant for the circumferential direction. In this case, the higher oriented layer appears near the inner wall and the thickness increases with increasing shear rate. The stress-optic coefficient $\boldsymbol{C}$ in this layer is chanted from the ordinal value and it shows this layer is consisted by the shear-induced structure.

Keywords: birefringence, shear binding, shear-induced structure, stress-optic coefficient, wormlike micelles

NOMENCLATURE

$\boldsymbol{C}$	$[Pa^{-1}]$	stress-optic coefficient
G'	$[Pa]$	storage elastic modulus
G''	$[Pa]$	loss elastic modulus
G_M	$[Pa]$	equilibrium elastic modulus
t	$[s]$	elapsed time
y	$[mm]$	radial distance from inner wall
α	$[deg.]$	orientation angle
$\Delta n'$	[-]	birefringence
$\dot{\gamma}$	$[s^{-1}]$	shear rate
$\eta*$	$[Pa.s]$	complex viscosity
λ	$[s]$	relaxation time
ω	$[rad/s]$	angular frequency

1. INTRODUCTION

In the steady Couette flow, Newtonian fluids show a constant shear rate across the whole flow field. On the other hand, some complex fluids, such as surfactant solutions, polymer solutions and liquid crystals, exhibit discontinuous velocity distribution and are formed some layers with different mechanical properties in parallel with the flow direction. This phenomenon that forms some layers is called "Shear-banding". Microscopic structure in each layer is not completely understood, especially in surfactant solutions. A surfactant solution of Cetyltrimethylammonium bromide: CTAB with a counter ion such as NaSal, which forms wormlike micelles, exhibits the shear-bands under specified conditions [1]. The wormlike micellar solution is expected to use various industrial applications not only detergent but thickening agent and drag reduction agent for turbulent flow. It shows strong viscoelasticity and has very complex flow behavior. The aggregation structure of the wormlike micelles solutions is changed to the other structure, namely

"Shear-Induced Structure (SIS)" [2] in high shear flow. The relationship between the shear-banding and the SIS is still not clear. According to these phenomena, the wormlike micelles solution shows a complex transient behavior in start-up regime of a step shear and the specific spatial flow patterns [3-5]. Furthermore, "Temporal shear stress oscillation" [1, 3-6] is also observed in the simple shear flow. The velocity distribution of the shear bandings was measured by the high-frequency ultrasonic speckle velocimetry [7] and the numerical and model analysis were applied to examine the mechanism of the shear banding [8, 9].

In this study, we investigate the microstructures of the wormlike micelles solution on the shear-banding phenomenon under a step shear flow and the relationship between Shear-banding, SIS and Temporal Shear Oscillations. Occurrence of an anisotropy of the microstructure of the wormlike micelles solution has been examined by laser, X-ray or neutron beams, such as an analysis techniques of Flow-birefringence [10], SAXS and SANS [11]. The local anisotropic information can be detected by these methods but the spatial distribution of the anisotropy across the flow field has not been reported yet. In order to observe the spatial distribution of the optical anisotropy, we develop a new technique that is calculated from a photograph taken by the crossed Nicols method with a digital camera [1]. This analysis technique can evaluate not only the distribution of the flow-birefringence and the orientation angle but also the stress-optic coefficient $\boldsymbol{C}$ that is a material function related to the molecular or aggregate structure. We evaluate the distribution of $\boldsymbol{C}$ and discuss about the micellar structure in each shear layer.

2. THEORY, EXPERIMENTAL DEVICE AND SAMPLE

An aqueous solution of 0.03M CTAB and 0.06M NaSal was used as a test fluid. All experiments were performed at 25 degrees Celsius. The rheological property of this sample was measured by the stress-controlled rheometer, Anton Paar MCR301, with the concentric cylinder flow cell. The result of the steady shear viscosity, the dynamic viscoelastic, and the step shear tests is shown in Fig.1. The lines in Fig.1(b) are G' and G" calculated by the one-mode Maxwell model as follows.

$$G' = G_M \frac{\omega^2\lambda^2}{1+\omega^2\lambda^2}, G'' = G_M \frac{\omega\lambda}{1+\omega^2\lambda^2} \tag{1}$$

Here, G_M is equilibrium elastic modulus and λ is relaxation time. In this case, G_M is 5.4Pa and λ is 1.2s. In the low shear regime, this sample coincides with the one-mode Maxwell model very well. However, when the shear rate exceeds the critical shear rate 1 s^{-1} of this sample, the SIS is generated and the property is changed from the Maxwell model. As seen in Fig.1(c), the shear stress larger than 5.0 s^{-1} shows periodic oscillation even in steady shear. It is the same as temporal shear stress oscillation [1, 3-5].

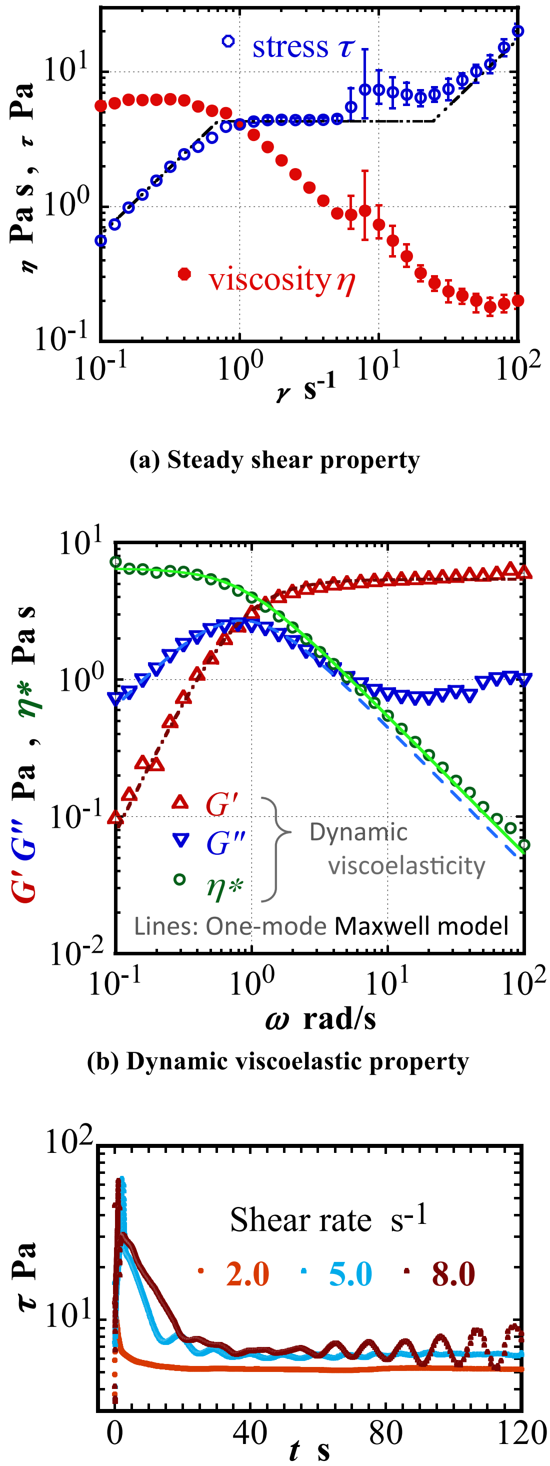

(c) Transient property for step shear

Figure 1. Viscoelastic property of test sample.

The flow birefringence distribution in the whole area of a concentric cylinder flow cell is visualized by the crossed Nicols polarizer method. Figure 2(a) and (b) show the schematic diagram of the birefringence visualization system and a sample image, respectively. The concentric cylinder flow cell that has a glass top and bottom plate was originally designed for this investigation. The bob and cup diameters and the annular gap of the flow cell are 32, 36 and 2.0 mm, respectively. The light source is the white LEDs and a diffuser filter is attached between the light source and the flow cell. The two polarizer-sheets are located at the top and bottom of the cell as a crossed Nicols arrangement. A digital camera is set at the bottom part. The entire flow field across both radial and circumferential direction can be observed, as shown in Fig.2(b). The magnitude of the birefringence $|\Delta n'|$ is evaluated by the hue profile reduced from the color profile of the visualized image. The four black areas in the visualized image are called the extinction angle that is related by the micelles orientation angle α. In the low shear rate region ($\dot{\gamma}<1\mathrm{s}^{-1}$), the birefringence and the orientation angle become almost constant across the radial direction. These values are linearly related to shear stress τ by the stress-optic rule [6], shown in Eq. (2).

$$\boldsymbol{\tau} = \boldsymbol{\sigma}_{12} = \left(\frac{1}{2C}\right) \times \Delta \boldsymbol{n}' \times \boldsymbol{sin}(2\boldsymbol{\alpha}) \qquad (2)$$

$\boldsymbol{C}$ is the stress-optic coefficient which is a constant of proportionality between the stress tensor and the refractive index tensor and is closely related to the molecular structure of the material or the micellar structure. In this sample, $\boldsymbol{C}$ is -2.7×10^{-7} Pa^{-1} at low shear rate.

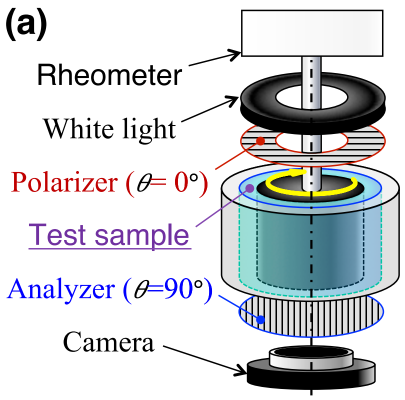

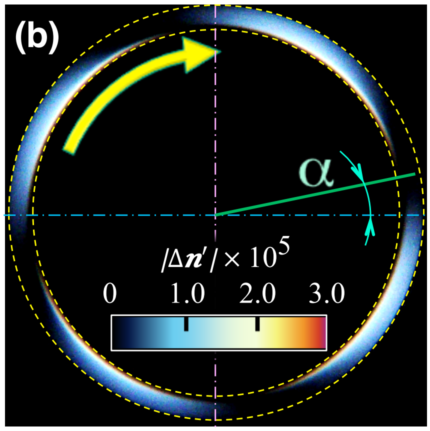

Figure 2. Schematic diagram of test section and visualized flow field.

In the case of polymer fluid that does not generate the shear-banding, the border of the black area of the extinction angle is along to the radial direction. As seen in Fig.2(b), however, the border of the extinction angle is shifted to circumferential direction. If the flow is in steady state and the shear stress is constant across the radial direction, it means that $\boldsymbol{C}$ is not constant but has a distribution to the radial direction. Therefore, we can evaluate the distribution of the stress-optic coefficient $\boldsymbol{C}$ from the visualized image. We reported that $\boldsymbol{C}$ of the wormlike micelles solution is changed by shear rate in the SIS state[7]. Then, we can examine the structure of the micelles in each band by evaluating $\boldsymbol{C}$.

3. RESULTS AND DISCUSSIONS

We drew a spatio-temporal chart using the re-slice function of image analysis software to visualize the shear-banding process at a certain cross section. A selected small region in the visualized image, which is 2.0mm length in the radial direction and 1 pixel ≈ 64 μ m in circumferential direction, is cut at every 1/30 s. These images of the small region are stacking to the x-axis direction side by side. One of the results is shown in Fig.3. The spatio-temporal charts named No.1 to 4 are captured in the first to the fourth quadrant of the visualized image as shown in Fig.2(b). The bottom of the image is the moving inner wall (y=0) and the top is the outer wall. At the start-up regime, the birefringence pattern is wavy but two layers are formed stably after 20 s. All of four charts show the same patter. It means that the flow is not changed along the circumference direction.

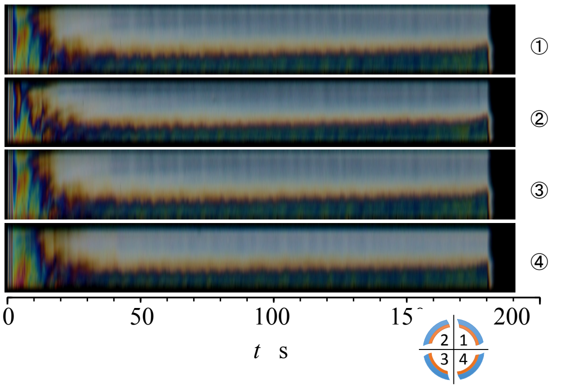

Figure 3. Spatio-temporal chart at shear rate 6s^{-1}.

Fig.4 shows the distribution of birefringence, the orientation angle and the stress-optic coefficient across the gap 2.0 mm at shear rate 2.0 s^{-1}. In these plots, $\boldsymbol{y}$=0 mm represents the moving wall. $\boldsymbol{\alpha}$=0 means that the orientation angle of micelles is equal to the flow direction. Assuming the shear stress keeps constant across the gap, $\boldsymbol{C}$ is calculated by Eq. (1). As seen in Fig.3, there are two layers in this state and the inner and the outer layers exhibit the different value in $\boldsymbol{C}$. This result suggests that the micelles in the layer near the moving wall changes to the SIS. The critical shear rate of the SIS in this sample is 1s^{-1} but it is found that only the inner layer changes the structure in this condition. We named this inner layer “SIS-band” and the other “orientation band”.

The temporal shear stress oscillation is observed when shear rate exceeds 5 s^{-1}. The shear stress shows a periodic oscillation in a constant shear rate 8.0 s^{-1}, as shown in Fig.5(a). The spatio-temporal chart at the same moment is shown in Fig.5(b). The blue color region in Fig.5(b) indicates the SIS-band. The interface between bands is changed slightly and the color in SIS-band is also changed in synchronization with the stress oscillation. These results show a strong relationship between the temporal shear stress oscillation and the time variation of the structure in the SIS-band. When the shear stress increases, the magnitude of the birefringence increases and the orientation angle goes to the flow direction. Fig.5(c) shows the time variation of average values of $\boldsymbol{C}$ at each band. The average value of $\boldsymbol{C}$ in the SIS-band changes syncronized with the stress oscillation. In summary, it is revealed that the temporal stress oscillation is caused by the periodical structure change of the SIS-band.

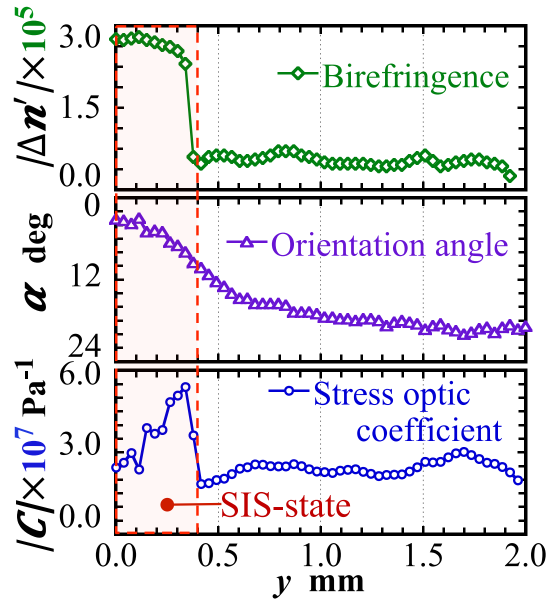

Figure 4. Distribution of birefringence, orientation angle and stress-optic coefficient to radial direction. The moving inner wall is zero and the outer wall is 2.0mm.

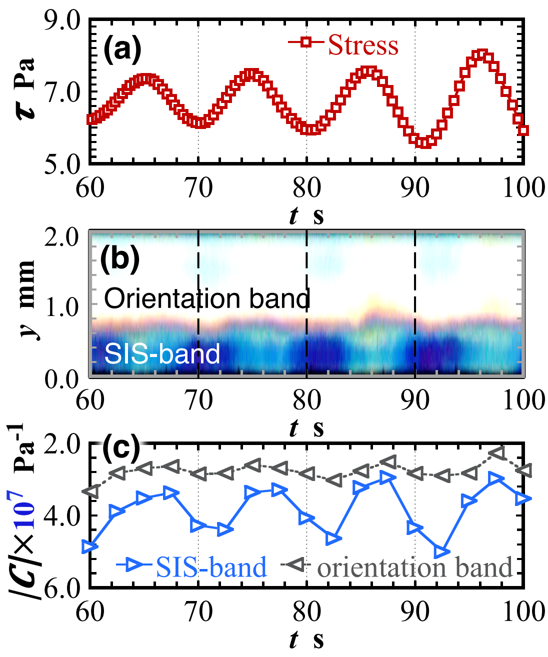

Figure 5. Relationship between temporal-stress oscillation, shear-bands and stress-optic coefficient.

4. SUMMARY

The newly developed technique to evaluate both the flow birefringence and orientation angle by the whole flow field visualization is very effective to examine the distribution of the stress-optic coeffeicent of the wormlike micelles soltution. It is clarified by this technique that the SIS-band is formed in the inner wall side and the other band is no changed to the SIS when the shear-bands are generated. It is also found that the temporal shear stress oscilation is closely related to the change of the miceller structre in the SIS-band.

REFERENCES

[1] M. Ito, Y. Yoshitake, T. Takahashi, 2014. Microstructure change of shear-bands in concentric cylinder flow of wormlike miceller solutions observed by birefringence profile, *Bulletin of The American Physical Society*, Nov, p. 33.

[2] T. Shikata, H. Hirata, T. Kotaka, 1987. Micelle formation of detergent molecules in aqueous media: viscoelastic properties of 3 aqueous cetyltrimethylammonium bromide solutions, *Langmuir*, **3**, May, pp. 1081-1086.

[3] E.K. Wheeler, P. Fischer, G.G. Fuller, 1998, Time-periodic flow induced structures and instabilities in a viscoelastic surfactant solution, *Journal of Non-Newtonian Fluid Mechanics*, **75**, Mar, pp. 193-208.

[5] H. Azzouzi, J. P. Decruppe, S. Lerouge, O. Greffier, 2005, Temporal oscillations of the shear stress and scattered light in a shear-banding-shear-thickening micellar solution, *The European Physical Journal E*, **17**, Aug, pp. 507-514.

[6] V. L., Bueno, J., Kohlbrecher, P., Fischer, 2013. "Shear thickening, temporal shear oscillations, and degradation of dilute equimolar CTAB/NaSal wormlike solutions". *Rheologica Acta*, **52**, Jan, pp. 297-312.

[7] S. Manneville, L. Bécu, A. Colin, 2004, High-frequency ultrasonic speckle velocimetry in sheared complex fluids, *Eur. Phys. J. Appl. Phys.*, **28**, Dec, pp. 361-373.

[8] S.M. Fielding, P.D. Olmsted, 2006, Nonlinear Dynamics of an Interface between Shear Bands, *Phys. Rev. Lett.*, **96**, Mar, 104502.

[9] M. Das, B. Chakrabarti, C. Dasgupta, S. Ramaswamy, A.K. Sood, 2005, Routes to spatiotemporal chaos in the rheology of nematogenic fluids, *Phys. Rev. E*, **71**, Feb, 021707.

[10] T. Takahashi, H. Sugata, M. Shirakashi, 2002, Rheo-Optic Behavior of Wormlike Micelles under a Shear-Induced Structure Formational Condition, *Nihon Reoroji Gakkaishi*, **30**, Jun, pp. 109-113.

[11] C. R. L. Barron, A. K. Gurnon, A. P. R. Eberle, L. Porcar, N. J. Wagner, 2014, Microstructural evolution of a model, shear-banding micellar solution during shear startup and cessation, *Physical Review E*, **89**, Apr, 042301 1-11.

Conference on Modelling Fluid Flow (CMFF'15)
The 16th International Conference on Fluid Flow Technologies
Budapest, Hungary, September 1-4, 2015

DISPERSION CHARACTERISTICS IN AN URBAN ENVIRONMENT

Eva BERBEKAR[1,2], Frank HARMS[3], Bernd LEITL[4]

[1] Corresponding Author. Meteorological Institute, University of Hamburg. Bundesstrasse 55, D-20146, Hamburg, Germany; Tel.: +49 40 4283855091; Fax: +49 40 428385452. E-mail: eva.berbekar@zmaw.de
[2] Department of Fluid Mechanics, Budapest University of Technology and Economics
[3] Meteorological Institute, University of Hamburg. E-mail: frank.harms@zmaw.de
[4] Meteorological Institute, University of Hamburg. E-mail: bernd.leitl@zmaw.de

ABSTRACT

When an airborne pollutant is released in a built-up area, the city geometry has a considerable effect on the dispersion. To investigate urban dispersion, results from boundary-layer wind tunnel measurements carried out in a model of an idealised European city centre were selected. The resulting concentration field of continuous tracer gas release from ground-level point sources was measured. A diversity of source locations and measurement positions provide a comprehensive dataset primarily designed for numerical model validation in the frame of the COST Action ES1006. Based on this dataset, the dispersion in lateral and longitudinal street canyons is investigated. Results show that the concentration profile in longitudinal street canyons follow exponential decay. The concentration profiles in lateral street canyons correspond well to a Gaussian fit; however the symmetry axis is in most cases not aligned with the source. The effect of the source location on the dispersion was also investigated. Releasing tracer gas from an open space inside the urban area shows similar results to sources located in street canyons. However, when the release location is inside a courtyard, the concentration relative to the distance from the source tends to be lower, than in case of sources located in street-canyons.

Keywords: concentration profile, continuous release, point source, street canyon, urban dispersion, wind tunnel

NOMENCLATURE

C	[-ppm$_V$]	measured concentration
C^*	[-]	dimensionless concentration
d_0	[m]	roughness length
H	[m]	building height
H_L	[m]	height of the lowest building
L_{ref}	[m]	reference length
Q	[m^3/s]	release flow rate
S	[m]	street-canyon width
U	[m/s]	mean wind velocity component parallel to the main wind direction of the approach flow
U_{ref}	[m/s]	mean wind speed at z_{ref} height
x	[m]	coordinate parallel to the direction of the approach flow
y	[m]	horizontal coordinate perpendicular to the direction of the approach flow
z	[m]	vertical coordinate (height)
z_{ref}	[m]	reference height
α	[-]	power exponent
σ_y	[m]	horizontal dispersion coefficient
σ_z	[m]	vertical dispersion coefficient

1. INTRODUCTION

Due to urbanisation, accidental releases inside cities affect more and more people. Therefore it is important to understand the phenomena of dispersion in an urban environment.

The Gaussian plume model [1] is often used to predict the transport of an airborne pollutant due to turbulent diffusion and advection in the atmospheric boundary layer. However when an airborne pollutant is released in a built-up area, the city geometry has a considerable effect on the dispersion [2,3].

Gaussian distribution describes well the lateral concentration profile above an open, flat terrain. In a symmetrically arranged built-up area, where the symmetry axis is parallel to the mean wind direction of the approach flow, the lateral concentration profile is also symmetric. The shape of the profile however is influenced by the geometry, therefore the Gaussian distribution does not necessarily fit to the concentration profile [4-6].

To investigate the dispersion characteristics in an urban environment, concentration measurements were carried out in a wind tunnel model ("Michelstadt"), resembling a Central-European city centre (Fig. 1). The measurements serve as a validation dataset used in the frame of the COST Action ES1006 to evaluate and improve local-scale emergency response tools [7]. Based on the dataset, the concentration distribution in street canyons parallel and perpendicular to the approach flow direction was studied and the effect of the source location was investigated.

2. WIND TUNNEL MEASUREMENTS

Results from wind tunnel experiments were evaluated to study the dispersion characteristics in an urban environment. The “WOTAN” boundary-layer wind tunnel (Fig. 2) located in the Environmental Wind Tunnel Laboratory in Hamburg has an 18 m long and 4 m wide test section. The height is adjustable between 2.75 and 3.25 m. The boundary layer is generated by turbulence generators at the inlet of the test section and by roughness elements placed on the floor of the wind tunnel. The approach flow can be characterised by the power law (Eq. 1) with a roughness length of $d_0 = 1.5$ m and an exponent of $\alpha = 0.27$, corresponding to a very rough boundary layer [8]. More information on the approach flow and the wind field within the model geometry can be found in [9].

$$\frac{U(z)}{U_{ref}} = \left(\frac{z - d_0}{z_{ref} - d_0} \right)^{\alpha} \qquad (1)$$

A 1:225 scaled model of Michelstadt was mounted in the test section of the wind tunnel [10]. The model has aspect ratios, building heights and street widths typical for many Central-European cities [11]. The model consists of 60 ring-shaped buildings. The three different heights (15 m, 18 m and 24 m in full scale) and the two street-canyon widths (18 m and 24 m) provides street-canyon aspect ratios (S/H) between 0.63 and 1.3.

Dispersion from sources with continuous and short-term releases (puffs) was measured. Ethane tracer gas was released from ground-level point sources represented by fast solenoid micro-valves. The concentration was recorded with high temporal resolution by a fast-Flame Ionisation Detector. Most measurements were taken at half-height of the lowest buildings (7.5 m). There are a limited number of elevated measurements at 52.5 m ($3.5H_L$) height for one source location. Seven vertical concentration profiles were also measured.

The dataset includes six source locations and two wind directions [12]. Concentration was measured at 352 locations for continuous releases and at 41 measurement points for puff releases. The uncertainty of the results was determined based on repetitive measurements. The minimum length of one continuous release dispersion measurement in full scale was 17 hours, ensuring the statistical representativeness of the data. The results are converted to full scale using the formula for the dimensionless concentration (Eq. 2)

$$C^* = \frac{C U_{ref} L_{ref}^2}{Q} \qquad (2)$$

The measurement results form a dataset to evaluate numerical models in the frame of the COST Action ES1006 [7, 13]. The main purpose of the measurements was to provide a high-quality dataset optimal for the validation of emergency response tools applied during an accidental release in an urban area. For this paper, the data is evaluated to investigate dispersion characteristics relevant for urban areas. For this purpose, the mean concentration field of continuous release dispersion is studied.

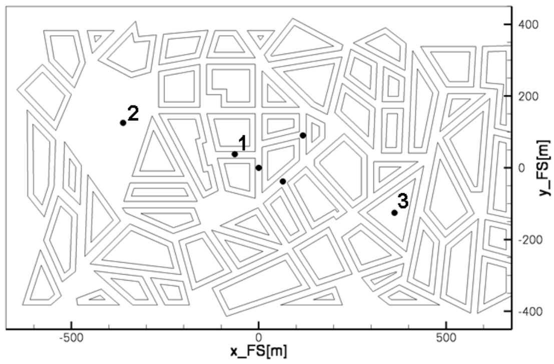

Figure 1. Layout of Michelstadt and the source locations.

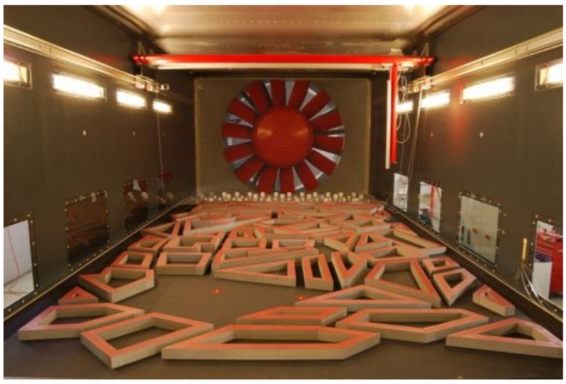

Figure 2. Model of Michelstadt in the wind tunnel

3. RESULTS

3.1. Concentration distribution in street canyons

The dispersion characteristics in street canyons perpendicular and parallel to the approach flow were analysed. The mean concentration field resulting from continuous releases was investigated. Fig. 3-4 show the concentration distribution along street canyons perpendicular to the approach flow direction, whereas on Fig. 5-7 the mean concentrations measured along lateral street canyons are plotted.

Exponential decay characterises the evolution of the mean concentration along parallel street canyons. The horizontal axis show the distance between the measurement location and the point of release. The exponential decay is even true, if the points do not lie in the same street canyon (Fig. 8.).

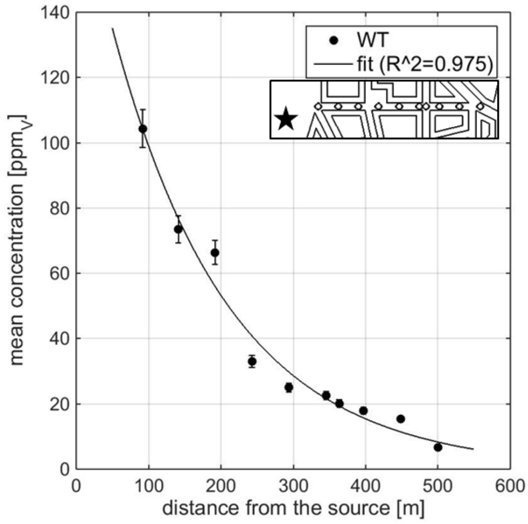

Figure 3. Concentration profile in a longitudinal street-canyon. Below the legend is the map of the geometry with the source (star) and the measurement points. The wind direction is from left to right.

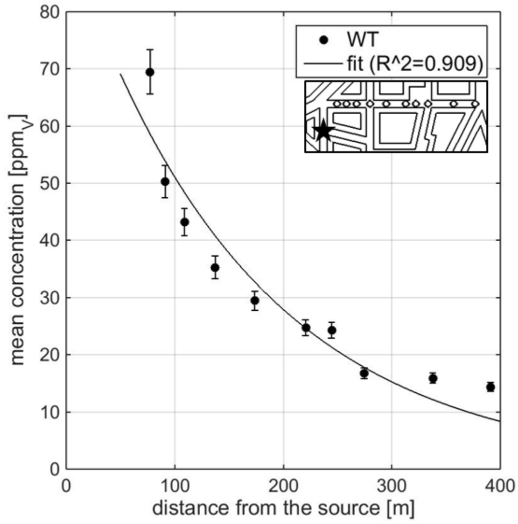

Figure 4. Concentration profile in a longitudinal street-canyon

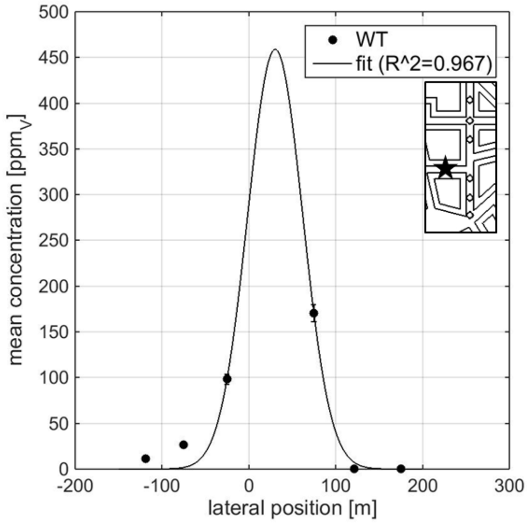

Figure 5. Concentration profile in a lateral street-canyon

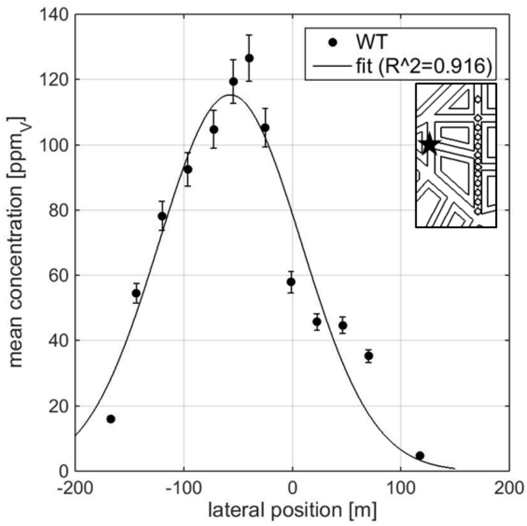

Figure 6. Concentration profile in a lateral street-canyon

The Gaussian function fits well to the lateral concentration profiles (Fig. 5-6), similarly to the profiles above a flat terrain. The lateral position related to the source location is plotted on the horizontal axis. Therefore, according to the Gaussian plume solution (Eq. 3.) of the advection-diffusion equation for ground-level point sources [14], the maximum concentration should occur at 0 position on the horizontal axis. Although the Gaussian function gives a good fit for the concentration distribution, the curve is shifted in comparison with the lateral concentration distribution in an open field or in a roughness with symmetrical layout.

$$C(x,y,z) = \frac{Q}{\pi \sigma_y \sigma_z U} \exp\left(- \frac{y^2}{2\sigma_y^2} - \frac{z^2}{2\sigma_z^2} \right) \quad (3)$$

The concentration distribution above the model resembles the dispersion characteristics of a flat terrain. Fig. 8 and 9 show results measured above the buildings of Michelstadt at $3.5H_L$ height. The source is located inside a courtyard. The longitudinal profile of the concentration corresponds to an exponential function (Fig. 8), whereas the lateral distribution of the concentration shows Gaussian-like behaviour (Fig. 9).

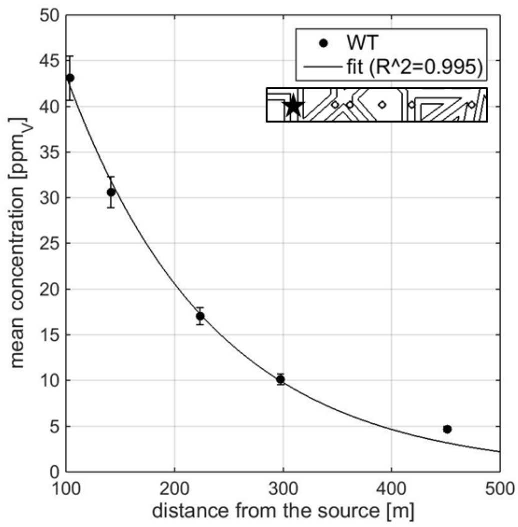

Figure 7. Longitudinal concentration profile

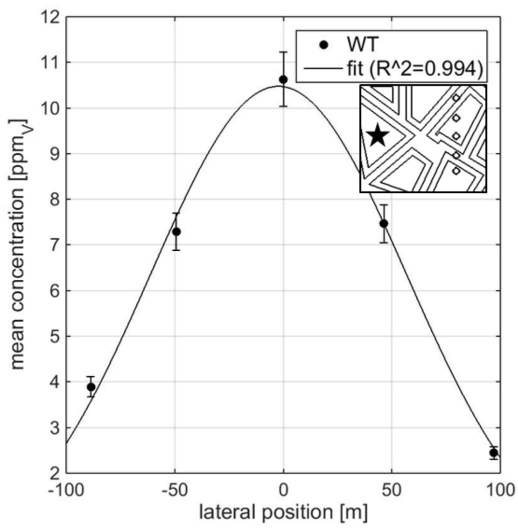

Figure 8. Lateral concentration profile at $3.5H_L$ height

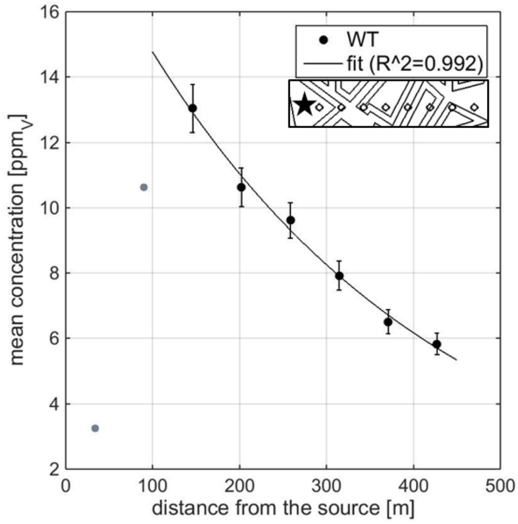

Figure 9. Longitudinal concentration profile at $3.5H_L$ height

3.2 Effect of the source location on the concentration field

The dataset contains results from six source locations (Fig. 1). The locations include an open area inside the urban environment, street canyons, intersections and a courtyard. Fig. 10-12 show the results of one source location, in comparison to the whole dataset. The envelope curve of the data has an exponential form, except for two outlier points (indicated with circles in Fig. 10). These were measured during a release from a street canyon parallel to the approach flow (marked as 1 in Fig. 1). The mean horizontal wind vectors in this area are shown in Fig. 11. The two points standing out from the dataset in Fig 10 are marked with circles in Fig 11.

The wind vectors indicate a strong channelling effect in the street canyons leading from the source to the measurement positions. This explains why the concentrations at these locations are higher than expected based on their distance from the source.

Fig. 12 shows the concentration values measured during the release from a source located in an open area (marked as 2 in Fig. 1), compared to the whole dataset. The results are fitting well to the dataset, not showing any outliers compared to the concentration measurements at sources located in street canyons.

The mean concentration values measured during the release from a point source located in a courtyard (marked as 3 in Fig. 1) are shown in Fig. 13. The concentration values measured during this case are considerably lower than those measured during releases from sources located in street canyons or intersections with the same distance from the source.

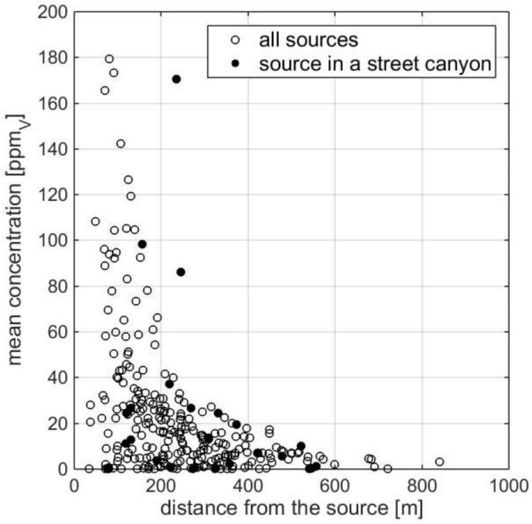

Figure 10. Mean concentrations measured during the release from a source located in a street canyon parallel to the approach flow direction in comparison with the whole dataset

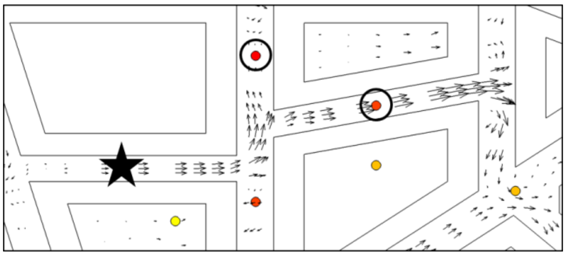

Figure 11. Mean horizontal wind vectors and concentration measurement points in the vicinity of the source 1 (marked with a star).

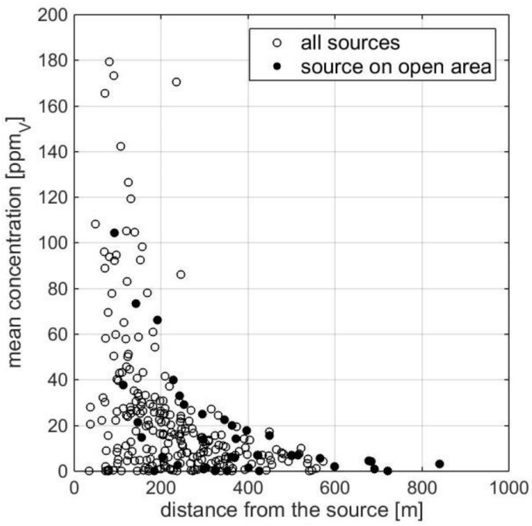

Figure 12. Mean concentrations measured during the release from a source located in an open square in comparison with the whole dataset

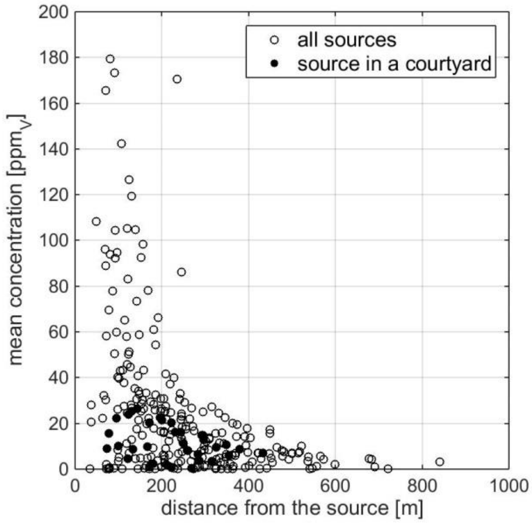

Figure 13. Mean concentrations measured during the release from a source located inside a courtyard in comparison with the whole dataset

4. CONCLUSIONS

Concentration measurements were carried out on a 1:225 scale model of an idealised Central-European city centre in a boundary-layer wind tunnel. The approach flow can be characterised as a very rough boundary layer [8]. The results of the measurements serve as a dataset for validation of numerical models in the frame of the COST Action ES1006 [7].

Dispersion characteristics in the urban environment were investigated based on continuous release measurement results. The dataset includes 352 measurements of dispersion from continuous releases. Six ground-level point sources and two wind directions were measured.

The characteristics of the mean concentration profiles in street canyons parallel and perpendicular to the mean direction of the approach flow were investigated. The Gaussian function gives a good fit for the mean concentration profiles measured in lateral street canyons. However, the symmetry axis is not aligned with the source location. The mean concentration profiles of longitudinal street canyons show exponential decay in the function of the distance from the source.

The dispersion from sources in different locations was also investigated based on the measurement results. When the source is located in a courtyard, the mean concentration field above the buildings (at $3.5H_L$ height) resembles the concentration field above an open terrain. When the source is located on an open space inside the urban area, the measured concentrations as the function of the distance from the source show similar values, as in case of sources located in street canyons or intersections. Concentrations of the tracer gas released from a source located in an inner courtyard are lower than in case of releases from street canyons or intersections.

ACKNOWLEDGEMENTS

The valuable guidance by COST Action ES1006 members during the measurements and data processing is very much appreciated. Support by the German Academic Exchange Service (DAAD) and the Deutsche Bundesstiftung Umwelt is gratefully acknowledged.

This work is connected to the project K 108936 “Flow and dispersion phenomena in urban environment” of the Hungarian Scientific Research Fund.

REFERENCES

[1] Stockie, J. M., 2011, „The Mathematics of Atmospheric Dispersion Modeling”, *SIAM Rev*, 53, 349–372.

[2] Branford, S., Coceal, O., Thomas, T. G., and Belcher, S. E., 2011, „Dispersion of a Point-Source Release of a Passive Scalar Through an Urban-Like Array for Different Wind Directions” *Boundary-Layer Meteorology*, 139(3), 367–394.

[3] Britter, R. E. and Hanna, S. R., 2003, „Flow and Dispersion in Urban Areas”, *Annual Review of Fluid Mechanics*, 35(1), 469–496.

[4] Coceal, O., Goulart, E. V., Branford, S., Glyn Thomas, T. and Belcher, S. E., 2014, „Flow structure and near-field dispersion in arrays of building-like obstacles”, *Journal of Wind Engineering and Industrial Aerodynamics*, 125, 52-68.

[5] Huq, P. and Franzese, P., 2013, „Measurements of Turbulence and Dispersion in Three Idealized Urban Canopies with Different Aspect Ratios and Comparisons with a Gaussian Plume Model” *Boundary-Layer Meteorology*, 147, 103–121.

[6] Huber, A. H., 1991, „Wind tunnel and Gaussian plume modeling of building wake dispersion”, *Atmospheric Environment Part A. General Topics*, 25(7), 1237–1249.

[7] Baumann-Stanzer and the members of the COST Action ES1006, 2015, „COST ES1006 Model evaluation case studies: approach and results”, *Available on http://www.elizas.eu*

[8] VDI Guideline 3783/12, 2000, „Environmental Meteorology—Physical Modelling of Flow and Dispersion Processes in the Atmospheric Boundary Layer—Applications of Wind Tunnels” *Beuth Verlag*, Berlin.

[9] Hertwig, D., Efthimiou, G. C., Bartzis, J. G. and Leitl, B., 2012, „CFD-RANS model validation of turbulent flow in a semi-idealized urban canopy”, *Journal of Wind Engineering and Industrial Aerodynamics*, 111, 61–72.

[10] Bastigkeit, I., 2011, „Erzeugung von Validierungsdaten für wirbelauflösende mikroskalige Strömungs- und Ausbreitungsmodelle”, *Ph.D. Thesis (in German). University of Hamburg, Germany*

[11] Di Sabatino, S., Leo, L.S., Cataldo and R.,Ratti, C.,Britter,R.E., 2010, „Construction of Digital elevation models for a southern European city and a comparative Morphological analysis with respect to northern European and North American cities” Journal of Applied Meteorology and Climatology 49, 1377–1396.

[12] Berbekar, E., Harms, F., Leitl, B., 2014, „Wind tunnel measurements of accidental gas releases in a simplified urban environment”, *16th International Conference on Harmonisation within Atmospheric Dispersion Modelling for Regulatory Purposes*, Varna, Bulgaria

[13] Efthimiou, G. C., Berbekar, E., Harms, F., Bartzis, J. G. and Leitl, B., 2015, „Prediction of high concentrations and concentration distribution of a continuous point source release in a semi-idealized urban canopy using CFD-RANS modeling”, *Atmospheric Environment*, 100, 48–56.

[14] Abdel-Rahman, A., 2008, „On the Atmospheric Dispersion and Gaussian Plume Model“,2nd International *Conference on waste management, water pollution, air pollution, indoor climate*, Corfu, Greece

Conference on Modelling Fluid Flow (CMFF'15)
The 16th International Conference on Fluid Flow Technologies
Budapest, Hungary, September 1-4, 2015

NUMERICAL SIMULATION OF BUBBLE DEFORMATION AND BREAKUP IN SIMPLE SHEAR FLOW

Mitsuhiro Ohta [1, 2], Ryohei Hotta [2], Yozo Toei [3], Mark Sussman [4]

[1] Corresponding Author. Department of Energy System, Institute of Technology and Science, Tokushima University. 2-1Minamijyousanjima-cho, Tokushima, Japan 770-8506. Tel. & Fax: +81 88 656 7366, E-mail: m-ohta@tokushima-u.ac.jp
[2] Department of Mechanical Engineering, Faculty of Engineering, Tokushima University.
[3] High Performance Plastics Company, Sekisui Chemical Co., Ltd. E-mail: toei@sekisui.com
[4] Department of Mathematics, Florida State University. E-mail: sussman@math.fsu.edu

ABSTRACT

Computational results for the deformation and breakup of a bubble, in immiscible viscous liquids undergoing simple shear flow, are presented. Our computations are implemented through a hydrodynamic scheme with formal second-order accuracy using the Moment-of-Fluid (MOF) method. From the numerical results, the appearance of bubble deformation and breakup is quite different from that for the drop. The first distinguishing factor for bubble breakup is that the magnitude of shear flow necessary to cause breakup is much larger than that in the drop system. In other words, a larger Reynolds number system is needed in order to induce bubble breakup. The second distinct feature of the bubble system versus the drop system, is that the bubble does not keep a stable deformed shape as the parameters of the system approach the critical "breakup" Reynolds number. It is asserted that the differences in morphology for a bubble undergoing breakup versus that of the drop is attributed to the density and viscosity ratio of the corresponding two-phase flow systems. The critical conditions for bubble breakup with respect to the Reynolds and capillary numbers are also presented for some cases.

Keywords: bubble deformation, bubble breakup, shear flow, CFD

NOMENCLATURE

B	[m]	half-breadth of the bubble
Ca	[–]	capillary number
D	[–]	Taylor deformation parameter
F	[–]	volume fraction
H	[–]	Heaviside function
L	[m]	half-length of the bubble
p	[Pa]	pressure
R	[m]	bubble radius
Re	[–]	Reynolds number
Re_C	[–]	critical Reynolds number
t	[s]	time
V	[m/s]	moving wall velocity
X	[m]	x-directional length of the domain
Y	[m]	y-directional length of the domain
Z	[m]	z-directional length of the domain
Γ	[1/s]	linear shear flow (= $2V/Z$)
η	[–]	viscosity ratio (= μ_B/μ_S)
κ	[1/m]	curvature
λ	[–]	density ratio (= ρ_B/ρ_S)
μ	[Pa·s]	viscosity
ρ	[kg/m^3]	density
σ	[N/m]	interfacial tension
ϕ	[m]	level-set function

Subscripts and Superscripts

B, C, S bubble, critical, suspending fluid

1. INTRODUCTION

The deformation and breakup of a drop in immiscible viscous liquids undergoing simple shear flow has been extensively investigated [1-5] as a basic study in connection with emulsion and materials processings, mixing and reaction devices etc. On the other hand, few studies for the deformation and breakup of a bubble have been carried out. In order to gain a fundamental understanding of the physical properties of fluids used in emulsion and materials processings, it is important to study the critical physical conditions in which breakup of a drop or bubble just occurs. In other words, it is important to identify the parameter regimes in which a system transitions from stable to unstable. In this study, the deformation and breakup of a bubble in insoluble viscous liquids undergoing simple shear flow are computationally examined using the Moment-of-Fluid (MOF) method [6-8]. We remark that for the study of bubble deformation in a shear flow, the density and viscosity ratios, λ and η, are negligible.

In this study, we specifically focus on the difference in the breakup process between the drop and the bubble, and we reveal distinguishing characteristics of the break-up process of the bubble.

2. NUMERICAL ANALYSIS

2.1. Computational System

Figure 1 shows a schematic of the computational system from a lateral view. The computational domain consists of a three-dimensional rectangular domain of $X = 24R$ (x) × $Y = 6R$ (y) × $Z = 6R$ (z). A spherical bubble is initially set at the center of the domain and is subjected to a linear shear flow Γ (= $2V/Z$) generated by the motion of top and bottom plates with velocity $\pm V$. Periodic boundary conditions are imposed in the x and y directions. The initial velocity condition is assumed to be a simple linear profile. One mesh size is set to $\Delta x = R/16$ in our computations. In this study, we ignore the effects of gravity in order to compare with previous results for a drop with $\lambda = \eta = 1$. The control dimensionless parameters are Reynolds and capillary numbers which are defined as follows:

$$Re = \frac{\rho_S \Gamma R^2}{\mu_S} \text{ and } Ca = \frac{\mu_S \Gamma R}{\sigma} \tag{1}$$

In the computations, for a certain Ca value, we determine the value of Re_C corresponding to the threshold for breakup.

2.2. Governing equations

The MOF method [6-8] is used to represent the liquid-gas interface. The MOF method is a generalization of the Volume-of-Fluid (VOF) method [9]. The fluids in our study are the bubble and the Newtonian suspending fluid. Both the bubble and the suspending fluid are governed by the continuity equation and the momentum equation. The governing equations including the surface tension force as a body force are written as follows:

$$\nabla \cdot \boldsymbol{u} = 0 \tag{2}$$

$$\begin{aligned} &\frac{\partial \boldsymbol{u}}{\partial t} + \left(\boldsymbol{u}\cdot\nabla\right)\boldsymbol{u} = \\ &\quad -\frac{\nabla p}{\rho} + \frac{1}{\rho}\nabla\cdot\left[\mu\left(\nabla\boldsymbol{u} + \nabla\boldsymbol{u}^{\mathrm{T}}\right)\right] - \frac{\sigma\kappa(\phi)}{\rho}\nabla H(\phi) \end{aligned} \tag{3}$$

Since the interface moves and deforms with the fluid, the time evolution of F is as follows:

$$\frac{\partial F}{\partial t} + \left(\boldsymbol{u}\cdot\nabla\right)F = 0 \tag{4}$$

We also use a level set function ϕ for tracking the interface as an auxiliary function for the VOF method.

$$\frac{\partial \phi}{\partial t} + \left(\boldsymbol{u}\cdot\nabla\right)\phi = 0 \tag{4}$$

ϕ satisfies,

$$\phi(\boldsymbol{x},t) = \begin{cases} >0 & \boldsymbol{x} \in \text{liquid} \\ \le 0 & \text{otherwise} \end{cases} \tag{5}$$

$H(\phi)$ is the Heaviside function defined as,

$$H(\phi) = \begin{cases} 1 & \phi \ge 0 \\ 0 & \text{otherwise} \end{cases} \tag{6}$$

ρ and μ are written as

$$\rho = \rho_S H(\phi) + \rho_B\left(1 - H(\phi)\right) \tag{7}$$

and

$$\mu = \mu_S H(\phi) + \mu_B\left(1 - H(\phi)\right). \tag{8}$$

The normal that points from gas to liquid and the curvature are

$$\boldsymbol{n} = \frac{\nabla\phi}{|\nabla\phi|} \text{ and } \kappa = \nabla\cdot\frac{\nabla\phi}{|\nabla\phi|}. \tag{9}$$

The governing equations are solved through a hydrodynamic scheme with second-order accuracy in the bulk fluid regions.

2.3. Moment of Fluid Method

In this section, we briefly mention the moment of fluid interface reconstruction. For a computational cell $\Omega_{i,j}$, the volume fraction F (zeroth-order moment) and centroid $\boldsymbol{x}$ (first-order moment) for suspending fluid are:

$$F = \frac{1}{|\Omega_{i,j}|}\int_{\Omega_{i,j}} H(\phi(\boldsymbol{x}))d\boldsymbol{x} \tag{10}$$

$$\boldsymbol{x}_S = \frac{\int_{\Omega_{i,j}} H(\phi(\boldsymbol{x}))\boldsymbol{x}d\boldsymbol{x}}{\int_{\Omega_{i,j}} H(\phi(\boldsymbol{x}))d\boldsymbol{x}} \tag{11}$$

The liquid-gas interface is reconstructed as a plane in three-dimensions (3d) and a line in two-dimensions (2d). This interface representation is called the piecewise linear interface calculation

(PLIC). Take a 2d case for example, an interface Π in cell $\Omega_{i,j}$ is represented by a straight line using the following vector form equation:

$$\Pi = \Omega_{i,j} \cap \left\{ \boldsymbol{x} \middle| \boldsymbol{n} \cdot \left(\boldsymbol{x} - \boldsymbol{x}_{i,j} \right) + b = 0 \right\} \tag{12}$$

where $\boldsymbol{n}$ is the interface unit normal vector, $\boldsymbol{x}_{i,j}$ is the cell center of $\Omega_{i,j}$ and b is the distance from $\boldsymbol{x}_{i,j}$ to the interface. Thus, the interface can be constructed when the normal vector $\boldsymbol{n}$ and distance b are known. In the MOF method, in order to find the slope and intercept of the reconstructed plane (line in 2d), we use the reference volume fraction, F_{ref}, and the reference centroid, $\boldsymbol{x}^{\mathrm{c}}_{\mathrm{ref}}$. The reference volume fraction and centroid correspond to the real interface which is not necessarily a straight line. The slope $\boldsymbol{n}$ and intercept b are selected so that the actual volume fraction function $F_{\mathrm{act}} = F_{\mathrm{act}}(\boldsymbol{n}, b)$ is equal to F_{ref} and the actual centroid, $\boldsymbol{x}^{\mathrm{c}}_{\mathrm{act}}(\boldsymbol{n}, b)$ is as close as possible to $\boldsymbol{x}^{\mathrm{c}}_{\mathrm{ref}}$. In other words, $\boldsymbol{n}$ and b are chosen in order to minimize E_{MOF} (Eq. 13) subject to the volume fraction constraint given in (Eq. 14):

$$E_{\mathrm{MOF}} = \left\| \boldsymbol{x}^{\mathrm{c}}_{\mathrm{ref}} - \boldsymbol{x}^{\mathrm{c}}_{\mathrm{act}} \left(\boldsymbol{n}, b \right) \right\|_2 \tag{13}$$

$$\left| F_{\mathrm{ref}} - F_{\mathrm{act}} \left(\boldsymbol{n}, b \right) \right| = 0 \tag{14}$$

Unlike the VOF method, the MOF interface reconstruction method only uses information from the computational cell under consideration. This property makes the MOF method more suitable for deforming boundary problems with sharp corners or slender filaments. Also, the MOF reconstruction algorithm makes itself more suitable for block structured dynamic adaptive mesh refinement since conditions at coarse/fine grid interface can be interpolated from the coarse grid using a stencil that does not depend circularly on the neighboring fine grid.

3. RESULTS AND DISCUSSION

Figures 2 and 3 show numerical results for the time evolution of the bubble interface when Ca = 0.3: Fig. 2 corresponds to the condition of Re = 65 and Fig. 3 corresponds to the condition of Re = 70. These figures show a cross-sectional slice in the *x-z* plane through the center of the bubble. In the case of Re = 65, the bubble does not breakup as can be seen from Fig.2. On the other hand, the bubble reaches breakup for the case of Re = 70 (Fig. 3). A distinguishing feature of bubble dynamics with no-breakup is that the bubble might not reach a stable deformed state like what one observes for the drop system [3-5]. In some parameter regimes, the bubble might oscillate between its maximum elongated shape and a slightly shortened geometry. This dynamic motion is not seen in previous studies for the drop [3-5]. When Re = 70, the bubble smoothly breaks up at the center through elongation. We assert that the condition of Re = 70 is the critical value (Re_{C}) for which the Ca = 0.3 bubble breaks up. A relatively large magnitude shear field is required for causing the breakup of the bubble in comparison to the drop case. Re_{C} for the drop with $\lambda = \eta = 1$ and Ca = 0.3 is about Re_{C} = 0.75 [3]. In the case of drop breakup with $\lambda = \eta = 1$, the volume of the ends of the deforming drop become large [3] which is in contrast to the bubble case. Large volume areas are not formed at the ends of the deforming bubble. The ends of the deforming bubble have cusped shapes and the bubble is linearly elongated with the same thickness.

Figures 4 and 5 show numerical results for the time evolution of the bubble interface for the case of Ca = 0.5: Figs. 4 and 5 correspond to the condition of Re = 47 and 50, respectively. For Ca = 0.5, the bubble does not breakup when Re = 47 but does breakup when Re = 50. We define the critical Reynolds number for this case to be Re_{C} =50. As with the Ca = 0.3 case, as the Reynolds number approaches the critical Reynolds number, we observe underdamped behavior in the length of the bubble. In comparing the results for Ca = 0.5 with those for Ca = 0.3, the bubble for Ca = 0.5 has a more elongated shape than that for Ca = 0.3 and the value of Re_{C} for Ca = 0.5 becomes smaller than that for Ca = 0.3. This is because the increase in Ca means the surface tension force becomes smaller relative to the viscous force. Accordingly, the bubble is more deformable as Ca is increased.

In Figure 6, we show numerical results of the time evolution of the bubble interface for the case of Ca = 0.8 and Re = 38. The value of Re = 38 can be regarded as Re_{C} for this case. The effects of the surface tension force are the least in this case. The constriction formed right before the breakup is barely-noticeable. Finally, the bubble ruptures after a very long elongation.

Figure 7 shows the time evolution of the Taylor deformation parameter D in the case of Ca = 0.3. D is defined by the following relation:

$$D = \left(L - B \right) / \left(L + B \right) \tag{15}$$

Here, we denote the half-length of the bubble as L and the half-breadth of the bubble as B. The upper panel is the case of Re = 65 and the lower panel is for the condition of Re = 70. In Figure 7, we plot the deformation parameter D versus the time for two contrasting cases in which the bubble does not break for case 1 (Ca = 0.3 and Re = 65) and the bubble does break for case 2 (Ca = 0.3 and Re = 70). We note from case 1 of this figure that the deformation function is underdamped near the critical Reynolds number which is in contrast to what is observed for the break-up of a drop in shear flow.

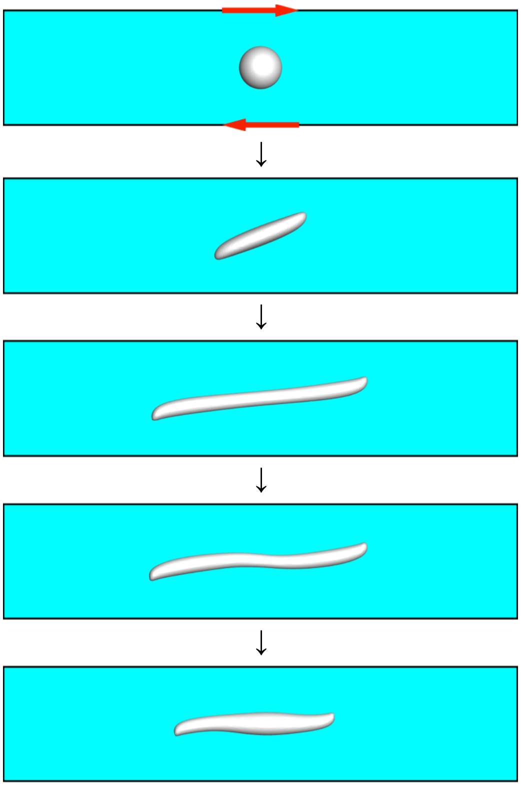

Figure 2. Time evolution of bubble interface at *Ca* = 0.3 and *Re* = 65.

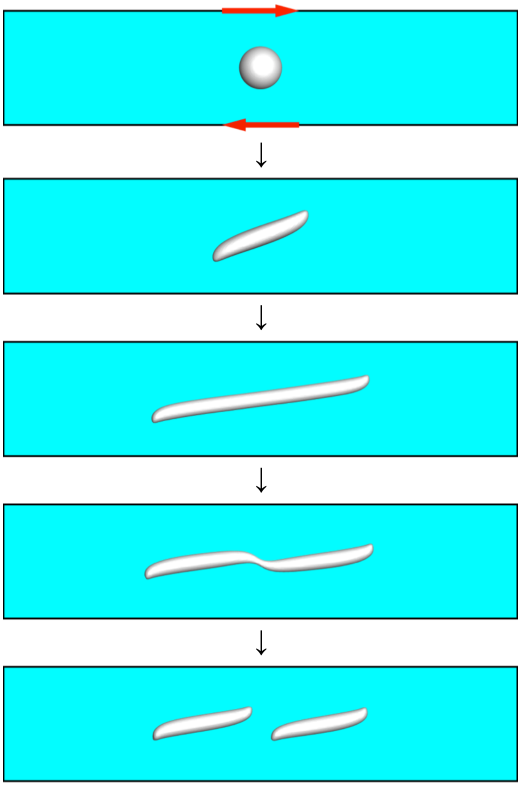

Figure 3. Time evolution of bubble interface at *Ca* = 0.3 and *Re* = 70.

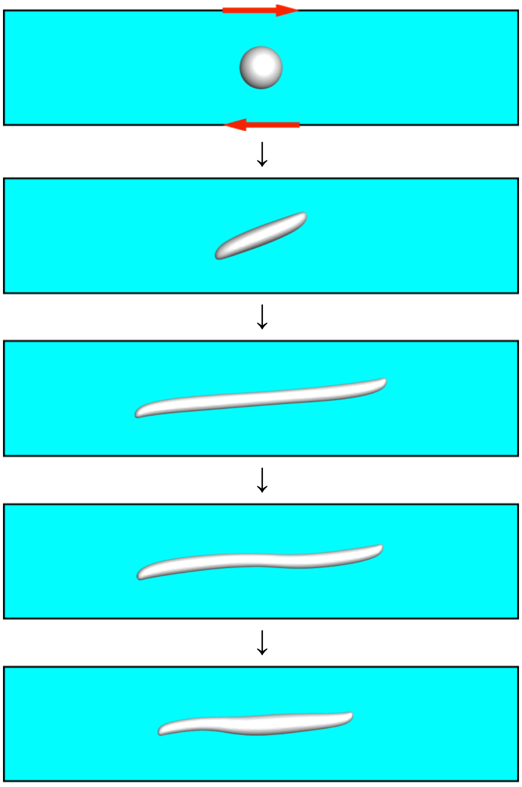

Figure 4. Time evolution of bubble interface at *Ca* = 0.5 and *Re* = 47.

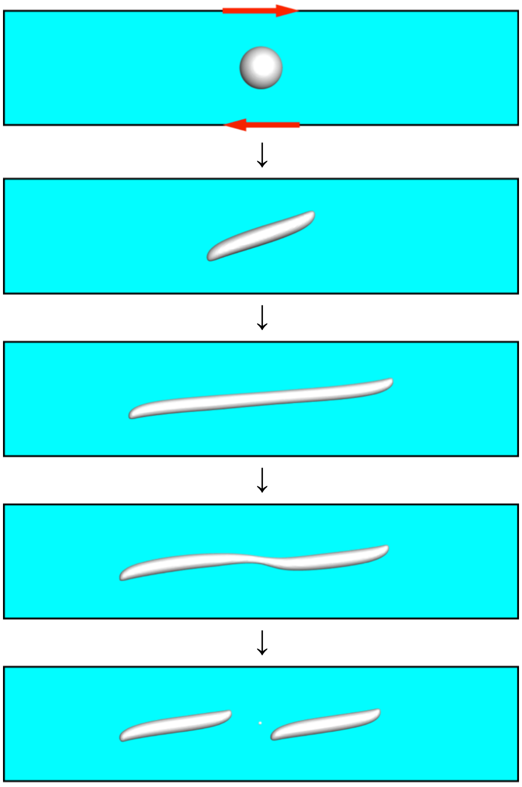

Figure 5. Time evolution of bubble interface at *Ca* = 0.5 and *Re* = 50.

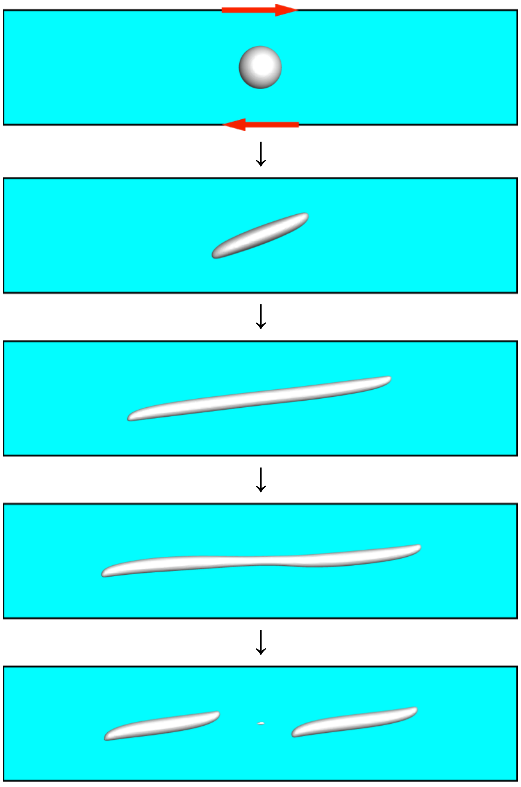

Figure 6. Time evolution of bubble interface at *Ca* = 0.8 and *Re* = 38.

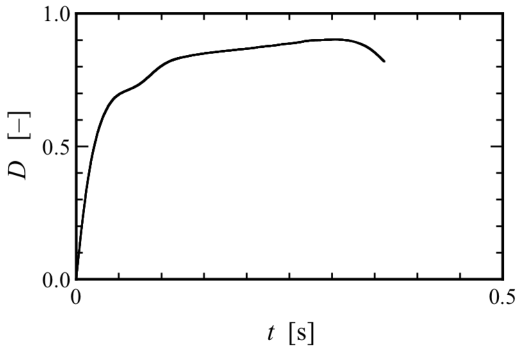

Ca = 0.3 and *Re* = 65

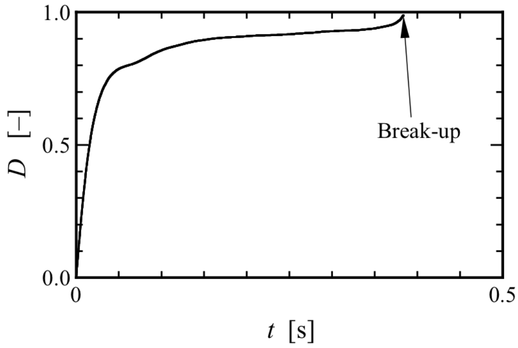

Ca = 0.3 and *Re* = 70

Figure 7. The change in the deformation parameter *D* as a function of time *t*.

5. CONCLUSIONS

By way of varying the Reynolds number and Capillary number, we discovered that the bubble deformation near the critical Reynolds number is more likely to exhibit pronounced underdamped behavior when compared to drop deformation. Also we found that the critical Reynolds number required in order to induce breakup was larger for the bubble than for the drop case.

ACKNOWLEDGEMENTS

The authors would like to thank Mr. Y. Suetsugu for his help with the computations and image processing.

REFERENCES

[1] Rallison, M., 1984, "The Deformation of Small Viscous Drops and Bubbles in Shear Flows", *Ann. Rev. Fluid Mech.*, Vol. 16, pp. 45-66.

[2] Stone, H. A., 1994, "Dynamics of Drop Deformation and Breakup in Viscous Fluids", *Ann. Rev. Fluid Mech.*, Vol. 26, pp. 65-102.

[3] Li, Y., Renardy, Y., and Renardy, M., 2000, "Numerical Simulation of Breakup of a Viscous Drop in Simple Shear Flow through a Volume-of-Fluid Method", *Phys. Fluids*, Vol. 12, pp. 269-282.

[4] Janssen, P. J. A., and Anderson, P. D., 2006, "Boundary-integral method for drop deformation between Parallel Plates", *Phys. Fluids*, Vol. 19, 043602.

[5] Komrakova, A. E., Shardt, O., Eskin, D., and Derksen, J. J., 2014, "Lattice Boltzmann Simulations of Drop Deformation and Breakup in Shear Flow", *Int. J. Multiphase Flow*, Vol. 59, pp. 24-43.

[6] Ahn, H. T., and Shashkov, M, 2007, "Multi-material Interface Reconstruction on Generalized Polyhedral Meshes", *J. Comput. Phys.*, Vol. 226, pp.2096-2132.

[6] Ahn, H. T., Shashkov, M., and Christon, M., 2009, "The Moment-of-Fluid Method in Action", *Commun. Numer. Methods Eng.*, Vol. 25, pp. 1009-1018.

[7] Jemison, M., Loch, E., Sussman, M., Shashkov, M., Arienti, M., Wang, Y., and Ohta, M., 2013, "A Coupled Level Set-Moment of Fluid

Method for Incompressible Two-Phase Flows", *J. Sci. Comput.*, Vol. 54, pp. 454-491.

[9] Hirt, C. W., and Nichols, B. D., 1981, "Volume of fluid (VOF) method for the dynamics of free boundaries", *J. Comput. Phys.*, Vol. 39, pp. 201-225.

Conference on Modelling Fluid Flow (CMFF'15)
The 16th International Conference on Fluid Flow Technologies
Budapest, Hungary, September 1-4, 2015

Entrance Region Flow in Concentric Annuli with Rotating Inner wall for Bingham Fluid

A.Kandasamy[1], Srinivasa Rao Nadiminti[2]

[1] Corresponding Author. Professor, Department of Mathematical and Computational Sciences, National Institute of Technology Karnataka, Surathkal, Mangalore, India. Tel.:+919449269793, Fax: +91824-2474033, E-mail: kandy@nitk.ac.in
[2] Department of Mathematical and Computational Sciences, National Institute of Technology Karnataka, Surathkal, Mangalore, India. E-mail: srinudm@gmail.com

ABSTRACT

Entrance region flow in concentric annuli with rotating inner wall for Bingham non-Newtonian fluid has been studied numerically. The inner cylinder rotates with a constant angular velocity ω, while the outer cylinder is stationary. A finite difference analysis is used to obtain the velocity components U, V, W and the pressure P along the radial direction R. With the Prandtl boundary layer assumptions, the continuity and momentum equations are solved iteratively using a finite difference method. Computational results are obtained for various non-Newtonian flow parameters and geometrical considerations. The development of the axial velocity profile, radial velocity profile, tangential velocity profile and pressure drop in the entrance region have been analyzed. Comparison of the present results with the results available in literature for various particular cases has been done and found to be in agreement.

Keywords: Concentric Annuli, Bingham Fluid, Entrance Region Flow, Finite Difference Method, Rotating Wall

NOMENCLATURE

m the number of radial increments in the numerical mesh network
p the pressure, Pa
p_0 the initial pressure, Pa
P the dimensionless pressure
r, θ and z the cylindrical coordinates, m
R, Z the dimensionless coordinates in the radial and axial directions, respectively
R1, R2 the radius of the inner and outer cylinders, respectively
B the Bingham number
Re, Ta the modified Reynolds number and Taylor number respectively
N the aspect ratio of the annulus, R_1/R_2
u, v, and w the velocity components in z, r, θ directions, respectively, m/s
u_0 the uniform inlet velocity, m/s
U, V, W the dimensionless velocity components
ρ the density of the fluid, kg/m^3
μ the apparent viscosity of the model, kg/m.s
μ_r the reference viscosity
$\overline{\mu}$ the dimensionless apparent viscosity
ω the regular angular velocity, rad/s
ΔR, ΔZ the mesh sizes in the radial and axial directions, respectively.

1. INTRODUCTION

The problem of entrance region flow in concentric annuli with rotating inner wall for non-Newtonian laminar flow is of practical importance in engineering applications. Many important industrial fluids are non-Newtonian in their flow characteristics and are referred to as rheological fluids. These include blood; various suspensions such as coal-water or coal-oil slurries, glues, inks, foods; polymer solutions; paints and many others. The fluid considered here is the Bingham model.

The problem of entrance region flow of non-Newtonian fluids in an annular cylinders has been studied by various authors. Mishra et al. [1] studied the flow of the Bingham plastic fluids in the concentric annulus and obtained the results for boundary layer thickness, centre core velocity, pressure drop. Batra and Bigyani Das [2] developed the stress-strain relation for the Casson fluid in the annular space between two coaxial rotating cylinders where the inner cylinder is at rest and outer cylinder rotating. Maia and Gasparetto [3] applied finite difference method for the Power-law fluid in the annuli and found difference in the entrance geometries. Sayed-Ahmed and Hazem [4] applied finite difference method to study the laminar flow of a Power-Law fluid in the concentric annulus.

The constitutive equation for Bingham fluid is given as Bird et al. [5]

$$\tau_{ij} = \left(\mu + \frac{\tau_0}{\varepsilon}\right)\varepsilon_{ij} \qquad (\tau \geq \tau_0) \tag{1}$$

where

$$\tau = \sqrt{\frac{1}{2}\tau_{ij}\tau_{ij}} \quad and \quad \varepsilon = \sqrt{\frac{1}{2}\varepsilon_{ij}\varepsilon_{ij}}$$

where τ_0 is the yield stress, τ_{ij} and ε_{ij} are the stress tensor and the rate-of-strain tensor, respectively. and μ is the viscosity of the fluid.

The problem of entrance region of Bingham fluid in concentric annulus has been investigated by Mishra et al. Kandasamy [6] investigated the entrance region flow heat transfer in concentric annuli for a Bingham fluid and presents the velocity distributions, temperature and pressure in the entrance region. Recently, Rekha and Kandasamy [7] have investigated the entrance region flow of Bingham fluid in an annular cylinder.

In the present work, the problem of entrance region flow of Bingham fluid in concentric annuli has been investigated. The analysis has been carried out under the assumption that the inner cylinder is rotating and the outer cylinder is at rest. With prandtl boundary layer assumptions, the equation of conservation of mass and momentum are discretized and solved using linearized implicit finite difference technique. The system of linear algebraic equations thus obtained and has been solved by the Gauss-Jordan method. The development of axial velocity profile, radial velocity profile, tangential velocity profile and pressure drop in the entrance region have been determined for different values of non-Newtonian flow characteristics and geometrical parameters. The effects of these on the velocity profiles and pressure drop have been discussed.

2. FORMULATION OF THE PROBLEM

The geometry of the problem is shown in Figure 1. The Bingham fluid enters the horizontal concentric annuli with inner and outer radii R_1 and R_2, respectively, from a large chamber with a uniform flat velocity profile u_0 along the axial direction z and with an initial pressure p_0. The inner cylinder rotates with an angular velocity ω and the outer cylinder is at rest. The flow is steady, laminar, incompressible, axisymmetric and of constant physical properties. We consider a cylindrical polar coordinate system with the origin at the inlet section on the central axis of the annulus, the z-axis along the axial direction and the radial direction r perpendicular to the z-axis.

Under the above assumptions and with the usual Prandtl boundary layer assumptions [8], the governing equations in polar coordinate system (r, θ, z) for

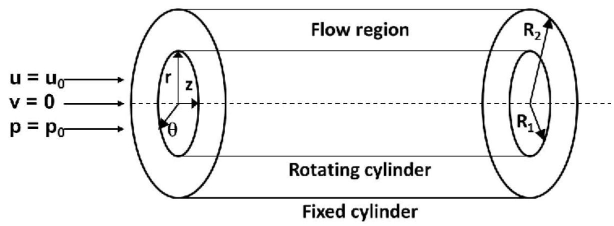

Figure 1. Geometry of the problem

a Bingham fluid in the entrance region are:

$$\text{Continuity equation}: \frac{\partial(rv)}{\partial r} + \frac{\partial(ru)}{\partial z} = 0 \tag{2}$$

$$r - \text{momentum equation}: \frac{w^2}{r} = \frac{1}{\rho}\frac{\partial p}{\partial r} \tag{3}$$

$$\theta - \text{momentum equation}: v\frac{\partial w}{\partial r} + u\frac{\partial w}{\partial z} + \frac{vw}{r} = \frac{1}{\rho r^2}\frac{\partial}{\partial r}\left(r^2\left[\tau_0 + kr\frac{\partial}{\partial r}(\frac{w}{r})\right]\right) \tag{4}$$

$$z - \text{momentum equation}: v\frac{\partial u}{\partial r} + u\frac{\partial u}{\partial z} = -\frac{1}{\rho}\frac{\partial p}{\partial z} + \frac{1}{\rho r}\frac{\partial}{\partial r}\left(r\left[\tau_0 + k\frac{\partial u}{\partial r}\right]\right) \tag{5}$$

where u, v, w are the velocity components in z, r, θ directions respectively, ρ is the density of the fluid, k is the coefficient of fluidity and p is the pressure.
The boundary conditions of the problem are given by

$$\begin{aligned} \text{for } z &\geq 0 \text{ and } r = R_1, v = u = 0 \text{ and } w = \omega R_1 \\ \text{for } z &\geq 0 \text{ and } r = R_2, v = u = w = 0 \\ \text{for } z &= 0 \text{ and } R_1 < r < R_2, u = u_0 \\ \text{at } z &= 0, p = p_0 \end{aligned} \tag{6}$$

Using the boundary conditions (6), the continuity Eqs. (2) can be expressed in the following integral form:

$$2\int_{R_2}^{R_1} rudr = (R_2^2 - R_1^2)u_0 \tag{7}$$

Introducing the following dimensionless variables and parameters,

$$R = \frac{r}{R_2}, U = \frac{u}{u_0}, V = \frac{\rho v R_2}{\mu_r}, W = \frac{w}{\omega R_1}, N = \frac{R_1}{R_2},$$
$$P = \frac{p - p_0}{\rho u_0^2}, Z = \frac{2z(1-N)}{R_2 Re}, B = \frac{\tau_0 R_2}{k u_0},$$
$$Re = \frac{2\rho(R_2 - R_1)u_0}{k},$$
$$T_a = \frac{2\omega^2\rho^2 R_1^2(R_2 - R_1)^3}{\mu_r^2(R_1 + R_2)}, where\ \mu_r = k\left(\frac{\omega R_1}{R_2}\right).$$

Here B is the Bingham number, Re Reynolds number, T_a Taylors number, μ_r is know as reference viscosity and N is known as aspect ratio of the annulus.

Eqs. (2) to (5) and (7) in the dimensionless form are given by

$$\frac{\partial V}{\partial R} + \frac{V}{R} + \frac{\partial U}{\partial Z} = 0 \tag{8}$$

$$\frac{W^2}{R} = \frac{Re^2(1-N)}{2(1+N)T_a}\frac{\partial P}{\partial R} \tag{9}$$

$$V\frac{\partial W}{\partial R} + U\frac{\partial W}{\partial Z} + \frac{VW}{R} = \frac{\partial^2 W}{\partial R^2} + \frac{1}{R}\frac{\partial W}{\partial R} - \frac{W}{R^2} + \frac{2B}{R} \tag{10}$$

$$V\frac{\partial U}{\partial R} + U\frac{\partial U}{\partial Z} = -\frac{\partial P}{\partial Z} + \frac{1}{R}.\frac{\partial U}{\partial R} + \frac{\partial^2 U}{\partial R^2} + \frac{B}{R} \tag{11}$$

and

$$2\int_N^1 RUdR = (1-N^2) \tag{12}$$

The boundary conditions (6) in the dimensionless form are:

$$\begin{aligned} \text{for } Z &\geq 0 \text{ and } R = N, V = U = 0 \text{ and } W = 1 \\ \text{for } Z &\geq 0 \text{ and } R = 1, V = U = W = 0 \\ \text{for } Z &= 0 \text{ and } N < R < 1, U = 1 \\ \text{at } Z &= 0, P = 0 \end{aligned} \tag{13}$$

3. NUMERICAL SOLUTION

The numerical analysis and the method of solution can be considered as an indirect extension of the work of Coney and El-Shaarawi [9]. Considering the mesh network of Fig.2, the following difference representations are made.

Here ΔR and ΔZ represents the grid size along the radial and axial directions respectively.

$$V_{i+1,j+1} = V_{i,j+1}\left(\frac{N+i\Delta R}{N+(i+1)\Delta R}\right) - \frac{\Delta R}{4\Delta Z}* \left(\frac{2N+(2i+1)\Delta R}{N+(i+1)\Delta R}\right)\left(U_{i+1,j+1}+U_{i,j+1}-U_{i+1,j}-U_{i,j}\right) \tag{14}$$

$$\frac{W^2_{i,j+1}}{N+i\Delta R} = \frac{(1-N)Re^2}{2T_a(1+N)}\frac{P_{i,j+1}-P_{i-1,j+1}}{\Delta R} \tag{15}$$

$$Vi,j\left[\frac{W_{i+1,j+1}+W_{i+1,j}-W_{i-1,j}-W_{i-1,j+1}}{4\Delta R}\right] + Ui,j\left[\frac{W_{i,j+1}-W_{i,j}}{\Delta Z}\right] + \frac{V_{i,j}W_{i,j}}{N+i\Delta R} = \frac{W_{i+1,j+1}+W_{i+1,j}-2W_{i,j+1}-2W_{i,j}+W_{i-1,j}+W_{i-1,j+1}}{2(\Delta R)^2} + \frac{W_{i+1,j+1}+W_{i+1,j}-W_{i-1,j}-W_{i-1,j+1}}{(N+i\Delta R)4\Delta R} - \frac{W_{ij}}{(N+i\Delta R)^2} + \frac{2B}{N+i\Delta R} \tag{16}$$

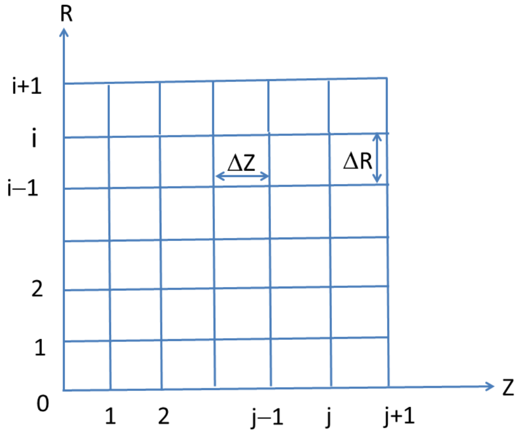

Figure 2. Grid formation for finite diffrence representations

$$Vi,j\left[\frac{U_{i+1,j+1}-U_{i-1,j+1}}{2\Delta R}\right] + Ui,j\left[\frac{U_{i,j+1}-U_{i,j}}{\Delta Z}\right] = -\left[\frac{P_{i,j+1}-P_{i,j}}{\Delta Z}\right] + \left[\frac{U_{i+1,j+1}-U_{i-1,j+1}}{(N+i\Delta R)2\Delta R}\right] + \left[\frac{U_{i+1,j+1}-2U_{i,j+1}+U_{i-1,j+1}}{(\Delta R)^2}\right] + \frac{B}{N+i\Delta R} \tag{17}$$

where i=0 at R=N and i=m at R=1.

The application of trapezoidal rule to equation (12) gives

$$\frac{\Delta R}{2}(NU_{0,j}+U_{m,j}) + \Delta R\sum_{i=1}^{m-1}U_{i,j}(N+i\Delta R) = \left(\frac{1-N^2}{2}\right)$$

The boundary condition (13) gives $U_{0,j} = U_{m,j} = 0$ and the above equation reduces to

$$\Delta R\sum_{i=1}^{m-1}U_{i,j}(N+i\Delta R) = \left(\frac{1-N^2}{2}\right) \tag{18}$$

The set of difference Eqs. (14) to (18) have been solved by the iterative procedure. Starting at the j = 0 column (annulus entrance) and applying Eq. (16) for $1 \leq i \leq m-1$, we get a system of linear algebraic equations. This system has been solved by using Gauss-Jordan method to obtain the values of the velocity component W at the second column j=1.

Then applying Eqs. (15) and (17) for $1 \leq i \leq m-1$ and Eq. (18), we get a system of linear equations. Again solving this system by Gauss-Jordan method, we obtain the values of the velocity component U and the pressure P at the second column j=1. Finally, the values of the velocity component V at the second column j=1 are obtained from Eq. (14) by Gauss-Jordan method using the known values of U. Repeating this procedure, we can advance, column by column, along the axial direction of the annulus until the flow becomes axially and tangentially fully developed.

4. RESULTS AND DISCUSSION

Numerical calculations have been performed for all admissible values of Bingham number B and aspect ratio N. The ratio of Reynolds number to Taylor number $Rt = Re^2/T_a = 20, 10$, $\Delta Z = 0.02, 0.03$ and $\Delta R = 0.1, 0.05$ has been fixed for N=0.3 and 0.8 respectively. The velocity profiles and pressure distribution along radial direction have been plotted for N =0.3, 0.8 and B =0, 10, 20, 30.

Figures 3 to 4 show the development of the tangential velocity profile component W for N=0.3, 0.8 and for different values of Bingham numbers B. The values of tangential velocity decrease from the inner wall to outer wall of the annulus. Also, it is found that with the increase of aspect ratio N, the tangential velocity profile increases. Further it is found that with the increase of Bingham number, the tangential velocity profile increases. The effect of the parameter Rt is negligible for the tangential velocity.

Figs. 5 to 6 show the development of the axial velocity profile component U for N=0.3, 0.8 and for different values of the Bingham numbers B. It is found that the velocity component U increases with the increase of Bingham number B as well as aspect ratio N. Also it is observed that the velocity profile takes the parabolic form when Bingham number B being zero (Newtonian fluid).

The radial velocity profile component V for N = 0.3 and 0.8, at different sections of the axial direction Z are show in Figs. 7 to 8. The values of radial velocity are negative in the region near the outer wall since it is in the opposite direction to the radial coordinate R and it has positive values near the inner wall because it has the same direction of the radial coordinate.

Figs. 9 to 10 show the distribution of the pressure P along the radial coordinate R for N=0.3 and 0.8. It is found that the value of P increases from a minimum at the inner wall to a maximum at the outer wall. Moreover, it is observed that the pressure does not depend on the radial coordinate in the region near the outer wall.

The present results are compared with available results in literature for various particular cases and are found to be in agreement. When the Bingham number B=0, our results match with the results corresponded to Newtonian fluid (Coney and El-Shaarawi [9]). In the case of stationary cylinders, the results of axial velocity components in our analysis are matching with that of the results of Kandasamy [6].

5. CONCLUSION

Numerical results for the entrance region flow in concentric annuli with rotating inner wall for Bingham fluid were presented. The effects of the parameters N and B on the pressure drop, the velocity profiles are studied. Numerical calculations have been performed for all admissible values of Bingham number B and aspect ratio N. The velocity distribution and pressure distribution along radial direction R have been presented geometrically. The present results are found in agreement with the results corresponding to various particular cases available in literature.

From this study, the following can be concluded.

1. Tangential velocity decrease from the inner wall to outer wall of the annulus.

2. Increasing the aspect ratio N, the axial velocity component U increases at all values of Bingham numbers B.

3. Radial velocity is found to be dependent only on the axial coordinate.

4. Pressure increases from a minimum at the inner wall to a maximum at the outer wall of the annulus and pressure does not vary so much with respect to the radial coordinate in the region near the outer wall.

Acknowledgements The authors would like to express our gratitude to the reviewers for their useful comments and suggestions which has helped to improve the presentation of this work.

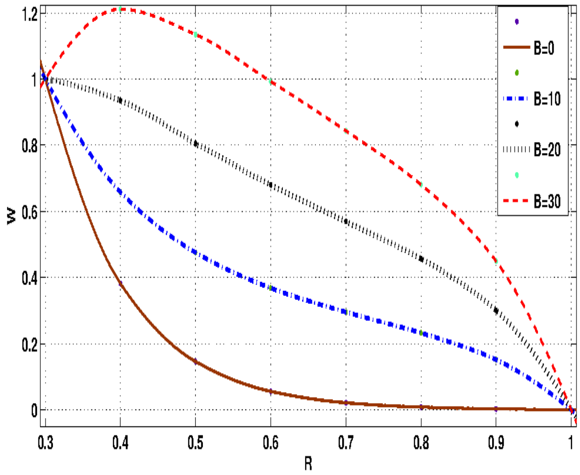

Figure 3. Tagential velocity profile for N=0.3

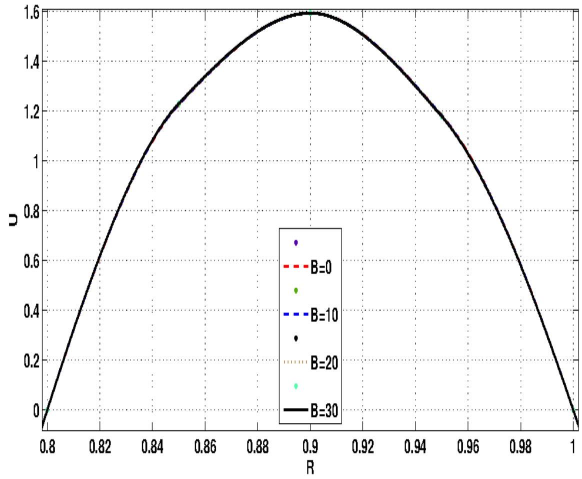

Figure 6. Axial velocity profile for N=0.8

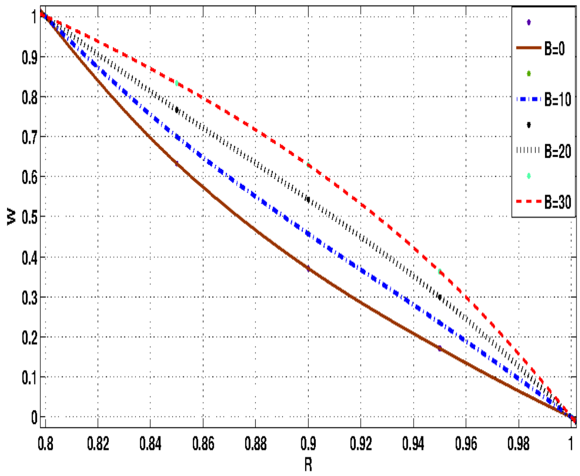

Figure 4. Tagential velocity profile for N=0.8

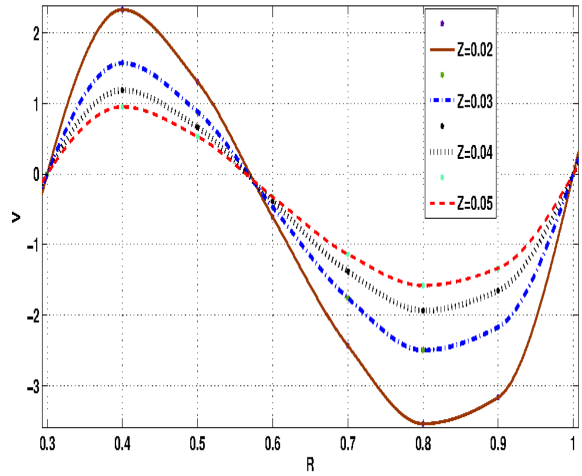

Figure 7. Radial velocity profile for N=0.3

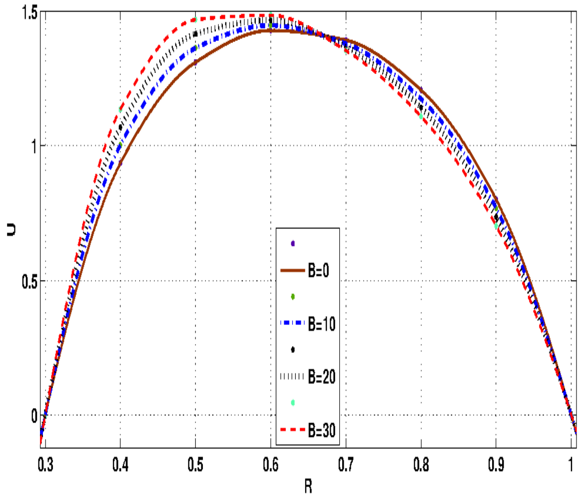

Figure 5. Axial velocity profile for N=0.3

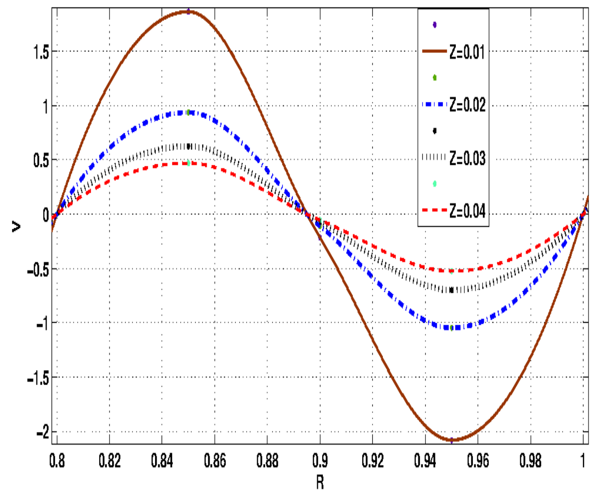

Figure 8. Radial velocity profile for N=0.8

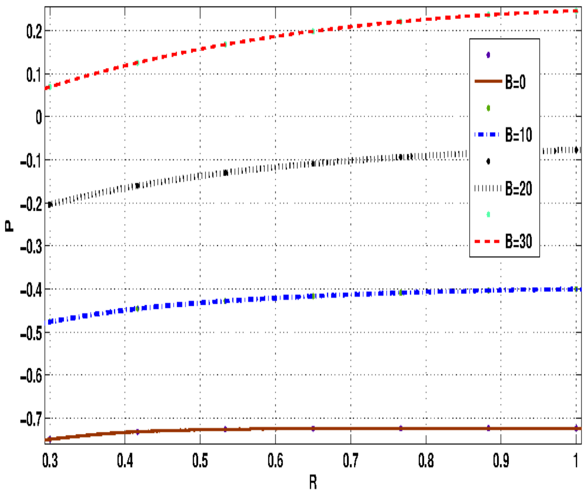

Figure 9. Pressure drop for N=0.3

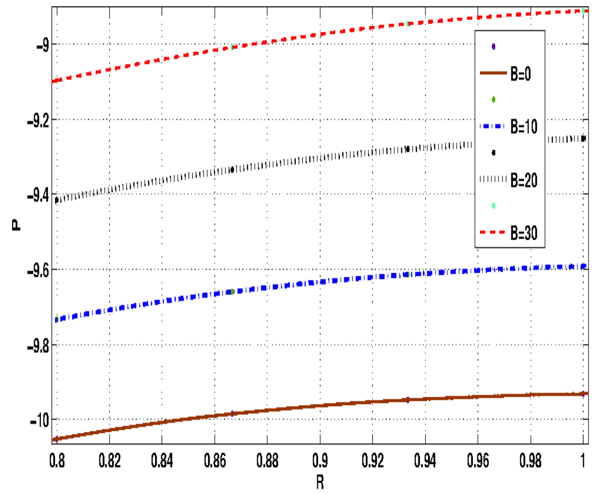

Figure 10. Pressure drop for N=0.8

REFERENCES

[1] Mishra I. M., Surendra Kumar and P Mishra, 1985, "Entrance Region Flow of Bingham Plastic Fluids in Concentric Annulus", *Indian Journal of Technology*, vol. 23, pp. 81-87.

[2] Batra, R.L. and Bigyani Das, 1992, "Flow of a Casson Fluid between Two Rotating Cylinders", *Fluid Dynamic Research*, vol. 9, pp. 133-141.

[3] Maia, M.C.A. and Gasparetto, C.A., 2003, "A numerical solution for entrance region of non-Newtonian flow in annuli", *Brazilian Journal of Chemical Eng.*, vol. 20, pp. 201-211.

[4] Sayed-Ahmed and M.E., "Hazem Sharaf-El-Din, 2006, Entrance region flow of a power-law fluid in concentric annuli with rotating inner wall", *International Communications in Heat and Mass Transfer*, vol. 33, pp. 654-665.

[5] Bird, R.D., G.C. Dai and B.J. Yarusso, 1982, "The rheology and flow of viscoplastic materials", *Rev. Chem. Eng.*, vol. 1, pp. 1-70.

[6] Kandasamy A., 1996, "Entrance region flow heat transfer in concentric annuli for a Bingham fluid", *Third Asian-Pacific Conference on Computational Mechanics*, Seoul, Korea, pp. 1697-1702.

[7] Rekha G. Pai and A. Kandasamy, 2014, "Entrance Region Flow of Bingham Fluid in an Annular Cylinder", *International Journal of Applied Engineering Research*, vol. 5, pp. 7083-7101.

[8] Schlichting H. and K. Gersten, 2000, *Boundary Layer Theory*, 8th ed., Springer.

[9] Coney, J.E.R. and M.A.I. El-Shaarawi, 1974, "A contribution to the numerical solution of developing laminar flow in the entrance region of concentric annuli with rotating inner walls", *ASME Trans. J. Fluid Eng.*, vol. 96, pp. 333-340.

[10] Round, G.F. and Yu. S., 1993, "Entrance laminar flows of viscoplastic fluids in concentric annuli", *Canadian J. Chem. Eng.*, vol. 71, pp. 642-645.

Conference on Modelling Fluid Flow (CMFF'15)
The 16th International Conference on Fluid Flow Technologies
Budapest, Hungary, September 1-4, 2015

NUMERICAL ANALYSIS OF MELTING PROCESS IN AN INDUCTION FURNACE FOR DIFFERENT POSITIONS OF INDUCTOR

Piotr BULIŃSKI[1], Jacek SMOŁKA[2], Sławomir GOLAK[3], Roman PRZYŁUCKI[4]

[1] Corresponding Author. Institute of Thermal Technology, Silesian University of Technology. Konarskiego 22, 44-100 Gliwice, Poland. Tel.: +48 32 237 14 60, E-mail: piotr.bulinski@polsl.pl
[2] Institute of Thermal Technology, Silesian University of Technology. E-mail: jacek.smolka@polsl.pl
[3] Silesian University of Technology. E-mail: slawomir.golak@polsl.pl
[4] Silesian University of Technology. E-mail: roman.przylucki@polsl.pl

ABSTRACT

The main purpose of this work was to develop a validated coupled mathematical model of metal melting process in an induction furnace. The technology allows for the efficient removal of impurities, thus the purity of final material is very high. Such materials can be applied in the advanced technologies as aviation, biotechnology, etc.

To mathematically describe the physical processes in a furnace, mutual interaction of electromagnetic and thermo-fluid fields needs to be considered. The coupled mathematical model of metal melting and rectification was implemented using two commercial codes: Ansys Mechanical APDL for electromagnetic field and Ansys Fluent for thermal and flow fields. The most important factors for this kind of modelling is a shape of free surface of the liquid metal, flow field in the melt, heat transfer in the crucible and transport of components in the liquid metal and further in the inert or protective atmosphere over crucible.

The final model can be used to identify the best operating parameters of the melting and rectifying process.

Keywords: CFD, coupled model, electromagnetism, induction furnace,

NOMENCLATURE

B	$[T]$	magnetic induction
F	$[N]$	force
J	$[A/m^2]$	current density
U	$[m^3/s]$	volume flux
V	$[m^3]$	volume
f	$[N/m^3]$	force density
g	$[m/s^2]$	gravity
p	$[Pa]$	pressure
r	$[m]$	radial coordinate
t	$[s]$	time
v	$[m/s]$	velocity
x	$[m]$	axial coordinate
α	[-]	volume fraction
μ	$[Pa{\cdot}s]$	dynamic viscosity or
	$[H/m]$	magnetic permeability
σ	$[S/m]$	electrical conductivity
ρ	$[kg/m^3]$	density
ω	$[rad/s]$	angular frequency

Subscripts and Superscripts

e	electromagnetic
f	face
n, n+1	previous and current time step
q	q^{th} phase
s	source
x, r	axial, radial (coordinate)

1. INTRODUCTION

The technology of metal melting in induction furnace allows for efficient removal of impurities, thereby yielding products of very high purity. Such materials can then be applied in cutting edge technologies as aviation (turbine blades), biotechnology (prosthesis, implants), to name but a few. To control these processes, measurements and numerical analysis can be conducted. In this paper, both experimental and numerical approaches were performed.

Induction furnaces produce pure metals and alloys of highest purity. Their feature is the ability of removing impurities in the melt. The units are fitted with a crucible consisting of electrically insulated material. The crucible is placed in a cylindrical inductor being a source of electromagnetic field.

Some experimental and simulation results addressed in this paper are available in the recent literature. Its review shows clearly that the experimental portion of the research is by far more advanced than its modelling counterpart. The reports on experiments on furnaces are available not only in laboratory but also in industrial scale units [1]. This reference reports on very efficient experimental methods of purification of alloys, while the scope of the numerical simulations are limited to coupled CFD model of temperature and velocity field in the charge.

More sophisticated models deal with coupling of electromagnetic and thermofluid phenomena [2-6]. The computational domain was, as a rule, axisymmetric [7] though reference [8] considers a 3-D segment with appropriately defined periodicity conditions [8]. The most important achievement of the last few years was the development of various techniques of modelling the dynamics of the free surface variation resulting from the alternating electromagnetic field in the induction furnaces [9-11]. Only few authors took into account the solidification of the metal in contact with the cold crucible [12]. Nonetheless, also in these works the influence of the geometry of the solidified metal, of significantly higher electrical conductivity, onto the electromagnetic field has been neglected.

A separate group of problems associated with metal melting in induction furnaces is the transport and evaporation of the impurities into the surrounding atmosphere. The available literature concerns standard crucible furnaces [13-15]. Reference [13] gives the analysis of the influence of the turbulence intensity in the near surface zone of the metal onto the evaporation of components of the melt. However, the paper studies only classic turbulence k-epsilon and its RND variant [16], while the current trend is to use more sophisticated techniques, able to reproduce the behaviour of the fluid in the near-surface domains. Large Eddy Simulations (LES) [17] and Reynolds Stress Model are good examples of such approaches.

The field of interest of the majority of papers dealing with numerical simulations was limited to the development of coupled electromagnetic – thermofluid models. The influence of the supply frequency, geometry of the inductor onto the behaviour of the melt in the fluid has not been analysed. The exception from this rule are references [18,19] authored by co-authors of this paper, where these aspects have been addressed. Additionally, the same team of authors investigated the influence of the shape and surface area of the free surface [20,21] in furnaces with ceramic crucibles. The possibility of controlling the shape of the surface of the molten metal in the furnace with cold crucible is a fundamental factor influencing the efficiency of the refining and loss of alloys components.

The aim of the work was the development of a validated, coupled mathematical model of a process of metal melting in classical induction furnaces. The developed mathematical description of process in the furnace encompassed sub-models of all constituent phenomena. To accomplish this, the algorithm account for mutual interactions of electromagnetic and thermofluid fields. In this work, the most important question was the evaluation of the complex shape of the free surface for three different positions of inductor.

2. EXPERIMENT

One of the most important part of every computational fluid dynamics paper is verification and validation process. Usually sensitivity analysis for spatial and time discretization are enough to verify developed model. Validation is a process of determination of differences between real phenomena and simulated.

Due to high temperatures and proximity of the crucible, carrying out measurements in liquid metal is not a trivial matter. Thus, the measurements should be conducted using contactless methods. In the course of the measurement campaign for a given current of the inductor, its position and filling fraction of the crucible, following parameters can be monitored:

1. Shape of the free surface and its linear profile. 3-D camera and laser can be used for these purposes.
2. Velocity on the surface of the liquid metal by tracking the local singularities and markers. This can be accomplished using high resolution, high speed camera. This measurement yields the quantities directly associated with the mass transfer on the metal-gaseous phase interface.
3. Temperatures field on the surface by IR camera or by two colour pyrometer.

Besides these measurements, it is possible to determine the chemical composition of the melt. Taking samples can be accomplished during the purification process. Thus, the investigation carried out can yield necessary data for the validation of the portion of the coupled model that concerns the transient transport of impurities of additives from the bath to its surrounding.

In order to perform validation of the numerical analysis, the measurement site was constructed. It was presented in “Figure 1”. The inductor was placed on the movable table, therefore it was possible to check the influence of its position on the liquid metal in the crucible. Several tests were carried out for different crucibles, currents, inductor positions, etc. In this work results for three positions of inductor was presented:

A. the bottom of inductor was 19,5 mm beneath the bottom of crucible,

B. the bottom of inductor was 20,5 mm above the bottom of crucible,
C. the bottom of inductor was 51,5 mm above the bottom of crucible,

Figure 1. Measurement site with the visible shape of the meniscus

3. MATHEMATICAL MODEL

The considered crucible is exposed to negligible both axis and tangential forces. Therefore, it was possible to simplify geometry of model to two-dimensional axisymmetric problem. The numerical domain was presented in “Figure 2”. It consisted of outlet, axis, side and bottom walls. The overall geometrical dimensions were the following: an outlet radius of 62 mm, a height of 200 mm and a bottom radius of 30 mm. The molten metal sample had reached 128 mm height of the crucible.

Once geometry was prepared, numerical discretisation had to be applied. Firstly, to verify created numerical model, three grids were computed with different number of quadrilaterals. The results for every mesh were examined and one of them were chosen for consecutive simulations. The smallest grid with 24 000 quadrilaterals was selected due to the lowest computing time and the similar results obtained for two other meshes. The employed numerical discretisation was shown in “Figure 2b”.

The coupled numerical model of the pure metal melting in the induction furnace was formulated using platforms of two commercial codes. Both these component programs were mutually connected in an effective coupling procedure developed by the co-authors of this paper. The following software was used for the particular data transfer between submodels:

1. Ansys Mechanical APDL 15 for the electromagnetic field to compute and transfer a non-uniform field of the source terms in the momentum equations of the CFD model. These source fields are the effects of the Lorentz force for liquid metal.
2. Ansys Fluent for the fluid flow to compute the new shape of the liquid metal domain. This quantity was used to compute an update of the electromagnetic field.

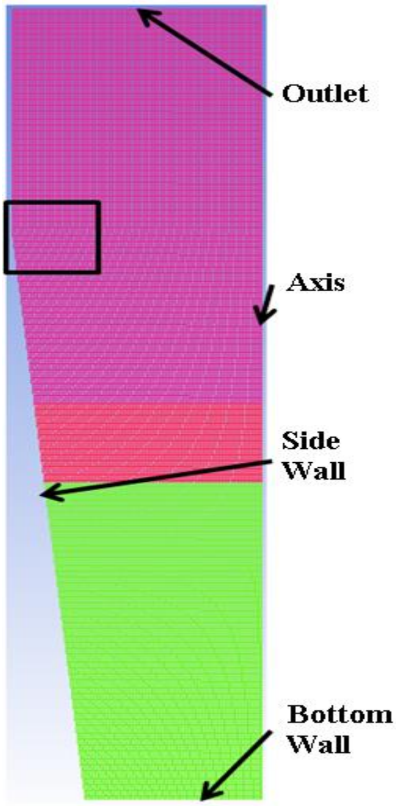

(a)

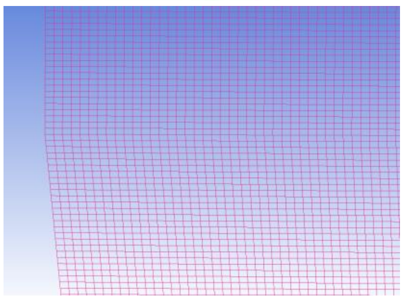
(b)

Figure 2. (a) Boundary conditions and (b) numerical grid in the developed coupled model

To predict a shape of free surface, it was necessary to solve the momentum conservation equations. For 2-D axisymmetric and unsteady flow, these equations take the following form:

$$
\begin{aligned}
&\frac{\partial}{\partial t}(\rho v_x)+\frac{1}{r}\frac{\partial}{\partial x}(r\rho v_x v_x)+\frac{1}{r}\frac{\partial}{\partial r}(r\rho v_r v_x)\\
&=-\frac{\partial p}{\partial x}+\frac{1}{r}\frac{\partial}{\partial x}\left[r\mu\left(2\frac{\partial v_x}{\partial x}-\frac{2}{3}(\nabla\cdot\vec{v})\right)\right]\\
&+\frac{1}{r}\frac{\partial}{\partial r}\left[r\mu\left(\frac{\partial v_x}{\partial r}+\frac{\partial v_r}{\partial x}\right)\right]+\rho\vec{g}+F_x
\end{aligned}
\tag{1}
$$

$$
\begin{aligned}
&\frac{\partial}{\partial t}(\rho v_r)+\frac{1}{r}\frac{\partial}{\partial x}(r\rho v_x v_r)+\frac{1}{r}\frac{\partial}{\partial r}(r\rho v_r v_r)\\
&=-\frac{\partial p}{\partial r}+\frac{1}{r}\frac{\partial}{\partial x}\left[r\mu\left(\frac{\partial v_r}{\partial x}+\frac{\partial v_x}{\partial r}\right)\right]\\
&+\frac{1}{r}\frac{\partial}{\partial r}\left[r\mu\left(2\frac{\partial v_r}{\partial r}-\frac{2}{3}(\nabla\cdot\vec{v})\right)\right]-2\mu\frac{v_r}{r^2}\\
&+\frac{2}{3}\frac{\mu}{r}(\nabla\cdot\vec{v})+F_r
\end{aligned}
\tag{2}
$$

where ρ is the density, t is the time, x and r are the axial and radial coordinates, respectively, v is the velocity, g is the gravity, μ is the dynamic viscosity and F is Lorentz force.

In this study, a multiphase flow was simulated using Volume of Fluid (VOF) model. Moreover, the explicit scheme was used. To track the interface between air and liquid metal, the mass conservation equation for the volume fraction was solved:

$$
\frac{\alpha_q^{n+1}\rho_q^{n+1}-\alpha_q^n\rho_q^n}{\Delta t}V+\sum_f\left(\rho_q U_f^n\alpha_{q,f}^n\right)=0 \tag{3}
$$

where α_q is the volume fraction of current (n+1) or previous (n) time step and U is the volume flux.

In the mass conservation equation, the specified density is referred to q^{th} phase. However, in the momentum conservation equation, the average density appears. In VOF model, all the material properties in this paper were averaged as follows:

$$
\rho=\sum\alpha_q\rho_q \tag{5}
$$

Energy equation was negligible because once aluminium was liquid, temperature field inside charge was uniform and during few seconds which were modelled it did not change.

To solve the defined set of the differential equations, material properties of air and metal had to be specified. The liquid metal parameters were: ρ = 2380 kg/m^3 and μ = 0.0015 $Pa\cdot s$, which are average values for liquid aluminium in 1500℃. To simplify model the air was examined as incompressible gas with ρ = 1.225 kg/m^3 and μ = 1.7894e-5 $Pa\cdot s$.

The last necessary information to achieve solution of the governing equations were source terms in the momentum conservation equations. They were computed in the electromagnetic solver Ansys Mechanical APDL. These source terms were introduced into the momentum conservation equations by means of the User-Defined Functions (UDFs).

The formulated two-dimensional, axially symmetric electromagnetic model was based on a commonly used equation where the magnetic vector potential is applied:

$$
\nabla\times\left(\frac{1}{\mu}\nabla\times A\right)+j\omega\sigma\cdot A=J_S \tag{6}
$$

where: μ, σ is the magnetic permeability and conductivity of aluminium, ω is the angular frequency and J_s is the current density source.

Based on the distribution of the magnetic vector potential A, a distribution of the magnetic induction (Eq. 7), the eddy current densities (Eq. 8) and the density of electromagnetic force that acts on a liquid metal (Eq. 9) can be determined:

$$
B=\nabla\times A \tag{7}
$$

$$
J=-j\omega\sigma\cdot A \tag{8}
$$

$$
f_e=\frac{1}{2}\mathrm{Re}\left(J\times B\right) \tag{9}
$$

4. RESULTS

For verification study, few cases with different grid and time steps were performed. This action allowed of the selection of the most appropriate model setups for the final simulations.

Then an effect of the inductor position was examined. Three different heights relative to crucible were considered. This yields three different Lorentz force fields in the liquid metal. Therefore, it was possible to choose the best position of inductor in order to control process of melting and purification of metal.

The preliminary results from the numerical simulations were presented in "Figure 3". The volume fraction fields were revealed. For the first case (Figure 3a), the value of the radial Lorentz force was the smallest. The shape of a free surface slightly differs from initial state without Lorentz force introduced. As a result, small convex meniscus was formed only. The second position of the inductor yielded medium values of source terms of momentum conservation equations (Figure 3b). The core of the liquid metal was around 10 mm higher than the connection point of wall and free surface. The last case had the highest value of the radial and axial forces. The convex meniscus that was formed was much bigger than that of the previous cases. The area where liquid metal is connected to the wall is smallest. This factor is important for the purity of final metal. However, for this case area of free surface is the largest so the protective gaseous atmosphere has to be ensured.

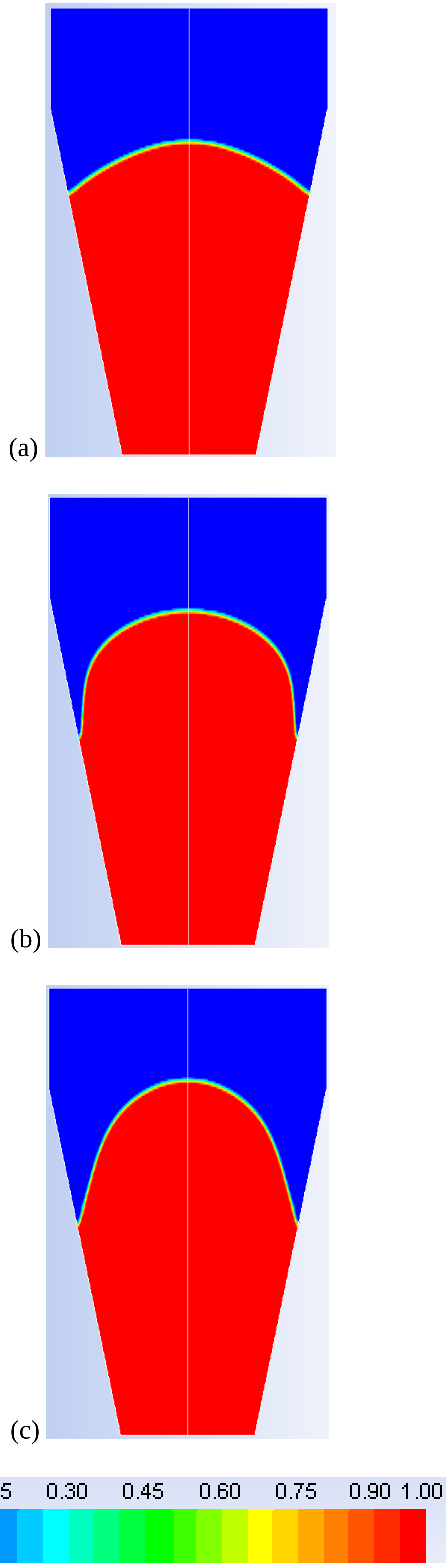

Figure 3. Volume fraction of aluminium in the numerical domain for three different positions of an inductor

Quasi steady state of the final shape of liquid metal was maintained by Lorentz forces. Direction and value of force vectors was presented in "Figure 4". Lorentz force acts only in the outer areas of numerical model. The maximum of the force occurs near contact angle of liquid metal and air and its value is around 500 thousands Newtons. According to electromagnetic field theory obtained distribution of Lorentz force is correct.

Applied force leads to the formation of eddies in the liquid metal domain. Velocity field and vectors coloured by volume fraction were presented in "Figure 5". There are two large eddies in the core of the aluminium charge and two smaller eddies in the top part. This behaviour of the flow is right if there is a large force applied in the two thirds of the domain. The highest velocity has value 0.62 m/s and it appears in the near wall area where the highest force is applied. It is not possible to compare this kind of numerical results to experiment due to behaviour of this phenomenon, but for the future measurements it is planned to examine velocities on the free surface of liquid metal. Markers on the surface of metal will be tracked and the it will be possible to calculate velocities on the free surface.

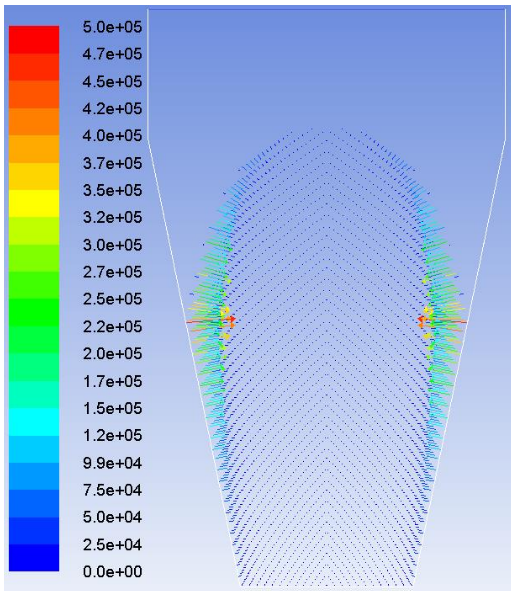

Figure 4. Vectors of Lorentz force (in *N*) in the numerical domain for position C of an inductor.

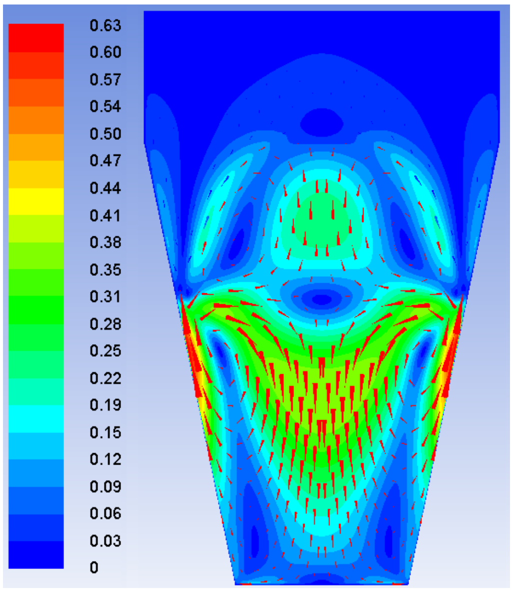

Figure 5. Velocity field (in *m/s*) in the numerical domain for position C of an inductor with vectors coloured by volume fraction.

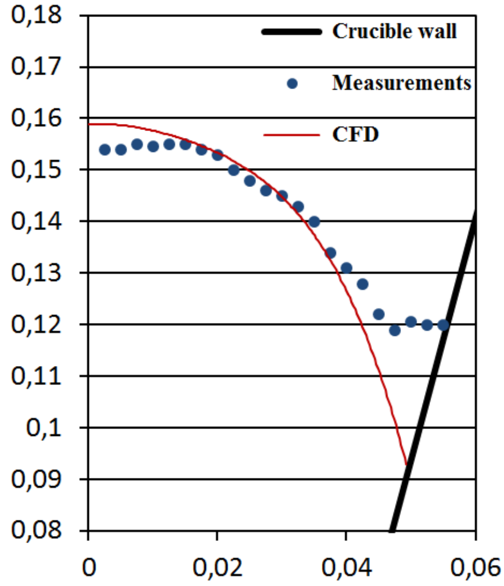

Figure 6. Comparison of measured and modelled meniscus for position C of an inductor.

Comparison between numerical analysis and experimental data was presented in "Figure 6". Red line denotes position of free surface for simulations, blue dots were obtained from measurements. CFD results are very accurate in the radius range of 0.02 m to 0.04 m from the crucible axis. There is a significant difference near wall of crucible. The reason of that is the oxidation process which occurs during experiment. Measurements were performed without atmosphere of inert gases and the products of the oxidation accumulated near the wall of crucible which leaded to flat area. In the numerical analysis chemical reactions were not modelled therefore oxides did not appear. There is also small difference between numerical and experimental results in the axis area. Metal melting process in crucible is very unsteady process, as a consequence, the free surface of liquid metal oscillating up and down. Hence, the results from measurements showed the field for a single given time instant while for numerical data it is average position of free surface over time.

5. SUMMARY

The aim of this work was to develop a validated coupled mathematical model of metal melting process in an induction furnace. The technology allows for the efficient removal of impurities, thus the purity of final material is very high.

Coupled numerical analysis was performed for three different positions of the inductor. Numerical results reflected experimental observations. The changes in the inductor position yielded different fields of Lorentz force in the examined material. It is necessary to perform velocity measurements of the liquid metal surface to completely validate numerical model.

REFERENCES

[1] T. Liu, Z. Dong, Y. Zhao, J. Wang, T. Chen, H. Xie, J. Li, H. Ni, D. Huo, 2012 “Purification of metallurgical silicon through directional solidification in a large cold crucible”, *Journal of Crystal Growth*, Vol. 355, pp. 145–150.

[2] V. Bojarevics, R.A. Harding, M. Wickins, 2003, “Experimental and numerical study of the cold crucible melting process”, *Proceeding of the Third International Conference on CFD in the Minerals and Process Industries*, CSIRO.

[3] J.H. Songa, B.T. Mina, 2005, “An electromagnetic and thermal analysis of a cold crucible melting”, *International Communications in Heat and Mass Transfer*, Vol. 32, pp. 1325-1336.

[4] S. Spitans, A. Jakovics, E. Baake, B. Nacke, 2010, “Numerical modelling of free surface dynamics of conductive melt in the induction crucible furnace”, *Magnetohydrodynamics*, Vol. 46, pp. 317-328.

[5] S. Spitans, A. Jakovics, E. Baake, B. Nacke, 2011, “Numerical modelling of free surface dynamics of melt in an alternate electromagnetic field”, *Magnetohydrodynamics*, Vol. 4, pp. 461-473.

[6] S. Spitans, A. Jakovics, E. Baake, B. Nacke, 2012, “Numerical modelling of free surface dynamics of melt in alternate electromagnetic field”, *Journal of iron and steel research international*, Vol. 19, pp. 531-535.

[7] J. Yang, R. Chen, H. Ding, J. Guo, J. Han, H. Fu, 2013, “Thermal characteristics of induction heating in cold crucible used for directional solidification”, *Applied Thermal Engineering*, Vol. 59, pp. 69-76.

[8] I. Quintana, Z. Azpilgain, D. Pardo and I. Hurtado, 2011, “Numerical Modeling of Cold Crucible Induction Melting”, *Proceedings of The COMSOL Conference*, Boston, USA.

[9] S. Golak, R. Przylucki, 2009, “A simulation of the coupled problem of magnetohydrodynamics and a free surface for liquid metals”, *WIT Transactions on Engineering Science*, Vol. 63, pp. 67-76.

[10] O. Pesteanu, E. Baake, 2011, “The Multicell Volume of Fluid (MC-VOF) method for the free surface simulation of MFD flows, Part I: Mathematical Model”, *ISIJ International*, Vol. 51, pp. 707-713.

[11] S. Matsuzawa, K. Hirata, T. Yoshimura, G. Yoshikawa, 2013, “Numerical analysis of cold crucible induction melting employing FEM and MPS method”, *IEEE Transactions on Magnetics*, Vol. 49, pp. 1921-1924.

[12] V. Bojarevics, K. Pericleous, 2004 “Modelling induction skull melting design modification”, *Journal of Materials Science*, Vol. 39, pp. 7245-7251.

[13] K. Adler, R. Schwarze, V Galindo, 2005, “Numerical modelling of the evaporation process of an electromagnetically stirred copper melt”, *Proceedings of the FLUENT CFD Forum 2005*, Bad Nauheim, Germany.

[14] L. Blacha, S. Golak, A. Jakovics, A. Tucs, 2014, “Kinetic analysis of aluminium evaporation from the Ti-6Al-7Nb alloy”, *Archives of Metallurgy and Materials*, Vol. 59, pp. 275-279.

[15] S. Golak, R. Przylucki, J. Barglik, 2014, “Determination of a mass transfer area during metal melting in a vacuum induction furnace”, *Archives of Metallurgy and Materials*, Vol. 59, pp. 287-292.

[16] T. Toh, H. Yamamura, H. Kondo, M. Wakoh, S. Shimasak, S. Taniguchi, 2007, “Kinetics Evaluation of Inclusions Removal during Levitation Melting of Steel in Cold Crucible”, *ISIJ International*, Vol. 47, pp. 1625-1632.

[17] A. Umbrasko, E. Baake, B. Nacke, A. Jakovics, 2008, “Numerical studies of the melting process in the induction furnace with cold crucible”, *COMPEL: The International Journal for Computation and Mathematics in Electrical and Electronic Engineering*, Vol. 27, pp. 359-368.

[18] R. Przylucki, S. Golak, B. Oleksiak, L. Blacha, 2012, “Influence of an induction furnaces electric parameters on mass transfer velocity in the liquid phase”, *Metalurgija*, Vol. 51, pp. 67-70.

[19] R. Przylucki, S. Golak, B. Oleksiak, L. Blacha, 2011, “Influence of the geometry of the arrangement inductor - crucible to the velocity of the transport of mass in the liquid metallic phase mixed inductive”, *Archives of Civil and Mechanical Engineering*, Vol. 11, pp. 171-179.

[20] S. Golak, R. Przylucki, 2010, “Inductor geometry modification for minimization of free surface shape area of melted metal”, *Przegląd Elektrotechniczny*, Vol. 86, pp. 310-312.

[21] S. Golak, R. Przylucki, 2008, “The optimization of an inductor position for minimization of a liquid metal free surface”, *Przegląd Elektrotechniczny*, 84, pp. 163-164.

Conference on Modelling Fluid Flow (CMFF'15)
The 16th International Conference on Fluid Flow Technologies
Budapest, Hungary, September 1-4, 2015

ANALYTIC SOLUTIONS OF HIGH-SYMMETRY GAS FLOW INDUCED BY SLOW DENSITY VARIATIONS

Andrei VEDERNIKOV[1], Daniyar BALAPANOV[2]

[1] Corresponding Author. Microgravity Research Centre, Université Libre de Bruxelles. Av. Franklin Roosevelt 50, CP 165/62, 1050 Brussels, Belgium. Tel.: +32 2 650 3128, Fax: +32 2 650 3126, E-mail: avederni@ulb.ac.be
[2] Microgravity Research Centre, Université Libre de Bruxelles. E-mail: dbalapan@ulb.ac.be

ABSTRACT

We present a method of analytical description of compressible fluid flows for the cases when the density variation time scale is much longer than the sound propagation characteristic time. Such variations may be resulted from time-dependent thermal boundary conditions, boundary motion and matter sources. The general solution for one-dimensional flow is obtained in homobaric approximation (low Mach number) and in assumption that the gas motion does not influence on the heat propagation (low Peclet number). The latter condition allows solving the energy equation independently. The mathematical model is closed by the mass conservation law and known equation of state. The gas velocity is expressed through the temperature, mass source terms and boundary motion laws.

This paper presents a set of analytic solutions considering various motion sources in different symmetries (central, axial and planar). The analytic solutions are validated by comparison with corresponding numerical solutions of full system of the conservation equations.

Keywords: analytic solution, low Peclet number, homobaric approximation, one-dimensional flows, microgravity, PIV

NOMENCLATURE

L	$[m]$	domain typical size
M	$[kg/mol]$	gas molar mass
R		the gas constant
T	$[K]$	temperature
j_i	$[kg/m^2/s]$	matter flux through i-th boundary
n	$[-]$	geometry factor, $0 \le n \le 2$
p	$[Pa]$	pressure
q_i	$[W/m^2]$	heat flux through i-th boundary
r	$[m]$	coordinate
r_i	$[m]$	location of the i-th boundary
t	$[s]$	time
u	$[m/s]$	gas velocity
λ	$[W/m/K]$	gas heat conductivity
ρ	$[kg/m^3]$	gas density
χ	$[m^2/s]$	gas heat diffusivity

Subscripts and Superscripts

EBT	equal boundary temperatures
i	boundary index, $1 \le i \le 2$
0	initial value
1	related to the 1st boundary
2	related to the 2nd boundary
·	time derivative
~	dimensionless variable

1. INTRODUCTION

Dynamics of compressible fluids deals with quick fluid density variation, characterized by high Mach number, and such phenomena as sound propagation, explosion and implosion, projectile aerodynamics, etc. since long time are the objects of extensive investigation. At the same time, gases by definition of their aggregate state assume existence of slow and nearly arbitrary density variation at low Mach number and thus practically uniform pressure.

This kind of gas flows, especially thermally-driven ones, can be found and in some cases play important role namely in microgravity experiments, because at normal gravity they are masked by natural convection. In microgravity there is no preferred direction in space and flows show high symmetry which simplifies their mathematical description and gives opportunity of finding analytical solutions facilitating quick analysis of the dependences on the task parameters, relative importance of the sources of gas motion.

For practical demonstration, one can refer to numerous experiments aimed at investigation of dust agglomeration in astrophysical processes mostly related to proto-planetary matter formation [1].

Similar conditions take place in the investigation of complex plasma. In both cases, the typical parameters are like the following. Micron-sized particles float in a rarefied gas at temperature of about 300 K and pressures between 50 and 200 Pa.

The centrosymmetric gas temperature variation is created as a component of thermal field in the volume of the thermophoretic trap developed within the European Space Agency project Interaction in Cosmic and Atmospheric Particle Systems, ICAPS [2]. The heaters are the rings that modulate directly the temperature of the gas with high rate (up to 500 K/s).

Most of the examples are related to the particles floating in the gas. Modern methods of particle tracking velocimetry provide high resolution of particle displacement measurements, routinely of the order of micrometre per second. As tracers, the particles may visualize the gas flow pattern. On the other hand, the particles may be subjected to the force under investigation, particularly, in various realizations of phoretic phenomena.

In some of the mentioned examples, the solution may be written straightforward after formulation of the problem, in many other cases it requires certain effort.

2. GOVERNING EQUATIONS

This paper considers highly symmetric flows having a single non-zero velocity component along some axis r. It can be a planar flow (n = 0), an axisymmetric flow (n = 1), or a centrosymmetric flow (n = 2). The flow domain $r_1(t) \le r \le r_2(t)$ is limited by the boundaries (see Figure 1), generally, in the state of displacement. The boundary r_1 may physically disappear being transformed into an element of symmetry at r_1 = 0.

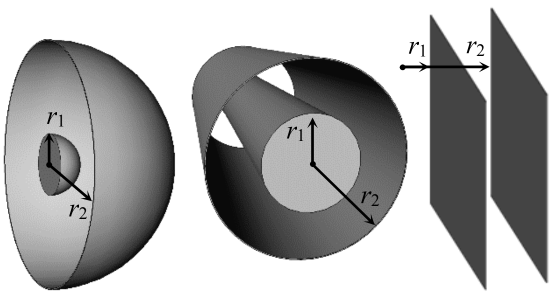

Figure 1. Example domains: (from left to right) in case of a centrosymmetric flow, in case of a planar flow and in case of an axisymmetric flow.

The system under consideration may be thermodynamically open. Generally, it contains volumetric heat sources and matter sources due to chemical reactions, phase transition, radiation sources, etc. as well as heat and matter fluxes through the boundaries.

The mathematical model of the flow is based on the following assumptions:

a) The convective heat transfer is negligible in comparison with the conductive one, i.e. the Peclet number is low: $Pe = uL/\chi << 1$. This assumption results in decoupling of the energy equation from the rest equation system.

b) The typical velocity is small in comparison with the sound speed c in the gas (Mach number $\mathrm{M} = u/c << 1$). As a result, the pressure can be treated as uniform $p = p(t)$. It is often denoted as “homobaric approximation”.

c) In the energy equation, the term responsible for the gas heating due to deformation can be neglected in comparison with the heat conduction term since $pu/L << \rho c_V \Delta T f$, where c_V is the isochoric specific heat and ΔT is characteristic temperature difference. Parameter f denotes the frequency of the periodic component or the inverse characteristic time in boundary conditions.

d) Viscous dissipation has negligible contribution to the internal energy variation in comparison with the heat conduction, which means that the Brinkman number is low: $Br = \mu u^2 / \lambda \Delta T << 1$, where μ is the dynamic viscosity.

e) The heat propagation is quasi-steady, i.e. the temperature profile establishes instantaneously on time variation of the boundary conditions or the heat source. In other words, the Fourier number is high: $\mathrm{Fo} = \chi / fL^2 >> 1$.

f) The thermo-physical properties of the gas are constant.

The equation of state is the one of the ideal gas

$$p = R\rho T/M \tag{1}$$

On application of the assumptions a) and c)-e), the energy equation reduces to the Poisson equation describing quasi-steady heat propagation

$$\frac{\chi}{r^n}\frac{\partial}{\partial r}\left(r^n \frac{\partial T}{\partial r}\right) = -Q \tag{2}$$

at, generally, time-dependent boundary conditions

$$\begin{aligned} T\big|_{r=r_1(t)} &= T_1(t) \quad \text{or} \quad -\lambda \nabla T\big|_{r=r_1(t)} = \underline{q}_1(t); \\ T\big|_{r=r_2(t)} &= T_2(t) \quad \text{or} \quad -\lambda \nabla T\big|_{r=r_2(t)} = \underline{q}_2(t) \end{aligned} \tag{3}$$

and time-dependent heat source term $Q(r,t)$. Eqs. (2)-(3) are solved independently from the others and give the temperature distribution in the gas.

T_1 and T_2 denote the actual temperatures on the boundaries $T(r_1,t)$ and $T(r_2,t)$ respectively; even for the boundary conditions of the second type.

The mass conservation law demands the whole mass of the gas within the boundaries to be equal to the initial gas mass plus the mass produced by the matter sources during the time interval from 0 to t:

$$\int_{r_1(t)}^{r_2(t)} \xi^n \rho(r,t)\,d\xi = \int_{r_1(0)}^{r_2(0)} \xi^n \rho(r,0)\,d\xi + \int_0^t S(\tau)d\tau \tag{4}$$

where

$$S(t) = I_J(r_2,t) + r_1^n j_1(t) - r_2^n j_2(t) \tag{5}$$

is the cumulative matter source intensity. In Eq. (5) j_i are the projections of $\underline{j}_i$ on the r-axis. Following three auxiliary functions are used here and further to shrink the equations:

$$I(r,t) = \int_{r_1(t)}^{r} \frac{\xi^n d\xi}{T(\xi,t)};$$
$$I_t(r,t) = \int_{r_1(t)}^{r} \frac{\dot{T}(\xi,t)\xi^n d\xi}{T^2(\xi,t)}; \tag{6}$$
$$I_J(r,t) = \int_{r_1(t)}^{r} J(\xi,t)\xi^n d\xi$$

The gas density in Eq. (4) can be expressed through gas pressure and known temperature using Eq. (1). The pressure comes out the integral operator because it does not depend on the coordinate and can be thus written explicitly:

$$p(t) = \frac{p_0}{I(r_2,t)}\left(I(r_2,0) + \frac{R}{p_0 M}\int_0^t S(\tau)d\tau \right) \tag{7}$$

Further on the arguments are omitted, i.e. $u(r,t) \equiv u$, $T_I(t) \equiv T_I$, $p(t) \equiv p$, etc., if not to highlight their particularity.

According to the differential form of the mass conservation law, the time derivative of the mass of a fixed material volume equals to the sum of instantaneous matter source intensities within this volume:

$$\frac{d}{dt}\int_{r_1}^{r} \xi^n \rho d\xi = r_1^n j_1 + I_J \tag{8}$$

Application of the Leibniz rule to Eq. (8) gives

$$\int_{r_1}^{r} \xi^n \dot{\rho} d\xi + r^n \rho u - r_1^n \rho(r_1,t)\dot{r}_1 = I_J + r_1^n j_1 \tag{9}$$

where we took into account that $\dot{r} \equiv u$ is the velocity in arbitrary point of the fluid volume that we need to find. Hereinafter the dot above a variable denotes the time derivative operation applied to the variable.

From Eqs. (1) and (9) the general solution for the velocity $u(r,t)$ can be retrieved, where the volume of mass conservation is chosen between the internal boundary $r_1(t)$ and the imaginary moving surface with coordinate r.

$$u = \frac{T}{r^n}\left\{ \frac{r_1^n}{T_1}\dot{r}_1 + I_t + \frac{R}{pM}\left(r_1^n j_1 + I_J\right) - \left[\frac{r_1^n}{T_1}\dot{r}_1 - \frac{r_2^n}{T_2}\dot{r}_2 + I_t(r_2,t) + \frac{RS}{pM} \right]\frac{I}{I(r_2,t)} \right\} \tag{10}$$

where S is given by Eq. (5).

Eq. (10) defines the gas velocity in arbitrary point with coordinate r, in the gas having temperature profile $T(r,t)$. It is important to note that limitations a)-f) should be valid in the volume, to which the mass conservation law is applied. Far away from the chosen volume, the geometry and motion parameters as well as sources distribution may substantially deviate.

The gas motion is a result of the displacement of the two boundaries, of the temperature variation and gas sources on both boundaries, and of the volumetric gas production intensity. The gas may contain dispersed second phase in the form of droplets or solid particles that may influence on the temperature profile between the boundaries and on the gas production intensity. Space distribution of the second phase should not necessarily be uniform and external agents like irradiation may modulate the temperature profile and gas production intensity.

As it was said above the model comprises several driving forces of gas motion, and there are particular cases for the external boundaries at infinity or internal boundary reduced to an element of symmetry. The solutions are quite different for different dimensionality n = 0, 1, or 2. As a result, there may be created nearly 500 combinations of sources (active or not) For particular combinations of sources, we present in the following section the exact and approximate analytical solutions along with the numerical results and comparative analysis.

3. TYPICAL FLOWS

In the present section the known solutions (see, for example, [3]) of Eqs. (2)-(3) with time-dependent boundary conditions in closed domains with static boundaries ($0 < r_1 \le r \le r_2$) are used to find the gas velocity field using the developed theoretical approach. Solutions are obtained for all three considered geometries (planar, axisymmetric and centre-symmetric). Gas motion created by moving boundaries and inflows/outflows through the boundaries is also considered. Exact analytical solutions and approximations are obtained.

3.1. Thermal boundary condition variations

This subsection is devoted to the problem of gas motion between two non-moving boundaries when one or two boundary conditions change in time. Due to relative simplicity of the quasi-static temperature distribution, it appeared possible to obtain exact analytical solutions for the gas velocity in all considered statements.

Virtually all of obtained solutions contain reciprocal $T_2 - T_1$ term that produces a singularity at equal boundary temperatures. Limit expressions at $T_1 \to T_2$ were found and it was realized that these expressions can be used as natural approximations of corresponding solutions if a condition of small temperature variation: $|1 - T_1/T_2| << 1$ is fulfilled at the studied time instant. This approximation is mentioned in further text as Equal Boundary Temperatures (EBT) approximation. The EBT-approximation of the velocity contains only T_2 since it is $T_1 \to T_2$ limit, but to improve the accuracy T_2 can be replaced by the volume averaged (or another reference) temperature.

3.1.1. Planar flow (*n* = 0)

Consider a gas motion between two parallel plates $r = r_1$ and $r = r_2$ having time-dependent temperatures $T_1(t)$ and $T_2(t)$. The distance between the plates is a sole possible typical length L. Assume $Q(r, t) = 0$, then the temperature distribution for Eqs (2)-(3) in the planar gap $r_1 \le r \le r_2$ is a linear function of r:

$$T = \frac{r - r_1}{L} T_2 + \frac{r_2 - r}{L} T_1 \tag{11}$$

From Eqs. (7) and (10) the pressure and the velocity are following:

$$\begin{aligned} p &= p_0 \frac{T_2 - T_1}{\ln T_2/T_1} \frac{\ln T_{20}/T_{10}}{T_{20} - T_{10}}; \\ p_{EBT} &= p_0 \frac{T_2}{T_{20} - T_{10}} \ln \frac{T_{20}}{T_{10}} \end{aligned} \tag{12}$$

$$\begin{aligned} u &= \frac{\dot{T}_2/T_2 - \dot{T}_1/T_1}{T_2 - T_1} L \left(\frac{\ln T/T_1}{\ln T_2/T_1} T - \frac{r - r_1}{L} T_2 \right); \\ u_{EBT} &= \frac{\dot{T}_2 - \dot{T}_1}{2T_2} \frac{r - r_1}{L} (r - r_2) \end{aligned} \tag{13}$$

Hereinafter T_{i0} designate the initial value of T_i.

Eqs (12)-(13) can be used as a solution for any type of thermal boundary condition replacing T_1 and T_2 by $T(r_1,t)$ and $T(r_2,t)$. The velocity profile in the coordinate system $x = (r - r_1)/L$ attached to the boundaries is scalable by the distance between the boundaries. It means that velocity x-profile for certain value of L can be derived from another profile at the same boundary conditions just by multiplication by the gap widths ratio.

As it will be proved in the end of the section the velocity sign at a time instant does not depend on the coordinate, i.e. the whole gas flows in the same direction. The velocity profile has single extremum whose location coincides neither with the domain center nor with the location of the zero of the temperature derivative by time:

$$r(u_{\max}) = r_1 + L \frac{T_1}{T_2 - T_1} \left\{ \exp\left(\frac{T_2}{T_2 - T_1} \ln \frac{T_2}{T_1} - 1 \right) - 1 \right\} \tag{14}$$

At $T_1 \to T_2$ the velocity extremum is located right in the middle of the region: $r(u_{\max}) - r_1 = L/2$. The extreme velocity value within the domain is:

$$\begin{aligned} u_{\max} = \frac{\dot{T}_2/T_2 - \dot{T}_1/T_1}{T_2 - T_1} T_1 L \Bigg\{ \frac{T_2}{T_2 - T_1} - \\ \exp\left(\frac{T_2}{T_2 - T_1} \ln \frac{T_2}{T_1} - 1 \right) \Bigg\} \end{aligned} \tag{15}$$

The velocity extremum is linearly proportional to the distance between the boundaries.

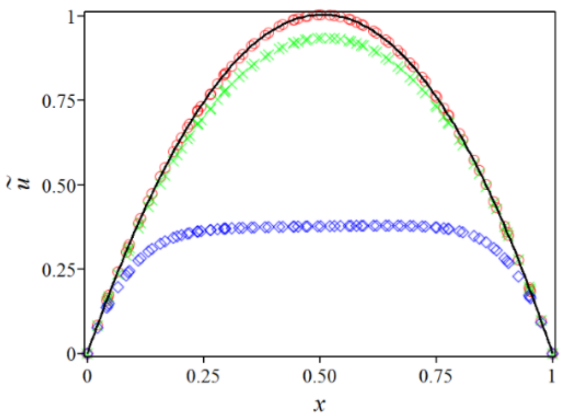

Figure 2. Comparison of the analytical (solid line) and three numerical solutions: at Fo = 10 (red circles), Fo = 1 (green crosses), and Fo = 0.1 (blue diamonds) in case of linear wall temperature variations.

On Figure 2 a comparison between numerical and analytic solutions in case of linear wall temperature variation $T_1 = T_0 + At$, $T_2 = T_0 - At$ is presented. The velocity is normalized by its initial maximum value $u_{\max}(t=0)=AL/4T_0$ and the dimensionless coordinate is $x=(r-r_1)/L$. One can show that in this statement the normalized velocity is completely defined only by x and dimensionless time $\tau=At/T_0$. The velocity profiles on Figure 2 are obtained for $\tau = 1/15$. The solution is defined at $\tau < 1$ because at $\tau = 1$ T_2 becomes zero and there the velocity has a singularity point. The velocity maximum moves to the right wall when $\tau \to 1$.

The numerical simulation is done for a set of values of the Fourier number defined as $\mathrm{Fo}=\chi T_0/AL^2$ and it is seen how the model loses its validity with growth of Fourier number.

ANSYS Fluent software was used for the CFD calculations and Gmsh software [C. Geuzaine and J.-F. Remacle, 2009] was used for meshing.

3.1.2. Axisymmetric flow (n = 1)

Let us consider a similar problem statement to the previous one in the axisymmetric geometry (n = 1). The general solution for the temperature distribution is:

$$T=\frac{\ln r/r_1}{\ln r_2/r_1}T_2+\frac{\ln r_2/r}{\ln r_2/r_1}T_1 \tag{16}$$

Explicit expressions for pressure and velocity through the boundary conditions are:

$$p=p_0\frac{T_2-T_1}{T_{20}-T_{10}}\frac{E(r_2,0)-E(r_1,0)}{E(r_2,t)-E(r_1,t)}\times \left(\frac{r_2}{r_1}\right)^{2\left(\frac{T_1}{T_2-T_1}-\frac{T_{10}}{T_{20}-T_{10}}\right)} \tag{17}$$

$$u=\frac{\dot T_2/T_2-\dot T_1/T_1}{T_2-T_1}\frac{\ln r_2/r_1}{\left(E(r_2,t)-E(r_1,t)\right)r}\times \Big[\left(r_2^2T_1-r_1^2T_2\right)E(r,t)T+\left(r^2T_2-r_2^2T\right)E(r_1,t)T_1+\left(r_1^2T-r^2T_1\right)E(r_2,t)T_2\Big] \tag{18}$$

where $E(r,t)=\mathrm{Ei}\left(\frac{2T(r,t)}{T_2(t)-T_1(t)}\ln\frac{r_1}{r_2}\right)$ and Ei(x) is the exponential integral function of a real argument.

Eqs (17)-(18) can be used as a solution for any boundary condition with T_1 and T_2 replaced by corresponding $T(r_1,t)$ and $T(r_2,t)$.

The general properties of the velocity distribution is similar to the plane case (n = 0).

Equal boundary temperature approximations for the velocity and pressure are:

$$\begin{aligned}u_{EBT}&=\frac{\dot T_2-\dot T_1}{2T_2r}\left[\frac{r_1^2r_2^2}{r_2^2-r_1^2}-\frac{r^2\left(r_1^2\ln r/r_1+r_2^2\ln r_2/r\right)}{\left(r_2^2-r_1^2\right)\ln r_2/r_1}\right]\\ p_{EBT}&=\frac{2p_0T_2}{T_{20}-T_{10}}\frac{r_2^2\ln r_2/r_1}{r_2^2-r_1^2}\times\left(E(r_2,0)-E(r_1,0)\right)\left(\frac{r_2}{r_1}\right)^{-\frac{2T_{10}}{T_{20}-T_{10}}}\end{aligned} \tag{19}$$

Figure 3 presents velocity profiles obtained for the problem statement identical to that in the subsection 3.1.1. The same approach of non-dimensionalization is used. Comparison of Figures 2 and 3 shows that the exteremum of the velocity distribution in the axisymmetric case is significantly shifted from the cell center as compare to the velocity distribution in the planar geometry. The shift depends on the cell geometry: the closer r_1 to zero the more the extremum is shifted, and the closer the walls to each other the less is the maximum shift. Also, the residual between exact solution and EBT-approximation is more significant in the axially-symmetric case.

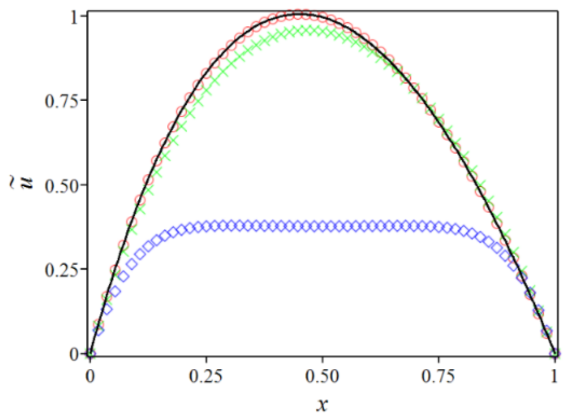

Figure 3. Comparison of the analytical (solid line) and three numerical solutions (red circles Fo=10, green crosses Fo=1, and blue diamonds Fo=0.1) in case of linear wall temperature variation. Axisymmetric flow.

3.1.3. Centrosymmetric flow (n = 2)

The general solution of the quasi-steady heat equation in spherical symmetry with first type boundary conditions is:

$$T=a+\frac{b}{r};\qquad a=\frac{r_2T_2-r_1T_1}{L};\quad b=r_1r_2\frac{T_1-T_2}{L} \tag{20}$$

where L is the distance between the boundaries.

In this subsection the solutions are expressed imlicitly through the auxiliary functions Eq. (6):

$$I=\frac{r^3-r_1^3}{3a}-b\frac{r^2-r_1^2}{2a^2}+b^2\frac{r-r_1}{a^3}-\frac{b^3}{a^4}\ln\frac{rT}{r_1T_1};$$

$$\begin{aligned}I_t&=\frac{\dot a}{a^2}\frac{r^3-r_1^3}{3}+\left(\frac{\dot b}{2}-\frac{b\dot a}{a}\right)\frac{r^2-r_1^2}{a^2}+\\&\left(\frac{3b^2\dot a}{a}-2b\dot b\right)\frac{r-r_1}{a^3}+\left(\frac{b^4\dot a}{a^4}-\frac{b^3\dot b}{a^3}\right)\frac{r-r_1}{r_1rT_1T}\\&+\left(\frac{3b^2\dot b}{a^4}-\frac{4b^3\dot a}{a^5}\right)\ln\frac{rT}{r_1T_1}\end{aligned} \qquad (21)$$

Eq. (10) yields following velocity distribution

$$u=\frac{T}{r}\left(I_t-\frac{I_t(r_2,t)}{I(r_2,t)}I\right) \qquad (22)$$

In the EBT-aproximation the pressure and the velocity have following simple form

$$\begin{aligned}p_{EBT}&=3p_0\frac{I(r_2,0)}{r_2^3-r_1^3}T_2;\\u_{EBT}&=\frac{\dot T_2-\dot T_1}{2T_2}\times\\&\frac{(r-r_2)(r-r_1)r_1r_2(r_1r_2+(r_1+r_2)r)}{(r_2^3-r_1^3)r^2}\end{aligned} \qquad (23)$$

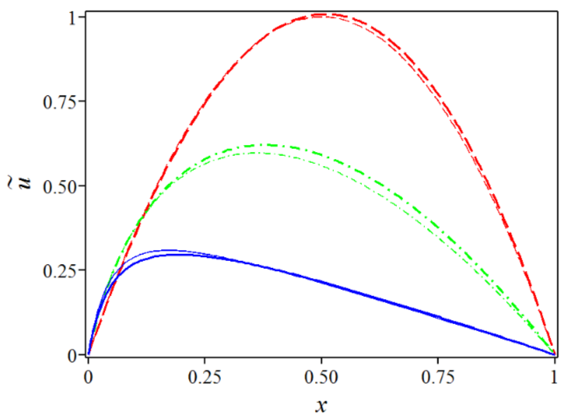

Figure 4. Comparison of the velocity distributions in planar case (dashed red line), in axisymmetric case (dash-dotted green line) and in centrosymmetric case (solid blue line) at similar boundary conditions. Thinned lines represent the EBT-approximations.

General properties of the velocity distribution are similar to the plane case (n = 0). It is seen from Figure 4 that the velocity profile at any n is always bell-shaped and do not have inflection points. The velocity maximum in the centrosymmetric case is shifted from the cell center even more than in the axisymmetric case. The velocity maximum decreases for higher n factor.

In addition, the EBT-approximation for each geometry is presented on Figure 4. The calculation is done again for the same statement described in the subsection 3.1.1. Corresponding value of the EBT-approximation validity criterion is $|1-T_1/T_2|=2/9$.

3.1.4. Velocity profile features

Solutions obtained in this subsection have one common property: the gas velocity at a certain instant of time has constant sign in the whole domain. In other words, there cannot be stagnant points, only in case when the velocity is zero everywhere. Let us prove this affirmation. The general solution for the velocity can be obtained from Eq. (10) by exclusion of the matter sources and boundary motion terms:

$$u=\frac{T}{r^n}\left(I_t(r,t)-I(r,t)\frac{I_t(r_2,t)}{I(r_2,t)}\right) \qquad (24)$$

where the multiplier T/r^n can be omitted as always positive one. We know that the velocity is zero at the boundaries. Therefore, to have no zeroes the velocity distribution should have not more than one extremum. Taking space derivative of the expression in the brackets in Eq. (24) and equating it to zero we obtain following condition:

$$\dot T=TC(t) \qquad (25)$$

where the function $C(t)$ is the ratio of the definite integrals in Eq. (24) and thus does not depend on coordinate. This equation has always only one solution due to monotonicity of the temperature by coordinate. It means that velocity has sole extreme that was need to be proved. Therefore, the gas moves in the same direction in the whole domain.

3.2. Boundary displacement and boundary mass sources

Supposing that the temperature is constant $T=T_0$ and there are no volumetric mass sources, the gas velocity driven by boundary mass sources comes from Eq. (10) as

$$\begin{aligned}u=\frac{1}{r^n}\Bigg\{&r_1^n\dot r_1+\frac{RT_0}{pM}\left(r_1^nj_1+I_J\right)-\\&\left[r_1^n\dot r_1-r_2^n\dot r_2+\frac{RT_0}{pM}S\right]\frac{r^{n+1}-r_1^{n+1}}{r_2^{n+1}-r_1^{n+1}}\Bigg\}\end{aligned} \qquad (26)$$

where S is defined in Eq. (5).

Boundary motion and boundary matter sources are identical for the generation of the gas motion and peculiarities of its pattern, with one note that the pressure should be calculated accordingly.

3.2.1. Boundary displacement

In absence of mass sources on the boundaries the pressure from Eq. (7) is:

$$p = p_0 \frac{r_{20}^{n+1} - r_{10}^{n+1}}{r_2^{n+1} - r_1^{n+1}} \tag{27}$$

where r_{10} and r_{20} are the boundary coordinates at t = 0. For the adiabatic approximation $p/p_0 = (\rho/\rho_0)^\gamma$

$$p = p_0 \left(\frac{r_{20}^{n+1} - r_{10}^{n+1}}{r_2^{n+1} - r_1^{n+1}} \right)^\gamma \tag{28}$$

Gas density in adiabatic case equals to that in isothermal case and the gas velocity in both cases is

$$u = \frac{\left(r^{n+1} - r_1^{n+1}\right) r_2^n \dot{r}_2 + \left(r_2^{n+1} - r^{n+1}\right) r_1^n \dot{r}_1}{\left(r_2^{n+1} - r_1^{n+1}\right) r^n} \tag{29}$$

It is always assumed that the boundary motion does not depend on pressure, temperature and gas velocity. It is easy then to combine moving boundaries and quasi-stationary heat conduction because in this case we have just to replace r_1 by $r_1(t)$ and r_2 by $r_2(t)$ in the expressions for p and u.

3.2.2. Boundary matter sources

In this paragraph, we consider the gas motion driven by the sources $j_1(t)$ and $j_2(t)$ on the boundaries in a closed domain with non-moving boundaries $r_1 \le r \le r_2$ and uniform temperature T_0. Practically such systems may be realized in a cavity with the some physico-chemical transformation on the walls, such as phase transition, absorption or catalytic reaction. In this case the pressure from Eq. (7):

$$p = p_0 + \frac{RT_0}{M} \frac{n+1}{r_2^{n+1} - r_1^{n+1}} \int_0^t \left[r_1^n j_1(\tau) - r_2^n j_2(\tau) \right] d\tau \tag{30}$$

Expressions for the gas velocity are the same as in the previous subsection.

In the illustrative case of the matter fluxes $j_1 = -j_2 = j$, equal by absolute value but oppositely directed we have

$$u = \left(\frac{jRT}{pM} \right) \left[\frac{(r_1 + r_2) r_2^n r_1^n - \left(r_1^n + r_2^n\right) r^{n+1}}{\left(r_2^{n+1} - r_1^{n+1}\right) r} \right] \tag{31}$$

The velocity profiles for the illustrative case are shown on Figure 5. The velocity is normalized by division by jRT/pM. So normalized velocity depends only on x and a geometry factor $G = r_2/r_1$. The calculations are done at G = 5. When the latter is large, in the second statement at n = 1 and n = 2, the dimensionless velocity profile in the almost the whole domain is described by linear function with the slope -1 that is twice less than at n = 0. And when G tends to unity the dimensionless velocity profiles at n = 1 and n = 2 are identical to that at n = 0.

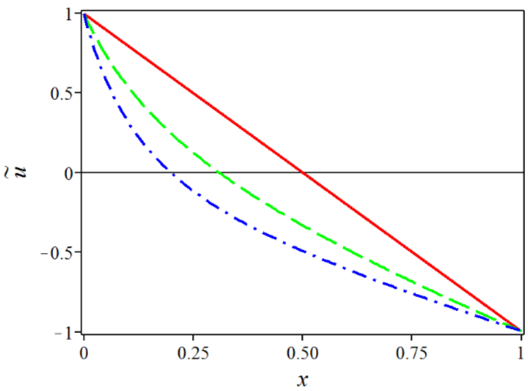

Figure 5. Profiles of the gas velocity in the case when $j_1 = -j_2 = j_0$ at n = 0 (solid red line), n = 1 (dashed green line) and n = 2 (dash-dotted blue line).

This kind of gas flow has a stagnant point (where u = 0), whose location is found from

$$x(u=0) = \frac{G^n}{G^n+1} \frac{G+1}{G-1} \left(\frac{G^{-n}+1}{G+1} \right)^{\frac{n}{n+1}} - \frac{1}{G-1} \tag{32}$$

5. CONCLUSIONS

In present work a mathematical model for the problem of one-dimensional fluid flow at low Mach and Peclet numbers has been developed and the general solution for the gas pressure and velocity has been obtained.

Particular solutions presented in the subsection 3.1 describe a gas flow in closed domains of different symmetry types at time-dependent thermal boundary conditions. An approximation for low temperature variation is obtained. It is found that under any conditions the gas moves in the same direction in the whole domain. The velocity profiles are similar for all the symmetries: they are bell-shaped and have always only extremum, location of which depends on the domain geometry. These analytic solutions are in excellent agreement with corresponding numerical solutions made in ANSYS Fluent software. The simulation are performed in a range of Fourier number to illustrate the area of the model applicability.

Gas flows driven by boundary matter sources and boundary motion are studied in the second block. The general solutions for arbitrary *n* are presented in isothermal statement. In case of inflows of equal intensity on the boundaries the location of the stagnant point is found. It is shown that in a large domain the velocity profile in the almost the whole domain is linear except a narrow zone near the internal wall.

The approach proposed allows obtaining reference analytical solutions to validate numerical methods in compressible fluid dynamics. The results are applicable in planning and processing of the experiments dealing with high accuracy measurements of the kinetic coefficients and particle transport properties, especially in microgravity conditions. A possibility to estimate gas creep component is important in bubble dynamics, aerosol physics, condensation/evaporation experiments, etc. The approach should be valuable in university coursework in fluid dynamics as it allows obtaining exact solutions and approximations for large variety of tasks using integral calculus.

ACKNOWLEDGEMENTS

ESA PRODEX program and the Belgian Federal Science Policy Office are greatly acknowledged.

REFERENCES

[1] Blum, J., et al., 2008, “Dust from Space,” *Europhysics News*, Vol. 39, pp. 27-29.

[2] Vedernikov, A., et al., 2012, “Cloud Manipulation System: Thermal Characterization and Drop Tower Experiment”, Proc. *63rd International Astronautical Congress,* Naples, Italy, IAC-12-A2.3.9.

[3] Carslaw, H. C., and Jaeger, J. C., 1959, *Conduction of Heat in Solids*, Oxford University Press.

[4] Geuzaine, C., and Remacle J.-F, 2009, “Gmsh: a three-dimensional finite element mesh generator with built-in pre- and post-processing facilities”, *International Journal for Numerical Methods in Engineering*, Vol. 79 (11), pp. 1309-1331.

Conference on Modelling Fluid Flow (CMFF'15)
The 16th International Conference on Fluid Flow Technologies
Budapest, Hungary, September 1-4, 2015

CALIBRATION OF ATP DAMPER'S MATHEMATICAL MODEL BY CFD SIMULATION

Siniša BIKIĆ[1], Maša BUKUROV[2], Robert-Zoltan SZASZ[3]

[1] Corresponding Author. Faculty of Technical Sciences, University of Novi Sad. Trg Dositeja Obradovića 6, 21000 Novi Sad, Serbia. Tel.: +381(21) 485 2397, Fax: +381(21) 454 026, E-mail: bika@uns.ac.rs
[2] Faculty of Technical Sciences, University of Novi Sad. E-mail: mbukurov@ uns.ac.rs
[3] Faculty of Engineering LTH, Lund University. SE-221 00, Lund, Sweden. E-mail: robert-zoltan.szasz@energy.lth.se

ABSTRACT

Dampers are used in HVAC (Heating Ventilation and Airconditioning) systems to control the air flow rate. Experimental studies confirmed that the moment (torque) characteristics of structurally altered dampers can be used for flow rate measuring. In this paper a mathematical model of an ATP (Air Torque Position) damper is presented. Such a damper measures air velocity indirectly by measuring the position of the blades and the moment of air acting on the blade. The considered damper is of square cross section, with a flat blade, and before and after the blade there are straight sections of pipeline, without local resistances. The calibration of the mathematical model of the damper was conducted by CFD (Computational fluid dynamics). CFD calibration would be applied for the purpose of validating the universal character of the developed mathematical model of the damper. The discretization of partial differential equations was done using the finite volume method; space discretization is done with unstructured polyhedral meshes, while the turbulence model was the standard k-ε model. Verification of the calibrated mathematical model was done experimentally. It was found that for several operating conditions the measurement error and the adequacy of the mathematical model for the case when it is calibrated by CFD is the same as in the case when it is calibrated using the experimental method.

Keywords: ATP damper, CFD, k-ε

NOMENCLATURE

A	[m^2]	cross section area
C_Q	[-]	flow coefficient,
D	[m]	diameter
F	[N]	force
G	[-]	correlation function
H	[m]	damper housing height
M	[Nm]	torque
R	[Ω]	electric resistance
$a, b,..h$	[m]	clearances between blade and damper housing
d	[m]	distance from the force point of attack D to blade axis C
g	[m/s^2]	gravitational constant
f	[m^2]	face surface
k	[J/kg]	turbulent kinetic energy
l	[m]	lever length
m	[kg]	mass
$\dot{m}$	[kg/s]	mass flow rate
r_f	[m]	position of face f relative to x_0
v	[m/s]	velocity
x	[m]	the longitudinal distance from the axle to the center of pressure
x_0	[m]	the point about which the moment is taken
y	[m]	the lateral distance from the axle to the center of pressure,

Greek symbols

α	[°]	angle of attack
δ	[m]	distance between center of axle and damper blade, normal to damper blade
Δ	[m]	distance between center of axle and damper blade, along to damper blade
Δv	[m/s]	difference between measured and modeled velocity
Δp	[Pa]	pressure difference
ε	[m^2/s^3]	turbulent dissipation
ρ	[kg/m^3]	air density
φ	[°]	angle of attack

Subscripts and Superscripts

I	first set of measurements
II	second set of measurements

a	longitudinal
c	contraction position
d	downstream position
f	face surface
h	hydraulic
l	lateral
n	normal
mer	measured
mod	modeled
p	pressure
u	upstream position
τ	shear

Abbreviations

ATP	Air Torque Position
HVAC	Heating Ventilation Air Conditioning

1. INTRODUCTION

An ATP damper (Air Torque Position) is a device that measures air velocity indirectly by measuring the blade angle of attack α and the air stream moment M acting on the blade, Figure 1:

$$v = f(M, \alpha) \tag{1}$$

The ATP damper concept comes from scientists' aspiration to predict the moment characteristics of butterfly valves. Initially, researchers predicted the moment characteristics of butterfly valves theoretically [1-4].

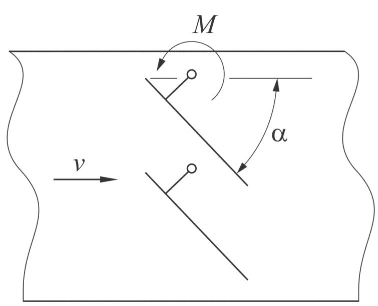

Figure 1. Operating parameters of ATP dampers

The first author who conducted experimental verification of the mathematical model of the moment characteristic of butterfly valve was Sarpkaya [5, 6]. Sarpkaya developed and verified the mathematical prediction model for the moment characteristic of a butterfly valve with a thin blade under the assumption that the air flow is irrotational and incompressible. Hasennpflug [7] corrected Sarpkaya's mathematical model using the theory of potential flow. Morris et al, [8] developed a mathematical model of the moment characteristic of the butterfly valve that takes into account the compressibility of the fluid.

Most of the knowledge about the prediction of the moment characteristic of the actuator element in a butterfly valve for the purpose of development of an ATP damper is based on the work of Federspiel [9]. He expanded the mathematical models of Sarpkaya and Hasennpflug for cases with several blades and when the axis of rotation is shifted from the axis of the blade in its longitudinal and transversal direction [9]. During the development of the mathematical model, Federspiel considered the case of irrotational and incompressible flow of air around a single blade damper, Figure 2. Since the velocities encountered are well below the sound speed, the mathematical modeling with the assumption of incompressible flow is acceptable for HVAC systems.

The mathematical model was developed on the basis of the continuity, Bernoulli and the momentum equations. Dampers on HVAC systems may be installed in three ways:

- with a straight pipe section positioned in front of a damper placed at the end of the pipeline;
- with a straight pipe section positioned after a damper placed at the entrance of the pipeline and
- with straight pipe sections positioned both in front of and behind the damper.

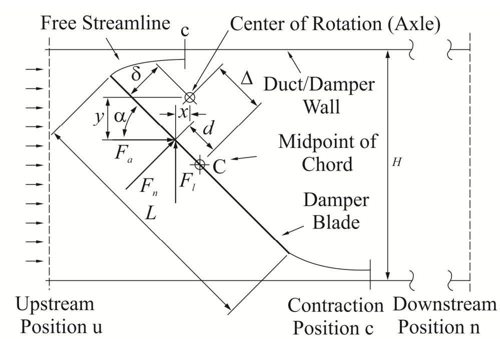

Figure 2. Schematic representation of ATP damper with single blade 'after]9]'

For all three possible positions of dampers in HVAC systems, Federspiel came to the same correlation between the air velocity directly in front of the damper, v, the angle of attack of the blade, α, and the moment of the air stream acting on the blade, M:

$$v|v| = G^2(\alpha)\frac{2M}{\rho A_u D_h} \tag{2}$$

By measuring the pressure and temperature of the air stream directly in front of the blade of the ATP damper, the density of the air stream ρ can be calculated from the equation of state of an ideal gas. In this way the air velocity can be measured with the ATP damper at different operating conditions.

The correlation function in equation (3) is as follows:

$$G(\alpha)=\left(\frac{D_h}{\frac{y}{C_{Q,a}^2}+\frac{x}{C_{Q,l}^2\cdot tg\alpha}}\right)^{\frac{1}{2}} \tag{3}$$

where: α represents the blade angle of attack, x is the longitudinal distance from the axle to the center of pressure, y is the lateral distance from the axle to the center of pressure, $C_{Q,a}$ is the longitudinal flow coefficient and $C_{Q,l}$ is the lateral flow coefficient.

Federspiel verified the mathematical model shown in Eq.(2) for a damper with the following characteristics: a square cross-section 0.61x0.61 m sides, with straight pipe section after the damper located at the entrance of the pipeline and with four oppositely driven straight blades (cascading blades). He verified the mathematical model that can be used for accurate measuring of the air velocity under different operating conditions. The difference between the measured and modeled velocity was ±10% of the measured velocity or ±5% of the full scale. He also found that, when ATP dampers are opened more than 70%, local resistance in front of the damper bears a significant impact on the accuracy of the measurement and applicability of the mathematical model [10].

Federspiel came up with a mathematical model of the ATP damper which has a potentially universal character. In order to confirm the universal applicability of the mathematical model, it is necessary to verify the mathematical model for dampers of different cross section, shape and number of blades and the manner of blade driving. It should also be investigated how the applicability of the mathematical model is influenced by the position of the damper in the system, damper hysteresis and local resistances in front of and behind the damper.

There is no doubt that the investigation of the universal character of the developed mathematical model of ATP damper requires more research. The authors believe that for further development of ATP dampers one should reduce the share of the experiments, and increase the share of computational fluid dynamics to reduce development costs. From that standpoint it is important to assess the possibility to apply computational fluid dynamics in the development of ATP dampers.

Computational fluid dynamics would be applied for the purpose of validating the universal character of the developed mathematical model of the damper. The aim of this paper is to calibrate the existing mathematical model of the ATP damper with the results of numerical simulations. Furthermore, the calibrated model will be validated by experimental measurements.

The damper used in this research was an ATP damper with one blade of square cross section, located between two straight pipeline sections, without local resistance. The number of blades being two, they cannot be assumed to form a cascade as it is often used in HVAC systems.

The clearances between the blades and damper housing used in the mesh of the numerical model of the ATP damper are sized to be realistic.

2. MATERIALS AND METHODS

2.1 Experimental setup

In order to validate the results of the CFD simulations used to calibrate the mathematical model (2) of the ATP damper a set of experiments have been carried out.

In the Laboratory of Fluid Mechanics at the Faculty of Technical Sciences of the University in Novi Sad, a laboratory facility for ATP damper testing was set up, according to the recommendations provided by the standard [11] for testing of dampers for the control of air flow rate in HVAC systems.

The measurement of air flow velocity was done with a hot wire anemometer; moment measurement was done with moment meter while the measurement of the blade angle of attack was done with a rotary potentiometer, Figure 3.

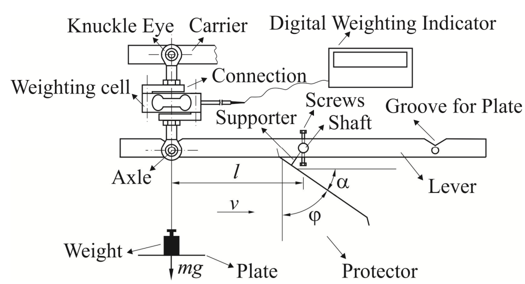

Figure 3. Schematic diagram of the ATP damper test rig

The moment meter is formed with a lever arm of length l=100 mm, mass m weighing cell manufactured by "HBM" model PW4MC3 (accuracy Class C3 and 0.5 g minimum resolution) and scaling electronics manufactured by "HBM" model WE2110 (classes 6000 d and measuring range from 0 to 3.5 mV/V) to display the measured moment M, Fig. 3. The blade is rigidly attached to the shaft, the shaft is bolted rigidly to the lever, and the lever is rigidly connected with a spherical joint to the weighing cell. In this way, the moment M of air acting on the blade is transferred to the moment meter.

The calibration of the moment meter is done with weights of known mass Fig. 3. Since the weighing cell for mass measurement has linear characteristic, the resulting characteristic of the moment meter is also linear, Figure 4.

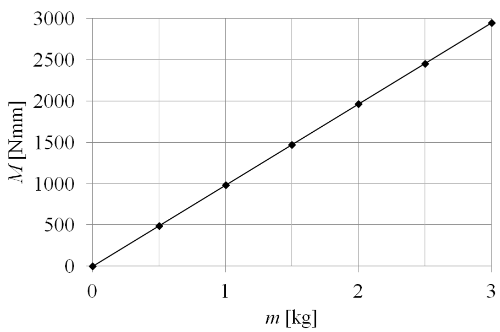

Figure 4. Calibration curve of the moment meter for lever arm length *l*=100 mm

In order to measure the damper blade angle of attack, a rotary potentiometer manufactured by "Dada electronics" model Tyco 10 (measuring range from 0 to 10 kΩ) and a digital multimeter were used. The rotary potentiometer was calibrated in accordance with the protractor that monitors the position of the blade with the rotation axis displaced from the axis blade, Figure 5. The blade position can be defined by the angle α (position of the blade defined in relation to the horizontal direction), or angle φ (position of the blade defined in relation to the vertical direction). According to Fig. 5, the sum of these two angles is 90°.

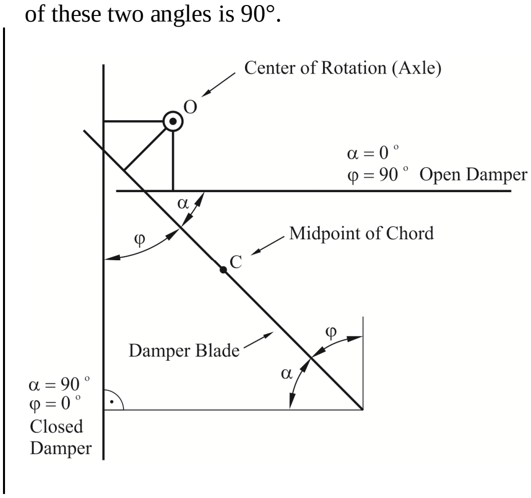

Figure 5. The ATP damper blade angle of attack with the axis of rotation displaced from the axis of the blades

The blade angle of attack α was used to measure the position of the blade. Figure 6 presents the formed protractor to measure the blades angle of attack of the ATP damper.

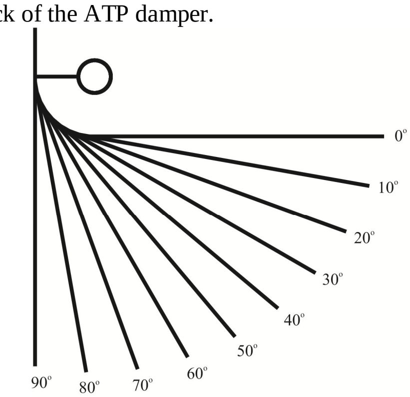

Figure 6. Appearance of the protractor formed for the purpose of measuring the blade angle of attack of the ATP damper

During the calibration of the rotary potentiometer, a 30° shift of potentiometer shaft was made and the field of non-linear characteristic of the potentiometer was abandoned. In this way, an approximately linear relationship between the blade angle of attack α and electric resistance of the rotary potentiometer R was achieved, Figure 7.

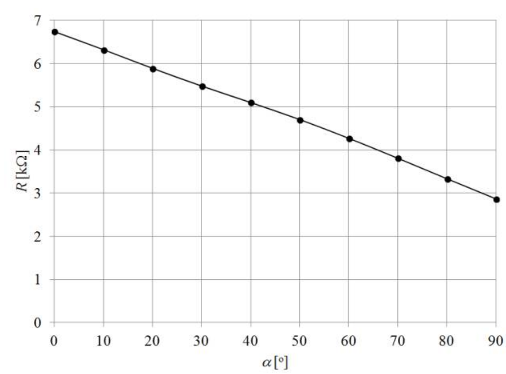

Figure 7. Typical calibration curve of the rotary potentiometer

The air velocity was measured with a hot wire anemometer manufactured by "Testo", model 425 (accuracy ± [0.03% + 5% of measured velocity]) with a one point method, in line with recommendations provided by the standard [12].

In front of the blade of the ATP damper sensors were placed to measure pressure and temperature. Based on the measured air pressure and temperature from the equation of state of an ideal gas the air density is determined. In the mathematical model of ATP damper (2) the compensation of air velocity for different operating conditions is done with the term for the air density.

Atmospheric pressure p_a was measured by a digital barometer manufactured by "PCE", model

THB 38 (with uncertainty of ±1.5% of measuring range up to 1000 mbar and ± 2% of the measuring range above 1000 mbar).

The measurement procedure was as follows. First, the laboratory facility was turned on, the fan unit was set to the desired air flow velocity. After reaching stationary air flow conditions, air temperature, gauge pressure, air velocity, atmospheric pressure and moment were measured.

Two independent series of measurements of ATP damper operating parameters at different operating conditions were performed. The air velocity ranged from 0 to 10 m/s, while the measurement range of the blade angle of attack was from 0 to 90°.

2.2 Laboratory ATP damper

The considered damper is of square cross section, with a flat blade, and before and after the blade there are straight sections of pipeline, without local resistances. The damper blades were made of aluminium. Their dimensions are presented in Figure 8.

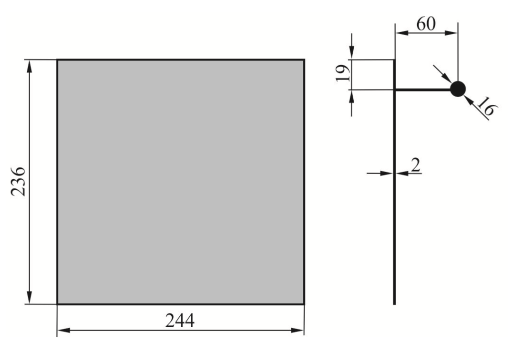

Figure 8. Dimensions of ATP damper blades

Figure 9 shows the dimensions of the clearances between the blade and the wall of the ATP damper.

Table 1. The clearance sizes between blade and damper housing in horizontal direction

α [°]	a [mm]	b [mm]	c [mm]	d [mm]
0	2.88	3.62	1.63	2.37
10	2.89	3.61	1.48	2.52
20	2.92	3.58	1.35	2.66
30	2.95	3.55	2.73	4.27
40	3.11	3.64	2.63	4.37
50	3.15	3.60	2.55	4.45
60	3.19	3.56	2.50	4.50
70	3.23	3.52	2.22	4.27
80	3.28	3.47	2.23	4.28
90	3.32	3.43	2.38	4.37

The clearance sizes for each blade angle of attack were obtained by measuring and are presented in Tables 1 and 2.

It can be noted that the physical model is asymmetric according to these values. The asymmetry of the physical model is due to its imperfect manufacturing and asymmetrical position of blades relatively to the axis of the channel.

Table 2. The clearance sizes between blade and damper housing in vertical direction

α [°]	e [mm]	f [mm]	g [mm]	h [mm]
0	82	83	168.24	167.26
10	77.79	78.76	131.48	130.51
20	71.83	72.81	97.7	96.72
30	64.34	65.31	67.91	66.94
40	55.65	56.63	43.03	42.05
50	45.79	46.77	23.8	22.82
60	35.18	36.13	10.81	9.84
70	24.15	25.12	4.71	3.74
80	12.67	13.65	5.19	4.22
90	2.14	3.11	12.61	11.64

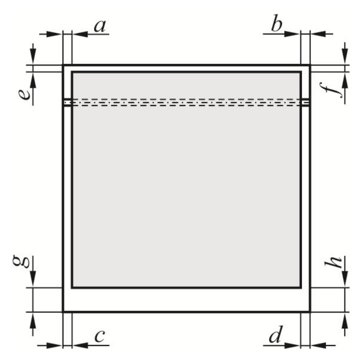

Figure 9. Dimensions of clearance between blade and ATP damper wall

2.3 Application of CFD

For the purposes of numerical simulation the commercial software package STAR CCM+ was used.

The work has been carried out in two stages. First the mathematical model (Eq. 2) has been calibrated. Two correlation functions, $G(\alpha)$, have been determined, one based on the first set of experimental data, and one based on numerical computations.

In the second stage, the correlation functions obtained experimentally and numerically were validated against a second, independent, set of experimental data. The algorithm of mathematical model calibration using the computational fluid dynamics and its experimental verification is shown in Figure 10. In Fig.10 the first set of measurements is denoted with the index I, while the second set of measurement is denoted with index II.

The boundaries of the numerical model are identical to the boundaries of the physical model, see Figure 11. The air flows through the channel and flows around the blade which is placed in a channel. The mass flow rate is set at the entrance to the channel, while at the exit of the channel it is assumed that the pressure difference is zero, Δp=0. Wall boundary conditions were set as smooth and no-slip. Boundary conditions for the turbulet quantities were set as: turbulent dissipation rate 0.1 m^2/s^3 and turbulent kinetic energy 0.001 J/kg.

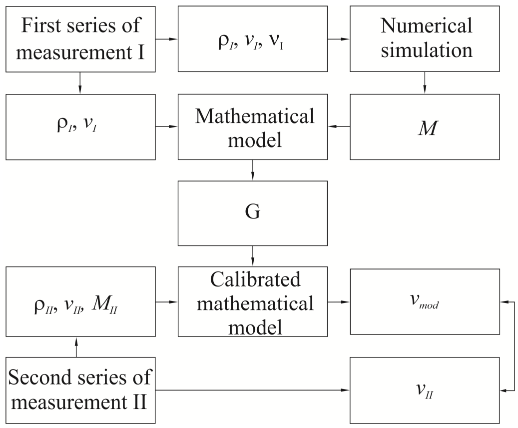

Figure 10. Algorithm of mathematical model calibration with the results of the numerical simulation and its experimental verification for one value of the blade angle of attack α

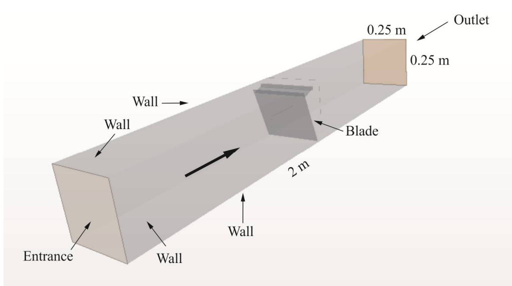

Figure 11. Boundaries of the mesh model

Space discretization is done with unstructured polyhedral meshes. Due to the observed asymmetry of the physical the whole geometry is taken into consideration. The parameters of the mesh were: number of cells 439180, average cell size 0.007 m, number of prism layers 2, prism layer stretching 1.5, prism layer thickness 0.0007 m, cell size close to the walls 0.00175 m and wall distance y+=3.4. The network model is formed so that it has the same clearance between the blade and damper housing like the physical model (Tab. 1 and Tab. 2).

The only approximation which was applied on the mesh model in relation to the physical model is the length of the straight sections of pipeline in front of and behind the blade. According to the recommendation of standards [11] this length should be 3 m and 2 m, in front of and behind the blade respectively for the physical model. The corresponding lengths of the straight sections for the mesh model were 1 m.

Discretization of the partial differential equations was done using the finite volume method while the turbulence model was the standard k-ε model. As in the derivation of mathematical model of the ATP damper (2), in the numerical simulation the air flow was treated as incompressible. In order to illustrate the flow of air through the ATP damper the velocity vector field is shown on the longitudinal plane obtained by numerical simulation for the air mass flow rate $\dot{m} = 0.21$ kg/s and for the blade angle of attack α=70^{o}, Figure 12. One can observe a pair of large scale recirculation zones developed downstream the blade. Furthermore, strong acceleration is seen at the clearances between the blade and the housing of the ATP damper.

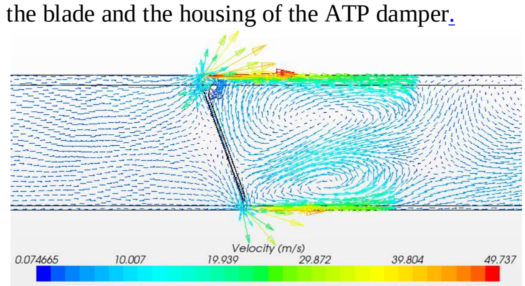

Figure 12. The velocity vectors field on the plane of symmetry for the air mass flow rate of 0.21 kg/s and for the blade angle of attack of 70 ^{o}

Two standard convergence criteria were selected for terminating the iterative procedure when the result is sufficiently accurate: the residues of iterative result and the magnitude of the physical property that is of interest.

According to the recommendation from the literature [13] the tendency was to keep the residues of iterative result in tolerance of 0.001.

As the physical property of interest, the airflow moment acting on a blade of ATP damper was observed. The moment of force on a surface about an axis is defined:

$$M = \sum_f \left[r_f x \left(F_{fp} + F_{f\tau} \right) \right] \cdot a \qquad (4)$$

where F_{fp} and $F_{f\tau}$ are the pressure and shear force vectors, a is a vector defining the axis through point x_0 about which the moment is calculated and r_f is the position of the face relative to x_0. This quantity was computed using the inbuilt functions in the flow solver.

In line with the literature, the result of the physical property of the interest was significantly smaller than 1% between the two last iterations [13].

We have chosen these tolerances because we needed to carry out a large number of computations and we wanted to save time. Furthermore, the results obtained are already good enough, so no stricter tolerances were needed. For the same reason we don't have any mesh resolution sensitivity study.

3. RESULTS AND DISCUSSION

Figure 13 presents typical moment curves for several inlet velocities for blade angle of attack of 70 degrees. In Figure 14 the dependence of the square of the correlation functions obtained by the experiments and computational fluid dynamics is presented. Correlation functions obtained by experiment and computational fluid dynamics overlap in the whole range of angles of attack.

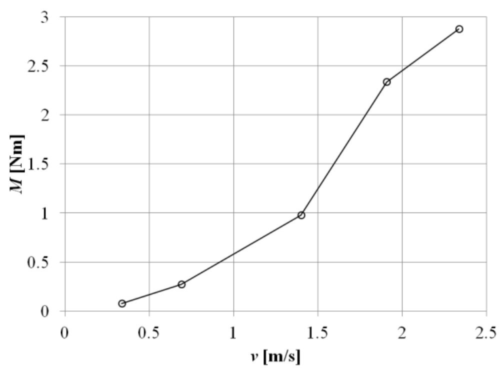

Figure 13. Predicted torque for several inlet velocities, for blade angle of attack α=70^o

Differences in the values of the correlation function obtained by the experiment and computational fluid dynamics exist only when the damper is completely open, when the blade angle of attack is 0^o.

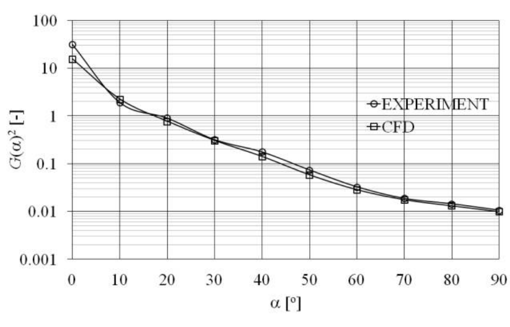

Figure 14. The square of correlation functions of the ATP damper obtained experimentally and with CFD results

Figure 15 presents the results of the experimental verification of the mathematical model of the ATP damper calibrated in two different ways: with experimental data and with computational fluid dynamics results. It can be observed that in both cases the difference between the model v_{mod} and measured v_{mer} velocity compared to the measured velocity is within the limits of ± 10%.

The obtained results are in favor of Federspel's theory assuming that the mathematical model of the ATP damper (2) is of universal character [9]. As one can see in Figure 15, the accuracy of the model used in the present work is similar to the accuracy of the model used by Federspel [???] who calibrated and verified the model using experiments.

In Fig. 15 one can observe that only a few points lie beyond the specified limits of ± 10%. Due to the differences in the results of the correlation functions obtained with experimental data and with computational fluid dynamics solutions when the ATP damper is fully open, it was suspected that the points that go beyond the limits are obtained for fully open damper.

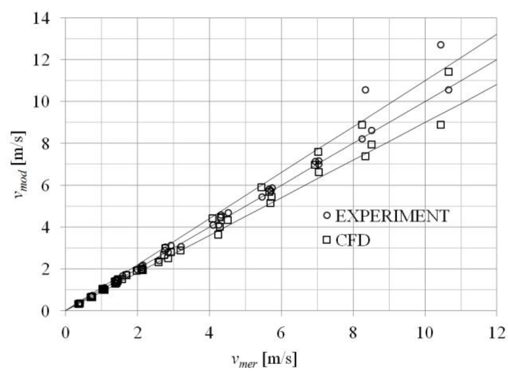

Figure 15. Results of experimental verification of mathematical model calibrated with experimental method and CFD results

In order to prove this assumption here is presented the dependence of the differences of measured and model velocity Δv as a function of the blade angle of attack α, for two different ways of mathematical model calibration, Figure 16.

It can be observed that in both methods of calibration the largest difference between the measured and model velocity appears at fully open blade of ATP damper, when the angle of attack is zero degrees.

When ATP damper is fully open, the moment of air flow acting on the blade is very small, and originates mostly from the effects of airflow to the blade carrier. For such a small value of moment, the mathematical model is incorrect and inadequate weather it is calibrated with experimental data or the results of computational fluid dynamics.

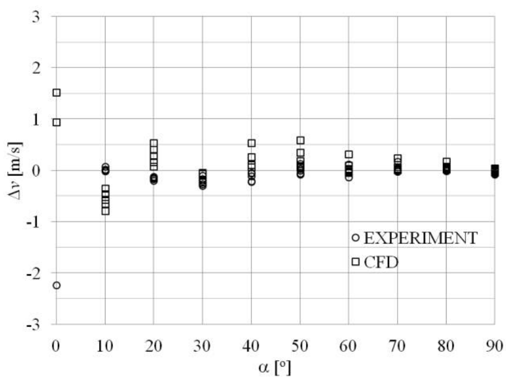

Figure 16. Results of the verification of the mathematical model calibrated with experimental data and with CFD results

4. CONCLUSIONS

Computational fluid dynamics was used to calibrate a mathematical model of an ATP damper. The results indicate, that numerical calibration lead to at least as good results as experimental calibration of the model. The difference between the measured and modeled velocity normalized with the measured velocity for both methods of calibration is in the range of ± 10%.

It is interesting that in both methods of calibration of the mathematical model of the ATP damper the difference between the measured and model velocity exceedes the above mentioned limits only when the damper is fully open. For this position of the blade, the airflow moment acting on the blade is too small to obtain accurate and adequate mathematical model for both methods of calibration.

Since the mathematical models calibrated with computational fluid dynamics results and with experimental data have the same accuracy, the share of experiments in the calibration of mathematical models of ATP dampers can be reduced significantly. Furthermore, the numerical approach can be applied already in the design phase.

It should be noted that to achieve such a good accuracy in the numerical model, the geometry of the device must be accurately reproduced in the computations. The size of the cleareances was found to be an important parameter in the computations.

Finally, it should be noted that the results of the verification of the mathematical model are in favour of the universality of the existing mathematical models. The same accuracy and adequacy of the mathematical model was obtained like in the literature [9].

ACKNOWLEDGEMENTS

This paper is a result of the research within the project TR31058, 2011-2014, supported by the Ministry of Education, Science and Technology, Republic of Serbia.

REFERENCES

[1] Bleuler, H., 1938, "Flow phenomena in hydraulic butterfly valves", *Esch-Wyss News*, Vol. 11, pp. 31-35.

[2] Cohn, S.D., 1951, "Performance analysis of butterfly valves", *Instruments*, Vol. 24, pp. 880-884.

[3] Gaden, D., 1951, "A contribution to study of butterfly valves", *Water Power Part I.*, Vol. 3, pp. 456-474.

[4] Gaden, D., 1952, "A contribution to study of butterfly valves", *Water Power Part II.*, Vol. 4, pp. 16-22.

[5] Sarpkaya, T., 1959, "Oblique impact of a bounded stream on a plane lamina", *Journal of the Franklin Institute*, Vol. 267, pp. 229–242.

[6] Sarpkaya, T., 1961, "Torque and cavitation characteristics of butterfly valves", *Journal of Applied Mechanics*, Vol. 28, pp. 511–518.

[7] Hassenpflug, W. C., 1998, "Free Streamlines", *Computers and Mathematics with applications*, Vol. 36, pp. 69–129.

[8] Morris, M.J. & Dutton, J.C., 1989, "Aerodynamic torque characteristics of butterfly valves in compressible flow", *Journal of Fluid Engineering*, Vol. 11, pp. 392–399.

[9] Federspiel, C., 2004, "Using the Torque Characteristics of Dampers to Measure Airflow Part I: Analysis and Testing", *HVAC&R Research*, Vol. 10, pp. 53-64.

[10] Federspiel, C., 2004, "Using the Torque Characteristics of Dampers to Measure Airflow, Part II: Model Development and Validation", *HVAC&R Research*, Vol. 10, pp. 65-72.

[11] ANSI/AMCA 500 D, (2007), "Laboratory Methods of Testing Dampers for Rating", *American National Standard Institute*.

[12] ISO 7145, 1982, "Determination of flowrate of fluids in closed conduits of circular cross – section. Method of velocity measurement at one point of the cross – section", *International Standard Organization*.

[13] Ferziger, J.H., and Perić, M., 2002 *Computational Methods for Fluid Dynamics*, Springer, 3rd edition.

Conference on Modelling Fluid Flow (CMFF'15)
The 16th International Conference on Fluid Flow Technologies
Budapest, Hungary, September 1-4, 2015

THE DETERMINATION OF THE DRAG COEFFICIENT IN POWER-LAW NON NEWTONIN FLUID OVER MOVING SURFACES

Gabriella BOGNÁR[1],

[1] Corresponding Author. Institute of Machine and Product Design, University of Miskolc. Egyetemváros, H-3515 Miskolc, Hungary. Tel.: +36 46 565 111, Fax: +36 46 563 584, E-mail: v.bognar.gabriella@uni-miskolc.hu

ABSTRACT

This paper deals with the solution to the boundary layer problem of a non-Newtonian power-law fluid flow along a moving flat surface. Two cases are investigated. One of them is when the surface is moving in a fluid flow, the other one is when the surface is moving through an otherwise quiescent fluid. Applying similarity transformation to the system of the governing partial differential equations, the boundary value problem of one nonlinear ordinary differential equation on $[0,\infty)$ is derived. Numerical solutions obtained for the velocity components and the drag coefficient parameter depending on the velocity ratio and on the power-law exponent are exhibited.

Keywords: Non-Newtonian fluid, boundary layer, moving surface, similarity method, iterative transformation method, spectral method

NOMENCLATURE

f	[-]	similarity velocity
g	[-]	function
h, h^*	[-]	parameters
K	$[Pa\ s^n]$	consistency coefficient
n	[-]	power-law exponent
u, v	[-]	non-dimensional velocity components
U_∞	$[m/s]$	fluid velocity
U_w	$[m/s]$	wall velocity
x, y	[-]	non-dimensional variables

Greek symbols

$\gamma, \sigma, \kappa, \mu$	[-]	parameters
Γ	[-]	function
η	[-]	similarity variable
ρ	$[kg/m^3]$	density of the fluid
ψ	[-]	non-dimensional stream function
τ_{yx}	$[Pa]$	shear stress
τ_w	$[Pa]$	wall shear stress
λ	[-]	velocity ratio
λ_c	[-]	critical velocity ratio

1. INTRODUCTION

In fluid dynamics, the drag force or force component in the direction of the flow velocity is proportional to the drag coefficient, to the density of the fluid, to the area of the object and the square of the relative speed between the object and the flow velocity. Blasius applied the similarity method to investigate the model arising for a laminar boundary layer of a Newtonian media [3]. Fluids such as molten plastics, pulps, slurries and emulsions, which do not obey the Newtonian law of viscosity, are increasingly produced in the industry. The first analysis of the boundary layer approximations to non-Newtonian media with power-law viscosity was given by Schowalter [17] in 1960. The author derived the equations governing the fluid flow. The numerical solutions to the problem of a laminar flow of the non-Newtonian power-law model past a two-dimensional horizontal surface were presented by Acrivos, Shah and Petersen [1]. When the geometry of the surface is simple the system of differential equations can be examined in details and fundamental information can be obtained about the flow behaviour of a non-Newtonian fluid in motion (e.g., to predict the drag). The production of sheeting material, which includes both metal and polymer sheets, arises in a number of industrial manufacturing processes. The fluid dynamics due to a continuous moving solid surface appears in aerodynamic extrusion of plastic sheets, cooling of a metallic plate in a cooling bath, the boundary layer along material handling conveyers, boundary layer along a liquid film in condensation processes, etc. Much theoretical work has been done on this problem since the pioneering papers by Sakiadis [16] and Tsou et al. [19], and extensive references can be found in the papers by Magyari and Keller [12, 13], Liao and Pop [11], and Nazar et al. [14].

Several numerical methods are developed and introduced for the solution of these type of fluid mechanics' problems.

It was shown in [4] that a non-iterative Töpfer-like transformation can be applied for the determination of the dimensionless wall gradient on a stationary flat surface. Our aim is to give numerical results on the drag coefficient in non-Newtonian media along moving flat surfaces for two cases and to introduce two numerical methods, an iterative transformation method and a spectral method, for the numerical evaluation.

2. MATHEMATICAL MODEL

Consider an incompressible uniform parallel flow of a non-Newtonian power-law fluid, with a constant velocity U_∞ along an impermeable semi-infinite flat plate whose surface is moving with a constant velocity U_W in the opposite direction to the main stream. The *x*–axis extends parallel to the plate, while the *y*-axis extends upwards, normal to it. Applying the necessary boundary layer approximations, the continuity and momentum equations are [2]:

$$\frac{\partial u}{\partial x}+\frac{\partial v}{\partial y}=0\,, \tag{1}$$

$$u\,\frac{\partial u}{\partial x}+v\,\frac{\partial u}{\partial y}=\frac{1}{\rho}\frac{\partial \tau_{yx}}{\partial y}\,, \tag{2}$$

where u, v are the velocity components along x and y coordinates, respectively. The shear stress and the shear rate relation is assumed to be the power-law relation $\tau_{yx}=K\left|\frac{\partial u}{\partial y}\right|^{n-1}\frac{\partial u}{\partial y}$, where K stands for the consistency and n is called the power-law index; that is $n<1$ for pseudoplastic, $n=1$ for Newtonian, and $n>1$ for dilatant fluids. Therefore, differential equation (2) is rewritten as

$$u\,\frac{\partial u}{\partial x}+v\,\frac{\partial u}{\partial y}=\frac{\partial}{\partial y}\left(\mu_C\left|\frac{\partial u}{\partial y}\right|^{n-1}\frac{\partial u}{\partial y}\right), \tag{3}$$

where $\mu_C=K/\rho$.

2.1. Fluid flow of velocity U_∞

In the first case, the surface is placed in a fluid flow of velocity U_∞. The wall is impermeable and no-slip boundary condition is supposed. For the investigated model, the boundary conditions are formulated such as

$$u\big|_{y=0}=-U_W,\quad v\big|_{y=0}=0,\quad u\big|_{y=+\infty}=U_\infty\,. \tag{4a}$$

2.2. Flow in an otherwise quiescent fluid

In the second case, the ambient fluid velocity is zero and we suppose that the plate is moving at a constant velocity; therefore:

$$u\big|_{y=0}=-U_W,\quad v\big|_{y=0}=0,\quad u\big|_{y=+\infty}=0\,. \tag{4b}$$

2.3. Introduction of stream function

The continuity equation (1) is automatically satisfied by introducing a stream function ψ as

$$u=\frac{\partial \psi}{\partial y}\ ,\qquad v=-\frac{\partial \psi}{\partial x}\,.$$

The momentum equation can be transformed into an ordinary differential equation by the similarity transformations

$$\psi(x,y)=\mu_C^{\frac{1}{n+1}}\left(U_\infty\right)^{\frac{2n-1}{n+1}}x^{\frac{1}{n+1}}\,f(\eta)\,,$$

$$\eta=\mu_C^{-\frac{1}{n+1}}\left(U_\infty\right)^{\frac{2-n}{n+1}}y\,x^{-\frac{1}{n+1}}\,,$$

where η is the similarity variable and $f(\eta)$ is the dimensionless stream function for the boundary value problem (1), (3) and (4a). Equation (3) with the transformed boundary conditions can be written as

$$\left(\left|f''\right|^{n-1}f''\right)'+\frac{1}{n+1}\,f\,f''=0\,, \tag{5}$$

$$f(0)=0\,,\quad f'(0)=-\lambda\,,\quad f'(\infty)=\lim_{\eta\to\infty}f'(\eta)=1\,, \tag{6a}$$

where the prime denotes the differentiation with respect to the similarity variable η, and the velocity ratio parameter is $\lambda=U_W/U_\infty$. Equation (5) is called the generalized Blasius equation and the case $\lambda=0$ corresponds to the Blasius problem. It should be noted that for $\lambda>0$, the fluid and the plate move in the opposite directions, while they move in the same directions if $\lambda<0$. Now, the dimensionless velocity components have the form:

$$u(x,y)=U_\infty\, f'(\eta)\,,$$

$$v(x,y)=\frac{U_\infty}{n+1} Re_x^{\frac{n}{n+1}}\,(\eta\, f'(\eta)-f(\eta))\,,$$

and $\eta = Re_x^{\frac{1}{n+1}}\, y/x$, where $Re_x = U_\infty^{2-n}\, x^n / \mu_c$ is the local Reynolds number.

For $U_\infty = 0$, λ is not defined. Here the momentum equation can be transformed into an ordinary differential equation by the similarity transformations

$$\psi(x,y)=\mu_c^{\frac{1}{n+1}} \left(U_w\right)^{\frac{2n-1}{n+1}} x^{\frac{1}{n+1}}\, f(\eta)\,,$$

$$\eta = \mu_c^{-\frac{1}{n+1}} \left(U_w\right)^{\frac{2-n}{n+1}} y\, x^{-\frac{1}{n+1}}$$

for the boundary value problem (1), (3) and (4b). The transformed form of equation (3) has the same form as (5), but the boundary conditions (4b) are formed by

$$f(0)=0\,,\quad f'(0)=1\,,\quad f'(\infty)=\lim_{\eta\to\infty} f'(\eta)=0\,. \tag{6b}$$

The dimensionless velocity components can be given as:

$$u(x,y)=U_w\, f'(\eta)\,,$$

$$v(x,y)=\frac{U_w}{n+1} Re_x^{\frac{n}{n+1}}\,(\eta\, f'(\eta)-f(\eta))\,,$$

and $\eta = Re_x^{\frac{1}{n+1}}\, y/x$, where $Re_x = U_w^{2-n}\, x^n / \mu_c$.

Since the pioneering work by Acrivos [1], different approaches have been investigated for $f''(0)=\gamma$ in the case of non-Newtonian fluids. It has a physical meaning in *drag force* or force due to *skin friction*. It is a fluid dynamic resistive force which is a consequence of the fluid and the pressure distribution on the surface of the object. The *skin friction parameter* γ originates from the non-dimensional *drag coefficient*

$$C_D = (n+1)^{\frac{1}{n+1}}\, Re^{\frac{-n}{n+1}} \left|\gamma\right|^{n-1} \gamma\ ,$$

and it is involved in the *wall shear stress*

$$\tau_w(x)=\left[\frac{\rho^n K U_\infty^{3n}}{x^n}\right]^{\frac{1}{n+1}} \left|\gamma\right|^{n-1} \gamma \quad \text{for } U_\infty \neq 0$$

and

$$\tau_w(x)=\left[\frac{\rho^n K U_w^{3n}}{x^n}\right]^{\frac{1}{n+1}} \left|\gamma\right|^{n-1} \gamma \quad \text{for } U_\infty = 0\,.$$

The boundary value problem (5), (6a) is defined on a semi-infinite interval. For Newtonian fluids ($n=1$), equation (5) is equal to the well-known Blasius equation:

$$f'''+\frac{1}{2} f\, f''=0\,. \tag{7}$$

For non-Newtonian fluids on steady surfaces ($\lambda = 0$), the boundary value problem (5), (6a) has been investigated in [4]. A non-iterative Töpfer-like transformation was introduced for the determination of γ, when

$$f(\eta)=\gamma^{(2n-1)/3} g\left(\gamma^{(2-n)/3}\eta\right)$$

and g is the solution of the initial value problem

$$\left(\left|g''\right|^{n-1} g''\right)' + \frac{1}{n+1} g\, g''=0\,,$$

$$g(0)=0\,,\quad g'(0)=0\,,\quad g''(0)=1\,.$$

By analogy with the Blasius description of Newtonian fluid flows [3], here our aim is to study the similarity solutions and investigate the model arising in the study of a two-dimensional laminar fluid flow with power-law viscosity. A Töpfer-like transformation is applied for the determination of γ.

3. PRELIMINARY RESULTS

The existence and uniqueness of Blasius' boundary layer solution to (7), (6a) with $\lambda = 0$ was rigorously proved by Weyl [20]. The properties of similarity solutions to the boundary layer problem on a moving surface ($\lambda \neq 0$) for Newtonian fluids, have been examined by Hussaini and Lakin [8], Hussaini *et al.* [9]. It turned out that for a semi-infinite plate, the existence of solutions depends on the ratio of the plate surface velocity U_w to the free stream velocity U_∞. When $n=1$, $\lambda \le 0$, the existence, uniqueness and analyticity of solution to (5), (6a) were proved by Callegari and Friedman [6] using the Crocco variable formulation. If $\lambda > 0$, Hussaini and Lakin [8] proved that there is a critical value λ_c such that solution exists to (7), (6a) only if $\lambda \le \lambda_c$ (see [8]). Dual solutions exist for $0 < \lambda < \lambda_c$. The numerical value of λ_c was found to be 0.3541... for $n=1$. The non-uniqueness and analyticity of solution for $\lambda \le \lambda_c$ has been proved by Hussaini et al. [8, 9].

For non-Newtonian fluids ($n \neq 1$) with $\lambda = 0$, the existence, uniqueness and some analytical results for problem (5), (6a) were established when $0 < n < 1$ by Nachman and Callegari [11]. The existence and uniqueness result for $n > 1$ was considered by Benlahsen et al. [2] via Crocco variable transformation. For non-Newtonian fluids the numerical calculations also show that there is a critical value λ_c for each n such that solution exists only if $\lambda \le \lambda_c$ (see [10]). The variations of $f''(0)$ and λ_c with λ for different values of n are given in [5].

In this paper our aim is to introduce an iterative transformation method for the determination of γ involved in the drag coefficient and the calculation of the boundary layer thickness for different values n and λ.

4. NUMERICAL SOLUTIONS

For the determination of the solution to boundary value problems (5)-(6a) and (5)-(6b) two different methods are applied. The problems are solved on truncated intervals instead on $[0,\infty)$.

4.1. Iterative transformation method for the case $U_\infty \neq 0$

This section is devoted to the application of the scaling concept to numerical analysis of (5), (6a). Solving this problem, we have to deal with a practically unsuited condition at infinity. In the case of $\lambda = 0$ a non-iterative transformation method called Töpfer or Töpfer-like method was be used for solving (5), (6a) either for $n = 1$ [13] or for $n \neq 1$ [5]. The figure of the velocity gradient parameter near the wall $f''(0)$ is exhibited in Fig. 1 depending on n [5].

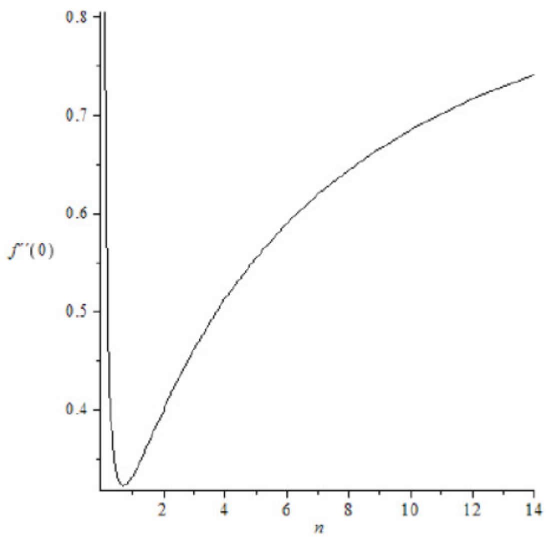

Figure 1. Velocity gradient parameter near the wall $f''(0) = \gamma$ depending on n for $\lambda = 0$

Here we describe an iterative transformation method. Non-iterative and iterative transformation methods for boundary value problems have been introduced by Fazio [8].

The idea behind the present method is to consider the "partial" invariance of (5), (6a) with respect to a scaling transformation in the sense that the differential equation and one of the boundary conditions at 0 are invariant, while the other two boundary conditions are not invariant. Therefore, we modify the problem by introducing a numerical parameter *h*. Now, equation (5) is to be solved with boundary conditions

$$f'(0) = -\lambda h, \; f(0) = 0, \; f'(\infty) = \lim_{\eta \to \infty} f'(\eta) = 1,$$

where *h* is involved, to ensure the invariance of the extended scaling group.

We introduce a Töpfer-like transformation $g = \sigma^{\kappa} f$, $\eta^* = \sigma^{\mu} \eta$ to convert the boundary value problem to an initial value problem. Equation (5) is scaling invariant if $(2-n)\kappa = (1-2n)\mu$. Then, one gets

$$\left(\left|g''\right|^{n-1} g''\right)' + \frac{1}{n+1} g\, g'' = 0. \tag{8}$$

Let us choose $\sigma = \gamma$, then $g''(0) = \gamma^{\kappa - 2\mu + 1}$ and with $\kappa - 2\mu + 1 = 0$ one can obtain the appropriate boundary conditions as $\kappa = (1-2n)/3$, $\mu = (2-n)/3$:

$$g(0) = 0, \;\; g'(0) = -\lambda h^*, \;\; g''(0) = 1, \tag{9}$$

where $h^* = \gamma^{-\frac{n+1}{3}} h$.

The initial value problem (8), (9) is solved with the so-called iterative transformation method. A numerical parameter h is applied so that the asymptotic boundary condition remains invariant. By starting with a suitable value of h^*, a root finder algorithm is used to define a sequence h_i^* for $j = 0,1,...$. The group parameter σ is obtained by solving numerically the initial value problem after the iterations. The sequence is defined by $\Gamma\left(h^*\right) = h - 1 = 0$. An adequate termination criteria must be used to verify whether $\Gamma\left(h_i^*\right) \to 0$ as $i \to \infty$. The solution of the original problem can be received by rescaling to $h = 1$.

It is important to note that similarity solution exists only for $-1 \le \lambda \le \lambda_c$. If $\lambda > \lambda_c$, then the flow separates, the boundary layer structure collapses and the boundary layer approximations are no longer applicable.

Figure 2 provides upper bound for the critical velocity parameter for non-Newtonian fluids.

The influences of λ and n on the skin friction parameter γ are represented in Fig. 3. It can be noticed that there are two solutions for $0<\lambda<\lambda_c$ (see Fig. 3.). Figures 4-6 show the influence of the positive parameter λ for different power-law exponent n on γ^n. We remark that f' monotonically increases from $-\lambda$ to 1 for both the lower and upper solutions. Our results are in good agreement with those reported in [10].

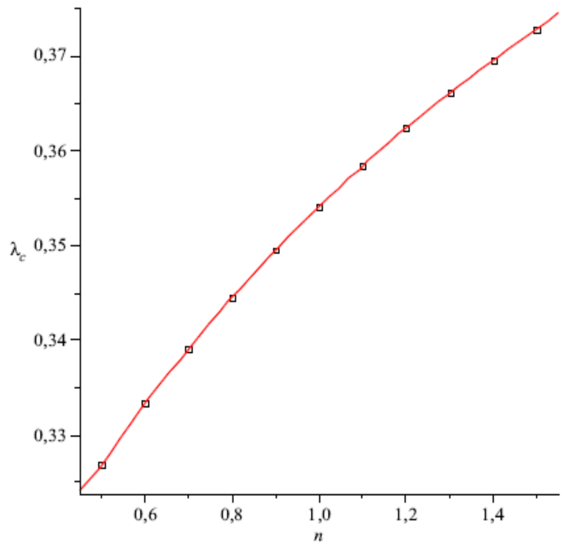

Figure 2. The graph of λ_c against n

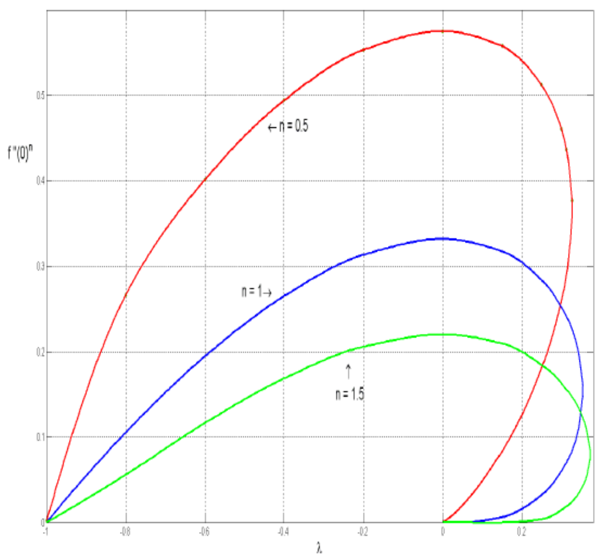

Figure 3. Drag coefficient parameter $[f''(0)]^n$ dependence with λ for different values of n

Figures 4-6 exhibit the upper and lower solutions for velocities $f'=u(x,y)/U_\infty$ as a function of η for some values of n and λ to show the effect of the velocity parameter λ and power-law exponent n. We remark that f' monotonically increases from $-\lambda$ to 1 for both the lower and upper solutions. This phenomenon shows that the velocity component u is monotonically increasing in the boundary layer.

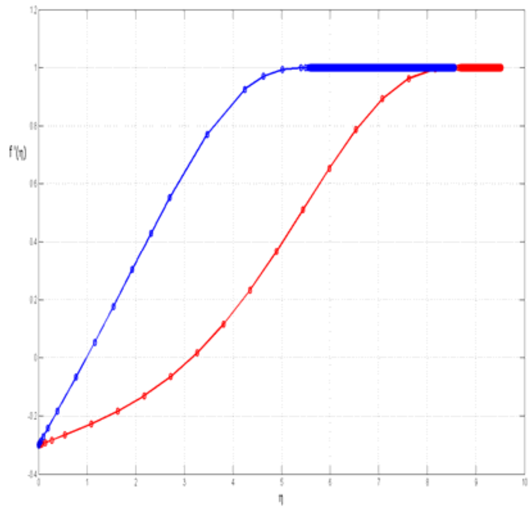

Figure 4. Velocity distribution for $n=1.5$ and $\lambda=0.3$

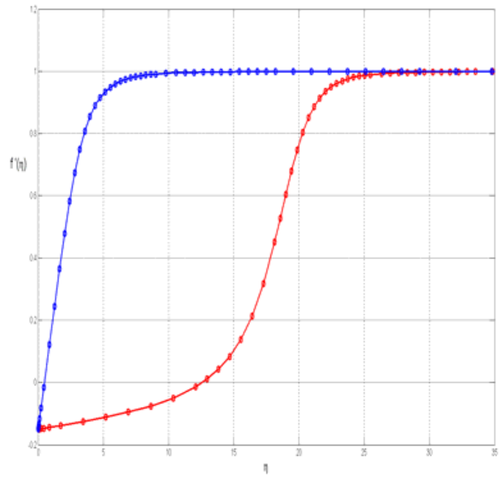

Figure 5. Velocity distribution for $n=0.5$ and $\lambda=0.15$

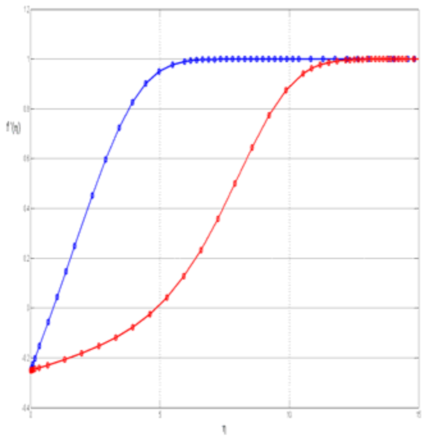

Figure 6. Velocity distribution for $n=1$ and $\lambda=0.25$

4.2. Spectral method for the case $U_\infty=0$

In this section a different method is introduced for the numerical solution to (5), (6b) as the iterative transformation method applied in Section 4.1 is not suitable for this case.

With the advent of the spectral element method, complicated domains can be handled. In spite of being mainly used in fluid mechanics, nowadays, these are more and more frequently utilized in biomechanics, astrophysics and in the study of electromagnetic waves.

We use a spectral method for the determination of the solution to (5)-(6b). Spectral methods are able to provide very accurate results when the solution is smooth enough. More precisely, if the solution is differentiable to all orders, an exponential (or infinite order or spectral) convergence is achieved.

All three versions of spectral methods (collocation, Galerkin and tau) belong to the method of weighted residuals and the main classification is carried out according to the type of trial functions used. Trial functions in the Galerkin method are the same as the weight functions and satisfy some of the boundary conditions. In spectral collocation, the trial functions are Dirac-delta functions located at the collocation points while the tau method, similarly to the Galerkin method, operates in the weak form but the trial functions generally do not satisfy the boundary conditions. In our calculations, the collocation method is used. During collocation we determine the function values of the interpolating polynomial at the collocation points (nodal approximation) as opposed to the other two methods which give result for the coefficients of the truncated approximating series (modal approximation).

The n-th order Chebyshev polynomial of the first kind, $T_n(x)$ is defined on [-1; 1] and can be expressed by the recursion

$$T_0(x)=1,\ T_1(x)=x,$$
$$T_n(x)=2xT_{n-1}(x)-T_{n-2}(x),\quad n>1.$$

The modal approximation of function $u(x)$ is calculated by $T_n(x)$. The nodal approximation of $u(x)$ can be evaluated in the Lagrange base. The spectral differentiation for Chebyshev polynomials can be carried out either by a matrix-vector product or by using the Fast Fourier Transform (FFT). We implement the matrix-vector multiplication method because of the relatively few number of collocation points. One of the methods for solving a boundary value problem on an infinite or semi-infinite interval is the so-called domain truncation. Performing the truncation and the linear mapping we have

$$\eta\in[0,\infty)\to\xi\in[0,L]\to\zeta\in[0,1]\to\bar{x}\in[-1,1].$$

Introducing $\bar{f}(\bar{x})=f(\eta(\bar{x}))$, the boundary value problem (5)-(6b) is written as

$$\frac{8}{L^3}\bar{f}'''-\frac{1}{n(n+1)}\left(\frac{4}{L^2}\right)\bar{f}\left|\bar{f}''\right|^{2-n}=0,$$

$$\bar{f}(-1)=0,\ \bar{f}'(-1)=L/2,\ \bar{f}(1)=0.$$

After the discretization, N+2 number of algebraic equations are at our disposal. The differential equation approximated at the N-1 inner nodes and the three boundary conditions. However, the number of unknowns is only N+1, therefore the resulting system is overdetermined. One possible solution is to take an interpolant that already satisfies some of the boundary conditions. Let us seek function k such that

$$\bar{f}(\bar{x})=P(\bar{x})k(\bar{x}),\ P(\bar{x})=a\bar{x}^2+b\bar{x}+c.$$

In case of $P(-1)=0,\ P'(-1)=L/2$ and $P'(1)=0$ are satisfied, a,b,c are obtained as

$$a=L/8,\ b=L/4,\ c=3L/8\,.$$

Now the differential equation is reformulated for k under boundary conditions

$$k(-1)=1,\ k'(1)=0.$$

The boundary value problem is solved with the Chebyshev spectral technique. After the discretization of $k(\bar{x})$ and its derivatives, the resulting system of nonlinear equations is solved with the Levenberg-Marquardt algorithm in Matlab. The numerical results for different power-law exponents are shown in Fig. 7, where f' is shown which is proportional to $u(x,y)$. The figure shows that with larger values of n the boundary layer thickness decreases and shorter interval is enough for the truncation. Because $f''(0)<0$, both the drag coefficient and the wall shear stress are influenced by $|f''(0)|^n$ and this is exhibited in Fig. 8.

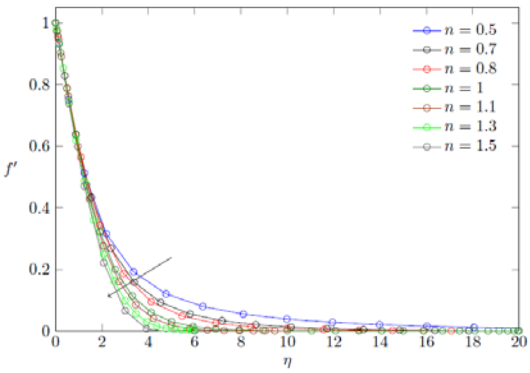

Figure 7. Velocity distribution for different values of n for $U_\infty = 0$

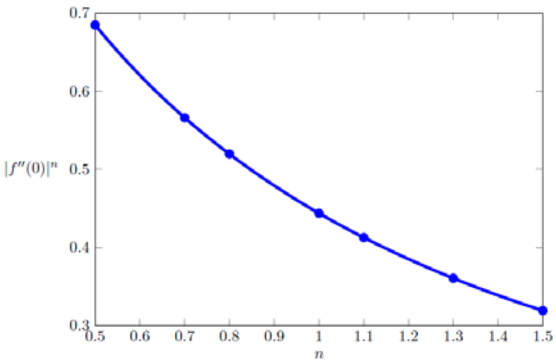

Figure 8. The values of $|f''(0)|^n$ for $n = 0.5 \ldots 1.5$

5. CONCLUSIONS

In this paper the determination of the drag coefficient is shown for two-dimensional, incompressible, laminar non-Newtonian fluid flow along a moving surface. The power-law non-Newtonian approximation is used. The governing partial differential equations are transformed into a third order ordinary differential equation together with the boundary conditions applying the similarity technique. Two main cases are considered: if the velocity U_∞ of the ambient fluid flow is zero or non-zero. For $U_\infty \neq 0$, an iterative transformation method is used for the determination of the numerical results. If $U_\infty = 0$, a spectral method is applied for the simulations. The values of $f''(0) = \gamma$ and the influence of the power-law exponent n and the velocity ratio λ on it are exhibited on Figs. 1-8.

ACKNOWLEDGEMENTS

The research work presented in this paper is based on the results achieved within the TÁMOP-4.2.1.B- 10/2/KONV-2010-0001 project and carried out as part of the TÁMOP-4.1.1.C-12/1/KONV-2012-0002 " Cooperation between higher education, research institutes and automotive industry" project in the framework of the New Széchenyi Plan. The realization of this project is supported by the Hungarian Government, by the European Union, and co-financed by the European Social Fund.

REFERENCES

[1] Acrivos A., Shah M.J., Peterson E.E.: Momentum and heat transfer in laminar boundary flow of non-Newtonian fluids past external surfaces, *AIChE J.*, **6** (1960), 312–317.

[2] Benlahsen M., Guedda M., Kersner R.: The generalized Blasius equation revisited, *Math.Comput. Model*, **47** (2008), 1063–1076.

[3] Blasius H.: Grenzschichten in Flussigkeiten mit kleiner reibung, *Z. Math. Phys.*, **56** (1908), 1–37.

[4] Bognár G.: Similarity solutions of boundary layer flow for non-Newtonian fluids, *Int. J. Nonlinear Sci. Numer. Simul.* **10** (2010), 1555–1566.

[5] Bognár G.: On similarity solutions of boundary layer problems with upstream moving wall in non-Newtonian power-law fluids, *IMA Journal of Applied Mathematics*, **77** No.4 (2012), 546-562.

[6] Callegari, A.J., Friedman M.B.: An analytical solution of a nonlinear, singular boundary value problem in the theory of viscous flows, *J. Math. Anal. Appl.*, **21** (1968), 510–529.

[7] Fazio R.: A novel approach to the numerical solution of boundary value problems on infinite intervals, *SIAM J. Numer. Anal.*, **33** (1996), 1473–1483.

[8] Hussaini M.Y., Lakin W.D.: Existence and nonuniqueness of similarity solutions of a boundary-layer problem, *Q. J. Mech. Appl. Math.*, **39** (1986), 177–191.

[9] Hussaini M.Y., Lakin W.D., Nachman A.: On similarity solutions of a boundary layer

problem with an upstream moving wall, *SIAM J. Appl. Math.,* **47** (1987), 699–709.

[10] Ishak A., Bachok N.: Power-law fluid flow on a moving wall, *European J. Scie. Res.,* **34** (2009), 55-60.

[11] Liao S. J., Pop I.: Explicit analytic solution for similarity boundary layer equations, *Int. J. Heat Mass Transfer,* **47** (2004), 75–85.

[12] Magyari E., Keller B.: Heat and mass transfer in the boundary layers on an exponentially stretching continuous surface, *J. Phys. D: Appl. Phys.,* **32** (1999), 577–585.

[13] Magyari E., Keller B.: Exact solutions for self-similar boundary-layer flows induced by permeable stretching walls, *Eur. J. Mech. B/Fluids,* **19** (2000), 109–122.

[14] Nazar R., Amin N., Pop I.: Unsteady boundary layer flow due to a stretching surface in a rotating fluid, *Mech. Res. Comm.,* **31** (2004), 121–128.

[15] Nachman A., Callegari A.J.: A nonlinear singular boundary value problem in the theory of pseudoplastic fluids, *SIAM J. Appl. Math.,* **38** (1980), 275–281.

[16] Sakiadis B. C.: Boundary layers on continuous solid surfaces, *AIChE. J.,* **7** (1961), 26–28, see also pp. 221–225 and 467–472.

[17] Schowalter W.R.: The application of boundary layer theory to power-law pseudoplastic fluids: Similar solutions, *AIChE J.,* **6** (1960), 24-28.

[18] Töpfer K.: Bemerkung zu dem Aufsatz von H. Blasius: Grenzschichten in Flüssigkeiten mit kleiner Reibung, *Z. Math. Phys.,* **60** (1912), 397–398.

[19] Tsou F., Sparrow E., Goldstein R.: Flow and heat transfer in the boundary layer on a continuous moving surface, *Int. J. Heat Mass Transfer,* **10** (1967), 219–235.

[20] Weyl H.: On the differential equations of the simplest boundary-layer problems, *Ann. of Math.,* **43** (1942), 381-407.

Conference on Modelling Fluid Flow (CMFF'15)
The 16th International Conference on Fluid Flow Technologies
Budapest, Hungary, September 1-4, 2015

FLUID AND HEAT FLOW BETWEEN TWO STRETCHABLE CYLINDRICAL CHANNELS WITH POROUS WALL IN THE PRESENCE OF AN EXOTHERMIC REACTION SOURCE

Suraju Olusegun AJADI[1], Saheed Ojo AKINDEINDE[2], Kazeem Babawale KASALI[3]

[1] Corresponding Author. Department of Mathematics, Obafemi Awolowo University. 220005, Ile-Ife, Nigeria. Tel.: +234 805 241 7120, E-mail: soajadi@oauife.edu.ng
[2] Department of Mathematics, Obafemi Awolowo University. 220005, Ile-Ife, Nigeria. Tel.: +234 708 698 3977, E-mail: soakindeinde@oauife.edu.ng
[3] Department of Mathematics, Obafemi Awolowo University. 220005, Ile-Ife, Nigeria. Tel.: +234 807 330 5461. E-mail: otbs4real@gmail.com.

ABSTRACT

In this work, we consider the flow and heat dynamics between two stretchable cylindrical channels enclosing an exothermic reaction source in the presence of an accelerated stretching velocity. The governing equations have been reduced to a system of similarity variables and subjected to analytical and numerical treatments. A parametric analysis using the stretching velocity parameter, reaction source term and other embedded parameters have been carried out. As a test case,in the absence of the Hartmann number($Ha = 0$) the numerical treatment has proved to be effective as known results have been recovered for the radial and axial velocity profiles [1]. The presence of the Hartmann number parameter showed a considerable effect of porosity on the velocity profiles when compared with known results. Graphical and tabular demonstration of the solutions are presented to shed more lights on the behaviour of the solutions.

Keywords: Exothermic Reaction source, Fluid and Heat flow, stretchable cylindrical channels, Porous wall

NOMENCLATURE

Ha	$[-]$	Hartmann number
G_r	$[-]$	Grashous number
P_e	$[-]$	Peclet number
ρ	$[kg/m^3]$	Fluid density

1. INTRODUCTION

Consider the flow of the axis-symmetric flow between two stretchable infinite disks with a distance d between them. If both sides are stretched in the radial direction with a velocity proportional to the radii, and assuming that the bottom disk is along $z = 0$ plane, while stretching velocity ratio of the upper disk to the lower one is γ. In dimensionless form, the governing equations for an incompressible fluid in the presence of suction, reaction term and viscous dissipation are

$$\frac{1}{r}\frac{\partial}{\partial r}(ru) + \frac{\partial v}{\partial z} = 0 \tag{1}$$

$$\frac{\partial u}{\partial t} + u\frac{\partial u}{\partial r} + v\frac{\partial u}{\partial z} = \frac{-1}{\rho}\frac{\partial p}{\partial r} + \nu\left(\frac{1}{r}\frac{\partial}{\partial r}\left(r\frac{\partial u}{\partial r}\right)\right. \tag{2}$$

$$\left. + \frac{\partial^2 u}{\partial z^2} - \frac{u}{r^2}\right) + G_r\theta - Ha^2 u \tag{3}$$

$$\frac{\partial v}{\partial t} + u\frac{\partial v}{\partial r} + v\frac{\partial v}{\partial z} = \frac{-1}{\rho}\frac{\partial p}{\partial z} + \left(\frac{1}{r}\frac{\partial}{\partial r}\left(r\frac{\partial v}{\partial r}\right) + \frac{\partial^2 v}{\partial z^2}\right) \tag{4}$$

$$+ G_r\theta - Ha^2 v \tag{5}$$

$$\frac{\partial \theta}{\partial t} + u\frac{\partial \theta}{\partial r} + v\frac{\partial \theta}{\partial z} = \frac{1}{p_e}\left(\frac{1}{r}\frac{\partial}{\partial r}\left(r\frac{\partial \theta}{\partial r}\right) + \frac{\partial^2 \theta}{\partial z^2}\right) \tag{6}$$

$$+ \phi + R(\theta, \delta, m) \tag{7}$$

where ϕ, the viscous dissipation expressed as

$$\phi = 2\left[\left(\frac{\partial u}{\partial r}\right)^2 + \left(\frac{u}{r}\right)^2 + \left(\frac{\partial v}{\partial z}\right)^2\right] + \left(\frac{\partial u}{\partial z} + \frac{\partial v}{\partial r}\right)^2.$$

and the reaction term

$$R(\theta, \delta, m) = \delta\theta^m e^{\beta\theta}$$

where δ and β represent the Frank-Kamenetskii parameter and the activation energy respectively.

2. SOLUTION METHODS

Let us introduce the similarity variables

$$\eta = \frac{(z+kt)}{d}, \quad F(\eta) = \frac{u}{rE}, \quad H(\eta) = \frac{v}{Ed}, \tag{8}$$

$$P = \rho E\nu\left(P(\eta) + \frac{\beta r^2}{4d^2}\right), \quad G(\eta) = \frac{\theta}{rE_\theta} \tag{9}$$

where $\eta = \frac{(z+kt)}{d}$. The quantity E is a parameter corresponding to the disk stretching strength and its unit is $1/s$, d is a characteristic length and parameter E_θ has dimension $\frac{K}{m}$.

Now substituting (8)-(9) into (1)-(6) gives the following system of coupled ordinary differential equations;

$$2F + H' = 0 \tag{10}$$

$$F'' - A_0F' - RF^2 - RHF' - A_1F - \beta + A_2G = 0 \tag{11}$$

$$H'' - B_0HH' - B_1H' - B_2P' + B_3G - B_4H = 0 \tag{12}$$

$$G'' + M_0F^2 + M_1(H')^2 + M_2G + M_3(F')^2 - M_4G' - M_5HG' + \bar{\delta}G^m e^{\bar{\beta}G} = 0 \tag{13}$$

with the initial-boundary conditions; initial conditions

$$t = 0, \quad \eta = 0, \quad F(0) = 0, \tag{14}$$

$$H(0) = 0, \quad G(0) = 0, \quad P(0) = 0; \tag{15}$$

the boundary conditions

$$t > 0, \quad \eta = 1, \tag{16}$$

$$F(1) = 1, \quad H(1) = 0, \quad G(1) = 1, \tag{17}$$

$$F(2) = \gamma, \quad H(2) = 0, \quad G(2) = 0. \tag{18}$$

In the above, the constants

$$A_0 = \frac{kR}{E}, \quad A_1 = \frac{d^2Ha^2}{\nu},$$

$$B_0 = \frac{R}{Ed}, \quad B_1 = \frac{kR}{E^2}, \quad B_2 = Ed,$$

$$B_3 = \frac{rRG_r}{Ed}, \quad B_4 = \frac{d^2Ha^2}{E\nu}, \quad M_0 = \frac{4\nu P_z}{r},$$

$$M_1 = \frac{2\nu RP_z}{r^2}, \quad M_2 = \frac{d^2}{r^2} - \nu P_e, \quad M_3 = 2rEP_e$$

$$M_4 = \frac{\nu RkP_e}{E}, \quad M_5 = \nu P_e$$

where P_e denotes the Peclet number and the constants $\bar{\delta} = rE_\theta\delta$ and $\bar{\beta} = rE_\theta\beta$.

By substituting (10) into (11), we obtain

$$H''' - A_0H'' + \frac{R}{2}(H')^2 - RHH'' - A_1H' - A_2G + \beta = 0 \tag{19}$$

with the associated boundary conditions

$$H(0) = 0, \quad H(1) = 0, \quad H(2) = 0 \tag{20}$$

$$H'(0) = 0, \quad H'(1) = -2, \quad H'(2) = -2\gamma. \tag{21}$$

By differentiating (19) with respect to η once, a simpler form of (19) is obtained as

$$H'''' - A_0H''' - RHH''' - A_1H'' - A_2G' = 0 \tag{22}$$

subject to the initial-boundary conditions

$$H(0) = 0, \quad H(1) = 0, \quad H(2) = 0 \tag{23}$$

$$H'(0) = 0, \quad H'(1) = -2, \quad H'(2) = -2\gamma \tag{24}$$

$$H'''(1) = -2R - \beta - 2A_1, \tag{25}$$

$$G(0) = 1, \quad G(\infty) = 0. \tag{26}$$

The model problem then becomes

$$H'''' - A_0H''' - RHH''' - A_1H'' - A_2G' = 0, \tag{27}$$

$$G'' + M_0F^2 + M_1(H')^2 + M_2G + M_3(F')^2 - M_4G' - M_5HG' + \bar{\delta}G^m e^{\bar{\beta}G} = 0 \tag{28}$$

with $F = -\frac{H'}{2}$ and subject to the conditions (23)-(26). In what follows, approximate analytical and numerical methods will be applied to solve the model problem. Once H and G have been obtained this way, equation (12) can be solved to obtain the expression for pressure P.

2.1. Perturbation methods

2.1.1. Traditional perturbation method

For a very small Reynolds numbers, that is $R \to 0$ the solution of the equation (22) with $A_2 = 0$ can be obtained as follows.

Assume an infinite series expansion of the form

$$H(\eta) = H_0(\eta) + RH_1(\eta) + R^2H_2(\eta) + ... + R^nH_n(\eta) + \dots$$

which for small R translates to

$$H(\eta) \approx H_0(\eta) + RH_1(\eta). \tag{29}$$

Now substituting (29) into (22) and collecting terms in zeroth-order and first-order systems to obtain

$$H_0'''' - A_0H''' - A_1H_0'' = 0, \tag{30}$$

$$H_1'''' - A_0H_1''' - H_0H_0''' - A_1H_1'' = 0 \tag{31}$$

with the initial-boundary conditions

$$H_0(0) = 0, \quad H_0(1) = 0, \quad H_0(2) = 0, \tag{32}$$

$$H_0'(0) = 0, \quad H_0'(1) = -2, \quad H_0'(2) = -2\gamma. \tag{33}$$

and

$$H_1(0) = 0, \quad H_1(1) = 0, \quad H_1(2) = 0, \tag{34}$$

$$H_1'(0) = 0, \quad H_1'(1) = 0, \quad H_1'(2) = 0. \tag{35}$$

The equations (30)- (35) is solved to obtain the solution components H_0 and H_1. Finally, a second order approximate solution of (30)- (35) is then obtained as

$$H(\eta) = H_0(\eta) + RH_1(\eta).$$

In what follows, the equations (30)- (35) are solved using MATHEMATICA software and report on approximate solutions shall be made.

2.1.2. Homotopy perturbation method(HPM)

In line with Ajadi and Zuilino[2], He[3 − 4], Chowdhury et al[5], we illustrate homotopy perturbation method for the nonlinear equation

$$A(u) - f(r) = 0, \quad r \in \Omega,$$

with the boundary conditions

$$B(u, \frac{\partial u}{\partial n}) = 0, \quad (r \in \partial\Omega),$$

where A is a general differential operator, B is a boundary operator, $f(r)$ is a known analytic function, and $\partial\Omega$ is the boundary of domain Ω. The operator A are generally divided into two parts; L and N, where L and N are linear and nonlinear parts of A respectively. Therefore, (10) may be written as

$$L(u) + N(u) - f(r) = 0.$$

We construct a homotopy $v(r, p) : \Omega \times [0, 1] \to \Re$ which satisfies

$$H(v, p) = [L(v) - L(u_0)] + pL(u_0)] + p[N(v) - f(r)] = 0,$$

or

$$H(v, p) = [L(u) - L(u_0)] + p[A(u) - f(r)] = 0.$$

where $p \in [0, 1]$ is called the homotopy parameter and u_0 is an initial approximation of (10). At the two extremes $p = 0$ and $p = 1$, we have

$$H(v, 0) = L(u) - L(u_0) = 0 \text{ and } H(v, 1) = A(u) - f(r) = 0.$$

In the interval $0 < p < 1$, then the homotopy $H(v, p)$ deforms from $L(u) - L(u_0)$ to $A(u) - f(r)$. Thus, the solution of $H1$-$H2$ may be expressed as

$$v = v_0 + pv_1 + p^2 v_2 + p^3 v_3 + \ldots$$

Eventually, at $p = 1$, the system takes the original form of the equation and the final stage of deformation gives the desired solution. Thus taking limit

$$u = \lim_{p \to 1} v = v_0 + v_1 + v_2 + \ldots$$

2.2. Numerical method

We solve (27)-(28) subject to the boundary condition (23)-(26) using the Matlab routine bvp4c which is based on finite difference implementation of the three-stage Lobatto formula. This collocation approach produces a continuously differentiable approximate solution that is fourth-order accurate.

In order to apply bvp4c to solve (22), the equation has to be transformed into a corresponding system of first-order ordinary differential equations. For that purpose, let $H = u_1$, $H' = u_2$, $H'' = u_3$, $H''' = u_4$ so that (27)-(28) become

$$u_1' = u_2,$$
$$u_2' = u_3,$$
$$u_3' = u_4,$$
$$u_4' = Ru_4 + Ru_1 u_4 + A_1 u_3$$

subject to appropriately renamed boundary conditions

$$u_1(0) = u_1(1) = 0, \quad u_2(0) = -2, \quad u_2(1) = -2\gamma.$$

3. RESULTS AND DISCUSSION

In this section, by applying the numerical method implemented on the Matlab package, we obtain the velocity profiles of the system and plotted for varying value of the defining parameters in the system. For the purpose of validating our results, as a test case, we consider the steady-state form of the system of equations by setting $A_0 = A_1 = 0$. The graphical demonstration of our results are in full agreement with known results in literature[1]. In the presence of the Hartmann number($A_1 \neq 0$), the radial and axial velocity profiles show a departure from the known results in literature.

3.1. Comparison with Existing Results in the Literature

The present work is an extension of the work of [1]. The steady-state model equation therein can easily be recovered from (22) by setting $A_0 = A_1 = A_2 = 0$. In Figure 1 the velocity profiles are obtained for Reynold's number $R = 2.0$ and varying values of the stretching velocity ratio γ of the upper disk to the lower one. The results are in perfect agreement with those reported in [1].

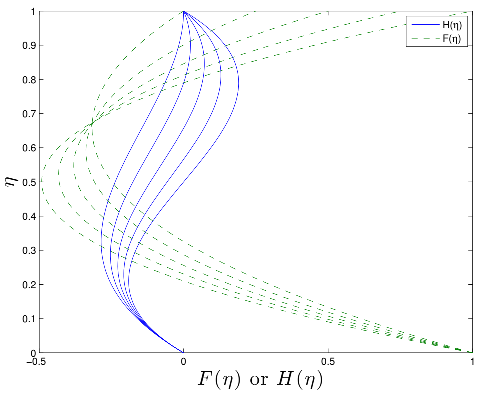

Figure 1. The recovered solution of [1] with $A_0 = A_1 = A_2 = 0$

Note that the term involving the constant A_0 in (22) comes from the temperature (unsteadiness) parameter introduced in our model. Hence, for the purpose of comparison with the steady-state model studied in [1], we will set A_0 and investigate the effect of the Hartmann number Ha embedded in the constant A_1. With $A_0 = 0$, we apply the bvp4c routine to obtain the following Figures.

4. CONCLUSION

In this article, we seek to obtain steady and unsteady state solutions for flow and heat transfer between two stretchable cylindrical channels enclosing an exothermic reaction source in the presence

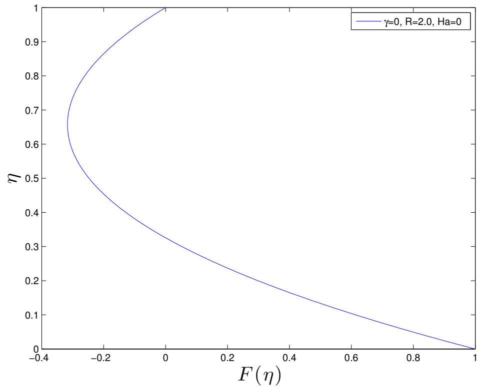

Figure 2. The solution profile in the radial direction for $\gamma = 0, R = 2.0$ and $Ha = 0$.

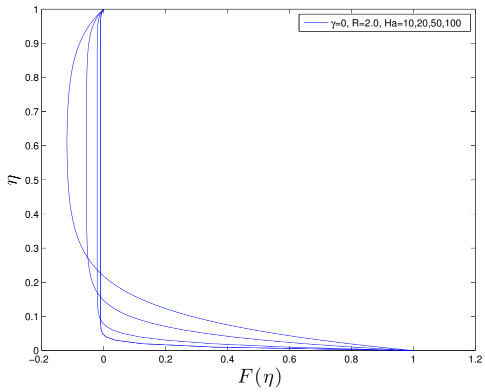

Figure 3. The effect of the Hartmann number Ha on the solution profile in the radial direction.

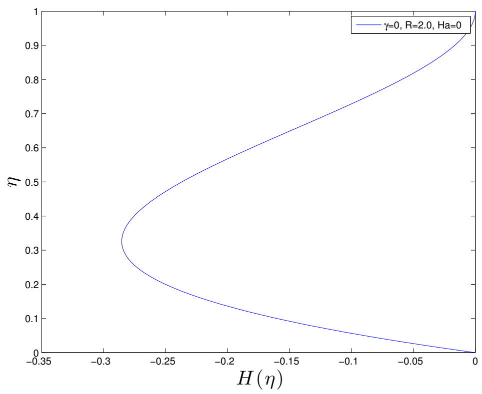

Figure 4. The solution profile in the vertical direction for $\gamma = 0, R = 2.0$ and $Ha = 0$.

of an accelerated stretching velocity. We subject our equations to perturbation methods and numerical solution for ease of comparison. In the interim, taking advantage of the numerical solution, we shall elucidate the effect of some parameters in the systems

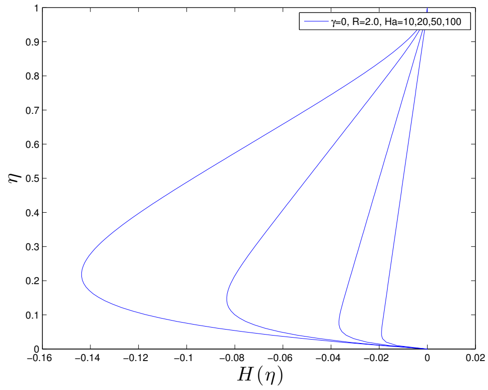

Figure 5. The effect of the Hartmann number Ha on the solution profile in the vertical direction.

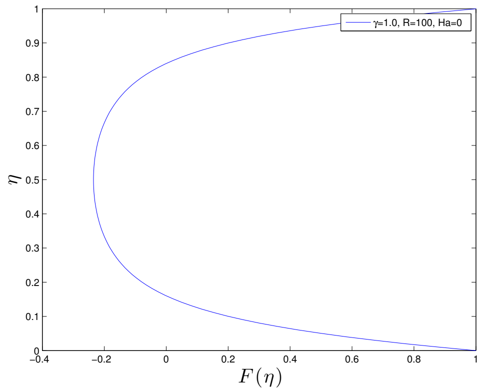

Figure 6. The solution profile in the radial direction for $\gamma = 1.0, R = 100$ and $Ha = 0$.

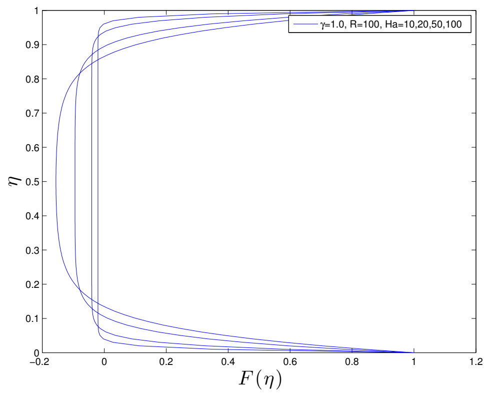

Figure 7. The effect of the Hartmann number Ha on the solution profile in the radial direction for $\gamma = 1.0, R = 100$.

on the flow and temperature profiles in the system. In particular, the effect of the porousity and reaction parameters on the heat and mass transfer is highly desirable. Graphical and tabular demonstrations of the solutions will be presented.

REFERENCES

[1] T. Fang and J. Zhang Flow between two stretchable disks - An exact solution of the Navier-Stokes equations. *International Communications in Heat and Mass Transfer*, 35 :892–895, 2008.

[2] S.O. Ajadi and M. Zuilino, Approximate analytical solutions of reaction–diffusion equations with exponential source term: Homotopy perturbation method (HPM), *Applied Mathematics Letters* 24(2011)1634–1639.

[3] J.H. He, Homotopy perturbation method: A new nonlinear analytical technique, *Applied Mathematics and Computation* 135 (2003) 73–79.

[4] J.H. He, Homotopy perturbation method for solving boundary value problems, *Physics Letters A* 350 (2006) 87–88.

[5] M.S.H. Chowdhury, T.H. Hassan, S. Mawa, A New Application of Homotopy Perturbation Method to the Reaction-diffusion Brusselator Model, *Procedia Social and Behavioral Sciences* 8(2010) 648–653

Conference on Modelling Fluid Flow (CMFF'15)
The 16th International Conference on Fluid Flow Technologies
Budapest, Hungary, September 1-4, 2015

INVESTIGATION OF RADIAL FORCES ACTING ON CENTRIFUGAL PUMP IMPELLER

Krzysztof Karaśkiewicz[1], Marek Szlaga[2], Waldemar Jędral[3], Ryszard Rohatyński[4]

[1] Corresponding author. Institute of Heat Engineering, Warsaw University of Technology. ul. Nowowiejska 25, 00-665 Warsaw, Poland; E-mail: kkara@itc.pw.edu.pl
[4] Corresponding author. Wrocław School of Banking, Wrocław. E-mail: rrohatynski.wez.uz.zgora.pl

ABSTRACT

Predictions of radial thrust in centrifugal pump with low specific speed were compared with measurements carried out for several rotational speeds. Apart from the predictions of the radial force, the calculations of axial thrust were also conducted, and correlation between thrust and the radial force was found. Similarity law of radial forces was checked within the range of the measured rotational speeds.

Keywords: axial thrust, centrifugal pump, CFD, radial force, radial thrust

NOMENCLATURE

d	[m]	diameter
F_a	[N]	axial force
F_r	[N]	radial force

1. INTRODUCTION

One of the important steps in the centrifugal pump design process is predicting hydraulic forces acting on the impeller. It enables to correctly select bearings in the centrifugal pump and to decide whether or not a balancing device should be used. If balancing disk or balancing drum is necessary the accurate value of axial force F_a (Eq. (1)) is essential.

$$F_a = \int_{r''}^{r_2}\int_0^{2\pi} p_{II}\left(r,\varphi\right) r dr d\varphi - \int_{r'}^{r_2}\int_0^{2\pi} p_I\left(r,\varphi\right) r dr d\varphi \pm \sum F_{remaining} \quad (1)$$

To decide whether a double volute instead of single volute should be used the accurate value of radial force is essential.

The components x and y of radial force depend on pressure distribution around the impeller.

$$F_{rx} = \int_{r'}^{r_2}\int_0^{2\pi} p_I\left(r,\varphi\right) tg\vartheta \cos\varphi r dr d\varphi + \int_0^{2\pi} p_2\left(\varphi\right) b'_2 r_2 \cos\varphi d\varphi \quad (2)$$

$$F_{ry} = \int_{r'}^{r_2}\int_0^{2\pi} p_I\left(r,\varphi\right) tg\vartheta \sin\varphi r dr d\varphi + \int_0^{2\pi} p_2\left(\varphi\right) b'_2 r_2 \sin\varphi d\varphi \quad (3)$$

where total radial force $F_r = \sqrt{F_{rx}^2 + F_{ry}^2}$.

The radial force depends on the head and on the diameter d and width b of the impeller. The pump head is a quadratic function of the rotational speed n so the force can be described as:

$$F_r \sim Hdb \sim n^2 d^3 b \quad (4)$$

The radial force is largest in high-speed pumps or pumps with large impeller diameters. Its value depends on the type of casing (single volute, double volute, diffuser) and is the function of the flow rate. The radial thrust reaches the highest values in single volute pumps at duty points far from the BEP. A pump operating outside acceptable flow range can suffer from bearing problems or even shaft breaking [1].

Pump designers readily refer to simple empirical formulas. The earliest one, based on one size of the pump only, was proposed by Stepanoff [2]. Agostinelli et al. [3] measuring radial thrust for sixteen different pumps extended the formula involving the effect of specific speed on radial force. Also Biheller [4] and the Hydraulic Institute

[5] proposed some other relationships. The values obtained by the HI were over-predicted for low specific speeds compared to those found by Agostinelli [3]. Later, the Hydraulic Institute corrected its values [6], so they comply well with the Agostinelli's ones [3]. The direction of the radial thrust cannot be found from theses relations.

Results of experimental and numerical investigations in this paper are presented for centrifugal pump with the rectangular cross-section volute.

2. MEASUREMENT METHOD

The tests were carried out on the test-bed presented in figure 1. The pump (3) with exchangeable impellers was the essential part of the test bed. In the tests, the impeller of specific speed n_s = 26 was used. The pump sucked water from tank (1) and delivered it to the same tank. Pressures before (4) and after (5) the pump, flow rate (6), rotational speed (7), torque (8) and radial force (11) were measured on the test-bed.

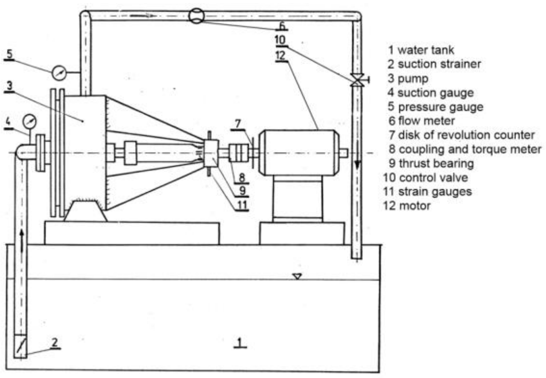

Figure 1. Pump test-bed

Volute casing of rectangular cross-section (Fig. 2) was made of wood, so it was easy to change its dimensions. In the presented investigations, the inlet volute width was b_3 = 40mm and was equal to the volute casing width b_4. The width of impeller outlet together with the shrouds was b_2 = 34mm and its diameter d_2 = 264mm.

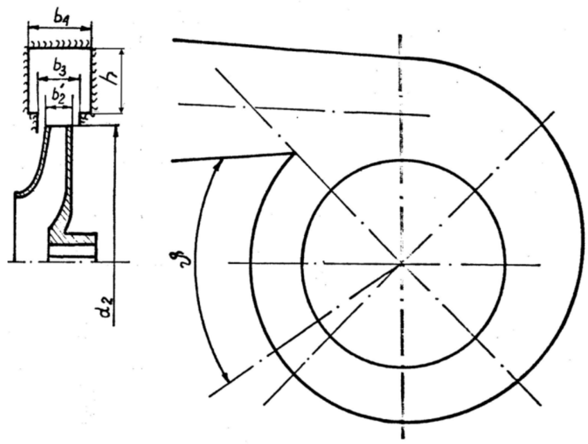

Figure 2. The volute casing of the pump tested

The radial force was measured with strain gauges attached to the shaft (p. 11 in Fig. 1).

The test stand is presented in Fig. 2. The shaft of pump tested (1) was supported by cylindrical (2) and ball (3) bearings. The radial force acting on the impeller is transmitted to the bearing bed (4) by the cylindrical bearing so the bed is bending.

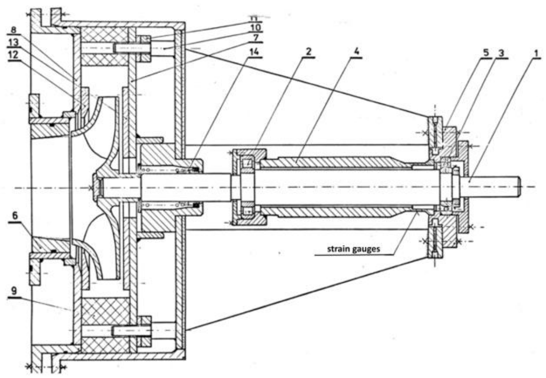

Figure 2. Test stand

In a bed part of the maximum bending moment the wall width is very thin, therefore largest is the strain. Two sets of the strain gauges were stick on over there for measurements of horizontal and vertical components of the radial force and this way the value and direction of the force.

The ball bearing (3), besides the radial force, balances the whole axial thrust therefore it can be heated to a high temperature. To avoid possibility of heating the strain gauges which are close to the bearing, the part (5) of the casing was cooled by water.

The shaft of the pump tested was coupled with motor shaft through double universal joint to protect against forces from the motor.

The mechanical shaft seal (14) was used to prevent the pump from leakage.

The accuracy of the measurements requires the shaft to be long enough in order to provide the large radial displacement of its end therefore the impeller was equipped with the radial seal instead of typical annular seal. The gap width of the seal was regulated by displacement of the diffuser inlet part (6).

Two disks (7) and (8) made the side walls of the volute (9). According to the width of the volute the disk (7) was displaced and fixed by distance elements (10)

The variations of the width of the volute inlet were possible because of the front (12) and rear (13) disks.

For calibration procedure, the shaft was lengthened to apply standard force G (Fig. 3). In this way the calibration curve was determined. The radial force F_r was calculated from the relationship (a= 310mm, b = 200mm, c = 640mm)

$$F_r = G\frac{a+b+c}{a+b} = 2{,}25G \qquad (5)$$

The uncertainty of calibration procedure was predicted from the equation

$$\delta_F = \frac{\Delta F}{F}$$

where $\Delta F = \left|\frac{\partial F}{\partial a}\right|\Delta a + \left|\frac{\partial F}{\partial b}\right|\Delta b + \left|\frac{\partial F}{\partial c}\right|\Delta c + \left|\frac{\partial F}{\partial G}\right|\Delta G$

Finally

$$\delta_F = \frac{G}{F}\left[\frac{c(\Delta a + \Delta b)}{(a+b)^2} + \frac{\Delta c}{a+b} + \frac{\Delta G(a+b+c)}{G(a+b)}\right]$$

For uncertainties Δa = Δb = 0,5mm, Δc = 1mm, $\Delta G/G$ = 0,002 the uncertainty δ_F = 0,4%

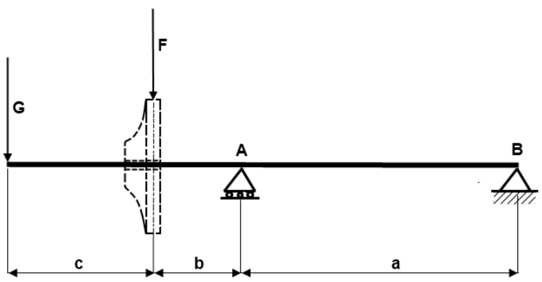

Figure 3. Schematic diagram of radial force *F* calibration

The investigations and predictions cover rotational speeds of n = 1150, 1300, 1450, 1600rpm for one volute casing.

3. COMPARISON OF NUMERICAL PREDICTIONS AND EXPERIMENTAL MEASUREMENTS

The ANSYS Fluent code was employed for numerical predictions of hydraulic forces acting on impeller. The grid covering the flow area consisted of 8.8x105 nodes. The mesh was made of tetrahedral cells. The minimum orthogonal quality of the mesh was 0.21 and the maximum aspect ratio was 24.5. A relatively coarse mesh was used, but it was found that it was enough to predict the pump H-Q curve properly. Therefore this kind of mesh was adopted to save CPU time. As a turbulence model, the standard k-ε model was used with standard wall functions. As for the boundary conditions, the mass flow rate was prescribed at the inlet of the computational domain and the outflow at the outlet of the pump. Figure 4 shows the 3D pump model with inlet part, impeller, volute and outlet channel and the corresponding grid.

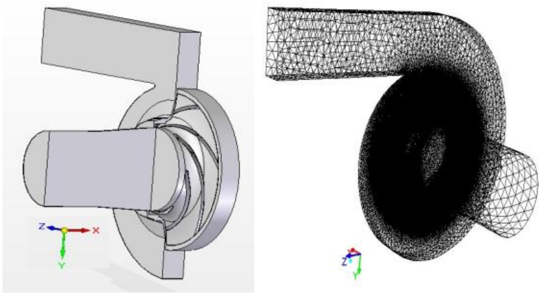

Figure 4. The pump model with corresponding grid

The predictions covered rotational speeds of n = 1300, 1450, 1600 rpm. The flow rate in Figures 6 is related to the rated (nominal) values Q_n taken from commercial data of the tested impeller.

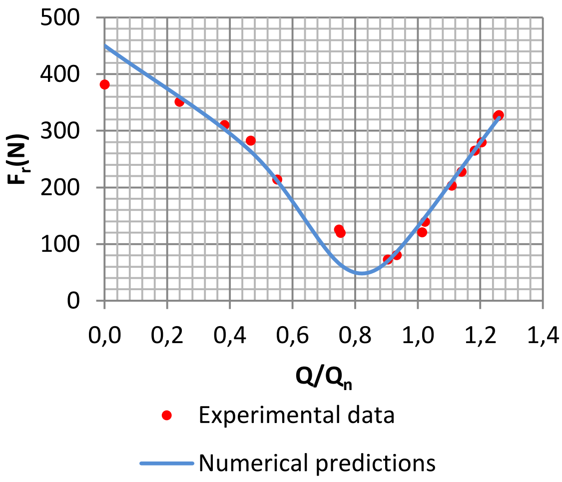

Figure 6a. Experimental and numerical investigations for n = 1300rpm

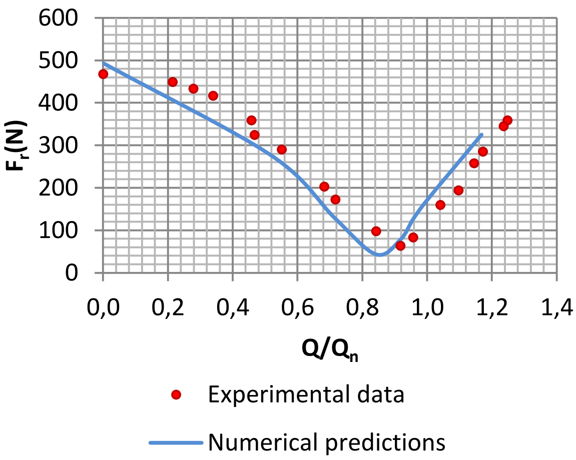

Figure 6b. Experimental and numerical investigations for n = 1450rpm

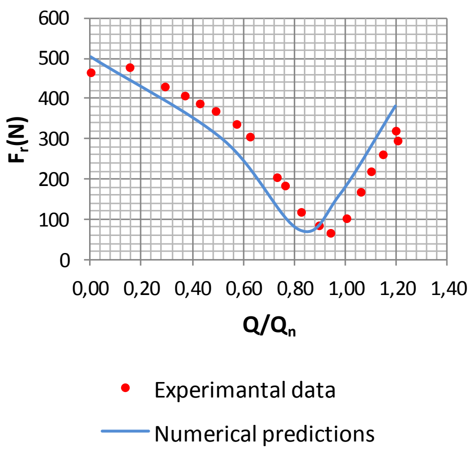

Figure 6c. Experimental and numerical investigations for n = 1600rpm

The predictions of the magnitude of the radial force are generally in accordance with the measurements. The value of the radial force for rotational speed n= 1300 rpm at shut off flow Q = 0 is over-predicted, but the shape of the radial force curve is very similar to that determined by measurements. The minimal values of the radial force both measured and predicted are below nominal flow rates. Figure 7 is showing efficiency curves predicted for the three speeds.

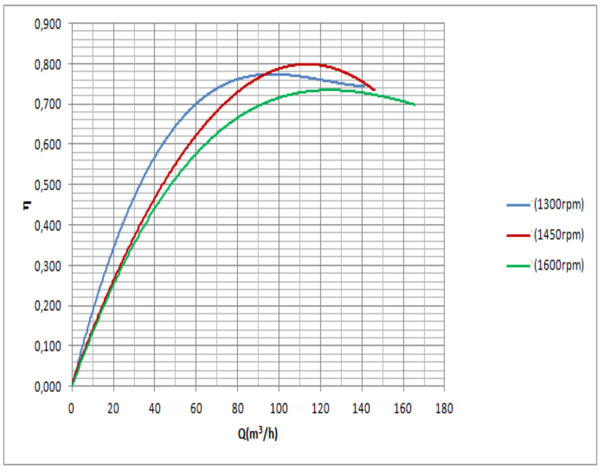

Figure 7. Efficiency curves predicted for different speeds

In Figures 6a,b,c the radial force is presented versus flow rate related to BEP values.

Correlation between minimal radial force and BEP is obvious from the figures.

Figures 8a,b shows direction of both measured and predicted radial force. The calculated results do not coincide well with measurements; however, satisfactory agreement was achieved between the magnitudes of experimental and calculated radial force. The calculations were made using the frozen rotor approach with one impeller blade positioned opposite to the tongue, which might have some influence on the pressure field between the rotor and the volute.

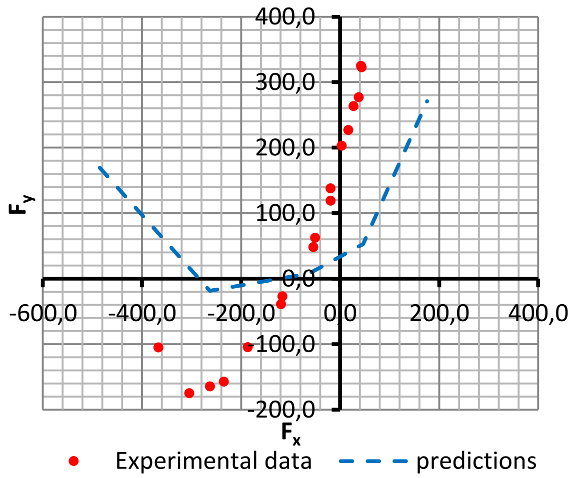

Figure 8a. The direction of radial force for n = 1300rpm

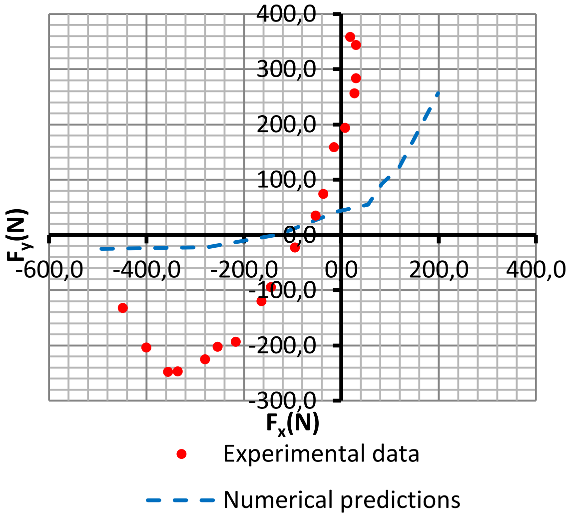

Fig. 8b The direction of radial force for n = 1450rpm

The frozen rotor scheme supports steady-state prediction in the local frame of reference on each side of the interface. This scheme is used for non-symmetric flow domain of volute. The relative circumferential position of the impeller with respect to the volute tongue is fixed in time. In this case, the solution provides a snapshot of the flow regime. The predictions thus depend on the rotor position, so one can obtain inadequate results for local flow fields.

The advantages of the frozen rotor model, compared to the unsteady calculations are robustness of the model and lower demand for computer resources. Steady state calculations can't capture unfortunately all interaction effects with complete fidelity.

Asymmetrical pressure distribution at the outlet of impeller produces not only the radial force and its bending moment acting on the shaft, but it also moves the axial thrust centre off the impeller axis, what creates an additional bending moment. Pressure asymmetry at the impeller outlet has an impact on the impeller sidewall gaps (Fig. 9) so one can expect that the moments of axial thrust and radial thrust have similar form.

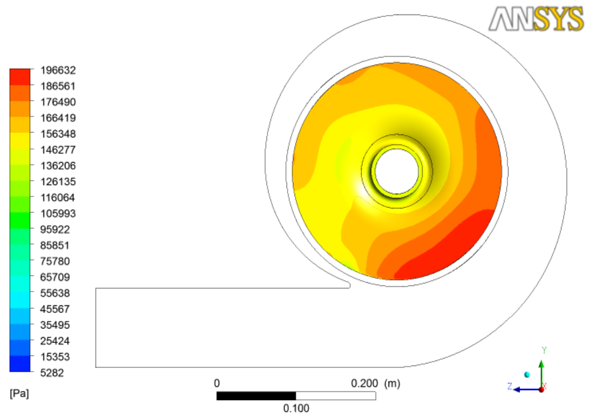

Figure 9. Static pressure distribution on rear shroud of impeller

This interesting correlation between both distributions is presented in Figure 10 for the rotational speed of n=1450rpm.

The presented data are in dimensionless form related to their maximum values for shut off flow. The phenomenon of axial thrust moment is usually ignored by pump designers when analysing shaft stresses. Luckily, this moment is opposite to the radial force moment, so it lessens the shaft load.

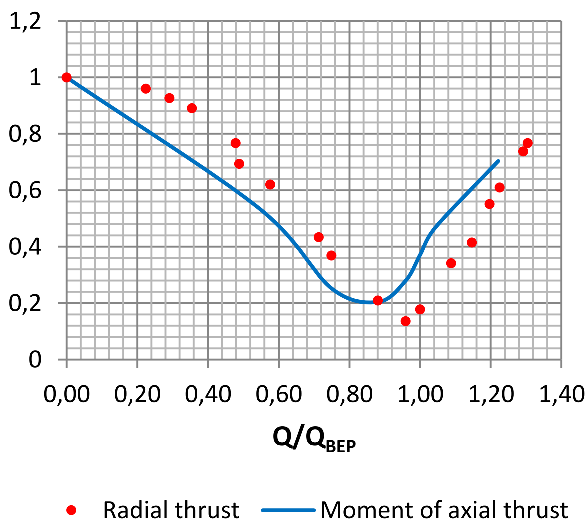

Figure 10. Comparison between radial thrust and axial thrust moment for rotational speed 1450rpm

One could expect similar characteristics of the radial force, since it depends on rotational speed for the same impeller geometry. Figure 11 presents distributions of force coefficient against flow coefficient for five different rotational speeds.

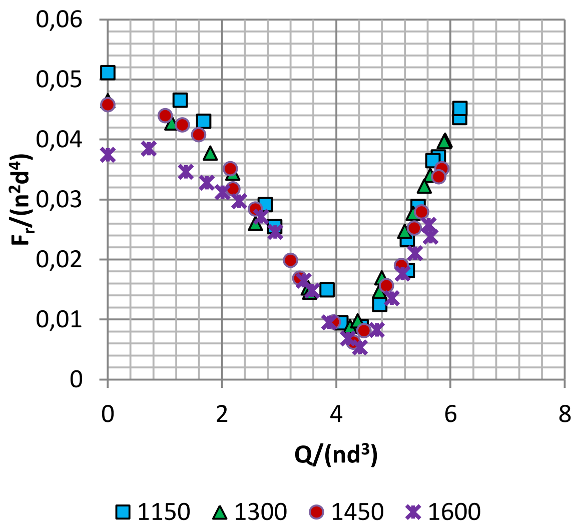

Figure 11. Force coefficient distributions for five rotational speeds

For rotational speeds equal to or less than nominal speed, the similarity law is quite well satisfied. The discrepancy appears at highest rotational speed for low flow coefficients and is caused by higher losses connected with higher speeds.

The components of radial force showing the force direction are presented in Figure 12.

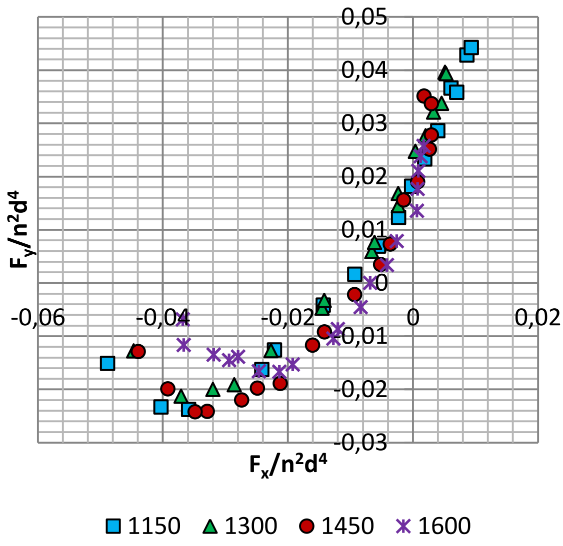

Figure 12. The direction of measured radial force

The discrepancies appear (as previously) at highest rotational speed for low flows, due to the same reasons as mentioned above.

4. CONCLUSIONS

The centrifugal pump of specific speed n_s=26 with the volute of the rectangular cross-section was tested and results of radial thrust for several rotational speeds were presented.

For pumps with speed control, radial thrust for different than nominal rotational speeds can be achieved based on similarity law. In the case of pump operating with speeds higher than nominal one, true radial thrust is lower than that estimated from the similarity law, so the predictions are on the safe side.

CFD with the frozen rotor scheme predicts with sufficient accuracy magnitude of radial thrust in the whole range of flows. When pump operates in the narrow range around nominal flow rate, optimization of pump designing is possible.

The frozen rotor approach may be the reason for erroneous prediction of the radial force direction. Therefore, several rotor positions should be calculated, and the results averaged for performance prediction, or predictions of one impeller position should be used as a starting point for a transient sliding-mesh simulation.

There is a correlation between distributions of radial force and axial thrust moment. It results from asymmetry of pressure distribution around the impeller, which causes asymmetry of the pressure field acting on the front shroud of the impeller.

REFERENCES

[1] I.Karassik, J.Messina, P.Cooper, C.Heald -*Pump Handbook*, Fourth Edition, McGraw-Hill Prof., 2008.

[2] A.J. Stepanoff - *Centrifugal and Axial Flow Pumps: Theory, Design, and Application*, John Wiley & Sons, 1957 also Krieger Publishing Company, 1992.

[3] Agostinelli, A., Nobles, D., and Mockridge, C. R., *An Experimental Investigation of Radial Thrust in Centrifugal Pumps*, ASME J. Eng. Power, 80, 1960, pp. 120–126.

[4] Biheller, H. J., *Radial Forces on the Impeller of Centrifugal Pumps with Volute, Semivolute, and Fully Concentric Casings*, ASME J. Eng. Power, 85, 1965, pp. 319–323.

[5] *Hydraulic Institute Standards For Centrifugal, Rotary & Reciprocating Pumps*, twelfth edition, 1969, Hydraulic Institute, New York, N. Y.

[6] *Hydraulic Institute Standards for Centrifugal, Rotary & Reciprocating Pumps*, Hydraulic Institute, Parsippany, N.J, 2009.

THE BEHAVIOUR OF MHD FLOW AND HEAT TRANSFER IN THE PRESENCE OF HEAT SOURCE OVER A STRETCHING SHEET

Matthew Oluwafemi LAWAL[1] and Suraju Olusegun AJADI[2]

[1]Corresponding Author, Department of Mathematics, Adeyemi Federal University of Education, P.M.B. 520, Ondo. Nigeria. Tel:+234 803 278 6997, e-mail: femathlaw@yahoo.com
[2]Department of Mathematics, Obafemi Awolowo University, Ile-Ife. Nigeria. e-mail: sajadi@oauife.edu.ng

ABSTRACT
This article is based on the study of the behaviour of MHD flow and heat transfer in the presence of heat source over a stretching sheet. The steady state two dimensional partial differential governing equations were subjected to dimensionless variables to elucidate some relevant dimensionless parameters in the system. The Homotopy Perturbation Method (HPM) was employed to solve the system of dimensionless equations and the approximate analytical solutions obtained were further analyzed using the MAPLE 17 symbolic platform. It was observed that the flow velocity within the boundary layer increases with increase in magnetic field. Further parametric analysis reveals that the temperature decrease with Hartmann number, Prandtl number and heat sink parameter, while it increases with heat source parameter. Graphical demonstrations of these solutions shed more lights on the behaviour of the system.

Keywords: chemical reaction, heat source, HPM, MHD boundary layer, pressure gradient, stretching sheet.

NOMENCLATURE

B_O	[-]	applied uniform magnetic field
C	[-]	species concentration
C_P	$[kgm^2/s^0C]$	specific heat capacity at constant pressure
C_∞	[mol/m^3]	concentration of the fluid far away from the sheet wall
C_w	[mol/m^3]	concentration at the wall
D	$[m^2/s]$	mass diffusion coefficient
M	[-]	Hartmann number
P	[Nm^{-2}]	Pressure
Pr	[-]	Prandtl number
Q_O	[-]	heat generation or absorption
Q	[J]	internal heat generation term
Re	[-]	Reynolds number
Sc	[-]	Schmidt number
T	$[^0C]$	temperature of the fluid
T_w	$[^0C]$	temperature of the sheet wall
T_∞	$[^0C]$	free stream temperature
U_e	$[m/s]$	free stream velocity
u, v	$[m/s]$	velocity components in x and y directions respectively
$\hat{u}$, $\hat{v}$	[-]	dimensionless velocity components in x and y directions respectively

Greek Symbols

α	$[m^2/s]$	thermal diffusivity
δ	[mol/s]	rate of chemical reaction
κ	[kgm/$^0Cs^3$]	fluid thermal conductivity
λ	[-]	heat source or sink Parameter
μ	$[kg/ms]$	coefficient of fluid viscosity
ν	$[m^2/s]$	kinematic fluid viscosity
ϕ	[-]	dimensionless concentration
ρ	[kg/m^3]	fluid density
σ	[$ohm^{-1}m^{-1}$]	electrical conductivity of fluid
τ	[-]	chemical reaction parameter
θ	[-]	dimensionless temperature

Subscripts and Superscripts

m	[-]	pressure gradient parameter
n	[-]	order of reaction
w	[-]	condition at the wall

1. INTRODUCTION

Simultaneous heat and mass transfer from different geometries embedded in porous medium has many engineering and geophysical applications such as geothermal reservoirs, drying of porous solids, thermal insulation, enhanced oil recovery, packed-bed catalytic reactors, cooling of nuclear reactors and underground energy transport. The science of magneto hydrodynamics (MHD) was concerned with geophysical and astrophysical problem for a number of years. In recent years, the possible use of MHD is to affect a flow stream of an electrically conducting fluid for the purpose of thermal protection, braking, propulsion and control. Ravikumar [1] observed from the point of applications, model studies on the effect of magnetic field on the convection flow have been made by several investigators. From technological point of view, MHD convection flow problems are also very significant in the field of stellar and planetary magnetospheres, aeronautics, chemical engineering and electronics.

Kandasamy [2] studied the effects of chemical reaction, heat and mass transfer on boundary layer flow over a wedge with heat radiation in the presence of suction or injection using an appropriate numerical solution.

Devi and Kandasamy [3] studied the effects of heat and mass transfer on nonlinear boundary layer flow over a wedge with suction or injection in which the effects of induced magnetic field is included in the analysis. Muthucumaraswamy [4] investigated the effects of heat and mass transfer on a continuously moving isothermal vertical surface with uniform suction. Sharma [5] discussed in detail the effect of variable thermal conductivity in MHD fluid flow over a stretching sheet considering heat source and sink parameter.

Yih [6] presented an analysis of the forced convection boundary layer flow over a wedge with uniform suction/ blowing, where as Watanabe [7] investigated the behavior of the boundary layer over a wedge with suction or injection in forced flow. Krishnendu [8] analyzed the effect of heat source/ sink on MHD flow and heat transfer over a shrinking sheet with mass suction by transforming the governing partial differential equations into self similar ordinary differential equations using similarity transformations which were then solved by finite difference method using quasilinearization technique and found that velocity inside the boundary layer increases with increase of wall mass suction and magnetic field and accordingly the thickness of the momentum boundary layer decreases.

Pijush *et al* [9] noticed that $0 \leq m \leq 1$ with $m = 0$ for the boundary-layer flow over a stationary flat plate which is the Blasius equation and from Dulal *et al* [10] $m = 1$ is for the flow near the stagnation point on an infinite wall, *x* and *y* coordinates measured along the surface of the wedge and normal to it. Baoheng [11] presented approximate analytical solution to Falkner-Skan wedge flow with the permeable wall of uniform suction; with the boundary conditions of $f(0) = \gamma > 0$, $f'(0) = 0$, $f'(+\infty) = 0$, i.e. the permeable wall mass transfer conditions of uniform suction, is given.

This paper is basically to study the behaviour of velocity profile in the presence of pressure gradient and to showcase the contribution of chemical reaction to temperature and concentration profile by employing Homotopy Perturbation Method (HPM) and the approximate analytical solutions obtained were subjected to further analysis taking advantage of the MAPLE 17 package. It also investigated the effect of various flow parameters such as Schmidt number, Prandtl number and Hartmann on the system.

2. FORMULATION OF THE PROBLEM

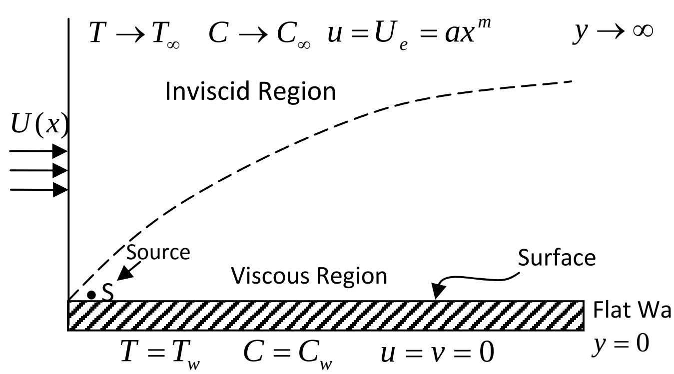

Figure. 1. Schematic Diagram of the Problem

We consider the non-isothermal, unsteady, two dimensional flow of a binary fluid in the system. The fluid properties ρ, μ, C_p, κ and D are considered constant, viscous dissipation is neglected, and there are no homogenous chemical reactions. $Q = Q_O(T - T_\infty)$ is the internal heat generation term.

The governing equations of the MHD boundary layer flow in the presence of uniform transverse magnetic field in the laminar region are

$$\frac{\partial u}{\partial x} + \frac{\partial v}{\partial y} = 0, \tag{1}$$

$$u\frac{\partial u}{\partial x} + v\frac{\partial v}{\partial y} = \upsilon\frac{\partial^2 v}{\partial y^2} - \sigma\frac{B_o^2}{\rho}u - \frac{1}{\rho}\frac{\partial P}{\partial x}, \tag{2}$$

$$u\frac{\partial T}{\partial x} + v\frac{\partial T}{\partial y} = \frac{\kappa}{\rho C_P}\frac{\partial^2 T}{\partial y^2} + \frac{Q_O}{\rho C_P}(T - T_\infty) + \frac{Q}{\rho C_P}C^n e^{-\frac{E}{RT}} \tag{3}$$

$$u\frac{\partial C}{\partial x} + v\frac{\partial C}{\partial y} = D\frac{\partial^2 C}{\partial y^2} - \delta C^n e^{-\frac{E}{RT}}. \tag{4}$$

The boundary conditions for the velocity components, temperature and concentration are given by:

$$u = 0 \ v = -v_W \text{ at } y = 0; u = ax^m \quad \text{as} \quad y \to \infty, \tag{5}$$

$$T = T_W \quad \text{at } y = 0; \qquad T \to T_\infty \quad \text{as} \quad y \to \infty, \tag{6}$$

$$C = C_W \quad \text{at } y = 0; \qquad C \to C_\infty \quad \text{as} \quad y \to \infty. \tag{7}$$

Where $a > 0$ is the shrinking constant and $v_W > 0$ is a prescribed distribution of wall mass suction through the porous sheet.

Introducing the stream function ψ, the velocity components *u* and *v* can be written as:

$$u = \frac{\partial \psi}{\partial y} \text{ and } v = -\frac{\partial \psi}{\partial x}. \tag{8}$$

We now introduced the following dimensionless quantities and parameters:

$$\psi = \sqrt{\upsilon a}\,x^{\frac{m+1}{2}} f(\eta), \quad \eta = \frac{y}{x}\sqrt{\text{Re}} = \sqrt{\frac{a}{\upsilon}}\,y x^{\frac{m-1}{2}},$$

$$U_e = ax^m, \quad \theta = \frac{T - T_\infty}{T_w - T_\infty}, \quad \phi = \frac{C - C_\infty}{C_w - C_\infty} \tag{9}$$

The transformed momentum Eq. (2) becomes

$$f''' + \frac{m+1}{2}ff'' + m\left(1 - (f')^2\right) - M^2 f' = 0, \tag{10}$$

$$f(0) = 0, \ f'(0) = 0, \ f'(\infty) = 1.$$

The energy Eq. (3) reduces

$$\theta'' + \Pr\left(\frac{m+1}{2}f\theta' + \lambda\theta\right) + \tau\phi e^{\theta} = 0, \tag{11}$$

$$\theta(0) = 1, \quad \theta(\infty) = 0$$

and the specie Eq. (4) gives

$$\phi'' + Sc\left(\frac{m+1}{2}f\phi' - \tau\phi e^{\theta}\right) = 0 \tag{12}$$

$$\phi(0) = 1, \quad \phi(\infty) = 0$$

Where primes denote the differentiation with respect to η such that $\text{Re} = \frac{xU_e}{\upsilon} = \frac{ax^{m+1}}{\upsilon}$,

$S_C = \frac{\upsilon}{D}$, $\tau = \frac{\delta v}{U^2}$, $\Pr = \frac{\mu C_P}{\kappa}$,

$M = \left(\frac{\sigma B_0^2}{c\rho}\right)^{\frac{1}{2}}$ and $\lambda = \frac{Q_O}{\rho C_P a}$.

3. MATHEMATICAL PROCEDURE AND SOLUTION

The Homotopy perturbation method (HPM) is based on the concept of topology, which has been discovered to be an effective and efficient tool for solving non-linear equations [12-14]. To illustrate Homotopy perturbation method, we consider the nonlinear equation:

$$A(u) - f(r) = 0, \ r \in \Omega \tag{13}$$

with the boundary conditions:

$$B\left(u, \frac{du}{dn}\right) = 0, \ (r \in \Gamma), \tag{14}$$

where *A* is a general differential operator, *B* is a boundary operator, $f(r)$ is a known analytic function, and Γ is the boundary of domain Ω. The operator A are generally divided into two parts; *L* and *N,* where *L* and *N* are linear and nonlinear parts of *A* respectively. Therefore, (4) may be written as

$$L(u) + N(u) - f(r) = 0. \tag{15}$$

We construct a Homotopy $v(r, p): \Omega \times [0,1] \rightarrow \Re$

$$H(v, p) = [L(v) - L(u_O)] + pL(u_O) + p[N(u) - f(r)] = 0, \tag{16}$$

Where $p \in [0,1]$ is called the Homotopy parameter and u_O is an initial approximation of Eq. (15). At the two extremes $p = 0$ and $p = 1$, we have

$$H(v,0) = L(v) - L(u_O) = 0 \text{ and } H(v,1) = A(u) - f(r) = 0 \tag{17}$$

In the interval $0 < p < 1$, then the Homotopy $H(v, p)$ deforms from $L(v) - L(u_O)$ to $A(u) - f(r)$. Thus, the solution of Eqs. (10), (11) and (12) may be expressed as

$$v = v_O + p^1 v_1 + p^2 v_2 + p^3 v_3 + p^4 v_4. \tag{18}$$

Eventually, at $p = 1$, the system takes the original form of the equation and the final stage of deformation gives the desired solution. Thus taking limits

$$u = \lim_{p \to 1} v = v_O + v_1 + v_2 + v_3 + v_4 \quad . \tag{19}$$

We start by applying the Homotopy perturbation technique to Eqs. (14)-(16) and we define the Homotopy as

$$f''' - f_0''' + pf_0''' + p\left(\frac{m+1}{2} ff'' + m\left(1 - (f')^2\right) - M^2 f'\right) = 0 \tag{20}$$

$$\theta'' - \theta_0'' + p\theta_0'' + p\left[\Pr\left(\frac{m+1}{2} f\theta' + \lambda\theta + \tau\theta e^{\theta}\right)\right] = 0, \tag{21}$$

$$\phi'' - \phi_0'' + p\phi_0'' + p\left(Sc\frac{m+1}{2} f\phi' - Sc\,\tau\phi e^{\theta}\right) = 0. \tag{22}$$

Suppose that the solutions of f, θ and ϕ take the form

$$\left.\begin{aligned} f(\eta) &= f_0(\eta) + pf_1(\eta) + p^2 f_2(\eta) + p^3 f_0(\eta) + \ldots \\ \theta(\eta) &= \theta_0(\eta) + p\theta_1(\eta) + p^2\theta_2(\eta) + p^3\theta_0(\eta) + \ldots \\ \phi(\eta) &= \phi_0(\eta) + p\phi_1(\eta) + p^2\phi_2(\eta) + p^3\phi_0(\eta) + \ldots \end{aligned}\right\} \tag{23}$$

Substituting Eq. (23) into Eqn. (10) and picking terms in order of *p*, we have

$$p^O : f_0''' - f_0''' = 0 \ , \tag{24}$$

$$p^1 : f_1''' + f_0''' + \frac{m+1}{2} f_0 f_0'' + m[1 - (f_0')^2] - M^2 f_0' = 0, \tag{25}$$

$$p^2 : f_2''' + \frac{m+1}{2}\left(f_0 f_1'' + f_1 f_0''\right) - m\left(2 f_0' f_1'\right) - M^2 f_1' = 0 \tag{26}$$

$$f(0) = 0, \ f'(0) = 0, \ f'(\infty) = 1.$$

From the momentum equation with the boundary conditions we take our initial guess to be

$$f_0 = \left(\eta - (1 - e^{-\eta})\right) \tag{27}$$

Solving equations (30)

Using the boundary condition we have

$$\begin{aligned} f_1 = &-\frac{1}{16}e^{-2\eta}m + \frac{1}{2}e^{-\eta}\eta m + 3me^{-\eta} + \frac{1}{16}e^{-2\eta} + \frac{1}{2}e^{-\eta}\eta + M^2 e^{-\eta} \\ &+ \frac{1}{6}M^2\eta^3 + \frac{1}{2}\left(\frac{1}{4}M^2 e^{-4} - \frac{9}{4}M^2 - \frac{1}{32}e^{-8}m + \frac{9}{8}e^{-4}m + \frac{1}{32}e^{-8} + \frac{3}{8}e^{-4}\right. \\ &\left. + \frac{3}{32} - \frac{19}{32}m\right)\eta^2 + \left(M^2 + \frac{19}{8}m - \frac{3}{8}\right)\eta - M^2 - \frac{47}{16}m - \frac{1}{16} \end{aligned} \tag{28}$$

The solutions of f_2, f_3 and f_4 are obtained but could not be written here for space sake.

The fourth order approximation is given by

$$f = f_O + f_1 + f_2 + f_3 + f_4 \ldots \tag{29}$$

Similarly Substituting Eq. (23) in Eq. (15) and picking terms in order of *p*, we have

$$p^{O}: \theta_0'' - \theta_0'' = 0 \qquad (30)$$

$$p^{1}: \theta_1'' + \theta_0'' + \frac{m+1}{2} f_0 \theta_0' + \lambda\theta_0 + \tau e^{\theta_0} = 0 \qquad (31)$$

$$p^{2}: \theta_2'' + \Pr \frac{m+1}{2}\left(f_0\theta_1' + f_1\theta_0'\right) + \lambda\theta_1 + \tau\theta_1 e^{\theta_0} = 0 \qquad (32)$$

$$\theta(0) = 0,\ \theta(\infty) = 0.$$

From the energy equation with the boundary conditions we choose our initial guess to be

$$\theta_0 = e^{-\eta}. \qquad (33)$$

The temperature being a decreasing function of chemical reaction. Energy is been absorbed for reaction to take place.

Solving Eq. (31) introducing Eqs. (27) and (33) using the boundary condition we have

$$\begin{aligned}\theta_1 = {} & -e^{-\eta} - \frac{1}{2}\Pr \eta m e^{-\eta} - \frac{1}{2}\Pr m e^{-\eta} - \frac{1}{2}\Pr \eta e^{-\eta} - \frac{1}{2}\Pr e^{-\eta} - \lambda e^{-\eta} \\ & - \tau e^{-\eta} - \frac{1}{8}\Pr m e^{-2\eta} - \frac{1}{8}\Pr e^{-2\eta} - \frac{1}{4}e^{-2\eta}\tau + \Big(\frac{5}{8}\Pr m e^{-4} \\ & + \frac{1}{32}\Pr m e^{-8} + \frac{5}{8}\Pr m e^{-4} + \frac{1}{4}\lambda e^{-4} + \frac{1}{4}\tau e^{-4} + \frac{1}{32}\Pr e^{-8} \\ & + \frac{1}{16}\tau e^{-8} + \frac{1}{4}e^{-4} - \frac{1}{4} - \frac{5}{32}\Pr m - \frac{5}{32}\Pr - \frac{1}{4}\lambda - \frac{5}{16}\tau\Big)\eta \\ & + \frac{5}{8}\Pr m + \frac{5}{8}\Pr + \lambda + \frac{5}{4}\tau + 1 \end{aligned} \qquad (34)$$

The solutions of θ_2, θ_3 and θ_4 are gotten but could not be written here for space and ambiguity sake.

The fourth order approximation is given by

$$\theta = \theta_O + \theta_1 + \theta_2 + \theta_3 \ldots \qquad (35)$$

Similarly Substituting (28) in (16) and picking terms in order of *p*, we have

$$p^{O}: \phi_0'' - \phi_0'' = 0, \qquad (36)$$

$$p^{1}: \phi_1'' + \phi_0'' + \frac{m+1}{2} Sc f_0 \phi_0' - \tau Sc \operatorname{Re} \phi_0 e^{\theta_0} = 0, \qquad (37)$$

$$p^{2}: \phi_2'' + \frac{m+1}{2} Sc\left(f_0\theta_1' + f_1\theta_0'\right) - \tau Sc \operatorname{Re} \phi_1 e^{\theta_0} = 0, \qquad (38)$$

$$\phi(0) = 0,\ \phi(\infty) = 0.$$

From the specie equation with the boundary conditions we choose our initial guess to be

$$\phi_0 = e^{-\eta}. \qquad (39)$$

Solving equations (47)

$$\phi_1'' = -\phi_0'' - \frac{m+1}{2} Sc f_0 \phi_0' + \tau Sc \operatorname{Re} \phi_0 e^{\theta_0} \qquad (40)$$

$$\phi_1'' = -e^{-\eta} + \frac{m+1}{2} Sc\left(\eta - (1 - e^{-\eta})\right)e^{-\eta} + \tau Sc \operatorname{Re} \phi_0 (1 + \theta_0 + \frac{\theta_o^2}{2})$$

The solutions of ϕ_1, ϕ_2, ϕ_3 and ϕ_4 are gotten but could not be written here for space and ambiguity sake.

The fourth order approximation is given by

$$\phi = \phi_0 + \phi_1 + \phi_1 + \phi_2 + .\phi_3 ..$$

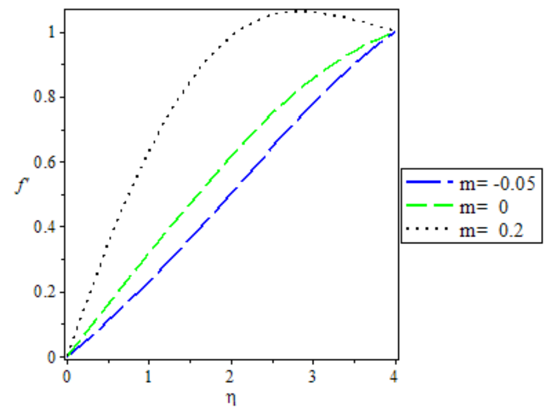

Figure 2. Graph of f' vs η for some m, $M=0.2$

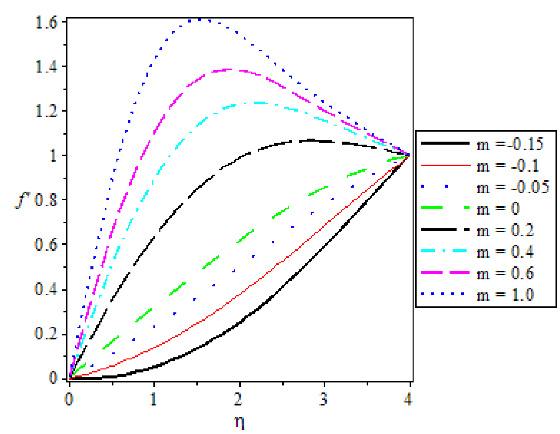

Figure 3. Graph of f' vs η for some m at *M=0.2*

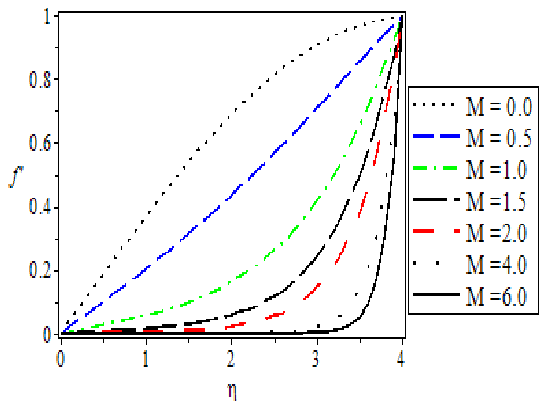

Figure 4. Plot of f' vs η for some M at m=*0.01*

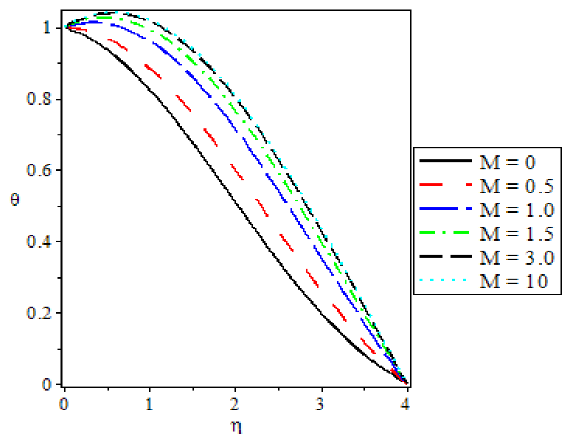

Figure 5. Plot of θ vs η for some M at *m=0.01, Pr=0.2,* $\lambda = 0.05$ and $\tau = 0.1$.

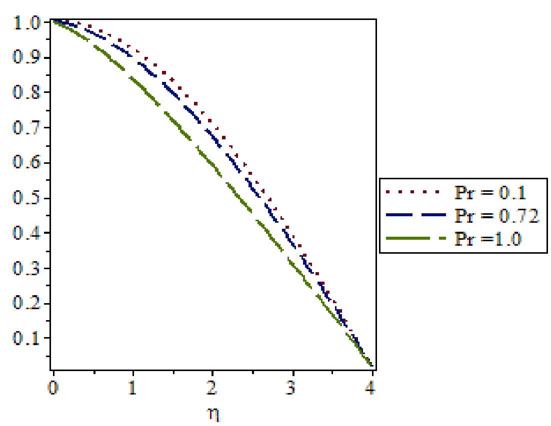

Figure 6. Plot of θ vs η without chemical reaction at $m = 0.01$ $Sc = 0.62$, $\lambda = 0.05$ and $\tau = 0$.

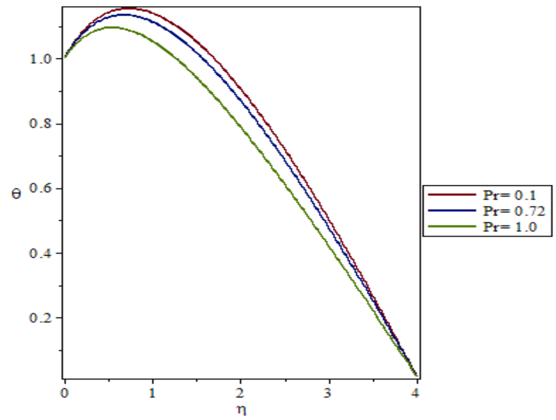

Figure 7. Plot of θ vs η, $m = 0.01$, $Sc = 0.62$, $\lambda = 0.05$ and $\tau := 0.5$.

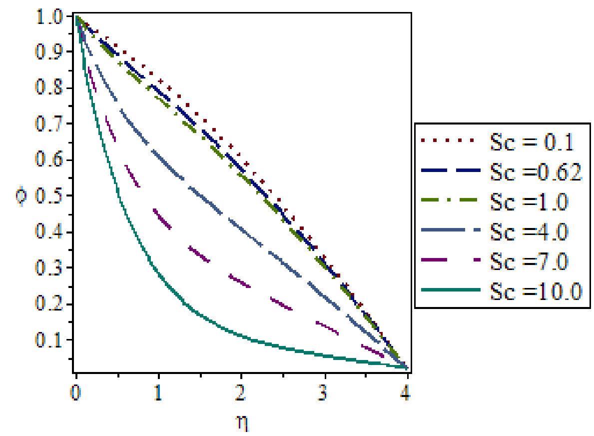

Figure 8. Plot of ϕ vs η for some Sc at $m = 0.01$, $\Pr = 0.72$, $\lambda = 0.01$, $M = 0.5$ and $\tau = 0.1$

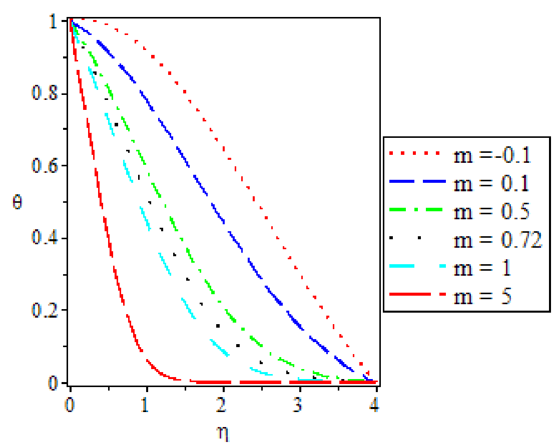

Figure 9. Plot of vs η for some m at $\Pr = 0.72$, $Sc = 0.62$, $\lambda = 0.05$, $\mathrm{Re} = 1$, $\tau = 0.1$ and $M = 0.1$

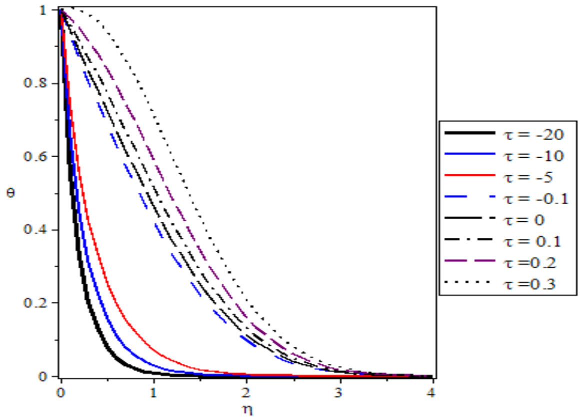

Figure 10. Plot of θ vs η for some τ at $m = 0.5$, $\Pr = 1$, $Sc = 0.62$, $\lambda = 0.01$, $\mathrm{Re} = 1$, $M = 0.1$

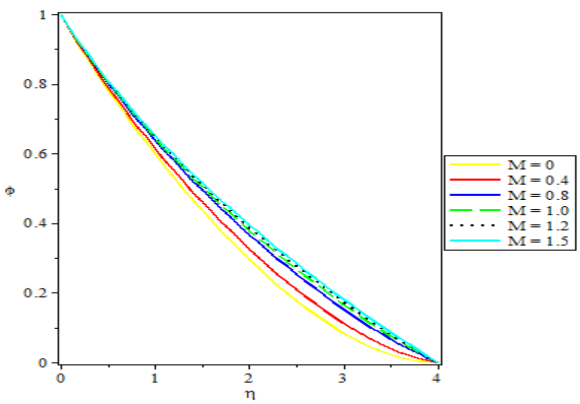

Figure 11. Plot of ϕ vs η for some M at $m = 0.01$, $\Pr = 0.72$, $Sc = 0.62$ $\lambda = 0.01$ and $\tau = 0.1$

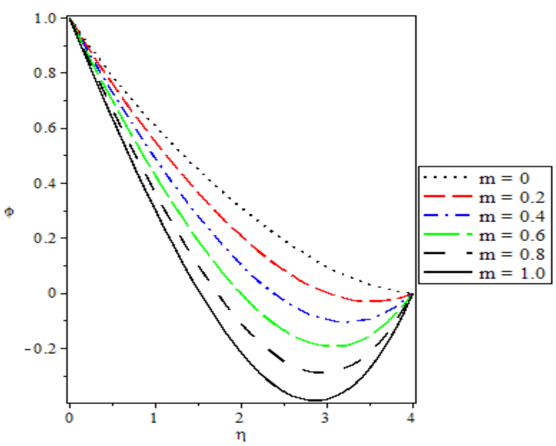

Figure 12. The Plot of ϕ vs η for some m at $M = 0.2$, $\Pr = 0.72$, $Sc = 0.62$ $\lambda = 0.05$ and $\tau = 0.1$

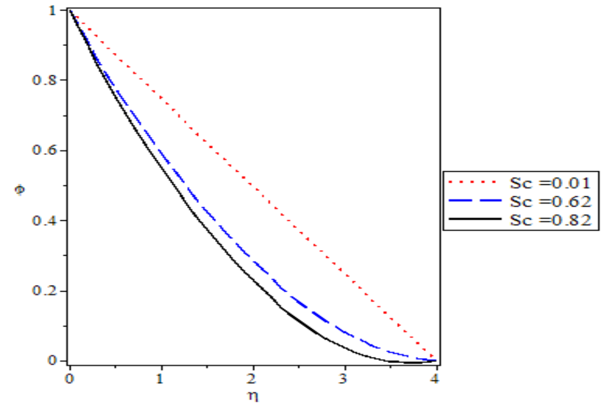

Figure 13. Plot of ϕ vs η for some Sc at $M = 0.2$, $\Pr = 0.72$, $\lambda = 0.05$ $\mathrm{Re} = 1$ and $\tau = 0.1$

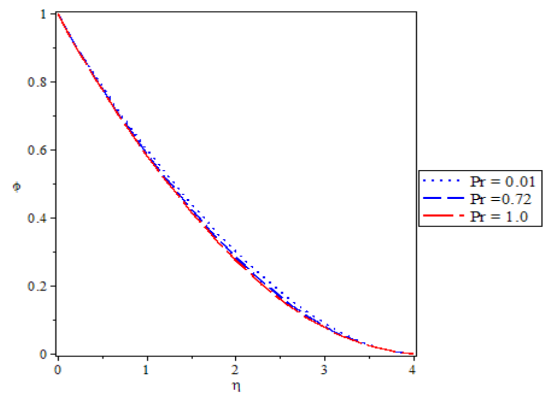

Figure 14. The graph of ϕ vs η for some Pr at $M = 0.2$, $Sc = 0.62$ $m = 0.01$, $\lambda = 0.05$ and $\tau = 0.1$

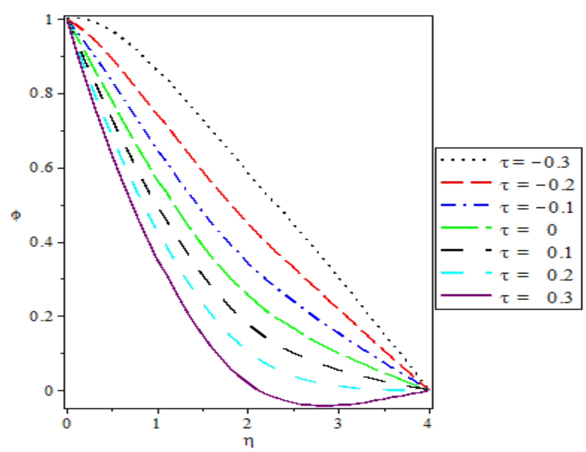

Figure 15. The graph of ϕ vs η for some τ at $\Pr = 0.72$, $Sc = 0.62$ $\lambda = 0.01$ $\mathrm{Re} = 1$ and $M = 0.1$

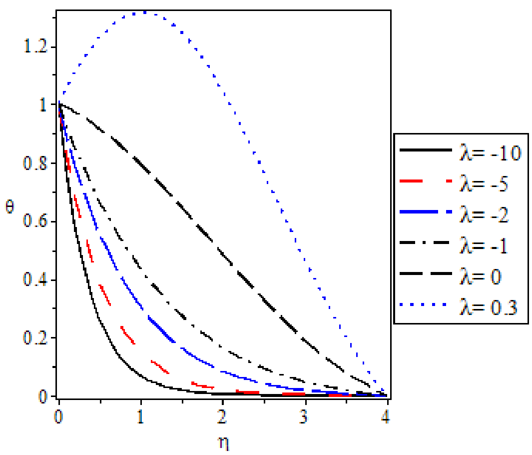

Figure 16. The graph of θ vs η for some λ at $\Pr = 1, Sc = 0.62 \ \ \tau = 0.1 \ \ \mathrm{Re} = 1, m = 0.5$ and $M = 0.1$

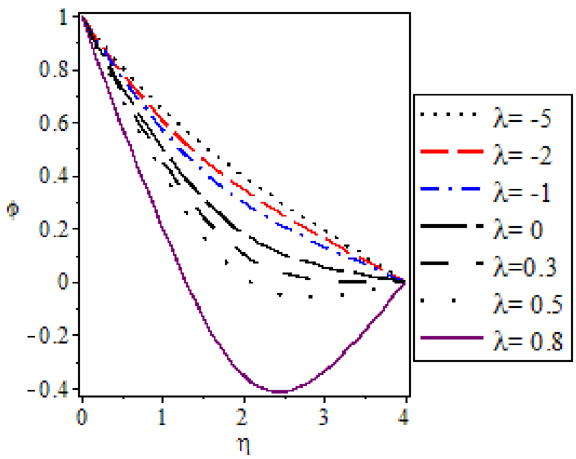

Figure 17. Plot of ϕ vs η for some λ at $M=0.1$, $\Pr = 1, \ Sc = 0.62 \ \ m = 0.5 \ \ \mathrm{Re} = 1$ and $\tau = 0.1$

4. CONCLUSION

This study investigated the flow and heat transfer of an incompressible boundary layer flow in the presence of a chemical reaction source over a stretching sheet.

It was observed in Figures 2 and 3 that the velocity profiles for $m > 0$ is higher than $m < 0$. This is because for a positive value of *m*, pressure gradient is negative and for a negative value of m, pressure gradient is positive. A negative pressure gradient is as a result of pressure decreases in the direction of fluid flow across the boundary layer. Thus the fluid within the boundary layer has enough momentum to overcome the pressure which is trying to push it backward and the flow accelerates. For a positive pressure gradient the pressure increases in the direction of flow, the fluid within the boundary layer has little momentum to overcome this pressure which could make the flow quickly brought to rest and possibly reversed in the direction. For a wide range of values of m, Figure 3 shows that the velocity profiles is convex for m>0 and concave for m<0.

The impacts of the Hartman number M on the velocity and temperature profiles are very significant in practical point of view. In Figs. 4 and 5, the variations in velocity field and temperature distribution for several values of M are presented. The dimensionless velocity $f'(\eta)$ increases with increasing values of M. This shows that increasing the magnetic force inhibits the flow velocity. On the other hand, Fig. 5 shows that the temperature ($\theta(\eta)$) profiles increases with increasing M. This may be due to the positive response of temperature to an increasing magnetic force in relation to the viscous force. Similarly behavior was observed in Fig. 11 for the concentration profiles($\phi(\eta)$).

The effect of Prandtl number on the temperature profile in the absence of chemical reaction was shown in Fig. 6. It was observed that an increase in the Prandtl number (Pr) decreases the temperature profile. This is justified in that higher values of Prandtl number are equivalent to decrease in the thermal conductivity of the fluid and therefore heat flow is reduced. Hence there is a reduction in temperature. Fig. 7 shows the same temperature profile pattern with increasing Prandtl number (Pr), except that the temperature peaks in the interval 0.5<η<1, which may be regarded as the reaction zone- a point wherein the reactant is completely consumed.

Fig. 8 shows the effect of Schmidt number on the concentration profile, it was observed that higher Schmidt number reduces the concentration profile. This may be due to the decreasing diffusivity of the reactant.

Fig. 9 shows that an increasing pressure gradient parameter (m) decrease the temperature profile. Similarly, in Fig. 12 shows the effects of pressure gradient parameter (m) on concentration profile in that as m increases the concentration profile decreases.

From Figs. 10 and 15, show that increasing the chemical reaction term increases the temperature profiles, while it decreases concentration profiles respectively. This is because an exothermic reaction involves the release of heat to the surroundings, while it enhances a depletion of the reactant.

Figs. 13 and 14 show that the concentration profiles decrease with increase in Schmidt number. This is because a large Schmidt number is as a result of decrease in mass diffusivity which reduces concentration across the boundary layer.

Figs. 16 and 17 show the variation of heat source parameter on the temperature and concentration profiles respectively. It is quite interesting to note that relatively high heat source term results into a very high temperature at the reaction zone, while it decreases the concentration profiles.

ACKNOWLEDGMENTS

This work has been supported in part by the Nigerian Tertiary Education Trust Fund (TETfund).

REFERENCES

[1] Ravikumar, V., Kaju M. C. and Raju G.S.S., 2012,"Heat and Mass Transfer Effects on MHD Flow of Viscous Fluid through Non-Homogeneous Porous Medium in Presence of Temperature Dependent Heat Source", *Intl. J. Contemp. Math. Sciences*, Vol. 7(32) pp. 1597 – 1604.

[2] Kandasamy R., Abd Wahid B., Raj Md and Khamis Azme B., 2006, "Effects of chemical reaction, heat and mass transfer on boundary layer flow over a porous wedge with radiation in the presence of suction or injection", *Theoret. Appl. Mech.,* Belgrade. Vol. 33(2) pp. 123 – 148.

[3] Devi Anjali S.P. and Kandasamy R., 2001, "Effects of heat and mass transfer on MHD laminar boundary layer flow over a wedge with suction or injection", *Journal of Energy Heat and Mass Transfer,* Vol. 2, 167.

[4] Muthucumaraswamy R., 2002, "Effect of a chemical reaction on a moving isothermal vertical surface with suction", *Acta Ciencia Indica* Vol. 155, pp. 65 – 70.

[5] Sharma P.R. and Singh G., 2008, "Effects of variable thermal conductivity and heat source/sink on MHD flow near a stagnation point on a linearly stretching sheet", *Journal of Applied fluid mechanics* Vol.2, pp. 13 – 21.

[6] Yih K. A., 1998, "Uniform suction/ blowing effect on force convection about wedge", *Acta Mech.,* Vol. 128, pp 173.

[7] Watanabe T., 1990, "Thermal boundary layer over a wedge with suction or injection in force flow", *Acta Mech.,* Vol. 83, pp 119.

[8] Krishnendu Bhattacharyya, 2011, "Effects of heat source/sink on MHD flow and heat transfer over a shrinking sheet with mass suction", *Chemical Engineering Research Bulletin,* Vol. 15, pp. 12-17.

[9] Pijush K. Kundu and Ira M. Cohen, 2008, *Fluid Mechanics.* Fourth edition, Elsevier, The Boulevard, Langford lane Kidlington, Oxford, UK pp. 346 – 359.

[10] Dulal Pal and Hiranmoy Mondal, 2009, "Influence of temperature-dependent viscosity and thermal radiation on MHD forced convection over a no-isothermal wedge", *Applied Mathematics and computation,* Vol. 212, pp. 194 – 208.

[11] Baoheng Yao, 2009, "Approximate Analytical Solution to the Falkner-Skan wedge flow with the permeable wall of uniform suction", *Commun Nonlinear Sci Numer Simulat* Vol. 14, pp. 3320-3326.

[12] Ajadi S. O. and Zuilino M., 2011, "Approximate analytical solutions of reaction-diffusion equations with exponential source term: Homotopy Perturbation method", *Applied Mathematics letters,* Vol. 24, pp. 1634-1639.

[13] Ajadi S. O., 2011, "Approximate analytical solution for critical parameters in a thermal explosion problem", *Applied Mathematics and computation,* Vol. 218, pp. 2005 – 2010.

[14] Taghipour R,. 2011, "Application of Homotopy perturbation method on some linear and nonlinear parabolic equations", *IJRRAS* Vol. 6(1), pp. 55 – 59.

Conference on Modelling Fluid Flow (CMFF'15)
The 16th International Conference on Fluid Flow Technologies
Budapest, Hungary, September 1-4, 2015

ADOPTION AND APPLICATION OF OPENFOAM MULTIPHASE SOLVER FOR THE REAL PRODUCT DEVELOPMENT

Dongjune KIM[1], Cheolu CHOI[2], Kyungjin KIM[3]

[1] Production engineering research institute, LG electronics, 222 LG-ro, Jinwi-myeon, Pyeongtaek-si, Gyeonggi-do, 451-713, Korea. Tel.: +82 31 8054 2137, E-mail: dongjune1.kim@lge.com
[2] HA research institute, LG electronics. E-mail: cheolu.choi@lge.com
[3] HA research institute, LG electronics. E-mail: kyungjin1013@lge.com

ABSTRACT

The product life cycle of electronics industry is becoming shorter and shorter, requires fast and efficient product development to survive in intense competition. Computational Fluid Dynamics (CFD) tool has advantages, capable of evaluating the product performance and minimize trial & error at the early stage of product development. And expectation and requirement on CFD has grown consistently, demanding solution of complicated and big sized problem. However, commercial CFD code is expensive and has limitations that the license cost increases with the number of CPU used for parallel computing. On the other hand, there are various open source CFD codes available, one of the most popular codes is OpenFOAM [1-3]. Combining OpenFOAM with super computing system gives benefit of saving resources and efficient CFD simulation in terms of time and software investment.

This study mainly demonstrates how OpenFOAM multiphase solver is adopted and applied to our real product development. The OpenFOAM based developed solver includes CFD techniques - multiphase, moving mesh, porous media, etc. Electric washer example is used for the validation and verification of the solver. Usability, scalability, and feasibility test has been conducted; also OpenFOAM simulation results are compared with the Fluent simulation results.

Keywords: CFD, OpenFOAM, multiphase, washer

NOMENCLATURE

F	$[N]$	force
g	$[m/s^2]$	gravitational acceleration
L	$[m]$	characteristic length
n	[-]	normal vector
p	$[Pa]$	pressure
U	$[m/s]$	velocity
α	[-]	fluid fraction
ρ	$[kg/m^3]$	density
κ	$[1/m]$	curvature
μ	$[kg/m{\cdot}s]$	viscosity

1. INTRODUCTION

CFD is a mature mechanical engineering field and there are many CFD tool around the globe that is widely used in the various industries. However, comparing to the structural analysis tools, CFD tools requires much more resources – hardware/software investment, time, manpower - for the accurate simulation. Furthermore, recent industry requires severe simulation condition in terms of calculation time and accuracy. Especially in the industry of electronics, the product lifecycle is extremely short, becoming shorter in the recent market competition. Moreover, there has been consistent attempt to design the product virtually which indicate the effort to locate the simulation process at the rudimentary stage of New Product Introduction (NPI) [4 and 5]. NPI is a framework of the product development process, from the concept design to the mass production (Figure 1). It is well-known that earlier stages of NPI influence larger portion of the efficient product development – less cost and fast production. Eventually, it is advantageous to apply CFD at the earlier stage of NPI process, concept design stage for instance. However, as the process become earlier, the available time for the simulation get shorter. Thus, the CFD tool is required to have robust convergence and fast calculation performance. And the commercial CFD software, for instance Fluent, CFX, Star-CCM+, satisfies these requirement of the industry with the numerical techniques that achieve robustness and calculation speed. However, the commercial CFD software is extremely expensive, especially when user tries to simulate big problem with multiple cores. The parallel computing is indispensable for the CFD simulation, because of the calculation speed and the complexity of recent given product development problems. On the other hand, various open-source CFD codes are developed with the General Public License (GPL) type license and there are a large number of communities and workshops studying and sharing the information. The most popular open-source CFD code is OpenFOAM, a pressure based solver implementing Finite Volume Method (FVM). OpenFOAM is equipped with sufficient solvers, utilities and libraries that can be applied to the wide range of problems. One of the most important advantages of OpenFOAM is that there are no extra costs with the parallel computing that can accelerate the simulation and product development. Nevertheless it is not a simple task to apply OpenFOAM to the real product development. Comparing to the commercial CFD tool, OpenFOAM is short of Graphic User Interface (GUI), convergence robustness and calculation speed where these factors are trivial in academia but the most important factors for the industry. This study aims to demonstrate the strategy and methodology of applying OpenFOAM to the real product development. The electronic washer problem is selected and the solver is validated with the Fluent simulation results.

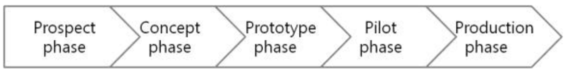

Figure 1. NPI process

2. STRATEGY

OpenFOAM certainly possess advantages but cannot completely supplant commercial software. Therefore, the strategy of targeting OpenFOAM application is necessary for the efficient and successful utilization. Comparing to the commercial CFD codes - Fluent, CFX, Star-CD –, OpenFOAM has disadvantages in terms of usability side especially for the novice CFD engineers. Although there are many developers making GUI or convenient tool boxes for OpenFOAM, user needs to find and apply these aids which take additional time and effort.

The strategy is to specify/fix the target problem and develop a solver based on OpenFOAM, thus the robustness of the solver can be guaranteed and usability can be improved with additional script or GUI. Based on current status of LG electronics, there are mainly three types of CFD tasks, spasmodic tasks, annual repetitive tasks and quality test related tasks. Spasmodic and quality related tasks demand high usability and accuracy to the solver, thus the annual repetitive type of task is considered to be appropriate target. The annual repetitive task can be once more subdivided into two types of problem. The first type is a routine and repetitive simulation where same process is repeated with minor change of the model. The second type of problem is time consuming simulations which require a large number of cores, for instance transient, big mesh and advanced model simulation. This study aims second type of CFD simulation.

2.1. Target problem

The target problem is an electronic washer simulation that account for the large number of cores because we model household washer with every holes located on the tub and pulsator– the second type of the problem. There are no laundries included in the model, but the pulsator/agitator rotates with time dependent speed. According to the rotation of pulsator/agitator, free surface of the water translates upward and downward. Therefore, the problem is transient, multiphase and moving mesh simulation which requires high calculation cost. Generally, the 5 seconds of the washer simulation is expected to take 1~2 days with more than 100 CPUs, which cost a lot of software license fee. Thus the substitution effect is expected to be high where making this study more profitable. The application process is described in Figure 2. Simple/full model simulation follows after solver development and the user interface is developed following solver validation.

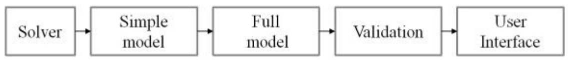

Figure 2. Application process

Table 1 shows the mesh specification of simple/full models. The simple model is created based on the full model, simplifying the shape of the pulsator/agitator and reducing the number of holes located at the pulsator/agitator and the inner tub. Case 1 and 2 has same type of filtration system, but case 3 is implemented with different type. Tetra type mesh is generated for each case.

Table 1. Simple/full model mesh specification

CASE	MODEL	CELL	NON-ORTHOGONALITY
1	SIMPLE	5.5 e4	-
2	FULL 1	8.3 e5	Max 71.65 Average 17.07
3	FULL 2	2.5 e6	Max 72.44 Average 17.07

3. NUMERICAL MODEL

OpenFOAM offers more than 80 standard solvers which can be categorized into basic, incompressible, compressible, multiphase, direct numerical simulation, combustion, heat transfer, particle tracking and etc. Among these standard solvers, interDyMFoam satisfies most of the requirements. interDyMFoam is a multiphase solver implement Volume Of Fluid (VOF) algorithm that captures the fraction of multiple phases and dynamic mesh technique that simulates rotation of the spinning domain where we are trying to simulate spinning pulsator with moving free surface.

3.1. Governing equations

Navier-stokes equation is calculated by the solver [3]. The fluid is considered to be incompressible and the time term is included on account of the time dependent pulsator/agitator rotation.

Conservation of mass

$$\nabla \bullet U = 0 \tag{1}$$

Conservation of momentum

$$\frac{\partial \rho U}{\partial t} + \nabla \bullet (\rho U U) - \nabla \bullet \mu \nabla U - \rho g = -\nabla p - F_S \tag{2}$$

The symbol *Fs* represents surface tension computed by equation 3. Value *n* is vector normal to the interface and kappa is representing curvature.

$$F_S = \sigma \kappa n \tag{3}$$

The flow is anticipated to be turbulent flow and k-omega model is selected to calculate the turbulence.

The filter in the washer is modelled as a porous media. Equation 3 shows the pressure drop phenomena.

$$\Delta p = -\left(\frac{\mu}{l} U + \frac{1}{2}\frac{1}{D}\rho U^2\right) L \tag{4}$$

VOF algorithm is represented by following equations 5-7. The alpha value is fluid fraction in a cell range from 0 to 1. It can be computed from transport equation as follows,

$$\frac{\partial \alpha}{\partial t} + \nabla \bullet (\alpha U) = 0 \tag{5}$$

$$\sum \alpha = 1 \tag{6}$$

OpenFOAM introduces extra artificial compression term into equation 4 to achieve the necessary compression of the free surface

$$\frac{\partial \alpha}{\partial t} + \nabla \bullet (\alpha U) + \nabla \bullet (\alpha (1 - \alpha) U_r) = 0 \tag{7}$$

The density can be calculated from weight averaged alpha value using equation 8.

$$\rho = \alpha \rho + (1 - \alpha) \rho \tag{8}$$

3.2. Numerical schemes

OpenFOAM provides several numerical schemes for the solver (Table 2) [6]. Each numerical scheme can be set with the upper/lower limit values so that the scalar values are strictly bounded. The Gauss scheme is the only choice for the divergence and laplacian discretisation scheme.

Table 2. List of numerical schemes

CLASS	SCHEME
Time	Euler, localEuler, CrankNicolson, backward
Gradient	linear, leastSquares, cellLimited, faceLimited
Divergence	upwind, vanLeer, linear, cubicCorrected
Laplacian	corrected, limited, uncorrected, bounded
Interpolation	linear, midPoint, pointLinear

Table 3 shows the default numerical schemes of "interDyMFoam". The numerical scheme affects stability of the simulation. There are a lot of choices and validating combination of these schemes requires enormous time. This is one of disadvantages using open-source CFD code; user needs to find the optimal solver settings.

Table 3. Default numerical scheme settings

CLASS	DEFAULT
Time	Euler
Gradient	linear
Divergence ρUU	upwind
Divergence $\alpha\rho U$	vanLeer
Divergence $\alpha\rho Ur$	linear
Laplacian	linear corrected
Interpolation	Linear

3.3. Pressure-velocity calculation

PIMPLE algorithm is selected for the pressure-velocity calculation of transient simulation. PIMPLE is an algorithm combination of SIMPLE (Semi-Implicit Method for Pressure Linked Equation) [7] and PISO (Pressure Implicit with Splitting of Operator) [8] algorithm to calculate pressure-velocity, where the specification of PIMPLE algorithm is described in Figure 3.

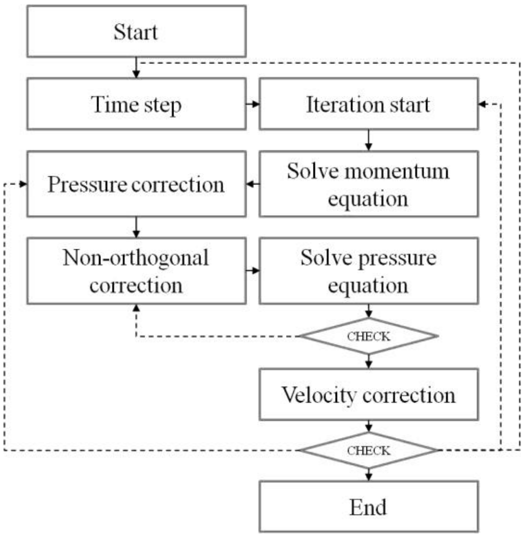

Figure 3. PIMPLE algorithm

PIMPLE is similar to PISO algorithm, but they are different in the existence of iteration loop right after the time step loop. There are three loop calculations except the time step loop and the iteration number of each loop can be specified in the solver settings. Combining with the time step size, these iteration numbers are critical to the simulation accuracy, convergence robustness and calculation speed.

4. RESULTS

The washer example is simulated by developed interDyMFoam based solver. The simulation result of CASE3 (Table 1) is presented in this chapter with normalized physical quantities.

4.1. Solver settings

This study aims to develop a solver that has convergence robustness thus it can be applied to the real product development. Thus, different numerical schemes are tested with same time step size, mesh, and different washer models. In addition, calculation speed cannot be ignored where both parameters are in a trade-off relationship. Case study of CASE1 (Table 1) shows time step size, numerical schemes and iteration numbers of pressure-velocity are critical to the solver stability and calculation cost.

The time step size 0.005~0.001 is calculated based on the maximum rotating speed of the washer pulsator/agitator. The default numerical scheme is working well with CASE1 and 2 but not with CASE3 (Table 1). CASE3 diverged in the time step range of 0.005 to 0.001. As a countermeasure, upwind scheme is utilized in the most of divergence schemes but the simulation still diverged. Thus the limit values are employed with second order schemes (Table 4).

Table 4. Numerical scheme settings

CLASS	SETTING
Time	Euler
Gradient	pointLinear 1
Divergence ρUU	limitedLinearV 1
Divergence $\alpha\rho U$	vanLeer01
Divergence $\alpha\rho Ur$	interfaceCompression
Laplacian	linear limited 0.5
Interpolation	pointLinear

There are three main iteration loop of PIMPLE algorithm – outer correction loop, pressure correction loop and Non-orthogonality correction loop. The several iteration numbers of each loop are tested and the iteration number of outer correction loop showed the most influence on the simulation convergence. Increasing the iteration number of outer correction loop take less calculation cost than decreasing time step size. In this study, interation number setting of SET2 is used for the simulation.

Table 5. Pressure-velocity variable settings

CORRECTION LOOP	DEFAULT	SET1	SET2
Outer	1	5	12
Pressure	3	1	2
Non-orthogonality	0	1	3

4.2. Result comparison

The simulation results are compared with Fluent results and the experimental results. Mesh is generated with Hypermesh and T-grid, converted with fluent3DMeshToFoam for the OpenFOAM. The other parameters are basically identical for the Fluent simulation – time step size, moving mesh, initial and boundary conditions. The important physical value of the washer simulation is flow rate at the holes and filter thus the flow rate is compared. Figure 4-7 describes the comparison result. The simulation result of developed solver is labelled by OpenFOAM.

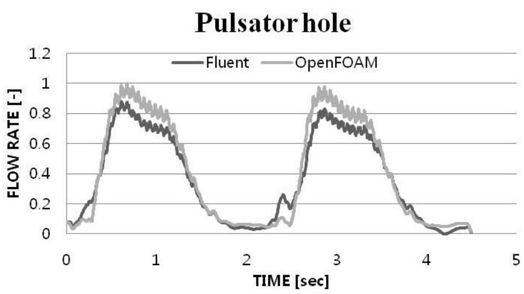

Figure 4. Pulsator hole flow rate comparison

The flow rate at the pulsator hole (Figure 4) shows flow rate of OpenFOAM result is higher than the Fluent result. Especially when the washer rotates at the maximum speed, OpenFOAM and Fluent shows maximum 10% difference of the flow rate.

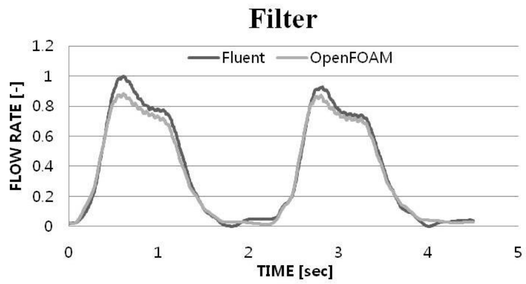

Figure 5. Filter flow rate comparison

The filter flow rate shows similar result to the pulsator hole flow rate, but in this case, Fluent result showed higher magnitude than the OpenFOAM simulation result (Figure 5).

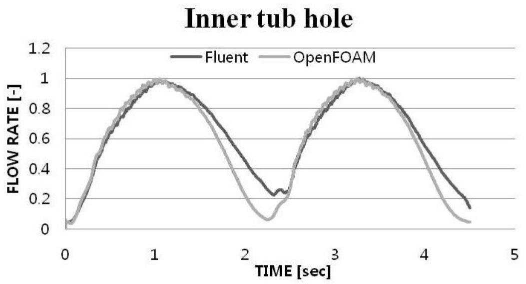

Figure 6. Inner tub hole flow rate comparison

The flow rate at the inner tub hole describes nice match of the maximum flow rate (Figure 6), but the result shows difference at the minimum flow rate.

Table 6. Simulation / experiment comparison

	Experiment	Fluent	OpenFOAM
Flow rate	0.460	0.453	0.444

Table 6 describes the OpenFOAM, Fluent and experiment comparison result. The compared value is time averaged flow rate at the filter. The result shows analogous match of three analyses where OpenFOAM shows relatively lower flow rate comparing with the other two analyses.

5. CONCLUSIONS

A multiphase solver is implemented based on OpenFOAM standard solver – interDyMFoam. The washer simulation is conducted and the result is verified with Fluent and experimental result. Comparison result showed similar trend of flow rate from both OpenFOAM and Fluent with maximum 10% difference in magnitude. The both simulation result is compared with the experiment result and they all present equivalent flow rate.

The feasibility of OpenFOAM is validated through this study. However, there are many future works left, for instance improvement of usability (user interface) and calculation speed.

The output of this study is on the application test stage; implemented solver is installed on the LG electronics hyper computing system and introduced to the electronic washer developers. We are expecting the solver contributes toward the efficient washer product development.

REFERENCES

[1] Jasak, H., 1996, “Error analysis and estimation in the Finite Volume Method with applications to fluid flows”, PhD thesis, *Imperial college, University in London*.

[2] Jasak, H., 2006, “Multi-physics simulations in continuum mechanics”, Proc. *Yokohama In proceedings of 5th International Conference of Croatian societ of Mechanics*, Trogir, Croatian Society of Mechanics.

[3] Jasak, H., Jemcov, A., and Tukovic, Z., 2007, “OpenFOAM: A C++ Library for Complex Physics Simulations”, *International workshop on Coupled Methods in Numerical Dynamics IUC*, Dubrovnik, Croatia.

[4] Day, G, S., 1981, “The product life cycle: analysis and application issues”, *Journal of Marketng*, 45 (4), pp. 60-68.

[5] Muffatto, M., 1999, “Platform strategies in international new product development”, *International Journal Of Operations & Production Management*, 19 (5/6), pp. 449-459.

[6] van Leer B., 1979, “Towards the ultimate conservative difference scheme. V. A second-order sequel to Godunov’s method”, *J of Computational Physics*, 32, pp. 101-136.

[7] Issa, R, I., 1986, “Solution of the implicitly discretizied fluid flow equations by operator-splitting”, *J. Comp. Physics*, pp. 62:40-65.

[8] Patankar, S, V., and Baliga, B, R., “A new Finite-Difference scheme for parabolic differential equations”, *Numerical Heat Transfer*, 178, pp. 1-27.

Conference on Modelling Fluid Flow (CMFF'15)
The 16th International Conference on Fluid Flow Technologies
Budapest, Hungary, September 1-4, 2015

STEADY FLOW AND HEAT TRANSFER OVER SIDE-BY-SIDE SQUARE CYLINDERS IN A LAMINAR REGIME

Aniruddha Sanyal[1], Amit Dhiman[2]

[1] Department of Chemical Engineering, Indian Institute of Technology Roorkee, Roorkee – 247 667, India.
[2] Corresponding Author. Department of Chemical Engineering, Indian Institute of Technology Roorkee, Roorkee – 247 667, India. E-mails: dhimuamit@rediffmail.com and amitdfch@iitr.ac.in; Tel.: +91-1332-285890 (office), +91-9410329605 (mobile).

ABSTRACT

A two-dimensional numerical study has been conducted to analyze forced convective confined flow and heat transfer from a pair of side-by-side square cylinders with a transverse gap ratio (defined as the ratio of the distance between the obstacles to the size of an obstacle) of 1.5. The flow is steady Newtonian flow in a viscous dominant flow field, investigated at Reynolds numbers (Re) ranging from 10 to 40 for Prandtl numbers (Pr) = 0.7 and 50. The present results are found in the excellent agreement with the literature, with a maximum deviation of 1.5%.

It is observed from the streamline contours that the wake formation in the downstream increases with Re. Isotherms are observed to be denser on the front surfaces of the square cylinders as compared to other surfaces, indicating higher Nusselt number. Onset of recirculation has been observed at Re = 7 and further a correlation connecting wake length with Re has been stated.

Keywords: Drag coefficient; Nusselt number; Side-by-side configuration; Square cylinders and Wake length.

NOMENCLATURE

β	[-]	ratio of the side of one square cylinder to the channel height (called here as a blockage ratio)
ρ	$[kg/m^3]$	fluid density
μ	$[Pa.s]$	viscosity of the fluid
ψ	[-]	stream function
$\boldsymbol{\tau}$	[-]	shear stress tensor
C_D	[-]	coefficient of drag
F_D	$[N/m]$	total drag force per unit length of the obstacle
F_{DF}	$[N/m]$	friction drag force per unit length of the obstacle
F_{DP}	$[N/m]$	pressure drag force per unit length of the obstacle
H	$[m]$	transverse height of the domain
L_r	[-]	recirculation length per unit length of the obstacle
Nu	[-]	Nusselt number
U_{max}	$[m/s]$	maximum velocity at the inlet
Pr	[-]	Prandtl number
Re	[-]	Reynolds number
St	[-]	Strouhal number
V	[-]	dimensionless velocity
T	[-]	temperature
X	[-]	distance between the obstacle boundary and inlet or outlet per unit size of the obstacle
c_p	$[J/kg.K]$	specific heat capacity of the fluid
d	$[m]$	width of a square cylinder
f	$[1/s]$	vortex shedding frequency
h	$[W/m^2.K]$	heat transfer coefficient
k	$[W/m.K]$	thermal conductivity of the fluid
p	[-]	pressure
s	$[m]$	gap between the two square cylinders
t	[-]	time
x, y	[-]	position of flow parameters in the domain

Subscripts

d	downstream
u	upstream
x	direction of vectors along horizontal axis
y	direction of vectors along vertical axis

1. INTRODUCTION

Ever since the inception of study for fluid flow and heat transfer past a bluff body in a confined domain, decades have gone by research mainly on experimental basis which has incurred huge cost. As a result several attempts were made to analyze this process through numerical modeling and simulation. Modern numerical methodologies like finite volume method (FVM), lattice Boltzmann method (LBM), optical density method, etc.; have profound applications in decoding the sets of complicated partial differential equations which define the flow and heat transfer processes. This field has heavy application in the process heat transfer equipments, structural dynamics and mechanical, chemical and other related engineering applications.

When two or more of such bodies/objects are placed in proximity, the intricacy in predicting momentum and heat transfer around it gets aggravated and interference effects are severe. As a result, the flow and thermal patterns differ from that of circular cylinders.

Valencia and Paredes [1] performed a numerical study to examine the flow and heat transport distinctiveness in a plane channel with two square cylinders (or square bars) placed side-by-side to the impending flow for a transverse gap ratio (*s/d*) ranging from 0 to 5 for Reynolds number (Re) varying from 25 to 125 at a constant blockage ratio (β) of 12.5% in an unsteady laminar flow regime. The mathematical outcomes divulge the complicated formation of the flow. The flow persists its steadiness at Re = 200; whereas, periodicity or unsteadiness is observed as the Re is further increased, and displays low frequency modulation at Re > 400; and transitional nature at Re = 1000. Peng [2] studied the fluid flow past two side-by-side square bluff bodies with a constant gap ratio of 2 in an unconfined domain by both mathematical simulation as well as investigational flow-visualization methods at Re = 100. They observed bi-stable flows, with both in-phase and anti-phase synchronized patterns, as a result of adjusting the initial conditions. Agrawal et al. [3] examined the flow over two side-by-side square cylinders using the LBM, discovered the subsistence of regimes with both synchronized and scattered vortex formation, and conferred the type of vortex shed from the square cylinder in either regime for a uniform flow field at the upstream. Numerical outcomes for two gap ratios of 0.7 and 2.5 for the fixed Re 73 and blockage 5.55% had been reported. Later, Rao et al. [4] carried out an extension work of Agrawal et al. [3] and performed quantitative study of the flow over two side-by-side square bluff bodies using LBM, for transverse gap ratio varying from 1 to 2.7 and Re varying from 73 to 200 at the blockage of 5.55%. They revealed that for transverse gap ratio lesser than 1.5, the flow demonstrates a flip-flop behavior known as chaotic; however, for *s/d* greater than 1.5, the flow tends to synchronize known as quasi-periodic and for *s/d* >4 synchronized flow was observed. The transition between chaotic and quasi-periodic regimes occurs at *s/d* = 1.5. It is useful to point out the fact that there is no mention on heat transfer behavior around similar configuration.

Sufficient information is now available in the literature on the flow around two side-by-side square cylinders in the turbulent regime. For instance, Wong et al. [5], Kolar et al. [6] and Alam et al. [7] executed experimental investigations of the wake formation around a pair of side-by-side square cylinders. Harichandan and Roy [8] displayed the strong dependence of flow characteristics on the transverse gap ratio and Reynolds number with former being more dominant over the later. Durga Prasad and Dhiman [9] analyzed the steady and unsteady laminar flow and heat transfer in a confined domain for a pair of side-by-side square cylinders for Re = 10 to 100 at Pr = 0.7 to 50 with the gap ratio from 1.5 to 10 in a transverse domain height of 18*d* [3, 4]. It was shown that the overall drag coefficient decreases with increasing Re and Pr for all values of gap ratios. The percentage enhancement in average Nusselt number was found more than 76% for the range of settings covered. This study has found the occurrences of in-phase and anti-phase flow past the square cylinders at various Re. They also found that beyond a gap ratio of 2.5 the steadiness in flow was observed till Re < 60 which was limited to Re =50 for a smaller gap ratio. Mizushima and Akinaga [10] studied wake interactions in a flow past a row of square bars by both numerical replication and experimental determination on the postulation that the flow is two-dimensional (2D), incompressible. Kumar et al. [11] reported the presence of synchronous, quasi-periodic, and chaotic flow regimes for *s/d* ranging from 0.3 to 12 for nine square cylinders in side-by-side arrangement at Re = 80. Along the same line, Sewatkar et al. [12] determined the effects of transverse gap ratio and Re on the flow around a row of square cylinders for Re ranging from 30 to 140 and *s/d* 1 to 4. Chatterjee et al. [13] executed numerical simulation for the flow around a row of five square bluff bodies kept at a side-by-side display for transverse gap ratios of 1.2, 2, 3, and 4 at Re =150.

Thus, from the foregoing argument, one can summarize that virtually no work is available on the confined flow around two side-by-side square cylinders in a cross flowing domain at low Reynolds numbers. Because the multiple bluff obstacles create a complex flow and thermal structures even at low Reynolds numbers, and owing to the engineering relevance in various applications (compact heat exchangers, plate type heat exchangers, etc.); the analysis of flow and thermal prototype is necessary. A close look on momentum and heat transfer processes in highly viscous force dominated steady laminar flow regime ($10 \leq Re \leq 40$) inside a confined domain has been attempted. It is also seen that very few papers have mentioned about the occurrence of recirculation zone quantitatively. Hence, an attempt has been made to study recirculation length from the flow field and domain parameters; Re = 10 to 40, Pr =

0.7, 50 and s/d = 1.5.

2. MATHEMATICAL FORMULATION AND SOLUTION METHODOLOGY

Any flow problem involves set of partial differential equations which need to be solved using CFD techniques. The sequence of approaching the solution methodology involves initial statement of the problem followed by mention of the governing equations coupled with its boundary conditions. Further, generation of an optimal grid is done which is solved using ANSYS FLUENT here. The basics regarding these topics are well explained in an article by Chhabra and Richardson [14].

2.1. Problem Statement

The following problem has been assumed to be a simplified case of a flow of a fluid past a pair of square cylinders in a 2D domain. Here, the square cylinders are assumed to be infinitely long in size along the neutral direction. The variation of physical process parameters along this direction is zero till Re less than 150 as per seen from literature. Following Durga Prasad and Dhiman [9], the domain has been set in a standardized format, where the upstream distance from the square cylinders, X_u is set at 8.5 and downstream distance, X_d as 16.5, which has an optimal grid and domain size. The size of a square cylinder, d is set as unity. The transverse gap ratio, s/d, is taken as 1.5 [15]. The following Figure 1 aptly depicts the aforesaid problem statement. The 2D approximation is well established in a highly viscous force dominant flow field along with a small thermal gradient which is significant enough to catch the change in flow and thermal patterns due to flow around a pair of side-by-side square cylinders with good numerical accuracy. The temperature difference is kept constant at 2 K so as to show the variations of flow parameters due to the heat transfer effect.

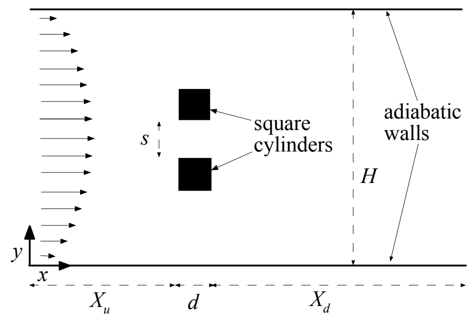

Figure 1. Schematic diagram for fluid flowing past side-by-side square cylinders

2.2. Governing Equations

For a two-dimensional forced convective laminar flow, the corresponding dimensionless equations are

Continuity equation for incompressible fluid flow

$$\frac{\partial V_x}{\partial x} + \frac{\partial V_y}{\partial y} = 0 \qquad (1)$$

Momentum equations neglecting the body forces

$$\frac{\partial V_x}{\partial t} + \frac{\partial V_x V_x}{\partial x} + \frac{\partial V_y V_x}{\partial y} = -\frac{\partial p}{\partial x} + \frac{1}{\mathrm{Re}}\left(\frac{\partial^2 V_x}{\partial x^2} + \frac{\partial^2 V_x}{\partial y^2}\right) \qquad (2)$$

$$\frac{\partial V_y}{\partial t} + \frac{\partial V_x V_y}{\partial x} + \frac{\partial V_y V_y}{\partial y} = -\frac{\partial p}{\partial y} + \frac{1}{\mathrm{Re}}\left(\frac{\partial^2 V_y}{\partial x^2} + \frac{\partial^2 V_y}{\partial y^2}\right) \qquad (3)$$

Energy equation neglecting viscous dissipation and considering a pure forced convection heat transfer process

$$\frac{\partial T}{\partial t} + \frac{\partial V_x T}{\partial x} + \frac{\partial V_y T}{\partial y} = \frac{1}{\mathrm{Re\,Pr}}\left(\frac{\partial^2 T}{\partial x^2} + \frac{\partial^2 T}{\partial y^2}\right) \qquad (4)$$

Further, Re = $\rho U_{max} d/\mu$ and Pr = $c_p\, \mu/k$. (5)

2.3. Boundary Conditions

At inlet: for a parabolic velocity inlet,

$V_x = 1 - (|1 - 2\beta y|)^2$ for ($0 \le y \le H/d$, $\beta = d/H$) and $V_y = 0, T = 0$ (6)

On the surfaces of the square cylinders, the standard no-slip condition is used,

$V_x = 0, V_y = 0, T = 1$ (constant wall temperature) (7)

On the upper and lower domain boundaries,

$$V_x = 0, V_y = 0, \frac{\partial T}{\partial y} = 0 \text{ (adiabatic)} \qquad (8)$$

At the exit boundary,

$\partial\phi/\partial x = 0$; where ϕ is a dependent variable, V_x or V_y or T. (9)

The output parameters are briefly summarized as follows

Total drag coefficient for a single square cylinder [16]:

$$C_D = \frac{F_D}{\frac{1}{2}\rho U_{\max}^2 d}$$

$$= \frac{F_{DF}}{\frac{1}{2}\rho U_{\max}^2 d} + \frac{F_{DP}}{\frac{1}{2}\rho U_{\max}^2 d} =$$

$$\frac{2}{\mathrm{Re}}\int_0^1 \left[\tau_t(x) + \tau_b(x)\right]dx + 2\int_0^1 \left[p_r(y) - p_f(y)\right]dy \qquad (10)$$

where b, f, r, t denotes bottom, front, rear and top surfaces of a square cylinder

Strouhal number: $St = fd/U_{\max}$ (11)

Nusselt number: $Nu = hd/k$ (12)

2.4. Grid Generation and Solution Technique

The following Figure 2a and 2b displays the overall grid structure and close view of the grid structure around the square cylinders, respectively. The grid, using quadrilateral cells, generated for this problem is non-staggered in nature. It is generated using the commercial grid generation tool ANSYS ICEM. A finer grid size is maintained near the square cylinders to capture the changes that occur in the flow around the square cylinders. The smallest grid spacing is kept around the square cylinders and confined walls is of 0.008d size, and the coarsest one is 0.5d which can be seen at the inlet or outlet part of the flowing domain. The number of grid points placed on each surface of the square cylinders is 100, following Durga Prasad and Dhiman [9]. The meshing procedure in the zone connecting the square cylinders and the confined walls are done in such a manner which can take into account of the wall effects in flow process. This is done by applying double ended first length configuration.

Following several literary articles [17, 18] and others, SIMPLE algorithm is used to avoid pressure velocity decoupling and it offers good convergence for the type of problem under consideration. The absolute convergence criteria set at 10^{-15} for flow parameters and 10^{-20} for thermal parameters.

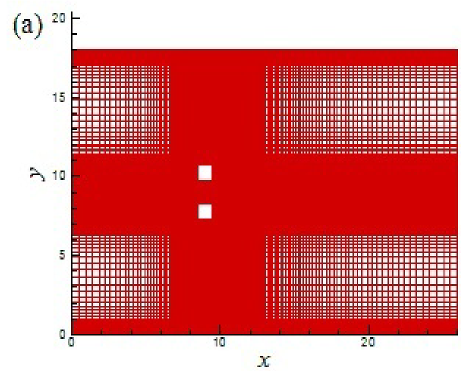

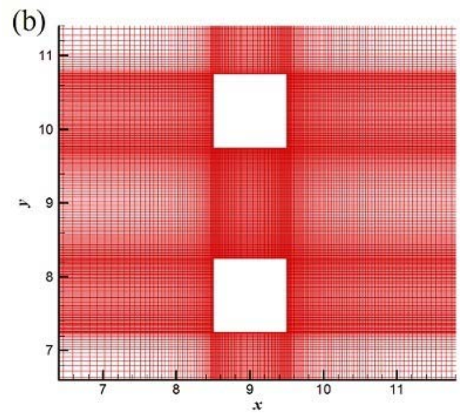

Figure 2. (a) The overall grid structure and (b) close view of the grid structure around the square cylinders

Discretization of the convective terms in the momentum and energy equations is done using QUICK, a third order upwind scheme.

3. RESULTS AND DISCUSSION

3.1. Validation

The validation of the results obtained applying the above numerical method with that of Durga Prasad and Dhiman [9] for the Re ranging from 10 to 40 at the Pr 0.7 (resembling air) and 50 (resembling organic polymer liquids) at a constant transverse gap ratio of 1.5. The following Tables 1 and 2 show that the values of coefficient of drag and Nusselt number stay well within 0.1% and 3.2% respectively of the previous works [9].

Re (s/d = 1.5)	C_D from Durga Prasad and Dhiman [9]	C_D from current simulation	% deviation
Pr = 0.7			
10	3.6034	3.6039	0.02
20	2.6151	2.6153	0.01
30	2.2001	2.1998	0.01
40	1.9646	1.9628	0.09
Pr = 50			
10	3.6034	3.6039	0.02
20	2.6151	2.6153	0.01
30	2.2001	2.1998	0.01
40	1.9646	1.9628	0.09

Table 1. Validation of drag coefficients with Durga Prasad and Dhiman [9] in a steady laminar flow regime

Re (at s/d = 1.5)	Nu from Durga Prasad and Dhiman [9]	Nu from current simulation	% deviation
Pr = 0.7			
10	1.4856	1.4918	0.42
20	2.0726	2.0913	0.90
30	2.4446	2.4713	1.09
40	2.7402	2.7749	1.26
Pr = 50			
10	6.0861	6.1320	0.75
20	8.4173	8.5673	1.78
30	10.2586	10.4862	2.22
40	11.6463	12.0215	3.20

Table 2. Validation of Nusselt number with Durga Prasad and Dhiman [9] in a steady laminar flow regime

In all the above cases, it was seen that the drag coefficient remained same for both the square cylinders because of the fact that the effect of gravity and the variation of the fluid's density with temperature have been neglected in this problem. The C_D values reported above are that of the upper square cylinder in the flow domain. It is also to be noted that the Nusselt number for both upper and lower square cylinders remains constant owing to the similar reasons.

3.2. Fluid Flow Patterns

Figure 3a-3d shows the streamline contours at s/d = 1.5 for Re = 20 and 40, at Pr = 0.7 and 50. The flow is found to be steady in this flow range and at the same time anti-phase (wake structures generated from both the square cylinders are equal and oppositely directed in a given plane) transitional pattern is seen. This pattern gradually glorifies as Re is increased from 20 to 40, which clearly depicts the approaching of unsteadiness in the downstream.

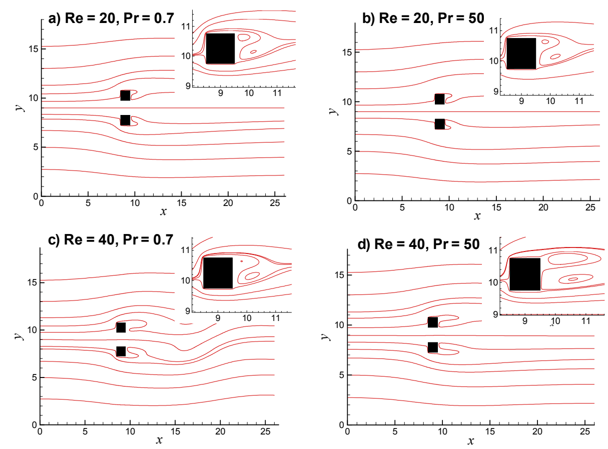

Figure 3 (a-d). Streamline contours along with the magnified views of upper square cylinder for a transverse gap ratio of 1.5

A close look at the magnified image of the contours reveals the formation of wakes at the rear part of the square cylinders, which widen with increasing Reynolds number but doesn't vary significantly with increasing Prandtl number. Further, it is also to be noted that there is no possibility of reverse flow in the domain. These streamlines also show a marginal interference of stream functions due to the presence of two square cylinders. As seen from previous literature [11], the transverse gap ratio falls under quasi- periodic flow regime is hence validated.

3.3. Thermal Patterns

Figure 4a-4d shows the isotherm contours of the fluid flowing past the pair of side-by-side square cylinders at the Re = 20 and 40 at the Pr = 0.7 and 50. Following Merkin [19], who said that during the flow process, cooling an obstacle brings about separation near the stagnation point is also evident in this case by the clusters of isotherms accumulating in front of the frontal surface of the square cylinders (despite the fact that the domain and flow structures are different from Merkin [19], the concept of high heat transfer in the front part of the obstacle stays intact irrespective of domain. In terms of magnitude factor, the results will always vary with configurations. The observation of the above pattern remains same in all the cases in the direction of flow). This eventually leads to an increased Nusselt number (Nu) and the heat transfer rates at the front surfaces compared to that of other surfaces. In fact, one can also conclude that the heat transfer is maximum in the front surface followed by the intermediate on surfaces parallel to the flow and the rear face has the least heat transfer rate. The isotherms also seem to be steady and symmetric along the centerline with almost no interaction at Pr = 50, but the interaction prevails at Pr = 0.7. This factor can be explained from the concept of boundary layer theory, where at Pr = 0.7 indicates that the hydrodynamic boundary layer is smaller than the thermal boundary layer, which means that the layers tend to move outward which lead to interaction of isotherms due to the presence of two square cylinders. But at Pr = 50, the thermal boundary layer is smaller than that of the hydrodynamic counterpart, as a result, the isotherms tend to die down at a close distance in the downstream from the rear surface of the square cylinders.

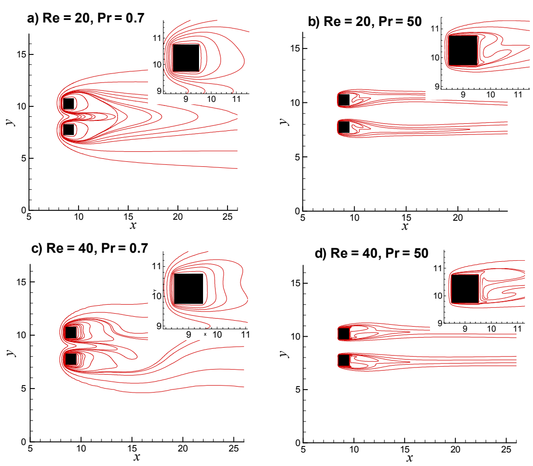

Figure 4 (a-d). Isotherms along with the magnified views of upper square cylinder for a transverse gap ratio of 1.5

The magnified views of the isothermal contours also point out the fact that the wakes formed at Re = 20 gradually increases in size at Re = 40. The above figures also explain clustering of isotherms near the rear surfaces of the square cylinders, which increases with increasing Reynolds and Prandtl numbers.

3.4. Recirculation Length

It is the distance from the rear surface of the obstacle to the point of attachment for the near closed streamline ($\psi = 0$) on the axis of symmetry. The following Figure 5 shows that the recirculation length varies linearly with increasing Re. It increases with Re and the results fit linearly with a mere 0.001% deviation.

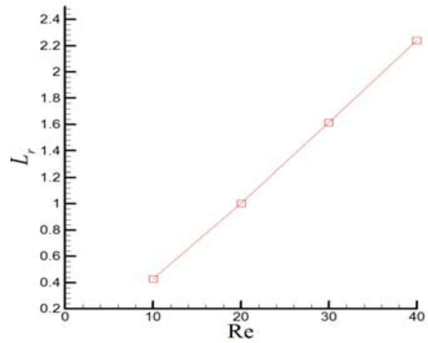

Figure 5. Variation of recirculation length with Reynolds number

The recirculation length varies almost negligibly with increasing Pr (Table 3).

Re	L_r (at Pr = 0.7)	L_r (at Pr = 50)
10	0.4276	0.4276
20	1.0039	1.0044
30	1.6146	1.6147
40	2.2406	2.2407

Table 3. Variation of recirculation length with Reynolds and Prandtl numbers

The following simple correlation is established for the calculation of wake length (L_r), for the intermediate values of physical parameters in the steady confined regime:

$$L_r = 0.06\text{Re} - 0.19 \text{ for } 10 \le \text{Re} \le 40 \quad (13)$$

This linearity in recirculation length versus Re plot has also been observed by Sharma et al. [20] for a single square cylinder.

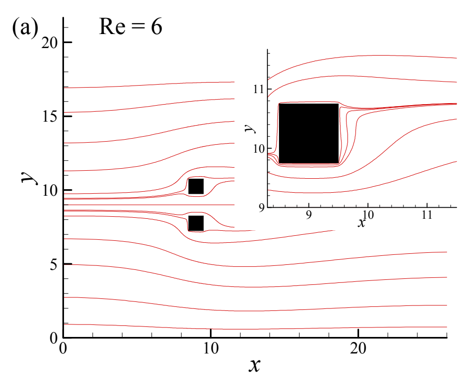

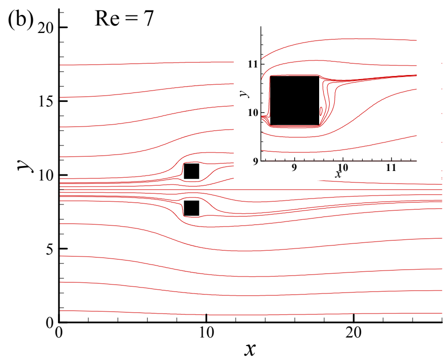

Figure 6 (a-b). Streamline contours along with magnified view of upper square cylinder showing absence of any wake at Re = 6 and onset of wake formation at Re =7

Furthermore, the onset of the flow separation is determined. It has been observed that there is no presence of recirculation wake at Re = 6; whereas, recirculation commences at Re = 7 (as shown in Figures 6a and 6b). Hence, one can infer that a higher the magnitude of viscous dominance in the flow field the lower or minimal is the recirculation or wake length formed in the rear side of the square cylinders.

4. CONCLUSIONS

Summarizing, the above study, one can make the observation that the coefficient of drag decreases with the increase in Re but remains unchanged with Pr, whereas the *Nu* increases with the increase in both Re and Pr as is evident from the stream function and isothermal contours. It has also been seen that the recirculation length increases linearly with the increase in Re in steady laminar flow regime from Re = 10 to 40. This paves a way for further determination of recirculation length for various flow regimes for a flow over a pair of side-by-side square cylinders. One can also correlate the results with that of cylindrical counterpart thereby leading to the appropriate justification of which choice of cylinder during various industrial operations. Finally, the onset of flow separation is determined for the current framework and it occurs between Re = 6 and 7 irrespective of the value of Pr.

REFERENCES

[1] Valencia A., and Paredes R., 2003, *"Laminar Flow and Heat Transfer in Confined Channel Flow Past Square Bars Arranged Side-By-Side"*, Heat and Mass Transfer, Vol. 39, pp. 721–728.

[2] Peng Y. F., 2004, *"On the Bi-Stabilities of Vortex Shedding Flows Behind a Pair of Square Solids"*, Journal of Chinese Institute Engineers, Vol. 27, pp. 385–393.

[3] Agrawal, A., Djenidi, L., and Antonia, R. A., 2006, "*Investigation of Flow Around a Pair of Side-By-Side Square Cylinders Using the Lattice Boltzmann Method"*, Computers and Fluids, Vol. 35, pp. 1093–1107.

[4] Rao Y., Ni Y., and Liu C., 2008, "*Flow Effect Around Two Square Cylinders Arranged Side-By-Side Using Lattice Boltzmann Method"*, International Journal of Modern Physics C, Vol. 19, pp. 1683–1694.

[5] Wong P. T. Y., Ko N. W. M., and Chiu A. Y. W., 1995, "*Flow Characteristics Around Two Parallel Adjacent Square Cylinders of Different Sizes"*, Journal of Wind Engineering and Industrial Aerodynamics, Vol. 54/55, pp. 263–275.

[6] Kolar V., Lyn D. A., and Rodi W., 1997, "*Ensemble-Averaged Measurements in the Turbulent Near Wake of Two Side-By-Side Square Cylinders"*, Journal of Fluid Mechanics, Vol. 346, pp. 201–237.

[7] Alam M. M., Zhou Y., and Wang X. W., 2011, "*The Wake of Two Side-By-Side Square Cylinders"*, Journal of Fluid Mechanics, Vol. 669, pp. 432–471.

[8] Harichandan A.B., and Roy A., 2012, "*Numerical Investigation of Flow Past Single and Tandem Cylindrical Bodies in the Vicinity of a Plane Wall*", Journal of Fluids and Structures, Vol. 33, pp. 19–43.

[9] Durga Prasad A.V.V.S., Dhiman A.K., 2014, "*CFD Analysis of Momentum and Heat Transfer Around a Pair of Square Cylinders in Side-By-Side Arrangement*", Heat Transfer Engineering, Vol. 35, pp. 398-411.

[10] Mizushima J., and Akinaga T., 2003, "*Vortex Shedding From a Row of Square Bars"*, Fluid Dynamics Research, Vol. 32, pp. 179–191.

[11] Kumar S.R., Sharma A., and Agrawal A., 2008, "*Simulation of Flow Around a Row of Square Cylinders"*, Journal of Fluid Mechanics, Vol. 606, pp. 369–397.

[12] Sewatkar C. M., Sharma A., and Agrawal A., 2009, "*On the Effect of Reynolds Number for Flow Around a Row of Square Cylinders"*, Physics of Fluids, Vol. 21, pp. 083602-1 – 083602-13.

[13] Chatterjee D., Biswas G., and Amiroudine S., 2010, *"Numerical Simulation of Flow Past Row*

of Square Cylinders for Various Separation Ratios", Computers and Fluids, Vol. 39, pp. 49–59.

[14] Chhabra R.P., and Richardson J.F., 1986, "*Co-Current Horizontal and Vertical Upwards Flow of Gas and Non-Newtonian Liquid"*, Encyclopedia of Fluid Mechanics, Vol. 3, Edited by N.P. Cheremisinoff, Gulf, Houston (USA), pp. 563-609.

[15] Denial A., and Dhiman A., 2013, "*Aiding Buoyancy Mixed Convection From a Pair of Side-By-Side Heated Circular Cylinders in Power-Law Fluids*", Industrial & Engineering Chemistry Research, Vol. 52, pp. 17294 - 17314.

[16] Sahu A.K., Chhabra R.P., and Eswaran V., 2010, "*Two-Dimensional Laminar Flow of a Power-Law Fluid Across a Confined Square Cylinder"*, Journal of Non-Newtonian Fluid Mechanics, Vol. 165, pp. 752-763.

[17] Muralidharan K., and Sundararajan T., 2004, *Computational Fluid Flow and Heat Transfer*, Narosa publication, second edition.

[18] Anderson J.D, Jr., 2000, *Computational Fluid Dynamics - the Basics with Applications*, McGraw Hill publication, second edition.

[19] Merkin J.H., 1977, "*Mixed Convection from a Horizontal Circular Cylinder"*, International Journal of Heat and Mass Transfer, Vol. 20, pp. 73 - 77.

[20] Sharma N., Dhiman A.K., and Kumar S., 2012, "*Mixed Convection Flow and Heat Transfer Across a Square Cylinder Under the Influence of Aiding Buoyancy at Low Reynolds Numbers"*, International Journal of Heat and Mass Transfer, Vol. 55, pp. 2601 - 2614.

Conference on Modelling Fluid Flow (CMFF'15)
The 16th International Conference on Fluid Flow Technologies
Budapest, Hungary, September 1-4, 2015

IMPROVEMENT OF MATHEMATICAL MODEL OF ULTRASONIC FLOWMETER FOR STUDYING ITS ERRORS IN DISTURBED FLOWS

Roman FEDORYSHYN[1], Yevhen PISTUN[2], Fedir MATIKO[3], Vitaliy ROMAN[4]

[1] Corresponding Author. Department of Automation of Heat and Chemical Processes, Lviv Polytechnic National University. S. Bandery St., 12, Lviv, 79013, Ukraine. Tel.: +38 032 258 25 16, Fax: +38 032 255 38 81, E-mail: romanfedoryshyn@yahoo.com
[2] Department of Automation of Heat and Chemical Processes, Lviv Polytechnic National University. E-mail: epistun@polynet.lviv.ua
[3] Department of Automation of Heat and Chemical Processes, Lviv Polytechnic National University. E-mail: fmatiko@gmail.com
[4] Department of Automation of Heat and Chemical Processes, Lviv Polytechnic National University. E-mail: roman_vitaliy@ukr.net

ABSTRACT

This paper deals with a mathematical model of an ultrasonic flowmeter (USM) for studying its errors in disturbed flows. The method of defining the position coordinates of the acoustic paths and their weighting factors was improved based on the Gauss-Jacobi method of integration (i.e. the weighting function was improved) which provided the possibility to raise the accuracy of the turbulent flow velocity integration. The effectiveness of the improved method was verified using the Salami functions. New methodology for improving the mathematical model of USM is proposed. According to this methodology the dependence of the calibration factor on the Reynolds number is introduced into the model. A technique for studying the errors of USM in disturbed flows was developed on the basis of the proposed methodology. The developed technique was verified by comparing the CFD simulation results for a 3D model of an acting USM with the experimental results for this meter obtained by means of a reference test rig. The deviation of the simulation results from the obtained experimental data is not more than 1 %. Recommendations on defining the pipe straight lengths for the double-path chordal flowmeters were developed on the basis of the investigation results.

Keywords: CFD, disturbed flow, error, flow rate, mathematical model, ultrasonic flowmeter

NOMENCLATURE

D	$[m]$	pipe internal diameter
K	[-]	compressibility factor
L	$[m]$	length of the acoustic path
N	[-]	number of the acoustic paths
PL	[-]	Lagrange polynomial
PJ	[-]	Jacobi polynomial
R	$[m]$	pipe internal radius
Re	[-]	Reynolds number
T	$[K]$	fluid temperature
T_h	$[m]$	width of the plane where the acoustic path is located
$W(x)$	[-]	weighting function of Jacobi polynomial
k	[-]	coefficient of weighting function of Jacobi polynomial
k_{cal}	[-]	calibration factor
l_{fit}	$[m]$	pipe straight length between USM and a fitting
n	[-]	Nikuradse number
p	$[Pa]$	fluid absolute pressure
q	$[m^3/s]$	volume flow rate
v_h	$[m/s]$	flow velocity along the chordal acoustic path
$w(i)$	[-]	weighting factor of i-th acoustic path
x	[-]	current radial position
$x(i)$	$[m]$	position coordinate of i-th acoustic path
δ	[%]	relative deviation
μ	$[Pa \cdot s]$	fluid dynamic viscosity
ρ	$[kg/m^3]$	fluid density
θ	[°]	integration angle
φ	[°]	angle of the acoustic path

Subscripts and Superscripts

CFD	based on CFD simulation
max	maximum
min	minimum
ref	reference value
s	volume in standard conditions
v	volume in operating conditions

1. INTRODUCTION

Ultrasonic methods and instrumentation for fluid flow rate and volume measurement are applied widely in various fields of industry including gas industry where natural gas metering is carried out during its transportation and supply to the consumers. The widespread application is caused by existence of new reliable ultrasonic flowmeters (USM) of gas providing high accuracy of measurement. For instance, multi-path USMs are developed for custody transfer of natural gas with the relative uncertainty of no more than ±0.15 % (USZ 08 of Honeywell RMG Company), ±0.2 % (FLOWSIC600 of SICK Company) or ±0.3 % (Daniel Senior Sonic of Emerson Company).

It is known that the metrological characteristics of flowmeters depend on the operating conditions (in particular, on how much the operating conditions are different from the calibration conditions). Based on the numerous experimental studies [1-4] it was defined that the flow disturbances in the pipe upstream of the USM lead to significant errors in flow rate measurement.

To provide a fully developed flow profile without a flow conditioner the pipe straight length of up to 50*D* may be needed to eliminate an asymmetric profile or up to 200*D* to eliminate a flow swirl according to ISO 17089-1: 2010 [1]. Such long pipe straight lengths not always can be provided in operating conditions. That is why it is important to study the effect of a flow disturbance on the error of USM and to develop the up-to-date means for simulation in order to work out recommendations on installation of USMs to eliminate the additional errors of flow rate measurement caused by flow disturbances.

A powerful instrument for studying the gas dynamical processes in pipes together with experimental studies is a computer simulation by means of Computer Aided Design (CAD) and Computational Fluid Dynamics (CFD) software. The models of fluid flows in pipes of complicated configurations can be built by means of the software with high accuracy. These models provide the possibility to study the pipe configurations and USM constructions for which the experimental studies were not carried out sufficiently.

The results of CAD/CFD simulation for studying the effect of a disturbed flow on the error of USM are presented and discussed in works [2-7]. Based on the analysis of these works it was defined that there are a lot of CAD/CFD software types both with open access and with licenses. There are different constructions of pipe fittings and positions of acoustic paths of USMs. That is why there is a need to develop a generalized methodology for application of CAD/CFD software to improve the mathematical model of USM and to study the effect of a disturbed flow on the error of USM.

2. MATHEMATICAL MODEL OF A FLOWMETER

A mathematical model of an USM was built on the basis of the equation of volume flow rate for chordal multi-path configurations of meters [7] and on the basis of Gauss-Jacobi numerical method of integration [8]. According to this method of integration the position coordinates $x(i)$ of the acoustic paths are defined by solving the recurrent equation of the Jacobi polynomial [7, 8]. The order of this polynomial is equal to the number of acoustic paths (N). After finding the position coordinates $x(i)$, the weighting factors of the acoustic paths $w(i)$ are defined by calculating the values of the Lagrange polynomial in the points $x(i)$ and by applying a special formula for integration were the following weighting function of Jacobi polynomial is used

$$W(x) = (1 - x^2)^k . \quad (1)$$

The value of the coefficient k in the classical method is equal to 0.5 [8]. It is proposed to improve the method for defining the $w(i)$ and $x(i)$ of the acoustic paths of USM by improving the weighting function (1). The coefficient k of the weighting function is improved on the basis of comparison of $W(x)$ values with the values of the power law of flow velocity distribution for a fully developed turbulent flow (see Figs. 1 and 2). The power law of flow velocity distribution in a relative form is presented by the following formula

$$\frac{v}{v_{\max}} = \left(1 - \frac{r}{R}\right)^{\frac{1}{n}} . \quad (2)$$

The Nikuradse number in (2) is defined as follows [9]

$$n = 1/[0.2525 - 0.0229 \lg(Re)] . \quad (3)$$

It can be seen from Figs. 1 and 2 that for k=0.2 the weighting function curve is closer to the power law of flow velocity distribution than for k=0.5.

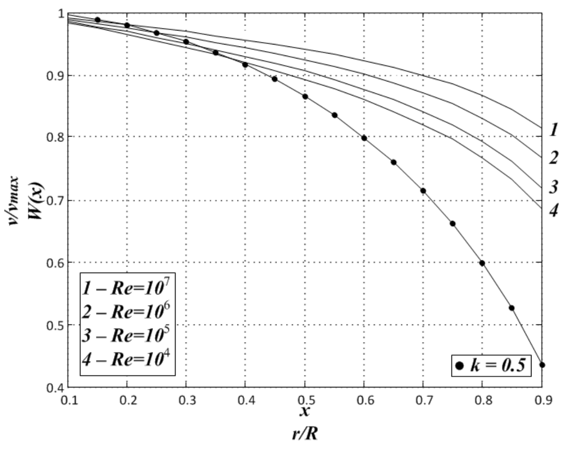

Figure 1. Comparison of the weighting function curve (–•–) for k=0.5 with the power law of flow velocity distribution (—)

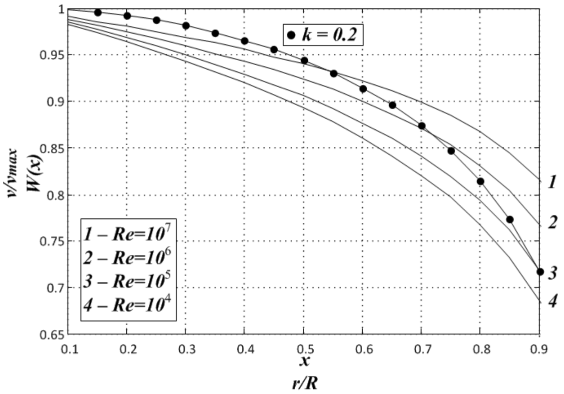

Figure 2. Comparison of the weighting function curve (–•–) for k=0.2 with the power law of flow velocity distribution (—)

For a number of values of k the standard deviation of $W(x)$ values from the values of the power law of flow velocity distribution were calculated for the values of Re from 10^4 to 10^7 and for the values of x from 0.1 to 0.9 [10]. Based on the calculation it was defined that the minimum standard deviation is reached for k=0.2.

The improved method for defining the $x(i)$ and $w(i)$ was also verified for a disturbed flow using the Salami function P09 [11]. The error of flow rate measurement result for a 4-paths chordal USM is reduced by 0.25 % when applying k=0.2 in comparison to k=0.5 (see Fig. 3). The error of flow rate measurement was calculated using the following formula

$$\delta_q = \frac{q_v - q_{v.Salami}}{q_{v.Salami}} \cdot 100 . \quad (4)$$

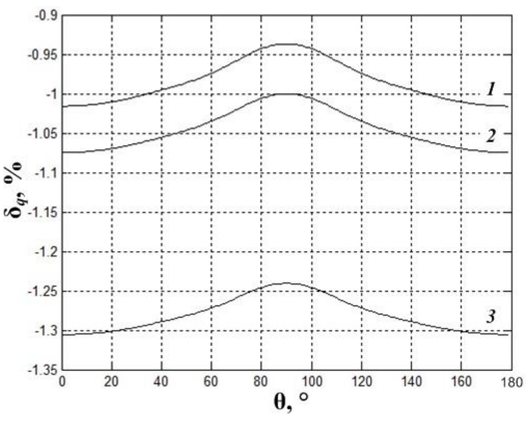

Figure 3. Flow rate measurement error versus integration angle for k=0.2 (curve 1), k=0.3 (curve 2) and k=0.5 (curve 3)

The mean flow velocities along each chordal acoustic path ($v_h(1)\ldots v_h(N)$) are the input variables of the mathematical model of USM. That is why the model can be applied together with a CAD/CFD software which provides the possibility to simulate the flow velocity profile and the mean flow velocities along each chordal acoustic path. The errors may take place during application of the mathematical model together with the CAD/CFD simulation software due to the following reasons.

1. Inaccurate drawing of the multi-path USMs and pipes which is caused by the complicated construction of the USM in the cases when the information on the geometrical dimensions of USM is absent or defined inaccurately (dimensions of the electro-acoustic transducers (EAT), their pockets, protection layer and length of the acoustic channel).

2. Inaccurate description of the behavior of the turbulent flow by the CAD/CFD software [3, 6].

To eliminate the errors of USM simulation it is proposed to improve the mathematical model of the meter by introducing the dependence of the calibration factor on the Reynolds number $k_{cal} = f(Re)$ into the model [12]. The values of k_{cal} are defined on the basis of the reference values of volume flow rate and flow parameters derived experimentally for specific values of Reynolds number according to the following formula

$$k_{cal} = q_{s.ref} / q_s . \quad (5)$$

The flow rate reduced to standard conditions is calculated as follows

$$q_s = q_v \frac{p_{CFD} T_s}{p_s T_{CFD} K(p_{CFD}, T_{CFD})} . \quad (6)$$

It should be stressed that the values of $q_{v.ref}$, p and T are used for setting the parameters of CFD simulation (boundary conditions) and the dependence $k_{cal} = f(Re)$ should be defined for an undisturbed flow.

Thus, the proposed methodology of improving the mathematical model of an USM consists in defining the dependence of k_{cal} on Re based on the results of CFD simulation and the available reference data on the measured flow rate and subsequent introduction of this dependence into the mathematical model. The generalized mathematical model of a multi-path USM with taking into account the proposed methodology and the improved method for defining the $x(i)$ and $w(i)$ is presented as follows

$$\begin{cases} q_v = k_{cal} \dfrac{\pi D^2}{4} \displaystyle\sum_{i=1}^{N} \dfrac{2\sqrt{R^2 - x(i)^2}}{\pi R} w(i) v_h(i); \\ k_{cal} = f(Re);\ Re_{\min} \le Re \le Re_{\max}; \\ k = 0.2;\ i = 1,\ 2, \ldots N; \\ w(i) = \dfrac{\displaystyle\int_{-R}^{+R} PL(x,\ x(i))(1 - x^2)^k\, dx}{(1 - x(i)^2)^k}; \\ PL(x,\ x(i)) = \displaystyle\prod_{\substack{j=0 \\ j \ne i}}^{N} \left(\dfrac{x - x(j)}{x(i) - x(j)} \right); \\ PJ = f(x, N, k);\ x(i) = roots(PJ). \end{cases} \quad (7)$$

The mathematical model of USM (7) together with the CAD/CFD software provides the possibility to carry out simulation in order to study the effect of the constructional parameters of multi-path USMs as well as the effect of flow disturbance on the results of flow rate measurement.

3. TECHNIQUE FOR STUDYING THE ERROR OF USM

Technique for studying the error of flow rate measurement was developed on the basis of the mathematical model of USM (7). This technique is presented in [12] and it consists of the following steps:

1) definition of the main and supplementary constructional parameters of the USM and the pipe (see Fig. 4);

2) definition of the parameters of the fluid flow (type of fluid, flow rate, p and T etc.);

3) design of k_{cal} of USM model (drawing of 3D model of the USM and the pipe by mean of CAD software (see Fig. 5); setting of parameters of 3D model in CFD software; development of the dependence of k_{cal} on Re);

4) study of the USM error in a disturbed flow.

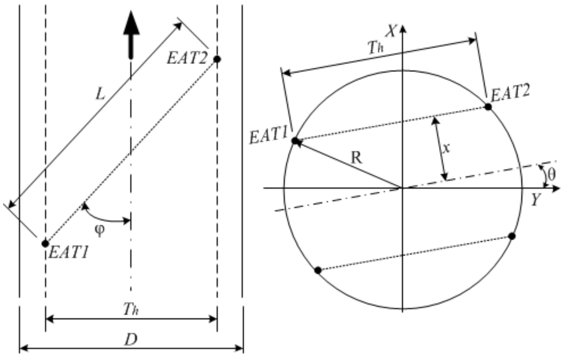

Figure 4. Simplified design diagram of a double-path chordal USM

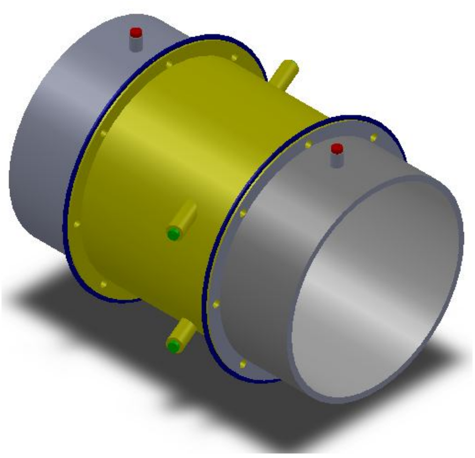

Figure 5. Three dimensional model of USM and pipe

The developed technique was verified on the basis of the results of experimental study of flow rate measurement error for an acting USM GUVR-011A2.2/VS in a gas test rig of “Energooblik” Company (Kharkiv, Ukraine) [12]. The working fluid was air. The picture of the test rig is presented in Fig. 6. It should be mentioned that both the experimental study and the simulation of USM were carried out without any flow conditioner according to the requirements specified by the flowmeter manufacturer in the operational documentation [13].

Figure 6. Picture of the test rig

Three dimensional model of the USM (see Fig. 5) together with the pipe and the fittings was built by mean of CAD software. The pipe straight lengths were set according to the diagrams in Figs. 7 and 8. The simulated flow rate values were compared to the experimental results of flow rate measurement by means of the USM installed downstream of two typical fittings (single 90° bend, Fig. 7, and two 90° bends in perpendicular planes (l≤5D), Fig. 8). This way the conclusion about the adequacy of the proposed technique was made.

The mathematical model of the double-path chordal USM GUVR-011A2.2/VS (8) was built by means of the proposed methodology. This model was applied for calculating the flow rate measured by the flowmeters presented in Figs. 7 and 8. Here the values $q_{v.et}$ were taken equal to the experimental values of flow rate measured by the reference gas meter in the test rig.

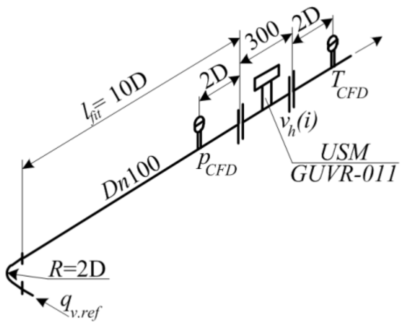

Figure 7. Axonometric diagram of pipe with USM installed downstream of a single 90° bend

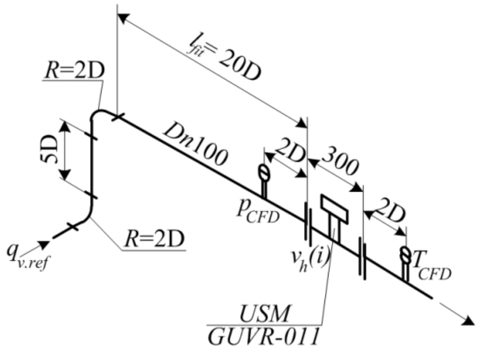

Figure 8. Axonometric diagram of pipe with USM installed downstream of two 90° bends in perpendicular planes (l≤5D)

$$\begin{cases} q_v = k_{cal}\dfrac{\pi D^2}{4}\dfrac{\sqrt{R^2-(0.5807R)^2}}{\pi R}[v_h(1)+v_h(2)]; \\ k_{cal} = \begin{cases} 38.79Re^{-0.7837} + \\ +1.01; \quad Re = 1\cdot 10^3 \div 5\cdot 10^3; \\ -1.148\cdot 10^{-10}Re^2 + 2.675\cdot 10^{-6}Re + \\ +1.049; \quad Re = 5\cdot 10^3 \div 1.5\cdot 10^4; \\ -3.567\cdot 10^{-8}Re + \\ +1.063; \quad Re = 1.5\cdot 10^4 \div 1.5\cdot 10^5; \end{cases} \\ Re = \dfrac{4q_{v.ref}\rho}{\pi\mu D}. \end{cases} \tag{8}$$

The values of flow rate calculated on the basis of the mathematical model (8) were compared to the experimental values of flow rate measured by means of USM GUVR-011A2.2/VS. To calculate the relative deviation between the calculated and the measured values of flow rate (δ_M) the values of flow rate were reduced to standard conditions by applying a similar formula to formula (6).

The relative deviation was calculated according to the following formula

$$\delta_M = \frac{q_{s.CFD} - q_{s.GUVR}}{q_{s.GUVR}} \cdot 100\,. \tag{9}$$

The curves of the relative deviation δ_M versus flow rate are presented in Figs. 9 and 10.

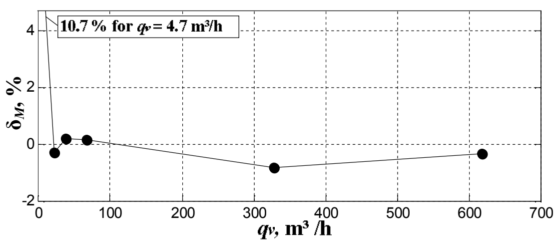

Figure 9. Relative deviation δ_M versus flow rate for USM installed downstream of 90° bend

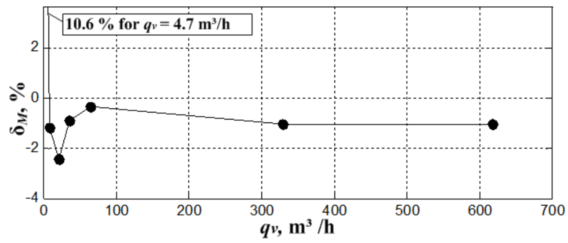

Figure 10. Relative deviation δ_M versus flow rate for USM installed downstream of two 90° bends in perpendicular planes (l≤5D)

As we can see from Figs. 9 and 10 the simulation results are close to the experimental values in the range of flow rate from $0.05q_{v.max}$ to $q_{v.max}$. For USM installed downstream of 90° bend the maximum value of δ_M is 0.86 % in the specified range of flow rate. And for USM installed downstream of two 90° bends in perpendicular planes (l≤5D) the maximum value of δ_M is 1.04 %. By means of these results the adequacy of the proposed technique is proved and the possibility of application of this technique for studying the effect of flow disturbances on the error of flow rate measurement by USMs is confirmed.

4. DEFINITION OF MINIMUM PIPE STRAIGHT LENGTHS

The developed technique was applied for studying the additional errors of USMs caused by flow disturbances downstream of typical fittings with relation to the distance between the fitting and the USM (l_{fit}). The following types of USM were taken to consideration:

1. USM1 – double-path chordal USMs with the angle of acoustic paths φ = 45°… 67°; calculation of the position coordinates and the weighting factors of the acoustic paths was carried out according to the improved method.
2. USM2 – double-path chordal USM GUVR-011A2.2/VS (G400, Dn100) with the angle of acoustic paths φ = 67°; the position coordinates and the weighting factors of the acoustic paths were set according to [13].
3. USM3 – double-path chordal USM with the angle of acoustic paths φ = 67°; calculation of the weighting factors of the acoustic paths was carried out according to the improved method.

The following fluid parameters were taken for simulation:

- type of fluid – air;
- fluid pressure and temperature – p = 400 kPa, T = 293.15 K (20 °C);
- reference values of flow rate: $q_v = q_{v.max}\times(0.025;\ 0.05;\ 0.1;\ 0.25;\ 0.5;\ 0.75;\ 1)$, $q_{v.max} = 650$ m^3/h.

The additional error of flow rate measurement caused by flow disturbance was calculated according to the following formula

$$\delta_A = \frac{q_s - q_{s.ref}}{q_{s.ref}} \cdot 100 \,. \qquad (10)$$

The results of δ_A calculation for various flow rates are presented in Fig. 11.

The minimum pipe straight lengths l_{min} between a fitting and USM (see Table 1) were defined on the basis of the simulation results with taking into account the following criteria:

- l_{min} is equal to the minimum length at which the value of δ_A error remains within the limits of the basic relative error of flow rate measurement declared by the manufacturer of USM;
- l_{min} is equal to the length at which prolonging the length by 10D would not lead to change of δ_A error by more than 0.3 %.

The greater value of l_{min} was accepted in each case when making the Table 1 based on the two criteria mentioned above.

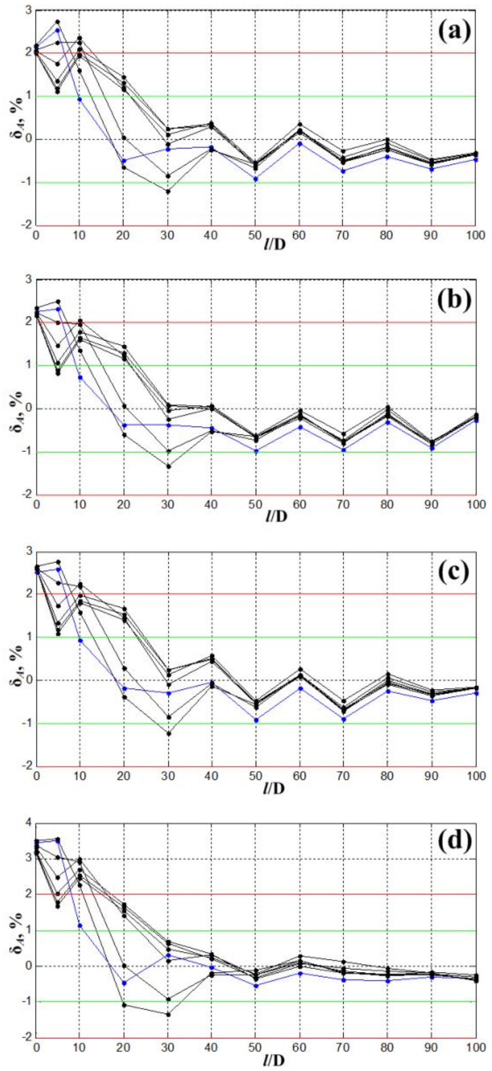

Figure 11. Relative error δ_A versus relative pipe straight length for USM installed downstream of two 90° bends in perpendicular planes (l≤5D): *a* – φ=45°; *b* – φ=55°; *c* – φ=55°; *d* – GUVR φ=67°

Table 1. Minimum pipe straight length for USM installed downstream of the fitting

No	Type of fitting	l_{min}, ≥ l/D		
		USM1	USM2	USM3
1	Single 90° bend	50	30	30
2	Two 90° bends in perpendicular planes (l≤5D)	40	40	30
3	Gagged tee with change of flow direction	50	50	40
4	Two 90° bends in the same plane: U-configuration (l≤10D)	50	50	40
5	Two 90° bends in the same plane: S-configuration (l≤10D)	60	60	50
6	Expander (80/100)D	20	20	20
7	Reducer (130/100)D	40	20	20

As we can see from Fig.11 the minimum pipe straight length l_{min} defined on the basis of the two criteria for USM installed downstream of two 90° bends in perpendicular planes (l≤5D) is 33D. The additional error of flow rate measurement δ_A is within the limits ±1 % for the double-path chordal USMs under consideration in the range of flow rate measurement from $q_{v.min}$ to $q_{v.max}$.

Based on the results presented in Table 1 we can say that the shortest pipe straight lengths are needed for USMs installed downstream of an expander. And the longest pipe straight lengths are needed for USMs installed downstream of two 90° bends in the same plane: S-configuration (l≤10D).

5. CONCLUSIONS

Thus, the method for defining the position coordinates and the weighting factors of the acoustic paths was improved which provided reduction of the error of flow rate measurement.

An improved methodology was proposed in order to build a mathematical model of an USM of any construction.

The technique for studying the error of flow rate measurement was developed and verified on the basis of the results of experimental study of flow rate measurement error for an acting USM GUVR-011A2.2/VS in a test rig.

The recommendations to the minimum pipe straight lengths for the double-path chordal USMs without a flow conditioner were defined.

REFERENCES

[1] Measurement of fluid flow in closed conduits – Ultrasonic meters for gas. Part 1: Meters for custody transfer and allocation measurement:

ISO 17089-1 : 2010. – [First edition 2010-11-15]. – Geneva (Switzerland) : International Organization for Standardization (ISO), 2010. – 100 pages. (International standard). http://www.iso.org/iso/catalogue_detail.htm?csnumber=41235.

[2] Ruppel, C., and Peters, F. (2004) Effects of upstream installations on the reading of an ultrasonic flowmeter. *Flow Measurement and Instrumentation*, **15**, 167–177. doi:10.1016/j.flowmeasinst.2003.12.004.

[3] Merzkirch, W., Gersten, K., Hans, V., Lavante, E.V., Peters, F., & Ram V.V. (2005). Fluid mechanics of flow metering. New York, USA : Springer.

[4] Voser, A. (1999). Analysis and error optimization of multipath strength acoustic flow measurement in water turbines. Unpublished master's doctoral dissertation, Swiss Federal Institute of Technology Zurich, Zurich, Switzerland.

[5] Hilgenstock, A., and Ernst, R. (1996) Analysis of installation effects by means of computational fluid dynamics – CFD vs experiments? *Flow Meas. Instrum*, **7 (¾)**, 161–171. doi:10.1016/S0955-5986(97)88066-1.

[6] In-service performance of ultrasonic flowmeters – Application and validation of CFD modelling methods : technical report no. 2002/72 / edit by N. A. Barton. – Glasgow : National Engineering Laboratory, 2002. – 43 pages. www.tuvnel.com/_x90lbm/Report_FDUS01.pdf.

[7] Staubli, T., Luscher, B., Senn F., and Widmen, M. (2007) CFD optimized acoustic flow measurement and laboratory verification. *Proceedings of the international conference HYDRO*, Granada, 14–18 October 2007, 7 pages.

[8] Press, W. H., Teukolsky S. A., Vetterling W. T., & Flannery B. P. (1995). Numerical Recipes in C (2nd ed.). Cambridge, England: Cambridge University Press.

[9] The Measurement, instrumentation, and sensors: handbook / edit by J. G. Webster. – Boca Raton (USA) : CRC Press, 1999. – 2630 pages.

[10] Roman V., Matiko F. Definition of weighting factors of acoustic paths of ultrasonic flow meters // Metrology and instrumentation . – 2014. – No 3(47). – p. 11-20 (in Ukrainian)

[11] Moore, P. I., Brown, G. J., & Simpson, B. P. (2000). Ultrasonic transit-time flowmeters modeled with theoretical velocity profiles: methodology. Meas. Sci. Technol, 11, 1802-1811.

[12] Pistun Y., Matiko F., Roman V., Stetsenko A. Investigation of the error of ultrasonic flow meters in disturbed flow based on CFD simulation // Metrology and instrumentation . – 2014. – No 4. – p. 13-23 (in Ukrainian)

[13] Ultrasonic Gas Meters GUVR-011: Instruction Manual 636128.310-1 RE / "Takhion" Private Company. – Kharkiv, Ukraine, 2013. – 58 p. (in Russian)

Conference on Modelling Fluid Flow (CMFF'15)
The 16th International Conference on Fluid Flow Technologies
Budapest, Hungary, September 1-4, 2015

CHALLENGES IN EVALUATING BEAMFORMING MEASUREMENTS ON AN INDUSTRIAL JET FAN

Bence TÓTH[1], János VAD[2]

[1] Corresponding Author. Department of Fluid Mechanics, Faculty of Mechanical Engineering, Budapest University of Technology and Economics. Bertalan Lajos u. 4 – 6, H-1111 Budapest, Hungary. Tel.: +36 1 463 2635, Fax: +36 1 463 3464, E-mail: tothbence@ara.bme.hu
[2] Department of Fluid Mechanics, Faculty of Mechanical Engineering, Budapest University of Technology and Economics. E-mail: vad@ara.bme.hu

ABSTRACT

The aim of this paper is to illustrate the difficulties that arise during the evaluation of phased array microphone measurements on ducted fans in an industrial environment, and draw attention to them. A case study was carried out, and the results were processed resulting in beamforming maps, but their interpretation is not straightforward. Firstly, some fine details are found that seem to correspond to true physical phenomena, but should not be dealt with as separate sources on the basis of the spatial resolution given by Rayleigh's criterion. These results together with some theoretical objections raise concerns about the validity of Rayleigh's criterion in case of beamforming. Secondly, in some frequency bins the noise peaks are found on the axis of revolution. Literature shows that this might truly be motor noise, but it might also be an artefact, that causes beamforming algorithms to falsely locate rotating noise sources onto the axis of revolution [1, 2]. Central noise source peaks might even result from the presence of axial duct modes [3]. These questions are to be answered before beamforming on industrial ducted fans may become a standard noise diagnostics tool.

Keywords: beamforming, fan noise, phased array microphone, Rayleigh criterion, spatial resolution

NOMENCLATURE

a	[m/s]	speed of sound
B	[dB]	beamform map value
BPF	[Hz]	blade passing frequency
D	[m]	diameter
f	[Hz]	frequency
L	[m]	minimum resolvable distance
N	[-]	number of blades
x	[m]	beamform map horizontal coordinate
y	[m]	beamform map vertical coordinate
z	[m]	rotor – microphone array distance
λ	[m]	wavelength
ν	[-]	hub-to-tip ratio
Θ	[rad]	angle between two sources

Subscripts and Superscripts

g	guide vane
mid	third-octave band mid-frequency
OPT	optical
r	rotor
S	Sparrow limit
t	rotor tip

Abbreviations

DS	Delay-and-Sum method
PAM	Phased Array Microphone
ROSI	Rotating Source Identifier

1. INTRODUCTION AND OBJECTIVES

Noise reduction is an important task in the 21st century, and regulations are becoming more and more stringent in connection with axial fans, too. Beamforming using phased array microphone (PAM) measurements presents means to localize sound sources even in a rotating reference frame. These source maps give invaluable information about the distribution of noise that can be related to its generation mechanisms.

Benedek and Vad [4-6] have investigated aerodynamic and acoustic properties of an unducted axial fan through a case study. Using on-site measurements and the PAM technique they have obtained spanwise distributions of boundary layer momentum thickness, and sound pressure level in third-octave bands. Analysis shows that these functions are in correlation for the dominating low frequency ranges. This suggests the possibility of reducing noise while improving efficiency in case of short ducted axial fans.

Similar tests on ducted fans are reported in [7, 8]. In [7] a turbofan engine is investigated using two microphone arrays, one in the inlet, and one in the bypass section of the duct. The source maps clearly show the periodicity related to the fan blades, and the location of maximum noise sources is visible. This measurement was however carried out in a special test rig in an anechoic chamber using wall-mounted microphones, therefore it is not applicable for on-the-field diagnostics. Such a measurement is described in [8] for a wind tunnel fan describing the difficulties of the experiments: reverberant space, high aerodynamic loading on the microphones, low spatial resolution, and the presence of other noise generating mechanisms.

In the current study the authors have implemented the same diagnostic methodology as in [4-6] for the case of ducted fans. This scenario however differs from the original one in several points. The duct length limits accessibility, and spatial resolution of the microphone array. Duct modes are also expected to form, and affect the measurements in different ways depending on duct geometry. The presence of coherent sources in the rotating frame of reference might also cause unrealistic results, in the form of false noise sources appearing on the axis of the rotor [1, 2]. In the following, this will be referred to as the “Mach radius effect”. These phenomena are investigated below.

The spatial resolution of beamforming appears to be a concern. It was tested in [9] for several algorithms, conventional and deconvolution-based, too. This investigation is different however, as our aim is to make practically relevant comments on the resolution when measuring turbomachinery acoustics instead of developing new beamforming methods.

This paper is considered as a Technical Note for the Workshop “Beamforming for Turbomachinery Applications” organized at CMFF’15, aiming at provoking a discussion on the topics outlined herein.

2. CASE STUDY

A ducted fan was investigated having a rotor tip diameter D_t=0.355 m, hub-to-tip ratio ν=0.57, N_r=8 rotor blades, and N_g=7 guide vanes. Rotor speed was 2856±1 RPM measured using a handheld stroboscope, corresponding to a rotor blade passing frequency BPF=381 Hz. Noise was measured from a distance of 2 d_t between the PAM and the fan inlet plane for 30 s with a sampling frequency of 44100 Hz on 24 channels on the suction side of the fan. The equipment used was an OptiNav, Inc., Array 24 multi-purpose portable array system. The PAM was placed perpendicular to the axis of rotation, with its centre coinciding with the rotor axis. Data was evaluated using an in-house beamforming software applying the “Rotating Source Identifier” (ROSI) [10] technique to localize rotating sources. Noise source maps of equal dynamic range were constructed showing the spatial distribution of beamform peak values in the fan inlet plane, together with the location of the hub and the annulus. Note that due to the lack of any rotor position transducer, the angular position of the rotor cannot be assigned to the noise source maps. However, with a knowledge of the accurate rotor speed, the ROSI processing algorithm principally enables the pitchwise resolution of the noise sources.

The authors have attempted to determine the most important noise generation mechanisms based on the source maps. They have however faced the problem of Rayleigh’s criterion for resolving power and the problem of noise maxima appearing on the axis of revolution. These problems are detailed in the following.

3. RESOLUTION

3.1 Rayleigh’s criterion

The applied ROSI method is basically an extension of the frequency-domain Delay-and-Sum (DS) beamforming technique with a special step called deDopplerization to place the rotating sources into a co-rotating reference frame, thus make them stationary. The step consists of adjusting the time delays and amplitudes in order to remove the effect of rotation from the measured noise signals.

In case of beamforming measurements the spatial resolution is of importance because it determines the smallest distance between two sources that can be regarded as separate ones. This way it also shows the minimum size of structures can be positively identified, since regions smaller than the resolution might be the effect of neighbouring source regions.

The spatial resolution is especially important in the case of rotor blades, for which an improper spatial resolution may lead to dissolving the contribution of the adjacent blades in the noise source maps.

Because the spatial resolution of the microphone array and the beamforming method is a very complex phenomenon, the spatial resolution of DS beamforming is usually determined by applying a simplified optical analogy.

The resolving power of an optical aperture is given using Rayleigh’s criterion [11]. Assume a point source radiating light of wavelength λ infinitely far from a perfect circular aperture, i.e. the wave fronts incident to the aperture are assumed to be planar waves. The diameter of the aperture is D_{OPT}. The image created by the aperture is the so-called Airy disk, a circularly symmetric diffraction pattern. In case of two sources of identical strength the image is the superposition of the two identical Airy disks. Rayleigh has defined the limit case of resolving the image when the intensity peak of one source falls into the first intensity minimum of the other source.

In such case for the Θ angle between the two sources the following holds:

$$\sin\Theta \approx 1.22\frac{\lambda}{D_{OPT}} \quad (1)$$

In between the two intensity peaks, the intensity of the resultant pattern drops to 73.7 % of the maximum value. The 26.3 % dip relative to the maximum is presumed arbitrarily in Rayleigh's criterion as being sufficient for the human eye in making a distinction between the two optical sources.

The minimum distance between two resolvable sources is usually given based on Eq. (1) by assuming a small angle between the sources. The measurement plane is parallel to the plane of the microphones and offset by z. The minimum resolvable distance is L [11, 12] assuming plane wave propagation:

$$L \approx z\Theta \approx 1.22\frac{z\lambda}{D_{PAM}} \quad (2)$$

Table 1 shows the minimum resolvable distances calculated using Eq. (2) for some representative third-octave frequency bands, being significant from the viewpoint of human audition. The spatial resolution L at a third-octave frequency range is calculated by taking the wavelength corresponding to the mid-frequency f_{mid} in the following way: $\lambda = a / f_{mid}$, then substituting it into Eq. (2) above. In this expression a is the speed of sound.

Table 1. Minimum resolutions in frequency bands, based on Rayleigh's criterion

f_{mid} [Hz]	L [m]	L/D_t [-]
2000	0.42	1.20
2500	0.34	0.96
3150	0.27	0.76
4000	0.21	0.60
5000	0.17	0.48
6300	0.13	0.38

The spatial resolution calculated using Rayleigh's criterion is quite weak due to the fact that the distance is the same order of magnitude as the size of the PAM, D_{PAM}=1 m. Each L/D_t value significantly exceeds 1) the rotor blade height of 0.22 D_t, 2) the rotor blade pitch (spacing) of 0.31 D_t at misdspan. These facts *anticipate the following limitations*, if one would take Rayleigh's criterion as a basis for the available spatial resolution: 1) Even the rotor annulus area, as a whole, could not be expected to be clearly distinguished from the rotor hub area as a noise source, if both sources are of equal magnitude, 2) No pitchwise resolution of noise sources related to the individual rotor blades would be expected at all.

Dougherty et al. also consider the Sparrow limit shown in Eq. (3) for the quantification of resolution [9]. This corresponds to the distance between two sources, at which the dip between their Airy disk diffraction patterns first appears.

$$L_S \approx z\Theta \approx 0.94\frac{z\lambda}{D_{PAM}} \quad (3)$$

The Sparrow limit is less conservative, than Rayleigh's one, by taking values that are roughly 80% of the latter. As customary in optics however, we focus our attention on Rayleigh's criterion.

3.2 Measurement results

In Figure 1 a source map is shown with 6 dB dynamic range showing the rotor from the upstream side in a co-rotating frame. This figure is a representative narrowband result taken from the third-octave band centred on 5 kHz. The two concentric circles indicate the fan annulus area: the inner one shows the hub, while the outer one corresponds to the tip diameter.

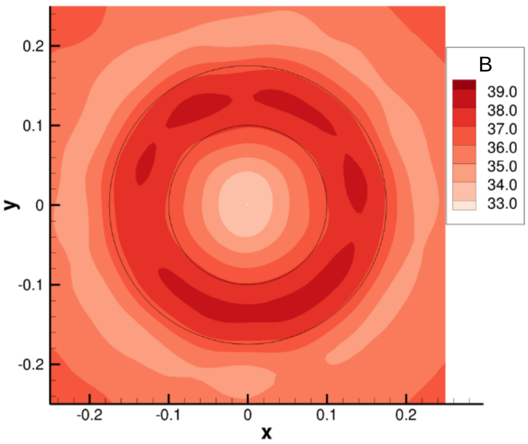

Figure 1. Rotor narrowband beamform map

Despite the anticipated limitations in spatial resolution, originating from Rayleigh's criterion, and formerly described in points 1) and 2), the following observations are made in Fig. 1, in contrast to those points.

1) The rotor annulus area – characterized by the minimum length scale being equal to the blade height of 0.22 D_t – is clearly distinguished from the hub area in the source map.

2) The periodicity in the source map corresponding to the rotor annulus, being in accordance with the eight rotor blades of midspan spacing of 0.31 D_t, is apparent in the upper half of the figure. Some small structures are detected in the

vicinity of the blade tips, whose size is much less than the calculated resolution of 0.48 D_t.

The above suggest that Rayleigh's criterion is a pessimistic approach in the case study presented herein, and, as such, it is to be treated with criticism.

3.3. Criticism of Rayleigh's Criterion

The above discussion suggests that Rayleigh's criterion exhibits some limitations in estimating the spatial resolution of PAM-based fan rotor noise source maps. This experimental finding described above is further supported by the following differences between optical systems and a PAM:

- In general, a microphone array does not necessarily represent a *circular aperture*. In references [1-3], the microphones of the array are arranged along a logarithmic spiral curve, where the shape of the aperture is not known. In case of a linear array however the aperture shape is certainly not circular.
- In the investigated frequency range no cut-on plane modes waves exist in the duct. Due to the proximity of the PAM plane wave propagation out of the duct is a poor approximation.
- The *distance* between the acoustic source and PAM is *finite*. It is often confined to the order of magnitude of some times the rotor tip diameter. Besides the current investigation, references [4-6] also report case studies in which the array was installed at a distance of ≈ *2* D_t from the fan inlet.
- The rotor noise sources to be resolved are not necessarily of *identical intensity*. The studies documented in [1-3] especially aimed at discovering the spanwise non-uniform intensity distribution of rotor noise sources.
- The criterion is based on the visibility of structure of optical diffraction patterns to the human eye, the applicability of which is doubtful from the viewpoint of human audition, and even more so in connection with microphones and digital signal processing.
- The 26.3 % dip in intensity is presumed *arbitrarily* as a quantitative criterion for resolution.

Note that besides these problems already the approximation $\sin\Theta \approx \Theta$ means an error of about 15 % in case of the large angles experienced in the current measurement.

4. ON-AXIS NOISE SOURCES

Besides the sources on the annulus regions several source maps show high peak levels on the axis of rotation. Such a source map is shown in Figure 2. It is a representative narrowband result taken from the third-octave band centred on 3000 Hz.

This peak might be attributed to motor noise. However, it is known from literature [3] that axial plane wave modes will appear in the duct. The beamforming method will localize these to the centre of the beamforming map.

Furthermore, Horváth et al. [1-2] have shown that beamforming measurements on a rotating object will falsely locate some coherent sound sources onto the axis of revolution when the PAM is perpendicular to the rotor axis. How to separate the contribution of real on-axis sources and the "Mach-radius effect" in these specific cases is an open question requiring further investigations.

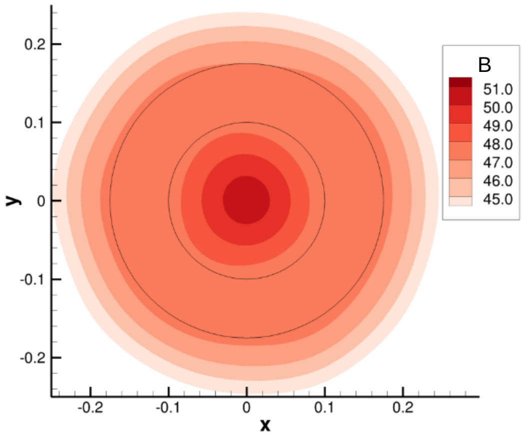

Figure 2. Narrowband beamforming map showing maximum values in the hub region

5. SUMMARY AND FUTURE REMARKS

Beamforming and phased array microphones present effective means of noise source localization that is a major step towards understanding and reducing noise generation. Using the ROSI algorithm rotating sources can also be dealt with effectively. A powerful application of this method is the investigation of industrial axial fans. However, in this case some special concerns arise.

The spatial resolution of beamforming maps obtained by PAM measurements is an important parameter, it is however quite difficult to obtain an expression describing this quantity. In several cases an analogy with wave optics is used, where the Rayleigh criterion is a classic result that presents a minimum distance between two sources if they are to be resolved separately.

While the criterion is well-known and accepted in optics, in the framework of beamforming its assumptions are at least questionable. Based on these reasons the authors consider Rayleigh's criterion in some cases ill-suited for the quantification of spatial resolution of beamforming measurements on rotating fans. The following question is arisen. What amount of dip between two peaks is to be considered as a practically relevant criterion for resolving two neighbouring sources in beamforming?

Another question is the case of noise sources appearing on the axis of beamforming maps. These might indicate true noise source positions on the axis, e.g. motor noise, but might also results from the "Mach radius effect". Possible causes of the phenomenon are the formation of axial duct modes and the interference of coherent sources in the rotating frame.

On the basis of above, some future tasks of departmental research on beamforming applied to industrial fans are as follows.

1) Elaboration of a widely applicable methodology for a realistic estimation of the spatial resolution of beamforming, with a special focus on rotating sources, as a critical revision of Rayleigh's pessimistic criterion. Comparison of resolution in case of stationary and rotating sources, e.g. DS and ROSI methods.

2) Elaboration of a systematic evaluation method for a comprehensive judgment on the origin of a local noise maximum apparent on / near the rotor axis, whether a) it is a virtual (physically non-existing) source, due to the Mach radius effect; or b) it is the representation of any duct modes; or c) it indicates indeed the local dominance of the hub as a noise source (e.g. due to the noise of the driving electric motor incorporated in the hub).

ACKNOWLEDGEMENTS

This work has been supported by the Hungarian National Fund for Science and Research under contract No. OTKA K 112277. Gratitude is expressed to Hungaro-Ventilátor Kft. for providing the test fan, and for making possible the tests at the premises of the company.

The work relates to the scientific programs "Development of quality-oriented and harmonized R+D+I strategy and the functional model at BME" (Project ID: TÁMOP-4.2.1/B-09/1/KMR-2010-0002) and "Talent care and cultivation in the scientific workshops of BME" (Project ID: TÁMOP-4.2.2/B-10/1-2010-0009).

REFERENCES

[1] Horváth, Cs., Envia, E., and Podboy, G. G., 2014. Limitations of Phased Array Beamforming in Open Rotor Noise Source Imaging, *AIAA Journal*, Vol. 52, No. 8, pp. 1810-1817.

[2] Horváth, Cs., Tóth, B., Tóth, P., Benedek, T., and Vad, J., 2015. Reevaluating Noise Sources Appearing on the Axis of Beamform Maps of Rotating Sources, *FAN 2015*, Lyon, France

[3] Tyler, J. and Sofrin, T., 1962. Axial Flow Compressor Noise Studies, *SAE Technical Paper 620532*, doi:10.4271/620532.

[4] Benedek, T., and Vad, J., 2015. An industrial on-site methodology for combined acoustic-aerodynamic diagnostics of axial fans, involving the Phased Array Microphone technique. *International Journal of Aeroacoustics* (accepted)

[5] Benedek, T., and Vad, J., 2015. Spatially resolved acoustic and aerodynamic studies upstream and downstream of an industrial axial fan with involvement of the phased array microphone technique. *Proc. 11th European Conference on Turbomachinery Fluid Dynamics and Thermodynamics (ETC'11),* Madrid, Spain, Submission ID 128. ISSN 2410-4833.

[6] Benedek, T., and Vad, J., 2014. Concerted aerodynamic and acoustic diagnostics of an axial flow industrial fan, involving the phased array microphone technique. *ASME Paper* GT2014-25916.

[7] Sijtsma, P., 2010. Using Phased Array Beamforming to Identify Broadband Noise Sources in a Turbofan Engine, *International Journal of Aeroacoustics*, Vol. 9, No. 3, pp. 357-374.

[8] Benedek, T., and Tóth, P., 2013. Beamforming measurements of an axial fan in an industrial environment, *Periodica Polytechnica Mechanical Engineering*, Vol. 57, No. 2.

[9] Dougherty, R. P., Ramachandran, R. C., and Raman, G., 2013. Deconvolution of sources in aeroacoustic images from phased microphone arrays using linear programming, AIAA Paper 2013-2210¸ *19th AIAA/CEAS Aeroacoustics Conference,* Berlin.

[10] Sijtsma, P., Oerlemans, S., and Holthusen, H., 2001. Location of rotating sources by phased array measurements, *National Aerospace Lab*., Paper NLR-TP-2001-135.

[11] Jenkins, F., A., and White, H. E., 1976. *Fundamentals of optics.* 4th Edition. McGraw-Hill Primis Custom Publishing, New York.

[12] Hald, J., 2005. Combined NAH and beamforming using the same array. *Brüel & Kjær Technical Note* (2005-1).

Conference on Modelling Fluid Flow (CMFF'15)
The 16th International Conference on Fluid Flow Technologies
Budapest, Hungary, September 1-4, 2015

INCOHERENCE OF BROADBAND DUCT MODES IN TURBOMACHINERY BEAMFORMING

Robert P. Dougherty[1]

[1] Corresponding Author. OptiNav, Inc. and the University of Washington. 1414 127th PL NE #106, Bellevue, WA, USA. Tel.: +1 425 891-4883, Fax: +1 425 467 1119, E-mail: rpd@optinav.com

ABSTRACT

In-duct mode measurement can be a useful method for characterizing the noise generation and radiation of turbomachinery. The usual approach is to locate a number of audio-frequency pressure transducers in the duct wall and process the data to infer the modal amplitudes. At high frequency, the number of cuton modes can exceed a reasonable number of transducers, invalidating the straightforward solution process for computing the amplitudes. In the broadband case, beamforming can be used to estimate the highest mode powers, but beamforming relies on the assumption that the sources to be measured are mutually incoherent. At first glance, it would appear that broadband duct modes could be coherent, for example if they were all produced by a single point source in the duct. Drawing inspiration from the observed incoherence that sometimes characterizes direct and reflected sources in free-space beamforming, it is shown that broadband duct modes can be forced to be mutually incoherent provided their axial group propagation velocities differ and the analysis bandwidth can be chosen to be wide enough, subject to the narrow relative bandwidth required for frequency domain processing. The decorrelation of a duct sound by choice of analysis bandwidth is demonstrated in a simple test.

Keywords: duct acoustics, beamforming, mode measurement, Sturm–Liouville, fan noise

NOMENCLATURE

$\underline{\underline{C}}$	[Pa^2]	Cross Spectral Matrix
$\underline{E}_j$	[-]	transverse eigenfunction
L	[s]	block length in FFT
M	[-]	number of cuton modes
N	[-]	number of microphones
R	[m]	distance
c	[m/s]	speed of sound
k_j	[m^{-1}]	axial wavenumber with index j
k_N	[m^{-1}]	eigenvalue of transverse equation
$\underline{g}$	[-]	steering vector
p	[Pa]	acoustic pressure
$\underline{p}$	[Pa]	acoustic pressure vector
q	[Pa m]	complex acoustic source strength
x	[m]	distance along the duct
$\underline{x_\perp}$	[m]	transverse coordinates
ω	[rad/s]	angular frequency

Subscripts and Superscripts

i	microphone or eigenvalue index
j	source basis function index
$'$	complex conjugate transpose
$*$	complex conjugate

1. INTRODUCTION

The noise generated turbomachinery commonly radiates along inlet and exhaust ducts before being radiated to the listeners. The extended shape of the ducts constrains the propagation to a certain set of cuton modes. Knowledge of the modal amplitudes is valuable for understanding and controlling the noise production mechanisms, predicting the radiation pattern, and designing noise treatments such as turbofan engine nacelle acoustic lining. A standard method for determining the modal amplitudes is to flush-mount a number of microphones in the duct wall so as to measure the unsteady pressure without disturbing the flow. Some of the fluctuating pressure signal is related to the excitation of the duct modes. An inversion procedure is used to infer the modal information from the acoustic part of the microphone data. Noise contamination by boundary layer turbulence must be rejected in the process.

Beamforming is an attractive processing technique for the high frequency part of the spectrum with many cuton modes. Since beamforming generally requires the sources to be mutually incoherent, it is important to understand where this requirement is met and, if possible, create favourable circumstances for mode incoherence.

2. MODE MEASUREMENT

Consider a uniform duct section with uniform flow and acoustic sources outside the section. Referring to [1] and converting the wave equation to the frequency domain, the narrowband sound field obeys the convected Helmholtz equation, Eq. (1).

$$\mathrm{L}p = 0 \tag{1}$$

Here $\mathrm{L} = \left(i\omega + cM_x \frac{\partial}{\partial x}\right)^2 - c^2\nabla^2$, ω is the angular frequency, c is the speed of sound, and M_x is the Mach number in the x direction, parallel to the duct. Using separation of variables, the pressure can be expanded in the form of Eq. (2), where $\underline{x_\perp}$ represents the transverse coordinates of the duct, t is the slowly varying time over which the random, complex, narrowband, quantities chage, k_j is the axial wavenumber, M is the number of cuton modes, and $E_j\left(\underline{x_\perp}\right)$ is transverse eigenfunction number $j \in [1, M]$.

$$p\left(x, \underline{x_\perp}, t\right) = \sum_{j=1}^{M} q_j(t) E_j\left(\underline{x_\perp}\right) e^{ik_j x} \tag{2}$$

The eigenvalue problem for $E_j\left(\underline{x_\perp}\right)$ is given by Eq (3), subject to the tranverse boundary conditions which relate to the duct shape and possibly acoustic lining.

$$(\nabla_\perp^2 + k_N^2)E_j = 0 \tag{3}$$

Combining Eqs. (1)-(3), the axial wavenumbers are given in terms of the transverse eigenvalue by Eq. (4).

$$k_j = \frac{\pm\alpha - M_x}{1 - M_x^2}\frac{\omega}{c}$$
$$\alpha = \left[1 - \left(\frac{k_N c}{\omega}\right)^2 (1 - M_x^2)\right]^{\frac{1}{2}} \tag{4}$$

The mode measurement problem is to deploy instrumentation and analysis techniques to determine at least the mean-square values of the modal amplitudes, $q_j(t)$, which are considered as stationary random variables. A common approach is to place microphones on the duct wall, measure the pressure time histories at the microphone locations, and attempt to determine the unknowns by a fitting the model to the mircrohone data [2,3]. See Figure 1.

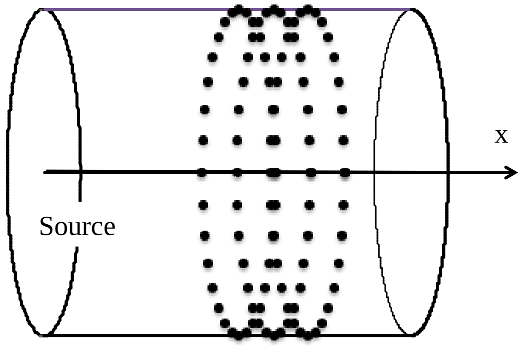

Figure 1: Mode measurement array

2.1 Mode coherence

At high frequency, the number of cuton modes typically becomes too large for a direct inverse procedure, so beamforming is applied. Beamforming has the advantage that it can function with more modes than microphones, can support nonuniform array designs that increase the efficiency of the use of the microphones [4], and advanced beamforming techniques such as CLEAN-SC and Functional Beamforming [5, 6]. An example of nonuniform array design is shown in Figure 2. With the partial exception of CLEAN-SC [7], beamforming requires the sources to be mutually incoherent. Clearly multiple tone modes at the same frequency would voilate the incoherence assumption and require a different procedure from beamforming. In the case of broadband noise, the sources are assumed to vary randomly in time, on a long time scale, which at least creates the possiblility that the modes could be mutually incoherent. It seems to be an intuitive result that if all of the modes were driven with a single source that they would all be coherent, since they can all trace their time histories to that source. Michalke et al. [8] analytically and experimentally proved that this can happen.

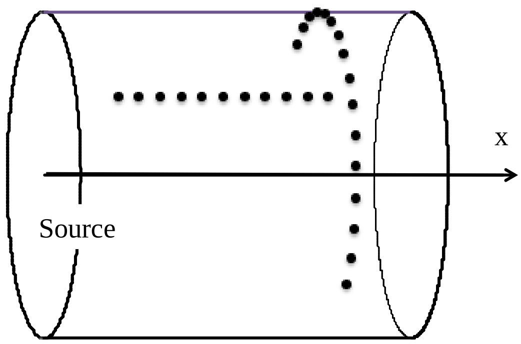

Figure 2: Thin mode measurement array

3. 2D BEAMFORMING REFLECTIONS

3.1 Classical beamforming

In free space beamforming, as opposed to mode measurement within a duct, the model source function is the free space Green's function given in Eq. (5).

.

$$p(x,y,z,t) = \sum_{j=1}^{M} q_j(t)\frac{e^{ik\frac{\omega}{c}R}}{R}$$
$$R^2 = \left(x - x_j\right)^2 + \left(y - y_j\right)^2 + \left(z - z_j\right)^2 \qquad (5)$$

Suppose the phased array has N microphones and the pressure measured at each is $p_i(t),\ i = 1, \dots N$. Stacking these functions gives the array data vector as shown in Eq. (6).

$$\underline{p}(t) = \begin{bmatrix} p_1(t) \\ \dots \\ p_N(t) \end{bmatrix} \qquad (6)$$

The array Cross Spectral Matrix (CSM), $\underline{\underline{C}}$, defined in Eq. (7), where the bracket notation refers to a time average: $\langle f(t)\rangle = \frac{1}{T}\int_0^T f(t)dt$.

$$\underline{\underline{C}} = E\left[\underline{pp'}\right] \approx \langle \underline{pp'} \rangle \qquad (7)$$

A grid of M potential source locations is defined, $\left(x_j, y_j, z_j\right), j = 1, \dots, M.$ For each grid point, an array steering vector is defined by evaluating N expressions of the form $\frac{e^{ik\frac{\omega}{c}R}}{R}$, where R is the distance from the grid point point j to microphone i, and stacking the N values and normalizing the result to 1 to form the N-dimensional steering vector $\underline{g_j}$. This is used to estimate the source strength for point j by the classical beamforming expression $b\left(\underline{g_j}\right) = \underline{g_j}'\underline{\underline{C}}\underline{g_j}$. The operation of the beamforming expression can be understood by supposing that a significant source, $s_k = E[q_k q_k^*]$ exists at point k. Then $\underline{\underline{C}}$ will contain a rank-1 contribution $s_k \underline{g_k}\underline{g_k}'$, and when the classical beamforming expression is applied to this part of $\underline{\underline{C}}$, the result is $s_k\left|\underline{g_k}'\underline{g_j}\right|^2$. The inner product has a peak of 1 at $j = k$, and the array is designed so that $\left|\underline{g_k}'\underline{g_j}\right|^2$ is small when the two grid points are far apart. This partially explains why a map of $b\left(\underline{g_j}\right)$ gives an image of the source distribution.

3.2 Reflected source

In free space beamforming, it frequently happens that the ground or a vertical wall creates a reflected image source so the array receives sound from both the direct and reflected sources, as indicated in Figure 3.

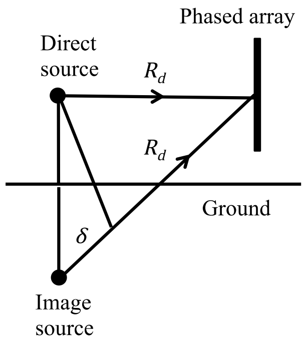

Figure 3: Reflection in free space beamforming

Suppose the array steering vector for the direct source in Fig. 3 is $\underline{g_D}$ and the steering vector for the image source is $\underline{g_I}$. The distance from the direct source to the centre of the phased array is R_D and the distance from the image source to the centre if the phased array is $R_D + \delta$. Also, suppose the source time history of the true (direct) source is $q_D(t)$. Because 3D spherical wave propagation is non-dispersive, the signal received at the array from the reflected source is the same as the signal from the direct source, except reduced slightly in amplitude by the additional spherical divergence and delayed by the additional time $\frac{\delta}{c}$. Ignoring the common propagation delay, the total signal received by the array is

$$\underline{p_{tot}}(t) = q_D(t)\underline{g_D} + \frac{R_D}{R_D+\delta} q_D\left(t + \frac{\delta}{c}\right)\underline{g_I} \qquad (8)$$

The estimate for the CSM is given in Eq. (9), where s is the strength of the direct source as seen at the array.

$$\underline{\underline{C}} = s\underline{g_D}\underline{g_D}' + s\left(\frac{R_D}{R_D+\delta}\right)^2 \underline{g_I}\underline{g_I}' + \frac{R_D}{R_D+\delta}\langle q_D(t)q_D^*\left(t + \frac{\delta}{c}\right)\rangle \underline{g_D}\underline{g_I}' + \frac{R_D}{R_D+\delta}\langle q_D\left(t + \frac{\delta}{c}\right)q_D^*(t)\rangle \underline{g_I}\underline{g_D}' \qquad (9)$$

In practice, the CSM is computed by Welch's method, which includes dividing the microphone time histories into blocks of length L, corresponding to an analysis bandwidth of length $\frac{1}{L}$, and taking the FFT of each block. For each pair of microphones in the CSM, the Fourier coefficients for one microphone are correlated with the complex conjugates of the Fourier coefficients for another microphone. This correlation is the integral indicated by $\langle \quad \rangle$ in the cross terms in Eq. (9). If the analysis bandwidth is very small so that the blocks are long and $\frac{\delta}{c} \ll L$, then $\frac{\delta}{c}$ will not affect the averages in Eq. (9), and the averages in the cross terms will both reduce to s. In this case, the direct source and the reflected source are coherent, $\underline{\underline{C}}$ will not have the expected form for any simple source, and the beamforming will fail. On the other hand, if L is a small compared with $\frac{\delta}{c}$, then the $\frac{\delta}{c}$ terms in the arguments of the cross terms will offset the time history of one copy $q_D(t)$ by more than the integration time. Each term in the sum that approximates the integral will contain a Fourier coefficient derived from one block of the time record from the direct source multiplied by the complex conjugate of the coefficient derived from a different time block of the function, where the two blocks are shifted so much that they do not overlap at all. Assuming that the broadband source is white noise, it is not correlated with a delayed copy of itself, so the cross terms will be 0, and the CSM for the direct source and the reflection will have the same form as it would for two independent sources, making beamforming an appropriate model. This is observed in practice. Processing with a bandwidth that is wide, but still less than 10% of the centre frequency, can make free space beamforming function correctly in the presence of reflections, in some cases.

4. DECORRELATING MODES

Within the analysis band $\Delta\omega = \frac{2\pi}{L}$, each duct mode has an envelope function, $q_j(t)$. As the mode propagates along the duct, the information contained in $q_j(t)$ is communicated at the group velocity $\frac{d\omega}{dk_j}$, where the axial wavenumber k_j is related to ω by the dispersion relation, Eq. (4). The time required for a wave packet to propagate from the source, say at $x = 0$, to x is $\frac{x}{\frac{d\omega}{dk_j}} = x\frac{dk_j}{d\omega}$. If two broadband modes with indices j_1 and j_2 are correlated at $x = 0$, then they will be decorrelated at x if the absolute value of the difference of their envelope propagation times, $x\left(\frac{dk_{j_2}}{d\omega} - \frac{dk_{j_1}}{d\omega}\right)$, exceeds L.

4.1 Example

Figure 4 shows a no-flow cylindrical duct, the Thematic Uniaxial Bladeless Environment (TUBE) with a diameter of 0.6 m and a length of 0.6 m. The source is a loudspeaker at the left end of the duct, positioned off centre. A phased array with 24 microphones is positioned at the right end of the duct. This arrangement of microphones differs from the wall mounting shown in Figs. 1 & 2, but still suffices to determine whether the sound field is coherent.

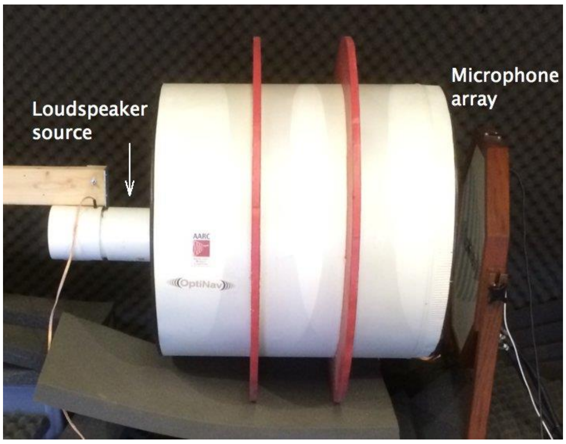

Figure 4: Duct example using the Thematic Uniaxial Bladeless Environment (TUBE)

The cuton modes for TUBE are shown Figure 5. The well-known modes for a hardwall cylindrical duct have spinning order m and the radial order n. In the foregoing, these are bundled into a single index, j. At each frequency in Fig. 5, the mode with the largest wavenumber is the plane wave mode with $k_{00} = \frac{\omega}{c}$. The number of cuton modes with lower wavenumbers increases with the frequency.

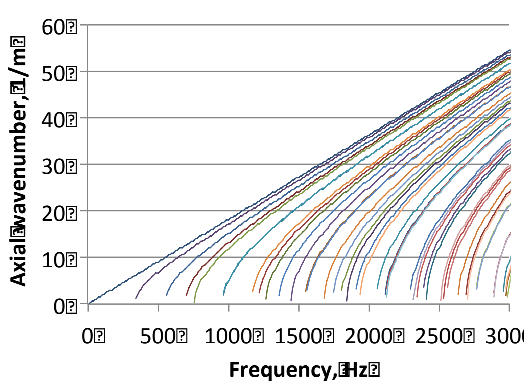

Figure 5: Cuton wavenumbers for TUBE

The group slowness, the reciprocal of the group velocity, for the modes in TUBE is shown in Figure 6. Modes that are barely cut on tend to have widely scattered group slowness values, suggesting that the decorrelation effect of finite analysis bandwidth will be powerful for these modes. Experience with mode measurements in turbofan engine suggests the barely cuton broadband modes are the ones with the highest amplitudes. Paul Joppa once explained that this occurs, intuitively, because the waves are trying to radiate away from the nacelle, and the duct confines them. The well cuton modes cluster toward the minimum slowness of $\frac{1}{c}$ = 0.0029 s/m.

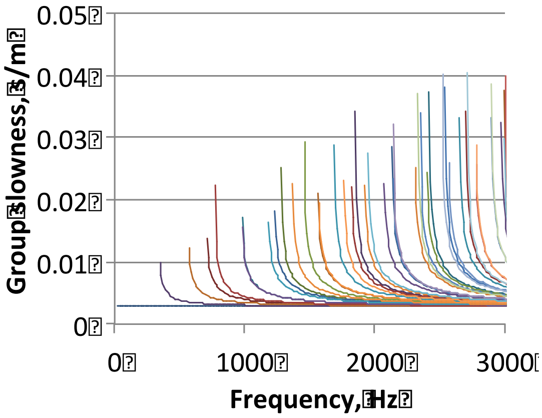

Figure 6: Array CSM eigenvalues at 3 kHz

In Figure 7, the degree of mode coherence is evaluated by the number of significant engenvalues of the array CSM at 3 kHz. When all the microphones in the array are coherent, there is only a single nonzero eigenvalue. This occurs for case with the duct removed, the green bar in the plot. Ideally, all of the microphones receive only direct radiation from the loudspeaker. The 128 point transform and a 96 kHz sample rate give L = 1.33 ms, correspoinding to a straight line propagation distance of 0.45. The geometry in the case with the duct removed is such the differences in the loudspeaker-microphone distances are much less than 0.45 m. The small relative values of eigenvalues 2 and 3 (0.046 and 0.026 respectively) may be related to reflections from the foam rubber absorber that was indended to create an anechoic environment. The case with the 4096 point transform and the duct present also has only one significant eigenvalue. (The relative second eigenvalue is 0.03.) This is consistent with very narrow band results of Michalke et al [8].

The red bars in Fig. 7 show a number of nonzero eigenvalues for the case with the duct installed and the 128 point transforms, indicating multiple independent modes. Referring to Fig. 6, the typical spacing of the group slowness at 3 kHz is about 0.01 s/m. Multiplying by the 0.6 m duct length gives a 6 ms shift between modes during duct propagation. This is longer than the 1.33 ms analysis block length, so mode decorrelation could be responsible for the multiple eigenvalues.

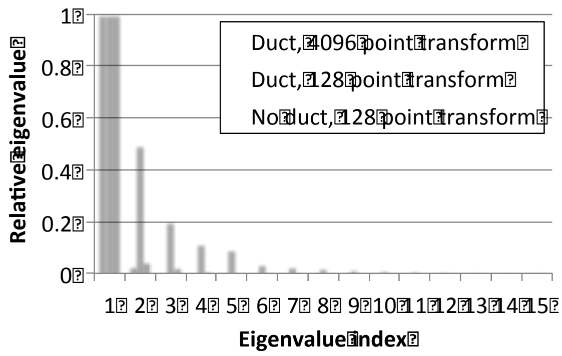

Figure 7: Array CSM eigenvalues at 3 kHz.

5. CONCLUSIONS

Broadband duct modes can sometimes be forced to be incoherent by choosing a wide analysis band and employing a long duct. This improves the applicability of beamforming for mode measurement and also makes the computation of sound power by summing the powers of the modes valid. Modes that are close to cutoff are more susceptible to decorrelation by this method.

Mode decorrelation is promoted by increasing the analysis bandwidth, which should be no more than 10% of the centre frequency for narrowband processing, and by increasing the distance between the sources and the microphone. A cross-shaped array such as Fig. 2 is made more feasible by decorrelation because it permits the use of beamforming and, especially, advanced techniques such as Functional Beamforming [6, 9]. The circumferential arm of a cross array should be positioned opposite the source to maximize decorrelation.

ACKNOWLEDGEMENTS

The construction of TUBE was supported by the Aeroacoustics Research Consortium.

REFERENCES

[1] Morfey, C., 1971, “Sound transmission and generation in ducts with flow,” *Journal of Sound and Vibration*, Vol. 14, No. 1, 37 – 55.

[2] Bolleter, U. and M.J. Crocker, 1972, “Theory and measurement of modal spectra in hard-walled cylindrical ducts,” *Journal of the Acoustical Society of America*, Vol. 51, 1439-1447.

[3] Joppa, P., 1978, “Acoustic mode measurements in the inlet of a turbofan engine,” *J. of Aircraft*, Vol. 24, No. 9, 587-593.

[4] Tapken, U., D. Gutsche, and L. Enghardt, 2014, "Radial mode analysis of broadband noise in flow ducts using a combined axial and

azimuthal sensor array", AIAA Paper 2014-3318, Atlanta, GA.

[5] Dougherty, R.P., B.E. Walker, and D.L. Sutliff, 2010, "Locating and quantifying broadband fan sources using in-duct microphones", AIAA Paper AIAA–2010–3736, Stockholm, Sweden.

[6] Marotta, T.R., L.S. Lieber, and R.P. Dougherty, 2014, "Validation of beamforming analysis methodology with synthesized acoustic time history data: sub-scale fan rig system," AIAA Paper 2014-3068, Atlanta, GA.

[7] Sijtsma, P., 2009, "CLEAN based on spatial source coherence," *Int. J. Aeroacoustics*, Vol. 6, No. 4, pp 357-374.

[8] Michalke, A., F. Arnold, and F. Holste, 1996, "On the coherence of the sound field in a circular duct with uniform mean flow," *Journal of Sound and Vibration*, Vol. 190, No. 2, 261–271.

[9] Dougherty, R.P., 2014 "Functional Beamforming for Aeroacoustic Source Distributions", AIAA Paper 2014-3066, Atlanta.

Conference on Modelling Fluid Flow (CMFF'15)
The 16th International Conference on Fluid Flow Technologies
Budapest, Hungary, September 1-4, 2015

Workshop on Turbomachine Optimization based on Computational Fluid Dynamics

László DARÓCZY[1], Gábor JANIGA[2], Dominique THÉVENIN[3]

[1] Corresponding Author. Lab. of Fluid Dynamics and Technical Flows, University of Magdeburg "Otto von Guericke". Universitätsplatz 2, D-39106 Magdeburg, Germany. Tel.: +49 391 67 18194, Fax: +49 391 67 12840, E-mail: laszlo.daroczy@ovgu.de
[2] Lab. of Fluid Dynamics and Technical Flows, University of Magdeburg "Otto von Guericke". E-mail: janiga@ovgu.de
[3] Lab. of Fluid Dynamics and Technical Flows, University of Magdeburg "Otto von Guericke". E-mail: thevenin@ovgu.de

ABSTRACT

CFD based optimization (CFD-O) is a strongly multidisciplinary field that significantly differs from analytical optimizations due to the costly function evaluations. CFD-O is especially difficult due to the fact, that for an appropriate optimization process every step of the objective function evaluation has to be automated, including geometry creation, mesh generation, CFD simulation and post-processing. CFD can be very time consuming in itself, but in an optimization the same computation has to be performed 100-100 000 times. For this reason, it is very important to (1) perform the CFD simulations with high fidelity, (2) to analyze and apply very efficient optimization algorithms.

Throughout the workshop, following an introduction, the most important fields will be discussed by the Invited Experts, including but not limited to Uncertainty Quantification (UQ), Robust Optimization (RO), Evolutionary Algorithms (EA), Multi-objective Optimization (MOO), gradient-based methods, adjoint methods and Surrogate or Meta-models. Several practical applications will be shown for wind turbines, flow channels and turbomachinery bladings.

Keywords: adjoint optimization, CFD-based optimization, metamodel, robust optimization

NOMENCLATURE

$\mathbb{X}$	$[-]$	feasible domain
g, h	$[-]$	equality/inequality constraint
x	$[-]$	design variable
y	$[-]$	objective function

1. INTRODUCTION TO OPTIMIZATION

In the followings, without any claim to completeness, the most important aspects of optimization will be addressed. Let us assume a problem with n independent variables:

$$\mathbf{x} = (x_1, ..., x_n)^{\mathrm{T}}, \quad \mathbf{x} \in \mathbb{X}, \tag{1}$$

where $\mathbf{x}$ is the design variable vector and $\mathbb{X}$ the feasible domain:

$$\mathbf{x} \in \mathbb{X} \iff \begin{cases} g_i(\mathbf{x}) = 0 \; (i = 1...k) \\ h_j(\mathbf{x}) \leq 0 \; (j = 1...l) \end{cases} . \tag{2}$$

Besides the variables m functions are defined:

$$\mathbf{y}(\mathbf{x}) = (f_1(\mathbf{x}), f_2(\mathbf{x}), ..., f_m(\mathbf{x}))^{\mathrm{T}} \tag{3}$$

Without any loss of generality the optimization can be defined as

$$\mathbb{O} : \begin{cases} \mathbf{y}(\mathbf{x}) \underset{\mathbf{x}}{\rightarrow} \min \\ \text{so that } \mathbf{x} \in \mathbb{X} \end{cases} . \tag{4}$$

2. CLASSIFICATION OF PROBLEMS

Table 1 summarizes the most important groups of optimization problems.

Table 1. Most important types of optimization problems

$k = l = 0$	unconstrained
$k \neq 0 \cap l \neq 0$	constrained
$m = 1$	single-objective
$m \geq 2$	multi-objective
$\mathbf{y}(\mathbf{X_1}) = \mathbf{y}(\mathbf{X_2}) \implies \mathbf{X_1} = \mathbf{X_2}$.	uni-modal
$\mathbf{y}(\mathbf{X_1}) = \mathbf{y}(\mathbf{X_2}) \not\implies \mathbf{X_1} = \mathbf{X_2}$.	multi-modal

An inherent difficulty of optimization is that one has to choose for each problem the appropriate optimization method. An algorithm, which is efficient for an unimodal problem with a single optimum might fail for noisy or multimodal problems. There is no algorithm that is efficient for all problems ("no free lunch" [1]). Additionally, it is usually very difficult to make a decision a priori, for which reason optimization software still heavily rely on expert knowledge.

3. DIFFICULTIES WITH CFD-O

In CFD-O [2], the objective function(s) are usually not known explicitly, but have to be computed using numerical simulations. This results in further complications:

- The evaluation of the objective function is very costly, one computation can require from several seconds up to several days.
- Due to numerical noise and model uncertainties, the objective functions are usually noisy.
- The geometry and mesh has to be created/morphed for each configuration in an automated and robust way.
- Different software (including proprietary commercial software) have to be coupled to cooperate for the optimization.

As a result, speed and efficiency is of key importance in CFD-O.

4. SPECIAL FIELDS OF CFD-O

4.1. Gradient-based and gradient-free methods

Optimization algorithms can be further classified as gradient-free or gradient-based methods. Gradient-based methods are usually local search methods (although gradient assisted global methods exist as well) and require the derivatives ($\frac{\partial y_i}{\partial x_j}$). These can be computed by n additional CFD computations for n variables (in a non-intrusive way), or by adjoint method [3]. The first method becomes unaffordable very fast due the "curse of dimensionality". With adjoint methods the flow solver has to be modified (increasing the implementation time), but the evaluation time remains quasi unchanged. This method is usually very fast, but can get trapped in a local minimum.

Gradient-free methods handle the CFD simulation as a black-box. The most popular methods are the different Evolutionary Algorithms, which are global search methods. These methods are able to find global optima, but require large number of CFD computations.

4.2. Robust and reliability based optimization

In the reality most values are not exact, but depend on some, usually unknown, uncertainty. E.g., the operating temperature variates slightly in a heat exchanger, the inflow wind speed varies around a wind turbine due to the wind gusts or the diameter of a pipe varies due to manufacturing imprecisions. This complicates the optimization, as some configurations might be optimal, but not robust. E.g, one turbine might be very efficient under low turbulence, but might fail for large intensities.

In robust design optimization (RDO) besides the objective function the variance of the objective function is minimized as well, while in reliability based design optimization (RBDO) a target reliability is defined which has to be satisfied in the optimization process. In RDO even more CFD simulations have to performed compared to normal optimization, as some kind of Uncertainty Quantification (UQ) methods have to be applied to quantify the risks (e.g., Monte Carlo, univariate reduced quadrature, Polynomial Chaos Expansion, etc.). The robust optimization of wind turbines is discussed e.g., in the work of Campobasso et al. [4].

4.3. Metamodel assisted optimization

Besides parallelization of the CFD evaluations, another possibility for speeding up the optimization process is to train metamodels [5]. In this case, an approximation of the objective functions is created ($\mathbf{y}(\mathbf{x}) \approx \mathbf{y}^{meta}(\mathbf{x})$), which can be updated in an on-line or off-line manner. Afterwards, the optimization can be executed on this reduced and usually very fast model ($\mathbb{O}^{meta} : \mathbf{y}^{meta}(\mathbf{x}) \underset{\mathbf{x}}{\rightarrow} \min$). However, for very complicated objective functions large number of training points might be needed to train the model. If the optimum of the reduced model does not correspond to an optimum of CFD simulations, new training points have to be added. The most popular surrogate models include Radial Basis Functions (RBF), Kriging, Artificial Neural Networks (ANN) or different Response Surface Models (RSM).

REFERENCES

[1] Wolpert, D., and Macready, W., 1997, “No free lunch theorems for optimization”, *Evolutionary Computation, IEEE Transactions on*, Vol. 1 (1), pp. 67–82.

[2] Thévenin, D., and Janiga, G. (eds.), 2008, *Optimization and Computational Fluid Dynamics*, Springer, Berlin.

[3] Papoutsis-Kiachagias, E., and Giannakoglou, K., 2014, “Continuous Adjoint Methods for Turbulent Flows, Applied to Shape and Topology Optimization: Industrial Applications”, *Archives of Computational Methods in Engineering*, pp. 1–45.

[4] Campobasso, M. S., Minisci, E., and Caboni, M., 2014, “Aerodynamic design optimization of wind turbine rotors under geometric uncertainty”, *Wind Energy*.

[5] Verstraete, T., Coletti, F., Bulle, J., Vanderwielen, T., and Arts, T., 2013, “Optimization of a U-Bend for Minimal Pressure Loss in Internal Cooling Channels—Part I: Numerical Method”, *Journal of Turbomachinery*, Vol. 135 (5).

Conference on Modelling Fluid Flow (CMFF'15)
The 16th International Conference on Fluid Flow Technologies
Budapest, Hungary, September 1-4, 2015

Shape optimization of U-bends for internal cooling channels: an overview

Tom Verstraete[1], Tony Arts[2], Filippo Coletti[3], Sebastian Willeke[4], Jing Li[5], Timothée van der Wielen[6], Jérémy Bulle[7]

[1] Corresponding Author. Turbomachinery Department, von Karman Institute for Fluid Dynamics. Waterloosesteenweg 72, 1640 Sint-Genesius-Rode, Belgium. Tel. +32 2 359 94 29, E-mail: tom.verstraete@vki.ac.be. Presently at Queen Mary University of London.
[2] Turbomachinery Department, von Karman Institute for Fluid Dynamics. E-mail: arts@vki.ac.be
[3] Aerospace Engineering and Mechanics, University of Minnesota. E-mail: fcoletti@umn.edu
[4] Institute of Dynamics and Vibration Research, University of Hannover. E-mail: willeke@ids.uni-hannover.de
[5] Pratt School of Engineering, Duke University. E-mail: jl477@duke.edu
[6] Cofely Services, GDF Suez. E-mail: timothee.vanderwielen@gmail.com
[7] Tractebel Engineering, GDF Suez. E-mail: jeremy.bulle@gmail.com

ABSTRACT

U-bends are found in various ducted applications in which the flow direction needs to be turned 180 degrees. The present work looks into the application of these U-bends for internal cooling channels inside turbine blades, where two major aspects need to be carefully addressed: pressure loss needs to be reduced while heat transfer needs to be enhanced.

An overview of different shape optimization studies is given with the aim to improve the performance of the standard U-bend consisting of two circular arcs. Different optimization methodologies were used in this study ranging from single-objective Evolutionary Algorithms (EA), with or without acceleration by surrogate model, to multi-objective EAs, to finally gradient based adjoint optimization. The difference in computational cost is compared for the different applications combined with their advantages and disadvantages, and finally one optimal configuration is experimentally verified and compared to the numerical predicted improvement.

Keywords: internal cooling channels, shape optimization, u-bend

NOMENCLATURE

ρ	$[kg/m^3]$	density
Obj	$[-]$	objective
Q	$[Watt]$	heat
D_h	$[m]$	hydraulic diameter
k	$[m^2/s^2]$	turbulence kinetic energy
p	$[N/m^2]$	pressure
P_{total}	$[Pa]$	total pressure
v	$[m/s]$	velocity
ϵ	$[m^2/s^3]$	turbulence dissipation rate

Subscripts and Superscripts

inlet	at the inlet of the domain
outlet	at the outlet of the domain
ref	reference value

1. INTRODUCTION

Turbine blades are since long equipped with internal cooling channels as an effective way to increase cycle efficiency of gas turbines by augmenting the firing temperature. These cooling channels are in a vast majority of cases implemented through a serpentine scheme, in which one single ducted flow passes multiple times the blade span. Near the extremities of the blade span the flow inside the duct is turned 180 degrees through U-bends. The coolant air is bled from the high pressure compressor which bypasses the combustor and enters the turbine blade through its root.

Since the coolant air needs to be pressurized while it does not participate in the work extraction in the turbine, it represents a loss in global cycle efficiency. As a result, the internal cooling channels need to simultaneously allow for a high heat transfer at the lowest possible pressure loss. The U-bends present in the serpentine cooling channels are responsible for up to 25% of the total pressure loss in the channel and merit a profound attention, as witnessed by numerous experimental studies [1, 2, 3, 4].

This paper presents an overview of several numerical optimization studies performed, including:

- Single-objective optimization with EA (2D)
- Single-objective optimization with EA accelerated by a surrogate model (3D)
- Multi-objective optimization by EA accelerated by a surrogate model (3D)

- adjoint based optimization (2D)

2. U-BEND TEST CASE

2.1. Geometry

The U-bend under investigation is typical of internal cooling channels. The baseline geometry is shown in Fig. 1. It consists of a circular U-bend with radius ratio of 0.76, a hydraulic diameter of 0.075 meter and an aspect ratio of 1. The Reynolds number is 40,000 and the Mach number of 0.05 allows using an incompressible assumption. The shape of the inner and outer curve is allowed to be changed but needs to remain inside the bounding box shown in the figure, which restricts the height and width of possible changes to account for structural limits. The distance between both cooling channels is not subject to optimization, as well as the hydraulic diameter.

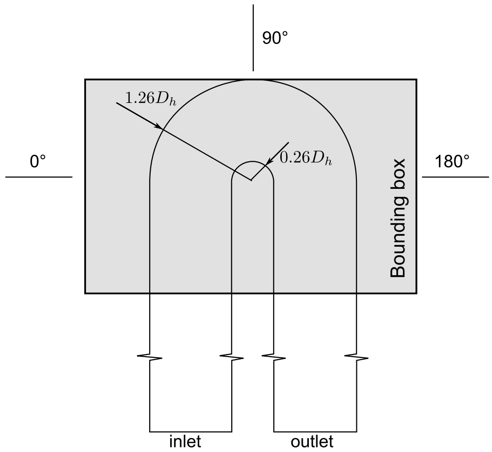

Figure 1. Baseline geometry, definition of the area in which the shape is allowed to change.

2.2. Parameterisation

The U-bend has been parameterised by Bézier curves for which the movements of the control points are the design variables. For the adjoint based optimization, both the inner and outer curve of the U-bend have been represented by two separate continuous curves containing 20 control points. This results in a total of 80 design variables (x and y coordinate of each of the 2 curves), which is unfeasible for the EA based optimization. Therefore, the EA based optimization uses a segmented approach, for which a total of 4 Bézier curves represent the inner or outer curve. Each Bézier curve only comprises of 4 control points, while relations between the control points are imposed to assure a sufficient degree of continuity between the curves. Figure 2 shows the parameterisation of the outer curve.

2.3. Performance evaluation

The simpleFoam solver from OpenFoam [5] is used to evaluate the incompressible Navier-Stokes equations. The mesh resolution has been adapted such that the maximum $y+$ value does not exceed

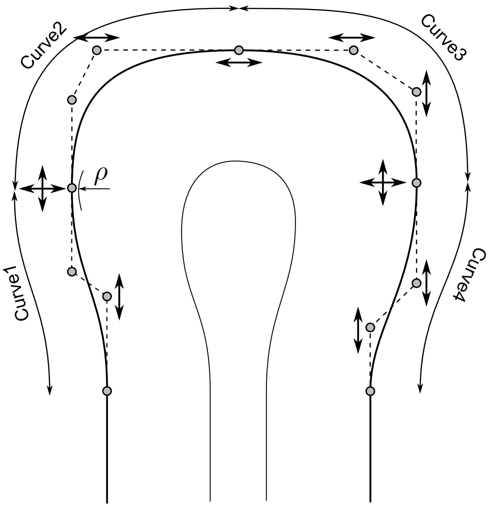

Figure 2. Parameterization of the outer curve.

2.2. The Launder-Sharma low-Reynolds k-ϵ turbulence model is used. The k-ϵ model "is arguably the simplest complete turbulence model" (Pope [6]), is implemented in most commercial software and is one of the most broadly employed at industrial level. Its performance is reasonably satisfactory in shear flows with small effects of streamwise pressure gradients and streamline curvatures, but far from these assumptions, it can fail badly. However it has been selected for the present application due to its large diffusion: given that the proposed methodology is apt for industrial problems, it was the intention to demonstrate its potential in conditions that are representative of real-life design practice.

At the inlet a fully developed velocity profile is imposed, together with values of k and ϵ for the turbulence model. Both are computed based on a turbulence intensity of 5% measured in the lab. At the outlet the static pressure is imposed.

The U-bend optimization is driven by the minimization of the pressure drop introduced by the U-bend and in case of the multi-objective optimization the maximization of the heat transfer is additionally considered. Both objective functions are defined as:

$$\text{Min} \quad Obj_1 = \frac{P_{total}^{inlet} - P_{total}^{outlet}}{\frac{1}{2}\rho \cdot v_{ref}^2} \tag{1}$$

$$\text{Max} \quad Obj_2 = \frac{Q}{Q_{ref}} \tag{2}$$

where Q is the total heat transferred to the fluid and P_{total} is the total pressure which is computed as the mass flow averaged quantity at the inlet respectively outlet of the domain, positioned 8 hydraulic diameters away from the U-bend. One single 3D evaluation is run in parallel on 5 cores which takes in average 2 hours.

3. OPTIMIZATION STRATEGIES

Two distinct optimization strategies have been used to the applied test case and allow comparison between the different techniques. On the one hand, Evolutionary Algorithms (EA's) are used as a non-deterministic optimization method. These methods benefit a wide community of users and are relatively easy to understand and implement, factors which have contributed to the large diffusion of the method. On the other hand, a deterministic gradient based optimization has been used, in which the gradient is computed efficiently through the adjoint method.

3.1. Evolutionary Algorithms

Evolutionary Algorithms (EA) have been developed in the late sixties by J. Holland [7] and I. Rechenberg [8]. They are inspired from Darwinian evolution, whereby populations of individuals evolve over a search space and adapt to the environment by the use of different mechanisms such as mutation, crossover and selection. Individuals with a higher fitness have more chance to survive and/or get reproduced.

This natural process is translated to engineering problems in several steps. First, the shape is parameterised (as discussed in section 2.2) which defines an analogy to the DNA of an individual. This ensures that a unique combination of design parameters will represent a unique shape. Next, the operations that enable EA's to generate offspring such as mutation and crossover need to be translated. There exists a wide variety of techniques for this, which give rise to various classes of EA methods. Genetic Algorithms (GAs) for instance usually allow two individuals from a parent generation to reproduce two children through a crossover process on the design variables with analogy from nature. In Differential Evolution (DE) on the contrary, as many as four individuals are required to produce one child per parent, here analogy with nature is lost. In a final step, a selection procedure needs to be introduced, imposing a pressure on the population in which fitter designs have more chance to be selected for reproduction, while non-fit designs have larger probability to become extinct and disappear in the next generation. Potentially, additional mechanisms can be introduced to increase convergence through keeping a healthy diversity among the individuals of the population and by making sure that good individuals do not get lost accidentally. Eventually, these algorithms can be easily modified to deal with multi-objective optimization problems, which identify the Pareto front.

EA methods are capable to work with noisy objective functions and can find global optima of multimodal problems. They however require a large number of function evaluations, which leads to unacceptable large computational costs in case the objective function depends on CFD evaluations. Especially for large design spaces the computational cost can be prohibitive, restricting the use of these methods to only a small design space. Typically, up to 20 or slightly more design variables can be considered, depending on the level of interaction between the different parameters.

To reduce the computational cost, very often a surrogate model is introduced, which is a sort of interpolation tool using the already analyzed individuals by CFD. The surrogate model performs the same task as the high fidelity CFD analysis, but at a very low computational cost. However, it is less accurate, especially for an evaluation far away from the already analyzed points in the design space.

The implementation of the surrogate into the optimization system depends on how the system deals with the inaccuracy of the model. The technique used in the present work uses the surrogate model as an evaluation tool during the entire evolutionary process. After several generations the evolution is stopped and the best individual is analyzed by the expensive analysis tool. This technique is referred to as the "offline trained surrogate model". The difference between the predicted value of the surrogate model and the high fidelity tool is a direct measure for the accuracy of the surrogate model. Usually at the start this difference is rather large. The newly evaluated individual is added to the database used for the interpolation and the surrogate model will be more accurate in the region where previously the EA was predicting a minimum. This feedback is the most essential part of the algorithm as it makes the system self-learning. It mimics the human designer which learns from his mistakes on previous designs.

3.2. Gradient based optimization

Optimization methods that use gradient information are iterative methods that continuously alter the shape with small perturbations. The basic idea behind these methods is that through the knowledge of the gradient the direction can be found in which the design variables need to be changed in order to obtain an improved design. Small modifications to the design variables are required, as the gradient will only provide a linear approximation to the real objective function and remains only valid in the neighborhood of the current design. The simplest gradient based optimization method is the steepest descent, which modifies the design variables in the direction of the steepest descent, given by the opposite direction of the gradient. Although it has the lowest convergence rate of all gradient based methods, it is still an attractive method and will also be used in this work

The most complex part of this type of method is however to compute the gradient information, especially for problems which require the solution of partial differential equations to compute the objective. This can be achieved through a forward method, such as for instance finite differences, complex variable perturbation or algorithmic differentiation. In brief, these methods perturb one by one each design variable and compute the difference with the unperturbed design. The main drawback is that the computational cost is proportional to the number of design variables, requiring n additional CFD computations for n design variables.

The computational cost can however be dramatically reduced by reverse or adjoint methods, which require a cost proportional to only one CFD computation to obtain the gradient information, irrespective the number of design variables. In the case of continuous adjoint methods, a new set of linear partial differential equations needs to be solved after convergence of the CFD analysis, as for instance derived in [9]. Then the gradient can be computed with small effort. It is evident that such methods are preferred, as they allow for an efficient computation of the gradient even for extremely large design spaces (literally every grid point on the boundary of the shape can become a design variable). They however require a large development and implementation cost, which has been one of the major reasons for their reduced usage compared to EA or other gradient free methods. Additional disadvantages of gradient based methods is the local search, which allows only to find the nearby local optimum in case of multimodal problems.

4. RESULTS

4.1. Single-objective EA

A single objective Differential Evolution *DE/rand/1/bin* algorithm is applied to the U-Bend optimization. Since DE requires a large number of evaluations when not supported by a surrogate model, the problem is viewed in 2D to reduce the cost per CFD computation. In Fig. 3 the convergence history of the optimization can be seen. A total of 100 populations of 40 individuals each need to be performed in order to obtain convergence. This means a total of 4000 CFD computations. A reduction 35% in total pressure loss could be achieved.

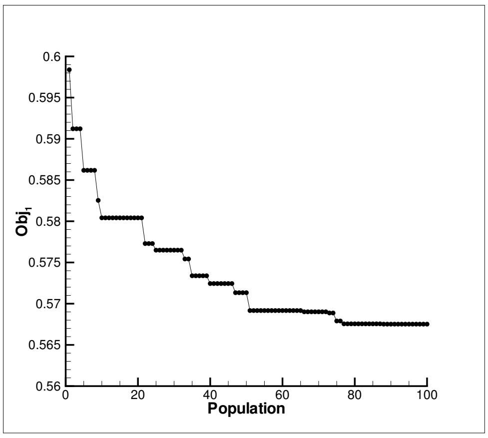

Figure 3. Convergence of the EA without surrogate model.

4.2. Single-objective EA assisted by surrogate model

A reduction in the computational cost can be obtained by using a surrogate model. In Fig. 4 the convergence history of a surrogate model assisted DE optimization is shown. It compares the surrogate model prediction (here a Kriging surrogate model was used) with the CFD evaluation for each iteration. An iteration within this method consists first of a training the surrogate model on the existing data, followed by a DE optimization using the surrogate model instead of the CFD evaluation, and a validation of the obtained best design by CFD. As can be seen, during the first iteration the surrogate model does not represent reality well, such that the DE optimization results in a design for which the surrogate model predicts a very large reduction in pressure drop. This is however not confirmed by the CFD validation, which shows that in fact a much larger pressure drop is obtained. This failure is added to the database after which a new iteration starts, consisting of retraining the surrogate model, optimizing the shape using the updated model and again verifying the result by CFD. As can be clearly seen, the surrogate model still overpredicts the reduction in pressure loss, but this time the prediction is already much closer to reality. Through adding the previous design to the database, the system has learned valuable information preventing the optimization algorithm to search further in this wrong direction. The newly found design is added again to the database after which a new iteration starts. Gradually the difference between the surrogate model and CFD prediction is reduced until the accuracy of the surrogate predictions are confirmed by CFD. Similar to the previous study a 36% reduction in pressure drop could be achieved, although in the present case a 3D CFD computation was used.

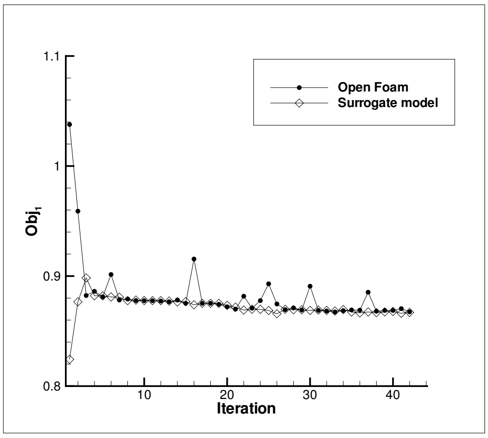

Figure 4. Convergence history of surrogate model assisted EA.

Prior to the optimization a total of 65 designs were analyzed by CFD to have an initial training set for the surrogate model. With an additional 40 calculations needed to find the optimum, only about 100

CFD computations are needed, which is an order less than for the DE without surrogate model assistance.

In Fig. 5 the optimal shape is shown. Careful analysis demonstrated that the reduction in pressure drop was achieved through a suppression of the separation on the inward surface of the bend. This was achieved by reducing the curvature near the wall, hence decreasing the velocity gradient normal to the wall and reducing the adverse pressure gradient in the second half of the inward surface.

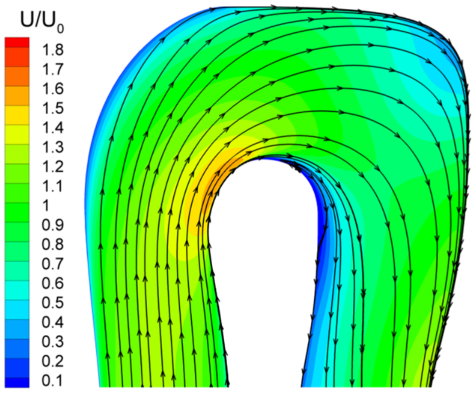

Figure 5. Optimal shape of the U-bend for minimal pressure loss.

4.3. Multi-objective EA assisted by surrogate model

So far only the pressure objective (Eq. 1) has been minimized. The U-bend in the present work however serves to cool down a turbine blade, and as explained in the introduction an increased heat transfer is an additional aim. Especially the tip of the blade is a critical area which may benefit from a better cooling. Therefore the objective expressed by Eq. 2 is introduced. Both objectives are conflicting and need a multi-objective optimization to obtain the optimal solution. The DE algorithm has been extended to this end to cope with multiple objectives based on the NSGA-II algorithm [10, 11].

In Fig. 6 the result of the optimization is summarized. It shows the total pressure drop versus the heat extracted for all 220 analyzed geometries. The baseline geometry consisting of the circular U-bend is indicated by a square, while the 65 samples generated for the initial database are represented by black dots. It is already apparent that these initial geometries perform better with respect to the total pressure drop objective, and most samples also perform better in the heat objective compared to the baseline.

The samples generated during a total of 32 iterations of the optimization phase are represented by diamonds. All of them are generated in the region of interest, i.e. with high heat transfer and low pressure drop. A clear Pareto front is formed, for which one cannot improve one objective without worsening the other. This clearly indicates that pressure loss and heat transfer are conflicting requirements, i.e. a physical mechanism is responsible to increase one and at the same time decrease the other.

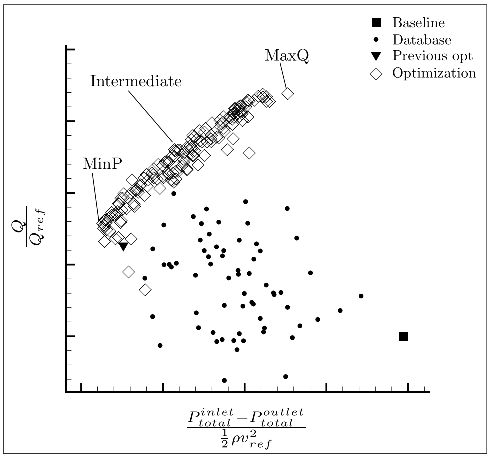

Figure 6. Results of the optimization plotted in the objective space.

Three candidate solutions are identified as “Min” which has the lowest total pressure drop, “MaxQ” which has the highest heat transfer, and “Intermediate”, which is in between both extremes. The performance of all three Pareto optimal geometries is summarized in Table 1. Finally, the optimal solution found during the single objective optimization, as presented in the previous section, is plotted as a gradient symbol. Although this optimization was not targeting any heat transfer objective, it improved the heat transfer compared to the baseline, as was also found during experimental validation.

Table 1. Objectives of the trade-off configurations.

	Obj_1	Obj_2
Baseline	1.22	1.00
MinP	0.84	1.08
Intermediate	0.93	1.13
MaxQ	1.07	1.17

In Fig. 7 the shapes corresponding to the three identified candidates are shown. The geometry with lowest pressure drop (“MinP”) resembles very closely the shape of the single-objective optimum (see Fig. 5). The increase in heat transfer by going to “MaxQ” is obtained by increasing the curvature of the external wall in the first 90 degrees and by increasing the internal wall width. Both actions increase the pressure loss and transform the smooth configuration into one that resembles a sharp u-bend configuration. Similar to what was found by Liou and Chen [12], a thicker divider wall is beneficial for the losses. Geometries with low pressure loss tend to have a smooth curvature change, and successfully suppress separation by increasing the radius of the turn and by carefully decelerating first and then accelerating the mean flow. As a consequence, less secondary flow motion is present and reduces the heat transfer potential. Geometries with high heat transfer on the other hand contain rapid changes of curvature and resemble close to sharp U-bends. Heat transfer is enhanced due to the impingement of the flow near the external wall, however increasing the losses.

The computational cost of the multi-objective optimization is with its 220 CFD evaluations slightly larger than the single-objective optimization of section 4.2. It however needs to be noted that for each of the 32 iterations 5 individuals need to be analyzed which is performed in parallel. This allows for a faster completion than the single-objective optimization, for which only 1 design is evaluated per iteration.

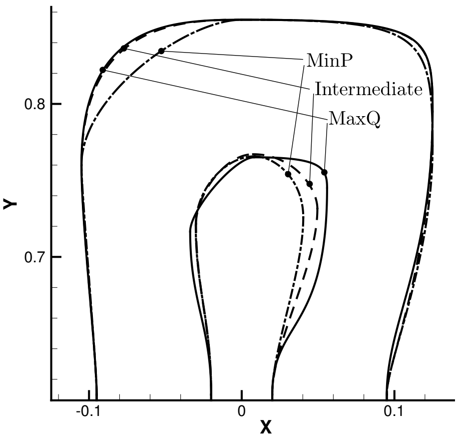

Figure 7. Comparison of the trade-off shapes.

4.4. Gradient based optimization

The same 2D single-objective optimization as performed in section 4.1 has been repeated with a gradient based optimization method, although with a different parameterisation as explained in section 2.2. The gradient has been computed using the continuous adjoint approach implemented in OpenFoam. In Fig. 8 the optimal shape is shown compared to the initial shape.

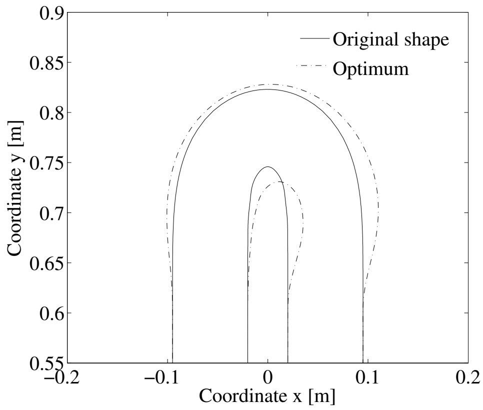

Figure 8. Comparison of baseline and adjoint optimization shape.

A comparison of the optimal shape from EA based optimization algorithms to the best performing design obtained by the steepest-descent method reveals that both U-bends exhibit similar geometrical features leading to a strong reduction of the total pressure drop. A direct comparison shows a slight advantage for the EA based optimization ($Obj_1 = 27Pa$ opposed to $Obj_1 = 35Pa$), however a different paramterisation has been used and a different starting point has been considered.

Both configurations feature an increased duct section in the first part of the bend resulting in a limited acceleration of the flow around the bend tip. In combination with increased radii of curvature along the internal and external walls, the reduced flow velocity leads to reduced centrifugal forces reducing the tendency of the flow to separate. In addition, the convex inner wall along the second leg of the bend is deformed such that it fills the space which is occupied by the separated flow in the original geometry. While present in the gradient-free optimized shape, this feature is even more pronounced by the gradient-based method. Considering the different geometry parameterisation resulting from the necessity to limit the number of design parameters for gradient-free optimization, the similarity of the optimal U-bend shapes obtained by differential evolution and steepest descent represents an unprecedented finding. This remarkable result demonstrates that the underlying objective function in the present case does not pose a multimodal problem as often assumed for engineering optimization problems. Consequently, both gradient-free and gradient-based optimization methods detect the global optimum demonstrating that the concern of getting trapped in a local minimum is of no relevance for the application of the latter. Therefore, by using a computationally efficient gradient-based optimization procedure a globally optimal U-bend shape is provided after only 30 design iterations where succeeding flow field computations benefit from previously converged solutions. The computational cost is thus almost an order of magnitude less than the EA, and this for a 4 times larger design space.

4.5. Experimental validation

An experimental investigation has been conducted for the baseline geometry consisting of 2 circular arcs and the shape shown in Fig. 5, which was obtained by a metamodel assisted EA optimization using 3D CFD. In terms of global performance, Table 2 summarizes the experimental obtained improvement and compares them to the numerical predictions. The agreement between experiments and calculations is good, and the improvement in aerodynamic performance (both measured as well as predicted) is very significant.

Detailed PIV measurements have however also been performed and reveal a small recirculation bubble, not present in the numerical result. Fig. 9

Table 2. Aerodynamic performance of the investigated U-bend configurations.

	ΔP baseline $[-]$	ΔP optimized $[-]$	gain [%]
Exp.	1.03 ± 0.03	0.65 ± 0.02	36.2 ± 3
CFD	1.01	0.63	37.6

shows the obtained velocity field, which can be compared to Fig. 5. It clearly demonstrates the limitations of the k-ϵ turbulence model in predicting flow separation in regions of adverse pressure gradients. Despite the differences in the flow details, however, the model allowed to predict well the global trends and combined with an optimization algorithm provides an extremely efficient methodology to improve the shape of the U-bend.

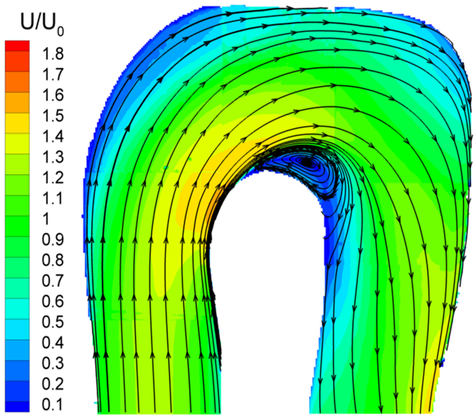

Figure 9. Mean velocity from PIV in the optimized geometry at mid height.

5. CONCLUSIONS

An overview was given of different studies attempting to improve the performance of a U-bend for internal cooling channels. It was shown that all methods lead to shapes with similar features, in which the curvature of the inner wall has been reduced to limit the velocity gradient across the passage. When heat transfer is introduced next to the pressure losses as a second objective, several trade-off solutions can be found. The physical process behind the conflict between both objectives is due to the secondary flow motion. To increase heat transfer, a stronger secondary flow motion is desired, which can be introduced by a smaller curvature, however increasing the mixing losses and hence increasing the pressure losses.

Comparison between the different optimization methods demonstrates that the use of surrogate models can drastically reduce the required number of CFD evaluations from 4000 to 100 only. Comparing further the surrogate model assisted EA with the gradient based optimization, it was found that similar shapes were obtained despite the fact that the gradient based method departed from a separated initial design. It is often believed that engineering problems facing separation represent a multimodal character, for which gradient based optimization algorithms can get trapped in local optima. In the present study however, results indicate that no such problems were present and seem to further feed the discussion as to which many engineering problems are unimodal of nature although easily thought multimodal

Finally, an experimental validation has proven the effectiveness of the optimization approach. In terms of global performance, the numerical predicted reduction in pressure losses was confirmed within measurement accuracy. Detailed PIV measurements however reveal a small separation which was not captured by CFD. It demonstrates that still further improvement should be possible, however beyond the capability of RANS approaches with their restriction on turbulence modeling.

REFERENCES

[1] Humphrey, J. A. C., Whitelaw, J. H., and Yee, G., 1981, "Turbulent Flow in a Square Duct with Strong Curvature", *Journal of Fluid Mechanics*, Vol. 103, pp. 443–463.

[2] Chang, S. M., Humphrey, J. A. C., and Modavi, A., 1983, "Turbulent Flow in a Strongly Curved U-Bend and Downstream Tangent of Square Cross-Sections", *Physico-Chemical Hydrodynamics*, Vol. 4, pp. 243–269.

[3] Monson, D. J., and Seegmiller, H. L., 1992, "Experimental Investigation of Subsonic Flow in a Two Dimensional U-Duct", *NASA report TM-103931*.

[4] Cheah, S. C., Iacovides, H., Jackson, D. C., Ji, H. H., and Launder, B. E., 1996, "LDA Investigation of the Flow Development Through Rotating U-ducts", *Journal of Turbomachinery*, Vol. 118, pp. 590–596.

[5] Open Foam, 2010, "Open Foam user guide", *Tech. rep.*, See also URL http://www.openfoam.com/docs/user/.

[6] Pope, S. B., 2000, *Turbulent Flows*, Cambridge University Press.

[7] Holland, J. H., 1975, *Adaption in Natural and Artificial Systems*, University of Michigan Press.

[8] Rechenberg, I., 1973, *Evolutionsstrategie — Optimierung technischer Systeme nach Prinzipien der biologischen Evolution*, Fommann-Holzboog, Stuttgart.

[9] Othmer, C., 2008, "A continuous adjoint formulation for the computation of topological and surface sensitivities of ducted flows", *Int J Num Meth Fluids*, Vol. 58, pp. 861–877.

[10] Abbas, H. A., Sarker, R., and Newton, C., 2001, "PDE: A Pareto-Frontier Differential Evolutio Approach for Multi-objective Optimization Problems", *Proceedings of the Congress on Evolutionary Computation*, Piscataway, New Jersey, Vol. 2, pp. 971–978.

[11] Madavan, N. K., 2002, "Multiobjective Optimization Using a Pareto Differential Evolution Approach", *Proceedings of the Congress on Evolutionary Computation*, Honolulu, Hawaii, Vol. 2, pp. 1145–1150.

[12] Liou, T.-M., Tzeng, Y.-Y., and Chen, C.-C., 1999, "Flow in a 180S Sharp Turning Duct With Different Divider Thicknesses", *Int J Num Meth Fluids*, Vol. 121, pp. 569–576.

Conference on Modelling Fluid Flow (CMFF'15)
The 16th International Conference on Fluid Flow Technologies
Budapest, Hungary, September 1-4, 2015

EVOLUTIONARY ALGORITHMS AND ADJOINT-BASED CFD OPTIMIZATION IN TURBOMACHINERY

K.C. Giannakoglou[1], V.G. Asouti[2], E.M. Papoutsis-Kiachagias[3]

[1] National Technical University of Athens. Iroon Polytechniou 9, 157 80 Athens, Greece. (+30)2107721636. kgianna@central.ntua.gr, web page: http://velos0.ltt.mech.ntua.gr/research/
[2] National Technical University of Athens. vasouti@mail.ntua.gr
[3] National Technical University of Athens. vaggelisp@gmail.com.

ABSTRACT

This paper deals with Computational Fluid Dynamics (CFD)-based shape optimization methods applied to gas and hydraulic turbomachines. In specific, two major optimization strategies, developed by the same group, are discussed: gradient–based methods (GBMs) supported by the continuous adjoint approach and metamodel–assisted evolutionary algorithms (MAEAs).

Regarding GBMs, the continuous adjoint method for the aero/hydrodynamic design of turbomachinery bladings is discussed. Full differentiation of turbulence models is considered. Recent developments allowing the computation of accurate sensitivity derivatives are presented in brief. Then, the continuous adjoint method is used for the shape optimization of two Francis turbine blades. The adjoint method for the optimization of thermal turbomachinery bladings, by taking into account conjugate heat transfer (CHT) effects, is also discussed.

Regarding MAEAs, emphasis is laid on the ways used to reduce the overall CPU cost of a CFD-based optimization. In particular, the efficient use of on–line trained surrogate evaluation models (or metamodels), the use of asynchronous search on multiprocessor platforms and the use of Principal Component Analysis (PCA) as remedies to the curse of dimensionality problem are discussed. MAEAs are demonstrated in the aero/hydrodynamic shape optimization of turbomachinery bladings.

Keywords: Computational Fluid Dynamics, Continuous Adjoint Method, Gradient–based methods, Metamodel Assisted Evolutionary Algorithms, Thermal and Hydraulic Turbomachines

NOMENCLATURE

F	[varies]	objective function
T	[K]	temperature
T_a	[F-related]	adjoint temperature
$\underline{b}$	[varies]	design variables
$\underline{u}$	[F-related]	adjoint velocity
$\underline{v}$	$[m/s]$	absolute velocity
$\underline{w}$	$[m/s]$	relative velocity
p	$[m^2/s^2]$	static pressure divided by density
q	[F-related]	adjoint pressure
λ	[-]	offsprings
μ	[-]	parents
ν	$[m^2/s]$	bulk viscosity
ν_t	$[m^2/s]$	turbulent viscosity
$\widetilde{\nu_a}$	[F-related]	adjoint turbulence model variable
$\widetilde{\nu}$	$[m^2/s]$	Spalart–Allmaras model variable

1. INTRODUCTION

During the last years, the cost benefits resulting from using CFD has given rise to an intense academic and industrial interest in the use of computational methods for the design/optimization of thermal and hydraulic turbomachines.

CFD–based optimization methods can be classified into deterministic and stochastic ones, according to the strategy used to compute the optimal set of design variables. Deterministic algorithms start with a given geometry and improve it iteratively based on the computed or approximated gradient of the objective function with respect to (w.r.t.) the design variables. Depending on the initialization, it is not unlikely for a GBM to be trapped into a local optimum. In such a case, the designer will get an optimized rather than an optimal solution. Though global optimal solutions are always the target, in practice local optima are highly welcome. The efficiency of GBMs greatly depends on the method used to compute the necessary gradient. In this respect, the adjoint method [1] has been receiving a lot of attention, since the cost of computing the gradient is, practically, independent from the number of the design variables. This makes the method an excellent choice for large scale industrial optimization problems. In this paper, recent advances in computing accurate sensitivity derivatives for turbulent flows using the continuous adjoint variant are discussed, [2]. In addition, a short discussion about adjoint methods for CHT applications is presented followed by industrial applications.

Evolutionary algorithms (EAs) are the most popular representative of stochastic population–based search methods. In EAs, entrapment to local minima is highly unlikely, unless the search is stopped early enough, since almost the entire design space can be explored. EAs are extremely flexible since the evolution operators do not interfere with the flow solver; so, in CFD–based optimization, no access to the source CFD code is required (black–box evaluation software). Furthermore, EAs can compute Pareto fronts of non-dominated solutions in multi–objective optimization (MOO) problems, with a single run. On the other hand, a great number of candidate solutions must be evaluated before reaching the optimal one(s), leading to a high optimization turnaround time, especially when the evaluation software is costly (such as in CFD applications). In addition, the number of evaluations required increases with the number of the design variables (curse of dimensionality). A number of remedies have been proposed in the literature to tackle the aforementioned two weaknesses of EAs. Among them is the use Metamodel–Assisted EAs (MAEAs), asynchronous search, performed on a cluster of many processors, and the use Principal Component Analysis (PCA) to identify correlations between the design variables, [3, 4, 5]. Industrial applications using the above techniques are presented.

2. ADJOINT METHODS

In this section, the formulation of the continuous adjoint PDEs, their boundary conditions and the sensitivity derivatives (gradient) expression are presented in brief. The development is based on the incompressible Navier-Stokes equations for a non-inertial Single Rotating Frame (SRF), though their extension to inertial reference systems, [2], exists too. The development for incompressible flows is based on OpenFOAM©. However, the same tools have been programmed also for compressible flows, [6], on an in–house CDF code, running on GPUs, [7].

2.1. Flow Equations

The mean flow equations together with the Spalart–Allmaras turbulence model PDE, [8], comprise the flow or primal system of equations that reads

$$R^p = -\frac{\partial w_i}{\partial x_i} = 0 \tag{1a}$$

$$R_i^w = w_j \frac{\partial w_i}{\partial x_j} + \frac{\partial p}{\partial x_i} - \frac{\partial \tau_{ij}}{\partial x_j} + \underbrace{2e_{ijk}\Omega_j w_k}_{C_R} + e_{ijk}\Omega_j e_{klm}\Omega_l x_m = 0 \tag{1b}$$

$$R^{\widetilde{\nu}} = \frac{\partial (w_j \widetilde{\nu})}{\partial x_j} - \frac{\partial}{\partial x_j}\left[\left(\nu + \frac{\widetilde{\nu}}{\sigma}\right)\frac{\partial \widetilde{\nu}}{\partial x_j}\right] - \frac{c_{b2}}{\sigma}\left(\frac{\partial \widetilde{\nu}}{\partial x_j}\right)^2 - \widetilde{\nu} P(\widetilde{\nu}, \Delta) + \widetilde{\nu} D(\widetilde{\nu}, \Delta) = 0 \tag{1c}$$

where w_i, Ω_j, x_m are the components of the relative velocity vector, rotational speed vector and position vector, respectively. The absolute (v_i) and relative (w_i) velocities are related through $v_i = w_i + e_{ijk}\Omega_j x_k$. Also, p is the static pressure divided by the constant density, $\tau_{ij} = (\nu + \nu_t)\left(\frac{\partial w_i}{\partial x_j} + \frac{\partial w_j}{\partial x_i}\right)$ are the components of the stress tensor, ν and ν_t the bulk and turbulent viscosity, respectively, $\widetilde{\nu}$ the Spalart–Allmaras model variable and Δ the distance from the wall boundaries. Details about the turbulence model constants and source terms can be found in [8].

2.2. General Objective Function

Let F be the objective function to be minimized by computing the optimal values of the design variables $b_n, n \in [1, N]$. A general expression for an objective function defined on (parts of) the boundary S of the computational domain Ω is given by

$$F = \int_S F_{S_i} n_i dS \tag{2}$$

where $\mathbf{n}$ is the outward normal unit vector.

Differentiating Eq. 2 w.r.t. to b_n and applying the chain rule yields

$$\frac{\delta F}{\delta b_n} = \int_S \frac{\partial F_{S_i}}{\partial w_k} n_i \frac{\partial w_k}{\partial b_n} dS + \int_S \frac{\partial F_{S_i}}{\partial p} n_i \frac{\partial p}{\partial b_n} dS + \int_S \frac{\partial F_{S_i}}{\partial \tau_{kj}} n_i \frac{\partial \tau_{kj}}{\partial b_n} dS + \int_S \frac{\partial F_{S_i}}{\partial \widetilde{\nu}} n_i \frac{\partial \widetilde{\nu}}{\partial b_n} dS + \int_S n_i \frac{\partial F_{S_i}}{\partial x_k} \frac{\delta x_k}{\delta b_n} n_k dS + \int_S F_{S_i} \frac{\delta (n_i dS)}{\delta b_n} \tag{3}$$

where $\delta\Phi/\delta b_n$ is the total (or material) derivative of any quantity Φ while $\partial\Phi/\partial b_n$ is its partial derivative. Operators $\delta()/\delta b_n$ and $\partial()/\partial b_n$ are related by

$$\frac{\delta \Phi}{\delta b_n} = \frac{\partial \Phi}{\partial b_n} + \frac{\partial \Phi}{\partial x_k}\frac{\delta x_k}{\delta b_n} \tag{4}$$

Computing the variation of the flow variables on the r.h.s. of Eq. 3, either through Direct Differentiation (DD) or Finite Differences (FD) would require at least N Equivalent Flow Solutions (EFS, i.e. as if the flow equations were solved instead). To avoid this computational cost that scales with N, the adjoint method is used, as presented in the next subsection.

2.3. Continuous Adjoint Formulation

Starting point of the continuous adjoint formulation is the introduction of the augmented function

$$F_{aug} = F + \int_\Omega u_i R_i^w d\Omega + \int_\Omega q R^p d\Omega + \int_\Omega \widetilde{\nu_a} R^{\widetilde{\nu}} d\Omega \tag{5}$$

where u_i are the components of the adjoint to the relative velocity vector, q is the adjoint pressure and

$\widetilde{\nu_a}$ is the adjoint turbulence model variable, respectively. Dropping the last integral on the r.h.s. of Eq. 5 would result to the so-called "frozen turbulence" assumption which neglects the differentiation of the turbulence model PDE(s). This assumption leads to reduced gradient accuracy, possibly even to wrong sensitivity signs, [9]. To avoid the "frozen turbulence" assumption implications, the Spalart–Allmaras model PDE has been differentiated, see [9]. A review on continuous adjoint methods for turbulent flows can be found in [2].

The differentiation of Eq. 5, based on the Leibniz theorem, yields

$$\frac{\delta F_{aug}}{\delta b_n}=\frac{\delta F}{\delta b_n}+\int_{\Omega}u_i\frac{\partial R_i^w}{\partial b_n}d\Omega+\int_{\Omega}q\frac{\partial R^p}{\partial b_n}d\Omega \\ +\int_{\Omega}R^{\widetilde{\nu}}\frac{\partial R^{\widetilde{\nu_a}}}{\partial b_n}d\Omega+\int_{S_W}(u_iR_i^w+qR^p+\widetilde{\nu_a}R^{\widetilde{\nu}})n_k\frac{\delta x_k}{\delta b_n}dS \tag{6}$$

Then, the derivatives of the flow residuals in the volume integrals on the r.h.s. of Eq. 6 are developed by differentiating Eqs. 1 and applying the Green-Gauss theorem, where necessary. Indicatively, the development of the C_R (Coriolis) term variation yields

$$\int_{\Omega}u_i\frac{\partial C_{R,i}}{\partial b_n}d\Omega=-\int_{\Omega}2e_{ijk}\Omega_ju_k\frac{\partial w_i}{\partial b_n}d\Omega \tag{7}$$

contributing an extra term to the adjoint momentum equations. The development of the remaining terms can be found in [9], [10] and [2].

In order to obtain a gradient expression which does not depend on the partial derivatives of the flow variables w.r.t. b_n, their multipliers in (the developed form of) Eq. 6 are set to zero, giving rise to the field adjoint equations

$$R^q=-\frac{\partial u_j}{\partial x_j}=0 \tag{8a}$$

$$R_i^w=u_j\frac{\partial w_j}{\partial x_i}-\frac{\partial(w_ju_i)}{\partial x_j}-\frac{\partial\tau_{ij}^a}{\partial x_j}+\frac{\partial q}{\partial x_i} \\ \underbrace{-2e_{ijk}\Omega_ju_k}_{C_{R_a}}+\widetilde{\nu_a}\frac{\partial\widetilde{\nu}}{\partial x_i}-\frac{\partial}{\partial x_l}\left(\widetilde{\nu_a}\widetilde{\nu}\frac{C_Y}{Y}e_{mjk}\frac{\partial w_k}{\partial x_j}e_{mli}\right)=0 \tag{8b}$$

$$R^{\widetilde{\nu_a}}=-\frac{\partial(w_j\widetilde{\nu_a})}{\partial x_j}-\frac{\partial}{\partial x_j}\left[\left(\nu+\frac{\widetilde{\nu}}{\sigma}\right)\frac{\partial\widetilde{\nu_a}}{\partial x_j}\right]+\frac{1}{\sigma}\frac{\partial\widetilde{\nu_a}}{\partial x_j}\frac{\partial\widetilde{\nu}}{\partial x_j} \\ +2\frac{c_{b2}}{\sigma}\frac{\partial}{\partial x_j}\left(\widetilde{\nu_a}\frac{\partial\widetilde{\nu}}{\partial x_j}\right)+\widetilde{\nu_a}\widetilde{\nu}C_{\widetilde{\nu}}+\frac{\partial\nu_t}{\partial\widetilde{\nu}}\frac{\partial u_i}{\partial x_j}\left(\frac{\partial w_i}{\partial x_j}+\frac{\partial w_j}{\partial x_i}\right) \\ +(-P+D)\,\widetilde{\nu_a}=0 \tag{8c}$$

where $\tau_{ij}^a=(\nu+\nu_t)\left(\frac{\partial u_i}{\partial x_j}+\frac{\partial u_j}{\partial x_i}\right)$ are the components of adjoint stress tensor. The term marked as C_{R_a} results from the differentiation of C_R and can be seen as the adjoint Coriolis acceleration. Eq. 8c is the adjoint turbulence model equation, from which the adjoint turbulence model variable $\widetilde{\nu_a}$ is computed.

The adjoint boundary conditions are derived by treating the flow variations in the boundary integrals (of the developed form of) Eq. 6, [9, 2]. Indicatively, at the inlet (S_I) and wall (S_W) boundaries, the following conditions are imposed

$$u_jn_j=u_{\langle n\rangle}=-\frac{\partial F_{S_{I-W,i}}}{\partial p}n_i \tag{9a}$$

$$u_jt_j^I=u_{\langle t\rangle}^I=\frac{\partial F_{S_{I-W,k}}}{\partial\tau_{ij}}n_kt_i^In_j+\frac{\partial F_{S_{I-W,k}}}{\partial\tau_{ij}}n_kt_j^In_i \tag{9b}$$

$$u_jt_j^{II}=u_{\langle t\rangle}^{II}=\frac{\partial F_{S_{I-W,k}}}{\partial\tau_{ij}}n_kt_i^{II}n_j+\frac{\partial F_{S_{I-W,k}}}{\partial\tau_{ij}}n_kt_j^{II}n_i \tag{9c}$$

where S_{I-W} stands for either S_I or S_W, depending on the boundary under consideration. In what follows, $\mathbf{t^I}$ is the unit tangent vector parallel to the velocity at the first cell centre off the boundary and the components of the second target vector $\mathbf{t^{II}}$ are given by $t_i^{II}=e_{ijk}n_jt_k^I$, where e_{ijk} is the Levi-Civita symbol. The outlet (S_O) conditions for the adjoint problem and boundary conditions for the $\widetilde{\nu_a}$ field can be found in [9, 2].

In industrial applications, the wall function technique is used routinely in analysis and design. When the design is based on the adjoint method, considering the adjoint to the wall function model becomes necessary. The continuous adjoint method in optimization problems, governed by the RANS turbulence models with wall functions, was initially presented in [11], where the adjoint wall function technique was introduced for the $k-\epsilon$ model and a vertex–centered finite volume method. The proposed formulation led to a new concept: the "adjoint law of the wall". This bridges the gap between the solid wall and the first node off the wall during the solution of the adjoint equations. The adjoint wall function technique has been extended to flow solvers based on cell-centered finite-volume schemes, for the $k-\omega$, [12], and Spalart–Allmaras , [2], models.

After satisfying the adjoint PDEs and their boundary conditions, the remaining terms in Eq. 6 yield the sensitivity derivatives

$$\frac{\delta F}{\delta b_n}=-\int_{S_W}\left[\tau_{ij}^an_j-qn_i+\frac{\partial F_{S_{W,k}}}{\partial w_i}n_k\right]\frac{\partial w_i}{\partial x_k}\frac{\delta x_k}{\delta b_n}dS \\ +\int_{S_W}n_i\frac{\partial F_{S_{W,i}}}{\partial x_k}\frac{\delta x_k}{\delta b_n}dS+\int_{S_W}F_{S_{W,i}}\frac{\delta(n_idS)}{\delta b_n} \\ -\int_{S_W}\left[\left(\nu+\frac{\widetilde{\nu}}{\sigma}\right)\frac{\partial\widetilde{\nu_a}}{\partial x_j}n_j+\frac{\partial F_{S_k}}{\partial\widetilde{\nu}}n_k\right]\frac{\partial\widetilde{\nu}}{\partial x_k}\frac{\delta x_k}{\delta b_n}dS \\ +\int_{S_W}(u_iR_i^w+qR^p+\widetilde{\nu_a}R^{\widetilde{\nu}})\frac{\delta x_k}{\delta b_n}n_kdS \\ -\int_{S_W}\left(-u_{\langle n\rangle}+\frac{\partial F_{S_{W_p,k}}}{\partial\tau_{lm}}n_kn_ln_m\right)\mathcal{TS}_1dS \\ -\int_{S_W}\frac{\partial F_{S_{W_p,k}}}{\partial\tau_{lm}}n_kt_l^It_m^I\mathcal{TS}_2dS \\ -\int_{S_W}\left(\frac{\partial F_{S_{W_p,k}}}{\partial\tau_{lm}}n_k(t_l^{II}t_m^I+t_l^It_m^{II})\right)\mathcal{TS}_3dS$$

$$-\int_{S_W} \frac{\partial F_{S_{W_{p,k}}}}{\partial \tau_{lm}} n_k t_l^{II} t_m^{II} \mathcal{TS}_4 dS \quad (10)$$

where $\mathcal{TS}_1$ to $\mathcal{TS}_4$ can be found in [2].

2.4. Differentiation of Turbulence Models: A Convincing Example

In the application of this section, the gain from overcoming the "frozen turbulence" assumption is discussed. In Figure 1, the sensitivity derivatives of the total pressure losses objective function,

$$F_{pt} = -\int_{S_{I,O}} \left(p + \frac{1}{2}v_k^2\right) v_i n_i dS$$

w.r.t. the coordinates of Bézier–Bernstein control points parameterizing a compressor cascade airfoil are illustrated. Here, the low-Re variant of the Spalart–Allmaras model is used. It can be seen that the "frozen turbulence" assumption leads to quite wrong sensitivities while the adjoint approach that takes into consideration the differentiation of the turbulence model reproduces the outcome of the reference method (FD). More on the gain in accuracy

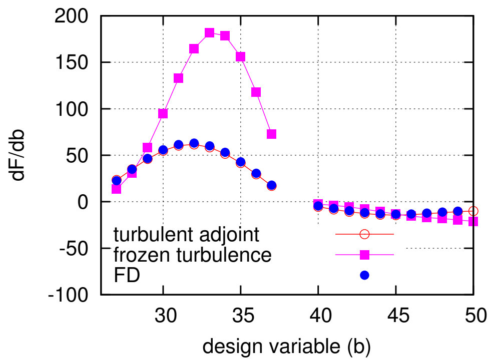

Figure 1. Shape optimization of a compressor cascade with $Re = 3.3 \times 10^5$. Sensitivity derivatives of the total pressure losses function F w.r.t. the coordinates of the Bézier–Bernstein control points parameterizing the suction (first half) and pressure (last half of the horizontal axis) airfoil sides.

from using the adjoint law of the wall when the flow simulation employs wall functions can be found in [2].

2.5. Continuous Adjoint for Conjugate Heat Transfer Analysis

This section discusses some points of the mathematical development and implementation of the continuous adjoint method to CHT applications. CHT comprises the concurrent solution of the mean flow and energy equations over the fluid domain and the energy equation over an adjacent solid domain. The fluid and solid domains communicate through the Fluid/Solid Interface (FSI). The conditions imposed along the FSI boundary, Figure 2, are (index F stands for fluid-related quantities and S for solid-related ones)

$$Q^S = -Q^F \Rightarrow k^S \left.\frac{\partial T^S}{\partial n}\right|_{FSI_S} = -k^F \left.\frac{\partial T^F}{\partial n}\right|_{FSI_F} \quad (11a)$$

$$T^S = T^F = T^{FSI} \quad (11b)$$

where Q is the heat-flux and $k^F = a_{eff} c_p$ is the thermal conductivity. Eq. 11a expresses the equality of heat fluxes along the FSI while Eq. 11b states that the temperature at the coinciding nodes of the solid and fluid meshes is the same.

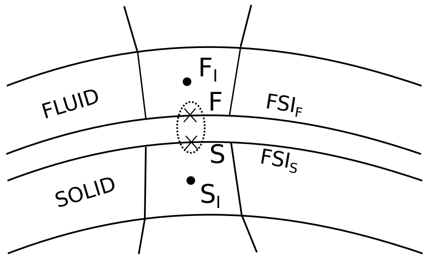

Figure 2. The fluid(F)/solid(S) interface. Faces F and S coincide. F_I and S_I are the centres of the first cells off the fluid and solid boundaries, respectively.

In the application examined, the optimization aims at minimizing the maximum temperature inside an internally cooled turbine cascade, Figure 3. Since such a min./max. objective can not be differentiated, a differentiable surrogate should be used. It is proposed to use a sigmoid function

$$F_T = \frac{\int_{\Omega_S} f_{sig} d\Omega}{\int_{\Omega_S} d\Omega}, \quad f_{sig} = 1 - \frac{1}{1 + e^{k_2(T - T_c) + k1}} \quad (12)$$

where Ω_S is the volume of the solid domain, T_c is a critical (high) temperature threshold and $T_s < T_c$ is a safety threshold to be defined by the designer. Constants k_1 and k_2 take on values that lead to $f_{sig}(T_s) = \epsilon$ and $f_{sig}(T_c) = 1 - \epsilon$, where ϵ is a user–defined infinitesimal positive number.

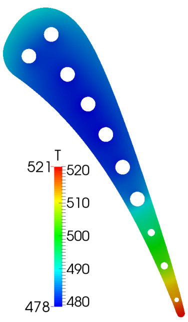

Figure 3. Temperature distribution inside an internally cooled turbine blade. The fluid (not shown in the figure) and solid domains are coupled based on the boundary conditions presented in Eqs. 11, while heat exchange between the solid domain and the cooling passages is simulated using a $1D$ heat exchange equation.

The augmented objective function for CHT optimization problems is written as

$$F_{aug} = F + \int_{\Omega_F} u_i R_i^w d\Omega + \int_{\Omega_F} q R^p d\Omega + \int_{\Omega_F} \widetilde{\nu}_a R^{\widetilde{\nu}} d\Omega + \int_{\Omega_F} T_a^F R^{T^F} d\Omega + \int_{\Omega_S} T_a^S R^{T^S} d\Omega \quad (13)$$

where R^{T^F}, R^{T^S} are the energy equation PDEs over the fluid and solid domains, respectively, and T_a^F, T_a^S are the corresponding adjoint temperatures. Following a process similar to that described in sections 2.2 to 2.4, the field adjoint equations, adjoint boundary conditions and sensitivity derivatives expression can be derived. In the interest of space, these are omitted herein. However, it is interesting to note that the adjoint boundary conditions at the FSI are of the same type as the primal conditions. Eq. 11. They include the conservation of the adjoint heat flux at the FSI and the same adjoint temperature values for both sides of the FSI. This remark holds only for objective functions which do not include the temperature values along the FSI.

The continuous adjoint approach to CHT problems was utilized to support a gradient-based algorithm to minimize F_T with $T_s = 515\ K$ and $T_c = 525\ K$ for the geometry presented in Figure 3; the turbine blade airfoil is parameterized using NURBS control points and the cooling holes are at fixed positions. The highest deformation is located close to the trailing edge, Figure 4, decreasing the maximum blade temperature by more than 2 K.

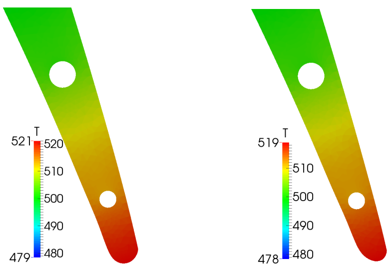

Figure 4. Shape optimization of an internally cooled turbine blade, targeting the minimization of the maximum temperature over the solid. Temperature distributions in a blow-up view close to the trailing edge of the initial (left) and optimized (right) geometries.

2.6. Turbomachinery Applications of Adjoint-based Optimization

Two industrial applications are presented in this section. The first one is concerned with the shape optimization of a Francis turbine runner in order to suppress cavitation, i.e. maximizing the minimum pressure on the blade surface. Following the same line of reasoning for differentiating a max./min problem as the one presented in section 2.5, a sigmoid function similar to Eq. 12 is used, by defining a cavitation threshold p_c and a safety threshold p_s. No shape parameterization was used. Instead, the normal displacements of the blade wall nodes acted as the design variables, after appropriately smoothing the computed sensitivity derivatives. The pressure distributions over the initial and optimized bladings are presented in Figure 5.

The second application deals with the multi-point design of a different Francis runner targeting the maximization of the weighted sum of the efficiencies at three operating points, ranging from 40% to 100% of the nominal mass flow rate Q_{nom}

$$F = 0.6F_{Q_{100}} + 0.25F_{Q_{71.5}} + 0.15F_{Q_{40}} \quad (14)$$

Blade shapes resulting after 8 optimization cycles of the multi-point as well as the three (separate) single-point optimizations (for the three mass flow rates) are depicted in Figure 6. The multi-point optimization deforms the blade in the same direction as the single-point optimization for the nominal flow rate, since this point has the highest weight in Eq. 14. The other two single-point optimizations for $Q = 0.715Q_{nom}$ and $Q = 0.40Q_{nom}$ deform the blade in the opposite direction. This clearly reveals the contradictory targets in multi-point optimization.

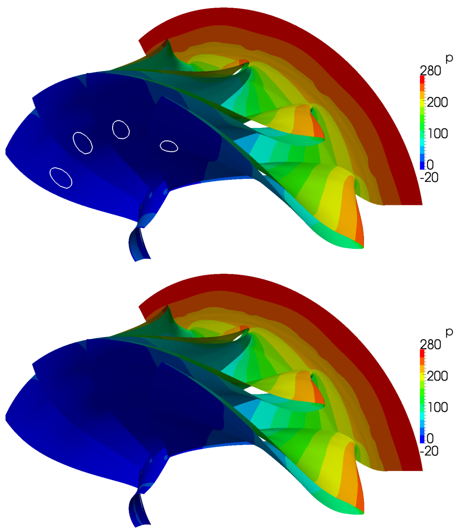

Figure 5. Optimization of a Francis runner blade targeting cavitation suppression. Top: pressure distribution over the initial blading; white isolines encircle the cavitated areas. Bottom: pressure distribution over the optimized blading.

3. OPTIMIZATION METHODS BASED ON EAS

Regarding EAs, emphasis is laid on ways to reduce the optimization turnaround time in large–scale applications. The most frequently used technique is the use of surrogate evaluation models (metamodels) giving rise to MAEAs. Either EAs or MAEAS can further be enhanced by the Principal Component Analysis (PCA) technique aiming at efficiently handling problems involving a great number of design

Figure 6. Multi-point optimization of a Francis runner Blades as seen from the trailing edge (left) and a blow–up view close to the shroud (right). The initial blade is depicted in grey, the result of the multi-point optimization in red, while the results of single-point optimizations at the three operating points are shown in green ($Q = Q_{nom}$), yellow ($Q = 0.715Q_{nom}$) and magenta ($Q = 0.4Q_{nom}$).

variables. Over and above to MAEAs (with or without PCA), the concurrent evaluation of the offspring of each generation on the available processors of a multi-processor system may further reduce the optimization turnaround time. Asynchronous EAs (AEAs), remove the synchronization barrier at the end of each generation, and fully exploit all the available computational resources. All these techniques are incorporated in the general purpose optimization platform EASY (Evolutionary Algorithm SYstem, http://velos0.ltt.mech.ntua.gr/EASY) developed by the authors' group.

On–line trained metamodels (radial basis function/RBF networks) for each candidate solution are used according to the Inexact Pre-Evaluation (IPE) technique, [3]. The first few generations are carried out as a conventional EA (with μ parents and λ offspring) and the MAEA starts once a user–defined number of entries have been stored in the database (DB) of already evaluated individuals. During the IPE phase all population members are pre–evaluated on the surrogate models trained on–the–fly. This training is carried out on the neighboring (in the design space) individuals in the DB. Then, based on the outcome of the pre–evaluations on the metamodels, a small number of the most promising members ($\lambda_{IPE} \ll \lambda$) are re–evaluated on the CFD model.

Metamodels can be also employed in AEAs (AMAEAs), after appropriately adapting the IPE scheme, [4], since the notion of generation does not exist anymore. Once an evaluation is completed and the corresponding processor is idle, a new individual is generated (using the evolution operators) and assigned to this processor. When the IPE is activated on an instantaneously idle processor, instead of generating a single individual, a small number (N_{IPE}) trial ones are generated. For each one of them, a local metamodel is trained and its objective function value is approximated. The best (according to the metamodel) among the N_{IPE} individuals is, then, re–evaluated on the exact model. An example of the gain in the optimization turnaround time by using AMAEA instead of MAEA, is shown in 7. This is concerned with the design of a peripheral compressor cascade for minimum viscous losses, where AMAEA and MAEA were allowed to perform up to 12 concurrent evaluations on a many–GPUs platform. The IPE was activated after 80 entries were gathered in the DB and $\lambda_{IPE} = 8$ members were re–evaluated on the exact tool for the MAEA. For the AMAEA, $N_{IPE} = 8$ trial members were generated before selecting the one to be re–evaluated on the idle processor.

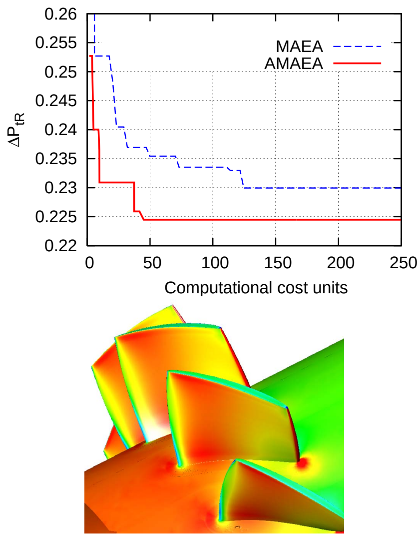

Figure 7. Optimization of a peripheral compressor cascade for minimum viscous losses. Top: Comparison of the convergence histories of MAEA and AMAEA. AMAEA outperforms MAEA which is known to perform much better than a conventional EA. Bottom: Pressure distribution on the optimal geometry.

EAs or MAEAs (along with their asynchronous variants), when applied to engineering optimization problems with a great number of design variables, suffer from the co–called "curse of dimensionality". A remedy to this problem is to process the elite set in each generation, using PCA and, based on the so acquired information to: (a) better guide the application of the evolution operators (to be referred as EA(PCA)) and (b) reduce the number of sensory units during the metamodels training (M(PCA)AEA), [5]. In (a), the design space is temporarily aligned with the principal component directions and the crossover and mutation operators are applied on the rotated individuals. This rotation according to the principal directions leads to a problem with as much as possible separable objective function, which is highly beneficial. In MAEAs, during the metamodel (RBF network) training, PCA can be used to reduce the dimension of the metamodels built. The variances of the design variables are used to identify the directions along which the elite members are less or more scattered. In the developed method, the RBF network sensory units corresponding to the directions of the design space with high variances are filtered out. Reducing the number of input parameters in the metamodel increases the prediction accuracy and accelerates the training process. The simultaneous use of PCA for both purposes is the so–called M(PCA)AEA(PCA).

An example of the use of PCA in both the metamodels and the evolution operators is shown in figure 8. This is concerned with the two–objective constrained design of a Francis runner parameterized using 372 design variables. The first objective (f_1) is related to the "quality" of the velocity profile at the runner outlet while the second one (f_2) to the blade loading. This case is studied with both MAEA and M(PCA)AEA(PCA) using a (μ,λ)=(20, 90) EA. During the IPE phase, $\lambda_{IPE} = 8$ members of each generation were re–evaluated on the CFD model. For the MAEA, the IPE phase was activated after 600 entries were stored in the DB, while for the M(PCA)AEA(PCA) only after 300 DB entries.

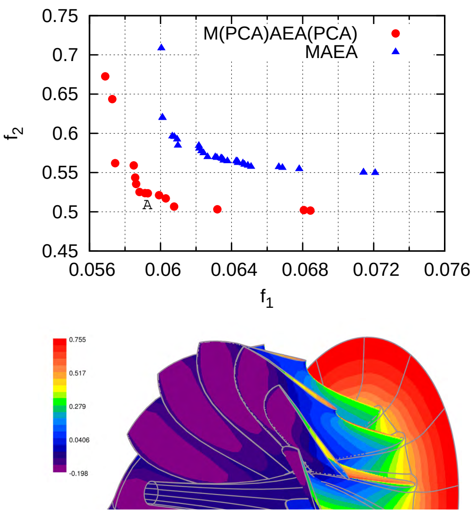

Figure 8. Two–objective design of a Francis runner at three operating points for optimizing the outlet velocity profile (min f_1) and the blade loading (min f_2). Top: Comparison of the fronts of non–dominated solutions computed by the MAEA and the M(PCA)AEA(PCA), at the same CPU cost. Bottom: 3D view and pressure field over the Francis runner, at the best efficiency operating point corresponding to non–dominated solution A.

4. USE OF EAS AND ADJOINT WITHIN THE RBF4AERO PROJECT

The aforementioned optimization methods, either stochastic (EAs) or gradient–based (adjoint) ones, are used for external aerodynamic optimization problems too. Some of these methods were appropriately adapted to fit the needs of the RBF4AERO, EU funded, project http://www.rbf4aero.eu/. The aim of the project is to develop the so–called RBF4AERO Benchmark Technology, an assembly of numerical (CFD, CSD solvers etc), morphing and optimization tools, capable of handling aerodynamic design/optimization problems. The morphing tool used is based on RBF networks and allows for fast morphing of the shapes to be optimized and the surrounding computational mesh, [13]. The optimization tool comprises both EAs and gradient–based methods assisted by the continuous adjoint method.

One of the cases to be studied within RBF4AERO is concerned with the minimization of the drag coefficient of a small aircraft underwing nacelle at two angles of attack, namely 0^o and 8^o. The nacelle is designed for the altitude of 2000m, with $M_\infty = 0.08$ and $Re_c = 3\times10^6$ based on the wing chord. The nacelle rotations around the y and z axes and the nacelle nose scaling were the three design variables used. Starting from a baseline geometry (figure 9 top), for each candidate solution the nacelle shape and the computational mesh was morphed using the customized RBF–based morphing tool of the RBF4AERO platform. The basic incompressible flow solver of OpenFOAM© (*simpleFoam*) was used as the evaluation tool, using the Spalart–Allmaras turbulence model.

In this paper, a (μ,λ)=(10, 30) MAEA was used for the optimization. The MAEA is capable of locating the Pareto front of non–dominated solutions after 100 evaluations on the CFD tool (Figure 9 bottom).

The limited range of the C_D values in the non–dominated front is due to the fact that, in all elite members, the two first design variables do not vary significantly and only the third design variable (i.e. the one related to the nose scaling) varies. This observation can be also backed-up by the magnitude of the drag force sensitivities w.r.t. the three design variables, presented in table 1 and computed using the continuous adjoint method.

b	y rot.	z rot.	scaling
dF/db	-1.9×10^{-4}	-4.4×10^{-7}	5.9×10^{-4}

Table 1. Sensitivity derivatives w.r.t. the three design variables parameterizing the nacelle shape, at 8^o farfield flow angle. It can be observed that the nose scaling has the greatest impact on the drag force value.

5. SUMMARY

This paper presented the use of either stochastic or gradient–based optimization methods in shape optimization of thermal and hydraulic turbomachines. Regarding continuous adjoint methods, some recent advances in the computation of accurate sensitivities were discussed and applied to industrial cases, lead-

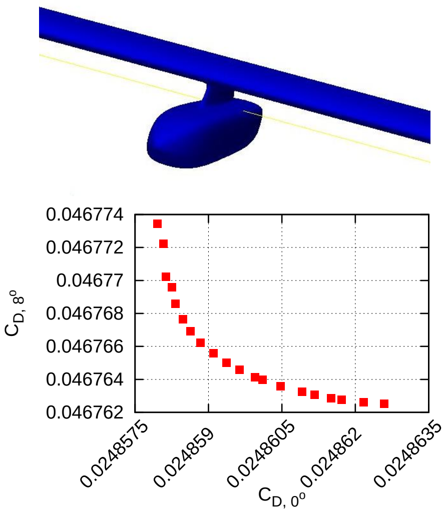

Figure 9. Two–objective optimization of an underwing nacelle (an RBF4AERO test case). Top: Baseline geometry. Bottom: Front of non–dominated solutions resulted after 100 **evaluations on the exact/CFD model.**

ing to the optimization of two Francis runners at a very small CPU cost (20 and 8 optimization cycles for each of the two cases). Regarding evolutionary algorithms, techniques involving surrogate evaluation models, asychronous search on multi-processor platforms and PCA have made the optimization of industrial cases with a great number of design variables and objectives possible.

ACKNOWLEDGEMENTS

Part of this work was funded by the RBF4AERO "Innovative benchmark technology for aircraft engineering design and efficient design phase optimisation" project funded by the EUs 7th Framework Programme (FP7-AAT, 2007-2013) under Grant Agreement no. 605396. The authors would also like to acknowledge contributions from Dr. Stylianos Kyriacou and Christos Kapellos.

REFERENCES

[1] Jameson, A., 1988, "Aerodynamic design via control theory.", *Journal of Scientific Computing*, Vol. 3, pp. 233–260.

[2] Papoutsis-Kiachagias, E., and Giannakoglou, K., 2014, "Continuous Adjoint Methods for Turbulent Flows, Applied to Shape and Topology Optimization: Industrial Applications", *Archives of Computational Methods in Engineering*, 10.1007/s11831-014-9141-9.

[3] Karakasis, M., Giotis, A., and Giannakoglou, K., 2003, "Inexact information aided, low-cost, distributed genetic algorithms for aerodynamic shape optimization", *International Journal for Numerical Methods in Fluids*, Vol. 43 (10-11), pp. 1149–1166.

[4] Asouti, V., Kampolis, I., and Giannakoglou, K., 2009, "A Grid-Enabled Asynchronous Metamodel-Assisted Evolutionary Algorithm for Aerodynamic Optimization", *Genetic Programming and Evolvable Machines*, Vol. 10 (3), pp. 373–389.

[5] Kyriacou, S., Asouti, V., and Giannakoglou, K., 2014, "Efficient PCA–driven EAs and metamodel-assisted EAs, with applications in turbomachinery", *Engineering Optimization*, Vol. 46 (7), pp. 895–911.

[6] Papadimitriou, D., and Giannakoglou, K., 2007, "A continuous adjoint method with objective function derivatives based on boundary integrals for inviscid and viscous flows", *Computers & Fluids*, Vol. 36 (2), pp. 325–341.

[7] Kampolis, I., Trompoukis, X., Asouti, V., and Giannakoglou, K., 2010, "CFD-based analysis and two-level aerodynamic optimization on Graphics Processing Units", *Computer Methods in Applied Mechanics and Engineering*, Vol. 199 (9-12), pp. 712–722.

[8] Spalart, P., Jou, W., Stretlets, M., and Allmaras, S., 1997, "Comments on the Feasibility of LES for Wings and on the Hybrid RANS/LES Approach.", *Proceedings of the first AFOSR International Conference on DNS/LES*.

[9] Zymaris, A., Papadimitriou, D., Giannakoglou, K., and Othmer, C., 2009, "Continuous Adjoint Approach to the Spalart-Allmaras Turbulence Model for Incompressible Flows", *Computers & Fluids*, Vol. 38 (8), pp. 1528–1538.

[10] Papoutsis-Kiachagias, E., Kyriacou, S., and Giannakoglou, K., 2014, "The Continuous Adjoint Method for the Design of Hydraulic Turbomachines", *Computer Methods in Applied Mechanics and Engineering*, Vol. 278, pp. 612–639.

[11] Zymaris, A., Papadimitriou, D., Giannakoglou, K., and Othmer, C., 2010, "Adjoint wall functions: A new concept for use in aerodynamic shape optimization", *Journal of Computational Physics*, Vol. 229 (13), pp. 5228–5245.

[12] Kavvadias, I., Papoutsis-Kiachagias, E., Dimitrakopoulos, G., and Giannakoglou, K., 2014, "The continuous adjoint approach to the k–ω SST turbulence model with applications in shape optimization", *Engineering Optimization, to appear.*

[13] Biancolini, M. E., "Mesh Morphing and Smoothing by Means of Radial Basis Functions (RBF): A Practical Example Using Fluent and RBF Morph", *Handbook of Research on Computational Science and Engineering: Theory and Practice (2 vol)*, pp. 347–380.

Conference on Modelling Fluid Flow (CMFF'15)
The 16th International Conference on Fluid Flow Technologies
Budapest, Hungary, September 1-4, 2015

Robust design optimization of wind turbine rotors

M.Sergio CAMPOBASSO[1]

[1] Corresponding Author. University of Lancaster, Department of Engineering. Engineering Building, Gillow Avenue, Lancaster LA1 4YW, United Kingdom. Tel.: +44 (0)1524 594673, E-mail: m.s.campobasso@lancaster.ac.uk

ABSTRACT

Wind turbine design is an inherently multidisciplinary task typically aiming at reducing wind cost of energy. In many cases the fulfillment of all design specifications and constraints is still accomplished using an iterative trial and error-based strategy. This may hinder the exploration of the feasible design space, lead to suboptimal solutions, and prevent the assessment of new and promising configurations. These shortfalls can be removed by using numerical optimization to optimize in an automated fashion wind turbine design. An additional challenge to turbine design arises from sources of uncertainty affecting wind turbine operation (e.g. wind variability), manufacturing, assembly and control (e.g. finite manufacturing tolerances and control system perturbations and faults), and the design process itself (e.g. uncertain accuracy of design tools). By adopting uncertainty quantification and propagation methods in the automated design process, the deterministic optimization becomes a probabilistic or robust design optimization process. This yields machines whose performance has reduced sensitivity to the abovesaid stochastic factors. The paper summarizes recent research work by the author and his group in the robust design optimization of horizontal axis wind turbine rotors, and it highlights some crucial areas of future research.

Keywords: wind turbine multidisciplinary design, computational aerodynamics, robust optimization

NOMENCLATURE

C_L	$[-]$	lift coefficient
N	$[rpm]$	rotational speed
P_e	$[kW]$	electrical power
U	$[m/s]$	wind speed
AEP	$[kWh]$	annual energy production
BM	$[kNm]$	bending moment
LCOE	$[\$/kWh]$	levelized cost of energy
PDF	$[-]$	probability distribution function
r	$[m]$	radial position
$x/c, y/c$	$[-]$	airfoil coordinates nondimensionalized by chord c
α	$[deg]$	angle of attack

1. INTRODUCTION

In recent years the exploitation of wind energy for producing electricity has been rapidly growing worldwide. This has been partly enabled by recent design technology advances, which have made possible substantial reductions of wind cost of energy (COE), one of the main metrics used to assess the viability of energy sources. The most widespread turbine type for heavy-duty on-shore and offshore installations is the horizontal axis wind turbine (HAWT). HAWT design, which typically aims at minimizing COE, is an inherently multidisciplinary task requiring the achievement of design specifications and the fulfillment of conflicting constraints dictated by aerodynamics, material engineering, structure mechanics and aeroelasticity, control, electrical and power engineering, and economic requirements. The characteristics of HAWT rotors, here intended as the set of turbine blades and the conversion control system from wind to mechanical power entering the drivetrain, play a major role in the design of the entire turbine, as they determine the steady and time-dependent structural loads on drivetrain, tower and foundations, and also the electrical power characteristics required for designing the power electronics subsystems. The main blade characteristics are their number, size, outer shape, internal geometry and material, while options available for power control include *a*) passive stall regulation for smaller HAWTs, and *b*) variable speed pitch-to-feather control for multimegawatt turbines.

The design of the rotor [1] as well as that of the entire turbine [2] is usually carried out using an iterative trial and error-based strategy. In rotor design, one starts by defining the outer blade shape, and this is followed by the definition of the internal structure which is modified in subsequent structural and aeroelastic analysis if found inadequate to withstand the aerodynamic loads. The iterative process may also yield the redefinition of the outer blade shape. One of the drawbacks of the manual iterative approach is the likelihood of incomplete exploration of the feasible design space, which may result in suboptimal solutions and prevent the scrutiny of radically new, potentially better configurations. A fully automated multidisciplinary design optimization (MDO) approach based on numerical optimization can avoid these pitfalls and yield substantial improvements of HAWT configurations.

In the area of turbine design Fuglsang *et al.* [3] developed a gradient-based HAWT MDO system to minimize COE, and used it to optimize the turbine design for site-dependent wind conditions. They showed that optimized site-specific designs achieved COE reductions of up to 15 % through annual energy production (AEP) increments and manufacturing cost reductions. Maki *et al.* [4] optimized the design of a 3-blade 1 MW HAWT using a multi-level system design to minimize COE. Their optimized configuration featured a reduction of about 29 % of COE, had higher rated rotational speed, larger diameter and lower rated power than the reference HAWT configuration. Their results also highlighted that COE had a minimum with respect to the rotor diameter and the rated rotational speed, and increased monotonically with the rated power. Ashuri *et al.* [5] used a gradient based optimizer to optimize the design of the National Renewable Energy (NREL) 5 MW virtual HAWT [6], reporting a 2.3 % COE reduction.

HAWT design and operation are affected by significant uncertainty caused by environmental, aerodynamic and engineering factors. Accounting for stochastic factors in the design optimization process yields a robust MDO (RMDO) process [7], whereby the deterministic estimates of objective functions and constraints are replaced by probabilistic estimates. Unlike deterministic designs, robust designs feature reduced performance sensitivity to stochastic variations of operation, control and engineering factors. RMDO is computationally more expensive than MDO because at each RMDO step multiple analyses of the same nominal design are required for propagating uncertainty [8] in the multidisciplinary analysis system. The recent development of numerically efficient uncertainty propagation methods [9] and the high performance of modern computers are making the computational burden of RMDO affordable.

HAWT RMDO is a very recent but extremely promising technology that can subsantially improve HAWT design and on which only a few advanced studies are available [10, 11, 12, 13] to date. This paper presents the research work carried out in this area by the author and his group. The options available for the modules of the multidisciplinary HAWT rotor analysis system are discussed in Section 2. Section 3 discusses the choice of methods for propagating uncertainty in the multidisciplinary analysis system, defines the objectives and constraints of HAWT rotor RMDO problem, and available approaches to its solution. Two sample applications of HAWT RMDO are presented in Section 4, while a summary with ongoing and future research trends is provided in Section 5.

2. MULTIDISCIPLINARY ANALYSIS

HAWT rotor MDO and RMDO rely on integrated multidisciplinary analysis (MDA) systems, made up of interlinked modules. For given rotor diameter and hub height, parameters defining the outer shape of the blades and their internal structure, power regulation, and wind parameters from cut-in to cut-out speeds, the MDA system returns the output required for the design optimization, such as AEP, COE, structural stresses and fatigue damage. MDA systems typically include: *a*) parametrized models of the blade outer and inner shapes, *b*) an aerodynamic module to determine the rotor power and the aerodynamic loads acting on the blades, *c*) an aero-servo-elastic subsystem for determining the aeroelastic characteristics of the rotor, and, in some cases, also the effects of blade deformations on power generation, *d*) a stress analysis module to determine the design-driving stresses of the blades subject to aerodynamic, weight and centrifugal loads.

2.1. Geometry parametrization

Both the outer shape of the blades and their internal structure need to be defined by suitable parametric representations. The input variables on which such parametrizations depend are the design variables.

As for the outer blade shape, most studies published in the last two decades parametrize and vary only the radial profiles of blade twist and airfoil chords during the optimization (a few design variables are associated to chord and twist at some radial positions, and cubic splines are used to define the complete radial profile of these two variables), while the blade airfoils are left unaltered [14, 15]. The adopted airfoils are chosen from among custom tailored HAWT or aircraft wing airfoil families for which reasonably reliable (usually experimentally measured) aerodynamic force data are available. As highlighted by Fuglsang *et al.* [16] and further discussed below, the reason for not parametrizing (and thus not designing) the blade airfoils within HAWT rotor design optimization is the difficulty in computing reliable estimates of abovesaid aerodynamic forces for the feasible arbitrary airfoil shapes generated when enabling airfoil geometry variations during the optimization. The same authors also recognized that significant improvements in HAWT design optimization can be achieved by enabling airfoil geometry variations in the optimization. In the light of the potential of new Computational Fluid Dynamics (CFD) to accurately predict transitional and stalled airfoil aerodynamics, new optimization studies start incorporating airfoil design in the 3D rotor design optimization [17, 12, 18, 19].

The airfoil geometry parametrization is often based on composite Bezier curves [12, 19], or even PARSEC parametrizations [17]. The author's group have used a composite 4-Bezier curve parametrization [13], sketched in Fig. 1. The composite parametrization features 14 control points, but the design variables are only 12 abscissas and ordinates of the 14 base points, since the remaining 16 abscissas are determined by fixing the position of the leading and trailing edges, and imposing suitable continuity conditions at the junctions between the 4 component curves.

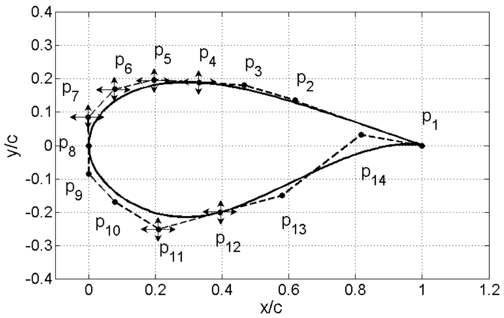

Figure 1. HAWT rotor airfoil parametrization based on composite Bezier curve.

The internal structure of HAWT blades typically consists of spar caps, spar webs and skin elements. Different levels of detail and approximation have been used in HAWT design optimization. Some studies model only the spar caps as they base the structural design on the bending load withstood by such components [14], whereas other studies model the complete internal structure, and use a shell element approach for calculating the stress field [20]. An important feature in HAWT rotor MDO is that the structural model used for the stress and the aeroelastic analyses (the aim of the latter is to determine deformations rather than stresses) are often different. More specifically, the structural model of the stress analysis often includes the 2D geometry of the blade sections, whereas the model of the aeroelastic analysis usually consists only of the radial distribution of section-averaged blade structural properties.

2.2. Aerodynamics

To compute the power generated by the rotor and the aerodynamic loads acting on its blades, a computational aerodynamics module is required. In HAWT rotor MDO and, even more, RMDO, computational speed is a crucial requirement. The blade-element momentum (BEM) theory [21] fulfills this requirement and is therefore widely used in wind turbine design. The BEM model combines the conservation of linear and angular momentum and classical lift and drag theory. Its main limitation is that the reliability of its assumptions and engineering models are questionable in many realistic HAWT rotor flows. Moreover BEM codes require knowledge of the lift and drag coefficients of the blade airfoils. Thus the accuracy of BEM analyses also depends on the source type of airfoil force coefficients.

In the automated RMDO environment, many airfoil geometries are scrutinized and their polars need to be determined very rapidly. In most cases, the viscous-inviscid panel code XFOIL [22] is used. In this code, laminar-to-turbulent transition, an important feature in HAWT rotor aerodynamics, is modeled with the e^N method. XFOIL enables the rapid calculation of the airfoil performance; the code, however, is known to usually overestimate the maximum lift coefficient [23], and is not meant to be used for reliable predictions of the force coefficients beyond the stall inception point. The near stall predictions of XFOIL appear to be particularly inaccurate for thicker airfoils [24]. Improved near-stall force predictions could be obtained with the proprietary code RFOIL, the variant of XFOIL developed at Delft University [23], or even using transitional Navier-Stokes (NS) CFD, which is reaching a level of maturity enabling it to accurately predict airfoil aerodynamics well beyond the angle of attack (AoA) of maximum lift [25]. At present, run-times of NS CFD, even in 2D simulations, are still excessive for their use in HAWT RMDO requiring hundreds or thousands of rotor analyses, but new highly-efficient computer processor architectures are enabling substantial run-time reductions of NS CFD for wind turbine analysis and design [26]. This is expected to accelerate the use of these technologies for wind turbine design.

In BEM models, the input 2D aerodynamic data are also corrected to account for the complex 3D flow physics of rotating blades, such as the Himmelskampf effect or centrifugal pumping effect [27]. Based on empirically derived equations, models like AERODAS [28] provide a method for calculating stall and post-stall lift and drag characteristics of rotating airfoils, using as input a limited amount of pre-stall 2D aerodynamic data (e.g. zero-lift AoA, AoA at maximum lift and drag, values of maximum lift and drag coefficients, slope of the linear part of the lift curve, and minimum drag coefficient). Other emprical corrections used in BEM codes include: *a*) Prandtl's tip and hub loss corrections [21], *b*) Glauert-type correction of the curve induction coefficient/thrust coefficient to account for the turbulent windmill state [29].

2.3. Aero-servo-elasticity and structural mechanics

Another functionality set of HAWT rotor MDA systems includes the determination of *a*) blade pitch angle and rotor angular speed (for pitch- and speed-regulated turbines), *b*) all time-dependent blade loads and deflections, *c*) generated power, and *d*) structural stress for each wind regime. The module or collection of interlinked modules implementing the first three functionalities forms the aero-servo-elastic analysis subsystem. Several choices are possible for this subsystem and the stress analysis module, depending primarily on the level of detail of the adopted model. The aero-servo-elastic subsystem used by the author's group is based on the NREL code FAST [30]. For given steady or time-dependent wind conditions, FAST models the aeroelastic behavior of the rotor using a modal representation of the blade displacements and velocities (the code can even model the entire turbine, including drivetrain and tower). In FAST, rotor aerodynamics is analyzed with AERODYN [30], a library implementing the BEM theory. For rotor analyses, the input of the code includes the aerodynamic force coefficients required by AERODYN to determine the aerodynamic loads, the mode-shapes and the radial distribution of the structural properties of the blades. The blade mode-shapes are determined with BMODES [30], a finite element code for calculating the mode-shapes of beams. For HAWT blades, the input of BMODES includes the radial profiles of the distributed structural and geometric properties of the blades and the rotor speed. The radial profile of blade structural properties used by FAST is determined with CO-BLADE [31], a structural analysis code custom-tailored for wind turbine blades. The input of CO-BLADE includes the detailed definition of the blade outer shape and internal structure. The latter includes the number and the orientation of the plies making up the laminates of spar caps, spar webs and skin. CO-BLADE also determines the 3D stress field in the blades using the aerodynamic loads of FAST/AERODYN, and the loads associated with the weight and the centrifugal forces of the blades. These stresses are required for sizing all structural components of the blades. The aero-servo-elastic and stress analysis framework described herein is that used for the RMDO of the 5 MW HAWT discussed in section 4.

3. UNCERTAINTY PROPAGATION AND HAWT RMDO

In HAWT RMDO, part of the design variables (e.g. rotor geometry characteristics) and/or design parameters (e.g. site- and time-dependent wind characteristics) are stochastic. Thus the turbine performance is no longer defined by deterministic but rather by probabilistic metric estimates. A numerical method for propagating the uncertainty affecting the input data is thus required. The two essential prerequisites of uncertainty propagation methods for RMDO are high execution speed and accuracy. These two requirements are conflicting, and case-dependent choices have to be made. When the underlying MDA systems feature low-levels of nonlinearity, first or second order moment methods based on truncated Taylor series [9] yield sufficiently accurate estimates of the statistical moments of the output of interest at low computational costs. For MDA systems featuring strong nonlinearities, conversely, computationally expensive Monte Carlo methods are often the only route to accurate estimates of the output functionals. The univariate reduced quadrature (URQ) method [9] yields an acceptable compromise between cost and accuracy.

The level and type of nonlinearity of the MDA system may be such that mean and standard deviation of the probability distribution function (PDF) of the output are insufficient to characterize the output PDF. This is illustrated in Fig. 2, taken from [11]. The two AEP PDFs of a small HAWT rotor refer to feasible turbines. However, one rotor has a nearly normal AEP PDF (left), whereas the other has a strongly skewed AEP PDF (right). In this circumstance, knowledge of the mean and standard deviation alone may lead to incorrect design choices, and more complex representations of the output PDF in the RMDO context should be used.

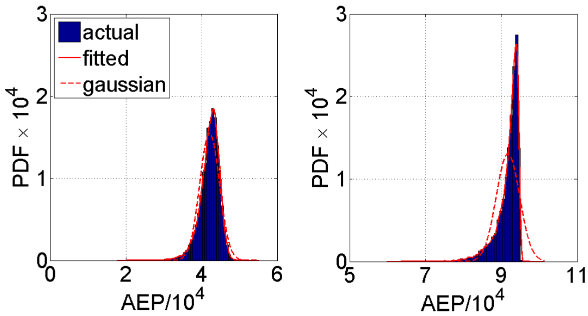

Figure 2. Encountered AEP [kWh] PDFs. Left: quasi-normal output. Right: non-normal output.

The most widely used objective function in HAWT and HAWT rotor MDO is the levelized cost of energy (LCOE) [16, 5, 13]. This variable is the ratio of the sum of all fixed (e.g. turbine and installation) and variable (e.g. operation and maintenance and land lease) costs, and the amount of energy generated over the turbine lifetime. All costs appearing in the definition are net present values. An interesting alternative to optimizing only LCOE is to optimize concurrently both the cost of energy and the annual energy production per unit area [14]. This formulation is particularly interesting when performing HAWT design optimization in the context of wind farm planning.

Structural, aeroelastic and aeroacoustic constraints are used in HAWT rotor design. Wind turbines must meet a large number of requirements for certification, which are coded by the International Electrotechnical Commission (IEC). Many recent HAWT rotor MDO studies derive their constraints from the IEC standards. Examples of structural and aeroelastic contraints include: *a*) maximum stress should not exceed material-dependent limits when the rotor is exposed to strongest foreseen wind in 20 or 50 years (depending on turbine specifications), *b*) maximum blade tip deflection should result in reduction of the blade tip/tower clearance not larger than specified values to avoid tower/blade interference, *c*) all components should achieve the target life of about 20 years despite all fatigue-inducing loads such as wind turbulence and blade weight. Aeroacoustic constraints often result in an upper limit for the rotor speed and some geometry constraints on the outer blade geometry.

Both gradient-based [16, 5, 19] and evolution-based [14, 18] optimizers are used for HAWT MDO. Gradient-based methods are faster but they have more limited capabilities of exploring the feasible design space. Evolution-based algorithms, conversely, require many more evaluations of the objective functions, but they can determine global optima. Moreover, they can also handle discontinuos functions.

Moving from MDO to RMDO, each objective function is estimated probabilistically. One simple approach is to replace the deterministic value of the output with its mean and standard deviation. Then one has to optimize the mean (minimize LCOE, maximize AEP), and minimize the standard deviation. Possible approaches to solving the probabilistic problem include *a*) solving a two-objective optimization, *b*) solving a one-objective optimization where a weighted sum of mean and standard deviation is optimized and *c*) solving a one-objective optimization where the mean is optimized and the standard deviation is a minimum inequality constraint. Using evolution-based optimizers in HAWT RMDO can yield a large computational burden because each probabilistic evaluation of a nominal design can require several deterministic evaluations and a very large number of nominal designs is scrutinized. Making use of sufficient computational resources and using uncertainty propagation methods requiring a small number of deterministic analyses for each probabilistic estimate, however, make the use of evolution-based optimizers viable also for HAWT rotor RMDO [11].

4. SAMPLE APPLICATIONS

4.1. AEP optimization of small HAWT rotor

The objective of this prototype HAWT rotor robust design optimization was to optimize the AEP of a 3-blade 12.6 meter-diameter speed-regulated rotor from cut-in to rated wind speed. The yearly frequency distribution of the freestream wind velocity U is taken to be a Weibull PDF with scale parameter of 7 m/s and shape parameter of 2, resulting in an average speed of 6.2 m/s. The blades feature the NACA4413 airfoil along their entire length. The effects of manufacturing and assembly errors are included in the analysis by assuming normally distributed geometric uncertainty affecting the radial profiles of chord and twist. The objectives of the rotor RMDO are to maximize the mean of AEP and minimize its standard deviation. The blades' nominal geometry is defined by 13 geometric design variables, and 7 control variables correspond to the rotor speeds for the considered wind speeds $U_i = (5 + i)\ m/s,\ i = 1, 7$. A structural constraint on the maximum bending moment (BM) and an aeroacoustic constraint limiting the maximum rotor speed are enforced, and XFOIL is used to determine required airfoil data for WINSTRIP, an in-house BEM code. The single-objective RMDO problem is formulated as a 2-objective deterministic problem requiring maximization of mean AEP and minimization of its standard deviation. URQ is used to propagate uncertainty, and the 2-objective optimization is solved with a 2-stage multi-objective evolution-based optimization strategy: a multi-objective Parzen-based estimation of distribution (MOPED) algorithm yields an initial estimate of the optimum solution, or the Pareto front if multiple optima exist, and an inflationary differential evolution algorithm refines the MOPED estimate [11].

To highlight the improvements achievable by using RMDO, the robust design is compared to the solution of the corresponding deterministic design optimization, which ignores uncertainty. The deterministically optimum rotor has nominal AEP of $96,20\ kWh$, AEP expectation $\mu_{AEP} = 89,97\ kWh$. and AEP standard deviation $\sigma_{AEP} = 4,99\ kWh$. The probabilistically optimum rotor has nominal AEP of $95,00\ kWh$, $\mu_{AEP} = 91,62\ kWh$ and $\sigma_{AEP} = 2,78\ kWh$. Thus, σ_{AEP} of the robust design is more than 44 % lower than that of the deterministic design. For both rotors, the left subplot of Fig. 3 compares the nominal and mean estimates of the amount of AEP accounted for by each wind speed U. Both mean curves also report error bars of size $\pm\sigma_{AEP}$. The deterministic optimum has better nominal AEP curve, but worse mean AEP curve than the robust optimum. More importantly, the σ_{AEP} values of the deterministically optimal rotor are significantly higher than those of the probabilistically optimal rotor. The right subplot of Fig. 3 refers to the root bending moment of the two rotors, and highlights that the root BM standard deviation of the probabilistic optimum is lower than that of the deterministic optimum for all considered speeds.

As reported in [11], the power curves of the two optima do not differ significantly. This is because the robust optimum has lower rotational speeds but higher loading at nearly all radii and wind speeds, due to its lower blade twist and its lower rotational speed. The power loss due to lower rotational speeds compensates the power enhancement due to higher loading. Thus, the AoA α over most of the blade is higher for the probabilistic than for the deterministic design. More specifically, for the probabilistic design, AoA is in a region where the slope of the lift-AoA curve is shallower than for the deterministic design. Consequently, variations of AoA due to pitch errors results in smaller variations of the lift coefficient, the power and the generated energy of the ro-

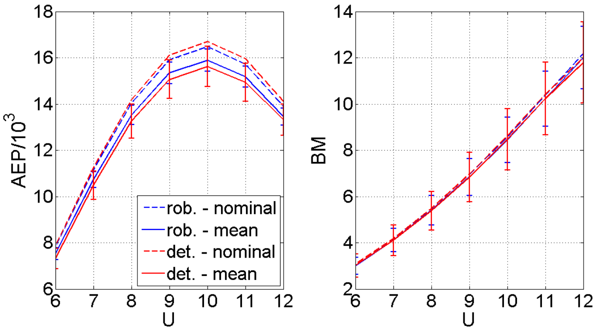

Figure 3. Performance of deterministic and robust small rotor designs. Left: proportion of AEP at each wind speed U $[m/s]$. Right: blade root bending moment $[kNm]$ against U.

bust design. This mechanism is highlighted by the mean and standard deviation of AoA and lift coefficient C_L of the two rotors reported in Fig. 4.

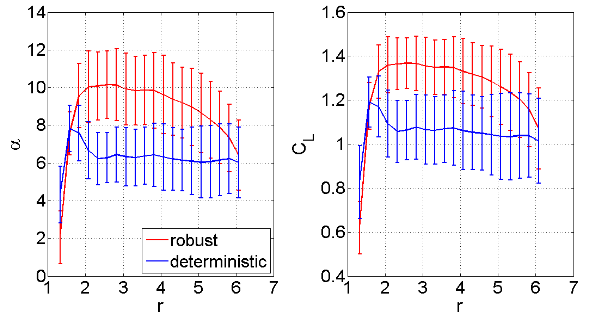

Figure 4. Performance of deterministic and robust small rotor designs at $U = 12$ m/s. Left: AoA α $[deg]$ against radius r $[m]$. Right: C_L against r.

4.2. COE optimization of 5 MW HAWT rotor

This study aimed at probabilistically minimizing the LCOE of the NREL 3-blade 5 MW 126 meter-diameter speed- and pitch-controlled turbine [6]. The uncertainty is due to the variability of the mean wind speed, arising either because the turbine is installed at sites with wind characteristics different from the design specification, or because of the long-term wind variability at a given site due to environmental factors such as climate change. The yearly frequency distribution of the wind velocity U at the hub height is taken to be a Weibull PDF with shape parameter of 2 and average speed varying between 7 and 13 m/s according to the uniform distribution. Composite Bezier curves are used to parametrize the airfoil geometry, and cubic splines are used to parametrize the radial distributions of blade pitch and chord. The considered 48 design variables are: 46 geometric parameters defining the blade outer shape, the tip speed ratio in the region between cut-in and rated wind speeds, and one scaling factor defining the relative thickness of all parts of the blade internal structure with respect to a reference structural design.

Structural constraints on ultimate loads, fatigue damage, buckling and maximum tip deflections are enforced. The aero-servo-elastic and stress analyses are performed using FAST, BMODES, and CO-BLADE, and the aerodynamic loads are determined with AERODYN using the force coefficients of XFOIL and AERODAS. The RMDO problem is solved by minimizing a weighted sum of mean and standard deviation of LCOE using the pattern search optimizer of MATLAB [13], a non-evolutionary deritative-free global search method. For each nominal design, mean and standard deviation of LCOE are computed using the analytical definitions of these two variables, and calculating the required integrals of LCOE over the given mean wind speed range.

The mean LCOE of the robust optimum is found to be about 6 % lower than that of the baseline turbine, and the LCOE standard deviation of the robust optimum is about 15 % lower than of the baseline. These improvements are achieved mostly through mass reduction and power curve enhancements of the robust optimum. The outer blade shape of the robust and baseline turbines differs significantly, as partly highlighted by the three subplots of Fig. 5, which compare the root, midspan and tip airfoils of the two turbines.

The left and right subplots of Fig. 6 report respectively the rotor speed and the electric power of the two turbines against the wind speed. One notes that the power extracted by the robust HAWT is higher than that of the reference turbine from cut-in to rated wind speed. It is also observed that the rotational speed of the robust turbine in this wind speed range is higher than for the reference turbine.

5. CONCLUSIONS

Numerous and significant sources of uncertainty in wind energy engineering demand the use of probabilistic design approaches, since a probabilistic definition of the producible wind energy is likely to better inform decision-making at scientific and governmental levels. This paper presented a brief description of the technologies used in HAWT rotor RMDO and the work performed by the author and his group in this area.

Important environmental uncertainty sources include the time- and space-variability of wind characteristics due to the vertical shear and the thermodynamic state of the atmospheric boundary layer (ABL) [32]. As an example, it was recently shown that omitting the effects of humidity fluxes in marine ABL thermodynamic state analyses can result in overpredicting by up to 4 % the mean wind speed at 150 meters, the hub height of several new large off-shore HAWTs [33]. The extent of these phenomena is expected to be strongly site-dependent, and such uncertainty ought to be accounted for in HAWT design.

Uncertain aerodynamic factors include the prediction of laminar-to-turbulent transition, near and

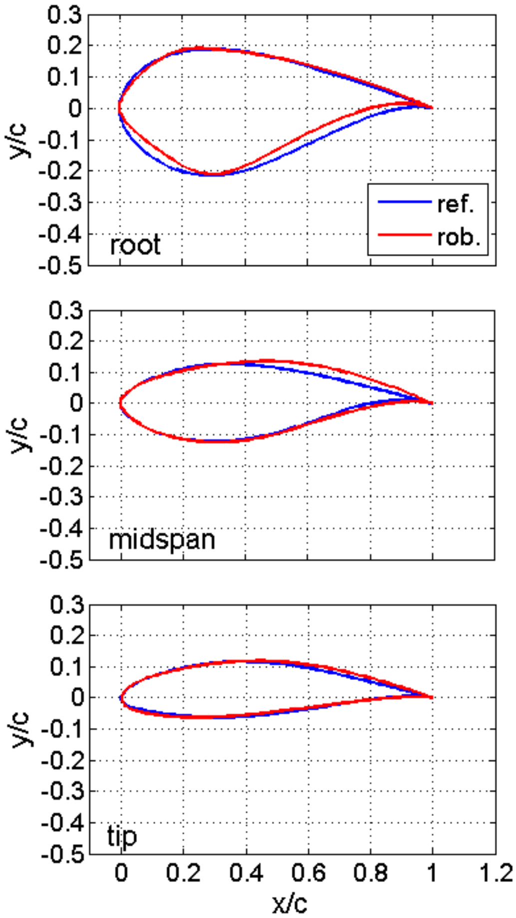

Figure 5. Comparison of airfoils of robust and conventional designs of 5 MW HAWT rotor.

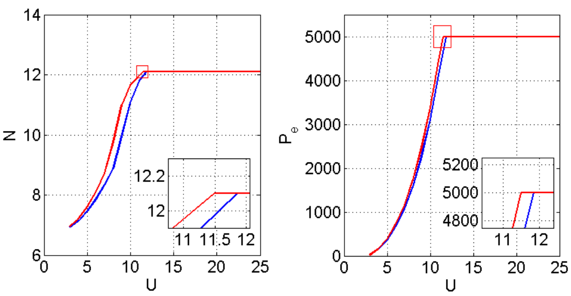

Figure 6. Regulation and power curve of robust and conventional designs of 5 MW HAWT rotor. Left: rotor speed N [rpm] against U. Right: electrical power P_e [kW] against U.

post-stall characteristics. Contributing factors to this uncertainty include the blade roughness levels varying during operation due to contamination, accretions and wear, and the turbulence intensity, but also the use of rapid but insufficiently accurate computational aerodynamics tools in HAWT design. Advances in this area, aimed at *a*) improving the prediction of the impact of transition and 3D flow effects on blade loads, and *b*) massively reducing the cost of the computational technologies needed to accomplish this are required.

Additional uncertainty to be considered in HAWT RMDO is that caused by input perturbations of the control system, such as inaccurate wind speed measurements, as well as insufficient accuracy of the HAWT models used to design the controller.

REFERENCES

[1] Bak, C., 2013, "Aerodynamic design of wind turbine rotors", W. Gentzsch, and U. Harms (eds.), *Advances in wind turbine blade design and materials*, Vol. 47 of *Energy*, Woodhead Publishing, Cambridge, UK, pp. 59–108.

[2] Jamieson, P., 2011, *Innovation in wind turbine design*, Wiley, Philadelphia, USA.

[3] Fuglsang, P., Bak, C., Schepers, J., Bulder, B., Cockerill, T., Claiden, P., Olesen, A., and van Rossen, R., 2002, "Site-specific design optimization of wind turbines", *Wind Energy*, Vol. 5 (4), pp. 261–279.

[4] Maki, K., Sbragio, R., and Vlahopoulos, N., 2012, "System design of a wind turbine using a multi-level optimization approach", *Renewable Energy*, Vol. 43, pp. 101–110.

[5] Ashuri, T., Zaaijer, M., Martins, J., van Bussel, G., and van Kuik, G., 2014, "Multidisciplinary design optimization of offshore wind turbines for minimum levelized cost of energy", *Renewable Energy*, Vol. 68, pp. 893–905.

[6] Jonkman, J., Butterfield, S., Musial, W., and Scott, G., 2009, "Definition of a 5-MW Reference Wind Turbine for Offshore System Development", *Tech. Rep. NREL/TP-500-38060*, NREL, Golden, CO, USA.

[7] Beyer, H.-G., and Sendhoff, B., 2007, "Robust optimization - A comprehensive survey", *Computer methods in applied mechanics and engineering*, Vol. 196, pp. 3190–3218.

[8] Lee, S., and Chen, W., 2009, "A comparative study of uncertainty propagation methods for black-box-type problems", *Structural and multidisciplinary optimization*, Vol. 37, pp. 239–253.

[9] Padulo, M., Campobasso, M., and Guenov, M., 2011, "A Novel Uncertainty Propagation Method for Robust Aerodynamic Design", *AIAA Journal*, Vol. 49 (3), pp. 530–543.

[10] Petrone, G., de Nicola, C., Quagliarella, D., Witteveen, J., and Iaccarino, G., 2011, "Wind turbine optimization under uncertainty with high performance computing", AIAA paper 2011-3806, 29th AIAA Applied Aerodynamics Conference, Honolulu, Hawaii.

[11] Campobasso, M., Minisci, E., and Caboni, M., 2014, "Aerodynamic design optimization of wind turbine rotors under geometric uncertainty", *Wind Energy*, dOI: 10.1002/we.1820.

[12] Caboni, M., Minisci, E., and Campobasso, M., 2014, "Robust aerodynamic design optimization of horizontal axis wind turbine rotors", D. Greiner, B. Galván, J. Periaux, N. Gauger, K. Giannakoglou, and G. Winter (eds.), *Advances in Evolutionary and Deterministic Methods for Design, Optimization and Control in Engineering and Sciences*, Vol. 36 of *Computational Methods in Applied Sciences*, Springer Verlag, ISBN 978-3-319-11540-5.

[13] Caboni, M., Campobasso, M., and Minisci, E., 2015, "Wind Turbine Design Optimization under Environmental Uncertainty", ASME paper GT2015-42674.

[14] Benini, E., and Toffolo, A., 2002, "Optimal Design of Horizontal-Axis Wind Turbines using Blade-Element Theory and Evolutionary Computation", *Journal of Solar Energy Engineering*, Vol. 124, pp. 357–363.

[15] Xudong, W., Shen, W., Zhu, W., Sørensen, J., and Jin, C., 2009, "Shape Optimization of Wind Turbine Blades", *Wind Energy*, Vol. 12 (8), pp. 781–803.

[16] Fuglsang, P., and Madsen, H., 1999, "Optimization method for wind turbine rotors", *Journal of Wind Engineering and Industrial Aerodynamics*, Vol. 80 (1), pp. 191–206.

[17] Kwon, H., You, J., and Kwon, O., 2012, "Enhancement of wind turbine aerodynamic performance by a numerical optimization technique", *Journal of Mechanical Science and Technology*, Vol. 26 (2), pp. 455–462.

[18] Vesel, R., and McNamara, J., 2014, "Performance enhancement and load reduction of a 5 MW wind turbine blade", *Renewable Energy*, Vol. 66, pp. 391–401.

[19] Bottasso, C. L., Croce, A., Sartori, L., and Grasso, F., 2014, "Free-form design of rotor blades", *Journal of Physics: Conference Series*, Vol. 524 (1).

[20] Jureczko, M., Pawlak, M., and Mezik, A., 2005, "Optimisation of wind turbine blades", *Journal of Materials Processing Technology*, Vol. 167, pp. 463–471.

[21] Jain, P., 2011, *Wind Energy Engineering*, McGraw-Hill, New York, NY, USA.

[22] Drela, M., 1989, "XFOIL: An Analysis and Design System for Low Reynolds Number Airfoils", *Low Reynolds Number Aerodynamics*, Springer Verlag, Vol. 54 of *Lecture Notes in Engineering*.

[23] Timmer, W., and van Rooij, R., 2003, "Summary of the Delft University Wind Turbine Dedicated Airfoils", *Journal of Solar Energy Engineering*, Vol. 125, pp. 488–496.

[24] Sørensen, N., 2009, "CFD Modelling of Laminar-Turbulent Transition for Airfoils and Rotors Using the $\gamma - \tilde{Re}_\theta$ Model", *Wind Energy*, Vol. 12, pp. 715–733.

[25] Aranake, A., Lakshminarayan, V., and Duraysami, K., 2015, "Computational analysis of shrouded wind turbine configurations using a 3-dimensional RANS solver", *Renewable Energy*, Vol. 75, pp. 818–832.

[26] Rinehart, T., Medida, S., and Thomas, S., 2014, "Computation of Two-dimensional Wind Turbine Airfoil Characteristics Using Advanced Turbulence and Transition Modeling Methods and a GPU-Accelerated Navier-Stokes Solver", AIAA paper 2014-1216, 32nd ASME Wind Energy Symposium, National Harbor, Maryland.

[27] Lindenburg, C., 2004, "Modelling of rotational augmentation based on engineering considerations and measurements", European Wind Energy Conference, London, UK.

[28] Spera, D., 2008, "Models of Lift and Drag Coefficients of Stalled and Unstalled Airfoils in Wind Turbines and Wind Tunnels", *Tech. Rep. NASA CR-2008-215434*, NASA, Cleveland, OH, USA.

[29] Buhl, M., 2005, "A New Empirical Relationship between Thrust Coefficient and Induction Factor for the Turbulent Windmill State", *Tech. Rep. NREL/TP-500-36834*, NREL, Golden, CO, USA.

[30] NREL, "National Wind Technology Center information portal: software.", Https://nwtc.nrel.gov/Software, accessed on 18 May 2015.

[31] Sale, D., "Co-Blade: Software for Analysis and Design of Composite Blades.", Https://code.google.com/p/co-blade/, accessed on 18 May 2015.

[32] Emeis, S., 2013, W. Gentzsch, and U. Harms (eds.), *Wind Energy Meteorology*, Green Energy and Technology, Springer Verlag, Berlin, Germany.

[33] Barthelmie, R., Sempreviva, A., and Pryor, S., 2010, "The influence of humidity fluxes on offshore wind speed profiles", *Annales Geophysicae*, Vol. 28, pp. 1043–1052.

Conference on Modelling Fluid Flow (CMFF'15)
The 16th International Conference on Fluid Flow Technologies
Budapest, Hungary, September 1-4, 2015

SMOOTHED PARTICLE HYDRODYNAMICS: TOWARDS ACCURATE LAGRANGIAN FLOW PREDICTION

Damien VIOLEAU[1]

[1]EDF R&D / LNHE and Université Paris-Est / LHSV. 6 quai Watier, 78400 Chatou, France. Tel.: +33 1 3087 7831, Fax: +33 1 3087 8086, E-mail: damien.violeau@edf.fr

ABSTRACT

We briefly describe the SPH (Smoothed Particle Hydrodynamics) Lagrangian numerical method for fluid modelling, using recent improvements proposed for boundary conditions. We explain the differences between the WCSPH (Weakly Compressible SPH) and ISPH (Incompressible SPH) variants. Validations prove that SPH performs as well as Finite Volumes in simple test cases. Applications are shortly presented in real hydraulic waterworks, like dam spillways, fish passes, etc.

Keywords: SPH, Lagrangian methods, particles, CFD, waterworks

NOMENCLATURE

D_a	$[\mathrm{m}^{-1}]$	discrete divergence operator
$\mathbf{G}_a$	$[\mathrm{m}^{-1}]$	discrete gradient operator
L_a	$[\mathrm{m}^{-2}]$	discrete Laplacian operator
V	$[\mathrm{m}^{d}]$	volume
a, b	[-]	particle labels
c_0	$[\mathrm{ms}^{-1}]$	speed of sound
$\mathbf{g}$	$[\mathrm{ms}^{-2}]$	gravity
h	[m]	smoothing length
m	[kg]	mass
$\mathbf{n}$	[-]	boundary unit normal vector
p	[Pa]	pressure
$\mathbf{r}$	[m]	position vector
$\mathbf{r}_{ab}$	[m]	vector linking two particles
r_{ab}	[m]	particle distance
$\mathbf{v}$	$[\mathrm{ms}^{-1}]$	velocity vector
w	$[\mathrm{m}^{-d}]$	kernel
Δt	[s]	time step
γ	[-]	boundary renormalization integral
μ	[Pa.s]	dynamic molecular viscosity
ρ	$[\mathrm{kg.m}^{-n}]$	density
ρ_0	$[\mathrm{kg.m}^{-n}]$	reference density

1. INTRODUCTION

SPH (Smoothed Particle Hydrodynamics) is a Lagrangian technique initially proposed in 1977 for astrophysical computations by Lucy [1] and Gingold and Monaghan [2]. In the early 90's, Monaghan [3] was the first to apply it to free-surface, almost incompressible flows, and since then it has increasingly been used with growing success in this field. Here we summarize the main two SPH approaches (hereafter referred to as WCSPH and ISPH, respectively) and present a few validation cases where it is proved to perform well when compared to recognized mesh-based techniques. We finally present a few real-life applications for hydraulics, showing that SPH has reached a certain maturity. SPH is now a classical tool in the community of computational fluid modellers, and should continue its growth with industrial applications.

2. SPH THEORY

2.1. SPH operators

The SPH method is based on discrete interpolations of the required fields and differential operators. The fluid domain is constituted of particles a, b, etc. making a discrete set F, with positions $\mathbf{r}_a$, $\mathbf{r}_b$, etc. (see Fig. 1) and moving with velocities $\mathbf{v}_a = \mathrm{d}\mathbf{r}_a/\mathrm{d}t$. The particle interactions are modelled through a kernel function denoted w and being a sole function of the inter-particle distance, with compact support of size proportional to the so-called smoothing length h, which is a measure of particle interaction distance (see [4, 5] for more details about standard SPH).

In the present SPH model, the walls are discretised using a skin mesh made of a set S of boundary elements s (*i.e.* segments in 2-D, triangles in 3-D). Vertex particles denoted by v are placed at the mesh vertices; they are truncated particles considered as being part of the set F (see Fig. 1).

The following discrete forms of the gradient **G**, divergence D and Laplacian **L** operators are then used [6, 7]:

$$
\begin{aligned}
(\nabla A)_a &\approx \mathbf{G}_a\{A_b\} \equiv \frac{\rho_a}{\gamma_a}\sum_{b\in F} m_b\left(\frac{A_a}{\rho_a^2}+\frac{A_b}{\rho_b^2}\right)\nabla w_{ab} \\
&\quad -\frac{\rho_a}{\gamma_a}\sum_{s\in S}\rho_s\left(\frac{A_a}{\rho_a^2}+\frac{A_s}{\rho_s^2}\right)\nabla\gamma_{as} \\
(\nabla\cdot A)_a &\approx D_a\{\mathbf{A}_b\} \equiv -\frac{1}{\gamma_a\rho_a}\sum_{b\in F} m_b\mathbf{A}_{ab}\cdot\nabla w_{ab} \\
&\quad +\frac{1}{\gamma_a\rho_a}\sum_{s\in S}\rho_s\mathbf{A}_{as}\cdot\nabla\gamma_{as} \\
(\nabla^2\mathbf{A})_a &\approx \mathbf{L}_a\{\mathbf{A}_b\} \\
&\equiv \frac{2}{\gamma_a}\sum_{b\in F} V_b\frac{\mathbf{A}_{ab}}{r_{ab}^2}\mathbf{r}_{ab}\cdot\nabla w_{ab} \\
&\quad -\frac{1}{\gamma_a}\sum_{s\in S}\left[(\nabla\mathbf{A})_a+(\nabla\mathbf{A})_s\right]\cdot\nabla\gamma_{as}
\end{aligned}
\tag{1}
$$

where A (resp. $\mathbf{A}$) is an arbitrary scalar (resp. vector) field, m_a denotes the particle masses and V_a their volumes. In the above equations, the subscripts a and b denote all quantities relative to a given particle, while we define $A_{ab} = A_a - A_b$, ∇w_{ab} being the gradient of $w(r_{ab})$ with respect to $\mathbf{r}_a$, and $r_{ab} = |\mathbf{r}_{ab}|$. Moreover, γ_a is the integral of the kernel:

$$\gamma_a = \int_\Omega w(|\mathbf{r}_a - \mathbf{r}'|)d^n\mathbf{r}' \tag{2}$$

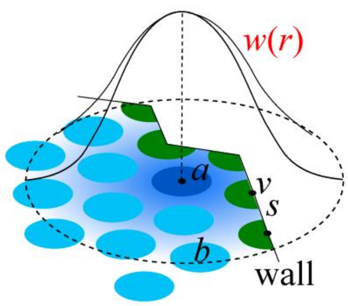

Figure 1. The discretization used in the present SPH method is based on fluid particles (a or b), vertex particles (v) and boundary elements (s). The truncation of the kernel is considered through the integral γ_a (shaded area).

with n the space dimension. This integral extends over the entire physical domain. Due to the compactness of the kernel support, however, it is restricted to the shaded area on Fig. 1. In the above equations, the subscripts s refer to boundary elements. $\nabla\gamma_{as}$ is the contribution of the boundary element s to the boundary terms, defined by a boundary integral over s:

$$\nabla\gamma_{as} = \int_s w(|\mathbf{r}_a - \mathbf{r}'|)\mathbf{n}_s d^{n-1}\mathbf{r}' \tag{3}$$

where $\mathbf{n}_s$ is the unit inward normal vector of the boundary element. Both γ_a and $\nabla\gamma_{as}$ can be computed analytically from the position of particle a and the position, size and orientation of the boundary element s [8].

2.2. WCSPH

The so-called Weakly Compressible SPH (WCSPH) method consist of using the above tools to solve the Lagrangian Navier–Stokes equations with no compressible terms in the momentum equation, the pressure being computed from a state equation [3]:

$$
\begin{aligned}
\dot{\mathbf{v}}_a &= -\frac{1}{\rho_a}\mathbf{G}_a\{p_b\} + \frac{\mu}{\rho_a}\mathbf{L}_a\{\mathbf{v}_b\} + \mathbf{g} \\
\dot{\mathbf{r}}_a &= \mathbf{v}_a \\
\dot{\rho}_a &= -\rho_a D\{\mathbf{v}_b\} + KL_a\{\rho_b\} \\
p_a &= \frac{\rho_0 c_0^2}{\xi}\left[\left(\frac{\rho}{\rho_0}\right)^{\xi} - 1\right]
\end{aligned}
\tag{4}
$$

where μ and ρ_0 are the fluid dynamic viscosity and reference density, while c_0 is the numerical speed of sound. The second term in the continuity equation (3rd line of eqn. (4)), where K is a diffusion coefficient, is meant to act as a density filter so as to avoid checker-boarding effects as in mesh methods (see *e.g.* [9]). When particles try to approach to each other, the continuity equation slightly increases the density, then the state equation leads to a higher pressure increase, which acts as a repulsive force in the momentum equation, preventing particle collapse. The particle interspacing then remains approximately constant, so that the fluid is only weakly compressible. This technique is used as a crude approximation of incompressible flows. The speed of sound is chosen as ten times the fluid velocity, so that the density fluctuations are order 1%.

Eqn. (4) is solved with a time integrator with time step Δt. Symplectic schemes are recommended, such as the second-order leapfrog (Monaghan, 2005). The time step is constrained for numerical stability; details about the stability criteria can be found in [10, 11].

2.3. ISPH and extensions

An alternative approach to WCSPH was originally proposed by Cummins and Rudman [12], today referred to as ISPH (Incompressible SPH). This method consists of computing the pressure through a Poisson equation, the velocity being updated with a predictor-corrector scheme, following Chorin (1968)'s method:

$$\frac{\mathbf{v}_a^* - \mathbf{v}_a^n}{\Delta t} = \frac{\mu}{\rho} \mathbf{L}_a \left\{ \mathbf{v}_b^n \right\} + \mathbf{g}$$

$$\mathbf{L}_a \left\{ p_b^{n+1} \right\} = \frac{\rho}{\Delta t} D_a \left\{ \mathbf{v}_b^* \right\} \qquad (5)$$

$$\frac{\mathbf{v}_a^{n+1} - \mathbf{v}_a^*}{\Delta t} = -\frac{1}{\rho} \mathbf{G}_a \left\{ p_b^{n+1} \right\}$$

where the superscripts refer to the time iterations, $\mathbf{v}_a^*$ being the predicted velocity. The Poisson equation (2nd line of eqn. (5)) is a linear system with unknowns p_b^{n+1}. It can be solved using any traditional numerical technique. Details about the boundary conditions can be found in [8]. Contrary to WCSPH, the ISPH technique provides an almost divergence-free velocity field, *i.e.* a truly incompressible flow, and then provides better pressure predictions [13, 14].

Additional features can easily be added to WCSPH or ISPH, such as turbulence (*e.g.* *k*–ε model, see [6, 8, 15, 16] or LES [17], or even more complex models [18]), temperature advection-diffusion with buoyancy effects and turbulence coupling [19], surface tension [20], etc.

Despite these relatively recent advances, key issues still remain in SPH, such as numerical stability, convergence, adaptive spatial refinement, and open boundary conditions. On the latter topic, one can refer to [21, 22].

Since 2008, the above developments are usually performed in a GPU framework (graphic cards) using the CUDA language. This method is particularly relevant to SPH, as already pointed out by Hérault *et al.* [23]. The reason is that in SPH, a given particle is connected to about 250 neighbouring particles in 3-D, which makes it useful to take advantage of the internal parallelism of graphic cards. The speed-up is typically around 50 in comparison with single CPU programming for SPH.

Note that many variations of the presently proposed SPH schemes exist in the literature. Reviews can be found in Monaghan [4] and Violeau and Rogers [24].

3. VALIDATION

3.1 Lid-driven cavity

The lid-driven cavity test-case is classical in fluid dynamics and is much used to validate numerical models. It consists of a square closed cavity of size *L* whose lid slides laterally at a constant velocity *V*, driving the fluid under the effect of the viscosity. For Reynolds numbers lower than about 7500, it reaches a steady-state after some time. Then, it is possible to compare the results between different computational fluid dynamics codes. In particular, the SPH results are compared to the ones obtained by Ghia *et al.* [25], and to the result obtained with with Code_Saturne [26], a widely validated code based on Finite Volumes (FV). Our SPH simulations were done with 500×500 particles and the FV simulations with 512×512 cells, for a Reynolds number of 1000. Fig. 2 shows that SPH performs well for velocity and pressure prediction in this standard case.

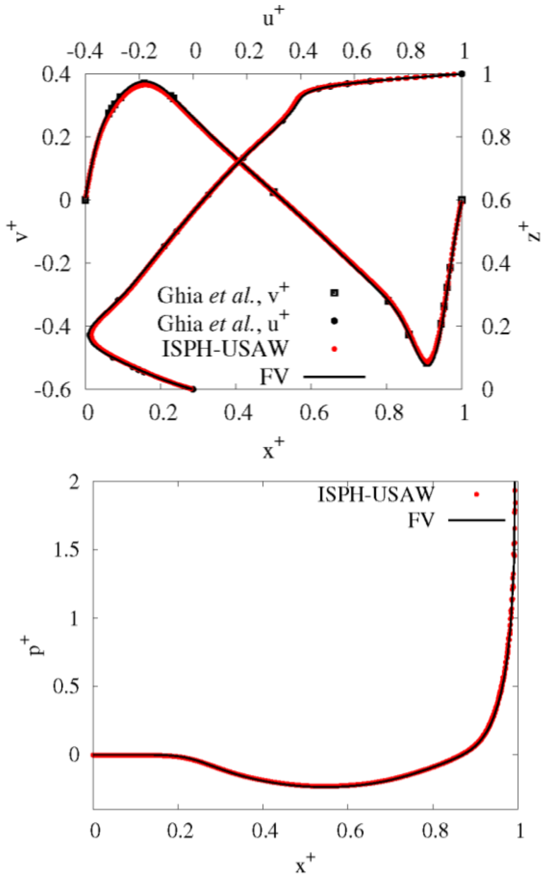

Figure 2. Lid-driven cavity: Incompressible SPH (ISPH) results compared to mesh methods, in particular FV. Top: horizontal and vertical velocity profiles; bottom: pressure profile on a diagonal section.

3.2 Heated lid-driven cavity

A differentially heated lid-driven cavity is tested by using the same geometry and setting different temperatures to the upper and lower walls [19]. Fig. 3 shows the shape of the velocity and temperature fields after convergence for a Rayleigh number of 10^5. One can see that SPH (here, ISPH) predicts fields in a very good agreement with FV, which is confirmed by Fig. 4, showing to temperature profiles for both methods.

Note that the model used here for wall boundary conditions was crucial in obtaining the above results, as explained by Leroy *et al.* [8, 19]. Generally speaking, WCSPH can be used for the above two applications, but with less success, as already explained. In particular, a closed cavity requires a small background pressure in the state equation, leading to additional care.

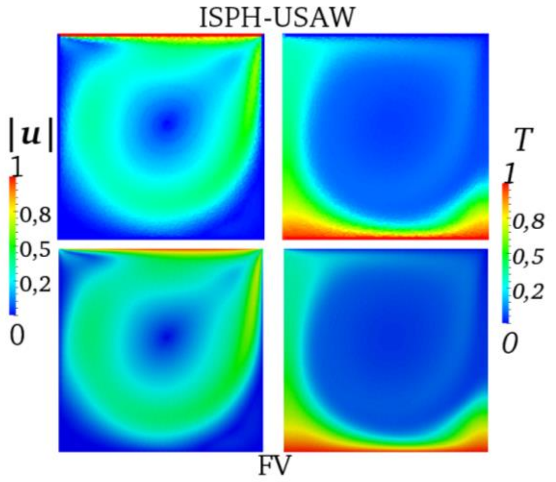

Figure 3. Heated lid-driven cavity: Incompressible SPH (ISPH, top) results compared to FV (bottom). Distributions of velocity magnitude (left) and temperature (right) after convergence.

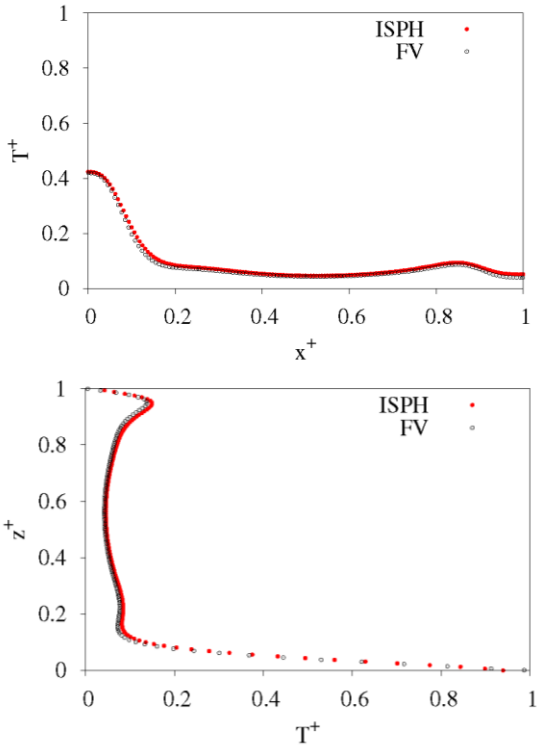

Figure 4. Heated lid-driven cavity: Incompressible SPH (ISPH) results compared to FV. Top and bottom: horizontal and vertical temperature profiles, respectively.

3.3 Turbulent channel flow

The SPH turbulent *k*–ε model is validated in [7, 8]. Fig. 5 depicts the velocity, turbulent kinetic energy and dissipation rate in a Poiseuille straight channel flow, showing that again SPH agrees with FV and fits the DNS data by Kawamura *et al.* [27] except in the viscous sub-layer (here no low-Reynolds correction was considered). In this case, WCSPH performs as well as ISPH.

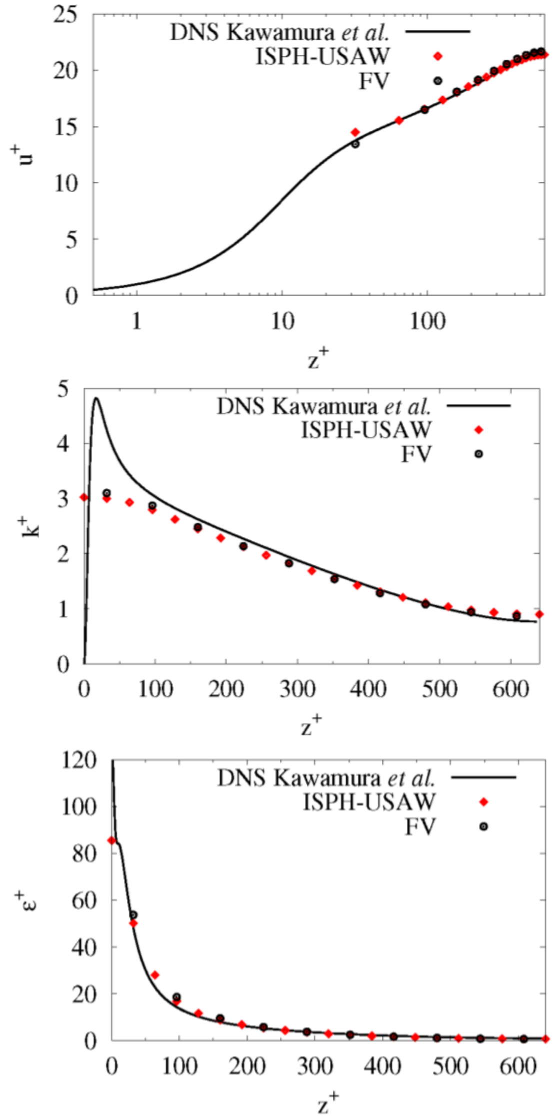

Figure 5. Turbulent Poiseuille channel flow: longitudinal Reynolds-averaged velocity, turbulent kinetic energy and dissipation rate (from top to bottom) along the channel section.

4. APPLICATIONS

4.1 Fish pass

With the above tools, SPH can be applied to real-world flows. As an example, Violeau *et al.* [28] show the flow in the vicinity of an oil spill containment boom.

The validations presented in the previous section proved that the quality of the predicted fields is comparable to standard mesh-based methods, with the advantages of SPH when modelling rapidly distorted free-surface flows. Besides, the GPU technique allows handling 3-D simulations with several million particles in a few hours on a single graphic card.

For the applications presented below, we use the GPUSPH open-source software (refer to http://www.gpusph.org/). In order to set the geometry of our computations, we built an appropriate pre-processing tool.

We first consider a pool fish pass with a vertical slot, using the geometry of the experimental installation used at the University of Poitiers [29], with length L = 0.75m and width B = 0.675m. The width of the slot is b = 0.075 m and the bed slope is 10%. We simulate only one pool, the flow being periodic. Fig. 6 shows a snapshot of the results. Comparisons against measurements are under progress.

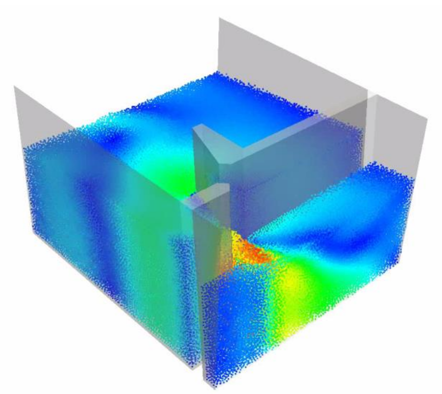

Figure 6. A vertical slot fish pass simulated with SPH.

4.2 Dam spillways

We consider the dam spillway of Goulours, on the Ariège river (France). A physical model has been built at EDF R&D with a scale factor equal to 20. Although this dam has two types of spillways, a ski-jump and a PK-weir (Piano-Key weir), only the ski-jump spillway is considered here for the present numerical study [30]. Fig. 7 shows four snapshots of the simulated flow. Validation against laboratory measurements will be done in the near future.

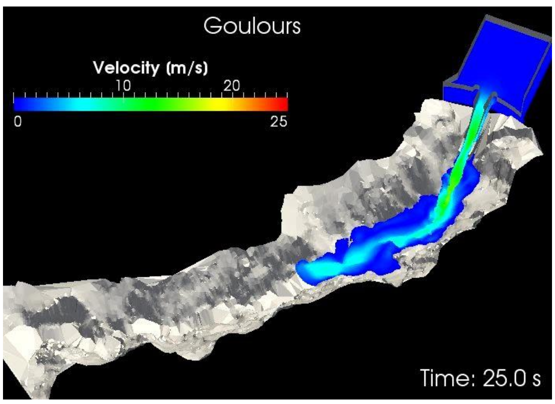

Figure 7. A dam spillway simulated with SPH (from Goulours dam, Midi-Pyrénées, France).

Finally, Fig. 8 shows a more complicated case where all the abovementioned SPH features are used: walls, inlet and outlet boundary conditions, turbulence closure, etc. It is a dam with crest weir-spillway. Comparisons with laboratory data are ongoing.

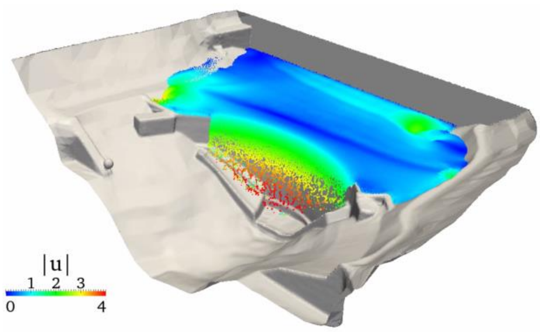

Figure 7. A crest-weir dam spillway simulated with SPH.

5. CONCLUSIONS

Thanks to numerical improvements and GPU-acceleration, the SPH method has considerably increased its ability to simulate real-life hydraulic flows. It is now more and more used for industrial design and prediction of complex waterworks. In the future, the coupling with mesh methods could further extend its field of application.

However, as mentioned in the text drawbacks subsist: there is still poor knowledge in SPH numerical stability, convergence properties and other mathematical issues. Ongoing major developments in SPH now concern variable particle size and multi-fluid flow modelling, among others. The reader may go to the SPHERIC (SPH European Research Interest Community) website to get informed about the progress in the SPH theory and applications, mainly in the field of hydraulics (https://wiki.manchester.ac.uk/spheric).

ACKNOWLEDGEMENTS

The Author acknowledges the SPH team of EDF R&D and the Saint-Venant Laboratory for Hydraulics, and particularly those who contributed to the simulations presented in this paper, *i.e*. M. Ferrand, Dr A. Leroy, Dr A. Joly. He also thanks Dr A. Mayrhofer (University of Natural Resources and Life Sciences, Vienna, Austria) and Dr A. Vorobyev (SNIIP Atom, Russia).

REFERENCES

[1] Lucy, L.B., 1977, “A numerical approach to the testing of the fission hypothesis”, *Astron. J.*, Vol. 82, pp. 1013–1024.

[2] Gingold, R.A., Monaghan, J.J., 1977, “Smoothed particle hydrodynamics: Theory and application to non-spherical stars”, *Mon. Not. R. Astron. Soc.*, Vol. 181, pp. 375–389.

[3] Monaghan, J.J., 1994, “Simulating free surface flows with SPH”, *J. Comput. Phys.*, Vol. 110, pp. 399–406.

[4] Monaghan, J.J., 2005, “Smoothed particle hydrodynamics”, *Rep. Prog. Phys.*, Vol. 68, pp. 1703–1759.

[5] Violeau, D., 2012, *Fluid Mechanics and the SPH Method. Theory and Applications*, Oxford University Press.

[6] Ferrand, M., Laurence, D., Rogers, B.D., Violeau, D., 2010, "Improved time scheme integration approach for dealing with semi-analytical wall boundary conditions in Spartacus-2D", Proc. *5th SPHERIC Int. workshop*, Manchester, UK, pp 389–393.

[7] Ferrand, M., Laurence, D., Rogers, B., Violeau, D., Kassiotis, C., 2012, "Unified semi-analytical wall boundary conditions for inviscid, laminar or turbulent flows in the meshless SPH method", *Int. J. Num. Meth. Fluids*, Vol. 71(4), pp. 446–472.

[8] Leroy, A., Violeau, D., Ferrand, M., Kassiotis, C., 2014, "Unified semi-analytical wall boundary conditions for 2-D incompressible SPH", *J. Comp. Phys*., Vol. 261, pp. 106–129.

[9] Mayrhofer, A., Rogers, B.D., Violeau, D., Ferrand, M., 2013, "Investigation of wall bounded flows using SPH and the unified semi-analytical wall boundary conditions", *Comput. Phys. Com*., Vol. 184, pp. 2515–2527.

[10] Violeau, D., Leroy, A., 2014, "On the maximum time step in weakly compressible SPH", *J. Comput. Phys*., Vol. 256, pp. 388–415.

[11] Violeau, D., Leroy, A., 2015, "Optimal time step for Incompressible SPH", *J. Comput Phys.*, Vol. 288, pp. 119–130.

[12] Cummins, S.J., Rudman, M.J., 1999, "An SPH Projection Method", *J. Comput. Phys*., Vol. 152, pp. 584–607.

[13] Lee, E.-S., Moulinec, C., Xu, R., Violeau, D., Laurence, D., Stansby, P., 2008, "Comparisons of weakly compressible and truly incompressible SPH algorithms for 2D flows", *J. Comput. Phys*., Vol. 227(18), pp. 8417–8436.

[14] Lee, E.-S., Violeau, D., Issa, R., Ploix, S., 2010, "Application of weakly compressible and truly incompressible SPH to 3-D water collapse in waterworks", *J. Hydr. Res*., Vol. 48(Extra Issue), pp. 50–60.

[15] Violeau, D., Piccon, S., Chabard, J.-P., 2002, "Two attempts of Turbulence Modelling in Smoothed Particle Hydrodynamics", *Advances in Fluid Modelling and Turbulence Measurements*, World Scientific, pp. 339–346.

[16] Violeau D., 2004, "One and two-equations turbulent closures for Smoothed Particle Hydrodynamics", Proc. *6th Int. Conf. Hydroinformatics*, Singapore, pp. 87–94.

[17] Mayrhofer, A., Laurence, D., Rogers, B.D., Violeau, D., 2015, "DNS and LES of 3-D wall-bounded turbulence using Smoothed Particle Hydrodynamics", *Comput. and Fluids*, Vol. 115, pp. 86-97.

[18] Violeau, D., Issa, R., 2006, "Numerical modelling of complex turbulent free surface flows with the SPH Lagrangian method: an overview", *Int. J. Num. Meth. Fluids*, Vol. 53(2), pp. 277–304.

[19] Leroy, A., Violeau, D., Ferrand, M., Joly, A., 2015, "Buoyancy modelling with income-pressible SPH for laminar and turbulent flows", *Int. J. Num. Meth. Fluids*, DOI: 10.1002/fld.4025.

[20] Hu, X.Y., Adams, N.A., 2007, "An incompressible multi-phase SPH method", *J. Comput. Phys*., Vol. 227, pp. 264–278.

[21] Kassiotis, C., Ferrand, M., Violeau, D., 2013, "Semi-analytical conditions for open boundaries in SPH", Proc. *8th SPHERIC Int. Workshop*, Trondheim, Norway, pp. 28–35.

[22] Leroy, A., Violeau, D., Ferrand, M., Joly, A., Fratter, L., 2015, "Open boundary conditions for ISPH with the unified semi-analytical boundary conditions", Proc. *10th SPHERIC Int. Workshop*, Parma, Italy.

[23] Hérault, A., Bilotta, G., Dalrymple, R.A., 2010, "SPH on GPU with CUDA", *J. Hydr. Res.*, Vol. 48(Extra Issue), pp. 74–79.

[24] Violeau, D., Rogers, B.D., "SPH for free-surface flows: past, present and future", submitted to *J. Hydr. Res*.

[25] Ghia, U., Ghia, K.N., Shin, C.T., 1982, "High-Resolutions for incompressible flow using the Navier–Stokes equations and multigrid method", *J. Comput. Phys*., Vol. 48, pp. 387–411.

[26] Archambeau, F., Méchitoua, N., Sakiz, M., 2004, "Code_Saturne: a finite volume code for the computation of turbulent incompressible flows – Industrial applications", *Int. J. Finite Vol*., Vol. 1, pp. 1–62.

[27] Kawamura, H., Abe, H., Shingai, K., 2000, "DNS of turbulence and heat transport in a channel flow with different Reynolds and Prandtl numbers and boundary conditions, Turbulence", Proc. *3rd Int. Symp. Turbulence, Heat and Mass Transfer*, pp.15–32.

[28] Violeau, D., Buvat, C., Abed-Meraïm, K., de Nanteuil, E., 2007, "Numerical modelling of boom and oil spill with SPH", *Coastal Eng*., Vol. 54, pp. 895–913.

[29] Wang, R.W., David, L., Larinier, M., 2010, "Contribution of experimental fluid mechanics to the design of vertical slot fish passes", Int. *J. Freshwater Ecosyst., Knowledge and Manag. Aquatic Ecosyst.*, Vol. 396, pp. 02.

[30] Violeau, D., Ferrand, M., Mayrhofer, A., Leroy, A., Vorobyev, A., Hérault, A., 2014, "Application of SPH to real-world free-surface flows", Proc. *3rd IAHR European Conf*., Porto, Portugal.

Conference on Modelling Fluid Flow (CMFF'15)
The 16th International Conference on Fluid Flow Technologies
Budapest, Hungary, September 1-4, 2015

WIND TUNNEL EXPERIMENTS OR ADVANCED CFD ... WHAT DO WE NEED FOR UNDERSTANDING FLOW AND DISPERSION IN THE LOWER ATMOSPHERIC BOUNDARY LAYER?

Bernd LEITL[1], Frank HARMS[2], Eva BERBEKAR[3], Gopal PATNAIK[4], Jay BORIS[5], Michael SCHATZMANN[6]

[1] Corresponding Author: Environmental Wind Tunnel Laboratory, Meteorological Institute, University of Hamburg, Bundesstrasse 55, D-20146 Hamburg, Germany. Tel.: +49 40 42838 5092, Fax: +49 40 42838 5452, E-mail: bernd.leitl@uni-hamburg.de
[2] Environmental Wind Tunnel Laboratory, Meteorological Institute, University of Hamburg, E-mail: frank.harms@uni-hamburg.de
[3] Environmental Wind Tunnel Laboratory, Meteorological Institute, University of Hamburg, E-mail: eva.berbekar@uni-hamburg.de
[4] U.S. Naval Research Laboratory, Washington DC, E-mail: gopal.patnaik@nrl.navy.mil
[5] U.S. Naval Research Laboratory, Washington DC, E-mail: jay.boris@nrl.navy.mil
[6] Meteorological Institute, University of Hamburg, E-mail: michael.schatzmann@uni-hamburg.de

ABSTRACT

Numerical modelling and physical modelling are often seen as competitors. Notably, this applies to the field of atmospheric physics and applied meteorology, where both types of models have to face severe restrictions with respect to the amount and complexity of physical processes to be captured in models. There is no doubt that substantial progress has been made, both in computational modelling and in the use of wind tunnels for simulating atmospheric flow and dispersion. Nevertheless, both approaches need to be combined in order to link model results with reality as it is measured. The paper illustrates some of the problems related to modelling and measuring flow and dispersion in the lower atmospheric boundary layer and intends to trigger at a conceptual level a discussion on how to combine specific strengths of both approaches to improve the understanding of flow and dispersion in the lower atmospheric boundary layer.

Keywords: model validation, atmospheric boundary layer flow, dispersion modelling, wind tunnel modelling, LES

1. INTRODUCTION

Fluid mechanics surely is among the well-elaborated fields of physics. Since the work of Navier and Stokes, a systematic framework of fundamental equations exists that is expected to describe fluid motion with necessary detail at the continuum level. Nevertheless, exact solutions of the system of nonlinear differential equations are rare and mostly limited to simplified problems or less complex flow phenomena. This applies particularly to the description of motion and transport in the lower atmospheric boundary layer, where the flow is predominantly turbulent with an exceptionally wide range of relevant eddy sizes. Although the statement made by Snyder (1981), that "Most mathematical models of turbulent diffusion in the lower atmospheric layer tend to ignore the fundamental fluid-dynamical processes involved in the dispersion of materials." might be softened nowadays, it still applies to atmospheric flow and dispersion modelling in general. The memory size and computing power available is still far too limited to keep track of the wide range of turbulent structures in corresponding flows.

Reynolds averaging enabled mean flow and dispersion fields to be calculated for a wide range of practical applications at reasonable computational costs. However, in complex urban geometries it remains a question whether RANS modelling approaches provide results representative for what can be observed within the lower atmospheric boundary layer at full scale. In this regard, verification and validation of RANS models still is a big challenge. A substantial step towards a more realistic numerical simulation of flow and dispersion in the lower atmospheric boundary layer is made by using Large Eddy Simulation techniques. LES is expected to provide at least the potential of properly accounting for turbulent fluctuations at relevant spatial and temporal scales. As numerous studies have shown, results from LES in complex urban environments seem to agree better with observations at full scale. However, model validation becomes even more challenging if validation is not just understood as replicating individual measurements. So-called micro-scale meteorological models are similar or equivalent to CFD-models, depending on the flow and dispersion problem to be simulated and CFD tools have been validated extensively for generic flow and dispersion scenarios. Nevertheless, the model approaches and parameterizations must also be proven to be suitable and valid for application within the lower atmospheric boundary layer and/or in complex urban environments, where models are increasingly applied and where many of the fundamental concepts of turbulence modelling cannot be applied in a strict sense.

Validating models is not a trivial task as far as the simulation of atmospheric boundary layer flow and dispersion is concerned because qualified reference data are more difficult to obtain in the lower atmosphere than for many technical flows. As meteorologists would prefer to use full-scale field data for model validation, Schatzmann and Leitl (2011) raised the question whether field data do represent the truth particularly in urban flow and air quality modelling. In order to decide how close models should get to measured field data, their representativeness needs to be evaluated carefully. Often, it must be stated that a perfect match of reference data from field experiments and simulation results is not proving a successful model validation but rather providing an example for successfully tuning simulation results. The variability inherently present in field data sets results in a large degree of freedom with respect to interpretation of measured values and assumed boundary conditions. This is because field data can almost never be collected extensively or densely enough to sample the full range of likely realizations of the real world during a short enough time that the underlying winds, sun angle, and weather have not changed appreciably. Obviously, there is a gap between what can be observed and measured at full scale and the well-defined world of a mathematical/numerical model.

Physical modelling in boundary layer wind tunnels can act as crucial mediator between full-scale field trials and computational modelling although it is a more or less simplified but homologous model itself. For example regarding the dynamics of turbulent structures, there is less trade-off between spatial resolution and model domain size in a physical model than in most of the CFD applications. Regarding boundary conditions, it is much easier in a controlled lab experiment to record and completely document all relevant boundary conditions in a representative way than what is possible in full-scale measurements. Many examples of this type can be given, promoting a combined approach to micro-scale meteorology. The following sections intend to illustrate challenges in linking computational modelling with real world data via fluid modelling for better understanding flow and dispersion in the lower atmospheric boundary layer.

2. PROBLEMS RELATED TO BOUNDARY CONDITIONS

As with any other flow and diffusion problem, transport phenomena in the lower atmosphere are defined by the corresponding physical and geometric boundary conditions. Nowadays the geometric boundary conditions are less difficult to be defined due to the availability of digital data for terrain and obstacles. For example it is possible now to get detailed digital data of an urban structure via digital information systems such as CAD/GIS. Defining a proper representation of buildings and other obstacles depends on the problem to be studied and it is difficult to decide what geometric detail is necessary from a physical point of view for a 'sufficiently accurate' representation of obstacles in a model. Furthermore, it depends on how structures in the urban canopy can be implemented in a discrete computational model. When large scale dispersion patterns from distributed emission sources such as car traffic are modelled, it might not be necessary to replicate all geometric detail of buildings or the cars in a simulation; the geometry data might sufficient even if provided at lower level of detail. The costs are substantially reduced and larger model domains become affordable if less detail is required in a computer simulation. Currently, different levels of detail are used ranging from simple block-like buildings to detailed and very precise CAD models. However, the more geometric simplification is applied the less simulation results can be taken as local data. This effect must be considered particularly when comparing usually pointwise measured field data with corresponding computational results. One could argue that, if a structured computational grid is used, the data of lower detail is sufficient because real geometry would be simplified anyway but this implies also that a distinct level of model uncertainty is introduced - independent from spatial resolution of the computational grid. This uncertainty is difficult to quantify without further systematic modelling.

The effects of geometric simplification can be quantified easily by laboratory physical modelling if a geometrically detailed model is replaced, for example, by a box-like simplified structure. Figure 1 shows a complex detailed urban model and its simplified representation both tested under identical approach flow conditions in a boundary layer wind tunnel. As reported in Leitl et al (2001), significant differences in flow and dispersion must be expected when comparing pointwise measured data, independent of the 'physical performance' of the model. Unfortunately, a general answer regarding the level of uncertainty cannot be given even for such a simple case because sensitivity of model results with respect to geometrical simplification strongly depends on wind direction and the size of the model domain.

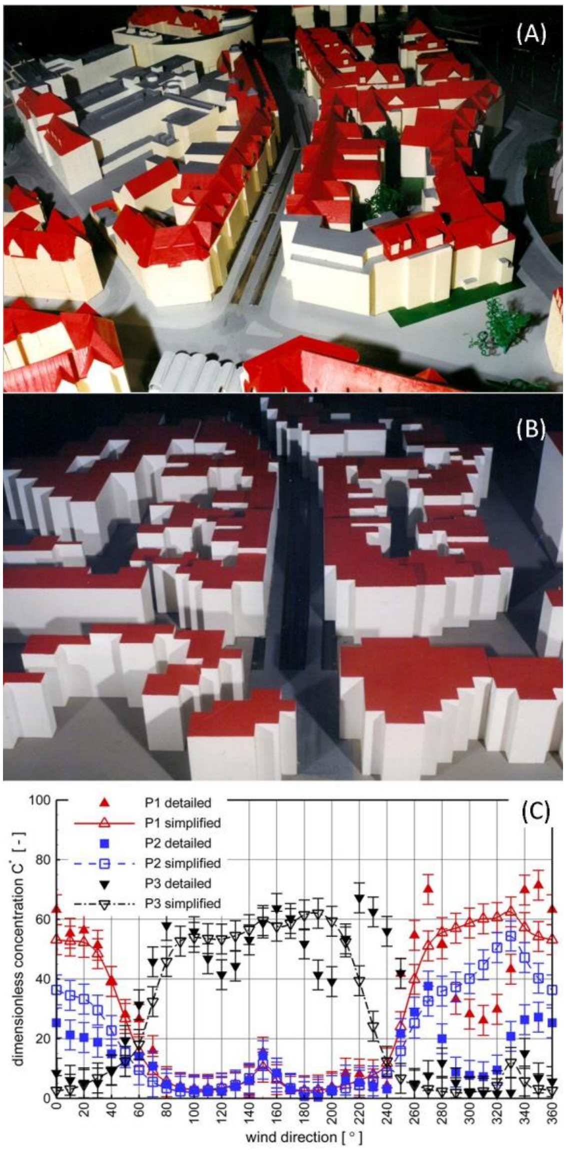

Figure 1. Effect of geometrical simplification on simulation results: (A) detailed model of urban geometry, (B) simplified block-structured geometry (C) comparison of results for detailed and simplified structure for three different measurement locations in the street canyon.

Substantially more problematic is an adequate characterization of the physical boundary conditions, such as the wind conditions driving flow and dispersion. CFD model simulations mostly rely on the concept of a quasi-stationary mean approach flow. However, at full-scale a representative mean wind profile does not exist for relevant time periods of, e.g., up to a few hours. The presence of turbulent structures in the atmospheric boundary layer and continuously changing meteorological boundary conditions prevent the forming of a statistically representative 'mean approach flow condition' at full scale. As field data show, the hourly mean values of wind speed and the shape of corresponding wind profiles are subject to substantial scatter, even if the long-term mean approach flow conditions can be assumed to be identical. Mean wind profiles as measured in reality must be understood as sub-samples of a bigger ensemble of possible variations even at a time scale of thirty minutes or one hour. Only if the mean wind profile as well as the underlying variability are properly derived from field data and properly replicated in a model experiment or simulation, similarity between model simulation and full-scale conditions can be assumed to be sufficient for translating simulation results to full scale or for comparing simulation data directly with corresponding field data.

This determination requires spatiotemporal analysis tools such as joint time frequency analysis, proper orthogonal decomposition or linear stochastic estimation to be applied for characterizing boundary layer wind flow conditions adequately. Field data are of rather limited value with regard to the application of such tools because they either lack either spatial or temporal resolution at the scales relevant for characterizing wind turbulence in the lower atmospheric boundary layer. On the other hand, such information is vitally important particularly for eddy-resolving numerical models, in order to ensure the proper spatiotemporal fluctuations of wind vectors to be replicated at the inflow boundary. Once again, physical modelling can assist in characterizing and synthesizing approach flow conditions for boundary layer flow modelling. Proper wind tunnel modelling is able to represent shear turbulence over the entire range of relevant eddy sizes at least within the lower part of the atmospheric boundary layer.

Once physically consistent and representative mean flow conditions can be documented for a modelled wind tunnel boundary layer flow, statistically representative wind velocity time series can be recorded. A mandatory convergence analysis of measured data reveals, that time series of several minutes must be recorded in a wind tunnel experiment in order to achieve acceptable statistical representativeness for a properly modelled boundary layer flow. Several minutes at model scale correspond to at least tens of hours at full scale. This duration is theoretically required for deriving representative mean wind conditions and the corresponding variability of results from field measurements and yet is practically impossible.

Nonetheless, dynamically similar quasi-stationary wind tunnel time series can be divided in sub-samples corresponding to full-scale time periods of tens of minutes or an hour. A subsequent analysis of short-term averaged samples enables the minimum expected variability of field data to be quantified with regard to statistical parameters such as mean and higher order moments. Furthermore, such analysis fosters the provision of physically consistent inflow boundary conditions for eddy-resolving computational models such as LES. Combining a spatiotemporal characterization of inflow turbulence derived from qualified wind tunnel data with a reference time series from corresponding field measurements acting as trigger or driver enables reconstruction / synthesis of physically consistent inflow boundary conditions for eddy resolving models such as LES.

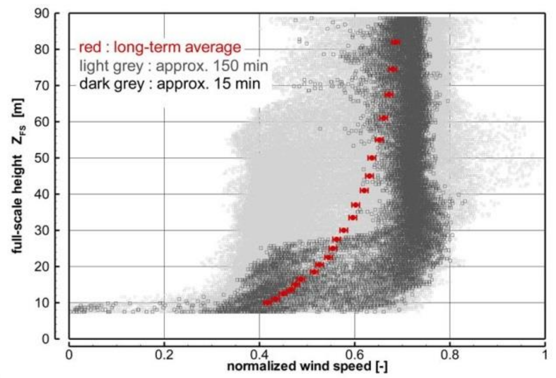

Figure 2. Variability of wind profiles near the ground. Circles represent the long-term mean wind profile, light grey symbols indicate wind profiles measured within an interval of 150 minutes, dark grey symbols illustrate wind profiles measured within an arbitrarily chosen time interval of 15 minutes.

Figure 2 illustrates the potential of such a combined approach at the example of sub-sample analysis of PIV measurements in an urban boundary layer flow. If all available wind profiles are averaged, a well-shaped mean wind profile is formed as indicated by the red symbols. The profile indicates the expected perfect equilibrium with the surface roughness located upwind of the measurement. However, if a subset of individually measured profile data is analysed over 150 minutes full-scale only, a significant scatter of the normalized wind profile data becomes visible (light grey scatter symbols). Most of the observed variability is caused by large turbulent structures generated in the shear flow above an urban roughness. Approach flow characterization becomes worse, if the time period for analysis is made shorter. In the example, a 15 minute interval is chosen in accordance to a typical instantaneous release experiment (puff dispersion measurement). As the dark grey symbols show, the short-term analysis sometimes indicates less scatter but clearly deviates from the long-term average profile. Subsequent analysis of the results revealed that wake flow effects of model buildings located more than 15 average building heights upwind of the profile location cause an erratic switching of the flow. This effect becomes visible in the data only if physically consistent information on the long-term mean flow is available. Considering that during a field experiment, if at all, only vertical and/or temporal averages of the dark grey symbols would have been measured, the question must be raised, what a 'proper' inflow profile for a corresponding simulation would be.

In practical applications, the problem of defining a 'proper' shape of a representative inflow profile is often transferred to the definition of a corresponding roughness length. This requires the boundary layer flow to be in equilibrium with the underlying roughness. What seems to be a pragmatic solution triggers further questions regarding the representativeness of data measured at full scale. The example given refers to the BUBBLE (Basel Urban Boundary Layer Experiment) data, which was extended by wind tunnel measurements from Feddersen et al. (2004). In the field, tall mast measurements were used to characterize the flow above the urban structure. Values of roughness length were derived from local measurements above roof level. If exactly the same scenario is replicated in a boundary layer wind tunnel, the assumption of equilibrium of the boundary layer flow with the underlying roughness must be questioned.

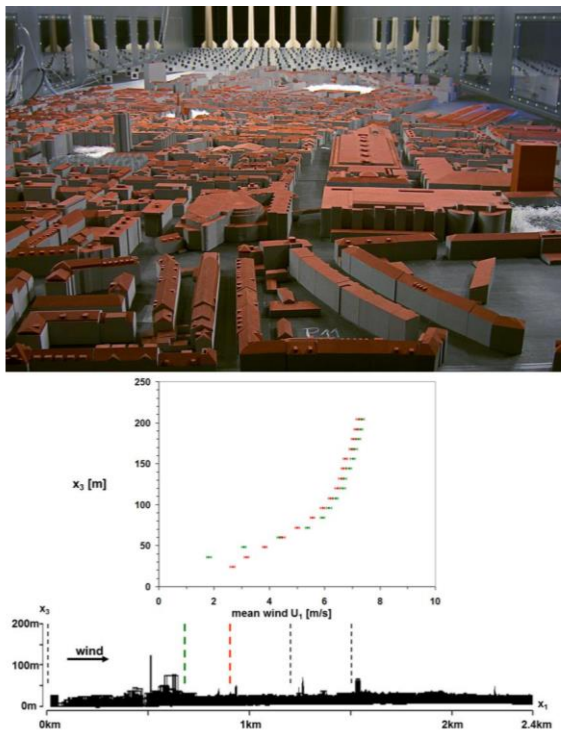

Figure 3. Adaptation of mean wind profiles measured above a city to changing urban roughness.

Figure 3 shows just two out of five measured vertical profiles along the domain modelled in the boundary layer wind tunnel. The upper part of the mean wind profile does not change substantially along the model, indicating equilibrium conditions of the overall boundary layer above the city. In contrast, the lower part of the profile quickly adapts to local changes in surface roughness, causing the related roughness length to scatter dramatically within a range of a few hundred meters. It becomes clear that the roughness length concept is not a proper approach to characterize wind conditions above a heterogeneous urban topography. It should be mentioned here, that an even higher local variability was observed in the turbulent momentum fluxes measured.

3. PROBLEMS RELATED TO SCALING OF RESULTS

From the illustrations presented we must conclude that field data require ensemble averaging to derive universal, representative results of flow and dispersion measurements. In order to unify measured data, non-dimensional functions can be derived via dimensional analysis. The use of generalized, dimensionless data enables not only results generated at different model scales to be compared with each other but also allows a unified presentation of data measured at different absolute values. However, non-dimensionalizing measured (or simulated) data requires representative reference quantities to be defined. In this context, the provision of a simple representative reference wind speed becomes a non-trivial task.

The following example has been extracted from a large field campaign conducted in 2003 in and around Oklahoma City. According to Allwine et al (2007) , one of the purposes of the Joint Urban 2003 field test was to provide quality-assured meteorological and tracer data sets "vital for establishing confidence that atmospheric dispersion models used to simulate dispersal of potential toxic agents in urban atmospheres are giving trustworthy results". For more than a month, extensive field measurements were carried out under fairly consistent environmental conditions using almost one hundred wind sensors including profile measurements by SODARs. The dataset obtained is perhaps the biggest and most complete of its kind and one would expect to be able to derive a representative reference wind speed from the data available.

Hertwig (2008) analysed the field data with respect to puff dispersion measurements and corresponding wind data to be unified. Out of the whole analysis, just two reference wind stations are considered in this example, one located upwind of the city and one at a more lateral position with respect to the mean approach flow and the city centre. Several so-called intense observation periods (IOPs) delivered results to be analysed and unified. Ideally, all measurement locations intended as reference stations should provide correlated data. However, as Figure 4 demonstrates, the exemplary 5 minute average data show a rather weak correlation only and no clear relationship between each other. Depending on the IOP chosen, systematic deviations in the measured wind speed and wind direction are observed.

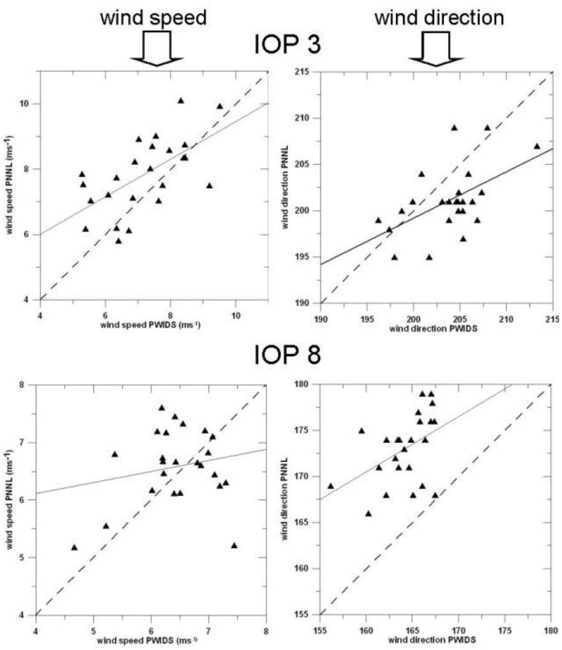

Figure 4. Correlation of wind speed (left plots) and wind direction (right plots) measured at two reference locations during the JU2003 field campaign. Two exemplary Intense Observation Periods (IOP 3 & 8) were selected.

Other reference stations indicate a similar behaviour thus a very large scatter is introduced to experimental results, depending on what reference conditions are assumed. For example, if the measured concentration data are properly non-dimensionalized by a reference length scale, source strength and reference wind speed, the data could be compared with data from a corresponding systematic wind tunnel test (e.g. Harms et al, 2011). Depending on the choice of the reference wind, the observed difference between field and laboratory data can vary between almost identical results and deviations of far more than 100% as illustrated in Figure 5. This automatically implies, that a comparison of field data with 'corresponding' simulations is leading to almost arbitrary results, and the degree of agreement can be tuned by the choice of reference conditions. Many examples of successful model validation based on the Joint Urban 2003 field data are presented in the literature but it remains an open question if the degree of agreement can properly document the quality of flow and dispersion models if the choice of reference conditions has that much impact. This is one of the reasons why more recent model validation concepts such as the COST 732 model validation protocol (Britter and Schatzmann, 2007) recommend partially blind tests and the use of quality-controlled laboratory data as validation data.

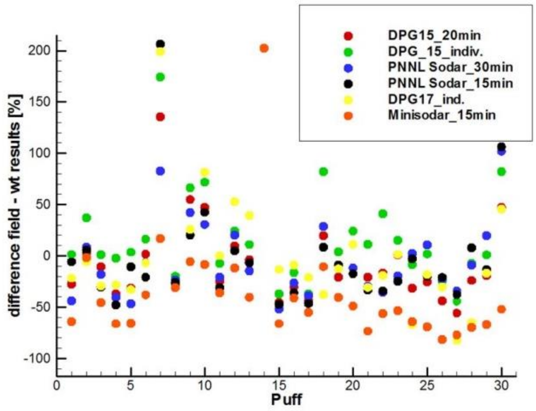

Figure 5. Relative difference between mean concentration values measured at full scale and in the corresponding laboratory experiment for different reasonably chosen reference wind data.

4. COMBINING COMPUTATIONAL AND PHYSICAL MODELLING

Constructing more and more complex physical models does not necessarily simplify model validation and model application. More complex models require provision of more complex model input data; it is not clear if a 'better model' provides 'better results' if model input data require more assumptions and simplifications to be made. Without elaborating further the question whether a more complex model is automatically a better one, a brief example is now given showing how combining computational and physical modelling can help develop a practical solution for the quite challenging problem of puff releases and dispersion within complex urban environments. Releases of toxic or potentially harmful substances pose a tremendous threat to the general public and big challenge to first responders particularly in densely populated urban areas. Within minutes after a release, decisions have to be made regarding possible safety measures such as evacuation. Emergency response personnel must be deployed and a scenario has to be managed in a way that reduces the exposure of the population. Models have to be applied to act and not just react to accidental releases and the models have to be chosen adequately with reference to the complexity of the problem.

Whereas in the past preference was given to simple flow and dispersion models, attempting to simulate releases on-the-fly, a more recent development is using LES for area-covering pre-calculations of turbulent wind fields driving instantaneous dispersion models in complex building arrangements. Based on the pre-calculated information, affected areas and other information relevant to first responders can be reconstructed instantly at literally any time during an accident (Patnaik et al, 2010). However, applying LES to a city of several hundreds of square kilometers and simulating wind fields for a sufficient number of possible wind directions quickly becomes a time-consuming and expensive task. In this regard it must be considered as well that urban structures tend to change continuously which means pre-calculations have to be updated from time to time. Hence, a 'sufficiently accurate' but preferably very efficient LES tool is desired.

Monotonically integrated LES (MILES) seems to provide a very good trade-off between efficiency and sufficient accuracy. However, as for any other model type, this modelling approach needs to be validated carefully for the intended application. Ideally, a model implementation is tested and improved for a series of test cases of different complexity before it is validated for a specific application, preferably in a blind test scenario. One of the few urban LES codes who have undergone this extensive procedure is the MILES based code Fast3D-CT, developed by Boris and Patnaik. Simulation results were compared for simplified test cases like cube array flows modelled in wind tunnels and at full scale and applied to several complex scenarios such as the Joint Urban 2003 wind tunnel and field data set before it was validated in a real blind test scenario in the course of developing a CT-Analyst version for the city of Hamburg in Germany.

While the laboratory experiments still were under preparation, numerical simulations already took place for a part of the city of Hamburg. Using truly the same reference in the wind tunnel and the numerical simulations enables the performance of the model to be evaluated. By intention no further manipulation of the gridded simulation results was applied before the data was compared with experimental results from within and above this complex and realistic urban model. A comprehensive description of the comparison can be found in Hertwig (2013). Figure 6 shows a part of the detailed wind tunnel model mounted in the large boundary layer wind tunnel facility at Hamburg University. The corridor shown in the Figure is aligned with one of the predominant wind directions observed in Hamburg because the chances for coincidence with a subsequent field trial were intended to be maximized.

Figure 6. Detailed wind tunnel model of a part of the inner city of Hamburg (Germany), mounted in the large wind tunnel facility at EWTL.

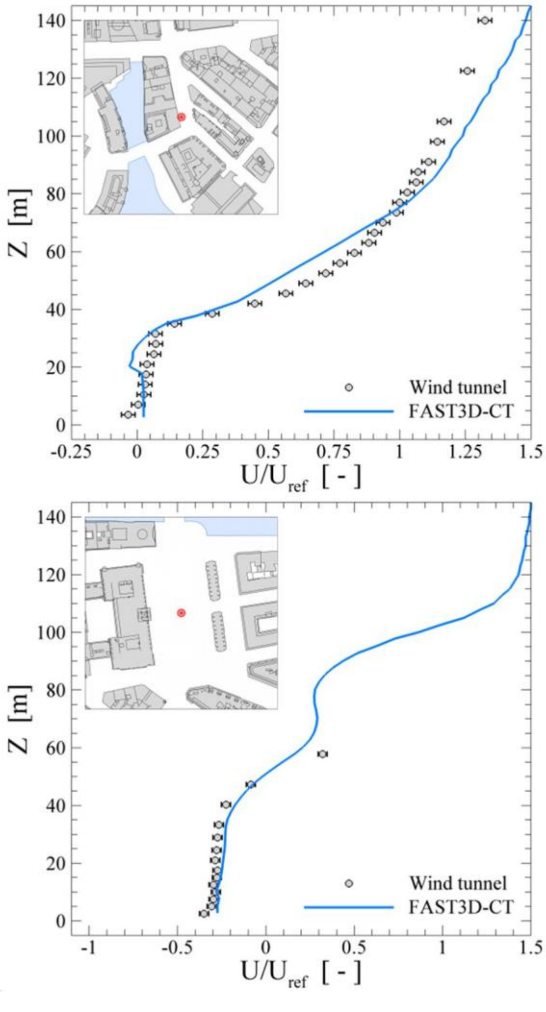

Figure 7. Comparison of simulated and measured mean wind profiles for two typical urban locations, solid line represents Fast3D-CT simulation results, symbols indicate corresponding wind tunnel results, and the building geometry surrounding the measurement location is illustrated by a map section.

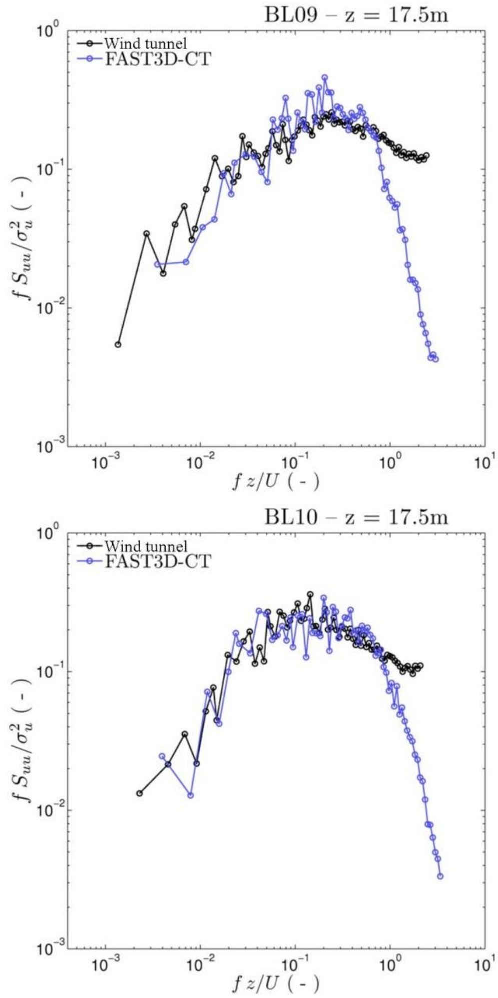

Figure 8. Turbulence spectra derived from LES simulations and measured wind tunnel data (black: wind tunnel, blue: Fast3D-CT results).

The model domain was 3.7 km long and 1.4 km wide in the wind tunnel, numerical simulations were carried out in a 4 km by 4 km square with 2.5 m resolution near the ground and a vertically stretched grid further above the urban structures. Sufficiently long time series of 4 hours real time needed to be simulated in order to restrict the remaining statistical uncertainty of comparison of data with corresponding laboratory result to approximately ±10%.

As typical results provided in Figure 7 indicate, the agreement of mean wind profiles is very good considering the complexity of the problem, a possible 'mismatch' of the location within ± 1.25 m horizontally and the blind test scenario with simulation results being submitted well before lab measurements took place.

The availability of area-covering reference data allows flow verification also at a very local scale where possible effects of geometric simplification can affect flow and dispersion modelling. Additionally, the availability of representative reference time series of flow measurements enables to validate the large-scale turbulence explicitly modelled with the MILES code. An example is provided in Figure 8, where the spectral distribution of turbulent kinetic energy is compared at two locations at approximately half of the mean building height. Bearing in mind the relatively coarse grid resolution of 2.5m and the intended use of the flow field data for dispersion modelling at scales from a couple of meters to a few kilometers, the spectral behavior documents a sufficient agreement of modelled and measured turbulent kinetic energy.

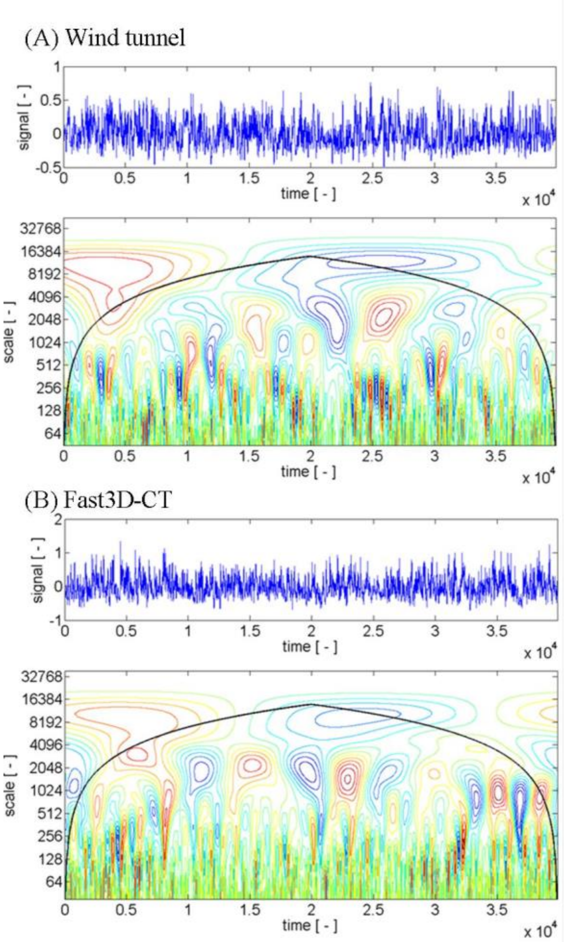

Figure 9. Comparison of wavelet-based JTFA for LES wind velocity time series (A) and corresponding measured wind tunnel data (B).

With qualified data being available, the model validation and insight in turbulent flow and transport can be pushed even further to a level almost impossible to achieve with full-scale data. Just as an example again, Figure 9 shows results of a wavelet-based joint time/frequency analysis as presented in Hertwig (2013). A Mexican hat wavelet was utilized to generate the corresponding correlograms. Already from visual inspection it becomes clear that the gross structure of turbulence is sufficiently well replicated by the fast-running and very efficient code Fast3D-CT.

5. SUMMARY

With respect to the question in the title of the paper, the answer still should be that both advanced CFD and wind tunnel modelling are needed to better understand flow and dispersion in the lower atmosphere. Despite the progress in computational modelling of flow and dispersion, physical modelling still can substantially contribute to better understand complex processes and phenomena observed in the lower atmospheric boundary layer. This applies particularly to urban flow and dispersion problems as they are of major concern with respect to urban climate modelling, ventilation studies or, as presented, in the context of local-scale emergency response. Although field measurements are an indispensable tool for capturing physical processes at local scale, numerical modelling is required to properly sort and interpret measured data because of the lack of resolution and representativeness of field data at this scale. On the other hand, we must state as well, that there is still a conceptual gap between what advanced numerical modelling and field measurements deliver, so combining both sources of information might look straightforward but in many respects it is not. Fluid modelling for example in specifically adapted boundary layer wind tunnels can help shape a more complete perspective on atmospheric flow and dispersion in complex environments by bridging this gap. Furthermore, physical modelling facilitates the further development and validation of efficient numerical simulation tools, providing data truly qualified for quantitative model testing which will not be available from field measurements.

ACKNOWLEDGEMENTS

Results and ideas presented in the paper were generated and developed in a series of projects supported by different funding agencies. The Joint Urban 2003 project was funded by the US Department of Homeland security. The LES Fast3D-CT model validation studies were partly sponsored by the U.S. Office of Naval Research Global and DTRA programs. The development of CT-Analyst Hamburg was funded by the German Federal Office of Civil Protection and Disaster Assistance (BBK) and the City of Hamburg.

REFERENCES

[1] Snyder, W.H., 1981, "Guideline for fluid modeling of atmospheric diffusion" *U.S. Environmental Protection Agency*, Environmental Sciences Research Laboratory, Research Triangle Park, NC 27711, EPA-600/8-81-009

[2] Schatzmann, M. and Leitl, B., 2011, "Issues with validation of urban flow and dispersion CFD models" *Journal of Wind Engineering and Industrial Aerodynamics*, Vol. 99, pp. 169-186.

[3] Leitl, B., Chauvet, C., Schatzmann, M., 2001, "Effects of Geometrical Simplification and Idealization on the Accuracy of Microscale Dispersion Modelling" Proc. *3rd Int. Conf. on Urban Air Quality*, March 19-23 2001, Loutraki, Greece

[4] Feddersen, B., Leitl, B., Rotach, M., Schatzmann, M., 2004, "Wind tunnel modelling of urban turbulence and dispersion over the City of Basel (Switzerland) within the BUBBLE project" Proc. *Fifth Symposium on the Urban Environment (AMS)*, Vancouver, Canada, August 23-28.

[5] Allwine, K. J., Leach, M. J. (Eds.), 2007 Editorial of Special Issue of the Journal of Applied Meteorology Climatology, Vol. 46, pp. 2017-2018

[6] Hertwig, D., 2008, "Dispersion in an urban environment with a focus on puff releases" *Independent Study Project*, University of Hamburg, Meteorological Institute.

[7] Harms, F., Leitl, B., Schatzmann, M., Patnaik, G., 2011, "Validating LES-based flow and dispersion models" *Journal of Wind Engineering and Industrial Aerodynamics*, Vol. 99, Issue 4, pp. 289-295

[8] Britter, R. and Schatzmann, M. (Eds.), 2007, Background and justification document to support the model evaluation guidance and protocol document. *COST Office Brussels*, ISBN 3-00-018312-4

[9] Patnaik, G., Moses, A., Boris, J., 2010, "Fast, accurate defense for Homeland Security: Bringing high-performance computing to first responders" Journal of Aerospace Computing, Information and Communication. 2010;7(7), pp. 210-220.

[10] Hertwig, D., 2013, "On Aspects of Large-Eddy Simulation Validation for Near-Surface Atmospheric Flows" PhD Thesis, *University of Hamburg*, Meteorological Institute, http://ediss.sub.uni-hamburg.de/volltexte/2013/6289/

Conference on Modelling Fluid Flow (CMFF'15)
The 16th International Conference on Fluid Flow Technologies
Budapest, Hungary, September 1-4, 2015

IMPROVING PHASED ARRAY MEASUREMENT TECHNIQUES FOR JET NOISE UNDERSTANDING

Robert P. Dougherty[1], Kenneth Brentner[2], Alan B. Cain[3], Philip J. Morris[4], Christopher C. Nelson[5]

[1] Corresponding Author. OptiNav, Inc. and the University of Washington. 1414 127th PL NE #106, Bellevue, WA, USA. Tel.: +1 425 891-4883, Fax: +1 425 467 1119, E-mail: rpd@optinav.com
[2] Department of Aerospace Engineering, The Pennsylvania State University. E-mail: ksbrentner@psu.edu
[3] Innovative Technology Applications Company. E-mail: abcain@itacllc.com
[4] Department of Aerospace Engineering, The Pennsylvania State University. E-mail: pjm@psu.edu
[5] Innovative Technology Applications Company. E-mail: ccnelson@ITACLLC.com

ABSTRACT

A research project to improve phased array beamforming techniques for gaining insight into the generation and radiation of high speed jet noise has been conducted. The work was led by the Innovative Technology Applications Company with contributions from Philip Morris and Kenneth Brentner at the Pennsylvania State University and Robert Dougherty at OptiNav, Inc. The approach was to apply Large Eddy Simulation and the Ffowcs Williams-Hawkings method to produce synthetic microphone phased array data and then develop and apply candidate array processing algorithms to the synthetic data. A wide range of algorithms were tested, along with several types of basis functions and coherent and incoherent source combinations. Ultimately, a hybrid technique that combines Orthogonal Beamforming, Functional Beamforming and incoherent combination of wavepackets emerged as a useful approach.

Keywords: jet noise, beamforming, wavepackets, LES, chevron nozzle

NOMENCLATURE

$\underline{\underline{C}}$	[Pa^2]	Cross Spectral Matrix
D_j	[m]	jet nozzle diameter
E	[-]	expectation value
M	[-]	number of sources
N	[-]	number of microphones
c	[m/s]	speed of sound
k_0	[m^{-1}]	wavenumber
$\underline{g}$	[-]	steering vector
p	[Pa]	acoustic pressure
$\underline{p}$	[Pa]	acoustic pressure vector
q	[Pa m]	complex acoustic source strength
$\underline{q}$	[Pa m]	acoustic source strength vector
$\underline{u}_i$	[-]	eigenvector of $\underline{\underline{C}}$
α	[m^{-1}]	axial wavenumber
α_i	[-]	inner product of vectors
ω	[rad/s]	angular frequency

Subscripts and Superscripts

i	microphone or eigenvalue index
j	source basis function index
$'$	complex conjugate transpose
$*$	complex conjugate
s	source

1. INTRODUCTION

Modern tactical military aircraft engines produce hot, high speed exhaust plumes with two primary noise production mechanisms: supersonic convection of the turbulence in the jet shear layer and shock-associated noise [1, 2]. The turbulence mixing source radiates in the downstream arc and is highly directive due to the matching of the axial phase velocity of the convection and the trace velocity of the radiated wave. Shock associated noise occurs when the jet is operating off design and the pressure mismatch at the nozzle creates a pattern of shock diamonds in the plume.

Over the last three years, the US Office of Naval Research engaged the Innovative Technology Applications Company (ITAC) to seek ways to improve microphone phased array processing techniques so as to increase the ability of the processing techniques to provide insight into high speed jet noise sources. ITAC performed Large Eddy Simulation (LES) of jet flows and used the Ffowcs Williams-Hawkings method to create virtual microphone array data. The Principal Investigator was Alan Cain, President of ITAC. OptiNav, Inc. was a subcontractor for this work. A high-aspect ratio, planar, 100-element array design was adapted from a separate OptiNav project and applied as the test case. The array was 55 jet diameters in length and located parallel to the jet at a sideline distance of 23.5 jet diameters. The large axial extent, combined with the nontrivial directivity of high speed jet noise, means that the array should be able project at least a portion of the directivity pattern of the jet. It also means that the incoherent monopole assumption usually employed in array processing may not be applicable. The technical approach to the beamforming analysis was to jump in with both feet. The simulations were performed and then many beamforming approaches were tried to determine whether any of them were practical for mapping source distributions and determining the far field polar arc microphone data. The actual far field directivity was also extracted from the LES results using the Ffowcs Williams-Hawkings integral technique to check the phased array results. This paper outlines the formulation and goals of acoustic beamforming in general, the methods that were attempted for the high speed jet noise problem, the hybrid beamforming approach that was developed, and sample results from the synthetic data.

2. VIRTUAL MICROPHONE DATA

ITAC simulated a baseline military-style faceted nozzle and a chevron nozzle variant. The results shown here are for the overexpanded condition with a nozzle pressure ratio of 3.0, a total temperature ratio of 3.0, a jet Mach number of 1.36, a ratio of jet temperature to ambient temperature of 2.19, and an acoustic Mach number of 2.01.

1.1 CFD solver

The Compressible High Order Parallel Acoustics (CHOPA) solver was used to compute the flow. The spatial descretization of CHOPA is the fourth-order Dispersion Relation Preserving (DRP) scheme of Tam and Webb [3], augmented by different methods for special parts of the geometry. An implicit dual time stepping method is used. Message Passing Interface (MPI) is applied to permit the code to run in parallel. CHOPA solves the Navier-Stokes equations on structured, multiblock grids with abutting boundaries. The Immersed Boundary Method (IBM) is applied to simplify the gridding of small details such as chevrons. Turbulence effects are modeled using variations of the Spalart-Allmaras one equation turbulence model [4].

1.2 CFD grid and example solution

An image of the chevron nozzle and the compuational grid is shown in Figures 1. Sample density contours are given in Figure 2.

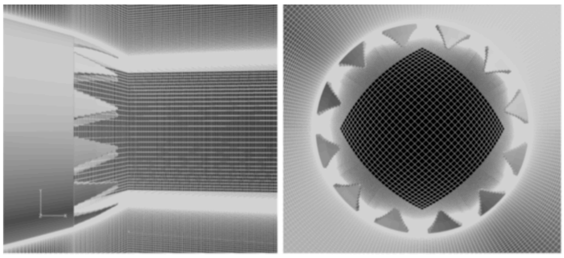

Figure 1: Computational mesh for chevron nozzle geometry

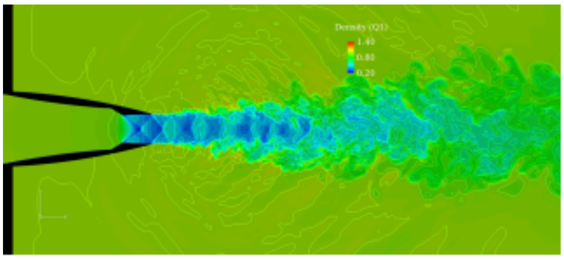

Figure 2: Density contours

1.3 Radiation to virtual microphones

A permeable Acoustic Data Surfaces (ADS) was defined as shown in Figure 3. The PSU-WOPWOP Ffowcs Williams–Hawkings (FW-H) code [5] was used to evaluate the acoustic pressure time history at far field microphones and the 100 microphones of the near field phased array as shown in Figure 4.

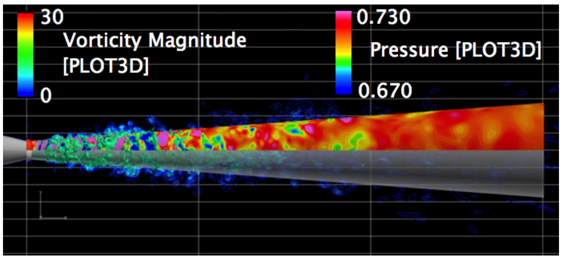

Figure 3: Iso-surface and centerline plane contours of vorticity with pressure contours plotted on the Acoustic Data Surface

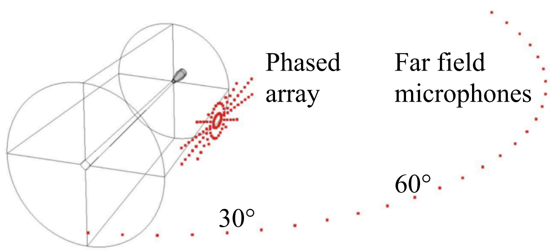

Figure 4: Virtual microphone arrays.

3. REVIEW OF ARRAY PROCESSING METHODS

3.1 Narrowband beamforming overview

In the present context, a phased array is a spatial arrangement of N microphones. The time history of the acoustic pressure is measured or simulated for the all of the microphones. The time records are divided into blocks and an FFT is used to determine the complex Fourier amplitude for each microphone, analysis frequency, and time block. The subsequent analysis concerns a single frequency bin, ω, with a bandwidth equal to the reciprocal of the block length. In the following, the symbol t represents the index of the time blocks. It varies slowly of the scale of the acoustic frequency, ω. The relative bandwidth should be 10% or less. The history of the complex Fourier amplitude of the acoustic pressure at microphone i is denoted $p_i(t),\ i = 1, \dots N$. Stacking these functions gives the array data vector as shown in Eq. (1).

$$\underline{p}(t) = \begin{bmatrix} p_1(t) \\ \dots \\ p_N(t) \end{bmatrix} \tag{1}$$

The covariance matrix of the $p_i(t)$ functions is the Cross Spectral Matrix (CSM), $\mathbf{C}$, defined in Eq. (2), where the bracket notation refers to a time average: $\langle f(t) \rangle = \frac{1}{T}\int_0^T f(t)dt$.

$$\underline{\underline{C}} = E\left[\underline{p}\underline{p}'\right] \approx \langle \underline{p}\underline{p}' \rangle \tag{2}$$

The error in the approximation above is proportional to $\frac{1}{\sqrt{T}}$, and T may be very short for simulated data. One dataset has T = 9 ms. At the peak jet noise frequency of about 16 kHz (St = 0.36), the width of the 1/12 octave analysis band is 941 Hz. The effective block length for the for the analysis is 1/(941 Hz) or about 1 ms. The estimate of the CSM can be considered to be based on 9 averages in this case. A typical goal for real data is 1000 averages

3.1.1 Basis functions

The is most elementary source for a radiated field is a simple source. With this assumption, each of the M sources for the phased array analysis is presumed to be located at a distinct location $\vec{x}_j$ and to vary on the slow time scale according to $q_j(t), j = 1, \dots, M$. The narrowband Fourier amplitude of the acoustic pressure at the analysis frequency ω is $p(\vec{x}, t) = \sum_{j=1}^{M} q_j(t)\frac{e^{ik_0R}}{R}$, where $R = \|\vec{x} - \vec{x}_j\|$, $k_0 = \frac{\omega}{c}$. Here t is again the slow time. The autopower of the pressure at a single point and the cross power of the pressure at two distinct points depend, in part, on the statistical relationship between the various $q_j(t)$ functions. In order for a monopole source ensemble to have a nontrivial far field directivity pattern, it is necessary for several sources to be at least partially correlated so that they can interfere constructively at some angles and destructively at other angles.

For $j \in \{1, \dots, M\}$, let $\underline{g_j}$ be an N-vector representing the phase and amplitude of source j at the microphone locations. The normalization of $\underline{g_j}$ is $\left\|\underline{g_j}\right\|_F^2 = \underline{g_j}'\underline{g_j} = 1$. The nature of the source vectors is not known a-priori. They may represent monopoles located at certain points or some other type or source. The source-receiver model is given in Eq. (3), where $q_j(t)$ is the slowly-varying time history of source j. The term $\underline{n}(t)$ represents noise picked up by the microphones that is incoherent between the microphones and not related to acoustic sources. It may reasonable to assume $\underline{n}(t) = \underline{0}$ for virtual microphones.

$$\underline{p}(t) = \sum_{j=1}^{M} q_j(t)\underline{g_j} + \underline{n}(t) \tag{3}$$

3.1.2 Coherent beamforming

Let the M vectors $\underline{g_j}$ be placed on the columns of an $N \times M$ matrix, $\underline{\underline{G}}$, and stack the source functions $q_j(t)$ into an M-vector $\underline{q}(t)$. The source-receiver model becomes $\underline{p}(t) = \underline{\underline{G}}\underline{q}(t) + \underline{n}(t)$, and the estimate of the CSM assumes the form given in Eq. (4), where $\underline{\underline{C_q}}$ is the CSM of the source functions.

$$\begin{aligned} \underline{\underline{C}} &\approx \langle \left(\underline{\underline{G}}\underline{q} + \underline{n}\right)\left(\underline{q}'\underline{\underline{G}}' + \underline{n}'\right) \rangle \\ &= \underline{\underline{G}}\underline{\underline{C_q}}\underline{\underline{G}}' + \langle \underline{n}\underline{n}' \rangle \end{aligned} \tag{4}$$

Coherent beamforming, also known as the generalized inverse method, consists of measuring $\underline{\underline{C}}$, creating an ansatz for $\underline{\underline{G}}$, and applying linear algebra to estimate $\underline{\underline{C_q}}$. The linear algebra usually involves a generalized inverse procedure, so the technique is known as the Generalized Inverse method. Nearfield Acoustic Holography is a special case in which the $\underline{g_j}$ vectors are constructed to be mutually orthogonal, such as plane waves with a regular array, which simplifies the algebra. The Generalized Inverse method described in [6] was initially applied for this project, but was abandoned for this application when it became clear that the ill-posed nature of the formulation constrained it to very low frequency.

3.1.3 Incoherent beamforming

Incoherent beamforming also begins with an ansatz for the M basis functions and their complex values at the microphone locations on the rows of $\underline{g}_j$, $\mathrm{j} = 1, \dots, M$. In this case, it is assumed that the source CSM matrix, $\underline{\underline{C}}_q$, is diagonal, and the objective of the beamforming is to estimate the autopowers $s_j = \langle |q_j|^2 \rangle$, $\mathrm{j} = 1, \dots, M$. Since the basis functions do not interfere coherently, any significant directivity features of the model need to be built into the basis functions, for example by using wavepackets. The diagonal self-noise term in the CSM, $\langle \underline{nn}' \rangle$, is harmful for the various beamforming formulas, so it will be assumed that a preprocessing step has been applied to replace the diagonal element of $\underline{\underline{C}}$ with minimum values that keep the matrix nonnegative definite.

The classical beamforming expression is $b\left(\underline{g}\right) = \underline{g}'\underline{\underline{C}}\underline{g}$. This is applied to construct the beamform map according to $s_j \approx b\left(\underline{g}_j\right)$, $\mathrm{j} = 1, \dots, M$. The expression can be derived as a least-squares fit of the model CSM for grid point j, $s_j \underline{g}_j \underline{g}_j{}'$, to $\underline{\underline{C}}$. This method is robust and fast, but suffers from poor resolution and high sidelobes, spurious peaks at points that do not correspond to true sources.

3.1.4 Deconvolution

The results from classical beamforming can sometimes be improved by postprocessing the classical beamform map to sharpen the peaks and reduce the sidelobes. Examples of deconvolution methods include DAMAS [7], CLEAN-SC [8] and linear programming [9]. These were investigated during this project, but Functional Beamforming was found to be more effective.

3.2 Functional Beamforming

Adaptive beamforming methods [10] are nonlinear formulas that attempt to improve the resolution and interference rejection of the classical formula. The Functional Beamforming formula [11, 12] is a new method of the adaptive type that offers better resolution and much higher dynamic range than conventional beamforming. The Functional Beamforming formula is given in Eq. (5), where where ν is a parameter between 1 and ∞.

$$b_\nu\left(\underline{g}\right) = \left[\underline{g}'\underline{\underline{C}}^{\frac{1}{\nu}}\underline{g}\right]^\nu \tag{5}$$

The expression reduces to classical beamforming for $\nu = 1$. The operation of raising $\underline{\underline{C}}$ to the power $\frac{1}{\nu}$ is implemented using the spectral decomposition shown in Eq. (6) where where $\underline{\underline{U}}$ is an orthogonal matrix with the eigenvectors of $\underline{\underline{C}}$, $\underline{u}_i, i = 1, \dots, N$, on the columns and the eigenvalue matrix is $\underline{\underline{\Sigma}} = \mathrm{diag}(\sigma_1, \dots, \sigma_N)$.

$$\underline{\underline{C}} = \underline{\underline{U}}\underline{\underline{\Sigma}}\underline{\underline{U}}' \tag{6}$$

The expression for $\underline{\underline{C}}^{\frac{1}{\nu}}$ is given in Eq. (7).

$$\underline{\underline{C}}^{\frac{1}{\nu}} = \underline{\underline{U}}\mathrm{diag}\left(\sigma_1^{\frac{1}{\nu}}, \dots, \sigma_N^{\frac{1}{\nu}}\right)\underline{\underline{U}}' \tag{7}$$

Negligible eigenvalues are excluded from this expression. Combining Eqs. 5 and 6 gives the alternative expression for Functional Beamforming shown in Eq. (8).

$$b_\nu\left(\underline{g}\right) = \left[\sum_{i=1}^{N} \alpha_i\, \sigma_i^{\frac{1}{\nu}}\right]^\nu \tag{8}$$

The α_i values, defined in Eq. (9) range from 0 to 1, and can be interpreted at the square of the cosine of the angle between the steering vector $\underline{g}$ and the eigenvector $\underline{u}_i$.

$$\alpha_i \equiv \left|\underline{g}'\underline{u}_i\right|^2, i = 1, \dots, N \tag{9}$$

3.3 Orthogonal Beamforming

In the Orthogonal Beamforming method [13] , the spectral decomposition of $\underline{\underline{C}}$ is computed and the $\alpha_i$values are computed according to Eq. (9) for all of the eigenvectors and all of the steering vectors. Each eigenvalue, eigenvector pair, $(\sigma_i, \underline{u}_i), i = 1, \dots N$, is assigned to the grid point, j, that maximizes the $\alpha_i\left(\underline{g}_j\right) = \left|\underline{g}_j{}'\underline{u}_i\right|^2$ over $j = 1, \dots M$. The source strength estimate for this grid point is set equal to σ_i. Grid points j, that do not maximize $\alpha_i\left(\underline{g}_j\right)$ for any eigenvector are assigned a source strength of 0. This produces a beamform map that conserves the integrated source strength of the CSM, since the sum of the source strength estimates over the beamforming grid equals the sum of eigenvalues of $\underline{\underline{C}}$, which also equals the trace of $\underline{\underline{C}}$, the sum of the microphone autopowers over the array. Dividing the map values by N would normalize the map so that the sum of the map values equals the array-average pressure-squared. Orthogonal Beamforming is good for some applications, but can give unexpected results for jet noise because an extended distribution of incoherent sources does not map 1-1 onto the eigenvalue, eigenvector pairs. That is to say it often happens that a given eigenvector, $\underline{u}_i$, gives rise to multiple peaks in $\left|\underline{g}_j{}'\underline{u}_i\right|^2$ at distinct grid points in the map. In this case, it is misleading to assign σ_i to one of these peak grid points and neglect the other peaks. For example, in a simulated line source of incoherent monopoles, the largest eigenvector will typically be assigned to a point in the center of the line. The second eigenvector will have two equal peaks of $\alpha_2\left(\underline{g}_j\right)$ for j corresponding to two points on either side of the center. The eigenvectors do not map neatly onto the grid points because the eigenvectors are forced to be mutually orthogonal, whereas the steering vectors for neighboring grid point are nearly parallel, even though they may have nonzero, uncorrelated, source strengths.

4. WAVEPACKET BASIS FUNCTIONS

Any source with a nontrivial directivity pattern requires a model that is more complicated than incoherent monopoles in order represent the radiation pattern in more than one direction at a time.

The wavepacket model used here is similar to previous work by Morris [14] and Papamoschou [15]. It is assumed that a large scale pressure field exists on the surface of a cylinder that encloses the flow. Let z be the donwstream axal coordinate of the cylinder and suppose the origin of the coordinate system coincides with a point to be considered as the center of an extended source. It is assumed, in the simplest case, that acoustic pressure is proportional to the symmetric Gaussian envelope function given in Eq. (10), where b is the axial width of the envelope and $\alpha = \frac{\omega}{u_c}$ is an axial wavenumber that is realated to the convection velocity of the wavepacket u_c.

$$G(z) = e^{-\left(\frac{z}{b}\right)^2} e^{i\alpha z} \qquad (10)$$

Making this assumption, using the Helmholtz equation outside the cylinder, and applying the method of stationary phase, the far field pressure of wavepacket takes the form given in Eq. (11), where θ is the polar angle of the observation point (the microphone) measured from the jet axis, R is the distance from the reference point at the origin to the microphone, and φ is the aximuthal angle of the microphone. The peak angle of the Gaussian envelope of the radiation pattern is characterized by $\cos\theta_0 \equiv \frac{\alpha}{k_0}$. The width of the peak in $cos\,\theta$ is $\beta \equiv \frac{b}{k_0}$. The radius of the cylinder is a. The circumferential eigenvalue, n, which gives the order of the Hankel function in the denominator, is taken as 0 for modes that are indepdent of φ.

$$p = \frac{q}{R} e^{-\left(\frac{\cos\theta_0 - \cos\theta}{2\beta}\right)^2} \frac{e^{ik_0 R} e^{in\phi}}{H_n^{(1)}(k_0\,\mathrm{a}\sin\theta)} \qquad (11)$$

As in the monopole case, the source q is considered to vary randomly in time at rate that is slow compared with the acoustic analysis frequency, ω. It is also assumed there are potentially a number of wavepacket source points along the jet axis at locations z_s indicated in Figure 6.

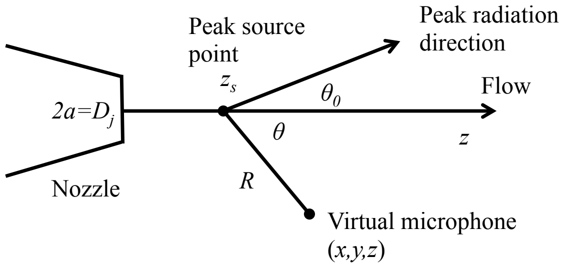

Figure 5: Wavepacket coordinates

5. HYBRID BEAMFORMING METHOD

The method ultimately developed in this research combines monopole and wavepacket steering vectors, Functional Beamforming, and ideas from Orthogonal Beamforming to tie the parts together. A composite beamforming grid is formulated as shown in Fig. 6. There are three Regions Of Interest (ROIs), monopole, upstream-radiating wavepackets, and downstream-radiating wavepackets

Like Orthogonal Beamforming, the method begins by computing the spectral decomposition of the CSM. The upper 50 of the 100 eigenvalues are considered and the lower 50 are discarded on the assumption that they are insignificant. Using the 50 retained eigenvectors, the squared inner products $\alpha_i\left(\underline{g}_j\right)$ are computed for $i = 1, \ldots, 50$ and $j = 1, \ldots, M$. An inner product threshold is determined (0.1 for this work). For each retained eigenvector, the largest $\alpha_i\left(\underline{g}_j\right)$ value is identified. If this maximum value of α exceeds the threshold, then the eigenvector is assigned to the ROI containing the steering vector that maximizes the inner product. This differs from Orthogonal Beamforming in that the eigenvector, eigenvalue pairs are only classified to ROIs, rather than being assigned to specific grid points. The motivation for this approach is that the steering vectors within a given ROI define a certain subspace of the array steering vector space, the span of these steering vectors. The various ROIs are supposed to be defined so as to contain sufficiently distinct types of steering vectors that each eigenvector can be uniquely classified into a certain ROI, i.e., the eigenvector is expected to fall within one or another ROI's subspace. The purpose of the threshold is to allow for the possibility that an eigenvector could have its origin in a process that is not associated with any of the ROIs.

After the first step, each ROI has had some, or no, eigenvectors assigned. Next, Functional Beamforming is applied for each ROI independently, using only the assigned eigenvalue, eigenvector pairs. Few additional calculations are required because the squared inner products and the eigenvalues are available from the first step. The Functional Beamforming results for each ROI are postprocessed by scaling so that sum of the scaled values equals the sum of the assigned eigenvalues divided by N. This compensates for peak width as well as the tendency of Functional Beamforming to yield unrealistic peak values in the case of inaccurate steering vectors. The final source strength estimates can be plotted to investigate the source characteristics and used with basis functions to the radiate the sound field to, for example, far field points.

The overview of the hybrid method is that Orthogonal Beamforming is used to assign the eigenvalues to ROIs and Functional Beamforming is used to distribute them within the ROIs. The ROIs used are intended to represent different physical processes: fine scale turbulence noise (monopole), large turbulent structures (downstream-propagating wavepackets), and shock associated noise (upstream-propagating wavepackets). This use of wavepacket basis functions to attempt to represent shock associated noise may not be strictly supported by the physical derivation of the wavepacket formula. For example, the appearance of the jet diameter in the Hankel function in the denominator may not be meaningful. In this case, the basis functions are being applied simply because they represent a set of anisotropic basis functions with directivity peaks in the broadside and upstream directions.

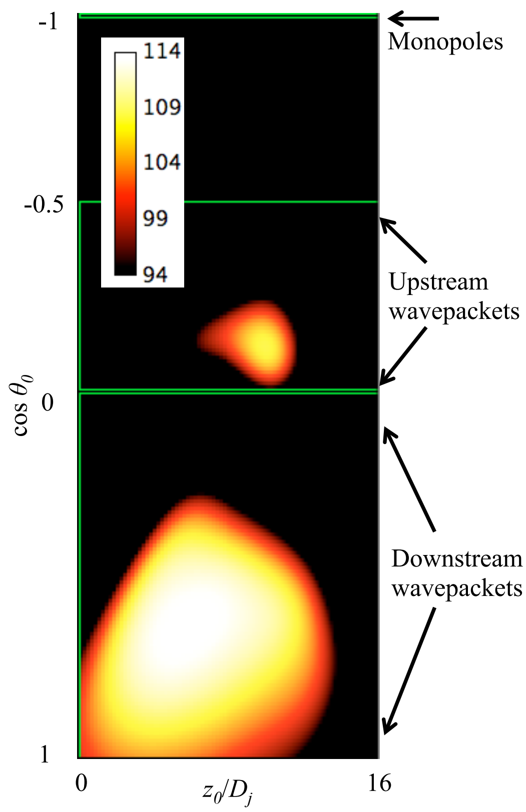

Figure 6: Wavepacket beamforming grid

6. RESULTS

6.1 2D Functional Beamforming with monopoles

Figure 8 gives octave band Functional Beamforming results for the cases studied. These plots were created by performing 1/12 octave band beamforming and incoherently summing the results to produce octave bands. The combination of continuously distributed sources and 50 dB dynamic range would not be possible with any known method other than Functional Beamforming. It is seen that the noise from the chevron case is weaker and slightly father aft.

6.2 Wavepacket results

Figures 8 and 9 show the octave-band downstream-propagating wavepacket source strength maps for baseline and chevron nozzles, respectively. As in the 2-D monopole plots in Fig. 8, the wavepacket source is weaker and located downstream relative to the baseline case. The peak wavepacket radiation direction is also shifted to larger angles in the chevron configuration. The octave-band upstream-propagating and monopole source maps are not shown because they do not display obvious trends.

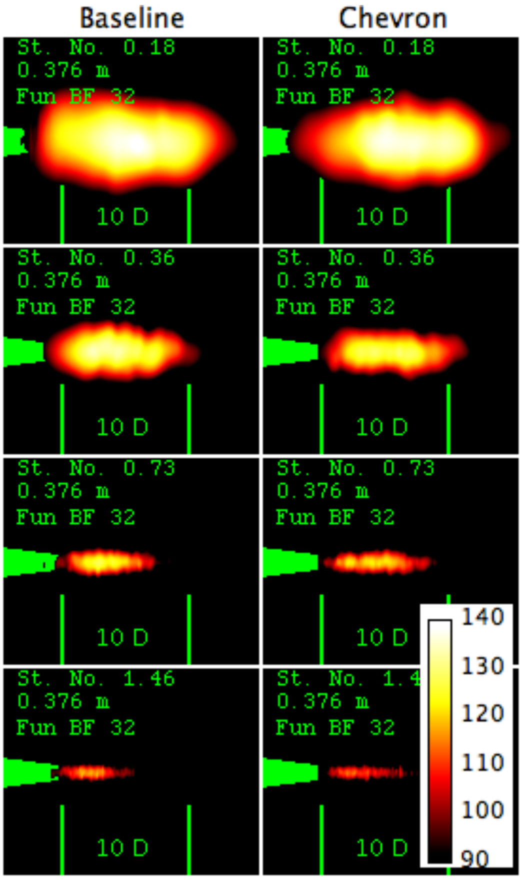

Figure 7: Two-dimensional, octave band, Functional Beamforming maps.

Figures 10 gives the array-average wavepacket source levels. Curves for upstream- and downstream-propagating wavepackets and the baseline and chevron configurations are shown. The upstream propagating wavepacket levels are about 20 dB below the downstream-propagating wavepacket levels. The difference decreases as the Strouhal number increases. Changing from the baseline to the chevron configuration reduces the downstream-propagating levels by 0-10 dB, with more reduction at higher Strouhal and Mach number. The levels of the upstream- propagating wavepackets are noisy and not seemingly changed by the chevron nozzle.

Figures 11 and 12 give the Ffowcs Williams-Hawkings (FWH) and wavepacket Functional Beamforming (WPFB) projected spectra at $\theta = 30°$ and $60°$, respectively. The difference between the FWH and WPFB results is typically about 2 dB. The WPFB results appear somewhat noisier than the FWH curves. The chevron projections are below the baseline projections by an amount that is larger at high frequency (St =1-2) at the 30° angle and larger at medium frequency (St = 0.3-0.5) at the 60° angle.

Figure 13 gives the projected Overall Sound Pressure Level (OASPL) for the FWH & WPFB projections and the baseline and chevron nozzles. In the peak angle range of 40°-50°, the difference between the two projection methods 1 dB or less. At very small angles, 10°-20°, the difference increases to as much as 3.25 dB, with the WPFB result consistently higher. The curves stop at 70° because the WPFB OASPL differ appreciably from the FWH curves for larger angles. The increased error in the WPFB result for angles away from the peak direction is believed to be related to the fact that largest density of microphones in the array was positioned between the source location and the peak directivity angle.

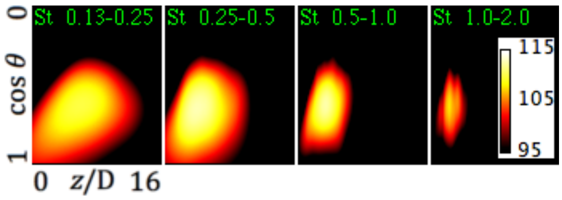

Figure 8 Downstream-propagating wavepacket source levels: baseline.

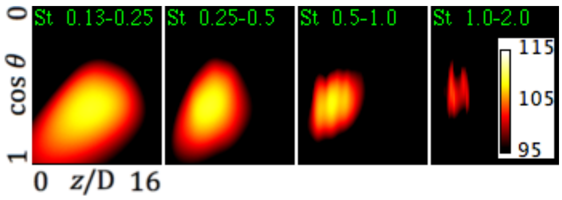

Figure 9: Downstream-propagating wavepacket source levels: chevron.

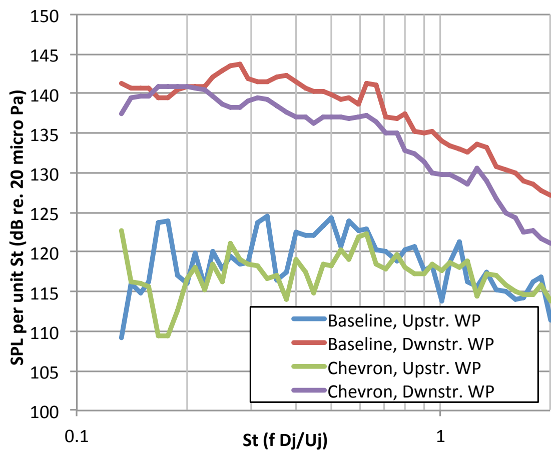

Figure 10: Array-average wavepacket source levels, $M_j = 1.36$

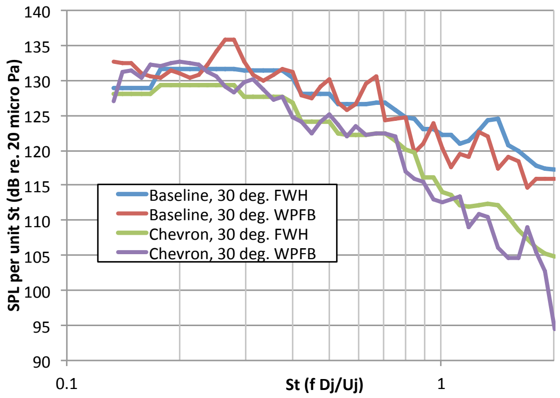

Figure 11: Projected spectra, $M_j = 1.36$, 30°

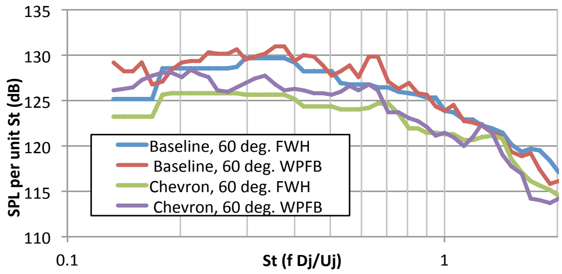

Figure 12: Projected spectra, $M_j = 1.36$, 60°

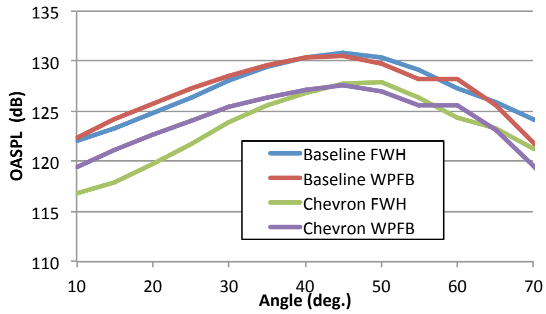

Figure 13: Projected OASPL

7. CONCLUSIONS

The method of developing phased array processing techniques using virtual microphone data from CFD can be successful. A hybrid beamforming technique that combines Orthogonal Beamforming with Functional Beamforming has been developed so as to take advantage of the strengths of both methods, as well as their common processing steps. Wave packets have been confirmed as a powerful basis set for beamforming high speed jet noise. A chevron nozzle for a high speed jet moves the primary location of the source large scale turbulence noise aft and the peak radiation angle of the source forward.

ACKNOWLEDGEMENTS

This work was supported by the Office of Naval Research under Contract N00014-12-C-0011.

The authors thank the Navy Technical Points of Contact (TPOC), Drs. Joseph Doychak and Brenda Henderson, for their support and encouragement during the execution of this contract.

REFERENCES

[1] Tam, K.W., 1995, "Supersonic jet noise", *Annu, Rev. Fluid. Mech*. 27, 17-43.

[2] Morris, P. J. and Viswanathan, K., 2013, “Jet noise,” in *Noise Sources in Turbulent Shear Flows*, ed. R. Camussi, Springer, 119-196.

[3] Tam, C. K. W., and Webb, J. C., 1993, "Dispersion-relation-preserving finite difference schemes for computational acoustics." *J. of Computational Physics*, Vol. 107, No. 2, pp. 262-281.

[4] Spalart, P., and Allmaras, S., 1992, “A One-Equation Turbulence Model for Aerodynamic Flows”, *Technical Report* AIAA-92-0439.

[5] Brès, G. A., 2002, “Modeling the noise of arbitrary maneuvering rotorcraft: Analysis and im- plementation of the PSU-WOPWOP noise prediction code,” M.S. thesis, Department of Aerospace Engineering, The Pennsylvania State University.

[6] Dougherty, R.P., 2012, “Improved generalized inverse beamforming for jet noise,” *Int. J. Aeroacoustics*, Vol. 11 No. 3-4.

[7] Brooks, T.F. and W.M. Humphreys, Jr., 2004 ,“A Deconvolution Approach for the Mapping of Acoustic Sources (DAMAS) determined from phased microphone arrays,” AIAA Paper 2004-2954.

[8] Sijtsma, P., 2009, "CLEAN based on spatial source coherence," *Int. J. Aeroacoustics*, Vol. 6, No. 4, pp 357-374.

[9] Dougherty, R.P., R.C. Ramachandran and G.Raman, 2013, "Deconvolution of Sources in Aeroacoustic Images from Phased Microphone Arrays Using Linear Programming," , AIAA Paper 2013-2210, Berlin, Germany.

[10]Johnson, D. H. and Dudgeon, D.E., *Array Signal Processing: Concepts and Techniques* Prentice-Hall, 1993.

[11]Dougherty, R.P., “Functional Beamforming”, Berlin Beamforming Conference, BeBeC 2014-1, 2014.

[12]Dougherty, R.P., 2014 "Functional Beamforming for Aeroacoustic Source

Distributions", AIAA Paper 2014-3066, Atlanta.

[13]Sarradj, E., 2010 “A fast signal subspace approach for the determination of absolute levels from phased microphone array measurements,” *Journal of Sound and Vibration* 329, 1553–1569,.

[14]Morris, P. J., 2009, “A note on the noise radiated by large scale turbulent structures in subsonic and supersonic jets,” *Int. J. Aeroacoustics*, Vol. 8, No. 4, pp. 301-316.

[15]Papamoschou, D., 2011, “Wavepacket modeling of the jet noise source,” AIAA Paper 2011-2835.

The birth of combustion science in France: Lavoisier, Berthelot, Vieille, Mallard, Le Chatelier, Jouguet and their impact on current research

Sébastien Candel[1] [2]

[1] Corresponding Author. CentraleSupélec, 92295 Chatenay-Malabry, France, Tel.: +33 1 41 13 10 83, E-mail: sebastien.candel@ecp.fr
[2] UPR288,CNRS, EM2C laboratory, 92295 Chatenay-Malabry, France.

ABSTRACT

This article provides a brief historical survey of the birth of combustion science with specific attention to the fundamental contributions of French scientists starting with the major discoveries due to Lavoisier, the founder of modern chemistry. Lavoisier was able to discard the so-called "phlogiston" theory and his immense contribution paved the way to the modern view of combustion. The paper then considers contributions of Berthelot, Vieille, Mallard and Le Chatelier who in the later years of the 19th century set the grounds of combustion science by performing fundamental experiments, deriving the first consistent theory of flames and demonstrating that the same mixture could support slow combustion waves (deflagration) and fast combustion waves (detonations) and demonstrating that the possible occurence of transition between deflagration and detonation. The early theory of detonations derived independently by Chapman and Jouguet is then briefly reviewed. Pioneering research carried out during this early period is then linked to current progress in combustion science.

Keywords: Combustion, explosions, detonation, flames, turbulent combustion

A Cross section area (m^2)
c_p Specific heat (J kg^{-1} K^{-1})
p Pressure (Pa)
S_L Laminar burning velocity (m s^{-1})
T_u Fresh mixture temperature (K)
T_b Burnt gas temperature (K)
T_i Ignition temperature (K)
U_D Detonation velocity (m s^{-1})
v Flow velocity (m s^{-1})
δ Flame thickness (m)
γ Specific heat ratio (-)

1. INTRODUCTION

Combustion is one of the oldest technologies known to man, it is at the root of civilization and is essential to the development of humankind. Combustion provides 85% of the primary energy, it assures most of the automotive transportation of persons and goods, it yields the energy required by aeronautical and space propulsion and is involved in many industrial processes like glass, cement and metal fabrication. But combustion also raises concerns as a source of fire, explosion, industrial risk and safety. Combustion also generates green house gases like carbon dioxide a species that is considered to be a major contributor to climate change. Pollutants generated by combustion have also become a major problem of modern technology and reduction of emissions constitutes an important objective in many applications.

It is clear that combustion science is playing an essential role in the present context and will continue to have considerable importance in the forseable future. It can be used to improve technologies, optimize systems and processes, reduce emission levels, enhance safety. Of course this is only a recent capacity. Fire has been known to man for for about half a million years, but that knowledge was essentially empirical. It took quite some time to learn how to ignite wood a capacity which is just about 30 000 years old. In comparison, combustion science itself is a very recent outcome and can be traced back to the work of Lavoisier (1734-1794) (Fig. 1). By performing careful combustion experiments Lavoisier was able to discard the phlogiston theory and lay the grounds of modern chemistry paving the way to combustion science.

This short article is focused on the early French contributions to combustion science and more specifically on those of Marcelin Berthelot, Paul Vieille, Ernest Mallard, Henry Le Chatelier and Emile Jouguet. It is quite fit to discuss this historic topic in the city of Budapest where some top level scientists were born

Figure 1. Lavoisier by Jacques Léonard Maillet, 1853. Palais du Louvre, cour Napoléon.

and educated and in this respect it is worth evoking the names of two immense personalities who contributed at a later stage to the theory of combustion and detonation : Theodore von Kármán and John von Neumann. In addition to their many other fundamental scientific contributions, Kármán and von Neumann notably advanced the theory of flames and detonations.

This article begins with a brief account of Lavoisier's foundation of modern chemistry. It proceeds with a short description of Berthelot and Vieille investigations of detonations. The theory of Mallard and Le Chatelier is described in the next section. The contributions of Jouguet are then discussed. The last section comprises a description of central issues in combustion science. Current progress is illustrated with a few examples which serve to show how much was accomplished in the more recent period.

2. LAVOISIER AND THE FOUNDATION OF MODERN CHEMISTRY

Combustion science begins with the work of Lavoisier, the founder of modern chemistry. Before Lavoisier, it was believed that fire constituted one of the four elements along with earth, wind and water. The "theory of the phlogiston" put forward in the 17th century prevailed among scientists. It implied that flames were formed by the flux of some kind of weightless substance which escaped from the burning material during the combustion process. This theory prevailed until the discoveries of Lavoisier who showed that a component of air which he later called oxygen reacted chemically with the combusting material generating heat and various products.

Through quantitative combustion experiments Lavoisier discarded previous explanations of combustion in his 1777 memoir, the beginning of which appears in Fig. 2 and in a lecture delivered at the Academy of sciences, Paris in 1783 [1]. The discovery of oxygen is also reported in this remarkable contribution. Later on Lavoiser demonstrated that water was formed by combining hydrogen with oxygen thus showing that water was not an element as previously believed but a composite. These advances are documented in his "Elementary treatise of chemistry presented in a new order after modern discoveries" [2]. It is quite regrettable that the French revolution put an end to his scientific discoveries by sending him to the guillotine at the age of 51.

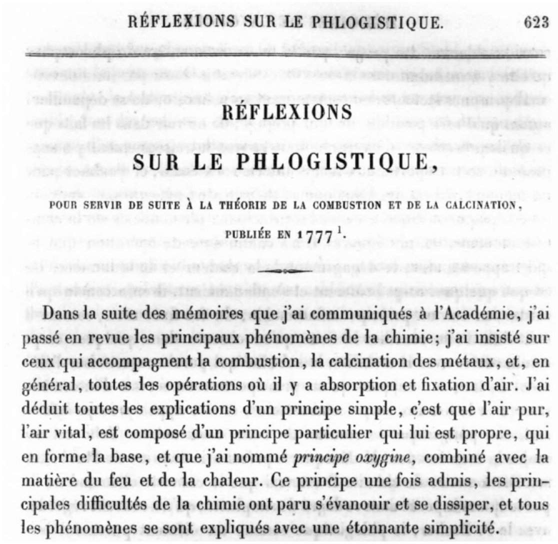

RÉFLEXIONS SUR LE PHLOGISTIQUE. 623

RÉFLEXIONS

SUR LE PHLOGISTIQUE,

POUR SERVIR DE SUITE À LA THÉORIE DE LA COMBUSTION ET DE LA CALCINATION, PUBLIÉE EN 1777 [1].

Dans la suite des mémoires que j'ai communiqués à l'Académie, j'ai passé en revue les principaux phénomènes de la chimie; j'ai insisté sur ceux qui accompagnent la combustion, la calcination des métaux, et, en général, toutes les opérations où il y a absorption et fixation d'air. J'ai déduit toutes les explications d'un principe simple, c'est que l'air pur, l'air vital, est composé d'un principe particulier qui lui est propre, qui en forme la base, et que j'ai nommé *principe oxygine*, combiné avec la matière du feu et de la chaleur. Ce principe une fois admis, les principales difficultés de la chimie ont paru s'évanouir et se dissiper, et tous les phénomènes se sont expliqués avec une étonnante simplicité.

Figure 2. The beginning of Lavoisier's memoir on the "Phlogiston" theory. [1]

3. THE LATER PART OF THE XIXTH CENTURY

Much progress in combustion science was accomplished during the 19th century. One may first evoke the contributions of Berthelot and Vieille and then examine those of Mallard and Le Chatelier.

3.1. The sensational discovery of gaseous detonations

Marcelin Berthelot (1827-1907) considered that chemical phenomena were not governed by some specific rules but followed the universal laws of mechanics. Berthelot synthesized a large number of organic compounds demonstrating that they could be obtained by standard chemical methods and that they followed the same principles as inorganic substances. His many experiments are reported in his books on "Mécanique chimique" (1878) and "Thermochimie" (1897). His investigations of explosives led to theoretical results collected in "Sur la force de la poudre et des matières explosives" (1872). During the siege of Paris (1870-1871), Berthelot was chairing the scientific defense committee and later on became chief of the French explosives committee. Experiments carried out with Paul Vieille [3, 4] on gaseous flames led to the sensational discovery of the fast mode of combustion in gaseous mixtures corresponding to detonations and to systematic measurements of detonation velocities in a variety of mixtures of gaseous fuels with different types of oxidizers. Incidentally, Paul Vieille (1854-1934) is also well known for his

invention of smokeless gun powder based on nitrocellulose (1884).
At the same time Ernest Mallard (1833-1894) and Henry Le Chatelier (1850-1936) observed the transition from deflagration to detonation by making use of a drum camera. This indicated that the two modes of combustion could be sustained in the same gaseous mixture. Mallard and Le Chatelier also suggested that the chemical conversion was initiated in the detonation wave by the adiabatic compression in the detonation front.
The different modes of combustion are sketched in Figure 3.

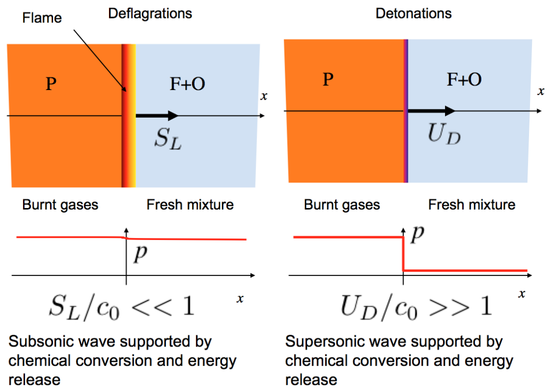

Figure 3. The different modes of combustion.

3.2. Early theory of flames

Starting from the work of Lavoisier, the scientific analysis of combustion was pursued in various directions by scientists like Volta, Bertholet, Berzelius, Dalton, Davy, Faraday and Bunsen. One important issue was that of mine explosions due to gas blasting. This led Davy to design a safety lamp using the principal of flame quenching by a fine metallic mesh. With the same motivation to reduce risk in coal mines, Mallard together with Le Chatelier carried out a comprehensive investigation of combustion, published in 1883 which reported what is considered to be the first theory of flame propagation. Former student from Ecole Polytechnique, Professor at the School of Mines in Saint-Etienne and later on at the School of Mines in Paris, Ernest Mallard is well known for his work on mineralogy and cristallography and for a Treatise on Cristallography published in 1879 with a second volume in 1884. At a later stage Mallard made a first attempt at deriving an expression for the burning velocity [5]. A few years later, Ernest Mallard with Henry Le Chatelier developed a set of fundamental investigations on combustion of explosive mixtures in relation with safety issues in mines [5, 6] reported in considerable detail in "Recherche expérimentales et théoriques sur la combustion des mélanges gazeux explosifs" while quite practical in its objective their research was however carried out in a scientific manner. Mallard and Le Chatelier both thought that progress of technical questions could be best achieved by studying the scientific basis. They understood that the burning velocity of explosive mixtures was a remarkably complex phenomenon and found important to identify the essential properties and dominant mechanisms like ignition and combustion temperature and the burning velocity. They identified the role of heat conductivity in this process and provided a clear demonstration that under certain conditions a regular regime of propagation at a constant burning velocity could be established. The theory is based on the idealized sketch shown in Fig. 4 adapted from Glassman [7] (see also Manson [8])

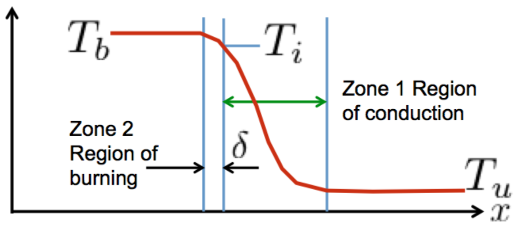

Figure 4. Schematic of the flame structure.

In the flame structure shown in Fig. 4 heat conducted from region 2 equals that required to bring the fresh mixture temperature to the ignition temperature:

$$\dot{m}c_p(T_b - T_u) = \lambda\frac{(T_b - T_i)}{\delta}A \tag{1}$$

$$\dot{m} = \rho A u = \rho S_L A \tag{2}$$

The burning velocity then takes the form

$$S_L = \frac{\lambda}{\rho c_p}\frac{T_b - T_i}{T_b - T_u}\frac{1}{\delta} \tag{3}$$

Now, this already provides a useful expression for the burning velocity but involves a quantity which is not easy to define precisely, the ignition temperature. In addition, one also has to estimate the thickness δ.
This was done later on by noting that the thickness of the burning region could be estimated in terms of the burning velocity and reaction time

$$\delta = S_L\tau = S_L/\dot{w} \tag{4}$$

Substituting the previous expression in that obtained by Mallard and Le Chatelier yields the following improved expression

$$S_L = [\frac{\lambda}{\rho c_p}\frac{T_b - T_i}{T_i - T_u}\dot{w}]^{1/2} \tag{5}$$

The burning velocity is now found to be proportional to the square root of the product of the heat diffusivity by the reaction rate

$$S_L \simeq (\alpha\dot{w})^{1/2} \tag{6}$$

Knowledge of the burning velocity is of importance as it gives access to the rate of heat release per unit flame area, a quantity of interest in the design of combustion systems. To see this one may consider a plane flame propagating in a fresh mixture of air and fuel as sketched in Figure 5. The mass fraction of fuel is Y_{fu} and its heating value per unit mass is Δh. It is then a simple matter to show that the rate of heat release per unit area is given by the mass flow rate of fuel converted in the flame times the heating value per unit mass:

$$\dot{Q} = \rho_u Y_{Fu} S_L \Delta h \tag{7}$$

It is instructive to use this expression to determine the heat released by a laminar flame propagating in stoichiometric mixture of air and methane. In this case $\rho_u \simeq 1.2\,\mathrm{kg\,m^{-3}}$, $(Y_{Fu})_{st} = 0.054$, $S_L(\phi = 1) \simeq 0.39\,\mathrm{m\,s^{-1}}$ and one finds that

$$\dot{Q} = 1.26\,\mathrm{MW\,m^{-2}}$$

.

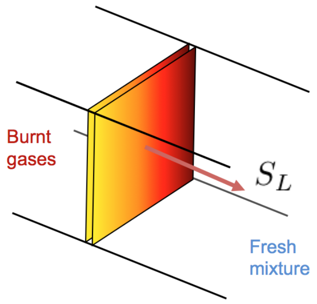

Figure 5. A methane air flame advances in the fresh mixture at a laminar burning velocity S_L.

4. EARLY XXTH CENTURY

4.1. The theory of detonations and the Chapman-Jouguet conditions

While propagation of detonations in gaseous mixtures was discovered by Berthelot and Vieille and transition from deflagration to detonation was observed by Mallard and Le Chatelier, the evaluation of the detonation velocity was considered by Chapman (1869-1958) [9] and Jouguet (1871-1943) [10, 11, 12]. The history of this topic is well covered by Lee [13] and in references cited in this book. Investigations of Chapman and Jouguet both rely on previous work on shock waves by Rankine [14] and Hugoniot [15, 16]. Use is made of the balance equations written for a one dimensional flow system undergoing chemical conversion. The initial state 1 designates the fresh mixture while the final state 2 corresponds to the reacted mixture. The chemical conversion of the fresh reactants in state 1 into burnt products in state 2 generates a certain amount of heat release per unit area and may be designated by q. One may assume that products in state 2 are in chemical equilibrium and determine the chemical composition of the fluid in state 2. Assuming for simplicity that the fresh and burnt mixtures behave as perfect gases so that $p_1 = \rho_1 r T_1$ and $p_2 = \rho_2 r T_2$ and that their specfic heats are constant and do not change, one may write the following balances of mass momentum and energy :

Mass balance

$$\rho_1 v_1 = \rho_2 v_2 \tag{8}$$

Momentum balance

$$p_1 + \rho_1 v_1^2 = p_2 + \rho_2 v_2^2 \tag{9}$$

Energy balance

$$c_p T_1 + \frac{1}{2} v_1^2 + q = c_p T_2 + \frac{1}{2} v_2^2 \tag{10}$$

One deduces from the previous expressions the Hugoniot relation which links the final state to the initial state and depends on the heat release q:

$$\frac{\gamma}{\gamma - 1}\left(\frac{p_2}{\rho_2} - \frac{p_1}{\rho_1}\right) - \frac{1}{2}(p_2 - p_1)\left(\frac{1}{\rho_1} + \frac{1}{\rho_2}\right) = q \tag{11}$$

When the heat release q is set to zero one retrieves the Hugoniot relation governing normal shock waves in a perfect gas. When q differs from zero, this expression provides conditions of the gas in state 2 as a function of conditions prevailing in state 1. In addition to this expression, a combination between mass and momentum balances yields the Rayleigh line defined by

$$\gamma M_1^2 = \left(\frac{p_2}{p_1} - 1\right)/\left(1 - \frac{\rho_1}{\rho_2}\right) \tag{12}$$

It is then convenient to draw the Hugoniot and Rayleigh lines in a diagram in which ρ_1/ρ_2 is the horizontal coordinate and p_2/p_1 is the vertical coordinate. The crossing points between these two lines correspond to solutions of the balance equations. Detonations correspond to the range $\rho_1/\rho_2 < 1$ while deflagrations are found for $\rho_1/\rho_2 > 1$.

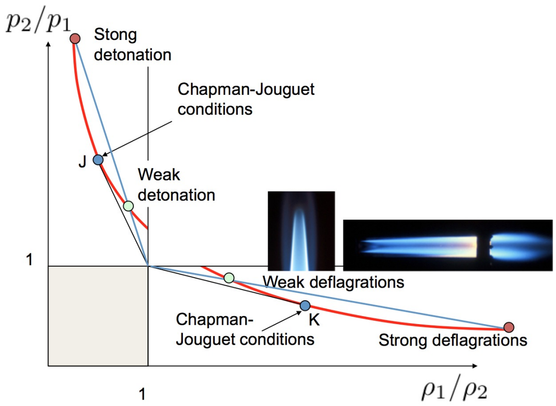

Figure 6. The Hugoniot and Rayleigh lines plotted in a $p - \rho$ diagram. C-J conditions correspond to the points where the Rayleigh line is tangent to the Hugoniot curve.

In contrast with the case of shock waves $q = 0$ which features a single solution and requires that the flow in state 1 be supersonic, there are two solutions when q differs from zero. In the detonation domain one finds a strong detonation solution such that the pressure p_2 and density ρ_2 are both larger than their counterparts corresponding to the weak detonation solution. The flow velocity on the downstream side (state 2) is subsonic with respect to the detonation wave in the strong detonation case while it is supersonic with respect to the wave in the weak detonation case. There is a point where these two solutions merge which corresponds to the case where the Rayleigh line is tangent to the Hugoniot line (point J) for detonations and another point K for deflagrations. Conditions at point J correspond to a minimum in the detonation velocity (as pointed out by Chapman) and to a miminum in entropy as demonstrated by Jouguet. Jouguet also found that the minimum entropy conditions at point J also led to sonic conditions of the flow in state 2and he proposed that the minimum entropy solution defined the characteristics of the detonation wave. The Chapman-Jouguet solution for detonations requires no knowledge of the internal structure of these waves. It only requires thermodynamic equilibrium calculations and provides reasonable estimates of detonation velocities which agree well with experimental data.Nevertheless, a physical interpretation of the C-J condition was missing but was later developed by Zelovich, von Neumann and Döring in what is called the ZND model for detonations (see [17, 13] for more details and recent developments).

5. RECENT PROGRESS IN COMBUSTION SCIENCE

In addition to issues considered by the early pioneers as evoked in previous sections, many other aspects need to be considered in the field of combustion. These arise from the fact that one has to cope with a wide range of applications including powerplants, gas turbines, industrial processes, automotive engines, rocket motors... introducing an extraordinary diversity in configurations, geometries and operational conditions. At the same time one has to consider a collection of difficulties resulting from the underlying disciplines and their coupling including fluid mechanics, themodynamics, chemical kinetics and transport phenomena. The corresponding scientific issues are linked with : (1) The many modes of combustion, (2) Complex kinetics, (3) Stiff reaction rates following Arrhenius laws, (4) The thin layer multicsale nature of flames, (5) The existence of critical conditions (ignition, extinction...), (6) Combustion of reactants in liquid or solid form (sprays, solid fuels...), (7) Interactions with boundaries, (8) High pressure, transcritical conditions, (9) Complex turbulent flows, (10) Essentially multiphysics (coupling with many other processes : acoustics, radiation...).

It is of course not possible to examine all these complications in this short article. This is done in a number of recent textbooks and in many review papers published in Progress in Energy and Combustion Science and in the plenary lectures delivered at the biannual International Combustion Symposia and appearing in the Proceedings of the Combustion Institute (see for example [17, 18, 19, 20, 21, 22, 23, 24]). We will only examine a few of these topics to illustrate progress accomplished since the early days of combustion science.

5.1. The theory of flames and complex kinetics

It is surprising to note that chemistry as a science is just a little more than two hundred years old and measure how much progress has been made over such a short period. This progress was also made possible by advances in thermodynamics, transport processes and fluid dynamics. The subdomain of combustion chemistry has also evolved quite remarkably as well allowing detailed analysis of flame structures which were carried out further during the XXth century. The governing equations describing the coupled combustion process were written in full detail only about fifty years ago and their computer application is even more recent. Initial attempts at obtaining numerical solutions for simple flames were made during the 1950's but detailed calculations of one dimensional flames were only completed during the late 70's. Multidimensional calculations of flames have become available during the 80's. Combustion reactions are now described with complex kinetic schemes involving tenths to hundreds species and hundreds to thousands elementary reactions.

About 60 years ago, in 1954 Karman and Penner [25] were able to treat the ozone decompostion flame by means of a two step reaction model

$$O_3 + M \rightarrow O + O_2 + M \tag{13}$$

$$O + O_3 \rightarrow 2O_2 \tag{14}$$

and determine the burning velocity of this relatively simple flame. They indicated in their report that their was hope that the more complicated chain reactions, such as the combustion of hydrocarbons, would also be made accessible to theoretical computations.

This has been accomplished well beyond what Karman and Penner were forseeing. Laminar flame calculations have now become routine and flame structures are being determined by including large kinetic schemes and detailed transport properties (see for example [26]). These calculations provide laminar burning velocities with great accuracy. Much work has also concerned strained flames formed in a counterflow, a configuration in which the flame is flat and the flow depends on a single transverse coordinate. This has allowed considerable progress in the analysis and determination of critical conditions defining extinction and ignition. Progress in the understanding of elementary mechanisms of flame initiation, propagation and instabilities has also been quite substantial (see for example [27]).

Advances on the theoretical side have also been quite substantial. The modern approach in the analysis of flame structures has mostly relied on activation energy asymptotics inspired by the early work of Zeldovich and Frank Kamenetski (see Zeldovich *et al.* [28]). Many theoretical investigations use the fact that the activation energy of the main kinetic step controlling the combustion process is large, so that the ratio $E/(RT_u)$ is large. Zeldovich and his colleagues were first to exploit this idea in a systematic fashion and it is now standard to define the Zeldovich number $E(T_b - T_u)/(RT_u^2)$ and consider asymptotic expansions in terms of large Zeldovich numbers. This is exemplified in the work Linan [29], Clavin (see [30, 31] for reviews), Sivashinsky [32], Buckmaster and Ludford [18], Williams [33, 34], Law [35, 36, 26] and Matalon [37, 38]. This track has been exploited extensively starting in the 1970s yielding a wealth of information on the structure and properties of many types of flames and on fundamental combustion processes like ignition and extinction.

5.2. Turbulent combustion

The interest in turbulent flames is more recent arising from the many technical applications of combustion. It is known that turbulent fluctuations occur in most practical flows but that "Turbulence is the most important unsolved problem of classical physics" as remarked by the famous Nobel prize winner Richard Feynman. Turbulent combustion introduces additional difficulties associated with the thin spatial scales correponding to the chemical conversion process in the flames and to the variety of temporal scales characterizing this process. In practical configurations this is compounded with many other complexities : injection of fuel as a spray, rotation imparted to the flow by swirlers, multiperforation of the boundary... One may then come to the conclusion that not much could be done with such complicated situations. This is not so, and much progress has been made in the analysis and modeling of turbulent flames. The key issue is of course the description of turbulence/combustion interactions ([22, 39]). There is no space to examine this topic in detail but one can safely consider that advances have been made because of the new simulation capacities in combination with detailed experimental investigations exploiting laser diagnostics and numerical imaging using high speed cameras. In the early days (in the 1970s) most turbulent flames were calculated with Reynolds Average Navier-Stokes equations (RANS). Considerable insights were then gained in the late 1980s and 1990s through Direct Numerical Simulations (DNS) (see [40, 41, 42, 43, 44]. These have provided useful information on many elementary processes of turbulent combustion. Starting in the 1990s the effort shifted to Large Eddy Simulations, a method in which the large scales of turbulence are calculated while the small scales are modeled. Results of LES are such that one can safely say that the future clearly lies in LES and that one can hope to deal with many practical applications and related issues (see [39] for a detailed presentation of issues and methods, [45] for a recent overview and [46] for a review of recent modeling tools in LES).

5.3. Ignition dynamics in annular systems

An example is now given to illustrate the state of the art in the simulation of turbulent flames. This example corresponds to the ignition process in a multiple-injector annular combustor designated as MICCA. This system comprises 16 swirling injectors which are fed with a mixture of propane and air. A view of the combustor under steady state operation is shown in Fig. 7. The combustor has transparent annular side walls allowing a direct view of the flame.

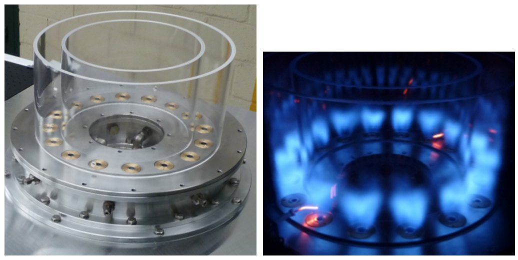

Figure 7. On the left multiple injector annular combustor MICCA. The lateral walls made of quartz allow a direct view of the combustion region. This device fed with a mixture of propane and air is seen under operation on the right.

Simulation of the ignition and light-round process are carried out with the AVBP flow solver developed by CERFACS and IFPEN and equipped with the F-TACLES combustion model derived in our laboratory. The computational domain includes the air/fuel injection manifold, plenum, swirling injectors, and the full annular space defined by the combustor backplane and sidewalls [47, 48]. A large volume is added at the exit of the combustor to represent the surrounding atmosphere. The mesh comprises 310×10^6 tetrahedra. Direct comparisons between numerical results and experimental data are shown in Fig. 8. The flame position is obtained in the experiment by recording the light intensity with a high speed camera.

A remarakable agreement is obtained between the simulated flame and the patterns observed in the experiment. The light-round delay is also well retrieved.

6. SUMMARY

By setting the basis of modern chemistry, Lavoisier made an essential step forward. His careful measurements allowed him to discard erroneous "theories"

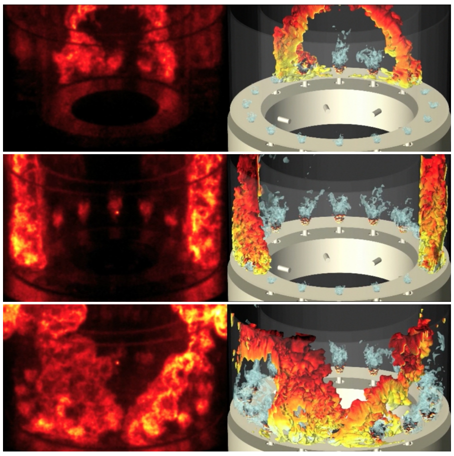

Figure 8. Ignition and light-round of a multiple injector annular combustor. On the left light emission detected by a high speed CCD camera. On the right results of Large Eddy Simulations. [47, 48].

like that of the phlogiston and to lay the grounds for combustion science. At a later stage Berthelot and Vieille in a sensational discovery demonstrated that there were two types of flames, one progressing at low speed designated as deflagration, the other much faster corresponding to detonation. During that same period corresponding to the later part of the XIXth century Mallard and Le Chatelier set the grounds for modern combustion theory by identifying the fundamental mechanisms controlling the propagation of deflagration and providing a reasonable mathematical expression for the burning velocity which could be used to explain many of their experimental observations. Mallard and Le Chatelier also demonstrated that combustion could take the form of slow flames propagating at low speed and fast flames corresponding to detonations and that transition could be observed between these two regimes. The existence of these two regimes was later analyzed independently by Chapman and Jouguet leading more specifically to the Chapman-Jouguet conditions for detonations which provided a relatively simple method for estimating detonation velocities. From these pioneering studies combustion has evolved into a broad field at the crossroads of four scientific disciplines including fluid mechanics, thermodynamics, transport phenomena and chemical kinetics. Following the initial steps made by these remarkable scientists, much progress has been made allowing considerable improvements of our understanding of combustion phenomena and a wide range of applications in a variety of fields. Still, much more remains to be done on a variety of topics including combustion modeling for large eddy simulation, application of these simulation methods to realistic configurations, computational efficiency, automatic reduction, tabulation methods, code coupling, multiphysics problems, combustion dynamics (ignition, extinction, flashback, instabilities), spray flames, pollutant prediction (soot, NOx...), transcritical combustion. Much remains to be done to deal with emerging challenges from novel combustion systems and technologies.

ACKNOWLEDGEMENTS

It is a pleasure to acknowledge the kind invitation of Professor Dominique Thévenin to give this lecture and the support provided to our research by CNRS, CNES, Safran and DGA.

REFERENCES

[1] Lavoisier, A. L., 1777, *Réflexions sur le phlogistique, pour servir de suite à la théorie de la combustion et de la calcination*, Académie des sciences, Paris.

[2] Lavoisier, A. L., 1789, *Traité élémentaire de chimie, présenté dans un ordre nouveau et d'après les découvertes modernes*.

[3] Berthelot, M., 1881, *Comptes Rendus de l'Académie des Sciences, Paris*, Vol. 93, pp. 18–22.

[4] Berthelot, M., and Vieille, P., 1883, *Ann Chim Phys*, Vol. 5è Série 28, p. 289.

[5] Mallard, E., 1875, "De la vitesse avec laquelle se propage l'inflammation dans un mélange d'air et de grisou et la théorie des lampes de sureté", *Annales des Mines*, Vol. 7, pp. 355–381.

[6] Mallard, E., and Chatelier, H. L., 1883, "Recherches expérimentales et théoriques sur la combustion des mélanges gazeux explosifs", *Ann Mines, Paris*, Vol. 4, pp. 274–561.

[7] Glassman, I., 1987, *Combustion*, Academic press, New York.

[8] Manson, N., 1988, "Some notes on the first theories of the flame velocity in gaseous mixtures", *Combustion and Flame*, Vol. 71, pp. 179–187.

[9] Chapman, D., 1899, "On the rate of explosion in gases", *Phil Mag*, Vol. 47, pp. 90–104.

[10] Jouguet, E., 1905, "Sur la propagation des réactions chimiques dans les gaz", *J Math Pures Appl*, Vol. 1, pp. 347–425.

[11] Jouguet, E., 1906, "Sur la propagation des réactions chimiques dans les gaz", *J Math Pures Appl*, Vol. 2, pp. 5–85.

[12] Jouguet, E., 1917, *La mécanique des explosifs*, O. Doin, Paris.

[13] Lee, J., 2008, *The detonation phenomenon*, Cambridge Univ Press, Cambridge.

[14] Rankine, W. J., 1870, "On the thermodynamic theory of waves of finite longitudinal disturbances", *Phil Trans of the Royal Soc London*, Vol. 160, pp. 277–288.

[15] Hugoniot, H., 1887-1889, "Mémoire sur la propagation des mouvements dans les corps et spécialement dans les gaz parfaits (première partie)", *J Ecole Polytechnique*, Vol. Cahiers 57, pp. 3–97.

[16] Hugoniot, H., 1889, "Mémoire sur la propagation des mouvements dans les corps et spécialement dans les gaz parfaits (deuxième partie)", *J Ecole Polytechnique*, Vol. 58, pp. 1–125.

[17] Williams, F. A., 1965 second edition 1985, *Combustion theory*, Benjamin/Cummings Publishing Co.

[18] Buckmaster, J. D., and Ludford, G. S. S., 1982, *Theory of laminar flames*, Cambridge Univ Press.

[19] Zeldovich, Y. B., Barenblatt, G. I., Librovitch, V. B., and Makhviladze, G. M., 1985, *The Mathematical Theory of Combustion and Explosions*, Consultants bureau, New York.

[20] Clavin, P., 1985, "Dynamic behavior of premixed flame fronts in laminar and turbulent flows", *Prog Energy Combust Sci*, Vol. 11, pp. 1–59.

[21] Candel, S., 2002, "Combustion dynamics and control: progress and challenges", *Proceedings of the Combustion Institute*, Vol. 29, pp. 1–28.

[22] Veynante, D., and Vervisch, L., 2002, "Turbulent combustion modeling", *Progress in Energy and Combustion Science* , Vol. 28, pp. 193–266.

[23] Westbrook, C. K., Mizobuchi, Y., Poinsot, T., Smith, P., and Warnatz, J., 2005, "Computational combustion", *Proceedings of the Combustion Institute* , Vol. 30, pp. 125–157.

[24] Poinsot, T., and Veynante, D., 2005, *Theoretical and Numerical Combustion (2nd Edition)*, Edwards.

[25] Kármán, T., and Penner, S. S., 1954, "Fundamental approach to laminar flame propagation", *Selected Combustion Problems, Part 1*, Butterworths Scientific Publications, London, pp. 5–41.

[26] Law, C. K., 2006, *Combustion physics*, Cambridge Univ Press.

[27] Jarozinski, J., Veyssiere, B., and Eds, 2009, *Combustion Phenomena : Selected Mechanisms of Flame Formation, Propagation, and Extinction*, CRC, Boca Raton.

[28] Zeldovitch, Y. B., Barenblatt, G. I., Librovitch, V. B., and Makhviladze, G. M., 1985, *Mathematical Theory of Combustion and Explosions*, (English translation), Plenum Press, New York.

[29] Linan, A., 1974, "The asymptotic structure of counterflow diffusion flames for large activation energies", *Acta Astronautica*, Vol. 1, p. 1007.

[30] Clavin, P., 1985, "Dynamic behavior of premixed flame fronts in laminar and turbulent flows", *Progress in Energy and Combustion Science* , Vol. 11, pp. 1–59.

[31] Clavin, P., 2000, "Dynamics of combustion fronts in premixed gases: from flames to detonations", *Proceedings of the Combustion Institute* , Vol. 28, pp. 569–586.

[32] Sivashinsky, G. I., 2002, "Some developments in premixed combustion modeling", *Proceedings of the Combustion Institute* , Vol. 29, pp. 1737–1761.

[33] Williams, F. A., 1985, *Combustion theory*, Benjamin Cummings, Menlo Park, CA.

[34] Williams, F., 1992, "The role of theory in combustion science", *Proceedings of the Combustion Institute*, Vol. 24, pp. 1–17.

[35] Law, C. K., 1988, "Dynamics of stretched flames", *Proceedings of the Combustion Institute*, Vol. 22, pp. 1381–1402.

[36] Law, C. K., and Sung, C. J., 2000, "Structure, aerodynamics and geometry of premixed flamelets", *Progress in Energy and Combustion Science* , Vol. 26, pp. 459–505.

[37] Matalon, M., and Matkowsky, B. J., 1982, "Flames as gasdynamic discontinuities", *Journal of Fluid Mechanics* , Vol. 124, p. 239.

[38] Matalon, M., 2009, "Flame dynamics", *Proceedings of the Combustion Institute* , Vol. 32, pp. 57–82.

[39] Poinsot, T., and Veynante, D., 2005, *Theoretical and numerical combustion*, R.T. Edwards, 2nd edition.

[40] Poinsot, T., Candel, S., and Trouvé, A., 1996, "Application of direct numerical simulation to premixed turbulent combustion", *Progress in Energy and Combustion Science* , Vol. 21, pp. 531–576.

[41] Poinsot, T., 1996, "Using direct numerical simulation to understand turbulent premixed combustion (plenary lecture)", *Proceedings of the Combustion Institute* , Vol. 26, pp. 219–232.

[42] Vervisch, L., and Poinsot, T., 1998, “Direct Numerical Simulation of non premixed turbulent flames”, *Annual Review of Fluid Mechanics* , Vol. 30, pp. 655–692.

[43] Thévenin, D., Gicquel, O., de Charentenay, J., Hilbert, R., and Veynante, D., 2002, “Two-versus three-dimensional direct simulations of turbulent methane flame kernels using realistic chemistry”, *Proceedings of the Combustion Institute* , Vol. 29, pp. 2031–2039.

[44] Thévenin, D., 2005, “Three-dimensional direct simulations and structure of expanding turbulent methane flames”, *Proceedings of the Combustion Institute* , Vol. 30, pp. 629–637.

[45] Candel, S., Durox, D., Schuller, T., Darabiha, N., Hakim, L., and Schmitt, T., 2013, “Advances in combustion and propulsion applications”, *Journal of Mechanics B-Fluids*, Vol. 40, pp. 87–106.

[46] Fiorina, B., Veynante, D., and Candel, S., Flow, Turbulence and Combustion, “Modeling combustion chemistry in Large Eddy Simulations of turbulent flames”, *2015*, Vol. 94, pp. 3–42.

[47] Philip, M., Boileau, M., Vicquelin, R., Schmitt, T., Durox, D., Bourgouin, J., and Candel, S., 2014, “Ignition sequence in a multi-injector combustor”, *Physics of Fluids*, Vol. 26, 091106, doi: 10.1063/1.4893452.

[48] Philip, M., Boileau, M., Vicquelin, R., Schmitt, T., Durox, D., Bourgouin, J., and Candel, S., 2015, “Simulation of the ignition process in an annular multiple-injector combustor and comparison with experiments”, *J Eng Gas Turbines Power (ASME)*, Vol. 137 (doi: 10.1115/1.4028265).

Conference on Modelling Fluid Flow (CMFF'15)
The 16th International Conference on Fluid Flow Technologies
Budapest, Hungary, September 1-4, 2015

TOWARDS A BETTER UNDERSTANDING OF TURBOMACHINERY BEAMFORM MAPS

Csaba Horváth[1], Bence Tóth[2]

[1] Corresponding Author. Department of Fluid Mechanics, Faculty of Mechanical Engineering, Budapest University of Technology and Economics. Bertalan Lajos u. 4 – 6, H-1111 Budapest, Hungary. Tel.: +36 1 463 2635, Fax: +36 1 463 3464, E-mail: horvath@ara.bme.hu
[2] Department of Fluid Mechanics, Faculty of Mechanical Engineering, Budapest University of Technology and Economics. E-mail: tothbence@ara.bme.hu

ABSTRACT

Beamforming processes developed specifically for rotating sources have provided a nonintrusive means by which turbomachinery noise sources can be localized. Investigations by Horváth et al. have shown that for unducted rotating coherent noise sources beamforming will localize the noise sources to their Mach radii rather than their true noise source positions. As a further step, Horváth et al. have shown that beamforming investigations utilizing beamforming processes developed specifically for the investigation of rotating noise sources in an absolute as well as a rotating reference frame need to take noise sources appearing on the hub into consideration in order to accurately identify all noise sources. The investigations showed that for certain frequencies this noise source can result from a combination of motor noise which is truly located on the hub, rotor-stator interaction noise radiating from along the rotor blade span, and even rotor-stator interaction noise radiating from along the span of the stationary guide vanes. The present investigation continues this study by investigating certain parameters and providing further guidelines for separating the beamform peak which is localized to the hub into its true noise source components, which are located on the axis as well as along the span of the rotor and the stator, making it possible to better understand turbomachinery beamform maps.

Keywords: axial flow turbomachinery, beamforming, Mach radius, tonal noise sources

NOMENCLATURE

B	[-]	blade count
L_B	[dB]	beamforming peak level
L_p	[dB]	sound pressure level
M_t	[-]	blade tip Mach number
M_x	[-]	flow Mach number
n	[-]	harmonic index
p	[Pa]	sound pressure
p_a, p_b	[Pa]	sound pressures of coherent noise sources
p_{ref}	[Pa]	reference sound pressure
p_t	[Pa]	total sound pressure
x	[-]	number of equal strength coherent in phase noise sources
y, z	[m]	coordinates in the plane of the fan
z^*	[-]	Mach radius
α	[°]	phase angle
Θ	[°]	angle of the viewer

Subscripts and Superscripts

one	contribution form one source
1	acoustic harmonic
2	loading harmonic

1. INTRODUCTION

As legislations and regulations have become more stringent along with the expectations of customers, the amount of research in the field of turbomachinery aeroacoustics has progressively increased. As a result of this, turbomachinery design requirements are continuously evolving, often pushing the limits of design practices. The drive to further increase efficiency and reduce noise levels is also pushing technology to develop at a fast pace. Design, simulation, and measurement technologies are therefore being refined and even radically reformed in the process. With regard to acoustic measurement technology, microphone technology has been improved, measurement techniques have been developed, and a combination of the two has helped us gain more information from the recorded acoustic data than ever before possible.

Traditionally, microphones have been set up and recorded individually, with the spectrum of the individual microphone signals providing a vast amount of information regarding the radiated noise field of the investigated phenomena. The development of phased array microphone beamforming technology has made it possible to extend these capabilities, simultaneously recording multiple microphone signals and then processing the results in order to learn more about the noise sources which are being investigated. Beamforming processes developed specifically for rotating sources have provided a nonintrusive means by which the noise sources of turbomachinery can be localized [1-3]. Utilizing phased array microphones and these advanced beamforming algorithms we are able to collect data for identifying turbomachinery noise sources, which is becoming a common practice [1-5]. On the other hand, the results are not so easily understood. Most beamforming algorithms assume that the noise is generated by compact incoherent noise sources, in most cases resulting in beamform maps which localize the noise sources to their true locations. If the investigated noise sources are coherent, the beamforming algorithms often have a hard time distinguishing one source from the other, resulting in the noise sources being incorrectly located on the beamform maps. This publication is one in a series that aims at understanding the beamform maps of various unducted turbomachinery applications. The goal is to first understand these beamform maps and then use the newly gained knowledge for developing methods of evaluating them, while in the long run taking this a step further and developing new beamforming methodologies specifically for the investigation of rotating noise sources. Questions which are addressed in this investigation are: If a noise source which is localized to the axis by beamforming is looked at in an absolute or rotating reference frame, will the source strength be the same? When we have multiple coherent noise sources which are localized to the same Mach radius position, how can we determine the individual contributions? With regard to the second question, only a few specific cases are looked at here, since there are many possibilities which need to be investigated.

The publications of Horváth et al. regarding unducted rotating coherent noise sources have shown that the noise sources are pinpointed to their respective Mach radii rather than their true locations by beamforming methodologies [6]. The name "Mach radius" or "sonic radius" refers to the mode phase speed, the speed at which the lobes of a given mode rotate around the axis, having a Mach number of 1 at the Mach radius (z^*, a normalized radius, where $z^* = 1$ refers to the blade tip) when examined from the viewpoint of the observer [7]. See Eq. (1). Based on these findings, Horváth et al. have explained the beamform maps of rotating coherent noise sources with regard to counter-rotating open rotors that are investigated from the sideline [8] as well as explaining why certain noise sources are localized to the axis in the case of a generic unducted axial flow fan test case which is investigated from the axial direction [9].

The investigation of a generic unducted axial flow fan test case by Horváth et al. focused on the noise sources appearing on the axis of the fan [9]. In many similar investigations, noise sources located on the axis have been associated with motor noise with no further investigations being considered [1, 5]. Taking into account what is known from [6] regarding unducted rotating coherent noise sources appearing at their respective Mach radii, it was shown that the noise sources appearing on the hub can for certain frequencies be resulting from noise sources located along the span of the rotor or the guide vane. This occurs when the wave fronts of coherent noise sources experience constructive and destructive interference, interacting with the phased array in the same manner as the wave front of a single monopole noise source located at the Mach radius of the given instance would. In the test case described in [9] the Mach radius is zero and therefore the noise source is localized to the axis. The Mach radius is calculated using Eq. (1), with n being the harmonic index, B being the blade count or guide vane count, M_t being the blade tip Mach number, M_x being the flow Mach number, and Θ being the angle of the viewer with regard to the axis (upstream direction referring to 0°), with subscripts 1 and 2 referring to the rotor or guide vane of the acoustic harmonic and loading harmonic, respectively. The equation is formulated for a turbomachinery system consisting of two rotors or one rotor and one guide vane which are moving relative to one another. Acoustic harmonic refers to the rotor or guide vane which is radiating noise while being loaded by the potential field and/or the viscous wake of the other, which is referred to as the loading harmonic. Both rows of rotors or guide vanes need to be considered as acoustic as well as loading harmonics in order to receive a complete and accurate sound field, since each blade row loads the other blade row and also radiates sound simultaneously [7].

$$z^* = \frac{(n_1 B_1 - n_2 B_2)}{(n_1 B_1 M_{t,1} + n_2 B_2 M_{t,2})} \frac{(1 - M_x \cos\Theta)}{\sin\Theta} \qquad (1)$$

The results presented in [9] therefore provide an explanation as to why the investigated noise sources appear on the axis. Three tonal components of unducted axial flow turbomachinery noise were investigated: motor noise, interaction noise radiating from the guide vanes as they interact with the rotors, and interaction noise radiating from the rotors as they interact with the guide vanes. The present report makes a further contribution to these results, providing information regarding how to distinguish between the contribution of the motor, each rotor, and each stator to the level of the apparent noise source appearing on the axis. This is done by individually investigating the effect of each of these noise sources on the beamform peak which is localized to the axis. In this way further guidelines are provided which will help in separating the noise source appearing on the axis into its components.

This investigation is motivated by a desire to better understand the beamform maps of unducted axial flow turbomachinery, which is necessary in order to accurately process the results of rotating coherent as well as incoherent noise sources which are processed using currently available beamforming methods, and which will provide the basis of a new beamforming investigation method designed specifically for the investigation of unducted rotating coherent noise sources.

2. TURBOMACHINERY NOISE SOURCES

In categorizing turbomachinery noise sources, they can be split into two main groups, tonal and broadband noise sources. Tonal noise sources are characterized by a discrete frequency, and are associated with the regular cyclic motion of the rotor blades with respect to a stationary observer and with the interaction of the rotors with adjacent structures [10]. These are referred to as Blade Passing Frequency (BPF) tones and interaction tones, respectively. With respect to the present investigation, the coherence of the noise sources also needs to be taken into consideration. Coherent noise sources are characterized by a time invariant phase relationship. While in most cases broadband noise sources are not coherent, many tonal turbomachinery noise sources often are. Broadband noise sources are characterized by a wide frequency range, and are associated with the turbulent flow in the inlet stream, boundary layer, and wake [10].

3. AXIAL FLOW FAN TEST CASE

In this investigation a synthetic axial flow fan test case is presented. The synthetic fan is used instead of a real fan in order to provide a means by which multiple noise sources can individually be investigated while easily manipulating certain variables. Figure 1 provides a schematic of the fan test case which is synthesized herein. An axial flow fan having a variable number of rotor blades (5 are pictured in the figure) and downstream guide vanes (1 is pictured in the figure) is investigated by a microphone phased array located 0.3 *m* in the upstream axial direction. The fan has a diameter of 0.4 *m*. The diameter of the phased array is 1m. The microphones of the array are arranged along a logarithmic spiral, based on the design used in the OptiNav Inc. Array 24: Microphone Phased Array System.

The following three components of turbomachinery noise are investigated: motor noise, guide vane noise radiating from the guide vanes as they interact with the rotors, and rotor noise radiating from the rotors as they interact with the guide vanes. The motor is represented by 1 stationary monopole noise source located on the axis. The guide vanes are represented by stationary coherent monopole noise sources located at the blade tips, and the rotors are represented by coherent rotating monopole noise sources located at the blade tips. Figure 2 shows a schematic of the monopole noise sources which replace the true noise sources. They are represented by small spheres in the figure.

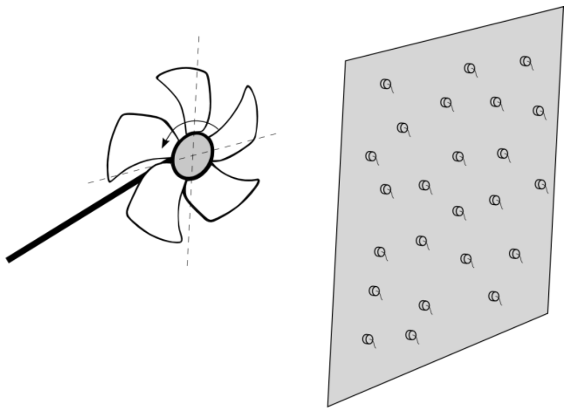

Figure 1. Schematic of the fan test case which is synthesized in the investigation.

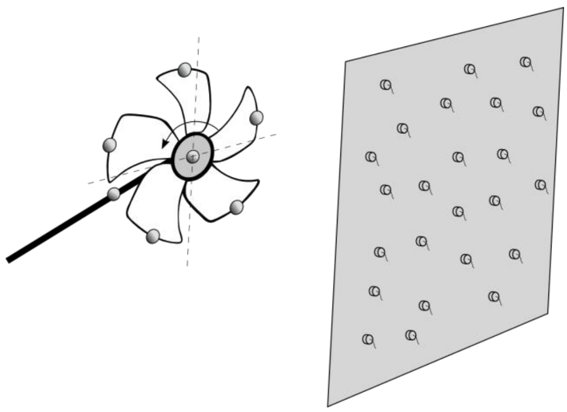

Figure 2. Synthetic fan test case, with monopole noise sources replacing the rotors, guide vanes and motor.

Only simulations of the synthetic test cases are presented in this investigation, but it should be mentioned that [9] showed that the simulations correctly localize the noise sources to their Mach radii and therefore these simulations can be used in further investigating other parameters. In order to account for the limited resolution of the finite aperture array, the investigated frequency is chosen as 3000 *Hz* for all test cases, and therefore the results provide beamform maps which clearly depict the investigated noise sources. Being a synthetic case, the sound pressure amplitude is defined at each noise source position instead of the sound power and whenever possible defined as having a sound pressure value which would be equivalent to a sound pressure level of 60 *dB* if measured at the source position. This investigation does not investigate the effect of phase difference at the source location, and therefore the phase of each noise source was set equal. The stationary monopole noise source located on the axis and representing the motor radiates at the investigated frequency, and should be considered as a harmonic of the motor noise. The stationary monopole noise sources representing the guide vanes also radiate at the same investigated frequency, as a result of the potential field and/or the viscous wake of the rotor blades rotating at a given RPM and interacting with the guide vanes or a harmonic of this tone. The coherent rotating monopole noise sources located at the blade tips and representing the rotors radiate at the same investigated frequency, which is resulting from the potential field and/or viscous wake of the guide vanes interacting with the rotor blades or one of its harmonics.

4. BEAMFORMING

For the simulations presented herein, in-house virtual noise source generation and propagation software is used for creating virtual microphone signals at the microphone positions. The in-house code is able to produce noise sources which are moving at subsonic speeds, while taking into account sound intensity attenuation with distance and the Doppler Effect. The simulation data is processed by versatile in-house beamforming software. Two types of algorithms are used: the classical frequency-domain based Delay & Sum (DS) method [11], which can localize incoherent stationary sources in an absolute reference frame, and the Rotating Source Identifier (ROSI) method [1], which can localize the incoherent sources which are stationary in a rotating reference frame. The results provide beamform maps, which display the magnitudes and the positions of the strongest sources located in the investigated plane for a given frequency range. The magnitudes of the beamform map sources are presented as levels which are calculated from sound pressure squared values which have been corrected for sound intensity attenuation with regard to distance. The values are therefore given with regard to the source position. The reference value used in the calculation of the levels is $2*10^{-5}$ *Pa*. Using these two algorithms, the sound sources originating from both the stationary and rotating elements of the fan can be localized.

Beamforming utilizes the phase differences measured between the microphone signals to determine the direction of arrival of the wave fronts. By adjusting the phase shifts (time delays) of the microphone signals relative to each other, a maximum correlation can be obtained between them. The corresponding phase shifts give information as to the direction of arrival of the wave fronts and hence the locations of the noise sources. This forms the basis of the DS beamforming method [11]. The method can be considered as forming a sensitivity curve, called mainlobe that is directed toward possible compact monopole noise source positions by phase adjustments. These possible source positions are defined by the user, providing focus points for the beamforming methodology, and the beamform maps display the strengths of the investigated sources.

The ROSI beamforming method is an extension of the DS method for rotating source models [1]. The main difference between the two methods is that the ROSI method applies a so called deDopplerization step in order to place the rotating noise sources into a rotating reference frame and hence make them stationary. The positions and velocities of the possible noise sources are accounted for by correcting the time difference and amplitude data with regard to each receiver position. The corrected source signals are then processed with a beamforming method that corresponds with the DS method. For a more detailed description of the ROSI method, see reference [1]. A more detailed description of the phased array microphone system and of the beamforming algorithms applied in the in-house code is available in [5].

In processing the test data the following parameters are applied. A sampling rate of 44100 *Hz* is used and 2 seconds worth of data are processed. A Hanning window is applied with a windowing size of 2048, which is applied with a 50% overlap. The narrowband beamform peak data is presented in the beamform maps and diagrams. It should be mentioned that the rotor noise sources were modelled in a rotating reference frame and when needed transferred into an absolute reference frame (making them rotating sources) by processing the data with the ROSI method. Vice versa, the stator noise sources were modelled in an absolute reference frame and when needed transferred into a rotating reference frame (rotating the stationary sources) by processing the data with the ROSI method.

5. RESULTS

As stated in the introduction, this paper further investigates turbomachinery noise sources which are localized to the axis by beamforming. The goal is to understand the effect of rotor blade number, stator blade number, and noise source amplitude on the resulting apparent noise source located on the axis, in order to help determine the contribution of each individual noise source.

The first test investigates the effect of motor noise source level on the level of the noise source located on the beamform map. The test examines changing the level of a single tonal noise source which is physically located on the axis and beamforming the results in both an absolute as well as rotating reference frame using the DS and ROSI beamforming methods. Figure 3 presents a diagram which compares the sound pressure level of the defined amplitude at the source location to the calculated beamform peak value, which is also calculated with regard to the source location. It can be seen that the values coincide well for the absolute and rotating reference frame results, having a constant difference of approximately 0.1 *dB*. This shows that the magnitude of the noise source which is physically located on the axis is independent from the coordinate system in which the noise source is investigated. Looking at Fig. 3, it can also be seen that with regard to the magnitude of the noise source there is a linear relationship between the source magnitude and the beamforming peak value. This suggests, as is customary in the beamforming literature, that for tonal sources physically located on the axis, the array can be calibrated with the help of a known source, after which the integral of the beamform map can be used in order to quantify results [11].

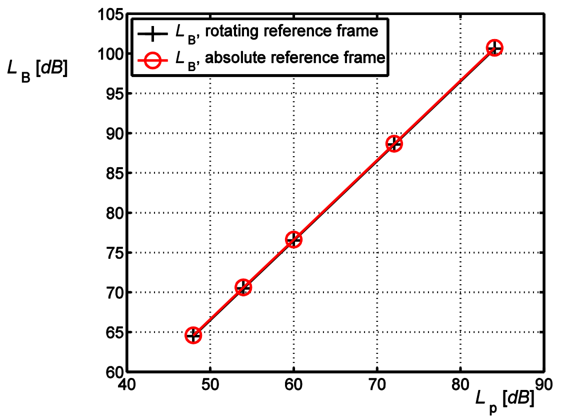

Figure 3. Relationship between the beamform peak level and the sound pressure level of the motor noise calculated with respect to the source.

The second test case investigates the effect of blade number on the level of the apparent noise source located on the axis. Multiple coherent in phase noise sources were evenly distributed around the axis. The noise sources were investigated in an absolute as well as rotating reference frame in order to investigate the effects of stationary sources (stators) in an absolute as well as rotating reference frame. (This is the same as investigating rotating sources (rotors) in a rotating and stationary reference frame, respectively, and therefore only one set of data is presented.) The number of sources was varied while keeping the frequency the same and therefore the rpm of the rotor was varied accordingly for each case. Source numbers ranging from 15-20 were investigated. Since this investigation does not look at the effect of phase difference between the sources, the number of rotors and stators is always kept equal and therefore the noise sources are always in phase.

Regarding coherent noise sources, it is known from classical acoustics that Eq. (2) can be used to determine the sound pressure level, L_p, of a single microphone measurement, where p_{ref} is the reference sound pressure and p_{t} is the total sound pressure, which can be determined according to Eq. (3) [12]. Here p_{a} and p_{b} refer to the sound pressures of two coherent noise source signals and α refers to the phase angle between them. The equation can be extended to take into account multiple sources. With regard to beamforming maps and superimposed apparent noise sources the authors have no information which can help in determining the contribution of each individual coherent noise source. This test is designed to give us a better understanding of these contributions.

$$L_p = 10\log_{10}\left(\frac{{p_{\mathrm{t}}}^2}{{p_{\mathrm{ref}}}^2}\right) \qquad (2)$$

$$ {p_{\mathrm{t}}}^2 = {p_{\mathrm{a}}}^2 + {p_{\mathrm{b}}}^2 + 2p_{\mathrm{a}}p_{\mathrm{b}}\cos\alpha \qquad (3)$$

Typical beamform maps from this multiple noise source test can be seen in Figures 4 and 5. The fan is viewed from the upstream direction, as depicted in Fig. 1, with the axis passing through the 0,0 position. Fig. 4 shows the beamform map of 15 equal strength rotating coherent in phase noise sources (stationary noise sources which have been processed using ROSI). Fig. 5 depicts the beamform map of 15 equal strength stationary coherent in phase noise sources (stationary noise sources processed using DS). As expected from the earlier investigations of Horváth et al. [9], the noise sources are always localized to the axis by beamforming. A summary of the coherent in phase noise source results can be seen in Figure 6, which depicts the beamform peak level of the apparent noise source which is localized to the axis for both the rotating as well as stationary coherent in phase noise sources as a function of source number.

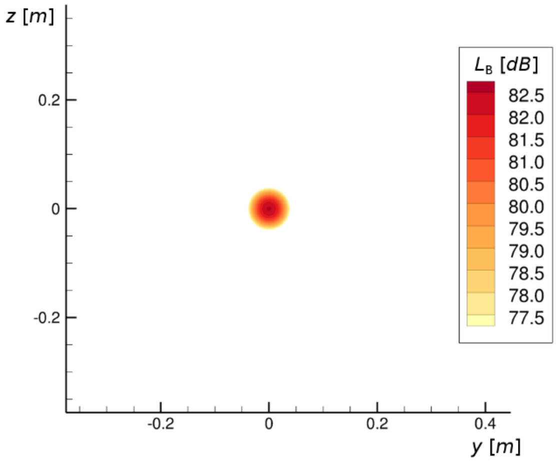

Figure 4. Beamform map of 15 stationary, coherent, in phase noise sources investigated in the rotating reference frame.

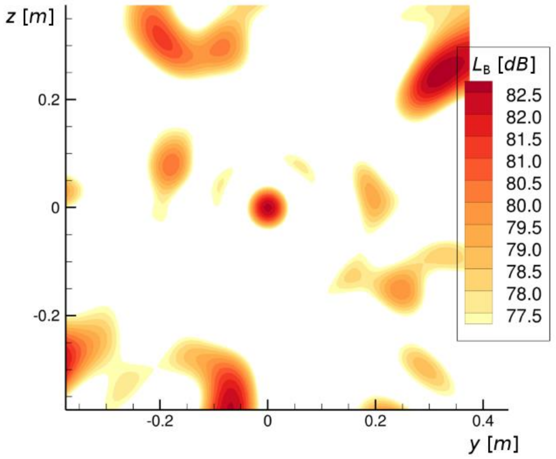

Figure 5. Beamform map of 15 stationary, coherent, in phase noise sources investigated in the absolute reference frame.

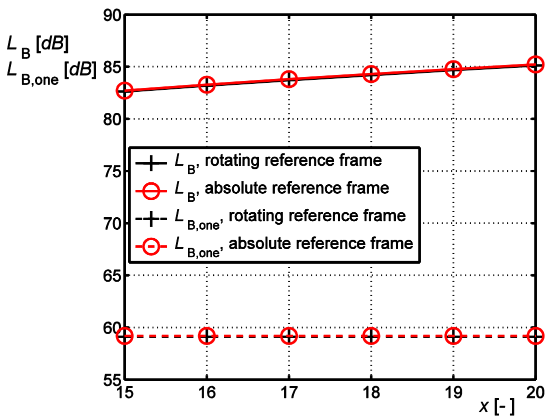

Figure 6. Beamform peak level of the equal strength coherent in phase apparent noise source as a function of source number.

In this investigation it is assumed that all of the coherent noise sources are of equal strength, which is known to be true in this case and generally true for axisymmetric turbomachinery noise sources. It is also known that the wave fronts of coherent noise sources experience constructive and destructive interference as they propagate, resulting in modes. In this test case a planar wave mode is traveling along the axis of the fan, the Mach radius of which is zero. Since the microphones used in the investigation are all relatively close to the axis and far enough away from the noise source for the planar wave mode to have already developed, it is expected that the contributions from each of the noise sources should be in the same phase at the in plane microphone positions as at the source positions. If this hypothesis is true, and the noise sources have the same phase difference at the microphones as they do at their source locations, then an equation which is analogous to Eq. (2) will describe the increase of beamform peak level at the Mach radius as a function of number of coherent in phase noise sources. According to the hypothesis, in this test case $\cos(\alpha)$ is equal to 1 since the phase of each noise source is the same, and Eq. (2) can be rewritten for the beamform peak level, L_B, of x coherent in phase noise sources of equal strength, as seen in Eq. (4). Here p_{one} refers to what would be the pressure amplitude of the beamform peak which could be calculated back from the beamforming results for one of the equal strength coherent in phase noise sources at the apparent source location. The equation can be rewritten for levels, as seen in Eq. (5). $L_{B,one}$ refers to the beamform peak level contribution from one of the equal strength coherent in phase noise sources at the apparent source location (Mach radius). Rearranging Eq. (5), one can solve for $L_{B,one}$, which should be equal for each instance investigated here, if the hypothesis is correct.

$$L_B = 10\log_{10}\left(\frac{p_{one}^2}{p_{ref}^2}\right) + 10\log_{10}\left(\frac{x^2}{p_{ref}^2}\right) \tag{4}$$

$$L_B = L_{B,one} + 20\log_{10}(x) \tag{5}$$

The values for $L_{B,one}$ are also plotted in Fig. 6 as a function of number of sources, where it can be seen that they are equal. It can therefore be concluded that though the noise sources are not physically located at the Mach radius position, the levels can be added using equations which are customarily used for the addition of coherent sound pressure levels. Taking advantage of this, one can determine the beamform peak amplitude contribution of one of the equal strength coherent in phase noise sources to the apparent noise source located at the Mach radius position.

The investigation is conducted in both the absolute as well as rotating reference frame with the help of the DS and ROSI methods, as can be seen in Fig. 6. Similar to the results for the noise source which is physically located on the axis, the difference between $L_{B,one}$ for DS and ROSI is approximately 0.1 *dB*. This shows that the results are independent of reference frame in which they are investigated, as was also the case for the noise source physically located on the axis.

Since the amplitudes of the noise sources used in the second test are defined as having a sound pressure level of 60 *dB* at the source position, they can be compared to the one case in the first test which also has a magnitude of 60 *dB*. The values of the beamform map peaks do not agree as can be seen in comparing Figs 3 and 6. Though beyond the scope of this investigation, further tests will investigate the relationship between the beamform peak level of one noise source which is physically located on the axis to the contribution from one of the noise sources which contributes to the apparent noise source which is located at the Mach radius.

6. CONCLUSIONS

This investigation is one in a series which looks at the beamforming results of coherent rotating noise sources through a turbomachinery fan test case. The goal is to better understand the beamforming results of currently available beamforming methods and to provide preliminary information which is needed in the development of a new beamforming method designed specifically for rotating coherent noise sources.

While earlier investigations provided information as to the localization of the rotating coherent noise sources to the Mach radius, which is the axis in this particular case, this investigation takes this a step further. The first test case investigates whether the level of a noise source which is physically located on the axis is affected by the choice of reference frame. The results show that the results are the same for the DS and ROSI investigations. The results also suggest that the results can be quantified by integrating the beamform maps, as is customary in beamforming investigations, though this is beyond the scope of the present investigation.

A second test investigates the contribution from equal strength coherent in phase noise sources to the magnitude of the apparent noise source located at the Mach radius. The noise sources are investigated in a rotating as well as absolute reference frame. The results show that the equations used in acoustics for adding levels can be applied in determining the contributions from equal strength coherent in phase noise sources to the apparent noise source located at the Mach radius. The results show that the same levels can be calculated for one test case independent of reference frame in which it is investigated. On the other hand, the beamforming peak level is dependent on whether the noise source is physically located at the given position or just an apparent noise source.

Though beyond the scope of this present report, further tests will investigate the relationship between the beamform peak level of one noise source which is physically located on the axis to that of the contribution from one of the noise sources which contributes to the apparent noise source which is located on the axis.

ACKNOWLEDGEMENTS

This work has been supported by the Hungarian National Fund for Science and Research under contract K 112277 and relates to the scientific program of the projects "Development of quality-oriented and harmonized R+D+I strategy and the functional model at BME" and "Talent care and cultivation in the scientific workshops of BME" under grants TÁMOP-4.2.1/B-09/1/KMR-2010-0002 and TÁMOP-4.2.2/B-10/1-2010-0009, respectively.

REFERENCES

[1] Sijtsma, P., Oerlemans, S., and Holthusen, H., 2001, "Location of Rotating Sources by Phased Array Measurements", *National Aerospace Lab. Technical Report* Paper NLR-TP-2001-135.

[2] Pannert, W., and Maier, C., 2014, "Rotating Beamforming – Motion-Compensation in the Frequency Domain and Application of High-Resolution Beamforming Algorithms", *Journal of Sound and Vibration*, Vol. 333, Issue 7, pp. 1899-1912.

[3] Herold, G., and Sarradj, E., 2015, "Microphone Array Method for the Characterization of Rotating Sound Sources in Axial Fans", Proc. *International Conference on Fan Noise, Technology and Numerical Methods*, Lyon, France, paper 026.

[4] Kennedy, J., Eret, P., Bennett, G., Sopranzetti, F., Chiariotti, P., Castellinni, P., Finez, A., and Picard, C., 2013, "The Application of Advanced Beamforming Techniques for the Noise Characterization of Installed Counter Rotating Open Rotors" Proc. *19th AIAA/CEAS Aeroacoustics Conference*, Berlin, Germany, Paper AIAA 2013-2093.

[5] Benedek, T., and Tóth, P., 2013, "Beamforming Measurements of an Axial Fan in an Industrial Environment", *Periodica Polytechnica Mechanical Engineering*, Vol. 57, No. 2, pp. 37-46.

[6] Horváth, Cs., Envia, E., and Podboy, G. G., 2014, "Limitations of Phased Array Beamforming in Open Rotor Noise Source Imaging", *AIAA Journal*, Vol. 52, No. 8, pp. 1810-1817.

[7] Parry, A. B., and Crighton, D. G., 1989, "Prediction of Counter-Rotation Propeller Noise", Proc. *AIAA 12th Aeroacoustics*

Conference, San Antonio, Texas, AIAA-89-1141.

[8] Horváth, Cs., 2015, “Beamforming Investigation of Dominant Counter-Rotating Open Rotor Tonal and Broadband Noise Sources”, *AIAA Journal*, Vol. 53, No. 6, pp. 1602-1611.

[9] Horváth, Cs., Tóth, B., Tóth, P., Benedek, T., and Vad, J., 2015, “Reevaluating Noise Source Appearing on the Axis for Beamform Maps of Rotating Sources”, Proc. *International Conference on Fan Noise, Technology and Numerical Methods*, Lyon, France, paper 013.

[10] Smith, M. J. T., 1989, *Aircraft noise*, Cambridge University Press.

[11] Mueller, T., Allen, C., Blake, W. K., Dougherty, R. P., Lynch, D., Soderman, P., and Underbrink, J., 2002, *Aeroacoustic Measurements: Chapter 3.*, Springer.

[12] Norton, M., and Karczub, D., 2003, *Fundamentals of Noise and Vibration Analysis for Engineers*, Cambridge University Press.

Conference on Modelling Fluid Flow (CMFF'15)
The 16th International Conference on Fluid Flow Technologies
Budapest, Hungary, September 1-4, 2015

CASE-SPECIFIC SEMI-EMPIRICAL GUIDELINES FOR SIMULTANEOUS REDUCTION OF LOSS AND EMITTED NOISE IN AN AXIAL FLOW FAN

Tamás BENEDEK[1], János VAD[2]

[1] Corresponding Author. Department of Fluid Mechanics, Faculty of Mechanical Engineering, Budapest University of Technology and Economics. Bertalan Lajos u. 4 – 6, H-1111 Budapest, Hungary. Tel.: +36 1 463 2464, Fax: +36 1 463 3464, E-mail: benedek@ara.bme.hu

[2] Department of Fluid Mechanics, Faculty of Mechanical Engineering, Budapest University of Technology and Economics. E-mail: vad@ara.bme.hu

ABSTRACT

The paper presents the semi-empirical investigation on the effect of the inlet axial velocity profile on the total efficiency and the upstream-radiated noise of an industrial axial flow fan rotor, installed in a free-inlet, free-exhaust setup. As a preliminary empirical diagnostics step, the emitted noise of the fan was measured by means of a Phased Array Microphone system, and the inlet axial velocity profile was taken with use of a vane anemometer. Supported by the measurements, the spanwise distribution of the emitted noise was estimated on the basis of the momentum thickness of the blade suction side boundary layer, being considered also as a loss indicator of the fan blading. The spanwise distribution of the momentum thickness was calculated with use of 2D empirical cascade correlations. The appropriateness of the applied rotor through-flow model was assessed by means of CFD simulation. Based on the semi-empirical model, the paper presents the method for surveying the dependence of the total efficiency and average sound pressure level for various inlet axial velocity profiles. Such method forms a basis for simultaneously reducing the loss and the emitted noise, while retaining the global aerodynamic performance of the fan.

Keywords: axial flow fan, efficiency, inlet velocity profile, noise, phased array microphone

NOMENCLATURE

A	[dB]	parameter in Eq. 4
d_t	[mm]	tip diameter
k	[-]	exponent in Eq. 5
L_P	[dB]	area-averaged SPL
$L_{P\Theta*}$	[dB]	Θ*-based approximation of SPL
$L_{\Theta*}$	[dB]	momentum thickness level
n	[RPM]	rotor speed
P	[Pa]	sound pressure
R	[-]	dimensionless radius
α	[°]	flow angle (from axial direction)
Φ	[-]	global flow coefficient
φ	[-]	local axial flow coefficient
η_t	[-]	total efficiency
ν	[-]	hub to tip ratio
ψ_{is}	[-]	local isentropic total pressure rise coefficient
ψ'_{sw}	[-]	local swirl loss coefficient
$\Theta*$	[-]	momentum thickness parameter
ω	[-]	local friction loss coefficient

Subscripts

1	rotor inlet
2	rotor outlet

Abbreviations

CFD	Computational Fluid Dynamics
PAM	Phased Array Microphone
ROSI	Rotating Source Identifier
SPL	sound pressure level
SST	Shear Stress Transport
2D	two-dimensional

1. INTRODUCTION

The inlet condition of an axial flow fan installed in an industrial environment often differs from the condition assumed in fan design or realized during the laboratory measurements forming the basis of fan catalogue data. The alteration in the inlet velocity profile influences the flow incidence to the blades, and has a major effect on the development of the boundary layer on the suction side of the fan blades. As noted in [1], the suction side boundary layer plays a key role in the generation of the aerodynamic loss over the blade surface. The boundary layer thickness can be used as an indicator of total pressure loss [2]. The suction side boundary layer is also one of the major aero-acoustic noise sources of the fan [3]. As reported in [4], the emitted noise relates to the boundary layer thickness. These findings can be summarized as follows. a) The inlet axial velocity profile substantially influences the condition of the blade boundary layer, *via* the angle of flow incidence to the blade sections. b) As such, it has a significant effect on the aerodynamic performance and noise of the fan. c) While retaining the global aerodynamic performance of the fan (flow rate, total pressure rise), the inlet axial velocity profile may be suitably tuned for simultaneously reducing the emitted noise and the total pressure loss (i.e. improving the total efficiency). Tuning the inlet axial velocity can be carried out by means of aerodynamically profiled rotor entry sections. For example, the ISO standard [5] prescribes the use of a bellmouth entry upstream of the fan in certain measurement installations – regardless of what type of inlet condition was assumed in the design of the rotor under consideration. The bellmouth entry aims at ensuring that the flow is uniform over the entire rotor intake section. Therefore, it is a means for realizing the "uniform axial inlet condition", often used in axial fan design as an idealized condition.

In the papers [6-8], Benedek and Vad presented a diagnostics method for discovering case-specific semi-empirical correlations between the spatial distribution of the aerodynamic properties and the noise sources of the fan blading. The diagnostic method, adaptable to on-site studies of industrial fans, is based on the following experimentation: a) measurement of the rotor inlet axial velocity profile, b) Phased Array Microphone (PAM) experiments. For the case study in [7-8], it was reported that the emitted sound pressure is proportional to the momentum thickness of the blade wake in the third-octave frequency bands that are the most important from the viewpoint of human audition.

In the present paper, the evaluation method related to the case study detailed in [7-8] is further developed, enabling the case-specific semi-empirical investigation on the effect of the inlet axial velocity profile on the aerodynamic loss and the emitted noise.

This paper is considered as a Technical note for the Workshop "Beamforming for Turbomachinery Applications" organized at CMFF'15. The paper aims at provoking a discussion on the topics outlined in the Summary.

2. THE FAN OF CASE STUDY, MEASUREMENT SETUP

The fan of case study is a ventilating fan with tip diameter d_t = 300 *mm*, hub-to-tip ratio ν = 0.3, tip clearance 6.6% relative to the span, and n = 1430 *RPM* rotor speed. The fan has 5 forward skewed blades and has no guide vanes. The fan was built in a short duct, in a free-inlet, free-exhaust setup (zero static pressure rise). The fan is equipped with a short, rounded inlet rim (photograph in [6]).

The inlet axial velocity profile was measured with use of a vane anemometer along two diameters being perpendicular to each other. The PAM measurement was performed from the upstream direction with use of an OptiNav Inc. Array24 microphone array. The distance between the PAM and the fan was 1.83 d_t, the PAM plate was set perpendicular to the axis of rotation, and the centre of the array coincided with the rotor axis. A more detailed description of the fan, the measurements and their evaluation can be found in [7-8].

3. SEMI-EMPIRICAL CALCULATION OF THE RADIAL DISTRIBUTION OF THE AERODYNAMIC PROPERTIES

3.1 The "simplified" through-flow model

In the papers [6-8], the aerodynamic properties were calculated along the span from the measured inlet axial velocity profile and from the geometrical data of the blading, using a two-dimensional (2D) cascade approach. In the aforementioned papers, the authors used the straightforward through-flow model inspired by reference [3] that the radial velocity component is *fully neglected* inside the rotor, i.e. the circumferentially averaged inlet and outlet axial velocity profiles are identical. This through-flow model is labelled herein as "***simplified" model***.

The "simplified" model enables the easiest treatment of through-flow in rotor analysis, and is directly consistent with the 2D cascade approach. Furthermore, it enables that the realistic angles of flow incidence to the blade sections are considered in the rotor analysis, determined directly from the measurement of the inlet axial velocity profile. Its obvious limitation is the inability to represent *any* rearrangement of the axial velocity profile through the rotor.

In the present paper, the "simplified" model is competed with a more sophisticated through-flow model, labelled herein as "***radial equilibrium" model***, and outlined in what follows.

3.2 The "radial equilibrium" model

In the case of axial flow rotors, the well-known radial equilibrium equation makes a connection between the outlet axial velocity profile and the radial distribution of total pressure rise of the blading. For further details, e.g. [3] is referred to. The dimensionless form of the radial equilibrium equation is the following:

$$\left(\eta_t - \frac{\psi_{is}(R)}{2 \cdot R^2}\right)\frac{d}{dR}\psi_{is}(R) = \frac{d}{dR}\varphi_2^2(R) \qquad (1)$$

The equation was implemented in the former calculation method [6] *via* an iteration algorithm. In the first step, the radial distributions of the aerodynamic properties were computed with use of the inlet axial velocity profile. Then, the outlet axial velocity profile was recalculated from the resulting isentropic pressure rise distribution using the continuity equation, and the radial equilibrium equation (1). In the following steps, the aerodynamic properties were calculated with the *average* of the inlet and the new outlet axial velocity profiles, to be consistent with the 2D cascade approach. The computation was continued until the relative difference between the outlet axial velocities derived from the last two iteration steps stayed below 1%.

The benefit of the "radial equilibrium" model is some (restricted) capability to represent the rearrangement of the axial velocity profile through the rotor, being of significance in certain axial fans. Its main limitations are as follows. a) By principle, the radial equilibrium equation is strictly valid only farther away from the blade row. Therefore, its applicability is theoretically doubtful for a short-ducted fan, such as the one in the present case study. b) The model allows for the presence of minor radial flow velocities, associated with the rearrangement of the axial velocity profile through the rotor. However, the radial velocity is neglected in Eq. (1). c) The annulus wall boundary layers are neglected further on, such as in the "Simplified" model. d) To be consistent with the 2D cascade analysis, an obligate modelling step is the averaging of the inlet and outlet axial velocity profiles. This tends to introduce unrealistic angles of flow incidence to the blade sections, being unfavourable in predicting the aerodynamic as well as acoustic behaviour of the rotor, especially near the leading edge. For example, flow separation may be presumed near the leading-edge – due to an erroneously predicted, extreme incidence angle –, that does not occur in reality.

A judgement is to be made whether the "simplified" or the "radial equilibrium" through-flow model is more realistic in the case study under discussion. As a reference case, approximating the realistic aerodynamic behaviour of the rotor, a Computational Fluid Dynamics (CFD) simulation was carried out.

3.3 CFD technique

A steady state CFD simulation was carried out for the fan with use of the Ansys FLUENT 15 software. In the model, the supporting struts were neglected, as a reasonable modelling simplification (in preliminary studies, the aerodynamic effect of the narrow downstream struts was found negligible). With this simplification, the geometry became rotationally periodic. Therefore, only one blade passage was modelled. The computational domain was distributed to three parts: the inlet and the outlet zones were steady, and the middle zone (the short duct including the rotor) was considered as a rotating zone. During the calculations, the frozen rotor method was used. The size of the inlet and the outlet zones was 5 times the rotor radius both in the axial and radial direction. On the inlet and outlet boundaries, identical and constant pressure was prescribed, according to the measurement setup. The turbulent phenomena were modelled with use of Menter's Shear Stress Transport (SST) model [9], which is widely used in the CFD simulations of turbomachinery [10-13]. The numerical mesh was a fully structured hexamesh, containing ~2.5 million elements in such a way that two-thirds of the cells were in the rotating zone. The appropriateness of the spatial resolution of the numerical mesh was checked with a grid sensitivity study.

Corresponding to the limitations in the aerodynamic measurement data available for the industrial fan setup, the validation of the CFD technique was confined to comparing the computational results with the following measurement-based data. a) The flow coefficient, Φ, representing globally the aerodynamic operation of the elemental rotor blade cascades. b) The inlet axial velocity profile, playing a key role in tailoring the aerodynamic as well as acoustic behaviour of the individual blade cascades along the radius [8][14-15].

The Φ data derived a) from preliminary fan performance curve measurements, b) from the vane anemometer measurements on the inlet axial velocity profile, and c) from CFD modelling as an output, are presented in **Table 1**. The CFD-based global flow coefficient is in good agreement with the experimental data. The discrepancy between the CFD- and measurement-based data is within the estimated range of experimental uncertainty of ± 4 % [6]. Therefore, it is concluded that the simulation accurately represents the aerodynamic co-operation of the individual rotor blade sections.

Table 1. The global flow coefficient for 0 *Pa* static pressure rise

	Φ
Performance curve meas.	0.313
Inlet axial velocity profile meas.	0.316
CFD	0.307

The inlet axial velocity profiles, measured by means of the vane anemometer, as well as those derived from the CFD computation, are presented in **Figure 1**. The measurement uncertainty is indicated using error bars. As demonstrated in the figure, the computation fairly well resolves the spanwise gradient of the inlet axial velocity (inlet axial velocity increasing along the radius), being of significance in developing the non-free vortex behaviour of the rotor [6]. The agreement between the computed and measured inlet axial velocity data is fair farther away from the annulus walls, i.e. in the spanwise region of R = 0.45÷0.85. Therefore, it is concluded that the simulation represents well the inlet condition of the individual blade sections in this region.

Based on the above, the CFD technique outlined herein is considered as a validated tool for representing the realistic behaviour of the rotor blade sections, with special regard to the spanwise region of R = 0.45÷0.85.

As Fig. 1 shows at R > 0.85, the simulation overpredicts the velocity deficit dedicated to flow separation anticipated at the periphery of the fan inlet section. As qualitative (wool tuft) experiments confirmed, the separation zone is considerably smaller than that predicted by the simulation.

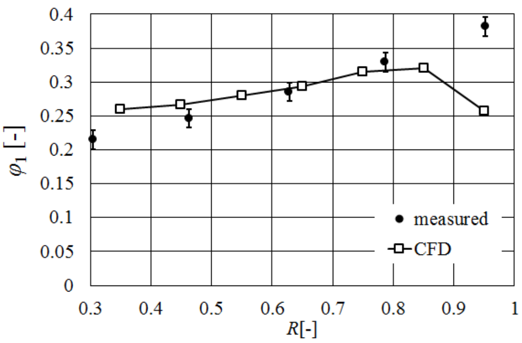

Figure 1. Inlet axial velocity profiles

3.4 Comparison between the through-flow models

In the classical 2D cascade analysis incorporated in the diagnostics method in [6-8], the inlet and outlet flow angles play a key role. In [7-8], the authors presented the correlation between the momentum thickness and the circumferentially averaged sound pressure. The wake momentum thickness is calculated in a 2D cascade approach, with use of the Lieblein diffusion factor [1], being the function of the inlet and outlet flow angles.

Therefore, the inlet and outlet flow angles are considered herein as the key indicators in investigating the appropriateness of the "simplified" and the "radial equilibrium" through-flow models.

Figures 2 to 3 present the spanwise distribution of the inlet and outlet flow angles, respectively, obtained with use of the "simplified" as well as the "radial equilibirum" model, in comparison with the CFD-based data. The semi-empirically modelled distributions obtained with use of the various through-flow models are equipped with error bars. These error bars represent the propagation of the measurement error of the axial inlet velocity – indicated in Fig. 1 –, as well as propagation of the measurement error of data on the blade geometry, in the semi-empirically modelled results.

Fig. 2 demonstrates that the "simplified" model better approximates the CFD-based inlet flow angle distribution. Taking the error bars into account, the quantitative agreement is fair in the region of R = 0.45÷0.85. The "radial equilibrium" model does not provide such a quantitative agreement over the entire region R = 0.45÷0.85.

As suggested by Fig. 3, the "radial equilibrium" model provides a better agreement with the CFD-based outlet flow angles away from the endwalls. However, investigating the region R = 0.45÷0.85, and considering the error bars as well, it is stated that the quantitative agreement between the "simplified" model and the CFD results is still satisfactory.

Based on the above observations, the following conclusion is made. Since a *single* throughflow-model is to be chosen that fairly well represents *both* the inlet and the outlet flow angle distributions, *the "simplified" model is better for the present case study*. Therefore, the "simplified" model, already applied in references [6-8], is utilised further on.

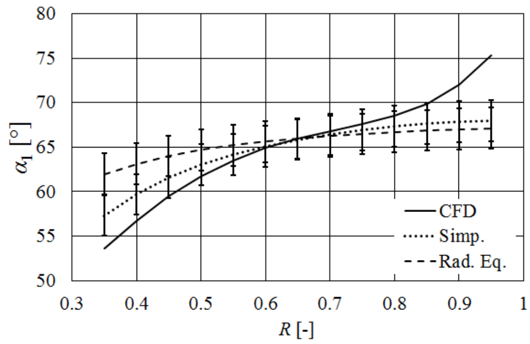

Figure 2. Inlet flow angle distributions

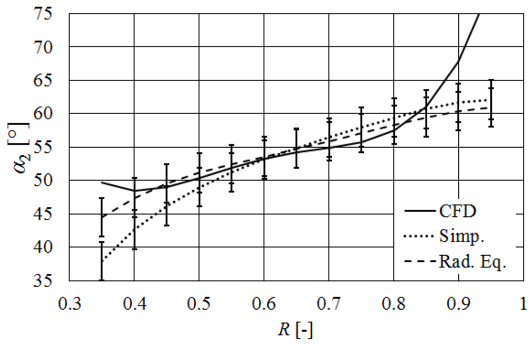

Figure 3. Outlet flow angle distributions

It is noted that a) none of the through-flow models are capable for treating the near-endwall phenomena, such as near-endwall blockage, b) the validity of the CFD tool is limited in the near-endwall region. Therefore, according to the expectations, the discrepancy between the CFD-based and semi-empirical data is increased near the annulus walls, for both the inlet (Fig. 2) and outlet (Fig. 3) flow angles.

4. CORRELATION BETWEEN THE NOISE AND THE AERODYNAMIC LOSS

The levels on a beamforming map represent the sound pressure level distribution in the investigation plane. [16] Based on that in the papers [6-8], the circumferentially averaged sound pressure level was calculated from the beamforming maps, with a third-octave band frequency resolution. At first, the noise source maps were calculated for each investigated frequency band using the Rotating Source Identifier (ROSI) [17] algorithm. Then the sound pressure values of the noise source maps in the rotor area were interpolated to an equidistant mesh. The mesh size was 100 cells both in radial and in circumferential direction. The sound pressure values were area-averaged along the circumference on this mesh, and the sound pressure level (SPL) at each radial location was calculated from the averaged sound pressure values. An example of the noise source map and the resultant SPL distribution is shown in **Figure 4**. The dashed-dotted line represents the hub radius. The circle in the upper-left corner of the map represents the estimated spatial resolution.

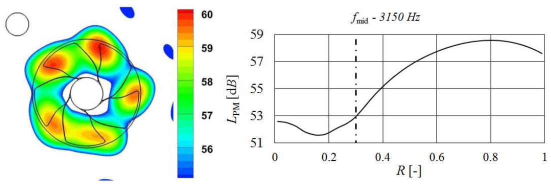

Figure 4. The noise source map, and the related averaged spanwise SPL distribution, for the frequency band of mid-frequency of 3150 *Hz*

In the papers [7] and [8], the following correlation was presented between the emitted noise and the momentum thickness of the blade wake:

$$P \propto \theta^{*} \quad (2)$$

By introducing the momentum thickness level

$$L_{\theta^{*}} = \log_{10}\left(\theta^{*}\right) \quad (3)$$

, the sound pressure level can be calculated using the following formula:

$$L_{P\theta^{*}} = A + 20 \cdot L_{\theta^{*}} \quad (4)$$

The spanwise distribution of the momentum thickness level is calculated. Afterwards, by best-fitting the trend functions of Eq. (4) to the PAM-based spanwise SPL distributions, the A values can be estimated for every third-octave bands for which the suction side boundary layer is the dominant noise source. In the present case, the third-octave bands of middle frequencies of 2000, 2500 and 3150 [*Hz*] were found as such frequency intervals. The A values for these frequency bands are presented in **Table 2**.

Table 2. The estimated *A* parameters

f_{mid} [*Hz*]	A [d*B*]
2000	106.3
2500	105
3150	98.2

5. EFFECT OF THE INLET VELOCITY PROFILE ON THE LOSS AND THE NOISE

The alteration of the inlet axial velocity profile modifies the aerodynamic behaviour of the individual blade sections. This is manifested in the alteration of the spanwise distribution of the momentum thickness. This represents the alteration of the global total pressure loss, and, *via* the trend in relationship (2), the alteration of the emitted noise as well.

In the following investigation, the global operational point of the fan is kept constant. This operating point, valid for the previous studies [6-8] as well, is characterised as follows. a) The flow rate, representing the user demand, is prescribed at Φ = 0.316. b) The static pressure rise is zero (free-inlet, free-exhaust). c) The useful total pressure rise is the dynamic pressure calculated with the mean axial velocity corresponding to the constant Φ.

It is investigated herein how the modification of the inlet axial velocity profile influences the global loss and noise of the fan. Since the operational point is prescribed, only *moderate changes* are assumed in the aerodynamic as well as acoustic behaviour of the individual blade sections. In mathematical sense, such *moderate changes* allow for the following assumptions. a) For each frequency band, the proportionality represented by the relationship (2) is valid further on, with unchanged factors of proportionality (linearization for moderate changes). b) This means that the A values presented in Table 2 are to be used further on in predicting the sound pressure level for the various bands *Via* Eq. (4), for altered momentum thickness values.

The inlet axial velocity profile is prescribed approximately as a power function of the radius:

$$\varphi_1(R) = \varphi_1(\nu)\left(\frac{R}{\nu}\right)^{k} \quad (5)$$

The shape of the velocity profile is tuned by modifying the value of the k exponent. The axial velocity at the hub, represented by $\varphi_1(\nu)$ in Eq. (5), is set in accordance with the integral condition of the prescribed Φ value.

As already noted, the “simplified” through-flow model was applied in the study reported below. The global total efficiency and the average sound pressure level were investigated as functions of k for the interval $k = 0 \div 1$, as demonstrated in **Figures 5 to 6**. $k = 0$ and $k = 1$ represent a uniform axial inlet condition, and a spanwise linearly increasing inlet axial velocity, respectively.

The global total efficiency (Fig. 5) is the mass-average of the local total efficiency over the span. The local total efficiency was calculated as presented in Eq. (6). It considers the blade friction loss (ω), calculated from the momentum thickness [1]; and the swirl loss (ψ'_{sw}), being equal to the mass-averaged dynamic pressure corresponding to the outlet swirl velocity.

$$\eta_t = \frac{\psi_{is} - \omega - \psi'_{sw}}{\psi_{is}} \qquad (6)$$

The average sound pressure level (Fig. 6) was calculated as follows. The spanwise-resolved sound pressure distributions were estimated using the Eq. (4). Then the sound pressure values were area-averaged over the annulus area for the individual frequency bands. The resultant average sound pressure has been presented in a logarithmic level form in Fig. 6.

The measured inlet velocity profile, presented in Fig. 1, and corresponding to the studies carried out so far [6-8], can be approximated using Eq. (5) with a substitution of $k = 0.45$. The results corresponding to this exponent – in what follows, referred to as "measured case" – are indicated in Figs 5 to 6 using dashed lines.

As Fig. 5 shows, the total efficiency increases with k. The main reason is the moderation of the swirl loss, being the dominant loss in Eq. (6), with increasing k values. With reference to the measured case, an efficiency deterioration of 1 % and an efficiency gain of 0.7% are predicted at $k = 0$ and $k = 1$, respectively.

In the literature [18], the classic formula by Regenscheit is proposed for estimating the emitted noise of the fan from the global aerodynamic properties. Considering that the global operational point is fixed in the present case study, the alteration of global efficiency, according to Fig. 5, is the only factor that influences the noise emission *via* the formula in [18]. Considering the efficiency deterioration of 1 %, the formula in [18] predicts an increase of noise of only ≈ 0.4 d*B* for the $k = 0$ case, relative to the measured case. This prediction is optimistic, in comparison with the results in Fig. 6, as discussed below.

The average SPL in Fig. 6 reaches its minimum at $k = 0.6$, being close to the measured case. The maximum SPL value can be found at $k = 0$, for which the increase of noise is ≈ 2 d*B* compared to the measured case – more than predicted on the basis of [18].

The above observations suggest that the fan in this case study exhibits favourable aerodynamic and acoustic features when the measured non-uniform axial inlet velocity profile ($k = 0.45$) is realized. The efficiency is at the middle of the investigated efficiency range of 81 ± 1 %, and the emitted noise is practically at the minimum.

Equipping the fan with an aerodynamically designed bellmouth entry, as proposed in [5], would approximate the uniform axial inlet condition of $k = 0$. Contrary to the expectations, the bellmouth entry is predicted herein to deteriorate the total efficiency by 1 %, and to increase the boundary layer related noise by 2 d*B*. These undesired changes are minor from a quantitative point of view, but draw the attention to the unwanted tendencies that may be more significant in other cases. The "myth" that the bellmouth entry contributes to the minimization of loss – and, as such, to the minimization of noise [18] – is to be replaced by a more systematic, tuned design of the rotor + its inlet section, for simultaneous reduction of loss and noise.

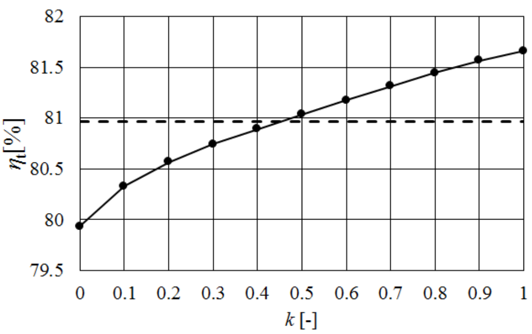

Figure 5. The total efficiency as a function of *k*

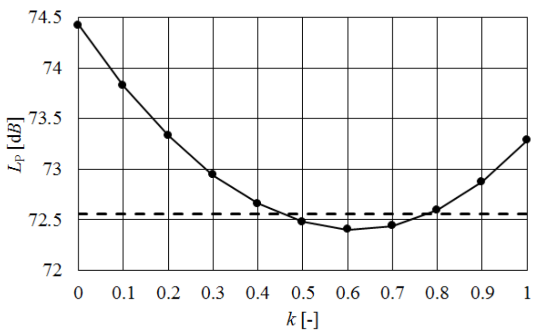

Figure 6. The average SPL as a function of *k*

CONCLUSION AND FUTURE REMARKS

In the paper, as continuation of research reported in [6-8], the effect of the inlet axial velocity profile on the total efficiency and on the upstream-radiated noise of an axial flow fan have been investigated, by means of a concerted aerodynamic-acoustic diagnostics method, incorporating PAM measurements. The results are summarized as follows, and some remarks are made for the continuation of the research programme.

1) The appropriateness of the “simplified” and the “radial equilibrium” through-flow models was investigated by comparing the modelled inlet and outlet flow angle distributions to computational results obtained by means of an experimentally validated CFD tool. In the present study, the “simplified” model, prescribing identical rotor-inlet and -outlet axial velocity profiles, was judged as being more realistic than the “radial equilibrium” model. Therefore, the “simplified” model has been used in the present case study. One important, generally valid advantage of the “simplified” model is that the realistic angles of flow incidence to the blade sections are considered in the rotor analysis, determined directly from the measurement of the inlet axial velocity profile. The proper modelling of inlet flow angles is essential in the concerted aerodynamic-acoustic analysis.

2) Based on semi-empirical correlations obtained in the previous research steps, a methodology was elaborated for a systematic investigation of the effect of the altered inlet velocity profile on the global total efficiency and the upstream-radiated average SPL. The inlet axial velocity profile was modelled by means of a power function, and the shape of the velocity profile was controlled by means of altering the power exponent k. Cases extending from the uniform axial inlet condition (k = 0) to spanwise linearly increasing axial inlet velocity (k = 1) were studied.

3) It has been found that the measured non-uniform inlet axial velocity profile provides a favourable aerodynamic and acoustic operation for the fan: the efficiency is at the middle of the investigated efficiency range of 81 ± 1 %, and the emitted noise is practically at the minimum.

4) Equipping the fan with an aerodynamically designed bellmouth entry would approximate the uniform axial inlet condition of k = 0. The bellmouth entry was predicted to deteriorate the total efficiency by 1 %, and to increase the emitted noise by 2 d*B*. This underlines the importance of systematic, tuned design of the rotor + its inlet section, for simultaneous reduction of loss and noise.

5) In the future, the predictions are to be confirmed by experiments. For this purpose, a bellmouth entry is to be designed and manufactured for realization of uniform axial velocity profile. The bellmouth entry is to be installed to the inlet of the case study fan, instead of the presently available short, rounded inlet rim. The aerodynamic and acoustic measurements are to be repeated for confirmation of the trends outlined in the previous point.

ACKNOWLEDGEMENTS

This work has been supported by the Hungarian National Fund for Science and Research under contract No. OTKA K 112277.

Gratitude is expressed to Ms. Anna Ilona Sipos for her help in programing, to Ms. Anna Tóth for the CFD simulations, and to Dr. Csaba Horváth and Mr. Bence Tóth for their useful comments.

The work relates to the scientific programs "Development of quality-oriented and harmonized R+D+I strategy and the functional model at BME" (Project ID: TÁMOP-4.2.1/B-09/1/KMR-2010-0002) and "Talent care and cultivation in the scientific workshops of BME" (Project ID: TÁMOP-4.2.2/B-10/1-2010-0009).

REFERENCES

[1] Vad, J., 2011, “Correlation of Flow Path Length to Total Pressure Loss in Diffuser Flows”, *Proceedings IMechE, Part A - J Power Energy*, Vol. 225, pp. 481-496.

[2] Lieblein, S., 1965, *Experimental Flow in Two-Dimensional Cascades, Chapter VI in Aerodynamic Design of Axial-Flow Compressors*, NASA SP-36, Washington D.C.

[3] Carolus, T., 2003, *Ventilatoren*, Teubner Verlag.

[4] De Gennaro, M., and Kuehnelt, H., 2012, “Broadband Noise Modelling and Prediction for Axial Fans,” Proc. *International Conference on Fan Noise, Technology and Numerical Methods (FAN2012)*, Senlis, France, ISBN 978-0-9572374-1-4.

[5] EN ISO 5801:2008 (E), “*Industrial Fans. Performance testing using standardized airways*”.

[6] Benedek, T., and Vad, J., 2014, “Concerted Aerodynamic and Acoustic Diagnostics of an Axial Flow Industrial Fan, Involving the Phased Array Microphone Technique,” *ASME Paper* GT2014-25916.

[7] Benedek, T., and Vad, J., 2015, ”Spatially Resolved Acoustic and Aerodynamic Studies Upstream and Downstream of an Industrial Axial Fan with Involvement of the Phased Array Microphone Technique,” Proc. *11th European Conference on Turbomachinery Fluid Dynamics and Thermodynamics*, Madrid, Spain, Paper # 128.

[8] Benedek T., and Vad J., 2015, “An industrial on-site methodology for combined acoustic-aerodynamic diagnostics of axial fans, involving the Phased Array Microphone technique”, *Int. J Aeroacoustics* (accepted)

[9] Menter, F.-R., 1993, "Zonal two equations k–ω turbulence models for aerodynamic flows", AIAA paper 93-2906.

[10] Reese, H., Carolus, T., and Kato, C., 2007, "Numerical prediction of the aeroacoustic sound sources in a low pressure fan with inflow distortion", Proc. *International Conference on Fan Noise, Technology and Numerical Methods (FAN2007)*, Lyon, France.

[11] Younsi, M., Bakir, F., Kouidri, S., and Rey, R., 2007, "Numerical and experimental study of unsteady flow in a centrifugal fan", *Proceedings IMechE, Part A - J Power Energy*, Vol. 221, pp. 1025-1036.

[12] Bamberger, K., and Carolus, T., 2012, "Optimization of axial fans with highly swept blades with respect to losses and noise reduction", Proc. *International Conference on Fan Noise, Technology and Numerical Methods (FAN2012)*, Senlis, France.

[13] Guédeney, T., and Moreau, S., 2015, "Unsteady RANS simulations of a low speed fan for analytical tonal noise prediction", Proc. *11th European Conference on Turbomachinery Fluid Dynamics and Thermodynamics*, Madrid, Spain, Paper # 123.

[14] Sharland, I. J., 1964, "Sources of noise in axial flow fans", *J Sound Vib*, Vol. 3, pp. 302-322.

[15] Carolus, T., Schneider, M., and Reese, H., 2007, "Axial fan broadband noise and prediction", *J Sound Vib*, Vol. 300, pp. 50-70.

[16] Koop, L., 2006, "Beamforming Methods in Microphone Array Measurements: Theory, Practice and Limitations," *VKI Lecture Series 2007/01: Experimental Aeroacoustics*, Rhode Saint-Genése, Belgium

[17] Sijtsma, P., Oerlemans, S., and Holthusen, H., 2001, "Location of Rotating Sources by Phased Array Measurements", AIAA Paper 2001-2167.

[18] VDI 3731 Blatt 2, 1990, "*Emissionkennwerte technischer Schallquellen. Ventilatoren.*"

Conference on Modelling Fluid Flow (CMFF'15)
The 16th International Conference on Fluid Flow Technologies
Budapest, Hungary, September 1-4, 2015

CHALLENGES IN EVALUATING BEAMFORMING MEASUREMENTS ON AN INDUSTRIAL JET FAN

Bence TÓTH[1], János VAD[2]

[1] Corresponding Author. Department of Fluid Mechanics, Faculty of Mechanical Engineering, Budapest University of Technology and Economics. Bertalan Lajos u. 4 – 6, H-1111 Budapest, Hungary. Tel.: +36 1 463 2635, Fax: +36 1 463 3464, E-mail: tothbence@ara.bme.hu
[2] Department of Fluid Mechanics, Faculty of Mechanical Engineering, Budapest University of Technology and Economics. E-mail: vad@ara.bme.hu

ABSTRACT

The aim of this paper is to illustrate the difficulties that arise during the evaluation of phased array microphone measurements on ducted fans in an industrial environment, and draw attention to them. A case study was carried out, and the results were processed resulting in beamforming maps, but their interpretation is not straightforward. Firstly, some fine details are found that seem to correspond to true physical phenomena, but should not be dealt with as separate sources on the basis of the spatial resolution given by Rayleigh's criterion. These results together with some theoretical objections raise concerns about the validity of Rayleigh's criterion in case of beamforming. Secondly, in some frequency bins the noise peaks are found on the axis of revolution. Literature shows that this might truly be motor noise, but it might also be an artefact, that causes beamforming algorithms to falsely locate rotating noise sources onto the axis of revolution [1, 2]. Central noise source peaks might even result from the presence of axial duct modes [3]. These questions are to be answered before beamforming on industrial ducted fans may become a standard noise diagnostics tool.

Keywords: beamforming, fan noise, phased array microphone, Rayleigh criterion, spatial resolution

NOMENCLATURE

a	[m/s]	speed of sound
B	[dB]	beamform map value
BPF	[Hz]	blade passing frequency
D	[m]	diameter
f	[Hz]	frequency
L	[m]	minimum resolvable distance
N	[-]	number of blades
x	[m]	beamform map horizontal coordinate
y	[m]	beamform map vertical coordinate
z	[m]	rotor – microphone array distance
λ	[m]	wavelength
ν	[-]	hub-to-tip ratio
Θ	[rad]	angle between two sources

Subscripts and Superscripts

g	guide vane
mid	third-octave band mid-frequency
OPT	optical
r	rotor
S	Sparrow limit
t	rotor tip

Abbreviations

DS	Delay-and-Sum method
PAM	Phased Array Microphone
ROSI	Rotating Source Identifier

1. INTRODUCTION AND OBJECTIVES

Noise reduction is an important task in the 21st century, and regulations are becoming more and more stringent in connection with axial fans, too. Beamforming using phased array microphone (PAM) measurements presents means to localize sound sources even in a rotating reference frame. These source maps give invaluable information about the distribution of noise that can be related to its generation mechanisms.

Benedek and Vad [4-6] have investigated aerodynamic and acoustic properties of an unducted axial fan through a case study. Using on-site measurements and the PAM technique they have obtained spanwise distributions of boundary layer momentum thickness, and sound pressure level in third-octave bands. Analysis shows that these functions are in correlation for the dominating low frequency ranges. This suggests the possibility of reducing noise while improving efficiency in case of short ducted axial fans.

Similar tests on ducted fans are reported in [7, 8]. In [7] a turbofan engine is investigated using two microphone arrays, one in the inlet, and one in the bypass section of the duct. The source maps clearly show the periodicity related to the fan blades, and the location of maximum noise sources is visible. This measurement was however carried out in a special test rig in an anechoic chamber using wall-mounted microphones, therefore it is not applicable for on-the-field diagnostics. Such a measurement is described in [8] for a wind tunnel fan describing the difficulties of the experiments: reverberant space, high aerodynamic loading on the microphones, low spatial resolution, and the presence of other noise generating mechanisms.

In the current study the authors have implemented the same diagnostic methodology as in [4-6] for the case of ducted fans. This scenario however differs from the original one in several points. The duct length limits accessibility, and spatial resolution of the microphone array. Duct modes are also expected to form, and affect the measurements in different ways depending on duct geometry. The presence of coherent sources in the rotating frame of reference might also cause unrealistic results, in the form of false noise sources appearing on the axis of the rotor [1, 2]. In the following, this will be referred to as the "Mach radius effect". These phenomena are investigated below.

The spatial resolution of beamforming appears to be a concern. It was tested in [9] for several algorithms, conventional and deconvolution-based, too. This investigation is different however, as our aim is to make practically relevant comments on the resolution when measuring turbomachinery acoustics instead of developing new beamforming methods.

This paper is considered as a Technical Note for the Workshop "Beamforming for Turbomachinery Applications" organized at CMFF'15, aiming at provoking a discussion on the topics outlined herein.

2. CASE STUDY

A ducted fan was investigated having a rotor tip diameter D_t=0.355 m, hub-to-tip ratio ν=0.57, N_r=8 rotor blades, and N_g=7 guide vanes. Rotor speed was 2856±1 RPM measured using a handheld stroboscope, corresponding to a rotor blade passing frequency *BPF*=381 Hz. Noise was measured from a distance of 2 d_t between the PAM and the fan inlet plane for 30 s with a sampling frequency of 44100 Hz on 24 channels on the suction side of the fan. The equipment used was an OptiNav, Inc., Array 24 multi-purpose portable array system. The PAM was placed perpendicular to the axis of rotation, with its centre coinciding with the rotor axis. Data was evaluated using an in-house beamforming software applying the "Rotating Source Identifier" (ROSI) [10] technique to localize rotating sources. Noise source maps of equal dynamic range were constructed showing the spatial distribution of beamform peak values in the fan inlet plane, together with the location of the hub and the annulus. Note that due to the lack of any rotor position transducer, the angular position of the rotor cannot be assigned to the noise source maps. However, with a knowledge of the accurate rotor speed, the ROSI processing algorithm principally enables the pitchwise resolution of the noise sources.

The authors have attempted to determine the most important noise generation mechanisms based on the source maps. They have however faced the problem of Rayleigh's criterion for resolving power and the problem of noise maxima appearing on the axis of revolution. These problems are detailed in the following.

3. RESOLUTION

3.1 Rayleigh's criterion

The applied ROSI method is basically an extension of the frequency-domain Delay-and-Sum (DS) beamforming technique with a special step called deDopplerization to place the rotating sources into a co-rotating reference frame, thus make them stationary. The step consists of adjusting the time delays and amplitudes in order to remove the effect of rotation from the measured noise signals.

In case of beamforming measurements the spatial resolution is of importance because it determines the smallest distance between two sources that can be regarded as separate ones. This way it also shows the minimum size of structures can be positively identified, since regions smaller than the resolution might be the effect of neighbouring source regions.

The spatial resolution is especially important in the case of rotor blades, for which an improper spatial resolution may lead to dissolving the contribution of the adjacent blades in the noise source maps.

Because the spatial resolution of the microphone array and the beamforming method is a very complex phenomenon, the spatial resolution of DS beamforming is usually determined by applying a simplified optical analogy.

The resolving power of an optical aperture is given using Rayleigh's criterion [11]. Assume a point source radiating light of wavelength λ infinitely far from a perfect circular aperture, i.e. the wave fronts incident to the aperture are assumed to be planar waves. The diameter of the aperture is D_{OPT}. The image created by the aperture is the so-called Airy disk, a circularly symmetric diffraction pattern. In case of two sources of identical strength the image is the superposition of the two identical Airy disks. Rayleigh has defined the limit case of resolving the image when the intensity peak of one source falls into the first intensity minimum of the other source.

In such case for the Θ angle between the two sources the following holds:

$$\sin\Theta \approx 1.22\frac{\lambda}{D_{OPT}} \tag{1}$$

In between the two intensity peaks, the intensity of the resultant pattern drops to 73.7 % of the maximum value. The 26.3 % dip relative to the maximum is presumed arbitrarily in Rayleigh's criterion as being sufficient for the human eye in making a distinction between the two optical sources.

The minimum distance between two resolvable sources is usually given based on Eq. (1) by assuming a small angle between the sources. The measurement plane is parallel to the plane of the microphones and offset by z. The minimum resolvable distance is L [11, 12] assuming plane wave propagation:

$$L \approx z\Theta \approx 1.22\frac{z\lambda}{D_{PAM}} \tag{2}$$

Table 1 shows the minimum resolvable distances calculated using Eq. (2) for some representative third-octave frequency bands, being significant from the viewpoint of human audition. The spatial resolution L at a third-octave frequency range is calculated by taking the wavelength corresponding to the mid-frequency f_{mid} in the following way: $\lambda = a / f_{mid}$, then substituting it into Eq. (2) above. In this expression a is the speed of sound.

Table 1. Minimum resolutions in frequency bands, based on Rayleigh's criterion

f_{mid} [Hz]	L [m]	L/D_t [-]
2000	0.42	1.20
2500	0.34	0.96
3150	0.27	0.76
4000	0.21	0.60
5000	0.17	0.48
6300	0.13	0.38

The spatial resolution calculated using Rayleigh's criterion is quite weak due to the fact that the distance is the same order of magnitude as the size of the PAM, D_{PAM}=1 m. Each L/D_t value significantly exceeds 1) the rotor blade height of 0.22 D_t, 2) the rotor blade pitch (spacing) of 0.31 D_t at misdspan. These facts *anticipate the following limitations*, if one would take Rayleigh's criterion as a basis for the available spatial resolution: 1) Even the rotor annulus area, as a whole, could not be expected to be clearly distinguished from the rotor hub area as a noise source, if both sources are of equal magnitude, 2) No pitchwise resolution of noise sources related to the individual rotor blades would be expected at all.

Dougherty et al. also consider the Sparrow limit shown in Eq. (3) for the quantification of resolution [9]. This corresponds to the distance between two sources, at which the dip between their Airy disk diffraction patterns first appears.

$$L_S \approx z\Theta \approx 0.94\frac{z\lambda}{D_{PAM}} \tag{3}$$

The Sparrow limit is less conservative, than Rayleigh's one, by taking values that are roughly 80% of the latter. As customary in optics however, we focus our attention on Rayleigh's criterion.

3.2 Measurement results

In Figure 1 a source map is shown with 6 dB dynamic range showing the rotor from the upstream side in a co-rotating frame. This figure is a representative narrowband result taken from the third-octave band centred on 5 kHz. The two concentric circles indicate the fan annulus area: the inner one shows the hub, while the outer one corresponds to the tip diameter.

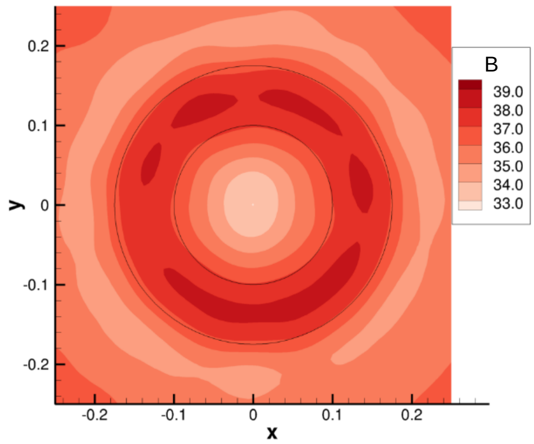

Figure 1. Rotor narrowband beamform map

Despite the anticipated limitations in spatial resolution, originating from Rayleigh's criterion, and formerly described in points 1) and 2), the following observations are made in Fig. 1, in contrast to those points.

1) The rotor annulus area – characterized by the minimum length scale being equal to the blade height of 0.22 D_t – is clearly distinguished from the hub area in the source map.

2) The periodicity in the source map corresponding to the rotor annulus, being in accordance with the eight rotor blades of midspan spacing of 0.31 D_t, is apparent in the upper half of the figure. Some small structures are detected in the

vicinity of the blade tips, whose size is much less than the calculated resolution of 0.48 D_t.

The above suggest that Rayleigh's criterion is a pessimistic approach in the case study presented herein, and, as such, it is to be treated with criticism.

3.3. Criticism of Rayleigh's Criterion

The above discussion suggests that Rayleigh's criterion exhibits some limitations in estimating the spatial resolution of PAM-based fan rotor noise source maps. This experimental finding described above is further supported by the following differences between optical systems and a PAM:

- In general, a microphone array does not necessarily represent a *circular aperture*. In references [1-3], the microphones of the array are arranged along a logarithmic spiral curve, where the shape of the aperture is not known. In case of a linear array however the aperture shape is certainly not circular.
- In the investigated frequency range no cut-on plane modes waves exist in the duct. Due to the proximity of the PAM plane wave propagation out of the duct is a poor approximation.
- The *distance* between the acoustic source and PAM is *finite*. It is often confined to the order of magnitude of some times the rotor tip diameter. Besides the current investigation, references [4-6] also report case studies in which the array was installed at a distance of ≈ $2\,D_t$ from the fan inlet.
- The rotor noise sources to be resolved are not necessarily of *identical intensity*. The studies documented in [1-3] especially aimed at discovering the spanwise non-uniform intensity distribution of rotor noise sources.
- The criterion is based on the visibility of structure of optical diffraction patterns to the human eye, the applicability of which is doubtful from the viewpoint of human audition, and even more so in connection with microphones and digital signal processing.
- The 26.3 % dip in intensity is presumed *arbitrarily* as a quantitative criterion for resolution.

Note that besides these problems already the approximation $\sin\Theta \approx \Theta$ means an error of about 15 % in case of the large angles experienced in the current measurement.

4. ON-AXIS NOISE SOURCES

Besides the sources on the annulus regions several source maps show high peak levels on the axis of rotation. Such a source map is shown in Figure 2. It is a representative narrowband result taken from the third-octave band centred on 3000 Hz.

This peak might be attributed to motor noise. However, it is known from literature [3] that axial plane wave modes will appear in the duct. The beamforming method will localize these to the centre of the beamforming map.

Furthermore, Horváth et al. [1-2] have shown that beamforming measurements on a rotating object will falsely locate some coherent sound sources onto the axis of revolution when the PAM is perpendicular to the rotor axis. How to separate the contribution of real on-axis sources and the "Mach-radius effect" in these specific cases is an open question requiring further investigations.

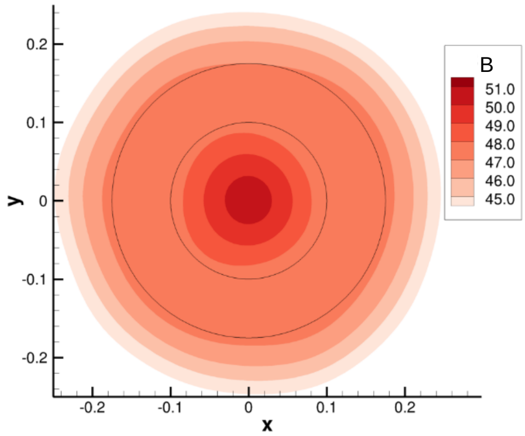

Figure 2. Narrowband beamforming map showing maximum values in the hub region

5. SUMMARY AND FUTURE REMARKS

Beamforming and phased array microphones present effective means of noise source localization that is a major step towards understanding and reducing noise generation. Using the ROSI algorithm rotating sources can also be dealt with effectively. A powerful application of this method is the investigation of industrial axial fans. However, in this case some special concerns arise.

The spatial resolution of beamforming maps obtained by PAM measurements is an important parameter, it is however quite difficult to obtain an expression describing this quantity. In several cases an analogy with wave optics is used, where the Rayleigh criterion is a classic result that presents a minimum distance between two sources if they are to be resolved separately.

While the criterion is well-known and accepted in optics, in the framework of beamforming its assumptions are at least questionable. Based on these reasons the authors consider Rayleigh's criterion in some cases ill-suited for the quantification of spatial resolution of beamforming measurements on rotating fans. The following question is arisen. What amount of dip between two peaks is to be considered as a practically relevant criterion for resolving two neighbouring sources in beamforming?

Another question is the case of noise sources appearing on the axis of beamforming maps. These might indicate true noise source positions on the axis, e.g. motor noise, but might also results from the "Mach radius effect". Possible causes of the phenomenon are the formation of axial duct modes and the interference of coherent sources in the rotating frame.

On the basis of above, some future tasks of departmental research on beamforming applied to industrial fans are as follows.

1) Elaboration of a widely applicable methodology for a realistic estimation of the spatial resolution of beamforming, with a special focus on rotating sources, as a critical revision of Rayleigh's pessimistic criterion. Comparison of resolution in case of stationary and rotating sources, e.g. DS and ROSI methods.

2) Elaboration of a systematic evaluation method for a comprehensive judgment on the origin of a local noise maximum apparent on / near the rotor axis, whether a) it is a virtual (physically non-existing) source, due to the Mach radius effect; or b) it is the representation of any duct modes; or c) it indicates indeed the local dominance of the hub as a noise source (e.g. due to the noise of the driving electric motor incorporated in the hub).

ACKNOWLEDGEMENTS

This work has been supported by the Hungarian National Fund for Science and Research under contract No. OTKA K 112277. Gratitude is expressed to Hungaro-Ventilátor Kft. for providing the test fan, and for making possible the tests at the premises of the company.

The work relates to the scientific programs "Development of quality-oriented and harmonized R+D+I strategy and the functional model at BME" (Project ID: TÁMOP-4.2.1/B-09/1/KMR-2010-0002) and "Talent care and cultivation in the scientific workshops of BME" (Project ID: TÁMOP-4.2.2/B-10/1-2010-0009).

REFERENCES

[1] Horváth, Cs., Envia, E., and Podboy, G. G., 2014. Limitations of Phased Array Beamforming in Open Rotor Noise Source Imaging, *AIAA Journal*, Vol. 52, No. 8, pp. 1810-1817.

[2] Horváth, Cs., Tóth, B., Tóth, P., Benedek, T., and Vad, J., 2015. Reevaluating Noise Sources Appearing on the Axis of Beamform Maps of Rotating Sources, *FAN 2015*, Lyon, France

[3] Tyler, J. and Sofrin, T., 1962. Axial Flow Compressor Noise Studies, *SAE Technical Paper 620532*, doi:10.4271/620532.

[4] Benedek, T., and Vad, J., 2015. An industrial on-site methodology for combined acoustic-aerodynamic diagnostics of axial fans, involving the Phased Array Microphone technique. *International Journal of Aeroacoustics* (accepted)

[5] Benedek, T., and Vad, J., 2015. Spatially resolved acoustic and aerodynamic studies upstream and downstream of an industrial axial fan with involvement of the phased array microphone technique. *Proc. 11th European Conference on Turbomachinery Fluid Dynamics and Thermodynamics (ETC'11),* Madrid, Spain, Submission ID 128. ISSN 2410-4833.

[6] Benedek, T., and Vad, J., 2014. Concerted aerodynamic and acoustic diagnostics of an axial flow industrial fan, involving the phased array microphone technique. *ASME Paper* GT2014-25916.

[7] Sijtsma, P., 2010. Using Phased Array Beamforming to Identify Broadband Noise Sources in a Turbofan Engine, *International Journal of Aeroacoustics*, Vol. 9, No. 3, pp. 357-374.

[8] Benedek, T., and Tóth, P., 2013. Beamforming measurements of an axial fan in an industrial environment, *Periodica Polytechnica Mechanical Engineering*, Vol. 57, No. 2.

[9] Dougherty, R. P., Ramachandran, R. C., and Raman, G., 2013. Deconvolution of sources in aeroacoustic images from phased microphone arrays using linear programming, AIAA Paper 2013-2210¸ *19th AIAA/CEAS Aeroacoustics Conference,* Berlin.

[10] Sijtsma, P., Oerlemans, S., and Holthusen, H., 2001. Location of rotating sources by phased array measurements, *National Aerospace Lab*., Paper NLR-TP-2001-135.

[11] Jenkins, F., A., and White, H. E., 1976. *Fundamentals of optics.* 4th Edition. McGraw-Hill Primis Custom Publishing, New York.

[12] Hald, J., 2005. Combined NAH and beamforming using the same array. *Brüel & Kjær Technical Note* (2005-1).

Conference on Modelling Fluid Flow (CMFF'15)
The 16th International Conference on Fluid Flow Technologies
Budapest, Hungary, September 1-4, 2015

Workshop on Turbomachine Optimization based on Computational Fluid Dynamics

László DARÓCZY[1], Gábor JANIGA[2], Dominique THÉVENIN[3]

[1] Corresponding Author. Lab. of Fluid Dynamics and Technical Flows, University of Magdeburg "Otto von Guericke". Universitätsplatz 2, D-39106 Magdeburg, Germany. Tel.: +49 391 67 18194, Fax: +49 391 67 12840, E-mail: laszlo.daroczy@ovgu.de
[2] Lab. of Fluid Dynamics and Technical Flows, University of Magdeburg "Otto von Guericke". E-mail: janiga@ovgu.de
[3] Lab. of Fluid Dynamics and Technical Flows, University of Magdeburg "Otto von Guericke". E-mail: thevenin@ovgu.de

ABSTRACT

CFD based optimization (CFD-O) is a strongly multidisciplinary field that significantly differs from analytical optimizations due to the costly function evaluations. CFD-O is especially difficult due to the fact, that for an appropriate optimization process every step of the objective function evaluation has to be automated, including geometry creation, mesh generation, CFD simulation and post-processing. CFD can be very time consuming in itself, but in an optimization the same computation has to be performed 100-100 000 times. For this reason, it is very important to (1) perform the CFD simulations with high fidelity, (2) to analyze and apply very efficient optimization algorithms.

Throughout the workshop, following an introduction, the most important fields will be discussed by the Invited Experts, including but not limited to Uncertainty Quantification (UQ), Robust Optimization (RO), Evolutionary Algorithms (EA), Multi-objective Optimization (MOO), gradient-based methods, adjoint methods and Surrogate or Meta-models. Several practical applications will be shown for wind turbines, flow channels and turbomachinery bladings.

Keywords: adjoint optimization, CFD-based optimization, metamodel, robust optimization

NOMENCLATURE

$\mathbb{X}$	[−]	feasible domain
g, h	[−]	equality/inequality constraint
x	[−]	design variable
y	[−]	objective function

1. INTRODUCTION TO OPTIMIZATION

In the followings, without any claim to completeness, the most important aspects of optimization will be addressed. Let us assume a problem with n independent variables:

$$\mathbf{x} = (x_1, ..., x_n)^{\mathrm{T}}, \quad \mathbf{x} \in \mathbb{X}, \tag{1}$$

where $\mathbf{x}$ is the design variable vector and $\mathbb{X}$ the feasible domain:

$$\mathbf{x} \in \mathbb{X} \iff \begin{cases} g_i(\mathbf{x}) = 0 \ (i = 1...k) \\ h_j(\mathbf{x}) \leq 0 \ (j = 1...l) \end{cases} . \tag{2}$$

Besides the variables m functions are defined:

$$\mathbf{y}(\mathbf{x}) = (f_1(\mathbf{x}), f_2(\mathbf{x}), ..., f_m(\mathbf{x}))^{\mathrm{T}} \tag{3}$$

Without any loss of generality the optimization can be defined as

$$\mathbb{O} : \begin{cases} \mathbf{y}(\mathbf{x}) \underset{\mathbf{x}}{\rightarrow} \min \\ \text{so that } \mathbf{x} \in \mathbb{X} \end{cases} . \tag{4}$$

2. CLASSIFICATION OF PROBLEMS

Table 1 summarizes the most important groups of optimization problems.

Table 1. Most important types of optimization problems

$k = l = 0$	unconstrained
$k \neq 0 \cap l \neq 0$	constrained
$m = 1$	single-objective
$m \geq 2$	multi-objective
$\mathbf{y}(\mathbf{X_1}) = \mathbf{y}(\mathbf{X_2}) \implies \mathbf{X_1} = \mathbf{X_2}$.	uni-modal
$\mathbf{y}(\mathbf{X_1}) = \mathbf{y}(\mathbf{X_2}) \not\Longrightarrow \mathbf{X_1} = \mathbf{X_2}$.	multi-modal

An inherent difficulty of optimization is that one has to choose for each problem the appropriate optimization method. An algorithm, which is efficient for an unimodal problem with a single optimum might fail for noisy or multimodal problems. There is no algorithm that is efficient for all problems ("no free lunch" [1]). Additionally, it is usually very difficult to make a decision a priori, for which reason optimization software still heavily rely on expert knowledge.

3. DIFFICULTIES WITH CFD-O

In CFD-O [2], the objective function(s) are usually not known explicitly, but have to be computed using numerical simulations. This results in further complications:

- The evaluation of the objective function is very costly, one computation can require from several seconds up to several days.
- Due to numerical noise and model uncertainties, the objective functions are usually noisy.
- The geometry and mesh has to be created/morphed for each configuration in an automated and robust way.
- Different software (including proprietary commercial software) have to be coupled to cooperate for the optimization.

As a result, speed and efficiency is of key importance in CFD-O.

4. SPECIAL FIELDS OF CFD-O

4.1. Gradient-based and gradient-free methods

Optimization algorithms can be further classified as gradient-free or gradient-based methods. Gradient-based methods are usually local search methods (although gradient assisted global methods exist as well) and require the derivatives ($\frac{\partial y_i}{\partial x_j}$). These can be computed by n additional CFD computations for n variables (in a non-intrusive way), or by adjoint method [3]. The first method becomes unaffordable very fast due the "curse of dimensionality". With adjoint methods the flow solver has to be modified (increasing the implementation time), but the evaluation time remains quasi unchanged. This method is usually very fast, but can get trapped in a local minimum.

Gradient-free methods handle the CFD simulation as a black-box. The most popular methods are the different Evolutionary Algorithms, which are global search methods. These methods are able to find global optima, but require large number of CFD computations.

4.2. Robust and reliability based optimization

In the reality most values are not exact, but depend on some, usually unknown, uncertainty. E.g., the operating temperature variates slightly in a heat exchanger, the inflow wind speed varies around a wind turbine due to the wind gusts or the diameter of a pipe varies due to manufacturing imprecisions. This complicates the optimization, as some configurations might be optimal, but not robust. E.g, one turbine might be very efficient under low turbulence, but might fail for large intensities.

In robust design optimization (RDO) besides the objective function the variance of the objective function is minimized as well, while in reliability based design optimization (RBDO) a target reliability is defined which has to be satisfied in the optimization process. In RDO even more CFD simulations have to performed compared to normal optimization, as some kind of Uncertainty Quantification (UQ) methods have to be applied to quantify the risks (e.g., Monte Carlo, univariate reduced quadrature, Polynomial Chaos Expansion, etc.). The robust optimization of wind turbines is discussed e.g., in the work of Campobasso et al. [4].

4.3. Metamodel assisted optimization

Besides parallelization of the CFD evaluations, another possibility for speeding up the optimization process is to train metamodels [5]. In this case, an approximation of the objective functions is created ($\mathbf{y}(\mathbf{x}) \approx \mathbf{y}^{meta}(\mathbf{x})$), which can be updated in an on-line or off-line manner. Afterwards, the optimization can be executed on this reduced and usually very fast model ($\mathbb{O}^{meta} : \mathbf{y}^{meta}(\mathbf{x}) \underset{\mathbf{x}}{\rightarrow} \min$). However, for very complicated objective functions large number of training points might be needed to train the model. If the optimum of the reduced model does not correspond to an optimum of CFD simulations, new training points have to be added. The most popular surrogate models include Radial Basis Functions (RBF), Kriging, Artificial Neural Networks (ANN) or different Response Surface Models (RSM).

REFERENCES

[1] Wolpert, D., and Macready, W., 1997, “No free lunch theorems for optimization”, *Evolutionary Computation, IEEE Transactions on*, Vol. 1 (1), pp. 67–82.

[2] Thévenin, D., and Janiga, G. (eds.), 2008, *Optimization and Computational Fluid Dynamics*, Springer, Berlin.

[3] Papoutsis-Kiachagias, E., and Giannakoglou, K., 2014, “Continuous Adjoint Methods for Turbulent Flows, Applied to Shape and Topology Optimization: Industrial Applications”, *Archives of Computational Methods in Engineering*, pp. 1–45.

[4] Campobasso, M. S., Minisci, E., and Caboni, M., 2014, “Aerodynamic design optimization of wind turbine rotors under geometric uncertainty”, *Wind Energy*.

[5] Verstraete, T., Coletti, F., Bulle, J., Vanderwielen, T., and Arts, T., 2013, “Optimization of a U-Bend for Minimal Pressure Loss in Internal Cooling Channels—Part I: Numerical Method”, *Journal of Turbomachinery*, Vol. 135 (5).

Conference on Modelling Fluid Flow (CMFF'15)
The 16th International Conference on Fluid Flow Technologies
Budapest, Hungary, September 1-4, 2015

SHAPE OPTIMIZATION OF U-BENDS FOR INTERNAL COOLING CHANNELS: AN OVERVIEW

Tom Verstraete[1], Tony Arts[2], Filippo Coletti[3], Sebastian Willeke[4], Jing Li[5], Timothée van der Wielen[6], Jérémy Bulle[7]

[1] Corresponding Author. Turbomachinery Department, von Karman Institute for Fluid Dynamics. Waterloosesteenweg 72, 1640 Sint-Genesius-Rode, Belgium. Tel. +32 2 359 94 29, E-mail: tom.verstraete@vki.ac.be. Presently at Queen Mary University of London.
[2] Turbomachinery Department, von Karman Institute for Fluid Dynamics. E-mail: arts@vki.ac.be
[3] Aerospace Engineering and Mechanics, University of Minnesota. E-mail: fcoletti@umn.edu
[4] Institute of Dynamics and Vibration Research, University of Hannover. E-mail: willeke@ids.uni-hannover.de
[5] Pratt School of Engineering, Duke University. E-mail: jl477@duke.edu
[6] Cofely Services, GDF Suez. E-mail: timothee.vanderwielen@gmail.com
[7] Tractebel Engineering, GDF Suez. E-mail: jeremy.bulle@gmail.com

ABSTRACT

U-bends are found in various ducted applications in which the flow direction needs to be turned 180 degrees. The present work looks into the application of these U-bends for internal cooling channels inside turbine blades, where two major aspects need to be carefully addressed: pressure loss needs to be reduced while heat transfer needs to be enhanced.

An overview of different shape optimization studies is given with the aim to improve the performance of the standard U-bend consisting of two circular arcs. Different optimization methodologies were used in this study ranging from single-objective Evolutionary Algorithms (EA), with or without acceleration by surrogate model, to multi-objective EAs, to finally gradient based adjoint optimization. The difference in computational cost is compared for the different applications combined with their advantages and disadvantages, and finally one optimal configuration is experimentally verified and compared to the numerical predicted improvement.

Keywords: internal cooling channels, shape optimization, u-bend

NOMENCLATURE

ρ	$[kg/m^3]$	density
Obj	$[-]$	objective
Q	$[Watt]$	heat
D_h	$[m]$	hydraulic diameter
k	$[m^2/s^2]$	turbulence kinetic energy
p	$[N/m^2]$	pressure
P_{total}	$[Pa]$	total pressure
v	$[m/s]$	velocity
ϵ	$[m^2/s^3]$	turbulence dissipation rate

Subscripts and Superscripts

inlet	at the inlet of the domain
outlet	at the outlet of the domain
ref	reference value

1. INTRODUCTION

Turbine blades are since long equipped with internal cooling channels as an effective way to increase cycle efficiency of gas turbines by augmenting the firing temperature. These cooling channels are in a vast majority of cases implemented through a serpentine scheme, in which one single ducted flow passes multiple times the blade span. Near the extremities of the blade span the flow inside the duct is turned 180 degrees through U-bends. The coolant air is bled from the high pressure compressor which bypasses the combustor and enters the turbine blade through its root.

Since the coolant air needs to be pressurized while it does not participate in the work extraction in the turbine, it represents a loss in global cycle efficiency. As a result, the internal cooling channels need to simultaneously allow for a high heat transfer at the lowest possible pressure loss. The U-bends present in the serpentine cooling channels are responsible for up to 25% of the total pressure loss in the channel and merit a profound attention, as witnessed by numerous experimental studies [1, 2, 3, 4].

This paper presents an overview of several numerical optimization studies performed, including:

- Single-objective optimization with EA (2D)
- Single-objective optimization with EA accelerated by a surrogate model (3D)
- Multi-objective optimization by EA accelerated by a surrogate model (3D)

- adjoint based optimization (2D)

2. U-BEND TEST CASE

2.1. Geometry

The U-bend under investigation is typical of internal cooling channels. The baseline geometry is shown in Fig. 1. It consists of a circular U-bend with radius ratio of 0.76, a hydraulic diameter of 0.075 meter and an aspect ratio of 1. The Reynolds number is 40,000 and the Mach number of 0.05 allows using an incompressible assumption. The shape of the inner and outer curve is allowed to be changed but needs to remain inside the bounding box shown in the figure, which restricts the height and width of possible changes to account for structural limits. The distance between both cooling channels is not subject to optimization, as well as the hydraulic diameter.

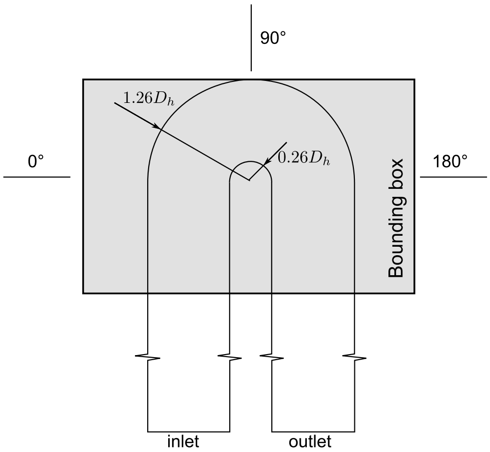

Figure 1. Baseline geometry, definition of the area in which the shape is allowed to change.

2.2. Parameterisation

The U-bend has been parameterised by Bézier curves for which the movements of the control points are the design variables. For the adjoint based optimization, both the inner and outer curve of the U-bend have been represented by two separate continuous curves containing 20 control points. This results in a total of 80 design variables (x and y coordinate of each of the 2 curves), which is unfeasible for the EA based optimization. Therefore, the EA based optimization uses a segmented approach, for which a total of 4 Bézier curves represent the inner or outer curve. Each Bézier curve only comprises of 4 control points, while relations between the control points are imposed to assure a sufficient degree of continuity between the curves. Figure 2 shows the parameterisation of the outer curve.

2.3. Performance evaluation

The simpleFoam solver from OpenFoam [5] is used to evaluate the incompressible Navier-Stokes equations. The mesh resolution has been adapted such that the maximum $y+$ value does not exceed

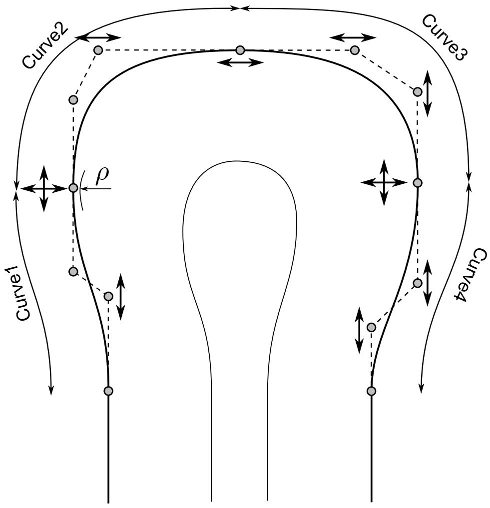

Figure 2. Parameterization of the outer curve.

2.2. The Launder-Sharma low-Reynolds k-ϵ turbulence model is used. The k-ϵ model "is arguably the simplest complete turbulence model" (Pope [6]), is implemented in most commercial software and is one of the most broadly employed at industrial level. Its performance is reasonably satisfactory in shear flows with small effects of streamwise pressure gradients and streamline curvatures, but far from these assumptions, it can fail badly. However it has been selected for the present application due to its large diffusion: given that the proposed methodology is apt for industrial problems, it was the intention to demonstrate its potential in conditions that are representative of real-life design practice.

At the inlet a fully developed velocity profile is imposed, together with values of k and ϵ for the turbulence model. Both are computed based on a turbulence intensity of 5% measured in the lab. At the outlet the static pressure is imposed.

The U-bend optimization is driven by the minimization of the pressure drop introduced by the U-bend and in case of the multi-objective optimization the maximization of the heat transfer is additionally considered. Both objective functions are defined as:

$$\text{Min} \quad Obj_1 = \frac{P^{inlet}_{total} - P^{outlet}_{total}}{\frac{1}{2}\rho \cdot v^2_{ref}} \tag{1}$$

$$\text{Max} \quad Obj_2 = \frac{Q}{Q_{ref}} \tag{2}$$

where Q is the total heat transferred to the fluid and P_{total} is the total pressure which is computed as the mass flow averaged quantity at the inlet respectively outlet of the domain, positioned 8 hydraulic diameters away from the U-bend. One single 3D evaluation is run in parallel on 5 cores which takes in average 2 hours.

3. OPTIMIZATION STRATEGIES

Two distinct optimization strategies have been used to the applied test case and allow comparison between the different techniques. On the one hand, Evolutionary Algorithms (EA's) are used as a non-deterministic optimization method. These methods benefit a wide community of users and are relatively easy to understand and implement, factors which have contributed to the large diffusion of the method. On the other hand, a deterministic gradient based optimization has been used, in which the gradient is computed efficiently through the adjoint method.

3.1. Evolutionary Algorithms

Evolutionary Algorithms (EA) have been developed in the late sixties by J. Holland [7] and I. Rechenberg [8]. They are inspired from Darwinian evolution, whereby populations of individuals evolve over a search space and adapt to the environment by the use of different mechanisms such as mutation, crossover and selection. Individuals with a higher fitness have more chance to survive and/or get reproduced.

This natural process is translated to engineering problems in several steps. First, the shape is parameterised (as discussed in section 2.2) which defines an analogy to the DNA of an individual. This ensures that a unique combination of design parameters will represent a unique shape. Next, the operations that enable EA's to generate offspring such as mutation and crossover need to be translated. There exists a wide variety of techniques for this, which give rise to various classes of EA methods. Genetic Algorithms (GAs) for instance usually allow two individuals from a parent generation to reproduce two children through a crossover process on the design variables with analogy from nature. In Differential Evolution (DE) on the contrary, as many as four individuals are required to produce one child per parent, here analogy with nature is lost. In a final step, a selection procedure needs to be introduced, imposing a pressure on the population in which fitter designs have more chance to be selected for reproduction, while non-fit designs have larger probability to become extinct and disappear in the next generation. Potentially, additional mechanisms can be introduced to increase convergence through keeping a healthy diversity among the individuals of the population and by making sure that good individuals do not get lost accidentally. Eventually, these algorithms can be easily modified to deal with multi-objective optimization problems, which identify the Pareto front.

EA methods are capable to work with noisy objective functions and can find global optima of multimodal problems. They however require a large number of function evaluations, which leads to unacceptable large computational costs in case the objective function depends on CFD evaluations. Especially for large design spaces the computational cost can be prohibitive, restricting the use of these methods to only a small design space. Typically, up to 20 or slightly more design variables can be considered, depending on the level of interaction between the different parameters.

To reduce the computational cost, very often a surrogate model is introduced, which is a sort of interpolation tool using the already analyzed individuals by CFD. The surrogate model performs the same task as the high fidelity CFD analysis, but at a very low computational cost. However, it is less accurate, especially for an evaluation far away from the already analyzed points in the design space.

The implementation of the surrogate into the optimization system depends on how the system deals with the inaccuracy of the model. The technique used in the present work uses the surrogate model as an evaluation tool during the entire evolutionary process. After several generations the evolution is stopped and the best individual is analyzed by the expensive analysis tool. This technique is referred to as the "offline trained surrogate model". The difference between the predicted value of the surrogate model and the high fidelity tool is a direct measure for the accuracy of the surrogate model. Usually at the start this difference is rather large. The newly evaluated individual is added to the database used for the interpolation and the surrogate model will be more accurate in the region where previously the EA was predicting a minimum. This feedback is the most essential part of the algorithm as it makes the system self-learning. It mimics the human designer which learns from his mistakes on previous designs.

3.2. Gradient based optimization

Optimization methods that use gradient information are iterative methods that continuously alter the shape with small perturbations. The basic idea behind these methods is that through the knowledge of the gradient the direction can be found in which the design variables need to be changed in order to obtain an improved design. Small modifications to the design variables are required, as the gradient will only provide a linear approximation to the real objective function and remains only valid in the neighborhood of the current design. The simplest gradient based optimization method is the steepest descent, which modifies the design variables in the direction of the steepest descent, given by the opposite direction of the gradient. Although it has the lowest convergence rate of all gradient based methods, it is still an attractive method and will also be used in this work

The most complex part of this type of method is however to compute the gradient information, especially for problems which require the solution of partial differential equations to compute the objective. This can be achieved through a forward method, such as for instance finite differences, complex variable perturbation or algorithmic differentiation. In brief, these methods perturb one by one each design variable and compute the difference with the unperturbed design. The main drawback is that the computational cost is proportional to the number of design variables, requiring n additional CFD computations for n design variables.

The computational cost can however be dramatically reduced by reverse or adjoint methods, which require a cost proportional to only one CFD computation to obtain the gradient information, irrespective the number of design variables. In the case of continuous adjoint methods, a new set of linear partial differential equations needs to be solved after convergence of the CFD analysis, as for instance derived in [9]. Then the gradient can be computed with small effort. It is evident that such methods are preferred, as they allow for an efficient computation of the gradient even for extremely large design spaces (literally every grid point on the boundary of the shape can become a design variable). They however require a large development and implementation cost, which has been one of the major reasons for their reduced usage compared to EA or other gradient free methods. Additional disadvantages of gradient based methods is the local search, which allows only to find the nearby local optimum in case of multimodal problems.

4. RESULTS

4.1. Single-objective EA

A single objective Differential Evolution *DE/rand/1/bin* algorithm is applied to the U-Bend optimization. Since DE requires a large number of evaluations when not supported by a surrogate model, the problem is viewed in 2D to reduce the cost per CFD computation. In Fig. 3 the convergence history of the optimization can be seen. A total of 100 populations of 40 individuals each need to be performed in order to obtain convergence. This means a total of 4000 CFD computations. A reduction 35% in total pressure loss could be achieved.

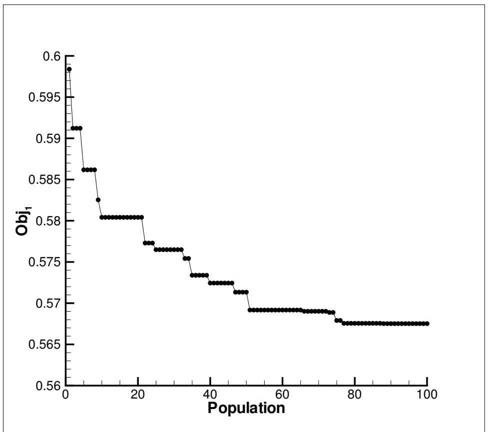

Figure 3. Convergence of the EA without surrogate model.

4.2. Single-objective EA assisted by surrogate model

A reduction in the computational cost can be obtained by using a surrogate model. In Fig. 4 the convergence history of a surrogate model assisted DE optimization is shown. It compares the surrogate model prediction (here a Kriging surrogate model was used) with the CFD evaluation for each iteration. An iteration within this method consists first of a training the surrogate model on the existing data, followed by a DE optimization using the surrogate model instead of the CFD evaluation, and a validation of the obtained best design by CFD. As can be seen, during the first iteration the surrogate model does not represent reality well, such that the DE optimization results in a design for which the surrogate model predicts a very large reduction in pressure drop. This is however not confirmed by the CFD validation, which shows that in fact a much larger pressure drop is obtained. This failure is added to the database after which a new iteration starts, consisting of retraining the surrogate model, optimizing the shape using the updated model and again verifying the result by CFD. As can be clearly seen, the surrogate model still overpredicts the reduction in pressure loss, but this time the prediction is already much closer to reality. Through adding the previous design to the database, the system has learned valuable information preventing the optimization algorithm to search further in this wrong direction. The newly found design is added again to the database after which a new iteration starts. Gradually the difference between the surrogate model and CFD prediction is reduced until the accuracy of the surrogate predictions are confirmed by CFD. Similar to the previous study a 36% reduction in pressure drop could be achieved, although in the present case a 3D CFD computation was used.

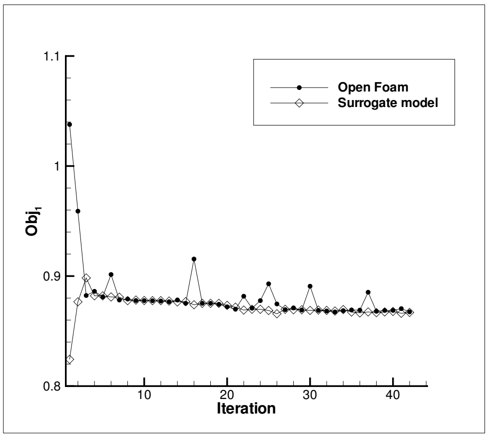

Figure 4. Convergence history of surrogate model assisted EA.

Prior to the optimization a total of 65 designs were analyzed by CFD to have an initial training set for the surrogate model. With an additional 40 calculations needed to find the optimum, only about 100

CFD computations are needed, which is an order less than for the DE without surrogate model assistance.

In Fig. 5 the optimal shape is shown. Careful analysis demonstrated that the reduction in pressure drop was achieved through a suppression of the separation on the inward surface of the bend. This was achieved by reducing the curvature near the wall, hence decreasing the velocity gradient normal to the wall and reducing the adverse pressure gradient in the second half of the inward surface.

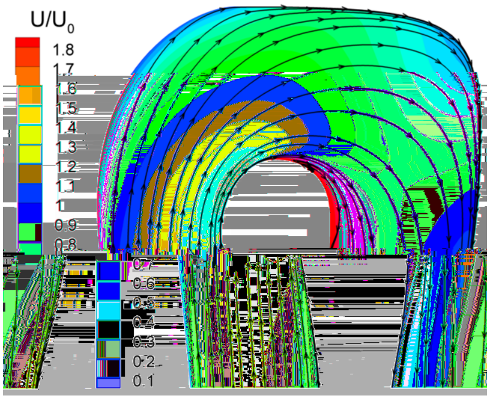

Figure 5. Optimal shape of the U-bend for minimal pressure loss.

4.3. Multi-objective EA assisted by surrogate model

So far only the pressure objective (Eq. 1) has been minimized. The U-bend in the present work however serves to cool down a turbine blade, and as explained in the introduction an increased heat transfer is an additional aim. Especially the tip of the blade is a critical area which may benefit from a better cooling. Therefore the objective expressed by Eq. 2 is introduced. Both objectives are conflicting and need a multi-objective optimization to obtain the optimal solution. The DE algorithm has been extended to this end to cope with multiple objectives based on the NSGA-II algorithm [10, 11].

In Fig. 6 the result of the optimization is summarized. It shows the total pressure drop versus the heat extracted for all 220 analyzed geometries. The baseline geometry consisting of the circular U-bend is indicated by a square, while the 65 samples generated for the initial database are represented by black dots. It is already apparent that these initial geometries perform better with respect to the total pressure drop objective, and most samples also perform better in the heat objective compared to the baseline.

The samples generated during a total of 32 iterations of the optimization phase are represented by diamonds. All of them are generated in the region of interest, i.e. with high heat transfer and low pressure drop. A clear Pareto front is formed, for which one cannot improve one objective without worsening the other. This clearly indicates that pressure loss and heat transfer are conflicting requirements, i.e. a physical mechanism is responsible to increase one and at the same time decrease the other.

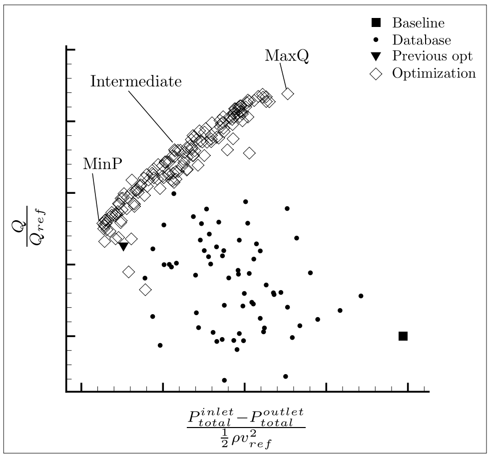

Figure 6. Results of the optimization plotted in the objective space.

Three candidate solutions are identified as “Min” which has the lowest total pressure drop, “MaxQ” which has the highest heat transfer, and “Intermediate”, which is in between both extremes. The performance of all three Pareto optimal geometries is summarized in Table 1. Finally, the optimal solution found during the single objective optimization, as presented in the previous section, is plotted as a gradient symbol. Although this optimization was not targeting any heat transfer objective, it improved the heat transfer compared to the baseline, as was also found during experimental validation.

Table 1. Objectives of the trade-off configurations.

	Obj_1	Obj_2
Baseline	1.22	1.00
MinP	0.84	1.08
Intermediate	0.93	1.13
MaxQ	1.07	1.17

In Fig. 7 the shapes corresponding to the three identified candidates are shown. The geometry with lowest pressure drop (“MinP”) resembles very closely the shape of the single-objective optimum (see Fig. 5). The increase in heat transfer by going to “MaxQ” is obtained by increasing the curvature of the external wall in the first 90 degrees and by increasing the internal wall width. Both actions increase the pressure loss and transform the smooth configuration into one that resembles a sharp u-bend configuration. Similar to what was found by Liou and Chen [12], a thicker divider wall is beneficial for the losses. Geometries with low pressure loss tend to have a smooth curvature change, and successfully suppress separation by increasing the radius of the turn and by carefully decelerating first and then accelerating the mean flow. As a consequence, less secondary flow motion is present and reduces the heat transfer potential. Geometries with high heat transfer on the other hand contain rapid changes of curvature and resemble close to sharp U-bends. Heat transfer is enhanced due to the impingement of the flow near the external wall, however increasing the losses.

The computational cost of the multi-objective optimization is with its 220 CFD evaluations slightly larger than the single-objective optimization of section 4.2. It however needs to be noted that for each of the 32 iterations 5 individuals need to be analyzed which is performed in parallel. This allows for a faster completion than the single-objective optimization, for which only 1 design is evaluated per iteration.

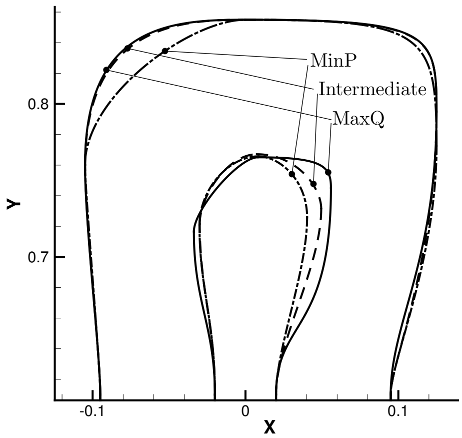

Figure 7. Comparison of the trade-off shapes.

4.4. Gradient based optimization

The same 2D single-objective optimization as performed in section 4.1 has been repeated with a gradient based optimization method, although with a different parameterisation as explained in section 2.2. The gradient has been computed using the continuous adjoint approach implemented in OpenFoam. In Fig. 8 the optimal shape is shown compared to the initial shape.

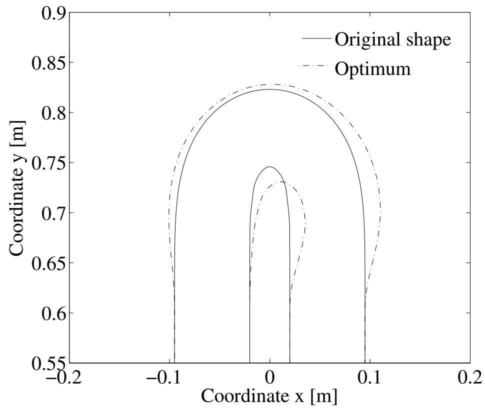

Figure 8. Comparison of baseline and adjoint optimization shape.

A comparison of the optimal shape from EA based optimization algorithms to the best performing design obtained by the steepest-descent method reveals that both U-bends exhibit similar geometrical features leading to a strong reduction of the total pressure drop. A direct comparison shows a slight advantage for the EA based optimization ($Obj_1 = 27Pa$ opposed to $Obj_1 = 35Pa$), however a different paramterisation has been used and a different starting point has been considered.

Both configurations feature an increased duct section in the first part of the bend resulting in a limited acceleration of the flow around the bend tip. In combination with increased radii of curvature along the internal and external walls, the reduced flow velocity leads to reduced centrifugal forces reducing the tendency of the flow to separate. In addition, the convex inner wall along the second leg of the bend is deformed such that it fills the space which is occupied by the separated flow in the original geometry. While present in the gradient-free optimized shape, this feature is even more pronounced by the gradient-based method. Considering the different geometry parameterisation resulting from the necessity to limit the number of design parameters for gradient-free optimization, the similarity of the optimal U-bend shapes obtained by differential evolution and steepest descent represents an unprecedented finding. This remarkable result demonstrates that the underlying objective function in the present case does not pose a multimodal problem as often assumed for engineering optimization problems. Consequently, both gradient-free and gradient-based optimization methods detect the global optimum demonstrating that the concern of getting trapped in a local minimum is of no relevance for the application of the latter. Therefore, by using a computationally efficient gradient-based optimization procedure a globally optimal U-bend shape is provided after only 30 design iterations where succeeding flow field computations benefit from previously converged solutions. The computational cost is thus almost an order of magnitude less than the EA, and this for a 4 times larger design space.

4.5. Experimental validation

An experimental investigation has been conducted for the baseline geometry consisting of 2 circular arcs and the shape shown in Fig. 5, which was obtained by a metamodel assisted EA optimization using 3D CFD. In terms of global performance, Table 2 summarizes the experimental obtained improvement and compares them to the numerical predictions. The agreement between experiments and calculations is good, and the improvement in aerodynamic performance (both measured as well as predicted) is very significant.

Detailed PIV measurements have however also been performed and reveal a small recirculation bubble, not present in the numerical result. Fig. 9

Table 2. Aerodynamic performance of the investigated U-bend configurations.

	ΔP baseline $[-]$	ΔP optimized $[-]$	gain [%]
Exp.	1.03 ± 0.03	0.65 ± 0.02	36.2 ± 3
CFD	1.01	0.63	37.6

shows the obtained velocity field, which can be compared to Fig. 5. It clearly demonstrates the limitations of the k-ϵ turbulence model in predicting flow separation in regions of adverse pressure gradients. Despite the differences in the flow details, however, the model allowed to predict well the global trends and combined with an optimization algorithm provides an extremely efficient methodology to improve the shape of the U-bend.

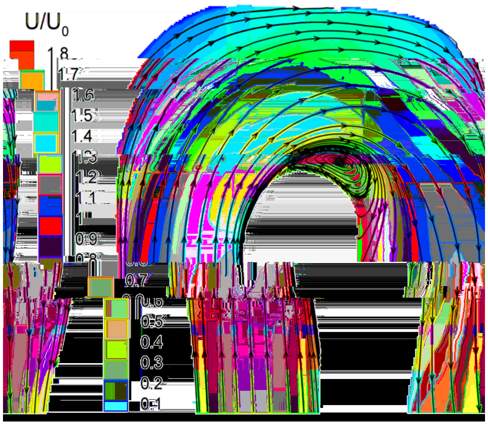

Figure 9. Mean velocity from PIV in the optimized geometry at mid height.

5. CONCLUSIONS

An overview was given of different studies attempting to improve the performance of a U-bend for internal cooling channels. It was shown that all methods lead to shapes with similar features, in which the curvature of the inner wall has been reduced to limit the velocity gradient across the passage. When heat transfer is introduced next to the pressure losses as a second objective, several trade-off solutions can be found. The physical process behind the conflict between both objectives is due to the secondary flow motion. To increase heat transfer, a stronger secondary flow motion is desired, which can be introduced by a smaller curvature, however increasing the mixing losses and hence increasing the pressure losses.

Comparison between the different optimization methods demonstrates that the use of surrogate models can drastically reduce the required number of CFD evaluations from 4000 to 100 only. Comparing further the surrogate model assisted EA with the gradient based optimization, it was found that similar shapes were obtained despite the fact that the gradient based method departed from a separated initial design. It is often believed that engineering problems facing separation represent a multimodal character, for which gradient based optimization algorithms can get trapped in local optima. In the present study however, results indicate that no such problems were present and seem to further feed the discussion as to which many engineering problems are unimodal of nature although easily thought multimodal

Finally, an experimental validation has proven the effectiveness of the optimization approach. In terms of global performance, the numerical predicted reduction in pressure losses was confirmed within measurement accuracy. Detailed PIV measurements however reveal a small separation which was not captured by CFD. It demonstrates that still further improvement should be possible, however beyond the capability of RANS approaches with their restriction on turbulence modeling.

REFERENCES

[1] Humphrey, J. A. C., Whitelaw, J. H., and Yee, G., 1981, "Turbulent Flow in a Square Duct with Strong Curvature", *Journal of Fluid Mechanics*, Vol. 103, pp. 443–463.

[2] Chang, S. M., Humphrey, J. A. C., and Modavi, A., 1983, "Turbulent Flow in a Strongly Curved U-Bend and Downstream Tangent of Square Cross-Sections", *Physico-Chemical Hydrodynamics*, Vol. 4, pp. 243–269.

[3] Monson, D. J., and Seegmiller, H. L., 1992, "Experimental Investigation of Subsonic Flow in a Two Dimensional U-Duct", *NASA report TM-103931*.

[4] Cheah, S. C., Iacovides, H., Jackson, D. C., Ji, H. H., and Launder, B. E., 1996, "LDA Investigation of the Flow Development Through Rotating U-ducts", *Journal of Turbomachinery*, Vol. 118, pp. 590–596.

[5] Open Foam, 2010, "Open Foam user guide", *Tech. rep.*, See also URL http://www.openfoam.com/docs/user/.

[6] Pope, S. B., 2000, *Turbulent Flows*, Cambridge University Press.

[7] Holland, J. H., 1975, *Adaption in Natural and Artificial Systems*, University of Michigan Press.

[8] Rechenberg, I., 1973, *Evolutionsstrategie — Optimierung technischer Systeme nach Prinzipien der biologischen Evolution*, Fommann-Holzboog, Stuttgart.

[9] Othmer, C., 2008, "A continuous adjoint formulation for the computation of topological and surface sensitivities of ducted flows", *Int J Num Meth Fluids*, Vol. 58, pp. 861–877.

[10] Abbas, H. A., Sarker, R., and Newton, C., 2001, "PDE: A Pareto-Frontier Differential Evolutio Approach for Multi-objective Optimization Problems", *Proceedings of the Congress on Evolutionary Computation*, Piscataway, New Jersey, Vol. 2, pp. 971–978.

[11] Madavan, N. K., 2002, "Multiobjective Optimization Using a Pareto Differential Evolution Approach", *Proceedings of the Congress on Evolutionary Computation*, Honolulu, Hawaii, Vol. 2, pp. 1145–1150.

[12] Liou, T.-M., Tzeng, Y.-Y., and Chen, C.-C., 1999, "Flow in a 180S Sharp Turning Duct With Different Divider Thicknesses", *Int J Num Meth Fluids*, Vol. 121, pp. 569–576.

Conference on Modelling Fluid Flow (CMFF'15)
The 16th International Conference on Fluid Flow Technologies
Budapest, Hungary, September 1-4, 2015

Evolutionary Algorithms and Adjoint-based CFD optimization in turbomachinery

K.C. Giannakoglou[1], V.G. Asouti[2], E.M. Papoutsis-Kiachagias[3]

[1] National Technical University of Athens. Iroon Polytechniou 9, 157 80 Athens, Greece. (+30)2107721636. kgianna@central.ntua.gr, web page: http://velos0.ltt.mech.ntua.gr/research/
[2] National Technical University of Athens. vasouti@mail.ntua.gr
[3] National Technical University of Athens. vaggelisp@gmail.com.

ABSTRACT

This paper deals with Computational Fluid Dynamics (CFD)-based shape optimization methods applied to gas and hydraulic turbomachines. In specific, two major optimization strategies, developed by the same group, are discussed: gradient–based methods (GBMs) supported by the continuous adjoint approach and metamodel–assisted evolutionary algorithms (MAEAs).

Regarding GBMs, the continuous adjoint method for the aero/hydrodynamic design of turbomachinery bladings is discussed. Full differentiation of turbulence models is considered. Recent developments allowing the computation of accurate sensitivity derivatives are presented in brief. Then, the continuous adjoint method is used for the shape optimization of two Francis turbine blades. The adjoint method for the optimization of thermal turbomachinery bladings, by taking into account conjugate heat transfer (CHT) effects, is also discussed.

Regarding MAEAs, emphasis is laid on the ways used to reduce the overall CPU cost of a CFD-based optimization. In particular, the efficient use of on–line trained surrogate evaluation models (or metamodels), the use of asynchronous search on multiprocessor platforms and the use of Principal Component Analysis (PCA) as remedies to the curse of dimensionality problem are discussed. MAEAs are demonstrated in the aero/hydrodynamic shape optimization of turbomachinery bladings.

Keywords: Computational Fluid Dynamics, Continuous Adjoint Method, Gradient–based methods, Metamodel Assisted Evolutionary Algorithms, Thermal and Hydraulic Turbomachines

NOMENCLATURE

F	[varies]	objective function
T	[K]	temperature
T_a	[F-related]	adjoint temperature
$\underline{b}$	[varies]	design variables
$\underline{u}$	[F-related]	adjoint velocity
$\underline{v}$	$[m/s]$	absolute velocity
$\underline{w}$	$[m/s]$	relative velocity
p	$[m^2/s^2]$	static pressure divided by density
q	[F-related]	adjoint pressure
λ	[-]	offsprings
μ	[-]	parents
ν	$[m^2/s]$	bulk viscosity
ν_t	$[m^2/s]$	turbulent viscosity
$\widetilde{\nu_a}$	[F-related]	adjoint turbulence model variable
$\widetilde{\nu}$	$[m^2/s]$	Spalart–Allmaras model variable

1. INTRODUCTION

During the last years, the cost benefits resulting from using CFD has given rise to an intense academic and industrial interest in the use of computational methods for the design/optimization of thermal and hydraulic turbomachines.

CFD–based optimization methods can be classified into deterministic and stochastic ones, according to the strategy used to compute the optimal set of design variables. Deterministic algorithms start with a given geometry and improve it iteratively based on the computed or approximated gradient of the objective function with respect to (w.r.t.) the design variables. Depending on the initialization, it is not unlikely for a GBM to be trapped into a local optimum. In such a case, the designer will get an optimized rather than an optimal solution. Though global optimal solutions are always the target, in practice local optima are highly welcome. The efficiency of GBMs greatly depends on the method used to compute the necessary gradient. In this respect, the adjoint method [1] has been receiving a lot of attention, since the cost of computing the gradient is, practically, independent from the number of the design variables. This makes the method an excellent choice for large scale industrial optimization problems. In this paper, recent advances in computing accurate sensitivity derivatives for turbulent flows using the continuous adjoint variant are discussed, [2]. In addition, a short discussion about adjoint methods for CHT applications is presented followed by industrial applications.

Evolutionary algorithms (EAs) are the most popular representative of stochastic population–based search methods. In EAs, entrapment to local minima is highly unlikely, unless the search is stopped early enough, since almost the entire design space can be explored. EAs are extremely flexible since the evolution operators do not interfere with the flow solver; so, in CFD–based optimization, no access to the source CFD code is required (black–box evaluation software). Furthermore, EAs can compute Pareto fronts of non-dominated solutions in multi–objective optimization (MOO) problems, with a single run. On the other hand, a great number of candidate solutions must be evaluated before reaching the optimal one(s), leading to a high optimization turnaround time, especially when the evaluation software is costly (such as in CFD applications). In addition, the number of evaluations required increases with the number of the design variables (curse of dimensionality). A number of remedies have been proposed in the literature to tackle the aforementioned two weaknesses of EAs. Among them is the use Metamodel–Assisted EAs (MAEAs), asynchronous search, performed on a cluster of many processors, and the use Principal Component Analysis (PCA) to identify correlations between the design variables, [3, 4, 5]. Industrial applications using the above techniques are presented.

2. ADJOINT METHODS

In this section, the formulation of the continuous adjoint PDEs, their boundary conditions and the sensitivity derivatives (gradient) expression are presented in brief. The development is based on the incompressible Navier-Stokes equations for a non-inertial Single Rotating Frame (SRF), though their extension to inertial reference systems, [2], exists too. The development for incompressible flows is based on OpenFOAM©. However, the same tools have been programmed also for compressible flows, [6], on an in–house CDF code, running on GPUs, [7].

2.1. Flow Equations

The mean flow equations together with the Spalart–Allmaras turbulence model PDE, [8], comprise the flow or primal system of equations that reads

$$R^p = -\frac{\partial w_i}{\partial x_i} = 0 \tag{1a}$$

$$R_i^w = w_j\frac{\partial w_i}{\partial x_j} + \frac{\partial p}{\partial x_i} - \frac{\partial \tau_{ij}}{\partial x_j} + \underbrace{2e_{ijk}\Omega_j w_k}_{C_R}$$
$$+ e_{ijk}\Omega_j e_{klm}\Omega_l x_m = 0 \tag{1b}$$

$$R^{\widetilde{\nu}} = \frac{\partial(w_j\widetilde{\nu})}{\partial x_j} - \frac{\partial}{\partial x_j}\left[\left(\nu + \frac{\widetilde{\nu}}{\sigma}\right)\frac{\partial \widetilde{\nu}}{\partial x_j}\right] - \frac{c_{b2}}{\sigma}\left(\frac{\partial \widetilde{\nu}}{\partial x_j}\right)^2$$
$$-\widetilde{\nu}P(\widetilde{\nu},\Delta) + \widetilde{\nu}D(\widetilde{\nu},\Delta) = 0 \tag{1c}$$

where w_i, Ω_j, x_m are the components of the relative velocity vector, rotational speed vector and position vector, respectively. The absolute (v_i) and relative (w_i) velocities are related through $v_i = w_i + e_{ijk}\Omega_j x_k$. Also, p is the static pressure divided by the constant density, $\tau_{ij} = (\nu + \nu_t)\left(\frac{\partial w_i}{\partial x_j} + \frac{\partial w_j}{\partial x_i}\right)$ are the components of the stress tensor, ν and ν_t the bulk and turbulent viscosity, respectively, $\widetilde{\nu}$ the Spalart–Allmaras model variable and Δ the distance from the wall boundaries. Details about the turbulence model constants and source terms can be found in [8].

2.2. General Objective Function

Let F be the objective function to be minimized by computing the optimal values of the design variables $b_n, n \in [1, N]$. A general expression for an objective function defined on (parts of) the boundary S of the computational domain Ω is given by

$$F = \int_S F_{S_i} n_i dS \tag{2}$$

where $\mathbf{n}$ is the outward normal unit vector.

Differentiating Eq. 2 w.r.t. to b_n and applying the chain rule yields

$$\frac{\delta F}{\delta b_n} = \int_S \frac{\partial F_{S_i}}{\partial w_k} n_i \frac{\partial w_k}{\partial b_n} dS + \int_S \frac{\partial F_{S_i}}{\partial p} n_i \frac{\partial p}{\partial b_n} dS$$
$$+ \int_S \frac{\partial F_{S_i}}{\partial \tau_{kj}} n_i \frac{\partial \tau_{kj}}{\partial b_n} dS + \int_S \frac{\partial F_{S_i}}{\partial \widetilde{\nu}} n_i \frac{\partial \widetilde{\nu}}{\partial b_n} dS$$
$$+ \int_S n_i \frac{\partial F_{S_i}}{\partial x_k} \frac{\delta x_k}{\delta b_n} n_k dS + \int_S F_{S_i} \frac{\delta(n_i dS)}{\delta b_n} \tag{3}$$

where $\delta\Phi/\delta b_n$ is the total (or material) derivative of any quantity Φ while $\partial\Phi/\partial b_n$ is its partial derivative. Operators $\delta()/\delta b_n$ and $\partial()/\partial b_n$ are related by

$$\frac{\delta \Phi}{\delta b_n} = \frac{\partial \Phi}{\partial b_n} + \frac{\partial \Phi}{\partial x_k}\frac{\delta x_k}{\delta b_n} \tag{4}$$

Computing the variation of the flow variables on the r.h.s. of Eq. 3, either through Direct Differentiation (DD) or Finite Differences (FD) would require at least N Equivalent Flow Solutions (EFS, i.e. as if the flow equations were solved instead). To avoid this computational cost that scales with N, the adjoint method is used, as presented in the next subsection.

2.3. Continuous Adjoint Formulation

Starting point of the continuous adjoint formulation is the introduction of the augmented function

$$F_{aug} = F + \int_\Omega u_i R_i^w d\Omega + \int_\Omega q R^p d\Omega + \int_\Omega \widetilde{\nu_a} R^{\widetilde{\nu}} d\Omega \tag{5}$$

where u_i are the components of the adjoint to the relative velocity vector, q is the adjoint pressure and

$\widetilde{\nu_a}$ is the adjoint turbulence model variable, respectively. Dropping the last integral on the r.h.s. of Eq. 5 would result to the so-called "frozen turbulence" assumption which neglects the differentiation of the turbulence model PDE(s). This assumption leads to reduced gradient accuracy, possibly even to wrong sensitivity signs, [9]. To avoid the "frozen turbulence" assumption implications, the Spalart–Allmaras model PDE has been differentiated, see [9]. A review on continuous adjoint methods for turbulent flows can be found in [2].

The differentiation of Eq. 5, based on the Leibniz theorem, yields

$$\frac{\delta F_{aug}}{\delta b_n} = \frac{\delta F}{\delta b_n} + \int_\Omega u_i \frac{\partial R_i^w}{\partial b_n} d\Omega + \int_\Omega q \frac{\partial R^p}{\partial b_n} d\Omega + \int_\Omega R^{\widetilde{\nu}} \frac{\partial R^{\widetilde{\nu_a}}}{\partial b_n} d\Omega + \int_{S_W} (u_i R_i^w + qR^p + \widetilde{\nu_a} R^{\widetilde{\nu}}) n_k \frac{\delta x_k}{\delta b_n} dS \tag{6}$$

Then, the derivatives of the flow residuals in the volume integrals on the r.h.s. of Eq. 6 are developed by differentiating Eqs. 1 and applying the Green-Gauss theorem, where necessary. Indicatively, the development of the C_R (Coriolis) term variation yields

$$\int_\Omega u_i \frac{\partial C_{R,i}}{\partial b_n} d\Omega = - \int_\Omega 2 e_{ijk} \Omega_j u_k \frac{\partial w_i}{\partial b_n} d\Omega \tag{7}$$

contributing an extra term to the adjoint momentum equations. The development of the remaining terms can be found in [9], [10] and [2].

In order to obtain a gradient expression which does not depend on the partial derivatives of the flow variables w.r.t. b_n, their multipliers in (the developed form of) Eq. 6 are set to zero, giving rise to the field adjoint equations

$$R^q = -\frac{\partial u_j}{\partial x_j} = 0 \tag{8a}$$

$$R_i^w = u_j \frac{\partial w_j}{\partial x_i} - \frac{\partial (w_j u_i)}{\partial x_j} - \frac{\partial \tau_{ij}^a}{\partial x_j} + \frac{\partial q}{\partial x_i} \underbrace{-2 e_{ijk} \Omega_j u_k}_{C_{R_a}} + \widetilde{\nu_a} \frac{\partial \widetilde{\nu}}{\partial x_i} - \frac{\partial}{\partial x_l} \left(\widetilde{\nu_a} \widetilde{\nu} \frac{C_Y}{Y} e_{mjk} \frac{\partial w_k}{\partial x_j} e_{mli} \right) = 0 \tag{8b}$$

$$R^{\widetilde{\nu_a}} = -\frac{\partial (w_j \widetilde{\nu_a})}{\partial x_j} - \frac{\partial}{\partial x_j} \left[\left(\nu + \frac{\widetilde{\nu}}{\sigma} \right) \frac{\partial \widetilde{\nu_a}}{\partial x_j} \right] + \frac{1}{\sigma} \frac{\partial \widetilde{\nu_a}}{\partial x_j} \frac{\partial \widetilde{\nu}}{\partial x_j} + 2 \frac{c_{b2}}{\sigma} \frac{\partial}{\partial x_j} \left(\widetilde{\nu_a} \frac{\partial \widetilde{\nu}}{\partial x_j} \right) + \widetilde{\nu_a} \widetilde{\nu} C_{\widetilde{\nu}} + \frac{\partial \nu_t}{\partial \widetilde{\nu}} \frac{\partial u_i}{\partial x_j} \left(\frac{\partial w_i}{\partial x_j} + \frac{\partial w_j}{\partial x_i} \right) + (-P + D) \widetilde{\nu_a} = 0 \tag{8c}$$

where $\tau_{ij}^a = (\nu + \nu_t) \left(\frac{\partial u_i}{\partial x_j} + \frac{\partial u_j}{\partial x_i} \right)$ are the components of adjoint stress tensor. The term marked as C_{R_a} results from the differentiation of C_R and can be seen as the adjoint Coriolis acceleration. Eq. 8c is the adjoint turbulence model equation, from which the adjoint turbulence model variable $\widetilde{\nu_a}$ is computed.

The adjoint boundary conditions are derived by treating the flow variations in the boundary integrals (of the developed form of) Eq. 6, [9, 2]. Indicatively, at the inlet (S_I) and wall (S_W) boundaries, the following conditions are imposed

$$u_j n_j = u_{\langle n \rangle} = -\frac{\partial F_{S_{I-W,i}}}{\partial p} n_i \tag{9a}$$

$$u_j t_j^I = u_{\langle t \rangle}^I = \frac{\partial F_{S_{I-W,k}}}{\partial \tau_{ij}} n_k t_i^I n_j + \frac{\partial F_{S_{I-W,k}}}{\partial \tau_{ij}} n_k t_j^I n_i \tag{9b}$$

$$u_j t_j^{II} = u_{\langle t \rangle}^{II} = \frac{\partial F_{S_{I-W,k}}}{\partial \tau_{ij}} n_k t_i^{II} n_j + \frac{\partial F_{S_{I-W,k}}}{\partial \tau_{ij}} n_k t_j^{II} n_i \tag{9c}$$

where S_{I-W} stands for either S_I or S_W, depending on the boundary under consideration. In what follows, $\mathbf{t^I}$ is the unit tangent vector parallel to the velocity at the first cell centre off the boundary and the components of the second target vector $\mathbf{t^{II}}$ are given by $t_i^{II} = e_{ijk} n_j t_k^I$, where e_{ijk} is the Levi-Civita symbol. The outlet (S_O) conditions for the adjoint problem and boundary conditions for the $\widetilde{\nu_a}$ field can be found in [9, 2].

In industrial applications, the wall function technique is used routinely in analysis and design. When the design is based on the adjoint method, considering the adjoint to the wall function model becomes necessary. The continuous adjoint method in optimization problems, governed by the RANS turbulence models with wall functions, was initially presented in [11], where the adjoint wall function technique was introduced for the $k - \epsilon$ model and a vertex–centered finite volume method. The proposed formulation led to a new concept: the "adjoint law of the wall". This bridges the gap between the solid wall and the first node off the wall during the solution of the adjoint equations. The adjoint wall function technique has been extended to flow solvers based on cell-centered finite-volume schemes, for the $k - \omega$, [12], and Spalart–Allmaras , [2], models.

After satisfying the adjoint PDEs and their boundary conditions, the remaining terms in Eq. 6 yield the sensitivity derivatives

$$\begin{aligned} \frac{\delta F}{\delta b_n} = &- \int_{S_W} \left[\tau_{ij}^a n_j - q n_i + \frac{\partial F_{S_{W,k}}}{\partial w_i} n_k \right] \frac{\partial w_i}{\partial x_k} \frac{\delta x_k}{\delta b_n} dS \\ &+ \int_{S_W} n_i \frac{\partial F_{S_{W,i}}}{\partial x_k} \frac{\delta x_k}{\delta b_n} dS + \int_{S_W} F_{S_{W,i}} \frac{\delta (n_i dS)}{\delta b_n} \\ &- \int_{S_W} \left[\left(\nu + \frac{\widetilde{\nu}}{\sigma} \right) \frac{\partial \widetilde{\nu_a}}{\partial x_j} n_j + \frac{\partial F_{S_k}}{\partial \widetilde{\nu}} n_k \right] \frac{\partial \widetilde{\nu}}{\partial x_k} \frac{\delta x_k}{\delta b_n} dS \\ &+ \int_{S_W} (u_i R_i^w + qR^p + \widetilde{\nu_a} R^{\widetilde{\nu}}) \frac{\delta x_k}{\delta b_n} n_k dS \\ &- \int_{S_W} \left(-u_{\langle n \rangle} + \frac{\partial F_{S_{W_p,k}}}{\partial \tau_{lm}} n_k n_l n_m \right) \mathcal{TS}_1 dS \\ &- \int_{S_W} \frac{\partial F_{S_{W_p,k}}}{\partial \tau_{lm}} n_k t_l^I t_m^I \mathcal{TS}_2 dS \\ &- \int_{S_W} \left(\frac{\partial F_{S_{W_p,k}}}{\partial \tau_{lm}} n_k (t_l^{II} t_m^I + t_l^I t_m^{II}) \right) \mathcal{TS}_3 dS \end{aligned}$$

$$-\int_{S_W} \frac{\partial F_{S_{W_{p,k}}}}{\partial \tau_{lm}} n_k t_l^{II} t_m^{II} \mathcal{T}\mathcal{S}_4 dS \qquad (10)$$

where $\mathcal{T}\mathcal{S}_1$ to $\mathcal{T}\mathcal{S}_4$ can be found in [2].

2.4. Differentiation of Turbulence Models: A Convincing Example

In the application of this section, the gain from overcoming the "frozen turbulence" assumption is discussed. In Figure 1, the sensitivity derivatives of the total pressure losses objective function,

$$F_{pt} = -\int_{S_{I,O}} \left(p + \frac{1}{2}v_k^2\right) v_i n_i dS$$

w.r.t. the coordinates of Bézier–Bernstein control points parameterizing a compressor cascade airfoil are illustrated. Here, the low-Re variant of the Spalart–Allmaras model is used. It can be seen that the "frozen turbulence" assumption leads to quite wrong sensitivities while the adjoint approach that takes into consideration the differentiation of the turbulence model reproduces the outcome of the reference method (FD). More on the gain in accuracy

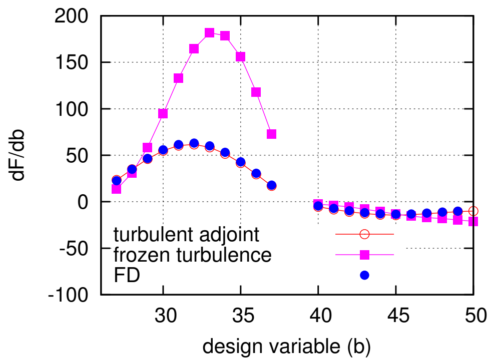

Figure 1. Shape optimization of a compressor cascade with $Re = 3.3 \times 10^5$. Sensitivity derivatives of the total pressure losses function F w.r.t. the coordinates of the Bézier–Bernstein control points parameterizing the suction (first half) and pressure (last half of the horizontal axis) airfoil sides.

from using the adjoint law of the wall when the flow simulation employs wall functions can be found in [2].

2.5. Continuous Adjoint for Conjugate Heat Transfer Analysis

This section discusses some points of the mathematical development and implementation of the continuous adjoint method to CHT applications. CHT comprises the concurrent solution of the mean flow and energy equations over the fluid domain and the energy equation over an adjacent solid domain. The fluid and solid domains communicate through the Fluid/Solid Interface (FSI). The conditions imposed along the FSI boundary, Figure 2, are (index F stands for fluid-related quantities and S for solid-related ones)

$$Q^S = -Q^F \Rightarrow k^S \left.\frac{\partial T^S}{\partial n}\right|_{FSI_S} = -k^F \left.\frac{\partial T^F}{\partial n}\right|_{FSI_F} \qquad (11a)$$

$$T^S = T^F = T^{FSI} \qquad (11b)$$

where Q is the heat-flux and $k^F = a_{eff} c_p$ is the thermal conductivity. Eq. 11a expresses the equality of heat fluxes along the FSI while Eq. 11b states that the temperature at the coinciding nodes of the solid and fluid meshes is the same.

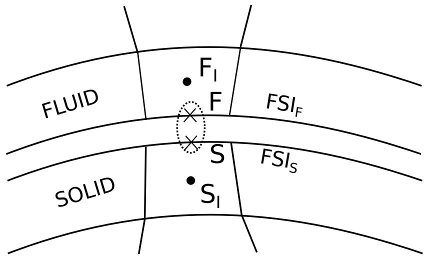

Figure 2. The fluid(F)/solid(S) interface. Faces F and S coincide. F_I and S_I are the centres of the first cells off the fluid and solid boundaries, respectively.

In the application examined, the optimization aims at minimizing the maximum temperature inside an internally cooled turbine cascade, Figure 3. Since such a min./max. objective can not be differentiated, a differentiable surrogate should be used. It is proposed to use a sigmoid function

$$F_T = \frac{\int_{\Omega_S} f_{sig} d\Omega}{\int_{\Omega_S} d\Omega} \,, \quad f_{sig} = 1 - \frac{1}{1 + e^{k_2(T-T_c)+k1}} \qquad (12)$$

where Ω_S is the volume of the solid domain, T_c is a critical (high) temperature threshold and $T_s < T_c$ is a safety threshold to be defined by the designer. Constants k_1 and k_2 take on values that lead to $f_{sig}(T_s) = \epsilon$ and $f_{sig}(T_c) = 1 - \epsilon$, where ϵ is a user–defined infinitesimal positive number.

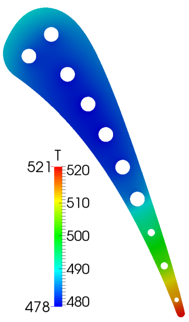

Figure 3. Temperature distribution inside an internally cooled turbine blade. The fluid (not shown in the figure) and solid domains are coupled based on the boundary conditions presented in Eqs. 11, while heat exchange between the solid domain and the cooling passages is simulated using a $1D$ heat exchange equation.

The augmented objective function for CHT optimization problems is written as

$$F_{aug} = F + \int_{\Omega_F} u_i R_i^w d\Omega + \int_{\Omega_F} q R^p d\Omega + \int_{\Omega_F} \widetilde{\nu}_a R^{\widetilde{\nu}} d\Omega + \int_{\Omega_F} T_a^F R^{T^F} d\Omega + \int_{\Omega_S} T_a^S R^{T^S} d\Omega \tag{13}$$

where R^{T^F}, R^{T^S} are the energy equation PDEs over the fluid and solid domains, respectively, and T_a^F, T_a^S are the corresponding adjoint temperatures. Following a process similar to that described in sections 2.2 to 2.4, the field adjoint equations, adjoint boundary conditions and sensitivity derivatives expression can be derived. In the interest of space, these are omitted herein. However, it is interesting to note that the adjoint boundary conditions at the FSI are of the same type as the primal conditions. Eq. 11. They include the conservation of the adjoint heat flux at the FSI and the same adjoint temperature values for both sides of the FSI. This remark holds only for objective functions which do not include the temperature values along the FSI.

The continuous adjoint approach to CHT problems was utilized to support a gradient-based algorithm to minimize F_T with $T_s = 515\ K$ and $T_c = 525\ K$ for the geometry presented in Figure 3; the turbine blade airfoil is parameterized using NURBS control points and the cooling holes are at fixed positions. The highest deformation is located close to the trailing edge, Figure 4, decreasing the maximum blade temperature by more than 2 K.

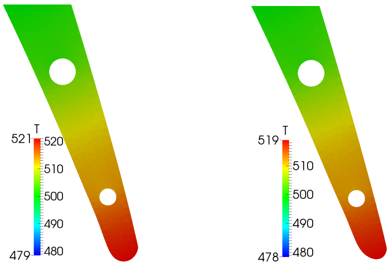

Figure 4. Shape optimization of an internally cooled turbine blade, targeting the minimization of the maximum temperature over the solid. Temperature distributions in a blow-up view close to the trailing edge of the initial (left) and optimized (right) geometries.

2.6. *Turbomachinery Applications of Adjoint-based Optimization*

Two industrial applications are presented in this section. The first one is concerned with the shape optimization of a Francis turbine runner in order to suppress cavitation, i.e. maximizing the minimum pressure on the blade surface. Following the same line of reasoning for differentiating a max./min problem as the one presented in section 2.5, a sigmoid function similar to Eq. 12 is used, by defining a cavitation threshold p_c and a safety threshold p_s. No shape parameterization was used. Instead, the normal displacements of the blade wall nodes acted as the design variables, after appropriately smoothing the computed sensitivity derivatives. The pressure distributions over the initial and optimized bladings are presented in Figure 5.

The second application deals with the multi-point design of a different Francis runner targeting the maximization of the weighted sum of the efficiencies at three operating points, ranging from 40% to 100% of the nominal mass flow rate Q_{nom}

$$F = 0.6F_{Q_{100}} + 0.25F_{Q_{71.5}} + 0.15F_{Q_{40}} \tag{14}$$

Blade shapes resulting after 8 optimization cycles of the multi-point as well as the three (separate) single-point optimizations (for the three mass flow rates) are depicted in Figure 6. The multi-point optimization deforms the blade in the same direction as the single-point optimization for the nominal flow rate, since this point has the highest weight in Eq. 14. The other two single-point optimizations for $Q = 0.715Q_{nom}$ and $Q = 0.40Q_{nom}$ deform the blade in the opposite direction. This clearly reveals the contradictory targets in multi-point optimization.

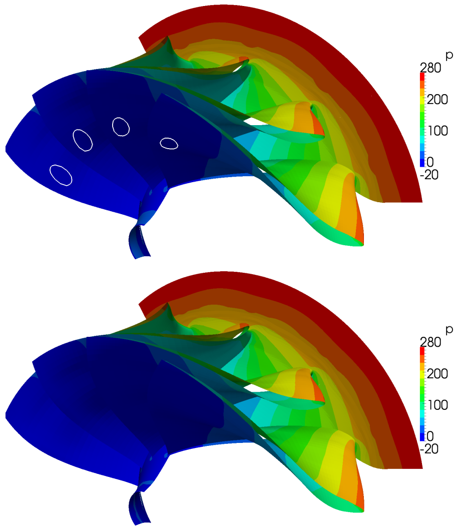

Figure 5. Optimization of a Francis runner blade targeting cavitation suppression. Top: pressure distribution over the initial blading; white isolines encircle the cavitated areas. Bottom: pressure distribution over the optimized blading.

3. OPTIMIZATION METHODS BASED ON EAS

Regarding EAs, emphasis is laid on ways to reduce the optimization turnaround time in large–scale applications. The most frequently used technique is the use of surrogate evaluation models (metamodels) giving rise to MAEAs. Either EAs or MAEAS can further be enhanced by the Principal Component Analysis (PCA) technique aiming at efficiently handling problems involving a great number of design

Figure 6. Multi-point optimization of a Francis runner Blades as seen from the trailing edge (left) and a blow–up view close to the shroud (right). The initial blade is depicted in grey, the result of the multi-point optimization in red, while the results of single-point optimizations at the three operating points are shown in green ($Q=Q_{nom}$), yellow ($Q=0.715Q_{nom}$) and magenta ($Q=0.4Q_{nom}$).

variables. Over and above to MAEAs (with or without PCA), the concurrent evaluation of the offspring of each generation on the available processors of a multi-processor system may further reduce the optimization turnaround time. Asynchronous EAs (AEAs), remove the synchronization barrier at the end of each generation, and fully exploit all the available computational resources. All these techniques are incorporated in the general purpose optimization platform EASY (Evolutionary Algorithm SYstem, http://velos0.ltt.mech.ntua.gr/EASY) developed by the authors' group.

On–line trained metamodels (radial basis function/RBF networks) for each candidate solution are used according to the Inexact Pre-Evaluation (IPE) technique, [3]. The first few generations are carried out as a conventional EA (with μ parents and λ offspring) and the MAEA starts once a user–defined number of entries have been stored in the database (DB) of already evaluated individuals. During the IPE phase all population members are pre–evaluated on the surrogate models trained on–the–fly. This training is carried out on the neighboring (in the design space) individuals in the DB. Then, based on the outcome of the pre–evaluations on the metamodels, a small number of the most promising members ($\lambda_{IPE} \ll \lambda$) are re–evaluated on the CFD model.

Metamodels can be also employed in AEAs (AMAEAs), after appropriately adapting the IPE scheme, [4], since the notion of generation does not exist anymore. Once an evaluation is completed and the corresponding processor is idle, a new individual is generated (using the evolution operators) and assigned to this processor. When the IPE is activated on an instantaneously idle processor, instead of generating a single individual, a small number (N_{IPE}) trial ones are generated. For each one of them, a local metamodel is trained and its objective function value is approximated. The best (according to the metamodel) among the N_{IPE} individuals is, then, re–evaluated on the exact model. An example of the gain in the optimization turnaround time by using AMAEA instead of MAEA, is shown in 7. This is concerned with the design of a peripheral compressor cascade for minimum viscous losses, where AMAEA and MAEA were allowed to perform up to 12 concurrent evaluations on a many–GPUs platform. The IPE was activated after 80 entries were gathered in the DB and $\lambda_{IPE}=8$ members were re–evaluated on the exact tool for the MAEA. For the AMAEA, $N_{IPE}=8$ trial members were generated before selecting the one to be re–evaluated on the idle processor.

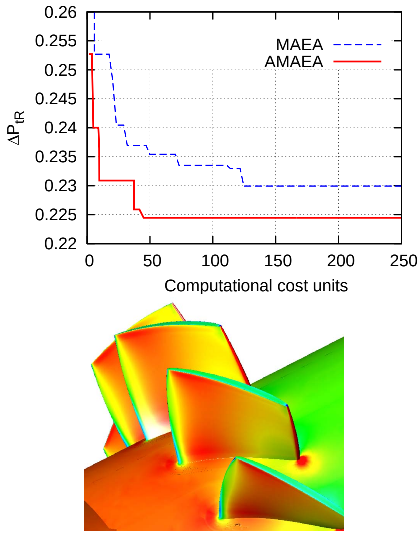

Figure 7. Optimization of a peripheral compressor cascade for minimum viscous losses. Top: Comparison of the convergence histories of MAEA and AMAEA. AMAEA outperforms MAEA which is known to perform much better than a conventional EA. Bottom: Pressure distribution on the optimal geometry.

EAs or MAEAs (along with their asynchronous variants), when applied to engineering optimization problems with a great number of design variables, suffer from the co–called "curse of dimensionality". A remedy to this problem is to process the elite set in each generation, using PCA and, based on the so acquired information to: (a) better guide the application of the evolution operators (to be referred as EA(PCA)) and (b) reduce the number of sensory units during the metamodels training (M(PCA)AEA), [5]. In (a), the design space is temporarily aligned with the principal component directions and the crossover and mutation operators are applied on the rotated individuals. This rotation according to the principal directions leads to a problem with as much as possible separable objective function, which is highly beneficial. In MAEAs, during the metamodel (RBF network) training, PCA can be used to reduce the dimension of the metamodels built. The variances of the design variables are used to identify the directions along which the elite members are less or more scattered. In the developed method, the RBF network sensory units corresponding to the directions of the design space with high variances are filtered out. Reducing the number of input parameters in the metamodel increases the prediction accuracy and accelerates the training process. The simultaneous use of PCA for both purposes is the so–called M(PCA)AEA(PCA).

An example of the use of PCA in both the metamodels and the evolution operators is shown in figure 8. This is concerned with the two–objective constrained design of a Francis runner parameterized using 372 design variables. The first objective (f_1) is related to the "quality" of the velocity profile at the runner outlet while the second one (f_2) to the blade loading. This case is studied with both MAEA and M(PCA)AEA(PCA) using a (μ, λ)=(20, 90) EA. During the IPE phase, λ_{IPE} = 8 members of each generation were re–evaluated on the CFD model. For the MAEA, the IPE phase was activated after 600 entries were stored in the DB, while for the M(PCA)AEA(PCA) only after 300 DB entries.

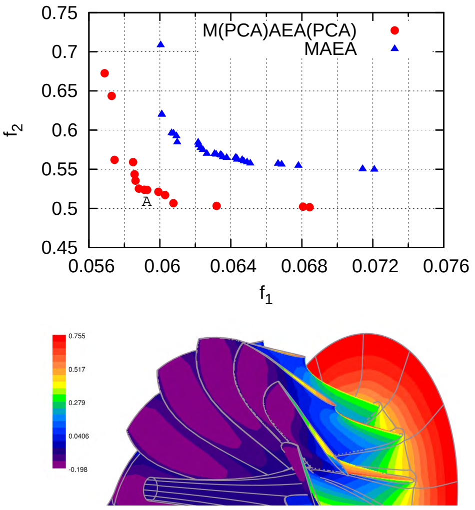

Figure 8. Two–objective design of a Francis runner at three operating points for optimizing the outlet velocity profile (min f_1) and the blade loading (min f_2). Top: Comparison of the fronts of non–dominated solutions computed by the MAEA and the M(PCA)AEA(PCA), at the same CPU cost. Bottom: 3D view and pressure field over the Francis runner, at the best efficiency operating point corresponding to non–dominated solution A.

4. USE OF EAS AND ADJOINT WITHIN THE RBF4AERO PROJECT

The aforementioned optimization methods, either stochastic (EAs) or gradient–based (adjoint) ones, are used for external aerodynamic optimization problems too. Some of these methods were appropriately adapted to fit the needs of the RBF4AERO, EU funded, project http://www.rbf4aero.eu/. The aim of the project is to develop the so–called RBF4AERO Benchmark Technology, an assembly of numerical (CFD, CSD solvers etc), morphing and optimization tools, capable of handling aerodynamic design/optimization problems. The morphing tool used is based on RBF networks and allows for fast morphing of the shapes to be optimized and the surrounding computational mesh, [13]. The optimization tool comprises both EAs and gradient–based methods assisted by the continuous adjoint method.

One of the cases to be studied within RBF4AERO is concerned with the minimization of the drag coefficient of a small aircraft underwing nacelle at two angles of attack, namely 0^o and 8^o. The nacelle is designed for the altitude of 2000m, with $M_\infty = 0.08$ and $Re_c = 3 \times 10^6$ based on the wing chord. The nacelle rotations around the y and z axes and the nacelle nose scaling were the three design variables used. Starting from a baseline geometry (figure 9 top), for each candidate solution the nacelle shape and the computational mesh was morphed using the customized RBF–based morphing tool of the RBF4AERO platform. The basic incompressible flow solver of OpenFOAM© (*simpleFoam*) was used as the evaluation tool, using the Spalart–Allmaras turbulence model.

In this paper, a (μ, λ)=(10, 30) MAEA was used for the optimization. The MAEA is capable of locating the Pareto front of non–dominated solutions after 100 evaluations on the CFD tool (Figure 9 bottom).

The limited range of the C_D values in the non–dominated front is due to the fact that, in all elite members, the two first design variables do not vary significantly and only the third design variable (i.e. the one related to the nose scaling) varies. This observation can be also backed-up by the magnitude of the drag force sensitivities w.r.t. the three design variables, presented in table 1 and computed using the continuous adjoint method.

b	y rot.	z rot.	scaling
dF/db	-1.9×10^{-4}	-4.4×10^{-7}	5.9×10^{-4}

Table 1. Sensitivity derivatives w.r.t. the three design variables parameterizing the nacelle shape, at 8^o farfield flow angle. It can be observed that the nose scaling has the greatest impact on the drag force value.

5. SUMMARY

This paper presented the use of either stochastic or gradient–based optimization methods in shape optimization of thermal and hydraulic turbomachines. Regarding continuous adjoint methods, some recent advances in the computation of accurate sensitivities were discussed and applied to industrial cases, lead-

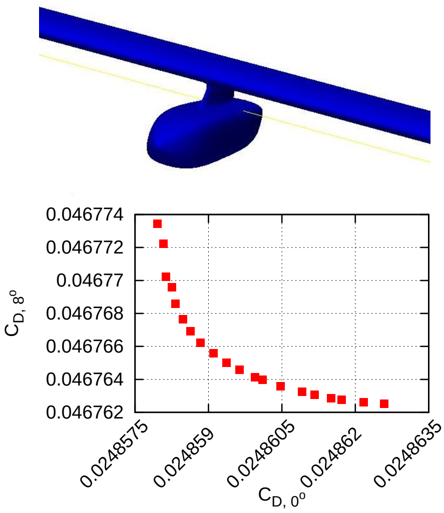

Figure 9. Two–objective optimization of an underwing nacelle (an RBF4AERO test case). Top: Baseline geometry. Bottom: Front of non–dominated solutions resulted after 100 **evaluations on the exact/CFD model.**

ing to the optimization of two Francis runners at a very small CPU cost (20 and 8 optimization cycles for each of the two cases). Regarding evolutionary algorithms, techniques involving surrogate evaluation models, asychronous search on multi-processor platforms and PCA have made the optimization of industrial cases with a great number of design variables and objectives possible.

ACKNOWLEDGEMENTS

Part of this work was funded by the RBF4AERO "Innovative benchmark technology for aircraft engineering design and efficient design phase optimisation" project funded by the EUs 7th Framework Programme (FP7-AAT, 2007-2013) under Grant Agreement no. 605396. The authors would also like to acknowledge contributions from Dr. Stylianos Kyriacou and Christos Kapellos.

REFERENCES

[1] Jameson, A., 1988, "Aerodynamic design via control theory.", *Journal of Scientific Computing*, Vol. 3, pp. 233–260.

[2] Papoutsis-Kiachagias, E., and Giannakoglou, K., 2014, "Continuous Adjoint Methods for Turbulent Flows, Applied to Shape and Topology Optimization: Industrial Applications", *Archives of Computational Methods in Engineering*, 10.1007/s11831-014-9141-9.

[3] Karakasis, M., Giotis, A., and Giannakoglou, K., 2003, "Inexact information aided, low-cost, distributed genetic algorithms for aerodynamic shape optimization", *International Journal for Numerical Methods in Fluids*, Vol. 43 (10-11), pp. 1149–1166.

[4] Asouti, V., Kampolis, I., and Giannakoglou, K., 2009, "A Grid-Enabled Asynchronous Metamodel-Assisted Evolutionary Algorithm for Aerodynamic Optimization", *Genetic Programming and Evolvable Machines*, Vol. 10 (3), pp. 373–389.

[5] Kyriacou, S., Asouti, V., and Giannakoglou, K., 2014, "Efficient PCA–driven EAs and metamodel-assisted EAs, with applications in turbomachinery", *Engineering Optimization*, Vol. 46 (7), pp. 895–911.

[6] Papadimitriou, D., and Giannakoglou, K., 2007, "A continuous adjoint method with objective function derivatives based on boundary integrals for inviscid and viscous flows", *Computers & Fluids*, Vol. 36 (2), pp. 325–341.

[7] Kampolis, I., Trompoukis, X., Asouti, V., and Giannakoglou, K., 2010, "CFD-based analysis and two-level aerodynamic optimization on Graphics Processing Units", *Computer Methods in Applied Mechanics and Engineering*, Vol. 199 (9-12), pp. 712–722.

[8] Spalart, P., Jou, W., Stretlets, M., and Allmaras, S., 1997, "Comments on the Feasibility of LES for Wings and on the Hybrid RANS/LES Approach.", *Proceedings of the first AFOSR International Conference on DNS/LES*.

[9] Zymaris, A., Papadimitriou, D., Giannakoglou, K., and Othmer, C., 2009, "Continuous Adjoint Approach to the Spalart-Allmaras Turbulence Model for Incompressible Flows", *Computers & Fluids*, Vol. 38 (8), pp. 1528–1538.

[10] Papoutsis-Kiachagias, E., Kyriacou, S., and Giannakoglou, K., 2014, "The Continuous Adjoint Method for the Design of Hydraulic Turbomachines", *Computer Methods in Applied Mechanics and Engineering*, Vol. 278, pp. 612–639.

[11] Zymaris, A., Papadimitriou, D., Giannakoglou, K., and Othmer, C., 2010, "Adjoint wall functions: A new concept for use in aerodynamic shape optimization", *Journal of Computational Physics*, Vol. 229 (13), pp. 5228–5245.

[12] Kavvadias, I., Papoutsis-Kiachagias, E., Dimitrakopoulos, G., and Giannakoglou, K., 2014, "The continuous adjoint approach to the k–ω SST turbulence model with applications in shape optimization", *Engineering Optimization, to appear*.

[13] Biancolini, M. E., "Mesh Morphing and Smoothing by Means of Radial Basis Functions (RBF): A Practical Example Using Fluent and RBF Morph", *Handbook of Research on Computational Science and Engineering: Theory and Practice (2 vol)*, pp. 347–380.

Conference on Modelling Fluid Flow (CMFF'15)
The 16th International Conference on Fluid Flow Technologies
Budapest, Hungary, September 1-4, 2015

ROBUST DESIGN OPTIMIZATION OF WIND TURBINE ROTORS

M.Sergio CAMPOBASSO[1]

[1] Corresponding Author. University of Lancaster, Department of Engineering. Engineering Building, Gillow Avenue, Lancaster LA1 4YW, United Kingdom. Tel.: +44 (0)1524 594673, E-mail: m.s.campobasso@lancaster.ac.uk

ABSTRACT

Wind turbine design is an inherently multidisciplinary task typically aiming at reducing wind cost of energy. In many cases the fulfillment of all design specifications and constraints is still accomplished using an iterative trial and error-based strategy. This may hinder the exploration of the feasible design space, lead to suboptimal solutions, and prevent the assessment of new and promising configurations. These shortfalls can be removed by using numerical optimization to optimize in an automated fashion wind turbine design. An additional challenge to turbine design arises from sources of uncertainty affecting wind turbine operation (e.g. wind variability), manufacturing, assembly and control (e.g. finite manufacturing tolerances and control system perturbations and faults), and the design process itself (e.g. uncertain accuracy of design tools). By adopting uncertainty quantification and propagation methods in the automated design process, the deterministic optimization becomes a probabilistic or robust design optimization process. This yields machines whose performance has reduced sensitivity to the abovesaid stochastic factors. The paper summarizes recent research work by the author and his group in the robust design optimization of horizontal axis wind turbine rotors, and it highlights some crucial areas of future research.

Keywords: wind turbine multidisciplinary design, computational aerodynamics, robust optimization

NOMENCLATURE

C_L	$[-]$	lift coefficient
N	$[rpm]$	rotational speed
P_e	$[kW]$	electrical power
U	$[m/s]$	wind speed
AEP	$[kWh]$	annual energy production
BM	$[kNm]$	bending moment
LCOE	$[\$/kWh]$	levelized cost of energy
PDF	$[-]$	probability distribution function
r	$[m]$	radial position
$x/c, y/c$	$[-]$	airfoil coordinates nondimensionalized by chord c
α	$[deg]$	angle of attack

1. INTRODUCTION

In recent years the exploitation of wind energy for producing electricity has been rapidly growing worldwide. This has been partly enabled by recent design technology advances, which have made possible substantial reductions of wind cost of energy (COE), one of the main metrics used to assess the viability of energy sources. The most widespread turbine type for heavy-duty on-shore and offshore installations is the horizontal axis wind turbine (HAWT). HAWT design, which typically aims at minimizing COE, is an inherently multidisciplinary task requiring the achievement of design specifications and the fulfillment of conflicting constraints dictated by aerodynamics, material engineering, structure mechanics and aeroelasticity, control, electrical and power engineering, and economic requirements. The characteristics of HAWT rotors, here intended as the set of turbine blades and the conversion control system from wind to mechanical power entering the drivetrain, play a major role in the design of the entire turbine, as they determine the steady and time-dependent structural loads on drivetrain, tower and foundations, and also the electrical power characteristics required for designing the power electronics subsystems. The main blade characteristics are their number, size, outer shape, internal geometry and material, while options available for power control include *a*) passive stall regulation for smaller HAWTs, and *b*) variable speed pitch-to-feather control for multimegawatt turbines.

The design of the rotor [1] as well as that of the entire turbine [2] is usually carried out using an iterative trial and error-based strategy. In rotor design, one starts by defining the outer blade shape, and this is followed by the definition of the internal structure which is modified in subsequent structural and aeroelastic analysis if found inadequate to withstand the aerodynamic loads. The iterative process may also yield the redefinition of the outer blade shape. One of the drawbacks of the manual iterative approach is the likelihood of incomplete exploration of the feasible design space, which may result in suboptimal solutions and prevent the scrutiny of radically new, potentially better configurations. A fully automated multidisciplinary design optimization (MDO) approach based on numerical optimization can avoid these pitfalls and yield substantial improvements of HAWT configurations.

In the area of turbine design Fuglsang *et al.* [3] developed a gradient-based HAWT MDO system to minimize COE, and used it to optimize the turbine design for site-dependent wind conditions. They showed that optimized site-specific designs achieved COE reductions of up to 15 % through annual energy production (AEP) increments and manufacturing cost reductions. Maki *et al.* [4] optimized the design of a 3-blade 1 MW HAWT using a multilevel system design to minimize COE. Their optimized configuration featured a reduction of about 29 % of COE, had higher rated rotational speed, larger diameter and lower rated power than the reference HAWT configuration. Their results also highlighted that COE had a minimum with respect to the rotor diameter and the rated rotational speed, and increased monotonically with the rated power. Ashuri *et al.* [5] used a gradient based optimizer to optimize the design of the National Renewable Energy (NREL) 5 MW virtual HAWT [6], reporting a 2.3 % COE reduction.

HAWT design and operation are affected by significant uncertainty caused by environmental, aerodynamic and engineering factors. Accounting for stochastic factors in the design optimization process yields a robust MDO (RMDO) process [7], whereby the deterministic estimates of objective functions and constraints are replaced by probabilistic estimates. Unlike deterministic designs, robust designs feature reduced performance sensitivity to stochastic variations of operation, control and engineering factors. RMDO is computationally more expensive than MDO because at each RMDO step multiple analyses of the same nominal design are required for propagating uncertainty [8] in the multidisciplinary analysis system. The recent development of numerically efficient uncertainty propagation methods [9] and the high performance of modern computers are making the computational burden of RMDO affordable.

HAWT RMDO is a very recent but extremely promising technology that can subsantially improve HAWT design and on which only a few advanced studies are available [10, 11, 12, 13] to date. This paper presents the research work carried out in this area by the author and his group. The options available for the modules of the multidisciplinary HAWT rotor analysis system are discussed in Section 2. Section 3 discusses the choice of methods for propagating uncertainty in the multidisciplinary analysis system, defines the objectives and constraints of HAWT rotor RMDO problem, and available approaches to its solution. Two sample applications of HAWT RMDO are presented in Section 4, while a summary with ongoing and future research trends is provided in Section 5.

2. MULTIDISCIPLINARY ANALYSIS

HAWT rotor MDO and RMDO rely on integrated multidisciplinary analysis (MDA) systems, made up of interlinked modules. For given rotor diameter and hub height, parameters defining the outer shape of the blades and their internal structure, power regulation, and wind parameters from cut-in to cut-out speeds, the MDA system returns the output required for the design optimization, such as AEP, COE, structural stresses and fatigue damage. MDA systems typically include: *a*) parametrized models of the blade outer and inner shapes, *b*) an aerodynamic module to determine the rotor power and the aerodynamic loads acting on the blades, *c*) an aero-servo-elastic subsystem for determining the aeroelastic characteristics of the rotor, and, in some cases, also the effects of blade deformations on power generation, *d*) a stress analysis module to determine the design-driving stresses of the blades subject to aerodynamic, weight and centrifugal loads.

2.1. Geometry parametrization

Both the outer shape of the blades and their internal structure need to be defined by suitable parametric representations. The input variables on which such parametrizations depend are the design variables.

As for the outer blade shape, most studies published in the last two decades parametrize and vary only the radial profiles of blade twist and airfoil chords during the optimization (a few design variables are associated to chord and twist at some radial positions, and cubic splines are used to define the complete radial profile of these two variables), while the blade airfoils are left unaltered [14, 15]. The adopted airfoils are chosen from among custom tailored HAWT or aircraft wing airfoil families for which reasonably reliable (usually experimentally measured) aerodynamic force data are available. As highlighted by Fuglsang *et al.* [16] and further discussed below, the reason for not parametrizing (and thus not designing) the blade airfoils within HAWT rotor design optimization is the difficulty in computing reliable estimates of abovesaid aerodynamic forces for the feasible arbitrary airfoil shapes generated when enabling airfoil geometry variations during the optimization. The same authors also recognized that significant improvements in HAWT design optimization can be achieved by enabling airfoil geometry variations in the optimization. In the light of the potential of new Computational Fluid Dynamics (CFD) to accurately predict transitional and stalled airfoil aerodynamics, new optimization studies start incorporating airfoil design in the 3D rotor design optimization [17, 12, 18, 19].

The airfoil geometry parametrization is often based on composite Bezier curves [12, 19], or even PARSEC parametrizations [17]. The author's group have used a composite 4-Bezier curve parametrization [13], sketched in Fig. 1. The composite parametrization features 14 control points, but the design variables are only 12 abscissas and ordinates of the 14 base points, since the remaining 16 abscissas are determined by fixing the position of the leading and trailing edges, and imposing suitable continuity conditions at the junctions between the 4 component curves.

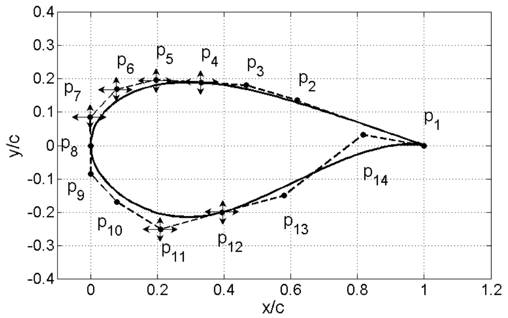

Figure 1. HAWT rotor airfoil parametrization based on composite Bezier curve.

The internal structure of HAWT blades typically consists of spar caps, spar webs and skin elements. Different levels of detail and approximation have been used in HAWT design optimization. Some studies model only the spar caps as they base the structural design on the bending load withstood by such components [14], whereas other studies model the complete internal structure, and use a shell element approach for calculating the stress field [20]. An important feature in HAWT rotor MDO is that the structural model used for the stress and the aeroelastic analyses (the aim of the latter is to determine deformations rather than stresses) are often different. More specifically, the structural model of the stress analysis often includes the 2D geometry of the blade sections, whereas the model of the aeroelastic analysis usually consists only of the radial distribution of section-averaged blade structural properties.

2.2. Aerodynamics

To compute the power generated by the rotor and the aerodynamic loads acting on its blades, a computational aerodynamics module is required. In HAWT rotor MDO and, even more, RMDO, computational speed is a crucial requirement. The blade-element momentum (BEM) theory [21] fulfills this requirement and is therefore widely used in wind turbine design. The BEM model combines the conservation of linear and angular momentum and classical lift and drag theory. Its main limitation is that the reliability of its assumptions and engineering models are questionable in many realistic HAWT rotor flows. Moreover BEM codes require knowledge of the lift and drag coefficients of the blade airfoils. Thus the accuracy of BEM analyses also depends on the source type of airfoil force coefficients.

In the automated RMDO environment, many airfoil geometries are scrutinized and their polars need to be determined very rapidly. In most cases, the viscous-inviscid panel code XFOIL [22] is used. In this code, laminar-to-turbulent transition, an important feature in HAWT rotor aerodynamics, is modeled with the e^N method. XFOIL enables the rapid calculation of the airfoil performance; the code, however, is known to usually overestimate the maximum lift coefficient [23], and is not meant to be used for reliable predictions of the force coefficients beyond the stall inception point. The near stall predictions of XFOIL appear to be particularly inaccurate for thicker airfoils [24]. Improved near-stall force predictions could be obtained with the proprietary code RFOIL, the variant of XFOIL developed at Delft University [23], or even using transitional Navier-Stokes (NS) CFD, which is reaching a level of maturity enabling it to accurately predict airfoil aerodynamics well beyond the angle of attack (AoA) of maximum lift [25]. At present, run-times of NS CFD, even in 2D simulations, are still excessive for their use in HAWT RMDO requiring hundreds or thousands of rotor analyses, but new highly-efficient computer processor architectures are enabling substantial run-time reductions of NS CFD for wind turbine analysis and design [26]. This is expected to accelerate the use of these technologies for wind turbine design.

In BEM models, the input 2D aerodynamic data are also corrected to account for the complex 3D flow physics of rotating blades, such as the Himmelskampf effect or centrifugal pumping effect [27]. Based on empirically derived equations, models like AERODAS [28] provide a method for calculating stall and post-stall lift and drag characteristics of rotating airfoils, using as input a limited amount of prestall 2D aerodynamic data (e.g. zero-lift AoA, AoA at maximum lift and drag, values of maximum lift and drag coefficients, slope of the linear part of the lift curve, and minimum drag coefficient). Other emprical corrections used in BEM codes include: *a*) Prandtl's tip and hub loss corrections [21], *b*) Glauert-type correction of the curve induction coefficient/thrust coefficient to account for the turbulent windmill state [29].

2.3. Aero-servo-elasticity and structural mechanics

Another functionality set of HAWT rotor MDA systems includes the determination of *a*) blade pitch angle and rotor angular speed (for pitch- and speed-regulated turbines), *b*) all time-dependent blade loads and deflections, *c*) generated power, and *d*) structural stress for each wind regime. The module or collection of interlinked modules implementing the first three functionalities forms the aero-servo-elastic analysis subsystem. Several choices are possible for this subsystem and the stress analysis module, depending primarily on the level of detail of the adopted model. The aero-servo-elastic subsystem used by the author's group is based on the NREL code FAST [30]. For given steady or time-dependent wind conditions, FAST models the aeroelastic behavior of the rotor using a modal representation of the blade displacements and velocities (the code can even model the entire turbine, including drivetrain and tower). In FAST, rotor aerodynamics is analyzed with AERODYN [30], a library implementing the BEM theory. For rotor analyses, the input of the code includes the aerodynamic force coefficients required by AERODYN to determine the aerodynamic loads, the mode-shapes and the radial distribution of the structural properties of the blades. The blade mode-shapes are determined with BMODES [30], a finite element code for calculating the mode-shapes of beams. For HAWT blades, the input of BMODES includes the radial profiles of the distributed structural and geometric properties of the blades and the rotor speed. The radial profile of blade structural properties used by FAST is determined with CO-BLADE [31], a structural analysis code custom-tailored for wind turbine blades. The input of CO-BLADE includes the detailed definition of the blade outer shape and internal structure. The latter includes the number and the orientation of the plies making up the laminates of spar caps, spar webs and skin. CO-BLADE also determines the 3D stress field in the blades using the aerodynamic loads of FAST/AERODYN, and the loads associated with the weight and the centrifugal forces of the blades. These stresses are required for sizing all structural components of the blades. The aero-servo-elastic and stress analysis framework described herein is that used for the RMDO of the 5 MW HAWT discussed in section 4.

3. UNCERTAINTY PROPAGATION AND HAWT RMDO

In HAWT RMDO, part of the design variables (e.g. rotor geometry characteristics) and/or design parameters (e.g. site- and time-dependent wind characteristics) are stochastic. Thus the turbine performance is no longer defined by deterministic but rather by probabilistic metric estimates. A numerical method for propagating the uncertainty affecting the input data is thus required. The two essential prerequisites of uncertainty propagation methods for RMDO are high execution speed and accuracy. These two requirements are conflicting, and case-dependent choices have to be made. When the underlying MDA systems feature low-levels of nonlinearity, first or second order moment methods based on truncated Taylor series [9] yield sufficiently accurate estimates of the statistical moments of the output of interest at low computational costs. For MDA systems featuring strong nonlinearities, conversely, computationally expensive Monte Carlo methods are often the only route to accurate estimates of the output functionals. The univariate reduced quadrature (URQ) method [9] yields an acceptable compromise between cost and accuracy.

The level and type of nonlinearity of the MDA system may be such that mean and standard deviation of the probability distribution function (PDF) of the output are insufficient to characterize the output PDF. This is illustrated in Fig. 2, taken from [11]. The two AEP PDFs of a small HAWT rotor refer to feasible turbines. However, one rotor has a nearly normal AEP PDF (left), whereas the other has a strongly skewed AEP PDF (right). In this circumstance, knowledge of the mean and standard deviation alone may lead to incorrect design choices, and more complex representations of the output PDF in the RMDO context should be used.

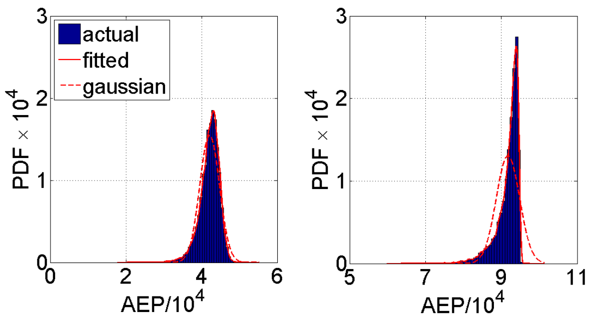

Figure 2. Encountered AEP [kWh] PDFs. Left: quasi-normal output. Right: non-normal output.

The most widely used objective function in HAWT and HAWT rotor MDO is the levelized cost of energy (LCOE) [16, 5, 13]. This variable is the ratio of the sum of all fixed (e.g. turbine and installation) and variable (e.g. operation and maintenance and land lease) costs, and the amount of energy generated over the turbine lifetime. All costs appearing in the definition are net present values. An interesting alternative to optimizing only LCOE is to optimize concurrently both the cost of energy and the annual energy production per unit area [14]. This formulation is particularly interesting when performing HAWT design optimization in the context of wind farm planning.

Structural, aeroelastic and aeroacoustic constraints are used in HAWT rotor design. Wind turbines must meet a large number of requirements for certification, which are coded by the International Electrotechnical Commission (IEC). Many recent HAWT rotor MDO studies derive their constraints from the IEC standards. Examples of structural and aeroelastic contraints include: a) maximum stress should not exceed material-dependent limits when the rotor is exposed to strongest foreseen wind in 20 or 50 years (depending on turbine specifications), b)

maximum blade tip deflection should result in reduction of the blade tip/tower clearance not larger than specified values to avoid tower/blade interference, *c*) all components should achieve the target life of about 20 years despite all fatigue-inducing loads such as wind turbulence and blade weight. Aeroacoustic constraints often result in an upper limit for the rotor speed and some geometry constraints on the outer blade geometry.

Both gradient-based [16, 5, 19] and evolution-based [14, 18] optimizers are used for HAWT MDO. Gradient-based methods are faster but they have more limited capabilities of exploring the feasible design space. Evolution-based algorithms, conversely, require many more evaluations of the objective functions, but they can determine global optima. Moreover, they can also handle discontinuos functions.

Moving from MDO to RMDO, each objective function is estimated probabilistically. One simple approach is to replace the deterministic value of the output with its mean and standard deviation. Then one has to optimize the mean (minimize LCOE, maximize AEP), and minimize the standard deviation. Possible approaches to solving the probabilistic problem include *a*) solving a two-objective optimization, *b*) solving a one-objective optimization where a weighted sum of mean and standard deviation is optimized and *c*) solving a one-objective optimization where the mean is optimized and the standard deviation is a minimum inequality constraint. Using evolution-based optimizers in HAWT RMDO can yield a large computational burden because each probabilistic evaluation of a nominal design can require several deterministic evaluations and a very large number of nominal designs is scrutinized. Making use of sufficient computational resources and using uncertainty propagation methods requiring a small number of deterministic analyses for each probabilistic estimate, however, make the use of evolution-based optimizers viable also for HAWT rotor RMDO [11].

4. SAMPLE APPLICATIONS

4.1. AEP optimization of small HAWT rotor

The objective of this prototype HAWT rotor robust design optimization was to optimize the AEP of a 3-blade 12.6 meter-diameter speed-regulated rotor from cut-in to rated wind speed. The yearly frequency distribution of the freestream wind velocity U is taken to be a Weibull PDF with scale parameter of 7 m/s and shape parameter of 2, resulting in an average speed of 6.2 m/s. The blades feature the NACA4413 airfoil along their entire length. The effects of manufacturing and assembly errors are included in the analysis by assuming normally distributed geometric uncertainty affecting the radial profiles of chord and twist. The objectives of the rotor RMDO are to maximize the mean of AEP and minimize its standard deviation. The blades' nominal geometry is defined by 13 geometric design variables, and 7 control variables correspond to the rotor speeds for the considered wind speeds $U_i = (5 + i)\ m/s,\ i = 1,7$. A structural constraint on the maximum bending moment (BM) and an aeroacoustic constraint limiting the maximum rotor speed are enforced, and XFOIL is used to determine required airfoil data for WINSTRIP, an in-house BEM code. The single-objective RMDO problem is formulated as a 2-objective deterministic problem requiring maximization of mean AEP and minimization of its standard deviation. URQ is used to propagate uncertainty, and the 2-objective optimization is solved with a 2-stage multi-objective evolution-based optimization strategy: a multi-objective Parzen-based estimation of distribution (MOPED) algorithm yields an initial estimate of the optimum solution, or the Pareto front if multiple optima exist, and an inflationary differential evolution algorithm refines the MOPED estimate [11].

To highlight the improvements achievable by using RMDO, the robust design is compared to the solution of the corresponding deterministic design optimization, which ignores uncertainty. The deterministically optimum rotor has nominal AEP of $96,20\ kWh$, AEP expectation $\mu_{AEP} = 89,97\ kWh$. and AEP standard deviation $\sigma_{AEP} = 4,99\ kWh$. The probabilistically optimum rotor has nominal AEP of $95,00\ kWh$, $\mu_{AEP} = 91,62\ kWh$ and $\sigma_{AEP} = 2,78\ kWh$. Thus, σ_{AEP} of the robust design is more than 44 % lower than that of the deterministic design. For both rotors, the left subplot of Fig. 3 compares the nominal and mean estimates of the amount of AEP accounted for by each wind speed U. Both mean curves also report error bars of size $\pm\sigma_{AEP}$. The deterministic optimum has better nominal AEP curve, but worse mean AEP curve than the robust optimum. More importantly, the σ_{AEP} values of the deterministically optimal rotor are significantly higher than those of the probabilistically optimal rotor. The right subplot of Fig. 3 refers to the root bending moment of the two rotors, and highlights that the root BM standard deviation of the probabilistic optimum is lower than that of the deterministic optimum for all considered speeds.

As reported in [11], the power curves of the two optima do not differ significantly. This is because the robust optimum has lower rotational speeds but higher loading at nearly all radii and wind speeds, due to its lower blade twist and its lower rotational speed. The power loss due to lower rotational speeds compensates the power enhancement due to higher loading. Thus, the AoA α over most of the blade is higher for the probabilistic than for the deterministic design. More specifically, for the probabilistic design, AoA is in a region where the slope of the lift-AoA curve is shallower than for the deterministic design. Consequently, variations of AoA due to pitch errors results in smaller variations of the lift coefficient, the power and the generated energy of the ro-

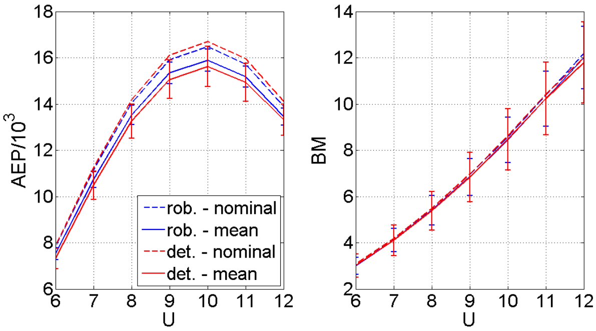

Figure 3. Performance of deterministic and robust small rotor designs. Left: proportion of AEP at each wind speed U $[m/s]$. Right: blade root bending moment $[kNm]$ against U.

bust design. This mechanism is highlighted by the mean and standard deviation of AoA and lift coefficient C_L of the two rotors reported in Fig. 4.

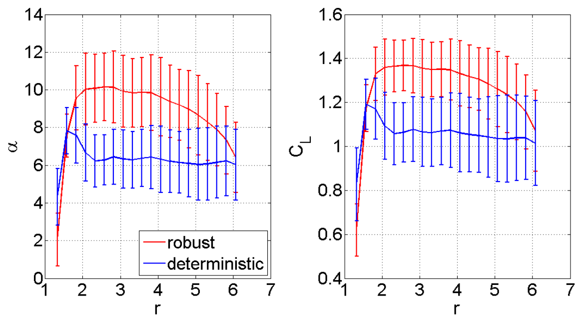

Figure 4. Performance of deterministic and robust small rotor designs at $U = 12\ m/s$. Left: AoA α $[deg]$ against radius r $[m]$. Right: C_L against r.

4.2. COE optimization of 5 MW HAWT rotor

This study aimed at probabilistically minimizing the LCOE of the NREL 3-blade 5 MW 126 meter-diameter speed- and pitch-controlled turbine [6]. The uncertainty is due to the variability of the mean wind speed, arising either because the turbine is installed at sites with wind characteristics different from the design specification, or because of the long-term wind variability at a given site due to environmental factors such as climate change. The yearly frequency distribution of the wind velocity U at the hub height is taken to be a Weibull PDF with shape parameter of 2 and average speed varying between 7 and 13 m/s according to the uniform distribution. Composite Bezier curves are used to parametrize the airfoil geometry, and cubic splines are used to parametrize the radial distributions of blade pitch and chord. The considered 48 design variables are: 46 geometric parameters defining the blade outer shape, the tip speed ratio in the region between cut-in and rated wind speeds, and one scaling factor defining the relative thickness of all parts of the blade internal structure with respect to a reference structural design.

Structural constraints on ultimate loads, fatigue damage, buckling and maximum tip deflections are enforced. The aero-servo-elastic and stress analyses are performed using FAST, BMODES, and CO-BLADE, and the aerodynamic loads are determined with AERODYN using the force coefficients of XFOIL and AERODAS. The RMDO problem is solved by minimizing a weighted sum of mean and standard deviation of LCOE using the pattern search optimizer of MATLAB [13], a non-evolutionary deritative-free global search method. For each nominal design, mean and standard deviation of LCOE are computed using the analytical definitions of these two variables, and calculating the required integrals of LCOE over the given mean wind speed range.

The mean LCOE of the robust optimum is found to be about 6 % lower than that of the baseline turbine, and the LCOE standard deviation of the robust optimum is about 15 % lower than of the baseline. These improvements are achieved mostly through mass reduction and power curve enhancements of the robust optimum. The outer blade shape of the robust and baseline turbines differs significantly, as partly highlighted by the three subplots of Fig. 5, which compare the root, midspan and tip airfoils of the two turbines.

The left and right subplots of Fig. 6 report respectively the rotor speed and the electric power of the two turbines against the wind speed. One notes that the power extracted by the robust HAWT is higher than that of the reference turbine from cut-in to rated wind speed. It is also observed that the rotational speed of the robust turbine in this wind speed range is higher than for the reference turbine.

5. CONCLUSIONS

Numerous and significant sources of uncertainty in wind energy engineering demand the use of probabilistic design approaches, since a probabilistic definition of the producible wind energy is likely to better inform decision-making at scientific and governmental levels. This paper presented a brief description of the technologies used in HAWT rotor RMDO and the work performed by the author and his group in this area.

Important environmental uncertainty sources include the time- and space-variability of wind characteristics due to the vertical shear and the thermodynamic state of the atmospheric boundary layer (ABL) [32]. As an example, it was recently shown that omitting the effects of humidity fluxes in marine ABL thermodynamic state analyses can result in overpredicting by up to 4 % the mean wind speed at 150 meters, the hub height of several new large off-shore HAWTs [33]. The extent of these phenomena is expected to be strongly site-dependent, and such uncertainty ought to be accounted for in HAWT design.

Uncertain aerodynamic factors include the prediction of laminar-to-turbulent transition, near and

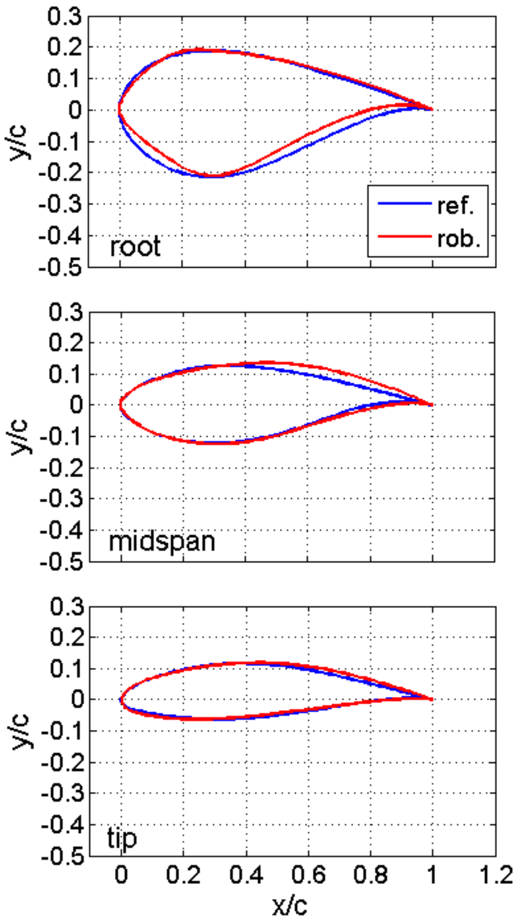

Figure 5. Comparison of airfoils of robust and conventional designs of 5 MW HAWT rotor.

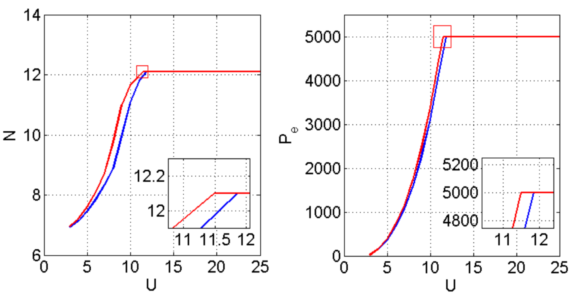

Figure 6. Regulation and power curve of robust and conventional designs of 5 MW HAWT rotor. Left: rotor speed N [rpm] against U. Right: electrical power P_e [kW] against U.

post-stall characteristics. Contributing factors to this uncertainty include the blade roughness levels varying during operation due to contamination, accretions and wear, and the turbulence intensity, but also the use of rapid but insufficiently accurate computational aerodynamics tools in HAWT design. Advances in this area, aimed at *a*) improving the prediction of the impact of transition and 3D flow effects on blade loads, and *b*) massively reducing the cost of the computational technologies needed to accomplish this are required.

Additional uncertainty to be considered in HAWT RMDO is that caused by input perturbations of the control system, such as inaccurate wind speed measurements, as well as insufficient accuracy of the HAWT models used to design the controller.

REFERENCES

[1] Bak, C., 2013, "Aerodynamic design of wind turbine rotors", W. Gentzsch, and U. Harms (eds.), *Advances in wind turbine blade design and materials*, Vol. 47 of *Energy*, Woodhead Publishing, Cambridge, UK, pp. 59–108.

[2] Jamieson, P., 2011, *Innovation in wind turbine design*, Wiley, Philadelphia, USA.

[3] Fuglsang, P., Bak, C., Schepers, J., Bulder, B., Cockerill, T., Claiden, P., Olesen, A., and van Rossen, R., 2002, "Site-specific design optimization of wind turbines", *Wind Energy*, Vol. 5 (4), pp. 261–279.

[4] Maki, K., Sbragio, R., and Vlahopoulos, N., 2012, "System design of a wind turbine using a multi-level optimization approach", *Renewable Energy*, Vol. 43, pp. 101–110.

[5] Ashuri, T., Zaaijer, M., Martins, J., van Bussel, G., and van Kuik, G., 2014, "Multidisciplinary design optimization of offshore wind turbines for minimum levelized cost of energy", *Renewable Energy*, Vol. 68, pp. 893–905.

[6] Jonkman, J., Butterfield, S., Musial, W., and Scott, G., 2009, "Definition of a 5-MW Reference Wind Turbine for Offshore System Development", *Tech. Rep. NREL/TP-500-38060*, NREL, Golden, CO, USA.

[7] Beyer, H.-G., and Sendhoff, B., 2007, "Robust optimization - A comprehensive survey", *Computer methods in applied mechanics and engineering*, Vol. 196, pp. 3190–3218.

[8] Lee, S., and Chen, W., 2009, "A comparative study of uncertainty propagation methods for black-box-type problems", *Structural and multidisciplinary optimization*, Vol. 37, pp. 239–253.

[9] Padulo, M., Campobasso, M., and Guenov, M., 2011, "A Novel Uncertainty Propagation Method for Robust Aerodynamic Design", *AIAA Journal*, Vol. 49 (3), pp. 530–543.

[10] Petrone, G., de Nicola, C., Quagliarella, D., Witteveen, J., and Iaccarino, G., 2011, "Wind turbine optimization under uncertainty with high performance computing", AIAA paper 2011-3806, 29th AIAA Applied Aerodynamics Conference, Honolulu, Hawaii.

[11] Campobasso, M., Minisci, E., and Caboni, M., 2014, "Aerodynamic design optimization of wind turbine rotors under geometric uncertainty", *Wind Energy*, dOI: 10.1002/we.1820.

[12] Caboni, M., Minisci, E., and Campobasso, M., 2014, "Robust aerodynamic design optimization of horizontal axis wind turbine rotors", D. Greiner, B. Galván, J. Periaux, N. Gauger, K. Giannakoglou, and G. Winter (eds.), *Advances in Evolutionary and Deterministic Methods for Design, Optimization and Control in Engineering and Sciences*, Vol. 36 of *Computational Methods in Applied Sciences*, Springer Verlag, ISBN 978-3-319-11540-5.

[13] Caboni, M., Campobasso, M., and Minisci, E., 2015, "Wind Turbine Design Optimization under Environmental Uncertainty", ASME paper GT2015-42674.

[14] Benini, E., and Toffolo, A., 2002, "Optimal Design of Horizontal-Axis Wind Turbines using Blade-Element Theory and Evolutionary Computation", *Journal of Solar Energy Engineering*, Vol. 124, pp. 357–363.

[15] Xudong, W., Shen, W., Zhu, W., Sørensen, J., and Jin, C., 2009, "Shape Optimization of Wind Turbine Blades", *Wind Energy*, Vol. 12 (8), pp. 781–803.

[16] Fuglsang, P., and Madsen, H., 1999, "Optimization method for wind turbine rotors", *Journal of Wind Engineering and Industrial Aerodynamics*, Vol. 80 (1), pp. 191–206.

[17] Kwon, H., You, J., and Kwon, O., 2012, "Enhancement of wind turbine aerodynamic performance by a numerical optimization technique", *Journal of Mechanical Science and Technology*, Vol. 26 (2), pp. 455–462.

[18] Vesel, R., and McNamara, J., 2014, "Performance enhancement and load reduction of a 5 MW wind turbine blade", *Renewable Energy*, Vol. 66, pp. 391–401.

[19] Bottasso, C. L., Croce, A., Sartori, L., and Grasso, F., 2014, "Free-form design of rotor blades", *Journal of Physics: Conference Series*, Vol. 524 (1).

[20] Jureczko, M., Pawlak, M., and Mezik, A., 2005, "Optimisation of wind turbine blades", *Journal of Materials Processing Technology*, Vol. 167, pp. 463–471.

[21] Jain, P., 2011, *Wind Energy Engineering*, McGraw-Hill, New York, NY, USA.

[22] Drela, M., 1989, "XFOIL: An Analysis and Design System for Low Reynolds Number Airfoils", *Low Reynolds Number Aerodynamics*, Springer Verlag, Vol. 54 of *Lecture Notes in Engineering*.

[23] Timmer, W., and van Rooij, R., 2003, "Summary of the Delft University Wind Turbine Dedicated Airfoils", *Journal of Solar Energy Engineering*, Vol. 125, pp. 488–496.

[24] Sørensen, N., 2009, "CFD Modelling of Laminar-Turbulent Transition for Airfoils and Rotors Using the $\gamma-\tilde{Re}_\theta$ Model", *Wind Energy*, Vol. 12, pp. 715–733.

[25] Aranake, A., Lakshminarayan, V., and Duraysami, K., 2015, "Computational analysis of shrouded wind turbine configurations using a 3-dimensional RANS solver", *Renewable Energy*, Vol. 75, pp. 818–832.

[26] Rinehart, T., Medida, S., and Thomas, S., 2014, "Computation of Two-dimensional Wind Turbine Airfoil Characteristics Using Advanced Turbulence and Transition Modeling Methods and a GPU-Accelerated Navier-Stokes Solver", AIAA paper 2014-1216, 32nd ASME Wind Energy Symposium, National Harbor, Maryland.

[27] Lindenburg, C., 2004, "Modelling of rotational augmentation based on engineering considerations and measurements", European Wind Energy Conference, London, UK.

[28] Spera, D., 2008, "Models of Lift and Drag Coefficients of Stalled and Unstalled Airfoils in Wind Turbines and Wind Tunnels", *Tech. Rep. NASA CR-2008-215434*, NASA, Cleveland, OH, USA.

[29] Buhl, M., 2005, "A New Empirical Relationship between Thrust Coefficient and Induction Factor for the Turbulent Windmill State", *Tech. Rep. NREL/TP-500-36834*, NREL, Golden, CO, USA.

[30] NREL, "National Wind Technology Center information portal: software.", Https://nwtc.nrel.gov/Software, accessed on 18 May 2015.

[31] Sale, D., "Co-Blade: Software for Analysis and Design of Composite Blades.", Https://code.google.com/p/co-blade/, accessed on 18 May 2015.

[32] Emeis, S., 2013, W. Gentzsch, and U. Harms (eds.), *Wind Energy Meteorology*, Green Energy and Technology, Springer Verlag, Berlin, Germany.

[33] Barthelmie, R., Sempreviva, A., and Pryor, S., 2010, "The influence of humidity fluxes on offshore wind speed profiles", *Annales Geophysicae*, Vol. 28, pp. 1043–1052.